ICF10

Honolulu (USA)

2001

Vol. A

ICF100591OR

2D AND 3D SELF-AFFINE CRACK PROPAGATION ON ALUMINUM ALLOYS

M. Hinojosa, E. I. Morales, X. Guerrero, J. Aldaco and U. Ortiz

Facultad de Ingeniería Mecánica y Eléctrica, Universidad Autónoma de Nuevo León, A.P. 076 Suc "F", Cd. Universitaria, San Nicolás de los Garza, N.L. MEXICO.

ABSTRACT

The self-affine exponents associated with the crack propagation phenomenon are evaluated on samples of aluminum alloys both on 2D and 3D experimental conditions. Fracture surfaces were generated by Charpy impact tests on samples of A319-type aluminum cast alloy. Roughness exponents and correlation length on the perpendicular and parallel directions with respect to the crack propagation direction were determined, this analysis was also performed for the arrested crack propagation front. In the two-dimensional case, cracks were propagated on notched tension specimens of aluminum foil and the resulting self-affine crack paths were recorded and analyzed, the self-affine parameters were determined for both longitudinal and perpendicular direction in order to investigate the effect of the microstructural anisotropy.

Self-affine analysis was carried out using the Zmax variable bandwidth method. The combined use of different techniques (SEM, AFM, Optical microscopy and stylus profilometry) enabled the analysis over up to seven decades of length scales. The results are analyzed in terms of recent crack propagation models and the self-affine parameters are found to be correlated with microstructural characteristic lengths.

KEYWORDS

Roughness exponents, self-affine crack paths, fracture surfaces, aluminum alloys, crack propagation.

INTRODUCTION

Crack propagation and the fracture of materials are catastrophic phenomena of considerable scientific, technological an economical importance [1-4]. Despite the scale of the problem and the considerable effort that has been undertaken by engineers and scientists of different disciplines, there is at present no clear understanding of the fracture process. In recent years much interest has been devoted to the self-affine character of fracture surfaces and crack propagation [5-7]. The fractal nature of fracture surfaces was first quantitatively studied in the mid-eighties [8]. At about the same time it was suggested that the fracture of heterogeneous media has some universal properties similar to critical phase transitions [9]. Later, experimental evidence led to the conjecture of the existence of a universal roughness exponent [10] for the fracture surfaces of many different materials [11], though this is still a controversial topic [7,12]. Anyway, it is now clearly established that fracture surfaces are self-affine objects that can be quantitatively described by self-affine parameters like one or more roughness exponents and one or more characteristic lengths such as cut-off lengths separating different scaling regimes, and the correlation length.

One of the main goals of materials scientists is to find clear and useful relationships between the microstructure of materials and their macroscopic properties. In our particular field of interest this traduces to finding quantitative relationships between the microstructural features and the relevant self-affine parameters associated with the fracture surface and the crack propagation process that led to its creation. From the statistical physics point of view the question is related to how disorder affects crack propagation considering that rupture is the culmination of a self-organization of cumulative damage and cracking characterized by power-law regimes which result from the fact that disorder is present at different length scales in the form of impurities, vacancies, grain boundaries, porosity, phase boundaries and so forth.

The first attempts to relate fractal parameters of the fracture surfaces [8] of maraging steels with mechanical properties were very promising and inspirational though unsuccessful, it is clear that the fractal dimension of a fracture surface is not clearly correlated with the toughness of the material. Moreover, fractal dimension is not an appropriate parameter to describe self-affine surfaces [13], the roughness or Hurst exponent should be used instead. At present [6, 7], results from experiments in a wide variety of materials tested in different kinetic conditions and analyzed with different topometric techniques over up to seven length scales [14] suggest the coexistence of two self-affine regimes, at high enough propagation speeds and/or large enough length scales the so-called *universal* exponent $\zeta \approx 0.78$ is detected, whereas at slow propagation conditions and/or small enough length scales the detected exponent has a value close to 0.5. The cut-off length separating these two regimes is apparently dependent on the propagation speed [15], it also appears to be affected by local plastic deformation at the crack tip in ductile materials. Neither of the two above mentioned exponents seems to be associated in any manner whatsoever with the microstructural features of the materials. Experiments in Al-Ti alloys suggested that the cut-off length might be linked to the size of intermetallic compounds embedded in the metallic matrix [16]. Recent results [17-19] have shown that the correlation length, *i.e.* the upper limit of the self-affine regime(s) is directly related with the largest heterogeneities in materials such as metals [14, 17, 18], polymers [19, 20] and certain glasses [19].

With the hope to provide more experimental evidence that can help to improve our knowledge and refine the existing theoretical models of crack propagation, in this work we report the experimental analysis of the self-affine parameters of fracture surfaces and crack paths in aluminum alloys. A cast aluminum alloy is broken in mode I and the three associated roughness exponents are recovered along with the respective correlation length is some cases. We have also tested an aluminum foil in 2D mode I condition and have analyzed the self-affine nature of the crack paths. In both cases special attention is paid to the possible relationships between the microstructural features and the self-affine parameters.

EXPERIMENTAL PROCEDURE

We have performed the self-affine analysis of the fracture surfaces of aluminum samples, the same analysis was done for the crack paths generated in mode I in 2D conditions using samples of aluminum foil. The quantitative analysis was carried out using height profiles which were recorded by different techniques. The resulting topometric data sets are processed using the variable bandwith method [21] in which the following quantity was calculated:

$$Z_{max}(r) = \langle \max\{z(r')\}_{x<r'<x+r} - \min\{z(r')\}_{x<r'<x+r} \rangle_x \propto r^{\zeta}$$

Where r is the width of the window and $Zmax(r)$ is the difference between the maximum and the minimum height z within this window, averaged over all possible origins x of the window. A log-log plot of $Zmax(r)$ *vs.* r gives a straight line for a self-affine profile.

The experimental details and results for the two cases considered in our work are presented below.

3D case, A319-type Aluminum alloy

The cast aluminum alloy employed for this part of our work is an A319-type alloy, which is commonly used in the automotive industry. The typical chemical compositon is as follows (wt %): Si:7.147, Cu:3.261, Fe:0.612, Zn:0.664, Mn:0.0374, Ni:0.041, Ti:0.154, Mg:0.313, Sr:0.014, Al: balance. Fig.1 shows the microstructure of this alloy as observed by optical microscopy, the dendrites of alpha aluminum-rich phase is observed along with a numbre of different phases in the interdendritic regions. There is also a grain structure which was revealed using a special preparation. Image analysis measurements showed that the largest heterogeneities were the dendrites and the grains, with characteristic lengths identified as the primary dendrite arm length (800 μm) and the grain size (950 μm).

Samples of this material were broken in Charpy impact tests according to ASTM standard E-23-93. The resulting fracture surfaces were examined by Scanning Electron Microscopy (SEM), Atomic Force Microscopy (AFM) and an stylus profilometer. These three techniques were used to obtain topometric profiles both in the perpendicular and parallel direction with respect to the crack propagation direction, see Fig. 2. Profiles of the arrested crack front were also recorded using a different procedure which is described later in this section. Using these profiles we were able to determine the perpendicular out-of-plane roughness exponent $\zeta_{\perp}$, the parallel out-of-plane roughness exponent $\zeta_{//}$, and the roughness exponent of the crack front ζ_f, Fig. 2.

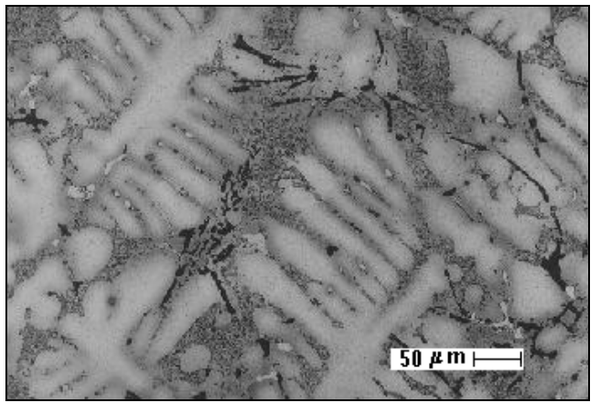

Fig.1 Optical micrography showing the microstructure of the A319-type alloy.

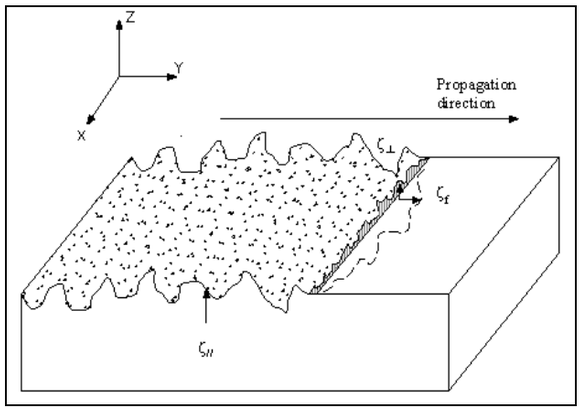

Fig. 2 Scheme illustrating the height profiles in the parallel and perpendicular directions with respect to the propagation direction, the crack front and the three roughness exponents are also included.

The SEM topometric profiles in the parallel and perpendicular directions were obtained by sectioning the surfaces previously plated with nickel, then SEM images are recorded using backscattered electrons and the profile is extracted by image analysis procedures. More details of these technique can be found in references [6, 15-17]. SEM profiles of 1024 points were obtained at magnifications ranging from 100X to 4000X. The AFM profiles are directly recorded by scanning the uncoated surfaces, we have used the contact mode in air. Profiles of 512 points with scan sizes ranging from 0.5 to a maximum of 6 μm were obtained. The stylus profilometer provided us with profiles of a maximum length of around one centimeter, a typical profile consisted of around 10,000 points with resolution of 0.25 μm.

Figures 3 and 4 show the self-affine curves obtained for the perpendicular and parallel directions, respectively. The exponents $\zeta_{\perp}$, $\zeta_{//}$ have very similar values: 0.81, 0.78, repectively.

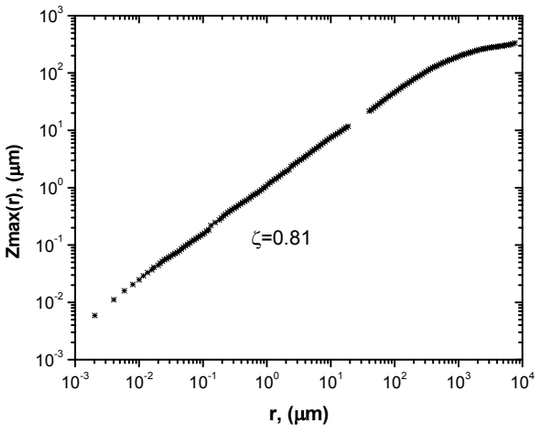

Fig. 3 Self-affine curve for the profiles in the perpendicular direction, the roughness exponent $\zeta_{\perp}$ has a value of 0.81.

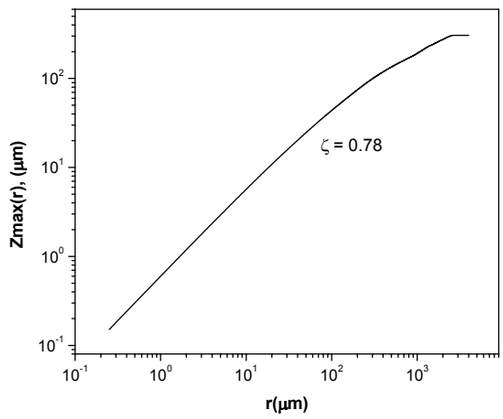

Fig. 4 Self-affine curve for the profiles in the parallel direction, the roughness exponent $\zeta_{//}$ has a value of 0.78.

Profiles of arrested crack fronts were obtained by a very different method, we have run interrumpted torsion tests over hollow cilindrical specimens then marked the crack front using a commercial penetrating die commonly used in crack inspection and failure analysis. The specimens were then broken in the torsion machine and the arrested crack front was registered by SEM using secondary electrons, profiles were extracted by image analysis. Figure 5 shows the self-affine plot for the crack front which has a roughness exponent $\zeta_f = 0.79$.

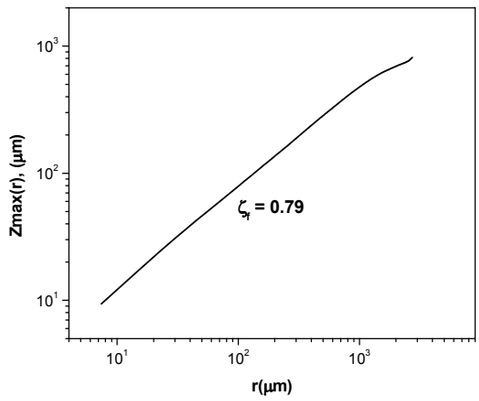

Fig. 5 Self-affine curve for the arrested crack front, the roughness exponent ζ_f has a value of 0.79

These self-affine curves permit only an estimation of the correlation length. However, as it can be observed, in all cases it has a value of the order of 1 millimeter, which is very close to the size of the largest dendrites and grains.

2D case: Self-affine crack propagation in aluminum foil

Tension specimens of aluminum foil (alloy 1145-O) were prepared as shown in Fig. 6, then fractured in 2D mode I condition. We have then performed the self-affinity analysis of the resulting crack paths. The purpose of these experiments was to evaluate the self-affine parameters paying special attention to the possible effect

that the anisotropic grain structure might have on the self-affine character of the crack paths. As it is shown in Fig. 7, the grains are elongated in the rolling direction, it is known that this causes anisotropic behavior of mechanical properties so one can expect an analogous effect on the self-affine parameters.

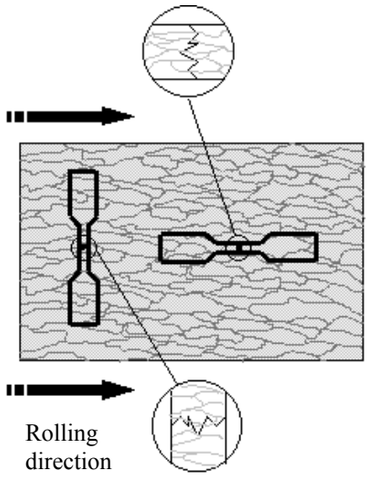

Fig. 6 Scheme showing the orientation of the tension specimen with respect to the rolling direction.

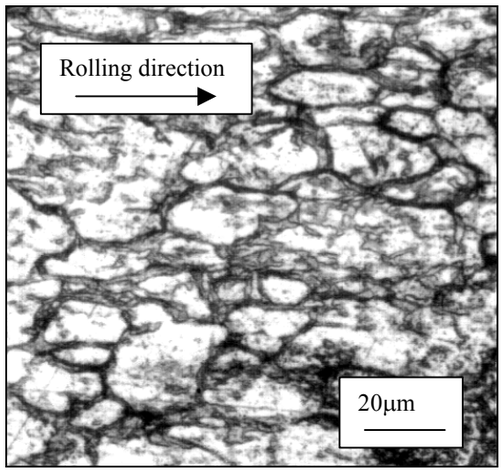

Fig. 7 Microstructure of the aluminum foil showing grains elongated in the rolling direction.

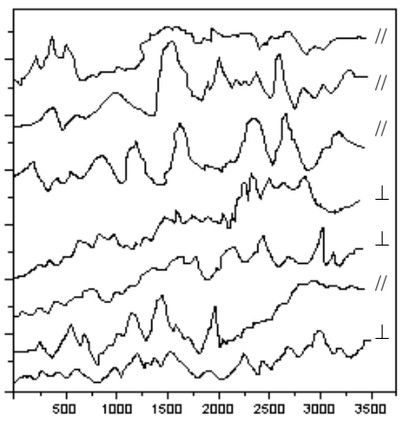

Fig. 8 Samples of the recorded crack paths in the rolling direction (//) and the perpendicular direction (⊥).

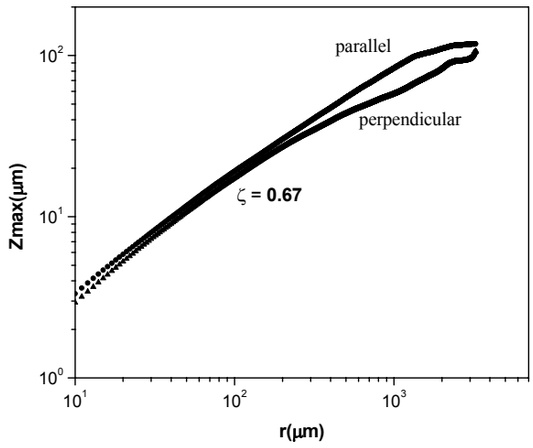

Fig. 9 Self-affines curves for the profiles in the parallel and perpendicular direction respectively, both curves reveal that the roughness exponent ζ has a value of 0.67

The crack paths obtained as a results of the tension test were recorded at various magnifications using SEM, optical microscopy and a conventional document scanner. Samples of the recorded self-affine paths are shown in Fig. 8 where paths belonging to cracks propagating in the rolling direction are “wider” and clearly distinguishable from those propagating in the perpendicular direction. The self-affine plot shown in Fig. 9 reveals that the roughness exponent has about the same value for both directions, $\zeta = 0.67$, this value is in good agreement with the results predicted by the random fuse model and a 2D simulation of crack propagation reported in reference [16]. It is not possible to estimate with good precision the correlation lengths but Fig. 9 suggest that this parameter is larger for the parallel direction compared to that of the perpendicular direction, one can speculate that this can be interpreted as an effect of the elongation of the grains caused by the rolling process.

CONCLUSIONS

We have determined the self-affine parameters of the fracture surface of a cast aluminum alloy. The parallel and perpendicular out-of-plane roughness exponents were determined with values of 0.78 and 0.79, respectively. The roughness exponent of the arrested crack front was also determined, with a value of 0.79. It was corroborated that the correlation length is in all the cases related to the size of the largest heterogeneities present in the complex microstructure. The analysis of the crack paths in aluminum foil as developed in 2D mode I loading allowed the determination of the respective self-affine parameters. It was found that the roughness exponent has a value of 0.67 for both the parallel and transverse direction of propagation with respect to the rolling direction. The anisotropy of the microstructure has an observable effect in the correlation length whereas the roughness exponent is apparently unaffected by this condition.

ACKNOWLEDGEMENTS

Author express their gratitude to E. Sánchez, E. Reyes, O. Garza, I. Suárez, L. Cruz, R. Colás and E. Velasco, the financial support of the Consejo Nacional de Ciencia y Tecnología and the UANL through the PAICYT program is also gratefully acknowledged.

REFERENCES

1. M. E. Eberhart, Scientific American, p. 44-51, Oct. 1999.
2. Hellemans, Science Vol. 281, p. 943-944, 14 August 1998.
3. MRS Bulletin, Vol. 25, No. 5, May 2000.
4. J.W. Hutchinson and A. G. Evans, Acta materialia Vol. 48 p. 125-135, 2000.
5. M. Marder and J. Fineberg, Physics Today Vol. 49, p. 24, 1996.
6. E. Bouchaud, J. Phys.:Condens. Matter Vol. 9, p. 4319-4344, 1997 and references therein.
7. A. Balankin, Engineering Fracture Mechanics Vol. 57, p. 135-203, 1997 and references therein.
8. B.B. Mandelbrot, Passoja, Paullay, *Nature* Vol 308 19 April 1984.
9. L. de Arcangelis, S. Redner, H.J. Herrmann, Journal de Physique Lettres 46, p. 585-590, 1985.
10. E. Bouchaud, G. Lappasset, J. Planes and S. Naveos, Phys. Rev. B, Vol 48, p. 2917 ,1993.
11. K. J. Maloy, A. Hansen, E. L. Hinrichsen and S. Roux, Phys. Rev. Lett., Vol. 68**,** p. 213-215, 1992.
12. X. Zhang, M.A. Knackstedt, D.Y.C. Chan and L. Paterson, Europhysics Letters, Vol. 34, p. 121-126, (1996).
13. J. Feder, *Fractals*, Plenum Press, New York, 1988.
14. M. Hinojosa, J. Aldaco, U. Ortiz and V. González, Aluminum Transactions Vol. 3, p.53-57, 2000.
15. P. Daguier, B. Nghiem, E. Bouchaud and F. Creuzet, Phys. Rev. Lett. Vol 78, p. 1062, 1997.
16. P. Daguier, Ph. D. Thesis, Paris University, Paris, 1997.
17. M. Hinojosa, E. Bouchaud y B. Nghiem, MRS Symp. Proc. Vol. 539, p. 203-208, 1999.
18. J. Aldaco, F.J. Garza, M. Hinojosa, MRS Symp. Proc. Vol. 578, p. 351-356, 2000.
19. M. Hinojosa, J. Aldaco, U. Ortiz and J.A. González, Euromat 2000, p. 1469-1474, 2000.
20. E. Reyes, Masters Thesis, Universidad Autónoma de Nuevo León, México (in Spanish), 1999.
21. J. Schmittbuhl, J. P. Vilotte and S. Roux, *Phys. Rev. E*, vol. 51, p. 131, 1995.

ORAL/POSTER REFERENCE: ICF10042OR

2D SIMULATION OF TENSILE BEHAVIOR OF FIBER-REINFORCED BRITTLE MATRIX COMPOSITES WITH WEAK INTERFACE

S. Ochiai, S. Kimura, M. Tanaka and M. Hojo

Mesoscopic Materials Research Center, Graduate School of Engineering,
Kyoto University, Sakyo-ku, Kyoto 606-8501, Japan

ABSTRACT

The shear lag analysis was combined with the Monte Carlo method, and applied to two-dimensional model composite to simulate the tensile behavior of unidirectional continuous fiber-reinforced brittle matrix composites with weak interface. The features particular to weakly bonded composites such as intermittent breakage of components and interfacial debonding, serrated stress-strain curve, pull-out of fibers, deleterious effects of residual stresses on strength of composite, overall unnotched strength determined by fiber bundle, longitudinal cracking arising from the tapered portion in unnotched specimen and from the notch tip in notched specimen and the notched strength given by the net stress criterion, were simulated well.

KEYWORDS: tensile behavior, simulation, unidirectional composite, weak interface, damage map

INTRODUCTION

When the interface in brittle fiber/brittle matrix composites is strong, the crack arrest-capacity is low and high strength and toughness cannot be achieved. Thus the interface is controlled to be weak. For the design and practical use, it is needed to describe and predict the behavior of weakly bonded composites.

Under tensile load, damages (breakage of fiber and matrix, and interfacial debonding) arise at many places, being distributed spatially. The damages interact mechanically to each other. Such mechanical interactions determine the species and location of the next damage, one after another. Thus the damage map and therefore the mechanical interaction among damages vary with progressing fracture. As a result of consecutive variation of them, mechanical properties such as stress-strain curve, strength and fracture morphology are determined. Thus, for description of the behavior of composites, as the damage map varies at every occurrence of new damage, the new interaction shall be calculated for the new damage map one after another

One of the tools to solve this problem may be the shear lag analysis [1,2]. However, the ordinary shear lag analysis have been developed using the approximation that only fibers carry applied stress and the matrix acts only as a stress-transfer medium. Due to this approximation, it had two disadvantages; it can be applied only to polymer- and low yield stress-metal –matrix composites but not to intermetallic compound- and ceramic-matrix ones; and the residual stresses cannot be incorporated. Recently, the authors [3-5] have proposed a modified method to overcome

these disadvantages, with which the general situation (both fiber and matrix carry applied stress and also act as stress transfer media) can be described and residual stresses can be incorporated, to a first approximation.

In the present study, the modified shear lag analysis mentioned above will be combined with the Monte Carlo method and be applied to 2D model, to simulate the tensile behavior of unidirectional weakly bonded brittle matrix composites.

MODELING AND SIMULATION METHOD

A two-dimensional model composite employed in the present work is shown in Fig.1. The components (fiber and matrix) were numbered as 1,2,…i,... to N from left to the right side. Each component was regarded to be composed of k+1 short component elements with a length Δx. The position at x=0 was numbered as 0 and then 1, 2, 3,...j... k+1 downward, in step of Δx.. The "i" component from x=(j-1) Δx to jΔx was named as the (i,j)-component-element, and the interface from x=(j-1/2) Δx to (j+1/2) Δx between "i" and "i+1" components as the (i,j)-interface-element. The displacement of the (i,j)-component-element at x=jΔx was defined as $U_{i,j}$. Two parameters ($\alpha_{i,j}$ and $\gamma_{i,j}$) were introduced to express whether (i,j)-interface is debonded ($\alpha_{i,j}$=0) or not ($\alpha_{i,j}$=1) and whether (i,j)-component is broken ($\gamma_{i,j}$=0) or not ($\gamma_{i,j}$ =1). From the spatial distribution of debonded interface-elements with $\alpha_{i,j}$=0 and broken component-elements with $\gamma_{i,j}$=0, the damage map was expressed. The values of $\alpha_{i,j}$ and $\gamma_{i,j}$ were determined at each occurrence of damage. The values of $U_{i,j}$ were calculated by the procedure elsewhere [3,4], from which the tensile stress $\sigma_{i,j}$ of each component and shear stress $\tau_{i,j}$ at each interface were calculated .

The simulation of the stress-strain behavior was carried out in the following procedure.

(1)The strength of each component $S_{i,j}$ was determined by generating a random value based on the Monte Carlo procedure using the Weibull distribution.

(2)Two possibilities arise for the occurrence of damage; one is the fracture of the component which occurs when the exerted tensile stress $\sigma_{i,j}$ exceeds the strength $S_{i,j}$ and another is the interfacial debonding which occurs when the exerted

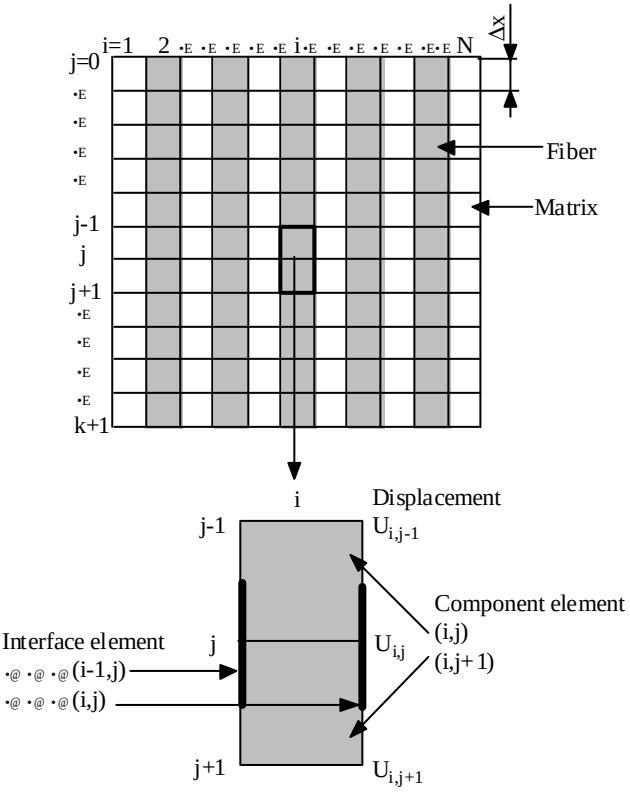

Figure1 Modeling for simulation.

shear stress $\tau_{i,j}$ exceeds the shear strength τ_c. To identify which occurs, $\sigma_{i,j}$ for all component elements were calculated and the component element having the maximum $\sigma_{i,j}/S_{i,j}$ -value, say (m,n)-component , was identified. Also, the interface element with the maximum shear stress, say (m',n'), was identified. (i)If $\sigma_{m,n}/S_{m,n}<1$ and $\tau_{m',n'}/\tau_c <1$, no breakage of component and no interfacial debonding occur. Thus the applied strain was raised. (ii)If $\sigma_{m,n}/S_{,m,n}>=1$ and $\tau_{m',n'}/\tau_c <1$, (m,n)-component-element is broken. If $\sigma_{m,n}/S_{m,n} <1$ and $\tau_{m',n'}/\tau_c>=1$, (m',n')-interface-element is debonded. If $\sigma_{m,n}/S_{m,n} >=1$ and $\tau_{m',n'}/\tau_c>=1$, (m,n)-component-element is broken when $\sigma_{m,n}/S_{,m,n}>\tau_{m',n'}/\tau_c$, while (m',n')-interface-element is debonded when $\sigma_{m,n}/S_{im,n} <\tau_{m',n'}/\tau_c$. In this way, what kind of damage occurs is identified. Then a similar process was repeated and the next damage was identified one after another. Such a procedure was repeated until no more occurrence of damage at a given strain.

(3)When no more damage occur, the applied strain ε_c was raised, and the procedure (2) was repeated until overall fracture of the composite.

RESULTS AND DISCUSSION

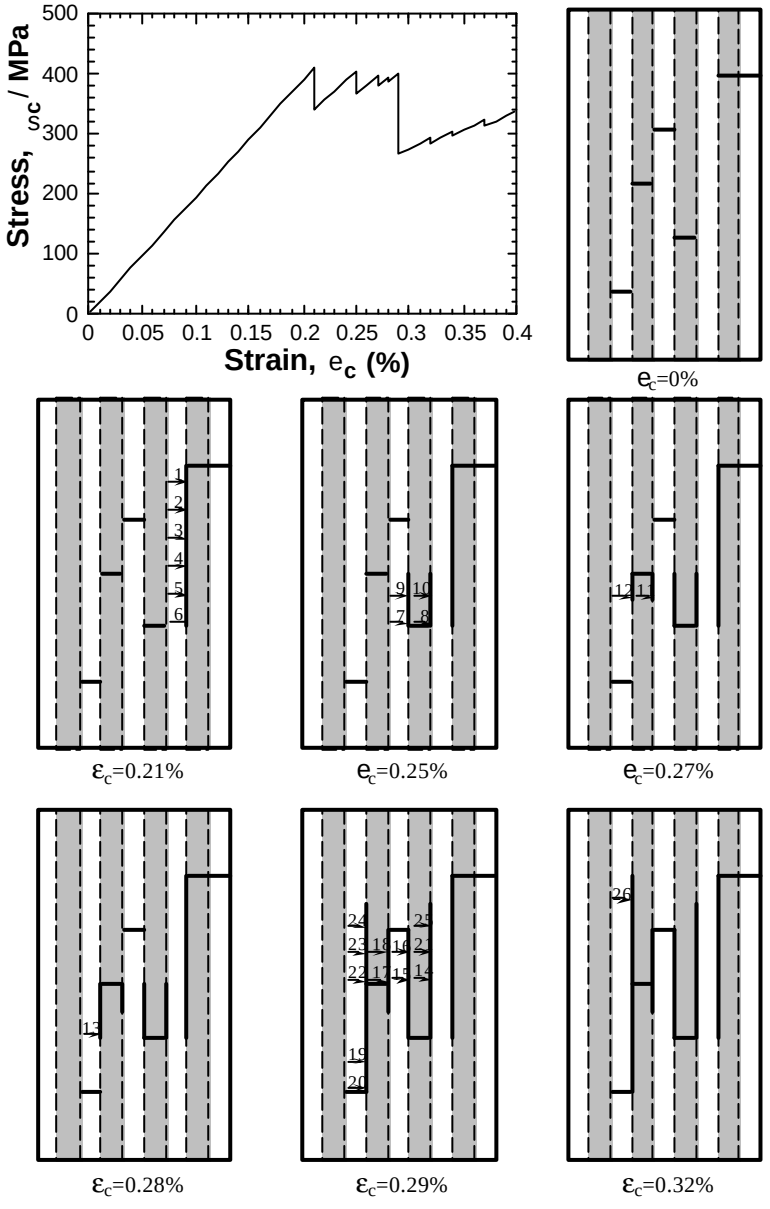

Figure 2 An example of the stress-strain curve and variation of damage map of the composite caused by progress of the interfacial debonding under the given geometry of the

broken components.

Progress of Interfacial Debonding and the Resultant Stress-strain Curve of the Composite with the Fixed Geometry of Broken Components

In this work, a mini sized model composite was used to describe the fundamental process of fracture, and following values were used for calculation: N=9, k=12, $d_f=d_m$=0.1mm, Δx= 0.2 mm (=$2d_f$), E_f=400GPa, E_m=200GPa, G_f=160 GPa, G_m=80GPa, τ_c= 50- 200 MPa. and τ_f =0 MPa.

First, in order to know the influence of pre-existent broken component element on the progress of debonding, the change of damage-map and overall stress-strain curve of composite was simulated under the given geometry of the broken components. In this case, it was assumed that no breakage of the components occurs. Figure 2 shows the stress (σ_c)-strain (ε_c) curve and damage map at various strains.

The feature of the debonding progresses is read as follows. The first debonding starts at ε_c=0.0021, followed by the 2nd to 6th debonding at the same strain, as indicated by 1 to 6. Then the debonding stops. Due to the progress of debonding at many interface-elements, the stress-carrying capacity of composite is reduced. The reduction of stress at ε_c=0.0021 in the curve corresponds to such an interfacial debonding-induced loss of stress carrying capacity. After occurrence of the 1st to 6th debonding at ε_c =0.0021, the overall debonding stops since the shear stresses of all bonded interface-elements become lower than the critical value at this strain. Beyond ε_c=0.0021, no debonding occurs and the composite stress increases up to ε_c=0.0025, at which the 7th to 10th debonding occur one after another, resulting in loss of stress carrying capacity. After the stoppage of debonding, the composite stress again increases with increasing strain. As shown in this example, the overall debonding progresses intermittently with repetition of growth and stoppage, resulting in the serrated stress-strain curve.

Stress-strain Curve of the Composite in Which Both Breakage of Components and Interfacial Debonding Occur

Figure 3 shows examples of the stress-strain curve of the composite in which both breakage of components and debonding of interface occur consecutively. (a) shows the case where the coefficients of thermal expansion of fiber(α_f) and matrix(α_m) are the same (5×10^{-6}/K) and therefore no residual stress exists and (b) the case where they are different(α_f =5×10^{-6}/K and α_m=10×10^{-6}/K) and the residual stresses are introduced by cooling from 1500K to 300K. As the number of elements of broken fiber (N_F), matrix (N_M) and interface (N_I) were quite different to each other and could not be clearly shown on the same scale, the normalized values with respect to the final values $N_{F,f}$, $N_{M,f}$ and $N_{I,f}$, respectively, are shown in this figure. Figure 4 shows the fracture process of unnotched composite with tapered grip portion. From Figs.3 and 4, following features are read.

(i)The stress-strain curve shows also serration due to the intermittent breakage of the components and interfacial debonding.

(ii)In case (b) in Fig.3, as $\alpha_f < \alpha_m$, the matrix and fiber have tensile and compressive residual stresses along fiber axis, respectively. In the example of Fig.3, the average failure strain of the matrix was taken to be comparable with that of fiber under no residual stresses. The authors [3,4] have shown that the tensile residual stress in the matrix enhances the breakage of matrix and also hastens the matrix breakage-induced debonding, while the compressive one in the fiber retards the fracture of fiber and also suppresses the fiber breakage-induced debonding. Comparing the variation of broken matrix-elements N_M and debonded interface-elements N_I with increasing applied strain in case (b) with that in case (a), the former evidently shifts to lower strain range. As known from such a difference under the existence of the present residual stresses, the matrix breakage and matrix breakage–induced debonding occur in the early stage, resulting in loss of stress carrying capacity and therefore low strength of composite. On the other hand, in the composite without residual stresses (a), the matrix is broken nearly at the same strain of breakage of fiber and the premature debonding does not arise so much until the ultimate stress, resulting in high strength. As the deleterious effect of the present residual stresses on the strength of weakly bonded composites, the strength of the composite with residual stresses (b) was 930MPa, which was far lower than 1500MPa of the composite without residual stresses (a).

(iii) In the case of (b) in Fig.3, the matrix breakage and the interfacial debonding have occurred in the early stage.

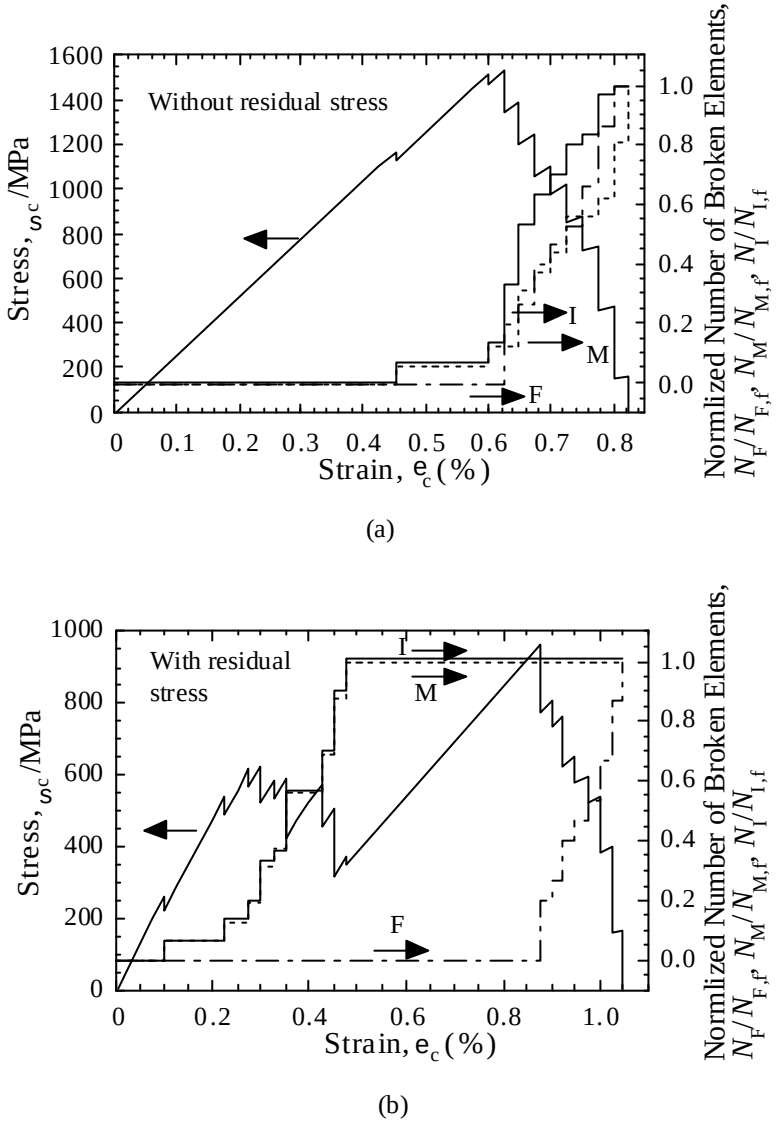

Figure 3 Comparison of the stress-strain curve, strength and accumulation process of damages between the composites (a) without and (b) with residual stresses.

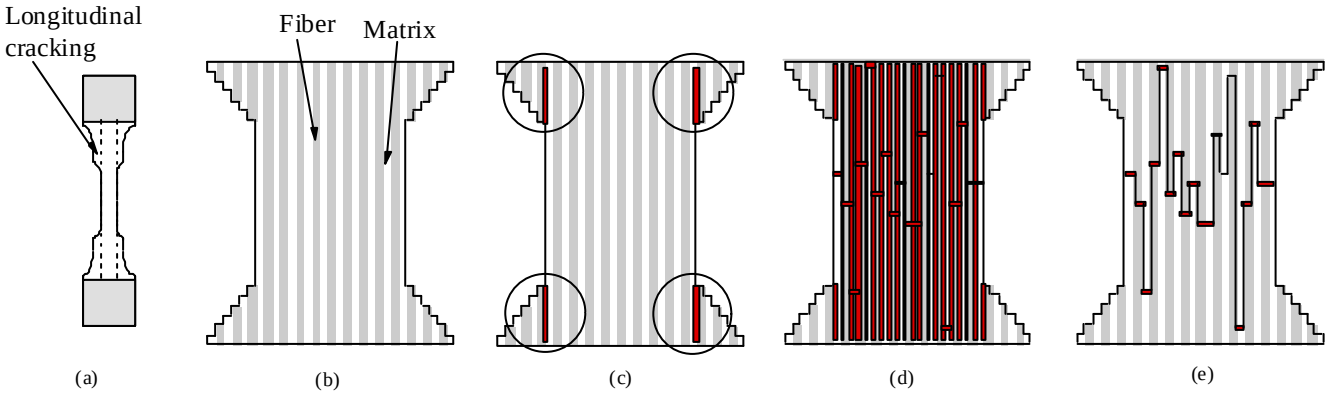

Figure 4 (a): Schematic drawing of the longitudinal cracking in the unnotched specimen. (b): Modeling for simulation. (c) to (e): Simulated fracture process accompanied with

longitudinal cracking and the fracture morphology

Once such a situation has occurred, the fibers are separated to each other and behave like a fiber bundle without matrix. Thus the strength of such composite is given by the strength of the fiber bundle. Further simulation using the low failure

strain-matrix composite without residual stresses showed the same feature.

(iv) It has been known that, in weakly bonded composites, longitudinal cracking occurs ahead of the notch. Furthermore, even in the unnotched samples, the longitudinal cracking between the parallel gage portion and the tapered one occurs (Fig.4(a)). Such a feature is also well realized in Fig.4 (b) to (e).

(v) It has been well known that the fiber is pulled-out in weakly bonded composites. The final fracture morphology of the composite, shown in Fig.4(e), describes such a feature also.

(vi) In notched samples, the longitudinal cracking occurs in the whole length between the grips at lower applied stress level than that in unnotched samples. Thus, the notch does not cause mode I type fracture but enhance longitudinal cracking. As a result, the strength of notched samples could be expressed by the net strength criterion.

CONCLUSIONS

The variation of the damage map, stress-strain curve, strength and fracture morphology of two-dimensional model composite with weak interface were simulated by combining the shear lag analysis with the Monte Carlo method. Following features of weakly bonded composites were described.

(1) Both of the breakage of components and interfacial debonding occur intermittently.

(2) As a result of (1), the stress-strain curve is serrated.

(3) When the fracture strain of matrix is low, the residual stresses (tensile and compressive stresses along fiber axis for matrix and fiber, respectively) enhance breakage of matrix and matrix breakage-induced debonding at low applied strain. As a result, the stress carrying capacity of the composite is reduced, resulting in low strength.

(4) The strength of weakly bonded composites whose matrix has low failure strain is practically given by the strength of the fiber bundle.

(5) Longitudinal cracking arises at the notch tip in notched specimens and also at the tapered corner in the unnotched specimens.

(6) The notched strength is given by the net stress criterion.

Acknowledgement

The authors wish to express their gratitude to The Ministry of Education, Science and Culture of Japan for the grant-in-aid for Scientific Research (No.11555175).

REFERENCES

1. Hedgepeth, J. M.. (1961). *Stress Concentrations in Filamentary Structures*. NASA TN D-882, Washington,.
2. Oh, K. P. (1979) *J. Comp. Mater.*, **13,** 311.
3. Ochiai, S., Okumura, I., Tanaka, M. and Inoue, T. (1998) *Comp. Interfaces*, **5**, 363.
4. Ochiai, S., Tanaka, M. and Hojo, M. (1998) *Comp. Interfaces*, **5**, 437.
5. Ochiai, S. Hojo, M. and T. Inoue. (1999) *Comp. Sci. Tech.*, **59**, 77.

A BOUNDARY ELEMENT BASED MESO-ANALYSIS ON THE EVOLUTION OF MATERIAL DAMAGE

H. Okada, Y. Fukui and N. Kumazawa

Department of Mechanical Engineering, Kagoshima University
1-21-40 Korimoto, Kagoshima 890-0065, JAPAN

ABSTRACT

In this paper, we present efficient numerical formulations for the analyses of particulate composites, underging meso-structural changes such as particle fracture, stress induced phase transformation, etc. The formulations are derived based on the homogenization method and the boundary element method (BEM). Proposed formulations can efficiently deal with problems, in which particles randomly distribute and orient in the composites, by combining analytical solutions for the ellipsoidal inclusions such as Eshelby's tensor and the boundary element method. Hence, there is no need to carry out any numerical integrations for the particles. Proposed numerical methods are computationally efficient and accurate. The formulations and numerical results for effective elastic moduli of composites and problems of particle fracture and stress induced phase transformation, are presented.

INTRODUCTION

In this paper, efficient boundary element formulations (see [1-6] for the boundary element method) for solids containing ellipsoidal inclusions/particles, as shown in Fig. 1, are presented (see Ashby [7] for various types of composite materials). First, a boundary element based formulation for homogenization analysis is discussed and is combined with analytical solutions for ellipsoidal inclusions in which constant initial strains are specified inside of them. A special case of the analytical solutions is given as the well known Eshelby's tensor [8,9]. The analytical solutions for ellipsoidal inclusions such as Eshelby's tensor, are based on the fundamental solution of linear isotropic elasticity, which is also used in the boundary element method as its kernel functions. The analytic solutions and boundary element formulation can easily be combined.

Homogenization method [10-12] based on the finite element method has been applied to a various class of problems, such as identifying macroscopic elastic moduli and nonlinear behavior of meso-structure for a prescribed macroscopic deformation mode. Homogenization method assumes that the microstructure of solid is spatially periodic, and finite element analyses for a unit of periodic structure (unit cell) are carried out. However, the homogenization method can not be applied to the problems of particulate composite materials in a straight forward manner, since the orientations and distributions of particles

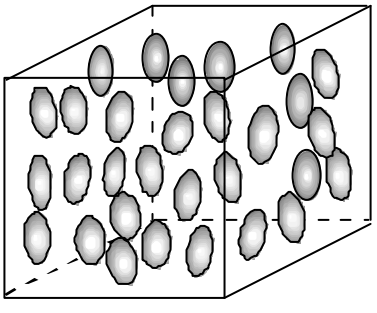

Figure 1: Particulate composite material

would be somewhat random. Therefore, defining a unit cell model containing one or a few particles may be an over simplification of the problem. To accurately model such solids, a unit cell containing many particles should be analyzed. Thus, one needs to build and carry out analyses for a unit cell model having tens and hundreds of particles. Finite element model, which is required for such analyses, would be gigantic. Generating the finite element model as well as solving the problem would pose many problems. However, mechanical interactions between the particles, and between matrix material and particles are fully accounted for, when the finite element method is adopted.

On the other hand, methodologies in micromechanics, such as self-consistent method [9,13,14] and Mori-Tanaka theory [9,15] have been presented. For particulate composites, Eshelby's tensor [8,9], takes a central role (see, for example, [9,16,17]). These methodologies have advantages over the finite element method such that the effective mechanical behaviors of composites can be estimated in a closed or semi-closed form, based on the elastic moduli of matrix and particles, the distribution, orientation and volume fraction of the particles. Large scale computations are not required. However the methods in micromechanics do not account for detailed mechanical interactions between the distributed particles. The mechanical interactions may have significant roles when the particles are densely distributed or when we attempt to account for the damage evolution or meso-structural changes, such as phase transformation of the particles.

Boundary element based homogenization formulation, which is developed in this paper, have advantages of both the above mentioned methodologies. Since the method is based on the boundary element method (BEM [1-6]), detailed mechanical interactions between all the material constituents can be accounted for. This nature is similar to that of the finite element method. A unit cell modeled by the boundary element method can contain many particles and the computation is simplified by using analytical solutions for ellipsoidal inclusions, such as Eshelby's tensor [8,9]. In this regard, proposed method is similar to the methodologies in micromechanics.

HOMOGENIZATION FORMULATION FOR PARTICULATE COMPOSITES

In this section, equation formulations for boundary element based homogenization analysis for particulate composites are briefly discussed (see [18,19] for homogenization method based on BEM). In homogenization method, the microstructure of solid is assumed to be spatially periodic, as shown in Fig. 2. A unit of the periodic microstructure is modeled by the boundary element method and is called "unit cell". As shown in Fig.1 in a two dimensional illustration, the size of the unit cell is represented by e. We introduce two different coordinate systems. One is x_i coordinate system, which is fixed in space and the other is y_i coordinate system, which is scaled by the size e of unit cell, as:

$$y_i = x_i / e + c_i \tag{1}$$

where c_i are the components of an arbitrary vector. Displacements u_i are expressed by the two scale asymptotic expansion, by following Guedes and Kikuchi [10], as:

$$u_i(\boldsymbol{x},\boldsymbol{y}) = u_i^o(\boldsymbol{x},\boldsymbol{y}) + e u_i^1(\boldsymbol{x},\boldsymbol{y}) + e^2 u_i^2(\boldsymbol{x},\boldsymbol{y}) + e^3 u_i^3(\boldsymbol{x},\boldsymbol{y}) + \cdots \tag{2}$$

For small deformation linear elasticity problem, Hooke's law and the equation of linear momentum balance are written to be:

$$\sigma_{ij} = E_{ijk\ell}\frac{\partial u_k}{\partial x_\ell} \quad , \qquad \frac{\partial \sigma_{ij}}{\partial x_i} + b_j = 0 \tag{3}$$

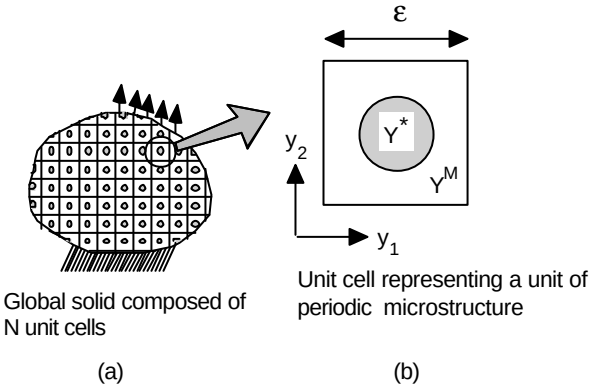

Figure 2: Two dimensional illustration for a solid whose microstructure is periodic and its unit cell.

where $E_{ijk\ell}$ are the fourth order tensor, representing Hooke's law. Based on Eqns. (2) and (3), it can be shown that $u_i^o = u_i^o(x)$ [u_i^o are the functions of x_i only.], and one can obtain an integral equation formulation for u_i^1 for the analysis of unit cell (see Okada et al. [19] for the derivation).

$$C_{pq}u_q^1\left(x_m^Y\right) = \int_{\partial Y} t_j^Y u_{jp}^*\left(y, x_m^Y\right)\mathrm{d}(\partial Y) - \int_{\partial Y} t_{kp}^*\left(y, x_m^Y\right)u_k^1\,\mathrm{d}(\partial Y) - \int_{Y^*} E_{ijk\ell}^M \bar{e}_{k\ell}\frac{\partial u_{ip}^*\left(y, x_m^Y\right)}{\partial y_j}\mathrm{d}Y^* - \frac{\partial u_k^o}{\partial x_m}\left[\int_{\partial Y} t_{kp}^*\left(y, x_m^Y\right)y_m\mathrm{d}(\partial Y) + C_{pq}x_q^Y\right] \tag{4}$$

where $\bar{e}_{k\ell}$ are the fictitious initial strains, which are defined by,

$$\bar{e}_{ij} = C_{ijmn}^M\left(E_{mnk\ell}^* - E_{mnk\ell}^M\right)\left\{\frac{\partial u_k^o(x)}{\partial x_\ell} + \frac{\partial u_k^1(x, y)}{\partial y_\ell}\right\} \tag{5}$$

Displacements u_i^1 at the source point x_m^Y is evaluated by the integral equation (4). A two phase composite material is assumed and elastic constants for matrix and second phase materials are represented by $E_{ijk\ell}^M$ and $E_{ijk\ell}^*$, respectively. u_{ip}^* and t_{ip}^* are the Kelvin solutions (see [4]). Y and ∂Y represent the domain and boundary of the unit cell. Y^* denotes the region of second phase material in Y.

We assume that the solid contains ellipsoidal particles as its second phase material and that the stresses and strains are constant values inside a particle, by following the result of Eshelby [8] and many of micromechanics analyses [9,17]. We then rewrite the volume integral term of integral equation (4), as:

$$\int_{Y^*}\frac{\partial u_{ip}^*\left(y, x_m^Y\right)}{\partial y_j}E_{ijk\ell}^M\bar{e}_{k\ell}\mathrm{d}Y^* = \sum_{I=1}^{N}\bar{e}_{ij}^I\int_{(Y^*)^I}\frac{\partial u_{ip}^*\left(y, x_m^Y\right)}{\partial y_j}E_{ijk\ell}^M\mathrm{d}\left(Y^*\right)^I = \sum_{I=1}^{N}\Lambda_{pij}^I\left(x_m^Y\right)\bar{e}_{ij}^I \tag{6}$$

where $\Lambda_{pij}^I\left(x_m^Y\right)$ are the analytical expressions for the integral (see Mura[9]) and $\bar{e}_{k\ell}^I$ are the fictitious initial strain in the *I*th particle. Thus, we write:

$$C_{pq}u_q^1\left(x_m^Y\right) = \int_{\partial Y} t_j^Y u_{jp}^*\left(y, x_m^Y\right)\mathrm{d}(\partial Y) - \int_{\partial Y} t_{kp}^*\left(y, x_m^Y\right)u_k^1\mathrm{d}(\partial Y) - \sum_{I=1}^{N}\Lambda_{pij}^I\left(x_m^Y\right)\bar{e}_{ij}^I - \frac{\partial u_k^o(x)}{\partial x_m}\left[\int_{\partial Y} t_{kp}^*\left(y, x_m^Y\right)y_m\mathrm{d}(\partial Y) + C_{pq}x_q^Y\right] \tag{7}$$

When the source point x_i^Y is at the interior of the *J*th particle, we can derive an integral equation for the displacement gradients $\partial\hat{u}_i/\partial y_j$, by differentiating Eqn. (7) with respect to x_i^Y, as:

$$\left(\frac{\partial\hat{u}_p}{\partial y_q}\right)^J = \int_{\partial Y} t_j^Y\frac{\partial u_{jp}^*\left(y, x_m^Y\right)}{\partial x_q}\mathrm{d}(\partial Y) - \int_{\partial Y}\frac{\partial t_{kp}^*\left(y, x_m^Y\right)}{\partial x_q}\hat{u}_k\mathrm{d}(\partial Y) - \sum_{\substack{I=1\\ I\neq j}}^{N}\Theta_{pqij}^I\left(x_m^Y\right)\bar{e}_{ij}^I - S_{pqk\ell}^J\bar{e}_{k\ell}^J \tag{8}$$

where $S_{pqk\ell}^J$ are the components of Eshelby's tensor [8,9] for the *J*th particle. Singular volume integrals, whose numerical evaluations are known to be troublesome, are replaced by the analytical formulae such as Eshelby's tensor. Therefore, proposed integral equations are computationally efficient and accurate.

Taking the last term in Eqn. (7) as the forcing term and following the standard boundary element analysis procedures by imposing the so called periodic boundary conditions on displacements u_i^1 and tractions t_i^Y, we can evaluate the displacements and tractions at the boundary of the unit cell. An initial strain iteration method is adopted to obtain the equilibrium (see [5,6] for the initial strain iteration for solving elastic-plastic problems using BEM). Thus, the solutions for given $\partial u_i^o/\partial x_j$ are obtained. We repeat the analyses for six times for a three dimensional problem to determine the responses of microstructure to all the macroscopic deformation modes (six strain modes). The characteristic functions $F_{ik\ell}(y)$, which relate $\partial u_i^o/\partial x_j$ to u_i^1, and the effective elastic moduli $E_{ijk\ell}^H$ of the composite are written to be:

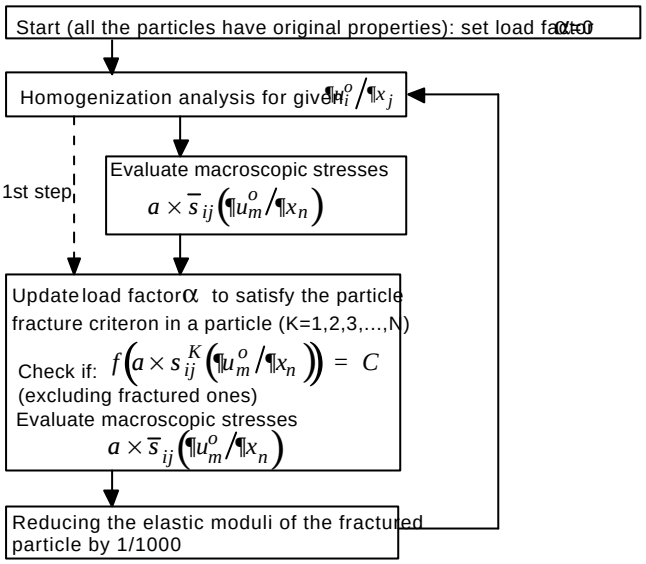

Figure 3: Algorithms for the analysis of problem of particle fracture

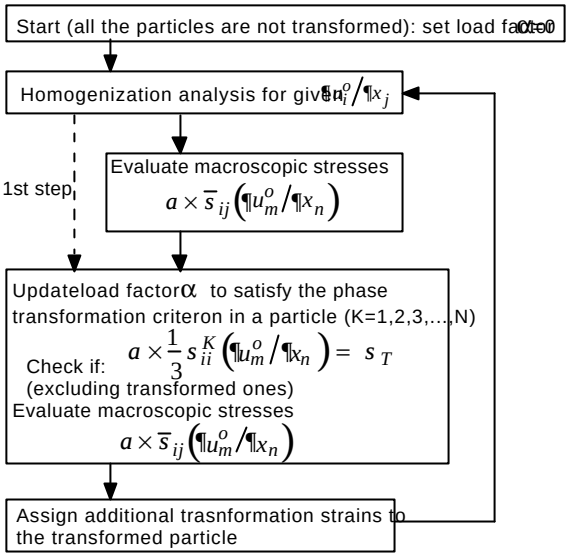

Figure 4: Algorithms for the analysis of problem of stress induced phase transformation

$$\begin{cases} E^H_{ijk\ell}(\boldsymbol{x}) = E^M_{ijk\ell} + \dfrac{1}{|Y|}\sum_{I=1}^{N}\left(E^*_{ijk\ell} - E^M_{ijk\ell}\right)Y_I^* + \dfrac{1}{|Y|}\sum_{I=1}^{N}\left(E^*_{ijk\ell} - E^M_{ijk\ell}\right)\left(\dfrac{\partial F_{mk\ell}(\boldsymbol{y})}{\partial y_n}\right)_I Y_I^* \\ u_i^1 = F_{ik\ell}(\boldsymbol{y})\dfrac{\partial u_k^o}{\partial x_\ell} \end{cases} \tag{10}$$

ANALYSIS FOR PROGRESSIVE DAMAGE (MESO-STRACTURAL CHANGE)

Here, we deal with the problems of particle fracture and of the stress induced phase transformation of particles (see [17,20] for stress induced phase transformation). We make small extensions on the integral equations (7) and (8), as follows.

Particle Fracture

An incremental analysis is carried out for the problems of particle fracture. The simplest scenario is assumed that when the stresses in a particle satisfy a criterion for particle fracture, the elastic modulus of the particle reduces to zero (in actual calculation, the elastic modulus is reduced to be 1/1000 of the original value). Therefore, the analysis is entirely based on the elastic analysis for the unit cell. The integral equations, which are developed in the previous section, are applied by specifying different elastic moduli for fractured and unfractured particles. Algorithms for the analysis are shown in Fig. 3.

Stress Induced Phase Transformation of Particles

The problems of dilatational stress induced phase transformation (see Okada et al. [17]) are considered and an incremental algorithm is adopted. It is assumed that at the instance, when hydrostatic stress ($s_{kk}/3$) inside a particle reaches a critical value, the particle transforms its phase and dilatational transformation strain is produced. The dilatational transformation strain is modeled as an additional initial strain. The integral equations [Eqns. (7) and (8)] are modified to include the effects of the transformation strain, as:

$$C_{pq}u_q^1(\boldsymbol{x}_m^Y) = \int_{\partial Y} t_j^Y u_{jp}^*(\boldsymbol{y}, \boldsymbol{x}_m^Y)\,d(\partial Y) - \int_{\partial Y} t_{kp}^*(\boldsymbol{y}, \boldsymbol{x}_m^Y)u_k^1\,d(\partial Y) - \sum_{I=1}^{N}\Lambda_{pij}^I(\boldsymbol{x}_m^Y)\bar{\bar{e}}_{ij}^I + \sum_{I=1}^{N} b^I \Lambda_{pij}^I(\boldsymbol{x}_m^Y)\bar{\bar{e}}_{ij}^I - \frac{\partial u_k^o(\boldsymbol{x})}{\partial x_m}\left[\int_{\partial Y} t_{kp}^*(\boldsymbol{y}, \boldsymbol{x}_m^Y)y_m\,d(\partial Y) + C_{pq}x_q^Y\right] \tag{11}$$

$$\left(\frac{\partial \hat{u}_p}{\partial y_q}\right)^J = \int_{\partial Y} t_j^Y \frac{\partial u_{jp}^*(\boldsymbol{y}, \boldsymbol{x}_m^Y)}{\partial x_q}\,d(\partial Y) - \int_{\partial Y} \frac{\partial t_{kp}^*(\boldsymbol{y}, \boldsymbol{x}_m^Y)}{\partial x_q}\hat{u}_k\,d(\partial Y) - \sum_{\substack{I=1 \\ I\neq j}}^{N}\Theta_{pqij}^I(\boldsymbol{x}_m^Y)\bar{\bar{e}}_{ij}^I - S_{pqk\ell}^J\bar{\bar{e}}_{ik\ell}^J + \sum_{\substack{I=1 \\ I\neq j}}^{N} b^I\Theta_{pqij}^I(\boldsymbol{x}_m^Y)\bar{\bar{e}}_{ij}^I + b^J S_{pqk\ell}^J\bar{\bar{e}}_{ik\ell}^J \tag{12}$$

where $\bar{\bar{e}}_{ij}^I$ are fictitious initial strains, which are related to the dilatational transformation strain e^t, as:

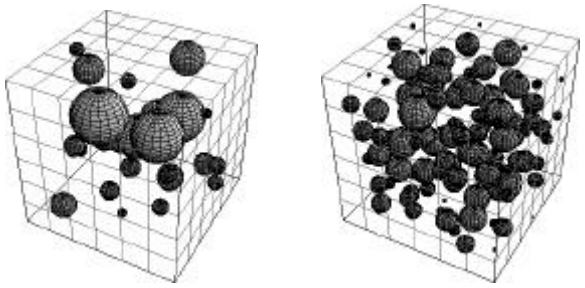

(a) (b)

Figure 5: Distributions of spherical particles in the unit cell. (a) 27 particles whose volume fraction is 0.1, (b) 125 particles whose volume fraction is 0.089

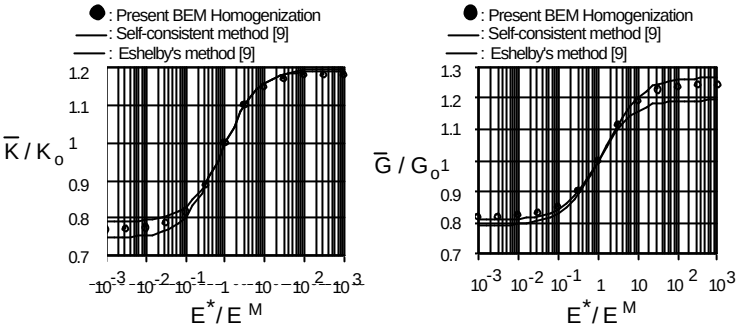

(a) (b)

Figure 6: The results for effective elastic moduli (125 particles). (a) Bulk modulus, (b) Shear modulus.

$$\bar{\bar{e}}_{ij}^{I} = C_{ijk\ell}^{M} E_{k\ell mm}^{*} \left(\frac{1}{3} e^{t} \right) \tag{13}$$

The effective stress for the solid can be given as average values of stresses in the unit cell, as:

$$\bar{s}_{ij} = E_{ijk\ell}^{M} \frac{\partial u_k^o}{\partial x_\ell} + \frac{1}{|Y|} \sum_{I=1}^{N} \left(E_{ijk\ell}^{*} - E_{ijk\ell}^{M} \right) \left(\frac{\partial \hat{u}_k}{\partial \ell} \right)^{I} - \sum_{I=1}^{N} b^{I} E_{ijkk}^{*} \left(\frac{1}{3} e^{pt} \right) \tag{14}$$

Algorithms for the analysis of the stress induced phase transformation problem are given in Fig. 4.

RESULTS OF NUMERICAL ANALYSIS

A limited number of numerical results are presented in this section due to the restriction of pages (results for the problem of particle fracture are omitted.). Unit cell models used for numerical computations are shown in Fig. 5. Randomly distributed spherical particles are assumed. The volume fraction of the particles is about 10%, and the number of the particles are 27 and 125. Linear quadrilateral boundary elements are used. Total number of boundary elements on each face of the unit cell is 36 (6 x 6).

Evaluation for Effective Elastic Moduli

The results are shown in Fig. 6. Isotropic elasticity is assumed for the particles and the ratio of Young's moduli of matrix and particles are varied from 10^{-3} to 10^{3}. Poisson's ratio is assumed to be 0.3 for both the material constituents. Results, which are analyzed by the 125 particle model, are presented.

For a comparison purpose, the results obtained by using self-consistent method and Eshelby's method theory (see Mura [9]) are also plotted in the figures. The results by three different methods are within an agreement. Though exact solutions are not known, three different methods are within a reasonable agreement and, therefore, the proposed technique is, at least, proven to be reliable.

Stress Induced Dilatational Transformation

Relationships between the effective hydrostatic stress ($\bar{s}_{kk}/3$) and effective dilatational strain ($\partial u_i^o / \partial x_i$), when Young's moduli of matrix and of particles are set to be the same, are shown in Fig. 7. Dilatational transformation strain is assumed to be $e_{kk}^{t} = 0.05$ and the phase transformation is assumed to take place when the hydrostatic stress in a particle reaches transformation stress s_T. The elastic moduli for matrix and particles are set to be the same in this case.

The stress-strain relationships follow zigzag paths and have negative slopes while the phase transformation is undergoing. The path is smoother for the 125 particle model than for the 27 particle one.

CONCLUDING REMARKS

In this paper, a new but simple method for the analysis of particulate composite material is presented. Though the numerical results, which are presented here, are rather limited, the method is proven to be quite effective. If one carried out a three dimensional analysis with 125 randomly distributed particles in a unit cell using the finite element method, a large scale computation must be carried out and the state of art mesh generation software would be necessary for the generation of analysis model. All the numerical analyses, which are presented in this paper are carried out using a workstation within a reasonable amount of computational time. Therefore, it can be concluded that present numerical technique can deal with the meso-mechanics problems of particulate composites effectively and efficiently.

REFERENCES

1. Cruse, T. A. (1969), *Int. J. Solid Structures* 5, 1259.
2. Cruse, T. A. (1987), *Comp. Meth. Appl. Mech. Engrg* 62, 227.-244, (1987).
3. Rizzo, F. J. (1967), *Q. Appl. Math.* 25, 83.
4. Banerjee, P. K. and Butterfield, R. (1981), *Boundary Element Methods in Engineering Science*, McGraw-Hill, London.
5. Okada, H. and Atluri, S.N. (1994), *Solids and Structures* 31, 12/13, 1735.
6. Okada, H., Rajiyah, H. and Atluri, S.N. (1988), *Computers & Structures* 30, 1/2, 275.
7. Ashby, M. F. (1993), *Acta. Metal. Mater.* 41, 5, 1313.
8. Eshelby, J. D. (1957), *Proceedings of Royal Society, London* A 241, 376.
9. Mura, T (1982), *Micromechanics of Defects of Solid*, Martinus Nijhoff.
10. Guedes, J. M. and Kikuchi, N. (1990), *Comp. Meth. Appl. Mech. Engrg.* 83, 143.
11. Kalamkarov, A. L. (1992), *Composite and Reinforced Elements of Construction*, John Wiley & Sons.
12. Hassani, B. and Hinton, E. (1998), *Computers & Structures* 69, 707.
13. Christensen, R. M. (1990), *J. Mech. Phys. Solids* 28, 3, 379.
14. Hill, R., *J. Mech. Phys. Solids* 13, 180.
15. Mori, T. and Tanaka, K. (1973), *Acta Metal.* 21, 571.
16. Nakagaki, M., Wu, Y. and Brust, F. W. (1999), *Computer Modeling and Simulation in Engineering* 4, 3, 186.
17. Okada, H. Tamura, T., Ramakrishnan, N., Atluri, S. N. and Epstein, J. S. (1992), *Acta. Metall. Materi.* 40, 6, 1421.
18. Kaminski, M. (1999), *Engineering Analysis with Boundary Elements* 23, 815.
19. Okada, H., Fukui, Y. and Kumazawa, N., In *Advances in Computational Engineering & Sciences*, pp. 1128-1133, Atluri, S. N. and Brust, F. W. (Eds.), Tech Science Press.
20. Ramakrishnan, N., Okada, H. and Atluri, S. N. (1991), *Acta. Metall. Mater* 39, 6, 1297.

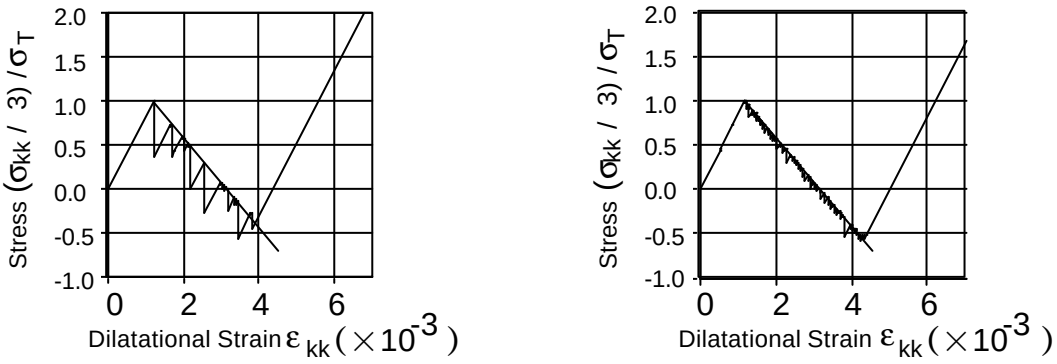

Figure 7: Hydrostatic pressure stress-dilatational strain curves for the problems of stress induced phase transformation. (a) 27 spherical particles, (b) 125 spherical particles. The straight lines are stress-strain curves following the results of Ramakrishnan, Okada and Atluri [20].

ICF100241OR

A COMPLEX VARIABLE FORMULATION FOR THE INTERACTIONS BETWEEN RIGID INCLUSIONS AND CRACKS

K.T. Chau[1] and Y.B. Wang[2]

[1]*Department of Civil and Structural Engineering, The Hong Kong Polytechnic University, Kowloon, Hong Kong, China*
[2]*Department of Mechanics, Lanzhou University, Lanzhou, China*

ABSTRACT

This paper summarizes the recent formulation by Wang and Chau [1] on a new boundary element method (BEM) in terms of complex variables for plane elastic bodies containing cracks, holes and rigid inclusions subjected to mixed displacement/ traction boundary conditions. A complex boundary function $H(t)$, which is a linear combination of the boundary traction and boundary displacement density, is introduced. The present Boundary Integral Formulation can be related directly to Muskhelishvili's formalism. Singular interpolation functions of order $r^{-1/2}$ (where r is the distance measured from the crack tip) are introduced such that singular integrand involved at the element level can be integrated analytically. The interaction between a rigid circular inclusion and a crack is investigated in details. Our results for the stress intensity factor are comparable with those given by Erdogan and Gupta [2] and Gharpuray et al. [3] for a crack emanating from a stiff inclusion, and with those by Erdogan et al. [4] for a crack in the neighborhood of a stiff inclusion.

KEYWORDS

Crack, Circular inclusions, Boundary element method, Complex variable

INTRODUCTION

In recent years, boundary element method (BEM) has widely been applied in solving linear elastic problems and fracture mechanics problems, and has been developed into a powerful numerical technique. In the traditional approach, boundary integral equations are derived by from the Somigliana's identity (e.g. Rizzo [5]; Cruse [6]; Lachat and Watson [7]; Brebbia [8]). The application of BEM has been focused mainly on traction boundary value problems (BVPs), and there is relatively few BEM studies on solving mixed BVPs,

to which displacements and tractions may be prescribed on disjoint portions or on the same segment of boundary but along different directions (e.g. Bonnet [9]; Gaul and Schanz [10]). Note, however, that the so-called "mixed BVPs" are sometimes simply referred as BVPs regardless of whether displacement or traction is prescribed on the boundary. A typical example of the mixed BVPs is the interaction between rigid circular inclusions and cracks in plane elastic bodies. There is no BEM that has been proposed in the literature for such problems. Therefore, Wang and Chau [1] recently proposed a robust BEM to solve this problem. This conference paper will present and summarize the main findings by Wang and Chau [1]. For the case of interactions between non-rigid circular inclusions and cracks, we refer to the works of Wang et al. [11], Erdogan et al. [4], Erdogan and Gupta [3], Isida and Noguchi [12], and Gharpuray et el. [3].

The present formulation closely resembles the Muskhelishvili [13-14] formalism. For mixed BVPs formulation in complex variables, we refer to the works by Sherman [15-18] and Lu [19]. These formulations, however, do not originate from the Somigliana's identity and, thus, their relationship to the classical BIE formulation is unclear. But this missing link between these formulations and the usual BEM was considered by Wang and Chau [1].

The main obecjtive of the present paper is to summarize the main findings by Wang and Chau [1]. The new BIE formulation originates from the Somigliana's identity and involves singular integrals of Cauchy type. The present BIE formulation is of the same mathematical form as that derived by Chau and Wang [20]. Thus, the numerical implementation proposed by Wang and Chau [21] will be adopted here for our BEM formulation. One main advantage of the present "complex" variable formulation over the traditional "real" variable formulations (e.g. Ghosh et al. [22]; Bonnet [23]; Frangi and Novati [24]) is that the kernal functions involved in the boundary integral equations are much simpler and, as shown by Wang and Chau [21], they can be dealt with analytically.

BOUNDARY INTEGRAL FORMULATION IN COMPLEX VARIABLE

By consider a two-dimensional linear isotropic elastic body containing *m* holes and *n* cracks of arbitrary shape under plane condition (see Figure 1), Chau and Wang [20] derived the following boundary integral formulation for stresses and displacements in terms of a complex unknown function $H(t)$:

$$\sigma_{11}+\sigma_{22}=2[\Phi(z)+\overline{\Phi(z)}], \qquad (z=x_1+ix_2\in\Omega \ \ and \ \ i=\sqrt{-1}), \tag{1}$$

$$\sigma_{22}-\sigma_{11}+2i\sigma_{12}=2[\bar{z}\Phi'(z)+\Psi(z)], \qquad (\bar{z}=x_1-ix_2), \tag{2}$$

$$2G(u_1+iu_2)=\kappa\varphi(z)-z\overline{\varphi'(z)}-\overline{\psi(z)}, \tag{3}$$

where

$$\Phi(z)=\frac{1}{4}(\sigma_1^{\infty}+\sigma_2^{\infty})+iC+\frac{1}{2\pi i}\int_{S+\Gamma}\frac{H(t)dt}{t-z}, \tag{4}$$

$$\Psi(z)=\frac{1}{2}(\sigma_2^{\infty}-\sigma_1^{\infty}+2i\sigma_{12}^{\infty})-\frac{1}{2\pi i}\int_{S+\Gamma}\left[\frac{\overline{H(t)}-\overline{q(t)}}{t-z}e^{-2i\alpha(t)}+\frac{\bar{t}H(t)}{(t-z)^2}\right]dt, \tag{5}$$

$$\chi(z)=\int\Phi(z)dz=\frac{1}{4}(\sigma_1^{\infty}+\sigma_2^{\infty})z+iCz-\frac{1}{2\pi i}\int_{S+\Gamma}H(t)\ln(t-z)dt+\gamma, \tag{6}$$

$$\psi(z) = \int \Psi(z)dz = \frac{1}{2}(\sigma_2^\infty - \sigma_1^\infty + 2i\sigma_{12}^\infty)z + \frac{1}{2\pi i}\int_{S+\Gamma}\left\{\left[\overline{H(t)} - \overline{q(t)}\right]e^{-2i\alpha(t)}\ln(t-z) - \frac{\bar{t}H(t)}{t-z}\right\}dt + \gamma', \tag{7}$$

$$H(t) = \frac{1}{\kappa+1}[q(t) + w(t)e^{-i\alpha(t)}] \qquad for\ t = y_1 + iy_2 \in S+\Gamma, \tag{8}$$

Before we continue to consider the boundary values of our complex functions, it is useful to note from (8) that *q(t)* can be expressed in terms of *H(t)* and *w(t)* as

$$q(t) = (\kappa+1)H(t) - w(t)e^{-ia(t)} \qquad for\ t = y_1 + iy_2 \in S+\Gamma. \tag{9}$$

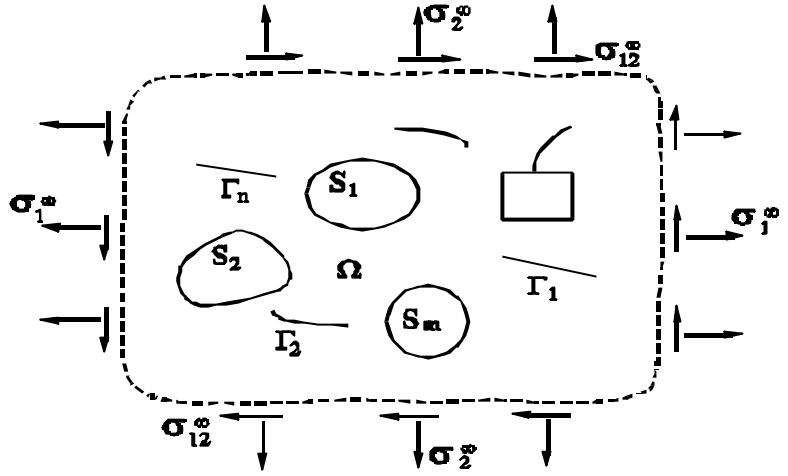

Figure 1: A sketch for an infinite elastic body containing *n* cracks $_j$ (j = 1,...,*n*) and *m* holes S_i (i=1,..., m) subjected to far field stresses σ_1^∞, σ_2^∞ and σ_{12}^∞.

In obtaining the above formula, we have let the outer boundary tends to infinity and the components of stress at infinity are given as σ_1^∞, σ_2^∞ and σ_{12}^∞. This formulation bears a close resemblance with Muskhelishvili's formalism (1975). In these formulas, S denotes the union of the holes $S_1, S_2, \ldots, S_m$, $C = 2G\varepsilon_\infty/(\kappa+1)$ with ε_∞ being the rotation at infinity, and the outer boundary S_0, and G the union of the cracks G_1, G_2, ..., G_n. The shear modulus and Poisson's ratio are denoted by G and respectively. The plane parameter equals 3 4 for plane strain or (3)/(1+) for plane stress. The angle between the tangent at *t* on S+ and the global coordinate axis ox_1 is denoted by (*t*). And $_{ij}$ and u_i (*i,j* =1,2) are the components of stress and displacement in the Cartesian coordinate system ox_1x_2, respectively. $_n$ and $_{ns}$ respectively are the normal and shear stresses on the boundary. The superscripts "+" and " " denote the upper and lower crack faces respectively. The complex integration constants and relate only to rigid displacements.

It is obvious that the only unknown function in the boundary integral formulation for (*t*), (*t*), (*t*) and (*t*) is *H*(*t*). Therefore, only one variable is needed in this complex formulation and this is one of the main advantage of using the present complex formulation.

MIXED BOUNDARY INTEGRAL EQUATIONS

The stresses and displacements shown above satisfy automatically the equilibrium equations and the displacement-strain relations. In addition, they must also satisfy the boundary conditions, which will lead to the boundary integral equations for the unknown boundary complex function $H(t)$. For infinite plane elastic bodies containing cracks and holes shown in Figure 1, Wang and Chau [1] obtained the following BIEs for mixed BVPs

$$\int_{S+G}\left\{\frac{H(t)}{t-t_0}-\frac{\overline{H(t)}}{\overline{t}-\overline{t}_0}e^{-2i\alpha(t)}+e^{-2i\alpha(t_0)}\left[\frac{H(t)}{\overline{t}-\overline{t}_0}+\frac{t-t_0}{(\overline{t}-\overline{t}_0)^2}\overline{H(t)}e^{-2i\alpha(t)}\right]\right\}dt$$
$$-(k+1)e^{-2i\alpha(t_0)}\int_{S_u+G_u}\frac{H(t)dt}{\overline{t}-\overline{t}_0}+e^{-2i\alpha(t_0)}\int_{S_u+G_u}\frac{w(t)e^{-i\alpha(t)}dt}{\overline{t}-\overline{t}_0}-e^{-2i\alpha(t_0)}\int_{S_t+G_t}\frac{q(t)dt}{\overline{t}-\overline{t}_0}=\pi i[f(t_0)-g_1(t_0)]$$
$$(t_0=x_{01}+ix_{02}\in S_t+G_t); \tag{10}$$

$$\int_{S+G}\left\{\frac{k H(t)}{t-t_0}+\frac{\overline{H(t)}}{\overline{t}-\overline{t}_0}e^{-2i\alpha(t)}+e^{-2i\alpha(t_0)}\left[\frac{k H(t)}{\overline{t}-\overline{t}_0}-\frac{t-t_0}{(\overline{t}-\overline{t}_0)^2}\overline{H(t)}e^{-2i\alpha(t)}\right]\right\}dt$$
$$-(k+1)e^{-2i\alpha(t_0)}\int_{S_t+G_t}\frac{H(t)dt}{\overline{t}-\overline{t}_0}-e^{-2i\alpha(t_0)}\int_{S_u+G_u}\frac{w(t)e^{-i\alpha(t)}dt}{\overline{t}-\overline{t}_0}+e^{-2i\alpha(t_0)}\int_{S_t+G_t}\frac{q(t)dt}{\overline{t}-\overline{t}_0}=\pi i[\nu(t_0)-g_2(t_0)]$$

,

$$(t_0=x_{01}+ix_{02}\in S_u+G_u); \tag{11}$$

where

$$g_1(t_0)=\sigma_1^{\infty}+\sigma_2^{\infty}+(\sigma_2^{\infty}-\sigma_1^{\infty}-2i\sigma_{12}^{\infty})e^{-2i\alpha(t_0)}, \tag{12}$$

$$g_2(t_0)=\frac{k-1}{2}(\sigma_1^{\infty}+\sigma_2^{\infty})-(\sigma_2^{\infty}-\sigma_1^{\infty}-2i\sigma_{12}^{\infty})e^{-2i\alpha(t_0)}+2(k+1)Ci; \tag{13}$$

and $f(t_0)$ and $\nu(t_0)$ are given BY Wang and Chau [1]. In deriving these BIEs, we have used the Plemelj formulas (Muskhelishvili [13-14]; England [25]) and the following formulas of $h_2(z)$ (Wang and Chau [1]):

$$h_2^{+}(t_0)=\frac{1}{2}H(t_0)e^{-2i\alpha(t_0)}+\frac{1}{2\pi i}\int_{S+G}\frac{\overline{t}-\overline{t}_0}{(t-t_0)^2}H(t)dt,$$
$$h_2^{-}(t_0)=-\frac{1}{2}H(t_0)e^{-2i\alpha(t_0)}+\frac{1}{2\pi i}\int_{S+G}\frac{\overline{t}-\overline{t}_0}{(t-t_0)^2}H(t)dt; \qquad (t_0\in S+G) \tag{14}$$

COMPATIBILITY CONDITION

In the case of multi-connected region, the unknown boundary function $H(t)$ for infinite bodies must satisfy the following compatibility conditions (Chau and Wang [20]):

$$\int_{S_k}H(t)dt=\frac{1}{k+1}\int_{S_k}q(t)dt \quad \text{for every hole } S_k \text{ (k=1,2,...,m)}, \tag{15}$$

$$\int_{G_j}H(t)dt=\frac{1}{k+1}\int_{G_j}q(t)dt \quad \text{for every embedded crack } {}_j \text{ (j=1,2,...,n)}. \tag{16}$$

The mixed BIEs (10-11) must be solved in conjunction with the compatibility conditions (15-16), either analytically or numerically by using BEM similar to those discussed by Wang and Chau [21]. Once the

boundary unknown $H(t)$ is obtained, the complex functions (z), (z), (z) and (z) can be determined. Subsequently, the stress and displacement components can be calculated.

NUMERICAL IMPLEMENTATION

The boundaries of any elastic body containing cracks and holes, either traction or displacement boundary, are discretized into a number of linear elements. Each element L_e is then mapped onto the interval 1 1. Linear shape functions are adopted for both complex variable t and the complex boundary function $H(t)$ on the non-singular crack elements. For crack tips, a square-root singularity is assumed (Wang and Chau [1]). In the case that the complex boundary function $H(t)$ on the hole's boundary, an additional constant is introduced for each hole such that the compatibility can be satisfied.

Once the solutions for the nodal unknowns are obtained by numerical calculations, the stress intensity factors can be determined from the following equations (Wang and Chau [21]):

$$K_I(a_j) - iK_{II}(a_j) = -\lim_{t \to a} \sqrt{2\pi|t - a_j|} \times iH(t), \tag{17}$$

$$K_I(b_j) - iK_{II}(b_j) = \lim_{t \to b} \sqrt{2\pi|t - b_j|} \times iH(t); \quad (j=1,2,...,n) \tag{18}$$

where a_j and b_j are two tips of the crack j .

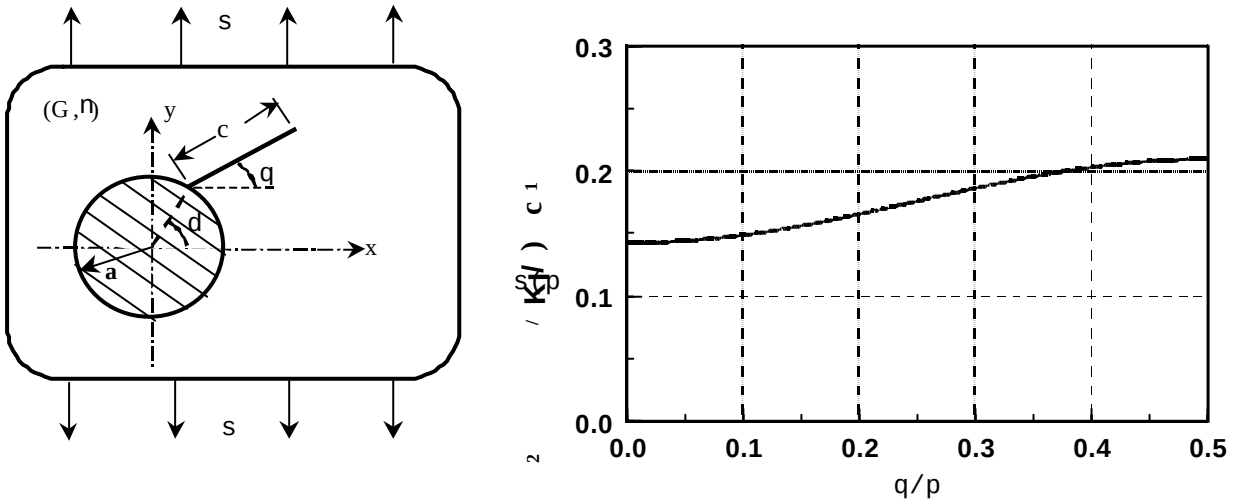

Figure 2: A crack of length c emanating from the interface of a circular rigid inclusion and an elastic matrix at the point measuring from the x-axis, and inclining at under tension . The mode I stress intensity factor is given for the case of =0.25, = and c=0.1a (after Wang and Chau [21])

NUMERICAL RESULTS AND CONCLUSION

Consider the case that a crack is emanating from a rigid inclusion (Fig. 2), the mode I crack tip stress intensity factor has been calculated by Wang and Chau [1]. Figure 2 plots the normalized mode I stress intensity factors for = and c=0.1a. Wang and Chau [1] also show that the present results are

comparable to Gharpuray et al. [3] when the inclusion is relatively rigid. Thus, the validity of the present BEM is demonstrated.

In this paper, the new BEM formulation by Wang and Chau [1] is presented. Although only the results for radial crack is presented here, the present BEM has also been applied to consider the interaction between a rigid circular inclusion and a crack, either an edge crack emanating from the interface or an internal crack in the elastic matrix (Wang and Chau [1]). For the case of rigid inclusion, Wang and Chau [1] has shown that our solutions are comparable to those by Erdogan et al. [4], Erdogan and Gupta [2], Isida and Noguchi [12], and Gharpuray et al. [3].

ACKNOWLEDGMENTS

The work was supported by the Research Grants Council of the Hong Kong SAR government with a Grant No. HKP 354/052 to The Hong Kong Polytechnic University through KTC and by the Natural Science Foundation of the Gansu Province under Contract No.ZQ-95-005 to Lanzhou University through YBW.

REFERENCES

1 Wang, Y.B. and Chau, K.T. (2001). *Int. J. Fracture* accepted, in press.
2. Erdogan, F. and Gupta, G.D. (1975). *Int. J. Fracture* 11, 13.
3. Gharpuray, V.M., Keer, L.M. and Lewis, J.L. (1990). *J. Biomedical Engineering* 112, 22.
4. Erdogan, F., Gupta, G.D. and Ratwani, M. (1974). *J. Appl. Mech.* 47, 1007.
5. Rizzo, F.J. (1967). *Quart. Appl. Math.*25, 83.
6. Cruse, T.A. (1969). *Int. J. Solids Struct*. **5**, 1259.
7. Lachat, J.C. and Watson, J.O. (1976). *Int. J. Num. Meth. Eng.* 10, 991.
8. Brebbia, C.A. (1984). *The Boundary Element Method for Engineers.* Pentech Press, London.
9. Bonnet, M. (1995). *Eng. Anal. Boundary Elements* 15, 93.
10. Gaul, L. and Schanz, M. (1997). *Meccanica* 32, 171.
11. Wang, C., Libardi, W. and Baldo, J.B. (1998). *Int. J. Fracture* 94, 177.
12. Isida, M. and Noguchi, H. (1983). *Transactions, JSME* 49**,** 147.
13. Muskhelishvili, N.I. (1975). *Some Basic Problems of the Mathematical Theory of Elasticity.* Noordhoff, Leyden, Netherlands.
14. Muskhelishvili, N.I. (1977). *Singular Integral Equations.* Noordhoff, Leyden, Netherlands.
15. Sherman, D.I. (1939). *Doklady, A.N. S.S.S.R.* **27,** 911 (in Russian).
16. Sherman, D.I. (1940a). *Doklady, A.N. S.S.S.R.* **28,** 29 (in Russian).
17. Sherman, D.I. (1940b). *Trudy Seismologiczesk Insts. A.H., S.S.S.R.*, No. 88 (in Russian).
18. Sherman, D.I. (1943). *Prikl. Mat. Mech.* 7, 413 (in Russian).
19. Lu, J.K. (1995). *Complex Variable Methods in Plane Elasticity*. World Scientific, Singapore.
20. Chau, K.T. and Wang, Y.B. (1999). *Int. J. Solids Struct*. 36, 2041.
21 Wang, Y.B. and Chau, K.T. (1997). *Int. J. Fracture* 87, 1.
22. Ghosh, N., Rajiyah, H. Ghosh, S. and Mukherjee S. (1986). *J. Appl. Mech.* 53, 69.
23. Bonnet, M. (1999). *Boundary Integral Equation Methods for Solids and Fluids*. Wiley, Chichester.
24. Frangi, A. and Novati, G. (1996). *Computational Mechanics* 19, 58.

25. England, A. H. (1971). *Complex Variable Methods in Elasticity*. Wiley-Interscience, London.

A J ESTIMATION SCHEME AND ITS APPLICATION TO LOW CYCLE FATIGUE CRACK GROWTH

G. G. Chell, R. C. McClung, and Y.-D. Lee

Materials Engineering Department
Southwest Research Institute
San Antonio, TX 78238, USA

ABSTRACT

A *J* estimation scheme is developed that combines the Electric Power Research Institute (EPRI) scheme with the Reference Stress (RS) approach. The hybrid EPRI-RS scheme is validated against elastic-plastic finite element results for small cracks at notches. Rules are given for converting *J* to an effective cyclic change in *J*, DJ_{eff}, for application to fatigue crack growth (FCG) under low cycle fatigue (LCF) conditions where cyclic plasticity may occur. The DJ_{eff} formulation includes the effects of crack closure. It is shown how the scheme can be modified to treat strain-controlled loading situations. The hybrid scheme is validated against laboratory specimen LCF tests and the results of full-scale fatigue tests on mechanically damaged pipes containing notches to simulate gouges.

KEYWORDS

J estimation scheme, reference stress, cracks at notches, constant cyclic strain, low cycle fatigue crack growth, crack closure

INTRODUCTION

Over the last decade, part of the fracture mechanics work at Southwest Research Institute (SwRI) has focused on developing practical *J* and *DJ* estimation schemes for use in the assessment of elastic-plastic fatigue crack growth (EPFCG) under low cycle fatigue (LCF) conditions involving cyclic plasticity. The driving force for this research has come from a number of different sources, but mainly because it is now widely recognized that FCG approaches based on linear elastic fracture mechanics (LEFM) are often non-conservative when applied to LCF situations. This has led to SwRI's involvement in providing practical solutions to a number of challenging industrial problems. For example, structural integrity issues in advanced space propulsion systems that experience a wide range of severe operating conditions [1], the enhancement of the LEFM based

FCG computer code, NASGRO [2], developed by Forman et al., [3] for NASA, and remaining life assessments of mechanically damaged gas transmission pipelines [4]. In addition to these, the developed methodology is finding direct applications in other industrial areas involving LCF of structures, such as the assessment of the effects of pipe reeling and straightening during the installation of offshore pipelines, and start-up and shutdown of industrial gas turbine engines.

Under small-scale yielding (SSY) conditions the *DJ* methodology reduces to LEFM approaches based on *DK*, the cyclic change in the stress intensity factor, *K*. The extension of the elastic-plastic fracture mechanics parameter, *J*, to EPFCG based on ΔJ was pioneered by Dowling [5,6]. The methodology presented herein employs a closure-corrected modification to *DJ* designated as DJ_{eff}, developed from the work of Newman [7]. The present paper briefly reviews recent efforts by SwRI in developing and validating DJ_{eff} estimation schemes for LCF applications involving cyclic loading of cracks at notches and cracks subjected to constant cyclic strains.

HYBRID EPRI-RS J ESTIMATION SCHEME

The proposed *J* scheme combines the EPRI approach [8] with the RS approach [9] and is herein referred to as the hybrid EPRI-RS method. *J* is resolved into elastic and plastic components, J_e and J_p, respectively,

$$J = J_e + J_p = \frac{K^2(a_e)}{E'} + mV\,J_e(a)\left[\frac{E\,e^p_{ref}}{s_{ref}}\right],\ s_{ref} = \frac{P}{P_o}s_o,\ e^p_{ref} = a\,\frac{s_o}{E}\left(\frac{P}{P_o}\right)^n \qquad (1)$$

Here $E' = E$, Young's modulus, for plane stress and $E/(1-\nu_e^2)$ for plane strain, where ν_e is Poisson's ratio. *P* is the applied load, P_o is the plastic limit load and *V* is a dimensionless engineering parameter and $m = 1$ for plane stress, $(1-\nu_p^2)/(1-\nu_e^2)$ for plane strain, where ν_p is the plastic Poisson's ratio. The strain e^P_{ref} is the plastic component of the reference strain corresponding to the reference stress, s_{ref}, on the stress-strain curve. The effective crack depth, $a_e = a + fr_y$, depends on a plastic zone size r_y and a load-dependent parameter f that are defined below for a Ramberg-Osgood material where $\frac{e}{e_0} = \frac{s}{s_0} + a\left(\frac{s}{s_0}\right)^n$ and a, s_o and n are material constants and $e_o = s_o/E$.

$$f = \frac{1}{1+\left(\frac{P}{P_o}\right)^2},\ r_y = \frac{1}{bp}\left[\frac{n-1}{n+1}\right]\left(\frac{K}{s_o}\right)^2 \qquad (2)$$

In this equation, b equals 2 for plane stress and 6 for plane strain.

The limit load P_o can be obtained from the EPRI handbooks of *J* solutions [10] or the review of solutions performed by Miller [11]. An optimization procedure proposed in [12] used 189 finite element analysis (FEA) solutions for J_p covering an extensive assortment of structures, crack shapes and sizes, and applied load types to determine values for P_o and *V* that gave the best fit between Eqn. 1 and the FEA results. This scheme enables Eqn. 1 to be generalized to arbitrary stress-strain behaviors. The mean value of *V* was 1.169, which is close to the value of 1 generally assumed in

the RS approach. The effectiveness of the optimization scheme in reproducing FEA generated J_p values for a range of crack shapes and sizes is demonstrated by the results shown in [13].

SMALL CRACKS AT NOTCHES

The hybrid EPRI-RS scheme captures in $J_e(a_e)$ first-order crack-tip plasticity effects that govern the transition from LEFM to fully-plastic behavior while providing a widely applicable scheme through the RS expression for J_p. This capability is shown in the following example calculations of J for small cracks at notches. The double edge notched tension (DENT) problems analyzed are described in detail in [14]. Plane stress FEA were performed for notches of constant depth $d=0.3b$ (where b is half the width of the plate) with various root radii, r. A wide range of J solutions were generated for various a/r and d/r values and for strain hardening exponents, n, of 5, 10, and 15. The FEA computations and the hybrid EPRI-RS solutions for J are displayed in Figure 1 for a/r ratios of 0.1195 and 0.115 and d/r ratios of 2.39 and 11.625 corresponding to elastic stress concentration factors (notch stress/remote stress) of 4.2 and 8.4, respectively. In the figure $J/J_e(a)$ is plotted against the normalized load, P/P_o. It is clear that the hybrid approach captures the influence of the high stresses near the notch root, but that the RS approach fails to do this. This point has been made previously by Smith [15].

STRAIN CONTROLLED LOADING

Under some circumstances, cracks may be subjected to constant strain LCF where the elastic strain is small compared to the plastic strain and the maximum load in the cycle decreases as a crack grows so that the term $Ee^p_{ref}/\sigma_{ref} = \Psi$ remains constant during growth, and $J_p = mV\, J_e(a)\Psi$. Examples are constant-strain LCF tests and the reeling and straightening of pipes as they are reeled on and off a large diameter spool as part of the pre-installation and at sea installation processes, respectively. The difference between J evaluated under constant load and strain conditions is illustrated in Figure 2.

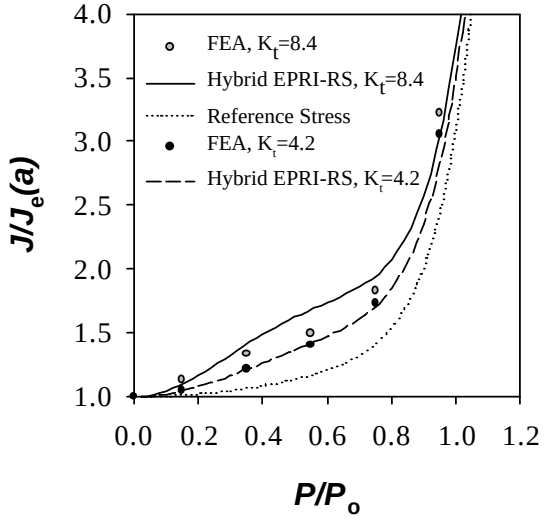

Figure 1: Comparison of J solutions for small cracks at notches.

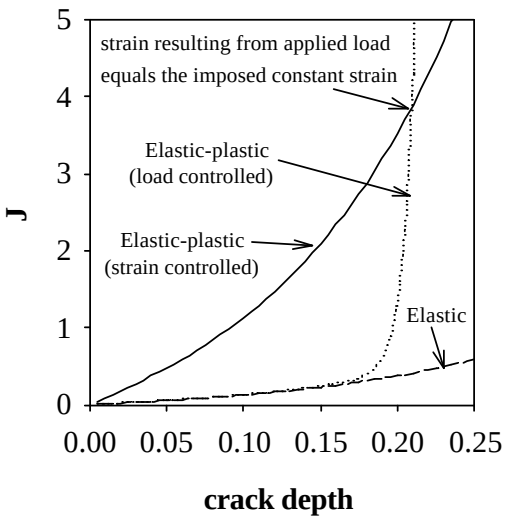

Figure 2: Schematic comparison of strain and load controlled J values.

RULES FOR DETERMINING ΔJ_{EFF} FROM J SOLUTIONS

The closure-corrected EPFCG parameter, DJ_{eff} , can be derived from J by employing a set of relatively simple rules, as shown below.

(1) Convert the monotonic s-e curve to the hysteresis Ds-De curve. For example, the Ramberg-Osgood equation becomes $\frac{\Delta e}{2e_0} = \frac{\Delta s}{2s_0} + a\left(\frac{\Delta s}{2s_0}\right)^n$.

(2) Convert the LEFM based FCG equation to a DJ_{eff} based equation which, in the case of the Paris equation, will take the form $\frac{da}{dN} = C\left(\Delta J_{eff}\right)^m$. (The Paris constants C and m can be estimated from LEFM FCG data [2]).

(3) Replace $J_e(a_e)$ by $\Delta J_{e,eff}(a_e^{\Delta})$, where

$$\Delta J_{e,eff}(a_e^{\Delta}) = \frac{[U\Delta K(a_e^{\Delta})]^2}{E'},\ a_e^{\Delta} = a + \Delta f^{\Delta}\Delta r_y^{\Delta}\ ,\ \Delta f^{\Delta} = \frac{1}{1+\left(\frac{\Delta P}{2P_o(a)}\right)^2}\ ,\ \Delta r_y^{\Delta} = \frac{1}{bp}\cdot\frac{n-1}{n+1}\left(\frac{U\Delta K}{2s_o}\right)^2$$

The closure parameter, U, is defined as

$$U = \frac{1 - K_{open}/K_{\max}}{1-R} \qquad\qquad R = \frac{K_{\min}}{K_{\max}}$$

where K_{open} is evaluated at the point the crack opens, and K_{min} and K_{max} are evaluated at the minimum and maximum loads in the cycle, respectively. A detailed expression for U derived from the work of Newman [7] is given in [14].

(4) Replace J_p by $\Delta J_{p,eff} = UmV\Delta J_e(a)\cdot\frac{E\Delta e_{ref}^p}{\Delta s_{ref}}$ where $\Delta s_{ref} = \frac{\Delta P}{2P_o}s_o$ and Δe_{ref}^p is the corresponding reference plastic strain range determined from the hysteresis stress-strain curve.

VALIDATION: LOAD CONTROL INCONEL 718 MATERIAL

The ΔJ_{eff} solutions were applied to calculating FCG rates and lifetimes in tests conducted by SwRI for NASA on surface cracks (SC), corner cracks (CC), and central through cracks (TC) in IN718 plates under SSY, intermediate- and large-scale yielding conditions [2]. A comparison between experimentally measured fatigue cycles to failure and predicted cycles is given in Figure 3. The term α_c appears in Newman's expression for U and takes a value of 1 under plane stress and 3 under plane strain conditions. The results in Figure 3 demonstrate that, in this case, the choice of value for α_c has little effect on the predicted cycles to failure. In general, all of the predictions are excellent, over a very wide range of cyclic lives. FCG rate data based on DJ_{eff} are shown in Figure 4 and demonstrate a very strong correlation of FCG rates over more than four orders of magnitude with DJ_{eff}.

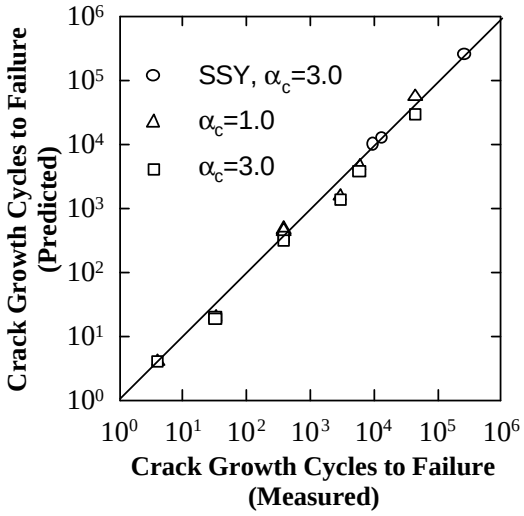

Figure 3: Comparison of predicted and measured cycles to failure.

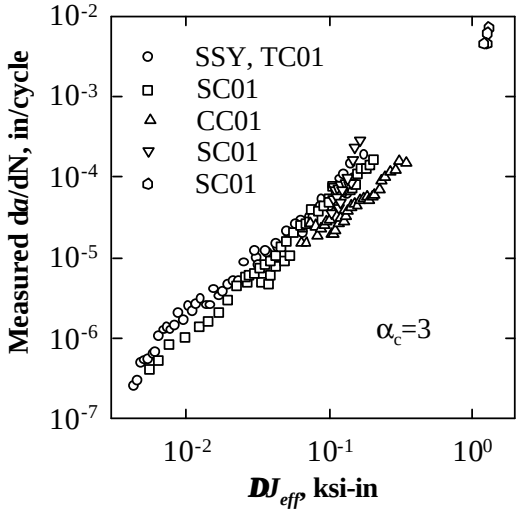

Figure 4: Correlation of measured FCG rates with calculated DJ_{eff} values.

VALIDATION: CONSTANT STRAIN LCF AND PRESSURIZED NOTCHED PIPES: X52 PIPE MATERIAL

As part of an investigation by SwRI for the Gas Research Institute (GRI) into the effects of mechanical damage on the remaining life of gas transmission pipelines, LCF tests were performed on X52 steel (see [4] for details). The tests were performed on round bars of diameter 2.54 mm (0.1 inches) under constant strain range conditions. Crack initiation was detected from the reduction in applied maximum load. The cycles to propagate initiated thumbnail cracks of depth 108 μm (4.25 mil) to failure were measured and an EPFCG equation was determined using the constant strain formulation for DJ_{eff}. The results, shown in Figure 5 as a plot of predicted against measured cycles to failure, provide a self-consistency check on the derived EPFCG equation and DJ_{eff}. The derived growth rate equation was then used to predict the remaining fatigue lives of dented pressurized pipes containing machined notches. The combined effects of the notch and the dent produced LCF conditions at the notch tip during pressure cycling. The predicted crack initiation and propagation cycles to cause a leak (defined as failure) are plotted against the measured cycles in Figure 6. As can be seen, under severe LCF conditions only a few pressure cycles are needed to initiate cracking at the notches, and the majority of the lives of the damaged pipes are spent in propagating the initiated cracks to failure. The results in Figure 6 demonstrate good agreement between the calculated and measured cycles to failure, verifying the proposed EPFCG methodology and DJ_{eff}-schemes for both the strain-controlled round bar tests and the analysis of the pressurized notched pipes.

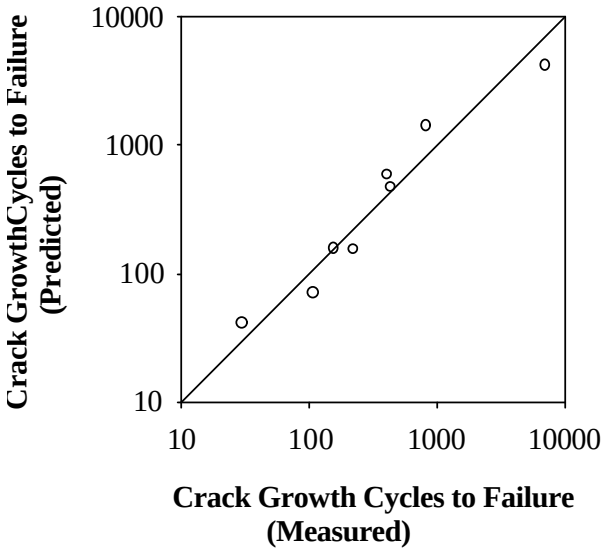

Figure 5: Comparison of predicted and measured cycles to failure under strain-controlled LCF conditions in round bar test specimens.

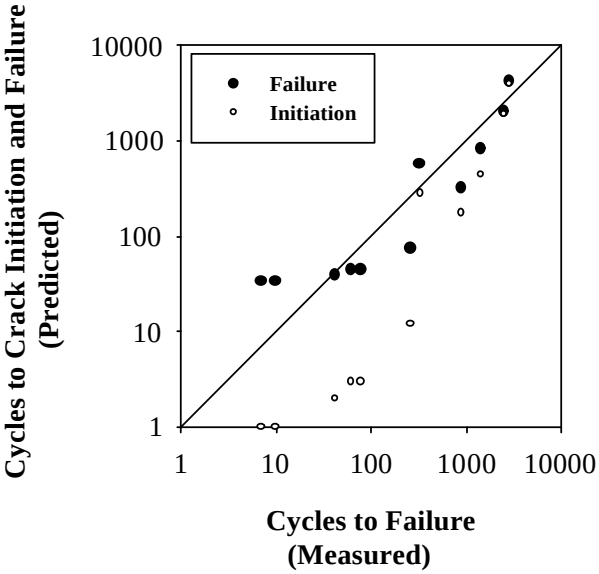

Figure 6: Comparison of predicted and measured cycles to failure of notches in mechanically damaged pipes.

REFERENCES

1. McClung, R.C., Chell, G.G., Russell, D.A., and Orient, G.E. (1997) *ASTM STP 1296*, pp. 317-337.
2. McClung, R.C., Chell, G.G. and Lee, Y.-D. (1999) FATIGUE 99: Proc. 7th Int. Fatigue Conf., Beijing, China, Vol. 1, pp. 433-438.
3. Foreman, R. G., et al. (1988) *ASTM STP 945*, pp.781-803.
4. Chell, G.G., et al. (2000) GRI Report GRI-00/0222, December, 2000 (available on GRI website).
5. Dowling, N. E., and Begley, J. A., (1976) *ASTM STP 590*, pp. 82-103.
6. Dowling, N. E., (1976) *ASTM STP 601*, pp. 19-32.
7. Newman, J. C., Jr., (1984) *Int. J. Fracture*, Vol. 24, pp. R131-R135.
8. Kumar, V. German, M. D. and Shih, C. F, (1981) EPRI Report NP-1931, July 1981.
9. Ainsworth, R.A. (1984) *Engng. Fract. Mech.*, Vol. 19, pp. 633-642.
10. Zahoor, A. (1989) EPRI Report NP-6301-D, Three Volumes.
11. Miller, A.G. (1988) *Int. J. Press. Ves. and Piping*, Vol. 332, pp. 197-323.
12. Chell, G.G., Kuhlman, C.J., Millwater, H.R. and Riha, D.S., (1997) *ASTM STP* 1297, pp. 54-73.
13. Chell, G.G., McClung, R.C. and Russell, D.A. (1995) ASME/JSME PVP Conference, Hawaii, July 1995, Vol. 304, pp. 475-485.
14. McClung, R.C., et al. (1999) NASA/CR-1999-209428.
15. Smith, E. (1996) *Int. J. Press. Ves. & Piping*, Vol. 69, pp. 203-206.

ORAL/POSTER REFERENCE: ICF100250PR

A LIMIT EQUILIBRIUM OF QUASIBRITTLE MATERIALS WITH THIN INCLUSIONS

M. M. Stadnyk[1], I. Y. Horbachevskyi [1]

[1] Department of Mathematics, Ukrainian State University of Forestry and Wood Technology, Lviv, 79057, Ukraine

ABSTRACT
A new effective approach to estimate a tensile strength of materials with inhomogeneities was proposed. As the example, the calculation of ultimate strength for cast irons with graphite inclusions or inclusions of phosphide eutectic was carried out. The comparison with the known experimental data was done and good coincidence was shown.

KEYWORDS
Inclusion, stressed state, plane strain, displacements, stress intensity factors, ultimate strength.

INTRODUCTION

The most of constructional materials are heterogeneous. They comprise cracks, cavities or impurities as the stress concentrators. Therefore, theoretical ultimate strength determination of materials in view of the presence of structural defects is an important scientific and technical problem.

PROBLEM DEFINITION

The elastic isotropic quasibrittle material with small volume content of structural defects is considered. We model such material by the infinite elastic body with the isolated cylindrical inclusion. It is assumed that G is the shear modulus, μ - Poisson coefficient for basic material (named as matrix), G_1 is the shear modulus for inclusion and μ_1 - its Poisson coefficient (the case of plane strain is supposed). Let's choose the system of rectangular Cartesian coordinates so that axis Oy coincides with a cylindrical axis of inclusion, and coordinate axes compound the right ternary. The inclusion cross section is described by the equation $z = \pm h(x)$, where $|x| \le a$, $|z| \le c$, $\lambda = a/c >> 1$, a and c are the semiaxes of cylinder. It is assumed, that during deformation the inclusion is rigidly linked to a base material. At infinity, the body is loaded by uniformly tensile forces p along z-axis. The problem is to determine the value $p = p_*$, for which the local fracture of a matrix or inclusion or separation process is begun.

MATHEMATICAL MODEL OF ELASTIC INCLUSION DEFORMATION

Using the model relationships [1], we obtain the following correspondences between stresses and displacements on the surfaces of the thin elastic inclusion under given loading:

$$\frac{2}{1-\mu_1}\frac{\partial}{\partial x}\left(u_x^1\right)_* + \frac{\mu_1}{G_1(1-\mu_1)}\left(\sigma_{zz}^1\right)_* + \frac{1}{G_1 h(x)}\int_{-a}^{x}\left[\sigma_{xz}^1\right]_* dt = 0,$$

$$\frac{\left(\sigma_{zz}^1\right)_*}{G_1} - \frac{2\mu_1}{1-2\mu_1}\frac{\partial}{\partial x}(u_x^1)_* - \frac{2(1-\mu_1)}{1-2\mu_1}\cdot\frac{[u_z^1]_*}{h(x)} = 0, \qquad (1)$$

where the symbols $[\ ]_*$ and $(\ )_*$ describe the jumps and sums of a function on passing through the surfaces of inclusion, i.e. $[A]_* = A^+ - A^-$, $(A)_* = A^+ + A^-$, $A^\pm = A\big|_{z=\pm h(x)}$, u_x^1, u_z^1 are the components of a displacements vector in inclusion; $\sigma_{xz}^1, \sigma_{zz}^1$ - are the constituents of a vector of stresses inside a defect. Eqn. 1 can describe all kinds of elastic inclusion deformations. If $G_1 = 0$ or $G_1 \to \infty$ the dependences for a cavity or an absolutely rigid inclusion respectively can be obtained from Eqn. 1. The system of dependences forms the mathematical model of elastic inclusion deformation.

STRESSED STATE DETERMINATION IN A BODY WITH INCLUSION

At first we present [2] the elastic problem for a body with thin inclusion as a composition of two problems: the problem a) for the homogeneous body under the given applied external loading inducing the vector of stresses $\vec{\sigma}_z^o\left(\sigma_{xz}^o,\ \sigma_{zz}^o\right)$, and the problem b) for the body with the cavity $\{z = \pm h(x), -\infty < y < \infty\}$ subjected to unknown stresses $\vec{\tilde{\sigma}}_z = -\vec{\sigma}_z^o + \vec{\sigma}_z^1$ on inclusion surfaces. We represent the displacement vector as the sum $\vec{u}(u_x, u_z) = \vec{\tilde{u}}(\tilde{u}_x, \tilde{u}_z) + \vec{u}^o(u_x^o, u_z^o)$. Using the supposition about thinness of inclusion we can replace [1] a task b) by the singular problem c) for the body with the mathematical cut $\{|x| \le a,\ -\infty < y < \infty\}$ with the stresses $\vec{\tilde{\sigma}}_z(\tilde{\sigma}_{xz}, \tilde{\sigma}_{zz})$ applied to it surfaces.

The solution of problem a) is known:

$$[u_z^o]_* = p(1-\mu)h(x)/G; \qquad (\sigma_{zz}^o)_* = 2p. \qquad (2)$$

Using Fourier integral transformation the solution of the problem c) can be obtained [3] in kind of such dependences concerning the stress and displacement jumps on the inclusions surfaces.

$$(\tilde{\sigma}_{zz})_* = \frac{G}{\pi(1-\mu)}\int_{-a}^{a}\frac{[\tilde{u}_z]_*'}{t-x}dt + \frac{1-2\mu}{2\pi(1-\mu)}\int_{-a}^{a}\frac{[\tilde{\sigma}_{xz}]_*}{t-x}dt;$$

$$\left(\tilde{u}_x\right)'_* = \frac{1-2\mu}{2\pi(1-\mu)}\int_{-a}^{a}\frac{[\tilde{u}_z]_*'}{t-x}dt - \frac{3-4\mu}{4\pi G(1-\mu)}\int_{-a}^{a}\frac{[\tilde{\sigma}_{xz}]_*}{t-x}dt. \qquad (3)$$

Here and further symbol prime means the derivate on *x*.

Substituting Eqn. 3 to Eqn. 1 we obtain the system of singular integro-differential equations for unknown vectors $[\vec{\tilde{\sigma}}_z]_*$ and $[\vec{\tilde{u}}]_*$ in such form

$$B_{11}\int_{-a}^{a}\frac{[\tilde{u}_z]_*'}{t-x}dt + B_{12}\int_{-a}^{a}\frac{[\tilde{\sigma}_{xz}]_*}{t-x}dt + B_{13}\int_{-a}^{a}[\tilde{\sigma}_{xz}]_* dt = -M_1;$$

$$B_{21}\int_{-a}^{a}\frac{[\tilde{u}_z]_*'}{t-x}dt + B_{22}\int_{-a}^{a}\frac{[\tilde{\sigma}_{xz}]_*}{t-x}dt - B_{23}\frac{[\tilde{u}_z]_*}{h(x)} = -M_2, \quad z = 0, \quad |x| \le a, \qquad (4)$$

where $B_{11}, B_{12}, ..., B_{23}$ - are known [4] coefficients depended by the elastic modules of inclusion; M_1, M_2 - are known functions defined by the solution of task a). When we'll solve Eqn. 4 we calculate the stress intensity factor K_I for the problem c) using the expression [1]

$$K_I = -\lim_{x \to -a} \sqrt{2\pi(a-x)} \left\{ \frac{G}{2(1-\mu)} [\widetilde{u}_z]'_* + \frac{1-2\mu}{4(1-\mu)} [\widetilde{\sigma}_{xz}]_* \right\}. \tag{5}$$

For a finding the stress distribution in basic material near the inclusion we use the formula [5]

$$\sigma_{zz} = \frac{2(\rho + \widetilde{x})K_I}{\sqrt{\pi(\rho + 2\widetilde{x})^3}} + \frac{\rho\sqrt{\rho}}{\sqrt{(\rho + 2\widetilde{x})^3}} \widetilde{\sigma}_{xx} + \sigma^o_{zz}; \qquad \widetilde{x} = x - a. \tag{6}$$

Here ρ is the radius of curvature in top of defect; $\widetilde{\sigma}_{xx}$ are the end stresses inside inclusion defined [5] by the stresses jump $[\widetilde{\sigma}_{xz}]_*$

$$\widetilde{\sigma}_{xx}(x) = -\frac{1}{2h(x)} \int_{-a}^{x} [\widetilde{\sigma}_{xz}]_* \, dt. \tag{7}$$

The normal stresses inside inclusion we obtain by means of Eqns. 2 and 3.

A LOCAL FRACTURE CRITERION

Using the first theory of strength we receive that in body a limit equilibrium state will be occur if even one of values the stress in a body near inclusion or inside defect else the stress on a intermediate contact surface attain their ultimate strength, i.e.

$$max \left\{ \frac{\sigma(p)}{\sigma_B^{(m)}}; \ \frac{\sigma^1(p)}{\sigma_B^1}; \ \frac{\sigma^{(c)}(p)}{\sigma_B^{(c)}} \right\} \Big|_{p=p_*} = 1, \tag{8}$$

where $\sigma(p)$, $\sigma^1(p)$, $\sigma^{(c)}(p)$ are maxima of stresses in a matrix, inside inclusion and on contact, respectively; $\sigma_B^{(m)}$, σ_B^1, $\sigma_B^{(c)}$ are values of corresponding ultimate strength.

SOLUTIONS OF APPLIED PROBLEMS

Using the results of pre-previous paragraph we'll obtain such formulae for stress concentration and stresses inside defect in the case of isolated elliptical $\left(h(x) = \sqrt{a^2 - x^2} \big/ \lambda \right)$ tunnel inclusion in infinite body.

Analysis of Eqn. 6 shows that in the case $G_1 < G$ maximum of stresses σ_{zz} is attained at points $x = \pm a$. Then

$$max\, \sigma_{zz} = \sigma_{zz}\big|_{x=\pm a} = 2K_I \big/ \sqrt{\pi\rho} + \widetilde{\sigma}_{xx}(a) + \sigma^o_{zz},$$

or for elliptical inclusion ($\rho = a/\lambda^2$) we find

$$\sigma_{zz}\big|_{x=\pm a} = p(1 + \Theta), \tag{9}$$

$$\sigma_{zz}^{1} = (1-\mu)\varepsilon p \frac{\varepsilon(\lambda(3-2\mu)+2(1-\mu))+\lambda(1-2\mu_1+2\lambda(1-\mu_1))}{\omega}, \qquad \varepsilon = \frac{G_1}{G}, \tag{10}$$

where designations were accepted as

$$\omega = 2\varepsilon(1-\mu)(1-\mu_1)(1+\lambda^2)+\lambda[\varepsilon^2(3-4\mu)-2\varepsilon\mu_1(1-2\mu)+1-2\mu_1)], \tag{11}$$

$$\Theta = \lambda\,\omega^{-1}\{2\lambda[\varepsilon\mu(\mu_1-\varepsilon\mu)+1-2\mu_1-\varepsilon(1-\mu-\mu_1)]+\varepsilon(1-\mu)[3-2\mu_1-\varepsilon(3-2\mu)]\}. \tag{12}$$

In the case $G_1 \geq G$ maximum of stresses σ_{zz} is attained at point $\tilde{x}_1 = -[3\rho\sqrt{\pi\rho}\,\tilde{\sigma}_{xx}(a)+4\rho K_I]/(2K_I)$ (see Eqn. 6) and it is equal to

$$max\,\sigma_{zz} = \sigma_{zz}\big|_{\tilde{x}=\tilde{x}_1} = \frac{2}{3\sqrt{3\pi\rho}}\sqrt{-\frac{K_I^3}{\sqrt{\pi\rho}\,\tilde{\sigma}_{xx}+K_I}}+\sigma_{zz}^{o}. \tag{13}$$

By means of Eqns. 8, 9, 10 and 13 the value of p_* can be calculated for given materials.

In the case of quasibrittle material with a great volume content of inclusions we shall use the model of infinite body with double periodical system of elliptic cylindrical inclusions, see Figure 1. Thus, at first we solve a problem for a periodic system of coplanar inclusions in a body. In this case the kern of Eqn. 4 $L(t,x) = 1/(t-x)$ was replaced by the kern $L_1(t,x,d_1) = \frac{\pi}{d_1} ctg \frac{\pi(t-x)}{d_1}$ and the problem solution was obtained by a little parameter decomposition method.

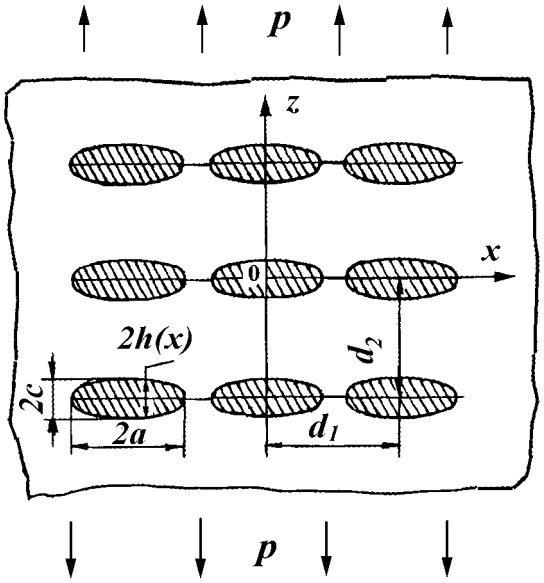

Figure 1: The schema of material with the great volume content of inclusions

Then we solve an elastic problem for a body with periodical system of parallel elliptical cylindrical inclusions. In this case the kern $L(t,x) = 1/(t-x)$ of Eqn. 4 will be replaced by the kern $L_2(t,x,d_2) = \frac{\pi}{d_2}\left[2cth\frac{\pi(t-x)}{d_2} - \frac{\pi(t-x)}{d_2} cosech^2\frac{\pi(t-x)}{d_2}\right]$. The solution of problem was obtained by the similar way. Thus using the method of boundary interpolation [6] we find the solution of the problem for a body with double periodical system of associated inclusions. If we shall assume that a quasibrittle matrix damages first of all (as experiments show) we get the values of the tensile strength for such material with the associated inclusions by means of Eqn. 8:

$$\sigma_B = \sigma_B^{(m)} \Big/ \Phi(\varepsilon, \lambda, \alpha_1, \alpha_2), \tag{14}$$

where

$$\Phi(\varepsilon,\lambda,\alpha_1,\alpha_2)=1+\Theta\,[1+F(\beta,\alpha_1,\alpha_2)], \qquad \alpha_1 = 2a/d_1; \qquad \alpha_2 = 2a/d_2;$$

$$F(\beta,\alpha_1,\alpha_2) = \frac{\alpha_1^2 - 3\alpha_2^2}{1+\beta}\cdot\frac{\pi^2}{3\cdot 2^3} - \frac{[(15\beta^2+52\beta+57)\alpha_1^4 + 15(5\beta^2+20\beta+27)\alpha_2^4]\cdot\pi^4}{(1+\beta)^2(3+\beta)\cdot 45\cdot 2^7} +$$

$$+\frac{[(210\beta^4+1877\beta^3+5597\beta^2+7495\beta+4125)\cdot\alpha_1^6 - 35(42\beta^4+409\beta^3+1433\beta^2+2149\beta+1785)\cdot\alpha_2^6]}{(1+\beta)^3(3+\beta)(5+\beta)}\cdot$$

$$\cdot\frac{\pi^6}{945\cdot 2^{10}} + o(\alpha_1^6, \alpha_2^6); \qquad \beta = \frac{2\varepsilon\lambda(1-\mu)(1-\mu_1)}{1-2\mu_1-\varepsilon\mu_1(1-2\mu)}, \quad \varepsilon < 1. \tag{15}$$

The comparison the theoretical values of tensile strength obtained by Eqn. 14 with famous [7] experimental data for cast-irons with graphite inclusions was carried out. Experimental results were obtained for different cast-iron alloys with 4% mass content of carbon and diverse forms of graphite inclusions – from circular to laminar mode (see symbols ∇, □, o at Figure 2). It is easy to convince somebody that there is a close correspondence between calculated and experimental results.

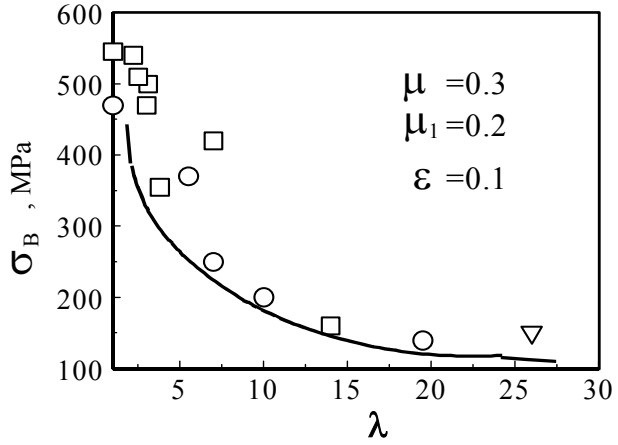

Figure 2: The comparison of theoretical tensile strength determination and experimental data for grey cast-iron with graphite inclusions

We also elaborated the estimation of tensile strength values for cast-irons with various mass content of phosphorus. At increasing a content of phosphorus the phosphide eutectic inclusions are formed. Experiments for grey cast-irons with phosphide eutectic were carried out at Technical University of Zaporizhzhya (Ukraine) under the leadership of prof. Volchok I.P. We made a comparison between the theoretical results and experimental data by means of such values of parameters: $\sigma_B^1 = 470\,MPa,\ \ \mu_1 = 0.1,\ G_1 = 165\,GPa,\ \mu = 0.25,\ G = 80\ MPa,\ \lambda = 1 \div 10$. A close correspondence between calculated and experimental results was obtained once again.

CONCLUSIONS

1. A mathematical model of elastic inclusion deformation of arbitrary relative rigidity was proposed.
2. A stressed state determination of a body with thin elastic inclusion was carried out.
3. A fracture criterion for quasibrittle materials with inhomogeneities was stated.

4. Using the methods of boundary interpolation and a little parameter decomposition the stress concentration in a material with double periodical system of associated elliptic inclusions was calculated.
5. The formula for the tensile strength determination of quasibrittle materials with great volume content of inclusions was proposed.
6. The comparison the theoretical values of tensile strength for cast-irons with graphite inclusions or the inclusions of phosphide eutectic with the known experimental data were carried out. A close correspondence between them was attained.

References

1. Stadnik, M.M. (1988). *Soviet Mater. Sci.* 24, 1, 49.
2. Cherepanov, G.P. (1979). *Mechanics of Brittle Fracture*. McGrow-Hill, New York.
3. Stadnyk, M.M. (1985). *Dokl. Akad. Nauk UkrRSR*. A, 3, 34. (In Ukrainian).
4. Stadnyk, M.M. and Horbachevskyi, I.Y. (1997). *Dopov. Nation. Acad. Nauk Ukr.* 8, 77. (In Ukrainian).
5. Stadnyk, M.M. (1994). *Physicochem. Mech. Mater.* 30, 6, 30. (In Ukrainian).
6. Panasyuk, V.V., Andreykiv, A.E. and Stadnik, M.M. (1983). *Ibid.* 19, 1, 3. (In Russian).
7. Volchok, I.P., Stadnik, M.M., Silovanyuk, V.P. et al. (1984). *Ibid.* 20, 3, 89. (In Russian).

ORAL REFERENCE: 128OR

A MESOSCOPIC THEORY OF DAMAGE AND FRACTURE IN HETEROGENEOUS MATERIALS

A. Carpinteri, B. Chiaia and P. Cornetti

Department of Structural Engineering and Geotechnics
Politecnico di Torino, 10128 Torino, Italy

ABSTRACT

Deformation patterns in solids are often characterized by self-similarity at the meso-level. In this paper, the framework for the mechanics of heterogeneous solids, deformable over fractal subsets, is briefly outlined. Mechanical quantities with non-integer physical dimensions are considered, i.e., the fractal stress [σ^*] and the fractal strain [ε^*]. By means of the *local fractional calculus*, the static and kinematic equations are obtained. The extension of the Gauss-Green Theorem to fractional operators permits to demonstrate the Principle of Virtual Work for fractal media. From the definition of the fractal elastic potential ϕ^*, the fractal linear elastic relation is derived. Beyond the elastic limit, peculiar mechanisms of energy dissipation come into play, providing the softening behaviour characterized by the fractal fracture energy $\mathcal{G}_F^*$. The entire process of deformation in heterogeneous bodies can thus be described by the fractal theory. In terms of the fractal quantities it is possible to define a *scale-independent cohesive law* which represents a true material property. It is also possible to calculate the size-dependence of the nominal quantities and, in particular, the scaling of the critical displacement w_c, which explains the increasing tail of the cohesive law with specimen size, and that of the critical strain ε_c, which explains the brittleness increase with specimen size.

KEYWORDS

Mesomechanics, fractals, fractional calculus, cohesive crack model, size-effects.

INTRODUCTION: FRACTAL STRESS AND FRACTAL STRAIN

The singular stress flux through fractal media can be modelled by means of a *lacunar* fractal set A^* of dimension Δ_σ, with $\Delta_\sigma \leq 2$. An original definition of the fractal stress σ^* acting upon lacunar domains was put forward by Carpinteri [1] by applying the renormalization group procedure to the nominal stress tensor [σ]. The fractal stress σ^*, whose dimensions are $[F][L]^{-(2-d\sigma)}$, is a scale-invariant quantity. For simplicity, a uniaxial tensile field is considered in Figure 1. Note that, for the definition of σ^*, exactly as in the case of the classical Cauchy stress, the limit:

$$\lim_{\Delta A^* \to 0} (\Delta P / \Delta A^*) \,, \tag{1}$$

is supposed to exist and, eventually, to attain finite values at any singular point of the support A^*. This is mathematically possible for lacunar sets like that in Figure 1 (and also for rarefied point sets like Cantor sets) which, although not compact, are dense in the surrounding of any singular point.

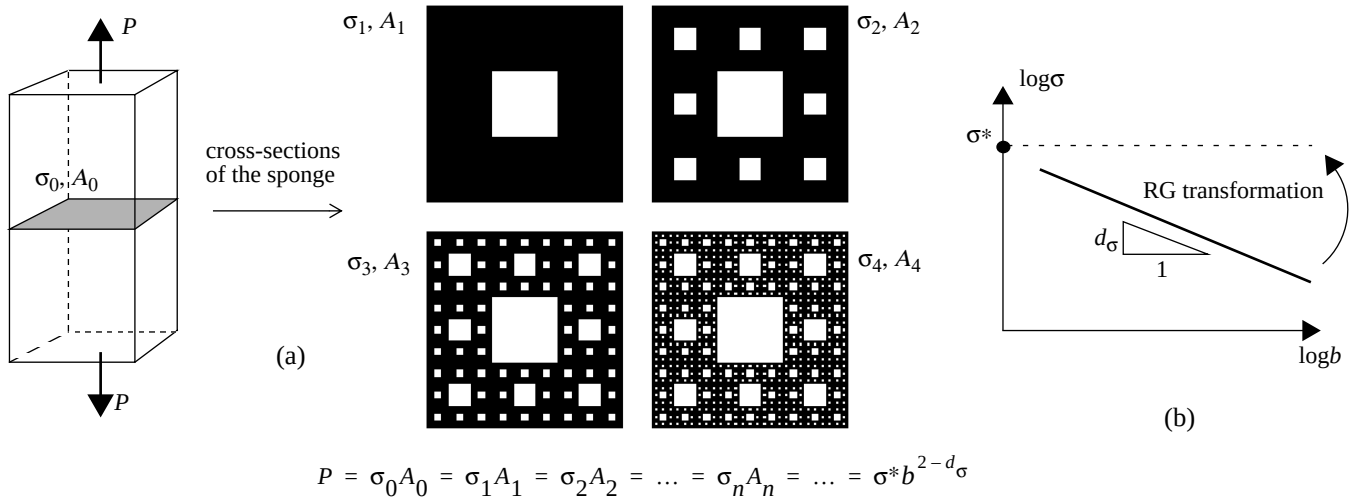

Figure 1. Renormalization of the stress over a Sierpinski carpet (a) and scaling of the nominal stress (b).

The kinematical counterpart of the fractal stress is the *fractal strain* ε*. The starting assumption is that displacement discontinuities can be localized on an infinite number of cross-sections, spreading throughout the body [2]. Experimental investigations confirm the fractal character of deformation, for instance in metals (*slip lines* with cantorian structure [3]), and in highly stressed rock masses (*plastic shear bands*).

Considering the simplest uniaxial model, a slender bar subjected to tension, it can be argued that the horizontal projection of the cross-sections where deformation localizes is a lacunar fractal set, with dimension between zero and one. If the Cantor set ($\Delta_\varepsilon \cong 0.631$) is assumed as an archetype of the damage distribution, we may speak of the *fractal Cantor bar* (Figure 2a). The dilation strain tends to concentrate into singular stretched regions, while the rest of the body is practically undeformed. The displacement function can be represented by a *devil's staircase* graph, that is, by a singular fractal function which is constant everywhere except at the points corresponding to a lacunar fractal set of zero Lebesgue measure (Figure 2b).

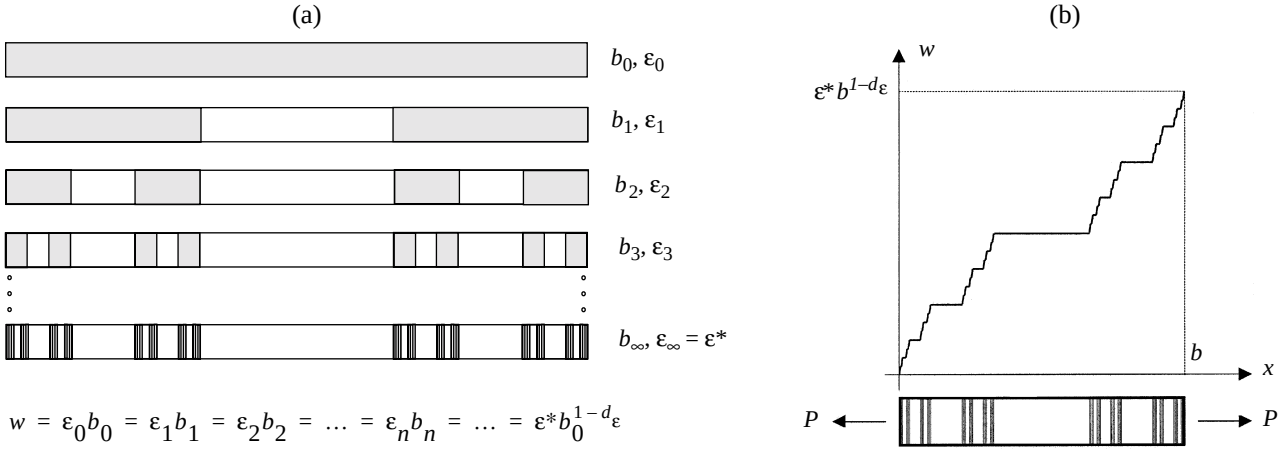

Figure 2. Renormalization of the strain over a Cantor bar (a) and singular displacement function (b).

Let $\Delta_\varepsilon = 1 - d_\varepsilon$ be the fractal dimension of the lacunar projection of the deformed sections. Since $\Delta_\varepsilon \leq 1$, the fractional decrement d_ε is always a number between 0.0 (corresponding to strain smeared along the bar) and 1.0 (corresponding to the maximum localization of strain, i.e., to localized fracture surfaces). By applying the renormalization group procedure (see Figure 2a), the micro-scale description of displacement requires the product of the fractal strain ε* times the fractal measure $b_0^{(1-d_\varepsilon)}$ of the support. The fractal strain ε* is the scale-independent parameter describing the kinematics of the fractal bar. Its physical dimensionality $[L]^{d_\varepsilon}$ is intermediate between that of a pure strain $[L]^0$ and that of a displacement [L], and synthesizes the conceptual transition between classical continuum mechanics ($d_\varepsilon = 0$) and fracture mechanics ($d_\varepsilon = 1$). Correspondingly, the kinematical controlling parameter changes, from the nominal strain ε, to the crack opening displacement *w*. By varying the value of d_ε (e.g. for different loading levels), the evolution of strain localization can be cap-

tured. The two limit situations are shown in Figure 3, the devil's staircase being an intermediate situation with $d_\varepsilon \cong 0.369$. While the first case represents the classical homogeneous elastic strain field, the second diagram shows a single displacement discontinuity, e.g., the formation of a sharp fracture.

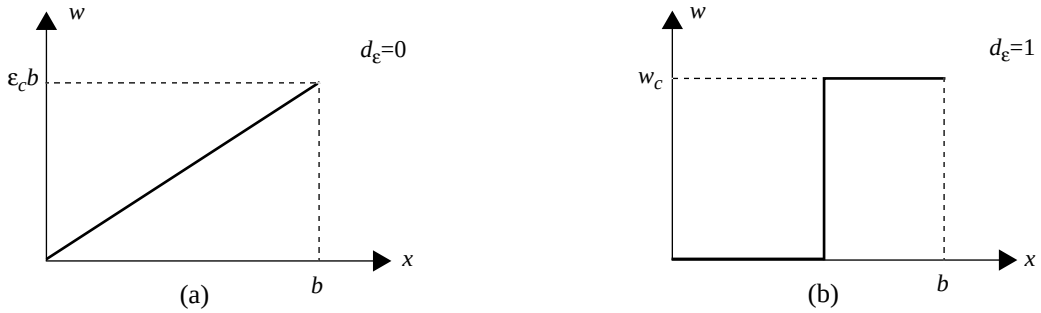

Figure 3. Homogeneous strain (a) and extremely localized deformation (b) over the bar (critical point).

During a generic loading process, the mechanical work W^* can be stored in the body as elastic strain energy (conservative process) or dissipated on the infinite lacunar cross-sections where strain is localized (dissipative process). In any case, the fractal domain Ω^*, with dimension $3–d_\omega$, where the mechanical work is produced, must be equal to the cartesian product of the lacunar cross-section with dimension $2–d_\sigma$, times its cantorian projection with dimension $1–d_\varepsilon$. Since the dimension of the product of two fractal sets is equal to the sum of their dimensions, one obtains: $(3-d_\omega) = (2-d_\sigma) + (1-d_\varepsilon)$, which yields the *fundamental relation* among the exponents as:

$$d_\omega = d_\sigma + d_\varepsilon \,. \tag{2}$$

STATIC AND KINEMATIC EQUATIONS FOR FRACTAL MEDIA

Classical fractional calculus is based on nonlocal operators. Recently, Kolwankar and Gangal [4] have introduced a new operator called *local fractional integral*. Let $[x_i, x_{i+1}]$, i=0, ..., N–1, x_0=a, x_N=b, be a partition of the interval [a, b], and x_i^* some suitable point of the interval $[x_i, x_{i+1}]$. Consider then a function *f(x)* defined on a lacunar fractal set belonging to [a, b]. The fractal integral of order α of the function *f(x)* over the interval [a, b] is defined as:

$$I^\alpha [f(x)]_a^b = \lim_{N\to\infty} \sum_{i=0}^{N-1} f(x_i^*) \frac{\mathrm{d}^{-\alpha} 1_{dx_i}(x)}{[\mathrm{d}(x_{i+1}-x_i)]^{-\alpha}} \,, \tag{3}$$

where $1_{dx_i}(x)$ is the unit function defined upon $[x_i, x_{i+1}]$. The fractal integral is a mathematical tool suitable for the computation of fractal measures. In fact, it yields finite values of the measure if and only if the order of integration is equal to the dimension of the fractal support of function *f(x)*. Otherwise, its value is zero or infinite, thus showing a behaviour analogous to the Hausdorff measure of a fractal set. Kolwankar and Gangal [4] introduced also the *local fractional derivative* (LFD) of order α, whose definition is ($0 < \alpha < 1$):

$$D^\alpha f(y) = \lim_{x\to y} \frac{\mathrm{d}^\alpha [f(x)-f(y)]}{\mathrm{d}(x-y)^\alpha} \,. \tag{4}$$

Differently from the classical fractional derivative, the LFD is a function only of the *f(x)* values in the neighborhood of the point y where it is calculated. The classical fractional derivative of a fractal function exists as long as its order is less than the Hölder exponent characterizing the singularity. Instead, in the singular points, the LFD (Eqn. (4)) is generally zero or infinite. It assumes a finite value only if the order α of derivation is exactly equal to the Hölder exponent of the graph. For instance, in the case of the well-known devil's staircase graph (Figure 2b) the LFD of order α=log2/log3 (i.e. equal to the dimension of the underlying middle-third Cantor set) is zero everywhere except in the singularity points where it is finite.

By means of the LFD, the fractal differential equations of kinematics and statics can be obtained [5]. The displacement field maintains the dimension of length. The noninteger dimensions of the fractal strain are: $[L]^{d_\varepsilon}$. Therefore, it can be obtained by fractional differentiation of the displacement vector $\{\eta\}$, according to the definition of LFD outlined above. The fractional differential operator $[\partial^\alpha]$ can be introduced, where the order of differentiation is $\alpha=1-d_\varepsilon$. Thereby, the kinematic equations for the fractal medium can be written, in the vector notation, as:

$$\{\varepsilon^*\} = [\partial^\alpha]\{\eta\}. \tag{5}$$

Classical strain is obtained when $\alpha=1$ ($d_\varepsilon=0$). Instead, when $\alpha=0$, strain is no longer homogeneously diffused and reduces to localized displacement discontinuities. The intermediate situations are described by generic values of α.

The static equations link the fractal stress vector $\{\sigma^*\}$ to the vector of body forces $\{F^*\}$, which assumes noninteger dimensions according to the fractal dimension of the deformable subset Ω^*, $[F][L]^{-(3-d_\omega)}$. On the other hand, the dimensions of the fractal stress are $[F][L]^{-(2-d_\sigma)}$. Therefore, the equilibrium equations can be written, in the vector notation, as:

$$[\partial^\alpha]^T\{\sigma^*\} = -\{F^*\}, \tag{6}$$

where the static fractional differential operator $[\partial^\alpha]^T$ is the transposed of the kinematic fractional differential operator $[\partial^\alpha]$. It is worth to observe that the fractional order of differentiation of the static operator in the fractal medium is $\alpha=1-d_\varepsilon$, the same as that of the kinematic operator (Eqn. (5)). This remarkable result is due to the fundamental relation among the exponents (Eqn. (2)), and represents the *Duality Principle for Fractal Media*. Finally, equivalence at the boundary of the body requires that the stress vector coincides with the applied fractal boundary forces $\{p^*\}$ (with physical dimensions $[F][L]^{-(2-d_\sigma)}$):

$$[N]^T\{\sigma^*\} = \{p^*\}. \tag{7}$$

In the case of fractal bodies, $[N]^T$ can be defined, *at any dense point of the boundary,* as the cosine matrix of the outward normal to the boundary of the *initiator* of the fractal body.

PRINCIPLE OF VIRTUAL WORK AND LINEAR ELASTIC LAW FOR FRACTAL MEDIA

Consider two arbitrary functions *f(x, y, z)* and *g(x, y, z)*, defined in a fractal domain Ω^*, with the same critical order α. The general formula of local fractional integration by parts has been obtained by the authors [5] as:

$$\{I^{(\beta-\alpha)}[gf]\}_{\Gamma^*} = \{I^\beta[gD^\alpha f]\}_{\Omega^*} + \{I^\beta[fD^\alpha g]\}_{\Omega^*}, \tag{8}$$

where Γ^* is the boundary of the domain Ω^*. This result extends the Gauss-Green Theorem to 3D fractal domains. Based on Eqn. (8), the Principle of Virtual Work for fractal media was demonstrated [5]. It reads:

$$\int_{\Omega^*(3-d_\omega)} \{F^*_A\}^T\{\eta_B\}d\Omega^* + \int_{\Gamma^*(2-d_\sigma)} \{p^*_A\}^T\{\eta_B\}d\Gamma^* = \int_{\Omega^*(3-d_\omega)} \{\sigma^*_A\}^T\{\varepsilon^*_B\}d\Omega^* \quad . \tag{9}$$

Both sides of Eqn. (9) possess the dimensions of work ([F][L]), since the operators are *fractional integrals* defined upon fractal domains. The external work may be done by fractal body forces $\{F^*\}$ and/or by fractal tractions $\{p^*\}$ acting upon the boundary Γ^* of the body. The internal work of deformation is defined as: $dW^* = \{\sigma^*\}^T\{d\varepsilon^*\}$, with dimensions $[F][L]^{-(2-d_\omega)}$. If the (initial) loading process is conservative (no dissipation occurs in the material), and stress is a univocal function of strain, a *fractal elastic potential* ϕ^* (function of the fractal strain $\{\varepsilon^*\}$) can be considered. The components of the fractal stress vector $\{\sigma^*\}$ can therefore be obtained by derivation:

$$\sigma_i^* = \frac{\partial \phi^*}{\partial \varepsilon_i^*} . \tag{10}$$

Note that these are canonical first-order partial derivatives in the space of the fractal strains $\{\varepsilon^*\}$. Performing the Taylor expansion around the undeformed state, and neglecting higher order derivatives, the following bi-linear form can be easily obtained:

$$\phi^* = \frac{1}{2}\{\varepsilon^*\}^T [\boldsymbol{H}^*]\{\varepsilon^*\}, \tag{11}$$

where $[\boldsymbol{H}^*]$ is the Hessian matrix of the fractal elastic potential. Dimensional arguments show that the anomalous dimensions of $[\boldsymbol{H}^*]$ are: $[F][L]^{-(2+d_\varepsilon-d_\sigma)}$. Thus, $[\boldsymbol{H}^*]$ depends on both the dimensions of stress and strain and, depending on the difference $(d_\sigma - d_\varepsilon)$, can be subjected to positive or negative size-effects. Each term in $[\boldsymbol{H}^*]$ is obtained as the second-order partial derivative of the elastic potential by the corresponding fractal strain:

$$\boldsymbol{H}^*_{ij} = \frac{\partial^2 \phi^*}{\partial \varepsilon_i^* \, \partial \varepsilon_j^*} . \tag{12}$$

From Eqns. (10) and (11), the linear elastic constitutive law for fractal media is provided as:

$$\{\sigma^*\} = [\boldsymbol{H}^*]\{\varepsilon^*\} . \tag{13}$$

SCALE INDEPENDENT COHESIVE CRACK LAW

After the initial elastic stage, when d_ε is close to 0, a nonlinear stage occurs, where damage and microcracking begin to spread and d_ε grows. In concrete-like materials, strain localizes quite soon in a band, and the softening stage comes into play. The cohesive law describes the decrement of the stress as a function of crack opening displacement w. The original model is based on the assumption that both the critical crack opening displacement w_c and the ultimate strength σ_u are independent of the structural size. Unfortunately, experiments show that this is not the case. Moreover, it is well-known that the area below the cohesive curve, i.e., the fracture energy $\mathcal{G}_F$, is subjected to relevant positive size-effects [6].

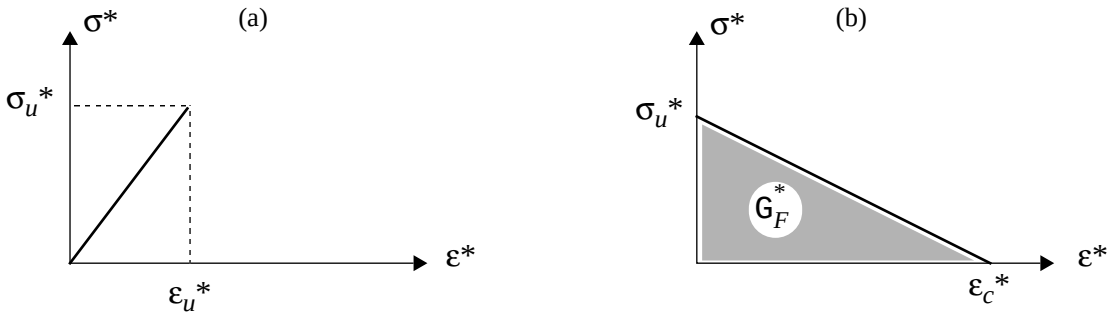

Figure 4. Fractal elastic law (a), and fractal cohesive law (b).

To overcome this limitation, the model associates to the fractal linear elastic law valid for the undamaged material (Figure 4a), a softening relationship between fractal stress and fractal strain, assuming that σ_u^* and ε_c^* are the true scale-independent limit parameters. It is interesting to note that the *fractal fracture energy* $\mathcal{G}_F^*$, defined in [1, 6], can be obtained, by a fractional integral, as the area below the fractal softening diagram (Figure 4b):

$$\mathcal{G}_F^* = \int_0^{\varepsilon_c^*} \sigma^* \, d\varepsilon^* . \tag{14}$$

During the softening regime, i.e. when most of the dissipation occurs, σ^* decreases from the maximum value σ_u^* to 0, while ε^* grows up to ε_c^*. In the meantime, the non-damaged parts of the bar undergo elastic unloading. We call the σ^*-ε^* diagram the *fractal cohesive law*, which is shown in Figure 4b. Contrarily to the classical cohesive law, which is sensitive to the structural size, this curve is scale-independent. Experimental tests by van Mier & van Vliet [7] have shown that, with increasing the specimen size, the peak of the curve decreases whereas the tail rises, i.e., tensile strength decreases while critical displacement increases. More in detail, w_c varies more rapidly than σ_u does. Therefore, an increase of the area beneath the cohesive law, i.e. of the fracture energy, is observed. Thus, the experimental trends of σ_u, G_F and w_c confirm the assumptions of the fractal model.

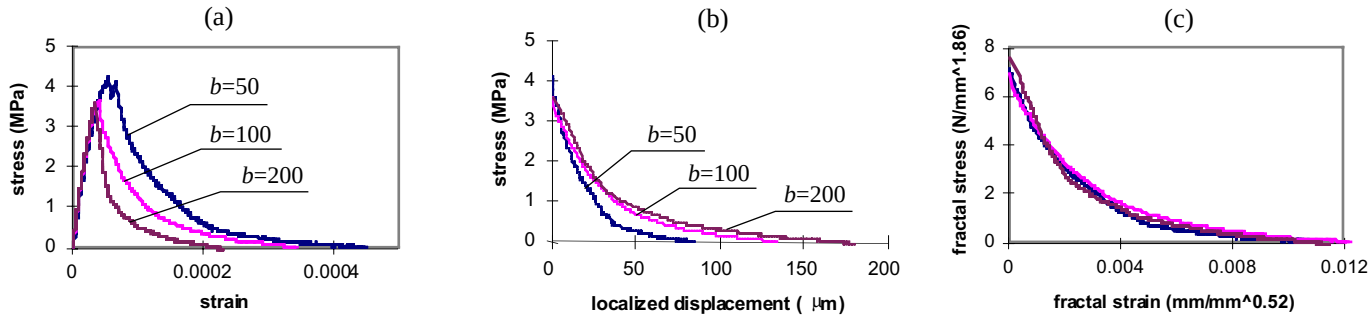

Figure 5. Size-effect tests [7]: stress-strain diagrams (a), cohesive curves (b) and fractal cohesive law (c).

The fractal model has been eventually compared with the uniaxial tensile tests described in [8]. The attention was focused on the size-effect on the ultimate tensile stress and on the fracture energy and their values interpreted by means of fractal assumptions. The exponents of the scaling laws were deduced by fitting the experimental results. In particular, they found the values $d_\sigma = 0.14$ and $d_G = 0.38$. The nominal σ - ε and σ - w diagrams are reported in Figure 5a and 5b. Here, w is the displacement localized in the damage band, obtained by subtracting from the total one the displacement due to elastic and inelastic pre-peak deformation. In addition, the value $d_\varepsilon = 0.48$ is provided by Eqn. (2), so that the fractal cohesive laws can be represented as in Figure 5c. As expected, all the curves related to the single sizes tend to merge in a unique, scale-independent cohesive law.

ACKNOWLEDGEMENTS

Supports by the Italian Ministry of University and Scientific Research and by the EC-TMR Contract N° ERBFMRXCT 960062, are gratefully acknowledged.

REFERENCES

1. A. Carpinteri (1994) *Mechanics of Materials* **18**, 89.
2. P. Cornetti (1999) *Fractals and Fractional Calculus in the Mechanics of Damaged Solids*, Ph.D. Thesis (in Italian). Politecnico di Torino, Torino.
3. T. Kleiser and M. Bocek (1986) *Zeitschrift für Metallkunde* **77**, 582.
4. K.M. Kolwankar and A.D. Gangal (1996) *Chaos* **6**, 505.
5. A. Carpinteri, B. Chiaia and P. Cornetti (2001) *Computer Methods in Applied Mechanics and Engineering*, in print.
6. A. Carpinteri and B. Chiaia (1995) *Material and Structures* **28**, 435.
7. J.G.M. van Mier and M.R.A. van Vliet (1999) *International Journal of Fracture* **94**, 195.
8. A. Carpinteri and G. Ferro (1994) *Materials and Structures* **27**, 563.

ORAL/POSTER REFERENCE: ICF100473OR

A METHOD FOR ACCELERATION OF DECREASING ΔK FCGR TESTS

S.Tarafder[1], S.Sivaprasad[1], M.Tarafder[1] and K.K.Ray[2]

[1] National Metallurgical Laboratory, Jamshedpur 831 007, INDIA
[2] Dept. of Met. & Mats. Engg., IIT, Kharagpur 721 302, INDIA

ABSTRACT

An alternative method of accelerating decreasing ΔK FCGR tests has been proposed in this paper in order to address experimental difficulties that are often faced when conducting such tests using the conventional technique. The equation for the envelope that is to be followed for reducing the ΔK level as the crack grows has been derived from considerations of decreasing the monotonic plastic zone size at a constant rate. Through experimental assessment of the alternative method and examination of crack closure effects, it has been shown that it does not lead to the accumulation of crack growth retardation effects. The new method has been shown to be particularly suitable for high strength materials. The employment of the method for obtaining threshold regime corrosion fatigue crack growth data has been demonstrated.

KEYWORDS

Fatigue crack growth, FCGR test method, Decreasing ΔK test, Crack closure, HSLA steel

INTRODUCTION

Decreasing ΔK fatigue crack growth rate (FCGR) tests are indispensable for obtaining fatigue crack growth resistance of materials at low levels of crack driving force. Conventionally such tests are conducted by a load-shedding procedure laid down in the ASTM standard E647 [1]. In this procedure, suggested by Saxena *et al.* [2], loads are progressively reduced as the crack length a increases such that the ΔK envelope of the test is forced to follow the relation

$$\Delta K = \Delta K_o \, e^{C(a-a_o)} \tag{1}$$

In the above equation, ΔK_o and a_o are the stress intensity factor (SIF) range and crack length respectively with which the test is started, and C is a negative constant (standardised at -0.08 mm^{-1}). Eqn. 1 was obtained based on the requirement that the fractional change in the monotonic plastic zone size associated with the fatigue crack remains constant with increase in a so as to preclude the accumulation of overload retardation effects. Figure 1 gives a schematic of the form of the ΔK vs a curve described by Eqn. 1.

From the nature of the conventional ΔK envelope shown in Figure 1, it can be envisaged that as lower ΔK values are achieved, cracks have to be grown through larger and larger increments in order to produce a given reduction in ΔK. Due to this, and because crack growth rates decrease as the ΔK is lowered, longer time intervals are required to produce progressive reductions in ΔK. For growing down to low values of ΔK

using the conventional technique therefore, fatigue cracks have to be grown through considerable length. In order to accommodate such cracks, specimens have to be sufficiently large. Also the number of cycles required to be imposed to grow a long crack at diminishing growth rates can often be very large, and it is often advantageous to conduct tests at high frequencies to cut down on the time requirement for tests.

To the experimentalist, using large specimens, carrying out tests through long periods, or conducting tests at high frequencies are often not viable options. This is especially true when product or component size restricts the dimensions of specimens, or when FCGR tests are to be conducted in corrosive media at low frequencies to study corrosion-fatigue behaviour. In order to cope with such experimental problems associated with conventional decreasing ΔK FCGR testing, a new relation for the decreasing ΔK envelope that considerably accelerates tests is presented in this paper. The derivation of this relation, and verification of the absence of unwanted retardation effects, notwithstanding the faster decrement rate of ΔK, is provided below. An application of the new method to obtain threshold regime corrosion fatigue crack growth data is also given.

DERIVATION OF ALTERNATE ΔK ENVELOPE

From studies on overload effects on fatigue crack growth (for example [3]) it is known that reduction of fatigue cycle amplitude can lead to retardation of crack growth rates. During decreasing ΔK FCGR testing, similar situations may arise due to the progressive reduction of load amplitudes, and cyclic loads must be reduced at a gentle rate in order to minimize retardation effects. As retardation effects are proportional to the relative decrease in the size of the monotonic plastic zone attending the crack tip, minimal retardation effects would be induced if the fractional change in the plastic zone size were very small. This requirement can be written as

$$\frac{-\Delta r}{r} = x\ ,\ x \perp 1 \tag{2}$$

where r is the plastic zone size and Δr denotes the change in the plastic zone size accompanying reduction of loads, its sign indicating a decremental change. The plastic zone size can be taken as per Irwin's definition [4] as

$$r = \frac{1}{2\pi}\left(\frac{K_{\max}}{\sigma_y}\right)^2 \tag{3}$$

in which $K_{\max}$ is the maximum SIF of the fatigue cycle and σ_y is the yield stress of the material under test.

Retardation after the imposition of overloads is known to be operative through a distance that is proportional to the extent of the overload plastic zone [3,5]. Crack growth rates recover to their original levels only after the fatigue crack has been grown out through this distance. For the case of decreasing ΔK FCGR testing, a comparable situation may arise if crack growth retardation effects are brought about by reduction of cyclic amplitudes. In order to avert the accumulation of retardation effects significantly affecting crack growth rates, it is necessary that cracks be grown out through multiples of prior plastic zone dimensions before subsequent reductions of cyclic amplitudes. This condition can be stated as

$$\Delta a = y\, r,\ y\, \pi\, 1 \tag{4}$$

in which Δa is the crack growth increment between reductions of load.

Eqns. 2 and 4 can be combined for the case of continuous reduction of cyclic amplitudes to write

$$\frac{\mathrm{d}r}{\mathrm{d}a} = -\frac{x}{y} \tag{5}$$

Substitution of Eqn. 3 into Eqn. 5 gives

$$K_{\max}\frac{\mathrm{d}K_{\max}}{\mathrm{d}a} = -\frac{x}{y}\pi\sigma_y^2 \tag{6}$$

which on integration with initial limits of a_o and K_{maxo} (the K_{max} of the fatigue cycle at start of test) produces

$$K_{max} = \sqrt{K_{maxo}^2 - Q\,(a\text{-}a_o)} \tag{7}$$

with

$$Q = 2\pi\sigma_y^2 \frac{x}{y} \tag{8}$$

For the case of tests with constant load ratio R, Eqn. 7 can be re-written as

$$\Delta K = \sqrt{\Delta K_o^2 - Q\,(1\text{-}R)^2\,(a\text{-}a_o)} \tag{9}$$

Eqn. 9, alongwith Eqn. 8, thus represents an alternate ΔK envelope that may be employed in conducting decreasing ΔK FCGR tests.

The conventional technique utilizes a ΔK envelope that is invariant for all types of materials and mean level of fatigue cycles. This is surprising considering that crack tip plasticity, which is thought to be responsible for retardation effects that may be induced, is majorly governed by the flow behaviour of the material and the mean load and amplitude of the fatigue cycle. In the proposed method for accelerating decreasing ΔK FCGR tests, the exact shape of the envelope is determined by the yield stress σ_y of the material under test (see Eqn. 8), and the R-ratio of the fatigue cycle (see Eqn. 9). A schematic of the ΔK envelope in Eqn. 9 is superimposed in Figure 1. It is not difficult to visualize that for appropriate choice of controlling factors, lower values of ΔK can be attained within much smaller extensions of crack length, as compared to the conventional technique. Having said that, it must be pointed out that despite the nature of the proposed envelope, it may not provide any advantage over the conventional technique in case of material with low σ_y or for tests at very high R-ratios.

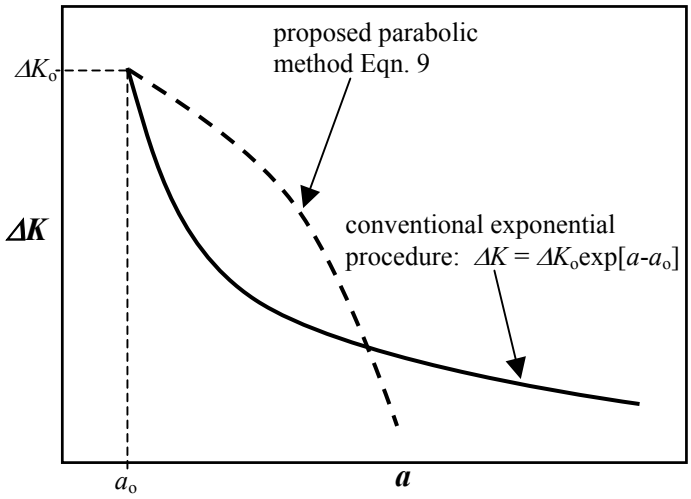

Figure 1: Schematic of reduction of ΔK with a as per conventional procedure and the proposed method

Other than the σ_y and R, x and y in Eqn. 8 will also determine the rapidity of the rate of decrease of ΔK. As an informed guess, x and y can be taken as 0.1 and 10 respectively, so that x/y is 0.01. Lumping a user preference parameter t through which the user may exercise control over the rate of ΔK decrement, Eqn. 8 can be explicitly re-written as

$$Q = 0.0628\ \sigma_y^2\ t \tag{10}$$

in which for t=1, x/y assumes a value of 0.01. In order to decide on a value of t that is optimum (i.e. one that allows the fastest rate of reduction of ΔK without inducing any retardation effects) for a given material, the effect of t must be experimentally verified. Such an exercise is detailed below for two varieties of Cu-strengthened HSLA steel that is used for naval structural applications.

EXPERIMENTAL VERIFICATION OF ACCELERATED TESTING PROCEDURE

Two varieties of Cu-strengthened HSLA steels, designated here as HSLA-80 and HSLA-100, were employed for carrying out validation FCGR tests. The HSLA-80 steel had a yield strength of 650 MPa, and the HSLA-100 steel had a yield strength of 840 MPa. The steels were available in the quenched and tempered condition. Standard SENB specimens in L-T orientation, of width 20mm and thickness 10mm were used for FCGR tests that were conducted on a 100kN closed loop servo-hydraulic testing machine. The machine was equipped with a digital controller, interfaced to a computer. Tests were controlled using a software in which the desired ΔK reduction scheme could be implemented. Crack lengths were monitored by the software using the compliance technique, which was based on location independent compliance crack length relations [6]. The software performed on-line crack closure measurements following the recommendations of ASTM task group E 24.04.04 [7].

Tests were carried out in air with R = 0.1 and at 10 Hz frequency. For conventional decreasing ΔK tests, Eqn. 1 was used to control the ΔK envelope, using C = -0.08 mm^{-1}. Tests based on the proposed method employed Eqn. 9, with Q calculated from Eqn. 10 using t = 1, 2 and 3, and the appropriate value of σ_y. The ΔK envelopes, normalised with respect to a ΔK_o of 25 MPa$\sqrt{m}$, arising from these values of t are shown in Figure 2 for both varieties of HSLA steels. The ΔK envelope for the conventional technique is also shown in the figure. It may be noted from Figure 2 that for HSLA-80, t=1 does not lead to any advantage in comparison to the conventional technique, as discussed earlier.

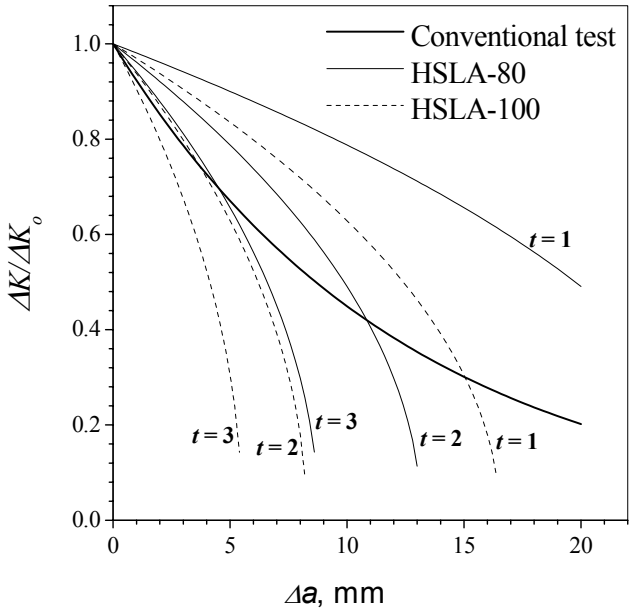

Figure 2: Normalised ΔK envelope obtained for various values of t in HSLA-80 and HSLA-100 steels

Figures 3(a) and (b) show Paris plots of the FCGR data obtained using the proposed method with t = 1, 2 and 3 for HSLA-80 and HSLA-100 steels respectively. The data obtained by employing the conventional technique are also included in the plots. As a first impression, it appears from the plots that the data obtained by the proposed method is compatible with the FCGR determined by the conventional technique. Data from the various tests lie within a small scatter band, which is thought to be acceptable. In order to comment conclusively on the acceptability of the data, it is necessary however to inspect the closure characteristics of the data generated. Figures 4(a) and (b) show plots of K_{cl}/K_{max} against the applied ΔK for the various tests conducted, for HSLA-80 and HSLA-100 steels respectively. K_{cl} is the crack closure SIF, corresponding to the load at 2% deviation from the open crack (i.e. linear) load-COD slope, that is determined on-line by the testing software. It can be seen from Figure 4(b) that for the HSLA-100 steel, K_{cl}/K_{max} for all tests follow the same path with reduction of ΔK. Hence for the higher strength HSLA-100 steel, variation of the rate of plastic zone size reduction, controlled by changing t, does not seem to affect crack closure behaviour. For the lower strength HSLA-80 steel, however, it is evident from Figure 4(a) that at the fastest rate of plastic zone size reduction (t=3), crack closure levels are higher, indicating that retardation effects have been manifested. It may be therefore be prudent to restrict the value of t to ≤ 2 for this steel.

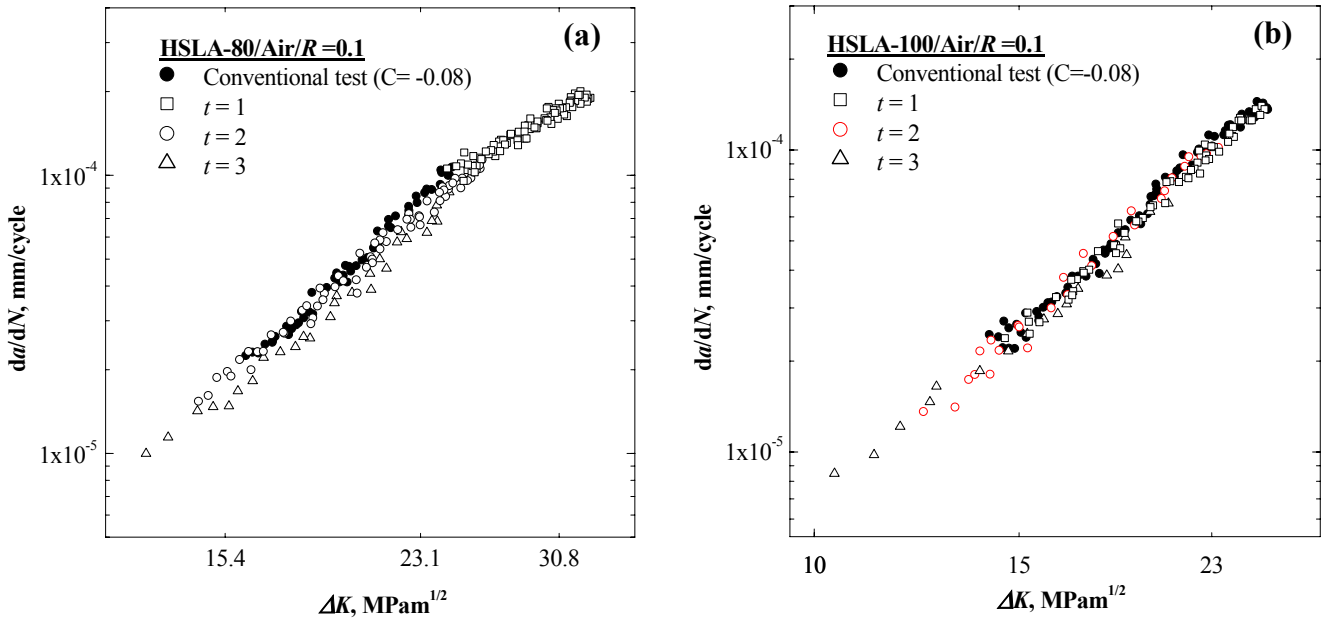

Figure 3: FCGR data of (a) HSLA-80 and (b) HSLA-100 steels obtained by using the proposed method with various values of t, and the conventional technique

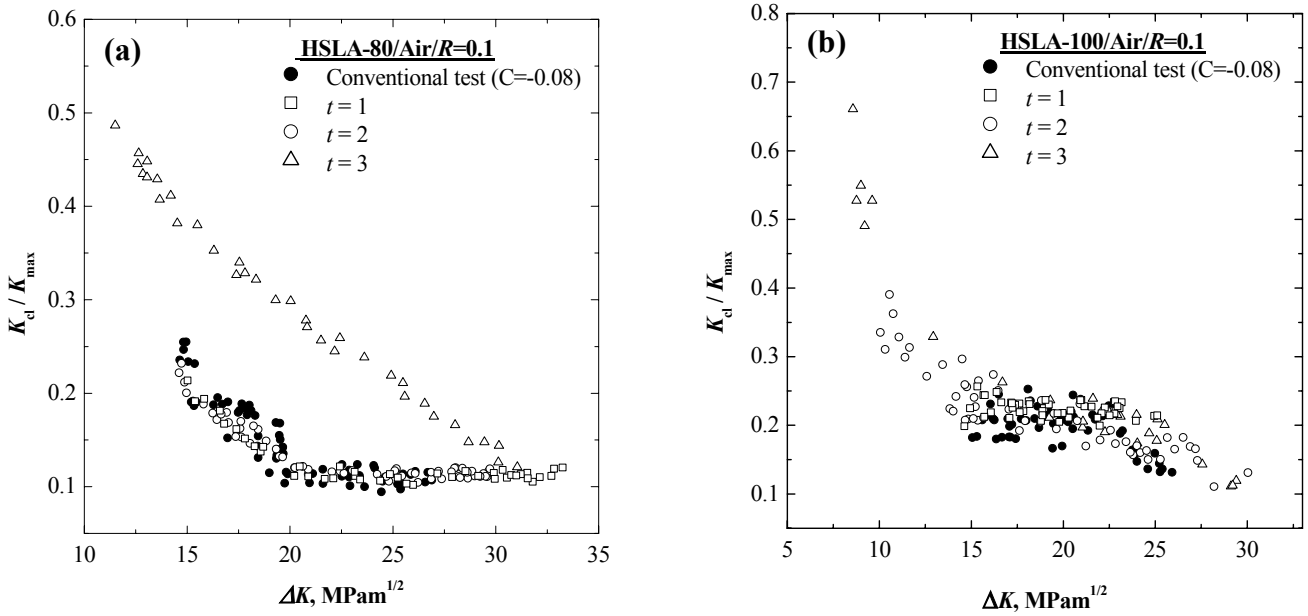

Figure 4: Crack closure behaviour in (a) HSLA-80 and (b) HSLA-100 steels during decreasing ΔK FCGR tests using proposed and conventional methods

From the validation studies described above it appears that the proposed scheme of ΔK reduction can be employed for conducting decreasing ΔK FCGR tests. It is also clear that the proposed method will lead to acceleration of tests only in the case of higher strength materials. An example of use of this new scheme for the generation of threshold level FCGR data is described below.

GENERATION OF THRESHOLD REGIME CORROSION FATIGUE CRACK GROWTH DATA

Corrosion fatigue crack growth rate (CFCGR) tests are typically conducted at low frequencies in aqueous environments. The time requirement for a test can often be prohibitively long if a test is stretched into the threshold regime. The proposed accelerating procedure is especially suitable for this situation.

CFCGR tests were carried out at a frequency of 1 Hz on Cu-strengthened HSLA-100 steel specimens using both the conventional technique and the proposed accelerating methodology with t = 2. The tests were

conducted with the same experimental tools as described earlier. Specimens were loaded within a bath containing 3.5% NaCl solution which was part of the load train of the testing machine.

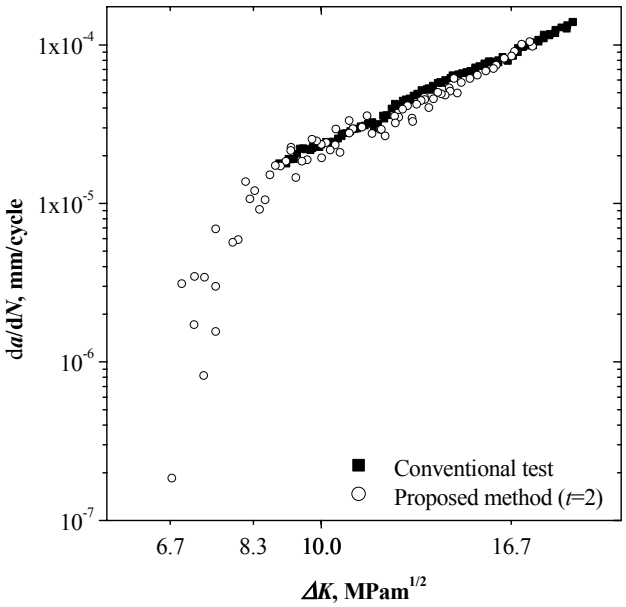

Figure 5: Corrosion fatigue crack growth behaviour of the HSLA-100 steel obtained by decreasing ΔK FCGR tests conducted by conventional and proposed methods

The results of the CFCGR tests are presented in Figure 5. It can be seen that for the common regime of ΔK in tests conducted by the conventional technique and the proposed method, the crack growth rates are comparable. Additionally it is evident that with the proposed method it is possible to achieve lower levels of ΔK covering a large part of the threshold regime as well for essentially the same extent of crack growth. It can be estimated that in order to grow down to ΔK of ~6.5 MPa$\sqrt{m}$ using the conventional testing procedure at 1 Hz test frequency, the test would have to continue for ~120 hours (not considering that it may not be possible to accommodate the crack length in the specimen). In comparison, the test conducted according to the proposed method required 21 hours. It is thus demonstrated that the proposed method of decreasing ΔK FCGR testing provides tremendous experimental advantage.

CONCLUSIONS

An alternative method of decreasing ΔK FCGR testing has been proposed in this paper which substantially shortens the time required to carry out such tests by the conventional procedure. The proposed method has been implemented on two varieties of HSLA steel, and it is shown that for judicious selection of the governing parameters (i.e. t), the integrity of FCGR data obtained can be assured. The method is particularly suitable for use with materials of high strength and in situations where limitations of specimen size are imposed or when the time required for experimentation can be expected to be long.

REFERENCES

1. E 647-93 (1994) *Standard test method for measurement of fatigue crack growth rates*. In: *Annual book of ASTM standards*, Vol. 3.01. American Society for Testing and Materials, Philadelphia, pp.569-596.
2. Saxena, A., Hudak S.J., Donald J.K., Schmidt D.W. (1978) *J. Testing and Eval.* 6, 167.
3. Kumar Raghuvir and Singh S.B. (1992) *Int. J. Press. Vessel & Piping* 51, 25.
4. Irwin G.R. (1968) *Eng. Fract. Mech.* 1, 241.
5. Gan D., Weertman J. (1983) *Eng. Fract. Mech.* 18, 155.
6. Tarafder S., Tarafder M. and Ranganath V.R. (1997) *Int. J. Fatigue* 19, 635.
7. Proposed Appendix X2: *Recommended practice for determination of fatigue crack opening load from compliance* (1990), ASTM Task Group E 24.04.04. Communication to members of Committee.

ORAL/POSTER REFERENCE: ICF100717PR

A Method for Variable Amplitude Lifetime Calculation in the High Cycle Regime

H. Zenner and S. Pöting

Institute for Plant Engineering and Fatigue Analysis
Technical University of Clausthal
Germany

Abstract

Lifetime predictions for components in the high cycle regime are still inadequate. A main reason for the inadequacy is the insufficient knowledge about the failure mechanisms and the lack of a simulation model.

Two different failure mechanisms have been reported in independent papers at the Euromech Conference from 1998 in Paris. The observed failures have been located on the surface and underneath the surface of specimens in a single test series. A simulation model describing these effects is not jet known. Other observations are suggesting a stepwise decreasing S-N-curve for constant amplitudes. None of the well-known modifications of the Miner-Rule are taking these effects into account.

An analysis of a wide database of variable amplitude tests on components leads to the conclusion that none of the Miner-Rule Modifications is capable to describe all test results. Another method to calculate the lifetime of components under variable amplitude loadings was introduced. This method is used to describe S-N-curves of components for variable amplitudes using a parameter to adjust the curve fit.

Therefore an investigation based on published data of variable amplitude fatigue tests has been made. A phenomenological description for variable amplitude test S-N-Curves has been evaluated on its accuracy to describe the test results.

Keywords

high cycle fatigue, lifetime prediction, lifetime calculation, variable amplitude test, spectrum loading

Introduction

Multiple components are used in structures and machines such as vehicles, offshore structures, as well as railway components and engines for more than 8 to 10 years. During their utilisation these components are exposed to 10^9 and more load cycles. In the high cycle regime failures of components have occurred even though the peak loads of the component's spectrum loading are just fairly above the fatigue limit. Even though components designed by the fatigue limit exposed to a few single overloads can fail in this regime. This leads to the question: Is there a fatigue limit and how can a lifetime prediction for variable amplitude loaded components be calculated more accurate in the high cycle regime?

For the lifetime designs there are two possible ways of strength verification: calculations and experiments. The experimental strength verification in the very high cycle regime is only in a few possible cases due to the long experiment time and high costs of testing. Due to these reasons there is only a limited number of test results available for the high cycle regime and experiments must carefully be monitored to gain the most possible information.

The lifetime calculation verification is based on various lifetime calculation models and modifications. Nevertheless, the calculated lifetimes are varying up to a factor of 200 in lifetime for spectrum loads with maximum stresses just above the fatigue limit. Therefore for spectrum loading is a high uncertainty in the predicted lifetime of a component.

Lifetime Calculation for Variable Amplitude

Constant Amplitude Component Stress Analysis

Lifetime prediction of components is based on stress analysis. These analyses are either base on nominal stress analysis, local stress analysis. In more complicated cases of complex components the finite element method (FEM) is used to determine the local stress distributions and to find the most claimed section of the component. A component, which shows no stress concentration, is considered a well-designed component because all sections of the component are equally stressed. The spots of stress maximums are called critical spots. These spots are considered the weakest spots of the design where the component is expected to fail.

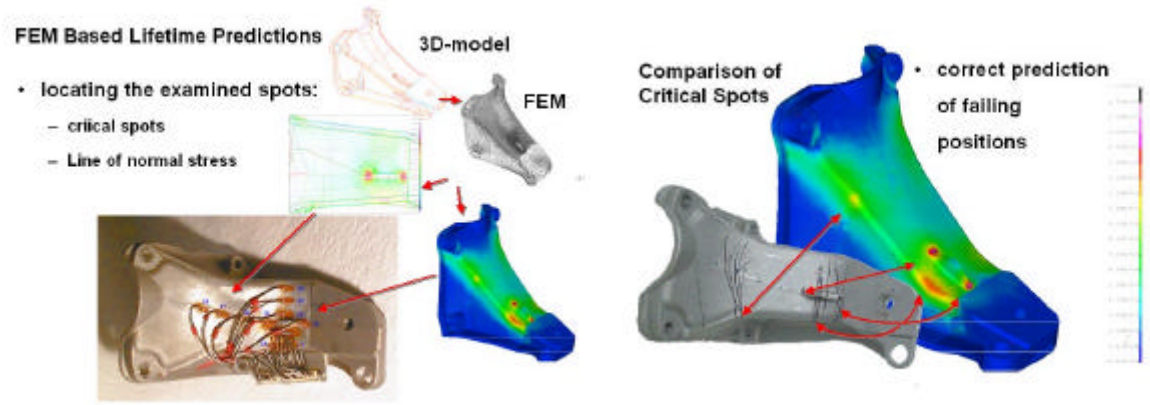

Figure 1: Elastic-Plastic Stress Analysis Compared to Strain Gauge Measurements

The FEM-analysis of such stress distribution can be verified using strain gauges to analyse local strains and calculate elastic stresses. These stresses can be compared with the analytical calculated local stresses on these spots. The accuracy of a FEM-model can be evaluated by a comparison of the calculated stresses by FEM analysis to the observed experimental stresses for elastic deformations.

Figure 2: Digital Video Test Observations of Multiple Surface Cracks

Based on the applied load the local stress or the nominal stress can be calculated. Compared with maximum applicable stress a lifetime prediction can be made for constant amplitude test. For constant amplitude test the lifetime calculations are quite satisfactory. They are based on S-N-curves of constant amplitude test with the same material properties as specimen properties such as load ratio, surface structure, material texture, e.g.. In case these S-N-curves do not exist the influences can be described by factors [2].

Variable Load Analysis

Machine parts today are subjected to variable amplitude loads during their lifetime. Long time load spectrum analysis of these components can be used to determine the frequency distribution of amplitude loads as well as a history of load amplitudes applied to the component during its life cycle.

In cases when a load history or a load spectrum of a component is not available generalised load spectrum can be used for experimental analysis. Standardised load spectra are commonly used for variable amplitude tests if it is not a specific load history for a component, which is tested [9]. A load history is the normalised load spectrum following a normal distribution. Another load history is a normalised straight-line load spectrum distribution. For aircrafts or rolling-mill components special standardised load spectrum histories like TWIST or WASA have been established.

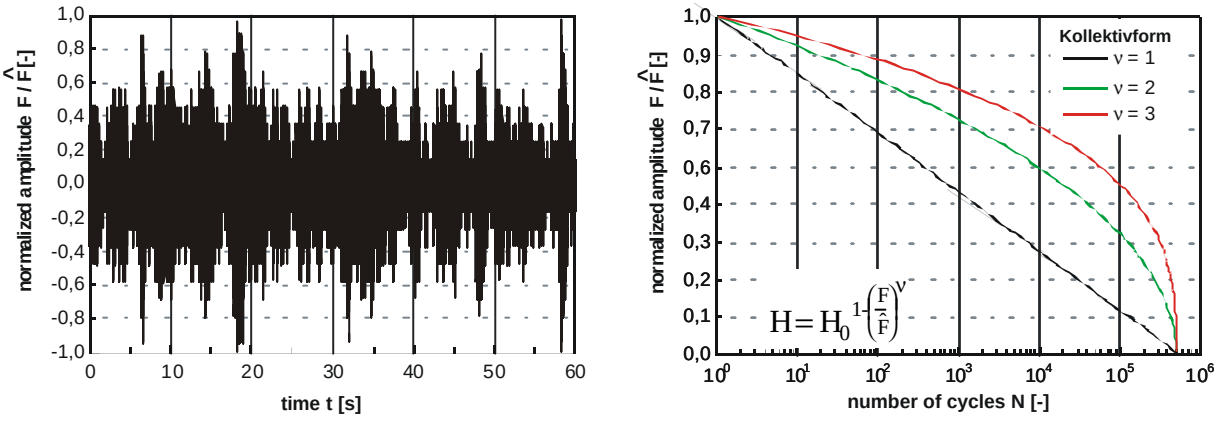

Figure 3: Loading Amplitude Time Plot and Frequency Spectra

It has been noticed that spectrum loads inducing stresses just below or above the fatigue limit can lead to component failures even though mostly subjected stresses are below the fatigue limit. Therefore the question is how do these loads attribute to the failure of such components and how can it be calculated?

Variable Amplitude lifetime Prediction

The linear damage accumulation is commonly used to calculate a cumulative damage sum using Miner's Rule and its modifications. For the original Miner's Rule is assumed that each load cycle has an average according to the description the slope of the S-N-curve for variable amplitudes [5, 6, 7, 11]. The linear damage accumulation assumes that each load at a certain level attributes a damage to the component, eqn. (1). Further more it is assumed that all cycles are contributing to the components damage equally and therefore the damage sum can be calculated by the sum of the damages of all cycles and failure occurs when the damage sum equals one [6].

$$D = \sum_{i=1}^{N} d_i \qquad d_i = h_i \cdot \frac{1}{N_i} \tag{1}$$

D: damage sum
d_i: damage sum of a
N_i: number of cycles to failure at a constant stress amplitude level i
h_i: number of cycles at a stress amplitude i

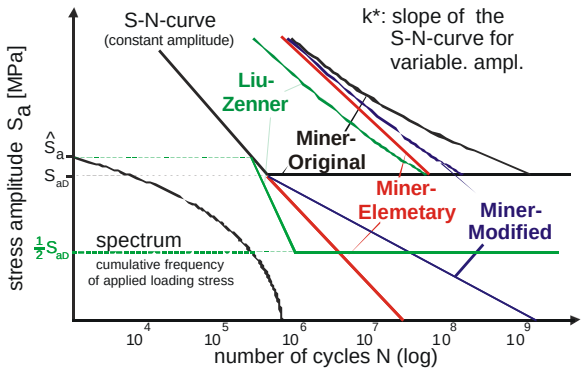

	$S_a \geq S_D$	$S_a < S_D$
original:	$k^* = k$	$k^* = \infty$
elementary:	$k^* = k$	$k^* = k$
modified by Haibach:	$k^* = k$	$k^* = 2\,k - 1$
modified by Liu/Zenner:	$k^* = (k + m) / 2$	$k^* = \infty$

k: slope of the S-N-curve for constant amplitude
m: slope of the crack growth S-N-curve for constant amplitude

Figure 4: Lifetime Predictions Using Miner Modifications

Current data analysis of variable amplitude tests has shown that components tend to fail at a mean value damage sum equal 0,3 for steel and 0,5 for aluminium [3, 4, 8, 11]. Therefore the relative Miner's Rule is introduced. Based on variable amplitude tests of components a different damage sum can be used to calculate the failure of a component. The analysis of the Miner' Rule and its modifications has proven that the modification by Liu/Zenner has the most accuracy. The different Miner's Rule modifications lead to longer or shorter calculated lifetimes [7].

Lifetime Predictions for Variable Amplitude Loads in the High Cycle Regime

In the high cycle regime the calculated lifetimes of variable amplitude tests differ magnificently for the different Miner's Rule modifications. The calculated lifetimes can differ depending on the spectrum, the slope k of the S-N-curve and the components up to a factor of 200 in lifetime. The modification leading to the shortest calculated lifetime is the Miner Modification by Liu/Zenner. The modification leading to the longest calculated lifetime is the Miner original modification. Compared to the experimentally investigated lifetimes the Miner elementary modification tends to lead to a safe and conservative lifetime calculation, the Miner original modification tends to lead to an unsafe and progressive lifetime calculation. For the experimental test results it was observed that the experimental lifetimes are in the range of the calculated lifetimes of the Miner elementary and original modification.

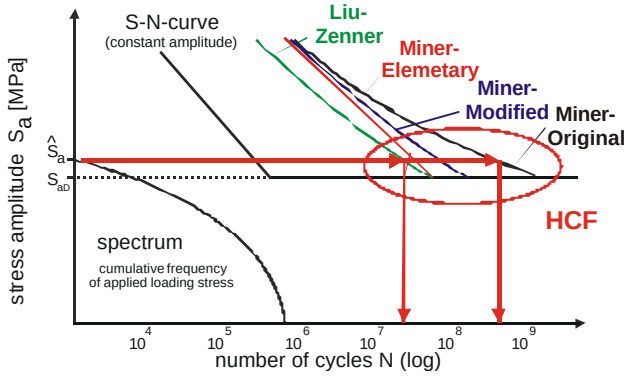

Figure 5: Difference in calculated lifetimes depending on Miner Modifications

Lifetime Prediction using a Form Parameter c

A method to describe a S-N-curve for variable amplitudes was published by [1]. The function describes any S-N-curve for variable amplitude tests in dependency of a single form parameter, eqn. (2). This function uses the point of the fatigue limit of the S-N-curve for constant amplitude loads as a reference point. The base point for the calculation is the limiting number of load cycles to the fatigue limit and the fatigue limit of the S-N-curve for constant amplitudes. The number of load cycles which can be applied to a component under variable amplitude loads of a spectrum with a maximum load $\hat{S}$ can be calculated by the use of the fatigue limit base point for constant amplitudes. The function for the finite life fatigue strength of constant

amplitude S-N-curves is used with a modified slope k^*. The modification of the slope k^* depends on the interval of the maximum spectrum load and the constant amplitude fatigue limit described by the form parameter c.

$$N = N_D \cdot \left(\frac{S_D}{\hat{S}} \right)^{k^*} \qquad k^* = k \cdot \left[1 + \frac{c}{\hat{S} / S_D - 1} \right] \tag{2}$$

S_D: constant amplitude fatigue limit
k: slope of constant amplitude S-N-curve
$\hat{S}$: spectrum maximum applied stress
c: form parameter

Setting the parameter to its extreme values the function describes the calculated lifetime curve of variable amplitude tests calculated by using the elementary or original Miner's Rule. The influence of the spectrum length and the spectrum load distribution can be described by this function. The experimentally observed effect of a lifetime reduction in case of a load spectrum with a greater number of higher loads can be described as well as the effect spectrum length.

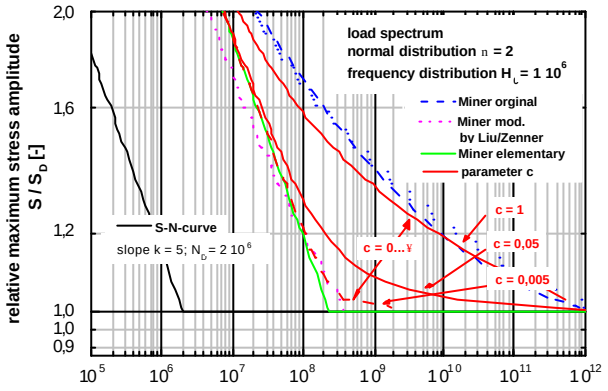

Figure 6: Capabilities of the Form Parameter c to Describe Variable Amplitude Lifetimes

From the analysis of the published data [8] of variable amplitude tests tendencies for the parameter c can be concluded. The results of the quantitative analysis are shown in table 1.

TABLE 1
INFLUENCE ON THE FORM PARAMETER C

influence factors	parameter indication	form parameter c
notch factor: K_t	high	↑
	low	↓
irregularity: I [11]	1	↓
	0	↑
stress ratio: R	-1	↑
	0	↓
slope of S-N-curve: k	steap	↓
	even	↑

This analysis leads to the following proposal of a function calculating the form parameter c in dependency of the above influence factors, eqn. (3).

$$c = f(K_t, I, R, k) \qquad (3)$$

Conclusions

This newly introduced function for variable amplitude lifetime prediction provides an easy method for a more accurate lifetime prediction. Based on constant amplitude tests and load analysis lifetime predictions can be made. More precise lifetime predictions can be made even for the high cycle regime.

Acknowledgements

Funding for the research project was provided by work community of industrial research union "AiF - Arbeitsgemeinschaft industrieller Forschungsvereinigungen "Otto von Guericke" e.V., Köln", the German Union for Welding and Related Processes "DVS - Deutscher Verband für Schweißen und verwandte Verfahren e. V., Düsseldorf " and the Research Union Propulsion Techniques "FVA – Forschungsgemeinschaft Antriebstechnik e.V., Frankfurt". Further support was provided by: VW – Volkswagen AG, Braunschweig; Corus Aluminium Technique, Bonn; Alstom LHB, Braunschweig; ADTranz, Berlin; DUEWAG, Duisburg.

References

1. Schütz, W; J. Bergmann; M. Hück (1988). *Gemeinschaftsarbeit Pkw-Industrie / IABG Relative Miner-Regel.* Technische Berichte TF–2022, Industrieanlagen-Betriebsgesellschaft mbH, Germany
2. Gudehus, H.; Zenner, H. (1995). *Leitfaden für eine Betriebsfestigkeitsrechnung.* ISBN 3-514-00445-5, Verein Deutscher Eisenhüttenleute, Düsseldorf, Germany
3. Eulitz, K.-G.; Döcke, H.; Esderts, A. (1994). *Lebensdauervorhersage I.* Forschungsheft 184, Jahrgang 1994, Forschungskuratorium Maschinenbau e.V., Frankfurt, Germany
4. Eulitz, K.-G.; Kotte, K. L.; Zenner, H. (1997). *Lebensdauervorhersage II*, Forschungsheft 227, Jahrgang 1997, Forschungskuratorium Maschinenbau e.V., Frankfurt, Germany
5. Miner, M. A. (1945). *Cumulative Damage in Fatigue*. ASME Journal of Applied Mechanics, Vol. 12, pp. 159 – 164, USA
6. Schütz, W.; Zenner, H. (1973). *Schadensakkumulationshypothesen zur Lebensdauervorhersage bei schwingender Beanspruchung.* Werkstofftechnik, book 1 and 2, pp. 25-33 and 97-102, Germany
7. Schütz, W.; Heuler, P. (2000). *Miner's Rule Revisited*. Materialprüfung Nr. 6, pp.245 – 251, Carl Hanser Verlag, Munich, Germany
8. Eulitz, K.-G.; Kotte, K. L. (1999). *Datensammlung Betriebsfestigkeit Teil 1 und Teil 2*. ISBN 3-8163-0383-8, VDMA Verlag GmbH, 1999, Frankfurt, Germany
9. Brune, M.; Eifler, D.; Heuler, P.; Schütz, D.; Schütz, W.; Ungerer, W.; Zenner, H. (1990). *Standardisierung von Lastfolgen und Verbesserung der Lebensdauervorhersage für Bauteile in Walzwerksantrieben*. VBFEh-Bericht Nr. 40, Vereins zur Betriebsfestigkeitsforschung, Düsseldorf
10. Zenner, H. (1997). *Lebensdauerberechnungskonzepte: Beschreibung – Kritik – Entwicklung*. DVM-Bericht Nr. 800, Deutscher Verband für Materialforschung und –prüfung e.V., Berlin, Germany
11. Haibach, E. (1989). *Betriebsfestigkeit – Verfahren und Daten zur Bauteilberechnung.* VDI-Verlag GmbH, Düsseldorf, Germany

ORAL/POSTER REFERENCE: **ICF100734OR**

A MULTISCALE FRACTURE MECHANICS MODEL FOR PREDICTING DAMAGE EVOLUTION IN LAMINATED COMPOSITES SUBJECTED TO IMPACT LOADING

David H. Allen

Aerospace Engineering Department
Texas A&M University
College Station, Texas 77843

ABSTRACT

Laminated polymeric composites are utilized in a variety of structural applications wherein impact loads are a common design consideration. In such circumstances damage is usually observed in the form of a variety of fracture modes including matrix cracking, delamination, and fiber fracture. Multiple cracks with significant energy dissipation are often observed experimentally before complete loss of structural integrity is attained. Therefore, since it is often possible to keep the part in service after the impact event, it is useful to develop models for predicting the post impact performance of the part.

The interaction of crack propagation makes it essential to model the evolution of these damage events during impact loading. In order to capture the physics of all of the fracture events both accurately and efficiently, it is possible to develop a multi-scale continuum mechanics framework in which successively larger scales are utilized to model each of the fracture modes. This approach is taken in the current paper to account for microscale damage ahead of delaminations, mesoscale matrix cracking, local scale delaminations, and global scale part response. The resulting micro-meso-local-global methodology utilizes ductile fracture mechanics on each scale to effect crack growth of the three types described above, with the smaller two scales developed analytically, and the larger two developed computationally by means of the finite element method. Linking between the four different scales is obtained by utilizing damage dependent homogenization theorems that account for energy dissipation due to fracture on the smaller scales.

KEYWORDS

laminated composites, damage evolution, fracture, multi-scale modeling

INTRODUCTION

Much effort has been devoted in recent years towards obtaining improved understanding of damage evolution in composites subjected to impact, as evidenced by numerous publications in the open literature.

Laminated composites impacted at low velocity by blunt objects are susceptible to the development of matrix cracks, fiber cracks, and interply delaminations[1]. While much of this damage may not be readily visible at the surface, it is capable of substantially reducing the residual strength and stiffness of the laminate. The resultant damage induced stress redistribution can lead to the failure of the component. Therefore, it is essential to be able to predict the damage evolution that occurs during the impact event so that the impact resistance, residual strength, and serviceable life of the laminate can be predicted.

While few papers have appeared which attempt to address the three dimensional problem of impact, noteworthy are those of Wu and Springer [2,3] and of Chang and coworkers [4,5]. In these works a three dimensional transient dynamic finite element analysis is presented for the study of impact. However, delamination is not modeled. To the knowledge of the author none of the delamination damage models found in the published literature accounts for the development of the process zone ahead of the delamination front and the resulting nonlinearity in the interfacial mechanical response.

Recently, the author has developed together with coworkers a micromechanics model for predicting the evolution of matrix cracking [6-8], and this model has previously been shown to be accurate when compared to experiment for polymeric composite plates subjected to quasi-static monotonic loading [9-12]. The problem of predicting the evolution of delaminations is much more complicated than that of matrix cracking. We have compared model predictions favorably to experiment for a variety of two dimensional examples [13,14]. While the problem of a single delamination in an elastic medium has successfully been solved [15], the prediction of multiple propagation of planar delaminations has only recently been considered. However, utilizing a cohesive zone model [6-24], the author and coworkers have been able to predict the evolution of up to seven simultaneous delaminations in a two dimensional setting [25], and this has been compared favorably to experimental results. Furthermore, the author and coworkers have also been able to predict the progression of multiple modes of damage in a two dimensional setting, as shown in Fig. 1. In addition, the algorithm has been utilized to predict multiple damage modes in a three dimensional plate with a circular cutout [26]. These predictions are among the most complex attempts known to date for predicting damage progression in composites subjected to impact.

SOLUTION METHODOLOGY

The model is three dimensional and computational in nature, utilizing the finite element method, and this model is implemented to the code SADISTIC [27]. Crack growth is simulated via the cohesive zone model currently under development by the author and coworkers [20-25]. The cohesive zone model for predicting damage evolution in laminated composite plates is cast within a three dimensional continuum finite element algorithm capable of simulating the evolution of matrix, fiber, and delamination cracking in composite structures subjected to ballistic impact. Cracking on vastly differing length scales is accounted for by employing global-local techniques, with appropriate damage dependent homogenization techniques introduced to bridge the disparate scales.

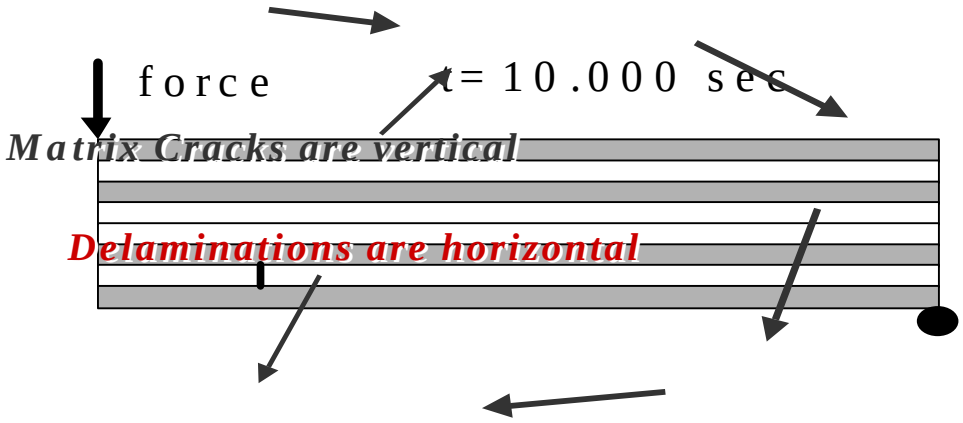

Fig. 1. Evolution of damage in right half plane of $[0,90,0,90]_s$ beam subjected to transverse loading

In order to describe this technique, consider a scenario in which damage exists simultaneously in a solid on two (or more) significantly different length scales. Of course, one way to analyze such a problem is to consider the possibility of cracks extending everywhere and at all length scales simultaneously in the continuum. However, this is untenable by both analytic and computational means for all but a few simple scenarios at the current state of the art. Alternatively, suppose we define the length scale of the microcracks to be l_1, and the length scale of the macrocracks to be l_2. Then, under the circumstance that $l_2 >> l_1$, it can be shown that continuum scale analyses can be carried out on the smaller and larger scales separately (so long as other geometric length scales are also widely separated) and linked together by a homogenization principle without significant loss of accuracy. This may be accomplished by completing the following tasks in succession: 1) perform a continuum scale analysis of the microscale problem; 2) homogenize the results of the microscale analysis, thus producing a damage dependent macroscale constitutive theory; and 3) solve the macroscale continuum problem (including crack propagation) using the damage dependent constitutive theory produced in 2). This procedure will obviate the presence of microscale induced stress concentrations on the macroscale, so that some loss of accuracy is inevitable. However, this loss of accuracy may not be significant when the length scales are significantly different. Furthermore, the savings in computational and/or analytical difficulties gained by employing homogenization techniques will in many cases make a heretofore untractable problem solvable. Note also that if the homogenization process is performed correctly, then the total energy dissipation predicted by the macroscopically homogenized constitutive equations will be identical to that predicted on the microscale, except that the homogenization process will result naturally in a dissipative damage parameter on the macroscale. Similar situations exist in other fields of applied physics, such as the process of linking continuum mechanics to molecular dynamics. Although temperature and entropy do not exist as state variables at the molecular scale, the process of homogenizing the effect of many molecular motions results naturally in the introduction of these variables at the continuum scale.

It is possible to employ this procedure on multiple scales at one time, where the number of scales, n, is essentially determined by the physics of the problem. Thus, we can say

$$l_{m+1} >> l_m \quad m=1,\ldots,n \qquad (1)$$

The solutions to the problems on each of these length scales is then linked to the solutions on the adjacent length scales by utilizing homogenization techniques such as those recently developed by the author and coworkers for damaged media [28-30]. These solutions can then be used to model damage evolution on several differing length scales simultaneously.

CONCLUSION

While the technique described herein is too complicated to present in detail in such a short space, the technique has been shown to lead to accurate solutions that are computationally efficient for several problems that involve damage evolution on widely differing length scales. The interested reader will find these results documented in references [20-30].

ACKNOWLEDGMENT

The author gratefully acknowledges the funding provided for this research by the U.S. Army Research Office under grant no. DAAG55-98-1-0119.

REFERENCES

1. Gilbert, D.G., Beaumont, P.W.R., and Nixon, W.C. (1983), “Direct Observations of the Micromechanisms of Fracture in Polymeric Solids Using the Scanning Electron Microscope,” *Mechanical Behaviors of Materials--IV, ICM4*, Vol. 2, pp. 705-710.
2. Wu, H.T., and Springer, G.S. (1988), “Measurements of Matrix Cracking and Delamination Caused by Impact on Composite Plates,” *Journal of Composite Materials*, Vol. 22, pp. 518-532.
3. Wu, H.T., and Springer, G.S., (1988), “Impact Induced Stresses, Strains, and Delaminations in Composite Materials,” *Journal of Composite Materials*, Vol. 22, pp. 533-560.
4. Wu, H.T., and Chang, F.K., (1989), “Transient Dynamic Analysis of Laminated Composite Plates Subjected to Transverse Impact,” *Computers and Structures*, Vol. 31, pp. 453-466.
5. Liu, S., Kutlu, Z., and Chang, F., (1993), “Matrix Cracking and Delamination in Laminated Composite Beams Subjected to a Transverse Concentrated Line Load,” *Journal of Composite Materials*, Vol. 27, No. 5.
6. Lee, J.W., Allen, D.H., and Harris, C.E., (1989), "Internal State Variable Approach for Predicting Stiffness Reductions in Fibrous Laminated Composites with Matrix Cracks," *Journal of Composite Materials*, Vol. 23, No. 12, pp. 1273-1291.
7. Lee, J.W., Allen, D.H., and Harris, C.E., (1991). "The Upper Bounds of Reduced Axial and Shear Moduli in Cross-Ply Laminates with Matrix Cracks," *Composite Materials: Fatigue and Fracture (Third Volume)*, ASTM STP 1110, T.K. O'Brien, Ed., Philadelphia, pp. 56-69.
8. Allen, D.H. and Lee, J.W. (1991). "Matrix Cracking in Laminated Composites under Monotonic and Cyclic Loadings," *Composites Engineering*, Vol. 1, No. 5, pp. 319-334, (also in *Microcracking Induced Damage in Composites*, G.J. Dvorak and D.C. Lagoudas, Eds., American Society of Mechanical Engineers, AMD Vol. 111, pp. 65-76, 1990).
9. Harris, C.E., Allen, D.H., Nottorf, E.W., and Groves, S.E., (1988). "Modelling Stiffness Loss in Quasi-Isotropic Laminates Due to Microstructural Damage," *Journal of Engineering Materials and Technology*, Vol. 110, No. 2, pp. 128-133.
10. Harris, C.E. and Allen, D.H., (1988). "A Continuum Damage Model of Fatigue-Induced Damage in Laminated Composites," *SAMPE Journal*, Vol. 24, No. 4, pp. 43-51.
11. Harris, C.E., Allen, D.H., and Nottorf, E.W., (1989). "Predictions of Poisson's Ratio in Cross-Ply

Laminates Containing Matrix Cracks and Delaminations" *Journal of Composites Technology and Research*, Vol. 11, No. 2, pp. 53-58.

12. Harris, C.E., Coats, T.W., Allen, D.H., and Lo, D.C., (1995). "Progressive Damage Analysis of Laminated Composites due to Tension Fatigue," *Proc. 2nd Pacific Int. Conf. on Aerospace Science and Technology*, Melbourne.
13. Lo, D.C., and Allen, D.H., (1994). "Modeling of Delamination Damage Evolution in Laminated Composites Subjected to Low Velocity Impact," *International Journal of Damage Mechanics*, Vol. 3, No. 4, pp. 378-407.
14. Lo, D.C., Costanzo, F., and Allen, D.H., (1995). "Delamination Evolution in Composites Using a Cohesive Zone Model," *Computational Mechanics '95 Theory and Applications*, S.N. Atluri, G. Yagawa, and T.A. Cruse, Eds., Springer, Berlin, pp. 1745-1750.
15. Tvergaard, V. and Hutchinson, J.W., "The Influence of Plasticity on Mixed Mode Interface Toughness", *J. Mech. Phys. Solids*, Vol. 41, 1993, pp. 1119-1135.
16. D.S. Dugdale, (1960). *Journal of the Mechanics and Physics of Solids*, 8, 100-104.
17. G.I. Barenblatt, (1962). *Advances in Applied Mechanics*, 7, pp.55-129.
18. Needleman, A., (1987). "A Continuum Model for Void Nucleation by Inclusion Debonding", *J. Appl. Mech.*, Vol. 54, pp. 525-531.
19. Tvergaard, V., (1990). "Micromechanical Modelling of Fibre Debonding in a Metal Reinforced by Short Fibres", *Proc. IUTAM Symp. Inelastic Deformation of Composite Materials*, (ed. G.J. Dvorak), Springer, New York, pp. 99-111.
20. Costanzo, F. and Allen, D.H., (1993). "A Continuum Mechanics Approach to Some Problems in Subcritical Crack Propagation," *International Journal of Fracture*, Vol. 63, No. 1, pp. 27-57.
21. Allen, D.H., and Searcy, C.R., (2000). "Numerical Aspects of a Micromechanical Model of a Cohesive Zone," *Journal of Reinforced Plastics and Composites*, Vol. 19, No. 3, pp. 240-248.
22. Yoon, C. and Allen, D.H., (1999). "Damage Dependent Constitutive Behavior and Energy Release Rate for a Cohesive Zone in a Thermoviscoelastic Solid" *International Journal of Fracture*, Vol. 96, pp. 56-74.
23. Allen, D.H. and Searcy, C.R., (2001). "A Micromechanical Model for a Viscoelastic Cohesive Zone," *International Journal of Fracture*, Vol. 107, pp. 159-176.
24. Allen, D.H., and Searcy, C.R., (2001). "A Micromechanically Based Model for Predicting Dynamic Damage Evolution in Ductile Polymers," to appear in *Mechanics of Materials*.
25. Allen, D.H., Lo, D.C., and Zocher, M.A., (1997). "Modelling of Damage Evolution in Laminated Viscoelastic Composites", *Int. J. Damage Mech.*, Vol. 6, pp. 5-22.
26. Phillips, M.L., Yoon, C., and Allen, D.H., (1999). "A Computational Model for Predicting Damage Evolution in Laminated Composite Plates," *Journal of Engineering Materials and Technology*, Vol. 21, pp. 436-444.
27. Allen, D.H., Jones, R.H., and Boyd, J.G., (1994). "Micromechanical Analysis of a Continuous Fiber Metal Matrix Composite Including the Effects of Matrix Viscoplasticity and Evolving Damage," *Journal of the Mechanics and Physics of Solids*, Vol. 42, No. 3, pp. 505-529.
28. Boyd, J.G., Costanzo, F., and Allen, D.H., (1993). "A Micromechanics Approach for Constructing Locally Averaged Damage Dependent Constitutive Equations in Inelastic Composites," *International Journal of Damage Mechanics*, Vol. 2, pp. 209-228.
29. Costanzo, F., Boyd, J.G., and Allen, D.H., (1996). "Micromechanics and Homogenization of Inelastic Composite Materials with Growing Cracks," *Journal of the Mechanics and Physics of Solids*, Vol. 44, No. 3, pp. 333-370.
30. Allen, D.H., and Yoon, C., (1998). "Homogenization Techniques for Thermoviscoelastic Solids Containing Cracks," *International Journal of Solids and Structures*, Vol. 35, pp. 4035-4054.

A NEW APPROACH FOR IDENTIFYING THE BENDING LOADS ON BEAM USING THE DISCRETE INTEGRAL METHOD

Hiroyuki Kisu[1], Guiming Rong[1] and Yoshihiro Kondo[2]

[1]Faculty of Engineering, Nagasaki University, Bunkyo-machi 1-14, Nagasaki 852, Japan
[2]Graduate School of Marine Science and Engineering, Nagasaki University

ABSTRACT

Analysis of inverse problems has already been performed in various fields. In many cases, assumptions for the solution is needed. It seems that the problems which need any assumptions cause a contradiction in the analysis.

On the other hand, we have developed the discrete integral method(DIM) utilizing the delta function. We have noticed that the DIM is one of the excellent schemes to solve the inverse problem since it can solve it without any assumptions. In this paper, we attempt to apply the DIM to one-dimensional inverse problems. Namely, we developed a scheme for identifying the external load distribution on a homogeneous beam without any assumption for the solution.

Through several examples, it is proved that the present scheme gives accurate and natural solutions.

KEYWORDS

Boundary element method, Discrete integral method, Inverse problems, Bending problems of beam

INTRODUCTION

In the analysis of Inverse Problem[1,2], many points of issue have been left yet even if problems with ill-conditions are excluded. One of them is concerning presumption. This means that, it is necessary to give assumption information such as the shape, the number, its size or position and so on, of the object to be treated, as supplementary information for identification. It is difficult to solve it as an inverse problem if several assumptions concerning priori information are not defined, for the subject to be estimated is a unknown existence. In addition, the unnatural equations must be used when the number of parameters is different from that of simultaneous equations which works as a deciding condition. These cause the difficulty to establish a general scheme in the analysis of inverse problems. For these reasons, it is important to establish a scheme for inverse problems without any assumptions of the solution.

In this study, the first time, the discrete integral method utilizing the delta function is developed and we try to apply this method as one of schemes to the analysis of inverse problem by boundary element method (BEM). It is shown that the identification is performed naturally without any assumptions of the solution by

using the present scheme. In this report, the present scheme is applied to one dimensional inverse problem, namely, the identification of external load distribution in bending problems of a homogeneous beam.

1. INSTITUTION OF ONE DIMENSIONAL INVERSE PROBLEM

1.1 *Integral equation of bending problem of beam by BEM*

It is convenient for the problem to identify external load distribution in bending problems of a beam to use the formulation of BEM. For a homogeneous beam under an external load of $q(x)$ as shown in Figure 1, the equation of the deflection W can be written as[3]

$$W(s) = [-WQ^* + \theta M^* - M\theta^* + QW^*]_0^L + \int_0^L q(x)W^*(x,s)dx \tag{1}$$

Where L is the length of the beam, s is the observation point, θ is the slope, M is the bending moment and Q is the share force, and parameters pointed with asterisk * are kernel functions. The inverse problem in this report is to identify the external load distribution applied on beam (i.e., $q(x)$ in the integral term of right side of Eqn.1) from the information of the deflection $W(s)$ which is monitored at observation point s as well as the information of boundary conditions at both ends of the beam.

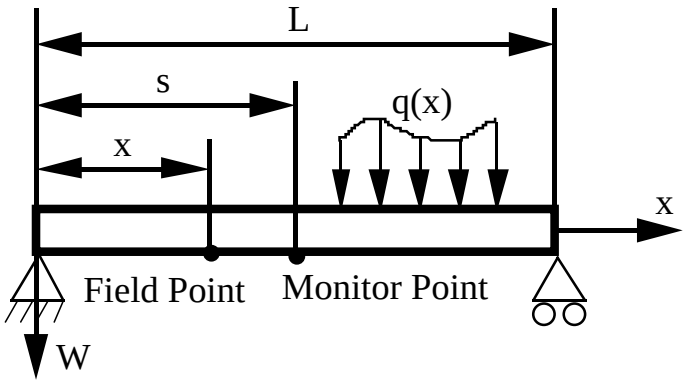

Figure 1: A homogeneous beam with external load $q(x)$

1.2 *Discrete integral method utilizing the delta function*

Here we will explain the discrete integral method utilizing the delta function, which forms the basis of this study. The following integration is considered.

$$\int_a^b f(x)K(x)dx \tag{2}$$

Here, $K(x)$ is a known function, $f(x)$ is a function which is treated as the target of interest (for example, in this case, it is the function of external load distribution), and it can be known or unknown value. The function $f(x)$ is usually approximated using the quadratic element. Instead of this, we approximate it using Dirac's delta function:

$$\nabla^n f(x) = \sum_{i=1}^{m} P_i \delta(x - x_i) \tag{3}$$

where ∇^n is the $n-$th Nabla differential operator, P_i is the strength of the delta function, namely, the strength of the virtual concentrated source, x_i is its applied position and m is the number of P_i.

Further, a function Z^* defined as the following equation is introduced:

$$\nabla^k Z^* = K^*(x) \tag{4}$$

It is supposed that the function Z^* is obtained by analytical operation. By substituting Eqn.4 into Eqn.2, and by integrating it by part, the Eqn.2 can finally be written as the following equations. Namely, in the case of $n = 2$,

$$\int_a^b f(x)K(x)dx = \int_a^b f(x)\nabla^2 Z^* dx = [f\nabla Z^* - \nabla f Z^*]_0^L + \sum_{i=1}^{m} Z^*(x_i)P_i \tag{5}$$

and in the case of $n = 4$, it becomes

$$\begin{aligned}\int_a^b f(x)K(x)dx &= \int_a^b f(x)\nabla^4 Z^* dx \\ &= [f\nabla^3 Z^* - \nabla f\nabla^2 Z^* + \nabla^2 f\nabla Z^* - \nabla^3 f Z^*]_0^L + \sum_{i=1}^{m} Z^*(x_i)P_i\end{aligned} \tag{6}$$

We found that the given integration is expressed by the quantities at the both ends of the beam and the strength of the delta function P_i, so the domain integral operation is never needed.

This scheme is regarded as a new discrete integral method, and will be introduced into the equation of beam which is expressed by Eqn.1.

1.3 *Construction of simultaneous equations for inverse problem*

Following equations are obtained when the Eqn.6 is substituted into the second term on the right side of Eqn.1 with $f(x) = q(x)$ and $K(x) = W^*(x, s)$:

$$\begin{aligned}W(s) &= [-WQ^* + \theta M^* - M\theta^* + QW^*]_0^L \\ &\quad + [q\nabla^3 Z^* - \nabla q\nabla^2 Z^* + \nabla^2 q\nabla Z^* - \nabla^3 q Z^*]_0^L + \sum_{i=1}^{m} Z^*(x_i)P_i\end{aligned} \tag{7}$$

In Eqn.7, the equation of BEM which gives the deflection is expressed using the strength of delta function P_i (unknown quantity). In addition to P_i, there are still the boundary values of physical quantities (the 4 parameters of W, θ, M, Q exist at each end of the beam, so the total amount is 8, and 4 of them are given by boundary conditions). Besides, the load distribution q and its differential quantity at both ends of the beam remain as unknown in the equations. To sum up, the total amount of the unknown values is $m+8$. To match with the number of the unknowns, m equations are obtained by monitoring the information of deflection at the m points where the delta function is applied. Further, 4 fundamental equations[4] to solve the bending problem of beam as a direct problem are used. For the rest 4 equations, the self-interpolated equation of q

$$q(s) = [q\nabla Y^* - \nabla q Y^*]_0^L + \sum_{i=1}^{m} P_i Y^*(x_i, s), (n = 2) \tag{8}$$

and its differential form are available. Therefore, the simultaneous equations, each has a natural form, can be constructed with the necessary number. When the simultaneous equations are solved, P_i and each unknown quantity at both ends can be calculated, then, we can calculate the external load distribution at any point of the beam using Eqn.8 directly because there is no unknown value on the right side of the equation.

2. EXAMPLES

In this section, analysis examples for model calculation are instituted, and the above identification method of external load distribution will be verified. The examples are calculated and showed by the following rules unless a special description is made:

1. The units: the dimensionless quantities are considered to fit any system of units. The length of beam L is 10.

2. The boundary condition(B.C.): a simply supported beam is treated.
3. The number of points m where the delta function is applied is 49 and they are arranged at even intervals except the both ends.
4. The order n of Nabla-operator: the equation of $n = 2$ is used.
5. In all graphs, the horizontal axis is in the length direction of beam (x axis), the vertical axis is the value of load. And, "Exact" means exact distribution, "Present" means present distribution of identified results. The rigidity EI is 100 in all examples.

Other boundary condition and the case for a Nabla-operator of order $n = 4$ will be discussed at the last.

2.1 *Identifying a concentrated load*

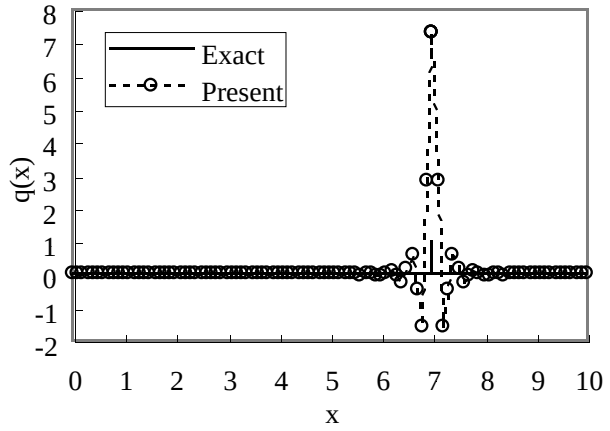

Figure 2: Identification of a concentrated load

First, the problem of a concentrated load is treated. The value of the concentrated load is 1 and it is applied at the point of $x = 7$. The result is shown in Figure 2. From this figure, it is seen that a sharp peak appears at the point of $x = 7$ and large overshoots exist near the peak. From this scene, we can ensure that a concentrated load exists there. However, the peak value differs very much from the exact value of 1. This occurs because the obtained value of q is expressed as a distributed load. Therefore, it is necessary to take attention that $q(s)$ must be integrated to identify the magnitude of the concentrated load. (This means that it is essentially impossible to distinguish a concentrated load from a distributed one in a very narrow range by only once identification using this analysis scheme. But in most cases, the integration will not be needed because practically most loads have a definite distributed range and therefore can be regarded as a distributed one. However, it will not be mentioned further.) From the above, the value of concentrated load (which may be the resultant force of distributed load in a very narrow range) is decided by the following equation in this analysis scheme:

$$F = \int_a^b q(\xi) d\xi \tag{9}$$

This equation can be integrated easily by Eqn.8, and the concrete expression can be obtained.

Table 1: Calculated load magnitude (Exact is 1)

Integration range	Integrated value
$6.8 \leq x \leq 7.2$	1.1423
$6.6 \leq x \leq 7.4$	0.9511
$6.4 \leq x \leq 7.6$	1.0205
$0.0 \leq x \leq 10.0$	0.9999

The magnitude of the concentrated load which was calculated by Eqn.9 for result of Figure 2 is shown in Table 1. Though the error is a little large in the range disturbed by overshoots, yet it is good enough as a estimated value. And, if we integrate it throughout the whole range, the value should become 1 because of the equilibrium condition of the force, as shown in the Table 1, so the extremely accurate value can be obtained.

2.2 *Identifying distributed load and its re-identifying*

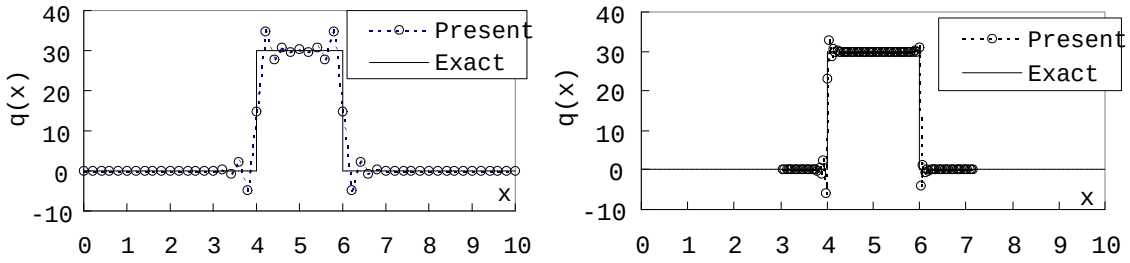

(a) Primary identification (b) Secondary identification

Figure 3: Refined identification of a localized quadratic distributed load

The left graph of Figure 3 is the identified result in the case that a step-shaped distributed load with strength of 30 exists in the range of $4 \leq x \leq 6$. Similar to the previous example, though rather large overshoots occur near $x = 4$ and $x = 6$ where the value changes abruptly, it is a very good identification as a whole. It seems that to avoid this overshoot is impossible, yet the error can be restrained to a small enough range to meet with the needed accuracy in practical use. For example, we can re-arrange the source point over a narrower region where we suppose the load probably exist from the first calculation, or use the larger number of source point. The right graph of Figure 3 is the result when we use 99 point source over a range of $3 \leq x \leq 7$. Compared to the left one, the outlook of the step is identified more clearly and the overshoots near the step becomes smaller, too.

Figure 4 is the result for two distributed loads, namely, a step-shaped linearly distributed load expressed by $q(x) = -x + 13$ is applied in the range of $1 \leq x \leq 5$, and a step-shaped constant distributed load with the magnitude of 2 is applied in $6 \leq x \leq 9$. This shows that each distribution can be identified with the accuracy as good as that in the case when each distribution is applied individually.

As shown in the above, it is proved that the load can be identified accurately by the method of this study without any assumptions such as those of the kind of load, the number of load and applied position.

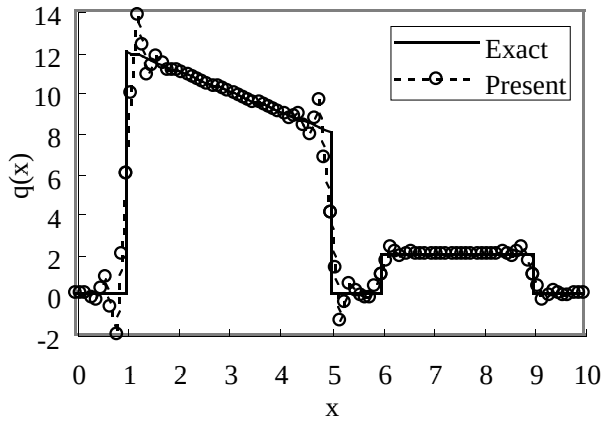

Figure 4: Identification of two distributed loads

2.3 ***Influence of order n of Nabla-operator and other boundary conditions***

All of the above results are obtained using equation of $n = 2$. If it is done with the equation of $n = 4$, the accuracy will be better. However, there is not so much difference as a whole because the overshoot near a step cannot be eliminate and the accuracy in the case of $n = 2$ is sufficient enough.

In all mentioned examples, the simple support boundary condition is used. Figure 5 is a problem which a beam has a roller at $x = 0$ and be fixed at $x = L$, the load distribution is shown in the figure. The behavior of the results is almost as same as in the (a) of Figure 3. So we can say that the difference in boundary condition has no influence to the new method.

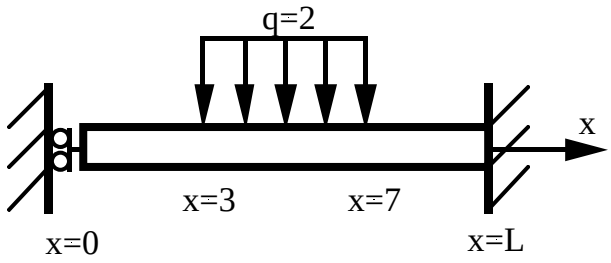

Figure 5: Analysis model with another boundary condition

CONCLUSIONS

In this paper, the discrete integral method utilizing the delta function was applied, and a new scheme to analyze the inverse problem using this method was demonstrated. In this report, identification problem of external load distribution on homogeneous beam was treated as an example of one dimensional inverse problem. By this analysis scheme, external load distribution can be identified accurately and naturally without any assumptions such as those of the kind of load, the number of load, and applied position. Further, the scheme is applicable to various boundary conditions. However, when the load to be identified is a concentrated one or has a steep change, the overshoot appears, and the errors apt to become larger round the edging point. It is possible to consider a practical scheme such as a re-identification using the result of the first identification to improve the accuracy. This analysis scheme can be expanded easily to a continuous beam.

The cases that ideal condition of identification can be instituted are treated in this paper. However, even for those problems with more complicated conditions, or of ill-conditions appeared in practical case, we consider that effective schemes can be developed based on the consideration of this analysis scheme.

References

[1] Kubo.(1998). "*Inverse Problem*", Baifu-Kan, Japan.

[2] Chrles W. Groetch.(1996) Translated by Kaneo and so on, "*Inverse Problem in Mathematical Science*", Separate Volume: Mathematical Science, Science-Sha, Japan.

[3] H. Kisu, G. Rong and C. Huang.(1999). In: *Advances in Engineering Software*, Vol. 30, No. 5, pp. 339-346, R.A. Adey, A.K. Noor and B.H.V. Topping (Eds). Elsevier, Oxford.

[4] H. Kisu and G. Rong. (2000). In: *JSME International Journal: Solid Mechanics and Material Engineering*, Series.A, Vol.43, No.3, pp. 268-274, *JSME*, Japan.

A NEW EXPERIMENTAL TECHNIQUE FOR DETERMINING THE FRACTURE ENERGY OF WOOD UNDER MODE II LOADING CONDITIONS

K. Frühmann[1], E.K. Tschegg[2] and S.E. Stanzl-Tschegg[1]

Christian Doppler Laboratory for Fundamentals of Wood Machining at the Institute of Meteorology and Physics, University of Agricultural Sciences, A 1180 Vienna, Austria
Material Science Laboratory, Institute of Applied and Technical Physics, Vienna University of Technology, A 1040 Vienna, Austria

ABSTRACT

Wood is a highly optimised natural composite material suitable for a number of different applications. Its orthotropic and inhomogeneous structure and non-linear behaviour during fracture leads to various differences in a fracture mechanical description compared to other materials. This study presents a new experimental technique for recording the complete load-displacement diagram for mode II loading conditions under stable crack-propagation. It allows the determination of various fracture mechanical parameters including stiffness, strength and specific fracture energy as well as an assessment of the fracture behaviour until complete separation of the specimen. The experiment is suitable for any crack propagation system in wood and requires only few raw material for specimen preparation which is advantageous for statistical significance and can be performed on any conventional testing machine. The experimental data of a first test series performed on spruce wood (*Picea abies* [L.] Karst.) in the RL (radial-longitudinal) direction is presented and compared with results in literature. The "size effect" is taken into consideration. Based on the experimental fracture mechanical data and fractographic observations in a light microscope and an Environmental Scanning Electron Microscope (ESEM) some basic principals of mode II fracture in wood are discussed and compared to other loading cases.

KEYWORDS

spruce wood, mode II loading, orthotropy, specific fracture energy, stable crack propagation, damage zone;

INTRODUCTION

Wood is a highly optimised and complex material being a multi-level fibre composite mainly consisting of tubular cells of 3-4 mm length and about 30 µm diameter oriented in the longitudinal direction of the stem. Seasonal differences in vegetation are causing repetitive gradual changes of the fibre-properties which are forming growth rings in the stem. The growth rings are causing a structure of

cylindrical orthotropy with three principal directions termed L (longitudinal, along the axis of the stem), R (radial) and T (tangential). In terms of a mechanical and fracture mechanical description anisotropy, hierarchic and cellular structure cause substantial differences compared to metals or artificial composite materials and require the modification of established concepts for describing fracture and crack propagation especially those using LEFM principles [1, 2, 3]. Recording the load and displacement data for a fracture mechanical experiment under conditions of stable crack propagation was found to be a very powerful method to investigate the fracture behaviour of wood. Material parameters like elasticity, fracture toughness or global strength as well as the energy consumed during the fracture process can be derived from the load displacement curves. Especially the determination of energy portions assigned to the different phases of crack propagation provides useful information about the fracture process itself.

To obtain load and displacement data it is necessary to apply experimental techniques which guarantee stable crack propagation until the complete separation of the specimen. For the mode I loading case a experimental technique was developed and applied to obtain fracture mechanical data for several wood species [4]. There is less information about in plane shear fracture of wood and only a few studies dealing with stable crack propagation under mode II loading conditions are available in literature [5, 6, 7]

The aim of this study is to present a new experimental procedure to record load and displacement data of fracture mechanical experiments on spruce wood (*Picea abies* [L.] karst.) under mode II loading conditions until ultimate fracture. The results of a first test series are described and some principal differences between mode I and mode II fracture are discussed.

EXPERIMENTAL TECHNIQUE

Specimen

A new technique has been developed using a notched bending beam (NBB) specimen as shown in Figure 1a. A beam fixed on one side and supported on the other is loaded by a single load close to a necked down cross section close to the support generating a vertical shear stress. After applying a sufficiently high vertical force a crack will start propagating throughout the cross section (ligament) until the pieces are separated. The fixed part is generating an elastic bending moment acting against the applied load which is preventing a too fast transfer of the energy elastically stored in the specimen and therefore supporting slow and stable crack propagation.

The experiments were performed on a conventional material testing machine which was equipped with the devices for fixing the beam at constant cross head displacement rates. Force and displacement are measured with a load cell and linear displacement sensor and recorded on a PC for later evaluation.

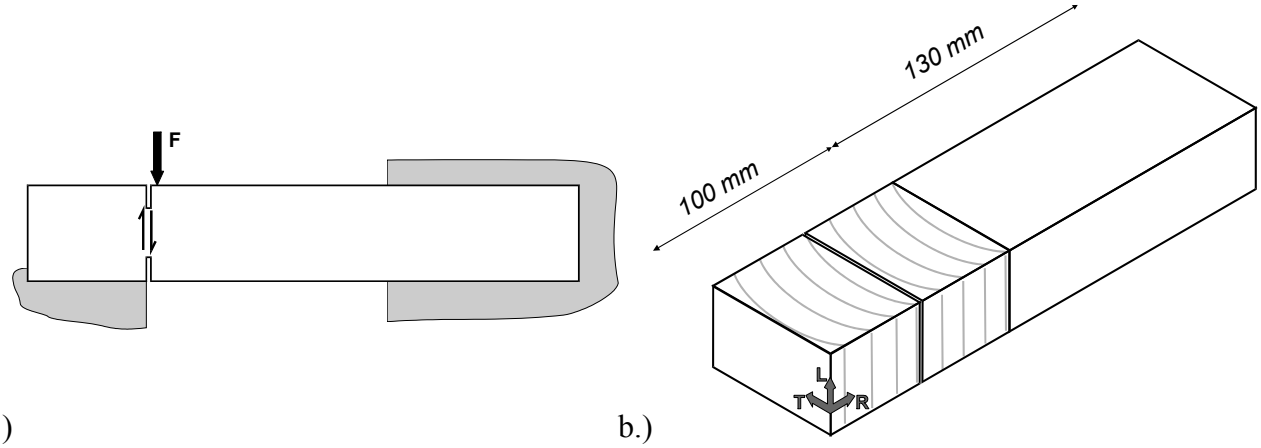

a.) b.)

Figure 1: (a) Principle of the notched beam specimen; (b) geometry of the notched beam specimen consisting of a bending part and a notched specimen part

The NBB specimen is made of two parts of clear spruce wood and has a total length of 230 mm and a cross section of 60×40 mm. The actual specimen part is 100 mm long and shows a RL crack propagation system where the first letter (R) indicates the direction of the crack plane normal and the second one (L) indicates the direction of crack propagation. The 130 mm long bending part is glued to the specimen part as shown in figure 1b. The rectangular ligament was cut with a band saw shortly before performing the experiment.
All pieces were obtained from a conventional board with an average density of 440 kg/m³ and stored until testing in an environment of 22°C and 60% relative humidity.
Tests with four different rectangular ligament areas between 400 and 720 mm² were performed.. Additional test series were carried out with a trapezoid ligament of 1.300 mm² to investigate the influence of ligament shape on the characteristic parameters. To obtain significant results when experimenting with wood an adequate number of experiments is required. Therefore the comparably low amount of raw material needed for these test series is advantageous. The number of replications for these tests was chosen to be eight for each of the five tested ligament geometries.

RESULTS

Load-displacement diagrams

Figure 2 shows an example for a typical load-displacement diagram. The upper curve represents the measured data for a sample of 720 mm². It includes also the load which is carried partly by the bending beam and doesn't influence the fracture process itself but need to be considered before analysis. To obtain the net load-displacement curve the elastic load-displacement behaviour of the beam was measured separately after the experiment and subtracted from the original data. The negative values for load and displacement are indicating compressive loads during the experiment.
At the beginning of the experiment the notched beam bending specimen shows a linear elastic behaviour followed by a short phase of non-elastic behaviour indicated by some deviation from the straight line before reaching the maximum load. After passing the maximum load some further energy consumption appears which is accompanied by a steep decrease of load and finally the complete fracture of the specimen as soon as the load reaches a plateau value. This plateau is caused by friction between the fractured surfaces which is still transmitting load between the two already separated specimen parts.

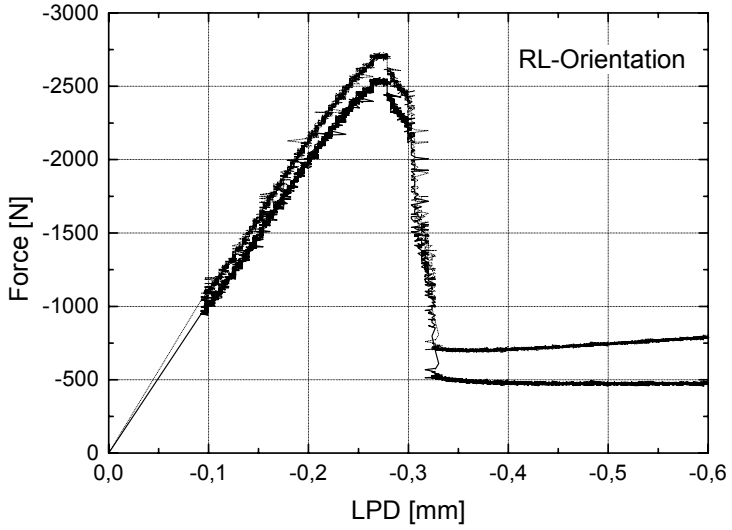

Figure 2: Typical load/displacement diagram showing original (upper curve) and net data (lower curve)

Fracture mechanical parameters

Analysing the load displacement curves several mechanical and fracture mechanical parameters can be derived. Among these the specific fracture energy is the most important one. It represents the total energy consumption during the fracture process related to the created fracture area and is determined according to Eqn. 1

$$G_f^{II} = \frac{1}{A_{lig}} \int_0^{LPD_{end}} F(LPD)dLPD\,. \tag{1}$$

Where A_{lig} is the ligament area and *F(LPD)* indicates the load versus load-point displacement. Although this characteristic parameter is related to the ligament area there are significant differences for the tested series showing an increase with growing fracture areas and a decrease for the biggest but trapezoid-shaped ligament (Figure 3).

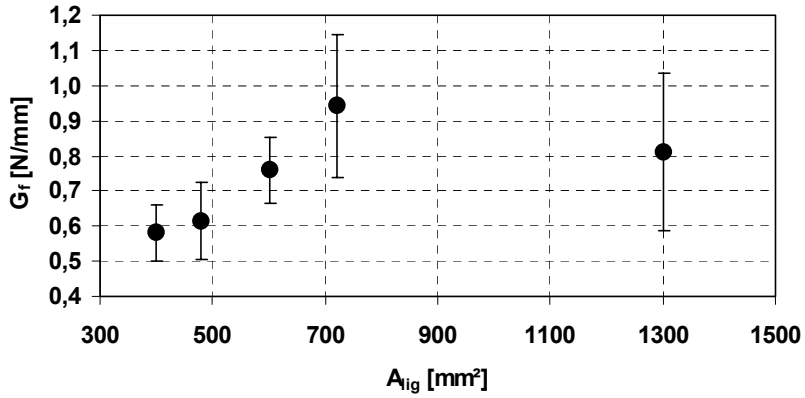

Figure 3: Specific fracture energy (G_f^{II}) versus Ligament area (A_{lig}).

DISCUSSION

Comments on testing method, Relevance of results

The results of this study demonstrate that the NBB specimen is appropriate to determine the characteristic parameters for mode II fracture mechanical experiments. The experiment is advantageous especially in comparison with other systems proposed in literature [4,5] because of its low consumption of raw material and its applicability for all six crack propagation systems in wood using the same geometry.

The decrease of load after passing the maximum load is sufficiently slow to collect enough data in this phase and to call crack propagation sufficiently stable and the specific fracture energy together with other fracture mechanical parameters can be calculated. Figure 3a shows the mean value of the specific fracture energy for all test series performed in this study compared to some results for spruce wood reported in the literature. (The results reported from Aicher *et al.* [7] vary depending on the evaluation method chosen for the experiment.)

The average specific fracture energy of 0,74 N/mm obtained in this study seems to be reasonable in comparison to other experiments especially regarding the comparably low ligament areas which have been considered for the mean value of the test series. In spite of the partly substantially bigger ligament areas of some of the experiments, the G_f^{II}–values of 0,94 N/mm and 0,81 N/mm for the biggest tested ligaments in this study are clearly in the range of the reported values which supports the assumption that the specific fracture energy is size independent for ligaments greater than 1.000 mm. However, a detailed investigation of this phenomenon has still to be done.

Compared to the other loading cases spruce wood fractured under mode II loads shows an about three times bigger specific fracture energy than under mode I loads whereas it is about 60% of G_f under mode III loading conditions (Figure 3b). The higher specific fracture energy indicates a less efficient fracture process for mode II cases compared to mode I fracture which can be seen also from the ESEM photographs of a mode II fracture surfaces. extruded fibres and parts of the longitudinal tracheids cover the surface and indicate substantial intracellular structural damage whereas mode I fracture surfaces were found to be smooth and less hairy [5]. The possible differences are discussed in the next paragraph.

Mode II fracture behaviour of wood

The fracture process of wood under mode II conditions is different to mode I loading conditions. In the later case the applied load generates a zone around the crack tip where the local material strength is exceeded and damage occurs. In this damage zone several micro cracks are formed and weaken the material until some of those micro-cracks join and form a macroscopic crack which is propagating. The damage zone has a finite extend and therefore a distinct crack tip within this volume cannot be determined exactly in wood which makes the application of conventional fracture mechanic concept very difficult. The formation of micro-cracks is an energy dissipating process and the amount of generated micro-cracks as well as the dissipated energy is proportional to the extension of the damage zone. Increasing loads cause macro-crack propagation and therefore a permanent shift of the damage zone into zones of lower stresses and intact material forming a band of weakened and damaged material beside the macroscopic crack path.

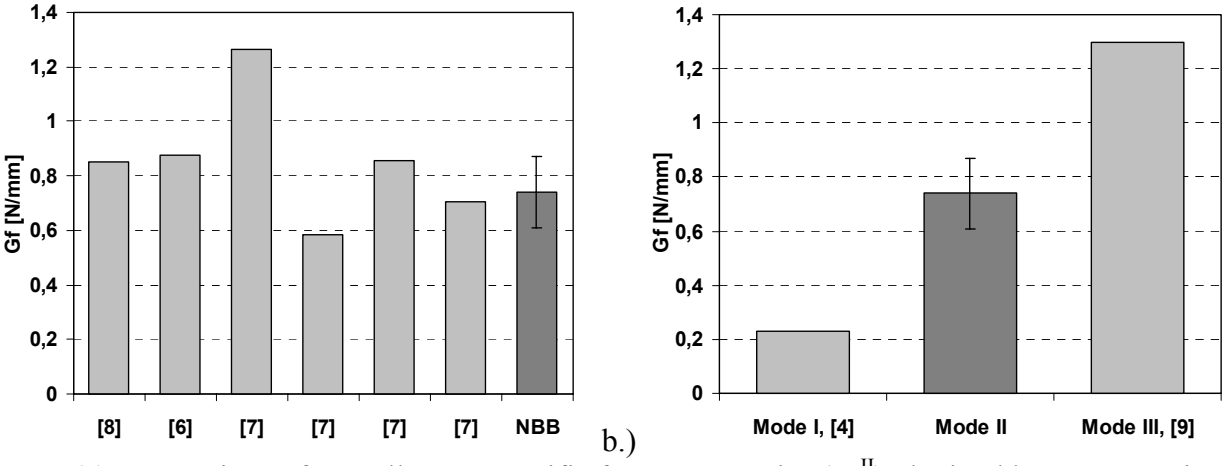

Figure 4: (a) Comparison of overall mean specific fracture energies (G_f^{II}) obtained by NBB specimens with values for spruce wood reported from literature [numbers]. (b) Mode II specific fracture energy (G_f^{II}) related to mode I and mode III loading conditions

In the mode II loading case the shear stresses along the complete ligament plane and not only in a small zone in front of the crack tip occur. The local material strength is exceeded in a much bigger volume ahead of the crack tip and micro-cracks are forming simultaneously in a much bigger damage zone now. It is also possible that additional macro-cracks are formed at different positions by those micro-cracks and growing independently of the actual macro-crack like shown in Figure 4b. Stanzl-Tschegg *et al.* [10] performed FEM analyses on mode II specimens for orthotropic materials and found the distribution of Mises equivalent stresses concentrated along the ligament which supports the assumption that the damage zone is elongated around the ligament plane.

The assumption of sudden and simultaneous wide spread damage in wood under mode II loads explains the steep load decrease after passing the maximum load in the load–displacement diagram. Once several micro-cracks exist the resistance for crack propagation is lowered drastically and the specimen can be separated easily contrary to the mode I loading case where a remarkable amount of energy is consumed during this last phase of crack propagation. Beginning with the deviation from the linear

elastic behaviour a complex fracture process is initiated where the various occurring effects do not appear necessarily in a sequential manner but happen simultaneously and de-localised.

a.) 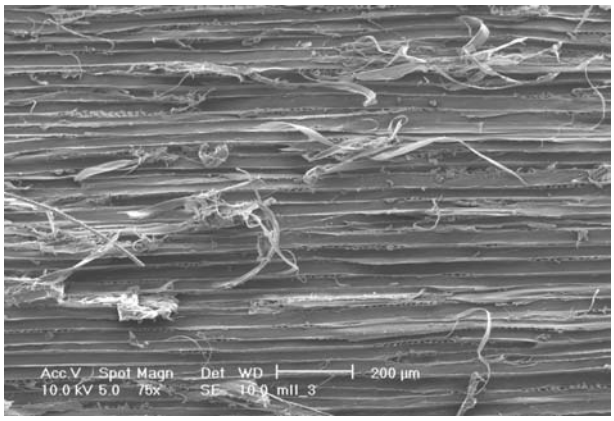

b.) 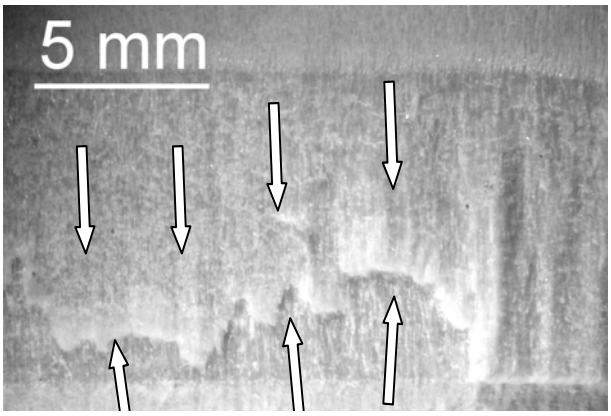

Figure 4: (a) ESEM image of mode II fracture surface of spruce wood; (b) Light microscopical image of mode II fracture surface. The arrows mark contrary crack propagation directions in different fracture planes.

CONCLUSIONS

A new testing method to study the fracture behaviour of wood under shear loads was developed and applied for a first test series on spruce wood in RL orientation.
Characteristic fracture mechanical parameters can be determined from the load-displacement diagrams recorded under sufficiently stable crack propagation. The specific fracture energy (G_f^{II}) can be calculated and shows results of 0,74 N/mm which is in reasonable accordance with values reported in the literature.
The mode II fracture process consumes more energy than the mode I case. The damage zone under mode II conditions is much bigger and extended along the ligament especially in an orthotropic material like wood. The mode II fracture process needs to be considered more as a cumulative event than a sequential procedure. A high stress along the entire ligament generates micro-cracks simultaneously and favours the formation of more than one macro-crack possibly with different propagation directions.

REFERENCES

1. Bodig, J. and Jayne, B.A., (1982) *Mechanics of wood and Wood Composites*. Van Nostrand Reinhold, New York.
2. Aicher, S., Reinhardt, H., (1993) *Holz als Roh- und Werkstoff* 51, pp 215-220
3. Barret, J.D., Foschi, R.O. (1977) *Engng. Fract. Mech.* 9, pp 371-378.
4. Stanzl-Tschegg, S.E., Tan, D.M., Tschegg, E.K., (1995) *Wood Science and Technology* 29, pp 31-50.
5. Tan D.M., Stanzl-Tschegg S.E. and Tschegg, E.K. (1995) *Holz als Roh- und Werkstoff* 53, pp 159-164.
6. Xu, S., Reinhardt, H.W., and Gappoev, M. (1996), *Int. J. of Fracture*, 75, pp 185-214
7. Aicher, S., Boström, L., Gierl, M., Kretschmann, D. and Valentin, G. (1997). *Determination of Fracture Energy of Wood in Mode II, RILEM TC 133 Report.* Swedish National Testing and Research Institute. SP Report 1997:13
8. Morel, S. and Valentin, G. (1996) *Journal de Physique IV, Colloque C6*, pp 385-394.
9. Ehart, R.J.A. (1998). Doctoral Thesis, Technical University of Vienna, Austria
10. Stanzl-Tschegg, S.E., Tan, D.M. and Tschegg E.K. (1996) *Mokuzai Gakkaishi* 42, pp 642-650.

ORAL/POSTER REFERENCE:ICF100724OR

A NEW MATERIAL MODEL AND ITS APPLICATION TO FRACTURE ANALYSIS IN FIBER PULL-OUT TESTS

S.E. Alexandrov, R.V.Goldstein, E.A. Lyamina

Institute for Problems in Mechanics, Russian Academy of Science,
Pr.Vernadskogo 101-1, Moscow, 117526, Russia

ABSTRACT

A new material model based on the assumption that the material consists of hard blocks and soft layers is proposed. In such materials, extensive plastic deformation develops within the soft layers whereas the blocks are rigid (elastic). The plastic deformation may lead to failure within layers. The dominated mode of deformation is shear. Assuming that the only non-zero deviatoric stress is a shear stress it is possible to obtain an analytical (semi-analytical) solution within the layer for quite an arbitrary constitutive law of the layer material. Using this solution the behavior of block/layer continuum may be described. To demonstrate the main features of the model the axisymmetric problem of the fiber pull-out is solved semi-analytically under simplified assumptions. In particular, the hard blocks and soft layers are circular cylinders of different thickness. The end effects are neglected. Based on these assumptions, the solution for arbitrary number of layers and blocks is given by induction. The material of the layers is assumed to be elastic/plastic, hardening. The evolution of damage is described by the Lemaitre law. The fracture condition is defined by a critical value of the damage variable. It is shown that the plastic zone develops in a jump-like manner and fracture initiates in the layer adjacent to the fiber. The displacement of the fiber at the initiation of fracture is determined. The effects of geometric and material parameters on the size of the plastic zone and fracture initiation are discussed.

KEYWORDS

pull-out test, elastic/plastic solids, composites, damage mechanics

INTRODUCTION

Studies of surfaces (including fracture surfaces) of samples of elastic/plastic materials demonstrated that at the micro- and meso scales zones of plastic deformations are alternated with zones of elastic deformation. In particular, it was shown in [1] that the process of deformation near interfaces consists of the formation of rigid blocks and thin zones where intensive straining occurs. This feature of the deformation process needs to be taken into account at evaluation of the limit deformation characteristics as well as fracture and damage parameters of structural elements. Note that such a deformation scheme is inherent to filled composites with compliant matrix and rigid inclusions at a high degree of filling.
The present paper is devoted to modeling of the aforementioned effect on the basis of a model proposed in [2] and its application to the analysis of fiber pull-out test.

MATERIAL MODEL

A general model for a continuum consisting of rigid blocks and elastic/plastic layers between the blocks has been proposed in [2]. Here the model is specialized to the case of anti-plane axisymmetric deformation using the assumption that all blocks are hollow cylinders with the same axis of symmetry. Then, all elastic/plastic layers are also hollow cylinders. Strains are small and are localized within the layers whereas the blocks can only move as rigid bodies along the axis of symmetry. A representative element of the continuum consists of an elastic/plastic layer and a rigid block adjacent to this layer as shown in Figure 1. Since another rigid block is adjacent to the layer at $r = a$, it is possible to assume,

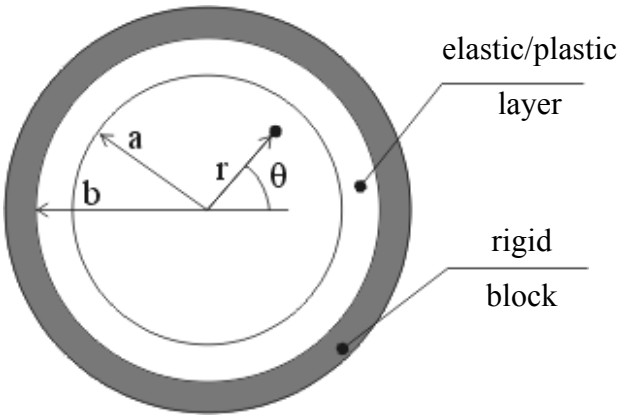

Figure 1: A representative element of the continuum

without loss of generality, that $u = -u_0 \ \ (u_0 > 0)$ at $r = a$ and $u = 0$ at $r = b$ where u is the axial velocity in the elastic/plastic layer. We will search for a solution with the only non-zero component of the stress tensor τ_{rz} in a cylindrical coordinate system whose z – axis coincides with the axis of symmetry of the blocks and layers. Then, for isotropic materials the only non-zero component of the strain tensor will be ε_{rz}. Using the definition for the equivalent strain and for the shear strain one can find

$$\varepsilon_{eq} = \left(2/\sqrt{3}\right)\varepsilon_{rz} = \left(1/\sqrt{3}\right)\partial u/\partial r \tag{1}$$

The only non-trivial equilibrium equation is $\partial \tau_{rz}/\partial r + \tau_{rz}/r = 0$ and its general solution is given by

$$\tau_{rz} = k_0 \rho / r \tag{2}$$

where k_0 is the initial shear yield stress and ρ is an arbitrary function of u_0.

If the entire layer is elastic then $\rho \le a$ and combining Eqn. 1, Eqn. 2 and Hooke's law leads to

$$\varepsilon_{eq} = \frac{1}{\sqrt{3}} \frac{k_0}{G} \frac{\rho}{r} \tag{3}$$

If the entire layer is plastic then $\tau_{rz} = k$ at each point of the layer. Here k is the current shear yield stress which is supposed to depend on the equivalent plastic strain ε_{eq}^{p} and a damage parameter D. A possible representation of this dependence is [3]

$$k = k_0 \left[1 + f\left(\varepsilon_{eq}^{p}\right)\right]\left(1 - D\right) \tag{4}$$

where $f\left(\varepsilon_{eq}^{p}\right)$ is an arbitrary function of ε_{eq}^{p} satisfying the following conditions, $df/d\varepsilon_{eq}^{p} > 0$ at any ε_{eq}^{p} and $f(0) = 0$. Since the hydrostatic stress vanishes, the damage evolution equation may be written in the form [3]

$$\dot{D} = \alpha \dot{\varepsilon}_{eq}^{p} \tag{5}$$

where the superposed dot stands for derivatives with respect to time and α is a material constant. For many materials $D = 0$ at $\varepsilon_{eq}^{p} = 0$ [3]. Using this condition, Eqn. 5 can be immediately integrated to give

$$D = \alpha \varepsilon_{eq}^{p} \tag{6}$$

Substituting Eqn. 6 into Eqn. 4 gives

$$k = k_0 \left[1 + f\left(\varepsilon_{eq}^{p}\right)\right]\left(1 - \alpha \varepsilon_{eq}^{p}\right) \tag{7}$$

Since $\tau_{rz} = k$, combining Eqn. 2 and Eqn. 7 results in

$$\rho / r = \left[1 + f\left(\varepsilon_{eq}^{p}\right)\right]\left(1 - \alpha \varepsilon_{eq}^{p}\right) \tag{8}$$

This equation determines ε_{eq}^{p} as a function of $\rho / r \equiv s$ in implicit form

$$\varepsilon_{eq}^{p} = \varphi(s) \tag{9}$$

Assuming that $\varepsilon_{eq} = \varepsilon_{eq}^{e} + \varepsilon_{pl}^{p}$, we arrive, with the use of Eqn. 3 and Eqn. 9, at

$$\varepsilon_{eq} = \varphi(s) + \frac{1}{\sqrt{3}} \frac{k_0}{G} s \tag{10}$$

If the elastic/plastic boundary is within the layer then its position is given by the equation $s = 1$, as follows from Eqn. 2. Therefore, the total equivalent strain is

$$\varepsilon_{eq} = m\varphi(s) + \frac{1}{\sqrt{3}} \frac{k_0}{G} s \tag{11}$$

where $m = 0$ at $s \le 1$ and $m = 1$ at $s > 1$. Thus Eqn. 2, Eqn. 3, Eqn. 10, and Eqn. 11 determine the dependence of τ_{rz} on ε_{eq} in the representative element in parametric form.

FIBER PULL OUT TEST

Neglecting end effects, fiber pull out test can be considered as an anti-plane problem. The fiber of radius r_f is assumed to be rigid. Its velocity is w_f ($u = -w_f$ at $r = r_f$). The material around the fiber is modeled by the continuum described in the previous section. It is assumed that $u = 0$ at $r = R_{max}$. The region $r_f \le r \le R_{\max}$ consists of N representative elements. The geometry of the element i is defined by $a = r_i$ and $b = R_i$ (Figure 1). Also, we will use the nomenclature $u = -w_i$ at $r = r_i$. Hence $r_1 = r_f$,

$R_N = R_{\max}$ and $w_1 = w_f$. The equivalent strain in each representative element is given by Eqn. 11. Since $\partial u/\partial r = -\left(s^2/\rho\right)\partial u/\partial s$, substituting Eqn. 11 into Eqn. 1 gives

$$u^{(i)} = -\rho \int_{\rho/r_i}^{\rho/r} \frac{\left[\sqrt{3} m \varphi(s) + k_0 s/G\right]}{s^2} ds - w_i \quad \text{at} \quad r_i \le r \le R_i \tag{12}$$

where $u^{(i)}$ is the velocity in the layer of the element *i*. Due to the continuity of velocity, Eqn. 12 leads to

$$w_{i+1} = \rho \int_{\rho/r_i}^{\rho/R_i} \frac{\left[\sqrt{3} m \varphi(s) + k_0 s/G\right]}{s^2} ds + w_i \tag{13}$$

Using Eqn. 13 it is possible to show by induction that

$$w_f = \rho \sum_{i=1}^{N} \int_{\rho/R_i}^{\rho/r_i} \frac{\left[\sqrt{3} m \varphi(s) + k_0 s/G\right]}{s^2} ds \tag{14}$$

where we have taken into account that $u = 0$ at $r = R_N$. The solution to Eqn. 14 determines the variation of ρ with w_f. Let r_* be the radius of the elastic/plastic boundary. It follows from Eqn. 2 that $r_* = \rho$ if ρ is within one of the intervals $r_i \le \rho \le R_i$. However, if $R_i \le \rho \le r_{i+1}$ then $r_* = R_i$. Therefore, the plastic zone develops in a jump-like manner. The damage parameter attains its maximum value at $r = r_f$. Using Eqn. 6 and Eqn. 11 at $s = \rho/r_f$ it is possible to find *D* at $r = r_f$ as a function of ρ in the following form

$$D = \alpha \left[\varphi\left(\frac{\rho}{r_f}\right) + \frac{1}{\sqrt{3}} \frac{k_0}{G} \frac{\rho}{r_f} \right] \tag{15}$$

Eqn. 14 and Eqn. 15 give the variation of *D* at $r = r_f$ with w_f in parametric form. In particular, assuming that $D = D_c$ the displacement of the fiber at which fracture starts, $w_f = w_f^{(f)}$, can be found.

NUMERICAL RESULTS AND CONCLUSION

The solution to Eqn. 14 has been found assuming that $r_f = 1$ (without loss of generality), $R_{\max} = 1.46$, $r_i = 1 + (i-1)(h+\delta)$, $R_i = 1 + h + (i-1)(h+\delta)$, $f\left(\varepsilon_{eq}^p\right) = 1.072\varepsilon_{eq}^p$, $\alpha = .3$, and $k_0/G = 3.3 \cdot 10^{-3}$. The mechanical properties are typical for a structural steel [4]. Figure 2 illustrates the development of the plastic zone with the displacement of the fiber. It is important to mention that the solution breaks down at $w_f = w_{\max}$. The same result has been obtained in [5, 6]. It is possible to show that this feature is independent of the hardening law and other material and geometric parameters involved in the calculation performed. Differentiating Eqn. 8 with respect to time at $r = r_f$ gives

$$\dot{\rho}/r_f = \left\{\left(df/d\varepsilon_{eq}^p\right)\left(1 - \alpha\varepsilon_{eq}^p\right) - \alpha\left[1 + f\left(\varepsilon_{eq}^p\right)\right]\right\}\dot{\varepsilon}_{eq}^p \tag{16}$$

For the plastic zone to develop at the initial instant, $\varepsilon_{eq}^p = 0$, it is necessary that $\dot{\rho} > 0$ and $\dot{\varepsilon}_{eq}^p > 0$. Using Eqn. 16 this necessary condition can be written in the form

$$df/d\varepsilon_{eq}^{p} > \alpha \quad \text{at} \quad \varepsilon_{eq}^{p} = 0 \tag{17}$$

If this inequality is not satisfied then no solution exists (the elastic solution does not exist because the

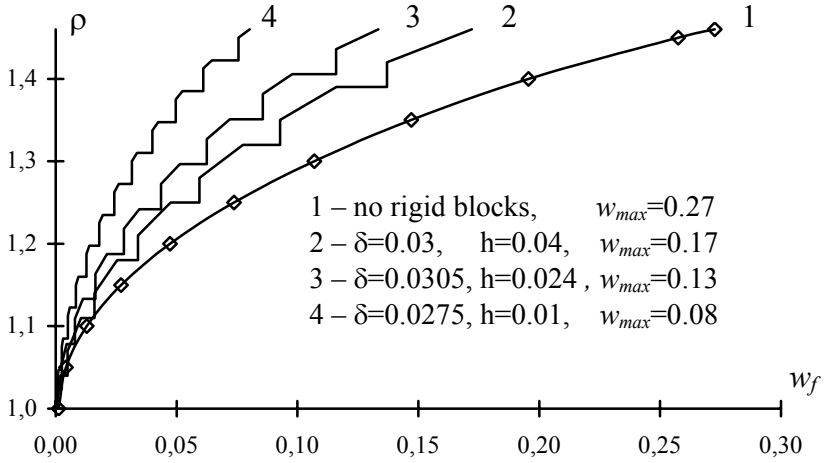

Figure 2: Variation of the elastic/plastic radius, ρ, with the displacement of the fiber, w_f

initial yield stress is attained, and the elastic/plastic solution does not exist because the plastic zone cannot develop). Assume that Eqn. 17 is satisfied. Then,

$$\left(df/d\varepsilon_{eq}^{p}\right)\left(1-\alpha\varepsilon_{eq}^{p}\right)-\alpha\left[1+f\left(\varepsilon_{eq}^{p}\right)\right]>0 \quad \text{at} \quad \varepsilon_{eq}^{p}=0 \tag{18}$$

On the other hand, it is clear that

$$\left(df/d\varepsilon_{eq}^{p}\right)\left(1-\alpha\varepsilon_{eq}^{p}\right)-\alpha\left[1+f\left(\varepsilon_{eq}^{p}\right)\right]<0 \quad \text{at} \quad \varepsilon_{eq}^{p}=1/\alpha \tag{19}$$

Therefore,

$$\left(df/d\varepsilon_{eq}^{p}\right)\left(1-\alpha\varepsilon_{eq}^{p}\right)-\alpha\left[1+f\left(\varepsilon_{eq}^{p}\right)\right]=0 \quad \text{at} \quad \varepsilon_{eq}^{p}=\varepsilon_{\max} \tag{20}$$

where $0<\varepsilon_{\max}<1/\alpha$. It follows from Eqn. 7 that k reaches its maximum value, $k_{\max}$, at $\varepsilon_{eq}^{p}=\varepsilon_{\max}$. Consider a possibility to obtain a solution if $\varepsilon_{eq}^{p}=\varepsilon_{\max}$ at a point $r=r_m$ of the interval $r_f<r<R_{\max}$. The distribution of k is shown schematically in Figure 3 (solid line). The plastic solution in the interval $r_f \le r \le r_m$ cannot exist because k is an increasing function of r (Figure 3) whereas τ_{rz} is a decreasing function of r, as follows from Eqn. 2, but $\tau_{rz}=k$ in the plastic zone. The elastic solution in the interval $r_f \le r \le r_m$ (dot line in Figure 3) cannot exist because τ_{rz} is a decreasing function of r and, therefore, $\tau_{rz}>k$ at $r<r_m$ that violates the yield criterion. Therefore, the solution breaks down if ε_{eq}^{p} attains the value of $\varepsilon_{\max}$ at $r=r_f$. Of course, it is possible that fracture occurs at $\varepsilon_{eq}^{p}<\varepsilon_{\max}$. However, since the critical value of damage, D_c, is an independent parameter, it is important to account for the possibility that the solution breaks down in numerical calculations. In particular, in the case of the material under consideration $w_{\max}=w_{\max 2}=0.13$ at $h=0.024$ and $\delta=0.0305$. The corresponding dependence D of ρ at $r=r_f$ found from Eqn. 14 and Eqn. 15 is shown in Figure 4 (solid line), and $D=0.33$ at $w=w_{\max}$. Since $D_c=0.22$ [4] for this material, fracture occurs at $w_f<w_{\max}$. However, for a material with a lower

strain-hardening modulus, say $a = 0.5$, $D = 0.18$ at $w_f = w_{\max 1} = 0.016$ (dot line in Figure 4, $h = 0.006$, $\delta = 0.004$). In this case the fracture condition is nowhere satisfied at $w_f = w_{\max}$ and the solution cannot be extended for $w_f > w_{\max}$.

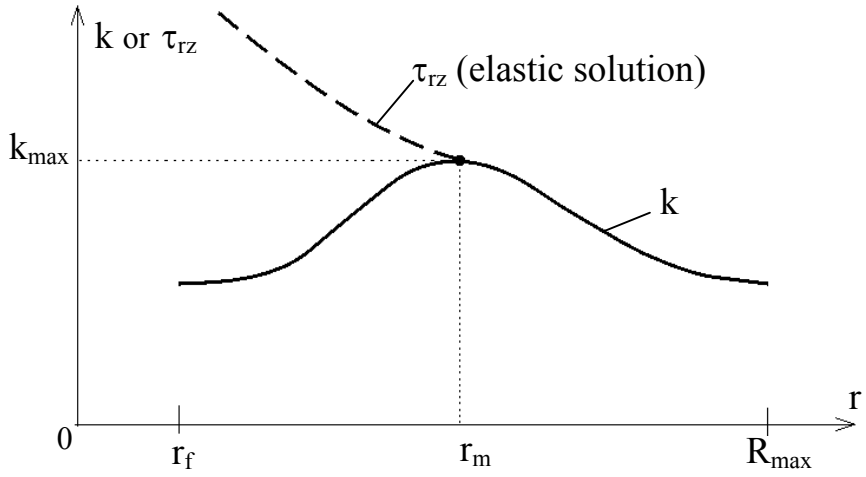

Figure 3: Schematic diagram illustrating non-existence of solution

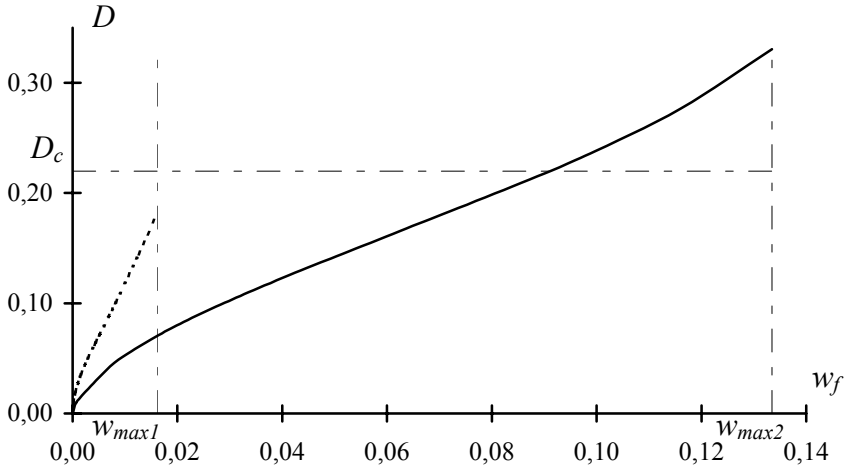

Figure 4: Evolution of the damage variable at $r = r_f$

Acknowledgement

This research was supported by the Russian Foundation for Basic Research (Grants 99-01-00926, 00-15-96066).

References

1. Panin, V.E. (1998). *Physical mesomechanics,* 5,22.
2. Alexandrov, S. and Goldstein, R.V. (1999). *Sov. Phys. Dok*. 368(6), 768 [in Russian].
3. Lemaitre, J. (1987). In: *Continuum Damage Mechanics: Theory and Applications*, pp. 37-89, Krajcinovic, D. and Lemaitre, J. (Eds). Springer, Wien - New York.
4. Prahl, U., Aboutayeb, M., Achenbach, U. and Wang, X. (1999). *Comp. Mater. Sci.* 16, 206.
5. Alexandrov, S. and Goldstein, R.V. (1999). *C. R. Acad. Sci*. Ser. IIb 327, 193.
6. Alexandrov, S. and Goldstein, R.V. (2000). *J. Appl. Math. Mech*. 64, 155.

A NEW NONLOCAL FRACTURE CRITERION

S. V. Suknyov

Institute of Physical-Technical Problems of the North, 677891, Yakutsk, Russia

ABSTRACT

The paper considers the problem of strength of a body containing an artificial flaw of a definite size and shape. The following questions are formulated: What is the range of allowable dimensions of a flaw of a given shape, which will not lead to the reduction in the strength of a body? How much will be the strength reduction in case when the flaw dimensions exceed the allowable ones? The known nonlocal fracture criteria such as the average stress criterion, the point stress criterion and the fictitious crack criterion can not be used for solving the linked problem of critical loading and critical size of a flaw stated above. To solve this problem the approach is suggested according to which the strength of a material in the stress concentration zone (local strength) is assumed to be dependent on its size. The corresponding fracture criterion is proposed. It is applied to estimating the tensile strength of composite laminates weakened by a single circular hole; the tensile strength of high strength steel bars with a circumferential notch and the tensile strength of polymethylmethacrylate plates with an angled elliptic hole. The expressions for the local-strength function and the failure stress are obtained and good agreement is found between the results of calculations and known experimental data.

KEYWORDS

Strength, brittle fracture, nonlocal criteria, stress concentration, size effect.

INTRODUCTION

The traditional approach to strength calculations is to compare the internal stresses, which occur in a loaded body with their limiting values. The strength condition has the form $\sigma_e < \sigma_0$, and failure occurs when

$$\sigma_e = \sigma_0, \tag{1}$$

where $\sigma_e = f(\sigma_{ij})$ and $\sigma_0 = \text{const}$. The equivalent stress σ_e characterizes the internal stress state of the body and is a function of the stress-tensor components σ_{ij} in the general case. The ultimate stress σ_0 characterizes the average mechanical properties of the body's field and it is assumed to be a material constant. So σ_0 is determined under conditions of the uniform stress state (for example, in uniaxial tension of unnotched specimen). In the traditional approach, strength of a solid in a given point is characterized by the value of equivalent stress in the same point without consideration of the stress state in neighboring points. This is the essence of so-called local strength conditions and corresponding local fracture criteria. They give a good description of experimental data when macro-stress variations are small enough on

dimensions of the order of the material structure scale. In other words, the range of application of the traditional approach is restricted to the cases where the dimension of the stress-uniformity zone is quite large to consider that $\sigma_0 = \text{const}$.

The nonlocal strength conditions and fracture criteria have recently been developed intensively [1–5]. The general approaches have been elaborated and the particular problems of strength of a body containing a stress concentrator have been considered. The general feature of nonlocal fracture criteria consists in the introduction of the characteristic length into the function of equivalent stress. That allows to describe the size effect on the strength of a body with a stress concentrator. The ultimate stress is assumed to be a material constant in nonlocal criteria as well as in traditional ones.

As a whole, the nonlocal criteria describe well the fracture initiation in the stress concentration zones. However, in some cases, their use gives rise to contradictory results. In particular, any small flaw located in a body gives rise to strength reduction according to the nonlocal fracture criteria. It is contrary to the modern knowledge about the real solid containing the pre-existing flaws inherent to it. Because of the inherent flaws existence, the small artificial flaws of the size comparable with the size of the inherent ones don't affect on the strength of a body until they rich a definite (critical) size [6–8].

PROBLEM STATEMENT

Consider a linearly elastic body of a brittle material containing an artificial flaw of a definite size and shape subjected to uniform loading. The following questions are formulated: What is the range of allowable dimensions of a flaw of a given shape, which will not lead to the reduction in the strength of a body? How much will be the strength reduction in case when the flaw dimensions exceed the allowable ones?

FRACTURE CRITERION

To solve this problem the approach is suggested [9], the essence of which is to assign the mechanical properties to a certain stressed region of finite dimensions rather than to the material as such, in contrast to the traditional and known nonlocal approaches. This means, in particular, that the strength of a material in the stress concentration zone (local strength) depends on its size.

The size of the highly stressed region is denoted by L_e; if it is quite large compared to the dimensions of the microstructural components of the material, including the inherent flaws, i.e., the conditions of averaging of the mechanical properties are satisfied, the value of the local strength differs little from σ_0. On the contrary, if L_e is comparable with the dimensions of the microstructural components, their influence on the local strength becomes noticeable. This influence is the stronger, the smaller the size L_e relative to the characteristic length of the material L_0. Thus, the local strength of the material should depend not only on the size of the highly stressed region L_e but also on the ratio L_0 / L_e. The fracture criterion can be stated as follows: The failure of a macroelement at the notch root is governed by the size of a highly stressed region to characteristic length of a material ratio. With allowance for this, we write the fracture criterion

$$\sigma_e = f(\sigma_0, L_0 / L_e). \tag{2}$$

Consider a tensile loaded body containing a smooth symmetrical stress concentrator as a basic problem for determining the local-strength function $f(\sigma_0, L_0 / L_e)$. Stress concentrator becomes a crack when $K_t \to \infty$ (K_t is the stress concentration factor). Asymptotic analysis of the critical (failure) stress $\sigma_c = f(\sigma_0, L_0 / L_e) / K_t$ behavior results in follows requirements:

$$\sigma_c = \sigma_0, \quad \text{for } K_t = 1; \tag{3}$$

$$\sigma_c \to \text{const} > 0, \quad \text{for } K_t \to \infty. \tag{4}$$

The requirement (3) ensures the transition of the nonlocal to the traditional criterion in the case of the uniform stress state. The requirement (4) ensures the relation between the nonlocal criterion and linear elastic fracture mechanics (LEFM). A constant in expression (4) depends on the cracking resistance of a material and the crack size and shape. We present the critical size of the flaw l_c in the form

$$l_c = l_0\left(1+\frac{\beta}{K_t}\right), \quad \beta \geq 0, \tag{5}$$

where l_0 is the critical size of the crack and β is a numerical parameter. The physically consistent values of β lie in the domain $\beta \geq 0$.

Since the local stress distribution in considered problem depends on the curvature radius of the concentrator to a large extent than on other geometrical parameters; therefore, in the first approximation, one can use the curvature radius of the concentrator ρ at a dangerous point to estimate L_e. For estimation of L_0, the critical size of the flaw l_c is used. We present the function $f(\sigma_0, L_0 / L_e)$ in the form

$$f(\sigma_0, L_0/L_e) = \sigma_0 f(l_c/\rho). \tag{6}$$

Bearing in mind that the stress concentration factor is an increasing function of l/ρ (l is the size of the concentrator)

$$K_t = f_t(l/\rho), \tag{7}$$

it is easy to see that it suffices to use the function f_t as $f(l_c/\rho)$ to satisfy the requirements (3) and (4):

$$f(l_c/\rho) = f_t(l_c/\rho). \tag{8}$$

The function given by Eqn. (8) is unique because $\sigma_c = \sigma_0$ for $l = l_c$, for any ρ. Thus, with allowance for Eqns. (6) and (8), the nonlocal fracture criterion takes the form

$$\sigma_e = \sigma_0 f_t(l_c/\rho). \tag{9}$$

Therefore, the critical stress is determined by the expression $\sigma_c = \sigma_0 \dfrac{f_t(l_c/\rho)}{f_t(l/\rho)}$, and the ratio $\dfrac{f_t(l/\rho)}{f_t(l_c/\rho)}$ can be regarded as an effective stress concentration factor.

EXAMPLES OF FRACTURE CRITERION APPLICATION

A plate with an elliptic hole under tension

The stress concentration factor can be presented in the form [10]

$$K_t = 1 + \sqrt{\alpha l/\rho}, \tag{10}$$

where α is a numerical coefficient which depends on the elastic constants of a material and the dimensions of a plate. For an infinite isotropic plate $\alpha = 2$ [10] and for an infinite orthotropic plate $\alpha = \sqrt{E_1/E_2} - \nu_1 + E_1/(2G)$ [11], where E_1, E_2, ν_1 and G are the elastic constants. The local-strength function $f(\sigma_0, L_0/L_e) = \sigma_0\left(1+\sqrt{\alpha l_c/\rho}\right)$. The critical stress has the form

$$\sigma_c = \sigma_0 \frac{1+\sqrt{\alpha l_c / \rho}}{1+\sqrt{\alpha l / \rho}}, \quad \text{for } l > l_c; \tag{11}$$

$$\sigma_c = \sigma_0, \quad \text{for } l \le l_c. \tag{12}$$

The critical size l_c

$$l_c = \frac{2K_c^2}{\pi\sigma_0^2}\left(1+\frac{\beta}{1+\sqrt{\alpha l / \rho}}\right), \quad \beta \ge 0, \tag{13}$$

where K_c is the critical stress intensity factor. To obtain the lower limit for σ_c or l_c that would define the margin of safety, the parameter β should be taken equal to zero. If K_c is unknown then l_c is found experimentally. With allowance for Eqn. (10) we can write Eqn. (11) in the form

$$\sigma_c = \sigma_0\left(\frac{1}{K_t}+\sqrt{\frac{l_c}{l}}\left(1-\frac{1}{K_t}\right)\right). \tag{14}$$

Eqns. (10)–(14) are also applicable to concentrators of non-elliptic shape, for which one can introduce the notion of equivalent elliptic hole or equivalent elliptic notch [10]. The latter concerns both flat and cylindrical specimens with a circumferential notch, including a V-shaped notch with a small opening angle.

An isotropic plate with angled elliptic hole under tension

Consider an isotropic plate with an elliptic hole, which is oriented at an angle ω to the direction of loading. The local-strength function for the basic problem in symmetric tension $\left(\omega = \frac{\pi}{2}\right)$ has the form

$$f(\sigma_0, L_0 / L_e) = \sigma_0\left(1+\sqrt{2l_c / \rho}\right). \tag{15}$$

The critical stress is determined by the expression

$$\sigma_c = \min\left\{\frac{f(\sigma_0, L_0 / L_e)}{\sigma_e / \sigma}\right\} > 0, \tag{16}$$

where σ is the tensile stress applied to the plate. We assume that failure determined by normal tensile stresses, i.e., $\sigma_e = \sigma_\theta > 0$ (σ_θ is the tangential stress on the hole boundary). The problem of σ_c determination is to find the minimum

$$\sigma_c = \min\left\{\sigma_0 \frac{1+m^2-2m\cos 2\theta+\sqrt{2l_c(1-m)/a}\,(1+m)(1+m^2-2m\cos 2\theta)^{1/4}}{1-m^2+2m\cos 2\omega-2\cos(2\theta-2\omega)}\right\} > 0. \tag{17}$$

Here the well-known expression for the stress σ_θ on the boundary of an elliptic hole [12] and the expression for the curvature radius of the hole boundary $\rho_\theta = a\frac{(1+m^2-2m\cos 2\theta)^{3/2}}{(1+m)^2(1-m)}$, where $m = \frac{a-b}{a+b}$; a and b are the major and minor semiaxes of the ellipse; θ is the varied parameter, were used.

COMPARISON BETWEEN PREDICTED AND EXPERIMENTAL DATA

Eqns. (14) and (17) for the critical stress, which were obtained on the basis of the nonlocal fracture criterion (Eqn. (9)), were used to estimate the strength of a plates with a circular or elliptic hole and bars with a circumferential notch subjected to uniaxial tension. The results of calculations are shown in Figs. 1–3.

A plate with a circular hole

Hyakutake, Hagio and Nisitani [8] tested quasi-isotropic FRP plates containing a circular hole of a different diameter. The critical stress variation with respect to the hole diameter given in Eqn. (14) is plotted in Fig. 1 (the solid curve) and compared with experimental data (points). The critical size (diameter) $l_c = 0.7$ mm was evaluated from best-fitting data. The dashed line was obtained with the use of the traditional criterion.

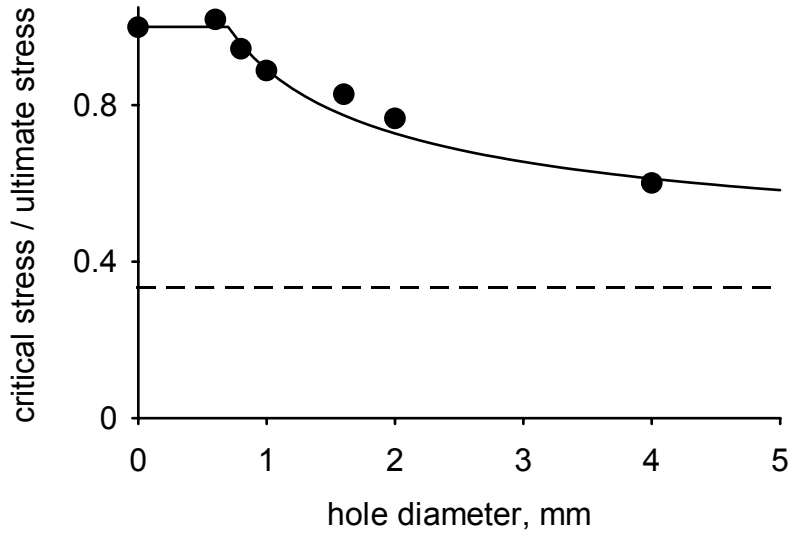

Figure 1: Critical stress variation with hole diameter.

A plate with angled elliptic hole

Wu, Yao and Yip [13] tested PMMA plates 380 mm long, 152 mm wide and 3.2 mm thick. The semiaxes of the elliptic hole were $a = 12.7$ mm and $b = 2.5$ mm. The failure stress for varying ω was experimentally determined. Fig. 2 shows experimental data (points) and the critical stresses calculated by Eqn. (17) for $\beta = 0$ (the solid curve). The dotted curve is calculated according to the traditional criterion.

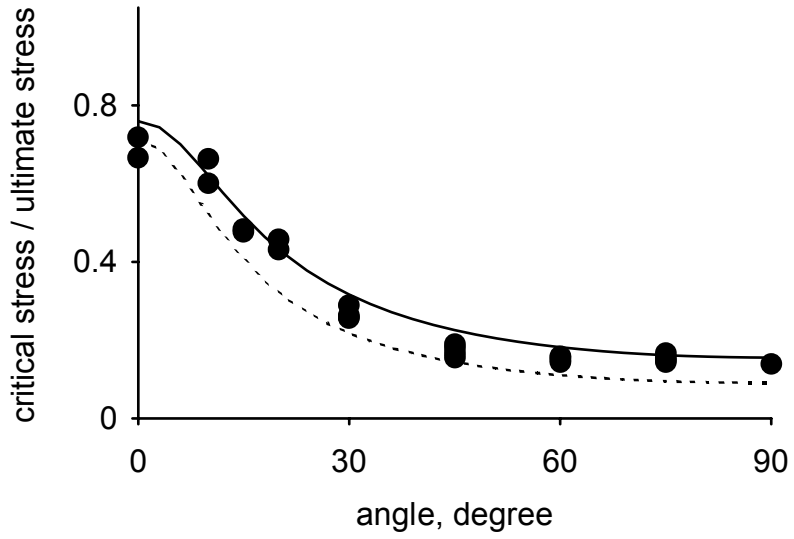

Figure 2: Critical stress variation with angle ω.

A bar with a circumferential notch

Nisitani and Noguchi [14] tested cylindrical bars made of high strength steel. The specimens had a circumferential V-shaped notch with opening angle $\psi = 60°$ and radius of curving ρ at the notch root. Specimens with notch depth $a = 0.2$ mm were tested by varying ρ within 0.056–2.1 mm. Fig. 3 shows the values of σ_c calculated by Eqn. (14), as a function of the stress concentration factor for $\beta = 0$ and $\beta = 1$ (curves 1 and 2). Curve 1 limits from below the domain of σ_c, and curve 2 approximates the experimental data represented by the points. As $K_t \to \infty$, the calculated curves approach asymptotically the value found in accordance with LEFM (dashed straight line). The dotted curve is calculated according to the traditional criterion.

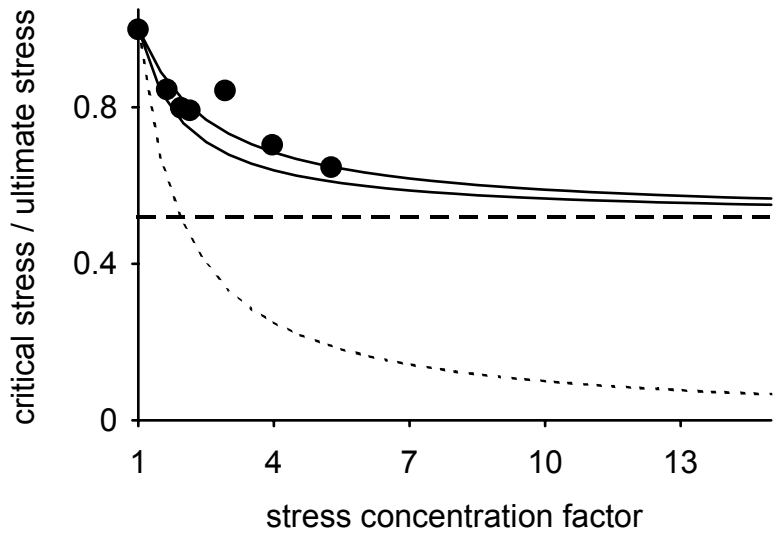

Figure 3: Critical stress variation with stress concentration factor.

The results of calculations are in good agreement with the experimental data on brittle fracture under conditions of stress concentration.

REFERENCES

1. Seweryn, A. and Mroz, Z. (1995). *Eng. Fract. Mech.* 51, 955.
2. Mikhailov, S.E. (1995). *Eng. Fract. Mech.* 52, 731.
3. Dyskin, A.V. (1997). *Int. J. Fract.* 83, 191.
4. Isupov, L.P. and Mikhailov, S.E. (1998). *Arch. Appl. Mech.* 68, 597.
5. Seweryn, A. (1998). *Eng. Fract. Mech.* 59, 737.
6. Sato, Y., Ohe, K. and Nagai, F. (1980). *Trans. Jap. Soc. Mech. Eng.* A46, 557.
7. Sato, Y., Susa, M. and Shigemura, T. (1980). *Trans. Jap. Soc. Mech. Eng.* A46, 564.
8. Hyakutake, H., Hagio, T. and Nisitani, H. (1990). *Int. J. Pres. Ves. & Piping.* 44, 277.
9. Suknev, S.V. and Novopashin, M.D. (2000). *Doklady Physics.* 45, 339.
10. Peterson, R.E. (1974). *Stress Concentration Factors.* John Wiley and Sons, New York.
11. Lekhnitskii, S.G. (1981). *Theory of Elasticity of an Anisotropic Body.* Mir Publishers, Moscow.
12. Sedov, L.I. (1972). *A Course in Continuum Mechanics.* Volters-Noordhoff, Groningen.
13. Wu, H.C., Yao, R.F. and Yip, M.C. (1977). *Trans. ASME: J. Appl. Mech.* 44, 455.
14. Nisitani, H. and Noguchi, H. (1986). *Trans. Jap. Soc. Mech. Eng.* A52, 1286.

A NUMERICAL STUDY OF CONSTRAINT AND RATE EFFECTS ON DYNAMIC CRACK GROWTH

Xi Zhang[1] and Yiu-Wing Mai[2,3]

[1] CSIRO Division of Petroleum Resources, PO Box 3000, Glen Waverley, VIC 3150, Australia
[2] Centre for Advanced Materials Technology (CAMT), School of Aerospace, Mechanical and Mechatronic Engineering J07, The University of Sydney, Sydney, NSW 2006, Australia
[3] MEEM, City University of Hong Kong, Tat Chee Avenue, Kowloon, Hong Kong

ABSTRACT

A transient finite element analysis has been carried out to provide insight into the dynamic crack growth behavior in viscoplastic materials under plane strain and small-scale yielding conditions. The fracture process is characterized by an embedded cohesive zone model in which the macroscopic fracture work is a function of crack opening rate and temperature rise on the crack flanks. The material is an isotropic hardening and thermal softening elastic-plastic von Mises solid. The computational model is developed to identify the individual roles of crack-tip constraint, loading rates and cohesive law properties. There is a sharp rise in the fracture resistance curves after a small amount of crack growth. The competition of strain-rate hardening and thermal softening in the fracture process zone can significantly change the fracture resistance curves. The effects of loading rates and crack-tip constraints have been examined. It is shown that the trend of increasing toughness due to the negative T-stress is greatly reduced when crack growth is fully developed. In addition, crack-tip constraint does not affect the limiting crack speed.

KEYWORDS

Dynamic fracture; Rate effect; Thermal effect; Constraint; Embedded cohesive zone model

INTRODUCTION

One class of models that serves as a bridge between the macroscopic and microscopic methods is that of the embedded cohesive zone model (ECZM). The fracture process is represented in terms of a traction-separation relation applied on the plane of fracture, while the bulk materials are considered by conventional continuum mechanics. Although this model cannot directly account for the interaction of the crack tip and the voids nearest to it, the implication of all these factors can be qualitatively put into a phenomenological cohesive law through some primary parameters [1]. It is more flexible than the cell model and easier for implementation of finite element methods. In addition, ECZM provides an illustrating and tractable way to include constitutive non-linearity into the continuum models.

Fracture behavior depends strongly on loading rate, material response and finite geometry change.

Emphasis is placed on dynamic crack growth such that inertia effect becomes significant. The class of materials considered here is hardened by increasing effective plastic strain rate and weakened by temperature rise. It is inferred that fast crack growth will have lower toughness since the elevated traction acts on the plane of separation due to strain-rate hardening. However, the inconsistent trend found in recent experiments by Du *et al* [2] and theoretical analyses [3,4] showed that rate-dependent materials must have a rate-dependent fracture process.

The effect of crack-tip constraint on fracture toughness has attracted a great deal of interest during the past decade. For stationary cracks in some specimen geometries, there is loss of J-dominance of crack-tip fields due to the non-uniqueness of hydrostatic stress [5,6]. The same problem has been extended to quasi-static crack growth in ductile materials by Xia and Shih [7] using a cell model and by Tvergaard and Hutchinson [1] using a cohesive zone model. However, crack-tip constraint effects on the dynamic fracture process have not been fully exploited.

The objective of the present paper is to consider the influences of crack-tip constraint, material inertia and thermal softening on the crack growth resistance. To this end, finite element simulations of mode I plane strain crack growth under small-scale yielding conditions are carried out for a range of material parameters. A rate- and thermal-dependent traction-separation relation is used to model the fracture process. The material considered is an isotropic hardening and linear thermal softening viscoplastic solid.

CONSTITUTIVE EQUATIONS OF THE SOLID AND THE FRACTURE PROCESS

We adopt a thermal-viscoplastic constitutive relation with linear thermal softening and power-law strain-rate hardening. The deformation rate tensor is decomposed into elastic, viscoplastic and thermal parts:

$$\mathbf{D} = \mathbf{D}^{e} + \mathbf{D}^{vp} + \mathbf{D}^{T} \tag{1}$$

For an isotropic hardening, viscoplastic solid, the plastic part of the deformation-rate tensor and the thermal dilatation take the forms:

$$\mathbf{D}^{vp} = (\frac{3\dot{\bar{\varepsilon}}}{2\sigma_e})\mathbf{S} \qquad \mathbf{D}^{T} = \alpha\Delta\dot{T}\mathrm{I} \tag{2}$$

where $\dot{\bar{\varepsilon}}$ denotes the equivalent plastic strain rate, $\mathbf{S} = \mathbf{t} - 1/3\mathbf{t}\cdot\mathbf{I}$ the deviator of Kirchoff stress $\mathbf{t}$, and $\mathbf{s}_e = \sqrt{3\mathbf{S}:\mathbf{S}/2}$ the equivalent stress, α the thermal expansion coefficient, ΔT the temperature rise and $\mathbf{I}$ the second order identity tensor. The constitutive relation can be written as:

$$\overset{\nabla}{\mathbf{t}} = \mathbf{L}:[\mathbf{D} - \mathbf{D}^{vp} - \mathbf{D}^{T}] \tag{3}$$

where $\overset{\nabla}{\boldsymbol{t}}$ is the Jaumann rate of Kirchoff stress tensor, $\mathbf{L}$ is elastic modulus tensor with Young's modulus E and Possion's ratio ν. The effective plastic strain rate becomes:

$$\dot{\bar{\varepsilon}} = \dot{\bar{\varepsilon}}_0[\frac{\sigma_e}{g(\bar{\varepsilon},T)}]^{1/m}$$
$$g(\bar{\varepsilon},T) = \sigma_0(1+\bar{\varepsilon}/\varepsilon_0)^{N}[1-\beta(T-T_0)] \tag{4}$$

where $\bar{\varepsilon} = \int_0^t \dot{\bar{\varepsilon}}dt$ denotes the equivalent plastic strain, $\dot{\bar{\varepsilon}}_0$ is reference strain rate, m rate sensitivity parameter, σ_0 yield stress, $\varepsilon_0 = \sigma_0/E$ reference strain, N strain hardening exponent, T_0 reference temperature, usually equal to the environmental temperature, abd β thermal softening coefficient.

The form of the static traction-separation law given by Tvergaard and Hutchinson [1] is adopted here. The parameters characterizing the traction-separation curves include the work of fracture per

unit area, the peak stress for separation $\hat{s}$ and three characteristic lengths, $\delta_1, \delta_2, \delta_c$. The shape parameters δ_1 and δ_2 are chosen so that $\delta_1 = 0.15\delta_c$ and $\delta_2 = 0.5\delta_c$. It is shown that these factors are of secondary importance in failure assessment [1]. The fracture work, $\Gamma_0 = \int_0^{\delta_c} \sigma(\delta, \dot{\delta}, T) d\delta = \hat{\sigma}(\delta_c + \delta_1 - \delta_2)/2$, is not a constant because of the effects of material inertia and thermal softening. Further, it is assumed that the rate and the thermal effects on the fracture work were incorporated into the model in terms of the changes in the peak traction $\hat{s}$. The cohesive strength is written as:

$$\hat{\sigma} = \hat{\sigma}_0 (1 + \frac{\dot{\delta}}{\dot{\delta}_0})^{r_1} [1 - r_2 (T - T_0)] \tag{5}$$

where r_1 and r_2 are material constants which describe the rate effect and thermal softening, $\dot{\delta}_0$ (=1 m/s) is reference separation rate and $\hat{s}_0$ is steady-state traction for the quasi-static cohesive zone model, and $T_0 = 20^0 C$.

COMPUTATIONAL MODEL

Finite element simulations described here are based on updated coordinate Lagrangian formulation. All physical quantities are functions of a set of moving coordinates x^i at time t. Consider an equilibrium crack in a body with current volume V, surface S_{ext} subjected to a velocity constraint and internal cohesive surface area S_{coh}. The weak form of the governing equations for mechanical fields yields the incremental form for the principle of virtual work on the current configuration [8]:

$$\int_V \tau^{ik} \delta D_{ij} dV - \int_{S_{coh}} S^i \delta \dot{u}_i dS = \int_{S_{ext}} T^i \delta \dot{u}_i dS - \int_V K^i \delta \dot{u}_i dV \tag{6}$$

where τ^{ij} are the Kirchoff stress tensor components equal to those of the Cauchy stress tensor s^{ij} in the current configuration, $D_{ij} = (\dot{u}_{i,j} + \dot{u}_{j,i})/2$ are deformation rate tensor components and $\dot{u}_i$ are displacement rate vector components. The kinetic energy $K_i = 0.5 r \P^2 u_i / \P t^2$ in which r is the mass density in the current configuration, T^i and S^i are the traction components on the external surface S_{ext} and internal cohesive surface S_{coh}. It should be noted that the Kirchoff stress is identical to the Cauchy stress if we take the current state as the reference configuration.

Also, the local balance of energy gives the following governing equation for the conduction of heat in a continuous medium:

$$r c_p \frac{\P T}{\P t} = k T_{,ii} + c w^p \tag{7}$$

where c_p is heat capacity, k is thermal conductivity and the parameter c specifies the fraction of plastic work ($w^p = s^{ij} D_{ij}^p$) that is converted to heat and is taken to have a value 0.90.

The crack growth analyses are carried out under small-scale yielding conditions. Due to symmetry about the crack plane only half of the solid needs to be analyzed. A semi-circular region with initial radius R_0 = 20 mm is used in the numerical computation. It is chosen so that $R_0 = 2000\Delta$ where Δ is the size of the smallest elements of the mesh at the crack-tip. $\delta_c = 0.1\Delta$ is selected to determine the minimum dimension of these elements if they are not specified. The mesh consists of 1584×4 triangle elements and a uniform mesh region with an initial length $L_0 = 48\Delta$ is used to model crack growth. A length twice L_0 can be taken as the uniform mesh zone since the mesh size is increased at a ratio near unity from the minimum size.

On the outer semi-circular boundary, the displacements, $\dot{u}_1$ and $\dot{u}_2$, are given by the external stress fields, according to small strain linear elastic fracture mechanics solutions. Thus, we have

$$\dot{u}_1(x^1, x^2, t) = \frac{2(1+\nu)\dot{K}_I}{E}\sqrt{\frac{R_0}{2\pi}}\cos\frac{\theta}{2}(1-2\nu+\sin^2\frac{\theta}{2})$$
$$\dot{u}_2(x^1, x^2, t) = \frac{2(1+\nu)\dot{K}_I}{E}\sqrt{\frac{R_0}{2\pi}}\sin\frac{\theta}{2}(1-2\nu+\cos^2\frac{\theta}{2}) \quad (8)$$

in which $R_0 = \sqrt{x_1^2 + x_2^2}$, $\theta = \tan^{-1}(x^2/x^1)$ for the points on the remote boundary in the current configuration, and $\dot{K}_I$ measures the incremental rate of the mode I stress intensity factor.

To minimize the wave effect, the initial velocities throughout the region are given by [9]:

$$\dot{u}_1(x^1, x^2, 0) = \frac{2(1+\nu)\dot{K}_I}{E}\sqrt{\frac{r}{2\pi}}\cos\frac{\theta}{2}(1-2\nu+\sin^2\frac{\theta}{2})$$
$$\dot{u}_2(x^1, x^2, 0) = \frac{2(1+\nu)\dot{K}_I}{E}\sqrt{\frac{r}{2\pi}}\sin\frac{\theta}{2}(1-2\nu+\cos^2\frac{\theta}{2}) \quad (9)$$

in which $r = \sqrt{x_1^2 + x_2^2}$.

At t=0, the non-singular stress term, T-stress, is applied uniformly. In this work, the T-stress T is applied together with the corresponding transverse stress $\sigma_{33} = \nu T$ under plane strain conditions. Its magnitude is taken to be such that the material remains elastic.

The Newark-β method with $\beta = 0$ and $\gamma = 0.5$ is used to integrate the discrete equation of motion. A lumped mass matrix is chosen since it is preferred for the explicit integration procedure. A fixed time step 5×10^{-11}s is employed, which is sufficient to ensure that the numerical solutions remain stable. In the calculations, all material parameters are kept fixed to be representative of AISI 4340 steel studied experimentally by Hartley *et al*. [10]. The properties are specified by: E =200 GPa, ν =0.3, σ_0 =1250 MPa, N =0.08, m =0.01, $\dot{\varepsilon}_0$ =0.001/s, ρ =7833 kg/ m^3, $\alpha = 1.3\times10^{-5}/^0C$, $c_r = 456J/kg^0C$, $k = 54w/m^{2\,0}C$ and $\beta = 0.0016$.

RESULTS

Effects of rate dependence and thermal sensitivity in traction-separation laws

Our first attention is focused on the effects of strain rate sensitivity and thermal softening factors in the cohesive zone model. Computations are carried out for specified material properties, $\hat{\sigma}_0 = 2.5\sigma_0$ and $\dot{K}_I = 10^7 MPa\sqrt{m}/s$ for different values of r_1 and r_2. Figures 1 and 2 show the R-curves for the two cases: (i) r_1=0.01 and r_2=0.001 and (ii) r_1=0.002 and r_2=0.001. The R-curves rise steadily after only a small amount of crack growth. It is seen that strain rate sensitivity plays a beneficial role in toughness enhancement, because higher magnitudes of toughness can be obtained at r_1=0.01 than at r_1=0.002. Physically, rate effect can act effectively through an increase in energy dissipation in the plastic zone since the fracture stress is enhanced by rate sensitivity in the fracture zone.

In Fig. 3, the variation of K_{Id} is plotted against $\Delta a/R_0$ for r_2=0.003 and r_1=0.002, so that the thermal effect becomes dominant over rate dependence. It is observed that at high r_2, crack growth resistance is much reduced. However, when $\Delta a/R_0$ >0.005, the slopes of the R-curves increase to the same order as those at small r_2. This is because, as the crack advances, the thermal softening is weakened severely and strain-rate hardening prevails.

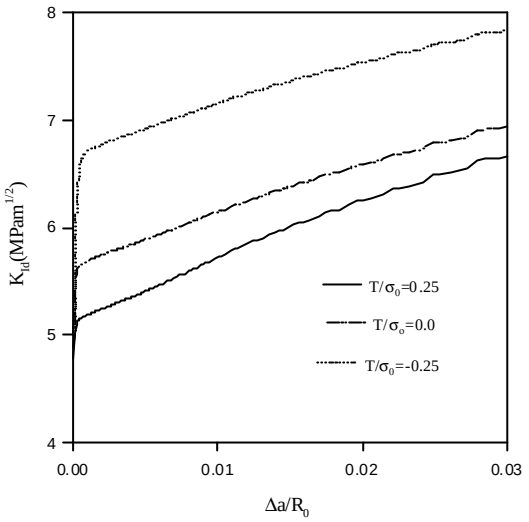

Fig. 1. Crack growth resistance curves for r_1=0.01, r_2=0.001 at three different T-stress

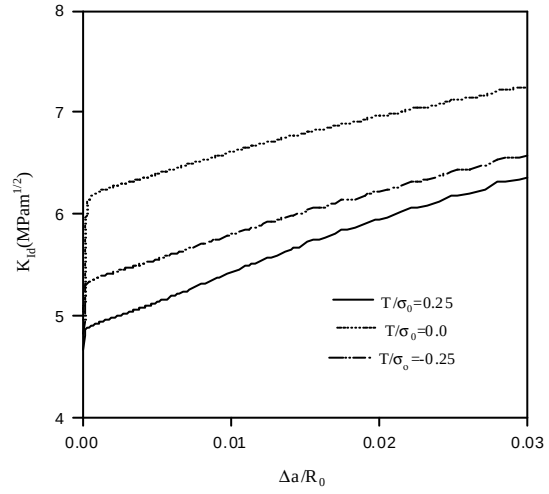

Fig. 2. Crack growth resistance curves for r_1=0.002, r_2=0.001 and $\hat{\sigma}_0$=2.5σ_0, at three different levels of T-stress and $\dot{K}_I = 10^7 MPa\sqrt{m}/s$.

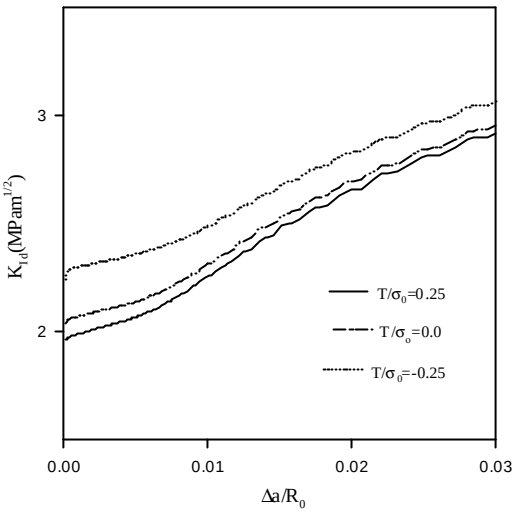

Fig. 3. Crack growth resistance curves for r_1=0.002, r_2=0.003 at three different T-stress

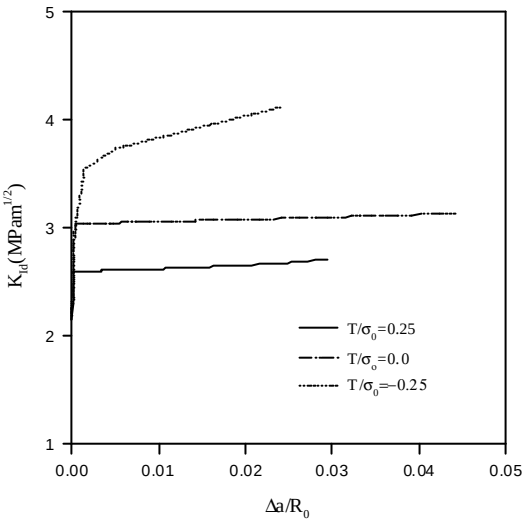

Fig. 4. Crack growth resistance curves for r_1=0.002, r_2=0.001 and $\hat{\sigma}_0$=2.5σ_0, at three different levels of T-stress and $\dot{K}_I = 10^6 MPa\sqrt{m}/s$.

Effects of loading rates

For comparison, two impact velocities $\dot{K}_I$ = 10^6 and $10^7 MPa\sqrt{m}/s$ are used with material constants r_1=0.002, r_2=0.001 and $\hat{\sigma}_0$=2.5σ_0. The R-curves at the higher impact speed are shown in Fig. 2, while those R-curves at the lower speed are shown in Fig. 4. There is a reduction in the fracture toughness with the lower impact speed. This is because high strain-rate increases the stress ahead of the crack-tip. Similarly, the fracture stress is enhanced by the rate-dependent cohesive law. Further, plastic deformation is restricted at low loading rates. The crack speed at different loading rates are examined in Figs. 2 and 4. It is found that the crack speed is larger at low impact speeds than at high impact speeds. The steady-state crack speed at $T/\sigma_0 = -0.25$ is 518m/s at the higher impact speed and 648m/s at the lower impact speed.

Effects of crack-tip constraints

Although the loss of crack-tip constraint plays an important role in the toughness enhancement of

cleavage fracture, the constraints cannot significantly affect the toughness at crack initiation for ductile fracture at low loading rates, as shown in Fig.4. The sensitivity of crack initiation toughness to T-stress can be found at high loading rates, as shown in Figs. 1 to 3. For example, the initiation toughness is 4.78 MPa $\sqrt{m}$ for T/σ_0 =0.25 and 5.03 MPa $\sqrt{m}$ for T/σ_0 =-0.25 in Fig. 1. In addition, negative T-stress can decrease crack speed during the early stage of crack growth.

Negative T-stress can increase fracture toughness significantly. There is a large difference in the R-curves between T=-0.025 and 0.25. At high loading rates, the difference in toughness mainly results from T-stress at the early stage and the trend is offset with crack advance. Upon full development of the crack speed, the slopes of the R-curves tend to be insensitive to the T-stress. (See Figs. 2 for example). This means that the steady-state crack speed is insensitive to the constraints. However, this is not the case at low impact rates. It is likely that the T-stress is still comparable to the fracture stress at lower loading rates.

CONCLUSIONS

(1) Crack initiation is suppressed as the rate-sensitivity factor r_1 in the cohesive law increases. The toughness is higher for larger r_1, irrespective of the impact speeds.
(2) Thermal softening caused by intense plastic deformation promotes ductile failure. This effect is more significant at the early stage of crack growth. After some crack extension, thermal effect at high r_2 is restricted and the R-curves increase at the same rate.
(3) Increasing the loading rate enhances the fracture toughness because the rate effect increases the flow strength and the fracture energy, as well as the kinetic energy. It is seen from Figs 2 and 4 that for low strain-hardening elastic-plastic materials, material inertia and rate sensitivity can increase the toughness by a factor of two.
(4) Fracture behavior is also strongly controlled by the constraint effect. However, it depends on the loading rate. Constraint does not change the crack initiation toughness at low loading rates, but it does at high loading rates. Importantly, change in the crack-tip constraint has no significant effect on the steady-state crack speed at high impact speeds.

ACKNOWLEDGEMENTS

We wish to thank the Australian Research Council (ARC) for the continuing support of this project. XZ was in receipt of an Overseas Postgraduate Research Award tenable at the University of Sydney and an ARC Research Scholarship funded from the project grant awarded to Y-W M.

REFERENCES

1. Tvergaard, V. and Hutchinson, J. W. (1992) *J. Mech. Phys. Solids* 40, 1377-1397.
2. Du, J., Thouless, M.D. and Yee, A. F. (2000) *Int. J. Fract*. 92, 271-285.
3. Langer, J. S. and Lobkovsky, A. E. (1998). *J. Mech. Phys. Solids* 46, 1521-1556.
4. Landis, C.M., Pardoen, T. and Hutchinson, J.W. (2000*) Mech. Mater*. 32, 663-678.
5. Hancock, J. W. Reuter, W. G. and Parks, D. M. (1993) In *Constraint Effects in Fracture*, ASTM STP 1171, American Society for Testing and Materials, Philadelphia, 21-40.
6. O'Dowd, P. and Shih, C. F. (1991) *J. Mech. Phys. Solids* 40, 989-1015.
7. Xia, L., Shih, C. F. (1995) *J. Mech. Phys. Solids* 43, 233-259.
8. McMeeking , R. M. and Rice, J. R. (1975) *Int. J. Solid Structures*, 11, 606-616.
9. Gao, X., Shih, C. F., Tvergaard, A. and Needleman, A. (1996) *J. Mech. Phys. Solids* 44, 1255-1282
10. Hartley, K. A., Duffy, J. and Hawley, R. H. (1987) *J. Mech. Phys. Solids* 35, 283-301.

ORAL REFERENCE: ICF100149OR

A POSSIBLE EXPLANATION OF SIZE EFFECT IN FATIGUE STRENGTH OF METALS

Andrea CARPINTERI, Andrea LANDINI, Andrea SPAGNOLI

Department of Civil Engineering, University of Parma, Parco Area delle Scienze 181/A, 43100 Parma, Italy

ABSTRACT

As is well-known, the experimental fatigue strength of metallic materials tends to decrease with increasing specimen size. Several theories on size effect, such as the Weibull statistical theory, have been proposed to explain this phenomenon. In the present paper, an attempt to analyse size effect in fatigue is made by considering the fractal nature of the reacting cross section of structures, that is, the renormalized fatigue strength is assumed to be equal to a force amplitude divided by a surface with a fractal dimension lower than 2. Such a dimensional decrement depends on a self-similar weakening of the material ligament, owing to the presence of cracks, defects, voids and so on (microscopic level). However, this decrement tends to gradually disappear by increasing the structure size (macroscopic level), this phenomenon being defined as multifractality. Relevant experimental results are examined in order to assess the reliability of the theoretical analysis presented.

KEYWORDS

Size effect; fatigue fracture phenomenon; metals; fractal geometry.

INTRODUCTION

According to well-known experimental findings, the fatigue strength of a given material is not a constant mechanical parameter, but it decreases by increasing the specimen size. Such a decrease can be dramatic for very large structures, by provoking sudden catastrophic failures with possible heavy losses of lives and resources involved. Size effect phenomenon was analysed by Griffith [1] for the glass filaments by assuming the presence of microcracks whose size is proportional to the diameter of the filament cross section, whereas Peterson [2] examined the size effect in the case of brittle fracture produced through fatigue loading. Then Weibull [3] proposed the statistical concept of the weakest link in a chain: by increasing the structure volume, the probability of failure increases owing to the higher probability of finding a critical microcrack provoking macroscopic fracture. More recently, the size of the most dangerous defect has been shown to be proportional to the structure size [4]. From such conclusions, it can be derived that the microscopic scale (material microstructure, grain size, microcracks, voids, inclusions, etc.) is significantly connected with the macroscopic scale (structure size), that is, the "disorder" of the material (heterogeneity and/or micromechanical damage) has to be considered when examining critical macroscopic phenomena (like for example fatigue fracture failure of structures).

In the present paper, the fractal nature of the material microstructure [5,6] and the renormalization group theory [7-9] can be considered to analyse the interactions between the two above levels (micro and macro), as has been proposed in Ref.[10]. In other words, the reacting cross section of a given structure shows a self-similar weakening due to the material heterogeneity, cracks, defects, etc., and therefore the fractal dimension of such a surface can be assumed to be lower than 2 [11,12]. Consequently, the damaged ligament of a heterogeneous solid may be modelled through a "lacunar" fractal set, analogous to the mathematical middle-third Cantor set, which presents Hausdorff dimension lower than that of the domain where it is contained. Then, new mechanical properties can be defined with physical dimensions depending on the fractal dimension of the damaged heterogeneous ligament (renormalization procedure), and such properties are scale-invariant constants. According to this approach, the renormalized fatigue strength could be represented by a force amplitude acting on a surface with a fractal dimension lower than 2, as is discussed in the following.

On the other hand, Mandelbrot [13] pointed out a non-uniform (multifractal) scaling of the *natural* fractals (different from the uniform one of the *mathematical* fractals), i.e. in the physical reality a transition occurs from a fractal (heterogeneous) regime for small structures to a Euclidean (homogeneous) one for structures large enough with respect to a characteristic microstructural size. In other words, the effect of the microstructural heterogeneity and/or damage (disorder) of a given material on the macroscopic mechanical behaviour gradually vanishes by increasing the structure size [14].

A monofractal scaling law for fatigue limit of metals is herein proposed, and some experimental results [15] are analysed to show how to apply the theoretical approach adopted.

FRACTAL NATURE OF FATIGUE FAILURE OF STRUCTURES

According to the concepts previously discussed, the reacting cross section of a disordered material is herein assumed to present a fractal dimension $\alpha = 2 - d$, with $0 \le d < 1$, where the decrement d depends on a self-similar microstructural weakening (heterogeneity and/or damage) [10-12], the value of d being higher when such a weakening is more significant. Let us consider two geometrically similar cylinders (A and B), made up of the same material, subjected to cyclic axial loading (Fig.1). On the basis of the theoretical approach proposed for static loading [10], the renormalized fatigue strength σ_a^* (the subscript a standing for amplitude) may be assumed as a material constant with physical dimensions given by $[F] \,/\, [L]^{2-d}$, and the following expression can be written :

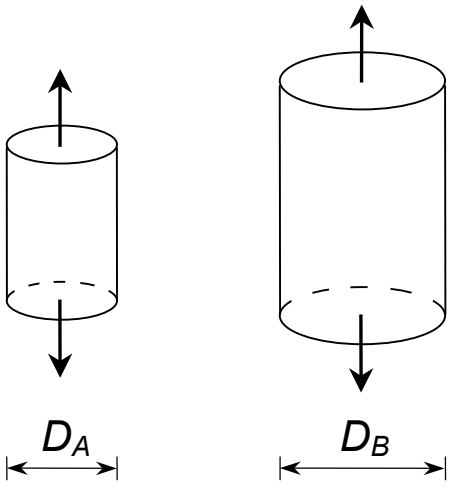

Figure 1: Geometrically similar cylinders under cyclic axial loading

$$\sigma_a^* = \frac{4\ F_{a,A}}{\pi\ D_A^{2-d}} = \frac{4\ F_{a,B}}{\pi\ D_B^{2-d}} \tag{1}$$

where $F_{a,A}$ and $F_{a,B}$ are the axial force amplitudes (acting on the two cylinders, respectively), which provoke fatigue fracture failure.

The apparent fatigue strengths for such bodies are equal to :

$$\sigma_{a,A} = \frac{4\ F_{a,A}}{\pi\ D_A^2} \tag{2}$$

$$\sigma_{a,B} = \frac{4\ F_{a,B}}{\pi\ D_B^2} \tag{3}$$

Therefore, recalling eqns (1) and (2), equation (3) becomes :

$$\sigma_{a,B} = \frac{4}{\pi\ D_B^2} \left\{ F_{a,A} \left(\frac{D_B}{D_A} \right)^{2-d} \right\} = \sigma_{a,A} \left(\frac{D_B}{D_A} \right)^{-d} \tag{4a}$$

and in a logarithmic form :

$$\ln \sigma_{a,B} = \ln \sigma_{a,A} - d\ \ln\left(D_B / D_A\right) \tag{4b}$$

By assuming $D_A = 1$ and $D_B = D$, where D is a generic value of the bar diameter, the last two expressions can be written in a more general form :

$$\sigma_a = \sigma_{a,1}\ \left(D\right)^{-d} \tag{5a}$$

$$\ln \sigma_a = \ln \sigma_{a,1} - d\ \ln D \tag{5b}$$

where the latter equation represents a straight line with slope equal to $-d$ in the diagram shown in Fig.2, $\sigma_{a,1}$ being the fatigue strength for a cylinder with $D = D_A = 1$.

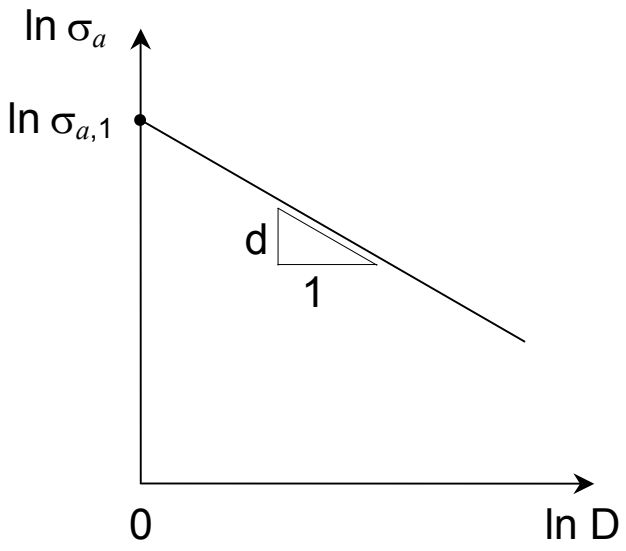

Figure 2: Monofractal scaling law for fatigue strength σ_a

In the case of $\sigma_a = \sigma_{af}$, where σ_{af} is the fatigue limit, equations (5) become :

$$\sigma_{af} = \sigma_{af,1} \left(D\right)^{-d} \tag{6a}$$

$$\ln \sigma_{af} = \ln \sigma_{af,1} - d \ln D \tag{6b}$$

with $\sigma_{af,1}$ equal to the fatigue limit for $D = D_A = 1$. Note that, through a reasoning similar to that described above, equations analogous to those for push-pull loading (eqns (1) to (6)) can be obtained in the case of rotary bending.

ANALYSIS OF SOME EXPERIMENTAL RESULTS

Now some experimental results are examined to show how to apply the above equations. As is well-known, several aspects (material properties, manufacturing process, specimen shape, testing conditions) play a role in determining the amount of fatigue limit decrease by increasing the structural size, but the analysis of the specific influence of each aspect is beyond the scope of the present paper.

Hatanaka et al. [15] performed fatigue tests on smooth specimens made up of two different materials : a cast steel (JIS SCMn 2A) originally including many defects (comparatively disordered material), and a forged steel (JIS SF 50) with a quite homogeneous microstructure (comparatively ordered material). The mechanical properties of these two types of steel are shown in Table 1.

TABLE 1 - Mechanical properties of two steels tested by Hatanaka et al. [15]

Material	*Yield stress (MPa)*	*Ultimate tensile strength (MPa)*	*Elongation (%)*
SCMn 2A	325	576	18.2
SF 50	283	484	39.1

Cylindrical smooth specimens with diameter D equal to 8, 20, 30 and 40 mm, respectively, were employed. The S-N curves for the two steels tested under rotating bending are shown in Ref.[15]. Note that, for both materials, the fatigue strength decreases by increasing the specimen size. In particular, the amount of decrease in the value of fatigue limit σ_{af} by increasing D from 8 to 40 mm is equal to about 24% for SCMn 2A steel and about 13% for SF 50 steel.

If experimental results of σ_{af} against D reported in Ref.[15] are plotted in a bilogarithmic diagram (Fig.3), two straight lines can be determined through the least squares method : the straight line slope, $-d$ (see eqn(6b)), for the cast steel is equal to – 0.162, whereas that for the forged steel (dashed line) is equal to – 0.085. Consequently, the reacting cross section presents a fractal dimension $\alpha = 2 - d$ equal to 1.838 and 1.915, respectively: in other words, the ligament for an ordered material is more similar to a two-dimensional Euclidean surface than that for a disorder material. Such a conclusion is consistent with the concepts discussed in the previous section. Furthermore $\ln \sigma_{af,1}$, defined in eqn(6b), is equal to 5.76647 for SCMn 2A steel and 5.63681 for SF 50 steel, that is, $\sigma_{af,1}$ is equal to 319.4 MPa and 280.6 MPa, respectively.

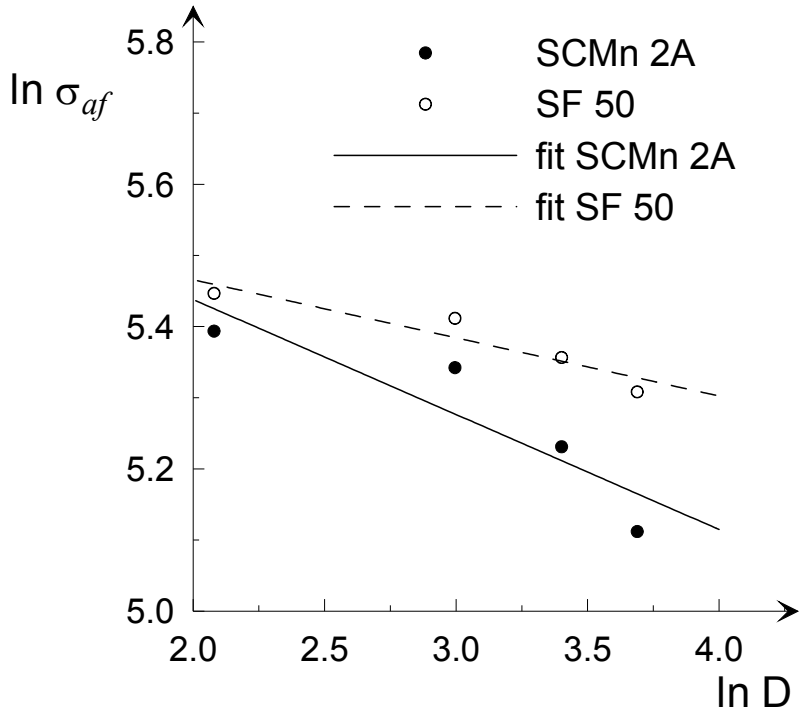

Figure 3: Monofractal scaling law for fatigue limit σ_{af} of two steels tested by Hatanaka et al. [15]

Note that the experimental points in Fig.3 are not perfectly aligned (the correlation coefficient is equal to 0.906 for the cast steel and 0.937 for the forged steel), which could mean that the monofractal scaling of σ_{af} is valid only in a narrow size range where the fractal dimension α is about constant. In other words, a non-uniform (multifractal) scaling of σ_{af} may be assumed, with a gradual decrease of d as the scale D increases. As a matter of fact, the material microstructure is independent of the macroscopic scale of the specimens tested; consequently, the influence of the microstructural disorder (heterogeneity and/or damage) on fatigue behaviour may progressively diminish by increasing the specimen size, and may become practically negligible for cylinder sizes large enough with respect to a characteristic microstructural size.

CONCLUSIONS

Experimental tensile strength and fatigue strength decrease by increasing the specimen size, and this decrease is more pronounced for comparatively heterogeneous and/or damaged materials, i.e. the so-called "disordered" materials.

The problem of size effect in fatigue has been herein analysed through fractal geometry concepts, by assuming a self-similar weakening of the reacting cross section of structures, due to the material disorder (microscopic level). A monofractal scaling law for fatigue limit σ_{af} has been proposed. The fatigue strength decrease may gradually tend to disappear by increasing the structure size D (macroscopic level) with respect to a characteristic microstructural size.

Experimental fatigue data related to two different steels have been examined to discuss the theoretical approach adopted. Such an approach seems to be a possible alternative method to analyse the size effect problem in fatigue fracture failure of structures.

ACKNOWLEDGEMENTS

The authors gratefully acknowledge the research support for this work provided by the Italian Ministry for University and Technological and Scientific Research (MURST) and the Italian National Research Council (CNR).

REFERENCES

1. Griffith A.A. (1921) The phenomenon of rupture and flow in solids. *Philosophical Trans. R. Soc., London,* **A221**, 163-198.
2. Peterson R.E. (1933) Model testing as applied to strength of materials. *J. Applied Mechanics* **1**, 79-85.
3. Weibull W. (1939) *A Statistical Theory for the Strength of Materials.* Swedish Royal Institute for Engineering Research, Stockholm.
4. Carpinteri Al. (1989) Decrease of apparent tensile and bending strength with specimen size: two different explanations based on fracture mechanics. *Int.J. Solids Struct.* **25**, 407-429.
5. Mandelbrot B.B. (1982) *The Fractal Geometry of Nature.* W.H. Freeman and Company, New York.
6. Falconer K. (1990) *Fractal Geometry: Mathematical Foundations and Applications.* Wiley, Chichester.
7. Wilson K.G. (1971) Renormalization group and critical phenomena. *Phys. Rev.* **B4**, 3174-3205.
8. Barenblatt G.I. (1979) *Similarity, Self-Similarity and Intermediate Asymptotics.* Consultants Bureau, New York.
9. Herrmann H.J. and Roux S. (Eds) (1990) *Statistical Models for the Fracture of Disordered Media.* North-Holland, Amsterdam.
10. Carpinteri Al. (1994) Scaling laws and renormalization groups for strength and toughness of disordered materials. *Int.J. Solids Struct.* **31**, 291-302.
11. Barenblatt G.I. and Botvina L.R. (1980) Incomplete self-similarity of fatigue in the linear range of crack growth. *Fatigue Fract. Engng Mater. Struct.* **3**, 193-202.
12. Mandelbrot B.B., Passoja D.E. and Paullay A.J. (1984) Fractal character of fracture surfaces of metals. *Nature* **308**, 721-722.
13. Mandelbrot B.B. (1985) Self-affine fractals and fractal dimension. *Phys. Scr.* **32**, 257-260.
14. Carpinteri Al. and Chiaia B. (1997) Multifractal scaling laws in the breaking behaviour of disordered materials. *Chaos, Solitons & Fractals* **8**, 135-150.
15. Hatanaka K., Shimizu S. and Nagae A. (1983) Size effect on rotating bending fatigue in steels. *Bulletin of JSME* **26**, 1288-1295.

ORAL/POSTER REFERENCE: ICF100545OR

A Potential Node Release Technique for Estimating Ductile Crack Growth in Metallic Materials

J.X.Zhang[1], H. Murakawa[2]

[1]Welding Research Institute, Xi'an Jiaotong University, Xi'an, China
[2] Joining and Welding Research Institute, Osaka University, Osaka, Japan

ABSTRACT

In order to estimate the ductile crack growth in metallic materials, a potential node release technique is proposed in finite element simulation by introducing a potential node release law in traditional node release technique. J-integral far from crack tip is taken as a fracture parameter and the criterion of node releasing is a crack driving force relating with ultimate fracture strain and stress triaxiality near crack tip. The ductile crack growth and affecting factors are investigated numerically for three-point bend specimen.

KEY WORDS: Damage Mechanics, Fracture Modeling, FEM

INTRODUCTION

It is a very important and complicated topic to estimate numerically the ductile crack growth in nonlinear fracture mechanics. There exist two kinds of methods to simulating the ductile crack propagation, i.e., generation phase and application phase [1]. The so-called generation phase is to study numerically the fracture mechanics parameters such as COD, CTOA, COA and J-integral based on the experiment relationship between load-point displacement and crack growth length. The application phase is to study the load-point displacement and crack growth according to the fracture criteria at crack tip. Most researches are concentrated in the generation phase. One of the most difficulties in numerical simulation is how to determine the fracture criterion for ductile fracture in large scale yielding as the crack propagation.

It is predicted from metallurgical researches that the nucleation and growth of voids play an important role for the fracture process of ductile metallic materials, which cannot be described by conventional continuum mechanics. In structural materials, voids nucleate mainly at second phase particles and inclusions. Usually, micro-voids can be divided into two families, larger voids and smaller voids. The larger voids nucleate from inclusions at relatively low strains and smaller voids nucleate from carbides or precipitates at considerably larger strains. Consequently, void growth takes place due to the plastic deformation of surrounding matrix material and final failure occurs when the larger voids coalesce with each other or link up with a nearby crack tip via a void sheet consisting of voids nucleated from smaller particles [2-3].

Combining the micro-void damage mechanics and macro-fracture mechanics, a model to estimate the ductile crack growth in ductile materials is proposed in this paper. Potential node release technique is developed in finite element simulation by introducing a potential node releasing law in traditional node release technique. The ductile crack growth and affecting factors are investigated numerically for three-point bend specimen.

COHENSIVE ZONE AND PNRT

The ductile fracture of mild steels can be described as a progressive process with the nucleation, growth and coalescence of voids or micro-cracks. At the vicinity of a pre-existing macro-crack, a large damage evolution occurs due to the high stress and strain concentrations. It has shown from experiments that the damaged zone is confined very near to the macro-crack tip. The fracture toughness, the crack resistance and tearing modulus of ductile materials may be considerably affected by the presence of such localized damages near the crack tip. The so-called cohesive zone model is proposed to incorporate more details of the separation process than the modeling with conventional continuum mechanics as. The region ahead of a growing crack tip is a narrow strip joining the two elastic-plastic bodies which interact with each other with a kind of separation law. In general, one-dimensional separation relation is assumed acting on the ligament for cases under mode I loading conditions.

The traditional node release technique is to modify the boundary condition by releasing simultaneously the node force. In this paper, a new kind of node release technique is proposed by introducing potential node release law letting the node force release gradually. The potential node release law can be arbitrary in some degree as well as it reflects some characteristics of failure. As shown in Fig.1, the distance of the node as releasing is denoted by δ. The mechanical characteristics of the node releasing are defined through a power exponent function F as shown in the following.

$$F = F_{\max} \exp\{-3(\frac{\delta}{\delta_c})^{\frac{1}{m}}\} \qquad (1)$$

where, F_{max} is the maximum force when the node is released, $\delta_c$the critical displacement when the new crack increment forms, and m the material constant.

In the model of cohesive zone, it is assumed that the maximum traction is given and related with the fracture stress. In fact, traction in the cohesive zone is changing with applied load. So it is important to keep that the traction in the cohesive zone is the same as predicted using the continuum mechanics. There are two parameters in Equ.1. It can be seen from Equ.1 that the larger the constant m is, the more difficult the separation of node and the higher the fracture tearing toughness will be. The constant *m* can be used to describing the fracture property in some degree.

NUMERICAL PROCEDURE

The three-point bend specimen was used in finite element simulation. The half specimen is meshed according to its symmetry. The meshes consisted of 1110 four-node isoparametric elements with 3435 nodes. In the large strain gradient zone the mesh was refined. The minimum mesh size near crack tip is about 1/400 of ligament length. The numerical evaluation of the J-integral was conducted incrementally throng Gauss-point integration of the elements on the path with standard weight function according to the reference [4]. The J-integral was calculated as the mean value for five different paths.

The procedure in the numerical simulations is simply as follows. Initially, the crack driving force expressed by parameter *U* increases with the increase of applied load[5]. The cohesive zone creates and the corresponding node begin to release when the calculated crack driving force *U* near the crack tip reaches to its critical value *U*c, which is the function of ultimate fracture strain ε_u and stress triaxiality near crack tip. In general, the traction at the nodes inside the cohesive zone has to follow the potential node release law as shown Equ.1. If the external applied load increases further, the cohesive zone grows. The new crack increment forms when node displacement gets to its critical value or the node

force reaches near zero. According to the crack increment and corresponding J-integral values, the development of J-integral as crack growth can be obtained.

RESULTS AND DISCUSSION

In this model of simulating ductile crack growth, there are five parameters to affect the J-resistance curve, i.e., yielding stress, strain hardening exponent, ultimate fracture strain, critical crack tip displacement and node release exponent. The yielding stress, strain hardening exponent and ultimate strain can be determined from tensile stress strain curve. And the critical crack tip displacement can be determined from void growth theory or from fracture toughness experiment. In order to check the potential node release technique in simulating the crack growth, it is important to understand the influences of the parameters in Equ.1.

The influence of critical crack tip displacement on J-resistance curve is illustrated in Fig.2. The yielding stress and strain hardening exponent of the ductile material used in calculation are 499MPa and 8.0 respectively. And the node force release exponent is kept the same value as 1.0. The ultimate fracture strain for node releasing is 0.2. It is well shown in figure 2 that the critical crack tip displacement affects not only the initial J-integral but also the J-resistance curve. It seems that the effect of the critical crack tip displacement on J-resistance curve is not linear. The larger the critical crack tip displacement is, the larger the initial J-integral and the slope of J-resistance line. As the assumption in the model, the critical crack tip displacement keeps the same as the crack growth. It is clear from the figure that the tendency of J-resistance curve becomes steeper as the critical crack tip displacement increasing. For the given critical crack tip displacement, the tendency of J-resistance curve becomes smaller as the crack growth. The critical crack tip displacement is a main factor influencing the initial J-integral.

The material constants are kept the same in the calculations in order to investigate the effect of node release exponent on the J-resistance curve. The yielding stress is taken as 490MPa. The strain-hardening exponent is 8.0. The ultimate fracture strain keeps 0.2. The critical crack tip displacement is 0.05mm. It is displayed in Fig.2 that the node release exponent m affects strongly on the J-resistance curve. The initial J-integral gets greater and the slope of J-resistance curve becomes steeper as the node release exponent decreasing. It can be obtained that the larger node release exponent expresses the lower crack growth resistance. In the potential node release technique, there are two parameters which can expresses the changes of the initial J-integral and J-resistance. These two parameters have some relations with the material properties, which can be determined from fracture toughness testing and tensile testing. From the micro-mechanics of ductile fracture, the critical crack tip displacement and node releasing exponent in the model should have some relation with void properties. Those need more detailed investigations.

The crack driving force U is taken as a crack growth criterion in this study. The critical values Uc is determined by the ultimate fracture strain and stress triaxiality near crack tip as mentioned above. The stress triaxiality is dependent on the state of crack body. The ultimate fracture strain can be determined from the maximum point in the tensile stress-strain line. The constants in potential node release law are kept the same in the calculations in order to investigate the effect of ultimate fracture strain on the J-resistance curve. The yielding stress is taken as 490MPa. The strain-hardening exponent is 8.0. The node release exponent is 0.5. The critical crack tip displacement is 0.05mm. It is displayed in figure 4 that the ultimate fracture strain affects significantly on the J-resistance curve. The initial J-integral gets greater and the slope of J-resistance curve becomes steeper as the ultimate fracture strain

increasing.

CONCLUSION

Based on the combination of micro-void mechanics and macro-fracture mechanics, a model to estimate the ductile crack growth in ductile materials is proposed. A potential node release technique is developed in finite element simulation by introducing a potential node releasing law in traditional node release technique. The ductile crack growth of three-point bend specimen is investigated numerically making use of self-developed finite element method. Conclusion shows that all the parameters in the model affect not only the initial J-integral but also J-resistance curve, that the node release exponent m, ultimate fracture strain and the strain hardening exponent are the main factors which influence the J-resistance slope, that the critical crack tip displacement, and yielding stress are the main factors affecting the initial J-integral.

REFERENCE

[1] Yoshimura-Shinobu, Yagawa-GGGenki, Pyo-Chang-Ryul, Simplified stable crack growth analyses of welded CT specimens - comparison study of GE/EPRI, reference stress and R6 methods. International Journal of Pressure Vessel and Piping, 1995, 63(3), 293-302.

[2] Leevers P.S. and Radon J.C., Inherent biaxiality in various fracture specimen geometries. International Journal of Fracture, 1982, 19,311-325.

[3] Barnby J.T., and Shi Y.W., Void nucleation in tensile deformation processes of a C-Mn structural steel, International Journal of Fracture, 1984, 25, 143-151.

[4] Oven D.R.J., and Fawkes A.J., Engineering Fracture Mechanics: Numerical Methods and Application, Swansea, Pineridge Press Ltd. 1983

[5] Zhang J.X., and Murakawa H., Numerical study of stress triaxiality and fracture driving force for notched specimen with mechanical heterogeneity. Trans. Of JWRI, 1990, 27, 81-87

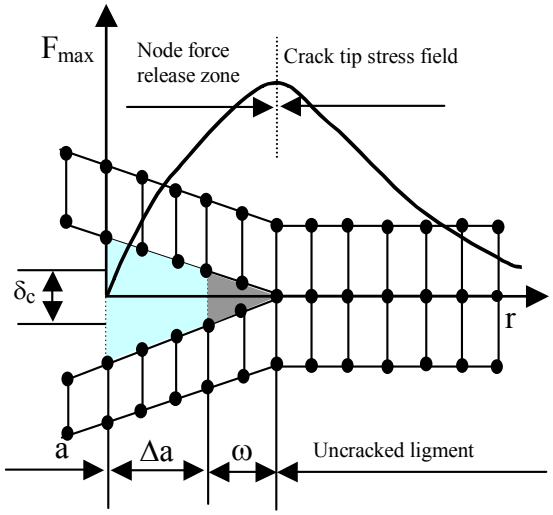

Fig.1 The simulating model for potential node release technique

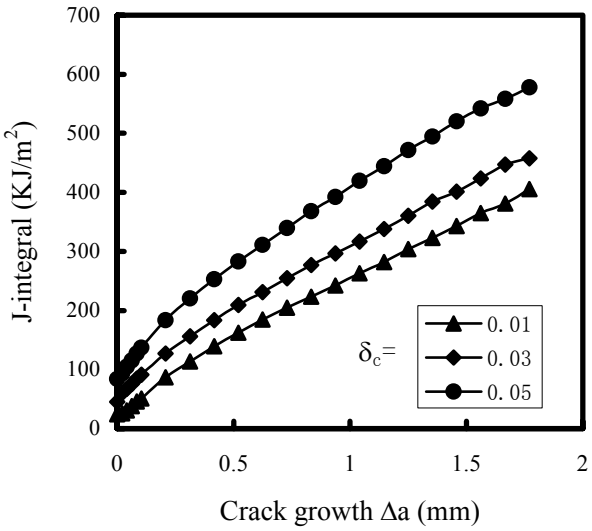

Fig.2 Effect of the critical crack tip displacement on J-resistance curve

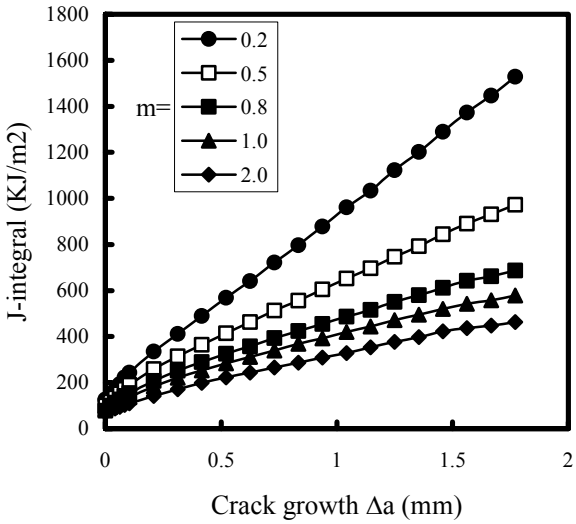

Fig.3 Effect of the node release exponent m on J-resistance curve

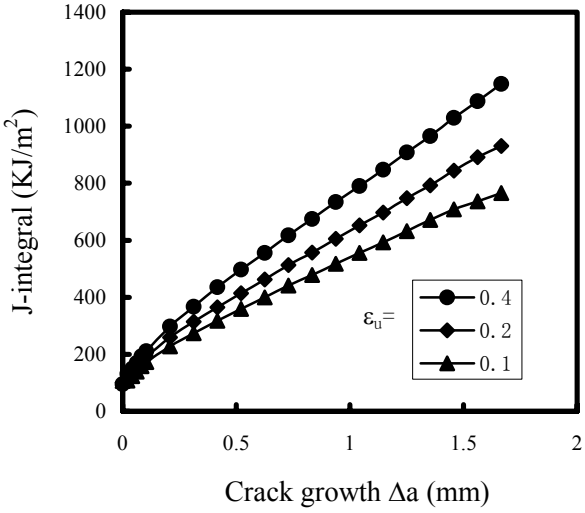

Fig.4 The effects of ultimate fracture strain on J-resistance curve.

ORAL/POSTER REFERENCE: IFC100255OR

A SIMPLE METHOD FOR TOPOLOGY OPTIMIZATION USING ORTHOTROPIC MATERIAL PROPERTIES

Zhiqiang WU[1], Yuji SOGABE[1], Yutaka ARIMITSU[1]

[1]Department of Mechanical Engineering, Ehime University,
3 Bunkyo-cho, Matsuyama, Japan

ABSTRACT

In this paper, a simple method for topology optimization of linearly elastic continuum structures is presented. For prescribed loading and boundary conditions, and subject to a specified amount of structural material, the optimum structural topology is determined from the condition of maximum integral stiffness, which is equivalent to minimum elastic compliance. The SIMP (Simple Isotropic Material with Penalization) is improved in order to save the computation time. Instead of using isotropic material with SIMP method, the material is assumed to be pseudo orthotropic continuum by setting the principal axis of the material to principal stress directions and introducing a new penalty function to the young's modulus at the minor principal stress direction. Numerical examples illustrate that the present method is more efficient than the SIMP method.

KEYWORDS

Topology optimization, Optimal design, Maximum stiffness structure, CAD

INTRODUCTION

The research in the area of topology optimization is extremely active recent years. Several topology optimization methods have been proposed, and used for the design of practical problem. However, there still exist a number of problems such as checkerboard, mesh-dependence, and local minima being investigated currently.

The topology optimization of continuum structures corresponds to finding the connectedness, shape and

number of holes such that the objective function is extremized. Using a density function ρ defined on design domain Ω to describe the material distribution, it can only takes the value 0 (void) or. 1 (solid), i.e.

$$\rho(x) = 0 \text{ or } 1, \forall x \in \Omega \tag{1}$$

It is well known that the 0-1 topology optimization problem lacks solutions in general. The reason is that given one design the introduction of more holes will generally increase the efficiency measure. A general approach to avoid this problem is that relax the 0-1 density constraint to a continuous variable as

$$0 < \rho(x) \le 1, \forall x \in \Omega \tag{2}$$

to achieve an approximate solution, and then use other techniques to approach a black/white design. Bendsøe and Kikuchi [1] introduced a periodic microstructure to the material through the use of so-called homogenization approach to topology optimization that allows the volume density of material to cover the complete range of values from 0 to 1 by changing the size of microstructure. To use this method, it is necessary to determine the effective material characteristic by homogenization, and results are obtained with large regions of perforated microstructure or composite materials ($0 < \rho < 1$). Another approach that is called density function method [2] disregards the details of the microstructure and defines the elasticity tensor as a function of density of material directly. The SIMP (Simple Isotropic Material with Penalization) approach [3] is kind of density function method, in which the stiffness tensor of the intermediate density material is penalized with an exponential function of density to somehow approach a 0-1 design. Using the SIMP approach the stiffness tensor of an intermediate density material is

$$C_{ijkl}(\rho) = C^0_{ijkl}\,\rho^p \tag{3}$$

where C^0_{ijkl} is the stiffness tensor of material and p is the penalization factor which ensures that the continuous design variables are forced towards a black/white solution. To control the value of p can control the speed of convergence and the rate of intermediate density material in the result design. It is a popular method and has also been widely used because of its simplicity.

In this study, the SIMP approach is improved in order to be more efficient in optimization process. Using the concept of Michell truss, we assume material to be a pseudo orthotropic continuum and introduce new penalties to the Yang's modulus. An example is attached at the end to show the validity of this approach.

FORMULATION OF OPTIMIZATION PROBLEM

In this paper, we treat the problem of maximum stiffness of structures with the given amount of material. Design for maximum stiffness of statically loaded linearly elastic structures is equivalent to design for minimum compliance defined as the work done bye the set of given loads against the displacements at equilibrium. Consider an initial domain Ω with a boundary Γ loaded with a static force $\mathbf{P}$. The optimization problem can be formulated as

$$\begin{aligned}
&\textit{Minimize} && \int_\Gamma P_i u_i \, d\Gamma \\
&\textit{Subject to} && \int_\Omega C_{ijkl} u_{k,j} v_{i,j} \, dx = \int_\Gamma P_i v_i \, d\Gamma \\
& && \qquad \mathbf{u} \in H^1(\Omega),\ \forall \mathbf{v} \in H^1(\Omega) \\
& && \int_\Omega \rho(x) \, dx \le M_0 \\
& && 0 < \rho(x) \le 1
\end{aligned} \tag{4}$$

where $\boldsymbol{u}$ is the displacement vector, $\boldsymbol{v}$ is the variation of $\boldsymbol{u}$, M_0 is the given amount of material. Using Lagrange multiplier method, this optimization problem can be rewritten to a stationary problem of a Lagrange functional as

$$L(\boldsymbol{u},\boldsymbol{v},\boldsymbol{r},\boldsymbol{L}) = \int_G P_i\, u_i\, dG - \int_W C_{ijkl} u_{k,j} v_{i,j}\, dx + \int_G P_i\, v_i\, dG - \boldsymbol{L}\left(\int_W \boldsymbol{r}(x)\, dx - M_0\right) \tag{5}$$

Taking the variation of the Lagrange functional, the optimality criterion of this problem can derived as

$$\int_W \left(\boldsymbol{L} - \frac{\partial C_{ijkl}}{\partial \boldsymbol{r}} u_{k,l} v_{i,j} \right) \dot{\boldsymbol{r}}\, dx = 0 \tag{6}$$

$$\int_W C_{ijkl} \dot{u}_{k,j} v_{i,j}\, dx = \int_G P_i\, \dot{u}_i\, dG \qquad \boldsymbol{u} \in H^1(W), \forall \boldsymbol{v} \in H^1(W) \tag{7}$$

Eqn.7 is an adjoint equation from which the adjoint variable $\boldsymbol{v}$ can be solved.

INTRODUCING ORTHOTROPIC MATERIAL PROPERTIES

As mentioned above, checkerboard problem is one of the problems occurring frequently in the topology optimization process. As shown in Figure 1, the result design consists of alternating solid and void elements so that it is not useful for practical purpose. To avoid the checkerboard pattern, the use of higher-order finite elements has been suggested [4]. However, this approach is the substantial increase in cpu-time because of not only the increasing of degrees but also the low convergence speed. A large penalty parameter p is used in general to reduce the cpu-time, but it has the possibility to decrease the performance of the structure. In this research, we try to find a new kind of penalty to the intermediate density material so that the optimization process is more efficient in finding the solution and converging to 0-1 material distributions with less performance loss of the result design. The hint is obtained from the so-called Michell truss [5] that is derived by Michell for a minimum weight truss of a plane structure. As shown in

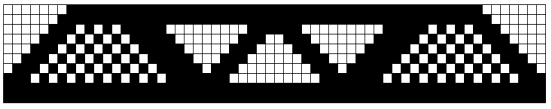

Figure 1: Checkerboard pattern

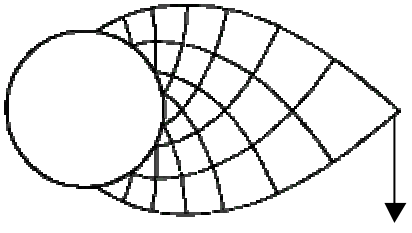

Figure 2: Michell truss

Figure 2, the Michell truss is an orthogonal net structure, in which each component extends in the direction of principal stress and crosses mutually with a right angle. Although this solution is impractical because it derived without the constraint on geometric shape and number of holes, the concept is applied in this paper. Instead of using isotropic material, the material is assumed to be pseudo orthotropic continuum and the principal axis of the material is set to principal stress directions. It is reasonable to consider that this approach will be efficient in generating the topology. In order to create pseudo orthotropic material, we introduce different penalty functions to the young's modulus at the major principal stress direction and that at the minor principal stress direction as

$$E_1 = E^0 \rho^p \tag{8}$$

$$E_2 = E_1 \left| \frac{\sigma_1}{\sigma_2} \right| \tag{9}$$

Where E^0 is the true Young's modulus, σ_1 and σ_2 are the major principal stress and the minor principal stress respectively ($|\sigma_1| \geq |\sigma_2|$), E_1 and E_2 are the Young's modulus at the directions of σ_1 and σ_2 respectively. Eqn.7 is the same penalty with SIMP method and Eqn.8 is a new penalty. The reason why give E_2 a harder penalty is that E_2 has less effect on the performance of the structure than E_1.

NUMERICAL RESULTS

In this section, a square plate example is performed in order to investigate the effect of the new penalties presented in this paper. As shown in Figure 3, the plate is computed for maximizing the stiffness, in which the left side is fixed and the right side is applied with a load. It is modeled by 8-node isoperimetric elements with the material properties Young's modulus E=2.10x10^{11} N/m^2 and Poisson's ratio =0.3. The volume constraint is set to 40% of the entire design domain. The penalty parameter p is raised from 1.0 to 2.0 with the step of 0.1 during the optimization process. Figure 4 shows an optimal result in the case of using isotropic material properties and Figure 5 shows an optimal result in the case of using orthotropic material properties. Comparing these two results, the obvious difference can be found. From Figure4, it is found that the clear topology didn't appear after 150 iterations. The clear topology appeared after 330 iterations. On the other hand, from results of Figure 5, it is found that the clear topology appeared after 150 iterations with p=1.4. It is similar to the result after 330 iterations and it is clear enough to use as a last result. Another fact can be confirmed that results of the two cases are almost the same; there is even no

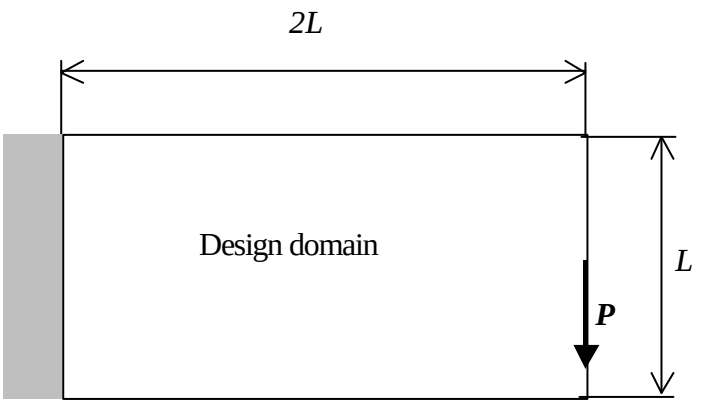

Figure 3: Design problem and boundary conditions

(a) After 30 iterations, p=1.0

(b) After 150 iterations, p=1.4

(c) After 330 iterations, p=2.0

Figure 4: Results for the use of isotropic material properties

(a) After 30 iterations, p=1.0

(b) After 150 iterations, p=1.4

(c) After 330 iterations, p=2.0

Figure 5: Results for the use of orthotropic material properties

difference of the values of two objective functions. This fact means that there is almost no extra loss of the efficiency of last design to use with new penalty functions.

CONCLUSION

In this paper, a simple method for topology optimization of linearly elastic continuum structures is presented. Instead of using isotropic material with SIMP method, the material is assumed to be pseudo orthotropic continuum by setting the principal axis of the material to principal stress directions. We introduce a new penalty function to the young's modulus at the minor principal stress direction. Numerical examples illustrate that the present method is more efficient than the SIMP method.

REFERENCES

1. Bendsøe, M.P. and Kikuchi, N. (1988). *Comp. Meth. Appl. Mech. Engng*. 71,197
2. Yang, R. J. and Chuang, C. H. (1994). *Comp. and Struct.* 52(2), 266
3. Zhou, M. and Rozvany, G.I.N. (1991). *Comp. Meth. Appl. Mech. Engng*. 89, 197
4. Diaz, A.R., Sigmund, O. (1995). *Struct. Optim*. 10, 40
5. Michell, A.G.M. (1904). *Philosophical Magazine*, Ser.6, 8, 589

ORAL/POSTAL REFERENCE: ICF100190OR

A STIFFNESS RELEASE (FINITE ELEMENT) MODEL FOR HIGH SPEED CRACK PROPAGATION ANALYSIS

N.N. Kishore, M. Siva Reddy and G.V. Deshmukh

Department of Mechanical Engineering, Indian Institute of Technology,
Kanpur – 208 016, India

ABSTRACT

In this paper, a finite element model for simulating dynamic crack propagation phenomenon is presented. The mesh is kept stationary and a 1-Dimensional elastic spring element is added at the crack tip node. The gradual propagation of crack is achieved by decreasing its stiffness value from a large (infinite) value to zero as the crack propagates to the next node within the element. This paper presents a model for the stiffness of the spring element and the crack tip element mass as a function of crack length. This method is applied to determine the dynamic energy release rate of DCB specimens made of glass-epoxy subjected to impact. Results show that the energy release rate gives stable and acceptable solution.

KEYWORDS

Computational Fracture mechanics, Dynamic Fracture, Composites, Impact

INTRODUCTION

An understanding of the mechanics of dynamic fracture is necessary for developing sound design methodologies. Nishioka and Atluri [1] gave elaborate information on the analysis of dynamic fracture using FEM. The most common ways to deal with the crack tip region was to simulate crack growth through gradual release of elemental nodal forces or embedding a moving element in which interpolation functions are determined by the continuum near tip fields at the crack tip in the mesh, and J-Integral consideration. Chiang [2] presented a numerical procedure based on eigen function to determine the dynamic stress intensity factor for a crack moving at steady state under anti-plane strain condition. Thesken and Gudmundson [3] worked with elasto-dynamic moving element formulation incorporating a variable order singular element to enhance the local crack tip description. Kennedy and Kim [4] incorporated micropolar elasticity theory into a plane strain finite element formulation to analyse the dynamic response of the crack. Beissel, Johnson and Popelar [5] presented an algorithm, which allows crack propagation in any direction but doesn't require remeshing or the definition of new contact surfaces. The edges of these failed elements simulate crack faces that can sustain only compressive normal traction In the present work an efficient 'Stiffness Release Model', method is proposed to simulate the crack propagation.

FORMULATION

In the present development of the stiffness release model, for Mode-I crack propagation a one-dimensional spring element is attached to the crack tip node, whose stiffness is reduced gradually as crack advances to the next node (Fig.1). The required spring stiffness is very large when crack tip is at the beginning of element and zero when crack tip reaches the other end. Amount of additional stiffness required is a function of crack length and is obtained from quasi-static crack propagation analysis. Fig. 1(a) shows a symmetric part of deformed 2-Dimensional plate in which crack is upto node B, and Fig. 1(b) shows the crack at at intermediate position between node B and node C. Fig.1(a) shows the additional spring element normal to the crack plane. Fig. 1(c) shows the crack reaching node C. Let, K_0 be the stiffness at node B of the original plate in the normal direction without the additional spring; and u_0 be the displacement of node when crack tip reaches the next node as the element opens up completely. The spring stiffness, K_s, corresponding to an intermediate displacement, u, can be found out from equilibrium conditions as

$$K_O(u_O - u) = K_S \tag{1}$$

which gives the equation,

$$K_S = K_O\left[\frac{u_O}{u} - 1\right] \tag{2}$$

Energy in the spring is given as

$$E_s = \frac{1}{2}K_s u^2 = \frac{1}{2}K_0\left[\frac{u_0}{u} - 1\right]u^2 \tag{3}$$

The energy in the system is released due to the decrease in the spring stiffness and thus, the energy release rate can be determined from

$$G = \frac{\Delta E}{\Delta A} \tag{4}$$

where ΔA is the increment in crack area. Defining a non-dimensional parameter, a, as, a = crack length (within element) / element length, d and B is the thickness of plate, the energy release rate for a double cantilever beam can be written as

$$G = \frac{\Delta E}{Bd\Delta a}$$

$$= \frac{1}{2}K_0(-u_0)\frac{1}{Bd}\frac{du}{da} \tag{5}$$

As the variation of G is linear with respect to a, it can be represented as,

$$G = C_1 + C_2 a \tag{6}$$

where C_1 and C_2 are constants. Therefore, from Eqs. (5) and (6) we get,

$$C_1 + C_2 a = -\frac{1}{2}\frac{K_o u_o}{Bd}\left(\frac{du}{da}\right) \tag{7}$$

On integrating Eq. (7) and using the conditions that at u=0 when a=0 and condition $u=u_0$ when a=1, we get

$$\frac{u}{u_o} = \frac{2C_1 a + C_2 a^2}{2C_1 + C_2} \tag{9}$$

which can be expressed in the form,

$$\frac{u}{u_0} = a + C\,(a - a^2) \tag{10}$$

Thus, the equation for the spring stiffness, (Eq. (2)), finally can be written as

$$K_S = K_o\left(\frac{1-f}{f}\right) \tag{11}$$

where $f=u/u_0$ as given by Eq. (10). Given the static stiffness, K_0, the energy release rate is determined using Eq. (5). Or, we can directly determine the dynamic energy release rate, G, using the basic equation

$$G\Delta A = \Delta W_{ext} - \Delta U - \Delta T \tag{12}$$

where ΔT is the increment in kinetic energy in the body. If the crack moves with velocity v, then,

$$G = \frac{1}{Bv}\frac{d}{dt}(W_{ext} - U - T) \tag{13}$$

Constant 'C' in Eq. (10) can be determined from the quasi-static case so as to get the energy release rate curve is continuous at element boundaries. For quasi-static case this value is very small. However it was observed that C has considerable effect in dynamic crack propagation. It can be seen that this constant, C, is affected by element size and time step Δt. For a given dynamic problem, its value need to be chosen so that final energy release rate curve is smooth without any fluctuation.

It is also important to take into account the changes in the effective mass of the crack tip element. In order to take into account the mass variation, shape function N_1 of the element at the crack tip is modified such that it is a function of crack length 'a' as,

$$N_1 = \left(\frac{1-\xi}{2}\right)^{\alpha}\left(\frac{1-\eta}{2}\right) \tag{13}$$

where , ξ and η are natural co-ordinates and α is chosen as,

$$\alpha = \left(\frac{10(1.1-a)}{a} \right)^{0.9} \tag{14}$$

$N_I=1$ at (ξ,η) is (-1,-1) and $N_I=0$ when $\xi=\eta=1$ and α is chosen such that, for a given crack length, a, within an element $N_I=1$ when $\xi=-1$, and $N_I=0$ when $\xi \geq (2a-1)$. Thus, as the crack advances mass of the element increases gradually. Finally when a=1 i.e., when crack is at the end of the element, shape function N_I take its usual bilinear form. Thus, crack node mass is zero when the crack is at the beginning of the element and increases gradually as crack reaches the end of the element.

RESULTS AND DISCUSSION

The important aspects of the results are: i) Determination of the constant C (Eq. (10)) for quasi-static crack propagation; ii) crack propagation analysis at constant speed under dynamic input force pulse; and iii) Crack propagation analysis of a DCB impact experiment. Material and geometric properties of the specimen are as follows: Length of specimen, L = 0.06m; width of specimen, W = 0.005m; Thickness of specimen, B = 0.024m; Crack length, a′ = 0.03m; Modulus of Elasticity, $E=210\text{x}10^9$ Pa; Poisson's ratio, $\nu = 0.3$. The DCB specimen is analysed using 4-noded isoparametric element. The mesh has 600 elements of 1.0 mm X 0.5 mm. Static stiffness, K_0, was determined for the given mesh by applying force at the node preceding crack tip node and determining corresponding displacement at that node. Energy release rate variation with crack length for different values of constant C are determined and it was observed that for C= -0.028, that the energy release rate curve was smooth within the element and continuous at element boundaries.

For dynamic crack propagation, a short pulse is applied on the specimen (Fig. 2). The pulse was modelled by $F(1-\cos(\omega t))$, where frequency is taken as 125KHz with a pulse duration of 8μs, amplitude of 50N. The crack was initiated after 8μs and moves at speed of 1500m/s and. The time steps used was $\Delta t=1.0\text{x}10^{-6}$sec. The value of C= -0.028 obtained for quasi static crack propagation case, if used for dynamic case of a crack velocity of 1500m/s gives energy release rate as shown in Fig 3. It can be seen that there are large oscillations at the element boundaries which shows that C value for the quasi-static case is not suitable for the dynamic case and has to be modified. C value is modified so that the energy release rate curve becomes smoother. Effect of change in C value on energy release rate curve is shown in Fig. 4. It can be seen that C=0.4 gives rise to less oscillations in G_I in comparison to other values and it is chosen for further analysis. Fig. 5 shows effect of averaging of 'f ' on energy release rate variation leading to a better solution. The effect of modification of crack tip element mass by changing the shape function N_I on energy release rate can be seen in Fig 6. This figure reveals that energy release rate curve has smoother variation within element and fairly stable solution across element boundaries It can be seen very clearly that solution with mass modification is better than one without mass modification.

The present method is applied to determine the dynamic G_I for the impact experiment on DCB specimen made of Glass Fabric/Epoxy DCB composite [6]. Following data was used as input for finding energy release rate. Density, $\rho = 1825\text{Kg/m}^3$; $E_L=26\text{x}10^9$ N/m^2, $E_T=6.6\text{x}10^9$N/m^2; $G_{LT}=3.5\text{x}10^9$N/m^2; $\nu_{LT}=0.21$; $\nu_{TL}=0.053$. Fig 7 give the dynamic G_I from the regular energy release rate determination. Fig. 8 shows the results by the present model. From these it can be seen that the present model is more accurate compared with the force release model.

CONCLUSIONS

A new model is proposed to investigate high speed crack propagation.

1. Model gives fairly smooth and more stable variation of energy release rate.
2. Experimental results reveal that unlike force release model energy release rate doesn't drop to a low value in just a few time steps but falls gradually which is a more practical result.
3. It can be observed that the size of the element and time step should be chosen such that the effective stiffness used in the integration scheme decreases fairly monotonically.

REFERENCES

1. Nishioka, T. and Atluri, S.N. (1986) *Computational Methods in Mechanics of Fracture*, Elsevier Pub.
2. Chiang, C.R. (1990) *Int. J. of Fract*, 45, pp 123-130.
3. Thesken, J.C. (1991) *Int. J. of Fract*, 52, pp 47-65.
4. Kneedy, T.C. and Kim, .B., *Eng. Fract. Mech.*, 27, pp 227-298.
5. Beissel, S.R., Johnson, G.R. and Popelar, C.H. (1998) *Eng. Fract. Mech.*, 61, pp 407-425.
6. Choudhary, H. (2000) M.Tech. Thesis, I.I.T., Kanpur

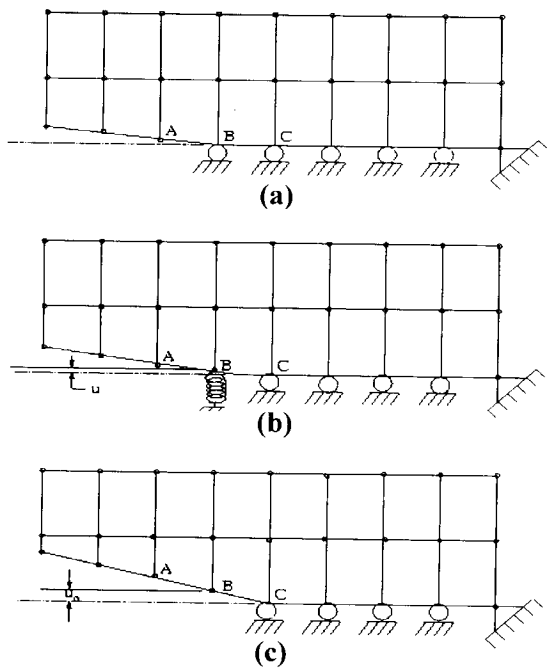

Fig. 1: Crack opening pattern in model

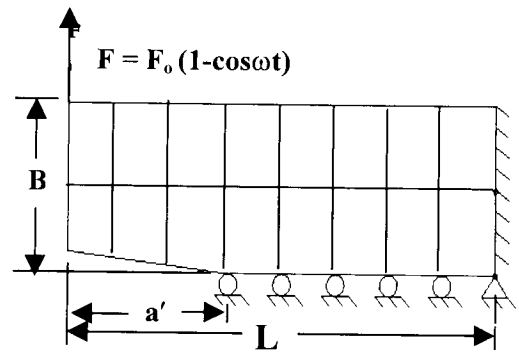

Fig. 2: DCB specimen (Half)

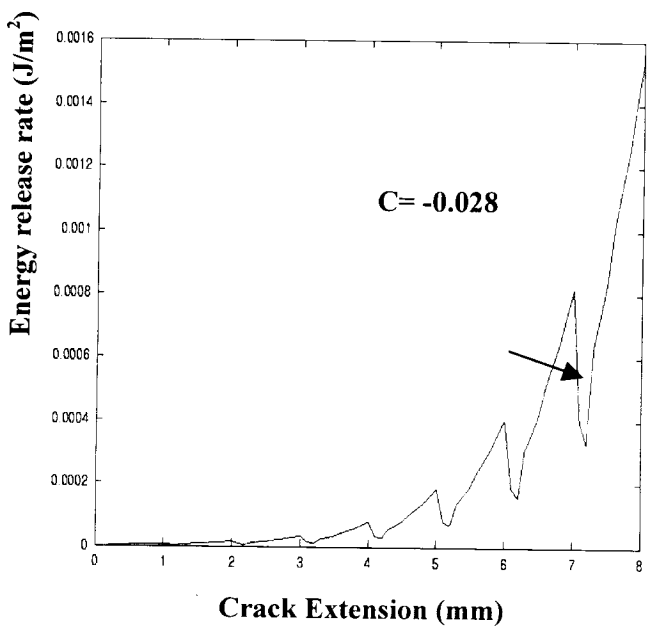

Fig. 3: Energy release rate variation for Crack-velocity 1500m/s

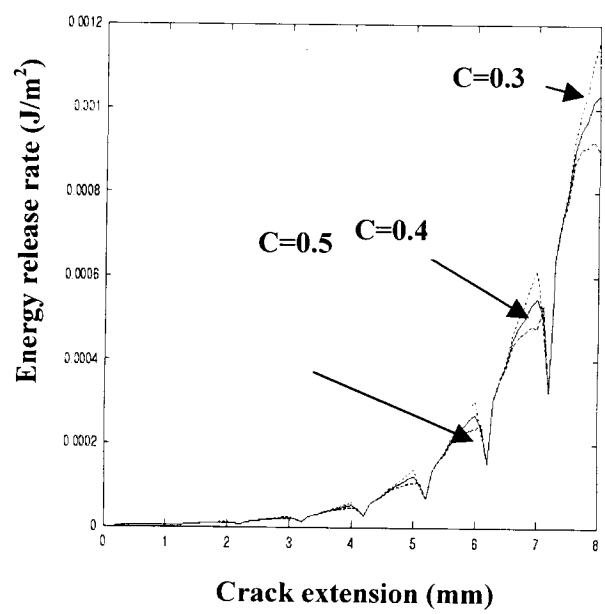

Fig. 4: Effect of change in C on energy release rate

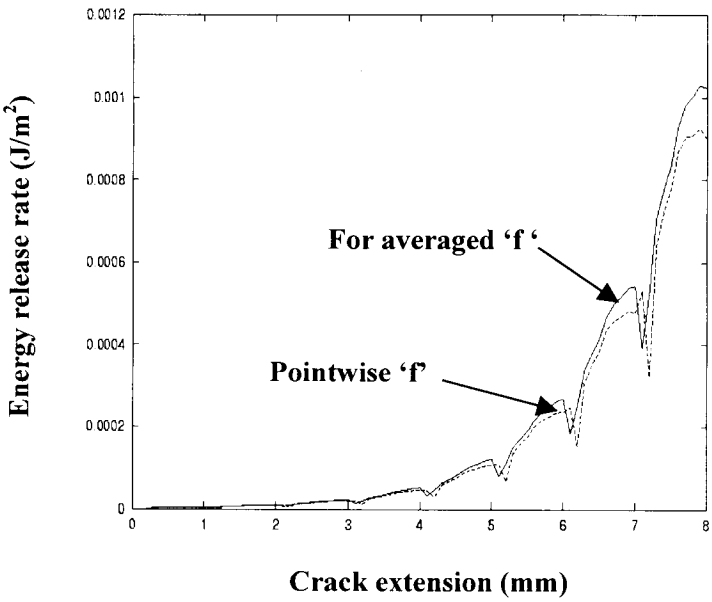

Fig. 5: Effect of averaging 'f' values on energy release rate

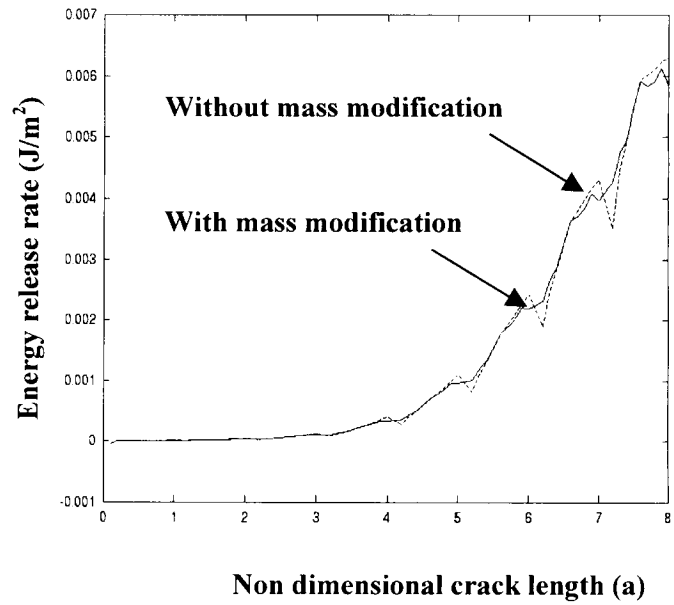

Fig. 6: Energy release rate for crack velocity 1250m/s

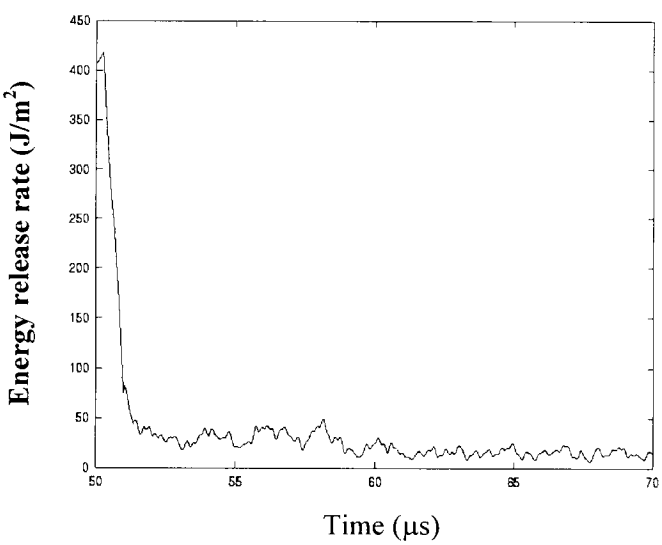

Fig. 7: Energy release rate for Expt. 1 [6] By Force release model

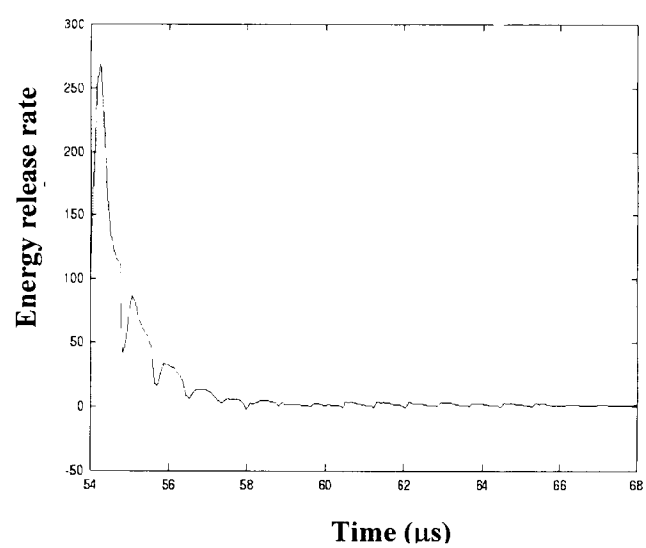

Fig. 8: Energy release rate for Expt. 1 (Present study)

ORAL/POSTER Reference: ICF100878OR

A STRAIN BASED APPROACH TO ASSESSING CREEP CRACK INITIATION AND CRACK GROWTH

D.J. Smith and A.J. Fookes

Department of Mechanical Engineering, University of Bristol, Bristol, BS8 1TR, UK

ABSTRACT

Recently, there has been considerable interest in studying creep crack growth in brittle materials. For example, the methodologies for assessing creep ductile materials, using fracture mechanics parameters like C^* and C_t, have been extended to include creep brittle materials. This paper begins by examining these recent developments and outlines the difficulties in adopting these methods. An alternative approach is then proposed in this paper. This new approach is based on recent work on development of a strain based failure assessment diagram (SBFAD). Experimental results from a series of tests on a simulated heat affected zone of a low alloy steel are examined. It is shown that the results agree well with the analysis using a SBFAD. The application of the methodology for assessing the initiation and growth of a defect in a creep brittle material is demonstrated.

KEYWORDS

Creep brittle, creep crack growth, Strain based failure assessment diagram, material resistance.

INTRODUCTION

Previous research [1-3] on characterising creep crack growth (CCG) has focussed on characterising the rate of creep crack growth in terms of C^*, the creep equivalent of the non-linear fracture parameter J. The bulk of this work has examined creep-ductile materials, in which CCG is accompanied by significant amounts of creep deformation. However, a more problematic class of high-temperature structural materials are creep-brittle materials where the extent of creep deformation is small compared to the total displacement.

In order to allow creep-brittle materials to be assessed using C^* the validity limits in the CCG testing standard [4] have been relaxed [5]. This includes decreasing the amount of creep deformation required and to widen the regime of creep crack extension. Alternatively the C_t parameter has been proposed to characterise CCG for small-scale creep conditions [6]. However, even with the reduction of the limitations there are still a number of observed shortcomings associated with using C^* for characterising creep crack growth. For example, the initial stage of CCG, and the subsequent steady CCG rate [6] cannot be described uniquely by C^*. In brittle alloys this can mean in many cases that

only the latter part of the test (usually less than 50% and sometimes as little as 10% of the remaining life of the test [8]) can be characterised. Consequently it is only the accelerating portion that is uniquely described by C^*. This is demonstrated clearly by [7,9-10]. In this latter stage it has also been suggested that measured values of C^* become equivalent to the CCG rate [11]. This is because, at large CCG rates, most of the displacement rate results from increases in the elastic compliance due to crack extension and not from creep deformation taking place within the specimen. With these concerns in mind this paper examines an alternative approach.

The development of the strain-based failure assessment diagram (SBFAD) is explored, which could potentially simplify the treatment of situations involving variable stress and variable temperature. A ferritic steel representative of the simulated heat affected zone of a low alloy steel is examined at 380^{o}C using the new SBFAD.

STRAIN BASED FAILURE ASSESSMENT DIAGRAM (SBFAD)

A high temperature time dependent failure assessment diagram (TDFAD) based on the well established low temperature R6 approach [12], has been developed which allows predictions of creep initiation time and times for small amounts of CCG [13]. The TDFAD uses a high temperature 'creep toughness' which replaces the fracture toughness used in the R6 procedure. This 'creep toughness' parameter may be examined directly from experimental load-displacement information or indirectly from CCG rates as a function of C*. A strain based failure assessment diagram (SBFAD) has recently been developed as an alternative to the stress based TDFAD for high temperature components [14]. Strain accumulation can be measured or calculated and could be used to provide a measure of the components continuing performance. This section very briefly describes the SBFAD.

The Option 2 FAD in R6 [12] may be extended to described a TDFAD [13] given by

$$K_r = \left[\frac{E\varepsilon_{ref}^T}{L_r \sigma_{0.2}^c} + \frac{L_r^3 \sigma_{0.2}^c}{2E\varepsilon_{ref}^T} \right]^{-1/2} \qquad (1)$$

where $K_r = K_{applied}/K_{mat}$, $L_r = \sigma_{ref}/\sigma_{0.2}^c$, ε_r is the reference strain corresponding to the reference stress σ_{ref}, and $\sigma_{0.2}^c$ is the stress at 0.2% strain from the isochronous stress-strain curve. It is possible to recast eqn 1 to give K_r as a function of normalised strain ε_r, where

$$K_r = 1/\sqrt{\left[\varepsilon_r + 0.5L_r^2/\varepsilon_r\right]} \qquad (2)$$

and ε_r is the ratio of the total to elastic strain at reference stress, $\left(\varepsilon_{ref}^T / \varepsilon_{ref}^e\right)$.

For a structure, a relationship between the reference strains and the load line displacements is required. Preliminary studies using the EPRI handbook solutions [15] have shown that for the compact tension (CT) specimen for a/W=0.5 and 0.75, where a is the crack length and W is the specimen width the normalised strain may be related to the load line displacement by

$$\varepsilon_r = \left(\frac{2.4\Delta_T}{\Delta_e} - 1.4 \right) \qquad (3)$$

where Δ_T is the total load line displacement and Δ_e is the elastic load line displacement.

Figure 1 shows a schematic SBFAD, with curves for K_r as a function of ε_r for L_r

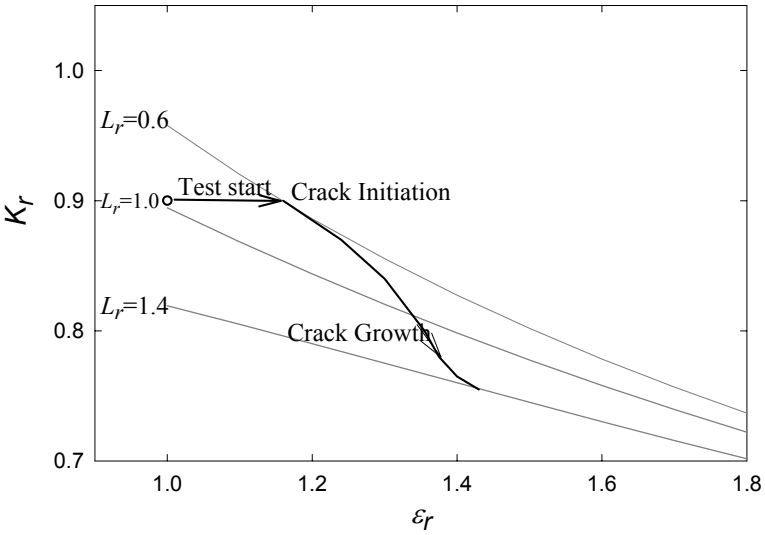

Figure 1, SBFAD Assessment of Creep Crack Growth

varying from 0.6 to 1.4. For large strains the SBFAD is reasonably independent of L_r. Now consider a cracked component subjected to a constant load corresponding to L_r=0.6 and K_r=0.9. At the start of the life (and assuming zero inelastic strain during loading) ε_r=1.0. Creep strain accumulation without crack growth corresponds to a horizontal line in figure 1. Crack initiation is assumed to occur when the horizontal line touches the SBFAD for L_r=0.6. Subsequent crack growth leads to increasing L_r and decreasing K_{mat}, and a locus of points are generated for increasing ε_r.

EXPERIMENTS AND RESULTS

To examine in more detail the applicability of the strain based approach results from CCG tests conducted on a simulated low alloy steel HAZ material at 380°C are explored in this section. The details of the tests and their results are given in [16]. The test programme used compact tension specimens subjected to constant load with the total displacements monitored throughout each test. Tests lasted from about 40 hours up to 1000 hours. In all tests there was very limited evidence of plasticity before the onset of creep.

In the absence of plasticity it is important to determine the elastic and creep displacements which can be separated by displacement partitioning presented earlier by Saxena and Landes [17]. At a given crack length the total displacement, Δ_t, is the sum of the elastic, Δ_e, and the creep, Δ_c, displacement, where

$$\Delta_t[a] = \Delta_e[a] + \Delta_c[a] \tag{4}$$

As the crack length, a, increases the elastic displacement is estimated using

$$\Delta_e[a] = \Delta_e[a_o]\frac{C_e[a]}{C_e[a_o]} \tag{5}$$

where C_e is the elastic compliance function and $\Delta_e[a_o]$ is the measured initial elastic displacement at the initial crack length, a_o. For the CT specimen the elastic compliance $C_e(a/W)$ expressed as a function of the normalised crack length, a/W [18] is:

$$C_e\left[\left(\frac{a}{W}\right)\right] = \frac{1}{EB}\left(\frac{1+(a/W)}{1-(a/W)}\right)^2\begin{bmatrix}2.163+12.219(a/W)-20.065(a/W)^2\\-0.9925(a/W)^3+20.609(a/W)^4-9.9314(a/W)^5\end{bmatrix} \tag{6}$$

The elastic displacement can therefore be determined for a growing crack using equation (5). The creep displacement is determined from

$$\Delta_c[a] = \Delta_T[a] - \Delta_e[a] \qquad (7)$$

Overall, the extent of cracking for all the tests was between 4 and 10 mm. This is very extensive compared to conventional ductile crack growth (tearing) tests. The calculated creep displacements using eqn 7 are shown in figure 2. For some tests (C, E and H) there is a consistent increase in creep displacement with increasing time. However, for other tests particularly for $t/t_f > 0.3$, where t_f is the failure time of the specimen, the estimated creep displacement decreased with increasing time.

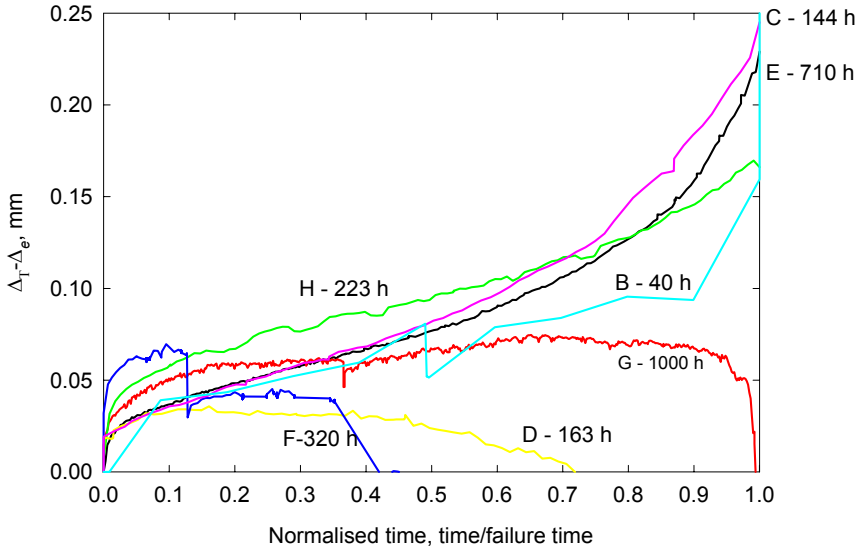

Figure 2, Total Displacement - elastic displacement for simulated HAZ material

In creep-brittle materials, the amount of creep deformation represents a very small percentage of the total displacement. Therefore, in the absence of plasticity the change of displacement caused by a change in elastic compliance is comparable to the total displacement. Consequently small errors in estimating the extent of cracking would lead to large errors in determining creep displacements. Tests D, F and G yielded negative apparent creep displacements. In these tests it is not possible to characterise CCG using C^*.

An alternative approach is to examine CCG in terms of material resistance. For ductile tearing involving rate independent processes the J-resistance curve has been adopted as a measure of a material's resistance to ductile crack growth. This approach is explored here. In general the total energy dissipated, during each test, can be determined from the sum of elastic, plastic and creep displacements. In order to determine the total J_T the elastic, plastic and creep terms were determined using the conventional J formulae, where,

$$J_T = J_e + J_p + J_c \qquad (8)$$

with

$$J_e = \frac{K^2(1-\nu^2)}{E}; J_p = \frac{\eta U_p}{B(W-a_o)}; J_c = \frac{\eta U_c}{B(W-a_o)} \qquad (9)$$

where η is a geometric factor, a_o is the initial crack length, and U_p and U_c are the areas under the plastic and creep parts of the load line displacement curves obtained from the experiments. To determine J_T from the creep crack growth tests it was necessary to obtain from the experiments not only the creep displacements but also the elastic and plastic displacements during initial load up. As

noted earlier the total displacements in the simulated HAZ material were dominated by elastic and creep displacements.

Material resistance curves derived using J_T are shown in figure 3. Each test generates a separate R-curve, with creep tests of short duration giving an R-curve which is generally higher than an R-curve for longer duration. From these results a measure of the material resistance for a given crack extension can be obtained as a function of time. This will be explored in later work.

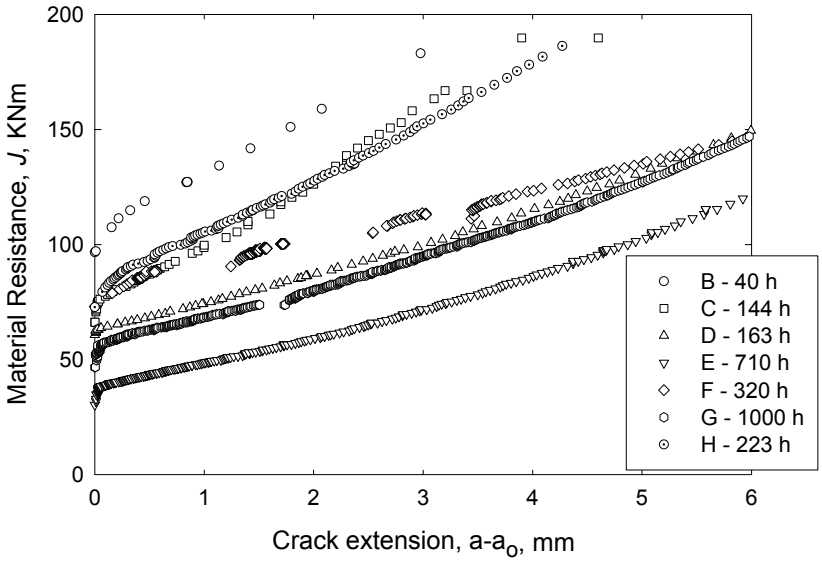

Figure 3, Resistance Curves for Simulated HAZ material

ASSESSMENT OF EXPERIMENTS USING THE SBFAD

In this section the results of the CCG tests on the simulated low alloy steel HAZ are assessed using the strain based failure assessment diagram (SBFAD). In each case K_r was determined using

$$K_r = \sqrt{\frac{K^2 / E'}{J_T}} \qquad (10)$$

where J_T has been obtained using the measured value for the elastic and creep displacements, using eqn 8. The rate ε_r has been obtained from eqn 3.

Figure 4 shows results from test E. A curve for K_r as a function of ε_r obtained from the experiment is shown. As the test progressed K_r decreased and ε_r increased. The position on the curve corresponding to crack initiation is shown on the curve. Also shown are two loci obtained from eqn 2. One locus is for L_r=0.52, corresponding to the initial applied load, assuming plane strain conditions and using the 0.2% yield strength from high temperature tensile test. The second locus is for variable L_r, where L_r was determined accounting for crack growth. The differences between the two loci are largest towards the end of the test. The experimental result closely follows the predicted strain based failure assessment curve given by eqn 2. It is also evident that there was a period of creep strain accumulation prior to crack initiation. Initiation occurred when the experimental curve crossed the assessment line. This is also illustrated schematically in figure 1. Subsequent crack growth occurred such that the experimental curve essentially followed the assessment line.

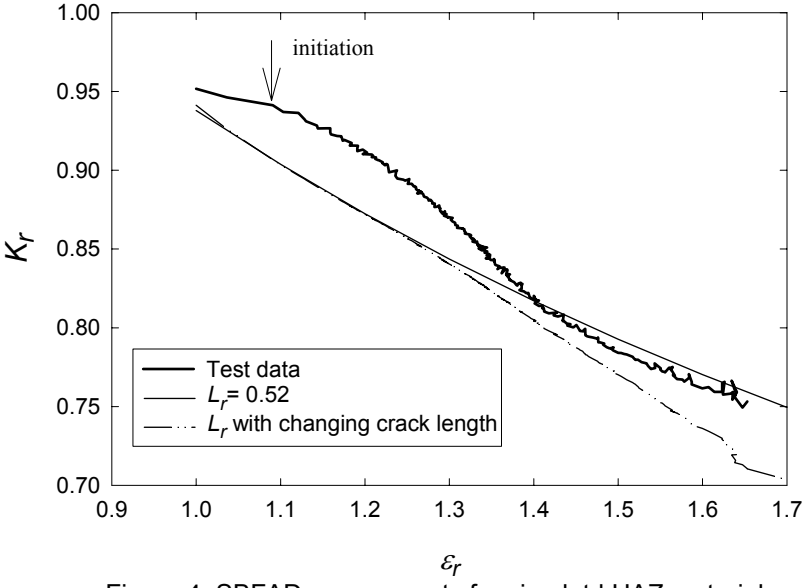

Figure 4, SBFAD assessments for simulatd HAZ material

CONCLUDING REMARKS

An alternative approach to characterising CCG using C^* has been proposed. The SBFAD provides a method of assessing the deformation throughout an entire test. The method uses the total accumulated material toughness and not the instantaneous creep rate to estimate the fracture parameter C^*. Experimental results for a creep-brittle simulated HAZ material have been used to demonstrate the principles of this new method.

REFERENCES

1. Gooch, D. J. and Kimmins, S. T. (1986). Journal of Strain Analysis. 21, 4, 231-242.
2. Webster, G.A. and Ainsworth, R.A. (1994). Chapman and Hall.
3. Ainsworth, R. A., Chell, G., Coleman, M. C., Goodall, W., Gooch, D. J., Haigh, J. R., Kimmins, S. T. and Neate, G. J. (1987). Fat. Fract. Eng. Mat. and Struct. 10, 2, 115-127.
4. ASTM E1457-92. (1996). ASTM 03.01, pp. 932-940.
5. Schwable, K-H., Ainsworth, R.A., Saxena, A. and Yokobori, T. (1999). Eng. Fract. Mech., 62, 1, 123-142.
6. Saxena, A. (1986). Fracture Mechanics-17, ASTM STP 905, pp. 185-201.
7. Tabuchi, M., Kubo, K., Yagi, K., Yokobori, Jr., A.T. and Fuji, A. (1999). Eng. Fract. Mech., 62, 1, 47-60.
8. Yokobori A.T. (1999). Eng. Fract. Mech., 62, 1, 61-78.
9. Yokobori A.T. (1998). Mat. at High Temp. 15, 2, 45-50.
10. Laiarinandrasana, L., Polvora, J.P., Piques, R. and Martelet, B. (1998). Mat. at High Temp. 15, 3/4, 181-186.
11. Bensussan, P., Piques, R. and Pineau, A. (1989). Non. Fract. Eng. ASTM STP 995, pp. 27-54. Saxena, A., Landes, J.D. and Bassani, J.L. (Eds). ASTM, Philadelphia.
12. Milne, I., Ainsworth, R.A., Dowling, A.R. and Stewart, S.T. (1988). Int. J. PVP, 32, 3-104.
13. Ainsworth, R. A. (1993). Fat. Fract. Eng. Mat. and Struct. 16, 10, 1091-1108.
14. Smith, D.J., Fookes, A.J., Dean, D.W. and Lamb, M. (1998). International Conference on Integrity of High Temperature Welds. pp. 355-370.
15. Kumar, V., German, M.D. and Shih, C.F. (1981). EPRI Report NP-5596, Electric Power Research Institute, Palo Alto, C.A.
16. Lamb, M. and Gladwin, D. N. (1998). BNFL, Magnox Generation, Confidential Report, M/TE/SXA/REP/0112/98.
17. Saxena, A. and Landes, J. D. (1984). Advances in Fracture Research, ICF-6, Pergamon Press, pp. 3977-3988.
18. Anderson,T.L. (1995). Fracture mechanics – Fundamental and Application. CRC Press, pp. 607.

A STUDY OF CRACK DEPTH EFFECT AND SCATTERING ON FRACTURE TOUGHNESS IN THREE POINT BEND COD SPECIMENS

M. TOYOSADA, K. GOTOH and S. NAKAYAMA

Department of Marine Systems Engineering, Kyushu University,
Hakozaki 6-10-1, Higashi-ku Fukuoka, 812-8581, Japan

ABSTRACT

Fracture toughness obtained under the same experimental conditions has the following two characteristic features: fracture toughness has the dependency of crack depth and shows a large scatter even though the same geometrical shaped specimens were applied to the tests, which derives from the sensitivity of micro structures of steel. Quantificational evaluation of these phenomena is performed by applying strain rate-temperature parameter in the fracture process zone (R_γ), which is the function of strain rate and temperature, as the evaluation parameter. Postulating that fracture toughness is a function of R_γ, it makes clear that there is no crack depth effect, namely the plastic constraint effect, on fracture toughness and that the scattering on fracture toughness decreases considerably. Moreover, the possibility which the dimensionless parameter derived from R_γ may be the universal parameter to characterize fracture toughness is indicated.

KEYWORDS

fracture toughness, scattering, crack depth effect, plastic constraint, strain rate, R prameter, three point bend COD spceimen

INTRODUCTION

Fracture toughness is affected by the crack depth, especially, in case that plastic zone grows large before the fracture generating. This phenomenon is known as the plastic constraint effect on fracture toughness.Although the explanation that the geometrical difference of specimen shapes generates this phenomenon is stated in many reports, it is difficult to quantify the phenomenon by applying this concept.

Some fracture parameters, e.g. T stress [1] and Q parameter [2], enable to describe the plastic constraint effect. Both parameters are, however, not practical ones to discuss the criteria of fracture because it is also difficult to identify a critical value at fracture generating.

By using the local approach which Weibull stress is the parameter to characterize this concept, clevage fracture strength could be estimated [3]. Moreover, Weibull stress was applied to explain many problems concerning fracture toughness, e.g. scattering [4], crack depth effect [5] and strain rate effect [6]. However, physical meaning of the shape parameter in the definition of Weibull stress has not been clear

yet. Identfying the precise stress/strain fields are a significant in order to calculate all the parameters mentioned above. Change of the strain rate in the vicinity of a crack tip caused by strain concentration affects the stress/strain fields considerably, because the constitutive relation of materials is a function of strain rate. Considering the strain rate effect on stress/strain fields is, therefore, necessary to identify the precise fields even though static loading condition. In most of analyses based on the local approach, strain rate effect on the stress/strain fields was ignored to calculate Weibull stress.
Authors [8] had shown that fracture toughness is the function of R parameter defined in Eqn. 1 [7] in fracture process zone.

$$R = T \ln(A/\dot{\varepsilon}) \tag{1}$$

where T: temperature [K], A: frequency factor ($= 10^8$ [s^{-1}]), $\dot{\varepsilon}$: strain rate [s^{-1}]. R parameter in fracture process zone denotes R_γ in the following sections. R_γ is a candidate to quantify the plastic constraint effect on fracture toughness, because a degree of the plastic constraint is directly reflected on the stress/strain fields in fracture process zone.
Large scattering exists in fracture toughness derived under the same experimental condition. This is one of a typical tendency on fracture toughness. Authors postulated that scattering of fracture toughness is caused by the difference of strain rate distribution in fracture process zone, because a certain scattering of pre-crack length in fracture toughness test specimens must remain even though the precracking condition was the same. Scattering of the strain rate in fracture process zone is ignored to evaluate fracture toughness in conventional methods in which fracture toughness is seemed as only function of ambient temperature. Large scattering of fracture toughness could be explained by applying R_γ as the characteristic parameter to control the brittle fracture.
Above the points of view, two types of three point bend COD spceimens which have different crack depth were used to clarify the crack depth effect on fracture toughness quantitatively. In addition, the scattering of fracture toughness caused by a little difference of initial crack depth was investigated by using COD specimens which precracking condition was the same.

FRACTURE TOUGHNESS TEST

Fracture toughness tests were performed in accordance with BS5762 [9].Three point bend COD specimens were made of mild steel (SM400B), which chemical composition and material properties are shown in Table 1.

Table 1 Chemical composition and material properties (plate thickness = 16[mm])

Chemical composition (Wt%)					Material properties			
C	Si	Mn	P	S	Y.S. [MPa]	T.S. [MPa]	El. [%]	${}_vE$ at 0[℃] [J]
0.15	0.20	1.05	0.009	0.002	299	452	33	260

Two types of the ratio of specimen breadth (W) to initial crack depth (a_0) were equiped for the experiment. One named standard specimen in this paper is that $a_0/W = 0.5$, the other named short cracked specimen in this paper is that $a_0/W = 0.1$. Fracture toughness tests by using standard specimen were performed under three ambient temperatures (-75, -60 and -40 ℃). These results were investigated to verify the hypothesis which the scattering was caused by the difference of strain rate in fracture process zone. The tests by using short cracked specimen were done only -75 ℃. By comparing fracture toughness of two types of specimens, crack depth effect on fracture toughness was also investigated. Both tests were performed under constant crosshead speed (about 0.04mm/s), which could be seen as static loading.
Round bar tension test were also performed by collecting test pieces from the same material of COD specimens. Crosshead speed (0.005mm/s) could be recognized as a static loading. Four ambient temperatures (-130, -80,-30 and 25 ℃) were set under the tests.

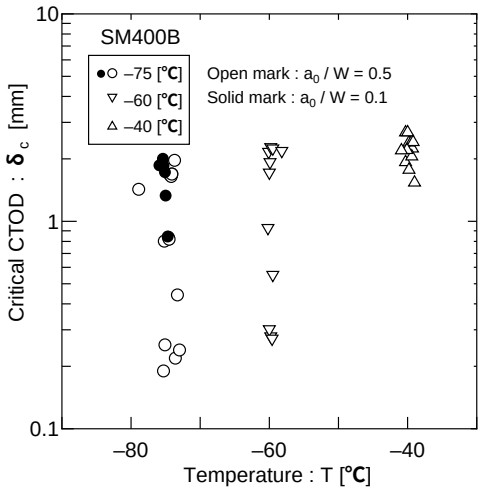

Figure 1 Relationship between ambient temperature and critical CTOD

EXPERIMENTAL RESULTS

Critical CTOD used as fracture toughness was calculated by using the conversion formula in BS5762 [9]. Measured values, mouth COD, crack length etc., at unstable fracture generating were applied to the calculation of fracture toughness, because the strain rate effect on the scattering and crack depth effect of fracture toughness at the moment of brittle fracture generating was highlighted in this paper. Crack length in calculating fracture toughness was equal to the sum of initial length and fibrous crack length grown by stable ductile fracture.

Figure 1 shows the relationship between ambient temperature and fracture toughness derived from the experiments. A noticeable scattering of fracture toughness can be recognized in Fig. 1. Fracture toughness of short cracked specimen shows a large value in the same ambient temprature. This is a same manner of ref.[5].

EVALUATION OF FRACTURE TOUGHNESS BY USING R PARAMETER

To evaluate the scattering and crack depth effect on fracture toughness, R parameter in fracture process zone (R_γ) at brittle fracture generating were calculated by the procedure stated in ref.[10]. Relationship

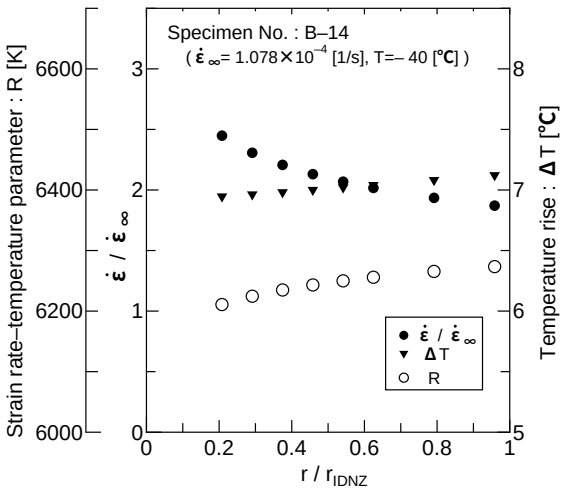

Figure 2 An example of R parameter, strain rate and temperature rise due to plastic work distributions in IDNZ

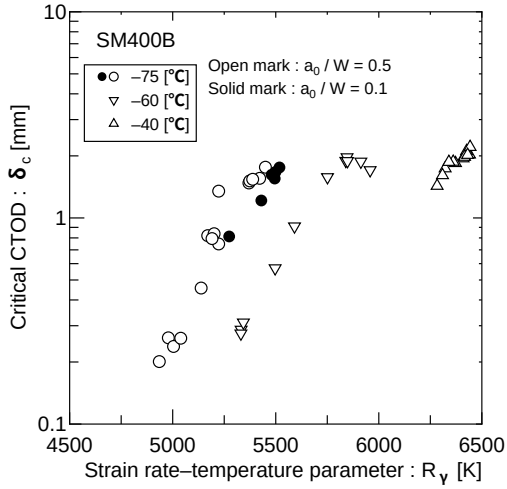

Figure 3 Relationship between R parameter in IDNZ and critical CTOD

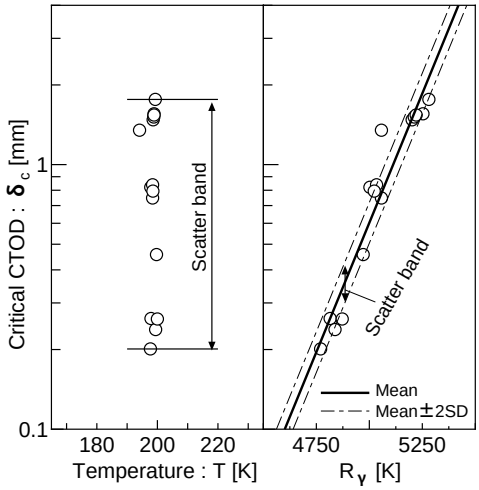

Figure 4 Comparison of R_γ and temperature as a parameter concerning the scattering of fracture toughness

between R parameter and yield stress (σ_Y) of the material had been provided from the round bar tension tests in advance. This relation is shown as follows.

$$\sigma_Y = 106.7 \exp(5607/R) \tag{2}$$

Unit in yield stress is MPa and in R parameter is abosolute temperature.
Figure 2 shows an example of R parameter distribution in IDNZ [11] which can be considered as fracture process zone. Abscissa in Fig. 2 is normalized by the distance from crack tip to the tip of IDNZ (r_{IDNZ}). The value of R parameter at the center of IDNZ was regard as R_γ in this paper, because R parameter in IDNZ keeps a approximately constant distribution at an arbitrary time throughout the loading. The calculation results of strain rate ($\dot{\varepsilon}$) normalized by the nominal strain rate ($\dot{\varepsilon}_\infty$) and of temperature rise (ΔT) due to plastic work are also shown in Fig. 2. Calculation procedure and the definition of nominal strain are explained in ref.[8] and [10]. As a result of the heat conduction, maximum value of ΔT appears in inside region apart from crack tip. This result was in agreement with the measuring result of temperature distribution near crack region [12] qualitatively. Strain rate in IDNZ increases more than about twice comparing with nominal strain rate. The strain rate increasing ratio in IDNZ showed a different value in each specimen.
Figure 3 shows the relationship between R_γ and fracture toughness. The different tendency of the relation can be recognized according to ambient temperature. However, the relation in Fig. 3 under each ambient temperature can be considered as an inherent relation. Comparison of R_γ and temperature as a parameter concerning the scattering of fracture toughness, which test temperature was -75 ℃, is shown in Fig. 4. Bold line and alternative long and short dash lines in the right side of Fig. 4

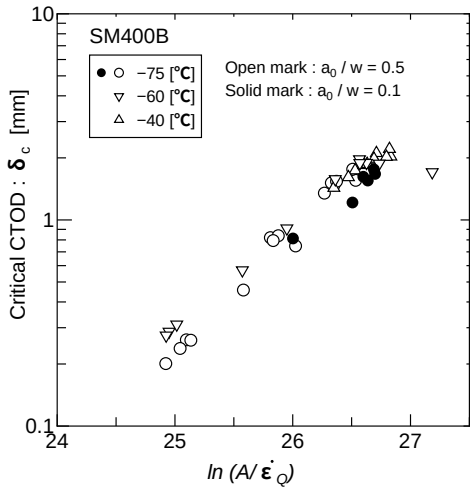

Figure 5 Relationship between dimensionless R parameter in IDNZ and critical CTOD

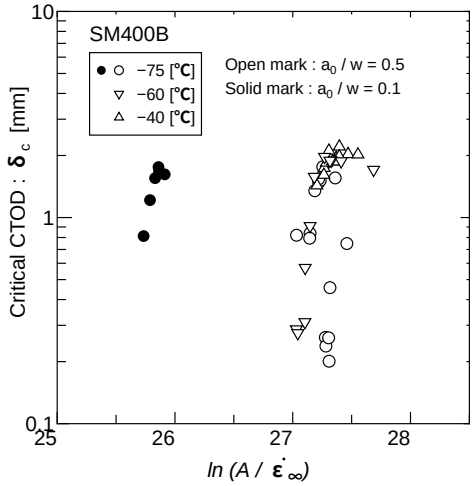

Figure 6 Relationship between dimensionless R parameter, based on nominal strain rate and ambient temperature, and critical CTOD

represent the mean line and $\pm 2SD$ (SD: standard deviation) ones of experimental results respectively. Figure 4 shows that the scattering of fracture toughness can be considerably reduced by using R_γ as a evaluating parameter for fracture toughness. This result indicates that the scattering of fracture toughness originates in the difference of strain rate in fracture process zone due to the difference of initial crack length.

The relationship betwen R_γ and fracture toughness of both standard specimens and short cracked specimens under the same ambient temperature can be seen identical in Fig. 3. Fracture toughness derived from the same ambient temperature can be considered as an inherent function of R_γ regardless of crack depth.

THE NEW PARAMETER CHARACTERIZING FRACTURE TOUGHNESS

An adequate parameter for possessing the universal relation to fracture toughness was studied. The dimensionless parameter (R_0) defined by Eqn. 3 was investigated as a candidate of the parameter.

$$R_0 = \ln(A/\dot{\varepsilon}_Q) \tag{3}$$

where, A: frequency factor ($= 10^8$ [s^{-1}]), $\dot{\varepsilon}_Q$: strain rate in fracture process zone [s^{-1}]. The midpoint in IDNZ was considered as the reference point of $\dot{\varepsilon}_Q$. Figure 5 shows the relationship between R_0

and fracture toughness. It can be recognized that fracture toughness is the inherent function of this parameter. On the othre hand, Figure 6 shows the relationship between the dimensionless parameter derived from substituting nominal strain rate for the term of strain rate in Eqn.3 and fracture toughness. The result in Fig. 6 remains the difference caused by the crack depth and the scattering on fracture toughness.
Figures 5 and 6 insist that the scattering and the crack depth effect, namely the plastic constraint effect, on fracture toughness are caused by the difference of strain rate in fracture process zone. The effect of temperature appears in value for the parameter in Fig. 5 indirectly, because the effect of strain rate and temperature on constitutive equation was considered to identify the stress/strain fields in the vicinity of a crack tip.
Yokobori [13] shows the relationship between activation free energy and applied stress as follows.

$$U \propto \ln(1/\sigma). \tag{4}$$

Comparing the form of Eqn. 3 with Eqn. 4, it can be expected that R_0 has a close relation to activation free energy in fracture process zone.

CONCLUDING REMARKS

Quantificational evaluation for the scattering and crack depth effect on fracture toughness is performed by considering the strain rate effect on fracture toughness. By postulating that fracture toughness is a function of R parameter in fracture process zone, it makes clear that the crack depth effect, namely the plastic constraint effect, and the scattering on fracture toughness can be explained by the difference of strain rate in fracture process zone. Moreover, the parameter defined by Eqn. 3 could be the universal parameter to characterize fracture toughness.

REFERENCE

[1] Betegón,C. and Hancock,J.W. (1991) *ASME J. Applied Mech.*, 58, 104

[2] O'dowd,N.P. and Shih,C.F. (1991) *J. Mech. Phys. Solids*, 39, 8, 989

[3] Beremin,F.M. (1983) *Metal. Trans. A*, 14A, 2277

[4] Tagawa,T.,Miyata,R. and Otuka,A. (1992) *J. Soc. Mat. Sci. Japan*, 41, 1227

[5] Minami,F., Ruggieri,C.,Ohata,M. and Toyoda,M. (1996) *J. Soc. Mat. Sci. Japan*, 45, 5, 544

[6] Tagawa,T.,Shimanuki,H.,Hagiwara,Y. and Miyata,R. (1999) *J. Soc. Naval Arch. Japan*, 185, 309

[7] Bennet,P.E. and Sinclar,G.M. (1966) *ASME J. Basic Eng.* 88, 2, 518

[8] Toyosada,M. and Gotoh,K. (1996) *Memo. Eng. Kyushu University*, 56, 273

[9] British Standard Institution BS5762 (1979)

[10] Toyosada,M. Gotoh,K. and Nakayama,S. (2000) *J. Soc. Naval Arch. Japan*, 188, 707

[11] Rice,J.R. and Johnson,M.A. (1970) *Inelastic Behavior of Solids*, McGraw-Hill, New York, 641

[12] Toyosada,M. Gotoh,K. and Sagara,K. (1992) *Proc. ISOPE*, 108

[13] Yokobori,T. (1952) *J. Applied Phys. (Letters to Eds.)*23, 1423

ICF100198OR

A study of fatigue cracking behavior dependent on the distance between two hole defects

Sam-Hong Song[1], Joon-Soo Bae[2] , Amkee Kim[3]

[1]Department of Mechanical Engineering, Korea University, Seoul, Korea
[2]Product Design Team, Samsung SDI, Suwon, Korea
[3]Department of Mechanical Engineering, Kongju National University, Kongju, Korea

ABSTRACT
The fatigue crack initiation and propagation behavior have been studied considering the distance between two hole defects in this work. The location of two hole defects is defined by an angle and the distance between two holes. The stress distribution around two holes is calculated by finite element method. The fatigue crack initiation is changed with the distance and the relative location of two holes. A parameter is introduced to predict the fatigue crack initiation life. This parameter contains the plastic deformation area and strain at stress concentrations.

KEY WORDS
Hole-defect, Crack initiation, Stress, Strain, Finite element method

INTRODUCTION

The life time of engineering materials can be associated with the size, the shape and the relative location of defects contained in the components. Thus, it is important to understand the fatigue crack initiation and propagation behavior in the vicinity of the defects under the complex stress field caused by those defects. When defects are located close to each other, the fatigue crack initiation life of material is very different from that of the material with sparsely distributed defects. The knowledge of fatigue crack initiation mechanisms from such interacting defects becomes a main concern of engineers engaged in fatigue life assessment. Song et al. [1] have studied the stress distribution and interaction around closely located two circular inclusions by the finite element method and experiments. The results indicate that interaction effect between two holes occurs at $s/r<2.2$. In other works, the interaction effects between flaws aligned perpendicular to the loading direction have been studied [2-3]. However it is hard to find the studies which deal with the fatigue crack initiation life at arbitrarily located defects. The life of crack initiation at simple notch has been predicted from the simple parameters such as stress concentration factor and local strain, but it is not fully understood that the parameters can always be applicable. In this study, the relative location of two hole defects with respect to the loading direction and the distance between hole defects are varied, and the fatigue

crack initiation life is investigated. A parameter based on the plastic deformation area and strain is proposed to predict the number of cycles to crack initiation.

EXPERIMENTAL PROCEDURE

The fatigue test was performed using a commercial bending testing machine (Model TB10). The crack was observed using an optical microscope. The material used in the test was ASTM Al-5086. The mechanical properties and chemical compositions of this material are shown in Tables 1 and 2. The geometries of specimen are illustrated in figure 1. The maximum applied stress was 90MPa and the stress ratio was $R(\sigma_{min}/ \sigma_{max})=-1$. The stress waveform was sinusoidal. Hole defects were machined by using a 0.5 mm drill. The depth of defect was 0.5 mm. The relative location of two holes is shown in figure 2. For examining crack initiation life, the angle between the line connecting two centers of holes and x-axis were chosen as θ =0°, 30°, 45°, 60° and 90°, and the distance between two centers of holes was chosen as l=3,4 and 5. Here, l=L/r. The stresses and the strains were analyzed by a commercial finite-element package [4].

Table 1 Mechanical properties of Al-5086

Yield stress (MPa)	Ultimate stress (MPa)	Elongation (%)	Elasticity modulus (GPa)	Poisson's ratio
190	260	22	62.4	0.32

Table 2 Chemical properties of Al-5086 (wt %)

Al	Mn	Mg	Cr
95.4	0.1	4.0	0.15

RESULTS AND DISCUSSION

When two hole defects are located close together, the crack initiation lives are affecte by the distance and relative locations of them. The stress concentration is varied with the distance of defects. The angle between the line connecting two centers of holes and x-axis was varied with θ=0°, 30°, 45°, 60° and 90°. Figure 3 shows the stress concentration factor(K_t) when the distances of two hole are l=3 and l=5. The stress concentration factors were calculated by two-dimensional finite element method. K_t is defined as the ratio of the y-direction maximum stress σ_{max} to the nominal stress σ_{nom}.

$$K_t = \frac{\sigma_{max}}{\sigma_{nom}} \qquad (1)$$

K_t is maximum at θ=30°, and minimum at θ=90°. K_t when l=3 is much larger than those when l=5 because the interacting effect of two holes are promoted by the adjacent hole. The crack initiation lives obtained experimentally are shown in figure 4. As seen from the figure 4, the crack initiation life strongly depends on the distance and the angle between two centers. Here, the fatigue crack initiation life is defined as the cumulative cycles up to crack length a=0.1 mm on the surface, because it is difficult to observe the crack initiation smaller than a=0.1 mm

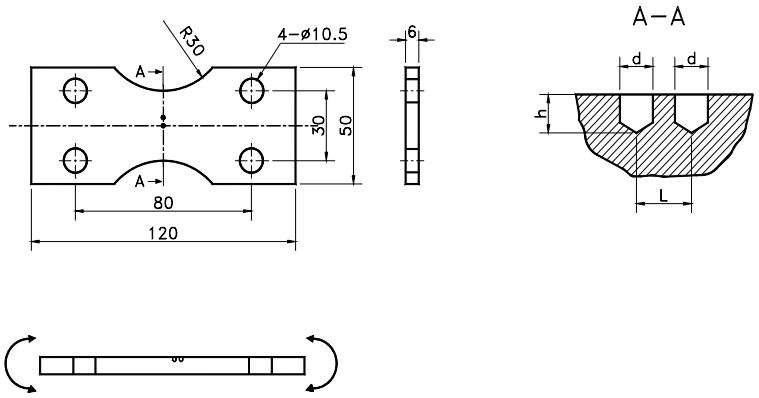

Figure 1: Geometries of test specimen

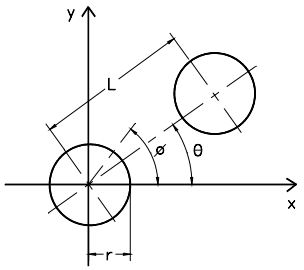

Figure 2: Position of two holes (l=L/r)

K_t is explicitly one of the main factor affecting crack initiation when the material behavior is supposed to be elastic. The relation of K_t and crack initiation life are drawn in figure 5. It shows the relation when l=3. The stress concentration factors and fatigue crack initiation lives is not correlated. Although the stress concentration factor at θ=30° was the largest, the crack at θ=0° was detected sooner. And the crack at θ =60° was detected sooner than the crack at θ=45°. This is attributed to the local stress that exceeds the yield stress as well as the difference of the stress gradient. Because of the rapid decrease of stress concentration with increasing distance from the defect and the existence of complex states of stress at a small distance from the defect, it is difficult to predict crack initiation life by using stress concentration factors. Strain-life concepts may be useful to estimate the crack initiation life when plasticity is dominant. The relation of post yield strain and crack initiation life is investigated. The equivalent strain is calculated by finite element method. The two-dimensional eight node plane stress element and full Newton-Raphson iterative scheme were used. The strain hardening of materials in finite element method was considered as elastic-piecewise linear, which was obtained

from the tensile test. The yield criterion is Von-Mises. The relation of strain and crack initiation life has the same tendency of K_t. Because there is no correlation between local strains and crack initiation lives like the case of stress, it needs more precise parameter to find correlation.

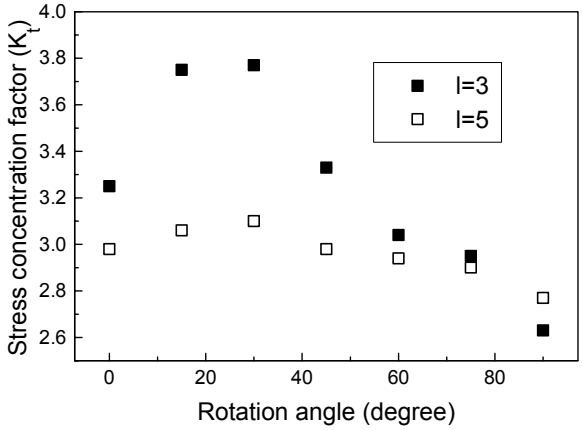

Figure 3: Stress concentration factor when l=3,5

The plastic strain area was also calculated to investigate the relation of crack initiation lives and stress distributions. In the experiment of this study, the plastic deformation area strongly played a role in the crack initiation life. A parameter is introduced to predict the fatigue crack initiation life. This parameter contains local strain magnitude and plastic deformation area as follows:

$$A_{p\varepsilon} = \varepsilon_l \times A^3 \qquad (2)$$

$$A = \frac{A_l}{A_1} \qquad (3)$$

ε_l : equivalent local strain obtained by F.E.M.
A_l : the area of plastic deformation occurred at each specimen
A_1 : the area of plastic deformation occurred at one hole notched specimen
At θ=0°, even though the magnitude of local strain is small, the plastic deformation area is so large that consequently the value of $A_{p\varepsilon}$ becomes large. At θ=0° and 45°, stress concentration factor is large but the plastic strain area is small, so that $A_{p\varepsilon}$ becomes small. Therefore crack initiation lives and $A_{p\varepsilon}$ for Al-5086 are fitted by the following equation:

$$N_i = \left(\frac{A_{p\varepsilon}}{9.0 \times 10^4} \right)^{-0.76} \qquad (4)$$

N_i : crack initiation life
The results are shown in log-log plot of Fig.8. If we find $A_{p\varepsilon}$, we can predict crack initiation life of the material used in this study.

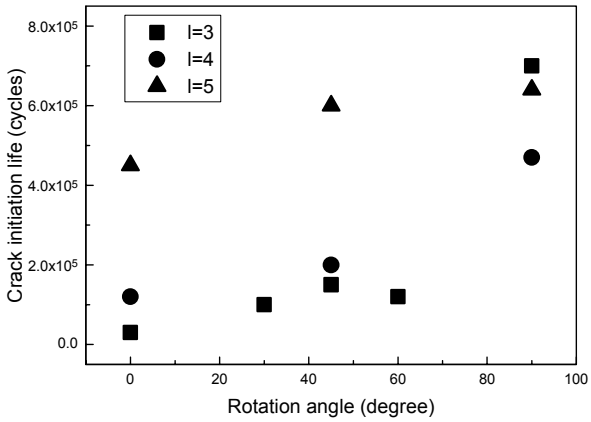

Figure 4: Relation between crack initiation life and relative location

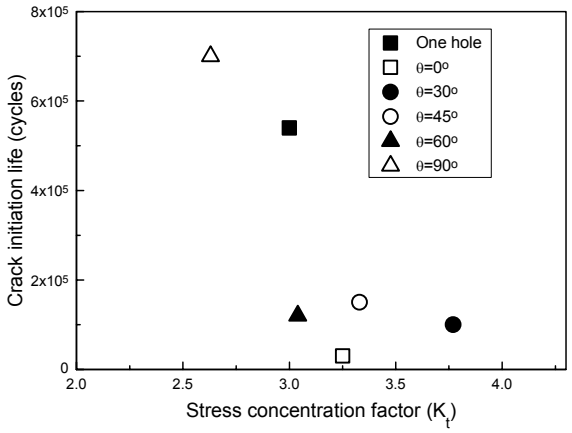

Figure 5: Relation between crack initiation life and stress concentration factor

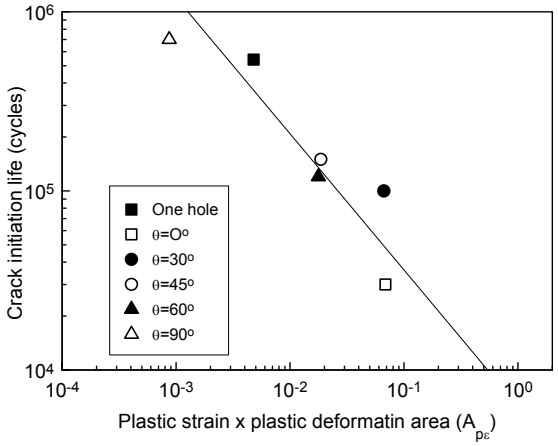

Figure 6: Relation between local strain and crack initiation life

CONCLUSIONS

In this study, the fatigue crack initiation and propagation behavior of Al-5086 with two interacting hole defects were investigated experimentally. The obtained results are as follows.

1. The relative location of two hole defects, the distance and angles, affects the crack initiation life.
2. When the defects are located close to each other, the fatigue crack initiation lives vary with the relative location of two hole defects. A new parameter is proposed for the prediction of fatigue crack initiation life. It contains an equivalent local strain magnitude and a plastic deformation area as follows.

$$A_{p\varepsilon} = \varepsilon_l \times A^3$$

REFERENCES

[1] S. H. Song and J. B. Kim (1994). Int. J. KSME, Vol. 18, No. 3, pp. 555-564
[2] Y. Murakami and S. Nemat-Nasser (1982). Engineering Fracture Mechanics, Vol. 16, No. 3, pp.373-386
[3] S.H.Song and J.S.Bae (1998). Experimental Mechanics, Vol.38, No.3, pp.161-166
[4] NISA finite element package, Engineering Mechanics Research Corporation, Troy, Michigan, USA

ORAL/POSTER REFERENCE:ICF100364OR

A STUDY OF FRACTURE FROM THE VIEWPOINT OF DILATATION

Y. Arimitsu, Y. Sogabe and Z. Wu

Department of Mechanical Engineering, Ehime University
3 Bunkyoucho Matsuyama, 790-8577, Japan

ABSTRACT

Solid materials possess two modes of elastic deformation to an external load. One is distortional and the other is dilatational. At the limit of elasticity, failure occurs by one of the two modes corresponding to respective elastic ones, i.e., yielding occurs as a limit of distortional deformation and fracture as a limit of dilatational one. Yield condition has been established with deviatric strain and stress in the theory of plasticity, but fracture has not been described with dilatation. In this paper, authors show close connection between dilatation and fracture, and proposes a criterion to predict the failure mode for a given material, non-elastic behavior, with the ratio of the elastic constants G/K, where G and K denote shear and bulk moduli, respectively.

KEYWORDS

Fracture criterion, Dilatation, Distortion, Brittle, Ductile, Elastic failure

INTRODUCTION

Fracture of materials has been discussed in terms of various physical quantities as summarized in Table 1.

TABLE 1
FRACTURE CRITERION FROM VARIOUS VIEWPOINTS

Viewpoint of fracture	Physical quantity	Criterion for fracture
Energy	Surface energy	Griffith's theory [1]
	Elastic energy	J-integral [2]
Stress space	Force	Crack extension force [3]
(Mechanical aspect)	Stress	Stress intensity factor [4]
Strain space	Displacement	Crack opening displacement [5]
(Geometrical aspect)	Strain	Dilatation (and Distortion)*
Property of matter	Elastic constant	Local elastic constant [6]

* The authors are proposing in this paper.

Fracture as a natural phenomenon is supposed to obey a universal principle, but we can describe it in many ways from various viewpoints. Each description is related to a view to visualize respective aspect of fracture through the employed physical quantity.

For example, Griffith's theory visualizes fracture through energics by noting that with an extension of a crack strain energy can be converted to surface free energy. Similarly, description in terms of stress concentration near the crack tip is related to the view that a solid is broken by a force (stress) beyond a critical value. Fracture may be related to degradation of materials around a crack tip, which involves the field of materials science in addition to mechanics. We can also consider fracture a geometrical problem as in the theory with the crack opening displacement. In this paper, we point out that dilatation of a solid body is closely connected with fracture and proposes a criterion to predict the failure mode for a given material as a first step toward establishing a fracture criterion in terms of dilation.

Elastic deformation can be classified into two modes, i.e., dilation (volumetric change) and distortion (shearing deformation). Isotropic solid bodies possess two independent elastic constants, shear modulus G and bulk modulus K, each of which represents resistance to distortion and dilatation, respectively. At the limit of elasticity, failure occurs by one of the two modes corresponding to respective elastic ones, i.e., yielding occurs as a limit of distortional deformation and fracture as a limit of dilatational one. Yield condition has been established with deviatric strain and stress in the theory of plasticity, but fracture has not been described with dilatation. We propose to classify other physical properties also in connection with those two modes as shown in Table 2.

TABLE 2
CLASSFICATION BASED ON THE DEFORMATION MODE

Deformation mode	Elastic constant	Strain energy	Property of material	Failure
Distortion	Shear modulus G	Distortion energy E_s	Ductility	Plastic deformation
Dilatation	Bulk modulus K	Dilatation energy E_v	Brittleness	Fracture

$E_s = G\,(\varepsilon_{ij}\varepsilon_{ij} - \varepsilon_{ii}\varepsilon_{jj}/3)$, $E_v = K\varepsilon_{ii}\varepsilon_{jj}/2$, where ε_{ij} is the strain component.

RELATED PHENOMENA

We can correlate the present idea with various behaviors of materials as follows:

1) Rubber is nearly incompressible materials [7]. It means that dilatation associated with deformation is negligibly small, hence we expect that deformation will not be easily terminated by fracture.

2) The volume of a body is nearly unchanged during plastic deformation, hence plastic deformation will not be easily terminated by fracture.

3) Materials become more ductile under hydrostatic pressure [8]. This can be interpreted as that fracture is prevented by constraining dilatation.

4) The thick specimen (plane stress) of a ductile material becomes more brittle than the thin one (plane strain). Under uni-axial tensile stress σ, volumetric strain ε_V with the plane stress condition becomes

$$\varepsilon_V = \frac{1-2\nu}{E}\sigma, \qquad (1)$$

and volumetric strain ε_V^* with the plane strain condition is

$$\varepsilon_V^* = \frac{1-\nu}{E}\sigma, \qquad (2)$$

where E and ν denote Young's Modulus and Poisson's ratio, respectively. When $0 \le \nu \le 0.5$, we get the

identical relation, $\frac{\varepsilon_V}{\varepsilon_V^*} = \frac{1-2\nu}{1-\nu} \le 1$. Therefore, dilatation with the plain stress condition is smaller than that with the plain strain condition.

5) In the fracture of brittle materials, voids are observed in tensile region at high temperature. It seems that dilatation is the driving force to form voids at high temperature, and that elastic dilatation influences fracture at room temperature.

The consideration given above suggests a possibility that the ratio G/K(=3(1-2ν)/2(1+ν), which decreases monotonously with Poisson's ratio ν) governs the failure mode, i.e., ductile vs. brittle behavior, of a given material. Table 3 summarizes the values for typical examples [9,10], and we see that this expectation in fact works. Materials which easily change volumes are brittle and materials which can be easily distorted are ductile. This tendency is independent of various classifications of materials such as metal vs. nonmetal, crystal vs. amorphous, and so on. Consequently, we can regard the ratio G/K (or Poisson's ratio) as a measure to predict the failure mode for a given material. It is called Pugh's rule [11]. Kelly et al. [12] pointed out the similar result that the ratio G/E is the index of ductile-brittle from comparison between shear and tensile stress. The ratio G/K and G/E are also the monotonous function of ν, hence both indices bring the same result. But the original viewpoint of each index is completely different.

TABLE 3
CORRELATION BETWEEN G/K AND FAILURE MODES

Material	E(GPa)	G(GPa)	ν	K(GPa)	G/K	
Quartz (fused)	73.1	31.2	0.170	36.9	0.846	
Glass (Crown)	71.3	29.2	0.22	41.2	0.709	↑
Cast iron	152.3	60.0	0.27	109.5	0.548	Brittle
Mild steel	211.9	82.2	0.291	169.2	0.486	
$Fe_{80}B_{20}$ (amorphous)	168.7	64.9	0.30	141	0.460	
Copper	129.8	48.3	0.343	137.8	0.351	
Aluminum	70.3	26.1	0.345	75.5	0.346	Ductile
Brass (70 Zn, 30 Cu)	100.6	37.3	0.350	111.8	0.334	↓
Gold	78.0	27.0	0.44	217.0	0.124	

NUMERICAL EVALUATION OF DILATATION AND DISTORTION NEAR CRACK

It is interesting to see how the difference in G/K affects the distribution of the strain and the strain energy density relevant to each of the two modes of deformation. Taking gold and crown glass as typical examples of ductile and brittle materials, we calculated the distributions by the finite element method for plates with cracks at their centers under 1% uniaxial tension with the plane strain condition. The results are given in Figs.1 and 2, in each of which a quarter of the plate is shown and the strain energy density is normalized with the total strain energy E_t stored in the entire plate. For gold, distortion energy density E_s is high along the 45 degrees direction from the crack tip over a wide region, while high values for dilatation energy density are limited to a small domain around the crack tip. On the other hand, in the case of glass, relatively large amount of strain energy is stored as the dilatation energy over a relatively wide region around the crack tip.

The distributions of distortion, represented by γ_{12} are almost the same for gold and glass because the plates are stretched by the same amount of strain (Fig.2(a)). On the other hand, distributions of dilatation, represented by ε_{ii} are very different between gold and glass (Fig.2(b)). Those numerical results suggest that materials with small G/K tend to fail plastically while materials with large G/K tend to have cleavage fracture.

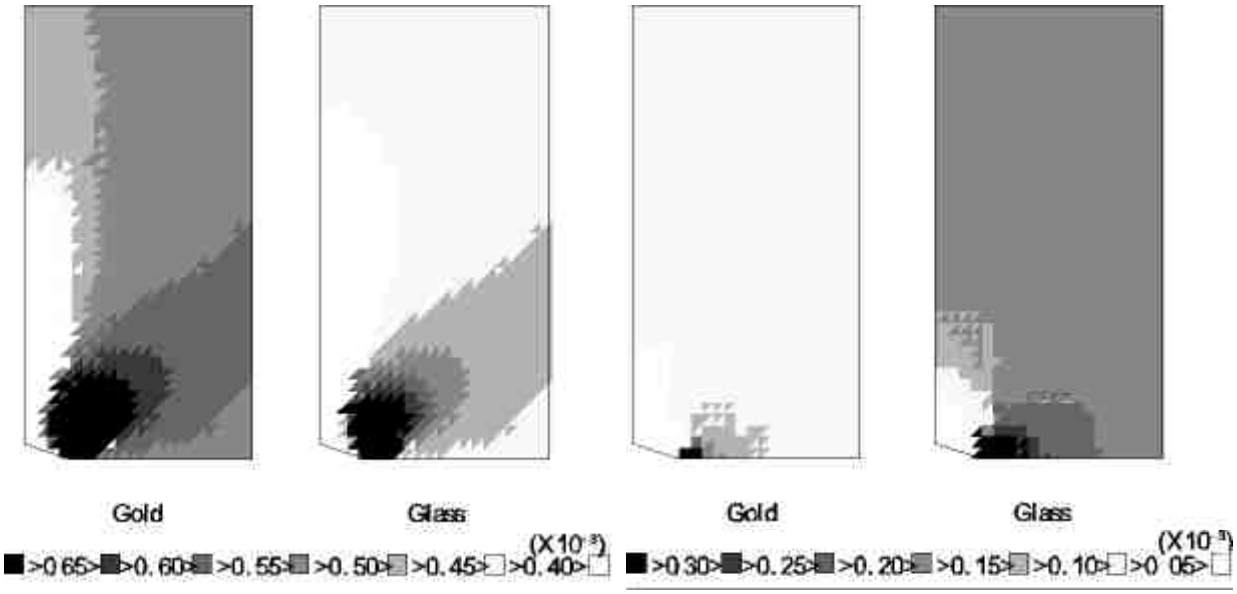

(a) Distortion energy density (b) Dilatation energy density

Figure 1: Distribution of strain energy density.

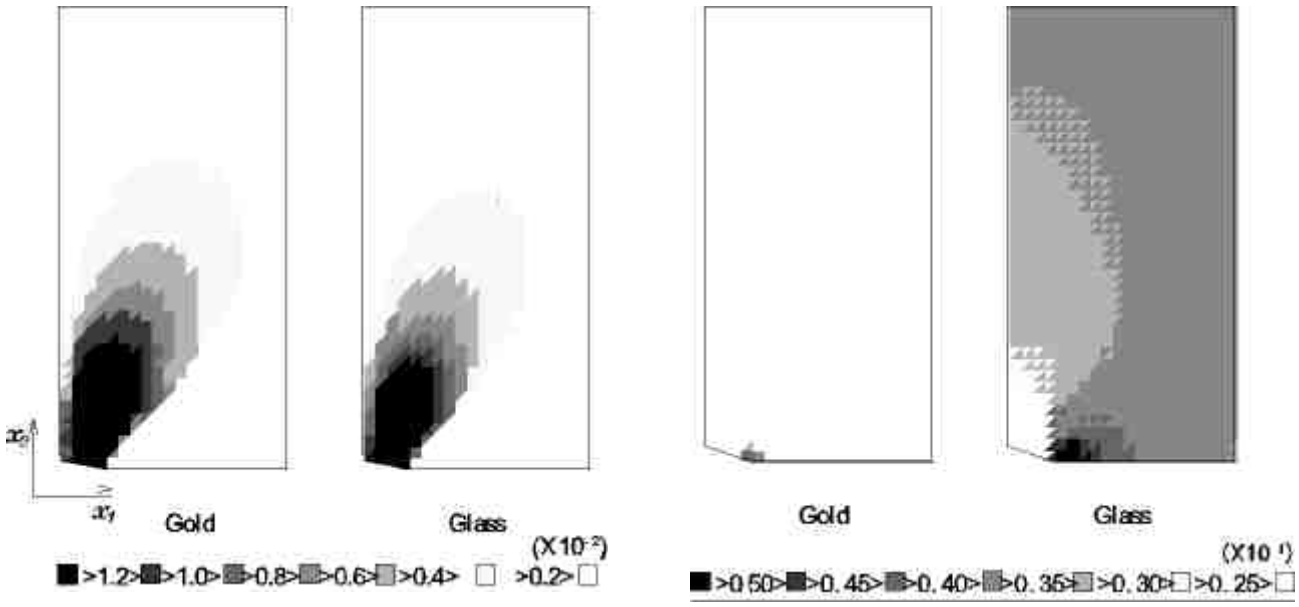

(a) Distortion γ_{12} (b) Dilatation

Figure 2: Strain distribution.

CONCLUSION AND DISCUSSION

We notice the close connection between the deformation mode (distortion and dilatation) and the failure mode (plastic deformation and fracture), and that brittleness and ductility are not only material property. In fracture mechanics, we ignore close connection between dilation and fracture. In the combined mode of fracture, we might discuss the singularity of dilation instead of the stress singularity near crack tip.

Microscopically, topology of atomic array changes in distortion, and many 'meta-stable states' appear in the process. Therefore, we should evaluate the yield condition by (distortion) energy. On the other hand, the inter-atomic distance increases in dilatation, and the 'critical state' appears. Therefore, we could evaluate fracture by (dilatation) strain. Furthermore, lattice defects are also classified into two categories; one is the dislocation,

which causes distortion, and the other is the vacancy, which causes dilatation. Therefore, it could be possible to establish new micromechanics from the viewpoint of the distortion and dilatation.

REFERENCES

1. Griffith, A.A. (1920) Phil. Trans. Roy. Soc. London, A221, 163.
2. Rice, J.R. (1968) Trans. ASME, J. Appl. Mech., 35, 379.
3. Irwin, G.R. (1957) Trans. ASME, J. Appl. Mech., 24, 361.
4. Irwin, G.R. (1958) Fracture, in S. Flugge (ed.) Handbook du Physik, 6, Springer, 551.
5. Dugdale, D.S. (1960) J. Mech. Phys. Solids, 8, 100.
6. Hata, K., Takai, T. and Nishioka, K. (1991) Molecular Simulation, 6, 343.
7. Williams, J.G. (1973) Stress Analysis of Polymers Longman, London.
8. Bridgman, P.W. (1952) Studies in Large Plastic Flow and Fracture McGraw-Hill, New York.
9. Kaye, G.W.C. and Laby, T.H. (1986) Tables of Physical and Chemical Constants 15th ed., Longman, London.
10. Chou, C.-P., Davis, L.A. and Hasegawa, R. (1979) J. Appl. Phys. 50, 3334.
11. Pugh, S.F. (1954) Phil. Mag. 45, 823.
12. A. Kelly, A., Tyson W.R. and Cottrell, A.H. (1967) Phil. Mag., 15, 567.

ORAL/POSTER REFERENCE: ICF100386OR

A STUDY OF HYDROGEN EMBRITTLEMENT IN AUTOMOTIVE FASTENER STEELS

B. Lonyuk[1*], R. Hop[2], D.N. Hanlon[1], S. van der Zwaag[3], J. Zuidema[3] and A. Bakker[3]

[1]Netherlands Institute for Metals Research, Rotterdamseweg 137, 2628 AL Delft, The Netherlands
[2]Koninklijke Nedschroef Holding N.V., Techno Centre, Kanaaldijk N.W. 71, 5707 LC Helmond, The Netherlands
[3]Laboratory of Materials Science, Delft University of Technology, Rotterdamseweg 137, 2628 AL Delft, The Netherlands

ABSTRACT

Fasteners exposed to hydrogen during processing can fail unpredictably at applied stress levels well below the fracture stress. The unpredictable nature of these failure mechanisms, which may be attributed to hydrogen concentrations of the order of a few parts per million, represents a serious safety hazard to the automotive industry. In this study the susceptibility of a commercial fastener steel has been investigated. All testing was performed using a slow strain rate tensile testing technique on fatigue pre-cracked cylindrical specimens. Results describing the effect of thermal treatment and coating on the susceptibility to hydrogen embrittlement are presented.

KEYWORDS

Hydrogen embrittlement, slow strain rate, fastener steel, stress intensity.

INTRODUCTION

High-strength fasteners are widely used in the automotive industry. However, in literature it has been reported brittle failure of high strength bolts sometimes occurs. Embrittlement in fasteners may occur as a result of hydrogen introduced into the material during processing [1]. This sort of failure is normally observed in electro-galvanized high strength steel bolts and the fracture is assumed to be caused by hydrogen which was introduced during bolt manufacturing, namely, during electroplating or during acid pickling before plating. This is referred to as internal hydrogen embrittlement (IHE) or delayed failure. Hydrogen that is absorbed is diffusible within the metal lattice and tends to accumulate in areas of high stress. It is at such locations that microcracking initiates and subsequently may proceed to catastrophic fracture. The susceptibility of high strength steels to IHE depends on alloy, strength level, microstructure, and the amount and distribution of the absorbed hydrogen. It is suggested that steels with yield strengths less than 1250 MPa, i.e. which are tempered at a high temperature, are resistant to delayed fracture due to hydrogen [2]. The purpose of this work is to assess

the susceptibility of a commercial fastener steel with yield stress of approximately 1100 MPa to IHE and to establish the effect of a typical low temperature annealing on the mechanical properties.

EXPERIMENTAL PROCEDURE

To evaluate the effects of low temperature annealing a series of experiments on pre-cracked specimens were performed. The materials were supplied by the Dutch fastener company Koninklijke Nedschroef Holding N.V. in a number of processing conditions, namely: a) quenched and tempered, b) quenched, tempered and electrolitically plated with zinc and c) quenched, tempered, plated and annealed. The final microstructure of the material is a heavily tempered martensite with scattered polygonal ferrite (Figure 1).

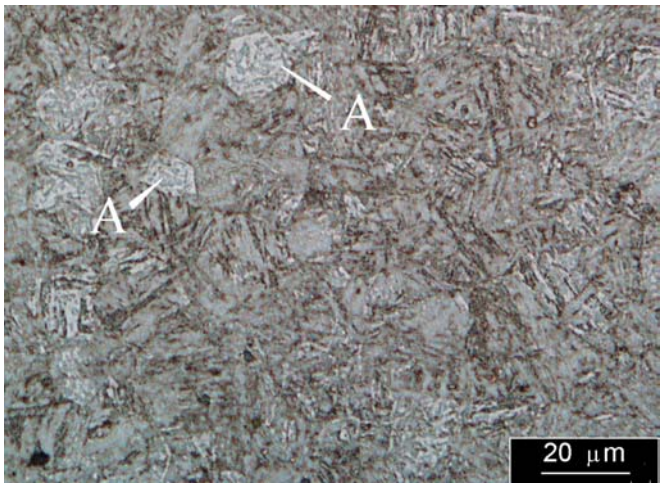

Figure 1: Photomicrograph of the tempered structure. The matrix composes mainly heavily tempered α' with some scattered polygonal ferrite *A*.

The composition of the material and mechanical properties after heat treatment are shown in the Table 1 and Table 2.

TABLE 1

COMPOSITION OF THE NEDSCHROEF STEEL

Element	C	Mn	P	S	Si	Cr	Ni	Mo	Ti	B
%	0.35	0.76	0.011	0.008	0.05	0.2	0.03	0.01	0.028	0.002

TABLE 2

MECHANICAL PROPERTIES OF THE NEDSCHROEF STEEL

Yield strength $\sigma_{0.2}$, MPa	Ultimate tensile strength σ_{UTS}, MPa	Fracture strain, ε, %	Reduction of area, ψ, %
1100	1190	13.2	63.2

The types of specimens used for mechanical testing were circumferentially notched cylindrical bar specimens (Figure 2). The fatigue precracking was performed on a four-point rotating-bending

machine. For most specimens the resulting precrack was not concentric. This necessitated, in order to determine the stress intensity factors, the application of a correction for eccentricity found by *Ibrahim et al* [3].

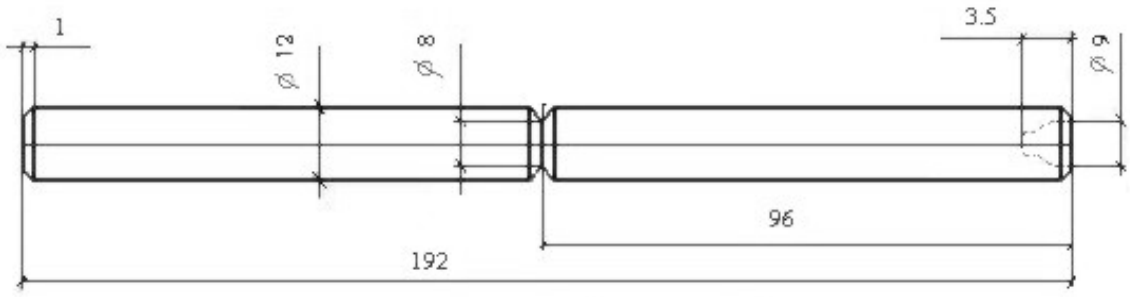

Figure 2: The specimen geometry used for fracture toughness testing

The fracture toughness tests were performed on a tensile machine in air either at the strain rate that is recommended by *ASTM E* 399-90 in fracture mechanics testing (1 mm/min) or at slow strain rate (0.001 mm/min) using fatigue pre-cracked specimens for all conditions. The test procedure of the slow strain rate test is described and compared with others in [4]. The fracture surfaces of tensile specimens were examined under both the optical microscope and scanning electron microscope (SEM).

RESULTS AND DISCUSSION

The mechanical properties of the materials investigated, measured at a strain rate of 0.001 mm/min by tensile testing are shown in Table 3.

TABLE 3

THE MECHANICAL PROPERTIES OF THE INVESTIGATED MATERIAL CONDITIONS.

Material	Yield strength $\sigma_{0.2}$, MPa	Ultimate tensile strength, σ_{UTS}, MPa	Fracture strain, ε, %	Threshold stress intensity factor, K_{1H} MPa $m^{1/2}$
Quenched and tempered	1064	1190	11.1	80
Quenched, tempered and plated	1027	1155	11.7	50
Quenched, tempered, plated and annealed	1019	1151	12.5	60

The series of fracture toughness tests, performed at a tensile strain rate of 1 mm/min, did not reveal a significant difference between samples which had been plated and those which were unplated. The values of the threshold stress intensity factors K_{1H} obtained at a tensile strain rate of 0.001 mm/min (Table 3) were considerably lower than the K_{1C} value (104 MPa $m^{1/2}$).

The microfractographic investigations of the fracture surfaces of slow strain rate failure specimens revealed three zones (Figure 3): fatigue precracking, slow-crack propagation and overload failure. The

region of stable, subcritical crack growth was observed for all conditions investigated (quenched and tempered; quenched, tempered and plated; quenched, tempered, plated and annealed). Microfractografic investigations of the fracture surfaces of samples tested at 1 mm/min showed no evidence of stable crack growth. Instead, the surfaces were composed of two regions: fatigue and overload.

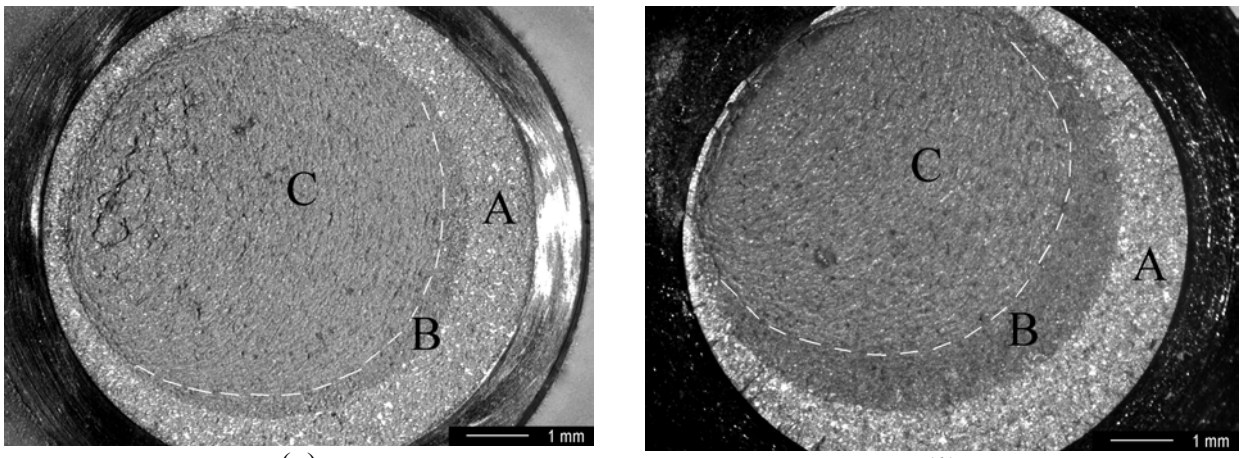

(*a*) (*b*)

Figure 3: Fracture surface of a slow strain rate failure samples: (*a*) – unplated material; (*b*) – plated material. A – fatigue precrack; B – slow-crack propagation area; C – overload failure.

Observation of the overload region of the fracture toughness samples subjected to fracture toughness testing at 1 mm/min revealed a ductile fracture mode due to microvoid nucleation and growth (Figure 3). Fast fracture areas of the slow strain rate failure samples indicated the same ductile type of fracture.

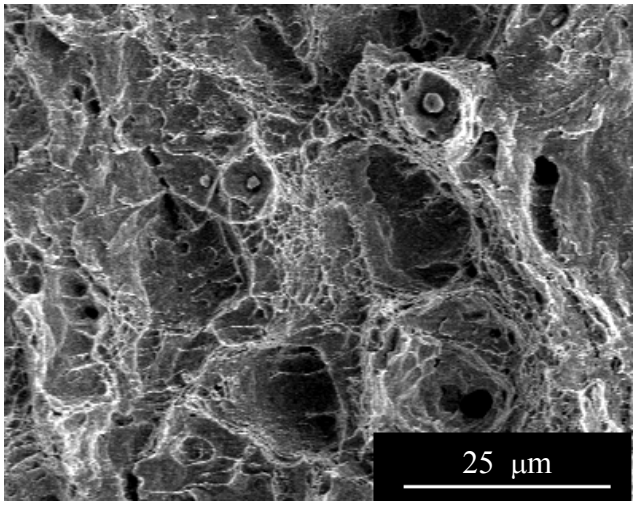

Figure 3: Fracture surface in the overload region close to the fatigue precrack for a sample failure at the 1 mm/min.

The most attention was paid to the investigation of the slow-crack propagation areas. Fracture surfaces were observed to comprise features indicative of brittle failure in this region. Many secondary cracks were also evident. It may be concluded that this embrittlement is due to either dissolved hydrogen (for the quenched and tempered material) or hydrogen introduced by the plating process (for plated material). It has been shown that for quenched and tempered material cracking was intergranular with respect to the prior austenite grain boundaries (Figure 4*a*). Whereas, the observed fracture mode for the plated material was quasicleavage (Figure 4*b*). The result shown in Figure 4 is not consistent with a known effect of hydrogen on the fracture mode. For plated material, where more hydrogen may be

expected, the failure along the prior austenite grain boundaries should be preferable. The contradiction can be explained on the basis of the following assumptions:

a) at a lower hydrogen content, H occupies mainly high-angle boundary sites (i.e. prior austenite boundaries) whereas at higher H contents more hydrogen occupies low-angle boundary sites (martensite laths) or microstructural heterogeneities (carbide precipitates, manganese sulphide, etc.) within grains;

b) continuum plasticity theory predicts that even at negligibly small load a maximum stress is attained ahead of the crack tip. For crack propagation the plastic zone size must exceed a critical value, which might be related to characteristic distances such as a prior austenite grain diameter, the mean distance between carbide precipitates, etc [5].

Therefore the observed intergranular fracture for quenched and tempered material is probably a consequence of hydrogen segregation to prior austenite grain boundaries and a resulting lower cohesive force in those regions. In this case the characteristic distance may be the prior austenite grain diameter. For plated materials the hydrogen at martensite laths, carbide precipitates, etc. may play a more important role and the characteristic distance could be related to the spacing of such microstructural heterogeneties.

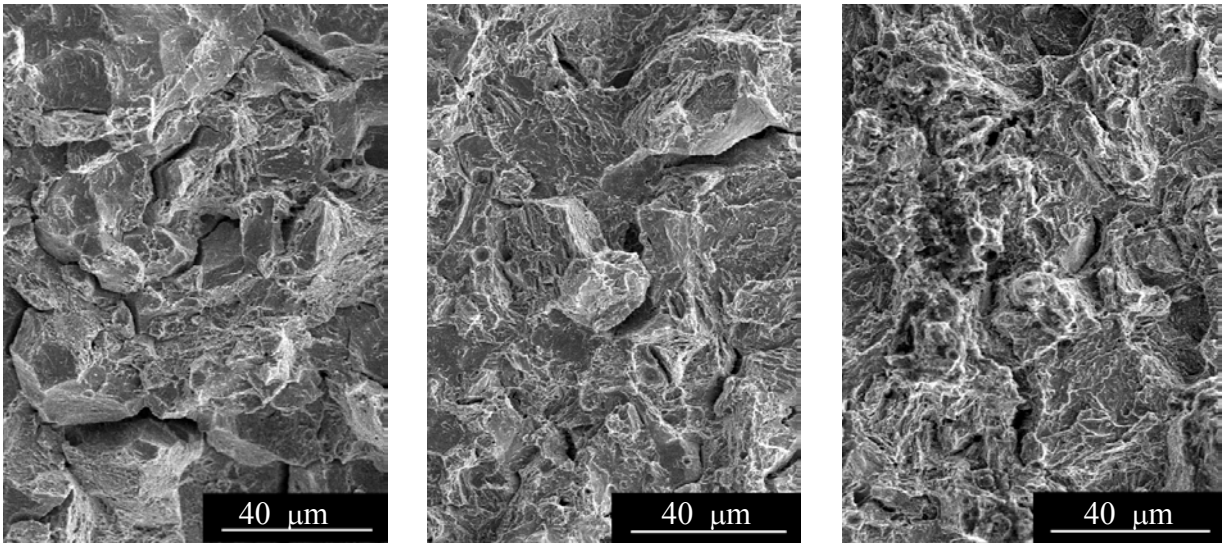

(*a*) (*b*) (*c*)

Figure 4: Slow-crack propagation area for quenched and tempered material (*a*), plated and unannealed (*b*) and plated and annealed (*c*) materials.

The application of a low temperature annealing on the material was observed to increase the threshold stress intensity factor (cracking started at higher stress level compared to unannealed material Table 3). The fracture surface for annealed samples was revealed to be similar to that for unplated material (Figure 4*b*).

The benefits of annealing in releasing the hydrogen introduced during plating have been investigated by *Rebak et al* [6]. It was shown that a zinc layer offered a strong barrier to hydrogen escape. In the light of this observation, the increase in resistance to hydrogen induced cracking may instead relate to a redistribution of hydrogen within the steel. According to *Townsend* [7] hydrogen, introduced during plating, is driven into deep trap sites where it loses mobility and is not available to affect embrittlement. The lower K_{1H} value for plated and annealed material compared to unplated material might be related to the generation of hydrogen at the crack tip via an electrochemical reaction with

moisture in the laboratory air due to the galvanocouple ‘zinc coating – steel’. This hydrogen exacerbates the effect of any internal hydrogen which may be present.

CONCLUSIONS

1. Embrittlement, which may be attributed to hydrogen, occurs during slow-strain rate testing in air in the steel under investigation.

2. An increase in hydrogen content during the application of a Zn coating during manufacture and possibly the generation of hydrogen via cathodic reaction during testing leads to embrittlement of the steel under investigation.

3. The mechanism of subcritical crack growth observed for quenched and tempered and plated materials is different. This change in mechanism may be attributed to a change in the critical crack tip plastic zone size which relates to a microstructuraly characteristic length scale.

REFERENCES

1. Grobin, A. W. Ir. (1990) *Materials Performance* 7, 71.
2. Fujita, T. and Yamada, Y. (1977). In: *Stress Corrosion Cracking and Hydrogen Embrittlement of Iron Base Alloys*, pp. 736 – 745, Hochmann, J. and Staehle, R.W. (Eds). National Association of Corrosion Engineers, Houston.
3. Ibrahim, R.N. and Stark, H.L. (1990) *International Journal of Fracture* 44, 179.
4. Ugiansky, G.N. and Payer, J.H. (1979). *Stress Corrosion Cracking – the Slow Strain Rate Technique, ASTM STP 665*. American Society for Testing and Materials, Philadelphia.
5. Rice, J.R. (1977). In: *Stress Corrosion Cracking and Hydrogen Embrittlement of Iron Base Alloys*, pp. 11 – 15, Hochmann, J. and Staehle, R.W. (Eds). National Association of Corrosion Engineers, Houston.
6. Rebak, R.B., Muchjin, L. and Szklarska-Smialowska, Z. (1997) *Corrosion* 53, 481.
7. Townsend, H.E. (1975) *Metallurgical Transactions A* 6A, 877.

ORAL REFERENCE: ICF100271OR

A STUDY OF MODE II FRACTURE TOUGHNESS TEST STANDARDISATION OF METALS

T. Tamilselvan, K. W. Lo, Y. B. Gong, and M. O. Lai

Department of Civil Engineering, National University of Singapore,
Singapore 119260

ABSTRACT

In LEFM, it has been predicted that under pure mode II loading a smooth test specimen would fracture at an angle of $_C$=–70.5°. However, for aluminum alloy 7075-T6, it has been found that $_C$=0 whether the specimen is grooved or not. This apparent inconsistency has now been resolved by adopting a specimen of appropriate geometry and loading configuration, which can distinguish between plastic and brittle fracture, thereby opening the way to standardisation of the mode II fracture toughness testing of metals. Accordingly, various studies have been conducted, both by FE analysis and laboratory testing, which address the selection of suitable test specimens, the requirements of specimen configuration and the analysis of test results. As a result, it may be concluded that the proposed specimen would be suitable and a grooved specimen would be needed in order to achieve true mode II fracture.

KEYWORDS

mode II, fracture toughness, fracture testing, crack shear displacement, groove, aluminum alloy 7075-T6, compact shear specimen, test standardisation

INTRODUCTION

Interest in K_{IIC} testing has increased in recent years and various mode II specimens have been proposed [1,2]. The two commonly-used criteria to evaluate the suitability of these specimens have been i) the intensity of normal stress ahead of the crack tip which would correspond to the error in measuring K_{IIC} and ii) the compactness of the test specimen which would provide for a lower fracture load and thus minimal plastic deformation.

The intensity of normal stress ahead of the crack tip of the test specimen may be determined from the value of the ratio of K_I/K_{II} under mode II loading. If $K_I>0$ indicating a tensile normal stress ahead of the crack tip, fracture due to mixed mode I-II loading could result. On the other hand, if $K_I<0$, the compressive stress at the pre-crack face behind the crack tip could give rise to friction and overestimation of the fracture toughness. From the point of achieving a pure mode II fracture, the absolute value of the ratio would have to be as small as possible.

The compactness of the test specimen may be determined by the normalised mode II stress intensity factor

K_{II} . A common form of the normalised mode II stress intensity factor, which is adopted in this study, is given by

$$K_{II}' = \frac{WT}{F\sqrt{\pi a}} K_{II}, \tag{1}$$

where F is the applied load, and T the thickness, a the crack length and W the width of the specimen respectively. Hence, specimens with similar dimensions of W, T and a but also smaller values of K_{II} would need higher loading to cause fracture. However, a higher load would result in greater plastic deformation during fracture testing, which is a source of error, hence K_{II} should be kept as large as possible.

Investigations [2,3,4] have shown that both the foregoing criteria have not been well satisfied in K_{IIC} testing. Firstly, the development of normal stresses ahead of the crack tip has seemed inevitable, and generally $K_I<0$ due to the effects of Poisson's ratio. As indicated in the foregoing discussion, fiction would develop as a result. Secondly, K_{II} has been generally small compared with K_I of mode I test specimens, where

$$K_I' = \frac{WT}{F\sqrt{\pi a}} K_I. \tag{2}$$

Thus, in taking into account the additional factor that K_{IIC} would probably be larger than K_{IC}, the fracture load in a K_{IIC} test might be expected to be much higher than that of a corresponding K_{IC} test.

Another problem in K_{II} testing has been the direction of crack extension. According to reports on brittle materials such as PMMA and tool steel [4,5], the crack would extend at an angle of about -70.5 with respect to the self-similar direction. Although this failure mode coincides with brittle fracture theory [6,7], the fracture mechanism is thought to be mode I by some researchers [7,8,9] because it is actually the near field tensile stress and not shear stress that causes the failure. On the other hand, for more ductile materials such as aluminum alloy, the crack tends to extend along the self-similar direction [10,11]. The load-displacement record in such test would become nonlinear at small loads [11], so the concepts of linear elastic fracture mechanics would not be applicable any more. Thus, a K_{IIC} value obtained under these circumstances would have some other connotation in terms of elastoplastic fracture.

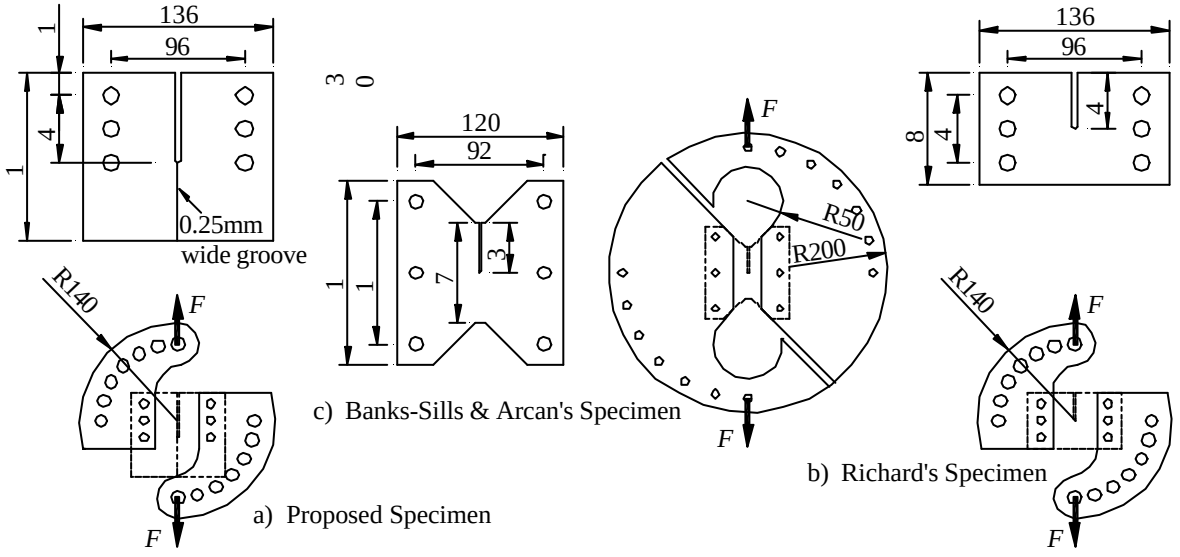

Figure 1: Mode II Fracture Specimens.

In view of the preceding considerations, a specimen for K_{IIC} testing is proposed herein which is essentially a modification of the mode II fracture test specimen originally proposed by Richard [12]. There are two aspects to this modification, as shown Figure 1(a). Firstly, the ligament length of the specimen has been

extended to produce a non-uniform shear stress distribution along it under mode II loading. With this modification, a considerable reduction in the value of $\frac{1}{2}K_I/K_{II}\frac{1}{2}$ as well as increase in K_{II} may be achieved. It was also found that brittle fracture could thereby be obtained under mode II loading for relatively ductile materials such as aluminum alloy, where the crack extended along the -70.5 direction. Secondly, a narrow groove was introduced in the normal direction to the face of the specimen, along the crack line and on both faces, so as to reduce the ligament thickness and assist in guiding the crack to extend along its self-similar direction and thus obtain a truly Irwin-type of brittle mode II fracture. The influence of the groove and relative stiffness of the loading fixture on the values of $\frac{1}{2}K_I/K_{II}\frac{1}{2}$ and K_{II} were also investigated. In an earlier investigation [13,14], the grooved specimen was found to be appropriate for fracture toughness testing as grooving was found to have no adverse influence on the distribution of the stress intensity factor along the crack front.

K_{IIC} test was carried out on aluminum alloy 7075-T6 using the proposed specimen. It is noteworthy that in the case of K_{IIC} testing, the "pop-in" phenomenon was observed.

TEST SPECIMEN

Proposed Mode II Test Specimen

The proposed specimen and its loading fixture are shown in Figure 1(a). The specimen is an adaptation of Richard's [12] specimen shown in Figure 1(b), with the exception that the ligament of the specimen has been extended and a 0.25 mm wide has been introduced along the crack line on both faces of the specimen and normal to the direction of each face. The extension of the specimen's ligament provided a non-uniform shear stress distribution along the ligament under mode II loading, in which the shear stress was highest near the crack tip and decreased at a significant rate away from it. This ensured that plastic deformation was localised within the near field of the crack tip while zones away from it remained largely elastic. Such circumstances would be more conducive to the development of brittle fracture.

The groove, on the other hand, was introduced to hinder the occurrence of brittle fracture at -70.5 under mode II loading. As a consequent and also due to the relative weakness of the reduced thickness of ligament in the plane, a crack extension in the self-similar direction would be more imminent. The depth of grooving required would, therefore, depend on its ability to deter the non self-similar crack extension under mode II loading. In the present study, the dimensions of the specimen adopted for analysis and testing are as shown in Figure 1(a). The thickness of specimen and depth of groove were varied.

Comparison of Mode II Test Specimens

Two commonly-used mode II test specimens are the ones proposed by Richard [12] and Banks-Sills and Arcan [4], as shown in Figures 1(b) and 1(c) respectively. In the present study, the suitability of the proposed specimen has been evaluated by comparing it against the two specimens whose dimensions adopted for analyses are shown in the same figures.

Two-dimensional (2-D) finite element analyses were carried on all three specimens using ABAQUS [15]. Eight-noded quadratic quadrilateral isoparametric elements were used and the singularity at the crack tip was simulated by triangular quarter-point elements formed by collapsing one face of the 8-noded quadrilateral element and relocating the mid-side nodes to respective quarter-points from the crack tip, as proposed by Barsoum [16]. The respective stress intensity factors were deduced from the displacements of the crack faces accordingly. The grooved specimen was idealised as a 2-D finite element model by modifying the Young's modulus of the elements at the ligament pro-rata to reflect its reduced thickness. This technique has been verified and found suitable in an earlier investigation [14].

In the present study, the material adopted for the three specimens and subsequently used for fracture testing of the proposed specimen was aluminum alloy 7075-T6 having a Young's modulus of E=72 GPa and

Poisson's ratio of =0.32. The loading fixtures of the three specimens were also presumed to be of aluminum alloy 7075-T6 for the purpose of comparison. The effects of stiffness of the loading fixture on the proposed specimen was analysed separately.

The three specimens were analysed for pre-crack lengths, a_f varying from 0.5 mm to 10 mm and corresponding values of $½K_I/K_{II}½$ and K_{II} are shown plotted against pre-crack length for the three specimen in Figure 2(a) and 2(b) respectively. Generally, the value of $½K_I/K_{II}½$ was lower while K_{II} was higher for the proposed specimen suggesting that it is the most compact specimen and at the same time experiences the least influence from a normal stress ahead of the crack tip. Furthermore, an optimal pre-crack length of approximately 3 mm is suggested in Figure 2(a) for the configuration of the proposed specimens at which the value of $½K_I/K_{II}½$ would be zero. This is not apparent in the case of the other two specimens. Also a pre-crack length of 3 mm would be appropriate from the point of view of Figure 2(b) as there would be no significant increase in the value of K_{II} with pre-crack length from then on. Hence, based on the foregoing considerations, it would appear that the proposed specimen would be the most suitable for mode II fracture testing.

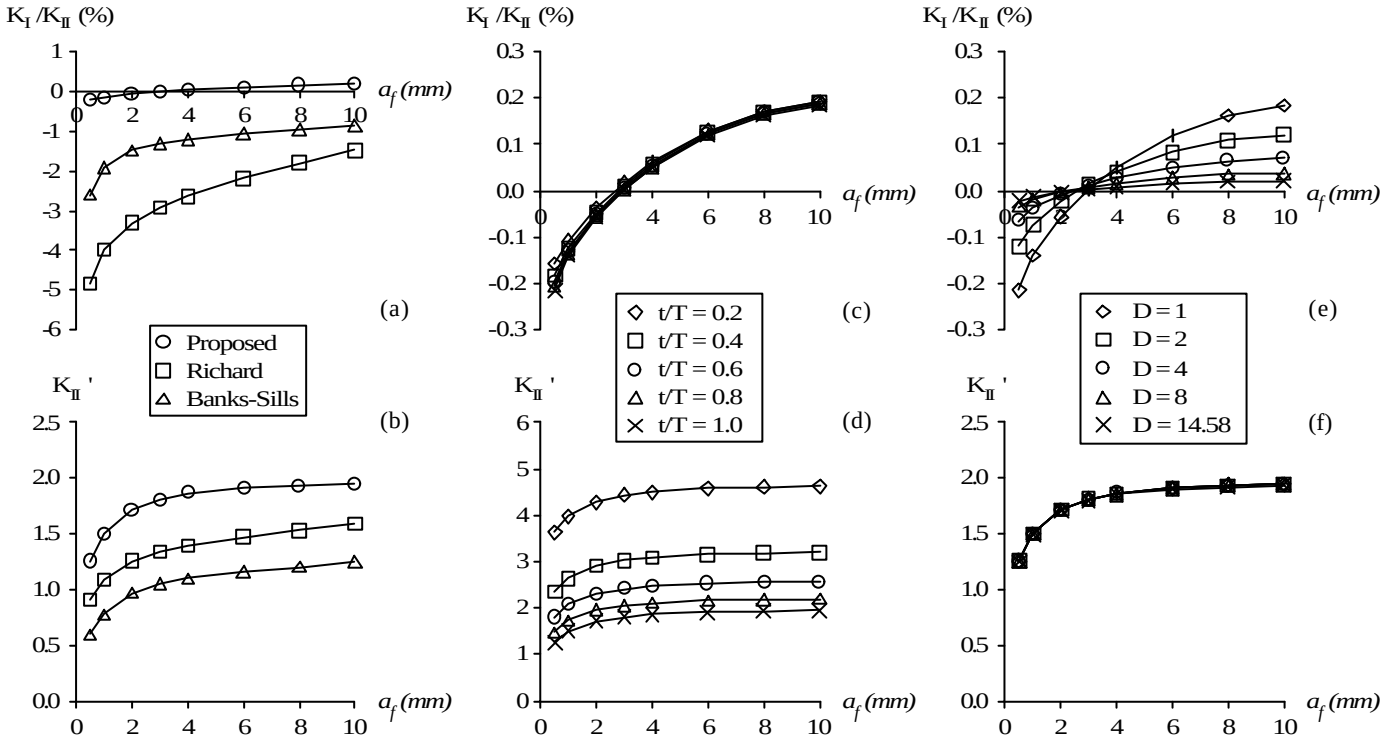

Figure 2: Analytical Results.

Investigation of Grooving and Loading Fixtures

As indicated in the foregoing discussion, the application of a groove to the faces of the proposed specimen would be a necessary feature of mode II fracture testing. Hence, the influence of grooving on the two characteristic parameters $½K_I/K_{II}½$ and K_{II} has been examined. In the analyses, the groove depth was varied such that the ratio of ligament thickness after and before grooving (t/T) ranged from 0.2 to 1. The results have been plotted in Figures 2(c) and 2(d). In Figure 2(c), it is apparent that grooving did not significantly influence the value of $½K_I/K_{II}½$ while on the other hand, as shown in Figure 2(d), K_{II} increased with depth of grooving, which, from the standpoint of compactness, would be advantageous. In both instances, the optimum pre-crack length of 3 mm was maintained.

The influence of the stiffness of the loading fixture was also examined, where the relative stiffness of loading fixture and the proposed specimen was specified as:

$$D = \frac{E_f\, T_f}{E\, T} \ , \tag{3}$$

in which E and E_f are the Young's modulus of the specimen and loading fixture respectively and T_f the thickness of the loading fixture. The analyses were carried out for relative stiffness D ranging from 1 to 14.58, where D=14.58 corresponds to the configuration used in subsequent fracture testing. The results have been plotted in Figures 2(e) and 2(f). In Figure 2(e), the value of $½K_I/K_{II}½$ decreased with increase in relative stiffness and furthermore, if a pre-crack of 3 mm were used, the relative stiffness would, in principle, have no effect on the value of $½K_I/K_{II}½$. However, since it is often not possible to control the pre-crack length, a stiffer loading fixture would be desirable. On the other hand, according to Figure 2(f), the relative stiffness would have practically no influence on $K_{II}¢$ at all. This would in turn suggest that $K_{II}¢$ may be taken to be a measure of compactness of the specimen as it would depend on specimen configuration alone.

FRACTURE TESTING

K_{IIC} tests were performed on aluminum alloy 7075-T6 based on the proposed specimen, a comprehensive account of which has been reported elsewhere [17]. The tests were carried out on both grooved and smooth specimens. The specimens were orientated in the LT direction of the metal and loaded via steel fixture in an MTS machine. The specimens were pre-cracked under mode I loading conditions according to the recommendations of ASTM E1820-96 [18] and thereafter grooved using a 0.25 mm wire cutter in an electro-discharge machine. The pre-crack length was kept close to 3 mm as suggested by the preceding analyses. During testing, the crack-mouth sliding displacement (CSD) was recorded using a clip gage attached to a knife edge which had been secured near the crack-mouth. Four set of grooved and one set of smooth specimens were tested in which the thickness of all specimens, T was 6 mm.

In the case of the smooth specimen, the crack extended in the –70.5 direction and in the load-CSD record of Figure 3(a), no "pop-in" was found. It is noteworthy that this observation has apparently not been reported on aluminum alloy before. In previous K_{IIC} testing [5,10,11], the crack invariably extended along the self-similar direction without satisfying brittle fracture theory. On the other hand, the proposed specimen herein is capable of developing brittle fracture even for a relatively ductile material such as aluminum alloy. Moreover, the result obtained would imply that it would not be feasible to obtain brittle mode II fracture on smooth specimen.

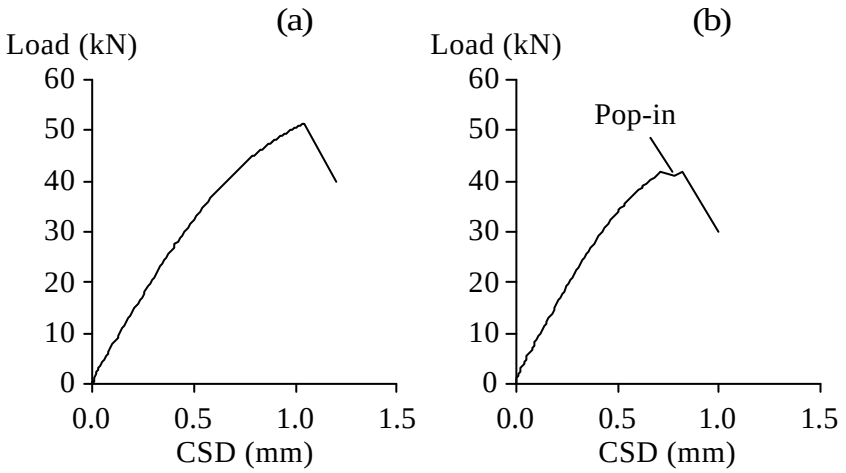

Figure 3: Experimental Results.

As for the grooved specimen for which t/T ranged from 0.68 to 0.8, the crack extended in the self-similar direction and similarly as the load-CSD record of Figure 3(b), "pop-in" was found in all tests. It is also noteworthy that this observation has apparently not been reported before in a K_{II} test. The "pop-in" load

was selected as the conditional load, P_Q to calculate K_{IIC} based on the recommendations for K_{IC} testing [18]. The K_{IIC} values obtained were consistent and independent of groove depth, which appears to indicate that the grooved depths adopted were within reasonable range. The average value of K_{IIC} was 63.7 $MPa\sqrt{m}$ which is approximately 2.1 times the known value K_{IC} for the metal.

CONCLUSIONS

A specimen is proposed for K_{IIC} testing, for which finite element analyses and fracture tests have been performed. As a result, the following findings have been made:-

1. In comparison with the K_{IIC} specimens of Banks-Sills and Arcan, and Richard, the proposed specimen is more compact and has significantly less intensity of normal stress ahead of the crack tip. Also the influence of the normal stress may be eliminated in principle by choosing the appropriate pre-crack length of 3 mm.
2. Grooving improves the compactness of the specimen while an increase in the stiffness of the loading fixture reduces the intensity of normal stress ahead of the crack tip.
3. In the K_{IIC} testing of a smooth specimen, the crack extends in the $_C$=–70.5° direction while for a grooved specimen, the crack can extend in the $_C$=0 direction. "Pop-in" has been found in the load-CSD records of all grooved specimens tested. These observations have apparently not been reported before.
4. For aluminum alloy 7075-T6, K_{IIC} was found to about 63.7 $MPa\sqrt{m}$ which is approximately 2.1 times the known value of K_{IC} for the metal.

REFERENCES

1. Richard, H.A., Tenhaeff, D. and Hahn, H.G. (1986). In: *The Mechanism of Fracture*, pp. 89-95, Goel, V. S. (Ed). ASM, USA.
2. Yuan, W. G., Lai, M.O. and Lee, K.H. (1994). Finite Elements in Analysis and Design, 18, 211.
3. Xu, S., Hans, W., Reinhardt and Gappoev, M. (1996). *Int. J. Fract.* 75, 185.
4. Banks-Sills, L. and Arcan, M. (1986). In: *Fracture Mechanics*, 17, pp. 347-363, ASTM-STP 905, Philadelphia.
5. Hiese, W. and Kalthoff, J.F. (1999). In: *Mixed-Mode Crack Behavior*, pp. 74-85, ASTM-STP 1359, West Conshohocken.
6. Erdogan, F. and Sih, G. C. (1963). *J. Basic Eng.* 85, 519.
7. Lo, K. W., Tamilselvan, T., Chua, K. H. and Zhao, M. M. (1996). *Eng. Fract. Mech.* 54, 189.
8. Buzzard, R. J., Gross, B. and Srawley, J. E. (1986). In: *Fracture Mechanics*, 17, pp. 329-346, ASTM-STP 905, Philadelphia.
9. Takao, U., Toshiaki, I., Hayato, O. and Katsuhiko, W. (1999). *JSME Int. J., Series A*, 42, 429.
10. Banks-Sills, L. and Sherman, D. (1991). *Int. J. Fract.* 50, 15.
11. Cowie, J. G. and Tuler, F. R. (1991). *Int. J. Fract.* 47, 229.
12. Richard, H. A. (1981). *Int. J. Fract.* 17, R105.
13. Lo, K. W., Lai, M. O. and Tamilselvan, T. (1997). In: *Advances in Fracture Research*, 5, pp. 2495-2502, Karihaloo, L., Mai, Y. W., Ripley, M. I. and Ritchie, M. O. (Eds). Pergamon, Great Britain.
14. Tamilselvan, T. (1998). PhD Thesis, National University of Singapore, Singapore.
15. Hibbit, Karlsson and Sorenson, Inc. (1995). *ABAQUS ver. 5.5*, USA.
16. Barsoum, R. S. (1976). *Int. J. Num. Methods Eng.* 10, 25.
17. Lo, K. W., Gong Y. B., Tamilselvan, T. and Lai, M. O. (2001). Submitted to *Int.J. Fract.*
18. American Society for Testing and Materials (1997). *Standard Test Method for Measurement of Fracture Toughness: Annual Book of ASTM Standards*, ASTM E1820-96, West Conshohocken.

ORAL REFERENCE: ICF100299OR

A THERMODYNAMIC CONSISTENT DAMAGE FORMULATION BASED ON A NONLOCAL DAMAGE ACTIVATION THRESHOLD

G. Borino[1], E. Benvenuti[2] and A. Tralli[2]

[1] Dipartimento di Ingegneria Strutturale e Geotecnica
University of Palermo, 90128 Palermo, ITALY

[2] Dipartimento di Ingegneria, University of Ferrara, 44100 Ferrara, ITALY

ABSTRACT

The paper deals with a formulation for nonlocal (integral) continuum damage models where the thermodynamic principles are consistently satisfied for nonlocal media. The nonlocal field is chosen to be an internal variable which describes the activation damage threshold. The present approach possesses several analogies with a recent one proposed by Polizzotto *et al.* [1,2] for elastic-plastic softening material models. The present choice shows that, when structural strain localization starts to develop, the amplitude of the damage band tends to become narrower and narrower as the damage loading proceeds, but the solution is kept objective with respect to mesh refinements. It is a remarkable fact that the amplitude of the damage band naturally evolves without introducing any "ad-hoc" rule for the evolution of the internal length. As a drawback, a nonlocal iteration procedure is required in order to establish the damage active region.

KEYWORDS

Damage, Nonlocal formulation, Thermodynamics, Localization.

INTRODUCTION

An effective way of modelling the constitutive behaviour of quasi-brittle materials is the so-called continuum damage mechanics, which is able to represent the overall volumetric degradation of the material elastic properties and eventually the induced strain softening state [3]. On the other hand, it is known that specific difficulties arise when strain softening regime develops, mainly related to constitutive instability matters [4]. Classical local theories lead to solutions in which strain fields localize in bands with zero width measure and, consequently, the collapse occurs with zero global energy dissipation. Such a physical meaningless condition has revealed to be an intrinsic limit of the traditional formulations applied to softening regimes. These difficulties can be removed introducing regularization techniques, which basically require a proper internal length scale parameter.
Among several regularization techniques, the most effective seem to be the gradient [5,6] and the nonlocal (integral) approaches [4,7-9], which have been developed, and successfully applied, by many researchers. Modern nonlocal formulations consider as nonlocal, i.e. obtained by a spatial integral averaging, only a suitable scalar measure associated to the dissipative softening process, preserving as local all the other involved variables. In this way, traditional field relations, like equilibrium and

compatibility, remain of local type, whereas, the nonlocality complexities are confined within the dissipative part of the constitutive relations.
The present contribution starts by selecting as nonlocal field a specific internal variable which is directly related to the yield limit of the damage activation function. This choice is alternative to the most common choices which selects as nonlocal field the damage, or its thermodynamic conjugate force, which is the energy released rate. The mechanical meaning of the present choice is that when a point suffers damage flow, the neighbour points register a reduction of their damage limit strength, so that a diffusion, or a nonlocal redistribution, of the damage is possible.
The present formulation also focuses on the thermodynamic consistency of the nonlocal model and a reasoning path, recently presented for nonlocal plasticity models [1,2], is considered. In fact, as a consequence of the nonlocality, the second principle of thermodynamics is enforced in an integral form all over the spatial domain occupied by the body. Its local form is still existing but it needs an additional term, the nonlocality residual, which is related to the energy exchanges of the mutually interacting particles.

FORMULATION

In order to derive a formulation which satisfy a-priori thermodynamic restrictions, let us consider an elastic-damage material for which the Helmholtz free energy is written as

$$\psi(\boldsymbol{\varepsilon}, d, \kappa, \bar{\kappa}) = \psi_e(\boldsymbol{\varepsilon}, d) + \psi_{in}^{l}(\kappa) + \psi_{in}^{nl}(\bar{\kappa}) = \frac{1}{2}(1-d)^2 \boldsymbol{\varepsilon} : \boldsymbol{C}_0 : \boldsymbol{\varepsilon} + \frac{1}{2} h_l \kappa^2 + \frac{1}{2} h_{nl} \bar{\kappa}^2, \tag{1}$$

where $\boldsymbol{\varepsilon}$ is the (infinitesimal) strain tensor, d is the damage variable, κ and $\bar{\kappa}$ are two internal variables which describe the damage evolution and are local and nonlocal, respectively. Isotropic damage is here considered, so that the damage d is a scalar variable ranging within the interval $[0, 1]$. $\boldsymbol{C}_0$ is the elastic moduli tensor of the undamaged material. In analogy with the elastic strain energy, ψ_e, the internal energies ψ_{in}^{l} and ψ_{in}^{nl} have been assumed as quadratic forms of the local and nonlocal internal variables and, consequently, linear hardening laws follow, where $h_l > 0$ and $h_{nl} < 0$ are the hardening/softening damage moduli. The nonlocality affects only the internal variable $\bar{\kappa}$ and the physical meaning is that, when damage develops in a point, its strength to further damage developments increases by local hardening $h_l\, \kappa$, whereas the strength of the neighbour points decreases by the nonlocal damage hardening $h_{nl}\, \bar{\kappa}$. A nonlocal operator $\mathcal{R}$ transforms the local scalar field $\kappa(\boldsymbol{x})$ in the nonlocal counterpart $\bar{\kappa}(\boldsymbol{x})$ by means of the following integral relation

$$\bar{\kappa}(\boldsymbol{x}) = \mathcal{R}(\kappa)\big|_x = \frac{1}{V_r(\boldsymbol{x})} \int_V \alpha(||\boldsymbol{x} - \boldsymbol{y}||)\, \kappa(\boldsymbol{y})\, dV(\boldsymbol{y}), \tag{2}$$

where $\alpha(r)$ is a spatial influence function, which is not negative and decrease with the distance $r = ||\boldsymbol{x} - \boldsymbol{y}||$. Moreover, $V_r(\boldsymbol{x})$ is the representative volume defined as

$$V_r(\boldsymbol{x}) = \int_V \alpha(||\boldsymbol{x} - \boldsymbol{y}||)\, dV(\boldsymbol{y}). \tag{3}$$

The influence function is usually chosen as the Gaussian error function, $\alpha(r) = \exp[-(kr/\ell)^2]$, where ℓ is the material internal length scale.
To enforce the satisfaction of the second principle of thermodynamics, let us write the Clausius-Duhem inequality in global form over the entire domain V

$$\int_V (\boldsymbol{\sigma} : \dot{\boldsymbol{\varepsilon}} - \dot{\psi})\, dV \geq 0. \tag{4}$$

Equation (4) can be written in a pointwise form after the introduction of the nonlocality residual function $P(\boldsymbol{x})$, [1,2,10], which takes in to account the energy exchanges between neighbour particles

$$\mathcal{D} = \boldsymbol{\sigma} : \dot{\boldsymbol{\varepsilon}} - \dot{\psi} + P \geq 0 \qquad \text{in } V, \tag{5}$$

where $\mathcal{D}$ indicates the intrinsic local dissipation. Assuming the body a thermodynamically isolated system, the following insolation condition holds

$$\int_V P\, dV = 0. \tag{6}$$

Substitution of (1) into (5) leads to

$$\mathcal{D} = \boldsymbol{\sigma} : \dot{\boldsymbol{\varepsilon}} - \frac{\partial \psi}{\partial \boldsymbol{\varepsilon}} : \dot{\boldsymbol{\varepsilon}} - \frac{\partial \psi}{\partial d}\dot{d} - \frac{\partial \psi}{\partial \kappa}\dot{\kappa} - \frac{\partial \psi}{\partial \bar{\kappa}}\dot{\bar{\kappa}} + P \geq 0 \qquad \text{in } V, \tag{7}$$

which holds for any, reversible or irreversible, deformation mechanism. Following standard procedures, it is possible to recognize the following state laws:

$$\boldsymbol{\sigma} = \frac{\partial \phi}{\partial \boldsymbol{\varepsilon}} = (1-d)^2\, \boldsymbol{C}_0 : \boldsymbol{\varepsilon}, \qquad\qquad Y := -\frac{\partial \psi}{\partial d} = (1-d)\boldsymbol{\varepsilon} : \boldsymbol{C}_0 : \boldsymbol{\varepsilon} \tag{8a,b}$$

$$\chi := \frac{\partial \psi}{\partial \kappa} = h_l\, \kappa, \qquad\qquad \chi_{nl} := \frac{\partial \psi}{\partial \bar{\kappa}} = h_{nl}\, \bar{\kappa} = h_{nl}\, \mathcal{R}(\kappa), \tag{8c,d}$$

so that the explicit form of the dissipation function reads

$$\mathcal{D} = Y\dot{d} - \chi\, \dot{\kappa} - \chi_{nl}\, \dot{\bar{\kappa}} + P \geq 0 \qquad \text{in } V. \tag{9}$$

The thermodynamic force Y, conjugated to the damage d, represents the energy release for unitary increment of damage. χ and χ_{nl} are the thermodynamic forces associated to the local κ and nonlocal $\bar{\kappa}$ internal variables, respectively. The dissipative irreversible mechanism associated to the damage is governed by the local fluxes $\dot{d}$, $\dot{\kappa}$. The dissipation $\mathcal{D}$ can therefore alternatively be written as the bilinear form

$$\mathcal{D} = Y\, \dot{d} - X\, \dot{\kappa} \geq 0 \qquad \text{in } V, \tag{10}$$

where X represents the equivalent nonlocal force that is associated to the increment of the local variable κ. By comparing eqs. (9) and (10), we can specify P as

$$P = \chi\, \dot{\kappa} + \chi_{nl}\, \dot{\bar{\kappa}} - X\, \dot{\kappa} \qquad \text{in } V. \tag{11}$$

The imposition of the insulation condition (6) leads to

$$\int_V \left(\chi\, \dot{\kappa} + \chi_{nl}\, \dot{\bar{\kappa}} - X\, \dot{\kappa}\right) dV = 0 \tag{12}$$

for each dissipative mechanism and then for each $\dot{\kappa}$. It can be shown that the following (Green) identity holds for the operator $\mathcal{R}$

$$\int_V \chi_{nl}\, \mathcal{R}(\dot{\kappa})\, dV = \int_V \mathcal{R}^*(\chi_{nl})\, (\dot{\kappa})\, dV, \tag{13}$$

where $\mathcal{R}^*$ is the adjoint operator of $\mathcal{R}$ defined by

$$\mathcal{R}^*(\chi_{nl})\big|_x = \int_V \frac{1}{V_r(\boldsymbol{y})} \alpha(||\boldsymbol{x}-\boldsymbol{y}||)\, \chi_{nl}(\boldsymbol{y})\, dV(\boldsymbol{y}). \tag{14}$$

By considering identity (13), eq. (12) turns out to be

$$\int_V \left[\mathcal{R}^*(\chi_{nl}) + \chi - X\right] \dot{\kappa}\, dV = 0. \tag{15}$$

Since (15) has to hold for any possible damage mechanism, and thus for any choice of $\dot{\kappa}$, it follows

$$X = \mathcal{R}^*(\chi_{nl}) + \chi \qquad \text{in } V. \tag{16}$$

After substitution of (16) in (10), the dissipation can be written in explicit form

$$\mathcal{D} = Y\,\dot{d} - [\chi + \mathcal{R}^*(\chi_{nl})]\,\dot{\kappa} \geq 0. \tag{17}$$

The structure of the dissipation in eq. (17) justifies the assumption of a damage activation function $\phi(Y, X)$, which, in the hypothesis of associative damage behaviour, gives the following flow rules:

$$\dot{d} = \frac{\partial \phi}{\partial Y}\dot{\lambda}, \qquad \dot{\kappa} = -\frac{\partial \phi}{\partial X}\dot{\lambda}, \qquad \text{in V.} \tag{18a}$$

Finally, the usual loading/unloading conditions complete the constitutive damage nonlocal relations

$$\phi(Y, X) \leq 0, \qquad \dot{\lambda} \geq 0, \qquad \phi\dot{\lambda} = 0 \qquad \text{in } V. \tag{18b}$$

Relations (18) are analogous to the correspondent relations characterizing local formulations for generalized standard materials [3]. At difference with the local case here, an extra term appears in the damage activation function, that is $\bar{\chi}^*_{nl} = \mathcal{R}^*(\chi_{nl})$ and, therefore, eqs. (18) is a system of spatially coupled relations. In the present paper, for sake of simplicity, the nonlocal damage activation function

$$\phi(Y, \chi, \bar{\chi}^*_{nl}) \equiv Y - \chi - \bar{\chi}^*_{nl} - Y_0 \leq 0 \tag{19}$$

has been assumed.

FINITE ELEMENT DISCRETIZATION

A nonlinear finite element structural analysis requires an iterative incremental solution procedure, in which the equilibrium, and the constitutive relations, are satisfied implicitly in a stepwise form, i.e.

$$\sum_{e=1}^{Ne} \int_{V_e} \boldsymbol{B}_e^T(\boldsymbol{x})\,\boldsymbol{\sigma}_{k+1}(\boldsymbol{x})\,dV = \boldsymbol{F}_{k+1}, \tag{20}$$

where Ne is the total number of elements, $\boldsymbol{B}_e$ is the compatibility matrix and $\boldsymbol{F}$ is the equivalent nodal load vector. Equation (20) is the equilibrium condition to be enforced using an iterative scheme of Newton type. Inside the equilibrium loop, the integration of the constitutive relations, between the previous equilibrium state, k, and the new one, $k+1$, has to be carried out. Indicating with Δ the increment of a quantity in the step, the discrete form of the constitutive relations (18) reads

$$\Delta d = \left.\frac{\partial \phi}{\partial Y}\right|_{k+1} \Delta\lambda = \Delta\lambda, \qquad \Delta\kappa = -\left.\frac{\partial \phi}{\partial X}\right|_{k+1} \Delta\lambda = \Delta\lambda, \tag{21a}$$

$$\phi_{k+1} \leq 0, \qquad \Delta\lambda \geq 0, \qquad \Delta\lambda\,\phi_{k+1} = 0. \tag{21b}$$

Due to the nonlocality nature of X_{k+1}, equations (21b) represent an integral complementarity problem that cannot be solved localwise, but it rather requires an inner iterative loop inside the equilibrium equations.

Iterative scheme

The iterative equilibrium procedure gives the increment displacement vector $\Delta\boldsymbol{u}$ and, consequently, the increment of total strains $\Delta\boldsymbol{\varepsilon}$.

The procedure that leads to the satisfaction of the nonlocal spatially coupled constitutive relations (21) is based on:

- a *predictor* phase: at each integration point the trial value of the damage activation function is evaluated as
$$\phi_{k+1}^{tr} = Y_{k+1}^{tr} - X_k - Y_0, \tag{22}$$
where $Y_{k+1}^{tr} = (1-d_k)(\boldsymbol{\varepsilon}+\Delta\boldsymbol{\varepsilon}) : \boldsymbol{C}_0 : (\boldsymbol{\varepsilon}+\Delta\boldsymbol{\varepsilon})$ and X_k is the nonlocal internal variable obtained at the previous equilibrium iteration. If, at some points $\phi_{k+1}^{tr} > 0$, then a corrector phase is necessary, otherwise a new equilibrium loop begins;
- a *corrector* phase: a further iterative inner loop is devoted to the identification of the damage active points as well as the damage increments. The procedure used closely follows the scheme originally proposed by Strömberg and Ristinmaa [11] for nonlocal plasticity.

The solution of the consistency condition $\phi_{k+1} = 0$ is then obtained iteratively. In fact, the solution requires at each point the knowledge of the unknown damage increments of the neighbour points. If a trial damage increment distribution is assumed, the set of equations $\phi_{k+1} = 0$ can be solved at each integration point and a new set of active damage points emerges, i.e. some new points can now be involved and some other can cease to be active. The new values are then assumed for a subsequent iteration until fulfillment of eqs. (21b)
The numerical strategy to solve the nonlinear equations $\phi_{k+1} = Y_{k+1} - X_{k+1} - Y_0 = 0$, where

$$X_{k+1}(\boldsymbol{x}) = h_l(d_k(\boldsymbol{x}) + \Delta d(\boldsymbol{x})) + h_{nl} \int_V \frac{\alpha(||\boldsymbol{x}-\boldsymbol{y}||)}{V_r^2(\boldsymbol{y})} \int_V \alpha(||\boldsymbol{y}-\boldsymbol{z}||)[d_k(\boldsymbol{z}) + \Delta d(\boldsymbol{z})]\, dV(\boldsymbol{z})\, dV(\boldsymbol{y}) \tag{23}$$

is based on a modified Newton-Raphson technique. The linearization of the consistency condition leads to

$$\phi_{k+1}(d + \Delta d + \delta d) = \phi_{k+1}(d + \Delta d) + \left.\frac{\partial \phi}{\partial\, \Delta d}\right|_{d+\Delta d} \delta d = 0, \tag{24}$$

which gives the correction increment

$$\delta d = -\left[\frac{\partial \phi}{\partial\, \Delta d}\right]^{-1}_{d+\Delta d} \phi_{k+1}(d + \Delta d). \tag{25}$$

Finally, instead of evaluating the Hessian, the following (local) approximation is adopted

$$\frac{\partial \phi}{\partial\, \Delta d} \approx [h_l + h_{nl} + (\boldsymbol{\varepsilon}+\Delta\boldsymbol{\varepsilon}) : \boldsymbol{C}_0(\boldsymbol{\varepsilon}+\Delta\boldsymbol{\varepsilon})] \tag{26}$$

so that eq. (25), which is spatially coupled, can be evaluated localwise.
Numerical tests have shown that this approach is quite effective, even if the nonlocal iteration loop inside the equilibrium iterations increases the overall computational cost of the analysis.

NUMERICAL APPLICATIONS

In order to investigate the capability of the proposed method, a simple application has been carried out. The analysis has been performed for a 1-D bar in a uniform state of stress. The length of the bar is 100 mm. In the middle part there is a zone, 10 mm long, where an initial damage has been imposed in order to trigger the damage localization. The material is characterized by the Young's modulus $E = 20000$ N/mm^2, the hardening parameters are assumed as $h_l = 0.0008$ N/mm^2 and $h_{nl} = -0.0004$ N/mm^2. Finally, the initial damage threshold is $Y_0 = 0.0001$ N/mm^2 and the internal length is $\ell = 5$ mm. The bar has been discretized by simple constant strain elements and the analysis has been performed with 20, 40, 80 and 160 elements. Figure 1a shows the load-displacement curves for the four different discretizations. It appears that the response is objective with respect to mesh refinement, at least until the very last part of the analysis. In Figure 1b, the damage distributions, at different levels of the loading process, are reported with reference to the analysis performed with

160 elements. It can be observed that the strain localization phenomenon is well regularized and, moreover, the damage band tends to shrink as the damage loading proceed. This aspect is quite remarkable, since it has been obtained without enforcing any special evolution law for the internal length parameter, which is kept constant in the analysis.
To conclude, numerical tests of 2-D structures are at the moment under study. It is expected that such analysis will confirm the above discussed properties of the presented thermodynamically consistent damage model.

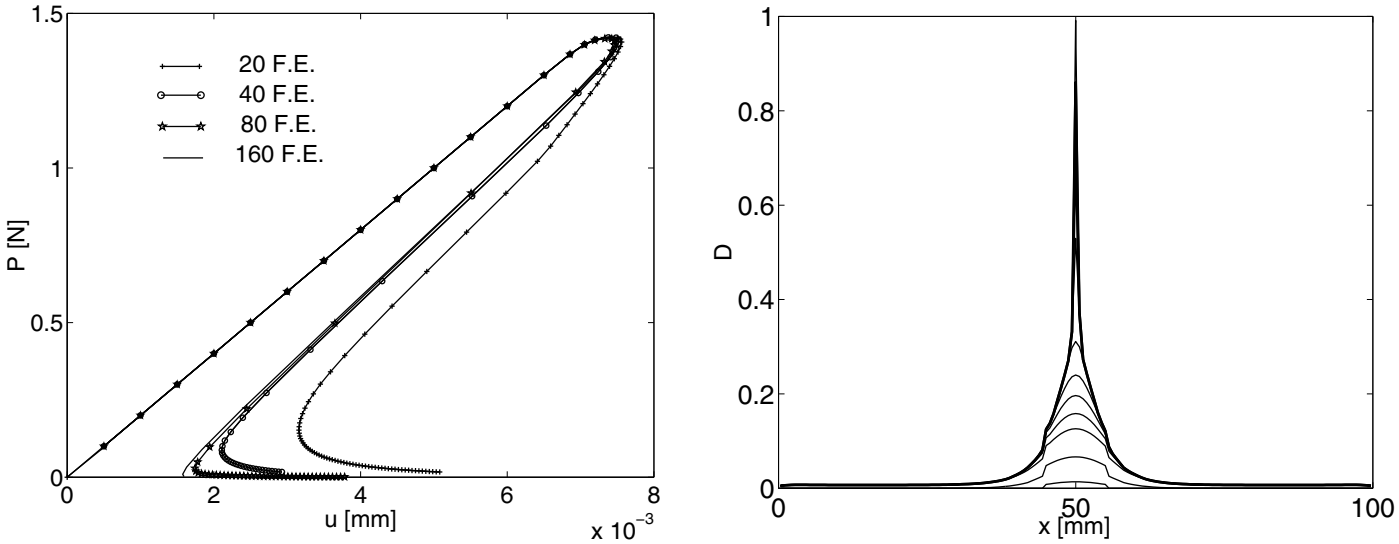

Fig. 1 (a) Load-displacement curves obtained with 20, 40, 80 and 160 elements. (b) Evolution of the damage profile at increasing damage loading steps. Results obtained with 160 elements.

REFERENCES

1. Polizzotto, C., Borino, G. and Fuschi, P. (1997), *Mech. Res. Com.* 25, 75–82.
2. Borino, G., Fuschi, P. and Polizzotto, C. (1999), *J. Appl. Mech.* 66, 952–963.
3. Lemaitre, J. and Chaboche, J.-L. (1990), *Mechanics of Solids Materials*, Cambridge University Press, New York.
4. Bažant, Z.P. and Pijaudier-Cabot, G. (1987), *J. Appl. Mech.* 55, 287–293.
5. Peerlings, R.H.J., de Borst, R., Brekelmans, W.A.M. and de Vree, J.H.P. (1996) *Int. J. Num. Meth. Engrg.* 39, 3391–3403.
6. Comi, C. (1999), *Mech. Cohesive Frictional Materials* 4, 17–36.
7. Pijaudier-Cabot, G. and Bažant, Z.P. (1987), *J. Engrg. Mech.* 113, 1512–1533.
8. Benvenuti, E., Borino, G. and Tralli, A. (2000), In: *CD Proc. ECCOMAS 2000*, Barcelona, Spain.
9. Benvenuti, E. (2001), Ph.D. Thesis, University of Ferrara, Italy.
10. Edelen, D.G.B. and Laws, N. (1971), *Arch. Rat. Mech. Anal.* 43, 24–35.
11. Strömberg, L. and Ristinmaa, M (1996), *Comp. Meth. Appl. Mech. Engrg.* 136, 127–144.

ICF100358OR

A TOUGHNESS STUDY OF THE WELD HEAT AFFECTED ZONE OF A MODIFIED 9Cr-1Mo STEEL

A. Moitra, K. Laha, P.R. Sreenivasan and S. L. Mannan

Materials Development Group
Indira Gandhi Centre for Atomic Research
Kalpakkam, Tamilnadu 603 102, India

ABSTRACT

Fracture properties of different microstructural regions of the heat affected zone (HAZ) of modified 9Cr-1Mo steel (tempered base metal, intercritical, fine grained, coarse grained with and without δ-ferrite) have been studied by Charpy impact test. Simulation technique is used to reproduce HAZ microstructures. The fine-grained region shows highest toughness and the coarse grained with δ-ferrite shows the lowest. The results have been analysed in terms of tensile properties and microstructural features. The inter particle distance seems to affect the energy absorbed up to fracture both in the tensile tests and Charpy impact test. The highest toughness is obtained for an optimum inter-particle spacing.

KEYWORDS

Modified 9Cr-1Mo steel, Weld, Microstructure, HAZ, Toughness

1. INTRODUCTION

Modified 9Cr-1Mo (grade T91/P91) steel in tempered martensitic condition is widely used in power plants for headers in steam generators and in tubing for heat exchangers due to excellent high temperature creep strength, high stress corrosion cracking resistance, low oxidation rate and good weldability. The steel is a modified version of the conventional 9Cr-1Mo alloy with controlled addition of niobium, vanadium and nitrogen [1]. It derives its high temperature strength from the complex microstructures consisting of a high dislocation density, sub-boundaries decorated with carbides and Nb-V carbo-

nitride precipitates of the type MX in the matrix [2,3]. However, welding modifies the microstructure of this steel locally (known as the Heat Affected Zone, HAZ) and hence the mechanical properties in this region are altered. Specifically the fracture toughness of the weldment is a matter of concern.

Microstructure in the HAZ is extremely complex and is controlled by interaction of thermal fields produced by heat input from the welding process, the phase transformations and grain growth characteristics of the material being welded [4]. A systematic study by Chandravathi et al. [5] reveals that the HAZ of modified 9Cr-1Mo is composed of coarse prior austenitic grained martensitic region with δ-ferrite (CPAGM-δ) adjacent to fusion line followed by coarse prior austenitic grained martensite (CPAGM), fine prior austenitic grained martensite (FPAGM) and intercritical region (ICR) merging with the tempered base metal (BM). However, the fracture properties of the different structures in the HAZ are difficult to obtain because of practical difficulties of fabricating samples of adequate dimensions with a single microstructure. The simulation of individual microstructure is a powerful method for studying the mechanical behaviour of HAZ [5]. The objective of the present study is to assess the fracture characteristics of the different microstructures likely to be encountered in the HAZ of modified 9Cr-1Mo steel weld joint. This paper reports Charpy impact properties of the steel in different microstructural conditions simulating different parts of HAZ. The results have been analysed in terms of tensile properties and microstructural features.

2. EXPERIMENTAL

Forged rounds (of 70 mm diameter) of a modified 9Cr-1Mo ferritic steel supplied by M/s. Midhani, Hyderabad, India in normalised (1060 ^{o}C/6 hrs/air cooled) and tempered (770 ^{o}C/4 hrs/air cooled) condition were used in this investigation. The chemical composition (in wt %) of the steel is: Cr-8.72, Mo-0.90, C-0.096, Mn-0.46, Si-0.32, V- 0.22, Nb-0.08, N-0.051, S-0.006, P-0.012, Ni-0.1, Fe-balance.

The microstructures of the HAZ have been simulated by isothermal heat treatments in different temperatures representing different phase fields. The details of the simulation technique and microstructures obtained are described in the earlier work by Chandravathi et al [5]. In the present study, the specimens were exposed for five minutes at five different temperatures (800, 850, 950, 1220 and 1350 ^{o}C) followed by oil quenching to reproduce the BM and ICR, FPAGM, CPAGM and CPAGM-δ regions of HAZ respectively. The tempering treatment at 760 ^{o}C/1hr has subsequently been carried out.

Charpy impact tests were carried out on a Tinius-Olsen make 358 J capacity machine using sub-size Charpy V-notch specimens (5x5x55 mm and 1 mm notch depth) in the temperature range of –156 ^{o}C to 61 ^{o}C following ASTM E23 [6] criterion. Scanning electron microscopy (SEM) was carried out on the fracture surfaces of the specimens tested –50 ^{o}C.

Tensile tests were carried out in air at room temperature at a nominal strain rate of $3x10^{-4}$ sec^{-1} on cylindrical tensile specimens of 26 mm gauge length and 4 mm diameter in an Instron 1195 universal testing machine.

3. RESULTS AND DISCUSSION

Charpy impact energies plotted against testing temperatures are shown in Figure 1.

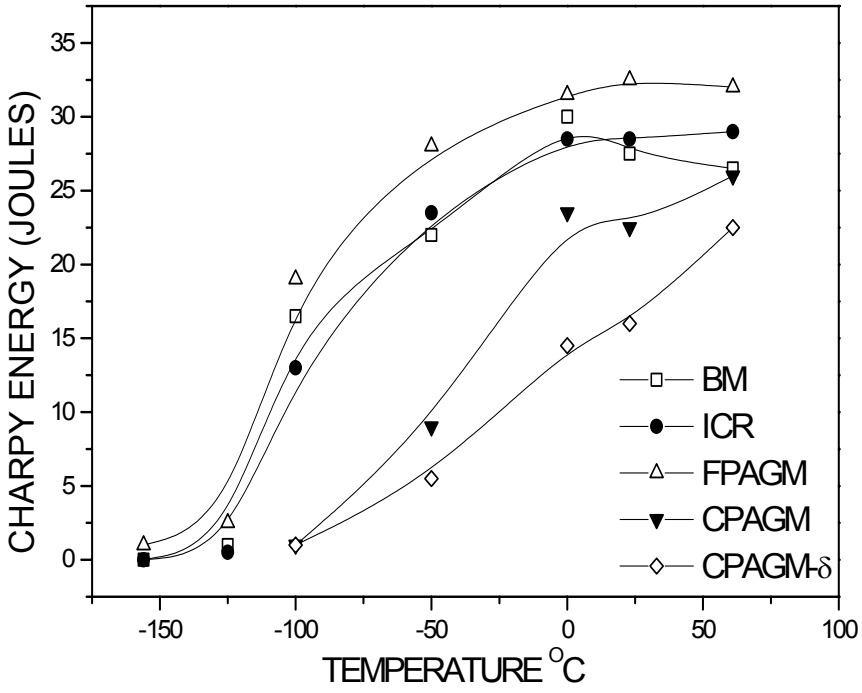

Figure 1: Charpy test results for simulated HAZ samples

Highest toughness in terms of the highest upper shelf energy and the lowest ductile to brittle transition temperature is observed for FPAGM and the lowest toughness is observed for CPAGM-δ. The toughness for BM and ICR are comparable and are higher than the coarse grained region CPAGM.

The results for the SEM study of the fractured surfaces are shown in Figure 2 (a and b). The fibrous appearance of the fracture surface from the FPAGM (fig. 2a) shows the ductile nature of the crack growth in this region. Similar fracture surfaces have been observed for the BM and ICR also. Void growth and coalescence is dominant in these samples. Contrary to the above, brittle cleavage mode of failure features in the fracture surface from CPAGM-δ (fig. 2b). The same has been observed for CPAGM also.

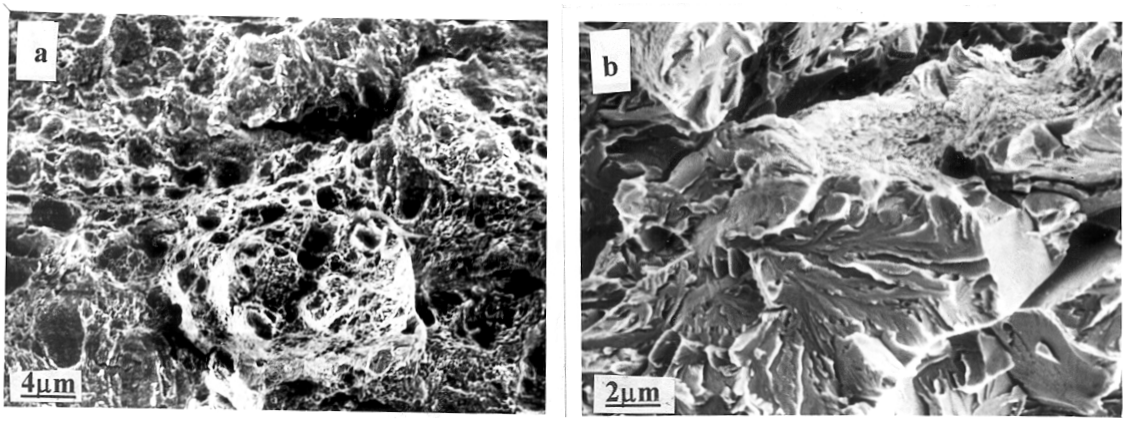

Figure 2 (a-b): The SEM pictures of the fracture surfaces from simulated HAZ samples; FPAGM (a) and CPAGM-δ (b)

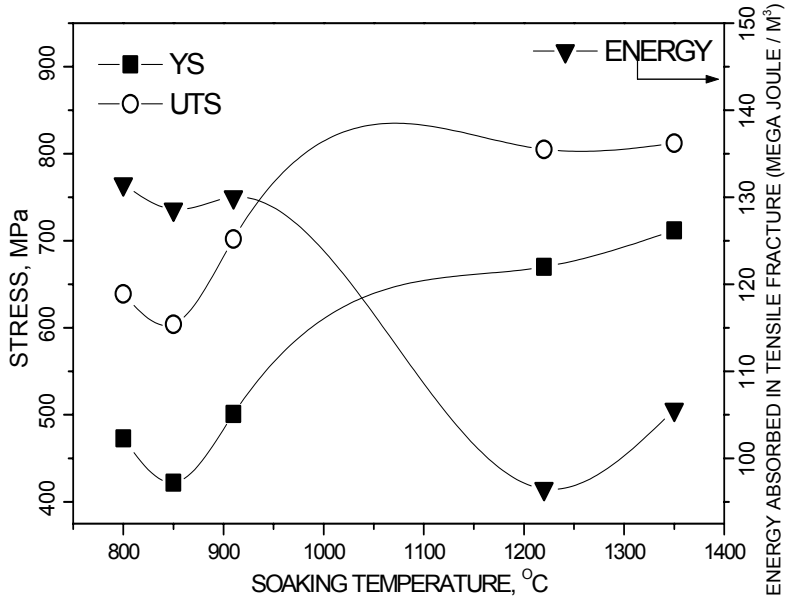

Figure 3: Tensile test results of simulated HAZ samples

The variations of yield stress, ultimate tensile stress and energy absorbed up to fracture (measured from the area under the stress-strain plots) with the heat treatment temperatures are shown in Figure 3.

It is evident that the ICR in the HAZ shows the lowest yield stress and the lowest ultimate tensile stress. The FPAGM shows reasonable combination of low yield stress

and high tensile strength. The peak in the energy absorbed up to fracture for the FPAGM confirms highest toughness for this region amongst the HAZ microstructures.

Estrin and Mecking's modified work hardening model [7] has been employed to assess the inter-particle spacing from the tensile curves obtained from different simulated HAZ microstructures. The Charpy upper shelf energies and the total energy absorbed in tensile failure were plotted against the estimated inter particle spacing, Figure. 4.

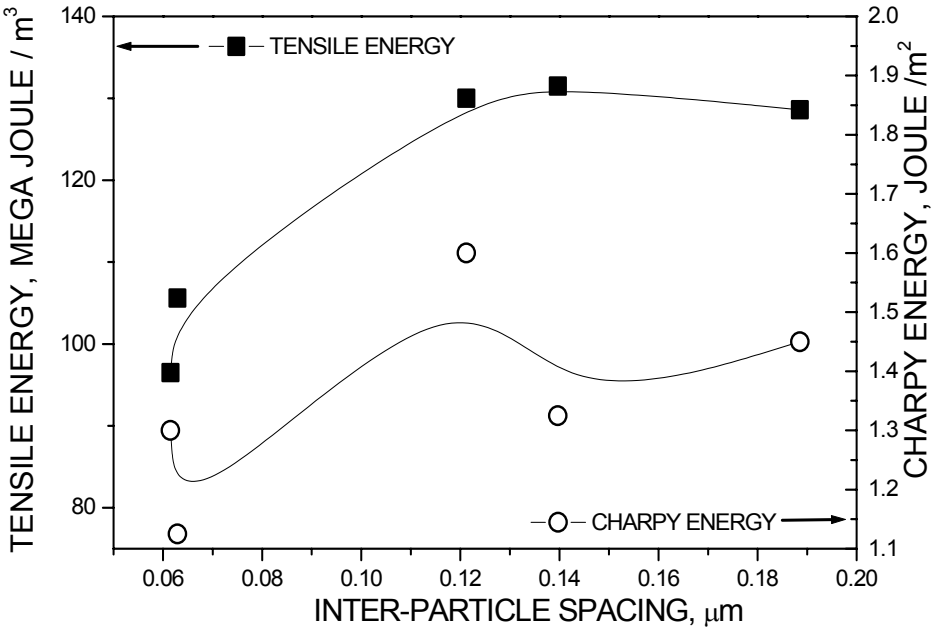

Figure 4. Variation of tensile and Charpy energies with inter-particle spacing

In the HAZ of modified 9Cr-1Mo steel, the general microstructural feature is tempered martensitic with various degrees of prior austenitic grain sizes, except the ICR where martensitic laths starts transforming to ferrites [5]. In these types of microstructures martensitic laths are arranged in packets of the size up to the half of the prior austenitic grain size [8]. The crystallographic orientation of the laths is such that they form low-angle grain boundaries between them [9]. This implies that the crack deviation is small for a crack propagation across the laths. On reaching the high angle packet boundary, a significant deviation of crack path may take place. In the FPAGM, the finer packet sizes contribute to more deviation in crack path, thus leading to the lowest ductile to brittle transition temperature. Also its high strength coupled with reasonably high ductility leads to the highest upper shelf energy (fig. 1). In the CPAGM-δ, slight increase in the energy absorbed (fig.3) during room temperature tensile fracture could be attributed to softer δ-ferrite formation which may blunt the propagating crack tip, initiated at carbide-matrix interfaces in the martensites. But this solute rich δ-ferrite could have lost its ductility more sharply with decreasing temperature and act as a probable crack initiation site (fig.2b), thus leading to the highest ductile to brittle transition temperature.

The inter-particle spacing plays an important role in determining the mechanical properties of steels. The systematic variation of the energy absorbed up to fracture in the tensile tests with the estimated inter-particle spacing indicates the existence of an optimum inter particle spacing for maximum toughness. In the case of Charpy upper shelf region, the same trend is observed with more amount of scatter. The high loading rate, constraints in crack propagation etc. may be contributing to the observed scatter.

CONCLUSIONS

1. The FPAGM is the toughest amongst the other microstructural regions present in the HAZ. This is attributed to its higher strength combined with reasonably higher ductility due to finer martensitic packet sizes.

2. The highest fracture energy is obtained for an optimum inter-particle spacing.

REFERENCES

1. Sikka, V.K. (1983) *Proc. Topical Conf. On 'Ferritic Alloys for Use in Nuclear Energy Technology',* Snowbird, Utah, June 19-23.
2. Vitek, J.M. and Klueh, R.H. (1983) *Metall. Trans.A,* 14A, 1047.
3. Jones, B.W., Hills,C.R. and Polonis, D.H. (1991) *Metall. Trans.A*, 22A, 1049.
4. Alberry, P.J. and Jones, W.K.C. (1977), *Metal Technol.* 4, 360.
5. Chandravathi, K.S., Laha, K., Bhanu Sankara Rao, K. and Mannan, S.L. accepted for publication in *Marerials Science and Technology.*
6. ASTM-E23, (1990) *Annual Book of ASTM standards,* Vol.03.01
7. Estrin, Y and Mecking, H. (1984) *Acta Metall*, 32, 57.
8. Zhang, X.Z. and Knott, J.F. (1999) *Acta Matall*. 47, 3483.
9. Gibson, G.P.(1988) *Review of cleavage fracture mechanisms in ferritic steels*, AEA Harwell Report AERE R 13227.

ORAL/POSTER REFERENCE:ICF100510PR

A VARIABLE-AMPLITUDE FATIGUE LIFE PREDICTION TAKING INTO ACCOUNT CRACK RETARDATION

Z.Perovic

Department of Mechanical Engineering, University of Montenegro,
81000 Podgorica, Yugoslavia

ABSTRACT

A bimodal concept for predicting a high-cycle fatigue life of the structural details subjected to a variable-amplitude loading is considered in this paper. The total fatigue life was separated into two phases: crack initiation and crack propagation. The portion of life spent in crack initiation was estimated by using S-N data obtained on smooth specimens. A fracture mechanics concept was used to calculate the portion of life spent in crack propagation. A modified Gray-Gallagher model was used to predict fatigue crack retardation following multiple overloads in a block spectrum. An original Gray-Gallagher model was proposed to predict fatigue crack retardation following a single overload, not taking into account either a delayed retardation or effect of multiple overloads. Both of these effects were incorporated in a modified Gray-Gallagher model used in this work. A computer program based on this model was applied to a welding joint subjected to a block spectrum loading and the results were compared with the experimental data reported in the literature.

KEY WORDS

Fatigue life prediction, crack initiation and propagation, retardation model, welded joint.

INTRODUCTION

Based on the previously determined stress distribution at the critical location, the fatigue life is calculated for each 'microelement' [Figure 1(*a*)] along the potential crack path, by using S-N data obtained on smooth specimens, as illustrated in Figure 1(b). The reciprocal derivative of this curve represents a rate of crack initiation in terms of dx/dN (x = distance from notch root; N = number of cycles), as shown in Figure 1(c). This rate may be interpreted as the rate at which the short crack grows due to the breaking of the microelements. It was proved [1] that the fatigue crack growth rate can be predicted on the basis of the smooth specimen data. A more consistent, but at the same time more complex, use of that approach would require a re-determination of the increased stress in each block when the crack tip reaches it and by taking into account the previous damage accumulation. It can be concluded that this method [1] should give a greater crack growth rate than the initiation rate obtained by the bimodal concept. However, an opposite effect is present during short crack growth, i.e. a gradual increase of crack closure level (decrease of ΔK_{eff}) which causes a decrease in crack growth rate. In this work, it is assumed, as a first approximation, that these two opposite effects are equal and so the estimated rate of crack initiation (or short crack growth) can be considered a reasonably accurate solution. The macrocrack growth rate da/dN (a = crack size; N = number of cycles) obtained by using fracture mechanics approach, is also shown in Figure 1(c). At some distance a_{i} , from the notch root, the rate of the crack initiation equals the rate of crack propagation. The upper zones of these curves, before and after this distance, indicate which of the mechanisms is more damaging. This distance a_{i}, when initiation is finished, may be regarded as the crack initiation size [2]. Determination of the crack initiation life N_{i} is based on the stress range at distance

a_i. The crack propagation life N_p is obtained by integrating the equation $da/dN = f(\Delta K)$ from a_i to a_f. The final crack size a_f can be determined from the fracture toughness of a material.

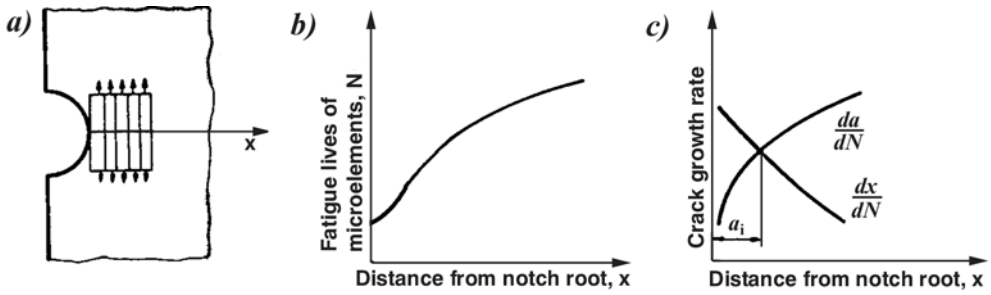

Figure 1: Schematic illustration of the bimodal concept. (*a*) Microelements; (*b*) Fatigue lives of microelements along the potential crack path. (*c*) Crack initiation and propagation rates and crack size a_i.

WELDED JOINT

The total fatigue life of non-load carrying, fillet-welded transverse stiffeners (Figure 2) subjected to spectrum loading, was determined by using the previously described bimodal concept. The specimens were welded by the automatic submerged-arc process. The mechanical properties of the steel (high-strength low-alloy structural steel, A588) plates are: σ_{ys} = 425 MPa, σ_{ts} = 569 MPa [3]. For simplicity, the influence of the microstructural heterogeneity was not considered in this paper. The S-N data, crack growth equation and relevant fracture mechanics parameters were assumed from Refs. [4-6] using average values for similar ferritic steels, i.e.
S-N curve for smooth specimens

$$log\, N = 13.785 - 3.178 log\, \Delta\sigma \tag{1}$$

The fatigue limit is $\Delta\sigma_{fls}$ = 227 MPa (stress ratio R = -1).

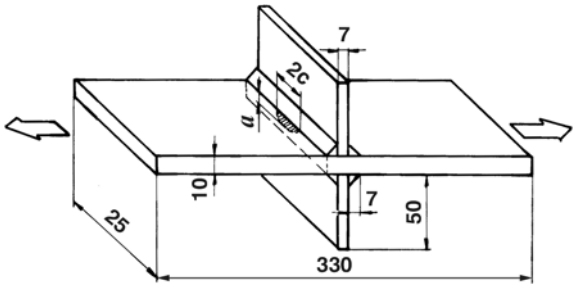

Figure 2: Welded joint; dimensions in mm.

Paris equation for the crack growth [7]

$$\frac{da}{dN} = C(\Delta K)^n \tag{2}$$

where $C = 4.8 \times 10^{-12}$, n = 3. Fracture mechanics parameters K_c = 55 MPa$\sqrt{m}$, the fracture toughness, ΔK_{th} = (3 to 8) MPa$\sqrt{m}$ (for R = 0.8÷0.1, respectively) threshold SIF range [8]. The threshold stress intensity range for various R ratios (changed by residual stress) was determined [9] by the equation:

$$\Delta K_{th} = (1 - R)^{\alpha}\, \Delta K_{th(0)} \tag{3}$$

where α is a material parameter, and $\Delta K_{th(0)} = \Delta K_{th}$, corresponding to R = 0. To get the best agreement with the experimental ΔK_{th} data [8], a value of α = 0.9 was assumed. The residual welding stresses cause a change in the R-ratio, thus influencing the fatigue strength. A typical residual welding stress pattern, through the specimen thickness along the section A-A, is shown in Figure 3(c) [curve 1]. The self-balancing stresses were assumed to vary from σ_r = 80% of the yield stress in tension at the weld toes to 40% of the yield stress in compression at the centre of the plate [10]. The load-induced elastic stress distribution in an uncracked detail, along section A-A, is given by curve 2 of Figure 3(c). To find the final stress distribution, curves 1 and 2 were superimposed, assuming identical elastic-perfectly plastic behaviour in tension and compression. Curve 3 shows the resulting

stress distribution at the top of the load cycle with the proper allowance for a redistribution of stresses in excess of yield to the adjacent elastic material. Curve 4 represents the stress distribution at the bottom of the load cycle. This curve was obtained by subtracting the elastic stress distribution, curve 2, from curve 3. If the residual stress distribution after the first cycle was unchanged, the actual stresses would cycle between curves 3 and 4. However, the mean stress relaxes during cycling; a process that is accelerated at higher stress (strain) ranges. The approximate procedure accounting for stress relaxation (described in Ref.[11]) was used in this paper.

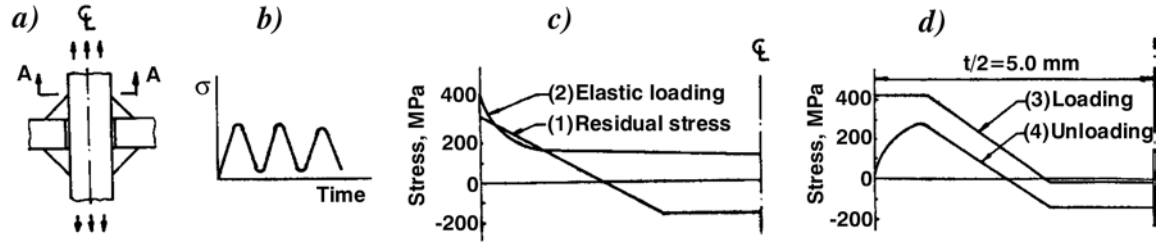

Figure 3: Superposition of residual and applied stresses

PREDICTION OF VARIABLE-AMPLITUDE FATIGUE LIVES OF A WELDED JOINT

The welded joint was subjected to block-spectrum loading (Figure 4) that simulates service loading. The normalized stress ranges ($\Delta\sigma_l/\Delta\sigma_{max}$) and the frequency of each stress level (f_l) are given in Table 1.

TABLE 1
DATA FOR BLOCK – LOADING SPECTRUM

Block number, l	1	2	3	4	5	6	7	8	9	10
Normalized stress range $\Delta\sigma_l/\Delta\sigma_{max}$	0.525	0.575	0.625	0.675	0.725	0.775	0.825	0.875	0.925	0.975
Frequency, f_l ,%	30.6	22.3	15.9	10.8	7.2	4.7	3.1	2.1	1.7	1.6

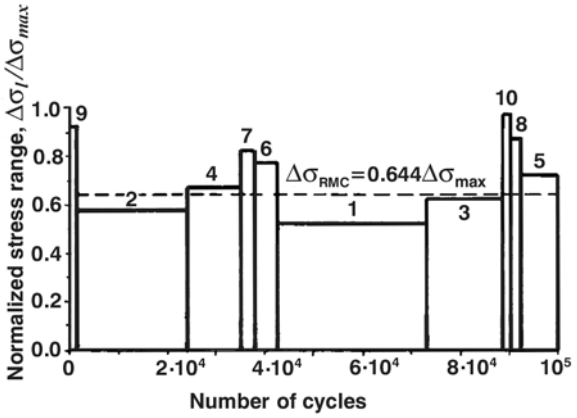

Figure 4: Block spectrum loading pattern

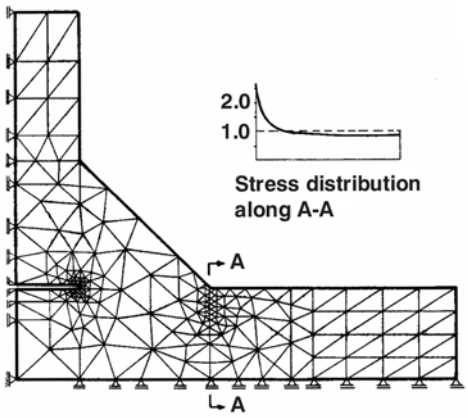

Figure 5: Finite elements mesh and stress distribution along potential crack path

The number of cycles per spectrum was 10^5 (at this block-spectrum size, the load interaction effects extend the fatigue life [12]). In order to check its reliability the bimodal concept was previously applied to the welded stiffener subjected to either constant-amplitude or spectrum loading (the spectrum size, 10^3 cycles, was chosen to avoid interaction effects as a consequence of 'delayed retardation', according to Refs [6,13]) [11]. Agreement between experimental test results and predictions was good.

Crack Initiation

The uncracked welded joint was first analysed. The stress distribution was obtained using the finite element method. Only one-quarter of the double symmetrical joint was modelled (Figure 5). A weld toe radius r = 0.5

mm (r/t = 0.05) was assumed in this work. The calculated value of the theoretical stress concentration factor is K_T = 2.6. Interaction effects, in this phase, were taken into account assuming that the residual stress relaxation during the first cycle was determined by the maximum stress range in the spectrum ($\Delta\sigma_{10}$), while the relaxation during subsequent cycling was determined by the root-mean-cube stress range ($\Delta\sigma_{RMC}$) level for the corresponding spectrum. The fatigue lives of the microelements were calculated using Miner's cumulative damage rule [14]:

$$\sum_{l=1}^{k} \frac{n_l}{N_l} = 1 \tag{4}$$

where n_l = number of cycles at stress range $\Delta\sigma_l$ in the spectrum, and N_l = number of cycles at constant stress range $\Delta\sigma_l$ that produces the failure. The fatigue life of the microelement can be obtained using Eqs. 1. and 4. to produce:

$$N = \frac{N_{10}}{\sum_{l=1}^{k} f_l \left(\frac{\Delta\sigma_l}{\Delta\sigma_{10}} \right)^{3.178}} \tag{5}$$

where N_{10} = number of cycles until failure at the highest stress range $\Delta\sigma_{10}$ in the spectrum. In these calculations Eqn. 1. was modified by Gerber's equation accounting for the effect of mean stress (changed by residual stress) on fatigue strength, i.e.

$$\Delta\sigma_{\mathrm{fs}} = \Delta\sigma_{\mathrm{fs}(0)} \left[1 - \left(\frac{\sigma_{\mathrm{m}}}{\sigma_{\mathrm{ts}}} \right)^2 \right] \tag{6}$$

where $\Delta\sigma_{\mathrm{fs}}$ = fatigue strength ($\sigma_{\mathrm{m}} \neq 0$), $\Delta\sigma_{\mathrm{fs}(0)}$ = fatigue strength ($\sigma_{\mathrm{m}} = 0$), σ_{m} = mean stress and σ_{ts} = tensile strength. Based on these values, the crack initiation rates dx/dN for the various values $\Delta\sigma_{\mathrm{RMC}}$ are calculated.

Crack Propagation

In order to take into account crack retardation following a single overload, Gray and Gallagher [15] expressed the rate of crack growth following the overload as

$$\frac{da}{dN} = C\left(\Delta K_{eff}\right)^n \tag{7}$$

where

$$\begin{aligned} \left(\Delta K_{eff}\right) &= \left(\frac{K_{max}}{K^*_{max}} \right)^{\frac{2m}{n}} \cdot \Delta K, \quad \text{if} \quad K_{max} < K^*_{max} \\ \left(\Delta K_{eff}\right) &= \Delta K, \qquad\qquad \text{if} \quad K_{max} \geq K^*_{max} \end{aligned} \tag{8}$$

K^*_{max} is given by

$$K^*_{max} = K_{max,OL} \left(1 - \frac{\Delta a}{Z_{OL}} \right)^{\frac{1}{2}} \tag{9}$$

where Δa is the crack increment since the overload and Z_{OL} is the size of the plastic zone due to the overload (load interaction zone). The shaping exponent m in Eqn. 8. was found to be:

$$m = \frac{n}{2} \left[\frac{log\left(\Delta K / \Delta K_{th}\right)}{log\left(K_{max,OL} / K_{max}\right)} \right] \tag{10}$$

An overload produces a complete crack arrest (in steel) when $S = K_{max,OL}/K_{max}$=2.3. Gray-Gallagher model predicts a sudden drop in da/dN after the overload application. However, other investigators observed that the lowest growth rate was reached after the crack had extended over approximately one eighth to one quarter of

the total overload plastic zone (this phenomenon is referred to as delayed retardation) [13]. To model the delayed retardation, it is assumed in this work, that the growth rate after an overload remains unchanged over an increment in crack length $\beta = \Delta a/Z_{OL}$. This increment decreases with increase of a number of overload cycles (for greater than 10 overload cycles, the minimum growth rate occurred almost immediately after the overload applications [16]). Because of that, it is assumed in this work that β varies from $\beta = 0.1$ for a single overload to $\beta = 0$ for greater than 10 overload cycles. The minimum value of da/dN in the load interaction zone decreases as the number of overloads increases [17]. This effect was modelled by assuming that the increase in closure level (changing ΔK_{eff}) is a function of the number of overload cycles applied [18]:

$$\gamma = \gamma_1 + (1-\gamma_1)\left(\frac{N_{OL}-1}{N_{sat}-1}\right) \tag{11}$$

where γ = ratio of the closure stress after N_{OL} overloads to the stabilized overload closure stress; γ_1 = the value of γ for $N_{OL} = 1$; N_{sat} = the number of overload cycles required to achieve saturation (that is beyond N_{sat} the addition of overload cycles produces no additional retardation). The effective stress range $\Delta\sigma_{\text{eff}}$, at lower stress level after multiple overloads, is then equal to the difference between the maximum stress, $\sigma_{\max}$, and the closure stress, σ_c:

$$\Delta\sigma_{eff} = \sigma_{max} - \sigma_c = \sigma_{max} - \sigma_{c1}\frac{\gamma}{\gamma_1} = \sigma_{max} - \left[\sigma_{max} - \left(\Delta\sigma_{eff}\right)_1\right]\frac{\gamma}{\gamma_1} \tag{12}$$

This equation can be expressed in terms of stress intensity factor:

$$\Delta K_{eff} = K_{max} - \left[K_{max} - \left(\Delta K_{eff}\right)_1\right]\frac{\gamma}{\gamma_1} \tag{13}$$

where $(\Delta K_{\text{eff}})_1$ = effective range of stress intensity factor in lower stress level following a single overload, calculated from the first of Eqs. 8. The stress intensity factor was calculated by the expression [19,20]:

$$K = F_G F \sigma\sqrt{\frac{\pi a}{Q}} \tag{14}$$

where:

$$F = \left[M_1 + M_2\left(\frac{a}{t}\right)^2 + M_3\left(\frac{a}{t}\right)^4\right] f_\varphi f_w g \;\; ; \;\; M_1 = 1.13 - 0.09\left(\frac{a}{c}\right) \; ; \; M_2 = -0.54 + \frac{0.89}{0.2+\frac{a}{c}}$$

$$M_3 = 0.5 - \frac{1.0}{0.65+\frac{a}{c}} + 14\left(1.0-\frac{a}{c}\right)^{24} \; ; \; f_\varphi = \left[\left(\frac{a}{c}\right)^2 cos^2\varphi + sin^2\varphi\right]^{\frac{1}{4}} \; ; \; f_w = \left[sec\left(\frac{\pi c}{2w}\sqrt{\frac{a}{t}}\right)\right]^{\frac{1}{2}}$$

$$g = 1 + \left[0.1 + 0.35\left(\frac{a}{t}\right)^2\right](1-sin\varphi)^2 \; ; \; Q = 1 + 1.464\left(\frac{a}{c}\right)^{1.65},$$

where c = major semi-axis of the elliptical crack; t,w = thickness and width of the main plate of a welded joint, respectively; φ = angle that describes the location at the crack front with respect to the major axis of the ellipse. The values of the crack axis ratio a/c were assumed from Ref. [5]. The geometry correction factor is

$$F_G = \frac{2}{\pi}\sum_{i=1}^{n}\frac{\sigma_{bi}}{\sigma}\left(arcsin\frac{b_{i+1}}{a} - arcsin\frac{b_i}{a}\right) \tag{15}$$

where σ_{bi} is the normal stress in a finite element between the distance b_{i} and $b_{\text{i+1}}$. This accounts for the effect on K of a stress concentration produced by a structural detail. Verreman *et al.* [21] used this method for determination of F_{G} factor of a cruciform-welded joint and compared it with the accurate solution obtained by using high-order crack tip elements with an inverse square root singularity. They reported differences smaller than 6%, so this method can be considered accurate for engineering purposes. The advantage of Albrecht's

method is that only one stress analysis needs to be made for each joint geometry, i.e. the stress analysis of an uncracked joint. The values of γ_1 and N_{sat} (γ_1 = 0.70; N_{sat} =500) were selected to provide the best fit of the predicted crack propagation life to the experimental data for the welded stiffeners (of the same material) with known initial cracks [5]. The crack propagation rate was calculated using Eqn. 7.

Total Fatigue Life

The crack initiation size a_i is determined by using the crack initiation rate curve and the crack propagation rate curve. The crack initiation life N_i is determined using Eqn. 5. with the stress range for the distance a_i. The crack propagation life N_p is calculated by solving Eqn.7. from a_i to a_f by the Runge-Kutta method (using the computer program). The total fatigue life is obtained by summing the initiation and propagation lives. The predicted fatigue lives for various equivalent stress ranges ($\Delta\sigma_{RMC}$ = 133; 196; 249 MPa) as well as experimental data [12] are shown in Figure 6.

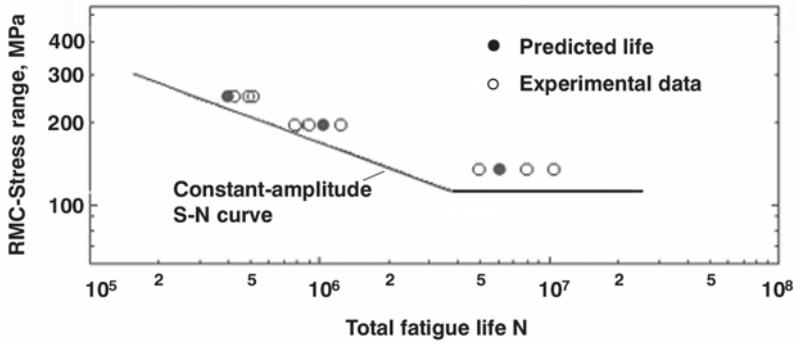

Figure 6: Comparison of predicted fatigue lives with experimental data

REFERENCES

1. Glinka, G. (1985) *Eng. Fract. Mech.* 21, 245.
2. Socie, D.F. Morrow, J. and Chen, W.C. (1979) *Eng. Fract. Mech.* 11, 851.
3. Albrecht, P. and Friedland, M. (1979) *J. Struct. Division, ASCE* 105(12), 2657.
4. Albrecht, P. and Rubeiz, C.G. (1987) *Variable Amplitude Load Fatigue.*Report No. DTFH61-86-C-0036-II, University of Maryland.
5. Albrecht, P. and Sahli, A. (1984) In: *Fracture Mechanics,*ASTM STP 833, pp.193-217, Sanford, R.J. (Ed).
6. Abtahi, A., Albrecht, P. and Irwin, G.R. (1977) In: *Mechanics in Engineering,* University of Waterloo Press, pp.313-334.
7. Paris, P.C. and Erdogan, F. (1963) *Trans. ASME, J. Basic Eng.,* 85(4), 528.
8. Paris, P.C., Bucci, R.J., Wessel, E.T., Clark, W.G. and Mager, T.R. (1972) ASTM STP 513, pp. 141-176.
9. Klesnil, M. and Lukas, P. (1972) *Mater. Sci. Eng.* 9, 231.
10. Abtahi, A., Albrecht, P. and Irwin, G.R. (1976) *J. Struct. Division,* ASCE 102(11), 2103.
11. Perovic, Z. (1998) *Fatigue Fract. Eng. Mater. Struct.* 21, 1559.
12. Albrecht, P. and Yamada, K. (1979) In: *Service Fatigue Loads Monitoring, Simulation and Analysis,* ASTM STP 671, pp. 255-277, Abelkis, P.R. and Potter, J.M. (Eds).
13. Von Euw, E.F.J., Hertzberg, R.W. and Roberts, R. (1972) In: *Stress Analysis and Growth of Cracks,* ASTM STP 513, pp. 230-259.
14. Miner, M.A. (1945) *J. Appl. Mech.* 12, *Trans.ASME,* 67, A-159.
15. Gray, T.D. and Gallagher, J.P. (1976) In: *Mechanics of Crack Growth,* ASTM STP 590, pp. 331-344.
16. Corbly, D.M. and Packman, P.F. (1973) *Eng. Fract. Mech.* 5, 479.
17. Trebules, V.W., Roberts, R. and Hertzberg, R.W. (1973) In: *Progress in Flaw Growth and Fracture Toughness Testing,* ASTM STP 536, pp. 115-146.
18. Bell, P.D. and Wolfman, A. (1976) In: *Fatigue Crack Growth Under Spectrum Loads,* ASTM STP 595, pp. 157-171, Wheeler, J. B. (Ed).
19. Newman, J.C. and Raju, I.S. (1984). NASA TM 85793, NASA Langley Research Center, Hampton, USA.
20. Albrecht, P. and Yamada, K. (1977) *J. Struct. Divis.,* ASCE 103(2), 377.
21. Verreman, Y., Bailon, J.P. and Masounave J. (1987) *Fatigue Fract. Eng. Mater. Struct.* 10(1), 17.

A VARIATIONAL PRINCIPLE FOR FINITE TRANSFORMATION GRADIENT PLASTICITY TO MODEL DUCTILE FRACTURE

E. Lorentz and V. Cano

EDF-R&D, 1 av. du Gal de Gaulle, 92141 Clamart, France

ABSTRACT

This paper presents an approach to predict ductile fracture of real-life structures. It relies on Rousselier's constitutive model to describe plastic void growth, a specific finite strain formulation that preserves energetic properties and a non local theory to deal with strain localisation. It is finally applied to the computation of a notched specimen.

KEYWORDS

ductile fracture, non local formulation, finite strain.

INTRODUCTION

This work proposes a model to predict ductile fracture of real-life steel structures, describing the inception of damaged zones, their propagation and the resulting final structural instability.

The physics of plastic void growth is modelled by Rousselier's model which has already proved its predicting capabilities compared to experimental results [1]. Its yield surface is :

$$\mathrm{F}\left(\boldsymbol{\tau},\, A\,;\, f\right) = \tau_{eq} + \sigma_1\, D\, f\, \exp\left(\frac{\mathrm{tr}\,\boldsymbol{\tau}}{3\sigma_1}\right) - \left(\sigma^{y} - A\right) \qquad \text{with} \quad \tau_{eq} = \sqrt{\frac{3}{2}\boldsymbol{\tau}^{\mathrm{D}} \cdot \boldsymbol{\tau}^{\mathrm{D}}} \tag{1}$$

$\boldsymbol{\tau}$ denotes Kirchhoff stress, f the porosity, A an isotropic hardening variable and σ^{y}, σ_1 and D material parameters. There are two main differences with Gurson model, see [2] : the elastic domain is unbounded in compression, as von Mises model, and the yield surface is singular on the hydrostatic axis in traction. Localisation phenomena are expected with such a model. To control them, the resulting high spatial gradients of mechanical fields in the localisation zone have to be explicitly taken into account ; this is achieved by introducing the gradient of the cumulated plastic strain in the model. This non local approach can be expressed as a variational principle for generalised standard materials. To ensure this property in the context of finite strain, a special formulation has to be stated, close to Simo and Miehe's one [3].

Part 1 is dedicated to this specific finite strain formulation while part 2 presents the two main steps of the non local theory. Finally, part 3 aims at demonstrating the operational character of the whole approach.

1. FINITE STRAIN FORMULATION

1.1 Application to Rousselier model

To provide a consistent framework with the variational principle we aim at, classical finite plasticity theory, based on Jaummann rate for instance, can not be used. Actually, we have to build a new theory, see [4], which relies mostly on Simo and Miehe's one [3] and extend the class of generalised standard materials to finite strain. As will be shown, it allows to express the integration of the constitutive relation as a minimisation problem, a crucial point for the application of our variational principle.

It begins with the introduction of a relaxed (stress free) configuration leading to the classical multiplicative split of the total deformation $\mathbf{F} = \mathbf{F}^{\mathbf{e}}\,\mathbf{F}^{\mathbf{p}}$. Then, the free Helmholtz' energy Φ_μ is assumed to be the sum of an elastic energy Φ^{el} that depends only on the elastic strain $\mathbf{e}$ yet to define (isotropic hyperelasticity) and a stored energy Φ^{st} that depends on a hardening internal variable p :

$$\Phi_\mu(\mathbf{e}, p) = \Phi^{\mathrm{el}}(\mathbf{e}) + \Phi^{\mathrm{st}}(p) \qquad \text{with} \quad \mathbf{e} = \frac{1}{2}\left(\mathbf{Id} - \mathbf{F}^{\mathbf{e}}\,\mathbf{F}^{\mathbf{e}^{\mathrm{T}}}\right) = \frac{1}{2}\left(\mathbf{Id} - \mathbf{B}^{\mathbf{e}}\right) \tag{2}$$

$$\begin{cases} \Phi^{\mathrm{el}}(\mathbf{e}) = \dfrac{1}{2}\left[K(\operatorname{tr}\mathbf{e})^2 + 2\mu\,\mathbf{e}^{\mathrm{D}}\cdot\mathbf{e}^{\mathrm{D}}\right] \\ \Phi^{\mathrm{st}}(p) = \displaystyle\int_0^p \mathrm{R}(s)\,ds \end{cases} \tag{3}$$

where K, μ and R denote respectively the bulk and shear moduli and the hardening function. The intrinsic dissipation can be derived for such a choice :

$$Diss = \left(\boldsymbol{\tau} - \mathbf{s}\,\mathbf{B}^{\mathbf{e}}\right)\cdot\mathbf{D} - \frac{1}{2}\mathbf{s}\cdot\left(\mathbf{F}\,\dot{\mathbf{G}}^{\mathbf{p}}\,\mathbf{F}^{\mathrm{T}}\right) + A\,\dot{p} \qquad \mathbf{G}^{\mathbf{p}} = \left(\mathbf{F}^{\mathbf{p}^{\mathrm{T}}}\,\mathbf{F}^{\mathbf{p}}\right)^{-1} \qquad \mathbf{s} \underset{\text{def.}}{=} -\frac{\partial\Phi_\mu}{\partial\mathbf{e}} \qquad A \underset{\text{def.}}{=} -\frac{\partial\Phi_\mu}{\partial p} \tag{4}$$

where $\mathbf{D}$ denotes the Eulerian strain rate. We can notice that a plastic strain measure $\mathbf{G}^{\mathbf{P}}$ and driving forces $\mathbf{s}$ and A associated to $\mathbf{e}$ and p are naturally defined in the process. As the dissipation is required to be zero for elastic evolution, the following stress - strain relation is obtained :

$$\boldsymbol{\tau} = \mathbf{s}\,(\mathbf{Id} - 2\mathbf{e}) \tag{5}$$

Moreover, to ensure a positive dissipation, we assume the principle of maximal plastic dissipation with respect to the yield surface characterised by $\mathrm{F}(\mathbf{s}, A\,; f) = 0$. We can notice that, compared to Eqn. (1), Kirchhoff stress $\boldsymbol{\tau}$ is replaced by the driving force $\mathbf{s}$. Here lies the difference with Simo and Miehe's approach. Nevertheless, thanks to the stress - strain relation Eqn. (5), $\boldsymbol{\tau}$ and $\mathbf{s}$ are close to each other while $\mathbf{e}$ remains small. Such a choice leads to the following evolution equations :

$$\begin{cases} -\dfrac{1}{2}\,\mathbf{F}\,\dot{\mathbf{G}}^{\mathbf{p}}\,\mathbf{F}^{\mathrm{T}} = \lambda\dfrac{\partial\mathrm{F}}{\partial\mathbf{s}} \\ \dot{p} = \lambda\dfrac{\partial\mathrm{F}}{\partial A} \end{cases} \qquad \text{with} \quad \lambda \geq 0 \quad \mathrm{F} \leq 0 \quad \lambda\,\mathrm{F} = 0 \tag{6}$$

Some insights on the advantages of such a formulation compared to a Jaumman rate one are given in [4]. Here, we only mention that these equations are objective (and incrementally objective) since the derivation with respect to time acts on $\mathbf{G}^{\mathbf{P}}$ which is a tensor defined on the initial configuration. Finally, the porosity evolution is based on an eulerian plastic rate :

$$\dot{f} = (1 - f)\,\operatorname{tr}\left(-\frac{1}{2}\,\mathbf{F}\,\dot{\mathbf{G}}^{\mathbf{p}}\,\mathbf{F}^{\mathrm{T}}\right) \qquad \text{with} \quad -\frac{1}{2}\,\mathbf{F}\,\dot{\mathbf{G}}^{\mathbf{p}}\,\mathbf{F}^{\mathrm{T}} = \mathbf{F}^{\mathbf{e}}\,\mathbf{D}^{\mathbf{p}}\,\mathbf{F}^{\mathbf{e}^{\mathrm{T}}} \tag{7}$$

1.2 Integration of the constitutive relation

From now on, we are interested in deriving the time integration of the constitutive behaviour over a single time step. Let us denote respectively by q^-, q and Δq the value of a quantity q at the beginning and the end of the time step, and its increment over the time step. Then, the integration procedure can be stated as : given $\mathbf{e}^-$ (or $\mathbf{G}^{\mathbf{p}^-}$), p^-, f^-, $\mathbf{F}^-$ and $\mathbf{F}$, find $\mathbf{e}$, p, f and $\boldsymbol{\tau}$. For the sake of simplicity, the porosity is treated in an explicit way, while the other variables are dealt with an Euler scheme, classical for plastic constitutive law, see [5]. Let us introduce now the solution for an elastic trial (q^E denotes the value of a quantity q during the elastic trial and $\Delta^E q = q - q^E$) :

$$\begin{cases} p^E = p^- \\ \Delta^E p = \Delta p \end{cases} \qquad \begin{cases} \mathbf{G}^{\mathbf{p}\,E} = \mathbf{G}^{\mathbf{p}-} \\ \Delta^E \mathbf{G}^{\mathbf{p}} = \Delta \mathbf{G}^{\mathbf{p}} \end{cases} \qquad \begin{cases} \mathbf{e}^E = \dfrac{1}{2}\left(\mathbf{Id} - \mathbf{F}\,\mathbf{G}^{\mathbf{p}^-}\,\mathbf{F}^{\mathrm{T}}\right) \\ \Delta^E \mathbf{e} = -\dfrac{1}{2}\mathbf{F}\,\Delta\mathbf{G}^{\mathbf{p}}\,\mathbf{F}^{\mathrm{T}} \end{cases} \qquad \begin{cases} f^E = f^- \\ \Delta^E f = \Delta f \end{cases} \tag{8}$$

Then, the non linear system corresponding to the integration of the constitutive relation reads :

$$\begin{cases} \Delta^E \mathbf{e} = \lambda \dfrac{\partial \mathrm{F}}{\partial \mathbf{s}}\left(\mathbf{s},\, A\,;\, f^-\right) \\ \Delta^E p = \lambda \dfrac{\partial \mathrm{F}}{\partial A}\left(\mathbf{s},\, A\,;\, f^-\right) \end{cases} \qquad \begin{cases} \mathbf{s} = -\dfrac{\partial \Phi_\mu}{\partial \mathbf{e}}\left(\mathbf{e},\, p\right) \\ A = -\dfrac{\partial \Phi_\mu}{\partial p}\left(\mathbf{e},\, p\right) \end{cases} \qquad \begin{cases} \lambda \geq 0 \quad \mathrm{F}\left(\mathbf{s},\, A\,;\, f^-\right) \leq 0 \\ \lambda\, \mathrm{F}\left(\mathbf{s},\, A\,;\, f^-\right) = 0 \end{cases} \tag{9}$$

We do not pay further attention to the resolution of this system, except to mention that special attention should be pay to the singular point of F (corresponding to $\sigma_{eq} = 0$). Finally, the porosity is explicitly computed by :

$$\frac{\dot{f}}{1-f} = \frac{\mathrm{tr}\,\Delta^E \mathbf{e}}{\Delta t} \qquad \Rightarrow \qquad 1 - f = \left(1 - f^-\right)\exp\left(-\,\mathrm{tr}\,\Delta^E \mathbf{e}\right) \tag{10}$$

As above mentioned, one of the advantage of such a finite strain formulation is the expression of the system Eqn. (9) as a minimisation problem. Let us introduce the dissipation potential, where I_K denotes the indicator function of the convex K ($+\infty$ outside K, 0 inside) :

$$\begin{aligned} \Delta_\mu\left(\mathbf{D}^{\mathbf{p}}, \dot{p}\right) &\underset{def}{=} \sup_{\substack{s,A \\ F\left(s,A;f^-\right)\leq 0}} \left(\mathbf{s}\cdot\mathbf{D}^{\mathbf{p}} + A\,\dot{p}\right) \\ &= \sigma^y \dot{p} + \sigma_1\,\mathrm{tr}\,\mathbf{D}^{\mathbf{p}}\left(\ln\frac{\mathrm{tr}\,\mathbf{D}^{\mathbf{p}}}{D\,f\,\dot{p}} - 1\right) + \mathrm{I}_{\mathrm{IR}^+}\left(\mathrm{tr}\,\mathbf{D}^{\mathbf{p}}\right) + \mathrm{I}_{\mathrm{IR}^+}\left(\dot{p} - \frac{2}{3}D^p_{eq}\right) \end{aligned} \tag{11}$$

Then, following [6], it can be shown that Eqn. (9) is equivalent to :

$$\Delta^E \mathbf{e},\, \Delta^E p \text{ are solutions of } \quad \min_{\Delta^E \mathbf{e},\, \Delta^E p}\left[\Phi_\mu\left(\mathbf{e}^E + \Delta^E \mathbf{e},\, p^E + \Delta^E p\right) \;+\; \Delta_\mu\left(\Delta^E \mathbf{e},\, \Delta^E p\right)\right] \tag{12}$$

2. NON LOCAL FORMULATION

2.1 Introduction of gradient terms

In Andrieux et al. [7], a homogenisation scheme was proposed to derive gradient constitutive relations from fully local (microscopic) ones. It allows to take into account potential spatial variations of the macroscopic mechanical fields which may occur with a length scale of the same order as the microscopic scale, that is the scale of an elementary representative volume for the microscopic constitutive relation. Such variations, which can namely occur in presence of singularities or localisation, are not compatible with the assumptions of quasi-periodic homogenisation. Let us apply the main steps of this homogenisation scheme to Rousselier model.

An elementary representative volume is introduced which is made of a collection of N microscopic cells of position $\mathbf{z}_i$, where $\Sigma\,\mathbf{z}_i = 0$. In each of these cells, the material state is described by a microscopic deformation tensor $\mathbf{F}_i$ and the microscopic internal variables $\mathbf{e}_i$ and p_i which obey a microscopic constitutive relation stated in terms of the microscopic potentials Φ_μ and Δ_μ. The simplest localisation relation introducing a spatial variation is assumed :

$$\mathbf{F}_i = \mathbf{F}_\bullet \qquad \mathbf{e}_i = \mathbf{e}_\bullet \qquad p_i = p_\bullet + \mathbf{z}_i \cdot \mathbf{p}_\nabla \tag{13}$$

where $\mathbf{F}_\bullet$, $\mathbf{e}_\bullet$, $p_\bullet$ and $\mathbf{p}_\nabla$ appear as a macroscopic variables. Then, a macroscopic free energy Φ and a macroscopic dissipation potential Δ are derived, depending on the macroscopic variables. Straightforward application of [7] and some simplifications for the dissipation potential (to allow practical computations) leads to :

$$\Phi\left(\mathbf{e}_\bullet, p_\bullet, \mathbf{p}_\nabla\right) = \frac{1}{2}\left[K\left(\operatorname{tr}\mathbf{e}_\bullet\right)^2 + 2\mu\,\mathbf{e}_\bullet^{\mathrm{D}} \cdot \mathbf{e}_\bullet^{\mathrm{D}}\right] + \int_0^{p_\bullet} \mathrm{R}(s)ds \;+ \frac{d\,\mathrm{R}}{dp}\left(p_\bullet\right)\mathbf{p}_\nabla \cdot \mathbf{J} \cdot \mathbf{p}_\nabla \tag{14}$$

$$\Delta\left(\mathbf{D}_\bullet^{\mathbf{p}}, \dot{p}_\bullet, \dot{\mathbf{p}}_\nabla\right) = \sigma^y \dot{p}_\bullet + \sigma_1 \operatorname{tr}\mathbf{D}_\bullet^{\mathbf{p}}\left(\ln\frac{\operatorname{tr}\mathbf{D}_\bullet^{\mathbf{p}}}{D\,f^-\,\dot{p}_\bullet} - 1\right) + \mathrm{I}_{\mathrm{IR}^+}\left(\operatorname{tr}\mathbf{D}_\bullet^{\mathbf{p}}\right) + \mathrm{I}_{\mathrm{IR}^+}\left(\dot{p}_\bullet - L_b\left\|\dot{\mathbf{p}}_\nabla\right\| - \frac{2}{3}D_{\bullet eq}^{p}\right) \tag{15}$$

$\mathbf{J}$ is a second-order symmetric tensor which introduces the so-called internal material lengths and depends on the spatial cell distribution. In the case of an isotropic cell distribution, with L_b the distance between the centres of two neighbour cells, it reads :

$$\mathbf{J} = \frac{2L_b{}^2}{13}\mathbf{Id} \tag{16}$$

Note that $\mathbf{z}_i$, $\mathbf{p}_\nabla$ and $\mathbf{J}$ are expressed in the initial configuration : they are lagrangian tensors. Therefore, the internal lengths are implicitly modified by the deformation (induced anisotropy for the non local terms). Finally, it is assumed that at the macroscopic scale, $\mathbf{p}_\nabla$ is equal to the gradient of $p_\bullet$, a choice which is consistent with Eqn.(13) :

$$\begin{cases} p_\bullet = p(x) \\ \mathbf{p}_\nabla = \nabla p(x) \end{cases} \tag{17}$$

2.2 Variational principle

Although the material behaviour is totally defined at the material point scale through the potentials Eqn. (14) and Eqn. (15), the boundary value problem stated over the structure generally does not admit solutions because the state variables $p_\bullet$ and $\mathbf{p}_\nabla$ are linked by relation Eqn. (17) and therefore they are no longer independent. This is however a strong requirement of generalised standard materials. Indeed, this nonlocal relation Eqn. (17) hinders the normality property at the material point scale.

To overcome this difficulty, we propose to put aside the local normality rule, over-constraining, while preserving the formalism of generalised standard materials at the scale of the structure, see [8]. First, the definition of state variables is extended : they become fields over the structure, so that the set of state variables is reduced to the fields $\mathbf{F}$, $\mathbf{e}$ and p. The former variables $p_\bullet$ and $\mathbf{p}_\nabla$ now appear only through different functional operations on the field p, see Eqn. (17). Then, global potentials are defined, which are functions of the state variable fields and their rates :

$$\mathrm{F}\left(\mathbf{e}, p\right) = \int_\Omega \Phi\left(\mathbf{e}(x), p(x), \nabla p(x)\right)\; dx \qquad \mathrm{D}\left(\mathbf{D}^{\mathbf{p}}, p\right) = \int_\Omega \Delta\left(\mathbf{D}^{\mathbf{p}}(x), \dot{p}(x), \nabla\dot{p}(x)\right)\; dx \tag{18}$$

where Ω denotes the body domain in the initial configuration. The generalised standard material formalism is preserved, so that a global constitutive relation can be derived from these potentials Eqn. (18). Thanks to the local character of the elastic strain, the former stress - strain relation is retrieved :

$$\boldsymbol{\tau}(x) = -\frac{\partial \Phi}{\partial e_{\bullet}}\left(\mathbf{Id} - 2\mathbf{e}(x)\right) \tag{19}$$

However, the evolution of the internal variables obeys a non local problem (where appear partial differentiations of functionals with respect to fields and a functional subgradient) :

$$\left(-\frac{\partial \mathrm{F}}{\partial \mathbf{e}}, -\frac{\partial \mathrm{F}}{\partial p}\right) \in \partial \mathrm{D}\left(-\frac{1}{2}\mathbf{F}\,\dot{\mathbf{G}}^{\mathbf{p}}\,\mathbf{F}^{\mathrm{T}}, \dot{p}\right) \tag{20}$$

In spite of the complexity of this evolution equation, the interesting minimisation property Eqn. (12) remains applicable. In the context of an implicit Euler scheme, time integration of Eqn. (20) results in the following minimisation (global) problem, while the evolution of the porosity keeps its former expression Eqn. (10) :

$$\Delta^E\mathbf{e}, \Delta^E p \text{ are solutions of } \min_{\Delta^E\mathbf{e},\, \Delta^E p}\left[\mathrm{F}\left(\mathbf{e}^E + \Delta^E\mathbf{e},\, p^E + \Delta^E p\right) + \mathrm{D}\left(\Delta^E\mathbf{e}, \Delta^E p\right)\right] \tag{21}$$

3. NUMERICAL APPLICATION

To examine the characteristics of such a non local model, a numerical simulation is carried out. A widely studied structure in the context of ductility is an axisymmetrical notched specimen submitted to tension, see figure 1 for the geometry, the loading and the material parameters. A first computation is made with the local model, a second with the non local one.

The integration in the former case is achieved in a classical fashion with a return mapping algorithm based on Eqn. (8) - (10). In the latter case, the integration of the non local constitutive relation relies on the resolution of the minimisation problem Eqn. (21). It presents severe difficulties :

- non differentiability of D (which is positive homogeneous of degree one),
- presence of non linear inequality constraints (indicator function that rules the growth of the cumulated plastic strain),
- large size (as many unknowns as the number of nodes in the mesh).

Therefore, a specific algorithm is required, see [9]. Without entering into further details, let us just mention that it is based on the explicit introduction of the fields $p_{\bullet}$ and $\mathbf{p}_{\nabla}$ at the Gauss points and the dualisation of the resulting constraint Eqn. (17), thus leading to an augmented lagrangian : the relaxed problem is then solved by means of a Newton's method, while BFGS with Wolfe line search is used for the dual one. That's why the expression of the integration as a minimisation problem appears essential. Note that such an algorithm has already proven its efficiency on brittle damage simulation.

The numerical results are presented in terms of the cumulated plastic field around the notch and the horizontal displacement at the notch tip versus the applied force (figure 2). By now, some convergence difficulties are encountered, so that the non local computation does not go as far as the local one. It appears that in this first stage, the results are very close, due to the small characteristic length ($30\,\mu\mathrm{m}$) compared to the characteristic size of the gradients triggered by the notch, as shown by the plastic field picture. To observe a significant difference between both models, we have to wait for localisation to appear, which is achieved with the local model but not yet with the non local one...

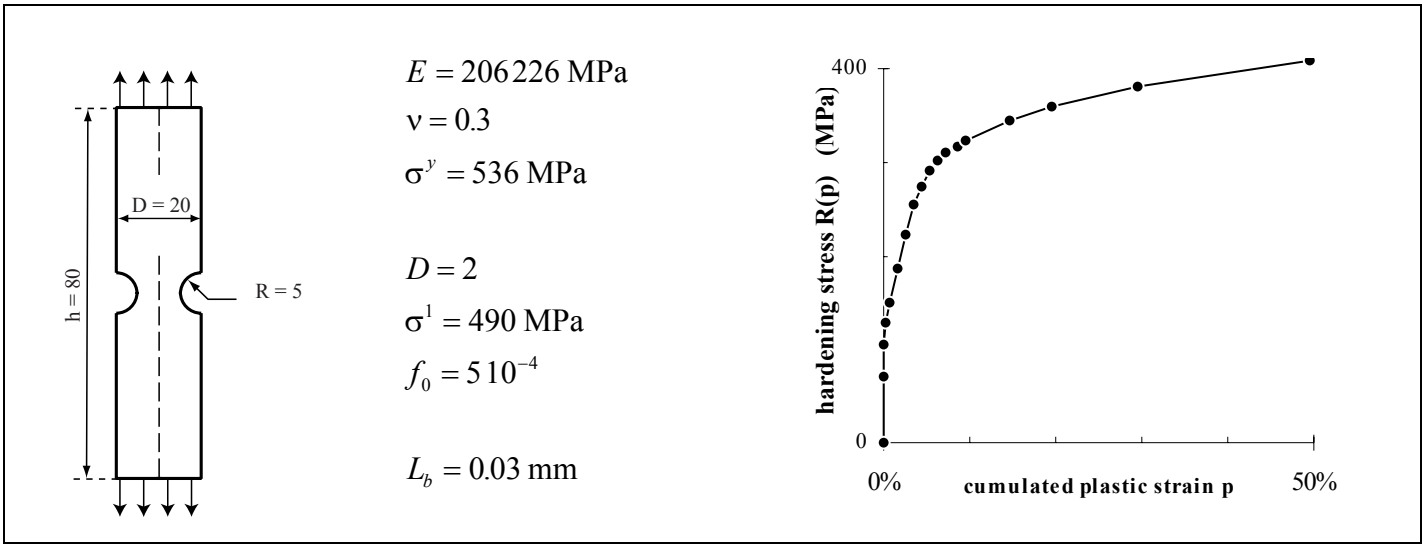

figure 1 - Test problem : geometry, loading and material parameters

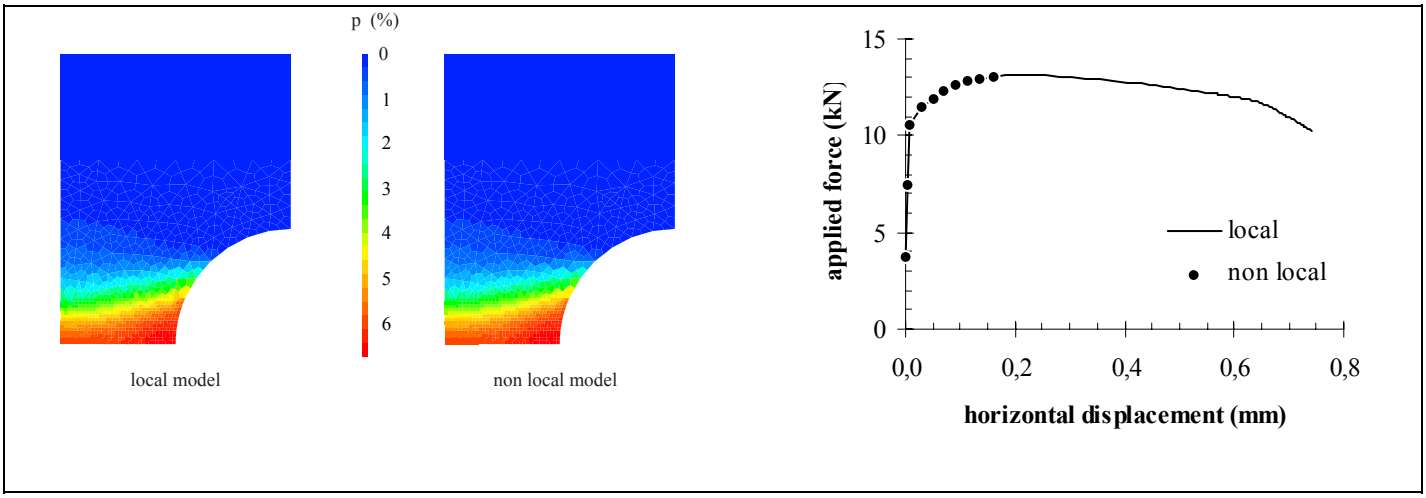

figure 2 - Test problem : local and global responses

REFERENCES

[1] Rousselier, G. (1981) Finite deformation constitutive relation including ductile fracture damage. In 3D constitutive relations and ductile fracture, ed. Nemat Nasser, North Holland, pp. 331-355.

[2] Gurson, A.L. (1977) Continuum theory of ductile rupture by void nucleation and growth : part 1 - yield criteria and flow rules for porous ductile media. ASME J. Eng. Mat. Tech., **99**, pp. 2-15.

[3] Simo, J.C. and Miehe, C. (1992) Associative coupled thermoplasticity at finite strains : formulation, numerical analysis and implementation. Comp. Meth. Appl. Mech. Eng., **98**, pp. 41-104.

[4] Lorentz, E. and Cano, V. (2001) An incrementally objective and easy implementing formulation for elastoplastic finite deformation, submitted to Comm. Num. Meth. Eng.

[5] Simo, J.C. and Taylor, R.L. (1985) Consistent tangent operators for rate-independent elastoplasticity. Comp. Meth. Appl. Mech. Eng., **48**, pp. 101-118.

[6] Ekeland, I. et Temam, R. (1974) Analyse convexe et problèmes variationnels. Dunod Gauthier-Villars, Paris.

[7] Andrieux, S., Joussemet, M. and Lorentz, E. (1996) A class of constitutive relations with internal variable derivatives : derivation from homogenisation. C.R. Acas. Sci., t. **323**, série IIb, pp. 629-636.

[8] Lorentz, E. and Andrieux, S. (1999) A variational formulation for nonlocal damage models. Int . J. Plas., **15**, pp. 119-138

[9] Lorentz, E., Gourcy, T. and Benallal, A. (2001) Gradient constitutive relations : numerical aspects and application to gradient plasticity, submitted to Comp. Meth. Appl. Mech. Eng.

ORAL REFERENCE: ICF100607OR

AB INITIO STUDY OF GENERALIZED STACKING FAULT ENERGIES IN MAGNESIUM

T. Uesugi[1], M. Kohyama[2], M. Kohzu[1] and K. Higashi[1]

[1] Department of Metallurgy and Materials Science, Osaka Prefecture University, 1-1, Gakuen-cho, Sakai, Osaka, 599-8531, Japan
[2] Department of Material Physics, Osaka National Research Institute, National Institute of Advanced Industrial Science and Technology, Ministry of Economy, Trade and Industry, 1-8-31, Midorigaoka, Ikeda, Osaka, 563-8577, Japan

ABSTRACT

The light weight and high specific strength magnesium alloys are important as structural materials. However, magnesium and magnesium alloys have low plastic formability and occur brittle fracture at room temperature, because their active slip systems are not sufficient. In the behaviors of slip deformation and dislocation motions, the critical and effective parameter is the generalized stacking fault (GSF) energy. The GSF energy is identified with the energy necessary to ideal slip, and shear strength of real materials should increase as the GSF energy increases. In HCP metals including magnesium, $\{0001\}<11\bar{2}0>$ basal slip and $\{10\bar{1}0\}<11\bar{2}0>$ prismatic slip with $1/3<11\bar{2}0>$ ***a*** dislocations are well known and basal slip is active and dominant in magnesium. We employ *ab initio* pseudopotential method for magnesium to study accurate the GSF energies on basal and prismatic plane and discuss the difference between basal and prismatic slip. It is also investigated from the GSF energy that the dissociation with stable stacking fault of ***a*** dislocations on prismatic plane is not so clear. The calculated GSF energy on basal plane is much lower than that on prismatic plane. This result agrees with that the observed main slip system is basal slip in real magnesium.

KEYWORDS

ab initio, pseudopotential, basal plane, prismatic plane, generalized stacking fault, stable stacking fault, dislocation, magnesium

INTRODUCTION

Recently the usage of magnesium alloys are increasing as light weight and high specific strength structural materials in automotive and aerospace industries. However, it is large problem that magnesium alloys have low plastic formability. The cause is that the active slip systems of magnesium are not sufficient near room temperature, and so it becomes low ductility. The ductility greatly depends on slip deformations and it is important to understand the deformation mechanism associated with the slip.

In HCP metals including magnesium, $\{0001\}<11\bar{2}0>$ basal slip with the dislocations along the shortest Burgers vector ***a***$=1/3<11\bar{2}0>$ (so called ***a*** dislocations) is the most commonly known plastic deformation mode and this slip system is active and dominant in magnesium. For a general loading, it is not only basal slip but also other independent slip systems are needed to deform the polycrystalline materials. It has been

reported that $\{10\bar{1}0\}<11\bar{2}0>$ prismatic slip, $\{10\bar{1}1\}<11\bar{2}0>$ first order pyramidal slip and $\{11\bar{2}2\}<\bar{1}\bar{1}23>$ second order pyramidal slip are also activated in magnesium at high temperature [1,2]. These slip systems are shown in Figure 1. Additionally, it is interesting that the dominant slip mode is different in HCP metals. For example, slip occurs preferentially on basal plane in Mg, Be, Cd and Zn, but prismatic slip is preferred in Ti, Y, Hf and Zr.

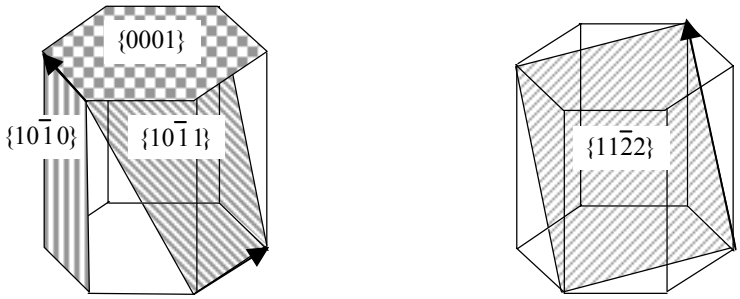

Figure 1: Slip systems in magnesium.

In slip deformations, the critical parameter is a property of the generalized stacking fault (GSF) energy which is also called γ-surface [3]. The GSF energy is defined as follows; a crystal is cut into two halves along the slip plane and one half is displaced relative to the other by the vector **t**. As this vector is varied, the energy changes and traces out the GSF energy $\gamma(\mathbf{t})$, which is normally defined as energy differences from bulk crystal. If this vector are varied along with Burgers vector, the GSF energy is identified with the potential energy necessary to ideal slip. So shear strength of real materials should increase as the GSF energy increases. There exists a relationship between the GSF energy and the dislocation density or Peierl's stress [4]. Especially, the stable stacking fault energy which is the minimum of the GSF energy play a major role in the behavior of dislocation core.

Legrand [5] calculated the GSF energy on basal and prismatic planes for various HCP metals including Mg using empirical pseudopotential method and tight-binding method. He found good agreements between the observed main slip system of various HCP metals and ratio of basal to prismatic stable stacking fault energy. It can be explained that the stable stacking fault energy is a dominant factor of the splitting width of the dislocation core and it is easy to slip as the energy is smaller. However, their calculations are based on the semi-empirical method and there is hardly quantitative and accurate investigations. Thus, in the present work we employ *ab initio* pseudopotential method for magnesium to study accurate GSF energy on basal and prismatic plane.

METHODS

All calculations presented in this paper were performed using Cambridge Serial Total-Energy Package (CASTEP). CASTEP is an *ab initio* pseudopotential method code for the solution of the electronic ground state of periodic systems with the wavefunctions expanded in plane wave basis using a technique based on density functional theory (DFT) [6,7]. The electronic exchange-correlation energy is given by the generalized gradient approximation (GGA) of Perdew and Wang [8] in the DFT. We use the norm-conserving pseudopotential of Troullier and Martins [9] in a reciprocal space. The pseudopotential is transformed to a separable form as suggested by Kleinman-Bylander [10]. The partial core correction [11] is also included in this pseudopotential. The electronic ground state is efficiently obtained using the conjugate-gradient technique [12]. The cutoff energy for the plane-wave basis is 4.36×10^{-17}J (20Ry) which is sufficient for all our purposes. The stable atomic configurations are obtained through relaxation according to the Hellmann-Feynman forces.

The supercells containing 10 basal atomic layers and 12 prismatic atomic layers are used for the calculation of the GSF energies on basal and prismatic plane, respectively (see Figure 2). For basal and prismatic supercells, Brillouin zone integration over k points are performed using $12\times12\times2$ and $11\times7\times3$ regular divisions of each axis in reciprocal space, respectively.

The slip deformation occurs with dislocations along Burgers vector, but dislocations are dissociated to

partial dislocations with stacking fault. Hence, it is important the GSF energy displaced by dissociated Burgers vector of partial dislocations, not simple Burgers vector of dislocations. We calculate the GSF energies displaced by vector **t** that changes continuously 0 to $\boldsymbol{b}_p$. The $\boldsymbol{b}_p$ is dissociated Burgers vector of partial dislocations. The atomic layers are cut into two half halves parallel to basal or prismatic plane and one half is displaced by displacement vector **t**. The GSF energy $\gamma(\mathbf{t})$ defined as

$$\gamma(\mathbf{t}) = \frac{E_{\text{fault}}(\mathbf{t}) - E_{\text{bulk}}}{2\mathbf{A}}, \tag{1}$$

where E_{bulk} is the total energy of supercell of magnesium bulk, $E_{\text{fault}}(\mathbf{t})$ is the total energy of supercell containing two generalized stacking faults displaced by vector **t** and **A** is the area of stacking fault per a supercell.

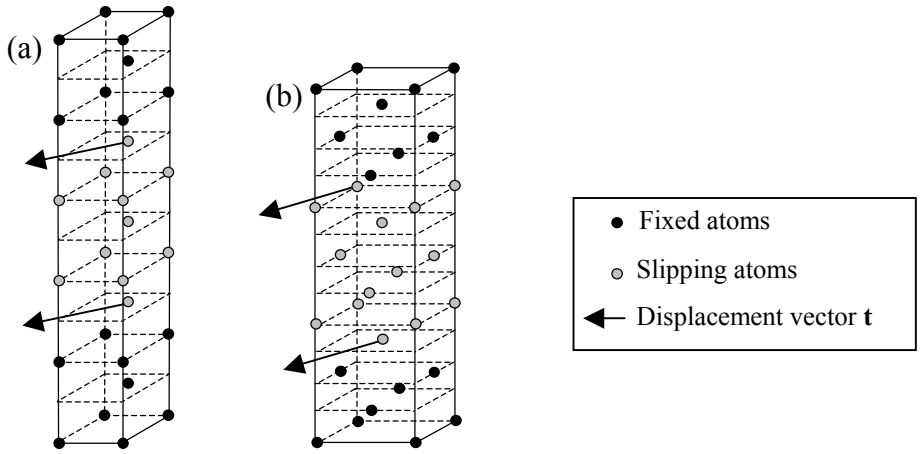

Figure 2: (a) Supercell for basal slip and (b) supercell for prismatic slip.

RESULTS

When considering dislocation splitting in HCP metals, the situation is clear for ***a*** dislocations on basal plane which can always dissociate into Shockley-type partials. The dissociation of ***a*** dislocations is the splitting on basal planes according to the reaction

$$\frac{1}{3}<11\bar{2}0>=\frac{1}{3}<10\bar{1}0>+\frac{1}{3}<01\bar{1}0>, \tag{2}$$

with the I_2 stacking fault between the partial dislocations. However, the dissociation of ***a*** dislocations on prismatic plane is not so clear. Using a hard-sphere model, Tyson [13] proposed the splitting

$$\frac{1}{3}<11\bar{2}0>=\frac{1}{6}<11\bar{2}1>+\frac{1}{6}<11\bar{2}\bar{1}>. \tag{3}$$

Vitek and Igarashi [14] suggest from the γ-surface calculations of empirical many-body potentials that the same dislocations may also split on prismatic planes according to the reaction

$$\frac{1}{3}<11\bar{2}0>=\frac{1}{6}<11\bar{2}\mathbf{x}>+\frac{1}{6}<11\bar{2}\bar{\mathbf{x}}>, \tag{4}$$

where **x** varies from material to material.

We calculate the GSF energies displaced by the vector $\boldsymbol{b}_p = 1/6[11\bar{2}\mathbf{x}]$, **x** is from 0 to 1.2, in order to examine the stable stacking fault point on prismatic plane. The results are shown in Figure 3. We find lowest

energy stable stacking fault point b_p=1/6[11$\bar{2}$**x**] , **x**=0.76. Vitek and Igarashi [14] calculated **x**=0.9 by empirical many-body potentials but their value is different from our value. This difference is based on the difference between the calculation methods. The stable stacking fault energy is 255.1 mJ/m^2 at **x**=0.76. From x=0.6 to x=0.9, this staking fault energy change little (~0.3 mJ/m^2) . The stable stacking fault on prismatic plane may exist in some extent range.

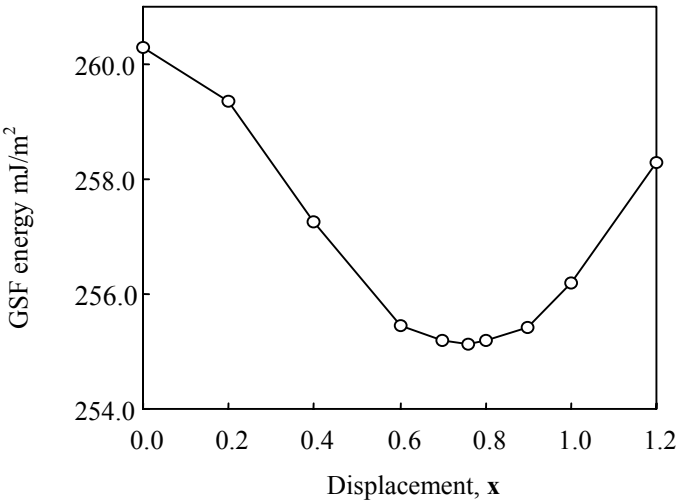

Figure 3: The stable stacking fault energy on prismatic plane.

Then, we calculate the GSF energies displaced by **t**=1/6[10$\bar{1}$0]u, with u from 0 to 1 on basal plane, and the GSF energies displaced by **t**=1/6[11$\bar{2}$**x**] u, **x** = 0.76, with u from 0 to 1 on prismatic plane. These are calculated by using the three different relaxation methods of atoms. First, the atomic relaxation perpendicular to the slip plane is allowed but parallel is not allowed at all. Second, the atoms of two layers constituting stacking fault are relaxed only perpendicular to the slip plane, while other atoms move freely in all directions. Third, the atoms of two layers constituting stacking fault are relaxed in all directions, while other atoms are relaxed only perpendicular to the slip plane. On both basal and prismatic plane, the GSF energies do not change very much by different three relaxation scheme. The results by third relaxation method are shown in Figure 4. The calculated GSF energy on basal plane is much lower than that of prismatic plane. This results agree with that the observed main slip system is basal slip in real magnesium.

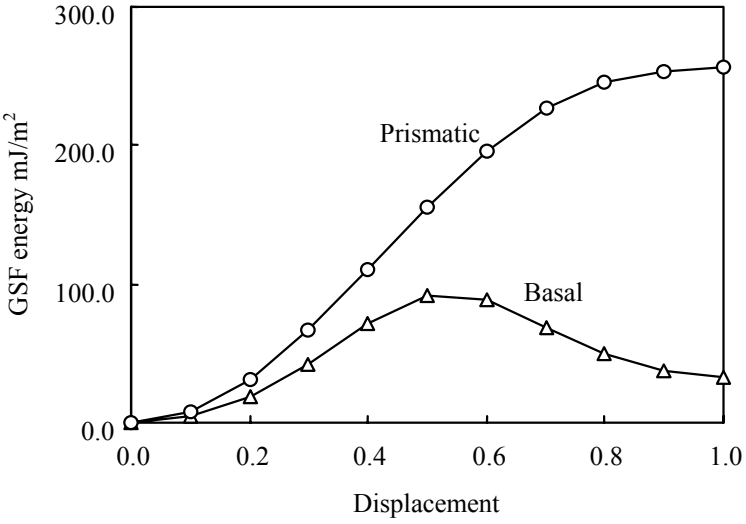

Figure 4: The GSF energies on basal and prismatic slip.

The stable stacking fault energy on basal plane, which is the minimum of the GSF energy path, is 32.4 mJ/m^2. On prismatic plane, it is different from basal plane, and stable staking fault point is the peak of the GSF energy path. We summarize the stable stacking fault energies in Table 1, which also includes other theoretical values.

TABLE 1
THE STABLE STACKING FAULT ENERGIES ON BASAL AND PRISMATIC PLANE

BASAL (mJ/m^2)	PRISMATIC (mJ/m^2)
32.4	255.1
44[a] [15]	
30[b] [5]	125[b] [5]

[a] *Ab initio* pseudopotential method [b] Empirical pseudopotential method

The result on basal plane is in good agreement with other theoretical values 30 mJ/m^2 by empirical pseudopotential method of Legrand [5] and 44 mJ/m^2 by *ab initio* pseudopotential method of Chetty and Weinert [15], while Chetty and Weinert calculated only the stable stacking fault energy, and not the GSF energies. However, the stable stacking fault energy on prismatic plane is 255.1 mJ/m^2, and it is much different from 125 mJ/m^2 by empirical pseudopotential method of Legrand [5]. In order to obtain accurate GSF or stable stacking fault energies, the precision is not sufficient by semi-empirical method, and so *ab initio* method is effective.

SUMMARY

The GSF energies on basal and prismatic plane in magnesium has been studied by *ab initio* pseudopotential method. It is also investigated that the dissociation with the stable stacking fault of $\boldsymbol{a}$ dislocations on prismatic plane is not so clear. We find the lowest energy stable stacking fault point $1/6[11\bar{2}\mathbf{x}]$, $\mathbf{x}$=0.76. The calculated GSF energy on basal plane is much lower than that on prismatic plane. This result agrees with that the observed main slip system is basal slip in real magnesium. The stable stacking fault energy, which is the minimum of the GSF energy, is 32.4 mJ/m^2 on basal plane and 255.1 mJ/m^2 on prismatic plane. In order to obtain accurate GSF or stable stacking fault energies, the precision is not sufficient by semi-empirical method, and so *ab initio* method is effective. In the future, much knowledge about slip systems will be obtained, if the similar calculations are performed on other slip planes or in other HCP metals.

ACKNOWLEDGMENTS

We are grateful to the financial support of "the Priority Group of Platform Science and Technology for Advanced Magnesium Alloys, Ministry of Culture, Science and Education" (Grant #11225209) and "The Light Metal Educational Foundation Inc.".

REFERENCES

1. Flynn, P. W., Mote, J. and Dorn, J. E., (1960) Trans. Met. Soc. AIME 218, 416.
2. Stohr, J. F. and Poirer, J., (1972) Phios. Mag. 25, 1313.
3. Vitek, V., (1968) Philos. Mag. 18, 773.
4. Juan, Y., and Kaxiras, E., (1996) Philos. Mag. 74, 1367.
5. Legrand, B., (1974) Philos. Mag. B 49, 171.
6. Hohenberg, P. and Kohn, W., (1964) Phys. Rev. 136, 864.
7. Kohn, W. and Sham, L. J., (1965) Phys. Rev. A 140, 1133.
8. Perdew, J. P. and Wang, Y., (1992) Phys. Rev. B 46, 6671.
9. Troullier, N. and Martins, J. L., (1991) Phys. Rev. B 43, 1993.
10. Kleinman, L. and Bylander, D. M., (1982) Phys. Rev. Lett. 48, 1425.
11. Louie, S. G., Froyen, S. and Cohen, M. L., (1982) Phys. Rev. B 26, 1738.
12. Teter, M. P., Payne, M. C. and Allan, D. C., (1989) Phys. Rev. B 40, 12225.

13. Tyson, W., (1967) Acta Metall. 15, 574.
14. Vitek, V. and Igarashi, M., (1991) Philos. Mag. A 63, 1059.
15. Chetty, N. and Weinert, M., (1997) Phys. Rev. B 56, 10844.

ORAL/POSTER REFERENCE: ICF100423PR

ABOUT THE CONNECTION BETWEEN THE CHARACTERISTICS OF THE LCF AND FCG

Gy. Nagy[1] and J. Lukács[1]

[1]Department of Mechanical Engineering, University of Miskolc
H-3515 Miskolc-Egyetemváros, Hungary

ABSTRACT

Characteristics determined for low cycle fatigue, high cycle fatigue or fatigue crack growth are different. The question arises, whether common mechanical and microstructural features can be found or not in this narrow field of loading types, based on which relationship between the materials constants can be assumed. The paper introduces the similarity of the stress and strain state, furthermore the dislocation structure having been developed during low cycle fatigue and fatigue crack growth. This can form a basis for the establishment of a connection between the material characteristics determined during the above mentioned two types of testing. The validity of the hypothesis has been illustrated here by comparing the test results determined for different material grades, steels (micro-alloyed and thermomechanically treated steels) and aluminium alloys (groups of different microstructure).

KEYWORDS

Low cycle fatigue (LCF), fatigue crack growth (FCG), Manson-Coffin equation, Paris-Erdogan law

INTRODUCTION

The behaviour and the properties of the different materials are determined by the quality of materials (chemical composition, type of atomic bonding, spatial arrangement of atoms, micro- and macrostructure), furthermore the stress state, the strain rate and the temperature. Due to the great variety of these influencing factors we do not have a general model for describing the behaviour of materials, thus we have to use several material constant to be able to characterise it. Even if we consider the fatigue loading of the possible loading conditions we have to determine more material constants to be able to provide sufficient data for sizing and control.

We determine different properties in case of low cycle fatigue, high cycle fatigue, and fatigue crack growth rate measurements. We can ask if there are common mechanical or microstructural properties – at such a relatively small area – that could be taken as a basis in order to build a connection between the materials constants.

The aim of this paper is to introduce the similarity of the mechanical stress state and the dislocation structure in case of low cycle fatigue (LCF) and fatigue crack growth (FCG) which can be the basis of the connection of the determined constants. The assumption is supported by the results measured and analysed

on the same steel and aluminium grades. Micro-alloyed and thermomechanically treated steels and aluminium alloys with different microstructure were used for the investigation.

COMPARISON AND SIMILARITY OF THE MECHANICAL STRESS STATE AND THE DISLOCATION STRUCTURE

Comparison of the mechanical stress state

In case of low cycle fatigue the load of the specimen is so large that the whole volume of measuring part of the specimen will suffer plastic deformation during the first half of the loading cycle. At the majority of the experiments the controlled parameter is the total strain amplitude and its time variation generally follows a sinus or a triangle function. Since the connection between the stress and strain is not linear in the region of plastic deformation, in case of total strain controlled low cycle fatigue the time dependence of the stress is influenced by the material, as well.

Figure 1 shows the time variation of the strain amplitude and the stress amplitude in case of low cycle fatigue with a saturated strain amplitude of $\varepsilon_a = \pm 1\%$. The difference is can be seen well. If the measuring part of the specimen is cylindrical with a uniaxial apprehension the same axial stress raises in each point of the cross section analysed.

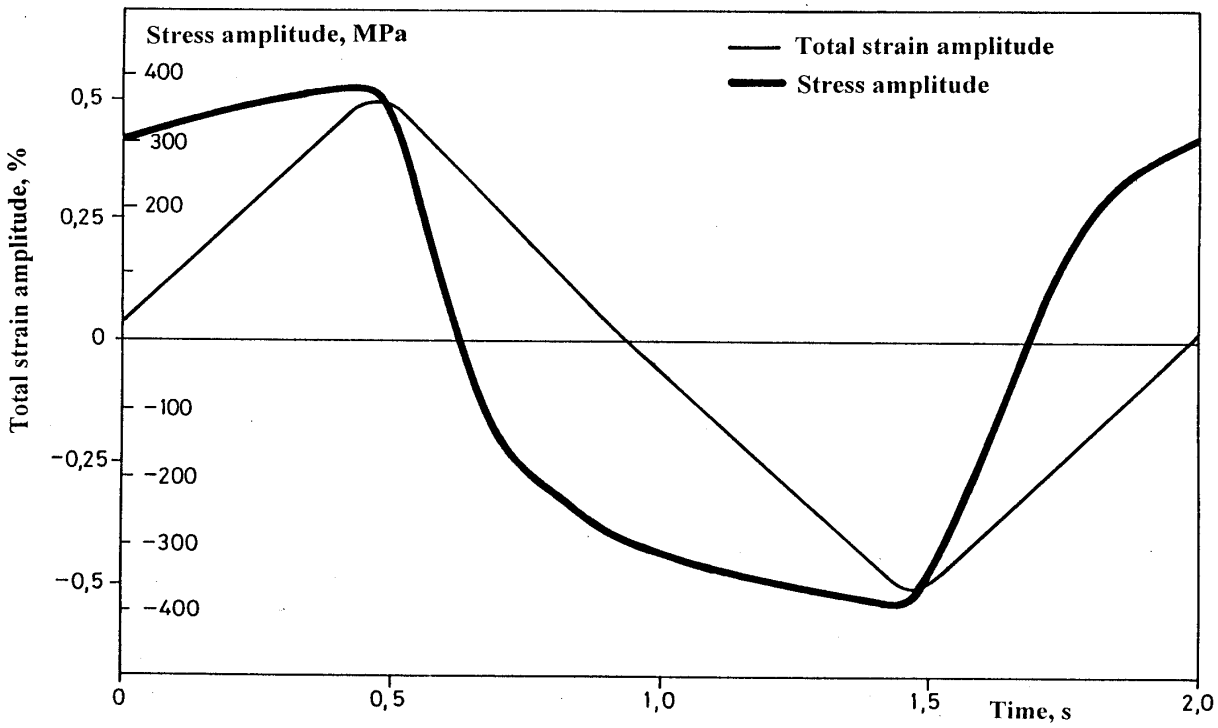

Figure 1: Time variation of the total strain amplitude and the stress amplitude in case of low cycle fatigue

Measuring the fatigue crack growth rate a plastic zone is forming at the crack tip during the first tensile cycle. The maximum size of the plastic zone (w) depends on the yield stress of the material (σ_0) and the stress intensity factor (K_I). Supposing an ideally elastic-plastic material and maximal loading the stress distribution in *y* direction in the function of the distance from the crack tip is going to form as shown in Figure 2 a). The maximum stress in the plastic zone is equal to the yield strength ($\sigma_y = \sigma_0$). Decreasing the load the stress distribution will change. When the load is zero again the stress distribution in *y* direction ahead of the crack tip is as shown in Figure 2 b), which demonstrates the reversed plastic zone, too.This means that a compressive stress arises in the plastic zone. Repeating the loading up (Figure 2 c)) and down the stress will be similar as experienced during low cycle fatigue.

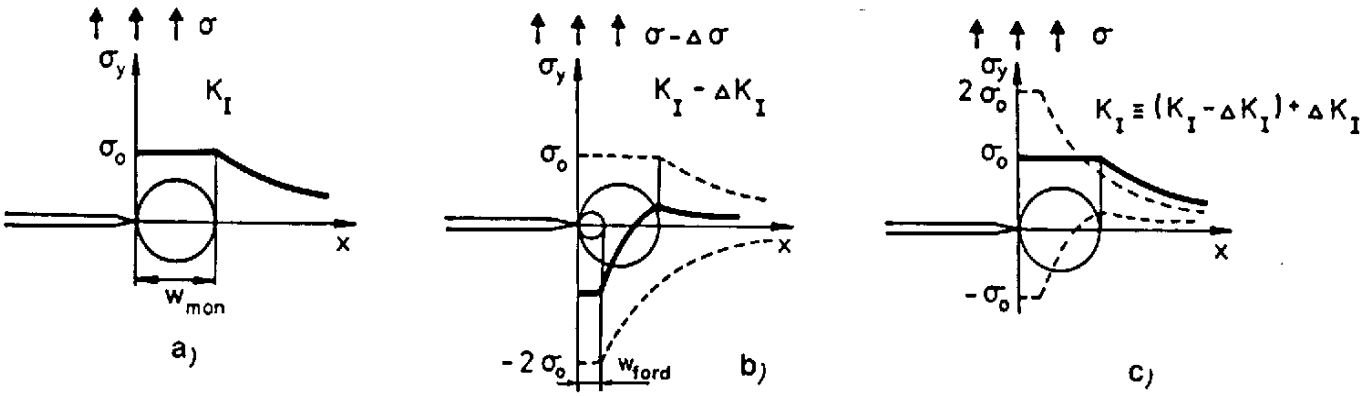

Figure 2: Stress distribution at the crack tip of the fatigue specimen

Comparison of the dislocation structure

Mild metals and alloys close to the equilibrium state can be characterized by a relatively small dislocation density ($10^{11} – 10^{13}$ m^{-2}) and a homogeneous dislocation distribution [1]. Under the influence of low cycle fatigue the dislocation density is growing and the dislocation distribution becomes heterogeneous even in the first cycle. At the early stage the edge dislocations, dislocation loops and dipoles, the labouring dislocation parts form uncondensed, blurred cell walls. With increasing number of cycles the number of multipoles and the dislocation density of the walls increases, the cell walls and the matrix will become more and more separated [1, 2]. At the beginning the cell size decreases with increasing the cycle number and after the dislocation density becomes stable the cell size will not change significantly. The orientation difference of the matrix crystal planes at the two sides of the cell-walls is increasing continuously during the entire fatigue process. The size of the cell is inversely proportional to the strain amplitude [7, 8].

In case of fatigue crack growth, a very large local plastic deformation will develop in front of the crack in the plastic zone, although its measure is different in the different points of the zone. Due to the large plastic deformation a cell structure will form [5, 6, 7]. In the crack vicinity the size of the cells is very small, while increasing the distance away from the crack their size is increasing. As well, the orientation difference of the planes of the neighbouring cells is the biggest near by the crack and getting more and more away the orientation difference is decreasing [8].

Based on these facts we can establish that the dislocation structure developing during low cycle fatigue is very similar to that which forms around the crack vicinity during fatigue crack growth.

INVESTIGATIONS AND RESULTS

For the experiments different micro-alloyed (37C, KL7D, DX52) and thermomechanically treated (X80TM, QStE690TM, StE690) steel grades (own tests and [9]) and aluminium alloys (AlMg3, AlMg5, AlMg5.1Mn, AlMg4.5Mn, 7075-T6) with different microstructure (own tests and [10], [11], [12]) were used. The chemical compositions of the examined materials are summarised in Table 1 and Table 2, the mechanical properties are listed in Table 3.

Low cycle fatigue tests have been executed in air, at room temperature, with total strain amplitude-control. The change of deformation was measured by a caliper, the time dependence of the load was a sinusoidal feature. The fatigue asymmetry factor was R = -1, the cycle number until failure was chosen at the 25% decreasing of the maximum tensile load. During the measurement the maximum values of the total strain and stress amplitudes and the hysteresis loop were recorded.

TABLE 1
CHEMICAL COMPOSITION OF THE TESTED STEELS, IN WT %

Material grade	C	Si	Mn	P	S	Al	Nb	V	Cr	Mo
37C	0.15	0.38	0.89	0.029	0.016	0.016	0.021	0.023	-	-
KL7D (1)	0.17	0.24	1.31	0.020	0.036	0.049	-	0.01	0.11	0.02
DX52 (2)	≤0.18	0.15-0.20	≤1.50	≤0.030	≤0.035	-	-	0.02-0.06	≤0.25	-
X80TM (3)	0.077	0.30	1.84	0.012	0.002	0.036	0.046	-	-	-
QStE690TM_FCG	0.08	0.29	1.75	0.011	0.002	0.041	0.04	0.061	0.037	0.32
StE690_LCF	0.15	0.53	0.87	0.011	0.004	0.038	-	-	0.63	0.22

(1) Ni = 0.08%, Ti = 0.0017%, Cu = 0.26%.
(2) Cu ≤ 0.30%.
(3) Ti = 0.018%, N = 0.005%.

TABLE 2
CHEMICAL COMPOSITION OF THE INVESTIGATED ALUMINIUM ALLOYS, IN WT %

Material grade	Si	Cu	Fe	Mn	Mg	Ti	Cr	Zr	Zn	Pb
AlMg3 (1)	0.179	0.022	0.310	0.2770	2.950	0.040	0.0430	0.0012	0.044	0.009
AlMg5_FCG	0.31	0.01	0.32	0.45	5.20	0.020	0.1	0.01	-	-
AlMg5.1Mn_LCF	<0.40	<0.10	<0.40	0.75	5.1	0.20	0.12	-	0.25	-
AlMg4.5Mn_FCG	0.21	0.01	0.27	0.77	4.53	0.015	0.1	0.03	-	-
AlMg4.5Mn_LCF	0.19	0.026	0.30	0.72	4.82	0.01	0.096	-	0.085	-
7075-T6_FCG	0.15	1.59	0.35	0.005	2.70	-	0.19	-	5.70	-
7075-T6_LCF	<0.4	1.2-2.0	<0.50	<0.30	2.1-2.9	<0.20	0.18-0.35	-	5.1-6.1	-

(1) Bi = 0.0150%, Be = 0.0018%, Al = 96.1170%.

TABLE 3
MECHANICAL PROPERTIES OF THE INVESTIGATED MATERIALS

Material grade	Yield strength R_y, N/mm^2	Tensile strength R_m, N/mm^2	Elongation A_5 %	Reduction of area Z %	Source
37C	269	405	33.5	63.5	own experiments
KL7D	392	535	≥19.0	-	own experiments
DX52	396	543	25.0	71.0	own experiments
X80TM	540	625	25.1	73.1	own experiments
QStE690TM_FCG	768	854	20.0	-	own experiments
StE690_LCF	743	885	-	57	[9]
AlMg3	127.7	217.9	27.0	-	[10]
AlMg5_FCG	185	288	14.5	-	[10]
AlMg5.1Mn_LCF	235	400	-	34.6	[12]
AlMg4.5Mn_FCG	230	296	18.0	-	[10]
AlMg4.5Mn_LCF	226	348	17.0	22.5	[12]
7075-T6_FCG	533	594	9.2	-	[11]
7075-T6_LCF	470	580	-	33.0	[12]

The results were evaluated by classical methods. The exponent ant the constant of the Manson-Coffin equation were determined by the following expression:

$$\varepsilon_{ap} = \varepsilon_f' N_t^c \tag{1}$$

where ε_{ap} is the plastic strain amplitude, N_t is the cycle number until failure, ε_f' and c are material constants. The calculated parameters, the material constants (c), for the different tested steel grades and aluminium alloys are listed in Table 4.

TABLE 4
PARAMETERS OF THE MANSON-COFFIN AND THE PARIS-ERDOGAN EQUATION

Material grade	Manson-Coffin equation, c	Paris-Erdogan equation, n	
		average	standard deviation
37C	-0.287	3.44	0.311
KL7D	-0.498	3.36	0.381
DX52	-0.784	3.11	0.140
X80TM	-0.478	2.49	0.561
QStE690TM_FCG	-	2.39	0.498
StE690_LCF	-0.659	-	-
AlMg3	-0.787	3.37	0.503
AlMg5_FCG	-	3.71	0.405
AlMg5.1Mn_LCF	-0.655	-	-
AlMg4.5Mn_FCG	-	3.57	0.444
AlMg4.5Mn_LCF	-0.755	-	-
7075-T6_FCG	-	2.13	-
7075-T6_LCF	-0.987	-	-

The fatigue crack growth rate measurements were made on compact tension (CT) and three point bending (TPB) specimens, in air, at room temperature, with a sinusoidal loading function and stress ratio of R = 0,1. The crack size was determined by optical method and using the compliance method. From the collected data and results of the fatigue crack growth measurements the exponent and the constant of the Paris-Erdogan equation have been determined:

$$\frac{da}{dN} = C\Delta K^n, \tag{2}$$

where da/dN is the fatigue crack growth rate, ΔK is the stress intensity factor range, C and n are material constants. In each case first we calculated the related part of the kinetic diagram of the fatigue crack growth (da/dN-ΔK diagram), then we determined the two material constants (C and n) with linear regression. From these results we calculated the average of the data measured on 5-26 specimens. The average and standard deviation values of the exponent are also listed in Table 4.

EVALUATION OF THE RESULTS

In our earlier works we showed that there is a correlation between the two parameters of both the Manson-Coffin and the Paris-Erdogan equation [13], therefore it is sufficient to study the relationship of the two exponents (c and n). Figure 3 shows the relation of these material constants.

Despite of the relatively few measurement data we can establish that there is an admissible connection between the exponents of the Manson-Coffin law characterising low cycle fatigue and the Paris-Erdogan equation describing fatigue crack growth.

The connection among the steel groups of different microstructure is different, which is demonstrated by the example of some micro-alloyed steels (37C, KL7D, DX52) and two grades of thermomechanically treated steels (X80TM, QStE690TM/StE690). The connection among the aluminium alloy groups of different microstructure is different, too, which is demonstrated by the example of some alloys (AlMg3, AlMg5.1Mn/AlMg5, AlMg4.5Mn) and one other alloy (7076-T6).

Comparison of the various material grades (e.g. micro-alloyed steels – aluminium alloys, or micro-alloyed steels – stainless steels) requires further investigations.

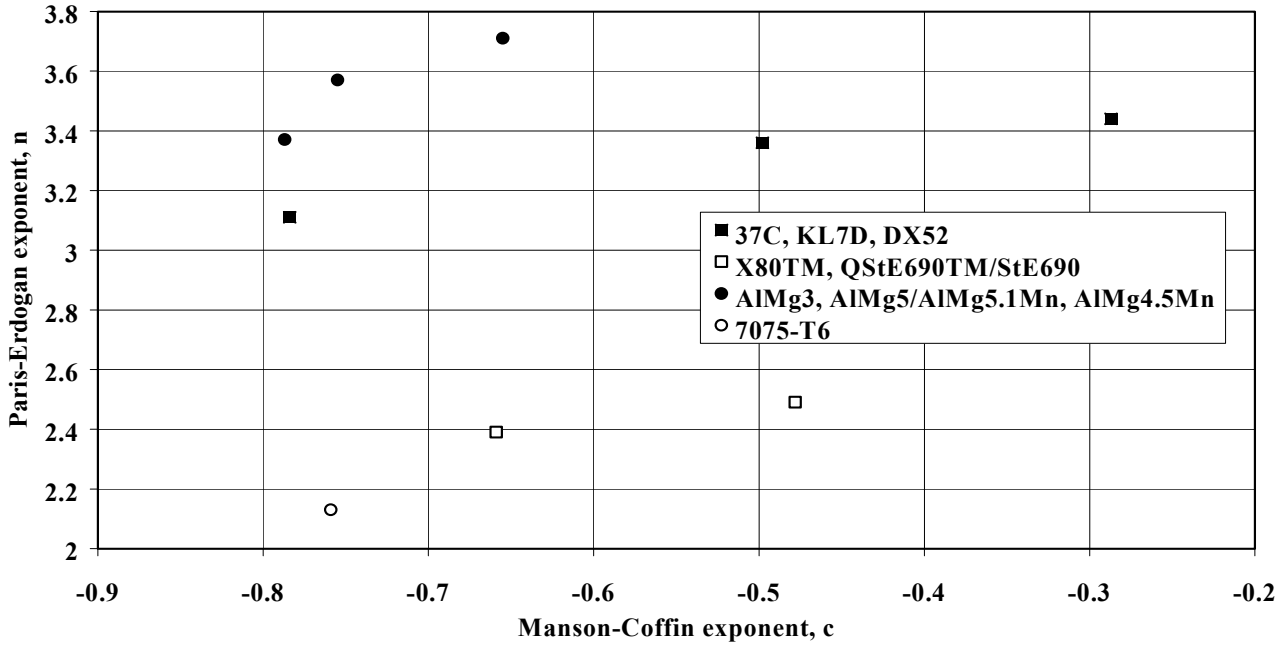

Figure 3: Connection between the exponents of Manson-Coffin and Paris-Erdogan equations

SUMMARY

Based on theoretical considerations and experiments the following establishments can be made. In the plastic zone in front of the crack tip the time dependence of the stress is similar in case of low cycle fatigue (LCF) and fatigue crack growth (FCG). The cyclic plastic deformation results in near the same cell type of dislocation structure. There is a connection between the exponents of the Manson-Coffin equation and the Paris-Erdogan law. The connection has been shown for different grades of steels and aluminium alloys.

ACKNOWLEDGEMENTS

The authors wish to acknowledge the assistance given by the National Scientific Research Foundation for supporting the research (OTKA F4418, OTKA T025428 and OTKA T022020).

REFERENCES

1. Klesnil, M. and Lukaš, P. (1980). *Fatigue of Metallic Materials*. Academia, Prague.
2. Feltner, E. and Laird, C. (1968). *Trans. Met. Soci. AIME.* 242, 1253.
3. Feltner, E. and Laird, C. (1967). *Acta Met.* 15, 1633.
4. Nahm, J. and Moteff, D. R. (1977). *Acta Met.*, 107.
5. Taira, S. and Tanaka, K. (1972). *Eng. Fract. Mech.* 4, 925.
6. Awatani, J., Katagiri, K. and Shiraishi, T. (1976). *Met. Trans.* 7A, 807.
7. Awatani, J., Katagiri, K. and Nakai, H. (1978). *Met. Trans.*, 111.
8. Lukaš, P., Klesnil, M. and Fiedler, R. (1969). *Phil. Mag.*, 799.
9. Boller, Chr. and Seeger, T. (1987). *Materials Data for Cyclic Loading. Part B: Low-alloy steels.* Elsevier, Amsterdam.
10. Török I. (1996). *Publ. Univ. Miskolc, Series. C, Mech. Engng*. 46, 33.
11. Lim, J.-K. Et al. (1966). In: *Proceedings of the Sixth International Fatigue Congress*, pp. 947-952, Lütjering, G. and Nowack, H. (Eds). Pergamon, Elsevier.
12. Boller, Chr. and Seeger, T. (1987). *Materials Data for Cyclic Loading. Part B: Low-alloy steels.* Elsevier, Amsterdam.
13. Tóth, L., Nagy, Gy. and Romvári, P. (1998). In: *Proceedings of the 7th European Conference on Fracture*, pp. 649-655, E. Czoboly (Ed). EMAS, Warley, West Midlands.

Ref. ICF100489OR

ACCOUNT OF PLASTICITY IN MACRO-MICROCRACK INTERACTION

V. Tamuzs[1], V. Petrova[2], S. Tarasovs[1]

[1] Institute of Polymer Mechanics, Riga, LV1006, Latvia
[2] Voronezh State University, Voronezh, Russia

ABSTRACT

Several papers during the last years were devoted to the problem of plastic zone growth for collinear cracks. In this work more general case was studied: plastic zone creation in isotropic, homogeneous elastic-perfectly plastic infinite plate containing crack and several microcracks near its tip. The macrocrack is subjected to a normal loading, acting at the infinity. The Dugdale model was used for plastic zones growing from the tips of macrocrack, microcracks are assumed to be elastic. The plastic zone length and crack opening displacement are found from asymptotic solution and compared with finite element solution.

KEYWORDS

Microcracks interaction, Dugdale model, crack opening displacement.

INTRODUCTION

The model of plastic zone ahead of the crack tip, introduced by Dugdale [1], is widely used in fracture mechanics. Many works were devoted to the problem of plastic zone creation in cracks interaction. Leonov and Onishko [2] considered the problem for two collinear equal cracks. The crack tips were supposed to close smoothly due to cohesive forces distributed along zones near the crack tips. The interior relaxed zones were coalesced. The review of Karihaloo [3] is devoted to the author's results on the fracture characteristics of elastic solids containing inhomogenities in the form of slitlike cracks with plastic zones. A perturbation solution was presented for widely spaced cracks. The numerical solution based on the Chebishev polynomials of the first kind was also obtained. Harrop [4] extended the Dugdale model for the case when plastic zones were being closed by cohesive parabolic stress distribution. Theocaris [5] studied the Dugdale model for two unequal collinear cracks. The theoretical and experimental works devoted to the modified Dugdale model were reviewed in the paper.

ASYMPTOTIC SOLUTION

The solution of Romalis and Tamuzs [6] for the problem of micro-macrocrack interaction was adopted in this work for macrocrack with plastic zones. Microcracks are assumed to be elastic.

Let an isotropic elastic-perfectly plastic plane contain a macrocrack and N microcracks of length $2a_k$. It will be assumed that all microcracks have the same length, i.e. $a_k = a$. Cartesian coordinates x and y are centered at the midpoint of the main crack with the crack along the x-axis. The local coordinate systems x_k , y_k are attached to each microcrack. The microcrack position is determined by its midpoint coordinate z^0_k and the inclination angle α_k to the x-axis.

The main crack consists from an open zone [- c_1 , c_2] and two plastic zones created at the vicinities of the crack tips - c_1 and c_2 such that the full length of the main crack is considered to be $2a_0$. In such case the lengths of the plastic zones are $|a_0 - c_1|$ and $|a_0 - c_2|$. The tensile stress T is applied at infinity while the plastic zones are closed by stress q which is normally identified with the yield stress of the material. The problem can be reduced to solving the problem with boundary conditions on the crack lines. For non-dimensional parameters $b = c_1/a_0$, $d = c_2/a_0$ and $\tau = x_k/a_0$ (k=0,1, …, N) the boundary conditions are written as

$$p_0(\tau) = \begin{cases} -T & -b < \tau < d \\ -T + q & -1 < \tau < -b \ \ and \ \ d < \tau < 1 \end{cases}$$
$$p_k(\tau) = -\frac{T}{2}\left(1 + e^{-2i\alpha_k}\right), \ \ |\tau| < a_k / a_0 \qquad (k = 1,2,..., N) \tag{1}$$

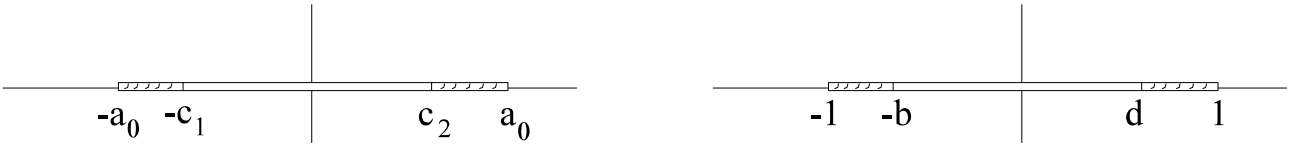

Figure 1: Coordinates of crack tips and plastic zones.

Singular integral equations for the system of cracks with self-equilibrium stresses on their faces have been derived by Panasyuk et al [7]

$$\int_{-a_n}^{a_n} \frac{g'_n(\tau)}{t - x} dt + \sum_{\substack{k=0 \\ k \neq n}}^{N} \int_{-a_k}^{a_k} \left[g'_k(t) K_{nk}(t,x) + \overline{g'_k(t)} L_{nk}(t,x) \right] dt = \pi p_n(x) \quad (n = 0,1,..., N) \tag{2}$$

where K_{nk} and L_{nk} are the regular kernels containing the geometric parameters of the problem [7]. The $g'_k(x)$ represents the derivatives of displacement jumps on the crack lines:

$$g'_k(x) = \frac{2\mu}{i(\kappa + 1)} \frac{\partial}{\partial x} ([u_k] + i[v_k]) = v'_k - iu'_k, \tag{3}$$

where $\mu = E/2(1+\nu)$ is the shear modulus, E Young's modulus, ν Poisson's ratio, $\kappa = 3-4\nu$ for the plane strain state and $\kappa = (3-\nu)/(1+\nu)$ for the plane stress state.

By using variables $t = a_k \tau$, $x = a_n \chi$ the system (2) can be reduced to a dimensionless form and the solution of it is sought as a power series with regard to the small parameter $\lambda = a/a_0$

$$g'_n = \sum_{p=0}^{\infty} g'_{np} \lambda^p, \ \ K_{nk} = \sum_{p=0}^{\infty} m_{nkp} \lambda^p, \ \ \ L_{nk} = \sum_{p=0}^{\infty} n_{nkp} \lambda^p \tag{4}$$

Inserting series (4) into Eqn. 2. and equating the expressions of like powers of λ, the recurrent relations are obtained for the subsequent determination of coefficients g'_{np}. We derived them by retaining terms up to λ^2 :

$$
\begin{aligned}
g'_{00}(\chi) &= -\frac{1}{\pi\sqrt{1-\chi^2}}\int_{-1}^{1}\frac{\sqrt{1-\tau^2}}{\tau-\chi}\,p_0(\tau)d\tau \\
g'_{02}(\chi) &= \frac{1}{\pi\sqrt{1-\chi^2}}\sum_{k=1}^{N}\int_{-1}^{1}\left[g'_{k0}(\tau)m_{0k1}(\tau,\chi)+\overline{g'_{k0}(\tau)}n_{0k1}(\tau,\chi)\right]d\tau \\
g'_{n0}(\chi) &= \frac{1}{\pi\sqrt{1-\chi^2}}\left\{-\int_{-1}^{1}\frac{\sqrt{1-\tau^2}}{\tau-\chi}\,p_n(\tau)d\tau+\int_{-1}^{1}\left[g'_{00}(\tau)m_{n01}(\tau,\chi)+\overline{g'_{00}(\tau)}n_{n01}(\tau,\chi)\right]d\tau\right\}
\end{aligned}
\tag{5}
$$

Taking into account the expression for $p_0(\tau)$ (1) the derivative of the vertical displacement on the isolated crack line is obtained by first two approximations of $v'_0 = \mathrm{Re}\{g'_0\}$.

$$
v'_{00}(\chi) = \mathrm{Re}\,g'_{00} = \frac{\chi(q-T)}{\sqrt{1-\chi^2}} + \frac{q}{\pi\sqrt{1-\chi^2}}\int_{-b}^{d}\frac{\sqrt{1-\tau^2}}{\tau-\chi}\,d\tau \qquad |\chi|\le 1,\ [-b,d]\subset[-1,1]
\tag{6}
$$

$$(b,d>0)$$

$$
v'_{02}(\chi) = \mathrm{Re}\,g'_{02} = \frac{1}{2\sqrt{1-\chi^2}}\sum_{k=1}^{N}\mathrm{Re}\left[(p_k+I_{k0})m'_{0k1}(\chi)+(\overline{p}_k+\overline{I}_{k0})n'_{0k1}(\chi)\right]
\tag{7}
$$

$$
\begin{aligned}
I_{k0} = \frac{T-q}{2}&\left[2-\frac{\overline{u}_k}{\sqrt{\overline{u}_k^2-1}}-\frac{u_k}{\sqrt{u_k^2-1}}+e^{-2i\alpha_k}\,\frac{u_k-\overline{u}_k}{(\overline{u}_k^2-1)^{3/2}}\right] \\
&+\frac{q}{2\pi}\left[\left(\frac{1}{\sqrt{\overline{u}_k^2-1}}+e^{-2i\alpha_k}\,\frac{u_k(\overline{u}_k-u_k)}{(\overline{u}_k^2-1)^{3/2}}\right)\int_{-b}^{d}\frac{\sqrt{1-t^2}}{t-\overline{u}_k}\,dt\right. \\
&\left.+\frac{1}{\sqrt{u_k^2-1}}\int_{-b}^{d}\frac{\sqrt{1-t^2}}{t-u_k}\,dt+e^{-2i\alpha_k}\,\frac{u_k-\overline{u}_k}{\sqrt{\overline{u}_k^2-1}}\int_{-b}^{d}\frac{\sqrt{1-t^2}}{(t-\overline{u}_k)^2}\,dt\right]
\end{aligned}
\tag{8}
$$

and

$$
\begin{aligned}
m'_{0k1}(\chi) &= \frac{e^{i\alpha_k}}{2}\left[\frac{e^{-i\alpha_k}(\overline{u}_k\chi-1)}{(\chi-\overline{u}_k)^2\sqrt{\overline{u}_k^2-1}}+\frac{e^{i\alpha_k}(u_k\chi-1)}{(\chi-u_k)^2\sqrt{u_k^2-1}}\right]; \\
n'_{0k1}(\chi) &= \frac{e^{-i\alpha_k}}{2}\left[(u_k-\overline{u}_k)e^{-i\alpha_k}\,\frac{-\chi^2+2\overline{u}_k^3\chi-3\overline{u}_k^2+2}{(\chi-\overline{u}_k)^3(\overline{u}_k^2-1)^{3/2}}+(e^{i\alpha_k}-e^{-i\alpha_k})\frac{\overline{u}_k\chi-1}{(\chi-\overline{u}_k)^2\sqrt{\overline{u}_k^2-1}}\right]
\end{aligned}
\tag{9}
$$

The derivatives of the vertical displacement discontinuities on the macrocrack line are written as

$$v_0'(\chi) = v_{00}'(\chi) + \lambda^2 v_{02}'(\chi), \qquad \lambda = a / a_0 \tag{10}$$

Then the stress intensity factors at the macrocrack tips -a_0 and a_0 are defined

$$k_I^{\pm} - ik_{II}^{\pm} = \mp \lim_{\chi \to \pm 1} \sqrt{1-\chi^2}\, a_0^{1/2} [v_0'(\chi) - iu_0'(\chi)] \tag{11}$$

The length of the unknown plastic zones will be calculated from the condition

$$k_I(\pm a_0) = 0, \tag{12}$$

which means that the crack faces are closed smoothly.

Solution for an Isolated Crack

Using the zero-th approximation of derivative of the vertical displacement for the symmetric case, Eqn. 6., the SIF for isolated crack is

$$k_{I00} = -\lim_{\chi \to 1} \sqrt{1-\chi^2}\, a_0^{1/2} v_{00}'(\chi) = a_0^{1/2} \left[T - q + \frac{2q}{\pi} \arctan \frac{b}{\sqrt{1-b^2}} \right] \tag{13}$$

The SIFs at right and left tips are equal for an isolated crack as well as the lengths of the plastic zones. The size (1-b) of the plastic zone is obtained by equating the expression of k_{I00} to zero

$$b = \cos \frac{\pi}{2} \frac{T}{q} \tag{14}$$

We obtain well known expression for an isolated relaxed crack with plastic zones of size (1-b) in an infinite solid (Dugdale, [1]). The value of CTOD can be determined by integrating $v_{00}'(\chi)$ and then calculating the obtained expression at χ=b

$$v_{00}(b) = -q \frac{2}{\pi} b \ln \left(\cos \left(\frac{\pi}{2} \frac{T}{q} \right) \right) \tag{15}$$

Solution for the Macrocrack Interacting with Microcracks

For the macro-microcrack system the derivatives of the normal displacements on the macrocrack line are determined by Eqn. 6-10. Consider the symmetrical case when the plastic zones have same length, i.e. b=d. We should determine the second term k_{I02} in the SIF.

$$k_{I02} = \mp \lim_{\chi \to \pm 1} \sqrt{1-\chi^2}\, a_0^{1/2} v_{02}'(\chi) \tag{16}$$

The equation for determination the plastic zones is

$$\left[\frac{T}{q} - \frac{2}{\pi} \arccos b \right] + \frac{\lambda^2}{2q} \sum_{k=1}^{N} \operatorname{Re} \left[\left(p_k + I_{k0}(T, q, u_k, b) \right) m_k + \left(\overline{p}_k + \overline{I_{k0}(T, q, u_k, b)} \right) n_k \right] = 0 \tag{17}$$

where

$$m_k = \frac{e^{i\alpha_k}}{2}\left[\frac{e^{-i\alpha_k}}{(\bar{u}_k \mp 1)\sqrt{\bar{u}_k^2 - 1}} + \frac{e^{i\alpha_k}}{(u_k \mp 1)\sqrt{u_k^2 - 1}}\right]$$
$$n_k = \frac{e^{-i\alpha_k}}{2}\left[(\bar{u}_k - u_k)e^{-i\alpha_k}\,\frac{2\bar{u}_k \pm 1}{(\bar{u}_k \mp 1)(\bar{u}_k^2 - 1)^{3/2}} + \frac{e^{i\alpha_k} - e^{-i\alpha_k}}{(\bar{u}_k \mp 1)\sqrt{\bar{u}_k^2 - 1}}\right] \tag{18}$$

The second term in the value of CTOD can be determined by integrating $v'_{02}(\chi)$ and then calculating the obtained expression at $\chi=b$

$$v_{02}(\chi) = \int v'_{02}(\chi)d\chi = \frac{1}{2}\sqrt{1-\chi^2}\sum_{k=1}^{N} \mathrm{Re}\left[(p_k + I_{k0})m^*_{0k1}(\chi) + (\bar{p}_k + \bar{I}_{k0})n^*_{0k1}(\chi)\right] \tag{19}$$

where

$$m^*_{0k1}(\chi) = e^{i\alpha_k}\,\mathrm{Re}\left[\frac{e^{i\alpha_k}}{(u_k - \chi)\sqrt{u_k^2 - 1}}\right]$$
$$n^*_{0k1}(\chi) = \frac{e^{-i\alpha_k}}{2}\frac{1}{(\bar{u}_k - \chi)\sqrt{\bar{u}_k^2 - 1}}\left[(u_k - \bar{u}_k)e^{-i\alpha_k}\,\frac{2\bar{u}_k^2 - \bar{u}_k\chi - 1}{(\bar{u}_k - \chi)(\bar{u}_k^2 - 1)} + e^{i\alpha_k} - e^{-i\alpha_k}\right] \tag{20}$$

The full value of CTOD is $v_0(b) = v_{00}(b) + \lambda^2 v_{02}(b)$.

NUMERICAL SOLUTION

Finite element method (FEM) was used to solve the problem. Plastic zones are modelled by introducing non-linear interface elements along the line of supposed plastic zone growth. The interface elements have user defined traction-opening relationship (constant traction equal to the yield stress of the material in the case of perfect plasticity).

RESULTS

As an example the macrocrack with two horizontal microcracks ahead of its tip was considered. Each microcrack is ten times smaller then macrocrack and geometry of the problem is presented in Fig.2. (distance between macrocrack and microcracks, d, and between microcrack and center line, h, is equal to the size of microcrack).

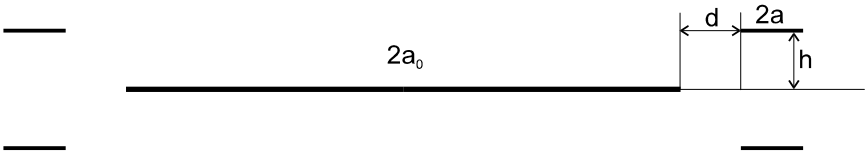

Figure 2: Geometry of the problem.

In Fig. 3-4 plastic zone length, C, and crack opening displacement, COD, are presented. The results are normalised with respect to plastic zone length and COD of single crack. The analytical results are compared with finite element solution.

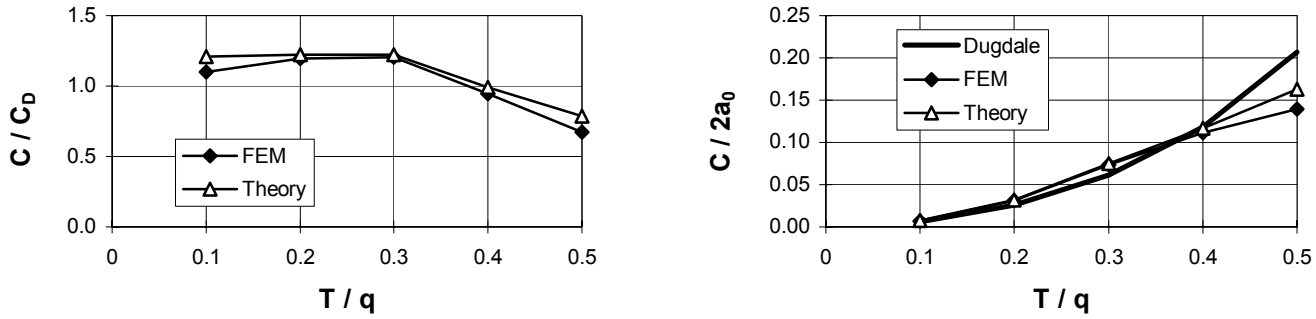

a) b)

Figure 3: Plastic zone length: a) results are normalised with respect to Dugdale solution, b) results are normalised with respect to the length of macrocrack.

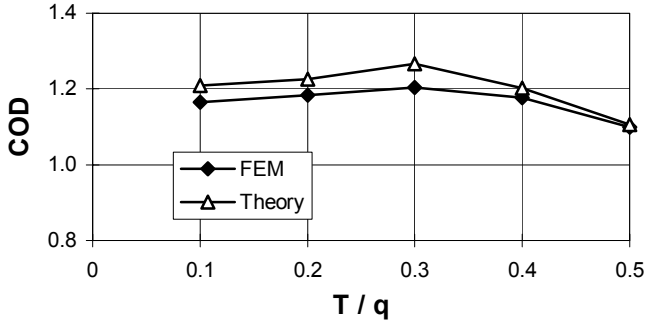

Figure 4: Crack opening displacement.

CONCLUSION

The pair of microcracks ahead of the crack tip increases the COD comparably with COD of a single crack whereas the plastic zone diminishes when it approaches to microcracks. So the defects ahead of the crack tip can enlarge the brittleness of material.

REFERENCES

1. Dugdale, D.S. (1960) *J. Mech. Phys. Solids.* 8, 100.
2. Leonov, M.Ya. and Onishko, L.V. (1962) In: *Teorija Plastin i Obolochek* (in Russian). Izd. AN Ukr.SSR, Kiev, pp. 200-203.
3. Karihaloo, B.L. (1979) *Eng. Frac. Mech.* 12, 49.
4. Harrop, L.P. (1978) *Eng. Frac. Mech.* 10, 807.
5. Theocaris, P.S. (1983) *Eng. Frac. Mech.* 18, 545.
6. Romalis, N. and Tamuzh, V. (1984) *Mechanics of Composite Materials.* 20, 35.
7. Panasyuk, V.V., Savruk, M.P., Dacishin, A.P. (1976) *Raspredelenie naprjazhenij okolo treschin v plastinah* (in Russian). Kiev.

Reference: ICF100909OR

ADVANCED COHESIVE ZONE MODELS FOR FRACTURE SIMULATION

Thomas Siegmund

School of Mechanical Engineering, Purdue University,
West Lafayette, IN 47907-1288, U.S.A.

ABSTRACT

Cohesive zone models (CZM) are attractive for fracture process simulation since they provide a link between failure at the micro-scale and macro-scale structural response. Throughout the recent past many successful applications of CZMs have been reported. To further expand the scope of CZM, the development of improved constitutive equations for the description of the mechanical processes during material separation are needed. The present paper reports on several recent developments on CZM that incorporate aspects such as triaxiality, rate dependence, damage accumulation during cyclic loading, as well as coupling to heat transfer.

KEYWORDS

Finite element modeling, Cohesive zone, Ductile fracture, Adhesive, Fatigue crack, Heat transfer

INTRODUCTION

In the recent past it has become evident that the framework of classical fracture mechanics – despite its significant success – possesses a series of limitations as a predictive tool [1]. To obtain a more fundamental view of failure it is necessary to adopt a concept in which the competing actions of (1) material separation processes in the cohesive zone at and near the crack front, *i.e.* in the cohesive zone, and (2) the deformation of material elements surrounding the fracture process zone, determine the observed behavior of a structure. This type of failure analysis becomes possible if the stress strain behavior of a material as well as the *material separation behavior* is described by an appropriate constitutive equation.

In the cohesive zone model (CZM) approach, the material separation behavior is described in a constitutive equation relating the crack surface tractions, $\mathbf{T}_{CZ}$, to the displacement jump across the crack, $\boldsymbol{\Delta}$. This law represents the physical processes of material deterioration in the fracture process zone. Its material parameter are the cohesive strength, σ_{max}, the peak traction, the cohesive length, δ, the value of displacement jump across the crack at which the stress carrying capacity has fallen to zero, and the cohesive energy, ϕ, the area under the traction-separation curve. Within the

mechanical equilibrium statement written as the principle of virtual work the cohesive zone elements are accounted for as internal surfaces:

$$\int_V \mathbf{s} : \delta\mathbf{F} \; \mathrm{d}V - \int_{S_{int}} \mathbf{T}_{CZ} \cdot \delta\boldsymbol{\Delta} \; \mathrm{d}S = \int_{S_{ext}} \mathbf{T}_e \cdot \delta\mathbf{u} \; \mathrm{d}S \tag{1}$$

Contributions in the volume and external surface terms (on V and S_{ext}) are described by the nominal stress tensor, $\mathbf{s}=\mathbf{F}^{-1}\det(\mathbf{F})\sigma$, with σ the Cauchy stress, the displacement vector, $\mathbf{u}$, the deformation gradient, $\mathbf{F}$, as well as by the traction vector, $\mathbf{T}_e$, on the external surface of the body. Traction vectors are related to $\mathbf{s}$ by $\mathbf{T}=\mathbf{n}\,\mathbf{s}$, with $\mathbf{n}$ being the surface normal. The cohesive surface contribution is described by the integral over the internal surface, S_{int}.

The concept of a cohesive fracture process zone abandons the failure criterion used in classical fracture mechanics and crack growth resistance of a structure is now viewed as the sum of the energy dissipated in the plastic zone and the energy spent in the actual separation process.

The basic concepts of CZM models are due to [2,3]. Current CZM models [4] differ from these classical models in that no initial crack needs to be defined and crack nucleation can thus be accounted for. Also, the length of the cohesive zone is not a parameter of the model. CZM models have been used in studies of monotonic or dynamic loading situations in homogeneous materials, composites and at interfaces. An overview paper [1] summarizes several examples of recent developments. Despite this success, few developments have been reported that aim at the development of improved traction separation laws. Such development can be accomplished if additional state variables are introduces into the CZM formulation [5]. The cohesive surface tractions are then no longer dependent on $\boldsymbol{\Delta}$ only. The present paper summarizes recent developments in this direction undertaken by the author. Approaches to computational modeling of ductile crack growth, rate dependency of failure, fatigue crack growth as well as fracture under thermo-mechanical loading are described.

TRIAXIALITY DEPENDENT CZM

Fracture of ductile materials is well known to be dependent on the level of constraint being present at the crack tip. Several prominent studies have clearly demonstrated that both the peak stress carrying capacity as well as the energy dissipated during void growth and coalescence can be characterized in terms of the stress triaxiality. While material models specifically geared towards failure based on void growth, *e.g.* the Gurson model [6], were specifically developed to account for the effect of triaxiality on material damage, CZMs have commonly assumed constant material parameter values for σ_{max}, δ or ϕ. This shortcoming can be overcome if these parameters are made dependent on the stress triaxiality. Since this quantity is not defined within the CZM itself, the effects of local crack tip constraint on the CZM parameters are introduced in dependence of the stress triaxiality in the solid elements adjacent to the crack line.

In a numerical study on ductile crack growth in a high strength structural steel, [7], the dependence of the CZM parameters on stress triaxiality was determined by unit cell simulations. The CZM parameters normalized by the flow strength of the material, σ_0, and the void spacing, X, respectively, are given in Fig. 1a in dependence of the maximum value of stress triaxiality reached during loading. Increasing triaxiality levels lead to an increase in σ_{max} and a decrease in ϕ. Subsequently, to study the effect of specimen size on the crack growth resistance a CZM with the CZM parameter dependence as of Fig. 1a was used. Both C(T) and M(T) specimens were analyzed. Figure 1b depicts the cohesive energy at Δa=20X normalized by (σ_0X) in dependence of the

normalized specimen size (W/X). The results clearly indicate that the cohesive energy, *i.e.* the energy needed to form new fracture surface, indeed is dependent on specimen size and geometry. The limit value of ϕ=0.5 (σ_{max} X) is reached only for fully developed crack tip constraint. Conventional CZMs cannot account for this effect.

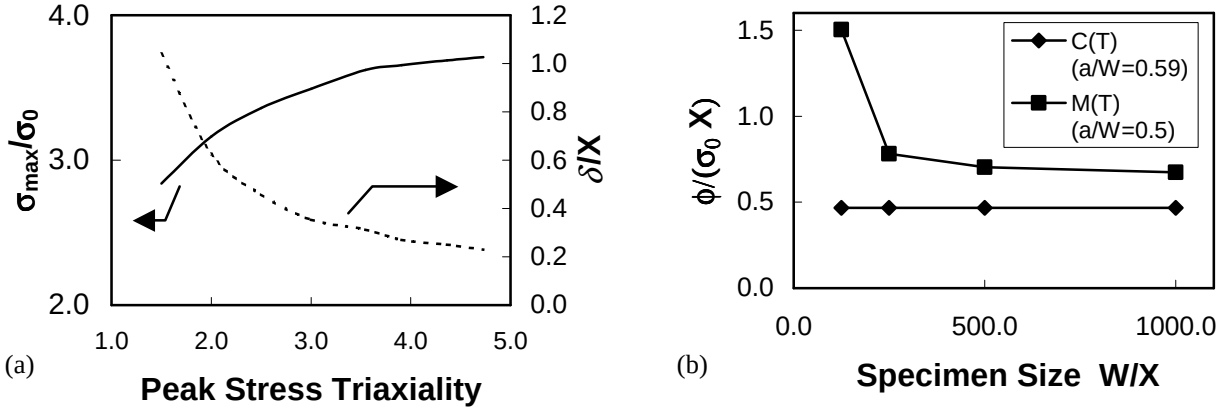

Figure 1: (a) Dependence of the normalized cohesive zone parameters on the peak value of stress triaxiality as obtained by unit cell computations of void growth, (b) Prediction of the normalized cohesive energy (Δa=20 X) in dependence of the normalized size for C(T) and M(T) specimens.

RATE DEPENDENT CZM FOR ADHESIVES

In studies of the integrity of adhesive bonds, CZM can conveniently be used to describe the combined deformation-failure behavior of the adhesive. To accurately describe polymeric adhesives it is necessary to account for the rate dependent fracture behavior exhibited by these materials.

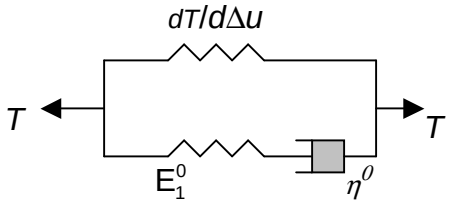

Figure 2: A rate-dependent CZM based on a standard linear solid model.

To capture such effects, a rate dependent CZM based on the standard linear solid was developed [8]. In this new CZM model (Figure 2), a rate-independent CZM, a secondary stiffness parameter, E_1^0 (force per displacement per area), and a viscosity, η^0, (force per velocity per area) characterize the adhesive. To calibrate these parameters, fracture tests on DCB specimen bonded by a HDPE adhesives were performed for a wide range of applied loading speeds, V. A total of three tests were necessary to determine all CZM parameters. Figure 3a compares measured and predicted peak loads for DCB fracture tests. Subsequently, the new dependent CZM model was applied to investigate DCB tests with stepwise constant applied loading speeds. Figure 3b depicts the result of one of these tests. A good agreement between the experimental data and the numerical predictions was obtained. Especially, the short-term stress relaxation behavior was well captured.

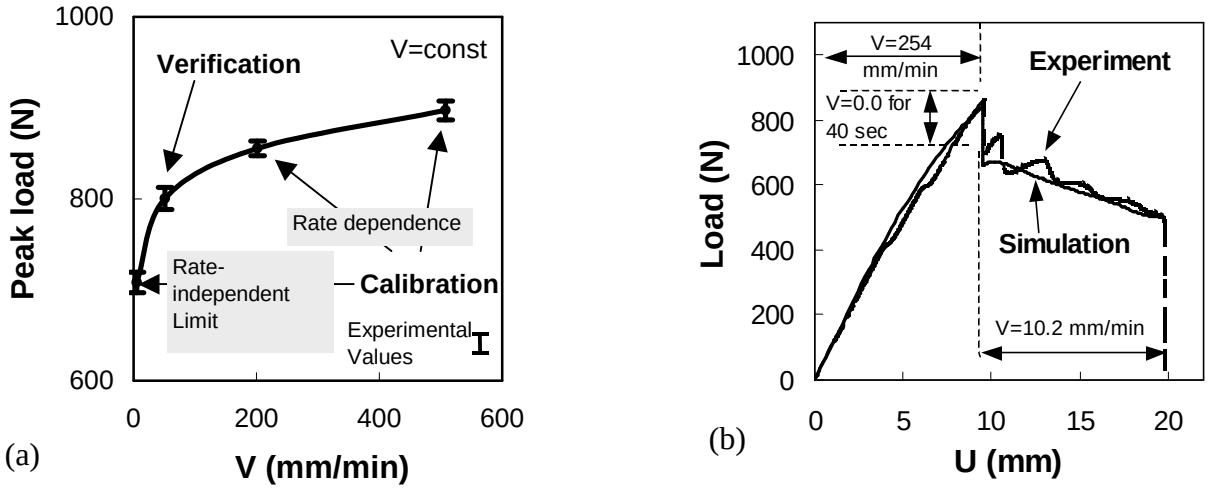

Figure 3: (a) Calibration of rate dependent CZM to peak loads of DCB tests at various crosshead speeds; (b) DCB test with three levels of crosshead speeds, simulation and experimental results.

CZM FOR FATIGUE CRACK GROWTH

For investigations of fatigue crack growth (FCG) the use of the Paris equation, $da/dN=A\ (\Delta G)^m$, to represent FCG data is a widely accepted approach [9]. However, this equation is empirical and provides a data correlation scheme rather than a predictive capability. This fact becomes especially important for interface FCG since experimentally determined ΔG-da/dN curves in this case depend on factors not of concern in homogeneous materials. Motivated by this need, it is attractive to extend CZMs to account for irreversible deformation, incorporate loading-unloading conditions and effects of accumulation of damage [10].

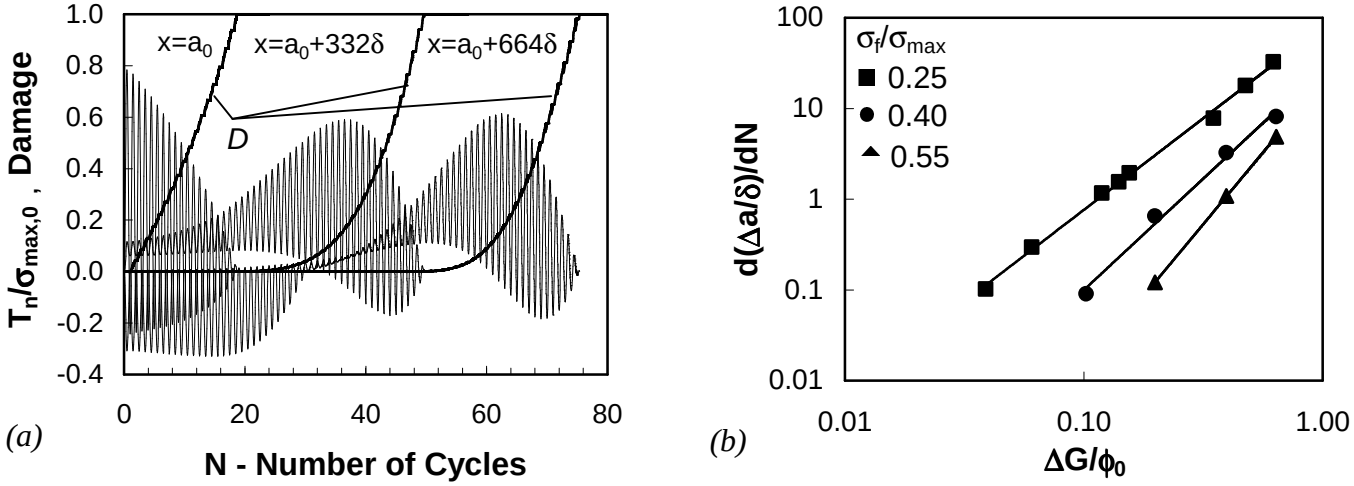

Figure 4: (a) The effective traction separation behavior accounting for unloading and damage dependent cohesive strength; (b) Numerically predicted fatigue crack growth rates for three values of the fatigue strength parameter, σ_f; cyclic loading with $R=0$.

For cyclic loading, the evolution of the cohesive strength of the FPZ is accounted for by the use of a damage variable, D. The current cohesive strength is given as $\sigma_{max} = \sigma_{max,0}\,(1\text{-}D)$, where $\sigma_{max,0}$ is the initial cohesive strength. For the case of mode I loading, the evolution of the damage variable, D, depends on the amount of the total accumulated displacement jump, Δ_{tot}, and on a fatigue limit stress, σ_f:

$$\dot{D} = \frac{\left|\dot{\Delta}_n\right|}{4\delta}\left[\frac{T_n}{\sigma_{\max}} - C\right] H\left(\Delta_{tot} - \delta\right) \;\text{ with }\; \sigma_f = C \cdot \sigma_{\max}\;,\; C < 1.0\;\; \Delta_{tot} = \int_t \left|\dot{\Delta}\right| dt \quad if \quad T_n > 0.0$$
$$\dot{D} = 0 \quad if \quad T_n \le 0 \tag{2}$$

A parametric study of fatigue crack growth in an adhesively bonded DCB specimen was performed using a formulation accounting for Eqn. 2. Figure 4a depicts the evolution of both the crack surface traction and the damage variable as a function of the number of applied load cycles for three locations in the FPZ. Figure 4b summarizes the numerically obtained crack growth rates in dependence on the normalized applied $\Delta G/\phi_0$ for three levels of fatigue strength, σ_f. The numerically obtained $d(\Delta a/\delta)/dN$ values can be described by the use of the Paris relation. For the present choices of the fatigue limit (C=0.25, 0.40, 0.55) the predicted values of the Paris exponent, m, are 2.0, 2.5 and 3.1, respectively.

HEAT TRANSFER CZM

Past applications of the CZM were directed towards the analysis of mechanical loading only. In many situations, however, fracture is coupled to and influenced by other physical processes. As an example of interest, consider the thermal gradient loading of a composite with crack bridging fibers [11]; see Fig. 5 for a schematic drawing.

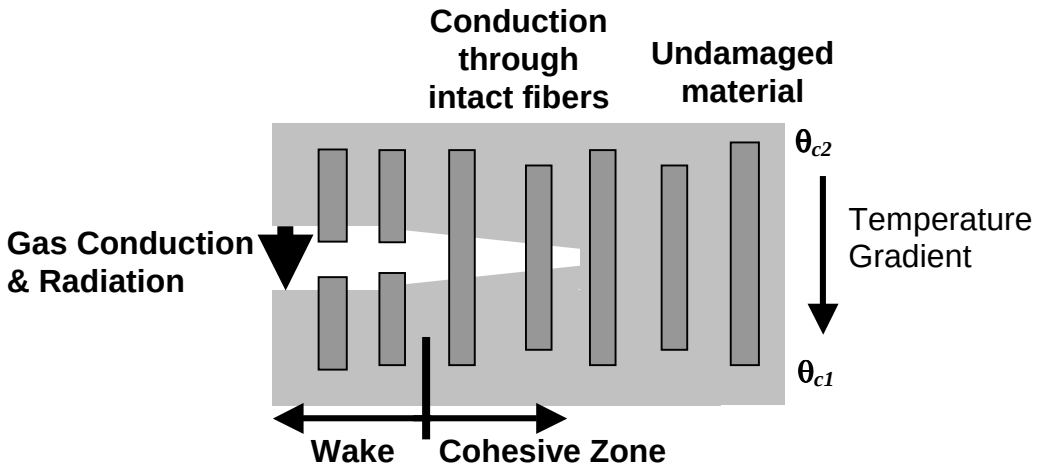

Figure 5: Thermo-mechanical processes during failure of a composite with bridging fibers.

A computational framework is required that allows for physically realistic fracture simulation for this thermo-mechanically coupled loading situations under the simultaneous consideration of crack growth and heat flux across the crack and the fracture process zone.

For a solution of this problem the system must fulfill thermodynamic equilibrium in addition to the mechanical equilibrium equation, Eqn. 1. In variational form and using Fourier's law, this can be expressed by:

$$\int_V \rho c_p \ (\partial_t \delta\theta) \ \delta\theta \ dV - \int_{S_{int}} h_{CZ} \Delta\theta \ \delta\Delta\theta \ dS + \int_V \frac{\partial \delta\theta}{\partial \mathbf{x}} \cdot \mathbf{k} \cdot \frac{\partial \delta\theta}{\partial \mathbf{x}} dV = \int_V \delta\theta \ r \ dV + \int_{S_{ext}} \delta\theta \ q \ dS \qquad (3)$$

The volume and external surface contribution (on V and S_{ext}) are described by the temperature field, θ, the material density, ρ, the heat capacity, c_p, the conductivity matrix, $\mathbf{k}$, the heat flux per unit area of the body flowing into the body, q, and the heat supplied externally into the body per unit volume, r. The cohesive zone contributions, representing the crack wake and the process zone in front of the crack tip, are again described by the integral described by the integral over the internal surface, S_{int}. Two quantities describe the conductance across the cohesive zone: the cohesive zone conductance, h_{CZ}, and the temperature jump across the cohesive surface, $\Delta\theta=\theta_{C1}-\theta_{C2}$, with θ_{C1} and θ_{C2} the temperatures of the opposite crack surfaces. The coupling between stress and heat transfer part of the fracture problem as described by Eqns. (1) and (3), occurs via the cohesive zone conductance, h_{CZ}. This quantity, in general, is dependent not only on temperature but also on both the traction as well as the displacement jump, $\boldsymbol{\Delta}$, across the cohesive surface:

$$h_{CZ} = h_{CZ}(\theta, \mathbf{T}_{CZ}, \boldsymbol{\Delta}) \qquad (4)$$

The conductance law, Eqn. 4, describes the energy transport across cracks or delaminations. In the process zone h_{CZ} depends on the level of material deterioration and changes from that given by the solid to the crack wake conductance. In the crack wake, h_{CZ} is dominated by gas conductivity or radiation as well as possibly by the contact conductance of the two crack surfaces. Fully coupled thermo-mechanical analyses with repeated non-uniform and non-steady heat flow as well as secondary mechanical loads are possible with this approach. It describes the creation of new free surface and thus accounts for the changing heat transfer boundary conditions due to crack growth.

ACKNOWLEDGEMENT

Funding for the work was provided by Sandia National Laboratories through the NSF Life Cycle Engineering program as well as by Purdue University. The author would like to thank W. Brocks, GKSS Research Center Geesthacht, Germany, as well as C. Xu and K. Ramani, Purdue University, for their collaboration.

REFERENCES

1. Hutchinson, J.W. and Evans, A.G. (2000) *Acta Mat.* 48, 125.
2. Barenblatt, G.I. (1962) *Adv. Appl. Mech.* 7, 55.
3. Dugdale, D.S. (1960) *J. Mech. Phys Solids* 8, 100.
4. Needleman, A. (1987) *J. Appl. Mech.* 54, 525.
5. Needleman, A. (1992) *Ultramicroscopy* 40,203.
6. Gurson, A.L. (1977) *ASME J. Engng Mater. Tech*. 99, 2.
7. Siegmund, T. and Brocks, W. (2000) *Eng. Fract. Mech.* 67, 139.
8. Xu, C., Siegmund, T. and Ramani, K., (2001) *Int. J. Adhesives Adhesion*, submitted.
9. Paris, P.C., Gomez, M.P. and Anderson, W.P. (1961) *The Trend in Engng* 13, 9.
10. Roe, K.L. and Siegmund, T. (2001). In *1st MIT Conference on Computational Fluids and Solids Mechanics*, in print, Bathe, K.J. (Ed). Elsevier.
11. Hutchinson, J.W. and Lu, T.J. (1995) *ASME J. Eng. Mater.* 117, 386.

Aircraft Structural Integrity: The Impact of Corrosion

P.K. Sharp[1], T. Mills[2] and G. Clark[1]

[1] Defence Science and Technology Organisation, PO Box 4331,
Melbourne, 3001, Australia
[2] Aerostructures Technologies PTY LTD

ABSTRACT
This paper discusses the development of methods, which will allow aircraft structural integrity to be maintained under conditions where an airframe is deteriorating through corrosion. The program discussed is exploring methods of assessing corrosion damage in terms which are compatible with existing life management approaches. In practical terms this involves relating the corrosion damage to an equivalent cracked condition, to determine the point at which corrosion would reduce the remaining fatigue life of the aircraft to an unacceptable level. While a number of types of corrosion are being examined this paper discusses only pitting and exfoliation corrosion.

KEYWORDS
Corrosion, structural integrity, aircraft, pitting, exfoliation

INTRODUCTION
In 1997, DSTO established a research program examining the effects of corrosion on aircraft structural integrity based on RAAF fleet observations detailed in [1] and worldwide research detailed in [2]. This research aims to provide a basis for introducing corrosion into the approaches used to manage aircraft structural integrity in the Australian Defence Force (ADF). This will allow the ADF to minimise both the cost and risk of owning and operating aircraft in which corrosion might become a threat to safety or fleet viability.

PITTING CORROSION RESEARCH
Both the F/A-18 and F-111 in RAAF service have had problems with pitting in structural components initiating fatigue failure [3,4]. However, in a number of cases pitting has also been observed that has not initiated fatigue cracks. The present airworthiness requirements call for the immediate removal of the pitting corrosion, in some cases tripling maintenance times or requiring component replacement. At the same time research at DSTO has shown that the use of certain corrosion protection compounds (CPC's), can greatly retard pitting corrosion [5].

The significant question in terms of improved fleet management is "can pitting corrosion be treated and left in place to a more suitable maintenance opportunity". To answer this question by equating a pit to a crack whose size gives it the same fatigue life, a number of matters need to be addressed; 1) what are the shape and dimension "metrics" of the corrosion pits, 2) what is the spatial distribution of the pits, 3) which critical pit "metric" can be correlated to fatigue life, and 4) how can this information be used in aircraft lifing models. Questions 1 and 2 can be determined from fractography and measurement of large numbers of pits. Questions 3 and 4 are more difficult. DSTO has adopted [6] an approach identified in early research conducted by the USAF on machining marks and their effect on fatigue initiation, which identified the possible use of an Equivalent Initial Flaw Size (EIFS) parameter. The EIFS approach, described in DSTO as

Equivalent Precrack Size (EPS), relies on identifying the crack size which gives the same fatigue life as the corroded specimen. It is important to note two things; 1) that the fatigue life of the cracked configuration is generally determined using a fatigue life prediction model and 2) that the EPS is not real and may bear no relationship to any physical dimension.

The F/A-18 has a number of structural components manufactured from thick (>100mm) rolled 7050-T7451 plate. This plate has a tendency to form very deep corrosion pits due to its microstructure [7]. To examine what effect this sort of pitting would have on a component's structural integrity an extensive test program was initiated. The specimens were flat dogbones, 30mm wide and 10mm thick with a 6mm-diameter hole in the middle to provide a stress concentration [7]. The specimens were all tested in a chamber to keep relative humidity below 20%. The corroded specimens had been subjected to 3.5%NaCl for 24hours [7]. The fatigue test results are shown in Figure 1.

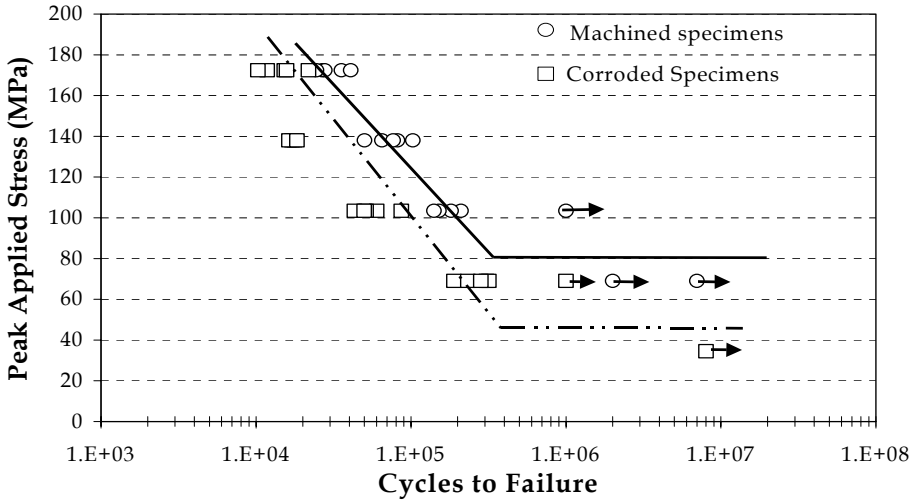

Figure 1: Comparison of machined specimen fatigue life with corroded specimen fatigue life.

Figure 1 clearly shows that the corrosion pits have two effects on fatigue: 1) a 50% reduction in the fatigue strength limit and 2) a general reduction in fatigue life which varies with stress. These results are very similar to results obtained by Pao [8] on the same material, but using a different specimen configuration (although with the same k_t) and a different corrosion time (>300hrs). Fractographic examination revealed large corrosion pits.

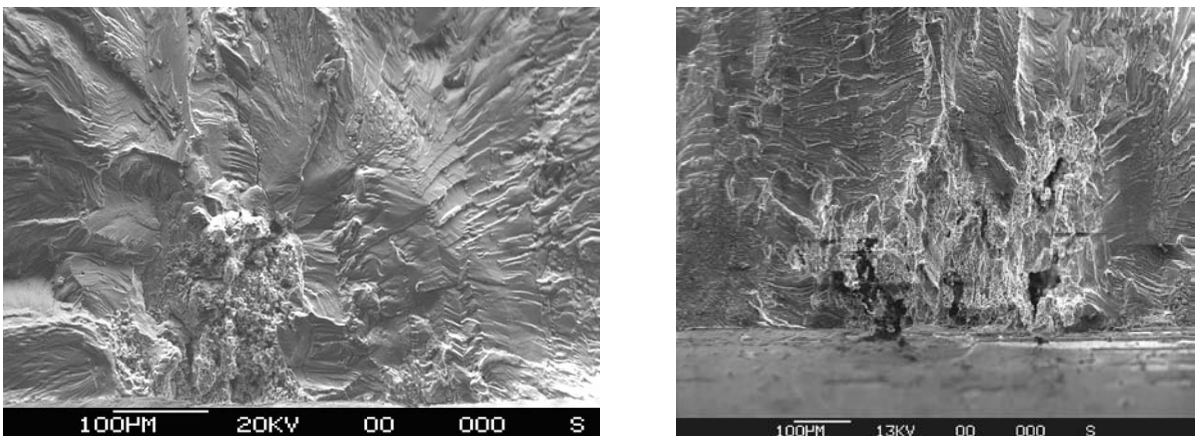

Figure 2: Typical 7050-T7451 corrosion pits on a coupon bore surface – 24hrs at 3.5%NaCl. In both cases the corrosion pits initiated a fatigue crack.

The corrosion pits "metrics" were measured from all pits that initiated a fatigue crack on the fracture surface. Also noted were the pit or pits that initiated the major crack. This provided a distribution of pit depths that initiated fatigue cracks, Figure 3. The distinction between pits and inclusions is blurred at depths below 100μm , and sizes below this are in fact usually inclusions and porosity; pit depths above 380μm are generally pit clusters where it is not possible to distinguish individual pits. Pit depth is only one of the "metrics" collected along with pit aspect ratio, pit tip radius, pit area and pit opening width.

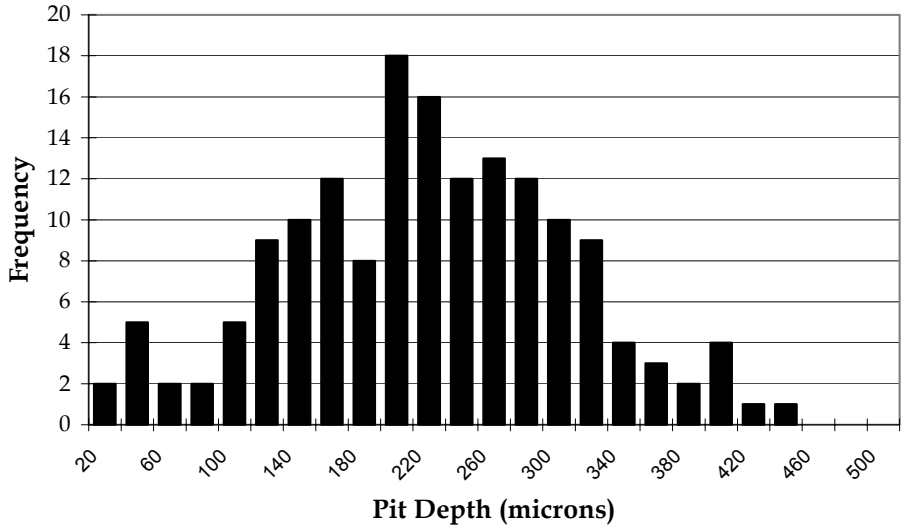

Figure 3: Distribution of depths for the flaws that initiated fatigue cracks. Below 100μm, these are generally inclusions and porosity, above 380μm, generally pit clusters.

The EPS modelling used AFGROW, a fatigue crack growth program developed by the USAF [9]. Several specimen geometries were examined; 1) a double corner crack, 2) a double surface crack and 3) a double through crack. A comparison of the pit depth vs EPS depth is shown in Figure 4. The best correlation between pit depth and EPS was with the double corner crack geometry. As can be seen there is a substantial amount of scatter in the relationship between pit depth and EPS, although the scatter is less than with pit width vs EPS and pit area vs EPS.

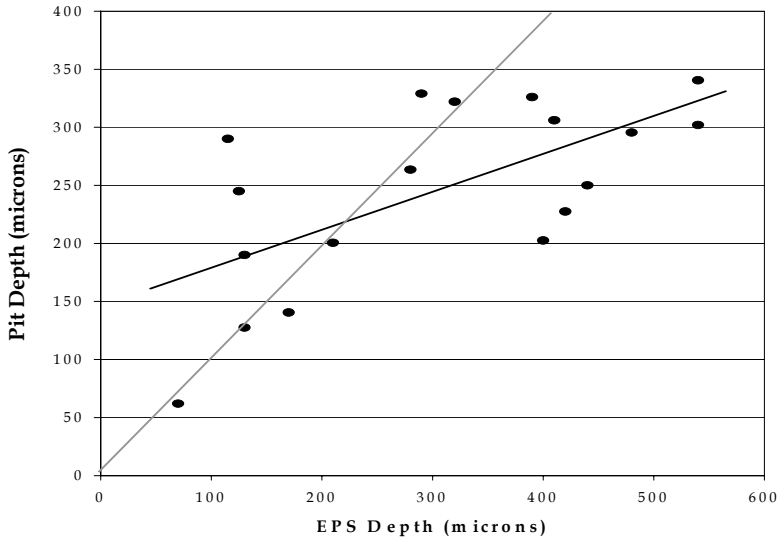

Figure 4: A comparison between pit depth and EPS depth. The dark line is the line of best fit and the light grey line is pit depth = EPS depth.

Research into the effect of pitting on structural integrity is also examining high strength steel, D6ac, which is used in the structural components of the F-111. While in its early stages the EPS approach appears to be substantially better, with higher correlations due to the reproducible and uniform nature of pitting in D6ac – all pits are close to hemispherical, Figure 5.

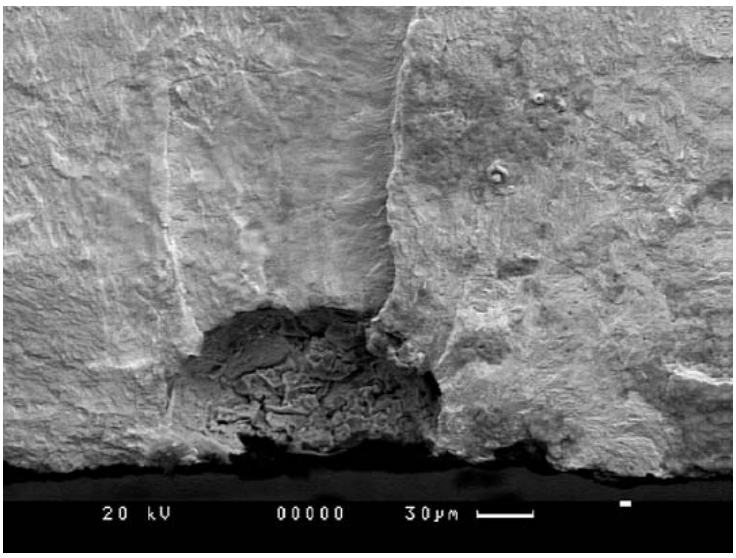

Figure 5: Corrosion pit and fatigue fracture generated in high strength steel fatigue specimen.

EXFOLIATION CORROSION RESEARCH

Flat dogbone test specimens, [10], were machined from 6mm thick 2024-T351 and 7075-T651 plates. In the centre of the 20mm wide gauge section, a circular region was exfoliated with EXCO solution (ASTM Standard G-34). Exposure times in EXCO ranged from 2-300 hours. Damage states ranged from mild pitting at short exposure times to severe flaking up to 400-550 μm deep at times approaching 300 hours. The specimens were fatigue tested at 240 MPa, R=+0.1 until fracture occurred and were tested in air at relative humidities of either <20%RH, f = 10 Hz or >90%RH, f = 2 Hz.

For both materials, there was a very rapid initial decrease in fatigue life with small exposure times (<10 hours) and then the gradual levelling out with longer exfoliation times. The results indicate that the major effect of the exfoliation corrosion on fatigue life is to cause a dramatic reduction in life with small corrosion depths, suggesting that most of the fatigue effect is associated with the introduction of small pits, rather than more general stress concentration associated with the bulk of the exfoliation attack.

Examination of the exfoliated region showed grain lift-off and separation typical of exfoliation. At the short exposure times, multiple distinct pit-like nucleation sites were present, but as the exposure time increased, these sites joined together to become one large exfoliated region. New pit-like discontinuities were visible at the base of the exfoliation. This observation forms the basis of an exfoliation/fatigue model discussed below.

Figure 6 is an example of corrosion damage in 7075-T651 aluminium after 48 hours exposure in EXCO. In most cases with the 7075, the pits that caused fatigue failure were approximately 60-100μm deep. Around the base of these pits, areas of intergranular attack could be seen, but these regions were quite small, 10 to 30μm in depth.

A number of models have been proposed to describe exfoliation corrosion. Russo et al. [10] undertook 2D modelling based on an Equivalent Precrack Size (EPS) approach. The approach was to predict the growth life of a crack-like defect that represented some geometrical feature of the gross or macroscopic exfoliation corrosion.

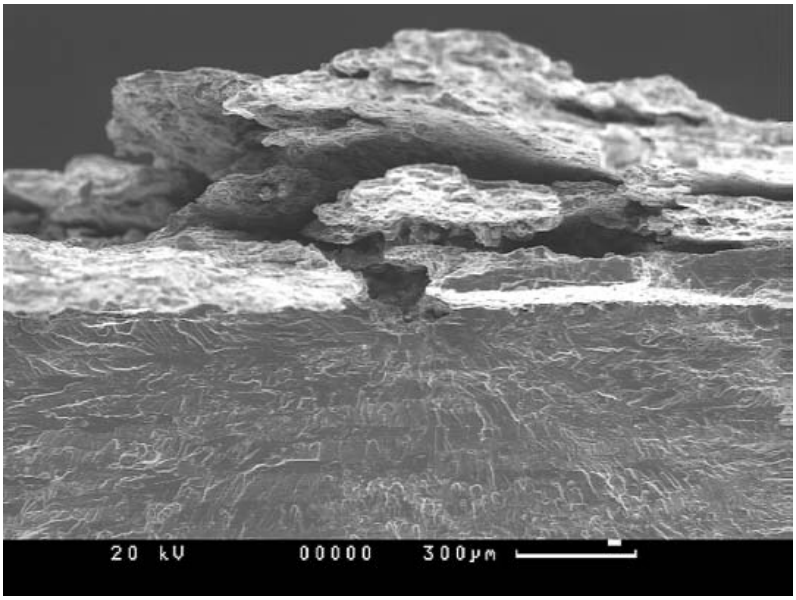

Figure 6: Fatigue crack origin under exfoliated grains, 7075-T651.

If this growth life were to be similar to that of the real corroded specimens, then the crack-like defect could be regarded as the EPS and could be substituted for the corrosion in further analyses. Three geometrical representations were considered:

1) a semi-elliptical crack with the same dimensions as a 2D slice through the exfoliation,
2) a semi-circular crack with a depth equal to that of the exfoliation, and
3) a geometric stress concentration, as though the exfoliation was blended out with a typical inclusion-sized starter crack (a=3µm and c=9µm) at the base.

The exfoliation/fatigue model was further refined based on the observation that the deepening exfoliation corrosion geometry has at its base pit-like intrusions from which intergranular cracks grow (model 4). The combination of a pit and crack represents a *process zone* that progresses through the material.

The proposed model is shown in Figure 7, where the process zone forms under environmental influences in the first few hours of exposure to EXCO. The authors postulate that for modelling purposes, the size of the zone stabilises and is followed by formation of the exfoliation stress concentrator.

To model the impact of the process zone on fatigue, notch (pit) and crack (intergranular attack) combinations derived from the experimental observations of different corrosion stages were input to FASTRAN II [11]. Figure 8 shows the three models used for 7075-T651 prediction, a range of initial crack sizes was explored based on experimental observations. In this case, model (4a) varies notch (pit) size with a 10µm crack, model (4b) varies pit size with a 20µm crack, and model (4c) varies pit size with a 30µm crack. All sub-models include the small effect of the overall material removal, which further reduces life for the more extensively corroded cases, and all give slightly unconservative results, close to the experimental data.

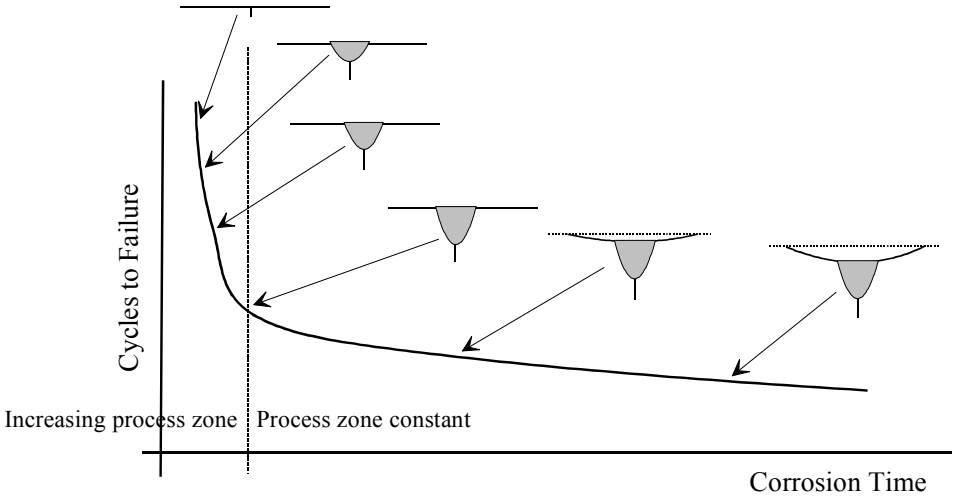

Figure 7: Concept of how process zone interacts with exfoliation over increasing corrosion time to affect fatigue life.

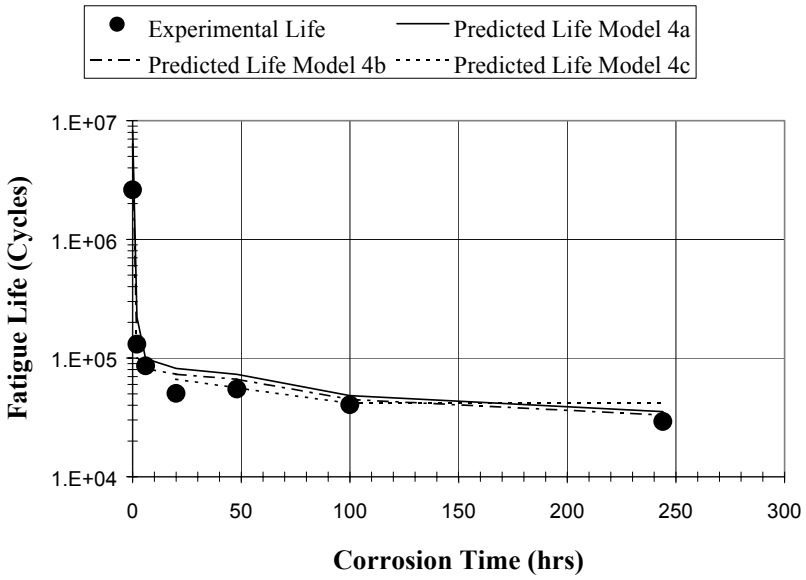

Figure 8: **Remaining Cycles to Failure vs. Corrosion Time for 7075-T651 aluminium along with the three variants in model 4 discussed in the paper.**

CONCLUSION

DSTO has developed models for the fatigue impact both pitting and exfoliation corrosion. To date the models have been tested with success on constant amplitude fatigue specimens. The next stage is to determine whether the models apply equally well for spectrum loading on laboratory specimens and whether the same approach can be extended to a wider range of materials, or aircraft components. In a number of special cases, real aircraft structure has been or is being tested containing either laboratory produced corrosion or real time environment corrosion.

REFERENCES

1. Clark G. and Hinton B., (1992) *Survey of ADF Aviation Materials-Related Problems*, General Document 35, DSTO Aeronautical Research Laboratory.
2. Cole G., Clark G. and Sharp K., (1997) *The Implications Of Corrosion With Respect To Aircraft Structural Integrity*, DSTO Research Report, DSTO-RR-0102.
3. Sharp P.K., Barter S.A., Athiniotis N., Bishop B.C. and Clark G.,(1995), *Investigation of F/A-18 Trailing Edge Flap Hinge-Lug Incident*, DSTO-TR-0124.
4. Cox, A.F., (1988) *Fatigue Cracking in the Upper Plate of Wing Pivot Fittings in F-111 Aircraft,* AR-005-567, DSTO Aeronautical Research Laboratory.
5. Chester R.J., Clark. G., Hinton B.R.W. and Baker A.A., (1993) '*Research into Materials Aspects of Aircraft Maintenance and life Extension-Part 1'*, Aircraft Engineering, Vol. 65, No. 1, p.2.
6. Manning, S. D., Pendley, B. J., Garver, W. R., Speaker, S. M., Henslee, S. P., Smith, V. D., Norris, J. W. and Yee, B. G. W., (1979) *Durability Methods Development Volume 1 Phase 1 Summary*, AF Wright Aeronautical Laboratories Technical Report AFFDL-TR-79-3118, Vol 1.
7. Sharp P.K. (2001), *EIFS Modeling of 7050 Aluminium Alloy Corrosion Pitting and its Implications for Aircraft Structural Integrity*, DSTO Research Report, In press to be published May.
8. Pao P.S., Gill S.J and Feng J.C.R, (1999), *Fatigue Crack Initiation from Corrosion Pits in Aluminium Alloys*, 3rd Joint FAA/DoD/NASA Conference on Aging Aircraft, Alburquque Sept 20th-24th.
9. Harter J., (1999), *AFGROW – USAF Fatigue Crack Growth Program*, Wright-Patterson AFB, Dayton, Ohio. Can be down loaded from http:\\fibec.flight.wpafb.af.mil/fibec/afgrow.html.
10. Russo, S., Sharp, P.K., Mills, T.B. and G. Clark(2000), *The Effects of Exfoliation Corrosion on the Fatigue Life of Two High-Strength Aluminium Alloys*., Fourth DoD/FAA/NASA Conference on Aging Aircraft, St Louis.
11. Newman J.C. Jr., (1992), *FASTRAN II - A Fatigue Crack Growth Structural Analysis Program*, NASA Tech Memo 104159.

ALTERNATIVE METHODS FOR DERIVING AND FITTING J-R CURVES: HOW THEY AFFECT STRUCTURAL INTEGRITY ASSESSMENT

J.R. Tarpani[1], A.A. Colafemea[1], W.W. Bose Filho[1] and D. Spinelli[1]

[1]Materials, Aeronautical and Automotive Engineering Department,
Engineering School of São Carlos, 13566-590, São Carlos-SP, Brazil

ABSTRACT

In this paper, results from Reese & Schwalbe's linear normalization (LN) methodology for deriving J-R curves are compared, related to J-Δ*a* (J-integral-ductile crack growth) data, to those obtained from traditional unloading elastic compliance (UEC) technique. Research results regarding to a nuclear grade steel exhibiting a wide range of elastic-plastic fracture resistance, agree quite well for both techniques until a certain level of toughness of the material. Below this critical level, linear normalization produces too conservative and inconsistent results for sub-sized compact testpieces. Power-law, linear and logarithmic fits were applied to the J-Δ*a* data points within well-known limits of validity of deformation-J (J_D). The results were assessed in terms of two typical J-integral criteria of the nuclear industry, namely, the crack initiation J (J_i) and the so-called Paris & Johnson's J_{50} for ductile instability of cracks. It was concluded that the logarithmic fit produces conservative values for both J_i and J_{50} criteria, when compared to power-law, whereas the linear fitting method provides the most non-conservative failure predictions.

KEYWORDS

Fitting and extrapolation methods, J-R curve techniques, Structural integrity assessment

INTRODUCTION

J-R Curves

The J-integral is the most important parameter for characterizing the elastic-plastic fracture resistance of structural materials and efforts have been continuously conducted to develop simplified methodologies for determining the so-called J-R curves. The most recent and promising trend in this field is the use of single-specimen normalization techniques, which simply demand the determination of the load versus displacement record and both initial and final crack lengths. Reese & Schwalbe [1] developed a method, named linear normalization (referred LN hereafter), which is based on the original Landes' work (LMN function [2]). LN is grounded upon the principle of load separation [3,4], which has been proved for all specimen geometry [5,6]. This principle allows the load, P, to be written as a function of the crack length, *a*, and the corresponding applied plastic displacement, v_{pl}, by two separate multiplicative functions:

$$P = G(a/W).H(v_{pl}/W) \quad (1)$$

W is the specimen width, and G(a/W) is the geometry calibration function, which is dependent on the specimen configuration and can be determined from the J calibration [5,6].

$$G(a/W) = B.W.(b/W)^{\eta_{pl}} \quad (2)$$

B is the specimen thickness, b the uncracked ligament length, $b = W - a$, and η_{pl} the geometry correction (plastic) factor, which is assumed to depend weakly on material properties. For compact specimens it is generally assumed the value of 2.13 [2,5,6].

Reese & Schwalbe focused their attention on the correlation between the change or gradient in normalized load, ΔP_N, and the respective crack extension, Δa. The gradient in the normalized load owing to a slight crack growth from the initial (pre)crack length (a_0) is:

$$\Delta P_{N(i)} = P_N(a_i) - P_N(a_0) = P/G(a_i/W) - P/G(a_0/W) \quad (3)$$

A well-defined linear dependency of $\Delta P_{N(i)}$ on $\Delta a_i = a_i - a_0 = b_0 - b_i$ has been shown for large amounts of crack growth in elastic-plastic fracture toughness testing (J-R curve) [1]. This linear relationship allows the complete J-R curve of these materials to be obtained by means of a special graphical procedure.

Fitting Methods

Power-law is the most widely employed method for both J-R curve fit and extrapolation [7,8], and it is even mandatory in current high demanding components codes [9]. J-R data extrapolation for higher levels of crack growth is used to compensate insufficiently extensive data obtained in laboratory testing, when the failure criteria, e.g., in the ductile instability assessment of a cracked component, is beyond the limits of validity of deformation-J (J_D), as defined on J-Δa space [10]. By virtue of the downwards concavity typically exhibited by J-R curves, which effect is further intensified by the J_D-saturation phenomena [11], extrapolation through power-law may be a quite non-conservative approach and the higher the degree of non-conservatism, the shorter is the crack extension level attained by fracture toughness testing [8]. In a previous paper [12], the authors have claimed that the logarithmic fit may be a worthwhile alternative method to the power-law, as long as it produces more conservative results with regard to predictions of ductile instability events for cracked components, specially when data extrapolation is necessary. Other methods used in some extent to fit J-R curves include polynomial and linear fits.

In this work, the performance of the methods for both J-Δa data determination and fitting are evaluated for a nuclear grade steel exhibiting microstructures with a wide range of elastic-plastic fracture resistance. None of the microstructures tested exhibited cleavage (catastrophic fracture) and in all cases unloading elastic compliance (UEC) provided confident results for dealing of close comparison between both techniques.

MATERIALS AND TESTPIECES

Seven miniaturized testpieces (0.4TC[S]) were machined from a thick forged plate of a nuclear grade steel in the as-received (AR) and several thermally embrittled (TE) conditions, the latter achieved by special heat treatments. They were fatigue precracked to an a_0/W ratio of 0.55, side grooved (SG) to a 20 or 33% reduction of their gross-thickness (B=10 mm) and thereafter tested at 300°C. The mechanical properties of the materials and the testpieces' specifications are listed in Table 1. Notice that the reduction in area of the tensile specimens precisely ranks the elastic-plastic crack resistance of the six tested microstructures.

EXPERIMENTAL AND ANALYTICAL PROCEDURES

Unloading Elastic Compliance (UEC)

J-R curve testing was conducted by clip-gage-controlling elastic unloadings, under a strain rate of 0.3 mm/min. J-Δa data points were obtained according to ASTM E1820 standard [10], i.e. corrected for crack growth. Initial and final crack length predictions by elastic compliance measurements loosely satisfied minimum accuracy requirements established by ASTM standard.

Linear Normalization (LN)

Linear-normalized J-R curves were derived by making use of the load versus load-line displacement diagrams resulting from compliance technique, and following the Reese & Schwalbe's analytical procedure, which is fully described elsewhere [1]. Initial and final crack lengths, a_0 and a_f, respectively, were obtained from the broken specimens, by means of observation in a stereo-microscopy. Figure 1 displays the linear dependence of ΔP_N on Δa, as described in Eqn. 3, for all steel structures and specimens tested in this study.

J-R Fitting Methods

Power-law, logarithmic and linear fits were applied to J-Δa data points within limits of validity of deformation-J (J_D), as delineated by exclusion off-set lines, at respectively 0.15 and 1.5 mm of crack growth. Given the reduced testpieces' size, only the specimen correspondent to the lowest fracture toughness level fulfilled both J maximum capacity and minimum thickness requirements established in Ref. 10. Once the J-R curves were fitted, the J value for crack initiation, J_i [10], and the so-called Paris & Johnson's J_{50} [13] for healthy conservative prediction of ductile instability of cracked components, were determined.

TABLE 1
MATERIALS AND TESTPIECES CHARACTERIZATION

Microstructural Condition	Testpiece Designation	SG (%)	Yield Strength (MPa)	Ultimate Strength (MPa)	Elongation (%)	Reduction in Area (%)
A (AR)	JRT7	33	362	548	11	77
A (AR)	JRT8	20	362	548	11	77
B (TE)	JRT27	20	361	621	17	71
C (TE)	JRT32	20	344	611	16	63
D (TE)	JRT36	33	370	620	12	54
E (TE)	JRT41	33	376	626	12	49
L (TE)	JRT86	33	701	810	08	44

$L_0 = 4\ D_0 = 40$ mm

RESULTS AND DISCUSSION

Incremental Crack Length

In this analysis, the number of load (P)-displacement (δ) data points, taken evenly spaced regarding to δ, was kept fixed and the incremental crack length extension ($da = d\Delta a$) was taken at the values of, respectively, 0.1, 0.01 and 0.001 mm on the fully computerized iterative data processing. Percentage differences among the three used approaches were then calculated. Figure 2 points out that crack increments smaller than 0.01 mm do not promote significant changes on J values. Higher errors invariably occurring post-maximum load capacity of the specimen, are certainly due to the effects of both spread plasticity and relatively large amounts of crack growth on data processing. However, even for the least accurate approach ($da = 0.1$ mm) such errors have never exceeded $\pm 0.06\%$, which is a very stringent criterion for purposes of comparing J values.

Number of Load-Load Line Displacement Data

For a fixed crack increment length of 0.01, J-R curves were generated by randomly choosing several different number of P-δ data points along the loading curve of the specimen. Figure 3 shows that, as a general rule, the larger the number of J (i.e., P-δ) data points, the higher is the J value for a constant Δa analysis. This can be explained in terms of the crack growth correction factor in the deformation-J (J_D) concept [3,10]. Thus, the larger the number of chosen P-δ data points, the smaller the average crack growth correction (i.e., reduction) factor and, consequently, smaller is its cumulative effect in lowering the J-R curve.

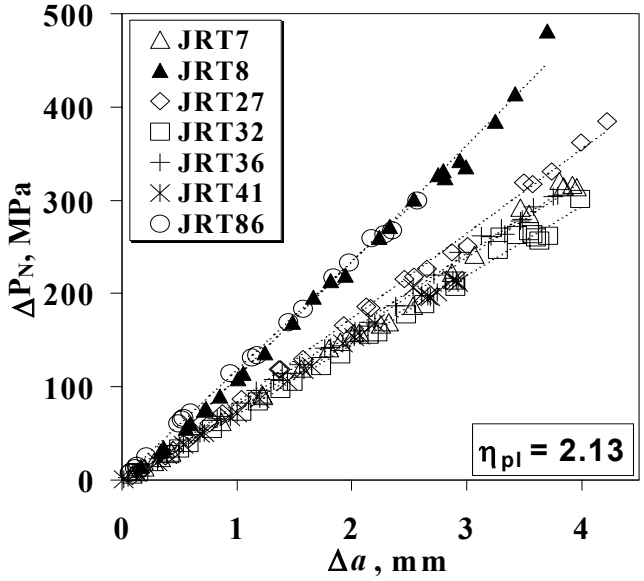

Figure 1: Linear relationship between ΔP_N and Δa, as determined by on-line UEC monitoring.

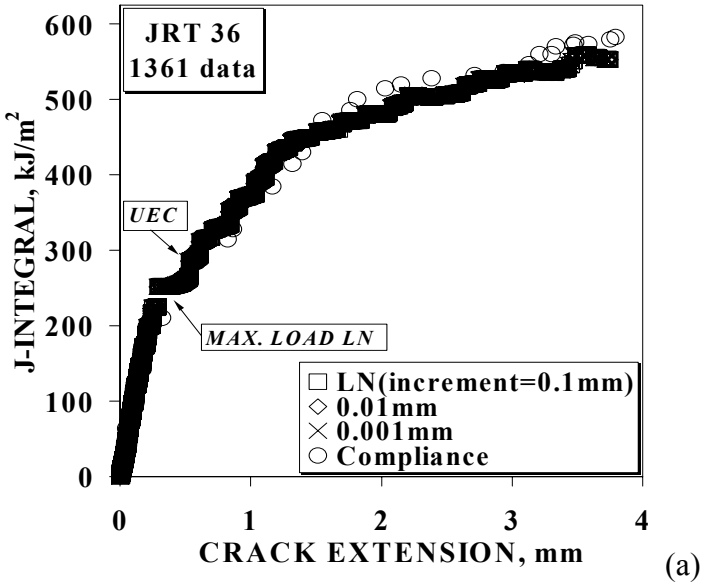

(a)

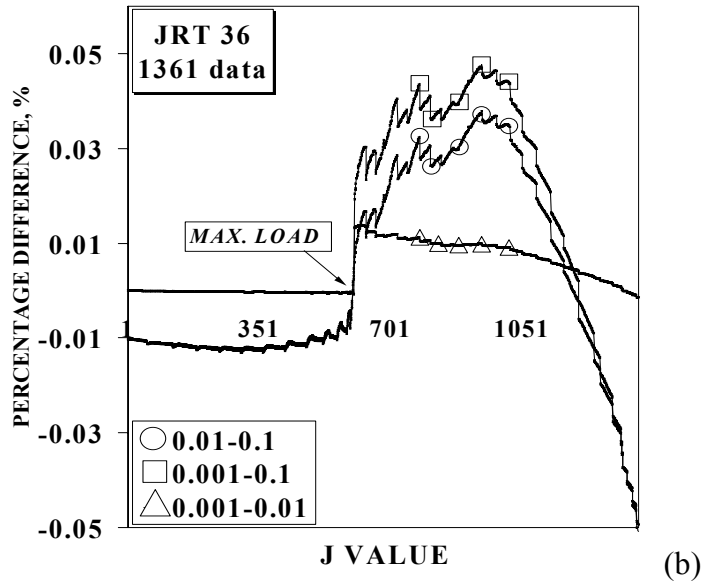

(b)

Figure 2: Incremental crack length affecting LN J-R curve. (a) Testpiece JRT36 with a large number of J data points. (b) Associated errors. Arrows indicate maximum load positions.

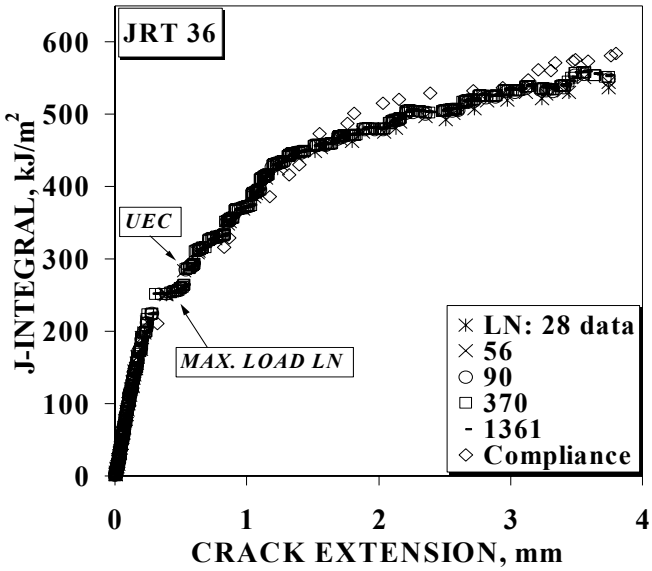

Figure 3: Number of P-δ (i.e., J) data points affecting LN J-R curves for an incremental crack length of 0.01 mm. Elastic compliance J-R curves are displayed as baseline.

The η_{pl} factor as an indicative of the LN worthiness

The applicability of the LN technique in the assessment of different fracture resistance behaviors was confirmed for very most of the microstructures tested. However, as shown in Fig. 4, LN failed in deriving the J-R curve for the least elastic-plastic fracture resistant microstructure. An η_{pl} factor of 2.13 was assumed for the miniaturized specimens herein tested. As a coincidence, or not, it was found out that good results regarding to the LN technique were obtained from testpieces which the best linear correlation between the normalized load gradient (ΔP_N) and the ductile crack extension (Δa) is achieved for $\eta_{pl} \leq 2.13$. Conversely, bad LN results were invariably associate to $\eta_{pl} > 2.13$, for a maximum ΔP_N-Δa linear correlation. This empirical rule could serve as an indicative of the applicability of the LN technique for this class of material.

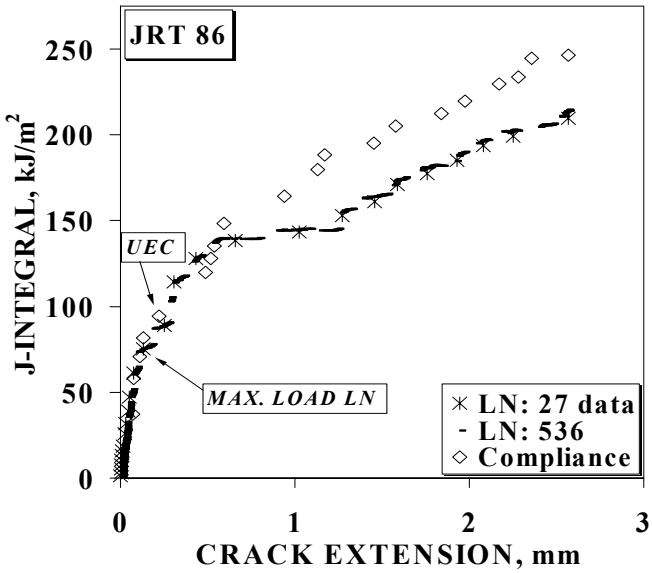

Figure 4: The inability of the LN technique in deriving J-R curve for the least tough microstructure.

J_i and J_{50} Criteria for Structural Integrity Assessment

The results concerning J_i and J_{50} criteria, obtained from both UEC and LN techniques, are furnished in Fig. 5. They are plotted against the Charpy impact energy of standard bend bar specimens precracked in fatigue with the same side-grooving level of the correspondent sub-sized compact J-testpiece. It can be seen that quasi-static fracture toughness results correlate rather well with the absorbed energy under dynamic

conditions. It is worthy of note that the LN methodology produces slight conservative results if compared to those obtained from the UEC technique. It is also observed that the degree of conservatism of both J criteria is strongly dependent on the fracture resistance of the tested microstructure.

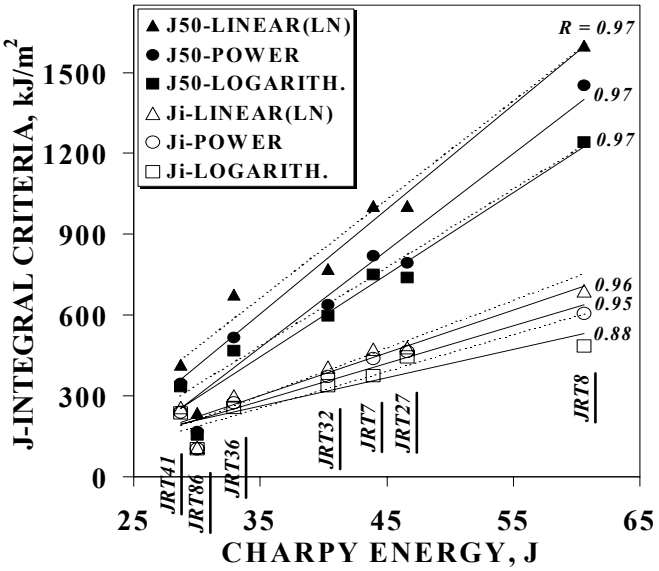

Figure 5: J_i and J_{50} criteria for all tespieces, as predicted by the LN technique. Dashed lines correspond to UEC results under the same testing conditions. *R* is the determination coefficient of the LN straight lines.

CONCLUSIONS

The following conclusions have been drawn during this comparative study:

1 – Computer programming renders to LN a trustworthy and very simple methodology for deriving J-R curves within a broad range of elastic-plastic fracture resistance of low-alloy steels.
2 – A simple empirical rule has been derived to determine the applicability of the LN methodology.
3 – A 0.01 mm crack increment is suitable, in the data processing, to produce precise LN J-R curves.
4 – Even a few load-load line displacement data points allow the generation of sufficiently accurate J-R curves through the linear normalization approach.
5 – There is a trend of LN technique in producing slightly conservative results of J-integral criteria for structural integrity assessment, as compared to elastic compliance method.

Acknowledgements: The authors are thankful for the funding provided by CAPES and FAPESP.

REFERENCES

1. Reese, E.D. and Schwalbe, K.-H. (1993) *Fatigue Fract. Engng Mater. Struct.* 16, 271.
2. Landes, J.D., Zhou, Z., Lee, K. and Herrera, R. (1991) *J. Test. Evaluation* 19, 305.
3. Ernst, H.A., Paris, P.C. and Landes, J.D. (1981). In: *ASTM STP 743*, pp. 476-502.
4. Ernst, H., Paris, P.C., Rossow, M., and Hutchinson, J.W. (1979). In: *ASTM STP 677*, pp. 581-99.
5. Landes, J.D. and Sharobeam, M.H. (1993) *Int. J. Fract.* 59, 213.
6. Landes, J.D. and Sharobeam, M.H. (1991) *Int. J. Fract.* 47, 81.
7. Neale B.K. (1993) *Fatigue Fract. Engng Mater. Struct.* 16, 465.
8. Wilkowiski G.M., Marschall C.W., and Landow M.P. (1990). In: *ASTM STP 1074*, pp. 56-84.
9. Rules for in-service inspection of nuclear power plant components (1996). *ASME Boiler and Pressure Vessel Code*, Section XI, Division I, Appendix NMA-K.
10. Standard test method for measurement of fracture toughness (1997) *ASTM Standards*.
11. Cayard, M.S. and Bradley, W.L. (1989) *Engng Fract. Mech.* 33, 121.
12. Tarpani, J.R. and Spinelli, D. (1997) *Int. J. Press. Vessels Piping* 74, 97.
13. Paris, P.C. and Johnson, R.E. (1983). In: *ASTM STP 803*, v.2, pp. 5-40.

ORAL REFERENCE: ICF10-083OR

AN ANALYTICAL TECHNIQUE FOR STUDYING INTERACTING BRANCHED CRACKS IN A PLATE

Stephanie C. TerMaath[1] and S. Leigh Phoenix[2]

[1] Department of Civil Engineering, Cornell University,
Ithaca, NY 14853 USA
[2] Theoretical and Applied Mechanics, Cornell University,
Ithaca, NY 14853 USA

ABSTRACT

An analytical method for studying interacting branched cracks in an infinite plate is developed. Based on superposition and dislocation theory, this method can be used to determine the full stress and displacement fields in a cracked material. In addition, stress singularities at both crack tips and wedges (created by crack branching) are calculated so that crack growth and initiation can be analyzed at all locations of possible crack propagation. A key concept of the method is the development of dislocation distributions that represent the opening displacements and capture the physical behavior of the cracks. Each distribution is a shaping series representing characteristic crack behaviors; therefore, development of effective distributions is a crucial aspect of this work. Branched cracks of complex shapes under general loading conditions can be evaluated with this method. Results show rapid convergence for few degrees of freedom (as measured by the number of dislocation distribution terms included in a particular analysis).

KEYWORDS

Dislocation distribution, superposition, stress intensity factor, branched crack

INTRODUCTION

Material imperfections, corrosion, and fatigue loading can create conditions that cause cracks to branch or grow in such a way that they have multiple crack tips. Damage zones containing cracks of such complex shapes, specifically many interacting branched cracks, pose a challenging problem when attempting to evaluate these areas for potential crack propagation and possible failure. To address this type of fracture, a two-dimensional analytical technique has been developed to study interacting branched cracks in an infinite plate. Based on superposition and dislocation theory, this method can be used to determine full stress and displacement fields in addition to stress intensity factors at crack tips and branch locations for a cracked plate. Previous researchers have used similar approaches to study these types of cracks [1-6], and an extensive review of this area of research has been performed [6].

OVERVIEW OF THE ANALYTICAL TECHNIQUE

To calculate the stress and displacement fields in an infinite plate containing an array of cracks of complex shape, each crack's opening displacement profile must be determined such that all crack faces are traction-free under the given loading conditions. (An opening displacement profile is the shape of a deformed crack.) Once the opening displacement profiles are known, this solution can also be used to determine the stress intensity factors at the crack tips and branch locations in order to study crack propagation. Superposition is applied at the global and local levels, and a dislocation distribution approach is utilized, to solve for the opening shapes of an existing crack array. Several excellent texts on this subject are available in the literature [7-9].

Superposition

To solve this boundary value problem, superposition is first applied at the global level by modeling the cracked plate as two separate problems (the trivial problem and the auxiliary problem) where the sum of their solutions equals the solution to the original problem. The trivial problem consists of the given plate under the specified far field loading but without the cracks. Meanwhile, the auxiliary problem is the given cracked plate, but without the far field loading. The loading conditions for the auxiliary problem are instead prescribed tractions applied to the crack faces that are calculated to be equal and opposite to the stresses induced in the uncracked material at the location of the crack faces. This loading insures that the crack faces are traction-free in the original problem when the stress field solutions to the trivial and auxiliary problems are summed. Obtaining a solution to the auxiliary problem, which constitutes the bulk of the analytical and computational effort, requires the development and superposition of certain solutions on the local level reflecting detailed crack geometric features.

To solve for the opening displacement profiles of the auxiliary problem, the first step is to subdivide cracks into a series of straight crack segments spanning from branch point to tip. For example, the branched crack of Figure 1 is divided into three crack segments, each with its own local coordinate system. Once the opening displacement profile for a single segment is determined, its effects on the full stress field can be evaluated separately from the other crack segments. Superposition of the local solutions for all of the respective crack segments yields the full solution to the auxiliary problem.

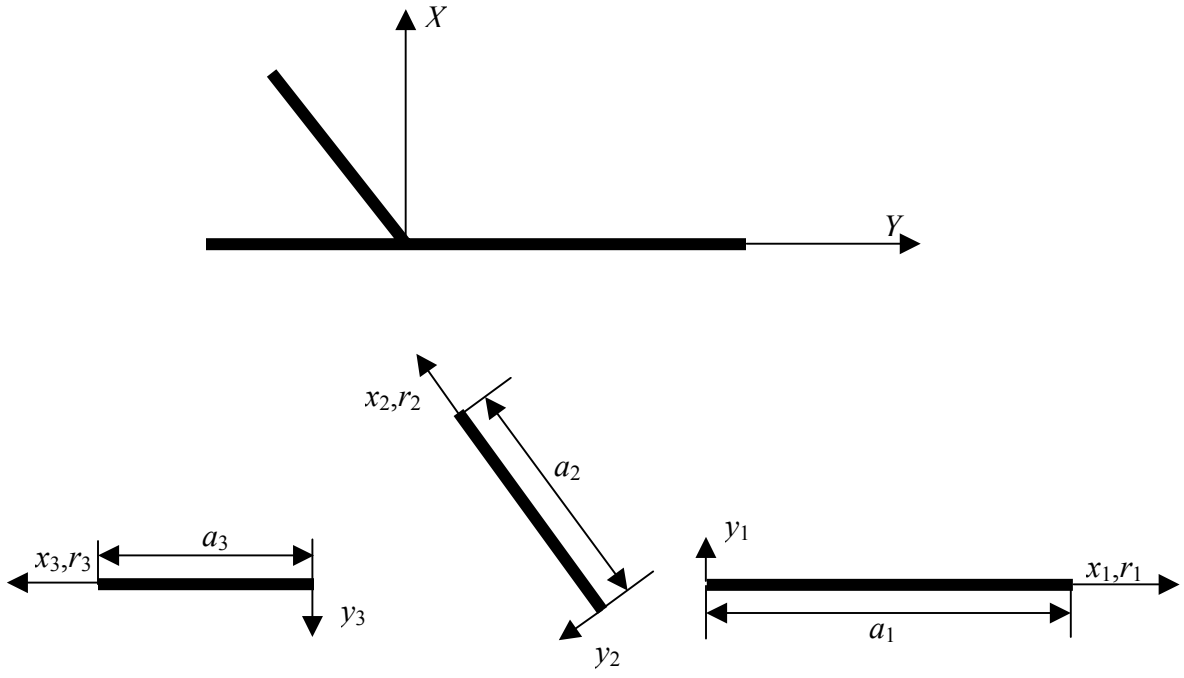

Figure 1: Global and local coordinate systems for a branched crack

Dislocation Distributions

Dislocation distributions are the means of describing the opening displacement profile of a crack segment and inducing the prescribed crack face tractions of the auxiliary problem. A dislocation distribution, $\mu_\eta(r)$, is defined as the derivative of a crack segment's opening displacement profile, where r is an axis coincident with the crack segment. To determine the stresses induced at a point (x,y) in the material caused by all of the crack segments, the individual effects of each must first be determined.

Consider crack segment i acting alone (as though all other crack segments are closed) in an infinite, linearly elastic, isotropic plate with local coordinate system (x_i, y_i) such that the x_i-axis lies along the crack segment which has length a_i. The distance along the x_i-axis is r_i and is measured from the origin. The dislocation distributions for a single crack segment are symbolized as $\mu_{1i}(r_i)$ and $\mu_{2i}(r_i)$. The subscripts 1 and 2 represent the tangential and normal directions respectively. The stress components caused by this individual crack segment at point (x,y) are written in terms of a complex variable formulation as

$$
\begin{aligned}
s_{xy}^{(i)} &= -\frac{2G}{\pi(1+\kappa)}\left\{ y\,\mathrm{Re}\left(Z_2^2\right) + \mathrm{Re}\left(Z_1^1\right) + y\,\mathrm{Im}\left(Z_2^1\right) \right\} \\
s_{yy}^{(i)} &= -\frac{2G}{\pi(1+\kappa)}\left\{ \mathrm{Re}\left(Z_1^2\right) - y\,\mathrm{Im}\left(Z_2^2\right) + y\,\mathrm{Re}\left(Z_2^1\right) \right\} \\
s_{xx}^{(i)} &= -\frac{2G}{\pi(1+\kappa)}\left\{ \mathrm{Re}\left(Z_1^2\right) + y\,\mathrm{Im}\left(Z_2^2\right) + 2\,\mathrm{Im}\left(Z_1^1\right) - y\,\mathrm{Re}\left(Z_2^1\right) \right\}
\end{aligned}
\tag{1}
$$

where G is the shear modulus of the material, ν is Poisson's ratio, and κ is Kosolov's constant ($3-4\nu$, for plane strain and $(3-\nu)/(1+\nu)$, for plane stress). These stresses are symbolized by s to indicate that they are created by a single crack segment and are oriented in its local coordinate system. Note that point (x,y) must also be converted to the local coordinate system for use in these equations. The full stress field due to all crack segments will be denoted by σ and is determined by summing the contributions from all individual crack segments after they are converted to the global coordinate system. The Z are Cauchy singular integrals to be evaluated in closed form in terms of the dislocation distributions and are given as

$$
\begin{aligned}
Z_1^\eta &= \int_0^{a_i} \frac{\mu_{\eta i}(r_i)\,\mathrm{d}r_i}{z - r_i} \\
Z_2^\eta &= \int_0^{a_i} \frac{\mu_{\eta i}(r_i)\,\mathrm{d}r_i}{\left(z - r_i\right)^2} = -\frac{\mathrm{d}}{\mathrm{d}z} Z_1^\eta
\end{aligned}
\tag{2}
$$

where $z = x + \mathrm{i}y$ and η = 1 or 2 referring to the tangential and normal directions respectively. For the cases where the point (x,y) falls along the crack segment, these integrals are evaluated as Cauchy Principal Value Integrals. Solutions to these integrals for given dislocation distributions can be found in [6].

The stress equations are functions of unknown dislocation distributions for the various crack segments. These dislocation distributions are approximated by summing together different types of series that each captures a fundamental crack or wedge behavior (such as singularities at branch locations and tips). The Cauchy singular integrals are evaluated analytically for each term of these series. The results from each particular term are then multiplied by an unknown weighting coefficient (or degree of freedom). Therefore, the stress equations for each crack segment are now captured through simple algebraic equations of unknown weighting coefficients.

Satisfying The Traction-Free Condition

Physical conditions dictate that the crack faces are traction-free in the full problem. To ensure this condition, the opening displacement profiles for each crack segment in the auxiliary problem must be exactly those caused by the prescribed tractions. Therefore, a series of equations to enforce traction-free crack faces in the tangential and normal directions is applied simultaneously at a given set of points along each crack segment. These equations take the form

$$\begin{aligned} \sigma_{xy}^{\infty} n_y + \sigma_{xx}^{\infty} n_x &= -n_y \sum_{i=1}^{N} s_{xy}^{(i)} - n_x \sum_{i=1}^{N} s_{xx}^{(i)} \\ \sigma_{yy}^{\infty} n_y + \sigma_{xy}^{\infty} n_x &= -n_y \sum_{i=1}^{N} s_{yy}^{(i)} - n_x \sum_{i=1}^{N} s_{xy}^{(i)} \end{aligned} \tag{3}$$

where N is the total number of crack segments. The left hand side of these equations represents the tractions induced at the crack faces by the loading conditions, while the right hand side represents the tractions caused by the opening displacements (dislocation distributions) of the crack segments. Also, n_x and n_y are the X and Y components, respectively, of the normal to the bottom (-) crack faces. The σ^{∞} are the far field stresses applied to the plate in the directions denoted by their subscripts.

Solving for the Unknown Coefficients

Satisfying the traction-free condition along the crack faces (Eqn. 3) at a suitably chosen set of points results in a system of equations. These equations are linear functions of the unknown weights of each term from each series. To calculate the weights a large matrix must be inverted; therefore, the use of efficient and physically realistic series is imperative to reduce the number of degrees of freedom to the smallest number possible. Solving this set of simultaneous equations requires the inversion of a large matrix. Selection of points and number of terms produces an over-determined matrix that is solved by a least squares fit. Once the weighting coefficients have been calculated, stress and displacement fields and stress intensity factors can be readily determined [6].

OPENING DISPLACEMENT SERIES

Different types of series (wedge, tip, and polynomial) are used to build the opening displacement profiles of the cracks. Emphasis was placed on creating efficient series to capture all necessary types of physical behavior while minimizing the number of degrees of freedom in an analysis. Wedge series based on singular eigenvalues [10-12] calculated at material wedges greater than 180° induced by crack branching will not be presented, since the example provided does not include a wedge of this type. It should also be noted that constraint equations are enforced at branch points to eliminate mathematical, but non-physical singularities, created by adjoining crack segments [6]. Each term of a series is multiplied by an unknown weighting coefficient, c, and each series is used independently in both the tangential and normal modes. Furthermore, each type of series must be applied to every crack segment.

Polynonial Series

Polynomial series, $P(r)$, provide flexibility in manipulating the overall opening displacement shape in addition to allowing for translation and rotation at branch locations. This series is formulated to constrain non-physical jump opening displacements and slopes at the tip end of a crack segment and takes the form

$$P(r) = \sum_{j=0}^{n-2} c_{jp} \left(\left(\frac{r}{a} \right)^{j} - (n-j) \left(\frac{r}{a} \right)^{(n-1)} + (n-j-1) \left(\frac{r}{a} \right)^{n} \right) \tag{4}$$

Tip Series

Tip series, $T(r)$, incorporate the ½ singularity and higher order behavior at crack tips. This series is developed to avoid non-physical jump opening and slope behavior at branch locations and is written as

$$T(r) = \sum_{j=0}^{n-2} c_{jt} \left(\left(\frac{a-r}{a} \right)^{\frac{2j+1}{2}} - (n-j) \left(\frac{a-r}{a} \right)^{\frac{2(n-1)+1}{2}} + (n-j-1) \left(\frac{a-r}{a} \right)^{\frac{2n+1}{2}} \right) \tag{5}$$

BRANCHED CRACK EXAMPLES

Rigorous testing for accuracy was performed using results of other researchers [13-16], and agreement was achieved in all cases studied [6]. Results available in the literature provided only stress intensity factors at crack tips, so this parameter formed the basis of the comparisons. However, overall results with this method demonstrated rapid convergence in terms of weighting coefficients, stress intensity factors, and tractions along crack faces as induced by the computed opening displacement profiles.

This method can be applied to branched cracks of any configuration and crack segment lengths. Cracks need not be symmetric nor limited to a certain number of crack tips or growth directions. Furthermore, loading is not restricted by type and can be any combination of shear and normal loading modes. As an example, results from one parameter study of two interacting branched cracks are provided.

For this particular case, two symmetric interacting branched cracks in an infinite plate under unit biaxial loading were evaluated. Branch segments were of unit length while the main crack segment had a length of 2. The branch angle, β, and the separation distance, d, were varied. Calculated values for K_I at the inner crack tips are shown in graphical form in Figure 3 as a representative sample of the results. Note that as the distance, d, was increased, the K_I values converged to those of a single, isolated, branched crack.

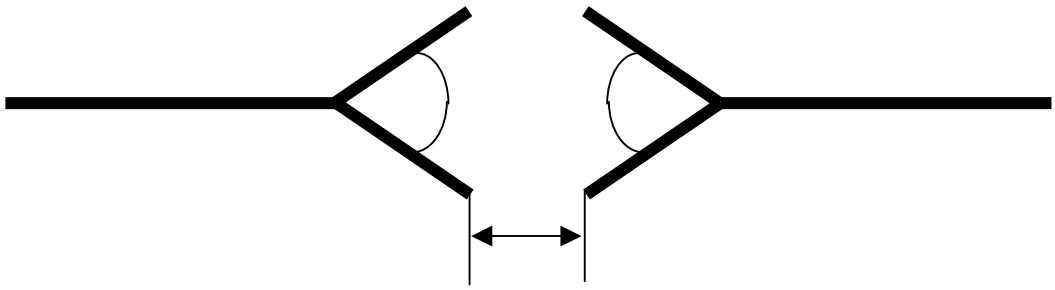

Figure 2: Two interacting branched cracks under unit biaxial loading

ACKNOWLEDGEMENTS

This work was performed under a fellowship from the American Association of University Women.

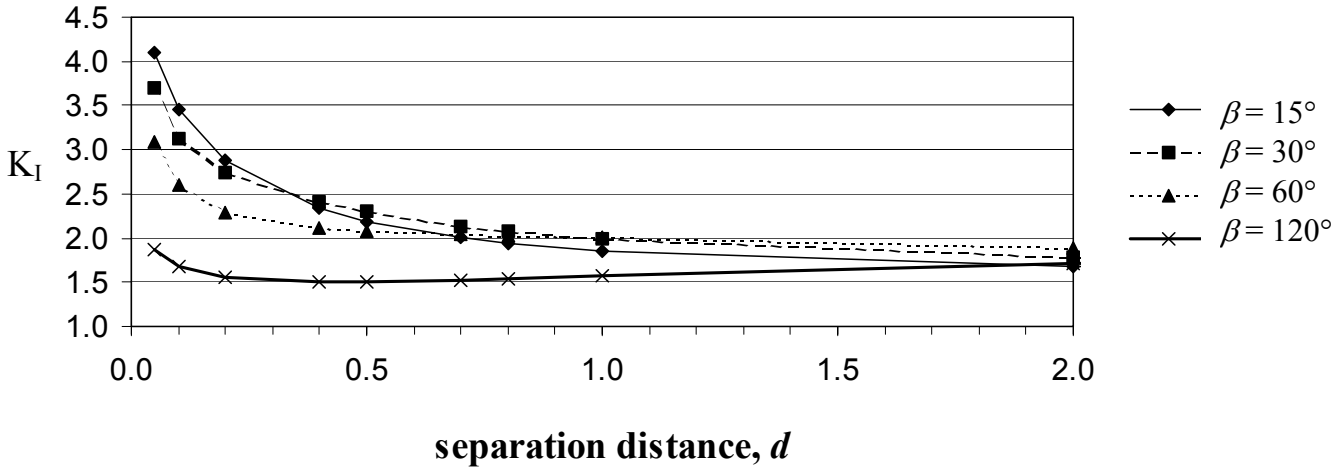

Figure 3: Mode I stress intensity factors for varying separation distances and branch configurations

REFERENCES

1. Vitek, V. (1977) *Int. J. Fract.* 13, 481.
2. Lo, K.K. (1978) *J. Appl. Mech.* 45, 797.
3. Niu, J. and Wu, M.S. (1997) *Eng. Fract. Mech.* 57, 665.
4. Burton, Jr., J.K. and Phoenix, S.L. (2000) *Int. J. Fract.* 102, 99.
5. TerMaath, S.C. and Phoenix, S.L. (2000) In: *Fatigue and Fracture Mechanics: 31st Volume, ASTM STP 1389*, 331, G.R. Halford and J.P. Gallagher (Eds). American Society for Testing and Materials, West Conshohocken.
6. TerMaath, S.C. (2000) Dissertation, Cornell University, USA.
7. Lardner, R. (1974) *Mathematical theory of dislocations and fracture*. University of Toronto Press, Great Britain.
8. Hirth, J. and Lothe, J. (1982) *Theory of dislocations*. John Wiley & Sons, New York.
9. Hills, D.A., Kelly, P.A., Dai, D.N., and Korsunsky, A.M. (1996) *Solution of crack problems: the distributed dislocation technique*. Kluwer Academic Publishers, Dordrecht.
10. Timoshenko, S.P. and Goodier, J.N. (1970) *Theory of Elasticity*, Third Edition, McGraw-Hill, New York.
11. Barber, J.R. (1992) *Elasticity*. Kluwer Academic Publishers, Boston.
12. Williams, M.L. (1952) *J. Appl. Mech.* 19, 526.
13. Theocaris, P.S. (1972) *J. Mech. Phys. Solids* 20, 265.
14. Kitagawa, H. and Yuuki, R. (1975) *Trans. Japan Soc. Mech. Engrs.* 41-346, 1641.
15. Isida, M. and Noguchi, H. (1983) *Trans. Japan Soc. Mech. Engrs.* 49-440, 469.
16. Chen, Y.Z. and Hasebe, N. (1995) *Eng. Fract. Mech.* 52, 791.

ORAL REFERENCE: ICF100194OR

An elasto-plastic damage model for cementitious materials

D. Addessi[1], S. Marfia[2] and E. Sacco[2]
[1]Dipartimento di Ingegneria Strutturale e Geotecnica, Università di Roma 'La Sapienza', Roma
[2]Dipartimento di Meccanica, Strutture, A. & T., Università di Cassino, Cassino

ABSTRACT
In the present paper, an elasto-plastic nonlocal damage model is proposed for studying the mechanical response of structural elements made of cementitious materials. An isotropic damage model, able to describe the different behavior in tension and in compression of the material is presented. To overcome the analytical and computational problems induced by the softening constitutive law, a regularization technique, based on the introduction of the damage Laplacian in the damage limit function, is adopted. A Drucker-Prager type of plastic limit function is proposed considering an isotropic hardening. A numerical procedure, based on an implicit 'backward-Euler' technique for the time integration of the plastic and damage evolutive equations, is developed and implemented in a finite element code. Some numerical examples are carried out in order to study the structural behavior of elements made of concrete and of fiber reinforced concrete.

KEYWORDS: Damage, Plasticity, Softening response, Nonlocal theory.

INTRODUCTION

Cementitious materials, such as concrete and masonry, are widely used in structural civil engineering. These materials are characterized by softening response coupled with plastic effects, due to the development of microcracks and of anelastic deformations.
The continuum damage mechanics represents an effective framework to model the softening behavior of cementitious materials [1], while the plasticity theory allows to take into account the anelastic material behavior [2]. Various macromechanical models have been proposed in literature to describe the mechanical response of structural elements made of cementitious materials. These models are mainly based on damage mechanics [3,4,5] and on plasticity theories [6,7].
In this paper, an elasto-plastic nonlocal damage model is proposed with the aim of developing an effective model able to predict the main features of concrete or masonry elements response. The stress-strain law accounts for damage and plastic effects.
The damage evolution process is controlled by a variable, which represents an equivalent deformation. The damage limit function considers the different response in tension and compression of the material.
In order to circumvent the pathological drawback due to strain and damage localization, a first gradient-enhanced theory is proposed. The nonlocal damage model is obtained by introducing the Laplacian of the damage variable in the loading function. The presence of the gradient term has a regularizing effect and avoids mesh-dependence when finite element analyses are performed.
The plasticity evolution law is governed by a plastic yield function with different threshold in tension and compression and with an isotropic hardening. The yield function and the plastic deformation evolution law depend on the effective stress.

The proposed model is implemented in the finite element code FEAP [8]. Some applications are developed to study the behavior of structural elements made of concrete and of fiber reinforced concrete.

AN ELASTO-PLASTIC NONLOCAL DAMAGE MODEL

The following stress-strain law is adopted for cementitiuos materials:

$$\boldsymbol{\sigma} = (1-D)^2 \mathrm{C}(\boldsymbol{\varepsilon} - \boldsymbol{\varepsilon}^P) \tag{1}$$

where $\mathbf{C}$ is the second order elastic isotropic constitutive matrix, $\boldsymbol{\varepsilon}^P$ is the plastic deformation, D is the damage variable that can vary in the range [0,1]; $D=0$ corresponds to the virgin material state and $D=1$ to the total damaged state.
The rate constitutive equation is obtained by differentiating equation (1) with respect to the time:

$$\dot{\boldsymbol{\sigma}} = (1-D)^2 \mathbf{C}(\dot{\boldsymbol{\varepsilon}} - \dot{\boldsymbol{\varepsilon}}^P) - 2(1-D)\dot{D}\mathbf{C}(\boldsymbol{\varepsilon} - \boldsymbol{\varepsilon}^P) \tag{2}$$

The elasto-plastic nonlocal damage model is based on the following assumption:

- the damage evolution is governed by the elastic strain $\boldsymbol{\varepsilon}^e = \boldsymbol{\varepsilon} - \boldsymbol{\varepsilon}^P$ in tension, and by the total strain $\boldsymbol{\varepsilon}$ in compression.
- the plastic deformation evolution is controlled by the effective stress $\tilde{\boldsymbol{\sigma}}$ defined as:

$$\tilde{\boldsymbol{\sigma}} = \frac{\boldsymbol{\sigma}}{(1-D)^2} \tag{3}$$

Nonlocal damage model
An isotropic nonlocal damage model is proposed. The damage evolution is controlled by the consistency condition with the classical Kuhn-Tucker conditions:

$$\dot{F}\,\dot{D} = 0 \tag{4}$$

$$\dot{D} \geq 0 \qquad F \leq 0 \qquad \dot{D}\,F = 0 \tag{5}$$

where $F(Y,D)$ defines the damage limit function and Y is the variable associated to the parameter D, which controls the damage evolution. In particular, the variable Y is defined as follows:

$$Y = \frac{Y_t}{Y_{0t}} + \frac{Y_c}{Y_{0c}} \tag{6}$$

where Y_{0t} and Y_{0c} are the initial damage thresholds in tension and in compression, respectively. The quantities Y_t and Y_c represents the equivalent tensile and compressive deformations and they are function of the elastic deformation and of the total deformation, respectively [7].
The following damage limit function is proposed:

$$F = (Y-1) - (aY + K)D + h\nabla^2 D \tag{7}$$

In formula (7) the nonlocal effect is due to the presence of the Laplacian of the variable D, i.e. $\nabla^2 \mathrm{D}$, in the damage limit function $F(Y,D)$. The parameter h is linked to the characteristic length of the material and controls the size of the localization region. The material constants K and a control the damage rate growth and the softening branch slope, respectively [7].

Plastic model

A plastic model with isotropic hardening, which takes into account the different strength in tension and in compression, is proposed. A plastic limit function $F_P = F_P(\tilde{\boldsymbol{\sigma}}, q)$, which depends on the effective stress $\tilde{\boldsymbol{\sigma}}$ (3) and on the thermodynamic force q, is introduced. The force q is associated to the internal hardening variable α by the rational relation:

$$q = -\frac{\alpha}{\alpha + \chi} \tag{8}$$

where χ is the hardening parameter.

The plastic deformation evolution is governed by the following equations:

$$\dot{\boldsymbol{\varepsilon}}_P = \dot{\lambda}_P \frac{\partial F_P}{\partial \tilde{\boldsymbol{\sigma}}} \tag{9}$$

$$\dot{\alpha} = \dot{\lambda}_P \frac{\partial F_P}{\partial q} \tag{10}$$

$$F_P \le 0 \qquad \dot{\lambda}_P \ge 0 \qquad F_P \, \dot{\lambda}_P = 0 \tag{11}$$

where $\dot{\lambda}_P$ is the plastic multiplier that can be evaluated from the classical consistency equation $\dot{F}_P \, \dot{\lambda}_P = 0$. In the present model the following yield function is considered:

$$F_P(\tilde{\boldsymbol{\sigma}}, q) = 3J_2 + (\sigma_c - \sigma_t) I_1 - \sigma_c \sigma_t \tag{12}$$

where σ_c and σ_t are the compressive and tensile yield stresses, respectively, I_1 is the first invariant and J_2 the second deviatoric invariant of the effective stress tensor $\tilde{\boldsymbol{\sigma}}$.

SOLUTION PROCEDURE

A numerical procedure, based on an implicit 'backward-Euler' technique for the time integration of the plastic and damage evolutive equations of the model, is developed. Each non-linear step is solved using a predictor-corrector iterative technique within the splitting method.

In the predictor phase, the elasto-plastic problem (8)-(12) is solved with the damage field frozen. In this phase the plastic evolution is computed through a further nested predictor-corrector phase based on a return-mapping algorithm.

In the corrector phase the strain field is taken frozen and the damage evolution is evaluated solving the problem defined by equations (4)-(7).

Hence, the solution algorithm consists in the following two steps:

- an elasto-plastic predictor phase;
- a damage corrector phase.

The equation governing the two phases are reported in the following scheme:

Elastic-plastic predictor	Damage corrector
$\dot{\boldsymbol{\varepsilon}}^P = \begin{cases} \dot{\lambda}_P \dfrac{\partial F}{\partial \tilde{\boldsymbol{\sigma}}} & if\ F_P \geq 0 \\ 0 & if\ F_P < 0 \end{cases}$ $\dot{\alpha} = \begin{cases} \dot{\lambda}_P \dfrac{\partial F}{\partial q} & if\ F_P \geq 0 \\ 0 & if\ F_P < 0 \end{cases}$ $F_P \leq 0 \qquad \dot{\lambda}_P \geq 0 \qquad F_P\, \dot{\lambda}_P = 0$	$\dot{\boldsymbol{\varepsilon}}^P = 0$ $\dot{\alpha} = 0$
$\dot{D} = 0$	$\dot{F}\, \dot{D} = 0$ $\dot{D} \geq 0 \qquad F \leq 0 \qquad \dot{D}\, F = 0$
$\dot{\boldsymbol{\sigma}} = (1-D)^2 \mathbf{C}(\dot{\boldsymbol{\varepsilon}} - \dot{\boldsymbol{\varepsilon}}^P)$	$\dot{\boldsymbol{\sigma}} = -2(1-D)\dot{D}\mathbf{C}(\boldsymbol{\varepsilon} - \boldsymbol{\varepsilon}^P)$

NUMERICAL APPLICATIONS

The plastic nonlocal damage model is implemented in plane-stress 3 and 4 node finite elements in the code FEAP [8].
Some numerical examples are developed in order to study the structural behavior of elements made of concrete and of fiber reinforced concrete (FRC).
In order to reproduce the concrete behavior the nonlocal damage model without plasticity is adopted; on the contrary to simulate the FRC response, characterized by the matrix softening and the fiber debonding and pull-out, the nonlocal damage model with plasticity is used. In fact, the adoption of a model characterized by a plasticity with rational hardening, reproduces the fact that when the matrix is completely damaged, the FRC response tends to a limit value corresponding to the fiber bridging action.
The material parameters used for the concrete nonlocal damage model and for the FRC plastic nonlocal damage model are:

- Concrete:

$$\mathrm{E_m} = 3.0 \cdot 10^4\ \mathrm{N/mm^2} \qquad \nu_m = 0.2$$
$$\mathrm{Y_{0t}} = 0.8 \cdot 10^{-4} \qquad \mathrm{Y_{0c}} = 0.8 \cdot 10^{-3}$$
$$K_t = 1.0 \cdot 10^{-4} \qquad K_c = 2.5 \cdot 10^{-3}$$
$$a_t = 0.97 \qquad a_c = 0.85$$
$$h = 1.0\ \mathrm{mm^2}$$

- FRC:

$$\mathrm{E_m} = 3.0 \cdot 10^4\ \mathrm{N/mm^2} \qquad \nu_m = 0.2$$
$$\mathrm{Y_{0t}} = 0.9 \cdot 10^{-4} \qquad \mathrm{Y_{0c}} = 0.9 \cdot 10^{-3}$$
$$\mathrm{K_t} = 1.5 \cdot 10^{-4} \qquad \mathrm{K_c} = 2.5 \cdot 10^{-3}$$
$$\mathrm{a_t} = 0.99 \qquad \mathrm{a_c} = 0.90$$
$$\mathrm{h} = 1.0\ \mathrm{mm^2}$$
$$\sigma_t = 100\ \mathrm{N/mm^2} \qquad \sigma_c = 200\ \mathrm{N/mm^2}$$
$$\chi = 1.0 \cdot 10^{-3}\ \mathrm{N/mm^2}$$

where K_t, a_t and K_c, a_c are damage materials parameter in tension and in compression, respectively. In order to take into account the beneficial effects of the fibers in improving the material mechanics response the values of the parameters K_t, K_c, a_t and a_c adopted for in the FRC model are higher than the ones used for the concrete.

Initially, some analyses are performed to set the values of the material parameters in order to reproduce the concrete and FRC behavior in the pure tensile and compressive states.

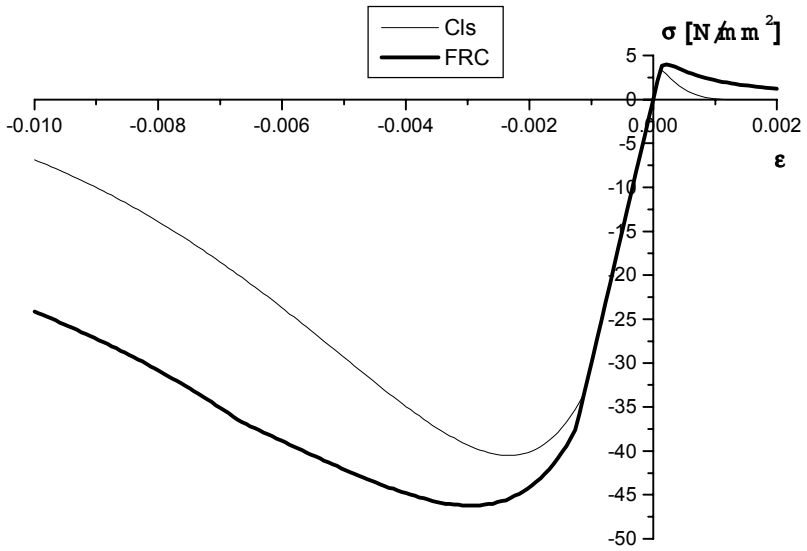

Figure 1: Tensile and compressive behavior of concrete and of FRC

In Figure 1 the stress-strain behavior in tension and in compression for the concrete and the FRC material is represented. It can be pointed out the beneficial effects of fibers in improving the mechanical response of concrete. In fact, in the post peak phase, when the fibers debonding and pull-out occurs the softening branch for FRC composite materials is less steep than for concrete.
The bending behavior of a concrete and of a FRC beam is investigated.
The geometrical parameters characterizing the analyzed beam are:

$$L = 800mm \qquad w = 250mm$$

where L is the length of the beam and w is the height of the cross section.
In Figure 2, the damage distribution in the FRC beam for different values of the prescribed displacement v is plotted.

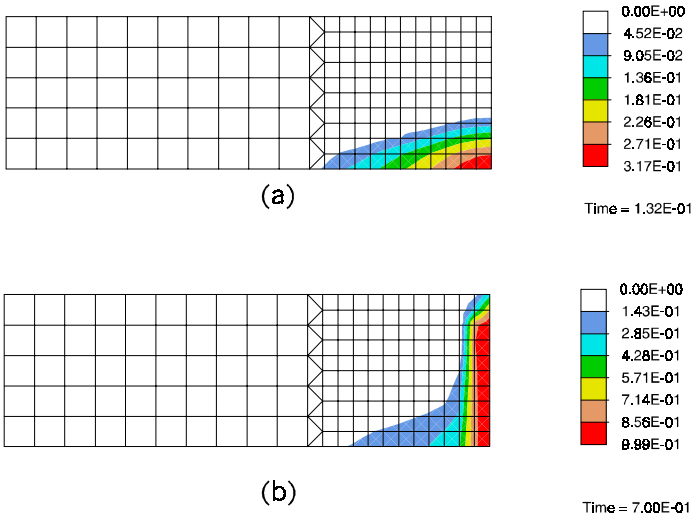

Figure 2: Damage evolution: a) *v=0.26 mm*, b) *v=1.4 mm*

It can be noted that the introduction of the damage Laplacian in the limit function F prevents the damage localization in the weakest point of the beam. The damage process starts at the bottom of the middle section (see Figure 2(a)), where the maximum tensile strains are concentrated. Then it propagates towards the topside of the beam when the compressive strain becomes significative (see Figure 2(b)).

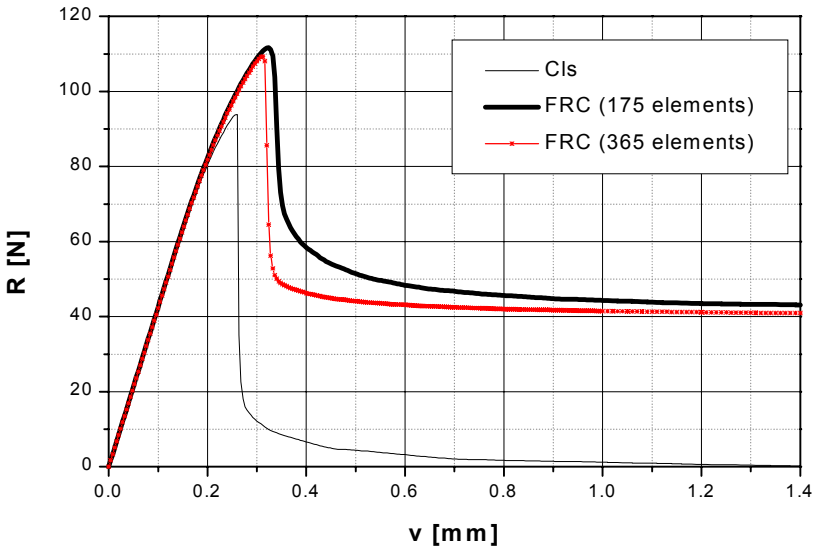

Figure 3: Load displacement curves for concrete and FRC

In Figure 3 the bending behavior of the concrete and the FRC beam is plotted. It can be pointed out that the plastic nonlocal damage model is able to reproduce the post-peak behavior of the FRC and the results are mesh independent.

CONCLUSIONS

A plastic nonlocal damage model for cementitious material is presented. The model is able to take into account the different behavior in tension and in compression of the material. To avoid the mathematical and numerical problems, due to the localization phenomenon, a gradient nonlocal model is adopted. The numerical results show the capability of the model in describing the mechanical behavior and the damage processes in concrete and FRC structural elements.

REFERENCES

[1] J. Lemaitre, J.L. Chaboche, Mechanics of solid materials, Cambridge University Press, 1990.

[2] J. Lubliner, Plasticity theory, Macmillan Publishing Company, New York, 1990.

[3] J.C. Simo, J.W. Ju, “Strain-and stress-based continuum damage models-I. Formulation”, Int. J. Solids Structures, Vol. 23(7), 821-840, 1987.

[4] M. Frèmond, B. Nedjar, “Damage, gradient of damage and principle of virtual power”, Int.J. Solids and Structures, Vol. 33(8), 1083-1103, 1996.

[5] C. Comi, “Computational modeling of gradient-enhanced damage in quasi-brittle materials”, Mechanics of Cohesive-Frictional Materials, Vol. 4(1), 17-36, 1999.

[6] Lee J., Fenves G., “ A plastic-damage concrete model for earthquake analysis of dams” Earthquake Engng. Struct. Dyn., Vol. 27, 937-956, 1998.

[7] D. Addessi, S. Marfia, E. Sacco, “A plastic nonlocal damage model”, submitted for publication on an international journal, 2000.

[8] O. C. Zienkiewicz, R. L. Taylor, The finite Element method, 4th edition, Mc GRAW-HILL, London, 1991.

ORAL REFERENCE: ICF 0824OR

An element-free Galerkin method for dynamic fracture in functional graded material

He Peixiang Li Ziran Wu Changchun
Department of Modern Mechanics, University of Science and Technology of China, Hefei, China

ABSTRACT

A improved element-free Galerkin method(EFGM) is used as the numerical tool for analyzing dynamic crack propagation problem in functional graded material(FGM). The Element-Free Galerkin Method(EFGM) suggested by T.Belytchko et al[1] is a meshless method, which uses the Moving Least-Squares(MLS) approximation based only on nodes. Since no element connectivity data is needed, the extension of the crack is then treated by the growth of the surfaces of the crack naturally and the remeshing is avoided. This makes the method particularly attractive for moving dynamic crack problems. In this paper, The shear modulus are assumed to vary continuously and Poisson's ratio to be constant. The variation of the material properties is simulated by adopting the material properties of the integration point when forming the stiffness matrix. The dynamic J integral is evaluated. Some numerical results are provided to demonstrate the utility and robustness of the proposed technique.

KEYWORDS

functional graded material, element-free Galerkin method(EFGM), dynamic J integral

INTRODUCTION

The functional graded materials(FGM) have been widely used in technological application . So, it is very important and necessary to study its mechanical behaviors, especially in the fracture mechanics. However the material properties of FGM vary with the coodinates, its mechanical behaviors is very complex. The analytical approach

can only deal with some simple and particular problems. Therefore, numerical methods for FGM have to be developed.

The Element-Free Galerkin Method(EFGM)[1] suggested by T.Belytchko et al is a meshless method, which use the Moving Least-Squares(MLS) approximation based only on nodes. Since no element method connectivity data is needed and the extension of the crack is then treated by the growth of the surfaces of the crack naturally, it is very convenient for modeling the crack propagation. This method provides a higher resolution localized derives of strains and stresses. Also it can adopt the material properties of integration points to simulate the variation of the material properties. So, it is very suitable to analyze FGM.

However, in EFGM, the interpolants constructed by the MLS method does not pass through the nodal parameter values, the imposition of boundary conditions on the dependent variables is quite awkward and the computational cost is quite burdensome, which makes EFGM not as fast as FEM. In this paper, the EFGM is coupled to FEM. EFG models are only used near the crack tip where their great versatility and high resolution is needed, FE models are applied in the other domains. Therefore, the boundary conditions can be treated easily and directly by FE models. Meantime, the computation efficiency can be great improved.

Jin and Noda[2] have shown that the singularity and the angular distribution of the stress and displacement near-tip fields for FGM are same as the ones of homogeneous materials. Erdogan and Wu[3] have presented the analytical result. Jian.C et al have given a modified static J integral for FGM. In this paper, based on Moran et al[4], a modified dynamic J integral for FGM is calculated. Numerical results are provided to demonstrate the utility and robustness of the proposed technique.

Element-Free Galerkin Method(EFGM) and Its Coupling to finite elements

The most difference between the EFGM and the FEM is the construction of the shape functions and test functions. In the EFGM, the field variable is approximated by moving least square(MLS) approximations, no element connectivity data is needed, which is necessary in the FE method. The shape functions of EFGM can be written as[1].

$$\mathbf{\Phi}(\mathbf{x}) = \mathbf{p}^T(\mathbf{x})\mathbf{A}^{-1}(\mathbf{x})\mathbf{B}(\mathbf{x}) = \begin{bmatrix}\varphi_1 & \varphi_2 & \cdots & \varphi_n\end{bmatrix} \tag{1}$$

The derives of $\mathbf{\Phi}(\mathbf{x})$ are expressed as:

$$\begin{aligned}\Phi(x)_{,i} &= [\mathbf{p}^T(\mathbf{x})\mathbf{A}^{-1}(\mathbf{x})\mathbf{B}(\mathbf{x})]_{,i} \\ &= \mathbf{p}^T(\mathbf{x})_{,i}\mathbf{A}^{-1}(\mathbf{x})\mathbf{B}(\mathbf{x}) + \mathbf{p}^T(\mathbf{x})\mathbf{A}^{-1}(\mathbf{x})_{,i}\mathbf{B}(\mathbf{x}) + \mathbf{p}^T(\mathbf{x})\mathbf{A}^{-1}(\mathbf{x})\mathbf{B}(\mathbf{x})_{,i}\end{aligned} \tag{2}$$

where

$$\mathbf{A}^{-1}(\mathbf{x})_{,i} = -\mathbf{A}^{-1}(\mathbf{x})\mathbf{A}(\mathbf{x})_{,i}\mathbf{A}^{-1}(\mathbf{x}) \tag{3}$$

To impose boundry conditions with as high a degree of accuracy and improve the

computation efficiency, the coupled EFG/FE approach is used.

In the meshless domain Ω_E, the MLS method is still adapted to construct the test function of $\mathbf{x}_{eI}$,

$$\mathbf{u}^h(\mathbf{x}_{eI}) = \mathbf{\Phi}(\mathbf{x})\mathbf{u}^* \tag{4}$$

In the non-interface FEM domain Ω_{FE}, the traditional FEM is used to construct the test function of $\mathbf{x}_{fI}$,

$$\mathbf{u}^h(\mathbf{x}_{fI}) = \sum_{i=1}^{ND} N_i \mathbf{u}_i^* \tag{5}$$

here ND is the number of element nodes.

For the FEM point $\mathbf{x}_{bI}$ in the interface zone Ω_B, we also use the MLS method,

$$\mathbf{u}^h(\mathbf{x}_{fb}) = \mathbf{\Phi}(\mathbf{x})\mathbf{u}^* \tag{6}$$

In the FEM domain, the test function can be expressed as,

$$\mathbf{u}^h(\mathbf{x}_{fI}) = \sum_{i=1}^{ND} N_i \mathbf{u}_i(\mathbf{x}_i), \qquad \mathbf{u}_i = \begin{cases} \mathbf{u}^*, \mathbf{x}_i \in \Omega_{FE} \\ \mathbf{\Phi}(\mathbf{x})\mathbf{u}^*, \mathbf{x}_i \in \Omega_B \end{cases} \tag{7}$$

With these test functions, mass matrix and stiffness matrix can be formed in general way, and boundary conditions can be enforced strictly. Since background finite element is used for quadrature in meshless domain, it is very convenient that in the procedure of numerical implementation, the material properties of the integration point are adopted not only in finite element domain but also in meshless domain.

NUMERICAL EXAMPLE

A single cracked panel (SECP, Fig.1) of unit thickness in elastic plane stress conditions is considered.

l and w are the length and the width of the plate. a is the edge crack. Poisson's ratio υ and mass density ρ are constant. Young's modulus is given by the following expressions:

$$E(x) = E_1 \exp(\frac{x}{h} \ln \frac{E_2}{E_1}) \tag{8}$$

In this paper, $l = 4, h = 1, a = 0.5$, $E_1 = 1.11 \times 10^{11}$, $E_2 = 2.22 \times 10^{11}$, $\upsilon = 0.3$, $\rho = 7800$ and $\sigma = 1.0$

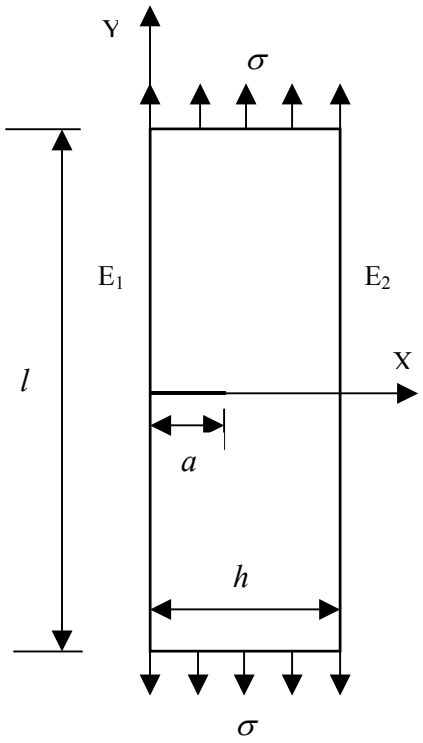

Fig.2 A single edge FGM panel

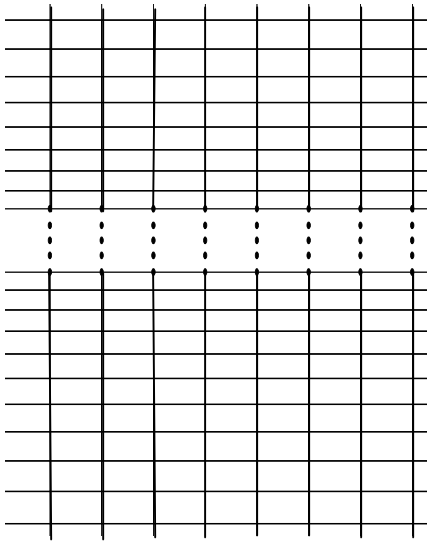

Fig.2 Node distribution

The distribution of nodes is like fig.2 . The plate is divided into 30×40 elements, including the background finite elements only for quadrature. The number of all nodes is 1271. The nodes of the EFGM is only distributed near the crack tip. The meshless domain is divided into 30×4 background finite elements mesh. The rest of the plate is divided into 30×36 finite elements. The nearer to the crack surface, the finer the nodes are distributed along Y. Otherwise, the material properties vary along X, so finer nodes are distributed along X than along Y.

J integral is often used to evaluate the stress intensity factor. Based on Moran[5], we obstaine modified dynamic J integral for FGM

$$J_t = \iint_S [-(W+L)q_{,1} + \sigma_{ij}u_{i,1}q_{,j} + \rho(\ddot{u}u_{i,1} - \dot{u}_i\dot{u}_{i,1})q - \frac{1}{2}(\varepsilon_{ij}D_{ijkl,1}\varepsilon_{kl} + \rho_{,1}\dot{u}_i^2)q]dS \quad (9)$$

It is obvious that the term $\iint_S \frac{1}{2}(\varepsilon_{ij}D_{ijkl,1}\varepsilon_{kl} + \rho_{,1}\dot{u}_i^2)qdS$ only exists for FGM. For

homogeneous materials, since $D_{ijkl,1} = 0$， and $\rho_{,1} = 0$， the term vanishes.

In term of (9), we evaluate the dynamic J integral for FGM on two different contour Γ_1 and Γ_2 with increment of the time step. The numerical results are drawn in

Fig. 3.

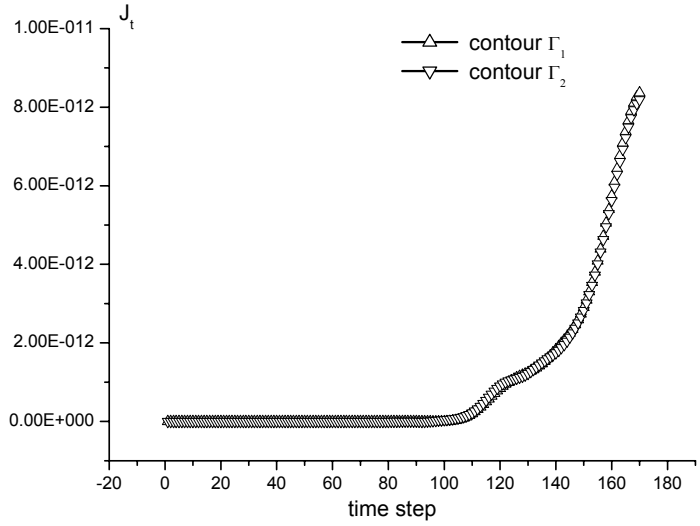

Fig.3 Variation of J integral with time step

These curves in fig.3 show that when the strength waves don't reach crack surface, the value of J integral is zero, when the strength waves reach crack surface, the value of J integral become increasing. Because the velocity of strength waves varies with the Young's modulus, a little difference between the J integral along Γ_1 and the J integral along Γ_2 exists. However, when the strength waves influence the whole area for evaluation, the values of the J integral on contour Γ_1 and Γ_2 are almost equal, namely the J integral is path independent. So, the trend of variation of the J integral is rational. The results show that the method in the paper is efficient for FGM.

CONCLUSION

In this paper, EFGM is used for analyzing dynamic fracture problem in FGM and meanwhile, EFGM is coupled to FE for enforcing boundry conditions strictly and improving the computation efficiency. The numerical results show that the technique is efficient. Otherwise, in the procedure of forming mass matrix and stiffness matrix and evaluating the dynamic J integral, we adopt the material properties of Gauss integration points. So, not as a great number of nodes are needed as in conventional technique for FGM. Not only computation efficiency is improved once again, but also high accuracy is achieved.

Since EFGM facilitates the modeling of growing crack problem, the technique

proposed in the paper is promising in dealing with dynamic crack propagation of FGM.

Although only Mode I cracks are reported, it is straightforward to employ this method to more complicated crack configurations.

REFERENCES

1 Belytschko T, Lu Y Y, Gu L. Element-free Galerkin methods. Int. J. Numer. Methods Engrg 1994,37:229~256.

2 Zhi-he Jin, Naotake Noda. Crack-tip singular fields in nonhomogeneous materials. ASME Journal of Applied Mechanics. 1994,61:738~740.

3 Erdogan F,Wu B H. The surface crack problem for a plate with functionally graded properties. Journal of Applied Mechanics. 1997,64:449~456.

4 Jian C, Linzhi W, Shanyi D. A modified J integral for functional graded materials. Mechanics Research Communication. 2000,27:301~306

5 B.Moran and C.F.Shih, Crack Tip and associated domain integrals from momentum and energy balance, *Engng.Fracture Mech.*,1987,27:615-642.

Examples of the Influence of Residual stresses on Fracture

W. Cheng[1] and I. Finnie[2]

Abstract Generally compressive residual stresses increase the resistance of a part to fracture while tensile residual stress degrades strength. It will be shown that the local compressive residual stresses and the subsurface cracks produced by scribing, at very low loads, are responsible for the low tensile strength of glass specimens. Also, if metal parts containing surface cracks are subjected to pressure such as shot-peening, which produces high near surface residual compressive stresses, the initial end of the crack will experience tensile loading. This paper explains these phenomena using procedures based on LEFM. A method for residual stress measurement using LEFM solutions is also reviewed.

1. BEAR, Inc.
Berkeley, CA 94710
e-mail: weilicheng@home.com

2. James Fife, Professor Emeritus
Dept. of Mech. Eng., University of California
Berkeley, CA 94720
e-mail: finnie@me.berkeley.edu

Introduction

The literature on cracking due to a sliding indenter, a process often referred to as scribing or scratching, goes back 80 years ago, when Griffith's classic work appeared. The scribing process will be described, and it is seen that "median" cracks propagate downwards, below the indenter, in glass at loads as low as 0.014 N. The present work is based on loading a sub-surface crack and analyzes the effect of loading rate in a moist environment in a different manner from previous work by others. The present wok estimates the strength of glass in the presence of subsurface flaws produced by scratching. An upper bound is observed by considering an inert environment. A lower bound is obtained for the strength of glass in moist air.

A related problem is the residual stresses induced by shot-peening or laser surface treatment. These are shown to have a profound effect on surface flaw detection. It is also shown that the solutions for LEFM leads to a new method for residual stress measurement.

The Strength of Glass Following Scribing

The scribing process shown in Fig. 1 introduces a zone of deformation under the indenter which we describe as "the plastic zone" due to a combination of compression and shear. The first crack to form, described as the median crack, propagates from the base of the plastic zone as shown in Fig. 2. Currently, the concept that surface flaws are inherent in glass is a common concept. For example, in the well known book by McClintock and Argon (1966) it is stated that "In some brittle solid, such as inorganic glass, cracks are formed only at the free surfaces". To study this assumption, we take a simple model in which the inherent flaw is treated as an edge crack and residual stresses are ignored. Taking a fracture toughness K_{IC} of 0.76 $MN/m^{3/2}$ and fracture stress of soda lime glass in a moist environment of 70 MPa leads to an estimate of crack size of $a = [K_{Ic}/(1.12\,\sigma)]^2/\pi = 30\ \mu m$. Immediately, we can draw two contradictory conclusions, first, such a flaw size should be detectable by optical or scanning electron microscope (SEM). Second, to our knowledge no such surface cracks have been observed directly. It is tempting by saying that the crack faces are touching. However, SEM examination of glass subjected to bending loads, which should separate the faces of a closed crack, has not revealed cracks. This suggests that strength impairing flaws are so close to the surface that they may be removed by surface melting or etching.

The most likely source of the damage described is scratching or scribing by small abrasive particles. As shown in Fig. 2 a median crack initiates at the base of the plastic zone. The lowest load we have observed for such median crack initiation is 0.014 N. Since the size of the median crack, as just over the threshold load, is only several micrometers, its influence on the fracture stress would be expected to be small if residual stresses are absent. However, scribing produces a high compressive stress in the plastic zone which prevents subsurface flaws from growing into the plastic zone. Also, the plastic zone exerts on opening force at the lower crack tip shown in Fig. 2. The fact that the median crack is often observed to grow after scribing shows the significance of the residual stress. In recent work, we have obtained the residual stress distribution below the plastic zone and have obtained the stress intensity factor for a subsurface flaw (Cheng and Finnie 1992) as shown in Fig. 3, the estimated fracture stress of soda lime glass is greatly reduced by the presence of the compressive residual stress near the surface. The prediction for moist and inert environments agrees well with the reported strength values in literature.

Surface and Near Surface Residual Stresses and Their Influence on Flaw Detection

We now consider the case of a flaw which exists before near surface residual stresses are introduced by shot peening. A typical distribution of residual stresses is shown in schematically in Fig. 4. The high compressive stresses near the surface greatly increase the resistence of a part to crack initiation. However, if a surface flaw is already present, the compressive stress near the surface effectively closes the mouth of the crack and may prevent its detection by dye penetrants. If the crack size is larger than the depth to which compressive stress is present, the crack tip will be subjected to tensile stresses. The displacement caused by releasing the compressive stress on the surface must be computed to estimate the force required to open the crack so that it can be detected.

To obtain the displacement/rotation due to a point load/moment for a cracked body, we use Castigliano's theorem (Teda et al. 1973). For two dimensional part of unit dimension normal to the x-y plane subjected to Mode I loading, the displacements v on the surface at a distance s from the crack plane may be obtained by introducing the virtual forces F, shown in Fig. 6. This leads to

$$v(a,s) = \frac{\partial U}{\partial F}_{F=0} = \frac{1}{E'}\int_0^a K_I(a)\frac{\partial K_I^f(a,s)}{\partial F}da \qquad \textbf{(1)}$$

where a is the crack length, $E' = E$ and $E/(1-\mu^2)$ for plane stress and plane strain respectively, U is the change of the strain energy due to the crack, K_I and K_I^f are the stress intensity factors for an arbitrary stress on the crack faces and the virtual force F respectively. Only the opening at the mouth of the crack is of interest (twice of v under load F) so s = 0. For simplicity, the residual stress due to shot peening is approximated by a uniform stress σ_r from a = 0 to b as shown in Fig. 3. The corresponding K_I is negative and hence fictitious but is needed to obtain the displacements required for subsequent calculation. Using the expressions for K_I and K_I^f given by Cheng and Finnie (1988) and Tada et al. (1973), Eq. (1) becomes

$$v_r(a) = 2.9\frac{F_r}{E'}aH\left(\frac{b}{a}\right) \quad with \quad H\left(\frac{b}{a}\right) = \frac{b}{a}\int_{b/a}^{1} f(z)\,dz \qquad a \geq b \qquad \textbf{(2)}$$

where

$$f(z) = 1 - \left(\frac{2}{\pi}\right)\left(1-\frac{3}{28}\frac{b/a}{z}\right)\cos^{-1}\left(\frac{b/a}{z}\right) \qquad \textbf{(3)}$$

In Eq. (3) the dummy variable z represents the ratio of any intermediate crack size to the final crack size. Displacement v_r would only appear when the crack is entirely opened by external loading. To open the crack, we apply a uniform tensile stress σ_o over crack faces and the resulting displacement v_o can be obtained by setting *b/a* = 1 in Eq. (3). Thus, the stress required for opening the crack is obtained by equating v_o and v_r. This leads to $\sigma_o = \sigma_r H(b/a)$. Figure 5 shows the ratio of σ_o/σ_r against *b/a*. It is seen that the opening stress required decreases as the size of the crack increases. Now it is possible to determine the tensile stress required to open the crack for detection.

The Crack Compliance Method for Through-the-Thickness Residual Stress Measurement

The inverse problem of determining residual stresses from measurements of strain, displacement or stress intensity factor as a crack is introduced into a part received little attention until the past decade. Vaidyanathan and Finnie [1971] showed that measurements of stress intensity factor as a function of crack length could be used to deduce the residual stress due to a butt-weld between two plates. However, the experimental technique using a photoelastic coating to measure the stress intensity factor, was time consuming and unsuited to general application. A more useful procedure, which was subsequently extended to a variety of configurations, was developed by Cheng and Finnie [1985]. This involved measurements of strain as a function of crack depth to deduce the axial residual stress in a circumferentially welded cylinder. We refer to this approach as the "crack compliance method" because it is closely related to the solutions for the compliance due to a crack. Similar procedures were presented later by Fett [1987], Ritchie and Leggatt [1987] and Kang, et al [1989].

To explain the basis of the method we consider the strip shown in Fig. 6 which contains residual stresses $\sigma_y(x)$. For near surface stress measurement, which will be discussed later, one or more strain gages are located close to the mouth of the crack. For through-the-thickness stress measurement a strain gage is located on the back face of the strip. In either case the normal strain $\varepsilon(a,y)$ at location y = s produced by introducing a crack of depth *a* is given by differentiating Eq. (2),

$$\varepsilon(a,s) = \frac{\partial v(a,s)}{\partial s} = \frac{\partial^2 U}{\partial F \partial s}\bigg|_{F=0} = \frac{1}{E'}\int_0^a K_I(a)\frac{\partial^2 K_I^f(a,s)}{\partial F \partial s}da \qquad \textbf{(4)}$$

Since strains can be measured very precisely with strain gages, Eq. (4) provides a more useful approach than displacement or stress intensity factor measurement.

Consider a body with a residual stress distribution expressed in terms of a series expansion of order n with amplitude factor A_i defined for the i^{th} order term. We now introduce a crack or a very thin cut of progressively increasing depth to the body while measuring the change of the strain at location *s* as shown in Fig. 6. From linear superposition K_I can be expressed as

$$K_I = \sum_{i=0}^{n} A_i K_I^i(a) \qquad \textbf{(5)}$$

where K_I^i is the stress intensity factor corresponding to the stress given by the i^{th} term in the series expansion. Equation (5), when combined with Eq. (4), leads to

$$\varepsilon_j = \sum_{i=0}^{n} A_i C_i(a_j, s) \quad \textit{with} \quad C_i(a_j,s) = \frac{1}{E'}\int_0^{a_j} K_I^i(a)\frac{\partial^2 K_I^f(a,s)}{\partial F \partial s}da \qquad \textbf{(6)}$$

where ε_j is the strain measured when crack depth equals a_j and C_i is crack compliance functions. When the number of the strain measurements is greater than n+1, the unknown A_i can be determined

using a least squares fit which reduces the average error over all data points to the minimum.

Crack compliance functions for through-thickness residual stress measurements have been obtained for a number of geometries. Figure 7 shows a residual hoop stress distribution measured in a water-quenched thick-walled ring. The agreement with numerical computation and X-ray measurement at the surface is very good. The method is especially useful when the stress to be measured varies rapidly both with the distance from the plane of the cut and with the depth of cutting. Such a situation arises for example at the toe of a fillet weld or at any other welded junction. X-ray and layer removal techniques are not well suited to such problems.

The Slit Compliance Method for Near-Surface Residual Stresses Measurement

In this case the width of the cut is usually not negligible, and the compliance functions for a slit instead of a crack are obtained using the body force method [Nisitani, 1978]. Similar to the hole-drilling method, strain gages are located on the surface near the cut. However, the actual distance measured from the strain gage to the cut is used in the computation of the compliance functions to eliminate the mis-alignment error which is often associated with the hole-drilling method. The strain response obtained by the slit compliance method has been shown to be more than twice of that obtained by the hole-drilling [Cheng and Finnie, 1993].

Residual stresses produced by surface treatment or cladding usually vary rapidly over a small distance below the surface. A least squares fit using a single continuous function may become unstable for numerical computation as the order of prediction increases. To solve this problem, we have developed a general procedure combining the least squares fit with lower order overlapping piecewise functions [Gremaud, et al. 1994] and implemented it for estimation of near surface stresses. Experimental results show that this procedure is capable of measuring stresses with a very steep gradient which failed to be detected by the X-ray diffraction method. Figure 8 shows a comparison of the residual stress distribution in a laser-treated specimen measured by the slit compliance and by the X-ray method with layer removal. The slit compliance method has also been used to measure the stress due to shot-peening and shows good agreement with X-ray measurements.

Using a specially made electrode for EDM, cuts of almost uniform depth can be introduced on a curved surface. Measurements can now be made at locations such as inside a valve body where other techniques would be impossible to implement without cutting the specimen apart.

Discussion

Griffith's classic work is revisited to show the influence of residual stresses on the tensile strength of glass in moist and inert environments.

The phenomenon of crack closure due to the residual stress in the wake of a propagating crack is familiar to those working in fatigue. However, the fact that surface compressive stresses may lead to closing of the crack mouth does not appear to have been fully appreciated in the area of non-destructive inspection for cracks.

The equivalence of energy release rate and the stress intensity factor, which is required to derive Eqs. (2) and (6), was shown in Irwin's classic paper in 1957. However, apart from a limited step in 1971, the use of LEFM for residual stress measurement has been developed only in the past decade. We have reviewed this recent work which appears to improve measurement procedures for many practical configurations.

References

Cheng, W. and Finnie, I., 1985, "A Method for Measurement of Axisymmetric Residual Stresses in Circumferentially Welded Thin-Walled Cylinders," ASME, J. of Eng. Mat. and Tech., **106**, 181-185.

Cheng, W. and Finnie, I., 1988, "K_I Solution for an Edge-Cracked Strip," Eng. Fracture Mech., **31**, 201-207.

Cheng, W. and Finnie, I, 1992, "A Prediction on the Strength of Glass Following the Formation of Subsurface Flaws by Scribing," J. of the American Ceramic Society, **75**, 2565-2572.
Cheng, W. and Finnie, I., 1993, "A Comparison of the Strains due to Edge Cracks and Cuts of Finite Width With Applications to Residual Stress Measurement", ASME J. of Eng. Mat. and Tech., **115**, 220-226.
Fett, T., 1987, "Bestimmung von Eigenspannungen mittels bruchmechanischer Beziehungen," VDI-Verlag GmbH, Düsseldorf , 92-94.
Gremaud, M., Cheng, W., Prime, M. B. and Finnie, I., 1994, "The Compliance Method for Measurement of Near Surface Residual Stresses - Analytical Background," ASME J. of Eng. Mat. and Tech. **116**, 550-555.
Griffith, A. A., 1921, "The Phenomena of Rupture and Flow in Solids," Phil Trans., **221A**, 163-198.
Kang, K. J., Song, J. H. and Earmme, Y. Y., 1989, "A Method for the Measurement of Residual Stresses Using a Fracture Mechanics Approach," J. of Strain Analysis, **24**, 23-30.
McClintock, F. A. and Argon, A. S., 1966, Mechanical Behavior of Materials, P. 496. Addision-Wesley, Reading, MA.
Nisitani, H., 1987, Stress Analysis of Notch Problems, Mechanics of Fracture Vol. 5, Edited by G. C. Sih, Noordhoff Int. Publishing.
Ritchie, D. and Leggatt, R. H., 1987, "The Measurement of the Distribution of Residual Stresses Through the Thickness of a Welded Joint," Strain, 61-70.
Tada, H., Paris, P. and Irwin, G., 1973, The Stress Analysis of Cracks Handbook, Del Research Corporation, PA.
Vaidyanathan, S. and Finnie, I., 1971, "Determination of Residual Stresses from Stress Intensity Factor Measurement," Trans ASME, J. Basic Eng. **93D**, 242-246.

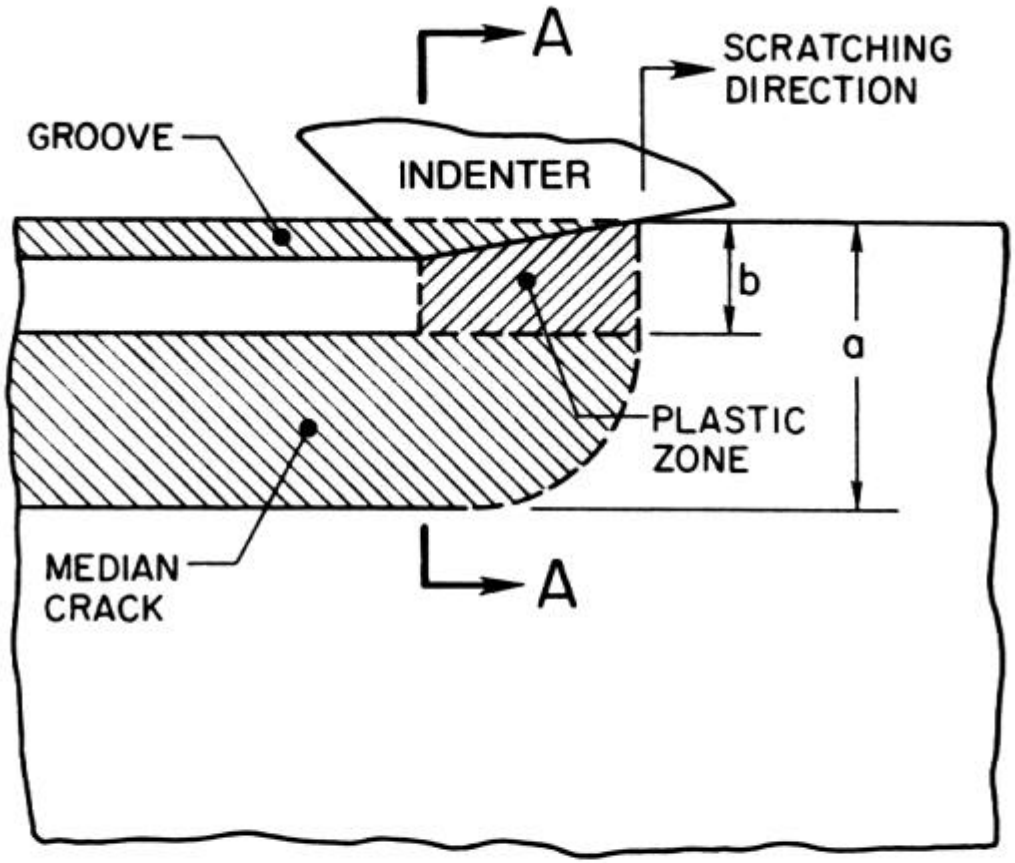

Fig. 1. Schematic cross section of scratching viewed perpendicular to scratching direction.

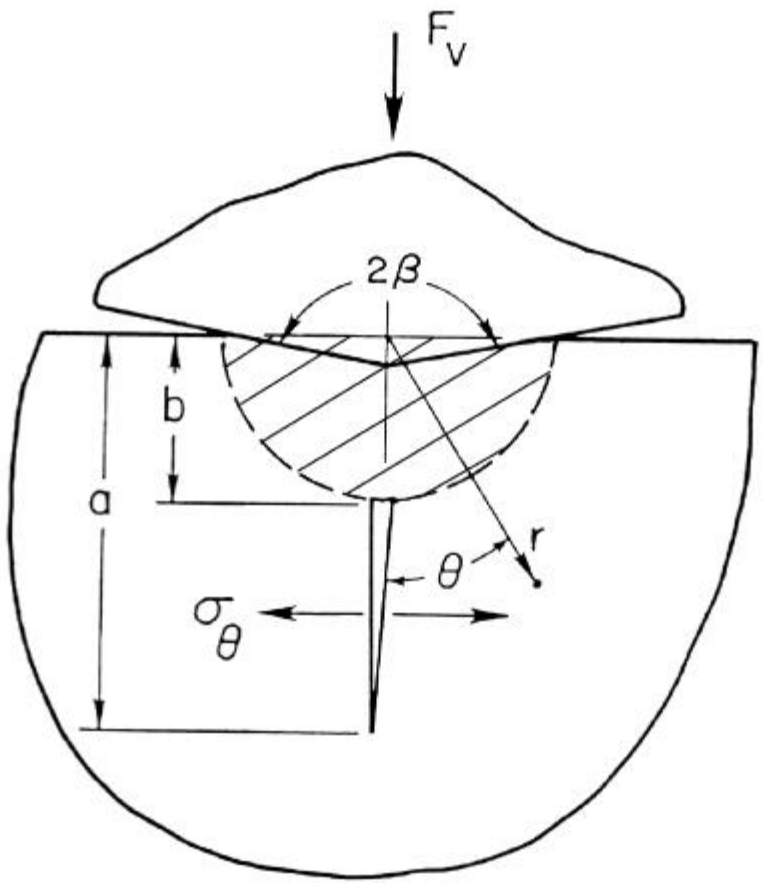

Fig. 2. Schematic view of the permanent deformation and a median crack looking in the direction AA shown in Fig. 1.

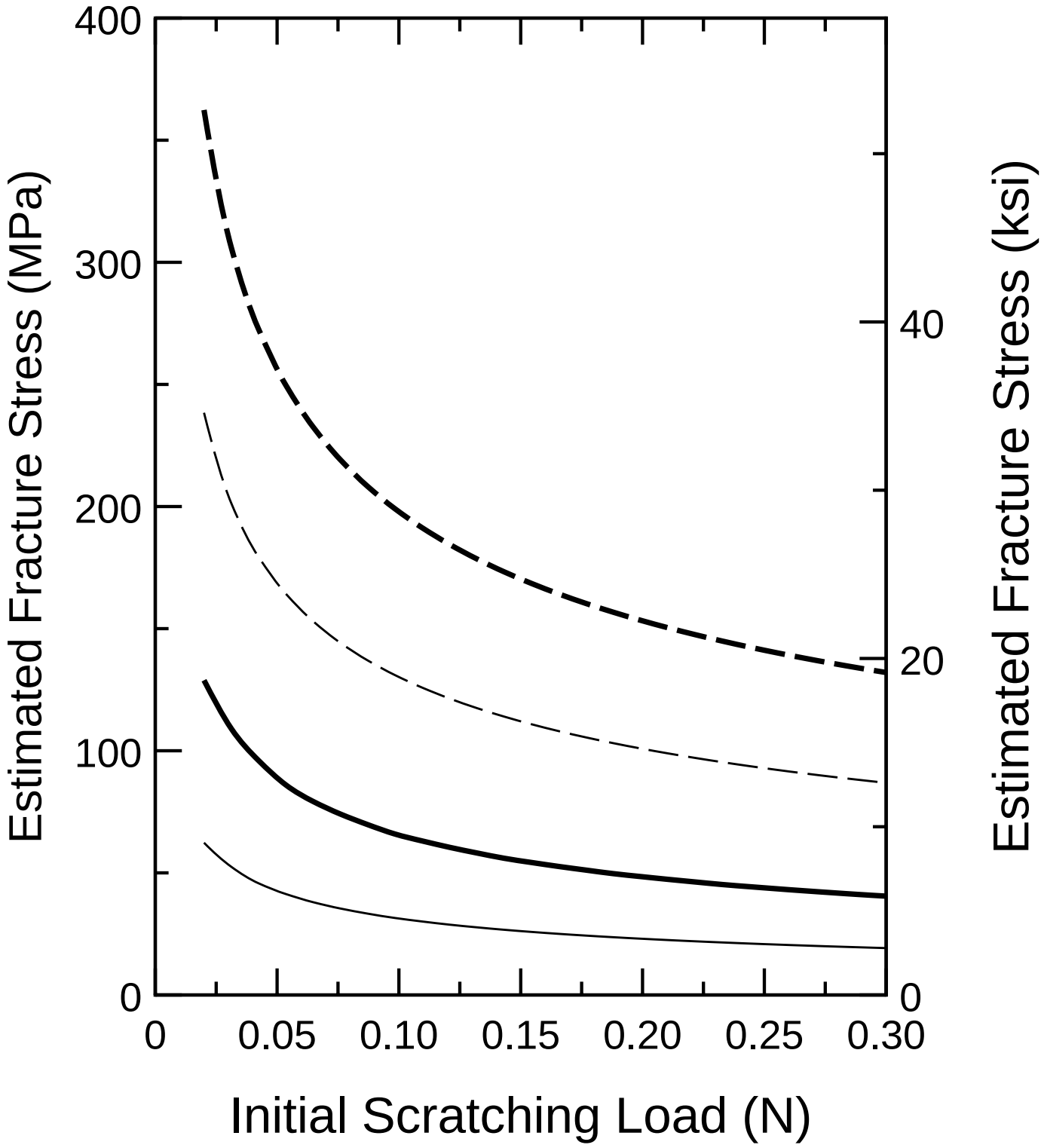

Fig. 3 Prediction of tensile strength of soda-lime glass as a function of scratching load dry air ignoring residual stress (heavy dashed line) and with residual stress (heavy solid line). For moist air the corresponding predictions are shown by the thin dashed and solid lines.

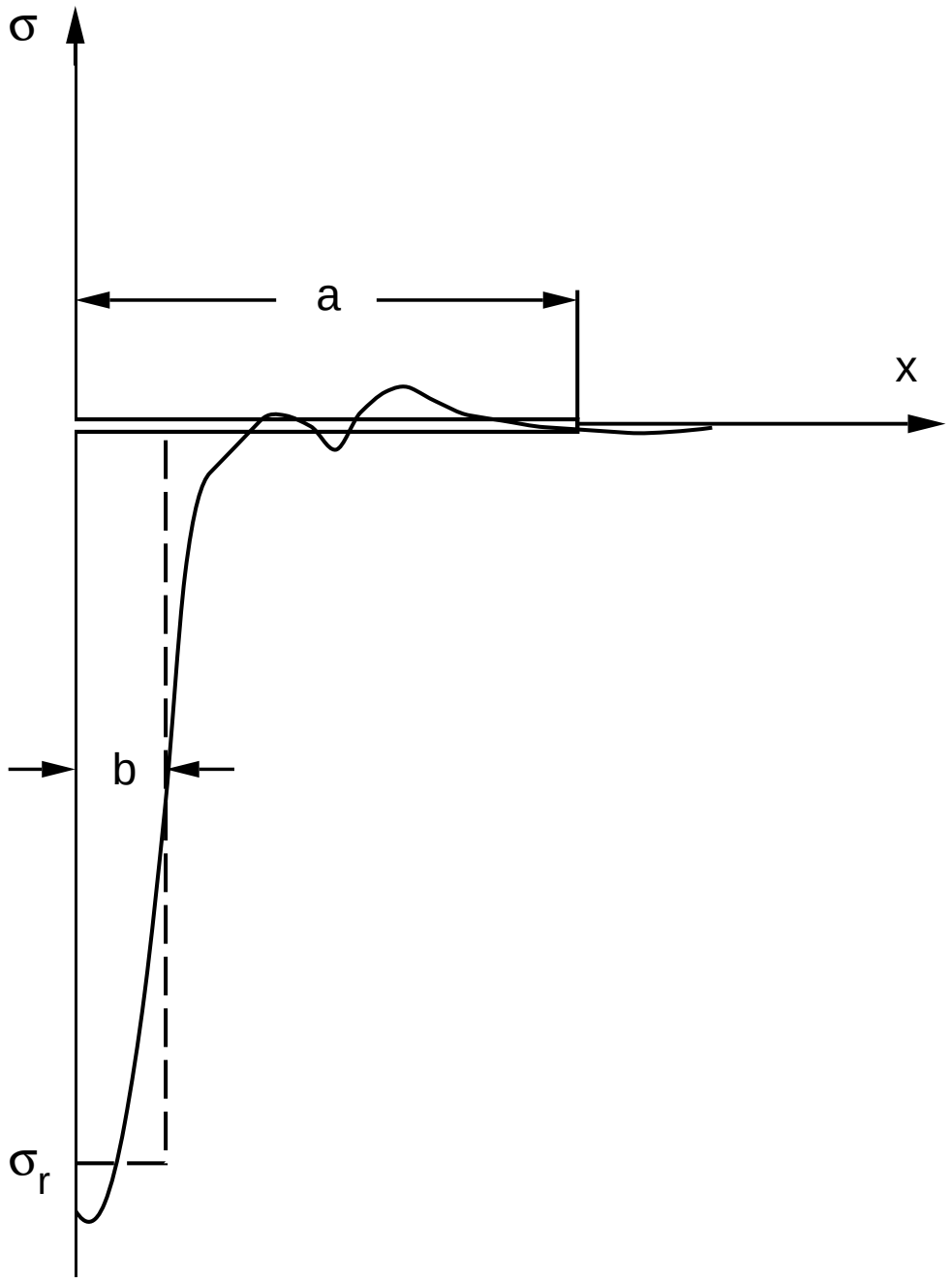

Fig. 4 Schematic of residual stress measured for a typical shot-peening application (solid line) and approximation by a rectangular distribution

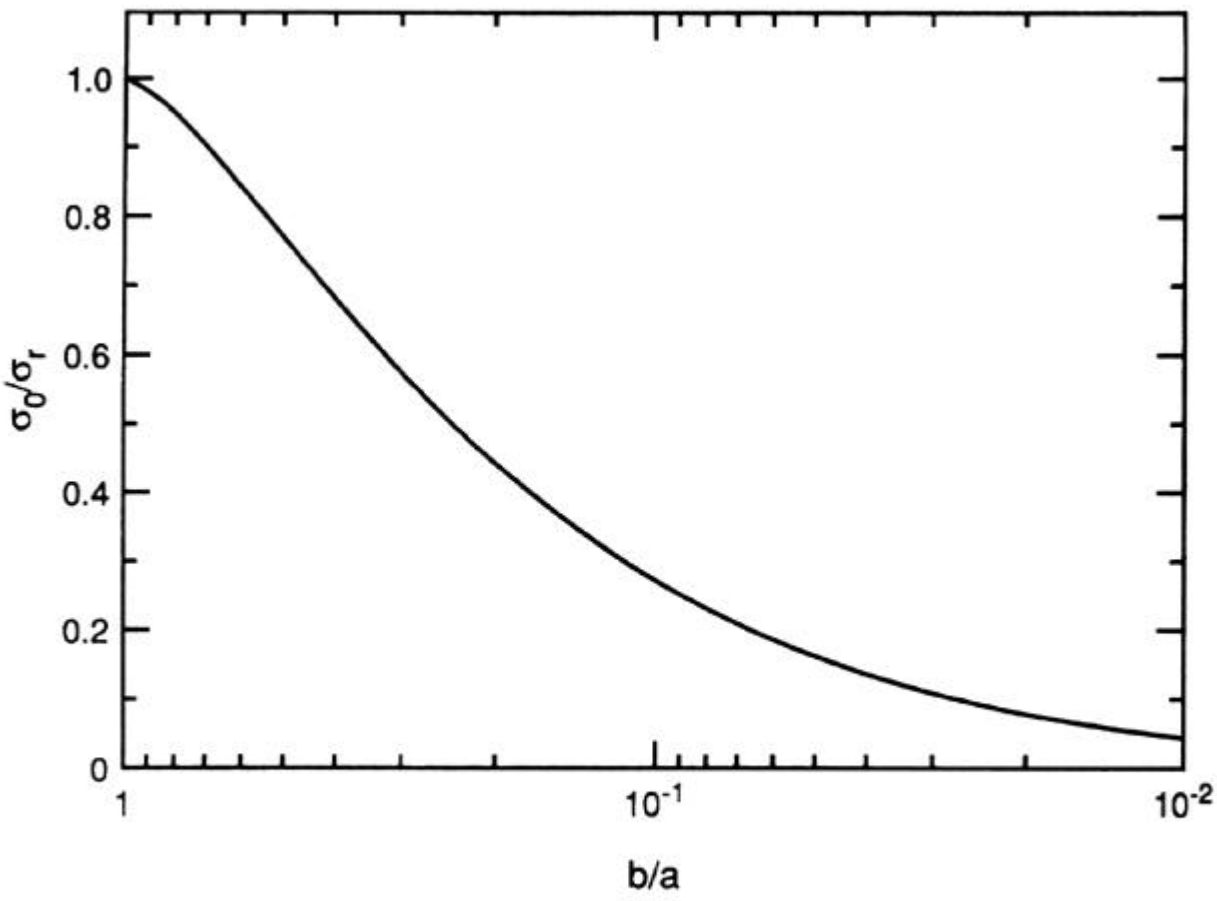

Fig. 5 The ratio of the opening stress to the magnitude of the residual stress as a function of *b/a*

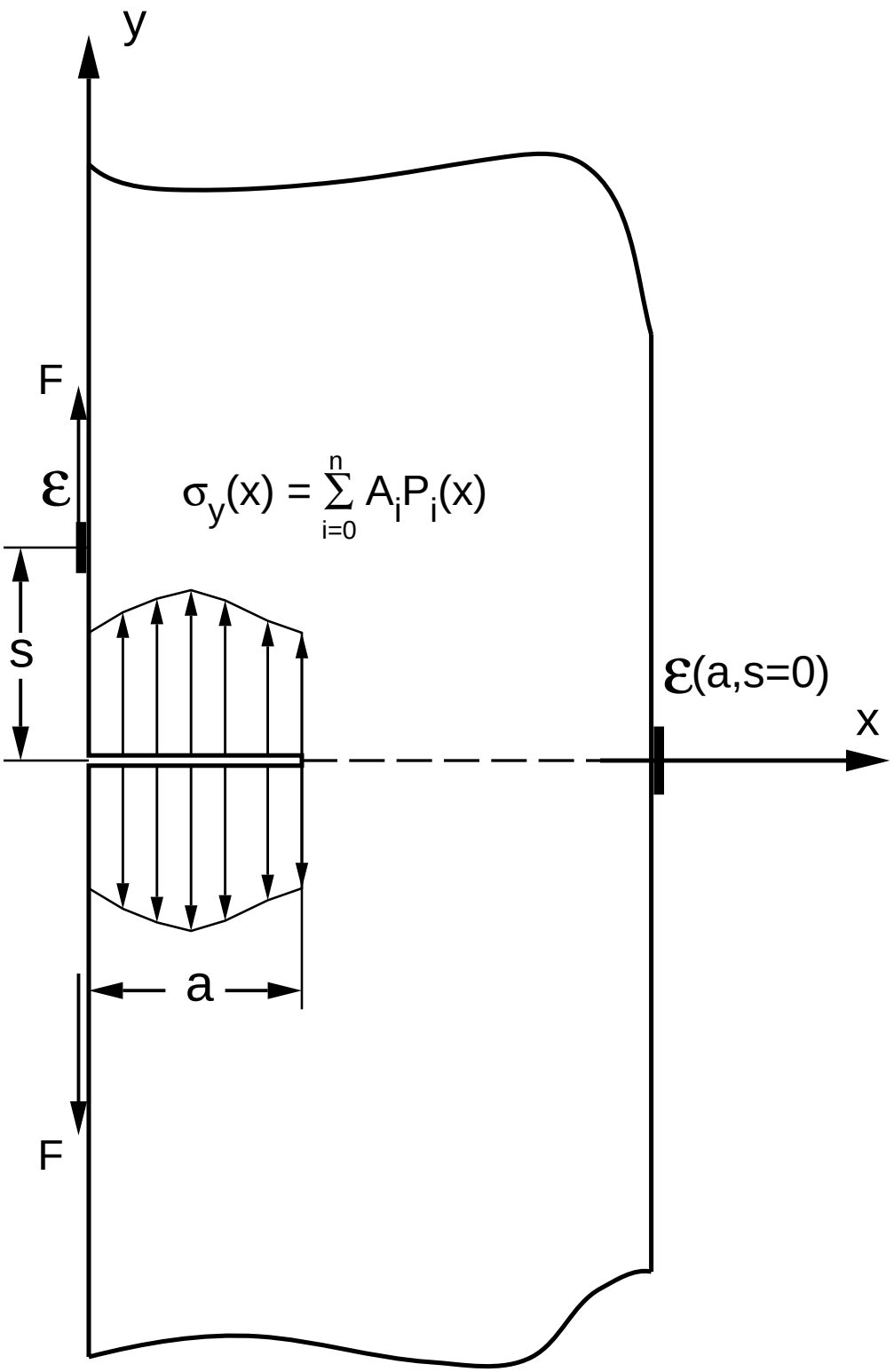

Fig. 6 A thin cut is introduced in a body with residual stress while strains are measured at selected locations

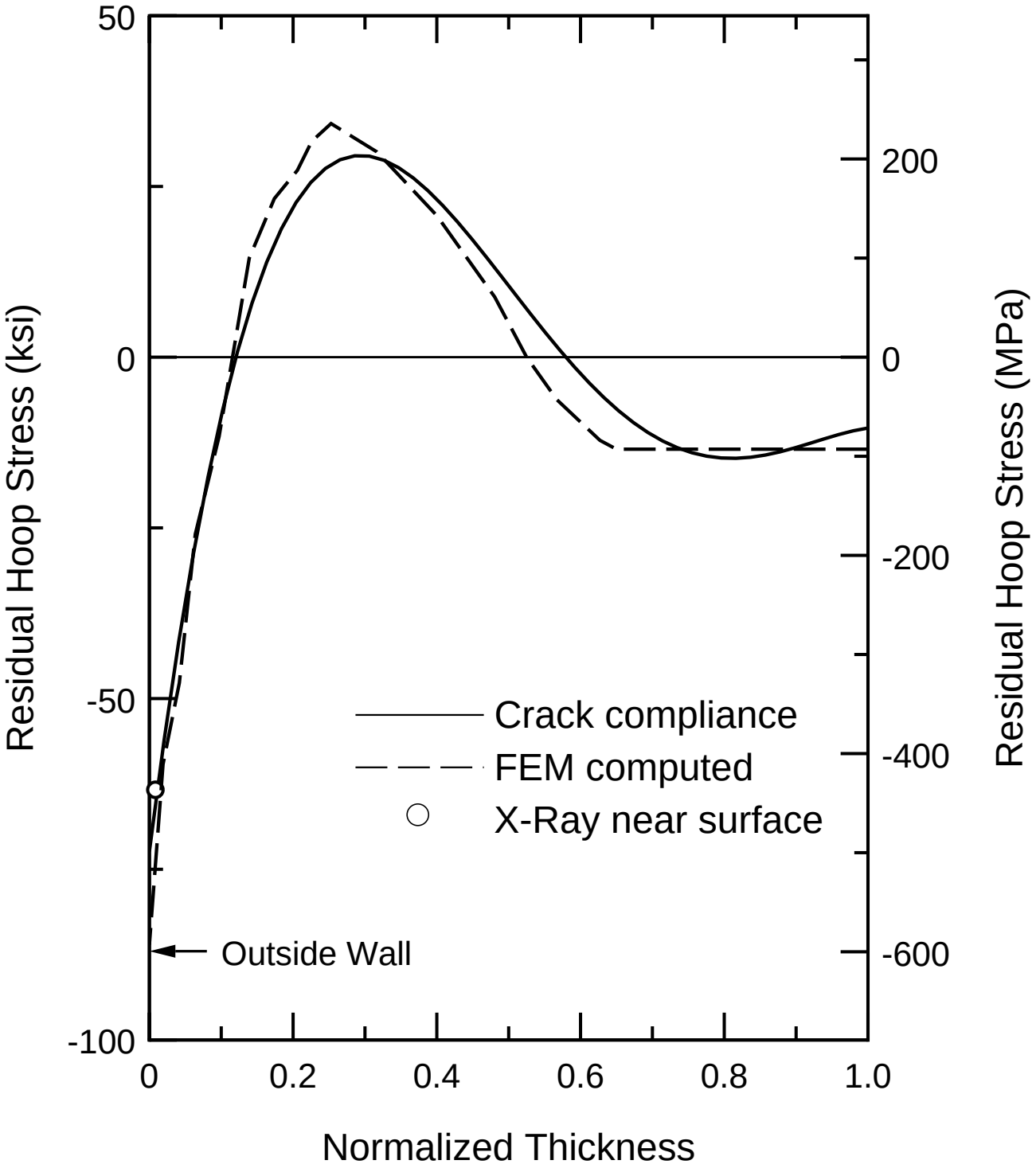

Fig. 7 Residual hoop stress in a water-quenched thick-walled ring measured by the present method (solid line) compared with numerical computation by FEM (dashed line). The near surface stress (data point) was measured by X-ray method.

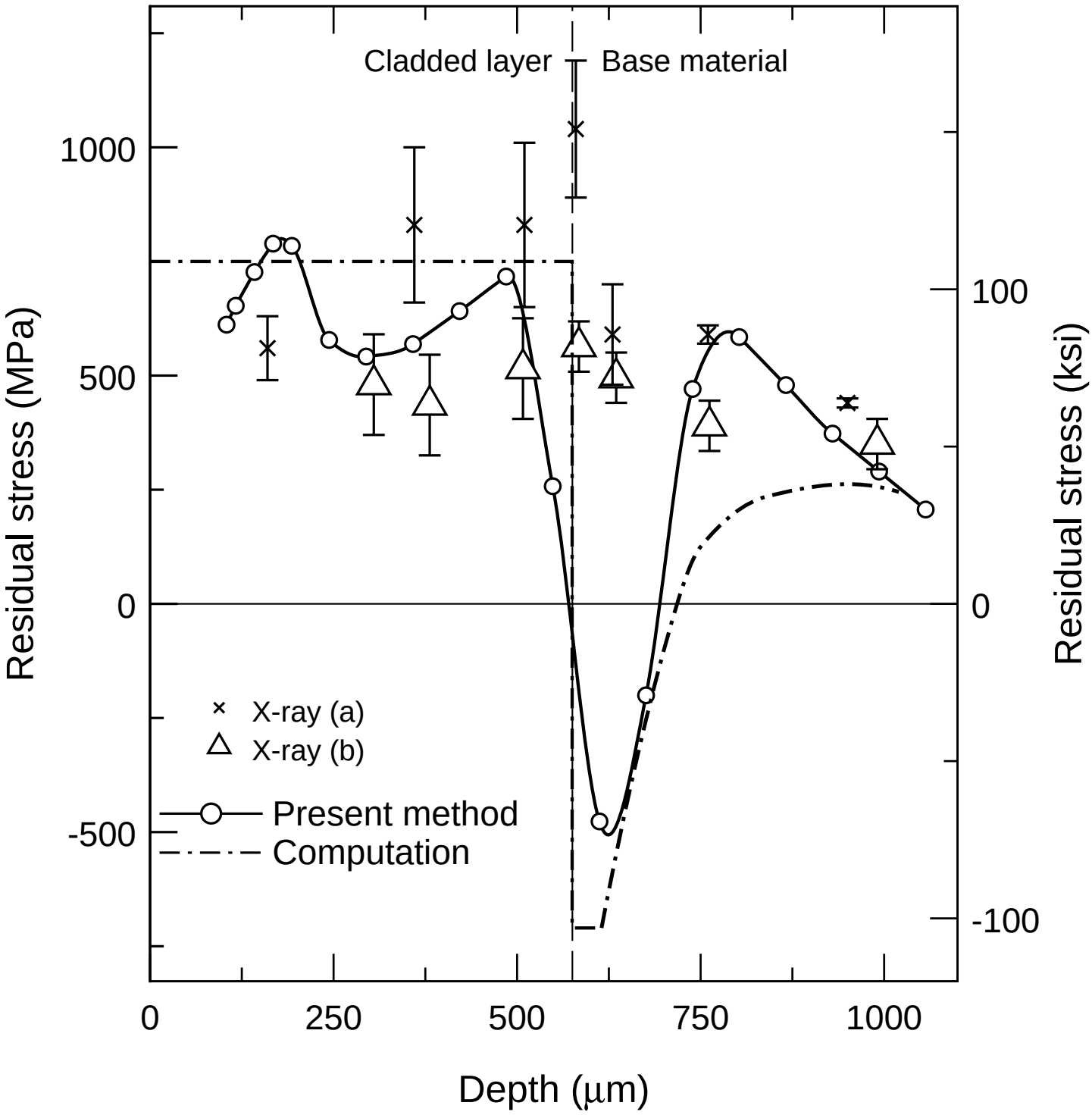

Fig. 8 Residual stress due to laser surface treatment measured by the present method and by the X-ray method from two independent laboratories. The dashed line represents approximate numerical computation

AN EXPERIMENTAL INVESTIGATION OF DYNAMIC INELASTICITY AND FRACTURE OF NANOSTRUCTURED COATINGS

H. D. Espinosa, Z. Wu and B. C. Prorok

Department of Mechanical Engineering, Northwestern University
Evanston, IL 60208-3111, USA

ABSTRACT

The strength and ductility of nanocrystalline WC-Co cermets was evaluated with a modified Kolsky torsional bar. The test specimen structure consisted of a thin walled Al7075-T6 substrate 250 μm thick coated with a 250 μm thick WC-Co layer with an average grain size of 100 nm. Dynamic torsion tests indicated the coating strength to be ≅ 200 MPa. The coated specimens exhibited quasi-ductile behavior in that, after diffuse microcracking and failure of the coating, the aluminum substrate takes control of the post failure behavior.

The use of high-speed photography showed that damage to the coating occurred at the point where maximum load was attained. A sudden drop in load carrying capacity was observed when cracks coalesced into a well-defined fracture plane. This drop was immediately followed by load reduction governed by plastic deformation of the Al substrate

INTRODUCTION

WC-Co cermets are employed mainly as wear resistant materials. Properties of high hardness and toughness have encouraged their widespread use in a variety of applications, including mining, grinding, and metal cutting. Conventional grades of these cermets possess grain sizes in the 1-10 μm regime, with a morphology composed of a hexagonal WC phase bound together with a Co phase. Mechanical properties are significantly influenced by this microstructure in that hardness increases with grain size in accordance with the Hall-Petch relation [1,2].

Recent work has indeed demonstrated that nanostructured cermets offer improved mechanical properties over their coarse-grained counterparts [3]. Nanostructured materials are of great interest in systems where nano-grained morphology may improve the yieldability of what would otherwise be brittle materials. As a result they possess high interface-to-volume ratios that can expand plasticity and strain to failure of normally brittle materials [4,5]. Nanostructured materials can also exhibit increased hardness that follows the Hall-Petch relation to a critical point prior to saturation [6,7]. These benefits stem from the large number of nano-sized grains per unit volume and their accompanying large interface-to-volume ratio [5,8]. The presence of porosity in a nanostructured material can result in a lower than expected hardness and affects various other mechanical properties as well [9,10]. For the WC-Co cermet material, properties of increased hardness and enhanced strain to failure are very desirable. These advantages have been well documented for other submicrometer-grain-sized ceramics [11-14].

The wear resistant applications of WC-Co cermets inevitably expose them to mechanical conditions involving local dynamic loading and high strain rates. Testing of materials under such loading conditions present special challenges [15]. Dynamic fracture toughness can be evaluated by a number of techniques that include: Charpy test [16,17], drop-hammer experiment [18], and plate-impact experiment [19]. In employing these methods, the energy applied to the specimens is considerable, resulting in unstable growth upon crack initiation. Similarly, damage and inelasticity can be addressed using dynamic testing with specimen recovery [20-22]. A further consequence of these methods stems from computational and theoretical considerations that make up the basis for identifying damage initiation and evolution [23-24].

It is essential for present and future application design that we are able to predict the high strain rate response of the cermet material. With this in mind, a simple and accurate technique for studying dynamic loading conditions is the modified split Hopkins pressure bar [25]. This method has the advantage of loading the material under nearly uniform stress and strain rate. The integration of high-speed photography allows for the continual monitoring of specimen shape during testing. By this approach, a correlation can then be made between failure initiation and the stress-strain state of the specimen. This work investigates the response of WC-Co nanostructured materials under high strain rate conditions and examines the effect of loading rate on failure mode. It also evaluates the strength and ductility of the nano-grain sized coatings with unique instrumentation and specimen configuration.

EXPERIMENTAL PROCEDURE

Materials and processing

Nanocrystalline WC-Co coatings of 250 μm thickness were produced by a proprietary spraying process developed by A&A Company, Inc., South Plainfield, NJ. In this study, the alloy Al7075-T6 was machined as a thin-walled tube and used as the substrate. Both coated and uncoated aluminum specimens were tested to evaluate the mechanical properties of the nanocoatings. The geometrical dimensions of the WC-Co nano-coated samples used in the dynamic torsion test are given in Figure 1(a). The Young's modulus and Poisson's ratio of WC-Co and Al7075-T6 are: E_C = 520 GPa, ν_C = 0.28, and E_{Al} = 70.9 GPa, ν_{Al} = 0.36, respectively. Figure 1 shows micrographs of (b) micro-sized (3-4 μm) and (c) nano-sized (100 nm) grain structures. The micro-sized material provided a basis for comparison in the micro- and nano-indentation experiments. Both materials had the same 11 percent cobalt content. The surfaces of the coated specimens were painted with a very fine speckle pattern that was essential for imaging by high-speed photography and for strain analysis by digital speckle correlation. The ends of the sample were fixed to the incident and transmission bars by means of a high strength and fast curing adhesive (DEVCON 5 minute epoxy).

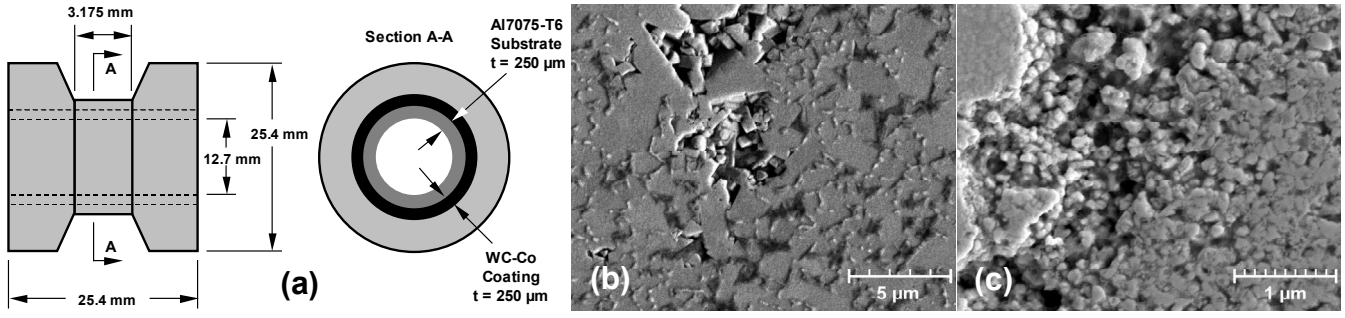

Figure 1: Schematic representation of WC-Co nanocrystalline coated dynamic torsion specimen (a). The dimensions of the Al7075-T6 substrate are identical for uncoated specimens. Photomicrograph of WC-Co (b) micro- and (c) nano-grain sized structures.

Mechanical testing

Our modified stored-energy Kolsky bar was used to obtain shear-stress / shear-strain curves at high strain rates [22,26,27]. The bar was integrated with a high-speed photography rig to observe deformation events and correlate them to specific points along the stress-strain curve.

High-speed photography

High-speed photography was used to independently monitor specimen inelasticity during testing. A Cordin Model 220-8 camera and K2 long distance microscope were used with a SUNPAK Auto 120J TTK high-power flash to acquire the images. Frames were captured at 20 μs intervals with exposure times of 1 μs. The incident pulse from the modified Kolsky bar was used to trigger the camera and flash.

Formulae

The functional dependence of strain rate on the incident, reflected, and transmitted shear strains for a single material specimen has been previously reported [28]. For a double-layered specimen, such as the WC-Co nano-coating on aluminum thin-walled substrate (see Figure 1(a)), the stresses and strains are obtained from the following equilibrium and compatibility relations:

$$T_T = G_{Al} \cdot I_{p,Al} \cdot \frac{\gamma_{Al}}{r_{Al}} + G_C \cdot I_{p,C} \cdot \frac{\gamma_C}{r_C} \quad , \quad \tau_{Al} = G_{Al} \cdot \gamma, \ \tau_C = G_C \cdot \gamma \tag{1}$$

$$\gamma_{Al} = \gamma_C = \frac{T_T}{G_{Al} \cdot 2\pi r_{Al}^2 t_{Al} + G_C \cdot 2\pi r_C^2 t_C} \tag{2}$$

where T_T is the transmitted torque, G is the shear modulus, I is the polar moment of inertia, γ is the shear strain, τ is the shear stress, r is the center line radius, and t is the shell thickness of the aluminum (AL) and of the coating (C). It is important to note that homogeneous deformation and compatibility in the double-layered specimens is violated when debonding at the aluminum-WC/Co interface or shear localization occurs.

RESULTS AND DISCUSSION

Dynamic Torsion

Shear stress – shear strain curves.

Three thin-walled sample configurations were selected for study. The first was an Al7075-T6 alloy thin-walled tube of thickness 250 μm coated with a 250 μm thick nanostructured WC-Co cermet. The second and third were uncoated Al7075-T6 thin-walled tubes of thickness 250 and 500 μm respectively, used comparatively for evaluating the nanocoatings mechanical properties.

The measured transmitted torque of the above samples is plotted as a function of time in Figure 2(a). For both uncoated Al7075-T6 specimens, (◇) denotes 250 μm thickness and (□) denotes 500 μm, the transmitted pulse has an extended steady state region at the top of the curve with large plastic deformations being recorded. However, for the WC-Co coated sample (◆), the transmitted pulse drops quickly after maximum transmitted torque is reached. This indicates that the WC-Co coating exhibits a quasi-brittle behavior and fractures at small inelastic deformations when compared to thin-walled Al7075-T6 specimens. The doubling of the wall thickness for the uncoated Al specimens translated into a doubling of the maximum transmitted torque as well as its steady state duration. The thin aluminum samples were found to be broken after the shear tests, a result of shear localization followed by fracture. This explains the reduction in transmitted pulse time to approximately one half of the pulse duration.

The WC-Co coating material is well bonded to the aluminum substrate. When this coating fails, the transmitted torque rapidly drops to a lower level before progressively decaying to zero. This indicates the inner-aluminum layer controls the post failure behavior. Furthermore, in view that the Young's modulus of WC-Co is much greater than that of Al7075-T6, the plastic deformation of the inner-aluminum layer is then constrained to a much narrower region. Thus, the total plastic deformation, on the whole specimen length, was smaller than in the case of the uncoated aluminum specimen. It can be expected that this sudden loss of load carrying capacity of the coating triggers shear localization in the aluminum substrate. This phenomenon was found to exist in all WC-Co nanocoated specimens subject to varying levels of incident

torque. Figure 2(b) is a plot showing transmitted torque signatures for specimens with incident torques of 200 Nm (●), 190 Nm (◆), 180 Nm (△), and 130 Nm (⊡). It should be noted that they are plotted on an arbitrary time scale to separate their signatures and that each data set lasted for a period of ≅ 250 μs. It is important to note that a higher incident torque did not always correspond to a higher transmitted torque. For example, the 180 Nm incident torque specimen exhibited the highest transmitted torque.

The shear stress and shear strain are easily obtained from the transmitted torque results via Eqs. (1) and (2). The shear stress and shear strain relationship that correspond to the experimental results in Figures 2(a) and 2(b) are plotted in Figures 2(c) and 2(d) respectively. Figure 2(c) compares the shear stress - shear strain relationship between the coated, (◆), and uncoated specimens, (◇) for 250 μm thickness and (□) for 500 μm. The 0.2 percent yield offset for both uncoated Al7075-T6 specimens was ≅ 185 MPa. The maximum shear stress was ≅ 220 MPa with corresponding shear strain of ≅ 20 percent and matches well with those reported in the literature. The results for the thin- and thick-walled samples are almost identical with exception to an extended plastic zone and a sharper decrease in shear stress toward failure.

For the coated specimen (◆), the maximum shear stress was ≅ 200 MPa. The abrupt drop after attaining maximum shear stress indicated that micro-cracking began with the offset of yielding by the substrate. As observed in the transmitted torque results discussed earlier, following the sudden drop in shear stress, the average plasticity leveled off and progressively decayed to complete failure. This is a clear indication that the inner-aluminum layer controls the post failure behavior.

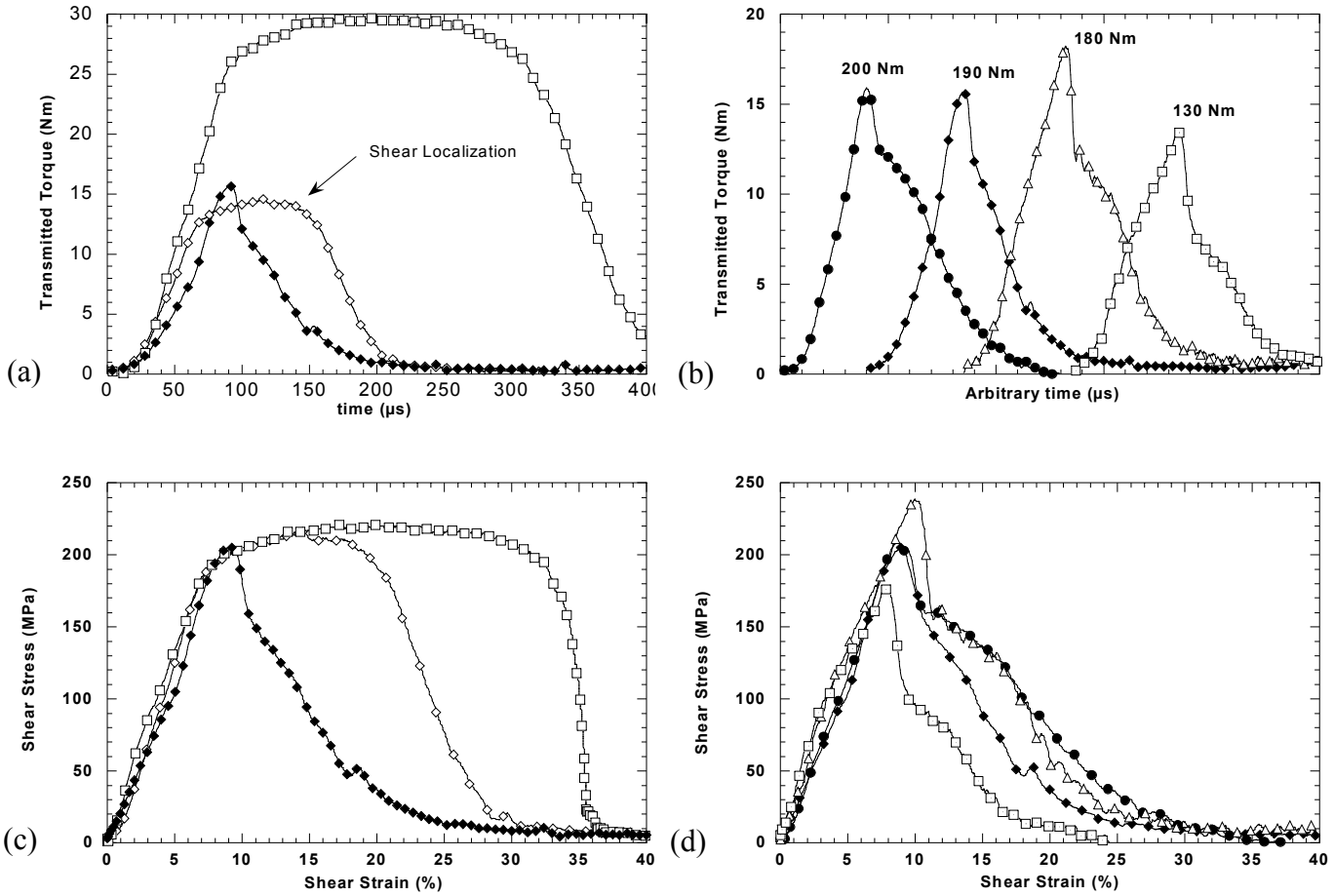

Figure 2: Transmitted torque-time signatures, (a) and (b), and the calculated shear stress - shear strain signatures, (c) and (d). Where (◆) denotes the nanocoated specimen, (◇) and (□) demote the uncoated Al7075-T6 thin-walled tubes of thickness 250 μm and 500 μm respectively, and various incident torques of nanocoated specimens are; 200 Nm (●), 190 Nm (◆), 180 Nm (△), and 130 Nm (⊡).

This transition in failure behavior was also observed in all coated samples with varying applied incident torque, Figure 2(d). In these data, the maximum shear stress attained for the coated specimens was ≅ 200 ± 30 MPa, reaching a maximum when the incident torque was 180 Nm. The absence of an extended strain to

failure region in the stress-strain curve for the nanocoated specimens is likely the result of extensive porosity in the coating material. This aspect was identified in the hardness discussion above.

The hardness of the micro- and nano-grain sized WC-Co was evaluated and revealed that hardness remained relatively uniform in the micro-indentation regime for both grain-size structures yielding values between 12–13 GPa. Nano-indentation revealed a significant change in behavior where the micro-sized material exhibited an increase in hardness to ≅ 20 GPa while the nano-sized material first showed hardness to be equivalent to the micro-indentation data at a depth of 500 nm and then increased to ≅ 20 GPa at a depth of 200 nm. Given the degree of coating porosity of the nano-sized material, the microstructure consists of hard agglomerates (clusters of nano-sized crystals strongly bonged together) that likely behave in a manner similar to the micro-grained material during the indentation tests.

High-speed photography.
Figure 3(a) is a series of images showing the surface of the coated thin-walled specimen. This series depicts a time sequence during torsional loading where a speckle pattern applied to the surface is used to determine the relative shear deformation experienced by the specimen. Two areas of the surface are denoted with a square (A) and a circle (B) that track the movement of specific speckles relative to each other. For the specimen in Fig. 9, the position of square A does not significantly change during the test. However, circle B was observed to displace continuously over time as a result of coating cracking and shear localization. After 70 μs circle B moved 21.2 μm relative to square A, resulting in an average shear strain of 2.85 percent. After 90μs the displacement increased to 105.8 μm and the average shear strain increased to 14.2 percent. There is also the initiation of a crack denoted by the arrow. Displacement and average shear strain increased with time until failure. These strains are a localized examination and differ from those calculated in Figure 2 under the homogeneous deformation assumption.

Synchronization of strain analysis and high-speed photography.
The data from dynamic torsion testing can be synchronized with the frames obtained from high-speed photography by matching their time scales. Figure 3(b) is a plot of the transmitted torque versus time for the coated specimen. Superimposed on this plot are the time markers for when each frame of Figure 3(a) was acquired during the test. Frames 1 (0 μs) and 2 (70 μs) were captured before the maximum transmitted torque was attained. When the microcracks coalesce into a dominant crack the coating fails and the aluminum substrate then governs the deformation behavior until failure.

CONCLUSIONS

Specialized equipment and specimens were developed to investigate strength and ductility of nanocrystalline WC-Co coatings. Dynamic torsion experiments with well-defined stress pulses were performed. These experiments revealed that the strength of WC-12%Co cermets, with an average grain size of about 100 nm, was about 200 MPa. The coating exhibits a quasi-ductile behavior as observed in deformation patterns. High-speed photography carried on in real time showed that coating damage occurred in the vicinity of the stress peak. Furthermore, the images revealed that a sudden drop in load carrying capacity coincides with micro-crack coalescence leading to the formation of a well-defined fracture plane in the coating. The stress peak in the coated material also coincides with the onset of large plastic deformation of the aluminum substrate. It is likely that shear localization in the aluminum thin-walled specimen is triggered by fracture of the coating and subsequently confined to the narrow region of the failed coating. The end result is the overall splitting of the specimen in two pieces.

Although the properties of the WC-Co nano-coating were far from optimum, a new methodology for investigating failure has been established. This methodology can be applied to examine the behavior of other advanced materials that can be manufactured as coatings on ductile substrates.

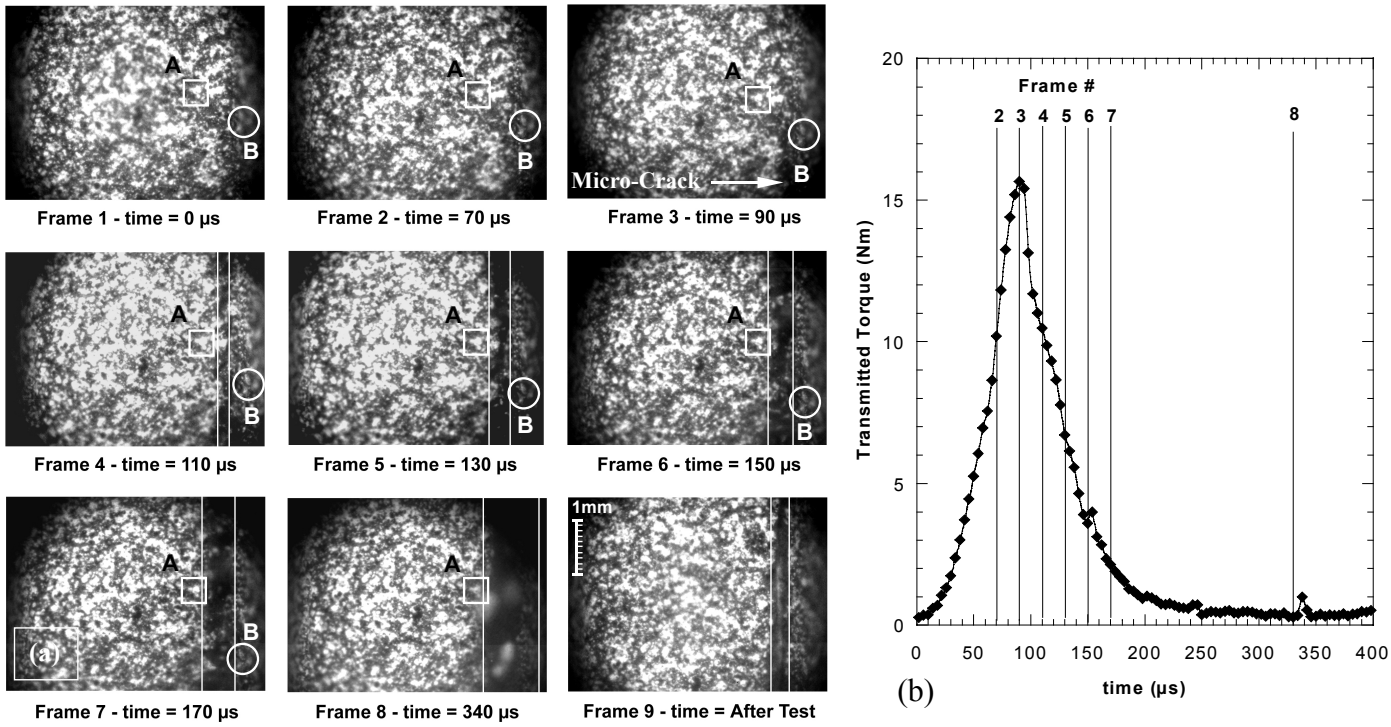

Figure 3: (a) High speed photography images taken during a dynamic shear test and (b) synchronization of frames with dynamic strain analysis data (b).

REFERENCES

1 Halls, E.O. (1951), *Proc. Phys. Soc. Lond.*, B64, 747.
2 Petch, N.J. (1953), *J. Iron Steel Inst.*, 174, 25.
3 Zhang, Z., Wahlberg, S., Wang, M., and Muhammad, M. (1999), *Nanostruc. Mater.*, 12, 163.
4 Kung, H. and Foecke, T., *ibid.*, 14.
5 Weertman, J.R., Farkas, D., Hemker, K., Kung, H., Mayo, M., Mitra, R., and van Swygenhoven, H. (1999), *MRS Bulletin*, 24(2), 44.
6 Nieh, T. G. and Wadsworth, J. (1991), *Scripta Metall. Mater.*, 25, 955.
7 Scattergood, R.O. and Koch, C.C. (1992), *ibid.*, 27, 1195.
8 Coble, R.L. (1965), *J. Appl. Phys.*, 34, 1679.
9 Mayo, M.J., Siegel, R.W., Narayamy, A., and Nix, W.D. (1990), *J. Mater. Res.*, 5, 973.
10 Mayo, M.J., Siegel, R.W., Liao, Y.X., and Nix, W.D. (1992), *ibid.*, 7, 1073.
11 Nieh, T.G., McNally, C.M., and Wadsworth, J. (1989), *J. Met.*, 31.
12 Maehara, Y. and Langdon, T.G. (1990), *J. Mater. Sci.*, 25, 2275.
13 Nieh, T.G., Wadsworth, J., and Wakai, F. (1991), *Int. Mater. Rev.*, 36, 146.
14 Mayo, M.J. (1997), *Nanostruc. Mater.*, 9, 717.
15 Espinosa, H.D. and Nemat-Nasser, S. (2000), *ASM Handbook, Mech. Testing and Evaluation*, 8.
16 Ruiz, C. and Mines, R.A.W. (1985), *Int. J. Fracture*, 29, 101.
17 Kobayashi, T., Yamamoto, I., and Niinomi, M. (1986), *Engineering Fracture Mechanics*, 24, 773.
18 Eftis, J. and Krafft, J.M. (1965), *J. of Basic Engineering, Trans. ASME*, 257, 89.
19 Prakash, V. and Clifton, R. (1993), *Trans. ASME*, 165, 412.
20 Subbash, G. and Ravichandran, G. (2000), *ASM Handbook, Mechanical Testing and Evaluation*, 8.
21 Nemat-Nasser, S., *ibid*.
22 Espinosa, H.D., Patanella, A., and Xu, Y. (2000), *Exp. Mech.*, 40(3), 1.
23 Espinosa, H.D., Zavattieri, P.D., and Dwivedi, S. (1998), *J. Mech. and Phy. of Sol.*, 46(10), 1909.
24 Zavattieri, P.D., Raghuram, P., and Espinosa, H.D. (2000), *J. Mech. and Phy. of Sol.*, 49, 27.
25 Kolsky, H. (1949), *Proc. Phys. Soc. Lon.*, B62, 676.
26 Espinosa, H.D., Patanella, A., and Fischer, M. (2000), *J. Tribology*, 122, 1.
27 Ibid. (2000), *Exp. Mech.*, 40(2), 138.
28 Meyers, M.A. (1994), *Dynamic Behavior of Materials*, John Wiley & Sons Inc., New York, 305.

AN EXPERIMENTAL MODEL OF VOID GROWTH AND COALESCENCE DURING DUCTILE FRACTURE

C.R. Colapietro[1], J.P. Bandstra[2], P.A. Kirkham[1,3], and D.A. Koss[1]

[1]Dept. Materials Science and Engineering, Penn State University, University Park, PA 16802, USA
[2]University of Pittsburgh at Johnstown, Johnstown, PA 15904
[3]Ryerson Tull, Inc., Chicago, IL 60540, USA

ABSTRACT

The strain-induced growth and interaction behavior between neighboring voids located within small clusters has been experimentally modeled by determining the thinning behavior of the ligaments between the cavities formed by blind-end holes that have (initially) hemispherical ends and that are contained within uniaxial tensile specimens. The key assumption is the strain-induced thinning and coalescence of the ligaments between the macro-scale cavities is similar to that between neighboring spherical microvoids. Results from Cu specimens containing 2 or 3 blind-end holes indicate strain-induced cavity growth and coalescence behavior that is more rapid for clusters of 3 cavities. For this case, cavity coalescence also results in the characteristic 3-fold symmetry pattern that frequently forms along the ridges on a dimpled ductile fracture surface. When compared to void growth predictions based on the strain-induced growth of isolated voids, these results indicate void interaction effects that are sensitive to cluster geometry such that the three-fold symmetry conditions created by 3 neighboring voids result in accelerated void growth induced by an elevated level of stress triaxiality within the inter-void ligament.

KEYWORDS: Void growth, void coalescence, ductile fracture

INTRODUCTION

Tensile fracture of ductile metals at low temperatures typically occurs by a damage accumulation process that involves microvoid nucleation, growth, and coalescence. For many metals, void nucleation at inclusions occurs at small strains, and fracture is dominated by void growth and coalescence. The strain-induced growth of isolated spherical voids was modeled initially by Rice and Tracey [1], and their predictions have been subsequently supported by computational studies [2,3]. However, for the case of closely spaced voids such as at high void volume fractions near coalescence or among those voids within the clusters, void interactions should result in accelerated void growth, as has been observed experimentally [4,5]. Despite two-dimensional modeling (both experimental and computational) as well as three-dimensional unit-cell models (the study of Thomson et al [6] is especially pertinent to this work), the detailed nature of such interactions among small void clusters, such as inter-void spacing effects or which void cluster geometry promotes strong interactions, is not well understood.

In this study, as shown conceptually in Figure 1, we utilize a novel specimen geometry to model experimentally the growth and coalescence among clusters of three neighboring spherical cavities. Specifically we employ tensile specimens containing three blind-end holes with hemispherical ends and subject the specimens to interrupted deformation in order to measure the ligament thinning behavior between

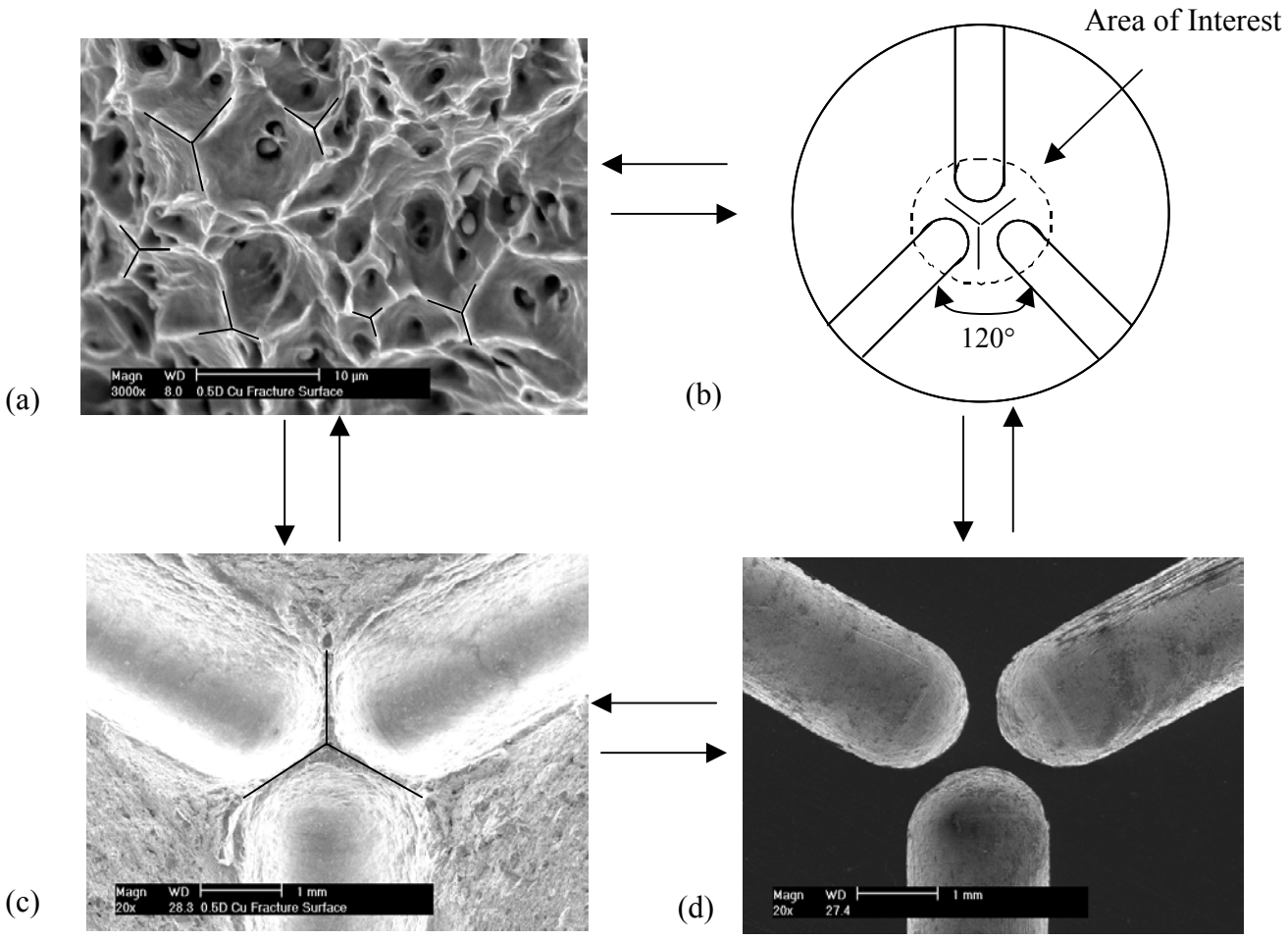

.Figure 1. (a) Ductile fracture surface illustrating "ridge-crater" shape formed by clusters of three voids. (b) Cross section of tensile specimen geometry employed to model clusters of three voids (c) Fracture surface created by our three-cavity cluster geometry. (d) Micrograph of a strained three-cavity cluster specimen that has been sectioned and polished.

the cavities formed by the hole ends [7]. We believe that the strain-induced thinning behavior of these inter-cavity ligaments is similar to that of the ligament between neighboring spherical voids located a similar relative distance apart. An important experimental advantage of this modeling approach is the ability to measure *directly* that the inter-cavity ligament width (and therefore the "cavity" growth behavior) as a function of strain. Using this modeling approach, we [7] have previously determined the ligament thinning behavior between two adjacent cavities. Geltmacher et al [8] subsequently established that tensile specimens with clusters of *three* blind-end holes failed such that the fracture surface between the cavities had the "ridge-crater" characteristic shape formed by void coalescence during microvoid fracture; however, no cavity growth measurements were performed in that effort. In this communication, we extend these two studies by utilizing copper tensile specimens containing either 2 or 3 co-planar holes with hemispherical ends to examine thinning behavior between these cavities and therefore to assess the "void growth" behavior within such small clusters of voids. The cavities formed by the hole ends form a triangular pattern and are contained on a plane normal to the tensile axis, and thus this cluster geometry differs considerably from those assumed in the three-dimensional computational modeling by Thomson et al [6]. In that study, their three-cavity cluster formed a linear array, as opposed to the triangular array here.

EXPERIMENTAL

The experimental basis for this study is a "blind-end hole" specimen shown in the three-hole configuration in Figure 1. Round bar tensile specimens with 15.5 mm gauge length diameters and 63.4 mm gauge lengths were machined from C11000 copper such that they contained either two or three coplanar holes into the mid section of each specimen. The holes, each with diameter = 1.59 mm, were drilled with a ball end-mill to produce *hemispherical cavity* at the hole end. For the two hole case, the holes were located in the same plane but opposite each other, while the three hole configuration had the hole axes separated by 120° to produce the Y geometry. The test specimens were fabricated with initial inter-cavity ligament widths of 0.79, 1.59, 3.18, 4.77, and 6.36 mm, which correspond to ligament widths of 0.5D, 1D, 2D, 3D, and 4D, respectively, where D is the hole diameter. Typical scatter in initial ligament widths was ± 0.04 D. Note that the inter-cavity ligament width dimension, W, is measured from the base of one hole to the base of another.
The material was C11000 copper, which was vacuum annealed at 375 °C for one hour after machining. The average grain size was 32 μm, which corresponds to greater than 20 grains across the minimum inter-hole ligament. The Cu had a yield stress of 220 MPa and a strain hardening exponent, $n = d\ln\sigma/d\ln\varepsilon$, of n = 0.28 for $0.01 \leq \varepsilon \leq 0.45$ as obtained from compression testing.

Inter-cavity ligament thinning was measured by deforming tensile specimens at room temperature at an initial strain rate of 10^{-3} s^{-1}. The specimens were strained in ≈ 0.015 far-field axial strain increments at which point a modified electronic depth indicator with rounded-end probes was used to measure hole depth using a procedure described elsewhere [7]. For the cases of the two-hole specimens, hole depth measurements could be used to determine the ligament width directly. For the three-hole specimens, inter-cavity ligament width was obtained from a straight-forward geometric analysis based on the determination of the distances from the geometric center of the specimen to the ends of two adjacent holes [9]. Five measurements were made of each dimension such that the ligament width was measured to within ±0.04D, where D is the hole diameter.

RESULTS AND DISCUSSION

As a measure of cavity growth, we have determined the inter-cavity ligament width, W, as a function of strain. These results, presented on the basis of the instantaneous ligament width, W, normalized to the initial ligament width, W_o, are shown for the case of three holes in Figure 2. In order to interpret these results, the choice of the strain axis in Figure 2 deserves a comment. The strain basis for Figure 2, $2\ln(d_o/d)_{local}$, relies on measurements of the initial and final specimen diameters, d_0 and d, respectively, in the plane of the holes and measured along a line inclined about 30^0 to the holes in order to avoid displacement effects along the barrels of the hole. We have also measured extensional strain values based on both scribe marks along the top and bottom of the holes and scribe marks along a 25 mm gauge section of the specimen; these extension-strain values coincide with the diameter-based strains until about 0.1 strain at which point specimen necking occurs in the section containing the holes. Thus, we have chosen the value of $2\ln(d_o/d)_{local}$ as the best measure of extensional strain in the vicinity of the cavities, despite the fact that strain-induced hole growth implies the extensional strain is somewhat greater than the $2\ln(d_o/d)_{local}$ -values reported in Figure 2.
Figure 2 shows that the normalized rate of thinning increases as the inter-cavity ligament width decreases, consistent with the fact that closely spaced voids coalesce at small strains during microvoid coalescence.
The special case of clusters of three cavities is also evident in Figure 1a, which highlights the formation of Y patterns along ridges formed by coalescence of groups of *three* microvoids. We believe that these Y patterns form because growth and therefore coalescence is rapid within groups of three voids. It is also likely that, given the small number of voids in such clusters, there is a relatively high probability that clusters of three voids are present so as to promote rapid growth (i.e., clustered roughly on a plane normal to the maximum principal strain axis).

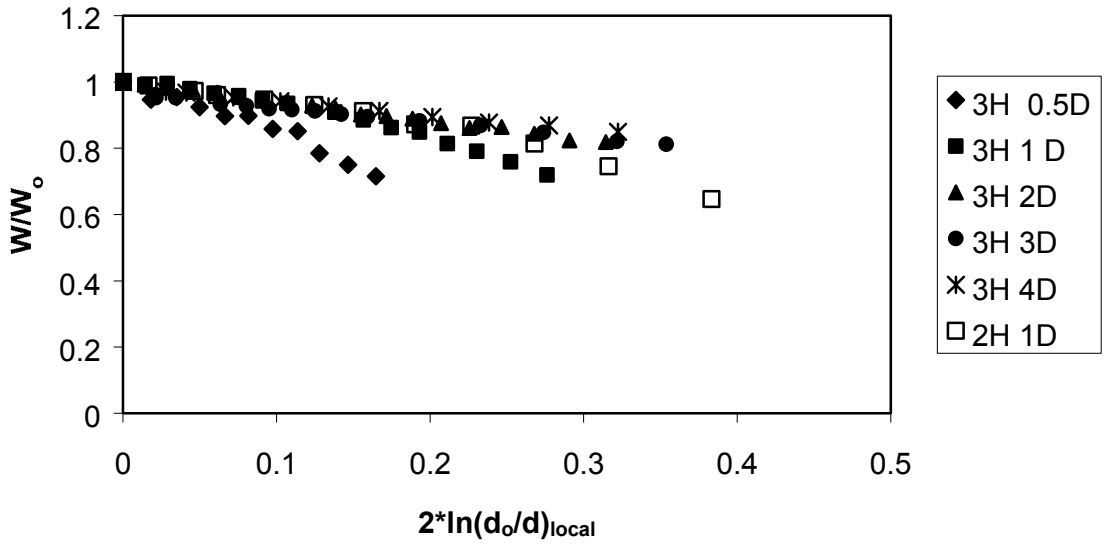

Figure 2. A comparison of normalized inter-cavity ligament thinning as a function of strain for five inter-cavity spacings in the three-cavity specimen. For comparison, the ligament thinning behavior of a two-cavity specimen (with an inter-cavity spacing of 1 cavity diameter) is also shown.

The ligament thinning data in Figure 2 is limited by the failure of the ligament between the cavities. As shown in Figure 1c, the fracture surfaces formed within the cluster of three closely spaced cavities (Figure 1c) mimic the Y ridge patterns formed among clusters of three microvoids in Figure 1a. In Figure 1c, there is sufficient ductility within the inter-cavity ligament at the 0.5D spacing such that the ligaments thin to knife-edges due to purely plastic failure. At larger inter-cavity spacings, an increased level of strain is required for the ligaments to thin to the knife-edge, and instead fracture of the ligament intervenes. In this latter case, there is sufficient constraint between the cavities to induce ligament fracture prior to the strain level necessary for the ligament to thin to a knife-edge.

Both the rapid thinning behavior and the manner of failure suggest that inter-cavity ligament deformation occurs under a level of constraint due to the notch-like geometry of the neighboring cavities. The implication is that the inter-cavity ligaments deform under stress triaxiality ratios higher than that of uniaxial tension. We therefore suggest that it is this locally elevated stress triaxiality that causes the rapid cavity growth and inter-cavity thinning depicted in Figure 2. Compared to the case of the growth of an isolated cavity/void under far-field uniaxial tension, these results suggest that cavity growth within a cluster is accelerated by the presence of a *triaxial* stress state within the ligaments.

As an initial attempt to analyze our results, we adapt the analysis procedure used by others [5,10] to analyze experimental void-growth behavior on the basis of the Rice and Tracey cavity-growth relationship [1]. As a first approximation, we assume spherical growth of cavities under a tensile deformation field at large stress triaxiality ratios that remain relatively constant during deformation. Under these conditions, the following relationship describes the radial growth of the cavities:

$$\ln(R/R_o) = \alpha\varepsilon_{eq}\exp(\beta\frac{\sigma_m}{\sigma_{eq}}) \qquad (1)$$

where R_o and R are initial and final cavity radii, ε_{eq} is the equivalent far-field strain, α and β are constants whose values should be $\alpha = 0.283$ and $\beta = 1.5$, according to Rice and Tracey [1]. A more recent analysis [11] indicates $\alpha = 0.427$ for $\sigma_m/\sigma_{eq} > 1$ and for $\sigma_m/\sigma_{eq} < 1$, $\alpha = 0.427\ (\sigma_m/\sigma_{eq})^{0.25}$.

In this study, we use straight-forward geometry to relate our ligament thinning measurements to cavity growth behavior. The following relationship between R/R_o and the normalized inter-cavity ligament width, W/W_o , is readily obtained:

$$\frac{R}{R_o} = 1 + \frac{W_o}{2R_o}\left(1 - \frac{W}{W_o}\right) \tag{2}$$

where in our case $2R_o$ is the hole/cavity diameter and equals 1.59 mm, while $W_o/2R_o$ is the initial inter-cavity spacing in terms of the diameter D.

Based on Equation 2 and assuming $\varepsilon_{eq} \cong 2\ln(d_o/d)_{local}$, Figure 3 tests the validity of Equation 1 by showing a nearly linear dependence of $\ln(R/R_o)$ on strain for both the two- and three-cavity cases. All of these data support the general form of Equation 1 as a basis for describing cavity growth within small cavity clusters. Small deviations from linear behavior in Figure 3 occur at large strains for the closely spaced cavities in which case linear behavior is observed initially and then followed by non-liner behavior as ligament thinning accelerates. Furthermore, a comparison of the cavity growth behavior in Figure 3 confirms that cavity growth is more rapid in the three-cavity cluster than in the two-cavity case.

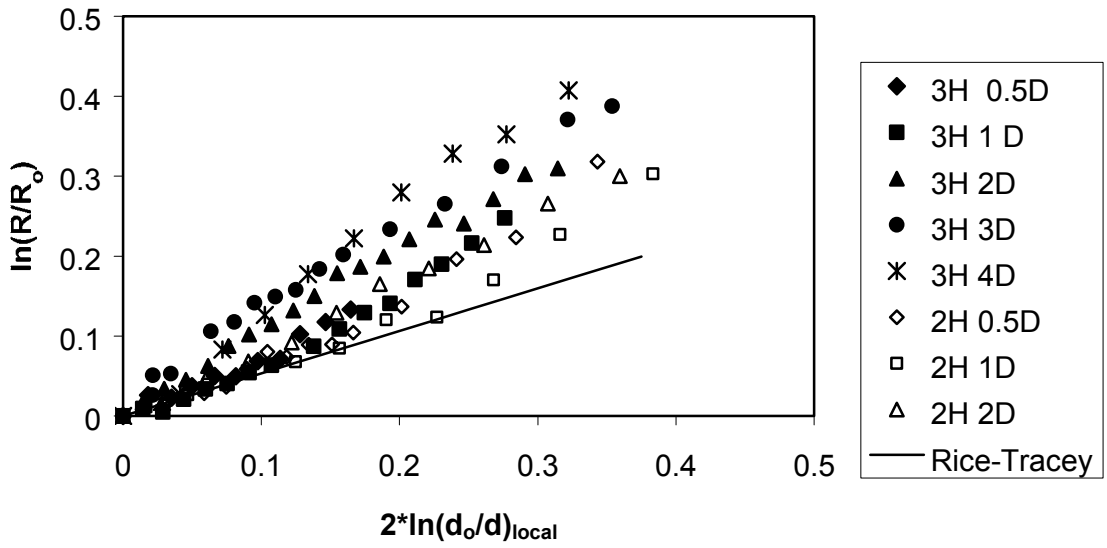

Figure 3. The dependence of cavity growth on strain for clusters of three cavities, designated 3H, and two cavities, designated 2H. Data are for a range of inter-cavity spacings from 0.5D to 4D.

It is also significant that increasing cavity spacing appears to be accompanied by an increase in cavity growth rates. While this effect is small in the case of the two-cavity condition, the cavities spaced far apart in the three-cavity clusters grow significantly faster than those closely spaced (i.e., at 0.5D and 1.0D). Such an effect is also consistent with the presence of elevated levels of stress triaxiality within the ligaments between the clustered cavities. For example, if the cluster of cavities is viewed as an incomplete circumferential notch, then the Bridgeman analysis [12] predicts increased stress triaxiality with increasing inter-cavity spacing.

The combination of the results in Figure 3 and Equation 1 can be used to test our hypothesis that an elevated level of stress triaxiality exists between the cavities and causes their rapid growth. If we assume $\alpha = 0.427$ for $\sigma_m/\sigma_{eq} > 1$ and for $\sigma_m/\sigma_{eq} < 1$, $\alpha = 0.427\ (\sigma_m/\sigma_{eq})^{0.25}$ [11] and $\beta = 1.5$ [1], then the cavity growth data in Figure 3 predict average stress triaxiality ratios within the inter-cavity ligaments that increase somewhat with strain but have values ranging from $\sigma_m/\sigma_{eq} \cong 0.6$ for three cavities spaced initially 0.5D apart to $\sigma_m/\sigma_{eq} \cong 0.8$ for the three cavities spaced 4D apart. Importantly, the predicted stress triaxiality between two cavities is

much less: $\sigma_m/\sigma_{eq} \cong 0.4$ to 0.5. While such stress triaxiality levels are significantly higher than the far-field value of $\sigma_m/\sigma_{eq} = 0.33$ characteristic of a uniaxial tension test, the elevated triaxiality values are similar to those imposed within circumferentially notched tensile specimens with very "mild" notch geometries. We are currently performing three-dimensional finite element analysis to examine this issue further [13].

The important implication of the above analysis is that it suggests that void growth within clusters of voids can be predicted on the basis of a straight-forward application of the Rice-Tracey void growth relationship *provided* that the stress triaxiality reflects the local condition within the deforming inter-void ligament. It appears that the clusters of three equal-sized voids with roughly three-fold symmetry and located on a plane normal to the maximum principal stress create elevated levels of stress triaxiality within the inter-cavity ligament (and therefore rapid void growth), *and* such clusters have a high probability of occurring in the optimum configuration/orientation.

SUMMARY

Utilizing copper tensile specimens containing either two or three blind-end holes, we have experimentally modeled the growth behavior of neighboring spherical cavities. Consistent with expectations from fracture surface observations of microvoid coalescence, the results indicate that inter-cavity ligament thinning is more rapid within a cluster of three cavities than between two cavities at the same inter-cavity spacing. Furthermore, the cavity growth within the three-cavity cluster is consistent with the void growth model of Rice and Tracey for a large range of inter-cavity spacings *provided* that the assumed stress triaxiality ratio is increased above that of uniaxial tension. As such, these cavity growth results strongly suggest the void interaction effects during ductile fracture can be understood on the basis of elevated levels of stress triaxiality within the inter-void ligaments.

AKNOWLEDGEMENTS

The authors appreciate the discussions with and comments of D. Goto, A. Geltmacher and P. Matic. We also appreciate very much the encouragement of George Yoder and the financial support of the Office of Naval Research.

REFERENCES

1. Rice, J.R. and Tracey, D.M. (1969) J. Mech. Phys. Solids 17, 201.
2. Budiansky, B., Hutchinson, J.W., and Slutsky, S. (1982) in Mech. of Solids, p. 13, Pergamon Press, Oxford.
3. Worswick, C.J. and Pick, R.J. (1990) J. Mech. Phys. Solids 38, 601.
4. Garrison, W.M. and Moody, N.R. (1987) J. Phys. Solids 48, 1035.
5. Marini, B., Mudry, F. and Pineau, A (1985) Eng. Fracture Mech. 22, 989.
6. Thomson, C.I.A., Worswick, M.J., Pilkey, A.K., Lloyd, D.J. and Burger, G. (1999) Mech. Phys. Solids 47, 1.
7. Goto, D. and Koss, D.A. (1996) Scripta Mater. 35, 459.
8. Geltmacher, A.B., Matic, P., and Harvey, D.P. (1996) J. Eng. Mater. Tech. 118, 515.
9. Colapietro, C.R., (2000), M.S. Thesis, The Pennsylvania State University.
10. Pardoen, T. and Delannay, F. (1998), Metall. and Mater. Trans.A 29A, 1895.
11. Huang, Y. (1991) J. Appl. Mech. 29, 1509.
12. Bridgeman, P.W. (1952), Studies in Large Plastic Flow and Fracture (McGraw-Hill, New York), p. 9.
13. Bandstra, J. and Koss, D.A., unpublished research, 2000.

ORAL REFERENCE ICF100910OR

AN EXTENDED VOID GROWTH MODEL FOR DUCTILE FAILURE – ASSESSMENT FOR NON RADIAL LOADINGS AND APPLICATION TO FRACTURE TOUGHNESS PREDICTION

T. PARDOEN[1], L. COUSIN-CORNET[1], and J.W. HUTCHINSON[2]

[1]Université catholique de Louvain, Département des Sciences des Matériaux et Procédés, PCIM, Bâtiment Réaumur, 2 Place Sainte Barbe, 1348 Louvain-la-Neuve, Belgium
[2]Division of Engineering and Applied Sciences, Harvard University, Pierce Hall, Cambridge MA 02138, U.S.

ABSTRACT

An extended Gurson model incorporating the effects of the shape and spacing of the voids on the growth and coalescence is proposed. The onset of void coalescence is modeled as a transition from diffuse plasticity to transverse localized plastic yielding in the intervoid ligament. A simple constitutive model for the coalescence stage is also developed. An assessment of the model is proposed by comparison with void cell computations under non-radial loading conditions. The effect of the void shape on the fracture toughness is addressed using the assumption of uniaxial straining state within the fracture process zone. The analysis reveals that the effect of the void shape on the fracture toughness becomes significant for initial porosity larger than 10^{-4} and this effect increases for increasing initial porosity.

KEYWORDS

Fracture toughness, ductile fracture, ductility, metal alloys, void growth, void coalescence

INTRODUCTION

Recent efforts in the development of computational models incorporating the void growth process has given rise to robust predictive methods for crack propagation in ductile solids, e.g. [1,2,3,4,5]. Most of these works employed the constitutive model initially proposed by Gurson [6], improved by Tvergaard [7], and finally extended by Needleman and Tvergaard [8]. Although good agreement with a range of experiments and void cells computations has been observed, the model as it currently stands still suffers from limitations which are though to arise partly because (i) *void shape* is not directly accounted for and (ii) *void coalescence* is not properly modeled. Hence, an enhanced void growth model incorporating void shape, void distribution et void coalescence effects has been developed by integrating contributions by Gologonu [9], Thomason [10] and new ingredients related to strain hardening and to the final coalescence stage [11]. The axisymmetric version of the model has been extensively validated by comparisons with void cell simulations performed under constant stress triaxiality in Ref. [11]. This report addresses two issues. First, the void growth model is again assessed by comparison with unit cell calculations, in the case of a constant strain biaxiality ratio. This mode of loading allows analyzing the pertinence of the model under non-radial loading. In the second part, the extended void growth model is used to draw qualitative features about the effect of void shape and void distribution on the fracture toughness of metal alloys.

Summary of the model. Only axisymmetric stress states are considered in the present work and the solid is made of a periodic distribution of the cylindrical representative volume element (RVE) defined on Fig. 1.

Void growth model. The extension of the Gurson model due to Gologanu *et al.* [9], which has been adopted here to describe behavior prior to void coalescence, gives a constitutive relation for a porous elastoplastic material containing (axisymmetric) spheroidal voids. This particular model, extended for strain-hardening, contains as state variables: the components of the mesoscopic stress tensor, $\boldsymbol{\Sigma}$, the porosity, f, the void aspect ratio, S, and an average yield stress for the matrix material, σ_m. The void aspect ratio is defined by $S = \ln(W)$ while $W = R_z/R_r$.

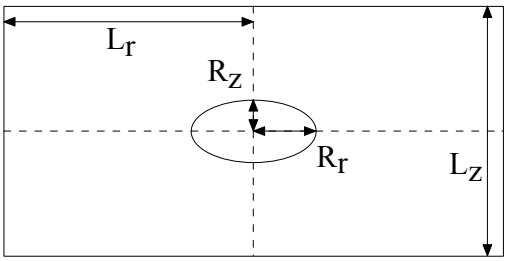

Figure 1: Representative volume element

The functional form of the model prior to coalescence is:

$$\Phi \equiv \Phi(\boldsymbol{\Sigma}, f, S, \sigma_m) = 0, \tag{1}$$

$$\dot{f} = (1-f)\dot{E}^p_{kk}, \tag{2}$$

$$\dot{S} \equiv \dot{S}(f, S, T), \tag{3}$$

$$\sigma_m \dot{\varepsilon}^p_m (1-f) = \Sigma_{ij}\dot{E}^p_{ij}, \tag{4}$$

$$\sigma_m \equiv \sigma_m(\varepsilon_e), \tag{5}$$

$$\dot{E}^p_{ij} = \gamma \frac{d\Phi}{d\Sigma_{ij}}, \tag{6}$$

where Φ is the flow potential; $\boldsymbol{E}^p$ is the mesoscopic plastic strain tensor; (2) and (3) are the evolution laws for f and S, respectively; (4) is the Gurson [6] energy balance for the plastic work allowing computation of σ_m using the effective stress-strain curve for the parent material (5); and (6) is the flow rule. The expressions for the functions such as Φ and the evolution of S are given in Ref. [9,11].

Criterion for the onset of void coalescence. Axisymmetric void cell computations [11,12] have shown that void coalescence consists in the localization of plastic deformation in the ligament between the voids, which, experimentally, gives rise to a flat dimpled fracture surface. Thomason [10] has studied the transition to localization for elastic-perfectly plastic solids by looking at artificially constrained localized solutions giving the load as a function of the void cell geometry. For axisymmetric geometry, Thomason has proposed that the average normal stress acting on the cell at the onset of localization occurs when Σ_z attains Σ_z^{loc} where

$$\frac{\Sigma_z^{loc}}{\sigma_0} = \left[1 - \left(\frac{R_r}{L_r}\right)^2\right]\left[\alpha\left(\frac{R_z}{L_r - R_r}\right)^{-2} + \beta\left(\frac{R_r}{L_r}\right)^{-1/2}\right], \tag{7}$$

where $\alpha = 0.1$ and $\beta = 1.2$. By comparing this expression with our numerical results for strain hardening materials [11], we also find that this expression provides an accurate estimate for the onset of localization within the cells, provided that σ_0 is replaced by an appropriate effective flow stress for the matrix, σ_m (see also [13]), and α and β incorporate a dependence on the strain hardening exponent n. The effective matrix stress, σ_m, is obtained using (4) and (5). A fitting procedure performed on a large number of void cell results [9] has revealed that the coefficient β is almost constant equal to 1.24 while $\alpha(n) = 0.1 + 0.22n + 4.8\,n^2$ ($0 \le n \le 0.3$). With relation (7), a new geometrical variable related to the void spacing has entered the model. For the sake of simplicity in the formulation of the model, we have chosen to use $A = \ln(\lambda) = \ln(L_z/L_r)$. The model thus depends on all the geometric characteristics of the representative void cell: f, A (or λ), S (or W).

In [11], the criterion (8) has proved to very accurately predict the onset of coalescence for porosity ranging between 10^{-2} and 10^{-4}, stress triaxialities between 1/3 and 5, void shapes W between 1/6 and 6, and void distribution λ between 1/2 to 16.

A model for the post-localization regime. Relation (7) still pertains after the onset of coalescence and Σ_z^{loc} is replaced by Σ_z, assuming the voids do not depart significantly from a spheroidal shape. The additional equations for the evolution of the state variables during the post-localization stage are obtained under the approximation that elasticity, as well as any reversed plasticity, are neglected. In agreement with the void cell results, the half-height of the localization zone is approximated as R_z (i.e. $h = R_z$, see Fig. 1).

ASSESSMENT OF THE VOID GROWTH MODEL FOR NON-RADIAL LOADINGS

The predictions of the void growth model under constant applied strain biaxiality ratio are compared to finite element void cell simulations performed with the same applied biaxiality ratio. Results are presented for a material with $f_0 = 10^{-2}$, $\lambda_0 = 1$, $\sigma_0/E = 0.002$, $n = 0.1$ and $W_0 = 1/6$, 1, 6. The strain biaxiality ratio $\beta = E_r/E_z$ ranges from –0.5 to 0. As the applied boundary conditions prevent plastic tensile localization, the void coalescence model has been turned off except for the uniaxial straining case (β=0). Thick lines correspond to the unit cell calculations and thin lines correspond to the model predictions. Figures 2 show the variations with overall straining of different quantities computed with the void growth model and with the finite element unit cell computations for initially spherical voids (W_0=1) : the overall axial stress in (a), the porosity in (b) and the void shape in (c). Figures 3 shows the variation of the overall axial stress as a function of the overall axial strain for voids initially (a) very oblate (W_0=1/6) or (b) very prolate (W_0=6).

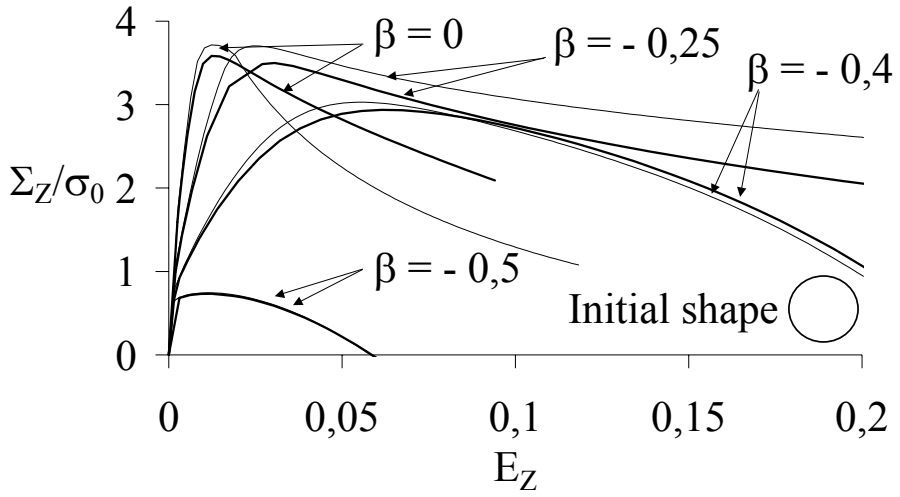

(a)

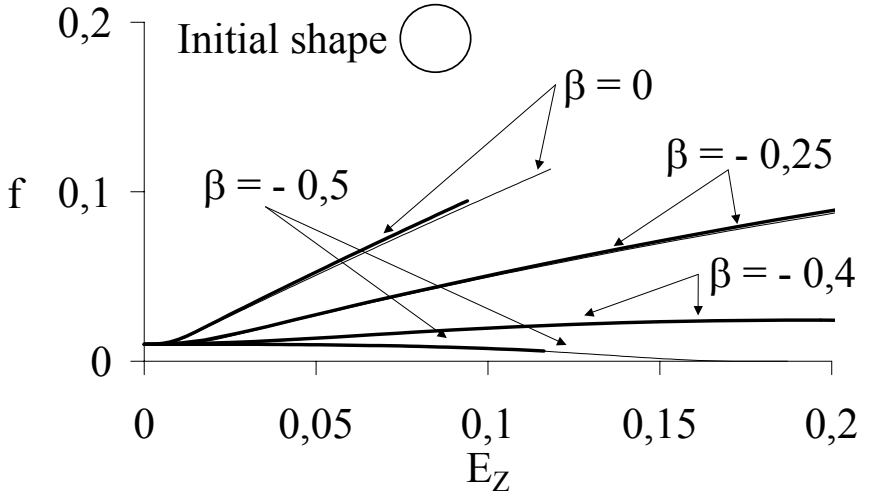

(b)

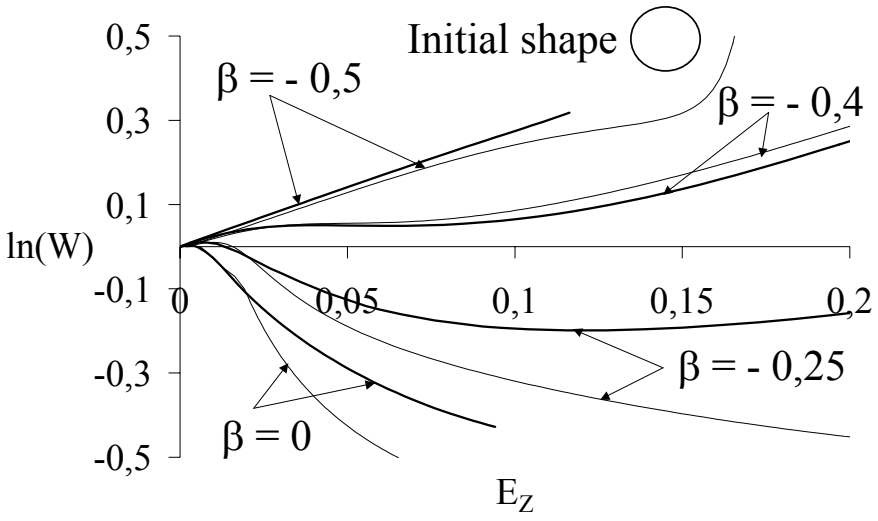

(c)

Figure 2: Variation as a function of the overall axial strain of (a) the overall axial stress, (b) the porosity, and (c) the void shape, for a material characterized by $f_0 = 10^{-2}$, $\lambda_0 = 1$, $\sigma_0/E = 0.002$, $n = 0.1$ and $W_0 = 1$.

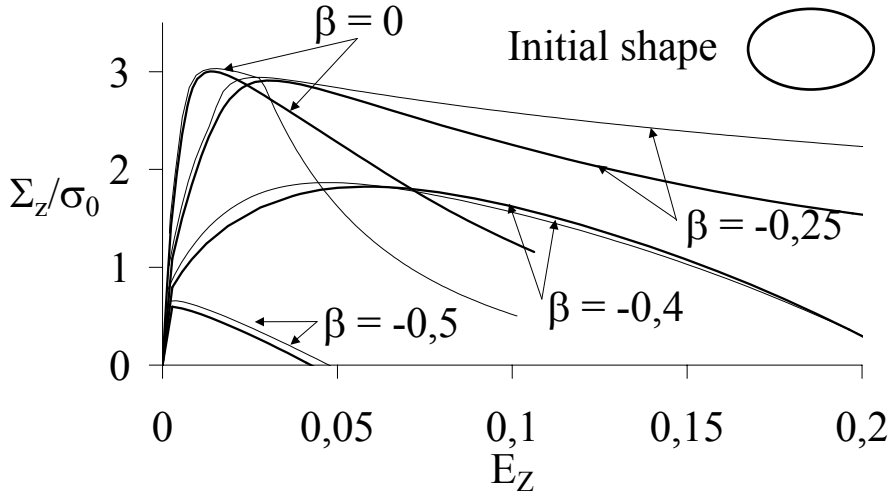

(a)

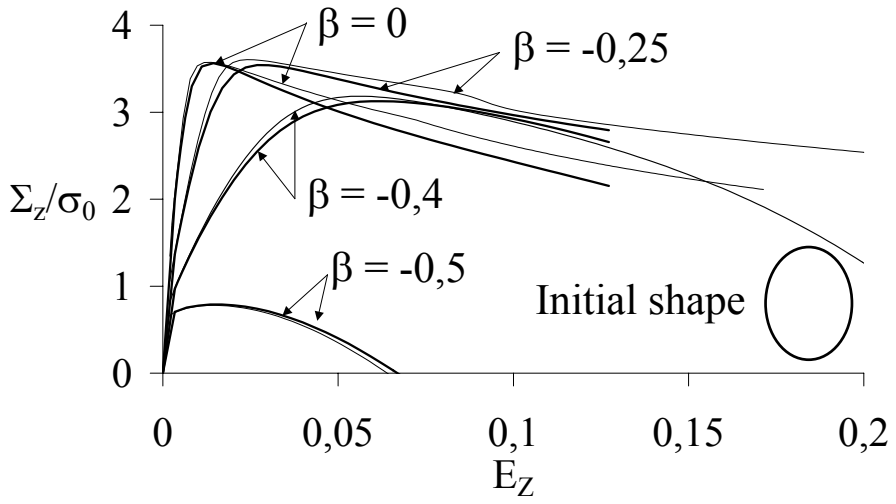

(b)

Figure 3: Variation of the overall axial stress as a function of the overall axial strain for a material characterized by $f_0 = 10^{-2}$, $\lambda_0 = 1$, $\sigma_0/E = 0.002$, $n = 0.1$ and (a) $W_0 = 1/6$ and (b) $W_0 = 6$ (a).

Figs. 2a and Figs. 3 show that the overall stress-strain behavior obtained with the model quantitatively agrees with the finite element unit cell solution. The most important characteristics, which are the maximum stress (the "strength" of the material) and the strain at final fracture (the "ductility" of the material), are predicted with an accuracy increasing when the strain biaxiality decreases. One should note that a constant strain biaxiality ratio involves marked variations of the stress triaxiality during deformation. In the case of large strain biaxiality ratio, the stress triaxiality sometimes reaches values larger than 5 or 6 for which other phenomena, such as unstable void growth may be expected.

FRACTURE TOUGHNESS PREDICTION

As initially proposed by Andersson [14] and then revisited by Tvergaard and Hutchinson [15], the fracture process zone at the tip of a sharp crack can be anticipated as a row of multiple interacting voids which, to a good approximation, are strained uniaxially during the major part of the void growth. Indeed, under large stress triaxiality, the fracture process involves early localization of the plastic flow in a planar zone of essentially one void spacing in thickness. Assuming spherical voids and isotropic void distribution, Tvergaard and Hutchinson [15] have shown that the fracture toughness, J_{Ic}, governing crack growth initiation can almost exactly be expressed as

$$J_{Ic} = \Gamma_0 \tag{9}$$

where Γ_0 is the work per unit area spent in the band until final failure. It can be computed from the Gurson model according to

$$\frac{\Gamma_0}{\sigma_0 L_{r0}} = F\left(\frac{\sigma_0}{E}, n, f_0\right) \tag{10}$$

where E is the Young's modulus. Xia and Shih [16] have shown that the uniaxial straining assumption is valid as long as f_0 is not too small. Typically, when f_0 becomes smaller than 0.1%, a one void - crack interaction mechanism takes place. In that case, the uniaxial straining assumption looses its pertinence. The analysis of Tvergaard and Hutchinson [15] has been extended by accounting for the effect of the void shape using the extended-Gurson model. Now, F generally writes $F = F(\sigma_0/E, n, f_0, W_0)$, assuming isotropic initial void distribution ($\lambda_0 = 1$). This extended model allows addressing the anisotropic fracture toughness of metal alloys. Indeed, since it accounts for the void shape, this model is able to capture variations of the fracture toughness with the orientation of the crack plane resulting from preferential orientation of the inclusions.

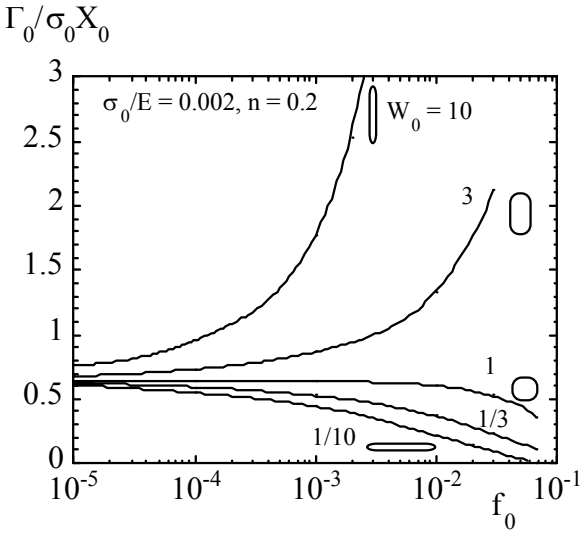

Figure 4: Variation of $F = \Gamma_0/\sigma_0 L_{r0}$ as a function of the initial porosity f_0 for various initial void shape

The variation of $\Gamma_0/\sigma_0 L_{r0}$ as a function of the initial porosity for various void shapes is shown in Fig. 4 (for n = 0.2 and σ_0/E = 0.002). The effect of the initial void shape is significant for porosity larger than about 10^{-4}. Prolate shape increases $\Gamma_0/\sigma_0 L_{r0}$ while oblate shape reduces it. For void shape departing from spherical,

$\Gamma_0/\sigma_0 L_{r0}$ cannot be considered anymore as independent of the initial porosity, it increases with f_0 for prolate voids and decreases with f_0 for oblate voids.

The results of Fig. 4 can be used to qualitatively understand and predict the variation of the fracture toughness as a function of the loading direction for rolled plates with preferential orientation of the second phase. From these results it is concluded that void shape effects (and the combined effect coming from the change in ligament length) can alone explain a factor two (or more) difference in the toughness of plates with elongated inclusions depending on the orientation of the crack plane. Note that this analysis is only qualitative because of the assumed axisymmetry. In other words, a 90° rotation of a prolate void with $W_0 = a$ does not give an oblate void with $W_0 = 1/a$.

CONCLUDING REMARKS

The new model only depends on the initial values of the state variable and thus avoids the use of critical porosities (for the onset of coalescence and for final separation). The two additional microstructural characteristics of the new model, the void initial shape S_0 and the initial void distribution λ_0, can be obtained from the same metallographic analysis performed to ascertain f_0 and L_0. The comparison with the void cell simulations in Ref. [11] for constant stress triaxiality and, in this report, for constant strain biaxiality has established that the full void growth/coalescence model is able to quantitatively account for variations of all the characteristic parameters of the representative volume element of Fig. 1: porosity, void shape, cell aspect ratio, stress triaxiality, for a wide range of matrix flow behavior. Consequently, the model naturally allows addressing issues such as the anisotropy in fracture toughness observed in many materials formed with large amounts of plastic strains. Most importantly, behavior at low and large stress triaxiality are adequately encompassed by the same model, giving thus the possibility to deal with failure of thin and thick structural parts within the same framework.

ACKNOWLEDGEMENTS

The work of JWH was supported in part by the NSF grant CMS-9634632 and in part by the Division of Engineering and Applied Sciences, Harvard University. This work was carried out in the framework of program PAI41 supported by SSTC Belgium.

REFERENCES

1. Mudry, F., di Rienzo, F., and Pineau, A., (1989). In: *Non-Linear Fracture Mechanics: Volume II - Elastic-Plastic Fracture*, ASTM STP 995, pp. 24-39, Landes, J.D., Saxena, A., and Merkle, J.G. (Eds). American Society for Testing and Materials, Philadelphia.
2. Xia, L., Shih, C.F., and Hutchinson, J.W. (1995). *J. Mech. Phys. Solids* **43**, 389.
3. Brocks, W., Klingbeil, D., Kunecke, G., and Sun, D.-Z. (1995). In: *Constraint Effects in Fracture Theory and Applications: Second Volume*, ASTM STP 1244, pp. 232-252, Kirk, M. and Bakker, A. (Eds). American Society for Testing and Materials, Philadelphia.
4. Ruggieri, C., Panontin, T.L., and Dodds, R.H., Jr. (1996). *Int. J. Fract.* **82**, 67.
5. Gao, X., Faleskog, J., and Shih, C.F. (1998). *Int. J. Fract.* **89**, 374.
6. Gurson, A.L. (1977). *J. Engng. Mater. Tech.* **99**, 2.
7. Tvergaard, V. (1981). *Int J. Fract*. **17**, 389.
8. Needleman, A. and Tvergaard, V. (1984). *J. Mech. Phys. Solids* **32**, 461.
9. Gologanu, M., Leblond, J.-B., Perrin, G., and Devaux, J. (1995). In: *Continuum Micromechanics*, Suquet, P. (Ed.). Springer-Verlag.
10. Thomason, P.F. (1990) *Ductile Fracture of Metals*, Pergamon Press, Oxford.
11. Pardoen, T. and Hutchinson, J.W. (2000) *J. Mech. Phys. Solids* **48**, 2467.
12. Koplik, J. and Needleman, A. (1988). *Int. J. Solids Struct.* **24**, 835.
13. Zhang, Z. L. and Niemi, E. (1994). *Engng. Fract. Mech.* **48**, 529.
14. Andersson, H. (1977). *J. Mech. Phys. Solids* **25**, 217.
15. Tvergaard, V. and Hutchinson, J.W. (1992) *J. Mech. Phys. Solids* **40**, 1377.
16. Xia, L. and Shih, C.F. (1995). *J. Mech. Phys. Solids* **43**, 1953.

Oral reference : ICF100425OR

AN IMPACT DAMAGE MODEL FOR CEMENTITIOUS COMPOSITES

Patricia VERLEYSEN[1] and Joris DEGRIECK[2]

[1] Doctor-Assistent, Ghent University, Faculty of Engineering,
Department of Mechanical Construction and Production,
Sint-Pietersnieuwstraat 41, 9000 Gent, Belgium
[2] Full Professor, Ghent University, Department of Mechanical Construction and Production.

ABSTRACT

Although in recent years a lot of research has been spent on the dynamic, tensile behaviour of cementitious composites, such as concrete, less attention has been paid to the modelling of this behaviour. In this contribution a model, developed within the framework of the continuum damage mechanics, is presented and the determination of the model parameters is dealt with. One of the essential characteristics of the approach is that the model distinguishes two stages : a first stage during which nucleation of damage is dominant and a second during which the existent damage propagates. The model was implemented in a finite element program, which was subsequently used for the simulation of split Hopkinson bar experiments. To validate the proposed material model and to determine the material parameters a series of experiments on concrete were performed. Comparison of the experimental and numerical results showed an excellent agreement for rates of deformation ranging from 1/s to 300/s.

KEYWORDS

cementitious composites, impact, damage model

INTRODUCTION

When a quasi-brittle material such as concrete is subjected to an increasing tensile stress, the initial linear elastic behaviour will soon be abandoned because of the creation of microcracks. The microstructure of the material will gradually degrade by the nucleation and propagation of these microcracks. In the beginning, the process of nucleation of microcracks is dominant; this is a stable stage. When the stress is further increased new microcracks develop and the size of the existing cracks grows. After a while propagation of existent microcracks becomes dominant; an equilibrium between stress and damage is only possible under decreasing stress. This process is unstable.

The dynamic, tensile behaviour of concrete differs significantly from its static behaviour; in experiments higher strengths, higher deformation capacities and higher energy-absorbing properties are observed at higher rates of strain [1][2][3][4][5]. This can be explained by the fact that, when the load is applied very slowly, the final rupture has the time to choose the way of least resistance; tougher aggregates are avoided and the fracture goes through the weakest zone of the matrix. The development of microcracks in other

zones is limited. In dynamic circumstances however, fracture has to develop in a very short time period. A lot of energy is put in the material in a very short time; as stresses are increasing very fast, cracks do not have the same time to search for the weakest path and have to develop along shorter paths with higher resistence; as a consequence higher strengths are observed. The high stresses in the material now also cause microcracking in other zones, resulting in higher deformations in dynamic experiments.

In this contribution a material model for the dynamic, tensile behaviour of concrete is proposed [6]. The description is based on damage mechanics. To validate the proposed material model and to determine the material parameters series of experiments on concrete were performed. Because of practical considerations a concrete 'on scale' (or microconcrete) was used. The results of the experiments are compared with simulated results, using the finite element program in which the material model is implemented.

DEVELOPMENT OF THE DYNAMIC DAMAGE MODEL FOR TENSION

One basic assumption of the continuum damage mechanics is the fact that the irreversible changes in the microstructure of a material due to the loading history and resulting in a degradation of the mechanical behaviour of the material, can be described by an internal variable (or variables); the *damage variable* d (or d_i, i=1, ..., n). Another essential assumption is that in the description of the mechanical behaviour of the material, this material can be replaced by a fictitious, homogenous and continuous material. The full set of all mathematical expressions describing the resulting mechanical behaviour of the fictitious material and the evolution of damage is a *damage model*. An adequate damage model is able to predict the onset and evolution of damage under variable circumstances.
The damage variables can be defined either in direct relation to the deficiencies which constitute the damage, or in relation to the observable reduction in mechanical properties which the damage brings about. The second, more phenomenological, approach is more often used, and was equally adopted here. In the developed one-dimensional model a scalar damage variable d is used. Its physical meaning is related to the reduction of stiffness of the damaged material, as follows :

$$E = E_0(1 - d) , \qquad \sigma = E\,\varepsilon \tag{1}$$

with E_0 the modulus of elasticity of the undamaged material, E the modulus of the damaged material, σ the uniaxial stress and ε the strain. Because of the irreversible nature of the degradation process d is always increasing, and its value is obviously limited to the interval [0, 1].
Next to the choice of an appropriate damage variable, a law describing the evolution of this variable is necessary : the *damage law*. The dynamic damage law presented in this paper starts from a static model. Essential is also the fact that damage growth consists of two distinct contributions : a nucleation part describing the creation of new microcracks and a propagation part describing the growth of the existent damage.
In [7] Lemaitre-Chaboche proposed the following function for the increment of damage of concrete :

$$\begin{aligned} d(d) &= \left(\frac{\varepsilon}{\varepsilon_0}\right)^s d\varepsilon \qquad && \text{if } \varepsilon > \varepsilon_{tr} \text{ and } d\varepsilon > 0 , \\ d(d) &= 0 \qquad && \text{in other cases.} \end{aligned} \tag{2}$$

ε_{tr} is a threshold value for the strain; below that value of the strain, no damage will occur. ε_0 and s are material constants.

When the strain is monotonicly increasing, the relation between stress and damage becomes :

$$\sigma = E_0(1 - d)\left(\varepsilon_0^s (s + 1)d + \varepsilon_{tr}^{s+1}\right)^{1/(s+1)} \tag{3}$$

This equation gives a unique relationship between applied stress and damage; no strain rate or other effects are taken into account. This equilibrium curve will only be followed during a static experiment with very low rates of loading and is therefore called the *static curve* (see figure 1).

In a dynamic situation the point representing the state of stress and damage in figure 1 will no longer be situated on the equilibrium curve, but above it; the damage evolution can't follow the stress. The point will tend to move down towards this curve. The higher the stress, or rather, the higher the available elastic energy, the faster this motion will be. It is therefore reasonable to take the rate of damage proportional to the difference in the square of the actual stress and the square of the stress of the equilibrium curve, both at the same amount of damage of course. Introducing the parameters C_1 and C_2 to scale the process of nucleation and propagation, this gives the following equation for the time derivate of the damage variable d :

$$\begin{aligned} \dot{d} &= \dot{d}_{nucleatie} + \dot{d}_{propagatie} \\ &= C_1 \left\langle \left(\frac{\sigma}{\sigma_{max}} \right)^2 - \left(\frac{\sigma_{stat}}{\sigma_{max}} \right)^2 \right\rangle + C_2 \left\langle \left(\frac{\sigma}{\sigma_{max}} \right)^2 - \left(\frac{\sigma_{stat}}{\sigma_{max}} \right)^2 \right\rangle \cdot d \end{aligned} \tag{4}$$

σ is the actual stress, σ_{stat} is the value of the static curve corresponding with the actual damage d and σ_{max} is the maximum value of the static curve (see figure 1). The brackets $\langle\ \rangle$ mean that negative values are replaced by zero, thus guaranteeing that only points above the static curve will cause damage growth.
The second term, the propagation term, is multiplied by a factor d, to express the simple fact that the more damage is already present, the greater the possibility for growth. This allows to take into account the instability of the growth process. Both terms are represented in figure 2 for a loading rate of 10/s. As can be seen, after a while the propagation term dominates the damage process.

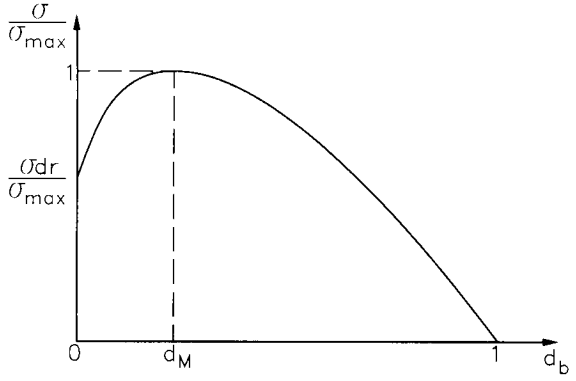

Figure 1: Static tensile curve for concrete derived from the model presented in [7].

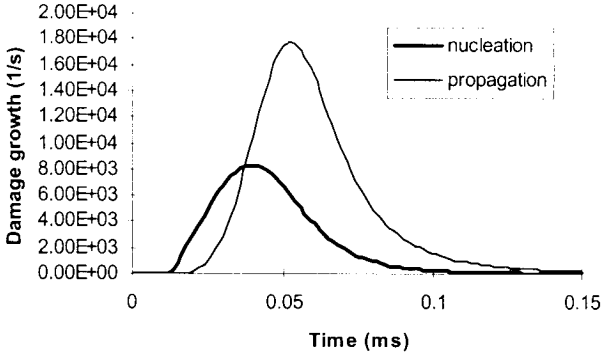

Figure 2: History of the contribution of the nucleation and propagation to the growth of damage. The rate of deformation is 10/s.

DETERMINATION OF THE MATERIAL PARAMETERS

The presented damage model contains 6 material parameters : E_0, ε_{tr}, ε_0 and s associated with the static behaviour, C_1 and C_2 related to the dynamic behaviour.
The static parameters were determined as follows : the value of E_0 is derived from a static uniaxial tensile test, for s the value 2 proposed in [7] is adopted, the value of ε_{tr} is derived from the value of the maximum stress σ_{max} observed in the static experiments. Indeed, during the static experiments an almost perfect linear behaviour is observed until 60 % of the maximum stress is reached. So, it can be concluded that under that limit no damage of any importance will appear. A good estimate of ε_{tr} was found to be :

$$\varepsilon_{tr} = \frac{0.6\,\sigma_{max}}{E_0} \tag{5}$$

ε_0 is also deduced from the maximum value of the stress. Indeed, the maximum stress σ_{max} can be written as a function of s, ε_{tr}, ε_0 and E_0 :

$$\sigma_{max} = E_0 \cdot \varepsilon_0^{\frac{s}{s+1}} \cdot \left(\frac{1 + s + \left(\frac{\varepsilon_{tr}}{\varepsilon_0} \right)^s \cdot \varepsilon_{tr}}{s + 2} \right)^{\frac{2+s}{s+1}} \quad (6)$$

For each set of values for s, ε_{tr}, σ_{max} and E_0 more than one value of ε_0 can be calculated from this expression, but only one ε_0 gives a value for d_M (damage corresponding with σ_{max}, see figure 1) in the interval [0, 1].

The damage model consisting of the equations (1) and (2) was implemented in the finite element program IMPACT. IMPACT is a one dimensional program using an unconditionally stable time integration algorithm. The program allows simulation of one-dimensional wave propagation problems. This enabled us to simulate the behaviour of a specimen during a split Hopkinson experiment. During such an experiment the specimen is subjected to a dynamic, uniaxial tensile load.
After incorporation in an optimisation routine, the simulated time histories were compared with experimental results, and the initial values of the dynamic material model parameters C_1 and C_2 are iteratively adapted [6]. Table 1 gives the values of the parameters for the microconcrete used in this study. With these parameters an excellent agreement with the experiments is observed with loading rates in the range of 2/s to 300/s, as will be shown in §4.

TABLE 1
MATERIAL MODEL PARAMETERS AND VALUE FOR σ_{max} DERIVED FROM STATIC AND DYNAMIC EXPERIMENTS

E_0 (MPa)	29 850	ε_0	$5.436\ 10^{-6}$
σ_{max} (MPa)	6.5	ε_{tr}	$1.306\ 10^{-4}$
C1	7 500	C2	45 000

EXPERIMENTAL TIME HISTORIES VERSUS NUMERICAL SIMULATIONS

As mentioned above split Hopkinson tensile bar experiments were performed on microconcrete specimen. During an experiment, a cylindrical disk of microconcrete is glued between two long bars, the Hopkinson bars, with the same diameter of the specimen. At the free end of one of the Hopkinson bars a tensile wave is generated. This wave travels through the bar towards the specimen. Once the wave reaches the specimen, the specimen is subjected to a dynamic, tensile stress, which is supposed to be purely uniaxial.

The history of the stress, the strain and the strain rate in a specimen during such an experiment is determined by the applied tensile wave and by the mechanical properties of the Hopkinson bars and of the specimen. The strain rate, strain and stress in a specimen during the experiment can be deduced from measurements on the Hopkinson bars [8][9]. Figure 3 gives a typical history of the strain rate for (micro)concrete. Notice that the strain rate is far from being constant in time. Figure 4 gives the corresponding strain. When loading of the specimen is started, strain and strain rate will be homogeneous over the length of the specimen, after a while the damage will concentrate in a small zone of the specimen, where also the deformation will localise. Thus, the measured strain and strain rate of figures 3 and 4 have to be seen as mean values over the length of the specimen. Figure 5 gives the stress history in the specimen. Figure 6 gives the corresponding stress-strain curve.

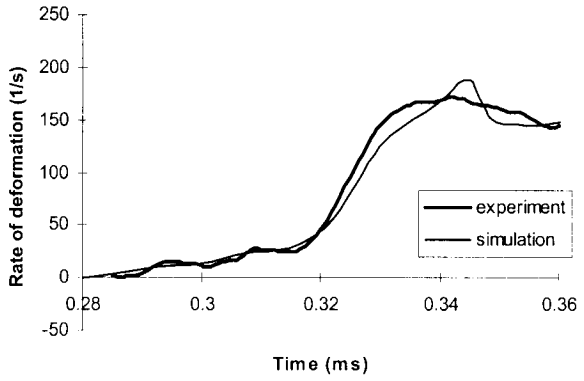

Figure 3: Simulated and experimental history of the rate of deformation in a specimen during a split Hopkinson bar tensile experiment.

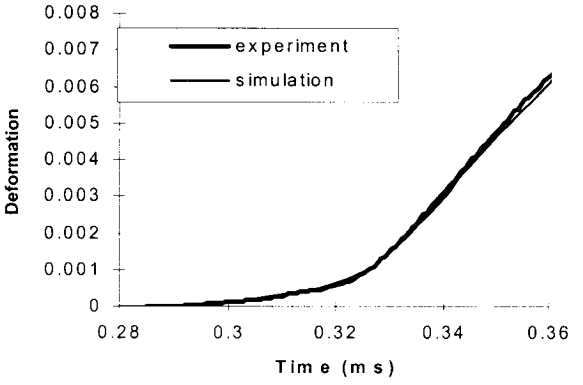

Figure 4: Simulated and experimental history of the deformation in a specimen during a split Hopkinson bar tensile experiment.

Next to the experimental values, in figures 3 to 6 also the simulated values are plotted. These simulations are obtained with the material constants mentioned in table 1 and 2. As can be seen an excellent agreement can be observed. A simular agreement between experiments and numerical simulations can be demonstrated for experiments conducted in other circumstances, and so other rates of deformation [6].

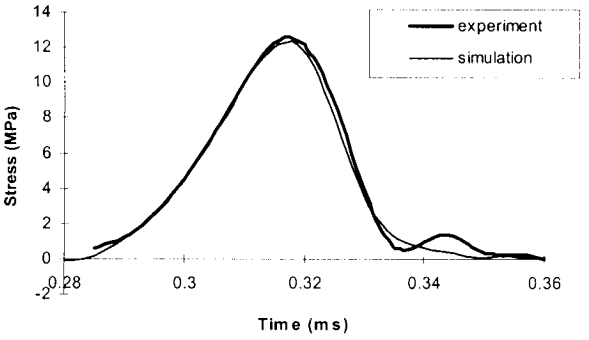

Figure 5: Simulated and experimental history of the stress in a specimen during a split Hopkinson bar tensile experiment.

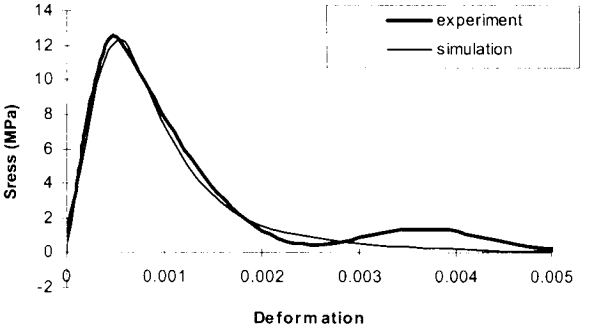

Figure 6: Simulated and experimental history of the stress as a function of the deformation in a specimen during a split Hopkinson bar tensile experiment.

Figure 7 gives the stress-strain curve for an experiment where lower rates of deformation are reached. Notice the smaller value of the maximum stress, the smaller the value of the deformation corresponding with the value of the maximum stress and the smaller the ultimate deformation. The experimentally observed strain rate dependence is well reflected by the material model.

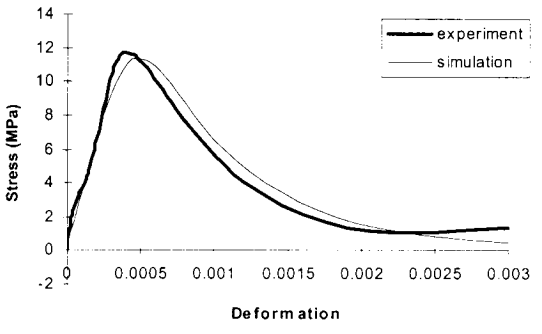

Figure 7: Simulated and experimental history of the stress as a function of the deformation in a specimen during a split Hopkinson bar tensile experiment.

CONCLUSIONS

An impact model within the framework of damage mechanics was developed for concrete. The model makes a clear distinction between the nucleation of new damage and the propagation of existent damage. The model starts from an existing static description. Future research will be performed to investigate if the approach can be extended for the description of the dynamic behaviour of other materials. After all, starting from a static curve valid for the considered material, the dynamic description can be derived in a simular way as for the concrete model presented in this paper.
The presented model is suitable for implementation in a numerical program. The model contains some parameters that were determined by means of experiments : static tensile tests allowed determination of the parameters associated with the time independent behaviour and, by means of a combination of numerical simulation and split Hopkinson tensile tests, the dynamic material parameters were determined.
The model proved to give an excellent agreement with experimental results. In the considered experiments loading rates from 1/s to 300/s were reached, thus it can be stated that the model is valid in this range of deformation rates.

ACKNOWLEDGEMENT

The presented research was performed in close collaboration with the Laboratory for Concrete Research of the Ghent University. The authors want to thank in particular prof. L. Taerwe and prof. G. De Schutter of this laboratory for the production of concrete and the static experiments.

REFERENCES

1. Ross, C.A., Thompson, P.Y. and Tedesco, J.W. (1989) Split-Hopkinson pressure-bar tests on concrete and mortar in tension and compression. *ACI mat jour* 86, nr. 5, 475-481.
2. Tang, T., Malvern, L.E. and Jenkins, D.A. (1992) Rate effects in uniaxial dynamic compression of concrete. *j. engrg. Mech.* 118, nr 1, 108-124.
3. Banthia, N., Chokri, K., Ohama,Y. and Mindess, S. (1994) Fiber-reinforced cement based composites under tensile impact. *Advn. Cem. Bas. Mat.*, 1, 131-141.
4. Rossi, P. (1994) Dynamic behaviour of concretes : from the material to the structure. *Materials and Structures*, 27, 319-32.
5. Reinhardt, H.W., Rossi, P. and Van Mier, J.G.M. (1990) Joint investigation of concrete at high rates of loading. *Mat. and Struc.*, 23, 213-216.
6. Verleysen, P.(1999) Experimental investigation and numerical modelling of the dynamic tensile behaviour of quasi-brittle and fibre reinforced quasi-brittle materials. Doctoral dissertation University of Gent (In dutch)
7. Lemaitre, J., Chaboche, J.-L. (1988) Mécanique des matériaux solides. Dunod.
8. Kolsky, H. (1949) An investigation of the mechanical properties of materials at very high rates of loading. *Proc. Phys. Soc.* Sec. B, **62**, 676-700.
9. Kolsky, H. (1963) Stress waves in solids. New York Dover Publications Inc..

ORAL/POSTER REFERENCE: ICF1001006PR

AN INTEGRATED EFGM-FEM FOR LINEAR-ELASTIC FRACTURE MECHANICS

B. N. Rao and S. Rahman

College of Engineering, The University of Iowa,
Iowa City, IA 52242

ABSTRACT

This paper presents a method for integrating the element-free Galerkin method (EFGM) with the traditional finite element method (FEM) for analyzing linear-elastic cracked structures. The EFGM is used to model material behavior close to cracks and the FEM in areas away from cracks. In the interface region, the resulting shape function, which comprises both EFGM and FEM shape functions, satisfies the consistency condition thus ensuring convergence of the method. Numerical examples are presented to illustrate the integrated EFGM-FEM. The stress-intensity factors predicted by this method compare very well with all-FEM or all-EFGM solutions. A significant saving of computational effort can be achieved due to coupling in the proposed method when compared with existing meshless methods.

KEYWORDS

Element-free Galerkin method, finite element method, fracture, stress-intensity factor, crack propagation.

INTRODUCTION

In recent years, a class of meshfree or meshless methods, such as the element-free Galerkin method (EFGM) [1,2], has emerged that demonstrates significant potential for solving moving boundary problems typified by growing cracks. Although meshless methods are attractive for simulating crack propagation, the computational cost of a meshless method typically exceeds the cost of a regular finite element method (FEM). Furthermore, given the level of maturity and comprehensive capabilities of FEM, it is often advantageous to use meshless methods only in sub-domains, where their capabilities can be exploited to the greatest benefit. In modeling crack propagation in a complex engineering structure with stiffeners, connections, welds, *etc.*, it is more effective to apply meshless methods at sites of potential crack growth and FEM in the remainder of the domain. Therefore, numerical methods need to be developed for combining meshless and finite element methods.

In this paper, a numerical technique integrating EFGM with the traditional FEM is presented for analyzing linear-elastic cracked structures. The EFGM is used to model material behavior close to cracks and the FEM in areas away from cracks. In the interface region, the resulting shape function, which comprises both EFGM and FEM shape functions, satisfies the consistency condition thus ensuring convergence of the method. Several numerical examples are presented to illustrate the proposed method.

THE ELEMENT-FREE GALERKIN METHOD

Consider a function $u(\boldsymbol{x})$ over a domain $\Omega \subseteq \Re^K$, where K = 1, 2, or 3. Let $\Omega_x \subseteq \Omega$ denote a sub-domain describing the neighborhood of a point $\boldsymbol{x} \in \Re^K$ located in Ω. According to the moving least-squares (MLS) [3], the approximation $u^h(\boldsymbol{x})$ of $u(\boldsymbol{x})$ is

$$u^h(\boldsymbol{x}) = \sum_{I=1}^{N} \Phi_I(\boldsymbol{x}) d_I = \boldsymbol{\Phi}^T(\boldsymbol{x})\boldsymbol{d} \tag{1}$$

where $\boldsymbol{d}^T = \{d_1, \cdots, d_N\}$ and $\boldsymbol{\Phi}^T(\boldsymbol{x}) = \{\Phi_1(\boldsymbol{x}), \cdots, \Phi_N(\boldsymbol{x})\}$ with d_I representing the nodal parameter for node I and $\Phi_I(\boldsymbol{x}) = \boldsymbol{a}^T(\boldsymbol{x})\boldsymbol{p}(\boldsymbol{x}_I) w_I(\boldsymbol{x})$ representing the MLS shape function corresponding to node I, $\boldsymbol{a}(\boldsymbol{x})$ is a vector of unknown parameters, which can be determined by imposing reproducibility or consistency conditions, $\boldsymbol{p}^T(\boldsymbol{x}) = \{p_1(\boldsymbol{x}), p_2(\boldsymbol{x}), \cdots, p_m(\boldsymbol{x})\}$ is a vector of complete basis functions of order m, $w_I(\boldsymbol{x})$ is a weight function associated with node I such that $w_I(\boldsymbol{x}) \geq 0$ for all $\boldsymbol{x}$ in the support Ω_x of $w_I(\boldsymbol{x})$ and zero where $\boldsymbol{x}_I$ denotes the coordinates of node I, and N is the total number of meshless nodes. According to the reproducibility condition,

$$\boldsymbol{p}(\boldsymbol{x}) = \sum_{I=1}^{N} \boldsymbol{p}(\boldsymbol{x}_I)\Phi_I(\boldsymbol{x}) = \sum_{I=1}^{N} \boldsymbol{p}(\boldsymbol{x}_I)\Phi_I{}^T(\boldsymbol{x}) \tag{2}$$

Substituting $\Phi_I(\boldsymbol{x})$ in Equation 2 gives,

$$\boldsymbol{p}(\boldsymbol{x}) = \left[\sum_{I=1}^{N} \boldsymbol{p}(\boldsymbol{x}_I)\boldsymbol{p}^T(\boldsymbol{x}_I) w_I(\boldsymbol{x})\right] \boldsymbol{a}(\boldsymbol{x}). \tag{3}$$

INTEGRATED EFGM-FEM

Consider the domain $\Omega = \Omega_{EFGM} \cup \Omega_{FEM}$, which comprises two non-overlapping subdomains Ω_{EFGM} and Ω_{FEM} and boundary Γ_b. Depending the location of a point $\boldsymbol{x} \in \Re^K$, the reproducibility condition given by Equation 3 can be written as follows:

Case 1: If $\boldsymbol{x} \in \Omega_{EFGM}$ and the shape function of all FEM nodes are zero at $\boldsymbol{x}$,

$$\boldsymbol{p}(\boldsymbol{x}) = \sum_{I=1,\, \boldsymbol{x}_I \in \Omega_{EFGM}}^{N} \boldsymbol{p}(\boldsymbol{x}_I)\Phi_I(\boldsymbol{x}). \tag{4}$$

Case 2: If $\boldsymbol{x} \in \Omega_{EFGM}$ and the shape function of some FEM nodes along boundary Γ_b are nonzero at $\boldsymbol{x}$,

$$\boldsymbol{p}(\boldsymbol{x}) = \sum_{I=1,\, \boldsymbol{x}_I \in \Omega_{EFGM}}^{N} \boldsymbol{p}(\boldsymbol{x}_I)\Phi_I(\boldsymbol{x}) + \sum_{J=1,\, \boldsymbol{x}_J \in \Gamma_b}^{M} \boldsymbol{p}(\boldsymbol{x}_J) N_J(\boldsymbol{x}). \tag{5}$$

A node on the boundary between EFGM zone and FEM zone Γ_b is treated as an FEM node if its FEM shape function value at the point $\boldsymbol{x}$ is nonzero or else it is treated as EFGM Node. In this case,

$$\boldsymbol{p}(\boldsymbol{x}) = \boldsymbol{A}(\boldsymbol{x})\boldsymbol{a}(\boldsymbol{x}) + \sum_{J=1,\, \boldsymbol{x}_J \in \Omega_{FEM}}^{M} \boldsymbol{p}(\boldsymbol{x}_J) N_J(\boldsymbol{x}). \tag{6}$$

Case 3: If $\boldsymbol{x} \in \Omega_{FEM}$,

$$\boldsymbol{p}(\boldsymbol{x}) = \sum_{J=1,\, \boldsymbol{x}_J \in \Omega_{FEM}}^{M} \boldsymbol{p}(\boldsymbol{x}_J) N_J(\boldsymbol{x}), \tag{7}$$

where the FEM shape function $N_J(\boldsymbol{x})$ can be obtained by Lagrange interpolation. Hence, the effective shape function for integrated EFGM-FEM, denoted by $\tilde{\Phi}_I(\boldsymbol{x})$, can be defined as

$$\tilde{\Phi}_I(\boldsymbol{x}) = \begin{cases} \Phi_I(\boldsymbol{x}), & \text{if } \boldsymbol{x}_I \in \Omega_{EFGM} \\ N_I(\boldsymbol{x}), & \text{if } \boldsymbol{x}_I \in \Gamma_b \text{ and } N_I(\boldsymbol{x}) \neq 0 \\ \left\{ \boldsymbol{p}(\boldsymbol{x}) - \sum_{J=1,\, \boldsymbol{x}_J \in \Omega_{FEM}}^{M} \boldsymbol{p}(\boldsymbol{x}_J) N_J(\boldsymbol{x}) \right\}^T & \\ \boldsymbol{A}^{-1}(\boldsymbol{x}) \boldsymbol{p}(\boldsymbol{x}_I) w_I(\boldsymbol{x}), & \text{if } \boldsymbol{x}_I \in \Gamma_b \text{ and } N_I(\boldsymbol{x}) = 0 \\ N_I(\boldsymbol{x}), & \text{if } \boldsymbol{x}_I \in \Omega_{FEM} \end{cases} . \tag{8}$$

The effective shape function $\tilde{\Phi}_I(\boldsymbol{x})$ strongly depends on the type of basis functions used. In this study, the fully enriched basis function was used for analyzing cracked structures [1,2].

VARIATIONAL FORMULATION AND DISCRETIZATION

For small displacements in two-dimensional, homogeneous, isotropic, and linear-elastic solids, the variational or weak form of equilibrium equation is

$$\int_\Omega \boldsymbol{\sigma}^T \delta\boldsymbol{\epsilon} d\Omega - \int_\Omega \boldsymbol{b}^T \delta\boldsymbol{u} d\Omega - \int_{\Gamma_t} \bar{\boldsymbol{t}}^T \delta\boldsymbol{u} d\Gamma - \delta W_u = 0 \tag{9}$$

$$\delta W_u = \sum_{\boldsymbol{x}_J \in \Gamma_u} \delta\boldsymbol{f}^T(\boldsymbol{x}_J)\left[\boldsymbol{u}(\boldsymbol{x}_J) - \bar{\boldsymbol{u}}(\boldsymbol{x}_J)\right] + \boldsymbol{f}^T(\boldsymbol{x}_J)\delta\boldsymbol{u}(\boldsymbol{x}_J) \tag{10}$$

where $\boldsymbol{\sigma}$ is the stress vector, $\boldsymbol{\epsilon}$ is the strain vector, $\boldsymbol{u}$ is the displacement vector, $\boldsymbol{b}$ is the body force vector, and $\bar{\boldsymbol{t}}$ and $\bar{\boldsymbol{u}}$ are the vectors of prescribed surface tractions and displacements, respectively. Using the integrated EFGM-FEM method, the displacement field can be approximated by

$$u_i^h(\boldsymbol{x}_J) = \sum_{I=1}^{N} \tilde{\Phi}_I(\boldsymbol{x}_J) d_I^{\,i} = \tilde{\boldsymbol{\Phi}}_J^{\,iT} \boldsymbol{d} \tag{11}$$

where $\tilde{\boldsymbol{\Phi}}_J^{\,iT}$ and $\boldsymbol{d}$ are vectors of integrated EFGM-FEM shape functions and nodal parameters displacements, respectively, and N is the total number of nodal points in Ω. For a single boundary constraint $\bar{u}_i(\boldsymbol{x}_J) = g_i(\boldsymbol{x}_J)$ applied at node J in the direction of x_i coordinate, when Equations 11 is invoked, the discretized form of Equations 9 and 10 becomes [2]

$$\begin{bmatrix} \boldsymbol{k} & \tilde{\boldsymbol{\Phi}}_J^{\,i} \\ \tilde{\boldsymbol{\Phi}}_J^{\,iT} & 0 \end{bmatrix} \begin{Bmatrix} \boldsymbol{d} \\ f_i(\boldsymbol{x}_J) \end{Bmatrix} = \begin{Bmatrix} \boldsymbol{f}^{ext} \\ g_i(\boldsymbol{x}_J) \end{Bmatrix} \tag{12}$$

where $\boldsymbol{k} \in \mathcal{L}\left(\Re^{2N} \times \Re^{2N}\right)$ is the stiffness matrix and $\boldsymbol{f}^{ext} \in \Re^{2N}$ is the force vector. When multiple boundary constraints are enforced, an augmented system of similar linear equation can be developed. The equilibrium equations can be solved using the method of Lagrange multipliers [1] or transformation methods [2].

COMPUTATIONAL FRACTURE MECHANICS

Consider a structure with a rectilinear crack of length 2*a* that is subjected to external stresses. Let K_I and K_{II} be the stress-intensity factors (SIFs) for mode-I and mode-II, respectively. The SIFs can be evaluated using the domain form of an interaction integral $M^{(1,2)}$, i.e.,

$$K_I = \frac{E'}{2} M^{(1,2)}, \tag{13}$$

where $E' = E$ for plane stress and $E' = E/(1-\nu^2)$ for plane strain, and

$$M^{(1,2)} = \int_A \left[\sigma_{ij}^{(1)} \frac{\partial u_i^{(2)}}{\partial x_1} + \sigma_{ij}^{(2)} \frac{\partial u_i^{(1)}}{\partial x_1} - W^{(1,2)} \delta_{1j} \right] \frac{\partial q}{\partial x_j} dA \tag{14}$$

where $W^{(1,2)}$ is the mutual strain energy from the actual mixed mode state for the given boundary conditions (superscript 1) and the super-imposed near-tip mode I auxiliary state (superscript 2), and *q* is another weight function chosen such that it is *unity* at the crack tip, *zero* along the boundary of the domain, and arbitrary elsewhere. Following similar considerations, K_{II} can be calculated from Equations 13-14, except that the near-tip mode II state is chosen as auxiliary state while computing $M^{(1,2)}$.

In order to simulate crack growth, the crack-path direction must be determined. There are a number of criteria available to predict the direction of crack trajectory. In this study, the crack-growth simulation is based on the maximum circumferential stress criterion [5]. When the values of K_I and K_{II} are known, the direction of crack-propagation can be easily solved using standard numerical procedures. Other criteria, which are not considered here, can be easily implemented into the proposed method.

NUMERICAL EXAMPLES

Example 1: Stationary Crack under Mixed-Mode

This example involves an edge-cracked plate in Figure 1, which is fixed at the bottom and subjected to far-field shear stress τ^{∞} = 1 unit applied on the top. The plate has length *L* = 16 units, width *W* = 7 units, and crack length *a* = 3.5 units. Figure 2 shows the domain discretization involving 324 uniformly spaced nodes, some of which are treated as meshless nodes and rest of them are treated as 4-noded quadrilateral finite elements. The elastic modulus and Poisson's ratio were 30×10^6 psi and 0.25, respectively. A plane strain condition was assumed.

Table 1 shows the predicted K_I and K_{II} for several values of L_{EFG}/L, where L_{EFG} is defined in Figure 2. The reference solutions for this problem are: $K_I = 34$ units and $K_{II} = 4.55$ units [6]. The predicted K_I and K_{II} values compare very well with the reference SIF values up to L_{EFG}/L = 6/14. However, the accuracy of the predicted values deteriorates and oscillates when $L_{EFG}/L \le 5/14$, possibly due to the smaller meshless zone. Figure 3 plots variation of CPU ratio, defined as the ratio of CPU time using integrated EFGM-FEM and CPU time using meshless method for the whole domain. It is evident from the plot that CPU time decreases with decrease in L_{EFG}/L, as expected. Hence combining meshless method with FEM can significantly reduce computational effort for solving fracture-mechanics problems.

Example 2: Experimental Validation of Crack Propagation

In this example, crack trajectories predicted by the proposed method are compared with the Pustejovsky's experimental data [7]. Pustejovsky performed a series of uniaxial tension tests on isotropic Titanium Ti-6Al-4V plates with oblique center-cracks of length 2*a* = 13.5 mm (0.53 inch) at $\gamma = 43^0$ and length 2*a* = 14.2 mm (0.56 inch) at $\gamma = 30^0$. The reported dimensions and material properties of the specimens were:

length, $2L$ = 304.8 mm (12 inches), width, $2W$ = 76.2 mm (3 inches), elastic modulus, E = 110 GPa (16,000 ksi) and Poisson's ratio, ν = 0.29. A far-field uniaxial tensile stress, σ^{∞} = 207 MPa (30 ksi) was applied on the top and the bottom of the specimen during meshless analysis. Figures 4 and 5 show the dimensions of the specimen and the meshless discretization, respectively. The domain discretization involves 1124 nodes, some of which are treated as meshless nodes and rest of them, are treated as 4-noded quadrilateral finite elements. A plane strain condition was assumed.

Figures 6 and 7 show the comparison of the predicted crack trajectories by using meshless method for the whole domain and by the proposed method when $L_{EFG} / L = 11/16$ and $7/16$, with the experimental data in a small region *ABCD* (see Figure 5) surrounding the crack. The results in Figure 6 corresponds to $2a$ = 13.5 mm (0.53 inch) and $\gamma = 43^0$ and the results in Figure 7 corresponds to $2a$ = 14.2 mm (0.56 inch) and $\gamma = 30^0$. The predicted crack trajectories by the proposed method are in good agreement with all-meshless results or the experimental data.

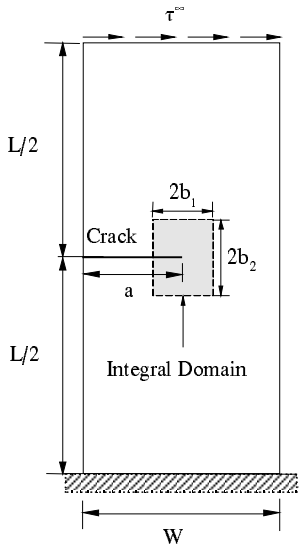

Figure 1. Edge-cracked plate

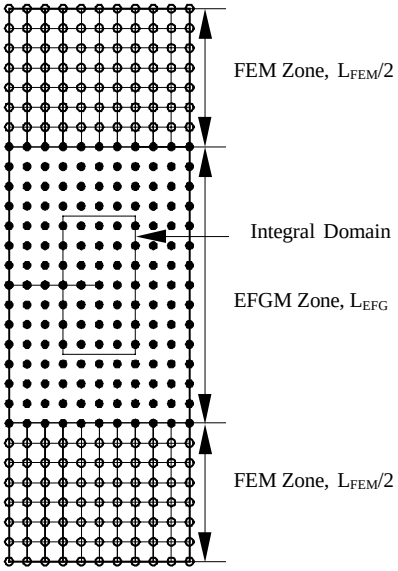

Figure 2. Domain discretization

TABLE 1
SIFs FOR EDGE-CRACKED PLATE

	Mode-I		Mode-II	
L_{EFG}/L	K_I	SIF Ratio[(a)]	K_{II}	SIF Ratio[(a)]
12/14	33.63	0.989	4.536	0.997
11/14	33.62	0.989	4.539	0.998
10/14	33.57	0.987	4.520	0.993
9/14	33.55	0.987	4.539	0.998
8/14	33.47	0.984	4.521	0.994
7/14	33.33	0.980	4.504	0.990
6/14	33.42	0.983	4.491	0.987
5/14	33.39	0.982	4.004	0.880
4/14	34.89	1.026	4.694	1.032
3/14	34.65	1.019	3.681	0.809
2/14	36.12	1.062	4.968	1.092

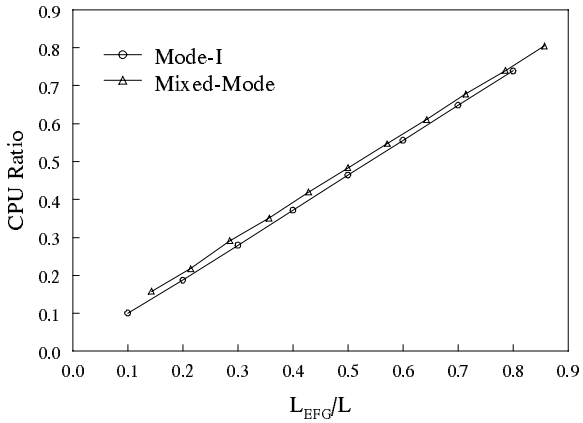

Figure 3. CPU time

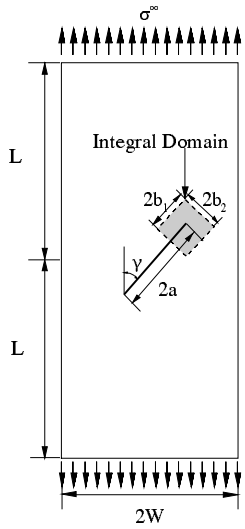

Figure 4. Angle-cracked plate

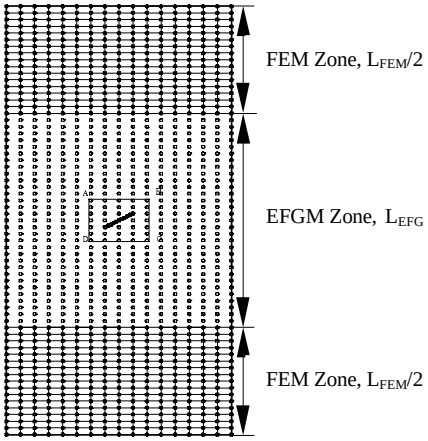

Figure 5. Domain discretization

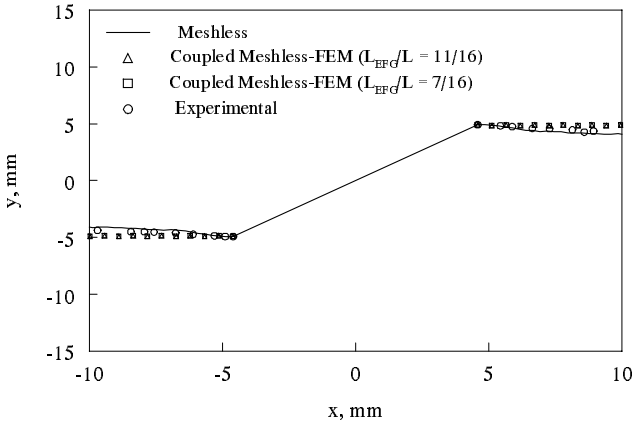

Figure 6. Crack propagation ($2a$ = 13.5 mm)

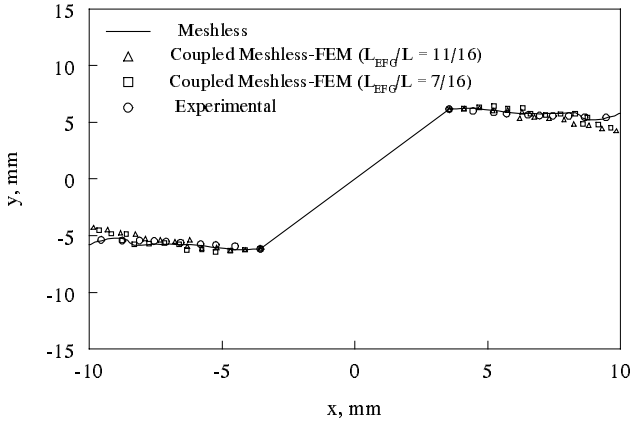

Figure 7. Crack propagation ($2a$ = 14.2 mm)

CONCLUSIONS

An integrated meshless-finite element method was developed for analyzing linear-elastic cracked structures subject to mixed-mode loading conditions. The EFGM was used to model material behavior close to cracks and the FEM in areas away from cracks. In the interface region, the resulting shape function, which comprises both EFGM and FEM shape functions, satisfies the consistency condition thus ensuring convergence of the method. Numerical examples show that the stress-intensity factors predicted by the proposed method compare very well with existing solutions obtained by all-FEM or all-EFGM analyses. A significant saving of computational effort can be achieved due to coupling in the proposed method when compared with existing meshless methods. The agreement between the predicted crack trajectories with those obtained from existing experimental data is excellent.

REFERENCES

1. Belytschko, T., Lu, Y., and Gu, L. (1995), *Engng. Frac. Mech.*, 51 (2), 295.
2. Rao, B. N., and Rahman, S. (2000), *Comp. Mech.*, 26, 398.
3. Lancaster, P. and Salkauskas, K. (1981), *Math. Comp.*, 37, 141.
4. Moran, B. and Shih,F. (1987), *Engng. Frac. Mech.*, 27, 615.
5. Erdogan, F. and Sih, G. C. (1963), *J. Basic Engng.*, 85, 519.
6. Wilson, W. K. (1969), *Ph.D. Thesis*, University of Pittsburgh, PA, USA.
7. Pustejovsky, M. A. (1979), *Engng. Frac. Mech.*, 11, 9.

Oral Ref. : ICF100210OR

AN INTEGRATED MULTISCALE COMPUTATION MODEL TO LINK ATOMIC AND CONTINUUM APPROACHES

Yufu Liu, Yoshihisa Tanaka and Chitoshi Masuda

National Institute for Materials Science (NIMS)*
1-2-1 Sengen, Tsukuba City, Ibaraki Prefecture 305-0047, Japan

ABSTRACT

Materials fracture often involves various length scales from dislocation evolution at the atomic scale level to crack propagation at the continuum levels. In this study, an integrated multi-scale model is proposed by concurrent coupling an atomic region, a meso-scale region and traditional continuum region. The meso-scale region is defined as a region with subcracks in comparison with a main large crack. The atomic region is solved by the molecular dynamics method and the meso-scale region is a finite element region where potentials in various forms may be introduced as fracture criteria. Cohesive-zone model with the cohesive law being the potential was used in the meso-scale region. This model has the advantage to simulate the complete process of a crack growth from the micro-, to meso- and then to the continuum regions. Unified description of the computation algorithm is presented. Simulation examples using a model with a primary crack and a subcrack located in front of the primary crack in bcc alpha-iron are given.

Key words: Multi-scale computation, Length Scale, Molecular Dynamics, Finite Element Method.

INTRODUCTION

Materials fracture often involves various length scales from dislocation evolution at the atomic scale level to crack propagation at the continuum levels. The current capabilities of atomic simulations are still restricted to nanoscale length of around 100nm order and are far from meeting practical demands of simulating various defects in solids, so a compromise between physical precision and computational feasibility is needed. In the large-scale atomic models, control of computation conditions and interpretation of the obtained results are difficult. Models by coupling

* Merger of National Research Institute for Metals and National Institute for Research in Inorganic Materials from April 2001.

various length scales and methods provide a means to solve such problems. Attempt in this direction has begun since 1970s. In the flexible-border or multi-region techniques, a fully atomic region is embedded into one or more outer regions and fully coupled atomistic [1] and finite element techniques to consider problems with complex nonlinearities were proposed [2-4]. An advantage of these models is natural inclusion of atomic potentials as a fracture criterion. Such models successfully explained some brittle microscopic fracture behavior of pure single crystals. More recently, the quasicontinuum method with a spatial mesh adaptively refined around highly energetic regions appears to be more promising [5]. Multiscale computation has been extended to include mean-field quantum mechanics in order to implement semiempirical tight-binding and molecular dynamics and finite element methods within one system [6].

The difficulty inherent in multiscale modeling is the treatment of mesoscale microstructure and how it is integrated and connected to micro (or nano)-scale and macro-scale microstructures. Computation at the mesoscale level itself involves multiple physical phenomena. For example, for pure materials of single crystals, dislocation nucleation and subsequent interaction and evolution are dominant factors, while void or micro-crack formation of various length dimensions and evolution are important in more engineering structural materials. In the case of composites, the interface between the reinforcement and matrix represents another microstructure and fracture length scales. The fracture behavior of brittle solids often involves the coalescence of many small cracks before linking with a main crack [see the review of Ref. (7) and references therein]. This subject has been studied extensively within the scope of continuum elasticity [7]. The interaction between individual cracks and the effective elastic properties with many cracks is of primary concern. These problems have not been treated on the atomic scale. Viewed from multiscale computation, the volume average quantities with regards to the problem having many cracks can be readily taken into account in the continuum region within the traditional treatment of coupling atomic and continuum models. This study is concerned with the interaction of individual cracks: a primary large crack and a small void-like crack. The primary crack tip region is deemed atomic, while a meso-scale region is introduced to describe the area with the sub-crack and this zone is based on the cohesive-zone concept where a fracture criterion is embedded automatically. This model has the advantage to consider crack growth interaction at different length scales while still maintaining atomic resolution in the most important region. Unified description of the computation algorithm is presented and simulation examples using bcc a iron are given.

MODEL AND FORMULATION

Fig.1 shows a central crack model used in the computation; only half of the model is plotted with the center of the main crack being a symmetrical axis. $a/l = 2.167$ is assumed as an initial geometrical condition. The details of the atomic crack tip region embedded within the continuum are shown later. The atomic region notch was created by removing three layers of atoms. The sub-crack region is called a meso-scale region where the cohesive zone theory is applied. The total energy of the system, E,

$$E[\mathbf{u}] = E(\text{atom}) + \int_{\Omega} W(\nabla \mathbf{u}) dV + \int_{\Sigma} \Phi(d) ds, \qquad (1)$$

where $E(\text{atom})$ is the total energy of the atomic region, $\mathbf{u}$ the displacement field, Ω the continuum domain, $W(\nabla \mathbf{u})$ the potential energy of the continuum; $\Phi(d)$ the cohesive-zone potential.

The material considered is *a* iron represented by Johnson's pair potential [8]. Molecular dynamics technique of the velocity Verlet algorithm is used to calculate atom movement with a time step of 1fs and the velocity scaling law to control temperature at 300K. The cohesive surface separation model [9] is used in the meso-scale region. The model relates cohesive tractions **T** to displacements by $\mathbf{T}=-\P f/\P\mathrm{D}$, where f is the potential and D is the displacement of cohesive points. f may be in various forms [9, 10] and a form giving linear cohesive relationship between **T** and D is introduced here for the brittle materials system, namely, $T_t = K_t\Delta_t$ and $T_n = K_n\Delta_n$, where the subscripts t and n represent quantities at the tangent and normal directions, respectively, and K_n and K_t are spring constant-like parameters. Such cohesive laws are then embedded into cohesive finite elements [5]. The cohesive elements are interspersed throughout the material of interest; here, the finite element region between the main crack tip and sub-crack tip is such a region to see how the main crack and sub-crack interact. In the atomic region, the crack plane is assumed to lie on {100} planes, the cleavage plane of BCC *a* iron.

Additional boundary conditions between the atomic region and meso-scale region are needed, i.e., the continuity of force and displacement of the atoms and finite element nodes at the boundary [4]. The atomic and continuum regions share a common boundary at the neighbor array of atoms and finite element nodes. Based on the virtual work principal, the continuum part in Eq (1) is discritized into finite elements. Quasi-static mode I loading, K_I, was applied in terms of the mode I main crack .

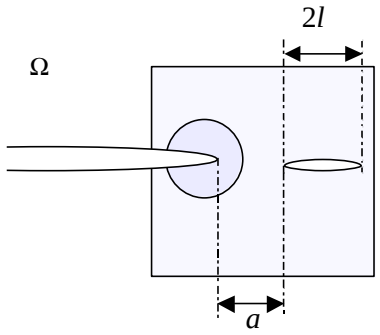

Figure 1 Central crack model with one sub-crack located in front of the main crack tip.

RESULTS, DISCUSSION AND SUMMARY

Figure 2 (a)-(d) shows a series of typical snapshots obtained in the simulation. Fig. 2 (a) demonstrates that both the atomic region and sub-crack region still undergo elastic deformation at an applied loading level of $K_I = 1.53\mathrm{MPam}^{1/2}$; it also indicates atom and finite element arrangement in these regions. Figs2. (b)-(d) are the results during subsequent loading for the case of $K_I = 2.37,\ 2.65$ and $2.7\ \mathrm{MPam}^{1/2}$, respectively. In Fig. 2 (b), atom movement to form crack-like extension, as indicated at Point A, within the atomic region is observed; the point A is slightly away from the initial notch plane. Meanwhile, the sub-crack also propagates towards the atomic region but is then stopped at a distance of about 2 lattice parameters in front of the atomic region. The loading level for this configuration of Fig. 2(b) is smaller than that reported in the literature [2]. This is may be due to the blunted initial notch tip, compared to the atomic sharpness crack tip in the literature. In Fig. 2(c), on further loading increase, the sub-crack propagates

completely across the continuum region to reach the atomic region and initiates a new crack in the atomic region as shown at Point A of Fig. 2(c). It is this new crack that governs the final failure path (Fig.2 (d)). Note that the system grows into unstable growth with additional small loading increment from the state shown in Fig.2(c). This clearly demonstrates the importance of the initial sub-crack. Further investigation regarding effects of lattice trapping and various parameters involved in the model is under way. In summary, the present study provides an effective method for simulating crack growth and crack interaction at different length scales.

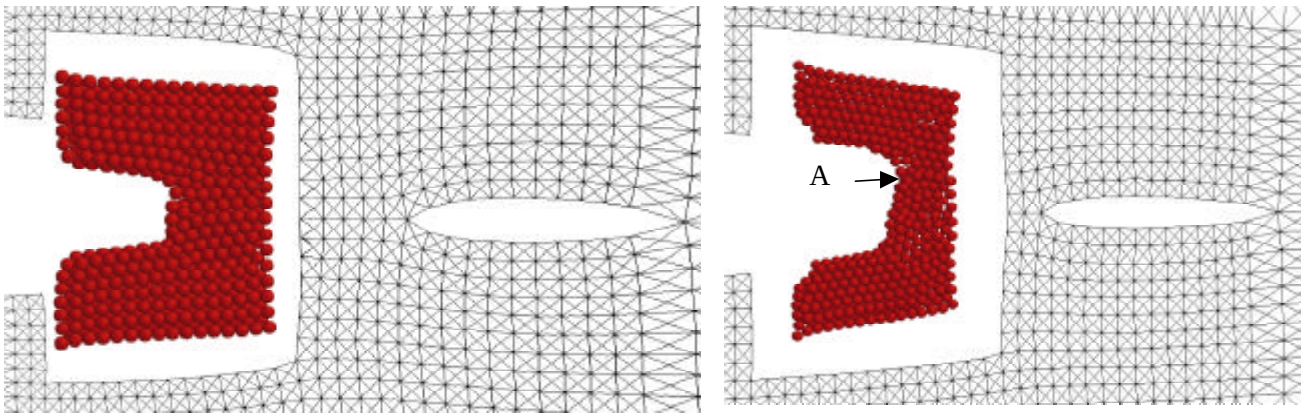

(a) $K_I = 1.53 \text{MPam}^{1/2}$ (b) $K_I = 2.37 \text{MPam}^{1/2}$

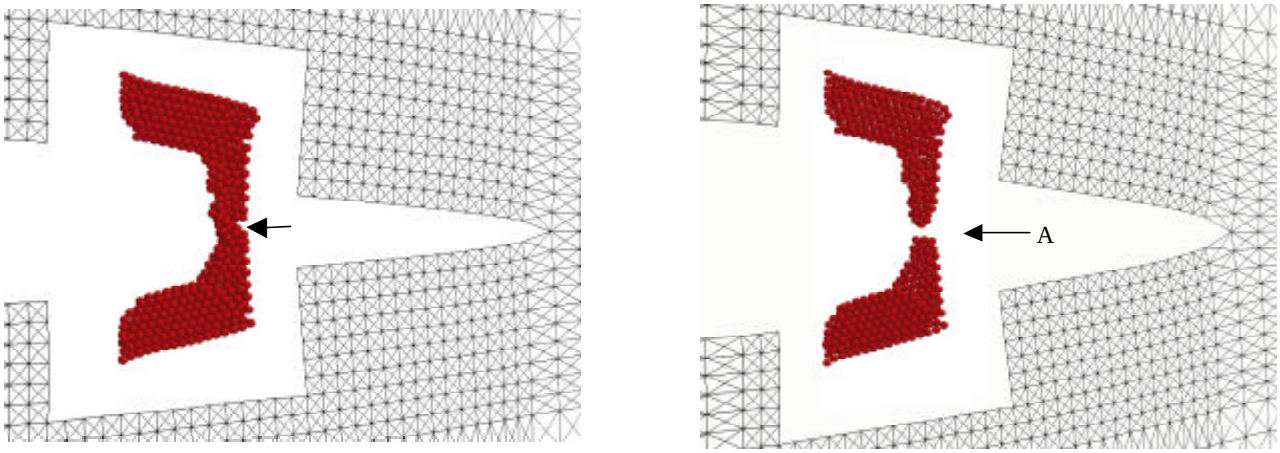

(c) $K_I = 2.65 \text{MPam}^{1/2}$ (d) $K_I = 2.7 \text{MPam}^{1/2}$

Figure 2 Simulation results for 4 loading levels (a) $K_I = 1.53 \text{MPam}^{1/2}$,(b) $K_I = 2.37 \text{MPam}^{1/2}$, (c) $K_I = 2.65 \text{MPam}^{1/2}$ (d) $K_I = 2.7 \text{MPam}^{1/2}$. Note that the deformation magnifications for the atomic region and continuum region are different.

ACKNOWLEDGEMENT

YF would like to thank Dr. Kusunoki of NIMS and Dr. Gumbsch of Max-Planck Institute for extensive discussion on MD and multi-scale computation and atomic modeling, and Prof. Nakatani of Osaka University for providing useful references that helped to verify the MD program reported here. Helpful communication with Prof. Sato of Akita Prefecture University is also gratefully acknowledged.

REFERENCES

1. Sinclair, J.E., Gehlen, P.G., Hoagland and Hirth, J.P. (1978), J. Appl. Phys. 49, 3890.
2. Kohlhoff, S., Gumbsch, P. and Fischmeister, H.F. (1991) Phi. Mag. A 64, 851.
3. Yang, W., Tan H.L. and Guo, T.F. (1994), Modelling Simu. Mater. Sci. Eng., 767.
4. Mullins, M. and Dokainish, M.A. (1982) Phi. Mag. A 46, 771.
5. Ortiz, M. and Phillips, R., in Advances in Applied Mechanics 36, pp.2-73, Giessen, E.. and Wu, T.Y. (Eds), Academic Press, UK.
6. Broughton, J.Q., Abraham, F.F., Bernstein, N. and Kaxias, E. (1999), Phy. Rev. B 60, 2391.
7. Kachanov, M. (1994) in Advances in Applied Mechanics 30, pp.260-438, Hutchinson, J.W. and Wu, T.Y. (Eds), Academic Press, UK.
8. Johnson, R.A. (1964), Phy. Rev. 134, A1329.
9. Ortiz, M. and Pandolfi (1999), A., Int. J. Numer. Meth. Eng. 44, 1267.
10. Needleman, A. (1987), J. App. Mech. 54, 525.

ORAL REFERENCE ICF100308OR

AN INTERFACE ELEMENT FOR THE NUMERICAL ANALYSIS OF FIBRE REINFORCED CONCRETE

Massimo Cuomo

Sezione di Ingegneria Strutturale
Dipartimento di Ingegneria Civile ed Ambientale
University of Catania – ITALY

ABSTRACT

A constitutive model for a joint element is developed based on a generalisation of the Cohesive Crack Model. The model uses a constitutive law based on dual external (tractions and crack opening vector), and internal variables, the latter of damage nature, responsible for the evolution of the softening cohesive. A potential energy of unilateral type couples the crack opening vector with the damage variables, whose evolution is ruled by two yielding modes, one accounting for the slippage of the fibres, the other for the deterioration of the material due to crack opening.

KEYWORDS

Damage Mechanics, Interface elements, Cohesive crack model, Brittle matrices, Fibre reinforced concrete

1. MOTIVATIONS, BACKGROUND AND OBJECTIVES OF THE MODEL PROPOSED

The occurrence of fractures causes two main phenomena that affects the mechanical modelisation: first, energy is dissipated in a domain of measure zero, since its physical dimension is smaller than the dimension of the structure (actually, its dimension is fractal); secondly, the displacement field ceases to be continuous, and finite jumps appear, so that the usual compatibility equations lose their validity, that is the vectorial space of the displacements changes from H_1 to BV. From a physical point of view, these phenomena give rise to an unstable behaviour at the material and structural level.

The numerical counterpart is that a simulation of the process with a continuum model suffers of numerical problems of mesh dependency, so that either a non-local media has to be used, or some form of enhancement of the displacement field has to be introduced. Enhanced elements, with embedded discontinuities, like the X-FEM recently developed by Belitschko are a promising example of the latter approach. An alternate methodology consists in introducing discontinuous interfaces in some predefined locations in the continuum. In the interface model the width of the process zone is assumed to reduce to zero, but the amount of dissipation is controlled, allowing a numerical treatment of the material instability. Tractions are directly related to the displacements jumps, so that there is no need to introduce generalised derivatives.

The latter approach is followed in this paper. Specifically, attention is focused on the constitutive behaviour of the interface model, disregarding the problem of refining the discretisation for better localising the fracture surfaces. Main objective of the paper is to modify an interface model previously proposed in the literature by Carol [1,2], that accounts for mode I and mode II fracture, based on the

definition of an intrinsic curve for the interface in the traction space, so that a plastic-like behaviour is assumed for the dual relative displacements. Cohesive forces are supposed to act after crack opening, and softening is introduced assuming a phenomenologically defined degradation of some material parameters. The model, thus, appears as a (non associated) elastic-plastic-softening model. Elasticity is introduced for numerical purposes. Still retaining the idea of an intrinsic curve and of its degradation as consequence of fracture evolution, the model proposed differs substantially from the original one in several aspects that will be now briefly introduced

1. The cohesive traction-displacement laws, as well as the softening behaviour of the interface, are defined on the basis of thermodynamic potentials, so that they can be easily implemented in a variational framework for numerical analysis.
2. The softening law is introduced through the dependency of the limit surface on a damage parameter, dual to the internal variable that rules the reversible loading-unloading. In this way the limit condition of the interface (yield surface) is defined in the extended space of the tractions and of the conjugated forces. The development follow closely a recently proposed model of continuum damage [3].
3. The first consequence of points 1,2 is that it is possible to obtain crack opening and reclosing, without permanent residual relative displacements, as in standard damage models. Furthermore, the thermodynamic framework allows to easily account for additional effects, like fibre bridging. It is sufficient to add an additional term in the internal energy, and additional dissipation mechanisms, that account for fibre slippage or yielding, in the dissipation potential.

2. PRESENTATION OF THE INTERFACE MODEL

The interface model is local, and is ruled by the following fields of dual variables:

$\mathbf{w} = (w_n, w_t) \in U$	*Relative displacements*	$\mathbf{t} = (\sigma, \tau) \in U'$	*Cohesive forces*
$\omega \in \Re$	*Internal damage variable*	$\zeta \in \Re$	*Conjugated damage energy*
$\alpha \in I$	*Hardening internal variable*	$\chi \in I'$	*Conjugated force*

$$h = (\mathbf{w}, \omega, \alpha) = (\mathbf{w}_e, \omega_e, \alpha_e) + (\mathbf{w}_p, \omega_p, \alpha_p) = h_e + h_p \qquad (1)$$

The indices *n,t* refer to normal and tangential components respectively. In the remaining of the paper only the 2-dimensional case will be addressed. It is underlined that a scalar damage mechanism is assumed, while the hardening variables can be in general vectors, so to account for anisotropic friction mechanisms. However, in this paper, they will not be explicitly considered. Following the Standard Generalised Material Model, the kinematic variables are partitioned in a reversible and an irreversible component, identified in (1) by the indices *e,p*, as done in [3] (the additive decomposition implies linear kinematic). The model is characterised by the functional of the internal energy *u*, that rules the reversible behaviour, and of the dissipation *d*, that accounts for irreversible phenomena. Denoting by $(\cdot)^c$ the conjugated potential, the constitutive equations are then obtained as

$$\begin{aligned} s &= (\mathbf{t}, \zeta, \chi) = \partial_{h_e} u(h_e) & s &\in \partial_{\dot{h}_p} d(\dot{h}) \\ h_e &= \partial_s u^c(s) & \dot{h}_p &\in \partial_s d^c(s) \end{aligned} \qquad (2)$$

The last of (2) are the flow rules for the irreversible kinematic variables.

2.1 The internal energy of the interface

The following form is assumed

$$u = \frac{1}{2}\mathbf{K}_\omega \mathbf{w}\cdot\mathbf{w} + \frac{1}{2}\mathbf{K}_f \mathbf{w}\cdot\mathbf{w} + \text{ind}\, W_n + \text{ind}\, \Omega$$
$$\mathbf{K}_\omega = \begin{bmatrix} K_n(\omega) & 0 \\ 0 & K_t(\omega) \end{bmatrix} \qquad \mathbf{K}_f = \begin{bmatrix} K_f & 0 \\ 0 & 0 \end{bmatrix} \qquad \mathbf{K}_\omega = \mathbf{K}_m\,(1+\omega_e)^n \tag{3}$$

In (3) K_m denotes the stiffness of the concrete matrix, while K_f is the stiffness of the fibre phase, assumed to act only in the normal direction. The damage mechanism is assigned only to the concrete matrix, but a further degradation, with the same or with another internal variable, can be introduced in the same way for the fibre properties. Introducing the set $W_n = \{w_n | w_n \geq 0\}$, the presence of the indicator function of W_n ensures the no compenetration condition. The set $\Omega = \{\omega^e | \omega^e \geq -1\}$ has been introduced in order to preserve the positivity of the damaged stiffness, so that the damage variable range from 0 to –1, as usually assumed. However, for the model (3) this term is not strictly necessary, since tends to –1 asymptotically, as will be shown later. Note finally that normal and tangential reactions are uncoupled.

The potential used, while preserves the unilateral character of the interface, does not fulfil the condition that no relative displacement develops until fracture occurs. Although the introduction of a fictitious elastic stiffness is usual in interface models [1], in the author's opinion it introduces serious drawbacks, that, however, will not be commented in this paper.

2.2 The dissipation potential

Following the developments in [3,4], in the time independent case considered in this model, the dissipation functional turns out to be conjugated to the complementary dissipation functional (plastic potential), that is given by the indicator function of the elastic domain *S*. Multiple dissipation mechanisms can then be included considering *S* as the convex hull of a finite number of domains S_i. The elastic domain is specified by means of a yield function. For the sake of clearness, the development of the model is followed step by step starting from the form assumed by Carol:

$$g_C = \tau^2 + (c - \mu\sigma_0)^2 - (c - \mu\sigma)^2 \tag{4}$$

with *c*, , $_0$ material constants. In the plane expression (5) represents an hyperbola having the Coulomb bilateral as asymptotes. The intersection of g_C with the co-ordinate axes are given by $\sigma = \sigma_0$, $2c/\mu - \sigma_0$, $\tau = \pm\mu\sqrt{\sigma_0(2c/\mu - \sigma_0)}$. Clearly, any fracture process occurs with irreversible displacements. In order to limit the phenomenon of dilatancy, the authors introduce a non-associative flow potential that becomes flat for compressive normal tension beyond a certain limit.

The first improvement consists in introducing the conjugate damage variable for definitely separating the irreversible plastic effects (due either to void development in the concrete or to fibres yielding or slipping) from the fracture phenomena which is associated mainly to damage. In the original model the parameters *c*, $_0$ where affected by the evolution of the fracture process, while was kept constant. A possible straightforward generalisation could then be to assume the yield function

$$g_C = \tau^2 + (c - \overline{\zeta} - \mu(\sigma_0 - \overline{\zeta})^2 - (c - \overline{\zeta} - \mu\sigma)^2 \qquad \overline{\zeta} = \zeta / w_0 \qquad w_0 = \sigma_0 / \left(K_n + K_f\right) \tag{5}$$

where the definition of the new damage variable is required for dimensionality reasons (note that has dimensions of a force per unit of length). The choice of (5) is motivated by the assumption that the damage affects equally the cohesion and the uniaxial limit stress. Expression (5) represents a lined surface, whose intersection with the plane =0 are the two straight lines

$$\sigma + \zeta = \sigma_0 \qquad (2-\mu)\,\zeta + \mu\sigma = 2c - \mu\sigma_0 \tag{6}$$

No physical damage mechanism is clearly associated t any of them. In an uniaxial process the initiation of the fracture can be found using the elastic law (2), as will be described soon. It is found that the limit values for the normal traction and the conjugated damage force are

$$\sigma_{\lim} = \frac{K_f + K_m}{K_f + K_m(1+n/2)}\,\sigma_0 \qquad \zeta_{\lim} = \frac{n}{2}\frac{K_m}{K_f + K_m(1+n/2)}\,\sigma_0 \tag{7}$$

so that neither $_0$ has a clear physical meaning, nor the value of the energy per unit area at the initiation of the fracture process matches the value that one would expect, i.e. ½ $_0$ w_0.

A further modification is then proposed, inspirited by the form (6) of the lined surface, that is it is proposed that the intersection of the limit surface with the plane =0 reduce to the two lines

$$\zeta - \zeta_0 = 0 \;\;,\;\; \sigma + \zeta = \sigma_k \;\;;\;\; \sigma_k = \sigma_0 + \zeta_0 - 2c/\mu \tag{8}$$

where the value $_0$ is the energy necessary for mode I fracture initiation if in the process only damage occurs. The expression for the limit surface takes the form

$$g = \tau^2 + \left(2c - \mu(\sigma_0 - \sigma)\right)^2 - \left(2c - 2\mu(\bar{\zeta}_0 - \bar{\zeta}) - \mu(\sigma_0 - \sigma)\right)^2 \tag{9}$$

The function (9) presents several differences with respect to (5). The intersection with the - plane is now a parabola, with $\tau \to \infty$ for $\sigma \to -\infty$, as before, but the tangent to the curve tends to 0, so that the problem of dilatancy is substantially reduced. The surface (9) is still a lined one, whose intersection with the plane =0 is given by the two straight lines (8), that intersect for the value $\sigma = 2\sigma_0 - c/\mu$, positive for the common values of the material parameters. The activation value of the conjugate damage energy will be discussed in the next paragraph in connection with the analysis of an uniaxial process. The surface (9) forms in the plane an hyperbola, whose sides are asymptotically tangent to a Coulomb bilateral with slope 1/|2|. Note that, although negative values of the damage conjugate variable are not called out by the admissibility condition (9), they are not attainable on the basis of the elastic relations. A sketch of criterion (9) and its section with the co-ordinate plane are given in figs. 1,2. The flow rules are given by the usual consistency rule, $\dot{h}_p = \lambda\,\partial_s g(s), \quad \lambda \in \partial\Re^-(g(s))$, and they take the forms

$$\dot{w}_{n_p} = \lambda^* 4\mu(\zeta_0 - \zeta) \qquad \dot{w}_{t_p} = \lambda^* 2\tau \qquad \lambda^* = \lambda/2\sqrt{g}$$
$$\dot{\omega}_p = \frac{\lambda^*}{w_0} 4\mu^2\left(2(\zeta_0 - \zeta) + (\sigma_0 - \sigma) - 2c/\mu\right) = \frac{\lambda^*}{w_0} 4\mu^2\left(\sigma_k - \zeta - \sigma\right) + \mu\frac{\dot{w}_{n_p}}{w_0} \tag{10}$$

It is stressed that the derivatives of the dissipation potential are continuous functions. Furthermore the permanent normal opening depends only on the difference between the current value of the damage energy and its limit value $_0$. When the latter is attained, the opening displacement becomes fully reversible, but damage still increases thanks to the other mechanism (first term in the latter of (10)). Additional dissipation mechanisms can be added in order to account for fibre yielding. The simplest choice could be $h_2 = \sigma + d\,\bar{\zeta} - \sigma_{0f} \le 0 \qquad d = K_f / K_m$, with $_{of}$ the limit tensile stress in the fibres. A sketch of the resulting domain in the uniaxial case is presented in fig. 3 First the matrix fails, then fibres plasticise, until pure separation of the interface is reached.

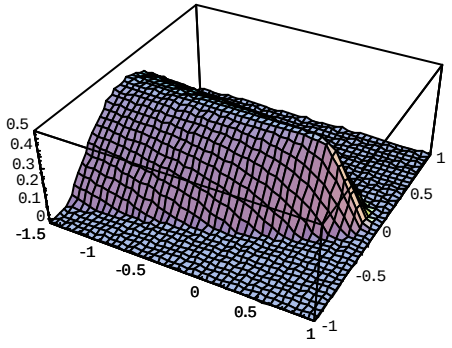

Figure 1 : Elastic domain

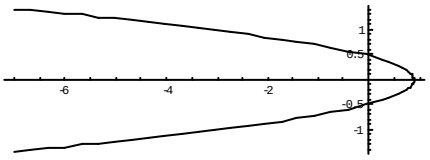

Figure 2 : section of the elastic domain

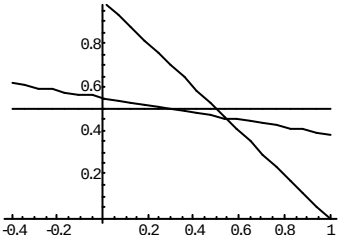

Figure 3 : uniaxial domain

3. EXEMPLIFICATION : UNIAXIAL RESPONSE TO MODE I FRACTURE

The characteristics of the model are investigated with reference to the special case of pure normal traction acting on the interface. Starting from a virgin state ($_e$=0), the elastic equations (2) furnish

$$\sigma = \left(K_m + K_f\right) w \; ; \quad \overline{\zeta} = \frac{n}{2} K_m \frac{w^2}{w_0} = \frac{n}{2} \frac{K_m}{\left(K_m + K_f\right)^2} \frac{\sigma^2}{w_0} \quad ; \quad \tau = 0 \tag{12}$$

Eqn.(12) is the parametric expression of a curve in the plane, that can intersect the limit surface in one of the 2 points that satisfy eqns. (8), according to the relative values of the material parameters ζ_0, σ_k. First is considered the case that the parametric curve (12) hits the limit surface on the line $=_0$, corresponding to a pure damage (reversible) process. Then one has

$$w_0 = \frac{2\overline{\zeta}_0}{K_m n} \quad ; \quad \zeta_{\lim} = \overline{\zeta}_0 w_0 = \frac{n}{2} K_m w_0^2 \qquad \sigma_{\lim} = \frac{2}{n} \frac{K_m + K_f}{K_m} \overline{\zeta}_0 \tag{13}$$

Therefore, in order to obtain the desired value for the fracture activation energy, it must be $\overline{\zeta}_0 = n/2\,\sigma_{0m}$, with $_{0m}$ the limit stress in the matrix. Indeed, substituting, it is found

$$w_0 = \frac{\sigma_{0m}}{K_m} \quad ; \quad \zeta_{\lim} = \overline{\zeta}_0 w_0 = \frac{n}{2} \sigma_{0m} w_0 \qquad \sigma_{\lim} = \frac{K_m + K_f}{K_m} \sigma_{0m} \tag{14}$$

where the stress in the last expression is relevant to the whole composite. Proceeding with the extension, the stress progressively decreases on the fracture surfaces, and tends to 0 asymptotically, as can be easily proved. This is in contrast with the cohesive model, that is based on the existence of a limit critical value of the crack opening. However, the energy for the entire process is finite, and it can be shown that it is equal to [4]

$$G_f = \frac{1}{2} \sigma_{0m} w_0 + \frac{n^2}{4} \zeta_0 = \left(\frac{1}{n} + \frac{n^2}{4}\right) \zeta_0 = \left(1 + \frac{n^3}{4}\right) \frac{\sigma_0 w_0}{2} \tag{15}$$

The previous equation can be used for estimating the value of n. For whatever value of n, the descending branch of the -w curve is always sublinear.

In the case the path (12) intersects first the second line (8) of the boundary, the following is found (note that in the case of absence of fibres, the limit stress coincides with the uniaxial limit tension of the matrix, and for the initiation energy one finds $\zeta_{\lim 1} = \overline{\zeta}_{\lim 1} w_0 = \left(\sigma_{0m} / K_m\right)\left(\sigma_k - \sigma_{0m}\right)$.

$$\begin{aligned}
w_{o1} &= \frac{2\overline{\zeta}_0}{K_m^2 n^2} \left(\sqrt{K_f^2 - 2nK_m^2 + n^2 K_m^2 \frac{\sigma_k}{\overline{\zeta}_0}} - K_f \right) \\
\sigma_{\lim 1} &= \sigma_{0m} \left(1 + \frac{K_f}{K_m^2 n} \left[\sqrt{K_f^2 + 2nK_m^2 \left(\frac{\sigma_k}{\sigma_{0m}} - 1 \right)} - K_f \right] \right) \\
\overline{\zeta}_{\lim 1} &= \frac{\overline{\zeta}_0}{K_m^2 n^2} \left[\sqrt{K_f^2 - nK_m^2 \left(2 - n \frac{\sigma_k}{\overline{\zeta}_0} \right)} - K_f \right]^2 \qquad \overline{\zeta}_0 = \frac{n}{2} \sigma_{0m}
\end{aligned} \tag{16}$$

Loading-unloading uniaxial processes are shown in fig. 4,5, comparing the cases of pure damage activation, and of mixed mechanisms. Fig.4 refers to plain concrete and fig.5 to a small addition of fibres. Note that no residual displacement is found after unloading in the pure damage mechanism, and the value of the damage parameter tends asymptotically to 1(full damaged state).

A different case is encountered if the limit surface is hit on the line $\sigma + \zeta = \sigma_0$. In this case some irreversible displacement is present, as it happens when fibres are present, and yielding occurs. At the same time the stiffness decreases, as damage develops. Increasing the relative displacement the stress decreases, and the state point moves on the limit curve until it eventually reaches the condition $_0$. At this stage the fibres start to slip, and no more permanent displacement is added, while damage in the matrix increases further. Note, however, that thanks to the hypothesis (2) the rigidity of the fibres remains constant, so that a residual plateau is finally reached with a residual stiffness.

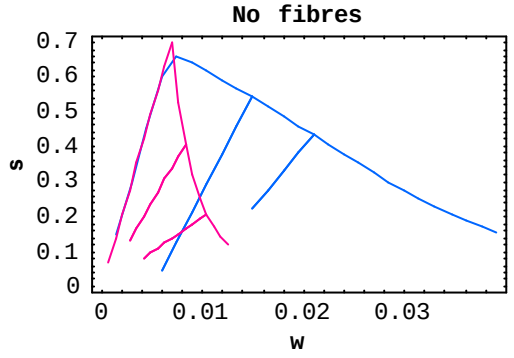

Figure 4 : Uniaxial fracture process for plain concrete

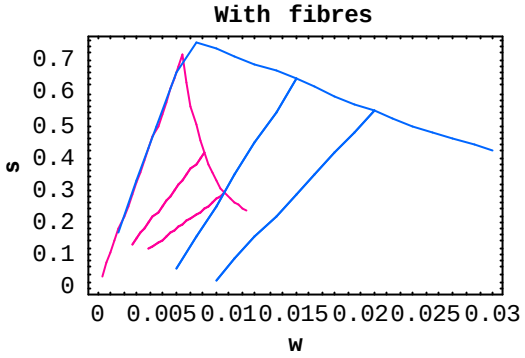

Figure 5 : Uniaxial fracture process for fibre reinforced concrete

4 FINAL COMMENTS

A constitutive model for a joint element has been developed based on a generalisation of the Cohesive Crack Model. The element is intended to be used for the microstructural analysis of fibre reinforced high strength concrete. The model is thermodynamically based, and differentiate both in the elastic energy and in the dissipation the contribution of the matrix and of the reinforcement. The unilaterality of the interface is guaranteed in compression, but some elastic opening is still admitted before fracture occurs. The choice of the elastic stiffness Kn is based on the energetic equivalence ½ $_0/K_m$ = $_0$, fracture activation energy. The author is conscious of the fact that the parameter is somewhat arbitrary, and that it introduces an internal length (the limit elastic opening w_0), that could affect the response of the model. A better model, where unilaterality is exactly fulfilled, can be implemented using a logarithmic damage law, and will be presented in a future paper.

In the paper only the simplest dissipation potential has been presented, but extra terms can be introduced, in the form of additional dissipation modes, for accounting explicitly for fibres yielding and other dissipative phenomena. However, the calibration of the parameters requires careful comparison with experimental data.

REFERENCES

[1] Carol, I., Prat, P.C., Lopez, C.M., Normal/shear cracking model: appliation to discrete crack analysis, *J. Engng. Mech.*, 123, 765-773, 1997

[2] Garcia-Alvarez, V.O., Gettu, R., Carol,I., "Numerical analysis of mixed model fracture in concrete using interface elements", Proceedings ECCOMAS 2000, Barcelona.

[3] Contrafatto, L., Cuomo, M., A new thermodynamically consistent continuum model for hardening plasticity coupled with damage, submitted to *Int. J. of Solids and Structures*.

[4] Cuomo, M., Forms of the dissipation function for some classes of viscoplastic models, submitted to *ZAMM*

AN OVERVIEW OF FAILURE MECHANISMS IN HIGH TEMPERATURE COMPONENTS IN POWER PLANTS

R. Viswanathan

Electric Power Research Institute, Palo Alto, CA 95070

ABSTRACT

The principal mechanisms of failure of high temperature components include creep, fatigue, creep-fatigue and thermal fatigue. In heavy section components, although cracks may initiate and grow by these mechanisms, ultimate failure may occur at low temperatures during startup-shutdown transients. Hence, fracture toughness is also a key consideration. Considerable advances have been made both with respect to crack initiation and crack growth by the above mechanisms. Applying laboratory data to predict component life has often been thwarted by inability to simulate actual stresses, strain cycles, section size effects, environmental effects and long term degradation effects. This paper will provide a broad perspective on the failure mechanisms and illustrate a few of the typical ones in boilers.

KEYWORDS:

Creep, Fatigue, Thermal Fatigue, Boilers, Steels, Fracture Toughness

1.0 INTRODUCTION

Reducing the cost of power production is paramount for staying competitive in the emerging utility market. Reducing capital costs by deferring replacement of expensive components and reducing operating and maintenance (O&M) costs by optimizing operation, maintenance and inspection procedures will both be key strategic objectives for utilities. This poses a significant challenge to the technical community since two apparently opposing needs will need to be reconciled. On the one hand, the need for improved plant efficiency and availability will dictate more severe and cyclic duty schedules which result in more severe creep-fatigue damage and warrant increased attention to the components. On the other hand, the need to reduce O&M costs may result in fewer, shorter and lower quality maintenance and inspection outages; thus, placing the components at greater risk of failure. The challenge to the technical community, therefore, is to develop tools and techniques that will permit more rapid, cost-effective and accurate assessment of condition of critical components, both off-line and on-line. In addition to assessing the current condition, these tools must also be capable of evaluating the impact of alternative strategies for operation, inspection and maintenance. It is crucial therefore that the high temperature research community be more intimately familiar with the specific needs of the industry. This paper will bring out some of the industry perspectives regarding high temperature failures and illustrate them with some failure examples pertaining to creep and thermal fatigue. A detailed review of the failure mechanisms affecting the integrity of utility and chemical plants can be found in Reference 1 [1]. Some critical industry perspectives are reviewed in detail in Reference 2 [2].

2.0 EXAMPLES OF HIGH TEMPERATURE FAILURES

Failure mechanisms at high temperatures include creep, thermal fatigue, corrosion, erosion, and hydrogen attack. In addition, embrittlement phenomena occurring at high temperatures, e.g. carbide coarsening, sigma phase formation, temper embrittlement, etc. can facilitate rapid brittle fracture at low temperatures during transient conditions. This section will describe issues associated with creep, thermal fatigue and embrittlement. Mechanisms affecting the integrity of fossil power plants may be found in Refs. 1and 2 [1,2].

2.1 Creep

Creep damage can take several forms. Simple creep deformation can lead to dimensional changes that result in distortions, loss of clearance, wall thinning etc. Examples are steam turbine casings, blades, and piping systems. Localised deformation can cause swelling and eventual leaks in headers, steam pipes and superheated reheater (SH/RH) tubes. Long term creep failures generally tend to be brittle failures involving cavitation and crack growth at interfaces and at highly stressed regions. The cavitation form of damage has been found in SH/RH tubes, rotor serrations, occasionally rotor bores, highly stressed areas in piping systems and at weldments. The most common weld failures have pertained to dissimilar welds in superheater/reheater tubing, welds in headers and in hot reheat and mainsteam piping.

2.1.A Failures in Headers at Girth Welds: A schematic illustration of a header is shown in Figure 1.

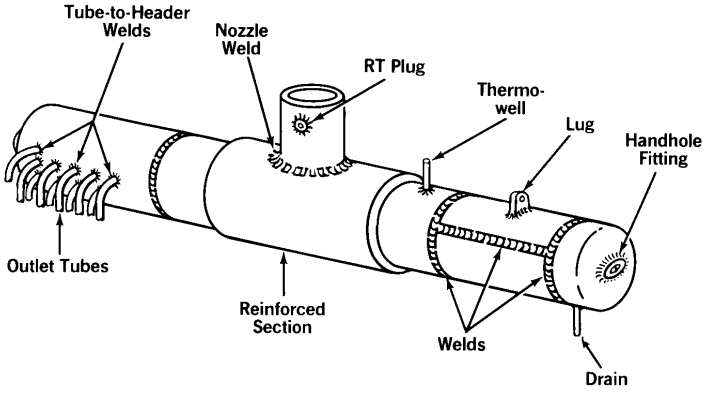

Figure 1: Schematic illustration of an elevated-temperature header (courtesy of B. W. Roberts, Combustion Engineering, Inc.)

Initial signs of creep-related distress in headers often appear at welds—welds at stub-tube inlets, long seams, header branch connections or girth butt joints. With the exception of some cases of long seam welds, and Type IV cracks in girth welds, creep damage in welds is invariably manifested on the outside surface as cavities, cracks, or, in extreme cases, steam leaks. Except in regard to long seam welds, concern about catastrophic bursts has been minimal. Although weld-related cracking is generally detectable and repairable, and although it does not have as great an impact on the over-all component life as does header-body base-metal deterioration, it is important from a life-assessment point of view for the following reasons: Because weld failures are often the forerunners of damage in the body, they can provide an index of creep damage and remaining life in the base metal. Failure of welds at crucial and multiple locations may constitute the end of the life of the header, regardless of the condition of the base metal. The need for frequent weld repair may prove uneconomical and justify retirement of a header. Due to these reasons, creep-damage assessment of welds has received considerable attention.

Four types of creep damage and cracking associated with weldments (for both headers or piping) have been cataloged by Chan et al. [3]. Each of the four creep damage types are identified below and shown schematically in Figure 2.

Type I — Damage which is longitudinal or transverse in the weld metal and remains entirely within the weld metal.

Type II — Damage that is longitudinal or transverse in the weld metal, but grows into the surround HAZ.

Type III — Damage in the coarse-grained region.

Type IV — Damage initiated or growing in the intercritical zone of the HAZ (the transition region between the fully-transformed, fine-grained HAZ, and the partially-transformed parent base metal).

Both axial and circumferential cracks have been observed in damaged girth butt welds, with cracking being found in the weld metal and/or the HAZ. The axial cracking has been attributed to internal pressure loading and pipe swelling, whereas the circumferential cracking has been associated with combined pressure and piping system loads. Several instances of girth weld cracking has been reviewed [4]. In one instance, circumferential cracking along the coarse-grain HAZ was attributable to stress-relief cracking prior to service. Axial creep cracking across the weld metal has been attributed to a combination of pipe swelling and poor weld ductility. Circumferential cracking in the intercritical regions of the HAZ has also been observed in both Cr-Mo-V and Cr-Mo steels. This type of cracking, known as Type IV cracking, occurs at the end of the HAZ adjacent to the unaffected parent metal. Type IV cracking is generally attributed to localized creep deformation in a "soft" zone in the intercritical region under the action of bending stresses. Field experience suggests that Cr-Mo-V steels may be more susceptible to cracking than Cr-Mo steels and that operation at 565°C (1050°F) rather than at 540°C (1000°F) might further exacerbate the problem. Because most of the headers in the United States are made of Cr-Mo steels and operate at 540°C (1000°F), the problem has not been encountered to any significant degree. More recently, Type IV cracking is emerging as a concern for P91 piping.

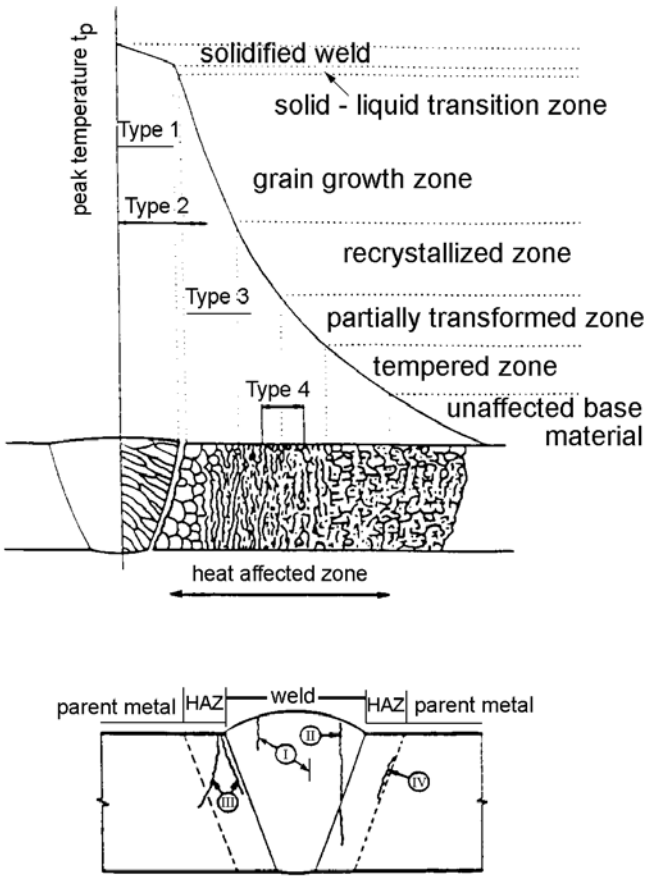

Figure 2: Four types of damage in girth welds in relation to microstructure [3].

2.1.B Failures in Seam Welded High Energy Piping:

Several categories of pipes carrying high temperature/pressure steam contain welds that may be of concern. Main steam pipes are pipes that carry steam at 538-565°C to the high pressure turbine. These pipes are small in diameter and do not contain seam welds. Hence, only girth welds are of concern. The mainstream pipes are however, often connected to the steam header using thick-walled seam welded piping. In addition, hot reheat pipes which carry steam at 538-565°C but at a lower pressure (than the main steam pipe) to the reheat IP turbine, and are frequently made of seal welded piping. Failure of seam welded pipes used in HRH piping as well as in header link piping has been of major concern to industry. Failure experience with respect to high energy piping has been reviewed by Wells and Viswanathan [5]. There have been at least 17 major instances of seam welded pipe failures including 3 cases of catastrophic rupture, 5 leaks and 9 incidents of major cracking. The failures are generally brittle with a fish mouth appearance.

In the cases of HRH pipes, the welds generally have a double V configuration and the pipes are generally subjected to a normalizing and tempering treatment. The cracking generally initiates subsurface at the cusp of the double V and then propagates along the fusion line towards the outside and inside, as shown in Figure 3. In the case of the thicker walled header leak pipes, the weld generally has a U geometry and is subjected to subcritical PWHT. A variety of cracking modes, including fusion line, Type I and Type IV cracking have been observed. Failures of most of the seam welded piping have occurred prematurely and could not be predicted based on simple life-fraction rule calculations. Failures occur due to unique combination of operating and metallurgical variables. Some of the contributing factors have been identified

to be operating temperature, pressure, cycling system stresses, and weld geometric factors such as configuration, cusp angle and roof angle, and welding practice employed; inclusion content and creep strength mismatch, etc. Currently two failure scenarios have been postulated. In one scenario, failure is proposed to involve crack initiation and propagation stages. In the alternative scenario cavities form and grow and eventually link up into a larger crack. Which of these is operative can determine whether NDE based monitoring is viable. A comprehensive review of the subject may be found elsewhere [6-8].

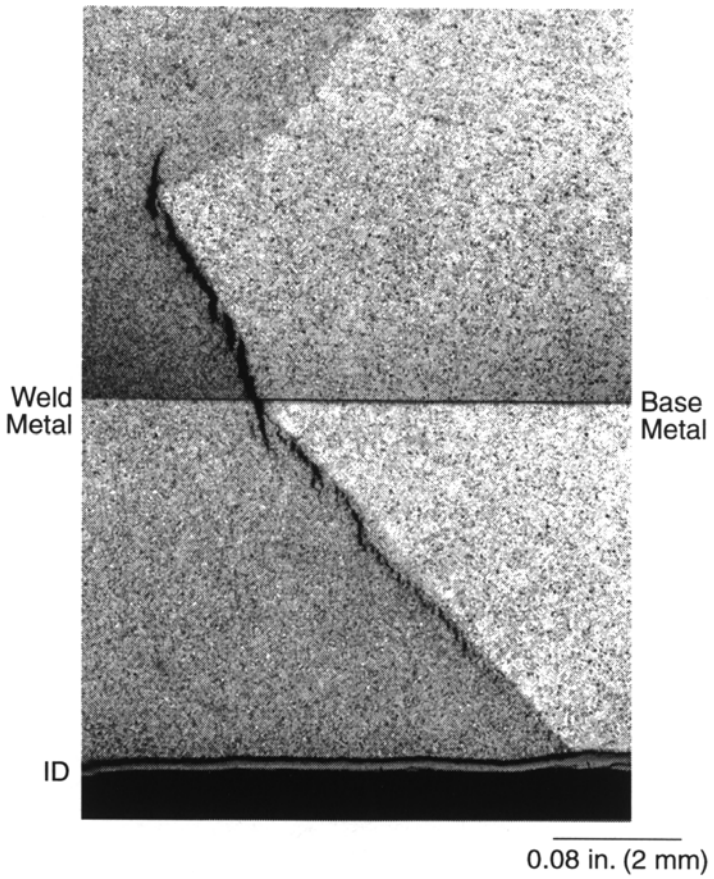

Figure 3: Macrograph of cross-section at location 6LS1, counter-clockwise side of weld sighting along flow; note ID-connected-cracking, located and detected by UT, and extent of cusp damage.

Since in many of the early instances of girth weld damage, the damage has consisted of evolution of creep cavities into cracks at the coarse grained heat affected zone (CGHAZ), assessment of damage consisted of simply classifying the damage and then recommending an appropriate action. Damage was classified as (A) isolated cavities, (B) oriented cavities, (C) linked cavities and (D) microcracking, as per the German practice. More quantitative correlations between the degree of cavitation and the creep life expended have been established based on EPRI research and have provided a clearcut basis for establishing re-inspection intervals. This approach is however valid only for Type III cracking in the CGHAZ. The evolution of damage in the other cases have not been sufficiently investigated.

While replication is very useful for detecting surface damage, many types of failures such as long seam weld and Type IV damage in girth welds originate sub-surface. In these cases, replication alone is not a reliable method to detect damage. In long seam welds in hot reheat piping and header link piping, high sensitivity conventional or automated UT, focused beam UT or time-of-flight diffraction UT methods are needed to ensure safety of the piping. In the case of girth welds however, conventional UT seems to be adequate.

Some forms of creep damage are more manageable than others. For example, if Type I, II or III creep damage is found, the subsequent action can range from record and monitor to some form of repair depending on the severity of damage. Advanced Type IV damage is characterized by profuse intergranular cavitation in the creep weak area of the HAZ. It has been suggested that the evolution of damage from the observation of cavitation (by replication) to macro-cracking can be swift and cannot be dealt with using the German system. In the absence of enough experimental evidence regarding damage evolution, the current approach is to replace completely the affected weldment, if any stage of Type IV damage is confirmed.

3.2 Creep-Fatigue Failures

Creep-fatigue damage induced by thermal stresses is of major concern with respect to the integrity of many high temperature components. The concern has been exacerbated in recent years due to cyclic operation of units originally designed for base load service. A sample list of fossil plant components in which creep-

fatigue has been a dominant failure mode has been published in Reference 2. A common form of cracking known as "Ligament Cracking" is described below.

Ligament cracking encountered in CrMo steel header pipes illustrated in Figure 4. Cracks initiate in the tube bore holes and are oriented parallel to the axis of the tube bore hole. Linking up of cracks between holes on the inside surface of the header leads to propagation to form cross ligament cracks. Presence of ligament cracking has been observed in a very large number of superheater headers in the U.S. The cracking mode has been identified as creep fatigue. A computer code, Boiler Life Evaluation and Simulation System (BLESS) developed recently, incorporates two alternate approaches for predicting crack initiation; one involving an inelastic linear damage summation method, and a second approach involving repeated cracking of oxide scale and oxide notching[9]. For a variety of cycle histories, the Code predicts crack initiation occurring in about 20,000 h by the oxide cracking mechanism. The creep-fatigue damage summation approach on the other hand, is inconsistent with the early initiation of cracks observed in headers. Metallography of cracked headers has shown numerous oxide spikes, see Figure 5, indicating oxide cracking to be the crack initiation mechanism. This example clearly illustrates the need for using appropriate thermomechanical fatigue data simulative of actual component cycles in predicting crack initiation life of components.

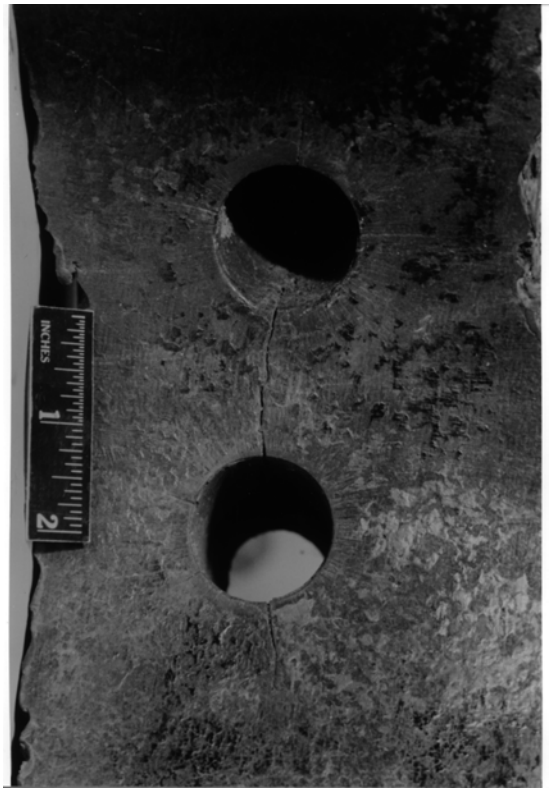

Figure 4: Ligament cracking at a tube bore hole viewed from the ID of a header.

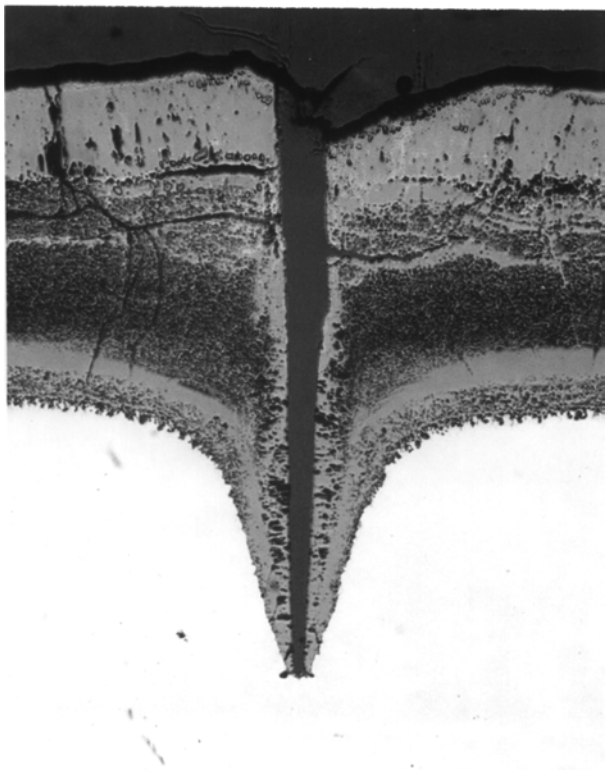

Figure 5: Oxide notching at ligament cracks.

4.0 SUMMARY AND CONCLUSIONS

Creep and creep-fatigue are the principal failure mechanisms affecting the integrity of components operating at elevated temperatures. Creep damage in weldments poses major challenges both in analytically calculating it and in experimentally reproducing it. Several alternative damage locations and mechanisms have been observed which are often difficult to reproduce in laboratory tests. Fusion line cracking and fine grain heat affected zones (FGHAZ) cracking has led to catastrophic failure of high energy piping. Thermomechanical fatigue (TMF or creep fatigue) affects many heavy section components as well as internally cooled components such as combustion turbine blades. It is important that researchers focus on component specific (rather than generic) life prediction models with a full understanding of the applicable failure definition,

failure scenario and relevant duty cycle. Future research needs to address advanced NDE techniques, on-line monitoring techniques, TMF mechanisms, and evolution of damage and growth of cracks in welds.

5.0 REFERENCES

1. Viswanathan, R., 1987, "Damage Mechanisms and Life Assessment of High Temperature Components," *ASM International Metals Park*, OH.
2. Viswanathan, R. and Stringer, J., 2000*, Failure Mechanisms of High Temperature Components in Power Plants*, ASME, J. of Engg. Materials and Technology, **122**, July 2000, pp 246-254.
3. Chan, W., McQueen, R. L., Prince, J., and Sidey, D., 1991, "Metallurgical Experience with High Temperature Piping in Ontario Hydro," ASME PVP, **21**, *Service Experience in Operating Plants*, ASME, New York.
4. Ellis, F. V. et al., 1988, *Remaining Life Assessment of Boiler Pressure Parts*, Final Report RP2253-1, Vol. 1-5, Electric Power Research Institute, Palo Alto, CA.
5. Wells, C. H., and Viswanathan, R., 1993, "Life Assessment of High Energy Piping," In *Technology for the 90s*, M. K. Au-Yang et al., Eds., ASME Pressure Vessels and Piping Division, New York, pp. 179-216.
6. Viswanathan, R., and Foulds, J., 1995, "Failure Experience with Seam-Welded Hot Reheat Pipes in the USA," ASME PVP, **303**, *Service Experience, Structural Integrity, Severe Accidents and Erosion in Nuclear and Fossil Plants*, S. R. Paterson et al., Eds., ASME, New York, pp. 187-207.
7. Foulds, J. R., Viswanathan, R., Landrum, L., and Walker, S. L., 1995, *Guidelines for the Evaluation of Seam Welded High Energy Piping*, Report TR-104631, Electric Power Research Institute, Palo Alto, CA.
8. Ellis, F., and Viswanathan, R., 1998, "Review of Type IV Cracking in Welds," ASME PVP Conference, July 1998, PVP, **380**, *Fitness for Service Evaluation in Petroleum and Fossil Plants*, pp. 59-76.
9. *Boiler Life Evaluation and Simulation System, BLESS Code and User Manual*, 1991, Report TR-103377, Vol. 4, Electric Power Research Institute, Palo Alto, CA.

ANALYSES OF SIZE EFFECTS IN THE CHARPY V-NOTCH TEST

A.A. Benzerga[1,2], R. Batisse[1], A. Needleman[2] and V. Tvergaard[3]
[1]Gaz de France, 361 Avenue du Président Wilson, La Plaine Saint–Denis 93211, France.
[2]Brown University, Division of Engineering, Providence, RI 02912, USA.
[3]Department of Solid Mechanics, The Technical University of Denmark,
2800 Lyngby, Denmark.

ABSTRACT

This paper addresses some issues related to the size dependence of both the upper shelf energy (USE) and the ductile–brittle transition temperature (DBTT) in the Charpy V-notch test. Two classes of pipe materials are considered. Emphasis is placed on the interplay between inertial, rate hardening and thermal softening effects. In a relatively high strength pipe steel, experimental results exhibit no size dependence of the DBTT. On the other hand, a significant shift in DBTT is obtained in a low strength steel. The difference between these two classes of steels is modeled. Calculations are carried out for Charpy specimens where only the ligament size is varied, as in available experiments. The extent to which the size effect is material dependent is investigated.

KEYWORDS

Impact loading, high strain-rate, adiabatic heating, ductile-brittle transition

INTRODUCTION

The absorbed energy versus temperature or strain rate in the Charpy V-notch test is often used to characterize the ductile-brittle transition in steels. Brittle fracture is found at lower temperatures and higher strain rates while ductile fracture occurs at higher temperatures and lower strain rates. The change from the lower shelf to the upper shelf with increasing temperature is mainly a result of the variation of flow strength with temperature, while the more brittle behavior under impact loading than under slow loading results from the material strain rate sensitivity. The basic issue investigated here is the extent to which the DBTT measured in the Charpy V-notch test is a material property or a structural property that depends on specimen size and geometry.

THEORY

A convected coordinate Lagrangian formulation is used with the dynamic principle of virtual work written as

$$\int_V \tau^{ij}\delta E_{ij}\,dV = \int_S T^i \delta u_i\,dS - \int_V \rho\frac{\partial^2 u^i}{\partial t^2}\,\delta u_i\,dV \tag{1}$$

$$\text{with} \qquad T^i = (\tau^{ij} + \tau^{kj}u^i_{,k})\nu_j \tag{2}$$

$$E_{ij} = \frac{1}{2}(u_{i,j} + u_{j,i} + u^k_{,i}u_{k,j}) \tag{3}$$

where τ^{ij} are the contravariant components of Kirchhoff stress on the deformed convected coordinate net ($\tau^{ij} = J\sigma^{ij}$, with σ^{ij} being the contravariant components of the Cauchy stress and J the ratio of current to reference volume), ν_j and u_j are the covariant components of the reference surface normal and displacement

vectors, respectively, ρ is the mass density, V and S are the volume and surface of the body in the reference configuration, and $(\,)_{,i}$ denotes covariant differentiation in the reference frame.

The constitutive framework is that for a progressively cavitating porous plastic solid, with the rate of deformation tensor written as the sum of an elastic part, $\mathbf{d}^e$, a viscoplastic part, $\mathbf{d}^p$, and a part due to thermal straining, $\mathbf{d}^\Theta$, so that

$$\mathbf{d} = \mathbf{d}^e + \mathbf{d}^p + \mathbf{d}^\Theta \tag{4}$$

Small elastic strains are assumed and the elastic and thermal properties are chosen to have representative values for steel; $E = 210$ GPa, $\nu = 0.3$ and $\alpha = 1 \times 10^{-5}/^\circ$K. The viscoplastic part of the rate of deformation, $\mathbf{d}^p$, is obtained from the flow potential (Gurson [1]; Pan *et al.* [2]),

$$\Phi = \frac{\sigma_e^2}{\bar{\sigma}^2} + 2q_1 f^* \cosh\left(\frac{3q_2\sigma_h}{2\bar{\sigma}}\right) - 1 - (q_1 f^*)^2 = 0 \tag{5}$$

where $\bar{\sigma}$ is the matrix flow strength, σ_e is the Mises effective stress, σ_h is the mean normal stress and q_1, $q_2 = 1.0$ are parameters introduced in [3, 4]. The function f^*, [5], accounts for the effects of rapid void coalescence at failure

$$f^* = \begin{cases} f & f < f_c \\ f_c + (f_u^* - f_c)(f - f_c)/(f_f - f_c) & f \geq f_c \end{cases} \tag{6}$$

where f is the void volume fraction. The constant $f_u^* = 1/q_1$ is the value of f^* at zero stress. As $f \to f_f$, $f^* \to f_u^*$ and the material loses all stress carrying capacity. For a power law strain rate hardening matrix

$$\dot{\bar{\epsilon}} = \dot{\bar{\epsilon}}_0 \left(\frac{\bar{\sigma}}{g(\bar{\epsilon}, \Theta)}\right)^{1/m} \qquad g(\bar{\epsilon}, \Theta) = \sigma_0 G(\Theta) \left[1 + \frac{\bar{\epsilon}}{\epsilon_0}\right]^N \tag{7}$$

The function $g(\bar{\epsilon}, \Theta)$ represents the effective stress *versus* effective strain response in a tensile test carried out at a strain rate $\dot{\bar{\epsilon}} = \dot{\bar{\epsilon}}_0$ and m is the strain rate hardening exponent. Here, $\dot{\bar{\epsilon}}_0 = 10^3\,\mathrm{s}^{-1}$ and $m = 0.025$. The temperature dependence specified through the function $G(\Theta)$ might depend on the material. In all calculations, the following form has been adopted

$$G(\Theta) = 1 + b\exp\left[-c(\Theta_0 - 273)\right]\left\{\exp\left[-c(\Theta - \Theta_0)\right] - 1\right\} \tag{8}$$

with b and c being material parameters and Θ and Θ_0 being given in Kelvin. Θ_0 is a reference temperature. A criterion for cleavage is used, which is based on a material dependent critical stress, σ_c, over a critical distance [6]. A plane strain model of the Charpy V-notch specimen is analyzed. For the standard specimen, the dimensions are $L = 55$mm, $B = 10$mm, $D = 2$mm, $R = 0.25$mm, $A = 40$mm and $\psi = 22.5^\circ$; see Fig. 1.

EXPERIMENTAL DATA

Charpy impact tests were conducted on two pipe steels which differ in both inclusion content and yield strength. Steel **A** is a low strength isotropic sheet with $\sigma_0 = 322$MPa along the transverse direction T, which contains mainly rounded manganese sulfide inclusions MnS with a volume fraction of 0.00186. Steel **H** is a hot–rolled sheet with $\sigma_0 = 500$MPa along T, and containing MnS stringers with an estimated volume fraction of 0.0004 along with some equiaxed oxide particles whose volume fraction is less than 0.0002. The presence of the elongated MnS inclusions results in directionality of the fracture properties. For instance, the upper shelf energy is about $106\mathrm{J/cm}^2$ in the loading configuration T–L, which is half the value measured for the L–T loading configuration. In addition, steel **H** has a low ductile-brittle transition temperature (DBTT) of about -138°C whereas steel **A** has a DBTT of about -12°C.

Although steel **A** is softer than **H**, it exhibits higher strain hardening with $N = 0.25$, while $N = 0.12$ in steel **H**. Also, tensile tests on smooth specimens were carried out at various temperatures in steel **H**. In the

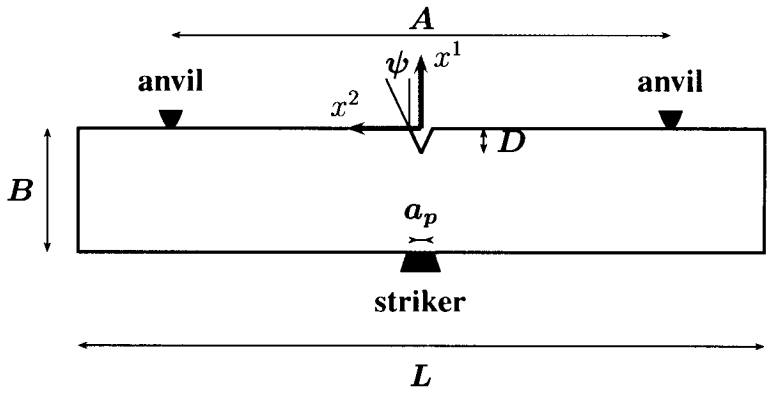

Figure 1: Geometry of the Charpy specimen with prescribed boundary conditions.

range 100°Cto 500°C, the rate of decrease of the yield strength is about 30 MPa every 100°C. This rate is representative of pipe steels with a ferrite–pearlite microstructure and hence applies to steel **A** as well. In addition, the increase in strength at -196°C may depend on the steel. The ratio $g(\epsilon_0, -196°C)/g(\epsilon_0, \Theta_0)$ was found to be equal to 2 for steel **H**. The same value is used for steel **A**. These data are enough to identify the thermal softening law (8) and the values $b = 0.2068$, $c = 0.009$ and $\Theta_0 = 273$K were then used for both materials.

Three geometries were tested in the T–L configuration for each steel. Each geometry is denoted CVNx where x refers to the value of specimen's width B; see Figure 1. The CVN10 specimen is the standard ASTM specimen. The notch depth D was also varied such that the ratio D/B was kept constant. It was found that the normalized upper shelf energy (USE) decreases with decreasing ligament size for both steels, with the decrease rate being enhanced in steel **H**. For example, USE values for the ASTM and CVN3 specimens were 106J/cm^2 and 66.5J/cm^2 respectively in steel **H** whereas they were 82J/cm^2 and 62.7J/cm^2 respectively in steel **A**. Most importantly, varying ligament size was found to affect the ductile to brittle transition temperature (DBTT) in steel **A** but not significantly in steel **H**. Halving the ligament size decreased the DBTT from -12°C to -31°C in steel **A**.

NUMERICAL RESULTS

For both steels, results are shown for two of the tested geometries: ASTM and CVN5. In the case of steel **H**, additional results are presented for a double size specimen, CVN20, for comparison. Typical meshes used in the simulations are shown in Figure 2. For a given material, the same finite element size was used for all specimen sizes in the region close to the notch. The element size, set equal to the average inclusion spacing

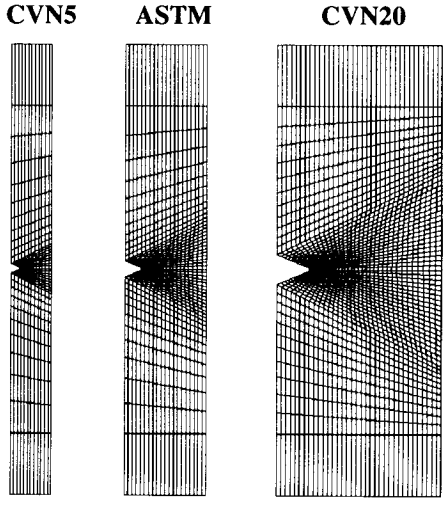

Figure 2: Typical finite element meshes used for steel **H**.

in the plane T–L, is about 240μm in steel **H** and 300μm in steel **A**. To confirm such values, quantitative metallography is under progress. The initial porosity is identified with the inclusion volume fraction assuming that instantaneous nucleation occurs uniformly at low strain. This is a reasonable approximation in steel **H** since the orientation of the major stress is perpendicular to the main inclusion length. In steel **A**, nucleation can be accounted for as in [7]. Corresponding results are presented elsewhere. Here, $f_0 = 0.0006$ in steel **H** and $f_0 = 0.002$ in steel **A**.

In order not to bias the numerical results towards the experimental data, the model parameters for ductile failure, f_c and f_f, are inferred from predictive approaches for coalescence [8, 9]. These have shown quite reasonable agreement with micromechanical unit–cell calculations [10, 11]. Assuming for the inclusions an initial isotropic distribution, the porosity at coalescence is $f_c = 0.018$ and $f_c = 0.022$ in steels **H** and **A** respectively, at an average stress triaxiality ratio of 2. The porosity at failure is $f_f = 0.10$ in **H** and $f_f = 0.17$ in **A**. These values of f_f are based on $q_1 = 1.35$ and $q_1 = 1.15$ for steels **H** and **A** respectively. As in [10], these values account for a strain hardening effect on void growth rates. It is difficult to infer the critical stress for cleavage from experimental measurements. Hence, the values $\sigma_c = 2450\,\mathrm{MPa}$ and $\sigma_c = 2025\,\mathrm{MPa}$ were used in steels **H** and **A** respectively to calibrate the DBTT in the ASTM specimen.

Figure 3 shows selected curves of normalized force plotted against imposed displacement. For each specimen and steel, the curves shown are representative of the upper and lower shelves together with the transition domain. Let us focus first on the lower shelf and transition range. In the ASTM specimens of both steels, Figs 3(a) and (c), the cleavage stress is attained shortly after initial yielding right at the notch tip, while the overall response is still linear. In the CVN5 specimens, however, general yielding slightly precedes the onset

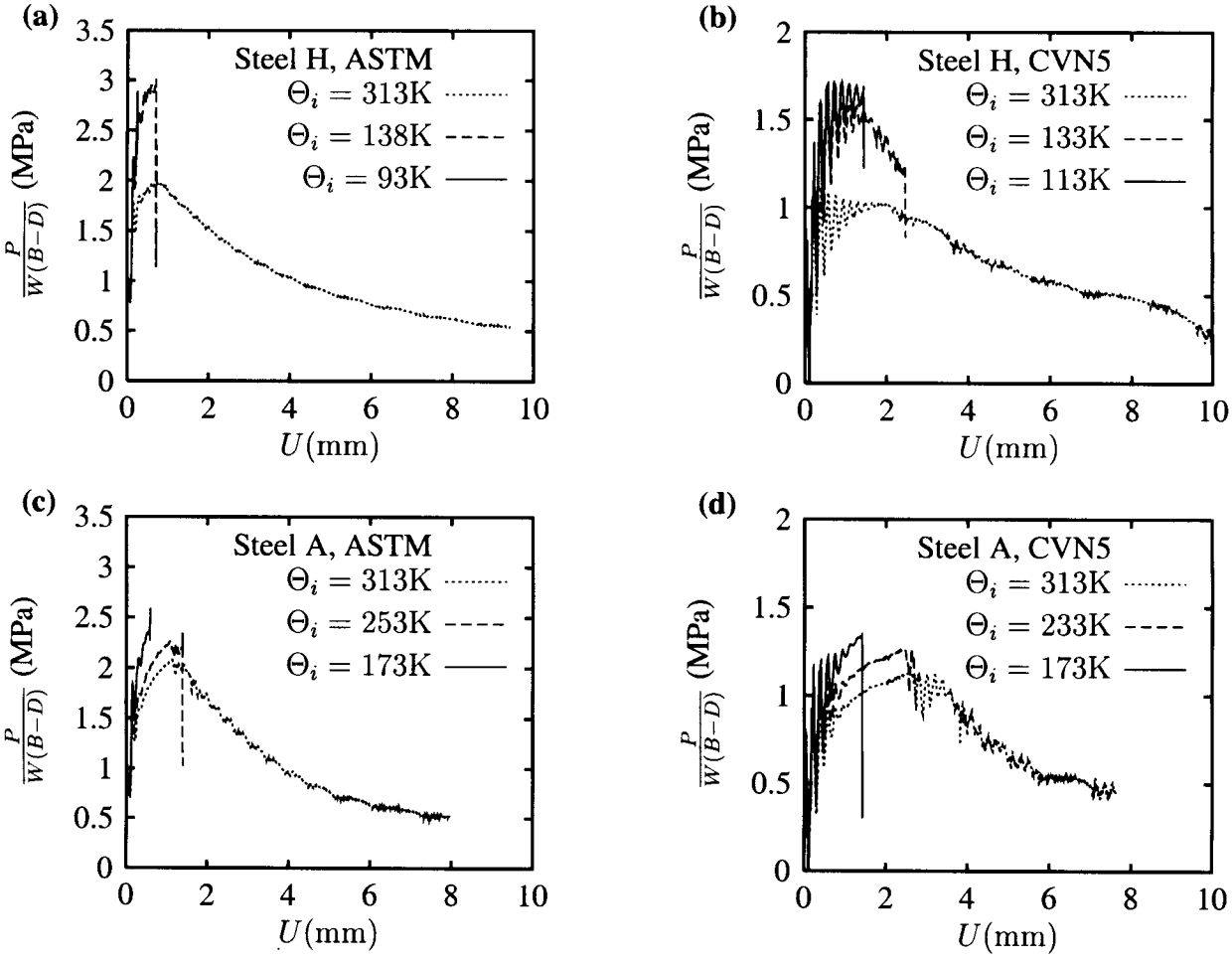

Figure 3: Representative curves of force, P, *vs* imposed displacement, U, for steel **H** and ASTM–specimen (a) or CVN5–specimen (b) and for steel **A** and ASTM–specimen (c) or CVN5–specimen (d).

of cleavage such that large bending of the specimen is observed, Figs 3(b) and (d). Moreover, cleavage does

not initiate at the notch root but at a distance of about five element sizes away from it. At higher temperatures, i.e. $\Theta_i = 313$K, plasticity spreads from the notch root to the opposite free surface and large scale yielding conditions are met. Pure ductile fracture then occurs across the specimen width. Calculations are terminated at $U = 9.5$mm and $U = 8$mm in the case of steels **H** and **A** respectively.

From the force, P, and the displacement, U, the total energy absorbed is computed. This is done for each initial temperature to obtain the computed transition curve. Absorbed energy versus initial temperature curves are shown for steel **H** in Figure 4 where results for the CVN20 specimen are also reported. A comparison with experimental results is shown in Table 1 for both steels in terms of the transition temperature and the upper shelf energy normalized by ligament area, K_{CV}. For steel **A**, the experimental shift in DBTT with ligament size is well reproduced. Increasing the ligament size is expected to have the following implications: (i) it increases the stress level through inertia; (ii) it increases the bending moment which tends to raise the strain level near the notch which leads to more thermal softening and (iii) increasing the ligament size decreases the nominal strain rate within the specimen. The effect of inertia is to increase the DBTT when the ligament size increases whereas the lower strain rate acts in the other direction. The increased bending moment increases the stress level which would tend to decrease the DBTT but it also increases the strain level which tends to increase the DBTT. For steel **A** the increase in stress largely due to inertia appears to be the dominant effect.

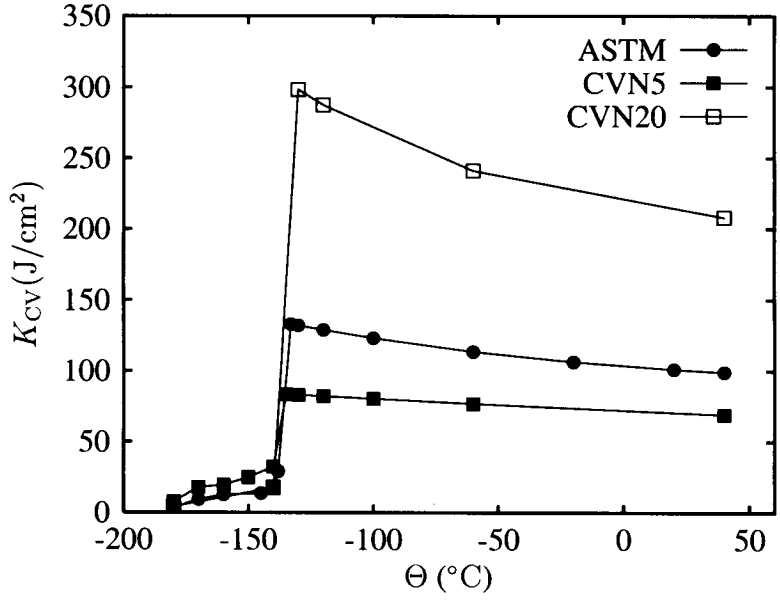

Figure 4: Calculated transition curves in steel **H** for three specimen geometries.

On the other hand, there is no shift of the DBTT in steel **H**, Fig. 4, which matches the experimental trend. In fact, the DBTT measured in specimen CVN3, not shown, is about -130°C, which is almost the same as for the ASTM specimen. Careful investigation of the numerical results shows that the thermal softening effect is here much more important than for steel **A** within the transition range. Indeed, at $\Theta_i = 133$K, the increase in temperature at the notch root is about 65 K in the CVN5 specimen, much lower than the $\Delta\Theta \approx 250$K encountered in a standard specimen at an approximately similar displacement. This counterbalances the effect of inertia and explains the trend in Figure 4.

The upper shelf energies are reasonably well reproduced, although the agreement in the case of steel **A** might be improved. As in the experiments, K_{CV} increases with increasing size. This is due to more plastic dissipation in the larger specimens. The fact that K_{CV} is size–dependent confirms that special care has to be taken when extrapolating Charpy V-notch energies to toughness predictions.

TABLE 1: EFFECTS OF LIGAMENT SIZE IN STEELS **H** AND **A**.

Specimen	DBTT (°C)		K_{CV}(J/cm^2)	
	exp.	calc.	exp.	calc.
H, ASTM	-138	-134	106	102
H, CVN5	-108	-136	77.1	78.5
A, ASTM	-12	-17	82.0	91.9
A, CVN5	-31	-27	65.8	60.8

CONCLUSIONS

Ligament size effects were investigated experimentally and numerically on two pipe steels. Full dynamic analyses were carried out. The upper shelf energy decreases with increasing size in general and this is due to the increased plastic dissipation in large specimens. The shift in the DBTT is found to depend on a subtle interplay between inertial effects and thermal softening effects. Steel **H** had a much lower transition temperature than steel **A** because of a higher resistance to cleavage initiation. As a consequence, thermal softening was more significant for steel **H** in the transition range because the softening law in ferritic–pearlitic steels exhibits a higher gradient at low temperatures. For both steels, the results give clear evidence of the effects of inertia in the Charpy V-notch test.

Acknowledgements
Support from the Office of Naval Research through grant N00014-97-1-0179 is gratefully acknowledged.

References

[1] A. L. Gurson. *J. Eng. Mat. Tech.*, 99:2–15, 1977.
[2] J. Pan, M. Saje, and A. Needleman. *Int. J. Frac.*, 21:261–278, 1983.
[3] V. Tvergaard. *Int. J. Frac.*, 17:389–407, 1981.
[4] V. Tvergaard. *Int. J. Frac.*, 18:237–252, 1982.
[5] V. Tvergaard and A. Needleman. *Acta metall.*, 32:157–169, 1984.
[6] R. O. Ritchie, J. F. Knott, and J. R. Rice. *J. Mech. Phys. Solids*, 21:395–410, 1973.
[7] A. Needleman and V. Tvergaard. *Int. J. Frac.*, 101:73–97, 2000.
[8] A. A. Benzerga, J. Besson, and A. Pineau. *J. Eng. Mat. Tech.*, 121(2):221–229, 1999.
[9] A. A. Benzerga. PhD thesis, Ecole des Mines de Paris, March 2000. parts in english.
[10] J. Koplik and A. Needleman. *Int. J. Solids Structures*, 24(8):835–853, 1988.
[11] T. Pardoen and J. W. Hutchinson. *J. Mech. Phys. Solids*, 2000. submitted.

ICF100503PR

ANALYSIS AND TESTING OF RUPTURE OF STEAM GENERATOR TUBING WITH FLAWS**

S. Majumdar,[1] K. S. Kasza,[1] J. Y. Park,[1] and J. Abou Hanna[2]

[1]Energy Technology Division, Argonne National Laboratory, Argonne, IL 60439
[2]Department of Mechanical Engineering, Bradley University, Peoria, IL 61625

February 2001

To be presented at the 10th International Conference on Fracture (ICF-10), Dec. 3–7, 2001, Honolulu.

**Work supported by the Office of Nuclear Regulatory Research, U.S. Nuclear Regulatory Commission

ICF100503PR

ANALYSIS AND TESTING OF RUPTURE OF STEAM GENERATOR TUBING WITH FLAWS**

S. Majumdar,[1] K. S. Kasza,[1] J. Y. Park,[1] and J. Abou Hanna[2]

[1]Energy Technology Division, Argonne National Laboratory,
Argonne, IL 60439
[2]Department of Mechanical Engineering, Bradley University,
Peoria IL 61625

ABSTRACT

A high-temperature (300°C), high-pressure (18 MPa), and high-leak rate (1500 L/min) facility, and a room temperature, high-pressure (52 MPa) test facility were used to test flawed steam generator tubes. Single and multiple rectangular flaws were fabricated by electro-discharge machining on the outside surface of the tubes. This paper briefly reviews analytical methods for predicting ligament rupture and unstable burst of tubes with single and multiple rectangular flaws. Test data are presented to validate the failure models. The ligament rupture pressures of specimens with mutiple flaws predicted by an "equivalent rectangular crack" method agree fairly well with measured data.

KEYWORDS

Steam generator tubes, axial flaw, ligament rupture, unstable burst

INTRODUCTION

Although steam generator (SG) tubes of pressurized water reactors (PWRs) are designed conservatively by following the ASME Boiler and Pressure Vessels Code and are made of highly ductile alloys such as Alloy 600, stress corrosion cracks (SCCs) have been detected in the SG tubes of several PWRs. Since SG tubes form part of the primary pressure boundary, it is important to be able to predict crack growth, tube failure or rupture, and subsequent leak rates of SG tubes from crack morphology, as measured nondestructively during in-service inspection. This paper is concerned with tests and analytical prediction of ligament rupture pressure and unstable burst pressure of SG tubes with initially part-throughwall axial flaws.

BACKGROUND

Significant literature [1- 12] is available on testing and analytical models for ligament failure and unstable burst of tubes with part-throughwall and throughwall rectangular flaws. Well-

**Work supported by the Office of Nuclear Regulatory Research, U.S. Nuclear Regulatory Commission

established criteria exist for predicting ligament rupture and unstable burst pressures of tubes with relatively long rectangular flaws. Some modifications of these criteria have been made for short and deep flaws based on recent tests at ANL [7].

The critical pressures and crack sizes for the unstable failure (burst) of a thin-wall internally pressurized cylindrical shell with a single rectangular throughwall axial crack can be estimated with an equation originally proposed by Hahn et al. [1] and later modified by Erdogan [2]:

$$p_{cr} = \frac{p_b}{m} = \frac{\bar{\sigma} h}{mR}, \tag{1}$$

where p_b is unstable burst pressure of unflawed tube, $\bar{\sigma}$ is the flow stress, and m is a bulging factor that depends on crack length, tube radius (R), wall thickness (h), and Poisson's ratio (e.g., see Ref. 7).

A general failure criterion for predicting rupture of the through-thickness crack tip ligament in a pressurized tube with a single rectangular part-throughwall axial crack can be expressed as follows:

$$\sigma_{lig} = m_p \sigma = \bar{\sigma}, \tag{2}$$

where σ_{lig} is the average ligament stress, σ is the nominal hoop stress, and m_p is a ligament stress magnification factor that depends on axial crack length and depth [7].

Although we can currently predict with some confidence failure pressures of tubes with rectangular flaws, such a morphology is not characteristic of much of the cracking currently observed in SGs. Stress corrosion cracks (SCCs) in SG tubes are generally nonplanar, ligamented, and have highly complex geometry.

TESTS WITH MUTIPLE FLAWS

As a first step toward understanding the behavior of more complex cracks, tests were conducted on 22-mm (0.875 in.)-dia, 1.27-mm (0.05 in.)-wall thickness Alloy 600 tubes with two part-throughwall axial rectangular notches. The yield and ultimate tensile strengths of the tube material at room temperature are 300 MPa (43 ksi) and 675 MPa (98 ksi), respectively. Two different configurations of axial notches were tested (Figure 1). Each notch was either 6 mm (0.25 in.) or 13 mm (0.5 in.) long and 80% deep with a ligament width of either 0.25, 1.27, or 2.54 mm (0.01, 0.05, or 0.1 in.). Pressure tests were conducted at room temperature in two stages. In stage 1, the specimens were tested without a bladder until ligament rupture occurred and the pump could not keep up with the leak rate. In stage 2, a bladder and brass foil were inserted in a few of the specimens to cover the notches, and the specimens were pressurized until unstable burst occurred. The effect of the bladder and foil on the burst pressures has been found to be minimal. Two tests with initially 100% deep notches (without bladder) were conducted in a high-flow-rate blowdown test facility. During stage 1 testing, the pressure was increased to the maximum limit of the facility. One of the two tests was conducted at 282°C with high-temperature pressurized water. A summary of the test results is given in Table 1 where, unless otherwise noted, all notches are 80% deep and tested at room temperature. After stage 1 testing, all of the axial ligaments in type 2 specimens were ruptured while all of the 2.54 mm (0.1 in.) ligaments in type 4 specimens survived. On the other hand, the 1.27 mm (0.05 in.) circumferential ligament of type 4 specimens ruptured during stage 1 testing with notch lengths of 12.7 mm (0.5 in.) but survived with notch lengths of 6 mm (0.25 in.). The axial ligament in the specimen with 100% deep notches survived stage 1 testing at room temperature (T24), but failed at 282°C (T25).

ANALYSIS OF TESTS

Part-Throughwall Notches

A simple empirical method for predicting rupture pressure of a through-thickness notch tip ligament is based on defining an equivalent rectangular crack whose depth is obtained by equating the total area of the two notches to that of a single rectangular notch of the same total length. Predicted vs. observed ligament rupture pressures for type 2 and type 4 specimens tested at room temperature are shown in Figures 2a-b. Except for a single type 2 specimen with two 13-mm (0.5 in.)-long notches, the observed rupture pressures of through-thickness notch tip ligaments are close to those predicted by the equivalent rectangular crack method. Note that the method predicts a minimum ligament width beyond which the two notches behave as two independent notches. However, the method cannot predict the rupture pressure of the axial or circumferential ligament separating the two notches. The tests showed that although the axial ligaments for all type 2 specimens ruptured at the final pressure in stage 1, some of the circumferential ligaments of type 4 specimens survived. In cases where the ligament between the notches ruptured after stage 1 testing (e.g., Figure 3a), the final stage 2 unstable burst pressure can generally be predicted quite well by Eq. 1 for single cracks. In other cases (e.g., Figure 3b), the specimen is left with two throughwall notches with a ligament after stage 1 loading.

Throughwall Notches

Nonlinear finite-element analyses with shell elements (ABAQUS) were performed for a type 2 specimen with two 100% deep, 6-mm (0.25 in.)-long notches separated by an axial ligament of varying width. A plot of the variation of average ligament thickness with pressure for a 0.25-mm (0.01 in.)-wide ligament is shown in Figure 4a. The accelerated decrease in thickness at a pressure of 17 MPa (2.5 ksi) indicates a necking-like behavior. A corresponding test (T24) conducted at room temperature did not experience ligament rupture. However, the ligament of an identical specimen (T25) tested at 282°C did rupture at 15.5 MPa (2.25 ksi), indicating that the room-temperature test was close to ligament rupture (flow stress at 282°C is 10% lower than at room temperature). Variation of the calculated ligament rupture pressure with ligament width is shown in Figure 4b, which also includes ligament rupture pressures calculated by Lee et al. [13] with a flow stress criterion (i.e., average ligament stress = flow stress = average of yield and ultimate tensile strengths). It is evident that a rupture criterion based on flow stress significantly underestimates the ligament rupture pressure because failure of the ligament occurs by necking. A failure criterion based on ultimate tensile strength would be more appropriate.

Results from a similar analysis for a type 4 specimen (Figure 5a) shows a similar reduction in average ligament thickness with pressure as in Figure 4a for a type 2 specimen. Because the calculated ligament rupture pressure (45 MPa) is greater than the unstable burst pressure of the resulting 13-mm (0.5 in.)-long throughwall crack, the specimen is predicted to burst unstably at 45 MPa, which is reasonably close to the reported stage 2 burst pressure of specimen OM159 (Table 1). Note that in contrast to type 2 specimen, the ligament in the type 4 specimen is subjected to high shearing deformation (Figure 5b).

CONCLUSIONS

Tests were conducted on steam generator tubes with two part-throughwall axial flaws arranged in two different configurations. Rupture pressure of a through-thickness notch tip

ligament can be predicted by an equivalent rectangular approach. Nonlinear finite-element analyses show that both the axial (type 2) and circumferential (type 4) ligaments between two axial throughwall notches fail by tensile necking. However, the type 4 ligament also experiences large shearing deformation. The calculated ligament rupture pressures are reasonably close to observed stage 2 burst pressures.

REFERENCES

1. Hahn, G. T., Sarrate, M. and Rosenfield, A. R., (1969) *Int. J. Fract. Mech*., 5, 187.
2. Erdogan, F. (1976) *Int. J. Pres. Ves. & Piping*, 4, 253.
3. Eiber, R.J., Maxey, W.A., Duffy, A. R. and Atterbury. T. J. (1971) *Investigation of the Initiation and Extent of Ductile Pipe Rupture*, BMI–1908, Battelle Memorial Institute.
4. Kiefner, J. F., Maxey, W. A R., Eiber, J. and Duffy, A. R. (1973). In *Progress in Flaw Growth and Fracture Toughness Testing*, ASTM Special Technical Publication 536, Philadelphia.
5. Flesch, B. and Cochet, B. (1988) *Int. Cong. on Press. Vess. Tech.,* Beijing.
6. Alzheimer, J. M., Clark, R. A., Morris, C. J. and Vagins, M.(1979). *Steam Generator Tube Integrity Program Phase I Report*, NUREG/CR–0718, PNL-2937, Richland, WA.
7. Majumdar, S., (1999) *Nucl. Eng. and Design*, 194, 31.
8. Ranganath, S. and Mehta, H. S. (1983). In *Fracture Resistance Curves and Engineering Applications*, American Society for Testing and Materials, ASTM Special Technical Publication 803, Philadelphia.
9. Kanninen, M. F., Zahoor, A., Wilkowski, G. M., Abou–Sayed, I., Marschall, C., Broek, D., Sampath, S., Rhee, C. and Ahmad, J. (1982). EPRI NP–2347 (Vol.1: Summary: Vol. 2: Appendices), Electric Power Research Institute, Palo Alto, CA.
10. Hasegawa, K., Shimizu, T. and Shida, S. (1985) *Nucl. Eng. and Design,* 87.
11. Kurihara, R., Ueda, S. and Sturm, D. (1988) *Nucl. Eng. and Design*, 106.
12. Cochet, B., Engstrom, J. and Flesch, B. (1990). Paper 4.1, *Steam generator tubes mechanical, LBRB, and probabilistic studies*, EDF, France.
13. Lee, J. H., Park, Y. W., Song, M. H., Kim, Y. J. and Moon, S. I. (2001) *Nucl. Eng. and Design,* 205

TABLE 1
SUMMARY OF TEST RESULTS

Tube ID	Notch type	Notch length (mm)	Ligament width (mm)	Stage 1 pressure (MPa)	Stage 2 pressure (MPa)
OM161	4	6	0.25	28.3	-
OM162	4	6	1.27	31.4	32.5
OM159	4	6	2.54	34.8	38.3
OM150	4	13	0.25	19.0	-
OM151	4	13	1.27	23.0	-
OM152	4	13	2.54	23.5	18.9
OM153[1]	2	6	0.25	34.8	-
T24[2, 3]	2	6	0.25	17.2	-
T25[2, 4]	2	6	0.25	15.5	-
OM160	2	6	1.27	32.3	-
OM149	2	13	2.54	27.0	-

[1]Notches in this specimen were 70% deep.
[2]Notches in this specimen were 100% deep.
[3]Axial ligament did not rupture in this test.
[4]This test was conducted at 282°C.

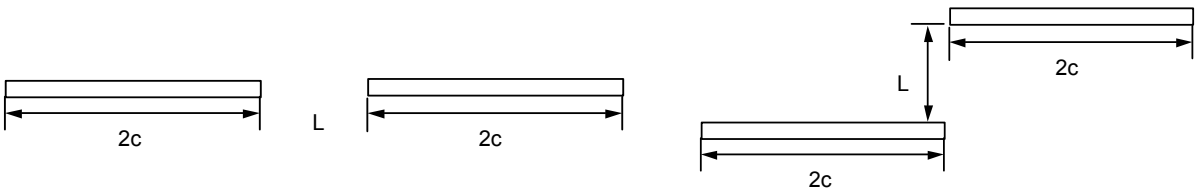

Axial Ligament (Type 2) Circumferential ligament (Type 4)

Figure 1: Type 2 and type 4 configurations of notches tested at ANL.

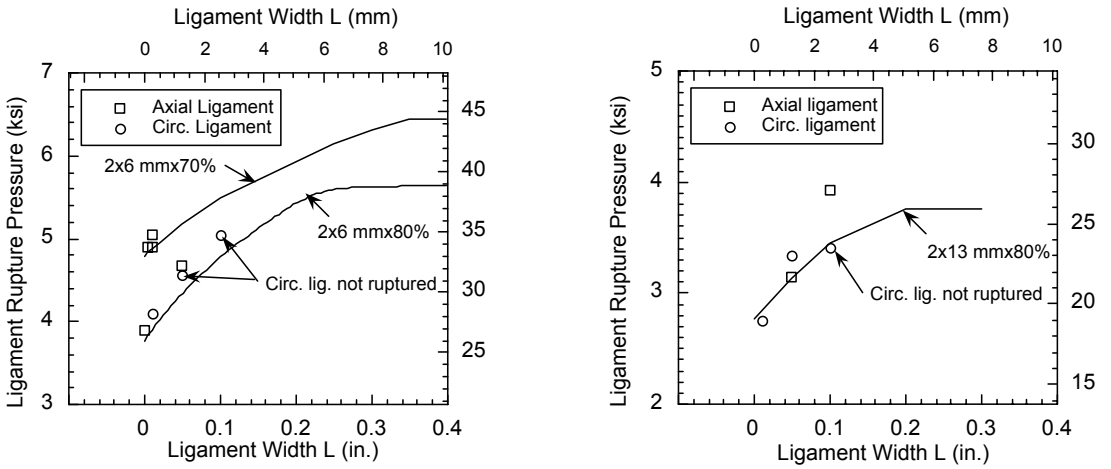

Figure 2: Predicted (lines) vs. observed (symbols) rupture pressures for through-thickness notch tip ligaments for type 2 (axial ligament) and type 4 (circumferential. ligament) specimens with (a) two 6 mm notches and (b) two 13 mm notches.

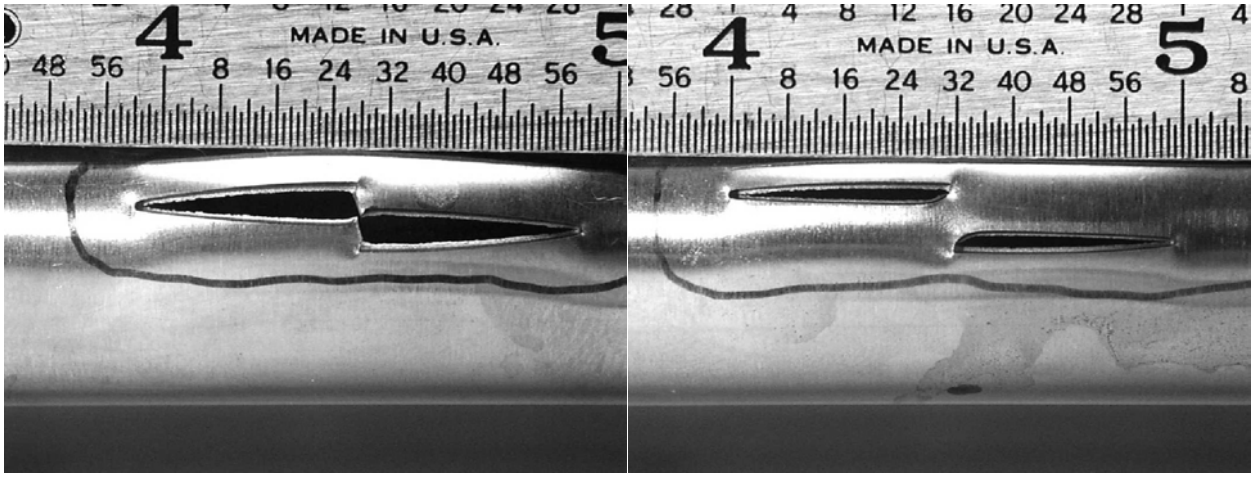

(a) (b)

Figure 3: Post-test (stage 1) photos of flawed tubes with two 80% deep, 13-mm (0.5 in.)-long notches separated by a (a) 1.27-mm (0.05 in.)-wide and a (b) 2.54-mm (0.1 in.)-wide ligament.

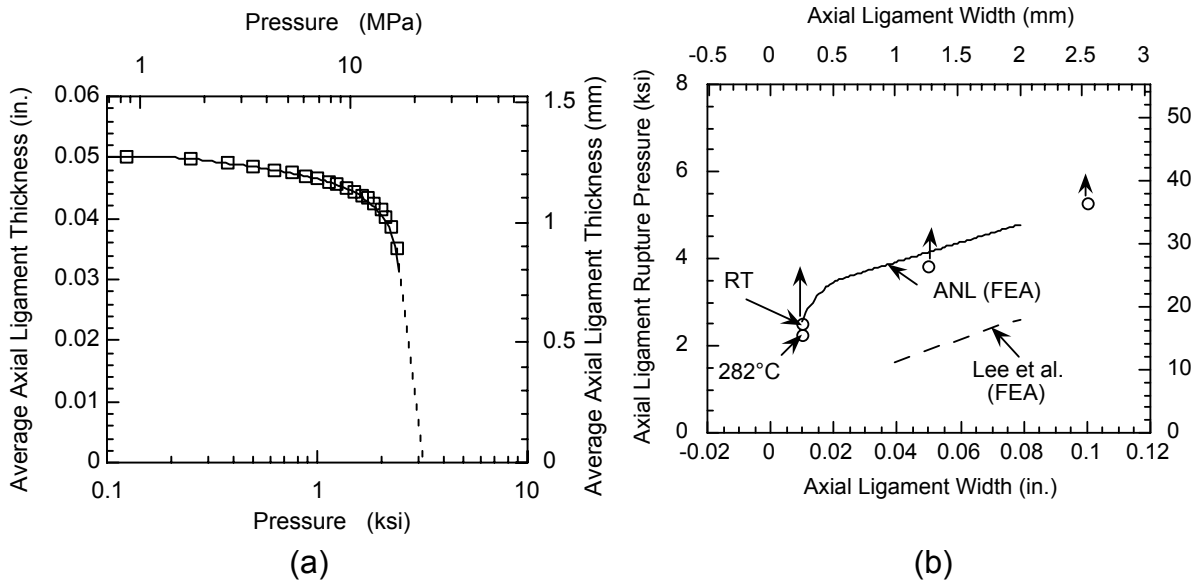

Figure 4: Results from FEA showing (a) variation of average axial ligament thickness with pressure for type 2 specimen with two 6-mm-long throughwall cracks separated by 0.25-mm-wide ligament, and (b) variation of ligament rupture pressure with axial ligament width for specimen with two 6-mm-long throughwall cracks. Symbols represent results from tests, with up arrow indicating no rupture of ligament. Dashed line is obtained from Ref. 13.

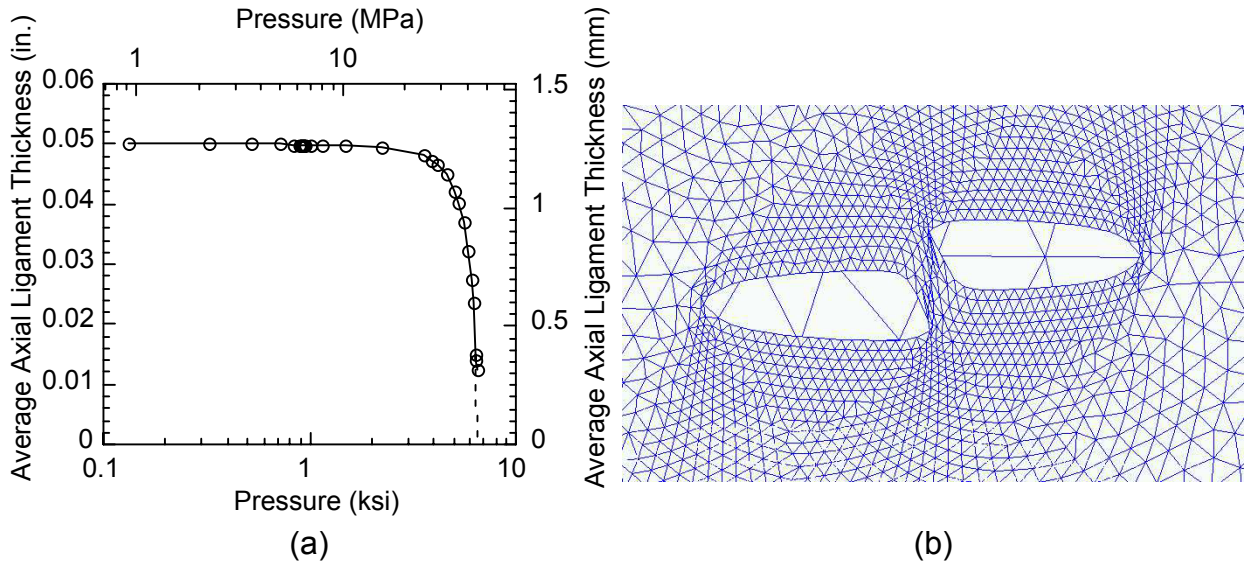

Figure 5: Results from FEA showing (a) variation of average axial ligament thickness with pressure and (b) deformed shape of type 4 specimen with two 6-mm-long throughwall cracks separated by 2.54-mm-wide ligament.

ANALYSIS OF A PENNY-SHAPED CRACK IN A TRANSVERSELY ISOTROPIC PIEZOELECTRIC MEDIUM

Ming-Hao Zhao, Pin Tong and Tong-Yi Zhang*

Department of Mechanical Engineering, Hong Kong University of Science and Technology
Clear Water Bay, Kowloon, Hong Kong, China, *E-mail: mezhangt@ust.hk

ABSTRACT

The present work analytically studies an ellipsoidal cavity and then a penny-shaped crack in a transversely isotropic piezoelectric medium under uniform remote mechanical and electrical loading. Three-dimensional (3D) analytic solutions are derived for the mechanical and electrical fields in the piezoelectric medium and for the electric field within the cavity. An effective dielectric constant of the material is introduced here, which involves the material dielectric, piezoelectric and elastic constants. The results indicate that the electric field within the cavity is uniform and its magnitude increases with decreasing the ratio β^* of the dielectric constant of the cavity to the 3D effective dielectric constant of the material. When the cavity is reduced into a penny-shaped crack, the crack mechanical and electrical fields depend on the ratio of α/β^*, where α is the ratio of the minor semi-axis to the major semi-axis of the ellipsoidal cavity. The electrically impermeable and permeable penny-shaped cracks are just two extreme cases of the present solutions, corresponding to $\alpha/\beta^* \to \infty$ and $\alpha/\beta^* \to 0$, respectively.

KEYWORDS

piezoelectric medium, penny-shaped crack, intensity factor, analytic solution

INTRODUCTION

In purely elastic fracture mechanics, a crack is usually treated as a mathematical slit without any thickness. To utilize this simplification for electrically insulating cracks in piezoelectric materials, one has to assume an electrically insulating crack to be electrically impermeable [1-10] or permeable [11, 12]. However, a real crack has a finite nonzero width and the crack geometry has a great influence on the fracture behavior of the materials [13]. Furthermore, the two-dimensional (2D) results show that the crack fields depend on the ratio of α/β [14, 15], where β is the ratio of the dielectric constant of the cavity (or crack) to the 2D effective dielectric constant of the material. The electrically impermeable and permeable boundary conditions along the crack faces are only two extreme cases, corresponding to $\alpha/\beta \to \infty$ and $\alpha/\beta \to 0$, respectively. In this paper, we will demonstrate the similar results for penny-shaped cracks.

BASIC EQUATIONS

In three-dimensional piezoelectric elasticity, the equilibrium equations, in terms of stress σ_{ij} and electric displacement D_i, are given by

$$\sigma_{ij,j} = 0, \quad D_{i,i} = 0, \qquad i, j=1, 2, 3. \tag{1}$$

The kinematic equations read

$$\varepsilon_{ij} = \tfrac{1}{2}(u_{i,j} + u_{j,i}), \quad E_i = -\phi_{,i}, \qquad i, j=1, 2, 3, \tag{2}$$

where ϕ, u_i, E_i and ε_{ij} denote the electric potential, displacement vector, electric field vector and the strain tensor, respectively. The constitutive equations take the form

$$\sigma_{ij} = c_{ijkl}\varepsilon_{kl} - e_{kij}E_k, \; D_k = e_{kij}\varepsilon_{ij} + \kappa_{kl}E_l, \quad i, j, k, l=1, 2, 3, \tag{3}$$

where c_{ijkl}, e_{kij} and κ_{kl} are the elastic, piezoelectric and dielectric constants, respectively.
Let the $r\theta$ - plane of the cylindrical coordinate system (r, θ, z) coincide with the isotropic plane of the transversely isotropic medium and the poling direction be along the z-axis. The displacements and the electric potential may be expressed by the four potential functions U_i (i=1, 2, 3, 4) [7, 11, 16, 17]

$$u_r = \sum_{i=1}^{3}\frac{\partial U_i}{\partial r} - \frac{1}{r}\frac{\partial U_4}{\partial \theta}, \quad u_\theta = \sum_{i=1}^{3}\frac{1}{r}\frac{\partial U_i}{\partial \theta} + \frac{\partial U_4}{\partial r}, \quad u_z = \sum_{i=1}^{3}k_{1i}\frac{\partial U_i}{\partial z}, \quad \varphi = \sum_{i=1}^{3}k_{2i}\frac{\partial U_i}{\partial z}, \tag{4}$$

where k_1 and k_2 are constants to be determined. Putting Eq. (4) into Eqs. (2), (3), and then (1) yields

$$\frac{\partial^2 U_i}{\partial r^2} + \frac{1}{r}\frac{\partial U_i}{\partial r} + \frac{1}{r^2}\frac{\partial^2 U_i}{\partial \theta^2} + \frac{\partial^2 U_i}{\partial z_i^2} = 0, \qquad i=1, 2, 3, 4, \tag{5}$$

where $z_i = s_i z$ and $s_i = 1/\sqrt{\lambda_i}$, and

$$\lambda_4 = \frac{2c_{44}}{c_{11} - c_{12}}, \tag{6}$$

and the other three roots λ_i (i=1, 2 3) are determined from the characteristic equation

$$A\lambda^3 + B\lambda^2 + C\lambda + D = 0. \tag{7}$$

In Eq. (7), the constants A, B, C, and D are combinations of material constants and given by

$$\begin{aligned}
&A = c_{11}(e_{15}^2 + c_{44}\kappa_{11}),\\
&B = 2e_{15}(e_{15}c_{13} - e_{33}c_{11}) + 2c_{13}(e_{15}e_{31} + c_{44}\kappa_{11}) - c_{44}(e_{31}^2 + c_{11}\kappa_{33}) + \kappa_{11}(c_{13}^2 - c_{11}c_{33}),\\
&C = e_{33}(e_{33}c_{11} + 2e_{15}c_{44}) - 2e_{33}(e_{15} + e_{31})(c_{13} + c_{44}) - \kappa_{33}(c_{13}^2 + 2c_{13}c_{44} - c_{11}c_{33}) + \kappa_{11}c_{33}c_{44} + c_{33}(e_{15} + e_{31})^2,\\
&D = -c_{44}(e_{33}^2 + c_{33}\kappa_{33}).
\end{aligned} \tag{8}$$

In Eq. (4) k_{1i} and k_{2i} (i=1, 2, 3) are constants related to λ_i by

$$\frac{c_{44} + (c_{13} + c_{44})k_{1i} + (e_{15} + e_{31})k_{2i}}{c_{11}} = \frac{c_{33}k_{1i} + e_{33}k_{2i}}{c_{13} + c_{44} + c_{44}k_{1i} + e_{15}k_{2i}} = \frac{e_{33}k_{1i} - \kappa_{33}k_{2i}}{e_{15} + e_{31} + e_{15}k_{1i} - \kappa_{11}k_{2i}} = \lambda_i. \tag{9}$$

Finally, we express the stresses and the electric displacements in terms of the potential functions

$$\sigma_{rr}=\sum_{i=1}^{3}\left[c_{11}\frac{\partial^2 U_i}{\partial r^2}+c_{12}\frac{1}{r}\frac{\partial U_i}{\partial r}+c_{12}\frac{1}{r^2}\frac{\partial^2 U_i}{\partial\theta^2}+(c_{13}k_{1i}+e_{31}k_{2i})\frac{\partial^2 U_i}{\partial z^2}\right]+(c_{11}-c_{12})\left(\frac{1}{r^2}\frac{\partial U_4}{\partial\theta}-\frac{1}{r}\frac{\partial^2 U_4}{\partial\theta\partial r}\right),$$

$$\sigma_{\theta\theta}=\sum_{i=1}^{3}\left[c_{12}\frac{\partial^2 U_i}{\partial r^2}+c_{11}\frac{1}{r}\frac{\partial U_i}{\partial r}+c_{11}\frac{1}{r^2}\frac{\partial^2 U_i}{\partial\theta^2}+(c_{13}k_{1i}+e_{31}k_{2i})\frac{\partial^2 U_i}{\partial z^2}\right]-(c_{11}-c_{12})\left(\frac{1}{r^2}\frac{\partial U_4}{\partial\theta}-\frac{1}{r}\frac{\partial^2 U_4}{\partial\theta\partial r}\right),$$

$$\sigma_{zz}=\sum_{i=1}^{3}\lambda_i(c_{44}+c_{144}k_{1i}+e_{15}k_{2i})\frac{\partial^2 U_i}{\partial z^2},$$

$$\sigma_{z\theta}=\sum_{i=1}^{3}\left[(c_{44}+c_{44}k_{1i}+e_{15}k_{2i})\frac{1}{r}\frac{\partial^2 U_i}{\partial z\partial\theta}\right]+c_{44}\frac{\partial^2 U_4}{\partial r\partial z},\tag{10}$$

$$\sigma_{zr}=\sum_{i=1}^{3}\left[(c_{44}+c_{44}k_{1i}+e_{15}k_{2i})\frac{\partial^2 U_i}{\partial r\partial z}\right]-c_{44}\frac{1}{r}\frac{\partial^2 U_4}{\partial\theta\partial z},$$

$$\sigma_{r\theta}=\sum_{i=1}^{3}\left[(c_{11}-c_{12})(\frac{1}{r}\frac{\partial^2 U_i}{\partial r\partial\theta}-\frac{1}{r^2}\frac{\partial U_i}{\partial\theta})\right]+\frac{1}{2}(c_{11}-c_{12})(\frac{\partial^2 U_4}{\partial r^2}-\frac{1}{r}\frac{\partial U_4}{\partial r}-\frac{1}{r^2}\frac{\partial^2 U_4}{\partial\theta^2}),$$

$$D_r=\sum_{i=1}^{3}\left[(e_{15}+e_{15}k_{1i}-\kappa_{11}k_{2i})\frac{\partial^2 U_i}{\partial r\partial z}\right]-e_{15}\frac{1}{r}\frac{\partial^2 U_4}{\partial\theta\partial z},$$

$$D_\theta=\sum_{i=1}^{3}\left[(e_{15}+e_{15}k_{1i}-\kappa_{11}k_{2i})\frac{1}{r}\frac{\partial^2 U_i}{\partial\theta\partial z}\right]+e_{15}\frac{\partial^2 U_4}{\partial r\partial z},\tag{11}$$

$$D_z=\sum_{i=1}^{3}\lambda_i(e_{15}+e_{15}k_{1i}-\kappa_{11}k_{2i})\frac{\partial^2 U_i}{\partial z^2}.$$

A ELLIPSOIDAL CAVITY UNDER REMOTE LOADING

Boundary conditions on the cavity surface

Figure 1 shows an ellipsoidal cavity in an infinite transversely isotropic piezoelectric medium under remote loading. The center of the cavity is located at the origin of the coordinate system. The ellipsoidal surface is

$$\frac{r^2}{a^2}+\frac{z^2}{b^2}=1 \tag{12}$$

or

$$\frac{r^2}{q^2-1}+\frac{z^2}{q^2}=C_0^2, \tag{13}$$

where $C_0^2=b^2-a^2$ and $q=b/C_0$, with the unit out normal $\{n_r, 0, n_z\}$,

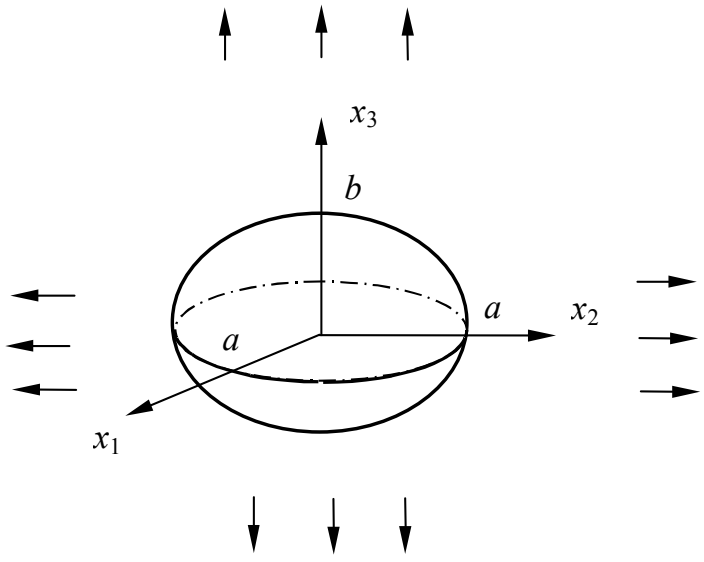

Fig. 1 Ellipsoidal cavity

$$n_r=\frac{r}{a^2N},\quad n_z=\frac{z}{b^2N},\quad N=\sqrt{\frac{r^2}{a^4}+\frac{z^2}{b^4}}. \tag{14}$$

The boundary conditions along the cavity surface

$$\begin{aligned}
&\phi = \phi^c \ \text{(continuity of electric potential)},\\
&\sigma_{rr}n_r + \sigma_{rz}n_z = 0,\ \sigma_{\theta r}n_r + \sigma_{\theta z}n_z = 0,\quad \sigma_{rz}n_r + \sigma_{zz}n_z = 0,\quad \text{(traction – free)},\\
&D_r n_r + D_z n_z = 0 \ \text{(surface charge – free)},
\end{aligned} \tag{15}$$

where the superscript "*c*" denotes a quantity inside the cavity.

Applied loads

For simplicity, we consider only the axisymmetric loading in the present work. Under the remotely uniform loads of $\sigma_{rr}^{\infty}, \sigma_{zz}^{\infty}$ and electric displacement D_z^{∞}, the corresponding displacements and electric potential are

$$u_r^{\infty} = \varepsilon_{rr}^{\infty} r,\ u_z^{\infty} = \varepsilon_{zz}^{\infty} z,\quad \varphi = -E_z^{\infty} z + \varphi_0, \tag{16}$$

where φ_0 is a reference electric potential, and

$$\begin{aligned}
&\sigma_{rr}^{\infty} = (c_{11}+c_{12})\varepsilon_{rr}^{\infty} + c_{13}\varepsilon_{zz}^{\infty} - e_{31}E_z^{\infty},\quad \sigma_{zz}^{\infty} = 2c_{13}\varepsilon_{rr}^{\infty} + c_{33}\varepsilon_{zz}^{\infty} - e_{33}E_z^{\infty},\\
&D_z^{\infty} = 2e_{13}\varepsilon_{rr}^{\infty} + e_{33}\varepsilon_{zz}^{\infty} + \kappa_{33}E_z^{\infty}.
\end{aligned} \tag{17}$$

Solution

Assume that the electric field strength inside the cavity is uniform with the electric potential,

$$\varphi^c = -\hat{B}z + \varphi_0^c, \tag{18}$$

where φ_0^c is another reference electric potential and $\hat{B}$ is a constant.

In this case,

$$U_4 = 0, \tag{19}$$

and the other three harmonic potential function U_i are given by [11]

$$U_i = A_i H(r, z_i),\quad i = 1, 2, 3, \tag{20}$$

with

$$\begin{aligned}
&H(r, z_i) = \frac{1}{2}\left[z_i^2\psi_1(q_i) + r^2\psi_2(q_i) - C_i^2\psi_0(q_i)\right],\\
&\psi_0(q_i) = \frac{1}{2}\ln\left(\frac{q_i+1}{q_i-1}\right),\quad \psi_1(q_i) = \frac{1}{2}\ln\left(\frac{q_i+1}{q_i-1}\right) - \frac{1}{q_i},\quad \psi_2(q_i) = -\frac{1}{4}\ln\left(\frac{q_i+1}{q_i-1}\right) + \frac{1}{2}\frac{q_i}{q_i^2-1},
\end{aligned} \tag{21}$$

where A_i, i=1, 2, 3, are constants and the independent variables $q_i(r, z_i)$, i=1, 2, 3, are defined implicitly by

$$\frac{r^2}{q_i^2 - 1} + \frac{z_i^2}{q_i^2} = C_i^2,\quad C_i^2 = (b^2/\lambda_i) - a^2. \tag{22}$$

Denoting $p_i^2 = b^2/(b^2 - \lambda_i a^2)$, we have $q_i = p_i$ for points (r, z) lying on the surface of the spheroid. Substituting the above expressions into the boundary conditions, i.e., Eq. (15), yields the equations to determine the constants A_i and $\hat{B}$

$$
\begin{aligned}
&E_z^{\infty} - \sum_{i=1}^{3} \frac{k_{2i}}{\lambda_i} \psi_1(p_i) A_i = \hat{B} \quad \text{(continuity of electric potential)},\\
&\sum_{i=1}^{3} \left[(c_{12} - c_{11}) \psi_2(p_i) - \frac{c_{44}(1+k_{1i}) + e_{15} k_{2i}}{\lambda_i} \psi_1(p_i) \right] A_i = -\sigma_{rr}^{\infty},\\
&2 \sum_{i=1}^{3} \left[c_{44}(1+k_{1i}) + e_{15} k_{2i} \right] \psi_2(p_i) A_i = \sigma_{zz}^{\infty} \quad \text{(traction – free)},\\
&2 \sum_{i=1}^{3} \left[e_{15}(1+k_{1i}) - \kappa_{11} k_{2i} \right] \psi_2(p_i) A_i = D_z^{\infty} - \kappa^c \hat{B} \quad \text{(surface charge – free)},
\end{aligned}
\tag{23}
$$

where κ^c is the electric permeability of the cavity. After the coefficients have been determined, the stress and the electric displacement field everywhere can be calculated from Eqs. (10) and (11).

If b approaches zero, i.e., $\alpha = b/a \to 0$, the cavity is shrunk to a penny-shaped crack. Using the kinematic and constitutive equations of Eqs. (2) and (3), the stress and the electric displacement in the crack plane can be obtained

$$
\sigma_{zz}(r,0) = \frac{2\sigma_{zz}^{\infty}}{\pi} \left[\frac{1}{\sqrt{(\tilde{r})^2 - 1}} + Arc\tan\sqrt{(\tilde{r})^2 - 1} \right], \quad \tilde{r} = \frac{r}{a} > a \tag{24}
$$

$$
D_z(r,0) = \frac{2(D_z^{\infty} - d^*)}{\pi} \left[\frac{1}{\sqrt{(\tilde{r})^2 - 1}} + Arc\tan\sqrt{(\tilde{r})^2 - 1} \right] + d^*, \tag{25}
$$

where

$$
d^* = D_z^{\infty} + \sigma_{zz}^{\infty} \tilde{M}_5 \quad \text{for a finite } \beta^* \text{ or } \beta^* \to 0 \text{ and } \alpha/\beta^* \to 0, \tag{26a}
$$

$$
d^* = \frac{D_z^{\infty} + \sigma_{zz}^{\infty} \tilde{M}_5}{1 + \dfrac{\alpha}{\beta^*}} \quad \text{for } \beta^* \to 0 \text{ and } \alpha/\beta^* \text{ has a finite nonzero value}, \tag{26b}
$$

$$
d^* = 0 \quad \text{for } \beta^* \to 0 \text{ and } \alpha/\beta^* \to \infty, \tag{26c}
$$

where

$$
\beta^* = \kappa^c / \kappa_{3D}^{eff}, \quad \kappa_{3D}^{eff} = \det[\mathbf{M}^{(1)}] / \det[\mathbf{M}^{(3)}], \quad \tilde{M}_5 = \det[\mathbf{M}^{(5)}] / \det[\mathbf{M}^{(3)}], \tag{27a}
$$

$$
\begin{aligned}
&M_{1i}^{(1)} = s_i \left[c_{44}(1+k_{1i}) + e_{15} k_{2i} \right], \quad M_{2i}^{(1)} = \frac{\pi i}{2} \left[c_{44}(1+k_{1i}) + e_{15} k_{2i} \right], \quad M_{3i}^{(1)} = \frac{\pi i}{2} \left[e_{15}(1+k_{1i}) - \kappa_{11} k_{2i} \right],\\
&M_{1i}^{(3)} = M_{1i}^{(1)}, \quad M_{2i}^{(3)} = M_{2i}^{(1)}, \quad M_{3i}^{(3)} = -s_i k_{2i},\\
&M_{1i}^{(5)} = M_{1i}^{(1)}, \quad M_{2i}^{(5)} = s_i k_{2i}, \quad M_{3i}^{(5)} = M_{3i}^{(1)}, \quad i = 1, 2, 3.
\end{aligned}
\tag{27b}
$$

Equation (27a) gives the effective dielectric constant of the material for the three-dimensional problems. The results indicate that the mechanical and electric fields are strongly dependent on the ratio of α/β^*, like the two-dimensional case in which the solution depends strongly on the ratio of α/β. The two extremes given by Eqs. (26a) and (26c) correspond, respectively, to the electrically permeable and impermeable boundary conditions along the crack faces.

Defining the Mode I intensity factors K_I^{σ} and K_I^{D}

$$K_I = \lim_{r\to a}\sqrt{2\pi(r-a)}\sigma_{zz},\ \ K_D = \lim_{r\to a}\sqrt{2\pi(r-a)}D_z, \tag{28}$$

one can obtain

$$K_I = 2\sigma_{zz}^{\infty}\sqrt{\frac{a}{\pi}},\quad K_D = 2(D_z^{\infty} - d^*)\sqrt{\frac{a}{\pi}}\ . \tag{29}$$

These results show that, as in the two-dimensional problems [14], the mode I stress intensity factor is the same as that in purely elastic media and independent of the applied electric displacement. The electric displacement intensity factor depends not only on the applied fields, but also on the material properties in terms of d^*. For the two limiting cases, we have

$$K_D = -2\sigma_{zz}^{\infty}\tilde{M}_5\sqrt{\frac{a}{\pi}} \tag{30}$$

for electrically permeable cracks and

$$K_D = 2D_z^{\infty}\sqrt{\frac{a}{\pi}} \tag{31}$$

for electrically impermeable cracks. Using the electrically permeable or impermeable boundary conditions, Kogan et al. [11] and Huang [12] obtained the intensity factors for electrically permeable cracks, while Wang [4], Zhao et al. [7, 8] and Chen et al. [9, 10] obtained the intensity factors for electrically impermeable cracks.

ACKNOWLEDGEMENTS: This work is supported by a grant from the Research Grant Council of the Hong Kong Special Administrative Region, China. MHZ thanks HKUST for the Post-Doctoral Fellowship Matching Fund.

REFERENCES

1. Deeg, W. F. J. (1980). Ph. D. Thesis, Stanford University.
2. Sosa, H. A. and Pak, Y. E. (1990) *Int. J. Solids Struct.* **26**, 1.
3. Wang, B. (1992) *Int. J. Solids Struct.* **29**, 293.
4. Wang, B. (1992) *Int. J. Engng. Sci*. **30**, 781.
5. Dunn, M. L. (1994) *Int. J. Engng. Sci*. **32**, 119.
6. Wang, Z. K. and Huang, S. H. (1995) *Theor. Appl.Fract. Mech*. **22**, 229.
7. Zhao, M. H., Shen, Y. P., Liu, Y. J. and Liu, G. N. (1997) *Theor. Appl. Fract. Mech.* **26**, 129.
8. Zhao, M. H., Shen, Y. P., Liu, Y. J. and Liu, G. N. (1997) *Theor. Appl. Fract. Mech.* **26**, 141.
9. Chen, W. Q. and Shioya, T. (1999) *J. Mech. Phys. Solids* **47**,1459.
10. Chen, W. Q. and Shioya, T. (2000) *Int. J. Solids Struct.* **37**, 2603.
11. Kogan, L., Hui, C. Y. and Molkov V. (1996) *Int. J. Solids Struct.* **33**, 2719.
12. Huang, J. H. (1997) *Int. J. Solids Struct.* **34**, 2631.
13. Zhang, T.-Y. (1994) *Int. J. Fracture* **66**, R33.
14. Zhang, T.-Y., and Tong, P. (1996) *Int. J. Solids. Struct.* **33**, 343.
15. Zhang, T.-Y., Qian, C.-F., and Tong, P. (1998) *Int. J. Solids Struct.* **35**, 2121.
16. Wang, Z. K. and Zheng, B. L. (1995) *Int. J. Solids Struct.* **32**, 105.
17. Ding, H. J., Chen, B. and Liang J. (1996) *Int. J. Solids Struct.* **33**, 2283.

ORAL REFERENCE: 0537

ANALYSIS OF BALLISTIC PROPERTIES OF MULTILAYERED SHIELDS USING APPROXIMATE MODELS

G. Ben-Dor, A. Dubinsky and T. Elperin

The Pearlstone Center for Aeronautical Engineering Studies, Department of Mechanical Engineering, Ben-Gurion University of the Negev, Beer-Sheva, 84105, P. O. Box 653, Israel

ABSTRACT

Recent results of analytical investigation of multilayered spaced and non-spaced shields using simplified models describing impactor-shield interaction are discussed. For targets consisting of plates manufactured from ductile materials the influence of the order of the plates and air gaps on ballistic limit velocity is investigated, and some problems of optimal arrangement of the plates in a layered shield are solved. Design of two-component ceramic-faced lightweight armors against ballistic impact is investigated, and approximate analytical formulas are derived for areal density and thicknesses of the plates in the optimal armor as functions of parameters determining the properties of the materials of the armor components, cross-section and mass of an impactor, and of the expected impact velocity.

KEYWORDS

Ballistic limit, impact, perforation, armor, shield, optimization.

INTRODUCTION

Sub-ordnance penetration and perforation of multilayered plates has been a subject of intensive research during recent years since non-monolithic configurations are considered feasible for the designing shields or elements of the shields. Simplified analytical models were derived and used for the analysis and optimization of the shields consisting of the layers manufactured from different materials, e.g., ductile multi-layered shields [1, 2-12], aluminum/Lexan combinations [11], ceramic-faced armors [12-17]. Qualitative laws that are obtained from approximate models can be very useful for further theoretical and experimental investigations. In order to obtain such laws the most appropriate are those models that allow to derive formulas determining the dependence of the ballistic limit velocity (hereafter BLV) on various factors affecting perforation, e.g., a shape of the impactor, simultaneous interaction between the impactor and different layers of the shield during motion of the impactor in a multilayered armor, properties of the materials of the layers, etc. In this respect localized-interaction models [18-19], cavity expansion approximations [20-21], Florence's model [13] appear to be very useful.

In this paper we discuss some our results on the multi-layered shields, and additional information can be found in Ben-Dor et al. [2-10, 12]. All the results for non-ceramic armor described here were derived rigorously using the adopted models for impactor-shield interaction. The obtained results (if not indicated differently) correspond to conical impactors with arbitrary shape of the cross-section. The determined ballistic properties of the shields are valid for any impactor in the considered class. Although validation of

the obtained results using the available experimental data in the literature is encouraging, specially designed experiments are required in order to determine the range of the validity of the obtained results.

BALLISTIC PROPETIES OF MULTILAYERED SHIELDS DETERMONED WITH THE AID OF THE LOCALIZED INTERACTION MODELS

Impactor-shield localized interaction model

Consider a high speed normal penetration of a 3-D rigid sharp impactor into an armor with a finite thickness and assume that the localized interaction model is valid, i.e., the impactor-armor interaction at a given location at the surface of the impactor which is in a contact with the armor can be described by the following equation:

$$d\vec{F} = \left[\rho\Omega(u)v^2 + \sigma\right]\vec{n}^0 dS, \quad u = -\vec{v}^0 \cdot \vec{n}^0 \qquad (1)$$

where $d\vec{F}$ is the force acting at the surface element dS of the impactor along the inner normal unit vector $\vec{n}^0$ at a given location at the surface of the impactor, $\vec{v}^0$ is the unit local velocity vector, Ω is function determining the particular model for the impactor-shield interaction. Equation (1) with constant parameters ρ,σ comprises the most widely used phenomenological models for homogenous targets (see, e.g., [18,19]). Usually parameters ρ,σ are density and distortion pressure of the armor, respectively, and $\Omega(u) = u^2$. We consider the armor consisting of N plates, the material of i-th plate is characterized by values ρ_i,σ_i. Often these parameters appear in our results as a combination $\chi_i = \sigma_i/\rho_i$. Thus the parameters ρ,σ in eqn (1) depend on the distance of the surface element from the front plane of the target. We assume that the adjacent plates are in contact and do not interact. If the "plate" with the number i is an air gap then $\rho_i = \sigma_i = 0$.

The total force $\vec{F}$ is determined by integrating the local force given by eqn (1) over the impactor-armor contact surface that depends on the position of the impactor inside the shield. This allows us to write equation of motion of the impactor in the normal direction and to determine the BLV that is defined as the initial velocity of the impactor required for its nose to emerge from the target with a zero velocity. Corresponding cumbersome expressions we do not write here (see, e.g., [2,8]).

Optimum multilayered shield. Plates with the same density and given thicknesses

For the shield consisting of several plates with the same density but having different values of distortion pressure perforated, generally, by a non-conical impactor the following properties are valid. If two adjacent plates in a multilayered armor are such that the value of the distortion pressure for the first plate is larger than that for the second plate, the BLV of the armor can be increased by interchanging these plates. The maximum BLV of the armor is achieved when the plates are arranged in the order of increasing values of the distortion pressure of the material of the plates; the minimum BLV is achieved when the plates are arranged in the armor in an inverse order.

Optimum two-layered shield. Plates of different densities and with given thicknesses

The maximum BLV for two-layered armor is attained when the plates are arranged according to the increase of the magnitude of the parameter $\chi = \sigma/\rho$.

Optimum multilayered shield. Plates manufactured from one of the two possible materials

Ballistic properties of multilayered shields are studied when the shield consists of the adjacent plates made from one of two possible materials and the total thickness of the plates manufactured from every material is fixed. The following ballistic properties of the shield are proved. The displacement of any plate inside the target in direction of penetration yields monotone change of the BLV of the shield and the criterion of increasing or decreasing of the BLV depends of the properties of the materials of the plates, namely, relocation of a plate with a larger (smaller) value of the parameter χ yields an increase (decrease) of the BLV. The maximum BLV is obtained for the two-layered shield without alternating the plates manufactured from different materials; the front plate in the optimum shield must be the plate manufactured from the material with the smaller value of the parameter χ.

Optimum multilayered shield with a given areal density and thickness. Plates manufactured from different materials

The problem is formulated as follows. There are several materials with different properties which can be used for manufacturing the plates in a mshield. The areal density of the shield (its mass per surface unit) and its thickness are given. The goal is to determine the structure of the shield (the order and the thicknesses of the plates from different materials) that provides the maximum BLV of the shield. It is proved that the shield with maximum BLV must consist of one or several adjacent plates (these cases are equivalent is point of view of the model) manufactured from the material with the maximum χ. The shield with minimum BLV consist of one or several adjacent plates manufactured from the material with the minimum χ. The values of BLV of different shields with given areal density and thickness are between these limiting values.

Optimum multilayered shield with large air gaps

It is assumed that the impactor perforates the plates in a multi-layered shield sequentially, i.e., it does not interact with two or several plates simultaneously. One would expect that this assumption is approximately valid if the length of the impactor is much less than the thickness of every plate. In the framework of the adopted penetration model this assumption corresponds to the spaced armor when the widths of the air gaps are greater than the length of the impactor. The set of plates is given. We proved that the maximum BLV is attained when the plates are arranged in the order of increasing values of χ.

Influence of air gap on the ballistic resistance of the two-layered shield

The following property is proved. If $\chi_1 > \chi_2 \, (\chi_1 < \chi_2)$ then the BLV decreases (increases) with increasing the air gap thickness from zero to the length of the impactor (BLV becomes constant with the further increase of the air gap thickness). If $\chi_1 = \chi_2$, i. e., the properties of the material of both plates are the same, the ballistic limit velocity does not depend on the thickness of the air gap. Numerical calculations performed for armors consisting of plates manufactured from different materials show that the developed model predicts a very negligible effect of an air gap upon the ballistic resistance.

Influence of the order of the plates on the ballistic resistance of a two-layered spaced shield

The maximum BLV of the armor with a fixed width of an air gap is attained when the plates are arranged in the order of the increasing values of parameter χ.

Influence of air gap on a ballistic resistance of a multilayered shield consisting of the plates are manufactured from the same material.

The BLV of the spaced shield is determined by the total thickness of the plates, i.e., it is independent of the air gap sizes between the layers, of the sequence of the plates in the shield and of the distribution of the total thickness among the plates. Monolithic and spaced shields are equivalent in the framework of the considered model.

Optimal shapes of 3D impactors.

We studied optimization of 3D impactors with a given longitudinal contour, length and volume. We determined the existence of the "universal" optimal impactor among the 3D conical and non conical slender impactors penetrating normally into non-homogeneous (layered) semi-infinite shield or into a shield with a finite thickness. The impactor having the minimum drag moving inside a homogeneous medium with a constant velocity penetrates to the maximum depth into a semi-infinite shield and has the maximum BLV when it penetrates into a shield with a finite thickness, regardless of the distribution of the properties of the material in the shield along the penetration path. Using the analogy with the hypersonic flow over the flying projectiles ($\Omega = u^2$ in eqn (1)) it is predicted that the optimal impactors have a star-shaped cross-section.

INFLUENCE OF AIR GAPS ON THE BALLISTIC PROPERTIES OF MULTILAYERED SHIELDS DETERMINED USING CAVITY EXPANSION MODEL

Cylindrical cavity expansion model (CCEM)

The model is based on the assumptions that the impactor (a body of revolution) moving in a shield causes hole expansion in every plane which is normal to the direction of its motion when it reaches this plane and

these layers do not interact. Expression for hole expansion vs. the time ($t = 0$ is the beginning of the hole expansion) at every plane reads (for details see, e.g., [20-21]):

$$p = \alpha \dot{R}^2 + \beta R \ddot{R} + \gamma \qquad (2)$$

where R is radius of the hole, p is a pressure applied in the normal direction at the part of the impactor's surface, coefficients α, β, γ depend on the properties of the material of the corresponding plate in the multilayered shield. Taking into account kinematic relation between the location of the impactor in the shield, its shape and the radius of the hole at every plane, the equation of motion of the impactor allows us to determine the BLV. Corresponding formulas can be found in [4]. It is important to emphasize that, even for conical impactor, in eqn (2) $\ddot{R} \neq 0$ and cavity expansion model does not reduce to the localized interaction model. Such special models for homogeneous metal shields can be found, e.g., in [21]. Thus, BLV depends, generally, of the parameters $\alpha_i, \beta_i, \gamma_i$ where the subscript i denotes the number of the plate in the shield.

Optimum multilayered shield consists of given plates. Large air gaps.

The following properties are proved. If two adjacent plates in a shield with large air gaps are such that the value of the parameter $\tilde{\chi} = \gamma/\alpha$ for the first plate is larger than that for the second plate, the BLV of the shield can be increased by interchanging these plates. The maximum (minimum) BLV of the shield is attained when the plates are arranged in the order of increasing (decreasing) values of the parameter $\tilde{\chi}$. The values β_i do not effect the optimal order of the plates.

Comparison of ballistic properties of monolithic and spaced shields

The simplified models that we use imply that monolithic target and the target consisting of several adjacent plates are equivalent if the total thickness of the plates and their material are the same. However, in contrast to localized interaction model, CCEM predicts the difference in BLV for monolithic and spaced shields. It was shown analytically (for large air gaps) that the BLV of a spaced shield is larger than that of a monolithic shield, and the BLV of the shield increases with the increase of the number of the plates with the same thickness while the total thickness of the plates is kept constant. Numerical simulation using the model [21] showed that the influence of air gaps on BLV of the shield is weak for slender conical impactors and can be more pronounced with the increase of the apex half angle of its nose and the density of the material of the shield.

OPTIMUM TWO COMPONENT CERAMIC ARMOR

Model description

Consider a normal impact by a rigid projectile on a two-layer composite armor consisting of a ceramic front plate and a ductile back plate. We employ the following model $v_*^2 = \alpha\varepsilon_2\sigma_2 h_2 z(Az + m)/\left(0.91m^2\right)$ where v_* is the BLV, m is a projectile's mass, R is a projectile's radius, h_1, h_2 are the plate's thicknesses, σ is the ultimate tensile strength, ε is the breaking strain, ρ is density, $A = \rho_1 h_1 + \rho_2 h_2$ is the areal density, $z = \pi\left(R + 2h_1\right)^2$; subscripts 1 and 2 refer to a ceramic plate and a back plate, respectively. For $\alpha = 1$ this model was suggested by Florence [13] and re-worked by Hetherington [14]. We generalized slightly this model introducing a coefficient α which can be determined using the available experimental data in order to increase the accuracy of the predictions.

The objective of our study is to find the thicknesses of the plates h_1, h_2 which provide the minimum areal density of the armor for a given BLV v_*.

Optimum two component armor

We found that using the dimensionless variables

$$\bar{h}_i = \frac{h_i}{R}, \bar{\rho}_i = \frac{\pi R^3 \rho_i}{m}, i = 1,2, \bar{w} = v_* \sqrt{\frac{0.91\rho_2}{\alpha\varepsilon_2\sigma_2}}, \bar{A} = \frac{\pi R^2 A}{m}$$

the problem is reduced to finding a positive $\bar{h}_1$ that provides the minimum $\bar{A} = \bar{A}(\bar{h}_1, \bar{\rho}_1, \bar{w})$. The dimensionless areal density $\bar{A}$ is a function of one variable $\bar{h}_1$ and depends on only two parameters, $\bar{\rho}_1$ and $\bar{w}$. Therefore, although the exact analytical solution of the problem does not exist, the latter property allows us to find the simple approximations for characteristics of optimum shield in a general case, namely, for arbitrary combination of materials of the plates. Such approximations (with the average accuracy of 3% in the range $0.04 \le \bar{\rho}_1 \le 0.1, 1 \le \bar{w} \le 10$) for the thickness of the ceramic plate and the areal density of the optimum armor are given by the the following expressions:

$$\bar{h}_1^{opt} = \frac{(0.04 + 1.12\bar{\rho}_1)\bar{w}^{1.895}}{\bar{\rho}_1(\bar{\rho}_1 + 1.29\bar{w}^{1.47} + 0.1)}, \quad \bar{A}^{opt} = (0.04 + 1.12\bar{\rho}_1)\bar{w}^{0.425}$$

The optimal thickness of metallic plate is $\bar{h}_2^{opt} = (\bar{A}^{opt} - \bar{\rho}_1\bar{h}_1^{opt})/\bar{\rho}_2$.

REFERENCES

1. Aptukov, V. N., Murzakaev, A. V. and Fonarev, A. V. (1992). *Applied Theory of Penetration*. Nauka, Moscow (in Russian).
2. Ben-Dor, G., Dubinsky, A. and Elperin, T. (1997) *Theoret. Appl. Fract. Mech*. 27, 161.
3. Ben-Dor, G., Dubinsky, A. and Elperin, T. (1998) *Int. J. Solids Str.* 35, 3097.
4. Ben-Dor, G., Dubinsky, A. and Elperin, T. (1998) *Int. J. Fract.* 90, L63.
5. Ben-Dor, G., Dubinsky, A. and Elperin, T. (1998) *Theoret. Appl. Fract. Mech.* 30, 243.
6. Ben-Dor, G., Dubinsky, A. and Elperin, T. (1998) *Int. J. Fract.* 91, L9.
7. Ben-Dor, G., Dubinsky, A. and Elperin, T. (1999) *Int. J. Impact Engng.* 22, 741.
8. Ben-Dor, G., Dubinsky, A. and Elperin, T. (1999) *Theoret. Appl. Fract. Mech.* 31, 233.
9. Ben-Dor, G., Dubinsky, A. and Elperin, T. (1999) *Composites-A.* 30, 733.
10. Ben-Dor, G., Dubinsky, A. and Elperin, T. (2000) *Int. J. Solids Str.* 37, 687.
11. Radin, J. and Goldsmith, W. (1988) *Int. J. Impact Engng,* 7, 229.
12. Ben-Dor, G., Dubinsky, A., Elperin, T. and Frage, N. (2000) *Theoret. Appl. Fract. Mech*. 33, 185.
13. Florence, A.L. (1969). *Interaction of projectiles and composite armor. Part 2*. Stanford Research Institute, Menlo Park, AMMRC-CR-69-15.
14. Hetherington, J.G. (1992) *Int. J. Impact Engng*. 12 , 229.
15. Wang, B. and Lu, G. (1996) J. *Mater. Proc. Techn.* 57, 141.
16. Woodward, R.L. (1990) *Int. J. Impact Engng.* 9, 455.
17. Zaera, R. and Sanchez-Galvez, V. (1998) *Int. J. Impact Engng.* 21, 133.
18. Bunimovich, A. and Dubinsky, A. (1995) *Mathematical Models and Methods of Localized Interaction Theory,* World Scientific Publishers, Singapore.
19. Recht, R. F. (1990) In: *High Velocity Impact Dynamics* (J.A. Zukas, ed.), Wiley, New York.
20. Forrestal, M. J., Luk, V.K. and Brar, N.S. (1990) *Mech. Mater.* 10, 97.
21. Sagomonian, A.Ya. (1988) *Dynamics of Barrier Perforation.* Moscow Univ. Publ. (in Russian).

Oral Reference: ICF100897

EXTENSION OF THE UNIFIED APPROACH TO FATIGUE CRACK GROWTH TO ENVIRONMENTAL INTERACTIONS

K. Sadananda[1], R. L. Holtz[1] and A. K. Vasudevan[2]

[1] Code 6323, Materials Science and Technology Division,
Naval Research Laboratory, Washington D.C. 20375
[2] Office of Naval Research, Washington D.C. 22217

ABSTRACT

According to the Unified Approach for Fatigue Crack Growth developed by the authors. K_{max} and ΔK are two intrinsic parameters simultaneously required for quantifying fatigue crack growth data. The two parameters lead to two intrinsic thresholds that must be simultaneously exceeded for a fatigue crack to grow. Environmental interactions being time and stress-dependent processes affect fatigue crack growth through K_{max} parameter. Based on an extensive analysis of literature data, we have classified environmental effects into four basic types. The Unified Approach provides also a true reference state to define an inert fatigue behavior based on which one can quantify the environmental effects.

KEYWORDS

Fatigue crack growth, Environmental effects, Unified Approach, Classification of environmental effects

INTRODUCTION

In our Unified Approach to Fatigue [1-5], ΔK and K_{max} provide two crack tip driving forces simultaneously required for crack growth to occur. There are two corresponding thresholds that must be exceeded for a crack to grow. Crack growth data in terms of a ΔK vs K_{max} curve, show an L-shaped curve with two limiting values corresponding to two thresholds. At any other crack growth rates, the L-shaped curve shifts with the asymptotic limiting values, ΔK^* and $K_{max}{}^*$ increasing with crack growth rate, as shown in Fig. 1a.

CRACK GROWTH TRAJECTORY

In the Paris regime, when crack growth is governed typically by striation mechanisms, R-ratio

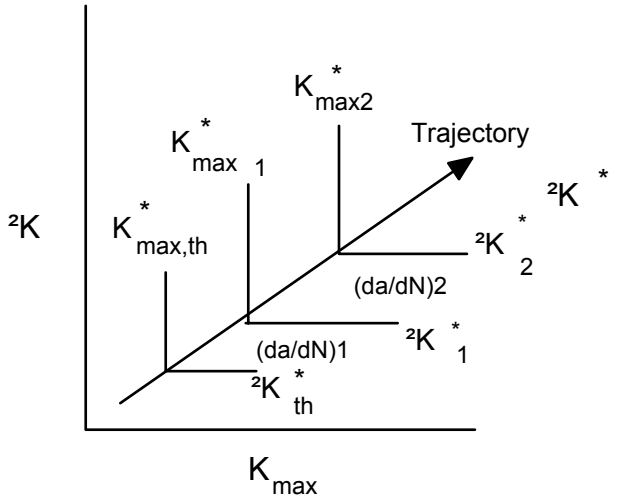

Fig. 1a. L-shaped curves defining ²K-Kmax limiting values at each crack growth rate

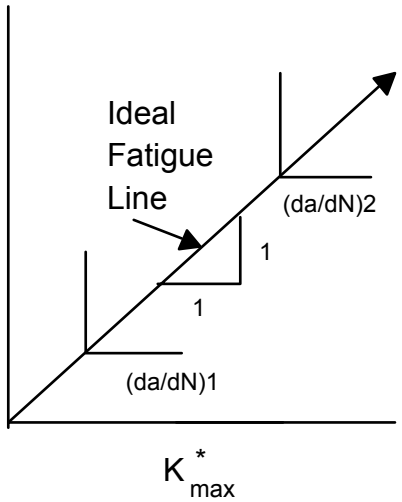

Fig. 1b. Trajectory of L-Shaped curves for an ideal fatigue case with no enviornmental effect

effects are minimal. Crack growth in this case is controlled purely by cyclic amplitude and

ΔK^* is nearly equal to K_{max}^*. Hence a plot of ΔK^* and K_{max}^* for different crack growth rates will be a straight line with $\Delta K^* = K_{max}^*$, as shown in Fig. 1b. The curve in Fig. 1b can be considered as a trajectory corresponding to crack growth mechanisms; the $\Delta K^* = K_{max}^*$ path characteristic of the pure-cycle controlled fatigue crack growth phenomenon. We refer to this as *ideal* fatigue behavior to separate it from other processes to be described below. Deviation from this line occurs if the crack growth mechanism changes. Empirically all deviations from ideal fatigue behavior occur with K_{max}^* being larger than ΔK^*, that is, all non-ideal behaviors fall below the line $\Delta K^* = K_{max}^*$. As the mechanisms become increasingly K_{max} controlled, the behavior swings more and more towards the K_{max}-axis.

CLASSIFICATION OF ENVIRONMENTAL EFFECTS

We have examined the available data in the literature for many different materials and environments, and arrived at some basic general classifications of the types of environmental interactions that are encountered during fatigue crack growth. We use the ΔK^*-K_{max}^* plot as a basis for the classification scheme. The plot represents the trajectory of crack growth behavior starting from threshold to unstable fracture as crack growth occurs, as suggested in Fig. 1a. For a given crack growth rate, the two values, ΔK^* and K_{max}^* represent the two limiting values in terms of the two parameters, ΔK and K_{max}, required for fatigue crack growth as defined in Fig. 1. The $\Delta K^* = K_{max}^*$ line represents the pure or ideal fatigue crack growth, Fig. 1b. This forms a reference line for the ideal inert behavior, which becomes a basis to classify the environmental contributions. This ideal behavior manifests only if the vacuum is very high or impurities in the so-called inert environments are very low and/or the materials are non-reactive to a given environment.

Fig 2 shows four types of basic behavior that are encountered. Type I behavior is typical of the true corrosion fatigue, wherein the environmental effects are maximum at low crack growth rates near threshold and decreases with increasing crack growth rate. At high crack growth rates, the reaction time is too short to have any significant environmental effect, and hence the behavior merges with that of ideal $\Delta K^*=K_{max}^*$ line. In a gas-metal system, four

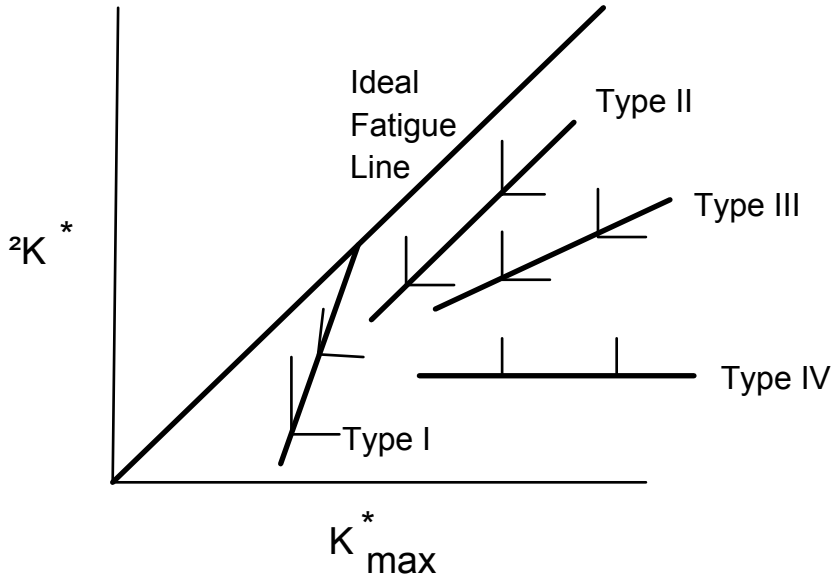

Fig. 2 Classification of Environmental Effects
Using Two-parameter aproach

sequential steps are considered[6]; transportation of aggressive species to the crack tip, reaction at the crack tip, transportation of the resulting hydrogen into the metal and finally the embrittlement of metal. In either case, with increasing crack growth rate, the Type I behavior is expected due to decreasing reaction time at the crack tip. Such a Type I behavior has indeed been observed.

The Type II behavior is indicated by the ΔK^*-K_{max}^* line parallel to the ideal behavior without merging with it. In this case, the environmental effects remain constant independent of crack growth rate or applied driving force, say K_{max}. Type II behavior is characterized by environmental effect that saturates extremely rapidly in relation to the transient crack advance times, and hence provides a constant contribution.

Type III behavior is opposite to Type I, wherein with increasing crack growth rate or K_{max}, the environmental contribution increases. Correspondingly the ΔK^*-K_{max}^* line swings towards K_{max}-axis. Here, transient time is not controlling, since with increasing crack growth rate or reduced time, the environmental contribution to fatigue crack growth actually increases rather than decreases. Since the deviation from ideal behavior of Type III increases with increasing stresses, it is associated with stress-enhanced or stress-driven environmental effects. Hence Type III may be more characteristic of stress corrosion fatigue process, Fig. 2b, in contrast to Type I and II. Increased effects of strain rates with increasing ΔK could also contribute to Type III.

Type IV is an extreme case of Type III behavior wherein the slope ΔK^*-K_{max}^* line approaches zero with ΔK^*-K_{max}^* trajectory running parallel to the K_{max}-axis, indicative of stress corrosion

crack growth rather than stress corrosion fatigue. The process is similar to static fatigue normally discussed with reference to ceramic materials. The role of cyclic stress in Type IV behavior may be to sharpen the crack tip, accentuating the stress-corrosion effect.

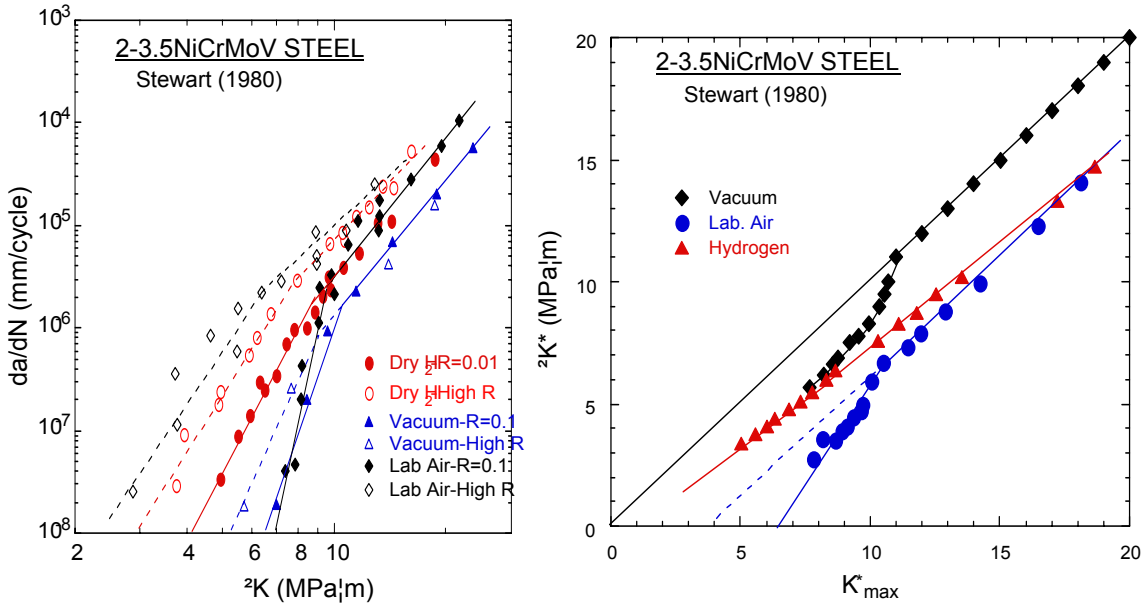

Fig. 3. A) Crack growth behavior in low alloy steel in ambient air, hydrogen and vacuum b) The analysis of the behavior in terms of ΔK*-Kmax* - trajectory map.

EXPERIMENTAL RESULTS

We show an example from the literature that illustrates a few of the types discussed above. To create the crack growth trajectory map similar to Fig. 2, both ΔK^* and K_{max}^* as a function of crack growth rate are needed. To determine these two values, crack growth rate data of a given material as a function of load ratio are needed. At the bare minimum, it is necessary to have data at R≈0 (e.g. R=0.05) from which we can estimate K_{max}^*, and the data at R ≈ 1 (e.g. R=0.9) from which we can estimate ΔK^*, since these are two asymptotic values at low and high R-values.

Fig. 3a shows the raw crack growth data in an ambient air, dry hydrogen and vacuum in low alloy steel (2-3.5Ni-Cr-Mo-V steel) measured by Stewart[7] at two R-ratios. The data may appear to be quite complex. However, since the data correspond to two extreme R-ratios, we can estimate the ΔK^* and K_{max}* values as a function of crack growth rate. These are plotted in the trajectory plot in Fig. 3b.

Considering first the data in vacuum, Fig. 3b shows that at low crack growth rates, the data deviate from the ideal fatigue behavior. But with increase in crack growth rates, the transient time decreases and the data slowly merge with that of the ideal fatigue behavior. The results demonstrate two important aspects. (a) The ideal fatigue behavior governed by the $\Delta K^*=K_{max}^*$ line can be observed in a material representing environment-free crack growth if the conditions are suitable. (b) The so-called vacuum tests do not ensure completely pure

inert environmental conditions since even very low partial pressures can have significant effect for some materials. This implies that care should be exercised in evaluating the environmental contributions using the vacuum tests as a reference. The vacuum data in Fig. 3b are consistent with the Type I behavior, that is decreasing environmental contribution with increasing crack growth rate until the data merge with the ideal fatigue behavior. The data are also consistent with Knudson flow[6] behavior where transportation of damaging species or the degree of crack-tip reaction reduces with the reduction in transient time due to increased da/dN and frequency or reduced partial pressure.

Examination of the laboratory air data of the same material shows somewhat different behavior from that of vacuum. It also shows initially a Type I behavior, but with increasing crack growth rate it converges to Type II behavior with data running parallel to the ideal line. Thus there is a definite change in the mechanism with increasing crack growth rate, stress or both. Here Type I leads to Type II behavior driven by applied stress, that is the mechanism in Type I should be such that it leads to a saturation stage at higher stresses or crack growth rates. One would expect that if the environmental effects are transportation control or reaction control then environmental contribution should decrease with increase in crack growth rate as in Type I. That is, one can have saturation effects at low crack growth rates due to larger reaction times available. From Fig. 2, saturation leading to unsaturation should result a Type II converging to Type I at high crack growth rates. One does not however expect an unsaturation leading to saturation that is a Type I behavior becoming Type II as the kinetics of the process are primarily time-dependent. On the other hand, if the process involves some complex roles of both time as well as stress, one can expect that it decreases due to decreasing time and stabilizing due to stress at some minimum value, causing a transition from Type I to Type II behavior. In order to establish the exact nature of the mechanism involved further analysis is required. Fig. 3, however, points out that controlling processes differ at ambient pressures from that observed in low vacuum.

The behavior in hydrogen environment differs from the previous two. At low crack growth rates the effect is comparable with that of partial vacuum and with increasing stress or growth rate the behavior converges to a constant effect similar to that of moist air. There is a small increase in environmental effect with crack growth typical of Type III, but that effect is very small. There is no Type I behavior observed at low crack growth rates in Hydrogen. Thus for the same material, three different environments show three different behaviors. Fig. 3 indicates that care should be exercised in interpretation of the data, particularly when there is change in the types of behavior in the same material and environment.

To understand the rate controlling process one has to examine in detail using above trajectory maps, the effect of frequency, composition and temperature (to evaluate the thermal activation process in each regime) supported by detailed fractographic analysis. Fig. 3, however, points to the fact one has to examine such trajectory map involving two crack tip driving forces, ΔK and K_{max}, to sort out the true contribution from environment in relation to the pure fatigue process. The micromechanism basis for each of the process has to be examined to have a better understanding of the mechanisms involved and how one mechanism can lead to the other with increasing crack growth rate. The analysis, however, points to the fact that environmental effects at the crack tip cannot be explained by a single mechanism for all crack growth rates, since they depend on both time and stress, as most of the corrosion process are. The reaction or transient time and the stress intensity at the crack tip have inverse relation

since the times are longer at low stresses and shorter at high stresses. Hence whether the process is dominated predominately by time or by stress will have significant effect on the resulting process and material response in the ΔK-Kmax* trajectory map. The Unified Approach points to the fact that ΔK-Kmax basis is fundamental for all fatigue crack growth process and the environmental effects have also to be examined from this perspective. Kmax parameter becomes a vehicle through which environmental effects get manifested, just as in the case of stress corrosion or sustained load crack growth processes. Analysis also provides a perspective in terms of the types of material behavior that one can expect, in addition to providing an environmentally pure fatigue behavior as a reference state.

SUMMARY AND CONCLUSIONS

We have extended the application of the Unified Approach to Fatigue Crack Growth to the analysis of environmental effects. It is shown that the two parameter approach is naturally amenable to the analysis since one of the governing driving force K_{max} is the characterizing parameter for the time-dependent environmental contributions. Based on this two-parameter approach we have developed a classification protocol for environmental contributions defining four types. This is discussed with reference to Fig. 3. Examples from the literature that exhibit the four types were shown.

REFERENCES

1. Vasudevan, A.K., Sadananda, K. and Louat, N., (1994), *Mater. Sci. Engrg*. 188, pp. 1-22.
2. Sadananda, K., and Vasudevan, A.K., (1993) in: *Fracture Mechanic,* Erodgan, R (Ed). ASTM-STP 1220, ASTM, 484-50.
3. Vasudevan, A.K. and Sadananda, K., (1995) *Met. Trans.A*, 26A, pp. 1221-34.
4. Sadananda, K. and Vasudevan, A.K., (1997) *Int. J. Fatigue*, 19, pp. S99-109.
5. Sadananda, K., Vasudevan, A.K., Holtz., R.L. and Lee, E.U., (1999) *Int. J. Fatigue*, 21, pp. S233-246.
6. Wei, R.P., and Simmons, G.W. (1981) *Int. J. Fracture*, 17, pp. 235-47
7. Stewart, A.T., (1980) *Engrg. Frac. Mech*., 13, pp. 463-78

Analysis of Fracture Mechanics and Fatigue Behavior for EC(T) Specimen

J.Z.LIU, X.R.WU, B.R.Hu and L.F.WANG
(Beijing Institute of Aeronautical Materials, Beijing 100095, China)

Abstract- In this paper, an approximate weight function (WF) for EC(T) specimen was given and verified. Using the WF, stress intensity factor and crack opening-displacement solutions for the specimen under pin loading and uniform pressure acting on the crack surface were obtained. The plastic-zone sizes from Dugdale model were calculated. Moreover, based on Dugdale model, a plasticity-induced crack-closure model for the specimen under fatigue loads was developed. Using the closure model, fatigue crack-closure behavior of the specimen was studied.

1. Introduction

Recently, an extended compact tension, EC(T), specimen, shown in Fig.1 has been developed for studying fatigue and fracture behavior of materials. The EC(T) specimen is considered an optimum design for laboratory fatigue-crack growth and fracture studies because of its distinct advantages compared to other cracked configurations, i.e. , standard compact tension, single-edge crack, and middle-crack tension specimens. These advantages are giving the experimenter additional working room, requiring low applied loads for an equivalent crack tip stress intensity factor, reducing the T-stress and crack fracture paths being self-similar, etc. [1]. The stress-intensity factor (SIF) solution and crack-surface opening displacements (CODs) at the crack mouth (x/c=0) and near the crack mouth (x/c=0.05) for the specimen under pin loading were derived by using the boundary-force method (BFM)[1,2]. Using an approximate method, the SIF solution for the specimen under pin loading was also obtained by Smith [3]. In this paper, following Smith's idea, an approximate crack surface weight function (WF) for the specimen is given. Using the weight function, SIF solution and CODs for the specimen under pin loading and uniform pressure acting on the crack surface are obtained. The plastic-zone sizes from Dugdale model are calculated. Moreover, based on Dugdale model, a plasticity-induced crack-closure model for the specimen under fatigue loads is developed. Using the closure model, fatigue crack-closure behavior of the specimen is studied.

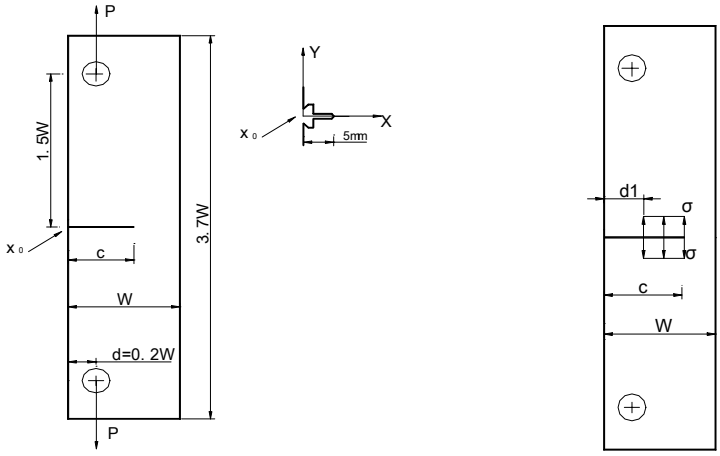

(a) (b)

Fig.1 Extended compact tension specimen (a). Pin loading and notch details, (b) Uniform segment pressure acting on the crack surface

2. Weight Function For EC(T) Specimen

The site of the load application is far enough away from the site of interest for the EC(T) specimen, the details of the method of load application are unimportant (colloquially, the principle of St. Venant).

Considering this and using the principle of superposition, Smith represented the EC(T) specimen with an edge-cracked long strip loaded by a direct remote end tension load, P, and end bending moment, M (where P is pin load and M=0.3PW) [3]. The SIF solutions by this method agree well with the results from Piasick, et al's BFM. Following this method, crack surface weight function of the EC(T) specimen is assumed to be equal to that of the edge-cracked long strip. That is [4],

$$m(\alpha,x)=\frac{1}{\sqrt{2\pi a}}\sum_{i=1}^{J+1}\beta_i(\alpha)\left(1-\frac{x}{a}\right)^{i-\frac{3}{2}} \tag{1}$$

where the $\beta_i(\alpha)$-function were given in [4,5].

3. SIFs and CODs under pin loading

3.1 SIF solutions

According to two-dimensional weight function theory, the stress intensity factor due to an arbitrary set of applied loads can be obtained by integrating over crack length a product of these loads with the weight function $m(\alpha,x)$ of the cracked body [4]:

$$K=\sqrt{W}\int_0^{\alpha}\sigma(x)m(\alpha,x)dx \tag{2}$$

where the term $\sigma(x)$ represents the stress distribution at the prospective crack site in the crack-free body. Under pin loading,

$$\sigma(x)=\frac{P}{BW}(2.8-3.6x) \tag{3}$$

Where P is pin loading, B and W are thickness and width of specimen, respectively. x=X/W. By substituting eqs(1) and (3) into eq(2), SIF solution can be gotten as follow:

$$K=\frac{P}{BW}\sqrt{\pi\alpha W}\,f(\alpha) \tag{4}$$

Where

$$f(\alpha)=\frac{2.8\sqrt{2}}{\pi}\sum_{i=1}^{5}\left[\frac{1}{2i-1}\beta_i(\alpha)\right]+\frac{7.2\sqrt{2}\alpha}{\pi}\sum_{i=1}^{5}\frac{\beta_i(\alpha)}{(2i-1)(2i+1)}$$

$$\alpha=c/W$$

Results from eq(4) and Piascik, et al's BFM[1,2] are given in Table 1, respectively, for comparison. Differences between the results are within 0.8%, very small. By fitting the their numerical solutions, Piasick ,et al got the following SIF expression:

$$K=\left[P\Big/\left(B\sqrt{W}\right)\right]F_{EC(T)} \tag{5}$$

Where

$$F_{EC(T)}=(2+\lambda)G\Big/\left[(1-\lambda)^{3/2}(1-d/W)^{1/2}\right]$$

$$G=1.15+0.94-2.48\lambda^2+2.95\lambda^3-1.24\lambda^4$$

$$\lambda=(c-d)/(W-d)$$

Where d is the distance from specimen edge to load line, d=0.2W here. For $0.1\le c/W\le 0.9$, eq(5) is within ±1.0 % of WF solutions.

3.2 COD solutions

The crack opening displacement between two crack surfaces can be computed by the following equation:

Where f(s) is the same as that of eq(4). $E'=E$ for plane stress and $E'=E/(1-\nu^2)$ for plane strain (E is

$$V(c,X)=2U(c,X)=\frac{2P}{E'B}\int_{\alpha_0}^{\alpha} f(s)\sqrt{\pi s}\,m(s,x)ds \tag{6}$$

Young's modulus and ν is Possion's ratio). $\alpha_0=X/W$.

Table 1 A comparison of normalized SIFs and crack-opening displacements under pin loading

C/W	$KBW^{1/2}/P$ (BFM)	$KBW^{1/2}/P$ (WF)	$E'BV_0/P$ (BFM)	$E'BV_0/P$ (WF)	$E'BV_1/P$ (BFM)	$E'BV_1/P$ (WF)
0.1	1.721	1.723	1.664	1.668	1.180	1.586
0.2	2.586	2.590	3.750	3.756	3.194	3.593
0.3	3.571	3.578	6.853	6.865	6.126	6.622
0.4	4.904	4.913	11.99	12.01	10 .96	11.68
0.5	6.907	6.919	21.33	21.34	19.74	20.93
0.6	10.25	10.28	40.30	40.20	37.59	39.71
0.7	16.67	16.73	85.51	84.76	80.21	84.20
0.8	32.21	32.39	227.6	222.3	214.5	221.7
0.84	45.90	46.25	379.4	367.3	358.2	366.6

Normalized displacements (E'BV/P) at crack mouth V_0(X/W=0.) and near the crack mouth V_1(X/c=0.05) from WF and BFM[1,2] , respectively, are also summarized in Table 1 as a function of c/W for comparison. For V_0, WF solutions are within 3.2% of the BFM's results. For V_1, WF solutions agree with those of BFM at 0.2<c/W≤0.84 (Error is within 8%). However, at c/W=0.1, WF solution is obviously different from that of BFM.

By fitting WF solutions, crack-surface-opening displacement expression under pin loading is obtained as follows:

$$V(c,X)=\frac{4P}{BE'}\sqrt{\frac{c-X}{2\pi W}}\left(A_0+A_1\left(1-\frac{X}{c}\right)+A_2\left(1-\frac{X}{c}\right)^2\right)F_{EC(T)} \tag{7}$$

Where $F_{EC(T)}$ is the same as that in eq(5)

$$A_0=0.150963+17.9227\alpha-85.4395\alpha^2+290.424\alpha^3-446.149\alpha^4+294.546\alpha^5$$
$$A_1=-10.0527+146.658\alpha-841.639\alpha^2+2358.52\alpha^3-3209.77\alpha^4+1767.36\alpha^5$$
$$A_2=0.874432-15.5152\alpha+114.107\alpha^2-382.732\alpha^3+599.264\alpha^4-369.882\alpha^5$$

When 0.2≤c/W≤0.7, eq(7) is within ±0.4% of WF solutions. At c/W=0.8, the errors are within 13.2%.

The compliance method, that is, by means of measuring crack-mouth-opening displacement to monitor crack length, can be used during EC(T) fatigue crack growth testing. By fitting BFM's solutions, Compliance, in terms of crack length, is given by Piascik, et al [3] as follows:

$$E'BV_0/P=[15.52\alpha-26.38\alpha^2+49.7\alpha^3-40.74\alpha^4+14.44\alpha^5]/(1-\alpha)^2 \tag{8}$$

Where α=c/W. Equation (8) is within 0.3% of the same BFM numerical results, within 3% of the corresponding WF solutions aty 0<c/W≤0.9. By fitting WF numerical results, the following expression with high accuracy is given:

$$E'BV_0/P=[-0.0864736+17.1971\alpha-35.1958\alpha^2+71.6459\alpha^3-64.2242\alpha^4+22.5789\alpha^5]/(1-\alpha)^2 \tag{9}$$

Equation (9) is within 0.6% of the same WF solutions for 0.1≤c/W≤0.9.

4. SIFs and CODs under a segment of uniform pressure in the wake of crack tip

4.1 SIF Solutions

According to eq.(2), let σ(x)=σ, SIF expression for the specimen under a segment of uniform pressure in the wake of crack tip, as shown in Fig.1 (b), is derived as follows:

$$K = \sigma\sqrt{\pi\alpha W}\, f(\alpha) \tag{10}$$

Where

$$f(\alpha) = \frac{\sqrt{2}}{\pi}\sum_{i=1}^{5}\frac{1}{2i-1}\beta_i(\alpha)\left(1-\frac{d_1}{c}\right)^{i-1/2}, \qquad \alpha = c/w$$

and

$$\beta_1 = 2.0$$

$$\beta_2 = (1.06326 - 3.76571\alpha + 74.003\alpha^2 - 270.01\alpha^3 + 574.281\alpha^4 - 743.859\alpha^5 + 523.98\alpha^6 - 155.07\alpha^7)/(1-\alpha)^{3/2}$$

$$\beta_3 = (0.784116 + 8.8676\alpha - 112.136\alpha^2 + 567.975\alpha^3 - 1471.26\alpha^4 + 2164.99\alpha^5 - 1672.5\alpha^6 + 532.822\alpha^7)/(1-\alpha)^{3/2}$$

$$\beta_4 = (0.0381597 - 11.516\alpha + 127.158\alpha^2 - 628.338\alpha^3 + 1674.3\alpha^4 - 2507.3\alpha^5 + 1964.73\alpha^6 - 634.102\alpha^7)/(1-\alpha)^{3/2}$$

$$\beta_5 = (-0.224561 + 4.32355\alpha - 42.822\alpha^2 + 22.819\alpha^3 - 574.885\alpha^4 + 867.481\alpha^5 - 683.491\alpha^6 + 221.584\alpha^7)/(1-\alpha)^{3/2}$$

Equation (10) is within 0.06% of the corresponding WF numerical results at $0.1 \le c/W \le 0.8$ and $0 < d_1/c < 1$. d_1 is the distance from crack mouth to initiating load position.

4.2. COD solutions

The crack opening displacement between two crack surfaces for the specimen under a segment of uniform pressure in the wake of crack tip, as shown in Fig.1 (b), can be also computed by substituting f(s) in eq(10) into eq(6) and letting $a_0=d_1/W$ in eq.(6). The WF solutions of normalized COD for the specimen with several d1/c at c/W=0.2 and 0.8, are shown in Fig.2. Unfortunately, it is very difficult to get a COD expression with high accuracy by fitting the corresponding WF numerical solutions under this loading case.

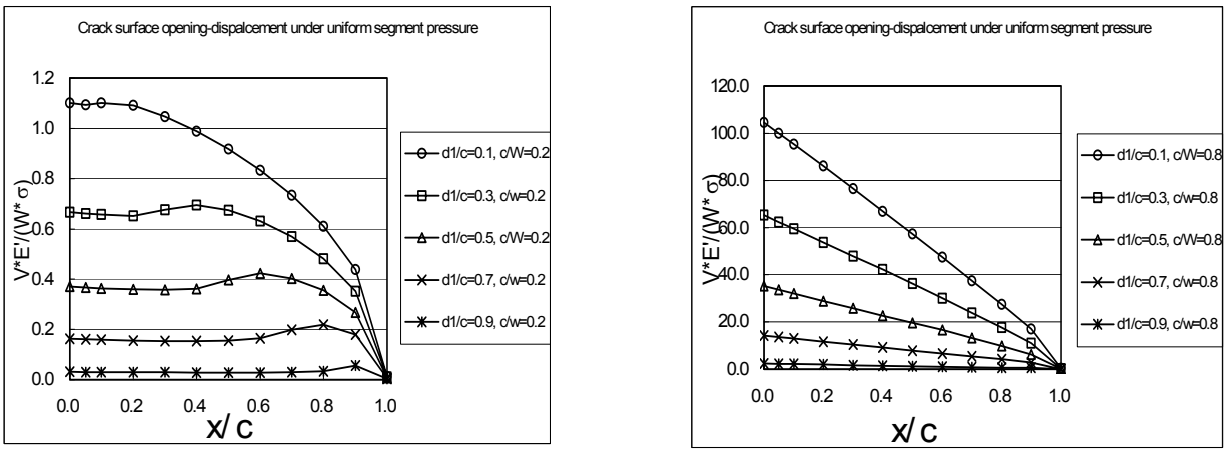

(a) (b)

Fig.2 Normalized crack-surface-opening displacement for EC(T) specimen with uniform pressure applied to crack wake for various d_1/c. (a) c/w=0.2, (b) c/W=0.8

5. Plastic-zone from Dugdale model for EC(T) specimen

The Dugdale model for EC(T) specimen requires that the "finiteness" condition of Dugdale be satisfied. This condition state that K at the tip of the plastic zone (at c+ρ) is zero. Thus,

$$\frac{P}{BW}\int_0^{\alpha}(2.8-3.6x)m(\alpha,x)dx=\int_{\alpha_0}^{\alpha}\sigma_0 m(\alpha,x)dx, \tag{11}$$

Where $\alpha=(c+\rho)/W$, $\alpha_0=c/W$, σ_0 is flow stress, which is taken to be an average of the yield and ultimate strength. By eq.(11), the plastic-zone size (ρ) is calculated for various c/W and $P/(BW\sigma_0)$ ratios. An equation is then fitted to these results and is

$$\frac{\rho}{a}=\frac{\pi W}{8c}\left(\frac{PF_{EC(T)}}{BW\sigma_0}\right)F_0 \tag{12}$$

Where

$$F_0=\left(\sum_{i=0}^{6}A_i\alpha^i\right)/(1-\alpha)^{3/2}$$

and A_0=1.2231, A_1 =-23.3888, A_2 =226.401, A_3 =-942.615, A_4 =2080.0, A_5 =-2301.44, A_6 =1036.04. Equation (12) is within 3% of the corresponding numerical results at $0.1\le c/W\le 0.8$ and $\rho/(W-c)\le 0.55$.

6. Fatigue crack closure behavior

Based on two dimensional weight function method, a new crack closure analytical model was developed by two of the present authors, Liu and Wu[4,5] in order to extend the Newman model to various cracked geometries. Following the method, using the weight function method as explained above, a crack closure model for EC(T) specimen was established. In the model, the applied stress level $P_o/(BW)$, at which the crack surfaces are fully open, is obtained on crack surface-opening displacement. To find the applied stress level needed to open the crack surface at any point, the displacement at that point due to an applied stress increment (Po-Pmin)/(BW) is set to equal to the displacement at that point due to the contact stresses at Pmin/(BW). Thus,

$$\left(\frac{P_o}{BW}\right)_i=\frac{P_{\min}}{BW}-\sum_{j=16}^{n}s_j g(x_i,x_j)/f(x_i) \qquad for \quad i=16 \quad to \quad n \tag{13}$$

Where $f(x_i)$ is the crack surface-opening displacement at the point x_i due to unit pin load P per unit thickness (B) and unit width (W). $g(x_i,x_j)$ is the displacement at the point x_j due to unit uniform stress acting on a segment of the crack surface with the center at x_i. n is the total number of elements modeling crack-tip plastic-zone and residual plastic deformation along the crack surface. The maximum value of $(P_o)_i$ gives the crack open load, P_o.

In this paper, EC(T) specimen is assumed to be made of 2024-T351 aluminum alloy. The mechanical properties of the material are UTS σ_u=457 MPa, yield stress σ_y=364Mpa, Young's modulus of elasticity E=69Gpa. Constraint factor, alf, ahead of crack tip is assumed to be equal to 1 and 1.73, respectively.

Normalized crack opening loads under different stress ratios and constraint factors were obtained by the model above, and are given in Fig.3. From the figure, it is found that obvious effect of both stress ratio and maximum stress on crack closure exists. Crack closure is more distinct under lower stress ratio. The effect of maximum stress on crack closure is significant at low stress ratio and small crack-tip constraint factor. These results can be used to explain fatigue crack growth behavior of EC(T) specimen at different stress ratio and specimen thickness.

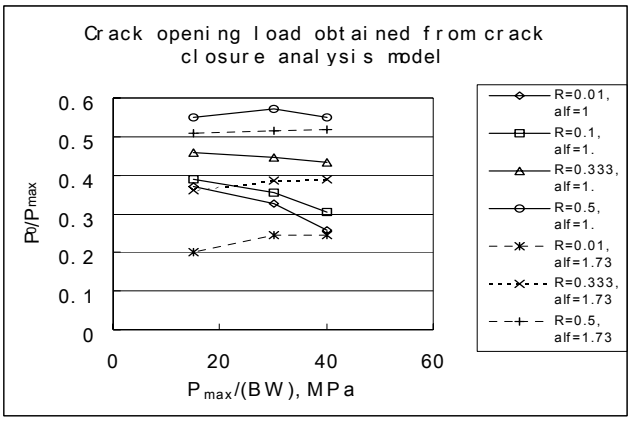

Fig.3. Normalized crack opening loads for EC(T) specimen made of 2024-T351 aluminum alloy under different stress ratios and constraint factors

7. Conclusions

(1) According to the principle of St. Venant, a crack-surface weight function of EC(T) specimen was assumed to be same as that of an edge-cracked long strip. Stress intensity factor and crack mouth opening-displacement solutions, obtained by using the WF, agreed well with the corresponding BFM's solutions. Thus, the WF is verified to be with high accuracy, can be used for EC(T) specimen.

(2) Using the WF, SIF and COD solutions of EC(T) specimen under pin loading and uniform pressure acting on the crack surface were obtained. The plastic-zone sizes based on Dugdale model were calculated. By fitting the numerical results, simple expressions with high accuracy were obtained for COD under pin loading, SIF under a segment of uniform pressure in the wake of crack tip, and the Dugdale plastic-zone size.

(3) A plasticity-induced crack-closure model for the specimen was developed. Using the model, fatigue crack closure behavior of the specimen was analyzed. The results showed that an obvious effect of both stress ratio and maximum stress on crack closure exists. Crack closure is more distinct at lower stress ratio. The effect of maximum stress on crack closure is significant at low stress ratio and small crack-tip constraint factor. These results can be used to explain fatigue crack growth behavior of EC(T) specimen at different stress ratio and specimen thickness.

References

[1] R.S.Piascik and J.C.Newman, Jr., An extended compact tension specimen for fatigue crack growth and fracture testing, Int. J. Fract., Vol.76: R43-R48, 1996

[2] R.S.Piascik, J.C.Newman, Jr and J.H.Underwood, The extended compact tension specimen, Fatigue Fract. Engng. Mater. Struct., Vol.20, No.4: pp.559-563, 1997

[3] R.A.Smith, Stress intensity factors for the extended compact tension specimen obtained by superposition, Fatigue Fract. Engng. Mater. Struct., Vol.20, No.4: pp.615-617, 1997

[4] X.R.Wu and A.J.Carisson, Weight functions and stress intensity factor solutions, Pergamon Press, 1991

[5] J.Z.Liu and X.R.Wu, Study on fatigue crack closure behavior for various cracked geometries, Engng. Fract. Mech., Vol.57, No.5, pp.475-491, 1997

[6] J.Z.Liu and X.R.Wu, Analysis of fatigue crack closure behavior for various cracked geometries, Key Engng. Mater., Vols.145-149, pp.691-698, 1998

[7] S.Mall and J.C.Newman, Jr., The Dugdale Model for compact specimen, ASTM STP868, pp.113-128, 1985

ORAL/POSTER REFERENCE: ICF100478OR

ANALYSIS OF MICROMECHANICAL TENSILE DAMAGE PROCESS FOR BRITTLE CERAMIC MATERIALS USING FEM

T. Niezgoda[1], J. Małachowski[1], Z. Smalko[2]

[1] Institute of Materials Science and Applied Mechanics, Military University of Technology
Kaliskiego Street 2, 00-908 Warsaw, Poland
[2] Warsaw University of Technology,
Pl. Politechniki 1, 00-661 Warsaw, Poland

ABSTRACT

The computer simulation of physical processes is one of the current directions of research development of body structures behaviour. The method, which was worked out (experimentally confirmed), gives an opportunity to analyse the same problems numerically, without expensive experiment. Recently the finite element method (FEM) has been used to investigate the above problems [1÷4]. The authors of this paper consider crack-face bridging, the stress field and the stress intensity factor ahead of the crack tip in the single-edge notched bend (SENB) ceramics specimen using FEM. In the FEM calculations the cohesive forces caused by the bridging effect were modelled using non-linear elastic springs. To solve this non-linear problem the incremental procedure was used. The results of this analysis are the stresses and displacements on the bridging crack and external load, which allow to compute the stress intensity factor and fracture energy.

KEYWORDS

Alumina ceramic, crack growth process, bridging effect, FEM simulation

INTRODUCTION

Ceramic materials exhibit several favourable properties (chemical inertness, high temperature capability, hardness stiffness and compressive strength, which make them products to be potentially employed in many different engineering applications. During the crack propagation in alumina ceramics a crack-border interaction zone develops directly behind the crack tip. In this zone, the two crack surfaces are not completely separated, and therefore, crack-surface interactions occur. The origin of this behaviour is well documented by authors [5,6] from the experimental point of view (see Figure 1): the microscopic observations of the crack path showed the existence of crack surface interactions and crack bridging due to serrated grains and unbroken ligaments. There is a compelling evidence of crack surface interaction by frictional tractions around bridging grains, which produces a strong toughening effect. To describe this kind of behaviour (two steps mechanism, see Figure 2) it is possible to use the bilinear softening curve. The curve responds to different mechanisms of energy

dissipation and takes into account the bridging effect of the fibres just behind the crack tip and refers to decohesion and pull out between fibres and matrix.

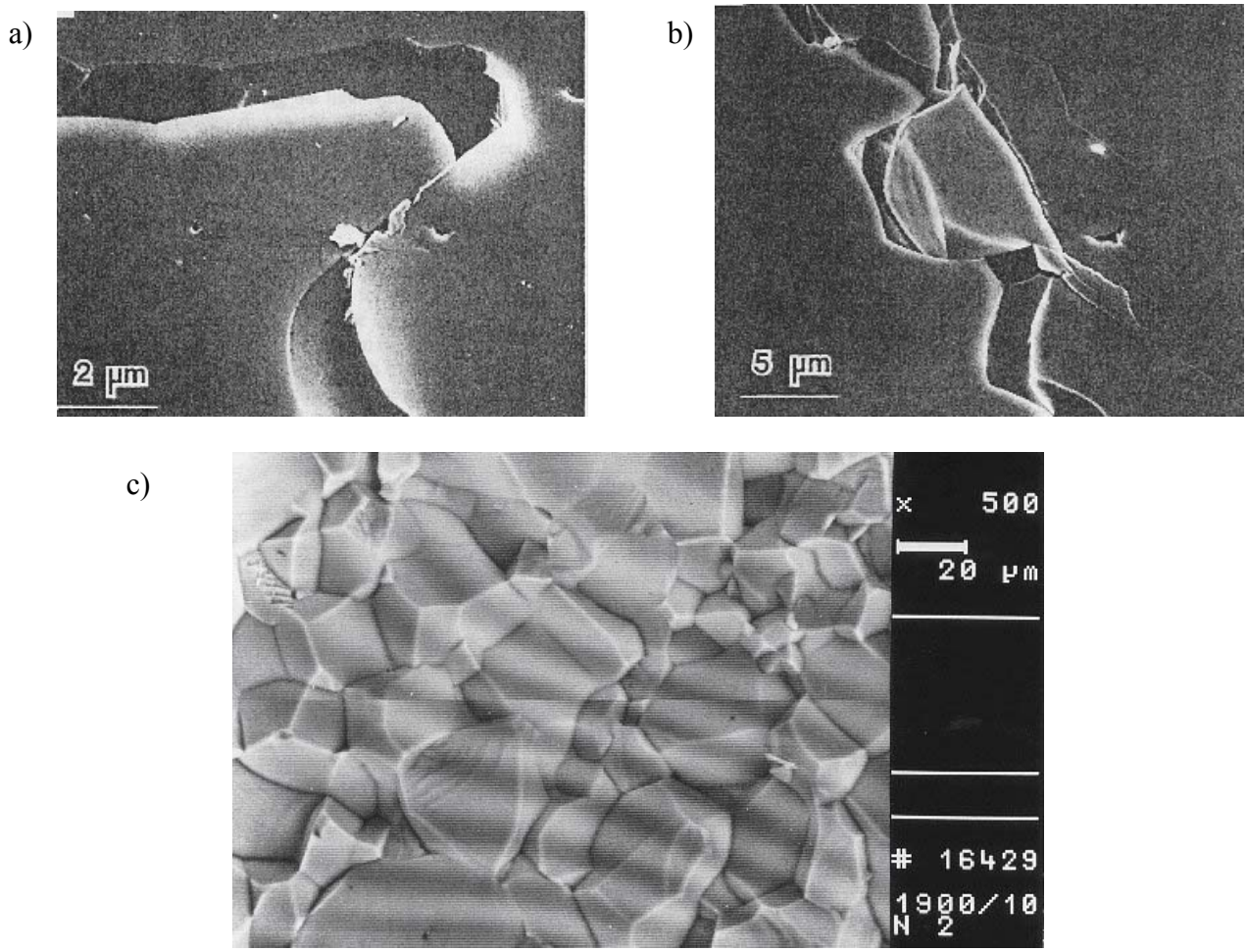

Figure 1: a) crack surface interactions process [5], b) crack bridging due to serrated grains [5] and c) view of the surface after fracture in Al_2O_3 ceramic

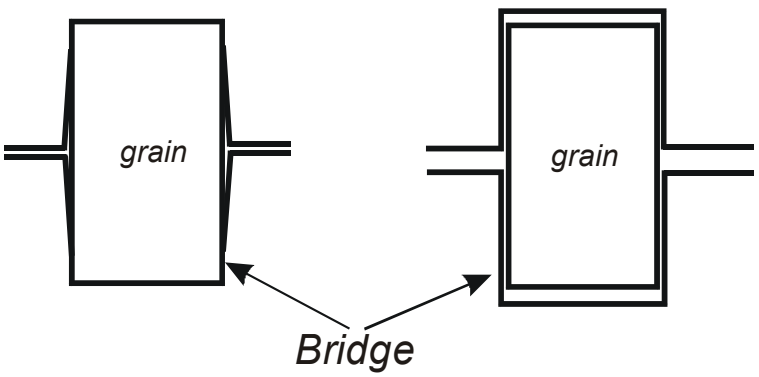

Figure 2: Two steps bridging process in ceramics:
a) break of a link between grain and matrix, b) pull out between grain and matrix

THEORETICAL FUNDAMENTALS

The theoretical analysis of crack growth process in alumina ceramic is described by authors [7÷11]. The algorithm of the analysis looks as follows. The existing interaction zone behind crack tip has capability to transmit stresses, which are called bridging stresses. The stresses transmitted due to the crack surface interactions are denoted by $\sigma_{br}(x)$, and they are superimposed by the external applied stresses resulting in:

$$\sigma(x) = \sigma_{appl}(x) - \sigma_{br}(x) \tag{1}$$

Authors of papers [7,10] indicated, that the stress intensity factor K_I for SENB loaded by stress distribution $\sigma(x)$ can be calculated using the fracture mechanical weight function method:

$$K_I = \int_0^a h\left(\frac{x}{a}, \frac{a}{W}\right)\sigma(x)\,dx \tag{2}$$

where h is the weight function depending on the geometry of the crack-component configuration. Integration of the equation proposed by Rice [12], which is presented as follows

$$h = \frac{H}{K_I}\frac{\partial\delta}{\partial a} \tag{3}$$

yields the crack opening displacements (COD) δ caused by stress σ. A detailed description was gathered from the handbook [13]. Taking into consideration the total stress (Eqn. 1) acting at the crack tip the obtained equation is as follows:

$$\delta = \frac{1}{H}\int_0^a \int_{\max(x,x')}^a h\left(\frac{a'}{W}, \frac{x}{a'}\right)h\left(\frac{a'}{W}, \frac{x'}{a'}\right)\left(\sigma_{appl} - \sigma_{br}\right)da'\,dx' = \delta_{00}\exp^{-1}\left(\sigma_{br}/\sigma_0\right) \tag{4}$$

where H = E (Young's modulus) for plane stress and H = E/(1-ν^2) (ν -Poisson's ratio) for plane strain, x is the coordinate of the displacement computed, x' is the location where the stress σ acts, δ_{00} and σ_0 are the fracture parameters [7,10]. The solution of the integral Eqn. 4 provides the distribution of the bridging stresses as the function of the stresses applied, and allows obtaining the stress intensity factor basing on the next equation:

$$K_{I\,tip} = K_{I\,appl} - K_{I\,br} \tag{5}$$

The evaluation of Eqn. 4 using successive approximation requires plenty of computer time. Authors of report [10] have prepared special strategies to limit the number of the computation.
The following procedure was applied to analyse the stress state and displacement of crack surface (COD) behind the crack tip in the single-edge notched bend (SENB) alumina ceramic specimen. The average grain size in analysed ceramic was 13 μm. The performed calculations provided the distribution of bridging stress as a function of crack opening displacement, see Figure 4a. The bridging crack intensity factor K_{Ibr} was obtained, see Figure 4b.

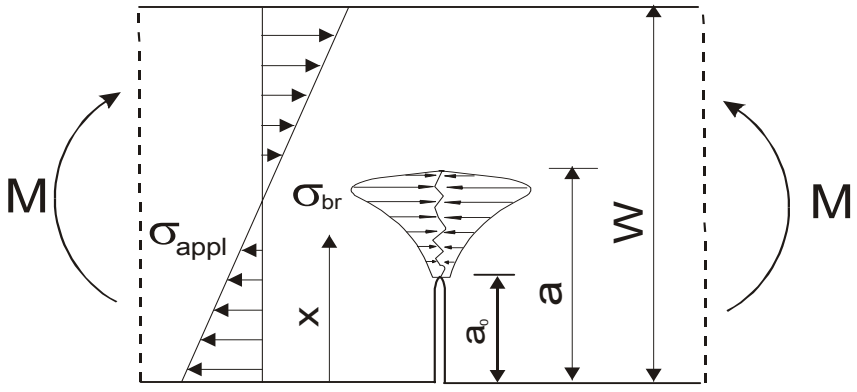

Figure 3: Crack starting from a notch in a bending test [7,10]

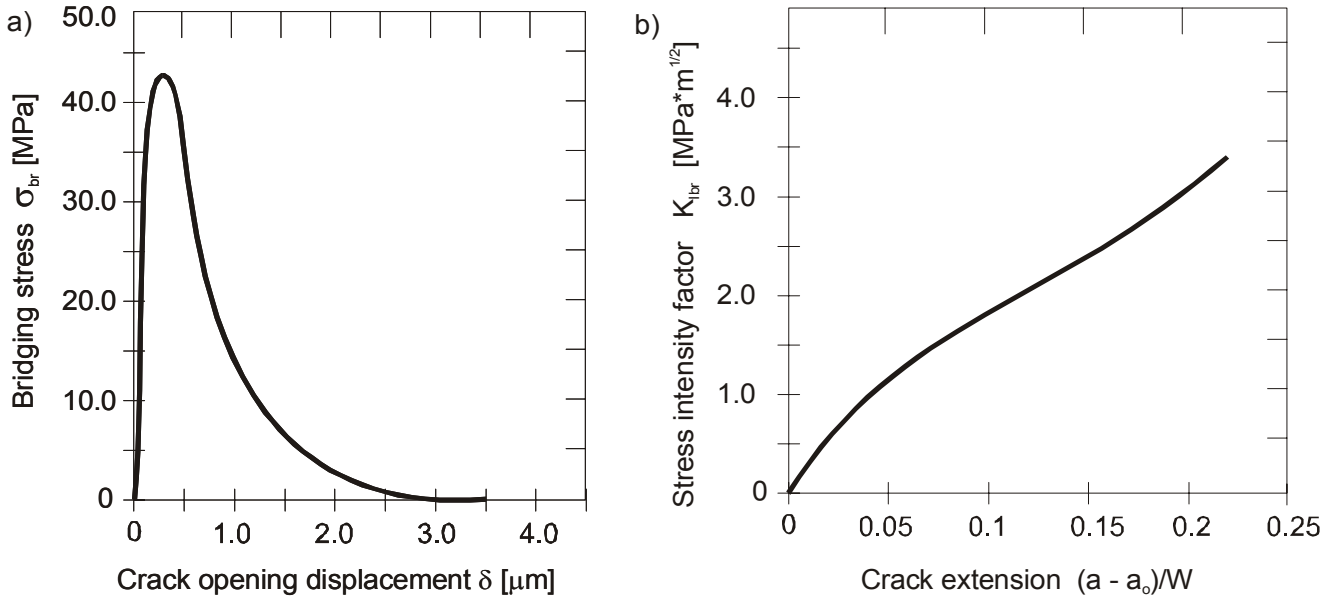

Figure 4: a) Distribution of bridging stress
and b) bridging stress intensity factor as a function of crack extension

NUMERICAL METHOD

The Finite Element Method was applied to crack growth process simulation in alumina ceramic. The structure's deformation under consideration is localised within the crack. The relationship between the crack opening displacement (COD) δ and the transferred stresses σ by bridging effect was described using the softening curve (see Figure 5). The authors of papers [9,11] indicated, that the curve must always fit some conditions. Firstly, when $\delta = 0$, the stresses transferred through the crack have to be equal to σ_c. Secondly, there is a critical value of δ, named δ_c, defined as follows if $\delta \geq \delta_c$ then $\sigma = 0$. Finally, the area under the softening curve is the fracture energy G_F, that is the energy needed by the unit area to create a new separated surface. The parameter σ_c was obtained from the three point bending test for the bars without the notch, and performed from the alumina ceramics being analysed. The value of the parameter σ_c is given in the Table 1. The critical value of the crack opening displacement δ_c was measured by the authors [9] for different grain size polycrystalline alumina. The authors have found out that it is equal to one quarter of the mean a grain size.

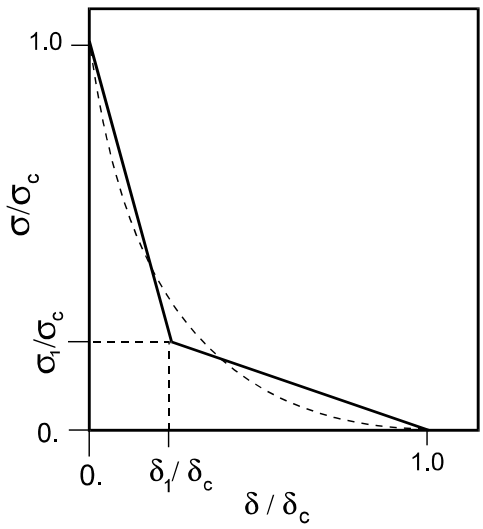

Figure 5: Strain softening curve (— bilinear, ---- exponential) [11]

The behaviour of the material behind the crack tip (influence between the newly separated surfaces due to the existing cohesive forces) was modelled using non-linear elastic springs. The profile of the

curve (relation force-displacement) was obtained basing on formula presented in papers [4,11]. Numerical model of the three-point bending bar was performed from 8-nodes plain stress elements. Due to the body symmetry (see Figure 6) one-half of the bar was analysed only.

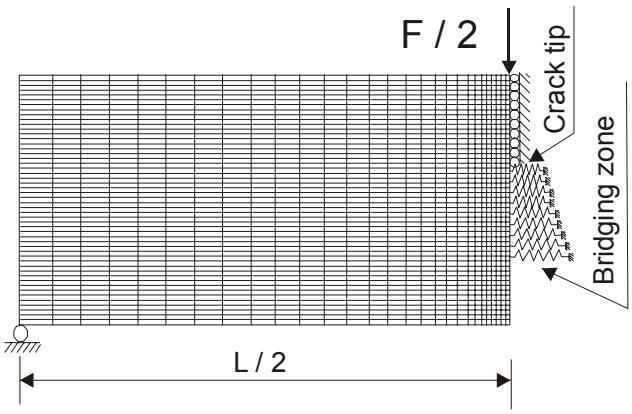

Figure 6: Finite element model with crack-face bridging during modelling crack growth process

TABLE 1
SOFTENING CURVE PARAMETERS FOR ALUMINA CERAMICS

Mean grain size (μm)	σ_c (MPa)	δ_c (μm)	σ_1 (MPa)	δ_1 (μm)
13	200	3.25	18.06	0.4

A finite element model for crack bridging systems has been proposed and performed in this work on the basis of the results from single-edge notch bend experiment. Existing in the process of the crack propagation bridging effect was modelled using non-linear springs elements (see Figure 6). It was used the incremental procedure to solving this problem. The results of this analysis are stresses and displacements on the bridging crack and external load. A numerical simulation of crack growth shows that the stress bridging zone movies along the crack, behind the crack tip.
Basing on obtained results the stress intensity factor was calculated and than R-curve was created. Typical profile of R-curve with existing toughening effect is presented on Figure 7. Bridging zone causes the increase of stress intensity factor ΔK_{Ibr}.
Initial value of stress intensity factor for analysed ceramics equals $K_I \approx 2{,}95$ MPa×m$^{1/2}$ (see Figure 8). From the performed calculations for alumina ceramics with different grain sizes it was apparent, that the value of K_I is strongly depended on grain size in analysed material. The values obtained from numerical analysis are in a good agreement with results, which were described by the authors [1,7,10].

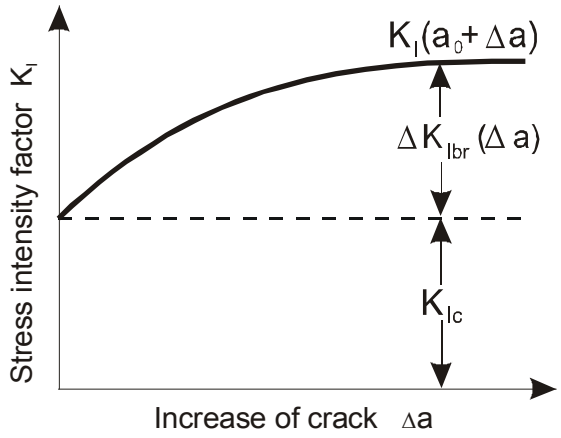

Figure 7: A profile of R-curve for materials with existing toughening effect (for instance bridging zone behind crack tip) [1]

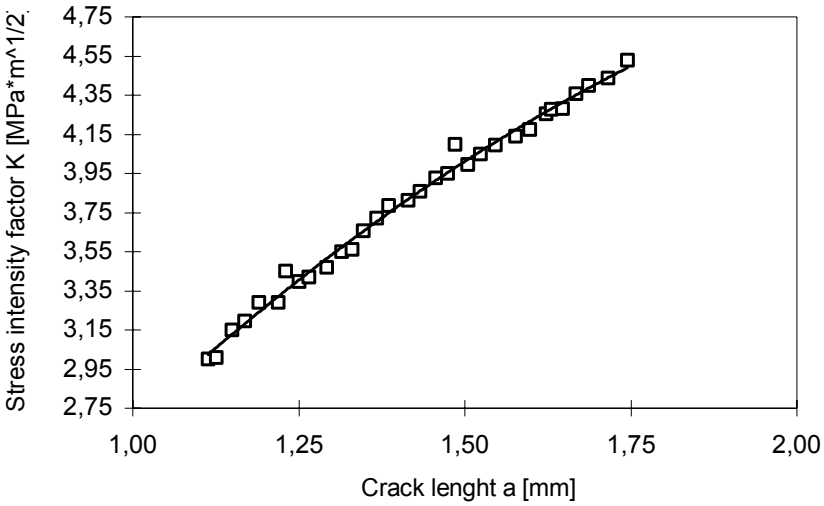

Figure 8: *R-curve* for alumina ceramics

SUBMISSION

The method of numerical analysis with the use of FEM proposed in this paper allows for reduction of analytical computation, which was presented in this paper. From the macroscopic point of view we have possibility take into consideration the effect, which appeared in the microstructure of alumina ceramics during the crack growth (bridging effect). This numerical method permits to analyse much more complex structures with real loading. There is also a possibility to obtain R-curve for alumina ceramic (see Figure 8).

Acknowledgements
We would like to express our gratitude to Dr. Marek Boniecki from Institute of Electronics Materials Technology in Warsaw for carrying out the experiment.

References

1. Cao, J.W., Sakai, M., (1996). *J. Mater. Res.*, Vol. 11, No. 6.
2. Sakaida, Y., Okada, A., Tanaka, K. and Yasutomi, Y., (1998). *Proceedings of the 9th CIMTEC Ceramics Congress and Forum on New Materials*, Florence, Italy.
3. Niezgoda, T., Małachowski, J. and Boniecki, M., (1998). *Ceramics International*, 24 pp. 359-364.
4. Niezgoda, T., Małachowski, J. and Boniecki, M., (1998). *Proceedings of the 9th CIMTEC Ceramics Congress and Forum on New Materials*, Florence, Italy.
5. Swanson, P. L., Fairbanks, C. J., Lawn, B. R., Mai, Y., Hockey, B. J. (1987). *J. Am. Ceram. Soc.* 70 [4], pp. 279-289.
6. Thouless, M. D. and Evans, A. G. (1988). *Acta metall.* Vol. 36, No. 3, pp. 517-522.
7. Fett, T. and Munz, D. (1993). *J. Mater. Sci*., 28 pp. 742-752.
8. Fett, T., (1996). , *Eng. Fract. Mech.*, Vol. 53 No. 3.
9. Reichl, A. and R. W. Steinbrech, R. W. (1988). *J. Am. Ceram. Soc.,* 71 [6] C-299-C-301.
10. Fett, T. and Munz, D. (1990). *Evaluation of R-curves in ceramic materials based on bridging interactions*, Kfk-Report 4940, Kernforschungszentrum Karlsruhe.
11. Llorca, J. and Steinbrech, R. W. (1991). *J. Mater. Sci.,* 26 pp. 6383-6390.
12. Rice, J. R. (1972). *Int. J. Solids Structures,* 8, pp. 751-758.
13. Tada, H., Paris, P.C. and Irwin, G. R. (1985). The Stress Analysis of Cracks Handbook, Del Research Corporation, St. Louis, Missouri.

ORAL/POSTER REFERENCE: ICF100936OR

ANALYSIS OF SUBSONIC INTERFACIAL FRACTURE USING STRAIN GAGES IN AN ISOTROPIC-ORTHOTROPIC BIMATERIAL

Vittorio Ricci[1], Kwang Ho Lee[2], Arun Shukla[3], and Vijay Chalivendra[3]

[1] Naval Undersea Warfare Center Division, Newport, RI 02841, USA
[2] Sangju National University, Republic of Korea
[3] Department of Mechanical Engineering, University of Rhode Island, Kingston, RI 02881, USA

ABSTRACT

An experimental study has been conducted in which strain fields were used to investigate the behavior of subsonic crack propagation along the interface of an isotropic-orthotropic bimaterial system. Strain field equations were developed from available field equations and critically evaluated in a parametric study to identify optimum strain gage location and orientation. Bimaterial specimens were prepared with PSM-1 polycarbonate and Scotchply® 1002 unidirectional, glass-fiber-reinforced, epoxy composite. Dynamic experiments were conducted using these specimens with strain gages mounted on the composite half to obtain values of the dynamic complex stress intensity factor (CSIF), $\mathbf{K^d} = K_1^d + iK_2^d$, in the region of the crack tip while photoelasticity was used on the PSM-1 half. Results show that the trend and magnitude of $\mathbf{K^d}$ obtained using strain gages compare favorably with those obtained using photoelasticity. Therefore, it is feasible to use strain gages to investigate interfacial crack propagation in isotropic-orthotropic bimaterials.

KEYWORDS

Strain gages, bimaterials, interface, orthotropic, fracture, subsonic crack propagation

INTRODUCTION

Because of their low cost and ease of use, the strain gage remains the predominant measuring device in industry. Thus, the development of strain gage techniques in bimaterial problems would greatly facilitate the analysis of such problems for practical application. Strain gage methods have been used in fracture research conducted on isotropic materials [1,2] and in orthotropic materials [3,4]. Substantial progress has been made in the study of dynamic interfacial fracture. Yang *et al.* [5] provided the asymptotic structure of the most singular term of the steady-state elastodynamic interfacial crack-tip fields. Deng [6,7] obtained a complete series solution for the stress field around a crack-tip for steady-state interface crack propagation. Liu *et al.* [8] provided a more general higher-order asymptotic analysis for unsteady interface crack propagation that accounted for transient effects. They also conducted experiments to support the need of such an analysis. Tippur and Rosakis [9] performed the earliest experimental study on dynamic crack initiation and growth in bimaterials. Lee *et al.* [10] developed the field equations for an orthotropic bimaterial. Lee [11] subsequently developed the field equations for an isotropic-orthotropic bimaterial.

To date, work on isotropic-orthotropic bimaterials and interface fracture using strain gages is limited at best. Ricci *et al.* [12] used strain gages and photoelastic techniques to evaluate interface fracture parameters in bimaterials under quasi-static loads. Thus, this study focuses on developing strain field equations and critically examining them via experimentation to demonstrate the feasibility of the strain gage method.

STRAIN FIELDS AROUND AN INTERFACIALLY PROPAGATING CRACK TIP

Crack growth along a bimaterial interface is generally referenced with respect to the material properties of the more compliant material, Material 1. (Material 2 is the stiffer material.) Crack propagation is considered subsonic for crack-tip velocities, v, below the shear wave velocity, c_s, of the more compliant material. From the governing equations for subsonic crack growth [5], the crack-tip stress field was found to be a coupled oscillatory field scaled by the dynamic complex stress intensity factor (CSIF), $\mathbf{K^d}$:

$$\sigma_{ij} = \frac{Re\left\{K^d\, r^{i\varepsilon(v)}\right\}}{\sqrt{2\pi r}}\,\tilde{\sigma}^1{}_{ij}(\theta, v) + \frac{Im\left\{K^d\, r^{i\varepsilon(v)}\right\}}{\sqrt{2\pi r}}\,\tilde{\sigma}^2{}_{ij}(\theta, v) \tag{1}$$

where r, θ are polar coordinates of a coordinate system translating with the crack tip at speed v, $\mathbf{K^d} = K_1{}^{\mathrm{d}} + iK_2{}^{\mathrm{d}}$ is the dynamic CSIF, and $\tilde{\sigma}^1{}_{ij}$ and $\tilde{\sigma}^2{}_{ij}$ are real, dimensionless angular functions [5]. The oscillatory index ε, which is the dynamic material mismatch parameter, is a function of crack tip speed ($\varepsilon = \varepsilon(v)$):

$$\varepsilon = \frac{1}{2\pi} \ln \frac{1-\beta}{1+\beta} \tag{2}$$

where, β is the generalized Dundurs' parameter [7,8].

Using existing field equations for subsonic crack propagation in an isotropic-orthotropic bimaterial [11], the strain field equations were developed. For the orthotropic material (Material 2):

$$\begin{aligned}(\varepsilon_x)_2 = {} & \frac{K_I}{2\sqrt{2\pi r}D_2\cosh(\varepsilon\pi)}\left\{p_l\left[e^{-\varepsilon(\pi+\theta_l)}\overline{A_2}\cos\left(\varepsilon\ln\frac{r_l}{a}-\frac{\theta_l}{2}\right)+e^{\varepsilon(\pi+\theta_l)}A_2\cos\left(\varepsilon\ln\frac{r_l}{a}+\frac{\theta_l}{2}\right)\right]f_l(\theta) - p_s\left[e^{-\varepsilon(\pi+\theta_s)}\overline{B_2}\cos\left(\varepsilon\ln\frac{r_s}{a}-\frac{\theta_s}{2}\right)+e^{\varepsilon(\pi+\theta_s)}B_2\cos\left(\varepsilon\ln\frac{r_s}{a}+\frac{\theta_s}{2}\right)\right]f_s(\theta)\right\} \\ & + \frac{K_{II}}{2\sqrt{2\pi r}D_2\cosh(\varepsilon\pi)}\left\{-p_l\left[e^{\varepsilon(\pi+\theta_l)}\overline{A_2}\sin\left(\varepsilon\ln\frac{r_l}{a}-\frac{\theta_l}{2}\right)+A_2\sin\left(\varepsilon\ln\frac{r_l}{a}+\frac{\theta_l}{2}\right)\right]f_l(\theta) + p_s\left[e^{-\varepsilon(\pi+\theta_s)}\overline{B_2}\sin\left(\varepsilon\ln\frac{r_s}{a}-\frac{\theta_s}{2}\right)+B_2\sin\left(\varepsilon\ln\frac{r_s}{a}+\frac{\theta_s}{2}\right)\right]f_s(\theta)\right\}\end{aligned} \tag{3a}$$

$$\begin{aligned}(\varepsilon_y)_2 = {} & \frac{K_I}{2\sqrt{2\pi r}D_2\cosh(\varepsilon\pi)}\left\{pq_l\left[e^{-\varepsilon(\pi+\theta_l)}\overline{A_2}\cos\left(\varepsilon\ln\frac{r_l}{a}-\frac{\theta_l}{2}\right)+e^{\varepsilon(\pi+\theta_l)}A_2\cos\left(\varepsilon\ln\frac{r_l}{a}+\frac{\theta_l}{2}\right)\right]f_l(\theta) - qq_s\left[e^{-\varepsilon(\pi+\theta_s)}\overline{B_2}\cos\left(\varepsilon\ln\frac{r_s}{a}-\frac{\theta_s}{2}\right)+e^{\varepsilon(\pi+\theta_s)}B_2\cos\left(\varepsilon\ln\frac{r_s}{a}+\frac{\theta_s}{2}\right)\right]f_s(\theta)\right\} \\ & + \frac{K_{II}}{2\sqrt{2\pi r}D_2\cosh(\varepsilon\pi)}\left\{-pq_l\left[e^{-\varepsilon(\pi+\theta_l)}\overline{A_2}\sin\left(\varepsilon\ln\frac{r_l}{a}-\frac{\theta_l}{2}\right)+A_2\sin\left(\varepsilon\ln\frac{r_l}{a}+\frac{\theta_l}{2}\right)\right]f_l(\theta) + qq_s\left[e^{-\varepsilon(\pi+\theta_s)}\overline{B_2}\sin\left(\varepsilon\ln\frac{r_s}{a}-\frac{\theta_s}{2}\right)+B_2\sin\left(\varepsilon\ln\frac{r_s}{a}+\frac{\theta_s}{2}\right)\right]f_s(\theta)\right\}\end{aligned} \tag{3b}$$

$$\begin{aligned}(\gamma_{xy})_2 = {} & \frac{K_I a_{66}}{4\sqrt{2\pi r}D_2\cosh(\varepsilon\pi)}\left\{\alpha_l\left[e^{-\varepsilon(\pi+\theta_l)}\overline{A_2}\sin\left(\varepsilon\ln\frac{r_l}{a}-\frac{\theta_l}{2}\right)-e^{\varepsilon(\pi+\theta_l)}A_2\sin\left(\varepsilon\ln\frac{r_l}{a}+\frac{\theta_l}{2}\right)\right]f_l(\theta) - \alpha_s\left[e^{-\varepsilon(\pi+\theta_s)}\overline{B_2}\sin\left(\varepsilon\ln\frac{r_s}{a}-\frac{\theta_s}{2}\right)-e^{\varepsilon(\pi+\theta_s)}B_2\sin\left(\varepsilon\ln\frac{r_s}{a}+\frac{\theta_s}{2}\right)\right]f_s(\theta)\right\} \\ & + \frac{K_{II}a_{66}}{4\sqrt{2\pi r}D_2\cosh(\varepsilon\pi)}\left\{\alpha_l\left[e^{-\varepsilon(\pi+\theta_l)}\overline{A_2}\cos\left(\varepsilon\ln\frac{r_l}{a}-\frac{\theta_l}{2}\right)-e^{\varepsilon(\pi+\theta_l)}A_2\cos\left(\varepsilon\ln\frac{r_l}{a}+\frac{\theta_l}{2}\right)\right]f_l(\theta) - \alpha_s\left[e^{-\varepsilon(\pi+\theta_s)}\overline{B_2}\cos\left(\varepsilon\ln\frac{r_s}{a}-\frac{\theta_s}{2}\right)-e^{\varepsilon(\pi+\theta_s)}B_2\cos\left(\varepsilon\ln\frac{r_s}{a}+\frac{\theta_s}{2}\right)\right]f_s(\theta)\right\}\end{aligned} \tag{3c}$$

where the coefficients, defined by Lee [11], are given as

$$A_2 = \alpha_S + (1+M_a)\eta \;,\; \overline{A_2} = \alpha_S - (1+M_a)\eta$$
$$B_2 = \alpha_l + (1+M_a)\eta \;,\; \overline{B_2} = \alpha_l - (1+M_a)\eta$$

Eqn. 3 completely describes the two-dimensional strain field for the orthotropic half and were used in a parametric study of the strains near the interfacial crack tip. To determine the strain at a gage rotated θ_g degrees from the x-axis, a coordinate transformation is done accordingly:

$$\varepsilon_{x'x'} = \varepsilon_{xx}\cos^2\theta_g + \varepsilon_{yy}\sin^2\theta_g + \gamma_{xy}\cos\theta_g\sin\theta_g \tag{4}$$

Eqn. 4 may be rewritten in terms of K_1^d and K_2^d. Then, substituting for the coefficients of K_1^d and K_2^d as C_1 and C_2, respectively, yields

$$\varepsilon_{x'x'} = C_1\left(\varepsilon, r, \theta, \theta_g, v\right)K_1^d - C_2\left(\varepsilon, r, \theta, \theta_g, v\right)K_2^d \tag{5}$$

The strain equations have three unknowns: K_1^d, K_2^d, and velocity v. The velocity is obtained experimentally by taking crack-tip position with respect to time; this is discussed below in the experiment section of this paper. The remaining two unknowns then require two strain measurements taken at the same time. Then, Eqn. 5 can be solved for K_1^d and K_2^d from two measured strains, $\varepsilon^{(1)}$ and $\varepsilon^{(2)}$; the superscript indicates the gage. Thus, the components of the complex stress intensity factor, K_1^d and K_2^d, are given as

$$K_1^d = \frac{C_2^{(2)}\varepsilon^{(1)} - C_2^{(1)}\varepsilon^{(2)}}{C_2^{(2)}C_1^{(1)} - C_2^{(1)}C_1^{(2)}} \qquad K_2^d = \frac{C_1^{(2)}\varepsilon^{(1)} - C_1^{(1)}\varepsilon^{(2)}}{C_2^{(2)}C_1^{(1)} - C_2^{(1)}C_1^{(2)}} \tag{6}$$

PARAMETRIC INVESTIGATION

A parametric study was conducted to understand the development of the strain field close to the crack tip. Subsequently, this information was used to optimize the location and orientation of the strain gages for the development of strain gage techniques used in this study to obtain the dynamic complex stress intensity factor $\mathbf{K^d}$ from a propagating interfacial crack.

Strain Gage Location

The effect of the dynamic CSIF, $\mathbf{K^d}$, on the strain fields was examined to determine the optimum locations for the strain gages. The bimaterial system chosen for this parametric study was PSM-1 polycarbonate and Scotchply 1002 unidirectional, glass-fiber-reinforced, epoxy composite. This bimaterial has a relatively high material mismatch, ε, on the order of 0.12. The material properties are given in Table 1. Also, it is noted that the fiber orientation angle, α, is the angle between the fiber direction and the x-axis (i.e. the interface).

TABLE 1
MECHANICAL PROPERTIES USED IN BIMATERIAL SPECIMENS

Property	**PSM-1***	**Scotchply® 1002****
Young's Modulus, E (GPa)	2.76	$E_L = 30$ $E_T = 7.0$
Poisson's Ratio, ν	0.38	$\nu_{LT} = 0.25$
Density, ρ (kg/m^3)	1200	1860
Material Fringe Value, f_σ (kN/m/fringe)	7.0	

* Manufactured by Measurements Group, Raleigh, NC, USA
** 3M® unidirectional, glass-fiber-reinforced epoxy

Since the crack travels along the interface, the position of the gages would be set at a distance of one half the plate thickness ($y \geq 0.5B$) from the interface. This satisfies the plane stress condition as well as avoids difficulties introduced by the plastic zone at the crack tip. This would also ensure that the gages would be within the singularity-dominated region such that the singular strain field solutions are valid.

Effects of Mixity and Velocity on the Strain Gage Orientation

Eqn. 4 above was used to study the strain fields around a propagating interfacial crack. To determine the optimal strain gage orientation angle, θ_g, a method was developed to examine the theoretical strain profiles of an interfacially propagating crack as sensed by a nearby strain gage. The strain gage profiles would be compared for various gage angles over suitable mixity, ϕ, and velocity, v, domains. (*Mixity* is the relative

strength K_2^d to K_1^d.) For given values of mixity and velocity, it was noted that, as θ_g was changed, the peak of the strain profile relative to the gage would shift along the interface (i.e. the x-axis). In this case, the coordinate system is fixed with respect to the gage with the y-axis passing through the center of the gage (i.e. x = 0 is on the interface directly below the gage – referred to hereafter as the *gage datum*). The crack tip propagates along the interface in the positive x-direction. Thus, θ_g could be selected such that the peak strain occurs when the crack tip is at or very near gage datum. Figure 1 illustrates the crack-tip position at peak strain as a function of mixity for varying velocity for $\theta_g = 55^o$ and $\alpha = 0^o$.

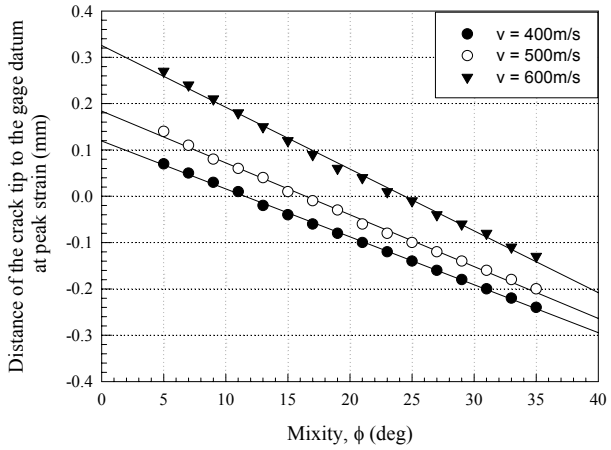

Figure 1. Location of crack tip relative to gage datum for varying mixity and velocity ($\theta_g = 55^o$; $\alpha = 0^o$).

For a given velocity, the crack tip position varies just 0.3 mm over the range of mixities. From preliminary model experiments, values for mixity were expected in the range of 10 to 30 degrees and velocity in the range of 500 to 600 m/s. That means the expected crack tip position would vary just 0.2 mm. It was further found that changes in θ_g result in the curves shifting significantly relative to gage datum. Thus, it is clear that the crack tip position is relatively insensitive to mixity and velocity and greatly influenced by θ_g. For fiber orientation angle, α, = 0^o, θ_g is 55^o, and for α, = 90^o, θ_g is 100^o.

Crack-Tip Position Uncertainty and Strain Error

The error in the complex stress intensity components, K_1^d and K_2^d, induced by an error in crack-tip position was investigated. By varying the crack-tip position from –1.0 to 1.0 mm around the gage datum, it was found that the variation in K_1^d is less than two percent and for K_2^d less than three percent. Ricci *et al*. [12] examined averaging error in the case of quasi-static loading as a function of radius and gage angle for various values of K_1^d and K_2^d for a Micromeasurements, Inc., USA, model CEA-06-015UW-120 strain gage, the same gage to be used in this study. It was found that for $r \geq 0.4B$, the averaging error was less than 0.2%. Similar error is assumed in the experiments herein.

EXPERIMENTAL PROCEDURE

The parametric study was followed by experimentation, in which strain gage techniques were used to obtain values of $\mathbf{K}^d$ from a propagating crack as it passed a series of strain gages. Results from the strain gage data were then compared to results obtained from photoelastic data conducted as part of these experiments.

Setup and Procedure

Experiments were designed and conducted using a PSM-1/Scotchply single edge notch tension (SENT) bimaterial specimen, shown in Figure 2. Four strain gages were mounted on the Scotchply half at an angle of 55^o ($\alpha = 0^o$) or 100^o ($\alpha = 90^o$) and 5 mm above the interface. The gages were hooked up to a Lecroy high-

frequency digitizer, which recorded the interface fracture data at a rate of 1 MHz. The specimen was placed into a Vishay loading frame and loaded until fracture.

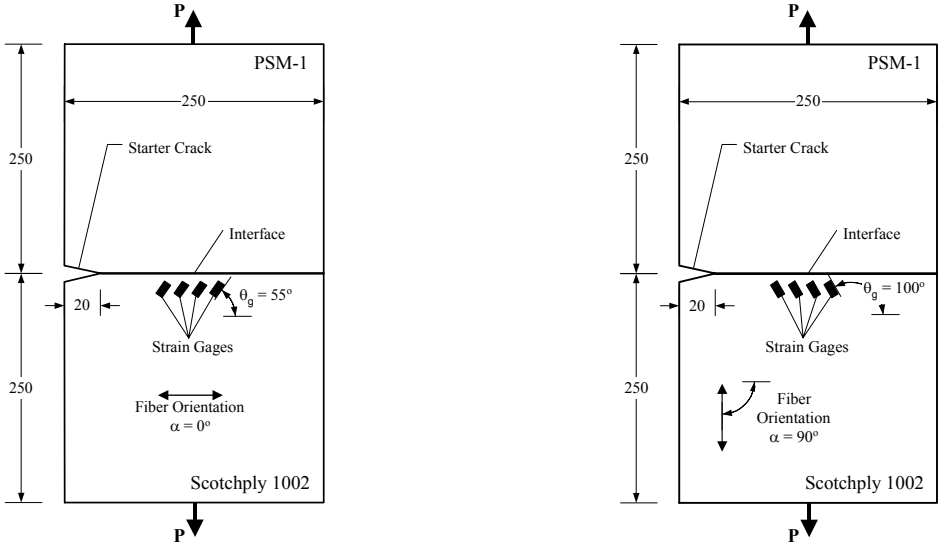

Figure 2. Single edge notch tension (SENT) bimaterial specimen: a) $\alpha = 0^o$ b) $\alpha = 90^o$.

RESULTS AND DISCUSSION

Experiments were conducted on the PSM-1/Scotchply bimaterial specimen described above. Figure 3 shows the experimental data obtained from an $\alpha = 0^o$ experiment. Figure 3a shows the strain gage data: four pulses that correspond to the four gages as the crack passed by. Assuming that the peak strain occurs when the crack is at gage datum, the crack-tip velocity, v, was determined to be 600 m/s, leaving just two unknowns: K_1^d and K_2^d. Figure 3b shows a frame of photoelastic data from the same experiment.

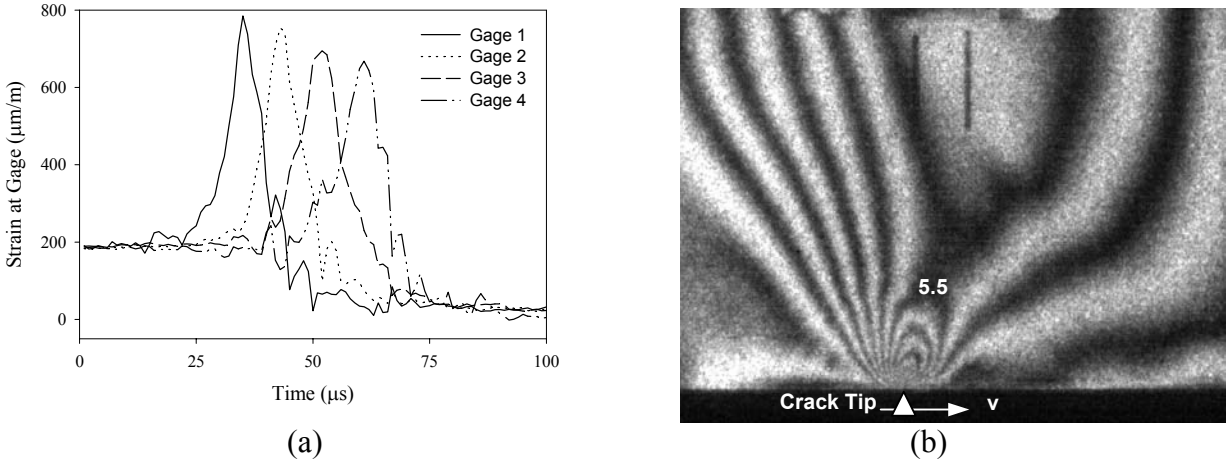

Figure 3. Experimental data from a propagating interfacial crack for $\theta_g = 55^o$ and $\alpha = 0^o$: a) Gage data showing strain pulses and b) Isochromatic fringes.

Using Eqn. 5, the strain gage data were analyzed to determine the magnitude of the CSIF. These values for $\mathbf{K^d}$ were compared to values obtained from photoelastic data for $\alpha = 0^o$ and $\alpha = 90^o$, shown in Figure 4a and 4b, respectively. There is reasonable correlation in the magnitude ($|\mathbf{K^d}| = \sqrt{\{(K_1^d)^2 + (K_2^d)^2\}}$)and trend of $\mathbf{K^d}$ for the strain gage results as compared to the photoelastic results. The strain gage analysis is a first-order

analysis based on the singular most term compared to a second-order photoelastic analysis. Thus, some error between the strain gage and the photoelasticity results is attributable to differences in the analyses.

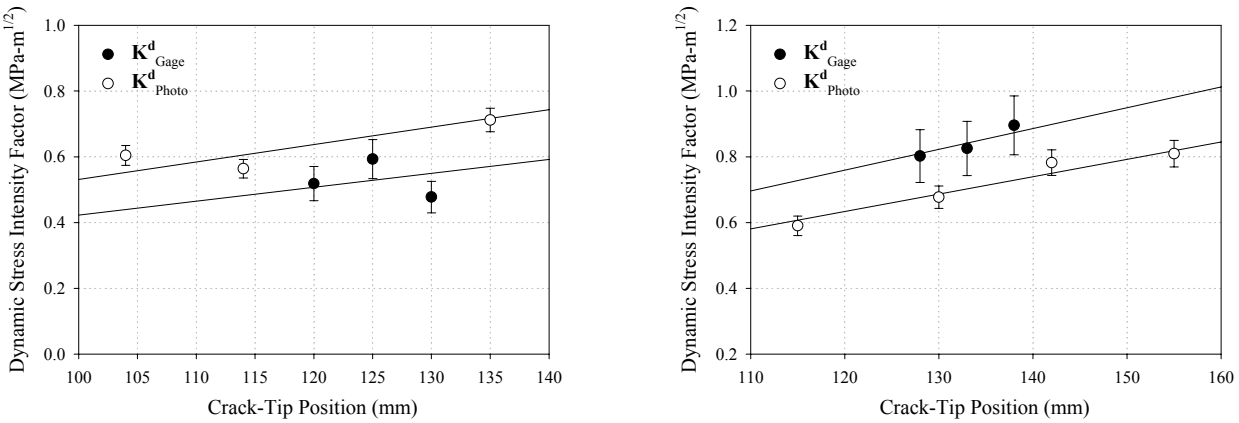

Figure 4. Dynamic Complex Stress Intensity Factor: a) $\alpha = 0^o$ b) $\alpha = 90^o$.

CONCLUSION

An experimental study was conducted in which strain fields were developed and used to investigate the behavior of cracks propagating along the interface of an isotropic-orthotropic bimaterial. Analytical work focused on the influence of the dynamic CSIF, $\mathbf{K^d}$, on the strain field surrounding a crack tip, which yielded the optimum strain gage orientation. In the experimentation that followed, $\mathbf{K^d}$ for a PSM-1/Scotchply bimaterial was determined using strain gages. The trend and magnitude of $\mathbf{K^d}$ obtained from strain gage analysis compared favorably with those from photoelastic analysis from the same experiment. Thus, it is feasible to use strain gages to study subsonic interfacial crack propagation in isotropic-orthotropic bimaterials. Differences in the methods and analyses are the subject of an on-going study.

ACKNOWLEDGEMENTS

The authors wish to acknowledge the support of the Naval Undersea Warfare Center ILIR, the Korean Science and Engineering Foundation (Grant No. 971-1003-017-2), and the National Science Foundation.

REFERENCES

1. Dally, J. W. and Sanford, R. J. (1987) *Experimental Mechanics* **27**, 381-388.
2. Shukla, A., Agarwal, R. K., and Nigam, H. (1988) *Engineering Fracture Mechanics* **31**, 501-515.
3. Shukla, A., Agarwal, B. D., and Bhushan, B. (1989) *Engineering Fracture Mechanics* **32**, 469-477.
4. Khanna, S. K. and Shukla, A. (1994) *Engineering Fracture Mechanics* **47**, 345-359.
5. Yang, W., Suo, Z., and Shih, C.F. (1991) *Proceedings of the Royal Society* (London) **A433**, 679-697.
6. Deng, X. (1992) *Engineering Fracture Mechanics* **42**, 2, 237-242.
7. Deng, X. (1993) *Journal of Applied Mechanics* **60**, 183-189.
8. Liu, C., Lambros, J., and Rosakis, A. J. (1993) *Jour. of Mech. and Phys. of Solids* **41**, 2, 1887-1954.
9. Tippur, H. V. and Rosakis, A. J. (1991b) *Experimental Mechanics* **31**, 243-251.
10. Lee, K. H., Hawong, J. S., and Choi, S. H. (1996) *Engineering Fracture Mechanics* **53**, 1, 119-140.
11. Lee, K. H. (1999) *Korean Society of Mechanical Engineers Journal (A)* **23**, 9, 1463-1475.
12. Ricci, V., Shukla, A., and Singh, R. P. (1997) *Engineering Fracture Mechanics* **59**, 4, 273-283.

ANALYSIS OF THE PHYSICO-CHEMICAL MECHANISMS RESPONSIBLE FOR HYDROGEN ATTACK

S. M. Schlögl and E. Van der Giessen

Koiter Institute Delft, Delft University of Technology, The Netherlands

ABSTRACT

The failure mode known as 'hydrogen attack' involves several processes which are active when steel components are exposed to high hydrogen pressures at elevated temperatures. In this paper, a microstructural model is presented which covers these processes through a combination of continuum mechanics with solid solution thermodynamics, kinetics and chemistry. The model is applied to study the response of 2.25Cr-1Mo steel consisting of a ferritic matrix and alloy carbides (e.g., M_7C_3, $M_{23}C_6$, M_6C, M_2C) to an exposure of 18MPa hydrogen pressure at a temperature of 530°C. The investigated microstructures vary in their carbide types and/or their carbide volume fractions. The numerical simulations show that the microstructure that does not contain M_7C_3 carbides is most resistant to hydrogen attack.

KEYWORDS

hydrogen attack, 2.25Cr-1Mo steel, diffusion, dissolution, methane pressure, creep, driving force

INTRODUCTION

2.25Cr-1Mo steel is a standard material for reactors used in the petro-chemical industries. In case of hydrocracking or hydrotreating applications, the material of the reactor is exposed to a high hydrogen pressure and to elevated temperatures. It is this combination that is responsible for the material degradation process called hydrogen attack (HA). During HA, carbon, present in the steel, and hydrogen, originating from the gas atmosphere inside the reactor, form methane molecules. These molecules are captured in cavities which have nucleated at the grain boundaries. Due to the presence of methane and hydrogen molecules, the cavities are internally pressurized. Consequently, the cavities grow and coalesce which finally results in intergranular fracture.

Carbon is present in the steel in two forms, namely interstitially dissolved in the ferritic matrix (α-Fe) and bonded in carbides. A standard 2.25Cr-1Mo steel contains various types of carbides, such as M_7C_3, $M_{23}C_6$, M_6C and M_2C [1]. The microstructure, characterized by the composition of the various alloy carbides and their volume fraction, depends on the heat treatment. Generally, the steel that is exposed to the high hydrogen pressure, does not possess a microstructure which is in equilibrium. So, the question arises whether this influences the susceptibility to hydrogen attack. Our recently developed microstructural model [2] enables us to shed some light on this issue. In this paper, we numerically study the response of non-equilibrium microstructures and compare their resulting methane pressures and void growth to the ones of the equilibrium microstructure.

MICROSTRUCTURAL MODEL

The microstructure is represented by a spherical unit cell of radius r_o, in which a total of N carbides with the radius ρ^j are embedded. The unit cell is also assumed to contain one already nucleated cavity of radius a. Inside this cavity, the hydrogen pressure is taken to be the same as the one in the gas atmosphere inside the reactor or autoclave. Our microstructural model includes several mechanisms that are potentially relevant during hydrogen attack. These processes can be gathered in three groups (see Figure 1): (i) carbide dissolution controlled by the diffusion of metal and carbon atoms in the ferritic matrix away from or to the carbides (Figure 1a); (ii) chemical reaction of carbon and hydrogen in the void going hand in hand with the diffusion of carbon atoms to the void (Figure 1b) and (iii) growth of the void by grain boundary diffusion and dislocation creep (Figure 1c). Each of these groups is treated in a submodel. In this paper we briefly summarize the main ideas of the concept; for a complete description we refer to [2].

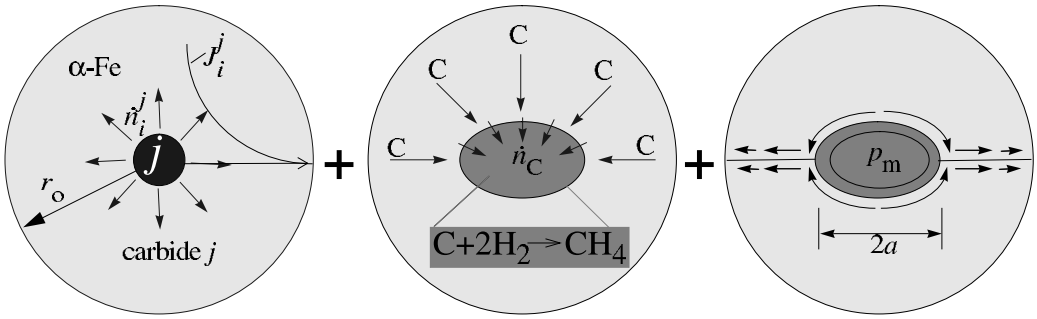

Figure 1: Submodels describing the processes leading to hydrogen attack. Submodel 1: dissolution of carbide j with radius ρ^j in the ferritic matrix together with the flux J_i^j leading to a homogeneous distribution in the ferrite (a). Submodel 2: chemical reaction of $\dot{n}_C^{cav}$ carbon atoms with hydrogen to methane (b). Submodel 3: cavity growth due to creep and grain boundary diffusion (c).

Submodel 1: Dissolution of carbides

During hydrogen attack, the average carbon composition in the steel decreases which results in a driving force for carbide dissolution, i.e. in a reduction of the Gibbs free energy G of the total system (α-Fe + carbides). Its rate, $\dot{G}$, is linearly related to the size change of the carbides via

$$\dot{G} \equiv \sum_{j=1}^{N} A^j \dot{\rho}^j . \tag{1}$$

The coefficient A^j depends on the actual radius ρ^j of the carbide j, the thermodynamic parameters of the phases α and carbide j, and on their composition. The exact expression of A^j and its derivation can be found in [2]. Here, it is sufficient to mention that all phases are described with the sublattice model [3, 4] where the corresponding thermodynamic parameters have been gathered from the literature (for a complete list see [5]).

During the dissolution of carbide j, $\dot{n}_i^j$ metal and carbon atoms (i = Fe, Cr, Mo and C) transfer across the matrix-carbide interface and diffuse within the ferritic matrix. As the alloy carbides possess a higher content of Cr, Mo and C than the ferritic matrix, these elements diffuse away from the dissolving carbide, while Fe diffuses towards the carbide. For the modelling, it is assumed that the diffusion of the substitutional elements controls the kinetics of the dissolution. Instead of directly solving Fick's second law of diffusion, we express the Gibbs energy dissipation $\dot{Q}_i^j$ associated with the diffusion of component i by [2]

$$\dot{Q}_i^j = \int_V \frac{RTV_m^{Fe}}{y_i^\alpha D_i^\alpha} (J_i^j)^2 dV. \tag{2}$$

with J_i^j the diffusive molar flux, T the temperature, y_i^α the composition of the ferrite, V_m^Fe its molar volume and D_i^α the diffusivity of component i. To bypass the large numerical effort to calculate the fluxes locally, we make the simplification that all k components are and remain homogeneously distributed in the ferritic matrix and that no diffusion takes place inside the carbides. As another simplification, we do not take into account the spatial arrangement of the carbides; instead we imagine that each carbide j sits in the center of our spherical unit cell. Under the assumption that the components remain homogeneously distributed during hydrogen attack, each flux should exhibit the radial dependence $J_i^j(r) = (\dot{n}_i^j/4\pi r^2)(1-r^3/r_\mathrm{o}^3)$, as is illustrated in Figure 1a. This allows us to integrate (2) over the volume of the unit cell. Since there exists a direct relation between $\dot{n}_i^j$ and $\dot{\rho}^j$, the total dissipation $\dot{Q} = \sum_{j=1}^{N}\sum_{i=1}^{k} \dot{Q}_i^j$ can be formulated as a function of the unknown $\dot{\rho}^j$. By inserting (2) and (1) into the condition $\dot{Q} + \dot{G} = 0$ [6] we obtain the size change $\dot{\rho}^j$ of each carbide.

Submodel 2: Chemical reaction

When $\dot{n}_\mathrm{C}^\mathrm{cav}$ carbon atoms in the cavity (located in the center of the unit cell, see Figure 1b) react with hydrogen molecules to form methane, the total Gibbs energy reduces according to

$$\dot{G}_\mathrm{C} = -\dot{n}_\mathrm{C}^\mathrm{cav}\Delta f = \dot{n}_\mathrm{C}^\mathrm{cav}(\mu_{\mathrm{CH_4}} - 2\mu_{\mathrm{H_2}} - \mu_\mathrm{C}^\alpha). \tag{3}$$

Δf represents the driving force and μ_x stands for the chemical potential of the component x. Knowing the actual composition of the ferritic matrix, the actual methane pressure in the cavity and the applied hydrogen pressure, we can calculate this driving force. Besides Δf, the availability of carbon atoms at the cavity-matrix interface plays an important role for the kinetics of the chemical reaction. The more and the faster carbon atoms diffuse in the ferritic matrix towards the cavity, the higher will be the rate of reaction, characterized by $\dot{n}_\mathrm{C}^\mathrm{cav}$. Like in submodel 1, the dissipation energy due to the diffusion of C atoms, $\dot{Q}_\mathrm{C}$, is equal to $-\dot{G}_\mathrm{C}$ which allows us to compute the number $\dot{n}_\mathrm{C}^\mathrm{cav}$ of methane molecules that are newly formed per unit of time.

Submodel 3: Void growth

The gas pressure p_m $(= p_{\mathrm{CH_4}} + p_{\mathrm{H_2}})$ causes the cavity to grow (Figure 1c). Grain boundary diffusion and dislocation creep (described by a Norton law) lead to an increase of the volume of the cavity, $\dot{V}^\mathrm{cav} = \dot{V}_\mathrm{diff}^\mathrm{cav} + \dot{V}_\mathrm{cr}^\mathrm{cav}$. A numerical and analytical analysis of the growth of a representative single cavity was performed by Van der Giessen *et al.* [7] leading to approximate yet accurate closed-form expressions for $\dot{V}_\mathrm{diff}^\mathrm{cav}$ and $\dot{V}_\mathrm{cr}^\mathrm{cav}$. For the sake of brevity we just mention that $\dot{V}_\mathrm{diff}^\mathrm{cav}$ depends linearly on p_m, while $\dot{V}_\mathrm{cr}^\mathrm{cav}$ is proportional to p_m^n with n the creep exponent. The exact expressions are given in [2, 5, 7, 8]. Under the condition that the cavity maintains its equilibrium spherical cap shape during growth, a relation exists between $\dot{V}^\mathrm{cav}$ and the rate of the cavity radius $\dot{a}$.

The outcome of the three submodels are the values for the rates $\dot{\rho}^j$, $\dot{n}_\mathrm{C}^\mathrm{cav}$ and $\dot{a}$. An explicit time integration scheme is applied to obtain the actual ρ^j, $n_\mathrm{C}^\mathrm{cav}$ and a as a function of the exposure time. Based on this information, we update the composition of the ferrite and the methane pressure at each new time instant.

RESULTS

Before we can apply the model, the material parameters (e.g. diffusion coefficients of all components, creep parameters), the operating and the initial conditions should be specified. For the material parameters we refer to [2]. We chose to simulate autoclave tests where 2.25Cr-1Mo steels with different microstructures are exposed to a hydrogen pressure of 18MPa at a temperature of 530°C. The alloy composition is fixed to 2.4at%Cr, 0.58at%Mo and 0.7at%C, while various carbide types and volume fractions are assumed in the calculations. Chao *et al.* [1] found the following carbide types and carbide composition (expressed in site fractions) in their investigation: M_7C_3 with 35%Fe, 60%Cr and 5%Mo; $M_{23}C_6$ with 55%Fe, 39%Cr and 6%Mo; M_6C with 45%Fe, 13%Cr and 42%Mo and M_2C with 3%Fe, 27%Cr and 70%Mo. Unfortunately, the total volume fraction f^carb is not mentioned, just their relative volume fractions: 43% of the total volume occupied by the carbides belongs to M_7C_3, 25% to $M_{23}C_6$, 10% to M_6C and finally 21% to M_2C. As we do not know the value for f^carb, we study two cases. In the first case (microstructure m1), f^carb possesses the maximum possible

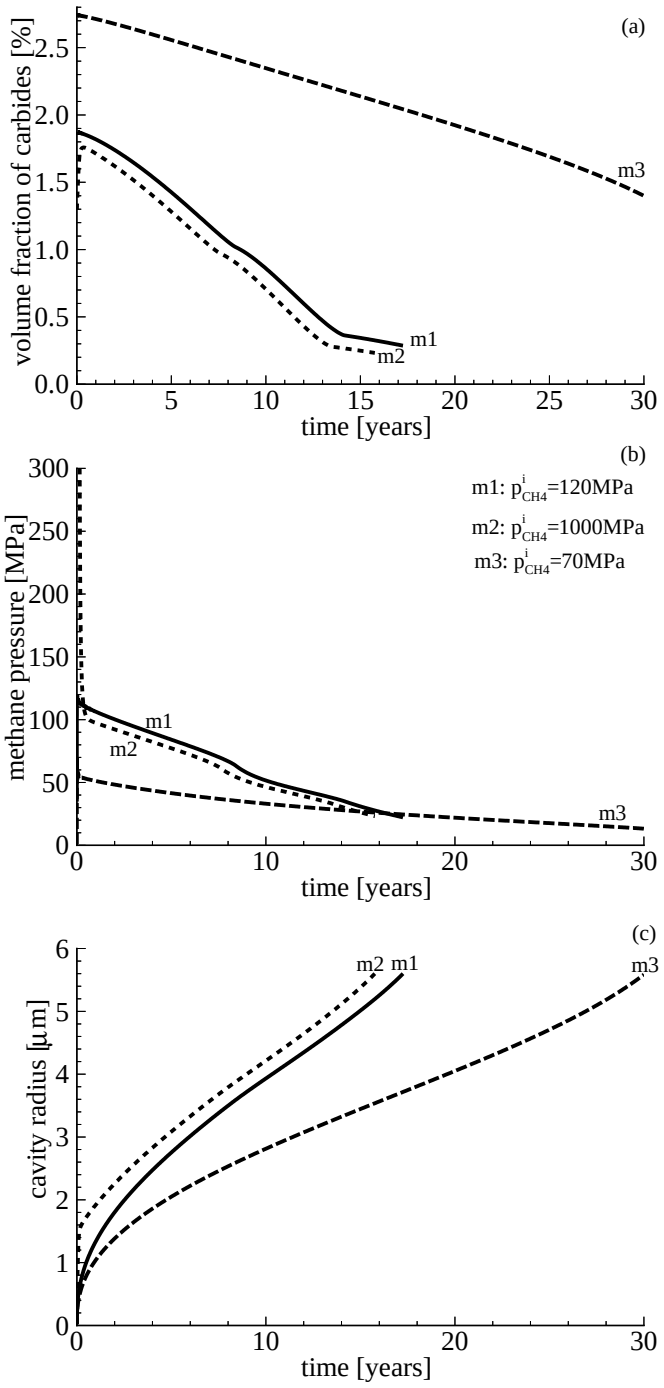

Figure 2: Evolution of the total volume fraction of carbides (a), of the methane pressure (b) and of the void radius (c) for various microstructures (m1, m2, m3) exposed to a hydrogen pressure of 18MPa at a temperature of 530°C.

value, namely $f^{\mathrm{carb}} = 1.87\%$ which then corresponds to the following composition of the ferritic matrix: 1.6%Cr, 0.16%Mo and 2.6×10^{-5}%C. To check the influence of f^{carb} on HA, the second microstructure (m2) contains a smaller carbide volume fraction, $f^{\mathrm{carb}} = 1.3\%$, and a ferritic matrix of 1.9%Cr, 0.29%Mo and 2.2×10^{-1}%C. Further input parameters are the total number of carbides N in the unit cell, their radius ρ^j and the size of the unit cell (r_{o}). For the sake of simplicity, we assume that in a unit cell of the radius $r_{\mathrm{o}} = 8\mu$m there are 100 carbides which all possess the same size. This means that $\rho^j = 0.46\mu$m in m1 and $\rho^j = 0.41\mu$m in m2. According to the measured relative carbide fractions, there are 43 M_7C_3 carbides, 25 $M_{23}C_6$ carbides, 10 M_6C carbides and 21 M_2C carbides in both microstructures. The third microstructure (m3) of interest here is the equilibrium microstructure. We used the thermodynamics program Thermo- Calc [9] to predict the equilibrium state of the 2.25Cr-1Mo steel at a temperature of 530°C in air. The outcome is a microstructure just containing two types of carbides, namely $M_{23}C_6$ (30.8%Fe, 56.5%Cr and 12.7%Mo) with a volume fraction

of $f^{\mathrm{M_{23}C_6}}$ of 2.6% and M_6C (35.6%Fe, 3.1%Cr and 61.3%Mo) with a volume fraction of $f^{\mathrm{M_6C}}$ of 0.16%. Again we assume that there are 100 equally sized carbides embedded in the unit cell. From $f^{\mathrm{M_{23}C_6}}$ and $f^{\mathrm{M_6C}}$ it follows that $\rho^j = 0.52\mu$m and that 94 $M_{23}C_6$ carbides and 6 M_6C carbides are present.

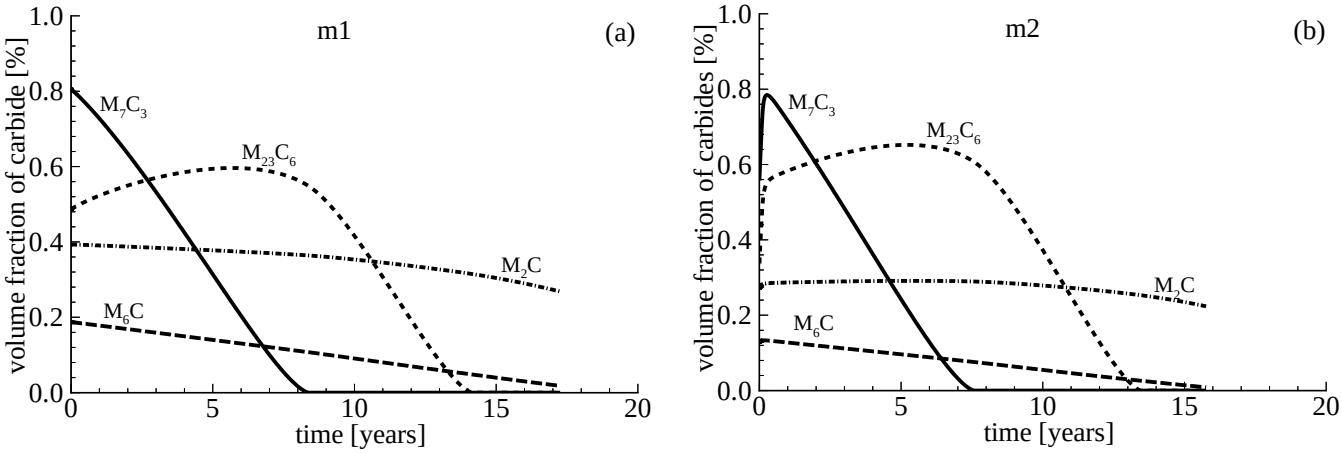

Figure 3: Evolution of the volume fraction of the various carbide types (M_7C_3, $M_{23}C_6$, M_6C, M_2C) during exposure at 530°C in microstructure m1 (a) and microstructure m2 (b).

The model is applied to simulate the response of these three microstructures to hydrogen exposure. Some selected results are shown in Figure 2 giving (a) the volume fraction of all carbides f^{carb}, (b) the methane pressure and (c) the cavity radius as a function of exposure time for each microstructure. Starting with microstructure m1, we see (Figure 2b) that a methane pressure of 120MPa is built up at the beginning of the exposure which leads to void growth (Figure 2c). In order to keep up the methane pressure in a bigger void, new carbon atoms should react with hydrogen to methane. First, the carbon atoms dissolved in the ferritic matrix react. Due to the initially very low carbon content of microstructure m1 (2.55×10^{-5}%C), the reacting carbon atoms mainly stem from the second source, the carbides. As seen in Figure 2a, their total volume fractions decreases. During this dissolution, carbon atoms transfer from the carbide to the matrix where they diffuse to the cavity to react. Carbide dissolution takes time since it is controlled by the diffusion of the substitutional elements Cr and Mo. It is not fast enough to keep the methane pressure at a constant value and indeed it is seen (Figure 2b) to decrease as the cavity grows. In microstructure m2, the ferritic matrix contains a high initial carbon content. As a first consequence, a high methane pressure ($p_{\mathrm{CH_4}} = 1000$MPa) is built up in the cavity and the cavity grows very quickly during the early stages of the exposure. A second consequence is that the carbides grow as long as the carbon content is high and as long as a driving force for precipitation exists. This results in an increase of f^{carb} from 1.3% to 1.9% as seen in Figure 2a. When the carbon content has reached a low value, the methane pressure drops quickly, the void growth slows down and the carbides dissolve similar to microstructure m1. Microstructure m3, which is initially in the equilibrium state, is much less susceptible to HA. The methane pressure (starting with 70MPa and decreasing to 20MPa) is quite low which results in a slow void growth. The carbides also dissolve very slowly.

Now, we have a closer look at the influence of the carbide type on HA. To find out whether they possess a different susceptibility, Figure 3 shows the volume fractions of each carbide type individually, both for microstructure m1 (a) and microstructure m2 (b). In m1, the M_7C_3 carbides dissolve by far the fastest, M_6C and M_2C dissolve much slowlier while the $M_{23}C_6$ carbides seem to be quite stable during the first years. They even grow for the first 6 years (Figure 3a). Except for the early beginning, the picture does not change for microstructure m2. Due to the high initial carbon content in the ferrite, all carbide types grow first and then they behave similar to m1. In microstructure m3 (not shown), the volume fraction of the $M_{23}C_6$ carbides decreases from 2.6% to 1.2% within 30 years while the volume fraction of M_6C remains the same (0.16%). It turns out that the relatively high resistance to HA of m3 is related to the absence of M_7C_3 carbides.

CONCLUSIONS

A microstructural model has been presented which covers the potentially relevant mechanisms responsible for hydrogen attack, such as diffusion of carbon and metal atoms, the chemical reaction to methane, grain boundary diffusion and dislocation creep. The simulation of autoclave tests of 2.25Cr-1Mo steels with different microstructures demonstrates that the methane pressure is not constant during HA, thus falsifying previous decoupled approaches to HA. Then, they show that the methane pressure at the beginning of the exposure is related to the initial carbon content of the ferritic matrix. Microstructure m2 with its high content of dissolved carbon in the ferrite possesses a very high methane pressure initially. Afterwards, the methane pressure drops in all cases, because the cavities grow and the carbides dissolve too slowly to supply sufficient carbon atoms for the reaction. Consequently, the decreasing methane pressure is responsible for a delay in void growth. Furthermore, the simulations reveal the big influence of the carbide types on the failure times. The equilibrium microstructure (m3) which contains just $M_{23}C_6$ and M_6C carbides fails after 30 years. The microstructures m1 and m2, where M_7C_3, $M_{23}C_6$, M_6C and M_2C carbides are present, give rise to failure times of 17 and 16 years. The higher resistance of m3 can be mainly attributed to the absence of M_7C_3, which dissolves quite easily in the other microstructures.

ACKNOWLEDGEMENTS

The work of S.M. Schlögl is supported through the FOM/NIMR research program “Evolution of the microstructure of materials”.

REFERENCES

[1] Chao, B.L., Odette, G.R. and Lucas, G.E. (1988). ONRI/Sub/82-22276/01 University of California, Santa Barbara, United States.

[2] Schlögl, S.M., Svoboda, J. and Van der Giessen, E. (2001), submitted to *Acta Mat.*.

[3] Hillert, M. and Staffansson, L.-I. (1970) *Acta Chem. Scand.* 24, 3618.

[4] Sundman, B. and Ågren, J. (1981) *J. Phys. Chem. Solids* 42, 297.

[5] Schlögl, S.M., van Leeuwen, Y. and Van der Giessen, E. (2000) *Metall. Mat. Trans. A*31, 125.

[6] Svoboda, J. and Turek, I. (1991) *Phil. Mag. B* 64, 749.

[7] Van der Giessen, E., Van der Burg, M.W.D., Needleman, A. and Tvergaard, V. (1995) *J. Mech. Phys. Solids* 43, 123.

[8] Van der Burg, M.W.D., Van der Giessen, E. and Brouwer, R.C. (1996) *Acta Mat.* 44, 505.

[9] Sundman, B., Jansson, B. and Anderson, J.O. (1985) *CALPHAD* 9, 1127.

ANALYSIS OF THE PROCESS ZONE AHEAD OF A CRACK TIP

J. Lemaitre
Prof. Em. Universite Paris 6
Laboratoire de Mécanique et Technologie
61 av. du président Wilson F-94235 CACHAN Cedex, FRANCE
and
R. Desmorat
Laboratoire de Modélisation et Mécanique des Structures
8, rue du Capitaine Scott, F-75015 PARIS, FRANCE

ABSTRACT

At the head of a crack tip of plane stress problem, the near far stress field is taken as the Westergaard equations for elasticity. Closer, it is given by the HRR plastic field. More closer, where damage occurs, it is given by a linear approximation of stress from the ultimate stress σ_u at the border of the damage zone to $\sigma_u(1-D_c)$ at the real crack tip where the damage reaches its critical value D_c. It is shown that the damaged zone is very small and homothetic of the plastic zone and that the ductile crack growth rate may be deduced from the plasticity and damage parameters. [1]

STRESS ANALYSIS AHEAD OF A CRACK TIP

Consider the simple reference case of fracture mechanics : a crack of length a loaded in mode I by a state of quasi-static monotic plane stress σ_∞ at infinity. Due to the properties of a material subjected to elasticity, plasticity and damage, the domain close to the crack tip is divided into three regions as shown in figure 1.

- A region E far from the crack tip where the behavior of the material is purely elastic. The state of stress not too far from the crack tip is given by the Westergaard analysis [1, 2].
- A region P closer to the crack tip where the behavior of the material is purely plastic. The state of stress is given by the H.R.R. field [3, 4].
- A region D surrounding the crack tip where the behavior of the material is elasto plastic softened by damage up to the crack tip where the damage reaches its value at fracture.

Elastic zone E

Using Westergaard equations the purely elastic domain is limited by a line along which the von Mises equivalent stress $\sigma_{eq} = \sqrt{\frac{3}{2}\sigma_{ij}^D\sigma_{ij}^D}$ reaches the yield stress σ_y of the material. Its distance from the crack tip along the x-axis is (G: strain energy release rate),

1. ICF 10 - March 2001

$$x - a = r_y = \frac{EG}{2\pi\sigma_y^2} = \frac{\sigma_\infty^2 a}{2\sigma_y^2} \qquad \text{for plane stress} \tag{1}$$

Figure 1: Elasticity, plasticity and damage ahead of a crack

Plastic zone P

The plastic property of the material is represented by the Ramberg-Osgood constitutive equation,

$$p = \left(\frac{\sigma_{eq}}{K}\right)^M \tag{2}$$

where $p = \sqrt{\frac{2}{3}\epsilon_{ij}^p \epsilon_{ij}^p}$ is the accumulated plastic strain and K and M are material parameters. Eq. (2) models plasticity as a nonlinear elasticity problem. It is valid as long as no unloading occurs and neglects the elastic part of the strain. Ramberg Osgood law is the constitutive equation used in the HRR analysis in order to determine the von Mises equivalent stress σ_{eq} and the equivalent plastic strain p along the x axis,

$$\sigma_{eq} = Const \cdot {\sigma_\infty}^{\frac{2}{M+1}} \left(\frac{a}{x-a}\right)^{\frac{1}{M+1}} \tag{3}$$

$$p = \left(\frac{Const}{K}\right)^M {\sigma_\infty}^{\frac{2M}{M+1}} \left(\frac{a}{x-a}\right)^{\frac{M}{M+1}} \tag{4}$$

$x = a + r_y$ is the abscisse corresponding to the yield limit where the yield stress σ_y is reached, or in an equivalent manner where p takes a conventional value, let us say $p_y = \sigma_y/E$, of the order of magnitude of $0.2 \cdot 10^{-2}$, and

$$p_y = \left(\frac{Const}{K}\right)^M {\sigma_\infty}^{\frac{2M}{M+1}} \left(\frac{a}{r_y}\right)^{\frac{M}{M+1}} \tag{5}$$

$x = a + r_D$ is the abscisse corresponding to the damage limit, i.e. $D = 0$ if $x > a + r_D$, $D \neq 0$ if $x < a + r_D$ considering the continuous damage variable D (surface density of microcracks or microcavities) as a scalar for

isotropic damage. The damage threshold p_D, below which $D = 0$, is generally loading dependent and related to the damage threshold in pure tension ϵ_{pD} characteristic of each material [5]. For simplicity we take here $p_D = \epsilon_{pD}$,

$$p_D = \left(\frac{Const}{K}\right)^M \sigma_\infty{}^{\frac{2M}{M+1}} \left(\frac{a}{r_D}\right)^{\frac{M}{M+1}} \tag{6}$$

This shows that the damage zone is homothetic to the plastic zone

$$\frac{r_D}{r_y} = \left(\frac{p_y}{p_D}\right)^{\frac{M+1}{M}} \tag{7}$$

In fact, this zone is very small. If p_y is of the order of 0.2 10^{-2}, ϵ_{pD} for metals is often of the order of 5 to 20 10^{-2} and M of 3 to 8,

$$r_D \approx \frac{r_y}{10 \text{ to } 100} \tag{8}$$

Damage zone D

The abscisse of the damage zone r_D is defined by $p = p_D$ which corresponds for most metals to an equivalent stress close to the ultimate stress σ_u [5]. Then $\sigma_{eq} = \sigma_u$ for $x = a + r_D$.

At the crack tip $x = a$, the damage reaches its critical value at mesocrack initiation $D = D_c$ ($D_c \approx 0.2$ to 0.5 depending upon the material). Considering the hardening saturated for $p > p_D$, the plasticity criterion coupled to damage by the effective stress concept is written as

$$\frac{\sigma_{eq}}{1 - D} - \sigma_u = 0 \tag{9}$$

which gives the value of the stress at the crack tip $x = a$

$$\sigma_{eq} = \sigma_u(1 - D_c) \tag{10}$$

Figure 2: Behavior of the material by zone

The damage zone being small, a linear variation of the stress σ_{eq} is assumed for $a < x < a + r_D$,

$$\sigma_{eq} = \sigma_u \left[1 - D_c \left(1 - \frac{x-a}{r_D}\right)\right] \tag{11}$$

The behavior of the material, elastic for $\sigma_{eq} < \sigma_y$, plastic by the Ramberg-Osgood law for $\sigma_y \leq \sigma_{eq} < \sigma_u$ is softened by damage for larger plastic strain p_u corresponding to σ_u. The hardening being saturated, the accumulated plastic strain, is in this range a linear function of the von Mises stress (figure 2) and

$$dp = -\frac{p_R - p_u}{\sigma_u D_c} d\sigma_{eq} \tag{12}$$

This allows to calculate the plastic evolution and the damage from its law of evolution taken as a function of the total elastic energy and of the accumulated plastic strain [6], two variables governing also the crack propagation [7]

$$dD = \left(\frac{\sigma_u^2 R_\nu}{2ES}\right)^s dp \qquad \text{if} \quad p > p_D \tag{13}$$

also from the plasticity criterion: $dD = -d\sigma_{eq}/\sigma_u$ E is the Young's modulus, S and s two material damage parameters. R_ν is the triaxiality function. The linearity of the plastic strain induces the linearity of the damage,

$$\frac{dD}{dx} = -\frac{D_c}{r_D} \qquad \text{and} \qquad D(x,a) = D_c \left(1 - \frac{x-a}{r_D(a)}\right) \tag{14}$$

CRACK GROWTH

Consider the loading σ_∞ at the level which has just created the crack of length a. The loading increment is noted $\delta\sigma_\infty$. It induces a virtual increment of the stress $\delta\sigma_{eq}$ but as the stress σ_{eq} is bounded by σ_u at $x = a + r_D$, this corresponds to a decrease $-\delta\sigma_{eq}$ which induces first an increment of the plastic strain, then an increment of the damage, and finally a real increment of the crack δa (a discontinuity of crack mechanics from continuous damage mechanics) as the Damage is bounded by D_c (Figure 3).

Figure 3: Crack increment

It is necessary to indroduce a link which can be an energetic equivalence $\mathcal{D}_a = \mathcal{D}_d$ between the crack growth dissipation $\mathcal{D}_a$ and the damage dissipation $\mathcal{D}_d$ [5, 8]. If $a(t_0) = a_0$ and $a(t) = a$,

$$\mathcal{D}_a = \int_{a_0}^{a} G h da \qquad \mathcal{D}_d = \int_{a_0}^{\infty} \int_{t_0}^{t} Y \dot{D} dt h^2 dx \tag{15}$$

where $G = \sigma_\infty^2 \pi a / E$ is the strain energy release rate, Y is the damage energy release rate density (a constant here $Y = Y_c = \sigma_u^2 R_\nu / 2E$), h is the size of the Representative Volume Element. The second integral is in fact an integral between a_0 and $a + r_D(a)$ as outside of the damage zone $\dot{D}$ remains equal to zero,

$$\mathcal{D}_d = h^2 Y_c \left(\int_{a_0}^{a+r_D(a)} D(x,a) dx - \int_{a_0}^{a_0+r_D(a_0)} D(x,a_0) dx \right) \tag{16}$$

Equations (1) and (8) may be combined in order to give r_D as:

$$r_D = \alpha G \qquad \alpha = \frac{E}{2\pi\sigma_y^2} \left(\frac{p_y}{p_D} \right)^{\frac{M+1}{M}} \tag{17}$$

Then

$$\mathcal{D}_d = \frac{1}{2} h^2 \alpha Y_c D_c \left[\left(1 + \frac{a - a_0}{\alpha G} \right)^2 G - G_0 \right] \tag{18}$$

Using the approximation $\mathcal{D}_a \approx h(a - a_0)(G + G_0)/2$ and anticipating the fact that the initial strain energy release rate does not have a quantitative effect, the energetic equivalence $\mathcal{D}_a = \mathcal{D}_d$ allows for the determination of G as

$$G \approx \sqrt{\frac{h Y_c D_c}{\alpha} (a - a_0)} \tag{19}$$

which is the equation equivalent to the one of the R-curve in Fracture Mechanics. Furthermore it gives the possibility to evaluate the danger of a damage crack initiation regarding to an increase of the loading.

Références

[1] H. M. Westergaard. *J. Appl. Mech.*, **A 49**, 1939.

[2] Irwin. Analysis of stress, strains near the end of a crack transversing a plate. *J. Appl. Mech.*, **24**:361–364, 1957.

[3] J. W. Hutchinson. Singular behavior at the end of a tensile crack in a hardening material. *J. Mech. Phys. Solids*, **16**:13–31, 1968.

[4] J. R. Rice and G. F. Rosengreen. Plane strain deformation near a crack tip in a power-law hardening material. *J. Mech. Phys. Solids*, **16**:1–12, 1968.

[5] J. Lemaitre. *A Course on Damage Mechanics*. Springer Verlag, 1992-96.

[6] J. Lemaitre, R. Desmorat, and M. Sauzay. Anisotropic damage law of evolution. *Eur. J. Mech., A/ Solids*, **19**:187–208, 2000.

[7] G. C. Sih. *Mechanics of fracture initiation and propagation*. Kluwer, 1991.

[8] O. Allix and P. Ladevèze. Damage mechanics of interfacial media: basic aspects, identification and application to delamination. *Damage and Interfacial debonding in Composites, Ed. G.Z. Voyiadjis and D.H. Allen, Elsevier Science B.V.*, pages 167–188, 1996.

ORAL/POSTER REFERENCE: ICF100832OR

ANALYSIS OF THREE-DIMENSIONAL INTERFACE CRACKING IN ELECTRONIC PACKAGES

A. O. Ayhan and H. F. Nied

Department of Mechanical Engineering
and Applied Mechanics, Lehigh University
Bethlehem, PA 18015-3085, USA

ABSTRACT

A technique for calculation of stress intensity factors for three-dimensional interface surface crack problems is presented. Of special interest, is the analysis of interface delamination observed in electronic packaging subjected to thermal cycling. Using a finite element approach, enriched 3-D interface crack tip elements are developed for direct computation of stress intensity factors along the crack front. The enriched 3-D crack tip elements contain the asymptotic displacement and strain fields for interface cracks. For cracks located between silicon and polymeric underfill materials in electronic packaging, the mode I and mode II stress intensity factors can be strongly coupled, since these materials yield relatively large values for Dunders' parameters. It is demonstrated that the enriched interface crack tip element approach is a very efficient technique for obtaining stress intensity factors and strain energy release rates for general three-dimensional interface crack problems. Of particular interest in this study are the stress intensity factors for semi-circular and quarter-circular surface cracks on the interface between silicon and epoxy. The enriched element approach is particularly effective for obtaining mode I, II and III stress intensity factors in the small zone near the free surface where the strength of the stress singularity is known to change.

KEYWORDS

Interface Cracks, Electronic Packages, Finite Element Method, 3-D Surface Cracks.

INTRODUCTION

One of the most important failure mechanisms that needs to be considered in the design of electronic packages, is interfacial cracking between the various layers of dissimilar electronic materials, e.g., silicon and epoxy. Such cracking can arise due to thermal cycling and/or moisture diffusion into the electronic package. Large differences in coefficients of thermal and hygroscopic expansion provide the driving forces necessary for interfacial cracking between material layers with inherently weak interfacial adhesion. Typically, such cracking originates at edges and corners where high stress concentrations are known to exist. The most severe stress concentrations tend to occur at three-dimensional corners [1], leading to the type of three-dimensional corner cracking shown in Figure 1. This figure depicts crack growth due to

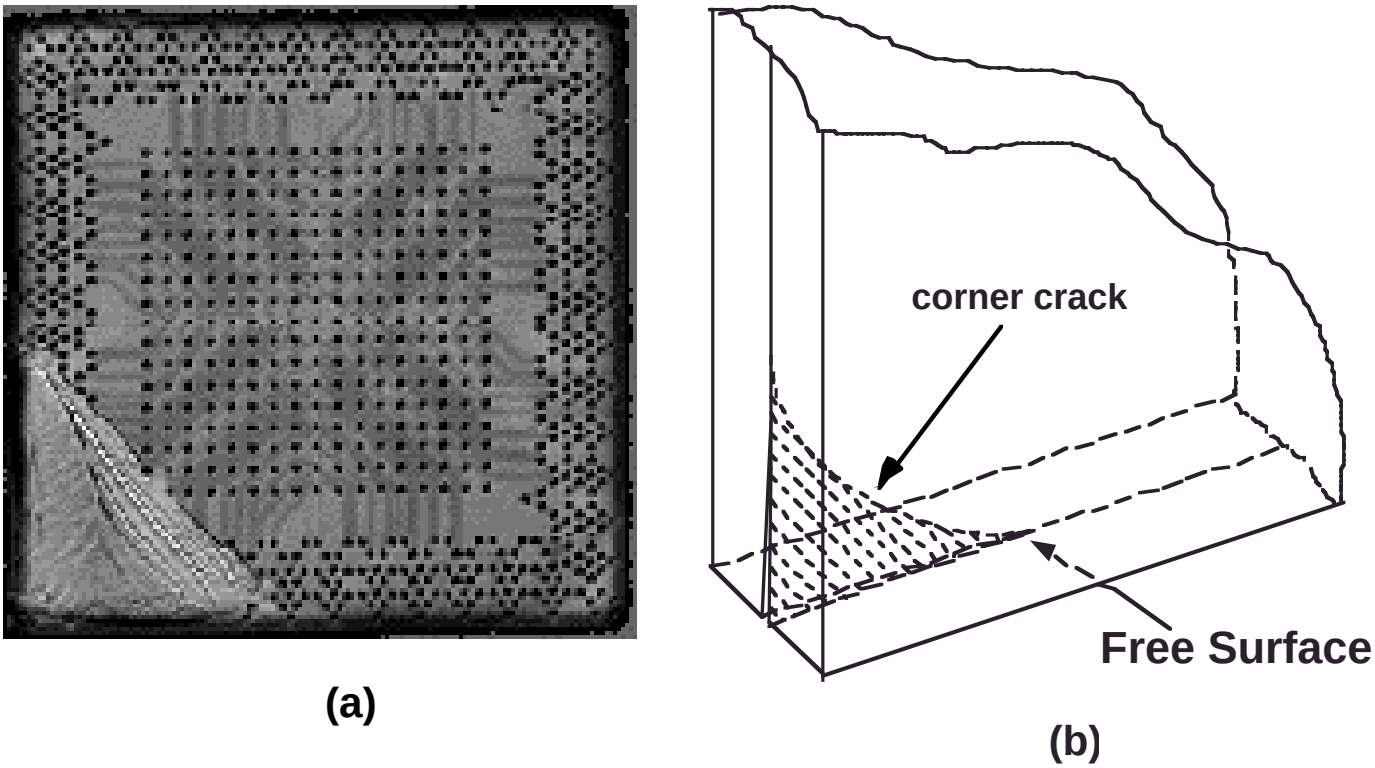

Figure 1: Interface cracking between silicon die and epoxy underfill in flip chip package. Crack emanating from corner after 300 cycles (-45°C - 125°C). Acoustic C-SAM image courtesy of David Peterson, Sandia National Laboratories.

thermal cycling between -45°C and +125°C. Crack growth under these conditions is inherently mixed-mode in nature with large mode II/III components. Application of interface fracture mechanics to predict debonding between layered materials has been extensively investigated and can serve as a basis for structural design for damage tolerance. This approach requires the accurate computation of stress intensity factors, K_I, K_{II}, and K_{III}, as well as strain energy release rates, G, for complex geometries and loading. The finite element method, suitably modified, can be used to compute these quantities for the complex interface cracking problems encountered in semiconductor packaging. A particularly effective approach is the use of "enriched" 3-D interface crack tip elements for direct computation of stress intensity factors [2]. The enriched crack tip elements contain the closed-form asymptotic solutions for displacements and strains in addition to the usual polynomial interpolation functions. Following this approach, the stress intensity factors are additional degrees of freedom computed directly in the same manner as the nodal displacements. One advantage of this approach is that there is no need for a special crack tip mesh, e.g., refined "tunnel" mesh or relocation of nodes to obtain a suitable singular solution. As long as the enriched elements are properly integrated and transition elements are used to maintain displacement compatibility, automatically generated meshes are adequate for highly accurate results.

FINITE ELEMENT FORMULATION

Enriched Crack Tip Elements

The enriched finite element formulation for interface crack problems is an extension of concepts introduced by Benzley [3] for conventional isotropic fracture problems. Application of the enrichment technique to interfacial fracture problems is relatively straightforward for two-dimensional problems once the asymptotic crack tip displacement and strain fields have been derived. In [4], an enriched crack tip element for interface cracks between dissimilar isotropic media is developed. Reference [5] documents a similar formulation for modeling interface cracks between orthotropic materials.

We have developed 3-D enriched elements for a variety of elements with various polynomial shape functions. For example, Figure 2a depicts a 32-noded enriched hexahedron element that uses cubic polynomial interpolation functions for displacements. In addition to the 96 displacement degrees of freedom

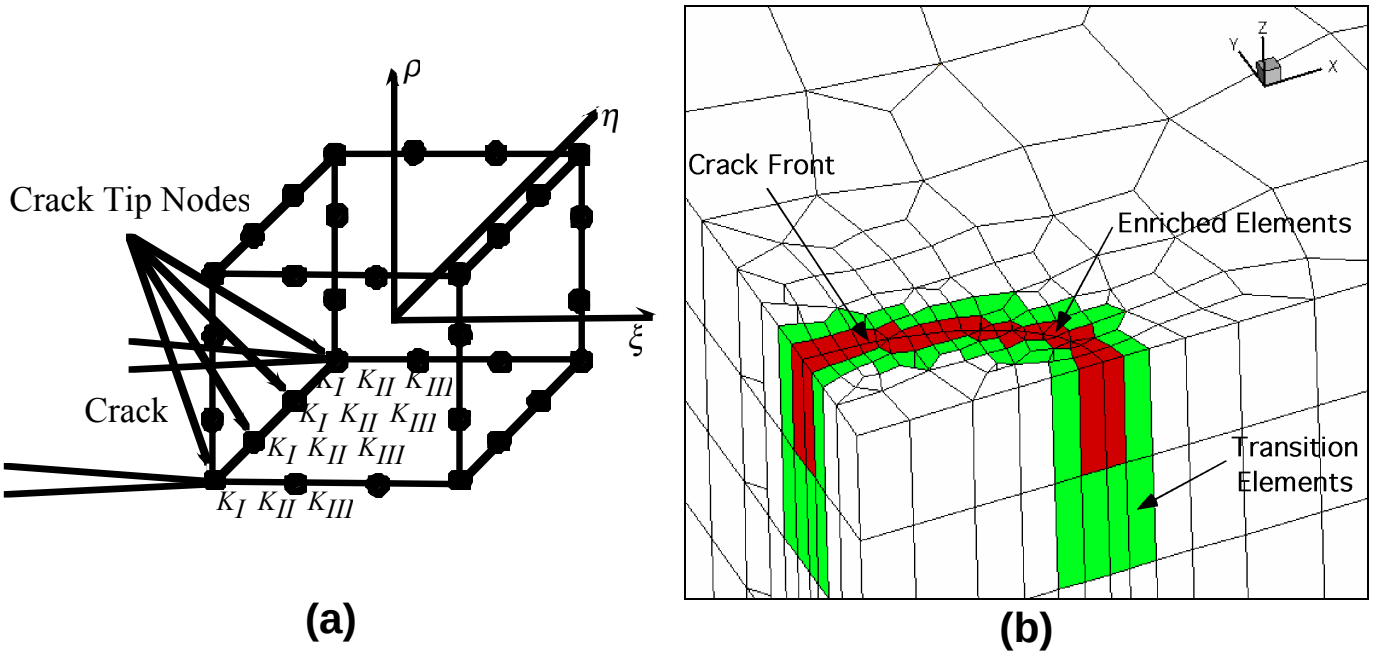

Figure 2: a) Enriched cubic hexahedron showing crack tip nodes. b) Semi-elliptic surface crack showing location of enriched crack tip elements and adjacent transition elements.

this element also has 12 unknowns representing the stress intensity factors K_I, K_{II}, and K_{III}, at nodes on the crack front. Thus, for this particular element there are 108 unknowns. Since the enriched crack tip element contains non-polynomial analytic terms, displacement compatibility cannot be ensured with neighboring elements that do not contain the asymptotic terms. To enforce displacement compatibility between all elements, transition elements should be used between the fully enriched crack tip elements and the regular elements. The location of these transition elements is shown in Figure 2b. Transition elements also contain the asymptotic fields for displacements and strains, but this contribution to the element stiffness matrix is linearly zeroed out across the volume of the element. The relevant details for 3-D transition elements are given by Ayhan in [6]. The components of displacement field for enriched 3-D elements of the type shown in Figure 2 are given by

$$u(\xi,\eta,\rho)=\sum_{j=1}^{nodel}N_j(\xi,\eta,\rho)u_j+Z_0(\xi,\eta,\rho)\sum_{i=1}^{ntip}N_i(\bar{\xi})K_I^i\left(f_1(\xi,\eta,\rho)-\sum_{j=1}^{nodel}N_j(\xi,\eta,\rho)f_{1j}\right)$$
$$+Z_0(\xi,\eta,\rho)\sum_{i=1}^{ntip}N_i(\bar{\xi})K_{II}^i\left(g_1(\xi,\eta,\rho)-\sum_{j=1}^{nodel}N_j(\xi,\eta,\rho)g_{1j}\right) \quad (1)$$

$$v(\xi,\eta,\rho)=\sum_{j=1}^{nodel}N_j(\xi,\eta,\rho)v_j+Z_0(\xi,\eta,\rho)\sum_{i=1}^{ntip}N_i(\bar{\xi})K_I^i\left(f_2(\xi,\eta,\rho)-\sum_{j=1}^{nodel}N_j(\xi,\eta,\rho)f_{2j}\right)$$
$$+Z_0(\xi,\eta,\rho)\sum_{i=1}^{ntip}N_i(\bar{\xi})K_{II}^i\left(g_2(\xi,\eta,\rho)-\sum_{j=1}^{nodel}N_j(\xi,\eta,\rho)g_{2j}\right) \quad (2)$$

$$w(\xi,\eta,\rho)=\sum_{j=1}^{nodel}N_j(\xi,\eta,\rho)w_j+Z_0(\xi,\eta,\rho)\sum_{i=1}^{ntip}N_i(\bar{\xi})K_{III}^i\left(h(\xi,\eta,\rho)-\sum_{j=1}^{nodel}N_j(\xi,\eta,\rho)h_j\right). \quad (3)$$

The first summation terms in (1)-(3) represent the usual displacements in regular isoparametric elements, i.e., N_i are the interpolation functions in element coordinates (ξ,η,ρ) and u_i,v_i,w_i, are the nodal displacements. Z_0. is the "zeroing function" that provides inter-element compatibility between the crack tip elements and the elements that surround the enriched elements. In a typical transition element, Z_0=1 at the nodal points where the transition element is adjacent to any of the crack tip elements, and is 0 when adjacent

to regular isoparametric elements. K^i_I , K^i_{II} , and K^i_{III} 's are the unknown stress intensity factors, for modes I, II, and III, respectively. For the cubic element, with four crack tip nodes, K^i_I , K^i_{II} , and $K^i_{I,}$ are interpolated using the cubic polynomial shape function associated with the displacements at these same nodes. The functions f_1, f_2, g_1, g_2, and h are the asymptotic displacement terms that are coefficients of the mode I, II and III stress intensity factors [3-5]. The terms f_{1j} , f_{2j} , g_{1j} , g_{2j} , and h_j are the asymptotic crack tip displacement expressions evaluated at the jth node in the element. It is well known that the asymptotic crack tip fields in three dimensions are identical to two-dimensional fields in plane strain, with the possible exception of points where the three-dimensional crack front terminates on a free surface. For three-dimensional analysis, the plane strain crack tip fields are evaluated in planes that are perpendicular to the crack front. Thus, during integration to calculate the element stiffness matrix, the perpendicular distance to the crack front r, as well as the angular orientation θ, with respect to the plane of the crack, must be determined for evaluation of the asymptotic displacements and strains. Since the element stiffness matrix is determined with respect to a global coordinate system, the asymptotic expressions computed in the local crack tip coordinate system must be transformed back to global coordinates.

Crack Tip Fields for Interface Cracks

The elastic singular stress field near the tip of an interface crack differs from that of a crack in a homogeneous material and exhibits an oscillatory behavior near the crack tip region. The singular stress field for a three-dimensional interface crack is given by

$$\sigma_{ij} = \frac{1}{\sqrt{2\pi r}}\left\{\mathrm{Re}\left[\mathrm{K}r^{i\varepsilon}\right]\tilde{\sigma}^{I}_{ij}(\theta,\varepsilon) + \mathrm{Im}\left[\mathrm{K}r^{i\varepsilon}\right]\tilde{\sigma}^{II}_{ij}(\theta,\varepsilon) + K_{III}\tilde{\sigma}^{III}_{ij}(\theta)\right\} \tag{4}$$

where r and θ are the polar coordinates in the local coordinate system that is located on the crack front in planes perpendicular to the crack front. The complex stress intensity factor **K** is defined by K_I+iK_{II} and $\tilde{\sigma}_{ij}$'s are the angular stress variation terms for different modes of loading. The complex singularity in (4) depends on the oscillatory index, ε, given by

$$\varepsilon = \frac{1}{2\pi}\ln\left[\frac{1-\beta}{1+\beta}\right] \ . \tag{5}$$

In (5) β is the second Dunders' parameter. Dunders' parameters for bimaterial problems are defined by

$$\alpha = \frac{\mu_1(\kappa_2+1)-\mu_2(\kappa_1+1)}{\mu_2(\kappa_1+1)+\mu_1(\kappa_2+1)}, \quad \beta = \frac{\mu_1(\kappa_2-1)-\mu_2(\kappa_1-1)}{\mu_2(\kappa_1+1)+\mu_1(\kappa_2+1)} \ , \tag{6}$$

with μ the shear modulus and κ=3-4ν for plane strain (ν is Poisson's ratio). The subscripts for μ, κ and ν in (6) identify the different materials on either side of the interface. For the silicon/epoxy materials used in this study, the oscillatory index ε=0.066 and Dunders' parameters are given by α = -0.8235, β=-0.2044.

RESULTS

In an effort to investigate interfacial crack solutions for three-dimensional (curved) crack fronts on silicon/epoxy interfaces, two different crack geometries are presented: 1) A semi-circular surface crack (Fig. 3a) and 2) A quarter-circular corner crack (Fig. 3b). Solutions are given for uniform tensile loading and thermal loading. A typical finite element model had 3400 elements consisting of 32-noded cubic hexahedrons and 26-node cubic pentahedrons with 26984 nodes. Because of the oscillatory form of the mode I and mode II interface stress intensity factors (4), the presented stress intensity factors are "rotated" using a procedure described by Rice [6], i.e.,

$$K^R_j = K_j L^{i\varepsilon} \ , \qquad j = 1,2 \tag{7}$$

$$K^R_{III} = K_{III} \ . \tag{8}$$

In (7) L is a constant arbitrarily set as 2 meters. In addition, the plotted results are normalized using the solution for a penny shaped crack, i.e., $K_{IR} = \frac{2}{\pi}\sigma_0(\pi a)^{1/2}$.

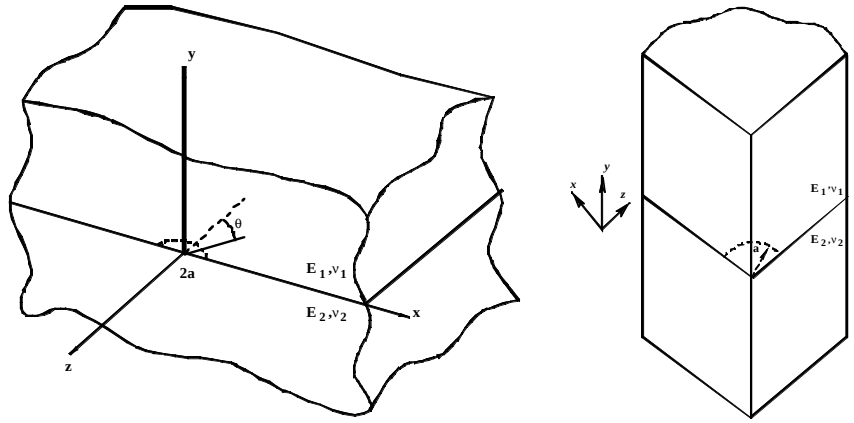

Figure 3: a) Semi-circular surface crack b) Quarter-circular corner crack.

Interfacial Surface and Corner Cracks Subjected to Uniform Tension

Figure 4a shows the normalized rotated stress intensity factors along the crack front for the case of a semi-circular surface crack on the interface between silicon and epoxy loaded in uniaxial tension. The results are given as a function of the angle θ measured from the plane of symmetry. Note that the mode I stress intensity factor increases significantly as the free surface is approached and in the neighborhood of this surface is 50% greater than the mode I stress intensity factor in the interior. K_{II}, on the other hand, decreases from the symmetry plane towards the free surface and K_{III} increases in magnitude having a negative sign. For the quarter-circular corner crack (Figs. 3b & 4b), the results are symmetric with respect to the θ=45^o plane. We also note that, although K_{II} remains almost constant along the front, a higher mode I stress intensity factor is seen near θ=45^o (middle region) than it was near the mid-plane (θ=0) for the interfacial semi-circular surface crack problem. In both problems, the mode III component of the stress intensity factor also takes its maximum value near the free surface region.

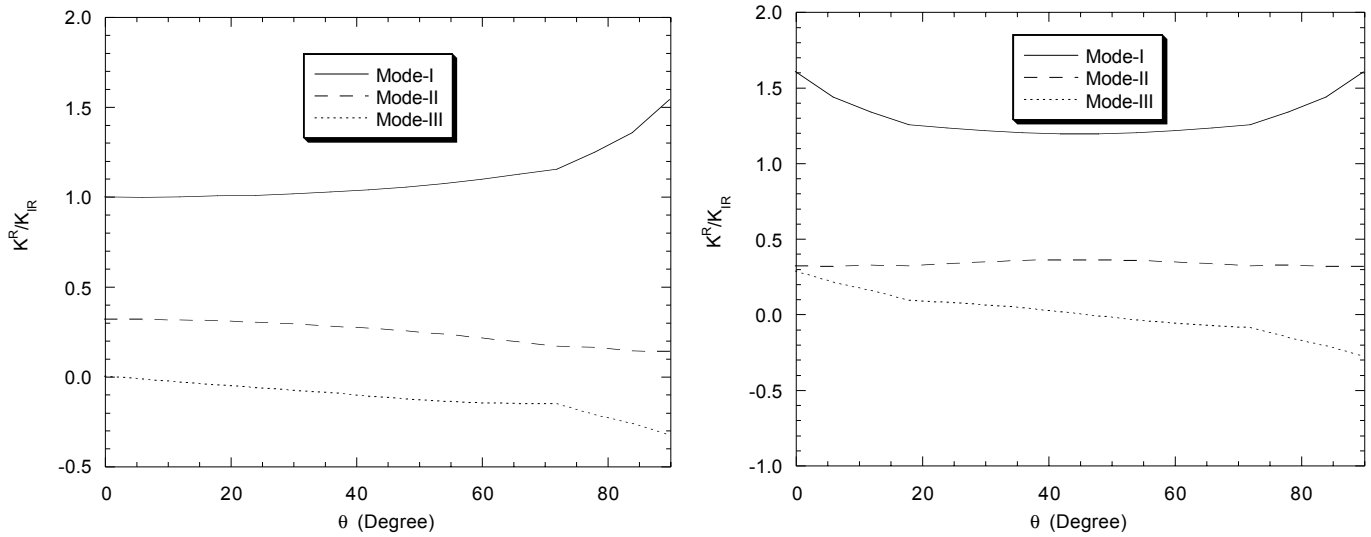

Figure 4: Normalized stress intensity factors for silicon-epoxy interface cracks subjected to uniform tensile loading. a) Semi-circular surface crack. b) Quarter-circular corner crack.

Interfacial Surface and Corner Cracks Subjected to Thermal Loading

Fig. 5a depicts the stress intensity factors along the crack front for the case of interfacial semi-circular surface crack subjected to -1^{o}C uniform cooling. There are no boundary restraints in either of these models. Normalization is again with respect to the penny shaped crack mode I solution with $\sigma_0 = 1$. As in the preceding case, K_I and K_{III} see a substantial increase as the free surface is approached. The other important point is that for thermal loading problems, the mode II and mode III stress intensity factors become as

important as the mode I component. This reflects the high mode mixity that occurs for this type of loading. It can be seen in the figures that K_{II} takes its maximum value on the symmetry plane (θ=0^o) whereas K_{III} becomes maximum in magnitude on the free surfaces. Note also that near the symmetry plane, K_I is negative. For a homogeneous crack problem this would indicate that the crack surfaces are in large-scale contact, but it is not so in this case. Because of the definition of the stress intensity factor in the bimaterial case, having a negative K_I does not always mean large scale crack surface contact, as it would in the homogeneous case. Of course, the asymptotic crack tip contact associated with the oscillatory crack tip behavior is present, but this is another matter. The stress intensity factors shown in Fig. 5b are for the case of a quarter-circular corner crack on the silicon-epoxy interface with a -1^{o}C uniform temperature change. Again, the results are symmetric with respect to θ=45^o plane and K_I and K_{II} have their maximum values near the free surface whereas K_{II} has a maximum value at θ=45^o. Comparing the results with the previous surface crack solution (Fig. 4), it can be seen that near the free surface region, the order of magnification in K_I and K_{III} are almost the same for both cases.

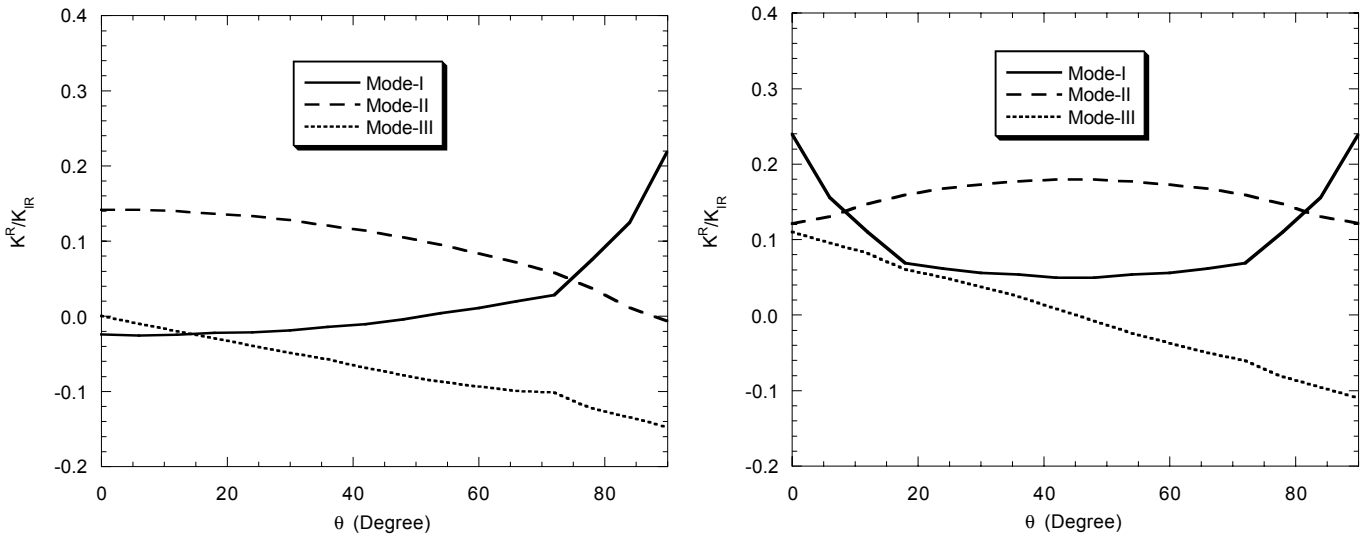

Figure 5: Normalized stress intensity factors for silicon-epoxy interface cracks subjected to -1^{o}C uniform cooling loading. a) Semi-circular surface crack. b) Quarter-circular corner crack.

ACKNOWLEDGEMENT

The support of the Semiconductor Research Corporation under Contract SRC 826.002 and a grant from General Electric's Corporate Research and Development Center is gratefully acknowledged.

REFERENCES

1. Xu, A. Q., and Nied, H. F., (2000), "Finite Element Analysis of Stress Singularities in Attached Flip Chip Packages," *ASME Journal of Electronic Packaging*, Vol. 122, pp. 301 - 305.
2. Ayhan, A. O., and Nied, H. F., (1999), "Finite Element Analysis of Interface Cracking in Semiconductor Packages," *IEEE Transactions on Components and Packaging Technology*, Vol. 22, No. 4, pp. 503 – 511.
3. Benzley, S. E., (1974) "Representation of Singularities with Isoparametric Finite Elements," *Int. J. Numer. Meth. Eng.*, vol. 8, pp. 537-545.
4. Chen, E. P., (1985) "Finite Element Analysis of a Bimaterial Interface Crack," *Theoretical Appl. Fracture Mech.*, vol. 3, pp. 257-262.
5. A. C. Kaya and H. F. Nied, (1993) "Interface Fracture Analysis of Bonded Ceramic Layers Using Enriched Finite Elements," *Ceramic Coatings*, MD-Vol. 44, edited by K. Kokini, Proceedings of the 1993 ASME Winter Annual Meeting, pp. 47-71.
6. Ayhan, A. O., "Finite Element Analysis of Nonlinear Deformation Mechanisms in Semiconductor Packages," (1999), Ph.D. Dissertation, Lehigh University.
7. Rice, J. R., "Elastic Fracture Mechanics Concepts for Interfacial Cracks," (1988), *J. of Appl. Mech.*, vol. 55, pp 98-103.

ANISOTROPIC MICROCRACK-BASED FRICTIONAL DAMAGE MODEL FOR BRITTLE MATERIALS

Luigi Gambarotta

Department of Structural and Geotechnical Engineering, University of Genova
Genova, 16145, Italy

ABSTRACT

An anisotropic constitutive model based on the assumption of linear elastic matrix weakened by microcraks is derived by assuming a tensorial description of the damage and of the unilateral and frictional effects on the displacement jump across the crack faces. Damage and sliding evolutions are obtained by defining proper limit conditions and associated flow rules. This treatment implies a different tensile-compressive response because under triaxial tensile stress states only the damage limit condition is effective, otherwise this condition must be coupled with the frictional sliding one. By considering monotonic loading paths, the constitutive equations provide limit strength domains; limit domains for the case of biaxial stress states are obtained and their dependence on the friction coefficient is shown.

KEYWORDS

Anisotropic damage, microcracked solids, friction, brittle materials, limit strength domain.

INTRODUCTION

Micromechanical models based on a representation of the material meso-structure as a population of growing microcracks embedded in an elastic matrix have been proposed by several Authors (see Krajcinovic [1]) in order to get suitable descriptions of the different response to tensile, compressive and mixed stress states exhibited by brittle materials. A direct approach, that ignores the interactions among microcracks, assumes a vector representation of the anisotropic damage and considers the unilateral frictional sliding between the crack faces; this allows a physical interpretation of the different response to tensile and compressive stress states, load and damage induced anisotropy and energy dissipation at constant damage. Unfortunately, these models involve a high number of internal variables making them useless in computational applications. As a consequence, micromechanically inspired constitutive models characterized by a reduced number of internal variables have been proposed [2,3]. On the other hand, several phenomenological models, involving a limited number of internal variables, have been proposed and applied. These models are based on both scalar-isotropic and tensorial description of damage and take into account the unilateral effect of the crack opening mechanisms by means of the concept of positive and negative projections of stress and strain tensors [4-7].
An attempt to derive a simplified damage model from a complete microcrack one [8] has been carried out by Brencich and Gambarotta [9] by assuming isotropic damage variables as a measure of the average crack size. In this model the opening/sliding effects in the microcracks were considered by two second

order tensors related to the overall normal and tangential traction on the crack faces. Moreover, the evolution equations of the internal variables were deduced by two limit conditions related to damage propagation and frictional sliding. Even if this model provides good results in terms of stress-strain response and limit strength domains, the assumption of isotropic damage implies several validity limits for the model, with particular reference to non proportional loading paths. An extension of the model to include an anisotropic damage description based on a tensorial representation was proposed in [10], but in this approach frictional effects were disregarded.

The model here presented is developed in order to describe both the anisotropic damage and the effects of frictional unilateral conditions on the displacement jumps across the crack faces. The constitutive equations are formulated in terms of a damage tensor evolving from the natural isotropic state and of tensors standing for the overall effects of normal and frictional contact traction on the microcrack faces. A further simplifying hypothesis on the representation of these tensors allows compact constitutive equations and the definition of the tensor of damage energy release rate in terms of the stress, normal and frictional tensors. Damage and sliding evolutions are obtained by coupling a damage and a frictional criterion that provide different evolution modes. Finally, the constitutive equations are applied in case of monotonic loading paths and limit strength domains for biaxial stress states, depending on the frictional parameter, are deduced; they seem to fit both the corresponding ones by the isotropic model [9] and the experimental results.

CONSTITUTIVE MODEL BASED ON THE CONCEPT OF DAMAGE PLANES

The hypothesis of representing brittle materials as an elastic solid containing a population of non-interacting microcracks, isotropically distributed at the natural state, allows the mean strain $\mathbf{E}$ to be expressed as the sum $\mathbf{E} = \mathbb{K}\mathbf{T} + \mathbf{E}_n + \mathbf{E}_t$ of the mean strain in the elastic matrix and the contributions $\mathbf{E}_n$ and $\mathbf{E}_t$ due, respectively, to normal and tangential displacement discontinuities across the crack faces, being $\mathbb{K}$ the fourth-order elastic isotropic compliance tensor and $\mathbf{T}$ the mean stress tensor. According to [8], these contributions to the mean strain may be expressed as follows:

$$\mathbf{E}_n = \frac{c_n}{2\pi}\int_{\Omega} \alpha_n^3 (\sigma_n - p_n)\ \mathbf{n}\otimes\mathbf{n} d\Omega \quad , \qquad \mathbf{E}_t = \frac{c_t}{2\pi}\int_{\Omega} \alpha_n^3 sym[(\boldsymbol{\tau}_n - \mathbf{f}_n)\otimes\mathbf{n}]\ d\Omega \quad , \tag{1}$$

where $\mathbf{n}$ is the unit vector normal to the crack plane on which the resolved stresses $\sigma_n = \mathbf{n}\bullet\mathbf{T}\mathbf{n}$ and $\boldsymbol{\tau}_n = (\mathbf{I} - \mathbf{n}\otimes\mathbf{n})\mathbf{T}\mathbf{n}$ act; c_n and c_t are the normal and tangential compliance parameters of the set of the plane crack systems not depending on $\mathbf{n}$ because the hypothesis of isotropy at the natural state; dΩ is the infinitesimal solid angle representing the neighborhood of the unit vector $\mathbf{n}$; Ω the unit hemisphere of all the orientations; p_n and $\mathbf{f}_n$ are the normal and tangential tractions acting on the crack faces; $\alpha_n (\geq 1)$ is the damage variable representing the ratio between the actual average size of $\mathbf{n}$-oriented cracks and the corresponding one at the reference state. In this approach, α_n and $\mathbf{f}_n$ play the role of internal variables, while the hypothesis of ignoring the sliding induced dilation allows the normal traction to depend on the normal stress $p_n = -\langle -\sigma_n \rangle$ by the MacAuley operator.

To get a simplified model based on a reduced number of internal variables some simplifying hypotheses are put forward. Firstly, the damage variable $a_n\ (=\alpha_n^3)$ related to each microplane is introduced and assumed to depend on $\mathbf{n}$ in the form $a_n = \mathbf{n}\bullet\mathbf{A}\mathbf{n}$, being $\mathbf{A}\ (a_{ij})$ a symmetric positive defined tensor, having $\mathbf{A}_0 = \mathbf{I}$ at the natural state. Integration of equations (1) on Ω implies:

$$\mathbf{E}_n = c_n\left(\mathbb{H}_n[\mathbf{A}]\mathbf{T} - \mathbb{P}^*\mathbf{A}\right) \quad , \qquad \mathbf{E}_t = c_t\left(\mathbb{H}_t[\mathbf{A}]\mathbf{T} - \mathbb{F}^*\mathbf{A}\right) \quad , \tag{2}$$

having introduced the positive defined fourth-order symmetric tensors:

$$\mathbb{H}_n[\mathbf{A}] = \mathfrak{H}_n\mathbf{A} = \frac{1}{105}\left\{\frac{7}{3}\ tr\mathbf{A}\ \left(\mathbf{I}\otimes\mathbf{I} + 2\mathbf{I}\boxdot\mathbf{I}\right) + 2\left(\mathbf{I}\otimes\mathbf{A}' + \mathbf{A}'\otimes\mathbf{I}\right) + 4\left(\mathbf{A}'\ \boxdot\mathbf{I} + \mathbf{I}\boxdot\mathbf{A}'\right)\right\} \quad , \tag{3}$$

$$\mathbb{H}_t\left[\mathbf{A}\right]=\mathfrak{H}_t\mathbf{A}=\frac{1}{105}\left\{7\ tr\mathbf{A}\ \left(\mathbf{I}\boxdot\mathbf{I}-\frac{1}{3}\mathbf{I}\otimes\mathbf{I}\right)-2\left(\mathbf{I}\otimes\mathbf{A}'+\mathbf{A}'\otimes\mathbf{I}\right)+3\left(\mathbf{A}'\boxdot\mathbf{I}+\mathbf{I}\boxdot\mathbf{A}'\right)\right\}\ ,\qquad(4)$$

being $\mathbf{A}'=\mathbf{A}-\frac{1}{3}(tr\mathbf{A})\mathbf{I}$, $(\mathbf{B}\otimes\mathbf{C})\mathbf{X}=\mathbf{B}(\mathbf{C}\bullet\mathbf{X})$ and $(\mathbf{B}\boxdot\mathbf{C})\mathbf{X}=\mathbf{B}(\mathbf{X}+\mathbf{X}^{\mathrm{T}})\mathbf{C}^{\mathrm{T}}/2$. The linear dependence of the previously defined tensors on the damage tensor **A** is expressed through the six order tensors $\mathfrak{H}_n$ and $\mathfrak{H}_t$ [1]:

$$\mathfrak{H}_{n,ijrshk}=\frac{1}{7}I_{ijrshk}\quad,\quad\mathfrak{H}_{t,ijrshk}=\frac{1}{20}\left(\delta_{ih}I_{kjrs}+\delta_{ik}I_{hjrs}+\delta_{jh}I_{kirs}+\delta_{jk}I_{hirs}\right)-\frac{1}{7}I_{ijrshk}\quad.\qquad(5)$$

The definitions (3) and (4) of the tensors $\mathbb{H}_n\left[\mathbf{A}\right]$ and $\mathbb{H}_t\left[\mathbf{A}\right]$ are particular cases of the general representation given in [11] because of the assumption of independence of the parameters c_n and c_t on **n** and of the damage description based on a second order tensor. Moreover, the fourth order tensors representative of the overall normal and tangential tractions on the crack faces are defined as follows:

$$\mathbb{P}^*=\frac{1}{2\pi}\int_\Omega p_n\mathbf{n}\otimes\mathbf{n}\otimes\mathbf{n}\otimes\mathbf{n}\ d\Omega\quad,\quad\mathbb{F}^*=\frac{1}{4\pi}\int_\Omega\left(\mathbf{f}_n\otimes\mathbf{n}\otimes\mathbf{n}\otimes\mathbf{n}+\mathbf{n}\otimes\mathbf{f}_n\otimes\mathbf{n}\otimes\mathbf{n}\right)\ d\Omega\quad;\qquad(6)$$

while the tensor $\mathbb{P}^*$ directly depends on **T**, the tensor $\mathbb{F}^*$ assumes the role of further internal variable of the constitutive model.

To limit the complexity of the formulation, it is assumed that the frictional contact traction may be expressed in terms of a symmetric traceless second order tensor $\mathbf{F}^*$ as follows $\mathbf{f}_n=(\mathbf{I}-\mathbf{n}\otimes\mathbf{n})\mathbf{F}^*\mathbf{n}$. A further simplifying assumption is based on the observation that when $\sigma_n\geq 0\ \ \forall\mathbf{n}$, then $\mathbb{P}^*=\mathbb{O}$ and when $\sigma_n\leq 0\ \ \forall\mathbf{n}$, then $\mathbb{P}^*=\mathfrak{H}_n\mathbf{T}$. Therefore it is assumed that tensor $\mathbb{P}^*$ may be expressed in the form $\mathbb{P}^*=\mathfrak{H}_n\mathbf{P}^*$, being $\mathbf{P}^*$ a symmetric tensor satisfying the conditions: $\mathbf{P}^*=\mathbf{0}$ if $\sigma_n\geq 0\ \ \forall\mathbf{n}$ and $\mathbf{P}^*=\mathbf{T}$ if $\sigma_n\leq 0\ \ \forall\mathbf{n}$. A possible choice for $\mathbf{P}^*$ suggested in [9] is:

$$\mathbf{P}^*=\frac{5}{2}\mathbf{P}-\frac{1}{2}(tr\mathbf{P})\mathbf{I}\quad,\quad\mathbf{P}=\frac{3}{2\pi}\int_\Omega p\mathbf{n}\otimes\mathbf{n}\ d\Omega\quad.\qquad(7)$$

Moreover, it may be easily observed by equation (4) that $\mathbb{H}_t\left[\mathbf{A}\right]\mathbf{T}=\mathbb{H}_t\left[\mathbf{A}\right]\mathbf{T}'$, being $\mathbf{T}'=\mathbf{T}-\frac{1}{3}(tr\mathbf{T})\mathbf{I}$ the stress deviator. On these hypotheses the constitutive equations are derived:

$$\mathbf{E}=\mathbb{K}\mathbf{T}+\mathbf{E}_n+\mathbf{E}_t\quad,\quad\mathbf{E}_n=c_n\mathbb{H}_n\left[\mathbf{A}\right]\left(\mathbf{T}-\mathbf{P}^*\right)\quad,\quad\mathbf{E}_t=c_t\mathbb{H}_t\left[\mathbf{A}\right]\left(\mathbf{T}'-\mathbf{F}^*\right)\ ,\qquad(8)$$

which depend on the damage **A** and friction $\mathbf{F}^*$ internal variable to be evaluated by means of proper evolution equations. Within this model the thermodynamic force associated to the damage variable is derived by the damage energy release rate and is described by the second order symmetric and positive defined tensor **Y** having components:

$$Y_{rs}=\frac{1}{2}c_n\ \mathfrak{H}_{n,hkrsij}\left(T_{ij}-P^*_{ij}\right)\left(T_{hk}-P^*_{hk}\right)+\frac{1}{2}c_t\ \mathfrak{H}_{t,hkrsij}\left(T'_{ij}-F^*_{ij}\right)\left(T'_{hk}-F^*_{hk}\right)\ ,\qquad(9)$$

besides the variable associated to the friction tensor is the sliding strain tensor $\mathbf{E}_t$. Once given the applied stress **T,** the damage tensor **A** and the sliding strain tensor $\mathbf{E}_t$, from equation (8.3) the tensor $\mathbf{F}^*$ is obtained.

EVOLUTION EQUATIONS AND LIMIT STRENGTH DOMAINS

The evolution equations are obtained by assuming both a damage and a frictional sliding criterion. The first one is based on the following assumption:

$$\phi_d\left(\mathbf{Y},\mathbf{A}\right)=\left|\mathbf{Y}\right|-R(\mathbf{A})\leq 0\quad,\qquad(10)$$

being $R(\mathbf{A})$ the overall damage toughness function to be properly chosen. When the limit condition $\phi_d = 0$ is attained then damage evolution equation is assumed:

$$\dot{\mathbf{A}} = \mathbf{V}_d \ \dot{d} \quad , \quad \mathbf{V}_d = \frac{\partial \phi_d}{\partial \mathbf{Y}} = \mathbf{Y} / |\mathbf{Y}| \quad , \qquad \dot{d} \geq 0 \quad , \tag{11}$$

that guarantees a positive energy dissipation $w_d = |\mathbf{Y}| \dot{d} \geq 0$. Moreover, the damage toughness function $R(\bullet)$ is assumed depending on the scalar variable $D = 1/3 |\mathbf{A}|^2$ ($D \in [1,\infty)$), providing a measure of the overall damage (at the natural state D=1 and $R(1)=0$). The progressive strength deterioration exhibited by brittle materials up to the limit strength and the following strain softening phase may be modeled by the toughness function, that must be chosen to attain a maximum value R_c followed by a decreasing phase for increasing damage as long as it attains vanishing values (see for instance [12]).

When compressive stress acts on some crack plane, the limit damage condition must be coupled with the frictional sliding condition. In this case tensor $\mathbf{P}^*$ does not vanish and $1/3 \mathrm{tr}\mathbf{P}^* < 0$ represents the average compressive stress on the set of compressed planes. As a result, the crack sliding is partially restrained by the frictional traction $\mathbf{f}$. In the frame of the present model, the limit condition should be formulated in terms of the global friction tensor $\mathbf{F}^{*\prime}$ and the average compressive hydrostatic pressure $1/3\ \mathrm{tr}\mathbf{P}^*$. A simplifying assumption could concern an overall frictional limit condition in a form analogous to the Drucker-Prager criterion [10]:

$$\phi_s = |\mathbf{F}^*| + \mu \ tr(\mathbf{P}^*) \leq 0 \qquad , \tag{12}$$

where μ plays the role of friction coefficient. In this case, when the limit condition is attained $\phi_s = 0$ the sliding rule is assumed:

$$\dot{\mathbf{E}}_t = \mathbf{V}_s \ \dot{\lambda} \qquad , \qquad \mathbf{V}_s = \frac{\partial \phi_s}{\partial \mathbf{F}^*} = \frac{\mathbf{F}^*}{|\mathbf{F}^*|} \qquad , \qquad \dot{\lambda} \geq 0 \ . \tag{13}$$

On these hypotheses it is possible to derive the evolution equations for the damage tensor and the friction tensor following two different possibilities depending on whether overall compression or tension is active.

In the case of tensile traction on any crack planes ($\sigma_n \geq 0$), it follows $tr\mathbf{P}^* = tr\mathbf{P} = 0$ and so also the friction tensor is vanishing $\mathbf{F}^* = \mathbf{0}$. Only the damage limit condition (10) must be considered; when the limit condition is attained $\phi_d = 0$, then the damage rate is obtained by solving the LCP:

$$\dot{\phi}_d = c_n \mathbf{T} \bullet \mathbb{H}_n[\mathbf{V}_d] \dot{\mathbf{T}} + c_t \mathbf{T}' \mathbb{H}_t[\mathbf{V}_d] \dot{\mathbf{T}}' - \tfrac{2}{3} R' \mathbf{V}_d \bullet \mathbf{A} \, \dot{d} \leq 0 \quad , \qquad \dot{d} \geq 0 \quad , \qquad \dot{\phi}_d \, \dot{d} = 0 , \tag{14}$$

that has a single stable solution if $R' = dR/dD > 0$. The condition $R' = 0$ define a limit state for the damage process corresponding to an upper limit for the stress rate; since it may be observed that this condition does not depend on the load history, it is here assumed as a limit strength condition and is expressed in the simple form $|\mathbf{Y}| = R_c$.

If a compressive traction is acting on some planes, it follows $tr\mathbf{P}^* < 0$ and the strain rate $\dot{\mathbf{E}}_t$ associated to the crack frictional sliding must be obtained by equation (13). In this case from equations (8), (11) and (13) one obtains:

$$\dot{\mathbf{T}}' - \dot{\mathbf{F}}^* = \tfrac{1}{c_t} \mathbb{H}_t[\mathbf{A}]^{-1} \left\{ \mathbf{V}_s \, \dot{\lambda} - c_t \mathbb{H}_t[\mathbf{A}] (\mathbf{T}' - \mathbf{F}^*) \, \dot{d} \right\} \quad , \tag{15}$$

that allow us to formulate the evolution equations according to four different possible initial states:

(a) *Elastic state*: $\phi_s < 0, \ \phi_d < 0$. In this case, being $\dot{\mathbf{E}}_t = \mathbf{0}$ it follows $\dot{\mathbf{F}}^* = \dot{\mathbf{T}}'$.

(b) *Friction limit state with stable damage*: $\phi_s = 0, \ \phi_d < 0$. The sliding rate $\dot{\lambda} \geq 0$ is obtained by solving the LCP:

$$\dot{\phi}_s = b_{ss}\,\dot{\lambda} + \dot{t}_s \le 0 \quad , \quad \dot{\lambda} \ge 0 \quad , \quad \dot{\phi}_s\,\dot{\lambda} = 0 \quad , \tag{16}$$

where

$$b_{ss} = \mathbf{V}_s \bullet \mathbb{H}\left[\mathbf{A}\right]^{-1}\mathbf{V}_s \quad , \quad \dot{t}_s = \mathbf{V}_s \bullet \dot{\mathbf{T}}' + \mu\, tr\,\dot{\mathbf{P}}^* \quad , \quad \dot{\mathbf{P}} = \frac{3}{2\pi}\int_\Omega \dot{p}\,\mathbf{n}\otimes\mathbf{n}\, d\Omega \quad , \tag{17}$$

that always provides a single solution. While the sliding strain rate is given by equation (13), the opening strain rate is not vanishing only if $\mathbf{P}^* \neq \mathbf{T}$ and in this case $\dot{\mathbf{E}}_t = c_n \mathbb{H}_n\left[\mathbf{A}\right](\dot{\mathbf{T}} - \dot{\mathbf{P}}^*)$.

(c) *Damage limit state with no sliding*: $\phi_d = 0,\ \phi_s < 0$. Since this implies $\dot{\mathbf{E}}_t = \mathbf{0}$, this possibility is meaningful only when some plane are compressed, that is $\mathbf{P}^* \neq \mathbf{T}$. In this case, remembering equation (15), the LCP (10) assumes the form:

$$\dot{\phi}_d = b_{dd}\,\dot{d} + \dot{t}_d \le 0 \quad , \quad \dot{d} \ge 0 \quad , \quad \dot{\phi}_d\,\dot{d} = 0 \quad , \tag{18}$$

where

$$b_{dd} = -\frac{1}{c_n}\tilde{\mathbf{E}}_t \bullet \mathbb{H}_t\left[\mathbf{A}\right]^{-1}\tilde{\mathbf{E}}_t - \frac{2}{3}R'\mathbf{V}_d \bullet \mathbf{A} \quad , \quad \dot{t}_d = c_n(\dot{\mathbf{T}} - \dot{\mathbf{P}}^*) \bullet \mathbb{H}_n\left[\mathbf{V}_d\right](\mathbf{T} - \mathbf{P}^*) \quad , \tag{19}$$

having defined $\tilde{\mathbf{E}}_t = \mathbb{H}_t\left[\mathbf{V}_d\right]\mathbb{H}_t\left[\mathbf{A}\right]^{-1}\mathbf{E}_t$. In the case $\mathbf{P}^* = \mathbf{T}$ no damage evolution is allowed. Moreover, the solution of problem (18) is unique until $b_{dd} < 0$ and the condition $b_{dd} = 0$, that depends on the load path, characterizes a limit for the stress rate.

(d) *Damage and friction limit state*: $\phi_d = 0,\ \phi_s = 0$. The evolution of the internal variables is obtained by solving the coupled LCP:

$$\begin{aligned} &\dot{\phi}_s = b_{ss}\,\dot{\lambda} + b_{sd}\,\dot{d} + \dot{t}_s \le 0 \quad , \quad \dot{\lambda} \ge 0 \quad , \quad \dot{\phi}_s\,\dot{\lambda} = 0 \quad , \\ &\dot{\phi}_d = b_{ds}\,\dot{\lambda} + b_{dd}\,\dot{d} + \dot{t}_d \le 0 \quad , \quad \dot{d} \ge 0 \quad , \quad \dot{\phi}_d\,\dot{d} = 0 \quad , \end{aligned} \tag{20}$$

where

$$b_{sd} = b_{ds} = \frac{1}{c_t}\mathbf{V}_s \bullet \mathbb{H}_t\left[\mathbf{A}\right]^{-1}\tilde{\mathbf{E}}_t \quad . \tag{21}$$

In this case the solution is unique for load control paths until:

$$\det\mathbf{B} = \frac{1}{c_t^2}\left[(\mathbf{V}_s \bullet \mathbb{H}_t\left[\mathbf{A}\right]^{-1}\mathbf{V}_s)(\tilde{\mathbf{E}}_t \bullet \mathbb{H}_t\left[\mathbf{A}\right]^{-1}\tilde{\mathbf{E}}_t) - (\mathbf{V}_s \bullet \mathbb{H}_t\left[\mathbf{A}\right]^{-1}\tilde{\mathbf{E}}_t)^2\right] + \frac{2}{3c_t}R'\mathbf{V}_d \bullet \mathbf{A} > 0\,, \tag{22}$$

a condition that is depending on the load history.

By substituting the sliding tensor rate $\dot{\mathbf{E}}_t$ and the damage tensor rate $\dot{\mathbf{A}}$ in the incremental form of equations (8) one obtains the complete constitutive equation to be applied in case of general loading histories. In the particular case of proportional load histories it is possible to obtain the limit strength condition defined as the maximum value of the stress intensity allowable by the model. In fact, when tensile stresses are acting on all crack planes ($tr\mathbf{P}^* = 0$) the limit stress state is path independent and corresponds to the condition $|\mathbf{Y}| = R_c$. If some or every crack planes are compressed ($tr\mathbf{P}^* < 0$), the limit strength domain is obtained by simultaneously imposing equations $\phi_d = 0,\ \dot{\phi}_d = 0$ and $\det\mathbf{B} = 0$, that corresponds to assume $\mathbf{F}^* = -\mu\left(tr\mathbf{P}\right)\mathbf{T}'/|\mathbf{T}'|$; this implies the limit strength criterion to be expressed in the general form $|\mathbf{Y}| = R_c$, being the internal variable in the definition (9) directly dependent on the stress tensor. It follows that the limit strength domain only depends on three material parameters: the ratio $\rho = c_t/c_n$, the friction coefficient μ and the uniaxial tensile strength σ_T. In order to show some features of the model, limit domains referred to biaxial stress states are shown in the diagrams of figure 1a.

Finally, a further simplifications can be obtained by assuming the scalar description of damage **A**=*a***I**, that provides the isotropic damage constitutive model proposed by Gambarotta and Brencich [9].

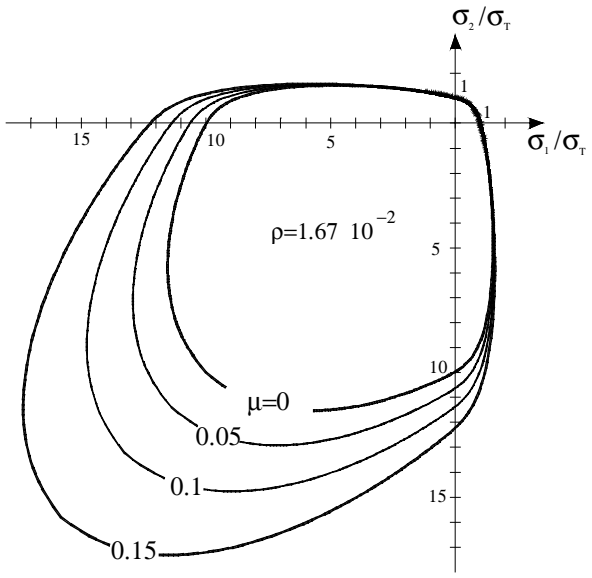

Figure 1: Biaxial limit strength domain for varying friction coefficient.

ACKNOWLEDGEMENTS

The present research was carried out with the financial support of the Department for University and Scientific and Technological Research (MURST) in the frame of the Joint Research Project "Structural integrity assessment of large dams".

REFERENCES

1. Krajcinovic D., *Damage mechanics*, Elsevier, Amsterdam, 1996.
2. Krajcinovic D., Basista M and Sumarac D., Micromechanically inspired phenomenological damage model, *J. Appl. Mech.*, **58**, 305-310, 1991.
3. Halm D. and Dragon A., Anisotropic model of damage and frictional sliding for brittle materials, *Eur. J. Mech. A/Solids*, **17**, 439-460, 1998.
4. Chaboche J.L., Damage induced anisotropy: on the difficulties associated with the active/passive unilateral condition, *Int. J. Damage Mechanics*, **1**, 148, 1992.
5. Chaboche J.L., Development of continuum damage mechanics for elastic solids sustaining anisotropic and unilateral damage, *Int. J. Damage Mechanics*, **2**, 311, 1993.
6. Lubarda V.A., Krajcinovic D. and Mastilovic S., Damage models for brittle elastic solids with unequal tensile and compressive strength, *Eng.ng Fracture Mechanics.*, **49**, 681, 1994.
7. Hansen N.R. and Schreyer H.L., Damage deactivation, *J.Appl.Mech.*, **62**,450, 1995.
8. Gambarotta L., Lagomarsino S., A microcrack damage model for brittle materials, *Int. J. Solids and Structures*, **30**,177, 1993.
9. Brencich A. and Gambarotta L., Isotropic damage model with different tensile-compressive response for brittle materials, *Int. J. Solids and Structures*, to appear, 2001.
10. Brencich A. and Gambarotta L., Anisotropic damage model for brittle materials with different tensile-compressive response, Murakami H and Luco J. (Eds.), *Proc. 12th Engineering Mechanics Conf.*, ASCE, 889-892, 1998.
11. He Q.C. and Curnier A., A more fundamental approach to damaged elastic stress-strain relations, *Int. J. Solids and Structures*, **32**, 1433-1457, 1995.
12. Gambarotta L. and Lagomarsino S., Damage models for the seismic response of brick masonry shear walls. Part II: the continuum model and its applications, *Earthquake Engineering & Structural Dynamics*, **26**, 441-462, 1997.

ORAL/POSTER REFERENCE: to be assigned

Anti-plane shear crack growth in piezoceramics: change of electric field and displacement direction

G.C. Sih[1,2,3], B. Liu[2], Z.F. Song[3], W.F. Ren[2,3]

[1] Institute of Mechanics, Chinese Academy of Sciences, Beijing 100080, China
[2] Institute of Engineering Mechanics, Hebei University of Technology, Tianjin, 300130, China
[3] School of Advanced Science and Technology, Xi'an Jiaotong University, Xi'an, 710049, China

ABSTRACT

Volume energy density factor is derived to evaluate the crack growth behavior under the electric field/shear stress boundary conditions for the PZT-4 and PZT-5H piezoelectric ceramics. Positive electric field is found to enhance anti-plane shear crack growth while negative electric field tends to retard crack growth. This result is similar to that obtained for in-plane crack extension. Crack growth solutions for electric displacement/shear strain boundary conditions, however, suggest that positive electric displacement would retard anti-plane shear crack growth while the opposite would occur for negative electric displacement. It is anticipated the same conclusion would hold for in-plane crack extension, a result that deserves future investigation.

KEYWORDS

Anti-plane shear, Crack growth, Electric displacement, Piezoelectric ceramics, Shear stress

1. INTRODUCTION

Anti-plane shear crack models have been used primarily as a guide for analyzing in-plane crack problems because they are simple to solve and behave similar to plane crack extension. Cracking of piezoelectric materials such as barium titanate and lead zirconate titanate ceramics has added complexities because of the electro-mechanical coupling effects. They possess the special features that when deform an electric field is produced and when subjected to an electric field deformation is pronounced. Such properties are induced through a process referred to as poling such that the materials become transversely anisotropic. In this spirit, the anti-plane shear crack model will be adopted in this work to better understand the in-plane crack growth enhancement and retardation behavior.

One of the unexplained cracking phenomena in piezoelectric ceramics is concerned with the situation that a crack tends to extend longer when the electric field is directed in the pole direction. If the electric field opposes the pole direction, the crack extends shorter. Past attempts [1-4] have provided many reasons why the theoretical and experimental results did not agree but failed to emphasize why they should. Only recently, the volume energy density criterion [5,6] gave results that are physically sound and did not contradict with observed data. The energy release rate remain unchanged if the electric field direction is

reversed with reference to that of the pole.
The vulnerable situation for a piezoceramic with a pre-existing crack under anti-plane is for the crack edge to be parallel with the axis of longitudinal shear and transverse anisotropic which coincides with the poling direction. In contrast to in-plane extension the applied electric field would be normal (anti-plane shear) to the pole direction rather than being parallel to each other (in-plane extension). Hence, positive and negative electric field should be referred to the coordinate axes rather than the poling direction. The difference between a positively and negatively applied electric field in anti-plane shear is to reverse the direction of poling. What is physically meaningful is to identify the combination of boundary conditions, applied field direction and material symmetry that would enhance or retard crack growth. Moreover, inappropriate use of fracture criterion could lead to results that would violate the first principle. The energy release rate criterion shows that a positive crack driving force could become negative by increasing the absolute value of the applied electric field [7,8].

2. ANTI-PLANE SHEAR CRACK

Consider the anti-plane shear of a line crack of length 2a in a transversely isotropic piezoelastic material. Referring to Fig. 1(a), the crack lies in the xy-plane while the poling direction coincides with the z-axis. At infinity, either the pair (τ_∞; E_∞) or (γ_∞; D_∞) are specified. The uniform shear stress and strain are τ_∞ and γ_∞, respectively whereas E_∞ and D_∞ are the uniform electric field and displacement, respectively.

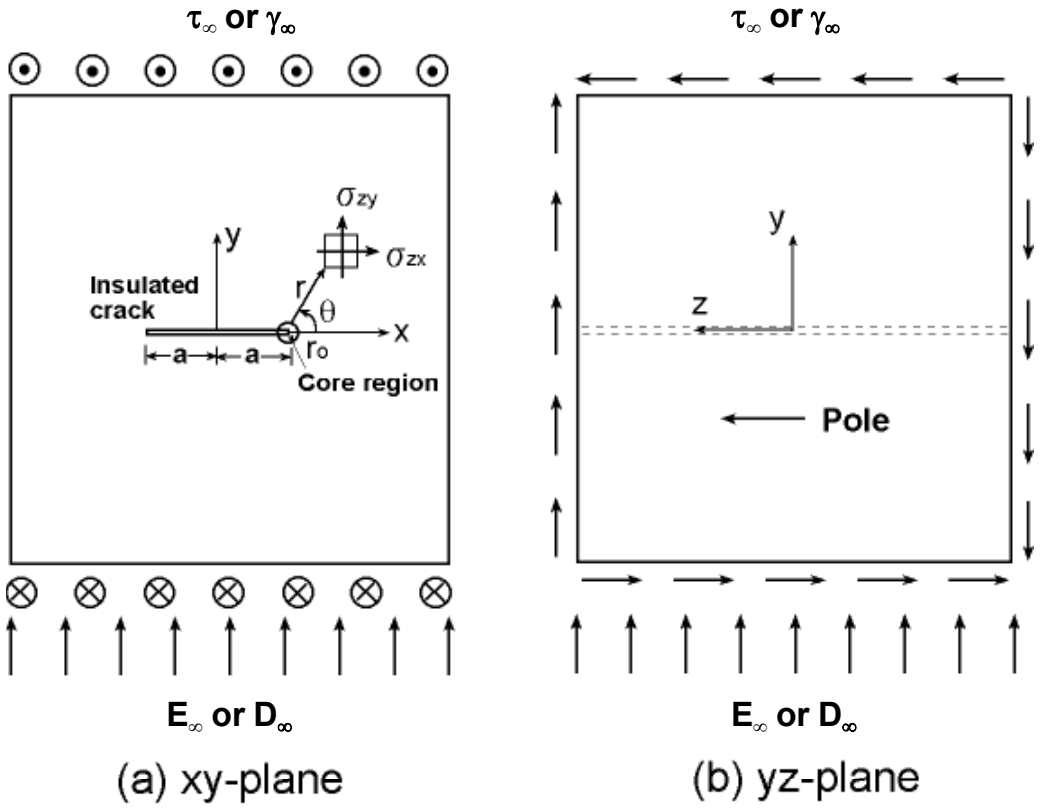

Fig. 1 Schematics of anti-plane shear crack and near tip element

2.1 Basic equations

Under anti-plane shear, there prevails only two pairs of stress and strain (σ_{zx}; γ_{zx}) and (σ_{zy}; γ_{zy}) which are functions of x and y. The in-plane electric and displacement field possess the components (E_x; E_y) (D_x; D_y), respectively. In the absence of body forces and charges, the equations of equilibrium are given by

$$\frac{\partial \sigma_{zx}}{\partial x} + \frac{\partial \sigma_{zx}}{\partial y} = 0, \qquad \frac{\partial D_x}{\partial x} + \frac{\partial D_y}{\partial y} = 0. \tag{1}$$

On the crack surface, the tractions T_z and/or surface charges q can be specified:

$$T_z = \sigma_{xy} n_x + \sigma_{yx} n_y, \qquad -q = D_x n_x + D_y n_y \tag{2}$$

where n_x and n_y are components of the unit normal vector. The constitutive relations take the forms

$$\sigma_{zx} = c_{44}\gamma_{zx} - e_{15}E_x, \qquad \sigma_{zy} = c_{44}\gamma_{zy} - e_{15}E_y \tag{3}$$

and

$$D_x = e_{15}\gamma_{xz} + \in_{11} E_x, \qquad D_y = e_{15}\gamma_{yz} + \in_{15} E_y. \tag{4}$$

only three material constants need to be specified; they are c_{44} (elastic), e_{15} (piezoelectric) and $\in_{11}$ (dielectric),

2.2 Conditions far away and on crack

Referring to Fig. 1(a), a uniform shear stress field τ_∞ or strain field γ_∞ together with uniform electric field E_∞ or electric displacement D_∞ can be specified, i.e.,

$$\sigma_{zy} = \tau_\infty \quad \text{or} \quad \gamma_{zy} = \gamma_\infty \quad \text{for} \quad x^2 + y^2 \to \infty, \tag{5}$$

and

$$E_y = E_\infty \quad \text{or} \quad D_y = D_\infty \quad \text{for} \quad x^2 + y^2 \to \infty. \tag{6}$$

Note that poling is in the positive z-direction.

The conditions on the crack surfaces are to be free of surface tractions and surface charges. They are written as

$$\sigma_{zy} = 0, \quad D_y = 0 \quad \text{for} \quad |x| < a; \quad |y| = 0. \tag{7}$$

The solution for this problem is well known [7,8]. The r and θ functions for those quantities referred to the x- and y- direction can be written as

$$\text{x-component:} \quad -\frac{1}{\sqrt{r}}\sin\frac{\theta}{2} + \cdots, \qquad \text{x-component:} \quad \frac{1}{\sqrt{r}}\cos\frac{\theta}{2} + \cdots. \tag{8}$$

Refer to Fig. 1(b) for the polar coordinates measured from the crack tip. The $1/\sqrt{r}$ singularity is the same as that found for the corresponding anti-plane shear crack in elasticity.

3. Volume energy density function and factor

The volume energy density in an element ahead of the crack, Fig. 1(b), can be computed from

$$\frac{dW}{dV} = \frac{1}{2}(\sigma_{xz}\gamma_{xz} + \sigma_{yz}\gamma_{yz}) + \frac{1}{2}(D_x E_x + D_y E_y). \tag{9}$$

Eq. (8) indicate that the singular term would dominate as $r \to 0$, the crack tip. It follows that dW/dV in eq. (9) would depend on 1/r and can be expressed as

$$\frac{dW}{dV} = \frac{S}{r}, \tag{10}$$

where r is the distance from the crack tip such that $r \geq r_o$. The core region with radius r_o is excluded from the analysis.

For the loading in Fig. 1(a), the crack would extend along the x-axis θ = 0 where dW/dV reaches a critical

value $(dW/dV)_c$ that is characteristic of the PZT material. In view of eqs. (8), all quantities referred to the x-direction would vanish and those referred to the y-direction for $\theta = 0$ can be expressed as

$$\sigma_{zx} = -\frac{K_{III}^{\tau}}{\sqrt{2\pi r}}, \qquad \gamma_{zy} = \frac{K_{III}^{\gamma}}{\sqrt{2\pi r}}, \qquad E_y = \frac{K_E}{\sqrt{2\pi r}}, \qquad D_y = \frac{K_D}{\sqrt{2\pi r}} \tag{11}$$

which can be substituted into eqs. (9). Comparing the result with eq. (10) gives the energy density factor

$$S = \frac{1}{4\pi}(K_{III}^{\tau}K_{III}^{\gamma} + K_E K_D). \tag{12}$$

For an element situated at $r = r_o$ and $\theta = 0$, the condition of $(dW/dV)_c$ is equivalent to $S = S_c$. The intensity factors in eqs. (12) stand for

$$\begin{aligned} K_{III}^{\tau} &= (c_{44}F_j - e_{15}G_j)\sqrt{\pi a}, \qquad K_{III}^{\gamma} = F_j\sqrt{\pi a} \\ K_D &= (e_{15}F_j + \in_{11} G_j)\sqrt{\pi a}, \qquad K_E = G_j\sqrt{\pi a} \end{aligned} \tag{13}$$

where j = I and II correspond to the two different types of boundary conditions (τ_∞; E_∞) and (γ_∞; D_∞) to be considered. They shall be referred to as Case I and II.

Case I specifies τ_∞ and E_∞. The contractions F_1 and G_1 in eqs. (13) given by [7]:

$$F_I = \frac{\tau_\infty + e_{15}E_\infty}{c_{44}}, \quad G_I = E_\infty \tag{14}$$

Putting eqs. (14) into (13) and normalizing eq. (12) with respect to $\tau_\infty^2 a/(4c_{44})$, it can be shown that

$$S/(\frac{\tau_\infty^2 a}{4c_{44}}) = 1 + 2e_{15}p + (c_{44}\in_{11} + e_{15}^2)p^2, \quad \text{Case I} \tag{15}$$

where $p = E_\infty/\tau_\infty$ is a load factor.

Case II specifies γ_∞ and D_∞. The quantities F_j and G_j in eqs. (13) for j = II are known from [7]. They can be put into eq. (12) to render

$$S/(\frac{\gamma_\infty^2 a}{4\in_{11}}) = (c_{44}\in_{11} + e_{15}^2) - 2e_{15}q + q^2, \quad \text{Case II} \tag{16}$$

where $q = D_\infty/\gamma_\infty$ is a load factor.

Eqs. (14) and (15) show that the volume energy density factor S could increase or decrease with reference to the ratios of the electric field to shear stress or electric displacement to shear strain depending on the properties of piezoelectric materials.

4. Crack growth criterion

The form of eq. (10) has been used as a criterion [9,10] for crack initiation and growth. A crack is assumed to grow in segments of $r_1, r_2, \ldots, r_j, \ldots, r_c$ after dW/dV in an element at $r = r_o$ shown in Fig. 1(b) has reached $(dW/dV)_c$, i.e.,

$$\left(\frac{dW}{dV}\right)_c = \frac{S_1}{r_1} = \frac{S_2}{r_2} = \cdots = \frac{S_j}{r_j} = \cdots = \frac{S_c}{r_c} = \text{const.} \tag{17}$$

The first increment r_1 is measured from the core region r_o. Hence, the half crack length would increase from a to $a+ r_o+ r_1$. Each subsequent step can be treated in the same way.

4.1 Effect of electric field and displacement reversal

The effect of electric field and displacement will be examined. Now, let the superscripts +, 0, - be attached to those quantities that refer, respectively, to E_∞ or D_∞ that are positive, zero, and negative. Positive E_∞ or D_∞ corresponds to the positive direction of the coordinate axis. The corresponding crack growth segments are r_j^+, r_j^o and r_j^- while the volume energy density factors are S_j^+, S_j^o and S_j^- where j = 1, 2, etc. It follows from eq. (17) that for the jth segment of crack growth yield the expression.

$$\frac{S_j^+}{r_j^+} = \frac{S_j^o}{r_j^o} = \frac{S_j^-}{r_j^-}, \qquad j = 1, 2, \text{etc.} \tag{18}$$

Once the energy density factors are known, the crack growth segments can be computed for different boundary conditions to examine how the direction of applied electric field displacement would affect crack growth. Numerical results will be made available for the PZT-4 and PZT-5H piezoelectric materials. Their elastic, piezoelectric and dielectric constants can be found in Table 1.

TABLE 1
Elastic piezoelectric and dielectric constants

Material	Material constants		
	$c_{44} \times 10^{10}$ (N/m^2)	e_{15} (C/m^2)	$\in_{11} \times 10^{-10}$ (C/Vm)
PZT-4	2.56	13.44	60
PZT-5H	3.53	17.00	151

4.2 Case I: Positive and negative electric field

Note from eq. (15) that a change in the sign of p, i.e., positive and negative E_∞ would affect the value of the energy density factor S. Using the case of E_∞= 0 or $S/(\tau_\infty^2 a/4c_{44}) = 1$ as reference, the ratio S_1^+/S_1^o and S_1^-/S_1^o can be calculated. This also gives r_1^+/r_1^o and r_1^-/r_1^o because they are directly proportional, eq. (18). The numerical results are summarized in Table 2 for different values of $p = E_\infty/\tau_\infty$. Plotted in Fig. 2 are the numerical values in Table 2. Both curves go through the coordinate p = 0 and $r_1^\pm/r_1^o$ =1. The crack growth segment is greater than r_1^o for positive E_∞ and smaller than r_1^o for negative E_∞. This indicates that $+E_\infty$ and $-E_\infty$ would enhance and retard crack growth. Such a trend continues to prevail for the subsequent crack growth segments because of the relation [11]

TABLE 2
. Normalized first crack growth segments $r_1^\pm/r_1^o$ for Case I (τ_∞; E_∞)

Material	$E_\infty/\tau_\infty \times 10^{-3}$ (Vm/N)						
	-15	-10	-5	0	5	10	15
PZT-4	0.672	0.765	0.874	1	1.143	1.302	1.478
PZT-5H	0.675	0.742	0.851	1	1.191	1.422	1.695

$$\frac{a}{r_1} = \frac{a + r_1}{r_2} = \frac{a + r_1 + r_2}{r_3} = \cdots = \text{const.} \tag{19}$$

The results $r_1^+/r_1^o > 1$ for $+E_\infty$ and $r_1^-/r_1^o < 1$ for $-E_\infty$ is similar to those found for in-plane crack extension [6]. A sign change in E_∞ alters the ways with which the electrical and mechanical properties of the material would interact with external disturbance. This causes the crack to grow longer for $+E_\infty$ and shorter for $-E_\infty$.

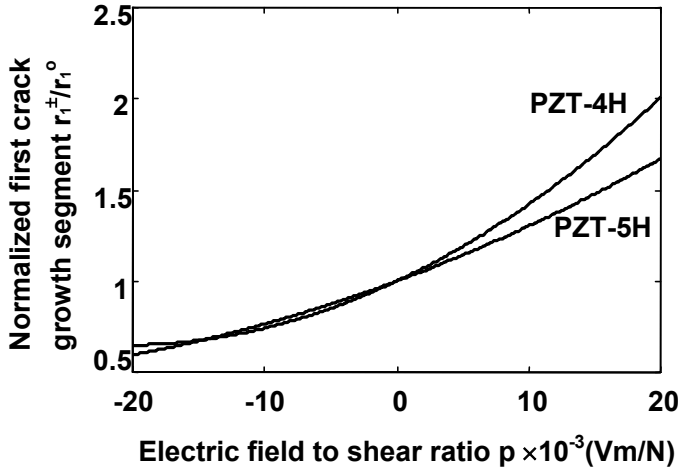

Figure 2: Normalized crack growth segment as a function of electric field to shear stress ratio

4.3 Case II: positive and negative electric displacement

When strain γ_∞ and electric displacement D_∞ are specified on the remote portion of the boundary, Fig. 1(a), the coupling of the electrical and mechanical properties would react differently when the direction of the electric displacement D_∞ is changed. This can be exhibited by solving for S in eq. (16) for the PZT-4 and PZT-5H materials. Following the exact procedure as discussed earlier for Case I and eq. (15), the numerical values of $S_1^{\pm}/S_1^o$ are first obtained. Application of eq. (18) gives $r_1^{\pm}/r_1^o$ from which eq. (19) gives the other growth steps $r_j^{\pm}/r_j^o$ for j = 2, 3, etc. The results for the first step are outlined in Table3.

TABLE 3

Normalized first crack growth segments $r_1^{\pm}/r_1^o$ for Case II (γ_∞; D_∞)

Material	D_∞/γ_∞ (C/m^2)						
	-15	-10	-5	0	5	10	15
PZT-4	2.880	2.103	1.477	1	0.673	0.459	0.467
PZT-5H	1.894	1.535	1.237	1	0.824	0.708	0.653

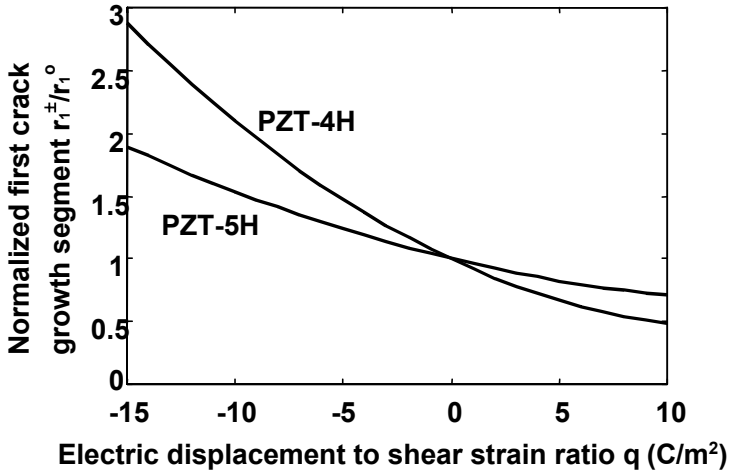

Figure 3: Normalized crack growth segment as a function of electric displacement to shear strain ratio

In contrast to Case I for specifying (τ_∞, E_∞), the crack growth behavior for Case II where (γ_∞, D_∞) are prescribed reacts in an opposite manner. Negative D_∞ decreases crack growth while positive D_∞ decreases crack growth. Such a trend is displayed in Fig. 3. The curves also intersect at q = 0 and $S/(\gamma_\infty^2 a/4 \in_{11}) = 1$. However, their slopes are negative instead of being positive as those in Fig. 2. For Case I. These results are new and are expected to prevail for in-plane a crack extension as well.

5. CONCLUSIONS

Further application of the volume energy density criterion show the enhancement/retardation behavior of crack growth in anti-plane shear is the same as that for in-plane crack extension [5,6]. However, when the stress/electric field boundary conditions are replaced, a reversal of the enhancement/retardation behavior is predicted. Using D_∞= 0 as the base, crack growth would be increased for negative D_∞ and decreased for positive D_∞. These effects are just the opposite to those for prescribing E_∞ and τ_∞.

Experimental verifications of the above findings for anti-plane shear crack growth are impractical because it is next to impossible for producing a pure longitudinal shear mode. Some degree of opening mode would always be present ahead of a tunnel crack especially for the ceramic-like materials that are hard and brittle. The aim of this work is to provide the motivation for solving the electric displacement/strain boundary-value problem for in-plane crack extension. Displacement boundary condition experiments could be designed and performed to show that positive D_∞ would retard crack growth whereas negative D_∞ would enhance crack growth. This is contrary to the observations made in [1,2] for crack growth under the electric field/stress boundary conditions.

References

1 Tobin and Y.E. Pak, Effects if electric fields on fracture behavior of PZT ceramics. Smart Materials, ed. V.K. Varadan, SPIE Vol.1916, pp.78-86, 1993.

2 Y. E. Pak and A. Tobin, On the electric field effects in fracture of piezoelectric materials. Mechanics of Electromagnetic Materials and Structures, AMD-Vol.161/MD-Vol.42, ASME, 1993.

3 H. Gao, T. Y. Zhang and P. Tong, Local and global energy release rates for an electrically yielded crack in a piezoelectric ceramic. J. Mech. Phys. Solids, 45 (1997), 491-510.

4 S. Park and C. T. Sun, Fracture criterion of piezoelectric ceramics. J. Am. Ceram. Soc., 78 (1995), 1475-1480.

5 J.Z. Zuo and G.C. Sih, Energy density formulation and interpretation of cracking behavior for piezoelectric ceramics, J. of Theoretical and Applied Fracture Mechanics, 34 (1) 2000, 17-33.

6 G.C. Sih, J.Z Zuo, Multiscale behavior of crack initiation and growth in piezoelectric ceramics, J. of

Theoretical and Applied Fracture Mechanics, 34(2000) 123-141.
7 Y.E. Pak, Crack extension force in a piezoelectric material, J. of Applied Mechanics, 57(1990) 647-653.
8 Y.E. Pak, Linear elecro-elastic fracture mechanics of piezoelectric material, Int'l J. of Fracture (54) (1992) 79-100.
9 G.C. Sih, Mechanics of Fracture, Volume I to VII, Sijhoff and Noordhoff International Publisher, The Netherlands, 1973-1981.
10 G.C. Sih, Mechanics of fracture initiation and propagation, Kluwer Academic Publishers, The Netherlands, 1991.
11 G.C. Sih, Fracture mechanics of engineering structural components, Fracture Mechanics Methodology, G.C. Sih, L. Faria, eds., Martinus Nijhoff Publishers, The Netherlands, 35-101 (1984).

ORAL REFERENCE: ICF100886OR

APPLICATION OF RISK-BASED MAINTENANCE WITH LIFE AND FINANCIAL ASSESSMENT ON FOSSIL-FIRED POWER PLANTS

Akio FUJI, Haruki EGUCHI, Chie FUKUOKA, Tatsuro TANOUE, Jun TAKAHASHI,
Yoshiaki OKATSUKA, Shigemitsu KIHARA

Research Laboratory, Ishikawajima-Harima Heavy Industries Co., Ltd.
3-1-15 Toyosu Koto-ku Tokyo, 135-8732 Japan

ABSTRACT

A risk-based maintenance (RBM) technique has been generated to optimize inspection and maintenance plans for fossil-fired power plants which will be deregulated in Japan. In the present study, technological advances and problems are considered that have resulted from the application of the RBM to actual boiler plants with operating times exceeding 100,000 hours. Risk is defined as the product of the likelihood of damage in plant components by the consequence due to failure of the components or system. The present study found that the RBM is a useful decision tool for determining inspection priority, mitigation of undesirable risk, extension of the inspection period, and other improvements in maintenance practice. At the same time, serious potential problems are brought out.

KEYWORDS

Risk-based maintenance, Fossil-fired power plant, Inspection, Likelihood, Consequence, Residual life prediction, Damage, High temperature component

INTRODUCTION

Risk-based maintenance (RBM) provides strategies for optimizing safety as well as maintenance costs for degraded components of boiler plants that have accumulated operating times exceeding 100,000 hours. The maintenance strategy consists of plans for inspections, repair, refurbishment, and replacement based on the risk assessment. The risk is defined as the product of likelihood of failure by the consequence severity. In Europe and the United States, major oil companies have already implemented RBI (Risk-based inspection) technique several years ago. As a result, several guidelines [1,2,3,4] have been published for RBI/RBM techniques. Some papers [5,6,7] were published on practical use of RBI/RBM to petrochemical plants and fossil-fired power plants. Furthermore, the practical guideline [8,9] and the standard [10] for nuclear power plants have also been published. In Japan, the RBI/RBM has lately attracted considerable attention as a new technique for maintenance planning of fossil-fired power and petrochemical plants that will be deregulated. In this study, the RBM technique has been provided as a systematic analysis of qualitative and semi-quantitative judgments for failure likelihood and consequence by calculating the risk ranking. As results of the application of RBM

intended for actual boiler plants with accumulated operating times exceeding 100,000 hours, many advances and problems of the technique are considered to frame optimized risk scenarios.

PROCEDURE AND RESULTS OF RBM INTENDED FOR THE 600MW BOILER PLANT

Procedure of RBM

The overall procedure of RBM is shown in Fig.1.

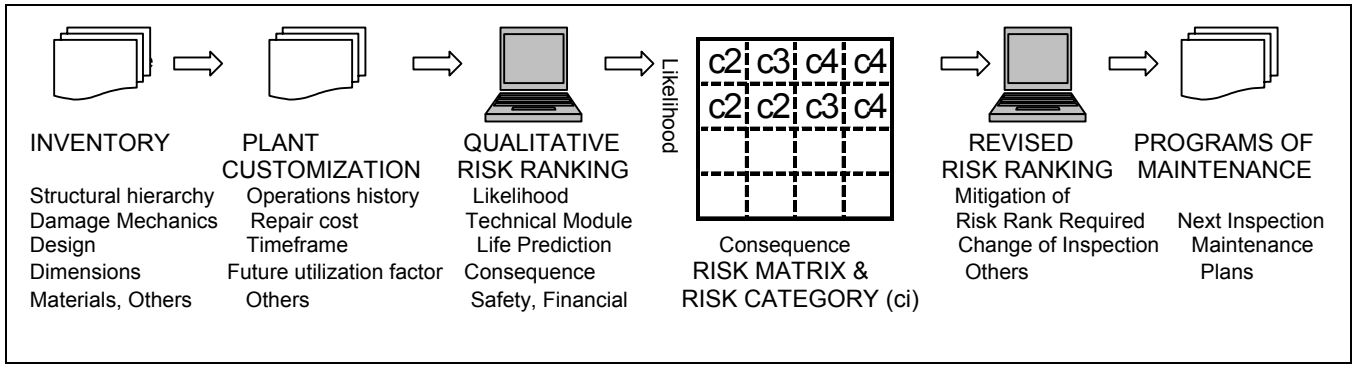

Figure 1: Procedure of RBM

Inventory and plant customization

The first step is to classify components and locations of a plant with a hierarchical structure in terms of the risk assessment and to define the risk of components and locations in the plant considering the operating conditions in terms of a standard rule. The aim of inventory is to include all relevant components, and identify all potential degradation locations. Table 1 shows the reheater system that consists of 8 components such as header, tube and so on in the 600MW boiler plant. Furthermore, those are divided into 43 locations as assessed locations with collection of each material specification, dimension, design data, and operating history and so on. Number of all locations in the 600MW boiler plant is about 500. Damage mechanisms to be fear at each location were defined for the risk assessment with inspection records and the residual life assessment data concerning the operating history.

TABLE 1

INVENTORY FOR THE ESTIMATED REHEATER SYSTEM IN THE 600MW BOILER PLANT

Unit	System	Component	Location (Number of Locations)
K- Power Plant No. N-Boiler	Reheater	Reheat inlet Header	Shell weld etc. (7)
		RH tube-Inlet short tube	Tube etc. (2)
		RH tube-Horizontal Lower Stage	Tube, Oval Tie Lugs etc.(4)
		RH tube-Horizontal Middle Stage	Tube, Oval Tie Lugs etc. (5)
		RH tube-Horizontal Upper Stage	Tube, Oval Tie Lugs etc. (4)
		Tube-Vertical Upper Stage	Tube (SUS321, STBA24) etc. (6)
		Tube-Unheated Region	RH outlet tube etc. (7)
		Reheat Outlet Header	Shell Seam and Circ weld etc. (8)
Total Number		8 Components	43 Locations

Table 2 shows the plant customization included the operating condition for the estimated boiler. The assessment time is defined as the number of operating hours expected to be accumulated up to the next but one inspection. In order to demonstrate the utility of the method for validation of extension to the inspection period, the risk assessment assuming that an extension of inspection period from 24 months to 48 months, can be carried out in this study.

TABLE 2

CUSTOMIZATION FOR THE ESTIMATED REHEATER SYSTEM OF 600MW BOILER

Item	Subject	
Operating history	Boiler On-Load	about 117,000 hours
	total number of hot starts, warm starts, cold starts	about 600 times
Assumed Current Inspection Plan	Outage Frequency	24 months
	Expected Utilization	70 %
	Service hours at next outage	about 137,000 hours
Assumed Revised Inspection Plan	Outage Frequency	48 months
	Expected Utilization	70 %
	Service hours at next outage	over 150,000 hours
Cost of one day outage		about ¥ 8 million

Risk Assessment

As mentioned before, the risk is defined as the product of likelihood of failure and the consequence. Likelihood of failure ($L=F$ x M) can be derived from multiplication of failure frequency (F) from the database based on general failure cases or personal experiences by a revised factor (M). The revised factor M can be obtained from considering factors of inspection program (monitoring), degradation of materials, conditions of construction, and operating conditions of the past and the future by following each module for judgment. The factor M needs to have weighting factors in terms of their likelihood. This idea is according to standard ideas in RBI/RBM through API [1,2] and ASME [3,4] guidelines. The consequence of failure can be calculated from safety consequence (injury or death) and financial consequence (plant outage, repair cost, and injury or death of plant operators). Financial consequence is usually expressed by cost or money.

Skilled engineers on the design, the maintenance, operating, inspection, metallurgy, and structural strength perform the risk assessment with the systematical judgment procedure under the following two steps.

Primary qualitative risk category of each location is decided in the timeframe of 24 months assumed as a current inspection period. Any potential degradation mechanism that can cause component failure is assessed using the qualitative / semi-quantitative risk ranking (QRR) procedure. This involved assessing the likelihood of failure, and separately, the consequence of failure of that specific location, by the damage mechanism. Safety risk ranking and financial risk ranking are both determined, using the risk matrix as shown in Fig.1. Following the risk category plotted in the matrix, actions to reduce the risk are required. The risk category and required actions are expressed as shown in Table 3.

TABLE 3
REQUIRED ACTIONS FOLLOWING THE RISK CATEGORYS WITHIN THE TIMESCALE

Risk Category (Fig.1)		Required Actions
Category 1	Acceptable	No inspection or other actions are required, considered unless to safety national legislative requirements
Category 2	Acceptable with controls	Define and implement an appropriate revised inspection, assessment strategy to support risk ranking judgment
Category 3	Undesirable	Mitigate to Risk Category 1 or 2 within the timescale of the next overhaul, in the following actions (1) Improved inspection procedures (2) Improve operating practices or controls (3) On-line plant monitoring (4) Engineering measures to mitigate consequence
Category 4	Unacceptable	Mitigate immediately to Risk Category 1 or 2 as above

Assessed locations with the high risk (Category 3 or Category 4) are considered to reduce the risk to Category 1 or 2 by effective inspection methods or actions. Consequently, necessary actions are determined to obtain “Acceptable or Acceptable with controls” conditions.

In the next step, revised qualitative risk ranking (RQRR) is carried out. In this study, the mitigation of the risk category with actions according to Table 3 is considered. At the same time, the risk change due to extension of the inspection period of 24 months to 48 months is assessed.

Results and consideration on RBM for 600MW boiler plant

Figure 2 shows the plots of risk matrices for assessment results on typical locations. Fig. 2(a) describes the risk ranking within the current inspection requirement (every two years for regular inspection). Most of the components in the matrix were ranked as "Category 1; Acceptable". Fig. 2(b) shows results of the revised risk ranking in assumption of the inspection period of every four years. Results shown in Fig. 2(b) expressed the effects of both extension of inspection period and the required actions considered in revised risk ranking (RQRR).

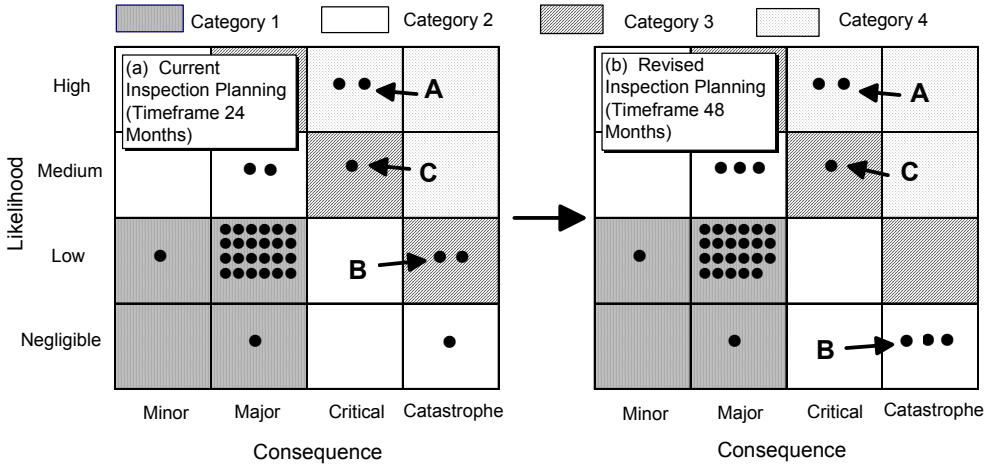

(a) Current Inspection Planning (b) Revised Inspection Planning

Figure 2: Examples of RBM assessment results on the reheater system of 600MW boiler

As shown in Fig.2 (b), almost of the locations were plotted in the "Category 1; Acceptable", even though extension of the inspection period from two years to four years was assumed. Risk at the location (B) in the figure was mitigated by the revised risk assessment. High risk at some locations (A, C) expresses not to change the Category after considering required actions or improvement of the inspection.

Details of assessment at the high-risk locations (A, B, and C in Fig. 2) are described as follows.

Location (A); Reheater Outlet Tube (STBA24 unheated tube) – thinning of wall

The residual life at this location was assessed to be just over two years by consideration of thinning rate at the tube wall due to both oxidation and calculating the creep life. Therefore, the result indicated that the risk was too high for the likelihood of failure. Although the safety consequence was "Negligible", the financial consequence was "High" according to the failure. Consequently, final risk assessment of the location was "Category 4; Unacceptable". In the revised risk assessment (RQRR) to clarify the problem, any solutions or actions to reduce the risk could not been found. Finally, urgent replacement of the component was decided as the only action to reduce the risk. This result was in consistent with the actual action that the component had been replaced at an outage recently.

Location (B); Reheater Outlet Header - creep damage of seam weld

At the location, initiation and growth of internal cracks due to circumferential stress have been reported in abroad. According to experiences in the oversea plant, the likelihood at the location should be ranked as "High". In Japan, there is, however, no experience of the failure at the location. Consequently, the risk rank as "Low" was considered. Furthermore, the current inspection methods of PT (Dye Penetrant Test) or MT (Magnet Particle Test) were not enough to assess the internal damage of the header wall. The financial consequence was ranked as "Catastrophe". According to this assessment, the risk of the component was assessed as "Category 3; Undesirable". In the revised risk assessment (RQRR), the risk ranking was reduced by improvement of the inspection technique, using UT (Ultrasonic Test, TOFD method) to be possible to detect the internal damage. Finally, the action allowed

the risk to be reduced to “Category 2; Acceptable with Controls”.

Location(C); Reheater Outlet Vertical Tube - damage by oxidation and creep

At the location, the excessive wall-thinning rate has been found recently with continuous periodic measurement of wall thickness by the ultrasonic equipment. Although problems in terms of inspection methods and locations of measurement concerning the reason of excessive thinning were considered, it was not possible to reduce the risk from “Category 3; Undesirable” to “Category 2; Acceptable with Controls” by any actions. Therefore, the replacement should be considered. Consequently, the obtained result in the assessment was consistent with the actual replacement of the component that had been replaced at a outage recently the same as reheater outlet tube plotted as A in Fig.2.

ADVANDAGES AND FUTURE TASKS OF RBM

As the results of RBM assessment, many advantages were found in the maintenance planning as follows.

(1) Covering all locations of a unit concerning the damage by inventory. (2) Effective information handed down from experiences of the experts in consistence with RBM results. (3) Improvement of the safety assessment with global standards and damage mechanisms (4) Decision making of maintenance items among several units of the plant based on the priorities decided by RBM. (5) Clarifying the reasons of inspections and repairs for reaching a consensus among the maintenance department, the investment department in the plant customer, public inspection organizations and others. (6) Omitting the current inspections at locations assessed as low-risk categories. (7) Smooth transition of inspection record stored by papers to the electric system. (8) Others.

At the same time, future tasks are justified on the basis of development of risk scenarios. The consequence scenarios concerning financial factors should include systematically the assets assessment due to the scale of power generation, the type of usage of the boiler (utility or industrial), financial strategy of the plant customer, and others as shown in Fig. 3. The quantitative judgment system that could reflect the subjective probability of expert opinions and experiences with the numerical data of the residual life assessment should be developed in the likelihood ranking.

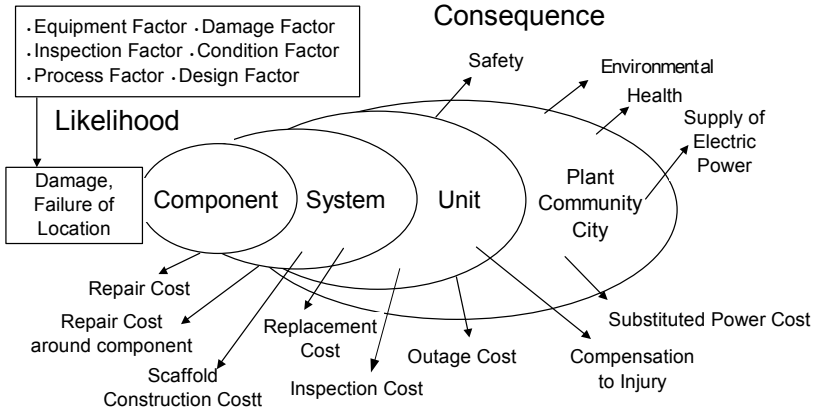

Figure 3: Development of consequence scenario

CONCLUSIONS

Risk based maintenance (RBM) technique has been applied to the actual fossil-fired power plants. As results, it is concluded that many advantages for the maintenance planning is expected. The

RBM could be attracted considerable attention as a new technique for maintenance planning of fossil-fired power plants that will be deregulated in Japan. At the same time, the systematic and quantitative method for framing risk scenarios such as the assets assessment should be developed. Valuable databases of failure cases and knowledge-based information by expert's experiences are also required to apply the RBM effectively to various plants and structural components.

ACKNOWLEDGMENTS

The authors are grateful to Mr. Bob Browne and Dr. David Worswick of AEA Technology for providing consultation while the study was being conducted.

REFERENCES

1. The American Petroleum Institute (1996). *Preliminary Draft API Publication* PD581
2. American Petroleum Institute (2000). *API Publication* 581
3. The American Society of Mechanical Engineering (1991). *CRTD* 20-1
4. The American Society of Mechanical Engineering (1994). *CRTD* 20-3
5. Reynolds J. T. (1998). *PVP conf., ASME*, 360, PP.63-71
6. Winter P.W. and Browne R. J. (1999). *IRR Int. Forum, London*
7. Munson R. E. et al. (1996). *PVP conf. ASME*, 336, PP.135-138
8. The American Society of Mechanical Engineering (1993). *CRTD* 20-2
9. Gosselin S. R. et al. (1997). *ICON-5, Nice*, 2641
10. The American Society of Mechanical Engineering (2000), *Sec. XI code case* N-560, N-578

Application of ultrasonic peening to improving fatigue properties of welded joints

Huo Lixing[1], Wang Dongpo[1], Zhang Yufeng[1], Chen Junmei[1]

[1]College of Material Science and Engineering, Tianjin University, Tianjin 300072, China

Keywords: Fatigue strength, Ultrasonic peening, Low carbon steel, Welded joints

ABSTRACT

Fatigue strength of welded joints in welded structures are much lower than that of base metals. Many experiments show that the fatigue crack normally initiates at welded toe, so that the fatigue strength can be increased dramatically by peening weld toe.[1,2,3]

Ultrasonic peening made by Tianjin University in China under the financial support of Natural Science Foundation of China is one of the most useful methods to improve fatigue behavior of weld toe due to improving toe geometry, removing defects and modifying the residual stresses distribution in this region.

For evaluating the ultrasonic peening performance carried out by our equipment, the fatigue tests were performed on butt and cruciform joints of Q235B steel both in the as-welded and peened condition. Test results are as follows:

1.Both butt and cruciform peened joints show a significant increase in fatigue life under different stress levels (high cycle fatigue). The results show that the fatigue life of the peened weld toe was 20~30 times as long as the as-welded joints, and in many cases the fatigue cracking initiation was transferred to the base metal instead of the weld toe.

2.The increase in fatigue strength (at 2×10^6 cycles)of the peened Q235B butt welded joints compared to the as-welded joints was 57%,and for the cruciform joints, the increase was 64~71%. The fatigue strength of both the butt and cruciform welded joints were no lower than that of the base metal. In such cases, weld joints is not the degense location any longer.

1. INTRODUCTION

Fatigue is one of the main forms of the failures of the welded structure. Many experiments show that the fatigue crack mainly initiates at the weld toe, so that the fatigue strength can be increased by treatment the welded toe.[1.2]

Ultrasonic peening made by Tianjin University in China under financial support of Natural Science Foundation of China is one of the most useful methods to improve fatigue life due to improving toe geometry, removing defects and introducing benefit compressive residual stress, as well as 1) It can be used not only for plate butt joints, but also for the tube joints, to which it is difficult by using other methods, such as TIG dressing. 2) It can be applied not only to the process of structure manufacturing in the working shop, but also to the field welding condition such as to bridges, oil platforms, ships and so on. 3) High treatment velocity (at the velocity of half meter per

minute). 4) Other advantages: it don't produce noise; the whole device is not heavy. (the peening unit weight is only several kilograms.)

Fig.1 is the picture of the ultrasonic peening device. One of the most important part in peening device is energy transform part, which based on piezoelectric ceramic transducer, is convenient to use for its small size, light weight, lower power to supply and easy to apply. The equipment is matched with the special ultrasonic power generator which used IGBT as the higher power component, matched with delicate frequency tracing system and the constant vibrating velocity control system, controls the quality of the ultrasonic peening results. The peening unit, named ultrasonic peening gun, consists of the sound system, shell and holder, and was designed to give high treatment velocity (at the velocity of half meter per minute) and strong peening force.

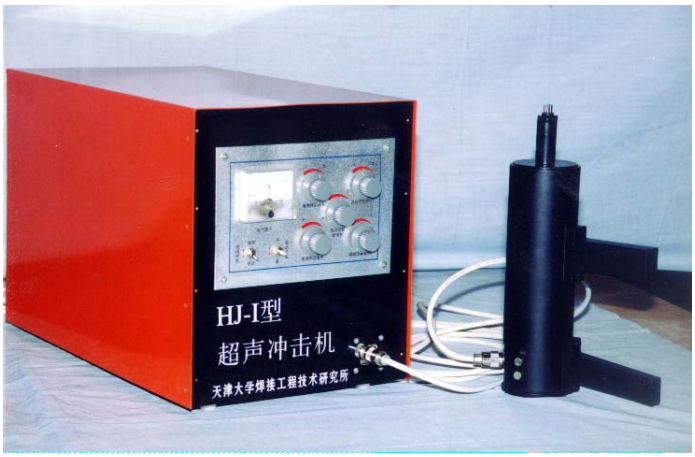

Fig.1.Ultrasonic peening device

2. MATERIAL, SPECIMENS AND TESTING CONDITION

Table 1.Mechanical properties of Q235B steel

material	σ_s /MPa	σ_b /MPa	δ
Q235B	267.4	435.5	26%

The material used in this research program is Q235B steel. Table 1 gives the mechanical properties of this steel. Both as-welded and peening conditions of the cruciform (under tensile) and the butt (under four-point bending) joints were considered in this study. The welding parameters are given in table 2.

2.1.Preparation of butt Welded Joints

On the surfaces of each piece of the specimen, a X groove was cutting and a thickness equity to 1mm was left in the middle of the specimen in order to prevent or reduce distortion. The welds were

Table 2. Welding process parameters

Joints	（1 pass）welding current（A）	（2 pass）welding current（A）	Welding Voltage（V）
Butt joints	110	120	24~30
Cruciform joints	130	150	25~30

produced in two passes by manual arc welding with J422 electrode.

2.2.Preparation of Cruciform welded joint:

A X groove with 60° angle was cutting for the load-carrying piece of the specimen. The welds were produced in two passes by same manual arc welding with J422 electrode. In order to prevent or reduce distortion, spot-fixing weld was accepted and opposite distortion was taken before welding.

2.3.Fatigue Tests:

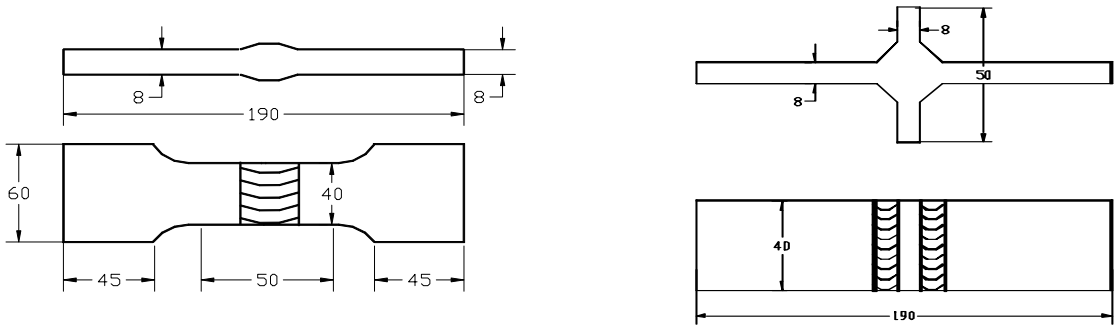

Fig.2.Shapes and dimensions of speci

The fatigue tests were performed on a high-frequency fatigue testing machine with a capacity of 100KN. For the butt joints subjected to tensile loads, a stress ratio R=0.1 was selected. For the cruciform joints subjected to four point bending, the stress ratio R=0.25 and R= - 0.5 were selected.

2.4.Ultrasonic Peening Operation

The peening gun was held approximately normal to the weld face and inclined at 45° to the base metal surface. The gun was move along the weld at an approximate speed of 0.5m/min and two times peening were used to obtain smooth weld toe geometry. The current of the device used is 0.5 ampere.

3.EXPERIMENTAL RESULTS AND DISCUSSIONS

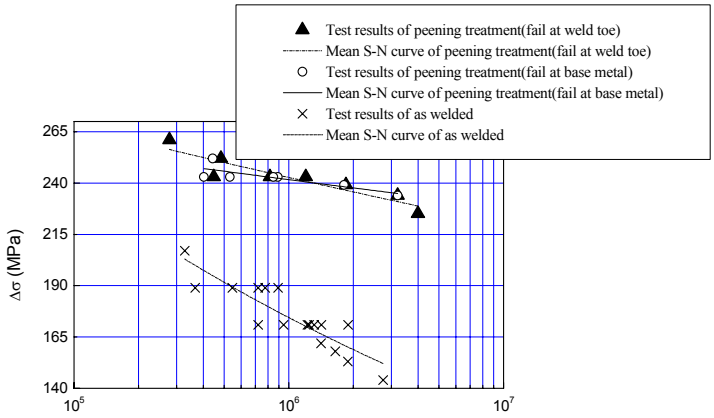

F ıtt joints (R=0.1)

p
c
tl

ınts of as-welded and peened condition were
tigue strength (at 2×10^6 cycles) of the butt and
re given. The fatigue limits were derived from
the mean v strength

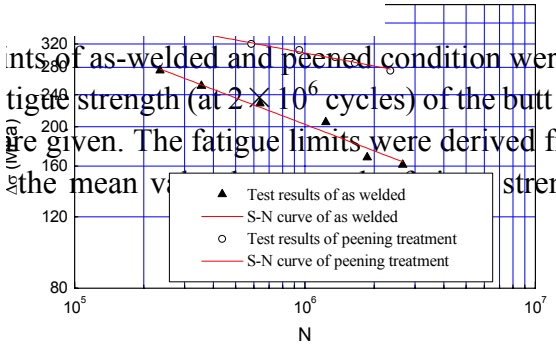

ig.5.S-N curves of cruciform joints (R= - 0.5)

corresponding to the specimen, whose life is just higher than 2×10^6 and the fatigue strength corresponding to
the specimen ,whose life is just lower than 2×10^6.

The results from S-N curves are as follows:

Compared with welded joints, the peened joints show significant increase in the fatigue life under different stress levels and the fatigue strength at a cycles 2×10^6.

On the butt peened joints, fatigue crack initiated at the weld toe under cycles much more than that on the as welded joints for some specimens, however for more specimens, fatigue crack initiation occurred in the base metal. The S-N curves of both crack initiation conditions are similar in the slope and fatigue stress levels, so that the fatigue strength of the peened joints can be considered as same as the base metal. Compared to the as-welded joints, the increase in fatigue strength (at 2×10^6 cycles) of the peened Q235B butt joints was 57%. For the cruciform peened joints, most cracks occurred in the base metal. The increase in fatigue strength of the peened cruciform joints tested with R=0.25 was 64%. For the specimen tested with R= -0.5, the increase was 71%.

Table 3. The fatigue limit of welded joints and with peening treatment joints

Type	Fatigue strengths (Δσ/Mpa)		
	As welded	Treatment	Improving degree/%
Butt joints	148.5	234	57
Cruciform joints （R=0.25）	142.5	234	64
Cruciform joints （R=-0.5）	165	282	71

Table 4 gives the fatigue life (under the same stress level) of the two series joints. According to the S-N curves (see from fig.3, 4, 5), the fatigue life of welded joints corresponding to the stress which comes from the peened joints corresponding to 2×10^7 cycles can be obtained. The results shows in Table 4.

Table 4 . The fatigue life of welded joints and with peening treatment joints

Joints	Condition	Stress	life
Butt joints （R=0.1）	As welded	228	1.65×10^5
	Treatment	228	1.0×10^7
Cruciform joints (R=0.25）	As welded	211	2.4×10^5
	Treatment	211	1.0×10^7
Cruciform joints (R= - 0.5）	As welded	235	5.12×10^5
	Treatment	235	1.0×10^7

Analysis of the results shows that the fatigue life of the peened joints was 40~60 times as long as the as-welded joints. Provided that the deviation of the test results were taking into consideration, the improvement was 20~30 times.

Test results reveal that the ultrasonic peening was an effective technique for improving the fatigue properties of the welded joints. The fatigue strength of the peened joints was nearly equal to the base metal. In such cases, welded joints is not the degense location any longer.

4.CONCLUSIONS

1) Both the butt and cruciform peened Q235B joints show a significant increase in fatigue life under different stress levels (high cycle fatigue), and also increase in fatigue strength under the same cycles. The difference in stress level was increasing with the increase of cycles.

2) The relative improvement in fatigue limit (at 2×10^6 cycles) caused by ultrasonic peening of the butt and cruciform joints were respectively 57%and 64%~71% compared with the as-welded condition.

3) The fatigue strengths of both the butt and cruciform welded joints were no lower than that of the base metal, when ultrasonic peening of the joints were carried out. Compares with the peened butt welded joint, the fatigue of cruciform welded joints after peened are increased more significantly.

4) The fatigue life of peened joints at least was 20~30 times as long as the as-welded joints.

ACKNOWLEGEMENTS

This project is supported by the National Natural Science Foundation of China, Project No. 59575061.

REFERENCES

1.J.Janosch, H.Koneczny, S.Debiez (France), E.C.Statnikov (Russia).V.J.Troufiakov and P.P.Mikhee (Ukraine), Welding in the world , 37(1996)p.72

2.T.R.Gurney, Fatigue of welded Structure, Cambridge University Press, England(1979)

3.P.P.Mikheev, A Ya Nedoseka, Automatic welding, march, 32(1984) p.37

ORAL REFFERENCE: ICF100331OR

ASSESSMENT OF FATIGUE STRENGTH OF LOW ALLOY STEELS FOR SHIPS' CRANKSHAFT

S. Omata and H. Matsushita

Research Institute, Nippon Kaiji Kyoki,1-8-3, Ohnodai, Midori-Ku, Chiba, Japan

ABSTRACT

Rotational bending fatigue tests for low alloy steels, KSFA80, KSFA110 were carried out to clarify the property of fatigue strength of high tensile forged materials. Fatigue fractures occurred even though the repeated stress exceeded 10^8 cycles, which started at an interior inclusion. Fatigue strength of forged materials show anisotropy depending on the relative direction of specimen to forged fiber flow, and it is shown that this anisotropy of fatigue strength is due to the projective shape and size of inclusions at crack origin to a plain perpendicular to the maximum stress direction. The effect of non-metallic inclusion to fatigue strength was estimated using the *area* parameter model.

KEYWORDS

High cycle fatigue, Low alloy steel, Forged steel, Crankshaft, Inclusion, Interior fracture.

INTRODUCTION

Recent years, the use of low alloy steels as material for crankshafts has gained for small and medium sized diesel engines, because of a demand for engines to be smaller and lighter in weight. Generally, fatigue design of products is based on the fatigue limit defined at 10^7 cycles of repeated stress, but for high speed engines, 10^7 cycles will be achieved in a short time and can not be enough to evaluate the fatigue limit. Therefore, the necessity for understanding the fatigue strength characteristic in the long life range of more than 10^7 cycles is recognized. But the fatigue data of low-alloy steels in the long life range are not enough under the present situation. In this study, fatigue tests of low alloy steels up to 10^8 cycles or more of repeated stress were performed to clarify the fatigue properties in the long life range. On the other hand, fatigue strength of forged products, like CGF (Continuous Grain Flow) crankshaft, are affected by the differences in the angle of the direction of applied stress and the direction of forged fiber flow, because fatigue strength of forged steels show anisotropy depending on the relative direction to the forged fiber flow. In this study, the effect of relationship between forged fiber flow and the direction of applied stress, and the effect of shape and size of inclusions in materials to fatigue strength were examined.

EXPERIMENTAL DETAILS

Four types of materials were subjected to fatigue testing, two types of KSFA80 and two types of KSFA110 (Class NK standards). The chemical compositions of each sample material are shown in table 1 and the

forging ratio and the heat treatment conditions are shown in table 2.

TABLE 1
CHEMICAL COMPOSITION OF MATERIALS

Material	C	Si	Mn	P	S	Ni	Cr	Mo	Cu
KSFA80A	0.43	0.26	0.73	0.011	0.005	0.44	1.07	0.22	0.08
KSFA80B	0.44	0.30	0.74	0.010	0.003	0.51	1.10	0.25	0.04
KSFA110A	0.37	0.27	0.40	0.009	0.003	2.82	1.61	0.41	0.05
KSFA110B	0.33	0.26	0.51	0.014	0.003	2.99	3.00	0.61	0.03

TABLE 2
FORGING RATIO AND CONDITIONS OF HEAT TREATMENT

Material	Forging ratio	Heat Treatment
KSFA80A	3.2S	870°C•2Hr OilQuenching & 640°C 15Hr AirCooling
KSFA80B	11.9S	870°C•9Hr OilQuenching & 635°C 20Hr FurnaceCooling
KSFA110A	3.1S	870°C•2Hr OilQuenching & 600°C 17Hr AirCooling
KSFA110B	6.8S	870°C•2Hr OilQuenching & 590°C 15Hr FurnaceCooling

Test specimens were cut out from round bar bulk materials having diameter of 320mm, and machined to hourglass type of shape with a minimum sectional diameter of 10mm. In the case of KSFA80A and KSFA110A, the test specimens were prepared which had a direction relative to the forged fiber flow of 0 degrees (referred to hereunder as being in the L direction), 45 degrees (referred to hereunder as being in the S direction) and 90 degrees (referred to hereunder as being in the T direction), while the test specimens of KSFA80B and KSFA110B were prepared which were in the L and T directions, respectively. Because the Vickers hardness distribution at a section of the bulk materials were almost constant from the surface to the center as shown in Fig. 1, the test specimens were cut out from each position of bulk materials including the center.

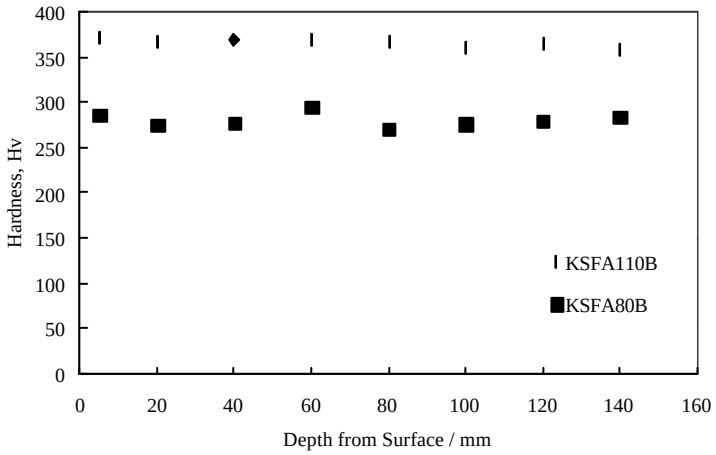

Figure 1: Vickers hardness of bulk materials, KSFA80B and KSFA110B

Fatigue tests were carried out on the test specimens using a canti-lever type rotational fatigue testing machines at 3,000rpm of rotating speed. Detailed observations of the fracture surfaces of each specimens were made using scanning electron microscope (SEM) and energy dispersive X-ray analyzer (EDX) thereby identifying inclusions that were the crack origin of fatigue fracture.

EXPERIMENTAL RESULTS

S-N properties

S-N diagrams of each sample material are shown in Figs. 2 and 3. In these figures, different plot symbols were used to indicate whether the fatigue crack started at the surface of test specimen (surface fracture) or at the interior of test specimen (interior fracture). Surface fracture means fatigue crack started at slip band or at a surface inclusion, and interior fracture means fatigue crack started at an interior inclusion. In Fig. 4, "**f**" mark was added to the plots for fish eye type fracture.

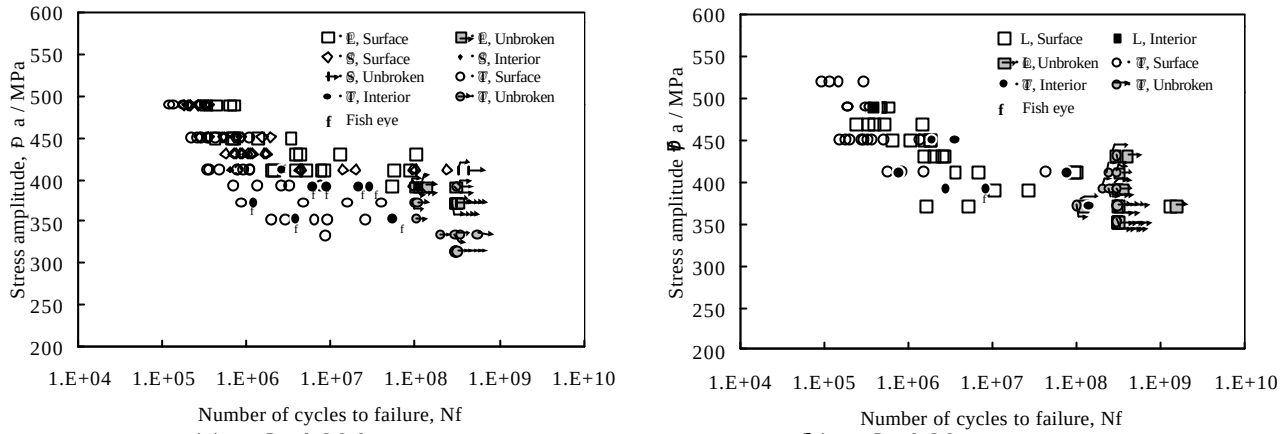

(a) KSFA80A (b) KSFA80B

Figure 2: S-N diagrams of KSFA80

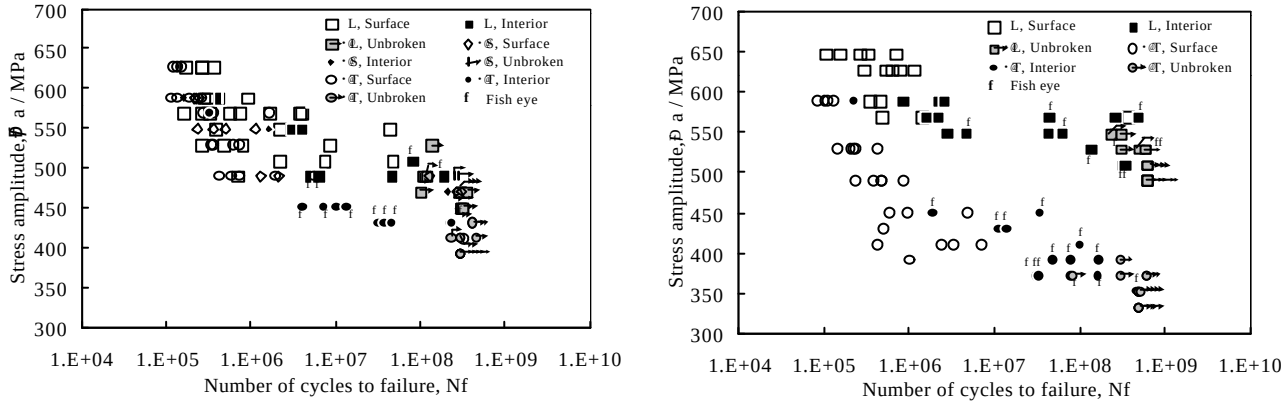

(a) KSFA110A (b)KSFA110B

Figure 3: S-N diagrams of KSFA110

The fatigue strength of KSFA80A, KSFA110A and KSFA110B in the T direction are lower than those in the L direction, namely, the anisotropy of fatigue strength appears clearly. This tendency is the most remarkable in KSFA110B. On the other hand, the fatigue strength of KSFA80B in the L direction and the T direction show almost equal values. The fatigue strength of KSFA80A and KSFA110A in the S direction are slightly lower compared with those in the L direction, but in the long fatigue life range, there seems no significant difference between them. As shown in Figs. 2 and 3, fatigue fractures occurred at even more than 10^7 cycles of repeated stress which generally regarded as fatigue limit, and most of these fatigue fractures started at an interior inclusion. This type of fracture is more remarkable in KSFA110 than KSFA80. Fatigue fractures starting at an interior inclusion in the long life range are reported in many papers [1,2] recent years in steels with an extremely high tensile strength like bearing steel (about σ_B=2,000MPa), but there seems no previous study using low alloy steel with the strength of the same level as the sample materials in this study. The above experimental results suggest that the interior fatigue fracture in the long life range occurs in steels having a tensile strength of more than 800MPa.

Effect of inclusion to fatigue strength

As described above, there is a tendency that fatigue fracture starts at an interior inclusion in the long life range in high strength low alloy steels, but the mechanism of that interior fatigue fracture has not completely clarified by now. As for the present experiment, compressive residual stress was confirmed in the surface thin layer of the test specimens using X-ray stress measurement method. This compressive residual stress is thought to be one of the causes of the interior fatigue fracture.

This compressive residual stress exists in the surface hardening layer introduced by grinding when test specimens were machined. It takes the maximum absolute value of 400MPa at specimen surface and decreases to 0MPa roughly at a depth of 50μm (see Fig. 4).

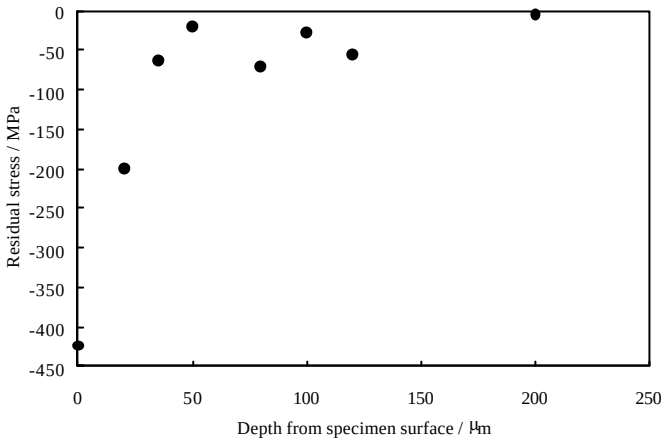

Figure 4: Residual stress distribution of test specimen (KSFA80B)

However, most of the surface inclusions of specimens in the T direction are much longer than the depth of the region where residual stress exists, therefore, it is difficult to explain the mechanism of the interior fatigue fracture only by the influence of the surface hardening layer. As another factor of the interior fatigue fracture, the difference of environment between the surface and the interior is assumed. For example, crack closure caused by oxidation takes place only at the surface. Moreover, the effect of hydrogen embrittlement around interior inclusions was proposed in a recent study [3]. To clarify the mechanism of the interior fatigue fracture, a quantitative examinations of these factors are necessary in the future.

Fig. 5 shows Two examples of SEM images of fatigue crack origins. These are fracture surfaces of the specimens fractured in the long life range, and fish eye type fractures are observed. The inclusion shown in Fig. 5(a) is observed at KSFA110B in the L direction, which has circle shape on the fracture surface. On the other hand, the inclusion shown in Fig. 5(b), observed at KSFA110B in the T direction, has thread-like shape on the fracture surface. The latter is clusters of many small inclusion grains. From EDX analysis, the inclusions at crack origins are mostly composed of Mg, Al, Si and Ca, and assumed to be an oxide type, while some MnS were also observed.

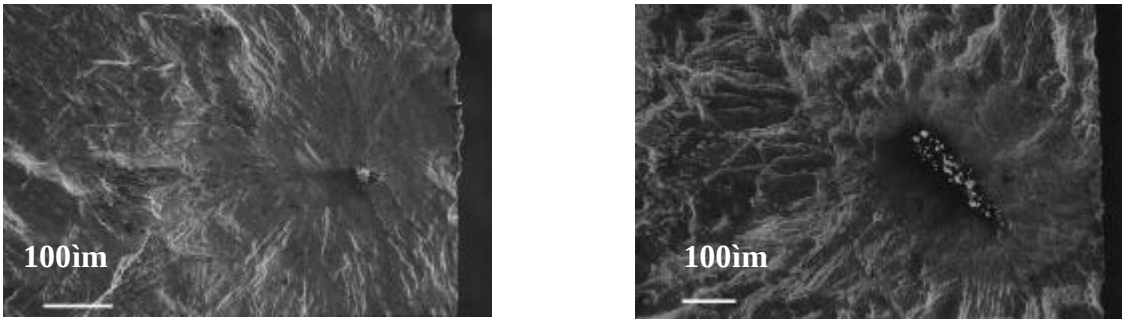

(a) KSFA110B-L (σ_a=568MPa, N_f=43,655,200) (b) KSFA110B-T (σ_a=372MPa, N_f=30,825,250)

Figure5: SEM images at crack origins

Table 3 shows the values of average and standard deviation of sizes of inclusions at crack origins, *a*, *b*, *(a+b)/2* and *a/b*, where *a* is a length of short side of circumscribed rectangular of the inclusion and *b* is a length of long side of the rectangular.

TABLE 3
AVERAGE VALUES OF SIZE AND ASPECT-RATIO OF INCLUSIONS

Mater.	Number of inc.	Size (μm)						Aspect -ratio	
		a		*b*		(*a* + *b*) / 2		(*a* / *b*)	
		Ave.	*Std. dev.*	**Ave.**	*Std. dev.*	**Ave.**	*Std. dev.*	**Ave.**	*Std. dev.*
80A-L	0	-	-	-	-	-	-	-	-
80A-S	11	**26**	*12*	**57**	*41*	**42**	*25*	**0.5**	*0.2*
80A-T	34	**37**	*16*	**295**	*203*	**166**	*104*	**0.2**	*0.1*
80B-L	9	**44**	*24*	**56**	*27*	**50**	*25*	**0.8**	*0.2*
80B-T	25	**51**	*21*	**69**	*38*	**60**	*25*	**0.8**	*0.2*
110A-L	27	**35**	*14*	**45**	*17*	**40**	*14*	**0.8**	*0.2*
110A-S	14	**34**	*13*	**67**	*33*	**51**	*18*	**0.6**	*0.3*
110A-T	29	**38**	*13*	**161**	*122*	**100**	*61*	**0.4**	*0.3*
110B-L	23	**21**	*6*	**34**	*15*	**27**	*9*	**0.7**	*0.2*
110B-T	34	**49**	*14*	**352**	*182*	**201**	*93*	**0.2**	*0.1*

In each material except for KSFA80B, inclusions have thread-like shapes running in the direction of forging, and average values of *a/b* are about 0.2-0.4 in the T direction specimens and are about 0.7-0.8 in the L direction specimens. Inclusions of KSFA80B have nearly circle shape on the fracture surface both in the L and the T direction specimens, and their average values of *a/b* are both 0.8. The anisotropy of the fatigue strength of each sample material appeared in the S-N characteristics of Figs. 2 and 3 depends on three-dimensional shapes of inclusions, and was remarkable in steels containing thread-like shape inclusions. For convenience, assuming *(a+b)/2* is a representative value of projected size of inclusion on the fracture surface, there is a tendency that the fatigue strength decreases as the average value of the size of inclusion becomes large.

Because the fatigue strength of steels depend on the size of inclusion at crack origin as mentioned above, It is expected that the fatigue strength could be estimated by the use of a parameter which combines stress with the size of the inclusion at crack origin, like initial stress intensity factor of micro crack initiated at the inclusion. Murakami et al [4,5] assumed proportional relationship between threshold stress intensity factor range of crack propagation, ΔK_{th} and cubic root of crack size, $(\sqrt{area})^{1/3}$ and proposed a method called *area* parameter model for estimation of fatigue limit as equations (1) .

$$\sigma_w = \frac{F(H_v + 120)}{(\sqrt{area})^{1/6}} \tag{1}$$

Where σ_w - fatigue limit (MPa), H_v - Vickers hardness (kgf/mm^2)
area - Square root of projected area of inclusion (μm)
F - Shape parameter
=1.43 for surface inclusion
=1.56 for interior inclusion

Fig. 6 shows a relationship between σ_a/σ'_w and N_f, where σ_a is stress amplitude and σ'_w is estimated fatigue limit calculated from equation (1) corresponding to the size of each inclusion observed at crack origin. For the calculation of σ'_w, *area* values were represented by ellipse for interior inclusions and by semi-ellipse for surface inclusions. As for extremely long inclusions, *area* values were of the ellipse which semimajor axis is five times of semiminor axis uniformly [6]. The values of Vickers hardness used for calculations were the average values of the measurement results shown in Figure 1. For each sample material, all the values of σ_a/σ'_w are above 1.0 except for one of KSFA110B. This means that almost all the specimens broke at higher

stress amplitude than estimated fatigue limits. And the difference between the lowest estimated value, σ'_w and applied stress amplitude, σ_a for each material is within 10% of σ_a. From these results, it is recognized that the equations (1) can estimate fatigue limits of forged low alloy steels approximately. As well as KSFA80B, almost same σ_a/σ'_w values are obtained for both in the L and the T direction in KSFA110B of which sizes of inclusions, *area* are largely different from each other. Displayed by "×" or "+" mark in Fig. 6(a) are data of unbroken specimens at 3×10^8 cycles of repeated stress. The σ_a/σ'_w values of these unbroken specimens were calculated using *area* of the inclusions observed at the crack origins on the compulsorily fractured surfaces. It is reasonable that these values of unbroken specimens were almost the minimum values in all data obtained in KSFA80B.

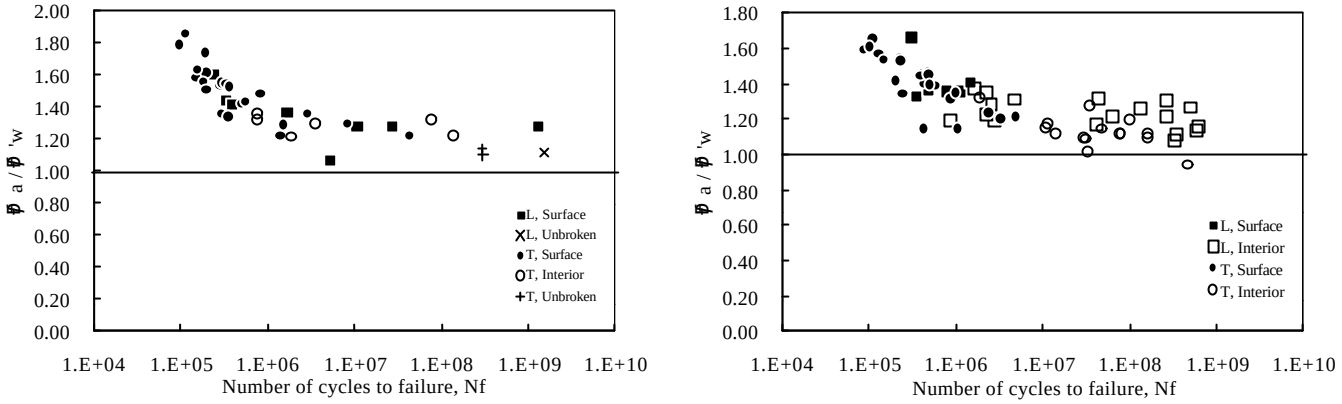

(a) KSFA80B (b) KSFA110B

Figure6: Relationship between σ_a/σ'_w values and N_f

From the above experimental results and considerations, it was shown that the fatigue strength of forged steels were affected by the shape and the size of inclusions and the anisotropy of fatigue strength of forged materials were explained by this. Therefore, it is clear that the most effective way to improve the fatigue properties of forged steel is to make the inclusions spherical and small.

CONCLUDING REMARKS

The experimental findings and the conclusions drawn from the present study are summarized as follows.

(1) Most of the inclusions at crack origins are oxidants composed of Mg, Al, Si and Ca, and even very small inclusion about 10μm acts as fatigue crack origin.
(2) In the long life range, fatigue crack initiates at an interior inclusion in high strength low alloy steel.
(3) Three-dimensional shape and size of inclusions in steel affect fatigue strength, and the anisotropy of forged material can be explained by this. The most effective way to improve the fatigue properties of forged steel is to make the inclusions spherical and small.
(4) Using the *area* parameter model, fatigue limit of forged low alloy steel can be approximately estimated.

REFFERENCES

1. Shiozawa, K., Lian-Tao, L. and Ishihara, S. (1999). *J. Soc. Mater. Sci. Jpn*. 48, 10, pp.1095-1100
2. Nishijima, S. and Kanazawa, K. (1999). *Fatigue Fract. Eng. Mater. Struct*. 22, pp.601-607
3. Murakami, Y., Nomoto, T. and Ueda, T. (1999). *Fatigue Fract. Eng. Mater. Struct*. 22, pp.581-590.
4. Murakami, Y. (1993). *Metal fatigue: effects of small defects and non-metallic inclusions*. Yokendo Ltd., Tokyo.
5. Murakami, Y., Takada, M. and Toriyama, T. (1998). *Int. J. Fatigue*. 16, 9, pp.661-667.
6. Murakami, Y and Endo, M. (1983). *Trans. Jpn Soc. Mech. Eng., Ser. A*. 49, 438, pp.127-136

ORAL/POSTER REFERNCE: ICF100850OR

ASSESSMENT OF FRACTURING TUNNEL LININGS WITH SMEARED CRACK MODEL

Z.S. Wu[1], J. Yin[1], T. Asakura[2] and Y. Kojima[3]

[1]Department of Urban & Civil Engineering, Ibaraki University, Japan
[2]Department of Earth Resources Engineering, Kyoto University, Japan
[3]Structural Technique Development Division, Railway Technical Institute, Japan

ABSTRACT

A finite element simulation is carried out to study the fracturing behavior of concrete tunnel linings with smeared crack model. To simulate the crack localization observed in experiment, a numerical strategy is introduced. Some weak elements as structural imperfections are inserted at critical positions of the tunnel linings to avoid the unrealistic crack distribution cracks due to the limitation of smeared crack model itself and the structural features of tunnel linings. It is found that the crack characteristics and structural performances of tunnel linings can be well simulated and predicted by smeared crack model with the numerical strategy on crack localization. In addition, the effect of a key material parameter, fracture energy, on the structural response of the tunnel linings is discussed.

KEYWORDS concrete tunnel linings, smeared crack model, fracture energy, crack localization, load-carrying capacity

INTRODUCTION

In Japan, there are currently thousands of railway and road tunnels in service. Many of them are being suffered from aging and external force, such as earthquake and traffic loading. Therefore, there exist serious problems on how to efficiently inspect and repair them to extend their service life. For this purpose, much work are being carried out experimentally [1,2], as well as numerical simulation [3], to study the mechanism of tunnel deformation and fracturing behavior. In this paper, the scale model experiments [1] is reviewed and referred. Smeared crack model is used to simulate the cracking behavior of the concrete tunnel linings. The objective is to obtain a general understanding of the effect of crack distributions on structural performance of plain concrete tunnel linings and the applicability of smeared crack model for the simulation on crack localization in such a structure.

EXPERIMENTAL REVIEW

A 1/3 scale model of plain concrete tunnel lining, as shown in Figure1, was tested. A tunnel lining specimen was supported by the I-shaped steel beams. No soil mass constrain outside the sidewalls was arranged. The external load was acted vertically down at the outside crown. This kind of load condition approximates the 2-dimension case.

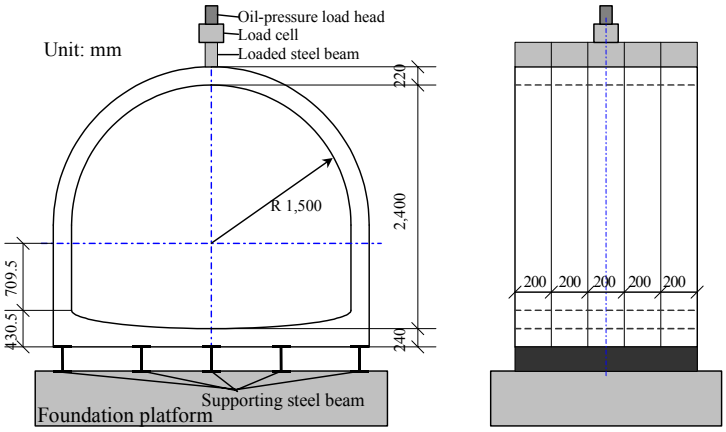

Figure 1: Cracks observed in experiments

According to the experimental observation [1], all the cracks that caused by the vertical load are flexural cracks. The first crack occurred in the crown (inside) followed by the ones occurring at the outside of sidewalls and the inside of bottom, as presented in Figure 2.

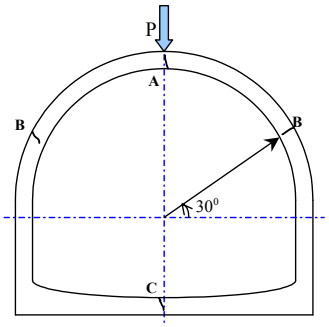

Figure 2: Cracking behavior observed in experiment

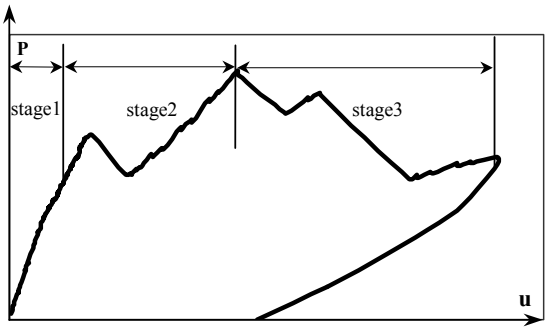

Figure 3: Four stages of tunnel lining response

From the load-displacement curve of experimental results, as shown in Figure 3, the structural stiffness decreased after the crack occurred at the inside of crown. But the tunnel lining could still resist the external load until the cracks happened at the outside of sidewalls. When the cracks at the sidewalls propagated to a certain extent, the tunnel lining began to lose its load resistance with the continuous deformation up to the ultimate collapse. A possible reason of the zigzag behavior in the experiment may result from unloading due to localized crack propagation. It can be seen that the structural response can be divided into 3 stages: 1)elastic stage with constant stiffness; 2)nonlinear stage after cracking occurrence with gradually decreased stiffness (but still positive); 3)strength degradation stage with negative stiffness until ultimate structural collapse.

The material properties obtained from identified uniaxial compression test are uniaxial compressive strength f_c = 26.2MPa, Young's modulus E=2.3×10^{4}MPa and Poisson ratio ν=0.17 [1]. As a reference property, the tensile strength f_t can be calculated through transformation equation f_t=0.23$f_c^{2/3}$=2.03MPa, based on the concrete design standard of JSCE.

SMEARED CRACK MODEL

A finite element formulation of smeared crack model [4] is used in the simulation. But, the treatment on the variation of shear modulus along the crack plane is modified by applying a softening curve rather than using conventional constant shear retention factor. The relation between the crack strain increment Δe^{ck} and the stress increment Δs can be defined as

$$\Delta s = D^{ck} \Delta e^{ck} \tag{1}$$

where D^{ck} contains the local stress-strain relations normal to and along the crack plane. It could be written as

$$D^{ck} = \begin{bmatrix} D^{I} & 0 \\ 0 & D^{II} (or D_0^{II}) \end{bmatrix} \tag{2}$$

in which D^I is mode I tensile softening modulus, D^{II} is mode II shear softening modulus and $D_0{}^{II}$ is the initial shear modulus before the mode II softening is entered, as shown in Figure 4. According to crack band theory [5], the actual discontinuous displacements on the crack plane, δ_n for opening and δ_t for sliding, are smeared over the a band of width h. Therefore, the crack strains $e^{ck}=\delta_n/h$ and $\gamma^{ck}=\delta_t/h$ are obtained. In the simple form, the crack band width h can be taken as an equivalent element size. For 2-dimension elements, h is approximated as $h=\sqrt{A}$, where A is the element area. Fracture energy is assumed to be a material property, defined as the energy required to bring a unit area to complete fracture. The areas below the local stress-strain curves at crack plane are the unit fracture energy over crack band h, G^I_f/h for mode I and G^{II}_f/h for mode II.

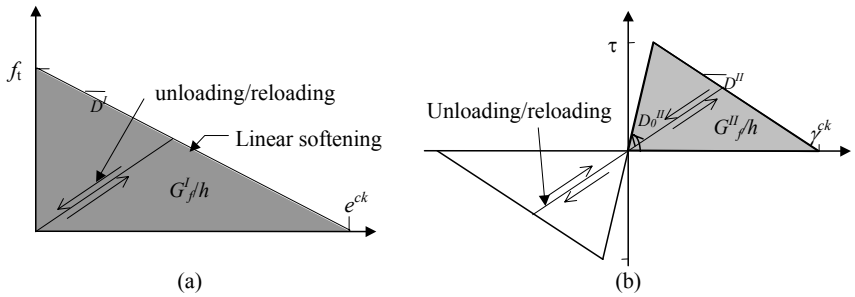

Figure 4: Softening models (a) Mode I tensile softening (b) Mode II shear softening

A linear tension softening curve is adopted for mode I fracturing. It is assumed that mode I fracture is initiated first when principle stress reaches the concrete tensile strength. Therefore, the shear stress across the crack is zero at the onset of cracking. That is why the shear stress-strain diagram in Figure 4(b) starts from the origin. Upon subsequent change of the principle stress axes the shear stress across the initial crack plane may increase until its maximum value τ, thereafter the shear softening branch is started. Different from the present treatment of mode II softening, in the traditional smeared crack model, a constant shear retention factor β is multiplied to the elastic shear modulus and kept unchanged in subsequent calculation. It may likely result in shear stress locking so as to lead to incorrect numerical results. Furthermore, the unloading and reloading are modeled by a secant path, which implies that the stress follows a linear path back to the origin.

NUMERICAL SIMULATION

A finite element code, in which smeared crack model is implemented, is used to carry out the numerical simulation. The structural model of tunnel lining, as shown in Figure 1, is discritzed by 4-node plane stress elements. Strain and stress are integrated at 4 Gaussian quadratic points.

Treatments of Shear Modulus on Crack Plane

First, the difference between the proposed shear softening model and the traditional constant shear retention factor is compared. The constant shear retention factor with β=0.5, 0.1 and 0.01 is used respectively for the traditional post-tension crack treatment of shear modulus. Other common material properties are concrete tensile strength f_t=1.8Mpa, mode I fracture energy G^I_f=0.15N/mm. For the shear softening model, initial shear retention factor is β=0.5, shear strength is τ=0.2MPa and mode II fracture energy is G^{II}_f=0.01N/mm. The results are shown in Figure 5.

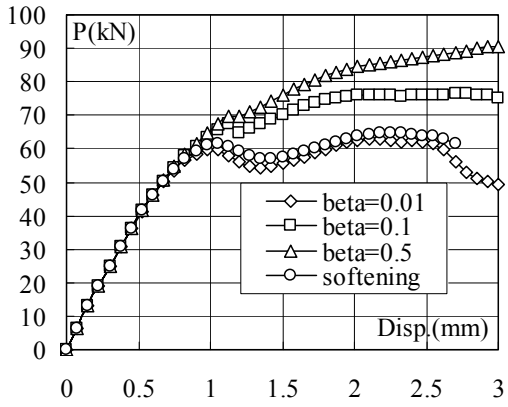

Figure 5: Different treatment of shear modulus

It is demonstrated that value of constant shear retention factor significantly influences the numerical results even though the mode II fracture is not dominant in the tunnel lining structure under such a load condition. Only the curve of case β=0.01 is close to the one of the shear softening model. In the viewpoint of concrete material behavior, the shear softening model is more physically reasonable because concrete is quasi-brittle material and the shear modulus dose not likely drop dramatically at the onset of the opening crack. In the following simulations, the mode II softening model is adopted.

Effect of Initial Imperfection

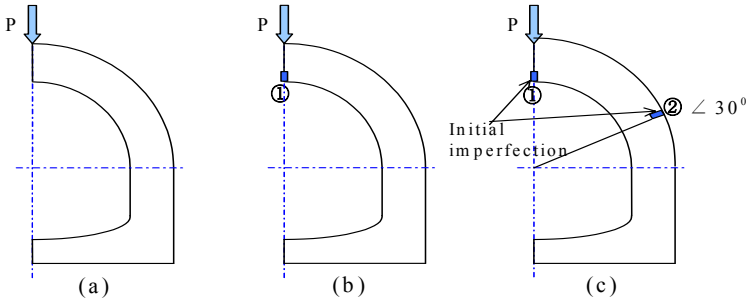

Figure 6: Initial imperfection at different positions

From the experimental observations, the localized cracks are mainly located at the following positions: 1)inside of crown, 2)outside of sidewalls, and 3)bottom of tunnel. Three cases are used to study the effect of the initial imperfection in the numerical simulation by smeared crack model, as shown in Figure 6: (a) without any initial imperfection, (b) with initial imperfection only at inside crown ① and (c) with initial imperfection positions ①+②. Since the crack that happens at the bottom does not further propagate, its effect on the structural behavior is not discussed in this paper. The initial imperfection is inserted by weakening one tip element with 1/2 concrete tensile strength and 1/4 fracture energy G^I_f of the normal ones. Concrete properties are tensile strength f_t=1.8MPa, mode I fracture energy G^I_f=0.15N/mm.

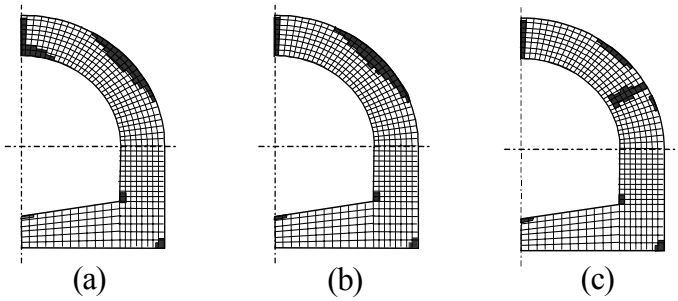

Figure 7: Crack patterns with and without initial imperfections

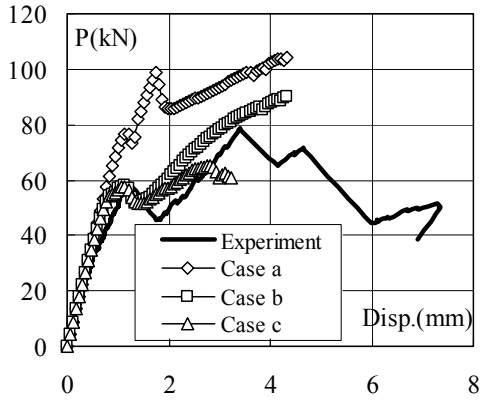

Figure 8: Load-displacement curve with and without initial imperfection

The simulation results of crack patterns and load-displacement curves are shown in Figure 7 and 8. Figure 7(a) (b) and (c) correspond to the case (a) (b) and (c) in Figure 6, respectively. Without any initial imperfection, cracks are widely distributed at the outside of sidewalls. Since the localized crack does not form, the local unloading behavior could not be found in load-displacement curve. This may result from two reasons. One comes from the deficiency of the smeared crack model, which smears a realistic crack over the whole finite element. This easily leads to the distributed crack. The second reason may be due to the gentle stress distribution in the tunnel lining under such a vertical load. The arch-shaped structure makes the stress gradient along the sidewalls relatively small. This also causes the difficulty during FE simulation of crack propagation. By using the numerical strategy with weak elements at critical positions, it is found that crack localization can be simulated by smeared crack model.

Concrete Fracture Energy

Fracture energy, G_f^I, is generally considered as a material property, which is defined as the amount of energy required to create a unit area of mode I crack. Because there is not much experimental data of the fracture energy, 5 cases with fracture energy G_f^I=0.10, 0.15, 0.20 0.40 and 1.0N/mm are simulated. The results are compared to the experimental one. Concrete tensile strength is f_t=1.8MPa.

The load-displacement curves are presented in Figure 9. It can be seen that when fracture energy is relatively small with G_f^I=0.10, 0.15, 0.20N/mm, cracks propagate rapidly after initiated. Because the stress on the crack plane releases rapidly, the local unloading behavior is apparently seen when cracks develop at crown and at sidewalls respectively. However, in the case of higher fracture energy G_f^I=0.40, 1.00N/mm, such an unloading behavior is not clearly shown out. With increase of fracture energy, not only the load-carrying capacity is enhanced, but the crack patterns also change even though the weak elements are inserted in the same critical positions as discussed previously. The area of cracked elements elsewhere also increases, as shown in Figure 10. Therefore, increasing the fracture energy of concrete by some means could effectively enhance the load-carrying capacity and prevent excessive crack localization in tunnel linings.

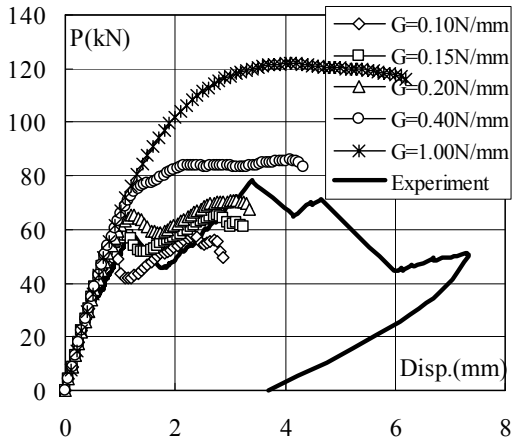

Figure 9: Load-displacement curve with different fracture energy

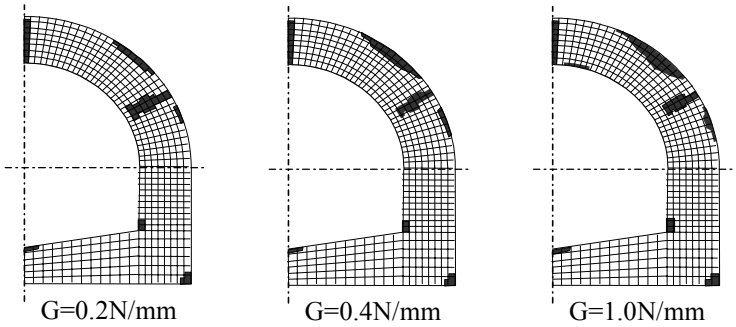

Figure 10: Change of crack patterns with increase of fracture energy

CONCLUSION

Through the numerical simulation with smeared crack model, the cracking behavior of concrete tunnel linings is studied. Shear softening model is used, in place of constant shear retention factor, as a rational approach to treat shearing behavior on the crack plane. As to smeared crack model, it is generally considered not so applicable to simulate localized cracking in complicated structures such as tunnel lining. But, by inserting weak elements at critical positions, such a disadvantage is overcome, and characteristics of cracking behavior and structural response are well simulated. In addition, the significance of fracture energy is discussed. Increasing the fracture energy of concrete tunnel lining intends to result in distributed crack so that it can effectively enhance the load-carrying capacity and deformation. This finding might be helpful to tunnel lining design in the future.

REFERENCE

1. Asakura, T., Ando, T. and Kojima, Y. (1998): Experiments of inner reinforced tunnel linings, *QR of RTRI,* Railway Technical Institute, Japan
2. Asakura, T., Kojima, Y., Ando, T., Sato, Y. and Matsuura, A. (1994) *J. of Geotech. Eng. JSCE* No.493/III-27, pp.79-88.
3. Yin, J., Wu, Z.S., Asakura, T. and Ota, H. (2001) *Structural Eng./Earthquake Eng. JSCE* Vol.18, pp.17-27.
4. de Borst, R. and Nauta, P. (1985): Smeared crack analysis of reinforced concrete beams and slabs failing in shear, *Proc. Int. Conf. on Computer Aided Analysis and Design of Concrete Struc.*, pp.261-273, Damjanic, F. et.al (Eds). Part 1, Prineridge Press, Swansea.
5. Bazant, Z. (1984) *J. of Eng. Mech. ASCE*, Vol.110, No.4, pp.518-535.

ASYMPTOTIC FIELDS AT A CRACK TIP IN FLAT PLATES

Jia LI

Laboratoire d'Etudes et de Recherches en Mécanique des Structures
Blaise Pascal University of Clermont-Ferrand
Avenue Aristide Briand, 03100 Montluçon, France

ABSTRACT

In this paper, we present a new approach to consider the near-tip fields of a crack in elastic flat plate subjected to bending forces. The Reissner assumptions of the plate theory were adopted. By introducing the dual variable vectors in the state space, the governing equations were established in the frame of the Hamiltonian system. Following problems were solved by using the present approach: (1): Cracks in elastic homogeneous plates. (2): Cracks formed by several homogeneous plates. Interface cracks between two dissimilar plates and cracks meeting an interface between two elastic plates are two special cases of this problem. (3): Cracks in orthotropic plates. (4): Cracks formed by several orthotropic plates. This work shows the efficiency and the simplicity of the present theory in studying the crack-tip asymptotic fields in plates.

KEYWORDS

Crack, plate, asymptotic analysis, near-tip fields, orthotropy, interface

1. INTRODUCTION

The principal theories studying the asymptotic fields near a crack tip in a plate loaded by bending forces were established in the 60's of the precedent century (Sih, 1965, Knowels and Wnag, 1960, Hartranft and Sih, 1968, 1970 etc.). Some of them were established on the basis of Poisson-Kirchhoff's thin plate theory, others on the basis of the Ressner theory. The Poisson-Kirchhoff theory provides rather simple mathematical procedures, but gives some physically incorrect behaviors about the near-tip fields. On the other hand, Ressner's thin plate theory gives physically more reasonable results, but the solution of the six-order differential equations remains difficult for some problems posed in this topic.

In this paper, we propose a new approach to find out asymptotic fields near a crack tip in thin plates loaded by bending. By choosing appropriate dual variables in the state space, we can establish the governing equations of the problem in the frame of the Hamiltonian system. All equations found are presented in the form of a system of first-order differential equations. Therefore, one can easily perform the separation of the variables and resolve the corresponding eigenvalue problems. The mathematical approaches are quite simple and a large range of problems in this domain can be dealt with.

2. FUNTAMENTAL EQUATIONS

Consider a semi-infinite crack in a thin elastic plate of thickness h. We adopt the hypothesis made by Reissner about the deformation of thin plates. (1): The strain and stress at the direction normal to the mid-plane are neglected, i.e.:

$$\sigma_z = \varepsilon_z = 0$$
$$w = w(r,\theta) \qquad (1)$$

(2): The in-plane displacements depend linearly on the thickness coordinate z:

$$u_r = z\widetilde{u}_r(r,\theta)$$
$$u_\theta = z\widetilde{u}_\theta(r,\theta) \qquad (2)$$

Where $\widetilde{u}_r$ and $\widetilde{u}_\theta$ are functions independent of the z coordinate. We write now the equilibrium equations in the cylindrical coordinate system:

$$\frac{\partial M_{rr}}{\partial r}+\frac{1}{r}\frac{\partial M_{r\theta}}{\partial \theta}+\frac{M_{rr}-M_{\theta\theta}}{r}=Q_{rz} \quad \frac{\partial M_{r\theta}}{\partial r}+\frac{1}{r}\frac{\partial M_{\theta\theta}}{\partial \theta}+\frac{2M_{r\theta}}{r}=Q_{\theta z} \quad \frac{\partial Q_{rz}}{\partial r}+\frac{1}{r}\frac{\partial Q_{\theta z}}{\partial \theta}+\frac{Q_{rz}}{r}=-q \qquad (3)$$

The relationships between the strain and displacement components are, according to assumption (2):

$$\varepsilon_r = z\frac{\partial \widetilde{u}_r}{\partial r} \quad \varepsilon_\theta = \frac{z}{r}\left(\frac{\partial \widetilde{u}_\theta}{\partial \theta}+\widetilde{u}_r\right) \quad 2\varepsilon_{r\theta} = z\frac{\partial \widetilde{u}_\theta}{\partial r}+\frac{z}{r}\left(\frac{\partial \widetilde{u}_r}{\partial \theta}-\widetilde{u}_\theta\right) \quad 2\varepsilon_{rz} = \widetilde{u}_r+\frac{\partial w}{\partial r} \quad 2\varepsilon_{\theta z} = \widetilde{u}_\theta+\frac{1}{r}\frac{\partial w}{\partial \theta} \qquad (4)$$

According to the Hooke law, we can directly write the relationships between the displacement and stress components:

$$z\frac{\partial \widetilde{u}_r}{\partial r}=\frac{1}{E}\left(\sigma_r-\nu\sigma_\theta\right) \quad \frac{z}{r}\left(\frac{\partial \widetilde{u}_\theta}{\partial \theta}+\widetilde{u}_r\right)=\frac{1}{E}\left(\sigma_\theta-\nu\sigma_r\right) \quad z\frac{\partial \widetilde{u}_\theta}{\partial r}+\frac{z}{r}\left(\frac{\partial \widetilde{u}_r}{\partial \theta}-\widetilde{u}_\theta\right)=\frac{2(1+\nu)}{E}\sigma_{r\theta}$$
$$\widetilde{u}_r+\frac{\partial w}{\partial r}=\frac{2(1+\nu)}{E}\sigma_{rz} \quad \widetilde{u}_\theta+\frac{1}{r}\frac{\partial w}{\partial \theta}=\frac{2(1+\nu)}{E}\sigma_{\theta z} \qquad (5)$$

We multiply the three first equations by z then perform integration through the thickness. For the two last equations, we just perform integration. We obtain:

$$\frac{\partial \widetilde{u}_r}{\partial r}=\frac{12}{Eh^3}\left(M_{rr}-\nu M_{\theta\theta}\right) \quad \frac{1}{r}\left(\frac{\partial \widetilde{u}_\theta}{\partial \theta}+\widetilde{u}_r\right)=\frac{12}{Eh^3}\left(M_{\theta\theta}-\nu M_{rr}\right) \quad \frac{\partial \widetilde{u}_\theta}{\partial r}+\frac{1}{r}\left(\frac{\partial \widetilde{u}_r}{\partial \theta}-\widetilde{u}_\theta\right)=\frac{24(1+\nu)}{Eh^3}M_{r\theta}$$
$$\widetilde{u}_r+\frac{\partial w}{\partial r}=\frac{2(1+\nu)}{Ehk}Q_{rz} \quad \widetilde{u}_\theta+\frac{1}{r}\frac{\partial w}{\partial \theta}=\frac{2(1+\nu)}{Ehk}Q_{\theta z} \qquad (6)$$

where $k = 5/6$ is a corrector constant in order to take the parabolic distribution of the shear stresses into account. Equation (3) and (6) are the fundamental equations we use in this work. The boundary conditions at the crack lips are written as following:

$$M_{r\theta}(\theta=\pm\pi)=M_{\theta\theta}(\theta=\pm\pi)=Q_{\theta z}(\theta=\pm\pi)=0 \qquad (7)$$

In order to solve these fundamental equations, we perform the following variable changes:

$$r=e^{\xi} \quad w=r\widetilde{w} \quad M_{rr}=\frac{\widetilde{M}_{rr}}{r} \quad M_{\theta\theta}=\frac{\widetilde{M}_{\theta\theta}}{r} \quad M_{r\theta}=\frac{\widetilde{M}_{r\theta}}{r} \qquad (8)$$

Then equations (3) and (6) become respectively:

$$\frac{\partial \widetilde{M}_{rr}}{\partial \xi}+\frac{\partial \widetilde{M}_{r\theta}}{\partial \theta}-\widetilde{M}_{\theta\theta}=e^{2\xi}Q_{rz} \quad \frac{\partial \widetilde{M}_{r\theta}}{\partial \xi}+\frac{\partial \widetilde{M}_{\theta\theta}}{\partial \theta}+\widetilde{M}_{r\theta}=e^{2\xi}Q_{\theta z} \quad \frac{\partial Q_{rz}}{\partial \xi}+\frac{\partial Q_{\theta z}}{\partial \theta}+Q_{rz}=-e^{\xi}q \qquad (9)$$

$$\frac{\partial \widetilde{u}_r}{\partial \xi}=\frac{12}{Eh^3}\left(\widetilde{M}_{rr}-\nu\widetilde{M}_{\theta\theta}\right) \quad \frac{\partial \widetilde{u}_\theta}{\partial \theta}+\widetilde{u}_r=\frac{12}{Eh^3}\left(\widetilde{M}_{\theta\theta}-\nu\widetilde{M}_{rr}\right) \quad \frac{\partial \widetilde{u}_\theta}{\partial \xi}+\frac{\partial \widetilde{u}_r}{\partial \theta}-\widetilde{u}_\theta=\frac{24(1+\nu)}{Eh^3}\widetilde{M}_{r\theta}$$
$$\widetilde{u}_r+\widetilde{w}+\frac{\partial \widetilde{w}}{\partial \xi}=\frac{2(1+\nu)}{Ehk}Q_{rz} \quad \widetilde{u}_\theta+\frac{\partial w}{\partial \theta}=\frac{2(1+\nu)}{Ehk}Q_{\theta z} \qquad (10)$$

3. TRANSFORMATION INTO THE HAMILTONIAN SYSTEM ON THE BASIS OF THE RADIAL COORDINATE

In this case, we note $\frac{\partial}{\partial \xi}=\left(\bullet\right)$, and then we define the dual variables as following:

$$\boldsymbol{v}=\left\{\boldsymbol{v}_1^T \quad \boldsymbol{v}_2^T\right\}^T \quad \boldsymbol{v}_1=\left\{\boldsymbol{q}_1^T \quad \boldsymbol{p}_1^T\right\}^T \quad \boldsymbol{v}_2=\left\{\boldsymbol{q}_2^T \quad \boldsymbol{p}_2^T\right\}^T$$
$$\boldsymbol{q}_1=\left\{\widetilde{u}_r \quad \widetilde{u}_\theta\right\}^T \quad \boldsymbol{q}_2=\widetilde{w} \quad \boldsymbol{p}_1=\left\{\widetilde{M}_{rr} \quad \widetilde{M}_{r\theta}\right\}^T \quad \boldsymbol{p}_2=Q_{rz} \qquad (11)$$

We eliminate from (10) the quantities that do not exist in the above dual variables, namely:

$$Q_{\theta z}=\frac{Ehk}{2(1+\nu)}\left(\widetilde{u}_\theta+\frac{\partial\widetilde{w}}{\partial\theta}\right)\quad \widetilde{M}_{\theta\theta}=\frac{Eh^3}{12}\left(\frac{\partial\widetilde{u}_\theta}{\partial\theta}+\widetilde{u}_r\right)+\nu\widetilde{M}_{rr} \tag{12}$$

By neglecting the terms of higher orders as $r\to 0$, we obtain the following dual differential equations:

$$\dot{\boldsymbol{v}}=\boldsymbol{H}\boldsymbol{v} \tag{13}$$

with:

$$\boldsymbol{H}=\begin{bmatrix}\boldsymbol{H}_{11} & \boldsymbol{0}\\ \boldsymbol{H}_{21} & \boldsymbol{H}_{22}\end{bmatrix}\qquad \begin{matrix}\dot{\boldsymbol{v}}_1=\boldsymbol{H}_{11}\boldsymbol{v}_1\\ \dot{\boldsymbol{v}}_2=\boldsymbol{H}_{22}\boldsymbol{v}_2+\boldsymbol{H}_{21}\boldsymbol{v}_1\end{matrix} \tag{14}$$

$$\boldsymbol{H}_{11}=\begin{bmatrix}-\nu & -\nu\dfrac{\partial}{\partial\theta} & \dfrac{12(1-\nu^2)}{Eh^3} & 0\\ -\dfrac{\partial}{\partial\theta} & 1 & 0 & \dfrac{24(1+\nu)}{Eh^3}\\ \dfrac{Eh^3}{12} & \dfrac{Eh^3}{12}\dfrac{\partial}{\partial\theta} & \nu & -\dfrac{\partial}{\partial\theta}\\ -\dfrac{Eh^3}{12}\dfrac{\partial}{\partial\theta} & -\dfrac{Eh^3}{12}\dfrac{\partial^2}{\partial\theta^2} & -\nu\dfrac{\partial}{\partial\theta} & -1\end{bmatrix} \tag{15}$$

$$\boldsymbol{H}_{22}=\begin{bmatrix}-1 & \dfrac{2(1+\nu)}{Ehk}\\ -\dfrac{Ehk}{2(1+\nu)}\dfrac{\partial^2}{\partial\theta^2} & -1\end{bmatrix}\qquad \boldsymbol{H}_{21}=\begin{bmatrix}-1 & 0 & 0 & 0\\ 0 & -\dfrac{Ehk}{2(1+\nu)}\dfrac{\partial}{\partial\theta} & 0 & 0\end{bmatrix}$$

The resolution of the governing equation (13) with the boundary conditions (7) is easy. We first write the solution under separable form:

$$\boldsymbol{v}=e^{\mu\xi}\boldsymbol{\psi}(\theta) \tag{16}$$

where μ is an eigenvalue. $\boldsymbol{\psi}(\theta)$ is the corresponding eigenvector. Substituting (16) into (13) gives:

$$(\boldsymbol{H}-\boldsymbol{I}\mu)\boldsymbol{\psi}(\theta)=\boldsymbol{0} \tag{17}$$

From (14), we remark that the solution of $\boldsymbol{v}_1$ is independent of $\boldsymbol{v}_2$. So we can first solve the eigenvalue problem (17) for $\boldsymbol{v}_1$. We can easily find the eigenvalues $\mu=0,\pm 1/2,1,3/2,\ldots$. In crack problems, only eigenvectors of $\boldsymbol{v}_1$ for positive eigenvalues exist. The singular fields for $\boldsymbol{v}_1$ can therefore easily be obtained, namely:

$$\begin{aligned}
u_r&=\frac{K_1 z}{2D}\sqrt{\frac{r}{2\pi}}\left[-\cos\frac{3\theta}{2}+(2\chi-1)\cos\frac{\theta}{2}\right]+\frac{K_2 z}{2D}\sqrt{\frac{r}{2\pi}}\left[3\sin\frac{3\theta}{2}-(2\chi-1)\sin\frac{\theta}{2}\right]\\
u_\theta&=\frac{K_1 z}{2D}\sqrt{\frac{r}{2\pi}}\left[\sin\frac{3\theta}{2}-(2\chi+1)\sin\frac{\theta}{2}\right]+\frac{K_2 z}{2D}\sqrt{\frac{r}{2\pi}}\left[3\cos\frac{3\theta}{2}-(2\chi+1)\cos\frac{\theta}{2}\right]\\
M_{rr}&=\frac{K_1}{4\sqrt{2\pi r}}\left[-\cos\frac{3\theta}{2}+5\cos\frac{\theta}{2}\right]+\frac{K_2}{4\sqrt{2\pi r}}\left[3\sin\frac{3\theta}{2}-5\sin\frac{\theta}{2}\right]\\
M_{\theta\theta}&=\frac{K_1}{4\sqrt{2\pi r}}\left[\cos\frac{3\theta}{2}+3\cos\frac{\theta}{2}\right]+\frac{K_2}{4\sqrt{2\pi r}}\left[-3\sin\frac{3\theta}{2}-3\sin\frac{\theta}{2}\right]\\
M_{r\theta}&=\frac{K_1}{4\sqrt{2\pi r}}\left[\sin\frac{3\theta}{2}+\sin\frac{\theta}{2}\right]+\frac{K_2}{4\sqrt{2\pi r}}\left[3\cos\frac{3\theta}{2}+\cos\frac{\theta}{2}\right]
\end{aligned} \tag{18}$$

where K_1 and K_2 are stress intensity factors, $D=Eh/12(1+\nu)$. From dimension analysis, we know that the eigenvalues for $\boldsymbol{v}_2$ may be negative, and the most negative eigenvalue is $\mu=-1/2$. Since the eigenvector of $\boldsymbol{v}_1$ for $\mu=-1/2$ is nil, from (14), we have:

$$\dot{\boldsymbol{v}}_2=\boldsymbol{H}_{22}\boldsymbol{v}_2 \tag{19}$$

The solution of (19) with the boundary solution (7) is:

$$w=\frac{h^2}{3D}\sqrt{\frac{r}{2\pi}}K_3\sin\frac{\theta}{2}\quad Q_{rz}=\frac{K_3}{\sqrt{2\pi r}}\sin\frac{\theta}{2}\quad Q_{\theta z}=\frac{K_3}{\sqrt{2\pi r}}\cos\frac{\theta}{2} \tag{20}$$

(18) and (20) are just the solution found out by Hartranft and Sih (1968) by using an integral transform technique. Here we find it with rather a simple approach.

4. TRANSFORMATION INTO THE HAMILTONIAN SYSTEM ON THE BASIS OF THE ANGULAR COORDINATE, MULTI-MATERIAL PROBLEMS

If we define the dual variables as follows:

$$\begin{aligned} &\boldsymbol{v} = \left\{\boldsymbol{v}_1^T \quad \boldsymbol{v}_2^T\right\}^T \quad \boldsymbol{v}_1 = \left\{\boldsymbol{q}_1^T \quad \boldsymbol{p}_1^T\right\}^T \quad \boldsymbol{v}_2 = \left\{\boldsymbol{q}_2^T \quad \boldsymbol{p}_2^T\right\}^T \\ &\boldsymbol{q}_1 = \left\{\widetilde{u}_r \quad \widetilde{u}_\theta\right\}^T \quad \boldsymbol{q}_2 = \widetilde{w} \quad \boldsymbol{p}_1 = \left\{\widetilde{M}_{r\theta} \quad \widetilde{M}_{\theta\theta}\right\}^T \quad \boldsymbol{p}_2 = Q_{\theta z} \end{aligned} \tag{21}$$

and we note $\frac{\partial}{\partial\theta} = (\bullet)$. We eliminate from (10) quantities that don't exist in the dual variables defined above, namely:

$$\widetilde{M}_{rr} = \frac{Eh^3}{12}\frac{\partial\widetilde{u}_r}{\partial\xi} + \nu\widetilde{M}_{\theta\theta} \quad Q_{rz} = \frac{Ehk}{2(1+\nu)}\left(\widetilde{u} + \widetilde{w} + \frac{\partial\widetilde{w}}{\partial\xi}\right) \tag{22}$$

We obtain another dual differential equations:

$$\dot{\boldsymbol{v}} = \boldsymbol{H}\boldsymbol{v} \tag{23}$$

with

$$\boldsymbol{H} = \begin{bmatrix} \boldsymbol{H}_{11} & \boldsymbol{0} \\ \boldsymbol{H}_{21} & \boldsymbol{H}_{22} \end{bmatrix} \quad \begin{aligned} \dot{\boldsymbol{v}}_1 &= \boldsymbol{H}_{11}\boldsymbol{v}_1 \\ \dot{\boldsymbol{v}}_2 &= \boldsymbol{H}_{22}\boldsymbol{v}_2 + \boldsymbol{H}_{21}\boldsymbol{v}_1 \end{aligned} \tag{24}$$

$$\boldsymbol{H}_{11} = \begin{bmatrix} 0 & 1-\frac{\partial}{\partial\xi} & \frac{24(1+\nu)}{Eh^3} & 0 \\ -1-\nu\frac{\partial}{\partial\xi} & 0 & 0 & \frac{12(1-\nu^2)}{Eh^3} \\ -\frac{Eh^3}{12}\frac{\partial^2}{\partial\xi^2} & 0 & 0 & 1-\nu\frac{\partial}{\partial\xi} \\ 0 & 0 & -1-\frac{\partial}{\partial\xi} & 0 \end{bmatrix} \tag{25}$$

$$\boldsymbol{H}_{22} = \begin{bmatrix} 0 & \frac{2(1+\nu)}{Ehk} \\ -\frac{Ehk}{2(1+\nu)}\left(\frac{\partial}{\partial\xi}+1\right)^2 & 0 \end{bmatrix} \quad \boldsymbol{H}_{21} = \begin{bmatrix} 0 & -1 & 0 & 0 \\ -\frac{Ehk}{2(1+\nu)}\left(\frac{\partial}{\partial\xi}+1\right) & 0 & 0 & 0 \end{bmatrix}$$

The solution of (23) gives the same results as those found in the precedent section.

The main advantage of this approach is its high capacity to deal with the multi-material problems. Imagine a crack or a notch formed by *n* homogenous plates, all interfaces between two of these plates intercept at the crack tip. The boundary conditions at the crack lip are therefore:

$$\boldsymbol{p}^{(1)}(\theta = \theta_0 = -\pi) = \boldsymbol{p}^{(n)}(\theta = \theta_n = \pi) = \boldsymbol{0} \quad \boldsymbol{p} = \left\{\boldsymbol{p}_1^T \quad \boldsymbol{p}_2^T\right\}^T \tag{26}$$

and the continuity conditions across the interfaces are:

$$\boldsymbol{v}^{(i)}(\theta = \theta_i) = \boldsymbol{v}^{(i+1)}(\theta = \theta_i) \tag{27}$$

where the superscript $^{(i)}$ indicates the quantities in the zone occupied by the plate *i*. It is seen that the variable vector $\boldsymbol{v}$ is continuous across all the interfaces. This makes the solution of the multi-material problems much easier. In each zone, we can establish the governing differential equation (23), namely:

$$\dot{\boldsymbol{v}}^{(i)} = \boldsymbol{H}^{(i)}\boldsymbol{v}^{(i)} \tag{28}$$

We look for only the eigenvalues leading to singular stress filed near the crack tip. According to the analysis made in the precedent section, the vectors $\boldsymbol{v}_1$ corresponding to negative eigenvectors are nil, while a singular vector v_2 requires negative eigenvalues. Therefore, we can divide (28) into two distinguish equations:

$$\dot{\boldsymbol{v}}_1^{(i)} = \boldsymbol{H}_{11}^{(i)}\boldsymbol{v}_1^{(i)} \quad \dot{\boldsymbol{v}}_2^{(i)} = \boldsymbol{H}_{22}^{(i)}\boldsymbol{v}_2^{(i)} \tag{29}$$

We can resolve (29) by writing $\boldsymbol{v}_1$ and $\boldsymbol{v}_2$ under separable form:

$$\boldsymbol{v}_1^{(i)} = e^{\mu_1\xi}\boldsymbol{\psi}_1^{(i)}(\theta) \quad \boldsymbol{v}_2^{(i)} = e^{\mu_2\xi}\boldsymbol{\psi}_2^{(i)}(\theta) \tag{30}$$

Substituting (30) into (29) gives:

$$\dot{\psi}_1^{(i)} = \boldsymbol{H}_{11}^{(i)}(\mu_1)\psi_1^{(i)} \quad \dot{\psi}_1^{(i)} = \boldsymbol{H}_{22}^{(i)}(\mu_2)\psi_1^{(i)} \tag{31}$$

where

$$\boldsymbol{H}_{11}^{(i)}(\mu_1) = \begin{bmatrix} 0 & 1-\mu_1 & \dfrac{24(1+\nu^{(i)})}{E^{(i)}h^3} & 0 \\ -1-\nu^{(i)}\mu_1 & 0 & 0 & \dfrac{12(1-\nu^{(i)2})}{E^{(i)}h^3} \\ -\dfrac{E^{(i)}h^3}{12}\mu_1^2 & 0 & 0 & 1-\nu^{(i)}\mu_1 \\ 0 & 0 & -1-\mu_1 & 0 \end{bmatrix} \quad \boldsymbol{H}_{22}^{(i)}(\mu_2) = \begin{bmatrix} 0 & \dfrac{2(1+\nu^{(i)})}{E^{(i)}hk} \\ -\dfrac{E^{(i)}hk}{2(1+\nu^{(i)})}(\mu_2+1)^2 & 0 \end{bmatrix} \tag{32}$$

The solution of (31) is immediately written as follows:

$$\psi_1^{(i)}(\theta) = e^{\boldsymbol{H}_{11}^{(i)}(\theta-\theta_{i-1})}\psi_1^{(i)}(\theta_{i-1}) \quad \psi_2^{(i)}(\theta) = e^{\boldsymbol{H}_{22}^{(i)}(\theta-\theta_{i-1})}\psi_2^{(i)}(\theta_{i-1}) \tag{33}$$

According to the continuity conditions (27), we obtain the relationship between the $\boldsymbol{\psi}$'s at the two crack lips:

$$\psi_1^{(n)}(\theta=\pi) = \boldsymbol{G}^1\psi_1^{(0)}(\theta=-\pi) \quad \psi_2^{(n)}(\theta=\pi) = \boldsymbol{G}^2\psi_2^{(0)}(\theta=-\pi) \tag{34}$$

with:

$$\boldsymbol{G}^1 = \prod_{i=n}^{1} e^{\boldsymbol{H}_{11}^{(i)}(\theta_i-\theta_{i-1})} \quad \boldsymbol{G}^2 = \prod_{i=n}^{1} e^{\boldsymbol{H}_{22}^{(i)}(\theta_i-\theta_{i-1})} \tag{35}$$

where $\boldsymbol{G}^1$ is a 4×4 matrix and $\boldsymbol{G}^2$ is a 2×2 matrix. According to the boundary conditions (26), we have finally the following conditions allowing calculation of the eigenvalues:

$$\det\begin{bmatrix} \boldsymbol{G}_{31}^1 & \boldsymbol{G}_{32}^1 \\ \boldsymbol{G}_{41}^1 & \boldsymbol{G}_{42}^1 \end{bmatrix} = 0 \quad \boldsymbol{G}_{21}^2 = 0 \tag{36}$$

Once the eigenvalues obtained, the corresponding eigenvectors can immediately be computed from (33).

5. ORTHOTROPIC PLATES

Anisotropy is a very important quality in composite plates. Now let us consider an orthotropic plate that is habitually used in engineering applications. If the mid-plane is perpendicular to the orthotropic axis, one can write the relationship between the stress and strain components in the cylindrical coordinate system:

$$\boldsymbol{\sigma} = \boldsymbol{C}\boldsymbol{\varepsilon}$$

$$\boldsymbol{\sigma} = \{\sigma_{rr} \quad \sigma_{\theta\theta} \quad \sigma_{zz} \quad \sigma_{r\theta} \quad \sigma_{rz} \quad \sigma_{\theta z}\}^T \quad \boldsymbol{\varepsilon} = \{\varepsilon_{rr} \quad \varepsilon_{\theta\theta} \quad \varepsilon_{zz} \quad 2\varepsilon_{r\theta} \quad 2\varepsilon_{rz} \quad 2\varepsilon_{\theta z}\}^T \tag{37}$$

$$\boldsymbol{C} = \begin{bmatrix} c_{11} & c_{12} & c_{13} & c_{14} & 0 & 0 \\ c_{21} & c_{22} & c_{23} & c_{24} & 0 & 0 \\ c_{31} & c_{32} & c_{33} & c_{34} & 0 & 0 \\ c_{41} & c_{42} & c_{44} & c_{44} & 0 & 0 \\ 0 & 0 & 0 & 0 & c_{55} & c_{56} \\ 0 & 0 & 0 & 0 & c_{65} & c_{66} \end{bmatrix}$$

The components of the stiffness matrix may be function of θ. From (37), one can easily find:

$$\begin{Bmatrix} \widetilde{M}_{rr} \\ \widetilde{M}_{\theta\theta} \\ \widetilde{M}_{r\theta} \\ Q_{rz} \\ Q_{\theta z} \end{Bmatrix} = \begin{bmatrix} \widetilde{c}_{11} & \widetilde{c}_{12} & \widetilde{c}_{14} & 0 & 0 \\ \widetilde{c}_{21} & \widetilde{c}_{22} & \widetilde{c}_{24} & 0 & 0 \\ \widetilde{c}_{41} & \widetilde{c}_{42} & \widetilde{c}_{44} & 0 & 0 \\ 0 & 0 & 0 & \widetilde{c}_{55} & \widetilde{c}_{56} \\ 0 & 0 & 0 & \widetilde{c}_{65} & \widetilde{c}_{66} \end{bmatrix} \begin{bmatrix} \partial/\partial\xi & 0 & 0 \\ 1 & \partial/\partial\theta & 0 \\ \partial/\partial\theta & 1+\partial/\partial\xi & 0 \\ 1 & 0 & \partial/\partial\xi \\ 0 & 1 & \partial/\partial\theta \end{bmatrix} \begin{Bmatrix} \widetilde{u}_r \\ \widetilde{u}_\theta \\ \widetilde{w} \end{Bmatrix} \quad \begin{matrix} \widetilde{c}_{ij} = \dfrac{h^3}{12}c_{ij} & i,j = 1,2,4 \\ \widetilde{c}_{ij} = khc_{ij} & i,j = 5,6 \end{matrix} \tag{38}$$

By choosing the following dual variable vectors:

$$\boldsymbol{v} = \begin{Bmatrix} \boldsymbol{q}^T & \boldsymbol{p}^T \end{Bmatrix} \quad \boldsymbol{q} = \{\widetilde{u}_r \quad \widetilde{u}_\theta \quad \widetilde{w}\}^T \quad \boldsymbol{p} = \{\widetilde{M}_{r\theta} \quad \widetilde{M}_{\theta\theta} \quad Q_{\theta z}\}^T \tag{39}$$

and by neglecting the high order quantities as $r \to 0$, we can find the following dual differential equations:

$$\dot{\boldsymbol{v}} = \boldsymbol{H}\boldsymbol{v}$$

$$\boldsymbol{H} = \begin{bmatrix} -\boldsymbol{C}_d^{-1}\boldsymbol{C}_{d1} & \boldsymbol{C}_d^{-1} \\ \boldsymbol{C}_{f1}\left(\boldsymbol{C}_{e1} - \boldsymbol{C}_e\boldsymbol{C}_d^{-1}\boldsymbol{C}_{d1}\right) & \boldsymbol{C}_f + \boldsymbol{C}_{f1}\boldsymbol{C}_e\boldsymbol{C}_d^{-1} \end{bmatrix} \tag{40}$$

with $\dfrac{\partial}{\partial\theta} = \left(\bullet\right)$ and

$$\boldsymbol{C}_{d1} = \begin{bmatrix} \widetilde{c}_{41}\dfrac{\partial}{\partial\xi} + \widetilde{c}_{42} & \widetilde{c}_{44}\left(\dfrac{\partial}{\partial\xi} + 1\right) & 0 \\ \widetilde{c}_{21}\dfrac{\partial}{\partial\xi} + \widetilde{c}_{22} & \widetilde{c}_{24}\left(\dfrac{\partial}{\partial\xi} + 1\right) & 0 \\ \widetilde{c}_{65} & \widetilde{c}_{66} & \widetilde{c}_{65}\dfrac{\partial}{\partial\xi} \end{bmatrix} \quad \boldsymbol{C}_d = \begin{bmatrix} \widetilde{c}_{44} & \widetilde{c}_{42} & 0 \\ \widetilde{c}_{24} & \widetilde{c}_{22} & 0 \\ 0 & 0 & \widetilde{c}_{66} \end{bmatrix}$$

$$\boldsymbol{C}_{e1} = \begin{bmatrix} \widetilde{c}_{11}\dfrac{\partial}{\partial\xi} + \widetilde{c}_{12} & \widetilde{c}_{14}\left(\dfrac{\partial}{\partial\xi} + 1\right) & 0 \\ \widetilde{c}_{55} & \widetilde{c}_{56} & \widetilde{c}_{55}\dfrac{\partial}{\partial\xi} \end{bmatrix} \quad \boldsymbol{C}_e = \begin{bmatrix} \widetilde{c}_{14} & \widetilde{c}_{12} & 0 \\ 0 & 0 & \widetilde{c}_{56} \end{bmatrix} \tag{41}$$

$$\boldsymbol{C}_f = \begin{bmatrix} 0 & 1 & 0 \\ -\left(1 + \dfrac{\partial}{\partial\xi}\right) & 0 & 0 \\ 0 & 0 & 0 \end{bmatrix} \quad \boldsymbol{C}_{f1} = \begin{bmatrix} -\dfrac{\partial}{\partial\xi} & 0 \\ 0 & 0 \\ 0 & -\left(1 + \dfrac{\partial}{\partial\xi}\right) \end{bmatrix}$$

Here again, we establish the standard form of the governing equation (40) in the Hamiltonian system. We can then perform the separation of the variables and solve the corresponding eigenvalue problem as described in the precedent section. As for the isotropic materials, cracks or notches formed by several anisotrapic plates can also be dealt with in a very similar manner.

6. CONCLUSIONS

In this paper, we have developed a new approach to deal with asymptotic fields near a crack tip in thin plates subjected to bending forces. Ressner hypothesis are used in this theory. By establishing dual differential equations in the frame of the Hamiltonian system, a large range of problems in this topic, some of them are often difficult to treat with the traditional techniques, can be solved in rather a simple way.

Reference:

[1] Knowels, J. K. and Wang, N. M., (1960). *J. Mat. And Phys*., Vol.39, 223
[2] Sih, G. C., (1965). *Proc. 1st Int.Conference on Fracture*, Vol.1, 391
[3] Hartranft, R. J. and Sih, G. C., (1968). *J. Mat. And Phys*., Vol.47, 276
[4] Hartranft, R. J. and Sih, G. C., (1970). *Int. J. Engng. Sci*., Vol.9, 711

ASYMPTOTIC FIELDS NEAR A CRACK TIP LOCATED AT INTERFACES OF SEVERAL ANISOTROPIC MATERIALS

Jia LI, Xiao-Bing ZHANG, Naman RECHO

Laboratoire d'Etudes et de Recherches en Mécanique des Structures
Blaise Pascal University of Clermont-Ferrand
Avenue Aristide Briand, 03100 Montluçon, France

ABSTRACT

In this paper, we studied the stress singularities near tip of a two-dimension notch, which could be a crack tip, formed from several elastic materials, each of them may be generally anisotropic. By introducing the dual variables in the state space, the basic equations governing the posed problem were established. We also proposed a numerical method to solve the governing equations. It was shown that the mathematical formulations advanced are quite simple and the numerical method proposed is easy and highly accurate.

KEYWORDS
Notch, crack, interface, multi-material, bimaterial, anisotropy, plane stress, generalized plane strain

1. INTRODUCTION

Knowledge about the stress concentration near the tip of a notch in anisotropic materials, or a crack as a special case, has a particular importance. The fracture behaviors of such a structure may be interesting for many engineering applications such as composites, crystals, welded structures or reinforced polymers etc. In this topic, one can note the pioneering works of Stroh (1958), Sih *et al*. (1965) or Hoenig (1982) concerning the asymptotic fields near a crack tip in homogenous orthotropic or general anisotropic materials. The next studies were carried out in determining the near-tip fields when the crack lying at or touching an interface between two anisotropic materials. Several basic crack problems have been solved (Gotoh, 1967, Clements, 1971, Willis, 1971, Delale and Erdogan, 1979, Ting and Hoang, 1984, Ting, 1986, Qu & Bassani, 1989, Suo, 1990, Gupta *et al*., 1992, Ting, 1996, Sung and Liou, 1996, Lin and Sung, 1997, Matntic *et al*., 1997 among others).

In all the studies mentioned above, the linear elastic anisotropy theory developed by Lekhnitskii (1953) and Eshelby *et al* (1953) were essentially followed. This theory provides explicit results for some problems such as cracks in homogenous materials or cracks lying at an interface etc. However, for more complex problems, the methods provided by this theory leads to long and difficult mathematical formulations.

In this paper, we propose to study the stress singularities near the tip of a notch formed from several generally anisotropic elastic materials. We will use, in this work, another methodology than that of Lekhnitskii and Eshelby. This new methodology consists in introducing the Hamiltonian system and the state space method into the continuum mechanics and has been successfully used in the reform of the elasticity theory (Zhong, 1995). In this work, we deduced the governing equations allowing the determination of the stress singularities and the asymptotic fields near the notch tip. The mathematical formulation is quite simple comparing with those currently appeared in the literature. We also proposed a

numerical method to solve the governing equations. It has been shown that this numerical method is simple and highly accurate.

2. GOVERNING EQUATIONS OF THE PROBLEM

Let consider a notch formed from several elastic anisotropic materials. We establish a Cartesian coordinate system and a cylindrical coordinate system with their origins at the notch tip and the *z*-axis representing the notch front. The material 1 occupies the sectorial domain $[\theta_0,\theta_1]$, named zone 1; the material 2 occupies the zone 2, bounded by $[\theta_1,\theta_2]$, and so on. Under remote loading, the stress concentration at the notch tip will take a mixed mode nature due to the anisotropy of the materials.

First, we write the stress components in the Cartesian system and in the cylindrical system as $\boldsymbol{\sigma}_{xyz} = \{\sigma_x \quad \sigma_y \quad \sigma_z \quad \tau_{xy} \quad \tau_{xz} \quad \tau_{yz}\}^T$ and $\boldsymbol{\sigma}_{r\theta z} = \{\sigma_r \quad \sigma_\theta \quad \sigma_z \quad \tau_{r\theta} \quad \tau_{rz} \quad \tau_{\theta z}\}^T$ respectively. The corresponding strain components are $\boldsymbol{\varepsilon}_{xyz} = \{\varepsilon_x \quad \varepsilon_y \quad \varepsilon_z \quad \gamma_{xy} \quad \gamma_{xz} \quad \gamma_{yz}\}^T$ and $\boldsymbol{\varepsilon}_{r\theta z} = \{\varepsilon_r \quad \varepsilon_\theta \quad \varepsilon_z \quad \gamma_{r\theta} \quad \gamma_{rz} \quad \gamma_{\theta z}\}^T$ respectively. In the Cartesian system, each material has a homogeneous and anisotropic elasticity:

$$\boldsymbol{\sigma}_{xyz} = \boldsymbol{C}_{xyz}\boldsymbol{\varepsilon}_{xyz} \qquad (1)$$

$\boldsymbol{C}_{xyz}$ is the stiffness matrix of the material. All its components c_{ij} (i, j = 1,6) are constant. In the cylindrical system, the stress and the strain components can be obtained from their corresponding quantities in the Cartesian system with a coordinate rotation, namely,

$$\boldsymbol{\sigma}_{r\theta z} = \boldsymbol{T}_\sigma\boldsymbol{\sigma}_{xyz} \qquad \boldsymbol{\varepsilon}_{r\theta z} = \boldsymbol{T}_\varepsilon\boldsymbol{\varepsilon}_{xyz} \qquad (2)$$

where $\boldsymbol{T}_\sigma$ and $\boldsymbol{T}_\varepsilon$ are the coordinate rotation matrices about the stresses and strains respectively. Therefore, the stress-strain relationship in the cylindrical system is:

$$\begin{aligned} &\boldsymbol{\sigma}_{r\theta z} = \boldsymbol{C}_{r\theta z}\boldsymbol{\varepsilon}_{r\theta z} \\ &\boldsymbol{C}_{r\theta z}(\theta) = \boldsymbol{T}_\sigma\boldsymbol{C}_{xyz}\boldsymbol{T}_\varepsilon^{-1}. \end{aligned} \qquad (4)$$

This shows that in the cylindrical system, the stiffness matrix is not a constant matrix but a function of θ. Hereafter we work exclusively in the cylindrical system, therefore the subscript $_{r\theta z}$ will be omitted in order to simplify the notations. At the present, we do not distinguish the different materials in the formulation.

We write now the fundamental equations of the anisotropic elasticity in the cylindrical system:

(a): *The equilibrium equations:* In the case when the stress components are independent of the *z*-axis, the equilibrium equations are:

$$\frac{\partial\sigma_r}{\partial r} + \frac{1}{r}\frac{\partial\tau_{r\theta}}{\partial\theta} + \frac{\sigma_r - \sigma_\theta}{r} = 0 \quad \frac{\partial\tau_{r\theta}}{\partial r} + \frac{1}{r}\frac{\partial\sigma_\theta}{\partial\theta} + \frac{2\tau_{r\theta}}{r} = 0 \quad \frac{\partial\tau_{rz}}{\partial r} + \frac{1}{r}\frac{\partial\tau_{\theta z}}{\partial\theta} + \frac{\tau_{rz}}{r} = 0 \qquad (5)$$

We perform the following variable changes:

$$\xi = \ln r \qquad r = \exp(\xi); \qquad (6)$$

and

$$\begin{aligned} &S_r = r\sigma_r \quad \sigma_r = S_r/r; \\ &S_{r\theta} = r\tau_{r\theta} \quad \tau_{r\theta} = S_{r\theta}/r; \quad \text{...etc} \end{aligned} \qquad (7)$$

Then by using the notation $(\cdot) = \dfrac{\partial}{\partial\theta}$, the equilibrium equations (5) can be rewritten as:

$$\dot{S}_{r\theta} = S_\theta - \frac{\partial S_r}{\partial\xi} \quad \dot{S}_\theta = -\frac{\partial S_{r\theta}}{\partial\xi} - S_{r\theta} \quad \dot{S}_{\theta z} = -\frac{\partial S_{rz}}{\partial\xi} \qquad (8)$$

We define the following variable vectors:

$$\boldsymbol{p} = \{S_\theta \quad S_{r\theta} \quad S_{\theta z}\}^T \quad \boldsymbol{p}_t = \{S_r \quad S_z \quad S_{rz}\}^T \qquad (9)$$

Hence, the equilibrium equations (8) can be rewritten as:

$$\dot{\boldsymbol{p}} = \boldsymbol{E}_1\boldsymbol{p} + \boldsymbol{E}_2\frac{\partial\boldsymbol{p}}{\partial\xi} + \boldsymbol{E}_3\frac{\partial\boldsymbol{p}_t}{\partial\xi} \qquad (10)$$

where

$$\boldsymbol{E}_1=\begin{bmatrix}0&-1&0\\1&0&0\\0&0&0\end{bmatrix}\qquad \boldsymbol{E}_2=\begin{bmatrix}0&-1&0\\0&0&0\\0&0&0\end{bmatrix}\qquad \boldsymbol{E}_3=\begin{bmatrix}0&0&0\\-1&0&0\\0&0&-1\end{bmatrix}$$

(b): *The displacement-stress relationship:* If the displacement components are independent of the *z*-axis, the relations between the strain and displacement components are:

$$\begin{aligned}&\varepsilon_r=\frac{\partial u_r}{\partial r}\qquad \varepsilon_\theta=\frac{1}{r}\left(u_r+\frac{\partial u_\theta}{\partial\theta}\right)\qquad \varepsilon_z=0\\&\gamma_{r\theta}=\frac{1}{r}\frac{\partial u_r}{\partial\theta}+\frac{\partial u_\theta}{\partial r}-\frac{u_\theta}{r}\qquad \gamma_{rz}=\frac{\partial w}{\partial r}\qquad \gamma_{\theta z}=\frac{1}{r}\frac{\partial w}{\partial\theta}\end{aligned}\tag{11}$$

By substituting (11) into (4) and by using the variable changes (6) and (7), one obtains:

$$\begin{Bmatrix}S_r\\S_\theta\\S_z\\S_{r\theta}\\S_{rz}\\S_{\theta z}\end{Bmatrix}=\begin{bmatrix}c_{12}&c_{14}&c_{16}\\c_{22}&c_{24}&c_{26}\\c_{32}&c_{34}&c_{36}\\c_{42}&c_{44}&c_{46}\\c_{52}&c_{54}&c_{56}\\c_{62}&c_{64}&c_{66}\end{bmatrix}\begin{Bmatrix}\frac{\partial u_\theta}{\partial\theta}\\\frac{\partial u_r}{\partial\theta}\\\frac{\partial w}{\partial\theta}\end{Bmatrix}+\begin{bmatrix}-c_{14}&c_{12}&0\\-c_{24}&c_{22}&0\\-c_{34}&c_{32}&0\\-c_{44}&c_{42}&0\\-c_{54}&c_{52}&0\\-c_{64}&c_{62}&0\end{bmatrix}\begin{Bmatrix}u_\theta\\u_r\\w\end{Bmatrix}+\begin{bmatrix}c_{14}&c_{11}&c_{15}\\c_{24}&c_{21}&c_{25}\\c_{34}&c_{31}&c_{35}\\c_{44}&c_{41}&c_{45}\\c_{54}&c_{51}&c_{55}\\c_{64}&c_{61}&c_{65}\end{bmatrix}\begin{Bmatrix}\frac{\partial u_\theta}{\partial\xi}\\\frac{\partial u_r}{\partial\xi}\\\frac{\partial w}{\partial\xi}\end{Bmatrix}\tag{12}$$

Similarly, we define a displacement vector

$$\{\boldsymbol{q}\}=\{u_\theta\quad u_r\quad w\}^T\tag{13}$$

By using the definitions (9) and (13), the relationship (12) can be rewritten as:

$$\boldsymbol{p}=\boldsymbol{C}_d\dot{\boldsymbol{q}}+\boldsymbol{C}_e\boldsymbol{q}+\boldsymbol{C}_f\frac{\partial\boldsymbol{q}}{\partial\xi}\quad \boldsymbol{p}_t=\boldsymbol{C}_{d1}\dot{\boldsymbol{q}}+\boldsymbol{C}_{e1}\boldsymbol{q}+\boldsymbol{C}_{f1}\frac{\partial\boldsymbol{q}}{\partial\xi}\tag{14}$$

Or :

$$\dot{\boldsymbol{q}}=\boldsymbol{C}_d^{-1}\left(\boldsymbol{p}-\boldsymbol{C}_e\boldsymbol{q}-\boldsymbol{C}_f\frac{\partial\boldsymbol{q}}{\partial\xi}\right)\quad \boldsymbol{p}_t=\boldsymbol{C}_{d1}\boldsymbol{C}_d^{-1}\boldsymbol{p}+\left(\boldsymbol{C}_{f1}-\boldsymbol{C}_{d1}\boldsymbol{C}_d^{-1}\boldsymbol{C}_f\right)\frac{\partial\boldsymbol{q}}{\partial\xi}\tag{16}$$

with:

$$\begin{aligned}&\boldsymbol{C}_d=\begin{bmatrix}c_{22}&c_{24}&c_{26}\\c_{42}&c_{44}&c_{46}\\c_{62}&c_{64}&c_{66}\end{bmatrix}\quad \boldsymbol{C}_e=\begin{bmatrix}-c_{24}&c_{22}&0\\-c_{44}&c_{42}&0\\-c_{64}&c_{62}&0\end{bmatrix}\quad \boldsymbol{C}_f=\begin{bmatrix}c_{24}&c_{21}&c_{25}\\c_{44}&c_{41}&c_{45}\\c_{64}&c_{61}&c_{65}\end{bmatrix}\\&\boldsymbol{C}_{d1}=\begin{bmatrix}c_{12}&c_{14}&c_{16}\\c_{32}&c_{34}&c_{36}\\c_{52}&c_{54}&c_{56}\end{bmatrix}\quad \boldsymbol{C}_{e1}=\begin{bmatrix}-c_{14}&c_{12}&0\\-c_{34}&c_{32}&0\\-c_{54}&c_{52}&0\end{bmatrix}\quad \boldsymbol{C}_{f1}=\begin{bmatrix}c_{14}&c_{11}&c_{15}\\c_{34}&c_{31}&c_{35}\\c_{54}&c_{51}&c_{55}\end{bmatrix}\end{aligned}\tag{18}$$

In (17) the relationship $\boldsymbol{C}_{e1}-\boldsymbol{C}_{d1}\boldsymbol{C}_d^{-1}\boldsymbol{C}_e=\boldsymbol{0}$ is used. Since the strain energy in solids is always positive, consequently, $\boldsymbol{C}_d$ is a positively definite matrix. Therefore, the inversion of the matrix $\boldsymbol{C}_d$ is permitted

(c): *The governing equations:* By substituting equation (17) into the equilibrium equation (10), the variable vector $\boldsymbol{p}_t$ is eliminated. Then we obtain, from (10) and (16), the following dual equations that govern the posed problem:

$$\dot{\boldsymbol{q}}=\boldsymbol{H}_{11}\boldsymbol{q}+\boldsymbol{H}_{12}\boldsymbol{p}\quad \dot{\boldsymbol{p}}=\boldsymbol{H}_{21}\boldsymbol{q}+\boldsymbol{H}_{22}\boldsymbol{p}\tag{19}$$

with:

$$\begin{aligned}&\boldsymbol{H}_{11}=\boldsymbol{E}_1-\boldsymbol{C}_d^{-1}\boldsymbol{C}_f\frac{\partial}{\partial\xi}\qquad \boldsymbol{H}_{12}=\boldsymbol{C}_d^{-1}\\&\boldsymbol{H}_{21}=\boldsymbol{E}_3\left(\boldsymbol{C}_{f1}-\boldsymbol{C}_{d1}\boldsymbol{C}_d^{-1}\boldsymbol{C}_f\right)\frac{\partial^2}{\partial\xi^2}\quad \boldsymbol{H}_{22}=\boldsymbol{E}_1+\left(\boldsymbol{E}_2+\boldsymbol{E}_3\boldsymbol{C}_{d1}\boldsymbol{C}_d^{-1}\right)\frac{\partial}{\partial\xi}\end{aligned}\tag{20}$$

In fact, it is more convenient to define a total vector $\boldsymbol{v}$ as variables in the state space:

$$\boldsymbol{v} = \left\{ \boldsymbol{q}^T \quad \boldsymbol{p}^T \right\}^T \tag{21}$$

such that the governing equations (19) become:

$$\dot{\boldsymbol{v}} = \boldsymbol{H}\boldsymbol{v} \tag{22}$$

with:

$$\boldsymbol{H} = \begin{vmatrix} \boldsymbol{H}_{11} & \boldsymbol{H}_{12} \\ \boldsymbol{H}_{21} & \boldsymbol{H}_{22} \end{vmatrix} \tag{23}$$

(d): *The boundary conditions and the continuity conditions:* Referring to Fig.1, we adopt the superscript $^{(i)}$ to indicate the quantities in the zone i , for example, $\boldsymbol{v}^{(i)}$, $\boldsymbol{H}^{(i)}$, etc.. The boundary conditions at the two free surfaces of the notch are:

$$\boldsymbol{p}^{(1)}(\theta = \theta_0) = \boldsymbol{0} \quad \boldsymbol{p}^{(n)}(\theta = \theta_n) = \boldsymbol{0} \tag{24}$$

The continuity conditions across the interfaces are:

$$\boldsymbol{v}^{(1)}(\theta = \theta_1) = \boldsymbol{v}^{(2)}(\theta = \theta_1) \quad \cdots\cdots \quad \boldsymbol{v}^{(n-1)}(\theta = \theta_{n-1}) = \boldsymbol{v}^{(n)}(\theta = \theta_{n-1}) \tag{25}$$

These relations show the advantage of the choice of the dual variables in the present study: the multi-material problem can be dealt with as a single material problem since the variable vector $\boldsymbol{v}$ is continuous across all the interfaces. This makes much easier the resolution of the governing equation (22).

If we suppose the stress component σ_z=0, from the third equation of (4), one deduces the strain component ε_z:

$$\varepsilon_z = -\frac{c_{31}}{c_{33}}\varepsilon_r - \frac{c_{32}}{c_{33}}\varepsilon_\theta - \frac{c_{34}}{c_{33}}\gamma_{r\theta} - \frac{c_{35}}{c_{33}}\gamma_{rz} - \frac{c_{36}}{c_{33}}\gamma_{\theta z} \tag{26}$$

Introducing (26) into (4) eliminates all components in the third colon and the third row of the stiffness matrix $\boldsymbol{C}$. The other components become:

$$c_{ij\ (plane\ stress)} = c_{ij} - \frac{c_{i3}c_{3j}}{c_{33}} \tag{27}$$

By adapting this new stiffness matrix, all formulations deduced for the generalized plane strain can directly be used for plane stress problems.

3. SOLUTION METHOD

By examining the governing equation (22), it is self-evident to try to solve it by using the variable separation method. We suppose that the variable vector $\boldsymbol{v}(\xi, \theta)$ can be written under separable form:

$$\boldsymbol{v}(\xi, \theta) = \exp(\lambda\xi)\boldsymbol{\psi}(\theta) \tag{31}$$

where λ is an undetermined eigenvalue, $\boldsymbol{\psi}(\theta)$ is a variable vector depending exclusively on θ. Then equation (22) becomes:

$$\dot{\boldsymbol{\psi}}(\theta) = \boldsymbol{H}(\theta)\boldsymbol{\psi}(\theta) \tag{32}$$

In (32), $\boldsymbol{H}$ is function of θ only,

$$\boldsymbol{H}(\theta) = \begin{vmatrix} \boldsymbol{E}_1 - \boldsymbol{C}_d^{-1}\boldsymbol{C}_f\lambda & \boldsymbol{C}_d^{-1} \\ \boldsymbol{E}_3\left(\boldsymbol{C}_{f1} - \boldsymbol{C}_{d1}\boldsymbol{C}_d^{-1}\boldsymbol{C}_f\right)\lambda^2 & \boldsymbol{E}_1 + \left(\boldsymbol{E}_2 + \boldsymbol{E}_3\boldsymbol{C}_{d1}\boldsymbol{C}_d^{-1}\right)\lambda \end{vmatrix} \tag{33}$$

The continuity conditions across the interfaces become:

$$\boldsymbol{\psi}^{(1)}(\theta = \theta_1) = \boldsymbol{\psi}^{(2)}(\theta = \theta_1) \quad \cdots\cdots \quad \boldsymbol{\psi}^{(n-1)}(\theta = \theta_{n-1}) = \boldsymbol{\psi}^{(n)}(\theta = \theta_{n-1}) \tag{34}$$

We believe that equation (32) may be solved by different ways. In this work, we propose a numerical method allowing the determination of the eigenvalue λ and the corresponding eigenvector $\boldsymbol{\psi}(\theta)$. First, we divide a zone, the zone i bounded by the interfaces $\theta=\theta_{i-1}$and $\theta=\theta_i$ for example, into N_i intervals of equal angle size by inserting N_i-1 points. In each interval, we integrate (32) by using the trapezoidal approximation:

$$\boldsymbol{\psi}_1^{(i)} - \boldsymbol{\psi}_0^{(i)} = \left(\boldsymbol{H}_0^{(i)}\boldsymbol{\psi}_0^{(i)} + \boldsymbol{H}_1^{(i)}\boldsymbol{\psi}_1^{(i)}\right)\frac{d}{2} \quad \cdots\cdots \quad \boldsymbol{\psi}_{N_i}^{(i)} - \boldsymbol{\psi}_{N_i-1}^{(i)} = \left(\boldsymbol{H}_{N_i-1}^{(i)}\boldsymbol{\psi}_{N_i-1}^{(i)} + \boldsymbol{H}_{N_i}^{(i)}\boldsymbol{\psi}_{N_i}^{(i)}\right)\frac{d}{2} \tag{35}$$

where d is the interval size. From (35), we have:

$$\boldsymbol{\psi}_1^{(i)} = \left(\boldsymbol{I}_6 - \boldsymbol{H}_1^{(i)}\frac{d}{2}\right)^{-1}\left(\boldsymbol{I}_6 + \boldsymbol{H}_0^{(i)}\frac{d}{2}\right)\boldsymbol{\psi}_0^{(i)} \quad \cdots\cdots \quad \boldsymbol{\psi}_{N_i}^{(i)} = \left(\boldsymbol{I}_6 - \boldsymbol{H}_{N_i}^{(i)}\frac{d}{2}\right)^{-1}\left(\boldsymbol{I}_6 + \boldsymbol{H}_{N_i-1}^{(i)}\frac{d}{2}\right)\boldsymbol{\psi}_{N_i-1}^{(i)} \qquad (36)$$

where $\boldsymbol{I}_6$ is a 6×6 unite matrix. Hence, we immediately obtain the relation between $\boldsymbol{\psi}_{N_i}^{(i)}$ and $\boldsymbol{\psi}_0^{(i)}$, namely:

$$\boldsymbol{\psi}_{N_i}^{(i)} = \boldsymbol{G}^{(i)}\boldsymbol{\psi}_0^{(i)} \qquad (37)$$

with:

$$\boldsymbol{G}^{(i)} = \left(\boldsymbol{I}_6 - \boldsymbol{H}_{N_i}^{(i)}\frac{d}{2}\right)^{-1}\left[\prod_{k=N_i-1}^{1}\left(\boldsymbol{I}_6 + \boldsymbol{H}_k^{(i)}\frac{d}{2}\right)\left(\boldsymbol{I}_6 - \boldsymbol{H}_k^{(i)}\frac{d}{2}\right)^{-1}\right]\left(\boldsymbol{I}_6 + \boldsymbol{H}_0^{(i)}\frac{d}{2}\right) \qquad (38)$$

According to the continuity conditions (34), one has:

$$\boldsymbol{\psi}_0^{(i)} = \boldsymbol{\psi}_{N_i}^{(i-1)} \qquad (39)$$

Hence, we obtain the relation between $\boldsymbol{\psi}^{(1)}(\theta = \theta_0)$ and $\boldsymbol{\psi}^{(n)}(\theta = \theta_n)$, namely,

$$\boldsymbol{\psi}^{(n)}(\theta = \theta_n) = \boldsymbol{G}\boldsymbol{\psi}^{(1)}(\theta = \theta_0) \qquad (40)$$

with

$$\boldsymbol{G} = \prod_{i=n}^{1}\boldsymbol{G}^{(i)} \qquad (41)$$

In practice, the trapeze method provides quite a poor accuracy in calculation of $\boldsymbol{G}$. The accuracy can considerably be improved by using the Richardson extrapolation technique.

Now we write (40) in the form of the dual vectors $\boldsymbol{q}$ and $\boldsymbol{p}$:

$$\begin{Bmatrix}\boldsymbol{q}\\ \boldsymbol{p}\end{Bmatrix}(\theta = \theta_n) = \begin{bmatrix}\boldsymbol{G}_{11} & \boldsymbol{G}_{12}\\ \boldsymbol{G}_{21} & \boldsymbol{G}_{22}\end{bmatrix}\begin{Bmatrix}\boldsymbol{q}\\ \boldsymbol{p}\end{Bmatrix}(\theta = \theta_0) \qquad (42)$$

Since $\boldsymbol{p}(\theta = \theta_0) = \boldsymbol{p}(\theta = \theta_n) = \{\boldsymbol{0}\}$, from the second equation of (42), one has:

$$\boldsymbol{G}_{21}\boldsymbol{q}(\theta = \theta_0) = \boldsymbol{0} \qquad (43)$$

This leads to:

$$\det(\boldsymbol{G}_{21}) = 0 \qquad (44)$$

Equation (44) is the condition required to determine the eigenvalues λ. Iteration techniques for roots finding can be used for the determination of λ. In this work, the Muler method is used because it can generate complex roots even if a real initial value of λ is chosen, and vice-versa. Once the eigenvalues determined, the vector $\boldsymbol{q}(\theta = \theta_0)$ is obtained from (43). Therefore, the boundary value problem posed becomes an initial value problem. Any numerical method providing a good accuracy can be used for solving equation (32). Otherwise the eigenvectors $\boldsymbol{\psi}$ can straightforwardly be given from (36), and all stress and displacement components can easily be obtained from (31) and (17).

5. CONCLUSIONS

In this work, we have established the general equations governing the asymptotic fields near a notch tip formed from several general anisotropic materials. These equations are expressed under the form of a system of first-order differential equations, instead of a high-order differential equation of a single variable as in the traditional methods. The dual variables chosen present important advantages in the resolution of the problems because of their continuity across all the interfaces. A numerical method has been proposed to solve the egeinvalue problem. This numerical method is simple and highly accurate comparing with results obtained in other existing analytical solutions. Consequently, the present method enables us to deal with a large range of problems in this topic with rather simple mathematical formulations and small numerical effort. Since the new materials developed recently present a large field in which the modeling of the anisotropy is important, we believe that the present work provides a new tool to study problems in this domain.

REFERENCES

Clements, D.L. (1971). A crack between dissimilar anisotropic media. *International Journal of Engineering Science* **9**, 257-265.

Delale, F. & Erdogan, F. (1979). Bonded orthotropic strips with cracks. *International Journal of Fracture* **15**, 343-364.

Eshelby, J. D., Read, W. T. & Shockley. W. (1953). Anisotropic elasticity with applications to dislocation theory. *Acta Metallurgica* **1**, 251-259.

Gotoh, M. (1967). Some problems of bonded anisotropic plates with cracks along the bond. *International Journal of Fracture Mechanics* **3**, 253-265.

Gupta, V., Argon, A. S. & Suo, Z. (1992). Crack deflection at an interface between two orthotropic media. *ASME Journal of Applied Mechanics* **59**, 79-87.

Hoenig, A. (1982). Near-tip Behavior of a crack in a plane anisotropic elastic body. *Engineering Fracture Mechanics* **16**, 393-403.

Lekhnitskii, S. G. (1953) Theory of an anisotropic elastic body. *Holden-Day, San Francisco.*

Lin, Y. Y. & Sung, J. C. (1997). Singularities of an inclined crack terminating at an anisotropic bimaterial interface, *International Journal of Solids and Structures* **34**,3727-3754.

Mantic, V. *et al*, (1997). Stress singularities in 2D orthotropic corners. *International Journal of Fracture,* **83,** 67-90**.**

Qu, J. & Bassani, J. L. (1989). Cracks on bimaterial and bicrystal interfaces. *Journal of Mechanics and Physics of Solids* **37**, 417-433.

Sih, G. C., Paris, P. C. & Irwin, G. R. (1965). On cracks in rectilinearly anisotropic bodies. *International Journal of Fracture Mechanics.* **1**, 189-203.

Stroh, A. N. (1958). Dislocations and cracks in anisotropic elasticity. *Philosophy Magazine* **3**, 625-646.

Sung, J. C. & Liou, J. Y. (1996). Singularities at the tip of a crack terminating normally at an interface between two orthotropic media. *ASME Journal of Applied Mechanics* **63**, 264-270.

Suo, Z. (1990). Singularities, interfaces and cracks in dissimilar anisotropic media*, Proceeding of the Royal Society of London* **A427**, 331-358.

Ting, T. C. T. & Hoang, P. H. (1984). Singularities at the tip of a crack normal to the interface of an anisotropic layered composite. *International Journal of Solids and Structures* **20**, 439-454.

Ting, T. C. T. (1986).Explicit solution and invariance of the singularities at an interface crack in anisotropic composites, *International Journal of Solids and Structures* **22**, 965-763.

Ting, T. C. T. (1996).Anisotropic elasticity, *Oxford University Press*

Willis, J. R. (1971). Fracture mechanics of interfacial cracks, *Journal of Mechanics and Physics of Solids* **19**, 353-368

Zhong, W. X. (1995). A new systematical methodology in elasticity theory (in Chinese). *Dalian Science & Technology University Press*.

ORAL/POSTER REFERENCE: ICF100923OR

ASYMPTOTIC MODE III AND MODE E CRACK TIP SOLUTIONS IN FERROELECTRIC MATERIALS

Chad M. Landis

Department of Mechanical Engineering and Materials Science, MS 321,
Rice University, P.O. Box 1892, Houston, TX, 77025
landis@rice.edu, ph: 713-348-3609, fax: 713-348-5423

ABSTRACT

Complete asymptotic solutions for the Mode III, longitudinal or anti-plane shear, and Mode E applied electric field cases are presented for idealized ferroelectric switching materials. The mathematical procedure required to solve these problems has been presented by Rice [1]. The purpose of this work is to compare and contrast the mechanical and electrical solutions. The constitutive behavior of the material is specified by an initial linear response, a segment of non-hardening switching behavior, i.e. perfect plasticity in the mechanical case, and finally a region where lock-up occurs. The crack tip solution is characterized by an outer solution with a standard $r^{-1/2}$ singularity that is not centered on the crack tip, a switching zone with the solution given by a simple radial slip line field, and an inner lock-up region which surrounds the crack tip.

KEYWORDS

Ferroelectric, dielectric, non-linear behavior, crack tip fields

1. INTRODUCTION

To reduce the mathematical complexity of analyzing the crack tip fields, the following assumptions are made. First, all electromechanical coupling effects including piezoelectricity are ignored. This assumption is not necessary for the purely mechanical anti-plane shear case. Second, the constitutive response, i.e. stress versus strain or electric field versus electric displacement, is taken to be completely reversible. This is to say that the stress or electric field is a unique function of the strain or electric displacement respectively. Borrowing the mechanics terminology, deformation theory plasticity is assumed. This assumption is used in preference to a more appropriate incremental theory in order to make the mathematics tractable.

The remainder of the paper will be devoted to presenting the equations governing the distributions of stress and strain or electric displacement and electric field and the solution to these equations very close to a crack tip. In order to emphasize the similarities between the mechanical and the electrical problems the equations will be presented concurrently.

2. GOVERNING EQUATIONS

Equilibrium and Gauss' law are given by

$$\frac{\partial \tau_x}{\partial x} + \frac{\partial \tau_y}{\partial y} = 0, \qquad \frac{\partial D_x}{\partial x} + \frac{\partial D_y}{\partial y} = 0 \tag{1}$$

where the shear stresses are $\tau_x = \tau_{xz}$ and $\tau_y = \tau_{yz}$, and the x and y components of the electric displacement are D_x and D_y.

The shear strains, $\gamma_x = \gamma_{xz}$ and $\gamma_y = \gamma_{yz}$, and electric field components, E_x and E_y, are derived from the gradient of the z displacement, w, or the electric potential, ϕ, respectively.

$$\gamma_x = \frac{\partial w}{\partial x} \text{ and } \gamma_y = \frac{\partial w}{\partial y}, \quad E_x = -\frac{\partial \phi}{\partial x} \text{ and } E_y = -\frac{\partial \phi}{\partial y} \tag{2}$$

Eqn. 2 implies the following compatibility condition for the shear strains and that the curl of the electric field is zero.

$$\frac{\partial \gamma_x}{\partial y} - \frac{\partial \gamma_y}{\partial x} = 0, \qquad \frac{\partial E_x}{\partial y} - \frac{\partial E_y}{\partial x} = 0 \tag{3}$$

The constitutive behavior of the material is assumed to be completely reversible, i.e. a deformation theory in mechanics terminology is used. For an isotropic material the stresses and strains or the electric field and electric displacement are collinear.

$$\frac{\tau_x}{\tau_y} = \frac{\gamma_x}{\gamma_y}, \qquad \frac{E_x}{E_y} = \frac{D_x}{D_y} \tag{4}$$

What remains is to specify the relationships between the magnitudes of the shear stress and shear strain and the magnitudes of the electric field and electric displacement. These magnitudes are given by

$$\tau = \left(\tau_x^2 + \tau_y^2\right)^{1/2} \text{ and } \gamma = \left(\gamma_x^2 + \gamma_y^2\right)^{1/2}, \quad E = \left(E_x^2 + E_y^2\right)^{1/2} \text{ and } D = \left(D_x^2 + D_y^2\right)^{1/2} \tag{5}$$

For the mechanical problem the stress is specified as a function of the strain and the electrical problem is characterized with the electric field as a function of the electric displacement.

$$\tau = \begin{cases} G\gamma & \text{for } \gamma \le \gamma_0 \\ \tau_0 & \text{for } \gamma_0 \le \gamma \le \gamma_L \\ \tau_0 + G\left(\gamma - \gamma_L\right) & \text{for } \gamma \ge \gamma_L \end{cases}, \qquad E = \begin{cases} D/\kappa & \text{for } D \le D_0 \\ E_0 & \text{for } D_0 \le D \le D_L \\ E_0 + \left(D - D_L\right)/\kappa & \text{for } D \ge D_L \end{cases} \tag{6}$$

The shear modulus and dielectric permittivity are G and κ, the shear yield stress and coercive field are τ_0 and E_0, and the lock-up strain and electric displacement are γ_L and D_L. The parameters γ_0 and D_0 are related to the yield stress and coercive field by

$$\gamma_0 = \frac{\tau_0}{G}, \qquad D_0 = \kappa E_0 \tag{7}$$

3. THE CRACK TIP

The crack tip solutions presented here along with the solution for a conducting crack are discussed in further detail by Landis [2]. Consider a semi-infinite crack with faces lying along the negative *x*-axis and tip at the origin. It is assumed that the size of the switching zone, as yet to be determined, is much smaller than the crack length or any other characteristic length in the geometry of the problem. In the mechanical case the crack faces are traction free. For the electrical case it is assumed that the permittivity of free space is zero and there is no normal component of electric displacement along the crack faces. The boundary conditions are then that

$$\text{for } y = 0,\ x < 0 \quad \tau_y = 0, \quad D_y = 0 \tag{8}$$

The solutions for the full fields with lock-up are now presented. The reader is referred to Rice [1] for the mathematical details of the solution procedure. For both the mechanical and electrical problems the switching regions are circles and the radii of the switching regions for the mechanical and electrical cases are

$$R_\tau = \frac{1}{2\pi}\left(\frac{K_{\mathrm{III}}}{\tau_0}\right)^2, \qquad R_E = \frac{1}{2\pi}\left(\frac{K_{\mathrm{E}}}{E_0}\right)^2 \tag{9}$$

The lock-up zones are also circular, surround the crack tip and are embedded within the switching zones. The radii of the lock-up zones are,

$$R_\tau^L = \frac{\gamma_0}{\gamma_L} R_\tau, \qquad R_E^L = \frac{D_0}{D_L} R_E \tag{10}$$

The solutions outside the switching region are given by

$$\text{mechanical} \begin{cases} \tau_y + i\tau_x = \dfrac{K_{\mathrm{III}}}{\left[2\pi\left(x - X_\tau + iy\right)\right]^{1/2}}, \ \text{for } \left|x - X_\tau + iy\right| \geq R_\tau \\ X_\tau = R_\tau\left[1 - 2\dfrac{\gamma_L/\gamma_0 - 1 + \ln\left(\gamma_0/\gamma_L\right)}{\left(\gamma_L/\gamma_0 - 1\right)^2}\right] \end{cases} \tag{11}$$

$$\text{electrical} \begin{cases} E_y + iE_x = \dfrac{K_{\mathrm{E}}}{\left[2\pi\left(x - X_E + iy\right)\right]^{1/2}}, \ \text{for } \left|x - X_E + iy\right| \geq R_E \\ X_E = R_E\left[2\dfrac{D_L/D_0 - 1 + \ln\left(D_0/D_L\right)}{\left(D_L/D_0 - 1\right)^2} - 1\right] \end{cases} \tag{12}$$

Here X_τ and X_E represent the x coordinate of the centers of the switching zones. The solution in the switching region is a radial slip line field. The solutions in these regions are

$$\text{mechanical} \begin{cases} \tau_{\bar\theta} = \tau_0,\ \tau_{\bar r} = \gamma_{\bar r} = 0,\ \gamma_{\bar\theta} = \dfrac{2R_\tau \gamma_0}{\bar r}\cos\bar\theta, \ \text{ for } \ 2R_\tau^L \cos\bar\theta \le \bar r \le 2R_\tau \cos\bar\theta \\ \bar r = \sqrt{\left(x - X_\tau + R_\tau\right)^2 + y^2}, \quad \bar\theta = \arctan\dfrac{\mathrm{y}}{x - X_\tau + R_\tau} \end{cases} \tag{13}$$

$$\text{electrical} \begin{cases} E_{\bar r} = E_0,\ E_{\bar\theta} = D_{\bar\theta} = 0,\ D_{\bar r} = \dfrac{2R_E D_0}{\bar r}\cos\bar\theta, \ \text{ for } \ 2R_E^L \cos\bar\theta \le \bar r \le 2R_E \cos\bar\theta \\ \bar r = \sqrt{\left(x - X_E - R_E\right)^2 + y^2}, \quad \bar\theta = \arctan\dfrac{\mathrm{y}}{x - X_E - R_E} \end{cases} \tag{14}$$

As drawn in Figure 1 and as indicated by the region of validity for Eqn. 13 and Eqn. 14 the lock-up zone is circular and it is tangent to the boundary of the switching zone. This point of tangency lies on the crack faces in the mechanical case and in front of the crack tip in the electrical case. The solution within the lock-up zone cannot be written in simple closed form with stresses or electric fields as functions of coordinates as in Eqns. 11-14. Instead the solution is given for the coordinates as a function of the strain or electric field components.

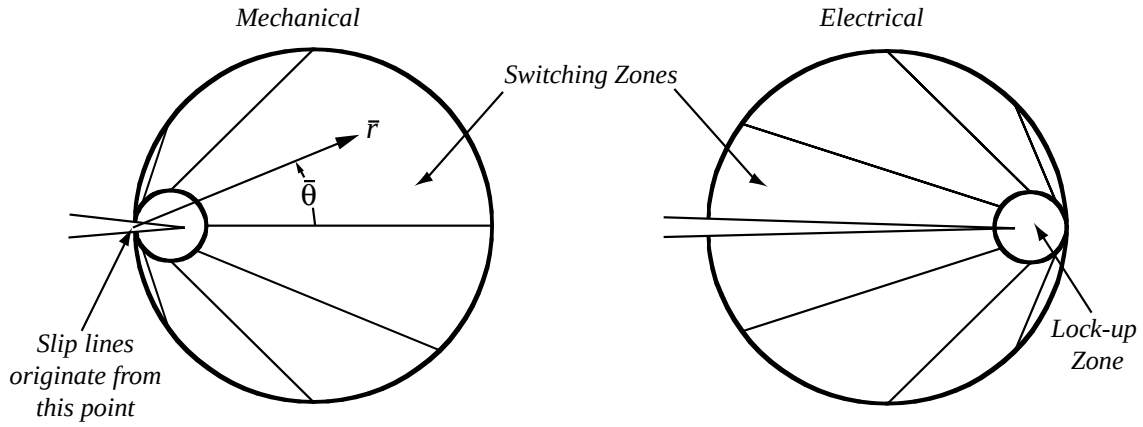

Figure 1: The switching and lock-up regions around a crack tip for the mechanical and electrical cases.

The crack tip solutions within the lock-up zones can be represented by contours of constant strain or electric field magnitude. The constant strain or electric field contours are circles that are not centered on the crack tip. The x and y coordinates along a given contour are then

$$x = X + R\cos 2\alpha \tag{15}$$

$$y = R\sin 2\alpha \tag{16}$$

where X is the x coordinate of the center of the contour and R is the radius of the contour. The angle 2α is the angle between a line drawn to a point along the contour and the x-axis. Then the components of shear strain or electric field at this point along the contour are

$$\text{mechanical:} \quad \gamma_x = -\gamma\sin\alpha, \qquad \gamma_y = \gamma\cos\alpha \tag{17}$$

$$\text{electrical:} \quad E_x = -E\sin\alpha, \qquad E_y = E\cos\alpha \tag{18}$$

The parameters $R(\gamma)$ and $X(\gamma)$ for the mechanical case will be presented first. For a given strain magnitude the radius and the *x* coordinate of the center of this circle are

$$\text{mechanical}\begin{cases} R(\gamma) = R_\tau \dfrac{1}{\gamma/\gamma_0\left(1+\gamma/\gamma_0-\gamma_L/\gamma_0\right)} \\ X(\gamma) = 2R_\tau\left[\dfrac{1-\gamma_L/\gamma_0+\gamma/\gamma_0\ln\left(\dfrac{\gamma/\gamma_0}{1+\gamma/\gamma_0-\gamma_L/\gamma_0}\right)}{\gamma/\gamma_0\left(\gamma_L/\gamma_0-1\right)^2}\right]-R(\gamma) \end{cases} \quad \text{for } \gamma \geq \gamma_L \tag{19}$$

For the electrical problem the radius of a constant electric field contour and the *x* coordinate of its center are,

$$\text{electrical}\begin{cases} R(E) = R_E \dfrac{1}{E/E_0\left(E/E_0+D_L/D_0-1\right)} \\ X(E) = 2R_E\left[\dfrac{D_L/D_0-1+E/E_0\ln\left(\dfrac{E/E_0}{E/E_0+D_L/D_0-1}\right)}{E/E_0\left(D_L/D_0-1\right)^2}\right]-R(E) \end{cases} \quad \text{for } E \geq E_0 \tag{20}$$

4. DISCUSSION AND IMPLICATIONS FOR NUMERICAL METHODS

The analyses presented in Section 3 are most applicable to initially unpoled ferroelectric ceramics. The analysis of poled ferroelectrics and in general full electromechanical coupling is beyond the scope of this work. The inclusion of coupling in the electrical and mechanical fields requires more detailed constitutive relations. Hence, due to the complexity that this type of coupling introduces it is likely that the solution to the crack tip problem will rely on numerical methods. The features appearing in the simple solutions of Section 3 will almost certainly appear in the more complicated fully coupled problem as well. For example, at the point of tangency between the switching and lock-up regions there is a large gradient of strain in the mechanical case and electrical displacement in the electrical case. This is an interesting issue for a numerical solution since from a mathematical standpoint, Eqn. 1 and Eqn. 3, these field variables are not equivalent. Hence, a standard finite element formulation that interpolates displacement and electric potential may be inferior to a mixed or hybrid formulation. At the very least the solutions presented in Section 3 offer an analytical check for any numerical method designed to solve field problems in ferroelectrics.

REFERENCES

1. Rice, J.R. (1967) *Journal of Applied Mechanics*, 34, 287-298.

2. Landis, C.M. (2001) submitted to *Engineering Fracture Mechanics*.

Abstract Reference Number:ICF100926OR

ATOMIC SCALE INVESTIGATION OF METAL/CERAMIC INTERFACE FRACTURE BY SUPER HIGH-RESOLUTION ELECTRON MICROSCOPY

H.Ichinose and H.Saito

Department of materials science, School of engineering, The University of Tokyo
7-3-1 Hongo, Bunkyo-ku, Tokyo, 113-0033 Japan

ABSTRACT

Interfacial atomic structure (chemical structure) of a Pd/ZnO hetero junction was investigated by atomic resolution high voltage transmission electron microscopy (ARHVTEM) in order to clarify the cause of thermal fracture of a metal/ceramic interface. A misfit dislocation, predicted by O-lattice model of Bollman, did not work as a stress accommodation mechanism in the ZnO(0001)/Pd(111) interface which was a polar interface. But in the non polar ZnO($\mathbf{10\bar{1}0}$)/(200) interface periodic stress localization occurred. The periodicity of the local strain coincided with that of misfit dislocation. Atomic structure image of the ARHVTEM showed that an atomic arrangement across the interface was in the order of O-Zn-Pd. It was shown that weakness of the ZnO(0001)/Pd(111) interface against cyclic heating is attributable to the absence of the periodic stress localization of the misfit dislocation.

KEY WORDS

thermal fracture, metal/ceramic interface, misfit dislocation, stress accommodation mechanism, bonding strength, high-resolution electron microscopy, chemical structure

INTRODUCTION

Although metal/ceramics hybrid materials are widely used, namely surface coating, electron device packages, and wirings to the semiconductor, a well known weak point problem still remains unsolved i.e. a metal/ceramic hybrid material is broken at the junction by cyclic heating during the work. A cause is known. The brittle junction has been attributed to large difference in thermal expansion coefficient between metal and ceramic. Expanded atomic distance across the hetero interface due to heating accidentally goes over the threshold of atomic bonding to produce a crack. Previously employed method to solve this problem was to insert a cushion material which has intermediate thermal expansion coefficient value. But, what ever cushion material is used it could not be the final solution of the problem. Melting point of the cushion was sometimes lower than that of the component metal. Mechanical strength of the cushion was not necessarily higher than any of the component materials in the other occasion. It rather provided a new additional problem. More credible solution based on a physical principle has been desired. Despite not few people have discussed so far to give a clear solution in atomic dimension either experimentally or theoretically, the problem still remains unsolved [1]. Major cause of the situation is attributed to the lack of an experimental tool to analyze the interface structure in real atomic dimension.

In the present work a ZnO/Pd interface is observed by our atomic resolution high voltage transmission electron microscope (ARHVTEM). This microscope enables us to observe even chemical structure of the hetero interface. The investigation is focused on the stress accommodation mechanisms of the interface in atomic dimension.

EXPERIMENTS

A high purity Pd sheet 100μm in thickness was alloyed by 2at% Zn. The alloy sheet was heated at 1273K for 100 hours to make Zn solute in Pd. Following diffusion treatment the Pd-Zn alloy sheet was internally oxidized at 1073K for 14～37 hours in the air to obtain a ZnO precipitate in the Pd matrix.
The precipitated sheet was mechanically thinned down to 10μm and then was thinned by Precision Ion Polishing System (PIPS). Incident angle of Ar ion of the PIPS was kept less than 4degree. Vacuum and acceleration voltage of the PIPS specimen chamber were respectively $\sim 10^{-6}$torr and 4kV. Damaged surface layer produced during the thinning was brown off by five minutes irradiation of Ar at 2.5kV acceleration.
The atomic resolution high voltage transmission electron microscope (ARHVTEM) was employed for the atomic structure investigation of the ZnO/Pd metal-ceramic hetero interface. The resolution of the microscope is 0.1nm at the optimum focus condition (so called Scherzer condition) and the information limit of this machine extends over 0.09nm [2], which are enough power to investigate the atomic structure of the ZnO/Pd hetero interface. Observation was performed at 1250kv acceleration and 39nm defocus, corresponded to the optimum focus condition. Not only atomic structure image but also ordinary lattice image was effectively employed depending on the required information level.

RESULTS

Chemical structure of ZnO crystal

Super high resolution of the ARHVTEM enabled to observe chemical structure of the ZnO crystal as shown in figure 1. The picture image was obtained from 3nm thick specimen at Scherzer focus condition so that atomic potential in the specimen was directly projected on the image in dark contrast (called as a projected potential image or atomic structure image)[3]. The atomic structure image is highly qualified for the atomic structure investigation in contrast to an ordinary lattice image which is obtained from thicker specimen and shows only periodicity of atomic potential. A line profile of darkness along the Zn-O atomic pair (bottom left) of the picture (bottom right) consisted of two peaks. The higher peak corresponded to Zn and the lower one to O i.e. Zn appeared in darker thick contrast and O in brighter thin contrast. The intensity profile of a simulated image computed by multi-slice method, shown in upper half of figure1, well coincided with that of experimental result.

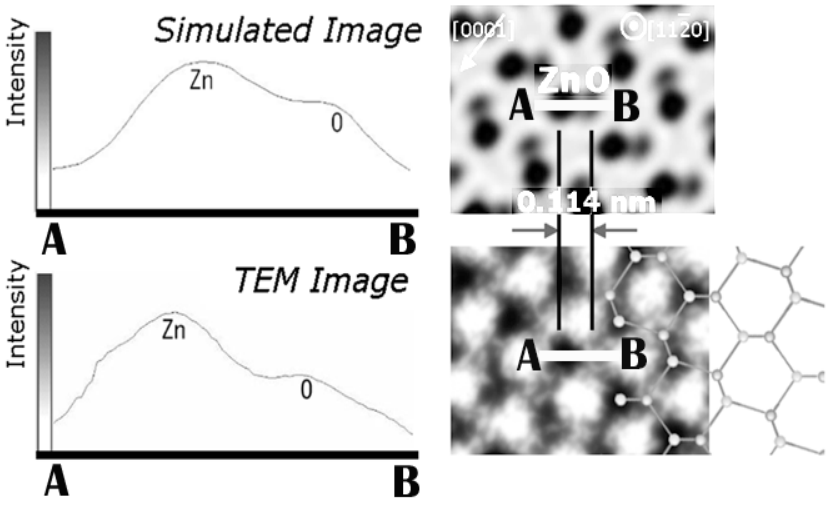

Fig.1. Identification of Zinc and Oxygen in the ARHVTEM atomic structure image. Zn appears in darker contrast and O in the thinner in both calculated image and picture. Projected inter atomic distance of Zn and O is 0.114nm.

Geometry of Pd/ZnO interface

The ZnO crystal and the Pd matrix were joined together by (0001) plane of the ZnO and (111) plane of the Pd. The (0001) plane is a polar interface stacked in turn by Zn-plane and O-plane. <110> axis of the Pd and <**11$\bar{2}$0**> axis of the ZnO were parallel to each other and to the electron beam too. (This interface is noted as ZnO(0001)/Pd(111) hereafter and is called as a polar interface.) Although most developed surface of a ZnO crystal grown in the free space is **(20$\bar{2}$1)** plane, the (0001) plan exceedingly developed in the present ZnO crystal precipitated in the Pd matrix (Fig.2). The development of (0001) plane of the precipitate ZnO is attributable to the energy reduction effect of the ZnO/Pd interface. Integrated inter atomic interaction energy over the interface area of the ZnO(0001)/Pd(111) junction must be lowest among the possible other ZnO/ Pd

interfaces to present. Morphology of the interface was flat (or straight) in atomic dimension, showing well defined atomic arrangement (Fig.3).

Absence of misfit dislocation in the ZnO(0001)/Pd(111) interface

Atomic arrangement shown by white dots in figure 3 is unusually straight everywhere in spite of 14% lattice mismatch at the interface. The 14% lattice mismatch, according to O-lattice model [4], must introduce a misfit dislocation at every eight (111) planes of Pd along the interface. The introduced dislocation is expected to localize the stress around the core to release the stress in the other region. The interface structure is stabilized by this mechanism. Additional thermal stress, if supplied, is absorbed by sliding of the dislocations. In the present interface, however, no periodic image contrast of the misfit dislocation was seen (Fig.2.). No evidence of atomic site shift parallel to the interface, corresponding to the strain field of the misfit dislocation, was observed even in the lattice image of high resolution TEM; every white dot in figure 3 ranged straight directing to the interface. No strain localization around the misfit dislocation seems present. An absence of the periodic strain localization means that no stress accommodation mechanism works in the interface. Under this situation inter atomic distance across the interface changes from place to place. If the ZnO/Pd junction is exposed to cyclic heating, the uppermost inter atomic distance may go over the threshold of local atomic bonding by thermal strain due to different thermal expansion coefficient. Repeated the process by the cyclic heating a fine crack may grow to break all the interface atomic bonding.

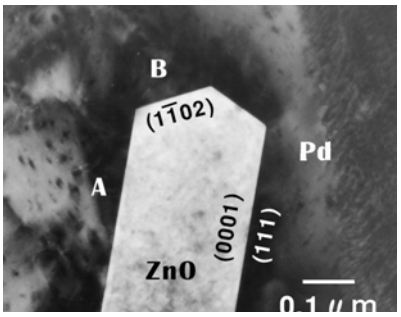

Fig.2. Well developed (0001) surface of ZnO.

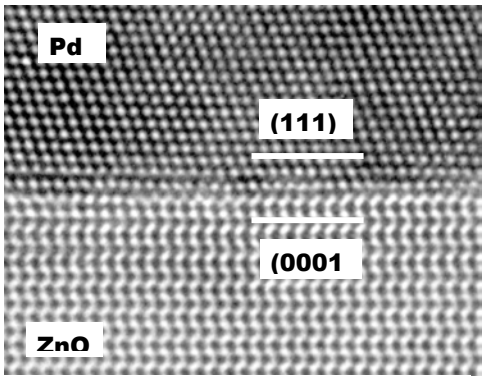

Fig.3.
Well defined ZnO/Pd interface. Interface is parallel to (111) plane of Pd and (0001) plane of ZnO.

Chemical structure of the ZnO/Pd interface

Employed an atomic structure image which is observed under strict condition, namely less specimen thickness than 30nm, a super high resolution TEM with 0.1nm resolution, strict optical axis alignment, an obtained data (picture) will be capable of not only atomic structure analysis but also chemical structure investigation [4].

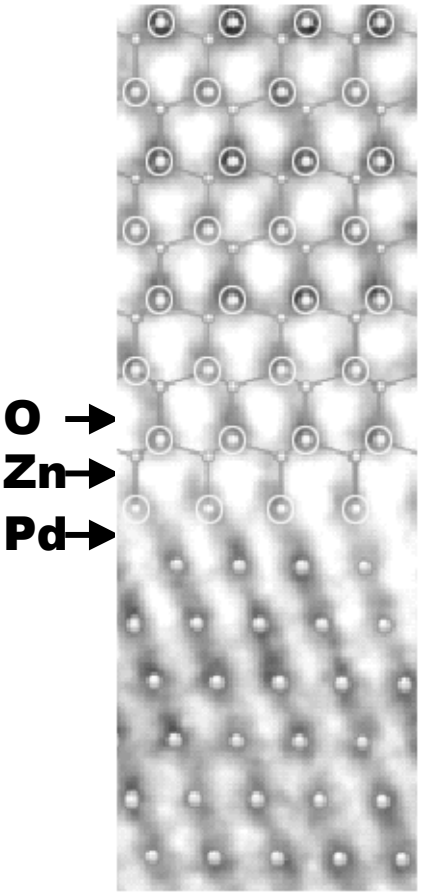

Fig.4. Well defined ZnO/Pd interface. Interface is parallel to (111) plane of Pd and (0001) plane of ZnO.

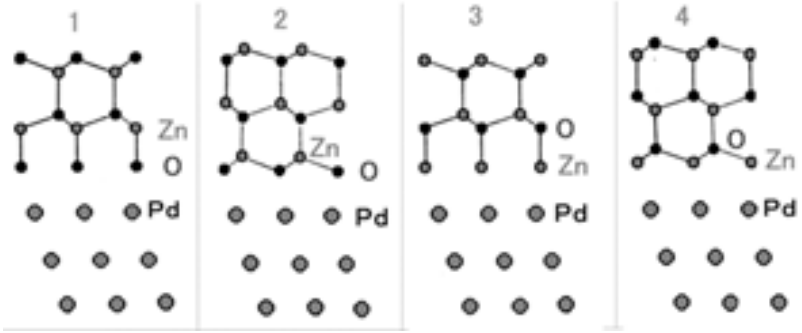

Fig.5. Four candidate structure models of the ZnO/Pd interface viewed from <**11$\bar{2}$0**> direction. #3 is the most likely structure.

Pictures shown in figure1 and figure 4 fulfill the required condition.

Chemical structure of the ZnO(0001)/Pd(111) interface was investigated by the image of figure 4 following the principle shown in figure 1. ◎ was put at Zn position, a darker spot in the ZnO region of the picture. Small dot was put at O position, a brighter spot. Medium size dot was put at Pd position in the bottom half region. As a result of this procedure an atomic network was completed (Fig.4). It was shown from the result that ZnO was terminated by Zn (not by O) at the interface even though there were four possible geometrical candidates as shown in figure 5. Although Zn connects to Pd also in the model #4, geometrical structure does not coincide with the present picture. The model #1 and #2 are totally not the case.

Periodic interface structure

Atomic structure image (projected potential image) in the wider region was inspected in order to see further precise structure which was hidden in figure 3 (lattice image). Atomic site was successfully pointed out in most area but in some small region the image contrast was not clear. An extent of the un clear diffused region was at most several (111) planes of Pd in diameter (encircled by doted line in figure 6). No other characteristic feature such as atomic site shift was detectable even in the clear image region. Each atomic plane which was either parallel or intersecting to the interface appeared straight. The straight atomic row tells that there is no local elastic strain field. A periodicity of the diffused region coincided with that of misfit dislocation.

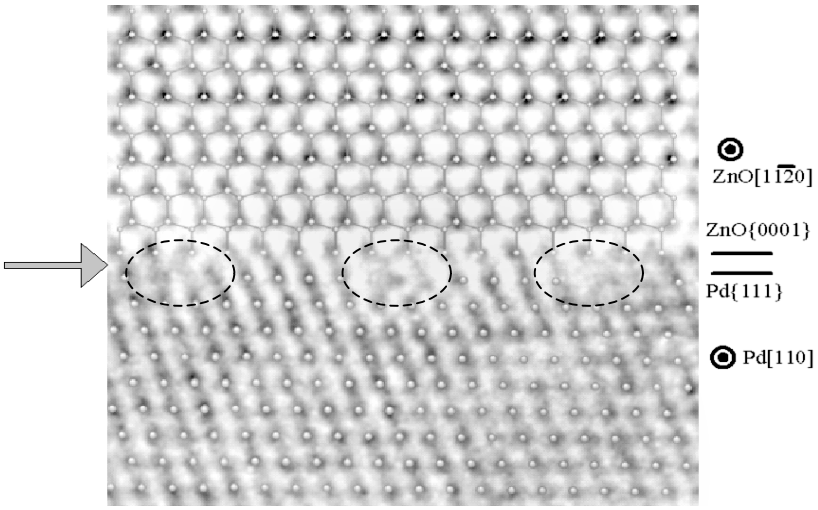

Fig.6. Atomic structure image of the ZnO/Pd junction. No local strain (stress) accommodation mechanism is recognized.

The diffused image in figure 6 is attributed to slight irregular atomic displacement. In this region, ordinary local atomic bonding may not be expected.

ZnO(1$\bar{1}$02)/Pd(200) non polar interface

A stress accommodation mechanism some times presented in the ZnO/Pd interface. In the case that the interface was parallel to (**1$\bar{1}$01**) plane of ZnO and (200) plane of Pd, periodic strain localization occurred (Fig.7(a)). An atomic arrangement of this structure is more apparent in the magnified image of encircled region of figure 7(a), shown in figure 7(b). Several (111) atomic planes of Pd in the vicinity of an extra half plane were apparently curved. Atomic rows in between the "dislocation" look straight showing that the extended strain over the interface was localized around the extra half plane or the dislocation core. A peric predicted by O-lattice model. The chanism.

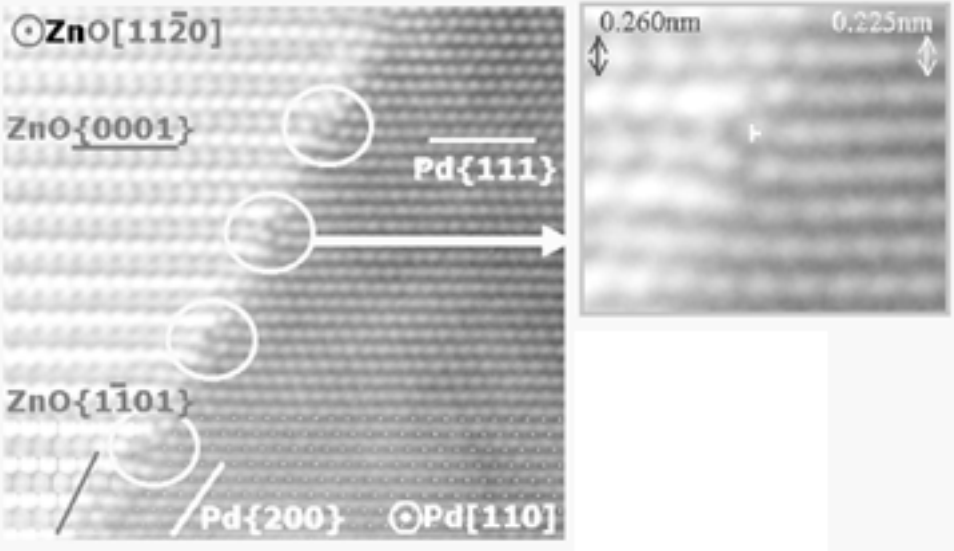

DIS

To b n the stress accommodation depe ss localization by the misfit dislo in the ZnO(**1$\bar{1}$01**)/Pd(200)

Fig.7. In the non polar interface parallel to ($\mathbf{1\bar{1}01}$) plane of ZnO
and (200) plane of Pd periodic strain localization occurs.

interface (Fig.7). Geometrical parameter seems to control the interface structure. However, the geometry can not be an essential cause in the physical phenomena. Physical contents which is adjoined (is represented) by the geometrical parameter must be essential cause. In the present system heterogeneous bonding nature and rigidity of ZnO crystal influenced on the result. Although a Pd crystal may show the heterogeneity, a ZnO crystal is more clearly orientation dependant. The reason why the strain localization did not occur at the dislocation core in the ZnO(0001)/Pd(111) interface is that atomic bonding across the interface was not enough to provide strong component force which was parallel to the interface to pull atoms to the dislocation core. In the other words, rigidity of the component materials in the direction parallel to the interface surmounted the applied component force and kept the original structure. If the atomic bonding across the interface is stronger and rigidity of the component material in the direction parallel to the interface is lower the misfit dislocation may concentrate the nearby strain to the core region to accommodate the misfit stress as is shown in the ZnO($\mathbf{1\bar{1}01}$)/Pd(200) interface.

SAMMARY

Well defined ZnO/Pd interface was produced and atomic structure was investigated employing ARHVTEM in order to see the cause of weakness of a metal/ceramic bonding against cyclic heating. The followings were shown. A misfit dislocation may not work as a stress accommodation mechanism in the ZnO(0001)/Pd(111) interface. However, it should work in the ZnO(1101)/Pd(200) interface. The atomic arrangement across the interface was in the order of O-Zn-Pd. It is suggested that the absence of stress (and strain) localization of the misfit dislocation may cause fragile interface.

REFERENCES

1)W.Mader: Mat. Res. Soc. Symp. Proc. Vol82 (1987) 403,P.LU and F.Cosandey;Acta.amet.Vol.40(1992)s259-266
T.Muschik and M.Ruhle; Phil.Mag.Vol.65(1992)263-388
2)H.Ichinose, H.Sawada, E.Takuma and M.Osaki: J.Electron Microscopy 48 (6) 887-891 (1999)
3)S.Horiuchi: High-resolution evaluation electron microscope, Kyoritsu Shuppan (1988)
4)W.Bollman: Crystal Defects and Crystalline Interfaces, Springer-Verlag (1980)

ATOMIC-FORCE MICROSCOPY OF CORROSION PITS AND CRACK INITIATION IN FATIGUE OF METALS

Y. Nakai, Y. Shimizu, S. Fujiwara and T. Ogawa

Department of Mechanical Engineering, Kobe University,
1-1, Rokkodai, Nada, Kobe 657-8501, Japan

ABSTRACT

In the present study, corrosion fatigue crack initiation of a 13Cr stainless steel and a high-strength aluminum alloy was investigated by using an atomic force microscope (AFM). The corrosion fatigue tests of 13Cr stainless steel were conducted in distilled water and dilute sodium chloride solution, and it was found that the corrosion fatigue life was affected by the environmental condition. The corrosion fatigue life was found to be shorter for higher concentration of sodium chloride. But no influence of dissolved oxygen was found on the corrosion fatigue life. From the surface observation by AFM, no corrosion pits were observed in 100 ppm sodium chloride solution before crack initiation. They formed after crack initiation. In 500 ppm solution, corrosion fatigue cracks were found to be initiated from surface inclusions. In this solution, corrosion pits were also found at the crack initiation site. The sizes of the pits just after initiation were almost independent of the concentration of sodium chloride. The growth rates of the pits, however, were higher for higher concentration of the solution. The fatigue strength of 7075-T651 alloy in 3% NaCl solution was also much lower than that in air. In this material, corrosion pits were observed prior to crack initiation, and corrosion fatigue cracks were found to be initiated either at corrosion pits or grain boundaries. For crack initiation at corrosion pits, it was not nucleated from the deepest point of the pit. The crack initiation site within the pit was also the grain boundary.

KEYWORDS

Corrosion fatigue, Corrosion pit, AFM, Stainless steel, High strength aluminum alloy

INTRODUCTION

Since microscopic observation is the most useful method to clarify the mechanisms of fatigue processes in materials, the progress of metal fatigue study has strongly depended on the development of new microscopic observation methods such as optical microscopy (OM), transmission electron microscopy (TEM), and scanning electron microscopy (SEM). Recently, we obtained a new microscope called as ”Scanning Probe Microscope (SPM)”, which gives us three-dimensional images of solid surfaces on the atomic scale. It has excellent capabilities for analyzing the topographic nature of solid surfaces. Recently, many types of the scanning probe have been developed. Among SPMs, scanning tunneling microscope (STM) and scanning atomic force microscope (AFM) are now widely employed for the studies of strength of materials because the surface morphology of materials can be observed with atomic scale resolution with these microscopes. By using STM

and AFM, Komai and others [1] observed the micro-crack initiation and growth behavior in stress corrosion cracking. Matsuoka and others observed cleavage fracture surface [2]. For fatigue micro-mechanisms, Ishii and others [3] observed fatigue slip band with STM. They also examined fatigue striation shape with AFM [4]. Yoon and others observed nucleation mechanism of intergranular cracks in high-cycle fatigue [5]. Ohgi and others observed crack initiation at grain boundary in low-cycle fatigue [6]. Nakai and his co-workers have been studied on fatigue slip bands, fatigue crack initiation, and the growth behavior of micro-cracks in a structural steel [7] and α-brass [8]-[12]. Nakai and Oida [13], Saxena and others [14], and Ogawa and Hatanaka [15] observed the change of surface roughness during fatigue test in air. Nakai and Shimizu studied corrosion pits and crack initiation mechanisms in corrosion fatigue of a stainless steel [16].

In the present paper, corrosion fatigue tests of 13Cr stainless steel and high strength aluminum alloy were conducted in sodium chloride solutions, and crack initiation mechanisms were observed by means of optical microscopy and scanning atomic force microscopy (AFM) to clarify corrosion fatigue crack initiation mechanisms.

EXPERIMENTAL PROCEDURE

The material for the present study was a 13Cr stainless steel, AISI 414, and a high strength aluminum alloy, 7075-T651. The chemical composition, mechanical properties, and heat treatment conditions of the materials were described elsewhere [16, 17]. Prior to the fatigue tests, the surface of specimens was polished by buffing. The specimen has a minimum cross section of width 8 mm and thickness 4 mm, and has weak stress concentration with the elastic stress concentration factor 1.03 under plane bending and 1.13 under push-pull loading [16]. The push-pull loading fatigue tests were carried out in a computer controlled electro-hydraulic fatigue testing machine, and a computer controlled electro-dynamic vibrator was employed for the plane-bending fatigue tests. They were operated at a frequency of 30 Hz under fully reversed cyclic loading ($R = -1$).

Since it was very difficult to identify in advance where fatigue cracks would be nucleated, we took replicas at the predetermined numbers of fatigue cycles. The replica films were coated by Au before observations. Although the height of the surface is reversed from the original surface by the replication method, the height of the replica film in the AFM images was reversed by an image processing technique. An scanning probe microscope (Seiko Instruments Inc.: SPA-350), which has large stage unit, was employed for the present AFM observation. The resolution of the microscope is 0.5 nm in the surface direction and 0.1 nm in the vertical direction. The region for AFM observation was determined by optical microscopy at a magnification of 2000 on a CRT monitor. In the present study, corrosion fatigue tests of the stainless steel were conducted in sodium chloride aqueous solution from 0 to 500 ppm, and the effect of sodium chloride concentration and dissolved oxygen on the corrosion fatigue life and crack initiation mechanism were examined. The corrosion fatigue tests of the aluminum alloy were conducted in 3% sodium chloride aqueous solution.

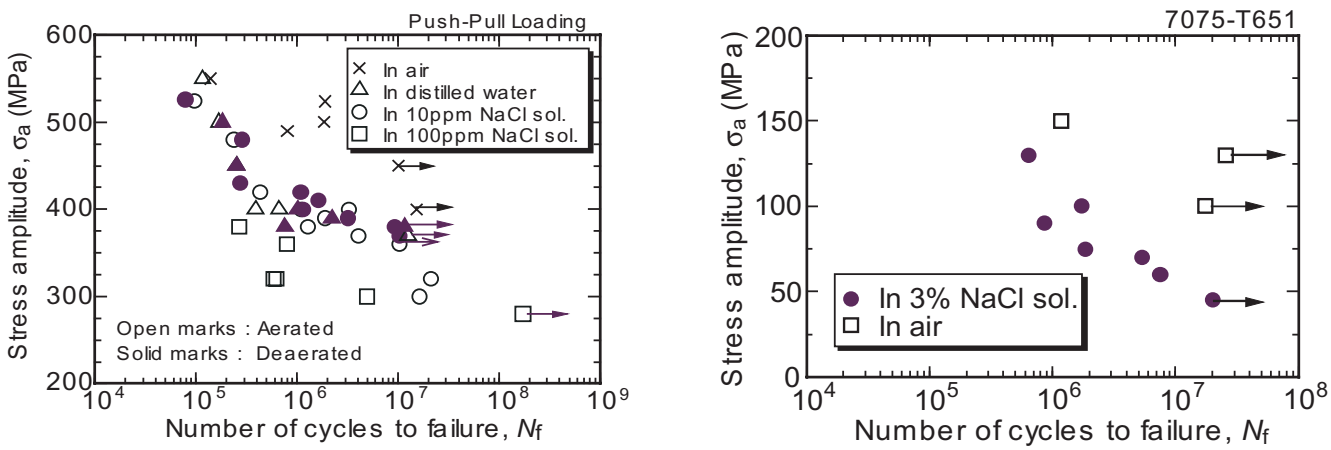

(a) 13Cr stainless steel (Push-pull loading).

(b) High-strength aluminum alloy (Plane bending).

Figure 1**:** S-N curves.

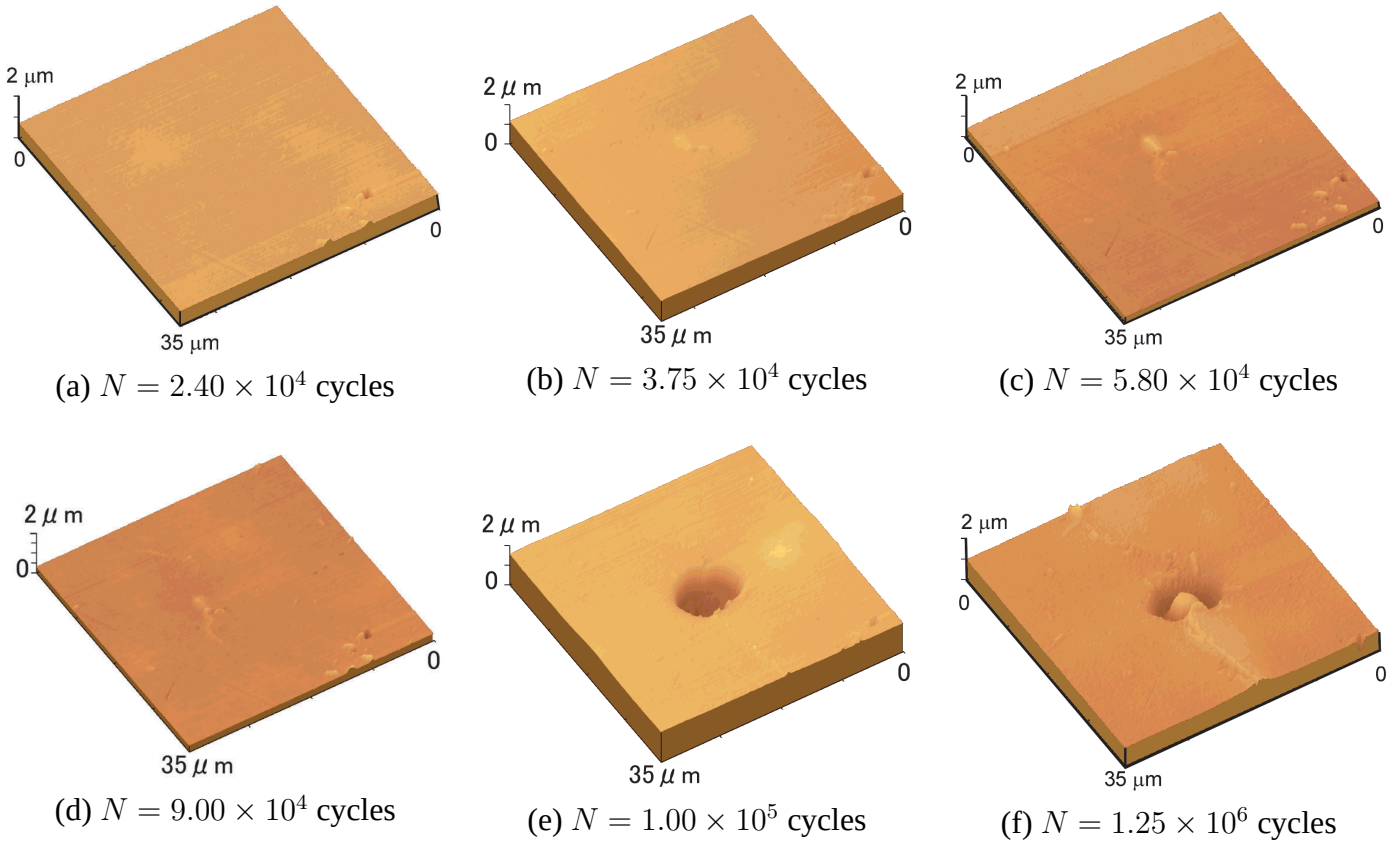

(a) $N = 2.40 \times 10^4$ cycles (b) $N = 3.75 \times 10^4$ cycles (c) $N = 5.80 \times 10^4$ cycles

(d) $N = 9.00 \times 10^4$ cycles (e) $N = 1.00 \times 10^5$ cycles (f) $N = 1.25 \times 10^6$ cycles

Figure 2**:** AFM images of surfaces in 100 ppm NaCl solution at σ_a = 430 MPa (13Cr stainless steel, Scanning area: 35 μm x35 μm).

EXPERIMENTAL RESULTS

S-N Curves

Figure 1 shows the relation between stress amplitude, σ_a, and number of cycles to failure, N_f. In either material, the fatigue life in aqueous environments was shorter than that in air. In 13Cr stainless steel, the fatigue life in 10 ppm NaCl solution was almost the same for that in distilled water. The fatigue life in 100 ppm NaCl solution, however, was shorter than that either in 10 ppm solution or in distilled water. For either concentration of NaCl solution, the fatigue life in aerated solution was almost the same for that in deaerated solution. In push-pull loading, some cracks were initiated from the cylindrically curved side surface. Since it was easier to make observation on the plane surface than on the curved surface when the magnification of the microscope was high, plane bending fatigue tests were conducted. There were no significant difference in fatigue life between plane bending and push-pull loading [16].

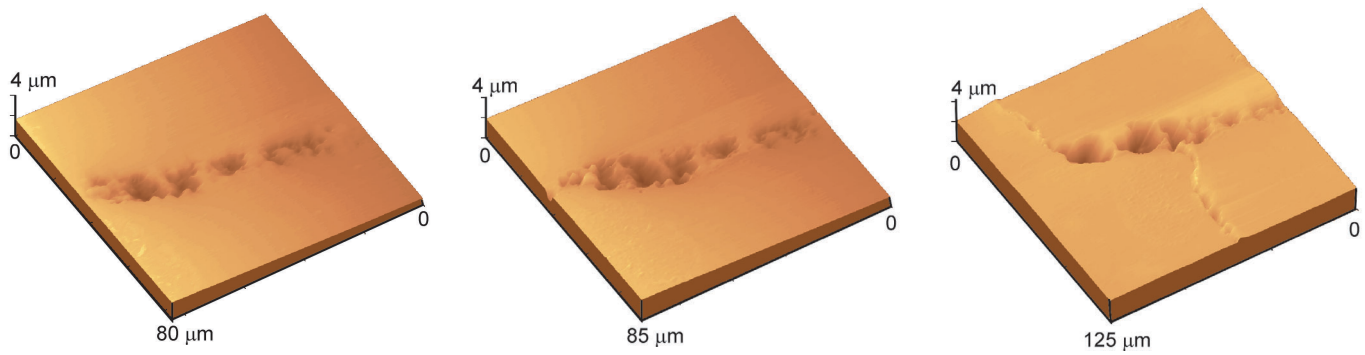

(a) $N = 3.70 \times 10^4$ (b) $N = 5.25 \times 10^4$ (c) $N = 3.18 \times 10^5$

Figure 3**:** AFM images of surfaces in 500 ppm NaCl solution at σ_a = 430 MPa (13Cr stainless steel).

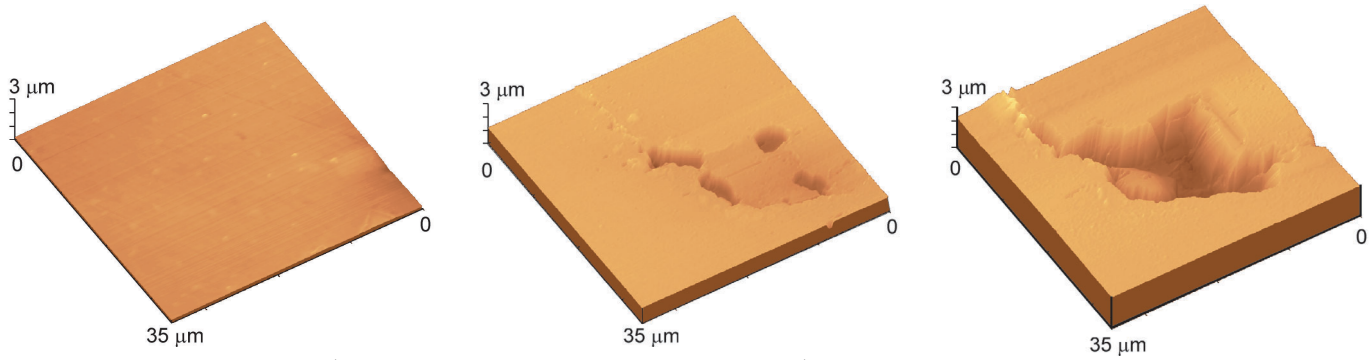

(a) $N = 3.70 \times 10^4$ (b) $N = 5.25 \times 10^4$ (c) $N = 3.18 \times 10^5$

Figure 4**:** Higher magnification AFM images of surfaces in 500 ppm NaCl solution (13Cr stainless steel, σ_a = 430 MPa).

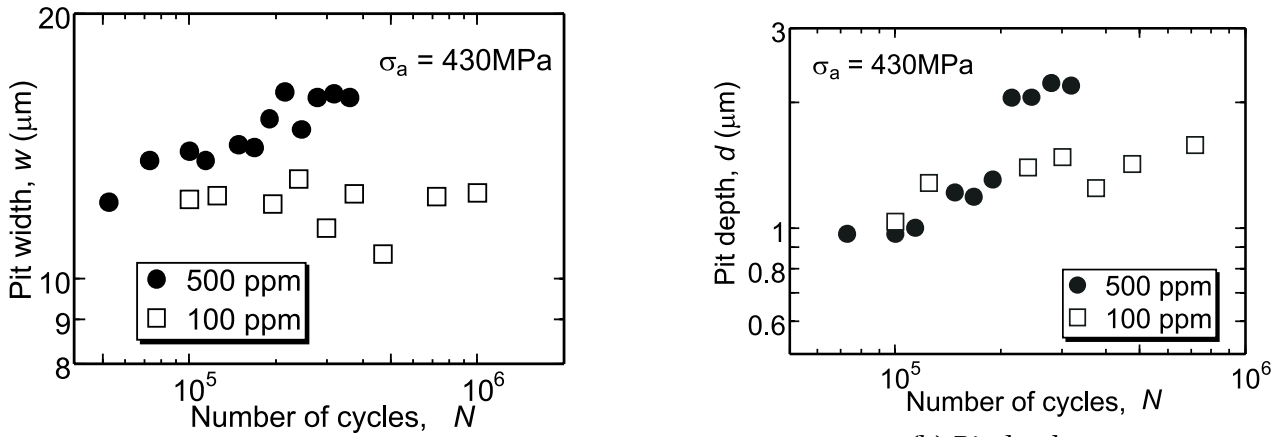

(a) Pit width. (b) Pit depth.

Figure 5**:** Change of pit sizes (13Cr stainless steel).

13Cr Stainless Steel

Crack initiation process

Either in distilled water and in 10 ppm sodium chloride solution, no cracks were initiated from corrosion pits, then the mechanism of crack initiation in these solutions may be similar to that in air.

AFM images of the specimen surface fatigued in 100 ppm solution are shown in Fig. 2. In these figures, extrusions are found in (b)($N = 3.75 \times 10^4$), and a crack was initiated from the extrusions in (c)($N = 5.80 \times 10^4$). The extrusion is considered to be corrosion product, which was formed at bare metal surface produced by a crack embryo. A corrosion pit was formed at the crack initiation site in (e)($N = 1.00 \times 10^5$). Then, it is evident from the AFM observation that the fatigue crack was initiated before the corrosion pit appeared, and a corrosion pit was found to be initiated along the crack, while optical micrographs showed that a crack was initiated from the corrosion pit. Therefore, it is important to notice that we sometimes misunderstand the corrosion fatigue crack initiation process from optical microscopy.

Figures 3 and 4 are AFM images of the corrosion fatigue process in 500 ppm sodium chloride solution at σ_a = 430 MPa, where images in Fig. 4 are higher magnification images of the crack initiation site of the inclusion. In this case, corrosion pits were appeared almost at the same time of the crack initiation. These results were consistent with those with optical microscopy. Inclusions also existed in specimens those were fatigued in 10 ppm solution, 100 NaCl solution, and in distilled water, but they were not crack initiation site in these environments.

Growth behavior of corrosion pits

Depth and surface width of a corrosion pit can be measured from cross-section geometry of the pits, which

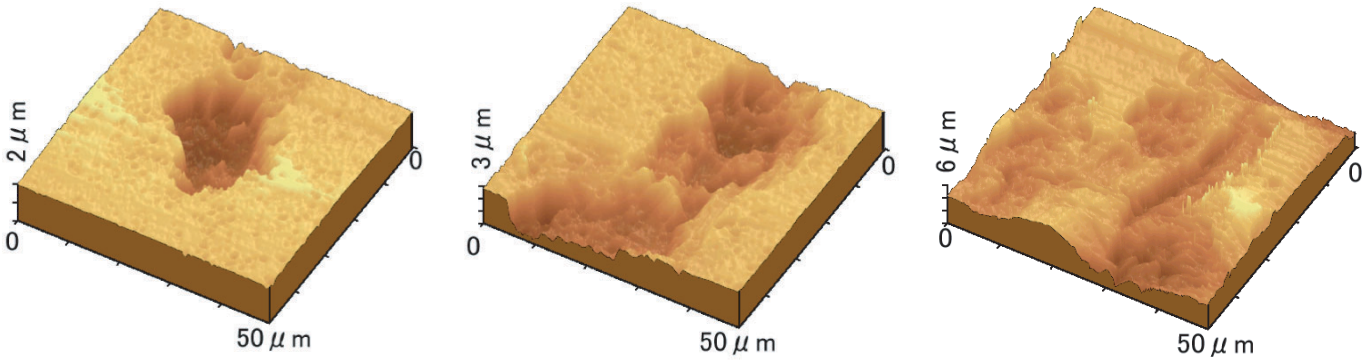

(a) $N = 9.4 \times 10^5$ (b) $N = 1.5 \times 10^6$ (c) $N = 2.5 \times 10^6$

Figure 6**:** AFM images of crack initiation from corrosion pit (High-strength aluminum alloy).

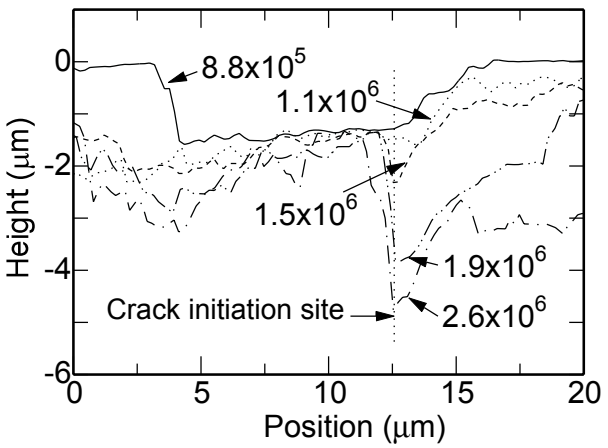

Figure 7**:** Change of geometry of a corrosion pit (High-strength aluminum alloy).

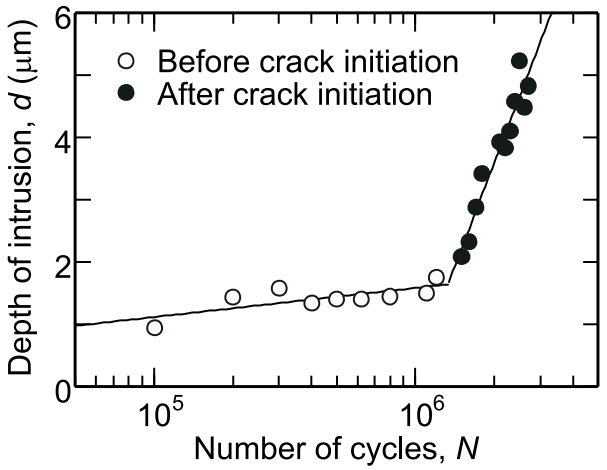

Figure 8**:** Change of intrusion depth in fatigue process (High-strength aluminum alloy).

can be obtained from AFM image. Changes in the size of corrosion pits are plotted as a function of number of cycles in Fig. 5, where the pit width was measured perpendicular to the loading direction. The stress amplitude for these observations was 430 MPa, and the concentration of NaCl was either 100 ppm or 500 ppm. Although the sizes of corrosion pits just after initiation was almost independent of the concentration of NaCl, the growth rate of the pits was higher for higher concentration of NaCl. The aspect ratio of corrosion pit was almost independent of the concentration of NaCl, and it gradually increased with number of cycles. The aspect ratio, however, remained 0.14 at the final stage of corrosion fatigue, then, the stress concentration by these pits were small.

High Strength Aluminum Alloy

AFM images of the specimen surface fatigue at a stress amplitude of 100 MPa were shown in Fig. 6, where arrows indicate the loading direction. The corrosion pit was initiated at very early stage of fatigue process, and it grew with number of cycles, and a crack was initiated from the pit. The crack initiation at $N = 1.5 \times 10^6$ could be identified clearly from AFM images. The change of the geometry of cross-section is indicated in Fig. 7. No cracks were initiated from the deepest point of the corrosion pit. It was initiated at a grain-boundary within the pit. As shown in Fig. 8, the growth rate of the intrusion depth at crack initiation site was accelerated with crack initiation.

Even for a crack whose optical micrographs showed that it was initiated from grain-boundary without corrosion pit, AFM images sometimes indicated that there was a small pit at the crack initiation site. In that case it was not clear whether the pit was nucleated after or before crack initiation [18].

CONCLUSIONS

Corrosion fatigue tests of a 13Cr stainless steel and a high strength aluminum alloy were conducted in sodium chloride solutions, and the initiation processes of cracks and corrosion pits were observed by means of optical microscopy and scanning atomic-force microscopy. The following results were obtained:

(1) In both materials, the fatigue life in aqueous environment was shorter than that in air. In the stainless steel, the corrosion fatigue life was shorter for higher concentration of sodium chloride. But no influence of dissolved oxygen was found on the corrosion fatigue life.

(2) In the stainless steel, no cracks were initiated at corrosion pits when the concentration of sodium chloride was less tham10 ppm. In 500 ppm solution, cracks were found to be initiated from surface inclusions. In this solution, corrosion pits were also found at the crack initiation site.

(3) In the aluminum alloy, cracks were initiated either at corrosion pits or grain boundaries. For crack initiation at corrosion pits, it was not nucleated from the deepest point of the pit. The crack initiation site within the pit was also the grain boundary.

REFERENCES

1. Komai,K., Minoshima, K., and Itoh, M. (1994). J. Soc. Mat. Sci., Japan, 43, 336.
2. Matsuoka, S., Sumiyoshi, H., and Ishikawa, K. (1990). Trans. Japan Soc. Mech. Eng., 56A, 2091.
3. Ishii,H., Yamanaka, S., and Tohgo, K. (1995). In: *ICM 7 (Proc. 7th Int. Conf. Mech. Behav. Mat.)*, pp.367-368, ESIS.
4. Choi, S. Ishii, H., and Tohgo, K. (1998) J. Mat. Sci., Japan, 47, 852.
5. Yoon, W. K., Inoue, T., Noguchi, H., and Higashida, K. (1998). Trans. Japan Soc. Mech. Eng., 64A, 1435.
6. Ohgi, J., Hatanaka, K., and Zenge, T. (1998). In: *Experimental Mechanics, Advances in Design, Testing and Analysis*, pp.1053-1058, Allison I. M. (Ed), Balkema, Rotterdam.
7. Nakai,Y., Fukuhara, S., and Ohnishi, K. (1997). Int. J. Fatigue, 19S,, 223.
8. Nakai, Y., Ohnishi, K., and Kusukawa, T. (1999). Trans. Japan Soc. Mech. Eng., 65A, 483.
9. Nakai, Y., Ohnishi, K., and Kusukawa, T. (1999). In: *Small Fatigue Cracks: Mechanics and Mechanisms*, pp. 343-352, Ravichandran, K. S., Ritchie, R. O., and Murakami, Y. (Eds), Elsevier, Oxford.
10. Nakai, Y., Kusukawa, T. and Hayashi, N. (1999). *ATEM'99 (Proc. Int. Conf. Adv. Tech. in Exp. Mech.)*, Vol. 1, pp.152-157, Jpn Soc. Mech. Eng.
11. Nakai, Y. and Kusukawa, T. (2001). Trans. Jpn Soc. Mech. Eng., 67A, 476.
12. Nakai, Y., Kusukawa, T., and Hayashi, N. (2001). In: *ASTM STP* (To be published).
13. Nakai, Y. and Oida, M. (1999). In: *Fatigue '99 (Proc. 7th Int. Fatigue Conf.)*, pp.2771-2776, EMAS, West Midlands, U.K..
14. Saxena, A., Yang, F., and Cretegny, L. (1999). *Fatigue '99 (Proc. 7th Int. Fatigue Conf.)*, pp.2777-2782, EMAS, West Midlands, U.K..
15. Ogawa,H. and Hatanaka, K. (1999). In: *ATEM'99 (Proc. Int. Conf. Adv. Tech. in Exp. Mech.)*, Vol. 1, pp.158-161, Jpn Soc. Mech. Eng.
16. Y. Nakai, Y. Shimizu, and N. Saeki (1999). In: *ICM8 (Progress in Mechanical Behavior of Materials)*, Vol. I, pp.364-369, Ellyin, F. and Provan, J. W. (Eds).
17. Nakai, Y., Kondo, K., and Ohji, K. (1992). Trans. Jpn Soc. Mech. Eng., 58A, 359.
18. Nakai,Y., Fujiwara, S., Ogawa, T., and Shimizu, Y. (2001). Materials Science Research International, STP-1, 101.

NEW SCENARIO FOR FRICTION

Eric Gerde and M. Marder

Computational and Applied Mathematics and Center for Nonlinear Dynamics
The University of Texas at Austin, Austin, TX 78712

ABSTRACT

We show that fixed-length cracks can race along an interface between two dissimilar crystals pressed together in compression and shear. These cracks permit one crystal to slide over the other as expected from Coulomb's laws of friction. We calculate the coefficient of static friction to be 0.2.

KEYWORDS

Fracture, friction, Coulomb's law, interfaces

INTRODUCTION

Many problems familiar to continuum mechanics can be studied in a new way when one decides to take into account explicitly the atomic structure of matter. Reluctance to take this path largely stems from the assumption that inclusion of atomic detail will create an impenetrable barrier to analytical progress. This assumption is best reversed by counter–examples. We show here that it is possible to calculate a coefficient of friction analytically starting with an atomic description of sliding surfaces.

Coulomb's laws of friction say that the force needed to slide a solid across a surface is proportional to the force with which the two are pushed together, but independent of the apparent area of contact. This fact is surprising. One would expect that solids in contact over larger areas would become more difficult to slide. Conventional explanations are based upon the fact that actual areas of contact are much smaller than apparent. The contacts are made through populations of asperities that jut out of the two solids, and the actual area of contact grows in proportion to the force pressing them together[1].

The complexities of this conventional explanation make it difficult to study in great detail. The asperities are treated in statistical fashion, and their individual properties are usually described phenomenologically. We therefore think it will be of interest to display a case where frictional sliding can be described analytically, and with a level of detail reaching down to the atomic scale.

We are able to accomplish this task because our scenario of frictional sliding is different from the conventional one. Our picture of solids in contact does not include asperities. Instead, we imagine two perfect crystals pressed into one another, weakly adhered across an interface, and ask what horizontal force is necessary for the first to begin to slide over the second. The answer is that sliding begins when the ratio of shear to compressive force reaches a critical value. At this point it becomes possible for fixed-length cracks to form at the interface, and propagate at a substantial fraction of the speed of sound, allowing one surface to slip over the other. Cracks of this sort were first described by Yoffe[2], for whom they were a mathematical artifact making it possible to describe dynamic cracks. The condition for these interface cracks to form is completely independent of the

area of contact of the two crystals. Therefore this scenario, like the conventional one, leads to a slipping rule in accord with Coulomb's law of friction.

The objection will naturally be raised that this scenario, even if correct, is irrelevant. Real surfaces are rough, the conventional picture applies, and ours is just a theoretical curiosity. To counter this objection, we appeal to experiment. Propagating modes similar in character to those appearing in our theories have been observed in laboratory studies of sliding[3, 4]. The idea that such modes exist plays an important role in geophysics, where traveling pulses of slip are invoked to explain anomalously low generation of heat during earthquakes[5, 6, 7, 8, 9, 10, 11, 12]. Thus while we agree that our calculations take place in an idealized setting, we believe that sliding of this sort can actually occur. We do not know how large is the domain of validity for our picture of sliding dominated by self-healing Yoffe cracks, as opposed to sliding dominated by the flow and failure of asperities.

CALCULATIONS

Establishing our idealized picture of friction involves combining information from several different calculations.

Our first calculation describes the motion of a semi-infinite crack along a weak interface between a crystal and a rigid substrate. This work is performed analytically for arbitrarily large systems, using Wiener-Hopf techniques as in Slepyan[13] and Marder[14]. The techniques must be generalized because certain symmetries present in the earlier problems are now lost. The Wiener-Hopf problem for interface cracks becomes a 2×2 system of coupled equations that can be solved using Wilson's algorithm[15]. The end result is an analytical description of the motion of every atom, and in particular a relationship between the speed of the semi-infinite interface crack and loading conditions far away.

Semi-infinite cracks traveling along interfaces exhibit the peculiar phenomenon of stress rotation, first found by Williams [16], and schematically shown in Figure 1 where the bottom material is assumed rigid for simplicity.

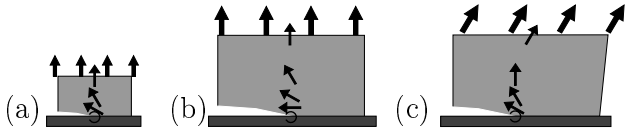

Figure 1: Stresses rotate near the tip of a crack separating dissimilar materials. Samples (b) and (c) are each twice the size of sample (a). The top boundaries in (a) and (b) have similar displacements while the the near-tip stress fields in (a) and (c) are similar.

Suppose one pulls straight up on a sample containing a crack as in Figure 1(a). Linear elastic theory predicts a counter-clockwise rotation of stress fields from the boundary to the crack tip. The rotation is logarithmically slow, progressing a constant amount as the distance to the tip is halved. The rotation halts just outside the tip, where the continuum approximation fails. Now consider a similar thought experiment on a sample twice as high [Figure 1(b)] but with the same inter-atomic separation. Because the continuum approximation is valid over a larger portion of the sample, there is more room for stress rotation, and as a result, the near-tip stress fields in Figure 1(b) are just a rotated version of those in Figure 1(a).

Because of the existence of stress rotation it is possible to construct cracks whose tip experiences tension even though far away the system is loaded in compression. In all such cases, the crack opens for some distance behind the tip, but the compressive loading then forces the upper and lower crack surfaces back into contact. Thus, these cracks are propagating regions of slip and separation of a sort first envisioned by Yoffe[2].

Our second calculation is an explicit computation of such cracks, using molecular dynamics simulations, as shown in Figure 2. Unfortunately, the systems that are accessible numerically are small, involving only millions of atoms. Increasing to billions of atoms is possible, but would not help much, since stress rotation is logarithmically slow.

Our third calculation is an analytical calculation for moving cracks of finite length on interfaces. We rederived and generalized the continuum solution of Dhaliwal, Saxena, Das, and Patra [17, 18] for a Yoffe crack

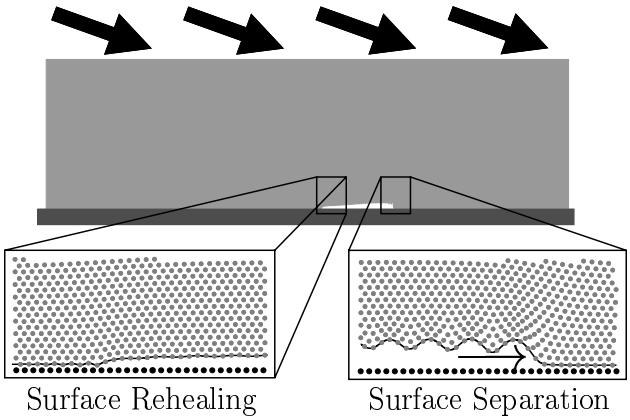

Figure 2: Numerical simulation of a self-healing Yoffe crack traveling through a compressed strip.

moving along an interface. In the continuum solution one chooses crack velocity v, crack length l, the total distance with which the surfaces slip Δu, and the far field stresses $(\sigma_{xy}^{\infty}, \sigma_{yy}^{\infty})$. These parameters determine a unique solution.

The history of self-healing Yoffe interface cracks has been controversial[19, 20, 21, 22, 23], because the continuum descriptions of these cracks contain disturbing features, including infinite numbers of self-intersection of opposing crack faces, and energy fluxes to crack tips in unphysical directions. We propose to resolve these controversies by locating those continuum cracks that are consistent with our atomic-scale solutions near the tips.

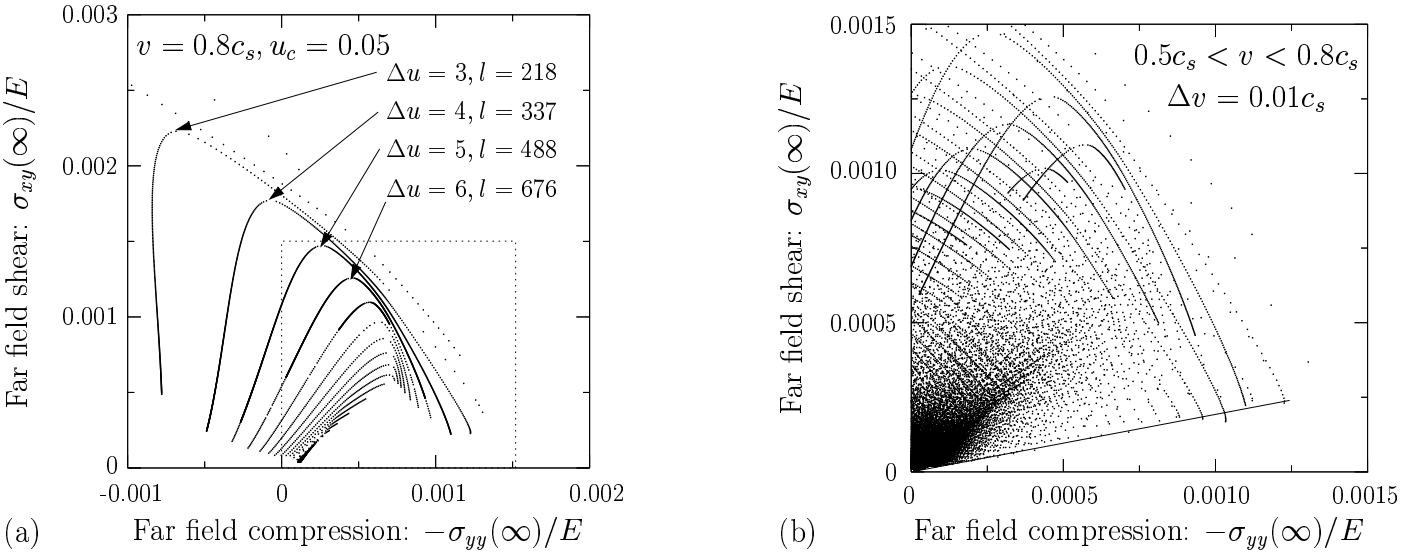

Figure 3: Shear and tensile stresses that support steadily moving Yoffe cracks. Stresses are normalized by Young's modulus E and velocities are normalized by shear wave speed c_s. Integral values of crack length l and total slip Δu lead to a discrete set of states for each velocity. (a) Solution set for $v = 0.8c_s$. Points that appear to form a curve have the same slip Δu but different crack lengths l. (b) Catalog of 120,000 interface crack states, for velocities between 50% and 80% of the shear sound speed, in increments of 1%. Notice that when the ratio of stresses $-\sigma_{xy}/\sigma_{yy}$ drops below around 0.2 there are no more states.

Thus our final calculation connects microscopic and macroscopic scales. We compute the far-field asymptotic stresses of the semi-infinite atomic interface cracks and demand that these stresses match the near-field asymptotic stresses for the continuum self-healing Yoffe cracks. Only a small fraction of the original continuum solutions turn out to be consistent with microscopic constraints on near-tip physics. We find that the original five-dimensional space of continuum solutions is reduced to a space indexed by one continuous parameter (the velocity) and one countably infinite parameter (crack length and slip).

The set of solutions shown in Figure 3(a) results from setting crack velocity $v = 0.8c_s$ (where c_s is the shear

wave speed) and exhaustively considering all possible crack lengths l and slips Δu. In Figure 3(b) we display all running crack states for velocities below 80% c_s, in increments of 1% c_s. When the ratio of horizontal shear to compressive shear $-\sigma_{xy}/\sigma_{yy}$ drops below around 0.2 there are no more states. Thus the condition for sliding to become possible corresponds to Coulomb's law of friction, with a coefficient of 0.2.

QUESTIONS

Many questions have still to be addressed. When does this mechanism of friction apply, and when does flow and fracture of asperities dominate? How do the conditions for initiation of these Yoffe cracks differ from conditions of propagation? Could such a difference account for a difference between coefficients of static and kinetic friction? How can effects of temperature and surface roughness be incorporated within this scenario?

This work was supported by the National Science Foundation (DMR-9877044), and by a fellowship from the Computational and Applied Mathematics program at The University of Texas at Austin.

REFERENCES

1. B. N. J. Persson (1998) *Sliding Friction: Physical Principles and Applications*. Springer, Heidelberg.
2. E. H. Yoffe (1951) Philos. Mag. **42**, 739.
3. S. R. Brown (1998), J. Geophys. Res. **103**, 7413.
4. J. N. Brune , S. Brown, and P. A. Johnson (1993) Tectonophysics **218**, 59.
5. T. H. Heaton (1990) Phys. Earth Planet. Interiors **64**, 1.
6. G. P. Cherepanov (1994) Eng. Fract. Mech. **47**, 691.
7. D. J. Andrews (1997), J. Geo. Res. **102B1**, 553.
8. Y. Ben-Zion and D. J. Andrews (1998) Bull. Seismol. Soc. Am. **88**, 1085.
9. P. Mora (1999) Geo. Phys. Res. Let. **26**, 123.
10. D. Place and P. Mora (1999) J. Comp. Phys. **150**, 332.
11. A. Cochard and J. R. Rice (2000) submitted to J. Geophys. Res.
12. K. Ranjith and J. R. Rice (2000) J. Mech. Phys. Solids, in press.
13. L. I. Slepyan (1982) Izv. Akad. Nauk SSSR Mekh. Tverd. Tela **16**, 101.
14. M. Marder and S. Gross (1995) J. Mech. Phys. Solids **43**, 1.
15. G. T. Wilson (1972) SIAM J. Appl. Math. **23**, 420.
16. M. L. Williams (1959) Bull. Seismol. Soc. Am. **49**, 199.
17. R. J. Dhaliwal and H. S. Saxena (1992) J. Math. Phys. Sci. **26**, 237.
18. S. Das and B. Patra (1996) Eng. Fract. Mech. **54**, 523.
19. J. Weertman (1975) Geo. Soc. Am. Mem. **142**, 175.
20. M. Comninou and J. Dundurs (1978) Int. J. Solids Struct. **14**, 251.
21. M. Comninou and J. Dundurs (1978) J. Appl. Mech. **45**, 325.
22. L. B. Freund (1978) J. Appl. Mech. **45**, 226.
23. J. Weertman (1980) J. Geo. Res. **85B3**, 1455.

ORAL/POSTER REFERENCE: ICF100575OR

ATOMISTIC SIMULATIONS OF THE MECHANICAL RESPONSE AND MODES OF FAILURE IN METALS AT FINITE STRAIN

J. Zhao[1,2], S. Chantasiriwan[1], D. Maroudas[2], and F. Milstein[1,3]

Departments of [1]Mechanical Engineering, [2]Chemical Engineering, and [3]Materials
University of California, Santa Barbara
Santa Barbara, CA 93106, U.S.A.

ABSTRACT

Isostress molecular dynamics and lattice statics methods have been used to compute theoretical responses of metals to various modes of loading at finite strain, with particular attention to elastic instabilities at points of bifurcation, as well as to post bifurcation phenomena leading to phase change or material failure. The example of nickel in [100] and [110] loading is presented in detail. Interatomic interactions are expressed both by simple Morse pair potentials and by more accurate semi-empirical embedded-atom-method potentials that have been parametrized specifically for studies of crystal elasticity at finite strain. The mechanical responses and failure modes are strongly influenced by crystalline symmetries and incipient bifurcations.

KEYWORDS

Crystals, molecular dynamics, stability, bifurcations, theoretical strength

INTRODUCTION

A number of years ago, Hill [1] observed that "Single crystals free from lattice imperfections are used increasingly as microstructural components. Perfect crystals are capable of elastic strains well beyond what can properly be treated as infinitesimal. Their response to general loading is virtually unknown and is doubtless complex…" In this context, Milstein and Chantasiriwan [2] noted that "Atomistic model computations can shed light on these complexities, particularly when comprehensive comparisons are made among different metals, crystal structures, and loading directions." Topics of current interest [2-4] include theoretical strength, stability, bifurcation, and failure modes at large strain. Here, we employ both the methods of lattice statics (LS), in which stable as well as unstable homogeneous deformation paths are studied, and the isostress molecular dynamics (IMD) ansatz Lagrangian of Parrinello and Rahman (P&R) [5], in which inhomogeneous bifurcations can occur naturally. Extensive series of LS [6a] and IMD [6b] simulations have been carried out; initial results have appeared elsewhere [2,4]. The LS

computations employ an embedded-atom method (EAM) [7] that reproduces identically all second and third order elastic moduli C_{ij} and C_{ijk}, atomic volume V, and cohesive energy E, and yields good theoretical pressure-volume and phonon-dispersion curves, when compared with experiment. The IMD simulations employ Morse interatomic potentials that were fit to two second order elastic moduli and atomic volume [8]; such potentials have been widely used in previous LS computations and yield large strain behavior in excellent qualitative agreement with more rigorous atomic models and experiment [8,9]. In this paper, we examine the behavior of nickel (Ni) under [100] and [110] loading as a particular example.

RESULTS AND DISCUSSION

Figure 1 shows the LS and IMD mechanical responses of the Ni Morse model; the LS behavior is typical of that previously observed for the complete family of Morse function crystals [8-10], as well as for quantum mechanically based pseudopotential models [11]; complete expositions of the LS response have appeared elsewhere [8,11]; a cursory description is provided here. The crystal structure on the primary path (solid line) of Fig. 1a (and throughout Figs. 1b-d) is tetragonal ($l_1 \neq l_2 = l_3$, in general), with uniaxial load l_1 (per unit reference area) applied parallel to the [100] direction; transverse loads $l_2 = l_3 = 0$. Uniaxial stress $s_1 = l_1 / l_2 l_3$, where l_i is the length of a fiber divided by its length in a reference state; the reference state here is the unstressed face centered cubic (fcc) configuration F on the primary path of Fig. 1a. The primary path contains two additional unstressed states, body centered cubic B and a special tetragonal configuration T, and two invariant branch points [8,12], at which the tetragonal crystal

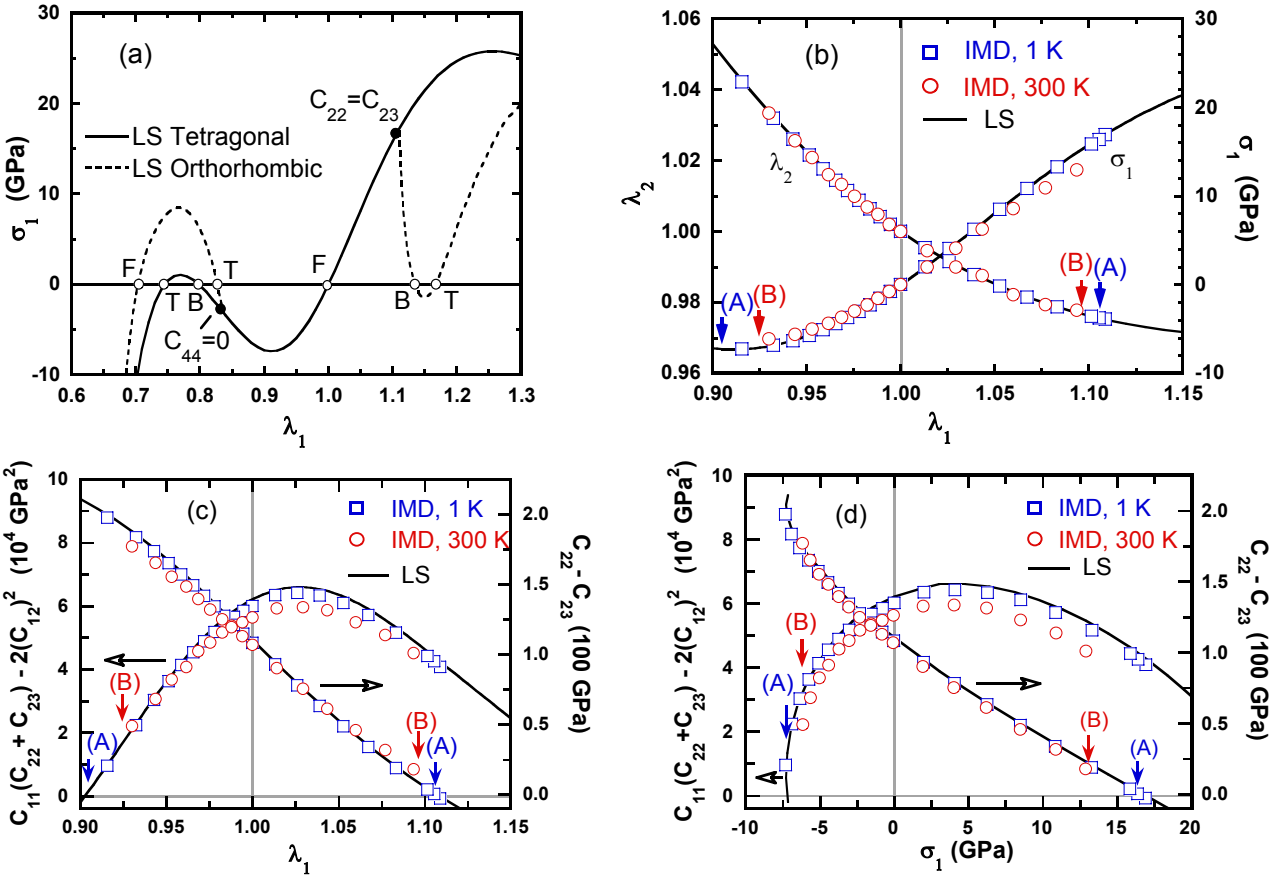

Figure 1: Mechanical response of Morse Ni in (a) [100] and [110] and (b)-(d) [100] loading

can bifurcate homogeneously, under strict uniaxial load, from the primary tetragonal path to a secondary orthorhombic path (dashed lines). Under such branching, second order moduli relations identify the branch points; relations with higher order moduli characterize the branching, as is discussed below, in connection with the EAM results. The primary path may be considered as face centered (fc) or body centered (bc) tetragonal. With the moduli reckoned to the fc axes (as in Figs. 1c,d), the left hand (lh) and right hand (rh) branch points occur respectively, at $C_{44} = 0$ and $C_{22} - C_{23} = 0$; conversely, if the moduli were reckoned to the bc axes, the lh and rh branch points, respectively, would coincide with $C_{22} - C_{23} = 0$ and $C_{44} = 0$ [8,11]. At a "$C_{22} = C_{23}$" eigenstate, to first order, the homogeneous eigendeformation is $dl_1 = 0, dl_2 = - dl_3$, with $dl_1 = dl_2 = dl_3 = 0$, where d indicates incremental change. The crystal thus becomes body centered orthorhombic (bco) on the lh secondary branch and face centered orthorhombic (fco) on the rh branch; the lh and rh secondary paths also contain, respectively, the unstressed F and B structures, although oriented with the load parallel to the [110] directions of *these* cubic structures. Thus, the respective secondary paths also represent primary paths of [110] uniaxial loading of the F and B crystals. The branch paths and symmetries have profound effects on crystal elasticity [8,9,11]; e.g., note the considerably smaller value of the (local) maximum in s_1 in [110] loading than in [100] loading of fcc Ni, owing to the incipient bifurcation at the lh branch point.

We turn next to the topic of stability. In the Morse model of Ni, states T and B are elastically unstable; the stable ranges in Fig. 1a are thus on the tetragonal and the bc orthorhombic paths, in the "neighborhoods" of states F. The use of elastic moduli in assessing stability at finite strain has been discussed elsewhere [1,8,12]; here we simply note that, as criteria for stability on the tetragonal path, "$C_{22} = C_{23}$" locates an invariant eigenstate (its location is independent of the choice of geometric parameters q_r in the definitions $C_{rs} = \partial^2 E / \partial q_r \partial q_s$) [12], while "$D^o \; C_{11}(C_{22} + C_{23}) - 2C_{12}^2 = 0$" occurs where the conjugate variable p_r in the relationship $dp_r = C_{rs}\, dq_s$ is stationary, and thus depends on the choice of q_s [12]. The C_{rs} represented in Figs. 1c,d are the Green moduli; and thus, in these figures, D=0 at the minimum value of the Green conjugate stress, which varies as l_1 / l_1.

Figures 1b-d compare the LS and IMD mechanical responses of Ni under [100] tensile ($l_1 > 1$) and compressive ($l_1 < 1$) loading. In the IMD simulations, the Ni crystal was first equilibrated in a tetragonal configuration at constant temperature T and constant uniaxial [100] stress. Either this equilibrated state remained stable indefinitely, or the crystal subsequently lost stability; both isothermal and adiabatic transformations were studied. The equations of motion in the IMD simulations were integrated using a fifth-order Gear predictor-corrector algorithm [13]. Isothermal conditions were maintained by rescaling the atomic velocities at each time step. The dimensionless fictitious supercell mass W in the P&R Lagrangian was taken to be $W = 20$. The time step size Δt was typically about 10^{-15} s; numerical accuracy and stability were tested for each thermodynamic state examined in our simulations. The initial configuration was an fcc crystal represented by a cubic supercell. For all of the IMD results reported in this paper, the simulation supercell contained 2048 atoms, periodic boundary conditions were employed, and the Morse potential cut-off distance was 5.6294 Å. Systematic convergence tests confirmed that this supercell size does not affect the mechanistic details of the transition under consideration. The C_{rs}, at finite temperature, were computed from canonical fluctuation formulae [14].

States (A) and (B) in Figs. 1b-d indicate where stability was first lost in IMD simulations at 1 and 300 K, respectively. At 1 K, the crystal becomes unstable very near the states $C_{22} = C_{23}$ in tension and $D = 0$ in compression (states (A)). At elevated temperature, the instabilities occur

earlier (states (B)), well before $C_{22} = C_{23}$ and $D = 0$; thus thermal activation "overcomes" the elastic strain energy barrier to bring about transformation.

We concern ourselves next with the tensile instability, which leads to fracture. (The compressive instability, which results in transformation to a hexagonal close packed (hcp) structure in adiabatic simulations, or to faulted hcp in isothermal simulations, will be discussed elsewhere [6b].) Previously, P&R [5] examined the behavior of the Morse Ni model in an adiabatic IMD simulation at and also found failure in the neighborhood of the $C_{22} = C_{23}$ state that was identified earlier by Milstein and Farber [10]. Here, we delve deeper into the failure phenomenon by examining (i) the influence of temperature and stress upon the elastic moduli and points of instability and (ii) the details of atomic movements during isothermal IMD simulations of failure.

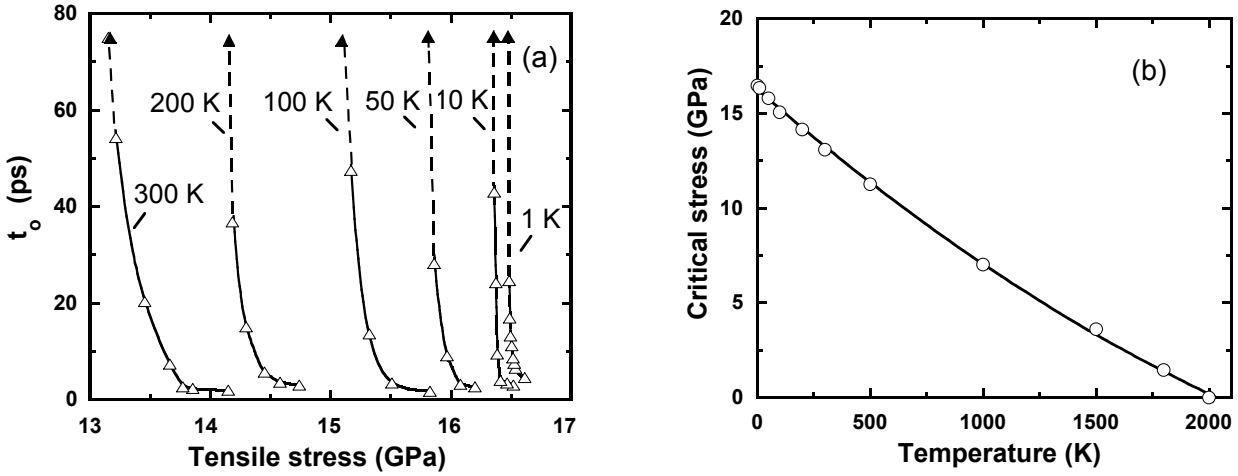

Figure 2: Determination of critical stress and its dependence on temperature

Figure 2a illustrates, for selected values of T, the stress dependence of the time t_o required for the onset of instability adiabatically, with T (of the equilibrated state) as a parameter; the asymptotic limits of stress at which the instabilities are not observed after "infinitely" long times are referred to as the critical stresses s_c. Values of s_c are indicated by solid triangles in Fig. 2a, and a complete set of s_c values is plotted vs T in Fig. 2b; s_c is seen to decrease continuously and monotonically with T, vanishing at the theoretical melting point of about 2000 K.

The mechanism of bifurcation is seen in Figs 3a-j, which show the computer generated evolution of the atomic configurations during an isothermal IMD simulation at 1 K and 17.05 GPa. This stress is slightly greater than the critical stress of 16.5 GPa at 1 K. The load is [100] uniaxial, and thus is perpendicular to the plane of the paper in Figs. 3a-d, and is vertical and parallel to the plane of the paper (i.e. the $(1\bar{1}0)$ plane) in Figs. e-j. At $t = 0$ ps, the crystal is face centered tetragonal, with lattice parameters $a_1 \neq a_2 = a_3$; the predicted bifurcation, $da_2 = -da_3$, $da_1 = 0$, is seen to have initiated in frame b, after about 10 ps. However, the bifurcation does not occur homogeneously throughout the crystal, but occurs in alternating domains that bifurcate with $da_2 > 0$, $da_3 < 0$ and $da_2 < 0$, $da_3 > 0$. In this stage, the atoms remain within their (100) planes, which in themselves remain fairly flat and parallel to each other, as seen in frame f. As the instability proceeds, however, the atoms tend to "shear" out of the (100) planes, which, in turn, leads to void formation and failure. The initial bifurcation is thus a precursor to the ultimate failure. The shearing is seen predominantly in frame h. Supercells containing as many as 16,384 atoms were tested and found to exhibit similar bifurcation and failure responses.

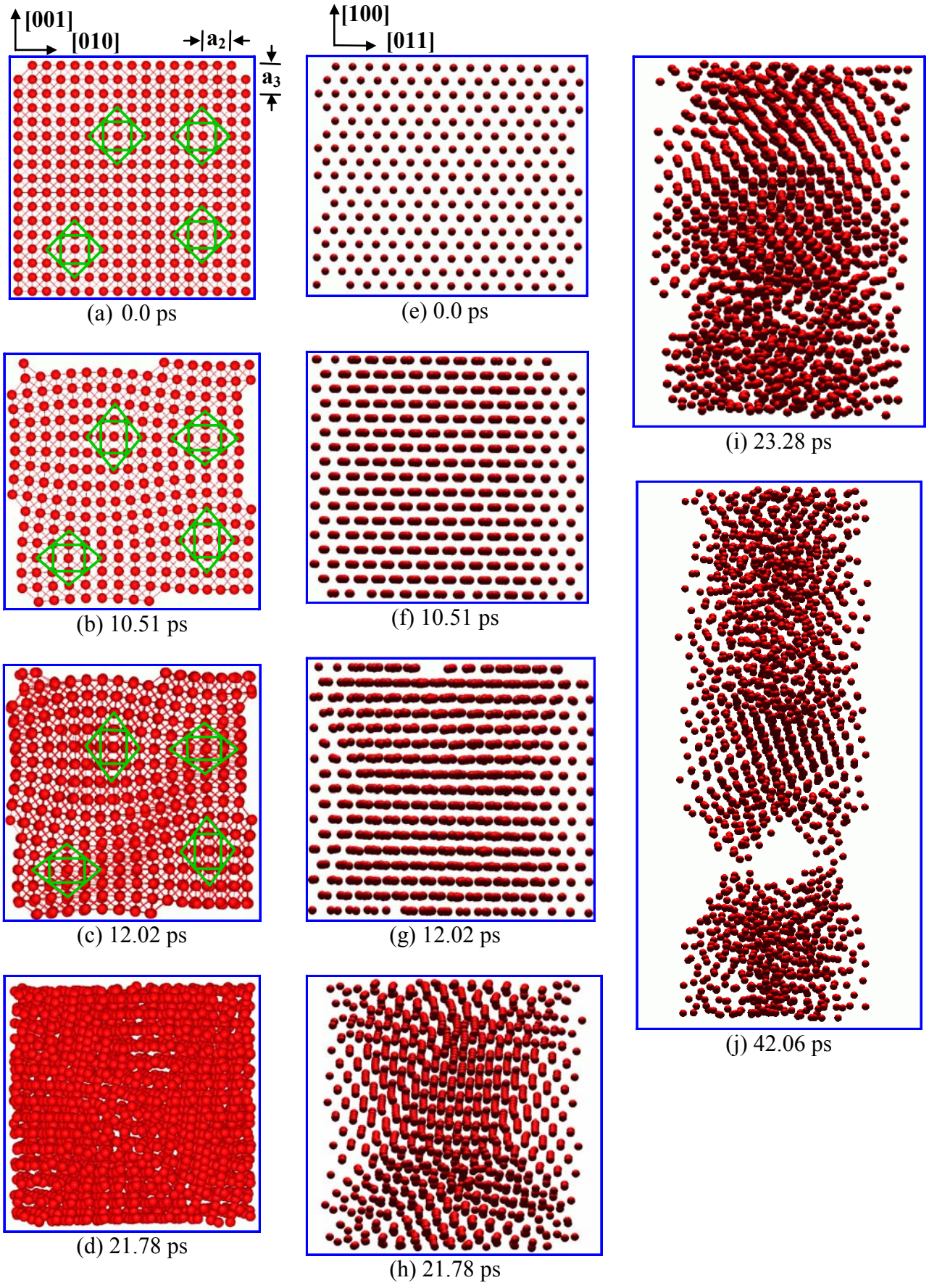

Figure 3: Evolution of atomic configurations during bifurcation and failure in an isothermal IMD simulation of Ni under 17.05 GPa [100] tensile stress at T=1 K

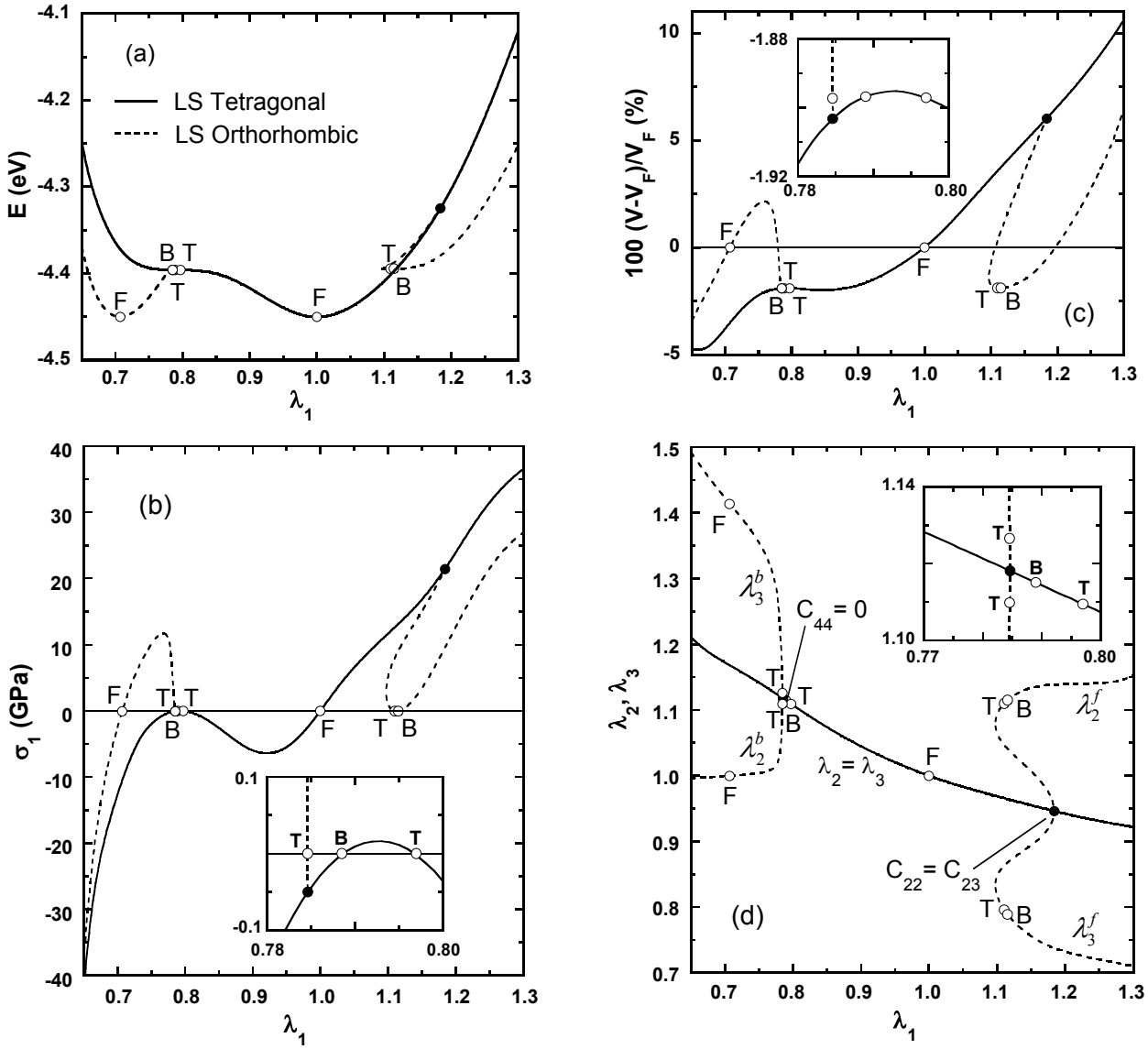

Figure 4: Mechanical response of the EAM model of Ni in [100] and [110] loading

Finally, we examine the LS behavior of the EAM model of Ni, and compare it to that of the Morse model. The EAM model is generally considered as more rigorous in that is has more substantial bases in theory. Also, its linear and non-linear elastic properties in the unstressed fcc state are identically in accord with experiment. As seen from Figs. 4, there is general agreement between the Morse and EAM models, in that both models: (i) exhibit bifurcations at $C_{44} = 0$ and $C_{22} = C_{23}$, leading to orthorhombic structures under uniaxial stress, (ii) contain the unstressed F and T states on the bc orthorhombic (lh) branch, and (iii) have the unstressed B and T configurations on the fc orthorhombic (rh) branch. Also, as in the case of the Morse model, in the EAM model, the crystal structures (and lattice parameters) in the states F, B, and T on the primary path are identical to the corresponding structures in states F, B, and T on the orthorhombic path, but differently oriented with respect to the loading direction; i.e., the loading direction is parallel to the [110] axes of the cubic crystals F and B that reside on the secondary paths.

There is also reasonable quantitative agreement, i.e. s_c is 17 and 21 Mpa, respectively, in the Morse and EAM models at the LS tensile instability (i.e. at $C_{22} = C_{23}$); the respective maximum stresses s_m on the primary path are 26 and 39 MPa, so s_c / s_m is 0.65 in the Morse

model and 0.55 in the EAM model. One noticeable difference, however, is the slope dl_1/dl_1 of the secondary path at the rh branch point, which is positive in the EAM model but negative in the Morse model; such branching, with positive slope, has not heretofore been observed in prior computations. Whether or not the slope of the fco branch path influences the IMD bifurcation response is yet to be determined. The slope on the secondary path at $C_{22} = C_{23}$ is given by [15]

$$\frac{dl_1}{dl_1} = \left\{ c_{11} - \frac{c_{12}^2}{c_{22}} - \left\{ \frac{[2c_{22}(c_{123} - c_{122}) + c_{12}(c_{222} - c_{223})]^2 / c_{22}}{2c_{22}(c_{2222} - 4c_{2223} + 3c_{2233})/3 - (c_{222} - c_{223})^2} \right\} \right\} \qquad (1)$$

where, $c_{ij..} \equiv \partial^2 E / \partial l_i \partial l_{j..}$. The term in brackets [ ] is the slope on the primary path at the branch point, which must be positive if branching terminates stability; thus the expression in the brackets { }, which contains the higher order moduli, must be less than $c_{11} - c_{12}^2/c_{22}$ for positive slope on the secondary path at $c_{22} = c_{23}$. We have used lattice summations to calculate the moduli in both the Morse and EAM models, to fourth order, and verified Eqn. 1 by comparison with the slope dl_1/dl_1, computed directly on the branch path at $c_{22} = c_{23}$.

CONCLUSIONS

Reasonably good agreement is found between the results of Morse model and (more sophisticated) EAM model lattice statics simulations of uniaxial loading of face centered cubic Ni single crystals. For both models, under [100] uniaxial loading, a branch point is found in tension at the invariant "$C_{22} = C_{23}$" eigenstate. The associated homogeneous eigendeformation leads to branching from the tetragonal crystal structure to body centered orthorhombic, via the bifurcation $\delta a_1 = 0$, $\delta a_2 = -\delta a_3$, with the load ℓ_1 remaining uniaxial, i.e., $\delta\ell_1 = \delta\ell_2 = \delta\ell_3 = 0$ (the 1-direction is coincident with the [100] axis, the transverse 2- and 3-directions are [010] and [001]).

In isostress molecular dynamics simulations of [100] loading of Morse model Ni crystals, it is also found that stability in tension is lost as elastic moduli C_{22} and C_{23} approach equality. However, the "predicted bifurcation" occurs locally, rather than uniformly; as shown by the computer generated evolution of the atomic configurations in the isothermal, isostress molecular dynamics simulations, during bifurcation and subsequent fracture. That is, the crystal's lattice parameters bifurcate inhomogeneously, with the $\delta a_1 = 0$ and, in alternating domains, $\delta a_2 = -\delta a_3 > 0$ and $\delta a_2 = -\delta a_3 < 0$. The bifurcation occurs as a precurser to failure. At elevated temperatures, thermal activation causes lattice instability prior to the convergence of C_{22} and C_{23}. The critical stress for failure σ_c is found to decrease continuously and monotonically with temperature, vanishing at the theoretical melting point of about 2000 K.

ACKNOWLEDGMENTS

The Campus Laboratory Collaborations Program of the University of California provided financial support for this work.

S. Chantasiriwan is currently at Thammasat University, Rangsit Campus, Khlong Luang, Pathum Thani 12121

REFERENCES

1. Hill, R. (1975) *Math. Proc. Cambridge Philos. Soc*. 77, 225.
2. Milstein, F. and Chantasiriwan, S. (1998) *Phys. Rev*. B 58, 6006.
3. Morris, J. W. Jr., Krenn, C. R., Roundy, D. and Cohen, M. L. (2000). In*: Phase Transformations and Evolution in Materials*, to be published, Turchi, P.E. and Gonis, A. (Eds). TMS, Warrendale, Pa., 2000.
4. Zhao, J., Maroudas, D. and Milstein, F. (2000) *Phys. Rev*. B 62, 13799.
5. Parrinello, M. and Rahman, A. (1981) *J. Appl. Phys*. 52, 7182.
6. (a) Chantasiriwan, S. and Milstein, F. (b) Zhao, J., Maroudas, D. and Milstein, F., to be published.
7. Chantasiriwan, S. and Milstein, F. (1998) *Phys. Rev.* B 58, 5996.
8. Milstein, F. (1982). In: *Mechanics of Solids,* pp. 417-452, Hopkins, H. G. and Sewell, M. J. (Eds). Pergamon, Oxford.
9. Milstein, F. and Rasky, D. J. (1996) *Phys. Rev*. B 54, 7016; Milstein, F. and Marschall, J. (1988) *Philos. Mag*. A 58, 365.
10. Milstein, F. and Huang, K. (1978) *Phys. Rev*. B 18, 2529; Milstein, F. and Farber, B. (1980) *Phys. Rev. Lett*. 44, 277.
11. Milstein, F. , Marshall, J. and Fang, H. E. (1995) *Phys. Rev. Lett*. 74, 2977.
12. Hill, R. and Milstein, F. (1977) *Phys. Rev*. B 15, 3087.
13. Allen, M. P. and Tildesley, D. J. (1990). *Computer Simulation of Liquids.* Oxford University Press, Oxford.
14. Ray, J. R. (1988) *Comput. Phys. Rep*. 8, 109.
15 Hill, R. (1982) *Math. Proc. Cambridge Philos*. *Soc*. 92, 167.

ORAL REFERENCE: ICF100445OR

AUTOMATIC CONTROL OF SECONDARY FLEXURE IN UNIAXIAL TENSILE TEST OF CONCRETE

H. Akita[1], D. Sohn[2], H. Koide[1] and M. Tomon[1]

[1] Department of Civil Engineering, Tohoku Institute of Technology, Sendai, 982-8577, Japan
[2] High Technology Research Center, Tohoku Institute of Technology, Sendai, 982-8577, Japan

ABSTRACT

When a uniaxial tensile test is performed to investigate tension softening behavior of concrete, a secondary flexure occurs inevitably because of the heterogeneous nature of concrete, even in the case of no eccentricity in the applied load. The secondary flexure causes a significant reduction in the observed peak load, and then makes the estimated observed tensile strength unreliable. Therefore, the prevention of the flexure occurrence is essential to obtain reliable experimental results. In order to meet this requirement, the authors have developed a unique test procedure, which consists of a manually operated adjusting gear system. Although the system has provided successful and informative results, it also has an intrinsic drawback, i.e. human related malfunction. The main objective of this study is to establish and to qualify automation for the prevention of the secondary flexure, using computer-controlled DC motors instead of manual operations. Consequently, the application of the automatic system on the uniaxial tensile test not only provides better test results but also reduces long time efforts.

KEYWORDS

Uniaxial tension, tension softening, secondary flexure, automatic control, test method, concrete

INTRODUCTION

The information of tension softening process is essential to analyze fracture behavior and to estimate concrete properties. One of the best ways to investigate the tension softening process is testing under uniaxial tensile loading because of simultaneous investigation of tensile strength and softening curves from single specimen. Additional tests or calculations, for instance the inverse analysis, are not required for the uniaxial tensile test. The authors had developed and reported a unique test procedure of uniaxial tensile test for concrete [1]. This test procedure provides solutions for four common problems of the test, such as unstable fracture, secondary flexure, multiple cracks and overlapping cracks. First, the problem of unstable fracture can be avoided by employing a deformation-controlled loading process with an appropriate measuring length. Second, a secondary flexure caused by

heterogeneous nature of concrete as well as unpredicted flexures due to load eccentricity are eliminated by equalizing reciprocally opposite lateral elongations. For this purpose, a specifically designed manual-operated adjusting gear system was developed. Next, multiple cracks are prevented by the application of primary notches on the middle of two identical laterals of a specimen. At last, overlapping cracks are avoided by adopting additional notches, called a guide notch, on the middle of other sides (cast and bottom laterals).

The prevention of the secondary flexure is the most significant among these four problems because the flexure, if it occurs, reduces the measured peak load up to 20%. Nevertheless, many researchers have paid little attention on the importance of the effect of the secondary flexure [2,3] or have sometimes failed in the prevention of it mainly because of insufficient experimental apparatus [4,5]. Thus, the main issue of this study is to establish the test procedure to prevent the secondary flexure in uniaxial tensile test of concrete.

MANUALLY OPERATED ADJUSTING GEAR SYSTEM

A secondary flexure is denoted as the induced flexure (namely lateral flexing) originated fundamentally in the heterogeneous material aspect of concrete. Even when there is no eccentricity in the applied load, the secondary flexure will occur. General causes of the secondary flexure are the effects of local softening at the weakest zone of a specimen and of non-symmetrical arrest of propagating cracks by aggregates. The secondary flexure produces strain gradient, making one half portion softened but the opposite half contracted relatively within the cracked section. The cohesive stresses in the softened zone decrease a little to compare with tensile strength, while the stresses at the opposite side are reduced much due to superposition of compressive stress by the flexure, as illustrated in Figure 1. Therefore, the peak load, which is the resultant force of these tensile stresses along the cross section, decreases considerably.

In order to control the secondary flexure, a specifically designed adjusting gear system was attached as illustrated in Figure 2. When a certain side of a testing specimen is elongated more than the opposite side, the longer side is contracted by manual turns of the adjusting gear on that side until balancing elongations, while the opposite side gear should be released completely. If the elongation of a certain side becomes longer than the opposite when the opposite side gear have already been tightened, the tightened side should be released until the balance. Without this release, the deformation of a specimen is too restricted to express a real softening phenomenon. When the measuring length of deformation is 70 mm and the maximum limit of the deformation is 0.35 mm, the four side deformations are monitored by a digital strain meter with the resolving power of 1 με. For the manual operation, it is inevitably required to use a human labor for continuous monitoring and controlling.

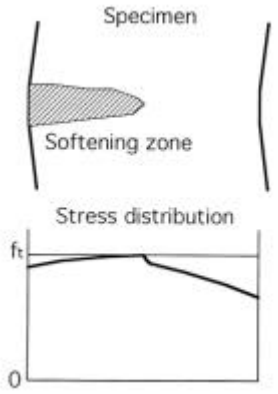

Figure 1: An illustrative explanation of a secondary flexure

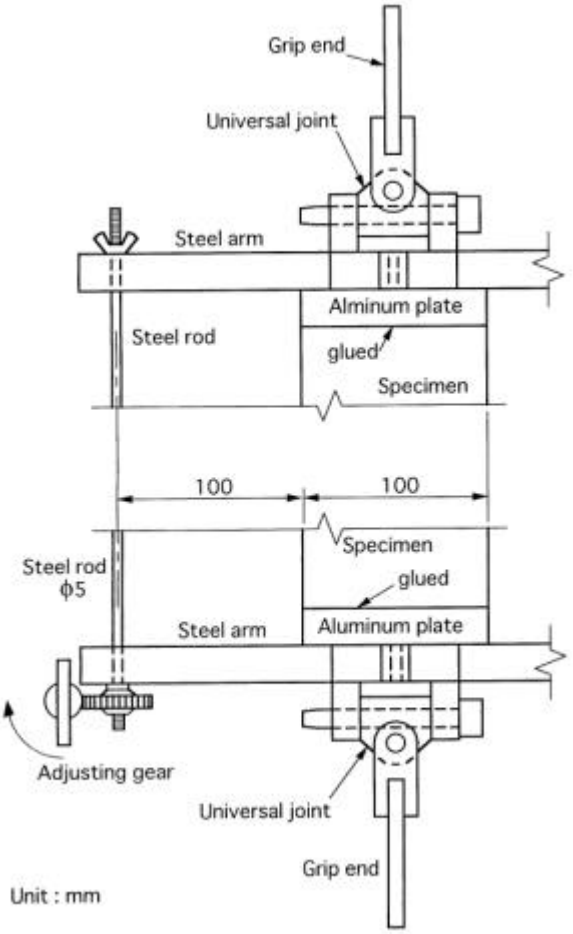

Figure 2: Apparatus to prevent secondary flexure

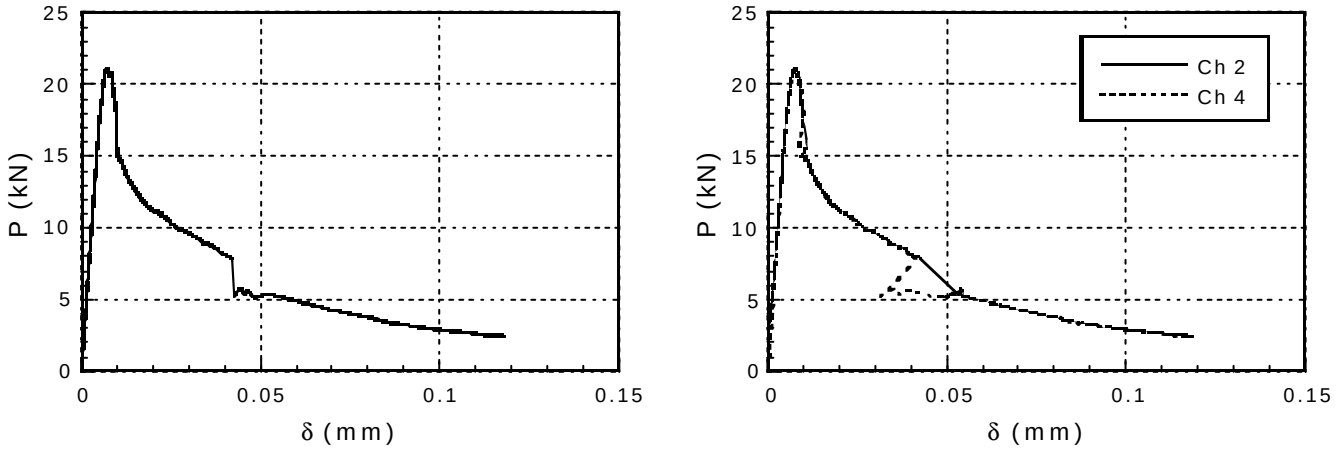

(a) average deformation (b) individual deformation of ch-2 and ch-4

Figure 3: Load-deformation curves by manual control

PROBLEM OF MANUAL OPERATION

Although the test procedure, mentioned in the previous section, shows great improvements of the uniaxial tensile test and provides much reliable information of tensile behavior of concrete, it has an inevitable weakness– employment of human operators as a kind of a controller. Outputs could sometimes be different even if ideally identical concrete specimens were tested because the controlling

patterns of human operators would be varied with respect to operator's skill and character, or date and time of testing. Fig. 3 shows the worst test result due to the mistake in the manual control. The radical drop at around δ=0.04 mm on the load-deformation (P-δ) curve in 3 (a) and corresponding contorted individual P-δ curves in 3 (b) might not be caused by the testing material itself but by the human mistake in controlling the adjusting gear. Thus, in order to establish fundamental and scientific basis for the test procedure, the kind of any uncontrolled and unpredicted factors should be excluded, and thus the development of an automatic adjusting gear system is required.

AUTOMATIC ADJUSTING GEAR SYSTEM

In order to improve manual operation, an automatic control system was developed. One DC 6V and 60 rpm motor controlled by a computer program is attached to each adjusting gear. The schematic diagram and photograph of the automatic system are shown in Figure 4 and 5, respectively. Figure 4

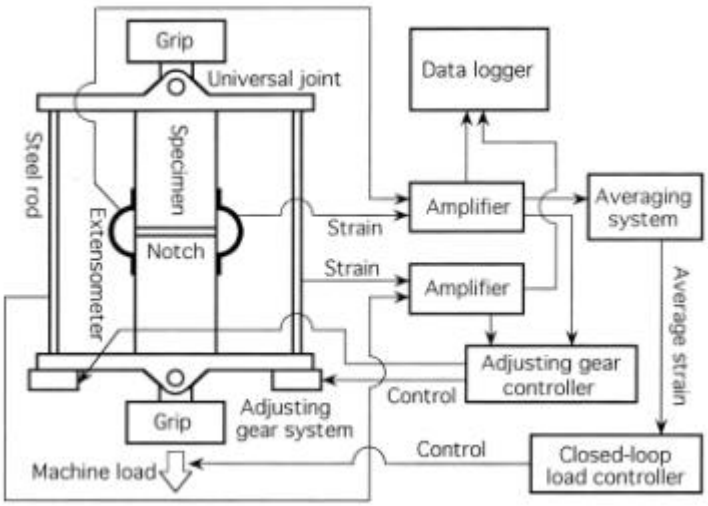

Figure 4: Controlling and recording system

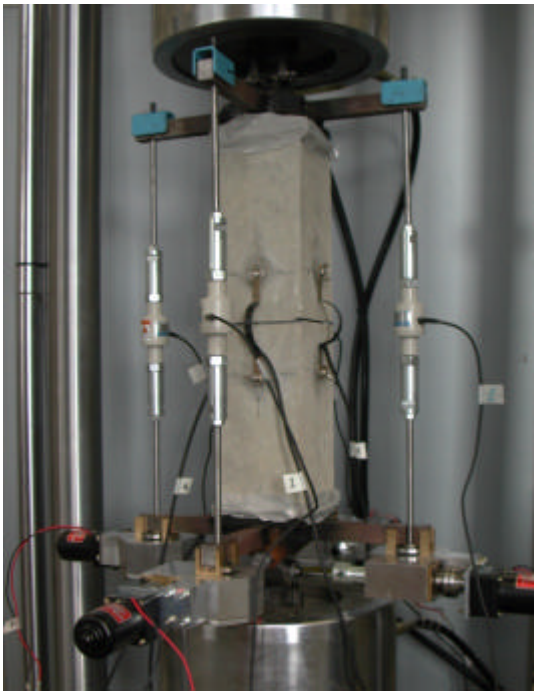

Figure 5: Experimental set-up

and 5 show upper and lower grips of loading machine, a prismatic specimen with notches, extensometers crossing the notches, load-cells connecting to rods and the adjusting gear system with motors. The only difference between the manual and the automatic system is the type of the adjusting gear controller in the Figure 5. The controller was human labor for the manual system, while that was a set of motors (See Figure 5) and a computer system. Both four side strains of the specimen and four strains of steel rods in the gear system are reflected for the control. The DC motor employed rotates clockwise or counterclockwise without speed variations. The computer program that controls the rotation of motors was written in the BASIC language, and the time duration of one cycle is 0.04 second. The algorithm of the computer program is shown in Figure 6. The motors begin to round when the deformation difference (Dif) exceeds a threshold (D), and an adjusting gear is judged whether it is

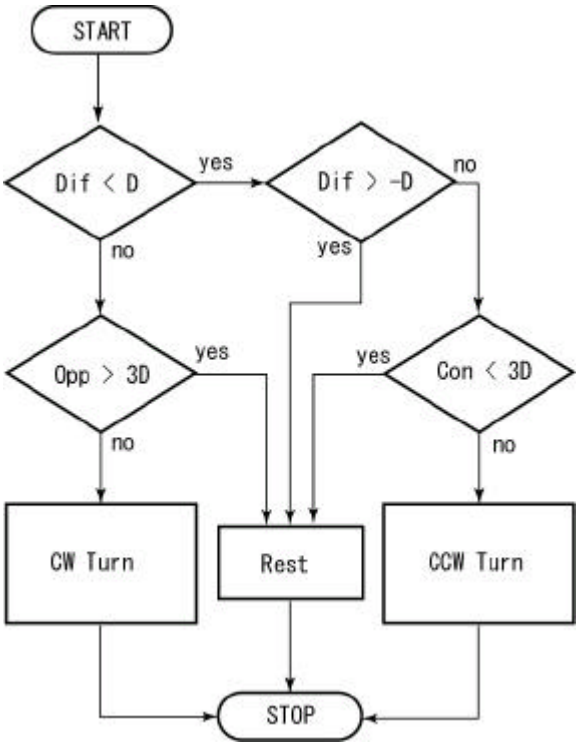

Figure 6: Flow-chart of controlling program

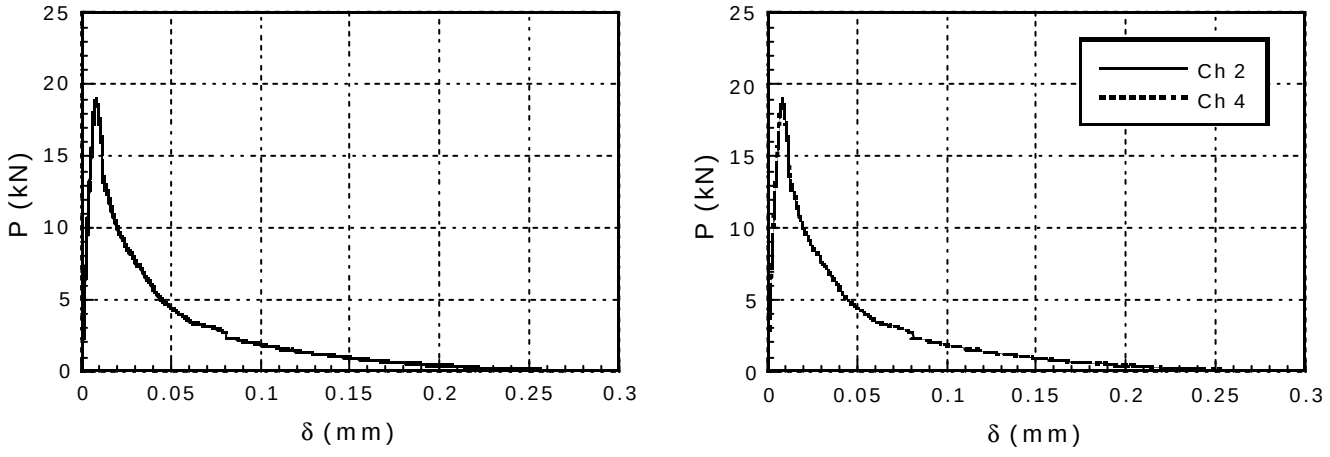

(a) for average (b) for ch-2 and ch-4

Figure 7: Load-deformation curves by automatic control

tightened or not by the comparison with the rod strain and other threshold (3D). The algorithm of the motor control consists of one turn and several time-unit-rests and the rest time is inversely proportional to the level of deformation difference. The rest is indispensable because of the delay in the response of the concrete specimen to the operation, especially at the load descending branch after peak load.

RESULTS AND DISCUSSIONS

Figure 7 are examples of P-δ curves obtained by the automatic control system. 7 (a) shows the relation with respect to the average deformation of four laterals, while 7 (b) to the individual deformation of ch-2 and 4. It is shown that the smooth and better curves are obtained by the automatic system in comparison with those obtained by the manual adjusting system. Both curves in 7 (b) are coincide all over the range. Thus, the automatic adjusting gear system enables to provide more reliable test results than manual operation.

CONCLUSIONS

An automatic adjusting gear system, which consists of four DC motors and a computer program, to control the secondary flexure in uniaxial tensile test of concrete is developed. The system shows a great improvement in controlling the secondary flexure and observing the tension softening behavior in comparison with the manual-operated system. Therefore, the automatic system provides an optimistic future in the field of the uniaxial tensile testing in concrete.

ACKNOWLEDGEMENTS

The authors gratefully acknowledge the financial support by Tohoku Construction Association through Technical Development Support Fund.

REFERENCES

1. Akita, H., Koide, H., Tomon, M. and Sohn, D. (in submitting) *Concr. Sci. Eng.*
2. Li, Z., Kulkarni, S. M. and Shah, S. P. (1993). *Exper. Mech.* 33, (3), 181
3. Li, Q. and Ansari, F. (2000). *ACI Mater. J.* 97, (1), 49
4. van Mier, J. G. M., Schlangen, E. and Vervuut, A. (1996). *Mater. Struct*., 29, 87
5. Hordijk, D. A., Reinhardt, H. W. and Cornelissen, H. A. W. (1987). In: *Fracture of Concrete and Rock*, pp. 138-149, Shah, S. P. and Swartz, S. E. (Eds), Soc. Exp. Mechanics, Bethel

BEAM THEORY AND WEIGHT FUNCTION METHODS FOR MODE I DELAMINATION WITH LARGE SCALE BRIDGING

R. Massabò [1] and B. N. Cox [2]

[1] Department of Structural and Geotechnical Engineering, University of Genova, Genova, 16145, Italy
[2] Rockwell Science Center, Thousand Oaks, CA 91360, USA

ABSTRACT

A nonlinear fracture mechanics model is formulated for analysis of mode I delamination of orthotropic double cantilever beam specimens in the presence of large scale bridging conditions. The model accounts for the presence of regions of contact along the wake of the crack, which may form due to the action of the bridging mechanisms. The problem is solved using a nonlinear integral equation approach in terms of stress intensity factors at the crack tip. An approximate weight function is proposed and validated numerically for a pair of concentrated forces acting on the surfaces of the delamination. The model is applied to investigate the influence of the orthotropy of the material on the fracture behavior and the validity of approximated solutions based on beam theory.

KEYWORDS: Nonlinear fracture mechanics, weight functions, delamination, strengthening mechanisms, anisotropic material, large scale bridging.

INTRODUCTION

Mode I and mixed mode delamination in large scale bridging conditions, such as those created by through thickness reinforcement in composite laminates, shows unusual phenomena of crack face closure, crack arrest and crack propagation with crack face contact, which have no precedent in the delamination of conventional tape laminates [1,2]. In [3] the authors considered a typical mixed mode geometry, the Mixed Mode Bending specimen proposed by Crews and Reeder, and explained these phenomena by means of a simple analytical model based on Timoshenko beam theory. The model treats the delaminated arms of the specimen as beams on an elastic, generally nonlinear, foundation of Winkler type with the constitutive laws of the springs given by the bridging law, which characterizes the bridging mechanism. The crack closure phenomenon is a manifestation of the oscillations of the function representing the deflection of the beams in the wake of the crack. The wavelength of the function, λ, sets the characteristic length scale of the problem, which in the case of linear bridging mechanisms is given approximately by $\lambda/4 = \pi/2 \sqrt[4]{4k_d / \beta_3}$, with β_3 the modulus of the foundation and k_d the flexural stiffness of the beam cross section. Once the limit configuration for crack tip closure is approached, the fracture response of the specimen will depend on the geometry and the loading conditions. In the case of a specimen symmetric about its midplane and in the absence of mode II loading, the crack will stop and the specimen will break by mechanisms other then delamination. In the presence of mode II loading or in asymmetric specimens, the crack will continue to propagate and the propagation will be opposed not only by the bridging mechanism but also by friction acting in the regions of contact.

The model proposed in [3] explains qualitatively all the problems associated with mixed mode large scale bridging delamination. However, the model makes strong assumptions which could affect the solutions quantitatively, namely it schematizes the specimen as a one-dimensional structure, it neglects the influence of the elastic material in front of the crack (built-in ends assumption) and it deals only approximately with regions of contact between the delaminated faces and the effect these regions may have on crack propagation driven by mode II loading.

In this paper a nonlinear fracture mechanics model is formulated for analysis of delamination crack growth which removes the above mentioned assumptions, assumes a two-dimensional deformation field and accounts for the orthotropy of the material. The problem is solved through an integral equation approach in terms of stress intensity factors at the crack tip. Since the crack closure phenomenon is controlled by the mode I response of the laminate, focus in this initial work is restricted to this problem.

FRACTURE PARAMETERS IN ORTHOTROPIC DOUBLE CANTILEVER BEAMS

Stress intensity factors

An exact solution for the stress intensity factor K_{IP} due to a pair of concentrated forces P applied per unit width onto the crack faces of a double cantilever beam at a distance d from the crack tip has been obtained by Foote and Buchwald [4]. They solved the problem by applying the Wiener-Hopf technique to an isotropic, arbitrarily loaded infinite strip and representing the concentrated loads in terms of the Dirac delta function. A simple formula approximating the exact solution, which has an accuracy of 1.1% and can be applied to double cantilever beams with an uncracked ligament $c > 2h$, is also given in [4]:

$$\frac{K_{IP}h^{0.5}}{P} = \sqrt{12}\left(\frac{d}{h}+0.673\right)+\sqrt{\frac{2h}{\pi d}}-\left[0.815\left(\frac{d}{h}\right)^{0.619}+0.429\right]^{-1} \tag{1}$$

where h is the half thickness of the specimen. For $d/h \geq 0.3$ the exact K_{IP} is well represented (error always lower than 4%) by Gross and Srawley's boundary collocation solution, approximately given by the first bracket term on the right hand side. The same limit solution is given by the modified beam theory of Kanninen, which removes the assumption of built-in ends to account for the elasticity of the uncracked ligament. For very large d/h, Eq. (1) approaches the elementary beam theory solution of a double cantilever beam with built-in ends, $K_I h^{0.5}/P = \sqrt{12}\, d/h$ [3]. For very small d/h the dimensionless K_{IP} of Eq. (1) approaches Irwin's solution for a semi-infinite crack in an infinite sheet, $K_I h^{0.5}/P = (2/\pi\, h/d)^{0.5}$. A lower limit for the normalized crack length a/h of the double cantilever beam specimen must be set for Eq. (1) to be valid for all d/h, $0 < d/h \leq a/h$. Irwin's solution for very small d/h is correct only if $a >> d$, and should be replaced by Tada's solution [5] for a finite crack of length a in a semi-infinite sheet when a/h also becomes very small. A conservative lower limit for a/h can be set as $a/h \geq 0.3$, so that when $d/h = a/h = 0.3$, the beam theory solution is already approached.

The stress intensity factor due to a pair of concentrated forces P_i applied on the crack faces of an orthotropic double cantilever beam at the coordinate $x_1 = x_{1i}$ (Fig. 1.a) can be deduced from the expression of the strain energy release rate $\mathcal{G}_I$ obtained by Suo et al. [6] making use of the orthotropic relationship $K_{Ii} = \sqrt{\mathcal{G}_I E_1^{'}}$. Plane stress conditions are assumed along with a principally orthotropic material with $E_1^{'} = (\sqrt{2E_1E_3}\lambda^{1/4})/\sqrt{1+\rho}$, $\lambda = E_3/E_1$ and $\rho = \sqrt{E_1E_3}/2G_{13} - \sqrt{\nu_{13}\nu_{31}}$ the orthotropic ratios [6], E_1 and E_3 the Young's moduli in the x_1 and x_3 directions, G_{13} the shear modulus and ν_{13} and ν_{31} Poisson's ratios. The dimensionless stress intensity factor is then given by:

$$\frac{K_{Ii}h^{0.5}}{P_i} = \frac{\lambda^{3/8}}{\sqrt{n}}\sqrt{12}\left(\frac{a-x_{1i}}{h}+Y_I(\rho)\lambda^{-1/4}\right) \tag{2}$$

where:

$$Y_I(\rho) = 0.677 + 0.146(\rho-1) - 0.0178(\rho-1)^2 + 0.00242(\rho-1)^3 \tag{3}$$

and $n = \sqrt{(1+\rho)/2}$. For an isotropic material ($\lambda = \rho = 1$), $Y_I(\rho) = 0.677$ and Eq. (2) coincides with Gross and Srawley's solution. The last term on the right hand side of eq. (2) describes the influence of the elasticity of the uncracked ligament ahead of the crack tip and it vanishes for large $(a\text{-}x_{1i})/h$, when the solution for an orthortropic beam with built-in ends is recovered. Equation (2), has 0.5% accuracy for all $(a\text{-}x_{1i})/h \geq 2\,\lambda^{-1/4}$ and $0 \leq \rho \leq 4$.

An exact solution for the stress intensity factor K_{Ii} when $(a\text{-}x_{1i})/h < 2\lambda^{-1/4}$ is not available in the literature. However, the method of orthotropy rescaling, the examination of Eqs. (1) and (2) and the observation that Irwin's solution for very small $d/h = (a\text{-}x_{1i})/h$ maintains its validity also in orthotropic sheets [7], suggest the following formula [10]:

$$\frac{K_{Ii}h^{0.5}}{P_i} = \frac{\lambda^{3/8}}{\sqrt{n}}\sqrt{12}\,\frac{(a-x_{1i})}{h}\left(1+Y_I(\rho)\lambda^{-1/4}\,\frac{h}{(a-x_{1i})}\right)+\sqrt{\frac{2h}{\pi(a-x_{1i})}} - \left[0.815\left(\frac{0.677}{Y_I(\rho)\sqrt{n}}\lambda^{1/4}\,\frac{a-x_{1i}}{h}\right)^{0.619}\lambda^{-1/8}+\frac{\sqrt{n}}{\lambda^{1/8}Y_I(\rho)\sqrt{12}}\right]^{-1} \tag{4}$$

which has the right asymptotic behaviors for large and small $(a\text{-}x_{1i})/h$. The validity of Eq. (4) for intermediate values of $(a\text{-}x_{1i})/h$ has been checked through finite element calculations for a range of λ and ρ typical of composite laminates, $0.025 \leq \lambda \leq 1$ and $0 \leq \rho \leq 5$, and the relative error has been found to be always lower than 2%. The lower limit for the normalized crack length for which Eq. (4) is valid can be defined by referring to the limit for an isotropic material and exploiting orthotropic rescaling of lengths [6], which yields $a/h \geq 0.3\,\lambda^{-1/4}$ with a 4% error in the case $\rho = 1$. When a reason exists for studying very small cracks as well as non-small cracks in numerical work, Eq. (4) can be combined very easily with Tada's result for the appropriate domains of a/h.

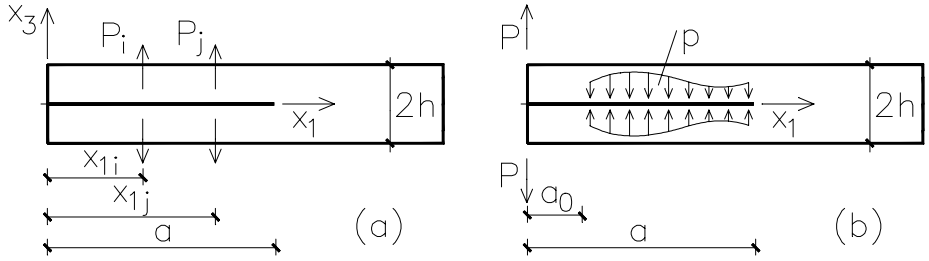

Figure 1: Schematic of the DCB specimen under different loading conditions.

Crack opening displacement

The crack opening displacement u_3 at the coordinate x_{1i} due to a pair of opening forces P_j acting at x_{1j}, Fig. 1, is obtained from the localized compliance $\lambda_{ij} = u_3(x_{1i}) / P_j$ which can be defined through an energy balance or Castigliano's theorem as shown in [8] for an isotropic body. The localized compliance is given by:

$$\lambda_{ij} = \frac{u_3(x_{1i})}{P_j} = \frac{2}{E_1'}\int_0^a \frac{K_{Ii}(a,x_{1i})K_{Ij}(a,x_{1j})}{P_iP_j}\,da \tag{5}$$

where E_1' is the orthotropic constant defined above, P_i is a pair of fictitious forces acting at x_{1i}, and K_{Ii} and K_{Ij} are the stress intensity factors at the crack tip due to P_i and P_j, respectively, given by Eq. (4), [10].

ORTHOTROPIC DOUBLE CANTILEVER BEAM WITH LARGE SCALE BRIDGING

The stress intensity factor at the crack tip of a double cantilever beam with tractions p acting along the bridged portion of the crack as shown in Fig. 1.b is given by:

$$K_{\mathrm{I}} = K_{\mathrm{IP}} + K_{\mathrm{Ip}} = K_{\mathrm{IP}} - \int_{a_0}^{a} \frac{K_{\mathrm{Ii}}(a, x_{1\mathrm{i}})}{P_{\mathrm{i}}}\, p[u_3(x_{1\mathrm{i}})]\mathrm{d}x_{\mathrm{i}} \tag{6}$$

where a_0 is the unbridged length of the crack, K_{IP} is the stress intensity factor due to the external loads P_{i} acting at $x_{1\mathrm{i}} = 0$, and K_{Ip} is the stress intensity factor due to opening tractions p; $K_{\mathrm{Ii}}/P_{\mathrm{i}}$ represents the Green's function of the problem and obtained from Eq. (4). The tractions p depend on the crack displacement and are a priori unknown in Eq. (6). If $u_3(x_{1\mathrm{i}}) > 0$, then $p[u_3(x_{1\mathrm{i}})] = p_3[u_3(x_{1\mathrm{i}})]$ is the closing traction developed by the bridging mechanisms. The value of p_3 as a function of u_3 is defined through the bridging traction law, $p_3(u_3)$, which is one of the data of the model. If $u_3(x_{1\mathrm{i}}) = 0$, then $p[u_3(x_{1\mathrm{i}})] = - p_{\mathrm{c}}[(x_{1\mathrm{i}})]$ is the opening traction depicting the effect of the contact pressure. The contact pressure and the size of the regions of contact are unknown a priori and can be determined through a compatibility condition for the crack opening displacement.

The crack opening displacement $u_3(x_{1\mathrm{i}})$ is obtained by applying the superposition principle and Eq. (6):

$$u_3(x_{1\mathrm{i}}) = u_3(x_{1\mathrm{i}})_{\mathrm{P}} + u_3(x_{1\mathrm{i}})_{\mathrm{p}} = \lambda_{\mathrm{iP}} P - \int_{a_0}^{a} \lambda_{\mathrm{ij}}\, p[u_3(x_{1\mathrm{j}})]\, \mathrm{d}x_j \tag{7}$$

which yields:

$$\begin{aligned} \frac{u_3(x_{1\mathrm{i}})}{h} = {} & \frac{2P}{E_1^{'} h} \int_0^{a/h} \frac{K_{\mathrm{IP}}(a/h)h^{0.5}}{P} \frac{K_{\mathrm{Ii}}(a/h, x_{1\mathrm{i}}/h)h^{0.5}}{P_{\mathrm{i}}}\, \mathrm{d}\left(\frac{a}{h}\right) \\ & - \frac{2}{E_1^{'}} \int_{a_0/h}^{a/h} \int_{\max[x_{1\mathrm{i}}/h, x_{1\mathrm{j}}/h]}^{a/h} \frac{K_{\mathrm{Ii}}(a/h, x_{1\mathrm{i}}/h)h^{0.5}}{P_{\mathrm{i}}} \frac{K_{\mathrm{Ij}}(a/h, x_{1\mathrm{j}}/h)h^{0.5}}{P_{\mathrm{j}}}\, \mathrm{d}\left(\frac{a}{h}\right)\, p[u_3(x_{1\mathrm{j}}/h)]\, \mathrm{d}\left(\frac{x_{1\mathrm{j}}}{h}\right) \end{aligned} \tag{8}$$

Note that the dimensionless $\mathrm{K_I}$'s appearing in Eq. (8) and in the equations that follow depend also on the orthotropic ratios, λ and ρ, as shown in Eq. (4).

Crack propagation in large scale bridging

At the onset of crack propagation the crack tip stress intensity factor of Eq. (6) is equal to the intrinsic fracture toughness, $K_{\mathrm{I}} = K_{\mathrm{Ic}}$, and the dimensionless critical load for crack propagation takes the form:

$$\frac{P_{\mathrm{cr}}}{K_{\mathrm{Ic}} h^{0.5}} = \frac{1}{\dfrac{K_{\mathrm{IP}}(a/h)h^{0.5}}{P}} \left\{ 1 + \frac{p_{30} h^{0.5}}{K_{\mathrm{Ic}}} \int_{a_0/h}^{a/h} \left[\frac{K_{\mathrm{Ii}}(a/h, x_{1\mathrm{i}}/h)h^{0.5}}{P_{\mathrm{i}}} \right] \frac{p[u(x_{1\mathrm{i}}/h)]}{p_{30}} \mathrm{d}\left(\frac{x_{1\mathrm{i}}}{h}\right) \right\} \tag{9}$$

where p_{30} is a normalizing value of the crack face tractions, p_3, given for instance by their maximum value. The dimensionless number on the right hand side of Eq. (9), $p_{30} h^{0.5} / K_{\mathrm{Ic}}$, is a measure of the brittleness of the structure. Recalling the expression for $E_1^{'}$ and that $K_{\mathrm{Ic}} = \sqrt{\mathcal{G}_{\mathrm{Ic}} E_1^{'}}$, Eq. (9) can be modified to allow direct comparison between isotropic and othotropic cases:

$$\frac{P_{\mathrm{cr}}}{\sqrt{\mathcal{G}_{\mathrm{Ic}} E_1 h}} = \frac{\lambda^{3/8}}{\sqrt{n}} \frac{1}{\dfrac{K_{\mathrm{IP}}(a/h)h^{0.5}}{P}} \left\{ 1 + \frac{p_{30} h^{0.5}}{\sqrt{\mathcal{G}_{\mathrm{Ic}} E_1}} \int_{a_0/h}^{a/h} \left[\frac{K_{\mathrm{Ii}}(a/h, x_{1\mathrm{i}}/h)h^{0.5}}{P_{\mathrm{i}}} \right] \frac{p[u(x_{1\mathrm{i}}/h)]}{p_{30}} \mathrm{d}\left(\frac{x_{1\mathrm{i}}}{h}\right) \right\} \tag{10}$$

The normalized crack opening displacement at the generic coordinate $x_{1\mathrm{i}}$ is obtained substituting $P = P_{\mathrm{cr}}$ into Eq. (8):

$$\frac{u_3(x_{1i})E_1'}{K_{Ic}h^{0.5}} = 2\frac{P_{cr}}{K_{Ic}h^{0.5}}\int_0^{a/h}\frac{K_{IP}(a/h)h^{0.5}}{P}\frac{K_{Ii}(a/h,x_{1i}/h)h^{0.5}}{P_i}\,d(\frac{a}{h})$$
$$-2\frac{p_{30}h^{0.5}}{K_{Ic}}\int_{a_0/h}^{a/h}\int_{\max[x_{1i}/h,x_{1j}/h]}^{a/h}\frac{K_{Ii}(a/h,x_{1i}/h)h^{0.5}}{P_i}\frac{K_{Ij}(a/h,x_{1j}/h)h^{0.5}}{P_j}\,d(\frac{a}{h})\frac{p[u(x_{1j}/h)]}{p_{30}}\,d(\frac{x_{1j}}{h}) \quad (11)$$

The statically indeterminate problem defined by the nonlinear integral equations (9) and (11) is solved for general bridging laws, $p_3(u_3)$, through a discretization. A self-consistent solution for the crack profile is obtained iteratively through a numerical procedure following the approach of [8,9].

Dugdale type bridging law, $p_3 = p_{30}$

In the special case of bridging mechanisms described by a Dugdale type bridging law, $p_3 = p_{30}$, Eqs. (9) and (11) simplify and Eq. (9) alone gives the dimensionless critical load for crack propagation. Beam theory predicts the absence of regions of contact for this case and this qualitative characteristic is confirmed by the more accurate calculations of the integral equation approach. Setting aside for this paper the interesting question of the nature of contact regions when they do occur (e.g., for linear bridging laws), a detailed assessment is made here of the limitations of elementary beam theory for predicting crack propagation in the presence of large scale bridging.

Figures 2.a, 2.b and 2.c show dimensionless diagrams of the critical load for crack propagation as a function of the normalized crack length in a double cantilever beam specimen with $a_0 = 0$. Three different values of p_3 are considered, as marked. The curves named (*a*), (*b*) and (*c*) in each diagram describe the response of an isotropic material, an orthotropic material with $\lambda = 0.1$ and $\rho = 3$ (e.g. a graphite epoxy laminate) and an orthotropic material with $\lambda = 0.05$ and $\rho = 5$ (e.g. a boron-epoxy laminate), respectively. The dashed curves depict the elementary beam theory solution (built-in ends, negligible shear deformations). The dotted curve in Fig. 2b, obtained using Timoshenko beam theory for an isotropic material and marked as $\gamma \neq 0$, highlights the influence of the shear deformations.

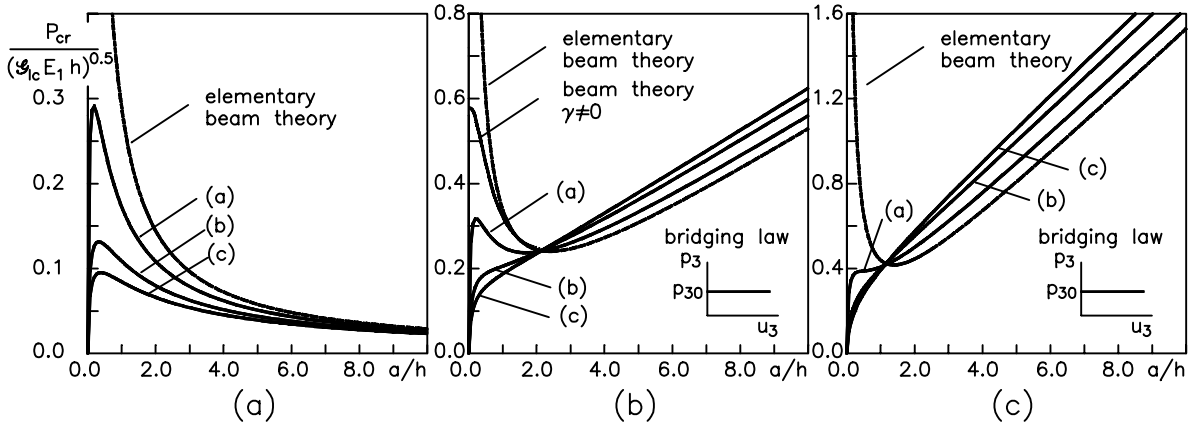

Figure 2: Dimensionless critical load versus normalized crack length in orthotropic DCB specimens. (a) No bridging. (b) Bridging tractions $p_3 = 0.1\sqrt{\mathcal{G}_{Ic}E_1/h}$. (c) Bridging tractions $p_3 = 0.3\sqrt{\mathcal{G}_{Ic}E_1/h}$.

Figure 2.a confirms the validity of elementary beam theory in unreinforced specimens when *a/h* is sufficiently high. The anisotropy of the material affects the response only for relatively small values of *a/h*. The influence of the anisotropy of the material on the structural response apparently seems to be more marked in members reinforced through the thickness (Figs. 2.b and 2.c). In this case, two different regimes of behavior are delineated by a transition value of $a/h = 1/(1.73p_{30}\sqrt{\mathcal{G}_{Ic}E_1/h})^{0.5}$, corresponding to the point where all curves cross each other. If *a/h* is smaller than the transition value, the anisotropy of the material strongly affects the response and the elementary beam theory solution does not describe the actual behavior even qualitatively. For *a/h* larger than the transition value, all curves tend to become parallel with a common slope given by $1/2\ p_{30}\sqrt{\mathcal{G}_{Ic}E_1/h}$ and the deviation between the correct solution and the elementary beam

theory solution becomes independent of the crack length and given by $1/2Y_I(\rho)\lambda^{-1/4} p_{30}\sqrt{\mathcal{G}_{Ic}E_1/h}$. However, the fractional error is $Y_I(\rho)\lambda^{-1/4}/(a/h)$, which is independent of the intrinsic fracture toughness of the laminate, $\mathcal{G}_{Ic}$, and the magnitude of the bridging tractions and coincides with the analogous fractional error of the case with no bridging. It depends only the crack length and the degree of anisotropy. This error is due to the assumption of neglecting the influence of the elastic material ahead of the crack tip and could be removed by using a modified beam theory (Kanninen's, Williams's).

CONCLUSIONS

An approximate weight function has been proposed and validated numerically for a pair of point forces acting on the surfaces of a delamination crack in a possibly thin orthotropic body. The weight function allows mode I large scale bridging problems in beams and plates to be formulated as integral equations without the limitations imposed on accuracy by beam theory approximations. In particular, the crack tip singularity will be properly represented. The integral equations can be solved using well-known, computationally efficient and accurate methods. The weight function strongly depends on the anisotropy ratio. This is a feature of the plate or beam geometry.

The first application of the new weight function to the problem of a large zone of uniform bridging tractions (the Dugdale bridging model) shows the ranges of crack lengths over which beam theories of different order succeed and fail. The presence of large scale bridging is found not to significantly increase the sensitivity of the solutions to the degree of anisotropy with respect to the case with no bridging.

While elementary beam theory will always be correct for sufficiently large crack lengths, a/h, there is a regime of small crack lengths, $a/h \lesssim 2$, where rigorous solutions are required, e.g. based on integral equation methods. Moreover, there is a regime of practical interest for laboratory specimens, $2 \lesssim a/h \lesssim 10$, where elementary beam theory yields only qualitatively correct trends and solutions based on integral equation methods or on modified beam theory are required for quantitative accuracy.

ACKNOWLEDGMENTS: RM was supported by the Italian Department for the University and for Scientific and Technological Research; BNC by the U.S. Army Research Office, Contract Number DAAD19-99-C-0042.

REFERENCES

1. D.D.R. Cartié and I.K. Partridge, (1999), Delamination Behaviour of z-Pinned Laminates, *Proc. ICCM12*, Paris, July, 1999, ed., T. Massard, Woodhead Publishing Limited, Melbourne.
2. Rugg, K.L., Cox, B.N. and Massabò, R. (2001), Mixed mode delamination of polymer composite laminates reinforced through the thickness by z-fibers, *Composites*, *part A,* in press.
3. Massabò R. and B.N. Cox (2001), Unusual characteristics of mixed mode delamination fracture in the presence of large scale bridging, *Mech. Comp. Mater. Structures,* 8(1), 61-80.
4. Foote, R. M. L., and Buchwald, V.T., (1985), An exact solution for the stress intensity factor for a double cantilever beam, *Int. J. of Fracture*, 29, 125-134.
5. Tada, H. (1985) *The Stress Analysis of Cracks Handbook*. Paris Productions Inc., St. Louis, Missouri.
6. Suo, Z., Bao, G., Fan, B., and Wang, T.C., (1991), Orthotropy rescaling and implications for fracture in composites, *Int. J. Solids Structures*, **28**(2), 235-248.
7. Sih, G.C., Paris, P.C., and Irwin, G.R., (1965), On cracks in rectilinear anisotropic bodies, *Int. J. of Fracture*, 1, 189-203.
8. Massabò, R., (1999), The bridged-crack model, book chapter in *Nonlinear Crack Models for Nonmetallic Materials,* (ed. A. Carpinteri), Solid Mechanics and its Applications Series (ed. G. Gladwell), Kluwer Academic Publishers, Dordrecht, The Netherlands, pp. 141-208.
9. Cox, B.N., and Marshall, D.B. (1991a) Stable and unstable solutions for bridged cracks in various specimens. *Acta Metall. Mater.* **39**, 579-89.
10. Massabò R., B.N. Cox and Brandinelli, L. (2001), in preparation.

POSTER REFERENCE: ICF100581PR

BENTONITE CONTAINING PELLETS MECHANICAL PROPERTIES VARIATION CAUSED BY OILY WASTES INCLUSION

E. A. de Carvalho, G. P. Souza and J. N. F. Holanda
Laboratório de Materiais Avançados
Universidade Estadual do Norte Fluminense
Av. Alberto Lamego, 2000 – Campos – RJ – 28015-620 – Brazil

ABSTRACT

Oily wastes are usual byproducts generated by oil industry. New and stricter environmental regulations had established that a permanent and sound solution must be found to these residues storage. Bentonite powder has been used to microencapsulate oily residues. However this new material containing residues cannot be buried or just piled up. The new material was found to be useful for the ceramic industry, therefore mechanical properties must be known. Several 10x10 mm cylindrical pellets containing residues amounts from zero up to 20% of the mixture were manufactured by forming pressure around 25 MPa and fired at 950 °C. Due to its geometry the only test that can be performed in order to determine strength and fracture limits is Brazilian Disk, which yields tensile strength by means of diametrical compression. A total of 25 pellets are tested and ultimate compressive strength and linear shrinkage for the different compositions presented. The effects of different contamination levels over fracture properties are discussed. A brief discussion on the uncertainty measurement is also presented.

KEYWORDS

Contact stresses, compressive strength, oily wastes, diametrical compression, ceramics properties

INTRODUCTION

Campos dos Goytacazes County, located at State of Rio de Janeiro (Brazil), holds extensive clay quarries presenting kaolinite as its main clay mineral [1]. Local ceramic plants exploit these clays as raw material for producing mostly hollow construction bricks and roofing tiles. On the other hand, Campos County has the largest Brazilian oil basin, which is responsible for more than 75% of the national oil production. However, during the process of oil extraction, transportation and storage, great amounts of toxic wastes are generated, among them an oily sludge residue. This waste in particular is sealed in tanks and brought to land to be mixed with an encapsulation substance, organophillic bentonite. Yet less harmful, the resulting material cannot be simply disposed in landfills or just pilled up. As a consequence, efforts have been made to find a permanent solution for the management of the referred waste, without causing major risks to the environment.

The Advanced Materials Lab, from Northern Fluminense State University (UENF) has tried to make the oil sludge waste inert by adding it in clayey ceramic pastes and firing it. Some of the most environmentally aggressive components are expelled during fire process. It is expected that the vitreous phase formed during the firing process completely inactivates the residue, and permits the use of this mixture as raw material for

the local ceramic industry, which will be paid by local oil companies to handle oily wastes. One possible use for this bentonite-oily wastes-clay mixture is as structural clay products. For this purpose, material is submitted to compressive pressures to take shape and density and fired afterwards. This work simulates manufacturing conditions by producing pellets under identical conditions. Important physical properties as ultimate compressive strength and linear shrinkage are determined to verify if the presented mixture is useful and the variations brought by means of different percentages of oily slurry addition.
Testing for mechanical properties present a challenge due to the pellet geometry. The height to diameter ratio is very close to one, eliminating the possibility of compressive testing use. The use of the Brazilian Disk [2,3] test solved the problem of consistent geometrical dimensions [4], but brought another one, namely localized fracture. The solution was to add an elastomeric foundation to the contact region and verify if the new stress field and uncertainty analysis correctly reproduces the test.

EXPERIMENTAL PROCEDURE

The clay sample employed in this work belongs to a quarry from Campos dos Goytacazes-RJ (Brazil). Previews characterization showed that the ceramic mass is kaolinitic, with illite, quartz and gibbsite as main impurities [5]. Chemical analysis revealed that the clay consists basically of SiO_2, Al_2O_3, and Fe_2O_3, the latter conferring a reddish color after firing, and TiO_2, MnO, MgO, CaO, K_2O and Na_2O in smaller amounts. The oil sludge waste chemical composition before bentonite encapsulation in average consists of 21% water, 62% solid material, 16% oil and 1% sulphur [6]. Waste granulometric analysis reveals that this material is essentially sandy silt.
Raw materials were crushed and sieved until the 60 mesh screen fraction passed. Ceramic masses containing clay and 0, 5, 10, 15 and 20wt% waste were prepared (5 each). The masses were mixed and homogenized, and 7wt% water was added in order to provide plasticity. Afterwards, the pastes were formed in a 10mm diameter steel die. The resulting 10 x 10mm cylindrical pellets were dried (110ºC for 24h) and fired at 950ºC for one hour. Heating and cooling rates have been controlled. Linear shrinkage (ABNT MB-305 [7]) and diametrical compressing strength [2] of the ceramic bodies were determined. Microstructure of the fracture surface was investigated using a DSM 962 Zeiss scanning electron microscope coupled with an Energy Dispersive Spectroscopy device.
A model 5582 INSTRON universal testing machine was used and both contact plates were covered with latex sheet. Crossbar speed was kept 0.5 mm/min for all tests. Specimens were placed between contact plates and a PC displayed a real time load x displacement graphic. At fracture load dropped very visibly, making quite easy to determine the ultimate compressive load. All pellets dimensions, after been fired, were recorded and used to determine individual ultimate compressive strength.

BRAZILIAN DISK TEST (DIAMETRICAL COMPRESSION)

Diametrical Compression Testing

Fired pellets presents an average 10 mm diameter and height. To correctly evaluate compressive strength limit, a compressive test is necessary but the pellets geometry do not allow the traditional compressive testing use, for it requires a height of 2 to 3 times the diameter size [8]. The solution is to use the Brazilian Disk Test, exploring diametrical compression as means to cause specimen fracture failure. In this test load is applied in two diametrically opposing points [9].

Stress Field

It is assumed that fracture initiates at the central point. Stresses acting over the horizontal diameter have the following form [10]:

$$\sigma_x = \sigma_1 = \frac{2P}{\pi Dt}\left(\frac{D^2 - 4x^2}{D^2 + 4x^2}\right)^2 \qquad (1)$$

$$\sigma_y = \sigma_2 = -\frac{2P}{\pi Dt}\left(\frac{4D^4}{\left(D^2 + 4x^2\right)^2} - 1\right) \quad (2)$$

$$\tau_{xy} = 0 \quad (3)$$

Where P is the applied load, D is the disk diameter, t is thickness and x is the horizontal position along disk diameter. For crack opening, only σ_x matters, because σ_y is a compressive type of stress. σ_1 component acting over the x direction and under the load line (x = 0) expression (1) is reduced to:

$$\sigma_x = \sigma_1 = \frac{2P}{\pi Dt} \quad (4)$$

Above expression ignores the existence of contact stresses acting near the points where loads are applied. Expression (4) is used in this work to determine Ultimate Compressive Strength (S_{uc}).

LOCALIZED FRACTURE

In the preliminary tests was observed that due to existence of contact stresses plus the fact that the contact area in this case is very small considered the body shape, localized stresses will fracture contact regions, thus altering stress distribution, crack initiation region and rendering useless expression (4) [11,12].

Controlling Localized Fracture

To avoid fracture initiation at the contact areas it was used an elastomeric rubber layer, applied to the contact region, to reduce magnitude of localized acting stresses. In this study latex was used and eliminated the problem. The used layer thickness measured 0.2 mm.

New Stress Distribution At Contact Area

The presence of that rubber layer is modeled as an elastic foundation and its presence alters stress distribution at contact region by increasing contact surface thus loading distribution area. Johnson shows that the new contact pressure distribution is paraboloidal rather than ellipsoidal as given by Hertz theory. Although localized stress field changes, at the center of the disk, where fracture is supposed to have started, no influence is felt, once contact stresses, regardless its shape, are expected to act at no more than up to 0.15D from the contact surfaces [13].

UNCERTAINTY MEASUREMENT

Uncertainty measurements, related to existing errors associated with the measurement system and material properties dispersion, for the proposed tests, are determined as described by ISO standards [14]. For the measurement system, these errors are originated from the load cell (ultimate compressive load) and the caliper (pellets dimensions). Both uncertainty sources combined and expanded to yield a 95% confidence level are called U_{95} and are represented by error bars on the following figures.

RESULTS AND DISCUSSION

Waste addition to the clayey ceramic mass clearly influences the ceramic pellets properties. Figure 1 shows the ceramic pellets Ultimate Compressive Strength (S_{uc}) variation as a result of the oil sludge waste addition. As can be noticed from this figure, the addition of oil sludge waste reduced the strength of the ceramic pellets. As shown in Figure 2, the pellets linear shrinkage is decreased with waste addition. Error bars size is

determined by U_{95}, as described before. According to the waste composition, the non-plastic materials present such as quartz may be contributing to these phenomena. Figure 3 (a) shows the fractured surface of a waste-free fired pellet. Comparing with the microstructure of waste containing pellets, Figure 3 (b) and (c), the present phases are relatively well distributed and inserted in a continuous matrix. A quartz particle found in a waste-containing pellet is outlined in Figure 3 (d), confirming the presence of non-plastic components. Moreover, quartz particles are likely to induce flaws to the sintered microstructure, acting like stress concentrators.

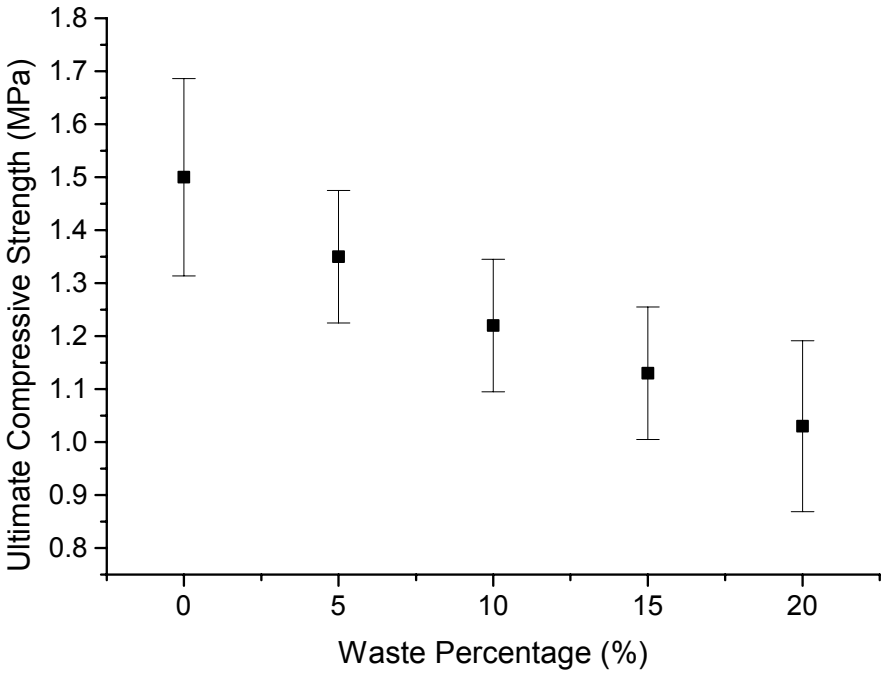

Figure 1: Compressive strength as a function of waste addition for the ceramic pellets.

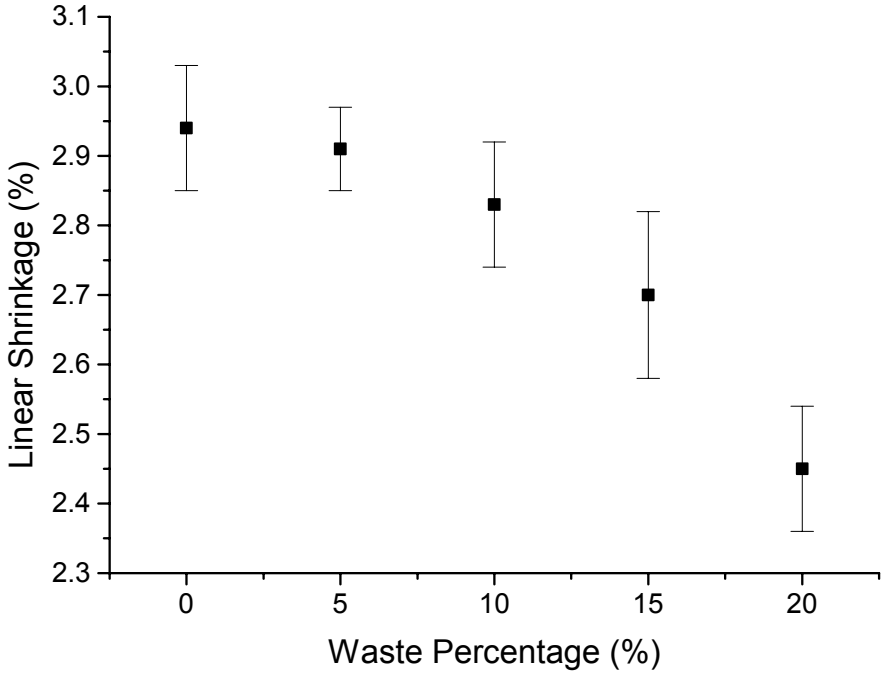

Figure 2: Linear Shrinkage as a function of waste addition for the ceramic pellets.

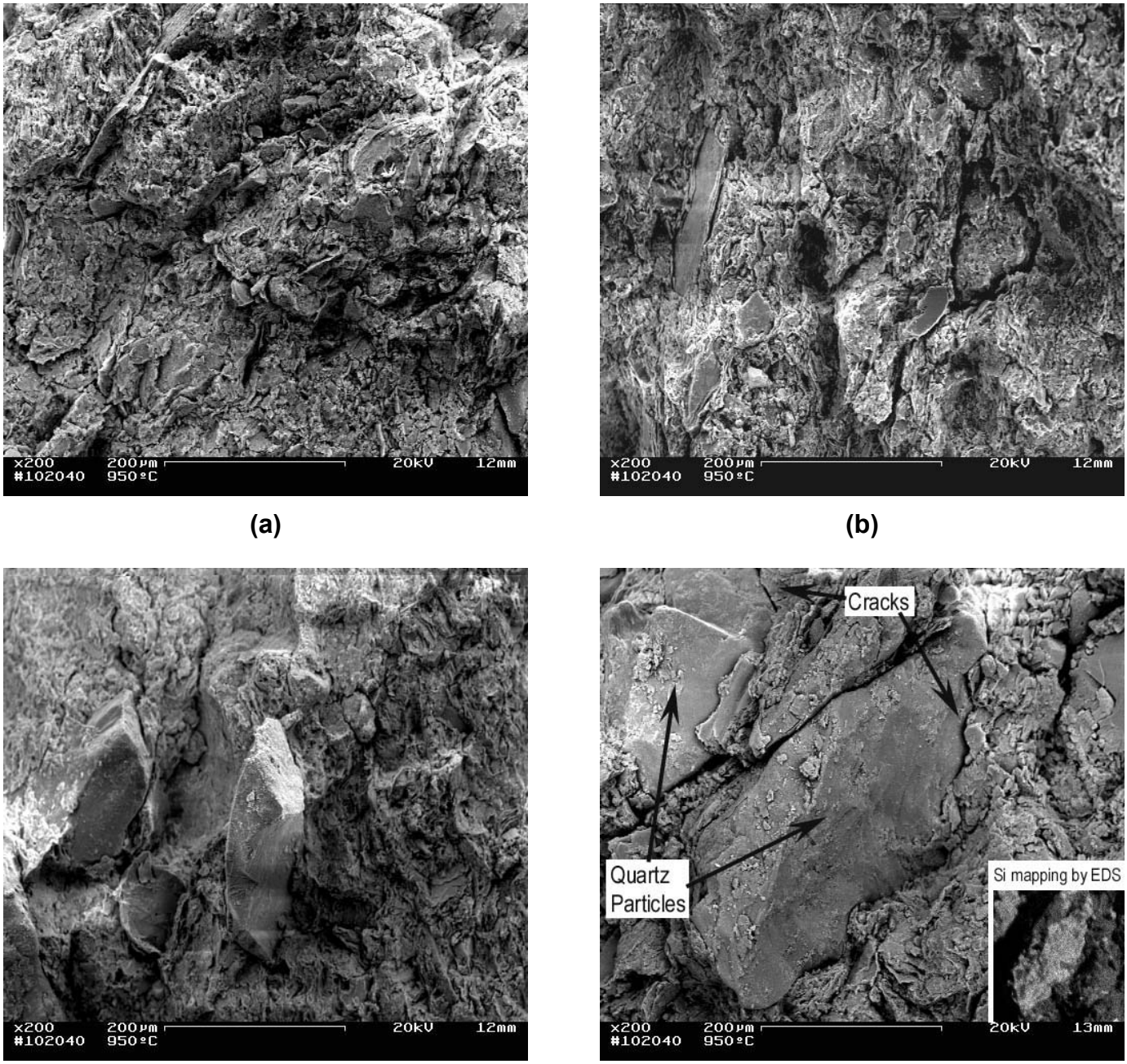

Figure 3: MEV micrographies showing (a) a waste-free pellet, (b) a 15% waste pellet, (c) a 20% pellet and (d) a detailed quartz particle bearing cracks. (a) through (d) magnification is 200x.

CONCLUSIONS

The chosen thickness for the elastomeric layer did not change significantly the stress field far from the contact region and solved the problem of fracture initiation in the contact area.

As the amount of waste increased, S_{uc} decreased. SEM pictures reveal an increasing amount of quartz crystals as waste amounts also increase and cracks initiating from their edges area are also observed.

Linear shrinkage reduces as waste amount increases, a desired effect for the tile industry. Although a limit for waste addition must be set, as to avoid a sharp decrease in S_{uc}.

The determined expanded uncertainty (U_{95}) shows that result dispersion for S_{uc} tends to be smaller for contaminated clay.

ACKNOWLEDGEMENTS

Authors gratefully thank FINEP (ref.: 77.98.0172.00) and FAPERJ (ref.: E-26/171.474/99 and E-26/171.475/99 – APQ1) for the financial support.

REFERENCES

1. Vieira, C.M.F. (1997). MSc Thesis, Northern Fluminense State University, Advanced Materials Lab, Campos dos Goytacazes-RJ, Brazil. (in Portuguese).
2. Fett, T. (1998). *International Journal of Fracture.* 89, 1: L9-L13.
3. Liu, C., Huang, Y., Lovato, M.L. and Stout, M.G. (1997). *International Journal of Fracture.* 87, 3: 241-263.
4. Krishnan, G.R., Zhao, X.L., Zaman, M. and Roegiers, J.C. (1998). *International Journal of Rock Mechanics and Mining Sciences.* 35, 6: 695-710.
5. Santos, R.S. (2001). MSc Thesis, Northern Fluminense State University, Advanced Materials Lab, Campos dos Goytacazes-RJ, Brazil, 97p. (in Portuguese).
6. Petrobras (1999). Oily Sludge Waste Treatment, Internal Report, Macaé-RJ, Brazil. (in Portuguese).
7. ABNT, NBR MB-305 (1984). Linear Shrinkage Determination. (in Portuguese).
8. ASTM (2000). In: *Annual Book of ASTM Standards, Section Three*, pp. 99-106, American Society for Testing and Materials, Conshohocken.
9. Liu, C., Huang, Y., Stout, M.G. (1998). *Acta Materialia,* 46, 16: 5647-5661.
10. Dally, J.W. and Riley, W.F. (1991). In: *Experimental Stress Analysis*, pp. 461-462, McGraw-Hill, Inc., New York.
11. Peterson, I.M., Pajares, A. Lawn, B.R., Thompson, V.P. and Rekow, E.D. (1998). *Journal of Dental Research,* 77, 4: 589-602.
12. Peterson, I.M., Wuttiphan, S., Lawn, B.R. and Chyung, K. (1998). *Dental Materials,* 14, 1: 80-89.
13. Johnson, K.L. (1996). In: *Contact Mechanics*, pp. 104-106, Cambridge University Press, Cambridge.
14. ISO (1995). In: *Guide to the Expression of Uncertainty in Measurement*, International Organization for Standardization (ISO), Genève.

BIFURCATION ASSESSMENT OF MIXED CRACK IN ELASTIC-PLASTIC MATERIALS

Xiao-Bing ZHANG, Naman RECHO, Jia LI

Laboratoire d'Etudes et de Recherches en Mécanique des Structures
Blaise Pascal University of Clermont-Ferrand
Avenue Aristide Briand, 03100 Montluçon, France

ABSTRACT

It is well kwon that the near-tip asymptotic stress field of an elastic-plastic crack in plane strain can be defined by two parameters, the *J*-integral and the plastic mixity parameter M^p (Shih, [5]). These two parameters for general yielding cracks can rapidly be calculated using a recently developed method based on the calculation of two associated *J*-integrals, J^{*I} and J^{*II} (Li, [3]). Many experimental studies showed that the crack growth under mixed mode loading can take place either in cleavage manner or in slip manner (Tohgo and Ishii [1], Aoki et al. [2]). Therefore, it is necessary to study the competition between these two kinds of crack growth in the frame of the J-M^p system.

In this paper, we carry out detailed numerical calculations of crack-tip fields in elastic-plastic materials in order to assess the bifurcation angle based on the calculations of the parameters J and M^p. Some specimens used by Aoki et al. [2] have been analysed by finite element modelling. The loading varies in order to produce fracture range from Mode I to Mode II. By using the numerical method developed recently (Li et al [3][4]), the *J*-integral and the plastic mixity parameter M^p were calculated and the theoretical HRR near-tip fields were obtained. The bifurcation angles were estimated then according to the maximum $\sigma_{\theta\theta}$ (circonferential opening stress) and the maximum $\tau_{r\theta}$ (shear stress) rules. The initial crack in the specimen was supposed to extend a small length in the two possible bifurcation angles. The competition between the cleavage growth and the slip one of cracks is discussed comparing with experimental tests carried out by Aoki et al. [2].

REFERENCES

[1] Tohgo, K. and Ishii, H., Elastic-plastic fracture toughness test under mixed mode I-II loading, *Eng. Fracture Mech*., 1992 Vol 4, 529-540
[2] Aoki, S., Kishimoto, K., Yoshida, M., and Richard, H. A., Elastic-plastic fracture behavior of an aluminum alloy under mixed-mode loading, *J. Mech. Phys. Solids,* 1990, Vol. 38, 195-213
[3] Li, J., Estimation of the mixity parameter of a plane strain elastic-plastic crack by using the associated J-integral, *Eng. Fracture Mech*., 1998 Vol 61, 355-368
[4] Li, J., Zhang, X. B., and Recho, N., Numerical method for determination of the mixed mode crack behavior in elastic-plastic materials, 12*th European Conference on Fracture,* Sheffield, UK, September 1998
[5] Shih, C. F., Small-scale yielding analysis of mixed mode plane strain crack problem. *ASTM STP* 1974, Vol. 560, 187-210

BIFURCATION ASSESSMENT OF MIXED CRACK IN ELASTIC-PLASTIC MATERIALS

Xiao-Bing ZHANG, Naman RECHO, Jia LI

Laboratoire d'Etudes et de Recherches en Mécanique des Structures
Blaise Pascal University of Clermont-Ferrand
Avenue Aristide Briand, 03100 Montluçon, France

ABSTRACT

Many experimental studies showed that the crack growth could take place either in cleavage manner (Tensile-type fracture) or in slip manner (Shear type fracture), see Tohgo and Ishii [1], Aoki *et al*. [2]. The purpose of this work is to study the competition between these two kinds of crack growth. We carry out the detailed numerical calculations of crack-tip fields in order to assess the bifurcation and propagation of the cracks in elastic-plastic materials. Some specimens used by Aoki et al. [2] have been analysed by finite element modelling. The loading varies in order to produce complete fracture range from Mode I to Mode II. By using the numerical method developed recently, the *J*-integral and the plastic mixity parameter M^p were calculated and the theoretical HRR near-tip fields were obtained. The bifurcation angles were estimated then according to the maximum $\sigma_{\theta\theta}$ (circonferential opening stress) and the maximum $\tau_{r\theta}$ (shear stress) rules. The initial crack in the specimen was supposed to extend a small length in the two possible bifurcation angles. The competition between the cleavage growth and the slip one of cracks is discussed comparing with experimental tests carried out by Aoki *et al.* [2].

KEYWORDS

crack bifurcation, crack propagation, mixed mode, stress analyses, *J*-Integral, energy release rate, elastic-plastic behaviour

1. INTRODUCTION

An elastic-plastic material can present two failure mechanisms. The first one, cleavage failure, is due to maximum circonferential opening stress $\sigma_{\theta\theta}$ or to the maximum energy release rate G (which can be presented as the *J*-integral). The failure occurs when the maximum $\sigma_{\theta\theta}$ (at certain distance r_c from the crack tip), *G* or *J* reach their critical values, respectively, σ_c, G_c or J_c. The second failure mechanism, slip failure, is due to very high local strains involving slip bands in the direction of the maximum shear stress $\tau_{r\theta}$. The failure mechanism occurs when $\tau_{r\theta}$ at certain distance r_c reaches τ_c. In order to analyse these two failure mechanisms, one has to know the near-tip stress field. The ratio $\frac{\sigma_{\theta\theta}}{\tau_{r\theta}}$ near the crack tip compared to $\frac{\sigma_c}{\tau_c}$ will determine the type of failure. Shih [5] showed that the near-tip asymptotic stress field of an elastic-plastic crack in plane strain can be defined by two parameters, the *J*-integral and the plastic mixity parameter M^p. A numerical method has been recently developed in order to determine these two parameters (Li *et al* [3][4]). This method is founded on the basis of the calculation of two associated *J*-integrals, J^{*I} and J^{*II} by introducing two auxiliary fields, a symmetric one and an anti-symmetric one with respect to the crack axis. Some studies have shown the validity of this method [4][6].

In the present work, we determine, using our numerical method, the near-tip stress fields in the specimens tested under mixed loading by Aoki et al. [2]. The experimental results are interpreted by the use of calculation results. The competition between the tensile-type fracture and the shear type fracture is discussed.

2. METHOD OF EVALUATION OF THE PARAMETERS *J* AND M^p

Shih [5] showed that, for a mixed mode crack lying in a power-law hardening material, the stresses, strains and displacements fields near the crack tip are dominated by the HRR singularity, and can be characterized by two parameters, the *J*-integral and a mixty parameter M^p. The later is defined as follows:

$$M^p = \lim_{r\to 0} \frac{2}{\pi} \tan^{-1} \left| \frac{\sigma_{\theta\theta}(\theta = 0)}{\sigma_{r\theta}(\theta = 0)} \right| \qquad (1)$$

The method to evaluate the parameter M^p has been reported in [3] [4] that we resume briefly. First, one defines an associated *J*-integral, the *J**-integral as follows:

$$J^* = \int_{\Gamma} \left(w^* n_1 - \sigma_{ij} n_j \frac{\partial u^*_i}{\partial x} \right) ds \qquad (2)$$

where Γ is an arbitrary path around the crack tip; σ_{ij} are the stress components of the actual field; u^*_i are the displacement components of an auxiliary field; w^* is the associated energy density defined as:

$$dw^* = \sigma_{ij} d\varepsilon^*_{ij} \qquad (3)$$

The auxiliary field can be constructed in terms of the actual field. Following the approach of Ishikawa *et al*. [8], one can decompose the actual field into symmetrical and anti-symmetrical parts with respect to the crack axis:

$$u^{*M}_i (x,y) = \frac{1}{2}\left[u_i(x,y) + (-1)^{i+M} u_i(x,-y) \right] \quad i = 1,2;\ M = I, II \qquad (4)$$

With these two auxiliary fields, we obtain two associated integrals J^{*I} and J^{*II}. It is clear that J^{*I} and J^{*II} are path independent. An equivalent elastic mixity parameter M^{*e} can be defined from J^{*I} and J^{*II}, namely:

$$M^{*e} = \frac{2}{\pi} \tan^{-1} \sqrt{\frac{J^{*I}}{J^{*II}}} \qquad (5)$$

By carrying out an asymptotic analysis near the crack tip, one can find the relationship between the M^{*e} and M^p. This relationship was given in [3]. Moreover, one can calculate the *J*-integral from J^{*I} and J^{*II}:

$$J = J^{*I} + J^{*II} \qquad (6)$$

This method is valid for any yielding cases.

3. EXPERIMENTAL RESULTS

An experimental investigation has been carried out by Aoki *et al* (1990 [2]). They used A5083-O aluminium alloy that the mechanical properties are given in Tab.1. A compact-tension-shear specimen attached to a special device, developed by Richard and Benitz [7], was employed (Fig.1). A mixed or pure mode fracture is obtained by applying the load in different hole numbers. A Mode I loading was performed using the No. 1 and No.1' holes in the loading device shown in Fig. 1.(b), and a Mode II loading was carried

out using the No. 7 and No. 7' holes. A fatigue crack was introduced up to $a_0 / w \approx 0.5$ (a_0 is pre-cracked length, w is specimen width) (Fig.1.(a)).

Young's modulus E (GPa)	68.65
0.2% Yield strength σ_0 (MPa)	142.1
Tensile strength σ_B (MPa)	308.6
Ultimate strength σ_f (MPa)	284.2
Reduction of area Ψ (%)	35.01

Tab.1 Mechanical properties of aluminium alloy A5083-O

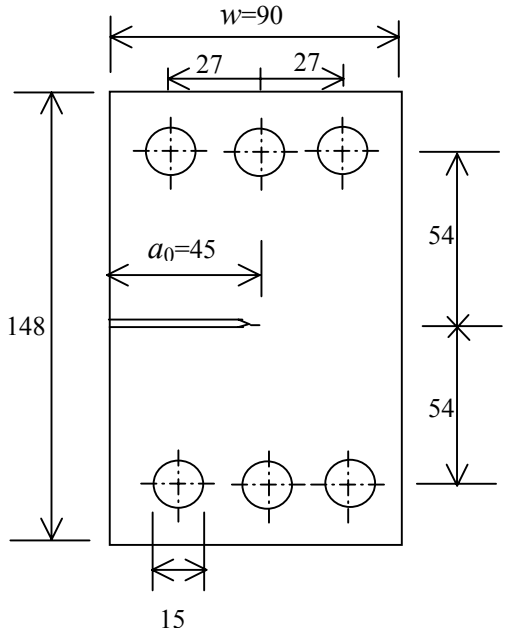

Fig.1.(a) Configuration of the specimen

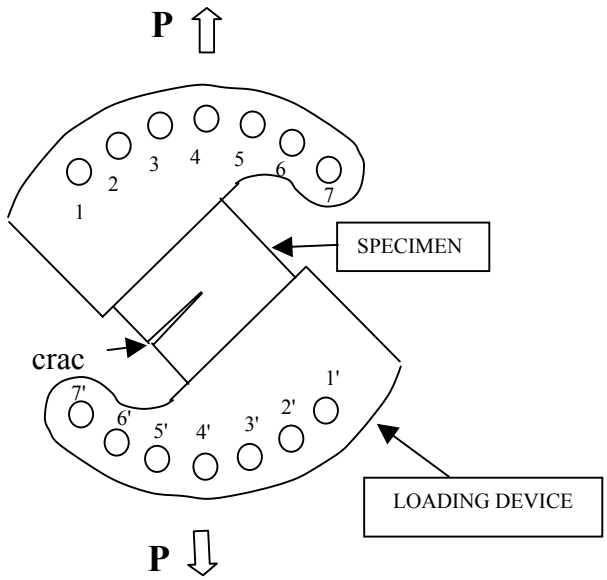

Fig.1.(b) Device for mixed mode loading

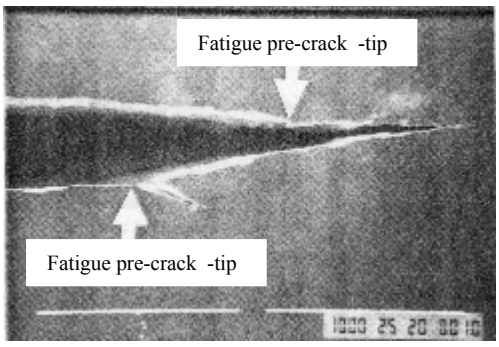

Fig. 2 Crack initiates in two directions (loading hole No. 6)

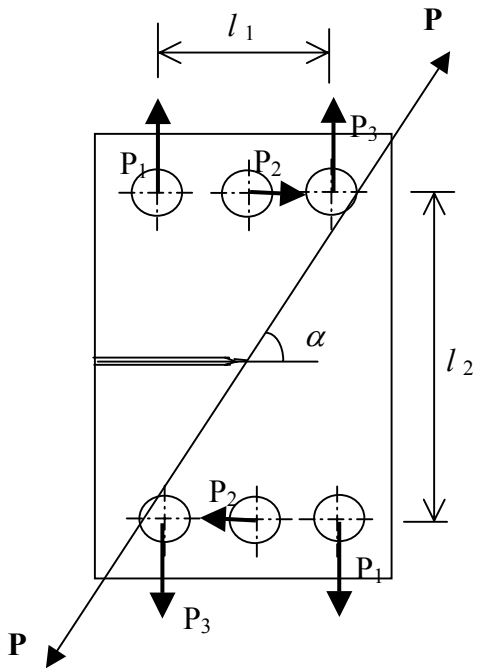

Fig. 3 Loads applied to a specimen

It was found that for the Mode I specimen (loading hole No. 1), the crack initiated from the centre of the blunted tip of the fatigue pre-crack and extended to the direction perpendicular to the loading axis. And for the Mode II specimen (loading hole No. 7), a crack due to shear type fracture is observed to extend in a

direction almost parallel to the fatigue pre-crack surface. Under mixed mode loading (loading hole No. 3-6), cracks due to shear type fracture (in slip manner) initiate at the sharpened corner of the pre-crack tip near the surfaces of a specimen, and then another crack due to tensile-type fracture (in cleavage manner) occurs at the midthickness. It develops more rapidly than the shear cracks and causes final fracture of the specimen. The cracks due to tensile-type fracture extend in the direction perpendicular to the loading axis (Fig.2).

4. NUMERICAL ANALYSES

Elastic-plastic finite element analyses are carried out by using a general-purpose finite element program, named CASTEM 2000 developed by CEA (Commessariat à l'énergie atomique – France). The analysis is based on small strain assumption and employs the flow theory of plasticity. Eight-nod and six-nod elements were used in the calculations. The finite element mesh is shown in Fig. 4. The loading conditions were approximated in such a way that the loads P_1, P_2 and P_3 were applied to the holes in the specimen as shown in Fig. 3. The magnitude of load was determined from following equilibrium equations:

$$P\cos\alpha = P_2, \qquad P\sin\alpha = P_1 + P_3, \qquad P_1 l_1 + P_2 l_2 = P_3 l_3 \qquad (7)$$

Where P is the load applied to the loading device shown in Fig.1 (b), and the lengths l_1, l_2 and the loading angle α are defined as shown in Fig. 3

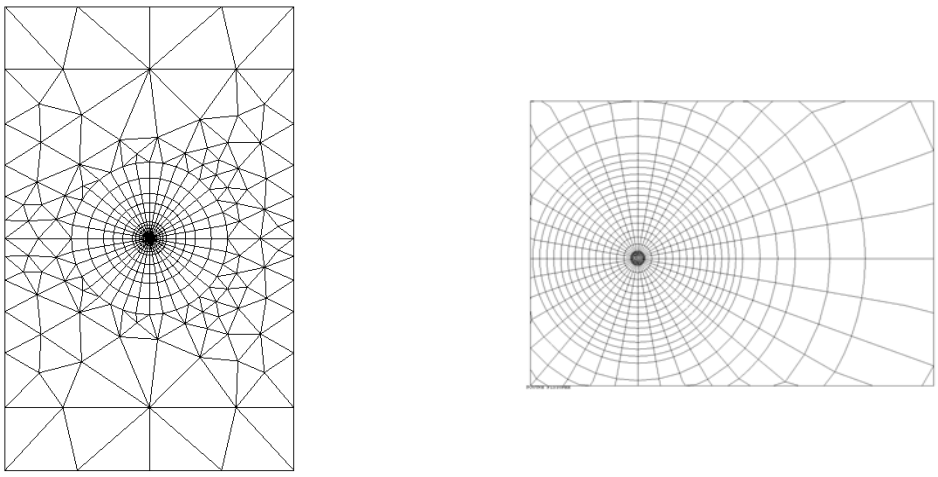

Fig. 4 Finite element mesh

5. NUMERICAL RESULTS AND DISCUSSIONS

After calculation of the two associated J-integrals J^{*I}, J^{*II} and the plastic mixity parameter M^p, the theoretical HRR near-tip stress fields are obtained for each specimen. The distributions of the stress components $\sigma_{\theta\theta}$, $\tau_{r\theta}$ near the crack tip and the J-integral value allow us to analyse the bifurcation angle and the propagation of the cracks.

According to bifurcation criteria, the tensile-type crack will propagate in the direction of maximum $\sigma_{\theta\theta}$, noted θ_σ (angle of bifurcation due to tensile-type fracture) and the shear type crack will propagate in the direction of maximum $\tau_{r\theta}$, noted θ_τ (angle of bifurcation due to shear type fracture). The Tab. 2 shows the

numerical results of the specimens under different loading: loading angle $\alpha = 0°$, 15°, 45° and 90°. $\sigma_{\theta\theta}$ and $\tau_{r\theta}$ are the maximum stress components at a distance $r = 2J/\sigma_0$ from the crack tip, J being the J-integral and σ_0 the yield stress.

Hole No.	7	6	4	1
Load P (N)	4850	4900	3500	2900
α (°)	0°	15°	45°	90°
$\sigma_{\theta\theta}$ (MPa) $\tau_{r\theta}$ (MPa)	395 292	467 266	426 177	497 153
$\sigma_{\theta\theta}/\tau_{r\theta}$	1.35	1.76	2.41	3.24
J^{*I} (N/mm) J^{*II} (N/mm) J (N/mm)	0 46 46	14.2 44.6 58.7	14.5 3.1 17.6	14.6 0 14.6
M^p	0	0.38	0.76	1
θ_τ (°) θ_σ (°)	0 -71	11 -61	40 -35	81 0
Experimental observation	Shear type fracture	Shear type fracture at the beginning and tensile-type fracture after		Tensile-type fracture

Tab. 2 Crack bifurcation angle versus loading angle

From experimental results, the critical values of J_{IC} and J_{IIC} are known. J_{Ic} is equal to 14.6 N/mm (loading angle $\alpha = 90°$). In order to obtain the value of J_{Ic}, the calculation shows that the load P has to be equal to 2900N. Under this load, the stress field is determined and the ratio $\sigma_{\theta\theta}/\tau_{r\theta}$ is than obtained ($\sigma_{\theta\theta}/\tau_{r\theta} = 3.24$). The critical value $\sigma_c = \sigma_{\theta\theta max}$ in this case. Similarly, from $J_{IIc} = 46$ N/mm, the ratio $\sigma_{\theta\theta}/\tau_{r\theta} = 1.35$ is obtained. The critical value $\tau_c = \tau_{r\theta max}$ in this case. The ratio σ_c/τ_c is then equal to 2.16 for this material. The criterion will be:

$\frac{\sigma_{\theta\theta}}{\tau_{r\theta}} > \frac{\sigma_c}{\tau_c}$ => tensile-type fracture , and $\frac{\sigma_{\theta\theta}}{\tau_{r\theta}} < \frac{\sigma_c}{\tau_c}$ => shear-type fracture

The table 2 shows that the ratio $\sigma_{\theta\theta}/\tau_{r\theta}$ is less important for $\alpha = 0°$ than for 15°, 45° and 90°. This can explain the shear type fracture observed in this case in which the crack bifurcation angle is equal to zero. In the case of $\alpha = 90°$, the ratio $\sigma_{\theta\theta}/\tau_{r\theta}$ becomes very high, so the crack will propagate in the direction of $\theta_\sigma = 0$ in a cleavage manner.

Now, in order to understand the growth behaviour of the crack when the two types of fracture are in competition, we assume that the crack extends simultaneously in two directions (θ_τ and θ_σ)(Fig. 5). This assumption is based on the observation of the experimental results (Fig.2). Let suppose that a_σ and a_τ lengths of small cracks due to tensile-type fracture and to shear type fracture respectively. These cracks are supposed to follow the bifurcation angles determined in Tab. 2.

The J-integrals, the mixity parameter M^p and the maximum stresses $\sigma_{\theta\theta}$ and $\tau_{r\theta}$ for each type of crack are shown in Tab.3 for different extended lengths of crack under the loading corresponding to $\alpha = 45°$ and $\alpha = 0°$. $\sigma_{\theta\theta_\tau}$, $\tau_{r\theta_\tau}$, are the maximum values of $\sigma_{\theta\theta}$ and $\tau_{r\theta}$ near the a_τ crack tip, $\sigma_{\theta\theta_\sigma}$, $\tau_{r\theta_\sigma}$, are maximum values of $\sigma_{\theta\theta}$ and $\tau_{r\theta}$ near the a_σ crack tip. J_τ, J_σ are the J-integral values for the a_τ crack and a_σ crack respectively.

Let suppose that the shear crack a_τ extends (experimental observation) and the extended length is 1mm. At the same time, the tensile crack a_σ initiates and then extends. Giving a_σ crack a extended length of 0.3, 0.4 and 1mm, we analyse the competition of a_τ crack growth and a_σ crack growth.

From Tab.3, one can observe that, in the mixed mode case (α = 45°, loading hole No.4), the value of $\tau_{r\theta_\tau}$ is important when a_σ is small (a_σ=0.3mm) and it decreases as a_σ grows. This can explain the fact that the shear type crack extends at first and stop after (experimental observation). In the other hand, $\sigma_{\theta\theta_\sigma}$ increases when a_σ grows. So the tensile-type crack grows until the final fracture of the specimen. In the Mode II case (α = 0°, loading hole No.7), $\tau_{r\theta_\tau}$ is more important for all length of a_σ. It is way the crack extends always in shear manner until the final fracture of the specimen.

		α =45°			α = 0°	
crack length (mm)	a_τ	1	1	1	1	1
	a_σ	0,3	0,4	1	0,3	0,4
stresses near a_τ (MPa)	$\sigma_{\theta\theta_\tau}$	430	420	310	340	300
	$\tau_{r\theta_\tau}$	170	160	140	270	260
stresses near a_σ (MPa)	$\sigma_{\theta\theta_\sigma}$	550	580	700	370	420
	$\tau_{r\theta_\sigma}$	165	170	180	160	180
J at a_τ (N/mm)	J_τ	14.1	12.4	5	18.5	17
J at a_σ (N/mm)	J_σ	21.3	25	40.7	7.5	10.9

Tab. 3 Maximum stresses near the tips of two cracks in competition and J values

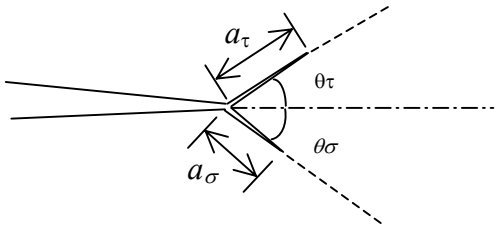

Fig. 5 Two cracks in competition

5. CONCLUSIONS

The numerical method developed recently allows us to obtain the theoretical HRR stress fields near the tip of a crack in elastic-plastic material under mixed mode loading. The numerical results obtained by using this method can explain the experimental results. The crack growth depends on the competition between the ratio $\sigma_{\theta\theta}/\tau_{r\theta}$ compared to the ratio σ_c/τ_c . this ratio could lead to a critical mixity parameter M^p.

Based on experimental observations, this competition was evaluated by numerical studies. More experimental and numerical studies will be necessary to establish suitable bifurcation criteria for a mixed mode crack in elastic-plastic materials.

REFERENCES

[1] Tohgo, K. and Ishii, H., Elastic-plastic fracture toughness test under mixed mode I-II loading, *Eng. Fracture Mech*., 1992 Vol 4, 529-540

[2] Aoki, S., Kishimoto, K., Yoshida, M., and Richard, H. A., Elastic-plastic fracture behavior of an aluminum alloy under mixed-mode loading, *J. Mech. Phys. Solids,* 1990, Vol. 38, 195-213

[3] Li, J., Estimation of the mixity parameter of a plane strain elastic-plastic crack by using the associated J-integral, *Eng. Fracture Mech*., 1998 Vol 61, 355-368

[4] Li, J., Zhang, X. B., and Recho, N., Numerical method for determination of the mixed mode crack behavior in elastic-plastic materials, 12*th European Conference on Fracture,* Sheffield, UK, September 1998

[5] Shih, C. F., Small-scale yielding analysis of mixed mode plane strain crack problem. *ASTM STP* 1974, Vol. 560, 187-210

[6] Zhang, X. B., Li, J., and Recho, N., Numerical analysis of a mixed mode crack in elastic-plastic material, 13*th European Conference on Fracture, ,* San Sebastian, Espagnal, September 2000, Ref:1U.27

[7] Richard H. A. and Benitz K., *Int. J. Fractue*., 1982 Vol 22, R55

[8] Ishikawa, H., Kitakawa, H. and Okamura, H., J-integral of a mixed mode crack and its applications. *Proc. 3rd Int. Conf. On Material*, Vol.3. Cambridge, 1978, 447

ORAL REFERENCE: ICF100269OR

BRITTLE FRACTURE OF HARD SOIL - SOFT ROCK MATERIALS

K. W. Lo, T. Tamilselvan and L. Yu

Department of Civil Engineering, National University of Singapore,
Singapore 119260

ABSTRACT

Hard soil - soft rock materials tend to fail along well-defined discontinuities. However, in the common practice of geotechnical engineering, such failure is implicitly modelled as uniform behaviour by smearing, and either based on elastoplasticity or empirically determined from laboratory test results. A model is presented herein which addresses the problem as one of brittle fracture of a three-phase material, where the matric suction exerted by the pore air/water phases on the solid phase is disrupted by tensile or shear loading, or a combination of both. There is therefore the added complication that the fracture toughness of the material medium would vary according to changes in the matric suction which is brought about by the application of test loading. Furthermore, it would be necessary to predict the development of non self-similar crack extension from a sharp corner in accordance with the observed behaviour of test specimens.

Accordingly, the problem of plane strain compression testing has been analysed using a hybrid BEM based on a combination of the displacement discontinuity and fictitious stress methods. The model has, moreover, been established for confirmation against the results of laboratory testing on unsaturated kaolin clay.

KEYWORDS

Brittle fracture, hard soil - soft rock, hybrid BEM, matric suction in plane strain, corner crack, unsaturated kaolin clay.

INTRODUCTION

Brittle hard soil - soft rock is often found in geotechnical engineering works such as tunnels, slopes, etc. These soils contain fissures or cracks which are the result of mechanical, thermal and volume-change-induced stresses. As a result of gravity, earthquake or water-pressure-induced loads, these flaws can develop stress concentrations which result in the non-uniform mobilisation of strength and ultimately lead to the catastrophic failure of the soil body as they propagate. Conventional failure criteria [1] of soils may be appropriate to plastic-yield-dominant behaviour, but not, in principle, to this category of brittle fracture. In view of the existence of fissures and cracks, such soils are non-uniform and therefore not amenable to analysis by continuum mechanics alone. On the other hand, fracture mechanical theory may be used to advantage to replicate their behaviour.

The first quantitative data on the role of fissures on the strength of clay appears to have been presented by Terzaghi [2] from a study of the instability of gentle slopes in fissured clay. Such failure occurred despite

the very high compressive strength of intact clay fragments. Terzaghi established that the overall strength of the fissured clay represented a fraction of the strength of the same clay without fissures. On the other hand, Bishop [3] and Skempton et al. [4] were apparently the earliest to suggest that fracture-mechanical concepts might shed light on the progressive failure of slopes made of stiff, fissured clays, although Bjerrum [5] also discussed progressive failure in terms of stress concentration at the tip of a slip surface. Saada [6] and Vallejo [7] subsequently applied the concepts of LEFM to investigate the mechanism of crack propagation in stiff clay.

A basic concept of fracture theory is that crack-like imperfections are inherent in engineering materials. These flaws act as stress raisers that can trigger fracture when subjected to critical loading. Unsaturated hard soil-soft rock materials, on the other hand, are three-phase media comprising air, water and solid. As such, the degree of saturation S of the material, and hence its matric suction $(u_a - u_w)$, could vary as it was loaded. Thus, it would be necessary to keep track of changes in the parameters at all stages of loading, since for brittle fracture to take place, the fracture toughness which is available would depend on their ambient values. In other words, unlike the generally-accepted material behaviour of fracture mechanics, during crack development, the applied loading would not only raise the level of total stresses required to cause further crack extension, but also influence the properties of the soil-rock medium which would determine whether the crack would extend.

In the following discussion, a model will be proposed for the brittle fracture of hard soil-soft rock, which is based on the above considerations. The model will be verified by conducting plane strain biaxial compression tests on a pre-cracked specimen, and thereafter comparing the test results with those obtained by using a hybrid BEM based on a combination of the displacement discontinuity and fictitious stress methods. Furthermore, it will be shown how the development of a secondary crack may be predicted in accordance with observed behaviour.

PROPOSED MODEL

Determination of Matric Suction

The matric suction $(u_a - u_w)$ is defined [8] as the difference between the pore air pressure u_a and pore water pressure u_w, which varies with load. It is required in order to determine the fracture toughness of the hard soil-soft rock test specimen. The pore pressures may, in turn, be deduced from their respective pore pressure parameters B_a and B_w, based on the following relationships:

$$du_a = B_a d\sigma_{ave} \tag{1}$$

and

$$du_w = B_w d\sigma_{ave} \ , \tag{2}$$

where

$$\sigma_{ave} = \frac{\sigma_1 + \sigma_3}{2} \tag{3}$$

and $_1$ and $_3$ are the major and minor principal stresses respectively. The pore pressure parameters are given by

$$B_a = \frac{R_2 R_3 - R_4}{1 - R_1 R_3} \tag{4}$$

and

$$B_w = \frac{R_2 - R_1 R_4}{1 - R_1 R_3} \ , \tag{5}$$

in which

$$R_1 = \frac{R_s - 1 - \left[(1 - S + hS)n / (\bar{u}_a m_{1p}^s)\right]}{R_s + (SnC_w / m_{1p}^s)}, \tag{6}$$

$$R_2 = \frac{1}{R_s + (SnC_w / m_{1p}^s)}, \tag{7}$$

$$R_3 = \frac{R_a}{R_a - 1 - \left[(1 - S + hS)n / (\bar{u}_a (m_{1p}^s - m_{1p}^w))\right]} \tag{8}$$

and

$$R_4 = \frac{1}{R_a - 1 - \left[(1 - S + hS)n / (\bar{u}_a (m_{1p}^s - m_{1p}^w))\right]}, \tag{9}$$

where

$$R_s = \frac{m_2^s}{m_{1p}^s}, \tag{10}$$

$$R_a = \frac{m_2^s - m_2^w}{m_{1p}^s - m_{1p}^w}, \tag{11}$$

h is the proportion of dissolved air in the water, $\bar{u}_a$ the absolute air pressure, n the porosity, C_w the water compressibility and $m_{1p}^s, m_2^s, m_{1p}^w$ *and* m_2^w the volumetric deformation coefficients which may be evaluated from the compressive indices C_t, C_m, D_t and D_m obtained from the constitutive surfaces of the hard soil-soft rock, as follows:

$$m_{1p}^s = \frac{0.435\, C_t}{(1 + e_0)(s_{ave} - u_a)_{mean}}, \tag{12}$$

$$m_2^s = \frac{0.435 C_m}{(1 + e_0)(u_a - u_w)_{mean}}, \tag{13}$$

$$m_{1p}^w = \frac{0.435 D_t G_S}{(1 + e_0)(s_{ave} - u_a)_{mean}} \tag{14}$$

and

$$m_2^w = \frac{0.435 D_m G_S}{(1 + e_0)(u_a - u_w)_{mean}}, \tag{15}$$

in which $(_{ave} - u_a)_{mean}$ and $(u_a - u_w)_{mean}$ are the averages of the initial and final net normal stresses and matric suctions over a load increment.

Determination of Fracture Toughness

At any given stage of crack development, it is necessary to obtain an update on the value of the fracture toughness K_c, which is generally dependent on the matric suction, or alternatively the degree of saturation of the soil medium, by way of the pore size distribution index . It is noteworthy that this dependency may be established fundamentally on the basis of Griffith's analogy of the critical rate of energy release G_c and the surface tension for glass, in which it may be shown that a relationship may be obtained between G_c, the matric suction $(u_a - u_w)$ and characteristic pore size D_p, given by

$$G_C = k \frac{(u_a - u_w) D_p}{4}, \tag{16}$$

where k is a parameter which reflects the mode of fracture. On this basis, the fracture toughness versus matric suction plot of Figure 1 has been determined by fracture testing of brittle kaolin clay specimens in

the mode I of deformation.

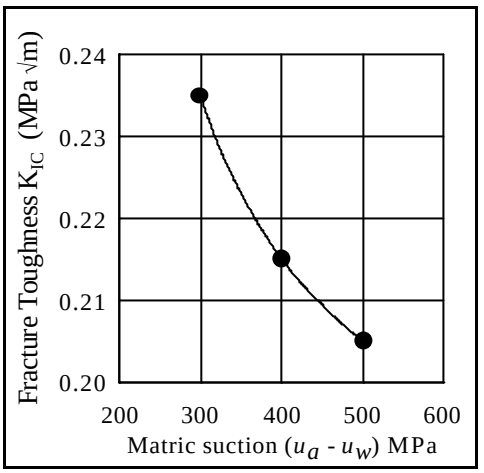

Figure 1: Fracture toughness versus matric suction.

Fracture Criteria

The fracture analysis of tensile loading of materials has been greatly aided by developments in fracture mechanics over the last 40 years or so. However, applied stresses are usually compressive rather than tensile in a geotechnical environment, and the fundamental fracture response of soil structures loaded in compression differs in a number of respects from its counterpart in tensile loading.

In the discussion which follows, the *unified model* [9] will be used as the basis of analysing how a crack would develop in this situation. Accordingly, the modes I and II stress intensity factors with respect to the generalised plane would be given by

$$K_{Iq} = K_I \cos^3\frac{q}{2} - 3K_{II}\sin\frac{q}{2}\cos^2\frac{q}{2} \tag{17}$$

and

$$K_{IIè} = K_I \sin^2\frac{q}{2}\cos^2\frac{q}{2} + K_{II0}\cos\frac{q}{2}\left(1 - 3\sin^2\frac{q}{2}\right), \tag{18}$$

while the criterion of fracture may be stated as

$$\frac{K_{Iè}^2}{K_{IC}^2} + \frac{K_{IIè}^2}{K_{IIC}^2} = 1\ . \tag{19}$$

In mixed mode loading where compression is applied, the stress field due to K_I and K_{II} can be tensile in the vicinity of the crack tip so that fracture can occur in a manner similar to the case of tensile loading, although if $K_{IC} > 1.15\ K_{IIC}$ shear or mixed mode fracture would in principle be possible too. However, unlike the case of the stress-free crack surface due to tensile loading, under combined shear and compressive stresses, the crack tip would develop a singularity due to relative shear displacement of the adjacent crack faces. Hence, some provision would have to be made to prevent the overlap of the material medium at the interface, and friction could also play a part in the fracture of the soil.

VERIFICATION OF PROPOSED MODEL

The problem adopted for verification consisted of a plane strain specimen of brittle kaolin clay, 72mm x 72mm in plan and 36mm thick, which was initially consolidated at 200kPa and then extruded and trimmed

to the required size. Thereafter, a pre-crack of length 20mm was formed centrally within the test specimen, and inclined at an angle of 45 as shown in Figure 2, following which the specimen was desaturated under a matric suction of 500 kPa by the application of cell pressure $_3$ = 550 kPa, back-pressure u_w = 50 kPa and pore-air pressure u_a = 550 kPa in a triaxial cell. Subsequently, the specimen was loaded monotonically by applying a constant rate of displacement of 0.5 mm/min under a constant cell pressure of $_3$ = 0.2N/mm^2. This rate of loading had been established from the consolidation stage to be sufficient to maintain an undrained condition in the test specimen.

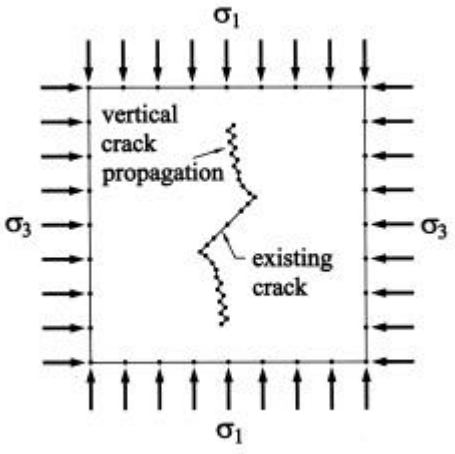

Figure 2: BE analysis of plane strain compression testing of a highly brittle soil.

During loading, the volume change of the soil skeleton, V_s, was monitored continuously by laser sensors and the axial displacement at the top of the specimen recorded automatically via a Wykeham Farrance AT2000 data-logger. Furthermore, the extension of the pre-crack was monitored in tandem with the applied loading. The loading was applied until the test specimen attained its ultimate condition.

A BE analysis was carried out on the extension of a pre-crack in the soil specimen, based on a combination of the displacement discontinuity and fictitious stress methods (Figure 2). The simulation, which was conducted over a total of 12 steps, employed the proposed soil-rock model, and was confirmed against the results of laboratory testing on unsaturated kaolin clay.

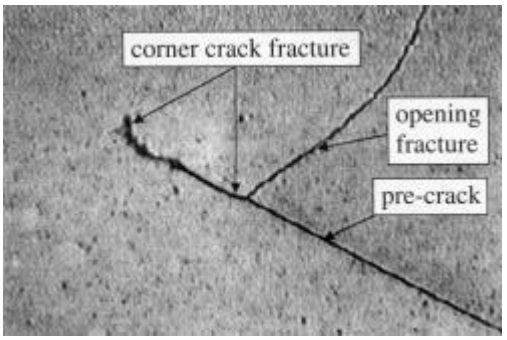

Figure 3: Opening and corner cracking of unsaturated kaolin clay.

Furthermore, it may be shown that the development of non self-similar crack extension from a sharp corner in accordance with the observed behaviour of test specimens (for example, Figure 3) may be determined from the mixed mode criterion

$$\frac{K_{a\text{I}\grave{e}}^{\ 2}}{K_{a\text{IC}}^{\ 2}} + \frac{K_{a\text{II}\grave{e}}^{\ 2}}{K_{a\text{IIC}}^{\ 2}} = 1 \ , \qquad (20)$$

where K_{IC} and K_{IIC} are the modes I and II fracture toughness at the corner, where the corresponding

generalised stress intensity factors, K_I and K_{II}, would be given by

$$K_{aq} = f_{11}K_{aI0} + f_{12}K_{aII0} \tag{21}$$

and

$$K_{aIIq} = f_{21}K_{aI0} + f_{22}K_{aII0} , \tag{22}$$

respectively, in which

$$f_{ij} = f(a, l, q) , \tag{23}$$

$$K_{aI0} = \lim_{q=0, r\to 0} [(2pr)^{1-l} s_{qq}(r, q)] , \tag{24}$$

$$K_{aII0} = \lim_{q=0, r\to 0} [(2pr)^{1-l} t_{rq}(r, q)] , \tag{25}$$

$$l \sin(2p - a) + \sin l(2p - a) = 0 , \tag{26}$$

and the included angle of the sharp corner.

CONCLUSIONS

Present-day geotechnical models in common usage tend to view the stress-strain behaviour of soils in terms of uniform point-to-point response of the material medium, implicitly. This is reflected in the use of continuum models of elastoplasticity coupled with the effective measurement of stress-strain parameters of soil specimens, when loaded, as smeared values. In an alternative approach, an empirical fit is made to the experimental data although the constraints of uniform behaviour and smeared values still persist.

However, it is a well-observed phenomenon that discontinuities, and hence the departure from uniform behaviour, often do develop in soils (that is, apart from highly plastic soils which exist on the "wet" side of critical state) when subject to loading, and may be expected to influence their stress-strain behaviour significantly. The fracture of brittle hard soils-soft rocks is an important case in point. Accordingly, a model has been proposed to deal with such materials which is based on LEFM, where the fracture toughness is related to the matric suction of the air-water-solid medium. As such, there is a departure from the generally-accepted material behaviour adopted in fracture mechanics, in that the fracture toughness is state-, and hence, load-dependent. The model has been applied to a laboratory test specimen which was subjected to biaxial compression with reasonably good agreement with observed behaviour.

REFERENCES

1. Atkinson, J. H. and Bransby, P. L. (1986). *The Mechanics of Soils: An Introduction to Critical State Soil Mechanics*. McGraw-Hill, London.
2. Terzaghi, K. (1936). In: *Proc First Int Conf on Soil Mech and Foundation Eng*, 1, pp. 161-165, Mass., Cambridge.
3. Bishop, A. W. (1967). In: *Proc Geotech Conf*, 2, pp. 142-150, Oslo.
4. Skempton, A. W., Schuster, R. L. and Petley, D. J. (1969). *Geotechnique*, 19, 205.
5. Bjerrum, L. (1967). *Journal of the Soil Mechanics and Foundations Division*, ASCE, 93, 1.
6. Saada, A. S. (1985). In: *Proc Eleventh Int Conf on Soil Mech and Foundatin Eng*, 2, pp. 637-640, San Francisco, Calif.
7. Vallejo, L. E. (1986). In: *Geotechnical Aspects of Stiff and Hard Clays*, ASCE, 2, pp. 14-27.
8. Fredlund, D. G. and Rahardjo, H. (1993). *Soil Mechanics for Unsaturated Soils*. John Wiley & Sons, Inc., New York.
9. Lo, K. W., Tamilselvan, T., Chua, K. H. and Zhao, M. M. (1996). *Eng. Fract. Mech.* 54, 189.

CALCULATION MODEL FOR CORROSION CALENDAR LIFE OF METAL PARTS

Zhang Fuze
Beijing Aeronautical Technology Research Center, Beijing 100076

ABSTRACT

A certain kind of approximate linear relationship is found between corrosive temperature (T) and corrosive time (H) for metal part within a certain range of temperature. It is called the T-H curve in this paper, which is similar to the S-N curve in the fatigue field. On the basis of T-H curve, the author deduces the formula of calendar life for corrosion damage of metal under many kinds of medium environment. As for the form, it looks like the Miner theoretical formula in fatigue field. Using this formula, the calendar life for corrosion damage of metal can be estimated simply under varied complicated medium surrounding.

Key words

T-H curve, calendar life, corrosion damage calculation model

INTRODUCTION

Up to now, there is not a applicable model which can be predicted at home and abroad, because the factors effecting on aircraft corrosion calendar life are complex. Therefore, the aircraft calendar life is not given scientifically in engineering, so that some great accidents often occur. In order to solve this difficult problem, this paper makes the study and gets following three respects of conclusion.

1. Approximate linear variation between corrosion damage amount and corrosion time for some of metals

This linear variation rule can be demonstrated not only by <Faraday law> but also by some tests. For example, 12 groups of curve shown in fig.1, between corrosion amount and corrosion time are approximate linear rule, which is useful for setting up an aircraft calendar life model.

2. A relation of corrosion temperature (T) and corrosion time (H)

A relation of corrosion temperature (T) and corrosion time (H) for some of metals appears the variation rule shown in fig.2. i.e. when some of metals in certain corrosion medium are corroded to the same corrosion amount

D, increasing corrosion on temperature T requires decreasing corrosion time H, decreasing corrosion temperatureT requires increasing corrosion time H. When the temperature decreases to a critical value T_c, the infinite corrosion time (no corrosion) is required, which is called corrosion T-H curve in this paper. This kind of variation rule is deduced by <Faraday Law>and also is verified by many groups of curve for high temperature corrosion test and middle-low temperature corrosion test, as shown in fig 4 to fig 7, which is useful for setting up an aircraft calendar life model.

Fig 1 Test curve of corrosion amount and corrosion time [2]

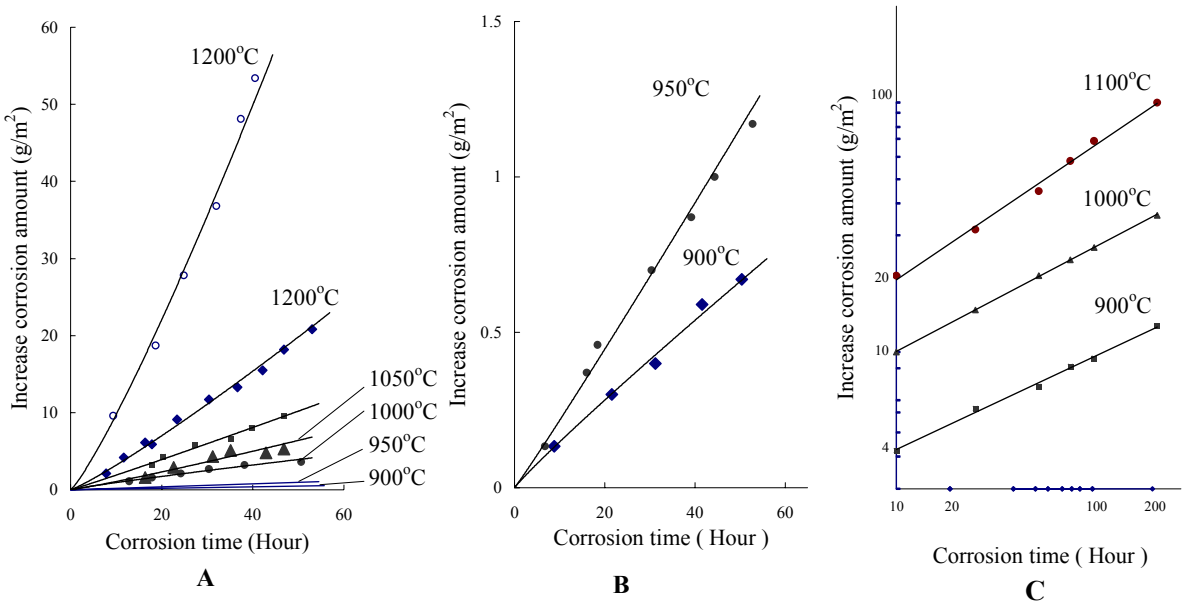

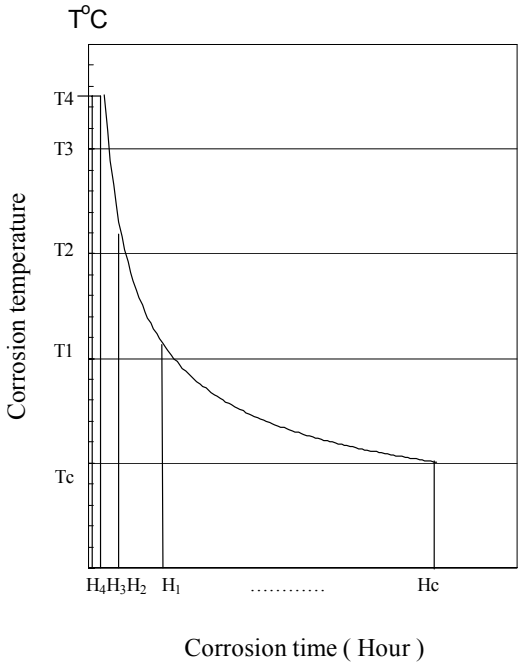

Fig .2 Standard T-H Curve to be deduced

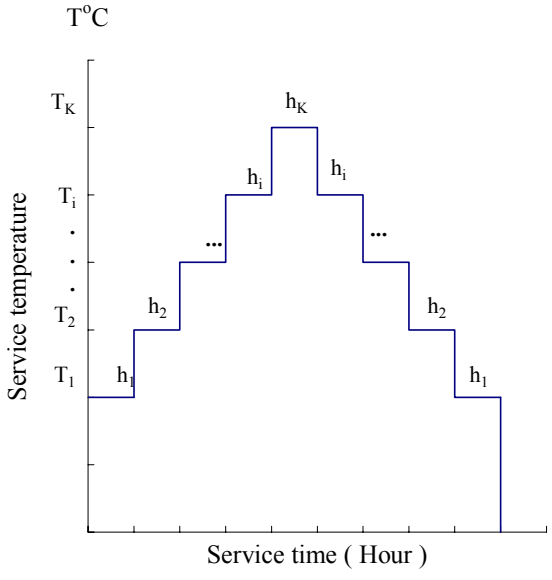

Fig.3 Assuming service temperature-time corrosion spectrum

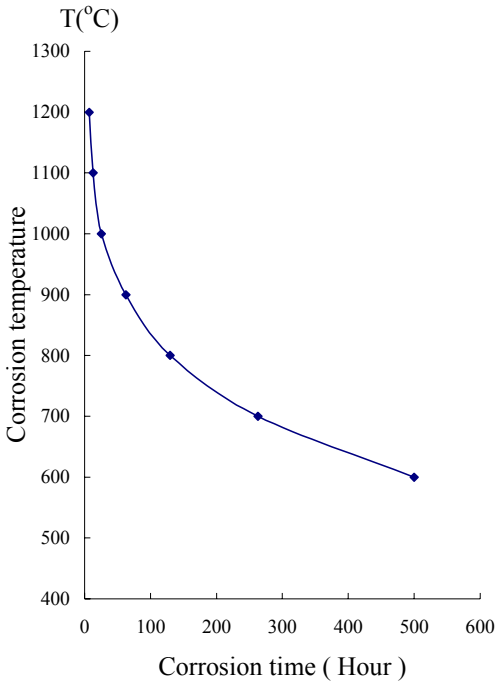

Fig.4 T-H test curves for 18 kinds of alloy[2]

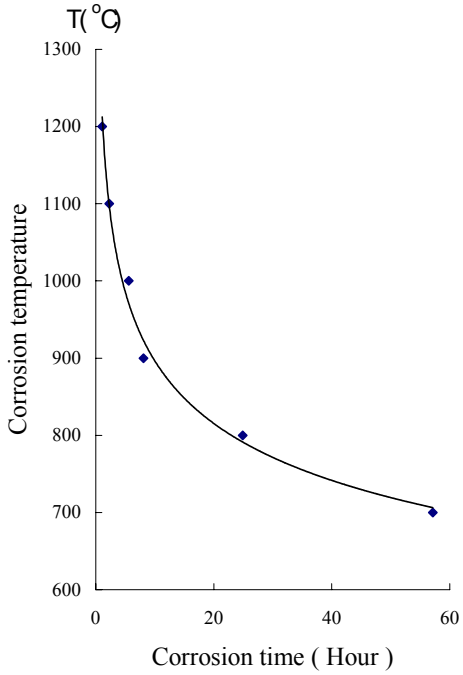

Fig.5 T-H test curves for 9 kinds of alloy[2]

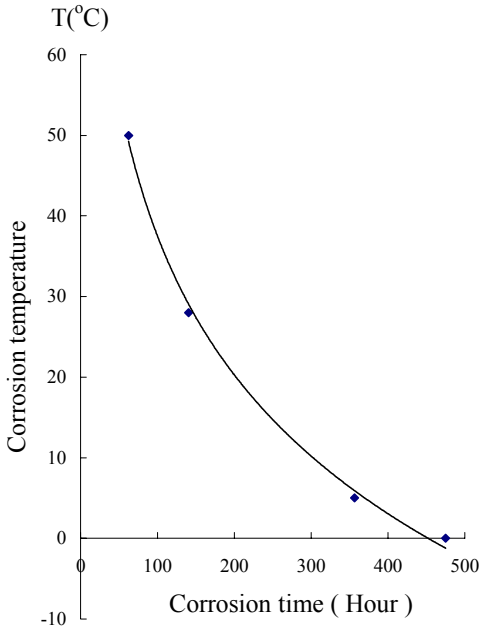

Fig.6 T-H test curve for Ly12C2 alloy

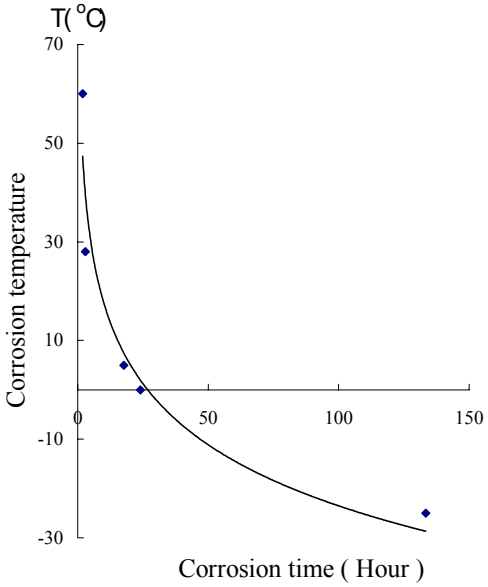

Fig.7 T-H test curve for 30CrMnSiA alloy

3.Calculation mathematical model of calendar life for corrosion damage of metal parts.

3.1 In order to get the calculation mathematical model of corrosion calendar life easily to use in engineering now assuming that：

① T_1—T_4 segment of the T—H curve shown in figure 2 is nearly straight line ,so it can be considered that corrosion amount caused at different temperature T can be accumulated linearly；

② any corrosion parts have a critical corrosion amount D_c, which can be corrosion area，volume，deep or corrosion loss amount and corrosion increments;

③ a part has a corrosion spectrum of using temperature T -- time H as shown in figure3；

④ when a part is corroded to critical corrosion amount $\mathbf{D_c}$, total cycle block number of corrosion temperature—time spectrum is λ，i.e. that is under acting at corrosion temperature—time spectrum，after passing λ cycles，the critical corrosion amount $\mathbf{D_c}$ will reach.

3.2. Calculation mathematical model for corrosion calendar life of metal parts

It can be got through analyzing complexly T - H curve shown in figure 2 and using temperature – time spectrum shown in figure 3 that in order to get corrosion amount D_c on T – H curve under temperature T_1,H_1 hours will be required, but in using temperature-time spectrum only h_1 hours will be exited under temperature T_1. Therefore, in according to the linear relation of corrosion amount and corrosion time under a certain temperature it only occupies h_1/H_1 of total corrosion damage amount, which is named corrosion damage degree.

Similarly, the corrosion damage degrees at T_2, T_I T_k can be got in using temperature - time spectrum, which are h_2/H_2 .h_i/H_i, h_k/H_k.In according to the assumption of linear accumulation of corrosion damage, the accumulation corrosion damage degree of a one corrosion temperature spectrum block is

$$\frac{h_1}{H_1}+\frac{h_2}{H_2}+\bullet\bullet\bullet+\frac{h_i}{H_i}+\frac{h_k}{H_k}=\sum_{i=1}^{k}\frac{h_i}{H_i}$$

which only occupies $1/\lambda$ of total cycle spectrum block damage degree, thus

$$\sum_{i=1}^{k}\frac{h_i}{H_i}=1/\lambda$$

that is $$\lambda\sum_{i=1}^{k}\frac{h_i}{H_i}=1$$

If corrosion parts are acted by using temperature – time spectrum for m kind of mediums at the same time, it can be got that

$$\lambda\left[\left(\sum_{i=1}^{k}\frac{h_i}{H_i}\right)_1+\left(\sum_{i=1}^{k}\frac{h_i}{H_i}\right)_2+\bullet\bullet\bullet+\left(\sum_{i=1}^{k}\frac{h_i}{H_i}\right)_i+\left(\sum_{i=1}^{k}\frac{h_i}{H_i}\right)_m\right]=1$$

that is $$\lambda\sum_{j=1}^{m}\left(\sum_{i=1}^{k}\frac{h_i}{H_i}\right)_j=1 \qquad (1)$$

where,

$\mathbf{H_I}$ is the hour number when corrosion parts are corroded to specified corrosion amount D in a certain medium environment under i stage of temperature;

$\mathbf{h_i}$ is the hour number corresponding to i stage of temperature in using temperature -time spectrum;

λ is the total cycle block number when corrosion parts acted together by m kinds of medium environment are corroded to specified corrosion amount D;

k is the stage number of a certain using temperature-time spectrum;

m is the number of corrosion medium

Formula (1) is a theoretical formula of corrosion damage accumulation which is got in this paper, that is, a calculation formula getting corrosion damage calendar life under m kinds of medium environment. A prediction of calendar life for two kinds of aircraft is made successfully by using this model and good results.

4. Conclusion

4.1 The linear accumulation theoretical formula (1) of corrosion damage is given through deduction and verification. As long as there is the T-H curve of metal corrosion and using corrosion temperature-time spectrum of a metal corrosion, the corrosion calendar life of the metal parts is calculated using formula (1).So the problem to predict complex corrosion calendar life of metal parts is reconverted into predicting “fatigue” life, which is a significant research. It is available and applicable for determining calendar life of metal parts which are in no loading or constant loading, for example, it is applicable for determining calendar life of aircraft which place on the earth’ s surface for long time.

4.2 The study range of this paper only is limited to corrosion conditions where the relation between corrosion time and corrosion amount is nearly linear, other conditions will remain to study further.

Reference

1. 周希沅.(1996).飞机结构的当量环境谱与加速试验谱.航空学报, ,17(5):613—616
2. 李金桂、赵闺彦主编,(1984). 航空产品腐蚀及其控制手册,北京:航空工业部第 621 研究所

ORAL/POSTER REFERENCE: *ICF100363OR*

CAN STRETCH ZONE MEASUREMENTS PROVIDE A GOOD ESTIMATE OF FRACTURE TOUGHNESS?

S. Sivaprasad[1], S. Tarafder[1], V.R. Ranganath[1], S. K. Das[1] and K.K. Ray[2]

[1] National Metallurgical Laboratory, Jamshedpur 831 007, INDIA
[2] Dept. Met. & Mat. Engg., IIT, Kharagpur 721 302, INDIA

ABSTRACT

Stretch zone measurement on the fracture surfaces is often used for ductile fracture estimations. However, it is not clear whether to use the stretch zone width or stretch zone depth for such evaluations. Both these dimensions have been used by several researchers for correlation with fracture toughness. While some researchers claim the use of stretch zone width, others recommend stretch zone depth for ductile fracture estimation. Moreover, a unified procedure for stretch zone depth measurement is not available in the literature. In this work, a method is proposed for stretch zone depth measurement and influence of prestrain on ductile fracture of two varieties of Cu-strengthened HSLA steels have been examined through both stretch zone width and stretch zone depth measurenments. Results are compared with the variation in fracture toughness (J_i) with prestrain. It is noted that the stretch zone depth measurements could predict the nature of variation in fracture toughness with prestrain for both the steels than the stretch zone width. It is therefore concluded that stretch zone depth measurements can be a useful method whenever the trend in the fracture toughness variation with respect to material/process parameter is to be examined. However, J estimated from stretch zone width provides a better approximation of the toughness and the nature of variation would also follow a similar trend as J_i only beyond the inhomogeneous yielding zone of these steels.

KEYWORDS

Fracture Toughness, Stretch Zone Width, Stretch Zone Depth, HSLA Steels

INTRODUCTION

Ductile fracture behaviour of materials is usually characterised by the J-integral – an elastic plastic fracture mechanics parameter. The procedure of ductile fracture toughness evaluation involves identifying a critical J value corresponding to a specific ductile crack extension on the J versus crack extension plot, known as the J resistance (J-R) curve. However, this procedure has been proven to be erroneous for high toughness materials when ASTM standards [1] are followed to characterise the critical fracture toughness J_{IC} [2-6]. An alternate method for such materials is to measure the extent of plastic blunting of the crack tip on the fracture surface of the tested specimen and correlate it to J_i on the J-R curve.

In an earlier work to study the influence of prior deformation on the ductile fracture behaviour of Cu-strengthened HSLA steels used for ship building applications [7], it was noted that the critical fracture

toughness, J_i, was retained up to 2% prestrain beyond which it was observed to be decreasing. This observation is significant, since normally one would expect the fracture toughness to decrease with prestrain. However, in order to confirm whether the initial retention in fracture toughness is real or the method of determination of J_i from the J resistance curve fails to take into consideration the effect of prestrain, the alternate method was explored.

The initiation regime fracture of ductile materials leaves an imprint of the phenomena in terms of a characteristic featureless region called the stretch zone followed by tearing which can be observed under a scanning electron microscope (SEM). This stretch zone represents the extent of crack tip blunting prior to actual crack extension and thus has a correlation with the initiation fracture toughness of the material. The size of this stretch zone is a characteristic of the material. Several attempts have been made to measure this stretch zone dimension and obtain an appropriate correlation with ductile fracture toughness [8-16]. Normally, in highly ductile materials, stretch zone would have two components *viz*., stretch zone width (*SZW*) and stretch zone depth (*SZD*). Both *SZW* and *SZD* are closely related to fracture toughness. However, there is no agreement on which of these stretch zone dimensions should be used for determining critical fracture toughness. Some researchers have used *SZW* [10-14] while others have used *SZD* [15,16] for obtaining ductile fracture toughness. Moreover, while *SZW* measurements can be made easily under SEM, direct *SZD* measurements are difficult due to complications in observing the specimen end-on under SEM. In this work, a procedure for *SZD* measurement is proposed, and an attempt is made to relate both *SZW* and *SZD* to ductile fracture toughness. The appropriateness of using *SZW* and *SZD* for ductile fracture determination is discussed by comparing the nature of variation of respective fracture toughness estimations with prestrain and that of J_i obtained from *J-R* curves.

EXPERIMENT

Material

The materials employed in this investigation are two varieties of quenched and tempered Cu-strengthened HSLA steels designated as HSLA-80 and HSLA-100. The chemical composition and the mechanical properties of the two steels are given in Table 1 and Table 2 respectively. The microstructure of HSLA-80 was acicular ferrite while that of HSLA-100 was observed to be tempered bainite. The materials were available in the form of 20mm (HSLA-80) and 25mm (HSLA-100) thick plates.

TABLE 1
CHEMICAL COMPOSITION OF HSLA STEELS IN WT. %

Steel	C	Mn	P	S	N	Si	Cr	Mo	Al	Nb	Ni	Cu
HSLA-80	0.05	1.00	0.009	0.001	0.01	0.34	0.61	0.51	0.025	0.037	1.77	1.23
HSLA-100	0.06	0.84	0.011	0.003	0.008	0.25	0.74	0.58	0.023	0.03	3.47	1.54

TABLE 2
MECHANICAL PROPERTIES OF HSLA STEELS

Steel	σ_{YS} MPa	σ_{UTS} MPa	%El	Uniform Elong. %#	%RA	n†	Hardness VHN	Charpy Energy J	YS/UTS
HSLA-80	650	715	24.2	10.5	75.8	0.12	250	218	0.91
HSLA-100	840	884	21.6	8.1	73.5	0.08	300	192	0.95

† obtained from $\sigma = k\varepsilon^n$, σ = true stress, ε = true strain, in plastic range
# over 25mm gauge length

Fracture Toughness Test

Specimen blanks of 5mm x 20mm cross-section were cut from the plates and single edge notch bend (SENB) specimens were prepared after prestraining them in tension to 1%, 2%, 3%, 4% and 5% of total strain. *J* tests were carried out by employing single specimen unloading compliance method. A location independent CCL relation was used for crack length measurements [17]. The *J* and the crack opening displacement, δ, values at each unloading were calculated and a plot of *J* versus Δa obtained. The departure of the *J* resistance curve from the experimental blunting line drawn to the initial linear region of the *J* resistance curve is taken as J_i.

Stretch Zone Measurement

Fracture surfaces extracted from the tested specimens are examined under SEM such that the plane of fracture is normal to the electron beam. A representative stretch zone feature is recorded at mid-thickness of the specimen. The specimen is then tilted through 45° about an axis through the crack front. While tilting, care is taken to ensure that there is no lateral shift of the specimen. A record of the stretch zone in this tilted view is also made.

The stretch zone boundaries in both untilted and tilted conditions are traced on to a transparency sheet. Horizontal grid lines are superimposed over these tracings and a number of (as many as 35) measurements made. Correspondence between untilted and tilted measurements is maintained by noting reference features in both the cases. The scheme is shown in Fig. 1. While the untilted view give *SZW*, *SZD* is calculated from a geometric inter-relation between the untilted and tilted conditions that is derived below with reference to Fig. 2.

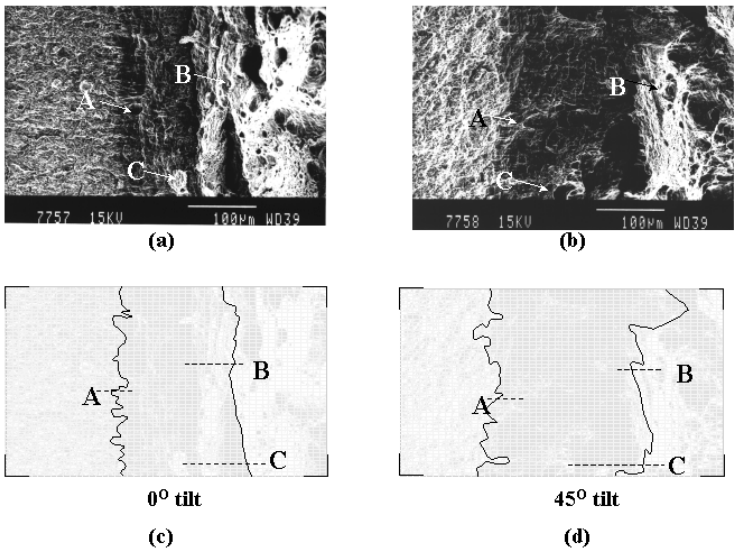

Figure 1: Typical stretch zone in (a) untilted and (b) 45° tilted view and (c) & (d) the measurement procedure with reference locations

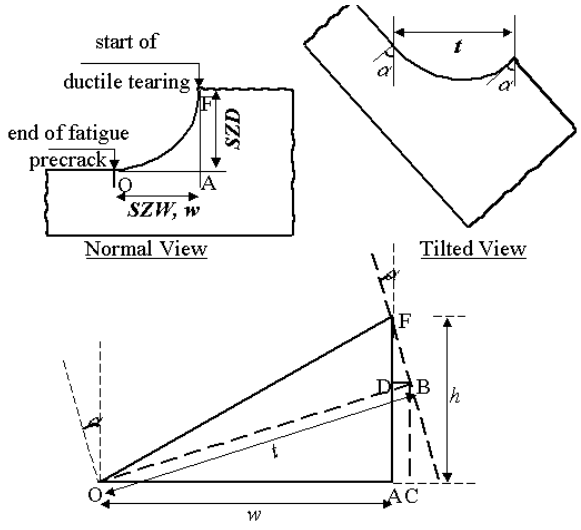

Figure 2: Geometrical inter-relation between normal and tilted configuration of specimen

From Fig. 2, $OC = OB\cos\alpha = t\cos\alpha$ since $OB = t$,

and $DB = AC = OC - OA = t\cos\alpha - w$ since $OA = w$

Similarly, $DA = BC = OB\sin\alpha = t\sin\alpha$,

and $$FD = \frac{DB}{\tan\alpha} = \frac{t\cos\alpha - w}{\tan\alpha}$$

F denotes the point at which the stretch zone ends and ductile tearing starts. Hence FA is the *SZD* of height *h*. Therefore, it can be written that

$$SZD = h = FD + DA$$

$$= \frac{t\cos\alpha + t\sin\alpha\tan\alpha - w}{\tan\alpha} + \tan\alpha \quad (1)$$

If the specimen is tilted through an angle $\alpha = 45^{o}$ the Eqn. 1 becomes

$$SZD = h = \sqrt{2}\,t - w \quad (2)$$

The measurements made in the untilted and tilted conditions thus refer to *SZW*, *w* and *t* respectively. Using Eqn. 2, the *SZD, h*, is calculated for each pair of *w* and *t* measured. Average of all the *w* and *h* measurements were considered as the *SZW* and *SZD* respectively. The exercise was carried out for both the steels at all prestrain levels.

Fracture Toughness from Stretch Zone Geometry

As *SZW* is equivalent to the critical value of Δa at which ductile fracture initiates, a vertical to the ordinate is drawn at $\Delta a = SZW$ on the experimentally derived J-Δa plot. Intersection of this vertical with the J resistance curve is taken as the initiation toughness from *SZW* measurements, J_{SZW}.

For evaluating the initiation toughness from *SZD* measurements, J_{SZD}, the J-δ plot for the same set of experimental data is constructed. A vertical at the ordinate corresponding to $\delta = 2SZD$ is drawn. Intersection of this vertical with the J-δ curve is noted as J_{SZD}.

RESULTS AND DISCUSSION

Effect of Prestrain on Stretch Zone Geometry

Variation of the mean *SZW* and *SZD* of HSLA-80 and HSLA-100 with prestrain is shown in Fig.3. The magnitude of *SZD,* for both the HSLA steels remained constant up to ~2% prestrain, beyond which it decreased markedly. This nature of variation is similar to the variation of J_i that was described earlier. However, the same is not true for *SZW*. In case of HSLA-80, *SZW* showed a decreasing trend while for HSLA-100, it showed an increasing trend with prestrain. The nature of variation of *SZD* with prestrain thus strongly qualifies the use of *SZD* for determining the fracture toughness.

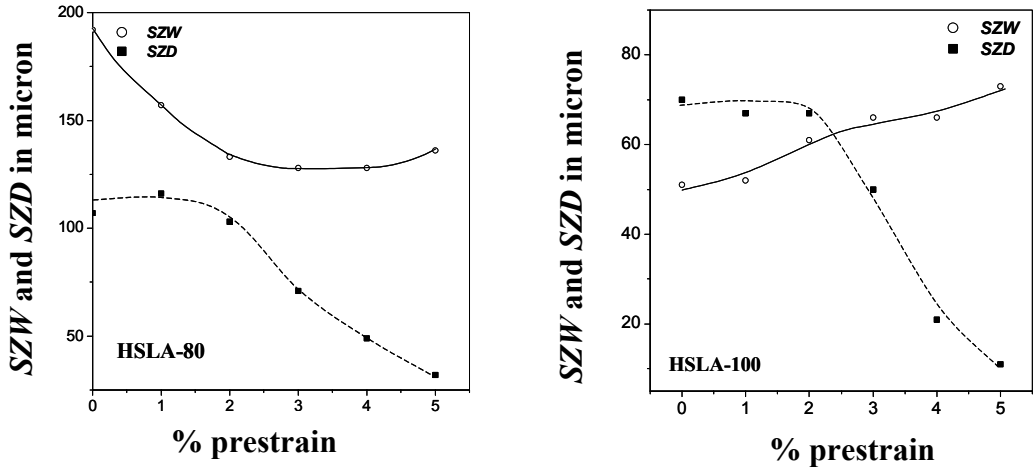

Figure 3: Variation of stretch zone dimensions with prestrain

Variation of J_{SZW} and J_{SZD} with Prestrain

The variation of J_{SZW} and J_{SZD} with imposed prestrains is depicted in Fig.4 and Fig. 5 for HSLA-80 and HSLA-100 steels respectively. Included in the plots are the J_i values at various prestrains for comparison. It may be noted from these figures that the nature of variation of J_{SZD} with prestrain is similar to that of J_i for both the steels. The magnitude of J_{SZD}, however, is lower than that of J_i through the entire range of prestraining investigated for both the steels. J_{SZW} in both the steel does not reflect the trend exhibited by J_i.

It decreases with prestrain for HSLA-80 and does not show a systematic variation (at least up to 2% prestrain) for HSLA-100 steel. Nonetheless, it is interesting to note that the magnitude of J_{SZW} compares well with that of J_i at prestrains greater than ~2% in both the steels. This is thought to be significant from the point of view that both the steels exhibit non-homogeneous deformation up to a strain level of about 1.5 to 2.5%, which is manifested in the form of Luders stretch (in HSLA-80) or low hardening rates (HSLA-100) during tensile deformation of the steels.

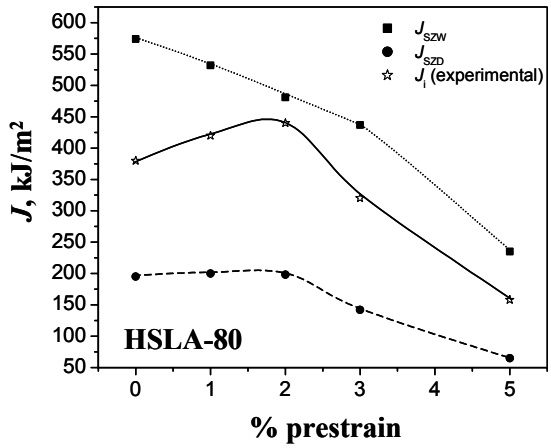

Figure 4: Variation of J_{SZW}, J_{SZD} and J_i with prestrain for HSLA-80 steel

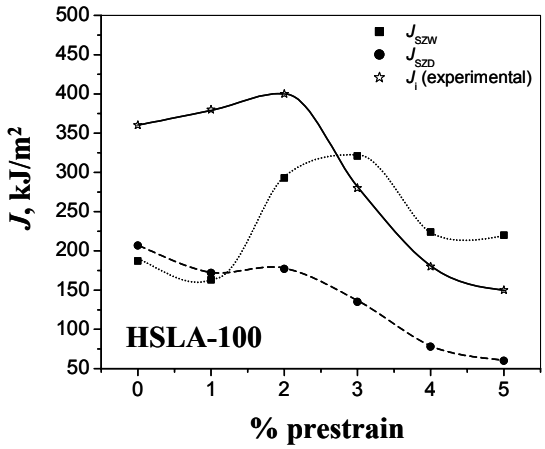

Figure 5: Variation of J_{SZW}, J_{SZD} and J_i with prestrain for HSLA-100 steel

The failure of *SZW* or *SZD* in predicting the trend and magnitude of J_i with prestrain can be attributed to a number of reasons. Inaccuracies in identifying the start and end of stretch zone extents may reflect in the measurement of w and t. Restricting measurements to the mid-thickness of specimens may produce significant contributions to the average stretch zone geometry originating from the flanks of the crack front. Minor errors will also be included due to non-consideration of elastic components of blunting/stretching that are recovered on unloading. By far the most important source of error can be traced to the occurance of secondary cracks within the blunted crack profiles (see Fig. 6) that have been observed in both the steels. Such cracks may influence the determination of J_{SZW} and J_{SZD} in the following ways:

(i) secondary cracks will contribute to the compliance of the specimen and result in the enhancement of the crack length measured during testing by the compliance technique. This will lead to a lower value of J_{SZW} and J_{SZD} to be read from experimental plots.

(ii) post test measurements of *SZW* and *SZD* are liable to be significantly different to the values existing at the time of testing.

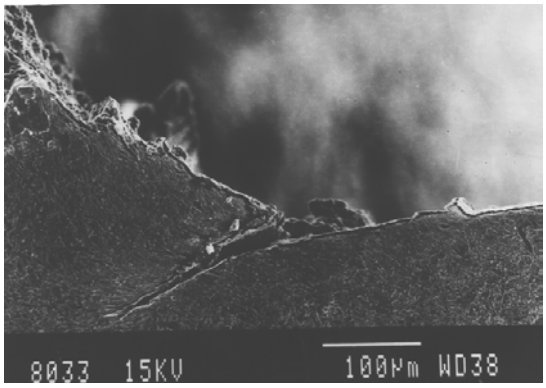

Figure 6: Presence of a secondary crack in the blunted profile of crack

CONCLUSIONS

From the investigation carried out on initiation toughness measurement via stretch zone geometry in HSLA steels, it can be concluded that

(i) use of *SZD*, in preference to *SZW*, provides a better appreciation of the trend of variation of ductile fracture toughness with external conditioning influence like prestrains.

(ii) SZW provides a better measurement of ductile fracture toughness when material deformation through non-homogeneous processes is absent.

ACKNOWLEDGEMENT

This investigation has been carried out as part of the work for the Office of Naval Research, USA, under Grant No. N00014-95-1-0015.

REFERENCE

1. E 813-89, Standard Test Method for J_{IC}, A Measure of Fracture Toughness (1994), Annual Book of ASTM standards, vol. 03.01, pp. 968-991, ASTM, Philadelphia, PA.
2. Kolednik,O. and Stuwe, H.P. (1986). *Eng. Fracture Mech*., 24, 277.
3. Prantl, G., *Int. J. Fract*., (1986), 32, R7.
4. Mills, W.J, James, L.A and Williams, J.A., *J. Test. Eval*., (1977). 5, pp. 446-451.
5. Tobler, R.L., *Cracks and Fracture, STP 601*, (1976) ASTM, Philadelphia, pp.346-370.
6. Berger, C. Keller, H.P. and Munz, D., Elastic-Plastic Fracture, STP 668, (1979). ASTM, Philadelphia, pp.378-405
7. Sivaprasad, S., Tarafder, S., Ranganath, V.R. and Ray, K.K. (2000) *J. Mater. Sci. Engg.*, A284, pp. 195-201.
8. Yin, S.W. and Gerbrands, R.A. (1983). *Eng. Fract. Mechanics*, 18, pp. 1025-1036.
9. Hopkins, P. and Jolley, G. (1983). *Eng. Fract. Mechanics*, 18, 239.
10. Ranganath, V.R., Kumar, A.N. and Pandey, R.K. (1991). *Mater. Sci. Eng.,* 132, pp. 153-160.
11. Amouzouvi, K.F. and Bassim, M.N. (1982). *Materl. Sci. Eng.*, 55, pp. 257-262.
12. Pandey, R.K., Sundaram, S. and Kumar, A.N. (1992). *J. Test. Eval.*, 20, pp. 106-113.
13. Srinivas, M., Kamat, S.V. and Rama Rao, P. (1994). *J. Test. Eval.,* 22, pp. 302-308.
14. Bassim, M.N., Mathews, J.R. and Hyatt, C.V. (1992). *Eng. Fract. Mechanics*, 43, pp. 297-303.
15. Sreenivasan, P.R., Ray, S.K., Vaidyanathan, S. and Rodriguez, P. (1996). *Fatigue Fract. Engg. Mater. Struct.,* 19, pp. 855-868.
16. Cao, Wei-Di and Lu, Xiao-Ping (1984). *Int. J. Fracture*, 25, pp. 33-52.
17. Tarafder, M., Tarafder, S and Ranganath, V.R. (1997). *Int. J. Fatigue*, 19, 635.

CHALLENGES IN CHARACTERIZING THE CRACK-TIP ENVIRONMENT AS A BASIS FOR PREDICTION OF CRACK GROWTH KINETICS

Alan Turnbull

National Physical Laboratory, Teddington, Middlesex, TW11 0LW, UK.

ABSTRACT

The challenges in improved mechanistically-based prediction of crack growth kinetics due to hydrogen embrittlement are discussed in relation to the local crack-tip environment, which, in context, embraces crack-tip chemistry and the hydrogen distribution ahead of the tip. Important advances have been made in modelling crack-tip electrochemistry and considerable insight obtained but the need for an electrochemical database of input parameters is paramount to ensure confidence in prediction. In modelling the crack-tip hydrogen distribution the use of generalised boundary conditions which link electrochemical processes and hydrogen atom transport in the crack-tip region has been an important advance but must be coupled to more realistic crack-tip stress and strain models. A validated model of this form linked with criteria for crack advance incorporating material property and microstructural parameters is a necessary precursor to meaningful quantitative crack growth prediction.

KEYWORDS

Environment assisted cracking, crack-tip environment, hydrogen embrittlement, modelling.

INTRODUCTION

Stress corrosion cracking and corrosion fatigue (collectively environment assisted cracking, EAC) pose major challenges in prediction because the interaction of the environmental, mechanical and material variables responsible for cracking occurs at a highly localised level. Cracks tend to initiate at microstructural and microchemical inhomogeneities, at stress concentrators, and at sites of local solution chemistry change. The latter is reflected for example in the importance of pitting, crevice attack, or intergranular corrosion as precursors to EAC for corrosion resistant alloys. Once a crack has initiated, the growth rate is determined or influenced strongly by the crack-tip environment and electrochemical kinetics. This applies also to hydrogen embrittlement, but here the concept of the crack-tip environment must be expanded to include the distribution of hydrogen atoms in the crack-tip process zone.

There is no mechanistic model for crack growth in aqueous solutions which properly accounts for the range of service variables and their time variation in a coherent manner although the simplest models based on slip-dissolution have had some limited engineering application, albeit with partial fitting [1,2]. Predicting threshold and crack growth kinetics for hydrogen embrittlement in an engineering context is a particularly formidable challenge [3]. In most service applications, transient variations in stress, temperature or environment chemistry will occur as part of normal operational service or be induced by scheduled excursions (e.g. shutdown) or unintentional fluctuation in system control (e.g. contamination); the character of the metal surface may change with time of operation (e.g. precipitation of a scale or deposit) and welding

quality may be variable. These pose a challenge to service prediction and would require extensive input data gathering representative of the change of conditions. It is perhaps best not to envisage mechanistic model development being undertaken for direct engineering prediction. Engineers will base predictions mainly on laboratory testing and field experience/measurement. Nevertheless, the value of modelling will be in sensibly interpreting short term data, in ensuring that testing is conducted with an informed awareness of the impact of operational variables and in providing some framework for prediction when test data are limited. To instil confidence in the industry, modelling has to improve and rigorous validation must be undertaken.

The component features of hydrogen embrittlement models are clear: crack-tip electrochemical kinetics, hydrogen transport in the stress/strain field at the crack tip, the interfacing between electrochemistry and transport, and a crack advance or failure criterion. These are interdependent to a large extent and a crack growth model must embrace all aspects in an integral fashion. A brief summary of the present position and the challenges in raising such models to the next level of sophistication is now described.

CRACK-TIP ELECTROCHEMISTRY

Characteristics

Conceptually, the crack electrochemistry system is now well understood and the principle processes are illustrated schematically for a Mode I crack in Figure 1. For completeness, the dissolution of alloying elements and the solubility limit for dissolved metal cations would also be included. Depletion of reactive species such as oxygen confines reduction of this species mainly to the external surface. Under open circuit conditions, the net anodic current emerging from the crack causes a depression in the corrosion potential in order to provide the balancing net cathodic current on the external surface. The key requirement for EAC prediction is to quantify the transient electrode kinetics for the partial anodic dissolution and cathodic hydrogen generation reactions at the crack tip. These cannot be determined directly but the functional dependency of the parameters, viz. maximum current density on bare surface and the refilming kinetics, can be determined from electrochemical experiments in simulated crack-tip environments and the values then used as input to the crack electrochemistry model.

Present position in prediction

Over the last two decades, the capability of modelling the various reaction processes in a crack together with mass transport by diffusion, ion migration and in the case of corrosion fatigue, fluid flow, has been established [4]. Models of crack chemistry of varying level of complexity exist for systems such as low alloy carbon steels in seawater, nickel-base alloys and stainless steels in nuclear environments, nickel in H_2SO_4. In relation to hydrogen embrittlement the advances made have led to clarification of several issues.

What we have learned

Relevance of bulk environment

- The bulk environment composition, including the species indicated in Figure 1 (O_2, H_2S, H^+ etc) will have an effect on the corrosion potential which can influence crack chemistry and potential for that reason, but, depending on crack size may not have a direct effect on crack chemistry because reactive species are consumed before they enter far into the crack.
- In very low conductivity chloride solutions, the potential drop in the bulk solution is often significantly greater than in the crack itself since dissolved metal ions increase the crack solution conductivity. A crack size effect on crack-tip conditions is predicted for low conductivity solutions but associated with the impact of crack depth on net current flow from the crack and the potential drop induced in the bulk solution [5].

Crack size effects

- In corrosion fatigue of low alloy high strength steels in seawater, acidic pH values of 4 can be achieved in short cracks compared to near neutral values for long cracks [4]; enhanced crack growth of the short crack would then be predicted and has been reported [6].
- Depletion of reactive species from the bulk solution such as H_2S will be greatest for deep cracks. For corrosion resistant alloys in the passive state, this may lead to a decrease of crack growth with increase in crack size, although testing remains to be done. For steels in the active state, this may result in bulk charging becoming the dominant source of hydrogen atoms for deep cracks [3].

Localised charging vs bulk charging

- As noted above, for alloys in the active state, bulk charging can become the predominant source of hydrogen atoms controlling crack growth when reactive species such as H_2S or H^+ in acid solutions are present in the bulk at significant concentrations but consumed readily in the crack and do not reach the crack tip. Bulk charging will also tend to be important under cathodic polarisation conditions because the potential drop and high pH in the crack limit hydrogen atom generation at the crack tip [4].
- For corrosion resistant alloys in the passive state, the oxide film is a major barrier to hydrogen entry at ambient temperatures. For that reason, hydrogen entry will be favoured where localised straining ruptures the film or where localised corrosion creates a local acidic metal chloride solution and correspondingly dissolves the film barrier. In the latter case, cracking may not ensue unless the critical pitting or critical crevice temperature is exceeded; simpler tests can then be used as a preliminary indication of cracking likelihood.

Fluid flow induced by cyclic loading

Fluid mixing induced by cyclic loading will result in dilution of the crack solution and generally permit more influence of bulk solution reactants. Even at a low frequency of 0.1Hz, fluid flow can result in a decrease in crack-tip metal ion concentration by more than two orders of magnitude [4]. Because of the lower conductivity, anodic polarisation will tend to be more difficult in a corrosion fatigue crack compared to a stress corrosion crack (assuming no major change in fracture mechanism which affects crack opening). In seawater, cathodic polarisation will be more difficult as buffering species are pulled into the crack by the fluid mixing and reduce the beneficial effect of high pH on the ease of polarisation.

Advances required

The limitation in modelling the crack-tip environment and predicting crack-tip kinetics for many systems is primarily the limited availability and quality of input parameters, including the transient electrode kinetics on initially bared surfaces which must be derived from separate electrochemical experiments using fast fracture or guillotine techniques. The establishment of an electrochemical database is essential and validation of model predictions by crack-tip chemistry and potential measurements is important. However, in some systems the crack-tip reactions may not have a significant effect on the local potential and chemistry and demonstration that the predicted crack tip reaction kinetics are valid may not be possible.

More attention to the crack-tip shape and opening for moving cracks and for intergranular cracks would add refinement. Concentrated solutions still pose some uncertainty in modelling; nevertheless, progress in being made. Modelling is still accessible to only a comparative few because of the complexity of development. A future can be envisaged where such models are accessed through the internet and run remotely with an individual's own dataset. Such schemes are already in place for other material performance models.

HYDROGEN TRANSPORT AND TRAPPING AT A CRACK TIP

Characteristics

The kinetics of hydrogen generation and entry will be varying around the crack tip from the highly reactive tip area to the crack walls and will be undergoing a complex time variation in response to film rupture and repair.

The hydrogen atoms generated will be absorbed and transported into the metal by lattice diffusion, grain boundary diffusion and by dislocation transport. Although there is some indication of enhanced grain boundary diffusion in pure nickel, for most commercial alloys the presence of impurities and precipitates at the grain boundary will provide local traps and hinder grain boundary diffusion. Dislocation transport of hydrogen certainly occurs but the relative significance is more hotly debated. However, the effectiveness of this process is inevitably constrained by microstructural barriers limiting the mean free path. Long range transport is not readily feasible but short range redistribution of hydrogen with possible dumping of hydrogen from dislocations to grain boundaries or to interfaces is likely. The hydrostatic stress field at the crack tip will create a gradient in chemical potential which will provide a driving force for localisation of hydrogen in the lattice. Trapping at microstructural trap sites will influence the diffusion rate through the matrix and may play a critical role in the fracture process. In addition, differential strain in the crack-tip region will create variations in dislocation trap density, and the varying plastic strain rate in the process zone will determine dislocation trap generation kinetics and dislocation transport kinetics.

In some systems, hydrogen atoms absorbed from the external surface will be diffusing to the crack-tip region. If that were not complicated enough, the crack advance process will result in a redistribution of crack-tip conditions. Cyclic loading will cause dynamic fluctuations in local entry kinetics, through the effect on crack-tip reduction kinetics and film rupture rate, and will affect the local concentration through the cyclic variation in hydrostatic stress.

Present position in prediction

Modelling of the time variation of the hydrogen distribution at a crack tip is a formidable problem but major advances have been achieved through the work of Sofronis and McMeeking [7,8], Turnbull et al [9], and Krom et al [10]. The modelling of Sofronis and McMeeking and of Krom et al represented a important step forward insofar as the models were two-dimensional, included elastic-plastic analysis combined with diffusion and trapping and accounted for trap generation associated with crack-tip straining. Simplified boundary conditions were used with no specific account of the distribution of the electrochemical kinetics between the tip and walls. Trapping of hydrogen was dealt with only in relation to low occupancy conditions. Also using a two-dimensional model, more appropriate boundary conditions were established by Turnbull et al which for the first time united the transport and electrochemical processes explicitly by including the reaction processes on the crack tip and walls in a generalised flux expression with no *a priori* assumption about surface or diffusion control of entry and transport. Reversible traps of varying occupancy and irreversible trapping were included. The other virtue of the model of Turnbull et al was the exploration of the imbalance between crack-tip charging rates and bulk charging rates. However, although a two-dimensional approach was used, an important limitation was the simplified Prandtl stress field used. The assumed crack-tip mechanics model has a critical impact on predictions and contrasting approaches such as that of Lii et al [11] based on a discretised dislocation model indicate the potential for very much larger hydrostatic stresses, at least in the single crystal system studied

What we have learned

Hydrogen localisation

Hydrogen atoms in the lattice are localised due to hydrostatic stress but the magnitude of the effect is modest for a blunting crack. However, since the crack-tip opening displacement for propagating cracks and for intergranular cracks tends to be smaller than predicted by the blunting model, the latter will tend to underestimate the crack-tip stresses and localised lattice hydrogen content. Nevertheless, the trapped hydrogen content ahead of the crack tip will be large. The trap binding energy will always lead to a local concentration significantly in excess of the lattice value, up to trap saturation level. Also, for hydrogen trapped at dislocations, the highly deformed nature of the crack-tip region means high trap densities.

Strain rate effects

A key conclusion from the work of Krom et al [10] and of Sofronis et al [8] was the demonstration that straining the material will cause depletion of lattice hydrogen because diffusion of hydrogen from the source at the tip is not fast enough to replenish hydrogen atoms lost to the newly created traps. This dilution of hydrogen

atom concentration would lead to the expectation of a reduced crack growth, which would be accentuated by increased strain rates. Krom et al give emphasis to the reduced lattice hydrogen concentration and models based on such in predicting the influence on cracking but inevitably the local trapped hydrogen concentration would be reduced also and a trapping-based model could not be excluded. Also, dislocation transport would provide an explanation for the strain rate behaviour but its inclusion in continuum models is difficult because it is inherently an inhomogeneous process. Correspondingly, there will always be uncertainty in the local distribution of hydrogen atoms at the microstructural level.

Surface reaction vs diffusion control

In alloys of low lattice diffusivity for hydrogen atoms, e.g. nickel-based alloys, entry and transport is inevitably diffusion control because the diffusion flux of hydrogen will be small compared to the charging and recombination fluxes at the crack tip. For iron-based ferritic alloys for which the lattice diffusivity is high, it is less apparent and conceptually, it would be expected to depend more critically on the concentration gradient. The particular advance of the model of Turnbull et al [9] was to show that the concentration gradient was high (and hence the flux high) because of the significant gradients in hydrogen induced by the marked difference in hydrogen generation kinetics between the crack tip and adjacent crack walls. Thus, the prediction was that crack growth would be surface reaction controlled, although a cautionary comment is required because of the simplified stress-strain model adopted. Since many of the models developed for crack growth kinetics are based on low alloy steel and often invoke diffusion control using a one-dimensional model this was an important step forward.

Bulk charging

The generalised boundary conditions adopted by Turnbull et al, which incorporated desorption fluxes as well as absorption fluxes, allowed exploration of the effect of pre-charging. In this case, significant *loss* of hydrogen atoms via the crack tip and walls can occur if the charging conditions at the tip are less significant than that associated with the precharging and especially so when testing in air. The latter deduction raises uncertainty in the interpretation of crack growth kinetics on cadmium-coated specimens once cracking has commenced and the coating barrier film locally damaged. Bulk charging is an important issue. Long term (150 days) pre-exposure of an AISI 4340 steel cathodically protected in seawater indicated corrosion fatigue crack growth rates much faster than obtained from conventional test (20 days) [3].

Advances required

There has to be integration of the best features of the models of Turnbull et al and those of Sofronis et al and of Krom et al but with crack-tip mechanics models more appropriate to growing stress corrosion and hydrogen embrittlement cracks. Multi-disciplinary interaction is required. A further step is to deal with the transient electrochemical parameters associated with a refilming material (rather than average crack-tip values). This is not so difficult to incorporate into a model but obtaining experimental data on the effect of refilming on the absorption and desorption input parameters, which determine C_0, presents a major challenge. In principle, it should not prove overly difficult to model some features of the effect of cyclic loading on hydrogen atom distribution provided we can define the impact on the stress and strain distribution on individual cycles and the cumulative impact. However, this would be on the basis of a non-propagating crack.. The biggest challenge is to account for the crack growth process itself, assuming that a criteria for the onset of cracking and for crack arrest (if crack growth is not a continuous process) has been established. With crack extension, new surface is created generating more hydrogen. The crack will have to be treated as a moving boundary and the evolution of the hydrogen distribution progressively recalculated. All of these steps are foreseeable with focused resource. Perhaps the greatest fundamental difficulty will be the incorporation of inhomogenous localised dislocation transport of hydrogen into the model.

These represent some of the challenges in improved modelling. Experimental validation is critical in models of such complexity and with so many variables. Direct measurement of crack-tip hydrogen concentration, lattice and trapped hydrogen, very close to the crack tip would be a fundamental test but presents major technical difficulties. Within the bounds of current test methods it is not easy to envisage how this might be achieved at the spatial resolution required.

CONCLUDING REMARKS

The potential exists for significant progress in modelling crack-tip electrochemistry and hydrogen transport in an integrated manner but as the complexity increases and the input database enlarges it becomes more important to seek direct experimental methods of validation such as crack chemistry or crack-tip hydrogen atom concentration measurement. Clearly, an integrated hydrogen generation and transport model will be a necessary input to models of cracking (although such modelling will inevitably be numerically based) but we have to build a more effective description of the failure process and its relationship to material properties and microstructural parameters.

REFERENCES

1. F. P. Ford and P.L. Andresen (1988). In: *Environmental Degradation of Materials in Nuclear Power Systems*, p 789, J.L. Theus, J.R. Weeks (Eds), The Metallurgical Society, Warrendale, PA.
2. Engelhardt, G.R., Macdonald D.D., and Urquidi-Macdonald, M. (1999), *Corros. Sci*., 41, 2267.
3. Turnbull, A. (2001), In: *Ageing Studies and Lifetime Extension of Materials*, L.G. Mallinson (Ed.), p. 397, KA/PP, New York, NY.
4. Turnbull, A. (2001) *Corrosion*, 57, 175.
5. Turnbull, A.(2001), In: *Corrosion 2001*, Paper no. 01237, NACE, Houston, Tx.
6. Gangloff, R.P (1985). *Metall. Trans. A ,* 16A, 953.
7. Sofronis, P. and McMeeking, R.M (1989). *J. Mechanics and Physics of Solids*, 37, 317.
8. Sofronis, P, and Taha, A. (2000). In: *Environmentally Assisted Cracking: Predictive Methods for Risk Assessment and Evaluation of Materials, Equipment and Structures*, p. 70, R.D. Kane (Ed.), ASTM 1401, West Conshohocken, PA.
9. Turnbull, A., Ferriss, D and Anzai., H. (1996). *Mater.Sci. Eng.,* A206, 1.
10. Krom, A.H.M., Koers. R.W.J. and Bakker, A.(1999). *J. Mechanics and Physics of Solids*, 47, 971.
11. Lii, M., Foecke, T., Chen. X., Zieliski W. and Gerberich, W.W., (1989) *Mater. Sci. Eng.*, A113, 327.

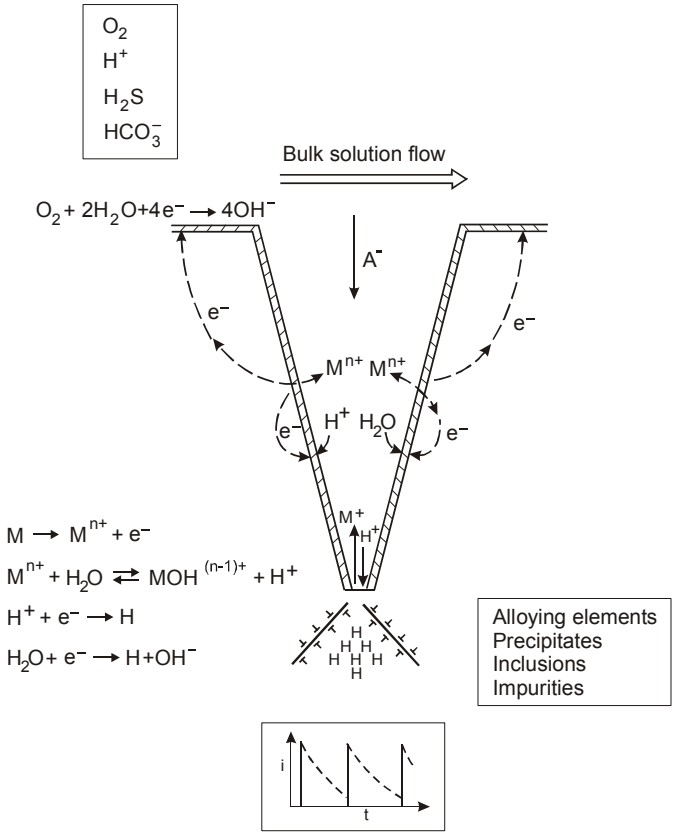

Figure 1: Schematic illustration of crack electrochemistry system indicating reactions in crack, transient current densities associated with film rupture at the tip, the possible impact of local material composition in determining kinetics (and fracture path) and accumulation of hydrogen ahead of the crack tip.

POSTER REFERENCE: ICF100760PR

CHARACTERISATION OF CRACK TOUGHNESS BEHAVIOUR OF UNFILLED AND FILLED ELASTOMERS

W. Grellmann[1], K. Reincke[1], R. Lach[1], G. Heinrich[2]

[1] Martin-Luther-University of Halle-Wittenberg, Department of Engineering Science, Institute of Materials Science, D-06099 Halle, Germany
[2] Continental AG, Strategic Technology Advanced Materials, D-30419 Hannover, Germany

ABSTRACT

With the help of the examinations described in this paper, possibilities should be shown to assess elastomer materials by different fracture mechanics methods. Vulcanizates on the basis of the statistical styrene-butadiene copolymer SBR 1500 with different sulphur and carbon black contents were investigated. Several fracture mechanics examination methods under cyclic, impact-like and quasi-static loading conditions were applied for describing the crack initiation and crack propagation behaviour. The so-called Tear and Fatigue Analyser was used to determine critical values of tearing energy. The instrumented tensile-impact test (ITIT) developed further for elastomer testing is described. By this test, the crack toughness behaviour related to resistance against unstable crack propagation can be examined. At last, a quasi-static fracture mechanics test was applied to the determination of stable crack initiation and crack propagation behaviour. The results of the different tests are discussed in dependence on structure, i.e. sulphur and carbon black content.

KEYWORDS

Fracture Mechanics – Elastomers – Crack Initiation and Propagation – Crack Resistance Curve

INTRODUCTION

Elastomer materials are used for a great number of applications from which defined requirements on material properties follow. Among others, for the application properties of tires for example, even under economic and ecological aspects, wet-skid stability, rolling resistance and wear resistance are important aspects. In the case of passenger car tires, the wear phenomenon mainly appearing is fatigue wear leading to abrasion losses within the tire tread. This is caused by initiation and propagation of cracks from which the application of fracture mechanics concepts for material assessment is derived. The use of fracture mechanics concepts for material characterisation of thermoplastic polymers has been proven to be very helpful in material development and optimization [1]. However, the transfer of these fracture mechanics concepts, such as *J*-integral or COD concept, to elastomeric materials is difficult because of their special, non-linear deformation behaviour. Therefore, fracture mechanics methods have to be modified partly and it is likely necessary to find new ways in analysis of test data recorded. By the experiments described below, it should be shown how usual fracture mechanics test methods work for elastomer testing.

EXAMINATION METHODS

The material behaviour under cyclic loading conditions was tested by using the Tear and Fatigue Analyser (TFA) of Coesfeld GmbH. This is a testing device which was specially developed for the examination of elastomers' fatigue behaviour. Up to ten specimens one-sided cut can be tested at the same time. During the experiment, various measuring parameters are recorded, such as current crack length, load and energy, which serve for subsequent analysis. From these tests, crack propagation curves for each material were plotted and critical tearing energies as a measure for the materials' resistance against fatigue crack propagation were determined. Instrumented tensile-impact tests (ITIT) can be used to investigate even such flexible materials like elastomers under impact-like loading conditions. In principle, a specimen is fixed between the unsecured crosshead and the secured clamp (see Figure 1). Then the specimen is loaded by the pendulum hammer that impacts the unsecured crosshead, and so the specimen is strained in direction of its longitudinal axis until it tears. At the same time the load–time curve is recorded, and afterwards through double integration the load-extension curve is calculated. In analogy to the instrumented *Charpy* impact test (ICIT) [2], characteristic parameters are used for analysis, and J values J_d were determined according to an evaluation method of Begley and Landes.

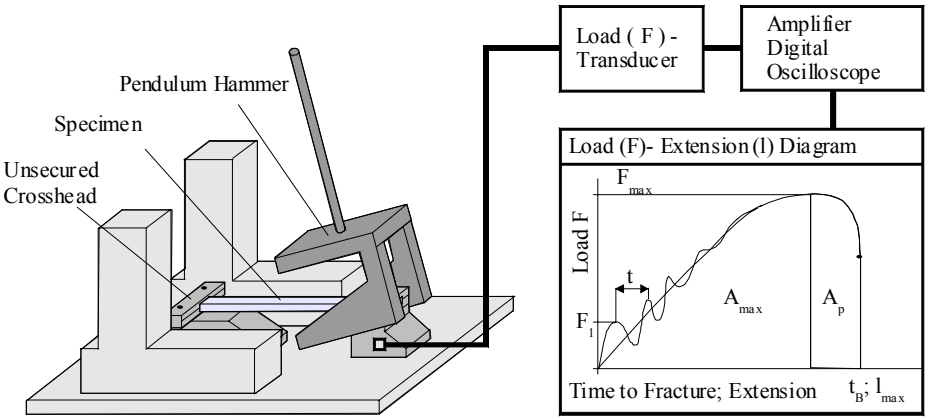

Figure 1: Schematic representation of the instrumented tensile-impact test

Besides these two methods described above, recording of crack resistance (R-) curves using a quasi-static fracture mechanics test took place. Following the stop-block method of the ICIT, the tests on several specimens (multiple-specimen method) were stopped after reaching different strain values to produce different amounts of stable crack growth. The fracture surfaces were investigated with a light microscope to determine the size of stable crack growth. From the recorded load–extension curves, energies for calculation of the loading parameter J for the R-curve were determined. Finally, the J–Δa data were plotted and regression functions were fitted and then used for subsequent analysis. Ascertainable parameters of the crack resistance curves are, for example, technical crack initiation values $J_{0.2}$ determined according to ESIS TC 4 recommendation [3] or the slope of the R-curve $dJ/d\Delta a$. These parameters supply quantitative criteria for a material comparison.

MATERIALS

Basis of the materials investigated is the statistical styrene-butadiene copolymer SBR 1500 with a styrene content of about 23 wt.-%. Crosslinking occurred with a sulphur–accelerator system. The sulphur content was varied in the range from 0.8 to 2.4 parts per hundred rubber (phr) with a constant sulphur–accelerator ratio to examine the influence of the crosslink density on the properties. For assessment of filler influence, vulcanizates with a constant sulphur content of 1.6 phr, but with different carbon black contents in the range from 0 to 50 phr were produced. Vulcanizates of this kind are used in different areas, for example in tires or conveyor belt materials. For these materials, network densities (see Figure 2) were determined on the basis of the Mooney-Rivlin equation using stress–strain diagrams. The physical network density shown in Figure 2 contains a primary network density as a result of chemical crosslinking and elastically active entanglements. In

the case of filled vulcanizates, a secondary apparent network density of the filler network can be estimated that is related to elastically effective filler-polymer interactions and to the contribution of the filler–filler networking above a certain percolation threshold.

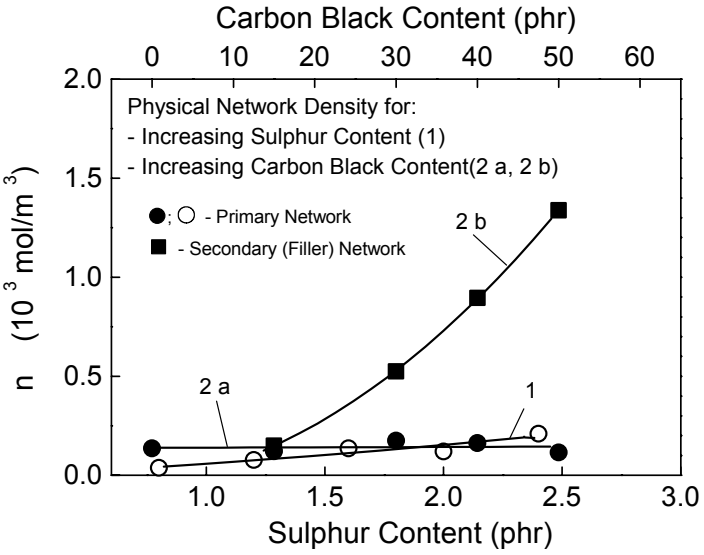

Figure 2: Network density of the elastomers examined

For the fatigue tests, SENT specimens were used with the dimensions of length l = 64 mm, width W = 15 mm and thickness B = 1.5 mm. The initial crack length was about 1 mm. For the tensile-impact tests and for the quasi-static fracture mechanics tests, DENT specimens were used which had the same dimension as for the fatigue tests, but the initial crack length was about 4 mm and 6 mm, respectively.

RESULTS

Critical tearing energy values T_c determined by the TFA measurements and the results of the instrumented tensile-impact test for the unfilled vulcanizates are shown in Fig. 3. Because T_c remains nearly constant up to a sulphur content of 2.0 phr, it can be said that the increasing network density (see Fig. 2) in this sulphur content range has no influence on T_c. Only a higher sulphur content decreases the critical tearing energy. The J values indicate a constant decrease of toughness, e.g. the resistance against unstable crack propagation is decreased with increasing network density.

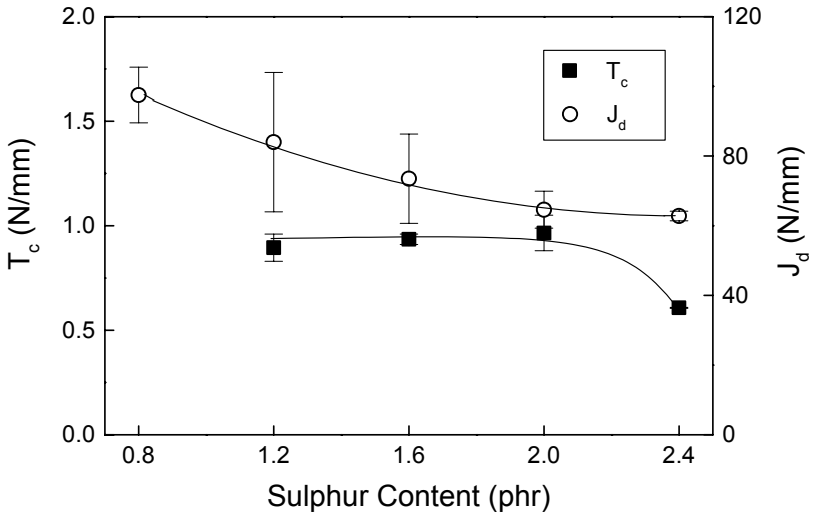

Figure 3: Results of the cyclic and impact tests for the unfilled vulcanizates

However, the T_c values and the J values of the filled vulcanizates are decisively influenced by changes in structure, i.e. by the rising carbon black content. This is attributed to reinforcing effects and the development of a filler network and increasing interactions between filler and polymer as well as filler and filler, respectively. For the J values of the filled materials a maximum was found at 40 phr carbon black. From the maximum loads and maximum extensions is derived that this maximum is strength-determined and shows that only a filler content up to 40 phr leads to an improvement of the crack growth behaviour of the observed material system. Possible causes for the decreasing parameter level with 50 phr carbon black are, on the one hand, reduction of effective network chain length due to the high filler content and a reduced extensibility in the area of stress concentrations within the material, which decrease the energy absorption capacity. On the other hand, an incomplete distribution of the carbon black particles and agglomerates, respectively or larger filler agglomerates are considered as inhomogeneities and work as crack starter due to unfavourable stress circumstances nearby.

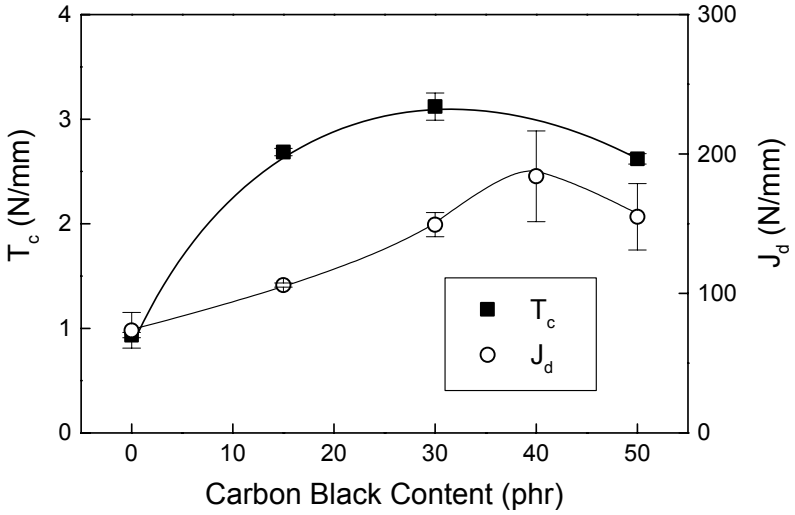

Figure 4: Influence of carbon black content on T_c and on J_d values related to resistance against unstable crack propagation

The results of the quasi-static fracture mechanics examination are shown in Figs. 5 and 6. Figure 5 represents the J–Δa curves, where a significant increase of the slope with rising carbon black content is visible. In comparison with the filled materials, only small differences resulted for the unfilled vulcanizates. This is reflected by the technical crack initiation values $J_{0.2}$ and the values of the slope of the crack resistance curves $dJ/d(\Delta a)$ at the point of maximum experimentally determined crack growth $\Delta a_{max\ (exp)}$ (Figure 6).

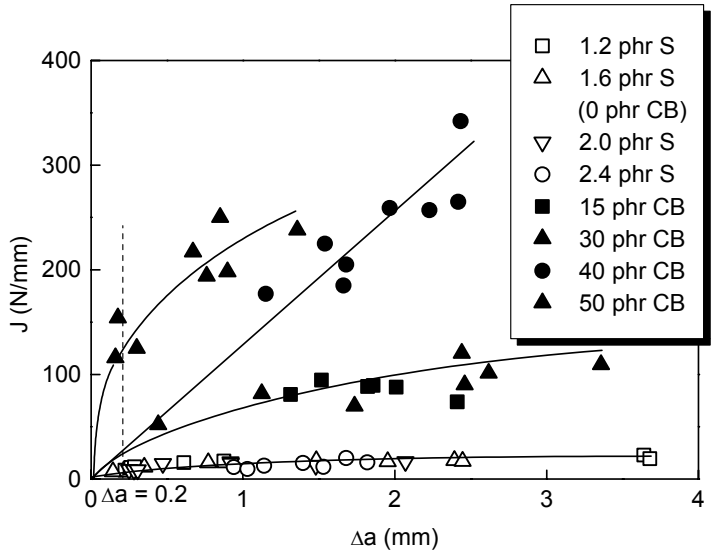

Figure 5: Crack resistance curves

The crack initiation and crack propagation behaviour is only slightly influenced up to a sulphur content of 2.0 phr, a still higher sulphur content of 2.4 phr leads to a lower crack initiation value, but to a higher resistance against crack propagation (see Figure 6a).
With an increasing carbon black content up to 30 phr, $J_{0.2}$ is slightly increased at first, then a strong increase of the resistance against stable crack initiation appears. Even the resistance against stable crack propagation characterised by $dJ/d(\Delta a)$ at $\Delta a_{max(exp)}$ rises slightly up to 30 phr filler and shows a maximum value at 40 phr. That means, more energy is necessary to initiate a stable crack within the 50 phr filled material, but in comparison with the 40 phr filled vulcanizate, the resistance against stable crack propagation is lower.
The observed differences of the crack initiation and propagation behaviour show that a multi-parametrical description of the fracture behaviour is necessary for an optimal material characterisation.

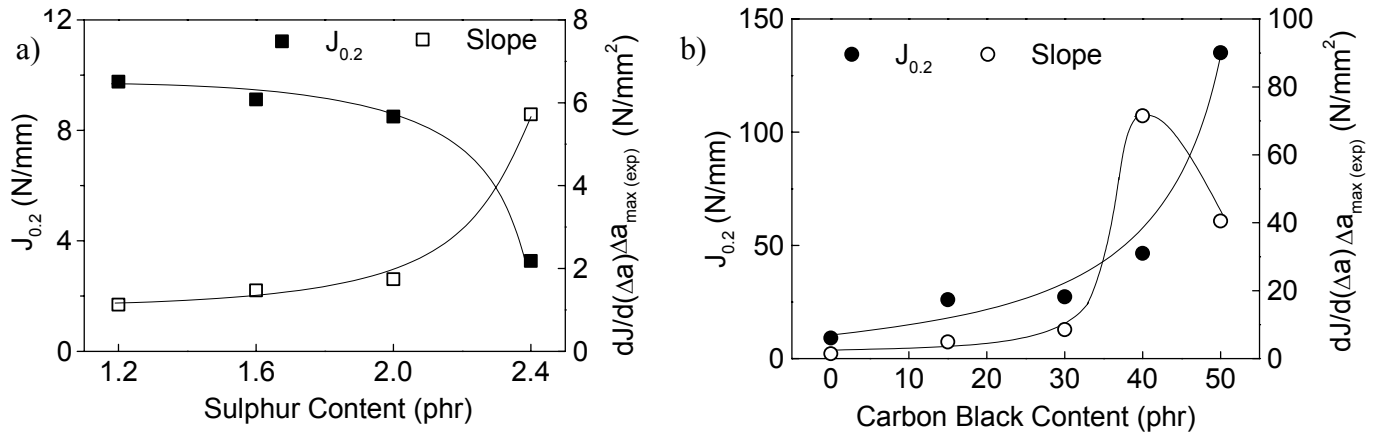

Figure 6 a, b: Influence of sulphur **(a)** and carbon black content **(b)** on the technical crack initiation value and the slope of the R-curves at the point $\Delta a_{max\ (exp)}$

CONCLUSIONS

With the examination methods described here, one can assess the toughness behaviour of the elastomer materials investigated. An increase of the sulphur content, this means an increase of crosslink density, leads, in some cases, to a considerable decrease of the toughness parameters determined under various loading conditions. In dependence on filler content, maximum values for the various toughness parameters, except for the technical crack initiation parameter $J_{0.2}$, were found at 30 and 40 phr filler content, respectively. Therefore, the addition of 30–40 phr carbon black shows in our study the optimal improvement of the crack initiation and propagation behaviour of this elastomer system in the filler content range investigated.

ACKNOWLEDGEMENTS

The authors gratefully acknowledge the Continental AG, Hannover (Germany) for providing the materials and for giving authorization for publication of the results.

REFERENCES

1. Grellmann W. (2001): In: Grellmann W., Seidler S. (Eds.): Deformation and Fracture Behaviour of Polymers. Springer Berlin Heidelberg: 3–26
2. Seidler S., Grellmann W., Hesse W. (2001): In: Grellmann W., Seidler S. (Eds.) Deformation and Fracture Behaviour of Polymers. Springer Berlin Heidelberg: 71–86
3. Standard Draft ESIS TC 4 (1995): A Testing Protocol for Conducting *J*-Crack Growth Resistance Curve Tests on Plastics.

CHARACTERIZATION OF FATIGUE CRACK FORMATION IN MECHANICALLY SURFACE TREATED AUSTENITIC STAINLESS STEEL

I. Altenberger [1], B. Scholtes [2], U. Noster [2], R. 0. Ritchie [1]

[1] Lawrence Berkeley National Laboratory, University of California, Berkeley, USA
[2] Institute of Materials Technology, University Gh Kassel, Kassel, Germany

ABSTRACT

Mechanical surface treatments such as shot peening or deep rolling are very effective tools to improve the fatigue life and endurance strength of cyclically loaded components. By introducing compressive residual stress and strain hardening in the surface layers, all stages of fatigue are significantly altered, from the first dislocation movements (cyclic hardening/softening) until the eventual propagation of micro- and macro-cracks.

Metastable austenitic stainless steels are particularly attractive for mechanical surface treatment as they exhibit very high strain hardening due to the martensitic transformation and a very complex near-surface microstructure, e.g. a thin two-phased surface layer of nanocrystallites.

In order to clarify the differences in crack formation of polished and of surface treated (shot peened or deep rolled) material states, scanning electron microscopy (SEM) studies have been carried out with conventional and high resolution instruments on samples of austenitic stainless steel AISI 304 fatigued under stress control.

The results clearly showed a distinct difference in damage mechanism depending on the surface state. Whereas polished surface states exhibited crack formation preferentially at sites of extensive multiple planar slip, cracks in mechanically surface treated states were mostly formed in a brittle manner without observable surface slip. Local loss of coverage during the shot peening process, however, led to microscopically non-peened regions which exhibited early crack initiation by formation of slip bands.

Interestingly, these preferential microcracks were rarely the crack sites from which fatal cracks originated, which suggests that the damage process is not only controlled by physical crack initiation but mainly by crack propagation conditions for microcracks. A slip line-induced microcrack formation can also be promoted in deep rolled specimens if thin surface layers of approximately 5-l 0 microns are elecrolytically removed prior to cycling, thus also removing the nanocrystalline surface regions which impede slip line formation.

KEYWORDS

shot peening, deep rolling, nanocrystallization, crack initiation

INTRODUCTION

Mechanical surface treatments can lead to very complex and depth-dependent microstructues in metastable austenitic stainless steels, such as AISI 304. A typical deformation mechanism in AISI 304 is deformation-

induced martensitic transformation [1,2,3] leading to typically 25-45% a'-martensite after deep rolling or shot peening, respectively, in near surface layers [4,5,6]. The formed martensite is lath-like and heavily twinned with high dislocation densities in the austenitic matrix. Additionally, deformation bands and nanocrystalline surface regions are formed with grains as small as 20 nms, extending into a depth of 1-2 microns (Fig. 1) [4].

Fatigue investigations on mechanically surface treated AISI 304 revealed pronounced lifetime and endurance strength improvements, especially after deep rolling [4]. Since the resultant near-surface compressive residual stress profile remained only partially stable in low cycle (higher strain) fatigue, in contrast to surface treatment-induced near surface microstructures which remained stable throughout cyclic loading, the fatigue life improvement can primarily be attributed to a higher microstructural fatigue resistance in near surface regions [4,7]. The specific role of different contributing microstructures for fatigue life-improvement of mechanically surface treated materials has not been defined in the literature. Therefore, in the present work an attempt is made to characterize the effect on fatigue of the most striking microstructural feature, -namely the nanocrystalline layer- in mechanically surface treated AISI 304 by investigating deep rolled specimens and specimens before and after the nanocrystalline layer has been removed electrolytically prior to cycling.

EXPERIMENTAL PROCEDURES

Rotation-symmetrical unnotched specimens of AISI 304, with a gage length of 10 mm and a diameter of 5 mm, were deep rolled with a "ball-point" rolling device, using a hydrostatic spherical rolling element and a rolling pressure of 150 bar (the composition and microstructure of the steel are given in ref. [4]). One set of specimens was then electrolytically polished for 20 seconds with a buthanol/perchloric acid-electrolyte in order to remove the surface treatment induced nanocrystalline surface layer. The surface roughness R_z before and after polishing was around 0.5 microns.

Tension/compression fatigue tests were performed under stress control without mean stresses (R = -1) with a cycling frequency of 5 Hz and a stress amplitude of 365 MPa. The fatigue tests were interrupted just before fracture at the onset of macro-crack propagation; practically this was done at the point where the hysteresis loops as measured with a clip-on extensometer began to buckle. The surface crack length was then approximately 1 mm. The specimens were then taken out of the servohydraulic testing device and the surface crack topography was investigated with a Camscan S4- and a LEO 1550 Gemini (Field emission)-scanning electron microscope (SEM).

RESULTS

The fatigue damage mechanisms in the polished, un-surface treated (reference) state is characterized by extensive slip line formation at the surface (Fig. 2). Typically, in AISI 304 multiple planar slip along (11 1)-planes occurs at high stress amplitudes. The planar slip character is due to the small stacking fault energy of AISI 304 which is around 20 mJm^{-2} [8]. It has been repeatedly shown that slip line formation is a precursor to microcrack formation in electrolytically polished AISI 304 [9]. Preferential cracks emanate from the border between slipped and unslipped material due to strain incompatibilities and stress concentration, as has been shown in SEM and atomic force microscopy [10].

In mechanically surface treated (e.g. deep rolled or shot peened) AISI 304 the surface fatigue damage mechanism is quite different (Fig. 3). Here, only an extremely low amount of surface plasticity (increase of surface roughness) around crack flanks and crack tips was detected. This lack of plasticity can be attributed to the surface treatment-induced nanocrystalline layer which effectively impedes dislocation movement and hence slip line formation. According to [1 1], dislocation pile-ups in nanocrystallites with a grain size of 20 nm or smaller are not effective enough to promote dislocation movement or Frank-Read-sources in neighbouring grains, thus only allowing the formation of brittle cleavage cracks [12] to relieve stress concentrations. Other characteristic features of fatigue damage in mechanically surface treated

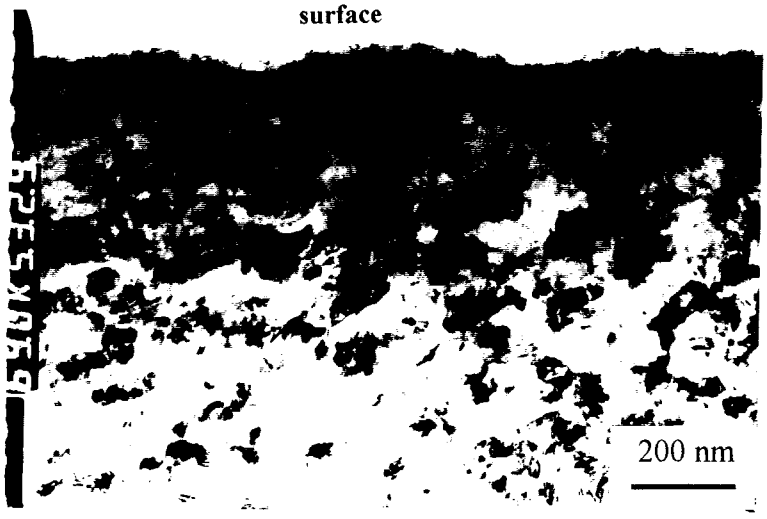

Fig. 1: Nanocrystalline layer in direct surface regions of shot peened (Almen intensity 0.175 mmA) AISI 304 (TEM-bright-field image)

Fig. 2: Typical planar (111)-slip lines in polished un-surface treated AISI 304 after high strain-fatigue, σ_a = 320 MPa, N = 1000 cycles (SEM-image, backscattering contrast)

AISI 304 compared to polished non-treated specimens are generally lower crack densities and lower crack openings as a consequence of compressive residual stresses. Crack formation without surface slip has also been reported for mechanically surface treated ferritic steels, where no nanocrystallites but extremely high dislocation densities in surface region existed [13,14].

Fig. 4 shows the microtopography of a fatigue crack in deep rolled and (prior to cyclic loading) electropolished AISI 304 for a stress amplitude of 365 MPa. The electropolishing treatment led to a layer removal of about 5-10 microns at the surface. In this case, the wake of the crack as well as the crack tip (Fig. 5) exhibit pronounced plasticity in form of slip lines that can be seen in high concentrations directly at the crack flanks but in lower density also as far away as 100 microns from the crack. Compared to Fig. 3, the surface roughening by plasticity is very pronounced here. Slip lines were found to initiate cracks but were also created by stress concentrations at the crack tip (Fig. 5). It should be noted that there was no significant difference in fatigue lifetime between this deep rolled state and the deep rolled state incorporating a

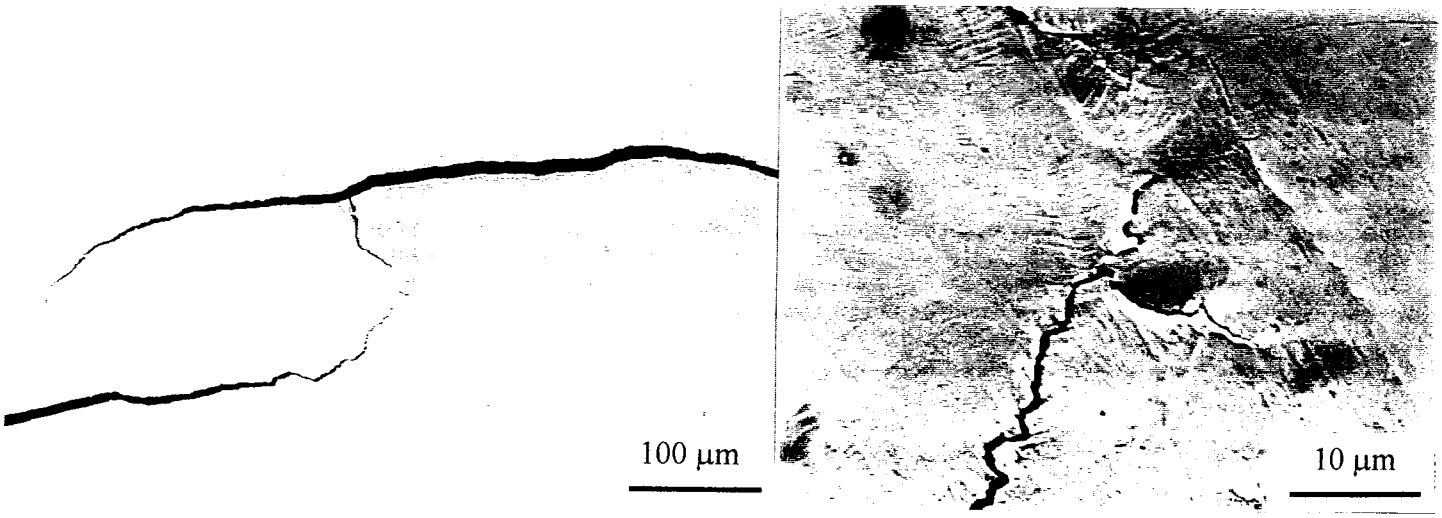

Fig. 3: Typical fatigue cracks in non-polished deep rolled AISI 304 (σ_a = 365 MPa, N = 68000 cycles)

Fig. 4: SEM-Micrograph of a typical fatigue crack in deep rolled and (prior to cyclic loading) electrolytically polished AISI 304, showing extensive slip-line formation (σ_a = 365 MPa, N = 82000 cycles)

nanocrystalline surface layer. The number of cycles to fracture was N_f = 82800 for the deep rolled and prior to cycling polished state compared to N_f = 71700 for the as deep rolled unpolished state. This is within the statistical scatter of fatigue life of this material. In short, we can summarize, that the nanocrystalline surface layer does not seem to have any positive effect on the fatigue behaviour of AISI 304 under stress controlled cyclic loading. This result is consistent to similar investigations on AISI 304, where the ratio of surface-strain hardened regions to soft core regions was smaller and where a different stress amplitude was used, resulting in shorter fatigue lives of approximately 10000 cycles[14].

It is not yet clear why a thin nanocrystalline surface layer does not signifcantly influence fatigue lifetime in spite of totally different surface damage processes. One possible explanation could be that crack initiation in deep rolled samples investigated here actually takes place beneath the surface, thus rendering the surface processes insignificant. In fact, hints for a subsurface crack formation at a depth of 2-5 microns beneath the nanocrystalline surface layer have been found in [14], where cross sections of deep rolled fatigued samples

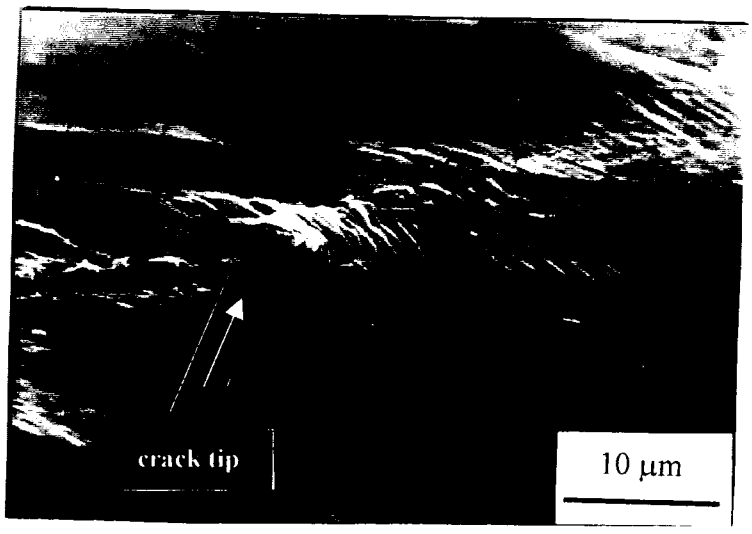

Fig. 5: Slip lines in the plastic zone of a fatigue crack tip in deep rolled and (prior to cyclic loading) electrolytically polished AISI 304 (σ_a = 365 MPa, N = 82000 cycles)

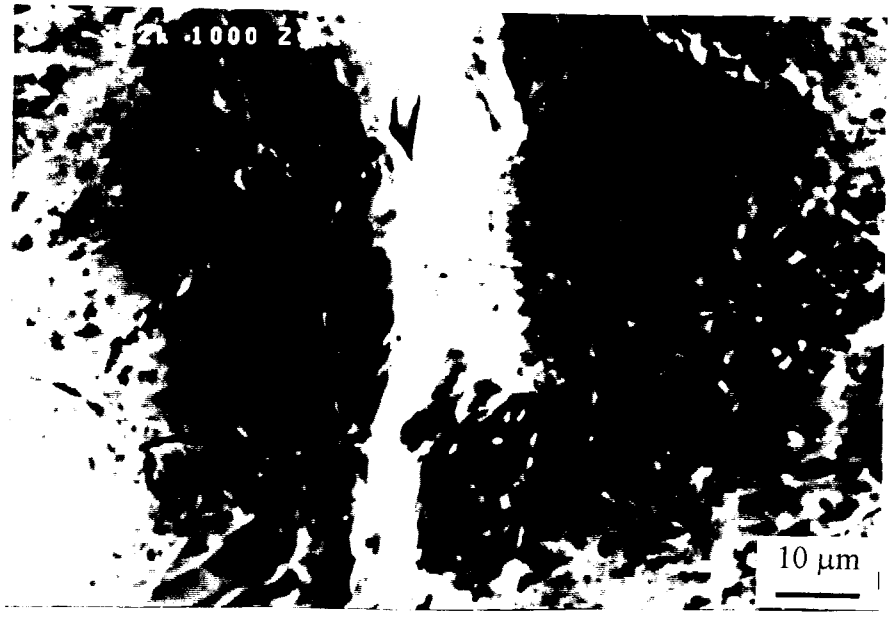

Fig. 6: Fatigue crack formation in an area of localized slip in shot peened (Almen intensity 0.175 mmA) and fatigued (σ_a = 320 MPa, N = 1000 cycles) AISI 304

revealed highest crack densities in these regions. Moreover, it has been shown in [15], that local fatigue life estimations for ductile mechanically surface treated materials are not as successful as concepts averaging over the fatigue behaviour of the whole sample like e.g. Manson-Coffin [16,17] or Smith Watson-Topper [18]. In the case investigated here, plastic strain amplitudes were identical for the polished and unpolished state, since the volume fraction of the removed layer was extremely small.

In practical applications, even in surface treated materials local plastic surface fatigue damage in form of slip lines can occur: For example, during shot peening a local loss of coverage can lead to locally non-strain hardened regions, which are prone to the same fatigue damage mechanisms as polished surfaces. Fig. 6 shows such a slip line-region in shot peened fatigued AISI 304 where a microcrack is readily formed. However, these cracks were not found to affect the fatigue life significantly and only rarely developed into 'fatal' cracks, since their propagation was retarded or stopped as soon as they encountered adjacent shot peened regions.

CONCLUSIONS

Mechanically surface treated specimens of AISI 304 exhibit brittle crack formation with little or no plasticity in direct surface regions in stress-controlled fatigue tests. This is attributed to a thin nanocrystalline surface layer. The totally different amount of surface plasticity of this layer, however, does not seem to have any significant influence on the extent of damage, since specimens without nanocrystalline surface layers exhibited quite similar fatigue lifetimes than those with nanocrystallites at the surface.
In shot peened specimens, regions not covered by the shot peening process could be found showing slip line formation similar to non-peened polished specimens. These regions were preferential sites for crack formation; however, only rarely would they develop into a fatal macro-crack, suggesting that local residual stress fields and microstructures play an important role in early crack propagation [19,20].

ACKNOWLEDGEMENT

Part of the work presented has been funded by the German Science Foundation (DFG) in form of financial support and the Emmy-Noether-programme

REFERENCES

1. Bayerlein, M., Christ, H-J. and Mughrabi, H. (1989) *Mater. Sci Eng. 114 A*, L11-L16.
2. Christian, J.W. (1965), *Theory of Transformations in Metals and Alloys*, Pergamon, Oxford.
3. D. Kirk (1982). In: *Proc. 1st Int. Conf. on Shot Peening*, p. 271, A. Niku-Lari (Ed.), Pergamon, Oxford.
4. Altenberger, I., Scholtes, B., Martin, U. and Oettel, H. (1999) *Mater. Sci. Eng.* 264 A, 1.
5. Martin, U., Altenberger, I., Scholtes, B., Kremmer, K. and Oettel, H. (1996). In: *Proc. 6th Int. Conf. on Shot Peening*, p. 142, J. Champaigne (Ed.), San Francisco.
6. Altenberger, I. and Scholtes, B. (2000) *Mater. Sci. Forum* 347-349, 382.
7. Altenberger, I., Martin, U., Scholtes, B. and Oettel, H. (1999). In: *Shot Peening - Present and Future* (Proc. 7th Int. Conf. on Shot Peening), p. 79, A. Nakonieczny (Ed.), The Institute of Precision Mechanics, Warsaw.
8. Dieter, G.E. (1988), *Mechanical Metallurgy*, McGraw-Hill, New York.
9. Lindstedt, U., Karlsson, B., Nystroem, M. (1998) *Fatigue Fract. Engng. Mater. Struct.* 21, 85.
10. Altenberger, I. (1999), PhD Thesis, University Gh Kassel, Germany.
11. Moelle, C. (1996), PhD Thesis, University Berlin (TU), Germany.
12. Stroh, A.N. (1957) *Adv. Phys.* 6, 418.
13. Natkaniec-Kocanda, D., Kocanda, S. and Miller, K.J. (1996) *Fatigue Fract. Engng. Mater. Struct.* 19, 911.
14. Busch, M. (1999), University Gh Kassel, Germany, unpublished results.
15. Scholtes, B., Altenberger, I. and Noster, U. (2000). In: *Proc. 3rd In. Conf. on Advanced Materials and Processes (Thermec 2000)*, Las Vegas, in print.
16. Manson, S.S. (1953) NACA-TN-2933.
17. Coffin, L.F. (1954) *Trans. ASME 76*, 931.
18. Smith, K.N., Watson, P. and Topper, T.H. (1979) *Journal of Materials 5*, 767.
19. Ritchie, R.O. and Lankford, J. (1986), *Mater. Sci. Eng. 84*, 11.
20. Turnbull, A., de Los Rios, E.R., Tait, R.B., Laurant, C. and Boabaid, J.S. (1998), *Fatigue Fract. Engng. Mater. Struct 21*, 1513.

Oral Reference Number: ICF100942OR

CHARACTERIZATION, ANALYSIS AND PREDICTION OF DELAMINATION IN COMPOSITES USING FRACTURE MECHANICS

T. Kevin O'Brien

U.S. Army Research Laboratory
Vehicle Technology Directorate
NASA Langley Research Center
Hampton, Virginia U.S.A

ABSTRACT

The state-of-the-art for characterizing, analyzing, and predicting delamination growth in composite materials and structures using a fracture mechanics approach will be reviewed. Techniques for measuring delamination fracture toughness and fatigue delamination onset data will be highlighted. The use of these data in finite element analyses utilizing fracture mechanics will be examined. The virtual crack closure technique for calculating strain energy release rates will be highlighted. The importance of capturing the physics of damage formation, accumulation, and growth will be emphasized. Application of this approach to delamination onset and life predictions for stiffener pull-off behavior in skin-stiffened regions and fatigue failure of composite rotor hub flexbeams will be highlighted.

KEYWORDS

composites, delamination, fracture mechanics, strain energy release rate, virtual crack closure technique, fatigue, stiffener pull-off

INTRODUCTION

One of the most commonly observed failure modes in composite materials is delamination, a separation of the fiber reinforced layers that are stacked together to form laminates. The most common sources of delamination are the material and structural discontinuities shown in figure 1. Delaminations occur at stress free edges due to the mismatch in properties of the individual layers, at ply drops where thickness must be reduced, and at regions subjected to out-of-plane loading such as bending of curved beams. Delaminations form due to some combination of three basic fracture modes shown in figure 2. These include the opening mode (mode I), the sliding shear mode (mode II), and the scissoring shear mode (mode III). The interlaminar fracture toughness (IFT) associated with each of the fracture modes must be characterized and the corresponding strain energy release rates for each mode associated with the configuration and loading of interest must be calculated to predict delamination onset and growth.

DELAMINATION CHARACTERIZATION

A mixed-mode I & II delamination failure criterion that is used for 2D problems is shown in figure 3. The IFT is determined as a critical value of the strain energy release rate, G_c, plotted as a function of the mixed-mode ratio, G_{II}/G_c. For the pure mode I opening case, $G_{II}/G_c=0$, whereas for the pure mode II case, $G_{II}/G_c=1$. These properties are determined using test methods that are being evaluated and standardized by the American Society for Testing and Materials (ASTM) and other national standards organizations, as well as the International Standards Organization (ISO) [1]. The pure mode I data are generated using a Double Cantilever Beam (DCB) specimen. The pure mode II data are generated using an End-notched Flexure (ENF) specimen. The mixed mode I&II data are generated using a Mixed-mode Bending (MMB) specimen. As shown in figure 3, the apparent toughness increases monotonically between the pure opening mode I case and the pure shear mode II case. Furthermore, due to the complex micro-mechanisms involved, the scatter is very large for the mode II case [2]. For cases where a mode III fracture toughness is required, the Edge-cracked Torsion (ECT) specimen is preferred.

Because delaminations often form and grow under cyclic loads, a fatigue characterization is also desired. The classical Paris Law for fatigue crack growth has often been generated. However, the exponents in these power laws are quite high compared to similar characterizations for metals. Hence, a no growth threshold approach is often proposed instead [3-6]. Furthermore, for mode I fatigue, fiber bridging typically develops in the unidirectional DCB specimens [1,4]. Fiber bridging can cause a growing crack to arrest artificially early yielding a non-conservative threshold value. Therefore, as shown in figure 4, an alternate G versus N onset curve is typically generated to achieve a threshold characterization for delamination onset [4-7].

DELAMINATION ANALYSIS

The strain energy release rate, G, associated with onset and growth must be determined to predict delamination. Typically, a plot of the G components due to the three unique fracture modes (G_I, G_{II}, G_{III}) and the total $G= G_I+G_{II}+G_{III}$ are calculated as a function of delamination length, a, using the Virtual Crack Closure Technique (VCCT) in a finite element analysis (FEA) [8,9]. The VCCT technique, depicted in figure 5, utilizes the product of nodal forces and the difference in nodal displacements to calculate the G components for each fracture mode. For predicting delamination onset under quasi-static or cyclic loading in 2D problems, the peak value of the G as a function of delamination length is compared to the delamination onset criteria shown in figures 3 and 4, respectively. The VCCT technique has also been extended to three dimensional problems [10,11].

DELAMINATION PREDICTION

Skin/stiffener debonding

In reference 12, the pull-off loads associated with separation of a hat stiffener from the skin of a composite part by delamination were predicted by comparing G's calculated from FEA using VCCT to mixed-mode delamination failure criterion. Subsequent studies led to the development of a simple specimen consisting of a skin bonded to a tapered flange laminate [13]. By applying various types of loads in a finite element analysis of the specimen, VCCT may be used to calculate G's and predict the onset of delamination from the matrix cracks. From this prediction, a failure criterion for combinations of bending and membrane loads may be generated.

Flexbeam Fatigue Life Prediction

Composite rotor hubs contain tapered flexbeams with large numbers of ply terminations, or ply drops, to taper the beam thickness. These ply drops act as initiation sites for delamination in the flexbeam under high combined tension and cyclic bending loads. In reference 14, flexbeams were tested and analyzed to determine the fatigue life. Fatigue delamination onset data were compared to G distributions determined from FEA and VCCT to predict the onset of unstable delaminations in these complex tapered laminates (figure 6).

CONCLUSIONS

Delamination fracture toughness and fatigue onset have been characterized using fracture mechanics. The virtual crack closure technique (VCCT) is commonly used in finite element analyses (FEA) to calculate strain energy release rates. Characterization data were used with VCCT in FEA to predict delamination onset and life in composite rotor hub flexbeams and stiffener pull-off behavior in skin-stiffener reinforced composites.

REFERENCES

1. O'Brien, T.K., (1998) *Composites: Part B, Engineering*, 29B, 57.
2. O'Brien, T.K., (1998) ASTM STP 1330, 3.
3. O'Brien, T.K., (1990) ASTM STP 1059, 7.
4. Martin, R.H. and Murri, G.B.(1990) ASTM STP 1059, 251.
5. O'Brien, T.K., Murri, G.B., and Salpekar, S.A.(1989) ASTM STP 1012, 222.
6. Murri, G.B. and Martin, R.H. (1993) ASTM STP 1156, 239.
7. ASTM standard D6115-97, (1997) 15.03, 338.
8. Rybicki, E.F. and Kanninen, M.F., (1977) *Eng. Frac. Mech.*, 9, 931
9. Raju, I.S., (1987) *Eng. Fracture Mech.*, 28, 251.
10. Raju, I.S., Shivakumar, K.N. and Crews, J.H., (1988) *AIAA J.*, 26, 1493.
11. Davidson, B.D., Krüger, R. and König, M., (1995) *Comp. Sci. Tech.*, 54(4), 385.
12. Li, J., O'Brien, T.K., and Rousseau, C.Q. (1997) *J. Amer. Hel. Soc.*, 42(4), 350.
13. Minguet, P.J, and O'Brien, T.K. (1996) ASTM STP 1274, 105.
14. Murri, G.B., O'Brien, T.K., and Rousseau, C.Q. (1998) *J. Amer. Hel. Soc.*, 43(2), 146.

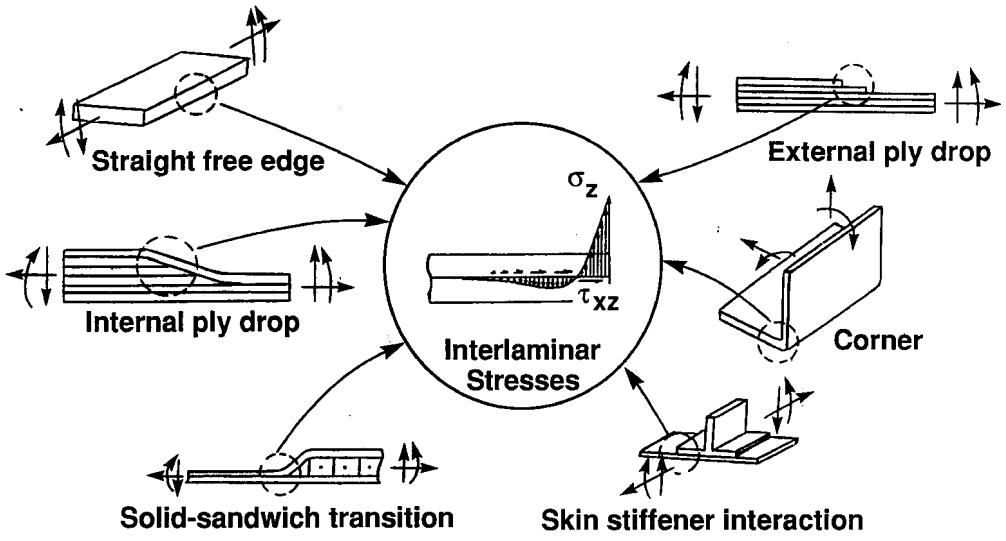

Fig. 1 Delamination Sources at Geometric and Material Discontinuities

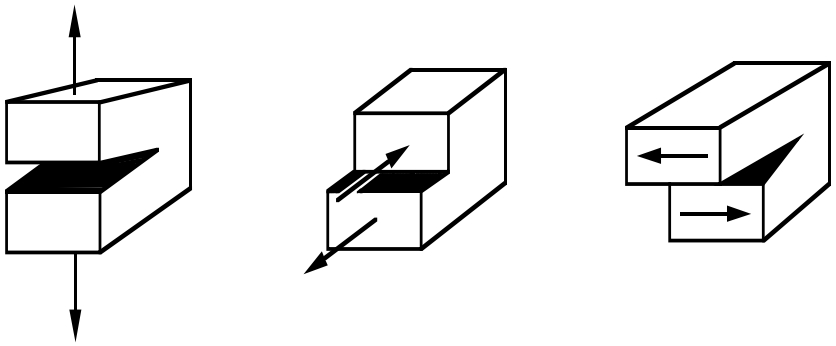

crack opening mode I | **sliding shear mode II** | **scissoring mode III**

Fig. 2 Three modes of delamination fracture

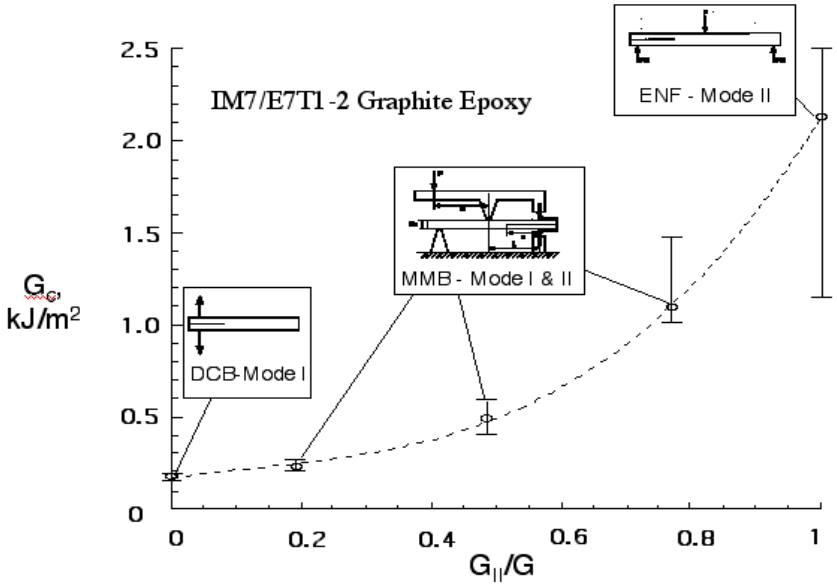

Fig.3 Mixed-Mode I & II Delamination Criterion

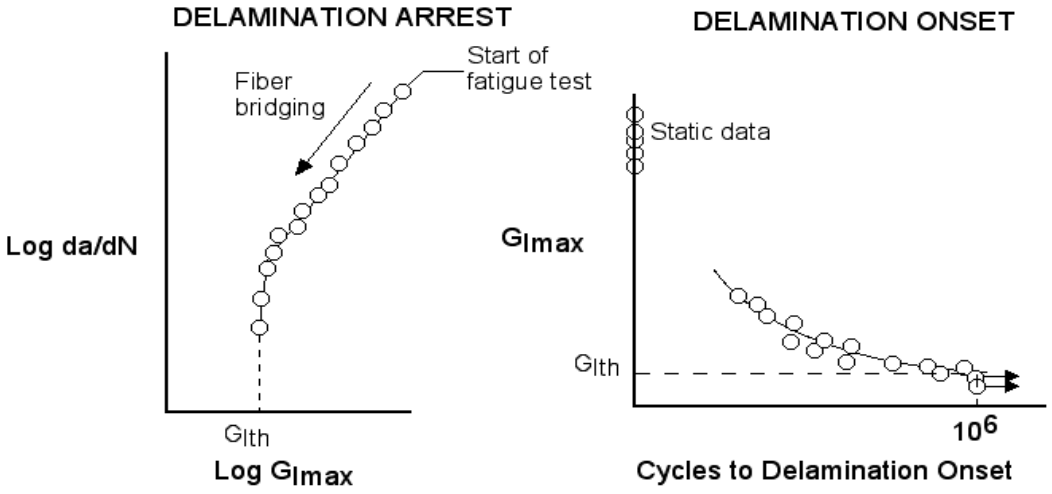

Fig.4 Experimental Technique to obtain a G Threshold for Delamination Onset

- **Eight-noded quadrilateral element**

$$G_I = \frac{1}{2\Delta a}\cdot\left(Y_i\cdot\Delta v_m + Y_j\cdot\Delta v_l\right)$$

$$G_{II} = \frac{1}{2\Delta a}\cdot\left(X_i\cdot\Delta u_m + X_j\cdot\Delta u_l\right)$$

- **Nonlinear Analysis**

$$G_I = \frac{1}{2\Delta a}\cdot\left(Y'_i\cdot\Delta v'_m + Y'_j\cdot\Delta v'_l\right)$$

$$G_{II} = \frac{1}{2\Delta a}\cdot\left(X'_i\cdot\Delta u'_m + X'_j\cdot\Delta u'_l\right)$$

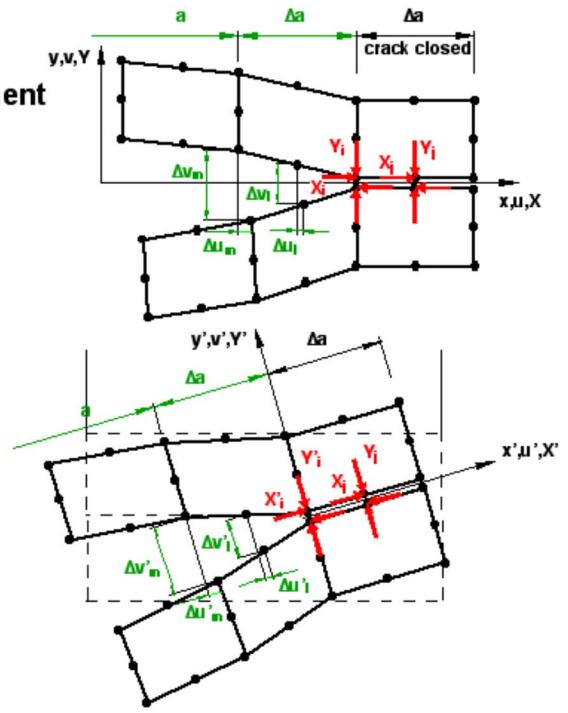

Fig. 5 Virtual Crack Closure Technique (VCCT)

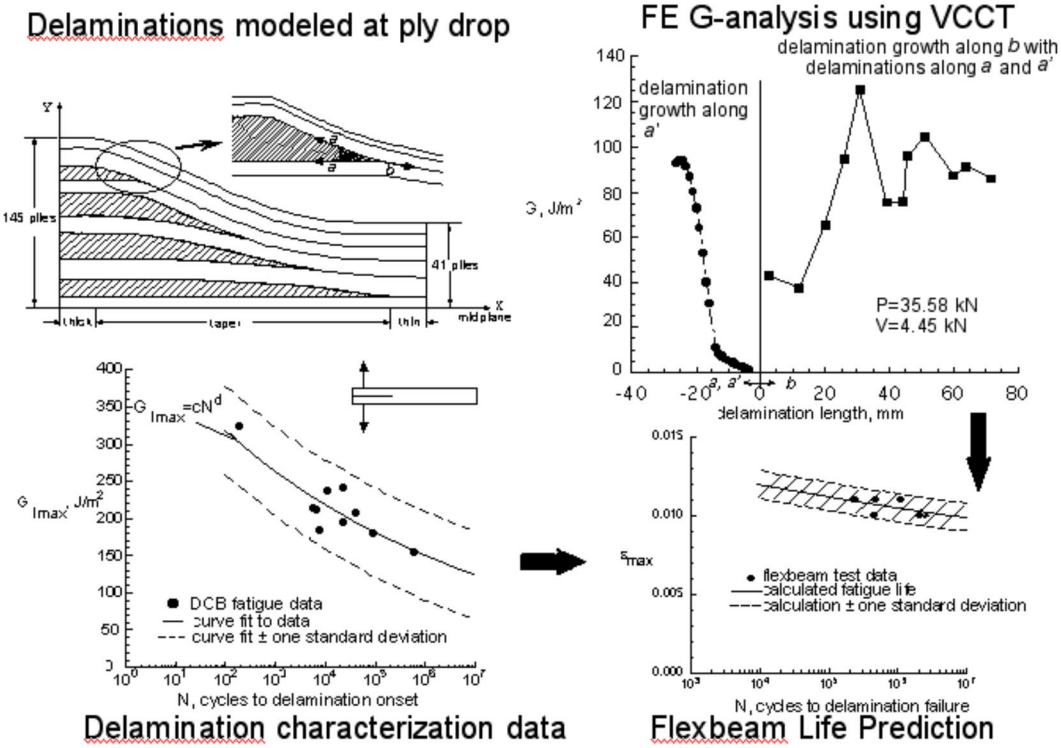

Fig. 6 Flexbeam Fatigue Life Prediction Methodology

Oral Reference: ICF1001085OR

CO-PLANAR CRACK INTERACTION IN CLEAVED MICA

J.C. Hill[1], S.J. Bennison[2], P.A. Klein[3], A. Jagota[2], S. Saigal[1]

[1]Department of Civil & Environmental Engineering, Carnegie Mellon University, Pittsburgh, (USA)
[2]CR&D, Experimental Station, The DuPont Company, Wilmington Delaware 19880-0356 (USA)
[3]Sandia National Laboratories, Livermore, California 94551 (USA)

ABSTRACT

This paper describes experimental work on cleavage of mica in a double cantilever beam (DCB) geometry in which the main crack induced by a wedge driven into one side of the specimen interacts with a pre-existing internal crack. The latter is introduced by inserting a fiber between the delaminating beams of the same mica specimen during a previous DCB experiment, followed by retraction of the wedge, which results in healing of the beams except for an internal crack wedged apart by the inserted fiber. The experiment has been simulated numerically using a cohesive zone model, implemented as cohesive elements, to represent the separating interface. As the main crack approaches the internal pre-existing crack, the two interact, resulting in mutual repulsion that manifests as an increase in apparent toughness. This feature of the experiment is captured very well by the model, independent of cohesive zone parameters other than the work of fracture. At a critical value of wedge displacement, the two cracks coalesce unstably, and the simulation captures this event as well. However, the instability condition depends on additional details of the cohesive zone law; by matching simulation to experiment one is able to extract a characteristic cohesive zone opening or peak cohesive stress.

KEYWORDS cohesive zone model, mica, instability, fracture.

INTRODUCTION

Cleavage experiments on mica by insertion of a wedge, a double cantilever beam (DCB) geometry, go back to the work of Obreimoff [1], have been re-visited often [2], and have contributed greatly to our understanding of the physics of fracture. Here we report on DCB experiments in mica in which a primary crack, induced by the wedge, interacts with a second, internal crack. These experiments build on the work of Wan *et al.* [3-5] on mica where, in particular, a repulsive interaction of co-planar cracks was observed. With increasing wedge insertion the two cracks coalesce eventually into one. The experiments have been simulated successfully using a cohesive zone model for the interfacial separation process. They reveal that the instability corresponding to crack coalescence depends on details of the cohesive zone model in addition to the fracture energy. By obtaining agreement between the experiments and simulation, one is able to extract a measure of the characteristic cohesive zone opening.

The cohesive zone approach to fracture, introduced originally by Barenblatt & Dugdale [6,7], has recently received considerable renewed attention [8,9,10]. It is especially powerful when implemented for numerical simulation of fracture, and is able to model different forms of inelasticity, crack nucleation and propagation. In particular, it has the potential to extend fracture analysis to small dimensions, and possibly to be a mechanism to bridge length scales. The cohesive zone approach requires the specification of a model that describes tractions resisting separation of material points at a crack tip. In an ideal elastic material, the macroscopic mechanics of a propagating crack when the cohesive zone is small compared to all dimensions are governed by the work of fracture alone [2]. Other cohesive zone parameters affect only the details of the stress and displacement fields near the crack tip. In inelastic materials, however, the work of fracture alone is insufficient; at least a second parameter is needed, such as peak separation stress or characteristic opening displacement. Even for a crack in an ideal elastic material, these details of the cohesive zone model can be important for crack initiation or certain instabilities.

EXPERIMENTAL PROCEDURE AND RESULTS

Material Selection and Preparation

Muscovite mica, an aluminum silicate, is a layered mineral with strong covalent intra-layer bonds and weak interlayer bonds. Because of this crystallographic structure, mica cleaves naturally. In addition, because muscovite mica is optically transparent, crack length measurements can be made by viewing interference fringes through the thickness. DCB specimens, 50 mm x 10 mm x 0.15 mm in dimension, were cut from single crystal muscovite mica sheets using a precision saw. To introduce an internal coplanar crack, the specimen was cleaved a distance of approximately 25 mm. A 7 μm carbon fiber was inserted across the width of the specimen and the cleaved mica was allowed to reheal. The fiber created a well-defined internal crack at the interface.

Experimental Test Procedure

Figure 1 illustrates the experimental apparatus. A crack was initiated in the prepared specimen using a 270 μm thick blade along the plane of the internal crack. Specimens with significantly asymmetric beams after crack initiation or with cracks on different cleavage planes were discarded. The cleaved mica was placed in the specimen holder and the wedge was adjusted vertically to minimize asymmetric displacements. A stepper motor pushed the mica specimen onto the blade in one-micron increments at a velocity of 20 microns per second. The crack propagation was viewed with an inverted optical microscope using green light with a wavelength of 550 nm. Crack lengths, measured from the fixed contact point of the wedge, were obtained using a micrometer attached to the microscope stage.

Fracture Energy Measurements

Based on beam theory, the relationship between the measured crack length c and the mechanical energy release rate G in a DCB configuration can be expressed as [11]

$$G = \frac{3Eh^3d^2}{4c^4}, \qquad (1)$$

where E is Young's modulus, $h = \left(\left(h_1^3 + h_2^3\right)/2\right)^{1/3}$ is the effective specimen thickness, and $2d$ is the wedge thickness. The modulus of elasticity for muscovite mica, as reported in the literature, varies from as low as 54.9 GPa [4] to as high as 196 GPa [1]. In this work, the Young's modulus has been taken to be 169 GPa, as measured by McNeil and Gremsditch [12] using Brillouin scattering.

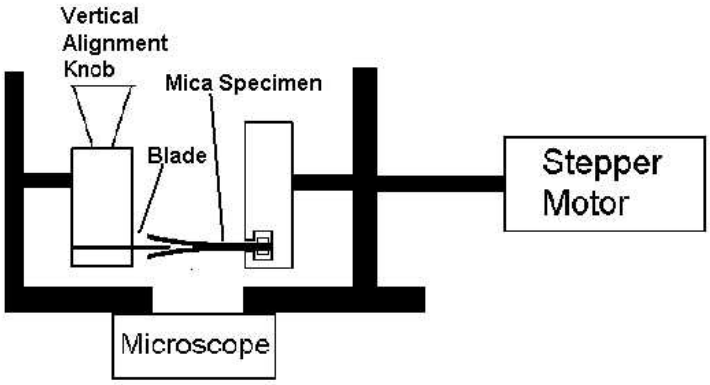

Figure 1: Constant displacement double-cantilever beam experimental apparatus. The vertical alignment knob is used to align the blade to create a symmetric crack. The stepper motor advances the mica specimen at 20 μm per second on the blade (~270 μm thick). The ensuing crack propagation is viewed using an inverted optical microscope.

Define an *apparent* fracture energy, G^*, as

$$G^* = \frac{3Eh^3d^2}{4c_1^4}, \qquad (2)$$

based on the length of the primary crack, c_1, due to the inserted wedge. G^* equals the fracture toughness G_c when the two cracks do not interact. When they do, it's departure from G_c measures the repulsion or attraction between the two cracks.

A typical crack interaction sequence is illustrated in Figure 2. Figure 2(a) shows the propagating DCB crack on the left approaching the crack front due to the inserted fiber, on the right. Note that in Figures 2(a) and 2(b), the distance between the two crack fronts remains roughly constant, though the crack front caused by the fiber has been repelled. In Figures 2(c-e), the distance between the two crack fronts continues to decrease until, just before Figure 2(f), the cracks coalesce.

Figure 3 shows the measured apparent fracture energy versus the wedge position. Initially, the apparent fracture energy G^* is approximately 800 mJ m^{-2}, its value for the healed interface. As the propagating crack front approaches the internal crack, the apparent fracture energy increases, then drops abruptly, and finally increases again to a value ≈ 1300 mJ m^{-2}, the fracture energy of virgin, uncleaved muscovite mica.

NUMERICAL SIMULATION

The experiment has been simulated numerically using the commercial finite element code, ABAQUS® [13], augmented with cohesive elements that model the separating interface [10]. The beams were modeled using two-dimensional plane strain elements; the simulation has been conducted as an implicit dynamic procedure to allow one to capture the instability. The dimensions and material properties reproduce the experimental specimen, i.e. length, L = 20 mm, beam thickness, h_1 = 133 μm, h_2, = 84 μm, wedge half-thickness, d = 133.5 μm, E = 169 GPa, ν = 0.3, G_1 = 820 mJ/m2, G_2 = 1250 mJ/m2.

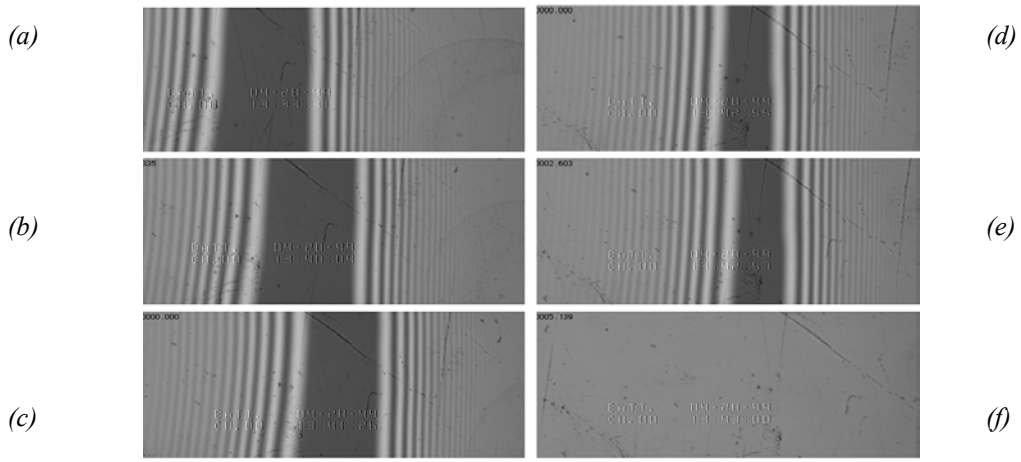

Figure 2: Series of experimental pictures illustrating crack repulsion. Crack front due to inserted wedge is on the left and crack front due to inserted fiber is on the right. Wedge positions relative to the fiber are (a) –9.51 mm, (b) –9.23 mm, (c) –8.98 mm, (d) –8.69 mm, (e) -8.64 mm, (f) –8.59 mm

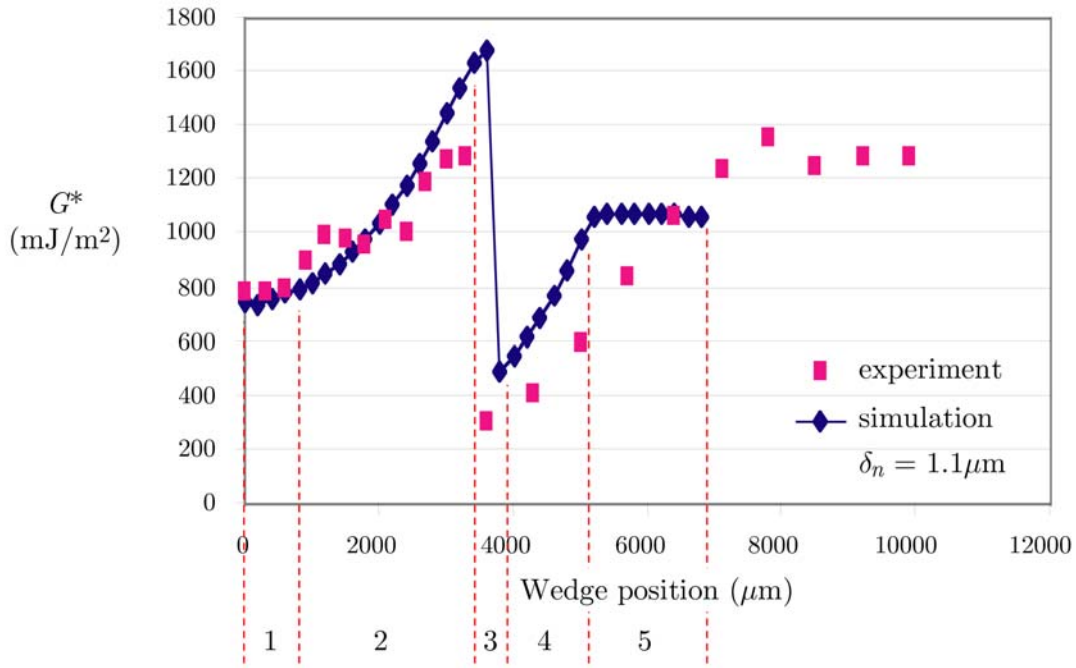

Figure 3: Measured and simulated apparent fracture toughness as a function of wedge position. Coalescence of the two cracks is simultaneous with the significant drop in apparent fracture energy. In the simulation, δ_{cr} = 1.1 μm.

The fracture zone has been modeled using a simplified version of the phenomenological cohesive law proposed by Xu and Needleman [8]. Tractions, T_n and T_t, resisting relative displacements in opening and shear are calculated from a potential function Φ, given as

$$\Phi(\Delta_n,\Delta_t)=\phi\left\{1-\exp\left(-\frac{\Delta_n}{\delta_{cr}}\right)\left[1+\frac{\Delta_n}{\delta_{cr}}\right]\exp\left(-\frac{\Delta_t^2}{\delta_{cr}^2}\right)\right\}, \qquad (3)$$

$$T_n = -\frac{\partial \phi}{\partial \Delta_n};\ T_t = -\frac{\partial \phi}{\partial \Delta_t}, \qquad (4)$$

where δ_{cr} is a characteristic opening of the cohesive zone, Δ_n and Δ_t are the normal and tangential relative displacements, and ϕ is fracture toughness. The maximum cohesive stress, σ_{max}, fracture toughness, and δ_{cr} are related through

$$\sigma_{\max} = \phi / \left(\delta_{cr} \exp(1)\right). \qquad (5)$$

The geometry used for the simulations was taken from measured specimen dimensions. A value of ϕ = 820 mJ/m^2 was used for the cohesive elements. This represents the measured fracture energy of the healed mica-mica interface, and is lower than that of uncracked mica. The carbon fiber inclusion was modeled by a circular rigid surface in contact with the continuum elements representing the beams. Wedge displacement was imposed by applying displacement boundary conditions to successive sets of nodes on the beams at the appropriate location, remote from the crack tip.

DISCUSSION & CONCLUSIONS

A comparison of simulated and experimental results is shown in Figure 3, for a critical cohesive zone opening, δ_{cr} = 1.1 μm. Also indicated in the figure are five notional stages. In stage 1, the interaction of the two cracks is minimal. In stage 5 there is only one crack in the system. In both, the apparent fracture toughness does not change with wedge location. Its value in stage 1 is estimated well by the simulation; this confirms that the simulation procedure is accurate enough to capture a simple DCB experiment. The under-prediction of fracture toughness in stage 5 is likely related to our use of a much coarser mesh in that region since the primary interest has been to capture the response prior to the instability, and the instability itself. Stage 2 represents the mutual repulsion between the cracks, which manifests as an increase in apparent toughness that is captured well by the simulation, although the simulated value exceeds the measured value. The simulation captures stage 3, the instability that leads to coalescence of the two cracks. After coalescence, the recovery to the uncleaved fracture energy is gradual, not immediate. We find, in the simulations, that the crack retains contact with the cylindrical fiber after coalescence, which results in a longer crack length than would be predicted due to the wedge alone, and hence a lower apparent fracture toughness. One may surmise that the same occurs in the experiment.

The numerical simulation captures all the features of the experiment very well qualitatively, with reasonably good quantitative agreement, generally. However, the value of critical opening parameter, δ_{cr}, required to do so, 1.1 μm, is much larger than might be expected for a brittle material. Figure 4 shows the effect of δ_{cr} on simulation results. Larger values result in earlier onset of the coalescence instability. It is interesting to note that whereas all other features of this experiment appear to be controlled solely by the energy release rate, the instability itself depends on additional parameters of the cohesive zone model. Two questions remain unanswered. Why is the value of δ_{cr} required to attain agreement between experiment and simulation so large? How do the conditions for coalescence instability scale with cohesive zone parameters? We have not resolved either satisfactorily at this time, but consider either capillary condensation or interaction between large charged domains as possible explanations for the former. Progress towards answering the latter question can likely be made by approximate analyses of the experiment using beam theory.

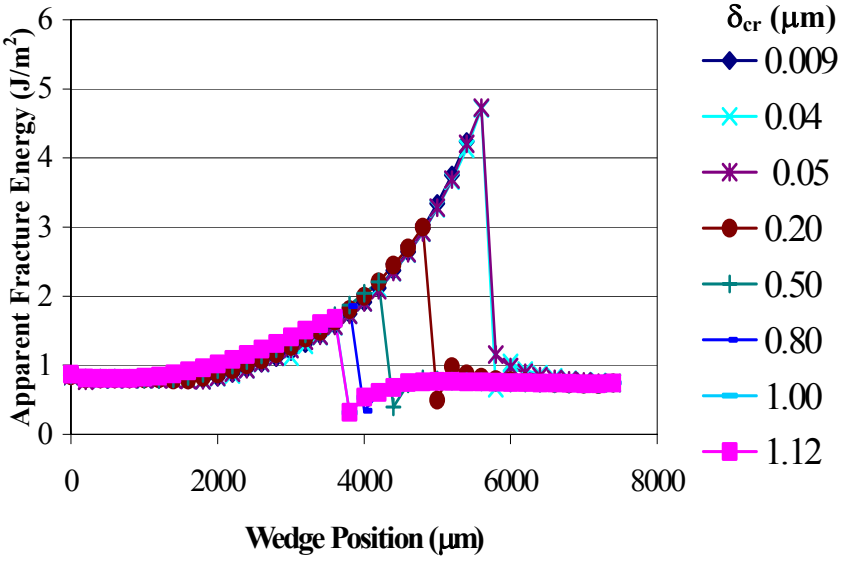

Figure 4: Effect of critical opening, δ_{cr} on the instability leading to coalescence of the two cracks.

ACKNOWLEDGEMENTS

This work was supported in part by the Computational Sciences Graduate Fellowship Program. Part of the work was carried out under the auspices of the Summer Institute of Sandia and under the NSF-Sandia Life Cycle Engineering Initiative. We'd also like to acknowledge the help with the experimental work of J.B. Brown & R.G. Bender at DuPont CR&D.

REFERENCES

1. Obreimoff, J.W. (1930) *Proc. Roy. Soc. Lond.* A217: 905.
2. Lawn, B. (1993), *Fracture of Brittle Solids*, Cambridge University Press.
3. Wan, K.T., Lathabai, S., & Lawn, B.R. (1990) *J. Eur. Cer. Soc.* **6**(4): 259-268
4. Wan, K.T. and B.R. Lawn. (1992) *Acta. Metall.* **40**(12).
5. Wan, K.T., Lawn, B.R., & Horn, R.G. (1992) *J. Mat. Res.* **7**(6): 1584-1588.
6. Barenblatt, G.I. (1959) *Appl. Math. Mech.* **23**: 622-636.
7. Dugdale, D.S. (1960) *J. Mech. Phys. Solids* **8**: 100-104.
8. Xu, X.-P. and Needleman, A. (1994) *J. Mech. Phys. Solids* **42**: 1397-1434.
9. Camacho, G.T. and Ortiz, M. (1996) *Int J Solids Structures* **33**:20-22: 2899-2938.
10. Rahulkumar, P., Jagota, A., Bennison, S.J., and Saigal, S. *Int. J. Solids Struct.*, **37** [13] 1873-1897 (2000).
11. Rice, J.R., (1968) in *Fracture*, Liebowitz H. (editor), Academic Press, 191-311.
12. McNeil, L.E., Grimsditch, M., (1993) *J. Phys.: Cond. Mat.* **5**(11): 1681-1690.
13. ABAQUS®, v 5.8, Hibbit, Karlsson & Sorensen, Inc., Pawtucket, Rhode Island (USA).

ICF1000673OR

COHESIVE AND ADHESIVE FRACTURE UNDER NANOSCALE CONTACTS: ENVIRONMENTAL AND MICROSTRUCTURAL EFFECTS

N.I. Tymiak*, A.Daugela*, M.Li**, T.J. Wyrobek*, and W.W. Gerberich**.

* Hysitron, Inc., Minneapolis, MN, 55439, USA
** University of Minnesota, CEMS, Minneapolis, MN, 55455

Present study evaluates fracture in ultra-small volumes utilizing nanoindentation combined with the nanoscale in-situ imaging and Acoustic Emission (AE) monitoring. Recently developed AE sensor integrated into an indenter tip provided a greatly increased sensitivity to contact loading induced transient processes. This enabled detection of AE events for the ultra-light contacts below 1 mN and assured an adequate basis for the AE signal analysis. Evaluated phenomena included fracture initiation in bulk materials, thin film cracking and film/substrate delamination. Indentation curves and in-situ images of the indented areas were correlated with the AE waveforms. Advanced procedures of AE signal decomposition provided additional information on separation of plasticity and fracture induced contributions of AE signals.

COHESIVE MODEL FOR THIN FILM/SUBSTRATE INTERFACIAL CLEAVAGE FRACTURE

Yu Shouwen Li Ran

(Department of Engineering Mechanics, Tsinghua University, Beijing 100084,China)

ABSTRACT Film/substrate structure is a basic structure widely used in microelectronic and materials science and technology. A modified three-parameter (Γ_0,σ/σ_y,t) cohesive model was used to investigate the cleavage fracture under plastic atmosphere. The model was also used to discuss the whole process of the initialization and extension of interface crack between uniform and functional graded metal thin film and ceramic substrate under residual stresses. This model was also used to analyze the interfacial crack extension between enhanced functional graded thin film and substrate. The characteristic of the interfacial crack in graded film/substrate was emphasized.

KEYWORDS embedded elastic zone, cohesive model, thin film/substrate structure, interfacial fracture

COHESIVE MODEL FOR CLEAVAGE FRACTURE UNDER PLASTIC ATMOSPHERE

Film/Substrate structure is a basic structure widely used in microelectronic and materials science and technology.. Liplin *et al.* [1] observed that the maximum separation stress can reach a high level, which was about 10 times of the yield stress. Tvergaard & Hutchinson [2][3] proved the results by using conventional plastic theory and EPZ model. At the same time, Hutchinson [4] pointed that for general metal/ceramic interface, the cleavage fracture toughness is about $1Jm^{-2}$,the macroscopic fracture toughness is about 400 Jm^{-2} to1000 Jm^{-2} and the crack tip keeps atomic scale keenness. There is great difference between these two fracture toughness.

It was considered that the fracture mechanism is atom separation. On the basis of this idea, SSV model has been proposed by Suo et al. [5], who assumed a dislocation-free strip present near crack tip. The SSV model was used by Wei et al. [6] Wei et al. [7] introduced a cohesive model in cleavage fracture process. This method was adopted and developed in this paper.

In EPZ and SSV model, two parameter were introduced to describe the fracture process zone. In EPZ model, the parameters are fracture toughness Γ_0 and maximum separation stress $\hat{\sigma}$,In SSV model, they are Γ_0 and the thickness of elastic strip, t. In cohesive model introduced by Wei [7] and used in this paper, SSV model and EPZ model were combined and three parameters, $\Gamma_0, \hat{\sigma}$ and t, were introduced to discuss the fracture process, which was shown in Fig.1.

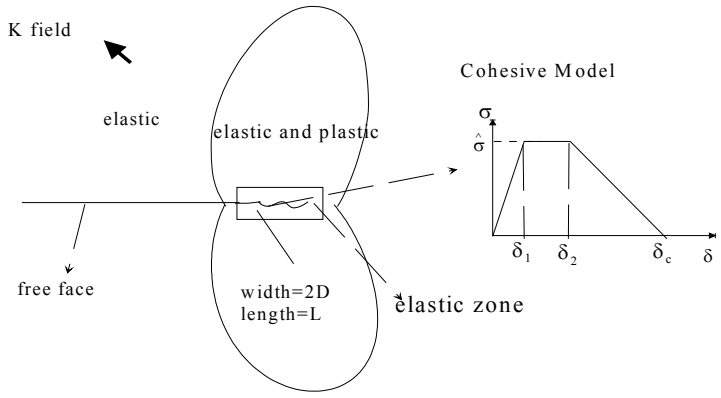

Fig. 1 Cohesive model for embedded elastic zone

INTERFACIAL FRACTURE OF UNIFORM FILM/SUBSTRATE STRUCTURE

Model for the residual stress induced interfacial fracture

In the machining process of film/substrate, the residual stress is often produced for the change of the temperature. The temperature of the film and the substrate is t_0 either. Aparently , there are residual stresses in the film, and the stress can induce the interface crack to initiate and propagate. It was assumed the film keeps plane strain restriction in x-y plane. Taking $T=t_1-t_0$, the residual stress can be express as

$$\sigma_R = \sigma_x = \sigma_z = \alpha ET/(1-\nu) \tag{1.}$$

Energy release ratio can be expressed as

$$G = \frac{1-\nu^2}{2E}\sigma_R^{\,2} h \tag{2.}$$

Taking $\delta_1/\delta_c=0.15$, $\delta_2/\delta_c=0.5$, $E/\sigma_y=300$, $k=\hat{\sigma}/\sigma_y$ and N=0.1, we can got the initial residual stress and initial temperature difference of crack propagation as below

$$\sigma_R^{\,0} = E\sqrt{\frac{4.5*10^{-3}}{(1-\nu^2)}}\sqrt{\frac{k\delta_c}{h}},\quad T^0 = \frac{1}{\alpha}\sqrt{\frac{4.5*10^{-3}(1-\nu)}{1+\nu}}\sqrt{\frac{k\delta_c}{h}} \tag{3.}$$

In brief, the module mismatch of film and substrate was ignored and we take $E_m= E_c$ and $\nu_m=\nu_c=0.3$. In the computation, we introduce nondimensional method for fracture process. When the results were changed to dimensional value with $\Gamma_0=1Jm^{-2}$ and $E=6\times10^{10}Pa$, we can acquire $\delta_c=7.407Å$, $R_0=0.1749\ \mu m$, t=8.74nm and h=0.3498um.

Resistance curve of crack propagation and the influence of the parameter on crack propagation

With $t/R_0=0.05$, $\hat{\sigma}/\sigma_y=10$ and $h/R_0=2$, the resistance curve can be calculated from the curve that Γ_s/Γ_0 approximately equals to 88.36. Compared with the results of infinite medium in which Γ_s/Γ_0 approximately equals to 400~1000, the plastic zone was restricted and can't develop completely for the scale of the thin film and the free upper surface.

The slopes of the two curves only have minor difference. The main differences are the critical σ_R^c and the critical length of crack propagation. The values of $h/R_0=4$ are much larger than that of $h/R_0=2$ because the plastic zone can more fully develop when the thickness of the film is larger. It can be concluded that when $h>>R_0$, the value of Γ_s will reach to the macroscopic fracture toughness of the interface between metal film and ceramic substrate.

INTERFACIAL FRACTURE OF GRADED FILM/SUBSTRATE STRUCRURE

Functionally graded structure is an important structure widely used in microelectronic and materials

science and technology. The continuous changes of materials' nature can greatly decrease the thermal and mechanical mismatch between different materials. In this paper, the enhanced thin graded film on ceramic substrate and the weakened graded film on metal substrate were discussed. The main purpose is to investigate the character of the propagation of interfacial crack under the drive force of residual stress and to make sure the effect of decreasing the mismatch. And the cohesive model and embedded elastic zone were used in the computation.

Enhanced graded film on ceramic substrate

The similar model showing above was introduced in this section. The process that residual stress induced crack to propagate was simulated. First we assume that the value E_m equals to E_c and v_m equals to v_c. T was taken as drive force for crack propagation. The T_0 was taken as the initial resistance force.

We take the calculation under plane strain conditions and $\delta_1/\delta_c=0.15$, $\delta_2/\delta_c=0.5$, $E(x)/\sigma_y(x)=300$, $v=0.3$, $t/R_0=0.05$, $\hat{\sigma}/\sigma_y=10$, $h/R_0=4$. For comparing with the result of the uniform film, the same T_0 in uniform film was taken. The relations between the true T_0 and the T_0 used in uniform film will be discussed later. We have

$$T^0=\frac{1}{\alpha}\sqrt{\frac{4.5*10^{-3}(1-v)}{1+v}}\sqrt{\frac{k\delta_c}{h}} \tag{4.}$$

The linear change of the mechanical and thermal parameter in the direction of thickness was assumed.For enhanced graded film ,we have $E_m>E_c$, $\alpha_m>\alpha_c$,, $\sigma_m>\sigma_c$ and take $E_m=2E_c$, $\alpha_m=2\alpha_c$, $\sigma_m=2\sigma_c$, and can get the results of stress distribution near crack tip.

We take $E_m=3E_c$, $\alpha_m=3\alpha_c$, $\sigma_m=3\sigma_c$ (signed 2), and compared the stress distribution near crack tip with the results of $E_m=2E_c$, $\alpha_m=2\alpha_c$, $\sigma_m=2\sigma_c$ (signed 1), which was shown in Fig. 2. It can be seen that there is only minor different between these two curves. On the basis Fig. 2, we can draw a conclusion that the graded structure in thin film has only a minor influence on the stress distribution and the three parameters of cohesive model have major influence on the distribution.

On the basis of the stress distribution, we can also acquire the displacement distribution. We take $E_m=2E_c$, $\alpha_m=2\alpha_c$ and $\sigma_m=2\sigma_c$ and plot the distribution in Fig. 3b. The similar conclusion can also be drawn that graded structure in thin film has only a minor influence on the displacement distribution.

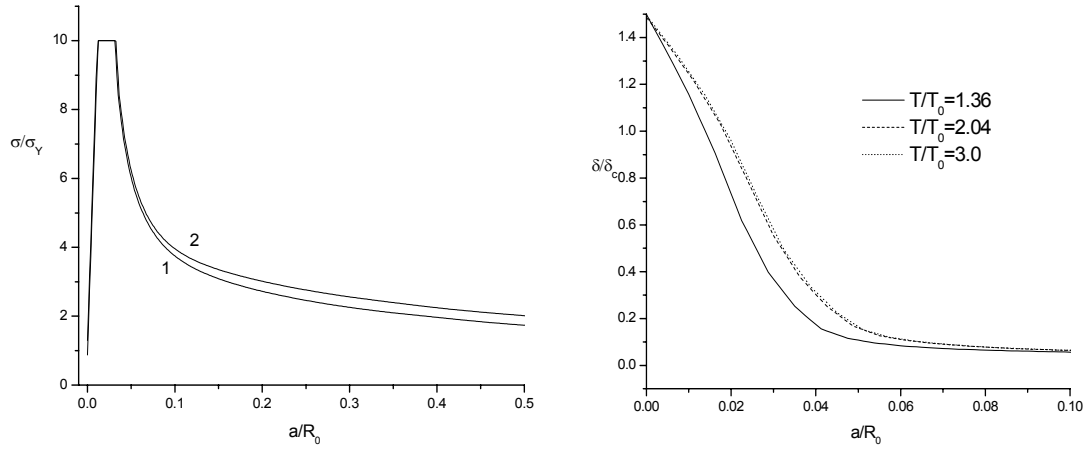

(a) (b)

Fig. 2 Stress and displacement distribution near crack tip

The different structures of graded films have influence on the resistance curve of crack propagation. First, we compared the results of the two structures, $E_m=3E_c$, $\alpha_m=3\alpha_c$, $\sigma_m=3\sigma_c$ (signed 2) and $E_m=2E_c$, $\alpha_m=2\alpha_c$, $\sigma_m=2\sigma_c$ (signed 1). The result was show in Fig. 4. In Fig.4a, the initial resistance force was discussed. It can be seen that the two structures have different initial resistance force. For structure (1), the true resistance force is about $0.855T_0$, which is the value in uniform film. For structure (2), the true value is $0.456T_0$. So It can be concluded that the crack between enhanced graded film and ceramic substrate is easier to propagate compared with that of the uniform film, and the more E_m/E_c, the easier to propagate. The reason is that the enhanced structure makes the film more difficult to come into plastic and easier to propagate. The similar result was acquired in crack propagation, which was shown in Fig. 3b. It can be seen that the graded film can greatly decrease the fracture toughness of interfacial crack propagation compared with the uniform film, and the more E_m/E_c, the more decrease. For example, for structure (1), the critical resistance force is about 40% of that of the uniform film. For structure (2), the critical resistance force is about 20% of that of the uniform film.

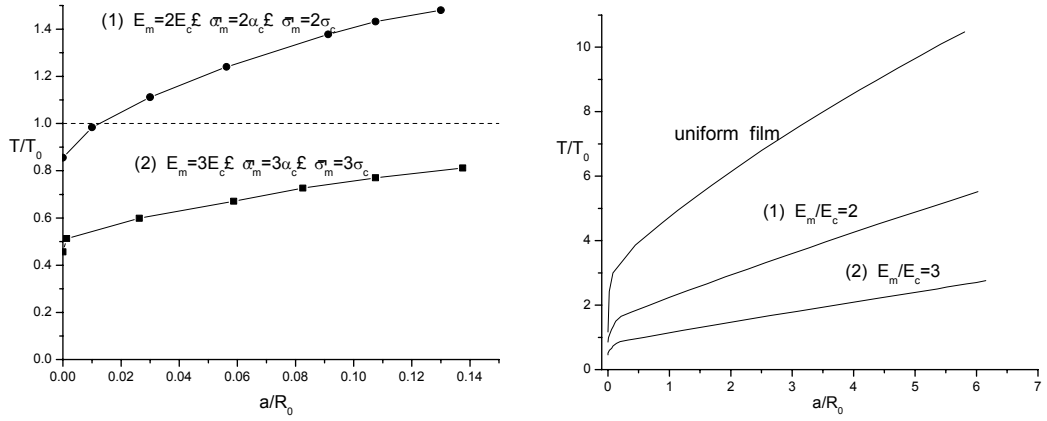

(a) (b)

Fig. 3 The influence of graded structure on crack initiation and propagation

In the process of making graded film on substrate, the rate of two materials can be controlled and different curve of parameter's change can be attained. The influence on the resistance curve will be discussed. We still take $E_m=2E_c$, $\alpha_m=2\alpha_c$, $\sigma_m=2\sigma_c$, and take different changing curves which were shown in Fig.4.

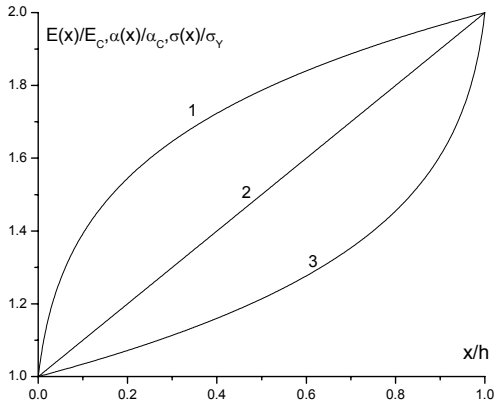

Fig. 4 Different changing curve

Curve 1 followed the expression below ($E(x)/E_c$, $\alpha(x)/\alpha_c$ and $\sigma(x)/\sigma_c$ are all equal to $f(x)$),

$$f(x) = 0.67951[640\frac{x}{h} + 10.159)]^{\frac{1}{6}} \tag{5.}$$

Curve 3 is symmetrical with curve 1 in point (0, 5, 1.5) and followed the expression below.

$$f(x) = 3 - 0.67951[640\frac{1-x}{h} + 10.159)]^{\frac{1}{6}} \tag{6.}$$

The three crack resistant curves were show in Fig. 5. It can be seen that in curve 1, the crack became unstable when initialing and propagating for a short distance. It is because that the elastic module and other parameters increase rapidly near the crack in thickness direction and the zone of the film near crack is difficult to come into plastic, the crack became unstable when the drive force is a little higher than the initial resistance force. But compared with uniform film, the structure expressed by curve 3 is difficult to propagate because the zone near crack is easier to come into plastic and more work will be dissipated in plastic yielding. But the critical fracture toughness of structure 3 is still much lower than uniform film because the upper part of the graded film was harder and more difficult to come into plastic and the plastic zone was restricted in a thin zone near crack tip.

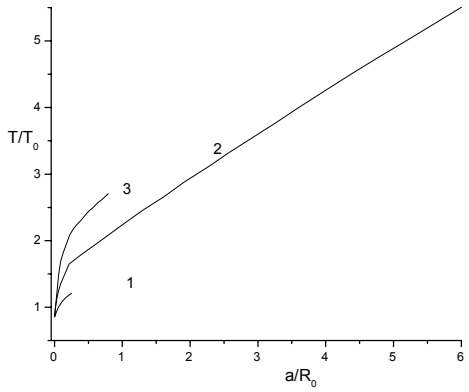

Fig. 5 The influence of different curves on resistance curve of crack propagation

On the basis of the discussion, we can draw a conclusion that for the enhanced thin film on substrate, the most critical fracture toughness and critical propagation length can be attained when the mechanical parameters (elastic module and yield stress) vary linearly. This result can do some favor for the optimizing the film structure and mechanical property.

The mechanical and thermal mismatched thin film on substrate was also investigated and compared with the graded film. The effect of the graded film on decreasing crack propagation between film and substrate was discussed. We also take $E_m=2E_c$, $\alpha_m=2\alpha_c$, $\sigma_m=2\sigma$. The resistance curve was plotted in Fig.6.

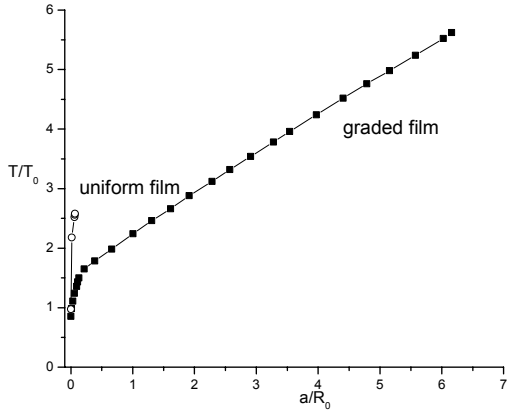

Fig. 6 The effect of graded film on decreasing interfacial crack propagation

It can be seen that because the parameter $\hat{\sigma}$ in mismatch uniform film is two times of that in graded film, the initial fracture toughness improved largely, which is about two times of the toughness in graded film. But the crack propagated in mismatch film became unstable when drive force exceeds the initial value very little. Compared with the mismatched film, the crack propagation of graded film has a much higher critical fracture toughness and a strong restrain on crack propagation.

CONCLUSIONS

A modified three parameter cohesive model embedded with elastic core was introduced to investigated

This model was used to analyze the interfacial crack extension between enhanced graded thin film and substrate. Compared with the uniform film/substrate structure mismatched in mechanical and thermal parameter, the graded film/substrate increased the critical fracture toughness and critical length of crack extension largely. The distribution of stress and displacement in fracture process zone are mainly determined by the parameters of process zone model and the deferent variation of the graded film has a minor influence on them.. The highest critical fracture toughness and critical length of crack extension can be acquired when the material parameters vary linearly on the graded thin film/substrate structure.

ACKNOWLEDGEMENTS

This project supported by National Natural Science Foundation of China (19891100(4)) and Tsinghua Fundamental Research Foundation.

REFERENCES

[1] Lipkin, D.M., Clarke, D.R. and Beltz, G.E.(1966) . *Acta Materialia.* 44. 4051.
[2] Tvergaard, V. & Hutchinson, J.W. (1992) *J. Mech. Phys. Solids*., 40,1377
[3] Tvergaard, V. & Hutchinson, J.W.(1993) *J. Mech. Phys. Solids*., 1993(41): 1119.
[4] Hutchinson, J.W. In *Advances in Fracture Research*.(1997) Sydney, Australia: ICF9, Vol.2,1~14,
[5] Suo, Z., Shih, C.F. and Varias, A.G.(1994) *Acta Metall. Mater.*, 41.1551.
[6] Wei, Y., Hutchinson, J.W.(1997) . *J. Mech. Phys. Solids.*, 45. 1137.
[7]Wei, Y. and Hutchinson, J.W.(1999) . *Inter. J. Fracture*, 95.1.

COHESIVE-ZONE MODELING OF DEBOND GROWTH AT ADHESIVELY BONDED INTERFACES IN AGGRESSIVE ENVIRONMENTS

Samit Roy*, D. Nagendra*, and K.M. Liechti**
***Mechanical Engineering Department, Oklahoma State University**
****Engineering Mechanics Department, University of Texas-Austin**

Abstract

In this study, a node-release algorithm based on a linear traction separation law was implemented in a test-bed finite element code that was developed to simulate normal (Mode I) and tangential (Mode II) crack growth at the interface. The combined effects of nonlinear viscoelasticity, temperature cycles, and moisture diffusion in the adhesive layer and their influence on crack-growth rates are included in the model. The particular values of the parameters of the traction-separation law can be determined through comparison with crack opening displacement data from test specimens following an iterative procedure previously established. The effect of crack length on mode mix and the existence of asymmetric shielding mechanisms can be accurately assessed using this procedure. Some preliminary benchmark results are presented.

Bond Durability Modeling Approach

One of the primary objectives of the current study is to be able to model the synergistic bond degradation mechanisms at the adhesive-composite interface. The following sections describe the details of the synergistic modeling approach.

Diffusion Controlled Crack Growth

Environmental cracking in a polymer typically occurs in the presence of a penetrant, such as moisture, and stress. It has been postulated that the mechanism involved in environmental crack growth in a polymer involves a small zone of craze formation and/or plasticization at the crack tip due to stress-enhanced moisture ingress. For the case of craze formation, Darcy's law for diffusion in porous media can be used to predict crack (or craze zone) growth. However, for thermoset resins, such as epoxy, energy absorption at the crack tip is primarily by a shear yielding process and not by crazing. Consequently, for a thermoset epoxy, the zone of plasticization ahead of the crack tip must be determined using a diffusion law for non-porous media, such as Fick's law. In the event of synergistic interaction between several processes, a crack will grow at the rate determined by the slowest controlling process and when this is diffusion, then there is diffusion-controlled crack growth.

Free Volume Constitutive Model

The free volume constitutive model [1,2] is based on the premise that the mechanical response of a viscoelastic polymer is dependent on the ability of its molecular chains to accommodate imposed deformations. Free volume may be conceptualized as the volume that is not occupied by the molecular chains in the material. Free volume is typically considered an indicator of molecular segmental mobility, where greater free volume provides the extra mobility needed to accommodate imposed deformations quickly.

Studies of the variables influencing the time scale of viscoelastic materials have shown that temperature, solvent concentration and mechanical dilatation all influence the time scale of the material in a similar manner. Hence the shift factor $a(T,c,\theta)$ can be represented as a function of temperature (T), solvent concentration (c) and mechanical dilatation (θ). Doolittle [3] defined a shift factor relating the fractional free volumes of a material at the current and reference states through the expression,

$$\log_{10} a = \frac{B}{2.303}\left(\frac{1}{f} - \frac{1}{f_0}\right) \quad \textbf{(1)}$$

where, B = a constant, f = fractional free volume at the current state, f_0 = fractional free volume at the reference state. Knauss and Emri [1,2] postulated the fractional free volume to depend on temperature (T), solvent concentration (c) and mechanical dilatation (θ). Therefore the fractional free volume can be expressed as,

$$f = f_0 + A.\alpha * dT + B.M(t) * \sigma_{kk} + C.\gamma(t) * dc \quad \textbf{(2)}$$

where, $\alpha(t)$ and $\gamma(t)$ are the volume coefficients of thermal and moisture expansion. In general, $\alpha(t)$ and $\gamma(t)$ are functions of T, c, the creep compliance $M(t)$ is a function of $\theta(t)$, V_0 is a reference volume, σ_{kk} is the first stress invariant, and A, B, C are constants to be determined. Note that the (*) notation used in eqn. (2) denotes Stieltjes convolutions representing the time history of the respective variables. For small changes in variables below the glass transition temperature of the polymer and the boiling point of the penetrant, it is assumed that $\alpha(t)$, $\gamma(t)$ and $M(t)$ are constants with respect to time. Further under such conditions, simple multiplicative relations can replace the convolutions in eqn. (2), giving,

$$f = f_0 + \alpha\Delta T + \gamma\Delta c + \delta\theta \quad , \quad \text{where } \theta = \varepsilon_{kk} \text{, and } \delta \text{ is a material constant} \quad \textbf{(3)}$$

Substituting eqn. (3) in eqn. (1) gives the nonlinear shift factor,

$$\log a(T,c,\theta) = -\frac{B}{2.303 f_0}\frac{\alpha\Delta T + \gamma\Delta c + \delta\theta}{f_0 + \alpha\Delta T + \gamma\Delta c + \delta\theta} \quad \textbf{(4)}$$

For negligible solvent concentrations and dilatation eqn. (4) reduces to the WLF equation. It was found from experimental data [4] that the value of δ was very close to unity, so henceforth the model assumes that δ = 1. In this model the nonlinear shift factor definition in eqn. (4) incorporates all the nonlinearity in the linear viscoelastic constitutive description of an isotropic solid under infinitesimal deformations. At reference conditions, the constitutive equations for a viscoelastic material are,

$$\begin{aligned} s_{ij} &= \int_{-\infty}^{t} 2\mu(t'-\tau')\frac{\partial e_{ij}}{\partial \tau}\, d\tau \\ \sigma_{kk} &= \int_{-\infty}^{t} 3K(t'-\tau')\frac{\partial(\theta+\alpha\Delta T+\gamma\Delta c)}{\partial \tau}\, d\tau \\ t'-\tau' &= \int_{\tau}^{t} \frac{d\xi}{a[T(\xi),c(\xi),\theta(\xi)]} \end{aligned} \qquad \textbf{(5)}$$

where s_{ij} and e_{ij} are components of deviatoric stress and strain tensors. The nonlinear set of equations (3) - (5) account for the temperature, solvent concentration, and dilatation histories and essentially comprise the free volume constitutive model.

Cohesive Zone Model

The cohesive zone interface model was developed by Needleman [5] in order to provide a unified description of crack initiation from initial debonding through complete separation and subsequent crack growth. The interface constitutive equation developed in the model was such that, with increasing interface separation, the traction across the interface of the crack reaches a maximum, decreases, and eventually vanishes so that complete decohesion occurs. The subsequent mechanical response of the crack is dependent on the strength of the interface, which is specified by the critical stress measure near the tip of the crack, and the work of separation per unit area. This interface model is based on the cohesive zone model developed by Dugdale and Barenblatt. Needleman introduces a characteristic length in order to determine the size of the cohesive zone where the tractions are to be applied, the equivalent of which is defined as the crack tip opening displacement in the Dugdale-Barenblatt model. The tractions at the interface are therefore a function of the crack tip opening displacement. Further investigations of crack growth in thin film blistering of polyimide film on aluminum substrate by Shirani and Liechti [6] made use of a simplified version of the Needleman interface model. In this case, the decay of tractions with the result of the traction separation law was simulated as non-linear softening springs attached to the nodes of the crack interface in the finite element model. This method has been referred to as "nodal relaxation" by several authors [7,8,9] due to the gradual decrease in traction force rather than the immediate release of the node due to debonding. The dependence of the

tractions on the crack tip opening displacement is considered invariant with respect to quasi-static propagation in a controlled environment as specified by Ungsuwarungsri and Knauss [10]. The use of the traction separation law as improvised by Shirani and Liechti has been successfully incorporated into a test-bed (NOVA-3D) finite element code to analyze tensile decohesion for elastic structures in two and three-dimensional cases. In this model, attention is directed towards the interface close to the crack that supports a nominal traction field **T** (force/unit reference area), which in general, has both normal and shearing components. Two material points A and B may be chosen which were initially on opposite faces of the interface and the interfacial traction is taken to depend only on the displacement difference vector across the interface, $\mathbf{\Delta u}_{\mathbf{AB}}$. Thus at each point on the interface, we may define normal and tangential components of displacements and tractions,

$$u_n = \mathbf{n} \cdot \mathbf{\Delta u}_{\mathbf{AB}}, \qquad u_t = \mathbf{t} \cdot \mathbf{\Delta u}_{\mathbf{AB}} \tag{6}$$

$$T_n = \mathbf{n} \cdot \mathbf{T}, \qquad T_t = \mathbf{t} \cdot \mathbf{T} \tag{7}$$

where, T_n = normal component of traction, T_t = shear component of traction, and positive u_n corresponds to increasing interfacial separation. This dependence of the traction magnitude on the amount of the separation between the interfaces can be expressed in terms of a potential $\phi(u_n, u_t)$, which is defined as,

$$\phi(u_n, u_t) = -\int_0^u [T_n du_n + T_t du_t] \tag{8}$$

As shown in Fig. 1, Needleman defined the model in such a way that as the interface separates, the magnitudes of the tractions increases, achieves a maximum and ultimately falls to zero when complete separation occurs. The model shown is defined for pure normal tractions on the interface with u_t being zero. Needleman has proposed to define the traction-separation curve in terms of the potential as,

$$\phi(u_n, u_t) = \frac{27}{4}\sigma_{\max}\delta\left\{\frac{1}{2}\left(\frac{u_n}{\delta}\right)^2\left[1 - \frac{4}{3}\left(\frac{u_n}{\delta}\right) + \frac{1}{2}\left(\frac{u_n}{\delta}\right)^2\right]\right\} \tag{9}$$

where, $\sigma_{\max}$= maximum traction carried by the interface undergoing pure normal separation, and, δ is a characteristic length. When $u_n > \delta$ then $\phi \equiv \phi_{sep}$, where ϕ_{sep} is the work of separation. The interfacial tractions for pure normal separation may be obtained by differentiating eqn. (9) and setting u_t=0 to give,

$$T_n = \frac{\partial \phi}{\partial u_n} = -\frac{27}{4}\sigma_{\max}\left\{\left(\frac{u_n}{\delta}\right)\left[1 - 2\left(\frac{u_n}{\delta}\right) + \left(\frac{u_n}{\delta}\right)^2\right]\right\} \quad \textbf{(10)}$$

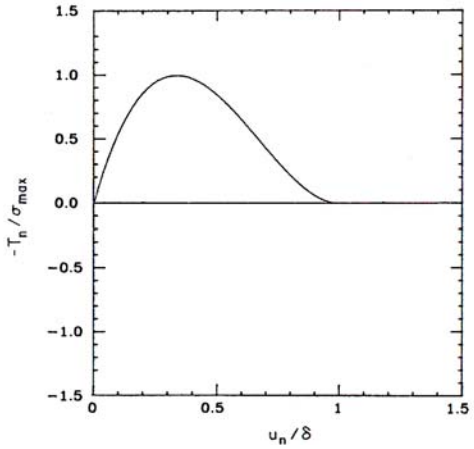

Figure 1. Normal tractions across the crack interface as a function of normal displacements

The fracture energy (work of separation) is defined as the area under the curve in Figure 1 and is given by,

$$\phi_{sep} = 9\sigma_{\max}\,\delta/16 \quad \textbf{(11)}$$

For a given fracture energy based on the material and stress at the crack tip, the value of δ may be computed using eqn. (11).

Preliminary Benchmark Results

Figure 2 depicts the strain energy release rate as a function of incremental crack length obtained from the analysis of an elastic Double Cantilever Beam (DCB) specimen employing the cohesive-zone crack growth model. The benchmark plot shows good agreement of the test-bed code (NOVA-3D) results when compared with crack growth data obtained from the commercial finite element code ABAQUS. Synergistic interfacial crack growth modeling in the presence of diffusing penetrants, material nonlinearities, and adhesive viscoelastcity is currently underway.

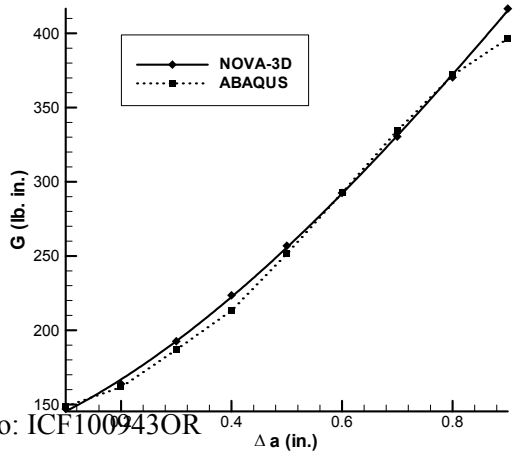

Figure 2. Strain energy release rate vs. incremental crack length, DCB steel specimen, constant load test, P = 600 lb.

Acknowledgement

The authors would like to thank the Automotive Composites Consortium, and the CMS Division of the National Science Foundation for supporting this research.

List of References

1. Knauss, W.G. and Emri, I., Non-Linear Viscoelasticity based on Free Volume Consideration, Computers and Structures, V.13, pp. 123-8, 1981.
2. Knauss, W.G. and Emri, I., Volume Change in the Nonlinearly Thermo-Viscoelastic Constitution of Polymers, Polymer Engineering and Science, V.27, pp. 86-100, 1987.
3. Doolittle, A.K., Studies on Newtonian Flow. II. The Dependence of the Viscosity of Liquids on Free-Space, Journal of Applied Mechanics, V.22, pp. 1471-5, 1951.
4. Knauss, W.G. and Kenner, V.H., On the Hygrothermomechanical Characterization of Polyvinyl Acetate, Journal of Applied Physics, V.51, pp. 5131-6, 1980.
5. Needleman, A., A Continuum Model for void Nucleation by Inclusion Debonding. Journal of Applied Mechanics, Vol. 54, pp. 525-531, 1987.
6. Shirani, A. and Liechti, K. M., A Calibrated Fracture Process Zone Model for Thin Film Blistering. International Journal of Fracture, Vol. 93, pp. 281-314, 1998.
7. Malluck J. F. and King W. W., Fast Fracture Simulated by Conventional Finite Elements: A Comparison of Two Energy-Release Algorithms, Crack Arrest Methodology and Applications, ASTM STP 711, G. T. Hahn and M. F. Kanninen, Eds., American Society for Testing and Materials, pp. 38-53, 1980.
8. Malluck J. F. and King W. W., Fast Fracture simulated by a Finite Element Analysis which accounts for crack tip energy dissipation. International Conference on Numerical Methods in Fracture Mechanics, pp. 648-659, 1978.
9. Rydholm G., Fredriksson B. and Nilsson F., Numerical investigations of rapid crack propagation. International Conference on Numerical Methods in Fracture Mechanics, pp. 660-672, 1978.
10. Ungsuwarungsri, T. and Knauss, W. G., The Role of Damage-Softened Behavior in the Fracture of Composites and Adhesives. International Journal of Fracture, Vol. 35, pp. 221-241, 1987.

ORAL/POSTER REFERENCE:ICF100928OR

COINCIDENCE DOPPLER BROADENING POSITRON ANNIHILATION SPECTROSCOPY IN DEFECTS IN IRON AND SILICON

M. Fujinami[1], T. Sawada[1], and T. Akahane[2]

[1]Department of Advanced Materials Science, The University of Tokyo,
Hongo, Bunkyo, 113-0033, JAPAN
[2]Advanced Materials Laboratory, National Institute for Materials Science,
Namiki, Tsukuba, 305-0044, JAPAN

ABSTRACT

Coincidence Doppler broadening (CDB) method in positron annihilation spectroscopy has been applied to chemical state analysis of the vacancy-impurity complexes in silicon and iron implanted with various ions. In Si implanted with oxygen $2x10^{15}/cm^2$ at 180 keV and hydrogen $1x10^{16}/cm^2$ at 60 keV, the defect structure has been discussed. CDB spectra reflect the character of elements coupled with vacancies very well, and enables us to estimate the number of impurities in the defects with combination of positron lifetime measurement. In Cu ion ($5x10^{15}/cm^2$ at 140 keV) implantation to Fe, it has been directly proved that vacancies and Cu atoms aggregate and that the inner wall of V-Cu complexes is covered with Cu atoms.

KEYWORDS

Positron annihilation spectroscopy, Coincidence Doppler broadening, Vacancy-impurity complexes, Chemical analysis, Silicon, Iron

INTRODUCTION

Positron annihilation spectroscopy is one of the most powerful techniques for studying the defects in solids and gives information on size and quantity in open-volume type defects. It is very important to observe the behavior of defects coupled with impurities because it is strongly dependent on a kind of impurity. Positron lifetime and shape of annihilation γ-rays spectrum strongly depend on them, although it is very difficult to extract the information of impurity from their measurements. A coincidence Doppler broadening (CDB) method in positron annihilation spectroscopy has been recently developed to carry out the chemical analysis of defects [1,2,3]. The positrons trapped at vacancy-impurity (V-I) complexes annihilate electrons due to impurity. Annihilation with core electrons gives larger Doppler shifts compared with valence electrons, so that it is possible to identify the impurity by analyzing the high electron momentum region. The CDB method improves the peak to background ratio in the annihilation spectrum to around 10^5 and fine structures due to core electrons

from impurity atom can be discussed. In this paper, with a combination of positron lifetime measurements, CDB method has been applied to study the defects in silicon and iron implanted with various kinds of ions.

EXPERIMENTALS

The samples were subjected to ion implantation and the subsequent annealing, and the defective layer was formed near the surface. The O ion implantation to CZ-Si wafer substrate was carried out at 180 keV with a dose of $2x10^{15}$ /cm^2, and the H ion at 60 keV with a dose of $1x10^{16}$ /cm^2. The iron sheet were implanted with Cu at 140 keV with a dose of $5x10^{13}$, 10^{14}, 10^{15} /cm^2. These implanted samples were annealed at various temperatures for 30 min. in a vacuum of 1 x 10^{-5} Torr. CDB measurements were performed using the low energy positron beam facility at NIRIM providing $1x10^5$ e^+/s in the energy from 0 to 30 keV. Around $1.5x10^7$ counts were accumulated for each spectrum, which was the diagonal cross section of the two-dimensional spectrum with a width of $2m_0c^2 - 1.2$ keV $< E_1 + E_2 < 2m_0c^2 + 1.2$ keV. The data are exhibited in terms of ratio-differences curves, in which the small change at high momentum region can be distinguishable. As a reference in Si, a spectrum of divacancy, V_2, induced by self-ion implantation ($2x10^{14}$ /cm^2, 100 keV) to Si, was used, while one of a defect-free Fe was used in Fe. Conventional Doppler broadening (S parameter) measurements and positron lifetime ones using a positron beam were also employed. The S parameter is defined as the ratio of the counts in a central region of the annihilation photopeak to those in the whole one and normalized to the value for bulk Si or Fe. The value of S generally increases due to an increase of the overlap of the positron density with (low-momentum) valence electrons when the positrons are trapped at vacancy-type defects.

RESULTS & DISCUSSION

Si implanted with O ions

An understanding of the behavior on oxygen-related defects in Si is essential to the fabrication of CZ-Si wafers, in which an oxygen concentration of around 10^{18} /cm^3 is introduced from the SiO_2 crucible used in the crystal-growth process. And the novel semiconductor substrate named SIMOX wafer has been proposed and the internal SiO_2 layer is formed between thin single crystal Si layer and Si substrate. Heavily ion implantation more than 10^{17} /cm^2 is employed in SIMOX fabrication, so that much attention has been paid to oxygen-related defects in Si. Some positron studies on them has been carried out and it has been reported that very low S value and short lifetime are responsible for oxygen-related defects in Si [4,5,6].

Figure 1 shows S-E curves for Si implanted with $2x10^{15}$ O ions/cm^2 at 180 keV and the samples after annealing. The mean projected range is around 380 nm, so that positron lifetimes at 5 keV stand for the information on the most defective layer. In the as-implanted sample, larger S is observed and the positron lifetime of 298 ps is longer that that, 219 ps, of the bulk and

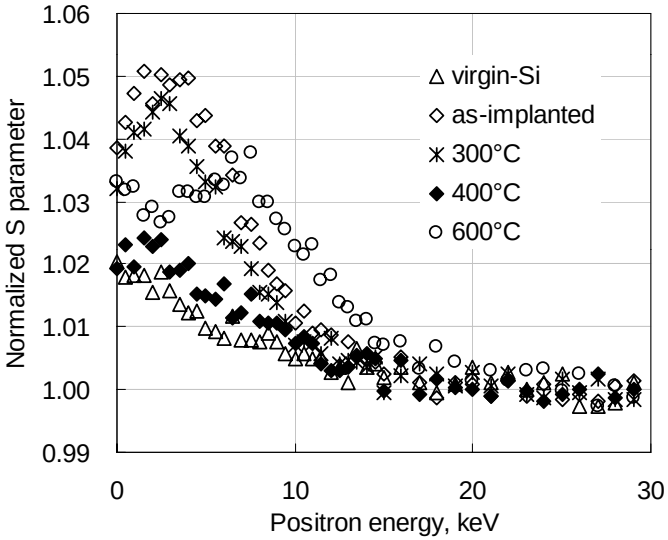

Figure 1: S-E curves for the O ion (180 keV, $2x10^{15}$ /cm^2) implanted Si and the samples annealed.

corresponds to that of divacancy in Si. In annealing at 600°C, drastic change takes place. Value of S is still large below positron energy of 2 keV, while that of S decreases in the region of more than 2 keV, and becomes lower than that of the bulk. If positrons annihilate electrons of matrix Si atoms, S value should not be lower than that of the bulk. This result suggests that a part of positrons annihilates electrons of the different kinds of atoms with matrix ones. The origin of lowering in S is considered to be due to the formation of V-O complex defects. The positron lifetime at 5 keV is estimated to be 330 ps (intensity: 97%), which corresponds to V_4, indicating that the defects formed are open-volume type. An anneal at 800°C gives rise to the minimum S, 0.93, at 6.5 keV and the long lifetime of 322 ps (97%). These results show that the size of open-volume is unchanged, while a fraction of positrons which annihilate electrons of non-Si atoms increases. The value of S strongly depends on the dose of oxygen implanted, so that it is concluded that vacancy-oxygen complexes are formed, and that positrons trapped at them give very low S due to electrons of oxygen.

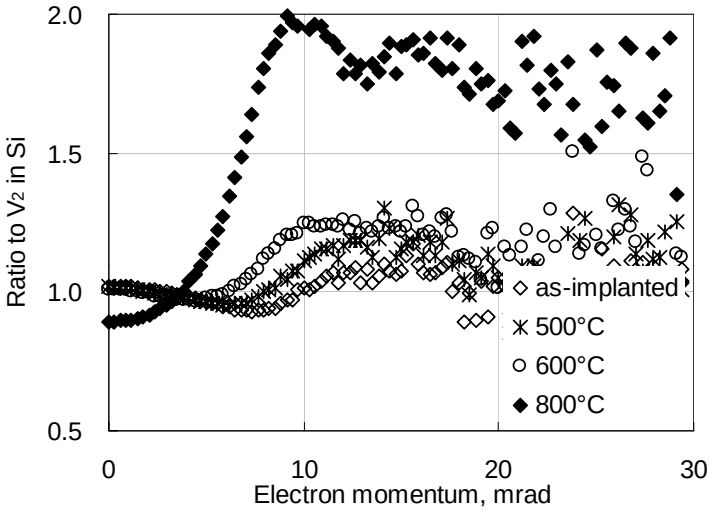

Figure 2: CDB spectra for the O ion (180 keV, $2x10^{15}$ /cm^2) implanted Si and the samples annealed.

To clarify their defect structures, CDB measurements at the positron energy of 5 keV have been carried out and the results are exhibited in Fig. 2. The CDB spectrum of the as-implanted sample does not coincide with that of V_2 in Si. The intensity in the range from 10 to 20 mrad due to oxygen atoms becomes larger, while that around 0 mrad is nearly unity. It is found that oxygen atoms are involved in the defects induced only by ion implantation and the size of the defects is almost same to V_2. As the annealing temperature rises, their intensity is increased, indicating that the number of oxygen atoms involved in the defects increases more and more. In combination of positron lifetime and CDB spectra, the following model on V-O defects can be summarized.

(1) Up to 500°C : The positron lifetime is around 300 ps and the CDB spectrum shows a slight large intensity in the range of 10 to 20 mrad. It is known that, in the relation of positron lifetime with the defect size, the lifetime of V_xI_y complex is same to that of V_{x-y} clusters and the lifetime of 300 ps coincides with that of V_2 in Si. It is, therefore, concluded that the formation of V_3O is dominant in the as-implanted sample and the samples annealed up to 500°C.

(2) 600°C : The lifetime is around 320 ps, which coincides with V_4 in Si, and the intensity in10-20 mrad in the CDB spectrum is increased. Hence the defects formed are considered to be V_6O_2 complexes, in consequence of a combination of two V_3O.

(3) 800°C : The lifetime is unchanged, compared with that of the sample annealed at 600°C, and the intensity in 10-20 mrad in the CDB spectrum is further greater. The magic numbers of vacancy cluster are well known to be 4, 6, 10, etc., so that the formation of $V_{10}O_6$ is acceptable.

Si implanted with H ions

The behavior of H atoms is very complicated in any materials. Hydrogen atoms are easily terminated at the dangling bond of defects in Si and stabilize them. These H property is utilized in amorphous Si:H and delamination of Si wafer. From the fact that S value for the Si implanted with H is similar to that for the bulk, it had been said that positrons were insensitive to H-related defects in

Si [7]. But the authors have found that the lifetime for the H-terminated defects is longer than that for the bulk and that positrons are trapped at them [8]. In this section, the behavior of H-related defects in Si is discussed from the CDB spectra.

The S-E curves for the H-implanted Si ($1x10^{16}$ H^+/cm^2 at 60 keV) and the annealed samples are shown in Fig. 3. For the as-implanted sample, large S and long lifetime of 280 ps (100%) at the positron energy of 7 keV are observed and the open-volume type defects are induced. The S-E curve for the sample annealed at 400°C returns to that for the virgin Si. This result can be interpreted with no defects in the sample, although the lifetime is still long and estimated to be 283 ps (100%). By annealing at 600°C, S value increases again and long lifetime component of 445 ps (62%) is taken, indicating that large vacancy clusters such as V_{10} are formed.

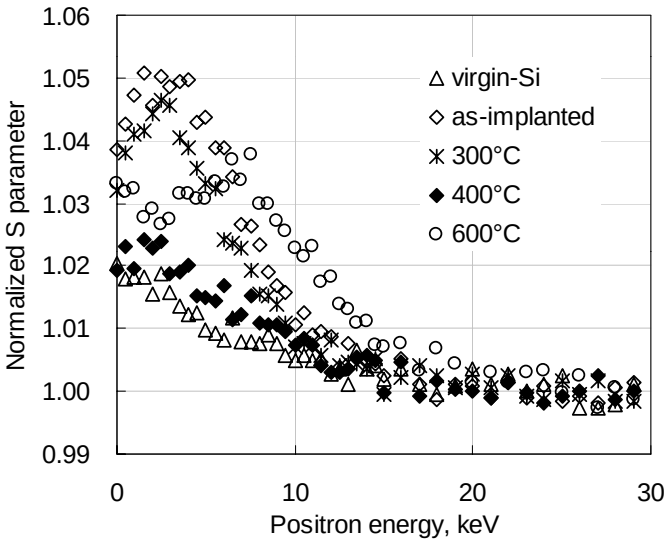

Figure 3: S-E curves for the H ion (60 keV, $1x10^{16}$ $/cm^2$) implanted Si and the samples annealed.

The CDB spectra at the positron energy of 6 keV are exhibited in Fig. 4. For the as-implanted sample, the intensity in the region of 5 to 15 mrad is larger than that for V_2 in Si. Annealing up to 400°C results in appearance of broad peak around 8 mrad. It is, therefore, considered that the H-terminated defects in Si are responsible for this peak and that the number of H coupled with vacancy is increased up to 400°C.

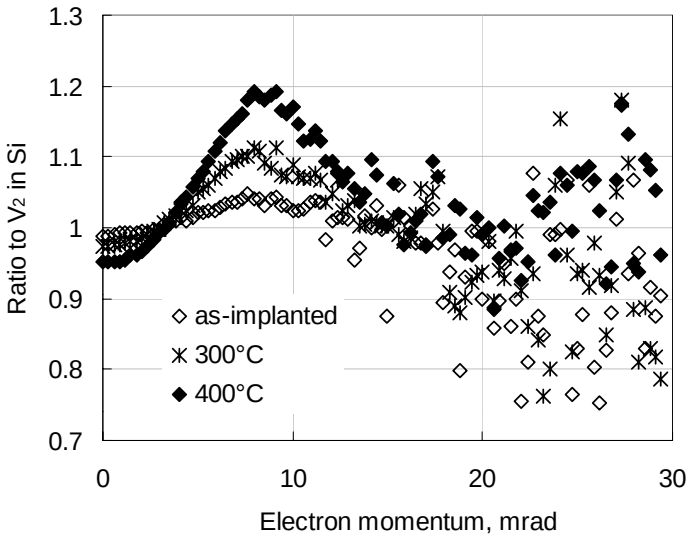

Figure 4: CDB spectra for the H ion (60 keV, $1x10^{16}$ $/cm^2$) implanted Si and the samples annealed.

The defect structure in this system is considered. The above-mentioned results indicate that the defect size is almost unchanged and H atoms are terminated to vacancies up to 400°C. Divacancy in Si is mobile around 230°C, but H termination prohibits the migration and the clustering of defects. If H terminated to defects do not affect the positron lifetime very much due to the small size, the implantation-induced defects may be attributed to be V_2H or V_2H_2 complexes, and the defects formed at 400°C V_2H_6.

It is very difficult to discuss the chemical state of defects coupled with impurities from only the positron lifetime and line shape parameter such as S, but it has been found that CDB technique enables us to estimate the number of impurities in the defects. For more detail discussion, theoretical calculation is required.

Fe implanted with Cu ions

The presence of impurity also results in the complexity in defect behavior in metal and CDB method is useful to study the interaction with impurity aggregations and vacancy. In this work, the reaction of Cu with vacancy, induced by Cu ion implantation to Fe, has been investigated. Hori *et al.* [9] suggested from the lifetime measurement the nucleation of copper precipitates was coupled with vacancy. Nagai *et al.* [10] reported that very-dilute Fe-Cu system irradiated by fast neutrons was studied by CDB technique and that ultrafine Cu precipitates were responsible for irradiation-induced embrittlement of RPV steels.

Figure 5 show the S-E curves for the Fe samples implanted with $5x10^{13}$, $5x10^{14}$, and $5x10^{15}$ Cu^{+}/cm^{2} at 140 keV and the samples annealed at 300°C. S value near surface is large in all of the samples, indicative of the formation of vacancy-type defects. Little difference between $5x10^{13}$ and $5x10^{14}$ Cu^{+}/cm^{2} samples is observed, while S is lowered in $5x10^{15}$ Cu^{+}/cm^{2} sample. Annealing at 300°C gives rise to the sudden lowering of S and it seems that the defects anneal out.

The CDB spectra of these samples at the positron energy of 3 keV are displayed in Fig. 6. No peaks appear for the $5x10^{13}$ and $5x10^{14}$ Cu^{+}/cm^{2} samples. In less than $5x10^{14}$ Cu^{+}/cm^{2} samples, the behavior of defects is very similar to that in pure Fe and we may consider only the simple vacancy-type defects in these systems. The broad peak around 22 mrad is observed in both of the $5x10^{15}$ Cu^{+}/cm^{2} sample and the annealed, and coincides with that of pure Cu [10], indicating that positrons annihilate electrons due to Cu. Further, the intensity of the peak increases by annealing at 300°C. These results are interpreted by the aggregations of vacancies and Cu atoms. Vacancies in Fe easily diffuse even at room temperature, and are consequently trapped with Cu. Due to the high binding energy between vacancy and Cu in Fe, V-Cu complexes migrate and are stabilized by a formation of large clusters. It is considered that the inner wall of micro voids is covered with Cu atoms, since Cu has a lower surface energy than Fe.

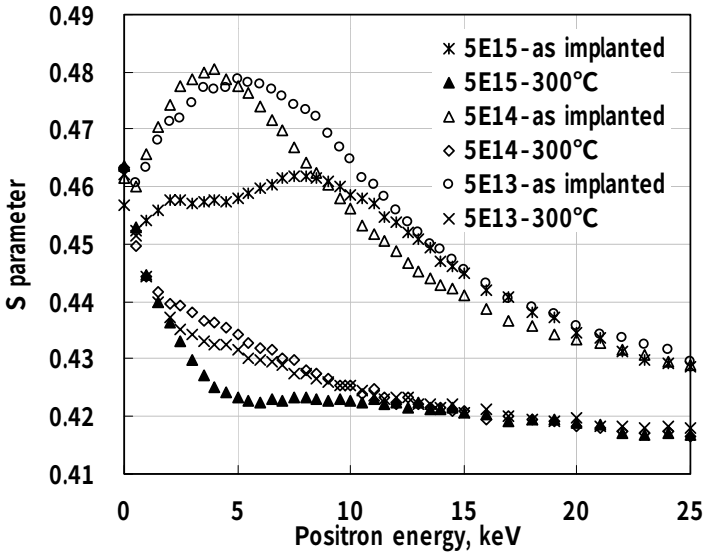

Figure 5: S-E curves for the Cu ion (140 keV, $5x10^{13}$, $5x10^{14}$, $5x10^{15}$ /cm^{2}) implanted Si and the samples annealed.

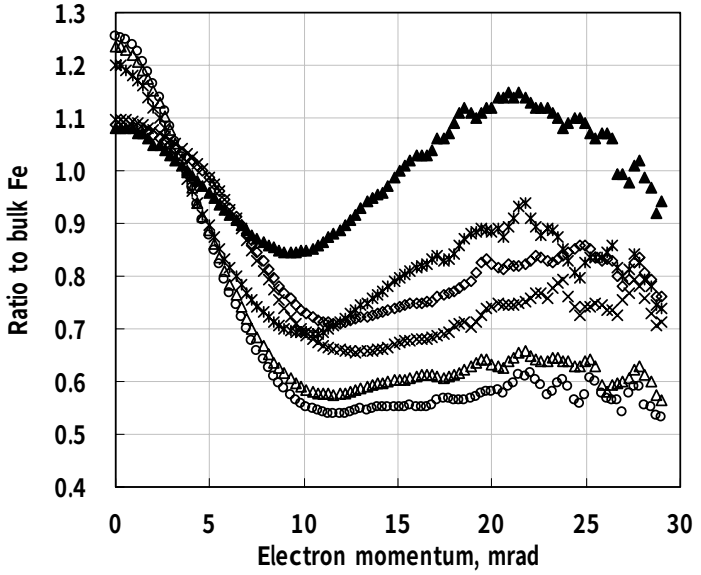

Figure 6: S-E curves for the Cu ion (140 keV, $5x10^{13}$, $5x10^{14}$, $5x10^{15}$ /cm^{2}) implanted Si and the samples annealed. The symbols are identical to those of Fig. 5.

ACKNOWLEDGEMENTS

The authors wish to thank Drs. R. Suzuki and T. Ohdaira for their measurements of positron lifetime using a pulsed positron beams at ETL. Financial support by Grant-in-Aid for Scientific Research (B)11450321 is gratefully acknowledged.

REFERENCES

1. Asoka-Kumar, P., Alatalo, M., Ghosh, V.G., Kruseman, A.C., Nielsen, B. and Lynn, K.G. (1996) *Phys. Rev. Lett.* 77, 2097.
2. Kruseman, A.C., Schut, H., van Veen, A., Mijnarends, P.E., Clemant, M. and de Nijs, J.M.M. (1997) *Appl. Surf. Sci.* 116, 192.
3. Nagai, Y., Hasegawa, M., Tang, Z., Hempel, A., Yubuta, K., Shimamura, T., Kawazoe, Y., Kawai, A. and Kano, F. (2000) *Phys. Rev. B* 61, 6574.
4. Dannefaer, S. and Kerr, D. (1986) *J. Appl. Phys.* 60, 1313.
5. Coleman, P.G., Chilton, N.B. and Baker, J.A. (1990) *J. Phys. Condens. Matter* 2, 9355.
6. Fujinami, M. (1996) *Phys. Rev. B.* 53, 13047.
7. Brusa, R.S., Naia, M.D., Zecca, A., Nobili, C., Ottaviani, G., Tonini, R. and Dupasquier, A. (1994) *Phys. Rev. B* 49, 7271.
8. Fujinami, M., Suzuki, R., Ohdaira, T. and Mikado, T. (1998) *Phys. Rev. B* 58, 12559.
9. Hori, F., Yunjia, A., Aono, Y., Takenaka, M. and Kuramoto, E. (1995) *Mater. Sci. Forum* 175-178, 379.
10. Nagai, Y., Tang, Z., Hasegawa, M., Kanai, T. and Saneyasu, M. (2001) *Phys. Rev. B* 63, 134110

Oral/Poster Reference: ICF100225OR

COMPARISON OF EXPERIMENT AND THEORY FOR CRACK TIP FIELDS IN DUCTILE SINGLE CRYSTALS

W. C. Crone and W. J. Drugan

Department of Engineering Physics
University of Wisconsin–Madison
1500 Engineering Drive
Madison, WI 53706 USA

ABSTRACT

We compare extremely detailed experimental studies of "plane strain" crack tip deformation fields for two symmetric crack orientations in a ductile single crystal of low hardening copper with new asymptotic analytical solutions employing single crystal elasto-plasticity. The experimental studies were motivated by the pioneering analysis of Rice [1] of crack tip fields in nonhardening ductile single crystals. Rice showed that, in contrast to crack tip fields in isotropic (polycrystalline) ductile materials, the single crystal crack tip fields consist of angular sectors of constant Cartesian stress components that are joined by rays of stress and radial displacement discontinuity. Rice's solutions assume yield is attained at *all* angles about the crack tip, which *requires* radial shear bands of both slip and kink type. The new experiments confirm several of Rice's predictions; however, there are several important differences. Our experimental observations and measurements show: an *absence* of kink-type shear bands; some sector boundary locations differing significantly from Rice's predictions; different near-tip fields for a 90° crack orientation change (in contrast to the theoretical prediction); and angular regions exhibiting no evidence of plastic slip and very low strain (as measured by Moiré microscopy). Based on these observations, we have derived new asymptotic analytical solutions that relax Rice's assumption that yield is attained at all angles about the crack tip; this permits derivation of solutions that do not require rays of kink-type shearing and that possess near-tip sub-yield angular sectors. Direct comparison of these solutions with the experimental observations and measurements show that the new asymptotic solutions agree quite well with the experiments. The result is enhanced fundamental understanding of ductile single crystalline crack tip fields as well as quantitative predictive capability.

KEYWORDS

crack tip fields; single crystal plasticity; optical interferometry; asymptotic analysis.

INTRODUCTION

Nonlinear fracture mechanics in its current state deals largely with isotropic materials; a main application is ductile polycrystalline materials whose grains are sufficiently small and randomly oriented that a macroscopic isotropic continuum theory suffices. However, structural components are increasingly being fabricated in single crystal form, for reasons including the avoidance of grain boundary defects and superior creep resistance. The fracture behavior of ductile single crystalline materials is as yet not well understood. Also, the fracture of more commonly employed polycrystalline materials involves, at the microscale, crack growth through (single crystalline) grains or along grain boundaries. To understand and predict the fracture behavior of such materials from a fundamental perspective, it is necessary to understand and be able to characterize the stress and deformation fields present at the tip of a crack in a single crystal.

In a pioneering paper, Rice [1] published an asymptotic study of crack tip stress and deformation fields for plane strain tensile cracks in elastic-ideally plastic single crystals. He showed that, unlike crack tip fields in *isotropic* elastic-ideally plastic materials, the single crystal crack tip fields in at-yield regions are comprised exclusively of angular sectors of constant Cartesian components of stress. For the stationary crack case, he showed that these are joined necessarily by stress and displacement discontinuities when, as he assumed, the stress state is at yield at all angles about the crack tip. Rice's solutions address the specific cases of a crack on the (0 1 0) plane pointing in the [1 0 1] direction, and a crack on the (1 0 1) plane pointing in the [0 1 0] direction, for both FCC and BCC crystals that flow according to the critical resolved shear stress (Schmid) criterion. Saeedvafa and Rice [2] extended Rice's [1] asymptotic analysis to incorporate Taylor power-law hardening.

The analyses of Rice and co-workers just summarized employed continuum elastic-plastic modeling of ductile single crystals, and analyzed crack tip fields via asymptotic analysis within an infinitesimal displacement gradient formulation. Rice et al. [3] performed full-field "small strain" numerical finite element calculations, using continuum crystal modeling; these solutions were in accord with Rice's [1] asymptotic analytical ones, confirming that the latter have a significant radius of validity. Mohan et al. [4] and Cuitino and Ortiz [5] employed finite deformation continuum theory to analyze (numerically) these crack tip fields, accounting for the full three-dimensional crystal geometry.

Several extremely careful and fascinating experimental studies of "plane strain" tensile crack tip fields have recently appeared, notably those of Shield and Kim [6], Shield [7], Crone and Shield [8] and Bastawros and Kim [9]. Also, very recently, numerical studies of plane strain tensile crack tip fields using discrete dislocation dynamics to model ductile materials containing substantial initial distributions of dislocations and dislocation sources have been conducted, the most recent by Van der Giessen et al. [10].

The solutions of Rice [1] involve rays of concentrated plastic shearing, of both slip (parallel to slip systems) and kink (perpendicular to slip systems) type, emanating from the crack tip. The recent experimental studies confirm Rice's predictions of the presence of discrete sectors near the crack tip, and also exhibit rays of slip-type concentrated plastic shearing. However, they do not appear to show kink-type concentrated plastic shearing. This motivated Drugan [11] to construct asymptotic solutions for stationary crack tip fields in elastic-ideally plastic ductile single crystals that do not contain kink-type rays of concentrated plastic shearing.

In the present paper, we provide direct comparisons of certain of Drugan's [11] solutions to the experimental measurements of Crone [12] and Crone and Shield [8] for cracks having two different orientations in FCC ductile single crystalline copper.

COMPARISON OF EXPERIMENT AND THEORY

Experimental Results

Single crystals of copper were grown with the Bridgman technique [13] and prepared as four-point-bend specimens [8]. The two crystallographic orientations were investigated with the interferometric method of Moiré microscopy to obtain detailed information about the surface strains [14] and the optical method of differential image contrast (DIC) to obtain general information about the surface deformations. Samples having a notch on the (101) plane and its tip along the $[10\bar{1}]$ direction are identified as Orientation I, while samples with a notch on the (010) plane and its tip along the $[\bar{1}01]$ direction are identified as Orientation II.

The formation of persistent strain localization bands, observed optically on the sample surface during testing and after unloading as shown in Figure 1, provide insight into the active slip systems within a sector and delineate the sector boundary angles. Slip band observations, refined by detailed Moiré microscopy strain measurements, suggest that certain sectors of the near-tip field may remain elastic. Although the details of the Moiré results [7, 8] are not presented here, they inform the discussion that follows.

The theoretical slip plane trace angle between the slip plane trace and the x_1 axis (see Figure 1) is of particular interest for comparison to the persistent strain localization band angles observed in experiments. Because FCC copper slips on {111} planes in <110> directions, the slip plane trace angles are 35°, 90°, and 145° from the x_1 axis for Orientation I. The related kink-like shear trace angles are 55°, 125°, and 180°. The slip and kink angles for Orientation II are interchanged. All of the persistent strain localization bands observed on the sample surface occur at orientations corresponding to the plane strain slip systems available. Thus all of the persistent strain localization bands observed are categorized as slip bands. No evidence of kink-type shear bands was observed in either orientation. If kink is not exhibited in these orientations, then the angles at which two plastic sectors may adjoin are greatly diminished.

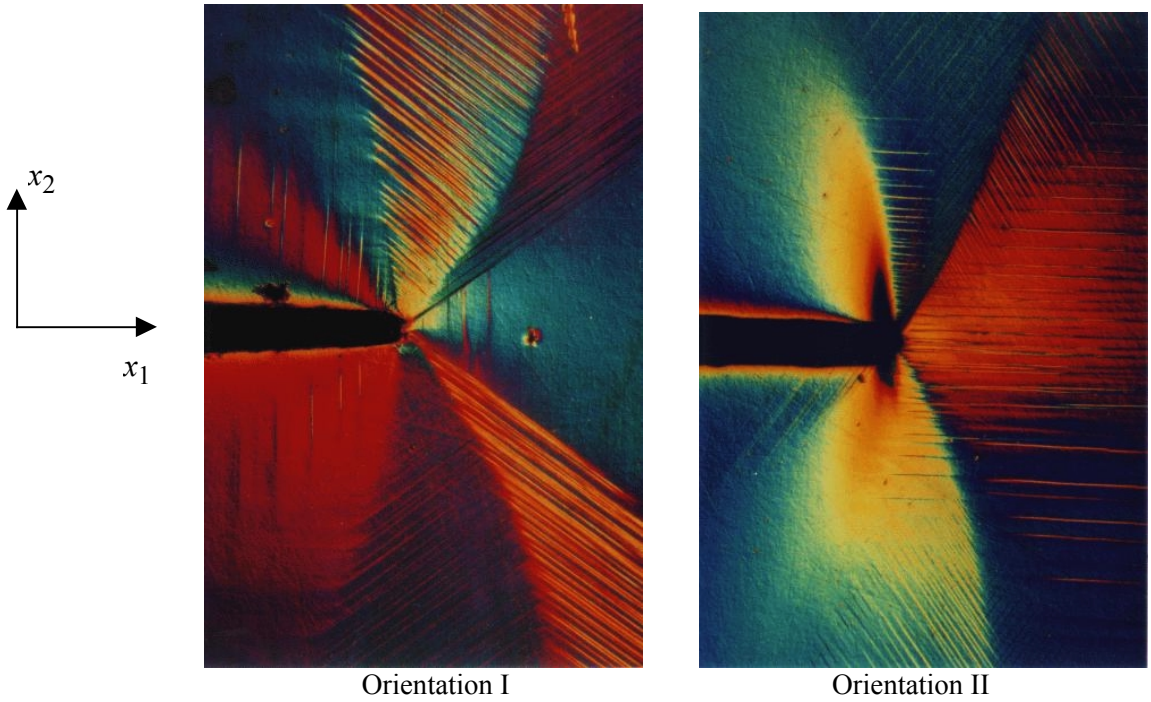

Figure 1. Optical micrographs were taken using a DIC microscope of FCC copper bend samples with Orientation I (left) [7] and Orientation II (right) [8]. The notch enters from the left. The lines in the sectors emanating from the notch tip are slip lines. Changes in color/shade indicate small changes in surface tilt. The black regions very near the tip are regions with larger out of plane deformation and thus larger tilt. The field of view is 2.7 by 1.8 mm.

Figure 1 shows slip bands at 90° (for Orientation I) and 180° (for Orientation II) occur ahead of the notch. However, Rice [1] proved that in nonhardening material, plastic sectors must have constant Cartesian stress components, and since we must have $\sigma_{12} = 0$ on $\theta = 0$ (i.e., the crack plane ahead of the tip) from symmetry, one expects $\sigma_{12} = 0$ in the entire sector ahead of the crack. However, it was observed during the experiments that these slip bands did not form until the final stages of loading; therefore, we hypothesize that they are the result of material hardening. Indeed, the results of Saeedvafa and Rice [2] show that even a low level of hardening permits nonzero σ_{12} everywhere in the front sector except at $\theta = 0$. Thus, for comparison to the perfectly plastic crack tip field solutions, the slip bands directly ahead of the notch will be ignored.

Rice's Fully Plastic Asymptotic Solutions

Rice's [1] solutions are illustrated in Figure 2 for the crack orientations shown in Figure 1. The near-tip sector assembly, the stress and displacement jump locations, and the stress field, are all identical for the two orientations. The solutions have rays of stress and displacement discontinuity at the following angles, measured counterclockwise from the crack plane ahead of the crack tip: θ = 54.74°, 90°, 125.3°. Importantly, the character of the deformation fields differs between the two orientations: In the Orientation II case, the rays at $\theta = 54.74°$ and 125.3° are sites of radial displacement discontinuities (concentrated plastic shearing) produced by slip on the crystal's slip plane traces, while $\theta = 90°$ is the site of a radial displacement discontinuity produced by a kinking mode of concentrated shear, since this direction is perpendicular, not parallel, to one of the crystal's slip plane traces. The situation is reversed for Orientation I: $\theta = 90°$ is the site of a slip-type concentrated shearing, while θ = 54.74° and 125.3° are sites of kink-type concentrated shearing. A comparison of Figure 2(a) with Figure 1 shows that neither of the experimental images appears to match completely Rice's [1] solution. [Since the experiments used notches, sharp-crack asymptotic solutions are expected to apply outside a radius of 2-3 times the notch radius.] Orientation II does seem to agree with Rice's solution for, say, $0 \le \theta < 90°$, but the experimental image shows slipping on both of Sector B's slip line traces significantly beyond $\theta = 90°$, as opposed to changing to Sector C behavior at $\theta = 90°$ as predicted by the analytical solution. Orientation I looks quite different from Rice's solution, except perhaps for the apparent sector boundary at $\theta \approx 54°$, but the experiments show no evidence of kink-type plastic shear there, as the analytical solution predicts.

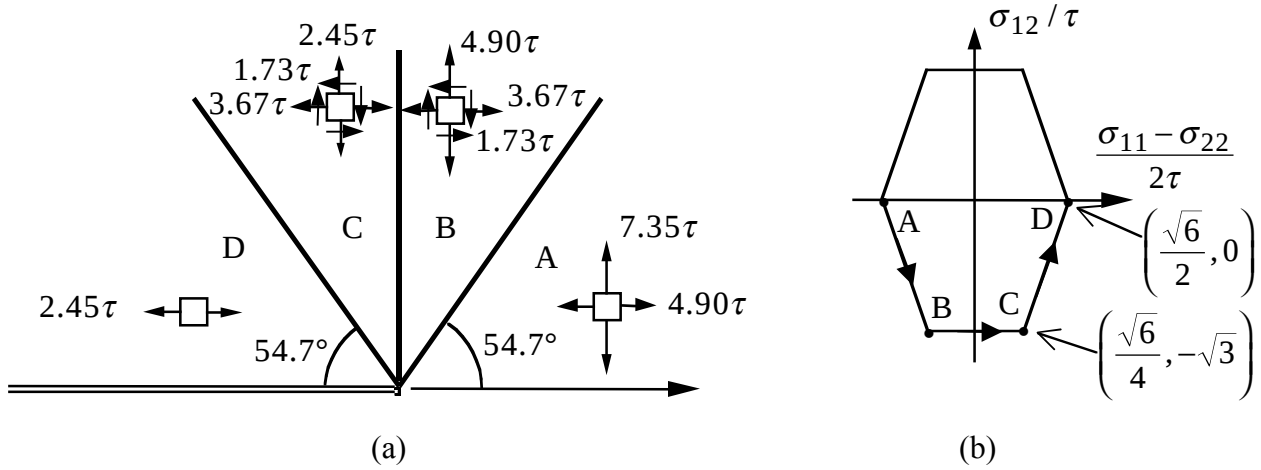

Figure 2. (a) Rice's [1] fully plastic stationary crack near-tip solutions for FCC crystals for the crack orientations discussed. The dark rays are sites of stress and displacement discontinuity; the angular sectors have constant Cartesian stress components corresponding to the points labeled on the yield surface shown in (b); τ is the critical resolved shear stress on {1 1 1}<110>.

New Elastic-Plastic Asymptotic Solutions Without Kink-Type Shear

Based in part on the observations and comparisons described above, Drugan [11] derived new asymptotic near-tip solutions that do not contain kink-type concentrated plastic shearing for cracks in nonhardening ductile single crystals. In contrast to Rice's [1] solutions, these new solutions necessarily contain sub-yield regions near the crack tip (treated as isotropic for simplicity). Here we select two of Drugan's [11] solution families that appear to agree well with the experimental images of Figure 1. These solutions are illustrated in Figure 3. Significant constraints exist on permissible near-tip elastic-plastic solutions; see Drugan [11].

We begin with Orientation II, as this appears to agree reasonably with Rice's [1] solution for $0 \le \theta < 90°$; however, for $\theta > 90°$, the experiments of Crone and Shield [8] clearly show the persistence of a Type B sector beyond 90°, after which there is an angular span of no apparent slip activity, and then finally some single slipping adjacent to the crack flank, as can be seen in the lower half of Figure 1. A simple solution of Drugan's [11] that is in accord with these observations is that illustrated in Figure 3(a). A constant stress at-yield sector of A type directly ahead of the crack joins by a stress and slip-type displacement jump to a B-type sector at $\theta = 54.7°$; this B-type sector extends until 98°, at which angle it joins, via full stress and displacement continuity, a sub-yield elastic sector. This extends to $\theta = 125°$, where it joins, with full stress and displacement continuity, a D-type sector, which persists to the crack flank. The sub-yield sector has Cartesian stress components that vary with angle, as illustrated in the stress plane. (This is actually one extreme member of a *family* of closely-related solutions, in which the angular extent of the elastic sector decreases until it becomes an elastic stress jump at $\theta = 112°$, which is the other extreme member of the family; see Drugan [11].)

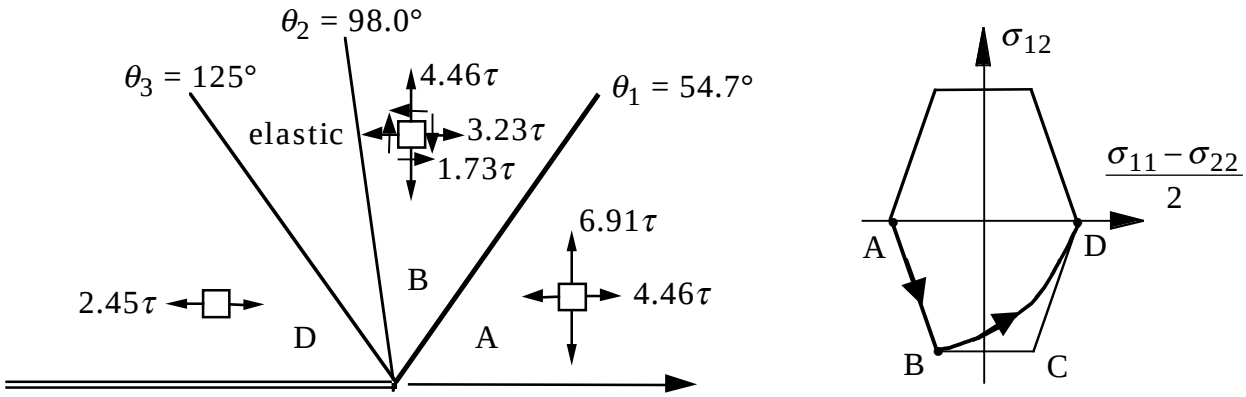

(a)

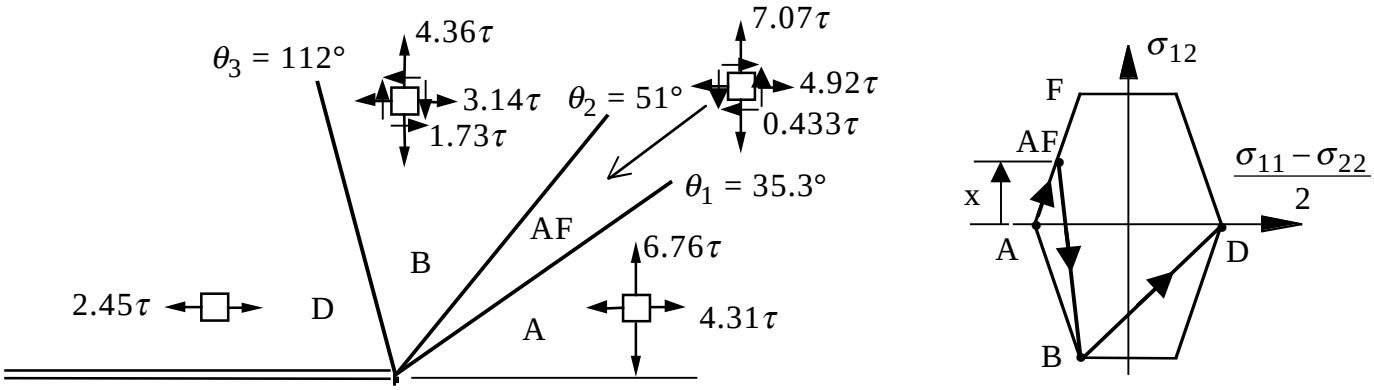

(b)

Figure 3. Drugan's [11] solutions that show good agreement with the experiments on:
(a) Orientation II; (b) Orientation I.

Orientation I differs significantly from Rice's [1] solution even ahead of the crack tip. As Figure 1 illustrates, the Crone [12] and Shield [7] measurements indicate a slip-type sector boundary at $\theta \approx 35°$, another sector boundary at about $\theta \approx 54°$, and a third at about $\theta \approx 111°$. A solution family of Drugan's [11] that agrees well with this experimental image is shown in Figure 3(b). This has a Sector A directly ahead of the crack tip, joined by a slip-type stress and displacement jump at $\theta = 35.3°$ to a Sector AF (whose stress state lies somewhere along the yield surface segment joining vertices A and F). This sector then joins a B-type plastic sector via an elastic stress jump. We illustrate the specific example having $x = 1/4$ in the stress plane of Figure 3(b), for which the solution shows $\theta_2 = 51°$. Sector B then persists until $\theta = 112°$, at which

angle it joins, via an elastic stress jump, a sector of D type. See Drugan [11] for details of the calculation. Figure 3 shows the stress states in each of the near-tip constant stress sectors. We emphasize that the experimental results do not provide definitive information about the near tip field behavior beyond about $\theta \approx 111°$, and thus that other asymptotic analytical solutions are possible having, for example in the solution of Figure 3(b), the material from the Sector B boundary all the way to the crack flank below yield. Further discussion of the possibilities, and constraints on these, is given in Drugan [11].

CONCLUSIONS

The combined investigation of new asymptotic analytical solutions and detailed experimental studies of "plane strain" crack tip deformation fields for symmetrically oriented cracks in a ductile FCC single crystal has produced interesting and encouraging new results. The *absence* of kink-type shear bands, and angular regions exhibiting no evidence of plastic slip and very low strain, in the experimental observations and measurements have guided the development of new analytical solutions employing single crystal elasto-plasticity. Direct comparison of these solutions with the experimental observations and measurements show that two new solutions agree quite well with the experiments on two crack orientations. Thus it appears that asymptotic crack tip field analysis within a "small strain" formulation of continuum single crystal elastoplasticity is capable of characterizing actual single crystal crack tip fields. The result is enhanced fundamental understanding of ductile single crystalline crack tip fields and quantitative predictive capability.

ACKNOWLEDGEMENTS

This research was supported by a grant from the University of Wisconsin Graduate School (WCC), and by the National Science Foundation, Mechanics and Materials Program, Grant CMS-9800157 (WJD).

REFERENCES

1. Rice, J. R. (1987) *Mechanics of Materials* 6, 317-335.
2. Saeedvafa, M., Rice, J. R. (1989) *Journal of the Mechanics and Physics of Solids* 37, 673-691.
3. Rice, J. R., Hawk, D. E. and Asaro, R. J. (1990) *International Journal of Fracture* 42, 301-321.
4. Mohan, R., Ortiz, M. and Shih, C. F. (1992) *Journal of the Mechanics and Physics of Solids* 40, 315-337.
5. Cuitiño, A. M. and Ortiz, M. (1996) *Journal of the Mechanics and Physics of Solids* 44, 863-904.
6. Shield, T. W., Kim, K. S. (1994) *Journal of the Mechanics and Physics of Solids* 42, 845-873.
7. Shield, T. W. (1996) *Acta Materialia* 44, 1547-1561.
8. Crone, W. C., Shield, T. W. (2001) "Experimental Study of the Deformation Near a Notch Tip in Copper and Copper-Beryllium Single Crystals." *Journal of the Mechanics and Physics of Solids*, in press.
9. Bastawros, A. F. and Kim, K-S. (2001) "Experimental Analysis of Near-Crack-Tip Plastic Flow and Deformation Characteristics (II): Hardened Copper Crystal." Submitted for publication.
10. Van der Giessen, E., Deshpande, V. S., Cleveringa, H. H. M. and Needleman, A. (2001) "Discrete Dislocation Plasticity and Crack Tip Fields in Single Crystals." *Journal of the Mechanics and Physics of Solids*, in press.
11. Drugan, W. J. (2001) "Asymptotic Solutions for Tensile Crack Tip Fields Without Kink-Type Shear Bands in Elastic-Ideally Plastic Single Crystals." *Journal of the Mechanics and Physics of Solids*, in press.
12. Crone, W. C. (1998) "Experimental Investigation of the Deformation Near a Notch Tip in Metallic Single Crystals." Ph.D. Thesis, University of Minnesota.
13. Crone, W. C. (2000) *Journal of Crystal Growth* 218, 381-389.
14. Shield, T. W., Kim, K. S. (1991) *Experimental Mechanics* 31, 126-134.

ORAL/POSTER REFERENCE: ICF100775OR

COMPARISON OF MEASURED FRACTURE TOUGHNESS AND SIZE-INDEPENDENT FRACTURE TOUGHNESS FOR CONCRETE

J. H. Hanson[1] and A. R. Ingraffea[2]

[1]Department of Civil and Environmental Engineering, Bucknell University, Lewisburg, PA 17837
[2]School of Civil and Environmental Engineering, Cornell University, Ithaca, NY 14853

ABSTRACT

Laboratory measured results from a broad-based experimental program have been combined with cohesive cracking simulations to determine the size-independent fracture toughness of two batches of concrete. The two batches of concrete used aggregate with a nominal maximum size of 22 mm. The batches had average compressive strengths of 36 and 52 MPa. The laboratory experimental program consisted of three sizes each of single edge (75 – 305 mm high) and round double beam specimens (305 – 1220 mm high). The two-parameter, size effect, Barker and inverse analysis data reduction methods were used to obtain measured values of fracture toughness from the test data. Each of the data reduction methods makes different assumptions about the effects of the process zone. Therefore, differences in measured fracture toughness values from the various data reduction methods are possible. The comparison shows that the single edge and round double beam specimens, up to 305 mm high, with the two-parameter, size effect and Barker data reduction methods do not produce fracture toughness values within 10% of the size-independent value. As expected, the accuracy of the various combinations of test specimen geometry, size, and data reduction method improved with larger test specimen sizes. Only the inverse analysis data reduction method produces accurate values in the range of specimen sizes that can be lifted by a single person.

KEYWORDS

concrete, fracture toughness testing, single edge specimen, round double beam specimen, two-parameter method, size effect method, inverse analysis, cohesive crack simulation

INTRODUCTION

At the scale of most civil engineering structures, macrocrack processes in concrete can not be predicted accurately using linear elastic fracture mechanics, LEFM. Fortunately, several models have been developed for use when there are non-linear fracture mechanics, NLFM, conditions. The size-independent fracture toughness, K_{Ic}, is a parameter common to all of these models for crack propagation. The size-independent fracture toughness is the value that would be obtained from a test specimen large enough that it experiences LEFM conditions. Testing specimens that large is not practical for most concrete mixes. Therefore, several data reduction methods have been developed based upon the models for crack propagation under NLFM conditions. In theory, the fracture toughness value obtained using one of these NLFM-based data reduction

methods, K_{Ic}^{method}, is the same as the size-independent value, K_{Ic}. In practice, the variation of K_{Ic}^{method} values for different test specimen geometries, specimen sizes, and data reduction methods indicates that at least some of the K_{Ic}^{method} values are not K_{Ic}. A difference in values occurs when assumptions made about the fracture process zone by the data reduction method are violated.

A broad-based experimental program has been undertaken in conjunction with cohesive cracking simulations in order to determine the size-independent fracture toughness, K_{Ic}, of two mixes of concrete. With the known values for K_{Ic}, the accuracy of the K_{Ic}^{method} values has been evaluated for the various combinations of test specimen geometry, size, and data reduction method.

Concrete Mixes

Both of the concrete mixes used in this investigation had a nominal maximum aggregate size of 22 mm. One of the batches, referred to as "Normal Strength", had an average compressive strength of 36 MPa at the time when fracture toughness tests were performed. The second batch, referred to as "High Strength", had an average compressive strength of 52 MPa. Detailed descriptions of the mix design and material properties for the batches can be found in [1].

Test Specimen Geometries

In order to determine the size-independent fracture toughness of a mixture of concrete without testing extremely large specimens, more than one test specimen geometry must be used. Different geometries result in different stress states around the crack front. Different stress states might cause the process zone to develop differently. Therefore, certain combinations of test specimen geometry and data reduction method might be more likely to produce the size-independent fracture toughness for a given size of specimens.

Two test specimen geometries were selected for this study: the single edge loaded in bending, SE(B) (Fig. 1), and the round double beam loaded in bending, RDB(B) (Fig. 2). The single edge specimen has been used extensively with concrete [2]. It is the geometry chosen for three proposed standard test methods for measuring fracture properties of concrete [3-5]. The specimen is rectangular with a straight notch. As the specimen is loaded, it exhibits linear elastic response until the process zone begins to develop ahead of the notch. The peak load is reached close to when the crack begins to propagate. Data reduction is performed on data obtained around the peak load. Therefore, the determining data is acquired after the process zone has begun to develop but before crack propagation has occurred.

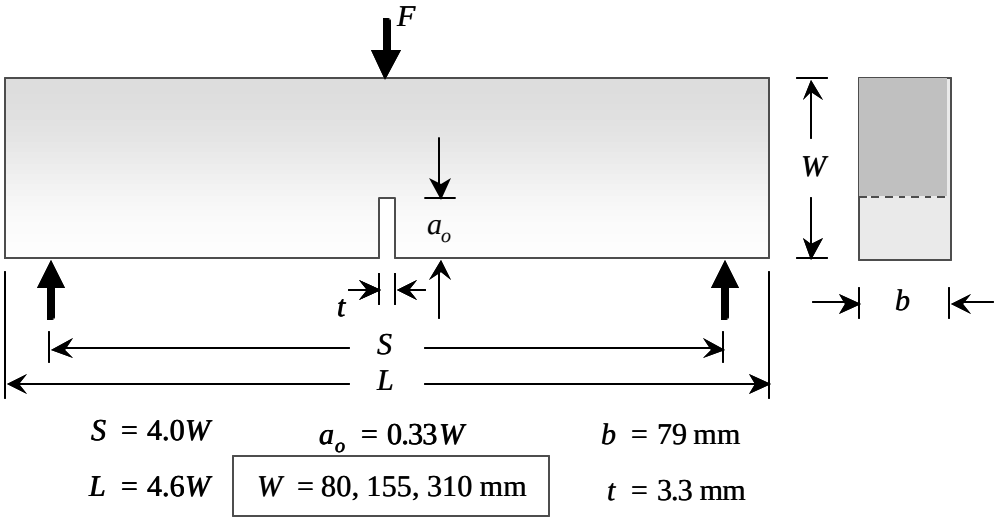

Figure 1. Single edge specimen loaded in bending, SE(B)

The round double beam is a specimen geometry used in a standard for measuring the fracture toughness of rock [6] and ceramics [7]. The specimen is cylindrical with a chevron shaped notch. Because of the chevron notch, the crack initially propagates in a stable manner during testing. When the crack reaches the

critical length, around mid-height, the peak load is reached and propagation becomes unstable in load control. Data reduction is performed on data obtained around this transition point. Therefore, the determining data is acquired after the process zone has begun to develop and stable crack propagation has occurred.

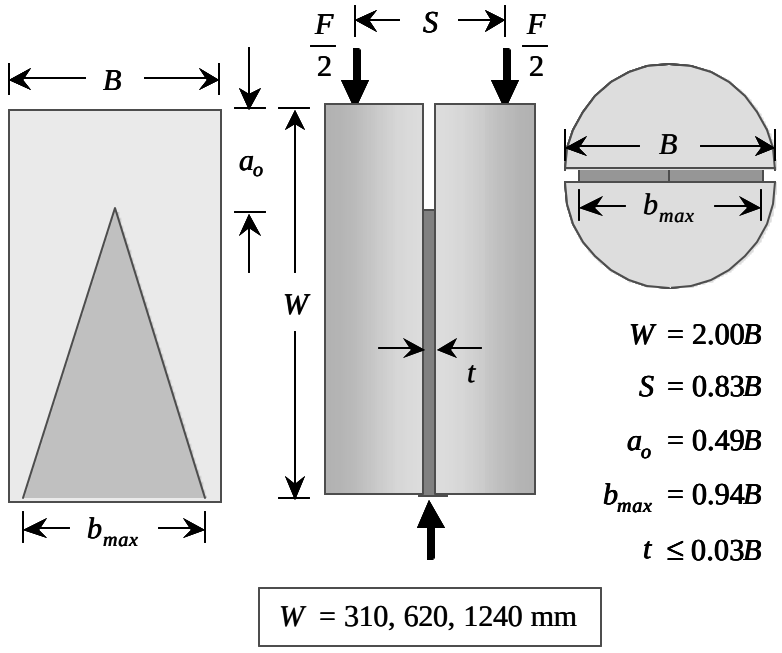

Figure 2. Round double beam specimen loaded in bending, RDB(B)

Data Reduction Methods

Each NLFM-based data reduction method makes different assumptions about the effect of the process zone when the determining data is acquired. Therefore, four data reduction methods were used in this study. The two-parameter data reduction method was used on each SE(B) result to obtain K_{Ic}^{TP} values. The method is based upon the two-parameter model for crack propagation [8]. The two-parameter method asserts that the global response of a structure with a crack experiencing NLFM conditions can be reproduced by considering the structure to have an effective crack experiencing LEFM conditions. Compliance is used to determine the effective crack length.

The size effect data reduction method was used on groups of SE(B) results to obtain K_{Ic}^{SZ} values. The method is based upon the size effect model for crack propagation [9]. The method assumes that the nominal strength of geometrically similar specimens is only a function of one specimen dimension. Linear regression is used to obtain the fracture energy or fracture toughness.

The Barker data reduction method was used on each RDB(B) result to obtain K_{Ic}^{BR} values. The method is based upon the Griffith energy criterion for crack propagation [10]. The method uses compliance to convert an LEFM-based K_{Ic}^{method} value into an NLFM-based value.

An inverse analysis data reduction method was used on groups of SE(B) and RDB(B) results to obtain K_{Ic}^{INV} values. The inverse analysis data reduction method used in this study is based on a cohesive crack model for crack propagation. The method selects the optimum cohesive zone properties to reproduce the behavior of all sizes of both specimen geometries for a single mix of concrete.

SIZE-INDEPENDENT FRACTURE TOUGHNESS VALUES

Determination of the size-independent value of fracture toughness, K_{Ic}, for concrete mixtures has been a significant challenge for the research community. Consistent results for a single size or single geometry or

single data reduction method do not ensure that the result is the size-independent value. To determine K_{Ic} with reasonable certainty requires consistent results from a variety of combinations of test specimen geometry, size and data reduction method.

In order to determine the K_{Ic} values for the two concrete mixes in this study, all of the measured K_{Ic}^{method} values were compared. The results are summarized in Figures 3 and 4. The K_{Ic}^{TP} values increased with SE(B) specimen depth for the range of specimens tested. The K_{Ic}^{BR} values increased with RDB(B) specimen depth until the 610 mm deep specimen results and possibly after. The K_{Ic}^{SZ} values are included; however, the scatter in the measured peak loads severely limits the precision of the data reduction method. The K_{Ic}^{INV} values are similar across all specimen sizes and geometries investigated for both mixes. For the Normal Strength mix, the K_{Ic}^{BR} values appear reach and remain near the K_{Ic}^{INV} value. In addition, the K_{Ic}^{BR} values are approaching the K_{Ic}^{INV} values for the High Strength mix.

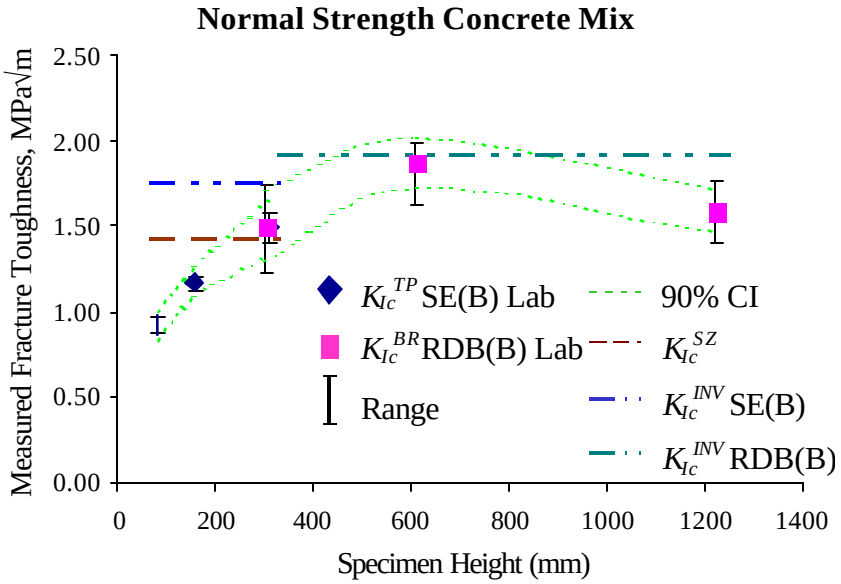

Figure 3. Measured fracture toughness value for specimens from the Normal Strength batch

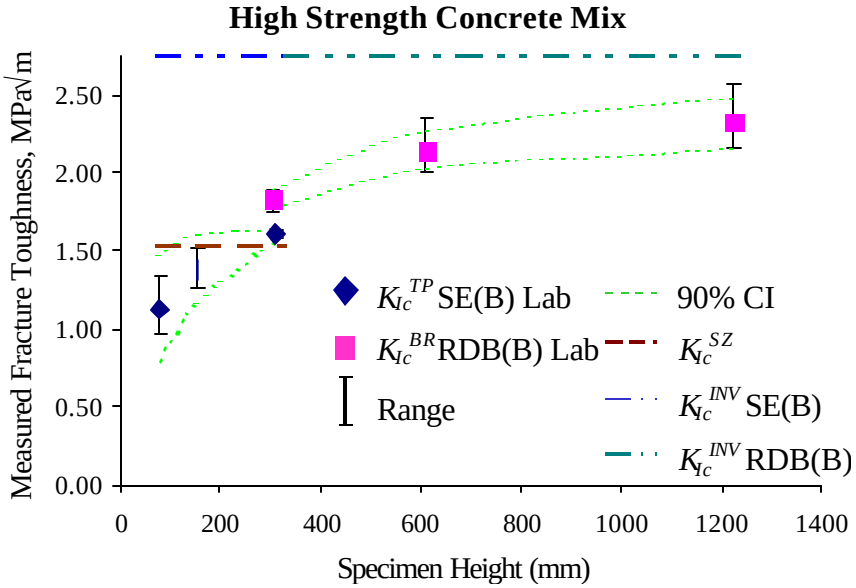

Figure 4. Measured fracture toughness value for specimens from the High Strength batch

Although such comparisons can not conclusively show what the K_{Ic} values are for these two mixes, one can reasonably argue that the K_{Ic} value for each mix is within 10-20% of the K_{Ic}^{INV} value. Therefore, for the purpose of comparing measured and size-independent fracture toughness values, the K_{Ic} value for the Normal Strength mix is taken to be 1.9 MPa√m. The K_{Ic} value for the High Strength mix is taken to be 2.7 MPa√m.

COMPARISON WITH MEASURED FRACTURE TOUGHNESS VALUES

The individual K_{Ic}^{method} values can now be compared to the size-independent K_{Ic} values. The accuracy of the measured values is calculated as the ratio K_{Ic}^{method}/K_{Ic}. The accuracies for the Normal Strength specimens are plotted versus specimen height in Fig. 5. The accuracies for the High Strength specimens are plotted in Fig. 6. The accuracy of the K_{Ic}^{INV} values is approximately 100% and was therefore omitted from the figures.

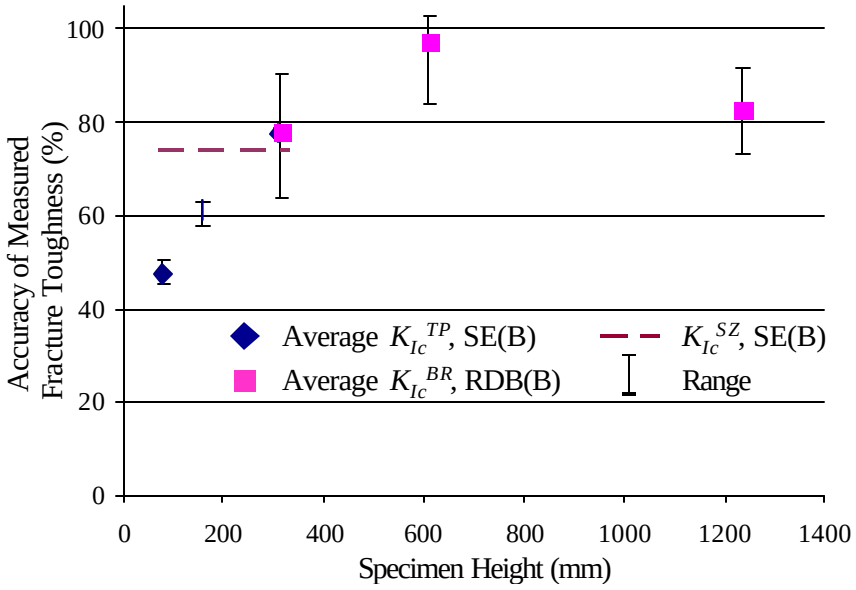

Figure 5. Accuracy of measured fracture toughness value for specimens from the Normal Strength batch

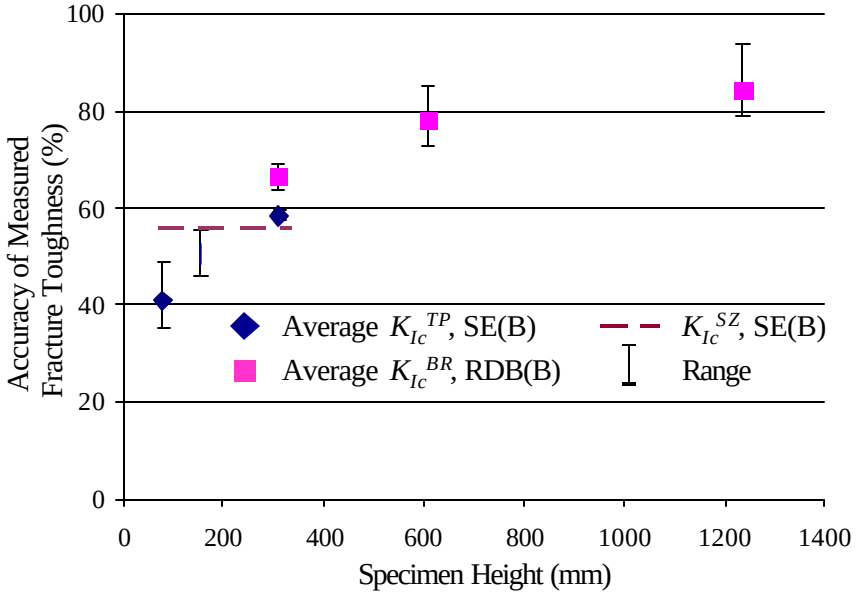

Figure 6. Accuracy of measured fracture toughness value for specimens from the High Strength batch

CONCLUSIONS

The poor accuracy of the K_{Ic}^{TP} and K_{Ic}^{SZ} values from the three sizes of SE(B) specimens clarifies the observations of Elices and Planas [11]. The results of their study implied that the critical energy release rate obtained from the two-parameter or size effect data reduction methods would be different from the energy release rate obtained from inverse analysis using a quasi-exponential tension softening diagram for typical laboratory sized SE(B) specimens. They predicted the difference would be approximately a factor of two. They were unable, however, to determine which of the data reduction methods would be more accurate. The results presented in Figs. 3 and 4 show that the inverse analysis data reduction method has produced the more accurate result.

The laboratory measured fracture toughness results from the Normal Strength batch of specimens appear to have converged to K_{Ic} with specimens that are 610 mm high. For the High Strength specimens, the results for the 1240 mm high RDB(B) are approaching K_{Ic}, but even larger specimens would be required to obtain K_{Ic} directly.

A practical test for measuring the fracture toughness of concrete will use specimens small enough to be carried by one person. Of the six sizes of specimens tested in this study, the largest that can be moved by a single person are the specimens 305 mm high. The average measured fracture toughness values for these and the smaller specimens are 20 – 60% below K_{Ic}. The systematic inaccuracies of the measured fracture toughness values have important implications for predicting crack propagation in concrete structures.

ACKNOWLEDGEMENTS

Much of the research detailed here was made possible through grants from the National Science Foundation, CMS-9414243, and the Alcoa Foundation.

REFERENCES

1. Hanson, J.H. (2000). PhD Dissertation, Cornell University, Ithaca, NY.
2. Karihaloo, B.P. and Nallathambi, P. (1991). In: *Fracture Mechanics Test Methods for Concrete: Report of Technical Committee 89-FMT*, pp. 1-86, Shah, S.P. and Carpinteri, A (Eds). Chapman and Hall, London.
3. RILEM (1985). *Materials and Structures*. 18, 106, pp. 285-290.
4. RILEM (1990). *Materials and Structures*. 23, pp. 457-460.
5. RILEM (1990). *Materials and Structures*. 23, pp. 461-465.
6. ISRM (1988). *Int. J. of Rock Mech. and Mining Sci. & Geomechanics Abst*. 25, 2, pp. 71-96.
7. ASTM (1987). B 771-87 in: *Annual Book of ASTM Standards*. 02.05, ASTM, Philadelphia.
8. Jenq, Y.S. and Shah, S.P. (1985). *Eng. Fract. Mech.* 21, 5.
9. Bazant, Z.P. and Pfeiffer, P.A. (1987). *ACI Mat. J.* 84, 6.
10. Barker, L.M. (1979). *Int. J. of Fract.* 15, 6.
11. Elices, M. and Planas, J. (1991). In *Analysis of Concrete Structures by Fracture Mechanics*, pp. 99-127., Elfgren, L. and Shah, S.P. (Eds). Chapman and Hall, London.

REFERENCE: ICF100376OR

COMPLEX COMPONENT FAILURE WITH LARGE DUCTILE CRACK GROWTH – HIGH QUALITY PREDICTION BY DAMAGE MECHANICAL SIMULATION AND EXPERIMENTAL VERIFICATION

W. Baer and D. Klingbeil

Division V.3 Service Loading Fatigue and Structural Integrity,
Federal Institute of Materials Research and Testing (BAM),
Unter den Eichen 87, D-12205 Berlin, Germany

ABSTRACT

A basic problem within the safety assessment of flawed components is the question of how to deal with large amounts of ductile crack growth. Conventional fracture mechanical concepts fail as their validity is restricted only to small amounts of ductile crack growth. The assessment tools for the elastic plastic material and component behaviour have been significantly improved by the development of micromechanical material models. Advantages of these models are geometry independent material parameters and their validity even with large amounts of ductile crack growth.
In the present study the micromechanical damage model of Gurson, Tvergaard and Needleman implemented in the FE code ABAQUS was applied to predict the complex crack growth and leakage behaviour of a large thinwalled pipe with 90°-external circumferential surface flaw under fourpoint bending (nominal pipe dimensions: length × outer diameter × wallthickness = 2000 × 273 × 17 mm³). The threedimensional elastic-plastic numerical simulation of the pipes failure behaviour including ovalization and leakage was performed up to ductile crack growth of about 200 mm in circumferential direction. A series of experimental pipe tests was carried out up to final cleavage failure after significant stable leak growth in order to gain detailed data on the failure behaviour for the verification of the FE simulation.
The numerically determined results were nearly identical to the respective experimental results. That especially applies to the crack front shapes, crack length, displacements and the leakage opening area. Therefore, it is outlined that even complex failure mechanisms of components with large ductile crack growth can be well assessed by application of damage models.

KEYWORDS

Component failure, large ductile crack growth, damage mechanical simulation, experimental verification

INTRODUCTION

A wellknown and basic problem within the safety analysis of components is the lack of valid crack resistance curves for large amounts of stable crack growth due to the validity limits in the relevant standard procedures and the uncertainty of how to extrapolate the curves correctly. Therefore, the present study

deals with the question of how to describe and predict complex component failure behaviour with large ductile crack growth by means of application of micromechanical damage simulation.

EXPERIMENTAL AND NUMERICAL INVESTIGATIONS

Material

The material under investigation was the german 15NiCuMoNb5 ferritic-bainitic high-temperature structural steel (WB36) in the form of thinwalled seamless pipes with nominal dimensions of length × outer diameter × thickness = 2000 × 273 × 16 mm³. Table 1 shows mechanical and fracture mechanical properties of the investigated material at ambient temperature together with Charpy impact energy values. Crack initiation toughness values J_i were determined on the basis of the critical stretch zone width from crack resistance curves of fatigue precracked and 20%-sidegrooved C(T)6.25 specimens in L-S orientation with an initial crack length ratio of 0.5 according to the ESIS P2-92 guideline [1] (L – axial direction in the pipe, T – tangential direction, S – wallthickness direction).

TABLE 1
MECHANICAL AND FRACTURE MECHANICAL PROPERTIES OF THE INVESTIGATED 15NiCuMoNb5 STEEL AT AMBIENT TEMPERATURE

	$R_{p0,2}$ [MPa]	R_m [MPa]	A [%]	K_V [J]	K_{VH} [J]	J_i [N/mm]
L- direction	515	672	27	-	-	-
T-L-position	-	-	-	105 [1]) (20 °C) 98 [2]) (20 °C)	159	-
L-S-position	-	-	-	133 ± 15 (22 °C, 8 specimens)	176	126

[1]) mean value of 3 specimens, [2]) lowest single value

Pipe Bending Tests

The pipe test program [2] covered tests on a pipe with no flaw and pipes with 90°- as well as 60°-external circumferential surface flaws each of which with an initial flaw depth ratio of 0.5 (Figure 1). Figure 1 gives a schematic outline of the test setup for pipe bending tests that was built up in a 20 MN servohydraulic testing machine. The pipes had been extensively instrumented with inductive linear position transducers and clip gages in order to provide a large set of purposefully determined data of deflection, ovalization and crack opening displacement (COD) that was needed for the development and verification of finite element models. Furthermore, a number of non-destructive testing methods were applied focussing on the investigation of the crack growth and leakage behaviour of the pipes. Ultrasonic testing, acoustic emission testing, direct current potential drop technique and an optical analysis delivered detailed data on the experimental pipe failure. Additionally, several engineering approaches were used to provide and to compare analytical predictions of the experimental pipe failure: Plastic Limit Load Concept, Concept of Local Flow Stress, R6 Procedure and Engineering Treatment Model. These investigations are reported in detail in [2].

Finite Element Analysis

All simulations of the component failure behaviour were performed by three-dimensional elastic plastic finite element analysis (FEA) with the FE code ABAQUS using the damage model of GURSON modified by NEEDLEMAN and TVERGAARD [3] for the simulation of ductile crack growth. With BAM division V.3 this model has been used very successfully for the simulation of ductile crack growth within a variety of problems during the past few years such as for instance different specimens geometries, structures and materials [4].

Table 2 summarizes the geometry independent material parameters of the applied damage model for the investigated steel 15NiCuMoNb5 at ambient temperature. These parameters were determined by fitting to experimental results of tensile tests on notched bars with different notch radii as well as to one fracture mechanics test on a C(T)6.25 specimen.

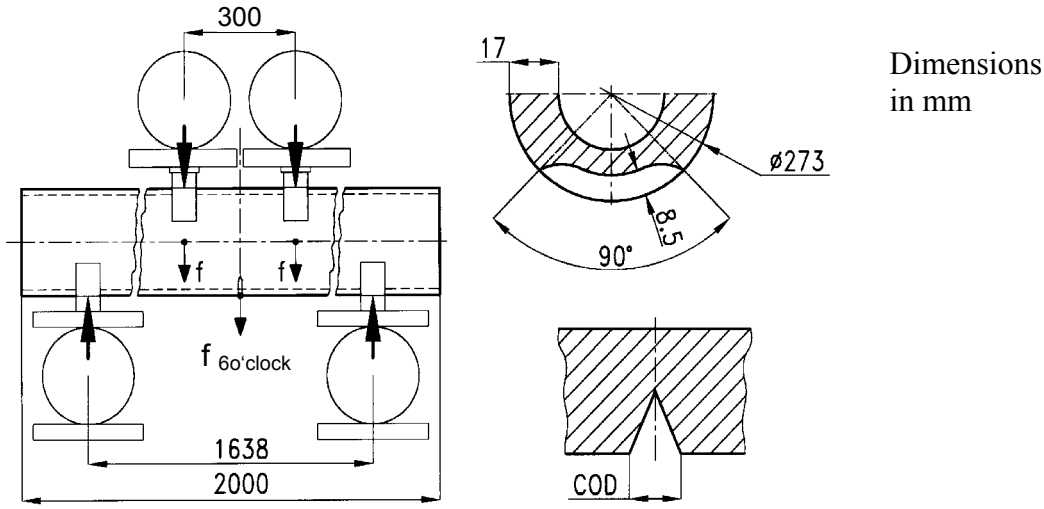

Figure 1: Schematic outline of the test stand for pipe bending tests and position of selected gauging points (f – deflection, COD – crack opening displacement)

TABLE 2
MATERIAL PARAMETERS DETERMINED FOR DUCTILE DAMAGE AND FAILURE OF 15NiCuMoNb5 STEEL AT AMBIENT TEMPERATURE

f_a	f_n	ε_n	s_n	f_c	f_f
0.0001	0.008	0.25	0.1	0.022	0.19

The geometry of the pipe and the bearings had to be modelled very exactly to achieve the experimentally measured forces and displacements and had therefore been optimized by experimental data of the test with an unflawed pipe. Due to the absolutely up-to date but limited available computer capacity the pipe with the 90°-flaw had to be meshed by relativ large elements compared to the model of the C(T)-specimen. The pipes mesh consisted of 14208 nodes and 10713 three-dimensional elements with linear shape functions and approximate edge length of 0.25 mm in radial (y) as well as axial (x) direction and 2.2 mm in tangential direction (z), see Figure 2.

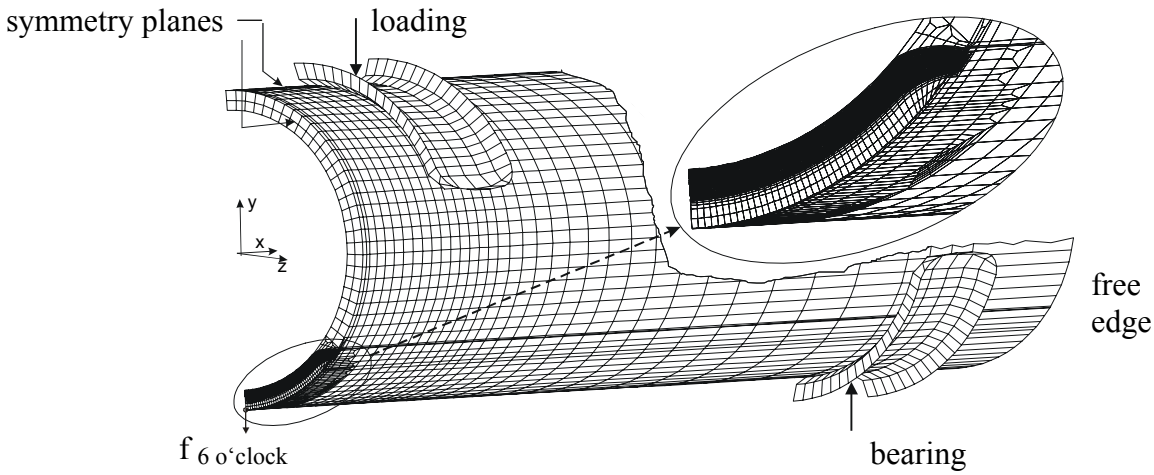

Figure 2: Finite element mesh of pipe no. 2 with 90°-external circumferential surface flaw, rigid bearings and contact

RESULTS AND DISCUSSION

The experimental failure behaviour of the pipes in the displacement controlled tests was characterized by ductile crack growth until full penetration of the wall thickness (leakage), stable growth of the leak and final instability by brittle fracture. The analysis of the fracture surfaces proved that stable crack growth in circumferential direction beyond the angle of the machined initial flaw did not occur. The cleavage fracture initiation region was always located in the area in front of the initial flaw angle.

The finite element analysis of the pipe with an 90°-external circumferential surface flaw was performed until a maximum displacement of about 18 mm at which the experimental failure by cleavage fracture was observed, see Figure 3. Due to the relativ stiff FE-mesh in the flaw region the simulation slightly overestimates the experimental maximum force. The experimental and numerical force records nearly coincide after the leakage had been initiated and thereby most of the comparable stiff elements in as well as near the ligament have failed. Furthermore, the start ot the leakage is remarkably well predicted by the simulation.

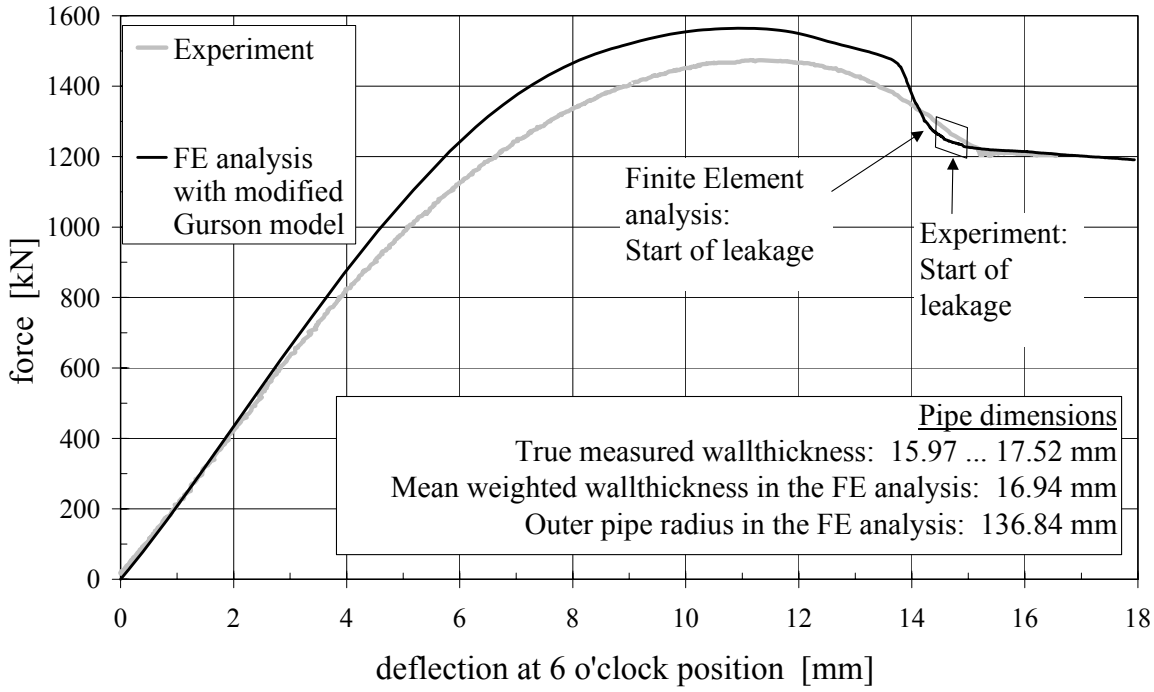

Figure 3: Experimental and numerical force - deflection at the 6 o'clock position - records

Within the FE analysis limits the simulated ductile crack growth led to a total leakage angle of about 70 ° in circumferential direction what equals the experimental result. It was proven by this that the experimental crack initiation and crack growth behaviour as well as the leakage behaviour of the flawed pipe was very well reproduced by the finite element analysis both in terms of the amounts of crack growth and the crack front shape. Figure 4 shows the leakage opening at the internal surface of the pipe in dependence on the circumferential angle at several levels of deflection at the 6 o'clock position. Under the conditions of increasing deflection the maximum of the leakage opening at 0 ° (6 o'clock position) increases up to a value of about 1.8 mm and the leakage enlarges up to an angle of 35 ° in circumferential direction. The numerically determined leakage opening profile in the moment of experimental failure at $f_{6o'clock}$ = 17.94 mm corresponds very well to the experimentally determined profile.

At a numerically determined leakage size of 36 ° ($f_{6o'clock}$ = 17.94 mm) there was the very high level of stress triaxiality in the ligament of about 4 determined in front of the end of the crack in the area of a circumferential angle of 40 to 45 °. This value of stress triaxiality was only determined at this position in the simulated structure and not until this stage of the simulation of the test. All other values determined are

significantly lower. As can be seen from Figure 5, the position of the highest stress triaxiality perfectly coincides with the area on the fracture surface, where cleavage fracture was initiated as indicated by the performed fracture surface analysis. Therefore, it is concluded that on the applied side the high stress triaxiality is responsible for the cleavage fracture that was initiated in the area in front of the crack at a circumferential angle of 40 to 45 °.

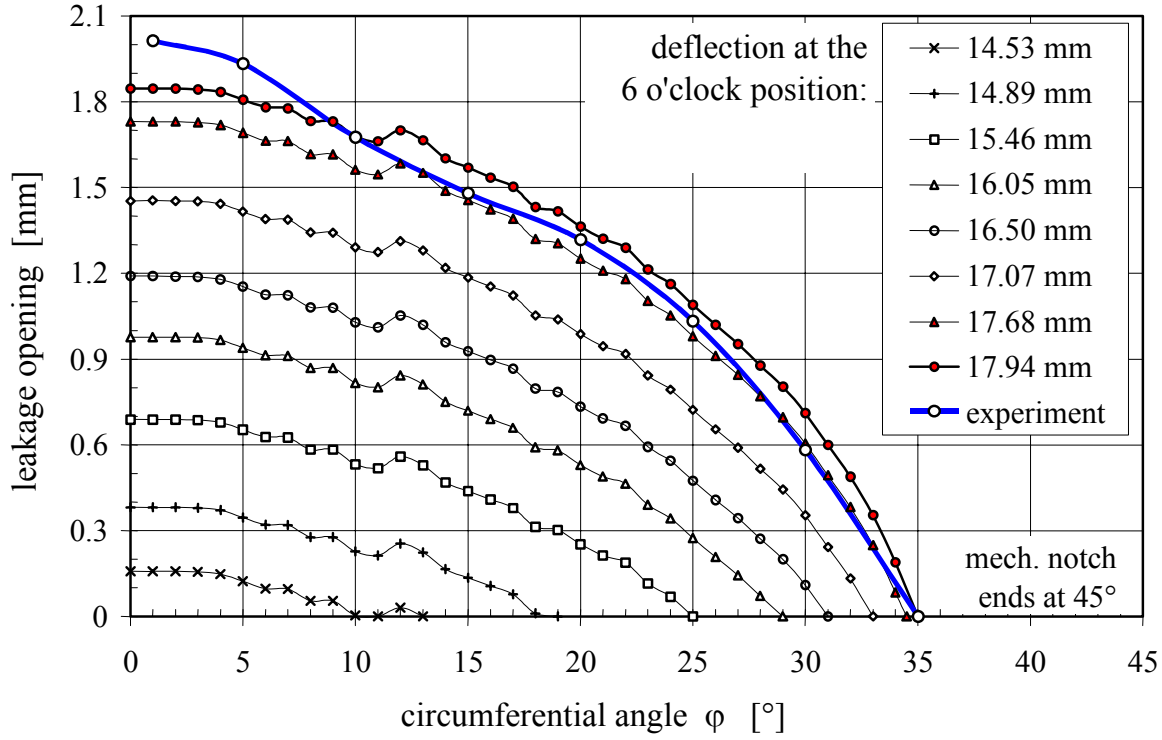

Figure 4: Pipe no. 2 with 90°-external circumferential surface flaw,
leakage opening profiles at different load levels in terms of deflection at the 6 o'clock position

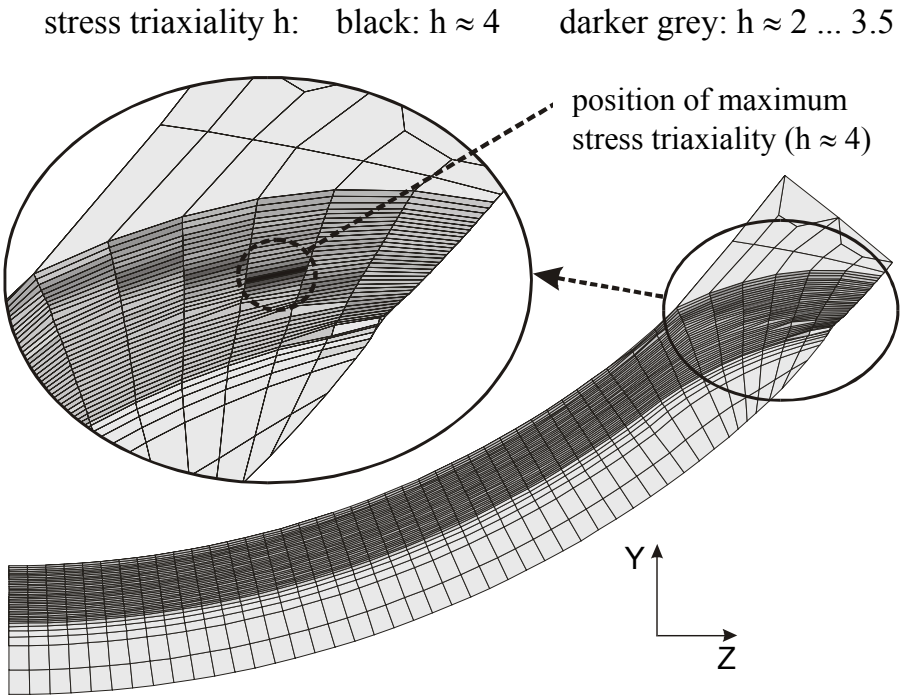

Figure 5: Pipe no. 2 with 90°-external circumferential surface flaw, maximum stress triaxiality in the ligament σ_h / σ_v at a deflection of $f_{6o'clock}$ = 17.94 mm, where experimental cleavage failure was observed

CONCLUSIONS

In the present investigations it could be shown by finite element analysis of large ductile crack growth that even complex failure of components can be modelled with high quality by use of damage mechanical simulation. It is pointed out that the problem could only be solved by damage models with geometry independent material parameters as conventional fracture mechanics concepts are not suited to be applied to large ductile crack growth. The high quality of the finite element analysis is underlined because experimental and numerical results are nearly identical, which applies especially to the crack opening area. For instance, this is regarded as an important prerequisite for the realistic assessment of effusion rates in damage cases and for the safety assessment of components in the field of power generating plants.

NOMENCLATURE

A	elongation at rupture
COD	Crack Opening Displacement
$f_{6o'clock}$	deflection at the 6 o'clock position
φ	circumferential angle (half of the total flaw angle)
J_i	crack initiation toughness
K_V	Charpy impact energy
K_{VH}	upper shelf of Charpy impact energy
L	axial direction (x-direction)
$R_{p0,2}$	0.2% offset yield strength
R_m	ultimate tensile strength
S	wall thickness direction (y-direction)
σ_h	hydrostatic stress
σ_v	Mises effective stress
T	tangential direction (z-direction)
f_n	volume fraction of void nucleating particles
ε_n	average plastic equivalent strain at which the nucleation of new voids reaches its maximum
s_n	standard deviation of the distribution which controls the nucleation of new voids
f_a	initial void volume fraction
f_c	critical void volume fraction
f_f	final void volume fraction

REFERENCES

1. European Structural Integrity Society: ESIS Procedure for Determining the Fracture Behaviour of Materials. ESIS P2-92, Delft, Jan. 1992
2. Analyse und Weiterentwicklung bruchmechanischer Versagenskonzepte; Schwerpunkt: Anwendung fortgeschrittener zähbruchmechanischer Konzepte; Bruchübergang, Abschlußbericht zum Forschungsvorhaben BMBF 1500 970, Forschungsbericht 232, BAM Berlin, 1999
3. Needleman, A.; Tvergaard, V.: An Analysis of Ductile Rupture in Notched Bars. J. Mech. Phys. Solids 32 (1984), pp. 461-490
4. Eberle, A., Klingbeil, D., Schicker, J.: The calculation of dynamic J_R-curves from the finite element analysis of a Charpy-test using a rate-dependent damage model, Nuclear Engineering and Design 198 (2000), pp. 75-87

COMPOSITE LAMINATES LEAST PRONE TO CRACKING UNDER COMBINED MECHANICAL AND THERMAL LOADS

J. Wang[1] and B. L. Karihaloo[2]

[1]Department of Mechanics and Engineering Science
Peking University, Beijing 100871, P. R. China
[2]Division of Civil Engineering, Cardiff School of Engineering
Cardiff University, Queen's Buildings, P. O. Box 686
Newport Road, Cardiff CF24 3TB, UK

ABSTRACT

This paper demonstrates the use of fracture mechanics based strength criteria and optimization techniques in the design of fibre-reinforced laminate configurations against cracking. The optimum configurations are sought for multidirectional fibre-reinforced composite laminates under combined in-plane mechanical and thermal loads. The design objective is to enhance the value of the loads corresponding to the first-ply-failure as judged by a transverse failure criterion which contains the *in situ* strength parameters proposed by the authors. The highly nonlinear optimization problems are solved using nonlinear programming incorporating a local-global algorithm of Elwakeil and Arora. It is found that the optimum designs under combined mechanical and thermal loads are not the same as those under pure mechanical loads for three of the four loading cases studied. For all cases the cracking loads are increased several fold in comparison with randomly chosen initial designs. The local-global algorithm can generally improve the computational efficiency of the pure multistart method for the considered optimum strength design of composite laminates.

KEYWORDS

Composite material, laminate, in situ strength, optimum design, thermal load, failure criterion, first-ply-failure, transverse cracking

INTRODUCTION

Most matrices of the advanced composite materials are brittle. They are prone to cracking under very low applied stresses. Cracking not only reduces the overall stiffness, but it can lead to disastrous failure of containers due to leakage. Another characteristic of these composite materials is their design tailorability. For this reason, a composite material or structure can be optimized, for given load conditions, in terms of one or a combination of the following properties: weight, stiffness, strength, toughness,

maximization for given material properties and volume, inevitably involve complicated fracture mechanics and/or failure analysis of heterogeneous materials. For this reason, the strength maximization of composite materials has not been as widely studied rigorously as the weight minimization, although optimum strength designs of continuous fibre-reinforced composite laminates have been pursued since the early days of these materials [1,2,3,4,5]. Daniel and Ishai [6] give an optimum design example of a composite material structure – the design of a pressure vessel based upon Tsai-Wu failure criterion and first-ply-failure.

The current failure criteria for fibre-reinforced composite laminates use the basic strength parameters that are measured using a unidirectional lamina (e.g. Daniel and Ishai [6]). Thus the configuration of a multidirectional laminate only influences the stress distribution in the multidirectional laminate. However, it is found that the transverse tensile and shear failure stresses of a unidirectional lamina depend upon the laminate configuration and the lamina thickness. This means that the conventional failure criteria need to be modified. They need to include the *in situ* strength parameters [7,8]. Moreover, in measuring the *in situ* transverse strength of unidirectional laminae in laminates, it was found by Flaggs and Kural [7] that the thermal residual stress resulting from the manufacturing process might consist of a large portion of the *in situ* strength (more than half for $[0_2/90_n]_s$ and $[\pm 30/90_n]_s$ for $n = 1, 2, ..., 8$). A composite structure will also experience temperature variations in service. Because of the remarkable difference in the thermal expansion coefficients as well as the stiffnesses of a unidirectional lamina in its longitudinal and transverse directions, the stresses caused by temperature variations may be quite significant in practice. It is obvious that the thermal stresses in a multidirectional laminate are functions of the laminate configuration, that is, functions of the ply angles in the laminate.

Given that most advanced fibre-reinforced composite laminates are prone to cracking and delamination but that the properties of laminates can be tailored, the present authors have attempted to apply fracture mechanics and optimization techniques to the optimum strength design of fibre-reinforced multidirectional composite laminates (Wang and Karihaloo [9,10,11,12,13]. It is well-known that optimization problems of composite laminates are highly nonlinear. The consideration of the *in situ* strength parameters complicates the problem. In the present paper, we shall demonstrate the optimum *in situ* strength design of multidirectional composite laminates subjected to combined mechanical and thermal loads. We shall first introduce the *in situ* strength parameters, and then incorporate them into the formalism of optimization problems. The optimization problems will be solved by a nonlinear mathematical programming technique incoporating the local-global algorithm proposed by Elwakeil and Arora [14].

IN SITU STRENGTH PARAMETERS

It has been observed in tests that the transverse tensile and shear strengths of a continuous fibre-reinforced unidirectional lamina, when situated in a multidirectional laminate, are functions of the thickness of the lamina itself and the ply angles of its neighbouring laminae (e.g. Flaggs and Kural [9]; Chang and Chen [15]). These strengths of a lamina in a laminate are generally larger than those measured using a thick unidirectional laminate. As a consequence, it is recognised that the transverse and in-plane shear strengths of a lamina cannot be regarded as its intrinsic property. Because of this observation, these strengths of a lamina are referred as *in situ* strengths, when the lamina is situated in a multidirectional laminate.

Chang and Lessard [8] proposed two formulas to calculate the *in situ* transverse and shear strengths by fitting experimental data

$$\frac{Y_t}{Y_t^0} = 1 + \frac{A}{N^B}\sin(\Delta\theta) \quad (1)$$

$$\frac{S_c}{S_c^0} = 1 + \frac{C}{N^D}\sin(\Delta\theta) \quad (2)$$

where Y_t^0 and S_c^0 are the transverse tensile strength and in-plane shear strength measured with a thick unidirectional lamina. A, B, C and D are to be determined by experiments. N is the number of unidirectional laminae in a multidirectional laminate. $\Delta\theta$ represent the minimum difference between the ply angle of a lamina and those of its neighbouring plies.

Wang and Karihaloo [10] studied the physics of the phenomenon of *in situ* strengths using fracture mechanics. Based upon the fracture mechanics analysis, they proposed two formulas to calculate the *in situ* strengths

$$\frac{Y_t}{Y_t^0} = 1 + \frac{A}{N^B} f_t(\Delta\theta) \quad (3)$$

$$\frac{S_c}{S_c^0} = 1 + \frac{C}{N^D} f_s(\Delta\theta) \quad (4)$$

Here, the two functions $f_t(\Delta\theta)$ and $f_s(\Delta\theta)$ represent the influence of the neighbouring laminae on the strengths of a lamina. They are given by

$$f_t(\Delta\theta) = \min\left[\frac{\sin^2(\Delta\theta_a)}{1+\sin^2(\Delta\theta_a)}, \frac{\sin^2(\Delta\theta_b)}{1+\sin^2(\Delta\theta_b)}\right] \quad (5)$$

$$f_s(\Delta\theta) = \min\left[\frac{\sin^2(2\Delta\theta_a)}{1+\sin^2(2\Delta\theta_a)}, \frac{\sin^2(2\Delta\theta_b)}{1+\sin^2(2\Delta\theta_b)}\right] \quad (6)$$

The parameters A, B, C and D in eqns. 3-4 are to be determined from experimental results. As these formulae also contain the ply angle influence functions, i.e. $f_t(\Delta\theta)$ and $f_s(\Delta\theta)$, the investigation of the dependence of A, B, C and D on the laminate configuration is very important. Their dependence upon the laminate configuration is discussed by Wang and Karihaloo [13].

In Figure 1, the *in situ* transverse strength predicted by eqns (1) and (3) are compared with the experimental results of Flaggs and Kural [7] for the material T300/934. In fitting the experimental data, different values of A are used in eqns (1) and (3) (1.7 and 3.4, respectively). Chang & Lessard [8] used $A = 1.3$ and $B = 0.8$ previously to fit the experimental data. It is seen that both of the theoretical formulas fit the experimental data reasonably well. The most important conclusion drawn from Figure 1 is that for the material and laminate configurations studied by Flaggs & Kural [7], the parameters A and B appear to be independent of the laminate configuration. They can therefore be treated as material constants. On the other hand, due to lack of experimental data, the dependence of the parameters C and D on the laminate configuration can not be judged. Chang & Lessard [8] found that formula (2) fits the experimental data well for T300/976 cross-ply laminates with $D = 2.0$ and $C = 1.0$ In the sequel, we shall use formula (3), which has a fracture mechanics basis, to calculate the *in situ* shear strength of laminae in multidirectional laminates with $C = 4.0$ and $D = 1.0$.

In most cases, transverse cracking is the first noticeable damage in a laminate. Although the transverse cracks generally do not result in the immediate failure of the whole laminate, they have the potential to induce failure by stress concentration and delamination. In the optimum strength design to follow,

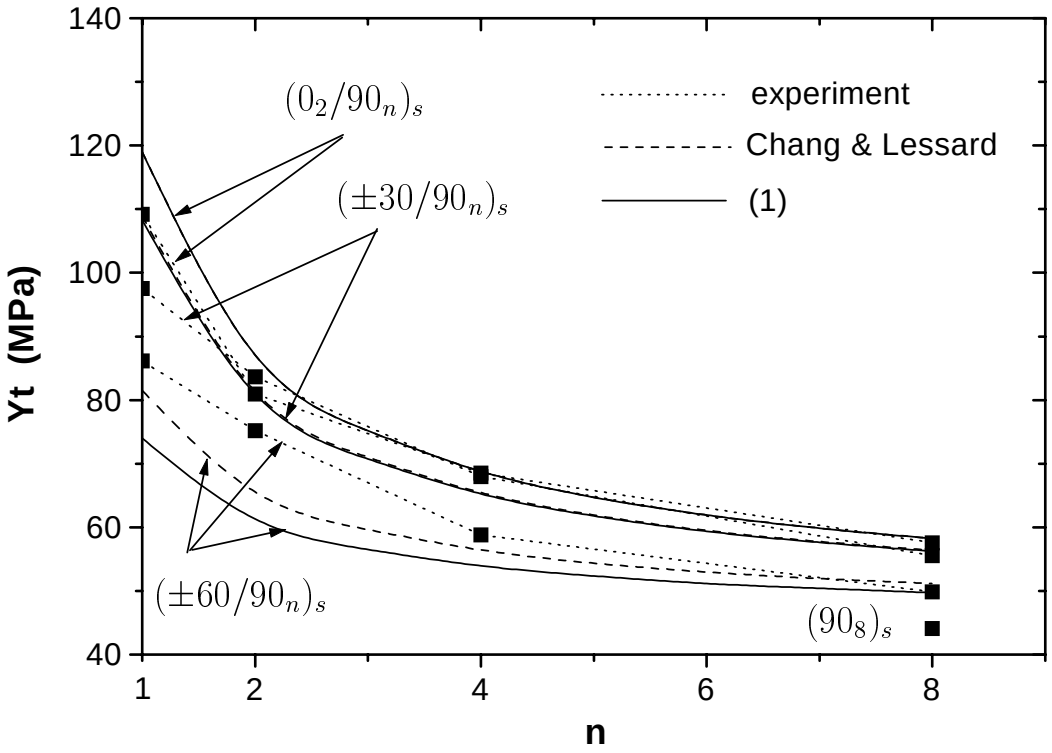

Figure 1: Comparison of theoretical and experimental results of the in situ transverse tensile strength. $A = 3.4$ and $B = 0.8$ are used in formula (1) (after Wang and Karihaloo [13]).

we shall use a transverse tensile failure criterion [8] to judge the transverse failure of a unidirectional lamina in a multidirectional laminate. This criterion, into which the *in situ* strengths are incorporated, is written as

$$q_i^2 \equiv \left(\frac{Y}{Y_t}\right)_i^2 + \left(\frac{S}{S_c}\right)_i^2 \leq 1; \qquad (i = 1, 2, ..., L) \tag{7}$$

where Y and S are the in-plane transverse and shear stresses in the lamina. L is the total number of unidirectional laminae in the laminate.

OPTIMUM DESIGN

For a composite laminate under given in-plane loads, if the ply angles and thicknesses of the constituent laminae are so chosen that the values of q_i^2 for all laminae are reduced, then the loads corresponding to the transverse cracking or failure will be enhanced. This objective is achieved by minimizing the maximum value of q_i^2. Following the procedure in the work by Wang and Karihaloo [11], the optimization problem is formulated as

$$\underset{\theta_i, t_i, \gamma}{\text{Min}} \quad \gamma \tag{8}$$

subject to

$$q_i - \gamma \leq 0 \tag{9}$$

$$-\frac{\pi}{2} \leq \theta_i \leq \frac{\pi}{2} \tag{10}$$

$$\sum_i t_i = h \qquad (i = 1, ..., L) \tag{11}$$

$$\underline{t} \leq t_i \leq \overline{t} \tag{12}$$

The optimization problem (8) is highly nonlinear with multiple local minima making the search for the global minimum difficult. Therefore, the above optimization problem is solved using nonlinear programming (constrained variable metric method) in conjunction with the so-called domain elimination method for global optimization proposed by Elwakeil and Arora [14].

The above optimization procedure was applied to the optimum design of an 8-ply symmetric multidirectional laminate $(\theta_4/.../\theta_1)_s$. The stiffness and strength constants used in the calculation of the *in situ* strengths are adapted from the work by Chang and Lessard [8] on T300/976. The thermal expansion coefficients are taken as those of T300/934 [7], i.e. $\alpha_L = 0.09\,\mu\text{strain}/^o\text{C}$, $\alpha_T = 28.8\,\mu\text{strain}/^o\text{C}$. The thickness of a single ply is assumed to be 0.14 mm. The temperature variation is taken as $\Delta T = -147^o\text{C}$, i.e. the temperature drop in the manufacturing process [7]. It can be arbitrary otherwise. Given a mechanical load $[N_1^0, N_2^0, N_6^0]$, the improvement in the design is represented by

$$k = \frac{1}{\max q_i}, \qquad (i = 1, 2, ..., 4) \tag{13}$$

The results of optimization with respect to the failure criterion (7) are shown in Figure 2 and Table 1. Figure 2 shows the changes of the load factor k during the optimization process for four in-plane loading combinations. Table 1 shows the initial, pseudo-randomly chosen guesses to ply angles, their final optimum values, and the optimum load factor k_{max}.

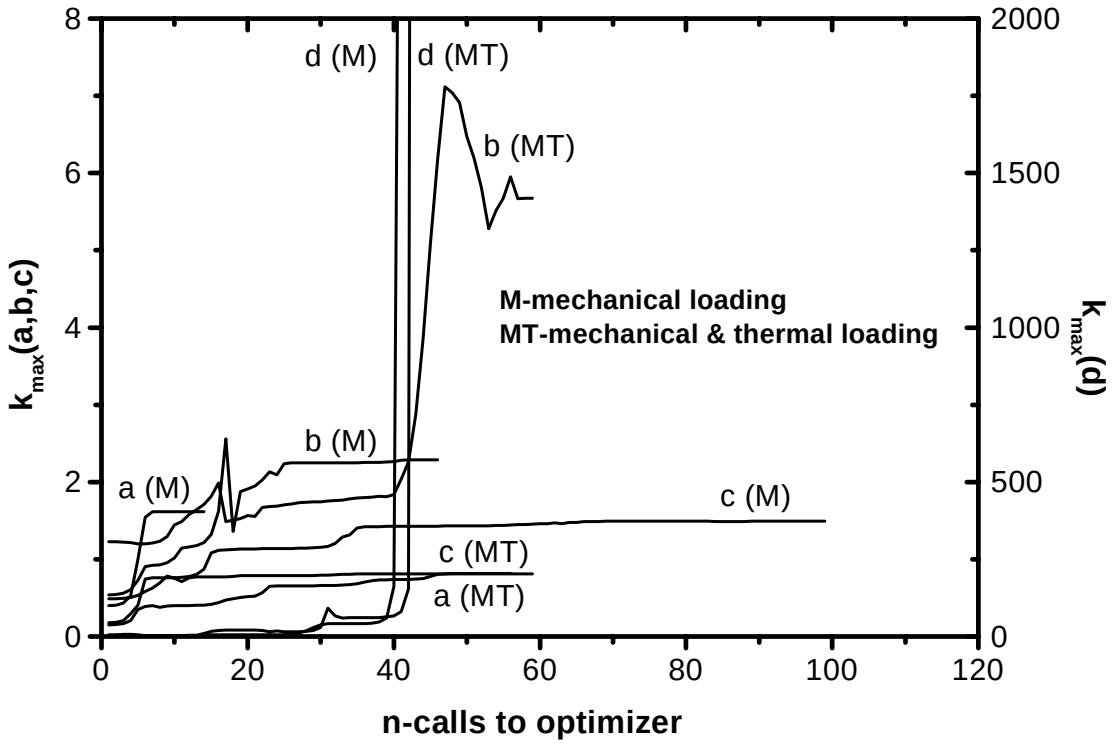

Figure 2: Evolution of load factor k for a symmetric laminate of 4 ply angles for four mechanical loading cases without and with thermal effect: (a) $[N_1^0, N_2^0, N_6^0]^T = [200, 200, 0]^T$ kN/m; (b) $[N_1^0, N_2^0, N_6^0]^T = [200, 0, 200]^T$ kN/m; (c) $[N_1^0, N_2^0, N_6^0]^T = [400, 200, 0]^T$ kN/m; (d) $[N_1^0, N_2^0, N_6^0]^T = [200, 200, 200]^T$ kN/m.

It is seen from Figure 2 that for each of the loading cases (a), (b) and (c), the mechanical load corresponding to the first-ply-failure in the optimally designed laminate is increased several fold compared

reached from many initial designs. It is hard to compare the results with and without thermal effect. However, the authors have previously found that for loading cases (a), (b) and (c), the same initial designs lead to different final designs for pure mechanical load and mixed mechanical and thermal load (Wang and Karihaloo [13]). For loading case (d), there is a global optimum design, namely, the configuration where all the ply angles are in the 45^0 direction. When the plies are so arranged, for the transverse criterion (7), the absolute global minimum value of the objective function is identically zero. This minimum value is captured by the optimizer. In all designs, in order to reduce the value of the objective function, the optimizer aims at reducing the transverse and in-plane shear stresses and distributing the stress in the fibre direction of a lamina in the laminate. The optimizer always distributes the stresses according to the strengths in different directions of the anisotropic material. An examination of the elimination procedure described above shows that the efficiency of the local-global algorithm depends upon the number of design variables, the elimination factor and the time taken to find a local minimum.

TABLE 1
SUMMARY OF OPTIMIZED PLY ANGLES IN A SYMMETRIC 8-PLY LAMINATE

without thermal effect				with thermal effect		
loading case	Initial design $\theta_1,\theta_2,\theta_3,\theta_4$	Final design $\theta_1,\theta_2,\theta_3,\theta_4$	k_{max}	Initial design $\theta_1,\theta_2,\theta_3,\theta_4$	Final design $\theta_1,\theta_2,\theta_3,\theta_4$	k_{max}
a	-43,-52,-47,5	-43,-86,-42,34	1.62	-74,-82,14,67	-36,-61,-42,45	0.8
b	-18,75,76,45	-58,32,86,32	2.3	-12,-34,40,13	32,-61,31,32	5.7
c	-62,60,-82,63	-36,50,-55,12	1.5	-74,-69,59,87	-44,51,-44,19	8.2
d	88,5,16,59	45,45,45,45	∞	47,29,29,49	45,45,45,45	∞

References

[1] Sandhu, R. S. (1969) TR-68-168, Air Force Flight Dynamic Laboratory, Wright-Patterson AFB.

[2] Brandmaier, H. E. (1970) *J. Compos. Mater.* 4, 422.

[3] Chao, C. C, Sun, C. T and Koh, S. L. (1975) *J. Compos. Mater.* 9, 53.

[4] Park, W. J. (1982) *J. Compos. Mater.* 16, 341.

[5] Fukunaga, H. and Vanderplaats, G. N. (1991) *Computers & Structures* 40, 1429.

[6] Daniel, I. M. and Ishai, O. (1994) *Engineering Mechanics of Composite Materials.* Oxfod University Press, New York.

[7] Flaggs, D. L. and Kural, M. H. (1982) *J. Compos. Mater.* 16, 103.

[8] Chang, F.-K. and Lessard, L. B. (1991) *J. Compos. Mater.* 25, 2.

[9] Wang, J. and Karihaloo, B. L. (1994) *Proc. Roy. Soc.*, London A444, 17.

[10] Wang, J. and Karihaloo, B. L. (1996a) *J. Compos. Mater.* 30, 1314.

[11] Wang, J. and Karihaloo, B. L. (1996b) *J. Compops. Mater.* 30, 1338.

[12] Wang, J and Karihaloo, B. L. (1997) *Composite Structures* 38, 661.

[13] Wang, J. and Karihaloo, B. L. (1999) *Composite Structures* 47, 635.

[14] Elwakeil, O. A. and Arora, J. S. (1996) *Int. J. Num. Methods Eng.* 39, 3305.

[15] Chang, F.-K. and Chen, M. H. (1987) *J. Compos. Mater.* 21, 708.

COMPRESSIVE FRACTURE OF ORTHOTROPIC LAMINATES CONTAINING OPEN HOLES DUE TO FIBRE MICRO-INSTABILITY

Constantinos Soutis

Department of Aeronautics, Imperial College of Science, Technology and Medicine
Prince Consort Road, London SW7 2BY, UK

ABSTRACT

The compressive strength and failure mechanisms are investigated for a wide range of filamentary composites. Static uniaxial compressive tests are performed on both notched and unnotched specimens made from four carbon fibres and three epoxy resins combined to give six different composite systems. In all cases the dominant failure mechanism is by fibre microbuckling (fibre kinking). An infinite band-kinking model is used to estimate the unnotched strength and a linear softening cohesive zone model is applied to estimate the open hole compression (OHC) strength.

KEYWORDS

Composite materials, laminate, fibre microbuckling, kinking, cohesive zone model, compressive strength.

INTRODUCTION

The compressive strength of long, aligned carbon fibre-reinforced plastics (CFRP) is significantly lower than the tensile strength of the material due to kink-band formation introduced by fibre instability (microbuckling). In contrast, the compressive strength of metallic materials equals or exceeds their tensile strength (by an order of magnitude for ceramics). From the literature on compressive fracture it is easy to get the impression that fibre microbuckling and kinking are two different competing mechanisms. In fact, the kink band is the outcome of fibre microbuckling failure, as observed experimentally in [1-3]. Fibre microbuckling occurs first, followed by propagation of this local damage to form a kink band. Many analytical models attribute the low compression strength and the mechanism of kink-band formation to initial fibre misalignment (waviness) but fibre and fibre-matrix interface properties may also play an important role. In a multidirectional laminate the supporting ply orientation on the stability of the 0° layer (ply-ply interaction) and the location of the 0° ply through the laminate thickness can also have a significant effect on the initiation and final failure. For instance, the failure strain of a laminate with 0° outer layers can be more than 10% lower than a similar lay-up with ±45° outer plies, due to out-of-plane fibre microbuckling [4]. The outer off-axis plies provide better lateral support to the 0° layers, permitting them to fail by in-plane microbuckling, which is a higher strain failure event.

In the present paper, compressive tests are reported for several carbon fibre-epoxy systems and lay-ups with and without holes; the failure mode is fibre microbuckling in all cases.

FRACTURE ANALYSIS

Unnotched Compressive Strength

It is now well established that the unnotched strength, σ_c, of unidirectional carbon fibre-epoxy laminates is governed by fibre microbuckling which is associated with non-linear shear of the polymer matrix initiating from regions of pre-existing fibre waviness (of magnitude only few degrees). For a rigid-perfectly plastic body Budiansky [5] showed that

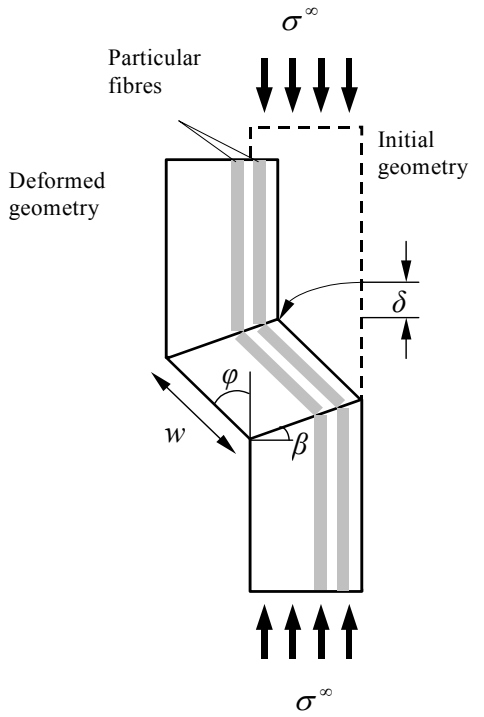

Figure 1. Fibre kink band geometry

$$\sigma = \frac{\tau_y \left[1 + \left(\frac{\sigma_{T_y}}{\tau_y} \right)^2 \tan^2 \beta \right]^{\frac{1}{2}}}{\phi_0 + \phi} \tag{1}$$

where τ_y and σ_{Ty} are the in-plane shear and transverse yield stresses of the composite, respectively. ϕ_0 is the assumed fibre misalignment angle in the kink band, ϕ is the additional fibre rotation in the kink band under a remote stress σ^∞, and β is the band orientation angle, Fig.1. The critical stress $\sigma=\sigma_c$ is achieved at $\phi=0$ in equation (1).

By using the above kinking theory, the unnotched strength of the unidirectional laminate can be obtained in terms of the shear properties of the composite and the initial fibre misalignment. Once the failure stress of the 0°-ply is known, the compressive strength of any multidirectional 0°-dominated lay-up can be estimated by the stiffness ratio method,

$$\sigma_{un} = \frac{\sigma_c}{NE_1} \sum_{k=1}^{N} n^{(k)} E_{x\theta}^{(k)} \tag{2}$$

where σ_{un} is the unnotched laminate strength, σ_c is the strength of the 0° lamina, N is the total number of the laminae in the laminate, E_1 is the 0° ply stiffness in the fibre direction, n is the number of plies of a given orientation θ, and $E_{x\theta}$ is the modulus of a ply of orientation θ in the loading direction (x).

Open Hole Compressive Strength

Soutis and co-workers [2, 6, 7] have developed a crack bridging model for the initiation and growth of compressive damage from the edge of a blunt notch such as an open hole. The microbuckled region (and associated plastic deformation in the off-axis plies and delamination between plies is treated as a compressive *Mode I* crack with a cohesive zone at its tip. A linearly softening spring law within the cohesive zone models damage: the crack bridging normal traction T is assumed to decrease linearly with increasing crack closing displacement (CCD) $2v$ from a maximum value (equal to the unnotched strength σ_{un} of the composite) to zero at a critical crack face displacement of $2v_c$. The intrinsic toughness at the tip of the cohesive zone is taken equal to zero, which is similar to the Dugdale analysis of plastic deformation in metals from the root of a notch [8]. Rice [9] has shown that the work done G_C to advance the crack equals the area under the crack traction versus crack displacement curve, giving $G_C=\sigma_{un}v_c$. The cohesive zone model may be used to predict the notched strength σ_n of any multidirectional laminate once the material parameters σ_{un} and G_C have been measured from independent compression tests [2, 6].

Alternatively, the unnotched compressive strength can be estimated from equations (1) and (2) and the critical crack closing displacement can be related to the kink band width w [5, 7], i.e.,

$$w = 2v_c = \frac{\pi d_f}{4}\left(\frac{V_f E_f}{2\tau_y}\right)^{\frac{1}{3}} \quad (3)$$

where d_f is the fibre diameter, E_f is the fibre elastic modulus, V_f is the fibre volume fraction and τ_y is the in-plane shear yield strength of the composite. Equation (3) implies that the broken fibres in the cohesive zone model rotate completely and do not lock up ($2v_c=\delta_c$, see Fig.1).

MATERIALS AND TESTING PROGRAMME

Four carbon fibres and three epoxy resins were combined to give six composites, as shown in Table 1. The materials were supplied in prepreg form by Hexcel Composites, and autoclave cured to produce a variety of laminates.

TABLE 1
COMPOSITE SYSTEMS STUDIED

Composite	Fibre	Matrix Resin
1	T800	922
2	T800	924
3	T800	927
4	T300	927
5	IMS	927
6	HTA	927

T800 (Torayca) and IMS (Tenax) are equivalent intermediate modulus fibres (about 290GPa) with tensile strain to failure of about 1.9%. T300 (Torayca) and HTA (Tenax) are equivalent low modulus fibres (about 235GPa) with tensile strain to failure of about 1.5%. The three Hexcel resins increase in tensile strength, failure strain and toughness from 922 through 924 to 927 [10, 11].

Unidirectional specimens were tested in compression according the Imperial College method [10], which uses a 10mm gauge length Celanese-style specimen, and according to the modified Celanese method [1, 3]. Collected results are given later. Notched specimens were tested in compression according to the ACOTEG standard ACO/TP/II [10, 11]. Specimens were 36mm wide and contained a 6mm diameter central hole. The laminates were nominally 3.5mm thick with the lay-up $[0/45/-45/0/90/0/45/-45/0/90/0/45/-45/0°]_s$. Specimens were supported in an anti-buckling guide to prevent overall buckling[2]. The extent of the internal damage in the specimens was assessed by ultrasonic scanning [10].

RESULTS AND DISCUSSION

Unidirectional Compression

The results from the unidirectional compression tests are presented in Table 2. The measured compressive strengths for the six composite systems examined are in very good agreement with the theoretical values, predicted by the Budiansky plastic fibre microbuckling model [5]. The model requires the knowledge of the initial fibre misalignment (ϕ_0), the shear yield stress (τ_y), the transverse tensile yield stress (σ_{Ty}) and the kink band inclination angle (β). Although the six composite systems demonstrate different ultimate shear strengths, their shear yield stresses, which mostly influence the unidirectional compressive response, are very similar at 65-70 MPa. Taking ϕ_0=3° (0.052 rad), τ_y=70MPa and β=15° (0.262 rad) gives a satisfactory overall prediction, as seen in Table 2. These values are close to values found from experimental observations for all materials. Of course, the effect of fibre strength and stiffness properties, fibre diameter and fibre/matrix interface, are not accounted for by the model and they may influence the composite

strength. A weak interface may trigger microbuckling prematurely, while a bigger fibre diameter will provide higher buckling resistance [4].

TABLE 2
STIFFNESS AND STRENGTH PROPERTIES OF A UNIDIRECTIONAL LAMINATE

Composite System	E_1 GPa	E_2 GPa	G_{12} GPa	ν_{12}	σ_c^{th} MPa	σ_c^{exp} MPa	difference %
T800/922	143.6 (158)#	9.9	3.98	0.29	1440	1410	-2.08
T800/924	141 (158)	8.6 (9.0)	4.12 (6.0)	0.33	1440	1350 (1448)	-6.25
T800/927	154	8.32	3.75	0.37	1440	1450	-
T300/927	116 (131)#	7.5 (8)#	3.56+	0.31	1440	1450	-
IMS/927	135 (175)#	8.2	3.56+	0.33	1440	1320	-8.3
HTA/927	118 (145)#	6.8 (8)#	3.24+	0.35	1440	1530	5.9
$\overline{\sum}$	137.4	8.3	4.02	0.33	1440	1435	-

Notes: ( ) Experimental data measured by Soutis et al [3,4]
+ Estimated values from the resin shear modulus and fibre volume fraction
# Expected values
σ_c^{th} Predicted strength
σ_c^{exp} Measured strength

Multi-directional Compression

The notched compressive strength (σ_n) of a multi-directional laminate is assessed with reference to the unnotched strength (σ_{un}). Details of the latter are given in Table 3. In the present study problems were experienced in the experiments due to the laminates failing adjacent to the grips, outside the region supported by the anti-buckling guides. The values given in the table will, therefore, be underestimates of the true value.

TABLE 3
PREDICTED STIFFNESS AND STRENGTH PROPERTIES OF A
$[0/\pm45/0/90/0/\pm45/0/90/0/\pm45/0]_s$ LAMINATE

Composite System	E_{xx} GPa	E_{yy} GPa	G_{xy} GPa	ν_{xy}	σ_{un}^{th} MPa	σ_{un}^{exp} MPa
T800/922	75.5	40.2	18.2	0.390	728	640.5 (±37)
T800/924	74.08	39.06	17.84	0.398	743.8	636.9 (±23)
T800/927	80.1	41.7	19.0	0.403	743.8	660.8 (±55)
T300/927	61.17	32.46	14.85	0.386	742.1	n/a
IMS/927	70.61	37.15	16.9	0.396	739.2	n/a
HTA/927	61.74	32.35	14.8	0.395	744.6	n/a

The theoretical compressive strength has been obtained by using Eq.(1) taking σ_{Ty}=100 MPa, τ_y=70 MPa, ϕ_0=3° and β=15° and Eq.(2). The measured unnotched strength is at least 15% lower than the predicted value due to premature (grip) failure. The stiffness ratio method predicts 728 MPa (assuming

σ_0=1440 MPa for all systems), while the result obtained from the maximum stress or strain criterion is 757 MPa (assuming σ_0=1440 MPa, or an average failure strain of 1%). The elastic stiffness properties in Table 3 are calculated values using ply properties (Table 2) and classical laminate theory.

TABLE 4
NOTCHED COMPRESSIVE STRENGTH OF A $[0/\pm45/0/90/0/\pm45/0/90/0/\pm45/0]_s$ LAMINATE (hole diameter=6mm, d/w=0.167)

Composite System	τ_y MPa	ϕ_0 ^{o}	β ^{o}	σ_{un}^{th} MPa	σ_n^{th} MPa	l_c mm	σ_n^{exp} MPa
T800/922	70	3	15	728	368.1	1.95	370.4 (±8)
T800/924	70	3	15	743.8	371.3	1.86	390.0 (±4)
T800/927	70	3	15	743.8	371.2	1.86	377.0 (±6)

The theoretical notched strength (σ_n) and critical microbuckling length (l_c) at the hole edges are simulated by the Soutis *et al* [2, 6] cohesive zone fracture model. For the T800 composite system, using equation (3) and material data (V_f=0.65, E_f=294 GPa, τ_y=70 MPa) a width of about 10 fibre diameters (≈60 μm) is obtained, which is representative of observed kink band widths of 60-80 μm [2, 6]. Using the theoretical unnotched strength (Table 3) and a value of v_c=40 μm appears to predict the notched strength of all three T800 systems very accurately, as seen in Table 4; similar good correlation is expected for the three other systems (T300-, IMS- and HTA-927). The predicted critical microbuckling length is also included in Table 4. When this value is reached the laminate is expected to fail catastrophically. Microbuckling lengths of 2-3 mm, depending on hole size and lay-up, have been observed experimentally [2, 6]. Microbuckling of the 0° plies nucleates at the sides of the hole at between 75-80% of the failure load and is accompanied by matrix cracking of the off-axis plies and delamination between neighbouring plies. This damage reduces the stress concentration at the edge of the hole and delays final failure to higher applied stresses. The OHC strengths of all these materials lie below the limit of notch insensitivity (where the net section failure stress equals the unnotched strength) but above the perfectly brittle limit (where the local stress at the root of the notch equals the unnotched strength). Applying the maximum stress failure criterion could underestimate the notched compressive strength by more than 30%, especially for small *d/w* ratios [6]. The material length l_c serves as a useful measure of laminate damage tolerance.

CONCLUDING REMARKS

The fibre kinking model by Budiansky [5] suggests that fibre microbuckling is a plastic rather than an elastic failure mode and that the strength of the unidirectional material is governed by the shear yield stress of the composite and the misalignment angle of the fibre. Applying the model to six different carbon fibre-epoxy systems tested in [10], a very good agreement is found. Although the six systems have different ultimate shear strengths, their shear yield stresses are very similar at 65-70 MPa. Once the failure stress of the 0°-ply is known, the compressive strength of any multidirectional laminate containing 0° layers can be determined on a ply-by-ply analysis using the laminate plate theory and the maximum stress failure criterion. For 0°-dominated lay-ups the strength can be accurately estimated by the stiffness ratio, equation (2). The 18-30% discrepancy observed between predictions and the measured multidirectional unnotched compressive strengths for the six systems examined in [10] is due to Euler bending that occurred during testing and thickness variation across the specimen width. Unnotched strength data are more difficult to generate than tensile data because compression testing is sensitive to factors such as Euler buckling, specimen geometric imperfections, specimen misalignment in the test fixture and fibre misalignment in the specimen.

The linear softening cohesive zone model of Soutis *et al* [2, 6] successfully predicts the effects of an open hole and lay-up upon the compressive strength and microbuckle zone size at failure. In the analysis, the inelastic deformation associated with fibre microbuckling and matrix plasticity developed at the hole edges is mathematically replaced with a line-crack loaded across its faces by a bridging normal traction that decreases linearly with the overlap displacement of the microbuckle. The model takes as its input the laminate unnotched strength and the critical crack closing displacement, which is related to the in-plane compressive fracture toughness of the laminate. A value of 40 μm appears to give an excellent correlation between predicted and measured OHC data for all systems and lay-ups examined in [10]. The cohesive zone approach offers a technique for the prediction of OHC strength, which is simple and easy to apply and has the prospect of being used as a preliminary design tool for laminated polymer composite structures.

ACKNOWLEDGEMENTS

The author would like to thank his research students for assisting with the collection of experimental data and the Engineering and Physical Sciences Research Council and the British Ministry of Defence for financial support.

REFERENCES

1. Soutis, C. (1991) *Comp. Sci. & Techn*., **42**(4), 373-392.
2. Soutis, C., Fleck, N.A. and Smith, P.A. (1991) *J Comp. Mat.*, **25**, 1476-1498.
3. Soutis, C. (1997). In: *Composite Materials: Testing & Design*, Thirteenth volume, ASTM STP 1242, S.J. Hooper, Ed., American Society for Testing & Materials, 168-176.
4. Berbinau, P., Soutis, C.,Goutas, P. and Curtis, P.T. (1999) *Composites A*, **30**(10), 1197-1207.
5. Budiansky, B. (1983) *Computers & Structures*, **16**(1), 3-12.
6. Soutis, C., Curtis, P.T. and Fleck, N.A. (1993) *Proc. R. Soc. London A*, **440**, 241-256.
7. Soutis, C. and Curtis, P.T. (2000) *Composites: Part A*, **31**, 733-740.
8. Dugdale D.S. (1960) J. Mech. Phys. Solids, 8, 100-104.
9. Rice, J.R. (1968). In: *Mathematical Analysis in the Mechanics of Fracture*, **2**, Academic Press, N.Y.
10. Smith, F.C. (2000) *PhD Thesis*, Imperial College, London, UK.
11. Soutis, C., Smith, F.C. and Matthews, F.L. (2000) *Composites: Part A*, **31**, 531-536.

COMPUTATIONAL MODELLING OF CRACKS IN VISCOPLASTIC MEDIA

G.N. Wells*, L.J. Sluys and R. de Borst

Koiter Institute Delft
Delft University of Technology
P.O. Box 5048, 2600 GA Delft, The Netherlands

ABSTRACT

A newly developed numerical model is used to simulate propagating cracks in a strain softening viscoplastic medium. The model allows the simulation of displacement discontinuities independently of a finite element mesh. This is possible using the partition of unity concept, in which fracture is treated as a coupled problem, with separate variational equations corresponding to the continuous and discontinuous parts of the displacement field. The equations are coupled through the dependence of the stress field on the strain state. Numerical examples show that allowing displacement discontinuities in a viscoplastic Von Mises material can lead to a failure mode that differs from a continuum-only model.

KEYWORDS

Displacement discontinuity, viscoplasticity, strain softening.

INTRODUCTION

Two distinct stages can be identified in the failure of quasi-brittle and ductile materials. The first stage involves the localisation of inelastic deformations into narrow zones. Later in the loading process, macroscopic displacement discontinuities across surfaces can be identified. Depending on the ductility of the material, this occurs at a point between the peak load and complete global failure. Computationally, failure is usually simulated using a continuum (regularised strain softening) or a discontinuous (cohesive zone, LEFM) model. Continuum models are well suited for modelling the inelastic deformations that develop early in the loading process, but are unable to represent the free surfaces that develop in a body prior to complete failure. Discontinuous models are well-suited for highly localised failure, but less adept at representing the distributed inelastic deformations near the peak load in quasi-brittle materials and the substantial plastic flow that occurs during the failure of ductile materials. A model is presented which is able to capture both stages of the failure process. Initial inelastic deformations are represented in the continuum using a regularised strain softening model, and the later development of discrete surfaces within a body is simulated by inserting a displacement discontinuity.

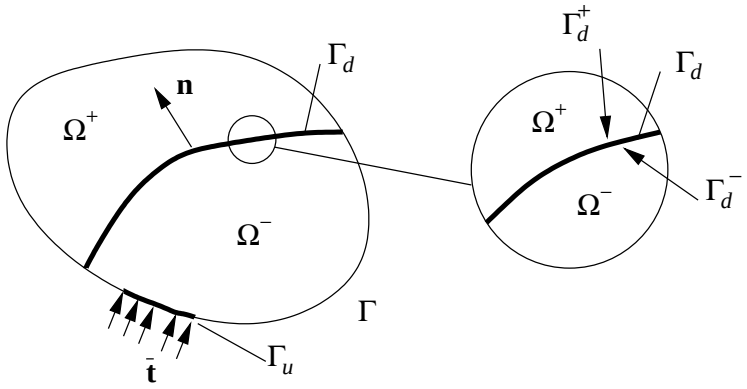

Figure 1: Body Ω crossed by a single discontinuity Γ_d.

To simulate strain softening in the continuum, a regularised continuum model must be used. In this work, a Perzyna viscoplastic model is used [1]. When the inelastic deformation at the tip of a discontinuity reaches a critical level, the discontinuity is extended. A displacement discontinuity is added to the underlying finite element interpolation basis using the partition of unity concept [2, 3]. Using the partition of unity concept, a displacement discontinuity can be modelled by adding extra degrees of freedom to existing nodes. The displacement field is decomposed into a continuous and a discontinuous part, with 'regular' nodal degrees of freedom representing the continuous part of the displacement field and 'enhanced' nodal degrees of freedom representing the discontinuous part of the displacement field. This method has been used successfully for simulating cracks in elastic bodies [4] and cohesive cracks under both static [5] and impact [6] loading.

To elaborate the model, the kinematics of a body crossed by a displacement discontinuity are first discussed. Aspects of introducing a displacement discontinuity in an inelastic continuum are then considered and the model is demonstrated through several numerical examples. The numerical examples highlight the influence of including a displacement discontinuity on the failure mode for a Von Mises material.

INCLUDING A DISPLACEMENT DISCONTINUITY

The proposed formulation allows a displacement discontinuity to be added to a finite element model, independently of the spatial discretisation. Rather than explicitly modelling a discontinuity through the mesh structure, a displacement jump is described mathematically using the Heaviside function.

Discontinuous displacement field

The displacement field $\mathbf{u}$ for a body crossed by multiple, non-intersecting displacement discontinuities can be described by:

$$\mathbf{u}(\mathbf{x},t) = \hat{\mathbf{u}}(\mathbf{x},t) + \sum_{i=1}^{k} \mathscr{H}_{\Gamma_{d,i}}(\mathbf{x})\tilde{\mathbf{u}}_i(\mathbf{x},t) \tag{1}$$

where $\hat{\mathbf{u}}$ and $\tilde{\mathbf{u}}_i$ are continuous functions, $\mathscr{H}_{\Gamma_{d,i}}$ is the Heaviside function centred at the ith discontinuity and k is the number of discontinuities. A body, crossed by a single discontinuity is shown in figure 1. The Heaviside jump is defined as $\mathscr{H}_{\Gamma_d}(\mathbf{x}) = 1,\ \mathbf{x} \in \Omega^+$ and $\mathscr{H}_{\Gamma_d}(\mathbf{x}) = 0,\ \mathbf{x} \in \Omega^-$, where the domains Ω^+ and Ω^- are shown in figure 1. The magnitude of the displacement jump at the ith discontinuity $[\![\mathbf{u}]\!]_i$ is given by $\tilde{\mathbf{u}}_{i,\mathbf{x}\in\Gamma_{d,i}}$. Taking

the symmetric gradient of equation (1), the strain field for the geometrically linear case is given by:

$$\boldsymbol{\varepsilon} = \boldsymbol{\nabla}^{\mathrm{S}}\mathbf{u} = \boldsymbol{\nabla}^{\mathrm{S}}\hat{\mathbf{u}} + \sum_{i=1}^{k} \mathscr{H}_{\Gamma_{d,i}} \left(\boldsymbol{\nabla}^{\mathrm{S}}\tilde{\mathbf{u}}_i\right) + \sum_{i=1}^{k} \delta_{\Gamma_d,i} \left(\tilde{\mathbf{u}}_i \otimes \mathbf{n}_i\right)^{\mathrm{S}} \tag{2}$$

with $\delta_{\Gamma_d,i}$ the Dirac-delta distribution centred at the *i*th displacement discontinuity and **n** is the normal vector to the discontinuity.

Variational formulation

The proposed model can be interpreted as a coupled problem, with one equation describing the continuous part of the displacement field, $\hat{\mathbf{u}}$, and a second describing the discontinuous part of the displacement field, $\mathscr{H}_{\Gamma_d}\tilde{\mathbf{u}}$. Following a Galerkin procedure, the weak governing equations can be formed by inserting the displacement decomposition in equation (1) into the virtual work equation. After some manipulations, two weak governing equations can be formed for a body crossed by a single discontinuity [5]:

$$\begin{aligned} &\int_{\Omega} \boldsymbol{\nabla}^{\mathrm{S}}\hat{\boldsymbol{\eta}} : \boldsymbol{\sigma} = \int_{\Gamma_u} \hat{\boldsymbol{\eta}} \cdot \bar{\mathbf{t}}\, d\Gamma \\ &\int_{\Omega^+} \boldsymbol{\nabla}^{\mathrm{S}}\tilde{\boldsymbol{\eta}} : \boldsymbol{\sigma} + \int_{\Gamma_d} \tilde{\boldsymbol{\eta}} \cdot \mathbf{t} = \mathscr{H}_{\Gamma_u} \int_{\Gamma_d} \tilde{\boldsymbol{\eta}} \cdot \bar{\mathbf{t}}\, d\Gamma \end{aligned} \tag{3}$$

where $\hat{\boldsymbol{\eta}}$ and $\tilde{\boldsymbol{\eta}}$ are admissible displacement variations, **t** is the traction acting at a discontinuity Γ_d and $\bar{\mathbf{t}}$ are tractions acting on the external boundary Γ_u. The unbounded Dirac-delta term has been eliminated by changing the volume integral containing the distribution to a surface integral over Γ_d.

Finite element implementation

The weak governing equations in equation (3) are solved in a similar manner to a coupled problem. Different sets of nodal degrees of freedom are used to represent the continuous and the discontinuous parts of the displacement field. In a discretised format, the displacement field is given by:

$$\mathbf{u} = \underbrace{\mathbf{Na}}_{\hat{\mathbf{u}}} + \mathscr{H}_{\Gamma_d} \underbrace{\mathbf{Nb}}_{\tilde{\mathbf{u}}} \tag{4}$$

where **N** is the standard matrix containing the element shape functions and the vectors **a** and **b** relate to the continuous and discontinuous parts of the displacement field, respectively. The discretised weak governing equations are formed by inserting the discretised displacement field in equation (4) and its gradient into equation (3).

The extra **b** degrees of freedom are added only to nodes close to a discontinuity. If the support of a node is crossed by a discontinuity, the **b** degrees of freedom are activated to describe the discontinuity. The addition of extra degrees of freedom to nodes whose support is not crossed by a discontinuity leads to a global stiffness matrix which is not positive definite since over the support of the node the Heaviside function is equivalent to a constant function, which is included in the span of the standard shape functions.

SIMULATING THE CONTINUUM-DISCONTINUOUS TRANSITION

A displacement discontinuity is extended when the inelastic deformation in the continuum at a discontinuity tip reaches a critical level. For the Perzyna viscoplastic model, a discontinuity is extended when the yield

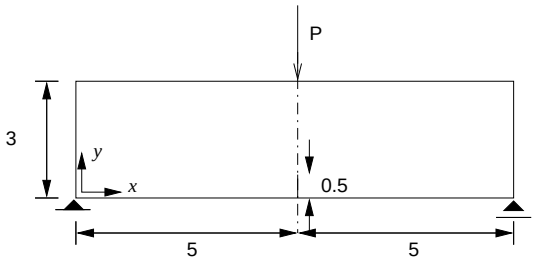

Figure 2: Three-point bending beam. All dimensions in millimetres (depth = 1mm).

strength of the underlying rate-independent model is exhausted. At this stage, the material is considered to have lost all coherence. Therefore, no tractions can be transmitted across an opening discontinuity. Since the rate-dependent constitutive model remains well-posed, it is not possible to draw on linear stability analysis to determine a discontinuity propagation direction. Therefore, a discontinuity is assumed to extend in the direction in which the effective stress is maximum. This is determined by a spatial weighting procedure around a discontinuity tip [7, 8]. Using an effective stress to determine the propagation direction is dependent on the chosen yield function and makes the procedure equally applicable to both mode-I and mode-II failure problems [8].

NUMERICAL EXAMPLES

To illustrate the combined continuum-discontinuous model, a three-point bending test (figure 2) is performed for a Von Mises material. A discontinuity propagates from a 0.5 mm long initial cut at the centre of the beam at the bottom edge. The material properties are initially taken as: Young's modulus $E = 1 \times 10^2$ MPa, Poisson's ratio $\nu = 0.2$, yield stress $\bar{\sigma} = 1$ MPa, viscosity $\eta = 2$ s and the hardening modulus $h = -200$ Nmm^{-2}. The beam is loaded via a constant downward velocity of 1 mms^{-1}, applied at the centre of the beam on the top edge. The analyses are performed under plane strain conditions and the six-noded triangle is used as the underlying finite element.

To illustrate the objectivity of the model with respect to finite element mesh structure, the beam is analysed using two different meshes. The first is a structured mesh composed of 4750 elements and the second is an unstructured mesh composed of 3631 elements. Figure 3 shows the equivalent plastic strain field and the discontinuity path for the two meshes near complete failure. The size and shape of the plastic zones are the same and a discontinuity has propagated through the beam towards the loading point. To examine more closely the failure mode, the evolution of the equivalent plastic strain field and displacement discontinuity are shown in figure 4. The failure mode is clearly mode-I dominated. A discontinuity propagates through the beam, with a plastic hinge forming only at the last stage of failure.

To highlight the influence of including a displacement discontinuity, the three-point bending test is re-analysed with an initial discontinuity which is not allowed to extend. The equivalent plastic strain field for this case is shown in figure 5. The failure mode differs fundamentally from the case of a propagating discontinuity. The beam has failed through the development of a plastic hinge, with the centre of the beam remaining elastic. The difference in response is due to the plastic incompressibility constraint for the continuum plasticity model. The introduction of a discontinuity implies the complete failure of the material and therefore no volumetric constraint can exist, making mode-I opening possible.

The three-point bending test is again analysed for a propagating discontinuity, but now for an increased hardening modulus of $h = -20$ Nmm^{-2}, ten times greater than for the previous example. The evolution of the equivalent plastic strain and the displacement discontinuity for this case are shown in figure 6. The failure

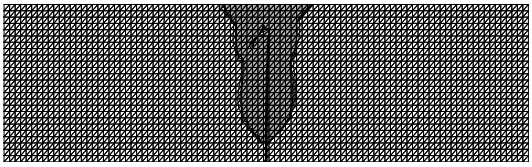

(a)

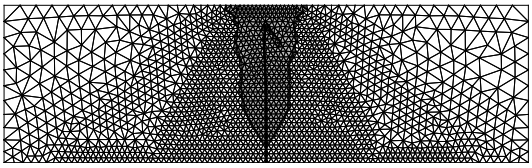

(b)

Figure 3: Equivalent plastic strain contours and discontinuity path for three-point bending test under plane strain conditions at $u = -0.4$ mm with (a) structured and (b) unstructured meshes.

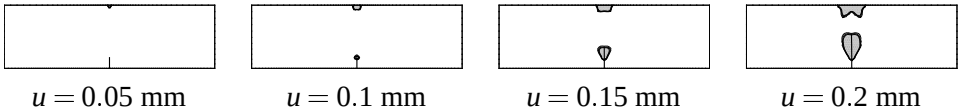

$u = 0.05$ mm $u = 0.1$ mm $u = 0.15$ mm $u = 0.2$ mm

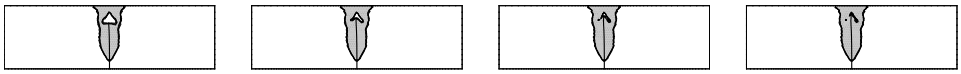

$u = 0.25$ mm $u = 0.3$ mm $u = 0.35$ mm $u = 0.4$ mm

Figure 4: Evolution of equivalent plastic strain contours and discontinuity for the three-point bending test under plane strain conditions.

mode for this example is different than that for the more brittle beam in figure 4. Rather than mode-I, the failure mode of the ductile beam is mode-II. The discontinuity has extended over only a short distance and a plastic hinge has formed. This example shows that when a discontinuity is introduced, for a Von Mises material the hardening modulus influences the failure mode.

CONCLUSIONS

Numerical examples have been presented which show the influence of including a propagating displacement discontinuity when simulating failure in a Von Mises material. The inclusion of a displacement discontinuity allows cleavage opening modes which are restrained by a continuum-only model through the plastic incompressibility constraint. The inclusion of a discontinuity makes mode-I dominated failure possible when using

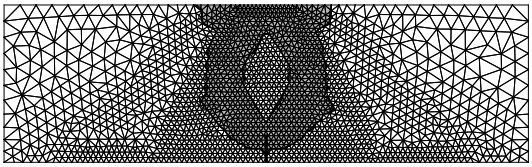

Figure 5: Equivalent plastic strain contours for a stationary discontinuity at $u = 1$ mm for the Von Mises yield surface.

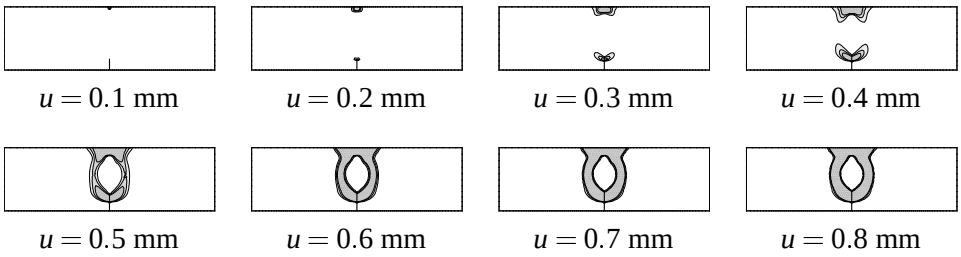

Figure 6: Evolution of equivalent plastic strain contours and discontinuity for the three-point bending test under plane strain conditions for a ductile beam. The hardening modulus h is equal to -20 Nmm^{-2}.

a continuum model that obeys a Von Mises flow rule.

ACKNOWLEDGEMENTS

This research is supported by the Technology Foundation STW, applied science division of NWO and the technology program of the Ministry of Economic Affairs and the Ministry of Public Works and Water Management, The Netherlands.

REFERENCES

1. Perzyna, P. (1966). Fundamental problems in viscoplasticity. In: *Recent Advances in Applied Mechanics*, volume 9, pp. 243–377. Academic Press, New York.

2. Babuška, I. and Melenk, J. M. (1997). The Partition of Unity Method. *International Journal for Numerical Methods in Engineering*, 40(4), 727–758.

3. Duarte, C. A. and Oden, J. T. (1996). H-p clouds – an h-p meshless method. *Numerical Methods for Partial Differential Equations*, 12(6), 673–705.

4. Belytschko, T. and Black, T. (1999). Elastic crack growth in finite elements with minimal remeshing. *International Journal for Numerical Methods in Engineering*, 45(5), 601–620.

5. Wells, G. N. and Sluys, L. J. (2001). A new method for modelling cohesive cracks using finite elements. *International Journal for Numerical Methods in Engineering*, 50(12), 2667–2682.

6. Wells, G. N. and Sluys, L. J. (2001). Discontinuous analysis of softening solids under impact loading. *International Journal for Numerical and Analytical Methods in Geomechanics*, 25(7), 691–709.

7. Wells, G. N., De Borst, R. and Sluys, L. J. (2001). An enhanced finite element method for analysing failure in elasto-plastic solids. In: *Trends in Computational Structural Mechanics* (CDROM), Wall, W. A., Bletzinger, K. U. and Schweizerhof, K., eds., pp. 397–406. CIMNE, Barcelona, Spain.

8. Wells, G. N., Sluys, L. J. and De Borst, R. (2001). Simulating the propagation of displacement discontinuities in a regularised strain-softening medium. *International Journal for Numerical Methods in Engineering*. (accepted).

COMPUTATIONAL MODELLING OF RESIDUAL STRESS EFFECTS ON CRACK INITIATION AND GROWTH IN DUCTILE MATERIALS

Noel P. O'Dowd, Yuebao Lei, Philip S. May and George A. Webster

Department of Mechanical Engineering
Imperial College, London, SW7 2BX, UK

ABSTRACT

In this work the effect of residual stress on fracture initiation and growth is examined numerically. A void growth and coalesence model is used to simulate the effect of local damage in the vicinity of a crack in a ductile material. It is seen that, for the cases examined, a J-based chararacterisation of the crack growth is still appropriate when residual stresses are present. The significance of the effect of residual stress on crack growth is examined for two material ductilities.

KEYWORDS

Fracture; residual stress; J-integral; finite element analysis.

INTRODUCTION

The J-integral has been adopted by most current structural integrity procedures for cracked bodies under combined secondary and primary loadings, *e.g.* R6 [**?**], BS 7910 [**?**] and EPRI [**?**] methods. The implicit assumption when applying these approaches is that the effect of the residual stresses may be accounted for through modification of the driving force, J, and the inherent toughness of the material remains unchanged. However, this assumption may not be valid in view of the well known effect of stress state (constraint) on the fracture toughness of materials, *e.g.* [**?**]. In this paper a numerical study is carried out to assess the influence of residual stress on the fracture of a ductile ferritic steel.

COMPUTATIONAL FRAMEWORK

A finite element analysis of a three point bend testing configuration is undertaken. The analyses have been carried out using the commercial finite element code ABAQUS V5.8 [**?**]. Full account is taken of material and geometric non-linearities with the resultant non-linear equilibrium equations being solved iteratively using Newton's method (see [**?**]). A typical finite element mesh, which is composed of about 2000 four noded isoparametric quadrilaterals, is shown in Fig. 1. Due to symmetry only half of the problem is analysed. The failure mechanism examined is that of void growth and coalescence, which is incorporated into the model using a Gurson-type failure model, developed for porous materials, ([**?**],

[**?**]). Within this model, the yield surface of the material, Φ, is a function of the evolving void volume fraction f,

$$\Phi \;=\; \left(\frac{\sigma_e}{\sigma_y}\right)^2 + 2\,q_1\,f\,\cosh\left(-q_2\,\frac{3\,p}{2\,\sigma_y}\right) - \left(1\,+\,q_1^2\,f^2\right) \;=\; 0 \;\;, \tag{1}$$

where σ_e is the equivalent stress, p the hydrostatic pressure and σ_y the yield stress of void-free material. The material parameters q_1 and q_2 depend on the hardening exponent n and on the ratio E/σ_y, where E is the Young's modulus [**?**].

The void growth rate is expressed in terms of the current value of f and the plastic strain rate tensor $\dot{\boldsymbol{\epsilon}}^P$ as

$$\dot{f} \;=\; (1-f)\,\dot{\boldsymbol{\epsilon}}^P : \mathbf{I} \;\;, \tag{2}$$

where $\mathbf{I}$ is the second order unit tensor. Finally, to completely define the material softening behaviour, the critical void volume fraction, f_e, at which the stress carrying capacity of the material is lost must also be specified. Once the void volume fraction, f, at a material point reaches this value, the stiffness at that point is gradually reduced to zero and the element is then removed from the analysis. If the removed element is directly ahead of the crack tip, the crack is considered to have grown by an amount equal to the element size. As seen in Fig. 1(b), ahead of the initial crack tip the finite element mesh consists of regular square elements. The use of an element removal approach to simulate crack growth introduces as an additional length scale into the problem, the size of these crack tip elements (see, *e.g.*, [**?**]). This characteristic length scale (*i.e.*, local mesh size) should be associated with a physically meaningful quantity such as the mean inclusion spacing or the CTOD of the material [**?**].

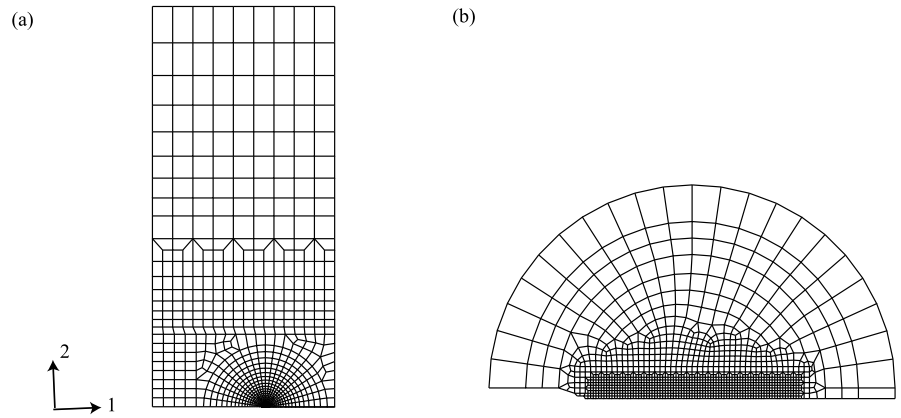

Figure 1: Finite element mesh used in the analysis (a) full mesh (b) near tip region

Evaluation of J integral

The evaluation of a path independent J integral value in the presence of residual stress has been discussed in [**?**]. A path independent J-integral equation can be obtained via,

$$J \;=\; \int_\Gamma \left(W\delta_{1i} - \sigma_{ij}\frac{\partial u_j}{\partial x_1}\right) n_i ds; + \int_A \sigma_{ij}\frac{\partial \epsilon^0_{ij}}{\partial X_1} dA \quad , \tag{3}$$

where A is the area enclosed within a contour Γ and W is the mechanical strain energy density,

$$W \;=\; \int_0^{\epsilon^m_{ij}} \sigma_{ij}\; d\epsilon^m_{ij} \;\; . \tag{4}$$

Note that $A \to 0$ as $\Gamma \to 0$ and implicit in this definition for J is the assumption that the initial strains, ϵ^0_{ij}, are bounded at the crack tip, [**?**].

The initial strains, ϵ^0_{ij} in Eq. 3, are determined as the difference between the total strains and the elastic mechanical strains at the initial state, *i.e.*

In this work, the residual stress in the specimen, before a crack has been introduced, is assumed to be available. This residual stress is then introduced into the finite element model as an initial condition and the effect of introducing a crack is represented by the removal of the symmetry boundary conditions along the crack plane (see [**?**]). The initial state, at which $\boldsymbol{\epsilon}^0$ is evaluated, is then the state after the initial residual stress is input, before the crack is introduced. This procedure has been shown to provide a path independent integral and, for linear elastic behaviour, results for J consistent with those obtained using linear superposition, [**?**]. In this analysis, to avoid loss of path independence on contours near to the growing crack tip, only the outer rings in the finite element mesh are used in the evaluation of J (outside the fine square mesh region illustrated in Fig. 1 (b)).

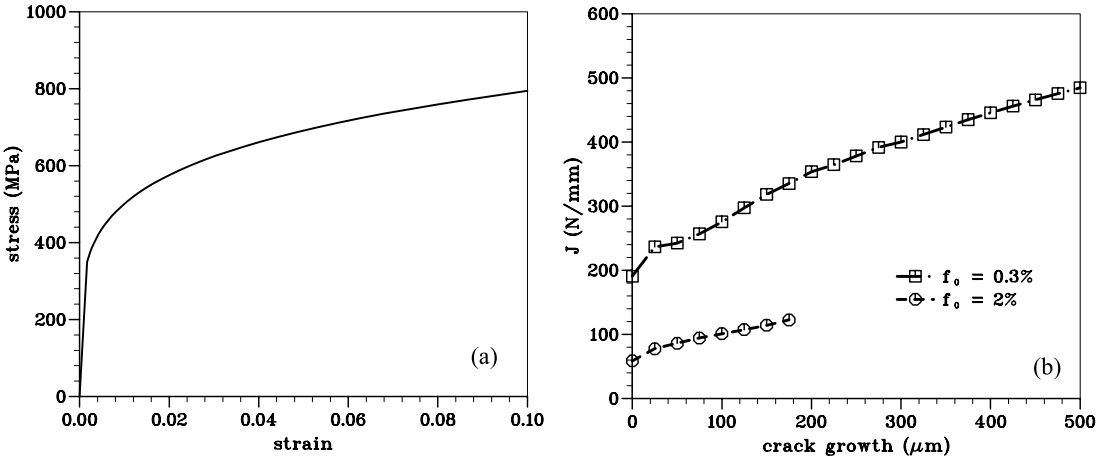

Figure 2: (a) Uniaxial stress-strain behaviour of the material (b) J-resistance curves with two values of initial void volume fraction, f_0

MATERIAL AND SPECIMEN PROPERTIES

The uniaxial stress-strain behaviour of the material is shown in Fig. 2(a). This behaviour is representative of a low strength offshore steel (BS 7191 Grade 355 EMZ), which is being studied as part of a larger overall program. The material has a yield strength of 350 MPa and the post yield strain hardening is represented here as a power law with $n = 5$.

The values of q_1 and q_2 related to the mechanics of void growth in Eq. 1 have been taken from [**?**] and are given by $q_1 = 2.0$ and $q_2 = 0.8$, respectively. The mesh size, D, (twice the size of the square elements in the crack tip region) used in the crack growth calculations is taken as 50 μm which is on the order of the measured CTOD for the BS 7191 Grade 355 EMZ steel. The sensitivity of the results to the mesh size is currently under investigation. The critical void volume fraction f_e is taken to be 10%.

The effect of the initial void volume fraction, f_0 on the predicted resistance curve behaviour is shown in Fig. 2(b). These results were determined from a study of a three point bend geometry with overall specimen width, W, of 50 mm and initial crack size, a, of 30 mm. The high toughness material with $f_0 = 0.3\%$ is representative of the toughness of the ferritic steel, (BS 7191 Grade 355 EMZ) at room temperature. The strong effect of f_0 is noted by comparison with the predicted resistance curve behaviour when $f_0 = 2\%$. Note that both materials have the same uniaxial stress strain behaviour, shown in Fig. 2(a). The analysis for $f_0 = 2\%$ terminates at $\Delta a = 200$ μm due to numerical difficulties. However, the trend of the behaviour is clear, even at this amount of crack growth.

EFFECT OF RESIDUAL STRESS ON RESISTANCE CURVE BEHAVIOUR

A representative residual stress distribution is examined in this paper. Future work will present results for measured residual stress distributions due to welding, [**?**]. The distribution examined is shown in

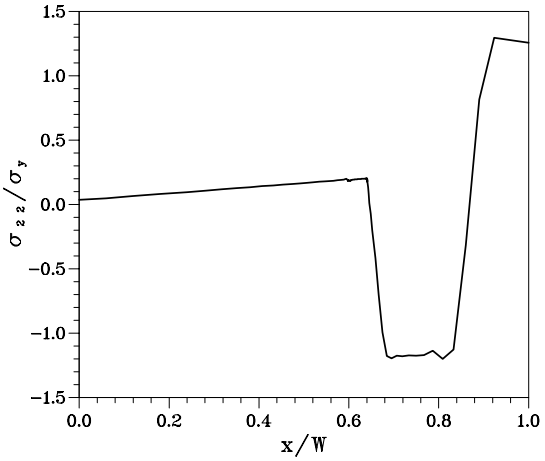

Figure 3: Residual stress distribution used in the analysis.

is shown. The value of a/W for the three point bend geometry is 0.6 so the crack tip is located at $x/W = 0.6$. This residual stress profile was chosen to provide a reasonably high fracture driving force due to residual stress. Note that, despite the fact that the uncracked body residual stress shown in Fig. 3 is close to zero along the crack faces, the J value due to the residual stress field determined from the finite element analysis is still significant (11 N/mm).

The resultant load *vs.* crack growth curves are shown in Figs. 4 (a) and (b) for the two material toughnesses. It is seen that for the high toughness material (Fig. 4(a)), there is a very small effect of residual stress on the load to cause crack initiation, (note that the J value due to residual stress is less than 1% of the initiation J) and after some crack growth, this effect almost disappears. For the low toughness material, Fig. 4(b), however, there is a strong effect of residual stress on the initiation load, though again the effect diminishes somewhat after crack growth. For the low toughness material, the load corresponding to $\Delta a = 50\mu$ m is about 20% lower when residual stresses are present. In Figs. 4(c) and (d) the J-resistance curves with and without residual stress are shown for the two materials examined. For the high toughness material (Fig. 4(c)), the resistance curves are almost indistinguishable. For the low toughness material (Fig. 4(d)), there is a small difference (maximum of 8%) between the resistance curves—the J resistance curve is slightly higher for the specimen with residual stress. If it is assumed that J retains its validity as a fracture parameter when residual stresses are present, any effects on the J resistance curve must be accounted through constraint arguments—the loss of J dominance in the specimen. At higher loads the effect of the residual stress is expected to diminish as the deformation is controlled by the applied mechanical load. Therefore constraint effects are expected to be more significant for lower strength materials as indeed is observed here. Similar trends have been observed in [**?**] where it was found that residual stress had a strong effect on the onset of brittle fracture but a much reduced effect on ductile fracture.

DISCUSSION AND CONCLUSIONS

The effect of residual stress on the fracture behaviour of a high and low toughness material have been examined numerically. A Gurson-type void growth model has been used to simulate the effect of damage ahead of a growing crack tip. It is seen that the $J-\Delta a$ behaviour of the material is relatively unaffected by the existence of the residual stress field for both materials. The damage introduced by the residual stress near the crack tip, is well accounted for by the use of J as the driving force for fracture. This implies that when residual stresses are present, it is acceptable to incorporate the residual stresses into the driving force and to assume that the material resistance is unaffected.

The geometry examined is a high constraint three point bend geometry and the residual stress field examined has a relatively low J and associated T stress. Different geometrical configurations, materials and residual stress distributions may lead to different results from those presented here. It should also

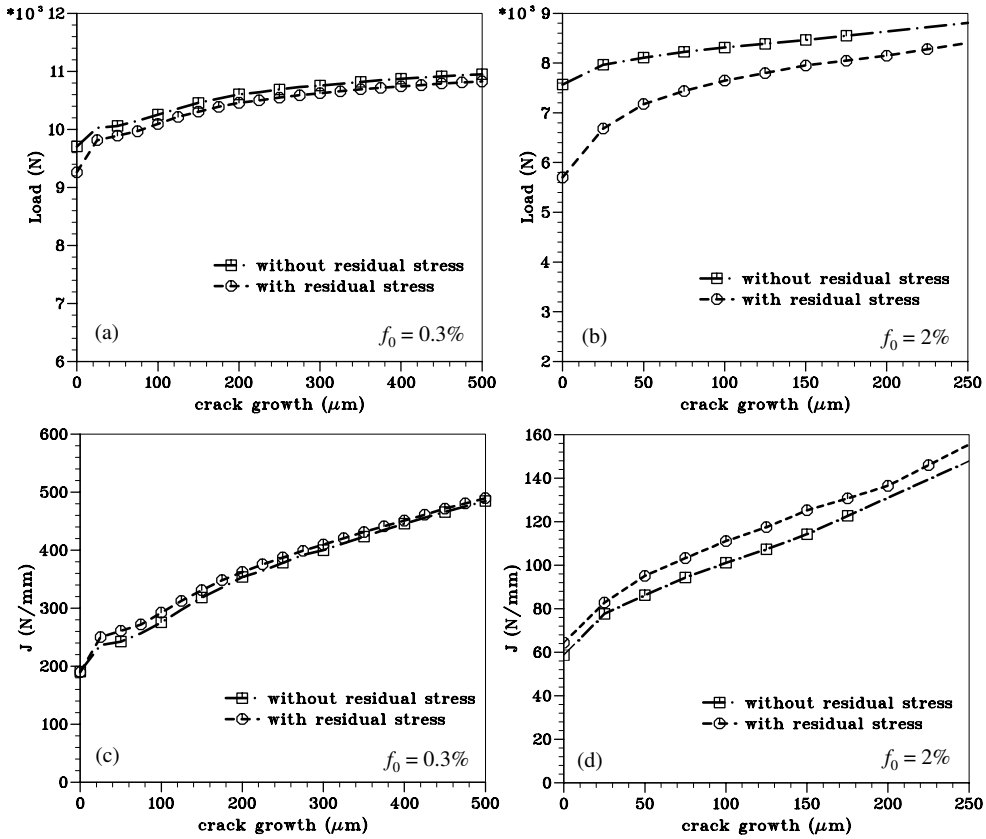

Figure 4: (a) and (b) Load vs crack growth for (a) high toughness material, (b) low toughness material; (c) and (d) J-resistance curves for (c) high toughness material and (d) low toughness material.

be pointed out that if the residual stress has been introduced due to welding or by a heat treatment there may be some effect on the material microstructure, in which case the intrinsic toughness of the material may change. Such effects have not been examined in this analysis.

ACKNOWLDEGMENTS

Financial support for this work, provided by the IMC, HSE, EPSRC and DERA, is gratefully acknowledged.

References

[1] British Energy Generation Ltd. (1998) Assessment of the Integrity of Structures Containing Defects, R/H/R6-Revision 3.

[2] British Standards Institution, 2001, Guidance on Methods for Assessing the Acceptability of Flaws in Welded Structures, BS7910, London, UK.

[3] Kumar, V., Schumacher, B. I. and German, M. D. (1984) Development of a procedure for incorporation secondary stress in the engineering approach, in *EPRI Report EPRI NP-3607*.

[4] O'Dowd, N. P. (1995) *Engng. Frac. Mechanics* **52** 3, 445.

[5] ABAQUS/STANDARD V. 5.8 (1999), Hibbitt, Karlsson and Sorensen Inc., Providence, RI.

[6] Gurson, A. L. (1977) *J. Engng. Mat. Tech.* **99** 2.

[7] Tvergaard, V. (1990) *Advances in Applied Mechanics* **27** 83.

[8] Faleskog, J., Gao, X. and Shih, C. F. (1998) *Int. J. Fracture* **89** 4, 355.

[9] Xia, L. and Shih, C.F. (1995) *J. Mech. Phys. Sol.*, **43**, 233.

[10] Lei, Y., O'Dowd, N. P. and Webster, G. A. (2000) *Int. J. Fracture* **106** 195.

[11] Ainsworth, R. A., Neale, B. K. and Price, R. H. (1978) In: *Proc. Int. Conf. on Tolerance of Flaws in Pressurised Components*, 171.

[12] May, P., Lei, Y., Webster, G. A., O'Dowd, N. P. (1998) Investigation of residual stresses in welded joints, Imperial College report, REF: MESMPN0228/MESMPR0374.

[13] Panontin, T.L and Hill, M.R. (1996) *Int. J. Fracture* **82** 317.

Constituent Effects on the Stress-Strain Behavior of Woven Melt-Infiltrated SiC Composites

G. N. Morscher[1] and J.I. Eldridge[2]

[1]Ohio Aerospace Institute; NASA Glenn Research Center, MS 106-5, Cleveland, OH 44135, USA
[2]NASA Glenn Research Center, MS 106-5, Cleveland, OH 44135, USA

ABSTRACT

The stress-strain behavior of 2D woven SiC fiber reinforced, melt-infiltrated SiC matrix composites with BN interphases were studied for composites fabricated with different fiber tow ends per unit length, different composite thickness, and different numbers of plies. In general, the stress-strain behavior, i.e. the "knee" in the curve and the final slope of the stress-strain curve, was controlled by the volume fraction of fibers. Some of the composites exhibited debonding and sliding in between the interphase and the matrix rather than the more common debonding and sliding interface between the fiber and the interphase. Composites that exhibited this "outside debonding" interface, in general, had lower elastic moduli and higher ultimate strains as well as longer pull-out lengths compared to the "inside debonding" interface composites. Stress-strain curves were modeled where matrix crack formation as a function of stress was approximated from the acoustic emission activity and the measured crack density from the failed specimens. Interfacial shear strength measurements from individual fiber push-in tests were in good agreement with the interfacial shear strength values used to model the stress-strain curves.

KEYWORDS

Ceramic matrix composites, Stress-strain behavior, Acoustic Emission

INTRODUCTION

Woven SiC fiber reinforced, SiC matrix composites are prime candidate materials for a high-speed civil aircraft combustor liner [1,2] as well as other high temperature engine components. A considerable amount of composite development has occurred in order to improve the performance of this material system including evaluating different fiber types, interphases, and matrices. For the reference 2 application, a composite system consisting of a Sylramic® (SYL) fiber (Dow Corning, Midland, MI), a BN interphase and a melt-infiltrated (MI) matrix was down-selected based on this system's superior strength, creep resistance, and thermal conductivity properties in comparison to other SiC/SiC systems (e.g. chemically vapor infiltrated SiC matrix). More recently, a further improvement to the SYL fiber has been developed via elevated temperature treatment in nitrogen containing atmospheres that results in an in situ-BN coating on the Sylramic® fiber [3,4] (referred to here as SYL-iBN). Composites processed with these treated fibers resulted in higher ultimate strengths and improved creep resistance over composites processed with as-produced SYL. However, to date, this latest improved composite has only been fabricated on a small scale.

In order for the SYL/MI-SiC matrix composite system to further mature and be used by designers, the stress-strain response of these materials needs to be well understood and modeled for a range of constituent volume fractions and specimen sizes. For example, components will vary in thickness, curvature, etc. This will

require varying numbers of woven fiber plies in specific locations or perhaps different fiber architectures. The most critical aspect of the stress-strain behavior of these types of composites is not necessarily the ultimate strength properties. Rather, the "knee" in the stress-strain curve, due to the formation of bridged matrix cracks may be more important. For example, the formation of through-thickness matrix cracks usually denotes the stress above which time-dependent strength degradation occurs at intermediate temperatures due to the oxidation of the fiber, interphase and matrix [5-7]. The purpose of this paper will be to compare and model the effect of varying fiber volume fraction on the stress-strain behavior for MI matrix composites using composites with different 2D woven fiber architectures, i.e., varying the numbers of fiber-tows per unit length, the number of plies, and the thickness of the composite specimens.

EXPERIMENTAL

Unload-reload tensile hysteresis tests were performed on over 20 different composite specimens that varied in fiber tow ends per unit length, number of plies, composite thickness or fiber type (SYL or SYL-iBN). Three different vintages of composites were tested in this study. The oldest vintage composites were from the early years of NASA's Enabling Propulsion Materials program [1] and were processed by Carborundum Corporation (Niagara Falls, NY). The next oldest vintage composites were from the latter years of the EPM program and were processed by Honeywell Advanced Composites (Newark, DE.) [2]. The newest vintage composites were processed under NASA's Ultra Efficient Engine Technology (UEET) program and were also fabricated by Honeywell Advanced Composites. The first two vintages consisted of only two different weaves, the same number of plies (8), and similar composite thicknesses (~ 2 mm). Whereas the latter vintage varied fiber tow ends per unit length, composite thickness, and number of plies by nearly a factor of two. This resulted in composite specimens that varied by a factor of two in fiber volume fraction in the loading direction. Table I lists the constituent variations for the composites tested.

TABLE 1
VARIATION IN PROCESSING PARAMETERS FOR DIFFERENT VINTAGE COMPOSITES

Vintage	Variation in Fiber* Tow Ends per Inch	Variation in Number of Five Harness Satin Plies	Variation in Composite Thickness, mm	Variation in Volume Fraction of Fibers in Loading Direction
1	18 or 22	8	2 to 2.3	0.17 to 0.2
2	18 or 22	8	2 to 2.3	0.17 to 0.2
3	12.5, 18, 20, or 22	4, 6, or 8	1.4 to 2.3	0.13 to 0.25

* Each fiber tow consisted of 800 fibers. The average fiber diameter was 10 μm.

Composite processing entails first stacking of the balanced five-harness pieces of cloth of SYL or SYL-iBN fiber, a BN interphase layer deposition (~ 0.5 μm) via chemical vapor infiltration (CVI), a SiC layer deposition via CVI, SiC particulate infiltration via slurry-infiltration, and finally, liquid Si infiltration [1-2].

The tensile tests were performed on specimens with a contoured gage section (dog-bone) using a universal-testing machine (Instron Model 8562, Instron, Ltd, Canton Mass.) with an electromechanical actuator. Glass fiber reinforced epoxy tabs were mounted on both sides of the specimen in the grip regions and the specimens were gripped with rigidly mounted hydraulically actuated wedge grips. A clip on strain gage, with a range of 2.5% strain over 25.4 mm gage length was used to measure the deformation of the gage section.

Modal acoustic emission (AE) was monitored during the tensile tests with two wide-band, 50 kHz to 2.0 MHz, high fidelity sensors placed just outside the tapered region of the dog-bone specimen. Vacuum grease was used as a couplant and mechanical clips were used to mount the sensors to the specimen. The AE waveforms were recorded and digitized using a 4-channel, Fracture Wave Detector (FWD) produced by Digital Wave Corporation (Englewood, CO). The load and strain were also recorded with the FWD. After the tensile test, the AE data was filtered using the location software from the FWD manufacturer in order to separate out the AE that occurred outside of the gage section. For more information on the AE procedure and analysis, see references 8 and 9.

Fracture surfaces were observed with a field emission scanning electron microscope (Hitachi S-4700, Tokyo, Japan). Since the compressive stress in the matrix closes the matrix cracks, to measure crack density,

sections of the tested tensile specimens in the gage section at least 10 mm long were polished and then plasma (CF_4) etched at 500 W for 30 minutes. The etchant reacts with the free Si in the matrix, removing much of it, making it impossible to observe cracks in the MI part of the matrix. Matrix cracks can only be observed in the dense CVI SiC layer between the BN and the MI matrix.

Push-in tests were performed on a few specimens from sections of the composite that were in the mechanical grips in order to measure the interfacial shear stress, τ, of the sliding interface. Specimens were cut and polished to a thickness of ~ 1mm. The procedure for the push-in technique, the apparatus used, and the analysis can be found in reference 10. The average τ was determined from at least 20 different fibers for each specimen.

RESULTS AND DISCUSSION

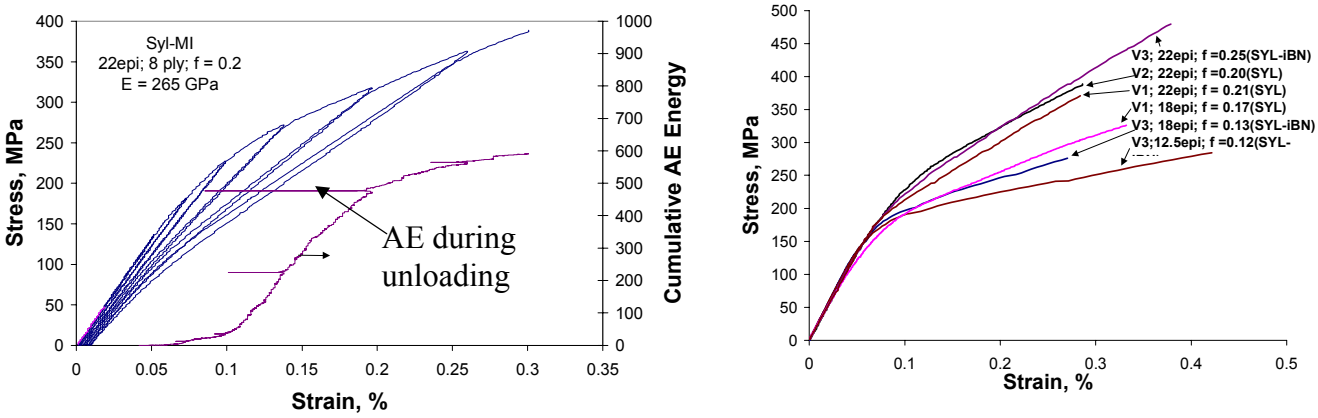

Figure 1: (a) Typical unload-reload stress-strain curve and cumulative AE energy for a vintage 2 SYL-MI composite. (b) Stress-strain curves (hysteresis loops removed) for composites with a variety of fiber volume fractions, f, in the loading direction and fiber tow ends per unit length (ends per inch) from all three composite vintages.

A typical hysteresis tensile stress-strain curve for a SYL-MI composite is shown in Figure 1a. All Sylramic-MI SiC composites stiffen during unloading due to matrix crack closure presumably due to residual compression in the matrix [11]. The AE activity is also plotted in Figure 1 in the form of cumulative AE energy. It was found in earlier studies that cumulative energy was the best AE parameter to correlate AE activity with matrix cracking [8-9]. Matrix crack formation and growth occurs in a similar fashion to that described in other studies [12-14] for 2D composites. At low stresses, microcracks form in the 90^o bundles and/or large matrix only regions (tunnel cracks). With increasing stress these cracks grow and become through-thickness matrix cracks and new cracks form. At higher stresses, the formation of matrix cracks diminishes and may cease altogether; however, for SYL-MI composites, matrix crack saturation was not always achieved.

Figure 1b shows a number of stress-strain curves with different fiber volume fractions. The elastic moduli were all similar for the composites in Figure 1b (265 to 280 GPa); however, elastic moduli as low as 220 GPa have been recorded. In general, an increase in fiber volume fraction results in an increase in the "knee" of the stress-strain curve as well as an increase in the slope of the stress-strain curve after the "knee" in the curve, as would be expected. Also, the SYL-iBN reinforced composites usually had higher ultimate strengths and strains for the same volume fraction/architecture when compared to SYL reinforced composites as was found in the other study [4]. The fracture surfaces of most specimens tested were observed using a field emission scanning electron microscope. For specimens corresponding to Figure 1a, it was verified that the fibers pulled-out between the fiber and the interphase (inside debonding) and had relatively short fiber pull-out lengths (Figure 2), typical of SYL-BN composites.

For some of the vintage 3 composites, debonding and sliding occurred between the interphase and the matrix (outside debonding, see Figure 3). For these composites, large pullout-lengths, higher strain to failure (Figure 4a) and lower elastic moduli (Figure 4a) were generally observed. However, some specimens with "outside debonding" had elastic moduli on the order of the "inside debonding" composites of Figure 1a but still had larger strains for a given stress at stresses above the "knee" in the stress-strain curve in comparison to "inside debonding" composites. This was the first time that debonding and sliding had been observed to occur on the outer interface between the interphase and the matrix for SYL reinforced composites. Presumably, this interface was

(a) (b)

Figure 2: Fracture surface from a SYL-iBN composite where the fibers debonded between the fiber and the interphase (inside debonding).

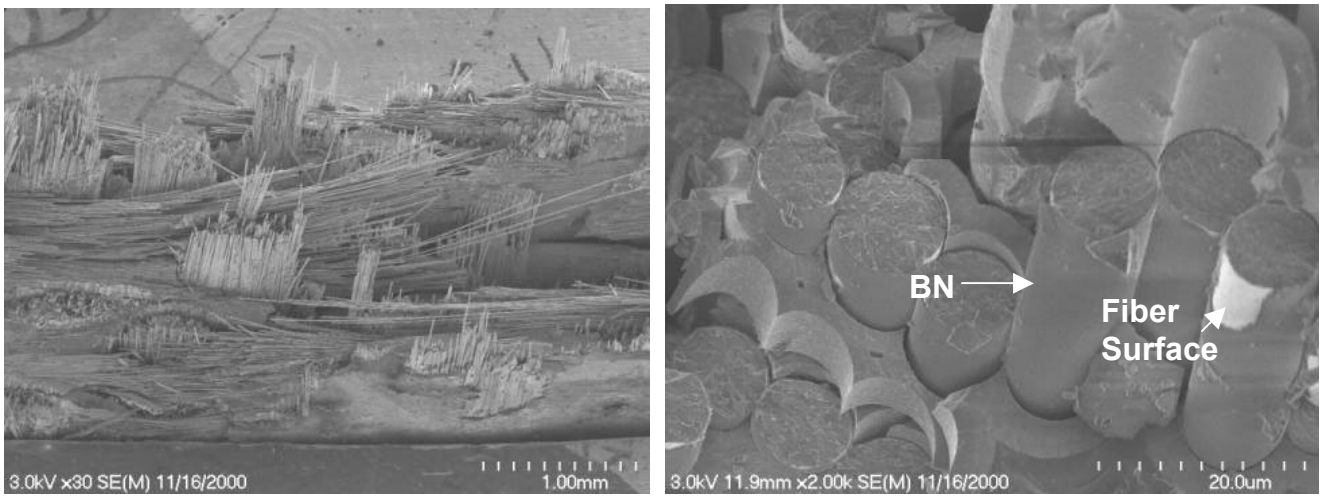

(a) (b)

Figure 3: Fracture surface from a SYL-iBN composite where the fibers debonded between the fiber and the interphase (outside debonding).

weaker and possibly debonded during cool down of the composite as the residual tension at the interphase increased with decreasing temperature. The residual compressive stress was estimated from intersection of the average slopes of the upper portions of the hysteresis loops (see Figure 1, after Steen [11]). It was found that for "inside debonding" composites, the residual stress was dependent on fiber volume fraction (Figure 4b). Many of the "outside debonding" composites had smaller residual compressive stresses for the same volume fraction compared to the "inside debonding" composites, especially for SYL-iBN composites (Figure 4b).

It was desired to model the stress-strain behavior in order to estimate the interfacial shear stress and to see if the "knee" in the stress-strain curve could effectively be accounted for. However, modeling the stress-strain behavior depends on accurately determining the stress at which matrix cracks will form and the extra displacement associated with the increased load applied to the fibers bridging the matrix crack. This was first done for unidirectional fiber reinforced composites assuming the matrix possessed an infinite Weibull modulus [15]. Later modifications incorporated the effects of residual stress due to thermal expansion mismatches between the fiber and the matrix [16]. However, for SiC/SiC composites, matrix fracture is dependent on the flaw population in the matrix [17]. Therefore, matrix cracking occurs over a range of applied stress. In addition, 2D lay-up or woven composites have been shown to possess different types of matrix cracks that originate either at pores in the matrix, in the 90° plies, or in the 0° plies with increasing stress, at least for CVI SiC matrix composites [12-14].

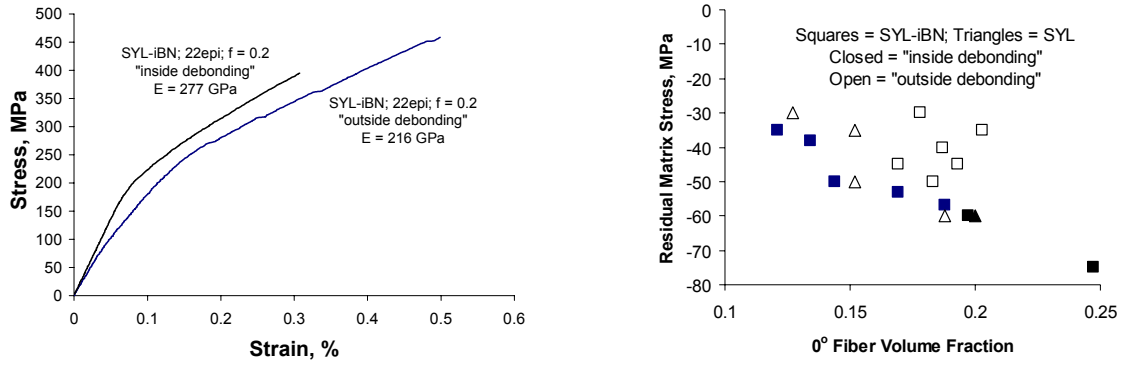

(a) (b)

Figure 4: Comparison of (a) stress-strain curves for two composites with identical fiber architectures (hysteresis loops removed) and (b) residual compressive stress in the matrix for composites with "inside debonding" (vintages 2 and 3) and "outside debonding" (vintage 3).

Cumulative AE energy has been related to the number of transverse matrix cracks [9]; however, it only gives the relative amount of cracking. In order to use AE energy for absolute crack densities, the AE energy must be calibrated to a known crack density at a specific stress. This was done for most of the composites after fracture. For composites where crack saturation was believed to occur, crack densities were measured to be 11.0 $\pm$ 4.0 and 8.7 $\pm$ 0.7 cracks/mm for "inside debonding" and "outside debonding" composites, respectively. However, there was no apparent relation between fiber volume fraction, specimen thickness, or ends per unit length and saturation crack density.

Composite strain was determined in the same fashion as Pryce and Smith [18]. Using the nomenclature of Curtin, et al. [19], composite strain can be modeled for equally spaced cracks:

$$\varepsilon = \sigma/E_c + \alpha\delta(\sigma)\rho_c/E_f \ (\sigma + \sigma_{th}); \qquad \text{for } \rho_c^{-1} > 2\delta \tag{1}$$

where the first part of the equation corresponds to the elastic strain response of an uncracked composite and the second part of the equation corresponds to the extra strain (displacement) of the fibers at and away from a through-thickness matrix crack dictated by the sliding length:

$$\delta = \alpha\, r\, (\sigma + \sigma_{th}) / 2\tau \tag{2}$$

where

$$\alpha = (1\text{-}f)\, E_m / f\, E_c \tag{3}$$

σ is the applied stress, σ_{th} is the residual (thermal) stress in the matrix (compression is negative), E is the elastic modulus, subscripts m, f and c refer to matrix, fiber, and composite, respectively, ρ_c is the matrix crack density, r is the fiber radius, and τ is the interfacial shear strength. Ec and σ_{th} were determined from the stress strain curves. E_f is 380 GPa and E_m was determined from the rule of mixtures. ρ_c was estimated from the AE energy based on the known crack spacing from the stress-rupture tests. Therefore, the only variable not known was τ which was adjusted in order to best fit the predicted stress strain curve to the experimental stress strain curve. For the case

where the sliding lengths overlap, Ahn and Curtin [20] showed that if the cracks are still equally spaced, the composite strain could then be modeled by:

$$\varepsilon = \sigma / (f E_f) + \alpha \sigma_{th} / E_f - \alpha (\sigma + \sigma_{th}) / [4 E_f \delta(\sigma) \rho_c]; \text{ for } \rho_c^{-1} < 2\delta \qquad (4)$$

Therefore, for higher applied stress conditions, if $\rho_c^{-1} < 2\delta$ was predicted, equation (4) was used.

Figure 5a to 5d show the room temperature experimental stress-strain curve, the AE activity, and predicted stress-strain curve using the best-fitted τ value and for τ values 20% greater and 20% less than the best-fit value for "outside debonding" and "inside debonding" composites. The ultimate stress was not predicted, the curves were only plotted to the known ultimate strength of the individual specimen. The predicted stress-strain curves are in good agreement with the experimental stress-strain curves. "Outside debonding" composites required lower τ values to model the stress-strain curve: 31±6 MPa for two SYL composite specimens and 15±4 MPa for two SYL-iBN composite specimens. "Inside debonding" composites required higher τ values: 64±1 MPa for two SYL composite specimens and 71±10 for four SYL-iBN composite specimens. Presumably, the lower τ for "outside debonding" composites is due to the smoother sliding interface. Average τ values had been measured for the SYL-iBN "outside debonding" specimen (Fig. 5a), SYL-iBN "inside debonding" specimen (Fig. 5b), and the SYL "inside debonding" specimen (Figure 5d) from push-in tests and were found to be 7 ± 5 MPa, 83 ± 25, and 64 ± 19 MPa, respectively. These values are in very good agreement with the τ values used to model the stress-strain curve for inside debonding composites.

The "knee" in the stress-strain curve was modeled very well using the AE data and final crack spacing to estimate the matrix crack distribution. The only exception was for the SYL "inside debonding" composite (Figure 5d), where the predicted stress-strain curve underestimated the strain at stresses corresponding to the "knee" in the

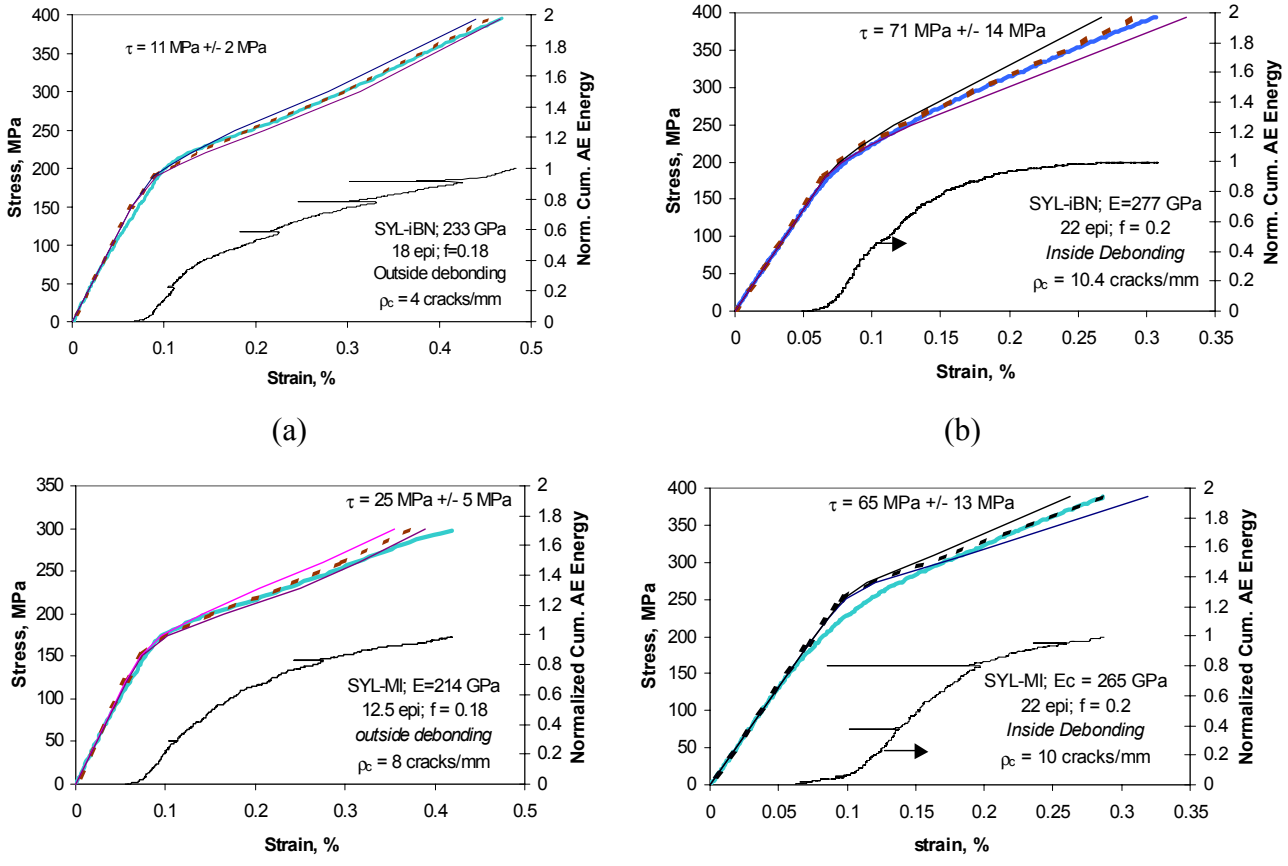

Figure 5: Experimental (thick solid line) and predicted (dashed and thin solid lines) stress-strain curves for an (a) SYL-iBN outside debonding, (b) SYL-iBN inside debonding, (c) SYL outside debonding , and (d) SYL inside debonding composites. Also shown is the normalized cumulative AE energy (AE energy normalized by the maximum cumulative AE energy).

stress-strain curve. The predicted stress-strain behavior for Figure 5d was the worst of all ten specimens modeled. The other SYL "inside debonding" composites was modeled similar to Figure 5b except with a $\tau = 63$ MPa.

CONCLUSIONS

The room temperature stress-strain behavior of Sylramic reinforced melt-infiltrated composites was shown to be most dependent on the volume fraction of fibers in the loading direction for various 2D architectures and composite thickness variations. Some specimens exhibited debonding on the outer interface between the BN interphase and the CVI SiC matrix-layer. This resulted in lower elastic moduli, in general, lower interfacial shear strengths, and higher strains to failure. It is unknown as to the benefits of such behavior at elevated temperature; however, the improvement in composite toughness is obvious. Outside debonding may also aid intermediate temperature properties since the environment would have to react through the interphase layer rather than having direct access to load-bearing fibers. However, interlaminar and high temperature creep/rupture properties still need to be determined in order to ascertain whether or not there is a benefit for this interfacial sliding behavior.

The composite stress-strain curves could be effectively modeled based on the approaches of references 18 and 20. However, this required several parameters to be directly or indirectly determined including the dependence of matrix cracking with stress from AE activity and final crack densities, composite elastic modulus, and matrix residual stress. The approach to best fit the predicted stress-strain curve to the actual data by varying τ provided a way of determining τ that was in very good agreement with measured values.

REFERENCES

1. Johnson, A.M., Bartlett, B.J., and Troha, W.A. (1997). In: *Thirteenth International Symposium on Air Breathing Engines*, pp. 1321-1328. Billig, F.S. (Ed.). American Institute of Aeronautics and Astronautics.
2. Brewer, D. (1999) *Mater. Sci. Eng.*, A261, 284.
3. Yun, H.M. and DiCarlo, J.A. (2000) *Ceram. Eng. Sci. Proc.*, 21, 347.
4. Yun, H.M. and DiCarlo, J.A. (2001) *Ceram. Eng. Sci. Proc.*, 22, in print.
5. Heredia, F.E., McNulty, J.C., Zok, F.W., and Evans, A.G. (1995) *J. Am. Ceram. Soc.*, 78, 2097.
6. Lipetzky, P., Stoloff, N.S., and Dvorak, G.J.,(1997) *Ceram. Eng. Sci. Proc.*, 18, 355.
7. Morscher, G.N., Gyekenyesi, J.Z., and Bhatt, R.T. (2000) In: *Mechanical, Thermal and Environmental Testing and Performance of Ceramic Composites and Components, ASTM STP 1392*, pp. 306-319. Jenkins, M.G., Lara-Curzio, E., and Gonczy, S.T. (Eds.), ASTM, West Conshohocken, PA.
8. Morscher, G.N. (1999) *Comp. Sci. Technol.*, 59, 687.
9. Morscher, G.N. (2000) *Review of Progress in Quantitative Nondestructive Evaluation*, Vol. 19A, pp. 383-390. Thompson, D.O. and Chimenti, D.E. (Eds.). American Institute of Physics, NY.
10. Eldridge, J.I., Bansal, N.P., and Bhatt, R.T. (1998) *Ceram. Eng. Sci. Proc.*, 19, 11.
11. Steen, M. and Valles, J-L. (1997) In: *Thermal and Mechanical Test Methods and Behavior of Continuous-Fiber Ceramic Composites, ASTM STP 1309*, pp. 49-65. Jenkins et al. (Eds.), ASTM, West Conshohocken, PA.
12. Domergue, J-M., Heredia, F.E., and Evans, A.G., (1996) *J. Am. Ceram. Soc.*, 70, 161.
13. Pluvinage, P., Parvizi-Majidi, A., and Chou, (1996) T.W., *J. Mater. Sci*, 31, 232.
14. Guilloumat, J. and Lamon, J. (1996) *Comp. Sci. Technology*, 56, 803.
15. Aveston, J., Cooper, G., and Kelly, A. (1971) *Proc. Natl. Phys. Lab.*, pp. 15-26. IPC Science and Technology Press, Surrey, U.K.
16. Budiansky, B., Hutchinson, J.W., and Evans, A.G. (1986) *J. Mech. Phys. Solids*, 34, 167.
17. Lissart, N. and Lamon, J., (1997) *Acta mater.*, 45, 1025.
18. Pryce, A.W. and Smith, P.A. (1993) *Acta metal. mater.*, 41, 1269.
19. Curtin, W.A., Ahn, B.K., and Takeda, N. (1998) *Acta mater.*, 46, 3409.
20. Ahn, B.K. and Curtin, W.A. (1997) *J. Mech. Phys. Solids*, 45, 177.

CONSTRAINT CORRECTION OF FRACTURE TOUGHNESS CTOD FOR FRACTURE PERFORMANCE EVALUATION OF STRUCTURAL COMPONENTS

F. Minami [1], T. Inoue [2] and K. Arimochi [3]

[1] Dept. Manufacturing Science, Osaka University, 2-1, Yamada-Oka, Suita, Osaka, JAPAN
[2] Nippon Steel Corporation, 20-1 Shintomi, Futtsu, Chiba, JAPAN
[3] Sumitomo Metal Industries, LTD., 1-8, Fuso-Cho, Amagasaki, Hyogo, JAPAN

ABSTRACT

Corrections of CTOD for constraint loss in large-scale yielding conditions are made on the basis of the Weibull stress fracture criterion. A CTOD ratio $\beta = \delta_{3P}/\delta_{WP}$ was introduced, where δ_{WP} is the CTOD of a wide plate component and δ_{3P} is an equivalent CTOD of the fracture toughness specimen at which the toughness specimen gives a compatible Weibull stress with the wide plate. CTOD toughness scaling diagrams with β are constructed, including effects of the work hardening property of materials, crack size in the component and the Weibull modulus m. The CTOD ratio β is decreased to a large extent after full yielding, which is more significant for a high yield ratio and short/deep crack. Case studies are presented on the fracture transferability assessment of high strength structural steels with different work hardening properties.

KEYWORDS

brittle fracture, constraint effect, transferability, CTOD toughness, fracture performance, Weibull stress

INTRODUCTION

The fracture mechanics approach to structural design and material selection relies on the stress intensity factor K, crack tip opening displacement (CTOD, δ) and J integral as the controlling parameters for stress fields ahead of a crack. In large-scale yielding conditions, however, the actual stress fields deviate from the K- and J-controlled fields and depend significantly on the crack size and geometry of specimens employed. This is due to the constraint effect on the crack-tip plasticity. A loss of constraint resulting from large-scale yielding relaxes the stress elevation for notched-tension panels and shallow-notch specimens, while deep-notch bend and compact specimens maintain a high level of crack tip constraint. Such constraint loss leads to an apparently increased fracture resistance K_c, δ_c and J_c for the former configurations. In order to characterize the constraint effect on the crack tip condition, the constraint parameters, T-stress and Q-parameter were implemented in the K- and J-controlled stress fields, respectively [1-4]. Nevertheless, these two-parameter characterizations posed an essential problem in the fracture assessment; the T-stress and Q-parameter at fracture are not material constants but depend on the geometry of specimens. On the other hand, Anderson & Dodds [5, 6] have proposed a toughness scaling model (TSM) to correct the fracture toughness for constraint loss in large-scale yielding conditions. This model insists a similarity between near-tip stress contours in different yielding conditions, and

transfer the fracture toughness in large-scale yielding to one under small-scale yielding with equivalent stressed areas ahead of a crack. For simplicity, the TSM does not reflect the variation of stresses within near-tip stress contours and not consider a statistical aspect of cleavage fracture. In order to overcome limitations of the TSM, a modified toughness scaling with the Weibull stress was developed [7, 8], which requires the attainment of a specified Weibull stress to cause cleavage fracture at the same probability in different specimen geometry. These methodologies focus the attention on toughness scaling in small-scale yielding conditions. From a structural design point of view, however, the fracture toughness to be used for the fracture performance evaluation in service conditions should be quantified in conjunction with the constraint state. This paper addresses the constraint correction of CTOD, based on the Weibull stress criterion, as a function of the deformation level of structural components. A parametric study is performed on the CTOD correction factors, including the work hardening property of materials, crack size in components and the Weibull modulus *m* related to a scatter in the material fracture toughness.

CTOD TOUGHNESS SCALING WITH THE WEIBULL STRESS

This paper constructs CTOD toughness scaling diagrams to correct a constraint loss in large-scale yielding conditions. The Weibull stress σ_W is used as a driving force for cleavage fracture. The Weibull stress σ_W is derived from a statistical characterization of instability of microcracks in the Local Approach [9, 10], and given by the integration of a near-tip stress σ_{eff} over the fracture process zone V_f in the form

$$\sigma_W = \left[\frac{1}{V_0} \int_{V_f} [\sigma_{eff}]^m \, d\, V_f \right]^{1/m} \tag{1}$$

where V_0 and m are a reference volume and a material parameter, respectively. The critical Weibull stress $\sigma_{W,cr}$ obeys the Weibull distribution with two parameters m and σ_u

$$F(\sigma_{W,\,cr}) = 1 - exp\left[- \left(\frac{\sigma_{W,\,cr}}{\sigma_u} \right)^m \right] \tag{2}$$

which is considered as a material property independent of the specimen geometry. This enables the fracture strength/toughness scaling among different specimen configurations. Figure 1 illustrates the process of CTOD scaling between the fracture toughness specimen with a high constraint level and a wide plate component. This paper defines the CTOD ratio β [11] as

$$\beta = \delta_{3P} / \delta_{WP} \tag{3}$$

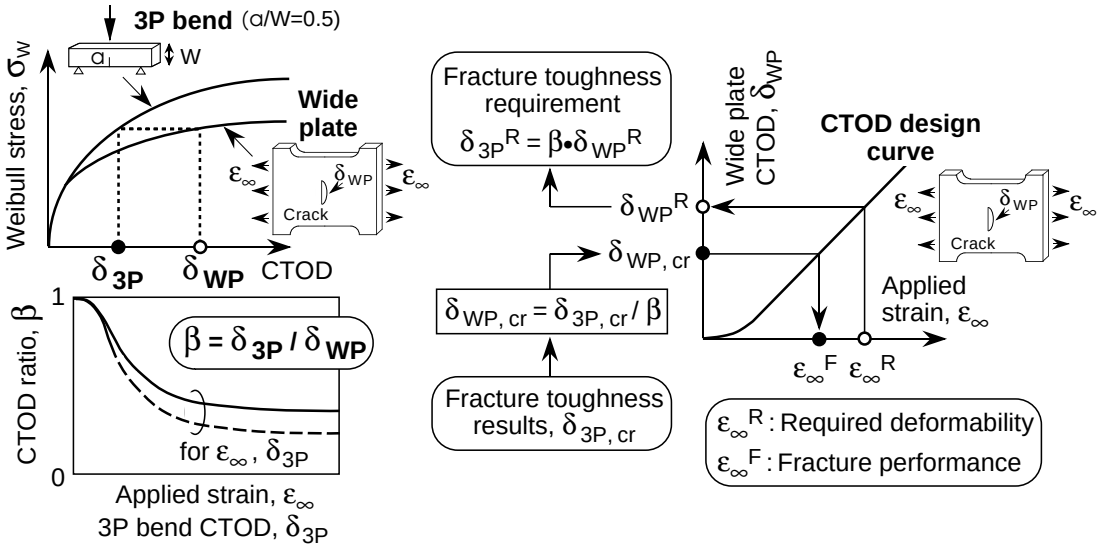

Figure 1 : CTOD toughness scaling between wide plate component and fracture toughness specimen.

where δ_{WP} is a wide plate CTOD, and δ_{3P} is an equivalent CTOD at which the fracture toughness specimen gives a compatible Weibull stress with the wide plate. The establishment of β as a function of (a) applied strain ε_∞ of wide plate and (b) CTOD δ_{3P} of toughness specimen enables the fracture control assessments with the CTOD design curve (relationship between ε_∞ and δ_{WP}) conventionally used in the structural engineering field:
- Determination of required fracture toughness $\delta_{3P}{}^R$ to meet a design solution $\varepsilon_\infty{}^R$ of structural components.
- Estimation of fracture performance $\varepsilon_\infty{}^F$ of structural components from fracture toughness test results $\delta_{3P,cr}$.
In this paper, an effective stress [12] considering a random spacial distribution of microcracks was employed as the near-tip stress σ_{eff} in Eqn. 1. The selection of V_0 does not affect the transferability analysis of fracture mechanics test results, although the absolute value of the Weibull stress depends on V_0. Furthermore, the Weibull modulus m has no connection with V_0. Hence, a unit volume was adopted as V_0 for convenience [12].

TRANSFERABILITY ANALYSIS OF FRACTURE MECHANICS TEST RESULTS

Firstly, advantages of the Weibull stress based approach to cleavage fracture are demonstrated for two structural steels with different work hardening properties. Materials used were high strength steels of 490 and 950 MPa class, HT490 and HT950, with a plate thickness of 25 mm. Table 1 shows the chemical composition and mechanical properties of these steels. Low and extremely high *YR* (yield-to-tensile ratio) values are noted for HT490 and HT950 steels, respectively. Figure 2 shows the configuration of test specimens used. Fracture toughness tests were conducted with compact and 3-point bend specimens. The compact and deep-notch bend specimens with $a/W = 0.5$ (a: notch length, W: specimen width) were of a standard type specified in the test standard, BS 7448 Part 1: 1991. A shallow notch of $a/W = 0.1$ was also prepared for the bend specimen. The tension specimen included a double-edge notch of $2a/2W = 0.3$, where the specimen width $2W = 100$ mm. The notch tip of each specimen was finished with a fatigue precrack of length 2.0 ~ 2.5 mm. Tests were conducted at -100 °C for both steels.
Test results were given in Fig. 3 in terms of cumulative distributions of the critical CTOD at brittle fracture initiation. The CTOD values were calculated according to BS7448 for the compact and deep-notch bend

TABLE 1 : CHEMICAL COMPOSITION AND MECHANICAL PROPERTIES OF STRUCTURAL STEELS USED.

	Chemical composition (mass %)										
	C	Si	Mn	P	S	Ni	Cr	Mo	Cu	V	Ceq
HT490	0.17	0.33	1.22	0.012	0.004	0.02	0.03	0.01	-	-	0.40
HT950	0.12	0.19	0.89	0.004	<0.001	2.61	0.58	0.55	0.30	0.05	0.60

Ceq=C+Mn/6+Si/24+Ni/40+Cr/5+Mo/4+V/14

	Mechanical properties (Rolling direction)			
	σ_Y (MPa)	σ_T (MPa)	YR=σ_Y/σ_T	ε_T (%)
HT490	356	520	68.3	13.8
HT950	1026	1036	99.1	6.2

σ_Y : Yield stress, σ_T : Tensile strength, ε_T : Uniform elongation

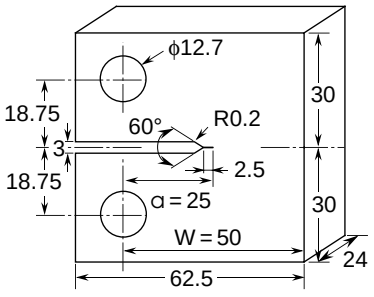

(a-1) Compact specimen for HT490

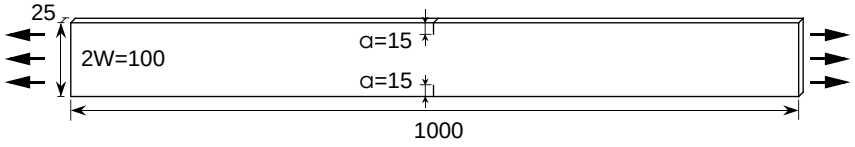

(a-2) Double-edge notched tension specimen for HT490

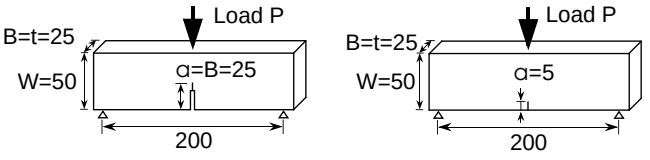

(b-1) 3-point bend specimens for HT950

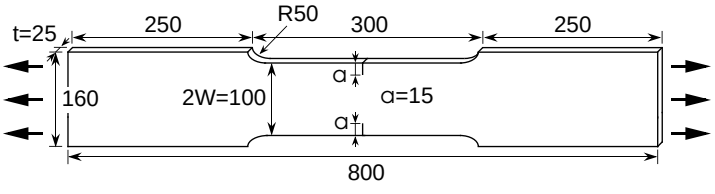

(b-2) Double-edge notched tension specimen for HT950

Figure 2 : Fracture mechanics specimens used in experiments.

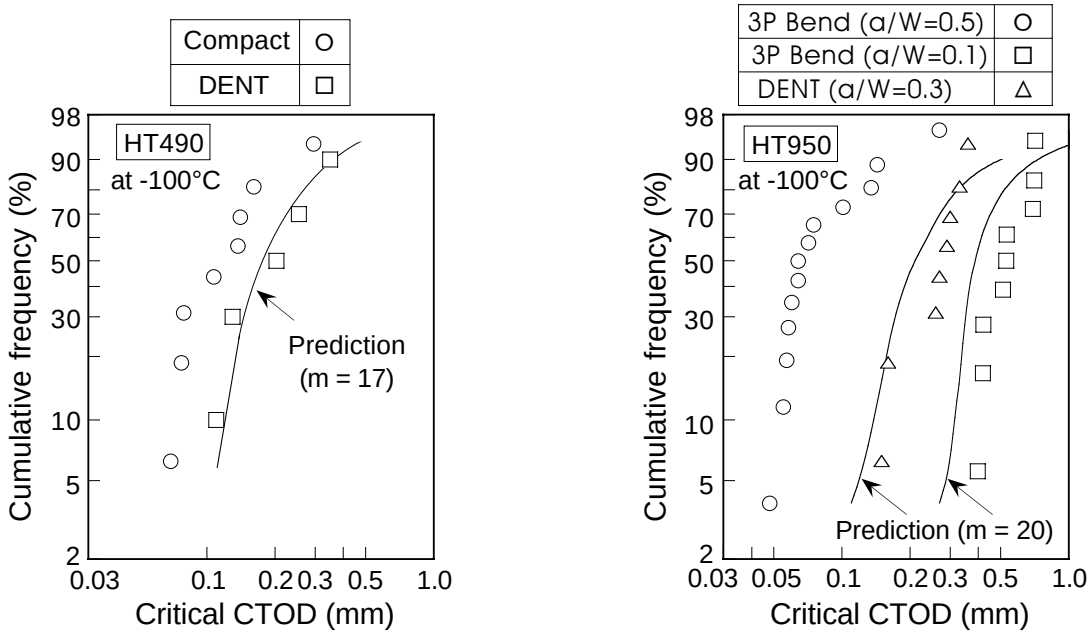

(a) HT490 steel (b) HT950 steel

Figure 3 : CTOD test results and estimation of critical CTOD of tension and shallow-notch bend specimens.

specimens and by the Dugdale model for the tension specimen. One for the shallow-notch bend was evaluated by a method proposed by Wang & Gordon [13], which is based on the area under the load versus CMOD record (CMOD: crack mouth opening displacement). A marked effect of constraint loss is observed in the tension and shallow-notch bend test results; larger critical CTOD than the standard fracture toughness specimen.

Using the CTOD results of the compact and deep-notch bend specimens, the critical CTOD values for the tension and shallow-notch bend specimens were estimated on the basis of the Weibull stress criterion; independence of $\sigma_{W,\,cr}$ on the specimen geometry. An iteration procedure [12] was employed for the determination of the *m*-value. The Weibull parameters *m* determined were 17 and 20 for HT490 and HT950 steels, respectively. The estimated results are drawn with a solid line in Fig. 3. A good agreement is found between the estimation and experimental data. One may argue the reliability of the *m*-value determined by the iteration procedure; non-uniqueness in small-scale yielding conditions [14]. In order to address this discussion point, a bias was introduced in the range $0.5\hat{m} \le m \le 1.5\hat{m}$, where $\hat{m}$ is the Weibull modulus determined by the iteration method ($\hat{m}$=17, 20 in this case). The numerical study with $m = \hat{m} \pm 0.5\hat{m}$ indicated that such bias hardly affected the estimation of the critical CTOD. Studies on the fracture transferability assessment of welded joints are published in the recent paper [11].

CTOD TOUGHNESS SCALING DIAGRAM

For applications of the Weibull stress approach to structural design and material selection, a framework begins in this paper to construct CTOD toughness scaling diagrams. A tension wide plate with a surface crack and a standard 3-point bend specimen of *a/W* = 0.5 were considered (Fig. 4). A parametric study was conducted on controlling factors of the CTOD ratio β. Table 2 gives basic variables used in the FE-analysis (3D FEM), which include the work hardening property, crack size in the wide plate and the Weibull modulus *m*;

- Work hardening property: The yield ratio *YR* ($=\sigma_Y/\sigma_T$) was varied in the range 0.60 to 0.95 with a given yield stress σ_Y= 583 MPa and tensile strength σ_T= 711 MPa. These σ_Y and σ_T values were referred to the mechanical properties of a high strength pipeline steel [15].
- Crack size; The crack length *2a* and depth *b* analyzed were in the range $16 \le a \le 100$ mm and $1 \le b \le 6$ mm.
- Weibull modulus *m*; The *m*-value ranged from 15 to 40, where *m* = 20 was used as a standard value.

The yield ratio *YR* exerted a large influence on the CTOD ratio β. Figure 5 shows the effect of *YR* on the CTOD ratio β for a surface crack of *2a* = 40 mm and *b*= 6 mm, where the results are given as a function of the non-

TABLE 2 : BASIC VARIABLES EMPLOYED IN PARAMETRIC STUDY OF CTOD RATIO β.

		Mechanical properties				Crack size		
		σ_Y (MPa)	σ_T (MPa)	YR $=\sigma_Y/\sigma_T$ (%)	ε_T (%)	2a (mm)	b (mm)	$2\bar{a}$ (mm)
Effect of YR	σ_T : const.	427~675	711	60~95	11.4	40	6	13.8
	σ_Y : const.	583	614~972	60~95	11.4	40	6	13.8
Effect of crack size	Crack length effect	583	711	82	11.4	100	6	18.2
						40		13.8
						30		12.0
						16		7.4
	Crack depth effect					40	1	2.5
							3	7.4
							6	13.8

$2\bar{a}$: Equivalent through-thickness crack size

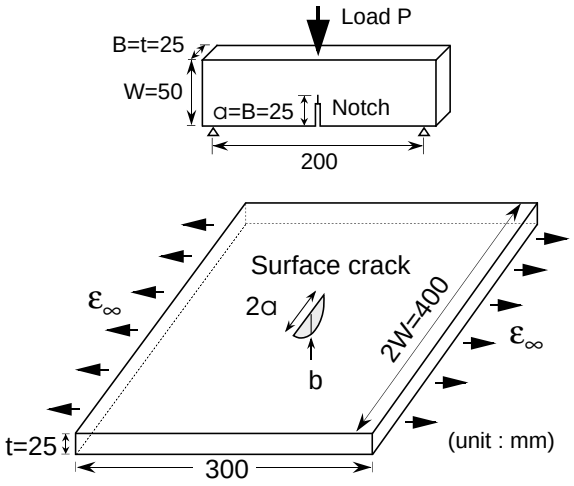

Figure 4 : Wide plate and 3-point bend specimen used for parametric study of β.

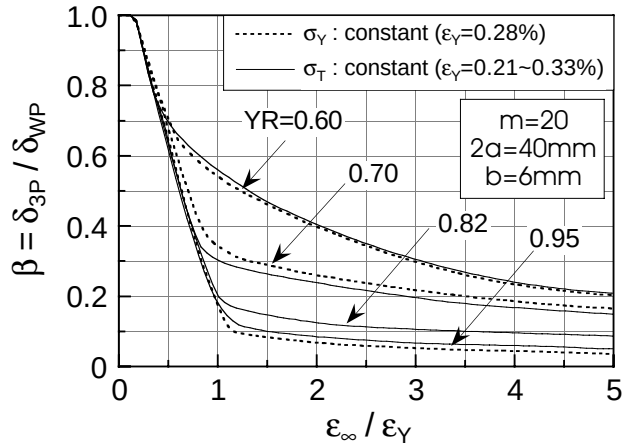

Figure 5 : Effect of yield ratio *YR* on CTOD ratio β.

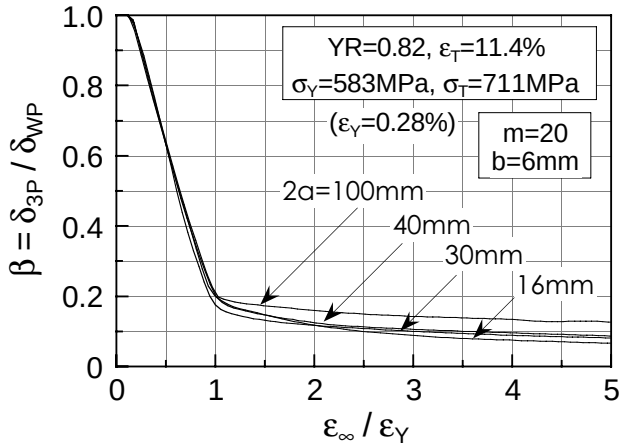

Figure 6 : Effect of crack length *2a* on CTOD ratio β.

dimensional overall strain $\varepsilon_\infty/\varepsilon_Y$ of the wide plate. The CTOD ratio β decreases to a large extent after full yielding of the wide plate, which is more significant for a high *YR*. This is mainly related to the crack opening behavior of the wide plate. Low work hardening (= high *YR*) yields a strain localization in the crack tip region, which produces a large CTOD δ_{WP} resulting in a low β. The change in *YR* under a constant σ_Y reached substantially the same results as under a constant σ_T. Similar effects were observed for another crack size.

Figure 6 shows the effect of crack length in the wide plate. The CTOD ratio β seems to be not so sensitive to the crack length. This is due to the following aspects: Longer crack provides a larger CTOD. At the same time, the fracture process zone V_f is enlarged with the crack front length, leading to amplification of the Weibull stress σ_W. Namely, the crack length 2*a* brings about two opposite influences on the CTOD ratio β. The positive and negative effects are almost evenly balanced, so that the CTOD ratio β seems to be insensitive to the crack length 2*a* in the range of calculations in this paper. The crack depth effect on the CTOD ratio β is presented in Fig. 7. A deep crack gives a low β, although the near-tip stress fields are activated in the deep crack. Low β for the deep crack was induced by a dominant action of crack opening; deep crack produces a large CTOD. However, the crack depth effect is weakened in a large-scale yielding range.

The influence of the Weibull modulus *m* is presented in Fig. 8. The CTOD ratio β was rather insensitive to the *m*-value. The exception was found in the results for a long crack of *2a*=100 mm. The Weibull stress σ_W consists of a stress term and a volume term. The stress term is given by $(\sigma_{eff}{}^m)^{1/m}$ and almost independent of *m*. On the other hand, the volume term includes the shape parameter *m* in the form $V_f{}^{1/m}$. The latter term becomes active, when a large process zone V_f is combined with a small *m*. Such volume effect elevated β slightly. Further work is in progress to establish the CTOD toughness scaling diagram.

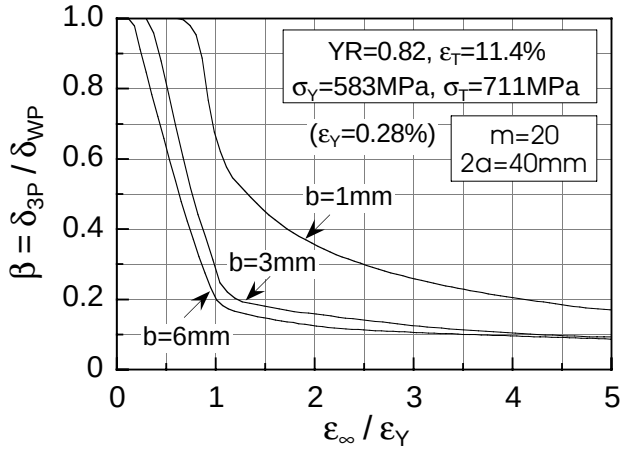

Figure 7 : Effect of crack depth *b* on CTOD ratio β.

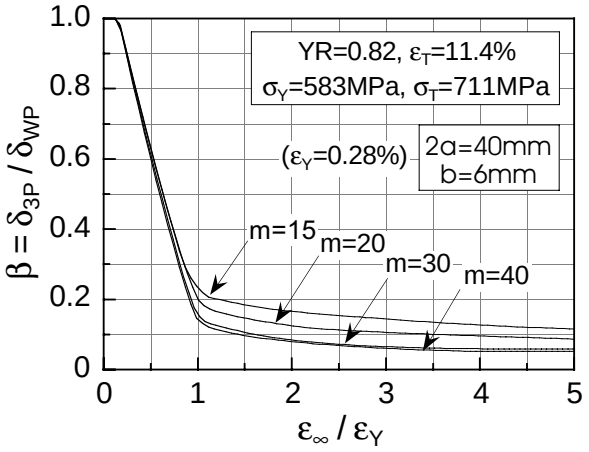

Figure 8 : Effect of Weibull modulus *m* on CTOD ratio β.

CONCLUSIONS

This paper presented the CTOD toughness scaling between structural components and fracture toughness specimens. Diagrams to correct the CTOD for constraint loss in large-scale yielding were constructed as a function of the deformation level of components, based on the Weibull stress fracture criterion. A CTOD ratio $\beta = \delta_{3P}/\delta_{WP}$ was introduced, where δ_{WP} is the CTOD of a wide plate component and δ_{3P} is an equivalent CTOD of the fracture toughness specimen at which the toughness specimen gives a compatible Weibull stress with the wide plate. Major factors controlling β were the work hardening property of materials and crack size in the component. A low β was related to a low work hardening (= high yield ratio) and a deep crack in the component. The CTOD toughness scaling diagrams enable a reasonable fracture assessment to eliminate an excessive conservatism in structural design and material toughness requirement.

REFERENCES

[1] Betegón, C. and Hancock, J. W. (1991). *Journal of Applied Mechanics*, **58**, pp. 104-110.

[2] Wang, Y.-Y. (1991). Ph. D. Thesis, Massachusetts Institute of Technology, USA.

[3] O'Dowd, N. P. and Shih, C. F. (1991). *Journal of Mechanics and Physics of Solids*, **39**, pp. 989-1015.

[4] O'Dowd, N. P. and Shih, C. F. (1992). *Journal of Mechanics and Physics of Solids*, **40**, pp. 939-963.

[5] Anderson, T. L. and Dodds, Jr. R. H. (1991). *Journal of Testing and Evaluation*, **19**, pp. 123-134.

[6] Dodds, Jr. R. H., Anderson, T. L. and Kirk, M. T. (1991). *International Journal of Fracture*, **48**, pp. 1-22.

[7] Gao, X., Ruggieri, C. and Dodds, Jr. R. H. (1998). *International Journal of Fracture*, **92**, pp. 175-200.

[8] Miyata, T., Tagawa, T. and Hongkai, Y. (2000). *Journal of Testing and Evaluation*, **28**, pp. 62-65.

[9] Beremin, F. M. (1983). *Metallurgical Transactions A*, **14A**, pp. 2277-2287.

[10] Mudry, F. (1987). *Nuclear Engineering Design*, **105**, pp. 65-76.

[11] Minami, F., Katou, T., Nakamura, T. and Arimochi, K. (1999). *Proc. 18th Int. Conf. on Offshore Mechanics and Arctic Engineering*, ASME, St. Johns, Newfoundland, OMAE99/MAT-2130.

[12] Minami, F., Brückner-Foit, A., Munz, D. and Trolldenier, B. (1992). *International Journal of Fracture*, **54**, pp. 197-210.

[13] Wang, Y.-Y. and Gordon, J. R. (1992). *Proc. Int. Conf. on Shallow Crack Fracture Mechanics, Toughness Tests and Applications*, TWI, Abington, Cambridge, Paper 28.

[14] Gao, X., Ruggieri, C. and Dodds, Jr. R. H. (1998). *International Journal of Fracture*, **92**, pp. 175-200.

[15] Minami, F., Ohata, M., Toyoda, M., Tanaka, T., Arimochi, K., Glover, A. G. and North, T. H. (1995). *Pipeline Technology*, **1**, pp. 441-461.

CONSTRAINT LOSS IN DUCTILE SOLIDS UNDER DYNAMIC LOADING

R.Narasimhan

Department of Mechanical Engineering,
Indian Institute of Science,
Bangalore 560012, India

ABSTRACT

In this paper, the evolution of T-stress and the constraint parameter Q in dynamically loaded fracture specimens are studied. The results show that typical fracture specimens exhibit significant constraint loss (i.e., negative Q) under dynamic loading irrespective of their static response. The implications of the above behaviour on the variation of fracture toughness with loading rate is discussed.

KEYWORDS

Ductile solids, constraint loss, dynamic loading, finite elements.

1. INTRODUCTION

The HRR solution [1,2] provides a one parameter characterization of the elastic-plastic crack tip fields based on the J integral. However, for certain specimen geometries like the centre cracked panel and shallow cracked bend specimen, the single parameter characterization has been found to be inadequate [3-5]. In other words, these specimens experience loss of HRR (or J) dominance, which is reflected in the reduction of stress triaxiality or crack tip constraint. In order to overcome the above limitation of the purely J based fracture methodology, two parameter description of the crack tip fields using the stress intensity factor K and the T-stress [3], or using J and a triaxiality or constraint parameter Q [4,5] have been proposed. In the former approach, T represents the second term in the series expansion for the elastic crack tip fields. In the latter method, Q is based on the difference between the actual near-tip stress field prevailing in a ductile specimen and the HRR solution. This difference field is found to be a slowly varying triaxial stress term in the region ahead of the crack tip [4]. A negative value of Q implies constraint loss in the specimen with respect to the high triaxiality HRR field. A one-to-one relation exists between Q and the elastic T stress under small scale yielding conditions [5], which indicates that the approaches based on K - T and J - Q are equivalent under these conditions. It must be emphasized that the above investigations pertain to quasi-static loading.

By contrast, only few investigations [6,7] have been carried out to understand loss of crack tip constraint in dynamically loaded ductile specimens. This issue assumes importance due to the following reasons. First, recent experimental studies [8-10] show that for many ductile materials the dynamic fracture toughness exhibits a strong increase over the static value for stress intensity rates $\dot{K} > 10^4$ Mpa$\sqrt{\text{m}}$/s. Secondly, numerical simulations [11,12] demonstrate that micro-void nucleation, growth and coalescence near a notch tip in ductile solids are retarded with respect to J when subjected to high loading rates. Hence, the objectives of this paper are to investigate the

evolution of T-stress and constraint loss in some fracture specimens under dynamic loading and to employ these results to understand the enhancement in fracture toughness with loading rate.

2. NUMERICAL MODELLING

In this work, a single edge notched plate under transient tensile loading (SEN(T)), and a three point bend specimen (TPB) subjected to impact loading are analysed. In Figs.1(a) and (b), schematic diagrams of these specimen geometries along with the loads and boundary conditions are shown.

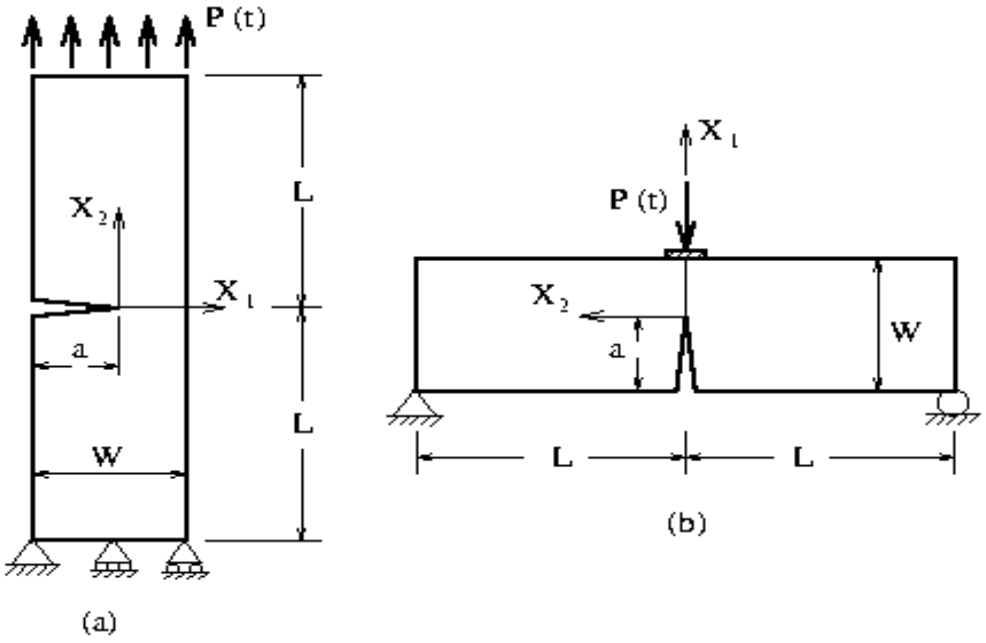

Figure 1: Schematic of **(a)** SEN(T) and **(b)** TPB specimen.

The applied load is chosen as a function of time t in the form $P(t) = \alpha t + \gamma t^2$. By varying the constants α and γ, a range of stress intensity rates $\dot{K}$ is achieved at the crack tip. The length 2L and width W of the specimens are taken as 160 and 40 mm, respectively. The analyses are conducted for different crack length to width, a/W, ratios. The material properties are assumed as E = 200 GPa, ν = 0.3 and ρ (density) = 7800 kg/m^3. In the elastic-plastic analyses reported in Sec.4, the initial yield strength σ_o and strain hardening exponent *n* are taken as 400 MPa and 10, respectively.

The 2D, plane strain, finite element meshes employed in the analyses are comprised of four-noded quadrilateral elements. They are well refined near the crack tip and are chosen after conducting mesh convergence studies. The finite element equations of motion are integrated using the explicit central difference method. The domain integral representation of the energy release rate J, proposed by Nakamura *et.al*. [13], is employed to compute the time history of J from the finite element results. The stress intensity factor K is obtained from J as $K = \sqrt{EJ/(1-\nu^2)}$.

3. T-STRESS UNDER DYNAMIC LOADING

In this section, the dependence of the T-stress on loading rate in a dynamically loaded SEN(T) specimen is examined. The time history of the T-stress is computed using a domain representation of the interaction integral [14,15].

In Fig.2, the evolution histories of the biaxiality parameter, $\beta = T\sqrt{\pi a} / K$, with respect to the stress intensity factor K are displayed for the SEN(T) specimen with a/W = 0.5, corresponding to three values of $\dot{K}$. Here, $\dot{K}$ is the average stress intensity rate which is obtained from the time history of K [15]. For comparison, the biaxiality parameter determined from the static analysis is marked on the ordinate axis in Fig.2.

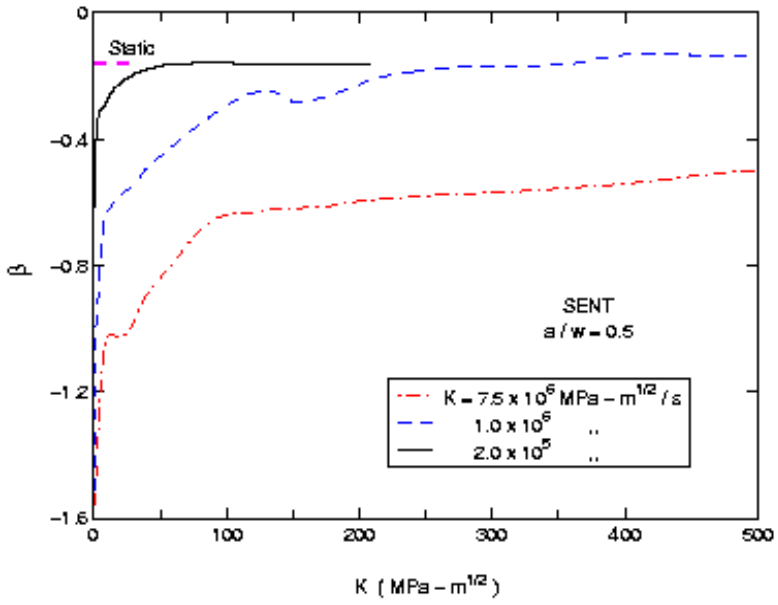

Figure 2: Evolution histories of biaxiality parameter β with respect to stress intensity factor K corresponding to different $\dot{K}$ for SEN(T) specimen with a/w = 0.5.

It can be observed from this figure that unlike the static case, where β is independent of load and has a fixed value for a given specimen geometry and crack length, β under dynamic loading varies strongly with K. During the early stages of dynamic loading (i.e., when the magnitude of K is small), β has a very large negative value, whereas the static biaxiality parameter has a much smaller magnitude. This behaviour is more pronounced at higher loading rates (see Fig.2) which implies that it is caused by inertial effects. Further, it is noted from Fig.2 that as the magnitude of K increases (i.e., at later stages of loading), β gradually approaches the static limit. Similar behaviour was observed from the analyses of SEN(T) specimens with other a/W ratios as well as the TPB specimen (see [15]). Since Q and T-stress are related [5], the above observations imply that Q will also be dramatically affected during the early stages of dynamic loading in ductile fracture specimens. This issue is examined below.

4. CONSTRAINT LOSS IN DUCTILE SPECIMENS

In this section, elastic-plastic dynamic finite element analyses of the specimens shown in Fig.1 under plane strain conditions are conducted. In Fig.3(a), the variation of normalized opening stress σ_{22}/σ_o with normalized radial distance $r/(J/\sigma_o)$ ahead of the crack tip corresponding to the SEN(T) specimen with a/W = 0.5 are shown. Results pertaining to different $\dot{K}$ values and at a fixed K = 50 MPa$\sqrt{m}$ are presented in this figure. Also shown are the variations obtained from static analysis of the above specimen and the analytical HRR solution [1,2].

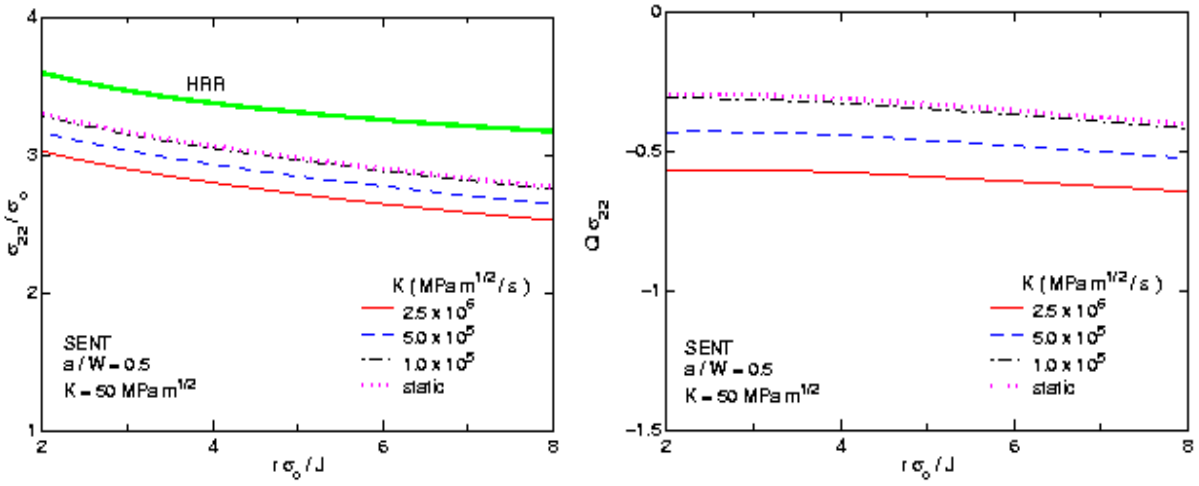

(a) (b)

Figure 3: Variation with respect to normalized distance $r/(J/\sigma_o)$ ahead of the tip of **(a)** normalized opening stress and **(b)** normalized difference stress for SEN(T) with a/W = 0.5.

It can be seen from this figure that with increasing $\dot{K}$, the opening stress ahead of the crack tip decreases in magnitude and falls well below the HRR solution. In order to quantify this discrepancy, the normalized difference stress field, introduced by O'Dowd and Shih [4], $Q\hat{\sigma}_{22} = (\sigma_{22} - \sigma_{22}^{HRR})/\sigma_o$ is plotted against normalized distance ahead of the tip in Fig.3(b) for the same cases as shown in Fig.3(a). It can be noticed from this figure that $Q\hat{\sigma}_{22}$ is negative for all cases and varies slowly with respect to r ahead of the tip. Its magnitude under static loading is quite small which corroborates with the small negative static biaxiality parameter associated with this specimen (see Fig.2). However, the magnitude of $Q\hat{\sigma}_{22}$ increases strongly from the static limit as $\dot{K}$ increases beyond 10^5 MPa$\sqrt{m}$/s. Further, it is found that $Q\hat{\sigma}_{11} = (\sigma_{11} - \sigma_{11}^{HRR})/\sigma_o$ also exhibits similar variation as discussed above. This implies that the difference stress field corresponds to a stress triaxiality term as observed by O'Dowd and Shih [4] for static loading.

Following O'Dowd and Shih [4,5], the constraint parameter Q is defined by the equation,

$$Q = (\sigma_{22} - \sigma_{22}^{HRR})/\sigma_o \quad (1)$$

at $r/(J/\sigma_o) = 2$ ahead of the crack tip. In Table 1, the values of Q obtained from the dynamic analyses of SEN(T) and TPB specimens with different a/W ratios corresponding to

$K = 50\ MPa\sqrt{m}$ and various average $\dot{K}$ values are summarized. The values of Q obtained from static analysis of the above specimens are also indicated in the table.

TABLE 1

VALUES OF Q AT $K = 50\ MPa\sqrt{m}$ FOR DIFFERENT SPECIMENS

SPECIMEN	STATIC	DYNAMIC $\dot{K}$ ($MPa\sqrt{m}/s$)		
		1×10^5	5×10^5	2.5×10^6
SEN(T) (a/W = 0.2)	-0.51	-0.52	-0.54	-0.59
SEN(T) (a/W = 0.5)	-0.31	-0.33	-0.45	-0.58
SEN(T) (a/W = 0.7)	-0.25	-0.28	-0.43	-0.68
TPB (a/W = 0.5)	-0.24	-0.26	-0.32	-0.80

It should first be noted that Q is negative under static loading for all cases shown in Table 1. However, for the SEN(T) specimen, the magnitude of Q under static loading increases as a/W decreases. This implies that the shallow cracked SEN(T) specimen suffers significant constraint loss under static loading which corroborates with the results of the earlier studies (see, for example, [3]).

Secondly, it can be observed from Table 1 that as $\dot{K}$ increases, Q becomes much more negative as compared to the static limit, particularly for deeply cracked specimens (with $a/W \geq 0.5$). The above effect which is attributed to material inertia corroborates with the large negative biaxiality parameter at high $\dot{K}$ noted in Sec.3 from the elastic analyses. Interestingly, Table 1 shows that enhancement in magnitude of Q with $\dot{K}$ is marginal for the shallow cracked specimen (at least up to $\dot{K} = 2.5\times10^6\ MPa\sqrt{m}/s$). It is clear from the above discussion that SEN(T) and TPB specimens, which are commonly used in dynamic fracture testing [8-10], display enhanced constraint loss as loading rate increases. This was further confirmed by examining the shape and size of the plastic zones, as well as the magnitude of the crack opening displacement, and comparing them with corresponding results from static, modified boundary layer analyses with negative T-stress [3-5].

5. DISCUSSION

An important consequence of the above noted constraint loss is the slowing down of micro-separation processes like void nucleation, growth and coalescence in the fracture process zone which is embedded inside the J-Q annulus at high loading rates as observed in [11,12]. This would result in enhanced fracture toughness as the loading rate $\dot{K}$ or $\dot{J}$ increases as reported in numerous experimental studies on ductile materials [8-10].

In order to illustrate this, the variation of J with Q for different applied load histories are superimposed along with a material-specific J_c versus Q failure locus in Fig.4(a).

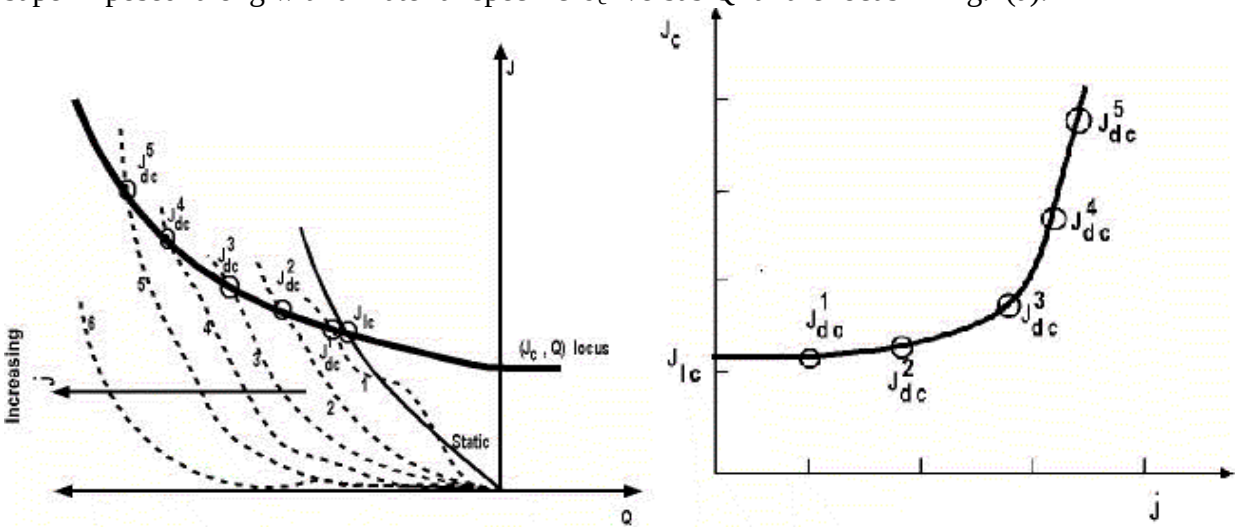

Figure 4(a): Schematic showing a material-specific J_c-Q failure locus along with J-Q variations corresponding to different loading histories. **(b)** Dynamic fracture toughness versus $\dot{J}$ predicted by the model.

The point of intersection of J versus Q trajectory pertaining to a certain loading rate $\dot{J}^{(i)}$ with the J_c-Q locus in Fig.4(a) yields the dynamic fracture toughness $J_{dc}^{(i)}$ corresponding to that loading rate. The variation of J_{dc} with $\dot{J}$ obtained by the above simple model can now be plotted as shown in Fig.4(b). This figure demonstrates that substantial enhancement in J_{dc} over the static limit will occur at high $\dot{J}$ as observed in the experimental studies [8-10].

REFERENCES

1. Hutchinson, J.W.(1968) *J. Mech.Phys.Solids* 16, 13.
2. Rice, J.R. and Rosengren, G.F. (1968) *J. Mech.Phys.Solids* 16, 1.
3. Al Ani, A.M. and Hancock J.W. (1991) *J. Mech.Phys.Solids* 39, 23.
4. O'Dowd, N.P. and Shih, C.F. (1991) *J. Mech. Phys. Solids* 39, 989.
5. O'Dowd, N.P. and Shih, C.F. (1992) *J. Mech. Phys. Solids* 40, 939.
6. Koppenhoefer, K.C. and Dodds, R.H. (1996) *Nuclear Engng. Design* 162, 145.
7. Basu, S. and Narasimhan, R. (2000) *J. Mech. Phys. Solids* 48, 1967.
8. Owen, D., Zhuang, S., Rosakis, A.J. and Ravichandran, G. (1998) *Int. J. Fracture* 90, 153.
9. Owen, D., Rosakis, A.J., Johnson, W.L. (1998). SM Report 98-22, GALCIT, California Institute of Technology, Pasadena, U.S.A.
10. Venkert, A., Guduru, P.R. and Ravichandran, G. (1998). SM Report 98-5, GALCIT, California Institute of Technology, Pasadena, U.S.A.
11. Basu, S. and Narasimhan, R. (1999) *J. Mech. Phys. Solids* 47, 325.
12. Basu, S. and Narasimhan, R. (2000) *Int. J. Fracture* 102, 393.
13. Nakamura, T., Shih, C.F. and Freund, L.B. (1986) *Engng. Fract. Mech.* 25, 333.
14. Sladek, J., Sladek, V. and Fedelinski, P. (1997) *Int. J. Fracture* 84, 103.
15. Jayadevan, K.R., Narasimhan, R., Ramamurthy, T.S. and Dattaguru, B.

(2001) *Int. J. Solids and Structures* 38, 4987.

CONSTRUCTION OF STRAIN-LIFE DIAGRAM BASED ON VARIABLE AMPLITUDE FATIGUE DATA

M. Endo and H. Miyata
Department of Mechanical Engineering, Fukuoka University
Jonan-ku, Fukuoka, 814-0180 Japan

ABSTRACT

A method is proposed that constructs a total strain range versus fatigue life curve ($\Delta\varepsilon_t$-N_f curve) based on variable amplitude loading data. In this method material parameters in the $\Delta\varepsilon_t$-N_f curve are determined by the least squares method on the assumption that fracture or crack initiation is occurred when the summation of life fractions estimated using Miner's rule reaches unity. Computer simulation of random loading fatigue test was first conducted to assure that the method is applicable to a wide variety of real materials. Constant and variable amplitude axial loading tests were carried out on annealed 0.37% carbon steel specimens. During the fatigue test, varying strain was measured by a strain gage and reduced to a frequency distribution of strain range using the rainflow method. The $\Delta\varepsilon_t$-N_f curve based on initiation of a crack was reasonably estimated by the proposed method. The procedure for obtaining the $\Delta\varepsilon_t$-N_f curve directly from an actual component subjected to service loading is also discussed.

KEYWORDS

Fatigue damage, Variable amplitude data, Miner's rule, Rainflow method, Inverse problem, Strain-life curve.

INTRODUCTION

One of the best ways for preventing fatigue failure of machines or structures is to monitor the fatigue damage accumulated in them. To do this it is necessary to measure the variable amplitude strain signal under the service condition where the component is used, and then to estimate the fatigue life by proper fatigue damage analysis. Service load fatigue phenomenon is so complicated that many problems have yet to be solved. Although study for understanding the essence of fatigue phenomena is important, development of practical technique for fatigue life estimate will become more important in the future.

Murakami et al. [1] have recently developed a small compact strain histogram recorder named Mini Rainflow Corder (MRC). In this device the rainflow method [2, 3] is used to decompose complex strain history into discrete strain ranges, related to fatigue damage, and the frequency is stored in the form of a histogram. In contrast, the authors [4] have developed user-friendly software that assists fatigue damage evaluation by analyzing the data obtained using MRC.

In usual fatigue life analysis, S-N curve or strain-life curve is necessary as basic material properties under cyclic loading. These relationships are usually obtained in a constant amplitude load or displacement fatigue

test where number of cycles to complete fracture of specimens or initiation of a crack with a definite length is examined. In general such a test requires an expensive testing machine and a skilled task. The purpose of this study is to propose a method to construct a basic relation of strain range versus cycles to failure from variable amplitude fatigue data. It is expected that using this method the relation can be obtained in an easy test with an inexpensive testing machine. In addition, this method may have a promising future in that field data reflecting particular effects of load spectrum, geometry of component, environment or other effects unforeseen in laboratory tests can be collected from actual components subjected to service load.

PROPOSED METHOD

Phenomenon on service load fatigue is not sufficiently elucidated now, and a unified method for damage or life assessment has not been established yet though many methods have been proposed. In this study, therefore, only well-known fatigue theories will be used to propose a new method. Usual process of fatigue damage assessment with MRC may be described as follows:

1. Strain range versus cycles to failure relationship (strain-life diagram) is obtained in a constant amplitude fatigue tests using small specimens in laboratory.
2. Varying strain signal is measured through a strain gage in a component or structure in service and the rainflow cycle counting is instantaneously made using MRC. The reduced strain history data is stored in MRC as frequency distribution of strain ranges, in which the maximum strain range is 7000×10^{-6} and it is divided into 256 discrete levels with the interval of 27×10^{-6} strain.
3. Fatigue damage summation is performed using Miner's rule. If consideration for stress concentration is necessary, local strain approach is employed with the aid of Neuber's rule, finite element analysis, etc.

If this process is grasped as a forward analysis, it is expected that a strain-life diagram may be reconstructed by a back analysis using output information of material; that is, frequency distribution of strain ranges, number of cycles to failure, etc.

For this analysis several assumptions are made in this study. First, it is assumed that strain-life diagram is stated as

$$\Delta\varepsilon = f(N_f), \tag{1}$$

where $\Delta\varepsilon$ is strain range, N_f is number of cycles to failure and $f(N_f)$ means a function of N_f. Failure means complete fracture, initiation of a crack with a given length, etc. Although the type of function can be arbitrarily determined depending on the purpose of life estimate, in this study the following equation is assumed:

$$\Delta\varepsilon_t/2 = A\ (2N_f)^B, \tag{2}$$

where A and B are material constants and $\Delta\varepsilon_t/2$ is total strain amplitude. Total strain may be convenient for practical use because it is directly measured by a strain gage. To deal with plastic strain we need the relation between stress and strain, which is usually changed with load cycling.

Second, it is assumed that a complex strain history is reduced by a certain cycle counting technique into a relation between strain range and its frequency. The rainflow algorithm [3] is used in MRC to provide the histogram.

Finally, it is assumed that fatigue damage is cumulated according to Miner's rule [5] expressed by

$$D = \sum d_i = \sum 2n_i / 2N_i\ , \tag{3}$$

where D : damage, i : level of strain range (i = 1~256 in MRC), d_i : damage fraction at level i, $2n_i$: number of reversals at level i and $2N_i$: number of reversals to failure when strain range of level i is cycled alone. Failure is assumed to occur when the summation of damage fractions, D, equals 1. Load sequence effects and mean stress effects are not taken into account in this analysis.

The following equation is obtained substituting Eqn. 2 into Eqn. 3 and setting D = 1.

$$\sum[2n_i(\Delta\varepsilon_i / 2\mathrm{A})^{-\frac{1}{\mathrm{B}}}]-1=0\,. \tag{4}$$

If giving linear forms by doing Taylor expansion for the left-hand side of Eqn. 4 as a function of variables A and B, the unknown values A and B will be computed by the least squares method. In this analysis, the solution of (A, B) is given as values converged by iteration starting the computation from a given set of initial values (A_0, B_0).

SIMULATION TESTS

The calculation ability of the proposed method can be examined by the following simulation test:

1. The values of (A, B) in Eqn. 2 are initially given as a correct solution.
2. A strain range level is randomly generated on a computer. For this strain range, damage fraction is calculated using Eqn. 2 and then summed up with the previous damage D using Eqn. 3. The number of reversals for the corresponding level is increased by 1.
3. If this work is continued until D = 1, a histogram of strain range frequency will be obtained.
4. For two or more sets of histograms obtained as above, a solution of (A, B) is given by applying the proposed method. The solution is compared with the correct solution initially given.

The calculable region of (A, B) is dependent on the initial values (A_0, B_0). The best values of (A_0, B_0) were obtained to be (0.002, – 0.6) through trial and error. Figure 1 shows the calculable region examined using (A_0, B_0) = (0.002, – 0.6) for the worst condition that the region becomes narrowest. The region is appeared to be broad enough to cover the regions corresponding to material constants of the Coffin-Manson relationship and Basquin's equation expected for a wide variety of real materials.

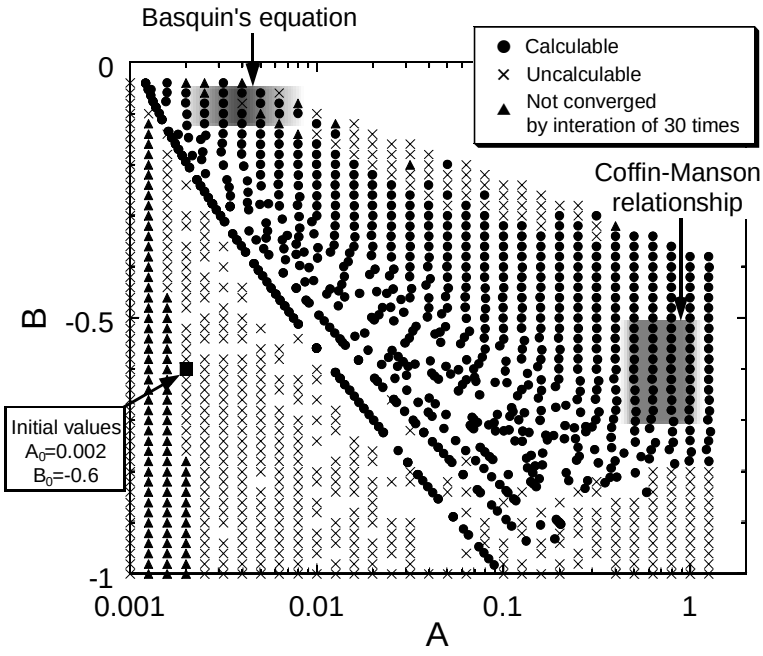

Figure 1 : Calculable region of (A, B) examined using (A_0, B_0) = (0.002, – 0.6)

FATIGUE TESTS

Material used is annealed 0.37% carbon steel. The chemical composition (wt %) is 0.37C, 0.21Si, 0.65Mn, 0.019P, 0.017S, 0.13Cu, 0.06Ni, 0.14Cr. The lower yield strength is 328 MPa, the tensile strength is 586 MPa, the reduction of area is 50.7 % and the Vickers hardness is 160. Specimen geometry is shown in Figure 2. The stress concentration factor K_t is 1.10. The specimens were electropolished to remove a surface layer of 40 μm in diameter. Axial load fatigue tests were conducted under load control using a 100 kN digitally-controlled servo-hydraulic testing machine, operating at 1-10 Hz. The alignment of specimen and machine axes was adjusted to minimize bending for each test using four strain gages at the positions indicated in Figure 2. The nominal stress amplitudes in constant load tests were 270, 290, 310 and 330MPa. The tests were performed under fully-reversed loading (R= –1). Stress is the nominal stress defined by the cross section area at notch root. It follows that the true stress has a tensile mean stress even for R = –1. The variable amplitude tests were carried out by block load tests using the stress histories shown in Figure 3. Note that there are three hysteresis loops with different stress and strain ranges in a block, as shown by schematic relationship between stress and strain. During the fatigue test the strain frequency was measured using an MRC. Notch root strain was numerically calculated using Neuber's rule, stress concentration factor K_t and the cyclic stress-strain curve estimated from the monotonic curve. Plastic replicas were taken during the tests to monitor crack growth.

RESULTS AND DISCUSSION

Figure 4a shows an example of the histogram of strain range frequency measured using MRC in block load tests. Figure 5 shows the strain-life diagrams constructed based on the definition that D = 1 when a 1000 μm

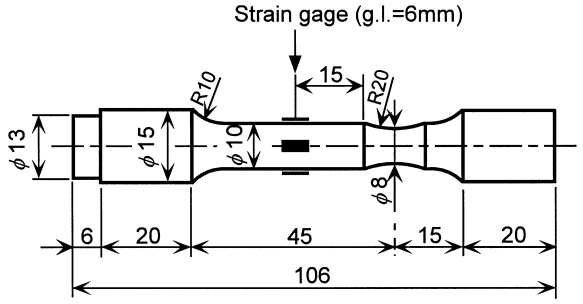

Figure 2 : Specimen geometry

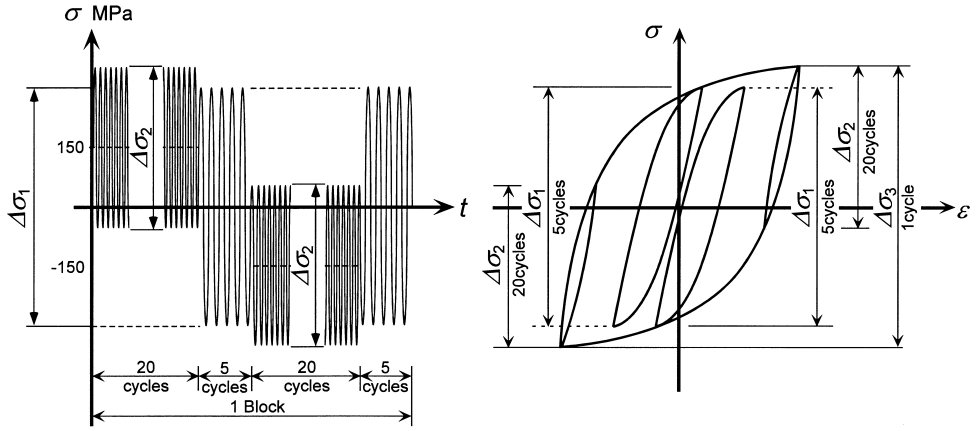

History	A	B	C	D
$\Delta\sigma_1/2$ (MPa)	340	320	300	280
$\Delta\sigma_2/2$ (MPa)	240	220	200	180

Figure 3 : Condition of variable amplitude load tests

crack is initiated. For small specimens shown in Figure 2, this definition is virtually equivalent to that for complete fracture. In this analysis damage below the fatigue limit was taken into account. The curve for variable amplitude is very close to that for constant amplitude. Table1 shows damage ratios for fatigue test results, which were computed using reconstructed curves. All ratios fall between 0.744 and 1.16. It may be concluded that the strain-life diagrams are well constructed from the variable amplitude data. Figure 4b shows histogram of damage fraction for the same data. The histogram has three populated groups, which may correspond to strain ranges of three hysteresis loops, see Figure 3. The scatter in the distribution may be mainly due to cyclic softening and hardening of material.

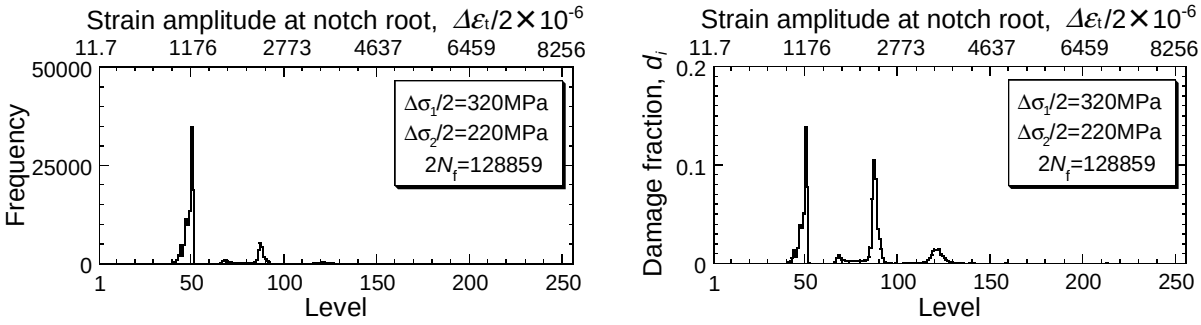

(a) Strain range frequency (b) Damage fraction

Figure 4 : Example of histogram obtained in block load test

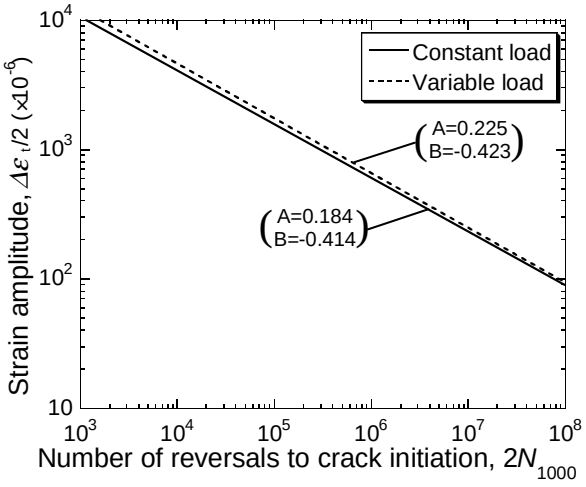

Figure 5 : Constructed strain-life diagrams

TABLE 1
DAMAGE RATIOS OF FATIGUE TEST RESULTS

(a) Constant amplitude test

Stress amplitude (MPa)	330		310		290		270	
Damage ratio	1.03	1.04	1.16	0.744	0.795	0.842	1.08	1.14

(b) Variable amplitude test

History	A	B	C	D
Damage ratio	1.06	0.842	0.995	1.07

The present method can be used also for the case that $D \neq 1$. Therefore, if certain physical damage observed in an actual component is correlated with D in the midst of its fatigue process, the data of strain-life relationship will be collected directly from the component subjected to service load. Although the term “fatigue damage” is often used in different ways by different researcher [6], in this study the length of a main crack leading the specimen to fracture was used as a measure of fatigue damage. Figure 6a shows the

relationship between surface crack length and damage D for the case of variable amplitude load tests. The value of D for a given crack length was calculated using the reconstructed strain-life curves and the strain range histogram corresponding to the length. Figure 6b shows the relationship between crack length and damage D normalized by the damage D_{1000} corresponding to the length of 1000 μm. All plots are within a narrow band. The values of D for cracks observed in a component may be defined using this relation.

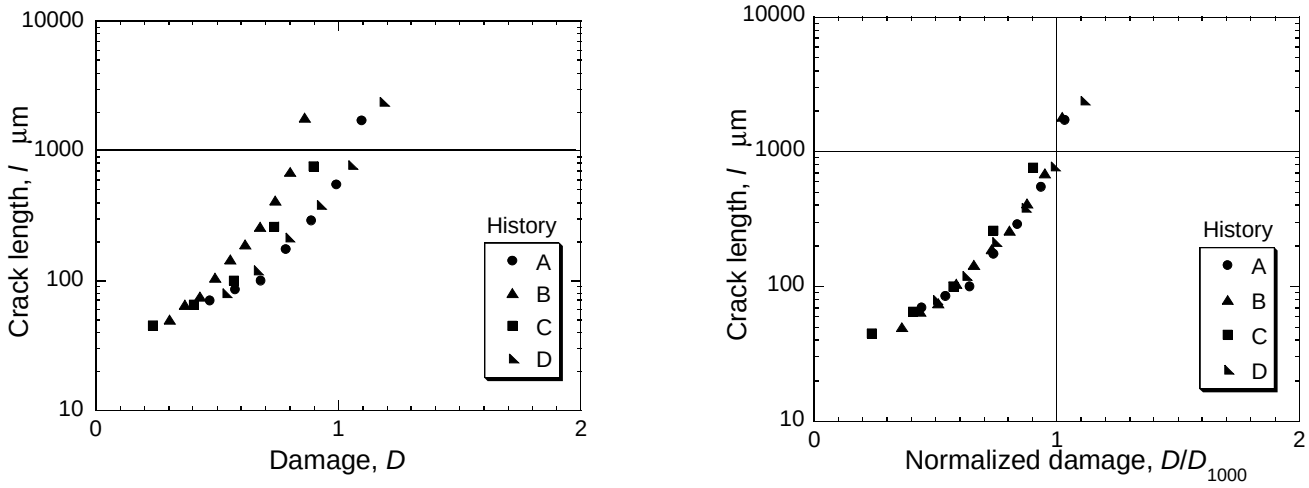

(a) Damage ratios

(b) Damage ratios normalized by D_{1000}

Figure 6 : Relationship between surface crack length and damage D

Several methods for constructing an S-N curve from variable amplitude fatigue data have previously been proposed. Nakamura et al. [7], Dowling [8] and Kikukawa et al. [9] used equivalent stress or plastic strain range to correlate the data between variable and constant amplitude loading. It is assumed in those methods that the value corresponding to B in Eqn. 2 equals the value obtained in constant amplitude fatigue tests. In contrast, the present method does not require such assumption. In addition it is applicable for the case that Eqn. 1 has two or more material constants.

CONCLUSIONS

A method for constructing a strain-life relationship from variable amplitude data was proposed. Computer simulation and fatigue tests were carried out to assure that the method is applicable to a wide variety of materials and complex strain history data. An idea for applying this method to an actual component subjected to service load was also presented.

REFERENCES

1. Murakami, Y., Morita, T. and Mineki, K., (1997) *J. Soc. Mater. Sci., Japan*, **46**, 1217.
2. Matsuishi, M. and Endo, T., (1968) *Preliminary Proc. of the Kyushu District Meeting, Japan Soc. Mech. Engrs*, pp. 37-40.
3. Anzai, H. and Endo, T., (1979) *Int. J. Fatigue*, **1**, 49.
4. Miyata, H. and Endo, M., (1999) *Preliminary Proc. of the Kyushu District Meeting, Japan Soc. Mech. Engrs*, **998**-3, pp. 25-26.
5. Miner, M. A., (1945) *J. Appl. Mech., Trans. ASME*, **12**, A159.
6. Lankford, J., Davidson, D. L., Morris, W. L. and Wei, R. P. (Eds.), (1982), *Fatigue Mechanisms: Advances in Quantitative Measurement of Physical Damage, ASTM STP 811*, ASTM, Philadelphia.
7. Nakamura, H. et al., (1973) *Trans. Japan Soc. Mech. Engrs*, **39**, 472.
8. Dowling, N. E., (1988) *Int. J. Fatigue*, **10**, 179.
9. Kikukawa, M., Jono, M. and Song, J., (1972) *J. Soc. Mater. Sci., Japan*, **21**, 753.

Oral Reference: ICF100546OR

CONTINUUM AND ATOMISTIC STUDIES OF INTERSONIC CRACK PROPAGATION

H. Gao[1], Y. Huang[2], and F. F. Abraham[3]

[1]Division of Mechanics and Computation, Stanford University, Stanford, California 94305
[2]Dept of Mechanical and Industrial Eng., University of Illinois, Urbana, Illinois 61801
[3]IBM Research Division, Almaden Research Center, San Jose, CA 95120-6099

ABSTRACT

Mechanisms of intersonic crack propagation along a weak interface under shear dominated loading are studied by both molecular dynamics and continuum elastodynamics methods. Part of the objective is to test if continuum theory can accurately predict the critical time and length scales observed in molecular dynamics simulations. To facilitate the continuum-atomistic linkage, the problem is selected such that a block of linearly isotropic, plane-stress elastic solid consisting of a two-dimensional triangular atomic lattice with pair interatomic potential is loaded by constant shear velocities along the boundary. A pre-existing notch is introduced to represent an initial crack which starts to grow at a critical time after the loading process begins. We observe that the crack quickly accelerates to the Rayleigh wave speed and, after propagating at this speed for a short time period, nucleates an intersonic daughter crack which jumps to the longitudinal wave speed. The daughter crack emerges at a distance ahead of the mother crack. The challenge here is to test if a continuum elastodynamics analysis of the same problem can correctly predict the length and time scales observed in the molecular dynamics simulations. We make two assumptions in the continuum analysis. First, the crack initiation is assumed to be governed by the Griffith criterion. Second, the nucleation of the daughter crack is assumed to be governed by a peak of shear stress ahead of the crack tip reaching the cohesive strength of the interface. Material properties such as elastic constants, fracture surface energy and cohesive strength are determined from the interatomic potential. Under these assumptions, it is shown that the predictions based on the continuum analysis agree remarkably well with the simulation results.

KEYWORDS

Continuum, Atomistic Models, Intersonic Crack Propagation

INTRODUCTION

This paper is a study of intersonic crack dynamics using both atomistic and continuum methods, with emphasis on the linkage between "mechanics" and "physics" modeling of fracture. Continuum mechanics is limited by its coarse view of physical phenomena and various assumptions adopted in its constitutive laws. On the other hand, atomistic methods, such as molecular dynamics (MD), is limited not just by the large number of degrees of freedom involved but also the time scale. There are only a few classes of problems to which

continuum and atomistic approaches can both be applied and the results directly compared. One of such problems is the simulation of dynamic crack propagation in a nanometer size crystal. The system is large enough for the continuum methods of dynamic fracture mechanics [1,2] to be applicable. On the other hand, the emergence of large scale parallel computers have also allowed MD simulations of crack propagation for system sizes reaching 1 billion atoms and time scales approaching nanoseconds [3]. Atomistic simulations provide an ab initio investigation of fracture by which the validity of continuum methods can be tested. Continuum mechanics analysis provides a conceptual framework in which MD simulation data can be analyzed and understood. It is in this spirit that we conduct a joint continuum and atomistic investigation of intersonic crack propagation along a weak interface.

Our present study is motivated by recent experiments on intersonic crack propagation by Rosakis et al. [4] who investigated shear dominated crack growth along weak planes in a brittle polyester resin under far field asymmetrical loading. They observed crack propagation as fast as the longitudinal wave speed. This experiment is interesting because it has been widely believed that a brittle crack cannot propagate faster than the Rayleigh wave speed. The origin for this belief stems from the vanishing of crack tip energy release rate and stress singularity at the Rayleigh wave speed predicted by continuum mechanics. The late arrival of laboratory experiments on intersonic fracture [4] is due, in part, to the fact that a crack in elastic homogeneous and isotropic solids always kinks or branches out, deviating from the initial crack plane and having a zigzag crack path, once the crack tip velocity exceeds only 0.3 ~ 0.4 of the shear wave speed [1, 5, 6]. A wavy crack instability occurs at low crack velocities and prevents an exploration of the full range of possible velocities. In fact, the only possibility of attaining intersonic crack propagation is to introduce a weak path (a layer of lower toughness) so that crack growth is confined to this path. Although the experiments of Rosakis et al. [4] have shown convincingly that a shear dominated crack can propagate with velocity up to the longitudinal wave speed, the question of whether such a crack has been accelerated from a subsonic crack or is nucleated directly as an intersonic crack has not been fully resolved by experiments.

A two-dimensional MD simulation was conducted to investigate the mechanisms of shear crack propagation along a weak interface joining two harmonic crystals [7]. The atomic bonds of the harmonic crystals are characterized by the harmonic interatomic potential with infinite cohesive strength. Crack propagation is forced to propagate along the interface which is characterized by the Lennard-Jones (LJ) potential. The two-dimensional crystal with pair interatomic potential assumes a triangular atomic lattice and behaves as a linear elastic isotropic sheet deforming under plane-stress conditions. Loaded by linearly increasing shear displacements along the boundary of the simulation block, a pre-existing notch is introduced to represent an initial crack which starts to grow at a critical time after the loading process begins. The main results in [7] can be briefly summarized as follows. A mode I crack never exceeds the Rayleigh wave speed. In comparison, a mode II crack initiates at a critical load level and accelerates very quickly to the Rayleigh wave speed. It travels at the Rayleigh speed for a short while and nucleates an intersonic daughter crack ahead of its tip. The daughter crack propagates near the longitudinal wave speed.

The objective of this paper is to test if continuum theory can accurately predict the critical time and length scales observed in molecular dynamics simulations [7]. We apply the dynamic elasticity methods [1] to solve the crack propagation problem subject to identical geometry and loading conditions in the molecular dynamics simulation. We determine material properties including Young's modulus, Poisson ratio, wave speeds, surface energy and cohesive strength from the interatomic potentials used in the atomic simulation. This precise knowledge of material properties allow us to use the simulation results to test the validity of continuum theories of fracture. We make two assumptions in the continuum analysis. First, the crack initiation is assumed to be governed by the Griffith criterion.

Second, the nucleation of the daughter crack is assumed to be governed by a peak stress ahead of the crack tip reaching the cohesive strength of the interface. Under these assumptions, we show that the predictions based on the continuum analysis agree remarkably well with the atomic simulation results.

ATOMIC SIMULATION RESULTS

The atomic simulation of intersonic shear fracture is based on molecular dynamics which is a computational method [8, 9] for predicting the motion of a given number of atoms by numerically integrating Newton's law for each atom. In the MD simulation, the mutual interactions among atoms are described by a continuous potential function. The details of MD simulations of intersonic shear fracture can be found in [7]. Here we briefly discuss the most relevant results that will be compared to the continuum analysis.

In accordance with the objective of studying crack propagation along a weak interface in a linear elastic isotropic solid, we consider a two-dimensional atomic lattice characterized by a pair potential. Atoms across a weak interface line are assumed to interact according to the LJ potential, $\varphi = 4\left(r^{-12} - r^{-6}\right)$. All results are expressed in terms of reduced units: lengths are scaled by the value of the interatomic separation for which the LJ potential is zero, energies are scaled by the depth of the minimum of the LJ potential, and mass is scaled by the atomic mass. A cut-off distance equal to *2.5* is assumed for the LJ potential. Atoms in the adjacent crystals are assumed to interact according to the harmonic potential $\varphi = k(r-d)^2/2$, where $d = \sqrt[6]{2}$ and $k = \varphi''(d) = 72/\sqrt[3]{2}$ such that the materials are elastically homogeneous across the interface. We note that the harmonic crystal has infinite fracture strength due to linear interactions among nearest neighbors. The only fracture path in this linear elastic homogeneous and isotropic solid is along the interface which has a finite cohesive strength associated with the LJ potential.

The total dimension of the simulation system under study is a 2D slab of atoms with *1424* atoms along the horizontal length defining the x_1 direction and with *712* atoms along the vertical length defining the x_2 direction. A horizontal slit of *200*-atom distance is cut midway along the left-hand vertical slab boundary. The 2D crystal has a triangular lattice with the slit parallel to the close packed direction along which atomic spacing is equal to the lattice constant $\sqrt[6]{2}$. To study a shear dominated crack, a shear strain rate of *0.00025* and a tensile strain rate of *0.00005* are imposed on the outer most rows of atoms defining the opposing horizontal faces of the two-dimensional slab. The crack is of mixed mode but dominantly shear. Linear velocity gradients are established across the slab initially. Then the loading process proceeds with constant shear and tensile velocities along the boundary, which leads to eventual failure of the material at the slit tip. The applied strain rates remain constant during the simulation, and the simulation is continued until the growing crack has traversed the total length of the slab. Simulations of a mode I crack is conducted with the same geometrical setup except only an opening strain rate is imposed.

The mode I crack in the atomistic simulations (Abraham and Gao, 2000) quickly approaches a constant velocity equal to the Rayleigh wave speed *4.83* of the harmonic crystal, which shows that the crack velocity is limited by the Rayleigh wave speed, consistent with the classical theories of fracture. The mode II crack initiates at a critical time estimated to be *65* and quickly approaches the Rayleigh wave speed of the harmonic solid. After propagating at the Rayleigh wave speed for a short while, the crack tip jumps to the longitudinal sound speed calculated to be *9*. The time for this velocity jump is estimated to be around *140*.

The mechanism for the mode II crack "jumping" over the forbidden velocity zone is the nucleation of an intersonic daughter crack ahead of the mother crack travelling at the

Rayleigh wave speed [7]. A sharp intersonic crack is nucleated at a small distance estimated to be around *22* ahead of the mother crack. Transverse Mach cones near the daughter crack are observed in atomistic simulations, and the angle of the Mach cone shows that the velocity of the daughter crack is consistent with the longitudinal wave speed. As the daughter crack moves ahead, the mother crack trails behind at the Rayleigh wave speed. The MD simulations demonstrate intersonic crack propagation and the existence of a "mother"-"daughter" crack mechanism for a subsonic shear crack to jump over the forbidden velocity zone. This mechanism is reminiscent of the mechanism of Burridge [10] and Andrews [11] based on continuum theories, although the continuum description cannot provide an ab initio description for crack formation. The birth of the daughter crack cannot be characterized by a critical energy release rate or a critical stress intensity factor near the mother crack because both these quantities vanish at the Rayleigh wave speed. It seems that the only possible mechanism by which the daughter crack can be nucleated is by the finite stress peak ahead of the mother crack and along the weak bonding line, as measured in the stress field and discussed by Burridge [10].

MATERIAL PROPERTIES

Material properties of importance to continuum descriptions of fracture include the elastic moduli, elastic wave speeds, surface energy and cohesive strength. In comparison with a laboratory fracture experiment, atomistic simulations have the advantage of providing a precise knowledge of these material properties from the interatomic potential.

A two dimensional triangular lattice behaves as a plane stress elastic sheet with the shear modulus $\mu = \sqrt{3}k/4$, Young's modulus $E = 2k/\sqrt{3}$, and Poisson's ratio $\nu = 1/3$ [12]. With the atomic mass taken as the unit of mass, the triangular lattice has density $\rho = \sqrt[3]{4}/\sqrt{3}$. The longitudinal, shear and Rayleigh wave speeds are $c_d = 9$, $c_s = 5.20$, and $c_R = 4.83$, respectively.

The fracture surface energy of the material is defined as the energy consumed in breaking atomic bonds as crack grows. For the MD simulations described in section 2, the crack is parallel to the close packed direction and atoms across the interface interact according to the LJ potential with a cut-off distance equal to *2.5*. Accounting for all the atomic interactions, four atomic bonds (2 between nearest neighbors and 2 between next nearest neighbors) are snapped per atom in the fracture process. The fracture surface energy is defined as half of the energy stored in these bonds and is equal to $\gamma = 0.956$ [12].

The cohesive strength of the weak interface under shear dominated loading is calculated as follows [13]. The cohesive failure of a single atomic bond is defined as the state when the interactive force between two atoms reach the maximum, which corresponds to $\varphi''(d_m) = 0$ and $d_m = \sqrt[6]{26/7}$ is the critical bond length at failure. Balance of forces parallel and normal to the interface gives the relation $\tau_{int} + 0.577\sigma_{int} = 2.04$ between shear and normal stresses along the interface at the cohesive limit, which is the cohesive strength criterion and has a strong coupling between shear and tensile stresses.

CONTINUUM ANALYSIS OF CRACK INITIATION AND PROPAGATION

The aforementioned entire process of crack initiation and propagation is studied via a transient, continuum analysis of dynamic fracture [13]. It is shown that the continuum analysis, in conjunction with the Griffith criterion, can determine the critical time for crack initiation rather accurately. The location and time at which the daughter crack is nucleated

are also determined rather accurately by the continuum analysis, together with a cohesive strength criterion.

An infinite plane-stress solid containing a semi-infinite crack on the negative x_1 axis is subjected to constant remote shear stress rate $\dot{\tau}_0$ and tensile stress rate $\dot{\sigma}_0$ normal to the crack. Consistent with the atomistic simulations, an initial velocity field at time $t = 0$ corresponding to the constant remote stress rates is imposed such that there are no waves coming from the remote field. The deformation field can be decomposed into the following two sub-problems. First, a uniform deformation field corresponding to constant shear stress-rate $\dot{\tau}_0$ and normal stress-rate $\dot{\sigma}_0$ in the same solid but without the crack; the initial velocity field is consistent with $\dot{\tau}_0$ and $\dot{\sigma}_0$ such that there are no waves from the remote field. The second sub-problem has constant shear and normal traction-rates, $\dot{\tau}_0$ and $\dot{\sigma}_0$, imposed on the entire crack faces (including the new ones generated by crack propagation) in order to negate the crack-face tractions from the first sub-problem. There is no initial velocity field. The crack tip remains stationary until a critical time, $t = t_{init}$, is reached at which the Griffith criterion is met. The crack tip then propagates in the crack plane at the Rayleigh wave speed c_R, consistent with the atomistic simulation discussed in section 2. It should be pointed out that stresses are indeed not singular near a crack tip propagating at the Rayleigh wave speed c_R. Instead, the shear stress has a peak that occurs at a finite distance ahead of the crack tip. Once the peak stress reaches the cohesive strength of the solid, the daughter crack is nucleated.

Griffith Criterion and Crack Initiation

We study first the critical time for crack initiation, $t = t_{init}$, at which the macroscopic crack tip starts to propagate. The plane-stress crack tip energy release rate for a stationary crack subjected to constant remote shear and normal traction-rates $\dot{\tau}_0$ and $\dot{\sigma}_0$ on the crack faces are given in [1]. The Griffith criterion predicts that the crack tip starts to propagate when the crack tip energy release rate reaches twice the surface energy, 2γ, which gives the critical time for crack initiation. Using the shear and normal strain rates in the atomistic studies given in section 2 as well as the elastic constants, wave speeds and fracture surface energy in section 3, we find that the critical time for crack initiation predicted by the continuum elasticity is $t_{init} = 70.3$ in the reduced unit, which is in good agreement with the corresponding result of *65* in the MD simulations. This analysis indicates that the Griffith criterion holds even down to the atomic scale.

Cohesive Strength Criterion and the Nucleation of Daughter Crack

The continuum analysis becomes much more difficult after the crack tip propagates at the Rayleigh wave speed c_R after time $t = t_{init}$. We follow the same method developed by Freund (1990) to solve this fully transient dynamic fracture problem involving both the dynamic crack-face loadings and the crack propagation. We skip details of the solution and present only the shear stress relevant to the nucleation of daughter crack. The shear stress has a very sharp peak at the shear wave front ahead of the moving the crack tip. This maximum shear and normal stresses have been determined in terms of the applied load, time, as well as the elastic constants and wave speeds. Using the cohesive strength criterion in section 3, we have determined the critical time and location for the nucleation of the daughter crack. For the material properties given in section 3 and the imposed strain rates in atomistic simulations (section 2), we find the critical time for the nucleation of the daughter crack predicted by classical elasticity is $t_{nucl} = 120$ in the reduced unit, which is in reasonable agreement with the counterpart of *140* in atomistic simulations. The corresponding location at which the daughter crack is nucleated ahead of the moving crack tip is the shear wave front and is found to be *18.2* in the reduced unit, which is once again in reasonable agreement with the estimate of *22* from atomistic simulations. This indicates that the

cohesive strength criterion seems to govern the nucleation of the daughter crack even down to the atomic scale, leading to intersonic crack propagation.

CONCLUSIONS

We have studied intersonic shear crack propagation along a weak interface by both molecular dynamics and continuum elastodynamics. The problem selected is a block of linearly isotropic, plane-stress elastic solid consisting of a two-dimensional triangular atomic lattice with pair interatomic potential loaded by constant shearing velocity along the boundary. The fracture process revealed by MD simulations shows the following sequence of events. The initial crack starts to grow at a critical time after the loading process begins. It quickly accelerates to the Rayleigh wave speed and, after propagating at this speed for a short time period, nucleates an intersonic daughter crack which immediately jumps to the longitudinal wave speed. The daughter crack emerges at a critical distance ahead of the mother crack. We solve the continuum elastodynamic problem of the same crack geometry under the same loading history to test if the continuum analysis can correctly predict the length and time scales observed in the atomic simulations. We assume that the crack initiation is governed by the Griffith criterion while the nucleation of the daughter crack is governed by the Burridge-Andrew mechanism of cohesive failure by a peak of shear stress ahead of the crack tip. We determine material properties including elastic constants, elastic wave speeds, fracture surface energy and cohesive strength from the interatomic potential used in the atomic simulations.

The critical time for initial crack growth predicted by the continuum elastodynamics and the Griffith criterion agrees with the atomistic simulation results within *10%*. Also, we find remarkably good agreement between continuum analysis and atomic simulations for the time and location of the nucleation of the daughter crack. From this comparison, we conclude that continuum mechanics can provides not only qualitatively useful insights into the mechanisms of intersonic shear crack propagation, but also gives quantitatively correct predictions for the times and locations of critical atomistic events. Effective linking between continuum and atomistic methods is expected to be a powerful way of studying a wide variety of nanoscale dynamic phenomena.

REFERENCES

1. Freund, L.B. (1990). *Dynamic Fracture Mechanics*. Cambridge University Press, Cambridge, England.
2. Broberg, K.B. (1999). *Cracks and Fracture*. Academic Press, San Diego.
3. Abraham, F.F., Brodbeck, D., Rudge, W.E., Broughton, J.Q., Schneider, D., Land, B., Lifka, D., Gerner, J., Rosenkrantz, M., Skovira, J. and Gao, H. (1998). *Modeling and Simulation in Materials Science and Engineering* 6, 639.
4. Rosakis, A.J., Samudrala, O. and Coker, D. (1999). *Science* 284, 1337.
5. Gao, H. (1993). *J. Mech. Phys. Solids* 41, 457.
6. Abraham, F.F., Brodbeck, D., Rafey, R.A. and Rudge, W.E. (1994). *Phys. Rev. Lett.* 73, 272.
7. Abraham, F. F. and Gao, H. (2000). *Phys. Rev. Lett.* 84, 3113.
8. Abraham, F.F. (1986) *Adv. Phys.* 35, 1.
9. Hoover, W.G. (1986). *Molecular Dynamics*. Springer-Verlag, Berlin.
10. Burridge, R. (1973). *Geophysical J. of the Royal Astronomical Soc.* 35, 439.
11. Andrews, D.J. (1976). *J. Geophys. Res.* 81, 5679.
12. Gao, H. (1996). *J. Mech. Phys. Solids* 44, 1453.
13. Gao, H., Huang, Y. and Abraham F.F. (2001). Continuum and atomistic studies of intersonic crack propagation. *J. Mech. Phys. Solids* (in the press).

CONTINUUM MODELS WITH RUPTURED/HEALED MICROSTRUCTURE

A. I. Leonov

Department of Polymer Engineering, The University of Akron
Akron, Ohio 44325-0301, USA

ABSTRACT

A continuum approach based on qualitative micro-structural physics and thermodynamic arguments has been elaborated for modeling of such interactive phenomena as yelding, thixotropy, nonlinear viscoelasticity, frozen memory, and stress localization. This type of modeling has been successfully applied to various systems, such as coagulating suspensions, highly filled polymers, concentrated solutions of surfactants, and elasto-viscoplasticity in metals. The mutual feature in these systems is the presence of a specific "structure" at rest, which can be destroyed at higher stresses and restored again after any type of unloading. Examples of this type modeling are presented in this paper. Several comparisons of calculations with experimental data will also be demonstrated in presentation.

KEYWORDS

Stress, strain, de-bonding, viscoelasticity, viscoplasticity, relaxation, yield, thixotropy.

INTRODUCTION

Many two-phase systems with small attractive colloidal particles display a peculiar mechanical behavior when the particle concentration is above a certain "gelation" (or a percolation) threshold. A simplest class of such systems is *dispersions* where solid colloidal particles with inter-particle attractive interaction are dispersed in a low molecular weight fluid. Many of them, such as lubricating greases, inks, pastes, foodstuffs, coal-water, and clay-water systems are of considerable industrial significance. Because of the attractive interactions, dispersions can create a particulate network, which is usually ruptured in flow with formation of "flocs", and restored again at rest. The general approach presented below, was successfully applied to dispersed systems in [1]. The *filled polymers* represent another example of such a system. They include a broad variety of cured and uncured rubber compounds employed in rubber and tire industries, as well as the micro-gels used in electronics. Here, depending on the type of polymer and filler, a dominant physical bonding can happen either between small particles of filler or between filler and polymer matrix. Again, this secondary network existing at rest can be destroyed by stresses, with a long restoration after unloading. Examples of our modeling of uncured systems are given in [2,3]. The third class of the

phenomena to which the general approach has been applied is the *elasto-viscoplasticity in metals* [4]. Here, beyond a critical (yielding) level of stresses, a sharp and time dependent transition from elastic behavior to plastic flow occurs in active loading, caused by the sliding of metallic "grains" along multiple dislocation lines. Also, a long time stress-strain relaxation with restoration of structure, its hardening, stress localization, and frozen memory effects happen in metals. Finally, the same approach with few modifications can also be employed to describe the rheological behavior of the concentrated solutions of *worm-like micelles*. Here, the long chains of micelles with relatively strong but still secondary inter-micelle forces present the structure. At low stresses, the system behaves as a polymer-like viscoelastic liquid, but at higher stresses, the chains of micelles are destroyed being restored again in any type of unloading [5]. No yielding exists in this system.

BODY OF PAPER

We demonstrate below the basic principles of the approach and its applications to the above four systems. For the sake of simplicity only the case of simple shearing with small viscoelastic deformations is considered. The general 3D approach with a complete geometric nonlinearity has also been developed and presented in the cited papers, where the comparison was made between calculations and data.

Basic Principles and Formulation

It is easy to illustrate the basic principles of the approach on the example of colloidal suspensions in viscous or viscoelastic liquid with interparticle attractive interactions. These interactions are of two major types.

(i) *Direct attractive interactions*, which create the particulate network and flocs. These interactions being elastic before yield and viscoelastic beyond it produce a specific macroscopic viscoelastic shear sub-stress $\sigma_p = G_p \gamma_p$. Here G_p is the elastic modulus and γ_p is the small (visco-) elastic strain. Two relaxation times are important here: a lifetime of flocs θ_p, and a restructuring time θ_o $(\theta_o \geq \theta_p)$ during unloading.

(ii) *Hydrodynamic interaction* between the flocs, as in a suspension of *inactive* particles, produces another type of sub-stress, σ_m, which depends on the rheological properties of matrix and such important parameters of suspension as particle concentration φ and size *d*. If the suspending matrix is a low molecular liquid, then $\sigma_m = \eta_m \dot{\gamma}$, where $\eta_m(\varphi, d)$ is the suspension viscosity. The function $\eta_m(\varphi, d)$ is approximately known from the rheology of suspension of inactive particles (see discussion in [2]). If the suspending matrix is a polymer liquid, the sub-stress σ_m is of viscoelastic nature (see details in [2,3]).

The total macroscopic shear stress σ is then represented as the sum of σ_p and σ_m. These are viewed as the contributions in the stress arising from specific matrix and particulate sub-media, or "modes" [2]. For high concentrated colloidal suspensions in low molecular matrices, the contribution σ_m in the total stress is negligible. Then the approach in this limit will also valid for the case of the elasto-viscoplasticity of metals [4]. Additionally, the normalized *debonding factor* ξ $(0 \leq \xi \leq 1)$ should also be introduced to characterize the process of rupture/restoration of flocs.

The formulation of the constitutive equations is then as follows [1,2]:

$$\sigma = G_p\gamma_p + \sigma_m \ (\sigma_m = \eta_m\dot{\gamma}) ; \quad \dot{\gamma}_p + f(\xi)\gamma_p / \theta = \dot{\gamma} ; \quad \theta_o\dot{\xi} + \xi = (1-\xi)|\dot{\gamma}|\theta / \gamma_* \qquad (1,2,3)$$

Here $\dot{\gamma}$ is the shear rate. Eqn.2 describes the evolution of elastic strain γ_p, and *kinetic equation* 3 describes the evolution of the debonding factor ξ. The *mobility function* $f(\xi)$ in Eqn.2 describes the effect of the floc rupture/restoration on the rheological properties of particulatee mode. The properties of $f(\xi)$ are assumed as follows:

$$f(\xi), f'(\xi) > 0; \ f \to f_0, \ \xi \to 0; \ f \to f_1 \ (< \infty), \xi \to 1. \qquad (4)$$

When $f_0 = 0$ the behavior of $f(\xi)$ near $\xi = 0$ is assumed as:

$$f = \xi + o(\xi), \ \xi \to 0 . \qquad (4a)$$

An example of (*ad hoc*) specification which captures the properties shown in Eqns.4 and 4a for $f(\xi)$, is proposed as:

$$f(\xi) = (f_o + k\xi)\exp(\beta\xi) \quad (k, \beta \geq 0) . \qquad (5)$$

Two asymptotic cases of Eqn.5, (i) $f_o \approx 1, k = 0$ and (ii) $f_o = 0, k = 1$, are considered below. The physical sense of Eqns.1-5 is easy to illustrate on the simple situation when contribution of the matrix mode in the stress is negligible, i.e. $\sigma \approx G_p\gamma_p$. This situation also describes the effects of elasto-viscoplasticity in metals and rheology of worm-like micelles.

1. The particulate mode in Eqns.1, 2 has a viscoelastic character, since it has elastic properties (due to attractive inter-particle interaction) and quasi-viscous properties (due to floc rupturing under stress action). The effective relaxation time in Eqn.2, $\theta^* = \theta / f(\xi)$, decreases with the increase in debonding factor ξ, i.e. with the floc rupture. Thus $f(\xi)$ should be an increasing function of ξ. In accordance with Eqn.4, parameter θ / f_1 has the sense of the ultimate viscoelastic relaxation time in the mode, when the flocs are completely ruptured. The parameter f_o in Eqn.4 reflects the importance of fluctuations in the floc network at rest. If $f_o \sim 1$, the system at rest has a viscoelastic character with initial relaxation time θ $(> \theta / f_1)$. This can describe the rheology of worm-like micelles. On the contrary, if $f_o << 1$, the value of f_o can be neglected and the floc network can be considered as "rigid". This is the case of dispersed systems in low molecular matrices, filled polymers and elasto-viscoplasticity, with yielding and sharp transition from solid-like behavior to flow. To guarantee the occurrence of such a sharp transition with yield behavior, the assumption shown in Eqn.4a is made about the behavior of $f(\xi)$ in the vicinity $\xi = 0$.

2. The phenomenological equation 3 is proposed here to capture the essence of the process of flocs rupturing and restoration. Here γ_* is the critical value of γ_p at which the intensive de-bonding process starts. When Eqn.4a is applicable, the parameter γ_* is associated with the elastic deformation at yielding point. It is easy to prove that Eqn.3 preserves the constraint $0 \leq \xi(t) \leq 1$. In thermodynamic interpretation [2] of floc de-bonding/re-bonding, the factor ξ is proportional to the free energy stored in flocs, ξ / θ_o is proportional to the rate of dissipation due to de-bonding and the

right-hand side of Eqn.3 is proportional to the average rate of work done by fluctuating micro-stresses on critical deformation γ_* [1,2].

3. For filled polymers, the matrix mode is viscoelastic and contributes a lot in the stress. Two cases are important here.

3a) In the simplest case, where the filler/filler interactions predominate, one can use along with Eqns.1-4, the multi-mode viscoelastic constitutive equations (Ces) for polymeric matrix. In our simplified case, these are the sum of linear Maxwell type modes with the relaxation spectrum $\{\hat{\theta}_k, \hat{G}_k\}$. Since the matrix mode is treated as a suspension of inactive particles in a polymer melt (or elastomer), there is the scaling relation [2]

$$\{\hat{\theta}_k, \hat{G}_k\} = \{\theta_k, G_k \chi\}, \quad \chi = \chi(\varphi, d) \tag{6}$$

between the matrix's viscoelastic spectrum and that for the pure polymer, $\{\theta_k, G_k\}$. The SBR elastomer filled with surface treated silica particles is an example of such a system.

3b) When the particle/polymer interactions predominate, more complicated particle/polymer secondary network and related flocs arise in the compound. At any instant, the polymer chains are classified here as either free or trapped to the particles; the total stress in the compound being the sum of the stresses in the two types of chains. During flow it is assumed that there is a dynamic balance between two competing structural processes - the debonding trapped chains from the particles, and the entrapment of free chains to the filler particles. The hydrodynamic effects of flow around the particles are lumped as in the case 3a), in the response of the free chains. The well-known examples of such compounds are the carbon black filled elastomers compounds [3]:

$$\sigma_f = G\gamma_f(\alpha + \xi)/(1+\alpha);\ \sigma_t = G\gamma_t(1-\xi)/(1+\alpha); \tag{7}$$

$$\sigma = \sigma_f + \sigma_t,\ \dot{\gamma}_f + \gamma_f/\theta = \dot{\gamma};\ \dot{\gamma}_t + f(\xi)\gamma_t/\theta = \dot{\gamma}. \tag{8}$$

Here σ_f (or σ_t) and γ_f (or γ_t) are stresses and elastic strains for free (trapped) chains. Also, the kinetic equation 3 with $\theta_o = \theta$ was assumed to be valid for every relaxation mode, with parameter γ_* being mode independent. The total stress is then represented as the sum of stresses over all the relaxation modes. Comparisons between calculations based on a completely nonlinear formulation and some data for uncured rubber compounds have been made [3].

Qualitative Predictions

We now illustrate the basic predictions of the approach on the simple example of the Eqns.1-3 with the use of Eqn.5, when the matrix sub-stress is negligible, i.e. when $\sigma \approx G_p\gamma_p$.

1. *Steady shearing*. Here $\dot{\gamma} = const$ and the solution of Eqns.2, 3, 5 can be found as follows:

$$\xi = \frac{z}{1+z},\ \hat{\sigma} = \frac{z(1+z)}{f_o(1+z)+kz}\exp\left(-\beta\frac{z}{1+z}\right),\ \ z = \frac{\dot{\gamma}\theta}{\gamma_*}. \tag{9}$$

Here $\hat{\sigma} = \sigma/(G_p\gamma_*)$. Eqn.9 displays a non-dimensional flow curve $\hat{\sigma}(z)$. Its non-Newtonian character is due to the floc rupture. Consider now two cases have been discussed above.

(i) When $f_o = 1$, $k = 0$, the asymptotic behavior of the flow curve at both the small and large shear rates is Newtonian. The maximum viscosity, $\eta_o = G_p\theta$, is reached at $\dot{\gamma} \to 0$, and minimum viscosity, $\eta_\infty = \eta_o e^{-\beta}$, at $\dot{\gamma} \to \infty$. If the numerical parameter β is large enough $(\beta > 2)$, the flow curve is non-monotonous, which predicts the occurrence of the stress localization. This behavior is similar to that known for worm-like micelles [5].
When $f_o = 0,\ k = 1,$ the asymptotic behavior of the flow curve at $\dot{\gamma} \to 0$ is *viscoplastic*, i.e: $\hat{\sigma} = 1 + (1-\beta)z + O(z^2)$, with the yield value, $Y = G_p\gamma_*$, and the Bingham plastic viscosity, $\eta_p = (1-\beta)G_p\theta$. When $\dot{\gamma} \to \infty$, the asymptotic behavior of flow curve is Newtonian with the limit viscosity, $\eta_\infty = G_p\theta e^{-\beta}$. When $\beta > 1,$ this model also predicts the occurrence of the stress localization near the yield stress. This behavior is similar to that known for dispersed systems [1]. Thus this analysis shows that the model predicts the occurrence of yield value without any yield criteria. The mechanism for this has been demonstrated in [1,2,4] and will be discussed in detail in Subsection 4 below.

2. *Start up shearing from the rest state*. Here the shear rate $\dot{\gamma}$ is constant at $t > 0$. A cumbersome transient solution for $\sigma(t)$ displays the well-known stress overshoot whose intensity increases and time location decreases with $\dot{\gamma}$ increasing. This demonstrates the effect *thixotropy*.

3. *Stress relaxation*. We assume that an active loading was applied at $t < 0$ and at the instant $t = 0$ the stress and de-bonding factor reached the values σ_o and ξ_o. For the more interesting case (ii), the model prediction of relaxation is:

$$\xi = \xi_o e^{-t/\theta}; \quad \sigma = \sigma_o \exp\left\{\frac{-\theta_o}{\beta\theta}[\exp(-\beta\xi_o e^{-t/\theta_o}) - e^{-\beta\xi_o}]\right\}. \tag{10}$$

Eqn.10 demonstrates the effect of incomplete relaxation (or "frozen memory") at $t \to \infty$. It is seen that the residual stress σ_∞ decreases with the increase in ξ_o. It happens since the rate of relaxation is higher when the flocs are more ruptured.

4. *Creep.* We consider here only interesting case (ii), when a constant stress σ_0 is applied at $t > 0$ to the elasto-viscoplatic body initially at rest. Eqns.2, 3, 5ii always have the *static solution*:

$$\dot{\gamma} = 0, \ \ \gamma = \gamma_p = \sigma_o / G_p, \ \xi(t) = 0. \tag{11}$$

It corresponds to the solid-like behavior. Another solution, describing the plastic behavior, may also exist. To find it, $\dot{\gamma}$ is expressed at $t > 0$ from Eqn.2 as: $\dot{\gamma} = \sigma_o e^{\beta\xi}\xi/(G_p\theta)$ and substituted into Eqn.3. Then the problem is reduced to the initial problem for the kinetic equation 3 rewritten in the form:

$$\theta_o\dot{\xi} = \xi(1-\xi)[e^{\beta\xi}\hat{\sigma} - 1/(1-\xi)], \ \xi_o \equiv \xi(0) = 1 - e^{-r\hat{\sigma}}. \tag{12}$$

Here $r = \theta/\theta_o < 1$, $\hat{\sigma} = \sigma_o / Y$, and $Y = G_p\gamma_*$ is the yield stress. Analysis of this problem reveals that depending on the value of parameter $\delta = e^{\beta\xi_o}\hat{\sigma}$, the following behavior of $\xi(t)$ happens at

$t \to \infty$. (i) If $\delta < 1$, $\xi(t) \to 0$, and (ii) if $\delta > 1$, the solution goes at $t \to \infty$ to a steady solution shown by Eqn.9. The case (i) is related to solid like behavior, and the case (ii), to the flow, and the transition between these is of a *bifurcational type*. In the realistic case $r << 1$, $\delta \approx \hat{\sigma}$. It means that the bifurcation happens when the stress in creep is closed to the yield value, i.e. $\sigma_o \approx Y$.

CONCLUSION

The approach presented in this paper, demonstrates many mutual features peculiar for such different systems as colloidal dispersions, filled polymers, worm-like micelles and metals. It was shown that in these systems, a simple and flexible kinetic model could capture common rheological effects, such as yielding, thixotropy, viscoelasticity, frozen memory, and stress localization. The key element in this model is the coupling between a specific kinetic equation, which describes the rupture/restoration of a "structure", and the equation of viscoelastic type for stress evolution. The remarkable feature of this approach is that it describes yielding as a bifurcation in the transition from solid-like behavior to flow. This gives this approach a computational advantage over those which employ an algebraic yield criterion, especially when solving complicated 3D problems.

REFERENCES

1. Coussot, P., Leonov, A.I. and Piau, J.-M. (1993) *J. Non-Newtonian Fluid. Mech*. 46,179.
2. Leonov, A.I. (1990) *J. Rheol*. 34**,** 1039.
3. Simhambhatla, M. and Leonov, A.I. (1995) *Rheol. Acta.* 34, 329.
4. Leonov, A.I. and Padovan, J. (1996) *Int. J. Engng Sci*. 34, 1033.
5. Berret, J.F., Porte, G.. and Decruppe J.P. (1997) *Phys. Rev. E.* 55, 1668.

ORAL REFERENCE: ICF100157OR

CONTINUUM-ATOMISTIC MODELING FOR CRACK INITIATION AND PROPAGATION IN POLYCRYSTALS

E. Iesulauro[1], K. Dodhia[1], T. Cretegny[2], C-S. Chen[1], C. Myers[3], and A. R. Ingraffea[1]

1 Department of Civil and Environmental Engineering, Cornell University, Ithaca, NY 14853 USA
2 Laboratory of Atomic and Solid State Physics, Cornell University, Ithaca, NY 14853 USA
3 Cornell Theory Center, Cornell University, Ithaca, NY 14853 USA

ABSTRACT

Current research efforts are developing simulation methods at the mesoscopic scale to study fatigue crack initiation and propagation in polycrystals. Geometric models of the microstructure are created using Voronoi tessellations. The grain material is modeled by statistically assigning lattice orientation and elastic or elastic-plastic material properties to each grain in a model. Grain boundaries then naturally arise in the model.

The focus is on the involvement of the grain boundaries in the fracture process and ways of characterizing their resistance to fracture based on atomic scale studies. The goal is to extract grain boundary properties (when possible as a function of their macroscopic parameters) out of atomistic simulations, then summarize and transfer this information across length scales. To model the behavior of the grain boundaries at the mesoscopic scale we consider a coupled, cohesive zone model, where the microscopic information is summarized in the form of traction-displacement relationships.

Finite element analyses are then conducted under monotonic and cyclic loading. Observations are made about where and when cracks initiate, their subsequent trajectory, and the sensitivity of the simulation to the grain and grain boundary constitutive models and their distributions in the polycrystal.

KEYWORDS

Fatigue Crack Initiation, Polycrystal, Multi-scale, simulation, cohesive model

INTRODUCTION

Assuming homogeneity at the macroscopic scale in a metallic component leaves out the details from smaller length-scales that precipitate fatigue crack initiation, a major concern in many applications. For these concerns the details at the polycrystal scale are the features that determine when and where fatigue cracks will initiate and which ones will grow to macro-cracks. As the macroscopic response results from the polycrystal-scale features, properties of polycrystal features such as grain boundaries are in turn dependant on the atomic-scale.

The work presented here investigates statistically modeling the polycrystal geometry and properties in order to study influences on the initiation of fatigue cracks. Outlined in the following section are how the polycrystal geometry is modeled and how the individual grains are constitutively modeled. Then, the coupled, cohesive zone constitutive model used for the grain boundaries is discussed. Finally, an example of a fatigue crack initiation simulation using FRANC2D/L is shown and the results and observations are discussed.

POLYCRYSTAL MODELING

Creating a polycrystal sample begins with defining the geometry of the grains. This is done using a Voronoi tessellation. Polygons are created from a random set of initiation points. Each polygon then represents a grain with an average size held to observed measures from electron back-scattering pattern scans (EBSP). Once the geometry is in place material properties are assigned. Four constitutive relationships for the grain material are currently being evaluated for their impact on the crack initiation process: elastic, isotropic; elastic, orthotropic; elastic-plastic, isotropic (von Mises); elastic-plastic, orthotropic (Hill). For the chosen material model each grain is assigned values of the appropriate parameters sampled from uniform distributions centered on the average macroscopic value. This allows each grain to be a separate realization of the material model.

COUPLED COHESIVE ZONE MODEL

The geometry created by the tessellation determines the locations of the grain boundaries while the material parameters introduce heterogeneity and possible anisotropy. Finally, a cohesive zone model (CZM) is used to describe the strength of the grain boundaries. The CZM is also used as a criterion for initiation of intergranular cracks. The GB's are allowed to decohere after reaching a critical combination of transmitted normal and shear stress, thus gradually initiating a crack. An advantage of using such a model is that initial cracks are not arbitrarily introduced at the beginning of a simulation. Instead cracks naturally occur due to the heterogeneous stress field throughout the sample caused by the geometry and property variations.

CZM's are traction-displacement relationships originally used to describe the damage that occurs in the plastic zone ahead of the crack [1]. In the present case the damage represented by the softening portion of the CZM is used to describe the decohesion of the GB's. The implementation being used in our simulation code, FRANC2D/L [2], is adapted from the coupled, cohesive zone model (CCZM) developed by Tvergaard and Hutchinson [3] where the normal and shear components of the traction and displacement are combined into single measures for each quantity, t and λ, respectively (Figure 1). A key characteristic of the relationship is the area under the curve, G_c, which represents the critical energy release rate.

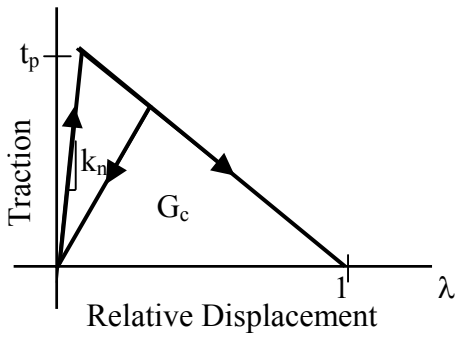

Figure 1: Coupled Cohesive Zone Model

The CCZM begins from a traction potential, Φ, (Eqn. 1) that is a function of the relative normal, δ_n, and tangential, δ_t, displacements between the faces of the GB. λ is a non-dimensional separation measure for the relative opening and sliding normalized to the relative critical displacement values, δ_n^c and δ_t^c, at which the separation is considered a true crack in pure Mode I and pure Mode II (Eqn. 2). When the value of λ reaches 1 this indicates the complete decohesion of the GB and the formation of a true crack. For a given relative displacement between two grains the combined traction, t, transmitted across the GB can be determined from the CCZM. The combined traction can then be decomposed into normal, T_n, and shear, T_t, components by differentiating Φ according to Eqns. 3 and 4, respectively. In the case in which the GB encounters unloading, the CCZM follows the path shown in Figure 1.

$$\Phi(\delta_n \delta_t) = \delta_n^c \int_\lambda t(\lambda')d\lambda' \tag{1}$$

$$\lambda = \left[\left(\frac{\delta_n}{\delta_n^c}\right)^2 + \left(\frac{\delta_t}{\delta_t^c}\right)^2\right]^{1/2} \tag{2}$$

$$T_n = \frac{\partial \Phi}{\partial \delta_n} = \frac{t(\lambda)}{\lambda}\frac{\delta_n}{\delta_n^c} \tag{3}$$

$$T_t = \frac{\partial \Phi}{\partial \delta_t} = \frac{t(\lambda)}{\lambda}\frac{\delta_n^c}{\delta_t^c}\frac{\delta_t}{\delta_t^c} \tag{4}$$

In our simulations the parameters describing the CCZM were determined to either be the same for all GB's in the sample, or to vary from GB to GB. For the orthotropic models, parameters were varied based on the misorientation angle, θ, across the GB shown in Eqn. 7 and Figure 2. For the isotropic grain material models, there is no physical misorientation across GB's. Therefore, the inclination angle, ψ, of the grain boundary with respect to the global X-axis (Figure 3) was chosen as an arbitrary measure with which to introduce variation in G_c. Assuming that G_c varies with the angle θ or ψ changes, the area under the CCZM varied according to Eqn. 5 or Eqn. 6, respectively, in which G_{avg} is the average value of the critical energy release rate and ΔG determines the range of values. The critical normal displacement, δ_n^c, is then held constant at 1μm so that the critical combined traction, t_p, for each GB could be determined.

$$G(\theta) = G_{avg} + \Delta G \cos(4\theta) \tag{5}$$

$$G(\psi) = G_{avg} + \Delta G \cos(4\psi) \tag{6}$$

$$\theta = \beta_1 - \beta_2 \tag{7}$$

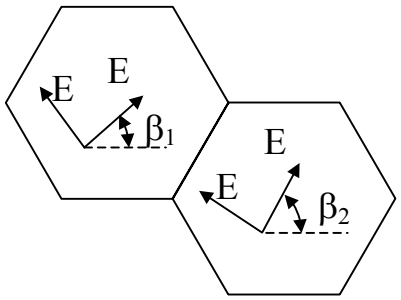

Figure 2: Misorientation angle, θ, calculated according to Eqn. 7 from the material orientation angles, β_i, of neighboring grains.

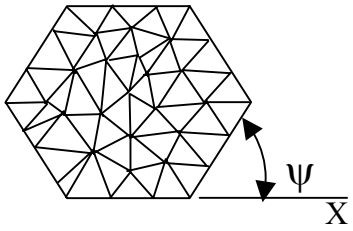

Figure 3: Grain boundary inclination angle measured with respect to the global X-axis.

The form of Eqns. 5 and 6 was chosen based on a Fourier expansion of spherical harmonics. In 3D any periodic function can be written using a Fourier expansion of spherical harmonics of which the present case is a 2D degenerative form. Holding the normal of each grain to be along the (100) direction forces cubic symmetry for a FCC crystal. This results in the cos 4θ(or ψ) form term seen in Eqns. 5 and 6.

In conjunction with this work are efforts to conduct atomistic and quasi-continuum simulations of the fracture of GB's and triple point junctions of grains. These results will be used to guide the determination of parameters of the CCZM as well as give insight into the shape of the CCZM curve and the form of variation as a function of misorientation between grains.

SIMULATION OF FATIGUE CRACK INITIATION

Simulations were run as part of a parametric study to observe the sensitivity of fatigue crack initiation due to the various parameters. Varied parameters included different realizations of grain geometry from the Voronoi tessellations, the four grain material models mentioned previously, different samplings from an orientation distribution function (ODF) for orientations of the orthotropic grains, variation in the range and mean values of the CCZM parameter ΔG, varying load conditions including monotonic and cyclic, and the presence of an initial stress field.

RESULTS

Results discussed here are for the grain geometry, boundary conditions and loading history shown in Figure 4. Individual results will be shown for the points indicated in Figure 4b. The grain material properties for the Hill material model and CCZM parameters are shown in Table 1. The parameters chosen result in the average peak combined strength of the GB's being equal to the average uniaxial yield stress of the grains. This will allow some of the GB's to reach their peak and begin softening, initiating fatigue cracks, before the grains begin to yield and absorb all of the damage to the polycrystal. The current implementation of the Hill yield criterion is limited to perfect plasticity.

As seen in Figure 4, the sample was loaded to 0.69% strain (98% of the macroscopic yield strain) and then unloaded. Figures 5a-c show the deformed mesh of the sample at 0.1%, 0.69%, and 0.2% strain corresponding to the points marked in the loading history (Figure 4b). The circled area in Figure 5b shows the opening of a grain boundary due to decohesion. Figures 5d-f show schematically the approximate corresponding location along the CCZM of the decohering GB's. Since λ has not reached a value of 1 this damaged GB has not yet completely fractured.

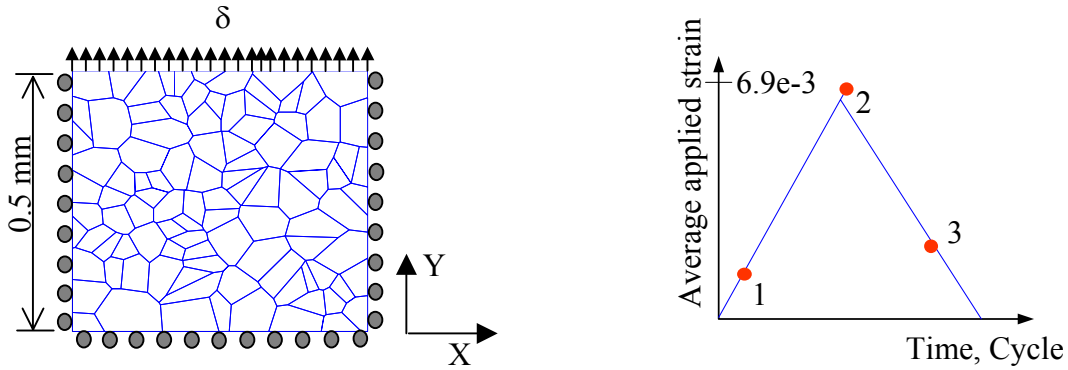

(a) (b)

Figure 4: (a) Boundary conditions and loading of polycrystal sample. (b) Loading history.

TABLE 1
GRAIN MATERIAL AND CCZM PARAMETERS

Grain Material		CCZM	
Type	**Elastic-Plastic, Orthotropic (Hill)**	**G_{avg}**	**250 Pa m**
E	**72 GPa**	**ΔG**	**100 Pa m**
σ_{yld1}	**505 MPa**	**Resulting t_{pavg}**	**500 MPa**
σ_{yld2}	**450 MPa**		
σ_{yld12}	**400 MPa**		

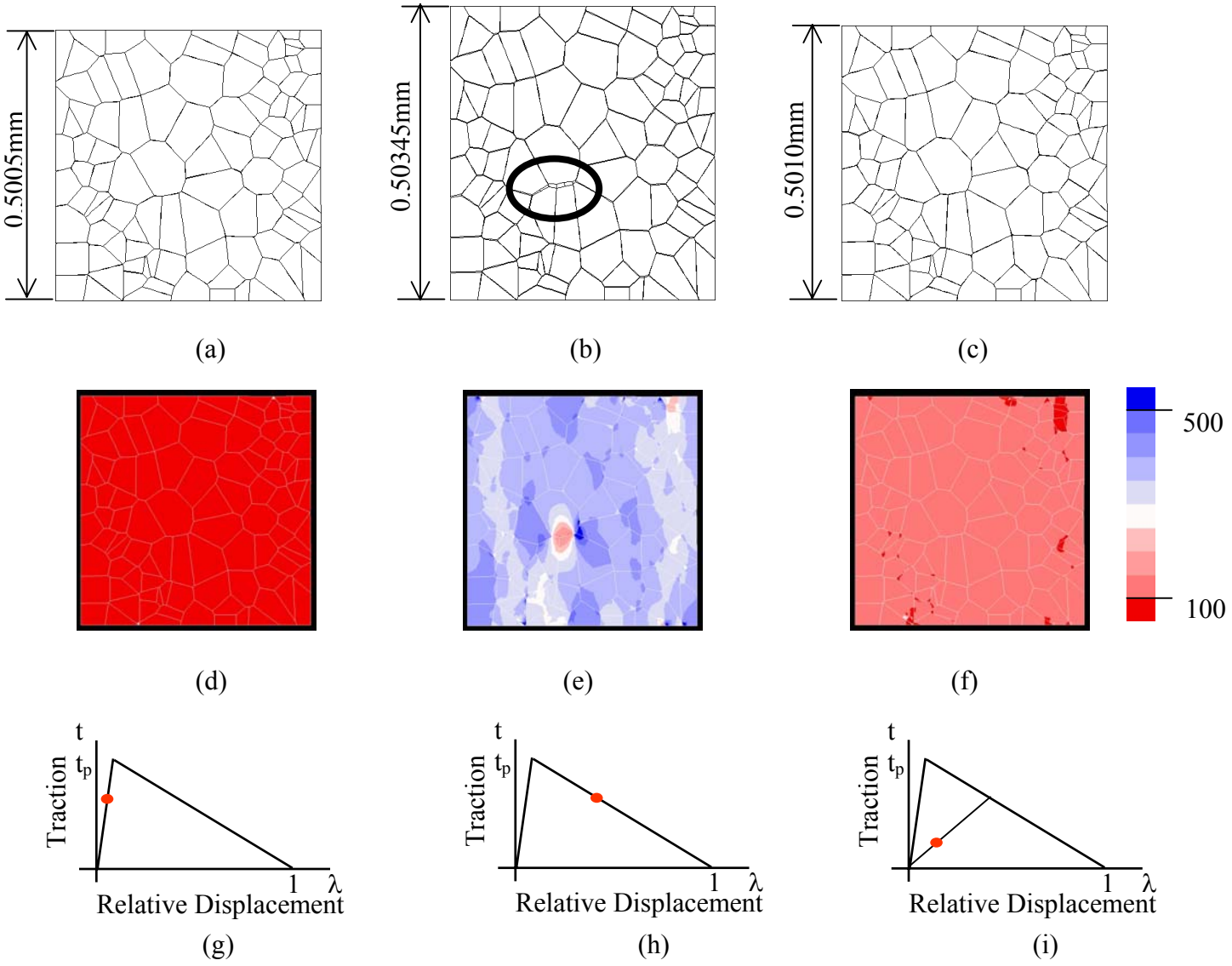

Figure 5: Deformed mesh at 2X magnification for (a) point 1 indicated in Figure 4. (b) point 2 in Figure 4. The circled grain boundaries have begun to decohere. (c) point 3 in Figure 4. (d) σ_{yy} contour plot corresponding to (a). (e) σ_{yy} contour plot corresponding to (b). (f) σ_{yy} contour plot corresponding to (c). (g) Schematic representation of the location on the CCZM of the opening GB at the first load point. (h) Schematic representation of the location on the CCZM of the opening GB at the first load point. (i) Schematic representation of the location on the CCZM of the opening GB at the first load point.

OBSERVATIONS AND CONCLUSIONS

Using a Voronoi tessellation, samples of polycrystalline geometry were created. The grains where statistically assigned material parameters from one of four material models. The GB's where assigned a statistically varying CCZM. Completed polycrystal samples were loaded monotonically and cyclically to observe damage and crack initiation.

In an example shown herein, damage occurs to the sample in the form of GB decohesion before any grains reach yield from macroscopic loading. Local yielding then follows due to stress re-distribution caused by the decohesion process. The use of the CCZM to describe the GB's allows for this type of damage to occur.

Other simulations to be reported include monotonically loaded samples strained to 3% or to failure due to the propagation of a through-crack. In samples using elastic material models damage began once the t_p was reached and progressed to failure as true cracks were created and propagated through the sample. Samples using elastic-plastic material models saw damage in the form of GB decohesion and plastic yielding of the grains. From these simulations the influence of t_p relative to the yield stress of the grains was observed. For the samples using the elastic-plastic, isotropic (von Mises) material model, which allowed for hardening within the grains, a shift from GB damage to grain hardening was observed as t_p was raised to from 0.8 to 1.5 times the average yield stress.

The current ongoing parametric study will yield additional sensitivities to modeling choices and parameter ranges. The collected observation will serve to reduce the parameter space when the current capabilities are transferred to a 3-D framework. Also, the accuracy of parameters for the CCZM, such as t_p or δ^c, needed will be determined though the observed sensitivity. This will guide future atomistic simulations of GB's.

ACKNOWLEDGEMENTS

Funding for this research is being provided through Grant F49620-98-1-0401 from the Air Force Office of Scientific Research and Grant 9873214 from the NSF.

REFERENCES

1. Dugdale, D. S. (1960). *Journal of Mech. Phys. Solids*. 8,100.
2. Bittencourt, T. N., Wawrzynek, P. A., and Ingraffea, A. R. (1996) *Engineering Fracture Mechanics.* 55, 321.
3. Tvergaard, V. and Hutchinson, J. W. (1992). *Journal Mech Phys Solids*. 40, 1377.

ICF100485PR

CORROSION CRACKING OF STAINLESS STEEL UNDER STRESS: THE PROBLEM AND ITS SOLUTION

Ata A. Miatiev and Galina V. Khil'chenko

Pro Scientific & Technical Service, Prague, Czech Republic

ABSTRACT

This study addresses the reasons behind stress corrosion cracking (SCC) of stainless steel and the lines of attack on this problem. The effects of different deposited oxide films on SCC were studied. These film coatings permitted the modeling of mechanical and chemical properties of the steel surface and surface layer. The understanding of the reasons behind SCC made it possible to suggest the ways of solving this problem. In particular, these films can increase the time-to-failure of steel under creep from 1 to 4575 h, while the average strain increases to 14–16%.

KEYWORDS

Stainless steel, deposited oxide films, chloride ion, corrosion cracking.

INTRODUCTION

Corrosion cracking of alloys depends on the level of mechanical stress [1]. In particular, corrosion tests of the SUS304 steel in a boiling (143°C) 42% $MgCl_2$ solution showed that (i) cracking did not take place at stresses below 110 MPa ($\sigma_{0.2}$= 244 MPa); (ii) at stresses 132–150 MPa, a crack issued from a corrosion center and propagated across a grain; (iii) at a stress of 180 MPa, cracking was of mixed character (intra- and intergranular); (iv) at stresses near the yield point, cracks formed at the junctions of three grains and rapidly propagated into the bulk along the grain boundaries. In the last case, the result was fatal, and brittle fracture proceeded rapidly, at virtually zero strains.

An abrupt increase in dislocation density in the surface layer accompanies the corrosion cracking of any alloy [2]. Brittle cracks propagate across dislocation pileups and twins and along grain boundaries loosened up (expanded) by dislocations.

As has been shown in [3], deposited oxide films can be used to control the dislocation density in the surface layer and the magnitude and sign of stress and to insulate the surface from an environment. In addition, film coatings permit the modeling of the stress–strain state of surface layers, with allowance for environmental effects, in SCC under virtually any conditions. This makes it possible to study all the processes that cause SCC and the reasons behind this phenomenon.

RESULTS

The tests were carried out with tubular pieces of 0.02C-16Cr-15Ni stainless steel under stress and creep in water with a chloride ion concentration of 100 mg /l and pH 3 at 340°C. The stress–strain state of the stainless steel surface was modified by deposited oxide films. This state was controlled by the following factors: (i) the sign of surface stresses (extension or compression); (ii) the intensity of surface stresses and relaxation effect; (iii) the surface energy barrier to dislocation egress; (iv) the lack of the surface energy barrier to dislocation egress; (v) insulation of the surface from environment. The testing cycle consisted of four stages. The first stage involved mechanical loading below the yield point; the second, third, and fourth stages involved creep at a rate of $1.06\ 10^{-4}$, $4.2\ 10^{-3}$, and $5.4\ 10^{-3}$ % h^{-1}, respectively. These test conditions may be thought of as of the severest ones. They were used to reliably assess the efficiency of films for solving the problem of SCC and to study the influence of these films on the process of SCC itself.

The time to failure under given conditions depends on the composition of a deposited film and its thickness [4]. It is obvious that these two factors do not give a comprehensive idea of the mechanism and protective action of deposited films. Therefore, the following parameters were considered to study the effects of deposited films:

1. ***Oxide film material.*** Both amorphous and crystalline metal oxide films (Zr, Y, Zr–Y, Zr–Ni–Fe, Sn, Ce, Sc, Fe, Ni, U), as well as layered oxide compositions, were used. Employing different film materials made it possible to modify the properties of the films and the properties of steel–film systems and resulted in various degrees of insulation of the specimen surface against ambient chloride ions.
2. ***Film thickness.*** The thickness of films was varied from 0.01 to 6 μm.
3. ***The intensity and sign of internal stresses in as-deposited films.*** As has been shown in [3], virtually all deposited films are characterized by considerable internal stresses. Film properties, including the intensity and sign of internal stresses, are able to considerably change the kinetics of deformation, hardening, and failure of substrate materials.
4. ***Relaxation effects in films***. This parameter determines the sign and intensity of the mechanical stress induced by a film in the surface layer of a substrate, both before and in the course of corrosion treatment.
5. ***Film deformability and imperfectness.*** Defects were monitored with a scanning electron microscope both in the as-deposited films and at the moment of test termination.

The time to failure and average strain of specimens were used as criteria for their stability toward corrosion cracking. In addition, the surfaces and fractures of selected specimens were examined at different stages of test. The test results are listed in Table 1.

TABLE 1

FORMAL RESULTS OF SCC TESTS OF STEEL SPECIMENS

No.	Specimen	Time to failure, h	Average strain, %
1	Uncoated steel	1 – 3	3.6 – 3.7
2	With an urania film	< 1	1.0 – 3.0
3	With an iron oxide film	1 – 1020	1.2 – 5.6
4	With a nickel oxide film	1 – 1980	2.2 – 7.6
5	With a zirconia film	200 – 1820	3.9 – 7.4
6	With a ceria film	500 – 1920	5.7 – 7.7
7	With a tin oxide film	1660 – 1880	7.3 – 9.0
8	With a zirconia–yttria film	340 – 1820	4.4 – 6.7
9	With a zirconia–iron oxide–nickel oxide film	1820 – 1980	6.4 – 13.1
10	With layered films	From 920 to 4575 without failure	5.0 – 14.0
11	With an yttria film	From 2140 to 4575 without failure	8.2 – 16.8
12	With a scandia film	From 1660 to 3600	6.3 – 12.6

Noteworthy is a large scatter of time-to-failure and average-strain values for specimens of the same set. However, there is no conflict here, since the above characteristics depend on the properties of the film and steel–film system and on the varied protective function of the film against a corrosive environment. Comprehensively studying the film-coated specimens of the same set have shown that both time-to-failure and ultimate strain correlate well with several factors that determine the process. The influence of these factors was studied for each specimen set.

The effects of the sign of mechanical stresses induced by a deposited film in the surface layer of steel. This influence follows the rule: tensile stresses provoke SCC, and compressive stresses inhibit SCC. In particular, urania films (set 2) (over the entire range of varying other parameters) and iron and nickel oxide films (sets 3 and 4, respectively) (in a portion of the range) created tensile stresses in steel. This resulted in a decrease in time-to-failure and ultimate strain, against uncoated steel. The remaining films (sets 5 and 6) created compressive stresses. This led to an increase in time-to-failure and ultimate stress, against uncoated steel.

The effect of the intensity of stresses induced by a film. The effect of tensile stress is quite definite: the higher the stress, the stronger the corrosion cracking caused by a film. The effect of compressive stress depends on stress intensity more complexly. With an increase in compressive stress, the resistance to corrosion increases, goes through a maximum, and then decreases. Figure 1 shows the plot of time-to-failure of coated specimens versus stress created by different films.

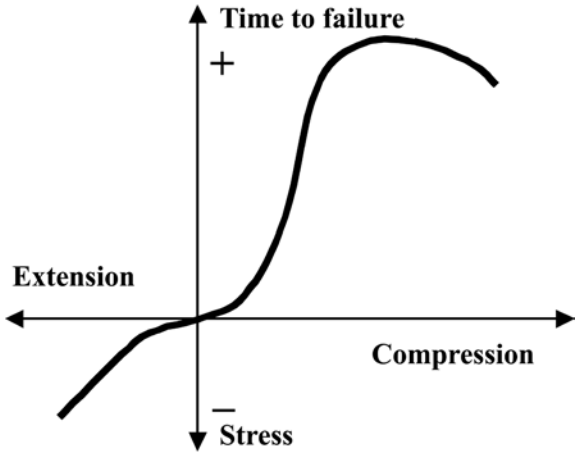

Fig. 1: Qualitative dependence of time-to-failure upon SCC on the magnitude of stresses created in the steel surface layer by a deposited film. Zero at the time coordinate axis corresponds to the time-to-failure of an uncoated steel specimen

We assume the following reason behind the effect of surface stresses on SCC: if a film, along with the external mechanical load, promotes the accumulation of deformation defects (for example, dislocations) in the surface layer of a steel specimen, this provokes brittle crack nucleation. In this case, the time-to-failure and ultimate-strain values decrease. Critical hardening of the steel surface layer can be realized even prior to corrosion tests (in the course of oxide film deposition). This is the case with a set of urania-coated specimens. If a film, due to compressive stresses, retards accumulation of deformation defects in the steel surface layer, a brittle crack forms at a later time, and the ultimate strain increases. However, given that a film creates large compressive stresses in the steel surface layer, the latter can be deformation-hardened by the film itself. Under external mechanical load and environment action, such a hardened layer can also be prone to brittle crack formation. However, the time-to-failure and ultimate strain values undoubtedly exceed those observed for tensile stresses.

The effect of the film thickness. It is quite reasonable to assume that an increase in the thickness of a deposited film should result in the buildup of its protective effect, for example, under the conditions of corrosion cracking tests. This general tendency was observed for some sets of specimens, but not for all of them. For specimens of the same set, the time-to-failure upon cracking is dominated by internal stresses in a film, which induce corresponding stresses in the steel surface layer, rather than by film thickness. This correlation is exemplified by an iron oxide film in Fig. 2a and by a zirconia film in Fig. 2b.

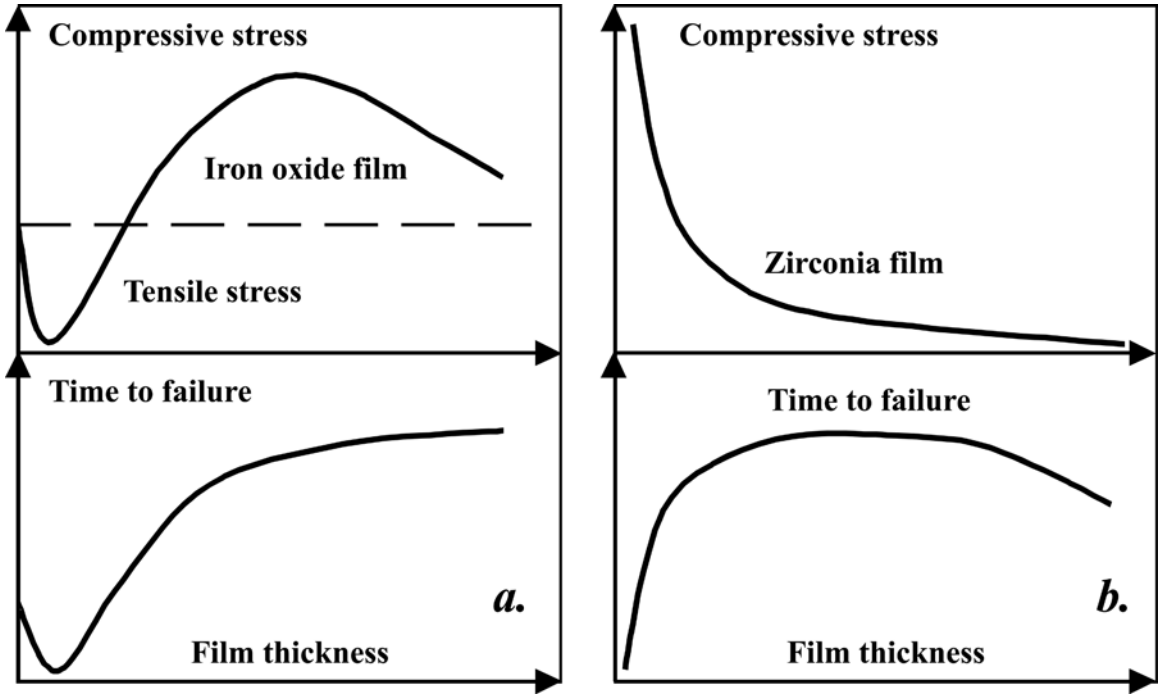

Fig. 2a: Correlation between internal stress in an iron oxide film and time-to-failure of film-coated steel specimens, depending on the thickness of the deposited film
Fig. 2b: Correlation between internal stress in a zirconia film and time-to-failure of film-coated steel specimens, depending on the thickness of the deposited film

Figure 2a shows that tensile stresses in iron oxide films up to 1 μm thick reduce the time to failure of the substrate. For compressive stresses, the time to failure abruptly increases for the film thickness ranging from 1 to 2 μm, and a further increase in film thickness has virtually no effect on the time to failure of the substrate.

Figure 2b shows that zirconia films with maximal compressive stresses considerably (hundredfold) increase the time-to-failure of film-coated steel specimens compared to the uncoated one. However, with an increase in film thickness and the corresponding decrease in internal stress, the time-to-failure increases still further, passes through a maximum, and then abruptly decreases.

Influence of relaxation in deposited films. Deposited films are characterized by structural relaxation [3]. Relaxation is a structural reconstruction, which changes stresses, continuity (imperfection), and many other film properties. In addition, relaxation effects in deposited films can considerably change the stress–strain state of the surface layer of substrates, their mechanical properties, and even the character of failure [3]. For the SCC problem under given test conditions, thermal, deformation, and adsorption relaxations are of crucial importance. Generally, relaxation can result in the decrease in internal stresses in films and in the enhancement of their influence on the steel surface layer; also, relaxation can lead to the crystallization of some films and to the formation of microcrack defects in these films. The most injurious effect is typical of adsorption relaxation. Adsorption relaxation, in the form of implantation of chloride ions in the film structure, usually results in additional tensile stresses in the film and, correspondingly, in the steel surface layer. This effect is most pronounced in iron, nickel, and uranium oxide films. Zirconia, tin oxide, and ceria films, as well as mixed Zr–Y and Zr–Fe–Ni oxide films, respond to the implantation of chloride ions to a lesser extent: tensile stresses in films decrease. For yttria and scandia films, adsorption relaxation does not manifest itself, at least, over a period of 1500 h.

Film deformability and imperfection. As shown by tests, all as-deposited films had no defects. In tests, crystalline films strained 1–1.5% cracked. In addition, crystalline films create a high barrier to dislocations, thus resulting in their concentration in the steel surface layer. Cracking these films promotes steel failure, regardless of the other properties of the surface and films. Therefore, crystalline films were not used in further tests.

In amorphous films, microcrack defects were observed in specimens coated by Zr, Zr–Y, Zr-Fe-Y, Ce, and Sn oxide films at an average strain of more than 5%. Noteworthy is that microcracks are uncommon in urania and nickel and iron oxide films, although the specimens coated by these films fractured rapidly at a

strain of less than 2.5%. Yttria and scandia films exhibit the highest deformability without defect formation. Examining the surface under the electron microscope indicates that these films are capable of deforming without failure up to strains of 8–12%. With an increase in test duration and deformation, these films crystallize and crack; however, hundreds of hours can elapse before failure.

Figure 3 shows a representative fracture. As a rule, the fracture section contains the region of brittle failure, in which cracks propagate along grain boundaries; the region of brittle–ductile failure, in which cracks propagate along the directions of stress localization; and the region of ductile failure, typical of ductile steel.

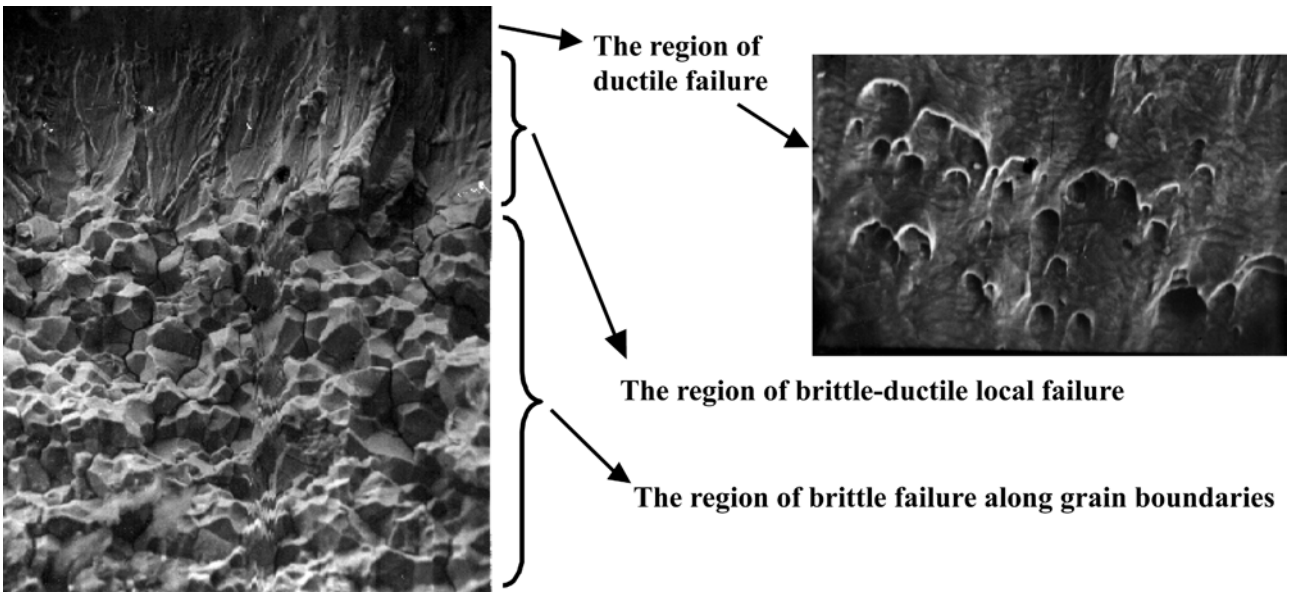

Fig. 3: Representative fracture of broken specimens

Reasons behind brittle failure upon SCC. Our findings and results reported in [3] allow us to argue that brittle failure is a result of the abnormal deformability of the surface layer, which accumulated deformation defects under an external mechanical load considerably lower than the yield strength of the bulk. The accumulated defects are localized in planes, and localization directions depend on the intensity of external mechanical stresses. This factor distinguishes intergranular brittle failure from intragranular one. The phase film that forms in water stimulates this process, since its formation is accompanied by an increase in volume, which results in additional tensile stresses in the surface layer. Chloride ions, being built into the structure of the phase film, induce even greater tensile stresses in the surface layer. The phase film and hardened surface layer represent an efficient barrier that prevents a "soft" drop of internal stresses and mechanical energy dissipation. Therefore, crack nucleation across dislocation pileups requires minimal energy consumptions. Brittle crack nucleation is a process of separation of a grain along the plane of dislocation pileups, or a process of separation of grains from one another along the grain boundaries. Embrittlement can propagate inward and can result in local deformation at stress concentrators upon stability loss of an entire specimen.

Ways of preventing SCC of steels.

To efficiently guard against SCC, the following measures are recommended:

1. To create internal compressive stresses, in the surface layer, which persist for a long time under material extension conditions;
2. To create conditions preventing accumulation of deformation defects in the surface layer, for example, by virtue of the dislocation and vacancy pump effect revealed and described in [3];
3. To insulate the surface against injurious environmental effects, in particular, against chloride ions.

Deposited oxide films can meet the above requirements. These films should have a complex of appropriate properties and characteristics, the most important being an amorphous layered structure, chemical stability in chloride-containing water, internal compressive stresses whose relaxation results in compression, and high adhesion and deformability.

References

1. Yagasaki, T., Kimura, Y., and Kunio, T., (1984) Dependence of Initial Stress Corrosion Damage in Austenitic Stainless Steel on Stress Level, *J. Soc. Mater. Sci. Jpn*., vol. 33, no. 373, pp. 1292–1297.
2. Levchenko, V.A. and Kuzyukov, (1986) The Effect of Substructure on Corrosion Crack Nucleation and Propagation in Austenitic Steel, *Fiz. Met. Metalloved.,* vol. 62, no. 4, pp. 829–832.
3. Miatiev, A.A. (2000) NEW ADVANCES IN SURFACE PHYSICS, CHEMISTRY, AND MECHANICS: MATERIALS WITH DEPOSITED OXIDE FILMS, Findings, Effects, and Applications. Izd. Mosk. Gos. Univ. Pechati, Moscow.
4. Miatiev, A.A., Khokhunov, A.N., Kmyazev, A.V., and Klimov, Yu.N., (1993) A Study of Protection of 02X16N15M3B Steel from Chloride Corrosion Cracking by Deposited Oxide Films, *Vopr. At. Nauki Tekh., Ser.: Materialoved. Novye Mater*., no. 2 (49), pp. 3–6.

CORROSION FATIGUE BEHAVIOR OF SHIP HULL STRUCTURAL STEELS

R. Ebara

Department of Advanced Materials Science, Kagawa University
2217-20, Hayashi-cho, Takamatsu, 761-0396, Japan

ABSTRACT

This paper seeks to describe on corrosion fatigue behavior of ship hull structural steels mainly based upon the author's recent experimental results. First it is described on general view of corrosion fatigue strength and corrosion fatigue crack propagation behavior of high strength steels. Then it is presented on corrosion fatigue strength of ship hull structural steel in ballast tank environment. It is demonstrated that tar epoxy resin coating effect on corrosion fatigue strength of KA32(TMCP) steel is observed in lower nominal stress range. Corrosion fatigue crack propagation behavior of ship hull structural steels in cargo oil environment is also presented. Fatigue crack propagation rate for KA36(TMCP) and KAS steel is accelerated in the region where ΔK is above about 16MPa $m^{1/2}$ in the sour crude oil containing 400ppm H_2S. A couple of future problems on corrosion fatigue research of ship hull structural steels are also touched in brief.

KEYWORDS

Corrosion fatigue strength, Corrosion fatigue crack propagation behavior, Ship hull structural steel, Ballast tank environment, Tar epoxy resin coating, Cargo oil environment, Hydrogen sulfide, Brittle striation

INTRODUCTION

Recently much attention has been focussed upon the improvement of corrosion fatigue strength and the evaluation of corrosion fatigue life for ship hull structural steels under ballast tank and cargo oil tank environment. The advantages such as lighter structures, increasing design stress and saving welding time were brought by use of higher strength steels for ship hull structures. However, the structure became more susceptible to corrosion fatigue. To evaluate ballast tank life evaluation of corrosion fatigue strength for ballast tank members is necessary under sea water environment with high temperature and high humidity. To evaluate corrosion fatigue life of cargo oil tank members it is necessary to understand corrosion fatigue crack propagation behavior of ship hull structural steels under cargo oil environment containing hydrogen sulfide.
In this paper it is briefly summarized on corrosion fatigue behavior of ship hull structural steels under sea water and sour crude oil environment mainly based upon the author's recent experimental results. It is demonstrated that corrosion fatigue strength of KA32 (TMCP) steel can be improved by tar epoxy resin coating. It is also demonstrated that an acceleration of corrosion fatigue crack propagation rate for KA36(TMCP) and KAS steel is observed in the higher stress intensity factor range under sour crude oil environment.

CORROSION FATIGUE STRENGTH OF HIGH STRENGTH STEELS

Fig.1 shows the conventional S-N diagrams for four kinds of high strength steels obtained by ISIJ round robin test [1]. Based upon the obtained more than one thousand S-N diagrams including those shown in

Fig.1, it was concluded that corrosion fatigue strength of tested high strength steels were almost same in the number of cycles of $2x10^4$ to 10^7. Thus it has been experimentally confirmed that corrosion fatigue strength of high strength steel is almost same as that of mild steel［2,3］. This means that an improvement of corrosion fatigue strength cannot be expected by use of high strength steels for ship hull structures. In Fig.1 it can be also observed that the S-N curves are inclined to drop to the offshore structures' design curves such as AWS-XX Improved and UK DOE Basic Sea Water design curve and are anticipated to drop into the lower than these allowable design curves in the long term S-N curves. Therefore, countermeasures such as cathodic protection and coating are absolutely necessary for safety use of high strength steels for ship hull structures.

In fact it was experimentally confirmed that the S-N curves for cathodically protected T type welded specimens for HT80 dropped in the upper side of the AWS-X and DOE design curve［4］. To keep the marine structures' maintenance free for long term services the complete cathodic protection system must be developed. The system should be taken stress gradient on the corrosion fatigue strength of the large scaled members such as ship hull structures and the connected tubular joints for offshore structures into consideration.

The most of the fatigue design rules for offshore structures are based upon the S-N diagrams. However, it is anticipated that brittle failure might occur from the corrosion fatigue crack initiated from the small defects of the welded joints in the low temperature sea water. Therefore many corrosion fatigue crack propagation tests for high strength steels have been conducted in sea water environment. Crack propagation tests of HT80 base metal and welded joints were conducted in low temperature sea water. Crack propagation rate of HT80 base metal in 4^0C synthetic sea water was almost four times faster than that in air at room temperature. It was also clarified that corrosion fatigue crack propagation rate in the heat affected zone was slower than that of the base metal. The da/dN of the heat affected zone might be enhanced due to hydrogen, however the higher hardness and corrosion resistant martensitic structure gave a slower da/dN in heat affected zone［5］. More than six thousand da/dN～⊿K curves were obtained in an artificial sea water in the aforementioned ISIJ round robin test. The acceleration of the da/dN was observed in sea water environment［6］.

Fig.1 S-N curves of four kind of high strength steels in synthetic sea water［Toyama et al.[1.]］.

To evaluate corrosion fatigue strength and corrosion fatigue crack propagation rate of high strength steels we have to consider about corrosion fatigue variables such as environmental, mechanical and metallurgical variables [7]. The principal environmental variables are bulk solution chemistries, temperature, dissolved oxygen content and wet-dry alternation. Further studies are required for wet-dry alternation on corrosion fatigue behavior of ship hull structural steels. Among the mechanical variables mean stress, frequency, stress mode, stress wave form and stress concentration factor are important to evaluate. The extensive studies on effect of stress mode, stress history and random loading on corrosion fatigue strength of high strength steels provide the useful data for ship hull structural design. As aforementioned any improvement of corrosion fatigue strength can be expected for high strength steels in sea water environment, the development of corrosion resistant high strength steels with higher corrosion fatigue strength is strongly desired. Whereas it has been indicated that the characteristics of weld metal depend not only metallurgical factor but also is strongly influenced by welding parameters［8］. Among the metallurgical variables the subjects of plate thickness and residual stress should be particularly investigated.

CORROSION FATIGUE BEHAVIOR OF TAR EPOXY RESIN COATED SHIP HULL STRUCTURAL STEEL

Fig.2 shows the effect of tar epoxy resin coating on corrosion fatigue strength of the ship hull structural steel KA32(TMCP) plate notched specimen by push-pull fatigue testing[9]. The coating thickness is 200 μ m and stress concentration factor of the plate specimen is 2.0. It is apparent that the effect of tar epoxy resin coating is observed in lower nominal stress range. An increase of corrosion fatigue life was 2.8 times higher than that of base metal specimen at nominal stress range of 199.8MPa. The lower the nominal stress range the coating effect increased. The influence of coating thickness with 50 to 300 μ m on corrosion fatigue life was also investigated. The thicker the coating thickness the longer the fatigue life was. Impedance/time curves were taken for tar epoxy resin coated specimen with 50 to 300 μ m thickness. Impedance of tar epoxy resin

Fig.2 S-N_f curve for tar epoxy resin coated specimen in artificial sea water［Ebara et al.[9]］.

coated with 50 and 100 μ m dropped tremendously after few days exposure into an artificial sea water. While the impedance of 200 μ m and 300 μ m tar epoxy resin coated specimen did not drop after exposure for 6000hrs. The impedance dropped slightly after exposure for 10^4 hrs. However the dropping rate was not prominent. From these results it can be mentioned that tar epoxy resin deteriorates due to the change of water absorption after long term exposure in sea water. The deterioration of the tar epoxy resin coating at the notched area of the coated specimen was influenced by the repeated stress. The decrease of the impedance at the notched area was bigger than that at the plane area［Fig.3］. These facts reached to the following mechanism of the deterioration of the tar epoxy resin coating. In higher nominal stress range corrosion fatigue crack initiate earlier at the notched area where stress concentrate and an improvement of corrosion fatigue strength cannot be expected when an interception effect against sea water disappear. The lower the nominal stress range an improvement of corrosion fatigue strength becomes to be observed by an interception effect due to the difficulty of crack initiation on the coating. An improving effect becomes to be smaller when water absorption rate increases and the coatings deteriorates as times go by. Since the deterioration of the tar epoxy resin coating is governed by the thickness of the coating, it can be mentioned that effective coating thickness to improve corrosion fatigue strength of the ship hull structures is at least 200 μ m. Considering the deterioration of the tar epoxy resin coating at the notched area, it can be easily reached to conclusion that the toe of the welded joints of ship hull structures is easily deteriorates due to the breakage and deterioration of the tar epoxy resin coating. To evaluate corrosion fatigue strength of the ballast tank members further studies on effect of sea water temperature on corrosion fatigue life of tar epoxy resin coated ship hull structural steels is necessary.

Fig.3 Impedance/Number of cycles curve for tar epoxy resin coated fatigue test specimen with 50 μ m thickness coating［Ebara et al.[9]］

CORROSION FATIGUE CRACK PROPAGATION BEHAVIOR OF SHIP HULL STRUCTURAL STEELS IN CARGO OIL TANK ENVIRONMENT

Corrosion fatigue crack propagation tests for the ship hull structural steels and their welded joints were conducted in sour crude oil containing 400 ppm H_2S. The crack propagation rate of the ship hull structural steels such as KA32(TMCP) and KAS steel in sour crude oil containing 400 ppm H_2S was remarkably accelerated in the higher ΔK region [Fig.4][11]. This acceleration was also observed on X65 line pipe steel in sour crude oil containing 1 to 4700ppm H_2S [12]. In the accelerated crack propagation area it was also found that the crack propagated predominantly on the cleavage fracture surface in association with brittle striation in the sour crude oil environment. The striation spacing per cycle, S obtained from the measured striation spacing ΔS versus ΔK curve was well coincident with the da/dN $\sim \Delta K$ curve in the accelerated crack propagation area. It can be assumed that hydrogen molecule (H_2) produced through the reaction of H_2S and H_2O in sour crude oil with ship hull structural steel turns into atomic hydrogen (H) ,which enters the plastic zone of the fatigue crack tip and accumulates there in large quantities causing the plastic zone to turn into the hydrogen embrittlement zone and thus resulting in acceleration of crack propagation rate as shown in Fig.5.Thus it can be concluded that the environmental enhancement of the fatigue crack propagation rate in sour crude oil is dependent on hydrogen evolved by reaction between H_2S and H_2O in the sour crude oil with structural steels. The crack propagation tests were also conducted for welded joints. The da/dN for weld metal (WM),heat affected zone (HAZ) and base metal (BM) in the sour crude oil were much faster than those in air[13]. The three stage crack propagation mechanism can be considered. In stage1 the fatigue crack opening is extremely small due to the compressive residual stress present in WM and HAZ. The corrosion products prevents of sour crude oil into the crack tip.

Fig.5 Schematic illustrations of corrosion fatigue mechanism in sour crude oil environment [Ebara et al.[11.]]

Fig.4 Fatigue crack propagation rate in sour crude oil (400 ppm H_2S) and in air [Ebara et al. [11.]]

Consequently, H_2S and H_2O are prevented from reaching crack tip and da/dN decelerated. In stage 2 the crack opening increases with associating fatigue crack propagation, causing the corrosion products itself to

crack. Consequently, sour crude oil gradually reached fatigue crack tip, allowing da/dN to approximate to the da/dN in the corrosive environment. In stage 3 the crack opening is large enough to permit sour crude oil to constantly reach the fatigue crack tip causing the fatigue crack propagation to proceed in the corrosive environment. It is also considered that the acceleration of corrosion fatigue crack propagation rate of the welded joints in sour crude oil is due to the effect of an atomic hydrogen resulting from a reaction between steel welded joints and H_2S, and H_2O in sour crude oil. For HAZ of the CT specimen in the sour crude oil, the relation between brittle striation spacing and ΔK shows a relatively good agreement with the da/dN $\sim$ ΔK curve in the region of high crack propagation rate as in the case of BM, showing the dominant influence of the brittle striation on the fatigue crack propagation behavior in the high ΔK region in the sour crude oil environment. In this tests that the effect of sour crude oil containing 400 ppm H_2S on the fatigue life of the round notched bar specimen was pronounced in the higher stress region and obviously tended to decrease as decreasing the stress. It was also assumed that atomic hydrogen accumulated in the plastic zone at the fatigue crack tip accelerated the crack propagation rate and hence causing the round notched bar specimen to fail shorter in the sour crude oil than in air [11].

CONCLUDING REMARKS

This paper has briefly summarized on corrosion fatigue behavior of ship hull structural steels. To develop a reasonable fatigue life design and fracture control design for ship hull structures much more information is needed about metallurgical, mechanical and environmental variables which influence on corrosion fatigue behavior of high strength steels. It is recommended to evaluate corrosion fatigue crack initiation life at the notched area and the welded toe of the ship hull structural steels. A quantitative evaluation of an influence of tar epoxy resin coating on crack initiation and propagation of the coated specimen is also desired. Clarification of water absorption mechanism for the tar epoxy resin coating and of an improving effect corrosion fatigue behavior in lower stress and long term region is future problem to be solved. It is also recommended to study on the effect of H_2S concentration ,plate thickness and microstructure on crack initiation and propagation behavior of ship hull structural steels in sour crude oil environment.

References

1. Toyama,K.,Ebara,R. and Okazaki,S.(1987) Proc. of the third Symposium on Environmental Strength of Steels. ISIJ,69.
2. Hirakawa,K.and Kitaura,I.(1980) Journal of the Iron and Steel Institute of Japan.66,A73.
3. Ishiguro,I.,Todoroki,R. and Sekiguchi,S.(1979) Journal of the Iron and Steel Institute of Japan,65,A179.
4. Ebara,R..,Yamada,Y.,Fujishima,K.,Nawata,T.,Soya,T.(1986) Proc. of the fifth International OMAE Symposium,ASME,288.
5. Ebara,R,Kino,H.,Nakano,S.,Hanzawa,M. and Yokota,H. (1981) Materials, Experimentation and Design in Fatigue, Westbury House,424.
6. Otsuka,A.,Mori,K.,Okamura,H.,Takano,T.,Iwadate,T. and Tanaka,Y. (1987) Proc. of the third Symposium on Environmental Strength of Steels,ISIJ,160.
7. Ebara,R. (1989) Proc. of EVALMAT 89,1033.
8. Wintermark,H. (1978) Criteria for Preventing Service Failure in Welded Structures, Japan Welding Society,83.
9. Ebara,R.,Yamada,Y., Kino,H.,Tada,M.,Hashimoto,M..,Imajo,Y.and Fushimi,A.(1996) Journal of the Society of Naval Architects of Japan,180,521.
10. Kobayashi,S. (1996) SR220 Report, Corrosion Fatigue of Ballast Tank, Japan Ship Research Committee,37
11. Ebara,R.,Yamada,Y.,Fushimi,A.,Sakai,D.,Watanabe,E.,and Yajima,H (1993) Journal of the Society of Naval Architects of Japan,173,337.
12. Vosikovsky,O. (1976) Corrosion,32,472.
13. Nakano,Y.,Matsumoto,S.,Sugie,E.,Yajima,H.,Ebara.,R. and Watanabe,E. (1993) Journal of the Society of Naval Architects of Japan,174,571.

CORROSION FATIGUE FRACTURE BEHAVIOR OF HIGH-STRENGTH Cu TROLLEY WIRE FOR HIGH-SPEED RAILROAD SERVICES

K. Minoshima, K. Miyazawa and K. Komai

Department of Mechanical Engineering, Kyoto University, Kyoto 606-8501, Japan

ABSTRACT

One of the limiting factors in an operation of a high-speed train is the wave propagation rate in trolley wire, because the current collecting performance is reduced when the speed of a train reaches the wave propagation rate. Therefore, an operation of a high-speed train requires trolley wire with high wave propagation rates. For this purpose, the trolley wire should be tightened up with high tension stress which in turn requires a high-strength property and/or should have less density, although the mechanical properties including wear and (corrosion) fatigue and other properties such as electric properties should be sufficient. In this investigation, fatigue and corrosion fatigue properties have been evaluated in a newly developed high-strength Cu-Sn trolley wire for an operation of a high-speed train. The influence of NaCl solution on corrosion fatigue life is negligible, because of relief of stress concentration due to initiation of multiple cracks, blunting of corrosion fatigue crack tip by dissolution, and decrease in total crack depth due to general corrosion on the wire. Therefore, the corrosion fatigue strength is determined by mechanical fatigue strength in air. Attention is also paid to crack initiation and corrosion behavior by using scanning electron and atomic force microscopy, and the mechanisms of corrosion fatigue are discussed.

KEYWORDS

Corrosion fatigue, Crack initiation, Atomic force microscopy, Trolley wire for High-Speed Railroad Services

INTRODUCTION

Continuous progress in science and technology creates increasing demands for further improved materials. The material degradation phenomennon, corrosion fatigue, is one of the most important issues for machine and structural design when the material is subjected to varying loads and a corrosive environment. One of the important processes of corrosion fatigue is that a crack is nucleated at a corrosion pit formed on the surface, and then it propagates to final failure. Some investigations into the mechanical condition of the crack initiation at a corrosion pit were already reported [1–3]. In order to analyze the initiation and propagation process of a corrosion fatigue crack, scanning electron microscopy is widely used, which has fascinating characteristics: i) a broad band of magnifications easily facilitates the correlation of macroscopic and microscopic images; ii) a high depth of field or focus is attained, and a rough surface such as a fracture surface is clearly imaged in a three-dimensional or panoramic manner. However, a drawback is that it is only capable of imaging in vacuum, and therefore serial, *in situ* imaging of a corrosion or crack initiation process is impossible, and that the vertical resolution is low for observing the very early stage of surface damage. In contrast with these, an atomic force microscope is capable of imaging the surface not only in vacuum, but also in air or in liquid, and thereby *in situ* high-magnification imaging is possible. Up to dates, it is applied to *in situ* observation of a growth process of a stress corrosion crack [6, 7], early fatigue crack initiation stage of a metal [8–10] and so on.

On one hand, speedup of railroad transportation of both Shinkansen lines and conventional lines is planned by Japanese railroad companies. In order to realize a high-speed electric train service, wave propagation velocity in the trolley wire must be increased. This is because when the train speed approaches the wave propagation velocity, the current-collecting performance is decreased owing to multi-pantograph induced resonance and uplift of the contact wire. Therefore, the maximum speed of the trains is limited to about 70% of the wave

propagation velocity. In order to increase the wave propagation velocity, two measures are utilized: one is to decrease the density of the trolley wire and the other is to increase the wiring tension. To increase the wiring tension, the strength of the trolley wire must be high enough for such high-tension during service. However, high-strength metallic materials are usually sensitive to stress corrosion cracking and corrosion fatigue, and therefore, the influence of environment on the strength must be clarified.

In this investigation, the fatigue tests in air and in a 3.5% NaCl solution were conducted in a newly developed high-strength Cu trolley wire for Shinkansen lines. In particular, the surface damage initiation and propagation were closely examined by a scanning electron microscope and an atomic force microscope, and the mechanisms of corrosion fatigue of the high-strength Cu trolley wire were discussed.

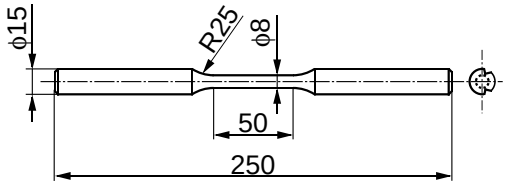

Figure 1: Shape and dimensions of smooth test specimens. All dimensions are in mm.

EXPERIMENTAL PROCEDURES

The material used was a newly developed Cu-trolley wire (Cu-0.36% Sn (O: 410 ppm, Ag: 8 ppm, other impurities (Fe, Co, Pb, Bi, Ni, Sb, As, and Te) less than 1 ppm), in mass). To achieve as much conductivity as that of the conventional Cu trolley wire and to increase the strength, the amount of Sn and the working are increased. This enables the high wiring tension of 19.6 kN for 160 mm^2-trolley wire, where the wave propagation velocity is about 410 km/h (≈ 114 m/s). The smooth round specimens shown in Fig. 1 were machined from the actual trolley wire. For the fatigue tests conducted at a lower stress, the specimen diameter of 6 mm is adopted to avoid fretting fatigue failure at a gripping position. The middle part of a sample was ground to #1500 by wet emery paper, and then finished by 1 μm diamond paste. In a corrosive environment, the middle part of 20 mm in gage length was exposed to an environment, and others were anti-corrosive coated. The corrosive environment was a 3.5% NaCl solution prepared by regent grade NaCl and ion-exchanged water whose relative resistance was larger than 1 MΩ•cm. The solution, which was kept at 298 ± 1 K, was circulated by a vane pump between a corrosion reservoir and a environmental cell attached to the specimen. The amount of the solution circulated was 10 L, and 3 L solution was exchanged every three days.

The testing machine employed was a computer-controlled, electro-hydraulic fatigue testing machine (Loading capacity: 98 kN). The tensile tests were conducted under displacement control: the displacement rate was 1 mm/min in laboratory air and 0.005 mm/min in a NaCl solution. Fatigue tests were conducted at a stress cycle frequency of 20 Hz with sinusoidal stress wave form. The tests were conducted at a constant mean stress of 115 MPa. This is because the trolley wire is used under tension of 19.6 kN, which gives the tensile stress of 115 MPa (cross sectional area: 170 mm^2). Two types of fatigue tests were conducted: one was to run the fatigue tests to final failure, and the other was an interrupted test, where the test was periodically interrupted and the surface damage was observed, until the specimen failed. When observing the specimen surface, the surface was ultrasonically cleaned in ethyl alcohol followed by in deionized water.

The specimen surface was observed by a scanning electron microscope. Some were closely examined by using an atomic force microscope (NanoScope IIIa and Dimension 3000 system, Digital Instruments, Ltd., USA), which has a large sample stage, and thereby the specimen surface was examined without cutting.

EXPERIMENTAL RESULTS AND DISCUSSIONS

Tensile Strength and Fracture Morphology

Table 1 summarizes the results of tensile tests conducted in laboratory air and in NaCl solution. The tensile strength obtained under a low strain rate in NaCl solution, (a slow strain rate test: SSRT), was the same as that conducted in laboratory air. The fracture in NaCl solution occurred in a cup-and-cone manner, similarly to the case of tensile tests in laboratory air. The microscopic fracture was dominated by dimples both in laboratory air and in NaCl solution. These indicate that the fracture occurred in a ductile manner in both environments, and the susceptibility to stress corrosion in a 3.5% NaCl solution is considered low.

TABLE 1
Mechanical properties of Cu trolley wire in laboratory air and in 3.5% NaCl solution.

	Tensile Strength	Elastic Modulus	Elongation at Break
Laboratory air	473 MPa	125 GPa	8%
3.5% NaCl soln	482 MPa	122 GPa	6%

Displacement rate: 1 mm/min (Laboratory air)
0.005 mm/min (NaCl solution)

Fatigue Fracture Behavior

Corrosion fatigue strength

Figure 2 illustrates the relationship between the stress amplitude and the number of cycles to failure (S-N

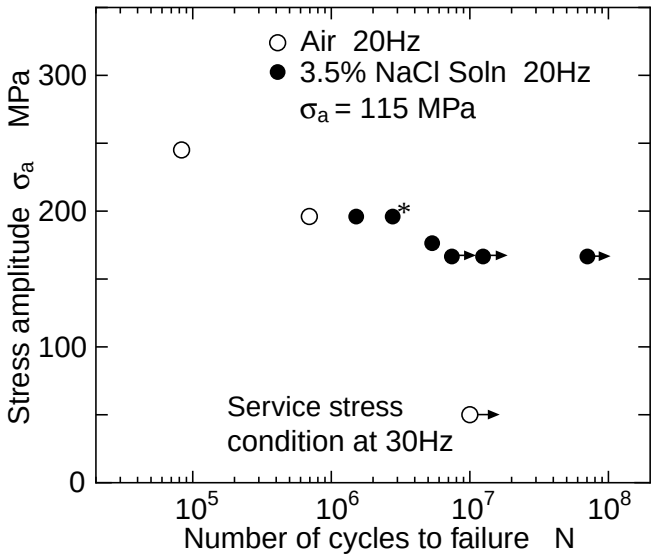

Figure 2: S-N curves of Cu trolley wire in laboratory air and in a 3.5% NaCl solution at 25°C. The tests were conducted under a mean stress of 115 MPa, corresponding to tension stress of the trolley wire in a service condition.

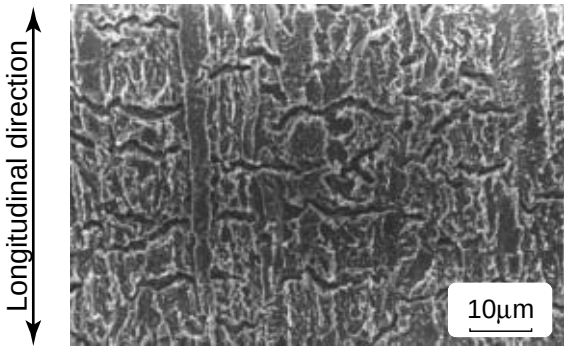

(a) Sample surface.

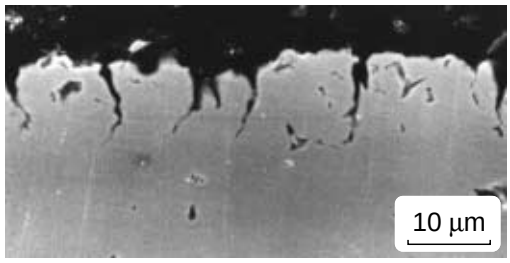

(b) Cross section along the longitudinal direction

Figure 3: Corrosion fatigue damage at σ_a = 196 MPa (σ_m = 115 MPa, $N_f = 1.5\times10^6$)

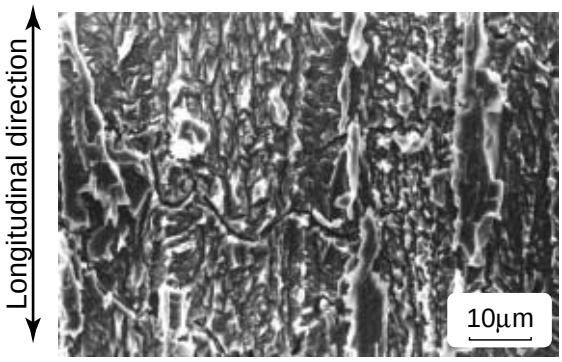

(a) Sample surface.

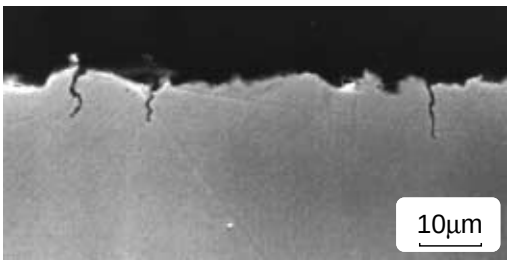

(b) Cross section along the longitudinal direction.

Figure 4: Corrosion fatigue damage at σ_a = 167 MPa (σ_m = 115 MPa, $N_f = 7.4\times10^6$)

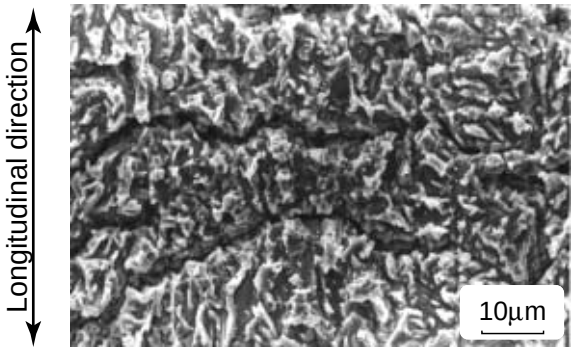

(a) Sample surface.

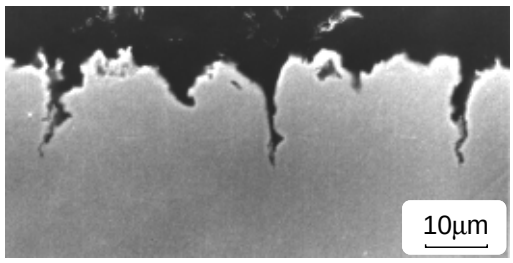

(b) Cross section along the longitudinal direction.

Figure 5: Corrosion fatigue damage at σ_a = 167 MPa (σ_m = 115 MPa, $N_f = 1.2\times10^7$)

curves) of fatigue conducted in laboratory air and in NaCl solution. The superscript "*" denotes the number of cycles to failure of an interrupted fatigue test mentioned before. Although the number of samples conducted in laboratory air is small, fatigue strength in NaCl solution was almost equal to that conducted in laboratory air. The run-out result conducted at a stress amplitude of 50 MPa was that of a simulated test of a service stress condition. These indicates that the trolley wire is strong enough for fatigue loading of a service operation. In a corrosive environment, the crack which led the final failure was initiated not at the exposed surface, but at the coated surface. This indicates that the fatigue fracture mechanism operating in a corrosive environment was the same as that of the fatigue conducted in laboratory air. Note that the failed specimen at a stress amplitude of 167 MPa was fractured at a gripping position due to fretting, and this is considered an exception.

Corrosion fatigue damage

Figures 3 to 5 illustrate the SEM images of corrosion-fatigued specimen surface and the cross sections along

the loading direction. It is clear that the specimen surfaces were subjected to general corrosion, and no corrosion pit that would induce the crack initiation was observed. The morphology of the general corrosion was influenced by the texture of the material owing to drawing. The amount of general corrosion increased with an increase in the number of cycles (compare Fig. 5 with Fig. 3).

In order to investigate the influence of the varying load on general corrosion, interrupted tests were conducted in samples with and without cyclic loading, and the changes in surface were examined by atomic force microscopy. The results are shown in Fig. 6 (under varying loads) and Fig. 7 (without loading). The longitudinal grooves that were observed in the virgin samples were due to final finish by diamond paste. From these AFM images and SEM images that are not shown here, the corrosion preferentially progressed along the longitudinal direction. This may be resulted from the influence of the longitudinal scratches induced by polishing and the longitudinal textures due to drawing. The second important thing which could be deduced from the figures is that the corrosion morphology was not influenced by varying load when the crack was not nucleated on the surface. Figure 8 illustrates the changes in roughness, root mean square roughness (RMS) and center plane roughness, R_a, measured with the AFM. Note that the unit used is nm. It is clear that the both roughness increased with an increase in testing duration, and no influence of varying load was observed. This indicates that although the corrosion behavior of this material was dependent on the microstructure, no influence of varying load was observed, as far as severe plastic deformation did not occur. When the testing duration was larger than 25 h, the roughness became smaller. This is due to measurement error owing to large roughness. The principle of the operation of the AFM is that the small, sharp tip positioned at the end of a micromachined small, weak cantilever is raster-scanned on the surface: the observed surface was so rough that the tip could not reach the bottom of the surface.

Corrosion fatigue crack

When the applied stress was high, multiple short transverse cracks were formed on the exposed surface (see Fig. 3(a)). Cross sectional views showed that the depth of these cracks remained short and was about 10 μm (Fig. 3(b)). The other noticeable point is that the crack wall was corroded, and this is in particular large near the surface. When the multiple cracks are formed on the surface, the stress concentration factors are increased or decreased depending on the distribution of surface defects. Ishida and Igawa [14] investigated the influence of multiple crack distribution on the stress intensity factor of a crack in a infinite body. They showed that the stress intensity factor is decreased when the cracks lined up, but increased when the cracks are distributed in a zigzag manner. From Fig. 3, the surface cracks tended to line up rather than to form in a zigzag manner. This indicates that the multiple crack formed on the surface may release the stress concentration, leading to lower crack growth rate.

As is discussed, multiple transverse cracks were nucleated, and then they grew due to coalescence (Figs. 4(a) and 5(a)). When multiple long cracks become long as shown in Fig. 5(a), the stress concentration factors are decreased. In addition, the crack walls were severely corroded, and the crack tip became blunt (Fig. 5(b)). From Fig. 4(b) and Fig. 5(b), it is clear that the extension of the crack toward the inside of the specimen was relatively short. The apparent crack growth rate computed was small, and was obtained at about 1.1×10^{-11} m/s ≈ 5.5×10^{-13} m/cycle. This was caused by the relief of the stress concentration due to crack blunting, and the crack growth rate became so much as that of general corrosion rate.

DISCUSSIONS

Corrosion fatigue mechanism can be summarized as follows [15]: in the case of a polycrystalline metallic material, the selective corrosion preferentially occurs at the deforming area, resulting in a corrosion pit. When the passive film or oxide film is formed, cyclic loading induces the breakage of the film owing to slip step formation, and the dissolution concentrates there. This may lead a corrosion pit initiation and progression. The corrosion fatigue crack is then initiated when the corrosion pit size, or depth, exceeds a critical value.

In the case of the Cu trolley wire tested here, however, the general corrosion prevailed on both cases of with and without cyclic loading, and the localized corrosion such as pitting did not occur. In the exposed area, multiple cracks were formed, and these yielded the relief of stress concentration. Severe general corrosion occurred, and this decreased the actual crack depth, and at the same time, caused crack tip blunting. These decreased the crack growth rate of both surface and depth directions. This is the reason why the final failure was brought about by the crack that was initiated at the anti-corrosive coated surface, where the mechanical factors dominated over the fracture, and the initiation and growth mechanism was the same as that of the fatigue in air. These may yield the speculation that when the entire part is exposed to a corrosive environment and a higher stress than the fatigue limit in air is applied, the corrosion fatigue strength would become higher than that in air. This is due to a decrease in corrosion fatigue crack growth rate. However, at a longer fatigue life region, i.e., larger than 1.0×10^8 cycles, the corrosion fatigue strength may be decreased from that conducted in

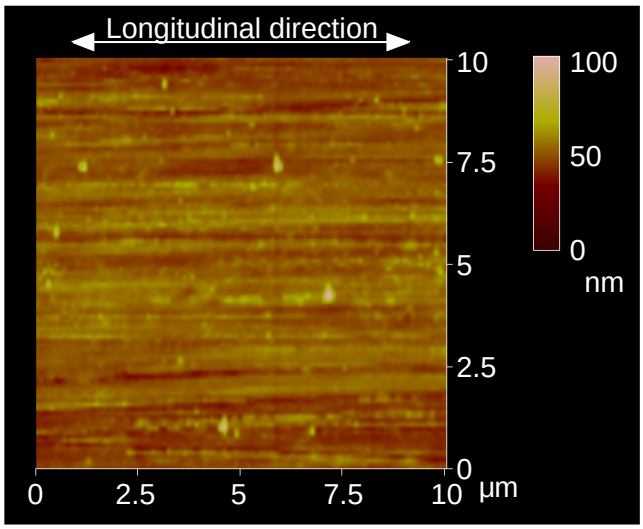

(a) Virgin sample surface

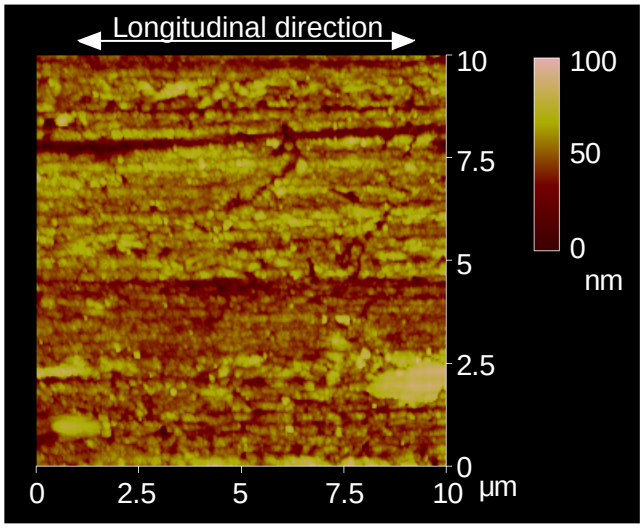

(b) n = 1.4×10^5, corresponding to two hour testing.

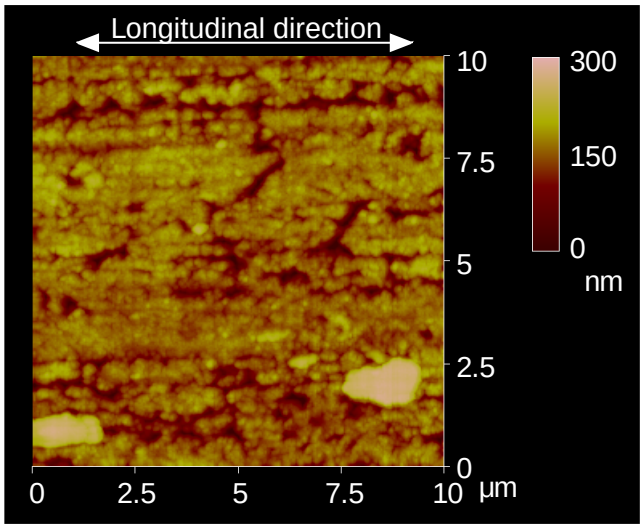

(c) n = 7.2×10^5, corresponding to ten hour testing

Figure 6: AFM imaging of the sample surface fatigued at σ_a = 196 MPa with σ_m = 115 MPa in a 3.5% NaCl solution. The test was periodically interrupted to observe the sample surface.

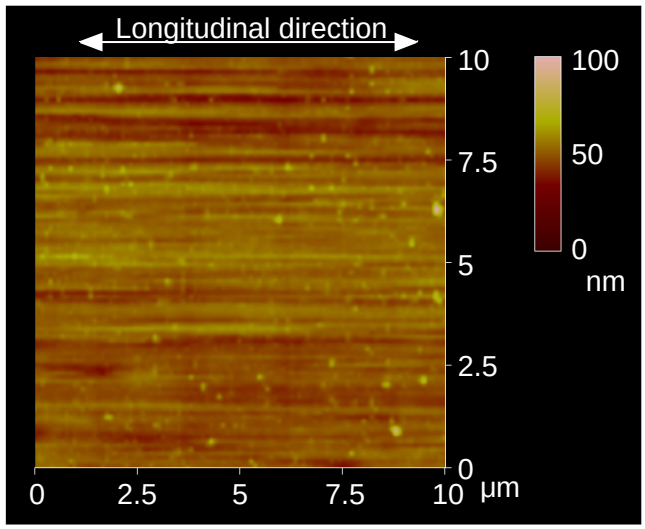

(a) Virgin sample surface

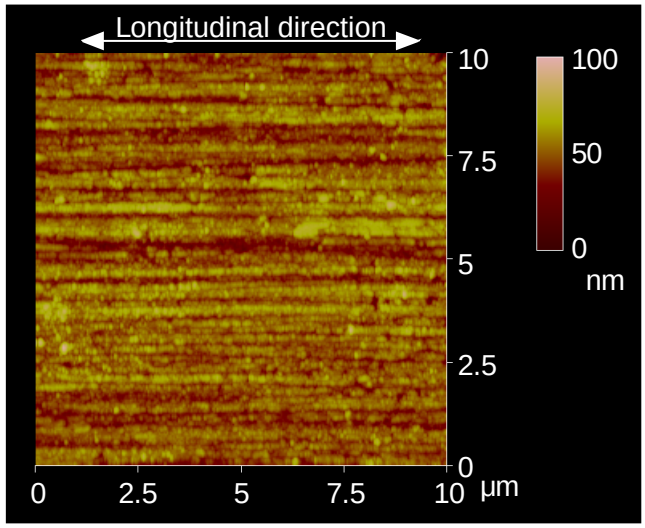

(b) Testing duration: two hours.

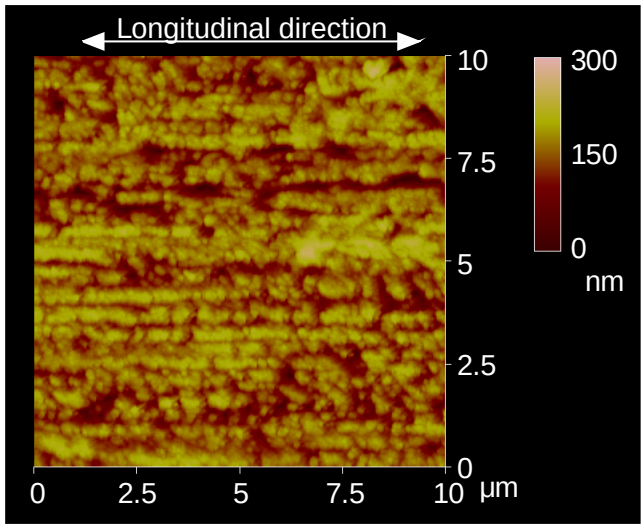

(c) Testing duration: ten hours.

Figure 7: AFM imaging of the sample surface without any loading in a 3.5% NaCl solution (Static corrosion). The test was interrupted periodically to observe the sample surface.

air, because the severe general corrosion causes a decrease in diameter of the wire itself. The amount of a decrease in the wire diameter due to general corrosion can be estimated at 5 to 8 %/ year of the virgin wire diameter of 15 mm. In a service operation, however, the design stress is σ_a = 50 MPa, and therefore, a decrease in fatigue strength due to a loss of wire diameter by general corrosion is considered small. Hence, it is concluded that the newly developed Cu trolley wire has a enough fatigue strength for a service operation.

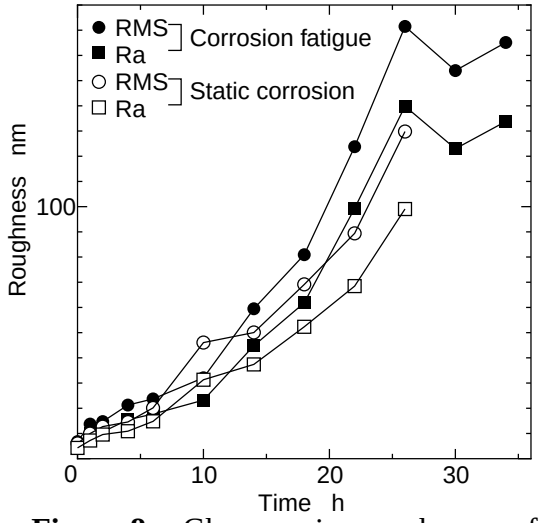

Figure 8: Changes in roughness of sample surface of corrosion fatigue and static immersion without loading.

CONCLUSIONS

Fatigue tests were performed in a newly developed Cu trolley wire in laboratory air and in NaCl aqueous solution. The corrosion damage was closely examined with a scanning electron and atomic force microscopy. The investigation yielded the following conclusions:

1. The corrosion fatigue strength of the Cu trolley wire in a 3.5% NaCl solution is as much as strong as that in laboratory air: the wire has enough fatigue strength in a service operation.

2. The surface exposed to NaCl solution suffers from general corrosion, and no localized corrosion such as a corrosion pit, that may cause the corrosion fatigue crack initiation, exists. Note that the amount of general corrosion increases with an increase in exposure time.

3. No influence of cyclic loading on the morphology and the amount of general corrosion is observed even in the nanometer order, when the applied stress is low and the plastic deformation or slip remains small.

4. The corrosion fatigue strength in NaCl solution is determined by the fatigue strength in laboratory air: a decrease in stress concentration due to multiple cracks formed on the exposed surface, crack tip blunting due to dissolution of the crack wake, and a decrease in crack depth due to general corrosion cause a decrease in corrosion fatigue crack growth rate. The final failure is then brought about by the crack that is initiated on the coated surface, where no environmental influence exists.

ACKNOWLEDGMENT

The authors wish to express their thanks to Mr. S. Amagumo, Sumitomo Electric Co, Ltd., for the donation of the test materials.

REFERENCES

1. Komai, K., Minoshima, K., Kinoshita, S. and Kim, G. (1988), *JSME International Journal*, 31, 606.
2. Kondo, Y. (1987), *Trans. Japan Soc. Mech. Eng., Series A*, 53, 1983.
3. Nakajima, M., Kunieda H., Tokaji, K. (1991), *Trans. Japan Soc. Mech. Eng., Series A*, 57, 2859.
4. Komai, K., Minoshima, K., and Kim, G. (1988), *J. Soc. Mater. Sci., Japan*, 36, 141.
5. Minoshima, K., Nagashima, I., and Komai, K. (1998), *Fatigue & Fracture Eng. Mater. & Technology*, 21, 1435.
6. Komai, K., Minoshima, K., and Itoh, M. (1994), *J. Soc. Mater. Sci., Japan*, 43, 336.
7. Komai, K., Minoshima, K. and Miyawaki, T. (1998), *JSME International Journal, Series A*, 41, 49.
8. Ishii, H., Miyazu, S., Nakura, K. and Tohgo, K. (1993), *Trans. Japan Soc. Mech. Eng., Series A*, 59, 3014.
9. Sriram, T.S. Ke, C-M and Chung, Y. W. (1993), *Acta Metall.*, 41, 2515.
10. Harvey, S. E., Marsh, P. G. and Gerberich, W. W. (1994), *Acta. Metall.*, 42, 3493.
11. Ikeda, K., Ito, S., Okada, T., Tenkumo, M., Yamamoto, M., Oku, G. and Maruyama, T. (1994), *Sumitomo Electric Review*, 145, 33.
12. Suto, H., Tamura, I. and Nisizawa, T. (1972), In: *Texture of Metallic Materials*, Maruzen Co. Ltd, Tokyo, Japan.
13. Nishida, M. (1973), In: *Stress Concentration*, Morikita Publishing Co., Ltd., Tokyo, Japan.
14. Isida, M. and Igawa, H. (1992), *Int. J. Fracture*, 53, 249.
15. Endo, K. and Komai, K. (1982), In: *Corrosion Fatigue of Metals and Strength Design*, Yokendo, Tokyo, Japan.

CORROSION FATIGUE MECHANISMS IN METALLIC MATERIALS

T. Magnin and D. Delafosse

Ecole Nationale Supérieure des Mines de Saint-Etienne, URA CNRS 1884,
158, Cours Fauriel 42023 Saint-Etienne Cedex 2, France

ABSTRACT

Classical approaches of corrosion fatigue damage according to the different electrochemical corrosion domains are presented through their interests and limits. A peculiar attention is paid on the necessity to integrate corrosion-deformation interactions to these modellings. A non exhaustive review of such interactions in corrosion fatigue is made and trends for further researches are emphasized.

KEYWORDS

Corrosion, fatigue, plasticity, electrochemistry, Corrosion-deformation interactions.

INTRODUCTION

The deleterious effect of aqueous environment on fatigue crack initiation and propagation in metals and alloys has been observed since a long time [1-3]. It is well known that slip bands, twins, interphases, grain boundaries and particles are classical sites for crack initiation and play a role on crack propagation. Moreover, persistant slip bands (PSB)/grain boundaries interactions are often observed to be preferential crack initiation sites during corrosion fatigue (CF), as well as localized pits around metallurgical heterogeneities.
The main need in corrosion fatigue modelling is related to the quantitative approach of local synergetic effects between environment and cyclic plasticity. In this article, quantitative approaches of corrosion fatigue damage from different electrochemical conditions are presented with respect to their interests and their limits. Then improvements of such models are given through corrosion-deformation interaction effects recently analysed.

Classical Approaches of Corrosion Fatigue Damage

Electrochemical corrosion can be schematised as an 'electronic pump or an electronic circuit' related to oxidation and reduction reactions :

$$M \rightarrow M^{n+} + ne^- \ : \text{ anodic dissolution}$$

$$\left.\begin{array}{l} 2H_2O + O_2 + 4e^- \rightarrow 4OH^- \\ 2H^+ + 2e^- \rightarrow H_2 \end{array}\right\} \text{ cathodic reactions}$$

together with cation hydrolysis reaction : $M^{n+} + nH_2O \rightarrow M(OH)_n + nH^+$.

M^{n+} is a solvated ion, e^- is an electron and *n* represents the ion state of charge. The electrons, liberated by the oxidation, must flow through the material M to be consumed in an appropriate cathodic reaction. Beyond a solubility limit, precipitates of hydroxide or hydrated oxide are formed, and this surface film can provide a barrier to further dissolution. In fact there are two film formation mechanisms : the dissolution / precipitation mechanism addressed before and also the solid state oxidation process $M + H_2O \rightarrow MO + 2H^+ + 2e^-$. Some films are named 'passive', for stainless steels or aluminium alloys for instance. Theses films will play an important role in environment sensitive crack initiation and fracture. Under thermodynamic equilibrium conditions, the film stability may be inferred from E = f (pH) diagrams, where E is the electrical potential related to the chemical free energy G by the relation : G = -n EF, and F is the Faraday's number. At equilibrium, one can define the 'electrode potential' (related to ΔG) and the current density I ($I \sim e^{-\Delta G^*/RT}$ where ΔG^* is the activation energy of dissolution). Thus corrosion fatigue damage is closely dependent of the electrochemical domaine from cathodic to anodic ones.

Crack initiation is often related to pits which act as stress concentrators during fatigue. If such pits reach a critical depth d_{CL}, a fatigue crack can develop. The critical depth is then a function of the applied stress range [4].

Let us suppose the following conditions :

- constant corrosion conditions (pH, concentration of bulk solution)
- constant alternating load, $d\Delta P/dt = 0$
- constant loading frequency $d\nu/dt = 0$

It is well established that growth kinetics of corrosion pits are determined by a simple power law :

$$d_L(t) = C\,(t - t_0)^{\beta},\ t > t_0 \tag{1}$$

where t_0 is the incubation time for pit nucleation. If the pit depth reaches the critical value :

$$d_L(t) = d_{CL} \tag{2}$$

corrosion fatigue crack initiation occurs. The critical pit depth d_{CL} depends on the applied stress range $\Delta\sigma_0$, cyclic yield strength σ_{FC} (which can be different than the tensile yield strength) fatigue crack growth threshold ΔK_0, and the geometry of the specimen, expressed in terms of a geometrical factor G. It can be calculated by elastic-plastic fracture mechanisms based on the Dugdale model [5]. d_{CL} is then given by the following equation :

$$d_{CL} = \frac{\cos\left(\pi\Delta\sigma_0 \,/\, 4\,\sigma_{FC}\right)\cdot \pi\Delta K_0^2}{32\,G^2\,\sigma_{FC}^2\left[1 - \cos\left(\Delta\pi\sigma_0 \,/\, 4\,\sigma_{FC}\right)\right]} \tag{3}$$

The number of cycles to initiate a corrosion fatigue crack under pitting conditions is, by combining the previous equations with $N = t.\nu$:

$$N_i = \nu\left[t_0 + \left(d_{CL} \,/\, C_2\right)^{1/\beta}\right] \tag{4}$$

Such approaches have been successfully applied to the fatigue crack initiation in a fcc Fe-Mn-Cr alloy cyclically deformed at low strain rate in a Cl^- solution. Nevertheless, the main problem is related to the fact that the coefficients C and β of the pit kinetics are often not constant during cycling : it is a clear example of a cooperative effect between plasticity and electrochemistry which needs finer analyses.

Crack propagation can be modelled in the same way. Anodic dissolution has been shown to occur preferentially in slip bands at the very near crack tip. This localized dissolution process is taken into account by the slip dissolution-model which is based on the fact that for many alloys in different solutions the crack propagation rate is proportional to the oxidation kinetics. Thus, by invoking the Faraday's law, the average environmentally-controlled crack propagation rates $\overline{V}_t$ for passive alloys is related to

oxidation charge density passed between film rupture events, Q_f : $\overline{V_t} = \frac{M}{n\rho F} Q_f \frac{1}{t_f}$ where t_f is the film rupture period. Thus $\overline{V_t} = \frac{M}{n\rho F} Q_f \frac{\dot{\varepsilon}}{\varepsilon_f}$ where $\dot{\varepsilon}$ is the strain rate and ε_f the strain for film rupture (about 10^{-3}). If we take a classical law for current transients at the crack tip,

$$Q_f = i_0 t_0 + \int_{t_0}^{t_f} i_0 \left(\frac{t}{t_0}\right)^{-\beta} dt, \tag{5}$$

Then, for $t_f > t_0$, $\beta > 0$,

$$\overline{V_t} = \frac{M i_0 t_0 \dot{\varepsilon}}{n\rho F(\beta - 1)\varepsilon_f}\left[\beta - \left(\frac{\dot{\varepsilon} t_0}{\dot{\varepsilon}_f}\right)^{\beta-1}\right] \tag{6}$$

Even if mechanical analyses give good approximations for $\dot{\varepsilon}$ at the crack tip, some problems still remain with the previous equation. In particular, the value of β evolves all along cycling [5]. But the main effect is in fact related to localized corrosion-deformation interactions. It has been shown that vacancy generation at crack tip due to localized dissolution can induce cyclic softening effects and that hydrogen absorption which can be also coupled to localized dissolution can also enhance the local cyclic plasticity [5]. It is why improvement of CF predictive laws are needed even if V_t can be adjusted from equation (6) which is still today very useful. Moreover, films related to solid state oxidation ($M + H_20 \rightarrow MO + 2H^+ + 2e^-$) can also play a role on crack advance. This needs further studies to be quantitatively precised.

Corrosion-deformation interactions

To improve previous modellings, corrosion-deformation interactions during fatigue must be taken into account. Following examples are given in this way.

Influence of cyclic plasticity on electrochemical reactions

PSB and intense slip bands are very prone to specific dissolution, not only for passivated alloys but also in conditions of generalised dissolution as shown on Figure 1 for copper single crystals in $NaClO_4$ solution [6].

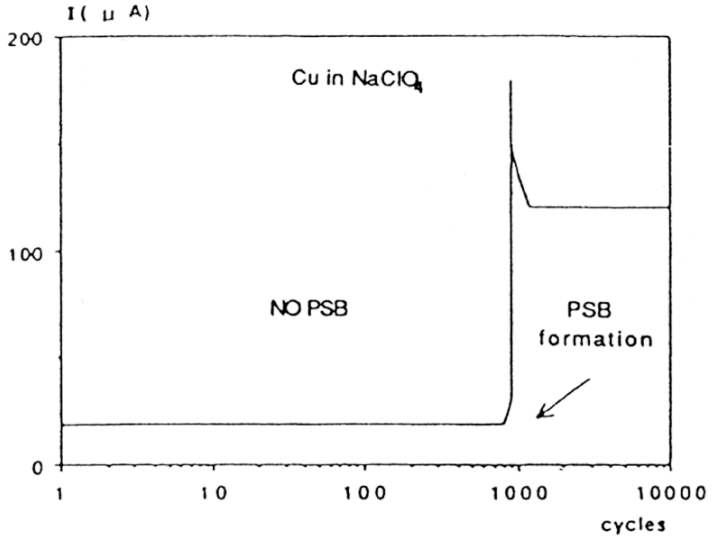

Figure 1: Influence of the PSB formation on the dissolution current for Cu single crystals in $NaClO_4$ [6].

As soon as the PSB form, the anodic current increases even though the applied plastic strain remains constant. This effect is not only related to the localisation of the cyclic plasticity but also to the influence of the dislocation microstructure of PSB on the free entergy of dissolution ($-\Delta G$) and the energy of activation (ΔG^*) [5]. Moreover cyclic plasticity has been also shown to often promote localised pitting well below the pitting potential without stress [5]. For the ferritic Fe-26 Cr-1Mo stainless steel in 3.5 % NaCl solution, a high strain rate $\dot{\varepsilon}$ promotes strain localisation at grain boundaries, which induces an intergranular pitting for an applied potential of about 400 mV below the pitting potential without stress effect [5].

The applied strain rate (or frequency) is a very sensitive parameter for CF damage, and particularly for crack initiation. The following example can be given for an Al-Li 8090 alloy in NaCl solutions. The number of cycles to crack initiation N_i is defined as the number of cycles to obtain a rapid 3% decrease of the saturation stress [5]. At high strain rate ($\dot{\varepsilon} > 5 \times 10^{-3} s^{-1}$), the anodic dissolution occurs at slip band emergence and induces an enhancement of the transgranular mechanical microcracking. At medium strain rate ($5 \times 10^{-5} s^{-1} < \dot{\varepsilon} < 5 \times 10^{-3} s^{-1}$), pitting is favoured and responsible for crack initiation. So when the plastic strain decreases, pitting is more profuse (because of time) and the reduction in the fatigue life to crack initiation is more pronounced in comparison to air. At low strain rate ($5 \times 10^{-6} s^{-1} < \dot{\varepsilon} < 10^{-5} s^{-1}$), the fatigue time to initiation increases by blunting of the mechanically formed microcracks because of generalised pitting which acts as general corrosion. At very low strain rate ($\dot{\varepsilon} < 5 \times 10^{-6} s^{-1}$) CF crack initiation occurs by intergranular stress corrosion due to localized dissolution at grain boundaries. The rapid occurrence of SCC induces a marked decrease of N_i.

Softening effect due to anodic dissolution

CF tests on smooth specimens were performed at room temperature on a 316 L austenitic stainless steel in a 0.5 N H_2SO_4 solution at different electrochemical potentials and for a prescribed plastic strain amplitude of 4×10^{-3} ($\dot{\varepsilon} = 10^{-2} s^{-1}$). The depassivation-repassivation process occurs in a very regular way, well before any microcracks can form [5]. It is of particular interest to follow the evolution of the maximum flow stress in the corrosive solution at free potential and at imposed cathodic potential, and to compare this evolution with that observed in air (Figure 2). It clearly appears that :

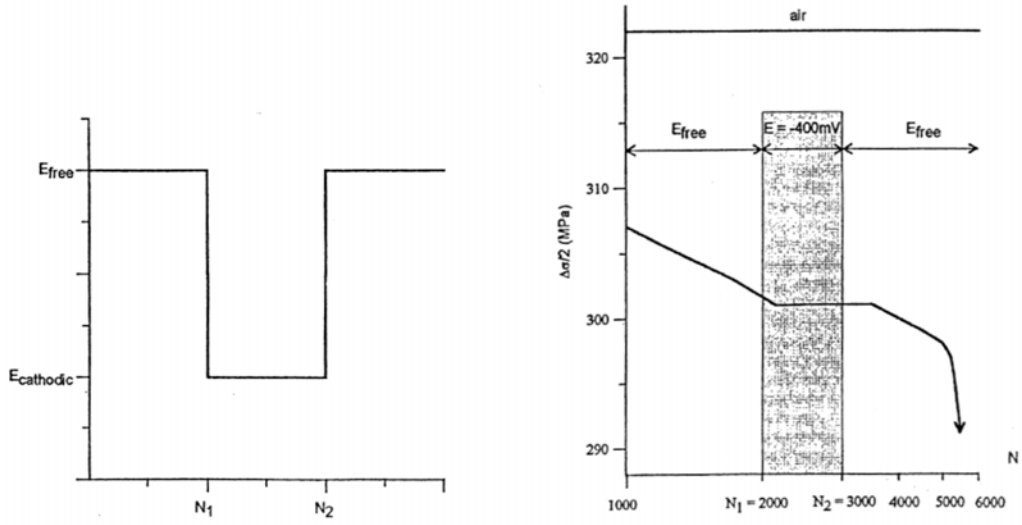

Figure2: Evolution of the peak stress $\Delta\sigma/2$ during cycling in a 0.5 N H_2SO_4 solution at free potential, for $\frac{\Delta\varepsilon p}{2} = 4x10^{-3}$ and $\dot{\varepsilon} = 10^{-2} s^{-1}$, compared to the air behaviour.

(i) a cyclic softening effect occurs at the free potential in comparison to the behaviour in air.
(ii) this softening effect disappears when the cathodic potential is applied (and the anodic dissolution is markedly reduced), after about 150 cycles.
(iii) the softening effect then occurs in the same way when the free potential is re-established.
(iv) a delay in the evolution of the flow stress with regard to the number of cycles for which a potential change is imposed can be observed for the free potential to the cathodic potential change (and vice-versa).
This effect has been also observed during creep in corrosive solutions for copper [5]. It corresponds to the time during which vacancies due to dissolution are still acting on the dislocation mobility. The macroscopic cycling softening effect observed in H_2SO_4 solution at room temperature (which is not due to microcracking) is very relevant to take quantitatively into account the local dissolution-deformation interactions which will lead to the fatigue crack initiation process.

An example of mechanical and electrochemical coupling effects : the CF crack initiation mechanisms of a two - phase stainless steel in NaCl solutions

Mechanical and electrochemical coupling effects are generally the key for understanding the crack initiation mechanisms in multiphase alloys. This is clearly illustrated for a duplex α/γ stainless steels (without nitrogen) in a 3.5% NaCl solution at pH 2 and free potential [5]. At low plastic strain amplitude, the softer γ phase is depassivated but this phase is cathodically protected by the non-plastically deformed α phase. This coupling effect reduces the dissolution of the γ phase and delays CF damage, which is not the case at higher strain amplitude when the α phase is also depassivated by slip band emergence.
Observations of the crack initiation sites by scanning electron microscopy show [5] that at low plastic strain amplitudes ($\Delta\varepsilon_p/2 < 10^{-3}$) for which the fatigue resistance of the α-γ alloy is close to that of the γ alloy, cracks nucleate only in the austenitic phase but, at higher strain amplitudes ($\Delta\varepsilon_p/2 > 10^{-3}$), the first cracks nucleate principally in the ferritic phase. The excellent CF resistance of duplex stainless steels (for $\Delta\varepsilon_p/2 < 10^{-3}$) can then be understood through the electrochemical and mechanical coupling effects on crack initiation processes.

Hydrogen effects on cyclic plasticity

Figure 3 shows the well-established cyclic stress-strain curves of nickel single crystals oriented for single slip, with a plateau region corresponding to persistant slip bands [7]. In the low amplitude range, the dislocation pattern is built up predominantly of elongated and fragmented edge dislocation dipole loops which frequently cluster into dense bundles (the veins). During cyclic hardening, the veins develop and become denser. At a critical threshold stress level, the vein structure becomes locally unstable and gradually gives thin lamellae of persistant slip bands (PSB's) which lie roughly parallel to the glide plane. Cyclic deformation becomes localized to a large extent in the PSB's which are softer than the so-called matrix of veins in which they are embedded.
Hydrogen has be shown to enhance the dislocation mobility in nickel [5] and to promote planar slip. Hovewer, the ease of cross slip is known to be an essential factor facilitating the development of PSB's [1]. The elimination of the screw dislocations by cross slip is a major prerequisite for providing the simple edge multipole dislocation arrangement that appears for undergoing the structural changes leading to PSB's. Moreover, the saturation stress in the PSB's regime is related to the equilibrium between multiplication and annihilation of dislocations which can then be modified by the presence of hydrogen.
Increasing strain amplitudes are applied (Figure 3) to obtain the cyclic stress-strain curves as a function of hydrogen content (from less than 1 ppm wt % in pure nickel to 23 ppm wt % in pre-charged specimens). The following remarks can be made : (i) A plateau region is observed whatever the hydrogen content, but the corresponding saturation stress is lowered in the presence of hydrogen. Moreover a sligth increase of the critical γp for the beginning of the plateau regime seems to be shown with hydrogen ; (ii) A more

marked difference in the value of the saturation stresses is observed in the vein structure region at low strain amplitudes than in the PSB's domain.
Because of a decrease of the cross slip ability in presence of hydrogen [8], nickel single crystals oriented for single slip exhibit different cyclic stress-strain curves according to the hydrogen content. In the low strain amplitude domain, saturation is reached faster in presence of hydrogen. Such effect can be interpreted in terms of new equilibrium between bundles and mobile screw segments between the veins, which leads to a lower value of the saturation stress. A softening effect due to hydrogen is observed when PSB are formed in the plateau region, whatever the applied strain amplitude. It can be interpreted in terms of decrease of the internal shear stress in PSB walls, which induces a decrease of τ_s.

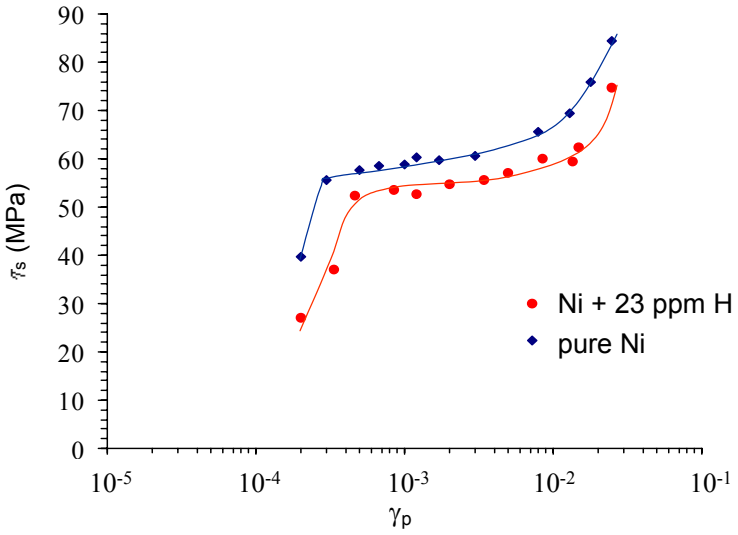

Figure 3: Effect of applied γp on the cyclic hardening curves of [153] nickel single crystals with and without hydrogen.

Such effects of hydrogen on plasticity must be taken to into account in modellings. Hydrogen assisted cracking is often invoked, particularly for bcc materials but also together with anodic dissolution for fcc alloys. Figure 4 schematizes a hydrogen assisted cracking event. Interactions between a discretized dislocation array and the crack tip under an applied stress produce a maximum stress field from behind the tip. When the hydrogen concentration reaches a critical value, a microcrack is nucleated because either the local cohesive strength is reduced, dislocation motion is blocked in the hydrogen-enriched zone, or both. The microcrack arrests about 1 μm ahead of the original location of the tip and these processes then repeat leading to discontinuous microcracking.
Other mechanisms have been proposed, particularly the hydrogen-induced plasticity model for precipitates containing materials such as Al-Zn-Mg alloys [9]. Absorbed hydrogen atoms weaken interactomic bonds at crack tip and thereby facilitates the injection of dislocations (alternate slip) from crack tip. Crack growth occurs by alternate slip at crack tips which promotes the coalescence of cracks with small voids nucleated just ahead of the cracks. In comparison to the behaviour in neutral environments, the CF crack growth resistance decreases as the proportion of dislocation injection to dislocation egress increases. More closely spaced void nuclei and lower void nucleation strains should also decrease the resistance to crack growth in CF. This mechanism is proposed for Al-Zn-Mg alloys and is highly supported by observations that environmentally assisted cracking can occur at high crack velocities in materials with low hydrogen diffusivities and that the characteristics of cracking at high and low velocities are similar.

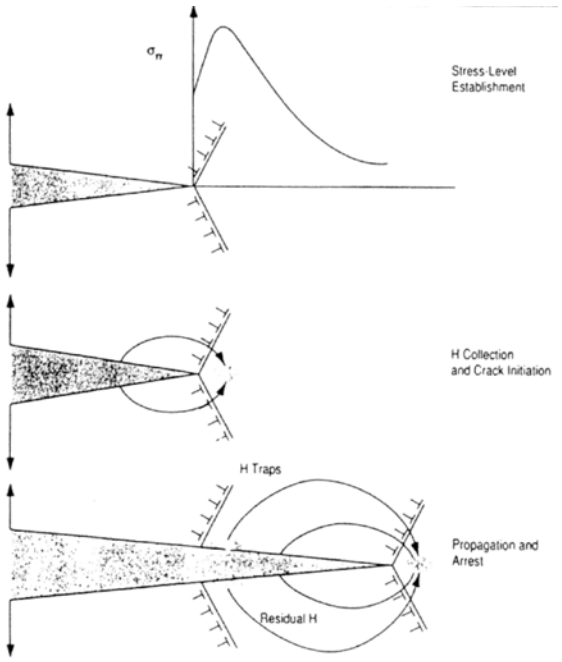

Figure 4: Schematic illustration of hydrogen assisted cracking mechanism [10].

CONCLUDING REMARKS

The analysis of CF micromechanisms related to anodic dissolution together with hydrogen effects is under progress but needs to be more quantitative through the localized corrosion deformation interactions. The trends for future researches are mainly related to :
(1) the modelization of crack tip chemistry,
(2) the quantitative analysis of corrosion-deformation interactions at CF crack tip (scale of 1 μm) according to the electrochemical conditions,
(3) a comparison between CF and SCC based on a detailed analysis of micromechanisms near the fatigue threshold,
(4) developments of numerical simulations at mesoscopic scales.
These researches are needed to propose more relevant predictive laws for CF damage based on physico-chemical controlling factors.

References

1. Laird, C. and Duquette, D.J. (1972) *Corrosion Fatigue*, Nace, New York.
2. Patel, C. (1977), *Corr. Sci.*, 21, 145.
3. Gangloff, R.P. and Duquette, D.J., in : *Chemistry and Physics of Fracture*, Nijhoff.
4. Mueller, M. (1982) *Met. Trans*, 13A, 649.
5. Magnin, T. (1996), *Advances in corrosion-deformation interactions*, Trans. Tech. Publ.
6. Yan, B.D., Farrington, G.C. and Laird, C. (1985) *Acta Met.*, 33, 9, 1593.
7. Mughrabi, H., Ackermann, F. and Herz, K. (1979) in : *Fatigue Mechanisms*, pp 69-105, J.T. Fong Ed., ASTM STP 675, Philadelphia.
8. Delafosse, D., Château, J.P. and Magnin, T. (1999) *J. Phys. IV*, 251.
9. Lynch, S.P. (1998) *Acta Met.*, 36, 2639.
10. Gerberich, W.W. (1993) in : *Corrosion-Deformation Interactions*, pp 325-354, T. Magnin and J.M. Gras Ed., Les Editions de Physique.

ICF100296OR

Corrosion Fatigue of High Pressure Die Cast Magnesium Alloys

W. G. Ferguson[1], Wu Liu[1] and John MacCulloch[2]

[1]The Chemical & Materials Engineering Department, The University of Auckland,
Private Bag 92019, Auckland, New Zealand
E-mail: wg.ferguson@auckland.ac.nz
[2]Magnesium Technology Ltd,
137 Captain Springs Rd, Onehunga, Auckland, New Zealand

Abstract:

To determine the effect of a coating on fatigue strength, three point bending fatigue tests of coated and un-coated specimens of AM50 and AZ91D magnesium high pressure die castings were made and S-N curves determined. Environments adopted were air, tap water and natural seawater. A difference in corrosion fatigue performance has been found, between AZ91D and AM50 and for both alloys performance in air was superior to both water environments. AZ91D has better corrosion fatigue resistance in tap water than in seawater; conversely, AM50 has better corrosion fatigue resistance in seawater than tap water. The results showed that the fatigue life was not reduced in these water environments for coated specimens, as the coating usually provided sufficient protection from corrosion
Key words: magnesium, high pressure die casting, fatigue, corrosion fatigue, coating

INTRODUCTION

Magnesium is the lightest of the commercial metallic construction materials. Die cast magnesium parts are rapidly replacing steel and aluminium structural components in automotive applications, as design engineers seek to reduce assembly costs, raise fuel efficiency, and improve safety. In addition to an excellent strength-to-weight ratio, magnesium die-castings offer good fatigue strength, high impact and dent resistance, good corrosion resistance, thermal and electrical conductivity. Corrosion resistance of magnesium alloys today is a less serious problem because of better control of alloying element contents.

The magnesium alloys used for this project are AZ91D and AM50 high-pressure die casting alloys. AZ91D die-castings have high values of fatigue strength and are among the most corrosion resistant of the magnesium alloys [1]. Many structural applications require an appreciable amount of energy absorption during service. Magnesium alloys having lower aluminium contents, such as AM50 have been found to be more ductile, especially during impact situations. AM50 alloy has been employed to fabricate prototype wheels for cars [2]. It is now possible to make large complex castings such as integral instrument panel/cross beam members for vehicles using AM60 [3] and high integrity crash sensitive components such as steering wheel frames in AM50 [4].

Corrosion is still a problem for these magnesium alloys for most applications. Magnesium alloys may be used under wet or chemical environments, thus a coating should be applied to improve corrosion resistance. There are two main reasons for the poor corrosion resistance of many magnesium alloys [5-7]. Firstly, there is internal galvanic corrosion caused by second phases or impurities. Secondly, the quasi-passive hydroxide film on magnesium is much less stable than the truly passive film which can form on metals such as stainless steels. This quasi-passivity causes poor pitting resistance in magnesium and its alloys.

A recently published review of the fatigue behaviour of magnesium alloys shows there are very few fatigue data available to the practising engineer [8]. Specifically, there is a lack of information concerning low cycle fatigue, cyclic stress-strain, mean strain-stress and fatigue crack growth behaviour. The literature on magnesium alloy fatigue behaviour is incomplete, covering only specific topics for some magnesium alloys. Examples of stress-life (S-N) curves are found for some alloys.
In many cases, metallic corrosion is governed by the characteristics of its surface films. For magnesium, the nature of the film is not well understood [9]. Hence, corrosion prevention is very important and essential for commercial applications. There are several ways to protect magnesium and its alloys from corrosion [10]: high purity alloys; new alloys; surface modification; protective films and coatings. In this project, an anodised coating is used to determine coating effects on corrosion fatigue performance for AZ91D and AM50.

Normally, corrosion fatigue is very sensitive to testing frequency, especially for structural steels. For magnesium alloys, it has been noted that: "frequency dependence of corrosion fatigue strength showed that the influence of a corrosion environment decreased with increasing frequency" [11]. However, no data showing the influence of frequency on fatigue performance of magnesium has been cited. Work on the effect of test frequency is in progress.

TEST MATERIAL AND ENVIRONMENT

Test specimens were 10mm×10mm cross-section bars, 50mm long with smooth die cast surfaces. These specimens, which were die cast to shape without heat treatment, allow three point bend fatigue tests to be conducted with a 40mm span. Bending fatigue tests were carried out with an MTS810 using constant load amplitude control, R-ratio of 0.25 and frequency of either 30 or 40 Hz. Tests were stopped when they reached 7.0E+06 cycles and at least three tests have been conducted for each test condition. Tests were performed in air, tap water and natural seawater. The natural seawater was taken from a local Auckland beach and the tap water from a tap in the MTS laboratory. Coated specimens were made to investigate the fatigue performance in seawater of magnesium alloys with or without coating. 5µm and 25µm thick coatings, and 5µm and 25µm thick organically sealed coatings were prepared at the site of Magnesium Technology Licensing Limited, who supplied a new anodising process, 'Anomag'.

RESULTS AND DISCUSSION

Environmental Influence on Fatigue Performance.

The fatigue performance of un-coated AM50 die cast alloy at various stress levels in air, tap water and natural seawater environments is shown in Figure 1. Maximum stress is plotted against the logarithm of the number of cycles to failure. The points with arrows are identified as "did not fail" at a certain stress level and number of cycles (tests were stopped when they reached 7.0E+06 cycles).

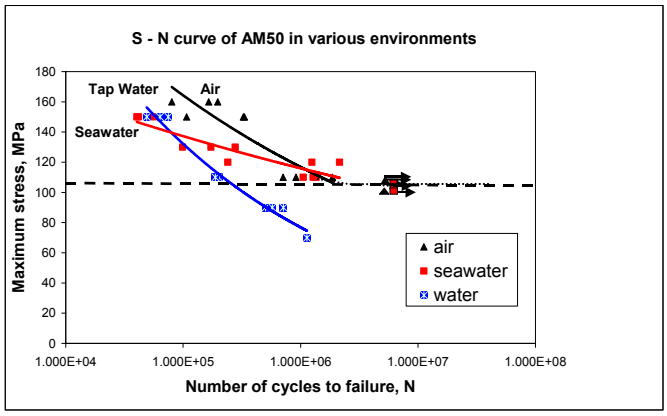

Fig.1 S-N curves of un-coated AM50 (40Hz, R=0.25, bending fatigue)

At high maximum stress, AM50 had best fatigue life in an air environment, with the effects of tap water and seawater environments being the same. For low maximum stress the curves for air and seawater drop slowly to an endurance limit of about 105MPa. All specimens, tested in air and seawater at a maximum stress of 105MPa, did not fail after 7.0E+6 cycles. However, the fatigue performance in tap water showed significantly different behaviour; the curve continues to decrease and shows no fatigue limit at 70MPa, where a specimen failed after 1.0E+6 cycles. It would appear that S-N curves have a 'knee' in air and seawater environments, but not in a tap water. These results are not consistent with our general knowledge of corrosion fatigue behaviour of magnesium alloys, in that it has been noted: "Sea water has a greater corrosive effect than tap water because chloride ions react with and remove the protective films from the surfaces of magnesium alloys" [12]. Eliezers et.al. [13] report similar behaviour for 5% NaCl solution and water environments where life depends on aluminium content with about 4% Al giving least life in a water environment.

It would appear that tap water is enhancing the fatigue process as expected with corrosion fatigue; but that seawater, which is assumed to be more corrosive, has a smaller effect on fatigue performance. The un-coated AM50 high pressure die castings have excellent corrosion fatigue behaviour in a seawater environment. A possible reason for the abnormal behaviour is that the more aggressive environment reduces crack initiation by decreasing or reducing the stress concentration at crack initiation sites, corrosion products may also cause crack blunting and reduce crack growth.

The fatigue performance of AZ91D die cast alloy at various stress levels in air, tap water and natural seawater environments is shown in Figure 2. It can be seen that the best fatigue life for AZ91D is in an air environment, while the effects of tap water and seawater environments within the fatigue scatter give similar but reduced performance. The S-N curve for air decreases sharply to a "knee" between 115MPa to 110Mpa being the fatigue endurance limit of AZ91D in an air. The fatigue performance in tap water and seawater is different to that in air. The fatigue resistance in tap water and seawater is significantly decreased, especially at low stress levels. The S-N curve in a tap water environment is slightly above the S-N curve in a seawater environment, which shows the slightly better fatigue resistance is in tap water compared with that in seawater. Both curves continue to decrease and possibly will not show a fatigue limit.

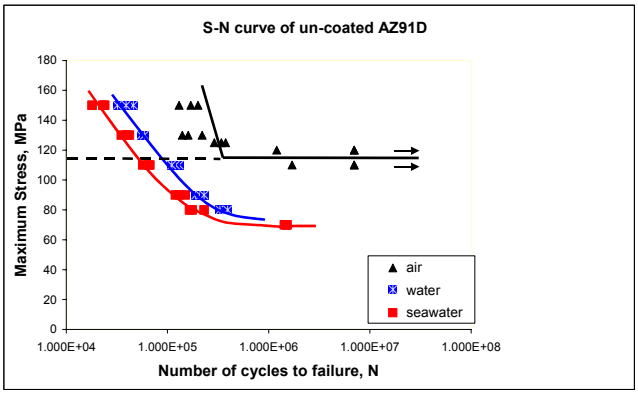

Fig.2 S-N curves of un-coated AZ91D (30Hz, R=0.25, bending fatigue)

Generally, the corrosion fatigue resistance for AM50 is always better than that for AZ91D in both tap water and seawater. The comparison of mean fatigue lives for these two alloys in both tap water and seawater are shown in figures 3 and 4. This result supports Eliezer et.al's work [13], in

which it was found that the less the aluminium content in magnesium alloys, the better the corrosion fatigue resistance. Eliezer et.al [14] also report that the sensitivity of AZ91D alloy to corrosion fatigue is higher than that of AM50 alloy when tested in 3.5% NaCl solution.

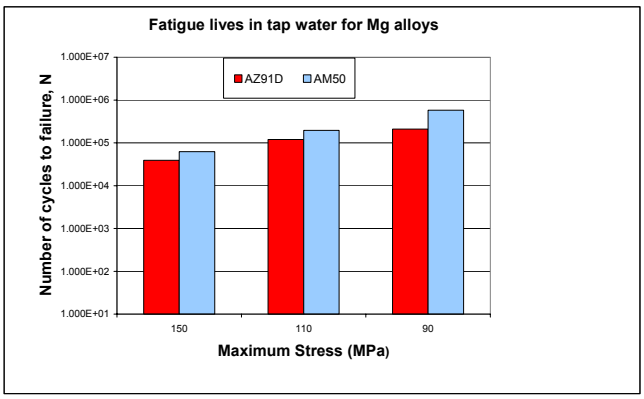

Fig.3 Fatigue lives in tap water for un-coated AM50 and AZ91D

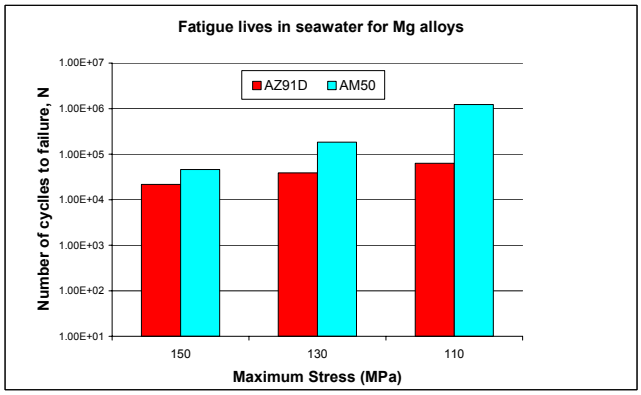

Fig.4 Fatigue lives in seawater for un-coated AM50 and AZ91D

Coating Influence on Corrosion Fatigue Behaviour

A special coating ('Anomag' anodising) has been used on AM50 and AZ91D die cast specimens to determine the influence of surface protection on fatigue performance in a seawater environment. The results of fatigue tests in seawater for coated and un-coated AZ91D and AM50 show that the special coating and coating & sealing ('Anomag') do not decrease the fatigue properties in the seawater environment (see figures 5 & 6). It has been noted that magnesium coating treatments, which are applied for corrosion protection, usually decrease the fatigue and corrosion fatigue resistance of materials in air, but not in seawater[15].

As the coating affects the number of cycles required to start a crack, the effect of coating on the total fatigue life should decrease with increasing stress amplitude. On the basis of this consideration, the most reliable estimate of the effect of the coating should be obtained from tests at low stress levels where the number of cycles to initiate cracking is large in comparison with the crack growth portion of the tests [16].

It can be seen from figure 5 that un-coated specimens in air have about the same fatigue resistance as coated specimens in seawater. The fatigue life of un-coated specimens in air is slightly higher than for the coated specimens at higher stress levels but at lower stress levels, there seems to be little difference in the fatigue life for all specimens. Considering the usual scatter of fatigue results, there is little difference between the S-N curves for un-coated and coated AM50 in seawater, at all stress levels. As un-coated AM50 has excellent corrosion fatigue resistance in seawater, the influence of a thin coating or sealing treatment should not show much improvement in fatigue performance.

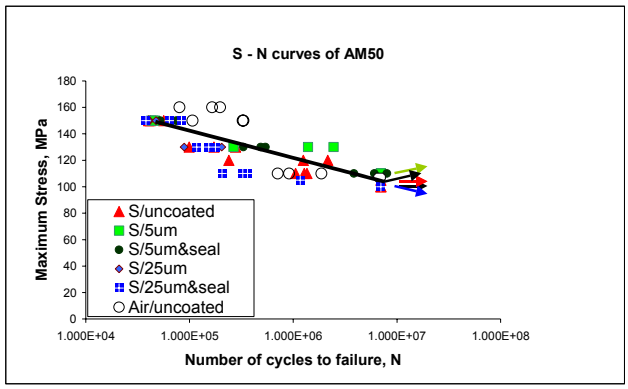

Fig.5 S-N curves of coated and un-coated AM50 in seawater (40Hz, R=0.25)

For AZ91D, it can be seen the coating treatment increases the corrosion fatigue performance, as the S-N data for coated specimens in seawater is always above the curve for un-coated specimens, but below the S-N curve of un-coated specimens in air (see figure 6). It can also be seen that the effect of coating increases with decreasing stress levels. There is little difference in fatigue life for coated and un-coated specimens in seawater at high stress levels, and the difference gets greater when the stress level decreases. As the stress decreases the life for 5 & 25 μm coated specimens approaches the air curve and then falls as the stress drops further. Similar behaviour has been reported by Beck [12] for tap water.

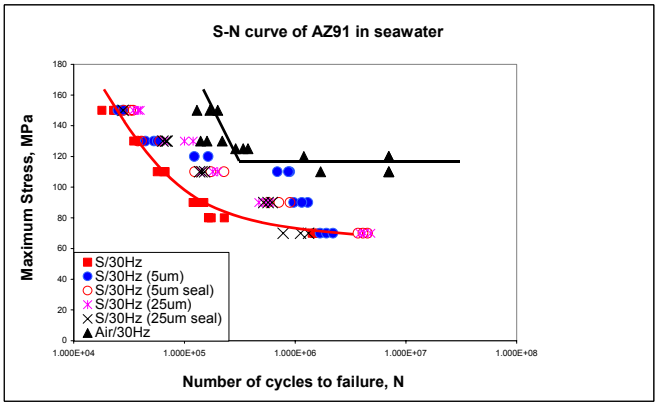

Fig.6 S-N curves of coated and un-coated AZ91D in seawater (30Hz, R=0.25)

It can be seen that the effect of coating or coating & sealing on corrosion fatigue performance in seawater is greater for AZ91D than for AM50. A possible reason is that the fatigue resistance for un-coated AM50 is much higher than that for un-coated AZ91D in a seawater environment.

CONCLUSIONS

- The endurance limits in bending for un-coated AM50 and AZ91D die cast alloys are about 105MPa and 115MPa (maximum stress), respectively.
- AM50 and AZ91D have different corrosion fatigue performances. There seems to no endurance limit for AM50 in tap water and for AZ91D in both tap water and seawater. Un-coated AM50 has a better corrosion fatigue resistance than AZ91D in water(tap & salt) environments but not in air.
- AM50 has excellent corrosion fatigue resistance in a seawater environment. The endurance limit (7×10^6) in seawater is about 105MPa (maximum stress), which is higher than that in tap water, but equal to that in air.

- There are no negative effects of coating and coating & sealing on fatigue performance in seawater for AM50, and a slight improvement in the performance for AZ91D.

REFERENCES

1. *Magnesium Casting Alloys,* SAE J465 JAN89, SAE standard 10.113.
2. F.H. Froes, *The Science, Technology and Applications of Magnesium,* JOM, Sept.,1998, 30-32.
3. K. Peete and L. Winkler, *Paper 930421*, Int. SAE Congress, Detroit, March, 1993.
4. W. Hirth, *Mg Alloys and their Applications*, DGM Conf., Germany, 1992, 375-379.
5. G.L. Makar, *J. Electrochem. Soc*., 137(2), 1990, 414-421
6. E.F. Emley, *Principles of Magnesium Technology*, Chapter XX, Pergamon Press, 1966
7. L.J. Polmear, *Light Alloys; Metallurgy of the Light Metals*, 2nd Edition, Edward Arnold, 1989
8. V.V. Ogarevic and R.I. Stephens, *Fatigue of Magnesium Alloys, Ann. Rev. Mater.Sci.*,1990, *20*
9. *Mechanical Testing,* Metals Handbook, ASM International, 9th Edition, Vol 8, 1985
10. G.L. Makar and J. Kruger, *International Materials Reviews*, 38930, 1993, 138-153
11. *Failure Analysis and Prevention,* Metals Handbook, ASM International, 9th Ed., Vol 11, 1986
12. A. Beck, *The Technology of Magnesium and its Alloy,* Hughes and Co, London, 1943
13. E.M Eliezer, E.Gutman, E. Abramov and E. Aghion, *Corrosion Reviews,* Vol. 16, No1-2, 1998
14. E. M. Gutman, Ya. Unigovski, A. Eliezer, E. Abramov and L. Riber, *Light Metals Age*, December, 2000, 14 - 20
15. H. T. Sumsion, *J. Spacecr. Rocket,* 5(6), 1968, 700-704.
16. J.A. Bennett, *Proc. Am. Soc. Test. Mater., 55,* 1955, 1015-19.

CORROSION-PIT-GROWTH BEHAVIOUR DURING THE CORROSION FATIGUE PROCESS IN ALUMINUM

S. Ishihara[1], T. Goshima[1], A. J. McEvily[2], S. Sunada[1]and S. Nomata[1]

[1]Department of Mechanical Engineering, Toyama University, Toyama, Japan
[2]Department of Metallurgy, University of Connecticut, Storrs, CT, USA

ABSTRACT

The fatigue strength of machines and structures operating under corrosive environment falls off remarkably in comparison with the fatigue strength in the ambient atmosphere. This decrease in fatigue strength is due to the easy initiation of fatigue cracks at corrosion pits in the early stage of the corrosion fatigue process. In order to make predictions of the lifetime of the machines and structures operating under corrosive environment, it is therefore important to understand the initiation as well as the growth characteristics of corrosion pits. However such kinds of research are few and limited, in contrast to the many studies of crack growth behavior during the corrosion fatigue process, which have been conducted. Furthermore, the existing data on corrosion pit growth are not always consistent, particularly with respect to the role of stress amplitude. In this study, plane bending fatigue tests of commercially pure aluminum were carried out in 3% NaCl solution, and the effects of stress amplitude and test frequency on the initiation and growth characteristics of corrosion pits were studied in detail. In addition the critical condition for the nucleation of a fatigue crack at a corrosion pit was considered.

KEYWORDS

Corrosion Pit, Pit Growth, Stress Amplitude, Cyclic Frequency, Crack Initiation, Aluminum.

INTRODUCTION

The fatigue strength of machines and structures exposed to corrosive environments is considerably reduced in comparison with that in the ambient atmosphere, and a fatigue limit may not exist. In the design of components for applications in corrosive environments allowance should be made for this degradation in fatigue properties. In the corrosion fatigue process it is known that corrosion pits arise in the initial stages of the fatigue process and that fatigue cracks develop at these pits. Therefore, it is important to clarify the generation and growth characteristics of corrosion pits as well as the process by which the cracks are generated in order to make reliable predictions of the corrosion fatigue lifetimes. Although there has been much research [1] on the generation and growth behavior of cracks during the corrosion fatigue process, relatively little work has been done on the generation and growth behavior of corrosion pits.

It has been reported that the following power law equation describes the growth law of a corrosion pit [2].

$$a = At^{\beta} \qquad (1)$$

where A and β are experimental constants. However, whether or not these experimental constants are dependent on stress amplitude and cyclic frequency has not been made clear.

The present study was carried out using commercially pure aluminum, which was cyclically loaded in plane-bending in a dripping 3% salt solution. Observations were made of the initiation and growth

characteristics of the corrosion pits throughout the corrosion fatigue lifetime in order to clarify the influence of stress amplitude and cyclic frequency. In addition, the critical stress intensity factor for fatigue crack growth from a corrosion pit was determined.

SPECIMEN AND EXPERIMENTAL METHOD

Specimen

The chemical composition of the commercially pure aluminum used in this study was 0.01% Si, 0.66% Fe, 0.15% Cu, 0.02 % Ti, 0.01% Mn, 0.01% Mg and 99.14% Al. The mechanical properties of the material were yield strength, 115 MPa, tensile strength, 125 MPa, and elongation, 20 %. The specimens were machined, planar-bending specimens, 15mm in width at the minimum section and 5mm in thickness. In order to facilitate the observations of the specimen surface, the specimens were polished to a mirror surface using diamond paste prior to testing. Except for the observation region the specimens, including the edges, were covered with a silicon resin so that corrosion pits and cracks would not be generated outside of the observation area.

Experimental Method

Fatigue machine used was a Schenck bending fatigue machine. The tests were carried out using sine wave loading at a stress ratio, R, of -1. The corrosive medium was a 3% salt solution, with tap water as the solvent. The experiments were carried out with the salt solution dripping onto the specimen surface at a drip rate of 10 cc per minute. In the study, four of stress amplitudes were used, namely 0, 54, 75 and 99 MPa and four cyclic frequencies, 0, 3, 15, and 30Hz were employed. The generation and growth behavior of corrosion pit were investigated by the observations made during the corrosion fatigue process. The experiments were interrupted periodically during the corrosion fatigue process in order to make replicas of the specimen surfaces. These replicas were then examined at 400x in an optical microscope (resolution: 1 micron) to obtain the dimensions and shapes of the corrosion pits. The depths of the corrosion pits were determined by the focused focal point method.

EXPERIMENTAL RESULT

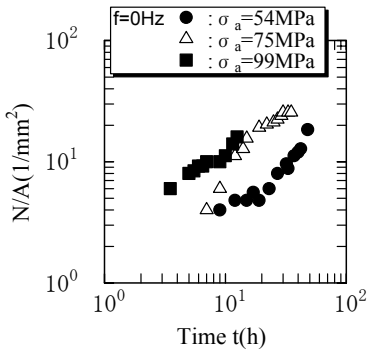

Figure 1: The corrosion pit density as a function of time under static loading.

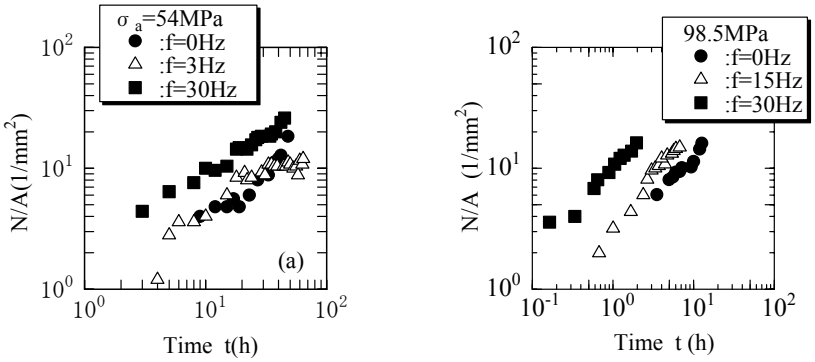

Figure 2: Corrosion pit density as a function of time under cyclic loading.

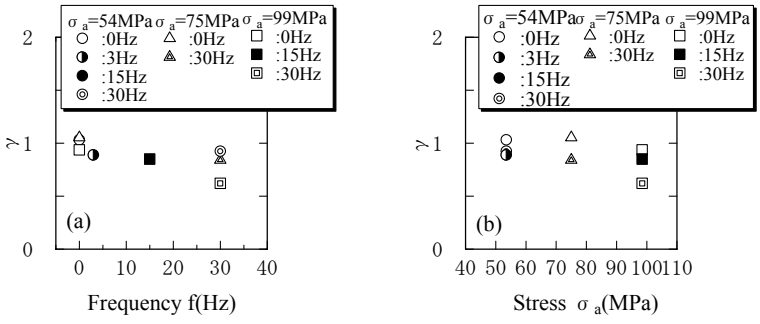

Figure 3: The constant γ as a function of the cyclic frequency and stress amplitude.

The Change in Time of the Corrosion Pit Density as a Function of Stress Amplitude and Frequency

Figure 1 shows the corrosion pit density as a function of time for pits at least 20 microns in size, which were

developed during static loading. As seen from this figure, corrosion pits develop within a few hours and their number increases with increase in stress level. Figure 2 shows the relationship between the corrosion pit density and cyclic frequency for stress amplitudes of 54 MPa and 99MPa. At low frequencies, 0 Hz and 3 Hz, there is little effect of cyclic frequency on the corrosion pit density. However, at the higher frequencies, 15 and 30 Hz, it is seen that pits initiate earlier and in greater numbers the higher the cyclic frequency. The change in corrosion pit density with time indicated in Figs, 1 and 2 can be approximated by the following equation:

$$N / A = Bt^{\gamma} \qquad (2)$$

where B and γ are experimental constants.

Fig. 3(a) shows the relationship between cyclic frequency and constant γ, and Fig. 3(b) shows the relation between stress amplitude and the constant γ. As seen from Fig. 3, the value of index, γ, is equal to about 1.0, independent of cyclic frequency and stress amplitude.

Growth Behaviour of Corrosion Pits

Growth Behavior of the Corrosion Pit in the Plane of the Specimen Surface

It was noted that some pits appeared to stop growing after reaching a certain size, whereas other pits continued to grow and serve as nuclei for fatigue cracks. In this study attention was directed at the growth behavior of the latter type of pits.

Figure 4 shows the relationship between the pit diameter, *2c*(m) and time, *t* (h), plotted on logarithmic scales for static loading. At static stress levels of 54 and 75MPa, there was a period during which corrosion pit growth was arrested, but later cracks were generated at the corrosion pits. At a static stress level of 99MPa, cracks developed at pits without a period of stagnation in corrosion pit growth. Further, the corrosion pits initiated earlier and grew more rapidly the higher the static stress level. A similar tendency was also observed for cyclic frequencies of 15 and 30 Hz as shown in Fig. 5 which shows the relationship between corrosion pit diameter, *2c* and time, *t*, plotted using logarithmic scales for stress amplitudes of 54 MPa and 99 MPa. As seen from this figure, the initiation time for a corrosion pit decreases and its growth rate increases the higher the cyclic frequency. The relation between pit size, 2c, and time in the static and cyclic tests can be approximated by the following equation:

$$2c = A_c t^{\beta_c} \qquad (3)$$

where, A_c and β_c are experimental constants. The relationship between cyclic frequency and the index β_c is shown in Fig. 6(a), and it is seen that the value of β_c increases from 0.2 to 1.0 with an increase in the cyclic frequency. Fig. 6(b) shows the relationship between stress amplitude and constant β_c, and β_c is seen to increase with an increase of stress amplitude. This trend was more pronounced at f=30Hz than at f=0Hz. We define the time for a pit of 10 microns diameter to develop as t_{ic}. The relationship between t_{ic} and cyclic frequency is shown in Fig. 7(a), and the relation between t_{ic} and stress amplitude is shown in Fig. 7(b). As seen from these figures, the generation time for a 10 micron sized corrosion pit decreases with increase in cyclic frequency and also with increase in stress amplitude.

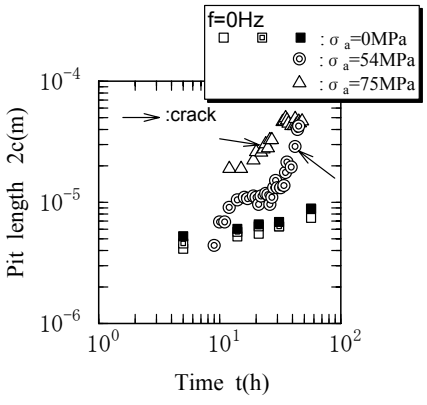

Figure 4: The corrosion pit diameter as a function of time under static loading.

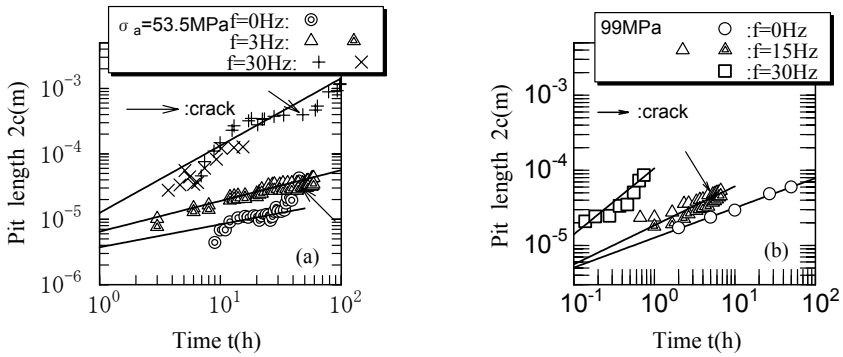

Figure 5: The corrosion pit diameter as a function of time under cyclic loading.

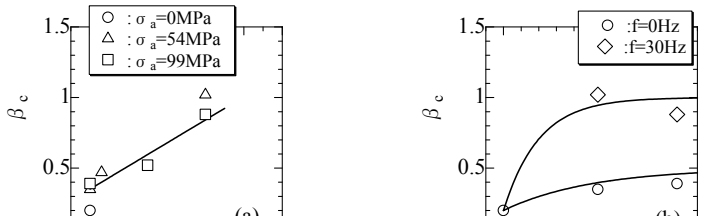

Figure 6: The constant β_c as a function of the cyclic frequency and stress amplitude.

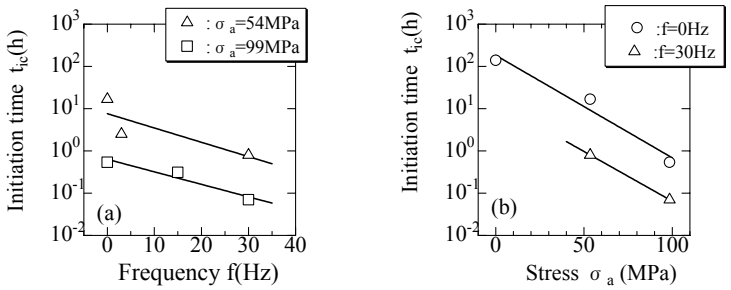

Figure 7: The time t_{ic} as a function of the cyclic frequency and the stress amplitude.

Growth Behavior of Corrosion Pits in the Depth Direction

In order to clarify the growth characteristic of corrosion pits, it is necessary to investigate not only the growth behavior of corrosion pits in the plane of the specimen surface but also in the depth direction. Figure 8 shows the relationship between time *t* (h) and corrosion pit depth *a* (m), under static loading conditions plotted on logarithmic scales, Fig. 9(a) and (b) show the relationship between time *t* (h) and depth *a* (m) for stress amplitude of 54 and 99MPa, respectively. From Figs, 8 and 9 it is seen that the corrosion pit depth increases with time and increase in cyclic frequency. In all cases the following type of relationship exists between the pit depth and the time, *t*:

$$a = A_a t^{\beta_a} \tag{4}$$

where, A_a and β_a are experimental constants.

Figure 10(a) shows exponent, β_a as a function of the cyclic frequency. With increase in the cyclic frequency, β_a increases from 0.2 to 1.0. In Fig. 10(b), the exponent β_a is shown as a function of stress amplitude. In the case of static loading no stress dependency of the exponent β_a is clearly apparent. However, at f =15 and 30 Hz, the exponent β_a increases from 0.3 to 1.0 with increase in the stress amplitude. Fig. 11(a) shows the relationship between the initiation time for a corrosion pit of 5 micron depth and the cyclic frequency, f, and Fig. 11(b) shows the relationship between this initiation time and the stress amplitude. From Fig. 11 it is seen that the initiation time decreases with an increase in cyclic frequency as well with increase in stress amplitude.

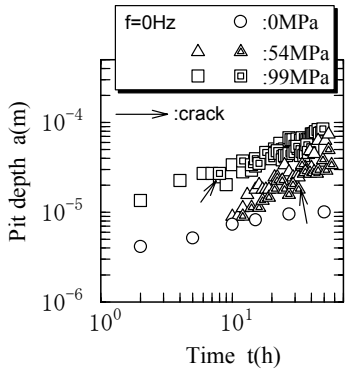

Figure 8: The depth of a corrosion pit under loading as function of time.

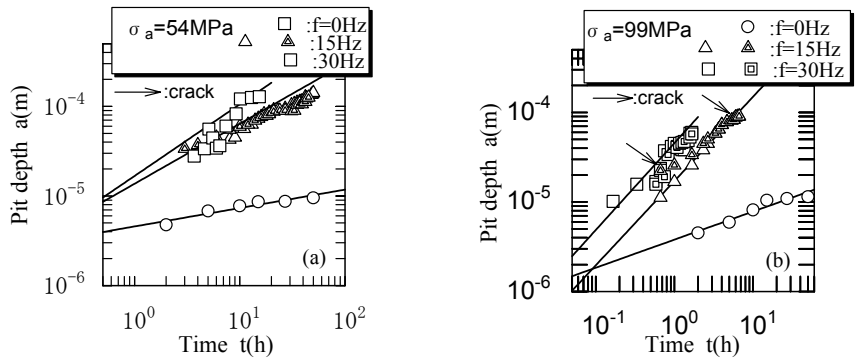

Figure 9: The depth of corrosion pit under cyclic loading static as a function of time.

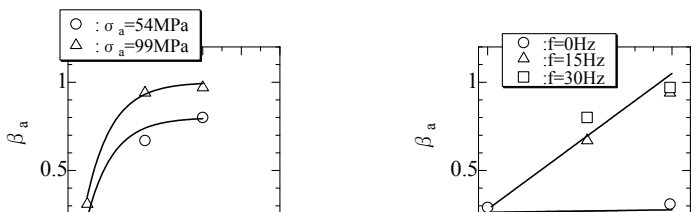

Figure 10: The constant β_a as a function of the cyclic frequency and stress amplitude.

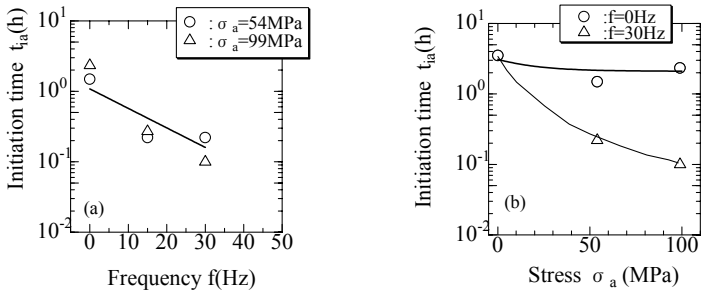

Figure 11: The time to generate a 5 micron deep corrosion pit as a function of the cyclic frequency and the stress amplitude.

The Condition for Crack Initiation at a Corrosion Pit.

In the design of components it is useful to have an understanding of the conditions for the initiation of a fatigue crack from a corrosion pit, and in this regard the $\sqrt{area}$ method proposed by Murakami and Endo [3] is helpful. In this method the effective length of a defect such as a corrosion pit is taken to be equal to the square root of the projected area of the pit measured perpendicular to the applied stress, i.e., in the depth direction. Upon substituting the projected area for a pit at which a fatigue crack is initiated as well as the associated stress into the following equation, a critical stress intensity factor for crack initiation can be determined:

$$K_{\mathrm{Im}ax} = 0.65\sigma_0\sqrt{\pi\sqrt{area}} \qquad (5)$$

where, σ_0 is the nominal stress.

The critical stress intensity factor at which a fatigue crack initiated is shown for each stress amplitude and cyclic frequency in Fig. 12. As seen from Fig. 12, the critical stress intensity factor for crack initiation from a corrosion pit takes on a value of about 0.4MPa$\sqrt{\ }$m, independent of stress amplitude or cyclic frequency. It is noted that Kondo [4] and Ishihara [5] have also previously found that the critical stress intensity factor at which a fatigue crack initiated at a corrosion pit takes on a constant value, independent of stress amplitude.

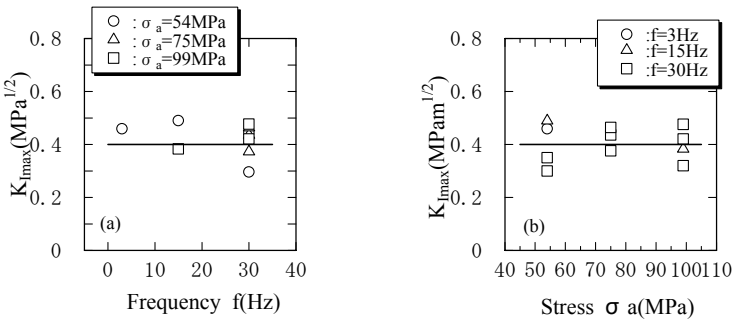

Figure 12: The critical stress intensity factor as a function of (a) the frequency, and (b) the stress amplitude.

Further, in a rotating bending test in 3% salt solution using an aluminum alloy, a value of 0.33MPa$\sqrt{\ }$m was obtained [6] for the threshold value of stress intensity factor range, $\triangle K_{th}$. This threshold value agrees quite well with the value of 0.4MPa$\sqrt{\ }$m, the value of critical stress intensity factor at which a crack initiates at a corrosion pit in the present investigation.

DISCUSSION

The commercially pure aluminum used in this investigation contained inclusions rich in iron and copper. When exposed to a 3% salt solution, these inclusions act as cathodes and the surrounding aluminum acts as an anode. The anodic aluminum near the cathodic particle corrodes and dissolves by a local battery reaction, and a corrosion pit is formed. SEM photographs confirm the above mechanism for the generation of corrosion pit formation. The following chemical reactions are involved in the formation of a corrosion pit:

$$2Al = 2Al^{3+} + 6e^{-} \quad (6a)$$

$$(3/2)O_2 + 3H_2O + 6e^{-} = 6OH^{-} \quad (6b)$$

The cathodic reaction, Eq. (6b), an oxygen-consumption-type of corrosion, was active in the experiments, with the rate of generation and growth of corrosion pits being governed by the oxygen content. Since the total anodic and cathodic currents must be equal, the oxygen content controls the rate of the anodic reaction as well. There are three factors, which contribute to the rate of corrosion pit generation. First of all, oxygen must be available, and in dripping experiment an ample supply of oxygen is present in the solution. Secondly, the inclusion acts as a stress raiser, and the higher the stress amplitude the more likely that the protective oxide film will be ruptured by local plastic deformation at an inclusion, thereby exposing the aluminum directly to the solution. Thirdly, an increase in cyclic frequency simply means that more cycles will be applied in a given time period, thereby contributing to the ease of fatigue crack nucleation within that time period. In addition, any corrosion products that might inhibit the corrosion reaction are washed away by the flow caused by the dripping action.

CONCLUSIONS

(1) Corrosion pits arise earlier in time and in greater numbers the higher the stress amplitude and the cyclic frequency.
(2) At a given stress amplitude and frequency the corrosion pit density is approximately proportional to the time of exposure to the 3% NaCl solution.
(3) The rate of growth of the corrosion pit diameter and the corrosion pit depth increases with stress amplitude and cyclic frequency. The relationship between the size of a corrosion pit and time can be expressed by a power law equation, with the exponent increasing from 0.3 to 1.0 as stress amplitude and cyclic frequency increase.
(4) The critical stress intensity factor for generating the crack from corrosion pit has a value of about 0.4MPa $\sqrt{}$m, independent of stress amplitude or cyclic frequency. This value is in close agreement with the threshold value for crack growth which was previously determined in corrosion-fatigue tests of an aluminum alloy.

REFERENCES

1. M. Nakajima *et al*, Trans. JSME, 58(1992) 2034.
2. H. P. Godard, Canadian J. Chemical Eng.38 (1960)167.
3. Y. Murakami and M. Endo, in The Behaviour of Short Fatigue Cracks, ed. by K. J. Miller and E. R. de los Rios, Mech. Engng. Pubs., London, (1986), 275-293.
4. Y. Kondo, Trans. JSME, 53 (1987) 1983.
5. S. Ishihara et al, Trans JSME, 57-540, A(1991),1775.
6. S. Ishihara and A. J. McEvily, Fatigue Fract. Eng. (1995), 1311.

ORAL REFERENCE: ICF100723OR

COUPLING OF ASYMPTOTIC SOLUTIONS WITH FINITE ELEMENTS AT INTERFACE CONFIGURATIONS IN PIEZOELECTRIC COMPOSITES

Matthias Scherzer and Meinhard Kuna

Freiberg University of Mining and Technology, Institute of Mechanics and Machine Components
Lampadiusstraße 4, D-09596 Freiberg, Germany

ABSTRACT

The present work is directed to the analysis of interface corner and crack configurations which occur in smart composite materials. It delivers a new technique for solving the corresponding piezoelectric boundary value problems by asymptotic eigenfunction expansions in connection with the conventional finite element method. This approach represents the extension to coupled electromechanical material behaviour of a method which was introduced for geometrical and physical linear and non-linear solid mechanics formerly [9, 10]. The proposed approach has the advantage that the asymptotic stiffness matrix does not depend on the distance to the tip and that oscillating terms of the asymptotics can be circumvented numerically but are still fully contained. Therefore, results can be achieved with much better accuracy than by means of regular finite elements.

KEYWORDS

Piezoelectric materials, fracture, asymptotic analyses, numerical methods

INTRODUCTION

Piezoelectric, ferroelectric and dielectric ceramics or polymers are widely applied in Micro Electro Mechanical Systems (MEMS) to supply the essential sensing and/or actuating functionality [5]. As a consequence of their integration into MEMS, problems of fracture and fatigue play an important role for the optimum design and reliable service performance of MEMS. Fracture mechanics analyses and safety concepts have to be applied to crack-like defects in piezoelectric bulk materials or in interface structures and lead to the corresponding asymptotic solutions at interface crack and corner tips with the associated coefficients of the eigenfunctions as fracture parameters.
First theoretical studies [3, 7, 14] about interface crack tips in piezoelectrics show that difficult singular oscillatory solutions can occur. According to its prior importance for many micromechanical applications, models of interface crack problems in dissimilar piezoelectric materials has been published recently with a fast-growing rate (see for instance [8, 15] and other and the references therein). Most of the authors use the Lekhnitzkij and Stroh formalisms or the Fourier transform technique in connection with dual boundary value problems including Cauchy-type-integrals for linear statements within infinite bodies. In this context it is interesting to note that the usual expecting singular oscillatory behaviour can change to solutions without oscillations for modified electric boundary conditions [4, 7, 14]. By means of the analytic solution in [2] it is shown that an interface crack tip between a piezoelectric

and a conductor produces three non-oscillating singular terms of the form $\xi^{(-0.5-\nu)}\tilde{\mu}_1(\theta)$, $\xi^{-0.5}\tilde{\mu}_2(\theta)$ and $\xi^{(-0.5+\nu)}\tilde{\mu}_3(\theta)$, whereby ξ is the distance to the tip, θ represents the polar angle and ν is defined through $\nu = 0.5 - h$ with $0 < h < 0.5$. This way, energetic possible solutions may have a singular behaviour which is stronger than -0.5.

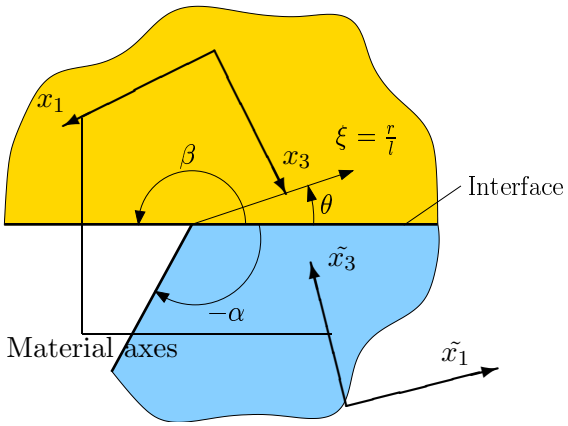

Figure 1: Interface corner configuration

The preponderant majority of the existing solutions at interface crack tips between piezoelectric materials represent linear boundary value problems for infinite bodies although real electromechanical materials show non-linear behaviour, too [6, 12]. But in general, the linear solution procedures mentioned above are not extensible to non-linear problems. Thus, there is a need to develop solution techniques filling this gap. The extension of the methods elaborated in [9, 10] to piezoelectric materials seems to be very hopeful in this sense. In the following, the approach of [9, 10] is applied to linear piezoelectric problems including interface cracks within finite body domains.

LINEAR PIEZOELECTRICITY AND ASYMPTOTIC ANALYSIS

In order to solve the complicated boundary value problem of interface configurations in connection with their difficult asymptotic features and to develop associated stable numerical methods for its handling, it is necessary to dispose of the complete eigenfunction expansions at interface corner and interface crack tips. We will restrict our analysis to the simplest approach for the constitutive laws in both material domains of the interface configuration. The main assumptions are:

1. Neglegtion of magnetic and time effects
2. Introducing the thermomechanical-electric coupling by the electric energy term in the first law of thermodynamics
3. Linearization of the ferroelectric hysteresis loop
4. Transversal isotropic piezoelectric behaviour

The governing relations describing this coupled electromechanical field problem are the equations of stress equilibrium, the compatibility equations and Gauss' law of electrostatics

$$\sigma_{ij,i} = 0, \quad S_{ij} = \tfrac{1}{2}(u_{i,j} + u_{j,i}), \quad D_{i,i} = 0, \quad \text{(i,j=1,2,3)} \tag{1}$$

as well as the equations of the linear piezoelectric material behaviour:

$$\begin{aligned}
\sigma_{11} &= c_{11}S_{11} + c_{12}S_{22} + c_{13}S_{33} - e_{31}E_3, \ \sigma_{21} = (c_{11} - c_{12})S_{21} \\
\sigma_{22} &= c_{12}S_{11} + c_{11}S_{22} + c_{13}S_{33} - e_{31}E_3, \ \sigma_{13} = 2c_{44}S_{13} - e_{15}E_1 \\
\sigma_{33} &= c_{13}S_{11} + c_{13}S_{22} + c_{33}S_{33} - e_{33}E_3, \ \sigma_{32} = 2c_{44}S_{32} - e_{15}E_2 \\
D_1 &= 2e_{15}S_{13} + \kappa_{11}E_1, \ D_2 = 2e_{15}S_{32} + \kappa_{11}E_2 \\
D_3 &= e_{31}S_{11} + e_{31}S_{22} + e_{33}S_{33} + \kappa_{33}E_3.
\end{aligned} \tag{2}$$

In (1) and (2) σ_{ij}, S_{ij}, u_i, E_i and D_i denote the stress and deformation tensor, the mechanical displacement vector, the negativ gradient of the electrical potential ϕ and the dielectric displacements, respectively. The material parameters c_{ij} (elastic), e_{ij} (piezoelectric) and κ_{ij} (dielectric) characterize transversly isotropic piezoelectrics with pooling-axis along the third direction of the chosen material co-ordinate system in (2). These material equations are written with regard to the material axes of each dissimilar material domain as shown in Figure 1 (x_1–x_3, $\tilde{x_1}$–$\tilde{x_3}$). The axes x_2 and $\tilde{x_2}$ are directed perpendicular to the plane of Figure 1.

Further simplifications lead to two-dimensional statements with the assumptions of plane strain:

$$S_{22} = S_{32} = S_{12} = E_2 = 0 \ (x_2 - \text{direction normal to the plane}) \tag{3}$$

and reduce the system (1) and (2) to

$$\left\{ \begin{array}{c} S_{11} \\ S_{33} \\ S_{13} \end{array} \right\} = \left(\begin{array}{ccc} a_{11} & a_{13} & 0 \\ a_{13} & a_{33} & 0 \\ 0 & 0 & \frac{d_{33}}{2} \end{array} \right) \left\{ \begin{array}{c} \sigma_{11} \\ \sigma_{33} \\ \sigma_{13} \end{array} \right\} + \left(\begin{array}{cc} 0 & b_{13} \\ 0 & b_{33} \\ \frac{b_{31}}{2} & 0 \end{array} \right) \left\{ \begin{array}{c} D_1 \\ D_3 \end{array} \right\} \tag{4}$$

$$\left\{ \begin{array}{c} E_1 \\ E_3 \end{array} \right\} = - \left(\begin{array}{ccc} 0 & 0 & b_{31} \\ b_{13} & b_{33} & 0 \end{array} \right) \left\{ \begin{array}{c} \sigma_{11} \\ \sigma_{33} \\ \sigma_{13} \end{array} \right\} + \left(\begin{array}{cc} \delta_{11} & 0 \\ 0 & \delta_{33} \end{array} \right) \left\{ \begin{array}{c} D_1 \\ D_3 \end{array} \right\} \tag{5}$$

$$\frac{\partial \sigma_{11}}{\partial x_1} + \frac{\partial \sigma_{13}}{\partial x_3} = 0, \ \frac{\partial \sigma_{13}}{\partial x_1} + \frac{\partial \sigma_{33}}{\partial x_3} = 0, \ \frac{\partial D_1}{\partial x_1} + \frac{\partial D_3}{\partial x_3} = 0 \tag{6}$$

$$\frac{\partial^2 S_{11}}{\partial x_3^2} + \frac{\partial^2 S_{33}}{\partial x_1^2} = 2 \frac{\partial^2 S_{13}}{\partial x_1 \partial x_3}, \ \frac{\partial E_1}{\partial x_3} - \frac{\partial E_3}{\partial x_1} = 0, \tag{7}$$

whereby the coefficients a_{11}, ..., b_{13}, ..., δ_{11} and δ_{33} ($b_{13} \neq b_{31}$) can be determined from the material parameters introduced above. In each material co-ordinate system the solution can be written in form of the potentials $U(x_1, x_3)$ and $\chi(x_1, x_3)$ [13]:

$$\begin{array}{rcl} \sigma_{11} & = & U(x_1, x_3)_{,33}, \ \sigma_{33} = U(x_1, x_3)_{,11}, \ \sigma_{13} = -U(x_1, x_3)_{,13} \\ D_1 & = & \chi(x_1, x_3)_{,3}, \ D_3 = -\chi(x_1, x_3)_{,1}. \end{array} \tag{8}$$

Finally, we end up in a linear partial differential equation of sixth order for $U(x_1, x_3)$. The general solution of this equation and therewith also the solution of the whole problem - because $\chi(x_1, x_3)$ follows from $U(x_1, x_3)$ by integration - has the form

$$U(x_1, x_3) = \sum_k \sum_{i=1}^{6} d_i(\lambda_k)(x_1 + \tau_i x_3)^{\lambda_k + 2}. \tag{9}$$

The complex variables $d_i(\lambda_k)$ are free coefficients to be determined from the overall solution and τ_i stands for the roots of the characteristic polynom (sixth order with real coefficients) of the partial differential equation. The numbers λ_j, which are in general complex ones, represent the roots of the solvability condition of the interface corner configuration together with the associated boundary and transition conditions. There exists the corresponding conjugate complex root $\overline{\tau_i}$ for each complex τ_i. Because $U(x_1, x_3)$ is a real function, terms of the form

$$\begin{array}{l} e_i p^{(\lambda_k + 2)} \cos\left[(\lambda_k + 2)(\kappa + \frac{\pi}{2})\right] + f_i p^{(\lambda_k + 2)} \sin\left[(\lambda_k + 2)(\kappa + \frac{\pi}{2})\right] \\ \text{with} \ \ p = \sqrt{(x_1)^2 + 2\tau_i^r x_1 x_3 + (x_3)^2[(\tau_i^i)^2 + (\tau_i^r)^2]}, \quad \kappa = \arctan\left((x_1 + \tau_i^r x_3)/(\tau_i^i x_3)\right) \\ \text{and} \ \ \tau_i = \tau_i^r + \sqrt{-1}\tau_i^i, \ d_i(\lambda_k) = e_i(\lambda_k) + \sqrt{-1} f_i(\lambda_k) \end{array} \tag{10}$$

occur for τ_i and $\overline{\tau_i}$ in (9). The solution representation (10) is valid for each material domain of the interface configuration which has its own material parameters, axes, τ_i and $d_i(\lambda_k)$. The construction of the associated eigenfunction expansion results in the following steps:

1. Transformation of the solutions (9) into the same polar co-ordinate system (ξ, θ) for both material regions ($0 \leq \theta \leq \beta$ and $0 \geq \theta \geq -\alpha$) of the interface corner configuration
2. Establishing the transcendental solvability condition according to the boundary and transition conditions

$$\Rightarrow \ Det(\lambda, ...) = 0 \tag{11}$$

The boundary and transition conditions have the usual form:
- Vanishing normal and tangent stresses $(\sigma_{\theta\theta}, \sigma_{\xi\theta})$ and vanishing normal dielectric displacements (D_θ) at $\theta = \beta, \ \theta = -\alpha$

- Continuity of normal and tangent stresses, both displacement components (u_ξ, u_θ), electric potential (ϕ, $E_1 = -\frac{\partial \phi}{\partial x_1}$, $E_3 = -\frac{\partial \phi}{\partial x_3}$) and normal dielectric displacements at $\theta = 0$
Other boundary conditions can be applied by the given solution technique, too. The only requirements are that they must result from physical reasons and have to give correctly formulated problems.

3. Numerical determination of λ: $\Rightarrow \lambda_k, k = 1, ..., \infty$ in (11)
4. For complex roots $\lambda_k = \nu_k + \mathrm{i}\mu_k$ the conjugate complex root $\overline{\lambda_k} = \nu_k - \mathrm{i}\mu_k$ exists:
$\Rightarrow$ terms of the quality $\xi^{\nu_k} \cos(\mu_k ln(\xi))$, $\xi^{\nu_k} \sin(\mu_k ln(\xi))$ occur
5. Determination of the associated eigenvectors and eigenfunctions (and removing of the energetic "useless" functions) to get the expansions

$$U(\xi, \theta) = \sum_{k=1}^{\infty} C_k \xi^{(\lambda_k + 2)} f_k^{(U)}(\theta, \lambda_k), \quad \sigma_{\xi\xi}(\xi, \theta) = \sum_{k=1}^{\infty} C_k \xi^{\lambda_k} f_{k\xi\xi}^{(\sigma)}(\theta, \lambda_k), ... \tag{12}$$

with the unknown coefficients C_k

For solving whole boundary value problems of components having interface corner configurations, the sole knowledge of the eigenfunctions introduced above is insufficient. The asymptotic eigenfunction expansion in the neighbourhood of the interface corner tip must be connected to the solution in the remaining part of the structure. Doing this, finite element nodes of a regular net can be established at a distance of $\xi = \xi_0$ from the corner together with the degrees of freedom $u_i(\xi_0, \theta_j)$ for the displacements and the electric potential ϕ (Figure 2).

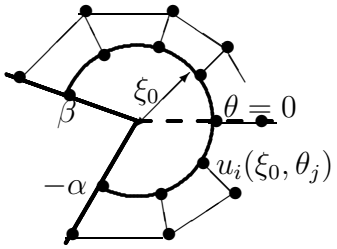

Figure 2: Neighbourhood of an interface corner together with the finite element nodes

The main idea of the presented approach (which was developed in [9, 10] for pure mechanical behaviour) consists in a replacement of the corner neighbourhood ($\xi < \xi_0$) effect to the surrounding body ($\xi > \xi_0$) by introducing a special stiffness matrix at $\xi = \xi_0$ which can be assembled in a conventional way together with the other element stiffness matrices to the global stiffness matrix. The description of this procedure cannot be given here because of the limited space. It is referred to [9, 10, 11] for more details. The main essentials of the proposed approach result in the facts that the asymptotic stiffness matrix does not depend on ξ_0 and the oscillating terms are circumvented numerically but still fully contained.

This makes it possible from the numerical point of view to "live" with the oscillatory asymptotic solutions at the interface crack tip if not any physical arguments forbid this behaviour from other reasons. To avoid the oscillations it is necessary to introduce the corresponding kinematical assumptions in the interface crack tip region.
Since the coefficients of the eigenfunctions C_k describe the electromechanical fields in the interface corner region completely they can be applied as fracture parameters and used to formulate failure criteria.

FIRST TEST EXAMPLES

The asymptotic stiffness matrix was calculated by the help of modern computer algebra systems and implemented as a user defined element within the commercial finite element code ABAQUS [1]. Results of test computations will be explained. An interface crack specimen (Figure 3) of two different piezoelectric materials (extension: 100*200 dimensionless units, crack in the middle of the specimen with a length of 50, plane strain (3) conditions) is strained homogenously at the upper specimen end and clamped right opposite. The electric potential is given at the right specimen side ($x_1 = 50$, $-100 \leq x_3 \leq 100$) with zero values. For this specimen the material parameters are introduced by:

Upper half (PZT-4):

$c_{11} = 1.39 * 10^{11} \frac{N}{m^2}$, $c_{33} = 1.13 * 10^{11} \frac{N}{m^2}$, $c_{12} = 7.78 * 10^{10} \frac{N}{m^2}$, $c_{13} = 7.43 * 10^{10} \frac{N}{m^2}$, $c_{44} = 2.56 * 10^{10} \frac{N}{m^2}$
$\kappa_{11} = 6.0 * 10^{-9} \frac{C}{Vm}$, $\kappa_{33} = 5.470 * 10^{-9} \frac{C}{Vm}$, $e_{15} = 13.44 \frac{C}{m^2}$, $e_{31} = -6.98 \frac{C}{m^2}$, $e_{33} = 13.84 \frac{C}{m^2}$

Lower half (hypothetical):

$c_{11} = 2.39 * 10^{11} \frac{N}{m^2}$, $c_{33} = 1.13 * 10^{10} \frac{N}{m^2}$, $c_{12} = 4.78 * 10^{10} \frac{N}{m^2}$, $c_{13} = 5.43 * 10^{10} \frac{N}{m^2}$, $c_{44} = 2.56 * 10^{9} \frac{N}{m^2}$
$\kappa_{11} = 4.0 * 10^{-9} \frac{C}{Vm}$, $\kappa_{33} = 2.470 * 10^{-9} \frac{C}{Vm}$, $e_{15} = 12.0 \frac{C}{m^2}$, $e_{31} = -4.98 \frac{C}{m^2}$, $e_{33} = 14.0 \frac{C}{m^2}$

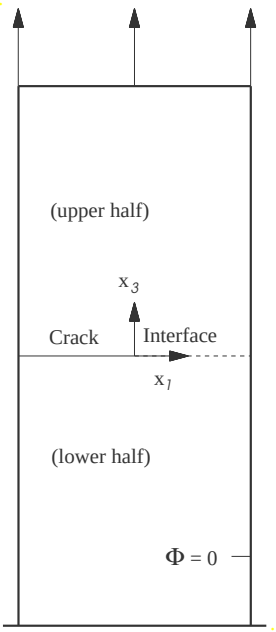

Figure 3: Piezoelectric specimen under tension

Both material domains have the same pooling directions (x_3). The homogenous boundary and transition conditions given above lead to the roots λ_k of the solvability condition (11) resulting in:

1. $-0.5 \pm \sqrt{-1} * 0.11733$, $0.5 \pm \sqrt{-1} * 0.11733$, $1.5 \pm \sqrt{-1} * 0.11733$, ...
2. -0.5, 0.5, 1.5, 3.5, 4.5, 5.5, ...
3. 0.0, 1.0, 2.0, 3.0, 4.0, 5.0, ...

Each pair of the conjugate complex roots (1.) produces two linear independent eigenvectors from the free constants $d_i(\lambda_k)$ while the second part of the roots (2.) have single eigenvectors and the third part (3.) generates three linear independent eigenvectors for each concrete value.
In Figure 4 the stress components σ_{33}, σ_{13} and the electric field E_3 are shown around the crack tip within a zoom radius $\xi_z = 1.0$. The crack comes from the left (negative x_1-axis) and the interface lies on the horizontal straight line (positve x_1-axis) on the ligament in front of the crack. The solutions of usual finite element computations ("without asymptotics") are compared with solutions following from the technique introduced above ("with asymptotics", $\xi_0 = 0.01$).

The results confirm the fact observed at pure mechanical analyses [9, 10] that the regular finite element method cannot give the correct solution at interface crack tips in general. The regular finite element representation of σ_{33} is familar to the asymptotic behaviour at a crack tip inside a homogenous isotropic material and cannot "feel" interface tip effects. Furthermore, the stress component σ_{13} of the same solution ("without asymptotics") fulfils the given boundary conditions on the crack surfaces very bad only. The differences between the solutions with and without asymptotics can also be seen on the representations of the electric variable E_3. The poor performance of regular finite elements in the vicinity of an interface crack tip may be explained by means of the fact that the polynomial shape functions cannot reproduce both the radial $\xi^{\nu_k}-$ asymptotics and the oscillating behaviour of the form $\cos(\mu_k ln(\xi))$ even if the element size is extremely diminished. Regular finite elements produce an asymptotic behaviour at interface crack tips which is severe different from that of the actual eigenfunctions.

References

[1] *ABAQUS Version 5.8.* Hibbitt, Karlsson & Sorensen, Inc. USA 1998.

[2] V.F. Bakirov, M. Scherzer and M. Kuna: *The problem of an interface crack between a piezoelectric and a conductor under electrical and mechanical loads.* (in preparation), 2001.

[3] H.G. Beom and S.N. Atluri: *Near-tip fields and intensity factors for interfacial cracks in dissimilar anisotropic piezoelectric media.* International Journal of Fracture 75(2), pp. 163–183, 1996.

[4] V.B. Govorukha and V.V. Loboda: *Contact zone models for an interface crack in a piezoelectric material.* Acta Mechanica 140(3-4), pp. 233–246, 2000.

[5] A. Heuberger (Editor): *Mikromechanik, Mikrofertigung mit Methoden der Halbleitertechnologie.* Springer-Verlag, Berlin Heidelberg New York, 1991.

[6] M. Kamlah, Böhle U. and D. Munz: *On a non-linear finite element method for piezoelectric structures of hysteretic ferroelectric ceramics.* Computational Material Science 19, pp. 81–86, 2000.

[7] C.-M. Kuo and D.M. Barnett: *Stress singularities of interfacial cracks in bonded piezoelectric half-spaces.* In J.J. Wu, T.T.C. Ting and D.M. Barnett, Eds., Modern Theory of Anisotropic Elasticity and Applications, pp. 33–50, Philadelphia 1991. SIAM Proceedings Series.

[8] Qing-Hua Qin and Yiu-Wing Mai: *Closed crack tip model for interface cracks in thermopiezoelectric materials.* International Journal of Solids and Structures 36(16), pp. 2463–2479, 1999.

[9] M. Scherzer: *Non-linear deformed interface corner stress characterization by effective parallel numerical methods.* In B.L. Karihaloo, Y.W. Mai, M.I. Ripley and R.O. Ritchie, Eds., Advances in Fracture Research, Proceedings of the 9th International Conference on Fracture 1-5 April 1997, Sydney, Australia, vol. 4, pp. 1959–1970, Pergamon Press.

[10] M. Scherzer: *Physikalisch und geometrisch nichtlineare Problemstellungen der Festkörper- und Bruchmechanik an Interface-Konfigurationen.* Habilitationsschrift, Technische Universität Bergakademie Freiberg 1999.

[11] M. Scherzer and M. Kuna: *Asymptotic analysis of interface problems in piezoelectric composite materials.* In K.-H. Hoffmann, Editor, Smart Materials, pp. 137–148, Berlin 2001. Springer Verlag, Proceedings of the first caesarium, Bonn, November 17–19, 1999.

[12] S. Shen, T. Nishioka, Z.-B. Kuang and Z. Liu: *Nonlinear electromechanical interfacial fracture for piezoelectric materials.* Mechanics of Materials 32(1), pp. 57–64, 2000.

[13] H. Sosa: *Plane problems in piezoelectric media with defects.* International Journal of Solids and Structures 28(4), pp. 491–505, 1991.

[14] Z. Suo, C.-M. Kuo, D.M. Barnett and J.R. Willis: *Fracture mechanics for piezoelectric ceramics.* International Journal of Solids and Structures 40(4), pp. 739–765, 1992.

[15] T.C. Wang and X.L. Han: *Fracture mechanics of piezoelectric materials.* International Journal of Fracture 98(1), pp. 15–35, 1999.

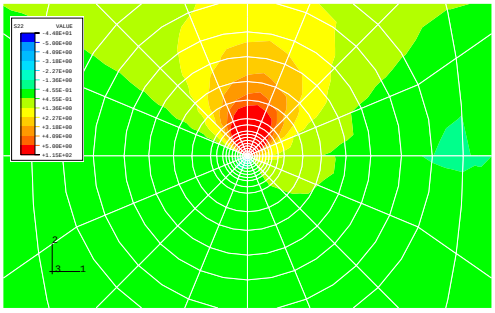

(σ_{33} with asymptotics)

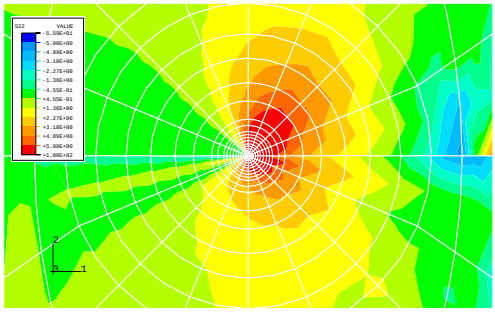

(σ_{33} without asymptotics)

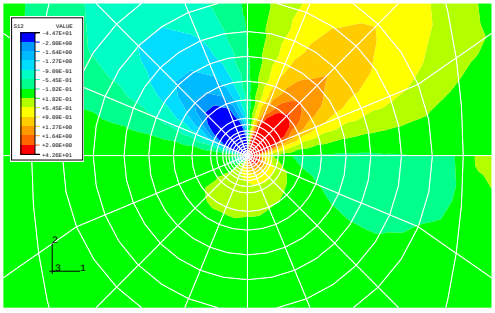

(σ_{13} with asymptotics)

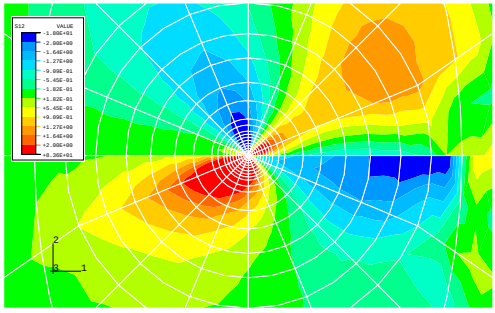

(σ_{13} without asymptotics)

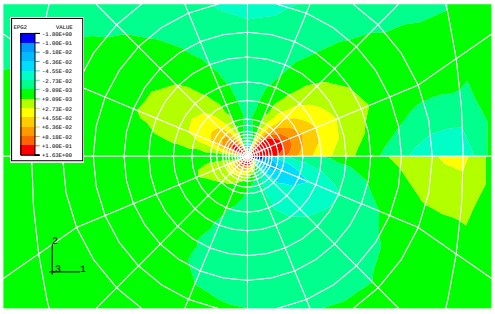

(E_3 with asymptotics)

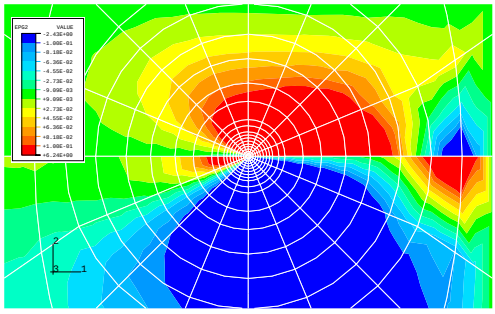

(E_3 without asymptotics)

Figure 4: Piezoelectric solutions at an interface crack tip under tension

ORAL/POSTER REFERENCE :

COUPLING OF DAMAGE MECHANICS AND PROBABILISTIC APPROACH FOR LIFE-TIME PREDICTION OF COMPOSITE STRUCTURES

Y. Bruner[1], J. Renard[1], D. Jeulin[2] and A. Thionnet[1]

[1]Centre des Matériaux Pierre-Marie Fourt, Ecole Nationale Supérieure des Mines de Paris
BP 87, F-91003 Evry Cedex, France
[2]Centre de Morphologie Mathématique, Ecole Nationale Supérieure des Mines de Paris
35, rue St Honoré 77305 Fontainebleau Cedex, France

ABSTRACT

We propose a damage model with a probabilistic approach for laminates made of unidirectional fibre reinforced plies. Statistical information is collected through multiple cracking tests. The defects are considered as transverse matrix cracks and we study them by examining $[0_3/90_3]_s$, $[0_2/60_2/-60_2]_s$ and $[0_2/90_2/-45_2/45_2]_s$ laminates.
Parameters of a cumulative distribution function of the failure strength are determined. Probabilistic parameters of the cumulative distribution are chosen to be independent of the ply thickness and multiaxial loading to have intrinsic values for describing the ply. Probabilistic parameters found previously are introduced into a finite element computation of laminates using a Statistical Volume Element (SVE). As experimental results, numerical ones present a dispersion of the failure stress.

KEYWORDS

Carbon/epoxy fabric laminates, composite laminates, defects statistics, crack density, transverse cracking, multiaxial loading, probabilistic failure criteria.

INTRODUCTION

The fracture behaviour of fibre reinforced composites has an inherent variability which results from the presence of defects in the constituents. A probabilistic model including failure criteria, taking into account the presence of defects for predicting the statistical fracture behaviour is proposed for a composite laminate under multiaxial loading.
The studied composite laminate is a stack of plies where each ply is made of unidirectional carbon fibre (T300) embedded in an epoxy matrix (914). Different stackings of composite laminates $[0_3/90_3]_s$, $[0_2/60_2/-60_2]_s$ and $[0_2/90_2/-45_2/45_2]_s$ are subjected to mechanical loads which lead to damage. The damage is known to consist of intralaminar cracks (fibre breaks, axial and transverse cracks) and interlaminar cracks formed by local separation of plies (delamination). We focus on transverse cracks which give a variability of fracture properties.

In order to predict failure stresses in composite laminates, it is necessary to take into account the probabilistic nature of defects. Such an approach consists of two parts: identification of a population of defects and simulation of the statistical behaviour of the material under multiaxial loading. The statistical aspect is introduced in finite element calculation with the Statistical Volume Element (SVE) described by Baxevanakis et al. [1]. The paper is organized in the following way. The first part describes the identification of transverse cracks and a multiaxial fracture criterion. The second part presents the numerical simulation of the fracture of a laminate composite.

TRANSVERSE CRACKING

Description of the test

The aim of the test is to estimate the population of defects that generates transverse cracks during the damage process of composite laminates. The material used in this study is a carbon fibre reinforced epoxy (T300, 914) with the ply properties reported on Tab. 1.

TABLE 1: MECHANICAL PROPERTIES OF CARBON/EPOXY PLY.

Material	E_L (GPa)	E_T (GPa)	G_{LT} (GPa)	ν_{LT}	σ_R (MPa)	ε_R (%)
Ply	140	9.5	3.2	0.31	2150	1.1

In a symmetric laminate, an axial load produces an in-plane stress state in off-axis plies consisting of normal stresses parallel and perpendicular to fibres and shear stresses. Following the orientation and the stacking, the stress state varies. To have different stress state we consider three laminates : $[0_3/90_3]_s$, $[0_2/60_2/-60_2]_s$, $[0_2/90_2/-45_2/45_2]_s$ laminates. Samples from the laminates are cut and tested in an Instron testing machine. Axial and transverse strains are measured using strain gauges. Once the edges of the specimens are polished, the specimens are loaded to a selected strain level. The position of every crack is measured in situ by a traveling optical microscope (Fig. 1). The position and the number of cracks are collected for each ply and for each level of deformation until the specimen fails.

Results

To determine the local failure stress state resulting from the global stress applied experimentally, we accurately simulate experiments by introducing cracks exactly at the positions and at the deformation levels they were found experimentally. Figure 2 shows how we calculate the stresses in each ply for a deformation level at which a crack appears.

We choose the damage variable defined by Thionnet [2] as $\Psi = d \times t$ (d : number of cracks per unit length and t : the thickness of the ply) and we define a quadratic criterion $\sigma_{eR} = \sqrt{\sigma_T^2 + a\tau_{LT}^2}$ (σ_T is the transverse stress and τ_{LT} is the shear stress in the local reference and a is a coefficient representing the effect of defects on shear) for describing the defect population in a ply (Fig. 3 a). These variables are chosen to describe the population of defects independently of the ply thickness and multiaxial loading. First from the curves of Fig. 3 a, we determine $a = 0.45$, this value is consistent to what is observed in literature for a deterministic mesoscopic Tsai-Hill criterion.

Next, we gather the information on defects coming from different plies. This is possible only if transverse cracks were observed just before the occurrence of the delamination because our pseudo-tridimensional calculation does not take into account this phenomenon. This is the reason why Figure 3 b) shows the addition of two populations in $[0_3/90_3]_s$ and $[0_2/60_2/-60_2]_s$ laminates. The population of cracks of $[0_2/90_2/-45_2/45_2]_s$ laminate is removed because the delamination appears at the same time as transverse cracks. Then, the possible model of distribution for the transverse cracks is a sigmoidal distribution represented by the Eq. 1 :

$$\Psi(\sigma_R) = A(1 - e^{(\frac{\sigma_R}{\sigma_\circ})^m}) \tag{1}$$

with $A = 0.47$ is the maximum number of defects (nondimensional),
$\sigma_\circ = 64.82$ scale parameter (MPa),

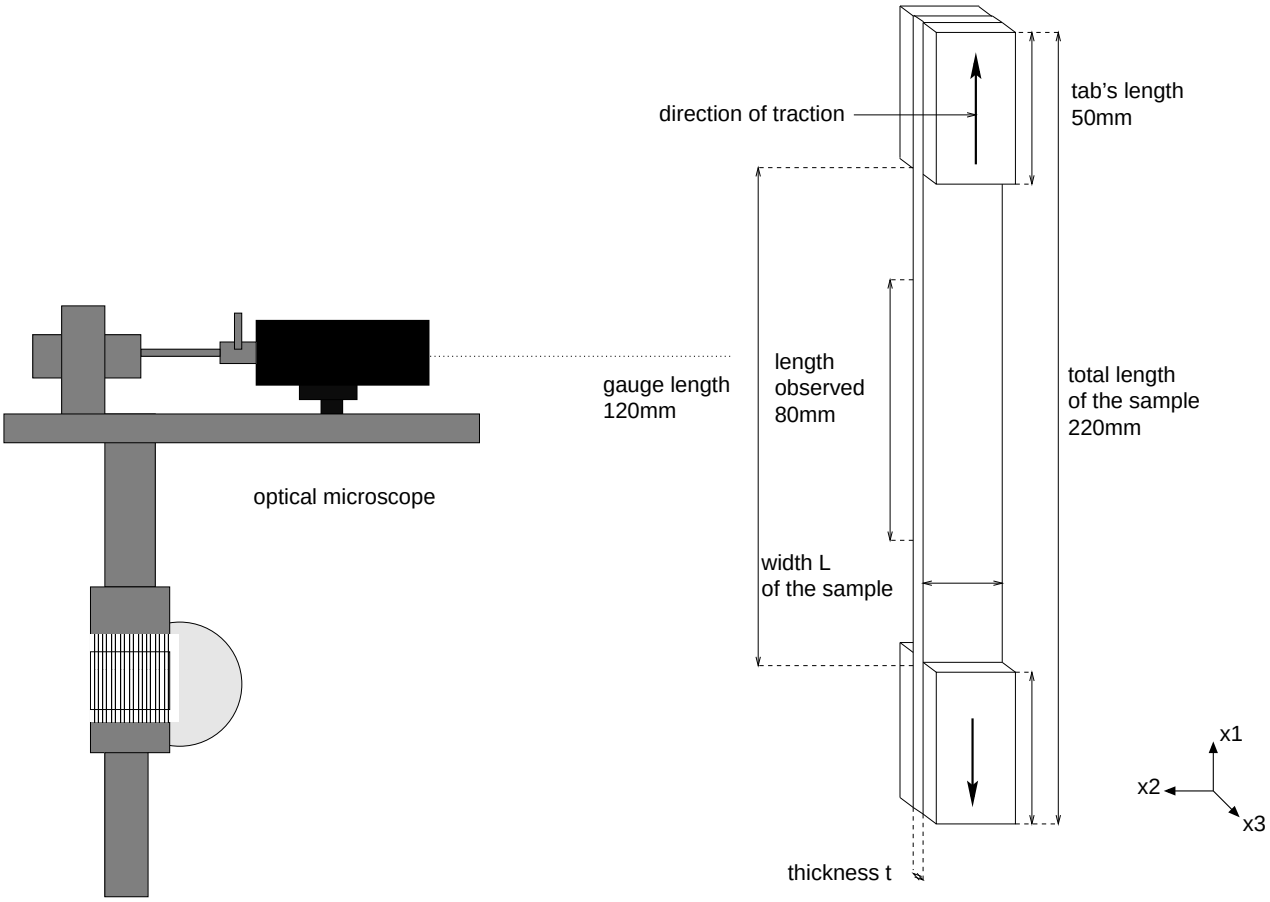

Figure 1: Counting cracks on the sample during the tension.

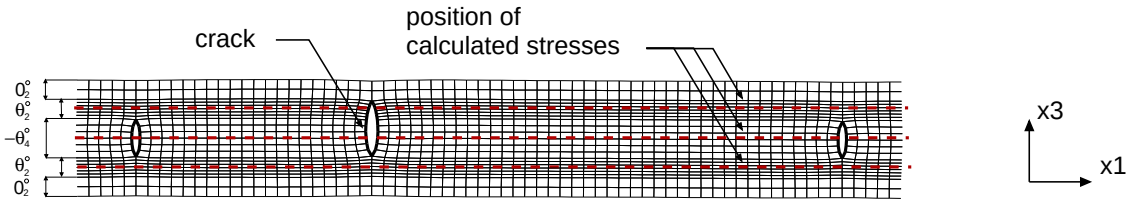

Figure 2: Mesh of the thickness of the laminate with cracks (pseudo-tridimensional calculation)

$m = 5.39$ a shape parameter (nondimensional).

SIMULATION OF THE FRACTURE OF A LAMINATE COMPOSITE

Statistical Volume Element (SVE)

The Statistical Volume Element (SVE) gives the possibility to introduce the stochastic aspect in the numerical simulation. It is defined as having one critical defect which is in our case a crack. During experiments, we observed that the geometry of the crack had the thickness of the ply (0.246 mm to 0.738 mm) and the width of the sample (25 mm). So two dimensions of the SVE are directly defined. The third dimension of the SVE is the intercrack spacing at saturation. Only the $[0_3/90_3]_s$ laminate has its cracks at saturation (1.41 mm), laminates with off-axis plies undergo delamination. Jeulin [3] assumes that defects are distributed according to a Poisson point process and that SVE breaks with the weakest link assumption described by Weibull [4] so its probability to break is given by Eq. 2:

$$P_r(\sigma_R) = 1 - e^{-\int_{SVE} \Psi(\sigma_R) dv} \tag{2}$$

Knowing $\Psi(\sigma_R)$ from the experimental study (Eq. 1) and using a uniform random variable P_r between 0 and 1, we associate to each SVE a fracture value σ_{RSVE} obtained by Eq. 3 :

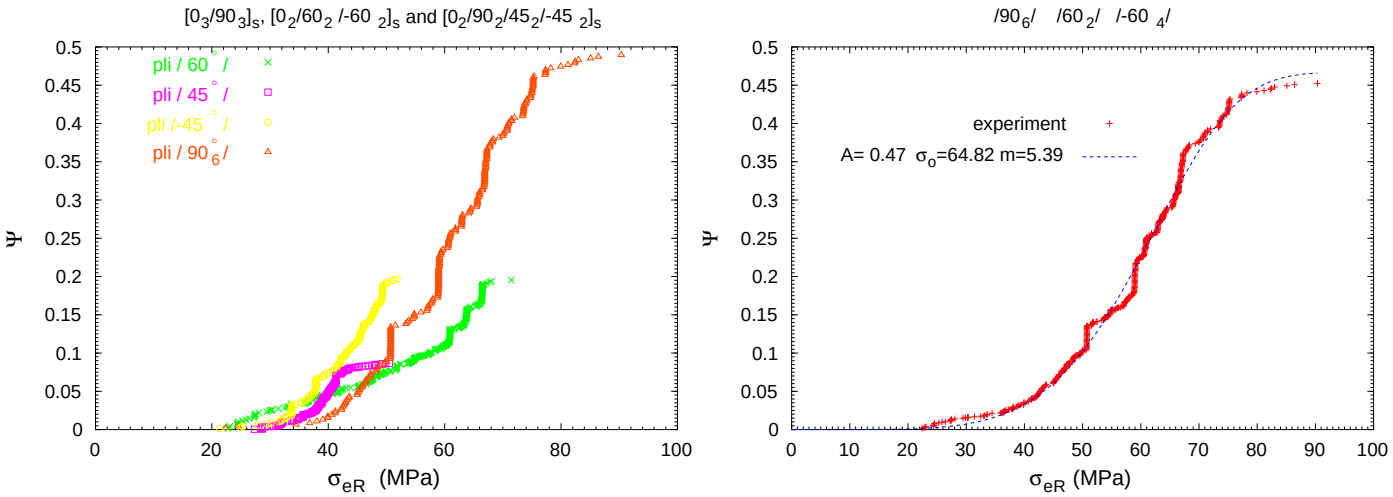

Figure 3: a) Cumulative damage variable Ψ for cracks in different laminates. b) Cumulative damage variable Ψ for cracks in $[0_3/90_3]_s$, $[0_2/60_2/-60_2]_s$ laminates.

$$\sigma_{RSVE} = \sigma_\circ \left[-ln\left(1 + \frac{ln(1-P_R)}{AV_{SVE}}\right)\right]^{\frac{1}{m}} \tag{3}$$

Damage model for numerical simulation

Figure 4 shows two meshes of a plate representing the sample studied experimentally : a finite element mesh and a statistical mesh. The finite elements are used to calculate under classical lamination theory [5] the stress and displacement states. The statistical mesh is made of SVE's which are introduced to give the failure stress variability of the sample. The different gray levels represent the values of the fracture criterion σ_{RSVE} associated with each SVE. The two meshes are superimposed to give the input for numerical calculation.

The appearance of damage in the laminate is simulated as follows. If in one SVE, the criterion σ_{eSVE} which is the mean of the criterion σ_{eiel} of all finite element which belong to the SVE reaches σ_{RSVE} according to Eq. 4, the damage of these elements is simulated numerically by a stiffness reduction described by Renard and Thionnet [6].

$$\sigma_{eSVE} = \sum \frac{v_{iel}\sigma_{eiel}}{V_{SVE}} > \sigma_{RSVE} \tag{4}$$

Numerical results

A numerical simulation is made on $[0_3/90_3]_s$ and $[0_2/60_2/-60_2]_s$ laminates with the model described previously, to compare it with experimental results. For both laminates we have a low variability on behaviour laws so the stress-strain curves are less interesting than the density of cracks represented in Fig. 5, where is plotted the damage variable (also called the cumulative density Ψ) against the criterion σ_{eR} ($\sigma_{eR} = \sigma_{RSVE}$ for numerical results). In the case of $[0_3/90_3]_s$ laminate, the SVE breaks in the same way as experimentally as shown in the Fig. 5 a).

In the case of $[0_2/60_2/-60_2]_s$ laminate (Fig. 5 b), the experimental and numerical curves are not similar, since we do not reach experimentally the saturation, the calculation being done with the size of the SVE of $[0_3/90_3]_s$ laminate. Numerically, by using the size of SVE of $[0_3/90_3]_s$ laminate, we introduce more cracks than there are in reality. In addition, the parameters used for the statistical model penalize this laminate configuration.

CONCLUSION

We proposed experimental and numerical schemes for the determination of defects population parameters in a ply. At the same time, we defined a multiaxial criterion $\sigma_e = (\sigma_T^2 + a\tau_{LT}^2)^{1/2}$, with $a = 0.45$. More

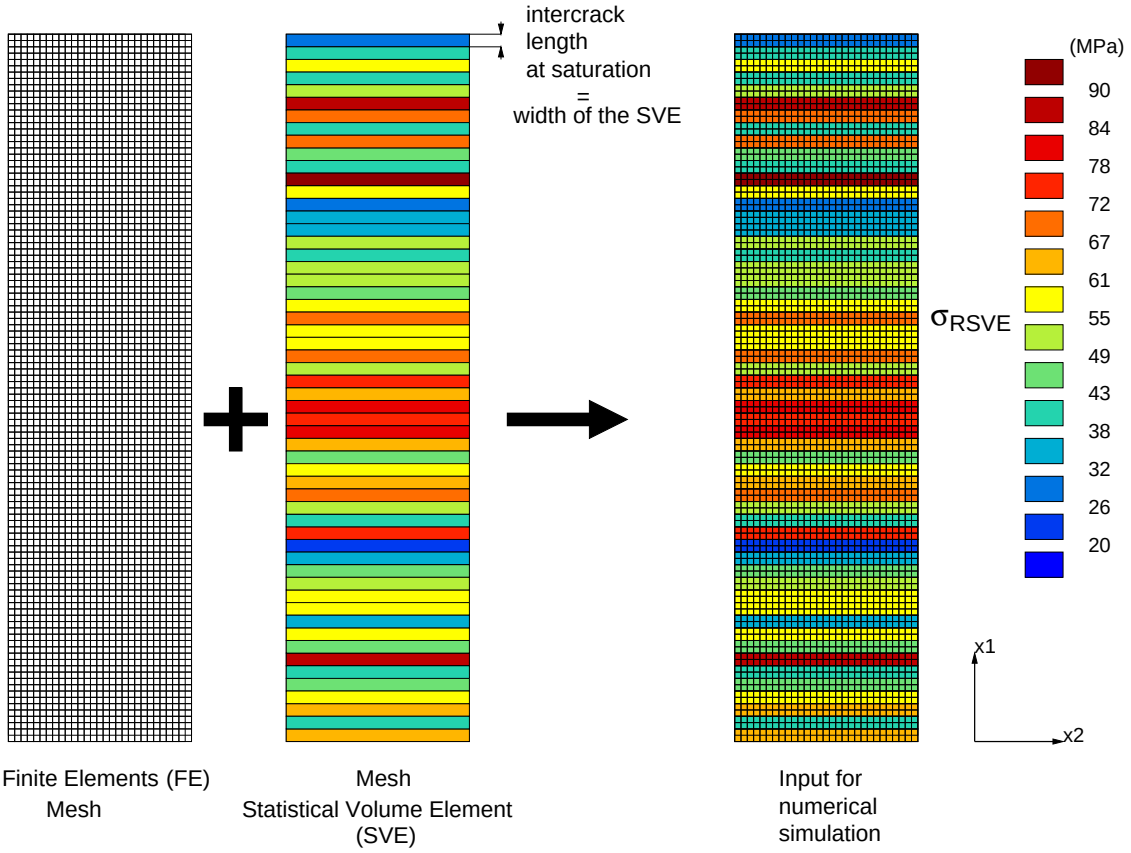

Figure 4: Input for the numerical simulation

we have information on defects more the parameters of population and the parameter a will be precise and realistic. Next, we built a probabilistic damage model by introducing stochastic failure stresses with the SVE. Numerical results $[0_3/90_3]_s$, gave a cumulative density similar to the experimental one. Concerning $[0_2/60_2/-60_2]_s$ laminate, the cumulative density was higher because of the choice of the size of the SVE. To model the cumulative density more precisely, we have to account for the tridimensional stress state, in order to include the delamination phenomenon so that the classical laminate theory assumptions could not be considered anymore.

The ongoing work is to apply the model for high stresses gradient zones (notched plates). Figure 6 shows the numerical input. The failure criterion is changed. Eq. 5 takes into account the fact that we have a higher probability to break in the vicinity of the circular hole.

$$\sigma_{eSVE} = \sigma_\circ \left[-ln \left[\sum_{iel}^{N} \frac{v_{iel} e^{-\left(\frac{\sigma_{iel}}{\sigma_\circ}\right)^m}}{V_{SVE}} \right] \right]^{\frac{1}{m}} > \sigma_{RSVE} \tag{5}$$

ACKNOWLEDGEMENTS

The authors wish to thank J.-C. Tesseidre and Y. Favry for the technical assistance in the experimental part of the study. This research was supported by Ministry of Defence.

REFERENCES

1. Baxevanakis, C., Jeulin, D. and Renard, J. (1995). *International Journal of Fracture*, 73, 149.
2. Thionnet, A. and Renard, J. (1993). *Composites Engineering*, 3(9), 851.
3. Jeulin, D. (1990). In: *Proceedings 32ème Colloque de Métallurgie*, pp. 99–113, volume 4, INSTN, Revue de la Métallurgie, France.
4. Weibull, W. (1951). *Journal of Applied Mechanics*, 18, 293.
5. Tsai, S. W. and Hanh, H. T. (1980). *Introduction to Composite Materials*, Technomics, CT, Stanford.

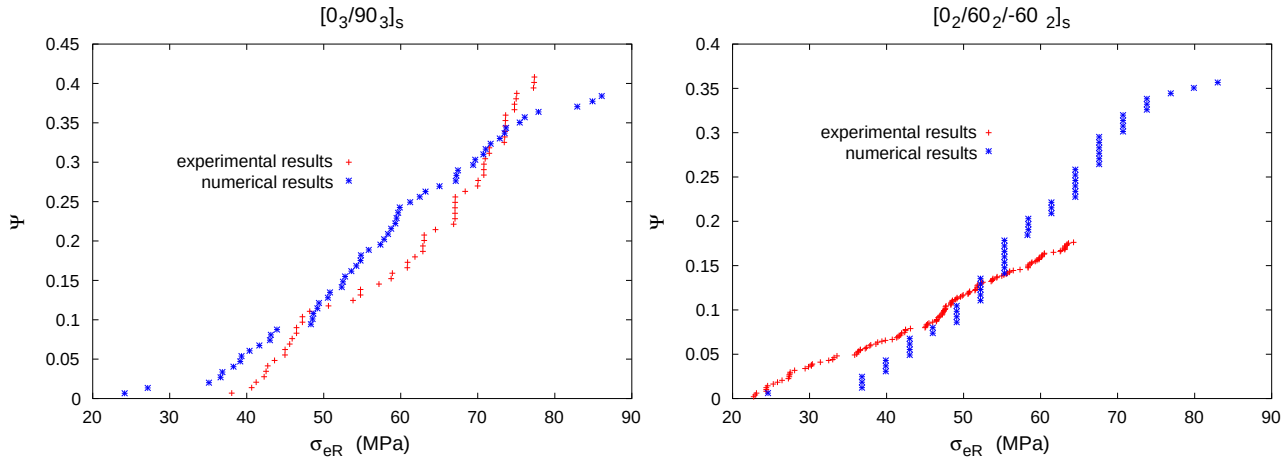

Figure 5: Comparison of numerical and experimental results for a) $[0_3/90_3]_s$ and b) $[0_2/60_2/-60_2]_s$ laminates.

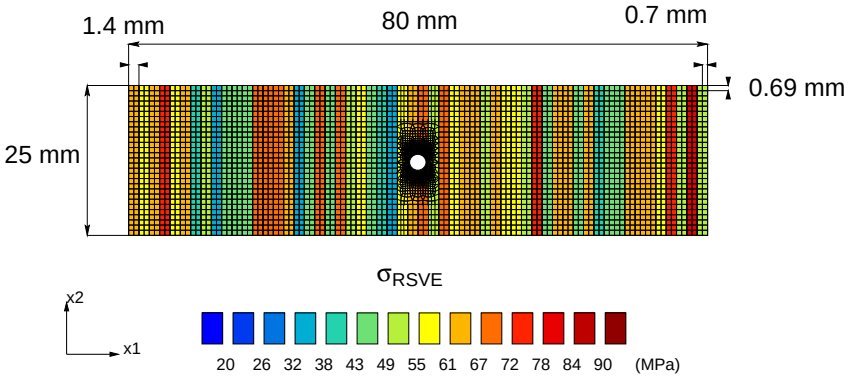

Figure 6: Example of realization of σ_{RSVE} for a notched plates.

6. Renard, J. and Thionnet, A. (1992). In: *Damage Mechanics in Composites*, pp. 31–39, Allen, D. H. and Lagoudas, D. C. (Eds.), volume 150, ASME Symposium, Anaheim, USA.

CRACK DEFLECTION IN LAYERED, GRADED COMPOSITES

J. Chapa-Cabrera and I. E. Reimanis

Metallurgical and Materials Engineering, Colorado School of Mines,
Golden, CO 80401, USA

ABSTRACT

Crack deflection in discretely layered, graded composites is examined through experiments and finite element modeling. Material and geometric parameters responsible for affecting crack deflection from an existing crack or notch are identified. Fracture experiments with Cu/W graded composites reveal that elastic mismatch between the layers, and layer thickness are key parameters in determining stress fields at the base of a notch. Numerical modeling indicates that the residual stress field, which is a function of the thermomechanical response (thermal expansion, elastic and plastic and behavior), has a significant effect on the crack deflection angle for most situations. These results are discussed in the context of developing predictive models for crack propagation in graded structures.

KEYWORDS

Graded, crack kinking, crack deflection, residual stresses.

INTRODUCTION

The first step in establishing failure criteria for compositionally graded composites is to determine the crack path. For cracks which lie asymmetrically within the gradient, a significant challenge to predicting crack paths lies in the fact that the crack tip stress field and the crack propagation criterion may change as a function of crack length. Thus, understanding which material and geometric parameters control the crack tip stress fields is ultimately required in the development of predictive fracture models for graded materials.

In this work, crack paths are examined experimentally, using Cu/W graded composites. These experimental observations comprise the first part of the paper. The tendency for crack kinking is then examined using a finite element model. The effects of residual stress on altering the crack kink angle are discussed.

EXPERIMENTAL OBSERVATIONS

Cu and W commercially obtained powders were mixed in the appropriate ratios, and layered in a graphite die for hot pressing to produce graded cylinders with discrete layers each consisting of Cu with either 60 % W, 40% W, 20 % W or 0 % W, where percentages are on a volume basis. Higher percentages of W were difficult to sinter to full density. Hot pressing was conducted at 940ºC for 12 h, in vacuum, under an applied load of 40 MPa. Details are available elsewhere [1,2]. The cylinders were cut into mechanical testing bars 3 x 8 x 30 mm, as illustrated schematically in Figure 1. The gradient was symmetric to facilitate mechanical testing. Each layer was either 2 mm or 4 mm in thickness. A 3 mm deep notch was placed using a diamond saw either within the center of the 20% W layer or the 40% W layer. The bar was then placed in four point bending, and the load was increased until a crack propagated from the base of the notch. After the test, the angle of crack deflection away from the loading axis was measured using scanning electron microscopy.

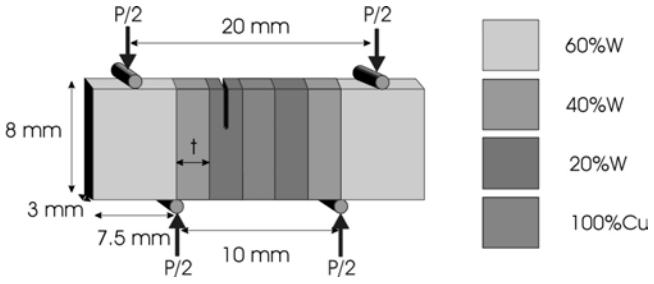

Figure 1: Cu/W graded composite mechanical test specimen. The 100 % Cu composition layer is located symmetrically in the center, to the right of the notch.

Figure 2 shows an example of a fractured bar in which the notch was situated within a 2 mm thick, 20% W layer, similar to the schematic in Figure 1. It is apparent that the crack path is relatively straight, except for the region in the vicinity of the interface between the 20 % W layer and the 0 % W layer, at which point the crack path eventually becomes parallel to the interface. The initial crack deflection angle (that nearest the base of the notch) was measured for each specimen configuration, and the results are shown in Table 1. Each reported measurement consists of an average of 3 tests for that configuration.

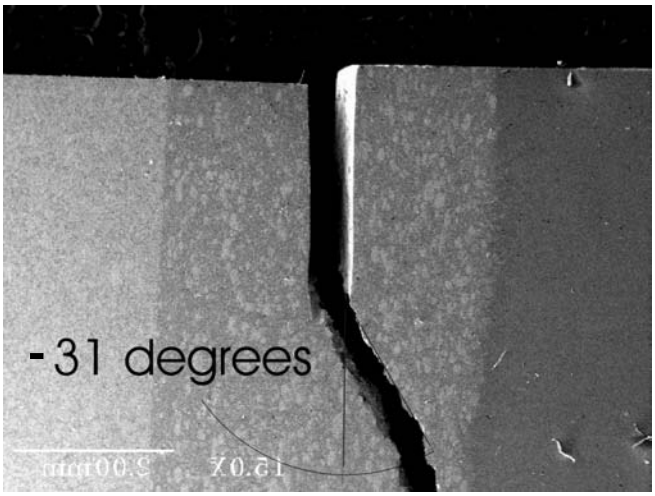

Figure 2: Scanning electron micrograph of bar containing 4 mm thick layers, fractured in four point bending. Notch was cut into 20 % W layer. Crack deflection by 31° towards the more compliant pure Cu layer to the right is apparent.

TABLE 1
Measured Crack Deflection Angles (in degrees). According to the convention used in the FE model, crack deflections towards the more compliant material (towards the right in Figure 2) are negative by definition.

Composition of Layer	Layer Thickness	
	2 mm	4 mm
20 % W	-50	-35
40% W	-25	0

FINITE ELEMENT RESULTS

Details of the finite element model are briefly described here; details are available elsewhere [3]. The commercially available code ABAQUS [4] was used. A four point bend beam (4PB) specimen geometry is analyzed here. The mesh is shown in Figure 3. Incremental FEA is used, allowing the application of mechanical loading to a body that is already deformed by residual stresses. The mesh is 25 mm long and 8 mm high. The discrete compositional gradient is formed by 11mm of pure copper, followed by 1 mm layers of 80%Cu-20%W, 60%Cu-40%W and 40%Cu-60%W, and by an 11 mm section with 20%Cu-80%W; all percentages are volumetric. A crack 3 mm long is cut perpendicular to the gradient in the center of the 60%Cu-40%W middle layer, as shown in Figure 3. Crack tip vicinity stresses resulting from two different conditions are superimposed. First, the thermal residual stresses resulting from thermal expansion coefficient mismatch and a change in temperature are obtained. Second, the stresses resulting from the applied load are evaluated. The residual stresses were obtained by applying an initial temperature of 300^{o}C to all the nodes and subsequently cooling down to 25^{o}C. The applied stresses reported correspond to the maximum stress on the tensile

surface of a homogeneous material. Quad second order elements with three nodes collapsed on the crack tip were used. The midside node immediately away from the tip was positioned to a ¼ of the element length to make the element square root singular. Stress intensity factors were obtained from FEA for the residual stresses and for each applied load with and without residual stresses. Standard rules of mixtures were used to estimate material properties [2].

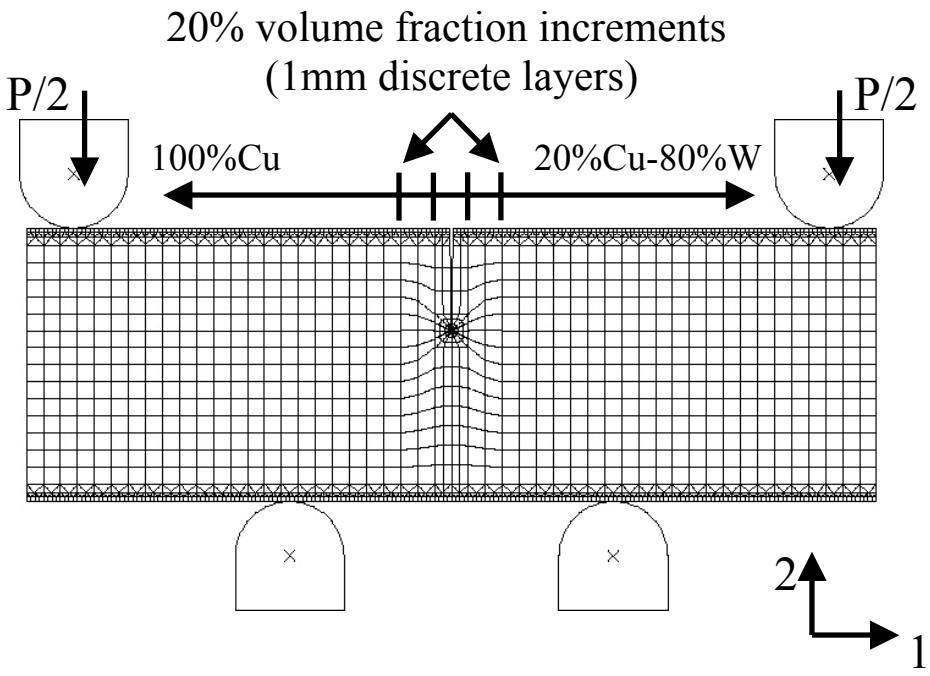

Figure 3: Four point bend (4PB) specimen geometry used for finite element analyses. Extensive mesh refinement is present at the contact surfaces and the crack tip region.

It was observed that the maximum principal stress around the crack tip exhibited a shallow maximum (over about 20°), and thus, a zero shear stress criterion was adopted. By fitting the numerical data with a curve, it was straightforward to determine the kink angle at which the shear stress became zero. It was observed that the predicted kink angle, θ_m, did not depend on the applied stress when no residual stresses were present. However, in the presence of residual stresses, θ_m depended strongly on the applied stress. To relate the results to toughness, the applied mixed mode crack tip stress was converted to an equivalent stress intensity factor [3], and the results plotted as a function of θ_m, as shown in Figure 4.

The dotted line in Figure 4 indicates the predicted value (-6.95°) when there is no residual stress. This value is approached at very high loads (higher than shown here). It is apparent that the effect of the residual stress is to rotate the crack tip stress field such that a positive crack kink angle is achieved for most applied loads. For very tough materials (e.g., $K_{IC} > 25$ MPa $m^{1/2}$), the effect of the residual stress diminishes.

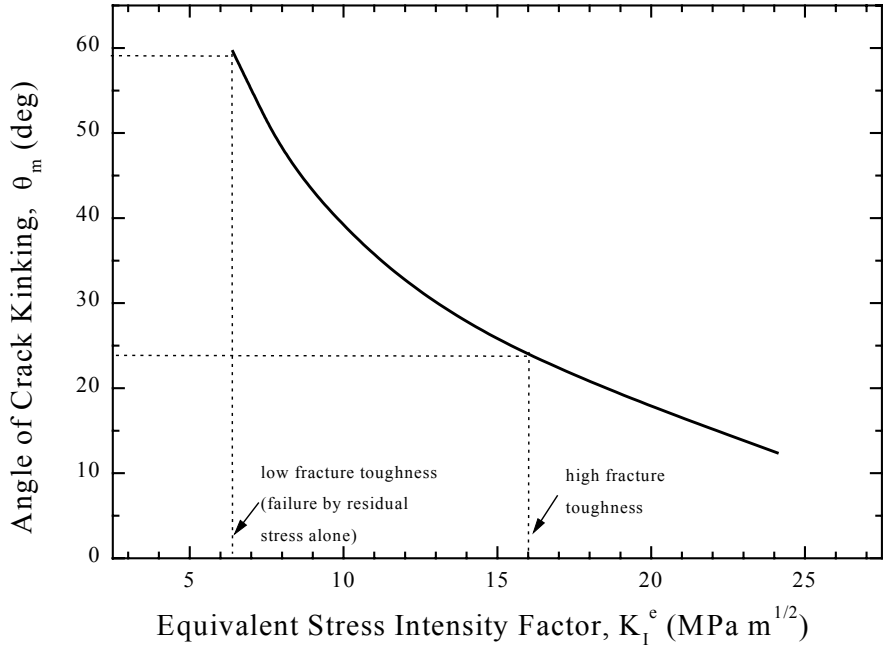

Figure 4: Predicted crack kink angle as a function of effective applied stress intensity factor. The positive crack kinking angles indicate that crack kinking towards the stiffer side of the composite.

The dependence θ_m on the applied stress intensity factor, when residual stresses are considered, is clear when one considers that the total mode I and mode II stress intensity factors are the superposition of the respective residual and applied stress intensity factors. Thus, the residual stress intensity factor rotates the stress field.

Relation of FEM Results to Experimental Observations

Two major differences exist between the experiments and the numerical modeling, making it difficult to compare results between the two. The first is that it is likely that plastic deformation is operative during the development of residual stresses, and during the applied loading, yet it is not accounted for in the numerical model. Second, the FEM specimen geometry is not identical to the experimental four point bend geometry. With these differences in mind, it is realized that the following comments are somewhat speculative.

It is noted that the crack is always experimentally observed to propagate towards the softer and more compliant material. In contrast, the numerical results indicate that in the presence of residual stresses, the predicted crack kink angle is positive, i.e., in the direction of the stiffer, less compliant material. If one assumes that the specimen geometry for the experiment and the numerical model (i.e., compare Figure 1 and Figure 3) is effectively the same, then it must be that plasticity substantially modifies the crack tip stress field. Plasticity is important during the development of residual stresses; obviously, in a graded material, its effect may be non-uniform across the sample, possibly

resulting in the rotation of stress fields. Plasticity may also be important during mechanical testing, an effect which would also be asymmetric in a graded material. FE models which account for plasticity in the copper are currently being developed to establish the precise role of plasticity.

CONCLUSIONS

The results here indicate that it is extremely important to take into account the effect of residual stresses when predicting the crack path in a graded composite. In the present case it was observed that without accounting for residual stresses, the crack is predicted to kink towards the more compliant side of the gradient, but in the presence of residual stresses, the predicted crack kink angle is towards the stiffer side. The reasons for this residual stress effect, and the dependence of the crack kink angle on the applied stress are obvious when one considers superposition of residual stress intensity factors and applied stress intensity factors. Specifically, the mode mixity of the residual stress is different from that of the applied stress. The result is that the predicted crack kink angle depends on the material toughness, with tougher materials exhibiting cracks that do not kink as much.

ACKNOWLEDGEMENTS

The authors would like to acknowledge the U.S. Department of Energy, Office of Basic Energy Sciences for funding this research under contract DE-FG03-96ER45575.

REFERENCES

1. Chapa, J., Rozenburg, K. and Reimanis, I. E., "Fracture in Ductile/Brittle Graded Composites", pp. 107-111 in Second International Conference on Processing Materials for Properties, edited by B. Mishra and C. Yamauchi, published by TMS, Warrendale, PA (2000).

2. J. Chapa-Cabrera, Elastic-Plastic and Residual Stress Effects on the Fracture Behavior of Graded Composites. Ph.D. Thesis, Colorado School of Mines (2001).

3. Chapa-Cabrera, J. and Reimanis, I. E, "Effects of Residual Stress and Geometry on Predicted Crack Paths in Graded Composites", to appear in *International Journal of Engineering Fracture Mechanics,* (2001).

4. Computer code ABAQUS (Hibbitt, Karlsson, and Sorensen, Inc., Providence, RI, (1992).

ORAL RFERENCE: ICF100547OR

CRACK FRONT WAVES IN DYNAMIC FRACTURE

J. Fineberg[1], E. Sharon[2] and G. Cohen[1]

[1] The Racah Institute of Physics, The Hebrew University of Jerusalem,
Givat Ram, Jerusalem 91904, Israel
[2]The Center for Nonlinear Dynamics, The University of Texas, Austin
78712, TX, USA.

ABSTRACT

A rapidly moving crack in a brittle material is often idealized as a one-dimensional object moving through an ideal two-dimensional material, where the crack tip is a singular point. In real three-dimensional materials, however, tensile cracks are planar objects whose tip forms a propagating one-dimensional singular front. Let us now consider a crack front propagating through a heterogeneous medium populated by an ensemble of localized inhomogeneities (asperities). The front is distorted by its interaction with each asperity. Can the crack front, after many such interactions, still be considered a single coherent entity, or, must the dynamics of failure be described by ensemble of individual cracks in all but the most homogeneous materials? Here we present laboratory measurements of a new type of wave, crack front waves, CFW, which are generated by asperities and propagate along crack fronts in tensile fracture. We will show that CFW are highly localized nonlinear entities that propagate along the front at approximately the Rayleigh wave speed, relative to the material. They possess a characteristic, inherently nonlinear shape, reminiscent of solitons. In glass, whose fracture energy is nearly independent of crack velocity, CFW are very long-lived whereas in PMMA, where the fracture energy increases with crack velocity, CFW decay. CFW serve to both transport and distribute the energy fluctuations, induced by asperities, throughout the entire front. In this way, these waves may allow a crack front to retain its coherence despite repeated interactions with randomly dispersed material inhomogeneities.

KEYWORDS Brittle fracture, localized waves, crack front waves, solitary waves

Dynamic crack propagation in brittle fracture has been the subject of much recent attention. Much of this work has been invested in studying the dynamics and stability of rapidly moving cracks in Mode I fracture. Experiments have shown that above a critical propagation velocity, v_c, of approximately $0.4V_R$, where V_R is the Rayleigh wave speed, a single crack becomes intrinsically unstable. At this speed, a single crack has been observed in brittle [1]becomes unstable to frustrated microscopic branching events. This instability . Qualitatively similar effects have also [11], and recently in crystalline materials[9, 10], glass [1-8]polymers , and molecular [16-18], finite element calculations [12-15]been observed in models of ideal crystals have also demonstrated that the equation of motion for a single [10]. Recent experiments [19, 20]dynamics , provides excellent quantitative agreement with [21]crack predicted by continuum elastic theory experiments in ideal quasi-2D amorphous materials both below and above v_c, whenever a *single-crack* state (single-crack states can occur *momentarily* when $v > v_c$) exists.

In the work summarized above only ideal (defect-free) quasi-2D materials were considered. The tip of a crack is idealized as a singular point progressing through an otherwise perfect two-dimensional material. As long as translational invariance exists in the third dimension, the above experiments have demonstrated that the assumption of two-dimensionality is justified. What happens, however, when the translational invariance in the "ignored" dimension is broken? Let us consider a crack progressing through an, initially,

ideal three-dimensional plate of finite thickness. Instead of a singular point, the "tip" of a crack is now a singular front, which extends throughout the sample's thickness. Let us now assume that the crack front meets an asperity, i.e. a localized inhomogeneity where the fracture energy is locally either higher or lower than in the surrounding medium. The asperity breaks the system's translational invariance in the direction normal to the crack's motion. We now consider its effect on the crack's motion.

have recently shown, analytically, that the crack's interaction with an asperity [22]Ramanathan and Fisher will induce a new type of wave that will propagate along the crack front. Their analysis was based on Willis calculation of the change in the energy release rate, G, induced by a localized [23]and Movchan's perturbation to a crack front in the propagation direction. This analysis indicated that an asperity could excite a wave, i.e. a local perturbation of the crack's velocity that could progress along the crack front at slightly less than v_R, relative to the asperity. This disturbance, predicted to exist within the fracture plane, was shown to be marginally stable for constant values of the fracture energy, Γ. The wave was predicted to [24, grow (decay) if Γ were a decreasing (increasing) function of the crack velocity, v. Morrissey and Rice have observed these waves in finite element calculations of tensile fracture in elastic 3D materials with a 25] constant fracture energy. They found that asperities along the crack path indeed generated persistent, localized waves of in-plane velocity fluctuations that propagated at velocities slightly below v_R. After an initial decay, these waves continued to propagate along the crack front with constant shape and amplitude.

Below we will describe experiments in which waves, similar in many respects to those predicted above, . In the tensile fracture of soda-lime glass and PMMA, we will show that the interaction [26]were observed of asperities with moving cracks indeed generates localized waves that propagate along the crack front at approximately v_R. The waves are stable in glass (nearly constant Γ) and decay in PMMA (Γ increasing with v). In contrast to the predicted waves, the crack front waves (CFW) observed in experiments have two surprising characteristics: these waves exist both within and normal to the fracture plane and CFW have a *unique* characteristic profile.

Our experiments were conducted in both PMMA and soda-lime glass plates of size 380×440 mm and thickness, h, between $2 < h < 6$ mm. The cracks were driven in Mode I by applying static tension at the sample's vertical boundaries. We define the x direction as the direction of propagation of the crack front, y as the direction of applied tensile stress ($0 < y < 440$mm), and z as direction along the crack front. The plates were initially defect-free. Asperities were generally introduced along the outer faces of the plate (z=0 or z=h). Asperities with fracture energy less than that of the material were formed by scribing a thin line in the y direction on the plate faces. Asperities with fracture energy greater than that of the material were formed by adhering thin glue lines on the plate faces along the y direction. Both types of disturbances generated CFW upon interaction with a moving crack. Instantaneous crack velocities were measured at the plate faces . Our velocity resolution at each point along the plate faces was [7]by the technique described in approximately 10 m/s in PMMA and 50 m/s in glass. Velocity measurements were performed at a 10MHz sampling rate enabling velocity measurements approximately every 0.2 (0.05) mm in glass (PMMA). The velocity measurements were later correlated with fracture surface measurements and optical photographs. The fracture surface profile was mapped to 10nm resolution in the y direction by the use of a modified Taylor-Hobson (Surtonic 3+) scanning profilometer with an x-z spatial resolution of 0.5 μm. The features on the fracture surface left behind by the CFW were also photographed by the use of incoherent illumination directed through the transparent samples. This light, passing through the fracture surface, was either focused or de-focused as it traversed through any surface features. This effect, similar in character to shadowgraph visualization, enabled the visualization of minute deviations from flatness of the fracture surface.

CFW have both an in-plane and *out-of-plane* character, in contrast to the *in-plane* deviations of the front . Evidence of the latter is in the residual tracks (normal to the fracture plane) [22, 24]velocity predicted by that CFW leave behind on the fracture surface. Examples of typical CFW tracks on the fracture surface are shown in Fig. 1. As Fig 1a shows, the tracks are deviations of the fracture surface height. These deviations can be either upward (away from the mean plane of the fracture surface) or downward (into the mean plane of the fracture surface). The direction of these height deviations has no significance, as tracks formed on the both fracture surfaces are mirror images of each other.

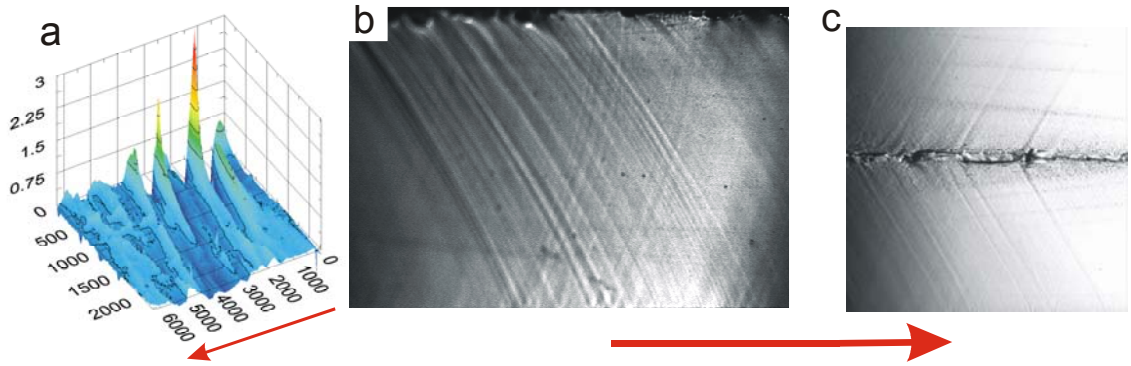

Figure 1. Typical crack front waves generated on a fracture surface. (a) Profilometer measurements (scales are in μm). The arrow shows the propagation direction. (b) Photograph of front waves generated, as in (a), by an external perturbation at the plate surface. Note both the initial decay (in (a)) and subsequent long lifetime of the waves as they are reflected at the plate surfaces. (c) Photograph of front waves generated by localized micro-branching events. The arrow below (b) and (c) is 3mm in length and denotes the propagation direction.

As the Fig. 1 shows, CFW are generated either by externally imposed asperities (Fig. 1a,b) on the plate surfaces or, intrinsically, by means of micro-branching events. In glass, micro-branching events are generally localized in the z direction and (as shown in Fig. 1c) occur along lines in the propagation direction . We can understand the initiation of CFW by micro-branching events since, as predicted by theory, the [27] origin of these waves is determined by local fluctuations in the fracture energy. When a micro-branching event occurs, energy is diverted into the daughter cracks that are bifurcating away from the main crack. Thus, from the perspective of the main crack, which was initially the sole source for dissipation in the system, a micro-branching event effectively increases the local value of the fracture energy in the system.

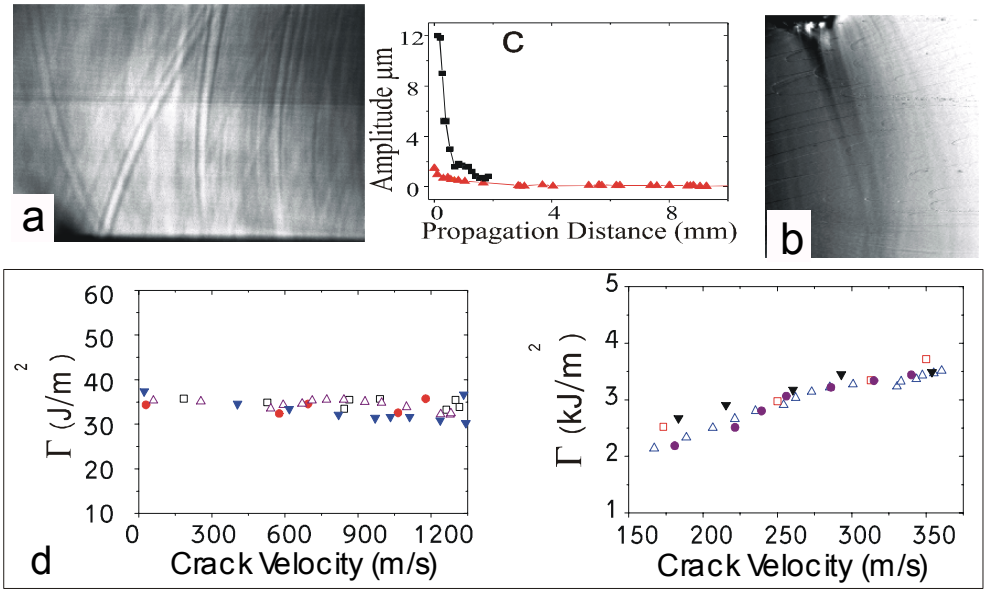

Figure 2. Photographs depicting the evolution of CFW generated by imposed asperities in soda-lime glass (a) and PMMA (b). Both cracks propagate from left to right and each photograph is 3 mm in height. The amplitude of the waves as a function of their propagation distance is shown in (c). CFW stably propagate in glass whereas in PMMA no stable propagation is observed. (d) The relative stability of CFW in these materials may be explained by the velocity dependence of the fracture energy, Γ, with v in (right) PMMA and (left) glass.

CFW are not limited to soda-lime glass. In PMMA, as shown in Fig. 2, CFW can also be generated by externally imposed asperities. In PMMA, however, the resulting waves are very quickly damped and have not been observed to stably propagate. In glass, CFW initially decay exponentially with a decay length

). The waves then stabilize with a constant amplitude [26]scaling with the size of the initial disturbance (see and are, subsequently, very long-lived (Fig. 2c). When impinging on the free [26]and unique shape boundary at a plate's surface, the waves reflect with very little loss of amplitude. We have observed CFW to undergo up to 7 reflections while traveling distances over an order of magnitude greater than their size.

had predicted that CFW are marginally stable if Γ is [22]As mentioned earlier, Ramanathan and Fisher *independent* of v. If Γ(v), on the other hand, is an *increasing* function of v - CFW are predicted to decay. The fracture energy dependences of glass and PMMA on v (see Fig. 2d) are consistent with this prediction. While Γ(v) for PMMA is a clearly increasing function, Γ is nearly constant for glass. The data shown were for velocities prior to the onset of the micro-branching instability. In PMMA we have found [10]obtained that the "bare" Γ(v) dependence after the instability. (*Effectively*, Γ(v) will increase for $v>v_c$ due to [8, 10] the increase in the total surface area formed by both the main crack and micro-branches.)

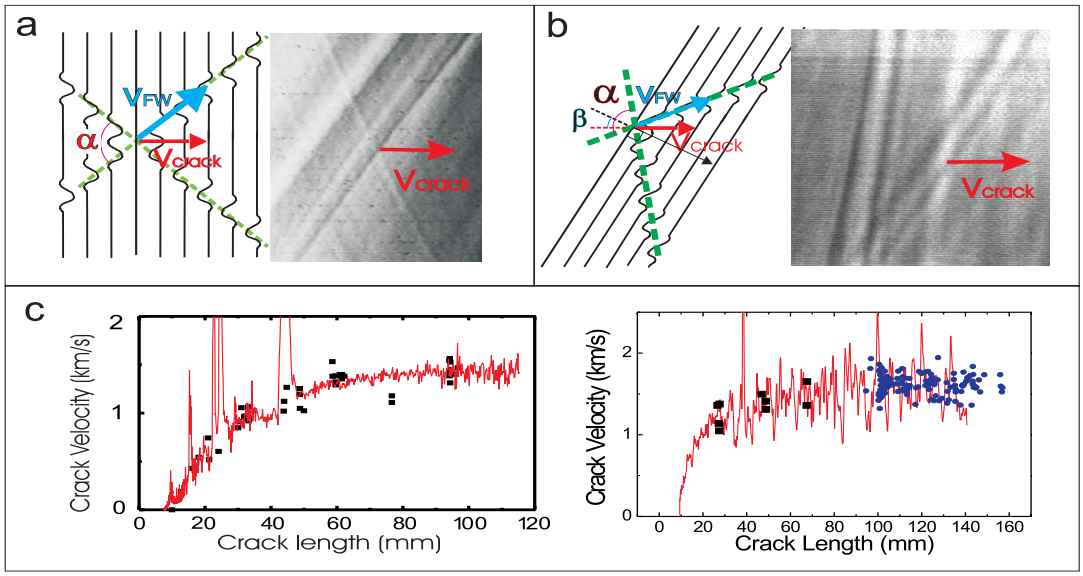

Figure 3. The front wave velocity can be determined via intersecting CFW tracks for (a) a case where the crack front is normal to the propagation direction and (b) where the front is inclined at an angle β relative to the propagation direction. Once $V_{FW} = (1 \pm 0.05)\ V_R$ is known, this method can be used to measure both the crack velocity, v, and the angle β at the point of intersection. (c) Two comparisons of the independent measurements (lines) of v with measurements (points) obtained by means of $v=V_{FW}\cos(\alpha/2)/\cos(\beta)$. The sharp peaks in v *prior* to v_c=1500 m/s (in glass) result from the crack's interaction with the arrival of asperity-induced front waves.

The velocity of CFW, V_{FW}, is very close to the Rayleigh wave speed, V_R, relative to the material. This is . We measure the CFW velocity by means of intersecting CFW tracks [24, 25] and [22]consistent with both on the fracture surface. The intersecting tracks are formed by two distinct counter-propagating CFW. As, in general, CFW can be formed whenever the crack front interacts with any localized material inhomogeneity, intersecting CFW are common. Two such intersections are illustrated in Fig. 3 for cases where the crack front is oriented normal to the propagation direction (Fig. 3a) and at an angle β relative to the propagation direction (Fig. 3b). Defining the angle α as the angle formed between two outgoing CFW tracks, V_{FW} is determined by:

$$V_{FW} = v\cos(\beta)/\cos(\alpha/2) \qquad (1)$$

that $V_{FW} = V_R(1 \pm 0.05)$. Once we have established the value of V_{FW}, we can invert [26]In this way we find Eq. 1 and use the values of V_{FW}, α and β to *measure* the instantaneous value of v at any point where two CFW tracks intersect. This is demonstrated in Fig. 3c, where independent velocity measurements are in excellent agreement with values of v obtained by inverting Eq. 1. In many applications where direct measurements of v cannot be performed, this new tool should prove to be useful.

in the fracture [28]The existence of the tracks left by CFW on fracture surfaces has been noted for decades literature, and identified as "Wallner lines". In most instances, however, their origin has been misinterpreted. Wallner lines are defined as lines imprinted on the fracture surface as a result of the interaction between a moving crack front and shear waves, generated by an external source. The markings on the fracture surface come about as a result of the momentary deflection of the stress field at a crack's tip generated by a passing shear wave. In the well-known Kerchof method, this interaction has been used to advantage as a tool for crack velocity measurement (using the patterns imprinted on the fracture surface by means of externally broadcast, ultrasonic shear waves). CFW however, are *not* Wallner lines. As illustrated by Fig. 4a, if the fracture surface markings were created by a radially propagating shear wave (generated by a point-like asperity), the tracks would have the following properties. Their amplitude would decrease as $1/r^2$, their propagation velocity would be that of shear waves, and they would not have a well-defined shape but, instead, mimic the initial conditions that created them. As we have shown (see Fig. 3), the propagation velocity of CFW is approximately V_R, which is more than 2σ less than the shear wave velocity in glass. We , CFW amplitudes stabilize [26]have also demonstrated (see Fig. 2) that after an initial *exponential* decay and these waves continue to propagate large distances with no appreciable change in amplitude. Last, as of the initial [26]shown in Fig. 4b, CFW have a unique, well-defined profile whose shape is *independent* conditions that formed them. Thus, although CFW are superficially similar to Wallner lines, the aforementioned properties show them to be qualitatively different entities.

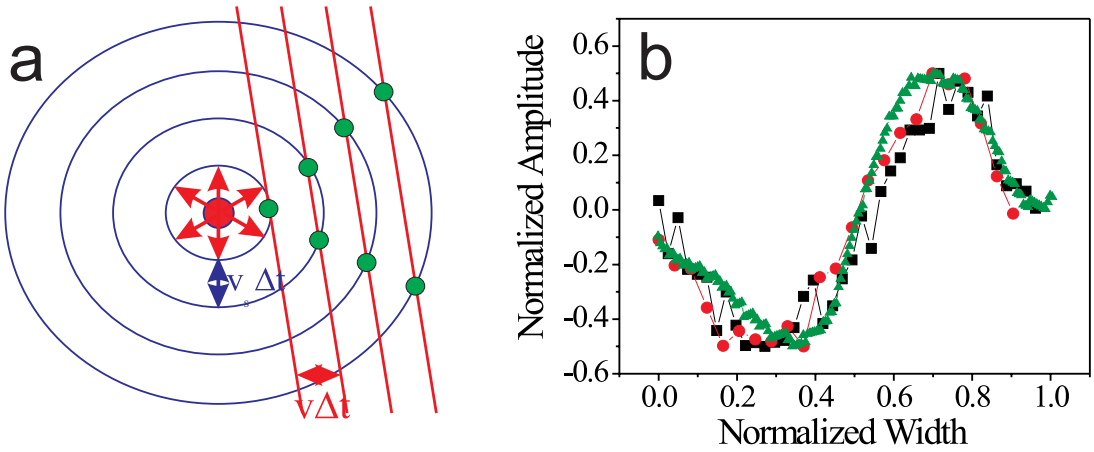

Figure 4. (a) A schematic picture depicting how surface markings might be formed by the interaction between the crack front and shear waves (i.e. the "Wallner line" mechanism). CFW properties are not . Shown are [26]consistent (see text) with this scenario. (b) CFW have a unique characteristic profile superimposed profiles of 3 different front waves. Each profile is scaled by the size of the initial asperity that formed it. The initial forms of the profiles used in (c) were very much different from their asymptotic profiles. The scales of the three profiles shown span over an order of magnitude.

In conclusion, crack front waves appear to be a new type of elastic wave. Although they "live" on a crack front, they move at a constant velocity of approximately the Rayleigh wave speed relative to the medium. CFW are not linear waves. Their characteristic shape provides evidence of a nonlinear, soliton-like character. Upon interaction CFW are not destroyed but retain both their shape and amplitude [26]. In addition, these highly localized waves transfer energy [27] throughout the fracture surface. This together with their propagating nature may enable them to allow a crack to remain a single coherent entity – even in highly inhomogeneous materials, since, statistically, any local changes to the crack front induced by a given asperity will, by means of CFW, be distributed throughout the entire front.

ACKNOWLEDGEMENTS: We wish to acknowledge the support of the US-Israel Binational Fund.

REFERENCES

1. Fineberg, J. and M. Marder, (1999) Physics Reports 313(1-2) p. 2.
2. Fineberg, J., *et al.*, (1991) Physical Review Letters 67(4) p. 457.
3. Fineberg, J., *et al.*, (1992) Physical Review B-Condensed Matter 45(10) p. 5146.
4. Hauch, J.A., *et al.*, (1999) Physical Review Letters 82(19) p. 3823.
5. Boudet, J.F., S. Ciliberto, and V. Steinberg, (1996) Journal De Physique II 6(10) p. 1493.
6. Sharon, E., S.P. Gross, and J. Fineberg, (1995) Physical Review Letters 74(25) p. 5096.
7. Sharon, E. and J. Fineberg, (1996) Physical Review B54(10) p. 7128.
8. Sharon, E., S.P. Gross, and J. Fineberg, (1996) Physical Review Letters 76(12) p. 2117.
9. Sharon, E. and J. Fineberg, (1998) Philosophical Magazine B78(2) p. 243.
10. Sharon, E. and J. Fineberg, (1999) Nature 397(6717) p. 333.
11. Cramer, T., A. Wanner, and P. Gumbsch, (2000) Physical Review Letters 85 p. 788.
12. Marder, M. and X.M. Liu, (1993) Physical Review Letters 71(15) p. 2417.
13. Marder, M. and S. Gross, (1995) Journal of the Mechanics and Physics of Solids 43(1) p. 1.
14. Kessler, D. and H. Levine, (2001) Physical Review E59 p. 5154.
15. Astrom, J. and J. Timomen, (1996) Physical Review B54 p. 9585.
16. Miller, O., L.B. Freund, and A. Needleman, (1999) Modelling and Simulation in Materials Science and Engineering 7(4) p. 573.
17. Xu, X.P. and A. Needleman, (1994) Journal of the Mechanics and Physics of Solids 42(9) p. 1397.
18. Johnson, E., (1992) International Journal of Fracture 57(2) p. R27.
19. Holland, D. and M. Marder, (1998) Physical Review Letters 80(4) p. 746.
20. Abraham, F.F., *et al.*, (1994) Physical Review Letters 73(2) p. 272.
21. Freund, L.B., *Dynamic Fracture Mechanics*. 1990, New York: Cambridge.
22. Ramanathan, S. and D.S. Fisher, (1997) Physical Review Letters 79(5) p. 877.
23. Willis, J.R. and A.B. Movchan, (1995) Journal of the Mechanics and Physics of Solids 43(3) p. 319.
24. Morrissey, J.W. and J.R. Rice, (1998) Journal of the Mechanics and Physics of Solids 46(3) p. 467.
25. Morrissey, J.W. and J.R. Rice, (2000) Journal of the Mechanics and Physics of Solids 48(6-7) p. 1229.
26. Sharon, E., G. Cohen, and J. Fineberg, (2001) Nature (to be published).
27. Sharon, E., G. Cohen, and J. Fineberg, (2001) (in preparation)
28. Wallner, H., (1939) Z. Physik 114 p. 368.

CRACK GROWTH BEHAVIOUR OF NICKEL-BASE HIGH TEMPERATURE ALLOYS AT 500 TO 1000°C

F Schubert, H J Penkalla, P J Ennis, L Singheiser

Research Centre Juelich
Institute for Materials and Processes in Energy Systems IWV-2
52425 Juelich, Germany

INTRODUCTION

Efficient and environmentally benign production of electrical power in fossil fired industrial gas turbines, either in single cycle or in combined cycle (gas turbine - steam turbine) plants will require components made of Ni-base alloys. Although such materials were developed and are extensively used in aero engines, the much larger dimensions of the components in stationary gas turbines mean that the impact of the much larger scale fabrication on the microstructure and the flaw tolerance of the materials must be investigated. Furthermore, the load cycles are very different; in aero gas turbines, full power operation is only required at take-off and landing, whereas industrial turbines must operate at full power for prolonged periods of time.

Only limited information exists in the open literature regarding the behaviour of technical cracks and the controlling mechanisms of crack growth in Ni-base alloys. Safe operation and estimation of the reliability and the allowable types and numbers of operational cycles require knowledge concerning crack growth initiation resulting from the local inhomogeneities expected in each component, and concerning the growth behaviour under operational loadings, especially creep and creep-fatigue cycles. The impact of the working environment on deformation behaviour is of specific importance. Three candidate alloys for the turbine rotors and discs , and one alloy for the turbine blading were investigated:

- solid solution hardened INCONEL 617;
- γ′ hardened alloy Waspaloy;
- INCONEL 706, precipitation hardened by γ′, γ′′ and η;
- single crystalline CMSX-4, hardened by a large volume fraction of γ′ precipitates.

EXPERIMENTAL DETAILS

Materials

The nominal composition and the microstructures of the four test materials are shown in Figure 1.The alloy INCONEL 617 is a Ni-Cr alloy solid solution strengthened by additions of Co and Mo and was originally developed as a sheet material for aero gas turbine combustion chambers. This alloy is a typical example of a forgeable material used in the solution heat treated condition. The material INCONEL 706 is a Nb containing Ni-Fe-base alloy with good forgeability for applications for large scale components. This alloy is strengthened by a complex structure of γ', γ'' and, dependent on the heat treatment, η phase precipitates. Waspaloy is a γ' hardened material with a low C content leading to a small amount on $M_{23}C_6$ precipitates on the grain boundaries. Because of the high Ti/Al ratio γ' precipitates in a bimodal size distribution of primary and secondary γ' particles. Both alloys may be candidates for applications as rotors or disks in steam turbines with very high steam temperatures of about 700 °C. Single crystalline superalloys, first developed for aero gas turbine blades, exhibit a significant improvement in creep and fatigue resistance over conventionally cast, equiaxed superalloys, allowing about 80C higher materials temperature in operation. Alloy CMSX-4 is a typical second generation, single crystal material with about 70 vol% γ′ and solid solution strengthening of the γ matrix by 3 wt.% Re.

alloy	nominal chemical composition in mass-%											hardening
	Ni	Cr	Fe	Co	Mo	Al	Ti	Nb	Ta	W	C	
IN 617	bal	23	<2	12	9	1	0.5	2.9	-	-	0.05	sol.hard.,carbides
Waspaloy	bal.	19	0.5	14	4.5	1.2	3.1	0.01	-	-	0.03	γ' phase
IN 706	bal.	16	37	-	-	1	1.5	3	-	-	0.01	γ', γ'', η phases
CMSX-4	bal	6.4	-	9.6	0.6	5.6	1	-	6.5	6.4	-	+3% Re,γ' phase

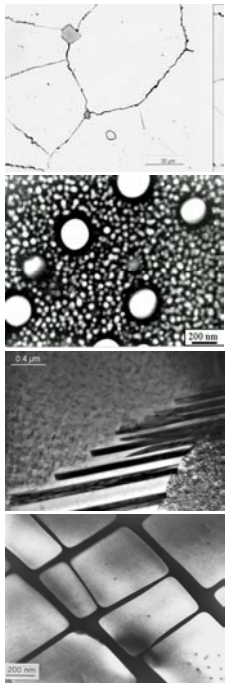

Figure 1: Nominal chemical compositions and microstructures of test materials

Test methods

12.7 mm CT specimens (ASME standards E 399 and E647) were machined from the wrought materials with guide notches if necessary (10% of the thickness of specimen, 60° angle). Specimens were fatigue pre-cracked at room temperature up to a depth-to-width ratio of 0.3 - 0.4. Assuming linear elastic fracture conditions [1,2], the results were interpreted using the stress intensity factor, K_I

$$K_I = \frac{F_{max}}{B \cdot W^{1/2}} \cdot f(a/w) \qquad (1)$$

where F_{max}= maximum of applied force, *B, W* = dimensions of the specimen, *a* = crack length and f(a/w) a geometrical factor.

INCONEL 617, Waspaloy and INCONEL 706 tested at 700°C or higher do not behave linear elastically, but viscoplastically. If the opening velocity $\dot{V}$ of the crack is considered, the integral of deformability (C*) is obtained by

$$C^* = \eta \cdot \sigma_{net} \cdot \dot{V} \qquad (2)$$

For CMSX-4, single edge notched (SEN) specimens were manufactured from <001> orientated cast plates. The K_I function for SEN specimens under stress load is normally given by

$$K_I = \sigma \sqrt{\pi a \cdot c} \qquad (4)$$

Specimens with corner cracks exhibit a much more complicated stress distribution ahead of the crack tip. This specimen represents the realistic crack geometry within a component due its three dimensionality. Mathematical results are given in [3,5,6], whereby a square edge crack surface area is estimated. One differentiates between the stress intensity factors along the surface of the specimen and in the direction of 45°. Then the stress intensity factor across the whole crack surface may be estimated by

$$K_{I\,mean} = \frac{K_{I\,45°} + K_{I\,surface}}{2} = \left(0.97 - 0.09\left(\frac{a}{w}\right)^2\right) \cdot K_{I\,surface} \qquad (5)$$

The approximations help in understanding the crack propagation of a corner edge crack [4]. The experimental observations indicate that for CMSX-4 the K_I-concept may be used at both test temperatures.

RESULTS

INCONEL 617 at 500°C

A comparison of the behaviour of creep crack either obtained by the evaluation as fatigue- or as creep-crack curves (Figure 2) shows: the values of ΔK_I in air and in vacuum are similar, the specimen in vacuum, however, developed a much higher resistance for creep deformation with higher ΔK_I- values. In the Paris regime of the crack curve the slope measured in both test atmospheres is similar. The behaviour of the crack growth curve in open air may be derived by a parallel transfer of the curve obtained in vacuum. The microstructure in the crack path consists of three regimes, whereby the fracture strain lines are observed to be stronger in open air than in vacuum.

After optimisation of the marker parameters [2,6], the marker lines are visible in the crack path surface. There are the same indications observed for this material at the test temperature. The crack initiation in air requires less stress intensity compared to vacuum; the Paris slopes are similar in both test environments, the end of deformability is higher in vacuum than in air (Figure 2).

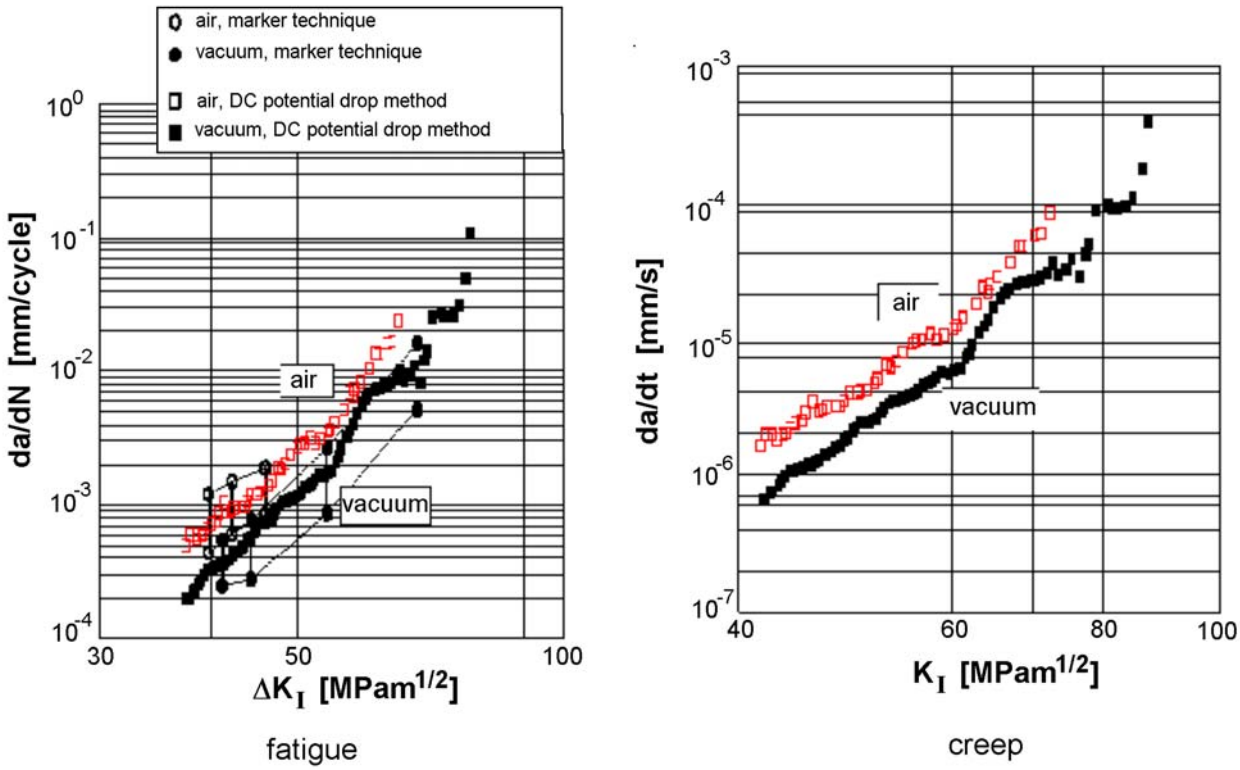

Figure 2: Results of crack growth experiments with INCONEL 617 in air and vacuum at 500°C, measurements by potential drop (PD) or by the marker technique [6]

Creep crack growth of wrought alloys

For the application of the wrought alloys INCONEL 617, INCONEL 706 and Waspaloy as large scale components, the creep crack growth behaviour becomes important. The results shown in Figure 3 demonstrate the influences of the temperature and of the environment on the creep crack growth resistance in the temperature range of 650 - 750°C. Figure 3a shows a comparison of the three alloys at 700 °C; for INCONEL 706, an η-free and an η-containing variant were investigated. The η phase precipitates as a cellular structure on the grain boundaries (see Figure 1) which results in an increase of the crack growth rate by a factor up to 10 compared with to the η free variant. Waspaloy shows the best creep crack growth resistance of the three alloys, with the highest K value for the crack initiation.

An example for the temperature dependence of the creep crack growth is given in Figure 3b. The exponent of the crack growth equation shows the highest value at 700 °C and the initial K value decreases with increasing temperature. The influence of the environment is demonstrated with the example of the η–free INCONEL 706 variant at temperatures of 650°C and 700°C in Figure 3c. The creep crack growth rate is higher in air than in vacuum, but with increasing temperature influence of test environment diminishes.

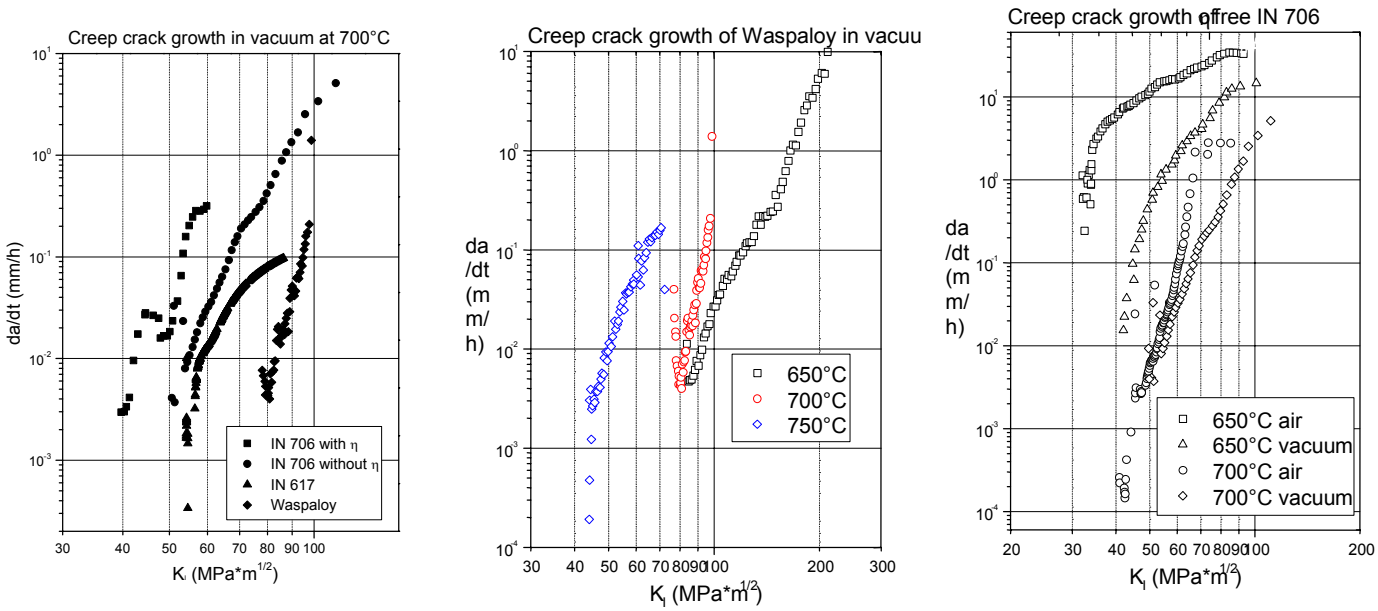

(a) (b) (c)

Figure 3: (a) Comparison of creep crack growth at 700°C in vacuum for INCONEL 617, INCONEL 706 (η-containing and η-free versions) and Waspaloy; (b) effect of temperature on creep crack growth rate of Waspaloy in vacuum; (c) effect of temperature and test environment on creep crack growth in η-free INCONEL 706.

SEN CMSX-4 at 750 and 1000°C

The results of fatigue crack growth experiments with SEN CMSX-4 specimens are summarised in Figure 4. At 750 and 1000°C, the fatigue crack growth behaviour of specimens with different orientations resulted in the expected functional behaviour ("Paris-Erdogan") of da/dN versus ΔK_I (the cyclic stress intensity factor [3]. At 750°C, the threshold values were higher and the slope of the Paris equation not so steep compared to the values at 1000°C. The influence of the crack path in an <001> oriented specimen seemed to be more marked at 750 than at 1000°C. Specimens with a <100> crack path orientation came to a sudden fracture by a spontaneous change to the {111} sliding planes. The <110> crack path orientation did not show this behaviour.

Figure 4 compares the fatigue and the creep fatigue behaviour at 1000°C. The edge crack specimen showed the same threshold values for both types of test, but the creep crack curves did not exhibit any changes in the crack growth rate. Therefore one may expect that creep-fatigue is more influenced by the deformation at the crack tip than by oxidation. If K as the stress intensity factor controlling the creep crack behaviour is used, the fatigue and the creep-fatigue results lie in the same range. At high K values and crack growth rates, the differences between fatigue and creep-fatigue became more significant. Because of these observations, one may conclude that creep dominates the crack growth process at low ΔK or K values, and fatigue at high ΔK or K values.

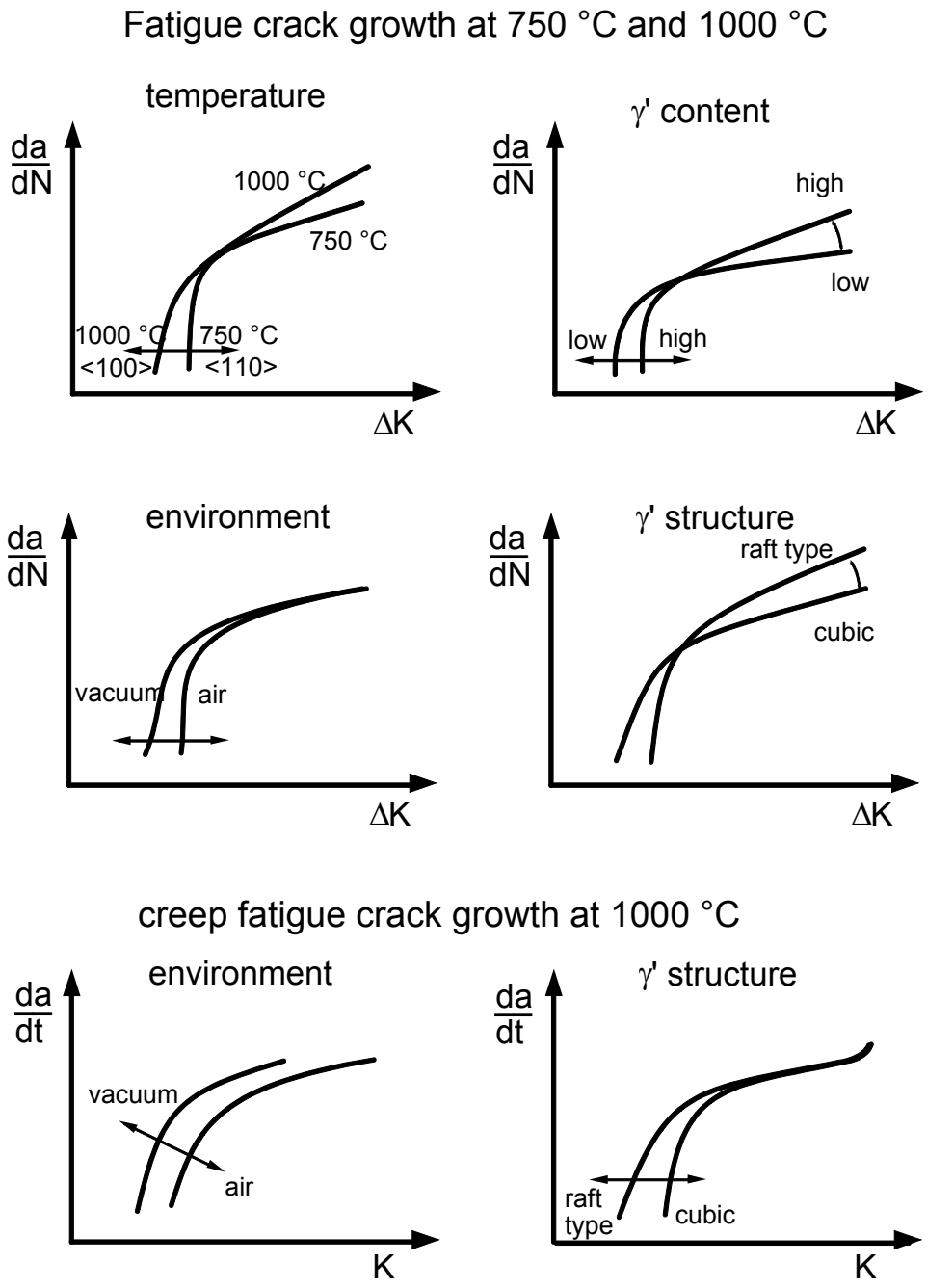

Figure 4 : Scheme of Crack growth behaviour of CMSX-4 in fatigue and creep fatigue crack growth tests [3].

Therefore, one may assume that the position of the crack front in relation to the {111} sliding planes is responsible for the observed brittle fracture. At 1000°C and for low ΔK values and low crack growth rates, the crack growth behaviour may be understood as typical crack behaviour of small cracks. This behaviour could be explained by the crack closure because of plastic deformation at the crack tip, oxidation and depletion of the crack surface areas and the start of the γ´ rafting process. These influences blunt the crack tip and the stress singularity decreases, so that the crack could be stopped or slowed down. At the low test temperatures, the influence of oxidation behaviour in the crack tip is not clearly demonstrated.

The oxidation behaviour at the crack tip became more important at the higher test temperatures. The comparison of the crack growth experiments in air and vacuum proved that the oxidation process influences significantly the crack initiation point or the initial stage of crack growth. Fractographic examinations using scanning electron microscopy (SEM) indicate for CMSX-4 (high volume fraction of γ´) a slightly different behaviour compared to equiaxed Ni alloys with γ´ volume fractions below 50%. In CMSX-4 at 750°C, high ΔK-values and high rates of crack growth, the fracture surface tended to shift to a {111} gliding plane, whereas at 1000°C

this was not observed. The crack surface of CMSX-4 at 750°C air followed at low ΔK-values the γ channels or the γ/γ´ interface region. At high ΔK-values, a change in the crack surface growth to be the {111} plane was observed and a cutting of γ´ occurred.

SUMMARY

The influences of test temperature and of the environment (air versus vacuum) have been investigated Ni-base alloys representing two different alloy types: solid solution hardened INCONEL 617 and the single crystal γ`-hardened CMSX-4. At test temperatures of 500 and 700°C there was no significant of test environment on the crack growth rate in the "Paris" region. However, a distinct influence of the environment on crack initiation was found.

The results of creep-fatigue crack growth experiments on the alloy CMSX-4, using single edge notched specimens at 750°C (maximum root-temperature) and for 1000°C (maximum airfoil temperature) showed that at 750°C and below the cracks, controlled by K concept, followed a zigzag line by changing the orientation along the {111} and {100} gliding planes. An influence of atmosphere was observed at the beginning and at the end of the crack growth. At high temperatures, such as 1000°C, crack propagation along the {100} planes was found.

REFERENCES

/1/ M Weber, Risswachstum in der PM-Nickelbasis-Legierung PM N18 bei Temperaturen zwischen 400 und 750°C unter statischer und zyklischer Belastung, Dissertation, RWTH Aachen, 1994

/2/ D Schwarze, Anwendbarkeit einer Marker-Technik zur Unterstuetzung von Risswachstumsuntersuchungen in sproeden und duktilen Ni-Legierungen bei 500 und 750°C, Dissertation RWTH Aachen, 1999

/3/ T. Rieck, "Wachstum kleiner Risse bei hohen Temperaturen und Zug-Schwellbeanspruchungen in den einkristallinen Superlegierungen CMSX-4 und SC 16", Diss. RWTH Aachen, Nov. 1999

/4/ /J. Newman, I. Raju, Stress intensity factor equations for cracks in three-dimensional finite radius subjected to tension and bending loads, NASA Langley Research Center, Hampton, TM 85793, Washington DC, 1984

/5/ F Schubert, T Rieck, P J Ennis, The growth of small cracks in the single crystal superalloy CMSX-4 at 750 and 1000°C, International Symposium on Superalloys: Superalloys 2000, 18-21 September 2000, Seven Springs, USA

/6/ D. Schwarze,J. Klabbers, F. Schubert, "Anwendbarkeit einer Markertechnik bei Untersuchungen zum Rißwachstum in Ni-Legierungen bei 500 und 750 °C", Zeitschr. F. Materialprüfung, DVM-Bericht 232,Juli 2000, pp 377-380

CRACK GROWTH CHARACTERISTICS UNDER HIGH TEMPERATURE FATIGUE-CREEP MULTIPLICATION CONDITION

Mitsuo Yoda [1],
Masayuki Kanou [2] ,
Osamu Yokota [1]
Toshimitsu Yokobori [3]

[1] Department of Mechanical Engineering, College of Engineering, Nihon University, Tamuramachi, Koriyama, Japan
[2] Graduate School, College of Engineering, Nihon University, [2]Tamuramachi, Koriyama,Japan
[3] Department of Mechatronics and Precision Engineering, Tohoku University, Aoba, Aramaki, Aobaku, Sendai Japan

Abstract

12 Cr heat-resisting steels have been developed for the high efficiency heat resisting steels of boiler and turbine and high temperature plant materials. These materials have been used under fatigue, creep and fatigue-creep multiplication conditions under corrosive environment and elevated temperature. It is necessary to clarify the effects of stress holding time, stress rising time, stress decreasing time, stress frequency on time-dependent fracture or crack growth under creep and fatigue-creep conditions at high temperatures. However, there are few papers in which each factor was systematically obtained.

In this paper, creep test and fatigue-creep multiplication condition test were conducted using compact tension (CT) specimens of HT1200 steel at high temperatures of 600 °C, 650 °C and 700 °C. In order to clarify strength mechanism of this material, both load line displacement and crack growth length were measured. Micro-structural and macro-structural fracture surfaces were also observed by optical microphotography and scanning electron microscope and so on.

Key words

Fracture, Crack growth rate, Load line displacement, High temperature, Fatigue-creep multiplication condition , Stress intensity factor, Scanning electron microscope, Activation energy.

1. Introduction

Many components in high temperature applications are subjected to variable loading patterns during service such as creep, fatigue and creep-fatigue. Creep-fatigue behavior is a complex problem of cyclically applied loading at high temperatures where time-dependent, thermally activated process can occur. The crack growth rate under the conditions of the creep-fatigue interaction will reflect the creep process and the fatigue process dominant near the crack tip. The majority of early work on high temperature structural alloys was concerned with static creep or fatigue testing. The crack growth rates in these cases were correlated with the parameters [1-3] such as the stress intensity factor, C^* integral, crack opening displacement and Q^* parameter.

Recently, the combined effects of temperature and frequency on the crack growth rate under creep-fatigue interaction have been determined and analyzed on the basis of the Arrhenius thermally activated process [4,5]. It has been shown that the activation energy thus obtained decreases with decreasing hold-time. The stress wave shapes such as triangular form and trapezoidal form have a strong effect on the crack growth rate. Similar effects of temperature and frequency were observed in terms of the failure life .

In this paper, the creep-fatigue tests were performed on the compact tension type specimens of 12 Cr steel at various combinations of temperatures and frequencies. The combined effects of temperature and frequency on the crack growth and the failure life were determined and analyzed based on the thermally activated processes.

2. **Specimens and Experimental Procedure**

The material used was 12 Cr steel (HR1200), and its chemical composition and mechanical properties are shown in Tables 1 and 2, respectively. The test specimens were of compact tension (CT) type with side grooves, as shown in Fig.1. The width W and the thickness B of the specimen were 50.8 and 25.4 mm, respectively. All the tests were performed using the lever-arm high temperature creep-fatigue machine, which could apply stress cycles involving various hold-times to the specimens. The amount of crack growth was measured using the electrical potential method and calculated by Johnson's formula. The stress wave form used for the creep-fatigue loading is shown in Fig.2. The gross stress σ_g and the frequency f are given as

$$\sigma_g = \frac{P}{B_1(W-a)}\left\{1+\frac{3(W+a)}{W-a}\right\} \qquad (1)$$

$$f = \frac{1}{(2t_R + t_H)} \qquad (2)$$

Table.1 Chemical composition (%)

	C	Si	Mn	Ni	Cr
12Cr-2.51W (HR1200)	0.10	0.06	0.46	0.25	10.21

Table.2 Mechanical properties

	Temperature (℃)	Yield stress (MPa)	Ultimate tensile strength (MPa)	Elongation (%)
12Cr-2.51W (HR1200)	20	705	853	19.3
	650	294	386	31.7

Mo	W	V	Nb	Co	N	B
0.14	2.51	0.21	0.07	2.44	0.017	0.013

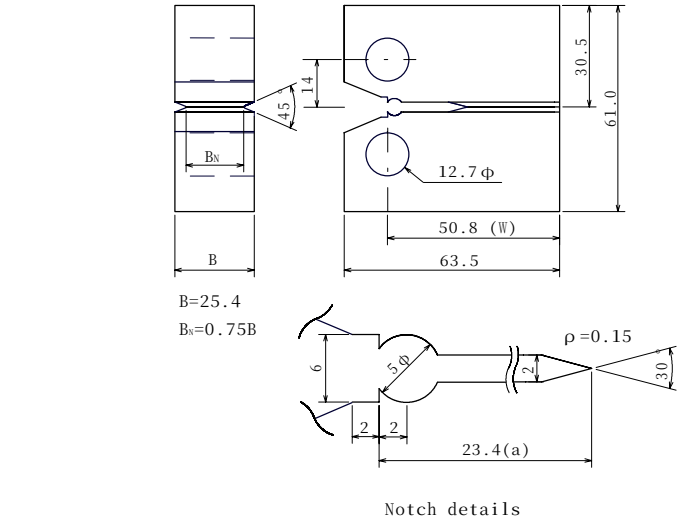

Figure 1 CT specimen geometry and size

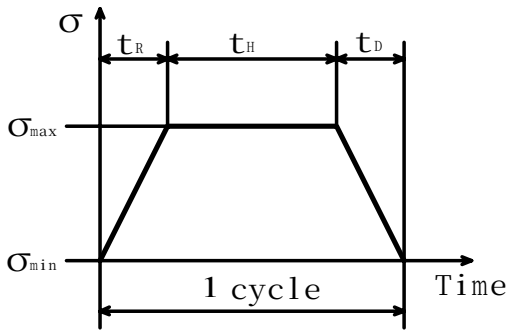

tR : Rising time (30s)
tH : Hold time
tD : Descending time(30s)

Figure 2 Stress wave form

where t_H is the hold-time, t_R the time for rising or descending stress rate. The tests were performed using four different hold-times t_H of 2, 10, 60 and 600s., resulting in frequencies of 1.6 x 10^{-2}, 1.4 x 10^{-2}, 8.3 x 10^{-3} and 1.5 x 10^{-3} Hz, respectively. The test temperatures were 600, 650 and 700°C and the temperature variation was ± 2 °C. The specimens were preheated, subjected to 10 % of the test load to maintain the alignment, at the test temperature for 16 hours and then loaded to a given stress cycle. The creep tests ($t_H = \infty$) were also performed under the constant stress at each temperature.

3. Experimental Results and Discussion

Figures 3 and 4 show the load line displacement Δδ and the crack growth Δa versus the time t normalized to the failure time t_f, respectively, at temperature 650°C. The load line displacement grows gradually until it is accelerated around $t / t_f = 0.8$. The $\Delta\delta - t / t_f$ curves fall on the same line independent of the hold times. However, the $\Delta a - t / t_f$ curves depend on the hold time. There is the region of nearly constant crack growth rate that occupied more than 60 % of the failure time t_f, as shown in Fig.4. The crack growth rate da/dt is plotted as a function of the load line displacement rate at

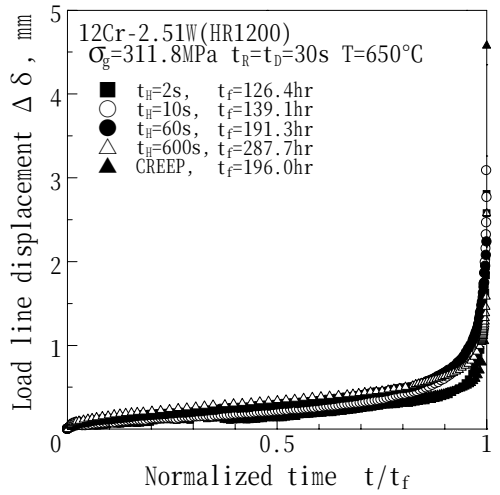

Figure 3 Load line displacement Δδ versus normalized time t/t_f (650 °C)

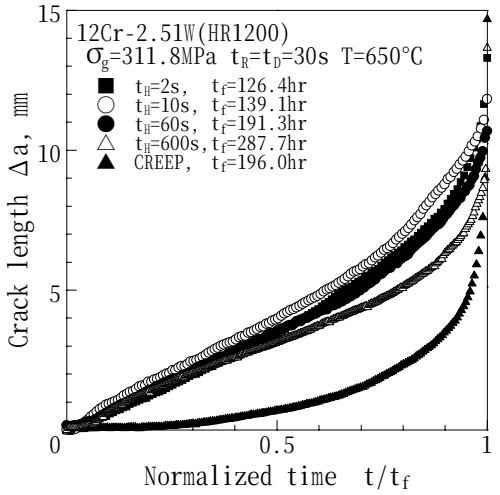

Figure 4 Crack growth Δa versus time t/t_f (650 °C)

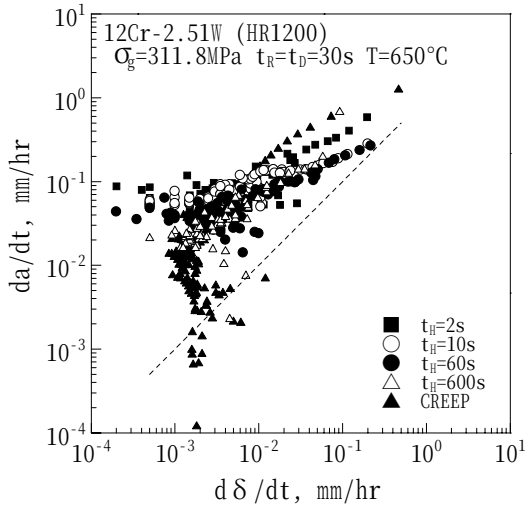

Figure 5 Crack growth rate da/dt versus load line displacement rate dδ/dt (650 °C)

temperature 650 °C in Fig.5. For creep ($t_H = \infty$) and t_H = 600 s, the da/dt – dδ/dt curves initially have a typical trend of nose-like shape and then da/dt is proportional to dδ/dt. For hold-times less than t_H = 60s, dδ/dt is accelerated more than da/dt over the entire range of the experiment.

The crack growth rate da/dt is plotted as a function of the stress intensity factor range ΔK for temperatures 650 and 700°C, in Figs.6 and 7, respectively. The stress intensity factor is given as follows.

$$K = \frac{P}{B_1\sqrt{W}} f(a/W) \qquad (3)$$

where

$$f(a/W) = \frac{(2+a/W)}{(1-a/W)^{3/2}}\{0.886 + 4.64(a/W) - 13.32(a/W)^2 + 14.72(a/W)^3 - 5.60(a/W)^4\}$$

It is evident that the crack growth rates, measured at each combination of temperature and frequency are largely different. As described above, there are two regions, region I for the constant crack growth rate expect for creep and region II for the accelerating crack growth rate. The constant or steady-state crack growth rate occupies more than 60 % of the failure life. Figure 8 shows the side view of fracture surface at the middle of the specimen thickness for t_H=2s. Crack branching deviating from the main crack can be observed to occur at many sites under the creep-fatigue condition, while there exists no crack branching under the creep condition. The constant crack growth rate may be attributed to crack branching.

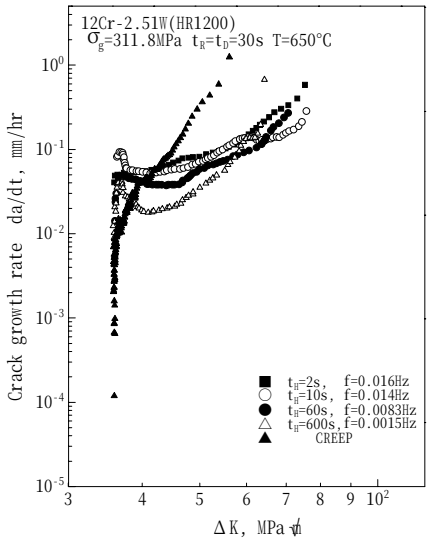

Figure 6 Crack growth rate da/dt versus stress intensity factor range ΔK(650 °C)

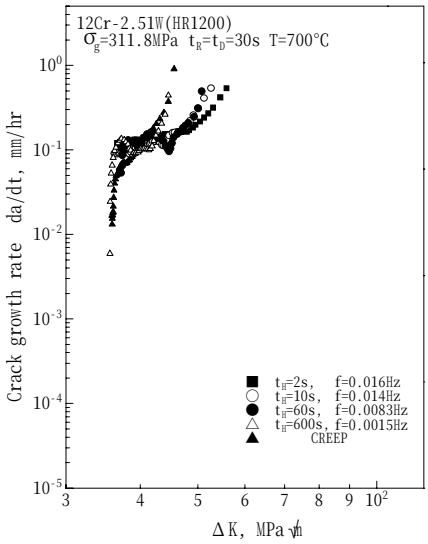

Figure 7 Crack growth rate da/dt versus stress intensity factor range ΔK(700 °C)

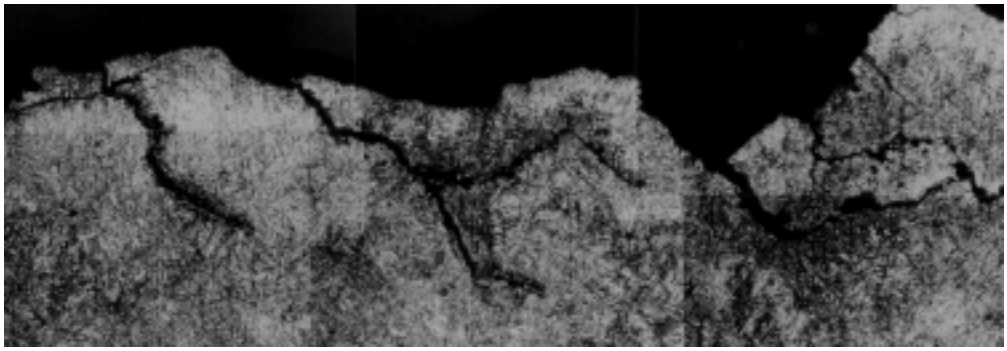

Figure 8 Side view of fracture surface at 650 °C

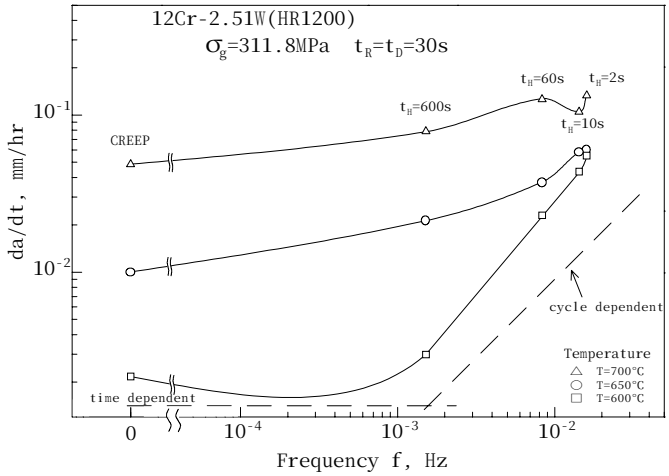

Figure 9 Dependence of constant crack growth rate da/dt on frequency f for various temperatures

The combined effects of temperature and frequency on the constant crack growth rate are shown in Fig.9. The dependence of the crack growth rate on frequency can be explained in terms of the following relationship between the crack growth per cycle da/dN and the crack growth rate da/dt

$$da/dt = f da/dN \qquad (4)$$

At high frequencies where da/dt is proportional to frequency, the crack growth per cycle is insensitive to frequency and cycle-dependent fatigue process is dominant. The da/dt decreases gradually with the decreasing frequency and the trend towards a horizontal line in Fig.9 at low frequencies corresponds with where da/dt is constant and time-dependent creep mechanisms will be expected to dominate. As the temperature increases, the difference of the crack growth rates between creep, fatigue and creep-fatigue interaction is small. Dependence of the constant crack growth rate on temperature can be explained on the basis of the thermally activated process, in terms of the relationship between da/dt and the reciprocal of absolute temperature T, as shown in Fig.10. The constant crack growth rate can be expressed as [5].

$$da/dt = AK_{in}^{n} \exp(-Q/RT) \qquad (5)$$

where A and n are the constants, K_{in} the initial stress intensity factor, Q the activation energy for the crack growth of the creep, and creep-fatigue interaction conditions, R the gas constant and T the absolute temperature. In this experiment, K_{in} is constant and the activation energy Q for each hold-time

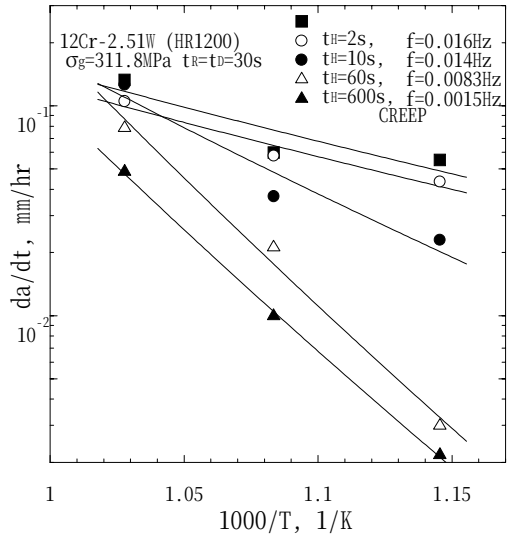

Figure 10 Dependence of constant crack growth rate da/dt on temperatures T

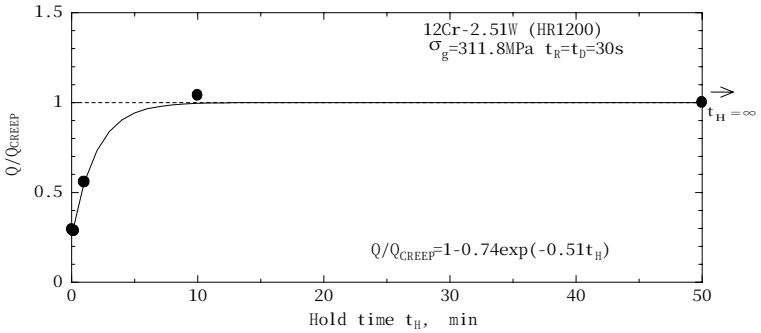

Figure 11 Variation of normalized activation energy Q/Q_{CREEP} with hold-time t_H

can be calculated from the slope of the curve. Although the activated energy tends to decrease as the temperature decreases for higher frequencies, the average value of Q over the range of the test temperatures can be obtained from the slope of the da/dt – l/T curve for each frequency. The value of Q normalized to the value of Q_{CREEP} for the creep crack growth is plotted as a function of the hold-time t_H in min, as shown in Fig.11. The normalized activation energy Q/Q_{CREEP} decreases with decreasing hold-time and the activation energy Q can be expressed as

$$Q = Q_{CREEP}\left[1 - A'\exp\left(-B't_H\right)\right] \qquad (6)$$

where, A' and B' are the constants. The value of Q_{CREEP} is 220.3 kJ/mol, the constants A' and B' are 0.74 and 0.51, respectively. The dependence of the constant crack growth rate on temperature can be described based on the thermally activated processes by taking account of the hold-time under the creep- fatigue interaction condition.

4. Conclusions

The creep, fatigue and creep-fatigue interaction tests were performed on the compact tension specimens of 12 Cr steel at three different temperatures. The crack growth rates were correlated by the stress intensity factor and there is the region of the constant crack growth rate that occupies more than 60 % of the failure life. At high frequencies where the constant crack growth is proportional to the frequency, cycle-dependent fatigue processes are dominant. The trend towards the horizontal line at low frequencies corresponds to the creep processes where the crack growth rate is independent of frequency. Dependence of the constant crack growth rate on temperature can be described on the basis of the thermally activated processes by taking account of hold-time.

References

1 J.D.Landes and J.A.Begley, 1976,ASTM STP590,pp128-148.
2 K.M.Nikbin, D.J.Smith and G.A.Webster, 1986, The Journal of Engineering Materials and Technology, Trans. ASTM'108, pp.186-191.
3 A.T.Yokobori, H.Tomizawa, H.Sakata, T.Kako and T.Kuriyama, 1987, Engineering Fracture Mechanics, 28, No.56, pp. 805-816.
4 A.T.Yokobori, H.Sakata, and T.Yokobori, 1980, Tans. Japan Soc. Mech. Engrs. 46, No.410, pp. 1062-1071.
5 A.T.Yokobori,Jr., T.Uesugi, T.Yokobori, A.Fuji, M.Kitagawa, I.Yamaya, M.Tabuchi and K.Yagi,1998, Journal of Materials Science 33, pp1555-1562.

ORAL REFERENCE: ICF0372OR

CRACK GROWTH IN A Ti6Al4V ALLOY UNDER MULTIAXIAL FATIGUE

Silva, F.S.; Pinho, A.C.M.

Department of Mechanical Engineering, University of Minho,
Campus de Azurém, 4800 Guimarães, PORTUGAL

ABSTRACT

The aim of this work is to identify the effect of steady torsion on crack growth. Crack growth was studied in a Ti6Al4V alloy at room temperature. Push-Pull tests (*R=-1*) with different levels of tension/compression were carried out with and without steady torsion. Round specimens according to ASTM E 606-80, with a pre-crack, were used and an assembly allowed to introduce the steady torsion. A Pulsed DCPD system with a very high resolution (less then 1 μm) was used to measure the crack growth.
At each level of tension, with and without steady torsion, the shape of the *da/dN-ΔK* curve was assessed. Closure effects, which are in Ti6Al4V alloys primarily associated with the roughness-induced mechanism, due to steady torsion were also assessed at different *R* (*R = -1; -0,23; 0,1 and 0,5*).
The fatigue threshold for small cracks was studied in relation to the mechanisms of propagation of short cracks with and without steady torsion.

Keywords: fatigue; crack growth; multiaxial; steady torsion.

INTRODUCTION

A combination of a steady torsion and an alternated tension is common in many practical problems such as power shafts and other rotating parts of cars, trains and airplanes.
The orientation of the principal axes associated with the alternating components remain fixed, and the steady torsion doesn't introduce a mean stress on the direction of the alternating component. Nevertheless, it's accepted that steady torsion changes the overall behavior of the components.
The role of steady torsion on the propagation behavior of specimens under alternated tension has been studied by several authors. Hourlier and Pineau [1-4] and Tschegg et al [5] used round specimens with a circunferencial crack on different alloys: Al alloys, steels, and titanium alloys. This authors detected a pronounced reduction on *mode I* fatigue crack growth rate, and imputed this effect to crack closure produced by the macrofaceted "factory roof" type fracture surface. Pinho [6] studied the influence of a steady torque on a high strength steel with a semi-elliptical crack shape and different concentration factors related to several concordance radius. The specimens didn't have a pre-crack. Pinho found the opposite behavior. Due to steady torsion, the mode I fatigue crack growth rate increases with steady mode III. Pinho also concluded that most of the cracks, in round specimens under alternated *mode I* and steady *mode III* are semi-elliptical. Only with high stresses and high stress concentrations factors the crack is circumferencial. And this happens only on a few specimens.

Tschegg et al [7] also studied the influence of steady torsion on the fatigue threshold, K_{th}. This author used a round 13 % chromium steel specimen with a circunferencial crack, and found that steady *mode III* increases the fatigue threshold.
In these studies, two mechanisms have been assumed as the causes of this behavior: work hardening at the crack tip; and closure effects. And the conclusion of most of the authors [1-5, 7] is that cyclic plastic behavior is not the dominant mechanism. Closure effect induced by roughness is assumed as the main mechanism. This effect is more relevant with an imposed steady *mode III*.
In Ti6Al4V alloys, in *mode I* crack growth, the closure mechanism is attributed mainly to roughness, Ogawa and Ravichandran [8,9].
In this work, the authors will try to explain that, under alternated tension and steady torsion, and a semi-elliptical crack, roughness may not play an important role as happens with circunferencial cracks, and cyclic plastic behavior of materials may be more relevant then roughness.

MATERIALS AND METHODS

Material and specimens

The material used in this investigation is a Ti6Al4V alloy. The chemical composition (wt.%) is Al:6,1; V: 4,21; Fe:0,20; Ni:0,01. The material was delivered on the mill annealed condition: 2h, 735±15ºC, air cool. The mechanical properties are listed in table 1. The specimens used are round specimens according to ASTM E 606-80, with a precrack. (fig.1). Stress concentration factors are respectively, for tension and torsion: 2,32 and 1,67.

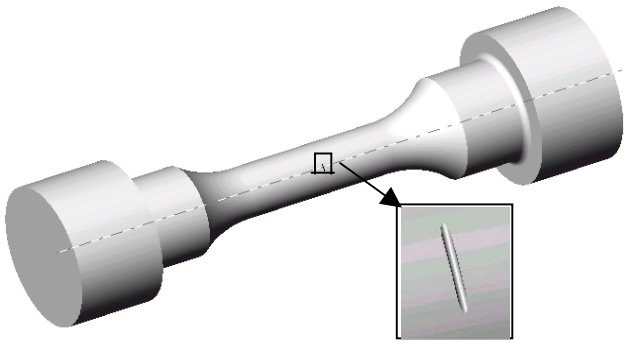

Figure 1 . Specimen geometry according to ASTM E 606-80, ∅=12 mm and L=133 mm. Pre-crack: a_0=100 μm; thickness = 300 μm; length = 2200 μm; curvature radius ρ=150 μm. K_t (tension)=2,32; K_t (torsion)=1,67

Table 1 : Mechanical Properties of Ti6Al4V

$\sigma_{ced\ (0,2\%)}$ *MPa*	σ_r *(MPa)*	*E (MPa)*
989	1055	$1,15*10^5$

Methods

Fatigue tests were conducted at two levels of alternated tension, $\Delta\sigma$, and one level of torsion, τ, as indicated in table 2, in laboratory air using a sinusoidal loading with different ratios of tension, (*R= -1; -0,23; 0,1*; and *0,5*) under loading control at a frequency of 8 Hz on a servo-hydraulic testing machine. The steady torsion was introduced using an assembly with dead weigth. At each level of tension and torsion the shape of the *da/dN-ΔK* curve was assessed. Tests presented in this work are representative tests of more than 50 tests. A Pulsed DCPD system with a resolution better than 1 μm [10] was used to measure the crack growth. Fracture surface examinations were made using an optical microscope.

Table 2 : Testing Conditions. Stresses don't include stress concentration factors.

Test	*R*	$\Delta\sigma$ *[MPa]*	τ *[MPa]*	$\sigma^{y}_{máx}$ *[MPa]*	σ_1 *[MPa]*
1	-1	698	0	349	349
2	-1	698	349	349	573
3	-1	884	0	442	442
4	-1	884	442	442	716
5	-1	1060	0	530	530
6	-1	1060	530	530	858
7	-0,23	698	0	575	575
8	0,1	698	0	796	795
9	0,5	411,5	0	823	823
10	0,5	411,5	349	823	951

RESULTS

The relationship between fatigue crack growth and ΔK, at different R levels is presented in fig. 2. (tests 1,2,7,8,9,10). Tests for $R=-1$ ($\Delta\sigma$ = 698 MPa) and $R=0,5$, with steady torsion are also at the same graphic.

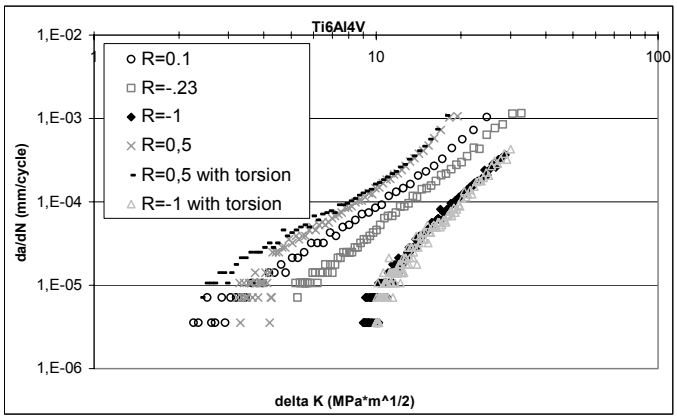

Figure 2 : Relationship between fatigue crack growth and stress intensity factor range, ΔK, at different R levels. Tests with R=-1 ($\Delta\sigma$ = 698 MPa) and R=0,5 are presented with torsion and without torsion.

The results can be summarized as follows:

1. When the R value increase, the fatigue crack growth curve *tend to the left*;
2. For $R=-1$ ($\Delta\sigma$ = 698 MPa) tests with steady torsion *tend slightly to the right*, mainly on small crack regime;
3. For $R=0,5$ (almost closure free), tests with steady torsion *tend slightly to the left*;
4. On the small crack regime, steady torsion seems to be more important for $R=0,5$ than for $R=-1$.
5. The fatigue crack Threshold, K_{th}, seems to decrease with steady torsion.

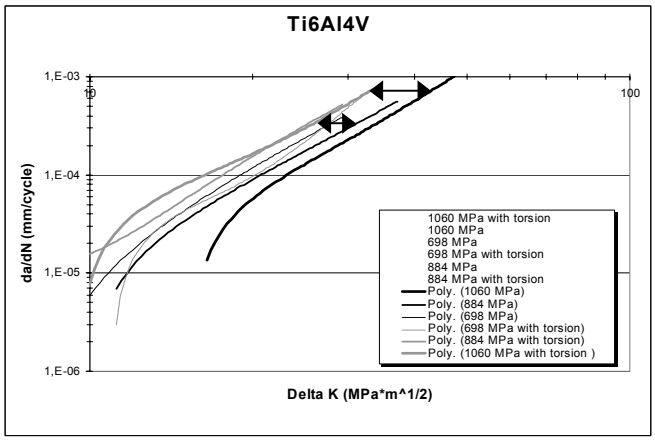

Figure 3 : Relationship between fatigue crack growth and stress intensity factor range, ΔK, at different levels of $\Delta\sigma$, and $R= -1$.

Fig 3 show the results of some other tests with different levels of alternated tension (tests 1-6) , under $R = -1$. Tests 2,4, and 6 have steady torsion.

a)

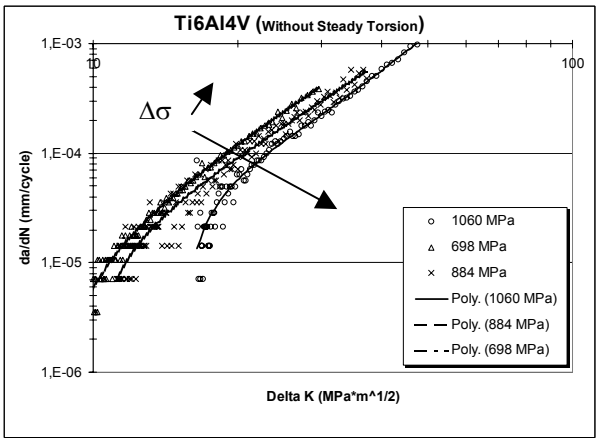

b)

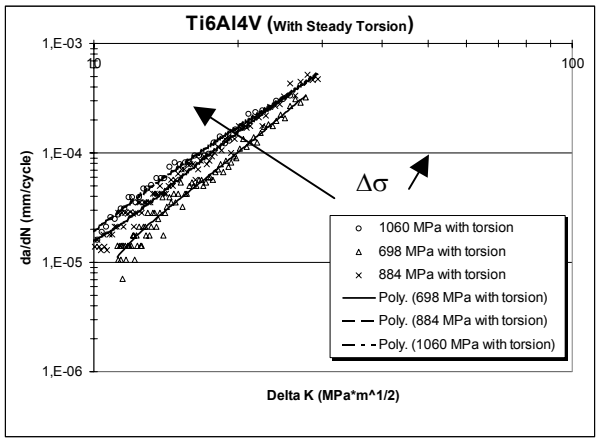

Figure 4 : Relationship between fatigue crack growth and stress intensity factor range, ΔK, at different levels of $\Delta\sigma$, and $R = -1$. a) Tests without steady torsion. b) Tests with steady torsion.

This results, for $R = -1$ can be summarized as follows:

1. Without steady torsion, as $\Delta\sigma$ increases, the fatigue crack growth curve *tends to the right* (fig.4 a). On the small crack regime the influence is more relevant and K_{th} increases with $\Delta\sigma$.
2. With steady torsion, as $\Delta\sigma$ increases, the fatigue crack growth curve *tends to the left* (fig.4 b). On the small crack regime the influence is more relevant and K_{th} decreases with $\Delta\sigma$.
3. As $\Delta\sigma$ increases, the difference on crack propagation rate between curves with steady torsion and without steady torsion, increases also (fig. 3);

Macroscopic observations of fracture surfaces

Figs. 5 - 6 show macroscopic photographs of fracture surfaces of tests with $R=-1$, with and without steady torsion. Fig. 6 have an alternated tension of 698 MPa, and fig. 7 have an alternated tension of 1060 MPa.

a)

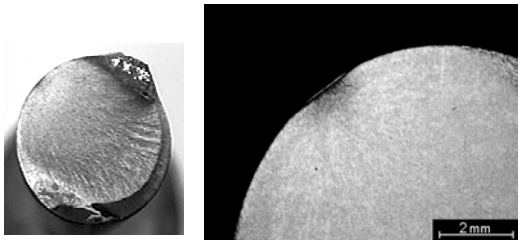

b)

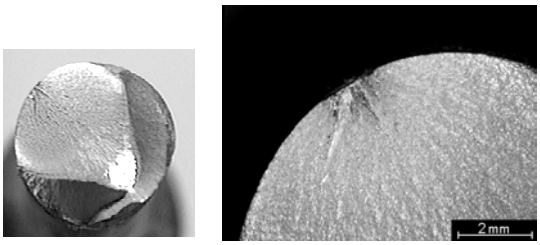

Figure 5 : Macroscopic appearance of fracture surfaces. $\Delta\sigma$ = 698MPa. a) without torsion; b) with torsion

a)

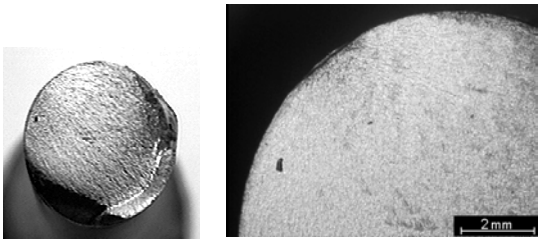

b)

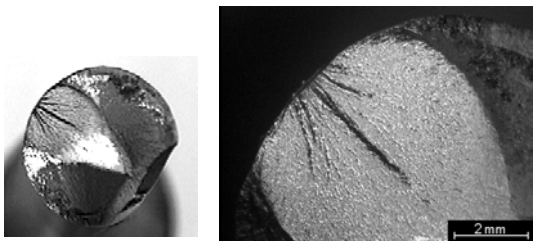

Figure 6 : Macroscopic appearance of fracture surfaces. $\Delta\sigma$ = 1060 MPa. a) without torsion; b) with torsion.

In fig. 7 we can observe macroscopic photographs of the fracture surfaces of tests with $R=0,5$, with and without steady torsion.

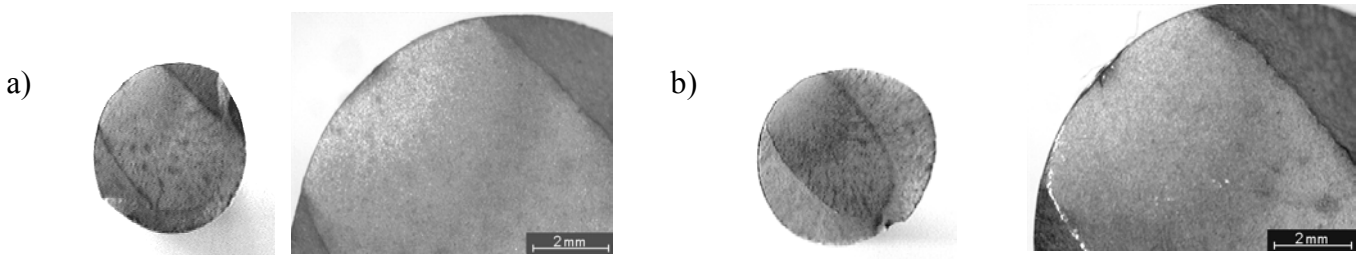

Figure 7 : Macroscopic appearance of fracture surfaces. *R=0,5.* a) without torsion; b) with torsion.

The results can be summarized as follows:

1. As the *R* value increase, the macroscopic fracture surface is smoother;
2. For *R=-1*, steady torsion produces the so called "factory roof" effect. This effect is more relevant as the level of $\Delta\sigma$ increases.
3. For *R=0,5* steady torsion doesn't introduce the "factory roof" effect;
4. "Factory roof" effect, at *R=-1*, seems to be present since the very beginning of the tests. For crack lengths less than 0,1 mm.

DISCUSSIONS

In terms of propagation life it's clear that decreasing *R* (fig.2) the fatigue crack growth curve tends to the left and it's observed that the fracture surface becomes smoother. This result is in accordance with theories [8-9,11-12]. When imposing steady torsion, the surface roughness increases because of the so called "factory roof" effect. This is true only for *R=-1*, and not for *R=0,5*. For *R=0,5* it's observed that the propagation rate with steady torsion is slightly higher than without steady torsion. If there is no effect of surface roughness one may conclude that another mechanism than surface roughness is responsible for this behavior. Let's assume that this mechanism is related with cyclic plastic behavior of this alloy (or plastic zone size).
For *R=-1* (fig.2) there is no significant difference on propagation rate in tests with and without steady torsion at an alternated tension of $\Delta\sigma$ = 698 MPa. When the amplitude of tension increases, curves of tests without steady torsion tend to the right (fig.4 a) while curves of tests with steady torsion tend to the left (fig.4 b). This could mean that cyclic plastic parameters push the curve to the left, but another mechanism, which may be surface roughness (without steady torsion) and "factory roof" effect, with steady torsion, pushes it to the right. As a result it's observed that those two mechanisms, surface roughness or "factory roof" effect, and cyclic plastic behavior compete with each other. It's interesting to observe that, without steady torsion, when stresses increase, roughness effect prevails, and curves tend to the right. This is because plastic effect is not relevant. When steady torsion is imposed, cyclic plastic effects become more important then roughness or "factory roof" effect. And this is more relevant when stresses are high. The difference between curves with and without steady torsion increase with increasing alternated tension (fig. 3).
On the small crack regime it's observed that the tendency of the threshold, K_{th}, is the same as for long crack regime, but it's even more relevant. This behavior is opposite to the behavior in the work of Tschegg, Pineau and Hourlier [1-5]. This authors worked with round specimens with a circumferential crack. Fig. 7 show the fracture surfaces of tests with a circumferencial crack and with a semi-elliptical crack. Both with steady torsion. As it's observed, it seems that with a circumferential crack, the effect of the faceted structure is greater, because the surface of the crack is much bigger. With a semi-elliptical crack the effect of the faceted structure may not be so relevant because the surface of the crack is smaller.

34CrNiMo6 with a cincumferencial crack [6]

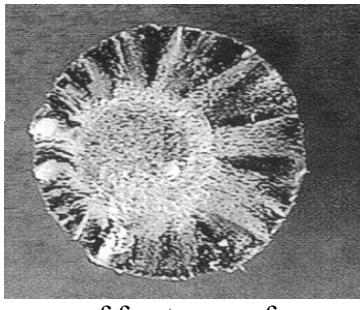

Ti6Al4V with a semi-elliptical crack

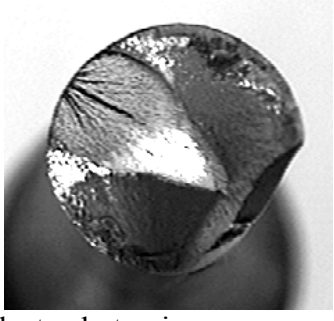

Figure 8 : Macroscopic appearance of fracture surfaces under a test with *R=-1* with steady torsion.

Maybe this is the reason why when imposing steady torsion, curves of crack propagation rate tend to the right, in work of Pineau, Hourlier and Tschegg, and tend to the left in this work.
Work of Tschegg [7] conclude that steady torsion increases threshold, K_{th}.This work concludes the opposite. The reason may be the same as for long crack regime.
Another possible explanation may be on cyclic plastic behavior of different materials with and without steady torsion. Steady torsion may have a softening or hardening influence on the cyclic plastic behavior of the materials. And this may be another possible reason for the behavior of this alloy in this work.
In high cycle fatigue, and with high frequencies, because plastic effects are small, roughness effect may prevail over cyclic plastic effects.

CONCLUSIONS

The main conclusions of this work can be summarized as follows:

1. With semi-elliptical cracks, between the two mechanisms which are present at the tip of the crack, cyclic plastic behavior seems to prevail over roughness or "factory roof" effect;
2. This effect causes crack propagation curves to move to the left with imposed steady torsion;
3. This tendency is more relevant for high stresses and in the small crack regime;
4. Fatigue threshold for small crack regime follows the same tendency.

References

1. Hourlier, F., Pineau, A., "Propagation of Fatigue Cracks Under Polymodal Loading", Fatigue Fract. Engng. Mat. Struct., 5, 1982, pp. 287-302
2. Hourlier, F., Pineau, A., "Fissuration par Fatigue Sous Solicitations Polymodales (Mode I ondulé + Mode III Permanent) d'un Acier Pour Rotors 26 NCDV 14", Mémoires Scientifiques Révue Metallurgie, 1979, pp. 175-185
3. Hourlier, F., Mclean, D., Pineau, A., "Fatigue Crack Growth Behavior of Ti5Al2.5Sn Alloy Under Complex Stress (Mode I + Steady Mode III), Metals Technology, 1976, pp.154-158
4. Hourlier, F., Hondt, H., Truchon, M., Pineau, A., "Fatigue Crack Path Behavior Under Polymodal Fatigue", ASTM STP 853, 1985, pp. 228-247
5. Tschegg, E.K., Stanzl, S.E., Mayer, H., Czegley, M.,"Crack Face Interactions and Near Threshold Crack Growth Fatigue", Fatigue Fract. Engng. Mat. Struct., 16, 1992, pp. 71-83
6. PINHO, A.C.M., "Fatigue Design of Power Shafts Using Fracture Mechanics", PhD Thesys, 1996
7. Tschegg, E.K., Mayer, H.R., Czegley, M., Stanzl, S.E., "Influence of a Constant Mode III Load on Mode I Fatigue Crack Growth Thresholds", ESIS 10, 1991, pp. 213-222
8. Ogawa, T; Tokaji, K., "The Effect of microstructure and fracture surface roughness on fatigue crack propagation in a Ti6Al4V alloy", Fatigue Fract. Engng. Mater. Struct., Vol. 16, nº9 (1993), pp. 973-982.
9. Ravichandran, K.S., "Near Fatigue Crack Growth Behavior of a Titanium Alloy: Ti6Al4V"" Acta Metall. Mater., 1991, 39 (3), pp. 401-410
10. Silva, F.S.; Pinho, A.C.M.; Peixinho, N.; Meireles, J., " Validation of a calibration procedure for fatigue crack growth measurement in circular section specimens" Damage and Fracture Mechanics VI (2000), Wit Press, pp. 353-364.
11. Finney, J.M., Deirmendjian, G.,"Delta K Effective: Which Formula?", Fat. Fract. Engng. Mater. Struct., 15, 1992, pp. 151-158
12. Katcher, M., Kaplan, M., **"**Effects of R-Factor and Crack Closure on Fatigue Crack Growth for Aluminum and Titanium Alloys", ASTM STP 559, 1974, pp. 264-282

ORAL/POSTER REFERENCE: ICF100579OR

CRACK GROWTH IN SOLID PROPELLANTS

E.E. Gdoutos and G. Papakaliatakis

School of Engineering, Democritus University of Thrace
GR-671 00 Xanthi, Greece

ABSTRACT

An analytical investigation of the growth behavior of an edge crack in a rectangular sheet specimen made of a solid propellant was performed. The specimen was subjected to a uniform displacement along its upper and lower faces. The solid propellant was simulated as a hyperelastic material with constitutive behavior described by the Ogden strain energy potential. A nonlinear finite deformation analysis of the stress and displacement fields was performed using the finite element code ABAQUS. A very detailed analysis of the stress field in the vicinity of the crack tip was undertaken. The deformed profiles of the crack faces near the crack tip were determined. The results of stress analysis were coupled with the strain energy density theory to predict the crack growth behavior including crack initiation, stable crack growth and final termination. Crack growth resistance curves representing the variation of crack growth increments versus applied displacement were drawn.

KEYWORDS

Crack growth, Solid propellant, Finite element analysis, Hyperelastic material, Nonlinear behavior, Finite deformations.

INTRODUCTION

Solid propellants are particulate composite materials, containing hard particles embedded in a rubber matrix. On the microscopic scale, a highly filled propellant can be considered as nonhomogeneous. When the material is strained, damage in the form of microvoids in the binder or debonding at the matrix/particle interface takes place. As the applied strain in the material is progressively increased the growth of damage takes place as successive nucleation and coalescence of the microvoids or as material tears. These processes of damage initiation and evolution are time-dependent and they are mainly responsible for the time-sensitivity of the nonlinear stress-strain behavior of solid propellants. Their mechanical response is strongly influenced by the loading rate, temperature and material microstructure.

A considerable amount of work has been performed by Liu and coworkers [1-3] to study crack growth behavior in solid propellants. They investigated the characteristics of damage zone near the crack tip and crack growth behavior in cracked specimens of a solid propellant. From experimental results they established that the damage characteristics have strong effects on crack growth behavior. Crack growth consists of crack tip blunting, resharpening and zig-zag crack growth.
The objective of the present work is to study the characteristics of the damage zone near the crack tip and

the crack growth behavior in edge and centrally cracked sheet specimens of a solid propellant. The stress field in the cracked plates is evaluated by modeling the solid propellant as an incompressible visco-hyperelastic material. A very detailed finite element analysis in the vicinity of the crack tip takes place. A methodology based on the strain energy density criterion is developed for the determination of the critical stress at the onset of crack initiation and the history of stable crack growth up to final instability.

CONSTITUTIVE BEHAVIOR

Solid propellants are modeled as hyperelastic materials. The behavior of hyperelastic materials is described in terms of a strain energy potential U(ε). The more frequently used forms of the strain energy potentials for modeling approximately incompressible isotropic materials are the polynomial form and the Ogden form.

The form of the polynomial strain energy potential is

$$U = \sum_{i+j=1}^{N} C_{ij}(\bar{I}_1 - 3)^i(\bar{I}_2 - 3)^j + \sum_{i=1}^{N} \frac{1}{D_i}(J_{e\lambda} - 1)^{2i} \tag{1}$$

where U is the strain energy per unit of reference volume, N is a material parameter, C_{ij} and D_i are temperature dependent material parameters, $\bar{I}_1$ and $\bar{I}_2$ are the first and second deviatoric strain invariants, defined as

$$\bar{I}_1 = \bar{\lambda}_1^2 + \bar{\lambda}_2^2 + \bar{\lambda}_3^2 \quad and \quad \bar{I}_2 = \bar{\lambda}_1^{(-2)} + \bar{\lambda}_2^{(-2)} + \bar{\lambda}_3^{(-2)}$$

with the deviatoric stretches $\bar{\lambda}_i = J^{-1/3}\lambda_i$, J is the volume ratio, λ_i are the principal stretches, and J_{el} is the elastic volume ratio without thermal expansion effects.

The form of the Ogden strain energy potential is

$$U = \sum_{i=1}^{N} \frac{2\mu_i}{\alpha_i^2}\left(\bar{\lambda}_1^{a_i} + \bar{\lambda}_2^{a_i} + \bar{\lambda}_3^{a_i} - 3\right) + \sum_{i=1}^{N} \frac{1}{D_i}(J_{e\lambda} - 1)^{2i} \tag{2}$$

N is a material parameter, and μ_i, α_i and D_i are temperature dependent material parameters. Because the powers α_i can be chosen by the user, the Ogden form usually provides a closer and more stable fit to the test data for a similar number of material constants in the strain energy function, especially at large strains. If all of the D_i are zero, the material is fully incompressible. If D_1 is equal to zero, all of the D_i must be equal to zero.

For cases where the nominal strains are small or only moderately large (<100%), the first terms in the polynomial series usually provide a sufficiently accurate model. The simplest form of the polynomial function is the form with N=1, which is the compressible form of the classical Mooney-Rivlin law:

$$U = C_{10}(\bar{I}_1 - 3) + C_{01}(\bar{I}_2 - 3) + \frac{1}{D_1}\left(J_{e\lambda} - 1\right)^2 \tag{3}$$

When C_{01}=0 the strain energy function corresponds to the compressible form of the neo-Hookean law.

FINITE ELEMENT ANALYSIS

The finite element method was used to solve the boundary value problem of an edge cracked specimen subjected to a uniform displacement along its upper and lower faces. The specimen is a rectangular sheet of width w=76.2 mm and height h=25.4 mm (Fig. 1). The thickness of the specimen was small enough to assume that conditions of plane stress prevail. An initial edge crack was introduced in the mid height of the specimen parallel to the specimen width. The crack length took the values a=2.54 mm, 15.24 mm and 30.48 mm. The specimen was made of a solid propellant. It was subjected to a uniform displacement u_0 along its upper and lower faces. The stress-strain curve of the propellant in tension is shown in Fig. 2.

A nonlinear large deformation analysis was performed by the ABQUS computer code. The discretization of a small region of the specimen crack tip are presented in Fig. 3. The applied displacement u_0 was increased incrementally. Results for the strain energy density, dW/dV, along the crack axis direction, are shown, in Fig. 4 for a=15.24 mm and for applied displacement u=0.0847 mm, 0.1694 mm and 0.2541 mm.

PREDICTION OF CRACK GROWTH

Crack growth consists of three stages: crack initiation, subcritical or slow growth and unstable crack propagation. These stages of crack growth will be addressed in a unified manner by the strain energy density criterion. The criterion was introduced by Sih , and it was used by Gdoutos and co-workers [4-6] for the solution of a host of problems of engineering importance.According to the strain energy density theory crack growth takes place when the strain energy density at an element ahead of the crack tip reaches a critical value. This value is calculated from the stress-strain curve of the material in tension.

$$\frac{dW}{dV} = \int_0^{\varepsilon_{ij}} \sigma_{ij} d\varepsilon_{ij} \tag{4}$$

where σ_{ij} and ε_{ij} are the Cartesian stress and strain components. Equation (1) applies to all materials either linear (nondissipative) or nonlinear (dissipative).For the case when material failure initiates from the tip of a preexisting crack in a solid propellant attention is concretrated on the distribution of the strain energy function along the circumference of a circle centered at the crack tip. This circle represents the process or core region in which the continuum model fails to describe the state of stress and strain. The crack will grow in the direction of the minimum strain energy density function, $(dW/dV)_{min}$. Onset of crack extension takes place when $(dW/dV)_{min}$ becomes equal to $(dW/dV)^c_{min}$ (referred to in sequel as $(dW/dV)_c$) which is directly determined from the area underneath the stress-strain diagram of the material up to the point of fracture. Crack growth initiation is expressed by

$$\left(\frac{dW}{dV}\right)_{min} = \left(\frac{dW}{dV}\right)_c \tag{5}$$

where $(dW/dV)_c$ is a material parameter.The value of the critical stress σ_i that triggers crack growth is determined from equation (5). The condition for stable crack growth is expressed by

$$\frac{dW}{dV} = \left(\frac{dW}{dV}\right)_c = \frac{S_1}{r_1} = \frac{S_2}{r_2} = \ldots = \frac{S_j}{r_j} = \ldots \frac{S_c}{r_c} \tag{6}$$

where r_m (m=1,2,...,j) are the crack growth increments. Crack growth becomes unstable when the critical crack increment r_c is reached. r_c is a material parameter and is calculated from $r_c=S_c/(dW/dV)_c$, where S_c is material parameter.The graphical procedure for the determination of the critical applied displacement u

for initiate of crack growth are presented in Fig. 4 for a crack length a=15.24 mm. In this figure r_0 is the radius of the core region within which the continuum model ceases to be able to represent the state of stress and strain. For analysis purposes in the present study r_0 was taken equal to r_0=0.014 mm. Based on the strain energy density criterion a series of crack growth increments are determined until the crack growth increment reaches the critical value r_c=1.6 mm. The R-curve for this case is shown in Fig. 5. The deformed profile of the crack face near the crack tip for applied displacement u=0.4235, 1.2705, 2.1175 and 2.9645 mm is shown in Fig. 6. Results for the critical stress for crack initiation and growth for various crack lengths is shown in Fig. 7.

ACKNOWLEDGEMENTS

The authors express their appreciation to Dr. C.T. Liu of the USAF, Phillips Lab., Edwards AFB for his encouragement, support and cooperation during the course of the present work.

REFERENCES

1. Liu, C.T. (1995) *J. Spacecrafts and Rock.* 32, 535.
2. Liu, C.T. (1992) *J. Spacecrafts and Rock.* 29, 713.
3. Liu, C.T. and Tang, B. (1995). *Proc. 1995 SEM Spring Conf.,* pp. 831-836.
4. Gdoutos, E.E. and Papakaliatiakis, G. (1986) *Ther. Appl. Fract. Mech.* 5, 133.
5. Gdoutos, E.E. and Papakaliatiakis, G. (1986) *Int. J. Fract.* 32, 143.
6. Gdoutos, E.E. and Papakaliatiakis, G. (1986) *Eng. Fract. Mech.* 25, 141.

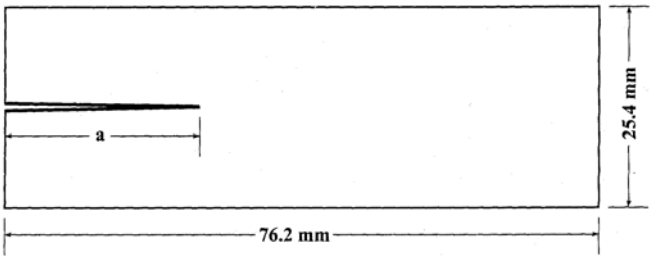

Fig. 1 Geometry of edge-cracked specimen

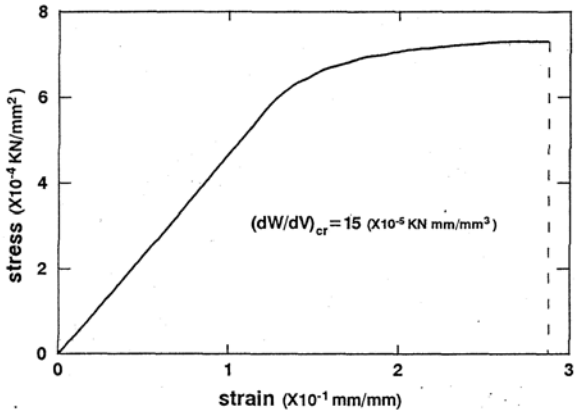

Fig. 2 Stress-strain curve of the solid propellant in uniaxial tension

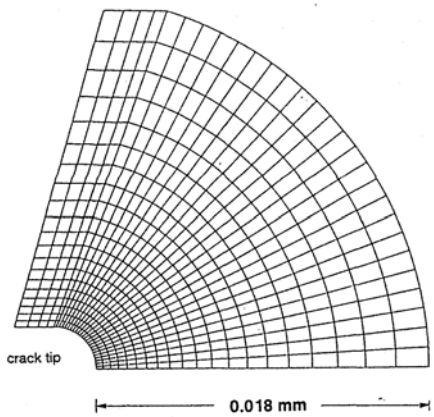

Fig. 3 Finite element grid pattern in a small region near the crack tip.

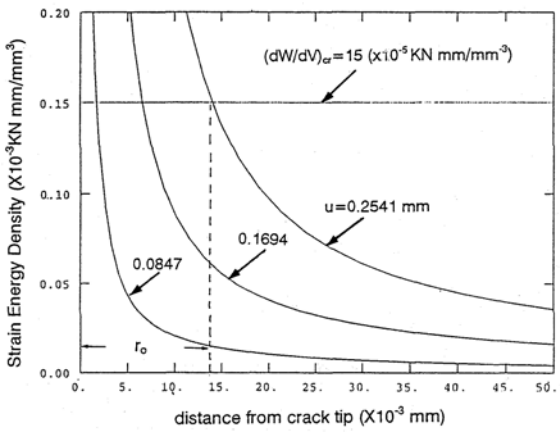

Fig. 4 Determination of the critical value of u at crack initiation

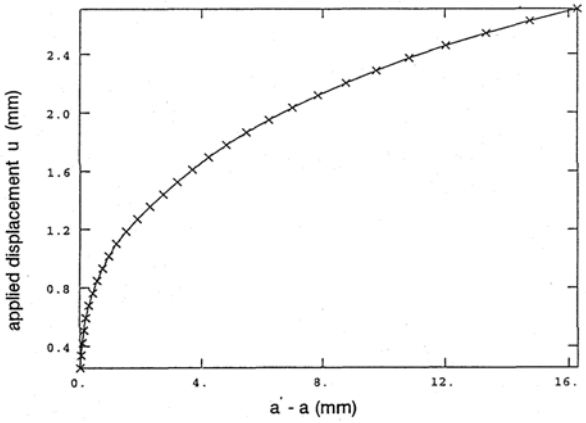

Fig. 5 Crack growth resistance curve.

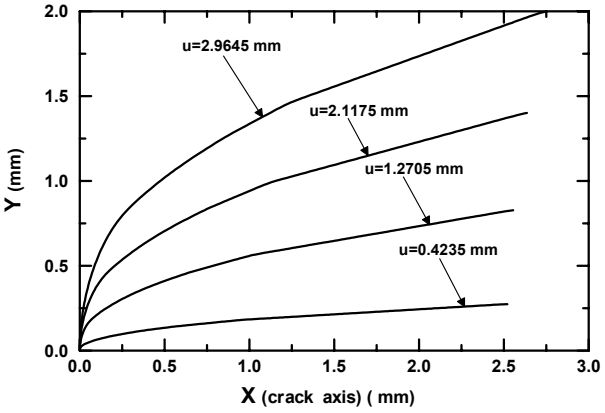

Fig. 6 Deformed profile of cracks faces near the crack tip for various values of the uniform applied displacement u.

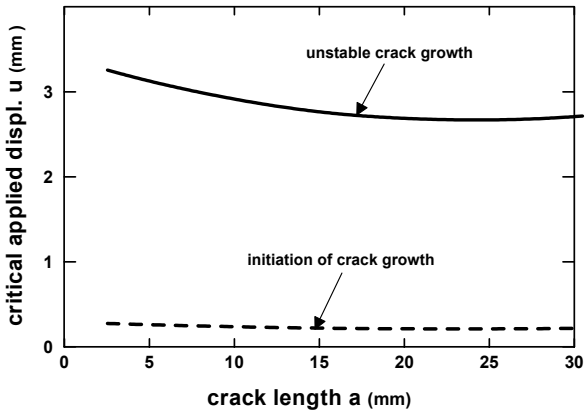

Fig. 7 Variation of the critical applied displacement u for crack initiation and unstable growth for various crack lengths

CRACK GROWTH RESISTANCE OF METAL FOAMS

I. Schmidt[1] and N.A. Fleck[2]

[1] Institut für Mechanik, TU-Darmstadt, Hochschulstr. 1, D-64289 Darmstadt, Germany
[2] Cambridge University Engineering Department, Trumpington Street, Cambridge CB2 1PZ, UK

ABSTRACT

This study investigates the crack growth initiation and subsequent resistance in ductile, open cell foams. We consider a macroscopic crack in a cellular structure in mode I loading and under small scale yielding conditions. The elasto-plastic response of the cell wall material is described by a bilinear stress-strain relation and fracture of the cell walls is characterised by a fracture energy per unit area. Suitable normalised problem parameters are identified in a dimensional analysis. Crack growth is simulated numerically by removing elements from a finite element model. In this way, evolving plastic zones and macroscopic K-resistance curves are calculated. Specifically, the dependence of the macroscopic fracture properties upon the parameters of the cell wall material is addressed. The results are compared with analytic estimates which are derived on the basis of simple considerations. The results include the findings that the toughness of the foam scales linearly with the fracture strength of the cell walls and quadratically with the relative density of the foam.

KEYWORDS

ductile fracture, crack resistance, R-curve, honeycombs, foams

INTRODUCTION

Metallic foams have unique property profiles and are considered for a number of engineering applications such as e.g. cores of sandwich constructions. An increasing use of such materials calls for an investigation of their failure mechanisms. Previous studies of the fracture properties of cellular materials seem to have been limited to the case of *brittle* base materials and to the prediction of a critical stress intensity factor. For example, Gibson & Ashby [1] derive an estimate for K_c by calculating the bending moment in a cell wall adjacent to the macroscopic crack tip from the asymptotic singular stress field of linear elasticity-theory. The local stresses associated with bending of the cell walls can then be expressed in terms of the applied K, and the fracture strength of the cell wall determines K_c. Similar approaches have been followed by Choi & Lakes [2] and Chen & Huang [3], where the

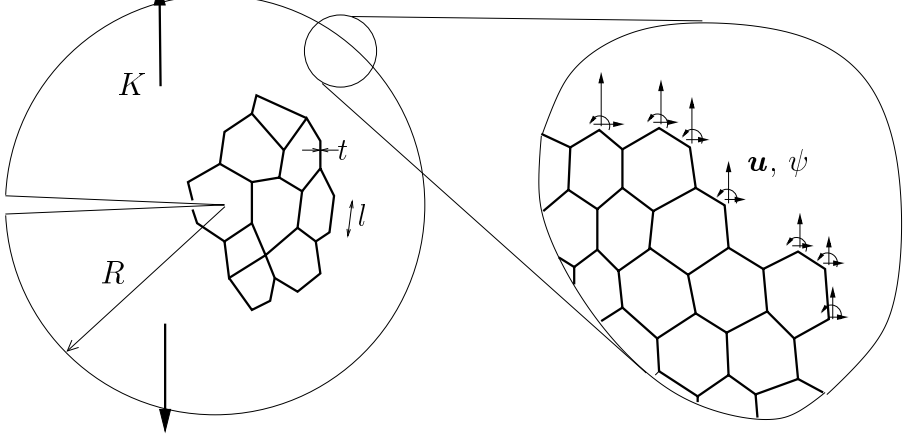

Figure 1: Cellular structure with a macroscopic crack under small-scale yielding conditions

latter used the crack tip asymptotics of a micro polar continuum theory. The authors are unaware of any micro-mechanical studies on the influence of the cell walls' ductility upon the macroscopic fracture properties of a cellular solid; this is the objective of the present paper. We consider two-dimensional irregular cellular structures as plane models for a metallic foam containing a macroscopic crack under mode-I loading and employ the assumption of small scale yielding. By introducing a local failure criterion, the initiation toughness, crack resistance curves and plastic zone evolution are then calculated numerically.

MODEL SPECIFICATION

We consider two-dimensional hexagonal structures with a macroscopic crack according to Figure 1. The beams (thickness t, average length l; termed 'cell walls' in the sequel) that make up the structure are assumed to be sufficiently slender so that their shear compliance can be neglected compared to their bending compliance ($t/l \ll 1$). The cell wall material is characterised by a uniaxial bilinear stress strain relation of the form

$$\begin{aligned} \epsilon &= \sigma/E & \sigma &< \sigma_{\mathrm{y}} \\ \epsilon &= \sigma_{\mathrm{y}}/E + (\sigma - \sigma_{\mathrm{y}})/H & \sigma &> \sigma_{\mathrm{y}} \end{aligned} \tag{1}$$

in terms of the true stress σ, true strain ϵ, Young's modulus E, yield strength σ_{y} and constant hardening modulus H. The assumption of small-scale yielding allows for the prescription of displacements on a boundary remote from the crack tip as given by the mode-I K-field. The applied K is gradually increased as a loading parameter until the stress in one of the beams attains the fracture strength σ_{f} of the cell wall material. This marks the beginning of a local fracture process which itself is not modelled in detail. Rather, we assume that it affects the macroscopic fracture response of the cellular material only through the amount of work dissipated due to the fracture of the beam. Thus, we take the fracture properties of the cell wall material to be sufficiently described through the fracture energy per unit area of beam cross section Γ_0. Crack propagation is then simulated by disconnecting a beam from the respective vertex with the requirement that the work of fracture equals Γ_0 times the cross section of the beam A.

NORMALISATION AND ESTIMATES

Stress intensity factor

A characteristic value for the fracture toughness which also serves as a normalisation for the stress intensity factor is introduced as

$$K_{\mathrm{Y}} = \sqrt{\pi l}\,\sigma_{\mathrm{y}}(t/l)^2 \quad . \tag{2}$$

This expression can be derived on the basis of elementary considerations by assuming that the local

deformation is bending dominated and that the displacement field around the crack tip is that of a linear elastic solid whose stiffness scales with $(t/l)^3$. The dimensionless stress intensity factor is then defined as $\tilde{K} = K/K_{\mathrm{Y}}$.

Dimensionless problem parameters

The parameters of the model allow for the following set of dimensionless quantities upon which the dimensionless fracture toughness depends.

$$\rho = t/l \ , \ \ \sigma_{\mathrm{y}}/E \ , \ \ \sigma_{\mathrm{f}}/\sigma_{\mathrm{y}} \ , \ \ H/E \ , \ \ \tilde{\Gamma}_0 = \Gamma_0/(E\sigma_{\mathrm{y}}^2 l) \quad , \tag{3}$$

where $\rho = t/l$, up to a factor of proportionality, can be interpreted as the relative density of the honeycomb; $\tilde{\Gamma}_0$ is, up to a constant factor, the work required to break a beam divided by the elastic strain energy contained in a beam under pure bending when the yield strain is attained at the outer fibres.

Plastic zone

A simple estimate for the plastic zone can be derived by introducing a yield function of the cellular material and inserting the asymptotic elastic stress field into it. In this way, a contour is defined inside of which the stresses exceed the yield value and which thus serves as an estimate for the plastic zone. Assuming a yield function quadratic in mean- and deviatoric stresses, which has been shown to be a good approximation for irregular hexagonal honeycombs Chen et al. [4], the above procedure leads to the estimate

$$r_{\mathrm{p}}(\varphi)/l = \frac{5.06}{2+\beta^2}\frac{\tilde{K}^2}{\kappa^2}[\sin^2(\varphi/2) + \beta^2(1+\cos\varphi)] \tag{4}$$

for the plastic zone contour in terms of polar coordinates centred on the crack tip. Here, β is related to the ratio of uniaxial to hydrostatic yield strength $\omega \equiv \sigma_u/\sigma_h$ via $\beta^2 = 2\omega^2/(4-\omega^2)$ and κ denotes the ratio of uniaxial yield strength for the irregular and regular honeycombs. In (4), the values $\omega = \beta = 0$ and $\kappa = 1$ correspond to a regular honeycomb.

NUMERICAL TECHNIQUE

The numerical evaluation of the above described model is performed with a finite element method. The beams are discretised with up to 7 cubic elements and the honeycomb slab is bounded by a circle of radius $R \approx 85l$ where the displacements are prescribed according to the mode-I K-field. When the fracture strength σ_{f} is reached in one of the elements, that element is removed from the finite element model – thereby disconnecting the fractured beam from a vertex. This element removal is performed with a built-in routine of the finite element code ABAQUS which first replaces the element with the forces and moments it exerts on its neighbouring nodes and subsequently reduces these section forces to zero over a prescribed load-parameter interval. By choosing this interval, i.e. ΔK, appropriately, $\tilde{\Gamma}_0$ can be adjusted to the desired value. In this way, crack propagation is simulated and K-resistance curves are calculated.

RESULTS

The following cell wall material parameters are chosen as representative of those for aluminium alloy foams:

$$\sigma_{\mathrm{y}}/E \ = 0.1\% \ , \ \ \sigma_{\mathrm{f}}/\sigma_{\mathrm{y}} \ = 2.0 \ , \ \ H/E = 0.1 \ , \ \ \tilde{\Gamma}_0 = 3.0 \quad . \tag{5}$$

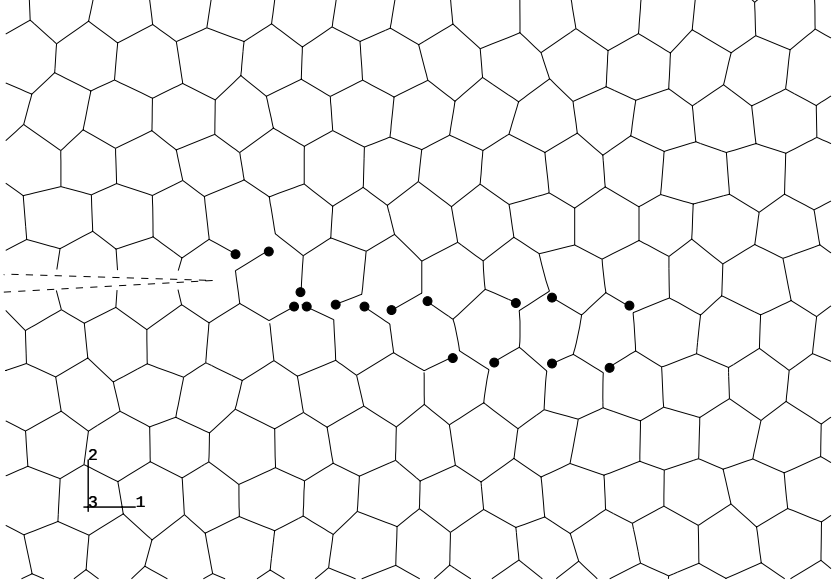

Figure 2: Predicted crack path in an irregular honeycomb

Crack path and plastic zones

A typical prediction of crack path is shown in Figure 2 with loading taken to the point where 15 cell walls have failed. This structure is generated by randomly perturbing the vertex positions of a regular hexagonal honeycomb, the amount of perturbation being uniformly distributed between -15% and $+15\%$ of the average beam length. Note that the broken beams do not form a continuous crack path with leading to a unique position of the macroscopic crack tip; the broken beams divide the structure into a multiply connected domain and this disconnected crack advance can be viewed as a crack bridging phenomenon. The plastic zones at initiation and at $\Delta a = 8l$ are shown in Fig. 3 together with the estimate (4), in which $\omega = 0.7$ and $\kappa = 0.8$ have been used (These values have been extrapolated from the calculations in Chen et al. [4] for the chosen level of imperfection in the foam.) The plots in Fig. 3 have been obtained by marking with a cross the plastic vertices of 5 different realisations of an irregular honeycomb in the same plot. Thus, the intensity of the markers can be viewed as the ensemble average for the magnitude of the plastic strain around the crack tip. The estimate (4) for the plastic zone is in reasonable agreement with the numerical results with regard to both shape and size.

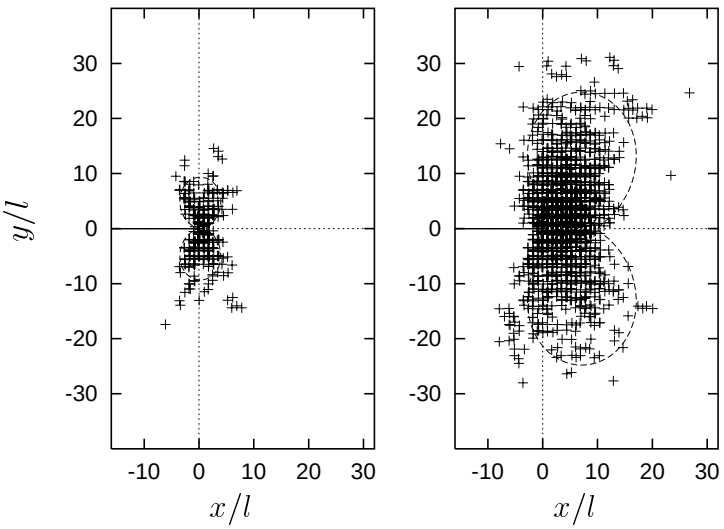

Figure 3: Plastic zones for the irregular honeycomb at initiation (left) and for $\Delta a = 8l$ (right)

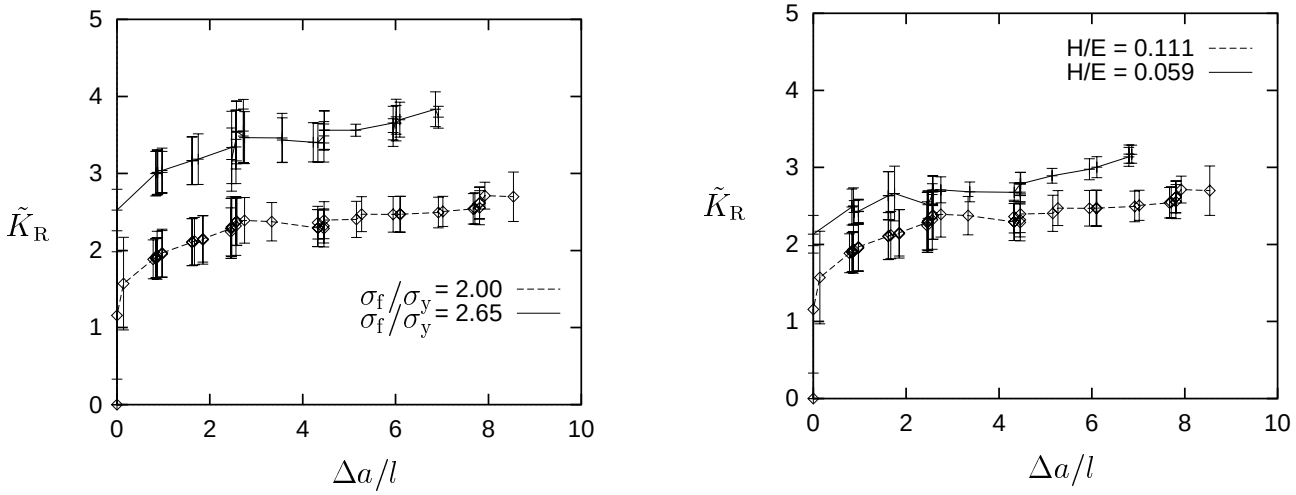

Figure 4: K-resistance curves for two values of fracture strength (left) and hardening modulus (right)

Crack resistance

Crack resistance curves in the form of a Stress intensity factor vs. crack elongation plots have been obtained by averaging, at each stage of the crack propagation, the K_{R}-values of 5 different realisations. Typical results are shown in Figure 4 where the error-bars indicate the standard deviation from the corresponding mean value. The left plot illustrates the influence of an altered cell wall fracture strength ($\sigma_{\mathrm{f}}/\sigma_{\mathrm{y}}$ 2.0 $\rightarrow$ 2.65) and the plot on the right that of an altered hardening modulus (H/E 0.11 $\rightarrow$ 0.059). As could be expected, increasing the former and decreasing the latter both leads to elevated K_{R} values: In the first case, a larger applied K is needed to break the first beam because these can sustain larger stresses. In the second case, the deformation of the mesh boundary and, hence, K needs to be larger for the stresses to reach the unaltered fracture strength.

Because the shape of the R-curves remains essentially the same in all of the plots in Figure 4, we can characterise the influence of the cell wall material parameters by calculating only the initiation toughness as a function of these parameters. The corresponding results are depicted in Figure 5 in a log-scale representation, showing that $\tilde{K}_{\mathrm{c}}$ increases linearly with the normalised fracture strength and decreases with the hardening modulus according to a power law with an exponent $\approx -1/3$.

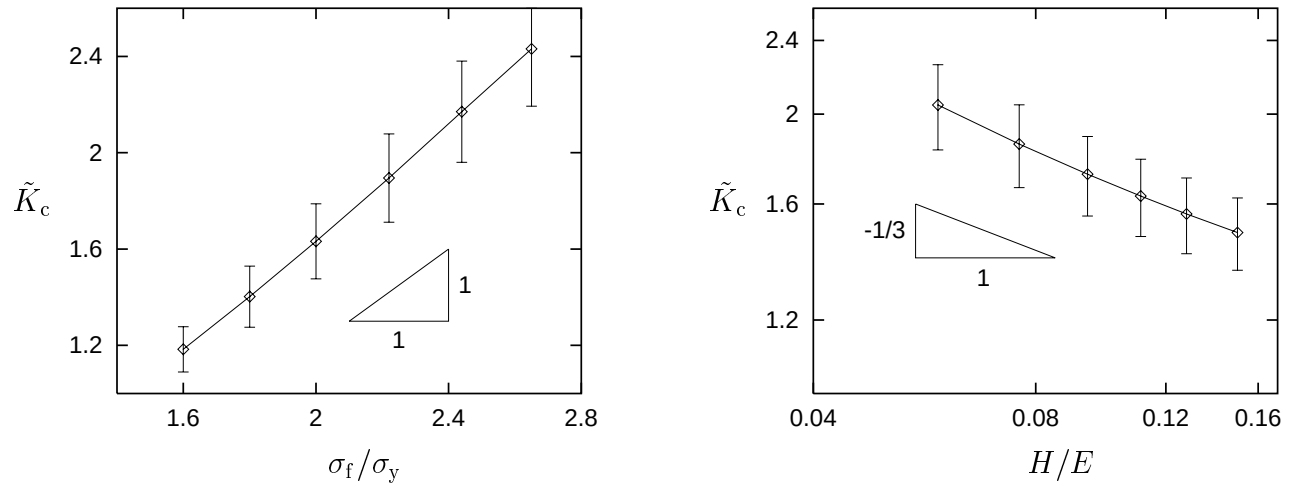

Figure 5: Initiation toughness vs. normalised fracture strength (left) and hardening modulus (right)

A result not shown here is that the dimensionless crack resistance remains practically unchanged upon changing the relative density ρ from 5% to 10%. This means that the influence of the relative density is adequately described through the normalisation introduced earlier, i.e. the dimensional fracture toughness of the honeycomb scales quadratically with ρ. Further results include the finding that, of the parameters listed in (3), the yield strain σ_y/E has negligible influence on the crack resistance. In contrast, numerical experimentation revealed that an increase in $\tilde{\Gamma}_0$ leads to large changes in the applied stress intensity factor during the process of removing an element (i.e. fracture of a beam) – with the effect that, at the end of a particular removal step, the stress may have attained the fracture strength in *several* other elements. In this case, the proposed method fails to describe the process adequately since it does not allow for the sequential fracture of beams at the crack tip. Nevertheless, we conclude that the slope of the R-curve will increase with increasing $\tilde{\Gamma}_0$.

REFERENCES

1. Gibson, L. J. and M. F. Ashby (1998) *Cellular Solids.* Pergamon Press.
2. Choi, J. B. and R. S. Lakes (1996) *Int. J. Fracture* **80**, 73–83.
3. Chen, J. Y. and J. S. Huang (1998) *J. Mech. Phys. Solids* **46**(5), 789–828.
4. Chen, C., T. J. Lu, and N. A. Fleck (1999) *J. Mech. Phys. Solids* **47**(11), 2235–2272.

CRACK INITIATION AND GROWTH IN GRADED MATERIALS DUE TO SLIDING CONTACT

F. Erdogan and S. Dag

Department of Mechanical Engineering and Mechanics, Lehigh University,
Bethlehem, PA 18015, USA

ABSTRACT

In this article, initiation and subcritical growth of surface cracks in graded materials due to sliding contact is considered. The investigation of the crack initiation process requires the evaluation of tensile cleavage stress on the surface, whereas subcritical crack growth is generally controlled by the stress intensity factors. After a brief introduction, the coupled crack/contact problem for a semi-infinite graded medium loaded by a rigid stamp is outlined, the stress intensity factors are calculated and some sample results are presented.

KEYWORDS

Graded Materials, sliding contact, crack initiation, crack/contact problem, stress intensity factors

INTRODUCTION

Graded materials, also known as *functionally graded materials* (FGMs) are multiphase composites with continuously varying volume fractions and, consequently, thermomechanical properties. Used as coatings and interfacial zones they reduce the stresses resulting from the material property mismatch, increase the bonding strength, improve surface properties and provide protection against adverse thermal and chemical environments. Many of the present and potential applications of graded materials involve contact problems. These are mostly load transfer problems in deformable solids, generally in the presence of friction. In such applications the concept of material property grading appears to be ideally suitable to improve the surface properties and wear resistance of the components that are in contact. From the standpoint of failure mechanics an important aspect of contact problems is surface cracking which is caused by friction forces and which invariably leads to fretting fatigue. In most applications material property grading near the surfaces is used as a substitute for ceramic coatings. Hence, the surface of the composite medium consists of one hundred percent ceramic. As a result the "maximum tensile stress" criterion may be used for crack initiation on the surface. The main objective of this study is to investigate the problem of contact mechanics and the associated fracture phenomenon in graded materials subjected to repeated loading by a rigid stamp. In particular the influence of the coefficient of friction and the material nonhomogeneity parameters on the stress intensity factors is examined. The problem is considered under the assumptions of plane strain and Coulomb friction.

Studies in contact mechanics were originated by Hertz [1]. A thorough description of the underlying solid mechanics problems in homogeneous materials maybe found for example in [2]. Sample results for

frictionless contact problems in a semi-infinite graded medium are given in [3]-[5]. The details of the analysis of contact mechanics for elastic solids with graded coatings and extensive results regarding the stress distribution are discussed in [6].

FORMULATION OF SLIDING CONTACT/CRACK PROBLEMS

The general description of a sliding contact/crack problem in a graded medium is shown in Figure 1.

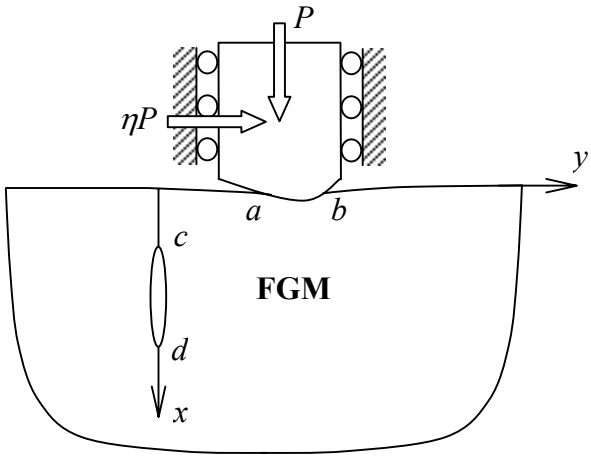

Figure 1: The general description of the crack/contact problem in a graded medium

The load is applied through a rigid stamp of arbitrary profile and it is assumed that the conditions of plane strain and Coulomb friction are valid and $h >> d$, $h >> |a|$, $h >> |b|$ where h is the thickness of the medium. Thus, the graded medium may be treated as being semi-infinite. In this study for simplicity it is further assumed that the shear modulus of the medium may be approximated by $\mu(x) = \mu_0 \exp(\beta x)$ and the effect of the variation of Poisson's ratio ν on such quantities as stress intensity factors is negligible [7]. In the coupled crack/contact problem described in Figure 1 the unknown functions are the crack surface displacements and the contact stresses defined by

$$f_1(x) = \frac{2\mu_0}{\kappa+1}\frac{\partial}{\partial x}\left[u(x,0^+) - u(x,0^-)\right], \qquad c < x < d, \tag{1}$$

$$f_2(x) = \frac{2\mu_0}{\kappa+1}\frac{\partial}{\partial x}\left[v(x,0^+) - v(x,0^-)\right], \qquad c < x < d, \tag{2}$$

$$f_3(y) = \sigma_{xx}(0,y) = \frac{1}{\eta}\sigma_{xy}(0,y) \qquad a < y < b, \tag{3}$$

where η is the coefficient of friction, $\kappa = 3 - 4\nu$ for plane strain and $\kappa = (3-\nu)/(1+\nu)$ for plane stress. The input functions are the crack surface tractions and the stamp profile given by

$$\sigma_{yy}(x,0) = \sigma_{xy}(x,0) = 0, \qquad c < x < d, \tag{4}$$

$$\frac{4\mu_0}{\kappa+1}\frac{\partial}{\partial y}u(0,y) = f(y) \qquad a < y < b. \tag{5}$$

By using the equations of elasticity and the definitions given by 1-5, the mixed boundary value problem described in Figure 1 may be reduced to a system of singular integral equations of the following form:

$$\int_c^d \left[\frac{1}{\pi}\frac{1}{t-x}+k_{11}(x,t)\right]g_1(t)\,dt+\int_a^b k_{13}(x,t)\,g_3(t)\,dt=0,\quad c<x<d, \tag{6}$$

$$\int_c^d \left[\frac{1}{\pi}\frac{1}{t-x}+k_{22}(x,t)\right]g_2(t)\,dt+\int_a^b k_{23}(x,t)\,g_3(t)\,dt=0,\quad c<x<d, \tag{7}$$

$$\int_c^d k_{31}(y,t)\,g_1(t)\,dt+\int_a^b k_{32}(y,t)\,g_2(t)\,dt+\int_a^b \left[\frac{1}{\pi}\frac{1}{t-y}+k_{33}(y,t)\right]g_3(t)\,dt-\eta\frac{\kappa-1}{\kappa+1}f_3(y)=f(y)$$

$$a<y<b, \tag{8}$$

$$\int_c^d g_1(t)\,dt=0,\qquad \int_c^d g_2(t)\,dt=0,\qquad \int_a^b g_3(t)\,dt=-P. \tag{9}$$

From Eqns. 6-8 the singular behavior of the unknown functions f_1, f_2 and f_3 is determined by using a function-theoretic method. The limiting case of $a=c=0$ is of some theoretical and physical interest. In this case by defining

$$f_1(x)=t^{\alpha}(d-t)^{\delta}g_1(x),\qquad f_2(x)=t^{\alpha}(d-t)^{\delta}g_2(x),\qquad f_3(x)=t^{\alpha}(b-t)^{\beta}g_3(x) \tag{10}$$

the condition of boundedness of $\sigma_{yy}(x,0)$, $\sigma_{xy}(x,0)$, $0<x<d$ and $f(y)$, $0<y<b$ would give the following characteristic equations to determine δ, β and α

$$\cot(\pi\delta)=0,\qquad \cot(\pi\beta)=\eta\frac{\kappa-1}{\kappa+1}=0, \tag{11}$$

$$\eta\sin^2(\pi\alpha)+\alpha^2+10\alpha+5+(\kappa-1)\cos(\pi\alpha)=\kappa(2\alpha+3)+(\kappa+1)\sin(\pi\alpha). \tag{12}$$

One may note that these results are independent of μ_0 and the material nonhomogeneity constant γ and dependent on η and κ only, meaning that the stress singularities for graded and homogeneous materials are identical. Generally the contact stresses are concentrated toward the trailing end of the stamp. For $c>0$ it may easily be shown that [6]

$$f_1(x)=(x-c)^{\theta}(d-x)^{\delta}g_1(x),\qquad f_2(x)=(x-c)^{\theta}(d-x)^{\delta}g_2(x)$$

$$\cot(\pi\theta)=0,\qquad \cot(\pi\delta)=0,\qquad f_3(y)=(y-a)^{\omega}(b-y)^{\beta}g_3(y)$$

$$\cot(\pi\omega)=\eta\frac{\kappa-1}{\kappa+1}=-\cot(\pi\beta),\quad \omega<0,\quad \beta<0. \tag{13}$$

Note that for $\eta>0$ the stress singularity at $y=a$ is greater than that at $y=b$. The powers of singularity at a, b, c and d for $c>0$, $a>0$ as well as at 0 for $a=c=0$ are shown in Figure 2 as functions of the friction coefficient η. From the standpoint of cracking $\eta>0$ is the physically meaningful case for which α is real and, for high values of η, can be greater than the corresponding uncracked value ω. This unusual result given by Eqn. 12 has also been verified independently by using Mellin transforms.

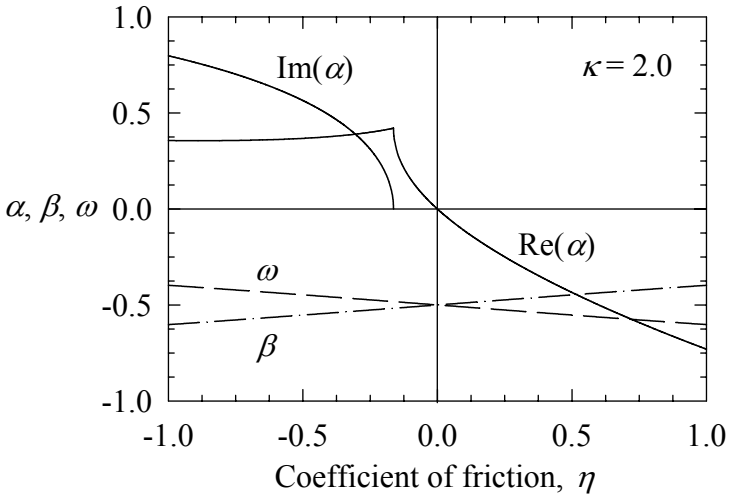

Figure 2: Variation of exponents α, ω and β with friction coefficient η

From Eqns. 7-9 it may be observed that the characteristic roots δ, θ, β, ω and α are multiple valued. The particular values of these exponents within the acceptable range $(-1, +1)$ are determined from physical considerations. For the crack $\delta = -1/2$ and $\theta = -1/2$ for $c > 0$ and $\theta = 0$ for $c = 0$. For $a = c = 0$ and $\eta > 0$ the dominant (and acceptable) root of Eqn. 12 is real and $\alpha < 0$. In the general stamp problem at an end point a (or b) ω (or β) is positive if the contact is smooth and negative if the stamp has a sharp corner [6].

Once the exponents δ, θ, β, ω and α are determined the weight functions $w_i(x)$ and the form of the solution of the integral equations may be obtained by normalizing the intervals $a < t < b$ and $c < t < d$ to $-1 < r < 1$ and by expressing the unknown functions as (see Eqns. 1-3 and 6-8)

$$f_i(t) = w_i(r)\sum_{0}^{\infty} C_{in} P_n^{(\beta,\theta)}(r), \quad i = 1, 2, \quad w_1(r) = w_2(r) = (1-r)^{\beta}(1+r)^{\theta},$$

$$f_3(t) = w_3(r)\sum_{0}^{\infty} C_{3n} P_n^{(\theta,\omega)}(r), \qquad w_3(r) = (1-r)^{\theta}(1+r)^{\omega}, \tag{14}$$

where P_n are the Jacobi polynomials associated with the weight functions w_j and C_{in} are unknown coefficients ($j = 1, 2, 3$). In the general form given by Eqn. 14 it is assumed that $c > 0$ (and $-\infty < a < \infty$). In the special cases of ($c = a = 0$) and ($c = 0,\ a > 0$) we have ($\theta = \alpha,\ \omega = \alpha$) and ($\theta = 0$), respectively, The integral equations are solved by truncating the series in Eqn. 14 and by using a suitable numerical method. After solving the integral equations, the quantities of physical interest, namely the stress intensity factors and the in-plane stress on the surface $\sigma_{yy}(0, y)$ may be obtained from

$$k_i(d) = -\lim_{x \to d} \exp(\pi\alpha)\sqrt{2(d-x)}\, q_i(x), \qquad k_i(c) = \lim_{x \to c} \exp(\pi\alpha)\sqrt{2(x-c)}\, q_i(x) \tag{15}$$

$$\sigma_{yy}(0, y) = \sum_{1}^{2} \int_{c}^{d} h_j(y, t)\, q_j(t)\, dt + \int_{a}^{b} h_3(y, t)\, q_3(t)\, dt, \tag{16}$$

where k_1 and k_2 are the modes I and II stress intensity factors and h_1, h_2 and h_3 are known kernels associated with the in-plane stress component $\sigma_{yy}(0, y)$. From the standpoint of crack initiation the critical

point on the surface is the trailing end ($y = a$, Figure 1) of the contact region where the cleavage stress $\sigma_{\theta\theta}(r,\theta)$ is positive and may be obtained from

$$\sigma_{\theta\theta}(r,\theta) = \sigma_{xx}\sin^2(\theta) + \sigma_{yy}\cos^2(\theta) - \sigma_{xy}\sin(\theta)\cos(\theta) \tag{17}$$

In the notation of Figure 1, from (17) it may be shown that $\theta_{cr} = 0$, and $\sigma_{\theta\theta cr} = \sigma_{yy}(0,a)$.

SAMPLE RESULTS

Some sample results giving the modes I and II stress intensity factors for a graded medium containing a surface crack of length d and subjected to a sliding rigid flat stamp are shown in Figure 3. (Figure 1, $c = 0$). The stiffness variation of the medium is given by $\mu(x) = \mu_0 \exp(\gamma x)$. On the top row of Figure 3 the full lines are obtained from the FGM solution for $\gamma d = 0.0001$, whereas the closed circles are given by the corresponding homogeneous medium. The results clearly show the strong influence of the stamp location a/d and the material inhomogeneity parameter γd on the stress intensity factors. Note that, as formulated the problem is one of mixed-mode. Consequently, crack growth would be curved. Also, in the absence of additional in-plane tension, k_1 could be negative, implying crack closure which can be treated in a straightforward fashion.

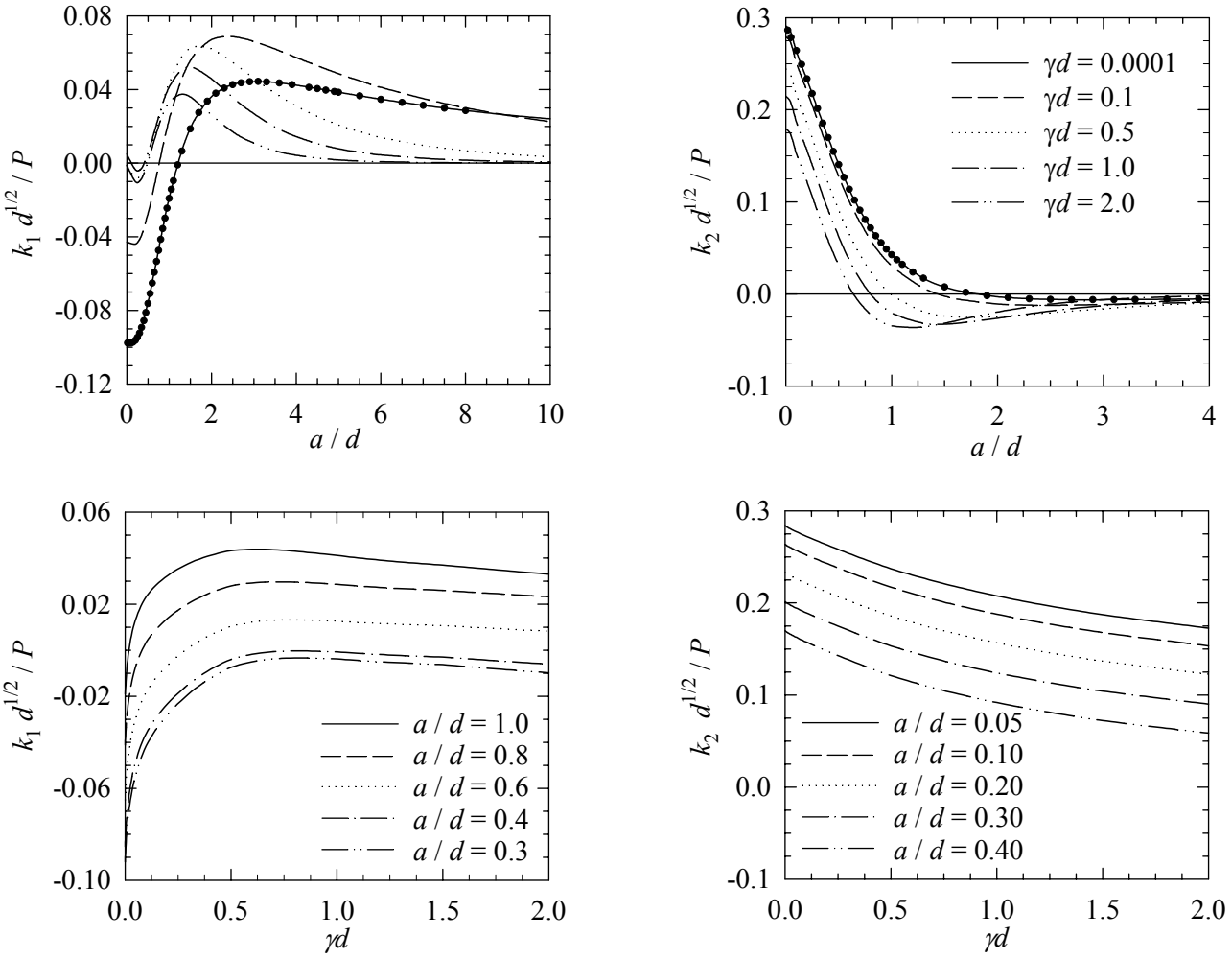

Figure 3: Stress intensity factors in an FGM half-plane with a surface crack loaded by a rigid stamp (Figure 1, $c = 0$), $\kappa = 2$, $\eta = 0.4$, $(b-a)/d = 0.1$.

For a graded medium in the absence of a crack and loaded by a sliding flat stamp the normal component of the contact stress $\sigma_{xx}(0,y)$, $a < y < b$, and the in-plane surface stress $\sigma_{yy}(0,y)$, $-\infty < y < \infty$, are given in Figure 4 for various values of γ and for $\eta = 0$ and for $\eta = 0.4$. Note that for $\eta = 0$ the stress distribution is symmetric, whereas for $\eta > 0$ $|\omega| > |\beta|$ and the stresses are concentrated near the trailing end $y = a$. Also, at $y = a$ $\sigma_{yy}(0,y)$ has a singularity of the order $(b - y)^{\omega}$, implying that $y = a$, is a likely location of crack initiation.

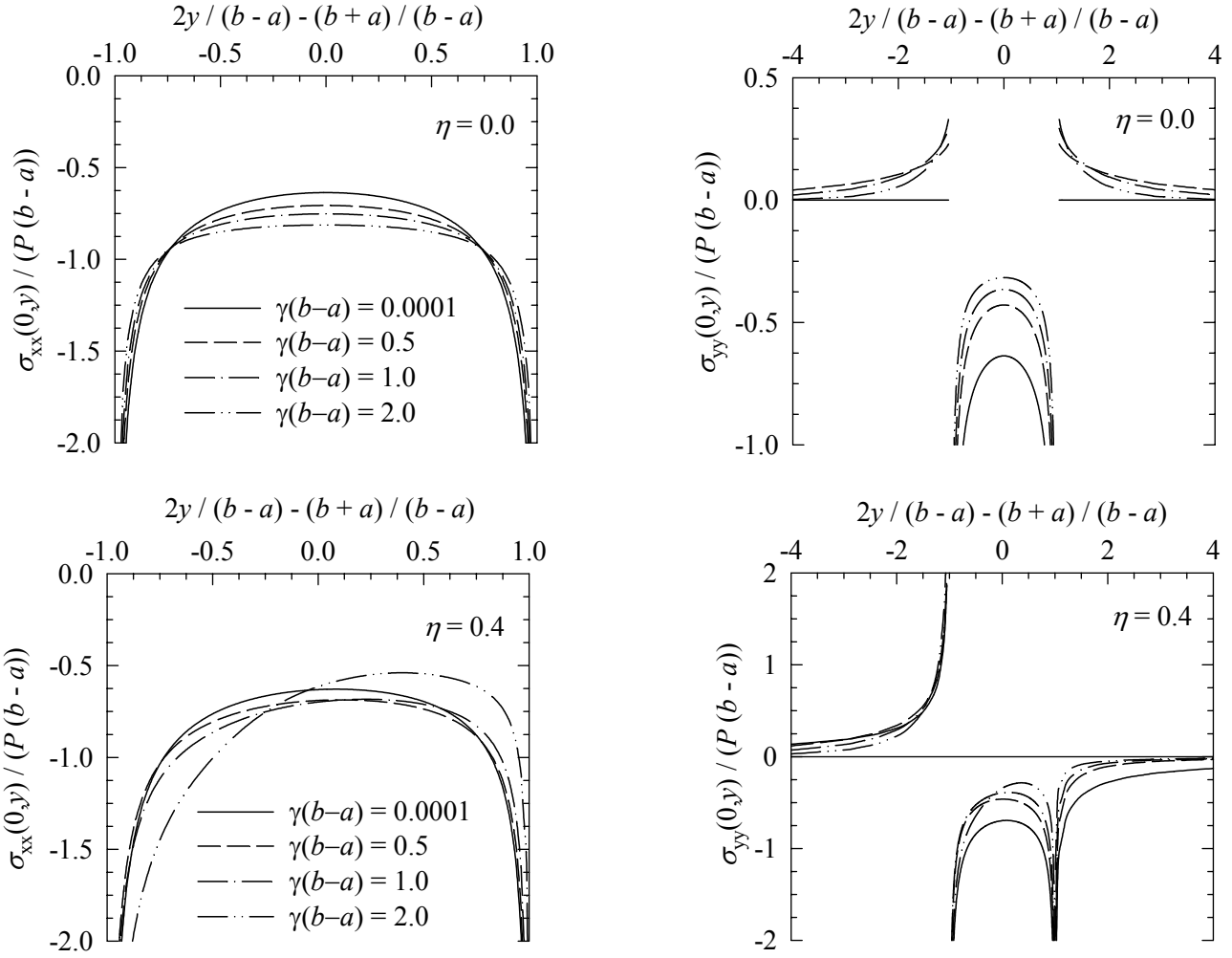

Figure 4: The contact stress $\sigma_{xx}(0,y)$ and the in-plane stress $\sigma_{yy}(0,y)$ on the surface of a graded medium loaded by a flat stamp.

REFERENCES

1. Hertz, H. (1882) *J. Reine und Augewandte Mathematik* 92, 156.
2. Johnson, K.L. (1985). Contact Mechanics. Cambridge University Press, Cambridge, UK.
3. Bakirtas, I. (1980) *Int. J. Engng. Sci.* 18, 597.
4. Giannakopoulos, A.E. and Suresh, S. (1997) *Int. J. Solids Structures.* 34, 2393.
5. Suresh, S., Giannakopoulos, A.E. and Alcala, J. (1997) *Acta Mater.* 45, 1307.
6. Guler, M.A. (2001). Ph.D. Dissertation, Lehigh University, Bethlehem, PA, USA.
7. Delale, F. and Erdogan, F. (1983) *ASME, J. Appl. Mech.* 50, 609.

ORAL/POSTER REFERENCE: 001053OR

Crack initiation behavior of piezoelectric ceramics: electro-mechanical interaction

B. Liu[1], Z.F. Song[2], G.C. Sih[1,2,3]

[1] Institute of Engineering Mechanics, Hebei University of Technology, Tianjin, 300130, China
[2]School of Advanced Science and Technology, Xi'an Jiaotong University, Xi'an, 710049, China
[3]Institute of Mechanics, Chinese Academy of Sciences, Beijing 100080, China

ABSTRACT

Crack initiation behavior in piezoelectric ceramics is examined for different choices of boundary conditions. They are referred to as the fundamental boundary-value problems when electric field/stress and electric displacement/strain are specified. The mixed boundary-value problems involve specifying electric displacement/stress and electric field/strain. Crack-growth is assumed to occur when the volume energy density function that accounts for interaction of mechanical and electrical effects reaches a threshold depending on the piezoelectric ceramic material properties. The crack driving force is shown to increase monotonically for positive and negative applied electric displacement or electric field. Such a trend prevails for the fundamental boundary-value problems as it is to be expected on physical grounds. The applied electric field and displacement have little influence on the energy density solution for the mixed boundary conditions.

KEYWORDS

Anti-plane shear, Crack growth, Electric-mechanical coupling, Piezoelectric ceramics, Shear stress

1. INTRODUCTION

Piezoelectric ceramics can be made to have "pole" directions where the dipole moments are aligned. These directions need not coincide with those of material anisotropy. Their interactions could involve a rotation and/or reflection of axes depending on whether the deformation is of the in-plane or out-of-plane type. A special feature of electrical and mechanical interplay is that a piezoelectric material could produce an electric field when deformed and vice versa. This makes piezoelectric ceramics attractive for making electronic devices that may include transducers, sensors, etc. Their reliability in service, however, can often be short changed by premature cracking. To this end, much attention has been given to analyzing the state of affairs near a sharp crack and the condition under which an existing crack would start to propagate. Past works [1-5] have reported inconsistencies between analytical and experimental results, particularly those concerned with application of the classical energy release rate concept. More recent works [6-10] showed that the energy density criterion had more success for resolving several of the previously unexplained fracture phenomena.

Solutions based on linear piezoelasticity theory have shown that the stress, strain, electric displacement and electric fields possess the inverse square root of r singularity at a sharp crack tip. Here, r stands for the radial distance measured from the crack front. The ways with which the aforementioned four boundary conditions

affect crack initiation have been discussed and analyzed using different approaches. Widely applied in the literature [1-5] is the energy release rate criterion. It relies on the exchange of global energy with the increase of local crack surface area. When electro-mechanical coupling effects are present, it is not apparent whether all the energy would be converted to the creation of new crack surface. This is similar to elasto-plastic fracture where the plastic energy being part of the total energy does not contribute to the increase of crack surface. It is involved only in a passive manner to reduce a portion of the total energy that would have otherwise be present in crack surface extension. Such a distinction is not and cannot be made in the energy release rate treatment. Linear theory has often been blamed as the scape goat for inadequacies that are embedded in the failure/fracture criterion, not because of the lack of nonlinearity.

The volume energy density criterion [11,12] does not have the inherent constraint of applying a global energy quantity to determine local crack driving force unless all of the energy is converted to the increase of crack surface. It focuses attention on the failure of a local element. Crack extension is regarded as the loci of failed elements. The global energy is not involved locally although the correct stress-strain analysis has to be made for determining the local stress and strain fields.

2. TRACTION AND CHARGE FREE CRACK

The anti-plane shear crack model has been used extensively in fracture mechanics because of its simplicity in formulation. Referring to Fig. 1(a), a line crack of length 2a is centered in a large body that is assumed to extend to infinity in all direction x, y, and z.

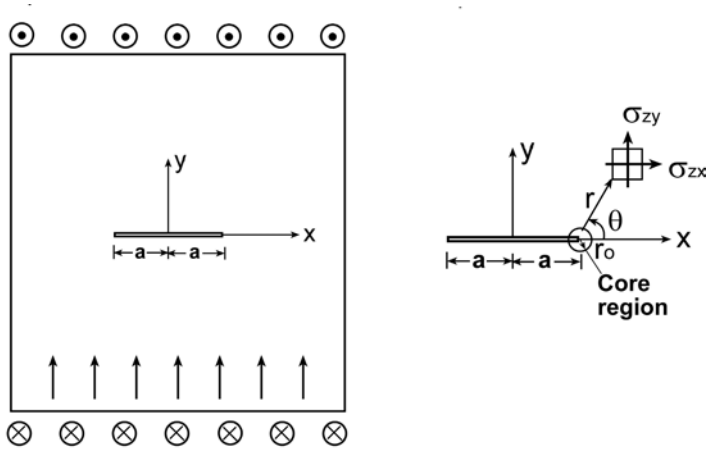

(a) Applied electric and mechaical load (b) Local coordinates

Fig. 1 Mode III crack line

2.1 Boundary conditions

The body is sheared at infinity with mechanical stress τ_∞ or strain γ_∞. Either electric displacement D_∞ or electric field E_∞ is applied in conjunction with the mechanical stress τ_∞ or strain γ_∞. The four possible combinations are $(\tau_\infty;E_\infty)$, $(\gamma_\infty;D_\infty)$, $(\tau_\infty;D_\infty)$ and $(\gamma_\infty;E_\infty)$. They will be referred to, respectively, as Case I, II, III and IV. This is summarized in Table 1. The corresponding quantities F_j and G_j (j = I, II, etc.) are given by

$$F_I = \frac{\tau_\infty + e_{15}E_\infty}{c_{44}},\ F_{II} = \gamma_\infty,\ F_{III} = \frac{\in_{11}\tau_\infty + e_{15}D_\infty}{c_{44}\in_{11} + e_{15}^2},\ F_{IV} = \gamma_\infty \qquad (1)$$

and

$$G_I = E_\infty,\quad G_{II} = \frac{D_\infty - e_{15}\gamma_\infty}{\in_{11}},\quad G_{III} = \frac{c_{44}D_\infty - e_{15}\tau_\infty}{c_{44}\in_{11} + e_{15}^2},\quad G_{IV} = E_\infty \qquad (2)$$

TABLE 3
Classification of boundary conditions

Cases	Specified quantities	Intensity factor coeff.
Fundamental problems		
I	τ_∞ and E_∞	F_I ; G_I
II	γ_∞ and D_∞	F_{II} ; G_{II}
Mixed problems		
III	τ_∞ and D_∞	F_{III} ; G_{III}
IV	γ_∞ and E_∞	F_{IV} ; G_{IV}

Eqs. (1) and (2) are coefficients that define the stress, strain, electric field and displacement factors in the work to follow.

More specifically, the boundary conditions are

$$\sigma_{zy} = \tau_\infty \quad \text{or} \quad \gamma_{zy} = \gamma_\infty \quad \text{for } x^2 + y^2 \to \infty \tag{3}$$

together with

$$E_y = E_\infty \quad \text{or} \quad D_y = D_\infty \quad \text{for } x^2 + y^2 \to \infty \tag{4}$$

For a crack free of surface tractions and charge (i.e., an insulated crack), the conditions are

$$\sigma_{zy} = 0, \; D_y = 0 \quad \text{for } |x| < a; \quad |y| = 0 \tag{5}$$

The pole is directed along the z-axis as shown in Fig. 1(b). Reversing the direction of E_∞ and D_∞ is equivalent to reversing the direction of poling.

2.2 Asymptotic solution

It can be solved for the two unknowns u_z and ϕ from which the stresses, strains, electric field and displacements throughout the medium can be obtained. For the present discussion, it suffices to consider the asymptotic expressions [5]:

$$\sigma_{zx} = -\frac{K_{III}^{\tau}}{\sqrt{2\pi r}}\sin\left(\frac{\theta}{2}\right), \quad \sigma_{zy} = \frac{K_{III}^{\tau}}{\sqrt{2\pi r}}\cos\left(\frac{\theta}{2}\right) \tag{6}$$

$$\gamma_{zx} = -\frac{K_{III}^{\gamma}}{\sqrt{2\pi r}}\sin\left(\frac{\theta}{2}\right), \quad \gamma_{zy} = \frac{K_{III}^{\gamma}}{\sqrt{2\pi r}}\cos\left(\frac{\theta}{2}\right) \tag{7}$$

and

$$E_x = -\frac{K_E}{\sqrt{2\pi r}}\sin\left(\frac{\theta}{2}\right), \quad E_y = \frac{K_E}{\sqrt{2\pi r}}\cos\left(\frac{\theta}{2}\right) \tag{8}$$

$$D_x = -\frac{K_D}{\sqrt{2\pi r}}\sin\left(\frac{\theta}{2}\right), \quad D_y = \frac{K_D}{\sqrt{2\pi r}}\cos\left(\frac{\theta}{2}\right) \tag{9}$$

The stress and strain intensity factors in eqs. (6) and (7) are defined by

$$K_{III}^{\tau} = (c_{44}F_j - e_{15}G_j)\sqrt{\pi a}, \quad K_{III}^{\gamma} = F_j\sqrt{\pi a} \tag{10}$$

where j = I, II, etc. The electric field and displacement factors in eqs. (8) and (9) are given by

$$K_E = G_j\sqrt{\pi a}, \quad K_D = (e_{15}F_j + \epsilon_{11}G_j)\sqrt{\pi a} \tag{11}$$

The electro-mechanical coupling effects are included by the factors in eqs. (10) and (11) via the constants F_j

and G_j given in eqs. (1) and (2). The local polar coordinates (r,θ) in eqs. (6) to (9) are measured from the crack tips; they are shown in Fig. 1(a). Note that all quantities possess the $1/\sqrt{r}$ singularity, a characteristic that is unaffected by piezoelectricity. In this case, the angular functions of the stresses and strains in eqs. (6) and (7) are also the same as those for purely elastic materials.

4. VOLUME ENERGY DENSITY APPROACH

According to the volume energy density criterion [9,10], attention is focused on the failure of an element nearest to the crack tip as shown in Fig. 1(a). Linear piezoelasticity provides the expression:

$$\frac{dW}{dV} = \frac{1}{2}\sigma_{ij}\gamma_{ij} + \frac{1}{2}D_iE_i \tag{12}$$

which simplifies considerably for anti-plane shear deformation:

$$\frac{dW}{dV} = \frac{1}{2}(\sigma_{xz}\gamma_{xz} + \sigma_{yz}\gamma_{yz}) + \frac{1}{2}(D_xE_x + D_yE_y) \tag{13}$$

Since the right hand side of eq. (13) are known from eqs. (6) to (9) inclusive, dW/dV can be computed with the aid of eqs. (1) and (2).

4.1 Crack initiation threshold

In view of the singular behavior of the quantities in eqs. (6) to (9), dW/dV is proportional to 1/r which tends to be become unbounded as $r\rightarrow 0$. Unboundness of dW/dV is excluded from the solution by letting $r\rightarrow r_o$ being the limit of r. For small values of r, the volume energy density can thus be written as

$$\frac{dW}{dV} = \frac{S}{r} \tag{14}$$

in which S is known as the energy density factor. It may be regarded as the crack driving force. For $r = r_o$, it suffices to examine S for the condition of crack initiation. if only mechanical shear stress τ_∞ is applied, then dW/dV can be computed simply as

$$\frac{dW}{dV} = \left(\frac{a\tau_\infty^2}{4c_{44}}\right)\frac{1}{r} \tag{15}$$

which gives $S = a\tau_\infty^2/(4c_{44})$. The onset of crack initiation would be assumed to coincide with $S = S_c$, a critical value while τ_∞ would correspond to the critical shear stress. for an isotropic elastic material c_{44} corresponds to the shear modulus of elasticity and $S = a\tau_\infty^2/(4G)$ [13].

4.2 Boundary-value problems

Let p_τ and q_γ stand for the ratios E_∞/τ_∞ and D_∞/γ_∞, respectively. By means of eqs. (13) and (14), S can be calculated from the asymptotic expressions in eqs. (6) to (9). the results for Case I and II in Table 1 take the forms

$$S = \frac{a}{4}\begin{cases} \dfrac{\tau_\infty^2}{c_{44}}[1 + 2e_{15}p_\tau + (c_{44}\in_{11} + e_{15}^2)p_\tau^2], & \text{Case I} \quad (16) \\ \dfrac{\gamma_\infty^2}{\in_{11}}[(c_{44}\in_{11} + e_{15}^2) - 2e_{15}q_\gamma + q_\gamma^2], & \text{Case II} \quad (17) \end{cases}$$

Similarly, let p_γ and q_τ stand for the ratio E_∞/γ_∞ and D_∞/τ_∞, respectively. In the same way, the S-factor expressions for Case III and IV are

$$S=\frac{a}{4}\begin{cases}\gamma_\infty^2[c_{44}+\in_{11}p_\gamma^2], & \text{Case III} \quad (18)\\ \dfrac{\tau_\infty^2}{c_{44}\in_{11}+e_{15}^2}[\in_{11}+c_{44}q_\tau^2], & \text{Case IV} \quad (19)\end{cases}$$

The condition of a uniform electric field can be more readily simulated at the surface of the piezoelectric material in contrast to the electric displacement boundary condition. Frequently used in the laboratory is Case I in eq. (16).

4.3 PZT-5H piezoceramic

A glance of eqs. (16) to (19) reveals that only three constants c_{44} , e_{15} and $\in_{11}$ are involved for the anti-shear problem. Their numerical values for the lead zirconate titante (PZT-5H) piezoceramic can be found in Table 2 [14].

TABLE 2
Constants of PZT-5H piezoceramic [14]

c_{44} (N/m^2)	e_{15} (C/m^2)	$\in_{11}$ (C/Vm^2)
3.53×10^{10}	17.0	151×10^{-10}

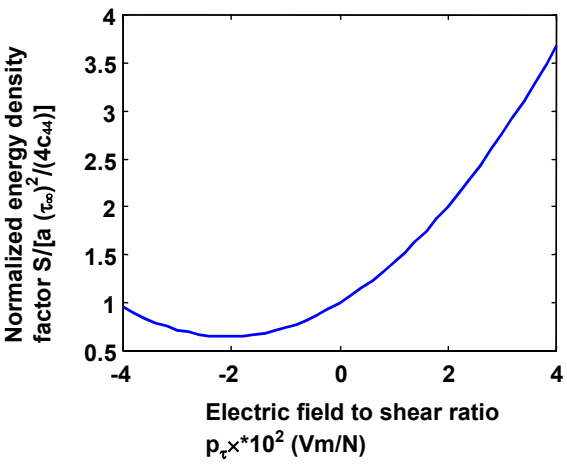

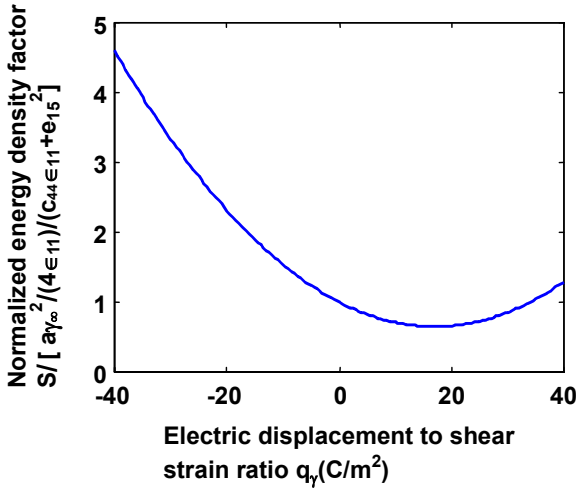

Figure 2: Normalized energy density factor versus E_∞/τ_∞ **Figure 3:** Normalized energy density factor versus D_∞/γ_∞

Plotted in Fig. 2 are the variations of the normalized volume energy density factor $S_c/(a\tau_\infty^2/4c_{44})$ with the load parameter E_∞/τ_∞. In general, the curve rises as p_τ is increased positively or negatively; it possesses a minimum for negative p_τ very close to the origin. On physical grounds, the crack driving force represented by S would increase with increasing applied electric field. Similar results are obtained for $S_c/(a\gamma_\infty^2/4\in_{44})$ versus D_∞/γ_∞ as shown in Fig. 3 where the minimum corresponds to positive q_τ near the origin. As it is to be expected, S increases for positive and negative applied electric displacements. The trends of the curves in Figs. 2 and 3 are opposite to those found in [5] by using the energy release rate criterion where the crack driving forces decrease and become negative when the applied electric field and displacement are increased. This is contrary to experimental observations.

Refering to the material parameters in Table 2, it can be seen that $\in_{11}$ is several orders of magnitude smaller than c_{44} in eq. (27) for Case III. Hence, S would remain nearly constant and not affected by the ratio E_∞/γ_∞. Case IV in eq. (19) yields a symmetric curve about $q_\tau = 0$ for the S versus q_τ plot. The mixed conditions in eqs. (18) and (19) are only of academic interest since they are difficult to produce in the

laboratory.

5. CONCLUSIONS

Anti-plane shear crack initiation behavior for piezoceramics is investigated to study the electro-mechanical interaction effects. Applied is the volume energy density criterion for analyzing how different boundary conditions would affect the crack driving force which remains positive definite under all conditions. This is a necessary requirement that must be satisfied on physical grounds. Numerical results are presented graphically for the PZT-5H piezoelectric material. These conclusions are contrary to those obtained from the energy release rate criterion [5] for the same problem. The crack energy release rate becomes negative as the electric field or displacement is increased, a condition that seems to contradict rational reasoning. In other words, it is inconceivable that a crack would arrest if the applied electric and/or mechanical load is increased. These unphysical predictions invalidate the usefulness of the energy release rate. Such contradictions do not arise when the volume energy density criterion is used.

REFERENCES

[1] Z. Suo, C. M. Kuo, D. M. Barnett and J. R. Willis, Fracture mechanics for piezoelectric ceramics. J. Mech. Phys. Solids, 40 (1992), 739-765.

[2] Y. E. Pak and A. Tobin, On the electric field effects in fracture of piezoelectric materials. Mechanics of Electromagnetic Materials and Structures, AMD-Vol.161/MD-Vol.42, ASME, 1993.

[3] H. Gao, T. Y. Zhang and P. Tong, Local and global energy release rates for an electrically yielded crack in a piezoelectric ceramic. J. Mech. Phys. Solids, 45 (1997), 491-510.

[4] S. Park and C. T. Sun, Fracture criterion of piezoelectric ceramics. J. Am. Ceram. Soc., 78 (1995), 1475-1480.

[5] Y.E. Pak, Crack extension force in a piezoelectric material, J. of Applied Mechanics, 57(1990) 647-653.

[6] S. Shen and T. Nishioka, Fracture of piezoelectric materials: energy density criterion, J. Theoretical Appl. Fract. Mech., Vol.33(1) (2000), 57-63.

[7] Z.T. Chen, Anti-plane mechanical and in-plane electric time –dependent load applied to two coplanar cracks in piezoelectric ceramic material, J. of Theoretical and Applied Fracture Mechanics, 33 (3) (2000), 173-184.

[8] B.L. Wang, N. Noda, Crack initiation in PZT-4 piezoelectric ceramic strip, J. of Theoretical and Applied Fracture Mechanics, 33 (1) (2000), 35-47.

[9] J.Z. Zuo and G.C. Sih, Energy density formulation and interpretation of cracking behavior for piezoelectric ceramics, J. of Theoretical and Applied Fracture Mechanics, 34 (1) 2000, 17-33.

[10] G.C. Sih, J.Z Zuo, Multiscale behavior of crack initiation and growth in piezoelectric ceramics, J. of Theoretical and Applied Fracture Mechanics, 34(2000) 123-141.

[11] G.C. Sih, Mechanics of Fracture, Volume I to VII, Sijhoff and Noordhoff International Publisher, The Netherlands, 1973-1981.

[12] G.C. Sih, Mechanics of fracture initiation and propagation, Kluwer Academic Publishers, The Netherlands, 1991.

[13] G.C. Sih, Fracture mechanics of engineering structural components, Fracture Mechanics Methodology, G.C. Sih, L. Faria, eds., Martinus Nijhoff Publishers, The Netherlands, 35-101 (1984).

[14] R.C. Pohanka, P.L. Smith, Recent advances in piezoelectric ceramics, Electronic Ceramics, L.M. Levinson, ed., Marcel Dekker, New York, 1988.

CRACK PATH DEVELOPMENT IN MATERIALS WITH NONLINEAR PROCESS ZONE AND COMPOSITES

Asher A. Rubinstein

Department of Mechanical Engineering, Tulane University
New Orleans, LA 70118, USA

ABSTRACT

Crack path development under mixed mode loading is an important and still not completely understood aspect of fracture process. A detailed understanding of this process could have several valuable benefits for failure prediction and for design of tougher materials using a crack path deflection toughening mechanism. The methods of linear fracture mechanics may give qualitative results, but do not accurately predict the crack path development, especially when the crack path is simulated for a certain distance due to a cumulative error. To improve the modeling process, nonlinear aspects of fracture process were introduced into consideration to determine the crack path direction criterion under more realistic conditions. A numerical procedure for solving this nonlinear problem has been introduced. A case illustrating the basic aspects of the solution method and the results is described using a deflecting line plastic zone as an example. The method is applicable to any nonlinear relationship within the deflecting process zone and is particularly useful for crack path analysis in composites.

KEYWORDS

Fracture, crack path, failure in composites, crack growth in nonlinear materials, crack growth in heterogeneous materials.

INTRODUCTION

The objectives of the presented investigation are aimed at determining the effect of nonlinear material behavior within the crack tip process zone on the crack path formation direction. The influence of the crack path deflection effect on the overall material toughness could be significant, as demonstrated by Rubinstein [1] for brittle materials. However, the current crack path prediction methods are not adequate for cumulative curvilinear crack path predictions. Generally, local crack path deflection in brittle materials is determined by one of three criteria: (*a*) maximal energy release rate, (*b*) maximal local K_I acting at the crack tip, or (c) zero local K_{II} acting at the crack tip. Most commonly used is criterion (*c*). Although physically all these criteria are similar, and one would expect them to predict the same crack path direction, there is a difference. For example [1], in case of a straight crack loaded under pure Mode II loading conditions, the resulting predictions would vary from a possible deflection in the direction of 75^o (criterion *a*) to 83^o (criterion *c*) depending on what criterion is used. For formation of a single crack kink the difference may be considered to be insignificant, but for continuous crack path curving and kinking over a finite distance, the difference will be noticeable. In a controlled experiment [2] with an accurate numerical analysis [3, 4], an attempt was

made to determine which of the three mentioned criteria actually controls the crack path development. It was found [4] that none of the mentioned criteria could be selected as the determinative one, and that the crack path actually does not follow any of them. Buzzard, Gross and Srawley [5] demonstrated that under certain conditions, the crack in fact could propagate under Mode II loading without changing direction. These observations led to assumption [4], that a nonlinear process zone, which is present in all considered cases [1, 5, 6, 7, 8], plays a significant role in crack path development even if in some cases the size of the process zone may appear to be insignificant on a large scale. Even in seemingly brittle materials, as observed by Chudnovsky et al. [1], a nonlinear process zone is present on microscale. The present investigation attempts to include the influence of the nonlinear process zone on crack path development. The nonlinear effects are of particular importance in the analysis of crack path development in composite materials, especially composite systems which exhibit linear elastic behavior everywhere and a special crack opening displacement - local traction relationship within the process zone, usually identified as a bridging zone.

The modeling principles of the crack path deflection mechanism presented here are aimed at application to materials which exhibit nonlinear behavior within the crack tip process zone while remaining elastic in the surrounding region. To include nonlinear material behavior within the crack tip process zone in the model, a proper computational procedure has been developed. Typically, the process zone in these materials is small as compared to the crack size; thus, some cases may be studied using small-scale analysis principles. A numerical procedure based on the integral equation technique has been developed for solving the resulting nonlinear problem. Several critical aspects typical for these nonlinear problems will be discussed. Specifically, the scaling problem, nonlinear zone size determination techniques, the numerical stability of the possible solution procedures, and ill-posed numerical schemes practiced for these types of problems will be discussed. Several solutions for kinked cracks under mixed mode loading will be presented and compared for different material properties exhibited within the process zone. The developed methods will be especially useful for failure modeling and crack path prediction in heterogeneous materials such as reinforced ceramics, concrete, and some metal alloys, and for development of smart materials.

The method developed in conjunction with this investigation is capable of handing various conditions within the process zone. However, as a representative example, primary attention in this report is given to the case of a process zone consisting of an inclined, under angle θ, rectilinear segment of a plastically deformed zone, Figure 1. The case of $\theta = 0$ is the well-known Dugdale plastic zone model [9]. Several interesting aspects of this nonlinear problem could be learned and understood based on this example. As is often the case in nonlinear numerical analysis, this problem may be easily misled into an ill-posed numerical scheme. This aspect of the analysis will be discussed in the following section.

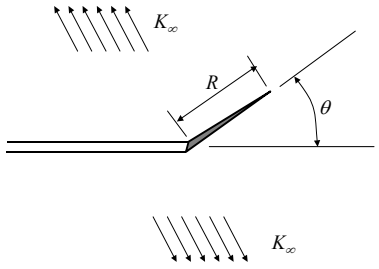

Figure 1. Considered problem

SOLUTION SCHEME

The considered problem has a specified remote load K_∞, which represents a mixed mode loading. The condition on the inclined segment, in this special case, states the yielding condition,

$$\sigma_{\theta\theta} = \sigma_y. \tag{1}$$

The inclination angle, θ, and the length of the inclined plastically deformed segment, R, are unknown variables. This simple fact is sometimes neglected and only the inclination angle is treated as an unknown variable, especially when a curvilinear crack path is simulated. Most typically for development of a direct numerical scheme, one needs to specify the length of the inclined segment or the inclination angle. Several examples could be presented wherein a finite element scheme was set with a specified length of inclined segment. In fact, the development of a direct computational scheme for this highly nonlinear problem could be complicated by convergence problems and mesh size dependency. To avoid that, the following indirect scheme is proposed, which allows the problem to be treated as a linear problem at every significant computational step.

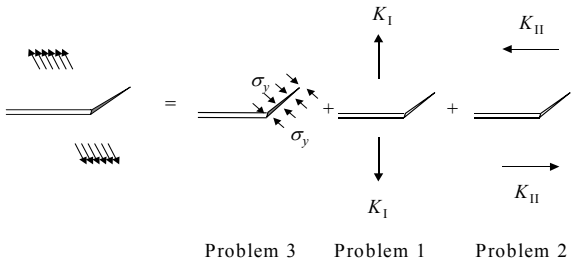

Figure 2. Superposition scheme.

The considered problem, as specified in Figure 1, can be represented as a superposition of three problems illustrated in Figure 2. Problem 3 has loading only on the kinked segment; Problem 1 is a problem of a kinked crack under Mode I loading; and Problem 2 is a problem of a kinked crack under Mode II loading. Problem 3 results in two local stress intensity factors, K_I^3 and K_{II}^3 at the tip of the kink Both of them must be compensated for by the local stress intensity factors of Problems 1 and 2, K_I^1, K_{II}^1 and K_I^2, K_{II}^2. The relationship between these three sets gives a set of two equations:

$$\begin{aligned} K_I^1 + K_I^2 + K_I^3 = 0 \\ K_{II}^1 + K_{II}^2 + K_{II}^3 = 0 \end{aligned} \tag{2}$$

The inclination angle, θ, determines the relationships between the applied load components K_I, K_{II}, and the corresponding local values of the stress intensity factors as

$$\begin{aligned} K_I^i = f_I^i(\theta) K_i \\ K_{II}^i = f_{II}^i(\theta) K_i \end{aligned} \tag{3}$$

i here runs values 1 and 2, and on the right hand side of (3) this index corresponds to the loading Mode. The functions $f^i_I(\theta)$ and $f^i_{II}(\theta)$ can be generated using a scheme given by Rubinstein [1], or used directly from the data given in [1].

Setting the length of the kink to a unit of length, substituting equations (3) into equations (2), one obtains a linear system for determination of the remote load that will generate a unit length plastic kink inclined at a specified angle θ, if solution of problem 3 is known. Thus, the following solution scheme can be employed using the inverse order for a unit length kink and a unit yield stress: (a) set a value for the inclination angle; (b) solve problem 3 and determine numerically the values of K_I^3 and K_{II}^3; (c) solve system (2) with (3) for K_I, K_{II}, using the given functions $f^i_I(\theta)$ and $f^i_{II}(\theta)$. The result is the load required to produce a unit length plastic kink at a specified angle, Figure 3. To obtain a general solution, these data in Figure 3 can be rescaled using the following relationship for the absolute value of the remote stress intensity factor, (4).

$$K_\infty = K_\infty(R=1, \sigma_y=1)\sigma_y\sqrt{R} \tag{4}$$

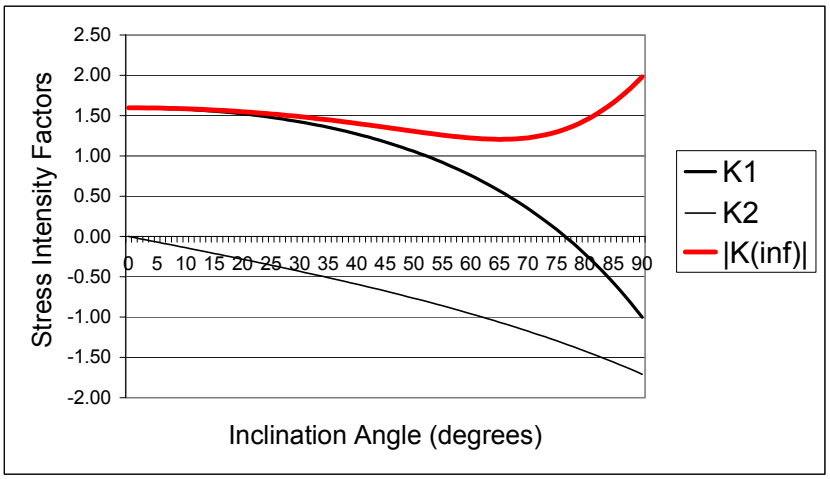

Figure 3. Applied load generating a unit-length inclined plastic zone (σ_y=1)

Relationship (4) uses the results of the scaling analysis for the described nonlinear case. This relationship is not a general one. Using the data in Figure 3, or the corresponding parametric form of that data and (4), one can determine the inclination angle and the length of the inclined plastic zone for an arbitrary loading. It is also convenient to use the loading stress intensity factor in a complex variable form. For the described case, the relationship between the loading phase and the inclination angle does not depend on the loading magnitude [10]. After one numerically generates the function representing this relationship, the inclination angle can be directly determined; then, using the data in Figure 3 and relationship (4), one obtains the length of the plastic kink.

CONCLUSIONS

A computational scheme for the analysis of crack kinking in materials with a nonlinear process zone has been developed. An example of the inclined Dugdale zone has been considered to illustrate the computational procedure. Further details of this procedure and examples could be found in [10].

ACKNOWLEDGMENT

This work was supported by the Department of Energy through the CERE project at Tulane University.

REFERENCES

1. Rubinstein, A. A. (1990) *Journal of Applied Mechanics*. 57, 97 -103.
2. Chudnovsky, A., Chaoui, K., and Moet, A. (1987) *Journal of Material Science Letters,* 6, 1033 - 1038.
3. Rubinstein, A. A., (1989) In: *Proceedings of the First Pan American Congress of Applied Mechanics.* pp. 162-165. Steele and L. Bevilacqua (Eds) J. Digorgio Rio de Janeiro.
4. Rubinstein, A. A. (1991) *International Journal of Fracture*, 47, 291 - 305.
5. Buzzard, R. J., Gross, B. and Srawley, J. E., (1986) In: *ASTM STP 905*, 329 - 346.
6. Smith, D. G., and Smith, C. W., (1972) *Engineering Fracture Mechanics,* 4, 357 - 366.
7. Smith, C. W. and Wiersma, S. J., (1986) *Engineering Fracture Mechanics,* 23, 229 - 236.
8. Yang, B. Ravi-Chandar, K. (2001) *Journal of the Mechanics and Physics of Solids*. 49, 91 - 130.
9. Dugdale, D. S., (1960) *Journal of the Mechanics and Physics of Solids*. 8, 100 - 104.
10. Rubinstein, A. A. Manuscript in preparation.

ORAL/POSTER PRESENTATION REFERENCE: ICF100666OR

CRACK PLANE INFLUENCE ON TIME-DEPENDENT FRACTURE OF BIMATERIALS

Ali P. Gordon[1] and David L. McDowell[1,2]

[1]The George W. Woodruff School of Mechanical Engineering, Georgia Institute of Technology, Atlanta, GA 30332-0405 USA
[2]School of Materials Science and Engineering, Georgia Institute of Technology, Atlanta, GA 30332-0405 USA

ABSTRACT

The behavior of a crack growing at or near the proximity of a bonded region has historically been approximated and modeled in a somewhat qualitative manner. To quantify how such cracks differ from those within homogeneous materials, parametric computational studies are performed for stationary cracks near a bimaterial interface. Finite element solutions for various compact tension [C(T)] specimen geometries under plane strain conditions are used to judge the limits of applicability of homogeneous creep fracture solutions. The bimaterial model is composed of two distinct isotropic, homogeneous materials that differ only by properties that describe the inelastic behavior. In most cases, an intermediate, finite heat-affected zone (HAZ) is included in the base metal (BM) to weld metal (WM) model. Previous investigations have limited this third material region to assignment of homogeneous properties; this study features a HAZ with a graded blend of base and weld metal properties. This numerical model more closely matches the fused region of actual in-service members, such as seam-welded high temperature steam pipes. Domain integral techniques are used to compute the *C(t)*-Integral and transition times for all cases. Predictions from parametric studies can then be consolidated using curve-fits of crack tip field parameters, transition times, etc. as a function of the HAZ thickness and position, inelastic property mismatches, and other independent model parameters. Results indicate that the incorporation of a functionally graded HAZ region leads to more conservative estimates of the fracture parameters.

KEYWORDS

Fracture, Creep, Functionally Graded Materials, Bimaterials, Finite Elements.

INTRODUCTION

Currently, many studies concerning time-dependent fracture of distinct or welded bimaterials have been limited to cases where the initial crack and its propagation are coplanar with the center of the weld material, Segle, et al. [1, 2]. However, since the predicted states of stress ahead of the crack tip are substantially influenced by the mismatch of properties of the surrounding materials, the nature of the local stress intensity is mixed-modal. The consequence is out-of-plane crack extension.

Functionally graded materials (FGMs) feature continuous variation of one or more material properties across one or more spatial directions. Typically they are interlayers, such as a HAZ, separating two larger material sections, each with negligible property variation. Most investigations that incorporate a transition layer approximate this HAZ with homogeneous properties that are derived from the average of the surrounding base and weld metals. In this study the HAZ is continuously graded in order to achieve more accurate descriptions of the stress and strain situation near the crack tip.

By conducting a parametric study of time-dependent fracture, we develop relationships for the influence of the crack plane-to-interface distance on the *C(t)*-domain integral. Also by obtaining the near tip stress fields, we use approximate means to understand the direction of crack bifurcation.

FINITE ELEMENT MODELING

Until recently, usual bimaterial fracture models were composed of two distinct perfectly-bonded, isotropic, homogeneous constituents. The initial crack was coplanar with their interface. The models used in this study are extensions of those used for the homogeneous case with several modifications. To more accurately represent a typical weldment, for example, models are composed of two bonded homogeneous, isotropic materials, each occupying either the region above or below the crack plane; however, in cases featuring a graded transition layer, a HAZ is introduced in a region between the homogeneous weld and base metal regions. This deviation from the standard homogeneous FEM model requires additional adjustments in the model.

Although the routine used to create these ABAQUS meshes has the capability of producing various model sizes with various stationary crack sizes and far-field and near-tip mesh densities, this study restricts the specimen size, $W = 25.4$ *mm (1.0 in)*, and initial crack size, $a = 12.7$ *mm (0.5 in)*. The thickness is $B = 6.35$ *mm (0.25 in)*. For the time-dependent cases the specimen is subjected to an ambient temperature, T_a = 538°*C*. The model is shown in Fig. 1.

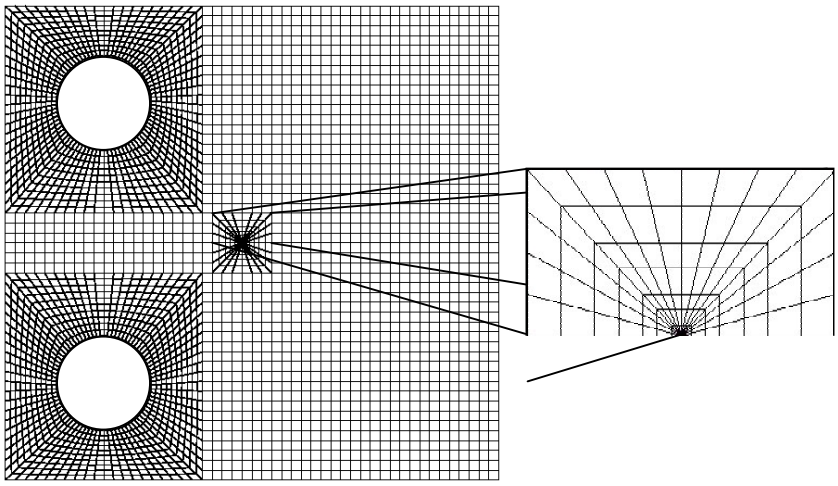

Figure 1: A finite element mesh used in the current investigation.

RESULTING FRACTURE PARAMETERS

In this time-dependent study, elastic-secondary creep behavior models were assumed. Slight variations of the base metal inelastic properties were assumed for the weld, while the HAZ metal was modeled with average properties of the weld and base metals. In every case the elastic properties are identical. The

commonly used 2¼Cr-Mo steel exhibits the following properties at close to one-third of its melting point, $T = 538°C$: elastic constants, $E = 160\ GP$ and $\nu = 0.3$, Norton secondary creep constants, $n = 4.7$ and $A = 2.0\times10^{-17}\ MPa^{-n}hr^{-1}$.

This elastic match and creep property mismatch should cause changes in the transition time and the steady-state value of the *C(t)*-Integral, *C**, only. Visualizations of the time-dependent effective stress fields were obtained for a variety of models and illustrated in Fig. 2. In the case of weldments, elastic matching permits the stress fields near the material interfaces to be initially symmetric with regard to the crack plane; however, as each of the materials relaxes over time, the steady state stress distribution is not symmetric. This stress re-distribution along each material interface is discontinuous due to the inelastic mismatch and is more intense in the more inelastically compliant, or softer, HAZ and WM regions. For cases where the transition layer or the eccentricity are small but positive, the intensity and variation of the stresses along the interface are greater.

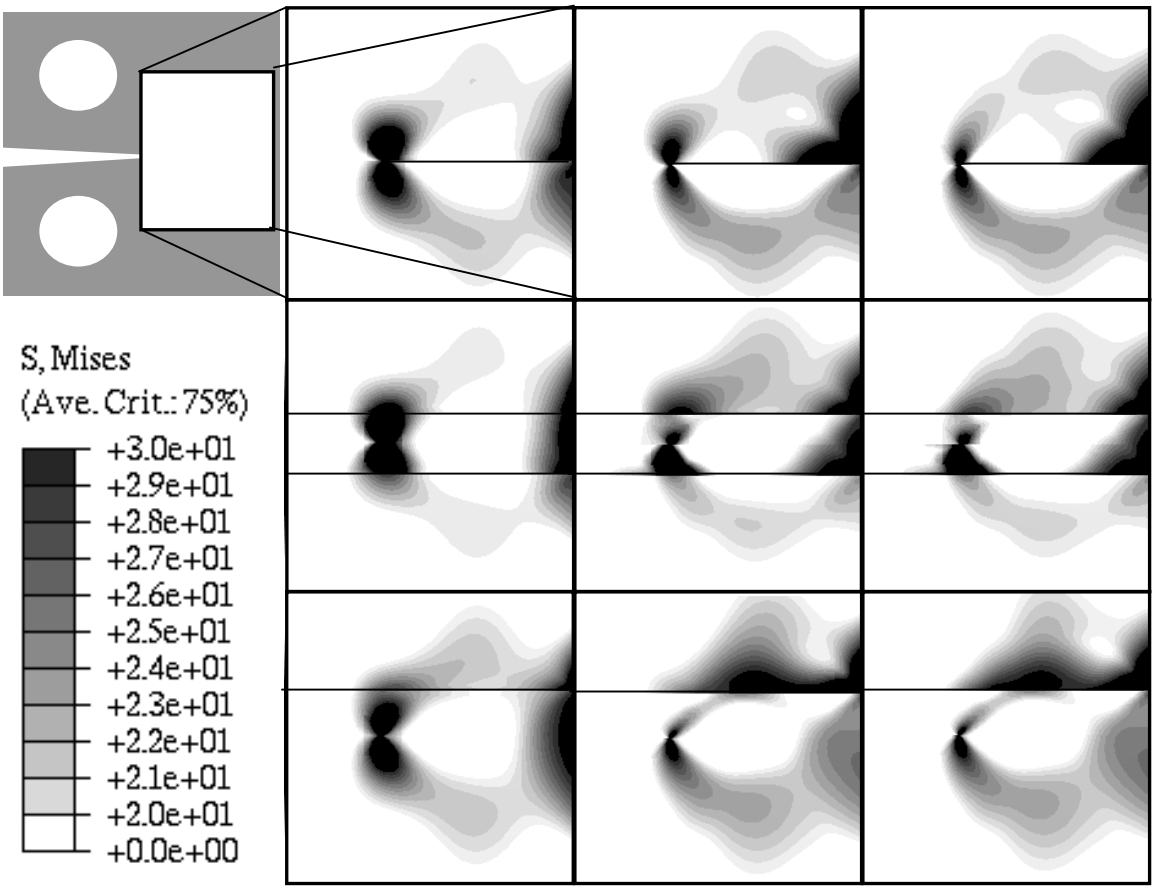

Figure 2: Stress (in ksi) evolution for bimaterial (first row), weldment with blended HAZ (second row), and eccentric bimaterial (third row) specimens. Each weldment specimen features an inelastic overmatch of $\chi_A = 100$ and $\chi_n = 1$ at T = 538°C. For each specimen the effective stress field is shown at various times: $t \approx t_{T_{WM}}$ (first column), $t \approx t_{T_{BM}}$ (second column), t □ $t_{T_{WM}}, t_{T_{BM}}$ (third column).

For simplicity, it is common to define the material property overmatch, χ, as the weld-to-base ratio of any material property, for example $\chi_A = A_{WM}/A_{BM} = 10$. For each behavior regime, the crack plane distance quantities, eccentricity, e, and transition layer thickness, t, are varied for particular material mismatches. As the eccentricity decreases, the initial crack is embedded more deeply within the base metal. The contour

integral approaches values that resemble those of base metal homogeneous model. Likewise, as the eccentricity reaches a large positive number, the C^* converge to C^*_{WM}, respectively. The variation of C^* can be related with a power law. For each of the material mismatch cases for perfect weldments, e = 0, the resulting C^* are observed to nearly follow the logarithmic average of the integral values of two material constituents; furthermore, as the HAZ region thickness increased the contour integral values move towards C^*_{HAZ}, exponentially. For most cases, the fracture parameters can be fit with the following exponential form:

$$\left.\begin{matrix} C^* \\ t_T \end{matrix}\right\} = b(\chi) e^{\frac{D(\chi)}{1.2W}\left\{\begin{matrix} e \\ t \end{matrix}\right\}}, \tag{1}$$

where b and D are the coefficient and exponent, respectively, which may be obtained explicitly via regression analysis. Each assumes the separate dimensions and should be influenced by the property mismatch. Function b takes on units of the ordinate fracture parameter $\{C^*, t_T\}$, while D is dimensionless. Using this relation, we can quantify b based on the results of the trivial bimaterial model. For $e = t = 0$, this quantity is close to the logarithmic average of the fracture parameters of the homogeneous members, and is usually bounded by these quantities.

FUNCTIONALLY GRADED MATERIALS

Most numerical fracture investigations model transition layers with homogeneous properties. This is not the most accurate depiction of in-service welded members. The majority of investigations that incorporate spatial dependence limit this gradation to only elastic mechanical properties. In a very small number of studies the yield strength is varied. The variation of material properties across a section is usually prescribed according to some linear function of distance. We extend this method to grade the hardening coefficients and exponent of the heat-affected zone.

The HAZ is sandwiched between materials that are homogeneous. Therefore, it is reasonable that the material behavior at each of its boundaries must match that of the weld and base metal. By replacing sharp property variations with continuous material functions, the states of stress and strain in actual service joints and members are perhaps more realistically represented. Micro-hardness tests of welded specimens show that the variation in Vickers hardness changes linearly between base and weld metal regions. Consequently, these sections, which encompass HAZs, correlate to linear yield strength variation from region to region. These indentation profiles, shown by Miyazaki et al. [3], can be combined with either Ramberg-Osgood or

TABLE 1
FRACTURE PARAMETERS FOR VARIOUS HAZ SECTIONS

HAZ Model	Normalized Transition Time, t_T/t_{TBM}	Normalized C(t)-Integral, $C(t)/C^*_{BM}$
No HAZ	0.0216	45.9654
Median HAZ	0.0327	29.4524
FG Linear HAZ	0.0366	25.9942
Base Metal	1	1
HAZ Metal	0.1	10
FG Exponential HAZ	0.0528	18.3862
Weld Metal	0.01	100
FG Continuous HAZ	0.0487	19.1354

Norton power law rules to indicate that the hardening coefficient exhibits exponential spatial dependence across the HAZ. Models with variation of strain hardening coefficient, $A_{HAZ}(y)$, have been simulated under

identical boundary conditions. These results are normalized by the homogeneous base metal results. The predicted C^* is higher for models using the blend or median method than models with functionally graded HAZs. Table 1 summarizes this conservative trend.

LOCAL PHASE ANGLE

The mode mixity for a bimaterial is uniquely described by a set of local phase angles. Introduced by Shih [4], the solid angle, ψ, which is also equivalently denoted as the mode mixity parameter, M_p, is found from the interface traction vector. It is given as

$$M_p = \frac{2}{\pi}\tan^{-1}\left[\lim_{r\to 0}\frac{\sigma_{xy}(r)}{\sigma_{yy}(r)}\right]_{\theta=0}. \qquad (2)$$

This expression effectively assigns non-dimensional values within the interval *(-1,1)* to distances ahead of the tip of the crack. Since cracks tend to propagate toward the traction vector that is perpendicular to the maximum normal stress, M_p is expected to indicate the direction of crack extension. Isotropic and homogeneous models always produce local phase angles equal to zero. Conversely, when the material constituents on either side of the crack are dissimilar, a non-trivial solution is always obtained. This phenomenon occurs for any material behavior regime. The results of Li et al. [5] show that the singularity fields near the crack tip are mixed mode, and the magnitude of the shearing mode increases with mismatch in properties.

Most investigations into the heterogeneous case have assumed that the crack is not only located on the interface, but is also restricted to growth along the weld line. Only recently have studies progressed to off-weld crack studies. By including this metric in parametric examination of numerically modeled C(T) specimens, we can further understand the influence of the initial position of the crack plane on the time-dependent fracture behavior of bimaterials. The stress fields in time-dependent bimaterials are primarily active between the transition times of the base and weld metals, t_{TWM} and t_{TBM}. This transient behavior is exemplified in M_p for models with various transition layer thickness, t, modeled with blended and functionally graded material properties.

The weld material occupies the upper region in the model; consequently, positive local phase angles indicate that the direction perpendicular to that of the maximum normal stress points toward this more creep strain compliant section. This is the case for each model studied. In Fig. 3, models with a finite HAZ thickness predict local phase angles that would favor crack bifurcation into the direction of the weld metal. When the fracture specimen is simulated with a graded section of some specified thickness, M_p is consistently increased by a factor, which varies based on the bimaterial overmatch. After the transition time of the base metal is reached, M_p smoothly converges to the steady state local phase angle, denoted by M_{pss}.

This technique is also applied to specimens that have eccentrically located cracks. The results indicate that for either negative or positive eccentricities, the local phase angle points toward the more creep strain compliant material. When the crack is located within the base metal (negative eccentricities), these values are (1) increased by at least a factor of two and (2) achieved at times closer to t_{TBM}. In addition, similar to models that include a HAZ, the factor is influenced by the level of the overmatch.

CONCLUSIONS

In addition to other fracture parameters, the mode mixity exhibits slight changes with respect to specimen dimensions and material property mismatch. This traction vector points toward the more compliant material for the subinterface and HAZ thickness models studied. By replacing a blended HAZ with a functionally graded HAZ, the stress concentrations at the interfaces are less extreme and the estimates for the predicted

fracture parameters are closer to the reference or base metal; however, the direction of the traction vector is increased by a factor. Collective consideration of a range of thickness or crack plane eccentricity values indicates that the crack is likely to kink into the softer material and then meander back towards the interface. Ultimately, this must be verified by a crack propagation analysis.

Most bimaterial studies limit crack propagation to the direction along the initial crack plane. Future studies featuring crack extension should incorporate propagation along a direction that is controlled by the evolution of the near tip stress and strain fields. The subject matter of interface fracture of non-linear and time-dependent materials needs more attention. Since there is no generalized analytical solution for the variation of the stress, strain, and displacement fields near the crack tip, the results of this study can only be confirmed and extended by performing branching crack analyses and experiments.

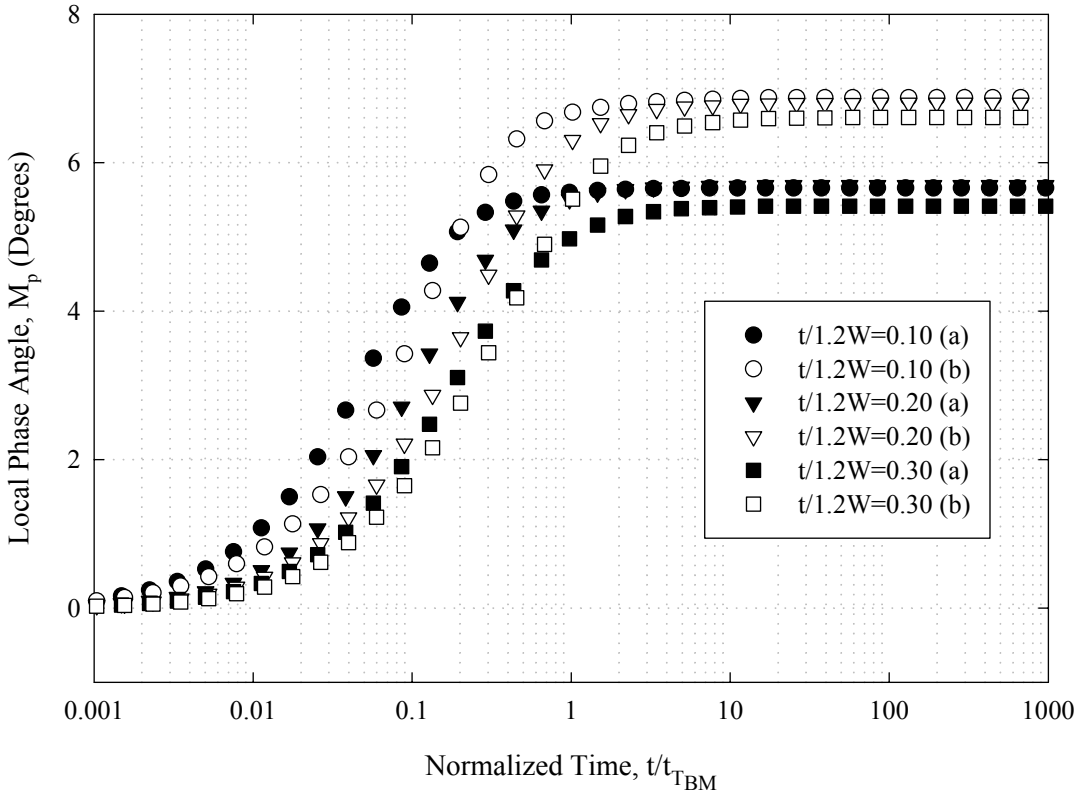

Figure 3: Convergence of local phase angles for median (a) and functionally graded (b) HAZ. χ_A=100 and χ_n=1 for each model.

REFERENCES

1. Segle, P., Andersson, P., Samuelson, L. Å , (1998), *Mat. High Temp.*, Vol. 15 No. 2, 63.
2. Biner, S. B., (1998), *Mat. Sci. and Eng.,* A, 233.
3. Miyazaki, N., Nakagaki, M., Sasaki, T., Sakai, T., Munakata, T., (1993), *JSME Int J., Series A: Mechanics and Material Engineering*, Vol. 36, No. 4, 361.
4. Shih, C. F., (1974), *Fracture Analysis, ASTM STP 560*, 187.
5. Li, F. Z. Needleman, A. and Shih, C. F., (1988), *Int. J. of Frac.*, Vol. 36, 163.

ORAL/POSTER REFERENCE : ICF100816OR

CRACK PROPAGATION IN CEMENTITIOUS MATERIALS BY ACOUSTIC EMISSION BASED ON FRACTURE MECHANICS

M. Ohtsu and Farid Uddin A. K. M.

Graduate School of Science and Technology, Kumamoto University
2-39-1 Kurokami, Kumamoto 860-8555, JAPAN

ABSTRACT

Acoustic emission (AE) techniques are applied to clarifying fracture mechanics in cementitious materials. Crack traces due to mixed-mode cracking are numerically analyzed by applying the boundary element method (BEM). Here, in order to determine the critical stress intensity factor prior to nucleating the fracture process zone, AE rate process analysis is applied to the three-point bending tests of notched concrete beams. AE-SiGMA analysis is implemented to characterize kinematics of cracks, classifying crack types and determining crack orientations. Thus, mixed-mode crack propagation in cementitious materials is clarified by AE analysis based on fracture mechanics..

KEYWORDS

Acoustic emission (AE), Boundary element method (BEM), Cementitious materials, Rate process analysis, SiGMA Analysis

INTRODUCTION

The increase of aging structures and the disastrous damage due to earthquakes updatedly demand for clarifying the failure mechanisms of concrete structures. To this end, crack propagation in cementitious materials has been recently studied on the basis of fracture mechanics. Acoustic emission (AE) techniques have been extensively studied in concrete engineering, where it is known that one promising approach is the application of AE to fracture mechanics. Concerning the theoretical treatment, the generalized theory of AE was established on the basis of elastodynamics [1]. It is already clarified that AE waves are elastic waves due to

dynamic crack motions in cementitious materials [2]. Based on these fundamental research, to classify crack types and determine crack orientation, the moment tensor analysis is implemented as the SiGMA (simplified Green's functions for the moment tensor analysis) code [3].

In the present paper, crack propagation in notched concrete beams is studied. The boundary element method (BEM) is applied to trace crack extension based on the linear elastic fracture mechanics (LEFM). The critical stress intensity factor K_{IC} is such a key parameter in the analysis that the value is estimated from AE rate process analysis [4]. Then, crack kinematics is clarified by applying the SiGMA analysis and compared with results of the BEM analysis.

THEORETICAL BACKGROUND

Rate Process Analysis

When concrete contains a number of critical microcracks, active AE occurrence is expected under compression due to crack propagation from the microcracks. In contrast, AE activity in sound concrete is known to be stable and low prior to final failure. Thus, to formulate AE activity under loading, the rate process theory was introduced [4]. Probability function f(V) of AE occurrence from stress level V(%) to V+dV (%) is formulated,

$$dN/N = f(V)\,dV. \qquad (1)$$

Assuming a hyperbolic function of the probability,

$$f(V) = a/V + b. \qquad (2)$$

.Eventually, a relationship between the number of total AE events N and stress level V(%) is derived as,

$$N = C\,V^{a} \exp(bV), \qquad (3)$$

where a and b are empirical coefficients and C is the integration constant. Then, a tangential equation is derived at the maximum stress level V = 100%, and an intersection with the stress level is determined as V',

$$V' = 1 - 1/(a + b) \qquad (4)$$

This stress level could correspond to initiation of crack propagation prior to nucleating the fracture process zone. Consequently, the load P' to determine the critical stress intensity factor K_{IC} is determined from the ultimate load P_{max} times V' ($P' = P_{max} \times V'$). As a result, K_{IC} is determined from the load level right before developing the fracture process zone in cementitious materials, satisfying the condition of small-scale yielding.

BEM Analysis

Elastic solutions of displacement $\mathbf{u}(\mathbf{x})$ are mathematically represented as,

$$C\,u_k(\mathbf{x}) = \int_S [G_{ki}(\mathbf{x},\mathbf{y})t_i(\mathbf{y}) - T_{ki}(\mathbf{x},\mathbf{y})u_i(\mathbf{y})]dS, \qquad (5)$$

where $\mathbf{u}(\mathbf{x})$ and $\mathbf{u}(\mathbf{y})$ are displacements, and $\mathbf{t}(\mathbf{y})$ are tractions. $G_{ik}(\mathbf{x},\mathbf{y})$ are Green's functions and $T_{ik}(\mathbf{x},\mathbf{y})$ are the associated tractions with Green's functions,

$$T_{ik}(\mathbf{x},\mathbf{y}) = G_{ip,q}(\mathbf{x},\mathbf{y})\,C_{pqjk}\,n_j. \qquad (6)$$

Here C_{pqji} are the elastic constants, and $G_{ip,q}(\mathbf{x},\mathbf{y})$ are the spatial derivatives of Green's functions. $\mathbf{n}$ is the normal vector to the boundary surface S. In BEM, eq. 5 is directly digitized and numerically solved, where C=1/2 and all points $\mathbf{x}$ and $\mathbf{y}$ are prescribed

on the boundary S.

According to LEFM, the angle of crack extension θ is obtained from the maximum circumferential stress [5],

$$K_I \sin\theta + K_{II}(3\cos\theta - 1) = 0. \qquad (7)$$

Here K_I and K_{II} are the stress intensity factors of mode I and mode II, which can be computed from the displacements on the crack-tip elements in BEM. Introducing the critical stress intensity factor K_{IC}, the initiation of crack extension is governed by,

$$\cos\theta/2[K_I\cos^2\theta/2 - 3/2(K_{II}\sin\theta) = K_{IC}. \qquad (8)$$

Implementing the above criterion of eqs. 7 and 8 into BEM, the automatic analysis of crack propagation in an arbitrary orientation has been developed by employing the two-domain BEM [6].

SiGMA Analysis

In order to model a crack as an AE source, the boundary surface S in eq. 5 is replaced by crack surface F. Taking into account the discontinuity, $\mathbf{b}(\mathbf{y},t)$, of displacements on the crack surface, eqs. 5 and 6 are reformulated as,

$$u_k(\mathbf{x},t) = \int_F T_{ki}(\mathbf{x},\mathbf{y},t) * b_i(\mathbf{y},t)\, dF = G_{kp,q}(\mathbf{x},\mathbf{y},t) * S(t)\, C_{pqij}\, n_j l_i \Delta V, \qquad (9)$$

where $\mathbf{l}$ is the unit direction vector and S(t) is the source-time function of crack motion. ΔV is the crack volume. Introducing moment tensor $M_{pq} = C_{pqkl} l_k n_l \Delta V$, eq. 9 is simplified,

$$u_k(\mathbf{x},t) = G_{kp,q}(\mathbf{x},\mathbf{y},t)\, M_{pq} * S(t). \qquad (10)$$

Based on the far-filed term in eq. 10, a simplified procedure suitable for a PC-based processor was developed. The procedure is implemented as a SiGMA (Simplified Green's functions for Moment tensor Analysis) code [3]. Since the moment tensor is symmetric and composed of six independent unknowns m_{pq}, multi-channel observation of the first motions at more than six channels is necessary and sufficient.

From AE waveform, the arrival time and the amplitude of the first motion are determined. In the source location procedure, location $\mathbf{y}$ is determined from the arrival time differences. From the amplitudes of the first motions at more than 6 channels, the components of the moment tensor are solved. The classification of a crack is performed by the eigenvalue analysis of the moment tensor. The eigenvalues of the moment tensor for a general case could be decomposed as X, Y, and Z which denote the shear ratio, the deviatoric tensile ratio, and the isotropic tensile ratio, respectively. AE sources of which the shear ratios are less than 40% are classified into tensile cracks. The sources of X > 60% are classified into shear cracks. In between 40% and 60%, cracks are referred to as mixed mode. In the eigenvalue analysis, three eigenvectors are also determined, and then the vectors $\mathbf{l}$ and $\mathbf{n}$ which are interchangeable are recovered.

EXPERIMENT

Three-point bending tests of notched concrete beams were conducted. To apply AE rate process analysis and SiGMA analysis, notched beams of dimensions 10 cm x 10 cm x 40 cm were made of concrete. By sawing the specimens, a notch of either 5 cm depth or 7 cm depth was made with 1 mm thickness. The compressive strength of concrete was 37.9 MPa, the tensile strength was 3.03 MPa and Young's modulus was 29.7 GPa after 28 day moisture-cure. The load was applied monotonously up to the final failure, monitoring AE events. AE sensor was of 1 MHz resonance. Total amplification was 60 dB and the frequency range was 10 kHz to 1 MHz. A sketch of the specimen and AE sensor array is given in Figure 1. AE rate process analysis was conducted in center-notched specimens (the notch of solid line) by employing one-channel system, while six-channel system was employed to

apply the SiGMA procedure to off-center notched specimens (the notch of broken line).

RESULTS AND DISCUSSION

The Critical Stress Intensity Factor

AE events were observed in the three-point bending tests of the center-notched specimens. Results are given in Figure 2. AE activity is approximated by eq. 3 and then the stress level V' is determined. As a result, the critical stress intensity factors were computed as 0.827 MPa $m^{1/2}$ for 5 cm notch and 0.723 MPa $m^{1/2}$ for 7cm notch. These values were checked by Barenblatt's criterion,

$$d > (K_{IC}/\sigma_t)^2, \qquad (11)$$

where d is the notch depth and σ_t is the tensile strength. It is obtained that d > 4.96 cm for 5 cm notch and d > 3.06 cm for 7 cm notch. The criterion is just satisfied in the case of 5 cm notch and completely for 7 cm notch.

To investigate an applicability of these values, BEM analysis was conducted for the center-notched specimens. Results are shown in Figure 3. In the case of 5 cm notch, an analytical result on the load versus crack-mouth opening displacement (CMOD) relation becomes unstable after reaching the peak value, while the relation of 7 cm notch is stable and in reasonable agreement with experimental results. Consequently, The value K_{IC} = 0.723 MPa $m^{1/2}$ is selected for the analysis of the off-center notch.

Crack Traces

Crack propagation was observed in the three-point bending of the off-center notched specimens. Three traces observed are given in Figure 4. BEM analysis was conducted to simulate the crack propagation. As can be seen, remarkable agreement with experimental results is observed. Thus, an applicability of eqs. 7 and 8 to analyze the crack trace of mixed-mode propagation. in concrete is confirmed.

Crack Kinematics

Results of SiGMA analysis for the off-center notched specimen is shown in Figure 5. Cracks identified are plotted at their locations. Those of tensile cracks are indicated by arrow symbol of which directions are identical to opening directions, while those of mixed-mode and shear are represented by cross symbol of which two directions correspond to the motion of crack and the normal vector to the crack surface.

Surface cracks observed at both the top and the bottom surfaces are indicated by broken lines. It is observed that both types of cracks are generated and fully mixed at their locations. Still, it seems that the shear cracks are observed as close as the final crack surface, indicating that the shear cracks are mostly generated along the existing crack surfaces. To compare with the analytical results by BEM, the ratios of the stress intensity factors K_I/K_{II} in the analysis are plotted against the crack extension length as given in Figure 6. It is clearly observed that the ratios are mostly larger than 1.0, implying that the dominant motions are of the opening mode. After propagating around 3.5 cm, the ratio abruptly decreases smaller than 1.0, indicating the presence of the dominant shear motions. Thus, the mixed nature of crack propagation in concrete is clarified, although the dominant mechanisms are of mode I.

CONCLUSION

Crack propagation in notched concrete beams is studied numerically and experimentally. Resulst are concluded, as follows:
(1) In the case of 7 cm notch, K_{IC} value estimated is fully satisfied with Barenblatt's criterion. The analytical result on the load-CMOD relation by BEM is stable and in reasonable agreement with experimental results. The feasibility of the procedure to estimate K_{IC} in cementitious materials is demonstrated.
(2) Crack traces observed in the off-center notched specimens are simulated by BEM. Remarkable agreement with experimental results on crack surfaces is observed. The applicability of LEFM to analyzing the mixed-mode crack propagation is confirmed.
(3) From SiGMA analysis, it is observed that both types of cracks are fully mixed during crack extension in the off-center notched beam. The ratios of the stress intensity factors K_I/K_{II} are studied brom the results of BEM analysis. It is found that cracking mechanisms are mostly of mode I, although there is a stage where mode II is dominant.

REFERENCES

1. Ohtsu, M. and Ono, K. (1984).*A Generalized Theory of Acoustic Emission and Green's Functions in a Half Space, Journal of AE*, 3(1), 124-133.
2. Ohtsu, M. (1982). *Source Mechanism and Waveform Analysis of Acoustic Emission in Concrete, Journal of AE*, 2(1), 103-112.
3. Ohtsu, M., Okamoto T. and Yuyama, S.(1998).*Moment Tensor Analysis of Acoustic Emission for Cracking Mechanisms in Concrete, ACI Structural Journal*, 95(2), 87-95.
4. Ohtsu, M. (1987). *Acoustic Emission Characteristics in Concrete and Diagnostic Applications,*
5. Erdogan, F. and G. C. Sih (1963).*On the Crack Extension in Plates under Plane Loading and Transverse Shear, J. Basic Engineering,* ASME, 12, 519-527.
6. Chahrour, A. H. and Ohtsu, M.(1994).*Crack Growth Prediction in Scaled –Down Model of Concrete Gravity Dam, Theoretical and Applied Fracture Mechanics,* 21, 29-40.

Figure 1: Experimental set-up and AE sensor array for an off-center notched specimen.

Figure 2: Results of AE rate process analysis in the three-point loading tests.

Figure 3: Results of load-CMOD curves and BEM analysis.

Figure 4: Crack traces.

Figure 5: Results of SiGMA analysis.

Figure 6: Ratio of the stress intensity factors K_I/K_{II} vs. crack length.

CRACK PROPAGATION IN CONCRETE ELEMENTS STRENGTHENED BY GFRP

B. Bonfiglioli, G. Pascale, E. Viola

DISTART - Department of Structural Engineering - University of Bologna
Viale Risorgimento, 2 – I-40136 BOLOGNA – ITALY

ABSTRACT

Fibre Reinforced Polymers (FRP) are a useful alternative to external strengthening with steel plates. Their typical applications are flexural and shear strengthening of reinforced concrete beams and wrapping of columns.
In this paper, a study of crack onset and propagation is reported, in order to improve knowledge of the global behaviour of r.c. beams strengthened by FRP.
The results of an experimental programme based on tensile tests on both unstrengthened and Glass Fibre Reinforced Polymer (GFRP) strengthened concrete specimens are proposed.
Based on Fracture Mechanics, a theoretical study of the stress field around the crack tip, and in particular at the concrete-FRP interface is presented. The Stress Intensity Factor at the interface are evaluated. The results afford an opportunity for some considerations about crack propagation: the first crack always appears in the concrete. Then the crack propagates to the concrete-composite interface. When the shear stress at the interface is low (applied load not high and crack edge displacement not big), the only way where the crack can propagate is into the concrete.

KEYWORDS

Concrete, Fibre Reinforced Polymer, Cracking, Fracture, Strengthening

INTRODUCTION

FRPs were first applied in the mechanical and aeronautical fields of engineering, and in recent years they have spread to civil and structural engineering. FRPs are a useful alternative to traditional steel reinforcement, because of their lightness,

corrosion resistance and very high tensile strength. Typical applications are flexural and shear strengthening of reinforced concrete beams [1,2,3] and wrapping of columns [4]. Both experimental and analytical-numerical researches have been performed in order to study the failure mechanisms. The first researches on the FRP application to civil structures involved a macroscopic scale [5],[6]. The principal failure modes found are:

- compression and shear failure of concrete,
- tensile rupture of FRP,
- peeling and debonding of FRP.

This macroscopic approach can give useful information about the global behaviour of concrete elements strengthened with FRP. But, especially in the last case, it is important to investigate the crack onset and propagation in order to follow the local crisis up to the global failure of the concrete element.

EXPERIMENTAL

The final goal is to study the effect of the FRP strengthening applied to the concrete structures in bending. This preliminary experimental programme is aimed at studying the correlation between the crack propagation in the concrete and the crack propagation at the interface.

Testing specimens

For this reason, tensile tests were carried out. In this way a simple case has been

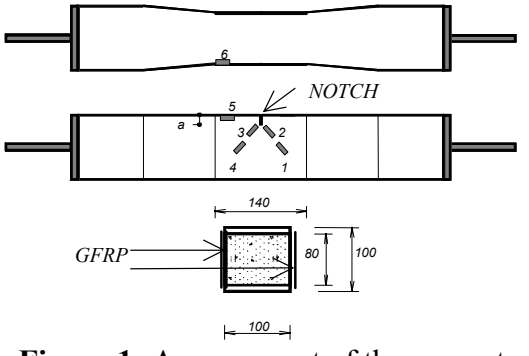

Figure 1: Arrangement of the concrete specimen tested in tension

studied, because the specimen has a very regular geometry and the loading arrangement is well defined. The shape and dimensions of the specimens are sketched in Figure 1. The particular shape was designed in order to have a stress state not disturbed by anchorage effects in the central part of the specimen. GFRP sheets were glued to the plain surfaces, on opposite sides. A notch was milled on one side, under the composite, to establish the crack starting point. Five similar specimens were tested. One plain concrete specimen was tested too.

Test set-up

The test set-up is shown on Figure 1. The specimens were instrumented with electrical strain gauges (ESG), 6 mm long, placed as follows:

- two ESGs on the same section, one on concrete and the other on GFRP (#5 and #6), in order to detect the difference between the strains during testing;
- two ESGs on the concrete (#2 and #3), close to the notch, 45° to the longitudinal axis;
- two ESGs (#1 and #4) as the previous ones, but at 20 mm from the notch.

Two displacement transducers LVDT-5 mm were used to measure of the elongation of the specimen.

Nevertheless, the local measurements supplied by the ESGs appeared to be unable to give sufficient information about the crack propagation direction around the cracking area. For this reason some photoelastic images were taken during the tests. The photoelastic sheet was glued to the concrete, in the area of interest. A digital video-camera was used to record the tests.

Experimental results

Photoelastic images

In figures 2.a and 2.c the most significant pictures from the video-camera are shown. Note the change in strain state during loading. Figure. 2.a shows the propagation of the first crack: an area of strain concentration localised close to the notch can be noted.

With loading increasing, the crack propagates into the concrete to the concrete-GFRP interface, as can be observed in Figure 2.c.

By means of the photoelasticity, it is easy to see the propagation direction: the fracture mode is a mixed mode at the start of the crack. Then, the crack propagates into the concrete towards the concrete-composite interface with mixed mode, too. This propagation mode has also been observed by other researchers [7]. Finally, the crack propagates in the concrete, perpendicular to the loading direction (Figure 2.c).

Strain measurements

In Figure 3 the readings from the two longitudinal strain gauges are plotted vs. load. The strain in the GFRP is higher than in the concrete, after the crack reaches the interface; this is because the concrete cracking causes a stress transfer from the concrete to the composite.

Figure 4 shows the diagonal strain in the concrete from the ESGs placed at +45° and –45° from the axis of the notch.

We can note higher strain values for the ESG #3. This difference can be caused by the strain localisation as pointed out by the photoelastic image (see Figure 2/a).

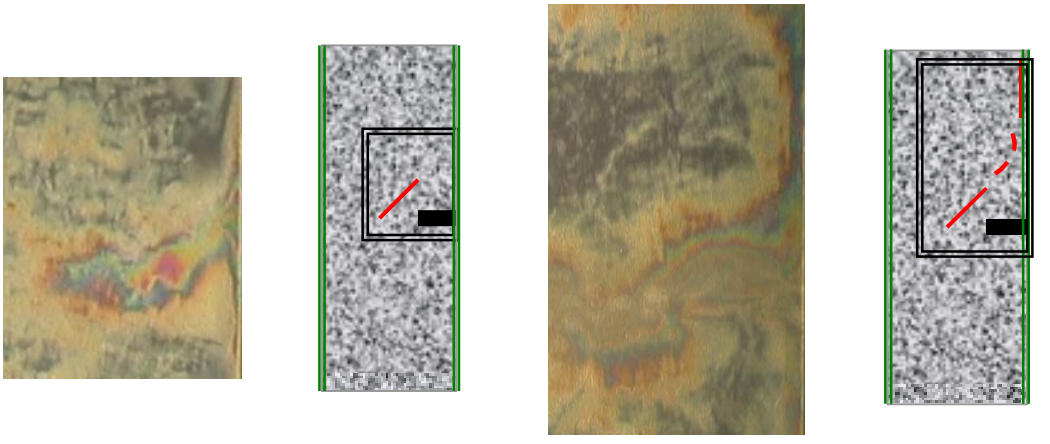

a: first crack in the concrete | **b:** sketch of the first crack onset | **c:** crack propagation | **d:** sketch of the crack propagation

Figure 2: Photoelasticity

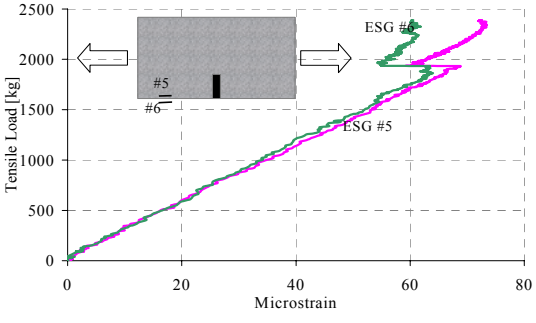

Figure3: Total Load vs. Longitudinal Strain

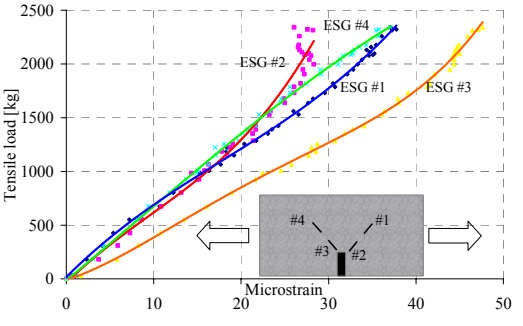

Figure 4: Total Load vs. Diagonal Strain

ANALYTICAL APPROACH

A simple analytical approach is presented, aimed at evaluating the Stress Intensity Factor for this experimental case.

An analogous problem has been analysed in [8] for a cracked beam element in r.c. beams.

In this case, a concentrated load P simulates the behaviour of the GFRP strengthening which hampers the opening of the crack. The existent models based on Fracture Mechanics [9,10] for a simple strip have been used and they are illustrated in Figures 5 and 6, respectively.

For a crack with a distributed tension, the stress intensity factor (SIF) is

$$K_{I\sigma} = \sigma\sqrt{\pi a}F(\xi),$$

where, $K_{I\sigma}$ is the stress intensity factor due to a distributed tension σ and ξ is the normalised crack height[9],

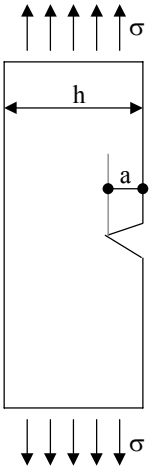

Figure 5: crack with distributed tensile stress

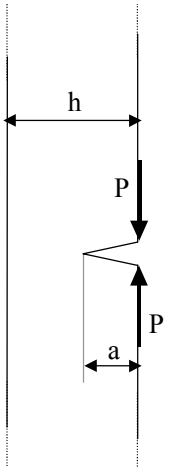

Figure 6: crack with concentrated load

$$F(\xi)=\sqrt{\frac{2}{\pi\xi}tg\frac{\pi\xi}{2}}\,\frac{0.752+2.02\xi+0.37\left(1-sin\frac{\pi\xi}{2}\right)^3}{\cos\frac{\pi\xi}{2}}\,.$$

For a crack with a concentrated load the value of the stress intensity factor is

$$K_{IP}=\frac{P}{h^{0.5}b}Y_P(\xi),$$

where K_{IP} is the stress intensity factor due to a concentrated opening load P, h, b are the height and the width of the specimen, respectively, and ξ is the normalised crack height[10],

$$Y_P(\xi)=\frac{3.52}{(1-\xi)^{3/2}}-\frac{4.35}{(1-\xi)^{1/2}}+2.13(1-\xi).$$

So, the final stress intensity factor K_{IT} can be evaluated as

$$K_{IT}=K_{I\sigma}-K_{IP}\,.$$

For the case under study, the calculated value of K_{IP} is higher than the value of $K_{I\sigma}$. For this experimental test, the load applied to the specimen is not too high to allow the crack propagation at the interface concrete-FRP strengthening. This could happen if the shear stresses reach critical values at the concrete-resin interface.
The crack propagation, as can be seen on the photoelastic images, takes place in the concrete, at the crack tip.

CONCLUSIONS

The first results of this research suggest that the crack propagation in the concrete strengthened by GFRP can be studied by means of Fracture Mechanics. The experimental tests give useful information about both the stress and strain state around the crack and the direction of the crack propagation. The values of SIF can be calculated and they suggest some failure mode of the concrete element strengthened. In particular, if the constraint of strengthening is good, the SIF suggest that the crack can not propagate at the interface and then it propagates around the other tip in the concrete. Research is still in progress in order to apply these preliminary results to the r.c. beams strengthened by FRP in bending, and then to define some correlation between the crack in the concrete and the crisis at the concrete-FRP interface.

ACKNOWLEDGEMENTS

Many thanks to all the staff of the Laboratory for Strength of Materials of the University of Bologna, in particular Mr. Davide Betti and Mr. Roberto Carli, for their diligence and enthusiasm in realising the experimental programme. The help of Mr. Maurizio Chendi of the Laboratory of DIENCA of University of Bologna has been very much appreciated. The financial support of the European TMR network, ConFibreCrete [contract N° FMRX-CT97-0135 (DG 12-MSPS)] and of the Italian Ministry of University and Scientific Research [contract N° MRST54] are gratefully acknowledged.

REFERENCES

1. Fam A.Z., Rizkalla S.H., Tadros G., (1997) *ACI Structural Journal* – 94(1) .
2. Stratford T.J., Pascale G., Bonfiglioli B., Manfroni O., (2000) Proceeding of *Mechanics of masonry structures strengthened with FRP-Materials – Modelling, testing, design, control* , pp. 19-30.
3. Triantafillou T.C., (1998) *Journal of Composites for Construction*, pp. 96-103.
4. Arduini M., (1999), *L'industria italiana del cemento* 11, pp. 100-112 (in Italian).
5. Arduini M., Nanni A., (1997) *Journal of Composites for Construction*, pp.63-70.
6. Arduini M., Di Tommaso A., Manfroni O., (1995) *2nd Int. Rilem Symposium (FRPCS-2)*, pp. 483-491.
7. Kamel A.S., Elwi A.E., Cheng J.J.R., (2000) Proceeding of advanced composite Materials in bridge and Structures (ACMBS-III), pp.61-68.
8. Carpinteri A., (1984), *J. Struct. Engin.*, 110, 3, , pp. 544-558.
9. Tada H., Paris P., Irwin G., *The Stress Analysis of Crack Handbook*, Paris Production Incorporated.
10. Massabò R., (1993) Ph.D Thesis, Politecnico di Torino, Italy (in Italian).

CRACK PROPAGATION IN MIXED MODE FRACTURE OF CONCRETE

P.C. Olsen[1]

[1]Man., Tech. Dir. Colberg Consult, Fasanvænget 124, 2980 Kokkedal, Denmark.

ABSTRACT

The paper is concerned with the application of the Hillerborg fictitious crack model in mixed mode I-II fracture of concrete. It is shown that the cohesive normal traction between opposite crack faces removes all stress singularities at the crack tip, provided that the direction of the crack propagation follows a path of minimum potential energy. In addition, the stresses at the crack tip are hydrostatic. Therefore, these stresses do not reveal a preferable direction of crack propagation. Also, as stresses are finite, stress intensity factors are all zero and K_I-K_{II} concepts cannot reveal a direction of propagation. A new concept of determining the direction of crack propagation based on a "predictor-corrector" principle is presented, in which, firstly, the crack is advanced tangentially into the uncracked concrete, the predictor. Thereafter the direction is updated using a corrector. Based on the *J, L* and *M* integrals of the conservation laws, two proposals for the updated direction are presented.

KEYWORDS

Non-linear fracture mechanics, fictitious crack model, mixed mode fracture, crack propagation, conservation laws, boundary element method.

INTRODUCTION

The original concept of the fictitious crack model proposed by Hillerborg [1] relies on the existence of a σ-δ relationship, i.e. a relationship between normal stresses and crack opening width, and that a crack propagates when the stress at the crack tip exceeds the tensile strength. Mixed mode fracture was not originally considered. However, Peterson [2], although investigating mode-I fracture only, implied that the fictitious crack model is valid also for mixed mode fracture, and proposed that the crack would propagate in a direction perpendicular to the first principal stress. Ingraffea and Samoua [3] applied the fictitious crack model using the FEM-method in mixed mode fracture, determining the direction of crack propagation based on K_I-K_{II} concepts.

However, by observing stresses and corresponding external loads, the author found in his research that the cohesive normal traction between opposite crack faces removes all stress singularities at the crack tip, provided that the direction of the crack propagation follows a path of minimum potential energy. In addition, the stresses at the crack tip are hydrostatic. Therefore these stresses do not reveal a preferable direction of crack propagation. Also, as stresses are finite, stress intensity factors are all zero and K_I-K_{II} concepts cannot

reveal a direction of propagation either. The direction of crack propagation determined by one of the principles above will therefore be coincidental, the paradox arising, that one gets an answer for an "incorrect" current crack tip position only, at which stresses are infinite and not hydrostatic.

The energy release rates for various changes in defects can be determined by evaluation of the *J, L* and *M* integrals as shown by Eshelby [4] and Budiansky/Rice [5]. Applying their results, the author presents two proposals for determining the direction of crack propagation based on a direction of maximum change in energy release rate, as determined by the *J, L* and *M* integrals. All results presented are based on the application of the boundary element method (BEM).

THE BEM-METHOD AS VEHICLE FOR THE FICTITIOUS CRACK MODEL

The basic equation in the boundary element method is the extended Somigliano's identity, valid for both internal points and for points on the boundary:

$$C_{ij}(s)u_j(s) + \int_\Gamma \overline{p}_{ij}(s,q)u_j(q)d\Gamma = \int_\Gamma \overline{u}_{ij}(s,q)p_j(s)d\Gamma + \int_\Omega \overline{u}_{ij}(s,q)b_j(q)d\Omega \qquad (1)$$

where $u_{ij}(s,q)$ and $p_{ij}(s,q)$ are the fundamental solutions for displacements and tractions respectively for a unit point load. $u_j(q)$ and $p_j(q)$ are the displacements and tractions respectively at the boundary. $b_j(q)$ is the body force, $C_{ij}(s)$ is a matrix depending upon the boundary shape, Ω is the domain considered and Γ the corresponding boundary. The reader is referred to literature for the fundamentals of the boundary element method, for example Brebbia et al [6]. Applying the multi-domain BEM-method, the fracture process zone could be embedded directly in the boundary element method by means of non-linear interface conditions, depicted by matrix ***S*** in Fig. 1. However, the principle of superposition as devised by Peterson [2] for mode-I fracture is more appropriate for the objectives in this paper. In this method the boundary element method merely serves as a device to determine influence coefficients.

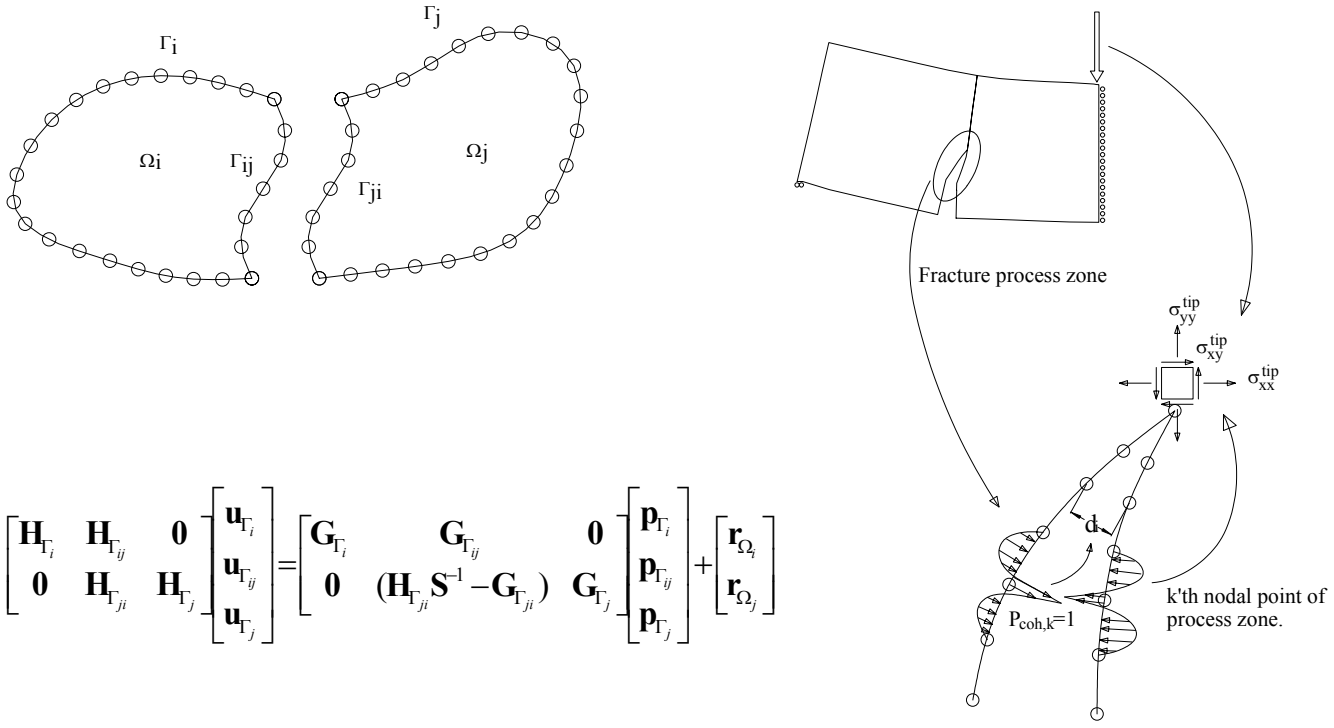

$$\begin{bmatrix} \mathbf{H}_{\Gamma_i} & \mathbf{H}_{\Gamma_{ij}} & \mathbf{0} \\ \mathbf{0} & \mathbf{H}_{\Gamma_{ji}} & \mathbf{H}_{\Gamma_j} \end{bmatrix} \begin{bmatrix} \mathbf{u}_{\Gamma_i} \\ \mathbf{u}_{\Gamma_{ij}} \\ \mathbf{u}_{\Gamma_j} \end{bmatrix} = \begin{bmatrix} \mathbf{G}_{\Gamma_i} & \mathbf{G}_{\Gamma_{ij}} & \mathbf{0} \\ \mathbf{0} & (\mathbf{H}_{\Gamma_{ji}}\mathbf{S}^{-1} - \mathbf{G}_{\Gamma_{ji}}) & \mathbf{G}_{\Gamma_j} \end{bmatrix} \begin{bmatrix} \mathbf{p}_{\Gamma_i} \\ \mathbf{p}_{\Gamma_{ij}} \\ \mathbf{p}_{\Gamma_j} \end{bmatrix} + \begin{bmatrix} \mathbf{r}_{\Omega_i} \\ \mathbf{r}_{\Omega_j} \end{bmatrix}$$

Figure 1 The multi-domain BEM-method for the fictitious crack model.

The objective is, for a given crack tip position, not necessarily the correct one, to determine an external load that complies with the following conditions: 1) the first principal stress in front of the crack tip equals the tensile strength and 2) normal stresses and crack widths in the crack process zone comply with the σ–δ relationship.

The external load naturally causes deformations and the crack to widen. On the other hand, the traction in the fracture process zone attempts to attract the two crack surfaces to each other. To determine the external

load, the stresses at the crack tip and the crack width along the crack surface are firstly determined for a unit external load. Secondly, for unit normal tractions at all the nodes along the crack surface, the stresses at the crack tip and the crack width along the crack surface are determined (see Fig. (1)). The total stress σ_{ij}^{tip} at the crack tip is thus composed of a linear combination of the stress from the external load and stresses from the cohesive tractions as follows:

$$\sigma_{ij}^{tip} = \lambda \sum_{k=1}^{n} \sigma_{ij,k}^{tip} p_{coh,k} + \sigma_{ij,p}^{tip} \tag{2}$$

where index p indicates the stresses from the unit external load and index k the stresses from the individual unit cohesive tractions along the process zone. Similarly, the crack width at the nodal points along the crack surface δ_i are composed of a linear combination of crack width from the external load and crack width from the cohesive tractions along the crack surface:

$$\delta_i = \lambda \sum_{k=1}^{n} \delta_{ik} p_{coh,k} + \delta_{i,p} \tag{3}$$

where $\delta_{i,p}$ are the crack width from the unit external load and δ_{ik} the crack width from the individual unit cohesive tractions along the process zone.

Having determined the influence coefficients above, the external load and the crack width profile that comply with the objectives above, can now be determined. This can only be accomplished iteratively. To assure convergence, a displacement-controlled procedure must be used. The crack opening opposite the crack tip, say δ_n, is used as control parameter. For a given value of the control parameter $\bar{\delta}_n$, the cohesive tractions $p_{coh,i}$ are firstly initialised, for example setting $p_{coh,i}=f_t$. With this initial guess, a load factor is determined from Eqn. 4:

$$\lambda = (\bar{\delta}_n - \sum_{i=1}^{n} \delta_{n,i} \times p_{coh,i}) / \delta_{n,p} \tag{4}$$

The crack openings δ_i at the other nodal points can now be determined and from the σ–δ relationship the cohesive tractions at the nodal points are updated. A new load factor is computed and so forth until the cohesive tractions stabilise. From Eqn. 5 the stress tensor at the crack tip is hereafter evaluated and the first principal stress is determined:

$$\sigma_1 = 0.5(\sigma_{xx}^{tip} + \sigma_{yy}^{tip} + \sqrt{(\sigma_{xx}^{tip} - \sigma_{yy}^{tip})^2 + 4\sigma_{xy}^{tip\,2}}) \tag{5}$$

The value of the control parameter is hereafter iteratively altered, for example using the bi-section method, until the requirement $\sigma_1=f_t$ is satisfied.

OBSERVING VARIOUS CRACK TIP POSITIONS

A three point bending beam with a flat notch placed in the shear zone is now considered. The depth of the beam is $d=400mm$, the width $b=1000mm$ and the length $l=1600mm$. The notch has a depth of $d'=100mm$ and is situated a distance $a=400mm$ from the centre line of the beam. The size of the support areas are $l_s=16mm$, whereas the point load at the centre of the beam is distributed over an area of $l_p=32mm$. Due to symmetry only half of the beam is modelled. A straight crack originating at the root of the notch, having a length of $h=100mm$ is considered. The concrete tensile strength is $f_t=4MPa$, the modulus of elasticity $E=40GPa$ and the fracture energy $G=100N/m$, the σ–δ relationship varying linearly.

Applying the principles described in the previous section, the stress distribution in front of the crack has been observed for various positions of the crack tip, expressed by means of the angle v, by which the crack direction deviates from vertical. In Fig. (2) the normal traction, the tangential traction and the tangential normal stress, all with respect to the sub-domain boundaries, are plotted for crack tip positions corresponding to $v=15°$, $v=20°$ and v=25º. It is easily recognized that for $v=15°$ and for $v=25°$ the tangential traction tends towards infinity, however, with opposite sign for the two crack tip positions. At $v=20°$, the tangential traction at the crack tip almost equals zero. The normal traction and the tangential normal stress

are almost continuous across the crack tip and it can be concluded that stress singularities are not present for this particular position of the crack tip.

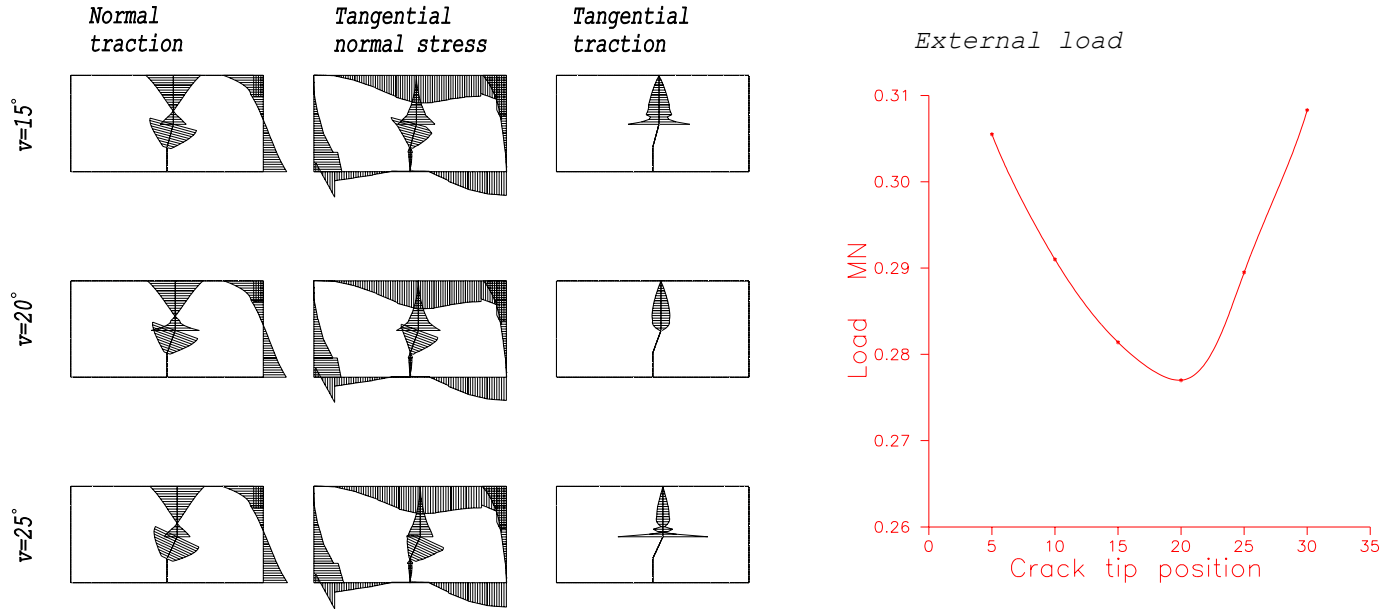

Figure 2 Observing external load and associated stresses for various crack tip positions.

In Fig. (2) the external load is plotted for the various crack tip positions as well. It is observed that the external load is minimal for $v=20^{o}$, i.e. for the crack tip position at which the stress singularities are all removed. The important observation is made that, following a crack path other than the one corresponding to continuous smoothness of stresses at the crack tip, one does not follow a path of minimum potential energy configuration.

DEFECT VARIATIONS AND RELATED ENERGY RELEASE RATES

The conservation laws are the direct consequence of the basic equations of the theory of elasticity. Knowles and Sternberg [7] have shown that, when these equations are all satisfied, the following integrals:

$$J_x = \int_S (Wn_x - (p_x \varepsilon_{xx} + p_y \frac{\partial u_y}{\partial x}))dS \tag{6}$$

$$J_y = \int_S (Wn_y - (p_x \frac{\partial u_y}{\partial x} + p_y \varepsilon_{yy}))dS \tag{7}$$

$$L = \int_S ((Wn_x - (p_x \varepsilon_{xx} + p_y \frac{\partial u_y}{\partial x}))y - (Wn_y - (p_x \frac{\partial u_y}{\partial x} + p_y \varepsilon_{yy}))x + p_x u_y + p_y u_x)dS \tag{8}$$

$$M = \int_S ((Wn_x - (p_x \varepsilon_{xx} + p_y \frac{\partial u_y}{\partial x}))x - (Wn_y - (p_x \frac{\partial u_y}{\partial x} + p_y \varepsilon_{yy}))y_x)dS \tag{9}$$

vanish for arbitrary closed integration paths S surrounding a homogeneous singly connected isotropic elastic domain. In Eqn. 6-9 W is the strain energy density, n_i is the unit outward normal vector of S, u_i is the deformation vector, ε_{ij} is the first order strain measure, p_i is the traction vector at S, corresponding to the unit outward normal vector and finally, x and y are coordinates of points at S. The subscripts refer to components in a global Cartesian reference frame (see Fig. (3)).

If a defect is present in the domain and the integration path S completely surrounds the defect, these integrals differ from zero and express energy changes in the domain corresponding to certain defect variations. Eshelby [4] has shown that the energy release rate for an infinitesimal translation $\boldsymbol{\delta r}$ can be determined by means of J_x and J_y, whereas Budiansky/Rice [5] have shown that the energy release rate for an infinitesimal rotation and an infinitesimal expansion can be determined by means of L and M. This may be summarized in the following formulae, which give the energy release rate associated with infinitesimal variations of defects:

Translation $\mathbf{r}' = \mathbf{r} + \boldsymbol{\delta}\mathbf{r}$ $\delta\Pi = \delta r_x J_x + \delta r_y J_y$ (10)

Rotation $\mathbf{r}' = \Omega\mathbf{r}, (\Omega = \delta\omega \begin{bmatrix} 0 & -1 \\ 1 & 1 \end{bmatrix})$ $\delta\Pi = -\delta\omega L$ (11)

Expansion $\mathbf{r}' = (1 + \delta f)\mathbf{r}$ $\delta\Pi = \delta f M$ (12)

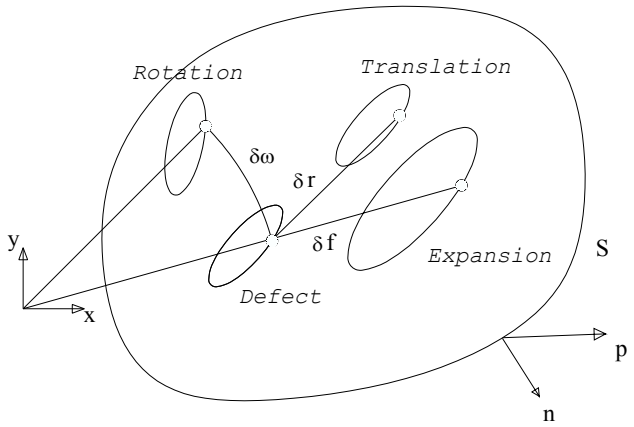

Figure 3 Various defect variations, translation, rotation and expansion, in an elastic domain.

PREDICTING THE DIRECTION OF CRACK PROPAGATION

Based on the energy release rates presented in the previous section, two proposals for predicting the direction of crack propagation are now made. The proposals are depicted in Fig.(4). The current crack tip is positioned such that the stresses are completely smooth. Firstly the crack tip is advanced a distance Δ in the tangential direction, a direction adhering to the $J_y=0$ or $L=0$ principles. For this predicted crack, the external load and the tractions in the process zone are determined, using the principle of superposition requiring the first principal stress to equal the tensile strength. Secondly, for this configuration the energy release rate with regard to the predicted crack is determined and the direction of crack propagation is derived from the virtual displacements of the predicted crack, as shown in Fig.(4). In proposal A the predicted crack is given virtual translations, whereas in proposal B the predicted crack is expanded and rotated. The energy release rate for the two proposals respectively is:

$$\delta\Pi = \begin{cases} J_x \delta r_x + J_y \delta r_y & \textit{Proposal A} \\ \Delta(M\delta r_x - L\delta r_y) & \textit{Proposal B} \end{cases} \tag{13}$$

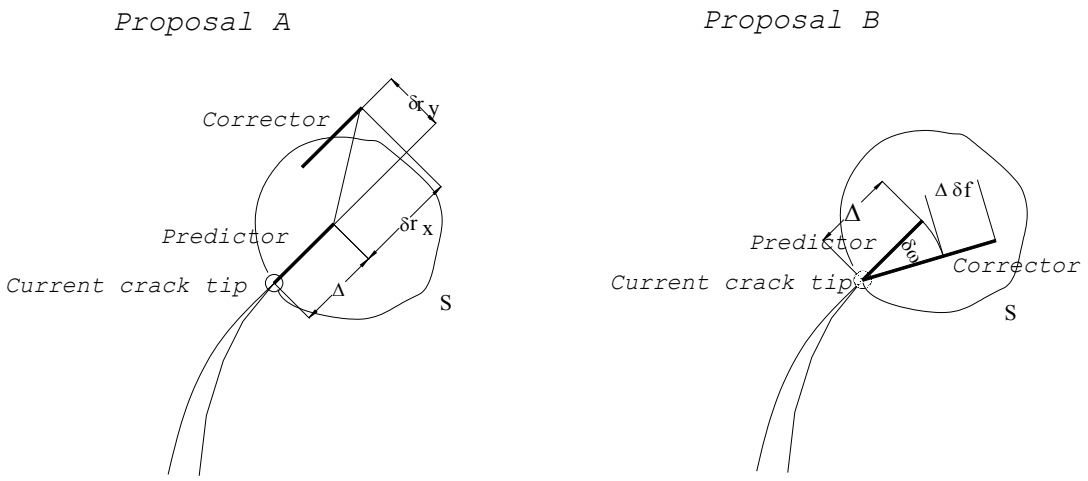

Figure 4 Proposals for predicting the direction of crack propagation.

From Eqn.(13), using the principle of maximum energy release rate, the direction of crack advance α is now determined from :

$$\alpha = Arctg \begin{cases} \dfrac{J_y}{J_x} & \text{Proposal A} \\ -\dfrac{L}{M} & \text{Proposal B} \end{cases} \tag{14}$$

For the beam studied previously, the direction of crack propagation is plotted in Fig.(5) for various directions of the crack predictor. It was seen previously that the minimum energy configuration was achieved for a crack tip position corresponding to approximately *v=20º*, with a rather flat functional variation within the interval *v=17° to v=22°*. With proposal A the corrected direction of crack propagation is rather insensitive to the direction of the crack predictor and lies in the interval *v=15.8-17.3º*, however, slightly below the expected direction of propagation. Proposal B is very sensitive to the direction of the crack predictor. However, within a range of ±3º, the proper direction of crack propagation is determined fairly accurately.

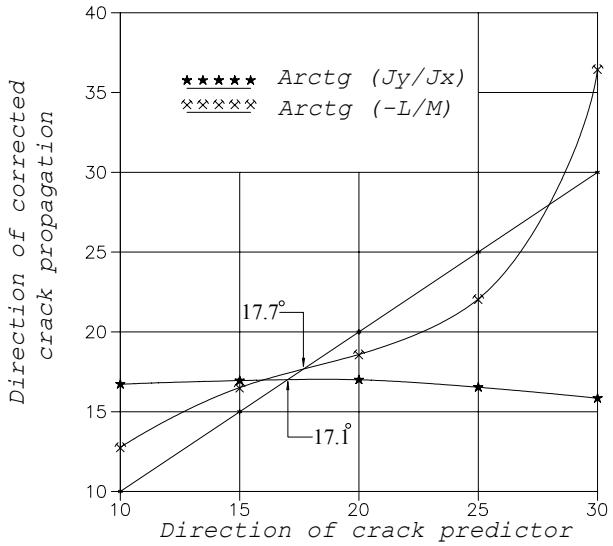

Figure 5 Prediction of the direction of crack propagation for various directions of the predictor.

CONCLUSION

In mixed mode fracture applying the fictitious crack model, the direction of crack propagation may be accurately predicted by evaluation of the *J, L* and *M* integrals. Directions based on $J_y=0$ and $L=0$ criteria are derived. These directions closely predict a path corresponding to minimum potential energy.

REFERENCES

1. Hillerborg, A, Peterson, P.E. : Analysis of crack formation and crack growth in concrete by means of fracture mechanics and finite elements. Cement and Concrete Research, 6:773-782,1976.
2. Peterson, P.E. : Crack growth and development of fracture zones in plain concrete and similar materials, TVBM-1006, thesis, Division of Building Materials, University of Lund, Sweden, 1981.
3. Ingraffea, A.R., Saouma, V. : Numerical Modeling of Discrete Crack Propagation in Reinforced and Plain Concrete, Fracture Mechanics of Concrete, Martinus Nijhoff Publishers, Dordrecht, pp.171-225, 1985
4. Eshelby, J.D. : Energy Relations and the Energy-Momentum Tensor in Continuum Mechanics, in Inelastic Behaviour of Solids, Ed. M.F. Kanninen et al, McGraw-Hill, New York, 1970, pp. 77-114.
5. Budiansky, B., Rice J.R. : Conservation Laws and Energy_Release Rates, J. Appl. Mech. No. 40, March 1973, pp. 201-203.
6. Brebbia, C.A., Telles J.C.F., Wrobel, L.C. : Boundary Element Techniques, Springer-Verlag, Berlin and New York, 1984.

REFERENCE: ICF100224OR

CRACK STABILITY IN UNIAXIAL TENSILE TESTS

C. Shi and J.G.M. van Mier

Micromechanical lab, Faculty of Civil Engineering and Geosciences,
Delft University of Technology, The Netherlands

ABSTRACT

In a series of uniaxial tensile test on single-edge-notched sandstone specimens, the effect of stiffness of the test set-up on the stability of crack propagation were studied. A specimen is loaded between cables to minimize restraint in the boundary conditions. Variation of cable length represents a variation of the machine stiffness. The cable length is 200 mm, 150 mm, 100 mm and 50 mm respectively. The tests were conducted under closed-loop deformation control. A new control system based on the maximum deformation rate near the notch was developed to achieve a stable test. A long distance microscope was employed to trace the crack propagation and the location of the crack tip. The results show that the cable length does affect the stability of crack propagation. In general, local instabilities occur inevitably for all four different cable lengths. In the cable test the loading situation is defined very well, and with known location of the crack tip, very accurate inverse analysis of softening stress-crack opening relation becomes possible.

KEYWORDS

Uniaxial tensile test, cable, deformation rate control, crack stability, energy balance, secondary flexure

INTRODUCTION

Many fracture models of brittle or quasi-brittle materials need tensile properties as input parameters. Uniaxial tensile tests are commonly used to determine these properties and parameters in such materials. The measurement of tension softening behavior often requires a single crack stably propagating through the specimen. In order to maintain stability after the peak load the tests can be controlled by LVDT's and the PID settings of the regulation amplifier. However, despite the feed back system, instability appears to occur frequently, like sudden load drop and snap-back in load-deformation diagrams. Crack stability in an experiment can be affected by several factors as composition of material, stiffness of test set-up, response of control system, boundary condition, loading rate, specimen size and measuring length of the control LVDT. Some attempts have been made to investigate the stability problems in a test of quasi-brittle material, such as [1,2,3,4]. However, the subject is still far from being well understood.

Freely rotating boundary conditions provide a clear loading condition for a specimen and allow for the propagation of a single crack. Flexure of hinged specimens has been identified as an important aspect of their post-peak failure behavior [5,6]. However, it is difficult to make perfect hinges and often some small constraint will be imposed in one or more directions. Since this constraint is fundamentally unknown it can be difficult to reproduce experimental results by fracture mechanics analysis or by means of finite

element computations. To further reduce the effects of constraints, cable supports have been developed and tested.

The objective of the study is to obtain a better understanding in the causes of instability in uniaxial tensile tests on brittle or quasi-brittle materials. A series of tensile tests has been performed on single-edge-notched sandstone specimens that were loaded between cables. Four different cable lengths were tested, which represent different stiffness of a test set-up. Some interesting phenomena observed from the test are reported.

SPECIMEN AND TEST SET-UP

Specimen Preparation

In this study, Yellow Felser sandstone was used to produce the specimens. This type of sandstone consists of clay matrix and aggregate particles (mostly quartz and feldspar) with size of 0.05 ~ 0.7 mm [7]. All the specimens were sawn from one large block in the same direction. The size of the specimen is 90*45*10 mm. The width is chosen as 45 mm in order to assure that the whole area where the crack is expected to propagate could be completely covered by the view of a long distance microscope. The thickness is chosen small so that three-dimensional effects could be avoided as much as possible. A single notch with 5 mm depth and 2 mm width was sawn for initiating a crack. After sawing, the specimens were stored in the lab for longer than 6 weeks in order to obtain constant moisture content. Furthermore, in order to improve visibility of the crack under a long distance microscope, the surfaces of the specimens were brightly painted before testing.

Test Set-up

The uniaxial tensile tests have been conducted in a servo-controlled hydraulic test machine (10 kN Instron 8872) as shown in figure 1. A specimen was glued on platens and loaded between two cables in order to eliminate boundary effect as much as possible, and to allow for the propagation of a single crack. In this series of test, four different cable lengths were used to investigate the effect of the stiffness of the set-up on the stability of crack propagation. The selected cable lengths are 200 mm, 150 mm, 100 mm, 50 mm, respectively. Three to five LVDT's were mounted on the specimen to measure the deformation in the middle region of a specimen where a crack is expected to develop. The vertical measuring length for a specimen is 15 mm. When five LVDT's were used, three of them were positioned on the rear face and two on the front face (microscope side) of the specimen to allow the microscope to follow the crack tip.

In addition, the vertical displacements of the top platen and bottom platen were measured in order to observe the rotation of the platens during crack propagation. For this purpose, two aluminum discs were connected to the rectangular specimen platen to provide for a sufficiently large measuring area. Three LVDT's are pointed to the upper disc and another three pointed to the bottom disc. A special frame has been built to mount these six LVDT's.

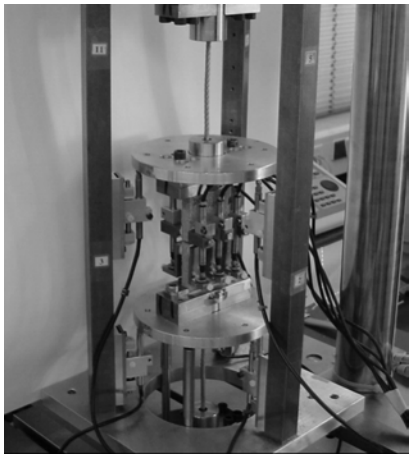

Figure 1: Test set-up

The control method plays a crucial role in the whole loading procedure to obtain a stable test. In earlier tests done by Van Vliet [9], the maximum deformation at any time was used as control variable. This system allowed for stable crack propagation studies in large sandstone and concrete specimens (up to 2400 mm long). Drawback was that manual adjustment of the PID settings was needed with decreasing stiffness of a fracturing specimen. In the present study, a new control system has been developed in which the system continuously compares the deformation rates of the two LVDT's close to the notch. Either of these LVDT's is active. The inactive LVDT will become active whenever its deformation rate is larger than that of the active LVDT plus some threshold value. For example, in Figure 2(a), LVDT 10 and LVDT 13 are the controlling LVDT's mounted next to the notch. LVDT 13 is at the front side of the specimen (microscope side) and LVDT 10 is at its rear side. Figure 2(b) shows which control signal being active at a specific moment in time. When output value is 0.95 the LVDT 10 provides the control signal and when the output value is 0.1 the LVDT 13 provides the control signal. The test results show that this control system gives a stable tensile test and it is even capable to handle snap-back behavior.

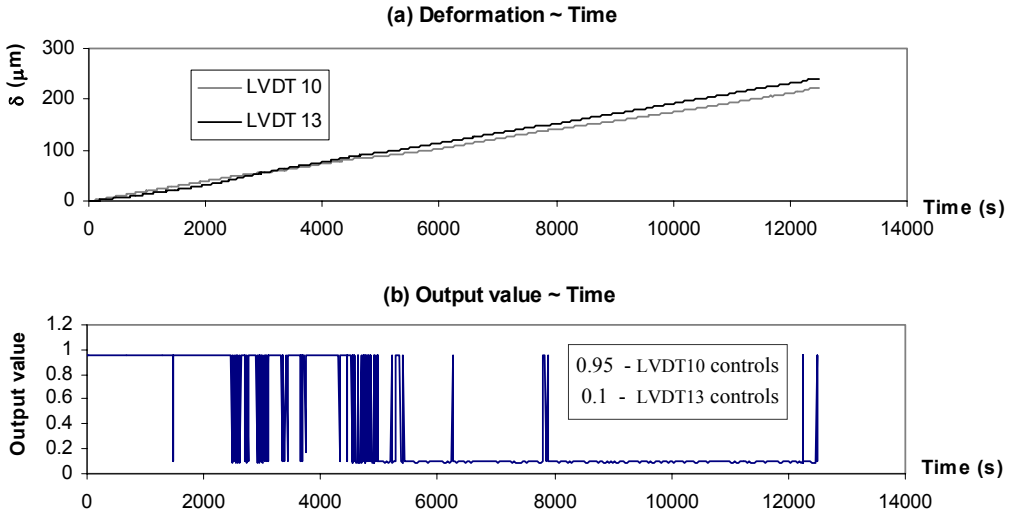

Figure 2: Control signal

In order to trace the crack propagation and location of the crack tip, a long distance optical microscope (Questar, QM100 MK-III) is employed in combination with a CCD camera. Reference [8] gives a detailed technical description on the Questar remote measuring system.

Horizontal Displacement of Cables

Theoretically, when a specimen is loaded in uniaxial tension through cables, no horizontal displacement will occur during crack opening. However, considering imperfections in the test set-up, it was felt that this should be checked. Therefore, a number of tensile tests were conducted in which the horizontal displacements of the cables were measured.

The longest cable (200 mm) was selected, which may show the most significant horizontal displacement. The horizontal displacements at the top of the lower cable were measured in-plane and out-of-plane of the specimen by means of two inductive transducers. This type of transducer uses a magnetic field to measure the distance between a cable and the head of the transducer. In order to distinguish between systematic errors and the real horizontal displacement of the cable, tests have been performed by loading both sandstone specimens (including cracking) and an aluminium specimen (deforming elastically without cracking). The results are shown in Figure 3 and table 1.

The results of sandstone tests show that the measured horizontal displacements of the lower cable are much smaller than in the aluminium tests. This indicates that the opening of a crack in the specimen does not introduce a horizontal displacement of the cables. The measured displacements are due to the elongation and rotation of the cable under tensioning. Therefore, in the subsequent experiments and data interpretation, it is assumed that the external load is properly aligned during the whole loading process.

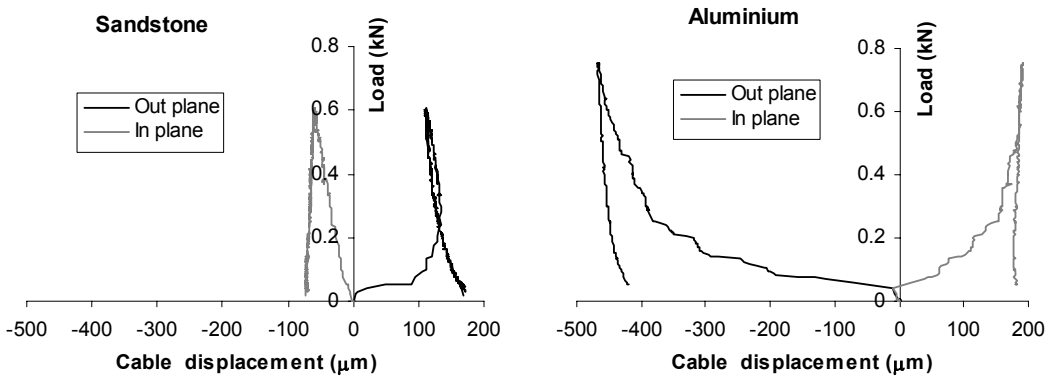

Figure 3: Load-cable displacement diagrams

TABLE 1
CABLE DISPLACEMENTS FROM TESTS OF ALUMINIUM AND SANDSTONE

Material	Test No.	Horizontal displacement of the cable (μm)	
		In-plane	Out-of-plane
Aluminium	Cable02	183.3	----
	Cable03	196.7	449.4
Sandstone	SS11	50.0	162.1
	SS13	73.4	171.3

EXPERIMENTAL RESULTS AND DISCUSSIONS

To investigate the effect of the cable length on stability of crack propagation, a series of 37 tests has been performed with cable length of 200 mm, 150 mm, 100 mm and 50 mm respectively. In these tests, the specimens were loaded in uniaxial tension under a constant loading rate of 0.02 μm/s until a sudden failure occurred. The following shows the typical results obtained from the successful tests.

Crack Propagation

For all the tests, load-deformation diagrams were recorded, which show that the shapes of the curves are not visibly affected by the cable length. By means of a remotely controlled long distance microscope, the crack path was followed during the whole loading procedure. The location of the crack tip was recorded under the selected magnification of the microscope. In most of the tests the cracks initiated at the notch and propagated straight through the middle area of the specimens, as shown in Figure 4. In the figure, the image has been enhanced to make the crack better visible. No correlation between the crack pattern and the cable length was observed. When the maximum deformation measured near the notch is approximately 150 μm, the crack propagation speed slows down gradually. Furthermore, when the deformation reaches about 200 μm, the crack opening continues to increase, but the crack tip appears to stop almost completely. Apparently, at this stage the stiffness of the intact segment becomes very low, and the eccentricity is large. Bending dominates the specimen behavior. The two segments of the specimen beyond the crack mainly rotate around the center of the intact area.

Figure 4: Example of the recorded crack pattern

Representative load-deformation diagrams for the tests using four different cable lengths are presented in Figure 5 (a) to (d). In these curves, δ is the average of the deformations measured by the two LVDT's close to the notch.

In general, it appears that the longer cables (200 and 150 mm) give a more stable crack propagation and larger crack opening at failure than the shorter ones (100 and 50 mm). This could be explained from the (small) flexural stiffness of the cables. Particularly the short cables have some flexural stiffness and provide some constraint in the out-of-plane direction.

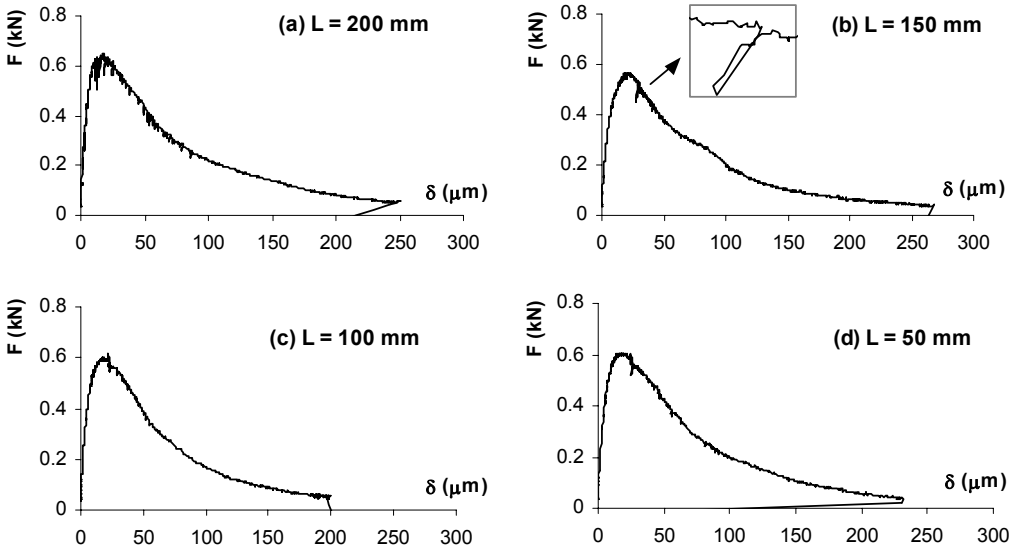

Figure 5: Load-deformation diagrams for four different cable lengths and an example of enlarged instability (snap-back) shown in the inset

Instability Phenomena

Local instabilities are visible in a load-deformation diagram as small dips. Tests with longer cables appeared to contain more instability than tests with the shorter cables (Figure 5). Evidently, in the longer cables more energy is stored which makes the set-up less sensitive to corrections of the control system. The control system first attempts small corrections but when these show to have little effect it will over-react and reduce the force strongly, producing a dip. In all tests the tail parts of the curves show to be smoother than the rest of the diagram. The reason is that at this stage the residual stiffness of the specimen becomes small due to the development of the crack, the stiffness of the cables does not dominate the control system any longer. The current control system therefore was considered an improvement to an earlier control system based on the maximum deformation in specimens used in [9].

A common feature of all load-deformation curves is that substantial drops are present around the peak-load. This indicates that the system experiences considerable changes at this stage. Just before the main crack formed, the biggest amount of strain energy is stored in the system of specimen and cables that requires higher sensitivity to react any sudden changes. When a crack is initiated a qualitative change occurs in the specimen. A big amount of energy releases suddenly at a high rate, and the system is not fast enough to follow the correction of the control system. As a consequence, over-reaction occurs in the system that results in bigger drops in the load-deformation diagrams.

Another distinct point showing instability is at the final stage just before failure. This behavior is possibly dominated by the secondary bending moment formed in the intact area in front of the crack tip due to gradually increased load eccentricity during crack propagation. In a uniaxial tensile test between cables, the stress distribution at the cross section of a crack can be schematized as shown in Figure 6 (a), (b) and (c) for subsequent stages of crack propagation. The stress at crack tip is assumed as tensile strength according to the fictitious crack model. Stress in the intact area in front of the crack tip is distributed linearly, whereas in the area behind the crack tip, the stress distribution follows softening behavior.

As the location of the applied force in the cable is exactly known (hardly any horizontal displacement of the loading cables were observed) and the location of the crack tip at failure is known to some accuracy, the test can be used for extracting softening data of the material to a high degree of accuracy. At present the analysis is in progress. As a result of the eccentric loading on the cracked specimen (Figure 6c) the area in front of the visible crack tip is loaded by the force F_{int} and the bending moment M_{int}. This situation will be used to assess the conditions just before final catastrophic failure.

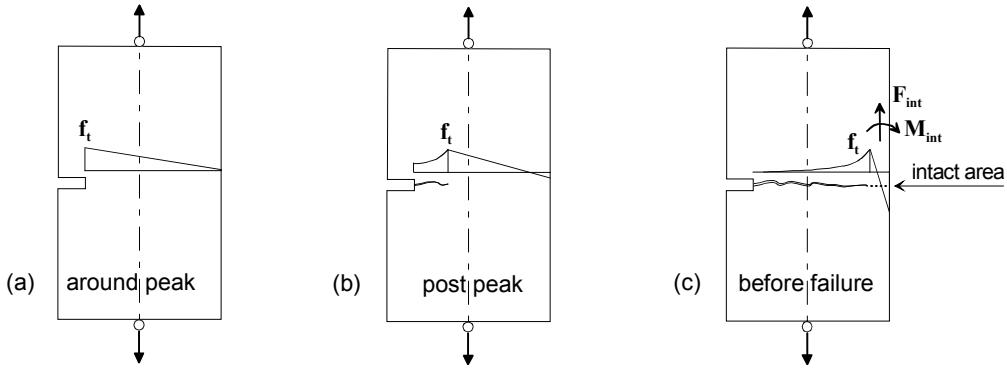

Figure 6: Stress distribution at different crack stages

CONCLUSIONS

1. The current control system, which is based on the rate of crack opening at the notch tip, is very well suited for obtaining stable load-deformation diagrams under uniaxial tension irrespective of the machine stiffness. The machine stiffness was varied through a variation of the length of the cables through which the specimen was loaded.
2. The tests showed local instabilities, which were successfully handled by the control system except for the catastrophic failure at large crack openings.
3. The loading situation in the specimen is very clear. The point of load application is well defined, and since the tip of the crack is known to some accuracy, inverse analysis of tension softening properties of the tested material is possible with high accuracy.

ACKNOWLEDGEMENTS

This research was supported by Dutch Technology foundation (STW) and the Priority Program Materials Research (PPM). The authors are indebted to Allard Elgersma for his invaluable assistance in carrying out the experiments.

REFERENCES

1. Tandon, S., Faber, K.T. and Bazant, Z.P. (1995). Mat. Res. Soc. Symp. Proc. Vol. 370, pp. 387-396.
2. Van Mier, J.G.M. and Schlangen, E. (1989). In: Fracture of Concrete and Rock – Recent Developments, pp. 387-396, Shah, S.P., Swartz, S.E. and Barr, B. (Eds). Elsevier, London/New York.
3. Hillerborg, A. (1989). In: Fracture of Concrete and Rock – Recent Developments, pp. 387-396, Shah, S.P., Swartz, S.E. and Barr, B. (Eds). Elsevier, London/New York.
4. Zhou, F.P. (1989). Report, Lund Institute of Technology, Sweden.
5. Van Mier, J.G.M. (1997). Fracture processes of concrete, CRC Press, Boca Raton (FL).
6. Cattaneo, S. and Rosati, G. (1999). Magaz. Concr. Res. 51, No. 5, 365.
7. Visser, J.H.M. (1998). Ph.D. Thesis, Delft University of technology, Netherlands.
8. Vervuurt, A.H.J.M. (1997). Ph.D. Thesis, Delft University of technology, Netherlands.
9. Van Vliet, M.R.A. and Van Mier, J.G.M. (1999), Int.J.Fract., 95, 195.

CRACK TIP DEFORMATION AND TOUGNESS IN POLYPROPYLENES

S. Seidler, T. Koch[1], I. Kotter and W. Grellmann[2]

[1] Inst. of Materials Science and Testing, Vienna University of Technology,
Karlsplatz 13, A-1040 Vienna, Austria
[2] Inst. of Materials Science, Martin-Luther University Halle-Wittenberg,
D-06099 Halle (S.), Germany

ABSTRACT

In-situ measurements were done to get information about crack tip deformation processes in different polypropylenes. For the measurements a conventional fracture mechanics test arrangement for three point bending tests coupled with a stereo microscope and a camera was used. In this way a directly correlation of load and deflection with crack extension and crack tip opening displacement is possible and crack resistance curves (R-curves) can be achieved. On principle the method is a single specimen method.
The influence of ethylene content and elastomer content on the crack opening displacement at the crack initiation point is demonstrated on different polypropylene (PP) materials: homopolymers, random copolymers, blends and heterophasic copolymers.

KEYWORDS

fracture mechanics, physical crack initiation, single specimen method, polypropylene

INTRODUCTION

The knowledge of the physical crack initiation process is the basis for the quantification of deformation determined fracture processes. It is generally well known that the fracture process is initiated by the crack tip blunting and stretch zone formation. The crack initiation occurs by opening the crack tip after exceeding a critical deformation. The blunting process depends on stress state, microstructure, testing velocity and temperature. Therefore, polymers show no unique crack tip blunting and initiation behaviour by reason of their structural variety and their specific critical behaviour which depends on testing velocity and temperature.
Crack tip blunting and initiation processes in polymers are a combination of crazing, local shear deformation and voiding, which depends on the structure, the material state and the testing conditions. For this reason crack initiation processes of polymers are not inevitable in accordance with the classical stretch zone concept [1,2]. Different investigations about crack tip blunting and crack tip deformation processes are done, e.g. in [3-6] for amorphous and in [3,7-13] for semicrystalline polymers. The process of transition from a blunted to a growing stable crack is controversial discussed for quite some time. In principle two mechanisms of crack tip deformation processes are provable. Both are influenced by the molecular structure. Results of different investigations exist which include problems of stretch zone determination on fracture surfaces [14-17].

EXPERIMENTAL

Materials

Different polypropylene (PP) materials were investigated: homopolymers, polyethylene (PE)/PP random copolymers, heterophasic copolymers with different interparticle distances A, and PP/EPR (ethylene propylene rubber) blends with different EPR content (Table 1). The average particle diameter of the elastomeric phase in the blends (≈ 2 μm) and in the heterophasic copolymers (≈ 1.5 μm) are comparable. Additionally the EPR phase of the heterophasic copolymers includes lamellas of crystalline PE [18,19].

TABLE 1
INVESTIGATED PP MATERIALS

term	material	description
PP 1, 2	homopolymers	polypropylene
RaCo 1, 2	random copolymers	4 mol.-% and 8 mol.-% ethylene
Blend 1, 2	PP/EPR blends	PP 1/EPR = 85/15 and 80/20
HeCo 1, 2	heterophasic copolymers	matrix PP 2, A = 2.12 μm and A = 1.38 μm

In-situ testing

For the in-situ tests a conventional fracture mechanics test arrangement for three-point bending tests was coupled with a stereo microscope and a camera. Uniform time-scale enables direct correlation between the load-time and deflection-time signals and the crack extension as well as the crack tip opening displacement.
Injection moulded single edge notched bend specimens with the dimensions 80 x 10 x 4 mm^3 were used. The specimens were notched with a razor blade. To prevent shear lips side-grooves (radius r = 0.1 mm) were mill-cut. Measurements were done using a support span of 40 mm and a strain rate of 0.001 s^{-1}.
The crack tip opening displacement (CTOD) δ and the stable crack growth Δa were taken from the recorded videos, J values were determined from the measured load-deflection curves (Eqn. 1) according to [20]:

$$J = \eta_{el}\frac{A_{el}}{B(W-a)} + \eta_{pl}\frac{A_{pl}}{B(W-a)}\left\{1 - \frac{(0.75\eta_{el}-1)\Delta a}{(W-a)}\right\}, \quad (1)$$

where A_{el} and A_{pl} are the elastic and the plastic part of generally deformation energy and η_{el} and η_{pl} are geometry functions.
The in-situ investigation allows the separation of the crack tip blunting process and the crack growth process. The blunting line was fitted using a linear equation (2). Crack growth curve was fitted with the help of a power law (3).

$$J = c\,\Delta a \quad (2)$$

$$J = C_1 (C_3 + \Delta a)^{C_2} \quad (3)$$

The crack initiation point was determined visually during analysing the video. This results were compared with results from δ-Δa curves, where the intersection of blunting line and crack growth curve was defined as crack initiation point.
For the investigation of deformation behaviour and damage in the crack tip region sections of about 5 μm were microtomed at – 100 °C using a MICROM microtome and a glassy knife. The investigated specimens were both fully unloaded and fixed in several bended states. The crack tip region of the latter ones was fixed with an embedding resin and cutting was done after curing of the resin. Microscopical observations were done at a ZEISS Axiolab Pol using crossed polars and a SEM PHILIPS XL 30.

RESULTS

Typical results of the measurements are shown in Fig. 1. Received load-deflection curves were normalized to the effective area, which depends on the actual crack length. The homopolymer breaks unstable at a crack length of about 0.6 mm whereas the modified materials do not break under the testing conditions chosen. Analysing the recorded video the crack initiation points were defined (see the arrows in Fig. 1). Crack initiation takes places below the maximum of the curves, but clearly above the linear region.

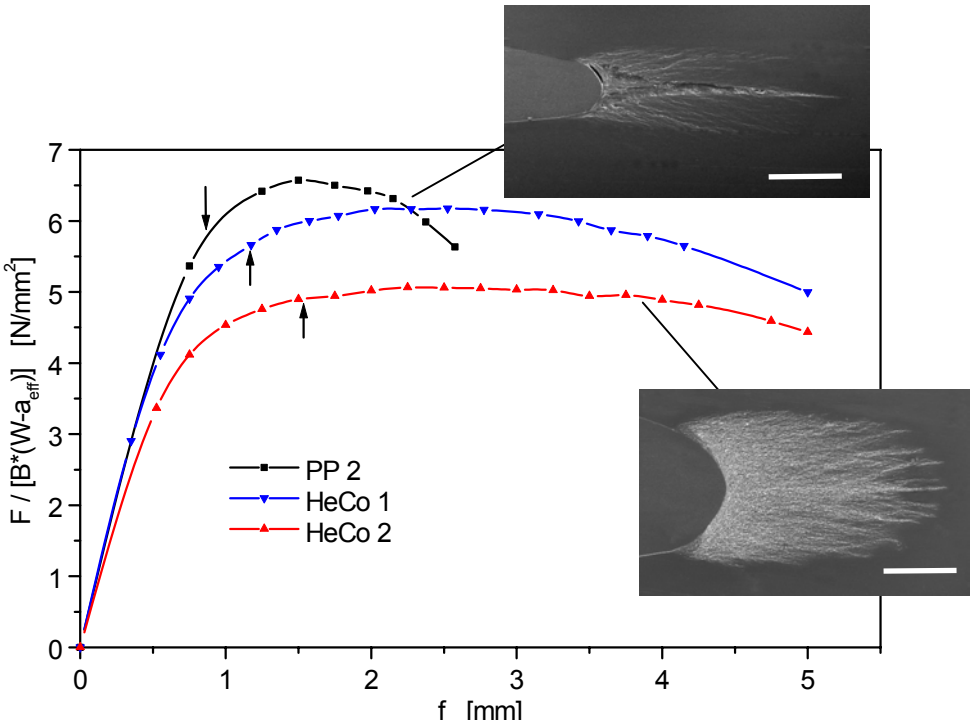

Figure 1: Normalized load vs. deflection for several PP-copolymers and the PP-homopolymer. Arrows indicate the visually defined crack initiation point. Scale bar length: 1 mm.

From the in-situ determined δ values and crack lengths δ-Δa curves can be plotted and crack initiation values were determined [21]. This single specimen method allows the determination of fracture mechanics values without relaxation and blunting effects, which is the main advantage in comparison with the partial unloading method. Furthermore the crack lengths are measured, not calculated.
CTOD at the in-situ determined crack initiation point depends on morphological and structural parameters (Fig. 2). For the heterophasic copolymers there is a critical value at a interparticle distance of about 2 µm.

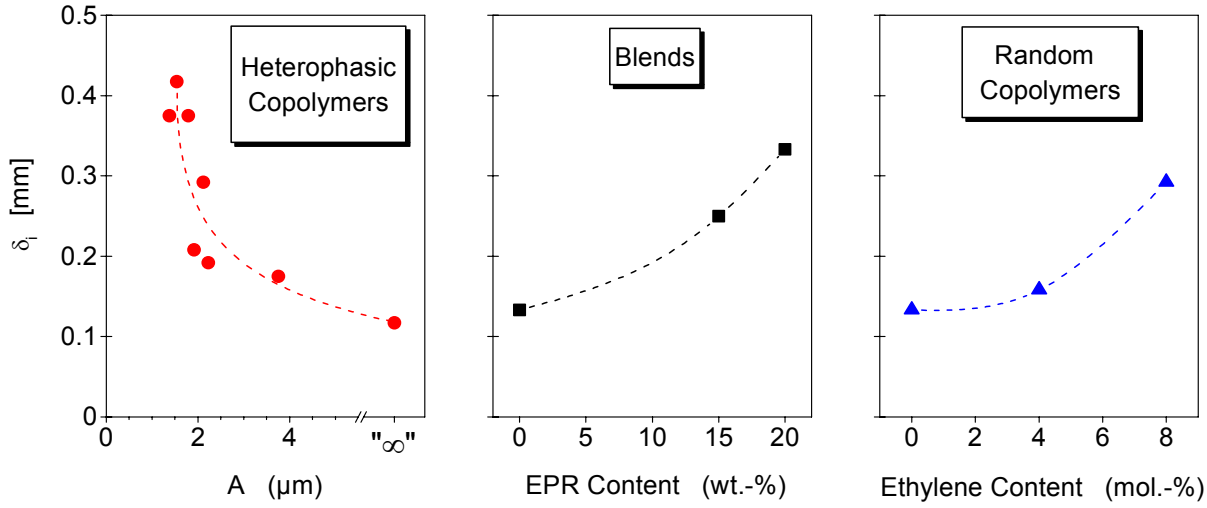

Figure 2: CTOD at the in situ determined crack initiation point δ_i in dependence on structural parameters.

Undergoing this value leads to a strong increase of δ_i –values. In dependence on EPR- and ethylene content the crack initiation values increase. Critical values are not able to determine due to the less number of investigated materials.
In conventional fracture mechanics tests the CTOD at crack initiation can be determined from δ-Δa curves as the intersection of the blunting line and the crack growth curve. Therefore the comparison of the CTOD values defined from δ-Δa curves with the visually defined ones (Fig. 3) is of a special interest. This procedure serves to check the experiment. For most of the investigated materials there is a good agreement between them.

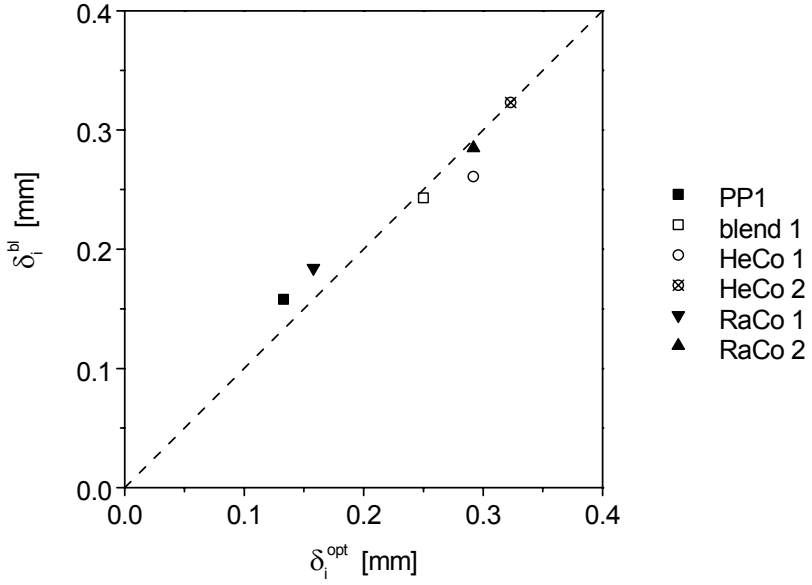

Figure 3: CTOD from δ-Δa curve δ_i^{bl} in dependence on visually defined CTOD at crack initiation point, δ_i^{opt}.

Figure 4 demonstrates that for polymers the elastic and viscoelastic deformation parts of general CTOD are very high. That means, that measurement of stretch zone dimensions on fracture surfaces can lead to an underestimation and blunting lines determined with this method are also underestimated. The quantity of the "error" in the first place depends on material and loading conditions.

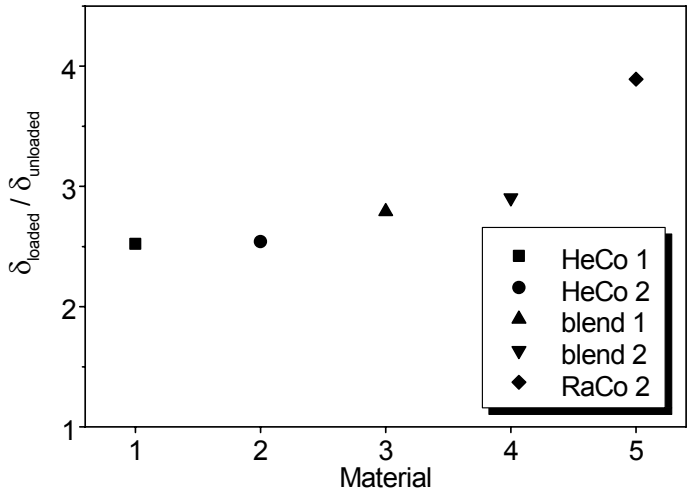

Figure 4: Ratio of the loaded and of the fully unloaded specimen for several PP-materials at a deflection of 5 mm.

The fracture process of the investigated PP- materials is demonstrated in Figure 5. In the first stage of blunting which corresponds to a seeming linear material behaviour in the load-deflection diagrams first damage occurs in front of the crack tip. For the homopolymers (Fig. 5/1a and b) and random copolymers deformations are of craze-like type. The whole blunting process (Figs. 5/1c and 5/2a) takes place without

translation of the crack tip and includes beside the seeming linear material behaviour a not neglectable non-linear part (see Fig. 1, position of the crack initiation points). The process is more a stretching in tension direction than a curving. Strong, large craze-like deformations are visible not only in the centre but also at the sharp edges between the blunted tip and the flanks of the initial razor notch (Figure 5/1c). The pre-crack flanks control shape of the large middle craze. The crack initiation is characterized by a more "gradual" than an abrupt transition from blunting to growing. The shape of the crack tip does not change clearly. The moving crack tip is not very sharp. Figures 5/1d and 5/2b show growing cracks in the different materials.

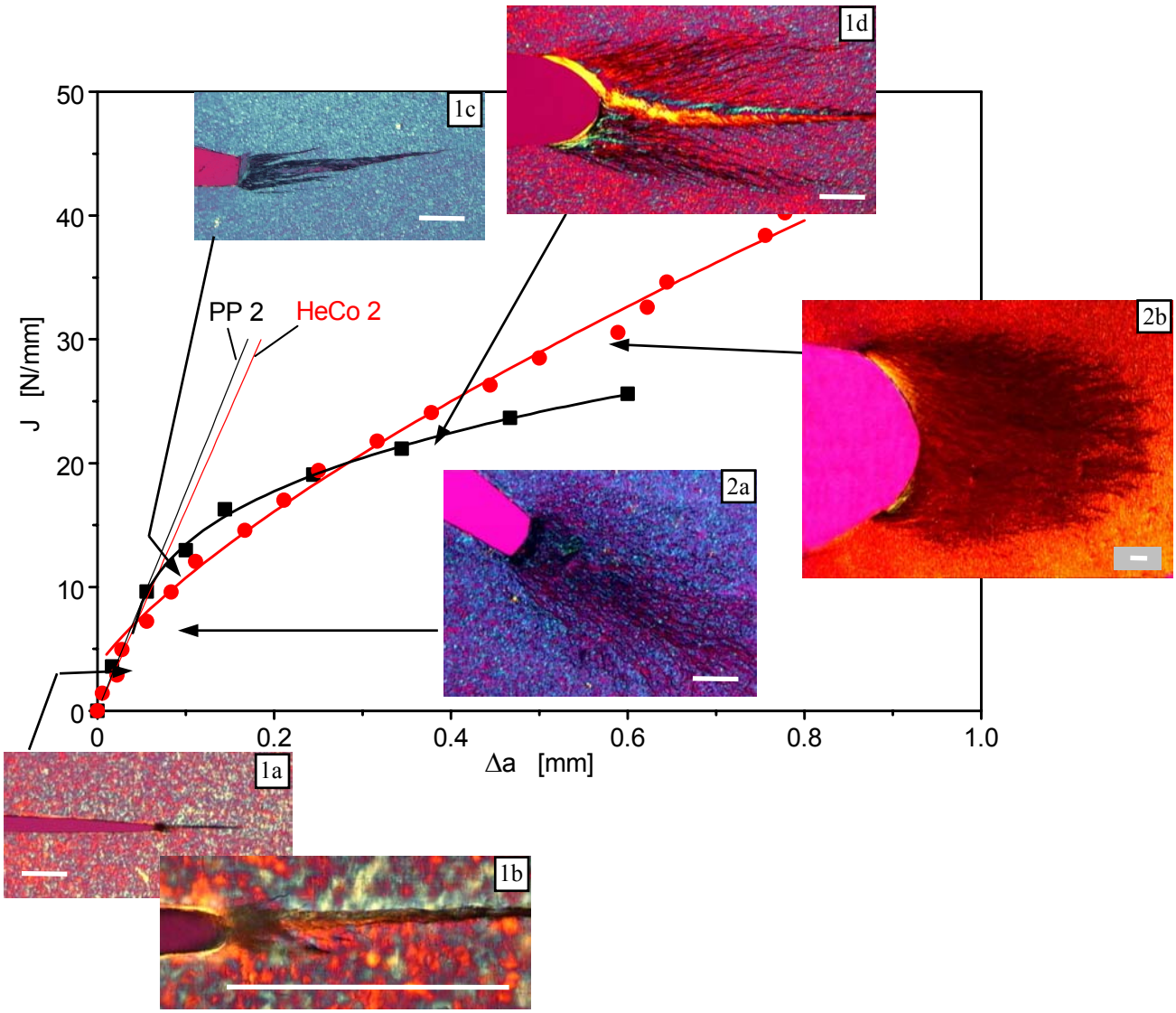

Figure 5: J-Δa curves of a PP-homopolymer and a heterophasic copolymer. Deformation states in the crack tip region: (1 a-d) homopolymer; (2 a,b) copolymer; scale bar length: 200 µm.

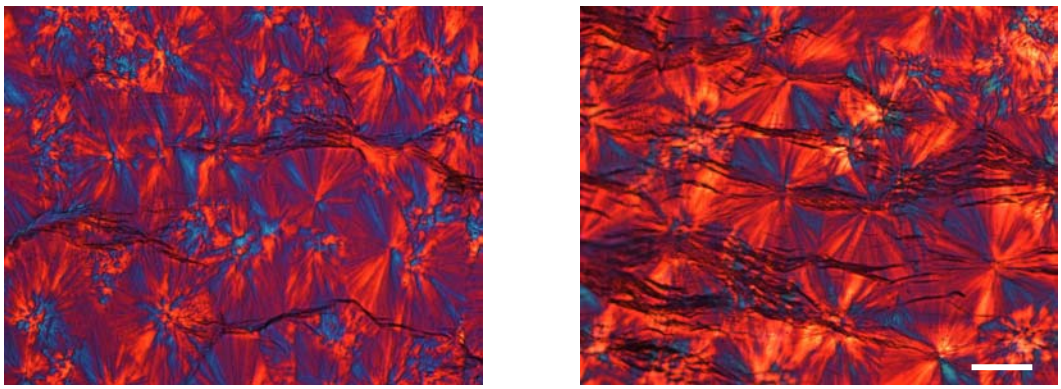

Figure 6: Crazing in the damaged region in front of the crack tip (scale bar length 50 µm)

Craze and microcrack paths in front of the crack tip are trans- and interspherulithic, which can be seen in Figure 6. For the elastomer modified materials the shape of the damaged region in front of the crack tip is different compared to the homopolymers (Figures 5/2a and b). Its shape is circular like and in the SEM failure of the rubber/matrix interphase can be seen. So-called "croids" are forming [18].

CONCLUSIONS

In-situ testing using a stereomicroscope is a suitable method to get information about deformation behaviour in front of the crack tip. It can be used as a single specimen method because the crack front of the side-grooved specimens is nearly linear, not round shaped.
Crack opening displacement at the visually defined crack initiation point was in good agreement with the CTOD determined from intersection of blunting line and fitted δ-Δa curve. The obtained crack initiation values depend on the ethylene content and on the elastomer content for the random copolymers and the blends or heterophasic copolymers respectively. For all materials crack initiation takes place without a clear change of tip shape. No stretch zone could be proved on fracture surfaces.
In homopolymers and random copolymers there is a crazed region in front of the crack tip in the elastomer modified materials, i. e. blends and heterophasic copolymers, however "croiding" was found.

REFERENCES

[1] Seidler, S. and Grellmann, W. (1995). In: *Impact and Dynamic Fracture of Polymers and Composites*., pp. 171-179, Williams, J. G. and Pavan, A. (Eds.), ESIS 19
[2] Seidler, S. and Grellmann, W. (1994). Proceedings of the 9th International Conference on Deformation, Yield and Fracture of Polymers, Churchill College, Cambridge, UK, 11.-14. 4. 1994, P108/1-P108/4
[3] Bandyopadhyay, S. (1984). *J. Mat. Sci. Lett*. **3**, 39-43
[4] Theocaris, P. S. et al (1989). *J. Mat. Sci*. **24**, 1121-1127
[5] Theocaris, P. S. and Kytopoulos, V. (1991). *J. Mat. Sci*. **26**, 3575-3580
[6] Tung, I. C. (1991). *Polym. Bull*. **25**, 253-255
[7] Mouzakis, D. E. and Karger-Kocsis, J. (1998). Proceedings of the EPS'98 „European Conference on Macromolecular Physics: Morphology and Micromechanics of Polymers" Merseburg, Germany, 45-48
[8] Bhattacharya, S. K. and Brown, N. (1984). *J. Mat. Sci*. **19**, 2519-2532
[9] Lu, X. et al (1991). *J. Mat. Sci*. **26**, 917-924
[10] Brown, N. et al (1991). *Macromol. Chem.: Macromol. Symp*. **41**, 55-67
[11] Dekker, J. C. and Bakker, A. (1994). Proceedings of the 10th European Conference on Fracture (ECF 10), Berlin, 20-23.9., Vol. 1, 571-580
[12] Strebel, J. J. and Moet, A. (1995). *J. Polym. Sci. Part B* **33**, 1969-1984
[13] Riemslag, A. C. (1997). Thesis, Delft University of Technology, Delft University Press
[14] Narisawa, I. and Takemori, M. T. (1988). *Polym. Eng. Sci*. **28**, 1462-1468
[15] Narisawa, I. and Takemori, M. T. (1989). *Polym. Eng. Sci*. **29**, 671-678
[16] Huang, D.D. and Williams, J.G. (1990). *Polym. Eng. Sci*. **30**, 1341-1344
[17] Huang, D. D. (1991). Proceedings of the 8th International Conference on Deformation, Yield and Fracture of Polymers, Churchill College, Cambridge, UK, 8.-11. 4.,
[18] Starke, J.U. et al (1998). *Polymer* **39**, 75-82
[19] Grellmann, W., Seidler, S., Jung, K., Kotter, I., *J. Appl. Polym. Sci.,* in press
[20] Seidler, S. (1998). *Fortschr. Ber. VDI*. No. 231. Series 18
[21] Seidler, S. et al (2000). Proceedings of the 13th European Conference on Fracture (ECF 13), San Sebastian, Spain, 6.9.-9.9.2000, Proceedings – CD- ROM, Polymer and Composites, No. 12

ORAL/POSTER REFERENCE: ICF100373OR

CRACK VELOCITY DEPENDENT TOUGHNESS IN RATE DEPENDENT MATERIALS

Chad M. Landis[1], Thomas Pardoen[2] and John W. Hutchinson[3]

[1]MEMS, MS 321, Rice University, PO Box 1892, Houston, TX 77251
[2]Département des Sciences des Matériaux et des Procédés, Université catholique de Louvain, PCIM, Lovain-la-Neuve, Belgium
[3]DEAS, Harvard University, Cambridge, MA 02138

ABSTRACT

Mode I, quasi-static, steady state crack growth is analyzed for rate dependent materials under plane strain conditions in small scale yielding. The solid is characterized by an elastic-viscoplastic constitutive law and the plane ahead of the crack tip is embedded with a rate dependent fracture process zone. The macroscopic work of fracture of the material is computed as a function of the crack velocity and the parameters characterizing the fracture process zone and the solid. With increasing crack velocity a competition exists between the strain rate hardening of the solid, which causes elevated tractions ahead of the crack tip that tend to drive crack propagation, and the rate strengthening of the fracture process zone which tends to resist fracture. Results for material parameters characteristic of polymers show that the toughness of the material can either increase or decrease with increasing crack velocity. To motivate the model, the cohesive zone parameters are discussed in terms of failure mechanisms such as crazing and void growth ahead of the crack tip. The toughness of rubber modified epoxies is explained by employing the fracture model along with micromechanical void cell calculations.

KEYWORDS

Steady state fracture, elastic-viscoplastic material, cohesive zone model

1. INTRODUCTION

In this work the toughness of a rate dependent material is determined as a function of certain intrinsic material properties. An elastic-viscoplastic constitutive law characterizes the bulk material deformation and a rate dependent cohesive zone law describes the separation ahead of the crack tip. A steady state finite element formulation, Dean and Hutchinson [1], is used to determine the stress and strain fields around the moving crack and to relate the critical applied energy release rate to the intrinsic material toughness.

Figure 1 is a schematic of a crack propagating in an elastic-plastic solid under Mode I, plane strain, small scale yielding, steady state conditions. The displayed shape of the plastic zone is the result of a calculation for an elastic-perfectly plastic, rate independent material. The plastic zone shape for rate dependent materials is similar in both size and shape. Far from the crack tip the stresses follow the Mode I elastic *K* field. As the crack propagates through the solid the crack tip is surrounded by active plasticity, elastic unloading and plastic reloading sectors, Drugan *et al*. [2]. Far behind the crack tip there is a wake of residual plastic strains where the material has unloaded elastically.

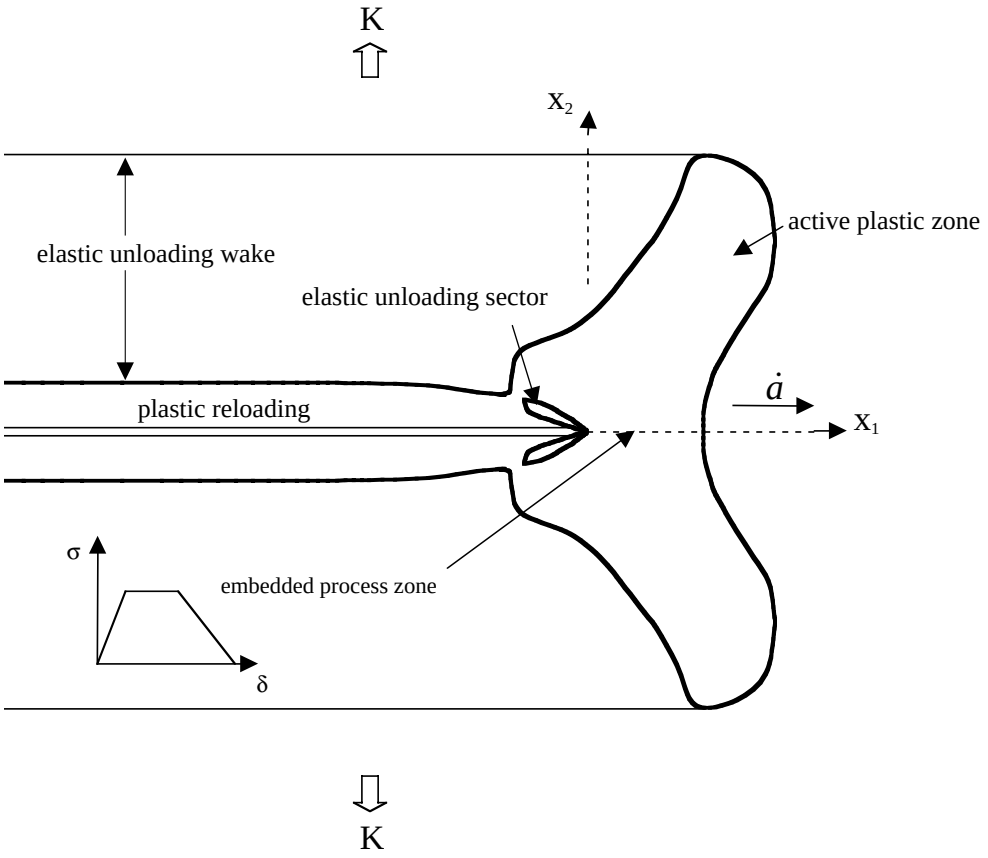

Figure 1: The plastic zone near a steadily propagating crack in an elastic-perfectly plastic material.

2. GOVERNING EQUATIONS

We adopt a rate dependent elastic-viscoplastic constitutive model of the form used by Marusich and Ortiz [3] and Xia and Shih [4],

$$\left(1+\frac{\dot{\bar{\varepsilon}}^p}{\dot{\varepsilon}_o}\right)=\left(\frac{\bar{\sigma}}{\sigma_y}\right)^m, \; if \; \bar{\sigma} \geq \sigma_y \tag{1}$$

$$\dot{\bar{\varepsilon}}^p = 0, \text{ if } \bar{\sigma} < \sigma_y \tag{2}$$

where $\bar{\sigma} = \sqrt{\frac{3}{2} s_{ij} s_{ij}}$ is the effective stress, $s_{ij} = \sigma_{ij} - \frac{1}{3}\sigma_{kk}\delta_{ij}$ is the deviatoric stress tensor, σ_y is the static tensile yield strength, $\dot{\bar{\varepsilon}}^p = \sqrt{\frac{2}{3}\dot{\varepsilon}_{ij}^p \dot{\varepsilon}_{ij}^p}$ is the effective plastic strain rate, $\dot{\varepsilon}_o$ is a reference plastic strain rate and *m* is the plastic strain rate sensitivity exponent.

The components of the plastic strain rate are then given by

$$\dot{\varepsilon}_{ij}^p = \frac{3}{2}\dot{\bar{\varepsilon}}^p \frac{s_{ij}}{\bar{\sigma}} \tag{3}$$

Finally, the elastic strain rates are given by

$$\dot{\varepsilon}_{ij}^e = \frac{1+\nu}{E}\dot{\sigma}_{ij} - \frac{\nu}{E}\dot{\sigma}_{kk}\delta_{ij} \tag{4}$$

where *E* and ν are the isotropic Young's modulus and Poisson's ratio. Notice that this form of the constitutive law allows for a well-defined region of elastic response which is required for the small scale yielding approximation to be used.

The rate dependence for the fracture process zone is taken to follow a similar functional form as that for the bulk solid. In order to facilitate the finite element calculations it is assumed that there is always an initial linear portion in the traction-separation law. Hence, the crack opening displacement, δ, is the sum of an elastic (linear) and a plastic part. The cohesive traction obeys

$$\dot{t} = \hat{\sigma}\lambda_1 \frac{\left(\dot{\delta} - \dot{\delta}^p\right)}{\delta_c} \tag{5}$$

where λ_1 is a shape parameter of the static traction-opening law (see Tvergaard and Hutchinson [5]), $\hat{\sigma}$ is the peak stress of the static form of the traction-separation law and δ_c is the critical crack opening where tractions drop to zero. The second shape parameter of the traction-separation law is λ_2. The plastic opening rate, $\dot{\delta}^p$, is described by

$$\left(1 + \frac{\dot{\delta}^p}{\dot{\delta}_o}\right) = \left(\frac{t}{t_o\left(\delta^p\right)}\right)^q \text{ for } t > t_o\left(\delta^p\right) \tag{6}$$

$$\dot{\delta}^p = 0 \text{ for } t < t_o\left(\delta^p\right) \tag{7}$$

$$t = 0 \text{ if } \delta > \delta_c \tag{8}$$

where $\dot{\delta}_o$ is a characteristic crack opening rate, *t* is the normal traction acting on the crack plane, *q* is the rate exponent of the fracture process zone and $t_o\left(\delta^p\right)$ represents the static form of the traction-separation law. We also impose the condition (8) requiring that the total crack opening, δ, must always be less than the critical crack opening, δ_c, for all applied opening rates otherwise the traction must drop to zero. A more detailed description of the traction-separation law can be found in Landis *et al*. [6].

3. RESULTS

Dimensional analysis suggests that the macroscopic steady state toughness depends on the following dimensionless parameters

$$\frac{\Gamma_{ss}}{\Gamma_o} = \overline{\Gamma}\left(\frac{\dot{a}}{R_o\dot{\varepsilon}_o}, \frac{\hat{\sigma}}{\sigma_y}, \frac{\dot{\delta}_o}{\delta_c\dot{\varepsilon}_o}, m, q, \frac{\sigma_y}{E}, \nu, \lambda_1, \lambda_2\right) \tag{9}$$

where $\dot{a}$ is the crack velocity and

$$R_o = \frac{1}{3\pi}\left(\frac{E}{1-\nu^2}\right)\frac{\Gamma_o}{\sigma_y^2} = \frac{1}{3\pi}\left(\frac{K_o}{\sigma_y}\right)^2 \tag{10}$$

is the approximate size of the plastic zone when the applied energy release rate, K, is equal to K_o, where K_o is related to Γ_o through (10). Previous studies on rate independent materials have demonstrated that the last 4 parameters in (9) are of secondary importance. For this study the parameters $E/\sigma_y = 50$, $\nu = 0.35$, $\lambda_1 = 0.15$ and $\lambda_2 = 0.5$ are used.

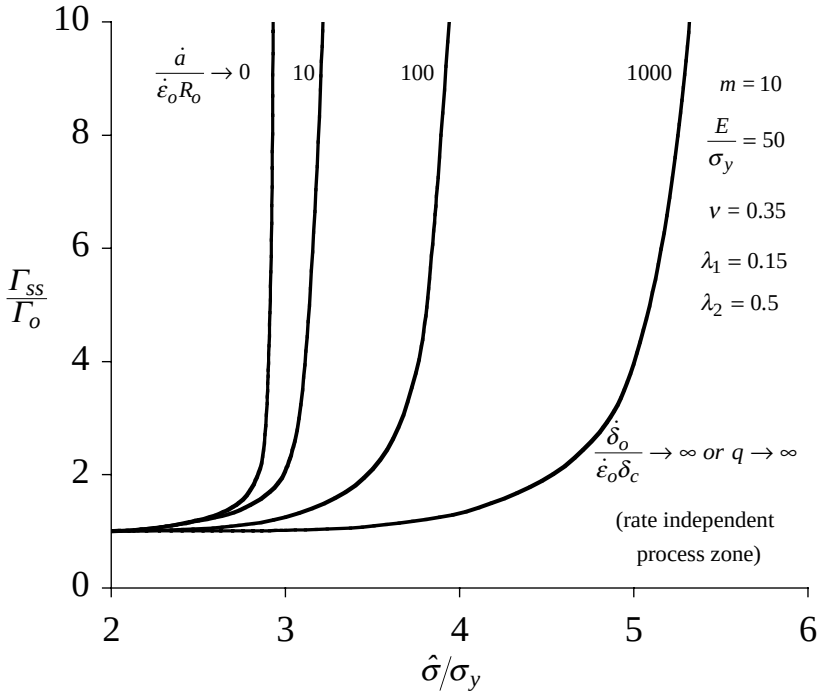

Figure 2: Steady state toughness versus peak cohesive strength for a rate independent cohesive zone law.

The first set of results shown in Figure 2 are for a solid with rate exponent $m = 10$ and a rate independent fracture process zone. The rate independent fracture process zone is a limiting case of Equations (6-8) with $\dot{\delta}_o/(\dot{\varepsilon}_o\delta_c) \to \infty$ or $q \to \infty$. Figure 2 plots the steady state toughness as a function of the peak cohesive stress in the fracture process zone. For values of $\hat{\sigma} < 2\sigma_y$ the plasticity in the bulk solid is not of sufficient intensity to induce a significant amount of dissipation and the steady state toughness is only slightly greater than Γ_o. For exceedingly slow crack velocities the model reduces to a rate-independent elastic-perfectly

plastic material where the solid cannot sustain normal tractions greater than approximately $2.96\sigma_y$ ahead of the crack tip. Hence, if $\hat{\sigma} > 2.96\sigma_y$ then the fracture process zone cannot separate and Γ_{ss} is infinite. At finite crack velocities the strain rate effects in the solid become relevant. Increasing crack velocities allow for elevated normal traction acting on the crack plane. However, the normal traction ahead of the crack tip cannot exceed $\hat{\sigma}$ which limits the intensity of the plastic deformation and hence the toughness of the material decreases as crack velocity increases. The effects shown in Figure 2 are analogous to strain hardening or strain gradient hardening effects in rate independent materials, Wei and Hutchinson [7]. The general trend is that material hardening elevates tractions ahead of the crack tip which promote the separation of the fracture process zone.

The introduction of a rate dependent fracture process zone sets up a competition between the hardening of the solid and the strengthening of the cohesive zone. As such, trends in the steady state toughness are not as straightforward as those for the rate independent fracture process. Furthermore, Γ_{ss} is sensitive to the two rate parameters associated with the fracture process, q and $\dot{\delta}_o$. It is likely that q and $\dot{\delta}_o$ will be difficult to measure directly, leaving their determination to micromechanical models of the fracture process.

Figure 3 plots Γ_{ss} as a function of $\hat{\sigma}$ for various crack velocities. The rate exponent for the fracture process was taken to be equal to that of the solid for these simulations, $q = m = 10$. Focusing first on the solid curves with the normalized reference crack opening rate $\dot{\delta}_o/(\dot{\varepsilon}_o\delta_c) = 1$, we note that steady state toughness now *increases* as the crack velocity increases. Within the range of Γ_{ss} shown, the strengthening of the fracture process dominates the hardening in the bulk solid. The two dotted lines on Figure 3 are results for a normalized crack velocity of $\dot{a}/(\dot{\varepsilon}_o R_o) = 100$ and reference crack opening rates of $\dot{\delta}_o/(\dot{\varepsilon}_o\delta_c) = 0.1$ and 10. For a given crack opening rate Eqn. (6) indicates that the traction acting across the crack faces decreases as $\dot{\delta}_o$ increases. Crudely, increasing $\dot{\delta}_o$ is similar to decreasing $\hat{\sigma}$ at a given opening rate.

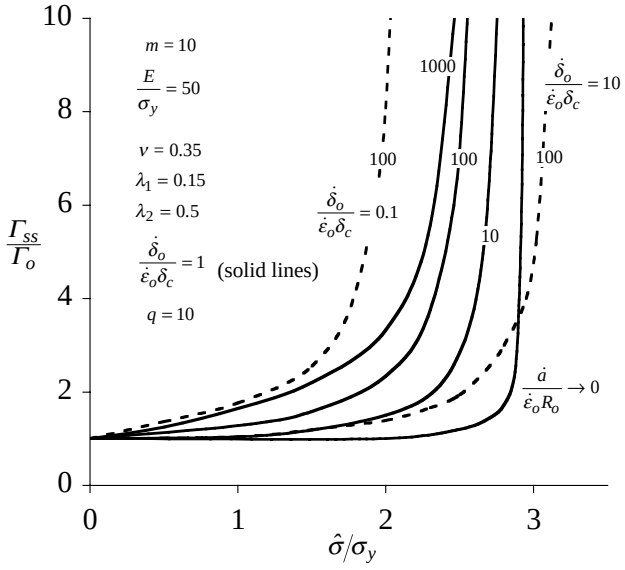

Figure 3: Toughness versus peak cohesive strength for a rate dependent traction-separation law with $q = m = 10$.

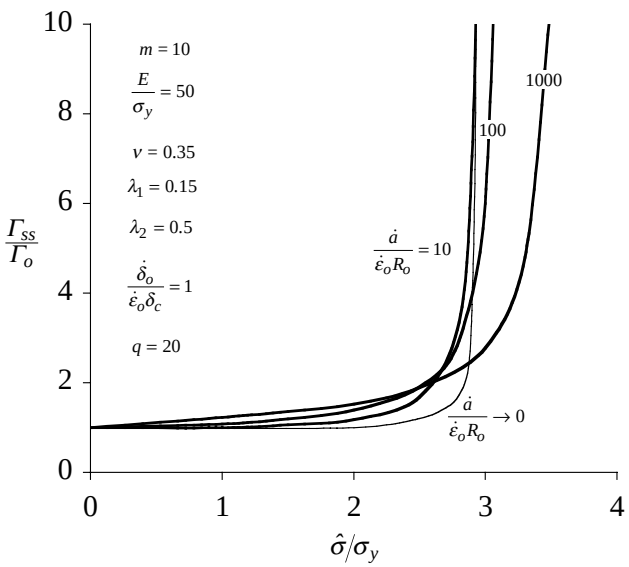

Figure 4: Toughness versus peak cohesive strength for a rate dependent traction-separation law with $q = 2m = 20$.

Notice that the solid curves in Figure 3 seem to approach the $\dot{a}/(\dot{\varepsilon}_o R_o) \to 0$ curve from the left as the crack velocity decreases. This appearance is due to the range of Γ_{ss} shown in the figure. Notice that the $\dot{a}/(\dot{\varepsilon}_o R_o) = 100$, $\dot{\delta}_o/(\dot{\varepsilon}_o \delta_c) = 10$ simulations cross over the $\dot{a}/(\dot{\varepsilon}_o R_o) \to 0$ curve. This is also the case for the $\dot{\delta}_o/(\dot{\varepsilon}_o \delta_c) = 1$ cases, however the crossover occurs at much higher values of Γ_{ss}. A similar change in the toughness versus crack velocity trend is evident for a value of $q = 2m$ to be presented next.

As we have stated throughout q and $\dot{\delta}_o$ could be obtained from a micromechanical analysis. Kramer and Berger [8] present a model for craze widening and under their assumptions the rate exponent for the craze widening is predicted to be twice that for bulk deformations. We note that their assumed form of the bulk constitutive law was power law viscous which is similar to Eqn. (1) except that no yield surface exists, i.e. the additive constant of 1 is removed from the left hand side of (1) and plastic straining occurs at all stress levels. For increasing levels of q Eqn. (6) indicates that for a given applied opening rate the traction acting across the crack surfaces decreases. As shown on Figure 2 the rate independent fracture process limit corresponds to $q \to \infty$. Hence, an increase in q will have similar effects on Γ_{ss} as an increase in $\dot{\delta}_o$. Figure 4 plots Γ_{ss} as a function of $\hat{\sigma}$ for three crack velocities and $q = 2m = 20$. Here again a crossover in the trend of toughness versus velocity occurs. For static peak cohesive stresses lower than approximately $2.7\sigma_y$, Γ_{ss} increases slightly as $\dot{a}$ increases. However, for $\hat{\sigma} > 2.7\sigma_y$ the toughness decreases dramatically as the crack velocity increases (within the range of velocities shown).

4. DISCUSSION

In this work a rate dependent bulk material was coupled with a rate dependent fracture process zone. When the fracture process is rate independent the rate hardening in the bulk solid allows the tractions ahead of the crack tip to elevate and overcome the strength of the cohesive zone. Hence, the toughness of the material decreases as the crack velocity increases. For a rate dependent fracture process zone where both the toughness and strength increase with increasing crack opening rate predictions of the model are more complicated. However, a simple rule of thumb could be proposed: if the peak cohesive stress is less than approximately $3\sigma_y$ then the steady state toughness will increase with increasing crack velocity while the opposite trend holds for $\hat{\sigma} > 3\sigma_y$. The coefficient of 3 is a remnant of the perfectly plastic description of the static stress-strain behavior and the introduction of strain hardening will change the magnitude of the peak stress where this transition occurs. Lastly, the rate of increase/decrease of Γ_{ss} with respect to crack velocity is quite sensitive to the q and $\dot{\delta}_o$ parameters of the fracture process.

REFERENCES

1. Dean, R.H. and Hutchinson, J.W. (1980) *In: Fracture Mechanics: Twelfth Conference*, 383-405.
2. Drugan, W.J., Rice, J.R. and Sham T-L. (1982) *J. Mech. Phys. Solids* 30, 447-473.
3. Marusich, T.D. and Ortiz, M. (1995) *Int. J. Num. Meth. Engng*. 38, 3675-3694.
4. Xia, L., Shih, C.F. (1995) *J. Mech. Phys. Solids*, 43, 1953-1981.
5. Tvergaard, V. and Hutchinson, J.W. (1992) *J. Mech. Phys. Solids*, 40, 1377-1397.
6. Landis, C.M., Pardoen, T. and Hutchinson, J.W. (2000), *Mech. Mater.*, 32, 663-678.
7. Wei, Y. and Hutchinson, J.W. (1997) *J. Mech. Phys. Solids*, 45, 1253-1273.
8. Kramer, J.K. and Berger, L.L. (1990) *Adv. Polym. Sci.*, 91/92, 1-68.

CREEP CRACK GROWTH ANALYSIS BASED ON MICROSCOPIC FRACTURE MECHANISM

M. Tabuchi[1], K. Kubo[1], K.Yagi[1] and A. T. Yokobori, Jr.[2]

[1]National Institute for Materials Science, Sengen, Tsukuba, 305-0047, Japan
[2]Tohoku University, Aoba, Sendai, 980-8579, Japan

ABSTRACT

Relationship between creep crack growth rate and microscopic fracture mechanism i.e., wedge-type intergranular, transgranular and cavity-type intergranular crack growth, has been investigated on Alloy 800H and 316 stainless steel. The growth rate of wedge-type and transgranular creep crack could be characterized by creep ductility. Creep damages formed ahead of the cavity-type creep crack tip accelerated the crack growth rate. Based on the experimental results, FEM code that simulates creep crack growth taking the fracture mechanism into account has been developed. The effect of creep ductility and void formation ahead of the crack tip on creep crack growth rate could be evaluated.

KEYWORDS

Creep crack growth, Alloy 800H, 316 stainless steel, Creep fracture mechanism, C^* parameter, FEM analysis, Vacancy diffusion

INTRODUCTION

Understanding of creep crack growth behavior is important for the reliability evaluation of high temperature structural components. Creep crack growth properties are affected by microscopic fracture mechanism dependent on temperature and loading condition. For the long-term services, evaluation of creep crack growth by grain boundary cavitation [1] is important. Type IV creep crack in heat affected zone of welded components grows accompanied by void formation ahead of the crack tip [2]. It would be necessary to evaluate the creep crack growth behavior, taking microscopic features such as damage formation into account, for the accurate life prediction.

In the present work, creep crack growth tests were conducted using CT specimen of Alloy 800H and 316 stainless steel at various temperature and loading conditions. Creep crack growth behavior was characterized in terms of microscopic creep fracture mechanism. In order to evaluate the relations between creep crack growth rate and fracture mechanism, FEM analysis taking the creep ductility and void formation into account was conducted.

EXPERIMENTAL PROCEDURES

Materials tested are Alloy 800H and 316 stainless steel plates. Chemical composition of Alloy 800H is given in Table 1. The solid solution heat treatment condition was 0.4h at 1443K. Creep crack growth tests were conducted using CT specimen of 50.8mm in width and 12.7mm in thickness. Fatigue pre-crack of 2.5mm was introduced at room temperature. After fatigue pre-cracking, side-grooves of 20% of thickness were machined. Creep crack length was measured using D.C. electrical potential technique. Load line displacement between upper and lower clevises, which connect the specimen with pull rods, was measured. The creep crack growth tests were conducted at temperature range from 873K to 1073K.

TABLE 1
CHEMICAL COMPOSITION OF ALLOY800H (MASS%)

C	Si	Mn	Fe	S	Ni	Cr	Cu	Ti	Al
0.06	0.4	1.0	45.4	0.001	31.9	20.0	0.03	0.46	0.35

RESULTS AND DISCUSSION

Creep Fracture Mechanisms

Figure 1 shows microscopic features of creep cracks observed in CT specimens of Alloy 800H. Three types of creep crack growth, wedge-type intergranular, cavity type intergranular and transgranular crack growth were observed depending on testing temperature and loading conditions. For higher stresses at lower temperatures, intergranular fracture due to the wedge-type cracking (W-type) was observed. It is considered that fine γ' precipitates hardened the matrix and brittle wedge-type fracture was occurred at this testing condition. For lower stresses at higher temperatures, intergranular fracture due to the formation of cavities at the interface between matrix and $M_{23}C_6$ precipitates on grain boundaries (C-type) was observed. Large creep damaged zone ahead of the crack tip was observed for C-type crack growth. Transgranular fracture (T-type) was observed between the temperature and loading conditions of W-type and C-type.

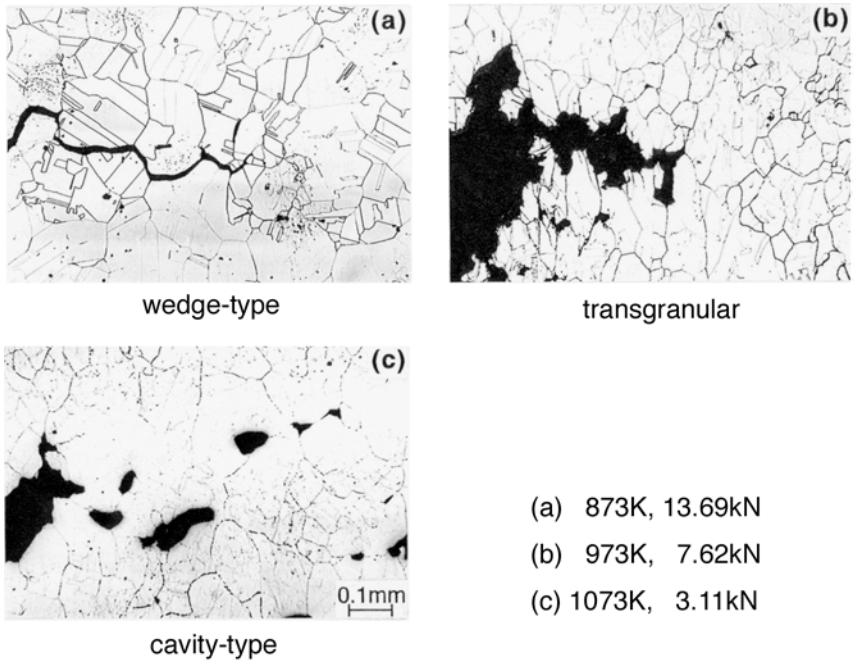

Figure 1: Microscopic features of creep cracks observed in CT specimens creep interrupted of Alloy 800H.

Relationship between Creep Crack Growth Rate and Fracture Mode

Creep crack growth rate was evaluated by C^* parameter calculated as follows [3];

$$C^* = \frac{n}{n+1} \frac{P\dot{\delta}}{B_N (W-a)} \left(\gamma - \frac{\beta}{n} \right) \qquad (1)$$

where, W is the specimen width, a is the crack length, P is the load, B_N is the net thickness, $\dot{\delta}$ is the load line displacement rate, n is the creep exponent in Norton's rule and γ and β are the function of a and W. The value of n was obtained from the relations between minimum creep rate *vs*. applied stress for round bar creep specimens.

The relationship between creep crack growth rate, *da/dt*, and C^* parameter obtained under relevant creep fracture mechanism condition for Alloy 800H is shown in Figure 2. The crack growth data of initial tail parts [4] were omitted in this figure. The *da/dt vs.* C^* relations depend on the microscopic creep crack growth mechanism. The creep crack growth rate for W-type and C-type fracture mode was higher than that for T-type fracture mode. The creep crack growth rate for C-type mode exists between the upper bound for W-type and the lower bound for T-type mode.

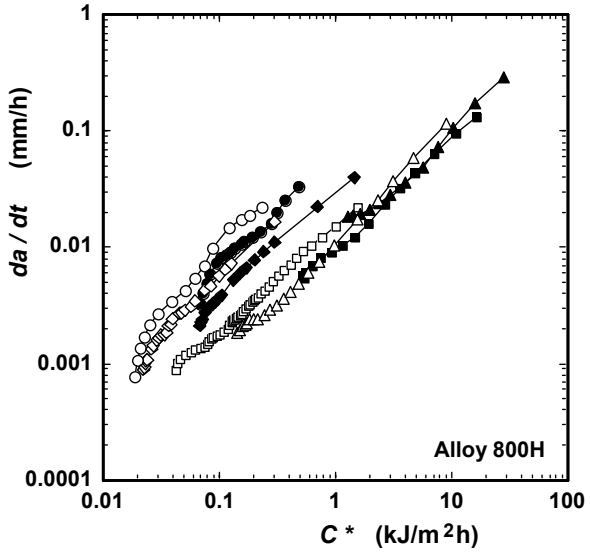

	Temp. (K)	Load (kN)	Fracture mode
●	873	13.69	W
○		11.47	W
▲	923	11.71	T
△		8.98	T
■	973	7.62	T
□		4.36	T
◆	1073	3.11	C
◇		2.61	C

Figure 2: Relationship between creep crack growth rate, *da/dt*, *vs.* C^* parameter.

Creep ductility was dependent on creep fracture mechanism, and that was lower for W-type, higher for T-type, and medium for C-type fracture mode. It is considered that difference of creep ductility between fracture modes is one of the reasons why *da/dt* depends on creep fracture mode. Figure 3 shows the relationship between creep crack growth rate at C^*=1 kJ/m^{2}h *vs.* reduction of area for round bar creep specimens of Alloy 800H and 316 stainless steel. These relations were dependent on creep fracture mechanisms. For W-type and T-type fracture mode, the *da/dt* was inversely proportional to creep ductility as shown with the solid curve in Figure 3. Creep crack growth rate for W-type and T-type mode could be written as follows [5];

$$\frac{da}{dt} = \frac{6.26 \times 10^{-3}}{\varepsilon_f^*} C^{*0.92} \qquad (2)$$

where, ε_f^* is the creep ductility.

For C-type fracture mode, however, *da/dt* was faster than that predicted from the equation (2). The *da/dt* was accelerated as the testing temperature and time was increased for C-type fracture mode. When creep voids are not formed ahead of the crack tip such as W-type and T-type fracture mode, the creep crack growth rate could be characterized by the creep ductility. When many voids and micro cracks are formed ahead of the main crack tip, the creep crack growth rate was accelerated than that predicted from creep ductility. In order to predict the creep crack growth rate under C-type fracture mode, it is necessary to consider not only creep ductility but also the effect of creep damages ahead of the crack tip. Vacancy diffusion and void formation accelerated under multi-axial condition at higher temperature should be taken into account.

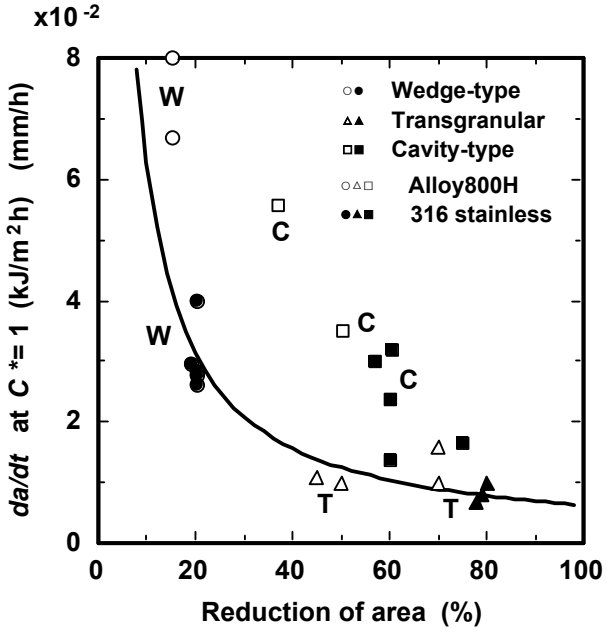

Figure 3: Relationship between *da/dt* at C^*=1 kJ/m^{2}h vs. creep ductility.

Computational Simulation for Creep Crack Growth

We attempted to simulate creep crack growth behavior taking the fracture mechanism into account on the basis of experimental results. The FEM analytical model of CT specimen is shown in Figure 4. For W-type and T-type fracture mode, the *da/dt* was inversely proportional to creep ductility, therefore the crack growth could be characterized by critical strain condition. The creep strain distribution of CT specimen model was calculated by FEM. When the equivalent creep strain ahead of the crack tip reached to the critical value, which is the creep ductility of round bar specimen, the coordinate of the crack tip node was moved according to he method proposed by Hsu et al. [6]. The C^* line integral was calculated for every time step.

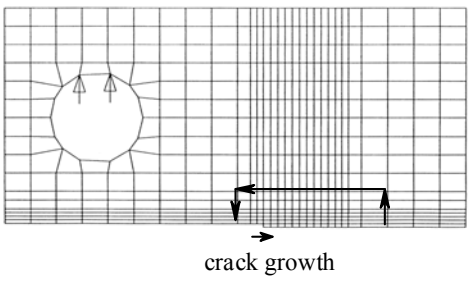

Figure 4: Analytical model for creep crack growth.

An example of computational and experimental relation of creep crack growth rate *vs.* C^*

integral is shown in Figure 5. The symbols indicate experimental data and the bold line shows the calculated results. In this case of T-type fracture mode, the crack growth rate could be predicted from Norton's creep rule and creep fracture strain. If we use half value of fracture strain for fracture criteria, the twice value of *da/dt* was obtained as shown with dashed line in Figure 5. These computational results coincide with the experimental ones that *da/dt* is inversely proportional to creep ductility.

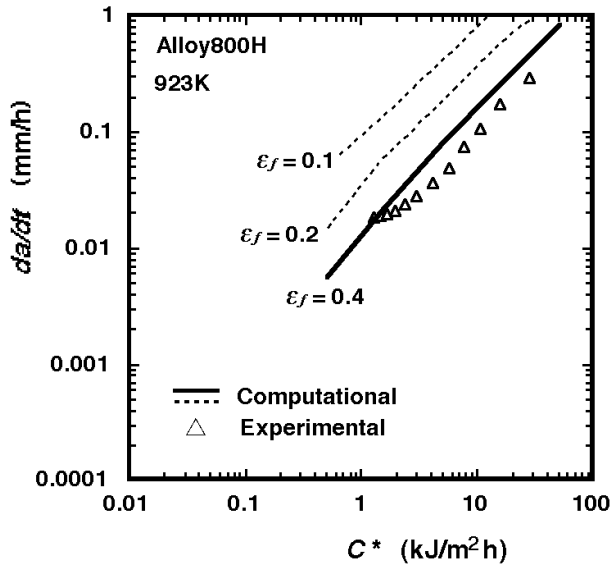

Figure 5: Comparison of experimental and computational relation between *da/dt vs. C** parameter.

For C-type fracture mode, which was observed at higher temperatures, *da/dt* was faster than others due to the formation of voids ahead of the crack tip. In order to evaluate the effect of void formation for C-type mode, it would be necessary to analyze the crack growth taking vacancy diffusion into account under multi-axial condition. The vacancy diffusion equation under stress gradient is given as follows [7, 8];

$$\frac{\partial C}{\partial t} = D\nabla\left(\nabla C + \frac{C\nabla V}{RT}\right) \tag{3}$$

$$V = -\sigma_p \Delta v \tag{4}$$

where, C is the vacancy concentration, D is the diffusion coefficient, σ_p is the hydrostatic stress and Δv is the volume changes by vacancy diffusion. In the present computational simulation, the vacancy

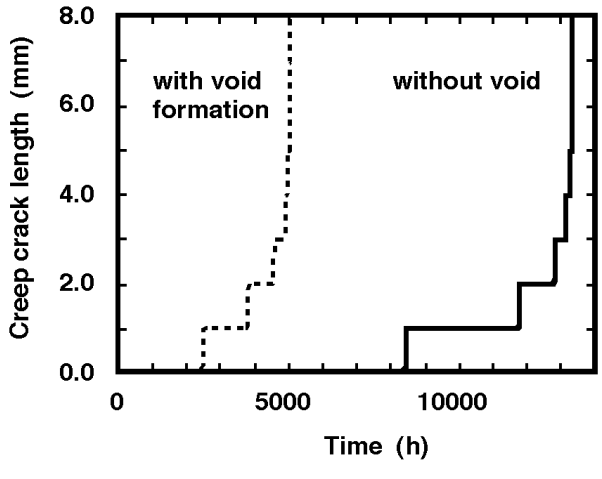

Figure 6: Example for simulation of creep crack growth
taking the diffusion into account.

concentration ahead of the crack tip is calculated by FEM according to the equations (3) and (4), and if that value reaches to the critical value, the stiffness matrix [K] is decreased step by step. The creep crack growth is simulated by combining the critical strain criteria and vacancy diffusion criteria. Figure 6 shows an example calculated by assuming that D=12.7e^{-11}(m^2/s), Δv=2.0e^{-6}(m^2/mol) and critical vacancy concentration C/C_0 =1.25. The qualitative results that creep crack initiation time and crack growth rate were accelerated were obtained while taking the void formation ahead of the crack tip into account. The quantitative evaluation for the effect of vacancy diffusion on crack initiation and growth under multi-axial condition should be the future work.

CONCLUSIONS

Creep crack growth tests have been carried out using CT specimens on Alloy 800H and 316 stainless steel at various testing conditions. The relationship between creep fracture mechanism and creep crack growth behavior has been investigated. The results are summarized as follows;
(1) Three types of creep crack growth mechanisms, i.e., wedge-type intergranular, transgranular and cavity-type intergranular, were observed for Alloy 800H and 316 stainless steel depending on testing conditions.
(2) Creep crack growth rate was dependent on microscopic creep fracture mechanism. The growth rate of wedge-type and cavity-type intergranular creep crack was higher than that of transgranular creep crack.
(3) The growth rate of wedge-type and transgranular creep crack could be characterized by creep ductility. The creep damages formed ahead of the cavity-type creep crack were considered to accelerate the crack growth rate.
(4) The FEM code, which simulates creep crack growth taking the fracture mechanism into account, has been developed. The effect of creep ductility and void formation ahead of the crack tip due to the vacancy diffusion on creep crack growth rate could be evaluated.

References

1. Riedel, H. (1986) *Fracture at High Temperatures,* Springer-Verlag, Berlin.
2. Tabuchi, M., Watanabe, T., Kubo, K., Matsui, M., Kinugawa, J. and Abe, F. (2000) *Proc. of 2nd HIDA Conference*, Stuttgart, Germany, S2-4.
3. Ernst, H.A. (1983) *ASTM STP* 791, I-499.
4. Yokobori, A.T. and Yokobori, T. (1988) *Eng. Frac. Mech.* 31, 931.
5. Nikbin, K.M., Smith, D.J. and Webster, G.A. (1986) *Trans. ASME, J. Eng. Mater. Tech.* 108, 189.
6. Hsu, T.R. and Zhai, Z.H. (1984) *Eng. Fract. Mech.* 20, 521.
7. Yokobori, A.T., Jr, Nemoto, T., Sato, K. and Yamada, T. (1993) *Japan Soc. Mech. Eng.* 59, 104.
8. Kikuchi, K. and Kaji, Y. (1995) *Proc. of 33rd Symposium on Strength of Materials at High Temperatures*, Yokohama, Japan, 1.

ABSTRACT REF NO: ICF1008810R

CREEP CRACK GROWTH PARAMETERS FOR DIRECTIONALLY SOLIDIFIED SUPERALLOYS

B. Gardner[1], A. Saxena[2], J. Qu[1]

[1]G.W.Woodruff School of Mechanical Engineering
[2]School of Materials Science and Engineering
Georgia Institute of Technology
Atlanta, 30332-0245, USA

ABSTRACT

Crack tip parameters used in nonlinear fracture mechanics are examined using finite element simulations for characterizing high temperature crack growth in directionally solidified (DS) Ni-base superalloys. The anisotropy in these materials is modeled as orthotropic materials in which the plastic and creep properties are different along the longitudinal and transverse directions. The elastic behavior of the material is modeled as isotropic. The loading direction is chosen along the longitudinal axis of the grains and the crack is located in the transverse plane. The analysis shows that C(t) characterizes the crack tip stress and strain as a function of time and also the evolution of the creep zone size and shape during the small-scale creep conditions. This leads to the conclusion that the parameters that characterize the crack growth rate in isotropic materials such as C^* and C_t are also suitable for DS materials for Mode I cracks when the loading axis coincides with one of the main material axis.

KEYWORDS: creep, fatigue, crack, DS Ni – alloys, C_t, C^*

INTRODUCTION

The performance of natural gas-fired gas turbines has steadily improved with the continuous development of advanced materials and design concepts for hot gas path components. The use of directionally solidified (DS) superalloy with adequate coatings has significantly improved the limitations inherent to equiaxed materials in the areas of oxidation and corrosion resistance, thermal and low cycle fatigue resistance, creep resistance and high cycle fatigue resistance [1]. A major aspect of any design or remaining (or residual) life assessment methodology for high temperature components is the ability to predict the creep and creep-fatigue crack growth behavior in these materials. This requires the use of nonlinear fracture mechanics concepts.

Directionally solidified materials by design are anisotropic because grain sizes in the longitudinal direction can be on the order of 100 mm and on the order of only a few mm in the transverse and the short transverse directions. The tensile and the creep data clearly show significant differences in the plastic and creep deformation behavior in the longitudinal and transverse directions. Thus, it is perhaps more accurate to represent them as orthotropic materials in which the creep deformation properties in the direction along the grain axis differ substantially from the properties in the transverse direction.

The crack tip parameters currently used for predicting creep and creep-fatigue crack growth are based on the assumptions that the material is isotropic. The purpose of this paper is to use finite element simulations to

explore the applicability and limitations of crack tip parameters such as C^*, C_t and C(t) for predicting crack growth in DS materials.

CRACK TIP PARAMETERS FOR CREEP CRACK GROWTH

We assume power-law creep behavior and that a cracked body is subjected to a static load under creep conditions and the load has been applied for sufficiently long time so that steady-state creep develops over the entire remaining ligament. Under these circumstances, the C^*- integral is shown to uniquely characterize the crack tip stress and strain rates through the Hutchinson-Rice-Rosengren (HRR) fields [2]. The C^*-Integral is defined as [2]:

$$C^* = \int_{\Gamma} W^* dy - T_i \left(\partial \dot{u}_i / \partial x\right) ds \qquad (1)$$

Where, Γ = a path that originates on the lower crack surface and ends on the upper crack surface enclosing the crack tip, $\dot{u}_i$ = displacement rate, T_i = components of the traction vector, W^* = stress-power density, ds = incremental distance along the path, Γ.

The validity of the C^*-integral is limited to extensive steady-state creep conditions. In practice, this condition may not always be realized because components contain stress and temperature gradients and are designed to resist widespread creep deformation. Therefore, it is necessary to derive the crack tip stress fields for the conditions of small-scale creep (SSC) and the transition creep (TC). Under SSC, the creep zone is restricted to a small region near the crack tip and is much smaller than the length dimensions such as crack size and the remaining ligament, and the surrounding material is under elastic conditions. Riedel and Rice [3] and Ohji, Ogura and Kubo [4] independently derived the nature of the crack tip stress fields under small-scale creep conditions as a function of time. The above analysis lends itself to the estimation of the creep zone size and transition time, t_T, which is the time needed for extensive creep conditions to develop from SSC conditions. Riedel and Rice [3] defined the creep zone boundary as the locus of points where time-dependent effective creep strains equal the instantaneous effective elastic strains in the cracked body. The transition time is the time when the small-scale-creep stress fields equal to the extensive steady-state creep fields characterized by C^*.

Bassani and McClintock [5] recognized that the crack tip stress fields under SSC can also be characterized by a time-dependent C(t)-integral, whose value is determined along a contour taken very close to the crack tip. C(t) is same as C^* except its value is determined close to the crack tip within a region where the creep strains dominate over the elastic strains. In contrast, the value of C^* can be determined along any contour which originates at the lower crack surface and ends on the upper crack surface enclosing the crack tip. Thus, determining the C(t)-integral requires accurate solutions of stress and strain near the crack tip. Bassani and McClintock [5] further related the value of C(t) with the HRR type stress fields. The validity of the C(t)-integral is not simply limited to the small-scale creep conditions because C(t) becomes equal to C^* for extensive steady-state creep with the additional property that its value becomes path-independent. Hence, C(t) can be said to be the amplitude of the HRR field for all conditions ranging from small-scale to extensive secondary-state creep and also including the transition creep conditions, in between. Therefore, to investigate time-dependent crack tip stress fields in DS materials, we will focus on the C(t)- integral and its value determined along a path taken very close to the crack tip.

C_t parameter [2] is different from C(t) in that it is uniquely related the stress power dissipation rate and the rate of expansion of the creep zone size in the small-scale-creep regime. In the extensive creep regime, C_t, C(t) and C^* all become identical by definition. The advantage of C_t over C(t) in the small-scale-creep regime is that it can be measured at the loading pins while C(t) cannot. Therefore, C_t has been widely used for correlating creep crack growth data over a wide range of conditions ranging from small-scale-creep to extensive creep [2]. The relationship between C_t and the rate of expansion of the creep zone size, $\dot{r}_c$ is given by the following equation [2]:

$$C_t = \frac{2K^2\left(1-\nu^2\right)}{EW}\beta\ (F'/F)\dot{r}_c \qquad (2)$$

Where, K= stress intensity factor, W = specimen width, E = elastic modulus, ν= Poisson's ratio, F = K-calibration function, F' = first derivative of F with respect to (a/W), and β = constant with a value of

approximately 0.33. The creep zone size in the above equation is referenced to its extent along 90 degrees from the crack plane.

FINITE ELEMENT ANALYSIS OF ORTHOTROPIC MATERIALS

In this study, the DS material is modeled as isotropic elastic and orthotropic creep with different creep properties in the longitudinal and transverse directions. The finite element method is used to investigate the development of the creep zone and to calculate the magnitude of C(t) for a stationary crack.

The orthotropic creep behavior was implemented in the numerical model using Hill's anisotropic yield function. The anisotropic yield function contains 6 constants for general loading. If we restrict loading to the principal axes, the number of constants can be reduced to three. The loading of the model is applied such that the principal axes are coincident with the longitudinal and transverse directions of the directionally solidified alloy. The equivalent deviatoric stress function based on Hill's anisotropic yield function in principal stress space is

$$\tilde{q}(\sigma) = \left[F(\sigma_2 - \sigma_3)^2 + G(\sigma_3 - \sigma_1)^2 + H(\sigma_1 - \sigma_2)^2\right]^{1/2} \tag{3}$$

where, F, G, and H are coefficients associated with the anisotropic creep properties.

The equivalent steady-state creep relationship is

$$\dot{\varepsilon}_{cr} = A\,\tilde{q}^{n} \tag{4}$$

Where, $\dot{\varepsilon}_{cr}$ is the equivalent steady-state creep rate, *A* is the equivalent creep coefficient, and *n* is the creep exponent. The constants *F*, *G*, and *H* are determined using the creep coefficients from three uniaxial creep tests, one in each of the principal directions. Substituting the equivalent deviatoric stress for each of the uniaxial creep tests yield

$$\dot{\varepsilon}_{icr} = A_i\,\sigma_i^{\,n} = A\,\tilde{q}^{n} \tag{5}$$

Where, i =1,2,3, $\dot{\varepsilon}_{icr}$ is the steady-state creep rate in the i-direction, A_i is the creep exponent in the i-direction, σ_i is the i^{th} principal stress, and n is the creep exponent. It is important to note that the use of this approach allows for different creep coefficients to accommodate the material anisotropy, but the creep exponent must be the same for each direction. Combining Eq. (3) and Eq. (5) for each of the uniaxial test yields the following relationships between the anisotropic creep coefficients and the equivalent creep coefficient.

$$\begin{aligned} A_x &= (G+H)^{n/2}\,A \\ A_y &= (F+H)^{n/2}\,A \\ A_z &= (F+G)^{n/2}\,A \end{aligned} \tag{6}$$

By setting $A=A_x$, the following equations are obtained for F, G, and H

$$\begin{aligned} F &= \frac{1}{2}\left[\left(\frac{A_y}{Ax}\right)^{2/n} + \left(\frac{A_z}{Ax}\right)^{2/n} - 1\right] \\ G &= \frac{1}{2}\left[\left(\frac{A_z}{Ax}\right)^{2/n} + 1 - \left(\frac{A_y}{Ax}\right)^{2/n}\right] \\ H &= \frac{1}{2}\left[\left(\frac{A_y}{Ax}\right)^{2/n} + 1 - \left(\frac{A_z}{Ax}\right)^{2/n}\right] \end{aligned} \tag{7}$$

A finite element model of a standard compact type (CT) specimen was created. The finite element model is 2-d, plane strain and consists of 15413 nodes and 4988 8-noded quadrilateral elements, Figure 1. Crack tip elements are used to ensure accurate representation of the stress and strain field at the crack tip. The use of crack tip elements is particularly important in the calculation of C(t) because its value is only valid as the dimension of the contour around the crack tip approaches zero. A detailed figure of the crack tip mesh is shown in Figure 2. A load of 2000 N is applied to the finite element model through the semi-rigid loading pins and the a/W ratio is 0.5. The stress intensity factor for this configuration is 109.2 $MPa(m)^{1/2}$. The finite

element model was analyzed using ABAQUS, which includes the anisotropic creep model based on Hill's function among its standard routines.

RESULTS

Three different finite element models were evaluated for comparison: isotropic (A_x=A_y), orthotropic - longitudinal bias ($A_y > A_x$), and orthotropic - transverse bias ($A_x > A_y$). The creep coefficient is 1.06×10^{-14} MPa^{-6}/hr and the creep exponent is 6 for the isotropic case. Using a load of 2000 N, the corresponding transition time is 430 hours for the isotropic case. The coefficients for the orthotropic models are shown in Table 1.

Table 1 – Orthotropic Creep Properties for Finite Element Model

	A_x(MPa^{-6}/hr)	A_y(MPa^{-6}/hr)	A_z (MPa^{-6}/hr)
Long. Bias	1.061×10^{-14}	4.897×10^{-14}	1.061×10^{-14}
Trans. Bias	1.061×10^{-14}	2.290×10^{-15}	2.290×10^{-15}

Figure 3 shows the resulting creep zone at 500 hours for all three finite element models. In this figure, the creep zone is defined as the boundary where the equivalent creep strain is equal to the largest principal elastic strain. The crack tip parameter C(t) was calculated during the finite element simulation. A plot of C(t) versus time for each of the three finite element models is presented in Figure 4. The most important result from this plot is the fact that the value of C(t) approaches a unique value as time increases for the two orthotropic cases evaluated. In the isotropic case, it is well known that $C(t) \rightarrow C^*$ as $t \rightarrow \infty$. This result shows that C(t)- Integral can be used for characterization of crack tip stress under extensive creep conditions for DS materials.

Figure 5 shows the development of the creep zone for the orthotropic – transverse bias (Ax > Ay) case. The results of the analytical study showed the creep zone does in fact grow in a self-similar fashion even with the orthotropic creep properties. Figure 6 shows a plot of the creep zone size as a function of time on a log-log scale for angles of 90 and 45 degrees from the crack plane. A line of slope of $2/(n-1) = 0.4$ for $n = 6$ is plotted through the data to compare the numerical results to the analytically predicted slope [2,3]. The good agreement between the numerical and analytical values attests to the validity of C_t for uniquely characterizing the creep zone expansion rate. This result has significant implications in regard to the use of C_t [6] parameter for characterizing the creep crack growth behavior in DS materials.

CONCLUSIONS

Finite element analyses of compact type specimens subjected to sustained load conditions made from orthotropic materials with different creep properties along the major axes show that crack tip stress and strain fields as a function of time and the evolution of the crack tip creep zone size and shape are characterized by the C(t)-Integral. Thus, the foundation has been laid for the use of parameters such as C^* and C_t for characterizing high temperature crack growth.

REFERENCES

1. Stringer, J. and Viswanathan, R., (1993) "Gas Turbine Hot-Section Materials and Coatings in Electric Utility Applications", Proceedings of ASM Materials Congress, Pittsburgh, 1.
2. Saxena, A., (1998) Nonlinear Fracture Mechanics for Engineers, CRC Press.
3. Riedel, H. and Rice, J.R., (1980), ASTM Special Technical Publication, STP 700, 112.
4. Ohji, K., Ogura, K., and Kubo, S., (1979), Transactions of Japan Society of Mechanical Engineering, 790-13, 18.
5. Bassani, J.L. and McClintock, F.A., (1981), International Journal of Solids and Structures, 17, 79.
6. Saxena, A. (1986), ASTM Special Technical Publication, STP 905, 185.

ACKNOWLEDGEMENTS

The authors wish to acknowledge the financial support of the General Electric Power Systems Company for the financial support of this study.

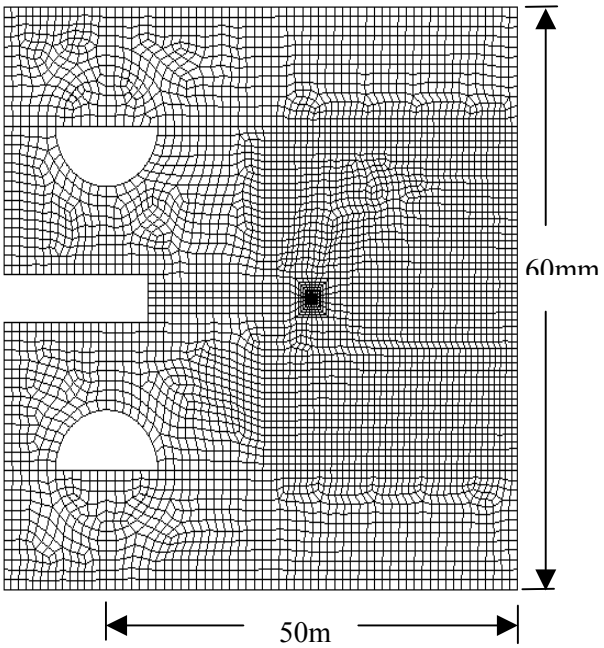

Figure 1: Finite Element Model of CT Specimen

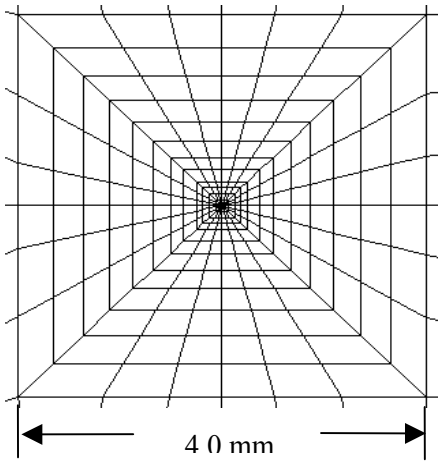

Figure 2: Close-Up View of Crack Tip Region in Finite Element Model

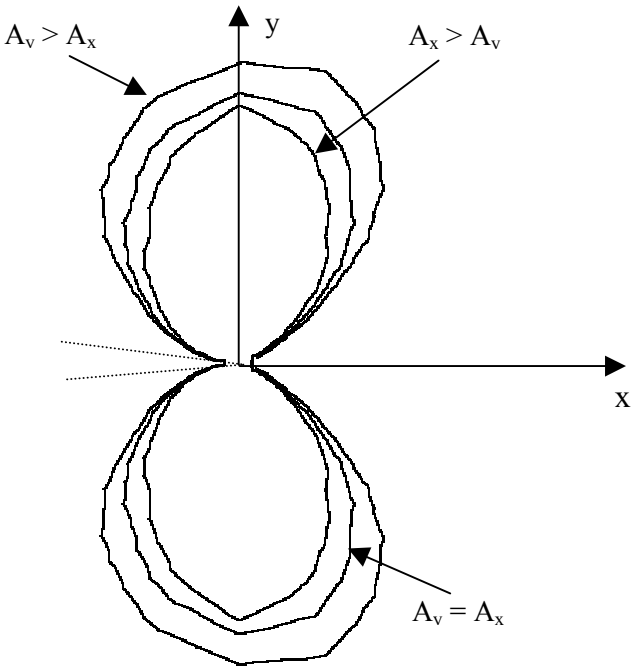

Figure 3: Boundary of creep zone at t=500hr for all three finite element models

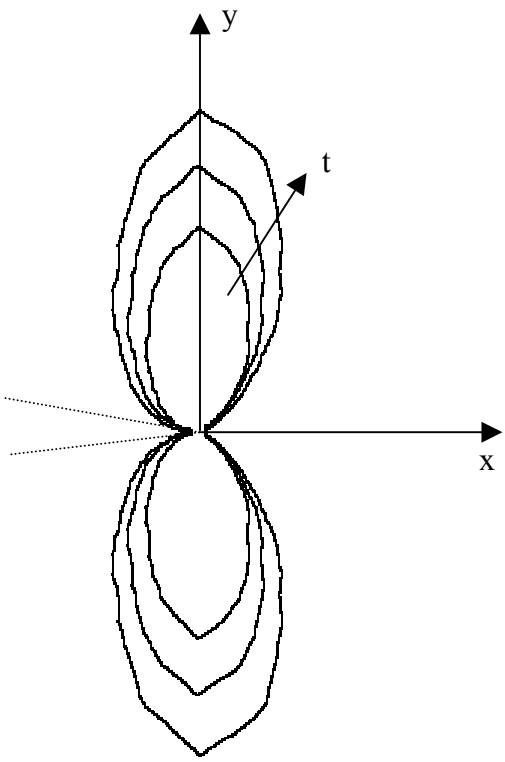

Figure 4: Evolution of Creep Zone for Orthotropic – Transverse Bias Case (t=200,500,1000 hr)

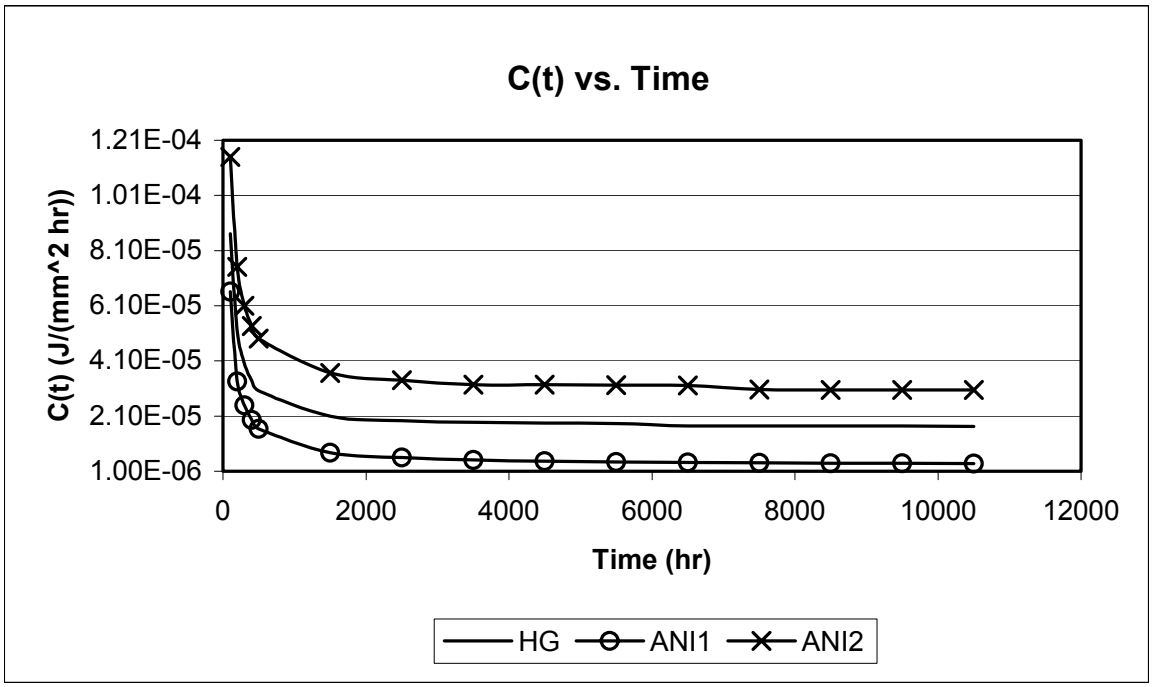

Figure 5: Comparison of C(t) vs. Time for each of the three finite element models

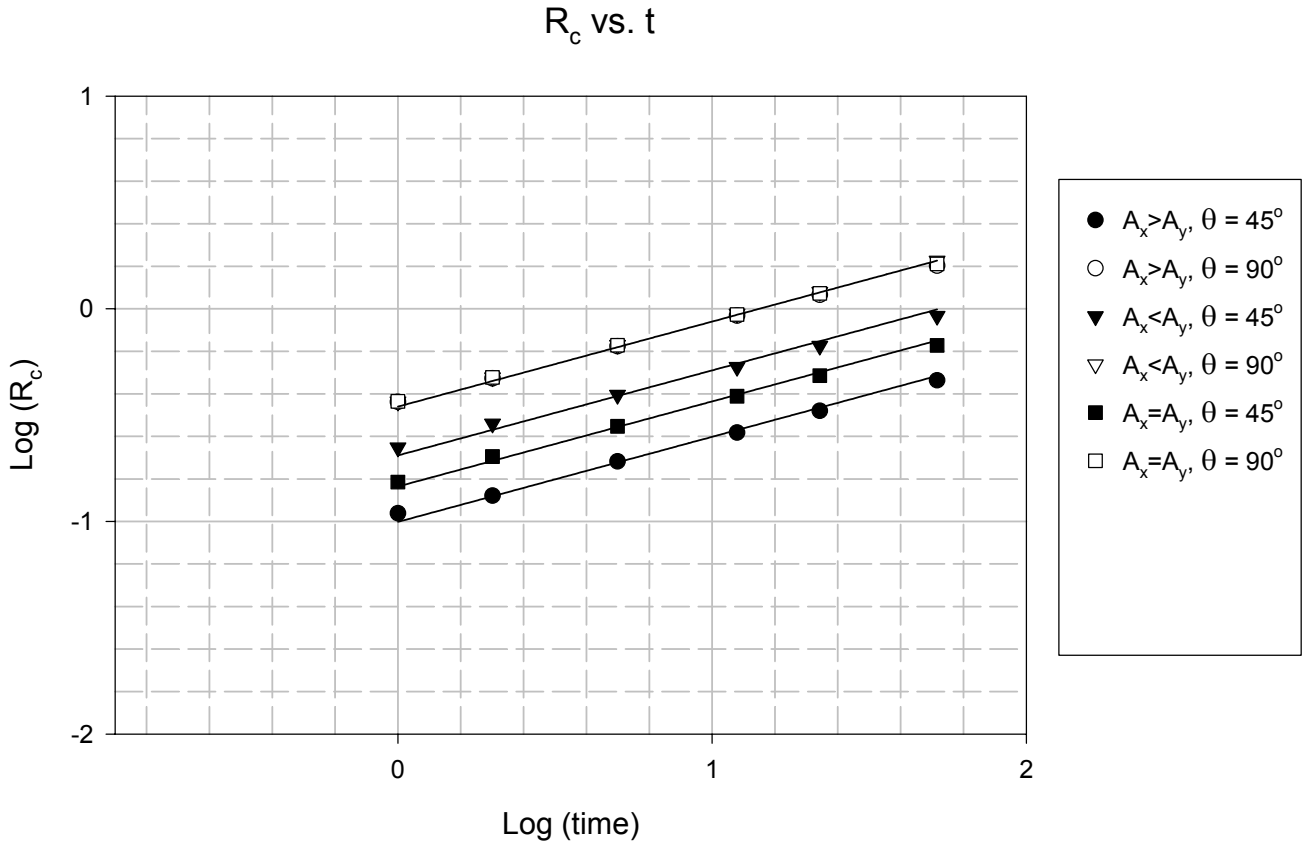

Figure 6: Plot of Creep Zone Radius vs. Time for angles of $\theta = 45°$ and $\theta = 90°$

CREEP DAMAGE ANALYSIS OF SHORT CRACKS USING A NARROW NOTCH SPECIMEN MADE FROM A NI-BASE SUPERALLOY AT 700^{o} C

T. H. Hyde, A. A. Becker and W. Sun

School of Mechanical, Materials, Manufacturing Engineering and Management
University of Nottingham, Nottingham NG7 2RD, UK

ABSTRACT

The results of damage mechanics finite element (FE) creep analyses were used to investigate the initiation and growth of short cracks using a 2D narrow notch model, under plane strain and plane stress conditions, with a uniform tensile loading. The material properties for a Ni-base superalloy (Waspaloy) at 700^{o} C were used. Damage distributions and growth near the notch, with time, were used to characterise and identify crack initiation and growth and to determine the direction of growth of the high damage zone, which was used to identify the crack growth direction. It was found that under plane stress conditions, the high damage zone was formed and grew inwards along the symmetric line of the notch, while under plane strain conditions, there was a bifurcation of the high damage zone, along a direction which was inclined at an angle to the notch. This angle was found to be dependent upon the tri-axial damage parameter α, reducing from 60^{o} to 35^{o} for α increasing from 0 to 0.3.

KEYWORDS

Short cracks, creep, damage, crack growth, crack direction

INTRODUCTION

The need to estimate the life of new components, or the residual life of components already in service, which operate at elevated temperature and may contain cracks, is important. For example, in the assessment of aeroengine components, an essential requirement is to study the high temperature failure and fracture behaviour of materials and components, under creep or creep/fatigue conditions. Results of laboratory testing using uniaxial, notched, compact tension specimens etc., are usually used to obtain information regarding material failure or crack propagation behaviour. In recent years, the investigations of crack growth have resulted in various parameters (e.g. K, C*, accumulated damage, ω, and critical strain, ε_c, etc) being proposed as parameters which govern creep crack growth. Numerical analyses, for example, the finite element (FE) method, are popularly used to assist with the detailed understanding of the behaviour at the advancing crack tips.

In this paper, the results of the continuum damage mechanics FE modelling have been used to assess the creep fracture behaviour of short cracks with a simplified 2D narrow notch model, using material properties

obtained for a Ni-base superalloy (Waspaloy) at 700° C. Damage distributions and accumulation near the notch, with time, were used to identify the crack initiation and its direction of growth.

FE MODEL, DAMAGE ANALYSIS AND MATERIAL PROPERTIES

FE Model

The 2D FE model used is shown schematically in Figure 1. The width of the specimen, L, is 7 mm, with a semi-circle narrow notch of length, a_o, of 0.5 mm at the edge, which has a radius, r, of 0.2 mm. A uniform tensile stress, σ_o, is applied to the end of the specimen. The FE mesh generated for damage analyses is shown in Figure 2, with 2-D axisymmetric, 8-node isoparametric, quadratic rectangular elements with reduced Gauss integration points (2×2). Local mesh refinement is used in the area near the notch.

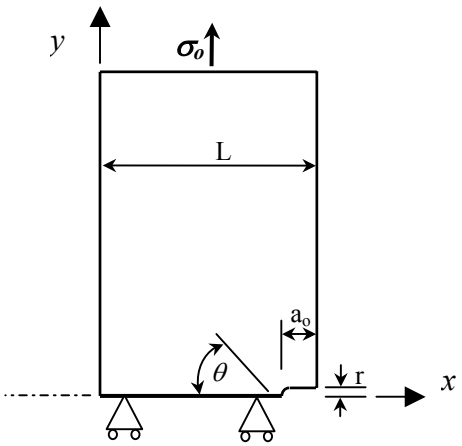

Figure 1: Schematic diagram of the short crack specimen (symmetrical half)

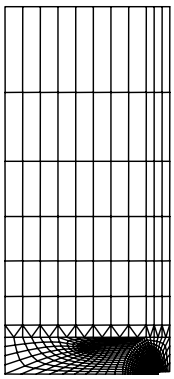

Figure 2: FE mesh of the narrow notch model

FE Damage Analyses

Creep damage constitutive equations of the type [1]

$$\dot{\varepsilon}_{ij}^{c} = \frac{3}{2} A \left[\frac{\sigma_{eq}}{1-\omega} \right]^{n} \frac{S_{ij}}{\sigma_{eq}} t^{m} \qquad (1)a \qquad \text{and} \qquad \dot{\omega} = \frac{M \sigma_{r}^{\chi}}{(1+\phi)(1-\omega)^{\phi}} t^{m} \qquad (1)b$$

in which $\sigma_r = \alpha\sigma_1 + (1 - \alpha)\sigma_{eq}$ were used in FE analyses to obtain the damage distributions, where σ_{eq}, σ_1 and σ_r are the equivalent, maximum principal and rupture stresses, respectively, ω is the damage variable and A, m, n, M, ϕ and χ are material constants. α is a material constant ($0 < \alpha < 1$) which describes the effect of the tri-axial stress state on the rate of damage of the material. FE creep damage calculations were performed using the user's material subroutine, UMAT, facility within the ABAQUS FE code [2, 3].

It should be noted that very high stress and strain concentrations occur at the notched region due to the small width of the notch. However, since the stress values in the high stress region will quickly reduce due to redistribution during creep, the local plastic behaviour was not taken into account in the current creep damage modelling.

Creep Properties

The material constants used in the FE analyses were related to the creep properties of a Ni-base superalloy (Waspaloy) at 700° C, which is used in the manufacture of aeroengine turbine discs [4]. The material constants, in equations (1), for the Waspaloy superalloy are given in Table 1. Young's modulus and the yield stress for the material at 700° C are 178×10^3 MPa and 860 MPa, respectively.

TABLE 1
MATERIAL CONSTANTS FOR THE NI-BASE SUPERALLOY (WASPALOY) AT 700° C [4]

A	n	m	M	ϕ	χ	α
9.226×10^{-34}	10.647	0.0	1.184×10^{-25}	13.0	8.133	0.15

RESULTS

Creep damage calculations were performed using the FE model shown in Figure 2, under both plane stress and plane strain conditions, using the material properties given in Table 1, with an applied stress, σ_o, of 400 MPa. Calculations were also performed with a range of other α values, in order to investigate the effect of the tri-axial stress state damage parameter on the damage behaviour of the specimen. Since the main purpose of this work was to identify the main factors affecting creep crack growth, an arbitrary damage level of 50% was chosen to represent the crack growth behaviour.

Stress, Strain and Damage Distributions and Direction of Damage Growth

The stress, strain and damage contours obtained from the FE analyses are used to illustrate the general behaviour of the specimen. The contours (near the notch) for the strain in loading direction, ε_y, rupture stress, σ_r, and damage at $\omega = 0.5$ under the plane stress condition, at different creep times, are shown in Figures 3(a) to 3(c), respectively. The corresponding results obtained from the plane strain analyses are shown in Figures 4(a) to 4(c), respectively. In all cases, it was found that the stress, strain and damage levels near the notch are significantly higher than those remote from the notch. The behaviours (strain, stress and damage distributions) illustrated by Figures 3 and 4 are consistent, i.e. in general, the high damage area is associated with the high strain area. When the damage level is high, the stress values in these areas reduce and the high stress regions move inwards to the region near the ends of high damage zones (similar to the behaviour at the tip of a crack), resulting in further growth of the high damage zones.

Results obtained under plane stress conditions, show that high damage initially occurs at the notch root, and then moves inwards, along the plane of symmetry of the notch, with increasing creep time, Figure 3(c). However, under the plane strain condition, the high damage zone, which initially occurs at the notch root, moves inwards along the plane of symmetry of the notch for a very short distance, before bifurcating and then continuing to grow in a direction inclined at an angle, θ, of about 45^o to the plane of symmetry of the notch, Figure 4(c).

Effect of the Tri-axial Stress State Damage Parameter, α

High damage growth direction

Calculations were also performed with α values (keeping the other material parameters in equations (1) the same), in the range of $0 < \alpha \leq 0.5$, in order to investigate the effect of the tri-axial stress state damage parameter on the distributions and growth of the high damage zones in the specimen. Results obtained from the calculations using the Waspaloy properties have shown that changing the α value in general will not change the trend of high damage growth for the plane stress specimen. However, for the plane strain case, increasing the α value will significantly reduce the inclination of the high damage zones to the plane of symmetry, θ, as illustrated in Figure 5.

Growth of the high damage zone

The variations of the crack growth, a, as indicated by the growth of the high damage zone, with the creep time, t, for a range of α values, under the plane stress condition, are shown in Figure 6. The results given in Figure 6 were obtained from the symmetric centre line of the specimen, at a damage level of $\omega = 0.8$ ($\omega = 0.5$ was used for most of the analyses presented), in order to obtain high accuracy. The crack length, a, was defined as the extent of 0.8 damage zone along the centre line, starting from the notch root.

Failure life estimation

Failure life was estimated, using the times at which the high damage ($\omega = 0.5$) zones reached a significant length (≥ 1 mm), compared to the width of the specimen. The lives, estimated in this way, with different α values, are presented in Table 2. In general, the failure lives estimated reduce with increasing α, which is similar to the behaviour indicated by calculations for a Bridgman notch bar made from the same material [4].

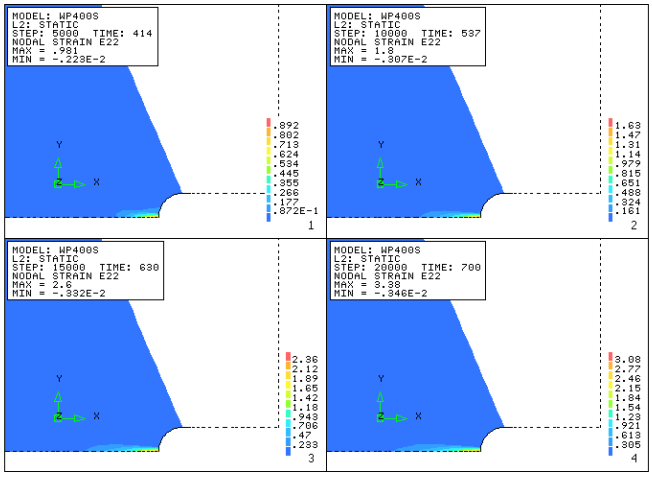

Figure 3(a): Distributions of axial strain, ε_y, for different times: plane stress case, $\alpha = 0.15$

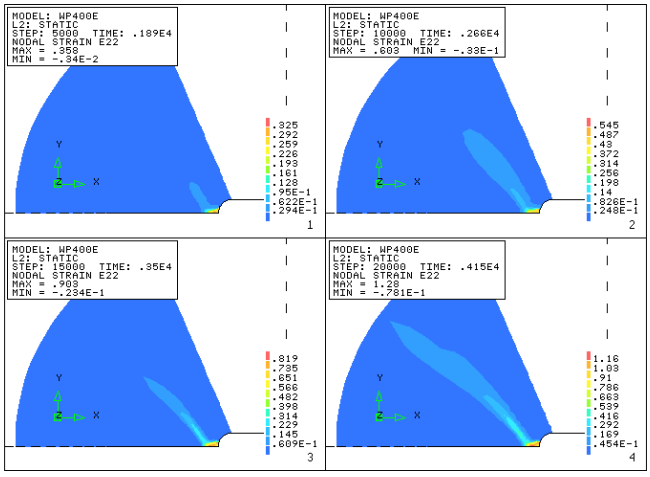

Figure 4(a): Distributions of axial strain, ε_y, for different times: plane strain case, $\alpha = 0.15$

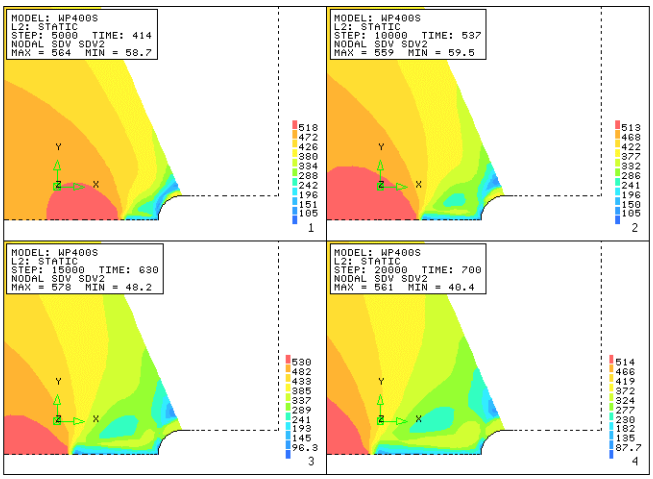

Figure 3(b): Distributions of rupture stress, σ_r, for different times: plane stress case, $\alpha = 0.15$

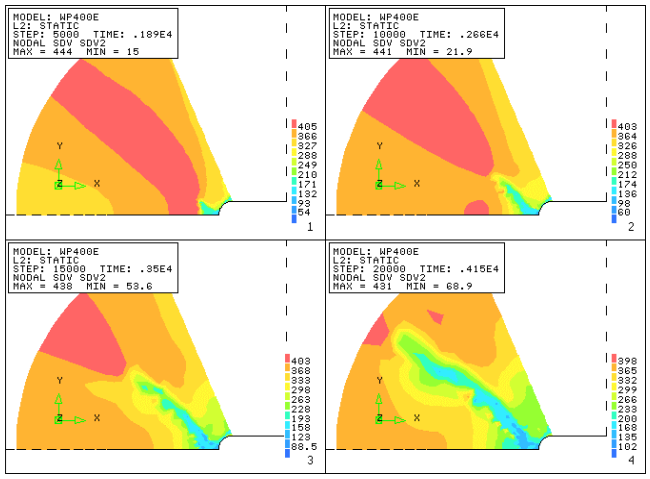

Figure 4(b): Distributions of rupture stress, σ_r, for different times: plane strain case, $\alpha = 0.15$

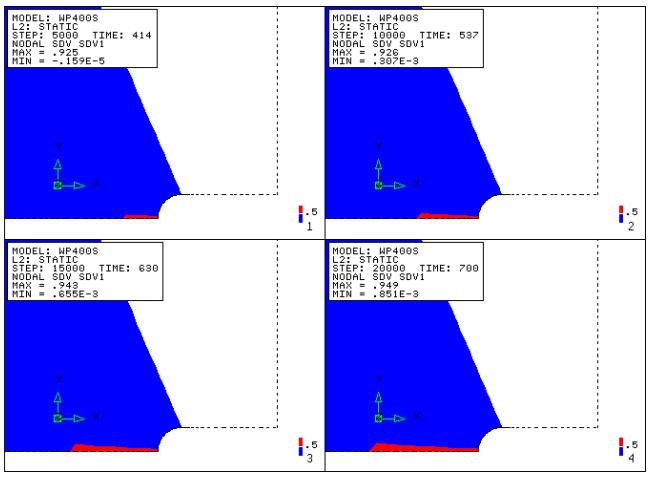

Figure 3(c): Distributions of damage, ω, for different times: plane stress case, $\alpha = 0.15$

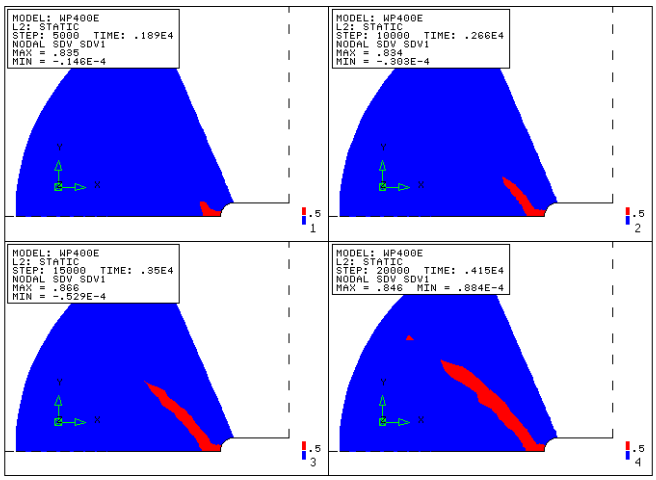

Figure 4(c): Distributions of damage, ω, for different times: plane strain case, $\alpha = 0.15$

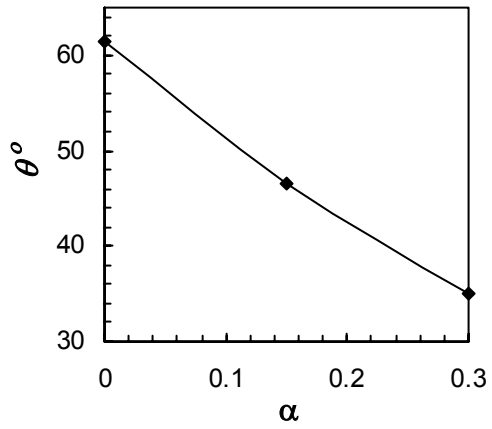

Figure 5: Variation of θ, with α, under the plane strain condition (σ_o = 400 MPa)

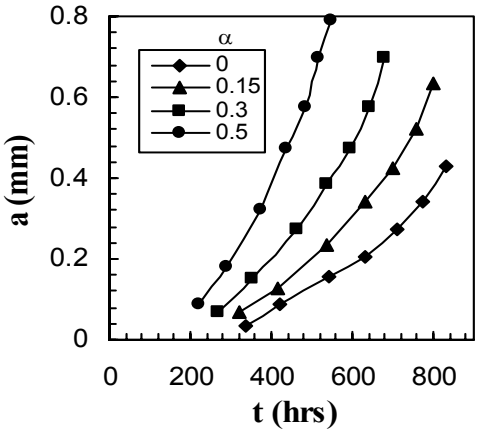

Figure 6: Variation of a, with t, for a range of α, under the plane strain condition (σ_o = 400 MPa)

TABLE 2
ESTIMATED FAILURE LIVES, t_f (hrs), FOR A RANGE OF α VALUES

	Waspaloy (σ_o=400 MPa)	
α	P Strain	P Stress
0.0	7063	1022
0.15	5665	634
0.3	----	773
0.5	----	612

The failure life obtained for a uniaxial specimen, using the Waspaloy properties at 400 MPa, is 5809 hrs. Therefore, it is obvious that under plane stress conditions, the existence of the narrow notch results in a significant reduction in life, while the failure lives of the narrow notch specimen under plane strain conditions are similar to those of the uniaxial specimen.

DISCUSSION AND CONCLUDING REMARKS

The results of the damage mechanics FE modelling have been used to assess the creep fracture behaviour of short cracks by using a 2D narrow notch model. The material properties used were related to a Ni-base superalloy (Waspaloy) at 700^o C. Damage distributions and accumulation near the notch, with time, were used to identify the crack initiation and its direction of growth. Since the main purpose of this work was to identify the trends of the crack growth, an arbitrary damage level of ω = 0.5 was chosen to represent the trends of crack growth and an arbitrary damage level of ω = 0.8 was used to obtain the crack growth with time. Failure life was roughly estimated using the times at which the high damage (ω = 0.5) zones reached a significant length (≥ 1 mm). These simplifications for crack growth and life estimate will not affect the general behaviour of the specimen.

The results obtained have shown that, under plane stress conditions, the high damage zone would be formed and would grow inwards along the plane of symmetry of the notch. Under plane strain conditions, bifurcating cracks would be formed, i.e. the high damage zone would grow in a direction inclined at an angle of between 35 and 60^o to the plane of symmetry of the notch, for α-values in the range of 0 to 0.3. The growth direction angle reduces significantly with increasing α, see Figure 5, and the inclined angle reduces to zero, when $\alpha \rightarrow 1$.

The results of the crack growth behaviour obtained, under plane strain conditions, Figure 6, have clearly shown the trends of the crack growth with time, i.e. crack growth occurs more rapidly with increasing time. It can be also seen that the failure lives estimated, Table 2 and Figure 6, reduce with increasing α, which is

similar to the behaviour indicated by results obtained for a Bridgman notch bar made from the same material [4]. However, in addition to this similarity, bifurcation behaviour was not observed in the damage modelling of the axisymmetric Bridgman notch model, where the failure damage initiated and grew along the minimum notch section, perpendicular to the direction of the applied axial load.

Although the local plastic behaviour was not taken into account and the crack growth was described by creep continuum damage modelling, the forms of the crack growth directions, obtained from the simplified plane stress and plane strain models, were found to be similar to the patterns of the plasticity zones, ahead of crack in a plate of finite thickness, subjected to tensile loading [5]. In this case, the stress state near the two free surfaces is close to that of plane stress and the stress state near the centre is close to plane strain [5]. Therefore, the difference in the crack growth direction between the plane stress and plane strain conditions is caused by the difference in the stress state or the creep strain constraint near the crack.

References

1. Hayhurst, D. R. (1983) In: *Engineering Approaches to High Temperature*, pp. 85-176, Wilshire, B. and Owen, D. R. J. (Eds). Pineridge Press, Swansea.
2. Moberg, F. (1995) Implementation of constitutive equations for creep damage mechanics into the ABAQUS finite element code, SAQ/FoU-Report 95/05.
3. Sun, W., Becker, A. A. and Hyde, T. H. (1999) 2D functions of ABAQUS UMAT damage code for creep continuum damage mechanics analyses, Internal Report, University of Nottingham.
4. Hyde, T. H., Xia, L. and Becker, A. A. (1996) *Int. J. Mech. Sci*. 38, 385.
5. Knott, J. F. (1973) *Fundamental of Fracture Mechanics*, Butterworths, London.

ORAL REFERENCE: ICF100658OR

EFFECT ON CREEP IN TENSILE FAILURE OF EARLY AGE CONCRETE

K.IRIYA and H. UMEHARA

Nagoya Institute of Technology
Gokiso-cho, Showa-ku, Nagoya, Japan, ZIP 466-0188

ABSTRUCT

The effects of stress-strength ratio and loading age on the tensile creep of concrete at early ages are elucidated on the basis of tensile creep experiments. Furthermore, effects of creep strain to failure are assessed by experiments. It is noted that the effects of stress-strength ratio are significant. It is concluded that capacity of tensile strain after loading is effected by loading age and stress and strength ratio. The results show that the strain capacity loaded at early ages is larger than others.

KEY WORDS

tensile creep, early age, stress- strength ratio ,creep failure

INTRODUCTION

This study has been carried out for rising accuracy of thermal stress analysis due to hydration heat of cement. The authors have already presented results of experimental creep studies of concrete at early ages, such as compressive creep [1] and creep during the unloading process [2]. They have also described a creep model [3] which is applicable to the prediction of thermal stress. Further, they have shown [4] the difference between compressive and tensile creep based on experiments at the same condition. In this paper, the effects of loading age and stress and strength ratio on tensile creep are investigated with the aim of presenting experimental data of tensile creep. An additional investigation is carried out on the effect of creep strain on tensile failure, in order to assess the effect of creep on cracking.

PROCEDURE OF TENSILE CREEP EXPERIMENTS

Procedure of tensile creep test is not defined in any standard. The method described in this paper is developed in the series of experiments. A dog-bone specimen is improved in order to observe creep failure and a embedded strain-meter is improved for dog-bone specimen.

The mix proportion used for this experiment was selected from candidates commonly

used in actual reinforced concrete work in NAGOYA and it has a compressive strength of used 30N/mm^2, a water cement ratio of 40%, and a sand ratio of 44.6%. The mix proportion is illustrated in TABLE 1. Concrete was mixed in a temperature controlled laboratory at 20℃ and cast in molds before storage under the same conditions for 24 hours. Specimens were then demolded and immediately sealed with an aluminum membrane in order to avoid diffusion of moisture. Specimen were cured in a temperature - and moisture - controlled room at 30 ℃ and 98% RH until loading, which took place at 1 to 7 days.

TABLE 1 MIX-PROPORTION

Slump (cm)	Air (%)	W/C (%)	s/a (%)	Unit weigh (kg/m^3)				
				W	C	S	G	AD
8.0	4.0	55.0	44.6	172	313	787	1015	1.16

The creep test apparatus was of lever type with a temperature and humidity controlled enclosure in the loading area [1]. Humidity of every case was controlled at 98%. The strain of an unloaded specimen made under the same condition was measured in order to compensate for shrinkage not caused by creep, such as automogenous shrinkage so on. Creep strain is calculated by extracting the measured strain of the unloaded specimen from the strain of the loaded specimen. Tensile strength at the loading age, which was needed to calculate the stress-strength ratio, was measured by a splitting test on an unloaded specimen cured under the same conditions as the loaded ones.

Loading was by pulling on the attachments fixed to top and bottom of a specimen. Although this creep test apparatus is able to directly apply tensile stress by means of a lever, but a bending moment might be generated due to shifting of the loading axis from the center of the specimen due to creep deformation. An automatic adjusting system was added to compensate for this effect. Since the embedded bolts or epoxy resin for the pulling attachment might lead to failure at surface of the attachment at early ages, such as 1 day, and at high stress-strength ratios such as 60%, a dog bone specimen was better for such experiments. Dog-bone specimen is shown in Fig.1.

Embedded strain meters modified to take measurements of concrete at early ages were

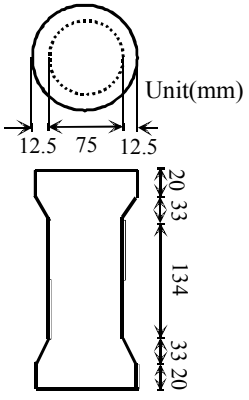

Fig.1 Dog-Bone Typed Specimen

TABLE 2 CASES OF THE EXPRIMENTS

Case No.	Loading age (day)	S/S (%)	Curing temp (℃).	Loading temp. (℃).
1	1	10	30	30
2	1	20	30	30
3	1	40	30	30
4	1	60	30	30
5	1	70	30	30
6	3	20	30	30
7	3	40	30	30
8	3	50	30	30
9	3	60	30	30
10	3	70	30	30
11	5	20	30	30
12	5	40	30	30
13	5	50	30	30
14	5	60	30	30
15	5	70	30	30
16	7	20	30	30
17	7	40	30	30

used for creep strain. Since the center section of the dog bone specimens is only 75 mm in diameter, the meter was improved to a more slender type in this case.

The experimental cases are shown in TABLE 2. The effect of stress-strength ratio (S/S) was investigated in cases 1 to 17. The loading period was basically 5 days.

EXPERIMENTAL RESULTS AND DISCUSSION

Tensile Creep

The relationships between creep strain with loading at 1 day, 3 days, and 5 days for several S/S value are shown in Figs.2~4. Although creep strain increased significantly for the 3 days after loading, it reached a steady state at 5 days. The loading period was chosen to be 5 days in this study, since creep strain at early ages is affected significantly by several factors during this period. Creep strain at early period immediately increases after loading and its increment is significant as at an early age and at high stress-strength ratio. The relationship between stress-strength ratio and final creep strain at several loading ages is shown in Fig. 5. No linear relationship passing through the zero point is obtained in Fig.5 up to S/S=40%. Creep strain at 1 day loading is larger than other ages at lower S/S values and the effect of S/S is not significant. Creep strain increases at 40% of S/S

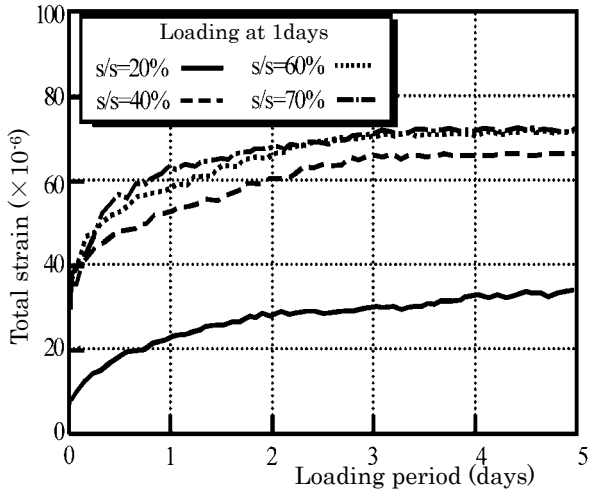

Fig.2 Effect of stress-strength

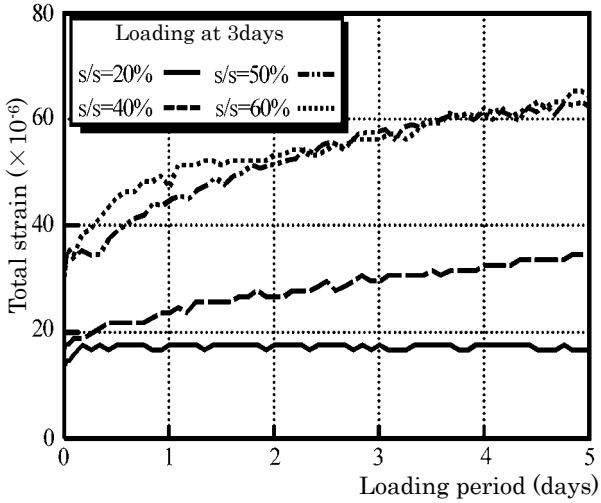

Fig.3 Effect of Stress-strength

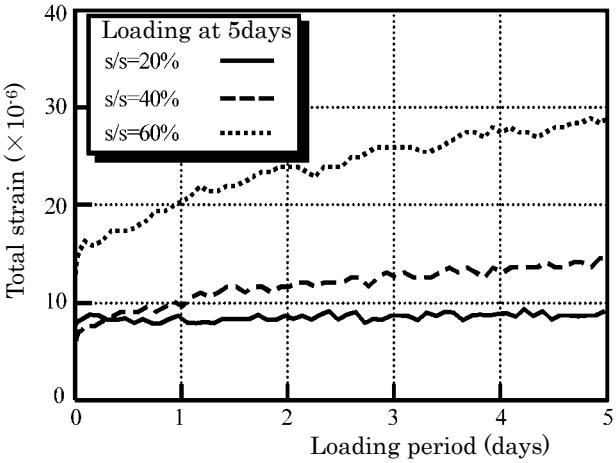

Fig.4 Effect of Stress-strength ratio

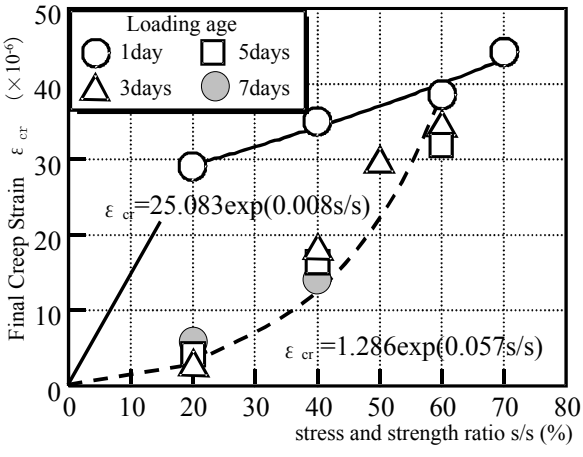

Fig.8 Stress-strength ratio and final creep strain

value in cases of loading at 3, 5, and 7 days. Final creep strain is strongly influenced by the stress-strength ratio in this study. Although tensile creep strain decreases with rising loading age, it is almost similar at other loading ages except 1 day in Fig.5. And the effect of loading age becomes smaller at higher S/S values in Fig.5. Loading stress increases with constant stress-strength ratio as loading age increases, since strength increases with age. Besides, creep decreases with rising loading age, since the matrix of cement paste hydrate becomes rigid as hydration progresses. The fall in creep strain with increasing loading age is nearly equal to the rise in loading stress due to hydration. This assertion is supported by Fig.6, in which the relationship between loading stress and final creep strain is shown for several loading ages. Relationship between loading age and final creep strain is shown in Fig. 7. The final creep strain decreases at greater loading ages in the case of loading at the same stress.

It can be concluded that factors which dominate the fall in tensile creep affect the rise in tensile strength as hydration progress and that both phenomena are caused by the rigidity of the cement paste matrix. Although the effect of loading age is insignificant at S/S values of more than 60%, the creep strain might reach to the deformation limit at these higher S/S ratios. It can be concluded that effect of deformation limit is more significant than effect of loading age. Creep failure might occur at such S/S ratios, if the stress were continuous. Although creep failure is described later, the possibility of creep failure is supported by the fact that tensile creep specimens failed within a day after loading at S/S=70% ~ 80%. The effect of stress-strength ratio at one day is smaller than at other loading ages and the final creep strain is smaller in this case.

Although creep strain is mainly generated by seepage of pore water of cement paste on compressive creep at a matured age, it is considered that creep strain is generated by defective zone and micro cracking at an early age due to weakness of cement paste. Since the results above mentioned show that large creep strain is generated with independence on stress-strength ratio in loading age of 1 day, defective zone might cause creep deformation upon tensile creep at an early age. The mechanism of tensile creep generation at one day is asserted slightly different from that at other ages.

Effect of creep strain on tensile failure

Creep strain is assumed to have no influence on steady tensile failure in thermal stress analysis, since it relaxes completely into constrained stress, such as thermal stress. However tensile creep might influence capacity of tensile strain, and this assumption is supported by observation of cracking at lower strain than 100 μ , which is ordinary tensile strain capacity, at continuous tensile loading.

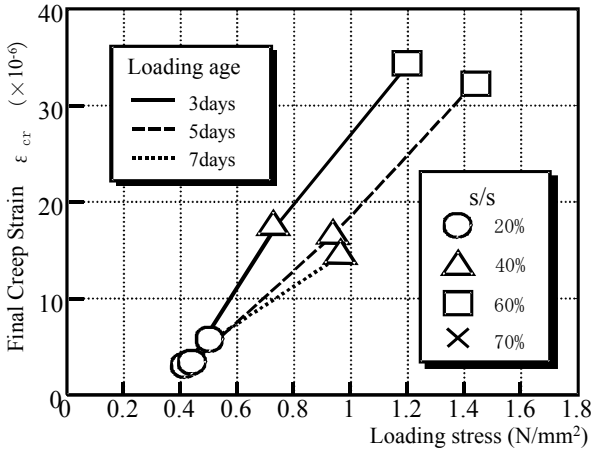

Fig.6 Loading stress and final creep strain

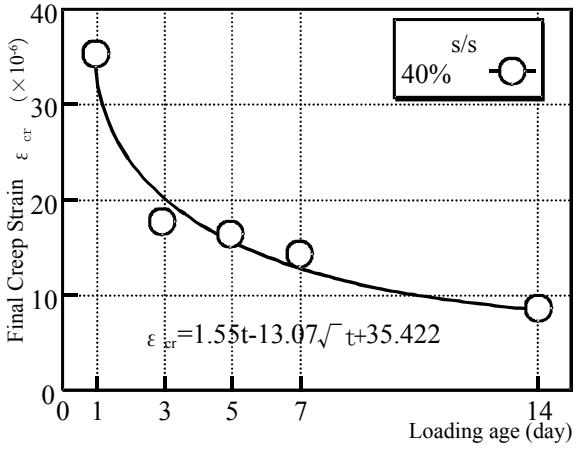

Fig.7 Loading age and final creep strain

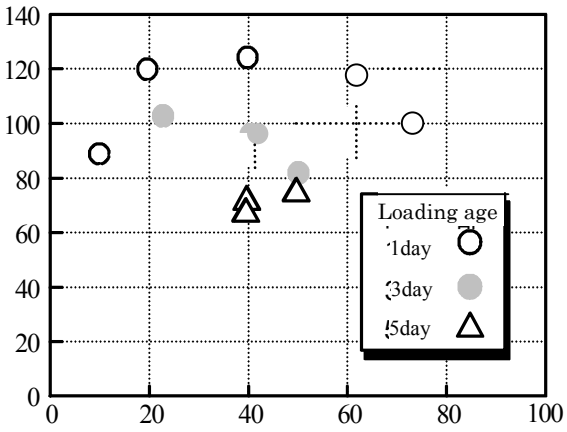

Fig.-8 Stress and strength ratio and strain capacity

Tensile failure tests were carried out by adding further stress after finishing the tensile creep tests in order to investigate the effect of creep strain on tensile failure.

Strain capacity after tensile creep test is defined as follows;

(strain capacity) = (total strain at failure) – (creep strain) –
(strain of unloaded specimen, consisting of automogenous shrinkage etc.) (1)

The relationship between strain capacity and stress-strength ratio in the creep tests is shown in Fig. 8. Regarding the effect of creep strain on the strain capacity, it should be noted that strain capacity is effected at higher S/S= 40%, although little effect is observed at less than 40%. And it is noted that significant decrement of strain capacity is observed at 70%. It can be pointed out that design tensile strain capacity should decreased by taking the effect of creep into account beyond S/S=40% from the results of this study. However, this effect hasn't been applied for prediction of cracking in thermal stress analysis. Specimens loaded at 1 day and 5 days with S/S = 80% failed in within 1 hour of adding all loads. Although it is considered that bending moment might be added by adjusting error of test apparatus, possibility of creep failure is not negligible. The relationship between strain capacity and generated creep strain is shown at each loading age in Fig.9. Although higher creep strain induces lower strain capacity in each loading

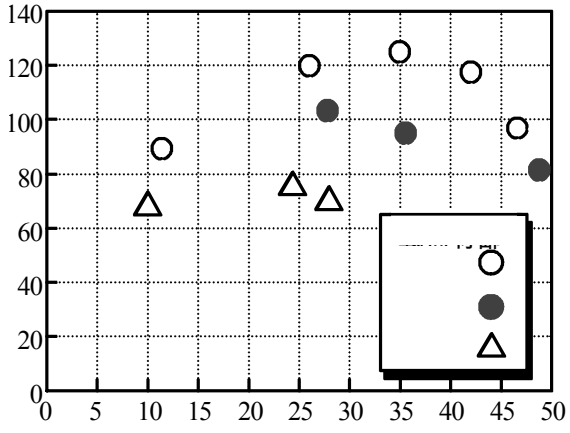

Fig.9 Creep strain and strain capacity

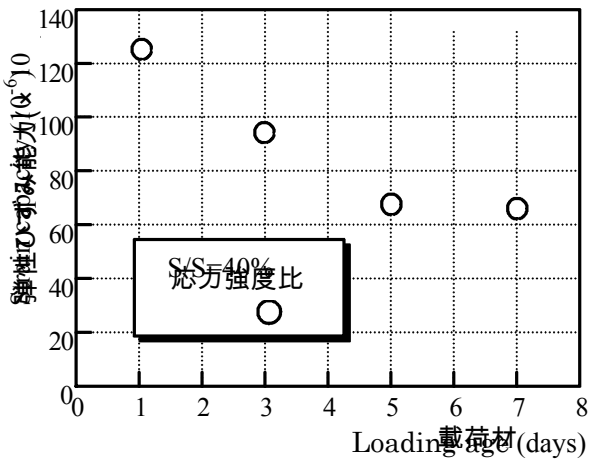

Fig.10 Loading age and strain capacity

age, no certain relationship is observed in investigation of all data. It is noted that strain capacity isn't effected by creep strain but by stress and strength ratio. This means that decrement of strain capacity is induced by generating defective zone at higher stress and strength ratio.

The relationship between strain capacity and loading age at S/S=40% is shown in Fig.10. It is noted that strain capacity decreased with rising of loading age. It seems to reach a stable value beyond 5 days, and the strain capacity after tensile creep at 5 days is approximate 60 μ . Although strain capacity of 1 day's loading is larger than others, which shows the highest creep strain due to generating defective zone, it is considered that healing at defective zone might be occurred corresponding to hydration at such a early age loading.

CONCLUSION

The results obtained in this study are described as follows.

1) The effects of stress-strength ratio on creep strain when loading takes place at 3 to 7 days of loading age are significant. No linear relationship was observed at low stress-strength ratios such as 20% ~40%. Creep strain significantly increased beyond S/S=60 %.
2) The creep strain with loading at 1 day is larger than that when loading takes place at 3 days ~ 7 days for low stress-strength ratios such as 20% ~40%. Furthers, the effects of stress-strength ratio with loading at 1 day are less significant than with loading at 3 ~7 days. It is considered that the creep strain with loading at 1 day is larger than in other cases, since micro cracking easily occurs due to weakness of the cement hydrate.
3) Tensile creep strain decreases at early age with loading age. However, this effect of loading age is smaller than that of stress-strength ratio.
4) Tensile strain capacity after creep test is effected by stress and strength ratio. Amount of effect is as small as early age loading.
5) Tensile creep strain induces little effect on tensile failure for S/S=20 ~ 40%. Certain effects can be observed in tensile failures at more than S/S=40 %, such as decreasing strain capacity to failure at high stress-strength ratio.

ACKNOWLEDGEMENT

Mr.Hattori.T, and Mr.Negi.T, and the students at NAGOYA Institute of Technology, are acknowledged for the support this experimental study.

REFERENCE

[1] Iriya,K., Hiramaoto,M., Hattori,T., Umehara,H. (1997):Creep Behavior for Early Aged Concrete, International Conference on Engineering Materials, CSCE & JSCE
[2] Iriya,K., Hattori,T, Negi,T., and, Umehara,H. (1999) : Study on creep behavior in the unloading process for early aged concrete, Journal of materials concrete structures and pavement, JSCE, V-42, pp.165~pp.174.
[3] Iriya,K., Negi,T., Hattori,T., and, Umehara,H. (2000):Study on Tensile Creep of Concrete at an Early Age, Concrete Library International, No.35, pp.135 ~ pp.150, JSCE
[4] Iriya,K., Hattori,T., and, Umehara,H. (1999) : Study on the arelationship Between Compressive Creep and Tensile Creep of Concrete at an Realy Age, Concrete Library International, No.33, pp. 185 ~ pp. 198,

CREEP FRACTURE OF CERAMIC-MATRIX COMPOSITES

B. Wilshire and H. Burt

Department of Materials Engineering, University of Wales,
Swansea, SA2 8PP, UK

ABSTRACT

The tensile creep and creep fracture properties in air at 1573K are compared for four composites produced with Al_2O_3 or SiC matrices, reinforced with interwoven bundles of either Nicalon™ or Hi-Nicalon™ fibres aligned at 0/90° to the stress axis. This analysis identifies the creep damage processes governing the strains and times to failure, suggesting avenues for development of improved SiC-fibre-reinforced ceramic-matrix materials.

KEYWORDS

Creep; Creep Fracture; Ceramic-Matrix Composites; Fibre Reinforcement.

INTRODUCTION

To combat the toughness deficiencies of monolithic ceramics, major R&D programmes have been directed to the manufacture and evaluation of ceramic-matrix composites (CMCs) reinforced with dispersions of ceramic whiskers or with arrays of ceramic fibres. However, for applications involving long periods of service without failure under load at high temperatures, fibre-reinforced CMCs display creep and creep fracture properties which are superior to those exhibited by whisker-reinforced products [1]. In seeking to interpret the creep behaviour patterns observed for fibre-reinforced composites, the damage processes leading to fracture have often been inferred [2-6] from the creep mismatch ratio (CMR) defined [2] as

$$CMR = \dot{\varepsilon}_F / \dot{\varepsilon}_M \tag{1}$$

where $\dot{\varepsilon}_F$ and $\dot{\varepsilon}_M$ are the creep rates of the fibres and matrices respectively. With this concept [2], when the creep resistance of the fibres exceeds that of the matrix (CMR < 1), the dominant damage mechanism is considered to be periodic fibre failure. Conversely, when the fibres have a lower creep strength than the matrix (CMR > 1), the principal damage process is seen as matrix cracking. Yet, even for nominally-identical fibre-reinforced materials, the fibres have been considered to be more creep resistant than the matrix [7] and *vice versa* [4]. For this reason, the comparative creep strengths of the fibres and the matrices are now assessed for a series of fibre-reinforced CMCs, anticipating that the mechanistic insights gained by understanding the processes governing creep damage accumulation and fracture will indicate practical avenues for development of improved product ranges.

MATERIALS

The strength characteristics of fibre-reinforced CMCs depend on load transfer to large volume fractions of high-modulus fibres, with weak fibre-matrix interfaces allowing intact fibres to bridge across the faces of cracks developing in the ceramic matrices [8-10]. To clarify the rôles of the fibres, matrices and fibre/matrix interfaces in determining the creep and creep fracture properties, the present study considers four CMCs, reinforced with various types of silicon carbide fibres, namely,

- a SiC-fibre-reinforced Al_2O_3-matrix composite [7], designated as SiC_f/Al_2O_3, and
- three SiC-fibre-reinforced SiC-matrix materials, now referred to as standard SiC_f/SiC [7], enhanced SiC_f/SiC [5] and $HNSiC_f/SiC$ [6].

The distinguishing compositional and microstructural characteristics of these four composites are summarized in Table 1, with the following comments made to amplify the descriptions given.

All materials were reinforced with ~0.4 volume fractions of ~12 to 15μm diameter SiC fibres, incorporated as bundles of ~500 fibres interwoven to form 2D layers of fabric, which were aligned and stacked to obtain multilayer samples having 0/90° fibre architectures. However, the standard SiC_f/SiC and enhanced SiC_f/SiC specimens were produced with plain woven bundle configurations, while the $HNSiC_f/SiC$ and SiC_f/Al_2O_3 were made with a satin weave. Compared with the plain woven arrays, the extent to which the fibres bend under load and the attendant risk of fibre damage should be lower with the satin weave.

In addition to differences in weave pattern, these 0/90° composites were reinforced with two types of SiC fibre. Thus, the SiC_f/Al_2O_3, standard SiC_f/SiC and enhanced SiC_f/SiC samples were produced using Nicalon™ NLM 202 fibres (Nippon Carbon Co., Tokyo, Japan). With these fibres, the presence of an amorphous oxycarbide ($SiC_{0.85}O_{0.15}$) phase results in a loss of creep resistance during long term exposure at elevated temperatures [11]. This deleterious amorphous phase can be eliminated by electron radiation under vacuum [12,13], giving the Hi-Nicalon™ fibre used to reinforce the $HNSiC_f/SiC$ product (Table 1). As well as possessing a higher modulus, these Hi-Nicalon™ fibres are expected to display better long-term creep strengths than Nicalon™ NLM 202 fibres.

The fibres in the SiC_f/Al_2O_3 material were coated with a thin BN layer before a ~5μm thick SiC coating was deposited by chemical vapour infiltration (CVI). The Al_2O_3 matrix was then introduced by *in-situ* directional oxidation of a liquid aluminium [14,15]. In contrast, with the three SiC-fibre-reinforced SiC-matrix composites (now collectively termed SiC_f/SiC type materials), thin carbon interface layers were obtained by decomposition of a hydrocarbon gas before the fibre preforms were CVI densified to produce the SiC matrices. Although the methods used to create the ceramic matrices were different, in all cases, the matrix porosities were ~15%.

Compared with the double BN/SiC interfaces in the SiC_f/Al_2O_3 samples, the carbon interfaces in the SiC_f/SiC type materials are more prone to oxidation during creep exposure. For this reason, the SiC matrices in the enhanced SiC_f/SiC and $HNSiC_f/SiC$ products contained boron-based particulate additives. These additives react with oxygen to form a borosilicate glass, which seals cracks developing in the 'enhanced' matrices [16,17]. In this way, the vulnerable carbon interfaces are protected by limiting oxygen penetration into the testpieces during creep.

TABLE 1

DISTINGUISHING CHARACTERISTICS OF THE SiC FIBRE-REINFORCED COMPOSITES

MATERIAL DESIGNATION	FIBRE TYPE	INTERFACE TYPE and THICKNESS	MATRIX TYPE	REF
SiC_f/Al_2O_3	Nicalon™ NLM 202	BN/SiC (~5μm)	Al_2O_3	7
Standard SiC_f/SiC	Nicalon™ NLM 202	Carbon (<0.5μm)	SiC	7
Enhanced SiC_f/SiC	Nicalon™ NLM 202	Carbon (<0.5μm)	Enhanced SiC	5
$HNSiC_f/SiC$	Hi- Nicalon™	Carbon (<0.5μm)	Enhanced SiC	6

RESULTS and DISCUSSION

The creep and creep fracture properties of the 0/90° fibre-reinforced CMCs (Table 1) can be compared using data obtained in tensile creep tests carried out in air at 1573K [5-7]. Under the test conditions studied, continuously decaying creep curves were recorded, i.e. after the initial strain on loading at the creep temperature, the creep rate decreased gradually with time towards a minimum value, with no well-defined secondary or tertiary creep stages apparent before fracture occurred. However, with the standard SiC_f/SiC samples, the creep strains to failure were low (~0.002) at all stress levels [7]. In contrast, with the other three materials, the creep ductility appeared to increase with decreasing stress, approaching values of ~0.03 in tests of around 3000 hours duration with the SiC_f/Al_2O_3 specimens [7].

Fibre Control of Creep and Fracture

At 1573K, the UTS for the SiC_f/Al_2O_3 samples is the same as the value (~230 MPa) recorded for the three SiC_f/SiC type products [5,6]. Moreover, broadly similar stress/minimum creep rate behaviour is found for all four CMCs (Figure 1a). Clearly, stresses about five times larger must be applied to Nicalon™ NLM 202 fibres [18] to achieve creep rates comparable with those observed for the Nicalon™-fibre-reinforced materials. Since the longitudinal (0°) fibres occupy about one fifth of the crosssectional areas of the testpieces, for all four 0/90° composites, the creep strength is determined by the longitudinal fibres.

Although the fibre reinforcements are similar for the four CMCs (Table 1), the creep and creep rupture strengths are comparable for the SiC_f/Al_2O_3, the enhanced SiC_f/SiC and the $HNSiC_f/SiC$ samples, but inferior properties are displayed by the standard SiC_f/SiC material (Figure 1). This seemingly-anomalous result is attributable to differences in creep ductility [7]. Thus, when continuously-decaying creep curves are observed in tension, the rupture life (t_f) can be defined as the time taken for the accumulated creep strain to reach the limiting creep ductility (ε_f). Simultaneously, the creep rate decays with time, reaching the minimum creep rate ($\dot{\varepsilon}_m$) as the curves terminate. The creep curves presented in Figure 2 then show that the initial variations in creep strain with time are similar for the standard SiC_f/SiC and enhanced SiC_f/SiC products, as would be expected for two materials having nominally-identical fibre reinforcement (Table 1). However, low ductility termination of the creep curves for the standard SiC_f/SiC samples (Figure 2) leads to minimum creep rates which are faster and rupture lives which are shorter than the values found when failure occurs at higher ductilities with the other three composites. (Figures 1 and 2).

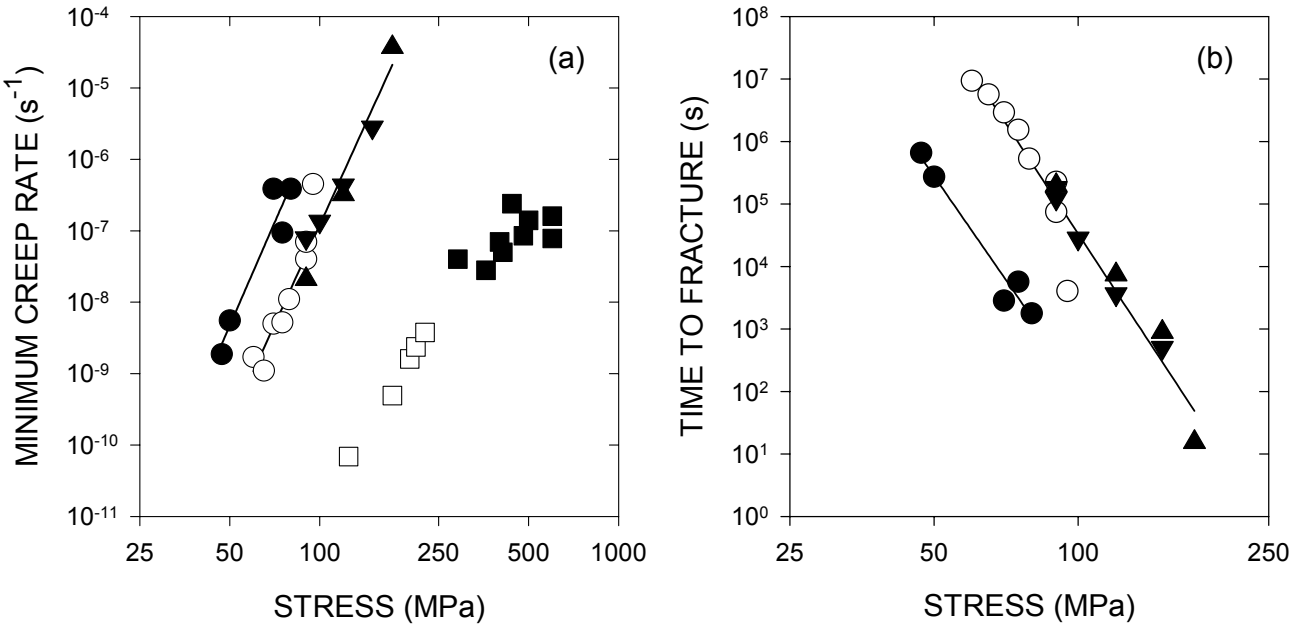

Figure 1. Variations of (a) minimum creep rate and (b) creep rupture life with stress for SiC_f/Al_2O_3 [○], standard SiC_f/SiC [●], enhanced SiC_f/SiC [▲] and $HNSiC_f/SiC$ [▼] composites at 1573K, together with creep data for Nicalon™ NLM 202 fibres [■] at 1573K and sintered silicon carbide [□] at 1773K.

Oxidation Effects During Creep

Since the creep ductility defines the point of creep curve termination (Figure 2), thereby affecting the minimum creep rates and rupture lives recorded (Figure 1), it is necessary to explain ductility variations in relation to the damage processes leading to fracture. For all CMCs considered (Table 1), the rates of creep strain accumulation are determined by the creep resistance of the longitudinal fibres, with creep of the fibres accompanied by cracking of the weak brittle matrices (Figure 3a). The developing matrix cracks can by-pass transverse fibres, but become arrested within the longitudinal fibre bundles. On progressing into the longitudinal bundles, the weak fibre/matrix interfaces allow the crack faces to be bridged by intact fibres. In turn, creep of the bridging fibres govern the rates of crack growth. Support for this view is then provided by the patterns of behaviour shown in Figures 1a and b, from which it can be shown that the times to fracture increase systematically with decreasing minimum creep rate. This creep rate dependence of the rupture life confirms that, since the longitudinal fibres control creep strain accumulation, these fibres also determine crack growth rates. However, the bridging fibres fail progressively as oxygen penetrates into the testpieces during creep exposure. As a result, the fracture surfaces of broken specimens show planar crack growth zones, characterized by in-plane oxidation-assisted fibre failure, together with regions where sudden failure occurs by fibre full out (Figure 3b). Yet, while this sequence of events is applicable to the four CMCs described in Table 1, differences in the susceptibility of the fibres to oxidation-assisted failure affect the observed creep ductility values.

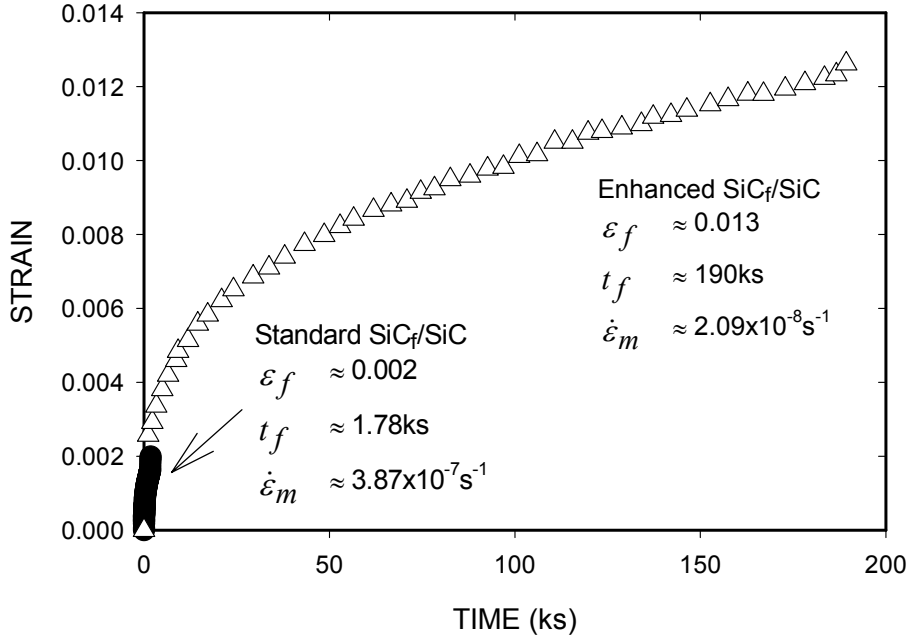

Figure 2. Creep strain/time curves at 90MPa for standard SiC_f/SiC and enhanced SiC_f/SiC at 1573K.

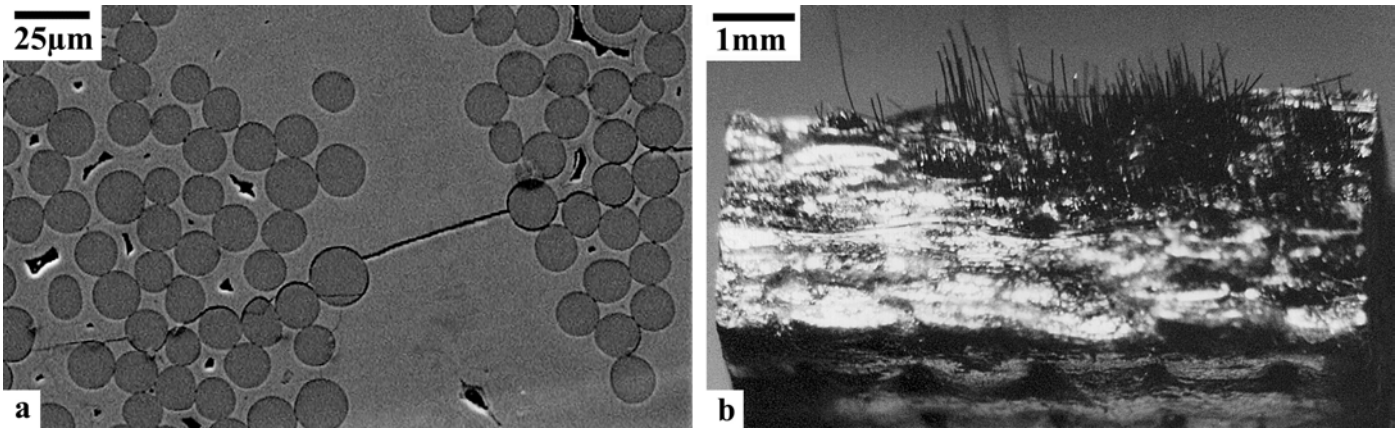

Figure 3. Micrographs showing (a) matrix cracking and (b) the planar crack growth zone and final fibre pull-out region on the fracture surface of a standard SiC_f/SiC sample.

With the standard SiC_f/SiC samples, cracks nucleate at macropores present in the matrix regions between the interwoven fibre bundles. These surface-nucleated cracks link up and grow, with oxygen penetrating directly along the opening crack. Rapid oxidation-assisted fibre failure then results in high crack growth rates, with low-ductility failure occurring when the cracks reach the size required to cause sudden failure by fibre pull out (Figure 3b). In contrast, with the enhanced SiC_f/SiC and $HNSiC_f/SiC$ materials, the glass-forming boron-based particles in the 'enhanced' matrices reduce the rates of oxygen penetration, oxidation-assisted fibre failure and crack growth. Consequently, creep must continue for longer times to reach higher strains (Figure 2) before the cracks attain the size needed for failure by fibre pull out.

With the SiC_f/Al_2O_3 composite, low rates of oxidation-assisted fibre failure also occur, but for different reasons. Firstly, residual-stress-induced microcracks present in the as-processed matrix [20] allow easy nucleation of many small cracks throughout the specimen gauge length, seemingly with oxygen ingress being relatively slow through the microcracked Al_2O_3 matrix. Secondly, the double BN/SiC interface layers are more resistant to oxidation than the carbon interfaces in the SiC_f/SiC type materials (Table 1). Hence, crack growth rates are lower and the creep ductilities are higher, resulting in creep rates and rupture lives comparable with those observed for the enhanced SiC_f/SiC and $HNSiC_f/SiC$ products (Figure 1).

Factors Affecting Creep Performance

The present analysis indicates several avenues for enhancement of the creep and creep fracture properties of fibre-reinforced CMCs. In particular, the longitudinal fibres control the rates of creep strain accumulation and crack growth, demonstrating that the development of new high-strength high-stability fibres of weaveable diameter (~15μm) is essential for future high-performance composites. Indeed, the data included in Figure 1a show that sintered silicon carbide displays creep strengths at 1773K [19] which match those of Nicalon™ NLM 202 fibres at 1573K, illustrating the potential for property improvement attainable with SiC fibres.

In this context, it is surprising that the creep properties of the $HNSiC_f/SiC$ samples produced with satin-woven bundles of Hi-Nicalon™ fibres are similar to those for the enhanced SiC_f/SiC product manufactured with plain-woven bundles of standard Nicalon™ fibres (Figure 1). However, the longest test reported for these materials lasted only ~100 hours [5,6], suggesting that long-term results are needed to quantify the benefits of incorporating satin-woven arrays of Hi-Nicalon™ fibres. Even so, the use of Hi-Nicalon™ fibres should offer advantages when double BN/SiC fibre/matrix interfaces are employed (Table 1). The BN coatings are less susceptible to oxidation than carbon interfaces [21,22], but the BN coating process [23] involves a high temperature treatment (> 1773K). Hi-Nicalon™ fibres should then avoid the property degradation expected with standard Nicalon™ fibres. Thus, recent studies have shown that no reduction in room-temperature strength of $HNSiC_f/SiC$ samples produced with 0.4μm thick BN interface layers occurred after exposure in air for 600h at 1673K, whereas significant strength reductions were found after 200h at 1273K with $HNSiC_f/SiC$ specimens manufactured with carbon interfaces [24].

While the matrices of the present SiC-fibre-reinforced CMCs contribute little to the overall creep strengths, the matrix compositions and microstructures affect the observed creep ductilities. Thus, the fracture modes exhibited by the standard SiC_f/SiC product indicate that the procedures adopted for densification of the fibre preforms must avoid the formation of macropores between the interwoven fibre bundles and large pores within the fibre bundles, which offer preferred sites for crack nucleation. Moreover, the matrices determine the rates of oxygen penetration into the composites during creep exposure, influencing the rates of oxidation-assisted failure of the crack-bridging fibres and the rates of crack growth. In this context, procedures such as the incorporation of boron-based particulate additives [16,17] are effective, resulting in the enhanced SiC_f/SiC and $HNSiC_f/SiC$ displaying creep and creep fracture properties substantially better than those found for the standard SiC_f/SiC samples (Figure 1). A further option could then be to employ surface coatings, just as the use of protective ceramic coatings extends the operational life of aeroengine turbine blades produced from nickel-base superalloys.

CONCLUSIONS

In contrast to the views expressed in earlier studies [4,5], the creep strengths of the reinforcing fibres exceed those of the matrices in SiC_f/SiC type materials, as proposed for the SiC_f/Al_2O_3 composite [7]. For the four SiC-fibre-reinforced CMCs considered (Table 1), the rates of creep strain accumulation are then controlled by the longitudinal fibres, with creep of the fibres accompanied by cracking of the weak porous matrices (Figure 3a). However, the creep strengths of individual fibres vary, as evident from the scatter in the data for Nicalon™ NLM 202 fibres (Figure 1a). Since the weakest fibre regions deform most easily, the creep rate decays with time as the stress is transferred to stronger fibres (Figure 2).

The rates of crack growth are also governed by the creep resistance of the longitudinal fibres which bridge the cracks developing through the longitudinal fibre bundles. Even so, oxygen penetration into the testpieces during creep exposure promotes oxidation-assisted failure of the crack-bridging fibres, affecting the creep strains at which fracture finally occurs by fibre pull out (Figure 3b). Fracture then terminates the decaying creep curves (Figure 2), with the creep ductility values influencing the minimum creep rates and rupture lives recorded (Figure 1). On this basis, the development of improved CMCs depends not only on the fibre reinforcement but also on the rates at which the matrices allow oxygen ingress and the susceptibility of the fibre/matrix interfaces to oxidation.

REFERENCES

[1] Wilshire, B. and Carreño, F. (1999) *Mater. Sci. Eng*. A272, 38

[2] Holmes, J. W. and Chermant, J.L (1993) In: *Proc. 6th European Conf on Composite Materials*, pp 633-647, Naslain, R., Lamon, J. and Doumeingts, D. (Eds). Bordeaux, France.

[3] Lamouroux, F., Steen, M. and Vallés, J.L. (1996) *Comp. Sci. Tech*. 56, 825.

[4] Zhu, S., Mizuno, M., Kagawa, Y., Cao, J., Nagano, Y. and Kaya, H. (1997), *Mater. Sci. Eng*. A225, 69.

[5] Zhu, S., Mizuno, M., Nagano, Y., Cao, J., Kagawa, Y. and Kaya, H. (1998), *J. Am. Ceram. Soc.* 81, 2269.

[6] Zhu, S., Mizuno, M., Nagano, Y., Cao, J., Kagawa, Y. and Kaya, H. (1999), *J. Am. Ceram. Soc.* 82, 117.

[7] Wilshire, B. and Carreño, F. (2000) *J. Eur. Ceram. Soc*. 20, 463.

[8] Prewo, K. M. (1986) *J. Mater. Sci*. 21, 3590.

[9] Brennan, J. J. (1986) *Mater. Sci. Res*. 20, 546

[10] Evans, A. G. and Marshall, B. D. (1989) *Acta Metall*. 37, 2657.

[11] DiCarlo, J. A. (1994) *Comp. Sci. Tech.* 51, 213.

[12] Bodet, R., Bourrat, X., Lamon, J. and Naslain, R. (1995) *J. Mater. Sci.* 30, 661.

[13] Chollon, G., Pailler, R., Naslain, R. and Olry, P. (1995) In: *High-Temperature Ceramic-Matrix Composites II: Manufacturing and Materials Development*. pp299–236, Evans, A.G. and Naslain, R (Eds). Amer. Ceram. Soc., Westerville, OH.

[14] Newkirk, M. S., Urquhart, A. W., Zwicker, H. R. and Breval, J. (1986) *J. Mater. Res*. 1, 81.

[15] Newkirk, M. S., Lesher, H. D., White, D. R., Kennedy, C. R. and Urquhart, A. W. (1987) *Ceram. Eng. Sci. Proc*. 8, 879.

[16] Elahi, M., Liao, K., Reifsnider, K. and Dunyak, T. (1995) *Ceram. Eng. Sci. Proc*. 16, 75.

[17] Fox, D. S., (1995) *Ceram. Eng. Sci. Proc*. 16, 877.

[18] Simon, G. and Bunsell, A. R. (1984) *J. Mater. Sci*. 19, 3670.

[19] Wilshire, B. and Jiang, H. (1994) *Brit. Ceram. Soc*. 93, 213.

[20] Heredia, F. E., Evans, A. G. and Andersson, C. A. (1995) *J. Am. Ceram. Soc*. 78, 2790.

[21] Prouhet, S., Camus, G., Labrugere, C., Guette, A. and Martin, E. (1994) *J. Am. Ceram. Soc*. 77, 649.

[22] Gonczy, S. T., Butler, E. P., Khasqiwale, N. R. and Tsakalakos, L. (1995) *Ceram. Eng. Sci. Proc*. 16, 433

[23] Moore, A. W., Sayier, H., Farmer, S. C. and Morscher, G. N. (1995) *Ceram. Eng. Sci. Proc*. 16, 37.

[24] Takeda, M., Imai, Y., Kagawa, Y. and Guo, S. Q. (2000) *Mater. Sci. Eng*. A286, 312.

ORAL REFERENCE: 100234OR

CRITICAL ENERGY RELEASE RATE OF A BIMATERIAL ASYMMETRIC DOUBLE CANTILEVER BEAM (ADCB) WITH AN ADHESIVE LAYER.

N.B. Kuipers[1)], A. Bakker[1)], G.E. Schoolenberg[2)], M. Janssen[1)]

[1]Department of Materials Science, Delft University of Technology,
Rotterdamseweg 137, 2628 AL Delft, The Netherlands
[2] Shell International Chemicals Badhuisweg 3
1031 BN Amsterdam The Netherlands

ABSTRACT

Goal of this research is to determine the relation between the composition of a PS-PEB block copolymer and the adhesion of a PS-LDPE interface with the block copolymer as adhesive layer. The focus of this paper is the improvement of the test method.

The Critical Energy Release Rate (G_C) of an interface between Polystyrene (PS) and Low Density Polyethylene (LDPE) is measured with an Asymmetric Double Cantilever Beam (ADCB). It was preferred to use the block-copolymers in their practical form. Therefore techniques to characterise the thickness of the block-copolymer layer which require deuteration (e.g. SIMS or FRES) could not be used and an alternative route applying ellipsometry and AFM was established.

G_C is determinated by inserting a wedge at the interface with a constant velocity. The equilibrium crack length is continuously measured during the test over the total interface length.
From the crack length and the compliance the G_C is calculated. Different models for calculating the compliance are used. The new model "beam on elastic foundation with a correction for shear deformation" is found to give the smallest variation of G_C as a function of both the beam thickness and the beam thickness ratio. Correction for non-linear elastic behaviour reduces the variation of G_C as function of the beam thickness and beam thickness ratio.

The test method is improved by:
- Developing a method to place a smooth block copolymer layer of known thickness at the interface.
- Correcting Gc calculations based on the "beam on elastic foundation" model.
- Correcting the G_C calculations for shear deformation.
- Making a start in correcting the G_C calculations for non-linear behaviour.

KEYWORDS

Critical Energy Release Rate; Asymmetric Double Cantilever Beam; Compliance model; Adhesion, Block Copolymers, Wedge Splitting Test.

INTRODUCTION

The adhesion between two different polymers is a subject of extreme relevance for many polymer applications, notably for heterogeneous polymer blending. Compatibilisation of the interface by block-copolymers is known to improve the level of adhesion. The strength of a polymer interface, reinforced by a block-copolymer, has been the subject of many investigations. Block copolymers turn out to form effective 'stitches' between the two adherents.

For practical blends, compatibilisation with thermoplastic rubber type of tri-block copolymers is often applied. In this situation both the adhesion between matrix and block-copolymer as a pure phase and its effect on the strength of the interface between matrix and dispersed phase is of importance. As a model system exemplary for such a blend, in this investigation we chose a combination of polystyrene (PS) and low-density polyethylene (PE) with a SEBS (styrene- ethylene butylene- styrene) type of block-copolymer as a compatibiliser.

Creton et al [1] developed the "wedge splitting test" which is very suitable for measuring adhesion between two rigid polymers (Fig.1). Johnson, Kendall en Roberts [2] developed the JKR test to measure the adhesion between two elastic materials. Brown [3] and Creton [4] used a JKR-type of test, which can measure the strength of an interface between a glassy polymer and a rubber reinforced with their di-block. The JKR test requires the softer component to be fully elastic up to the annealing temperature, which is not the case for PE or SEBS. Therefore the wedge splitting test was chosen. However, so far this has been applied to polymers where stiffness differed no more than 10-20 %. The Young's modulus, E, of PS and PE differ a factor of about 20.

Creton et al [1] measured the adhesion between two rigid polymers with the ADCB-test. Their results show that adhesion per block copolymer chain increases with increasing block length. A considerable increase in the adhesion was found for block copolymers with sufficient long blocks to form entanglements with the adherent substrates. Up to this block length only a small increase in adhesion was measured due to the increase in chain pull out energy with increasing chain length. If the blocks are long enough to form entanglements the fracture mechanism is chain scission with of without plastic deformation of the substrate.

Effects of and number of chains per surface area have been systematically investigated by Brown [5] for glassy, amorphous polymers reinforced by their block copolymers. His results show that interfacial adhesion increases with increasing chains per surface until the surface is saturated.

EXPERIMENTAL

Materials

One beam is made of Polystyrene (PS) the other beam is made of Low Density Polyethylene (LDPE).
The interface is reinforced with block copolymer consisting of block polystyrene, a block hydrogenated polybutadiene (PEB) and another block polystyrene. PEB has a vinylpercentage of 40-45%.

The mean molair mass between entanglements, Me, is according to Wu [6] for PS 18.7 kg/mol and for PE 1.39 kg/mol.
The moleculair weight of the PS block is 7.3 kg/mol. This is 0,4 x Me_{PS}. The moleculair weight of the PEB block is 33,9 kg/mol. With a vinylpercentage of 40 this gives a moleculair weight of the back bone of PEB of 27,1 kg/mol. This is 19,5 x Me_{PE}.

Sample preparation

The sample preparation procedure was as follows. The PS and PE material were compression moulded to the required thickness in a vacuum mould. The temperature was 220°C.
One side of the mould was covered with a smooth chromed metal plate as is used for photographic purposes. Plates were then machined to produce beams of the proper dimensions (width: 10 mm, length 45 mm), taking care that the smooth surface was not damaged or polluted.

The block copolymer was dissolved in toluene and spin coated on a silica wafer at standard spinning conditions. The thickness of the layer was measured by ellipsometry. The layer was then picked up from the wafer by placing the PS beam (dried at 90°C) with its smooth surface on the wafer and annealing in an oven at 130°C (under nitrogen, 150 mbar) for 1 hour. AFM images of the wafer clearly show that this procedure practically removes all the block-copolymer from the wafer. The layer thickness measured with AFM is equal to the ellipsometry measurement.
Thickness variations were obtained by changing the concentration.

After applying the block-copolymer to the PS, the PE part of the specimen was stacked on the interface, and the whole specimen was annealed in an oven (48 hours at 130 °C, 125 mbar nitrogen) to obtain adhesion.

Experiments
The wedge splitting test is used (see figure 1), as mentioned in the introduction.

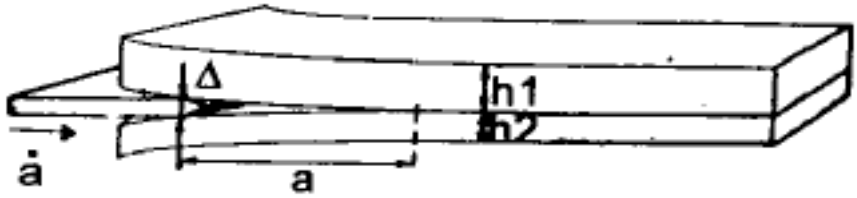

Figure 1: Wedge splitting test with an Asymmetric Double Cantilever Beam specimen.

The specimen is called "Asymmetric Double Cantilever Beam" because both beams have different thickness (h1 and h2 in figure 1) to minimise the tendency of the crack to propagate in a mode II direction. In order to test the most suitable ratio between the thickness (h) of both homopolymer beams several combinations of h_{PE} and h_{PS} were tested.
To determine G_C a wedge is inserted at the interface with a constant velocity of 0.1 mm/min. The equilibrium crack length is continuously measured during the test over 12 mm of the total interface length.
A video recording of 2 seconds is made every 1.51 minute, resulting in about 60 recordings of the crack length.

The inserting force on the wedge is measured during the experiment. It is found that this force is constant if the crack length is in equilibrium. An interval of 2.5 mm is choosen in which the inserting force fluctiations are minimal. During this interval 16 recordings of the equilibrium crack are made. These recordings are used for measuring the crack length.
The crack length is measured in the middle and on both sides (at a distance of the side of 20% of the specimen width). The avarage crack length is calculated from these meassurements. This avarge value is the avarage of the measurements of both sides and the measurement in the middle.
From the crack length, a, and the compliance, C, the critical energy release rate, G_C is calculated for each beam:

$$G_{C_i} = \frac{\Delta^2}{2b(C_1 + C_2)^2}\frac{dC}{da} \qquad (1)$$

In which Δ is the wedge thickness and b is the sample width.
Summation (i = 1..2) gives the G_C of the specimen.

The deflection of the beam and the load on the beam are not measured. Therefore a model is needed to calculate the compliance.

One model is the "simple beam model" in which the beams are considered to be clamped at the crack tip. The equation for G_c based on the "simple beam" model is:

$$G_C = \frac{3\Delta^2}{8a^4}\frac{\Pi E_i h_i^3}{\Sigma E_i h_i^3} \tag{2}$$

During the experiments other models are developed (see next section).

RESULTS: INFLUENCE OF BEAM THICKNESS (RATIO) AND COMPLIANCE MODEL ON G_C

Rutten has tested several combinations of h_{PE} and h_{PS} with a block copolymer (see materials) layer of about 21 nm [unpublished graduation thesis, Hogeschool Venlo HLO polymeerchemie, the Netherlands, in co-operation with Shell].
The layer thickness is uncertain because the method to place a smooth block copolymer layer of known thickness at the interface (see sample preparations) was not yet established by that time.
Rutten spincoated the block copolymer layer on the smooth PE surface. To estimate the layer thickness a block copolymer layer was spincoated under the same conditions on a silica wafer. The thickness of this layer is measured by ellipsometry.
Rutten used specimens with beam thickness of 2, 4 and 8 mm. Creating specimen with h_{PE}/h_{PS} of 2/8, 4/8, 2/2, 4/4, 8/2 and 8/4. Two specimen of each geometry.

His data were used to determine the most suitable ratio between the thickness (h) of both beams. The G_C-value of these specimens were calculated applying the equations based on the Kanninen's elastic foundation model [7] proposed by Creton [1]. In a similar range of thickness ratio data Creton showed that a minimum occurred, which was attributed to the lowest tendency of the crack to propagate in a mode II direction at this minimum. However our data showed a monotonously increasing Gc as a function of the thickness ratio.
When investigating the possible cause for this difference the original elastic foundation solution by Kanninen was revisited. It was found that where Creton relates the stiffness of the beam foundation to the stiffness of the beam under consideration. The stiffness has to be related to the stiffness of the opposite, supporting beam as originally intended by Kanninen. The equation for G_C based on the "beam on elastic foundation" model then change to:

$$G_C = \frac{3\Delta^2 E_1 h_1^3 E_2 h_2^3}{8a^4}\left(\frac{E_1 h_1^3 (1+0.64\frac{h_1 S_1}{a})^2 + E_2 h_2^3 (1+0.64\frac{h_2 S_2}{a})^2}{\left(E_1 h_1^3 (1+0.64\frac{h_1 S_1}{a})^3 + E_2 h_2^3 (1+0.64\frac{h_2 S_2}{a})^3\right)^2}\right) \tag{3}$$

with

$$S_{1,2} = \left(\frac{E_{2,1} h_{2,1}^3}{E_{1,2} h_{1,2}^3}\right)^{\frac{1}{4}} \tag{4}$$

Figure 2 shows the results of this calculation. Every point is the average of 2 measurements (2 specimens of each geometry).

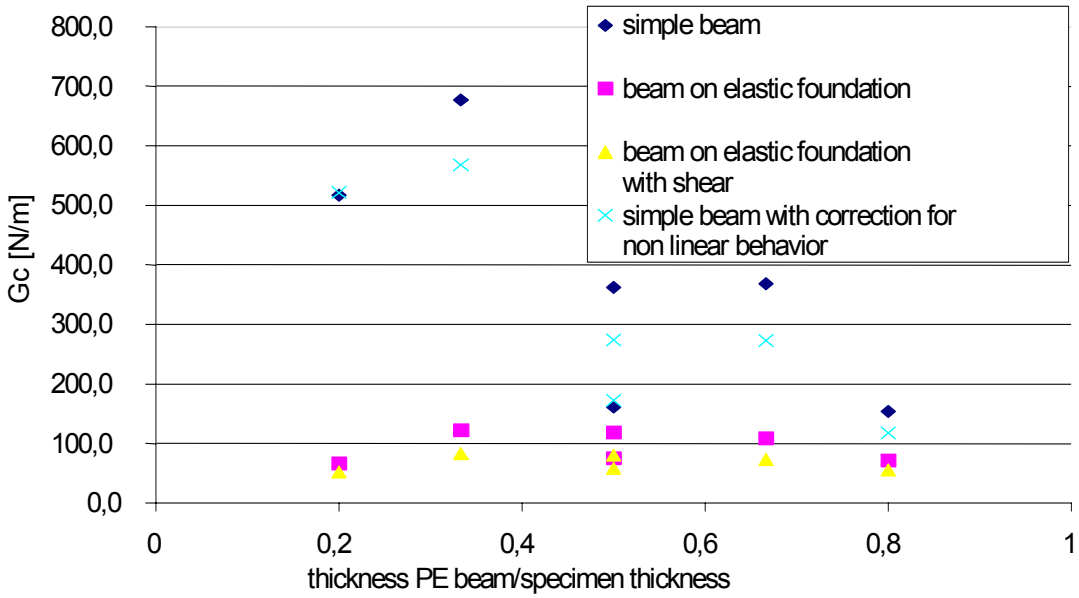

Figure 2: Critical energy release rate for different beam thickness ratio's and different compliance models. For thickness ration ratio's of 0,2 (h_{PE}/h_{PS} = 2/8), 0,33 (h_{PE}/h_{PS} = 4/8), 0,5 (h_{PE}/h_{PS} = 2/2 and h_{PE}/h_{PS} = 4/4 the lowest values of Gc at this thickness ratio are the values for 2/2), 0,66 (h_{PE}/h_{PS} = 8/4), 0,8 (h_{PE}/h_{PS} = 8/2),

Instead of showing a minimum a maximum is found. Furthermore data are still varying strongly with thickness and thickness ratio. It was then decided, given the relatively small ratio between beam length and thickness to include shear deformation in the elastic energy term. Resulting in the equation for C for beam 1 and 2 based on the "beam on elastic foundation with correction for shear stress" model:

$$C_{1,2} = \frac{4\left(\frac{aS_{1,2}}{0.64h_{2,1}}+1\right)^3}{E_{1,2}bh_{1,2}^3\left(\frac{S_{1,2}}{0.64h_{2,1}}\right)^3} + \frac{1.2a}{G_{1,2}bh_{1,2}} \tag{5}$$

Combination with equation 1 gives the energy release rate of each beam.
Beside the shear deformation the non-linear behaviour is another complication. Tensile tests show that PS behaves linear under the ADCB test conditions. The behaviour of PE however is non-linear. The beginning of the stress strain curve (tensile test acc. to DIN 53455-5, 50 mm/min) can be described by a power law:

$$\sigma = E_0 \varepsilon^n \tag{6}$$

In which σ is the stress, ε is the strain, E_0 and n are fitparameters. Fitting the stress strain curve from ε = 0.003 up to ε = 0.008 results in: E_0 = 4.02 (±0.82) x 10^7 N/m^2 en n = 0.663 ± 0.040.

Combination of this power law and the equation that Williams [8] derived for a DCB gives the energy release rate of one beam:

$$G = \frac{2n}{b(n+1)} P^{\frac{n+1}{n}} \left(\frac{2(n+2)}{bE_0h^{n+2}}\right)^{\frac{1}{n}} a^{\frac{n+1}{n}} \tag{7}$$

In which P is the force on the beam at the wedge. Summation gives the total G.

P has to be determinded by iteration:

$$(P_1 C_{n1})^{\frac{1}{n_1}} + (P_2 C_{n2})^{\frac{1}{n_2}} = \Delta_1 + \Delta_2 = \Delta_{tot} \tag{8}$$

The results of the Gc calculations are shown in figure 2 for every model. Every point is the average of 2 measurements (2 specimens of each geometry, 16 x 3 measurements pro specimen). The data still vary with thickness and thickness ratio. Table 1 shows the variation for each model.

Table 1:
Variation of Gc with thickness ratio, varation of Gc for given thickness ratio (h_{PE}/h_{total} = 0,5) but different beam thicknesses (h_{PE}/h_{PS} = 2/2 and h_{PE}/h_{PS} = 4/4) and the maximum variation of Gc for two specimen with identical geometry calculated with the four models.

Model	Gc variation with thickness ratio	Gc variation for same thickness ratio (= 0.5)	Meassurement variation
Simple Beam	523	200	145
Simple Beam with correction for non linear behavior	450	101	102
Beam on Elastic Foundation	56	43	36
Beam on Elastic Foundation with corr. for shear defformation	31	22	21

The new model "beam on elastic foundation with a correction for shear deformation" is found to give the smallest variation of G_C as a function of both the beam thickness and beam thickness ratio. Both variations are less than 150% of the maximum measured variation in Gc for two specimens with identical geometry.

Correction for non-linear elastic behaviour reduces the variation of G_C as function of the beam thickness.

The optimal optimal beam thickness ratio (pure mode I) is not derived from these experiments. Decided is to use a beam thickness ratio for which the compliamce of both beams is equal according the "simple beam model" (beam thickness: PE 5.5 mm, PS 2 mm).

CONCLUSIONS

- A method is established to place a smooth block copolymer layer of known thickness at the interface without deuteration.
- The new model "beam on elastic foundation with a correction for shear deformation" is found to give the smallest variation of G_C as a function of both the beam thickness and beam thickness ratio.
- Correction for non-linear elastic behaviour reduces the variation of G_C as function of the beam thickness.

REFERENCES

1. Creton, C. and Kramer, E.J.(1992)Macromolecules, 25, 3075.
2. Johnson, K.L., Kendall, K. and Roberts A.D., (1971) Proc. R. Soc. Lond. A, 324, 301.
3. Brown, H.R., (1993)Macromolecules 26, 1666.
4. Creton, C., Brown, H.R. and Shull, K.R., (1994) Macromolecules, 27, 3174.
5. Brown, H.R., (1989)Macromolecules 22, 2859.
6. Wu, S.(1989)J. of Polymer Science B 27, 723.
7. Kanninen, M.F., (1973)Int. J. of Fract., 9, 83.
8. Williams, J.G.(1987) Fracture Mechanics of Polymers, Ellis Horwood limited, Chichester, 31-35.

CRITICAL LENGTH OF SHORT FATIGUE CRACKS

Alan Plumtree[1] and Nils Untermann[2]

[1]Department of Mechanical Engineering, University of Waterloo
Waterloo, ON, Canada N2L 3G1
[2]Institut fur Werkstoffkunde, Technsiche Universitat Braunschweig, Germany

ABSTRACT

A model is presented that predicts the fatigue limit of a metal by determining the critical crack length. The threshold stress range for short fatigue crack growth is related to the strain intensity factor range by taking into consideration surface strain distribution and crack closure. In particular the surface strain concentration factor has been carefully evaluated. This factor decreases, together with an increase in crack closure, as crack length increases within the short crack range. The resulting threshold stress for crack growth increases to a maximum that corresponds to the fatigue limit stress. This occurs at the critical crack length. In addition to successfully predicting the fatigue limit stress, the model is capable of determining the crack initiation stress range and depth of non-propagating cracks as a function of material, grain size and stress ratio.

KEYWORDS

Critical crack length, threshold stress, short fatigue cracks.

INTRODUCTION

On cycling a polycrystalline metal each surface grain will experience a different amount of strain according to its orientation relative to the loading axis. Large, favourably oriented grains represent preferred sites for crack initiation because of localized slip. With increasing depth, the constraints and strain compatibility requirements become more severe, leading to a lower local strain range. The initial high local strain range, Äå, decreases, approaching the nominal strain range, Äe. The strain concentration factor, $Q_å$, decreases with the projected crack length, a, according to [1]:/

$$Q_å = Äå/Äe = 1+q \exp [a(-á/D)] \quad (1)$$

where q is a constant, á is a material constant depending upon deformation character and represents the ease of cross-slip. The function for the decay of $Q_å$ gives an average continuous description of short crack behaviour

allowing a relatively simple model to be applied although it is recognized that short crack behaviour may be discontinuous and strongly affected by microstructural features such as grain boundaries [2]. The depth at which $Q_{å}$ is effectively equal to unity determines the extent of the surface-affected zone, L_i. When a = 0, $Q_{å}$ =1+q represents the strain concentration factor at the free surface, $Q_{åS}$. Originally, Abdel-Raouf et al [1] concluded that q=5.3, based on the probability of slip at the surface. This gave a value of $Q_{åS}$ = 6.3. Reconsidering this original work, $Q_{åS}$ yielded a value of approximately 8.7. Using a slightly different probabilistic approach, the strain concentration factor at the surface was found to vary between 6.1 and 7.2 [3].

Another approach has been to consider the strain in Persistent Slip Bands (PSBs). In this case, the values for the strain concentration factor at the free surface ranged between 4.7 and 10.0 [4,5] and the weighted average value for eleven different set of data was 8.4.

By means of the Neuber approach $Q_{åS}$ varied between 5.9 and 8.1 if the cyclic yield limit were considered as the applied stress. The average values for twelve steels and seven aluminum alloys were 6.9 and 7.0 respectively, indicating material independence[6]. Hence, for simplification, Q_{eS} will be applied using a single value of 7.0.

INTRINSIC THRESHOLD STRESS RANGE

In the absence of crack closure, the intrinsic strain intensity factor range, can be expressed as follows:

(2)

where E is the modulus of elasticity and F is the geometrical crack factor.

When the nominal applied strains are elastic, $ÄeE = ÄS_i$ where is the intrinsic component of the applied stress range, the intrinsic stress intensity factor range simplifies to:

(3)

At high stress ratios (R= minimum/maximum stress ≥ 0.6) $ÄK_i$ can be assumed to be the intrinsic threshold stress intensity factor $ÄK_{ith}$. According to DuQuesnay [7] no closure effects were present at a stress ratio of R = 0.6 for aluminum alloy Al 2024-T351 with $ÄK_i$ = 2.2 MPa $m^{1/2}$.

The intrinsic threshold stress range, $ÄS_{ith}$ can be calculated at any crack depth using Eq. 3. As expected, a linear relationship with a slope of -0.5 exists between log $ÄS_{ith}$ and log a for long cracks ($a \geq L_i$) when $Q_{å}$ = 1, since linear elastic fracture mechanics (LEFM) applies. However, for short cracks ($a < L_i$), the curve deviates from linearity and their behaviour is under microstructural control.

The maximum value for $ÄS_{ith}$ represents the nominal stress range required to maintain continuous crack propagation, i.e. the fatigue limit of the material for the intrinsic condition when closure is absent. For the Al2024-T351 alloy, the crack initiation stress range, $ÄS_c$, had a value of 96 MPa at the minimum crack depth of 3 ìm and the maximum value for $ÄS_{ith}$ was determined to be 110 MPa which is in good agreement with the experimental value of 125 MPa. This occurred when a_c = 190 ìm (3.8D). Since the calculated fatigue limit $ÄS_{FL}$ is slightly smaller than the actual fatigue limit stress at the stress ratio of R=0.6 the crack may not have been fully open.

Figure 1: Nominal threshold stress range, as a function of crack depth and stress ratio for Al 2024-T351.

a_e = a-0.4D, q = 6.0, á = 1.0, D = 50 ì m, = 2.2MPa $m^{1/2}$, k=20 mm^{-1}, F (a=3ì m), = 1.12 and F (a=200ì m) = 0.72

CLOSURE

The stress intensity factor range (ÄK = K_{open} - K_{min}) required to open a closed crack increases with crack depth to a steady-state level, representative of long crack development. Hence at lower stress ratios when closure is present, the threshold stress intensity factor range must include a crack opening component in addition to the intrinsic component. This is achieved by introducing the closure development factor, H_{cl} representing the ratio of the total stress range to the open portion of the stress range, which increases the threshold stress intensity factor range, ÄK_{th}, and is expressed by [2, 8, 9]:

(4)

or with the corresponding expression for stress:

(5)

H_{cl} is given by:

(6)

The factor è′ is expressed by:

(7)

where k is a material constant describing the rate of crack closure development and a_c is an effective crack depth

a_c=a-0.4D since closure starts to build up about half-way into the surface grain [2].

For small cracks, H_{cl} is approximately unity and Eq. (4) yields $\Delta K_{th} = \Delta K_{ith}$, indicating that the crack is fully open. For long cracks, however, the steady state value of H_{cl} is invariant with crack length. Its magnitude increases as the stress ratio decreases.

The values of K_{th} at steady-state are listed in Table 1 for the corresponding stress ratios.

FATIGUE CRACK MODEL

Combining Eqs. (3) and (5) leads to the final equation describing the variation of the threshold stress range with crack length in the short and long fatigue crack regime:

$$\Delta S_{ith} = H_{cl}\, \Delta K_{ith} / (Q_{\text{å}}\, F \qquad) \tag{8}$$

The three mechanisms involved in the present model are incorporated in Eq. (8) and are as follows: i) the closure parameter H_{cl} ii) the inherent strain concentration factor $Q_{\text{å}}$ and iii) the LEFM-contribution. The crack length appears three times in Equation (8) through H_{cl}, $Q_{\text{å}}$ and a. It is the only unknown variable. Stress ratio is taken into account by H_{cl}.

FATIGUE LIMIT PREDICTION

The experimental data for 2024-T351 aluminum alloy is available from previous work [7, 8, 9] and applied to the present model. The important mechanical and microstructural material properties are given in Table 1.

The plot of Eq. (8) versus crack depth is seen in Figure 1. This illustrates the relationship between the nominal threshold stress range and the crack depth for three different stress ratios. The threshold stress range has a local maximum value, representing the stress range required for continuous crack growth, which defines the fatigue limit. For stress ratios less than 0.6, the magnitude of the threshold stress range at the fatigue limit increases with decreasing stress ratio due to an increase in the contribution of crack closure.

TABLE 1
Material Properties of 2024-T351 Aluminum Alloy [7, 8, 9]

Material Property	Stress Ratio	Value
ΔK_{th} for long-crack propagation	R = -1	4.4 MPa $m^{1/2}$
ΔK_{th} for long-crack propagation	R = 0	3.4 MPa $m^{1/2}$
ΔK_{th} for long-crack propagation	R = 0.6	2.2 MPa $m^{1/2}$
ΔS_{FL} at 2×10^7 cycles	R = -1	246 MPa $m^{1/2}$
ΔS_{FL} at 2×10^7 cycles	R = 0	170 MPa $m^{1/2}$
ΔS_{FL} at 2×10^7 cycles	R = 0.6	125 MPa $m^{1/2}$
Grain size in crack growth direction	-	50 ìm

Table 2 summarizes the predicted fatigue limit stress range, the critical crack length at the local maximum, a_c, the

experimental fatigue limit stress range and the relative deviation. The critical crack is about four grain diameters in length. The predicted and experimental values of the fatigue limit stress are in good agreement. However, the results are very sensitive to the closure parameter. A small deviation in the experimentally determined threshold stress intensity factor ranges can lead to a large scatter in the prediction.

TABLE 2
Predicted Fatigue Limits for Different Stress Ratios

R	a_c [ìm]	$\Delta\sigma_{FL}$[MPa]	Experimental $\Delta\sigma_{FL}$ [MPa]	Relative deviation [%]
0.6	188 (3.8D)	110	125	-12.0
0	194 (3.9D)	167	170	-1.76
-1	198 (4.0D)	214	246	-13.01

The fatigue limit stress range may be predicted using an alternative approach based on the experimentally determined ΔK_{th} (Table 1) without having to consider the closure parameter. Since, at a given stress ratio, ΔK_{th} accounts for closure development at the steady-state level and the critical crack length at the fatigue limit stress is known from the previous analysis, the following expression leads to the fatigue limit stress range for that stress ratio:

(9)

The critical crack depth a_c is taken as 4D. For the stress ratios of R=0.6, R=0 and R=-1 the fatigue limit stress ranges are then determined to be $\Delta\sigma_{FL}$ = 111 MPa, $\Delta\sigma_{FL}$ = 171 MPa and $\Delta\sigma_{FL}$ = 221 MPa, respectively. These values agree with those obtained in the previous section. It is important to note if the extreme values of 5 and 8 for q are considered, then the variation in $\Delta\sigma_{FL}$ is only in the range of 5% for a given stress ratio.

If a specimen were cycled with a stress range larger than $\Delta\sigma_c$ yet lower than $\Delta\sigma_{FL}$, the crack will grow to a depth corresponding to the threshold stress range given in Fig. 1 and become non-propagating. Due to the difference in closure levels the crack would stop growing at a shorter depth if the stress ratio were lower. The model is capable of predicting the depth of non-propagating cracks. This has been observed in smooth specimens cycled at low stress ratios [2] where there is a larger difference between $\Delta\sigma_c$ and $\Delta\sigma_{FL}$.

SUMMARY

The fatigue limit stress can be predicted accurately with the current model. The information required is the average grain size, the intrinsic threshold stress intensity factor range and the closed portion of the stress range for a long crack at a given stress ratio. The threshold stress curve may then be plotted against crack depth and its maximum corresponds to the fatigue limit stress range. The model is capable of predicting the development of non-propagating cracks when cycled at constant amplitude stress ranges lower than the fatigue limit.

ACKNOWLEDGMENTS

Financial support by the Natural Science and Engineering Council of Canada (NSERC) through grant OGP (0002770) is gratefully acknowledged. The authors wish to thank Marlene Dolson for typing the manuscript.

REFERENCES

1. Abdel-Raouf, H., Topper, T.H., Plumtree, A., (1991), Scripta Metallurgica et Materialia, Vol. 25, pp. 597-602.
2. Plumtree, A., (1999), In Engineering Against Fatigue, pp. 55-61, J.H. Beynon, M.W. Brown, R.A. Smith, T.C. Lindley, B. Tomkins, Eds. A.A. Balkema, Rotterdam, NL.
3. Untermann, N., (2000), Research Report, University of Waterloo, Canada.
4. Winter, A.T., (1974), Philosophical Magazine, Vol. 30, pp. 719-738.
5. Mughrabi, H., (1978), Materials Science and Engineering, Vol. 33, pp. 207-223.
6. Baumel, Jr., A., Seeger, T., (1990), Materials Science Monographs 61, Supplement 1, Elsevier.
7. DuQuesnay, D.L., (1991), PhD Thesis, University of Waterloo, Canada.
8. Abdel-Raouf, H., DuQuesnay, D.L., Topper, T.H., Plumtree, A., (1992), International Journal of Fatigue, Vol. 14, pp. 57-62.
9. DuQuesnay, D.L., Abdel-Raouf, H., Topper, T.H., Plumtree, A., (1992), Fatigue, Fatigue Fract. Engng. Mater. Struct., Vol. 15, pp. 979-993.

ORAL REFERENCE: ICF100624OR

CROSS-SECTIONAL NANOINDENTATION: A NOVEL TECHNIQUE TO MEASURE THIN FILM INTERFACIAL ADHESION

Brad Sun[1], Tracey Scherban[2], Daniel Pantuso[2], Jose M. Sanchez[3], Reyes Elizalde[3], J.M. Martinez-Esnaola[3]

[1] Intel Corp., Santa Clara, California, USA
[2] Intel Corp., Hillsboro, Oregon, USA
[3] CEIT, San Sebastian, Spain

ABSTRACT

Thin film interfacial adhesion is a critical material property in assessing the thermo-mechanical reliability of microelectronic components. Cross-sectional Nanoindentation (CSN) is a novel technique developed to characterize the adhesion of thin film interfaces. The technique consists of indenting a cross-sectional sample with a Berkovich diamond indenter using a Nanoindenter System. The indentation is made normal to the cross-section at a specific distance from the interface of interest. This produces a controlled bending of the thin film structure. The onset of interfacial delamination is related to sudden steps in the load-displacement curve. From optical and SEM micrographs, the delamination crack paths are directly observable. Based on the crack lengths, a relative determination of interface fracture toughness can be made. CSN results correlate to fracture toughness values obtained with the four-point bending technique(3).

KEYWORDS

Cross-sectional Nanoindentation (CSN), Interfacial adhesion, Microelectronics, Thin film, Berkovich indentation

INTRODUCTION

The microelectronics industry is running on an increasingly complex treadmill that requires novel materials to be integrated to meet electrical performance targets. The path to success requires the integration of new metal and dielectric interconnect materials that may increase the risk of thin film delamination. Lack of chemical affinity and large differences in thermal expansion coefficients of the various thin films, together with the presence of defects or residues at the interface, are some of the causes of interfacial delamination.

It is of critical importance that accurate, quantitative techniques are available to assess the mechanical integrity of thin film interfaces. More sophisticated methods are needed to replace older techniques such as the tape test and stud pull test [1-2] which are not generally applicable. The technique of four-point bending has recently been used to obtain quantitative values of thin film interface fracture toughness [3-5]. However, lengthy sample preparation is required and the technique is limited to blanket thin film samples.

Nanoindentation has been widely used to measure materials properties such as hardness and modulus[6-8]. It has also been used to study delamination by top-down indentation of thin films[9]. However, the interface at which delamination occurs is not clearly distinguishable. CSN represents the first application of the indentation technique to the study of thin film interface adhesion using cross-sectional samples. It allows direct observation of the delaminated interface. Due to the simplicity of sample preparation and the quick turn-around time (approximately four hours), CSN has the potential to be used as a quick-turn monitor for the fabrication engineers. A significant advantage of the technique is its application to patterned as well as blanket thin film samples.

EXPERIMENTAL PROCEDURE

Sample preparation

Blanket thin film samples consisting of 1 μm silicon nitride on 1 μm silicon oxide were studied. The silicon oxide was deposited using a chemical vapor deposition (CVD) process. The silicon nitride thin films were deposited using various processes: plasma-enhanced chemical vapor deposition (PECVD), high density plasma (HDP) and low deposition rate CVD. A test chip was analysed as part of CSN tests on patterned material. This consisted of a two metal layer integrated short loop with silicon nitride passivation, polyimide (PI) and Controlled Collapsible Chip Connectors (C4) bumps.

Sample preparation was a simple cross-sectioning using diamond scribing to initiate a precrack then cleaving with glasscutters' pliers. This produced a clean and flat cross section ready for indentation. In the case of the patterned material, the cleave was made through metal lines near the die's edge to determine if they would arrest cracks due to corner blunting.

CSN test procedure

The CSN test configuration used for the silicon nitride /silicon oxide blanket samples is illustrated in Fig. 1. The orientation of the three-sided Berkovich diamond tip and its positioning with respect to the interface are critical parameters for controlled delamination. The optimum orientation of the diamond tip is that depicted in the figure, where one of the sides of the triangular indentation mark is parallel to the interface. The optimum distance to the interface (d) is 1 to 5

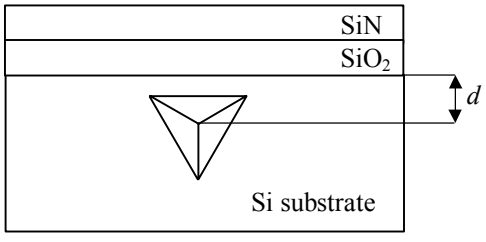

Figure 1: Thin film structure and orientation of Berkovich indenter with respect to thin film interface.

micrometers. The optimum load range for delamination was found to be 30 mN to 200 mN.

Indentations were made using a well-calibrated Berkovich diamond indenter (Nanoindenter II and Nano XP, MTS Nano Instruments, Inc.) with a load resolution of about 50 nN and a z-axis displacement resolution of 0.01 nm. The resolution of the diamond tip positioning system in the x-y directions is 0.5 μm. CSN tests were carried out using strain-rate control with a tip displacement rate of 10 nm/s. Load vs. tip displacement curves were recorded during the tests (data acquisition rate: 45 Hz). After the indentation experiments, SEM micrographs were collected to measure crack lengths and delamination areas.

CSN Fracture Interpretation

A 3D view of the CSN experiment is shown in Figure 2. Figure 3 shows a SEM image of the indentation zone. Cracking begins at the two corners of the indentation that are closer to the interface. These radial cracks, characteristic of brittle materials loaded with pyramidal indenters[10-11], propagate on loading through the silicon substrate and the strong silicon/silicon oxide interface, producing a wedge (shown in Fig 2).

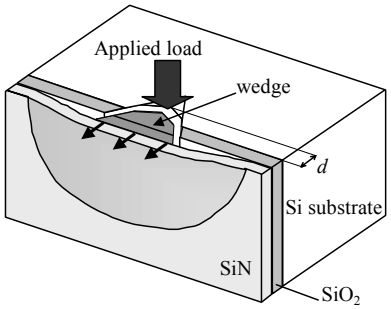

Figure 2: Sample cross-section showing location of applied load and bending of thin film structure producing delamination

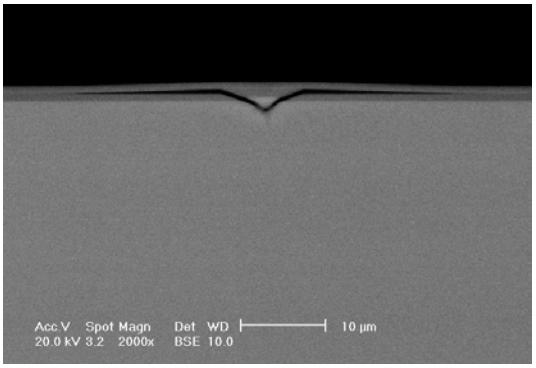

Figure 3: SEM micrograph of silicon nitride/silicon oxide thin film sample after cross-sectional indentation.

However, when the cracks reach the weak silicon oxide/silicon nitride interface, they tilt out of their original planes following the Si_xN_y/SiO_2 interface.

Delamination produces a sudden movement of the diamond tip that is registered as a step in the load vs. tip displacement (Fig. 4). Such a step is not detected when the maximum indentation load is lower than that required for delamination. In this case, the load vs. tip displacement curve is similar to that obtained in a hardness test of silicon.

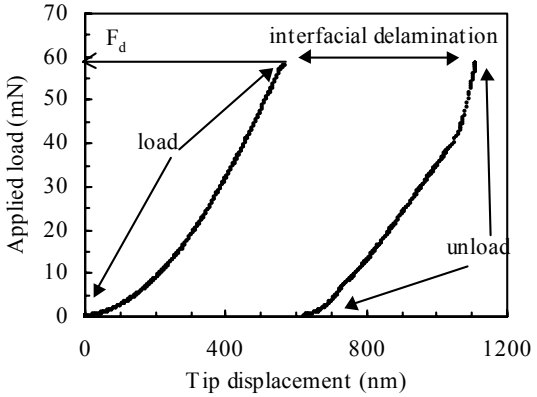

Figure 4: Load-displacement curve showing sudden jump corresponding to thin film delamination.

RESULTS

Blanket Thin Film Analysis

Adhesion of silicon nitride to silicon oxide blanket thin films was characterized for three nitride deposition processes, plasma-enhanced chemical vapor deposition (PECVD), high density plasma (HDP) and low deposition rate CVD. For each process, results with and without a plasma pretreatment are compared. The crack lengths at the interface were measured after indenting to a load of 100 mN. Results are given in Table 1, showing that the PECVD nitride deposition process produces the strongest interface. In this case, the interface could not be debonded. In general, CSN results are well-correlated to adhesion results obtained with the four-point bending technique[3].

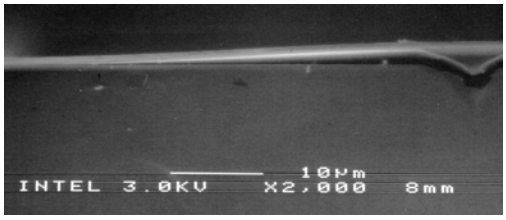

Figure 5a: CVD Silicon Nitride; crack Length = 27 μm

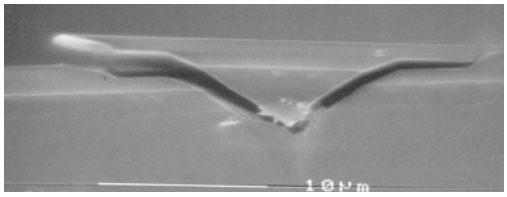

Figure 5b: HDP Slicon Nitride; crack Length = 4.7 μm

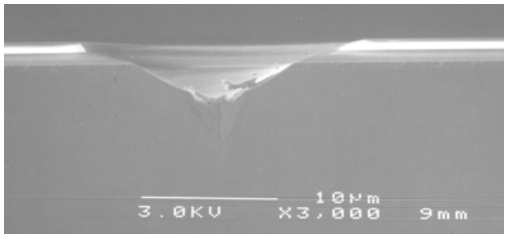

Figure 5c: PECVD Sillicon Nitride; no debonding

TABLE 1: COMPARISON OF CSN AND FOUR-POINT BENDING ADHESION RESULTS FOR SILICON NITRIDE/SILICON OXIDE SAMPLES WITH DIFFERENT PROCESSING CONDITIONS.

Nitride Dep Process	CSN Crack Length (um)	Four-point bend interface energy (J/m2)
CVD (Fig 5a)	28	2.84 ± 0.93
HDP (Fig 5b)	4.7	7.23 ± 0.97
PECVD (Fig 5c)	No debond	No debond

Patterned Thin Film Analysis

CSN measurments were carried out on a patterned test chip. The purpose of the study was to characterize polyimide thin film to silicon nitride thin film adhesion and the effect of metal lines on delamination at this interface. Indentations were made in the silicon substrate in two locations: in an open area and directly below the edge of the metal lines. The thin film stack in the open area consists of polymer / silicon nitride / silicon oxide / silicon substrate and in the locking structure location consists of polymer / silicon nitride / patterned aluminum /silicon oxide / silicon substrate.

SEM results for an indentation made in an open area of the scribeline are shown in Figure 6. Note the symmetry of debonding. This shows that the crack initially propagates to the silicon nitride / silicon oxide interface before jogging into the weaker polymer / silicon nitride interface. Figure 7 shows SEM results for the indentation made below the patterned metal lines. Note that the cracking is asymmetric. On the left side, the crack is shorter, being arrested due to corner blunting of the patterned metal line. The crack initially propagates to the metal / silicon oxide interface and then to the polymer / silicon nitride interface before stopping at the edge of a metal line.

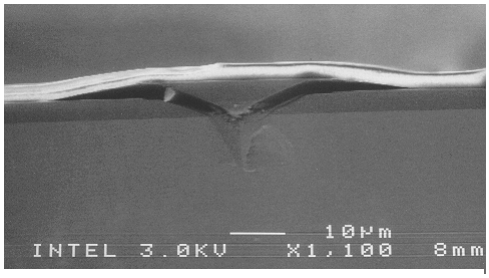

Figure 6a: Low mag image: CSN in open area

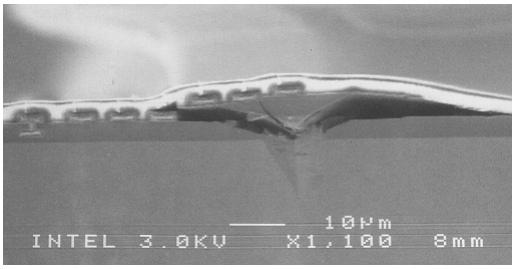

Figure 7: CSN below patterned lines

The repeatabilty of the indentation results was measured by conducting multiple CSN tests on samples from the same wafer. Tests were carried out under identical loading conditions (100 mN) and at the same distance from the Si/ silicon oxide interface (3±1 μm). Wafer-to wafer repeatability was also tested by conducting tests on different wafers from different lots. The results are consistent, showing that the crack length at the polymer / silicon nitride interface is significantly lower in the case of indentation made below patterned metal lines. Table 2 summarizes results.

TABLE 2: CSN REPEATABILITY RESULTS FOR PATTERNED MATERIAL

Sample ID	Crack Length (μm) for indent below patterned lines	Crack Length (μm) for indent in open area
Lot 1, sample 1	1.25	18
Lot 1, sample 2	2.5	16
Lot 1, sample 3	2	8
Lot 2, sample 1	2	12.5
Lot 3, sample 1	2	5

Discussion/Conclusions

Cross-sectional nanoindentation results for blanket thin film samples clearly show that the technique is capable of resolving differences in adhesion strength. Using crack length at the interface as a relative measure of adhesion strength, it has been shown that CSN results correlate well with four-point bend results. In order to obtain quantitative values of interface fracture toughness using the CSN technique, modeling is required. A model based on the elastic plate theory has been developed and applied to ceramic-ceramic systems[12]. In order to make the CSN technique fully quantitative, further model refinements are needed.

The application of the CSN technique to patterned thin film samples shows the great value of the technique in distinguishing differences in delamination behavior due to local geometry effects. The direct observation of crack blunting at patterned metal lines provides compelling evidence of the effectiveness to stop crack growth at the polymer to ceramic interface.

The electronic industry's silicon and packaging processes will need to fully comprehend thermal mechanical issues. As devices become faster and hotter and as novel materials are incorporated into an increasing number of interconnect layers, a comprehensive understanding of interfacial adhesion is critical. The cross-sectional nanoindentation technique has been demonstrated to be a reliable test method. Its advantages are ease of sample preparation, quick turn-around time, direct observation of delamination, and application to patterned and blanket thin films.

References

1. Chalker, P.R, Bull, S.J. and Rockerby, D.S., *Mater. Sci. Eng.,* 1991, **A140**, 583.
2. Kendall, K., *J. Mat. Sci.,* 1976, **11**, 638.
3. Ma, Q., Bumgarner, J., Fujimoto, H., Lane, M. and Dauskardt, R. H., *Mat. Res. Soc. Symp. Proc*., 1997, **473**, 3.
4. He, M. Y., Xu, G., Clarke, D. R., Ma, Q. and Fujimoto, H., *Mat. Res. Soc. Symp. Proc*. 1997, **473**, 15.
5. Lane, M., Ware, R., Voss, S., Ma, Q., Fujimoto, H. and Auskardt, R.H*., Mat. Res. Soc. Symp. Proc,* 1997, **473**, 21.
6. Pharr, G.M., Oliver, W.C., Brotzen, *J. Mater. Res*., 1992, **3**, 613.
7. Nix, W.D., *Metall. Trans. A*, 1989, **20A**, 2217.
8. Cook, R. F. and Pharr, G. M., *J. Hard Mater.*, 1994, **5**, 179.
9. Ritter, J. E. et al.; J. Appl. Phys. Vol 66 (8) Oct. 1989.
10. Ponton, C.B. and Rawlings, R.D., *Mat. Sci. and Tech.*, 1989, **5**, 865.
11. Evans, A.G. in "Fracture Mechanics Applied to Brittle Materials," ASTM. (ed. S.W. Frieman), 1979, **STP 678**, 112.
12. J.M. Sanchez, S. El-Mansy, B. Sun, T. Scherban, N. Fang, D. Pantuso, W. Ford, M.R. Elizalde, J.M. Martinez-Esnaola, A. Martin-Meizosa, J. Gil-Sevillano, M. Fuentes and J. Maiz, *Acta. Mat.,* 1999, Vol 47, No. 17, pp. 4405-4413.

Acknowledgments

The authors would like to thank Qing Ma and Quan Tran for four-point results. Jeff Bielefeld and Sridahr Balakrishnan for providing samples used in this work. Finally, we would like to thank Wayne Ford, Jose Maiz and Sadasivan Shankar for mentoring this project.

CRYSTALLOGRAPHIC ANALYSIS OF SURFACES AFTER BRITTLE FRACTURE IN FERRITIC STEELS

Valerie Randle, Paul Davies and Owen Williams

Department of Materials Engineering, University of Wales Swansea, Swansea, UK.

ABSTRACT

Recently considerable advances have been made in devising robust experimental methodologies for crystallographic analysis of fracture surfaces, and applying them to materials such as steels. There are two main practical thrusts: precision sectioning through the polished side of a specimen, perpendicular to the average fracture surface, and quantitative photogrammetry directly from the fracture surface. The second of these approaches is particularly novel since it allows electron back-scatter diffraction (EBSD) data to be obtained concurrently with the spatial coordinates, both in a scanning electron microscope. In this paper examples of some preliminary investigations in which these procedures have been used to produce valuable results will be described.

KEYWORDS

Electron back-scatter diffraction, quantitative fractography, fracture facet, stereo-photogrammetry.

INTRODUCTION

Brittle fracture in ferritic steels can occur intergranularly, especially in the presence of embrittling species such as phosphorus, or transgranularly on cleavage planes of low surface energy in the lattice. Unambiguous identification of which of these two processes is operating, and detailed analysis of the characteristics of the fracture phenomenon, relies crucially on knowledge of the local crystallography. There are two primary and separate requirements for the experimental measurement of facet crystallography on the fracture surface of polycrystalline materials [1]:

- the *positional coordinates* of a fracture facet in space
- the *crystallographic orientation* of the facet

both measured relative to the *same* reference axes. Electron back-scatter diffraction (EBSD) in a scanning electron microscope (SEM) is the forefront technique to provide crystallographic information [2], although there are several challenges regarding its accurate application to fracture surfaces. Equally, obtaining precise spatial coordinates for the positional orientation of a facet is taxing.

Recently considerable advances have been made in devising robust experimental methodologies in this area and applying them to real materials, namely steels. There are two main practical thrusts: precision sectioning through the polished side of a specimen, perpendicular to the average fracture surface, and quantitative photogrammetry directly from the fracture surface. The second of these approaches is particularly novel since it allows EBSD data to be obtained concurrently with the spatial coordinates. In this paper examples of some preliminary investigations in which these procedures have been used to produce valuable results will be described.

EXPERIMENTAL METHODOLOGIES

Essentially the experimental strategies divide into two approaches: some or all of the measurements are taken *directly* from the fracture surface, or some or all of the measurements are taken from a surface adjacent to the fracture surface, i.e. *indirectly*.

The crystallographic orientations of facets - or any other planar surface such as some internal interfaces - may be determined by a totally indirect approach. Orientations are obtained by EBSD from a polished section perpendicular to the overall fracture surface, coupled with fracture surface profile analysis from optical or SEM images of at least two serial sections through a plane perpendicular to the fracture. This information defines the crystallographic facet orientation. The procedures and applications are discussed in detail elsewhere [3]. Indirect crystallographic analysis of facets in this manner from serial sections has the distinct advantage that the orientation data are straightforward to obtain by EBSD, because they are taken from a flat polished section. Drawbacks are that it is an inherently destructive technique, it is restricted to materials with average grain size greater than approximately 100μm, and the procedures are very labour-intensive.

A variant of the indirect approach is to obtain data from a single polished section only. Useful information can be gleaned by performing EBSD on a 'matched fracture' specimen. Here the specimen is fractured into two halves, then the two halves are realigned, mounted together as they were prior to fracture, and polished as if they were a single specimen. The alignment and mounting procedure requires considerable care to maintain the specimen geometry. The merit of this procedure is that intergranular and transgranular fracture surfaces can be immediately identified from evidence of colour matching across the fractured interface in the crystal orientation map. Subsequently, proportions of intergranular and transgranular (cleavage) fracture can be quantified. Another piece of information which can be obtained from a single section is the crystallographic trace vector which defines the fracture edge. This direction must lie in the fracture plane, and so can be used to test the probability that, for bcc steel, the plane is a {001} cleavage plane.

In contrast to the indirect techniques, direct techniques have the advantage of being non-destructive although they still generally require accurate correlation between the crystallographic and macroscopic orientation of the facet. Probably the first experiment which combined photogrammetry and EBSD was employed by Slavik and coworkers [4] to determine the fracture facet crystallography using quantitative tilt fractography of an Al-Li-Cu (AA2090) alloy. The grain orientation was measured by EBSD from a polished surface, perpendicular to the average fracture plane, and combined with the facet orientation, which was aligned such that the co-ordinate system was identical for the tilt fractography and the EBSD analysis. A series of SEM fractographs (i.e. images of the fracture surface) were acquired at different tilts and a series of measurements made of projected lengths between features on the fracture surface. The data were then combined to determine the fracture facet crystallography.

An extension of photogrammetry is stereo-photogrammetry, where images of a rough surface, taken at least two different tilt angles, are combined to produce a three-dimensional (3D) reconstruction of the surface. In the last few years computer assisted stereo-photogrammetry, in real time in an SEM, has greatly expanded the potential of this technique to facet analysis, and there have been some pilot experiments to couple stereo-photogrammetry with EBSD [5,6] and, recently, those reported in this paper.

EXAMPLES OF CRYSTALLOGRAPHIC ANALYSIS OF SURFACES

Here we will present an example of both the indirect and direct techniques for facet analysis which have recently been performed on two steels as part of ongoing investigations..

Samples of an alloy having composition Fe-0.06wt%P-0.002wt%C were cut to 5mm × 5mm × 30mm and a notch of ¼-thickness depth was cut into one of the faces. The sample was held under liquid nitrogen and fractured by an impact on the face opposite the notched face. After fracture the two halves were realigned and mounted. An EBSD map was then obtained from the fractured region as if it were still a single specimen. Figure 1 shows an example of a 'matched fracture' specimen. In this case the crystallographic orientation map has been superimposed on the secondary electron image. It can be seen that for much of the map the colours match across the fracture surface, indicating cleavage fracture. There are also some cases where the colours do not match across the fracture surface, indicating an intergranular, accommodation fracture facet. As the ageing temperature increased so the proportion of facets on the brittle fracture surface showing colour match across the fracture (i.e. cleavage facets) increased.

Measurements directly from the fracture surface will be illustrated here by reference to recent investigations on a C-Mn alloy which had fractured predominantly in the transgranular mode. A previous investigation, using single crystals, into the accuracy of EBSD measurements obtained directly from fracture surfaces had revealed a large associated error, >25°. This is because although EBSD is calibrated for parallelism between the camera screen and the specimen surface (an individual fracture facet in this case), a large deviation away from the parallel condition can be tolerated before the diffraction pattern becomes unindexable by the software. This difficulty can be overcome somewhat by searching for 'local minima', but this technique is tedious and only suitable for small sample populations [6].

A more promising approach to direct crystallographic analysis of fracture surfaces than EBSD alone is computer-assisted stereo-photogrammetry, which was carried out in the present ongoing research using 'Stereo Facet' software, commercially available from Oxford Instruments. Validation of the stereo-photogrammetry procedure was achieved by a series of tests on a surface feature of known geometry, namely a Vickers hardness indent where the angle between the faces of the pyramidal indent is 136°. Stereo images were acquired separately, tilted at +5° and -5° with respect to the primary beam direction. The parallax shift data for each pixel is calculated using a digital-image correlation analysis routine provided by the software, which was subsequently used to construct a '3D-elevation model' of the indent.

Having validated the stereo-photogrammetry procedure, it was then used to determine the positional orientation of fracture planes in space and correlate the measurement with the crystallographic orientation obtained by EBSD. A 3D-elevation model of the fractured facet was produced using the stereo images and measurements of the cleavage plane orientation were then correlated with the crystallographic information determined using the automated EBSD application of Crystal Orientation Mapping (COM). The region of fracture surface, which is shown in figure 2a, was used to produce an 'anaglyph', i.e. a 3D visual representation of the surface that combines two stereo-images. A selected region of fracture surface was then successfully modelled using the stereo-photogrammetry software to produced a 3D-elevation model of the selected area enclosed by the rectangle on figure 2a (figure 2b) and a line profile of surface heights was acquired along the line bisecting the rectangle (figure 2c). Transferring the EBSD-measured crystal axes to the 3D-elevation model, where the reference plane is positioned perpendicular the normal direction, the deviation from the exact [001] direction correlates with the positional co-ordinates of the plane, indicating that the actual crystallographic orientation of the cleavage facet is exactly [001].

The principal advantage of direct techniques for crystallographic analysis of fracture surfaces is that the fracture surface remains intact, and so is available for further investigation. [7]. Computer assisted stereo-photogrammetry can yield accurate crystallographic data which, combined with its powerful imaging and visualisation capabilities, proves it to be a powerful technique for fracture surface analysis. However, only certain facets, where the image contrast is excellent, are candidates for analysis and the analysis procedure is quite lengthy.

CONCLUSIONS

There are several approaches to crystallographic analysis of fracture surfaces. These are:

- Indirect techniques: 'matched fracture' specimens where a fractured specimen was reassembled and EBSD performed across the fracture surface; serial sectioning; a single-surface section to obtain the trace vector of the fracture edge.
- Direct techniques: EBSD from the untreated fracture surface itself; computer-assisted stereo-photogrammetry combined with EBSD of the fracture surface.

There are merits and drawbacks for both the direct and indirect methods. A common feature is that both methods for crystallographic fracture analysis are experimentally difficult and challenging, although they are worthwhile to pursue because they yield valuable information about the fracture process.

REFERENCES

[1] Hull, D. (1999) *Fractography; Observing, Measuring and Interpreting Fracture Surface Topography*. University Press, Cambridge.

[2] Randle, V. and Engler, O. (2000) *Introduction to Texture Analysis: Macrotexture, Microtexture and Orientation Mapping*. Gordon and Breach Science Publishers, Amsterdam.

[3] Randle, V. and Hoile, C. (1998) *Mats Sci Forum*, 273, 183.

[4] Slavik, D.C., Wert, J.A. and Gangloff, R.P. (1993) *J. Mater. Res*. 8, 2482.

[5] Semprimosching, G.O.A., Stampfl, J., Pippan, R. and Kolednik, O. (1997) *Fat. Fract. Eng. Mater. Struct*. 20, 1541.

[6] Davies, P.A., and Randle, V. *Submitted to J. Micros.*

[7] Williams, O., Randle, V., Spellward, P. and Cowen, J. (2000) *Mat. Sci. Tech*., 16, 1372.

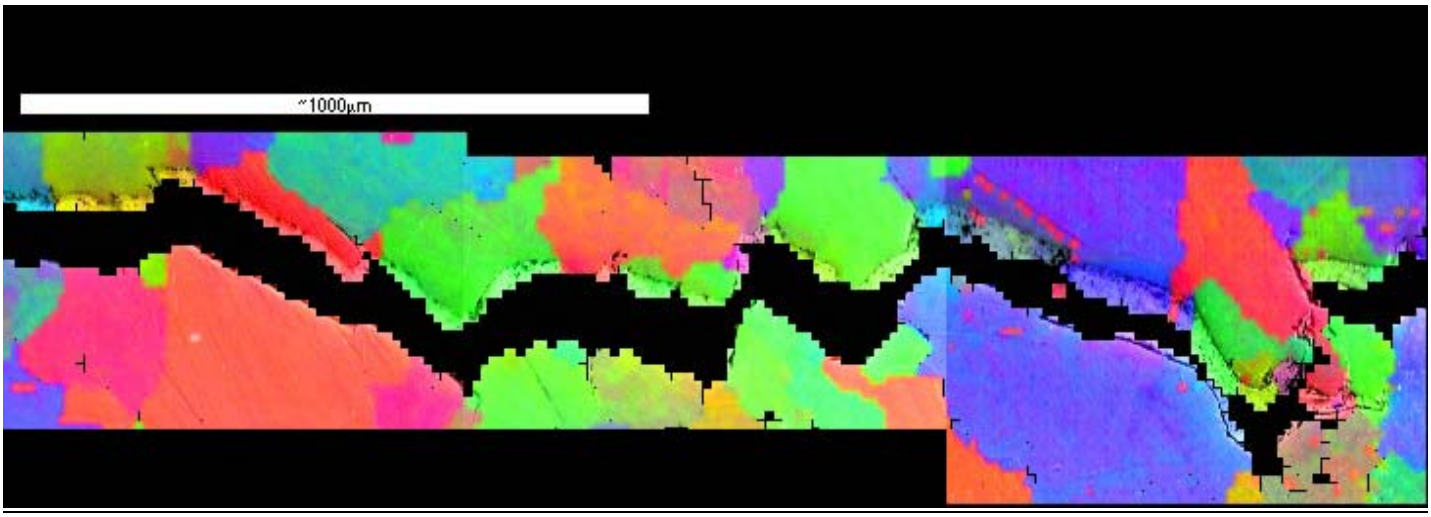

Figure 1 A 'matched fracture' specimen from an Fe-P-C alloy. The colours correspond to crystallographic orientation and are superimposed on a secondary electron image.

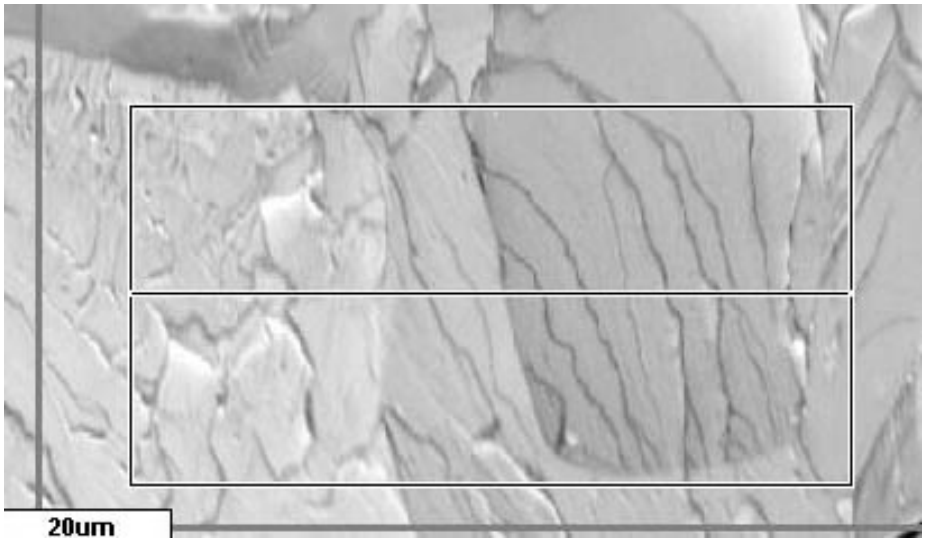

(a)

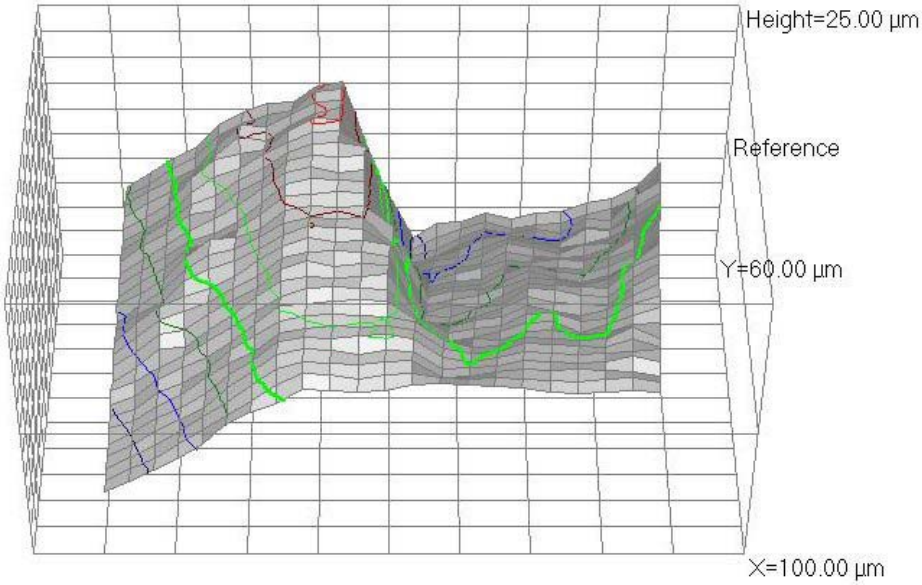

(b)

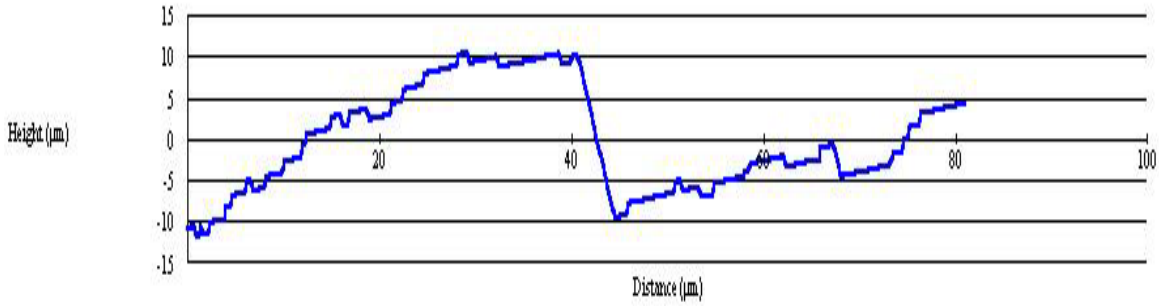

(c)

Figure 2 (a) Micrograph of a region on a fracture surface of a C-Mn steel. The region enclosed by the rectangle was selected to produce a 3-D elevation model and a horizontal line, bisecting the rectangle, was selected to produce a height profile. (b) 3-D elevation model of the region shown in (a). (c) Height profile along the line shown in (a).

ORAL REFERENCE: ICF10058OR

CURVED CRACK PATH PREDICTION BY THE MVCCI-METHOD AND EXPERIMENTAL VERIFICATION FOR A SPECIMEN UNDER LATERAL FORCE BENDING

H. Theilig[1] and F.-G. Buchholz[2]

[1]Department of Mechanical Engineering, University of Applied Sciences Zittau/Görlitz,
D-02763 Zittau, Germany
[2]Institute of Applied Mechanics, University of Paderborn
D-33098 Paderborn, Germany

ABSTRACT

In this paper it is shown that the curved crack path simulation can be improved considerably in accuracy by using a new predictor-corrector procedure that results in a piece by piece parabolic approximation of the simulated crack path in combination with the **M**odified **V**irtual **C**rack **C**losure **I**ntegral (MVCCI) method. In order to show the superiority of the proposed crack path simulation method in relation to the well established basic strategies, experiments of non-coplanar fatigue crack growth are carried out with a special specimen under lateral bending. In all cases considered the computationally predicted crack trajectories show an excellent agreement with the different types of curved cracks obtained experimentally.

KEYWORDS

Crack path simulation, curved increment, predictor-corrector procedure, virtual crack closure integral method

INTRODUCTION

Failure of structures and components is often caused by cracks that frequently originate and extend in regions characterised by complicated geometrical shapes and asymmetrical loading conditions. In such cases the developing crack paths are found to be curved. Several simulation methods have been proposed for crack path predictions based on step-by-step analyses by using finite elements or boundary elements (Bergquist and Gnex[1]; Sumi[2,3]; Portela and Aliabadi[4]). In the present paper, attention is focused on a new predictor-corrector procedure that results in an incremental parabolic approximation of the crack path on the basis of quantities which the straightforward Modified Virtual Crack Closure Integral Method can provide (Theilig, Döring and Buchholz[5]). In order to show the significance of the proposed technique computational results are compared with findings from experimental investigations obtained by the aid of a specially designed specimen under lateral force bending.

TWO-DIMENSIONAL CRACK PATH PREDICTION

Consider a crack in a two-dimensional linear elastic body under proportional mixed-mode loading conditions. The stresses ahead of the crack tip are given by

$$\begin{aligned}
\sigma_{11}(x_1,0) &= \frac{k_I}{\sqrt{2\pi x_1}} + T + b_I\sqrt{\tfrac{x_1}{2\pi}} + O(x_1),\\
\sigma_{22}(x_1,0) &= \frac{k_I}{\sqrt{2\pi x_1}} + b_I\sqrt{\tfrac{x_1}{2\pi}} + O(x_1),\\
\sigma_{12}(x_1,0) &= \frac{k_{II}}{\sqrt{2\pi x_1}} + b_{II}\sqrt{\tfrac{x_1}{2\pi}} + O(x_1),
\end{aligned} \tag{1}$$

where k_I and k_{II} are the stress intensity factors (SIFs). T, b_I and b_{II} are the included higher order stress field parameters. It is known that in such a situation the crack will propagate in a smoothly curved manner after an abrupt deflection out of its original plane (Figure 1). For several mixed-mode fracture criteria the initial direction φ_0 depends only on the ratio k_{II}/k_I of the SIFs of the original crack, whereas for others a further dependence on Poisson's ratio ν is found. But for small ratios k_{II}/k_I practically the same values $\varphi_0 = -2\, k_{II}/k_I$ are predicted by all criteria. This direction results in the state of local symmetry at the actual crack tip ($K_{II} = 0$). The generalisation of the local symmetry criterion can be regarded as the basis for the evolution of the crack path. Therefore the state of stress ahead of the deflected new crack tip exhibits no K_{II} and is given by

$$\begin{aligned}
\sigma_{11}(x_1^*,0) &= \frac{K_I}{\sqrt{2\pi x_1^*}} + T^* + b_I^*\sqrt{\tfrac{x_1^*}{2\pi}} + O(x_1^*),\\
\sigma_{22}(x_1^*,0) &= \frac{K_I}{\sqrt{2\pi x_1^*}} + b_I^*\sqrt{\tfrac{x_1^*}{2\pi}} + O(x_1^*),\\
\sigma_{12}(x_1^*,0) &= b_{II}^*\sqrt{\tfrac{x_1^*}{2\pi}} + O(x_1^*).
\end{aligned} \tag{2}$$

It can be stated that continuous crack deflections can only be caused by the existing non-singular stresses. According to Sumi[2,3] the crack path prediction can be performed by using the first order perturbation solution of a slightly kinked and curved crack.

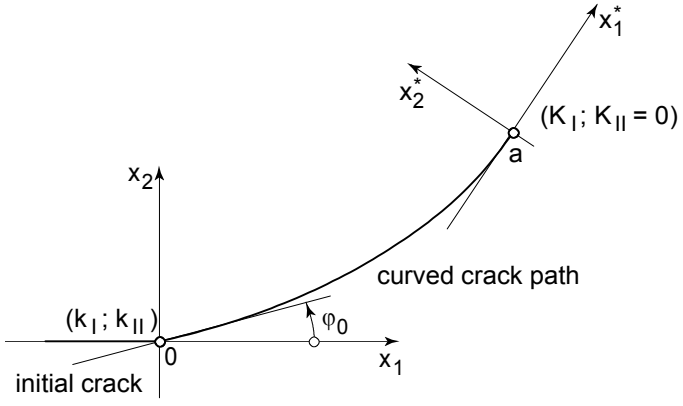

Figure 1: A kinked and curved crack

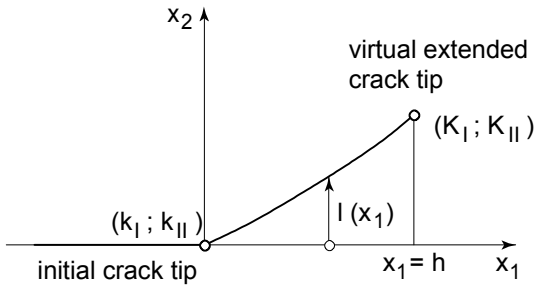

Figure 2: A slightly kinked and curved virtual crack

A virtually extended slightly kinked and smoothly curved crack path profile (Figure 2) is assumed in the form

$$l(x_1) = \alpha x_1 + \beta x_1^{3/2} + \gamma x_1^2 + O(x_1^{5/2}), \tag{3}$$

where α, β and γ are the shape parameters. As the consequence of the crack propagation criterion of local symmetry the SIF K_{II} vanishes along the smooth crack path and the shape parameters of the natural crack geometry are obtained as

$$\alpha = -2k_{II}/k_I\,,\ \beta = \frac{8}{3}\sqrt{\tfrac{2}{\pi}}\frac{T}{k_I}\alpha\,,\ \gamma = -\left(k_{II}\bar{k}_{22}+k_I\bar{k}_{21}+\frac{b_{II}}{2}\right)\frac{1}{k_I}+\left\{\left[k_I\left(2\bar{k}_{22}-\bar{k}_{11}\right)+\frac{b_I}{2}\right]\frac{1}{2k_I}+4\left(\frac{T}{k_I}\right)^2\right\}\alpha\,. \quad (4)$$

where the quantities $\bar{k}_{11},\bar{k}_{21},\bar{k}_{22}$ represent the effects of the far field boundary conditions to the crack growth. If we consider a straight crack under local symmetry at the initial crack tip, i.e. $k_{II} = 0$, we find $\alpha = \beta = 0$. Therefore the parabolic crack profile

$$l(x_1) = \gamma x_1^2\,,\ \gamma = -\left(\frac{b_{II}}{2}+k_I\bar{k}_{21}\right)\frac{1}{k_I} \quad (5)$$

is holding. In this case the crack will propagate without kinking with a continuous deflection. But in the case of a self-similar virtual crack extension of the postulated straight crack the SIF's

$$\bar{K}_I = k_I+\left(\frac{b_I}{2}+k_I\bar{k}_{11}\right)h,\ \bar{K}_{II} = \left(\frac{b_{II}}{2}+k_I\bar{k}_{21}\right)h \quad (6)$$

are obtained. Further $K_I(h) = \bar{K}_I(h)$ is found in consequence of the considered slightly curved crack extension. Finally one gets for a selected increment Δh the following information of the real crack path

$$\Delta\varphi = -2\frac{\Delta\bar{K}_{II}}{k_I}\,,\ \Delta l = -\frac{\Delta\bar{K}_{II}}{k_I}\Delta h\,,\ \Delta a \approx \Delta h\left[1+\frac{2}{3}\left(\frac{\Delta\bar{K}_{II}}{k_I}\right)^2-\frac{2}{5}\left(\frac{\Delta\bar{K}_{II}}{k_I}\right)^4\right]. \quad (7)$$

It is seen that under the local symmetry criterion $K_{II} = 0$ the change of the slope and the locus of the crack tip can be interpreted as the consequence of $\Delta\bar{K}_{II} \neq 0$ for a virtual tangential crack extension Δh (Figure 3).

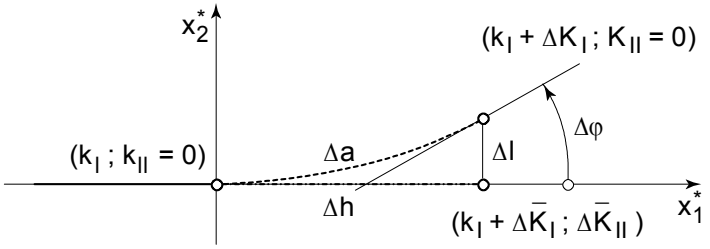

Figure 3: Curved crack propagation

Therefore, in the case of proportional loading conditions the analysis of a smooth crack path can be carried out by a small virtual tangential crack extension as the predictor-step in combination with a finite change of the crack path as the corrector-step. Due to the predictor-step the calculation of $K_I = \bar{K}_I$ and $\Delta\bar{K}_{II}$ is necessary in conjunction with the related tangential crack extension Δh. This can be done by using the finite element method. From Eqs.(7) the need for an efficient numerical mode separation technique in conjunction with the step-by-step analysis can be seen.

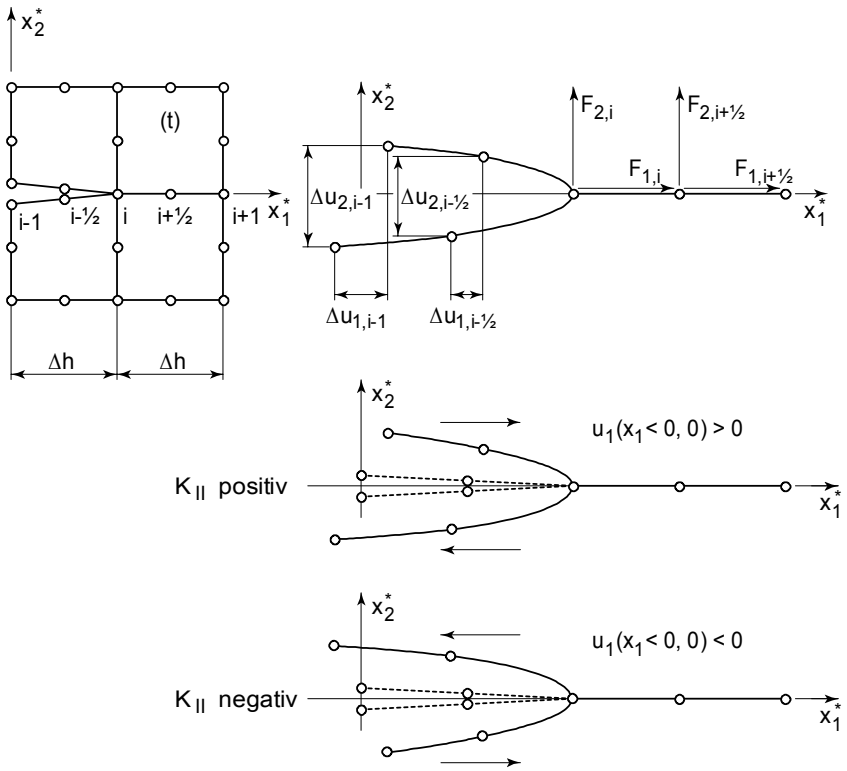

Figure 4: Modified virtual crack closure integral method

With respect to this requirement the MVCCI-method has proved to be highly advantageous, because it delivers the separated strain energy release rates of two modes simultaneously without any additional effort. For 8-noded quadrilaterals at the crack tip (Figure 4), which are necessary to model the parabolic curved increments of the crack path, the following finite element representation of Irwin's crack closure integral relations can be given (Buchholz[6])

$$\overline{G}_I = \frac{1}{2\Delta h t}\left(F_{2,i}\Delta u_{2,i-1} + F_{2,i+½}\Delta u_{2,i-½}\right),\ \Delta\overline{G}_{II} = \frac{1}{2\Delta h t}\left(F_{1,i}\Delta u_{1,i-1} + F_{1,i+½}\Delta u_{1,i-½}\right). \tag{8}$$

CURVED FATIGUE CRACK GROWTH TESTS

In order to evaluate the validity and the efficiency of the proposed higher order crack path simulation method with respect to the well established basic strategies, experiments of non-coplanar fatigue crack growth are carried out with a specially designed specimen under **l**ateral **f**orce **b**ending (LFB)[7]. The LFBH-specimen has been designed with a **h**ole in the centre in order to produce a non-homogeneous stress field (Figure 5).

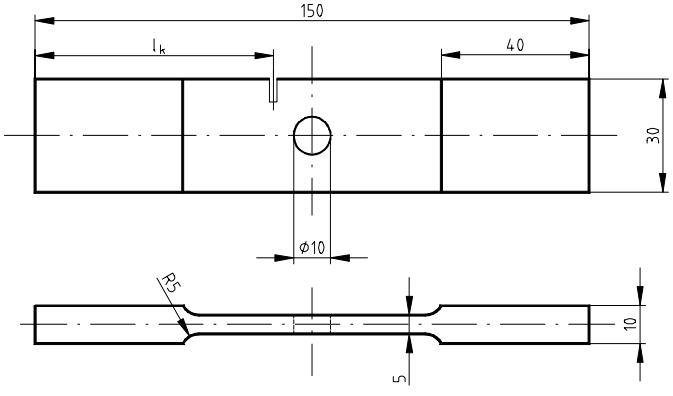

Figure 5: Dimensions and notch position of the LFBH-specimen

Crack initiations from notches at different positions l_K along the tensile loaded edge of these specimens are investigated to produce different crack interactions with the hole. In particular l_K = 65, 75 and 85 mm were selected. The notches have been manufactured with a width of 0.3 mm and a maximum depth of 3 mm. In Figure 6 two broken LFBH-specimens are shown with an experimentally obtained curved fatigue crack path, respectively for two of the three tested notch positions. In the experimental findings given in Figure 7 it can be recognised that the small differences of the notch positions with respect to the bore and the local positions of the pre-cracks in the roots of the notches essentially determine the experimental scattering.

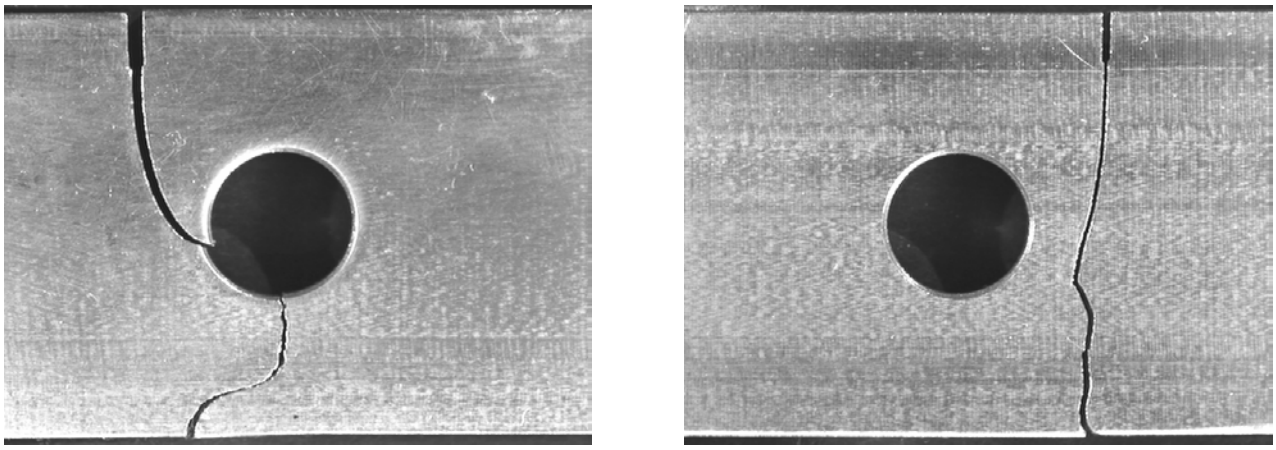

(a) (b)

Figure 6: Experimental fatigue crack paths of the LFBH-specimen with the notch position (a: l_K = 65 mm; b: l_K = 85 mm)

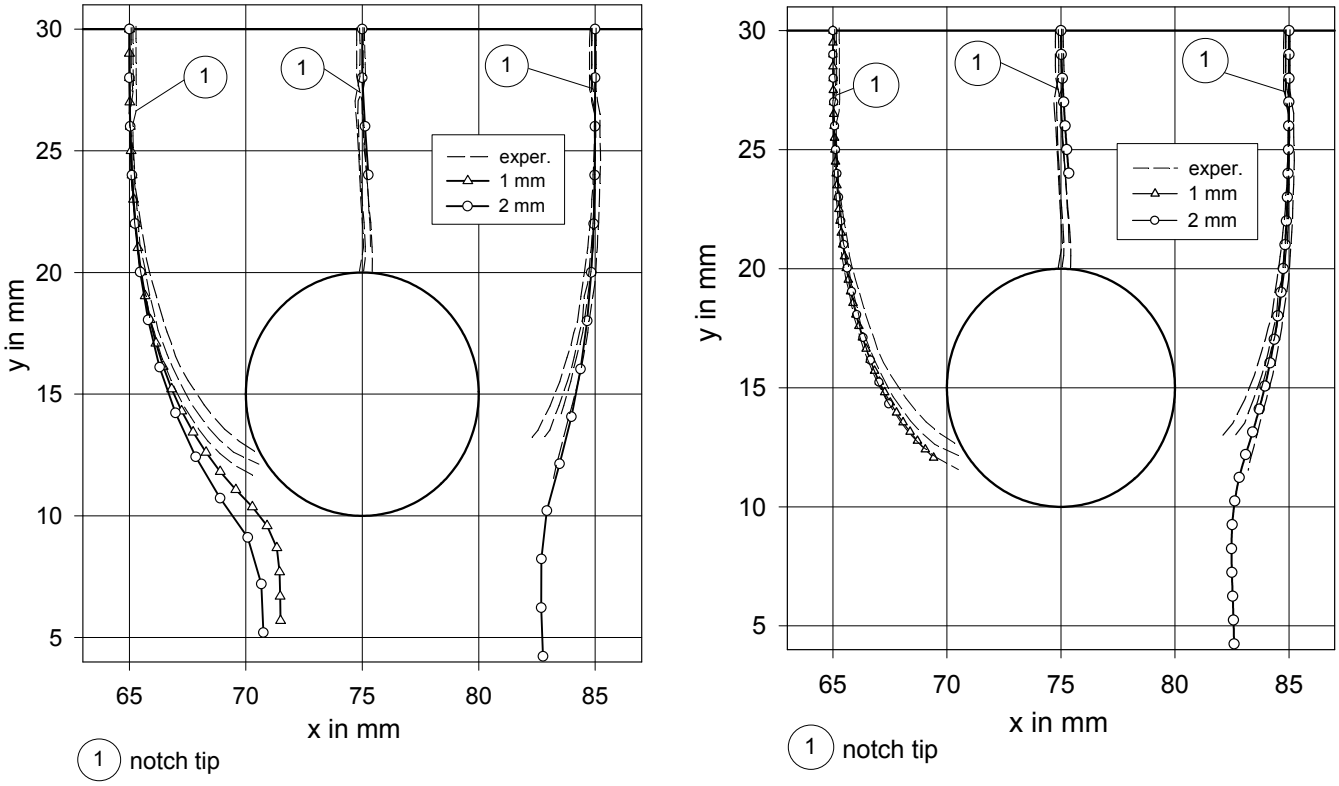

(a) (b)

Figure 7: Simulated and experimentally obtained crack paths of the LFBH-specimen (a: straight incremental steps; b: curved incremental steps with marked mid-side nodes)

NUMERICAL CRACK PATH PREDICTION

For the finite element calculations the model are chosen in accordance with the design of the LFBH-specimen and the available test assembly. After each predictor step of virtual tangential crack extension by Δh a re-meshing is necessary in such a way, that the corrector step is realised in order to model the curved crack surfaces and that together with the following predictor-step new crack tip elements are generated providing additional nodes. All calculations were carried out with the FE-code ANSYS. In Figure 7 the numerical results of the notch position l_K = 65, 75 and 85 mm and the experimental findings are given. For all chosen increments Δh (2 mm, 1 mm) an excellent agreement is found. Additional calculations were carried out without the proposed corrector step (straight increments) in order to verify the improved convergence of the new method. In particular for the critical notch position l_K = 65 mm the new method results in an accurate evaluation of the final fracture mode of the cracked specimen whereas, in this case, the other method fails to simulate the correct crack path.

SUMMARY

This investigation has shown that the new predictor-corrector procedure in combination with the MVCCI-method provides excellent crack path simulation results with 8-noded quadrilaterals and only moderately refined finite-element-meshes around the crack tip. The step-by-step higher order simulation process with a piece by piece parabolic curved approximation of the crack path offers an excellent way for the numerical analysis of fatigue crack growth in complex two dimensional structures under proportional loading conditions. From the excellent agreement of the numerical and experimental results one can also conclude that the applied criterion of local symmetry provides a correct and reliable basis. The proposed predictor-corrector-method in conjunction with the evaluation by the MVCCI-method provides a powerful numerical tool for a general computational approach to the fracture analysis of complex crack configurations and loading conditions.

ACKNOWLEDGMENT

The authors are grateful to Dipl.-Ing. R. Döring, who provided most of the computational results presented in this work.

REFERENCES

1. Bergkvist, H. and Gnex, L. (1978). Curved crack propagation. *International Journal of Fracture* 5, 429-441.
2. Sumi, Y.(1985).Computational Crack Path Prediction. *Theoretical and Applied Fracture Mechanics* 4, 149-156.
3. Sumi, Y. (1990), Computational Crack Path Predictions for Brittle Fracture in Welding Residual Stress Fields. *International Journal of Fracture* 44, pp. 189-207.
4. Portela, A. and Aliabadi, M.H. (1992), Crack Growth Analysis Using Boundary Elements. Computational Mechanics Publication Publisher , Southhampton, UK.
5. Theilig, H., Döring, R., Buchholz, F.-G.(1997). A Higher Order Fatigue Crack Paths Simulation by the MVCCI-Method. In: *Advances in Fracture Research, ICF9*, Volume 4, pp.2235-2242, B. L. Karihaloo, Y.-W. Mai, M. I. Ripley, R. O. Ritchie, (Eds.). Pergamon, Amsterdam-Oxford-New York-Tokyo-Lausanne.
6. Buchholz, F.-G.(1984). Improved Formulae for the Finite Element Calculation of the Strain Energy Release Rate by the Modified Crack Closure Integral Method. In: *Accuracy, Reliability and Training in FEM-Technology*, pp. 650-659, Robinson, I. (Ed.). Robinson and Associates, Dorset.
7. Kittelmann, T.(1993). Diploma Thesis, Technische Hochschule Zittau, Germany.

CYCLIC COMPRESSION OF JACKETED REINFORCED CONCRETE COLUMNS

M.A.G. Silva, F.C.T., Universidade Nova de Lisboa
D. Krajcinovic, MAE, Arizona State University, USA

ABSTRACT

Retrofitting reinforced concrete (RC) columns jacketed by carbon fibre reinforced plastics (CFRP) is one of the most frequent strategies to increase the life of damaged structures in civil engineering. This study focuses on the experimental research on the deformation during cyclic uniaxial compression of jacketed columns. Damage mechanics is used to interpret experimental data and initiate the second phase of this research.

The experimental studies of jacket effects on the strength and macro-ductility of the column concrete were conducted on 27 circular columns of 750-mm height and 150-mm diameter. Both CFRP and RC were utilised as well as different spacing of stirrups. All tested specimens were macroscopically identical.

Analysis of available data obtained for low values of the aspect ratio, λ=height/diameter, typically λ=2, raises considerable doubts on the generalisation of those results. Besides known shortcomings of such scaling for compressive tests based on which failure modes are to be analysed, the relative stiffness of the outer composite shell vs. concrete appears overestimated. This is a serious objection that the present study avoided by selecting an aspect ratio λ=5 for the tests reported herein.

The preliminary conclusion based on the experiment data on CFRP reinforced concrete columns subjected by cyclic compression suggest that the spacing of stirrups affects the strain localisation threshold. The primary objective of the developed continuum damage mechanics model, based on the thermodynamics of dissipated deformation processes and fracture mechanics, is to provide physical underpinning of the process of damage evolution.

1. Introduction

Reinforced concrete columns strengthened by CFRP display obvious advantages, but require further studies both experimental and analytical to establish reliable models for better engineering. Compression tests have shown that large strength and ductility enhancements become possible, but many earlier data are based on cylinders of small diameter vs. thickness of composite wrap and/or for low aspect ratio, typically 2, raising substantial doubts on the conclusions on failure modes. Adequate jacket stiffness is crucial, since lower values made jacket useless whereas very high values make the rupture very brittle. A reasonable compromise that avoids these pitfalls, e.g. [1-3], was attempted using H=750mm and D=150mm throughout the tests.

Results on loading of RC columns confined with FRP are scarce due to the complexity of interaction of between the confinement provided by stirrups to the concrete outer layer and the influence of the stiffness of the FRP shell. Extrapolation from confinement provided by steel reinforcement to that due to FRP is very dubious. Pressure provided by FRP jackets increases continuously till rupture, in association with their linear-brittle

constitutive law, while yielding of steel transverse reinforcement induces a different pattern of response.

Models that assume a constant radial pressure simulate the case of steel transverse reinforcement, given that such steel yields and produces a constant confining pressure proportional to the yield stress, area and spacing of the hoops. A better model used in study considers the increasing confining stress due to the actual dilation of the concrete core and fits better the concrete confined by a linear elastic shell. Correlation between confinement and current dilation can be deduced from an incremental model by record increment load, evaluate dilation and calculate confinement pressure and state of stress. Hoppel et al. [4] proposed a linear elastic relation between the hoop strain in the shell, the confining pressure and the axial stress in the concrete. Mirmiran and Shahaway [5] submitted an incremental method, based on a cubic relation relating the change in radial strain with the axial strain. The coefficients of the expression were generated from the unstressed and the ultimate jacket failure and considered a variable Poisson's ratio for the enclosed concrete according to Elwi and Murray [6]. The variable Poisson's ratio was obtained from unconfined concrete coupons and the confining pressure calculated from the jacket hoop modulus, geometry and radial expansion of the core. A constant pressure confinement model is used to predict the concrete axial stress and results have been considered reasonable for jackets only with hoop fibres, low axial stiffness and low Poisson's ratio in axial direction.

Available results on cyclic loading of concrete exist for over 30 years, e.g. at Rice University [7], as well as on confinement provided by steel reinforcement, leading to results and models [8-12] documented and used with success in existing Codes.

However, data are scarce for the case of specimen confined by FRP with the inner core reinforced by stirrups (RC) and subjected to axial cyclic loading. Added to the mentioned factors that make studies harder for loading of RC columns confined with FRP, i.e. contribution of stirrups, concrete outer layer and the FRP shell itself one has to account for the load-unload effects, interpret and explain results.

In order to attain these objectives, tests were made on 27 circular columns, of 750 mm-height and 150 mm diameter, jacketed with CFRP, under axial cyclic compression. Columns without jackets were also used for comparison, illustrating plain concrete behaviour. Results for these cylinders with longitudinal and transverse steel reinforcement are also reported elsewhere in detail. Representative results are described in the text and micromechanics considered only for the interpretation of results.

2. Material Parameters

Concrete, tested in standard cubes, had an average cylindrical strength f_{cm}=37.7Mpa; though, for design equations, values based on cylinders of 750mm were used in tests. Concrete columns were either of plain concrete, or were reinforced longitudinally with 6ϕ6mm or both longitudinally and transversely. In the latter case, stirrups ϕ3mm were placed at s=5, 10 or 15cm. The sample of columns consisted of 11 columns confined with 2 plies of CFRP. The elastic modulus of tested epotherm resin was E=1768 MPa, ultimate tensile strength σ_{tu}=23.7 MPa, strain at maximum force 4.99% and ultimate strain 13.53%. Parameters of Replark 30 carbon fibres were E=230GPa, σ_t= 3400MPa, t_{ply}=0.167mm. Laboratory tests data were E=210GPa, σ_{tu}=3371MPa, strain for maximum force 2.8% and ultimate strain 3.0% for coupons with 2 plies of CFRP.

3. Test Data

Three specimen are selected for the initial part of this communication, due to their clear rupture away from plates and completeness of data, hereafter identified as C3, C4, C26.

This choice allows the comparison of plain concrete with columns jacketed with two layers of CFRP, the latter either under monotonic loading or cyclic loading; all the reported specimen without steel reinforcement. The values of f'_{co}, ε_{co}, which correspond to maximum unconfined stress and corresponding strain in concrete, were respectively 32.2 MPa and 0.2%; f'_{cc} maximum confined stress in concrete; ε_z is vertical strain and ε_r maximum circumferential strain. For identification, C3 is unconfined, plain concrete, whereas C4 and C26 are externally wrapped with two layers of CFRP. Only the loading on specimen C26 was cyclic. The increase of maximum stress f'_{cc} was from 32.2 to 73.6MPa for C4 and to 81.0 MPa when loading was cyclic. Axial strain increased from 0.20% to 1.20 and 1.03%, respectively. Recorded hoop strain appeared reliably recorded for specimen C4 where it was found 0.74%.

A comparison of the results for the three cases in terms of σ–ε curve is depicted in Fig.1. Similar data were obtained for glass fibre wraps. Elastic parameter of the material acquired from FYFE Corporation was E_c=27.6 Gpa. The maximum stress was 552 MPa and the ultimate strain 2.0 %, based on the composite thickness per ply of 1.2954 mm. According to laboratory measure the ultimate strain was ε_u=3.75% .

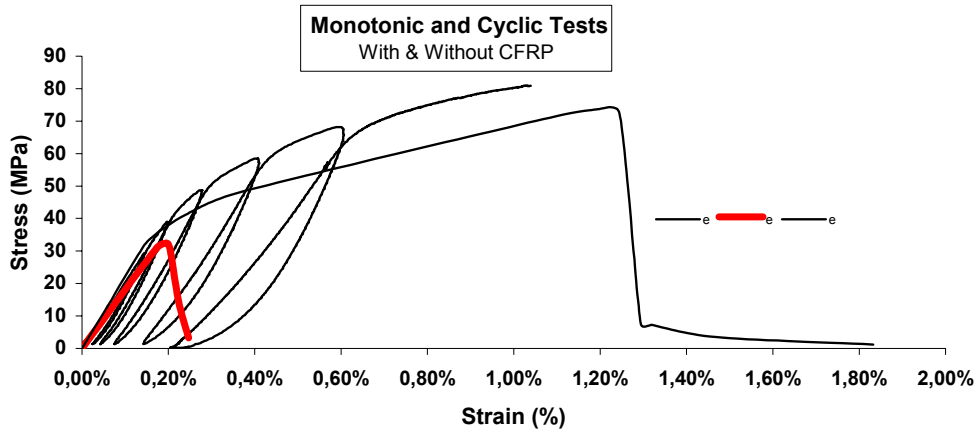

Fig. 1 – Unconfined column and confined under monotonic load and cyclic load (CFRP)

Results for specimens C22 and C27, wrapped with 3 layers of GFRP according to techniques recommended by FYFE, are plotted in Fig. 2, and compared with plain concrete. The behaviour of columns wrapped with CFRP (2 plies) and GFRP (3 plies) for cyclic loading can be compared in Fig. 3.

The influence of transversal steel reinforcement on results, as well as the importance that wider spacing of stirrups confers to the jackets was also examined. Preliminary results suggest that the importance of jacketing is greater when stirrups spacing increases. As mentioned above these results will be reported in a later text.

For CFRP strengthening, the monotonic loading curves were found to be below the envelope for static cyclic loading, for all three different cases of stirrups (5,10 and 15 cm apart). The part of axial strain curves when ε_z is approximately 0.2%, after concrete failure, are consistent to increases of the ratio $|\varepsilon_r/\varepsilon_z|$ that is often referred as the Poisson's ratio. The volumetric strain, $\varepsilon_v = 2\varepsilon_r+\varepsilon_z$, for cyclic loading, that increases for

large deformations, is associated to the deformation between the post-rupture of the concrete core and the failure of the RC columns.

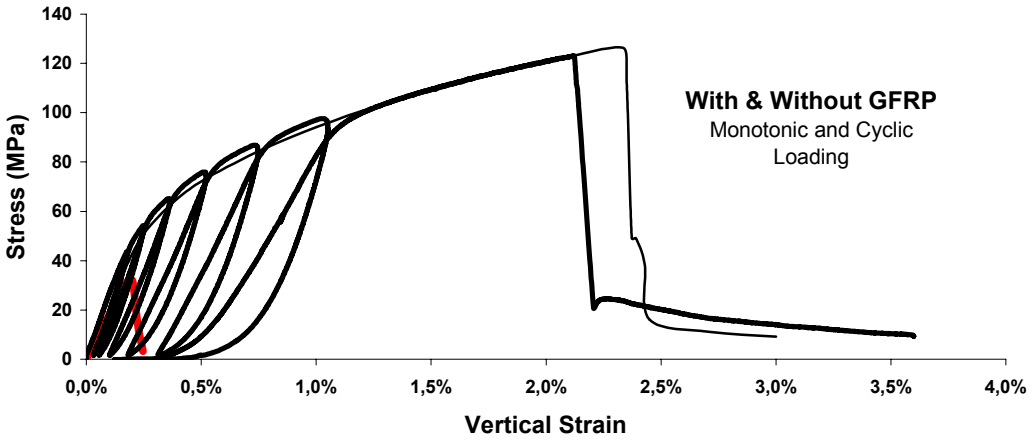

Fig. 2 – Unconfined column and confined under monotonic and cyclic load (GFRP).

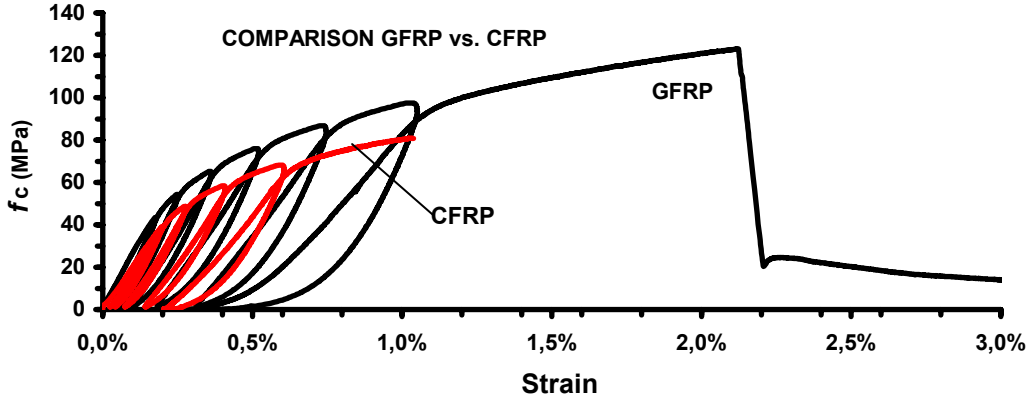

Fig. 3 – Stress-strain curves for confined columns subject to cyclic loading

4. Analytical Model

The macroscopic normal stresses in laterally confined concrete column subjected to quasi-static increased axial direction are all positive. Hence, the cracks are, at least in beginning, only nucleated and propagated in the plane of maximum shear stress. Useful models are discussed in [14]. However, these models can be used only when the material is statistically homogeneous, i.e. in the hardening phase of the deformation, which is also the failure when the applied stresses are controlled.

A continuum model for the FRC columns was developed by authors, that can be generalised to take in consideration column size on failure and seems to be rather

useful. A 3-dimensional micromechanics model would be very complex but still possible. Using the assumptions from [4] the micromechanics models the models will be quasi-two dimensional which will minimise the computational aspects of the model. Similar to [15] the ring shaped regions starting from radius zero to the external surface are elastic, process zone of increasing damage in concrete, zone in which the concrete is comminuted into smallest particles and the jacket zone which can be divided into elastic and plastics parts. Some stresses at the interfaces between two zones of different stiffness may be discontinuous. The stress discontinuity can be derived from the mass and momentum conservation equations [5].

Further tests and analytical modelling will interrogate the impact of composite jackets on the safety and on increased damage capability of the columns. The present small contribution to this goal indicates answers to some questions and rises new questions. The need for more precise micro-scale test data is one of the most important requirements that must pursued, in order to create needed conditions to explore further the potential of micromechanical modelling with a better precision.

5. Acknowledgments

Support was provided by the Portuguese Foundation for Science and Technology under Project CEG 3/3.1/2572-95. Writers are also grateful to Mr. C. C. Rodrigues, graduate student at UNL, who performed laboratory tests.

6. References

[1] Demers, K.W., "The strengthening of structural concrete with an aramid woven fiber/epoxy resin composite", Proc. Advanced Composite Mat. In Bridges & Struct., pp435-442, 1995

[2] Harmon, T.G. and Slaterry, K.T., "Advanced composite confinement of concrete", ditto, CSCE, pp292-302, 1992

[3] Nanni, A. et al. "Lateral confinement of concrete using FRP reinforcement", ACI SP 138, pp193-209, 1992.

[4] Hoppel, C.P.R., Bogetti, T.A., Gillespie, J.W. Jr. , Howie, I., Karbhari, V.M. "Analysis of a Concrete Cylinder with a Composite Hoop Wrap", Proc. ASCE Materials Engineering Conference, San Diego, CA, , pp 191-198, 1994.

[5] Mirmaran, A., Shahaway, M. "A Novel FRP-Concrete Composite Construction for the Infrastructure" Proceedings 13th Structures Congress, ASCE, New York, NY, pp1663-1666, 1995.

[6] Elwi, A. A., Murray, D. W. "A 3D Hypoelastic Concrete Constitutive Relationship", , Journal of the Engineering Mechanics Division, Proceedings of the American Society of Civil Engineers, Vol. 105, EM4, August, pp 623-641, 1979.

[7] Karsan, I.D. and Jirsa, J.O.; "Behaviour of concrete under compressive loadings". Journal of the Struct, Die., ASCE, 95 (ST12), 1969, 2543-63, 1969.

[8] Mander, J.B., Priestley, M.J.N. e Park, R., "Theoretical stress-strain model for confined concrete", J. Structural Engineering, vol. 114, N.8, pp.1804-1826, 1988.

[9] Shah, S.P., Fafitis, and Arnold, R.; "Cyclic loading of spirally reinforced concrete". Journal of Struct. Engng, ASCE, 109 (7), 1695-1710, 1983.

[11] Harmon, T.G., Gould, P.L.,Wang, E., and Ramakrishnan, S., "Behavior of confined concrete under cyclic loading". Proc. Advanced Composite Mat. In Bridges & Struct., pp398-409, 1998

[12] Bahn, B.Y.B., Hsu, C. T. T., “Stress strain behavior of concrete under cyclic loading”, ACI Materials Journal,V.95, N.2, March-April 1998.
[13] Rodrigues, C.C., Silva, M.A.G., ”Experimental Investigation of CFRP Reinforced Concrete Columns Under Uniaxial Cyclic Compression”, Proc. Composites Conf., Cambridge, July 2001
[14] Krajcinovic, D., Damage Mechanics, North-Holland Series in Applied Mathematics and Mechanics Vol. 41, Elsevier, 1996.
[15] Mastilovic, S. and Krajcinovic, D. “High velocity expansion of a cavity within a brittle material”, J. Mech. Phys. Solids, V 29, pp. 585-592, 1999.

ORAL REFERENCE: ICF100420OR

CYCLIC CRACK TIP DEFORMATION – THE INFLUENCE OF ENVIRONMENT

E. Gach and R. Pippan

Erich-Schmid-Institute of Materials Science,
Austrian Academy of Sciences, A-8700 Leoben, Jahnstraße 12

ABSTRACT:

Fatigue in metals is controlled by the cyclic plastic deformation at the crack tip. A simple direct observation of the crack tip deformation in the midsection of a specimen is not possible and the surface observation is usually not representative for the process along the crack front. We applied a stereophotogrammetric method to measure the real shape of the crack tip in the midsection of specimens. In this study the influence of ultrahigh-vacuum and a 3.5-% NaCl-solution on the crack growth behavior is reported. We determined both, the influence of environment on fatigue crack growth rate as well as the variation of the real shape of the crack tip in vacuum and saltwater in the midsection of a specimen. The examined materials were a cold-rolled austenitic stainless steel and an aluminum alloy 7020. It will be shown that the environment does not influence the cyclic crack tip opening displacement. The differences in crack growth rate are induced by changing of the shape of the crack tip during blunting.

KEYWORDS: cyclic crack tip deformation, environment, stereophotogrammetric method, crack growth rate

INTRODUCTION

A lot of different models, which try to explain the fatigue crack propagation behavior, can be found in the literature. These models are usually based on measured mean crack growth rate and (or) fractographic observations. However these experimental facts do not permit to decide which model describe the fatigue crack propagation behavior in a certain case. The only way to overcome this problem is to determine the deformation of the crack tip and the fracture processes directly. Such observations are not difficult at the surface, except in case of very small crack tip deformations. However the surface behavior is not representative for the deformation along the crack front, because the stress state in the vicinity of the crack tip at the surface differs from the midsection. In order to overcome this problem we have developed a special technique to determine the shape of the tip in the midsection of a specimen [1,2,3]. The aim of this paper is to investigate the effect of environment on the crack tip deformation and fatigue fracture process by direct observation in the midsection of the specimens.

MATERIAL AND ENVIRONMENT

Tests were performed in an austenitic stainless steel and an aluminum alloy 7020. The composition of this materials are shown in Tables 1 and 2. The fatigue crack growth tests were performed in ultrahigh-vacuum ($p < 10^{-7}$ Torr) and in 3.5-% NaCl-solution. The results were then compared with behavior in air.

The chosen ΔK was 70 and 20 MPa√m in austenitic stainless steel and the aluminum alloy, respectively. The stress ratio R in both cases was 0.05.

TABLE 1:
Composition of the used austenitic stainless steel (weight-%).

El.	C	Cr	Ni	Mo	Si	Mn	P	S	W	Cu	Al	N
%	0.018	17.24	14.53	2.56	0.61	1.71	0.018	0.001	0.07	0.11	0.03	0.068

TABLE 2:
Composition of the aluminum alloy 7020 (weight-%)

El.	Al	Zn	Mg	Cr	Mn	Si	Zr	Fe
%	93.59	4.48	1.08	0.17	0.16	0.11	0.09	0.03

DEFORMATION BEHAVIOR IN AIR

Figure 1 a) shows the real shape of the crack tip in the midsection of specimen at maximum load in a constant amplitude test. The investigated material was a austenitic stainless steel, cycled at ΔK=70 MPa√m and R=0.05. The determination of this 3D-image of the crack tip is shortly described later and for more details see [1,3,4,5].
Clearly visible are the striations on the fracture surface. The blue marked region, for example, corresponds to the striation which was formed in the last cycle. The red marked area is the blunting region which was formed during loading to the maximum load. In order to visualize what happens during a fatigue cycle the shape of the crack tip was determined at different loads [1,2]. From these images the crack tip opening displacement was easy to determine at different distances behind the crack tip during a load cycle, which is depicted in Figure 1 c). Figure 1 b) shows schematically the variation of the shape of the crack tip during one load cycle. At minimum load the crack tip is sharp. At a stress intensity of about 25 % of K_{max} the crack tip opens. The additional loading causes then a blunting of the crack. This blunting process continues till one reaches the maximum load. The shape of the crack looks like a V-notch. During unloading the crack resharpens, at first at the tip of the V-notch. At about 25 % the crack closes, which is also clearly visible in Figure 1 c), in the load vs. COD curve. From this observation we can see that the crack growth in air during loading by blunting (formation of a new fracture surface) and the unloading causes only a resharpening of the crack tip.

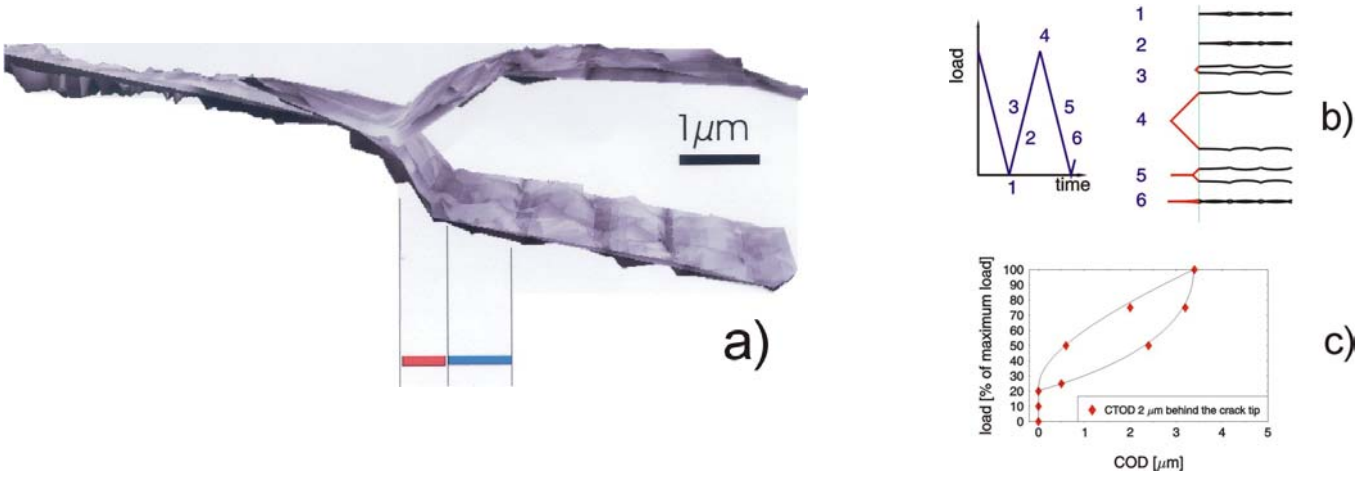

Figure 1: 3D-image of the shape of the crack tip in the midsection of the specimen at maximum load in a constant amplitude fatigue crack growth test (ΔK=70 MPa√m, R=0.05 – a)), the schematic crack tip deformation during a load cycle (b) and the variation of COD during a load cycle (c).

RESULTS AND DISCUSSION

Influence of environment on the crack growth rate

After failure of the specimen we observed the fracture surfaces in a scanning electron microscope. The crack extensions in different environments were clearly distinguishable. Hence, the crack growth rate could be determined.

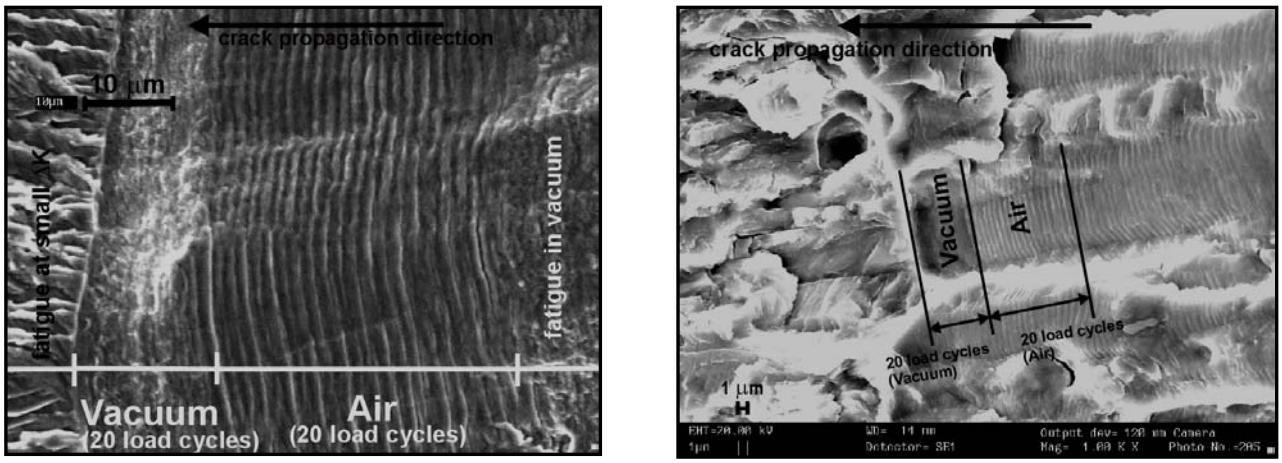

Figure 2: SEM-images from the fracture surface of an austenitic stainless steel (left) and an aluminum alloy 7020 (right). It shows a certain sequence of the constant amplitude test – approximately in the midsection of the specimen.

Figure 2 shows two SEM fractographs from a fatigue test. The fracture surface produced during 20 load cycles in air and 20 load cycles in vacuum at about 10^{-8} Torr is shown. In air clearly visible striations were formed at a constant load amplitude of ΔK=70 MPa$\sqrt{m}$ and a R-value of 0.05 in austenitic stainless steel, and ΔK=20 MPa$\sqrt{m}$ (R=0.05) in aluminum alloy 7020. By measuring the extensions of the crack produced in the different environments on the fracture surface and dividing through the number of load cycles we were able to calculate a mean value of the crack growth rate per cycle. In air we can control this result by determining the striation spacing at high magnifications in the SEM, because the width of one striation corresponds to the local crack growth rate da/dN. In the austenitic steel the crack growth in air is approximately two times larger than in vacuum. In the aluminum alloy 7020 the crack growth rate in air is roughly 2.30 times lager than in vacuum. In vacuum no striations were found. This result is well known from the literature. Pelloux have carried out experiments in aluminum alloys in vacuum and he also found no striations. He argued that the deformation in vacuum is more reversible as in air [6]. In air the new built fracture surface oxidize immediately and the formed oxide layer prevents a reversible deformation at the slip planes. As a result adjacent slip systems will be activated during unloading and one striations will be built [6]. Pelloux found that in aluminum alloys the crack growth rate in air is three times larger than in vacuum [6], which agrees relative good with our observations.

Influence of environment on the cyclic crack tip deformation

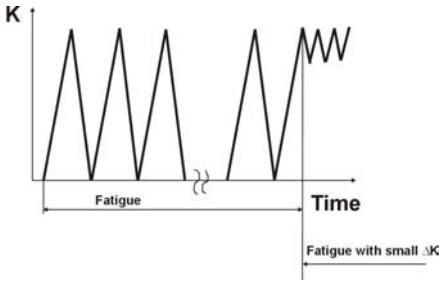

Figure 3: Experimental procedure to determine the crack tip deformation in the midsection of specimen at maximum load in a constant amplitude test.

For the determination of the cyclic crack tip deformation in the midsection of a specimen our fatigue test was interrupted at a chosen load, in this particular case at maximum load. Then a constant amplitude sequence with very small load amplitude was applied till the specimen failed. This small cyclic loading was used to fracture the specimen without changing the shape of the crack tip. Then the corresponding crack tip regions of both broken specimen halves were reconstructed. This was done by analyzing stereoscopic electron images of the two halves with an automatic image processing system [1,2,3]. Therefore we made an image from the fracture surface region and then an image from the same region of the tilted specimen. The tilting angle was 5 degree. We did that for both specimen halves. With an image processing system we got a three-dimensional model of both fracture surfaces. Now we were able to lay together the two 3D-models as in Figure 1 a) or to determine the height profiles along two corresponding lines. Fitting together the two corresponding height profiles give us the real shape of the crack tip. Figure 4 and 5 show two examples:

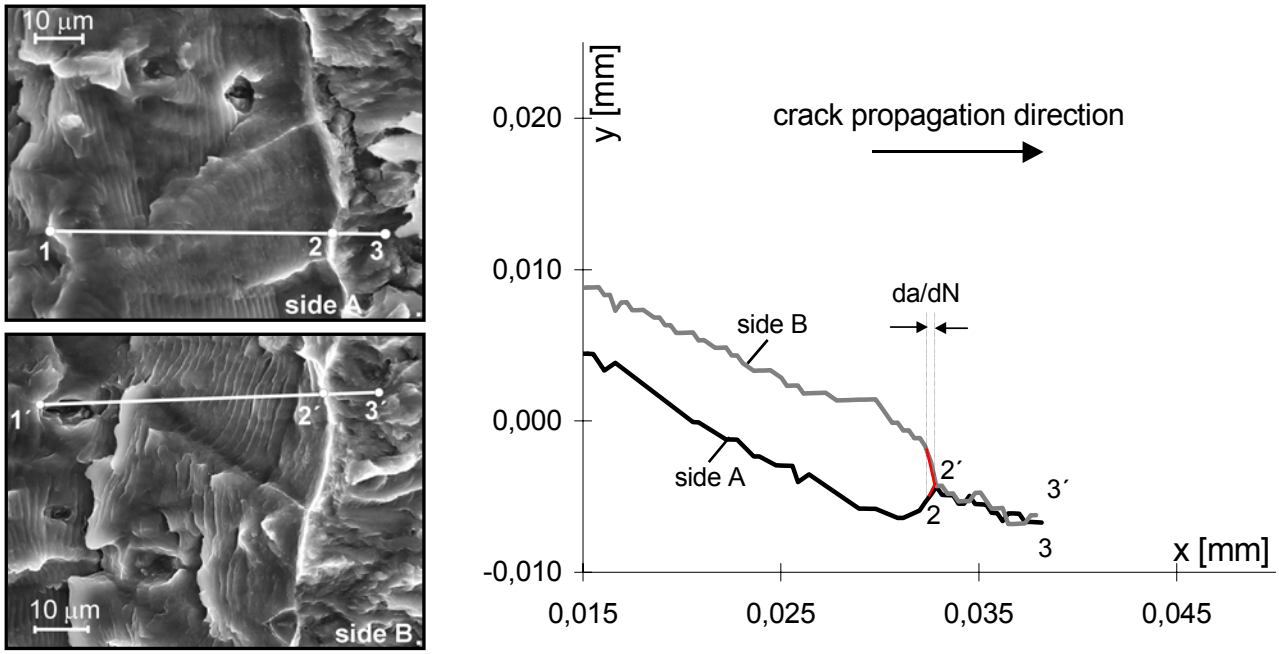

Figure 4: SEM-image from two corresponding fracture surfaces (aluminum alloy 7020) on both specimen halves. The determined height profiles gives the shape of the crack tip at the maximum load in vacuum.

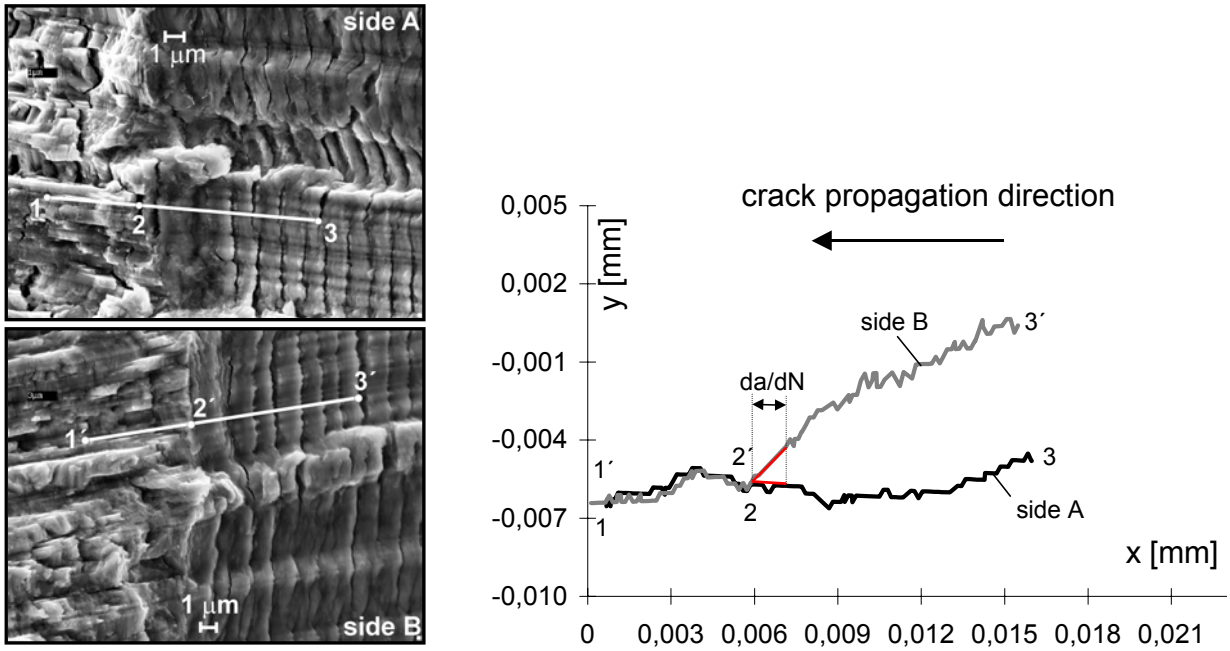

Figure 5: SEM-image from two corresponding fracture surfaces (austenitic stainless steel) on both specimen halves. The determined height profiles along the indicated line shows the shape of the crack tip at the maximum load in 3.5-% NaCl-solution.

Table 3 and 4 summarizes the results from the performed crack growth rate measurements and characteristic values from the determined shape of the crack tip in different environments, for both examined materials.

TABLE 3:
Crack tip opening displacement (CTOD) 3 and 7 μm behind the crack tip, crack tip opening angle (CTOA) or blunting angle, crack growth rate and relative crack growth rate for the austenitic stainless steel (ΔK=70 MPa√m, R=0.05) in different environments.

medium	**CTOD 3 μm behind crack tip**	**CTOD 7 μm behind crack tip**	**CTOA**	**crack growth rate da/dN [μm/loadcycle]**	**Relative crack growth rate (vacuum as reference medium)**
vacuum	4.30	4.60	≈ 105°	0.50	1.00
air	3.30	4.30	≈ 90°	1.00	2.00
saltwater	3.50	4.70	≈ 60°	1.10	2.20

TABLE 4:
Crack tip opening displacement (CTOD) 3 and 7 μm behind the crack tip, crack tip opening angle (CTOA) or blunting angle, crack growth rate and relative crack growth rate for aluminum alloy 7020 (ΔK=20 MPa√m, R=0.05) in different environments.

medium	**CTOD 3 μm behind crack tip**	**CTOD 7 μm behind crack tip**	**CTOA**	**crack growth rate da/dN [μm/loadcycle]**	**Relative crack growth rate (vacuum as reference medium)**
vacuum	4.00	5.00	≈ 130°	0.30	1.00
air	3.30	4.30	≈ 90°	0.70	2.30
saltwater	3.90	4.70	≈ 20°	1.70	5.70

It is evident from the depicted shapes of the crack tip and their determined characteristic values that the environment changes only the shape of the crack tip. The crack tip opening displacement at larger distances behind the crack tip remains constant. The determined differences are typical values for the scatter, which may be caused by small differences in the applied stress intensity range, real acting local stress intensity range in the investigated location or a small variation of the yield stress. A variation of crack closure stress intensity would also change crack tip opening displacement, however at this large ΔK, where only plasticity induced closure is important, this effect does not play a role. The effect of vacuum in both alloys is approximately the same. In vacuum the crack tip opening angle increases (or in other words, the shape of the crack tip changes from a V-shape notch to a more blunted notch). The effect of the NaCl-solution is also the same, however in the aluminum alloy the decrease in crack tip opening angle is much larger and hence also the increase in the crack growth rate is much larger.

CONCLUSIONS

Figure 6 shows a schematic summary of the crack tip deformation and the change of the relations between the crack growth rate (da/dN), the crack tip opening angle (CTOA) and crack opening displacement (COD) in the different environments.

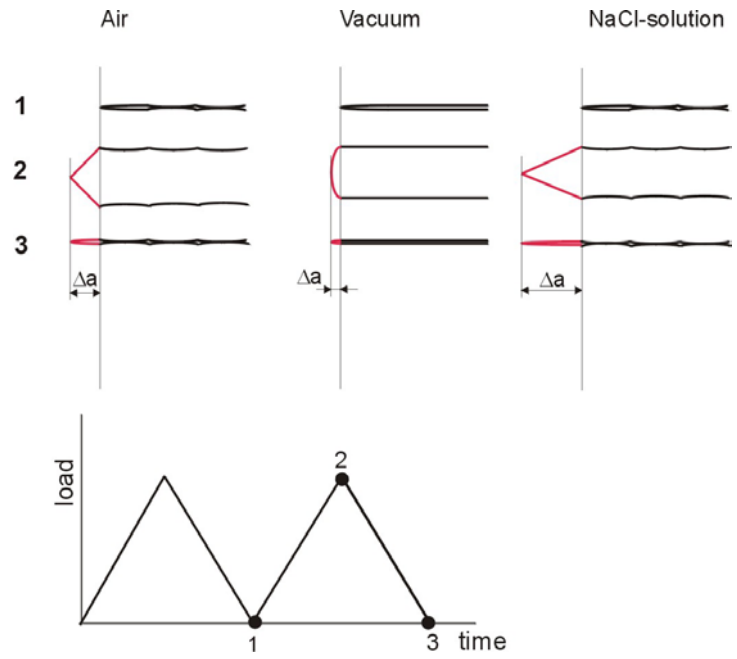

Figure 6: Schematic presentation of the shape of the crack tip at maximum load in different environments.

In all cases the crack propagation mechanism seems to be the same. It is a blunting and resharpening mechanism. However the environment significantly changes the shape of the crack tip during the blunting.

- In vacuum it seems that blunting, with a relative large crack tip opening angle and a relative small crack extension can be occurred.
- In air the blunting or crack tip opening angle decreases, which may be induced by a fracture of the oxide layer or nano fracture of volume elements immediately in front of the tip of crack (tip of the V-notch). This induces the increase in the crack growth rate. The effect is similar in both alloys.
- In 3.5-% NaCl-solution this additional "fracture" at the crack tip of the notch increases, which induces an decrease of the crack tip opening angle and an increase of the crack extension during blunting. In austenitic stainless steel this effect was relative small and very large in aluminum alloy.

REFERENCES

1. Bichler, C. and Pippan, R., Direct Observation of the Formation of Striations, *Proc. Engineering against fatigue* (J.H. Beynon, M.W. Brown, T.C. Lindley, R.A. Smith & B. Tomkins), pp. 211-218.
2. Bichler, C., *Thesis*, University Leoben, 1997
3. Siegmund, Th., Kolednik, O. and Pippan R., Direct Measurement of the Cyclic Crack-Tip Deformation, *Zeitschrift für Metallkunde*, Vol. 81, (1990) pp. 677 –683.
4. Stampl, J., Scherer, S., Berchtaler, M., Gruber, M. and Kolednik, O., *International Journal of Fracture*, Vol. 78, 1996, pp. 35-44.
5. Kolednik, O., *Practical Metallogr.* , Vol. 18, 1981, pp. 562-573.
6. Pelloux, R.M.N., Mechanism of formation of ductile fatigue striations, *Trans. ASM* 62 (1969) 281-285.

ORAL/POSTER REFERENCE: ICF100398OR

CYCLIC PLASTIC DEFORMATION OF PIPELINE STEEL

C.H.L.J. ten Horn[1], A. Bakker[1], R.W.J. Koers[2], J.T. Martin[2], J. Zuidema[1]

[1] Materials Science, Delft University of Technology, Rotterdamseweg 137, 2628 AL Delft, The Netherlands
[2] Shell Global Solutions International B.V., Badhuisweg 3, 1031 CM Amsterdam, The Netherlands

ABSTRACT

In the oil and gas industry, one way of laying pipes on the seafloor is by the reeling process. In this process the pipe is subjected to a cyclic plastic deformation. Due to this plastic deformation the mechanical properties of the material are changed. In this study cyclic plastic deformations are applied to laboratory specimens and alongside these experiments finite element calculations are performed to see if the material behaviour can be predicted. The specimens were subjected to 1% and 2.5% strain amplitude during several cycles. The experiments show that the material exhibits a lowering of the yield strength and an apparent slow transition from elastic to fully plastic behaviour after the first half cycle. To describe this in the finite element calculations three hardening models were tested: isotropic hardening, kinematic hardening and the fraction model. In the fraction model several material fractions are loaded in parallel, which allows for more complex material responses. From the calculations it followed that the isotropic and kinematic hardening models can not describe the cyclic plastic deformation of pipeline steel. Both failed to predict the lowering of the yield strength and the slow transition from elastic to fully plastic behaviour. The fraction model on the other hand can describe both phenomena.

KEYWORDS

Cyclic deformation, fraction model, pipeline steel, finite element method, reverse plasticity, low cycle fatigue

INTRODUCTION

For the investigation into the cyclic plastic deformation of steel, the reeling of steel pipelines was chosen as a test case. In the oil and gas industry the reeling and unreeling of pipelines is one of the ways to install pipelines on the seafloor. The reeling process involves four distinct stages: the reeling, the unreeling, the alignment and the straightening. In the reeling stage an initially straight pipeline is reeled onto a large drum. Once the ship is in position at sea, the pipe is pulled from the drum and it will straighten more or less. In the next stage the pipe is aligned to the correct angle for laying the pipe and it is also bend again but now to a constant radius of curvature. This is done to aid the final stage: the straightening of the pipe. These four stages and the corresponding deformations that occur are shown schematically in figure 1.

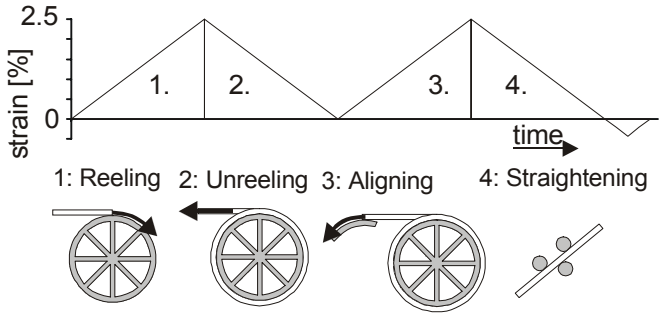

Figure 1: The reeling process and the corresponding deformations that occur

To investigate the influence of cyclic plastic deformation on the material, tests were performed on laboratory specimens. The bending of the pipe now being substituted for axial loading of the small specimens.
In order to predict the behaviour of the material, the cyclic plastic deformation was modelled using the finite element method. In order to achieve a good description several workhardening models were tested.
The material for the experiments was taken from a steel pipe with a diameter of 200 mm and a wall thickness of 21 mm. As the circumferential direction of the pipe is the most critical for failure during operation, the specimens were taken in the circumferential direction from the pipe.

EXPERIMENTS

For the experimental work two types of specimen were used: the tensile specimen geometry and the low cycle fatigue specimens.
The tensile tests were performed according to the ASTM E-8M standard. The specimen geometry can be seen in figure 2.

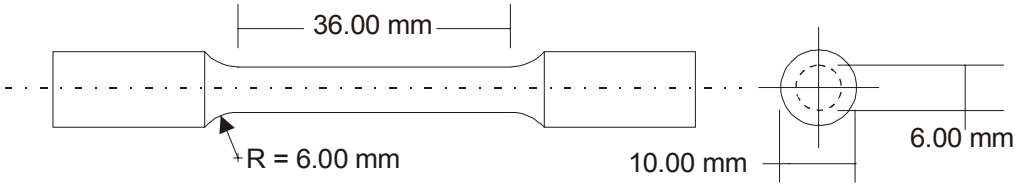

Figure 2: The tensile specimen geometry

In order to obtain the true stress – true strain curve for the material, the deformation of the specimen was monitored using a video camera attached to a computer. From the pictures the diameter of the specimen could be measured right up to fracture.
The low cycle fatigue tests were performed according to the ASTM E-606 standard for strain-controlled fatigue testing. The test section of the specimen was kept as short as possible to avoid buckling. The specimen geometry and its dimensions can be seen in figure 3. To measure the strain accurately strain gauges were glued to the test section of the specimens. The specimens were loaded with a ramp-wave of 0.005 Hz and a strain amplitude of 1% and 2.5%.

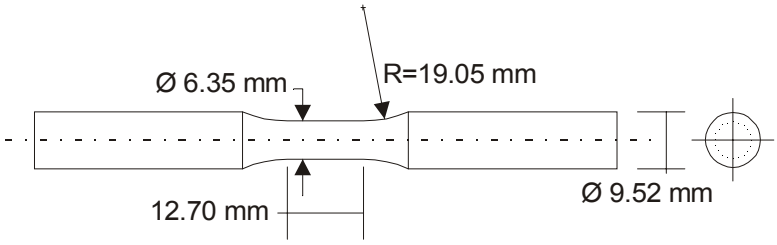

Figure 3: The low cycle fatigue specimen geometry

FINITE ELEMENT CALCULATIONS

For the finite element calculations the general finite element package MARC was used. The specimens geometry's as used for the experiments were modelled using axisymmetric elements.

Hardening models

In the finite element method two hardening models are regularly used: isotropic and kinematic hardening [1]. In this paper also a third model is used: the fraction model [2]. In the fraction model the material is thought to consist of different components or fractions with their own weight and mechanical properties. As a consequence the yielding behaviour of the material is the result of the yielding behaviour of all the fractions combined and their interaction with each other. For simplicity the fractions are to be loaded in parallel.

As Besseling et al. [2] have shown, kinematic hardening can also be modelled as a two fraction model. By enlarging the number of fractions more complex hardening behaviour can be obtained.

The fractions in this model may not be identified with certain microstructural components. This is because the parameters for the model cannot be identified uniquely and because in the model all fractions are loaded in parallel while in the real material the microstructural components are subjected to a combination of parallel and serial loading.

The mechanical behaviour of the fractions itself is kept simple. The fractions have a von Mises yield surface with isotropic hardening. For added simplicity and ease of parameter identification the fractions are assumed to exhibit linear workhardening.

In this study 4 fractions shall be used. The fraction model was implemented in the von Mises yield criterion allowing the calculation of the stresses in all fractions and combining them. A schematic graphical representation can be seen in figure 4.

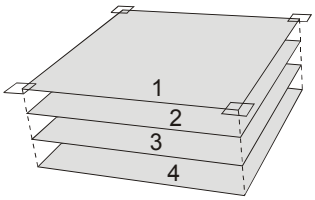

Figure 4: A schematic representation of how the fractions are implemented

Yield Elongation

One of the characteristics of steel is the yield elongation. As the workhardening rate during yield elongation is approximately zero, this means that the workhardening of the fraction responsible for the yield elongation has to account for the elastic responses of the other fractions. This in turn means that the rate has to be negative. At the end of the yield elongation the workhardening rate increases and this means that the rate of the fraction responsible for yield elongation has to increase. The implementation to achieve this is shown in figure 5, where σ_{y1} is the initial yield point, σ_{y2} is the lower yield point and E_{t2} is the secondary workhardening rate. For this study the yield elongation was modelled using two fractions exhibiting this behaviour.

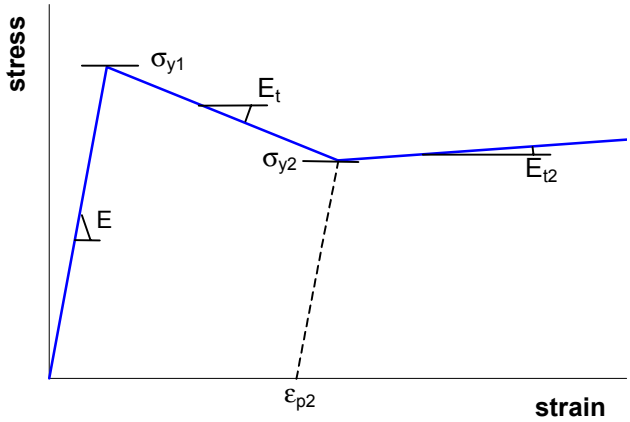

Figure 5: Yield behaviour of the fraction responsible for yield elongation

Parameter Identification

For a 1-dimensional model the parameters of the fraction model can be obtained directly from the tensile test results. The tensile results are approximated by a piece-wise linear representation. The start of the linear pieces coincides with the start of yielding of a fraction.

For 2-D and 3-D models the identification of the parameters involves an iterative approach. This is needed because of the interaction between the different fractions during yielding. The approach taken started with the 1-D parameters and modifying them until the response coincided with the piece-wise linear representation of the experimental tensile results.

RESULTS

The results of the tensile tests on the pipeline steel can be seen in figure 6 clearly showing the yield elongation.

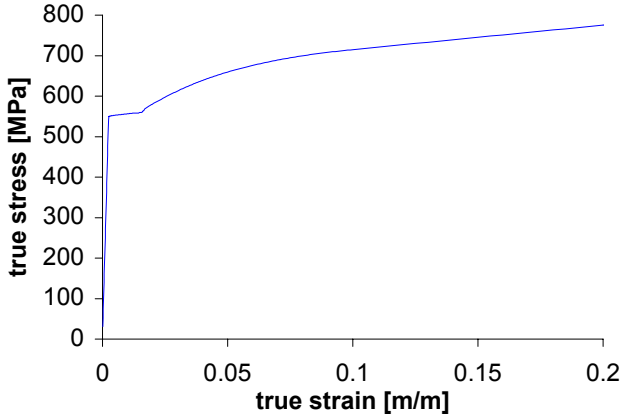

Figure 6: The tensile test results up to 20% strain

The results for the low cycle fatigue tests are shown in figure 7. Figure 7a shows the first 4 cycles at 1% strain amplitude while figure 7b shows the first 4 cycles at 2.5% strain amplitude. These figures clearly show a reduction in yield strength in both compression and tension direction after the first half cycle and that virtually no cyclic strain hardening occurs. Also the slow transition from elastic to fully plastic behaviour after the first half cycle is apparent.

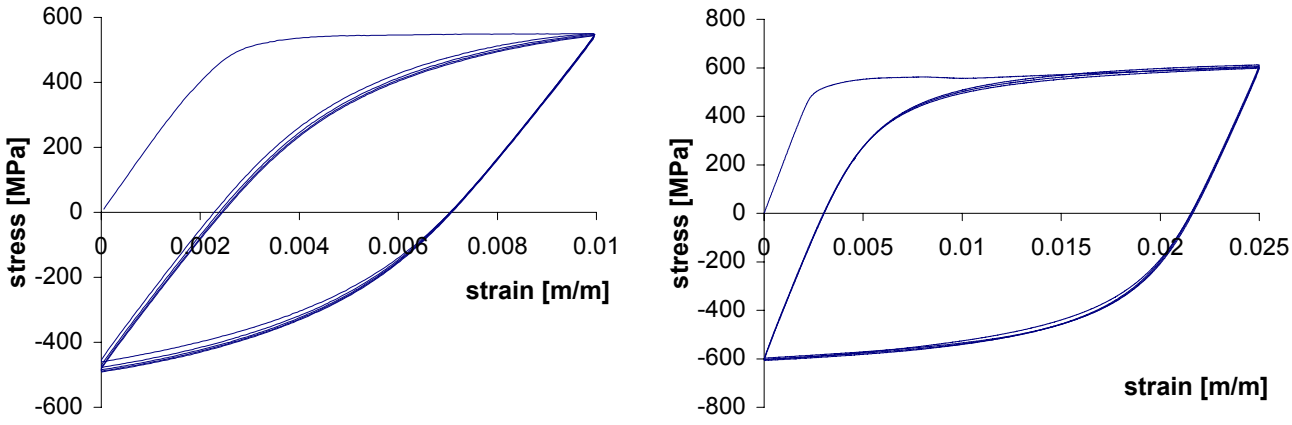

a. b.

Figure 7: The low cycle fatigue results for 1% and 2.5% strain amplitude

FINITE ELEMENT CALCULATIONS

As a first step the results from the isotropic and kinematic hardening are shown in figure 8. It is clear that the isotropic hardening model (fig. 8a.) is not appropriate for these cyclic plastic deformation tests at 1% or

2.5% strain amplitude. The strain hardening that occurs in the model is too high compared with the experiments. Isotropic hardening also neither shows the drop in yield strength nor the slow transition from elastic to fully plastic. The kinematic hardening model (fig. 8b.) also fails on these characteristics but the strain hardening is more realistic.

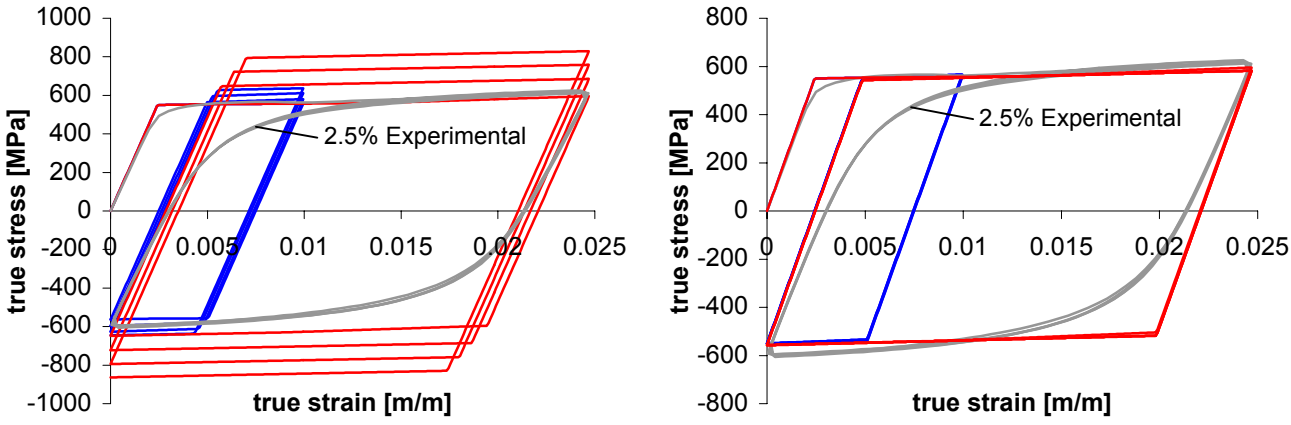

a.

b.

Figure 8: The results from the isotropic (a.) and kinematic (b.) hardening model for 1% and 2.5% strain amplitude

The Fraction Model

As there are many parameters to be identified for the fraction model, the influence of each parameter was investigated. The different parameter sets that are used, are shown in table 1.

TABLE 1: THE FRACTION MODEL PARAMETER SETS

	Fraction	Weight	E [GPa]	σ_{y1} [MPa]	E_t [GPa]	ε_{p2} (%)	E_{t2} [GPa]	σ_{y2}/σ_{y1}
Set 1	1	0.5	398	965	-56	0.407	0	0.76
	2	0.3	82	536	-8.5	0.832	2.2	0.87
	3	0.1	20	305	20			
	4	0.1	13.4	533	3			
Set 2	1	0.5	356	863	-88	0.455	0	0.54
	2	0.3	146	955	-15	0.831	2.2	0.87
	3	0.1	38	580	14			
	4	0.1	13.4	533	3			
Set 3	1	0.5	356	863	-88	0.455	0	0.54
	2	0.3	146	955	-15	0.831	0	0.87
	3	0.1	38	580	28			
	4	0.1	13.4	533	3			
Set 4	1	0.8	222.5	539	-55	0.455	0	0.54
	2	0.1	438	2861	-45	0.831	0	0.87
	3	0.05	76	1160	60			
	4	0.05	26.7	1066	4			

Parameter sets 2 and 3 are shown in figure 9a. indicating that the secondary workhardening rate (E_{t2}) of the fractions responsible for the yield elongation determines the amount of hardening that occurs during the cyclic loading. Whereas the ratio between the lower yield point (σ_{y2}) and the initial yield point (σ_{y1}) determines the yield strength after the first half cycle, this is shown in figure 9b using parameter sets 1 and 2. The ratio of σ_{y2}/σ_{y1} of the second fraction responsible for yield elongation determines the strain at which a kink occurs in the yield curve. The results from parameter sets 3 and 4 are identical, indicating that as long as the parameters fit the tensile test, the σ_{y2}/σ_{y1} ratios are identical and the secondary workhardening slopes are 0, then the weight of the individual fractions does not play any role. The influence of the weight of the fractions is only visible through its influence on the secondary workhardening rates.

The results of parameter set 1 is compared with the experimental low cycle fatigue behaviour in figure 10. From this figure it is clear that the fraction model can describe the drop in yield strength and the slow

transition from elastic to fully plastic behaviour much better than either isotropic or kinematic hardening can.

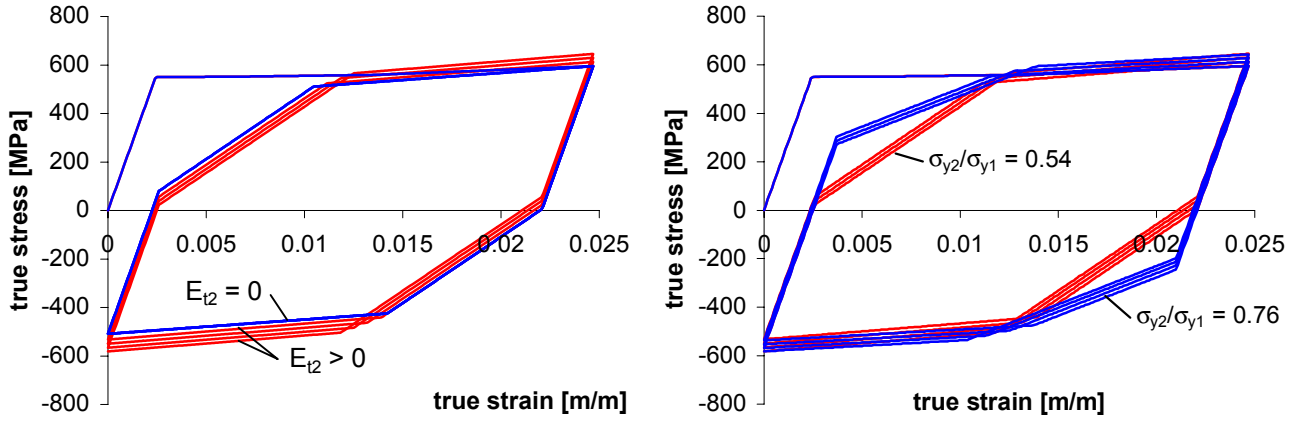

a. b.

Figure 9: The influence of E_{t2} and σ_{y2}/σ_{y1} on the yield behaviour

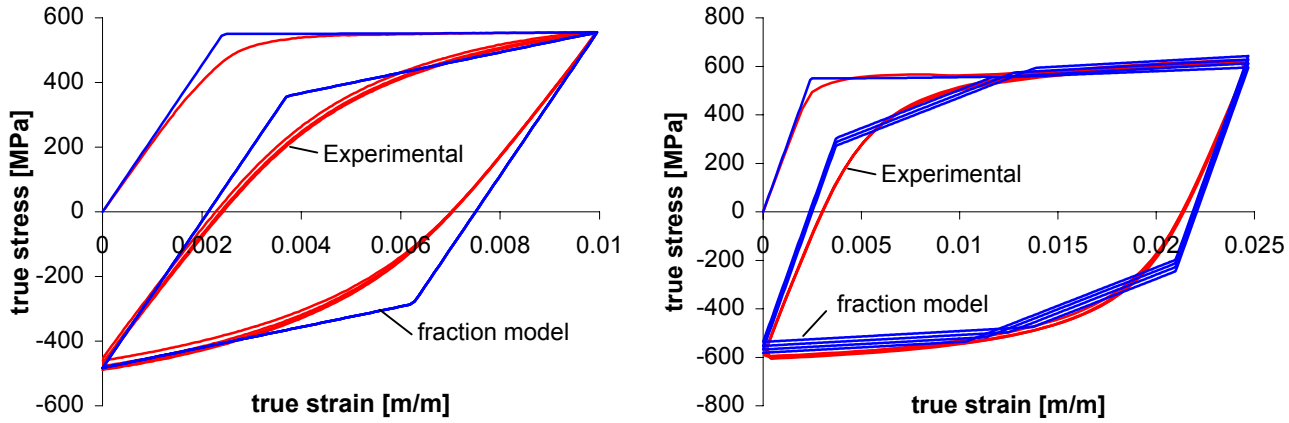

a. b.

Figure 10: The results from the fraction model for 1% (a.) and 2.5% (b.) strain amplitude.

CONCLUSIONS

From the experimental results it is clear that upon cyclic plastic deformation of pipeline steel the yield strength is reduced and that it shows an apparently slow transition from elastic to fully plastic behaviour while virtually no cyclic strain hardening is observed.

From the finite element calculations it is concluded that the isotropic and kinematic hardening models are not appropriate for cyclic plastic deformation of pipeline steel. Both models fail to describe the drop in yield strength and slow transition from elastic to fully plastic behaviour. The fraction model on the other hand does describe the yielding behaviour of the material better. As it shows both characteristics seen in the experiments. By extending the number of fractions that are used, the material can be modelled more accurately.

The parameters used in the fraction can not be uniquely identified. When the parameters are fitted to the tensile test results, the σ_{y2}/σ_{y1} ratio of the first fraction responsible for yield elongation describes the yield strength after the first half cycle while the weight of the fractions plays only a minor role.

REFERENCES

1. MSC.Marc2000 Manuals, (2000) MSC.Software Corp.
2. J.F. Besseling and E. van der Giessen, ”Mathematical Modelling of Inelastic Deformation”, Chapman & Hall London, 1994.

ICF1009580R

CYCLIC THERMAL LOADING OF CERAMIC MATRIX COMPOSITES: CONSTITUTIVE MODELS AND DESIGN STRATEGIES

A.C.F. Cocks[1] , M.E Booker[1] and F.A. Leckie[2]

[1] Department of Engineering, University of Leicester, Leicester LE1 7RH, UK
[2] Department of Mechanical and Environmental Engineering, University of California in Santa Barbara, CA 93106, USA

ABSTRACT

In this paper simple strategies are presented for the design of ceramic matrix composite (CMC) components which are subjected to cyclic thermo-mechanical loading histories. Simple constitutive models are described for the steady cyclic response which capture the major characteristics of the material behaviour. Analytical procedures are described which evaluate the component response in the cyclic state. The approach is illustrated by analysing the classical Bree problem assuming material properties which are representative of a SiC/SiC composite. Interaction diagrams are presented which identify safe operating conditions and the extent of damage in the component.

KEYWORDS

Cyclic thermo-mechanical loading, CMCs, SiC/SiC composites

INTRODUCTION

Decisions during the early stages of traditional design procedures are based on a small number of material properties and the results of simple calculations. Refinement of the design is accompanied by increasingly complex analyses which are based on a more detailed description of material behaviour. This approach has been very successful, but it is characterised by a slow and expensive development which is inconsistent with the need for designers to respond to the rapid increase in the availability of new materials. When dealing with any material it is important to identify those features of the material response which are likely to dominate in a given situation and to develop constitutive laws which allow the relationship between material behaviour and component performance to be clearly identified.

In this paper we attempt to establish a design method for SiC/SiC Ceramic Matrix Composites (CMCs), which are candidate materials for use in components subjected to severe cyclic thermal loading. We develop a simple phenomenological model of material behaviour, guided by the extensive studies of material scientists on the deformation and failure mechanisms. We limit our consideration here to situations in which the loading is largely uniaxial and the fibres within the body are aligned with the principal loading direction. Approximations to the material behaviour are introduced by concentrating on the cyclic state and excluding mechanisms which are known to have little effect on the overall material behaviour. It is then not necessary to develop evolution laws for the state variables which define the material response. Here we present the

results of a set of calculations for the classical Bree problem and construct simple interactive diagrams which give a clear description of the behaviour of the component and which can be employed readily in design.

IDEALISED MATERIAL BEHAVIOUR

There has been significant progress in the development of constitutive models for the mechanical behaviour of CMCs in recent years. The micromechanical processes which determine the macroscopic response are described by Zok et al [1,2] for monotonic loading and cyclic loading conditions respectively. The understanding gained from these studies has guided the development of macroscopic constitutive laws for the material behaviour. Burr et al [3,4] have examined the behaviour within a thermodynamic framework to develop a damage mechanics model which considers the different contributions to the degradation process in a consistent manner. Models of this type require extensive experimental data in order to properly calibrate them. They are useful in the final stages of design where both the material properties and component geometry need to be optimised. During the early stages of design, however, it is important to develop an understanding of the interaction between the material and structural phenomena, which combine to determine the overall structural response and to identify those features of the material behaviour which most critically influence the component performance. Here we describe a simple material model which captures the dominant features of the material response under cyclic loading histories. We are primarily interested in the material response after thousands of cycles. We assume that a cyclic state is reached for the class of loading histories of interest here and develop simple models which describe the steady cyclic response of the material.

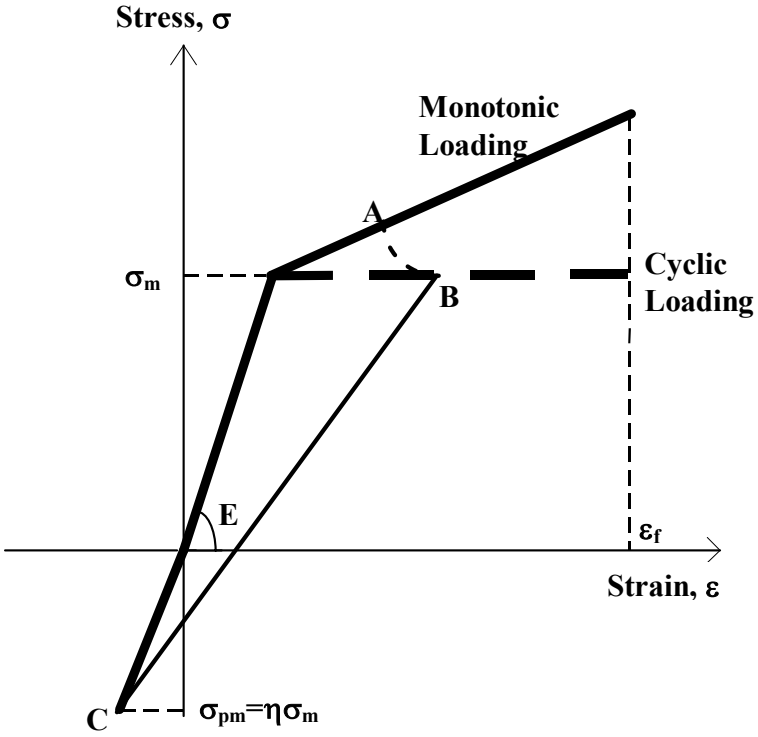

Figure 1 Idealised stress/strain response of a SiC/SiC composite

The idealised response of a SiC/SiC unidirectional composite is shown in Figure 1. During monotonic loading the response follows that indicated by the solid line in the Figure. If the stress exceeds the matrix cracking stress, σ_m, then during subsequent cyclic loading the inferface between the fibre and matrix gradually wears away. As a result, the compliance of the material gradually decreases and the maximum stress experienced during a cycle at a point in the component follows a trajectory similar to that illustrated

by the path AB, until the stress reaches a threshold value, below which no further deterioration of the mechanical response occurs. In situations where a component experiences a large number of cycles during its life (typically greater than 1000) a cyclic state is achieved, with the peak stress lying along the cyclic loading curve of Figure 1, where the stress is coincident with the threshold stress for strains above the matrix cracking strain. For simplicity, the threshold stress in Figure 1 is taken equal to the matrix cracking stress. This is a valid approximation for many SiC/SiC composites. Provided the strain accummulated during this process is less than a critical strain ε_f, damage within the body remains as discrete microcracks. If, from equilibrium considerations, the maximum stress at a point in the body is required to exceed the threshold stress the component will eventually fail. In the cyclic state, if the stress is reduced from the peak value the unloading line BC is followed until a compressive stress $\sigma_{pm}=\eta\sigma_m$ is achieved. At this point all the microcracks are closed and further unloading follows the elastic line for the virgin material. All unloading lines pass through the same point C on this line. The magnitude of σ_{pm} depends on the residual stresses induced in the material during processing.

The material response represented by Figure 1 can be characterised by specifying the modulus of the virgin composite, E, the matrix cracking stress, σ_m, the crack closure stress, $\eta\sigma_m$ and the strain to failure, which we normalise to define the quantity $\beta = E\varepsilon_f / \sigma_m$.

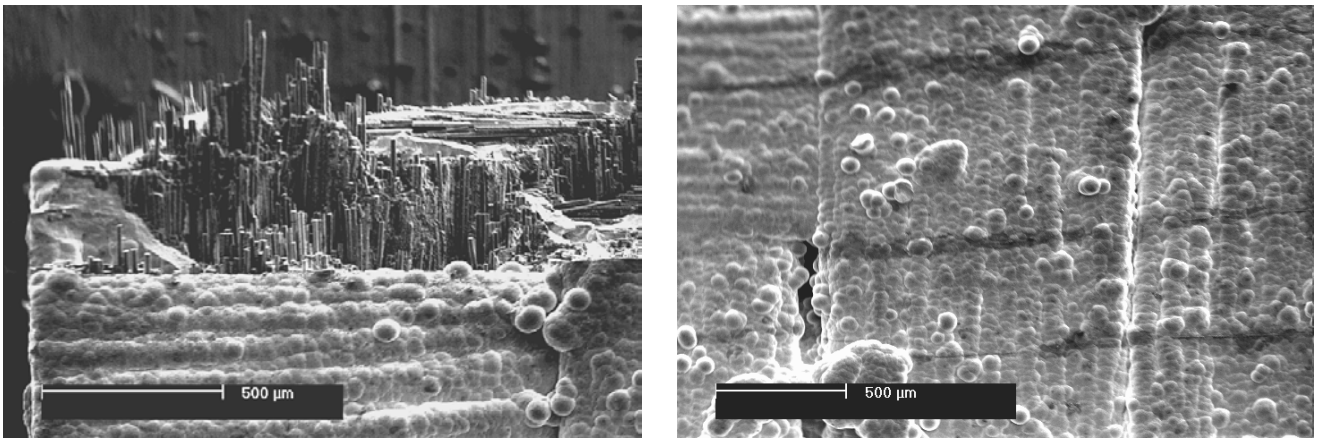

(a) (b)

Figure 2 (a) The failure surface of a SiC/SiC composite subjected to a constant axial load and cyclic thermal loading history involving through thickness temperature gradients. (b) A micrograph of the surface of the specimen within the thermally cycled region away from the failure plane, showing microcracks hich developed during the thermal loading history

THE BREE PROBLEM

In this paper we restrict our consideration to situations in which there is a through-thickness temperature gradient in the component. There are two possible mechanisms of failure for thermal loading histories of this type. Failure can either be determined by the growth of delamination cracks [5,6], or by the growth of microcracks through the thickness of the sample [7], followed by fibre failure and pull-out. Booker [8] has recently conducted a series of tests on a number of different SiC/SiC composites in which plane specimens were subjected to a constant axial load. A small region on the surface of the sample was heated using three focused infrared lamps, while the opposite face was cooled using a chiller unit. This set-up allowed the specimen to be subjected to a cyclic thermal loading history during which the maximum temperature difference across the plate was of the order of 800°C, with a staedy state temperature variation of 450°C. A typical failed component is shown in Fig 2. In all the tests there was no evidence of delamination and failure occurred by general micracking and fibre failure. It is therefore appropriate to analyse this class of loading history using the material model described in the previous section, which is based on matrix cracking, interface degradation and fibre failure and pull-out.

In order to gain insight into the relationship between material behaviour and structural performance we use the idealised model of Figure 1 to analyse the classical Bree problem represented in Figure 3, where the plate is subjected to a constant axial stress σ_p and a cyclic thermal loading history, whereby one side of the plate experiences a constant temperature θ_o, while the temperature of the opposite side is subjected to a temperature which is cycled between θ_o and $\theta_o + \Delta\theta$. The temperature is assumed to be cycled sufficiently slowly so that it varies linearly across the plate througout the cycle. We can characterise the thermal loading in terms of the maximum thermo-elastic stress experienced during a cycle, $\sigma_t = \frac{1}{2} E\alpha\Delta\theta$, where α is the linear coefficient of thermal expansion.

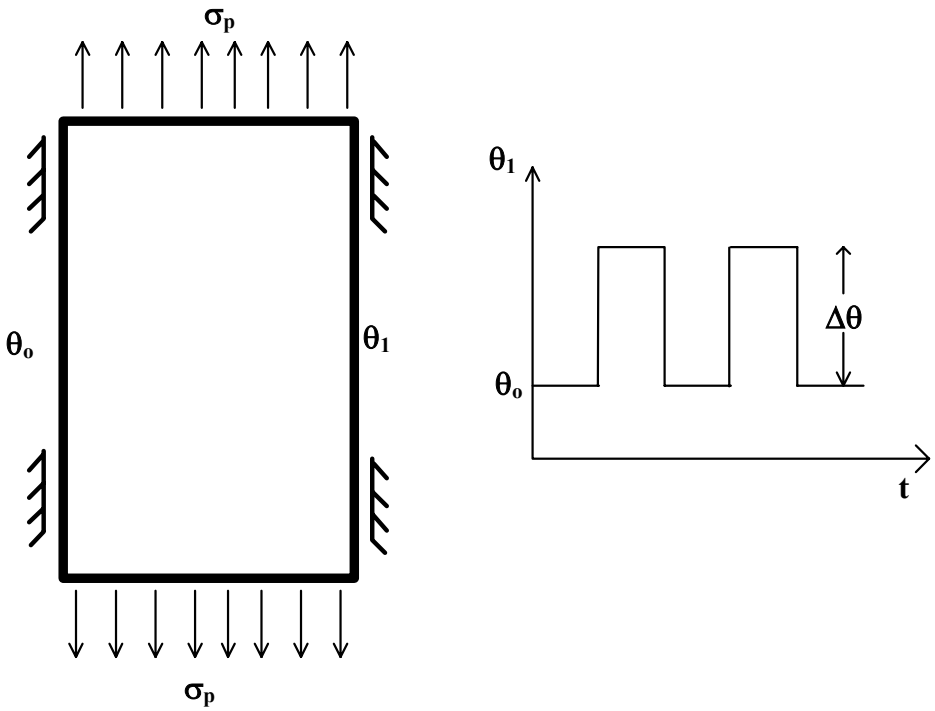

Figure 2 Classical Bree cyclic thermal loading problem

We assume that failure occurs when the strain in any part of the plate reaches the critical value ε_f. The analysis is quite lengthy, but the results can be presented in a simple graphical form. The critical strain is first achieved on the cold side of the plate when there is a temperature gradient. The combination of σ_p and σ_t which result in failure is shown as a solid curve in Fig 3 for β=6.93 and η=0.2, which are typical values for a SiC/SiC composite. The dashed line in this figure represents the combination of thermal and mechanical loading at which matrix cracking first occurs. This is often interpreted as the design limit. It is evident from this plot, however, that by taking into account the full effects of matrix cracking a much higher design limit is predicted for the component. There are three major contibutions to this large increase in load carrying capacity: the actual strain to failure is almost seven times the strain at the start of matrix cracking; the residual stress and its influence on crack closure; and most importantly, the influence of material damage on Young's modulus, which results in a decrease in the stress range experienced during cyclic thermal loading.

The analysis also provides information about the extent of microcracking in the plate. Three different regimes of behaviour can be identified as illustrated in Figure 4. In regime I, which occurs at high mechanical loads, the entire body is microcracked and the stresses are tensile throughout the cycle, such that these cracks are always open. In regime II, the entire body is microcracked, but the hot side of the plate goes into compression when there is a temperature gradient. In the remainder of the benign cracking regime only part of the plate is cracked. The chained lines of Figure 4 represent the fraction of the plate which has

experienced microcracking. The microcracked zone spreads in from the cold side of the plate. Thus there are no cracks growing in from the hot side of the plate. If the maximum temperature experienced in the microcracked zone is less than the so called "pest temperature" [9] then environmental degradation of the interface and fibres is not likely to occur, even though part of the plate is above this temperature

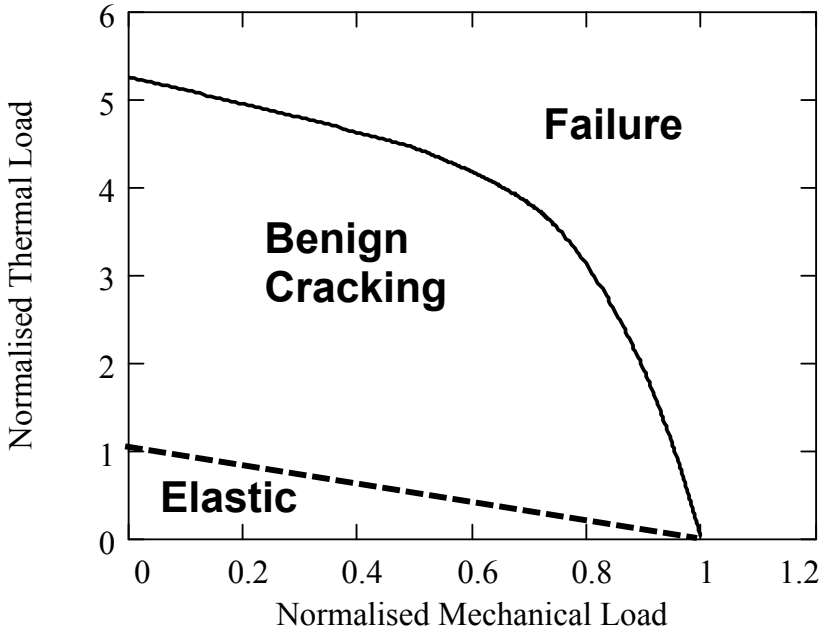

Figure 3 Interaction diagram for the problem of Fig 2

By varying the values of β and η and the magnitude of the threshold stress for fatigue damage we can examine the influence of each of these on the position of the limit boundary and the extent of microcracking in the cyclic state. For high thermal loads β and η are the most important parameters, with large values of β (ie large ductilities) and small values of η (small closure stresses) producing the best performance. Although the model of Figure 2 is a simplification of the actual response it reflects the major features of the material response and is consistent with predictions based on micromechanical models of the internal degradation processes which lead to failure. Use of these micromechanical models allows the parameters which have been identified as being important in this situation to be related back to microscopic features of the material, which can be controlled during processing to produce an optimum material for a given application. For example, a small value of η requires a large matrix cracking stress or small residual stresses. Calculations of this type, therefore, do not only provide valuable information to the designer, but they also provide important information to the material producer by identifying the most important macroscopic properties and the microstructural features that most strongly influence these properties.

CONCLUDING COMMENTS

In this paper we have developed a simple material model for the macroscopic response of a composite material based on an understanding of the micromechanical processes which result in damage development. It is possible to relate certain features of the macroscopic stress/strain curve to the internal degradation processes and to identify which of these processes dominate and largely determine the material response. We have analysed a simple representative structural problem in which the component is subjected to a combination of thermal and mechanical loading. Significant relaxation of the thermally induced stresses occur due to the influence of material damage on the instantaneous modulus. Design calculations which take this relaxation of stress into account provide design limits which are substantially in excess of elastic procedures which do not permit the development of any matrix cracking.

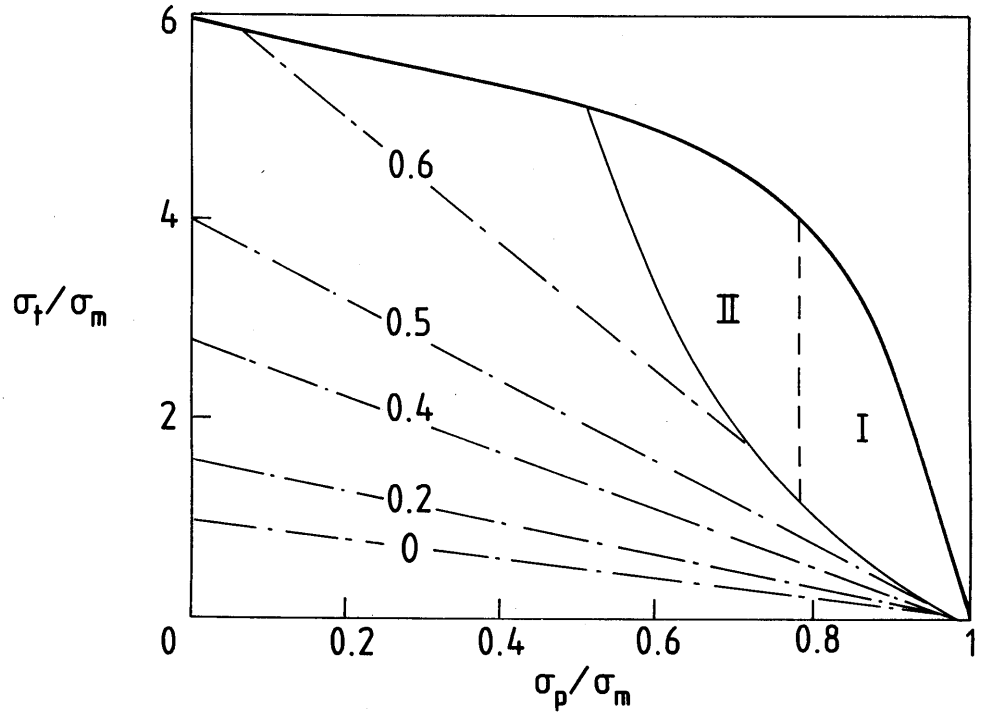

Figure 4 Interaction diagram fro the Bree problem of Figure 2. The chained lines represent the fraction of the plate which has experienced general microcracking

ACKNOWLEDGEMENT

MEB is grateful to EPSRC for financial support during the course of this research

REFERENCES

1. Evans, A.G. and Zok, F.W. (1994) *Solid State Phys. –Adv. Res. Appl*. 47, 177.
2. Evans, A.G., Zok, F.W. and McMeeking, R.M. (1995) *Acta Met. Et Mat.*, 43, 859.
3. Burr, A., Hild, F. and Leckie, F.A. (1997) *Eur. Jnl. Mech. A-Solids*, 16, 53.
4. Burr, A., Hild, F. and Leckie, F.A. (1998) *Mat. Sci. Eng. A,* 250,256.
5. Hutchinson, J.W. and Lu, T.J. (1995) *Jnl. Eng. Mat. Tech.*, 117, 386.
6. McDonald, K.R., Dryden, J.R., Majumdar, A. and Zok, F.W. (2000) *Jnl. Am. Cer. Soc.*, 83, 553.
7. Burr, A., Hild, F. and Leckie, F.A. (1998) *Comp. Sci. Tech.*, 58, 779.
8. Booker, M.E. (2001) PhD Thesis, University of Leicester, UK.
9. Evans, A.G., Zok, F.W., McMeeking, R.M. and Du, Z.Z. (1996) *Jnl. Am. Cer. Soc.*, 79, 2345.

DAMAGE AND FRACTURE IN CREEP OF MAGNESIUM ALLOY-BASED COMPOSITES

V. Sklenicka, M. Pahutova, M. Svoboda, K. Kucharova and I. Podstranska

Institute of Physics of Materials, Academy of Sciences of the Czech Republic
Zizkova 22, CZ-616 62 Brno, Czech Republic

ABSTRACT

A comparison between the creep characteristics of AZ 91 and QE 22 alloys reinforced with 20 vol.%Al_2O_3 short fibres and unreinforced matrix alloys shows that creep strengthening in the composites arises mainly from the existence of an effective load transfer. High values of load transfer estimated for the composites indicating good fibre/matrix interface bonding together with no substantial breakage of fibres during creep exposure lead to the conclusion that the use of alumina short fibres is very effective in improving the creep properties of Mg-based composites. However, the abrupt fracture occuring shortly after the end of the lengthy primary stage of creep at very high stresses implies the existence of a critical weakening and/or damage of the matrix/fibre interface corresponding to the ultimate state of load transfer.

KEYWORDS

Mg-based composite, short-fibre composite, creep, creep damage, creep fracture, fibre breakage, load transfer, interface debonding.

INTRODUCTION

There has been a dramatically increased usage of magnesium alloys in the past ten years by the automotive industry. This usage is projected to continue a large growth as automakers continue to strive for better fuel economy with reduced emission [1]. To achieve further substantial increase in usage in automotive industry, magnesium alloys must be utilized in engine and transmission components. These applications require better high temperature strength and creep resistance than it is possible with currently available commercial magnesium alloys.

A considerable improvement in the creep properties of magnesium alloys can be potentially achieved by short-fibre ceramic reinforcements (discontinuous metal matrix composites - MMCs) [2-4]. The creep properties of Mg-based composites [3-5] have received only limited attention. However, these studies are sufficient to allow some preliminary predictions on the deformation mechanisms which are significant in the creep process in Mg-based composites. By contrast, very little information is available on the creep damage mechanisms and creep fracture processes in discontinuous magnesium matrix composites.

This work reports the experimental results obtained in an investigation of the high temperature creep fracture behaviour of AZ 91 and QE 22 magnesium alloys reinforced with 20 vol.%Al_2O_3 (Saffil) short fibres. The objective of the present research is a further attempt to clarify the creep damage and fracture mechanisms in short-fibre reinforced magnesium-based composites.

EXPERIMENTAL DETAILS

All experimental materials used in the study were fabricated at the Department of Materials Engineering and Technology, Technical University of Clausthal, Germany. Short fibre reinforced and unreinforced blocks of the most common alloy AZ 91 (Mg-9wt%Al-1wt%Zn-0.3wt%Mn) and the high strength silver-containing alloy QE 22 (Mg-2.5wt%Ag-2.0wt%Nd rich rare earths-0.6wt%Zr) were produced by squeeze casting. The fibre preform consisted of planar randomly distributed δ-alumina short fibres (Saffil fibres from ICL, 97% Al_2O_3, 3%SiO_2, ~ 3 μm in diameter with varying lengths up to an estimated maximum of ~ 150 μm). The final fibre fraction after squeeze casting in both composites was about 20 vol.%. For convenience, the composites are henceforth designated AZ 91 - 20 vol.%Al_2O_3(f) and QE 22 - 20 vol.%Al_2O_3(f) where f denotes fibre. An unreinforced AZ 91 matrix alloy and its composite were subjected to a T6 heat treatment (anneal for 24 h at 688 K, air cool and then age for 24 h at 443 K). The QE 22 monolithic alloy and its composite were given the following T6 heat treatment: anneal for 6 h at 803 K, air cooling and ageing for 8 h at 477 K. Flat tensile creep specimens were machined from the blocks so that the longitudinal specimen axes were parallel to the plane in which the long axes of the fibres were preferentially situated for the squeeze-cast composites. Constant stress tensile creep tests were carried out at temperatures from 423 to 523 K and at the applied stresses ranged from 10 to 200 MPa [3,5]. Creep tests were performed in purified argon. The creep elongations were measured using a linear variable differential transducer and they were continuously recorded digitally and computer processed. Following creep testing, samples were prepared for examination by transmission electron microscopy (TEM). Observations were performed using a Philips CM 12 TEM/STEM transmission electron microscope with an operating voltage of 120 kV, equipped with EDAX Phoenix X-ray microanalyser. Fractographic details were investigated using light microscopy and scanning electron microscopy (Philips SEM 505 microscope).

EXPERIMENTAL RESULTS

Creep results

Figure 1 shows selected creep curves in the form of strain, ε, versus time, t, for the AZ 91 alloy and its composite for the creep tests conducted at an absolute temperature T of 423 K under comparable levels of the applied stress σ. As demonstrated by the figure, significant differences were found in the creep behaviour of the composite when compared to its matrix alloy. First, the presence of the reinforcement leads to a substantial decrease in the creep plasticity, which is proved by the values of the total strains to fracture for the composite. Second, the composite exhibits markedly longer creep life than the alloy at the entire stress range used. Third, the shapes of creep curves for the composite and the alloy differ considerably. It should be mentioned that the creep curves shown in Fig. 1 do not clearly indicate the individual stages of creep. However, these standard ε vs. t curves can be easily replotted in the form of the strain rate, $\dot{\varepsilon}$, versus time, t, as shown in Fig. 2, Fig. 2a presents the log $\dot{\varepsilon}$ - t curves for a temperature of 423 K and a stress of 100 MPa for both materials. It is apparent that neither curve exhibits a well-defined steady stage. In fact, this stage is reduced to an inflection point of the $\dot{\varepsilon}$ versus t curve. Despite this similarity, the occurrence of a primary stage followed by a tertiary stage of creep in the matrix alloy is in a striking contrast with the nature of the creep curve in the composite. The latter curve shows the primary stage is fairly extensive and represents practically the whole creep test. A minimum in the creep rate is reached just before final fracture and the presence of a tertiary stage is not well-defined. This difference in the shapes of the $\dot{\varepsilon}$ - t creep curves in the matrix alloy and in the composite is confirmed and perhaps more clearly illustrated in Fig. 2b for the tests conducted at the same temperature of 473 K and stress of 80 MPa. Inspection suggests that creep in the composite is again dominated by fairly extensive primary stage. On the other hand, an extremely short primary creep in the matrix alloy is followed by a lengthy tertiary stage. The creep data of the AZ 91 alloy and the AZ 91 - 20 vol.% Al_2O_3(f) composite and the QE 22 alloy and the QE 22 - 20 vol.%Al_2O_3 composite at 423, 473 and 523 K are shown in Fig. 3 where the minimum creep rate, $\dot{\varepsilon}_m$, is plotted against the applied stress, σ, on a logarithmic scale. Inspection of the creep data in Fig. 3 leads to two observations. First, the composites exhibit better creep resistance than the monolithic alloys over the entire stress range used; the minimum creep rate for the composite is about two to three orders of magnitude less than that of the

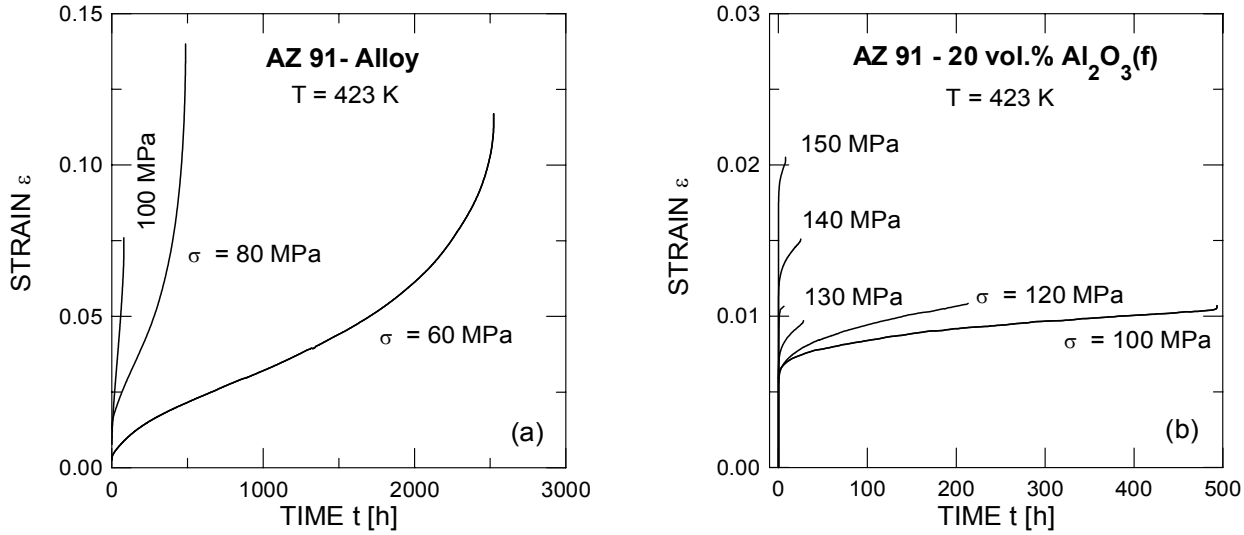

Figure 1a,b: Creep curves at 423 K for (a) the AZ 91 alloy, and (b) the AZ 91-20 vol.%Al_2O_3(f) composite.

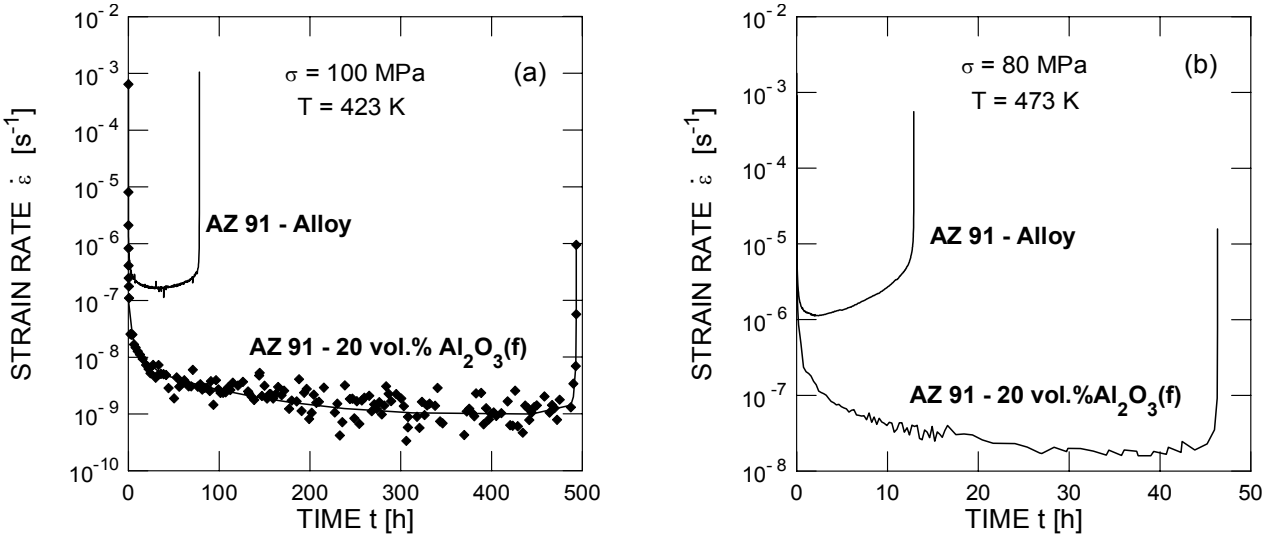

Figure 2a,b: Strain rate versus time for the AZ 91 alloy and the AZ 91-20vol.%Al_2O_3(f) composite (a) at 423 K and 100 MPa, and (b) at 473 K and 80 MPa.

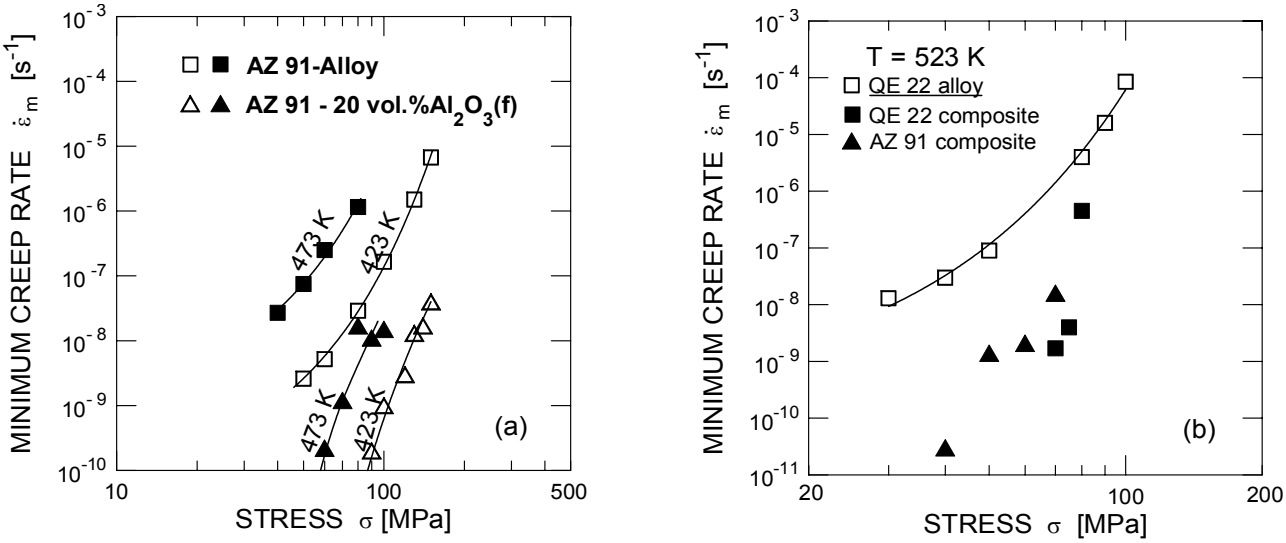

Figure 3a,b: Stress dependences of minimum creep rate for (a) AZ 91 alloy and its composite at 423 and 473 K, and (b) QE 22 alloy and both composites at 523 K.

unreinforced alloy. Second, as depicted in Fig. 3a, the stress dependences of the minimum creep rates for both materials are different in trend, which is clearly demonstrated by the characteristic curvatures on the inherent curves at low stress. While the slopes and therefore the apparent stress exponents, $n_a = (\partial \ln \dot{\varepsilon} / \partial \ln \sigma)_T$, for the alloy slightly decrease with decreasing applied stress, the curvatures for the composite increase with decreasing applied stress. Such an increase of the apparent stress exponent at low stresses is usually considered to be indicative of the presence of a threshold stress representing a lower limiting stress below which creep cannot occur [3,4]. Third, the creep resistance of the QE 22 - 20 vol.% Al_2O_3(f) composite seems to be essentially equal to the creep resistance of the AZ 91 - 20 vol.%Al_2O_3(f) composite (Fig. 3b). The double logarithmic plots of the time to fracture t_f as a function of the applied stress σ at a temperature of 423 and 473 K are shown in Fig. 4a for the AZ 91 alloy and its composite. It is clear from these plots that the creep life of the AZ 91 - 20 vol.%Al_2O_3(f) composite is an order of magnitude longer than that of the unreinforced AZ 91 alloy. However, this difference consistently decreases with increasing applied stress and there is a tendency for the reinforcement to have no significant effect on the lifetime at the higher stresses. In fact, inspection of Fig. 4a reveals that at stresses higher than 200 MPa the creep life of the composite is essentially equal to that of the monolithic AZ 91 alloy. The same conclusion can be drawn from Fig. 4b. Independent of the testing temperature, both composites (AZ 91 - 20 vol.% Al_2O_3(f) and QE 22 - 20 vol.%Al_2O_3(f)) exhibit superior creep resistance compared to their unreinforced alloys. It should be noted that no substantial difference in lifetime was found between both composites under the same creep loading conditions. The presence of the reinforcement leads to a substantial decrease in the creep plasticity. The values of the strain to fracture in both composites are only 1 - 2%, independent of stress and temperature. By contrast, the values of the strain to fracture in the monolithic alloys are markedly higher, typically 10 - 15% in the AZ 91 alloy and up to 30% in the QE 22 alloy.

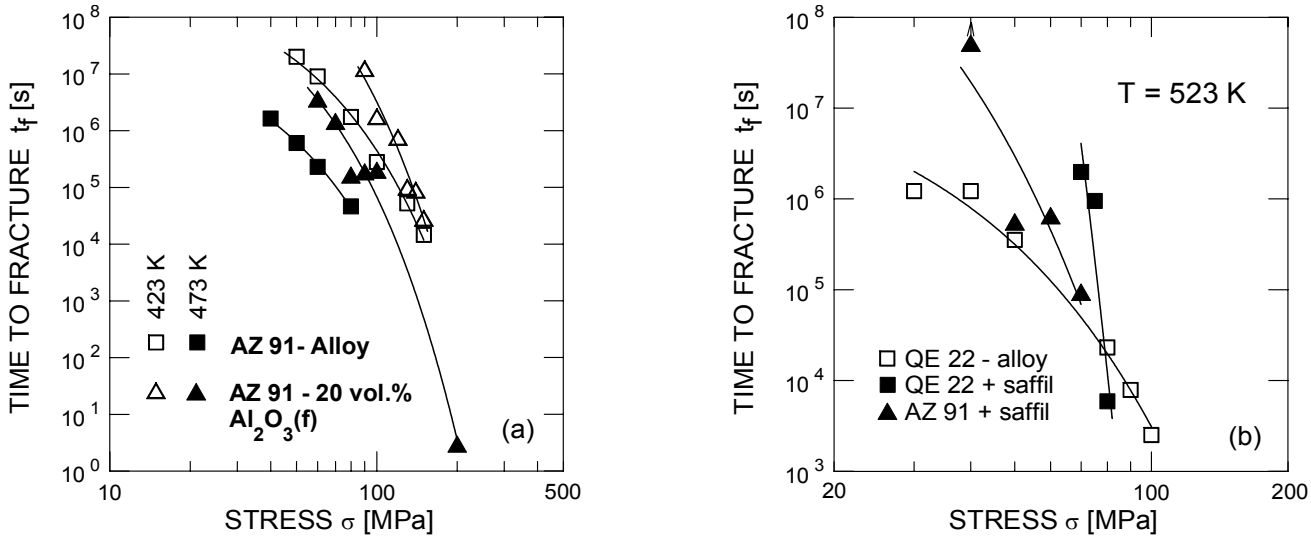

Figure 4a,b: Stress dependences of times to fracture for (a) AZ 91 alloy and its composite at 423 K and 473 K and (b) QE 22 alloy and both composites at 523 K.

Fractography

Creep behaviour and the creep plasticity of material can be substantially influenced by the development of creep damage and fracture processes. The longitudinal metallographic sections cut from the gauge length of creep fractured specimens were examined using optical microscopy and SEM to evaluate creep damage. No intergranular creep cavitation has been revealed in the monolithic alloys; all the specimens failed in intergranular and/or interdendritic manner without necking. Fractographic investigations of the composites did not reveal either substantial creep fibre cracking and breakage or any debonding at the interface between the fibres and the matrix due to creep (Figure 5). It should be emphasized that these effects were restricted to a region very near the fracture path (Figure 6) suggesting that fibre breakage occurs by the propagation of the main creep crack during the final stage of the creep fracture process. Even careful investigation of the fibre-matrix interface by TEM revealed no extensive debonding (Figure 5c). Rather, the enhanced precipitation of the β phase on the alumina fibres and some interconnection of fibres by the massive β-phase

bridges were found in the AZ 91 - 20 vol.%Al_2O_3(f) composite [3]. A thicker zone in contact with the fibres was identified as fine magnesium (MgO) particles (Figure 5c), [3,5].

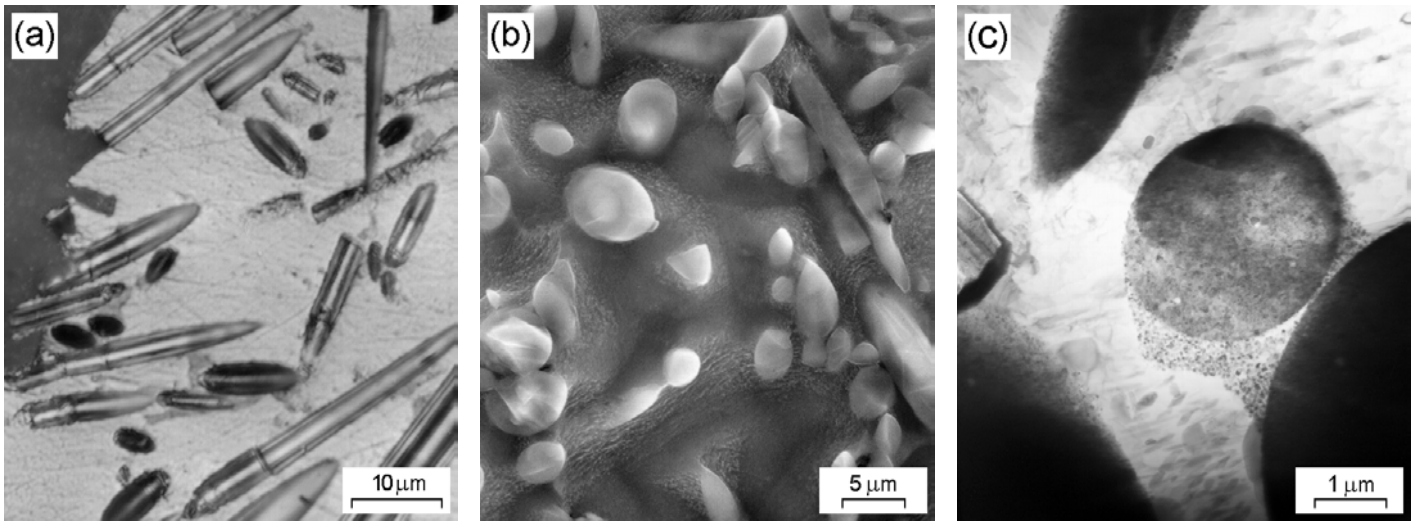

Figure 5a,b,c: Micrographs of the AZ 91-20 vol.%Al_2O_3 (f) composite after creep: (a) fracture path (OM), (b) matrix-fibre interfaces (SEM, etched metallographic section), (c) matrix-fibre interfaces (TEM, foil).

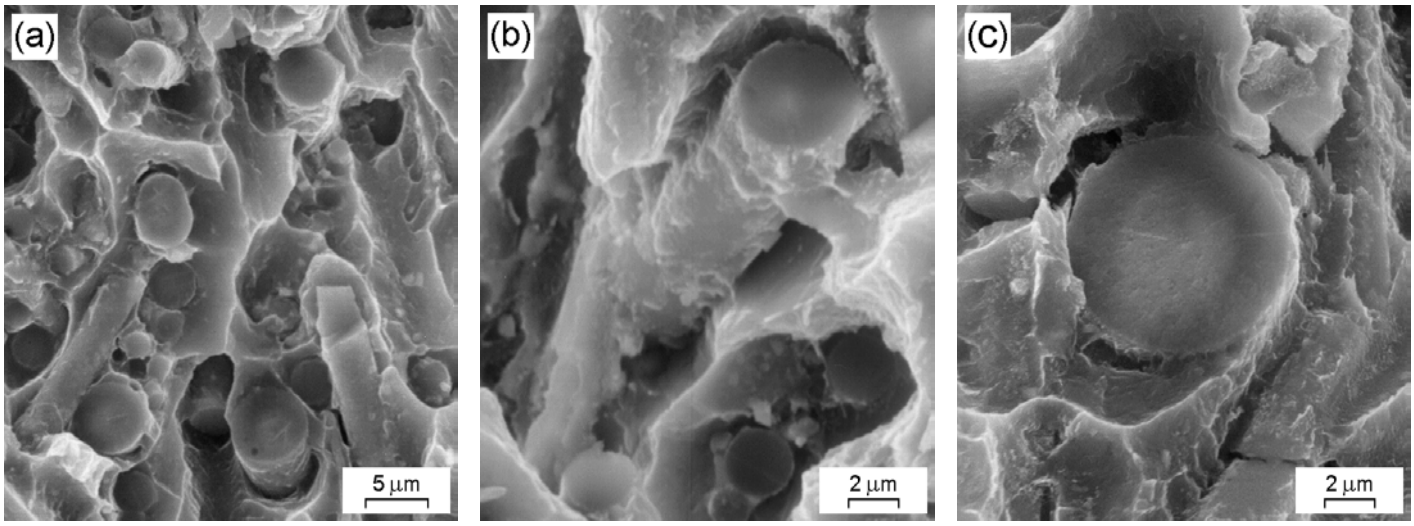

Figure 6 a,b,c: SEM micrographs of the QE 22-20vol.%Al_2O_3 (f) composite showing creep fracture surface.

DISCUSSION

It is relevant to discuss first the reason for different shapes of creep curves for the composite and the monolithic matrix alloy (Figs.1 and 2). The dominant primary stage apparent in the creep curves of the composite (Fig. 2) can be a result by non-linear visco-elastic deformation of the highly-stressed central regions of the fibres; this leads to a steady state due to matrix flow about the fibres when they are fully stretched elastically. Further, the occurrence of a lengthy primary stage of creep in the composite is probably associated with the additional secondary phase precipitation and with gradual change in the precipitate morphology during the creep exposure. Lastly, the observed long primary stages are not indicative of the initiation of any debonding at the interfaces between the matrix and the reinforcement and/or creep fibre breakage in accordance with the metallographic and fractographic observations. On the other hand, the tertiary creep behaviour should result from fibre fracture leading to a reduction in the fibre aspect ratio or the development of ductile tearing with off-loading of stress to the sound composite material, both factors leading to an acceleration in the creep rate. Thus, the observed extremly lengthy primary stage apparent in the creep curves of the composite in the present work does not support the prediction of the simplified

mechanistic model of creep in short fibre reinforced metal matrix composite [6] derived from the creep experiments and microstructural observations on short fibre reinforced alluminium alloys and based on three elementary microstructural processes including a multiple fibre breakage starting early in creep life. A possible explanation for this different creep behaviour in aluminium and magnesium short fibre reinforced metal matrix composites may lie in the different strength of the fibre-matrix interface (bonding) and load transfer during the creep of both composite materials.

As depicted in Fig. 3 the composites exhibit better creep resistance than the unreinforced matrix alloy; the presence of short-fibre reinforcement leads to reduced creep rate in the composite by two to three orders of magnitude. Such difference can arise when significant load transfer partitions the external load between the matrix and the reinforcement [3,4,7]. In the presence of load transfer the creep data may be successfully reconciled by putting the ratios of the creep rates of the composite and the matrix alloy equal to a factor given by $(1-\alpha)^n$, where α is a load transfer coefficient having values lying within the range from 0 (no load transfer) to 1 (full-load transfer) [3,4]. The values of α inferred from the data in Fig. 3 using $n = 3$ [3] are within the range of 0.79 to 0.90. It is interesting to correlate these experimentally determined values α with an analytical treatment. Kelly and Street [7] proposed a shear-lag approach that predicts the tensile creep behaviour of discontinuous fibre-reinforced composites. Subsequently, Nardone and Prewo [8] suggested a modified shear-lag model by considering the load transfer effect at the end of short fibres and various reinforcement geometries and arrangements (volume fraction, aspect ratio). The values of α predicted from the modified shear-lag model with 20 vol. pct of short-fibre reinforcement are $\alpha \cong 0.75$ and $\alpha \cong 0.84$ for an experimentally observed fibre aspect ratios S (diameter/length) ~ 30 and 50, respectively. Thus, the predicted values are in resonable agreement with the experimental values of α.

CONCLUSIONS

The creep resistance of squeeze cast AZ 91 and QE 22 magnesium alloys reinforced with 20 vol.% Al_2O_3 short fibres is shown to be considerably improved compared to unreinforced matrix alloys. The direct strengthening effect of short fibre reinforcement arises mainly from effective load transfer. Direct strengthening dominates the creep behaviour of the composites due to good fibre/matrix interfacial bonding together with no substantial breakage of fibres during creep loading.

ACKNOWLEDGEMENTS

Financial support for this work was provided by the Academy of Sciences of the Czech Republic under the Project K 1010104, by the Grant Agency of the Academy of Sciences of the Czech Republic under Grant A 2041902 and by Grant Agency of the Czech Republic under Grant 106/99/0187.

REFERENCES

1. Edgar, R.L.(2000). In: *Magnesium Alloys and Their Applications*, pp. 3-8, Kainer,K.U.(Ed.), Weinheim.
2. Mordike, B.L. and Lukac, P.(1997).In: *Proc.3rd Int. Magnesium Conference*, pp.419-429, Lorimer G.W.(Ed), IOM, London.
3. Sklenicka, V., Pahutova, M., Kucharova, K., Svoboda, M. and Langdon, T.G. (2000). *Key Eng. Materials*, 171-174, 593.
4. Li, Y. and Langdon, T.G.(1999). *Metall.Mater.Trans*. 30A, 2059.
5. Pahutova, M., Sklenicka, V., Kucharova, K., Svoboda, M. and Langdon, T.G. (2001). In: *Proc.9th Int. Conference on Creep and Fracture of Engineering Materials and Structures*, Parker J.D. (Ed), University of Wales, Swansea, in press.
6. Dlouhy, A., Eggeler, G. and Merk, N. (1995). *Acta Met. Mater.*, 43, 535.
7. Kelly, A. and Street, K.N.(1972). *Proc. R. Soc. London*, 328A, 267.
8. Nardone, V.C. and Prewo, K.M.(1986) *Scripta Metall.*, 20, 43.

ORAL/POSTER REFERENCE: ICF100232OR

DAMAGE ASSESSMENT FOR CONCRETE-STRUCTURES USING AE/UT TECHNIQUE

K. IWAKI [1], T. SHIOTANI [1] and M. OHTSU [2]

[1] Research Institute of Technology, Tobishima Corporation,
5472 Kimagase, Sekiyado, Higashi-Katsushika, Chiba 270-0222, Japan
[2] Graduate School of Science & Technology, Kumamoto University
2-39-1 Kurogami, Kumsmoto-City, Kumamoto 860-8555, Japan

ABSTRACT

In the present study, damage processes of concrete specimens under load repeated are investigated by applying a scalar damage based on damage mechanics. In order to estimate the damage, acoustic emission (AE) and ultrasonic testing (UT) are applied for five stages of damage degree. The propagation-attenuation of elastic waves is discussed in regard with adequate components of frequency for evaluating microcracks. As shown in Figure 1 (left), the result of AE activity is in good agreement with the scalar damage up to the Stage IV. As approaching yield point, higher AE activity is observed, although obvious growth of scalar damage is not obtained. Applicability of AE technique for not only damage process but also fracture progress is thus confirmed. In UT technique as shown in Figure 1 (right), the increase of propagation-attenuation in the filtered waves is evident with the scalar damage during Stage II-IV. It is resulted that the damage degree could be evaluated by the attenuation of adequately filtered elastic waves. Since the scalar damage based on damage mechanics is physically correlated with the volume of microcracks, it is confirmed that the AE/UT technique would be a promising method to evaluate the initiation and growth of microcracks.

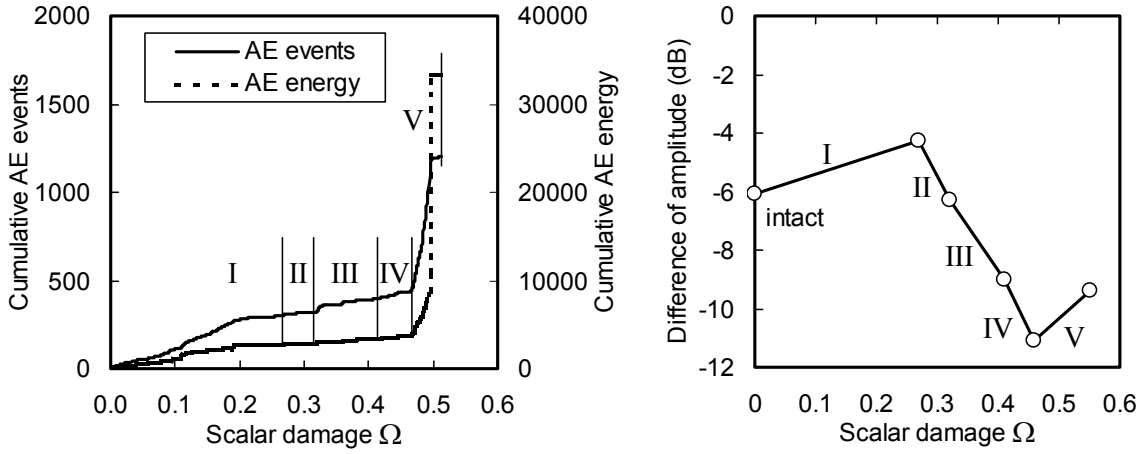

Figure 1: Results (left: relationship between scalar damage and cumulative AE parameters and right: relationship between scalar damage and attenuation of filtered waves)

ORAL REFERENCE:ICF100869OR

DAMAGE ACCUMULATION AND FATIGUE CRACK GROWTH CHARACTERISTICS UNDER MIXED-MODE LOADING CONDITION

T. Isogai [1] and A. T. Yokobori Jr. [2]

[1] Department of Mechanical and Precision Systems, Teikyo University Utsunomiya, 350-8551, JAPAN
[2] Fracture Research Institute, Tohoku University, Sendai, 980-8579, JAPAN

ABSTRACT

Using thin-walled cylindrical specimens subjected cyclic tension and torsion, fatigue crack growth tests under mixed-mode loading conditions were conducted. The characteristics of the fatigue crack growth rate (FCGR) were identified. By comparing the experimental results with the results of FE analyses, it was found that the characteristics of the FCGR were related to fatigue damage accumulation before initial crack growth. Based on these results, fatigue life prediction under mixed-mode loading was proposed. Damage analyses is indispensable for characterization of the fatigue crack growth and fatigue life prediction.

KEYWORDS

mixed-mode loading, fatigue crack growth rate, plastic deformation, finite element analyses, fatigue damage, life prediction

INTRODUCTION

Many studies have been conducted on fatigue crack behavior under mixed-mode loading conditions [1-9]. Among several experimental methods, a method in which combined tension and torsion are applied to a thin-walled cylindrical specimen has the advantage to achieve mixed-mode loading ranging pure mode-I to mode-II [5-9]. Using this method, fatigue crack growth tests were conducted and the characteristics of crack growth behavior were identified. Moreover, in order to discuss the effect of fatigue damage on mixed-mode crack growth, elastic-plastic FE analyses were carried out. Fatigue life prediction was also discussed.

CRACK GROWTH TESTS UNDER MIXED-MODE LOADING

The experiments on fatigue crack growth behavior under mixed-mode loading conditions were conducted [5-9]. Tensile and torsional stresses in the same phase were applied to thin–walled hollow cylindrical specimens of 5083P-O aluminum alloy. Using this method, mixed-mode fatigue load ranging from mode-I to mode-II can be applied to an initial crack, which was introduced in the circumferential direction of the specimen. Details of the experimental procedure are described elsewhere [5-7].

After fatigue crack initiation, the crack propagates in the direction perpendicular to the maximum principal stress, σ_1 (called ϕ_1-direction), as shown in Figure 1 [5-9]. The characteristics of fatigue crack growth rate (FCGR), db/dN, in region II were found to be divided into two regions, that is, region IIa followed by region

IIb, as shown in Figure 2. In each region, the FCGR can be expressed in the form of Paris law :

$$\frac{db}{dN} = A\Delta K_{Ib}{}^{m} \tag{1}$$

where, ΔK_{Ib} ($=\Delta\sigma_1\sqrt{\pi b}$, $\Delta\sigma_1$: maximum principal stress range) is the stress intensity range corresponding to the crack length, b, projected on the line of the ϕ_1-direction. In each region, m and A of Eqn. 1 are constants depending on loading condition. The value of m shown in Figure 3 can be expressed as:

$$\text{Region IIa} \qquad m = \begin{cases} 3.05 + 6.89(\sigma_2/\sigma_1) & (0.0 \le |\sigma_2/\sigma_1| \le 0.15) \\ 1.66 - 2.10(\sigma_2/\sigma_1) & (0.15 \le |\sigma_2/\sigma_1| \le 1.0) \end{cases} \tag{2a}$$

$$\text{Region IIb} \qquad m = \begin{cases} 3.11 - 7.31(\sigma_2/\sigma_1) & (0.0 \le |\sigma_2/\sigma_1| \le 0.47) \\ 9.34 + 5.58(\sigma_2/\sigma_1) & (0.47 \le |\sigma_2/\sigma_1| \le 1.0) \end{cases} \tag{2b}$$

where, σ_2/σ_1 is the ratio of the minimum and maximum principal stresses, which is a function of mixed-mode condition, $\Delta K_{II0}/\Delta K_{I0}$. It should be noted that the values of m are independent of stress ratio, R ($=\sigma_{min}/\sigma_{max}$).

The effect of the stress ratio, R on the FCGR is significant under mixed-mode loading condition, as shown in Figure 2. It was found that the FCGR in region IIa is accelerated by the static tensile stress component $\sigma_{st.}(=\sigma_{\min.})$ of mixed-mode fatigue loading, while the FCGR in region IIb is not affected by the R-ratio [9] . By considering these effects, the fatigue crack growth law can be expressed as the following equation [9]:

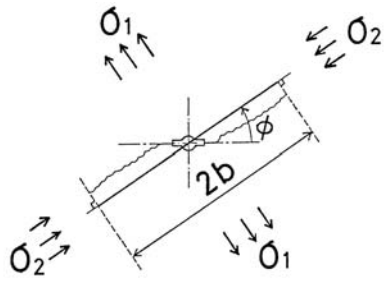

Figure 1: Crack length, b, projected to the line perpendicular to the σ_1 .

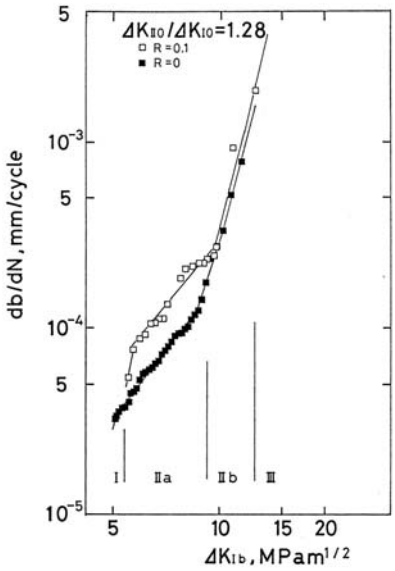

Figure 2: Characteristics of the db/dN under mixed-mode conditions.

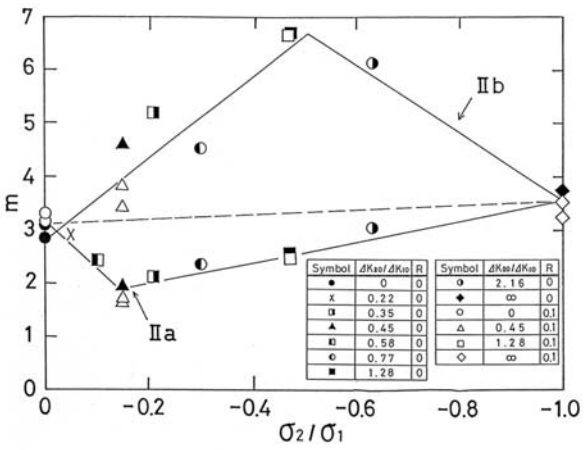

Figure 3: The effect of mixed-mode loading condition on the power coefficient, m, in Paris law in regions of IIa and IIb.

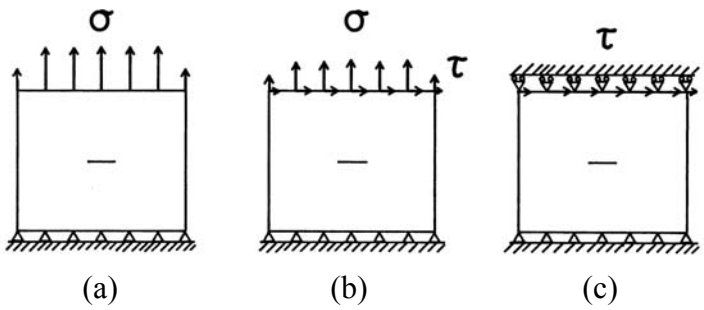

Figure 4: Model for mode I, mixed-mode and mode II conditions for the elastic-plastic FE analyses :
(a) $\Delta\tau / \Delta\sigma = 0$ (b) $\Delta\tau / \Delta\sigma = 0.45$, 1.28
(c) $\Delta\tau / \Delta\sigma = \infty$.

$$\frac{db}{dN} = \left(A^{R=0}\right)^{1/r^*} \Delta K_{Ib}{}^{m} \tag{3}$$

$$r^* = 1 + \frac{1}{7}\left(\sigma_{st.}/\Delta\tau\right)^{1/2} \qquad \text{(Region IIa)} \tag{4a}$$

$$r^* = 1 \qquad \text{(Region IIb)} \tag{4b}$$

where, $A^{R=0}$ is the value of A for R=0. In Eqn.3, r^* is a parameter which represents the effect of the R-ratio. The relationship between constants $A^{R=0}$ and m is given by:

Region IIa $$A^{R=0} = 2.16 \times 10^{-5} \times 0.230^{m} \tag{5a}$$

Region IIb $$A^{R=0} = 3.64 \times 10^{-6} \times 0.147^{m} \tag{5b}$$

By substituting Eqns. 2, 4 and 5 into Eqn. 3, the fatigue crack growth rate under mixed-mode loading conditions can be formulated as a function of ΔK_{Ib}, σ_2/σ_1 and $\sigma_{st.}/\Delta\tau$. In the crack growth law, constant m represents the effect of mixed-mode condition, $\Delta K_{\mathrm{II0}}/\Delta K_{\mathrm{I0}}$, while r^* represents the effect of the R-ratio.

EFFECT OF DAMAGE DUE TO PLASTIC DEFORMATION

The dominant mechanical factor of the FCGR under mixed-mode loading is now investigated. Mixed-mode crack growth has different characteristics from mode-I crack growth in which the direction of the maximum tangential stress, $\sigma_\theta^{\max}$ in the vicinity of the crack is the same as the direction of σ_1. Therefore, mode-I fatigue crack propagates in the same direction as it initiates, and the FCGR accelerates monotonically even though the effect of the global damage contributes it. On the contrary, under mixed-mode loading, as the direction of $\sigma_\theta^{\max}$ is not the same as the direction of σ_1, the crack growth direction shifts as the crack propagates [5-9]. Therefore, the crack growth behavior changes during its propagation. This transition of the crack growth is affected by the accumulated damage due to cyclic loading. It has been shown that plastic deformation increases with increase of the contribution of the shearing stress component [10]. Hence, analyses of fatigue damage are indispensable to understand crack growth behavior under mixed-mode loading.

To clarify the effect of the damage due to plastic deformation on the FCGR, elastic-plastic FE analyses were conducted under cyclic loading conditions. Plastic stress-strain relation is assumed to be linear hardening. Total strain is given by sum of the elastic strain and the plastic strain. As the yielding condition, the von Mises criterion was employed. The original elastic-plastic FE program developed by Yamada *et.al.* [11] was modified so that cyclic loading can be applied to a model. Analyses were carried out for $\Delta\tau/\Delta\sigma$= 0, 0.45, 1.28, ∞. The applied equivalent stress range, $\Delta\sigma_{eq}$ was kept constant throughout the analyses. Cyclic tensile and shear stresses were applied to center cracked models (shown in Figure 4), which simulate the situation where mixed-mode loading is applied to a crack before the initiation. Material constants of 5083 aluminum alloy were used for the analyses. The analyses were conducted up to 10 cycles, under plane stress condition.

From the FE analyses, the shapes of plastic zone for each condition were obtained, as shown in Figure 5. Using these results, the length, r_ϕ of the plastic zone in the ϕ_1-direction was determined (see Figure 6). The value of r_ϕ takes the maximum value for $\Delta\tau/\Delta\sigma$ =0.45 and its value is small under mode-I and mode-II conditions. For large value of r_ϕ, the crack closure might become eminent because the plastic zone around a crack could contribute plastic-induced crack closure. Experimentally, the crack closure under mixed-mode loading was more substantial than that under mode-I condition [7]. From this point of view, the characteristics of a/r_ϕ are in good agreement with the value of m in region IIa shown in Figure 3. Therefore, the deceleration of the FCGR in region IIa can be attribute to the effect of plastic-induced crack closure.

For quantifying the fatigue damage, the value of plastic strain energy, W_p was calculated. Figure 7 shows the change of the W_p against number of the loading cycles. It was shown that the value of W_p takes the maximum value for $\Delta\tau/\Delta\sigma$=1.28. The values of the W_p for the first cycle are presented in Figure 8. This result is in good agreement with the characteristics of the m in region IIb, as shown in Figure 3. Therefore,

acceleration

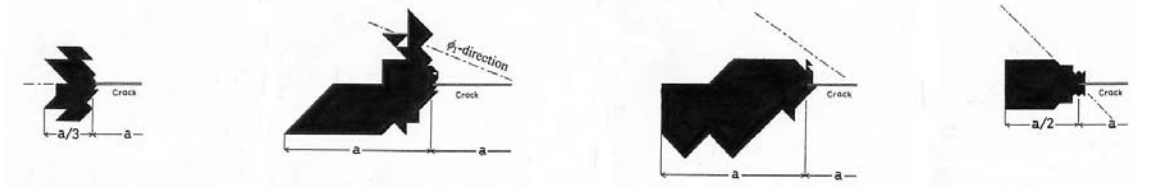

(a) $\Delta\tau/\Delta\sigma$=0 (b) $\Delta\tau/\Delta\sigma$=0.45 (c) $\Delta\tau/\Delta\sigma$=1.28 (d) $\Delta\tau/\Delta\sigma$=∞

Figure 5: Plastic zone ahead of a crack tip at maximum load for N=1, where a is half of the crack length.

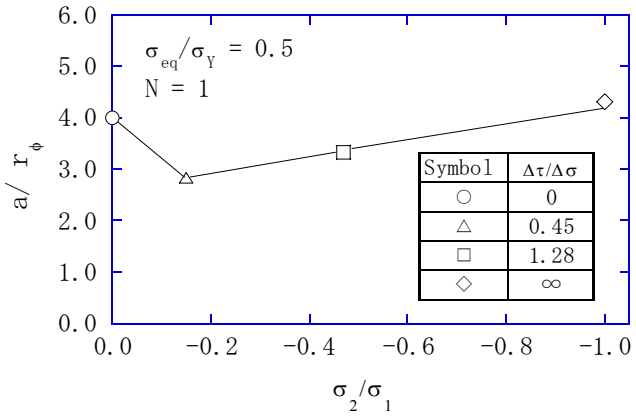

Figure 6: Effect of mixed-mode loading on the length, r_ϕ, of the plastic zone along the direction of the main crack growth.

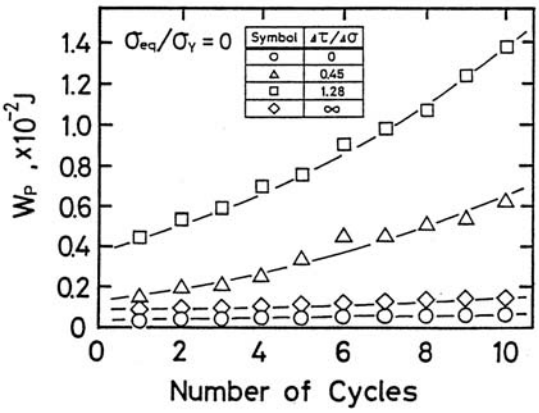

Figure 7: Accumulation of the plastic strain energy, W_p due to cyclic loading under mixed-mode conditions.

of the FCGR in region IIb might be dominated by the accumulation of the plastic strain energy, which is measure of the fatigue damage due to cyclic loading. This result indicates that fatigue damage around the initial crack has significant effect on the fatigue crack growth behavior under mixed-mode loading condition.

The effect of plastic deformation around an inclined main crack is also examined. Under mixed-mode conditions, after the fatigue crack initiates, it changes the growth direction to that nearly perpendicular to the maximum principal stress, σ_1 (see Figure 2). After this transition, the biaxial stress conditions are developed, where σ_1 perpendicular to the crack plane and the compressive principal stress, σ_2 parallel to the crack plane are applied to the inclined main crack. The FE analyses were also conducted for this case. Biaxial stresses $\Delta\sigma_1$ and $\Delta\sigma_2$ are applied to the same FE model. The values of $\Delta\sigma_1$ and $\Delta\sigma_2$ are determined so that the equivalent stress, $\Delta\sigma_{eq}$ takes the same value as that for the previous analyses. From the analyses, the characteristics of the W_p under biaxial loading are found to be very small compared with that obtained by the application of $\Delta\sigma$ and $\Delta\tau$ to the initial crack model. From these results, the fatigue damage accumulated around the main crack is found to be very small compared with that accumulated around the initial crack.

The FE results presented in this work reveal the effect of mixed-mode loading on fatigue damage accumulation. The characteristics of the FCGR, which is represented by the constants m and A in Eqn. 3, are closely related to formation of the fatigue damage around the initial crack due to mixed-mode loading.

FATIGUE LIFE PREDICTION UNDER MIXED-MODE LOADING CONDITIONS

Here, life prediction based on fatigue crack growth law is discussed. The experimental results of the fatigue failure life, N_f tends to increase as increase of $\Delta K_{II0}/\Delta K_{I0}$ [12]. However, other effects including the effects of the stress ratio, R and the initial stress intensity range, ΔK_{Ib0} might exist. Ratio of crack initiation life, N_i to the failure life, N_f is shown in Figure 9. Except shearing stress condition, crack initiation life, N_i is

approximately 10 percent of the failure life, N_f. Therefore, the life for crack propagation is significant within the total life and N_f could be estimated by the crack propagation life using the fatigue crack growth law.
It seems that life prediction based on fatigue crack growth law is complicated under mixed-mode conditions. The region II of the stable crack growth can be divided into two regions, that is region IIa followed by region IIb. In each region, the FCGR expressed by Eqn. 3 shows different characteristics, as shown in Figure 3. Although the fatigue failure life, N_f could be predicted by integrating the crack growth law of Eqn.3 from the beginning to the end of the test, this procedure includes consideration of the crack growth law during both regions IIa and region IIb. Moreover, this method requires the experimental results of the stress intensity range, ΔK_{Ibt} at the transition from region IIa to region IIb, and the stress intensity range, ΔK_{Ibf} just before the final failure. The relationship between ΔK_{Ibt} and ΔK_{Ibf} for various mixed-mode conditions is presented in Figure 10. This relationship indicates that ΔK_{Ibt} has the similar effect of mixed-mode loading as ΔK_{Ibf}. This result could be related to the similarity between N_f and the crack initiation life, N_i presented in Figure 9.

It should be noted that the FCGR during region II is closely related to formation of the fatigue damage around an initial crack due to mixed-mode loading. Experimentally, fatigue failure life, N_f is proportional to the crack initiation life N_i as shown in Figure 9. Therefore, the crack propagation at the first stage is important for life prediction. From this point of view, crack propagation life until the transition from region IIa to region IIb is to be examined. By integrating the crack growth law of Eqn. 3 between the beginning of the test and the transition, the following expression can be obtained:

$$N_t = \int_0^{N_t} dN = \int_{b_0}^{b_t} \frac{db}{(A^{R=0})^{1/r^*} \Delta K_{Ib}{}^m} \tag{6}$$

where, N_t is the crack propagation life and b_t is the half-length of the crack until the transition from region IIa to region IIb, respectively. By integrating, the following expression was obtained:

$$N_t = \frac{2}{\Delta\sigma_1{}^2 \pi} \frac{(\Delta K_{Ib0}{}^{2-m} - \Delta K_{Ibt}{}^{2-m})}{(A^{R=0})^{1/r^*} (m-2)} \tag{7}$$

The value of N_t is now compared with the experimental results. By substituting Eqns. 2(a), 4(a) and 5(a), and the experimental results of ΔK_{Ibt} into Eqn. 7, the value of N_t can be determined for each condition. The comparison between the experimental results of the fatigue failure life, N_f and the value of N_t is presented in Figure 11. It was found that the N_f is approximately proportional to the N_t. Hence, the total life, N_f seems to be controlled by the FCGR of region IIa, which is closely related to formation of the fatigue damage around the initial crack. The failure life, N_f under mixed-mode loading can be predicted by following expression:

$$N_f \approx \frac{3}{\Delta\sigma_1{}^2 \pi} \frac{(\Delta K_{Ib0}{}^{2-m} - \Delta K_{Ibt}{}^{2-m})}{(A^{R=0})^{1/r^*} (m-2)} \tag{8}$$

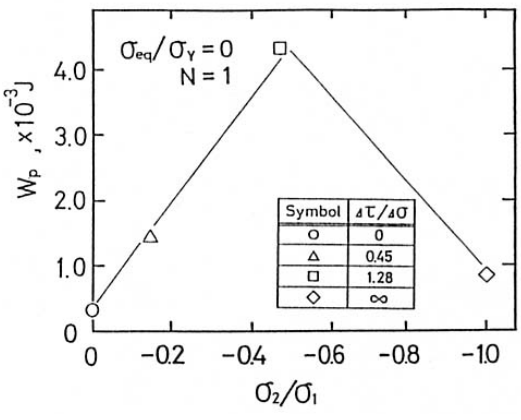

Figure 8: Effect of mixed-mode loading on the plastic strain energy, W_p, at the end of first unloading process.

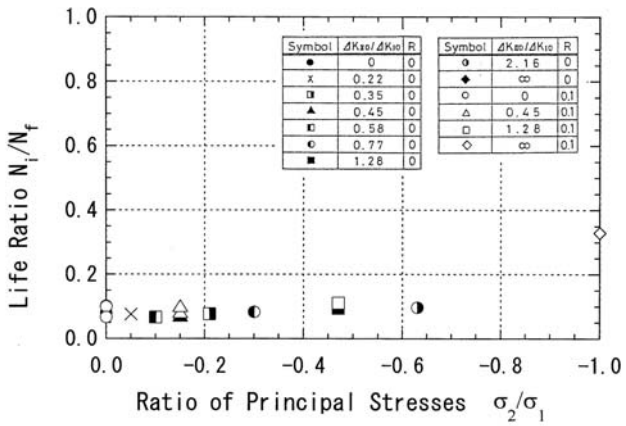

Figure 9: The characteristics of the life ratio, N_i/N_f under mixed-mode conditions.

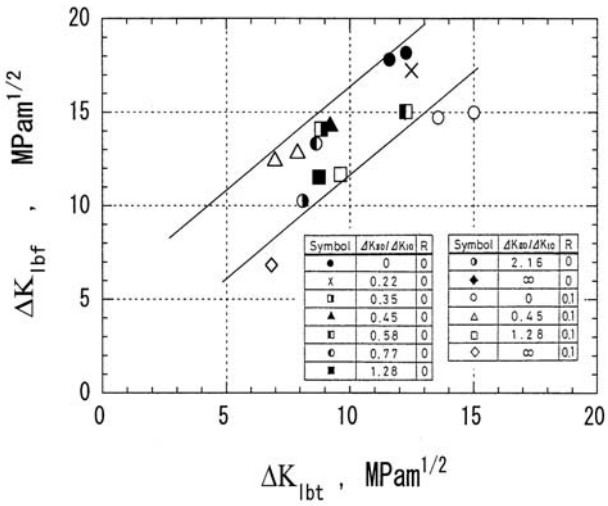

Figure 10: The relation between ΔK_{Ibf} and ΔK_{Ibt} under mixed-mode loading conditions.

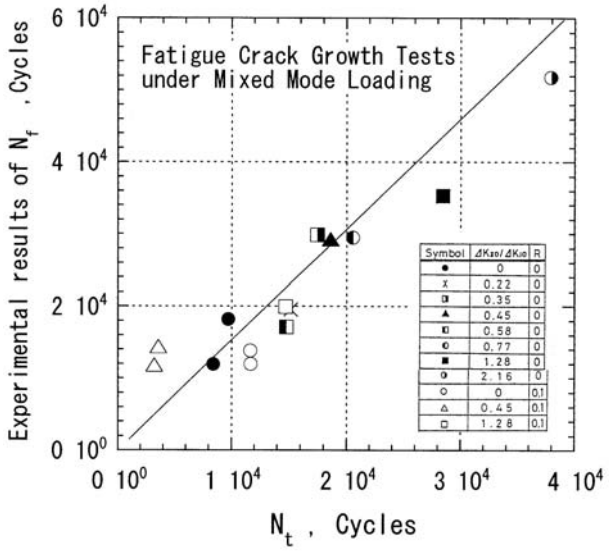

Figure 11: The prediction of the fatigue failure life, N_f under mixed-mode conditions.

In this prediction, the effect of the fatigue damage on N_f is represented by the constants, $A^{R=0}$ and m, which can be described as Eqns. 2a and 5a. The effect of the R-ratio on N_f is represented by the value of r^*.

CONCLUTION

When shearing stress is applied to an initial crack, plastic damage accumulated before initial fatigue crack growth affects significantly the characteristics of fatigue crack growth rate. Under mixed-mode loading conditions, the life for the initial crack growth dominates fatigue failure life. Damage analyses is indispensable to characterize the fatigue crack growth and to predict failure life.

ACKNOWLEGEMENT

Acknowledgement should be made to the financial grant in-aid from the JSPS-RFTF under the project No.97R12901. Acknowledgement also should be made to the Second Branch of Device and System Design Workshop (Mrs. T. Kawabata, K. Yaegashi and N. Ohga), Faculty of Engineering, Tohoku University for the skilful machining of the thin-walled hollow cylindrical specimens.

REFERENCES

1. Richard, H.A. (1989) In: *Biaxial and Multiaxial Fatigue, EFG3*, pp.217-229, Brown, M.W. and Miller, K.J. (Eds.), Mechanical Engineering Publications, London.
2. Quian, J. and Fatemi, A. (1996) *Engng. Fract. Mech. 33*, 969.
3. Brown, G. H. and Miller, K. J. (1982) *Fat. Fract. Engng. Mat. Struct. 5*, 1.
4. Otsuka, A., Mori, K. and Tohgo, K. (1985) *M. R. Series 1,* pp.127, Soc. Mat. Sci. Japan.
5. Yokobori, T., Kamei, A. and Yokobori, A. T. Jr. (1976) *Int. J. Fract. 12*, 158.
6. Yokobori, A.T.Jr., Yokobori, T., Satoh, K. and Shoji, K. (1985) *Fat. Fract. Engng. Mat. Struct. 8*, 315.
7. Yokobori, A.T.Jr., Koizumi, Y. and Isogai, T. (1991) In: *Mechanical Behavior of Materials-VI, Proc. of Sixth International. Conference 4*, pp.481-487, Jono, M. and Inoue, T. (Eds.), Pergamon Press, Oxford.
8. Yokobori, A. T. Jr., Isogai, T (2000) *Int. J. Fract. 102,* L47.
9. Yokobori,A.T.Jr., Isogai, T, Yokobori, T. and Koizumi, Y. (1990) *J.Soc.Mat.Sci. 39*, 1106 (in Japanese).
10. Yokobori, T., Yamanouchi, H. and Yamamoto, S. (1965) *Int. J. Fract. Mech. 1*, 3.
11. Yamada, Y (1972), *Plasticity and Viscoelasticity*, Bauhukan Publisher (in Japanese).

12. Yokobori,A.T.Jr., Isogai,T, and Koizumi, Y. (1991) *J.Jpn.Soc.Streng.Fract.Mat. 25*, 109 (in Japanese).

ORAL/POSTER REFERENCE: ICF100963OR

DAMAGE EVOLUTION AND DAMAGE TOLERANCE IN CERAMIC MATRIX COMPOSITES: EMPIRICAL MEASUREMENTS AND ANALYTICAL/NUMERICAL MODELING

Michael G. Jenkins

Department of Mechanical Engineering, University of Washington
Mechanical Engineering Building, Box 352600, Stevens Way
Seattle, WA 98195-2600

ABSTRACT

Ceramic matrix composites (CMCs) and continuous fibre ceramic composites (CFCCs) were developed to possess the desirable attributes of monolithic ceramics while exhibiting inherent damage tolerance through nonlinear energy absorption mechanisms. Empirical measurements and mathematical (analytical and numerical) models of this damage absorption have contributed to understanding the thermo-mechanical behaviour of CMCs. From this understanding have developed better test methods, greater predictive modeling capability of material behaviour, more appropriate processing methods, and finally design methods for utilizing CMCs. This paper presents background on CMC damage, discusses damage measurement and damage models and finally alludes to the role of damage mechanics in future developments/uses of CMCs.

KEYWORDS

ceramic matrix composites, damage tolerance, damage mechanics, modeling, testing

INTRODUCTION

Ceramic Matrix Composites

Ceramic matrix composites (CMCs) comprise a maturing subset of the broader genre of engineering materials known as composites. CMCs have potential applications in advanced engineering applications because they possess ceramic materials' high-temperature strengths, corrosion/erosion resistances, high stiffnesses, and low densities, while avoiding the brittle, catastrophic failure preventing monolithic ceramics' acceptance in modern designs [1]. In particular, for those CMCs 'reinforced' with continuous fibres, the synergistic micromechanical interaction of fibers, fiber coatings (a.k.a., interphase), matrix, and overcoats give these CMCs much greater resistance to catastrophic failure than for monolithic ceramics.

Because fibre-reinforced CMCs possess greater 'toughness' (i.e., energy absorption without catastrophic failure macroscopically measured as the area under the tensile stress-strain curve) they exhibit increased reliability and damage tolerance. While these CMCs offer greater 'toughness' than monoliths, their strengths can be much less (see Figure 1), thus necessitating still-evolving and different approaches to mechanical design with CMCs. Despite this limitation, numerous industrial, power generation and aerospace uses have been identified for CMCs including filters, heat exchangers, combustor liners, vanes, and nozzles [1].

It is important to note that design of and design with advanced materials are distinct but not always separate areas of modern engineering efforts. Early CMCs were discouragingly 'not tough' because micro mechanisms that lead to successfully 'tough' and damage tolerant materials were not well understood or appreciated. Eventually, mechanicians identified micro mechanisms and developed mathematical models [e.g., 2-11] such that design of modern CMCs now includes predictive micromechanical models to develop 'tough' high performance materials. Furthermore, significant strides have been made in CMC standard test

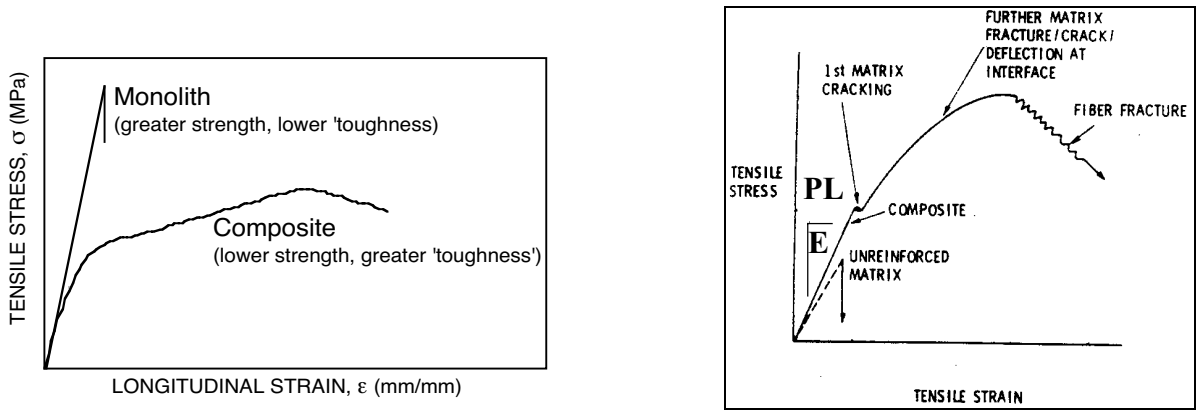

a) Comparison of stress-strain curves b) Details of stress-strain curve for CMC

Figure 1: Engineering stress-strain curves for monolithic and composite (CMC) ceramics

methods [12] with rudimentary design/codes [13] for CMCs now being implemented. These strides have allowed engineers to begin introducing well-designed CMCs in trial, short-term applications. The next major step yet to be achieved in utilizing CMCs is to understand and accommodate long-term behaviour.

As a starting point for long-term predictive design tools, it is useful to examine a CMC quasi-static tensile engineering stress strain curve (Figure 1b). Although Figure 1b is representative of many CMCs and appears quasi-ductile (linear region followed by a nonlinear region before peaking at the ultimate tensile strength, UTS), there is a critical difference between the behaviors of CMCs and those of ductile metals. Specifically, in CMCs the onset of nonlinearity (a.k.a., proportional limit, PL) does not represent the yield point and onset of work hardening as it does in ductile metals. In CMCs the PL is associated with the macro-manifestation of first matrix cracking (or crack opening) and onset of the cumulative damage process.

The still-evolving design codes for CMCs [13] have yet to describe how engineers are to account for the PL. One approach adopts conventional static failure theories based on 'yield' that dictates, for example comparing the stress state, σ_h, to the PL through a factor of safety, FS, such that FS=PL/ σ_h. (note that FS>1 for a 'safe design'). Although this conservative approach exploits only the linear regime of material behaviour, it addresses neither long-term behaviour/durability or the lauded damage tolerance of CMCs.

Continuum Damage Mechanics

The cumulative damage of CMCs, whether in the short-term nonlinear stress-strain curve (Figure 1) or over long periods times (e.g., creep deformation or cyclic fatigue failure) is a progressive physical process during which the matrix cracks, the interphase shears, and fibres fracture. Continuum damage mechanics (CDM) is the study, through thermo-mechanical variables, of the deterioration of the continuum of material [14, 15]. CDM does not require individual failure mechanisms, but rather it includes the response of the bulk material.

At the microscale, deterioration of the continuum is the accumulation of micro stresses and strains at defects or interfaces and the initiation and growth of microcracks.. At the mesoscale of a representative volume element, the growth and coalescence of these microcracks can form a single crack. At the macroscale, the single crack can propagate to cause final fracture. Damage variables and CDM can be used to describe material behaviour at the microscale and mesoscale while fracture mechanics can be used at the macroscale.

In applying CDM, it is important to distinguish between corresponding consecutive states of the material: deformation, damage and crack propagation. The irreversible deformation of plasticity is not complete (Figure 2a), because the material can be 're-deformed' to restore its original shape/state. However, damage corresponds to material degradation. Complete deformation is comprised of a negligible plastic component plus combined damage and elastic components (Figure 2b). The damage

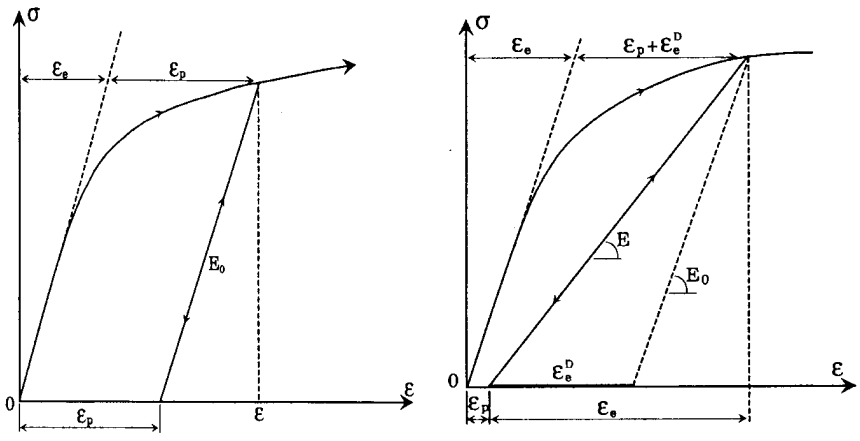

a) Plastic and elastic deformation b) Plastic, elastic and damage deformation

Figure 2: Stress-strain response due to a) plastic and elastic deformation and b) plastic, elastic and damage deformation [16]

component contributes to decreased elastic modulus and inability to return the material to the original state by 're-deformation' [16].

The evolution of design and analysis philosophies indicates that use of damage tolerance (e.g., CDM) is a recent occurrence [15]. For example, in aircraft design, methods involving static strength spanned ~1900 to 1950, safe life (a.k.a., fatigue crack initiation) methods spanned ~1950 to1960, fail-safe life (fatigue crack detection and accommodation) methods spanned ~1960 to 1975, and damage tolerant (residual strength, rate of damage growth, damage detection, and CDM) spanned the time from ~1975 to present.

It is interesting to note that the maturation of CMCs and CDM have occurred concurrently (~1970's to present). However, the applications of the concepts of CDM to CMCs have been limited even though the quasi-brittle behaviour of CMCs makes them an apparently ideal candidate for CDM-based analyses. In the following sections, some examples of the applications of CDM concepts to CMCs are described first for damage measurements then for damage models (both analytical and numerical).

DAMAGE MEASUREMENTS

Having described the concept of damage mechanics, it is useful to describe methods for actually measuring damage in materials. Four types of measurements have been identified [16]: a) Measurement of remaining life (e.g., cycles to failure in fatigue, time to failure in creep, etc.); b) Microstructual measurements (e.g. volume fraction of defects, cavities, microcracks, etc.); c) Measurement of physical parameters (e.g., density, resistivity, acoustic emission, etc.); and d) Measurement of mechanical behaviour (e.g., change in elastic modulus, etc.)

For mechanical modeling of damage, measurements of mechanical behaviour are best. Two approaches to assess mechanical behaviour of damage have been used for determining stress: net stress based on the net section and effective stress that accounts for stress concentration near defects. For the uniaxial case, the net stress is $\sigma^* = \sigma/(1-\omega)$ [16] where σ = true normal stress and ω = average reduction in section area due to microcracks and voids. The effective stress is $\tilde{\sigma} = \sigma/(1-D)$ [16] where D is macroscopic damage.

The variation in mechanical behaviour can be measured through the variation of application-specific parameters. For example, variation in elastic modulus, E, is used such that $D = 1-(\tilde{E}/E)$ where $\tilde{E}$ is the actual damaged elastic modulus. Similarly variation of microhardness, H, can be used such that $D = 1-(\tilde{H}/H)$ where $\tilde{H}$ is the actual damaged microhardness. A summary (Figure 3) of the 'quality' of physical and mechanical damage measurement methods/parameters has been given by Lemaitre [14].

An example of the use of a nondestructive characterization (NDC) method applied to assess damage is shown in Figure 4 for a CMC. An infrared measurement system coupled to laser flash excitation method was used to measure thermal diffusivity as a function of power generation use time [17]. Variation in grayscale (Figures 4a-4d) can be linked to through-thickness variation in thermal diffusivity (i.e., loss of structural integrity or damage). Change of thermal diffusivity with thermal cycles is shown in Figure 4e.

Acoustic emission (AE) can be linked to damage evolution in CMCs. During monotonic and/or cyclic loading of CMC test specimens, the 'number of counts' from the AE system is related to 1) onset of nonlinearity (e.g., matrix cracking) and 2) increasing nonlinearity (continued matrix cracking and fibre fracture) of the stress-strain curve. The unload/reload stress-strain curves (Figure 5a) and the AE cumulative counts vs stress (Figure 5b) show this relationship between nonlinearity and damage for a CMC.

An example of a newly proposed mechanically-based damage parameter for CMCs based on slope and energy information from the monotonic tensile stress-strain curve is given by [19]:

Mechanical/Physical Parameter	Damage Parameter	Brittle	Ductile	Creep	Low cycle fatigue	High cycle fatigue
Micrography	$D = 1-\left(\partial S_D/\partial S\right)$	Try to see	Good	Good	Try to see	Try to see
Density	$D = 1-\left(\bar{\rho}/\rho\right)^{2/3}$	Do not try	Good	Try to see	Try to see	Do not try
Elastic Modulus	$D = 1-\left(\bar{E}/E\right)$	Good	Very good	Very good	Very good	Do not try
Ultrasonic Wave	$D = 1-\left(\bar{V}_L^2/V_L^2\right)$	Very good	Good	Good	Try to see	Try to see
Cyclic Stress Amplitude	$D = 1-\left(\Delta\sigma/\Delta\sigma^*\right)$	Do not try	Try to see	Try to see	Good	Try to see
Tertiary Creep	$D = 1-\left(\dot{\varepsilon}_p^*/\dot{\varepsilon}_p\right)^{1/N}$	Do not try	Try to see	Very good	Try to see	Do not try
Micro-Hardness	$D = 1-\left(H/H^*\right)$	Good	Very good	Good	Very good	Try to see
Electrical Resistance	$D = 1-\left(V/\bar{V}\right)$	Try to see	Good	Good	Try to see	Try to see

Figure 3: 'Quality' chart of methods of damage measurement [14]

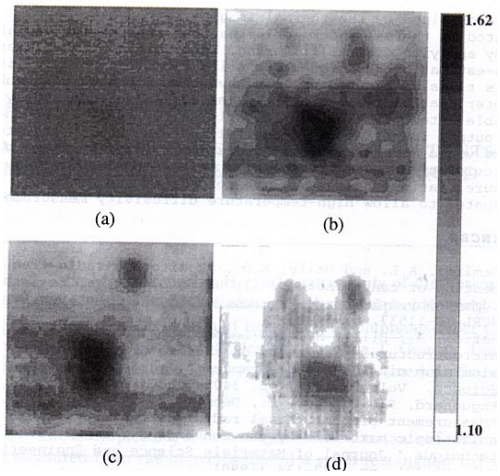

a-d) Raw thermal image, processed thermal image, diffusvity image, and enhanced diffusivity image, respectively.

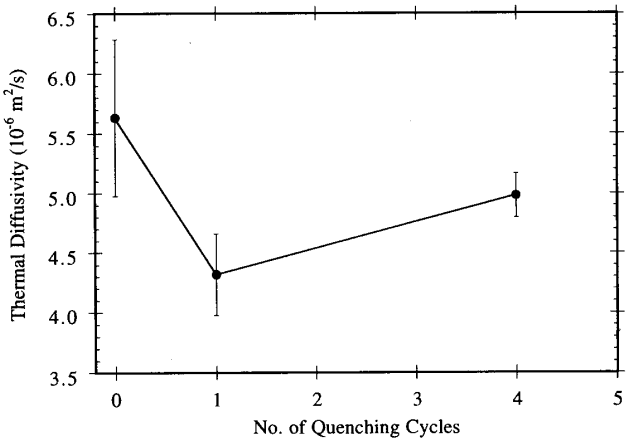

e) Effect of number of quench cycles (ΔT=800°C)

Figure 4: Infrared imaging to assess damage in a SiC fibre-reinforced SiC matrix CMC [17]

$$\tilde{D}(\sigma_i) = \left(1 - \frac{(d\sigma_c/d\varepsilon_c)_i}{(d\sigma_c/d\varepsilon_c)_0}\right)\left(\frac{U_{p,i}}{U_p^*}\right) \quad (1)$$

where $(d\sigma_c/d\varepsilon_c)_i$ is the tangent modulus at i-th point in the monotonically-loaded tensile stress-strain (σ_c-ε_c) curve,(for i-th stress, σ_i, and strain, ε_i), $(d\sigma_c/d\varepsilon_c)_0$ is the tangent modulus in the linear region of the tensile stress-strain curve where $(d\sigma_c/d\varepsilon_c)_0 \approx E_0$, $U_{p,i}$ is inelastic energy absorption at σ_i during the tensile test and U_p^* is the inelastic portion of the total energy absorption during the tensile test just up to the UTS, σ_{cu}.

Figure 6 compares D from Equation 1 to the simple model based on D=1-($\tilde{E}/E_o$) where $\tilde{E}$ is the tangent modulus using the monotonic stress-strain tensile stress curves of a CMC. D determined from Equation 1 reflects the rapidly increasing cumulative damage as the nonlinearity of the stress-strain curve increases whereas the simple damage model based on elastic modulus seems to have a series of plateaus.

DAMAGE MODELS

Analytical

CDM has been developed generally along the concepts of the theory of irreversible processes with internal variables. Total strain is divided into the sum of elastic, plastic and thermal expansion strains from which the elastic and thermal strains are combined into a single reversible, thermoelastic strain (i.e. a state variable). From the total observed strain and the temperature, the local state method develops the framework of CDM from the thermodynamic state of material. The first principle of thermodynamics expresses energy conservation while the second principle of thermodynamics expresses the irreversibility of the entropy production giving an interpretation of the energies stored as heat or stored in the material (see Figure 7). Note that the energy stored by hardening corresponds to an increase in free energy (i.e. internal energy) whereas the energy dissipated by damage is lost by the material (i.e., irreversible decrease in free energy).

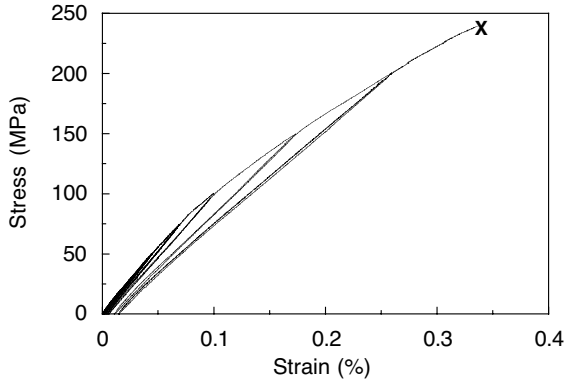

a) Unload/reload stress strain curve

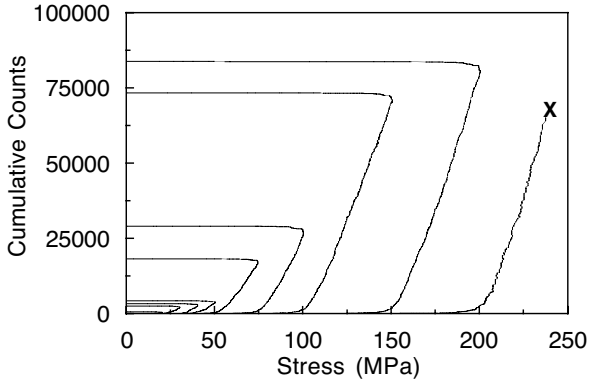

b) Cumulative AE counts for hysteresis loops

Figure 5: Correspondence of AE cumulative counts and the nonlinearity of the stress-stain curves for a SiC fibre-reinforced SiC matrix CMC [18]

From these bases, many 'special' case isotropic CDM models have been introduced for damage equivalent stress (plasticity and viscoplasticity) and strain damage (plasticity and viscoplasticity). For CMCs, anisotropic material damage models include maximum principal stress, 2nd order damage tensor, 4th order damage tensor, and double scalar variable. One such example includes [17]:

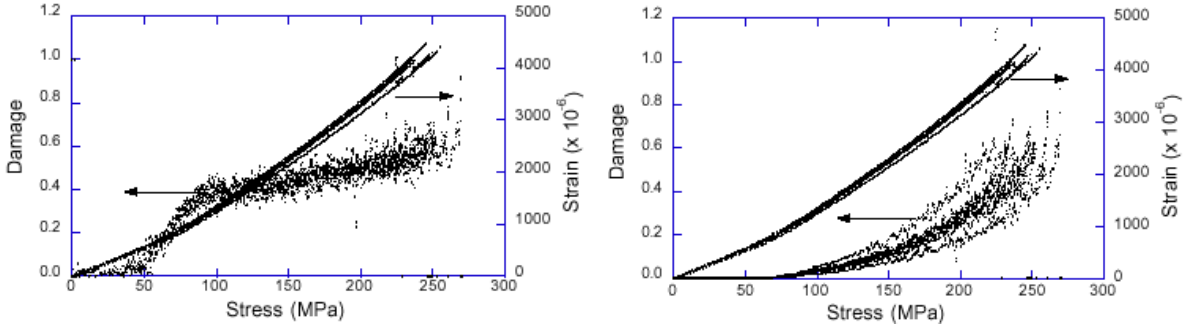

a) Damage=f(tangent modulus) only b) Damage=f(tangent modulus and inelastic energy)

Figure 6: Comparison of damage parameters and strain-stress curves for a Si-C-O fibre reinforced Si-C-N-O matrix CMC [20]

$$\Psi = \frac{1}{2}\left\{\{\varepsilon\} - \{\varepsilon^p\}\right\}[C_o]\left\{\{\varepsilon\} - \{\varepsilon^p\}\right\} + \frac{1}{2}\left\{\{\varepsilon\} - \{\varepsilon^c\}\right\}\left[\Delta C^{eff}\right]\left\{\{\varepsilon\} - \{\varepsilon^c\}\right\} \quad (2)$$

and

$$\{\sigma\} = \frac{\partial \Psi}{\partial \{\varepsilon\}} = \left[[C_o] + \left[\Delta C^{eff}\right]\right]\left\{\{\varepsilon\} - \{\varepsilon^c\}\right\} + [C]\left\{\{\varepsilon^c\} - \{\varepsilon^p\}\right\} \quad (3)$$

where Ψ = free energy, $\{\varepsilon\}$ = total strain vector, $\{\varepsilon^p\}$ = plastic strain vector, $\{\varepsilon^c\} = \{\varepsilon\} - \{\varepsilon^p\}$,

$[C_o]$ = undamaged stiffness matrix, $\left[\Delta C^{eff}\right]$ = damaged, reduced stiffness matrix, $\{\sigma\}$ = stress vector

Employing a hierarchical approach (e.g., Equations 2 and 3) along with constitutive constants from uniaxial tension and compression tests the multiaxial damaged stress-strain response of a CMC was predicted using strain as the independent state variable. The modeling is sophisticated but has been implemented in industrial design codes, with good agreement with actual experimental results for this CMC (see Figure 8).

Numerical

Many examples of numerical damage models could be related. These models may be as direct as applying linear damage models sequentially (e.g., Miner's Rule) or as involved as those that employ finite element analysis (FEA) programs 'drive' the accumulation of damage. Two FEA examples follow.

FEA model of an unnotched beam

In this study [21], a double meshed (i.e., one set of nodes, but two sets of elements, fibre and matrix) FEA model was constructed of a flexure test specimen geometry that had been used to strength test a three-dimensionally braided CMC [22]. A macrocode was written for the commercial FEA code such that matrix or fibre elements were 'killed' if the maximum principal stress in the respective elements exceeded the UTS of the respective materials. Good agreement between empirical and numerical results is shown in Figure 9. Note that most matrix elements have failed by the test's end, leaving only fibre elements to carry the load.

FEA model of a notched beam

In this study [23], an FEA model with macrocode was constructed using the same double meshing procedure and methodology [21, 22]. A single edge notched beam was modeled to compare the numerical results to R-curve behaviour in a unidirectionally-reinforced CMC. In this case matrix elements substantially failed not only near the notch tip but also distributed in the CMC. Fibres failed only near the notch region.

DISCUSSION AND CONCLUSIONS

Nonlinear monotonic tensile stress-strain curves are speculative and analytical foci used to describe the mechanical behaviour of CMCs and attendant micromechanics. In attempts to describe and extract additional information from these tensile tests, such methodologies as unload/reload tensile tests [e.g.,24-27] have been proposed. These methodologies provide information about in-situ mechanical properties of constituent materials but still require detailed knowledge and modeling of the micromechanics.

CDM, although a relative 'newcomer' for describing the mechanical properties and performance of CMCs, has the major advantage of simplifying the analysis of mechanical behaviour by reducing the requirements

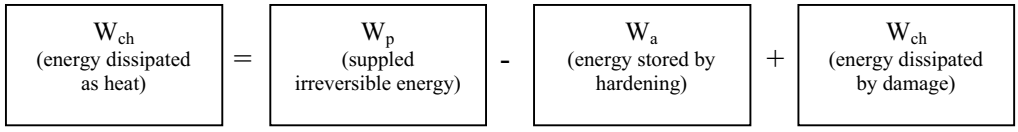

Figure 7: Illustration of the dissipation during plastic flow/deformation and damage [17]

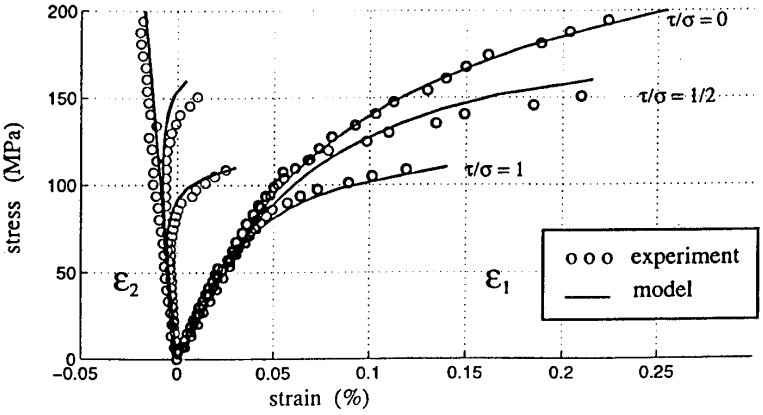

Figure 8: Comparison of experimental and damage model prediction results for a SiC fibre / SiC matrix CMC [16]

for knowledge about the individual micro mechanisms of failure and properties and performance of the constituent materials. CDM describes the cumulative damage process inherent in quasi-brittle CMCs as reflected by their nonlinear stress-strain curves and fracture surfaces.

In applying CDM to CMCs under ambient conditions, both analytical and numerical approaches have successfully described mechanical behaviour in complex stress states. With modifications, time/environmental aspects of constituent materials and bulk CMCs can be integrated into the damage models to describe long-term durability.

ACKNOWLEDGEMENTS

This work was sponsored by the U.S. Department of Energy, Assistant Secretary for Energy Efficiency and Renewable Energy, Office of Industrial Technologies, Industrial Energy Efficiency Division and Continuous Fiber Ceramic Composites Program, under contract DE00OR22725 with UT-Battelle, LLC.

REFERENCES

1. Karnitz, M.A., Craig, D.A., Richlen, S.L. (1991) *Ceram. Bull.,* 70, 430.
2. Aveston, J., Cooper, G.A., Kelly, A. (1971) In, *The Prop of Fibre Comp*, NPL, IPC Press, Teddington, U.K., 15.
3. Rice, R. W. (1981) *Ceram. Eng., Sci Proc.* 2, 661.
4. Marshall, D.B., Cox, B.N., Evans, A.G. (1985) *Acta Metall.,* 33, 2013.
5. Rice, R. W., (1985) *Ceram. Eng., Sci Proc.* 6, 589.
6. Budiansky, B., Hutchinson, J.W., Evans, A.G. (1986) *J. Mech. Phys. Solids,* 34, 167.
7. McCartney, L.N. (1987) *Proc. R. Soc. London, A.,* 409, 329-350.
8. Evans, A. G., Marshall, D. B. (1989) *Acta Metall.* 37, 2567.
9. Curtin, W. A. (1991) *J. Amer. Ceram Soc.,* 74, 2837.
10. Inghels, E, Lamon, J. (1991) *J. Mater. Scienc.* 26, 5403 and 5411.
11. Evans, A. G., Zok, F. W. (1994) *J. Mat. Scienc.* 29, 3857.
12. Jenkins, M. G. (1999) *Advanced Composite Materials,* 8, 55.
13. CMCs, Vol 5, MIL-HDBK-17, (Yellow Pages) (2000) DoD Handbook, Secretariat: MSC, Fort Wash., Penn..
14. Lemaitre, J. (1996) *A Course on Damage Mechanics,* Springer Verlag, Berlin.
15. Krajcinovic, D. (1996) *Damage Mechanics*, Elsevier, Amsterdam.
16. Chaboche, J.-L. (1999) In, *Creep & Damage in Materials & Structures,* Springer-Verlag, New York, 209.
17. Ahuya, S., Ellingson, W.A., Steckenrider, J. S., (1997) In, STP 1309, ASTM, W. Conshohocken, Penn., 209.
18. Jenkins, M.G., Piccola, J.P. Jr., Lara-Curzio, E. (1996) In, *Frac Mech of Ceramics*, Plenum, New York, 267.
19. Mamiya, T. Kagawa, Y., Jenkins, M.G. (2001) In, *Proc. 2001 SEM Annual Conf,* SEM, Bethel, Conn., 566.
20. Kessler, B. S., Jenkins, M.G. (2001) In, *Proc. 2001 SEM Annual Conf.*, SEM, Bethel, Conn., 430.
21. Jenkins. M.G., Mark. K.Y. (2001) *J. Materials Design and Analysis,* in press.
22. Jenkins, M.G., Mello, M.D. (1996) *Mater. Manuf. Processes,* 11, 99.
23. Kwon, O.H., Jenkins, M. G., (2001) Univ. of Wash. Report.
24. Burr, A., Hild, F., Leckie, F. A. (1997) In, STP 1315*,* ASTM, W. Conshohocken, Penn.
25. Evans, A. G., Domergue, J.-M., Vagaggini, E., (1994) *J. Am. Ceram. Soc*., 77, 1425.
26. Steen, M., Valles, J. L., (1996) In, *,* STP 1309, ASTM, W. Conshohocken, Penn, 49.
27. Campbell, C. X., Jenkins, M. G., (2000) In, STP 1392, ASTM, W. Conshohocken, Penn, 118.

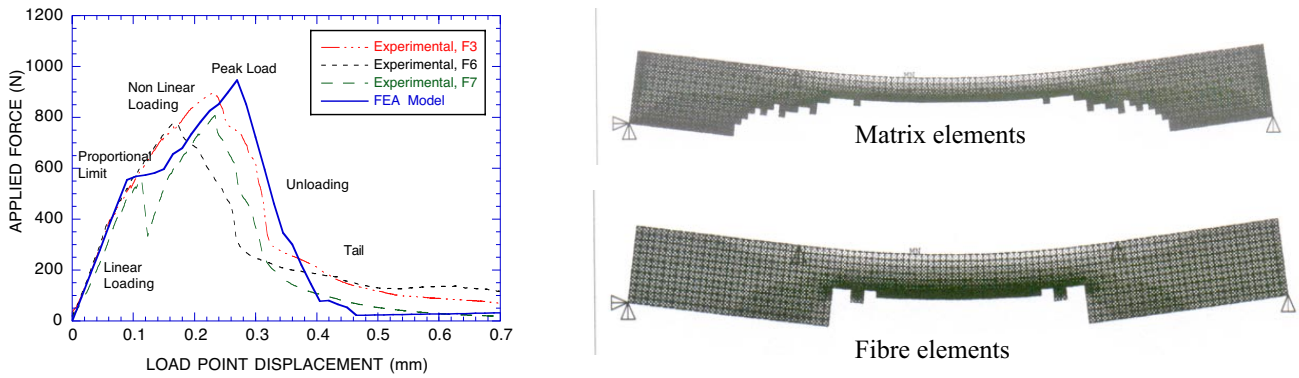

a) Load-displacement results b) 'Unkilled' elements at end of test

Figure 9: Results of FEA modeling of a CMC four-point flexure test specimen using element 'kill' commands for a 3-D braided SiC fibre reinforced SiC matrix CMC

DAMAGE EVOLUTION AND FRACTURE OF VISCOELASTIC COMPOSITES UNDER TIME-VARYING LOADS

J. Varna[1], A. Krasnikovs[2] and R. Talreja[3]
[1] Luleå University of Technology, Luleå, Sweden
[2]Riga Technical University, Riga, Latvia
[3]Georgia Institute of Technology, Atlanta, GA 30332-0150, USA

1. Introduction and Problem formulation

Symmetric $[0_n, 90_m]_s$ cross-ply laminate with transverse cracks in 90-layers is shown in Fig. 1. Layers in the (x,y,z) -system are homogeneous, orthotropic and linearly viscoelastic with constitutive relations given by,

$$\sigma^i(t) = \int_0^t E^i(t-\tau)\frac{d\,\varepsilon^i}{d\tau}d\tau \qquad (1)$$

where the superscript i =0, 90 designate the layer and ε^i, σ^i and E^i denote the strain, stress and stiffness tensors, respectively. In general, stresses and strains are functions of the position ξ characterized by dimensionless coordinates x/d and z/d. In the following, stress, strain and stiffness symbols without the superscript stand for averages over the entire laminate. Lower index, if given, specifies the component under consideration. For simplicity residual thermal stresses are not included in analysis. It is also assumed that all stresses arising during the formation of cracks have relaxed and the laminate before the displacement application is stress free.

Plane stress formulation is used and the only applied loading is time dependent displacement in x-direction, see Fig.1, $u_x(t) = \varepsilon_x(t)\,l_0$.

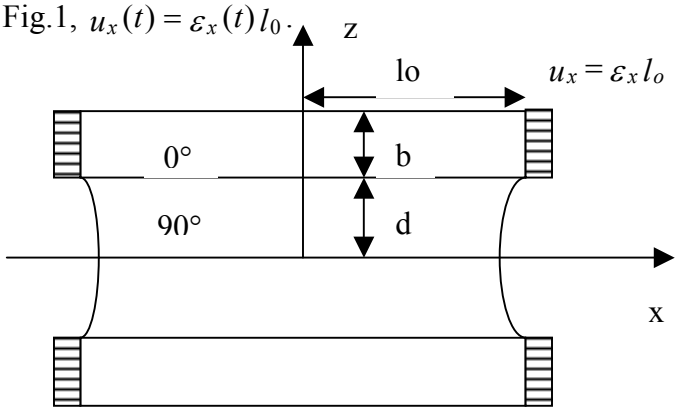

Fig. 1 Schematic showing the cross ply-laminate with cracks in the 90-layers.

For the assumed constant spacing of cracks the solution must satisfy:

1. Stress equilibrium equations

$$\frac{\partial \sigma^i_{kl}}{\partial x_l} = 0 \qquad (2)$$

2. Strain-displacement relationships

$$\varepsilon_{kl}^{i} = \frac{1}{2}\left(\frac{\partial u_k^i}{\partial x_l} + \frac{\partial u_l^i}{\partial x_k}\right) \tag{3}$$

3. Boundary conditions.

Based on symmetry considerations only a quarter of the full repeating unit (Fig. 1) is used. Symmetry conditions are on sides $x = -l_0, z \in [d, h]$ and $x \in [-l_0, 0], z = 0$. Traction free-conditions are on $z = h = d+b$ and on the crack surface $x = -l_0, z \in [0, d]$, applied constant displacement in *x*-direction, on $x = 0, z \in [0, h]$.

4. All stresses and strains at $t \le 0$ are zero.

2. Theoretical analysis

The expressions needed for calculation of stress-strain dependence in an arbitrary point for a general loading ramp are derived using Laplace transform technique and applying the linear viscoelastic correspondence principle. This principle states that the solution of a given viscoelastic problem in Laplace domain may be obtained using the solution of the corresponding elastic problem. The only modification is that instead of elastic constants the Carson transforms of the corresponding relaxation functions are used. We denote by $\overline{f}(\xi, s)$ the Laplace transform of an arbitrary stress-strain state characteristic $f(\xi, t)$ and the Carson transform of the set of relaxation functions by $\widetilde{E}(s)$. Here s is Laplace parameter. Due to linearity $\overline{f}(\xi, s)$ is proportional to the applied average strain $\overline{\varepsilon_x}$:

$$\overline{f}(\xi, s) = \Psi\left(\xi, \widetilde{E}^k(s)\right)\overline{\varepsilon_x}(s) \tag{4}$$

Considering relaxation test with unit applied strain, $\overline{\varepsilon}_x = \frac{1}{s}$ and denoting all time dependent functions with index R we have,

$$\overline{f}_R(\xi, s) = \Psi\left(\xi, \widetilde{E}^k(s)\right)\frac{1}{s} \tag{5}$$

The inversion to time domain in this case becomes trivial if we realize that in relaxation test all stress-strain state characteristics are monotonous functions of time with a small curvature in log*t* scale and, hence, satisfy Schapery's conditions for simple transformation [1]:

$$f_R(t) = \left(s\overline{f}_R(s)\right)_{s=0.56/t} \tag{6}$$

leading to

$$f_R(\xi, t) = \Psi\left(\xi, E^k(t)\right) \tag{7}$$

Function Ψ is given by the linear-elastic solution using values of elastic constants equal to relaxation moduli in the particular instant t.

The expression for the general strain ramp, Eq. (4), may now be rewritten in terms of functions in relaxation test:

$$\overline{f}(\xi, s) = \Psi\left(\xi, \widetilde{E}^k(s)\right)\frac{1}{s}s\overline{\varepsilon_x}(s) = \overline{f}_R(s)s\overline{\varepsilon_x}(s) \tag{8}$$

Inverse transformation to time domain leads to

$$f(\xi, t) = \int_0^t f_R(\xi, t-\tau)\frac{d\,\varepsilon_x}{d\tau}d\tau \tag{9}$$

Stress state characteristics for laminates with cracks subjected to given strain ramp are

1. Macro-response (laminate stress) of the laminate

$$\sigma_x(t) = \int_0^t \sigma_{xR}(t-\tau)\frac{d\,\varepsilon_x}{d\tau}d\tau \tag{10}$$

2. Stress in defined points ξ in layers where fracture may occur:

$$\sigma_x^i(\xi,t)=\int_0^t \sigma_{xR}^i(\xi,t-\tau)\frac{d\,\varepsilon_x}{d\tau}d\tau \qquad (11)$$

3. Average crack opening displacement normalized by the 90-layer half-thickness *d*: (Since the presented calculations are for open cracks, this parameter is needed to check the validity of the method.)

$$u_{an}(t)=u_a(t)/d \qquad u_a=\frac{1}{d}\int_0^d u_x(z)dz \qquad u_{an}(t)=\int_0^t u_{anR}(t-\tau)\frac{d\,\varepsilon_x}{d\tau}d\tau \qquad (12)$$

From Eqs (10)-(12) the response of a damaged laminate to an arbitrary strain ramp can be easily calculated if the corresponding functions are known for relaxation test. The procedure to determine the characteristics in relaxation test follows. According to Eq. (7) functions from relaxation test may be obtained by solving a sequence of elastic problems corresponding to varying parameter t. It may be done using FE method or by developing approximate analytical models. In this paper the macro-response of the damaged laminate (relaxation of laminate stress and average crack opening) is calculated using closed form expressions for elastic case [2,3].

Average crack opening displacement may be calculated using the simple power law which, based on FE parametric analysis, was obtained in [3] as

$$u_{anR}(t)=0.01\frac{E_x(t)}{E_{x0}(t)}u_n(t) \quad \text{with} \qquad u_n(t)=A+B\left(\frac{E_x^0(t)}{E_x^{90}(t)}\right)^{-n} \qquad (13)$$

Here $A=0.955$, $B=0.9102+0.3413\dfrac{d-b}{b}$ and $n=-0.0169\left(\dfrac{d}{b}\right)^2-0.0041\dfrac{d}{b}+0.9074$

The $\dfrac{E_x(t)}{E_{x0}(t)}$ for normalized crack density $\bar{\rho}=d/2l_0$ may be calculated using the following [2],

$$\frac{E_x(t)}{E_{x0}(t)}=\frac{1}{1+2\dfrac{E_x^{90}(t)d}{E_x^{90}(t)d+E_x^0(t)b}u_n(t)\bar{\rho}} \qquad (14)$$

Laminate stress: $$\sigma_{xR}(t)=0.01E_x(t) \qquad (15)$$

Stress in location ξ at a given instant of time t is obtained solving the elastic problem by FEM, using elastic constants equal to the relaxation moduli at this instant of time.

3. **Numerical example**

We consider three-step loading as shown in Fig.2. In all steps the strain rate is constant, ε_0/t_1, and strain is first linearly increasing until $\varepsilon_0=1\%$, then decreasing to $\varepsilon_2=0.05\%$ and finally increasing again. Results are presented for CF/EP [0/90$_2$]s laminate.

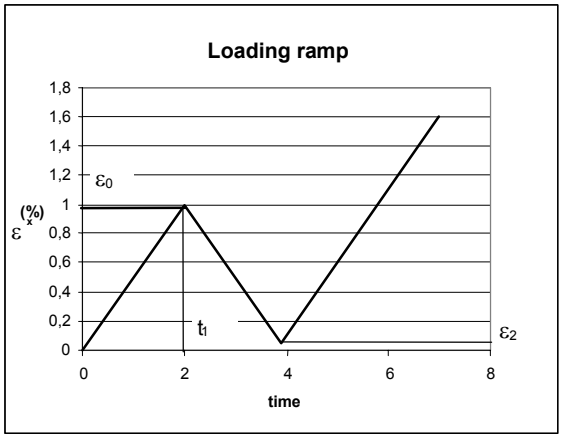

Fig.2 Three-step loading ramp with the same ramp rate in all steps applied to laminates.

Relaxation moduli of unidirectional lamina are shown in Fig 3. In relaxation test with the applied strain $\varepsilon_x = 1\%$, the laminate stress relaxation follows Eqs (15). For a given crack density we use Eq.(14) for relaxation modulus. This expression includes the crack opening displacement $u_n(t)$ which is calculated using the power law Eq.(13). The calculated laminate stress and COD relaxation curves are presented in Fig.4. Fifth order polynomials are used to fit the calculated data. These fitting polynomials are used in Eqs. (10)-(12) for modeling stress response in the loading case shown in Fig.2.

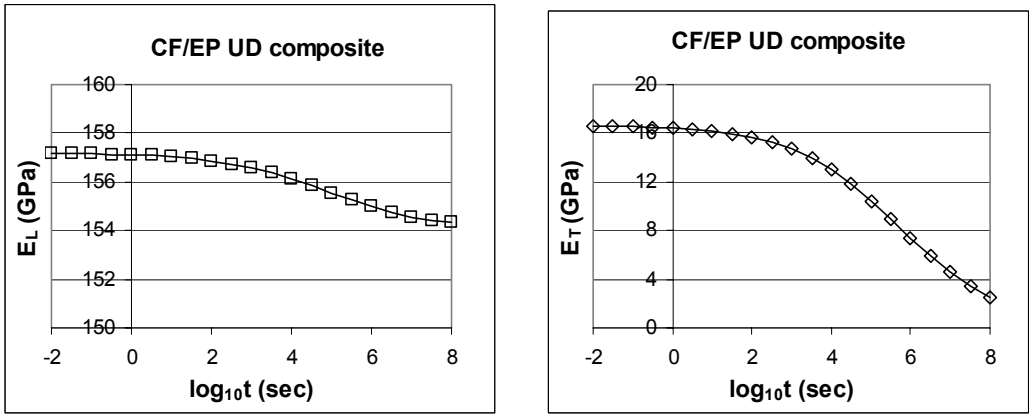

Fig.3 Relaxation functions of the unidirectional CF/EP composite

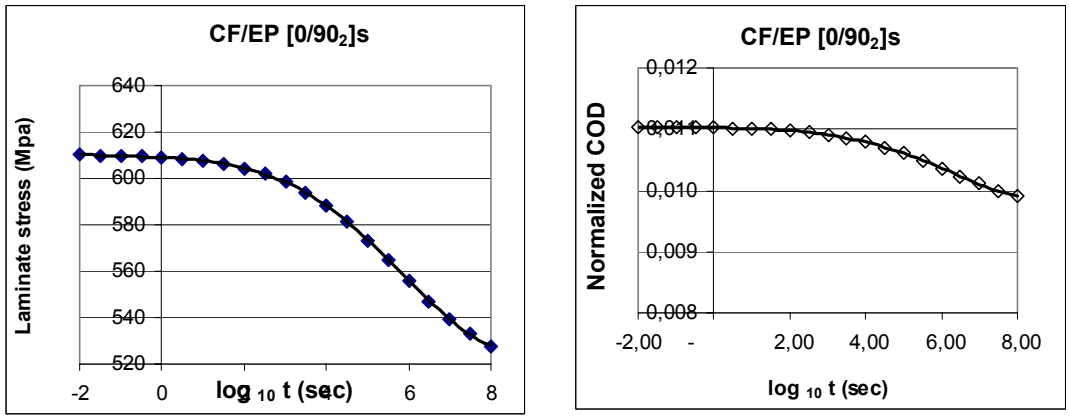

a) b)

Fig.4 Macro-response of [0/90-2]s CF/EP laminate in relaxation test. Applied strain $\varepsilon_x = 1\%$ *. Laminate with transverse crack spacing* $l_0/d = 5$. *a)* $\sigma_{xR}(t)$ *; b)* $u_{anR}(t)$

As a critical site for further damage development we consider a) x=0, z=0 where the next transverse crack is expected, and b) the fibers in the 0-layer which are located at the tip of the transverse crack for possible fiber fracture. Stress relaxation at these points is shown in Fig.5. The polynomial fit to all time dependent functions in relaxation test is used to calculate the response to strain ramp shown in Fig.2. Expressions (10)-(12) are used.

Before the response of the damaged laminate was simulated, the crack opening was inspected to insure that cracks remained open at all times. If due to hysteresis cracks would close, the used analysis becomes invalid. The calculated macro-response of the damaged laminate is

shown in Fig.6. Note, that in case of fast loading (t_1=10) the loading, unloading and reloading curves almost coincide. For the low strain rate (t_1=2e7), the unloading curve is below the loading curve and following reloading leads to slope which is higher than the initial loading slope, thus building a hysteresis loop.

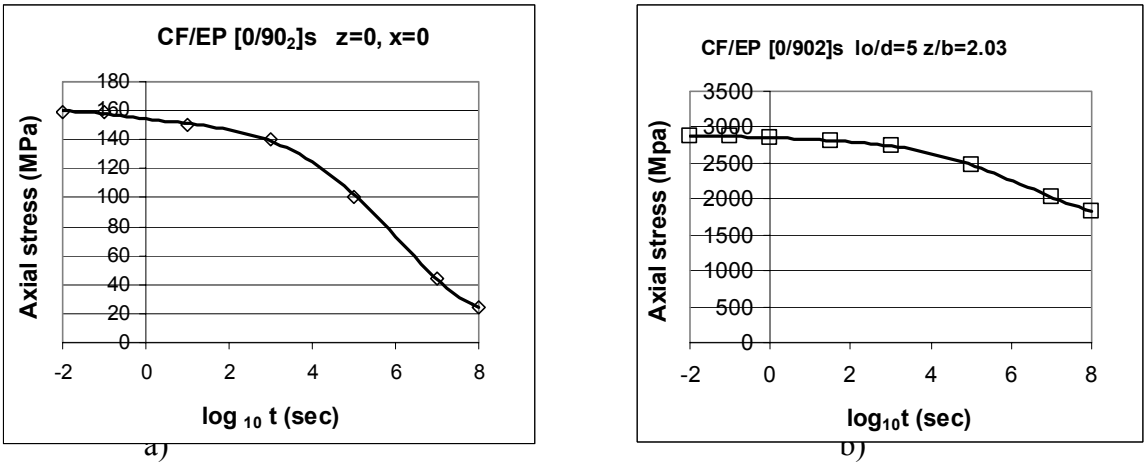

Fig.5 Axial stress $\sigma_x^i(t)$ *in CF/EP [0/90₂]s laminate. Relaxation test at applied strain* $\varepsilon_x = 1\%$. *Crack spacing* $l_0/d = 5$. *a)* $\sigma_x^{90}(t)$ *in 90-layer at x=0, z=0; b)* $\sigma_x^0(t)$ *in 0-layer (average over the first closest the crack fiber).*

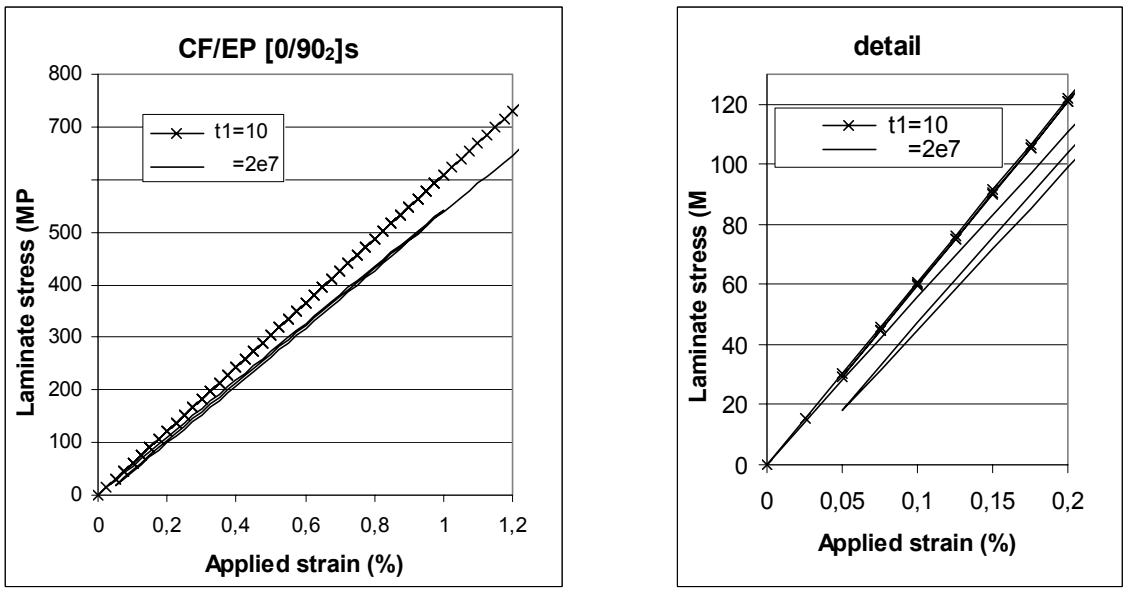

a) b)

Fig. 6 Stress-strain curve of [0/90₂]s CF/EP laminate with crack spacing $l_0/d = 5$*) obtained using the loading ramp shown in Fig.2. Strain rates t1=10 and t1=2e7 are used. a) the whole loading-unloading-reloading curve; b) detail at small strains.*

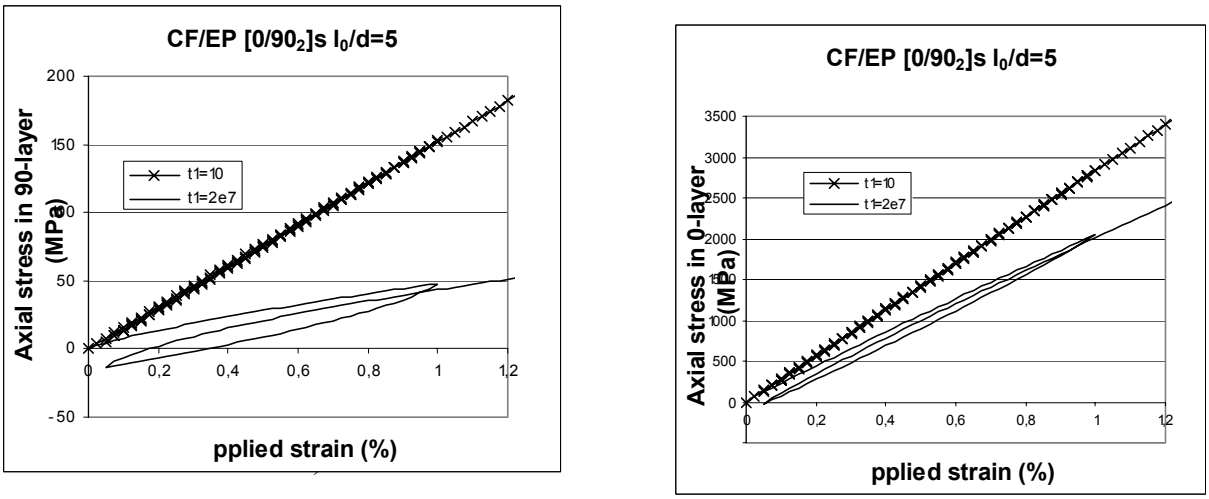

Fig. 7 a)Stress σ_x^{90} in the middle of 90-layer (x=, z=0) ; b) Average stress σ_x^0 in the closest fiber to the crack tip (x=0, z/b=2.03) in 0-layer.

Fig.7a shows the x-axis stress response at mid-distance between two preexisting cracks due to the applied strain ramp. The hysteresis loop is remarkably large leading to compressive stresses (remember that the applied strain is positive at all times). The fact that stress at the considered point is compressive, while cracks are still open, is remarkable. Loading rate has a huge effect on the obtained stress level. Finally, Fig 7b shows the stresses in the 0-layer. The position considered is at the tip of the transverse crack. This stress, which is the average over the closest fiber diameter (layer thickness), gives an indication of possible fiber fracture due to stress concentration at the crack tip. Stresses are very high, approaching the fiber strength. They are much higher than predicted by commonly used analytical stress models. Slower loading allows for stress relaxation and stresses are lower.

4. Conclusions

The stress response of a damaged laminate to an arbitrary applied strain ramp may be predicted by simple integration, provided the corresponding stress response in relaxation test is known.

The time dependence of stresses in relaxation test is obtained using Schapery's inversion method for Laplace transforms. To accomplish this, a sequence of elastic problems must be solved.

5. References

1. R. A. Schapery, *Approximate methods of transform inversion for viscoelastic stress analysis"*, Proceedings of the 4th U.S. National Congress of Applied Mechanics, ASME, 18-21 June, 1962, Berkeley, CA, pp. 1075-1086.
2. R. Joffe and J. Varna*, "Analytical modeling of stiffness reduction in symmetric and balanced laminates due to cracks in 90° layers"*, Composites Science and Technology, 59, 1999,1641-1652.
3. Varna J., Joffe R. and Krasnikovs A., " *COD based simulation of transverse cracking and stiffness reduction in [S,90n]s laminates*," Composites Science and Technology, 2001, in press.

ORAL/POSTER REFERENCE: ICF100470PR

DAMAGE FORMATION IN TRANSFORMATIONS IN HTSC DURING COMPACTION AND SINTERING

I. A. Parinov

Mechanics and Applied Mathematics Research Institute, Rostov State University, Rostov-on-Don, 344090, Russia

ABSTRACT

Three sub-problems which are able to advance the problem of an optimization of the manufacture techniques and high-temperature superconducting (HTSC) compositions, namely: (i) a yield criterion which can describe both the bulk movement and the consolidation of powder in a compaction process, (ii) a carbon segregation which embrittles intergranular boundaries, and (iii) a void transformation during sintering, are considered. In the proposed yield criterion, an effect of volume change on the strain of the powder during the compaction process is considered by adding the first invariant of stress tensor in the criterion. The carbon segregation processes are associated with slow, fast and steady states of the dislocation-screened crack growth. The phenomenological models of pore drag, shrinkage, coarsening and coalescence at the grain boundaries and a possible pore breakaway are developed by considering the third sub-problem.

KEYWORDS

HTSC, compaction, sintering, damage, yield, carbon, diffusion

INTRODUCTION

It is obviously, that an optimization of the manufacture techniques and material compositions is the most important to obtain HTSC with improved and more controlled structure-sensitive properties. The techniques used to prepare the HTSC bulks are very complex and usually include some intermediate stages, the goal of which is to obtain a highly connected and align grain structure. During concrete thermal and pressing treatments the secondary phases and segregations form into the composition, rendering, generally, non-simple effect on the final HTSC properties. For example, the melt-processing has been successfully applied to prepare the large-grain superconductive $YBa_2Cu_3O_{7-x}$ (YBCO) ceramics with decreased content of the intergranular boundaries and improved critical current density (J_c) [1]. However, there are great problems connected with preparation of the optimum compositions, thermal and pressing regimes. Then, in order to rise J_c into $(Bi, Pb)_2Sr_2Ca_2Cu_3O_{10}$ (Bi-2223) compositions a silver dispersion is inserted into calcinated powder and the intermediate cold or hot pressings are fulfilled [1]. At the same time, there is considerable problem of carbon which segregates to the intergranular boundaries and embrittles them.

It is the aim of this paper to consider the next sub-problems which could help to improve the processing techniques and compositions for above HTSC systems: (i) a yield criterion which can describe the bulk movement and the consolidation of powder in a compaction process, (ii) a carbon segregation which embrittles intergranular boundaries, and (iii) a void transformation during sintering.

POWDERED HTSC COMPACTION AND YIELD CRITERION

The computer models of the structure sintering, shrinkage, cooling and also the grain recrystallization for different YBCO and Bi-2223 compositions have been developed by using the finite difference method and Monte-Carlo procedures [2-6]. The more powerful finite element methods need detailed information on the critical characteristics and microstructure features. During the powdered HTSC compaction the mechanism of densification involves two processes, namely bulk movement and plastic deformation of particles. Because of the compact consists of numerous particles, one may be considered as a homogeneous continuum. Then, it is necessary to find a limiting condition or a yield criterion to describe the deformation during the compaction. Successful yield criterion is able to help in advance to optimum HTSC compositions. The deformation due to a grain slip results to an increase of volume in the compaction, while the yielding due to a consolidation leads to a volume decrease. At the transition point or critical state, the volume remains constant. Various yield criteria for the loose, porous and granular materials have been reviewed. However, as rule, these criteria do not take into account the effect of density on deformation. Moreover, due to the volume inconstancy during compaction the effect of hydrostatic pressure should be included in the yield criterion. At the same time, the limiting envelopes, stated by the Mohr-Coulomb's and related criteria, suggest an infinitely large shear stress to cause slip at compression, but this is not applied to granular materials. Therefore, the yield criterion for powdered compaction should suppose a closed limiting envelope (e.g., in the elliptic form), with asymmetrical conditions of the compressive and tensile stresses, because powders are not able to sustain tensile loading. Following to [7], for isotropic case of the powdered HTSC compaction it is considered 3D yield criterion in the form

$$f = \alpha\,(I_1 + s)^2 + I_2 = \beta\, Y^2 \tag{1}$$

where α, β and s are the material constants depended on the sample density, Y is the yield stress of the fully dense material, I_1 and I_2 are the first and second invariants of the stress tensor, respectively. Eqn. 1 can be represented in the terms of normal (σ) and shear (τ) stresses as

$$\frac{(\sigma + s/3)^2}{\left(\sqrt{(1+12\alpha)/9\alpha}\,\sqrt{\beta}Y\right)^2} + \frac{\tau^2}{\left(\sqrt{\beta}Y\right)^2} = 1 \tag{2}$$

By using the yield function f as the plastic potential, the associated flow rule is obtained from the normality condition between the plastic strain increments, $d\varepsilon_{ij}$ and the yield surface in the form

$$d\varepsilon_{ij} = d\lambda[2\alpha(\sigma_{kk} + s)\delta_{ij} + \sigma'_{ij}] \tag{3}$$

where δ_{ij} is the Kronecker delta, σ_{kk} and σ'_{ij} are the hydrostatic and deviatoric stresses, respectively. Find the proportionality constant, $d\lambda$, from Eqns. 1 and 3 as $d\lambda = \left[d\varepsilon_V^2/(18\alpha) + d\varepsilon'_{ij}d\varepsilon'_{ij}\right]^{1/2}/(\sqrt{2\beta}Y)$, where $d\varepsilon_V$ and $d\varepsilon'_{ij}$ are the volumetric and deviatoric strain increments. The material constants α, β and s can be found from the shear test [8]. For this, the yield locus is represented at the σ - τ plane by the ellipse with Eqn. 2. Due to the assumption of isotropic deformation the transition point approximately coincides with the apex of the minor axis of the ellipse. Then the inclined angle (ψ) of the critical state line against the abscissa (σ), and the ratio (R) of the ellipse major axis to the minor one can be treated as material constants, and from Eqn. 2 they have forms: $\tan\psi = \sqrt{\beta}Y/(s/3)$ and $R = \sqrt{(1+12\alpha)/9\alpha}$. Finally, as the third necessary equation we take the dependence between the density of a powder compact and pressure needed to achieve that density [9], namely: $KP = \ln[(1-\rho_0)/(1-\rho)]$, where P is the applied pressure, ρ_0 and ρ are the average densities of the loose powder and the presspowder, respectively, and K is an experimental constant. Then, taking into account the relationship: $P = s/3 + R\sqrt{\beta}Y$, the experimental constants ψ, R and K can be used to determine the values of α, β and s as

$$\alpha = \frac{1}{(9R^2 - 12)}; \quad s = \frac{3}{K(1 + R\tan\psi)} \ln\frac{1-\rho_0}{1-\rho} \quad \text{and} \quad \beta = \frac{1}{\mathrm{Y}^2}\left[\frac{\tan\psi}{K(1 + R\tan\psi)} \ln\frac{1-\rho_0}{1-\rho}\right]^2. \qquad (4)$$

A satisfactoriness of the proposed criterion to compaction of the HTSC precursors can be verified by using, e.g. the triaxial compaction test. However, it should be noted, that the triaxial compaction tests of sand, concrete and rock have shown that associated plasticity cannot describe experimental data satisfactorily [10]. At the same time, this issue has not been discussed for the powdered HTSC compaction.

CARBON SEGREGATION AND HTSC FRACTURE

Carbon can be introduced into yttrium and bismuth HTSC ceramics by carbon-containing gases or liquids. During the processing it is possible to form nanometer-scale carbon inclusions with superconductor grains and enhance flux pinning substantially [11]. However, it is well known, that carbon or carbon dioxide segregated to the grain boundaries can degrade them and transport properties, respectively [12]. The segregation processes can be studied by using the microscopic models of the equilibrium slow and fast propagation, and also a steady state growth of a dislocation-screened crack.

Equilibrium Slow and Fast Crack Growth

Consider an intergranular crack with the length, $2a$, in a carbonated HTSC. The crack lies along x axis in an elastic-plastic isotropic body with shear modulus, G, Poisson ratio, ν, yield strength, σ_y, and work hardening factor, n. The body is loaded by a remote stress, σ_a, parallel to the y axis at a constant temperature, T. At the x axis two linear dislocation arrays with the length r_y locate at the distance d from the crack tips. It is assumed, the size of the arc-shaped crack tips, q, remains constant during plastic deformation. The condition of the local equilibrium at the crack tip is that one must be screened by dislocation field and maintains a dislocation free zone with the size d. The loaded system "crack - dislocation arrays" maintains a local stress, σ_d, in the dislocation free zone and produces the next stress intensity [13, 14]

$$\sigma_{yy} = \sigma_d \ \text{ at } \ a < |x| < a + d \ \text{ and } \ \sigma_{yy} = \beta\sigma_y (K_a / \sigma_y)^{2n/(n+1)} (|x| - a)^{-n/(n+1)} \ \text{ at } \ a + d < |x| < a + d + r_y \qquad (5)$$

where K_a is the applied stress intensity, and β is the factor depended on the elastic and plastic deformation properties. The carbon segregation is found by the crack tip profile and the stress field ahead of the crack tip. The chemical potentials of C and HTSC can be stated following to [15] in various interface zones, namely: I - zone not affected by the stress intensity ($|x| > a+d+r_y$), II - zone of screening dislocations ($a+d < |x| < a+d+r_y$), III - dislocation free zone ahead of the crack tip ($a < |x| < a+d$), IV - arc-shaped crack tip zone ($a-q < |x| < a$) and V - parallel flat crack surface zone ($|x| < a-q$). At equilibrium, the chemical potentials of carbon and superconductor must be the same in the all regions. So, the equilibrium carbon segregation depends on the binding energies and crack tip conditions. The binding energies of C at grain boundaries and crack surfaces $(H_B)_b$ and $(H_B)_s$, respectively, are found by the standard chemical potentials of C and HTSC as

$$(H_B)_b = (\mu_{m0})_C - (\mu_{b0})_C - (\mu_{m0})_{HTSC} + (\mu_{b0})_{HTSC} \ \text{ and } \ (H_B)_s = (\mu_{m0})_C - (\mu_{s0})_C - (\mu_{m0})_{HTSC} + (\mu_{s0})_{HTSC}. \qquad (6)$$

Here and further the subscripts of different parameters indicate the next: m is the matrix, b is the grain boundary, and s is the crack surface. The basic assumption of the model is that the embrittlement occurs as a reduction of the interface energies due to the carbon segregation. Moreover, it is taken into account that slow and fast fractures occur by maintaining the constant chemical potentials and the same carbon concentration between the crack surface and the grain boundary, respectively. Then, from the thermodynamic theory of [16, 17] it can be obtained the variation of the ideal works, expended in slow (γ^s) and fast (γ^f) fracture as

$$\gamma^s = \gamma_0 - RT(2C_V / \Omega_s - C^s_{III} / \Omega_b) \qquad \text{and} \qquad \gamma^f = \gamma_0 - (C^f_{III} / \Omega_b)\Delta\mu \qquad (7)$$

where the equilibrium carbon concentrations at zones III and V have forms

$$C_{III} = \frac{C_m \exp\left\{\left[(H_B)_b + \sigma_d V_h - \frac{\sigma_d^2 V_h}{4G(1+\nu)}\right]/(RT)\right\}}{1 - C_m + C_m \exp\left\{\left[(H_B)_b + \sigma_d V_h - \frac{\sigma_d^2 V_h}{4G(1+\nu)}\right]/(RT)\right\}} \text{ and } C_V = \frac{C_m \exp[(H_B)_s/(RT)]}{1 - C_m + C_m \exp[(H_B)_s/(RT)]} \quad (8)$$

here C_m is the bulk carbon concentration, V_h is the molar volume of carbon, R is the gas constant, $1/\Omega_i$ is the carbon coverage at interfaces, C_{III}^s and C_{III}^f are the critical values of carbon concentration at zone III required, for slow and fast fracture, respectively, γ_0 is the ideal work of intergranular fracture in the absence of carbon, and $\Delta\mu$ is the chemical potential difference between the crack surface and the stressed grain boundary. The equations for constant carbon concentrations also can be found at zones I and IV. At the same time, due to the variable stress distribution (see Eqn. 5) the carbon content at zone II is not constant. The relationship between critical stress intensity required to propagate the crack (for slow, fast or steady state fracture) and the ideal work change due to the carbon segregation is stated by using the local energy balance condition [15]: $-(1-\nu)K_d^2/2G + \gamma^c \le 0$, where K_d is the local stress intensity factor, connected with the dislocation free zone ahead of the crack tip (d) and local stress (σ_d) in this zone by the equation $\pi d = (K_d/\sigma_d)^2$, the superscript c corresponds to definite fracture state. Then the threshold stress intensity, K_{th}^c, is given by [15]

$$K_{th}^c = K_0(\gamma^c/\gamma_0)^{(n+1)/4n}(\delta_{c0}/\delta_c^c)^{(1-n)/4n} \quad (9)$$

where K_0 is the fracture toughness, δ_c^c is the critical crack opening displacement (CCOD) required for various fracture processes (superscript c), and δ_{c0} is the CCOD in the absence of carbon, defined as

$$\delta_{c0} = \frac{[4G(1+\nu)\gamma_0]^{(n+1)/(1-n)}}{[2\pi(1-\nu^2)]^{2n/(1-n)}\beta^{2(n+1)/(1-n)}\sigma_y^2 K_0^{4n/(1-n)}} \quad (10)$$

Steady State Crack Growth

Assume, that the carbon diffusion along stressed boundaries and crack surfaces is the mechanism that controls the intergranular embrittlement and affects the crack growth rate. By this, the bulk diffusion effects are neglected. Under the geometrical and loading conditions of above considered equilibrium crack growth problem, the steady state case indicates the crack growth with constant velocity. Taking into account the five grain boundary and crack surface zones (I-V) the fluxes of carbon in these regions, J_i^j, can be stated as

$$J_i^j = -\frac{D_i C_i^j}{RT}\frac{d\mu_i^j}{d(x \text{ or } s)} \quad (11)$$

where D_i is the diffusivity of carbon, C_i^j is the carbon concentration, i is the subscript indicating b or s, and j is the superscript indicating various interface zones, μ_i^j are the corresponding chemical potentials. The differentiation with respect to s is carried out only at zone IV, by this, s is the variable arc length at the correspondent part of the arc-shaped crack tip. The continuity equation of fluxes is

$$\frac{dC_i^j}{dt} + \frac{dJ_i^j}{d(x \text{ or } s)} = 0 \quad (12)$$

where t is the time. Based on the Eqns. 5, 11 and 12, and also the relationship between the interface energies, γ_i^j, and the amounts of carbon, C_i^j, in the various zones, derived from the Gibbs theory and dilute solute approximation as $\gamma_i^j = \gamma_{i0} - (RT/\Omega_i)C_i^j$, the second-order differential equations, controlling the carbon diffusion in the intergranular cracking regions, can be obtained, analogously to [18]. It is assumed, the steady

state crack growth maintains the equilibrium values at the crack center and at the triple point of grain boundaries ahead of the crack. The interface conditions find that the chemical potentials and fluxes of carbon must be the same at each interface in order to maintain the continuity of the carbon flux. So, it is stated the boundary value problem for solution of which some relationships defined in the equilibrium crack growth are used. The carbon effect is determined by the ideal work of steady state fracture as

$$\gamma^{\bullet} = \gamma_0 - RT(2C_V^{\bullet}/\Omega_s - C_{III}^{\bullet}/\Omega_b) + (C_V^{\bullet}/\Omega_s + C_{III}^{\bullet}/2\Omega_b)\Delta\mu^{\bullet} \tag{13}$$

where $C_V^{\bullet} = (C_s^V)_{x=a-q}$, $C_{III}^{\bullet} = (C_b^{III})_{x=a}$ and $\Delta\mu^{\bullet} = \mu_{b0} - \mu_{s0} + RT\ln(C_{III}^{\bullet}/C_V^{\bullet}) - \sigma_d^{\bullet}V_h + \dfrac{\sigma_d^{\bullet 2}V_h}{4G(1+\nu)}$,

the superscript $\bullet$ indicates the steady state fracture. The boundary value problem can be solved numerically, e.g. by using the Runge-Kutta method. The boundary conditions at the triple points allow to study the effects of grain sizes. Then, the model of the steady state crack growth caused by the carbon segregation can be added to previously developed modeling of the toughening mechanisms, acting into HTSC structures [3-6]. At the same time, the size effects can not be estimated in the cases of the equilibrium slow and fast cracks.

VOID TRANSFORMATIONS DURING SINTERING AND CRITICAL CURRENT

As it has been shown in [19] the critical current in the monofilamentary Bi-2223/Ag tape, at first, increases with annealing time, attains maximum value and then decreases with reaction time. This behavior has been connected by authors with action of competing mechanisms, which initially improve the grain boundary quality and then lower pinning strength. The last has been explained by the lead expelling during sintering. However, during BSCCO/Ag tape processing considerable porosity due to CO_2 release can be observed, in particular leading to bubbles arising and the critical current decrease. For example, 200 ppm of carbon has caused up to 36% porosity in the core of Bi-2212/Ag tapes [12]. In the phenomenological analysis the grain growth and corresponding motion of pores located initially at triple grain junctions are assumed. The complete separation of a pore from a grain boundary occurs after the pore displacement at two-grain interface. It is accompanied by the grain disappearance and coalescence of the triple grain junction pores during the grain growth. The motion of the pore together with grain boundary takes place because of inducing a flux of atoms from leading to trailing surface of the pore. This approach allows to describe different pore motions accompanying grain growth, namely pore drag, shrinkage, coarsening, coalescence and breakaway. Though a grain size observed in the monocore Bi-2223/Ag tapes has remained constant during various durations (from 40 to 240 hours) of annealing [19], nevertheless, the grain size distribution should be different in the various cases. This is supported by considerable lead expelling monotonously increasing with annealing time [19]. But then these additions heterogeneously distributed into material can inhibit only a local grain growth in the Bi-2223 core. Moreover, the phenomenological analysis has shown, that for shrinkage of grain boundary pores and averting of pore separation there are two main conditions: (i) a small grain boundary mobility, and (ii) a large boundary diffusivity. However, simultaneously both these conditions can only be satisfied in the presence of appreciable addition drag, throughout the grain disappearance process. Finally, as it has been shown in the modeling of fracture processes in YBCO the size distributions play more important role to compare with the mean sizes [4]. Hence, a preservation of the grain size value in the different annealing times, generally does not allow to assert an absence of grain growth and microstructural alterations. In discussion of pore breakaway, at first it should be noted, that a pore attached to a grain boundary decreases due to grain boundary diffusion, but when the pore separates from the grain boundary and displaces into grain, one can shrinkage only thanks to much more slow diffusion of crystalline lattice. Further, the steady growth of a pore is possible at the dihedral angles of $\Psi < \pi$, and the pore stability rises with decrease of Ψ. In Bi-2223 core there is a spectrum of dihedral angles, connected with various grain boundary structures which form during processing. This spectrum corresponds to critical size interval of pores, as rule located at the low angle boundaries (those especially are character for Bi-2223/Ag tapes, where effective misalignment angle between grains is equal to approximately 7.5^{o} [19]). Then, the distributions of different diffusivities and grain boundary mobilities exist thanks to heterogeneous distributions of additions. The material and structure property changes which suppress pore separations can

be estimated by comparing the critical pore size with trajectories of pore and grain sizes at the final stage of annealing. The approach developed allows to determine intervals of pore size change for avoidance of pore separation. It is most desirable behavior in annealing when grain boundary mobility, initial pore size (a_0) and boundary diffusivity are very small. In this case a peak size of pore for the process of pore and grain coarsening coincides with initial pore size in precursor sample. Then the pore coarsening excludes during annealing. In other case, it is necessary to consider processes of optimum pore coarsening and averting of pore separation. The phenomenological analysis states that a lower limit for pore separation size, a_c, at all reasonable values of a_0/R (where R is the grain radius) is given by $a_c^2 \approx 2D_s\delta_s\gamma_s\Omega^{1/3}(3-\Psi)/(\sqrt{3}M_b kT\gamma_b)$, where $D_s\delta_s$ is the surface diffusion parameter, Ω is the atomic volume, γ_s and γ_b are the surface and grain boundary energies, respectively, M_b is the grain boundary mobility, k is Boltzmann constant, T is the annealing temperature. By selecting above parameters as following [19, 20]: $\Omega = 2.2*10^{-30}$ m^3, $D_s\delta_s = 2.5*10^{-21}$ m^3/s, $\gamma_s = 2\gamma_b$, $\Psi_{max} = \pi/2$, $T = 1110$K (here some parameters have been taken for Al_2O_3, because of their absence for Bi-2223), we obtain a very high value of $M_b \cong 7000$m/(Ns) even for $a_c = 100$nm. More grain mobility is demanded for less pores separated from grain boundary. Obviously, the size of pores which can separate from grain boundaries during annealing on some orders of value more than coherence length ($\cong$ 1nm) in Bi-2223. Then, these separated pores can not serve as effective pinning centres and because of percolation features they must considerably diminish the critical current. Thus, the lead expelling causes a decrease of critical current in long reaction, but rather due to pore transformations occured during calcination, than thanks to decrease of the pinning efficiency in the grains, assumed in Ref. [19].

So, the solutions obtained in this paper can be used in the finite element formulations by which the stress-strain states and damage parameters during compaction and sintering of the HTSC powders can be predicted.

ACKNOWLEDGEMENTS

This work was supported by the Russian Department of Common and Professional Education (Program of Basic Researches in Physics).

REFERENCES

1. S. Sengupta (1998) *JOM* 50, 19.
2. I. A. Parinov (1992) *Cryogenics* 32, 448.
3. I. A. Parinov and L. V. Parinova (1994) *Supercond. Phys. Chem. Techn.* 7, 79.
4. I. A .Parinov , E. V. Rozhkov and C. E. Vassil'chenko (1997) *IEEE Trans. Appl. Supercond.* 7, 1941.
5. I. A. Parinov , E. V. Rozhkov and C. E. Vassil'chenko (1998) *Adv. Cryog. Eng.* (*Mater.*). 44b, 639.
6. I. A. Parinov and Y. A. Kozinkina (1998) *Adv. Cryog. Eng.* (*Mater.*). 44b, 449.
7. F.-K. Chen (1998) *Appl. Mech. Eng.* 3, 413.
8. H. Tsunakawa and R. Aoki (1982) *Powder Tech.* 33, 249.
9. R. W. Heckel (1961) *Trans. Metal. Soc. AIME* 221, 671.
10. P. A. Vermeer (1998). In: *Physics of Dry Granular Media*, pp. 163-195, Herrmann, H. J., Hovi, J.-P. and Luding, S. (Eds). Kluwer Academic Publishers, Dordrecht.
11. S. Sengupta, V. R. Todt, K. C. Goretta, et al. (1997) *IEEE Trans. Appl. Supercond.* 7, 1727.
12. W. Zhang, M. Polak, A. Polyanskii, et al. (1998) *Adv. Cryog. Eng*. (*Mater*.). 44b, 509.
13. J. W. Hutchinson (1968) *J. Mech. Phys. Solids*. 16, 13.
14. J. R. Rice and G. F. Rosengren (1968) *J. Mech. Phys. Solids*. 16, 1.
15. J. Kameda (1986) *Acta Metall*. 34, 867.
16. M. P. Seah (1976) *Proc. R. Soc. Lond*. A349, 539.
17. J. P. Hirth and J. R. Rice (1980) *Metall. Trans. A*. 11A, 1809.
18. J. Kameda (1986) *Acta Metall*. 34, 883.
19. F. Marti, G. Grasso, J.-C. Grivel and R. Flukiger (1998) *Supercond. Sci. Technol*. 11, 485.
20. J. R. Porter, W. Blumenthal and A. G. Evans (1981) *Acta Metall.* 29, 1899.

DAMAGE, FRACTURE AND FATIGUE FOR THE PIEZOELECTRIC AND FERROELECTRIC MEDIUM

Shou wen YU and Wei Yang
(Tsinghua University, Beijing 100084, P.R.China)

ABSTRACT

Damage and dynamic fracture of the piezoelectric medium is an important branch of the fracture of smart materials and structures. Some new solutions for the damaged medium with micro-crack and micro-void are addressed and several solutions of dynamic fracture, wave scattering of crack weakened piezoelectric-medium under mode III and mode I for the response of electrical-mechanical impact are given**.** Two different boundary conditions of the surface for impermeable and perfect electric contact of crack surface are discussed.

Domain polarization switch near the tip of a flaw plays a critical role on the fracture and fatigue behavior of ferroelectric ceramics under electrical and/or mechanical loading. We will discuss three types of experiments, and propose the pertinent meso-mechanics models based on domain switching to explain the data.

1. DAMAGE ANALYSIS OF PIEZOELECTRIC PROPERTIES

Electromechanical coupling is known to be inherent in piezoelectric materials. They are used in actuators and transducers for a variety of applications..By way of Stroh's formula and the property on the root of multiplicit in piezoelectricity, the logarithmic singularity at a crack tip in homogeneous piezoelectric materials was investigated by Qin and Yu [1].Then a plane problem of a crack terminating at the interface between two piezoelectric solids was studied by using the concept of axial conjugate the technique of singular integral equations [1 , 2]. Further, the singular crack tip behavior for thermoelectroelastic problems was also studied. By application of Fourier transformations and extended Stroh's formula. Considering the above theoretical results, the formulation for estimating effective material parameters developed for thermopiezoelectric solids with microcracks or microvoids of various shapes deduced by Qin,Mai and Yu [3,4].These Models are capable to determinate the effective

properties such as the conductivity,electrelastic modulu, thermal expansion and pyroelectric coefficients. Mori-Tanaka techniques give explicit estimates of the effective thermoelectroelastic moduli. Electromechanical coupling is known to be inherent in piezoelectric materials.

2. TRANSIENT RESPONSE UNDER MECHANICAL_ELECTRICAL IMPACT

mode III case

In applications, piezoelectric materials are often required to resist dynamic loads. The anti-plane problems of a finite length crack and a semi-infinite crack subjected to sudden electromechanical disturbances can be found in the papers of Chen and Yu [5,6,7]. It was shown that the dynamic stress intensity factor(SIF) depends not only on mechanical impact, but also on the electrical impact, piezoelectric constants and dielectric constants. The dynamic stress intensity factor (DSIF) and the dynamic energy release rate (DERR) are shown to depend on the ratio of crack length to strip width and the combination of loading parameters.

Mode I case

For Mode I, the results of transient response are shown in Wang and Yu [10] also depend on the boundary conditions and the loading parameter λ. Compared with Mode III, the boundary conditions tend to couple SIF and EDIF even if the loading is static. DEDIF exhibits a dynamic behavior owing to the more complicated coupling effect. For the crack driving force, the results also show that DERR (instead of DSIF) could shed information on crack extension. The dynamic electric displacement intensity factor (DEDIF) for Mode I exhibits the dynamic effect such that the electromechanical coupling effect tends to weaken the quasi-static approximation for electric fields.

In addition,a problem of propagated Yoffe-crack is solved by Chen and Yu[11],other solutions of propagated Griffith Crack can be found in the paper of Chen,Yu and Karihaloo[12].

3. SCATTERING OF INCIDENT WAVES BY A DEBONDED PIEZOELECTRIC INCLUSION

For the scattering of incident waves by a crack, the dynamic stress intensity factor and electric field intensity factor were given by Wang and Yu in [6] by application of the solutions of singular integral equations. Considered also is the scattering problem of SH waves by a debonded piezoelectric inclusion. Two types of material combinations are treated, namely, epoxy/piezoelectric and piezoelectric/piezoelectric. Near-field exhibits low frequency resonance behavior. Large sub-resonant peaks for the piezoelectric/piezoelectric far-field solution appear frequently in the high frequecy region[13,14].

4. CRACK TIP DOMAIN SWITCHING AND UNCONVENTIONAL DOMAIN PLATE ASSEMBLIES

Ferroelectric ceramics exhibit peculiar behaviors such as fracture and fatigue cracking near defects or electrodes under electric load. Reliability is a major concern that calls for a better understanding of their degradation mechanisms. Though the fracture of ferroelectrics appears as the outcome of the electrical loading, the crack extension itself is driven by stress concentration due to the incompatible switching strain. Recent work in [15] explored switch-toughening of ferroelectric ceramics. The intensive electric field near a crack tip stimulates local domain polarization switching. The switched domains generate incompatible strain under the constraint of un-switched material and consequently alter the stress distribution near the crack. To verify the theory by experiment, the specimens were poled to eliminate previous domain band structures. Cracks are introduced after poling. Lateral electric field was applied to cause field concentration near the crack tip. Domain switching occurs near the crack tip and its microscopy reveals banded structures [16], Fig. 1.

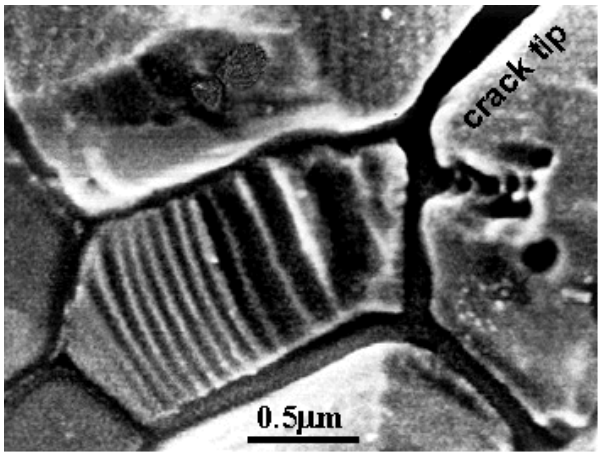

Fig. 1. SEM showing 90^{o} domain switching zone near a crack tip under lateral electric field

The observed band orientation indicates that the domain assembly near the crack tip is unconventional, caused by the highly localized crack tip electric field. An energetic and kinetic framework is proposed to quantify the parameters for the unconventional assembly and to take into account the embryos of domain structures. The elastic mismatch energy for a partially switched ferroelectric grain embedded in a polycrystalline ferroelectric matrix is formulated as a banded Eshelby inclusion. The domain wall energy is derived for unconventional domain structures via arrays of misfit dislocations, given a value of 0.023J/m^2 for Γ_{90}, the 90° domain wall energy. Micromechanics analysis quantifies various characteristics of unconventional domain band structures near a crack tip. The orientation of the domain wall is described by:

$$-\cos\phi\sin\phi x_1 + \cos^2\phi x_2 \pm \sqrt{\frac{1+\cos^4\phi}{2}}x_3 = 0\,. \qquad (1)$$

where $\phi = 70°$ is the measurable inclination angle. The volume fraction of the switched domain is:

$$V_{90} = \frac{C}{Y}\left(\frac{a}{c-a}\right)^2 P_s E_{app}. \qquad (2)$$

The constraining coefficient C is $15(1-\nu^2)/(7-5\nu)$ for a spherical grain constrained in all directions, and $16(1-\nu^2)/3$ for long cylindrical grains unconstrained along the cylinder axis. For the "soft" ferroelectric ceramics used in this test, the relevant physical constants are $Y = 33\text{GPa}$, $\nu = 1/3$, $c/a = 1.013$, $E_c = 1.1\times10^6\,\text{V/m}$ and $P_s = 0.3787\text{C/m}^2$. The calculation gives $V_{90} = 0.249$ for fully constrained spherical grain and $V_{90} = 0.474$ for cylindrical grain unconstrained along its axis. They provide bounds for actual value of V_{90}, as assessed from Fig. 1 as $V_{90} \approx 0.35$. The thickness of the switching plates is given by:

$$t = \sqrt{\frac{\pi^3 \Gamma_{90} D}{1.8\left[\frac{P_s^2}{\varepsilon} + \frac{2(1-\nu)Y}{(1+\nu)(3-4\nu)}\frac{(c-a)^2}{a^2}\frac{1+2\cos^2\phi+5\cos^4\phi}{(1+\cos^2\phi)^2}\right]}}. \qquad (3)$$

Substitution of above data, plus $\varepsilon = 1800\varepsilon_0 = 1.593\times10^{-8}\,\text{F/m}$, into (3) gives a predicted domain wall spacing of $t = 0.2178\mu\text{m}$, that is at the same order but larger than the measurement of Fig. 1.

5. FRACTURE TOUGHNESS OF POLED FERROELECTRICS

Experiments are conducted for SENB specimens of polycrystalline ferroelectrics when poled in longitudinal, vertical and through the thickness directions. Fracture toughness anisotropy is observed: the specimens poled along the longitudinal direction (normal to the crack front) has the least fracture toughness of $0.94\text{MPa}\sqrt{\text{m}}$; the ones poled along the vertical direction (parallel to the crack) has the intermediate fracture toughness of $1.08\text{MPa}\sqrt{\text{m}}$; and the ones poled out-of-plane has the highest fracture toughness of $1.24\text{MPa}\sqrt{\text{m}}$. The wakes of domain switching serve to raise the apparent fracture toughness. A model based on small scale domain switching is described in [17]. For a concrete calculation, we take the material parameters for PZT-5 furnished in the previous section. The toughening effect is given by:

$$K_{\mathrm{IC}} \approx \frac{K_{\mathrm{intrinsic}}}{1-5.277\Omega}. \qquad (4)$$

Under a poling field of $2.5\mathrm{kV/mm}$, the calculations [15] indicated that $\Omega = 0.022$ for samples poled longitudinally and $\Omega = 0.044$ for samples poled along the height. The difference explains the fracture toughness anisotropy reported in the literatures. For the case of anti-plane poling, the dimensionless quantity Ω would be about 0.079 for PZT-5 if the specimen were composed of a mono-domain crystal directed in the thickness direction. The actual domain configuration under an anti-plane poling of strength $2.5\mathrm{kV/mm}$, however, would lead to rather even polarization distribution within a cone from -45 to 45 degrees with respect to the thickness direction. Then the Ω value should be scaled by a factor of $8/\pi^2$, and become 0.064.

An intrinsic fracture toughness of $0.83\mathrm{MPa}\sqrt{\mathrm{m}}$ is taken to fit three sets of experimental data. The present analysis predicts K_{ss} values of $0.939\mathrm{MPa}\sqrt{\mathrm{m}}$, $1.081\mathrm{MPa}\sqrt{\mathrm{m}}$ and $1.253\mathrm{MPa}\sqrt{\mathrm{m}}$ for the specimens poled in the longitudinal, height and thickness directions. The switching induced stress intensity factors for the ferroelectric specimens poled in different directions quantify our experimental data of Fang and Yang [18].

Vickers indents of single crystal ferroelectrics undergone in-plane or anti-plane poling are conducted, the theory of domain switching is able to explain the intrigue cracking patterns under different directions of poling, Fig. 2.

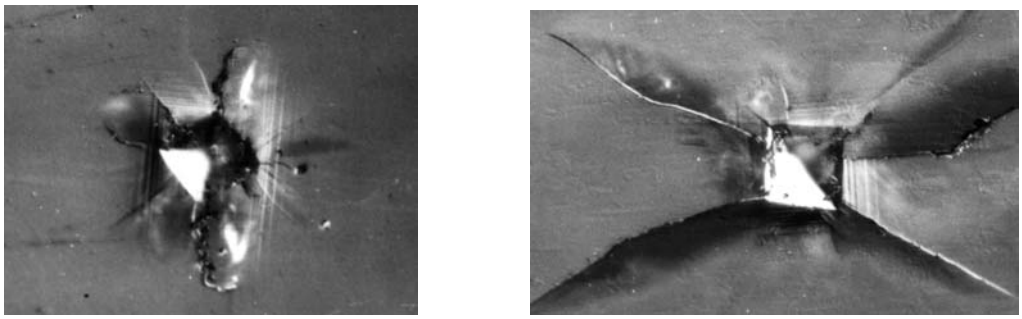

Fig. 2 Vickers indents for single crystal PLZT after anti-plane and vertical poling

6. FATIGUE CRACK GROWTH UNDER ALTERNATING ELECTRIC FIELD

The previous work by Cao and Evans reported fatigue crack growth in ferroelectrics by an alternate field whose amplitude is beyond the coercive value. By applying an alternate field with rectangular waveform, we observed [19] substantial fatigue crack growth even when the field amplitude is below the coercive field. Small scale switching model was proposed to link the fatigue crack growth to the unique domain switching sequence [20]. Our recent experiments indicate the important influence on the crack growth rates by the waveforms of the alternating field. For example, by changing the rectangular waveform to the sinusoidal waveform, the fatigue crack growth rate will

reduce about two orders of magnitude. This finding may lead to many possibilities to suppress the fatigue growth rates by modulating the field wave patterns. The previous model [20] is modified to accommodate the case of arbitrary waveforms. Its prediction, without any fitting parameters, is compared with the electric fatigue cracking data.

ACKNOWLEDGEMENTS

This project supported by National Natural Science Foundation of China (19891100(3)) and Tsinghua Fundamental Research Foundation.

REFERENCES

[1] Yu S.W and Qin Q.H.,(1996) , *Theoretical and Applied Fracture Mechanics*, Vol.25, 263.

[2] Yu S.W. and Qin,Q.H.1996, *Theoretical and Applied Fracture Mechanics*, 1996, Vol.25, 279.

[3] Qin Q.H..Mai,Y.W. and Yu S.W.,1998 *Int. J. of Fracture*, Vol. 91, 359.

[4] Qin ,Q.H.and Yu S.W.,(1998) *Int. J. Solids and Structures*, Vol. 35, 5085.

[5] Chen ,Z.T.and Yu S.W.(1997), *Int. J. Fracture,* 1997, Vol.85, L3.

[6] Chen ,Z.T.and Yu S.W**.,**(1997)**,** *Int. J. Fracture,* 1997, Vol.86, L9.

[7] Chen,Z.T. Yu S.W. and Karihaloo.B.L.,,(1997)*Int. J. Fracture,* 1997, Vol.86.L9.

[8] Yu S.W. and Chen,Z.T.,(1998) *Fatigure & Fracture of Materials & Structures,*Vol.21, 1381.

[9] Wang X.Y. and Yu S.W.,(1999) *Int. J. Solids and Structures* ,vol37,5795.

[10] Wang Xuyue and Yu Shouwen,(2001) *Mechanics of Materials*, Vol.33,11.

[11] .Chen,Z.T. and Yu S.W.**,**(1997) *Int. J. Fracture,* Vol.84, L41.

[12] Chen ,Z.T.Yu S.W. Karihaloo,B.L.,(1999) *Int.J.Fractuer,* Vol.91,197.

[13]Yu,S.W.andWangX.Y.,(2000),In*Mesomechanic2000*,Vol.II.,pp975-981.G..C.Sih,et.al.,(Eds) Tsinghua Univ. Press.Beijing.

[14] Wang,X.Y. and Yu S W,(1999), *Int.J.Fracture*,Vol.100,L35.

[15] Yang,W. and Zhu,T.,(1998) , *J. Mech. Phys. Solids* 46, 291.

[16] Fang,F., Yang,W., and Zhu,T.,(1999) *Journal of Materials Research*, 14 .

[17] Yang W, Fang F, Tao M (2001). *Int. J. Solids & Structs.*, (in press).

[18] Fang F, Yang W.(2000) *Materials Letters,* 46: 131.

[19] Zhu T, Fang F, Yang W.(1999), *Journal of Materials Science Letters,* 18: 1025.

[20] Zhu T, Yang W. (1999),. *J. Mech. Phys. Solids,* 47: 87.

ORAL REFERENCE:ICF100868OR

DAMAGE IN HIGH TEMPERATURE COMPONENTS AND THE LIFE ASSESSMENT TECHNOLOGIES

K. Fujiyama[1] and T. Fujiwara[2]

[1]Power and Industrial Systems R&D Center, Toshiba Corporation,
Tsurumi-ku, Yokohama 230-0045, Japan
[2]Keihin Product Operations, Toshiba Corporation, Tsurumi-ku, Yokohama 230-0045, Japan

ABSTRACT

Damage modes of steam turbine and gas turbine components are summarized and life assessment methods based on damage measurement are presented. For steam turbine high temperature components, typical damage modes are creep, thermomechanical fatigue(TMF) and creep-fatigue, which are enhanced by material degradation. For gas turbine high temperature components, the same damage modes are observed, coupled with severe oxidation, corrosion, erosion, wear and microstructural change than steam turbine. The damage-based life assessment approaches are 1)Trend analysis, 2)Cumulative damage rule, and 3)Damage parameter and simulation analysis. Trend analysis correlates damage data with operation history to obtain damage trend curves. Cumulative damage rule is modified to reflect the effect of material degradation in the material life prediction. Damage parameters are selected to be consistent with physical quantities, and are correlated with imposed cycle/time as well as the stress/strain. Damage simulation analysis is used for validating the damage model and predicting the future trend. Those approaches will contribute to the condition-based life management or risk-based maintenance because the plant specific and probabilistic assessment can be accomplished.

KEYWORDS

Damage, Degradation, Steam turbine, Gas turbine, Creep, Fatigue, Life assessment

INTRODUCTION

As the number of fossil power plants in long-term use increases, demand for life extension and cost-effective maintenance is becoming greater. Accurate life assessment methods can provide a basis of realizing rational maintenance and life management. Thus, various kinds of life assessment methods have been proposed[1], which are divided into three categories, i.e. analytical methods, non-destructive

methods and destructive methods. A comprehensive understanding of damage modes in actual components is indispensable for establishing an effective life assessment approach. Therefore, damage modes of steam turbines (including pipes) and gas turbines are summarized as the typical examples. Then, life assessment methods are presented in relation to a way of quantitative analysis of damage and degradation. They are, 1)Trend analysis, 2)Cumulative damage rule, 3)Damage parameter and simulation analysis. The importance of statistical analyses of actual damage data is demonstrated in regard to the on-conditioning life management and risk-based maintenance.

DAMAGE MODES IN STEAM TURBINE COMPONENTS

Figure 1 shows typical modes of damage and degradation in steam turbine components[2]. Steam turbine materials often show softening due to both creep/fatigue damage and thermal aging. Softening reduces material tensile, creep and fatigue strength. For high-pressure (HP) and intermediate-pressure (IP) turbine rotors, creep damage is accumulated in the bore and the dovetail hook. In the dovetail hook contacted area, creep softening reduces the fatigue strength, which leads to the high cycle or fretting fatigue under vibratory stress. Another degradation mode is embrittlement that enhances crack sensitivity. In the strain concentrations of casings and valves, cracks initiate due to TMF in the cyclic operation and then tend to grow due to creep under internal pressure. In this case, crack initiation and growth are assisted by softening and by embrittlement. For steam pipe weldments, creep damage is non-uniformly distributed depending on the microstructural inhomogeneity. In some cases, TMF cracking is experienced due to water induction from drain into the steam flow[3]. For low pressure turbine rotors, corrosion fatigue or SCC under centrifugal and vibratory stress are typical damage modes.

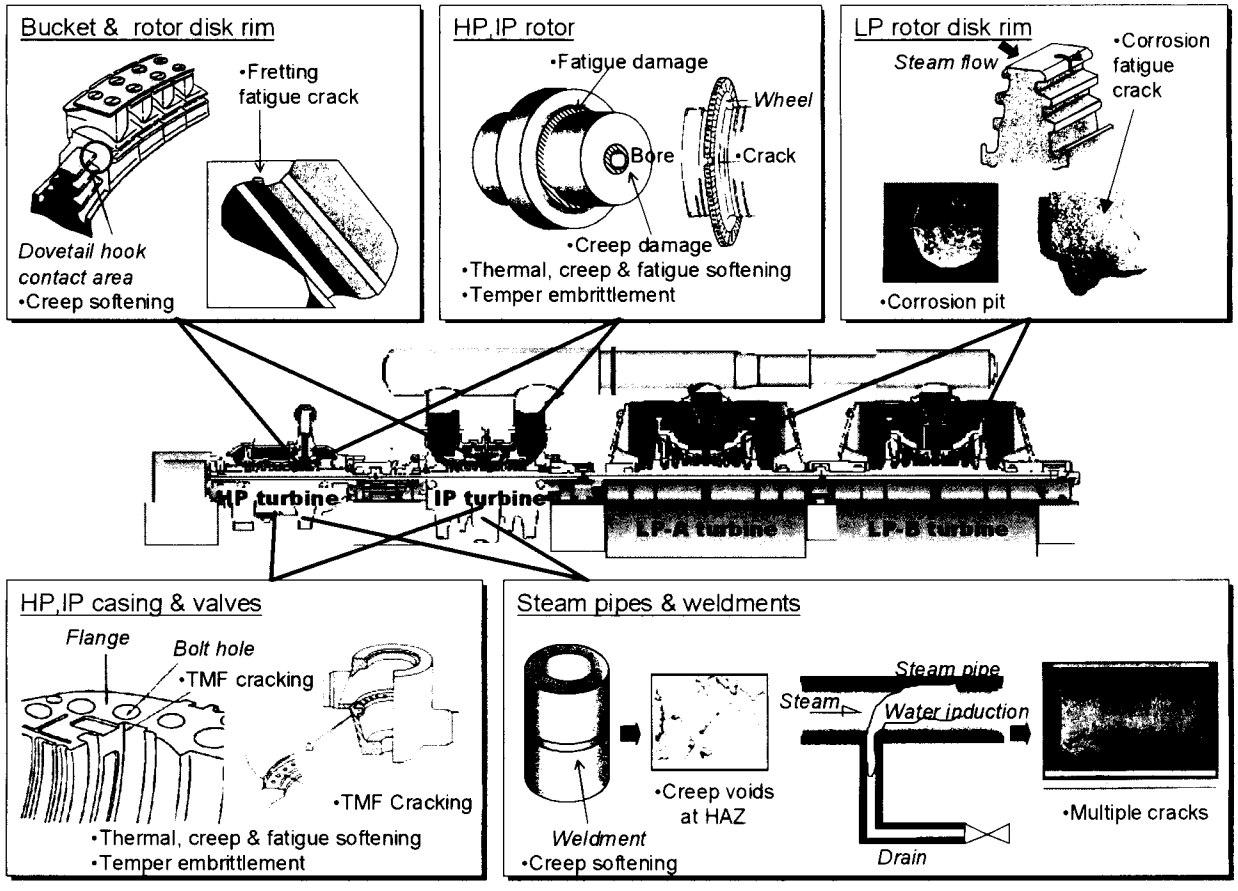

Figure 1: Damage modes of steam turbines and steam pipes

DAMAGE MODES IN GAS TURBINE COMPONENTS

Figure 2 shows the modes of damage and degradation in gas turbine components[4]. Hot gas flow may cause oxidation, corrosion and erosion depending on the gas composition and temperature. TMF is introduced during cyclic operation under severe thermal gradient due to internal cooling. Coating layer suffers from oxidation, hot corrosion, erosion, TMF cracking, spalling and degraded phase formation. If the oxides and cracks develop in the coating layer, they will grow into the substrate. For stage 1 nozzles, TMF cracking is the primary damage mode. Material degradation causes the reduction of ductility and toughness, but they can be refurbished by heat treatment. For stage 2 and 3 nozzles, creep deflection is significant. For combustion liners, TMF cracks are observed in the welded portion and sometimes grow by vibratory stress. Wear occurs in the support parts due to vibration. For transition pieces, creep deformation and TBC spalling also occur.

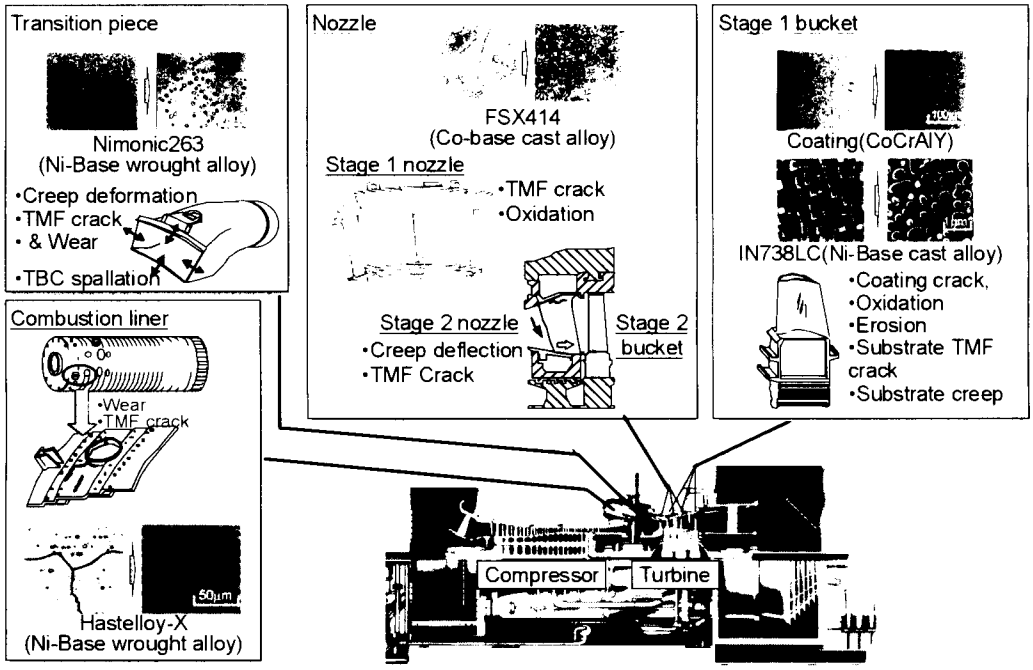

Figure 2: Damage modes in gas turbine components (1,100°C-class)

LIFE ASSESSMENT METHODS

To utilize the damage information of actual components for life assessment, trend analysis, cumulative damage rules, damage parameter and simulation analysis are implemented.

Trend Analysis

Trend analysis[4] correlates the measured damage quantities with operation history. Figure 3 shows the trend analysis flow for gas turbine nozzle vane cracks. These are the followed up data of individual cracks for periodic inspections. The maximum crack length a_{max} seems to obey the LCF crack growth law and the subsequent retardation is attributed to thermal stress relief by the cracks. On the other hand, the total crack length Σa increases monotonically with cycles. Another approach is the statistical trend analysis. As the crack length data of nozzles obey log-normal distribution, the statistics (mean, variance and number) are obtained and expressed as the functions of cycles. The maintenance management is conducted using a_{max} and Σa as the measure of structural integrity and repair amount, respectively.

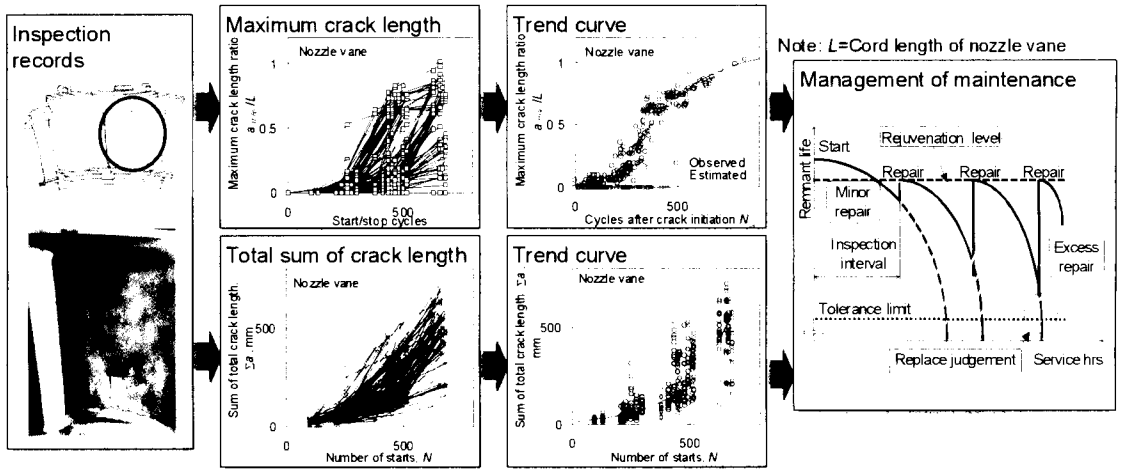

Figure 3: Trend analysis of TMF cracks for gas turbine nozzles

Cumulative Damage Rule

The conventional cumulative damage rule is described as follows.

$$\Phi_f = \sum_i \frac{n_i}{N_{fi}}, \quad \Phi_c = \int \frac{dt}{t_r}, \quad \Phi_f + \Phi_c = D_c \tag{1}$$

where, Φ_f: fatigue damage, Φ_c: creep damage, n_i: number of start-stop cycles of the operation mode i, N_{fi}: cycles to failure in the operation mode i, t_r: time to creep rupture, t: operation time, D_c: critical value of total damage. For long term operation, softening due to either thermal aging or damage may occur, which affects material life itself[2]. Figure 4 shows the modified cumulative damage rule based on hardness measurement. If the hardness HV_a is measured at the thermal aged portion, material creep life t_{ra} is estimated by HV_a. Therefore, creep damage is calculated as follows.

$$\Phi_c = \int \frac{dt}{t_{ra}(\sigma, T, HV_a(t,T))} \tag{2}$$

If the hardness HV_D is measured at creep damaged portion, HV_D represents creep damage effect and is correlated with the remnant creep life t_{rD}[5]. Therefore, the cumulative damage is calculated as follows.

$$\Phi_c = \frac{t}{t + t_{rD}(\sigma, T, HV_D(t,\sigma,T))} \tag{3}$$

Those definitions of damage should not be mixed up with one another.

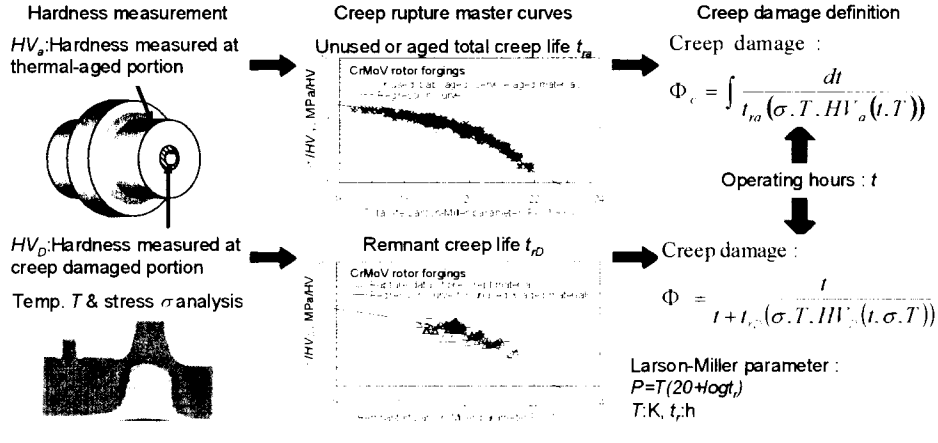

Figure 4: Cumulative damage evaluation procedures based on two cases of hardness measurement

Damage Parameter and Simulation Analysis

Parameters converted from measured physical damage are correlated with stress, strain, temperature, imposed cycles and time. The simulation analysis is used to verify or predict the damage evolution process obtained by damage parameter equations and trend analysis based on the stochastic damage model.

Fatigue damage

Figure 5 shows damage parameter evaluation for TMF cracks of gas turbine nozzle vane[4] and that of stem pipe with water injection[3], as well as the related damage simulation analysis[4]. The damage parameters selected are the maximum crack length a_{max} and the crack length density l. The damage equation for a_{max} is expressed by the following equation.

$$a_{\max} = E\exp(F\frac{N}{N_f}) \tag{4}$$

where, N is imposed cycles, N_f is cycles to failure (usually defined for 25% peak stress drop from steady-state value for LCF or TMF testing) and E,F are constants.

As l is closely related to the cumulative probability of multiple crack initiation, the damage equation is expressed by the following equation using the form of standard normal distribution function $\Phi()$.

$$\frac{l}{l_c} = \Phi\left[\left\{\ln\left(\frac{N}{N_f}\right) - \mu_{Le}\right\}\Big/\sigma_{le}\right], \qquad \Phi(u) = \frac{1}{\sqrt{2\pi}}\int_{-\infty}^{u}\exp\left(-\frac{u^2}{2}\right)du \tag{5}$$

where, l_c, μ_{Le}, σ_{Le} are constants determined through the regression of experimental data. From Eqn. 4 and Eqn. 5, If we know a_{max} and l, N and N_f can be determined. The plastic strainrange $\Delta\varepsilon_p$ can be calculated from N_f by the Coffin-Manson law[1]. Simulation analysis is applied to nozzle vane cracks. Discrete mesostructure model is used for assigning material resistance distribution for the superalloy. Crack initiation, growth and coalescence process is calculated by Monte-Carlo simulation, using stochastic damage model derived from experimental observation. The maximum crack growth trend is stepwise due to crack coalescence, but is similar to trend analysis and the damage parameter approach.

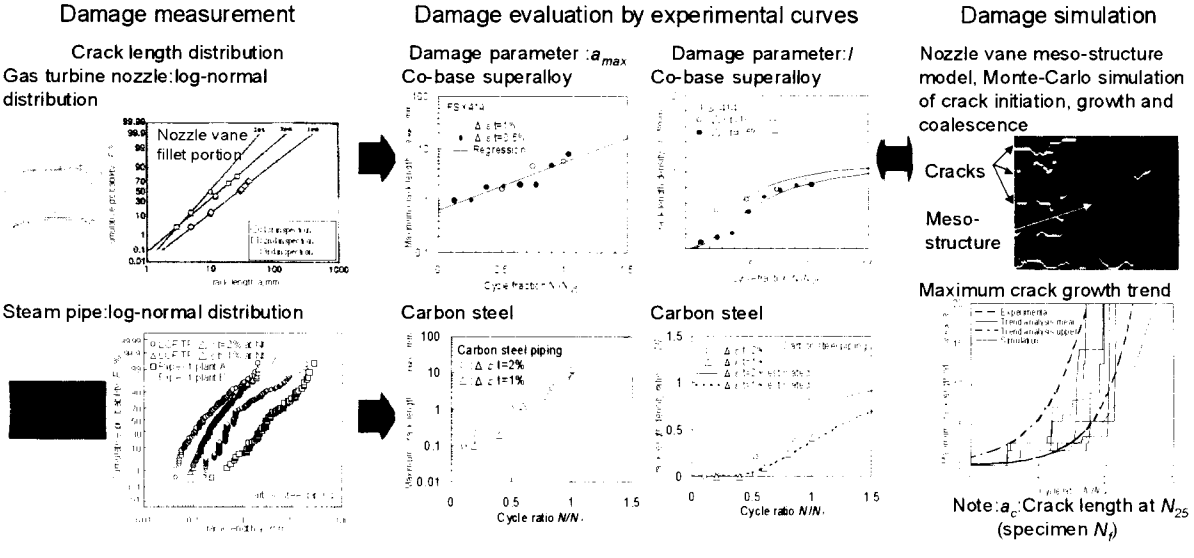

Figure 5: Damage evaluation by experimental curves and simulation analysis

Creep damage

For low alloy steels, creep damage is characterized by creep cavity formation and hardness change. Figure 6 shows the damage assessment methods for the weldment of low alloy steel piping[5]. The creep cavity A-parameter method[1] and the hardness method are applied. Softening curves have been provided for the weld portion from laboratory creep interruption testing data based on the carbide coarsening mechanism or the dislocation substructure recovery mechanism. The hardness method can be applied to the entire portion of weldments. Creep cavities are observed by scanning electron microscope for the replicas taken from actual components. Creep cavity formation depends on the material microstructure, the chemical composition (carbon contents) and the stress redistribution. These two approaches compensate each other for the creep life assessment of long term used components.

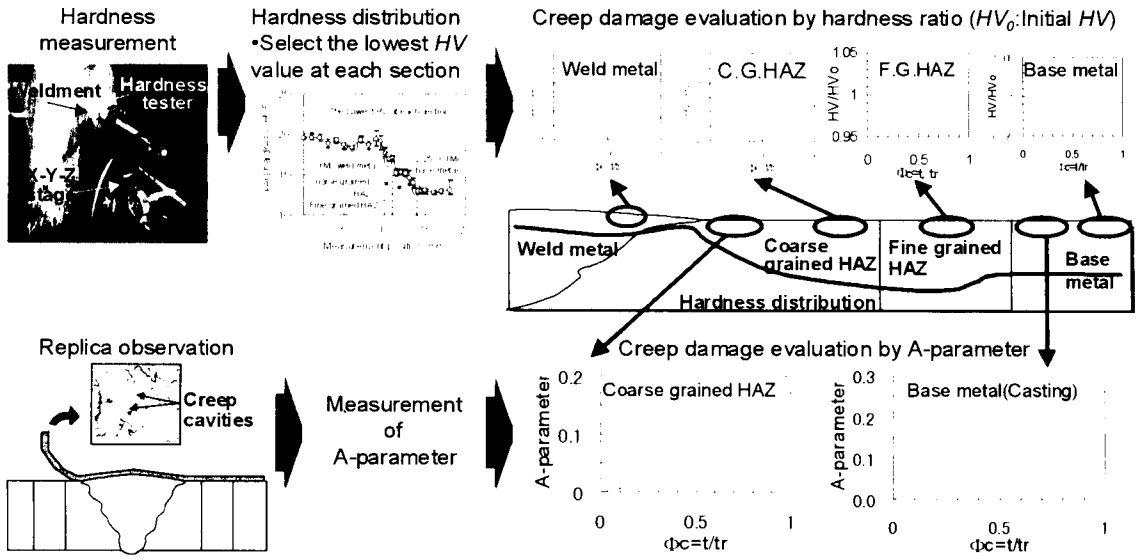

Figure 6: Creep damage assessment of weld portion of steam pipes

CONCLUDING REMARKS

It is demonstrated that the comprehensive knowledge of damage modes in actual components is effective for establishing practical life assessment methods. As the life assessment approaches presented here are based on the statistical treatment of damage data, they can be applied to probabilistic life prediction. The damage simulation analysis is a useful tool for investigating and modeling the stochastic nature of damage. Those approaches can contribute to life management and risk-based maintenance.

References

1. Viswanathan, R. (1989). *Damage Mechanisms and Life Assessment of High Temperature Components*. ASM International, Materials Park, OH.
2. Fujiyama, K., Kimura, K., Muramatsu, M., Kashiwaya, H., Tsunoda, E. and Ayano, S. (1988). *Int. Conf. Life Assessment and Extension II*, pp. 20-30, The Hague.
3. Nakatani, Y., Fujiyama, K., Ahiko, N. and Ito, Y. (2001). *Fourth Int. Congress on Thermal Stresses THERMAL STRESSES 2001*, pp. 375-378, Osaka.
4. Honma, T., (1999). *Proc. Int. Gas Turbine Congress*, pp.5-13, Kobe.
5. Fujiyama, K., Saito, K., Harada, S., Ahiko, N. and Itoh, Y. (2001). *Proc. 7th Int. Conf. on Creep and Fatigue at Elevated Temperatures*, pp.69-74, Tsukuba.

ORAL/POSTER REFERENCE: ICF100495OR

DAMAGE INITIATION AND EVOLUTION IN A HETEROGENEOUS MATERIAL

C. Liu[1], M.G. Stout[1] and B.W. Asay[2]

[1]MST-8, Materials Science and Technology Division
[2]DX-2, Dynamic Experimentation Division
Los Alamos National Laboratory
Los Alamos, NM 87545, USA

ABSTRACT

Heterogeneity and heterogeneity-induced damage in a high explosive simulant material are studied. In contrary to common practice, where it is assumed that the uniaxial compression sample is undergoing homogeneous deformation, we find that the strain field within the sample at each loading level is a distribution due to the heterogeneous nature of the material. As deformation proceeds, this distribution evolves, which indicates the initiation and evolution of damage. It is also shown that damage initiation occurs well before the applied load reaches its maximum value. The driving force that triggers the initiation of damage is identified and estimated based on a theory that explicitly treats the high explosive as a heterogeneous composite.

KEYWORDS

Heterogeneity, heterogeneity-induced damage, damage initiation, and damage evolution.

INTRODUCTION

High explosive (HE) materials are heterogeneous at the microscopic level and this heterogeneity plays a vital role in attaining the desired structural response in such areas as strength, stiffness, constitutive response, and fracture resistance. Consequently, the ability of providing accurate quantitative estimates of the constitutive behavior and flaw tolerance of HE materials is a direct concern for safety. HE materials, such as the PBX 9501, are composed by two phases: the energetic crystal and the polymeric binder. Under uniaxial loading, we found that the responses of the PBX 9501 high explosive in tension and in compression are quite different. In tension, the PBX 9501 specimen fails at relatively low strain level and failure occurs in a very narrow band normal to the loading axis. This behavior is similar to that of typical brittle solids. In compression, failure happens at relatively high strain level. Failure is also accompanied by massive internal cracking and the majority of the crack is parallel to the loading axis. The Poisson's ratio, as usually defined, is found to be an increasing function of the total axial deformation before the load reaches maximum value. Based on the conventional uniaxial stress test, if the PBX 9501 is viewed as homogeneous, there will be no driving force to generate the cracks observed in experiments. This concludes that the conventional way of conducting and interpreting uniaxial stress experiment cannot provide any explanation of what we see in the experiment. It is the objective of this investigation to observe the initiation and evolution of damage in a

high explosive simulant material under uniaxial compression, and to identify the driving forces that trigger the damaging process.

MATERIAL DESCRIPTION AND TESTING TECHNIQUE

A high explosive simulant material, referred to as PBS 9501, was used in the present investigation. The PBS 9501 simulant material is composed of 94wt% C&H granulated sugar and 6wt% polymeric binder, which in turn, is composed by 50% estane and 50% nitroplasticizer. The reason of choosing such a material is that PBS 9501 can simulate, at the macroscopic level, the mechanical behavior of the PBX 9501 high explosive, which is composed by the HMX energetic crystal and a polymeric binder, as a function of strain rate and temperature. Also, the sugar crystal and the HMX crystal are both monoclinic, so they are similar microscopically as well. Both the PBS 9501 and the PBX 9501 have the same polymeric binder system.

When a heterogeneous material is subjected to homogeneous boundary condition, below certain length scale, the deformation field will become non-uniform due to the heterogeneous nature of the material. Hence, to experimentally study the heterogeneity and heterogeneity-induced damage, one would need a technique that is able to monitor the full-field deformation throughout the entire sample. We developed an optical technique called dot-matrix deposition & mapping. In principle, this technique is very similar to the image correlation method [1], but avoids the ambiguity regarding the reflectivity of the specimen surface during the deformation process, especially, when damage is involved. Before experiment, a matrix of dot pattern is deposited on the surface of the specimen and the pattern is photographed at different moments during deformation. One of such photographs is shown in Figure 1(a). This image is then processed to

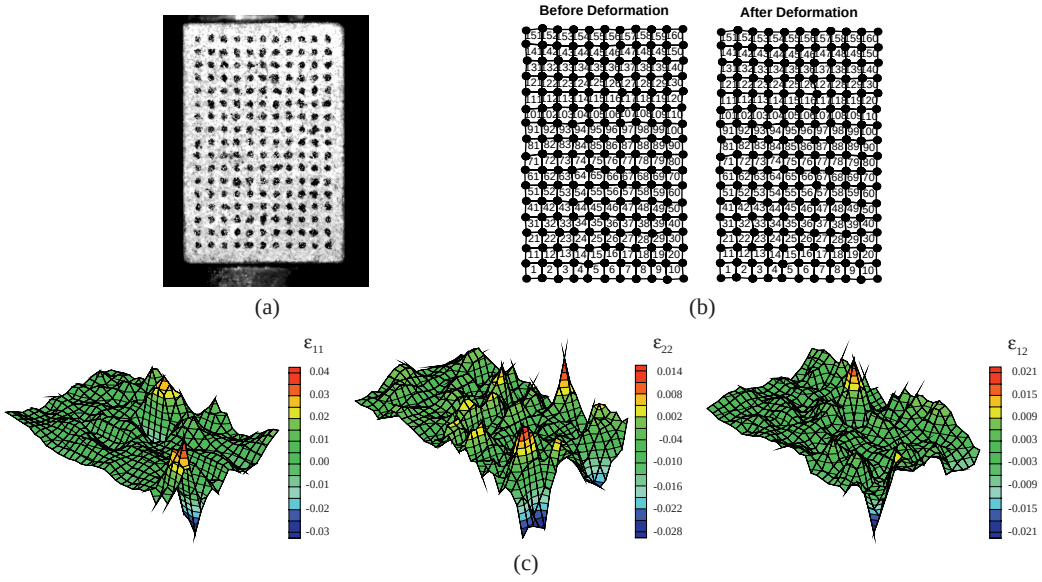

Figure 1: Dot-matrix deposition & mapping technique.

identify the exact location of the center of each dot. Based on the coordinates of each dot, an element mesh, as shown in Figure 1(b), for the moments of before and after deformation can be constructed. By assuming that each element is undergoing homogeneous deformation, all three in-plane strain components can be calculated using the coordinates of those four nodes. The field plot for each strain component that corresponds to the deforming state in Figure 1(b) is shown in Figure 1(c). The formulation for obtaining the strain components of each element is valid for finite deformation. Therefore, the technique we developed in this study is able to deal with local large deformation associated with damage.

EXPERIMENTAL OBSERVATIONS

The specimen we studied has a rectangular shape with the width and the thickness of 12.7mm. The height of the sample is 19.0mm. The specimen was loaded in compression at an equivalent strain rate of

$1.7\times10^{-4}\,\mathrm{sec}^{-1}$. The size of the element as shown in Figure 1(b) is about $1\mathrm{mm}\times1\mathrm{mm}$. Based on the technique described in the previous section, in-plane strain components of each element are calculated at each loading level. In the following we only present the result for the lateral strain component ε_{11}.

In Figure 2, the lateral strain component ε_{11}, at two moments during the early stage of loading is shown. One plot is a scatter plot showing the strain magnitude of each element and the other is a distribution plot showing the percentage of elements that experience certain strain. If the material is indeed homogeneous,

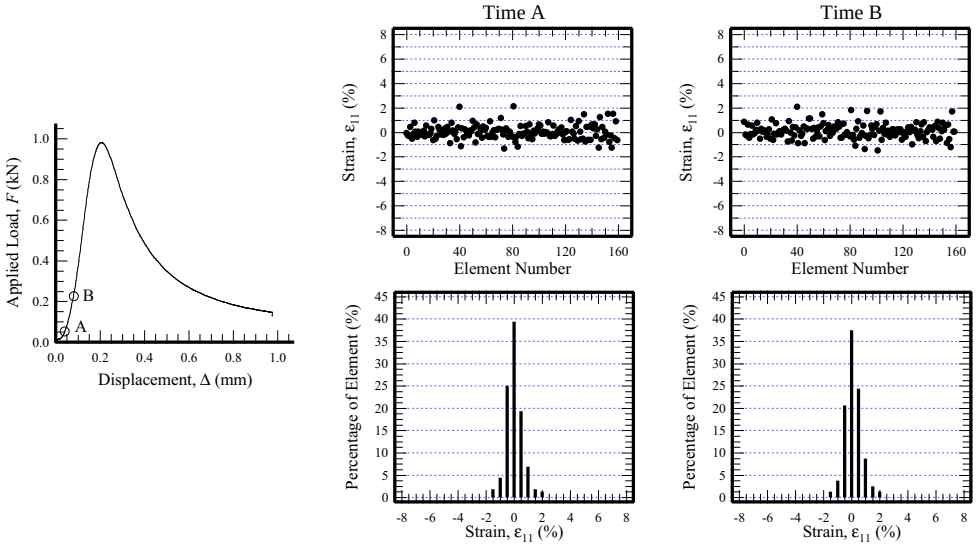

Figure 2: Strain distribution showing heterogeneous deformation during early stage of loading.

every element should deform exactly the same amount at the same time. Therefore, for a homogeneous material, all the data points in the scatter plot should fall on a horizontal line, and in the distribution plot we will only have a vertical line. However, in Figure 2, we can see that the deformation of the elements is scattered around a mean value. Also for the early stage of loading the overall shape of the distribution plot remains the same; only the mean value shifts responding to the overall deformation the entire specimen being subjected to. The shape of strain distribution, therefore, indicates the heterogeneous nature of the material. Note that the size of the element is about $1\mathrm{mm}\times1\mathrm{mm}$, which is much larger than the average diameter of the crystals.

In Figure 3, we study two consecutive moments along the loading curve. At time C, the compressive load is

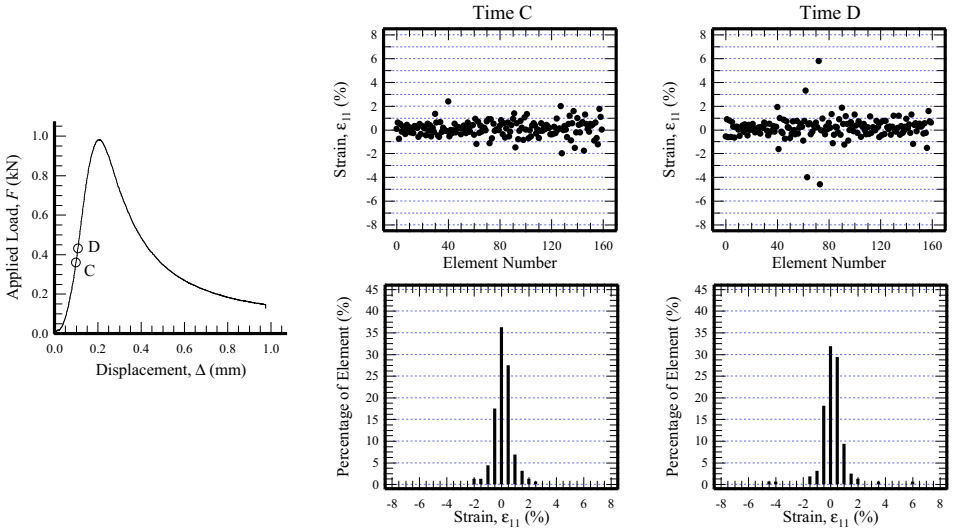

Figure 3: Indication of damage initiation in the specimen under compression.

360N and at time D, the compressive load increases to 432N. During such a small increment of loading, the distribution of the lateral strain component ε_{11} exhibits a drastic change that indicates the initiation of

damage within the test specimen. At time C, the shape of the distribution of ε_{11} is the same as those shown in Figure 2. At time D, several elements experience a much larger strain compared to the rest of elements. Two of these elements experience larger tensile strain and other two experience larger compressive strain. Simple analysis showed that the cracking of a material element under compression causes additional strain increment in the lateral direction. Therefore, those two elements that exhibit larger tensile strain must also experience cracking within the elements. At time D, where damage initiation is detected, the compressive stress $\sigma = 0.44\sigma_C$ where σ_C is the compressive strength of the material. Also, note that the two elements that experience a larger compressive strain are located next to the ones that exhibit larger tensile strain. When internal cracking occurs in an element, it will tend to expand more in the lateral direction. As a result, the element next to the cracked element has to be compressed in order to keep the overall deformation compatible.

Another observation can be made based on the results shown in Figure 3. At time D, if we ignore the elements that exhibit larger strains compared to other elements, we find that the distribution of the strain component ε_{11} is similar to that at previous moments. This suggests that the damage is confined within the individual element. On the other hand, if the region of damage extends over several elements, we will see a change in the overall shape of the strain distributions. This is demonstrated in Figure 4 where strain

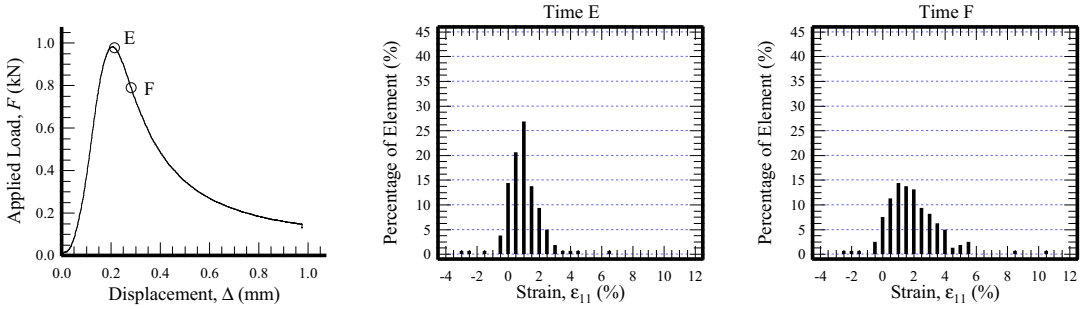

Figure 4: Indication of damage accumulation and evolution in the specimen under compression.

distributions at times after damage initiation. As a result, the broadness of the strain distribution provides a mean for monitoring damage evolution in the specimen.

DISCUSSIONS

Many theoretical investigations were conducted to explain the appearance of the splitting cracks in compression of brittle solids, e.g., [2]. These theories require pre-existing cracks within the sample. Although in most of brittle materials, microcracks do exist prior to the loading due to processing, the accurate description of the distribution of cracks proves to be very difficult if not impossible. Meanwhile, most of these micromechanical analyses treat the matrix material as homogeneous. From the experimental observations shown in previous section, we see that the strain distribution clearly indicates the heterogeneous nature of the material prior to the initiation of damage. It would be more appropriate of applying a theory, which treats the simulant material as a heterogeneous composite, to study the initiation of damage in compression.

Ortiz [3] proposed a general framework for the constitutive modeling of concrete starting from the first principles of mechanics based on the theory of interacting continua or mixture theory, and a rate-independent theory of damage. An important feature of this framework is that the concrete is treated explicitly as a mixture comprising two distinct phases: mortar and aggregate. A conclusion of this framework is that the externally applied stresses distribute unequally between the two phases. The average stresses acting in mortar and aggregate must jointly equilibrate the applied loads but may be vastly different from each other. Here we will adopt a very simple version of this mixture theory to show that purely compressive uniaxial load will induce tensile stress normal to the loading axis within the crystal, and the tensile stress is high enough to initiate damage before the overall compressive load reaches its peak value.

Consider a material element where the volumetric fractions of the crystal and the binder are f_1 and f_2, respectively. Let σ_1 and σ_2 be the average or phase stresses acting in crystal and binder, and σ the applied stress. The requirement that σ_1 and σ_2 jointly equilibrate σ can be expressed as

$$\sigma = f_1\sigma_1 + f_2\sigma_2 . \tag{1}$$

In order to make it more apparent about the fact that lateral tensile stress can be induced when HE material is subjected to uniaxial compression we consider a "virgin" HE specimen and assume that both crystal and binder are isotropic and elastic. As a result, the phase stresses σ_1 and σ_2 can be related to the applied stress σ through

$$(\sigma_\alpha)_{ij} = \frac{1}{3}\left(\frac{k_\alpha}{k} - \frac{\mu_\alpha}{\mu}\right)\sigma_{mm}\delta_{ij} + \frac{\mu_\alpha}{\mu}\sigma_{ij}, \qquad \alpha = 1,2, \tag{2}$$

where k_α and μ_α are the bulk and shear moduli of each constituent and k and μ are the bulk and shear moduli for the composite. Under uniaxial compression, where external stress is characterized by $\sigma_{ij} = -\sigma\delta_{i1}\delta_{j1}$ and $\sigma > 0$ is the magnitude of the applied compressive stress, the phase stress within crystal σ_1 has the following form

$$(\sigma_1)_{ij} = \begin{bmatrix} \sigma_{\mathrm{L}} & 0 & 0 \\ 0 & \sigma_{\mathrm{T}} & 0 \\ 0 & 0 & \sigma_{\mathrm{T}} \end{bmatrix}, \qquad \sigma_{\mathrm{L}} = -\frac{1}{3}\left(\frac{k_1}{k} + \frac{2\mu_1}{\mu}\right)\sigma, \qquad \sigma_{\mathrm{T}} = \frac{1}{3}\left(\frac{\mu_1}{\mu} - \frac{k_1}{k}\right)\sigma. \tag{3}$$

Experimental measurements have shown that the binder material is almost incompressible, i.e., its Poisson's ratio $\nu_2 \approx 0.5$. Then, one can show that

$$\frac{\sigma_{\mathrm{T}}}{\sigma} = \frac{1}{3f_1}\left\{1 + \frac{2(1+\nu_1)}{3}\cdot\frac{f_2E_2}{f_1E_1}\right\}^{-1}, \tag{4}$$

where ν_1 is the Poisson's ratio of the crystal, E_1 and E_2 are the Young's modulus of crystal and binder, respectively. For the simulant material PBS 9501, $f_1 \approx 0.96$ and the Poisson's ratio of crystal $\nu_1 \approx 0.2$. Meanwhile, within a wide strain-rate regime, the ratio of E_2/E_1 is in the order of 10^{-3}. As a result, the second term in the braces of the above expression is negligible that leads to $\sigma_{\mathrm{T}}/\sigma \approx 1/3f_1 = 0.35$. One can also show that the lateral stress within the binder is almost zero.

In a typical uniaxial compression test of the PBS 9501, the apparent stress-strain curve is shown as the solid line in Figure 5. The applied uniaxial stress is a monotonic increasing function of the axial strain before reaching the maximum value. After this point, stress decreases gradually as the deformation continues to proceed. If we take a crystal element from the compressive sample, the phase stress within the crystal is characterized by σ_{L}, compressive and parallel to the externally applied load and by σ_{T}, tensile and normal to the loading axis. The variation of the lateral tensile stress σ_{T} is shown as dash-dotted line in the figure. Experimental measurement also showed that the tensile strength of the PBS 9501 material is only about 15% of its compressive strength. If we assume that in tension, failure is mainly due to crystal cracking, we may conclude that microcracks start to develop in crystals when $\sigma_{\mathrm{T}} \approx 0.15\sigma_{\mathrm{C}}$. The onset strain for microcrack initiation within the compressive sample is indicated by the vertical dash-line in the figure. Therefore, damage initiation would occur when the compressive stress $\sigma \approx 0.42\sigma_{\mathrm{C}}$. This prediction matches the experimental observation shown in Figure 3 very well.

Immediately after damage initiation, microcracks within the sample are so few that they do not interact with each other. The enlargement of those cracks remains stable due to stress redistribution between crystal and binder, and the applied stress keeps increasing as deformation proceeds. However, when the size or the

density of microcracks becomes large enough that the stress redistribution cannot ensure stable crack growth any more, unstable crack propagation follows and this is the direct cause of the characteristic descending branch of the uniaxial compressive stress-strain curve in Figure 5.

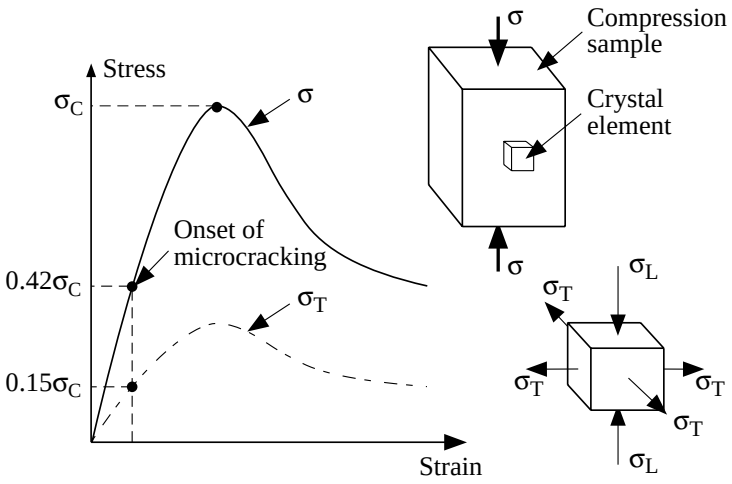

Figure 5: Driving force for triggering damage initiation in compression.

In this study, damage initiation and evolution in a high explosive simulant material are observed experimentally. Such damage is the direct consequence of heterogeneity, or the significant mismatch of the elastic constants between crystal and binder. The mixture theory, which explicitly treats the material as a heterogeneous composite, correctly predicts failure in uniaxial compression sample without resorting to any other artificial mechanisms.

ACKNOWLEDGEMENTS

This study was funded by the Department of Energy and the Department of Defense/Office of Munitions under the Joint DoD/DOE Munitions Technology Development Program.

REFERENCES

1. Chu, T.C., Ranson, W.F., Sutton, M.A. and Peters, W.H. (1985), *Exp. Mech.* 25, 232.
2. Nemat-Nasser, S. and Horii, H. (1982), *J. Geophys. Res.* 87, 6805.
3. Ortiz, M. (1985), *Mech. Mater.* 1, 67.

POSTER REFERENCE: *ICF100799PR*

DAMAGE OF NICKEL BASE SUPERALLOY SUBJECTED TO LOW CYCLE FATIGUE WITH HOLD PERIODS

J. Zrník, J. Semenak and V. Vrchovinsky

Department of Materials Science, Technical University of Košice
Park Komenského 11, 040 01 Košice, Slovak Republic

ABSTRACT

The approach to a life time prediction presented in this paper is based on the review the of data received from laboratory realised low cyclic creep fatigue experiment with respective nickel base superalloy. The cyclic creep fatigue tests were run with relatively simple trapezoidal wave loading at temperature of 650°C. The tensile hold periods imposing on the fatigue stress have been introduced into load control low cycle fatigue. The time to failure, the time to failure corresponding to maximum applied load, and number of cycles to failure have been the criteria to evaluate the deformation behaviour of alloy subjected to creep fatigue loading. To make an attempt of alloy life prediction to the respective types of applied load the modified Kitagawa's the linear damage criterion has been used. The two regression functions for respecting applied hold time interval were expressed to calculate the time to failure. The formulae can be used to predict the life of nickel base superalloy subjected to cyclic creep loading.

KEYWORDS

Nickel superalloy, cyclic creep, tensile hold time, damage evaluation, life prediction, structure

INTRODUCTION

Various components of industrial gas turbines and aircraft experience periods of both fluctuating and steady stress, due to complex situation of mechanical and thermal stress. Those components are subjected to operate under complex stress conditions, involving creep, fatigue and thermal fatigue. In deformation process both creep and fatigue can contribute to material damage. It was recognised that static creep and/or conventional fatigue test conditions approach cannot always assess the deformation process and life of the component.

In the past two decades considerable effort has been brought to characterise the deformation process of nickel base superalloys that were stressed under the conditions of time-dependent load at elevated temperatures [1,2,3,4]. In such cases both creep and fatigue can contribute to degradation of the material The hold periods constitute the creep stress component in the fatigue cycle. Deformation characteristics under the creep-fatigue stress can differ considerably from those of the static creep.

The study presents results gathered at deformation process of wrought nickel base superalloy EI 698 VD subjected to creep fatigue loading. The evaluation of deformation process and the life prediction of the alloy were done in relation to the hold periods introduced into low fatigue stress cycle at upper stress level. The

service life prediction in relation to the respective type of applied stress is expressed by modified Kitagawa's criterion being suitable for static and cyclic creep.

EXPERIMENTAL

The wrought nickel base superalloy EI 698 VD was selected as an experimental material. This alloy is suitable for manufacturing of discs and shafts of aircraft engines operated at temperatures up to 750°C. Chemical composition of the alloy in mass % is as follow: C max. 0.08, Cr 13-16, Mo 2.3-3.8, Nb 1.8-2.2, Ti 2.3-2.7, Al 1.3-1.7, Fe max. 0.2, balance Ni. Microstructure of alloy after finishing heat treatment consists of the equiaxed grain structure strengthened by coherent gamma prime precipitates. The alloy also contains MC and $M_{23}C_6$ carbides that do not contribute substantially to the strengthening.

The tensile stress cycling load controlled tests were conducted at temperature of 650°C. The cyclic creep tests were of trapezoidal wave pattern. The seven different hold times $\Delta t = 0$ (pure fatigue), 1, 3, 7.5, 15, 30, and 60 minutes at peak stress $\sigma = 740$ MPa were introduced in the tensile part of the load cycle. The net effect of these hold times is to systematically impose a creep stress component on the fatigue load cycling. The cycling frequency range was between 5.5×10^{-3} and 2.7×10^{-5} Hz and stress ratio R = 0.027. The stress ramp rate in one cycle, either during on-load or the off-load period, was 7.4 kN/min. No hold time was maintained at reduced load level of 20 MPa. The specimen longitudinal deformation, the failure lifetime or total time of the cyclic test, the number of cycles to failure, and the time at maximum load during cyclic test were recorded and compared with static creep.

RESULTS AND DISCUSSION

The results on the total time to fracture (TTF), time corresponding to maximum load (MLT), and numbers of cycles to failure (NCF) received at the cyclic creep experiment are summarised in Table 1.

TABLE 1
EXPERIMENTAL DATA RECEIVED AT CYCLIC TEST

Parameter	Hold time [minute]							
	fatigue	creep	1	3	7.5	15	30	60
TTF [min]	44 268	2 500	54 972	18 942	30 300	13 896	5 662	3 406
MLT [min]	-	2 500	10 741	8 003	19 591	10 911	4 981	3 188
NCF [min]	22 120	-	10 778	2 668	2 612	728	166	53
ε_f	3.2	6.3	3.3	3.5	3.6	3.1	3.9	6.9

The strain-time to failure dependencies, measured when strain was at the maximum load, corresponding to the initial stress of 740 MPa, for all hold times are illustrated in Figure 1. The low cycle fatigue test and static creep test results were conducted as well, and results are stated also in Table 1. As can be seen from the diagram in Figure 1 the introduction of stress reduction introduced into the creep process, and/or the introduction of cyclic stress component in static creep, resulted in life increase and decrease in the strain rate ε of the alloy in comparison with static creep. The time to failure was proportionally extended with decreasing of the hold period.

In order to evaluate the creep fatigue resistance of tested nickel base superalloy the time criteria, such as time to failure or time to failure corresponding only to the maximum applied load can be used for this purpose. The evaluation of deformation behaviour according to the time to failure corresponding to the sum of hold periods at maximum load (MLT) is presented in Figure 2. The corresponding hold period of $\Delta t = 7.5$ minutes at maximum load seems to have specific influence on the deformation behaviour of alloy. Probably, in the cyclic creep with the hold time shorter than 7.5 minutes, in damage process more fatigue would participate at crack nucleation and its propagation. If hold time is over this critical dwell the life prediction dominating role in damage process would be taken over by creep. Comparing these results with the results

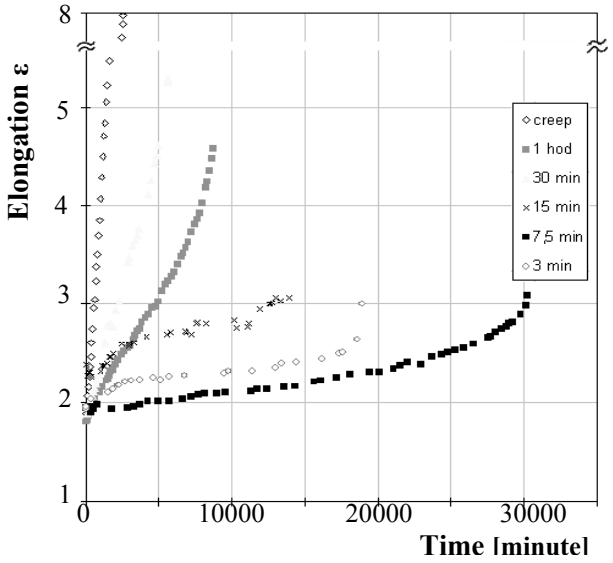

Figure 1: Strain-time to failure dependencies

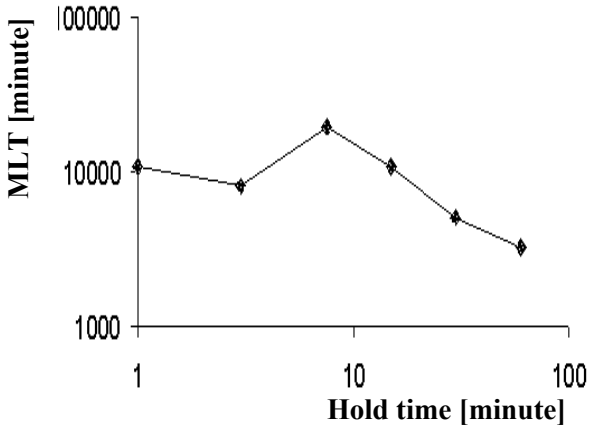

Figure 2: Plot of time to failure corresponding to applied load as the function of hold time

received on total time to fracture, the contradiction appeared. The longest life was corresponding to the test with hold time of Δt =1minute. In case that total number of cycles to fracture was the criterion to evaluate the deformation behaviour of the alloy the plot representing the dependence is documented in Figure 3. Regardless the fact that there is observed continuous decrease in number of cycles to failure with increasing hold time Δt the relationship can not be interpreted generallyy as prior creep damage effect on the fatigue mechanisms and/or as influence of creep on cycles reduction. The main reason not to follow such interpretation is the fact that creep damage which is time-controlled process will simply dominate at longer hold times. That is why it would therefore be illogical to explain such behaviour to apply the concept of the major damage mechanism to influence the minor one. Besides that, the resulted number of cycles to failure which showed continuous decreasing tendency with increasing hold time just it does not need to be the result of creep fatigue interaction. It can be accepted only as pure mathematics relation between time to failure and corresponding cycles number causing the creep damage.

Another interesting result of experiment was observed in case of applied hold times of Δt =3 and 7.5 minutes. The resulted number of cycles to failure showed very small difference. To verify the finding these tests were repeated and results were proved to be correct and were not an effect of random data scattering. Considering this fact, the explanation on such deformation behaviour could be based on the balanced creep and fatigue participation in damage at these applied hold times.

The application of stress of reductions in creep turns the respective process into a cyclic deformation process where besides time-controlled creep process also fatigue process would participate in damage process. The life extension, observed when the hold periods were introduced in cyclic process would have been a result of several additional aspects contributing to deformation process and modifying it. Among these aspects might be included, the alternating stress higher and lower than the yield point for the respective stress amplitude, the effect of introducing the cyclic deformation onto the creep process and vice versa, repeated storage of reversible anelastic creep deformation preceding the process of irreversible creep, and recovery of the stored deformation energy and release of anelastic deformation in time of the offs of the load. In this respect these facts make more difficult the prediction of life for actual test condition. It is known that during the creep fatigue the each other stress component mutual interactions are involved in damage process. However, in order to predict the cyclic service life of structural part there is not need to have knowledge how to estimate the individual creep and fatigue stress contribution in deformation process. For effective evaluation of their contribution would be more convenient to incorporate both of them into the one parameter.

To predict creep fatigue life of an alloy under considered laboratory test condition the linear damage summation rule [5] would be hardly appropriate to use it in case when creep damage may arise due to the

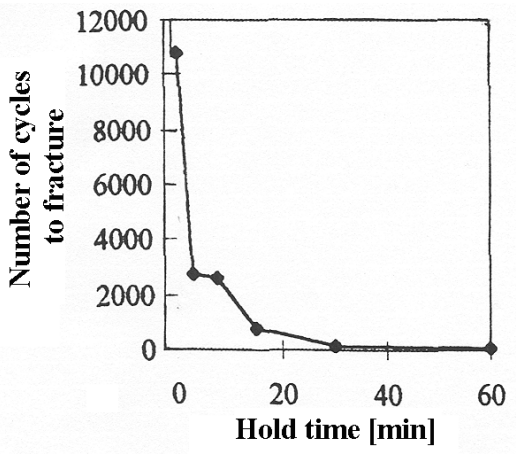

Figure 3: The dependence of hold time on the number of cycles to failure

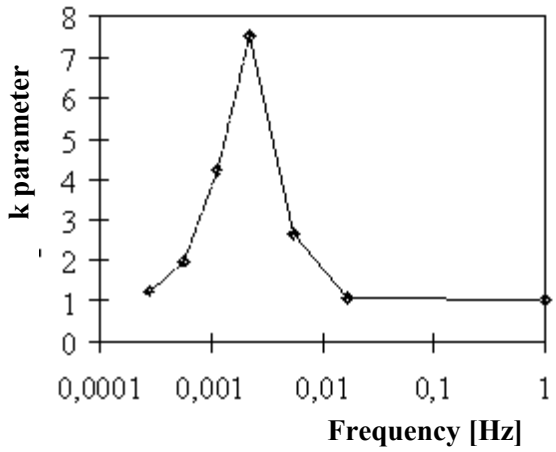

Figure 4: Frequency dependence of **k** parameter

cyclic loading condition. To separate the creep caused by the applied stress and the creep damage caused by the strain accumulation the equation of Kitagawa et al. [6] which is a modification of the linear rule of damage accumulation is more practical to use. The Kitagawa's equation can be written than in the following form where the frequency dependence of **a** parameter is assumed:

$$\left(\frac{N}{N_f}\right)+\left(\frac{t}{t_{rcyc}}\right)+\boldsymbol{a}\left(\frac{\varepsilon}{\varepsilon_{stat}}\right)=1 \tag{1}$$

where N is total number of cycles to failure, N_f is number of fatigue cycles to failure corresponding to pure fatigue, t is the total time to failure at cyclic creep, ε_{stat} is creep ductility, and **a** is Kitagawa parameter is considered to be frequency dependent, i.e. expressing a process frequency dependence.

This equation assumes explicitly that the creep life modification under the cyclic creep condition, however, it fails in evaluation of fatigue degradation by creep, i.e. by the time-dependent process. The parameter $\boldsymbol{a}$ can be expressed as $\boldsymbol{a} = 1 - 1/\boldsymbol{k}$. Parameter $\boldsymbol{k}$ determines the difference in a material life exposed in condition of cyclic creep and can be stated as $\boldsymbol{k} = t_{rcyc}/t_{stat.}$, where t_{rcyc} is the life corresponding to the conditions of cyclic creep when only creep process is considered, and t_{stat} is life corresponding to the course of static creep. Regarding these parameters the equation can be adjusted to the following form:

$$\left(\frac{N}{N_f}\right)+\left(\frac{t}{kt_{stat}}\right)+\left(1-\frac{1}{k}\right)\left(\frac{\varepsilon}{\varepsilon_{stat}}\right)=1 \tag{2}$$

The equation expresses the simplest modification of the linear damage summation rule that enables to evaluate the creep fatigue interaction when life increase is involved. The only limitation of using it for life evaluation was an assumption that creep damage resulting from hold period and from on-load and off-load period in one cycle was taken equal. To summarise the creep damage resulting from fluctuating load, creep damage resulting from constant load and fatigue damage the modified equation can be written as:

$$\left(\frac{N}{N_f}\right)+\left(\frac{N}{kN_c}\right)+\left(\frac{t_h}{kt_f}\right)=1 \tag{3}$$

where N -applied cycles number, N_f -cycles to failure under fatigue, N_c -number of cycles representing pure creep when fluctuating load is applied, t_h -sum of holds at maximum load, t_f-time to failure at applied static creep, k –parameter to characterise the different behaviour of material under cyclic and static creep.

If we consider the cyclic creep as deformation process where fatigue and (cyclic) creep participate there with respect to time-controlled degradation, then the resulting degradation should arise due do superposition of these contributions. Of course, we cannot generalise this assumption to whole frequency reductions interval of the applied stress because at low frequencies of load reduction exclusively simple static creep would control the degradation process only. That is why any important changes between the parameters t_{cyc} and t_{stat} can not be expected and there a continuous transition them must exit due to the change in stress reduction frequency. Kitagawa resolved the problem of ***a*** parameter frequency dependence by introducing a third member into the equation 1. In order to validate this equation over the entire frequency interval the limitation on admission only a negligible contribution resulting from cyclic deformation to total deformation must be introduced. It would be therefore more advantageous, to satisfy above limitation, to use only the first two terms of Eqn. 2 and to assume the frequency dependence of the ***k*** parameter. However, in order to simplify the calculation procedure the creep process was separated in to the periods of hold time and periods of ramping time and the number of cycles was formally used as a parameter of damage, although time-controlled process was involved. After these adjustments and using the data for creep life corresponding to maximum load and data from pure fatigue test to calculated the number of cycles to fracture corresponding to fluctuating load the following equation was received for applied loading:

$$\left(\frac{N}{60000}\right)+\left(\frac{N}{k.13000}\right)+\left(\frac{t_h}{k.2500}\right)=1 \tag{4}$$

The realised laboratory test did not provide the satisfactory data for precise determination of the time during which the creep at static load does not contribute to damage accumulation. However, according to the deformation dependencies in Figure 2 it can be assumed that hold times of Δt =1 and 3 minutes are involved to comply with this assumption. In order to guarantee the stated prediction, the calculation was based on an extreme hold limit that is for Δt = 1 minute, when the effective period of static creep will be the longest. After subtracting this value from applied hold time the effective hold times related to maximum load were calculated and they are presented in Table 2.

TABLE 2
FRACTURE EFFECTIVE DWELL TIME AT THE MAXIMUM LOAD

Δt	1 min	3 min	7.5 min	15 min	30 min	60 min
MLT_{ef}	0	5 335	16 979	10 183	4 815	3 153

To substitute this effective hold time to Eqn. 4 and utilising additional experimentally obtained data the ***k*** parameter and ***a*** parameter as a function of hold time at the maximum load was determined. The results of this calculation are presented in Table 3.

TABLE 3
PARAMETERS ***k*** AND ***a*** AS A FUNCTION OF HOLD TIME

Δt	1 min	3 min	7.5 min	15 min	30 min	60 min
k	1.03	2.62	7.5	4.2	1.95	1.25
a	0.03	0.62	0.87	0.76	0.48	0.2

It was already stated that ***k*** and ***a*** parameters are frequency dependent. The frequency dependence of ***k*** parameter can be related to frequency dependent process corresponding to, for example, the ability of storing and recovery of anelastic creep deformation. It is possible to assume that, in process of cyclic creep it should be a defined frequency at which the maximum dissipation of deformation energy resulting from the storing and recovery of anelastic creep deformation will be reached, because the frequency effect was introduced into the loading process as a result of different hold periods. Another possible example of the ***k*** parameter frequency dependence is equilibrium frequency dependence of hardening and softening process due to stress relaxing in off-times. The frequency dependence of ***k*** parameter, which was introduced into process by load reduction or by introduction of hold time onto low cycle fatigue, is presented in Figure 4.

To model the life prediction behaviour of alloy the modified Eqn. 4 of the linear rule of damage was used. For applied load – temperature conditions to calculate the time to failure (MTF) as a function of the applied hold time t_h at the maximum load with respect to ***a*** and ***k*** parameters the following explicit formula was determined:

$$\text{MTF} = \frac{60937.5k(t_h)}{24.375(t_h - 1) + 4.6875}\ t_h \qquad (5)$$

For other parameters, which may be suitable for life prediction, the following relations were calculated:

$$\text{NCF} = \text{MLT}/t_h \quad \text{and} \quad \text{TTF} = \text{MLT} + 4\ \text{NCF} \qquad (6)$$

To calculate the ***k*** parameter values it is not easy to find the regression function, which would describe its value with good reliability for whole interval of the applied hold times. That is why for interval of used short hold times t_h < 7.5 minutes and for interval of longer hold times, interval t_h > 7.5 minutes the different regression function has been used. The discontinuity at the boundary of the interval corresponding to hold time of Δt = 7.5 minutes in plotted curve presenting the alloy model life prediction was the result. For the shorter hold time regression function of $\boldsymbol{k}$ = 1.0105 t_h – *0.1567* and for longer hold time $\boldsymbol{k}$ = 44.53 $t_h^{-0.8862}$ were determined.

If these regression functions expressing the ***k*** parameter dependence on hold time would be substituted into the equation (5) the following formulae for life prediction, to differentiate the effect of shorter and longer hold time on superalloy behaviour subjected to cyclic creep would be resulting:

$$\text{MTF} = \frac{\check{z}60937.5(1.0105\ t_h - 0.1567)}{24.357(t_h - 1) + 4.6875 + (1.0105t_h - 0.1567)} t_h \quad \text{for } t_h < 7.5 \text{ minutes} \qquad (6)$$

$$\text{MTF} = \frac{60937.5(44.53t_h^{\ -0.8862})}{24.375(t_h - 1) = 4.6875 + (44.53t_h^{\ -0.8862})} t_h \quad \text{for } t_h > 7.5 \text{ minutes} \qquad (7)$$

The graphic presentation of the model life parameters prediction MTF and NCF for defined testing condition of cyclic creep using the Eqn. 6 and Eqn.7 are shown in Figure 5 and Figure 6.

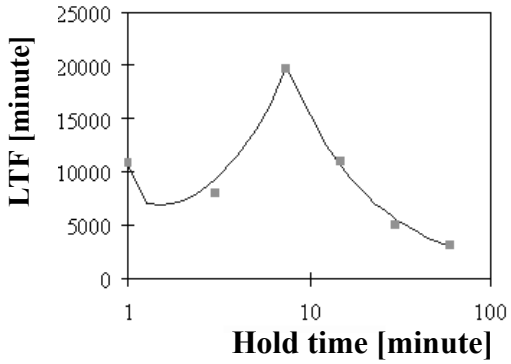

Figure 5: The plot of alloy model life prediction in condition of cyclic creep

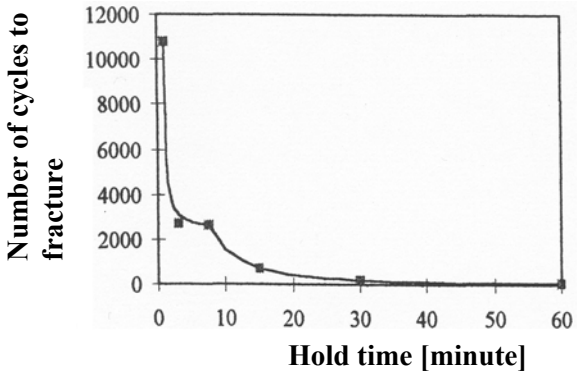

Figure 6: Model prediction dependence of number cycles to fracture as function of hold time

CONCLUSION

The application of short repeated reductions of the applied stress of 740 MPa to reduced stress level of 20 MPa resulted in change of deformation behaviour of alloy. By introduction of stress reductions onto creep the decrease of strain rate was observed and it was followed with life increase in comparison to static creep. For the laboratory tests condition the modified linear rule of damage summation was used to model the life prediction. The formulae differenting the effect of hold time at the applied maximum load with respect to ***a*** and ***k*** frequency dependent parameters to calculate time to failure were determined. These formulae

respecting the applied hold time interval and introducing limitations they can be used to predict the life of nickel base superalloy subjected to cyclic creep loading.

References

1. Härkgard, G. and Guedon, J.Y. (1998). In: Proceedings of the 6th Liege Conference on Materials for Advanced Power Engineering, Belgium, 913.
2. Gabb, T.G. and Welsch, G., (1998) Acta Metall. 37, 2507
3. Portela, P.D., Bertram, A., Fahlbusch, E., Frenz, H. and Kinder, J. (1996). In: Fatigue'96, 795, Lütjering, G., Nowack, H. (Eds). Beijing.
4. Bosimer, D.A. and Sheitogolu, H. (1989) Trans. ASME, 112, 205.
5. Taira, S. (1962). Creep in structures, pp. 96, Nicholas, H. J. (Eds). Academic Press, N.Y.
6. Kitagawa,M., Tamura, K. and Ohtomo, A. (1983) J. of SMSJ, 32-357, 662

ICF100882OR

Damage Progression Behavior under High Temperature Creep and Fatigue Conditions

A.T.Yokobori,Jr.[1] Y.Kaji,[2] and T.Kuriyama[3]

[1] Fracture Research Institute, Graduate School of Engineering Tohoku University
Aoba 01,Aramaki, Aoba-ku Sendai-shi,980-8579,Japan
[2] Japan Atomic Research Institute, Tokai-mura, Ibaraki, 319-11, Japan
[3] Faculty of Engineering Yamagata University, 992-0038, Japan

Abstract

The effect of high temperature damage progression on crack growth and the life were clarified under creep –fatigue interaction and multiplication conditions. The following results were obtained.Damage progression behaviors initiated around a notch tip show different characteristics depending on applied load frequency and creep ductility. It dominates the life of creep crack growth and high temperature fatigue fracture toughness.

Key words: creep-fatigue interaction and multiplication, damage, crack growth rate, crack growth life, SUS304stainless steel, Cr-Mo-Vsteel

1. Introduction

To clarify the effect of high temperature creep and fatigue interaction on the characteristics of crack growth behavior is important as a problem of phenomenal matter and to predict the life of crack growth. As a method of clarification of these matters, the characteristics of the effect of load frequency(f) on crack growth rate and the life are separately estimated into time dependent and cycle dependent mechanism[1-3]. Furthermore, the crack growth life is dominated by creep and fatigue damage under high temperature condition[2,3]. To clarify the characteristics of damage progression, the machine system was designed to enable automatic observation of the mechanical behavior of deformation and damage progression around a crack tip during fatigue and creep loading under computer control and some results have been obtained for SUS304 and Cr-Mo-V steels[2-4].

In this paper, on the basis of these results, the effect of high temperature damage on crack growth rate and the life were clarified and some analyses were performed.

2. Testing method and specimens

The machine system was designed and developed to enable automatic real-time observational experiments with CCD microscope. This microscope can be moved in x, y and z direction with a specified displacement value and time interval under computer control. It can take pictures of deformation and damage progression around a crack tip. These pictures are digitized and analyzed by computer image analytical system.

A specimen is a V type double notched specimen with 4mm width and 1mm thickness. Notch opening angle is 30° and notch tip radius, ρ is 0.05mm. Experiments were conducted under the vacuum condition of less than 10^{-5}torr.Detailed method was written in another literatures [5-7].

3. Damage progression characteristics of SUS304 stainless steel under creep, fatigue and creep-fatigue interaction and multiplication

Behavior of damage progression around a notch tip under high temperature creep-fatigue interaction for various values of load frequency, f were plotted against non-dimensional time as shown in Fig.1 Where D is damage area, t_f is fracture life for each specimen. These results show remarkable extension of creep damage is observed before creep crack initiation and after that, it saturates to some specified value. Under fatigue condition(1Hz), however, damage area is small at the stage of crack initiation, it lineally increases after crack initiation. This behavior is different from that under creep condition. Even though f decreases, this behavior does not saturates to that under creep condition as shown in the result for f=0.0017Hz.

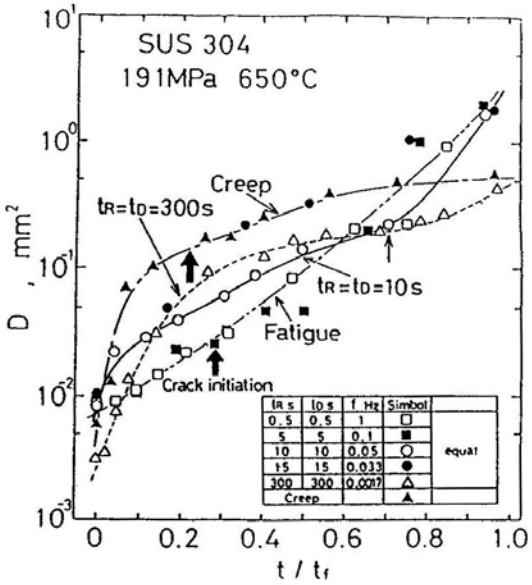

Fig. 1 Behavior of damage progression around a notch tip under high temperature creep-fatigue interaction for various values of *f*.

The results of in situ observation of damage progression behavior under creep and fatigue conditions were shown in Figs.2 and 3. The dark region around a notch tip is damage region. Tensile load is applied in the horizontal direction. Under creep condition, damage spreads over the wide area of specimen and notch opening displacement becomes large.

On the other hand, for the case of fatigue condition with 1Hz, damage localizes around a crack

and the value of crack opening displacement is smaller than that for a creep crack. Even though f decreases, for example, f=0.0017Hz, this fatigue effect is also observed in the morphology of damage region.

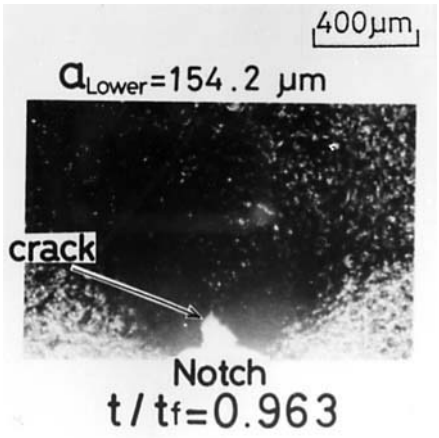

Fig. 2 The results of in situ observation of damage progression behavior under creep condition.

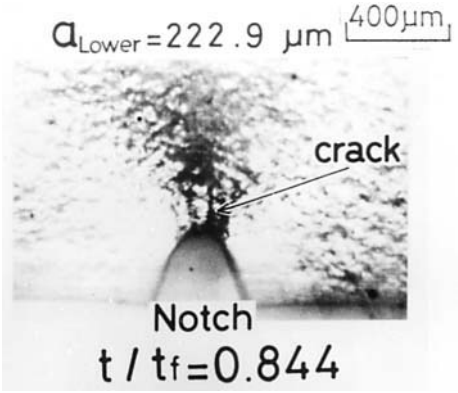

Fig. 3 The results of in situ observation of damage progression behavior under fatigue condition (f=1Hz).

The characteristics of damage progression behavior under creep and fatigue multiplication conditions with stress hold time, t_H were plotted against non-dimensional time as shown in Fig.4.

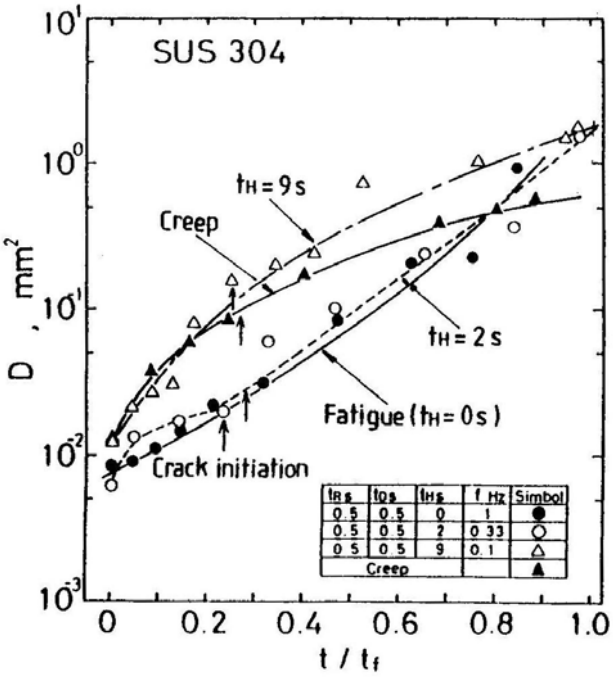

Fig. 4 The characteristics of damage progression behavior under creep and fatigue multiplication conditions with stress hold time, t_H.

These results show, with increase in t_H, that is, $t_H \geqq 9$s, the characteristic is in good agreement with that under creep condition and the definite transition from fatigue to creep occurs, which is different from the characteristics of f under fatigue condition(creep-fatigue interaction).

4. The characteristics of f on crack growth rate(CGR), its life and fatigue fracture toughness under creep-fatigue interaction and multiplication condition for SUS304 stainless steel

The effect of f and stress hold time on CGR and its life were plotted against f(=1/(t_H+2t_R) as shown in Figs.5(a),(b) and 6(a),(b). Where t_R is stress increasing and decreasing time. The characteristic of f on the life of each crack growth is qualitatively in good agreement with each characteristics of f on the low CGR when a crack starts to grow. Furthermore, even though f decreases, the characteristics of f on CGR and inverse value of the life do not saturate to those under creep condition and it was affected by fatigue effect as shown in Figs5(a) and (b).

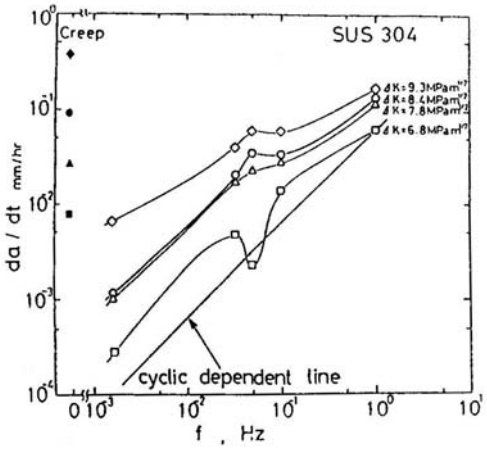

Fig. 5(a) The effect of *f* and stress hold time on CGR

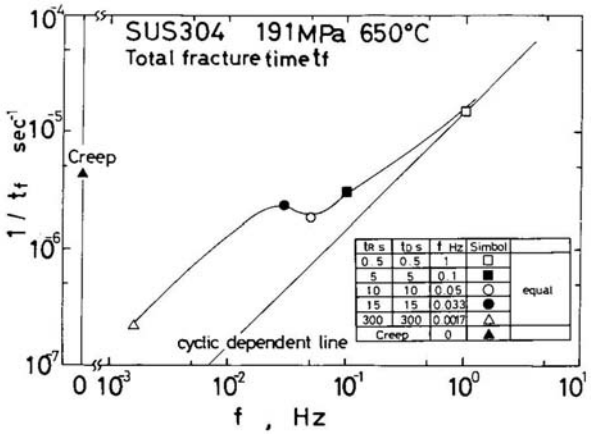

Fig. 5(b) The effect of *f* and stress hold time on CGR

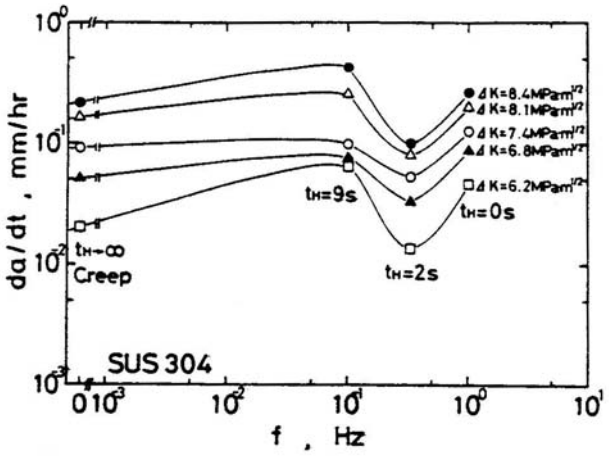

Fig. 6(a) The effect of *f* and stress hold time on CGR

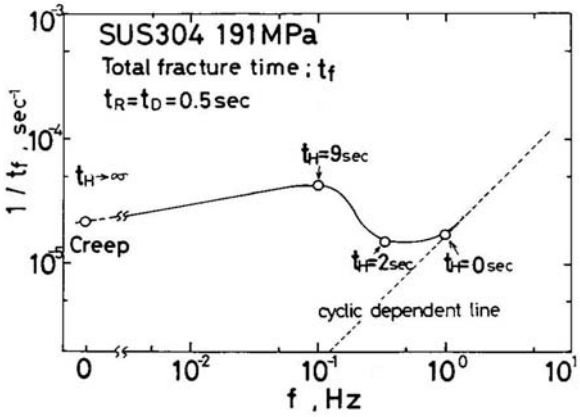

Fig. 6(b) The effect of *f* and stress hold time on CGR

On the other hand, with increases in t_H, both characteristics saturates to those under creep condition as shown for the case of $t_H \geqq 9s$ in Figs6(a) and(b). These characteristics are in good agreement with that of damage progression as shown in Fig.4.

The inverse value of damage area accumulated in the low ⊿K region is plotted against f as shown in Fig.7 which is in good agreement with the characteristics of low CGR and $1/t_f$ as shown in Figs.5(a) and (b). The relationship between Da and fatigue fracture toughness, K_{fc}(stress

intensity factor when final fracture occurs) was shown in Fig.8 which shows good correlation each other. That is, K_{fc} is found to be dominated by Da.

Therefore, under creep-fatigue interaction, low CGR, crack growth life and K_{fc} are found to be dominated by Da. These results were observed also for the case under creep-fatigue multiplication condition, that is, t_H effect. These results show damage progression behavior in the initial creep crack growth region dominates the crack growth life and K_{fc} under high temperature creep-fatigue interaction and multiplication conditions.

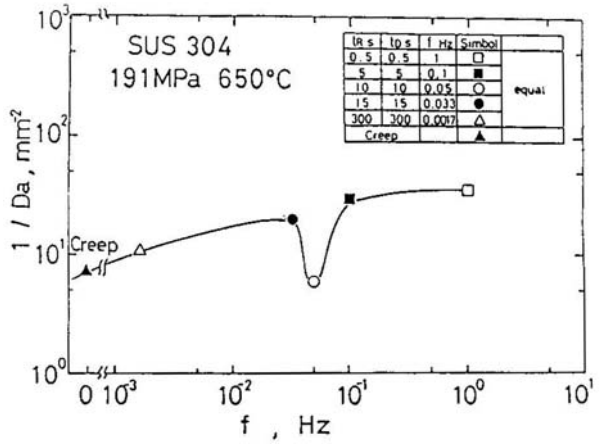

Fig. 7 The inverse value of damage area accumulated in the low ⊿K region.

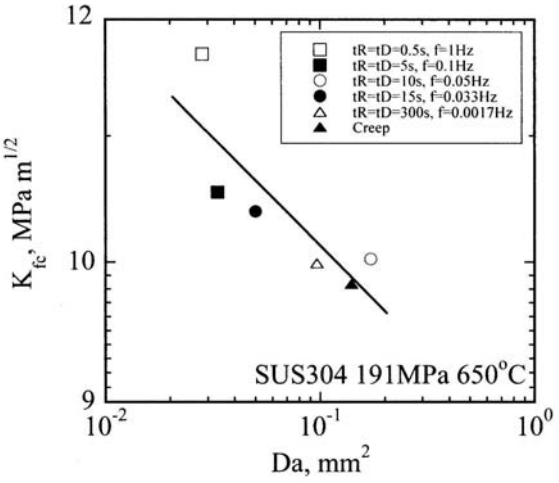

Fig. 8 The relationship between Da and fatigue fracture toughness, K_{fc}.

5. The characteristics of f on the life of creep crack growth and damage progression under creep-fatigue interaction conditions for Cr-Mo-V steel

The inverse values of the life of creep crack growth, $1/t_f$, under creep-fatigue interaction condition for Cr-Mo-V steel were plotted against f as shown in Fig.9[4]. With decrease in f, this characteristic saturates to that under creep condition, that is, time dependent mechanism. The characteristic of f on damage progression obtained by in situ observation is shown in Fig.10[8].

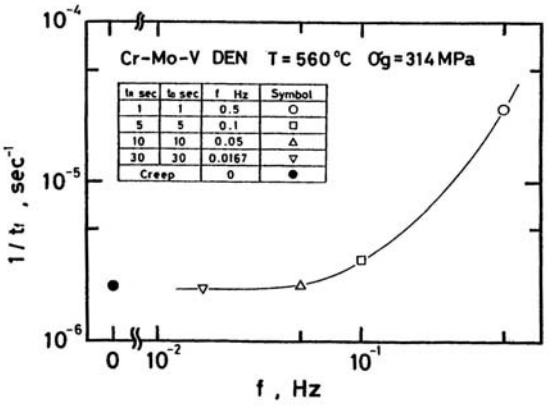

Fig. 9 The inverse values of the life of creep crack growth, $1/t_f$, under creep-fatigue interaction condition for Cr-Mo-V steel.

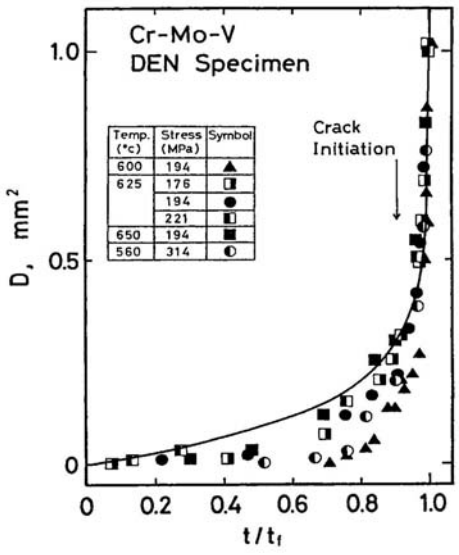

Fig. 10 The characteristic of *f* on damage progression obtained by in situ observation

It is well represented by concave damage law based on Kachanov-Rabatonov theory[9,10] given by eqn.(1). These characteristics are different from that for SUS304 stainless steel as shown in Figs.1 and 5. This will be due to the difference of creep ductility between Cr-Mo-V and SUS304 steels. These results show Kachanov-Rabatonov law will be applicable to that for creep ductile materials such as Cr-Mo-V Steel.

$$D = 1 - (1 - \frac{t}{t_f})^{1/7} \qquad (1)$$

6. Conclusions

Under creep-fatigue interaction and multiplication conditions, damage progression behavior initiated around a notch tip show different characteristics depending on applied load frequency and creep ductility. It dominates the life of creep crack growth and high temperature fatigue fracture toughness.

Acknowledgements

Thanks should be made for financial aid to the Japan Society for promotion of Science(JSPS) of the RFTF program 97R12101. We also appreciate the fruitful discussion about this work by Prof.Takeo Yokobori.

References

[1] T.Yokobori,A.T.Yokobori,Jr., and N.Takasu, Mechanical Behaviour of Materials-Ⅳ,J.Carlsson and N.G.Ohlson Eds, Pergamon Press, (1984)pp967-981

[2] A.T.Yokobori,Jr., Y.Kaji, T.kuriyama and T.Yokobori, Trans. of the Japanese Soc. of Mech. Engineers, A.54(1988)pp1304-1311

[3] A.T.Yokobori,Jr., Y.Kaji, T.kuriyama and T.Yokobori, Trans. of the Japanese Soc. of Mech. Engineers, A.57(1991)pp2349-2354

[4] A.T.Yokobori,Jr., T.Uesugi and A.Ohnogi, Trans. of the Ann. Meet. of Japanese Soc. for Strength and Fract. of Mat.(1995)pp64-71

[5] T.Yokobori and H.Sakata, Engng. Fract. Mech. 13,3(1979)509-522

[6] A.T.Yokobori,Jr., H.Takeda, T.Adachi, J.C.Ha and T.Yokobori, ASTMSTP1290,C.J.Spragg and L.T.Drzal Eds(1996)152-167

[7] D.Kobayashi and A.T.Yokobori.Jr., Trans. of the Ann. Meet. of Japanese Soc. for Strength and Fract. of Mat.(2001)

[8] A.T.Yokobori,Jr., Engng Fract.Mech. 62(1999)61-78

[9] L.M.Kachanov, Izv.Akad.Nauk. SSSR, Otd.tekhn.nauk8(1958)26

[10] Yu.N.Rabatnov, Vopr. Prochn. Mat. I Konstr.Izd.AN.SSSR, Moscow(1959)

Deformation Characteristics on Creasing of Paperboard Under Shallow Indentation

S.Nagasawa[1], Y.Fukuzawa[1], D.Yamaguchi[1],
S.Nagae[1], I.Katayama[2], and A.Yoshizawa[3]

[1] Department of Mechanical Engineering, Nagaoka University of Technology, 1603-1 Kamitomioka, Nagaoka, Niigata 940-2188 JAPAN
[2] Katayama Steel Rule Die Co.Ltd., 3-7 Higashigoken, Shinjuku, Tokyo 162-0831, JAPAN
[3] Yoshizawa Industry Inc., 318-8 Ogi, Izumozaki, Niigata 949-4332 JAPAN

Abstract

This paper reports on a fundamental deformation behavior and fracture modes of coated paperboard creased. The creasing condition was a shallow and loose indentation and the transition region on the occurrence of surface cracks under a folding test was revealed by observing the nominal shearing strain as initial crease. By reviewing the bending moment resistance, the initial gradient of bending moment as rigidity and the saturated bending moment at the crease, the correlation between the occurrence of surface cracks and the bending moment characteristics were founded.

Keywords: die creasing, paperboard, fracture mechanics, composite material, shear deformation

1. Introduction

Paperboard die cutting, which includes creasing, is wide spread in many fields such as foods, stationery packaging. For the improvement of productivity or the improvement of quality on die cutting[1,2], the estimation of endurance on die tools and the estimation of material properties on paperboard are required[3]. Creasing is one of most important mechanical behavior or processing technique for paperboard die cutting[4]. However, the working ability and the deformability of paperboard are different from isotropical elasto-plasticity such as many ductile metals and their work characteristics are complicated. Because the creasing work of paperboard includes deformation of laminates, fracture mechanics of fibers and non-linear contact forming with elasto-plasticity as anisotropy. In the past, since the creasing work was based on empirical knowledge of experts, any optimal condition of the work and the fracture mechanics in paper fibers are not almost revealed.

In this study, the uniaxial round-edge creaser and the square channel on the counter die plate was applied to determine the creasing property of a coated paperboard. The range of possible creasing states of a specified paperboard was investigated by varying the channel width of counter die and by varying the clearance between the creaser edge and the channel bottom under shallow indentation.

Mechanical properties of paperboard creased was compared in macroscopic with the strength of plain paperboard, by seeing the bending resistance of creased part. While the status of cracks at the crease was observed, the correlation between the generation frequency of surface cracks and the stroke of creasing rule was discussed by varying the channel width.

2. Experimental condition

2.1 Creasing model and working condition

When paperboard is creased, it results in a partial internal change of the material, and the permanent deformation is generated so as to obey the profile of creasing rule. The stiffness of the paperboard at the crease is substantially reduced and a hinge is created. **Figure 1** illustrates the geometrical relationship between a creasing rule, a paperboard creased, and a channel die. Since the crease part is altered mechanically by folding the paperboard, we call the first crease produced by the creasing rule as the "initial crease" for identifying the first one and the altered one, here. Although there are usually rubber fixtures adjoining to each creasing rule in commercial products, any rubber fixtures were not implemented in this experimental apparatus.

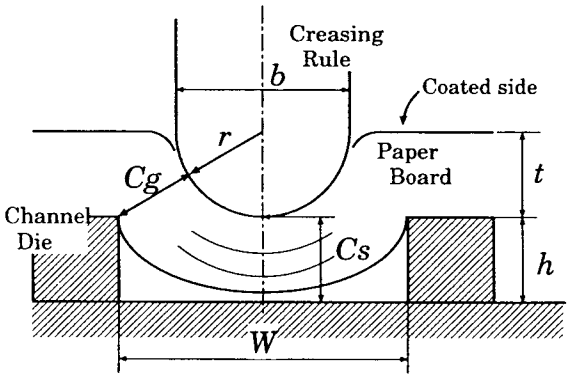

Fig.1 Creasing model and geometrical parameters

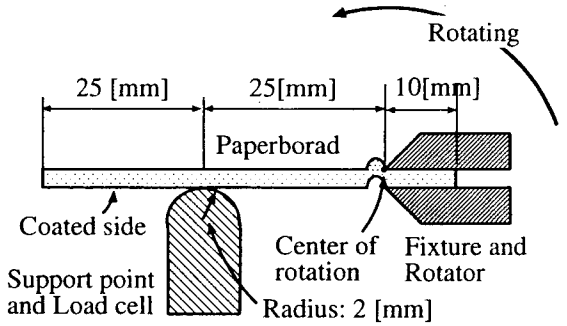

Fig.2 Schematic diagram of bending test

Nomenclature

b: thickness of creasing rule
r: tip radius of creasing rule
W: width of channel die
h: depth of channel die
t: thickness of paperboard
C_s: clearance on stroke direction
C_g: groove clearance between channel edge and creasing rule
$(C_g = \sqrt{(W/2)^2 + (C_s - h + r)^2} - r)$

Specification of creasing rule was as follows: thickness $b = 0.72$ [mm], height of rule = 23.1 [mm], tip radius $r = 0.364$[mm], length of rule = 40[mm]. The material of creasing rule was a steel of which the hardness was 175[HV]. The depth h and the width W of channel die were chosen as 0.5×1.5, 0.5×1.7, 0.5×1.9, 0.6×2.1, 0.6×2.3, 0.8×2.5, 0.8×2.7, and 0.8×3.0[mm], respectively. They were made by a polyester resin tip(the hardness: 120[HRC]) that was attached to a steel counter plate. The depth h is considered as $h > t$, and the width W is empirically chosen as $W \approx b + 2t$. The average thickness of specified paperboard t was 0.438[mm], while the basis weight ρ_S was 364.0 [g/m^2]. The nominal tensile strength σ_B of paperboard in the machine direction(MD) and the nominal strain corresponded ε_B were 38.14[MPa] $\times$ 2.05[%], while σ_B and ε_B in the cross direction(CD) were 15.80[MPa] $\times$ 4.72[%] (as average of five specimens, based on JIS-P8113, the cross head speed: 1 [mm/min.]). The side length and the width of paperboard specimen were 60.0[mm]$\times$40.0[mm] for the creasing test in MD and CD respectively. In this paper, when the crease line is transverse to MD, the material of paperboard is symbolized as "Transverse", and when the crease line is parallel to MD, it is symbolized as "Parallel". Here, all the specimens of paperboard were pre-processed: being kept for more than 24 hours at the room temperature 23[degree], the humidity 50[%]. The creasing test was carried out at the room temperature 20.5~22.5[degree], the humidity 39~40[%], and the cross head speed 1 [mm/min.].

2.2 Measured targets and evaluation method

The minimum stroke clearance C_s is empirically chosen as $C_s \approx h$. In this work, the variable C_s was varied from $C_s = t + h$ down to $C_s = h$, while the channel width was chosen as 1.5, 1.7, 1.9, 2.1, 2.3, 2.5, 2.7, and 3.0[mm] for the purpose of investigating the effect of groove clearance C_g and the effect of shearing deformation onto the creasing characteristics. This condition is shallow and loose indentation at the aspects of shearing deformation. By using the paperboard creased at an arbitrary C_s, the bending moment resistance M [Nm/m] of initial crease was firstly measured as shown in **Figure 2**. The hinge root of paperboard creased was cramped by the fixture and the paperboard was bended to 90 [degree] by the fixture, where the support point of the paperboard was at 25.0[mm] from the rotation center. Here, the concave surface of crease was considered to be an outside corner. From the response curve of M and the rotation angle θ, since there is usually a local maximum resistance, we have focused on the local maximum moment M_{max} and also on the initial gradient(rigidity) $dM/d\theta(= G_i)$. Three specimens were inspected for each clearance C_s.

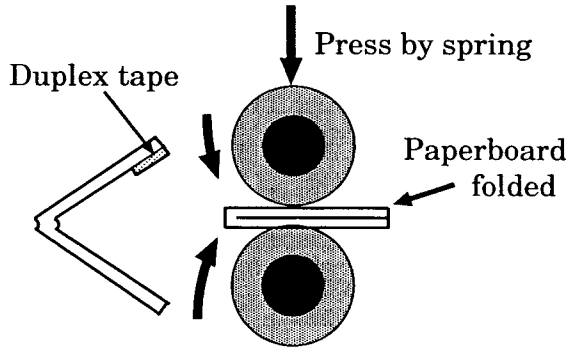

Fig.3 Schematic diagram of folding test

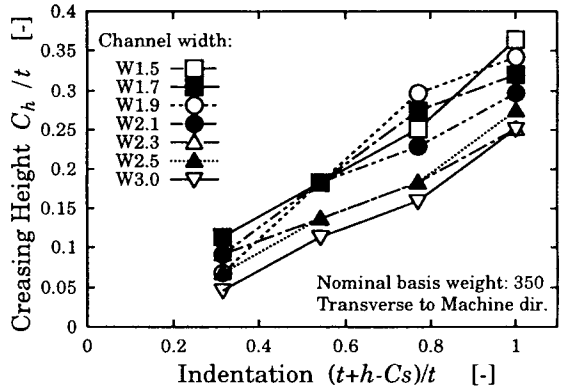

Fig.4 Creasing height and indentation of rule

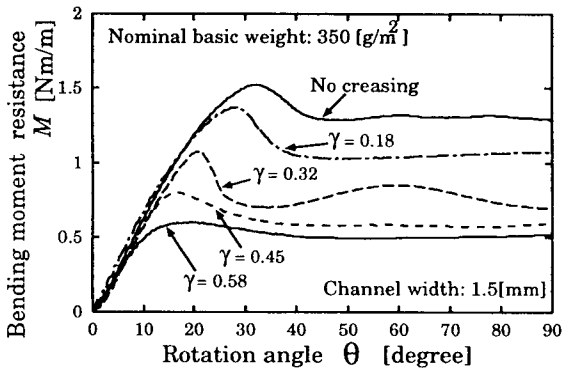

Fig.5 Relationship between rotation angle and bending moment resistance with Transverse paperboard

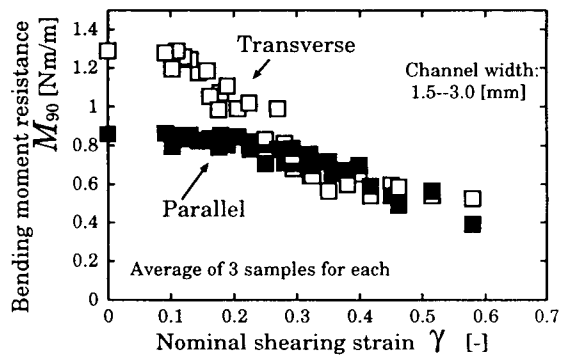

Fig.6 Effect of initial shearing strain on the saturated bending moment resistance (at θ= 90[degree])

Secondly, the paperboard was folded completely at the crease by using the two high roller shown in **Figure 3** for observing any crack generated on the surface of crease. The folding rollers were made by a hard rubber, and their diameter was 20[mm]. The pressing force 14.8[N] was applied to the folding rollers previously. After the initial creasing, the specimens were folded by hand so as to form a hinge without crushing the crease, and the both ends of paperboard were bonded by glue. By passing through the folding rollers, the crease of paperboard was crushed and a crushed hinge was completely formed. After that, the surface of crease was observed whether any cracks occur on it or not. Ten specimens were inspected for each clearance C_s respectively, and if any cracks were observed on the surface of crease, the occurrence was counted as one for each specimen. For inspecting the status of cracks, a section cut across the crease and the outer surface of the crease were observed.

3. Results of experiment

Figure 4 shows the relationship between the normalized indentation in the stroke direction $(t+h-C_s)/t$ and the normalized creasing height of initial crease C_H/t. The creasing height was measured at the convex surface, and increased with the indentation of creasing rule, almost linearly.

Figure 5 illustrates examples of the bending moment resistance at crease with Transverse paperboard. There was a local maximum M_{max} at a certain angle larger than 15[degree] and less than 30[degree] for Transverse. M_{max} becames disappeared by increasing the nominal initial shearing strain $\gamma = 2(t+h-C_s)/W$. The initial crease changes the mechanical structure and the inner state of crease. However, any cracks did not appear obviously on the outer surface of crease. For Parallel paperboard, there was also a local maximum M_{max} at a certain angle larger than 25[degree] and less than 60[degree]. The bending moment resistance with Transverse was apt to be larger than that with Parallel. This tendency is supposed to correspond to the anisotropic property of paperboard, such as the difference of σ_B. Since M is apt to be saturated at the rotation angles θ being larger than 60 [degree], the relationship between γ and M at θ= 90 [degree] was shown in **Figure 6**. The difference between Transverse and Parallel paperboard becomes disappeared as γ increasing.

By sampling M_{max} and G_i from Figure 6 and other data, the relationship between γ and the normalized bending moment resistance M_{max}/M_0 with Transverse paperboard is shown in **Figure 7**, while the relationship between γ and the normalized initial gradient G_i/G_0 is shown in **Figure 8**. Here, M_0 is M_{max} with the paperboard that was not creased initially. Similarly, G_0 is G_i with the paperboard

that was not creased initially. By applying the linear normal equation to these data approximately, the coefficients of normal equations were gotten as **Table 1**.

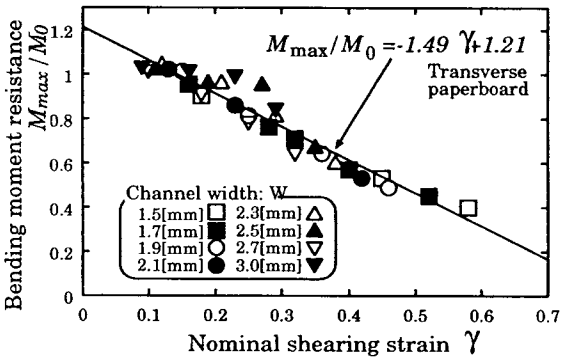

Fig.7 Effect of initial shearing strain on the bending moment resistance

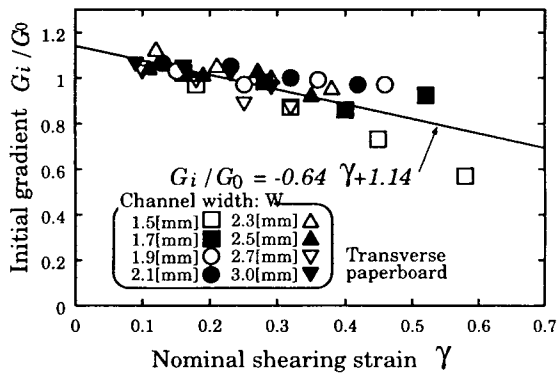

Fig.8 Effect of initial shearing strain on the rigidity of crease

$$M_{max}/M_0 = k_b\gamma + m_b \quad (1)$$

$$G_i/G_0 = k_t\gamma + g_t \quad (2)$$

Table 1 Coefficients of normal equation(1),(2)

Material	k_b	m_b	k_t	g_t
Transverse	-1.49	1.21	-0.64	1.14
Parallel	-0.71	1.08	0.14	0.91

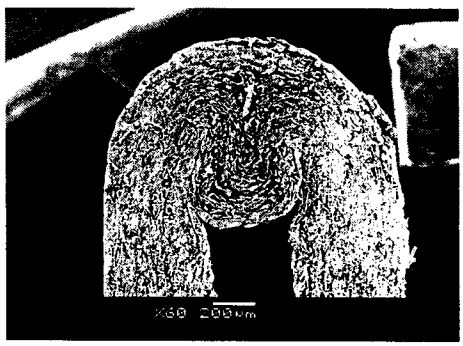

(a) γ= 0.184

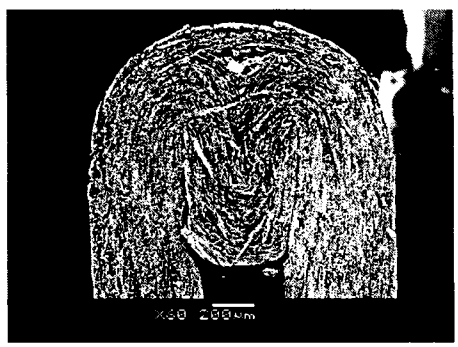

(b) γ= 0.58

Fig.9 Section of crease with Transverse paperboard after passing through folding rollers

(a) γ= 0.184

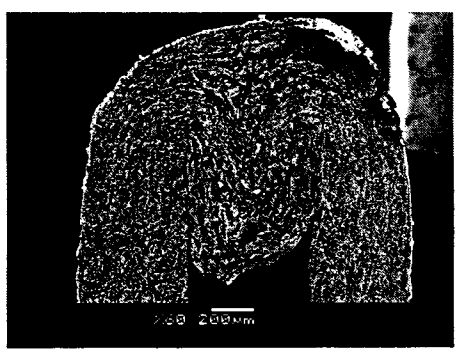

(b) γ= 0.58

Fig.10 Section of crease with Parallel paperboard after passing through folding rollers

Since this approximation is for all the range of channel width W, it is clarified that the inner change of crease relies on the initial shearing deformation. According to the article[4], the clearance C_g is said to be important to decide the creasing characteristic. Observing M_{max}/M_0 and G_i/G_0 with C_g, as all the data were separated by W, to focus on the initial shearing strain is suitable arrangement in this work. From Figure 8 and Table 1, as the variation of $k_t\gamma$ is smaller than g_t, G_i/G_0 can be roughly simplified as a constant value when $\gamma < 0.58$. Although k_t was calculated as -0.64 for Transverse and

calculated as +0.14 for Parallel, the latter can be understood that G_i/G_0 does not depend on γ and the plus of value includes the error measured, while the former shows slightly the dependency of γ to G_i/G_0. **Figure 9(a),(b)** show the section across the crease formed a hinge with Transverse paperboard (the indentation: $(t+h-C_s)/t$= 1.0, 0.315, the channel width: W= 1.5[mm]), and **Figure 10(a),(b)** show the one with Parallel paperboard. **Figure 11(a),(b)** show a top view of the outer surface at the crease after passing through the folding rollers ($(t+h-C_s)/t$= 0.315, W= 1.5[mm]). The depth of burst layer was roughly 0.1[mm].

(a) Transverse paperboard (b) Parallel paperboard

Fig.11 Outer surface of crease after passing through folding rollers (γ= 0.184)

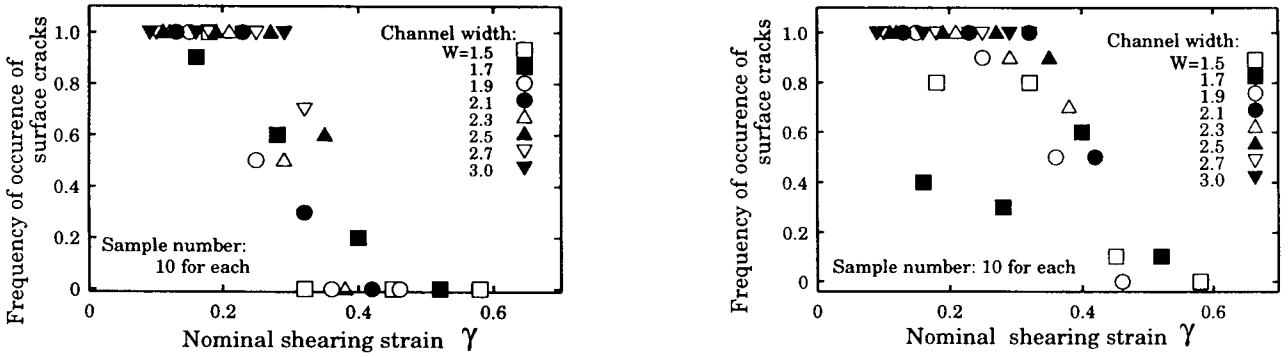

(a) (Transverse paperboard) (b) (Parallel paperboard)

Fig.12 Effect of shearing strain on the occurrence of surface cracks

The shapes of folded hinge were remarkably different from each other by varying γ as shown in Figure 9, and also they were different in Figure 10. When the indentation as initial crease is small relatively, since the inner delamination is little, the bulge of hinge becomes small for the both of Figure 9 and Figure 10. Here, Figure 9(a) and Figure 10(a) are quite different from each other, while Figure 9(b) and Figure 10(b) are almost similar profiles as formed hinge. This is supposed to be a reason why the anisotropy of bending moment resistance of paperboard disappeared with creasing in Figure 6. Namely, the bending moment resistance saturated depends on the geometrical profile of folded hinge. When the indentation is not sufficient for the inner delamination, the outer surface layer of crease is apt to be broken by folding the paperboard. This burst almost occurred at the first layer which delaminated with the thickness 0.1[mm] roughly. Since the tensile strength σ_B of paperboard in MD is larger than the one in CD, it is supposed that the initial bending strength of Transverse paperboard is apt to be larger than that of Parallel paperboard. Moreover, the inner delamination (local buckling of inner layer) of Transverse paperboard is apt to concentrate to a narrow region, while the inner delamination of Parallel paperboard is apt to be decentralized in the creased region. Namely, M_{max} depends on σ_B and the bending stiffness of paperboard.

Figure 12(a),(b) show the effect of shearing strain γ on the occurrence of surface cracks for Transverse and Parallel paperboard, respectively. From these figures, there is the critical shearing strain at which the surface cracks become increased remarkably for a certain transition region: $\gamma \approx 0.3 \sim 0.5$.

Comparing Figure 6 with Figure 12, it is supposed that there is a correlation between the occurrence of surface cracks at the crease and the convergency of saturated resistance. Namely, the hinge formed at the crease becomes changed so as to extrude the inner side layer delaminated and to reduce the surface tension stress at the outer side layer.

4. Conclusion

The characteristic of creasing for a coated paperboard, of which the nominal basis weight was 350[g/m^2], was investigated by varying the channel width of counter plate under the constant indentation of creasing rule. The results are summarized as follows:

1) The bending moment resistance at the crease has a correlation with the initial crease height, and also relies on the nominal shearing strain γ, while the initial gradient as rigidity is almost invariant when γ is less than 0.58.
2) The saturated bending moment resistance with Transverse paperboard differs remarkably from the one with Parallel paperboard when γ is less than 0.3.
3) The shapes of hinge formed are altered by the specified initial crease, namely the indentation of creasing rule affects to the mechanical inner change of crease or the state of delamination at crease.
4) The occurrence probability of surface cracks at crease has the transition region at $\gamma = 0.3 \sim 0.5$. Namely, when $\gamma > 0.3$, the surface cracks become disappeared and any surface cracks can not be almost observed under $\gamma > 0.5$.

References

[1] Grebe,W.,Hofer,H.: Allgemeine Papier-Rundschau, 9, (1973), 292-300.
[2] Hofer,H.,Wurth,V.: Papier+Kunststoff Verarbeiter, 10, (1994), 33-38.
[3] Fellers,C.,Fredlund M.,Wagberg,P.: Tappi Journal, 4, (1992), 103-109.
[4] Carey B.K.: Packaging Productivity, 1-1, (1992), 16-21.

Oral Reference: ICF100814OR

Deformation Behavior of [001] NiTi Single Crystals

Huseyin Sehitoglu[1], D. Canadinc[1], I. Karaman[2], Y. Chumlyakov[3], H. J. Maier[4], K. Gall[5]

[1]Department of Mechanical and Industrial Engineering, University of Illinois,
Urbana, IL 61801, USA
[2]Department of Mechanical Engineering, Texas A&M University,
College Station, Texas 77843, USA
[3]Siberian Physical-Technical Institute, Revolution Sq. 1, Tomsk, 634050, Russia
[4]University of Paderborn, Lehrstuhl f. Werkstoffkunde, D-33095 Paderborn, Germany
[5]Department of Mechanical Engineering, University of Colorado,
Boulder, Colorado 80309, USA

Abstract

We report on the unusual deformation behavior of [001] single crystals of NiTi alloys in compression. Two compositions of NiTi with Ni contents (50.8 and 51.5% at. Ni) were examined. Pseudoelastic deformation occured at both 25°C and 167°C in compression loading. The reason for the higher pseudoelastic behavior temperature range is attributed to the suppression of slip due to the lack of favorable slip systems in the [001] orientation. The results point that with suitable orientation control the pseudoelastic behavior can be extended to high temperatures. The transformation strains for the 50.8% at. and 51.5% at. Ni alloys were established via temperature cycling under compressive stress as 4.0% and 2.5% respectively. The 50.8%Ni results compared favorably with the theoretical prediction of 4.38%.

Keywords

Shape memory, phase transformation, pseudoelasticity, austenite,martensite, slip, temperature cycling

Introduction

The NiTi alloys are a special class of materials which exhibit reversible transformations from austenite(B2) to martensite (B19') and then martensite (B19') to austenite (B2). The transformation can be induced via a change in temperature or the application of stress at temperatures exceeding the martensite start temperature, M_s. In both cases the transformation depends on the crystal orientation, and the loading direction because the habit planes associated with the transformation are of low

symmetry and the transformation is directional. Most experimental work confirm that Type II <011> twins have been established in the B19' martensite [1]. Theoretical calculations have been carried out to predict the twin types and the associated habit planes[2]. It has been shown [2] that if slip deformation occurs during transformation, this reduces the transformation strains. The slip deformation occurs readily with loading along certain crystal orientations but is difficult in specific orientations. The [001] orientation can not slip due to the lack of available slip systems. Experimental studies [3] have shown that <001>{100} and <001>{110} are the dominant slip systems in the B2 phase of NiTi alloys. Also, the B2 phase has been shown to undergo twinning at high temperatures [3]. Therefore, the [001] orientation is particularly attractive to achieve transformation at elevated temperatures where slip restricts the transformation.

Another factor that plays a significant role in the transformation process is the presence of precipitates in the material. These precipitates lower the transformation stress (in the peak aged condition) due to the coherency stress fields. In the overaged case, they provide barriers to dislocation motion and also reduce the Ni content in the matrix domains increasing the martensite start and austenite finish temperatures. For example, for the 51.5%Ni alloys the martensite start temperature increases from <-200°C (77K) in the solutionized case to –37°C (236K) for the overaged case. The increase in martensite start temperature with aging for the 50.8% is less dramatic and this increase is from -98°C (175K) in the solutionized case to -55°C(218K) for the overaged case.

The purpose of the present work is to demonstrate the stress-strain response of binary NiTi single crystals with two different compositions under compressive loads. By choosing the orientation ([001]) that minimizes slip deformation, both compositions exhibited pseudoleastic deformation behavior over a temperature range near 200°C which is a factor of two higher than the early works in NiTi alloys [4]. The paper also establishes the transformation strains upon temperature cycling under stress for the 50.8% at. Ni and 51.5% at. Ni compositions as 4.0% and 2.5% respectively. These experiments also provide insight into the martensite and austenite start and finish temperatures for the two compositions under thermomechanical loads.

Experimental Results

Single crystal Ti-50.8 and 51.5% at. Ni samples were prepared from ingots cast by Special Metals Co. The single crystal samples were grown by the Bridgman technique in an inert gas atmosphere. The orientation of single crystal specimens was determined by using electron back-scattered diffraction patterns. Solutionizing of the specimens was conducted at 1000°C(1273K) for 2 hours in an inert gas atmosphere. Then, the specimens were aged at 550°C(823K) for 1.5 hours and this treatment is designated as 'overaged'. The precipitate size is in the range 300-400nm for the 50.8%Ni case while it is about 750nm in the 51.5%Ni case. The introduction of Ni near 51.5% increases the volume fraction of the precipitates considerably with concomitant increases in overall strength of the austenite and martensite phases. Figure 1(a) is transmission electron microscopy (TEM) bright field image that illustrates the precipitates. There are four variants of precipitates but only two are visible under the imaging conditions employed to record this picture. In Figure 1(b) the precipitates after the same aging treatment are shown for the 50.8%Ni composition.

There are two ways to evaluate the behavior of transforming alloys. The first method is to investigate the stress-strain response under loading and unloading at a constant temperature. The second method is to cycle the temperature under constant stress and monitor the strains. In Figure 2, the stress-strain response at 25°C(298K) and 167°(440K) is shown for the 51.5% at.Ni and 50.8% at. Ni cases. The loading and unloading paths are illustrated with the arrows. Three observations are noteworthy.

Firstly, the strength levels where pseudoelasticity is observed extends to stresses as high as 1500MPa at 440K which is unusually high for NiTi alloys. Secondly, pseudoelasticity is observed at room temperature 25°C as well as at 167°C for both compositions with pseudoelasticity of 100% for the 51.5%Ni composition. Thirdly, the transformation region in 50.8%Ni material extends to higher strains compared to the 51.5%Ni case as seen in the 25°C data. This point is further elaborated in Figure 3.

In Figure 3, the strain-temperature behavior is presented under temperature cycling conditions. The strain temperature path is illustrated with the arrows upon cooling and heating. The transformation strains for 50.8% and 51.%Ni compositions were determined as 4% and 2.5% respectively. The stress level was maintained constant during the experiments. This stress level was chosen high enough to produce the growth of the most favorably oriented variant with respect to others and low enough to minimize inelastic deformation and ratchetting of the strains during thermal cycling. Some ratchetting in the compressive strain direction has occurred in the 50.8% Ni case (Figure 3) and this is subtracted from the overall strain range to determine the transformation strain. The stress levels applied for the two compositions differ considerably, and the level of stress is primarily dictated by the flow properties near the martensite start temperature. Since the resistance to transformation is lowest near the M_s temperature, the application of high stress levels near M_s could produce inelastic flow altering the transformation strain trends. The transformation strains from these experiments are summarized in Table 1 where the theoretical value for transformation in compression for the [001] orientation is also listed as 4.38%.

We note that the martensite start temperatures can be determined accurately from Figure 3 by observing the rapid change in strain with spontaneous transformation. The levels are near -28°C for the 51.5%Ni and –47°C for the 50.8%Ni case. These results are consistent with the slightly lower transformation stress observed for the 51.5% at. Ni case in Figure 2 compared to the 50.8%at. Ni case. Some degree of difference between DSC and the transformation temperatures under stress is expected based on the thermodynamics considerations as well as the preferred variant formation corresponding to the stress-induced transformation. A comparison of the transformation temperatures based on the DSC measurements and the strain-temperature tests are compared in Table 3. We note that the M_s temperatures for the 51.5%Ni is consistently higher compared to the 50.8%Ni case using both the DSC and the strain-temperature measurement techniques. The austenite finish, A_f, temperature is slightly below room temperature for most cases producing a single crystalline cubic structure at room temperature.

Summary

The stress-strain response of aged NiTi alloys with two different Ni compositions is reported. It is noted that both NiTi compositions exhibit pseudoelastic deformation over an unusually high range of temperatures. Theoretical calculations of transformation strains have been undertaken in our previous study [2] and the result is provided in Table 1 as 4.38%. This is in close agreement with the experimental values obtained for the 50.8%Ni case. The transformation strains for the 51.5% Ni case are 2.5% which is lower than the theory. This difference can be explained based on the high volume fraction of precipitates which are untransformable. The results of the temperature cycling experiments were particularly insightful because they pointed out the transformation temperatures under stress and relative hysteresis in the two materials. The results in Figure 3 confirm that the material is in the fully austenitic state at room temperature and also that the hysteresis in the 50.8% case is significantly higher than the 51.5%Ni composition.

We note that the stress-strain response shown in Figure 2 does not exhibit a flat plateau region over which transformation occurs. Instead, the stress levels increase continuously during the transformation. This behavior has been observed in previous studies and point out the presence of multiple variants of martensite during transformation which mutually interact and increase the difficulty for further transformation. The complete reversibility of transformation was observed for the T=25°C (298K) cases and the T=167°C (440K) 51.5%Ni case. For the T= 167°C (440K) 50.8%Ni case the transformation is partially recoverable while it is fully recoverable for the 25°C (298K) case.

References

1. Nishida, M., Ohgi, H., Itai, I., Chiba, A. and Yamauchi, K. (1995) *Acta Mater*., 43(3), pp. 1219-1227
2. Sehitoglu, H., Karaman, I., Anderson, R., Zhang, X., Gall, K., Maier, H.J. and Chumlyakov, Y. (2000) *Acta Mater*., 48(10), pp. 3311-3326.
3. Surikova, N.S. and Chumlyakov, Y.(2000) *Phys. Metals Metal.,* 89 (2), pp. 196-205
4. Funakubo, H., *Shape Memory Alloys* (1984). Gordon and Breach Science Publishers.

TABLE 1

EXPERIMENTAL VALUES OF TRANSFORMATION STRAINS COMPARED WITH THE THEORETICAL VALUE IN [001] COMPRESSION

Material	Transformation strain, [001] Compression
NiTi	4.38%- Theoretical [1] (Type II-1 twinning)
51.5% at. Ni-Ti	2.5%- Experimental (Figure 3)
50.8% at. Ni- Ti	4.0%- Experimental (Figure 3)

TABLE 2

SUMMARY OF TRANSFORMATION TEMPERATURES FROM THE DSC MEASUREMENTS AND FROM THE STRAIN-TEMPERATURE RESPONSE UNDER STRESS

		M_s	M_f	A_s	A_f
DSC	51.5%Ni at.	-37°C	-51°C	11°C	25°C
	50.8%Ni	-55°C	-42°C	-7°C	2°C
Strain-Temperature Tests	51.5%Ni	-28°C	-47°C	-6°C	3°C
	50.8%Ni	-47°C	-65°C	-20°C	15°C

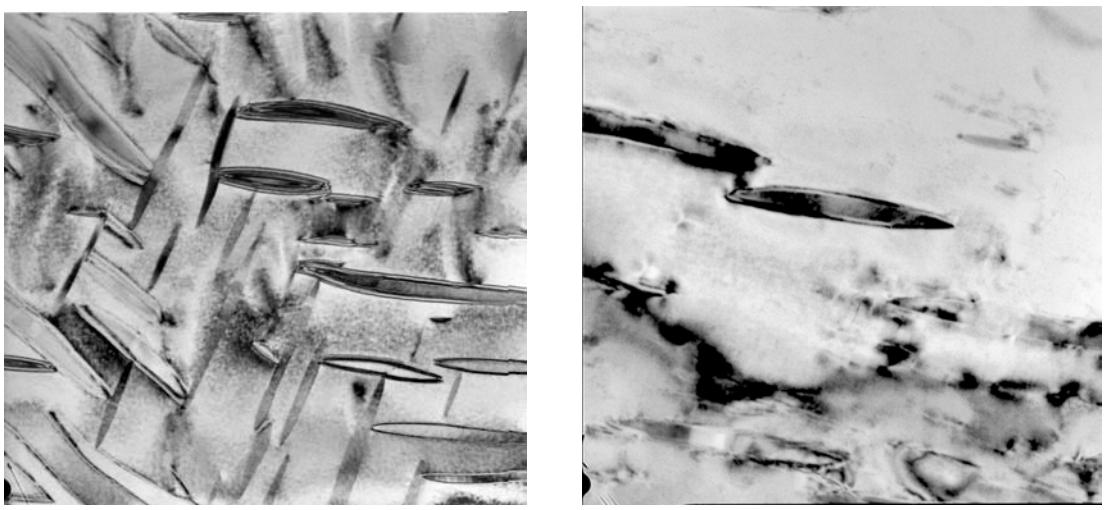

Figure 1: The Microstructure of the (a) 51.5% at. Ni and (b) 50.8% at. Ni NiTi alloys in the overaged state

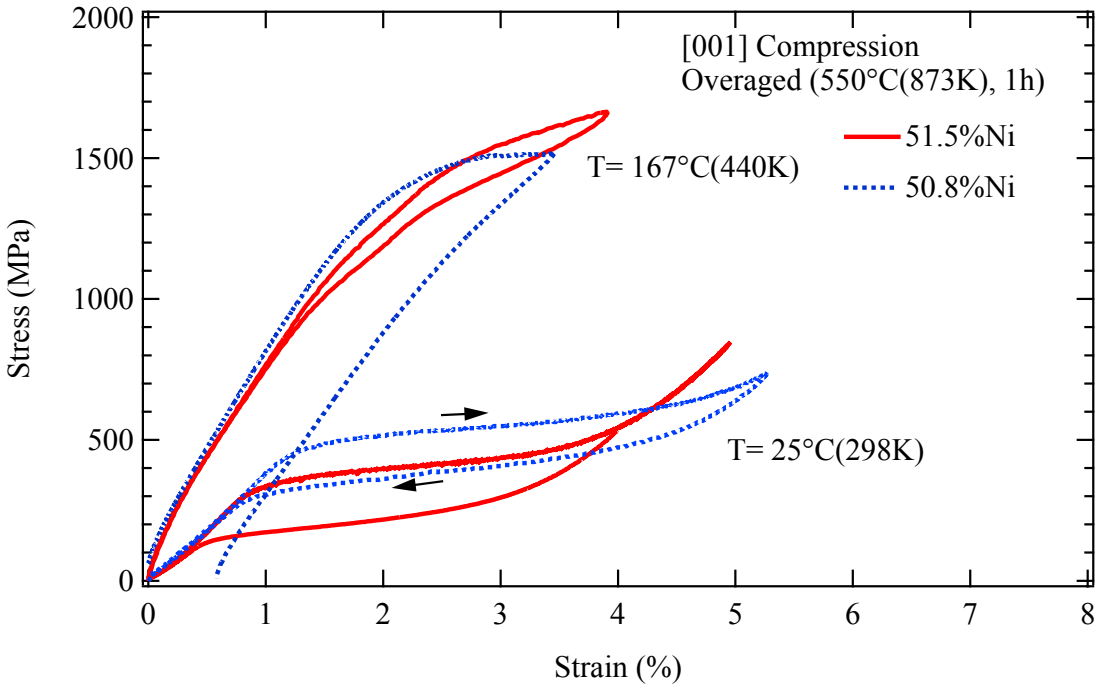

Figure 2: Compressive stress-strain response of 51.5% and 50.8Ni NiTi alloys at 25°C(298K) and 167°C(440K) in the [001] orientation.

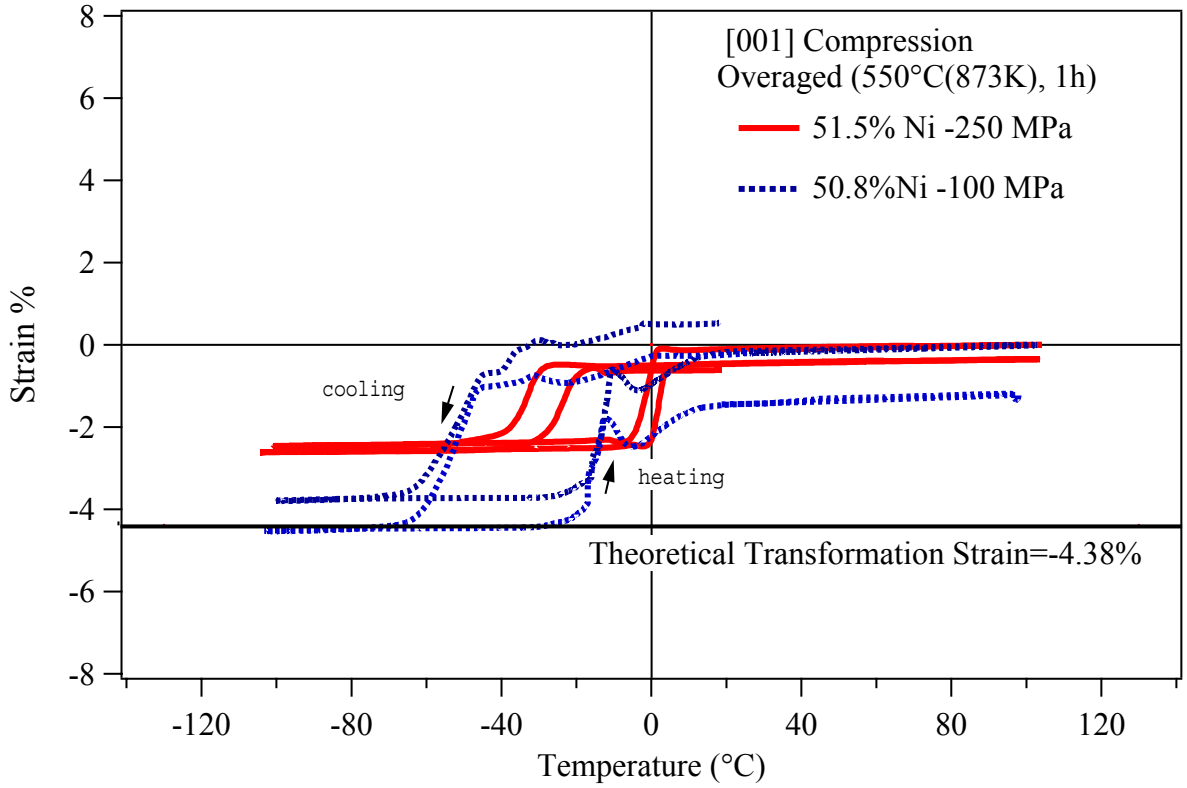

Figure 3: Strain-temperature behavior of two NiTi compositions under temperature cycling with a constant compressive stress.

POSTER REFERENCE: ICF100288PR

DESCRIPTION OF MULTIPLE CRACKING IN UV-DEGRADED STRESSED POLYETHYLENE USING PERCOLATION APPROACH

Ihor D. Skrypnyk[2], Natalia V. Bilyk[1], Jan L. Spoormaker[2]

[1] Karpenko Physico-Mechanical Institute, National Academy of Sciences of Ukraine,
5, Naukova st., 79601, Lviv, Ukraine
[2] Faculty of Design, Engineering and Production, Delft University of Technology,
9, Jaffalaan, 2628 BX, Delft, the Netherlands

ABSTRACT

Description of an evolution of damage, spread in bulk of material, remains for the time being a complex problem. The fracture mechanics approach is not capable to deal with the problem in general, since for the large ensembles of defects it requires lot of information and becomes too cumbersome. As a compromise the use of some physical theories, for instance percolation theory, can be suggested. These theories neglect some information related to individual characteristics of defects (in the other words they operate with the parameters of groups of defects).

Percolation theory deals with so-called "disordered systems", predicting behavior and certain properties of these systems, based on the properties of their elements. For simulation of cracking phenomenon, the possibility "to fail" is assumed for arbitrary element of this system. Then, using percolation theory approach, it is possible to study the dependencies between the probability of element' failure and formation of cluster of "failed elements", which connects opposite sides of the system (splitting it apart).

In frames of the traditional percolation theory it is assumed, that the elementary failure events should be independent. However, the damage evolution is affected by the long-scale stress-strain field, which, in turn, depends on the present distribution of damage. Hence, the percolation theory should be adapted to account for the long-scale fields (i.e. correlation of events). In this paper the elements of simulation approach, which includes both: elements of percolation theory and damage mechanics, is outlined. The approach is demonstrated by modeling surface cracking of high-density polyethylene due to it UV-degradation under mechanical loading.

KEYWORDS

Percolation approach, Finite Element analysis, damage evolution, surface cracking, UV-degradation

INTRODUCTION

The fracture mechanics' approach is not capable to describe the multiple cracks, developing quasi-uniformly in the bulk of material. Recently, in order to cope with the problem the percolation approach is employed [1 – 7] more and more intensively. The main attention here is paid to the process of formation of crack'

networks, connectivity of such networks and also to parameters, which can characterize these structures, like: percolation threshold, correlation radii [8] or excluded volume [7].

Although these studies have been performed on different geometrical objects (discrete and continuous) and have had different subjects (i.e. parameters) to be investigated, there are some features that are common for these studies. The "elementary failure events" have been assumed to be independent: in the other words, in all the cited papers only geometrical aspects of the crack' networks have been studied. In reality, however, the cracks grow, while affected by the long-scale stress field as well as by the other cracks. In order to account for this feature of the crack' networks evolution, the percolation theory approach should be modified. In this paper the elements of simulation approach, which includes elements of both: percolation theory as well as damage mechanics, is outlined. The approach is demonstrated for the case of modeling of surface cracking of High-Density Polyethylene (HDPE), degraded under UV-radiation and mechanical loading.

MAIN ELEMENTS OF PERCOLATION SIMUALTION APPROACH

Percolation theory [8] is an interdisciplinary field of research that constitutes mathematical method for the theory of critical phenomena and phase transitions [9]. It deals with the properties of so-called "disordered systems" (it can be a spatial lattice or a random spatial distribution of geometrical objects), which rise as the collective properties of its elements.

In order to model development of intergranular damage in polycrystalline material, the Voronoi tessellation was chosen as the object for percolation simulations, since the principle of formation of this tessellation is accordant with the principles that constitute the formation of a polycrystalline solid. The "possibility to fail" is assigned to every element in the tessellation. Using random numbers seed an "elementary failure" is drawn for every element. Next, clusters (i.e. sets of connected "failed" elements), their properties and evolution are to be monitored. Further, the lattice is scanned for a "percolated cluster", which connects two opposite sides of the tessellation, i.e. splits the object studied into two parts. The probability of percolated cluster formation (and corresponding "percolation thresholds") is to be evaluated.

There are several studies [10 – 12], where the Voronoi tessellation is being considered as the object for percolation studies. All of them, however, consider non-correlated percolation and none of them consider percolation as the model for fracture phenomenon of a polycrystalline solid. The elements of cluster labeling (in the other words: preparation for clusters' generation) for random lattices is given in [13, 14]. Further we will describe only some elements, related to simulation of correlated percolations. As mentioned above the "elementary failure" events in this model are correlated, but not directly – only through the long-scale field (namely stress-strain field). In order to construct such relation the stress-strain field should be calculated (for instance using Finite Element method) and mapped into the Voronoi tessellation (Fig. 1). Further the results of percolation simulations on the Voronoi tessellation at the end of every increment should be again mapped into Finite Element package. The above exchange of data was arranged in real time regime: in the other words, the Finite Element program and program for percolation simulations were waiting on each other at the moment, when the data from the other program are not yet calculated.

Unlike in the investigations [14, 15], where direct percolation was studied, the decision about "elementary failure occurrence" was derived, based on the completion of deformational criterion:

$$\varepsilon_{crystall} + \varepsilon_{external} = \varepsilon_c , \tag{1}$$

here $\varepsilon_{crystall}$ is a deformation of material due to internal stresses, $\varepsilon_{external}$ denotes external deformation and ε_c means the critical deformation level. The stochastic data concerning the failure of elements of the Voronoi tessellation were transformed to the continuous damage field ω by averaging of the results of percolation simulations over the λ-size regions [15].

This approach was used to study the surface cracking in UV-degraded and mechanically loaded HDPE.

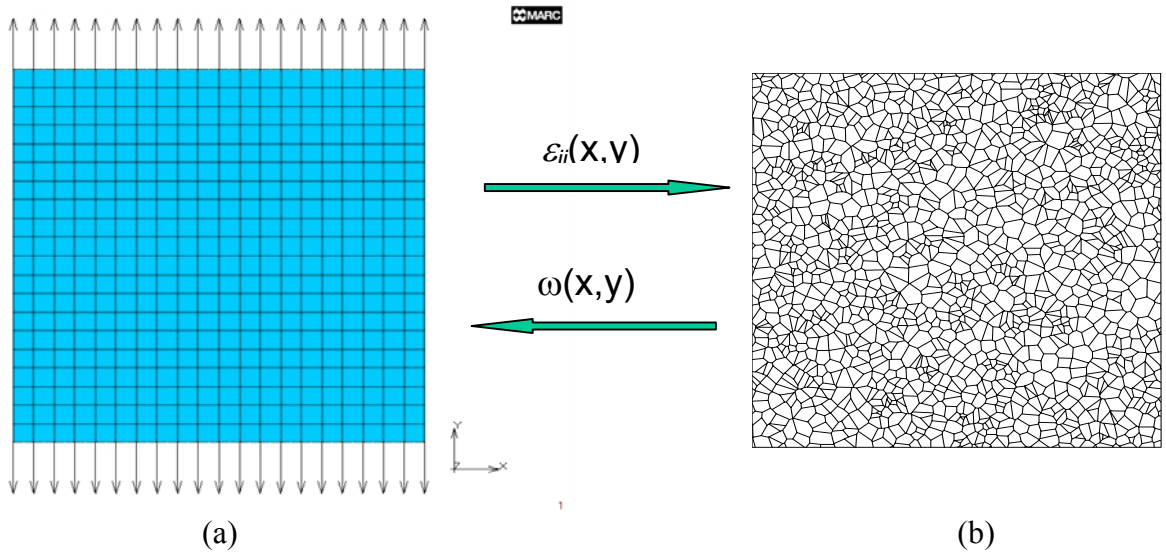

Figure 1. The scheme of data exchange between two parts of simulation process: FE modelling (a) and percolation simulation (b).

SOME ASPECTS OF BEHAVIOUR OF UV-DEGRADED HDPE

The main physico-chemical features of ultra-violet (UV) degradation of HDPE, which relate to surface cracking of material, are given in [14, 15]. Substantial drop in the material ductility with time (fig. 2,a) inevitably leads to the moment, when the critical strains ε_c become lower, than the local strains in polymer. In other words the deformational failure criterion $\varepsilon = \varepsilon_c$ turns out to be locally feasible, what results in the cracking along the crystallites' boundaries. These local strains ε might be the result of either mechanical loading (let us call them "external strains") or microstructural changes induced by UV-degradation of polymer ("internal strains"). Latter might be resulted by so-called "shrinkage due weathering" [16, 17].

The micromechanism of this phenomenon is as follows. The UV-degradation of polymer leads to additional crystallization of material: i.e. the amorphous regions that are closest to the crystalline lamellas transform into crystalline regions with the time passing by. The example of crystallinity' evolution in 0.2mm HDPE film during UV-degradation test is presented in fig. 2b. Since the density of HDPE crystalline phase (ρ_c=1.001·10 ^{6} g/m^3) is higher, than that of amorphous phase (ρ_a=0.856·10 ^{6} g/m^3) [18], the crystallinity growth leads to rise of total density of degraded material, which can be calculated as follows [19]:

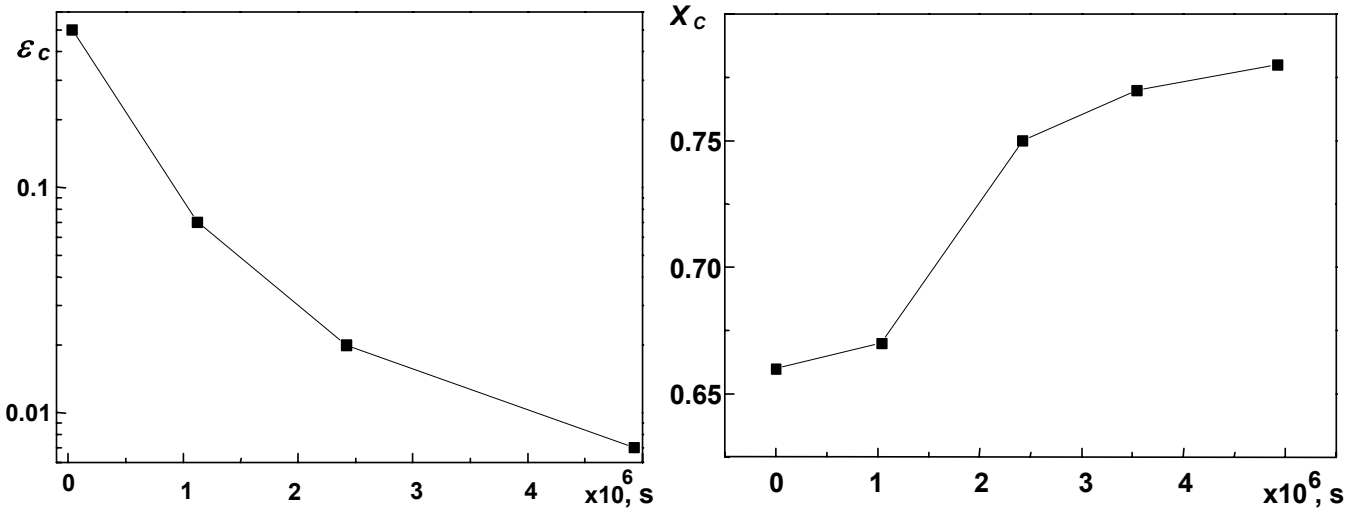

Figure 1. Strain failure, (a) and crystallinity X_c (weight fraction), (b) versus time of exposure to UV-radiation for 0.2mm HDPE film. Strain at failure registered for tension rate 3·10^{-6} s^{-1}, [19].

$$\rho_{tot} = \rho_c \rho_a \left[\rho_a X_c + \rho_c \left(1 - X_c\right) \right]^{-1}. \quad (2)$$

Assuming that the mass growth of polymeric material due to oxidation is small, the increase in density should lead to drop in volume of degraded polymer (i.e. degraded material "shrinks").

It should be noted that since UV-degradation requires constant replenishment of oxygen in material from surface, the spatial distributions of solved oxygen (as well as of the products of oxidation reactions) are formed [19]. In other words, the near-surface regions in polymers are most subjected to the UV-degradation and, hence, additional crystallization. Since these near-surface layers are tied with the bulk material, which does not suffer from these phenomena, the bulk material prevents these near-surface regions from shrinkage, what certainly will induce straining of outer surfaces:

$$\varepsilon_0(t) = \left[V_0 - V(t) \right] / V_0. \quad (3)$$

Here V_0 is the original volume (and the constant volume of bulk material, linked to considered part of surface); $V(t)$ denotes the variation of volume of degraded surface layer due to shrinkage. Taking into account the above assumption about the stability of polymer mass during weathering and, that the volume of a whole part consists of volume of amorphous and crystalline parts, the eqn. (3) can be rewritten as follows:

$$\varepsilon_0(t) = 1 - \left[\left(1 - X_c(t)\right)\rho_c + X_c(t)\rho_a \right] \times \left[\left(1 - X_c(0)\right)\rho_c + X_c(0)\rho_a \right]^{-1}. \quad (4)$$

Based on these phenomenological relations earlier [15] the simulation of surface microcracking in UV-degraded HDPE using percolation approach was performed. That study, however, accounted only for the internal strains as the possible reason for microcracking (i.e. correlation due to the long-scale field was neglected).

For simulation of the evolution of strain' field in UV-degraded HDPE the generalized Schapery model of relaxation type was modified in order to account for a continual damage parameter ω:

$$\varepsilon_{total} = \varepsilon_{ve} + \varepsilon_{pl}; \qquad \frac{\partial \varepsilon_{pl}}{\partial t} = C\left(\frac{\sigma - \sigma_0}{1 - \omega} \right)^{\chi}; \quad (4)$$

$$\sigma(t) = E_0 g_0(\varepsilon_{ve})(1 - \omega) + \sum_i D_i (1 - \omega) \exp(\beta_i \varepsilon_{ve}) \int_0^t \exp[-\lambda_i (\zeta_i - \zeta_i')] \frac{\partial [(\varepsilon_{ve})^{\alpha_i}]}{\partial \xi} d\xi; \quad (5)$$

$$\zeta_i(\xi) = \int_0^{\xi} \frac{d\xi}{a_i(\varepsilon_{ve})}; \qquad \zeta_i'(t) = \int_0^t \frac{dt}{a_i(\varepsilon_{ve})}; \qquad a_i(\varepsilon_{ve}) = \exp[\gamma_i \varepsilon_{ve}]. \quad (6)$$

The model parameters used for FE simulation of visco-elastic behavior of HDPE are given in Table 1 [20]. The details of the implementation of the model (4) – (6) in FE package MARC [21] are given in [22]. For this the user subroutine HYPELA [23] was employed.

Table 1. The set of model parameters for description of creep-recovery behaviour of HDPE

i	D_i	α_i	β_i	γ_I	λ_i
1	$.5976498 \cdot 10^3$	$.1145182 \cdot 10^1$	$-.259844 \cdot 10^2$	-	10^{+1}
2	$.140191 \cdot 10^3$	.8490412	$-.1368976 \cdot 10^2$	$.1786815 \cdot 10^1$	1
3	$.9025508 \cdot 10^3$	$.132205 \cdot 10^1$	$-.1379134 \cdot 10^2$	.9235095	10^{-1}
4	$.8507839 \cdot 10^2$	.8708816	$-.2221988 \cdot 10^2$	-	10^{-2}
5	$.1189788 \cdot 10^3$	.9295784	$-.1058856 \cdot 10^2$	$.5253887 \cdot 10^1$	10^{-3}
6	$.1578546 \cdot 10^3$	.9738781	$-.494870 \cdot 10^2$	-	10^{-4}
7	$.5585853 \cdot 10^2$	.9941104	$-.1252381 \cdot 10^2$	$.7399315 \cdot 10^1$	10^{-5}
8	$.6601488 \cdot 10^3$	.9040428	$-.1707527 \cdot 10^2$	$.5363343 \cdot 10^1$	10^{-6}
9	$.2640200 \cdot 10^2$	$.123677 \cdot 10^1$	$-.4865952 \cdot 10^2$	$.129430 \cdot 10^2$	10^{-7}

D_0	α_0	E_0	C	χ	σ_0
$.520395 \cdot 10^2$	.7241752	$.1036215 \cdot 10$	$.1499238 \cdot 10^{-5}$	$.121962 \cdot 10^1$	$.9810459 \cdot 10^1$

RESULTS OF MODELING

As the example for simulations an HDPE square plate, subjected for uniaxial tension and UV-degradation, is considered (fig. 1). Since the size of the Voronoi tessellation (i.e. number of elements in the tessellation) influences the results of percolation simulation (scaling effect), it is necessary to perform simulation for a set of lattices of different size. Next, using specific extrapolation technique [8], the conclusions concerning the behavior of infinitely large meshes can be derived. In this study the simulation was performed for 4 levels of stresses: 1, 3, 6 and 10 MPa. It was shown that for this model the percolation threshold $\boldsymbol{p_c}$ weakly depends on the stresses level (Table 2).

Table 2. Percolation threshold p_c of UV-induced microcracking in HDPE depending on the stress level

Stress level, MPa	-	1	3	6	10
Percolation threshold $\boldsymbol{p_c}$	0.6307	0.6363	0.6627	0.6773	0.6821

In the fig. 3 the variation of strain field and distribution of failed elements on the Voronoi tessellations versus stresses, applied to square plate, is given for the final moment of simulation at three stress levels: 10 MPa (Fig. 3, a), 3MPa (Fig. 3, b) and 1MPa (Fig. 3, c). The comparison of these fragments demonstrates an increase of the role of effective strains with the growth of the stress level: with the growth of stresses applied the formed clusters orient along the maximal shear strain direction.

REFERENCES

1. Balberg, I. (1985) *Phys. Rev.* **B, 31,** 4053.
2. Charlaix, E. (1986) *J. Phys. A*: *Math. Gen.* **19,** L533.
3. Balberg, I. (1987) *Phil. Mag.* **B, 56,** 991.
4. Chiles, J.P. (1988) *Math. Geol.* **20,** 631.
5. Berkowitz, B. (1995) *Math. Geol.* **27,** 467.
6. Sahimi, M. (1995) *Flow and Transports in porous Media and Fractured Rock,* Weinheim: VCH.
7. Huseby, O., Thovert, J-F., and Adler, P.M. (1997) *J. Phys. A*: *Math. Gen.* **30,** 1415.
8. Stauffer, D. and Aharony, A. (1994) *Percolation theory,* London: Taylor and Francis.
9. Stanley, H.E. (1971) *Introduction to phase transitions and critical phenomena*, Oxford University Press.
10. Noever, D.A., Cronise, R.J., Matsos H.C., Nikora V.I. (1995) *J. Phys. A*: *Math. Gen.* **28,** L115.
11. Hinrichsen, H., Schliecker, G. (1998) *J. Phys. A*: *Math. Gen.* **31,** L451.
12. Pittet, N. (1999) *J. Phys. A*: *Math. Gen.* **32,** L611.
13. Hoshen, J. and Kopelman, R. (1976) *Phys. Rev.* **B 14,** 3438.
14. Skrypnyk, I., Bilyk, N., Spoormaker, J. (2000) *Eur. Conf. on Fracture, ECF-13.*
15. Skrypnyk, I., Spoormaker, J. (1999) *Physico-Chemical Mechanics of Materials,* **35, № 4,** 73.
16. Bhateja, S.K. (1982) *Polym. Comm.* **23,** 654.
17. Brujin, J.C.M. de (1992) *The failure behaviour of high density polyethylene with an embrittled surface layer due to weathering*, Ph.D. Thesis, TU Delft, the Netherlands.
18. Moy F.H., Kamal M.P. (1980) *Polym. Eng. Sci.*, **20,** 957.
19. Hoekstra H.D. (1997) *The Mechanical behavior of UV-degraded HDPE: Consequences for Designers*, Ph.D. Thesis, TU Delft, the Netherlands.
20. Skrypnyk, I., Spoormaker, J. (2000) *ANTEC 2000 – Proc. of the 58th Ann. Tech. Conf. & Exhib.*, **XLVI**, 1504.
21. MARC (1997) *Theory and User Information*, Volume **A**, Rev. K.7, MARC Analysis Research Corp.
22. Skrypnyk I.D., Spoormaker J.L., Vasyljkevych T.O. (1999) *Report № K387 of Faculty of Design, Engineering and Production,* TU Delft.
23. MARC (1998) *User subroutines and special routines,* Volume **D**, Rev. K7, MARC Analysis Research Corp.

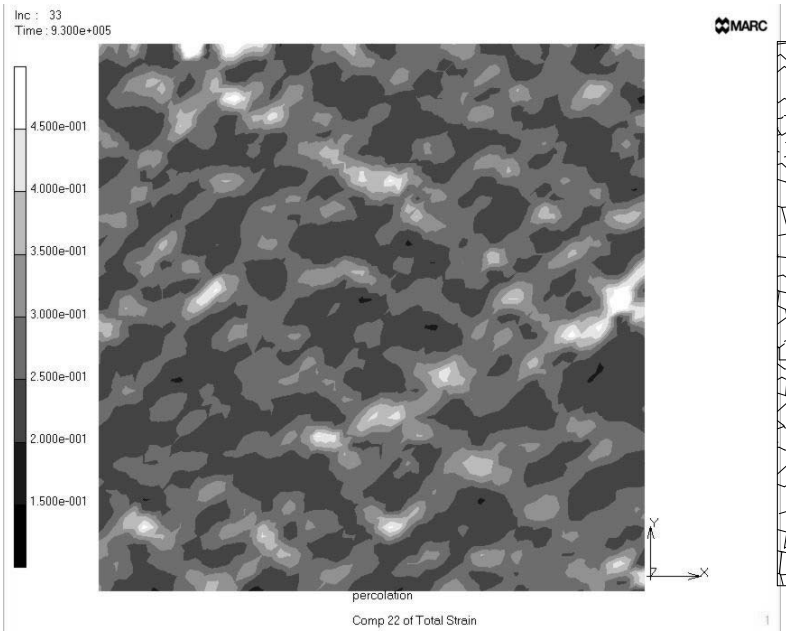

Figure 3, a.

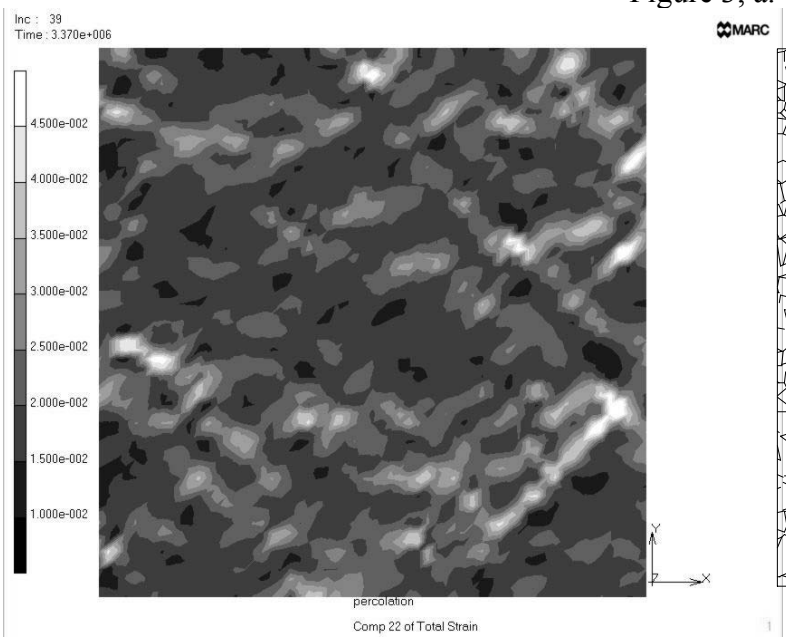

Figure 3, b.

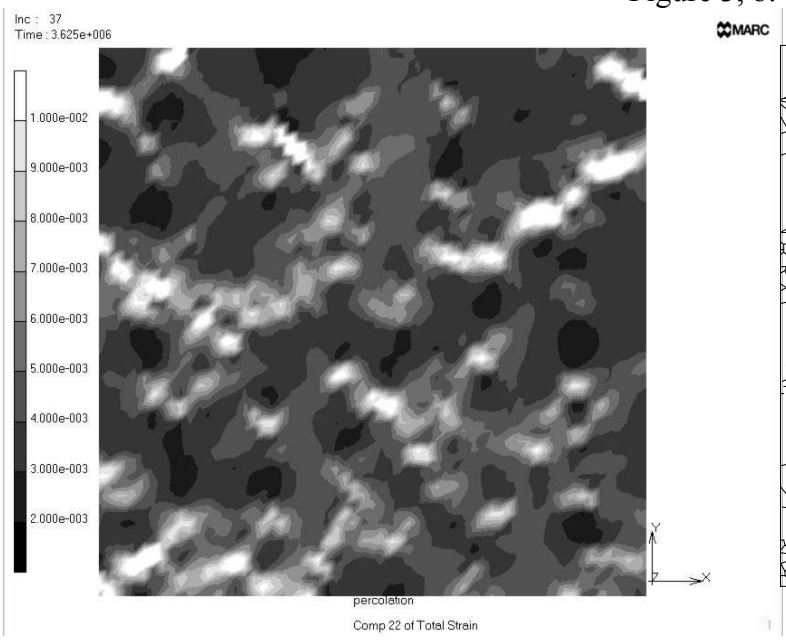

Figure 3, c.

POSTER REFERENCE: ICF 100380PR

Design of experiments for reliability assessment of active mechanical structures

R.Kouta*, H.Fall, W.Charon

Mécatronique3M, UTBM, rue du château 90010 Belfort, France

ABSTRACT

In recent years, significant activity around the world has been directed toward active control of mechanical structures. The goal of much of this research is to increase the reliability and safety of these structures against dynamic loadings. However, the design of most systems is done under conditions of uncertainty. If the uncertainties are not properly considered in the design of a control strategy, an absolute assurance cannot be given about the performance of the controlled structure. Such assurance can only be given in terms of a probability of failure in satisfying a criterion of performance: it is the reliability. This paper proposes a method to determine active mechanical structures effectiveness while assessing their estimated reliability, using design of experiments. Models joining active mechanical structures theories and those of reliability, and design of experiments method are presented. Numerical examples are provided through a controlled panel subjected to white noise excitation, to illustrate the effectiveness of the method.

KEYWORDS

Reliability, active control, vibration, design of experiments, white noise, LQG-control.

INTRODUCTION

Last decade has seen significant activity in the area of active control for mechanical structures against dynamic loading [1-3]. The principle of active control consists in attenuating a noise or a vibration while superimposing, with the initial amplitude, secondary amplitude of the same amplitude, but having an opposite sign. However, the design of most systems is done under conditions of uncertainty. The presence of such uncertainties can degrade control performance and can even lead to structural instabilities. To ensure such a performance, to study the reliability of these systems seemed a measurement necessary [4-7]. In this article, we propose to improve the active reliability of the structures by using the methods of the experimental designs. Initially we point out the various phases of the active systems design, the principle of evaluation of reliability, the methods of the experimental designs. Numerical examples on a panel subjected to an excitation of noise of white, are presented.

ACTIVE MECHANICAL STRUCTURES THEORY

There has been much research and many developments on active mechanical structures. Various methods incorporate concepts of modern control theory, and the active vibration control using piezoelectric sensors and actuators has drawn attention due to their higher applicability to real structures. Locations of both sensors and actuators have been determined with consideration of controllability, observability and spillover prevention. In the present case, the LQG-control technique is chosen, for the design of the controller [1-3,8-9].

One considers a deadened linear mechanical system disturbed by a white noise W, of which the equation representative is written:

$$M\ddot{q}+H\dot{q}+Kq=Dw \tag{1}$$

The equation of output or observation relating to this system is given by:

$$y=Cq \tag{2}$$

With $E\{w\} = 0$; $E\{w(t)w(\underline{t})\} = W\,\delta(t - \underline{t})$ and M, H, K are respectively the matrices of masses, damping, and stiffness. D, C are respectively the matrices of localization of the disturbances, and the exits. $q, \dot{q}, \ddot{q}$ are the vector displacement and its derivative. The equations (1) and (2) give a representation of the state of the following relationships:

$$\begin{cases} \dot{x}=Ax+\underline{D}w \\ y=\underline{C}x \end{cases} \tag{3}$$

With x which indicates the state of the system

The control of the system is done in closed loop, by observation of his state; as shown in figure 1:

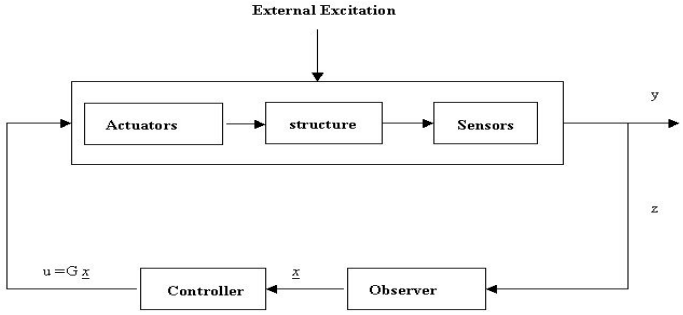

Fig 1. Schematic diagram of active control

The various phases of this technology of design lead to the following equations:
For the mechanical structure:

$$\dot{x}=Ax+\underline{B}u+\underline{D}w \tag{4}$$

$$y=\underline{C}x \tag{5}$$

$$z=\underline{M}x+v \tag{6}$$

For observer

$$\dot{\underline{x}}=A\underline{x}+\underline{B}\ \underline{u}+F(z-\underline{M}\ \underline{x}) \tag{7}$$

For controller

$$\underline{u}=G\underline{x} \tag{8}$$

$$u=\underline{u}+\tilde{n} \tag{9}$$

With $\underline{M}$: localization matrix of sensors, $\underline{x}$: the estimated state, z: the measurement of sensors, F: filter matrix, v: noise of measurement, G: gain matrix, B localization matrix of actuators, u: control vector, $\tilde{\eta}$: white noise, E $\{\tilde{n}\}$ = 0 and E $\{\tilde{n}(t)\ \tilde{n}(\underline{t})\} = \tilde{N}\delta(t-\underline{t})$.
According to the equations of (5) to (10) we obtain for the global system, the following equations:

$$\dot{x} = Ax + Dw \tag{10}$$

$$y=Cx \tag{11}$$

The covariance of output is expressed by:

$$Y=\underline{C}\chi\underline{C}^{T} \tag{12}$$

With χ the covariance of the state solution of the equation of Lyapounov

$$\chi A^{T} + A\chi + DWD^{T} = 0 \tag{13}$$

RELIABILITY ANALYSIS

This paper proposes to study the robustness of the laws of controls in the presence of uncertainties around the parameters of design of an active mechanical system. These uncertainties influence the stability and the performance of the controlled system. In the literature, a great importance is attached to the evaluation of the reliability of these types of systems [4-6]. Let us consider X = (X1, X2... Xn) the vector of the characteristic variables of the studied system. The first stage towards the evaluation of its reliability is to establish the functional relation binding these variables. This noted function G (X) is called function of state or function of absolute limit [10].

$$G(X) = G(X_1, X_2 \ldots X_n) \tag{14}$$

This function makes it possible to distinguish two fields: the field of safety or reliability called S (Sure) with G (X) > 0, and the field of failure called F (Failure) with G (X)<0. G (X)=0 is the surface of absolute limit. The reliability of the structure, noted PF is the probability that vector X is in an unfavorable position with the structure.

$$P_f = P[G(X) \leq 0] \tag{15}$$

$$P_f = \iiint_{G(X)\leq 0} \ldots \int f_{X1,X2\ldots Xn}(x_1, x_2 \ldots . x_n)\, dx_1 dx_2 \ldots dx_n \tag{16}$$

$f_{X1,X2,\ldots Xn}(x_1,x_2,\ldots x_n)dx_1\ldots.dx_n$ indicate the density of joined probability of the basic variables. Two methods are used to solve the integral (16): techniques of simulations of Monte Carlo or methods of approximations (FORM/SORM) [7]. Theoretical complexity for the installation of this type of method around the active systems led us to apply an experimental step. This step is based on the theory of the experimental designs.

DESIGN OF EXPERIMENTS METHOD

The method of the experimental designs helps in the study of the behavior of a complex system. It showed its effectiveness in different field from mechanics.
This method proposes a total model of behavior at the base of a series of experiments. This model is valid in the field of definition of the experiments. The number of experiments is depending on the number of the studied factors and the number of the methods chosen for each one. Each experiment of the plan brings information on the behavior of the studied system. The total analysis associated each experimental design is single. This analysis shows the influence of each factor on the total behavior of the answer (fig. 2). Concerning the study presented in this paper, it is reasonable to adopt a numerical step of experimentation in order to limit the number of experiments to be led to the laboratory.

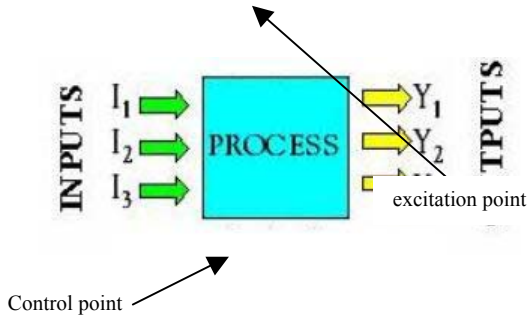

Fig 2 Process of Design of Experiments

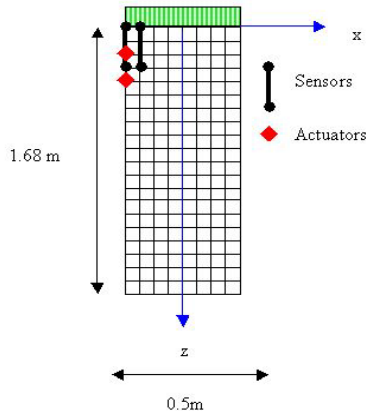

Fig 3 Configurations end dimensions of the Panel

This paper presents the study of the active control of a vibrating panel which undergoes a white noise excitation (fig 3). The study is carried out with the method of the experimental designs. The whole of the undertaken experiments is numerical. Calculations are done with a software for modeling of structures developed under MATLAB.
Concerning the application presented in this paper the objective is to determine the conditions of control of the standard deviation (σ_y) of clearance at the studied point. This standard deviation must be lower than 10E-3m (covariance=1E-6).
It is about clearance according to the direction perpendicular to the plan of figure 3 (y). However, in the presence of the observer and of the regulator σ_y is 1.51E-3 (covariance=2.27E-6).
The objective of the experimental step presented in this paper is to determine the adjustments of the factors of design to control the dispersion of the clearance measured with the node indicated on figure 3. This adjustment is carried out in a configuration given concerning the positioning of the sensors and the actuators.
The experimental design carried out relates to three factors. These factors and their level are presented in table 1. In this case the number of experiments is 27. Table 2 presents the plan used as well as the results obtained.

Table 1

Factors	Level			Units
	1	2	3	
A: width of the Panel	0.5	0.55	0.6	m
B: Young Modulus	7.1981E+10	7.2E+10	7.2019E+10	N/m²
C: Thickness of the Panel	1.8	2.0	2.2	Mm

The statistical analysis of the results for the experimental design confirms the importance of factors A, and C. At the same time, it reveals a strong presence of an interaction between these two factors. The nonlinear character of the results is with the results observed when A is on level 1 and C on level 1. This particular case is a configuration not wished for in design. Figure 4 shows the behavior of the factor A, B, C like that of the interaction AC.

Number of test	A width of the Panel	B Young Modulus	C Thick of the Panel	Y	σ_y
1	1	1	1	7,10E-06	2,67E-03
2	1	1	2	3,83E-06	1,96E-03
3	1	1	3	3,43E-06	1,85E-03
4	1	2	1	7,04E-06	2,65E-03

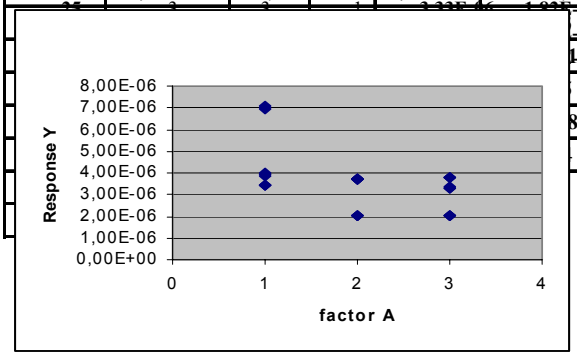

Table 2

Factors	variability	%	d.o.f	variance	experimental Fisher
A	1,71E-11	33,63	2	8,56E-12	5177,58

Table 3 : Variance analysis

Fig. 4-1: effect of A

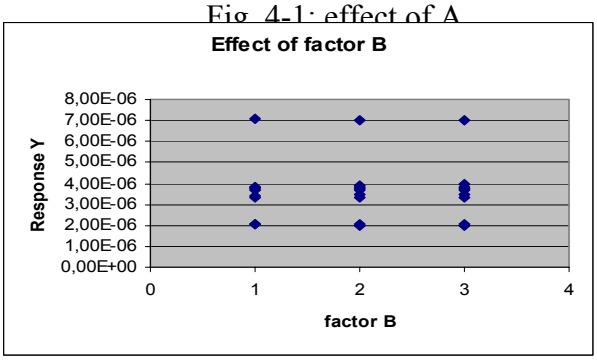

Fig. 4-3: effect of B

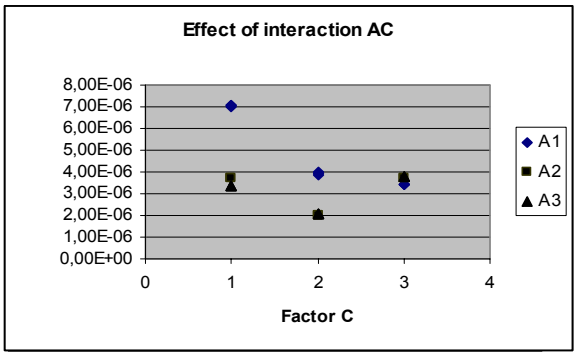

Fig. 4-3: effect of C

Fig. 4-4: effect of AC

The mathematical modeling suggested by the method of the experimental designs shows that it is possible to obtain levels of answers closer to the desired objective (σ_y < 1.51E-3 thus a covariance < 2.27E-6). Indeed, the strong influence of the interaction AC disturbs the level of the results.

Thus two configurations were retained to carry out experiments complementary with A to the level 0.575mm, B on level 7.210E+10 N/m2 and C on the levels 19mm and 21mm. The two results obtained are: with C with 19mm σ_y = 1.42E-3 (covariance=2.019E-6) and for C to 21 mm σ_y = 1.49E-3 (covariance = 2.227E-6).

Thus the configuration which consists in locking A on the level 0.575mm, B on the level 7.210e+10 N/m2 and C on the level 19mm lead to an interesting technological solution. Indeed it is about a thin plate with an optimized width and an average Young modulus.

The mathematical model resulting from the method of the experimental design shows in this configuration that the standard deviation of the clearance of the studied point lies between [1.4E-3 and 1.44E-3] with a confidence of 95%. Thus probability P_f (probability of failure) is in this case is 5%.

CONCLUSION

The evaluation of the reliability of an active structure is difficult to obtain according to steps employed today for the passive mechanical structures. Indeed, the use of the theoretical methods is not easy. The methodology of the experimental designs A made it possible to explore various configurations of design and to retain the best without the obligation to change the strategy of control adopted with the design. It remains to explore the possibility of controlling the parameters of manufacture of this type of structure (roughness, surface treatment...) and their interactions with the active character of the structure.

REFERENCES

1 Charon, W.(1991) “Actuators Positionning within the Mechanical Design of Active Structures” Paper 91-143., Int. Forum on Aeroelasticity & Struct. Dyn., Aachen., June 3-6

2 Charon, W. and Baeir, H. (1995) “ Active Mechanical Compononents as a Step toward Adaptive Structures in Space” J. of Intell. Mater. Syst. And Struct. Vol 6, pp 396-402.

3 Meirovitch, L.,(199) “Dynamics and Control of Structures” New York: Wiley.

4 Spencer, B.F., Sain, M.K., Kantor, J.C., and Montemagno, C. (1992) “Probabilistic Stability Measures for Controlled Structures Subjected to Real Parameter Uncertainties”. Int.Smart Materials and Structures, vol. 1, pp.294-305.

5 Spencer, B.F., Sain, M.K., and Kaspari D.C. (1994) “Structural Control Design: A Reliability-Based Approch” Proceeding of the American Control Conference, Baltimore, Maryland. June

6 Venini, P., and Mariani C. (1999) “Reliability as a measure of active control effectiveness”. Computers & Structures. Vol 73, pp 465-473.

7 Mahadevan, S.,(1988) “Stochastic Finite Element-Based Structural Reliability Analysis and Optimization” Ph.D thesis, Georgia Institute Of Technology, Atlanta.

8 Jae-Hung Han., and In Lee., (1999) “Optimal Placement of Piezoelectric Sensors and Actuators for Vibration Control of a Composite Plate Using Genetic Algorithms” Smart Mater. Struct. Vol 8, pp 257-267.

9 Lim K.B., (1992) „ Method for Optimal Actuator and Sensor Placement for Large Flexible Structures” J. Guidance Control Dyn., Vol 15, pp 49-57.

10 Madsen, H.O., Krenk, S., and Lind, N.D. (1986) “Methods of Structural Safety”, Prentice-Hall, Inc., Englewood Cliffs, New Jersey.

11 Hicks, C. R. (1982). Fundamental Concepts in the Design of Experiments, 3rd. ed., Holt, Rinehart and Winston, New York, NY, USA.

12 Montgomery, D. C. (1991). Design and Analysis of Experiments, 3rd. ed., John Wiley and Sons, New York, NY, USA.

ORAL REFERENCE: ICF100834OR

DETERIORATION PROPERTIES OF DAMAGED CONCRETE DUE TO FREEZING AND THAWING

M. Saichi[1] and H. Mihashi[2]

[1]Department of Architecture, Tohoku Institute of Technology,
Sendai, 982-8577, Japan
[2]Department of Architecture and Building Science,
Graduate School of Engineering, Tohoku University,
Sendai, 980-8579, Japan

ABSTRACT

This paper presents a study on statistical feature of internal cracks developed in frost-damaged concrete. Concrete specimens were observed for internal cracking by means of digital microscope after they were subjected to a series of rapid freezing-and-thawing cycles. The intensity of cracking was estimated by means of the intersections of traverse line and cracks. The agreement of shapes between normal distribution and observed histogram of intersects was verified. Furthermore, the expedience of using intersections for quantification as well as applying a probability distribution to the estimation of cracks was substantiated. Although, in this paper, observed cracks were restricted to those observed on the cut surface perpendicular to the direction of length, consequent findings might provide useful information for assessing the feature of damaged concrete due to freezing and thawing.

KEYWORDS

Concrete, frost damage, freezing-and-thawing test, normal distribution, statistical analysis

INTRODUCTION

In our study, the focus of interest is originally put on the field of damage assessment of concrete in existing reinforced concrete (RC) structures. This paper presents a study conducted as a part of series of investigation that was made to reveal the feature of internal cracking caused by frost damage.

Relation between damages and internal cracks

RC structures constructed in a cold district are possible to subject many freezing-and-thawing cycles during their design lives, and concrete is known to be deteriorated after a certain cycles. It has long been recognized that concrete is damaged by the internal pressure caused by freezing of the contained water [1,2]. Many investigators have implied that the intensity of damage is related to irreversible cracking within concrete. These and similar studies underscore the important role of internal cracking for the disruptive behavior and/or life of the concrete structures. On the other hand, in case of the frost-damaged concrete, research interests have been mainly focused on the nature of freezing effects, and little research has been done on the internal cracking.

Microscopic observation of internal cracks

While progressive cracking has mainly been observed by means of indirect examinations such as dynamic elastic modulus, direct observation is preferable because this would provide the precise information pertinent to the mechanism of cracking: for example, the location, the exact size of internal cracks, and so on. The use of powerful microscopes has been able to study the formation of internal cracks [3], and some insight features have been obtained on the change in concrete. A direct observing method by means of microscope for studying microstructure and crack growth within concrete was introduced by Hsu [4] and Shah and Sanker [5]. As demonstrated by them, a meso-level microscopic observation could be a useful tool for detecting distributed internal cracks. The most apparent properties of internal cracks are the number and the size including length, width and depth. In practice, however, the most widely used characteristic is the length of cracks developed on the surface during and/or after the freezing-and-thawing cycles.

The purpose of this paper is to estimate the deteriorated properties of frost-damaged concrete by means of microscopic observation of internal cracks. Statistical features of the cracks are also analyzed.

EXPERIMENTAL WORK

Specimen preparation

The specimens used were concrete prisms whose dimensions were $100 \times 100 \times 400 mm^3$. The nominal value of compressive strength was 30MPa. Ordinary Portland cement was used. The coarse aggregate was crushed gravel with the maximum size of 20 mm and the fine aggregate was crushed sand. No chemical or mineral admixtures were applied to the concrete mix. Approximately 48 hours after casting, specimens were removed from the steel molds and transferred to a standard water curing room where curing was continued at approximately 20℃ until the day freezing and thawing tests started.

Frost damage simulation

A series of rapid freezing-and-thawing test was carried out in this study for frost-damage simulation. The freezing-and-thawing cycles were applied according to the ASTM specification, "C 666, Procedure A". The cycle consists of alternately lowering the temperature of the specimens from 5 to -18 degree Celsius and raising it from –18 to 5 degree Celsius in 4 hours.

The tests were started when specimens were reached at an age of 14 days. Immediately after the curing period, specimens were weighed, and measured for fundamental transverse frequency, in accordance with the method of ASTM C 215, on the basis of which the frost damage levels were identified. After these measurements, the freezing and thawing cycles were started. The specimens were removed from the apparatus at intervals of 30 cycles. After rinsing out the container as well as adding clean water, they were returned to random positions in the apparatus with upside-down basis. In each interval, one specimen having a role in fixing the data of particular cycle was selected and kept out. The specimen was tested again for fundamental transverse frequency, weighed, and took procedures of preparation for microscopy. The freezing-and-thawing cycles were applied until the number of cycles was reached more than 300.

Preparation for microscopy

Since microscopy requires the specimen of a suitable size, a piece of cube (100mm in length) was taken from the frost-damaged prism. A transverse section, perpendicular to the longitudinal direction, was cut out directly through near the center of the prisms: thus the block of specimen has the size of 100 mm square in the section.

In total 7 concrete prisms were used to observe the cross section under a microscope. Each section was observed for internal cracking by means of optical microscope, which equipped with a high-resolution CCD digital camera and storage devices. Since this microscope did not require thin sections, time-consuming preparations of those samples could mostly be omitted. Cross sectional area was ground carefully by precision grind machine until no trace of saw could be seen. A red liquid for penetration was sprayed over the area for the staining. This was done to distinguish more clearly between cracks at

the interface and those through the matrix. After several times, mortar surface became a color of light pink, and deep red lines representing internal cracks could be clearly distinct in the view. The stained surface was then ground again on a grinding wheel. The sections were then slowly dried in room where the atmosphere was kept at 20℃ and approximately 65 percent relative humidity. Neither the sawing process nor the drying process on specimens was considered to significantly affect the measured characteristics of cracking because their effects were verified to be negligible through the preparatory tests.

Observed areas

The observed area used for the microscope observation was 6350mm^2 in total per section so that a sufficiently wide range of size could be covered. The observed data presented herein were obtained from the sample areas determined by dividing the observe area into 10×12 segments. Each segment has the dimension of 6.4×8.4mm^2, and is designated as "sample area" in this paper (see, Figure 1). At first, the feature of each sample area was recorded on a MO-media as a digital image. Subsequently, all images (in total 840) were processed.

EXPERIMENTAL RESULTS AND DISCUSSION

General feature of the internal cracks observed in the sample areas

At the beginning of the observation, relevant sample area was served onto the PC monitor from the MO media. The sample area was composed of matrix and inclusions, as shown in Figure 2. When observed at the previously mentioned magnification, those compositions are regarded to be in the scale of meso-level. The observation indicated that many internal cracks were identified in the sample area, regardless the intensity of the frost damage. Cracks through the mortar area, so called mortar cracks, began to increase noticeably and form continuous crack patterns from initial cycles whereas they would be developed at about 70～90 percent of the ultimate load in case of mechanically damaged concrete [4, 6]. Since internal cracks were shaped like a network pattern similar to cracks of parched earth, and their lengths were spread over a considerable extent, those cracks were not allowed to identify individually. Therefore, neither counting nor tracing of cracks was practicable. Hence, newly devised procedure for quantification would be required. As described later, intersections of traverse line and cracks were used in this paper as a parameter for estimating the intensity of internal cracking.

Relation between internal cracking and intensity of frost damage

Equivalent freezing-and-thawing cycle

Since specimens did not necessarily show the correspondence of damaged feature with nominal number of freezing-and-thawing cycle, the term "equivalent freezing-and-thawing cycle" was introduced to indicate the real stage of intensity of the frost damage. The equivalent freezing-and-thawing cycle was defined as the estimated value led from the correlation between nominal freezing–and-thawing cycle and dynamic Young's modulus of elasticity. The former was indicated by the apparatus, and the latter was calculated from the fundamental transverse frequency measured by the reference specimens. Frost damaged specimens were calibrated according to the established correlation, and the respective equivalent freezing-and-thawing cycle was determined. Hereafter, in this paper, the equivalent number of freezing-and-thawing cycle will be used for representing the number of freezing-and-thawing cycle.

Intersections as a parameter for quantification

Three linear-traverse-lines, which were referred to as test lines in this paper, were first drawn and were superimposed on each sample area as shown in Figure 3. Subsequently, intersections of test lines and cracks were counted. Since this process was repeated for every sample area, in total 360 test lines per observed area were drawn. These procedures were processed by using software, which enables to generate graphics as well as to perform some calculations.

Relation between damage intensity and extent of internal cracking

Figure 4 shows the comparison of extent of cracks within each sample area for sound and damaged specimens. For clarifying, results relating to three specimens are presented. Each bar represents total number of intersections included in respective sample area. Compared damaged specimens (Figure 4-b and c) with sound one (Figure 4-a), it is obvious that damaged specimens produce a higher extent of internal cracking. Figure 4-a also showed that cracks densely distributed are contained widely even in the sound (0cycle) concrete. This is a manifestation of the well-known phenomenon of existing cracks observed experimentally and/or microscopically by many investigators.

Statistical distribution of intersects

Figure 5 illustrates typical relation between damage intensity and increasing feature of intersects for three different freezing-and-thawing cycles. Although other diagrams were omitted to save the space, they showed essentially a similar trend. Each bar represents the number of test lines counted for the certain rank of intersections, and the line superimposed is drawn according to the normal distribution law. As shown in each diagram, there is an interesting agreement between bars and the line, and the Chi-square test carried out on each group of data did not reject the agreement at the usual significance level. These results suggest that the distribution of intersects could be approximated by a normal distribution.

Practical quantification of internal cracks

As intersections are essentially dimensionless data without perceptible area or length, the term "density of cracks" that is estimated by the Eqn. 1 is introduced for the practical quantification:

$$L_A = P_{Lx} = \int_0^{Ly} p_{Lx}(y) \cdot f(y)\, dy \qquad (1)$$

where, L_A is the estimated density of cracks (mm/mm^2); P_{Lx} is the expected density of intersects (points/mm), which is practically estimated by the average value; Ly is the longitudinal length of the sample area; $p_{Lx}(y)$ is the total number per test line at the position on the sample area; and $f(y)$ is the probability of appearance of the test line at the increment of dy .

Figure 7 represents the estimated density of cracks as a function of the freezing-and-thawing cycle increases. As shown in Figure 7-a, internal cracks increased with two stages that are a steeply increasing stage in lower cycles less than 30, and a gradually increasing stage in more than 30 cycles. The relation might be approximated by a bi-linear function when cycles were converted into logarithmic numbers as shown in Figure 7-b. The cyclic number of the break point was in the vicinity of 150 cycles.

CONCLUSIONS

Based on the results of this study, the following conclusion can be made.

1. Mortar cracks began to increase and form continuous patterns even in the initial cycles.
2. Cracks were not allowed to be identified individually since internal cracks were shaped like a network pattern similar to cracks of parched earth, and their lengths were spread over a considerable extent.
3. Damaged specimens produce a higher extent of internal cracking, and those cracks increase as the freezing-and-thawing cycles increase.
4. Intersects of a test line and cracks were utilized for crack quantification, and their distribution could be approximated by a normal distribution.
5. Internal cracks were increased with two stages that are a steeply increasing stage in lower cycles less than 30, and a gradually increasing stage in more than 30 cycles. The relation might be approximated by a bi-linear function, when cycles were converted into logarithmic numbers.

REFERENCES

1. Powers, T.C. (1945). *Journal of the ACI*, 16 (4), 245.
2. Powers, T.C. (1975). In: *Durability of concrete in service:* pp.1-11, ACI Committee, SP-47-1.
3. Wang, K., Monteiro, P.J.M., Rubinsky, B., and Arav, A. (1996). *ACI Materials Journal*, 93 (4), 370.
4. Hsu, T.T.C., Slate, F.O., Sturman, G.M., and Winter, G. (1963). *Journal of the ACI*, 60 (2), 209.
5. Shah, S.P. and Sanker, R. (1987). *ACI Materials Journal*, 84-M22, 200.
6. Carrasquillo, R.S. and Slate, F.O. (1983). *Cement, Concrete, and Aggregates*, 5 (1), 54.

POSTER REFERENCE: ICF100452PR

DETERMINATION OF DIFFERENT FRACTURE MODES STRESS INTENSITY FACTOR WITH VIRTUAL CRACK EXTENSION METHOD

B. Zafošnik, M. Ulbin and J. Flašker

University of Maribor, Faculty of Mechanical Engineering,
Smetanova ul. 17, 2000 Maribor, Slovenia

ABSTRACT

There are many methods for determination of stress intensity factors K_I, K_{II}. Evaluation of stress intensity factors determination using maximum energy release rate theory and complex J integral is the main purpose of the paper. A number of numerical analyses using the Compact Tension Shear (CTS) specimen were performed for determination of stress intensity factors. Virtual extension method (VCE) in framework the finite element method was used for crack propagation analysis. Calculated crack propagation angles with VCE method were compared to experimental results and crack propagation angles calculated using a maximum tangential stress criterion. Accuracy of determination crack propagation angles using virtual crack extension method was evaluated for different fracture mode.

KEYWORDS

Mixed Mode fracture, CTS specimen, Virtual Crack Extension method, Stress Intensity Factor

INTRODUCTION

For general, cracked structures it is necessary to consider the combined effects of mode I, II and III loading in linear elastic fracture investigations. In fact, mode III is largely separable and can be dealt with in an independent manner, but the combined effect of modes I and II, under tensile and shear loading, presents difficulties in analysis. Several mixed-mode fracture criteria exist, and they can be generally divided into two groups, depending on their scopes. Some criteria are concerned only with the local information at or around the crack tip (local approach) whereas others consider the global or total information about the whole body containing the crack (global approach). In the local approach, one needs to choose a parameter (or physical quantity) that measures the severity experienced by the local material particles at or around the crack tip. Widely used parameters include the maximum principal stress, the maximum circumferential stress ($\sigma_{\theta max}$) and the minimum strain energy density (S_{min}). The local approach appears to be based on a choice of the parameter through intuition. In contrast, the global approaches are based on the total potential (strain) energy of the system. The fundamental physical quantity in the global approach is the strain energy release rate G, which is the sole fracture parameter that governs the behaviour of the crack. G represents the strain energy that is lost by the system through unit surface extension of the crack. Richards [1] showed the most accurate criterion for crack propagation on CTS specimen is MTS criterion.

VIRTUAL CRACK EXTENSION METHOD (VCE)

The Virtual Crack Extension method, originally proposed by Hellen [2], is based on the criteria of released strain energy dV per crack extension da

$$G = -\frac{\mathrm{d}V}{\mathrm{d}a} \tag{1}$$

which serves as a basis for determination of the combined stress intensity factor around the crack tip

$$K = \begin{cases} \sqrt{E \cdot G} & \text{plane stress;} \\ \sqrt{\dfrac{E \cdot G}{(1-\nu^2)}} & \text{plane strain.} \end{cases} \tag{2}$$

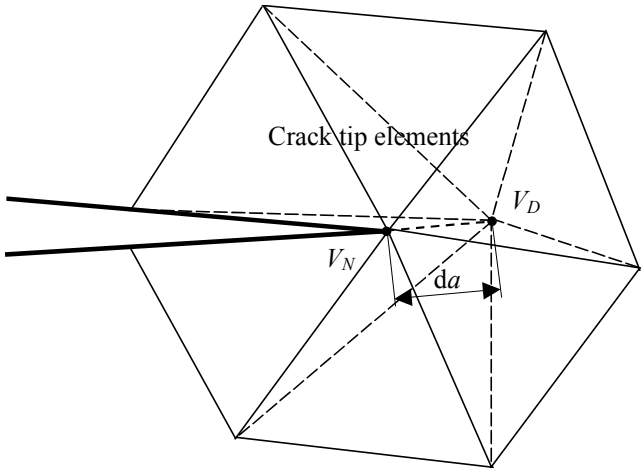

Figure 1: Initial and extended crack tip configuration

If V_C is the strain energy obtained for all degrees of freedom not present in the crack tip elements, and V_N is the energy in the crack tip elements when the tip is not extended, while V_D is the energy in these elements when the tip is extended, Figure 1, then the total energies of the initial and altered bodies, V_N^T and V_D^T, respectively, are equal to

$$V_N^T = V_C + V_N \quad \text{and} \quad V_D^T = V_C + V_D \tag{3}$$

Thus for a virtual crack extension δa it follows

$$\frac{\mathrm{d}V}{\mathrm{d}a} = \frac{V_D^T - V_N^T}{\delta a} = \frac{V_D - V_N}{\delta a} \tag{4}$$

which is clearly independent of V_C. It follows that only strain energies V_N and V_D in the crack tip elements need to be calculated for every possible crack extension. This results in a very efficient method for determination of the instantaneous energy release rate and thus the stress intensity factor for any given crack extension. Following the same argument, the energy release rate G and the stress intensity factor K can be easily determined for several different possible crack extension directions for a cluster of points on an arc around the initial crack tip with radius da, see Figure 2a

$$\left(\frac{\mathrm{d}V}{\mathrm{d}a}\right)^j = \frac{V_D^j - V_N}{\mathrm{d}a^j}. \tag{5}$$

Assuming the validity of the maximum energy release criterion, the crack will propagate in direction corresponding to the maximum value of $(\mathrm{d}V/\mathrm{d}a)^j$, *i.e.* in the direction of the maximum stress intensity factor

K^j. Computational procedure is based on incremental crack extensions, where the size of the crack increment is prescribed in advance. The virtual crack increment should not exceed 1/3 of the size of crack tip finite elements. For each crack extension increment the stress intensity factor is determined in several different possible crack propagation directions and the crack is actually extended in the direction of the maximum stress intensity factor, which requires local remeshing around the new crack tip. The incremental procedure is repeated until full fracture occurs or until the stress intensity factor reaches the critical value K_c, when full fracture is imminent. For improved numerical results, special fracture finite elements are used in the first circle of elements around a crack tip, with ordinary elements elsewhere, Figure 2b. In these special fracture finite elements, the displacements are proportional to the square root of the distance from the tip. Since the tip stresses are singular, they are not calculated at the crack tip node.

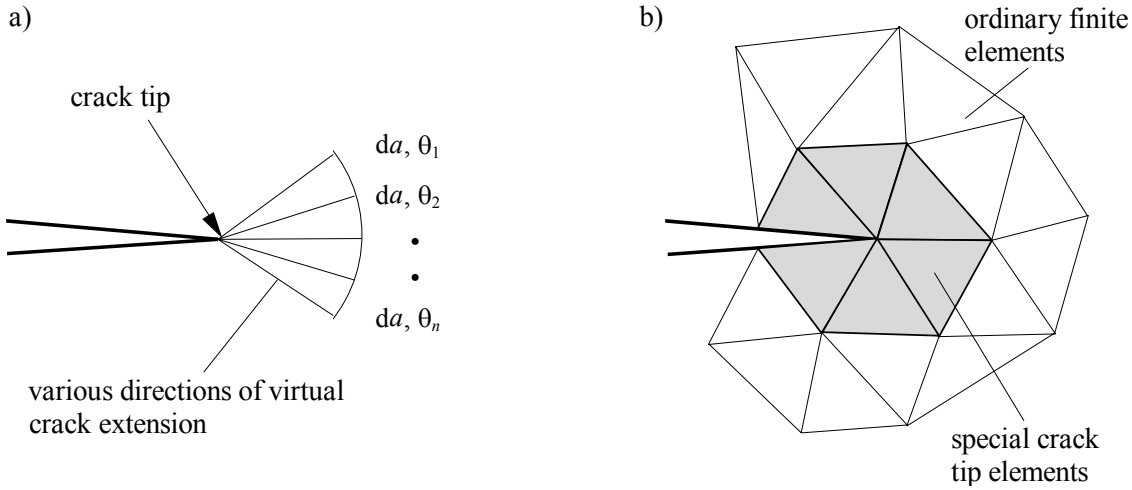

Figure 2: Virtual crack extensions of the crack tip

Following the above procedure, one can numerically determine the functional relationship $K=f(a)$ and the critical crack length a_c at $K=K_c$ from the computed values of K at discrete crack extensions a.

DETERMINATION OF CRACK PROPAGATION

Maximum Energy Release Rate using the Complex J Integral (MERRJ)

The maximum energy release rate criterion is based on the assumption that the energy release rate may be expressed as a function of the J_1 and J_2 integrals [4]. This theory is of particular practical interest since it compliments the finite element VCE method for mixed mode situations. Since J is equivalent to G for the linear elastic case, the values of stress intensity factors are

$$K_I^2 = \frac{2E}{(1+\nu)(1+\kappa)}\left(J_1 + \sqrt{J_1^2 - J_2^2}\right) \text{ and } K_{II}^2 = \frac{2E}{(1+\nu)(1+\kappa)}\left(J_1 - \sqrt{J_1^2 - J_2^2}\right) \tag{6}$$

where J_1, J_2 are energy release rate for crack extensions parallel and perpendicular to the crack, $\kappa = 3 - 4\nu$ for plain strain and $\kappa = (3-\nu)/(1+\nu)$ for plain stress. The maximum energy release rate is for a crack extending at the angle θ_0:

$$\theta_0 = \arctan\left(\frac{2K_I K_{II}}{K_I^2 + K_{II}^2}\right) \qquad \text{or} \qquad \theta_0 = \arctan\left(\frac{J_2}{J_1}\right) \tag{7}$$

to the plane of the crack and has magnitude

$$G(\theta_0) = \frac{(1+\nu)(1+\kappa)}{4E}\sqrt{K_I^4 + 6K_I^2 K_{II}^2 + K_{II}^4} \tag{8}$$

The Maximum Tangential Stress criterion (MTS)

Erdogan and Sih [3] used the stress equations for determination of direction of crack propagation. The crack propagates in direction of maximum tangential stresses calculated on a circle of sufficiently small radius around the crack tip. Angle of crack propagation θ_0 is determined with:

$$\tan\frac{\theta_0}{2} = \frac{-2K_{II}}{K_I + \sqrt{(K_I)^2 + 8(K_{II})^2}} \tag{9}$$

For opening-mode loading $(K_I \neq 0, K_{II} = 0)$, equation (9) yield $\theta_0 = 0$, while for sliding-mode loading $(K_I = 0, K_{II} \neq 0)$, it results in $\theta_0 = -70{,}6^{\circ}$.

NUMERICAL ANALYSES

Different crack propagation methods were evaluated for the CTS specimen shown on Figure 3.

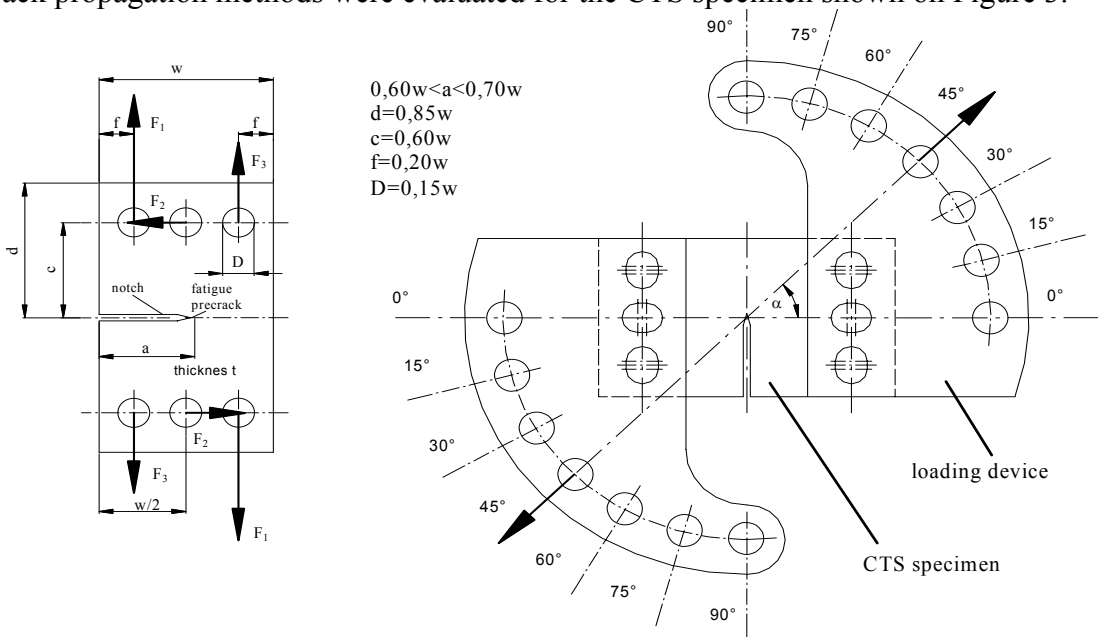

Figure 3: CTS specimen with loading device

A 2,5 mm fatigue pre-crack is on the end of the 52,5 mm long notch. The CTS specimen is loaded with a static load of 15 kN. In computational analysis this load is replaced with three equivalent nodal forces in x-y direction as shown on Figure 3. Different load cases for load angles between 0° and 90°, with a step of 15°, were used to simulate different fracture mode conditions. Pure Mode I condition was simulated with load angle of 0° while pure Mode II was simulated with load angle of 90°. The mixed mode conditions are simulated using load angles between 15° and 75°.

RESULTS

Figure 4 shows distribution of strain energy release rate G around the crack tip. The curve is seen to be sinusoidal, showing clearly that the directions of maximum G and minimum G are opposite. There are two directions of no energy release. Between them the energy release rate is negative, therefore crack extension is physically impossible in these directions. The value of G depends primary on K_I, resulting in highest value of G at pure Mode I, while G has the lowest value at pure Mode II.

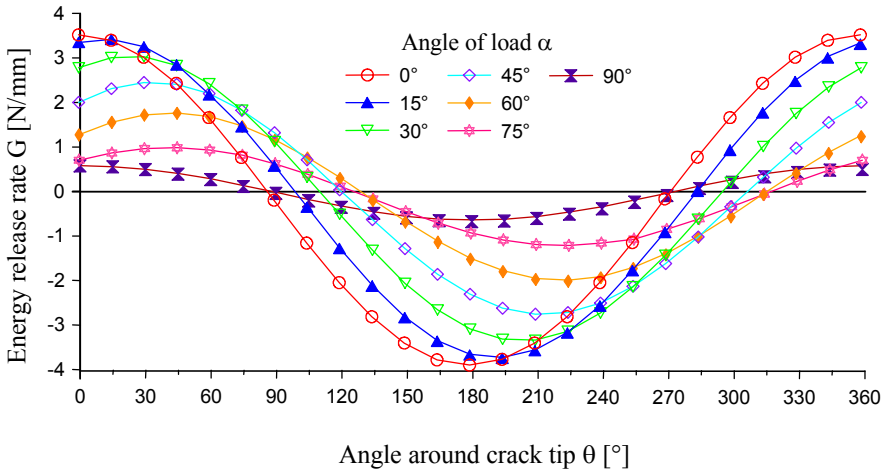

Figure 4: Plot of G against angle θ

The stress intensity factors K_I, K_{II}, shown in Table 1, were determined from Eqn. 6 using VCE method for determination of J_1 and J_2. At the start of crack propagation a kink in crack path is observed under mixed mode loading. The results in Table 1 are therefore given for a loaded initial crack configuration. In experimental testing [6] it has been observed that the crack propagation angle is $\theta_0 = 24°$ for load angle $\alpha = 30°$, $\theta_0 = 46{,}2°$ for $\alpha = 60°$ and $\theta_0 = 52° \pm 2°$ for $\alpha = 75°$.

TABLE 1: STRESS INTENSITY FACTORS K_I, K_{II}

	0°	15°	30°	45°	60°	75°	90°
K_I	549,85	531,29	476,67	389,79	279,05	138,32	0,09
K_{II}	0,19	56,49	109,24	153,73	186,20	217,28	222,58

The results of computational analyses show a reasonable agreement between VCE method and MERRJ criterion for crack propagation is shown on Figure 4:

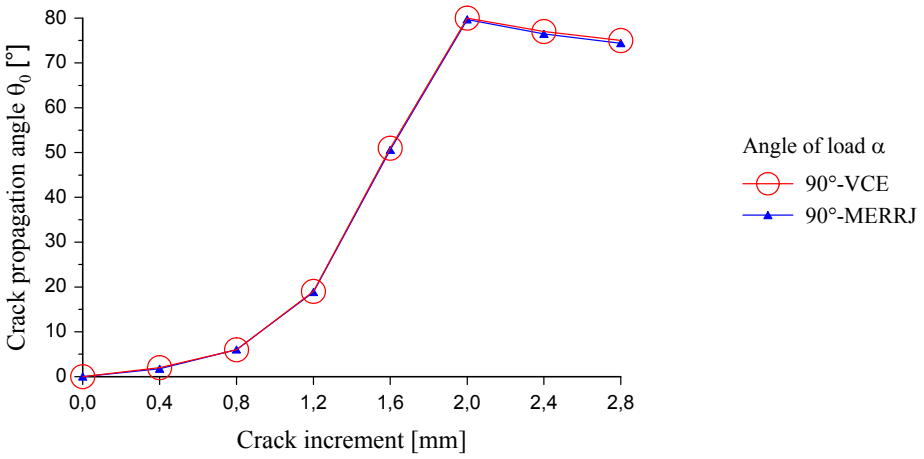

Figure 4: Plot of θ_0 against crack increment

Crack propagation angles calculated using VCE method are shown on Figure 5 while crack propagation angles calculated using MTS criterion are shown on Figure 6. Comparison between experimental crack propagation angle θ_0 and calculated crack propagation angle θ_0 shows that the MERRJ criterion is less accurate when $K_{II}>K_I$ as crack does not kink immediately. Crack propagates to the experimental value after a few increments.

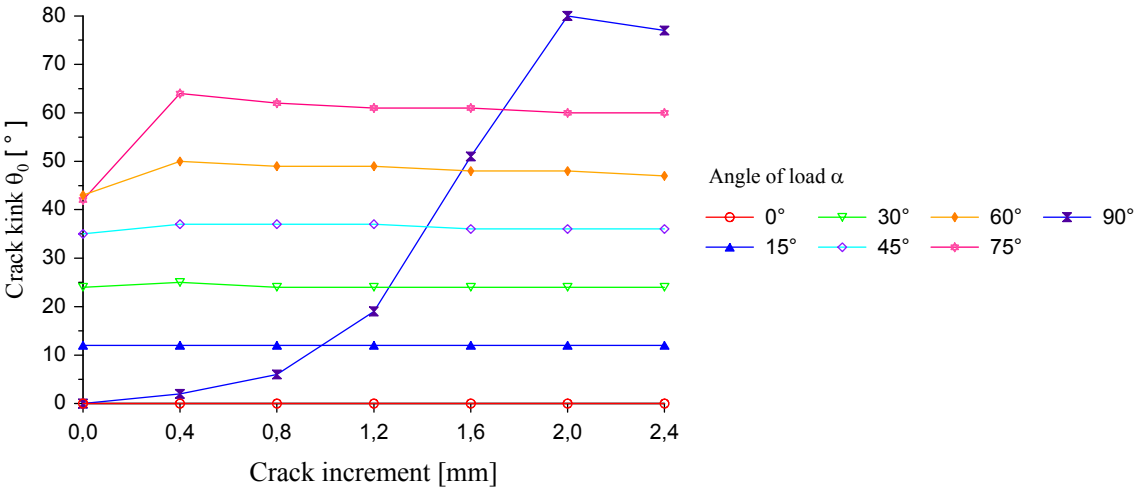

Figure 6: Crack propagation angle for MERRJ criterion

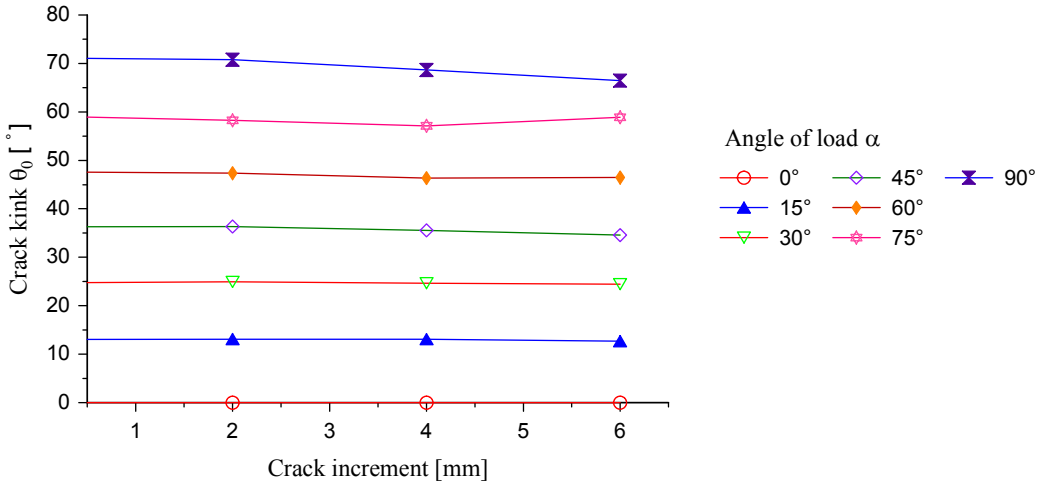

Figure 7: Crack propagation angle for MTS criterion

CONCLUSIONS

There are several criterions for determination of stress intensity factor K_I, K_{II} and crack propagation angle. Determination of stress intensity factor K_I, K_{II} using VCE method was evaluated. It can be observed that for cases where K_{II} is dominant the VCE method is less accurate. Therefore special care should be considered using this method for determination of crack propagation angle.

REFERENCES

1. Richard, H. A. (1985). *Bruchvorhersage bei überlagerter Normal- und Schubbeanspruchung von Rissen.* VDI Fortschungsheft 631, Düsseldorf: VDI Verlag.
2. Hellen, T.K., (1975). On the method of virtual crack extension. *Int. J. Numer Meth Engng,* **9**, 187-207.
3. Sih, G.C. (1974). Strain-energy-density factor applied to mixed-mode crack problems, *International Journal of Fracture*, **10**, 305-321.
4. Hellen, T.K., Blackburn, W. S. (1975). The calculation of stress intensity factors for combined tensile and shear loading. *Int. J. of Fracture* **11**, 605-617.
5. Schillig, R. (1990). *Ein Beitrag zur Ermüdungsrissausbreitung bei gleichphasiger Mixed-Mode Belastung*. VDI Fortschungsheft 86, Düsseldorf: VDI Verlag.

PAPER REFERENCE: ICF100741PR

DETERMINATION OF FRACTURE PROPERTIES OF HIGH-CHROMIUM WHITE CAST IRON

M. Janssen[1], M.B. van Leeuwen[1] and M.F. Mendes de Leon[2]

[1] Department of Materials Science, Delft University of Technology,
Rotterdamseweg 137, 2628 AL Delft, The Netherlands
[2] IHC Parts & Services, Post-box 50, 2960 AA Kinderdijk, The Netherlands

ABSTRACT

High-chromium white cast iron essentially consists of chromium carbides embedded in a matrix of high alloy steel. The carbides yield an excellent wear resistance, but also bring about a very low fracture toughness. The work described here concerns the experimental determination of the dynamic fracture properties of hypo-eutectic cast iron and the specific experimental problems that arise from its brittleness. Research is performed on how a sufficiently discriminative and reproducible measure for the fracture toughness of the cast iron can be obtained using Charpy-like specimens in combination with an instrumented drop-weight impact tower. It is found that a compliant tup causes the least load oscillations and that at low impact velocities, the measured K_{Id} values correspond well with those measured with a static test. However energy measurements with a compliant tup are troublesome: the total fracture energy is overestimated due to the kinetic energy attained by the specimen. Furthermore, to calculate the energy at fracture initiation the elastic compression of the tup should be taken into account. The results seem not to be affected by using a notch instead of a crack.

KEYWORDS

High-chromium white cast iron, Fracture toughness, Charpy impact test, Instrumented drop-weight test, Fracture energy, Notch geometry, Brittle material

INTRODUCTION

High-chromium white cast iron is a composite material which in the hypo-eutectic form consists of a network of eutectic carbides embedded in a martensitic or austenitic matrix [1]. The material is primarily used because of the excellent wear resistance provided by the eutectic carbides. This type of white cast iron has poor fracture properties, both static and dynamic. This is mainly attributed to the network of eutectic carbides, providing a low energy route for cracks to extend.

The long-term objective of this research is to gain insight in the factors that determine the dynamic fracture properties of this material in order to be able to control these to a certain extent. In the first instance the research is aimed at the use of an instrumented drop-weight impact tower using Charpy-like specimens as a discriminative, reproducible and easy technique for determining the low (dynamic) fracture toughness of high-chromium white cast iron.

In this paper experiments are described on a hypo-eutectic high-chromium white cast iron. The development is outlined of a drop-weight test suitable for this material, with an emphasis on the experimental obstacles and the considerations which led to the final set-up.

MATERIAL

Table 1 summarizes the approximate chemical composition of the high-chromium white cast iron investi-

gated. This composition represents a hypo-eutectic alloy. The material was cast in ingots of which the dimensions, i.e. length × width × height, are 250 × (80-89) × 125 mm. Using electric discharge machining, slabs were taken from the middle of these ingots normal to the length direction with a thickness of 10 mm. The macrostructure in these slabs depends on the distance to the ingot surface. Since solidification starts at this surface a columnar structure is present in the outer region of the slab with an orientation normal to the surface. In the center no obvious orientation is visible, a structure known as equi-axed. All specimens are taken from the center part of the ingot.

TABLE 1
CHEMICAL COMPOSITION OF THE WHITE CAST IRON [WEIGHT %]

C	Cr	Si	Ni	Mo	Mn	Cu
2.0	17.1	0.29	0.93	0.91	0.72	0.18

Figure 1 shows the as-cast microstructure of the material as it is tested. The white phases are the eutectic carbides. In-between the carbides martensite is found, while in the remaining matrix pearlite (black), ferrite and retained austenite are present.

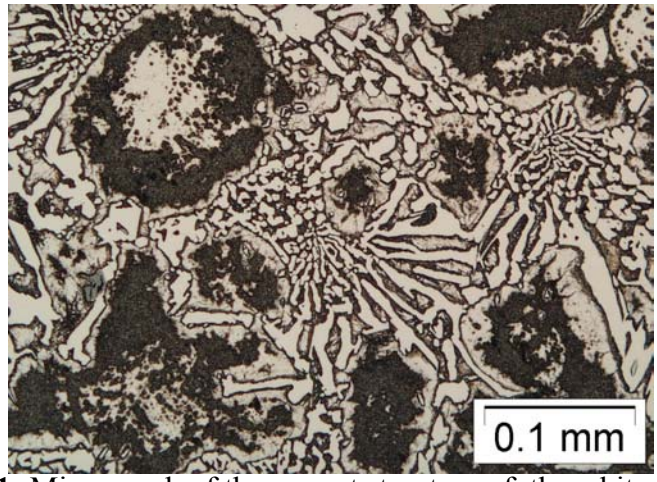

Figure 1: Micrograph of the as-cast structure of the white cast iron

EXPERIMENTAL SET-UP

The static fracture properties of a material with the brittleness of high-chromium white cast iron can be obtained by measuring the plane strain fracture toughness, K_{Ic} according to ASTM E399 [2]. This well-defined test method does, however, involve the costly and time-consuming preparation of suitable specimens, including the introduction of pre-fatigue cracks. To determine dynamic properties the standardized Charpy impact test [3] is available, which only uses a notched bar of 10×10×55 mm dynamically loaded in 3-point bending and therefore is much less expensive and faster to perform. However, from a fracture mechanics point of view, the standard Charpy test has a number of disadvantages.

1. For materials that exhibit a distinct amount of plastic deformation a plane strain condition at the notch tip is not guaranteed. This, however, will not be a problem for the white cast iron considered here, since plasticity is limited.
2. In the standard Charpy test only the total energy needed to fracture the specimen is determined. Therefore no information about crack initiation is obtained. This can be overcome by using an instrumented test set-up capable of monitoring the load.
4. The effect of the loading rate cannot be investigated in a pendulum set-up. However, a drop-weight test set-up does provide this versatility.

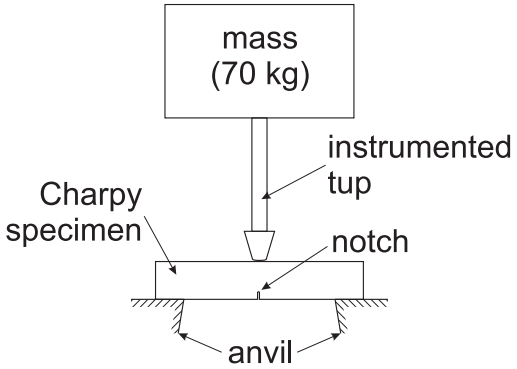

Figure 2: Set-up of instrumented drop-weight impact test

These considerations led to the use of an instrumented drop-weight impact tower for performing the test (see Figure 2). It consists of a mass of approximately 70 kg that loads the specimen by dropping it from a certain height. The load is transferred to the specimen by means of a tup and is digitally monitored as a function of time through a set of strain gauges mounted on the tup.

The dynamic fracture toughness, K_{Id}, is derived from the load at which crack extension initiates. For the brittle cast iron this is assumed to be the maximum load, P_{max}. Thus, from [4],

$$K_{Id} = \frac{P_{max} S}{B W^{3/2}} \cdot \frac{3\sqrt{\frac{a}{W}}\left[1.99 - \frac{a}{W}\left(1 - \frac{a}{W}\right)\left\{2.15 - 3.93\left(\frac{a}{W}\right) + 2.7\left(\frac{a}{W}\right)^2\right\}\right]}{2\left(1 + 2\frac{a}{W}\right)\left(1 - \frac{a}{W}\right)^{3/2}}, \quad (1)$$

where S = specimen span,
B = specimen thickness,
W = specimen height,
a = notch length.

In order to calculate energy values, the load versus time record is converted to load versus displacement data, a conversion which is based on the velocity during the test. In turn this velocity is calculated using the initial impact velocity and by considering the forces acting on the drop weight, i.e. gravity and the specimen load. Note that for the brittle material tested here and the relatively high impact energy of the drop weight, the velocity during the test will typically only drop slightly below the initial velocity.

Two energy values are assessed: the energy needed to initiate crack growth, E_i, and the total energy to fracture the specimen, E_f. These are calculated by integrating the area under the load-displacement curve until maximum force and under the whole curve respectively. To account for small differences in specimen dimensions the energies are divided by the area of the net section.

EXPERIMENTS TO EVALUATE IMPACT TEST

There are a number of experimental aspects that need to be clarified before reliable impact tests on the white cast iron can be performed:

1. The energy involved in the fracture of a material as brittle as white cast iron is very low. The question arises whether the test set-up is capable of determining such low values accurately.
2. Impact testing brittle material involves a relatively short time to fracture. Immediately after impact the load signal will inevitably oscillate. Also because plasticity in the specimen is only limited, it will take some time before these are damped. This can possibly mask crack initiation, thereby disabling the measurement of K_{Id} en E_i.
3. In standard Charpy specimens a V-notch (0.25 mm tip radius) or a U-notch (1 mm tip radius) is introduced. The workmanship with which this notch is machined will vary and it is uncertain whether the tip radius is small enough to simulate a natural crack. Introducing a fatigue crack would be preferable, but this is cumbersome in the white cast iron considered here and also contrary to the objective in this research, i.e. the development of an easy test method.

These aspects are assessed by performing the tests described below.

Tup Capacity

Tests are performed at a velocity of 3.4 m/s using a small-capacity tup (15 kN) and a high-capacity tup (220 kN). Specimens were prepared with a notch with 0.2 mm tip radius (see below). The resulting load-displacement curves, shown in Figure 3, differ considerably. The high-capacity tup causes the load to increase more rapidly and to a considerably higher value, resulting in a displacement at maximum force that is much smaller. Furthermore, the load oscillations are significantly larger and take longer to damp.

Table 2 summarizes the numerical results. The fracture toughness and the total fracture energy are strongly affected by the tup used. The initiation energy seems unaffected.

TABLE 2
RESULTS OBTAINED AT 3.4 M/S WITH TUPS WITH DIFFERENT LOAD CAPACITIES

Tup capacity [kN]	K_{Id} [MPa√m]	E_i [kJ/m^2]	E_f [kJ/m^2]
15	30.6	4.6	12.1
220	62.8	4.6	5.8

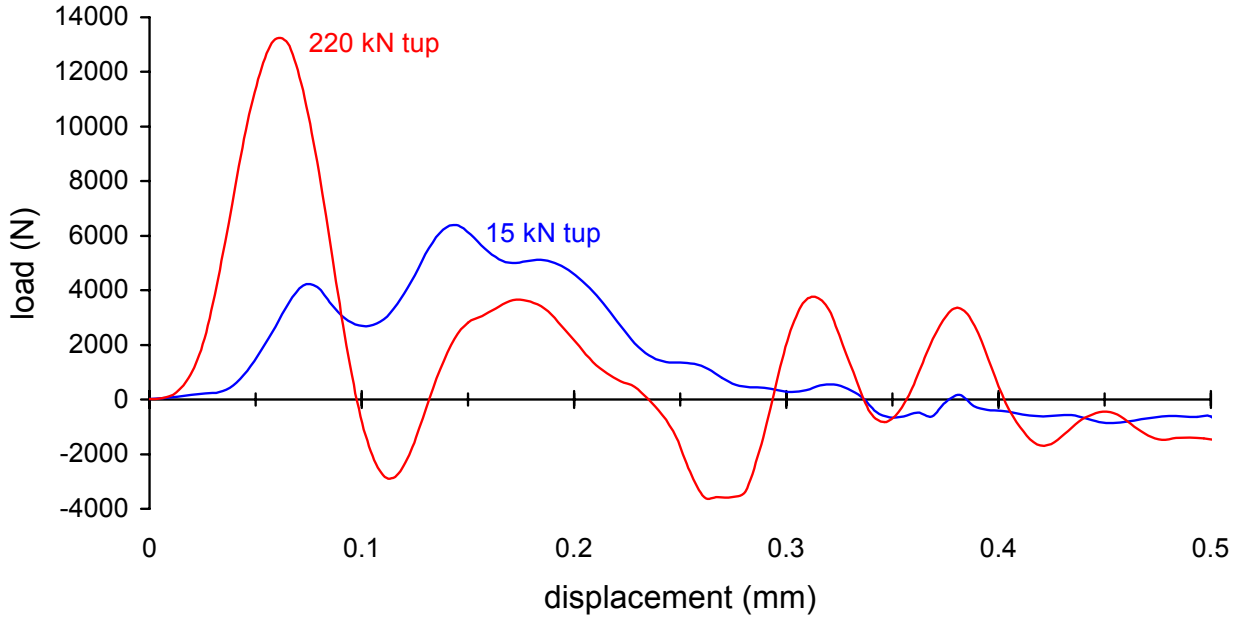

Figure 3: Load-displacement curves at an impact velocity of 3.4 m/s using different tups

Impact velocity

Using the 15 kN tup, tests are performed at different impact velocities, i.e. 1, 2, 3 and 5 m/s on specimens with a notch with 0.2 mm tip radius (see below). Furthermore, some static tests are performed using an electro-mechanical tensile machine. Figure 4 shows two examples of load-displacement curves obtained at 1, 2 and 5 m/s respectively. The values for the maximum load are affected by the velocity. Only at 1 m/s the oscillations are damped well before the maximum load is reached.

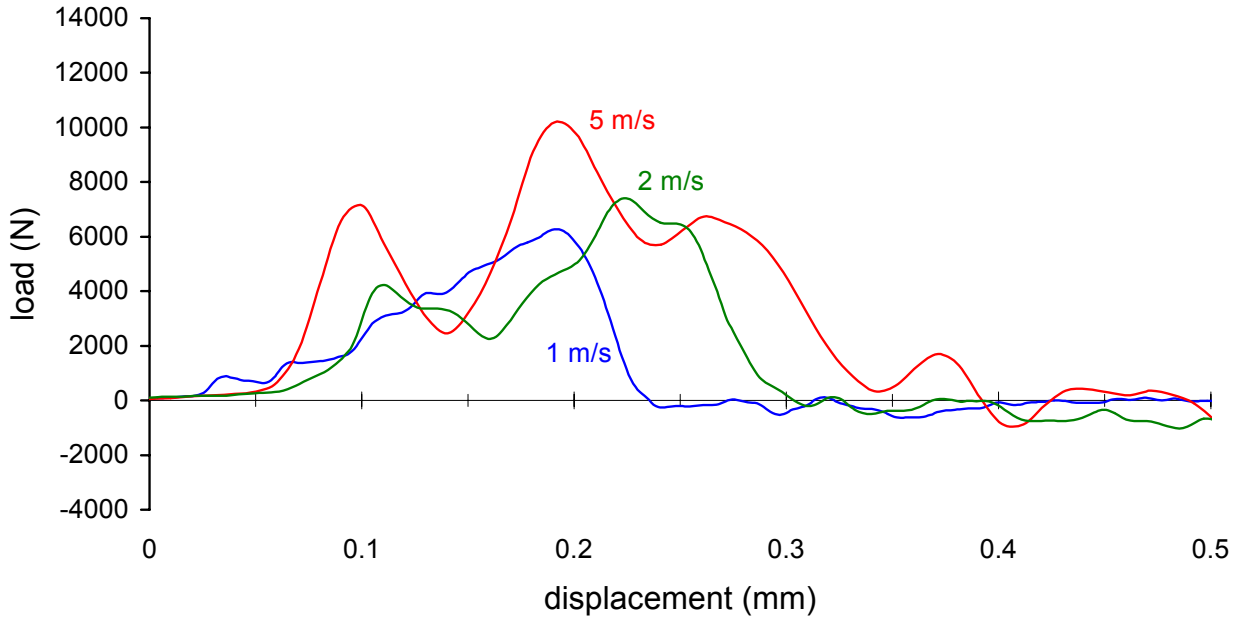

Figure 4: Load-displacement curves at different impact velocities using 15 kN tup

In Table 3 the average fracture toughness and energy values are summarized, including the number of tests and the 95% reliability interval. All measured values tend to increase with impact velocity.

TABLE 3
RESULTS OBTAINED AT DIFFERENT IMPACT VELOCITIES WITH 15 KN TUP

Velocity [m/s]	N° of tests	K_{Id} [MPa√m]	E_i [kJ/m^2]	E_f [kJ/m^2]
static	2	25± 5	7.9±2.4	–*
1	2	27±26	6.1±1.2	7.5±0.1
2	2	31± 9	7.1±1.0	10.1±6.7
3	1	29	8.3	11.4
5	1	45	9.3	–**

* specimen not completely broken
** measurement interrupted shortly after fracture

Notch geometry
Specimens are prepared with different notch geometries. Notches are introduced by electric discharge machining (EDM) using wire diameters of 0.3 mm and 0.15 mm, thus creating notch tip radii of 0.2 and 0.1 mm. Furthermore, pre-fatigue cracks are introduced in some specimens. Both static tests are performed as well as impact tests with the 15 kN tup at a velocity of 1 m/s. This velocity is chosen to be sure that K_{Id} and E_i can be measured. In Table 4 averaged results are summarized, including the number of tests and the 95% reliability interval. From these results no obvious effect of the notch geometry can be deduced.

TABLE 4
RESULTS OBTAINED FOR DIFFERENT NOTCH GEOMETRIES

Notch	N° of tests	K_{Id} [MPa√m]	E_i [kJ/m^2]	E_f [kJ/m^2]
Static test (1 μm/s)				
crack	2	22±21	6.2±5.1	–*
r = 0.1 mm	2	21± 8	6.8±3.4	–*
r = 0.2 mm	2	25± 5	7.9±2.4	–*
Impact test at 1 m/s using 15 kN tup				
crack	3	27.0±9	6.0±3.3	7.7±3.5
r = 0.1 mm	7	28.2±0.9	6.0±0.5	8.3±1.4
r = 0.2 mm	2	27.0±26	6.1±1.2	7.5±0.1

* specimen not completely broken

DISCUSSION

Tup Stiffness
The effect of the tup capacity on the load-displacement curves (Fig. 3) can be understood by considering the stiffness of the tups. For the 15 kN tup the stiffness is calculated to be 200 N/μm, while the 220 kN tup is estimated to have a stiffness that is at least 5 times higher. During loading the tups will become shorter. For example the 15 kN tup will be more than 30 μm shorter at maximum load. This means that the actual specimen displacement is the measured displacement minus the compression of the tup. Thus the actual loading rate applied to the specimen is lower for the 15 kN tup than for the 220 kN tup. This is an explanation for the smaller load oscillations and the larger displacement at maximum load found for the 15 kN tup.

Obviously, the calculation of energy values should in principal be based on actual specimen displacements rather than measured values. The fact that in Table 2 the energies for crack initiation, E_i, are the same, is believed to be more of a coincidence. E_i is not only influenced by using incorrect displacements, but also by the impossibility to correctly determine the moment of crack initiation. Due to load oscillations the maximum force is no longer a good measure. This also makes it impossible to determine meaningful K_{Id} values. From Figure 4 it can be concluded that at velocities of 2 m/s and above no reliable K_{Id} and E_i values can be obtained.

The total energy E_f should in principle not be affected by compression of the tup or by load oscillations, since these are elastic phenomena. The area under the measured load-displacement curve is equal to that under the actual curve if it is determined over a period that starts before impact and ends when the load signal has permanently returned to zero. The reason is that at these instants the tup is not compressed and the measured load corresponds exactly to the actual load. The fact that Table 2 suggests a large effect of the tup stiffness on E_f is explained below.

Kinetic Energy
The energy transferred from the tup to the specimen is not only used to fracture the specimen, but also to accelerate it. A fair estimate of this kinetic energy can be made if one simply assumes that the load point, i.e. the contact point between tup and specimen, has a velocity equal to the impact velocity. At 3.4 m/s this amounts to 0.17 J. Divided by the net section area, this corresponds to 2.1 kJ/m^2, a value that cannot be neglected compared to the energies measured (see Table 2).

A correction for the kinetic energy attained by the specimen during impact would be feasible. However the elastic compression of the tup causes the load-point velocity to deviate from the nominal impact velocity. Initially, due to the rising load, the load-point velocity is somewhat lower. From the moment the crack initiates and the load drops, the load-point velocity increases and rises above the nominal impact velocity. These velocity changes depend on the tup stiffness. For a stiff tup the kinetic energy the specimen ultimately attains will be close to the estimate given above, whereas for a compliant tup this value can be considerably higher. To quantify this, extensive calculations would be required, but it is believed that this effect does ex-

plain the large difference found in E_f for the two tups.

From Table 3 it can be seen that E_f increases with impact velocity. This can also be explained by the kinetic energy that the specimen ultimately acquires due to impact. It must be noted that it is impossible to establish whether in this case the material behavior is also partly responsible.

Notch geometry
The results in Table 4 indicate that an EDM notch with a tip radius of 0.2 mm simulates a real crack quite well. From Figure 1 it can be seen that the coarseness of the carbide structure of the cast iron is of the same order as this tip radius. It could be argued that in all cases there will be pores or crack-like defects close to the notch tip that become critical at approximately the same load level as a sharp pre-fatigue crack would.

Preferred Test Set-up
Because of the smaller oscillations, it seems favorable to use a low-stiffness tup. However, to obtain a more accurate value for the specimen displacement and thus for E_i, a correction is necessary. This can be done by subtracting the compression of the tup from the measured displacement. An estimate for the tup compression, discarding possible dynamic effects, follows from the load divided by the tup stiffness.

For the measurement of the total fracture energy, E_f, a high-stiffness tup is advantageous since then the kinetic energy of the specimen is only slightly enhanced after fracture. However at low velocity, e.g. 1 m/s, this effect is expected to be small. For instance the kinetic energy before fracture at 1 m/s is only 0.015 J (corresponding to 0.18 kJ/m^2). When measurements are performed at a single (low) impact velocity and they only have a comparative nature, a low-stiffness tup could be acceptable.

Clearly, to obtain K_{Id} or E_i for the cast iron, measuring at low velocities is essential. It is uncertain whether such values are also representative for the behavior of the cast iron at higher velocities. Measuring at high velocity would require alternative techniques to detect the moment of crack initiation and to account for load oscillations.

CONCLUSIONS

The following conclusions are drawn with respect to obtaining the fracture properties of high-chromium white cast iron using an instrumented drop-weight impact tower with Charpy-like specimens:

1. By using a compliant tup, the loading rate and the load oscillations are decreased, but the amount of kinetic energy transferred to the specimen is increased.
2. Values for K_{Id} or the energy involved in crack initiation, E_i, can only be measured at low velocity ($\leq$ 1 m/s).
3. For a compliant tup E_i can only be accurately determined by accounting for compression of the tup.
4. The total energy, E_f, is strongly affected by the amount of kinetic energy transferred to the specimen.
5. The increase in E_f with impact velocity is attributed to an increase in kinetic energy that is ultimately transferred to the specimen.
6. An EDM notch with a tip radius of 0.1 or 0.2 mm yields the same results as a pre-fatigue crack.

REFERENCES

1. Tabrett, C.P., Sare, I.R. and Ghomashchi, M.R. (1996) *International Materials Reviews* **41/2**, 59.
2. ASTM Standard E399 (1997). *Plane-Strain Fracture Toughness of Metallic Materials*. ASTM West Conshohocken, Philadelphia.
3. ASTM Standard E23 (1997). *Standard Test Methods for Notched Bar Impact Testing of Metallic Materials*. ASTM West Conshohocken, Philadelphia.
4. Ewalds, H.L. and Wanhill, R.J.H. (1991). *Fracture Mechanics*. Edward Arnold, London.

ORAL/POSTER REFERENCE: 518OR

DETERMINATION OF FRACTURE TOUGHNESS OF ROCK UNDER IN-SITU CONDITIONS USING SEMI-CIRCULAR SPECIMEN

M.D. Kuruppu[1] and M. Seto[2]

[1] Curtin University of Technology, PMB 22, Kalgoorlie, WA 6430, Australia
[2] National Institute for Resources and Environment, 16-3 Onogawa, Tsukuba, Ibaraki 305-8569, Japan

ABSTRACT

Fracture toughness of several types of rock is determined using the semi-circular bend (SCB) specimen and the single edge-cracked round bar in bending (SECRBB). The methodology for the evaluation of level I and level II fracture toughness and K-resistance curve using a single specimen is presented. K-resistance curve is shown to yield true fracture toughness even when under-sized specimens are employed. In order to simulate the in-situ conditions, tests were also done at elevated temperatures, high confining pressures, and different moisture levels. Fracture toughness of Kimachi sandstone increases moderately with increasing temperature up to 200^0C. In addition, it increases rapidly with increasing confining pressure before reaching a steady value. Increasing moisture content was found to reduce the fracture toughness.

KEYWORDS

Fracture toughness, rock, K-resistance, elevated temperature, confining pressure, moisture content, pore pressure

INTRODUCTION

The fracture behaviour of rocks is different from those in most man made materials due to their inherent properties. Sedimentary rocks such as sandstone and oil shale can be categorised as transversely isotropic as their properties are uniform in the plane of bedding, but may differ from those in the direction normal to bedding [1]. In addition, rocks behave nonlinearly under stress. They are subjected to explosive as well as non-explosive fragmentation for resource extraction. Fracture toughness is a valuable property in predicting the behaviour of material during fracture processes. A number of test specimens and methods have been suggested to determine the fracture toughness of rock materials [2-4]. The chevron-notched bend specimen [3] and the short rod specimen [2] have been incorporated into a standard method for the fracture toughness measurement of rock by the International Society for Rock Mechanics (ISRM) [5]. The semi-circular bend (SCB) specimen proposed by Chong et al. [6] and the single edge-cracked round bar in bending (SECRBB) specimen [7] are complimentary to the standard method. For example, the SCB specimen can be used as a third specimen for the complete characterisation of fracture toughness from a single core in materials such as sedimentary rocks [6]. It is suitable for measuring the plane strain fracture toughness of materials undergoing substantial nonlinear deformation before failure [8]. Lim et al. [8] has successfully used the

specimen to measure the fracture toughness of a synthetic mudstone which is a relatively weak rock behaving nonlinearly.

In past most rock fracture toughness tests have been performed under ambient conditions. However, it is essential that the measurements be carried out at in-situ conditions such as elevated temperatures and pressures, and in wet environments. This paper presents the methodology of determining levels I and II fracture toughness using the SCB specimen. Level II fracture toughness is especially required for materials behaving nonlinearly. Furthermore, methods of determining fracture toughness of rock at elevated temperatures and high confining pressures are given. Tests were done over a wide range of temperatures varying from ambient conditions up to 200^0C. It was observed that the effect of increasing confining pressure on the fracture toughness dies down at moderately high pressures. Therefore, the confining pressure of the tests was restricted to a maximum value of 7.5 MPa.

TEST PROGRAM

Most tests were done using SCB specimen. However, SECRBB specimen was also used for comparison and verification of some of the results. Both specimens are core based and therefore easy to prepare. The testing program covered the following areas:

(a) Fracture toughness of Kimachi sandstone was determined at ambient condition using 100 mm diameter SCB specimens. Fracture toughness was also measured according to the ISRM standard method.
(b) Effect of elevated temperatures on fracture toughness was measured using a custom built test system that facilitated loading the specimen in three-point bending while immersed in an oil bath. The oil bath can be heated to a desired temperature up to 200^0C. SCB specimens of 60 mm diameter and SECRBB specimens of 30 mm diameter were tested.
(c) The effect of confining pressure on fracture toughness was measured using the same test rig described in b above. The jacketed oil bath containing the test specimen was subjected to a confining pressure up to 7.5 MPa. However, the test specimen was not heated simultaneously.
(d) The effect of moisture content on fracture toughness of Kimachi sandstone was determined using dry as well as partially wet test specimens.

Specimens are made such that the notch is aligned with one of three principle orientations known as the arrester, the divider and the short transverse (ST) [6]. Specimens are prepared by slicing rock cores while noting the direction of bedding. Each core disc is then split into two halves producing two specimens having almost identical properties. Finally, a straight notch is introduced using a diamond impregnated wire saw or a thin circular saw. A circular saw having a thickness of 0.3 mm was used to cut the notch during this test program. SECRBB specimens were also made of cores with their notches oriented in the arrester and the ST orientations. Very little machining is required as only a straight edge-notch is introduced. The specimens were oven dried at 60^0C for a few days and all dimensions were recorded prior to testing.

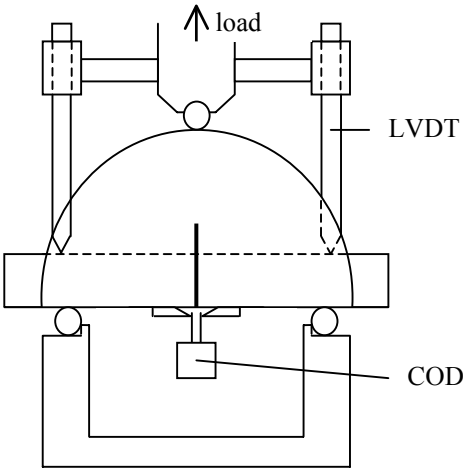

Figure 1: Fracture toughness test rig including SCB specimen

Tests at Ambient Conditions

SCB specimens made of Kimachi sandstone were tested using a MTS closed loop servo hydraulic test system (Figure 1). The sizes of specimens were approximately 100 mm diameter, 25 mm thickness and a crack length to radius ratio, a/R, of 0.5. A special fixture was used to load the specimen in three-point bending. The fixture allows the two support rollers to rotate and move apart slightly as the specimen was loaded, thus permitting roller contact and minimising frictional effects. The top loading pin was attached to the upper platen of the load frame. This fixture helps to achieve the proper alignment in the load transfer system. In addition, the SCB specimen must be properly aligned parallel to the axes of the loading pins as the pins make line contact with the specimen. A crack opening displacement (COD) gauge was attached to the specimen using knife-edges positioned across the mouth of the notch. The load-line displacement was measured by taking the average reading of two linear variable differential transducers (LVDTs) that were placed between the top and the bottom loading platens. Tests were done using COD control mode at a constant rate of 0.06 mm/min. At least one partial unloading was done before reaching the peak load and a number of partial unloading-reloading cycles were done in the post-peak region (Figure 2). The high stiffness of the test frame enabled recording the complete post-peak behaviour in each test. In addition, a number of tests in the ST orientation was done using partially wet Kimachi sandstone specimens.

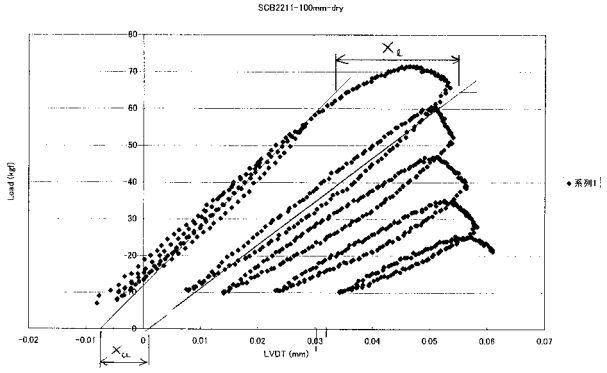

Figure 2: Typical load-displacement record illustrating the determination of p factor

Measurement of Fracture Toughness at Elevated Temperatures and Pressures

The machine facilitates testing specimens under three-point bending while immersed in a jacketed oil bath that can be subjected to hydraulic pressures up to 30 MPa and temperatures up to 200^0C. It can accommodate a number of different types of specimens including SECRBB and SCB specimens. SCB specimens of 60 mm diameter and 25 mm thickness as well as SECRBB specimens of 30 mm diameter were used for these tests. Kimachi sandstone specimens prepared in all three orientations were included in the test program. The notches of the specimen were covered with either several layers of taped paper (for high-pressure applications) or aluminium foil (for high temperature applications). Knife-edges for the COD gauge were attached and the specimens were covered with a layer of silicone to prevent any oil contamination. The specimens were placed in the loading platform with COD gauge attached and then immersed in the jacketed oil bath. In the case of elevated temperature tests, the oil bath was heated to the desired temperature and allowed approximately 2 hours to stabilize the conditions of the specimen. Specimens were then tested to failure under either LVDT or COD control. LVDT measured the load-line displacement. Partial unloadings were done at regular intervals before and after the peak load similar to the tests done at ambient conditions. The strain rate of each of the tests was 0.075 mm/min.

Method of testing at high confining pressures was similar to that of elevated temperature except that a desired confining pressure was applied instead of raising the temperature of the oil bath containing the test specimen. Most tests were done under LVDT control while a few was performed under COD control. As the silicone layer does not permit pressures to be applied on the free surfaces of the notch, the resulting closure of the crack due to the confining pressure was measured using the COD gauge. The load, load-point displacement and the crack opening displacement were recorded as a function of time during each test.

EVALUATION OF RESULTS

The level I fracture toughness, K_I, is determined using the peak load, the non-dimensional stress intensity factor and the specimen dimensions [5]. For the SCB specimen it may be given as

$$K_I = Y\, F\, (\sqrt{\pi\, a}) / 2Rt \tag{1}$$

where Y is a non-dimensional stress intensity factor, F is the peak load, a is the crack length, R is the specimen radius and t is the thickness. The span to diameter ratio is 0.8. The stress intensity factor Y is a function of the crack length to radius ratio, α. The best fit curve for Y is given by [6,9]

$$Y = 5.6 - 22.2\alpha + 167\alpha^2 - 576\alpha^3 + 929\alpha^4 - 506\alpha^5 \tag{2}$$

The stress intensity factor for SECRBB specimen is given in reference [10]. For level II testing, a nonlinearity correction factor is incorporated. The evaluation closely followed the procedure adopted in the ISRM standard method. As shown in Figure 2 the displacement ratio

$$p = X_u / X_l \tag{3}$$

defines the degree of nonlinearity. The two chosen unloading lines must span the maximum load. In addition, the average value of loads at unloading positions must be as close as possible to the peak load. Then the nonlinearity corrected fracture toughness is determined from the following equation:

$$K_{Ic} = \sqrt{(1+p)/(1-p)}\; K_I \tag{4}$$

The corrected fracture toughness is equivalent to the upper limit of the K-resistance curve of the rock. If specimens smaller than those satisfying the minimum dimensional requirements are employed, fracture toughness must be evaluated using a K-resistance curve instead of using level II value [11]. If the crack length is known, using Eqn. 2 the stress intensity factor can be determined for each cycle. Then the K-resistance for each cycle can be derived as

$$K_{I,R} = \sqrt{(1+p)/(1-p)}\; K_{Ii} \tag{5}$$

where K_{Ii} is a level I value determined using the non-dimensional stress intensity factor and the load at the unloading point of the cycle. In this case, p is taken as the average degree of nonlinearly of the given cycle and two adjacent cycles. The crack length is measured using the experimentally determined compliance. The non-dimensional compliance, C' is given as

$$C' = E'DC \tag{6}$$

where C is the compliance, which is the ratio of the load-point displacement and the load, D is the diameter and $E' = E/(1-\upsilon^2)$. E and ν are Young's modulus and Poisson's ratio respectively. For example, for SCB specimen the relation between the non-dimensional compliance and the crack length is given by

$$C' = 1366\,\alpha^3 - 867\,\alpha^2 - 51.9\,\alpha + 129.4 \tag{7}$$

Fracture Toughness at Ambient Conditions

Table 1 gives fracture toughness of Kimachi sandstone. Figure 3 shows a K-resistance curve derived using a single SCB specimen. The curve reaches a limit of 1.0 $\mathrm{MPa}\sqrt{\mathrm{m}}$. This value is higher than the level II toughness. It also agrees with the fracture toughness measured using chevron bend specimen according to ISRM standard, which yielded 0.99 $\mathrm{MPa}\sqrt{\mathrm{m}}$. Furthermore, this result agrees with that published by

Matsuki et al. [11]. This observation further reiterates the minimum specimen size requirement unless a K-resistance curve is used to determine the fracture toughness. Also, fracture toughness of Kimachi sandstone decreases almost linearly with increasing moisture content. At about 8% water content the fracture toughness is only about 33% of its value for dry material. This decrease is usually attributed to the build up of pore pressure that reduces the inter-particle bonds between grains in the process zone.

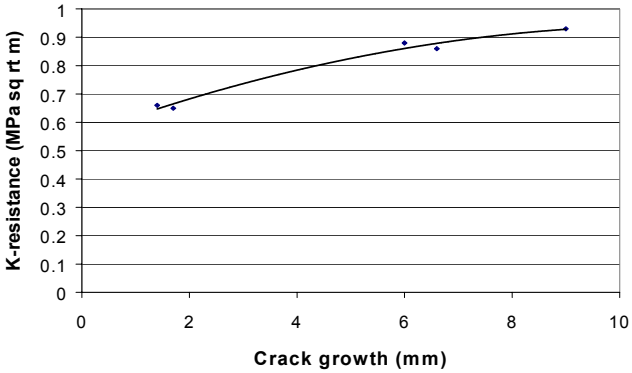

Figure 3: K-resistance curve for Kimachi sandstone

TABLE 1
FRACTURE TOUGHNESS OF KIMACHI SANDSTONE

Orientation	No. of specimens	Level I fracture toughness (MPa√m)	Level II fracture toughness (MPa√m)
Divider	6	0.45	0.65
Arrester	6	0.48	0.69
ST	9	0.41	-

Tests at Elevated Temperature and High Confining Pressure

Figure 4 gives the level I fracture toughness of Kimachi sandstone at elevated temperatures. Note that this result for ST orientation was produced using both SCB and SECRBB specimens. Fracture toughness shows a gradual increase with temperature. There is nearly 50% increase compared to the value at room temperature.

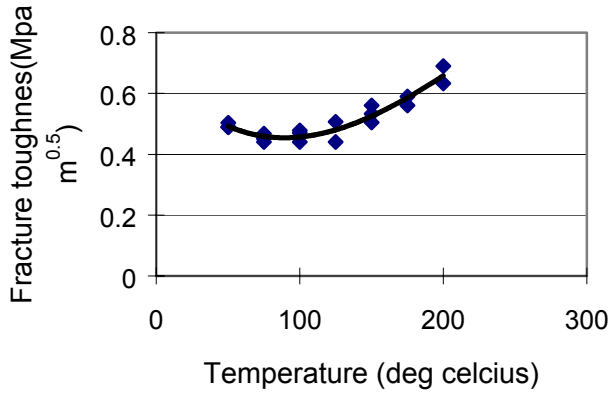

Figure 4: Fracture toughness of Kimachi sandstone at elevated temperature

Figure 5 shows fracture toughness of sandstone subjected to confining pressure (Note: mostly level I). Fracture toughness is quite significantly influenced by the confining pressure. In addition, it reaches a steady value when the confining pressure is about 4 MPa. This may be caused by the closure of the pre-existing microcracks and other discontinuities within the material due to the application of the confining

pressure. Once that happens, rock behaves as if it has a uniform matrix and the fracture toughness remains constant. However, this limit value is several orders of magnitude higher than the fracture toughness of unconfined rock. As the silicone layer prevents the hydraulic pressure act on the notch, the notch tends to close due to the pressure on the remaining surfaces. This was adjusted using a suitable mathematical formulation [12]. Notch closure measured using the COD gauge assisted the adjustment.

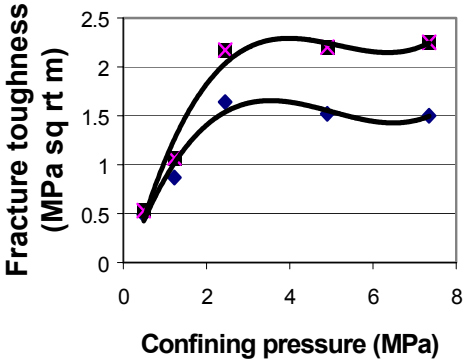

Figure 5: Variation of fracture toughness of Kimachi sandstone with confining pressure. Upper and lower graphs are for ST and divider orientations respectively

CONCLUSIONS

Fracture toughness tests were performed using SCB and SECRBB specimens. Firstly, level I and level II fracture toughness was measured for Kimachi sandstone. The crack growth was determined using the elastic unloading compliance measured at regular intervals of each test. Following a procedure similar to the analysis of level II fracture toughness, the crack growth resistance was measured using the unloading-reloading cycles following the peak load. This result in combination with crack growth data enabled the construction of K-resistance curve using a single specimen. The methodology also yields fracture toughness unaffected by the specimen size.

The fracture toughness of Kimachi sandstone increases moderately with increasing temperature. The level I fracture toughness increased by approximately 50% at 200^0C compared to the value at ambient temperature. The elevated temperatures appear to make the rock tougher and allow it to absorb more strain energy prior to failure. Fracture toughness was also found to increase substantially with increasing confining pressure. For example, for the divider orientation, fracture toughness of Kimachi sandstone increases from 0.45 $\text{MPa}\sqrt{\text{m}}$ at atmospheric pressure to 1.5 $\text{MPa}\sqrt{\text{m}}$ at a confining pressure of 2.5 MPa, an increase of 230%. However, it reaches a steady value and is not affected by further increase of confining pressure.

References

1. Chong, K.P. and Smith, J.W. (1984) *Mechanics of oil shale*, Elsevier, London.
2. Barker, L.M. (1977) *Eng. Fracture Mech*., 9:361-369.
3. Ouchterlony, F. (1986) *Proc. 27th U.S. Symp. Rock Mech*., SME Littleton, CO, pp.177-184.
4. Fowell, R.J., Hudson, J.A., Xu, C., Chen, J.F. and Zhao, X. (1995) *Int. J. Rock Mech. Min. Sci. & Geom. Abstr*., 32:57-64.
5. Ouchterlony, F. (1988) *Int. J. Rock Mech. Min. Sci. & Geom. Abstr*, 25:71-96.
6 Chong, K.P., Kuruppu, M.D. and Kuszmaul, J.S. (1987) *Eng. Fracture mech*. 28(1):43-54.
7. Ouchterlony, F. (1980) Report DS1980:17, Swedish Detonic Research Foundation, Stockholm.
8. Lim, I. L,, Johnston, I.W. and Choi, S.K. (1994) *Int. J. Rock Mech. Min. Sci.*31:3, 185-197.
9. Basham, K.D. (1989) PhD dissertation, Dept. of Civil Engineering, The University of Wyoming.
10. Underwood, J.H. & R.L. Woodward (1989) *Experimental mech.* 29(2):166-168.
11. Matsuki, K., Hasibuan, S.S. and Takahashi, H. (1991) *Int. J. Rock Mech. Min. Sci.*, 28(5):365-374.
12. Seto, M., Kuruppu, M.D. and Funatsu, T. (2001) *Proc. DC Rocks*, ARMA, to appear.

ICF1001026OR

DETERMINATION OF MICROSTRUCTURAL PARAMETERS FOR MODELING OF FATIGUE BEHAVIOR OF CERAMICS

M. Boudrare[1], R. D. Geraghty[2], C. Ortiz[3] and Kenneth W. White[4]

[1,4] Department of Mechanical Engineering, University of Houston,

Houston, TX, 77204-4792, U.S.A.

[2]Calpine Corp., Houston, TX

[3]Johnson Space Center, NASA Houston, TX

ABSTRACT

This study examines the microstructural role of crack face bridging mechanisms in a monolithic ceramic, subjected to cyclic loading conditions at room and high temperatures. By utilizing a unique post-fracture-tensile experiment, the fatigue properties of a commercially available alumina are examined. Based on the current results, one will conclude that the wake zone bridging consists of a combination of bridging by frictional and unbroken ligaments. At room temperature, when the peak loads, initial crack opening displacement and number of cycles are held below values which cause grain sliding, no fatigue damage is evident. Above the threshold values, however, notable damage may be observed. This cumulative wear process reduces the effectiveness of the bridging. At high temperature, it was found that the relaxation of normal forces due to the softening of the grain boundary phase gives a rise to ratcheting behavior. For the quasistatic bridging problem, accumulation of damage has been related to grain size features, but apparent from data in this study, fatigue related damage depends upon damage to sub-grain size features.

KEYWORDS

Ceramics, Toughness, Bridging mechanism, Fatigue, Thermal expansion Anisotropy.

INTRODUCTION

In the past, ceramics were considered to be immune to fatigue damage from cyclic loading due to their low dislocation mobility and corresponding lack of crack-tip plasticity [1]. Despite several early observations to the contrary [2,3], enhanced crack propagation under cyclic loading was commonly attributed to environmentally induced stress corrosion cracking [4]. However, recent work has demonstrated a true fatigue effect in many ceramics, such as Al_2O_3 [5-13] and Si_3N_4 [10,13-17], where subcritical crack growth rates, under cyclic loads, can greatly exceed growth rates under static loads at equivalent stress intensity levels. As a part of this new interest the question arises - what role does the microstructure play in the behavior, and specifically, how do the bridging grains contribute to fatigue crack growth resistance?

It is now well recognized that the toughness of many non-transforming monolithic ceramics, under monotonic loading often increases as the crack extends, resulting in a rising crack growth resistance (R) curve [18]. This toughening behavior is primarily due to grain bridging in the wake zone of the advancing crack, which reduces the effective stress intensity factor at the crack tip [19-21].

During cyclic loading, it has been suggested that the degradation of such toughening mechanisms promotes fatigue crack growth. Indeed, recent work [9-12,17,23] has indicated that in grain bridging ceramics, repetitive sliding wear of the bridging grains, under cyclic loading, reduces the load bearing capacity of these wake zone elements and lowers the toughness of the material. Lathabai, *et al* [23], modeled the decreased bridging capacity under cyclic loading by assuming a reduction in the frictional coefficient between the bridging grains and their sockets in the surrounding material. Also, a frictional wear mechanism was proposed by Dauskardt [10] in which a micromechanical model was developed to relate the reduction in grain pullout stresses to material removed by wear processes at the grain/socket interface. Indirect evidence for this mechanism of fatigue crack growth has also come from examination of fracture surfaces where wear tracts and wear debris have been observed [11,17,23].

The purpose of the present study is to examine the cyclic loading behavior in room and high temperature conditions of a monolithic alumina, which shows significant R-curve toughening by grain bridging. By utilizing an experiment called the post-fracture-tensile (PFT) test, developed by Hay and White [24-27], we are able to isolate discrete elements of the crack wake zone for detailed study. Previously, the PFT experiment has proven effective for the evaluation of the wake process zone resulting from quasistatic crack extension [24,26,27]. Of particular interest here is the damage induced by repeated loading and unloading of the bridging grains.

PROCEDURES

Material and Specimens

The alumina used in this study is a commercial 99.7% alumina, obtained through Johnson Matthey, and is the same as that characterized previously [24,27,30]. The average grain size, found from a polished and etched surface, is approximately 18 μm and a majority of the grains (~90%) are less than 35 μm. A monotonically loaded fracture surface, shown

in Figure 1 (a), indicates the size, morphology and spatial arrangement of the grains. The grain size distribution for this alumina, obtained from polished and etched surfaces, is shown in Figure 1 (b).

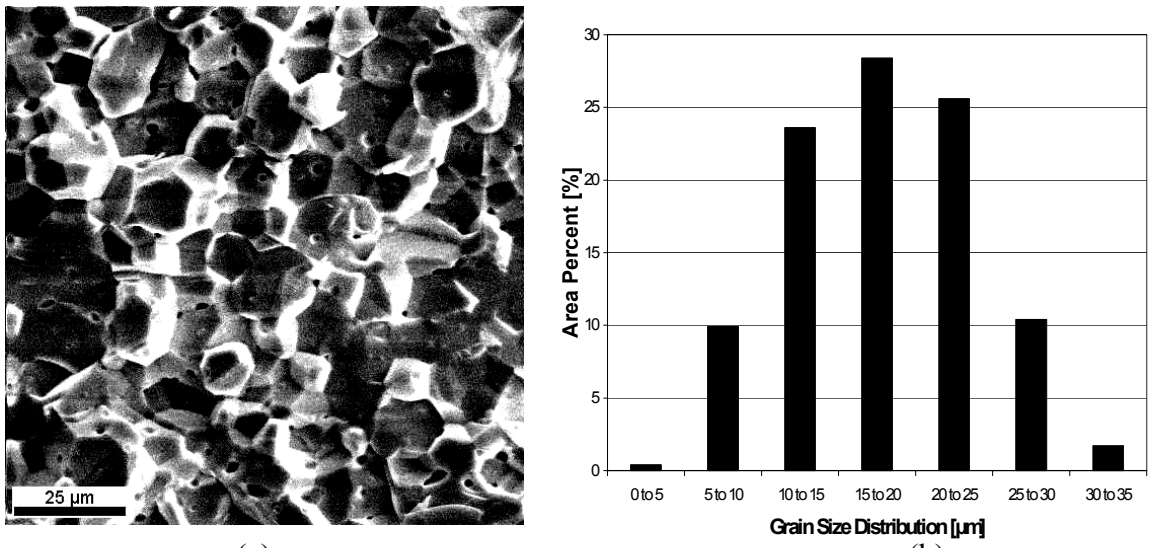

(a) (b)

Figure 1: Fracture surface (a) and grain size distribution (b) of material studied

PFT Experiment

To obtain R-curve information, and to provide specimens for the second stage of testing, double cantilever beam (DCB) specimens were cut from bulk plates measuring 50 mm x 100 mm x 4 mm. A schematic of the specimen is shown in Fig. 2(a), where h=8.5mm, w=4mm, w'=2mm, L=48mm, and a_0=13mm. A half-thickness side groove down the center of the specimen restricts crack deviation from the desired fracture plane. Specimens were fractured on an Instron testing machine at a displacement rate of 0.75 µm/min. Crack lengths were observed optically and crack growth was arrested by load removal when the crack had grown approximately 16 mm. Figure 2(b) shows the R-curve data obtained for this microstructure, where a plateau K_R value of 4.6MPa.m^{½} is reached after 9mm of crack extension.

The second part of the experiment, referred to as the post-fracture tensile (PFT) test, requires the machining of tensile specimens from the cracked DCB specimen for the direct characterization of the bridging mechanism. The PFT technique provides a unique tool to isolate incremental segments of the crack-wake. Shown in Figure 2(a), the region behind the crack tip is sliced into several 1mm wide strips. Each strip is through-cracked and held together only by bridging elements as shown by the schematic in Figure 3b. The two side grooves, which were machined prior to slicing, facilitate tensile loading on two knife-edges. We have examined the effects of introducing these PFT loading grooves prior to, or following the fracture test. Since the PFT data obtained by both methods are indistinguishable, we conclude the grooving step does not adversely affect the wake.

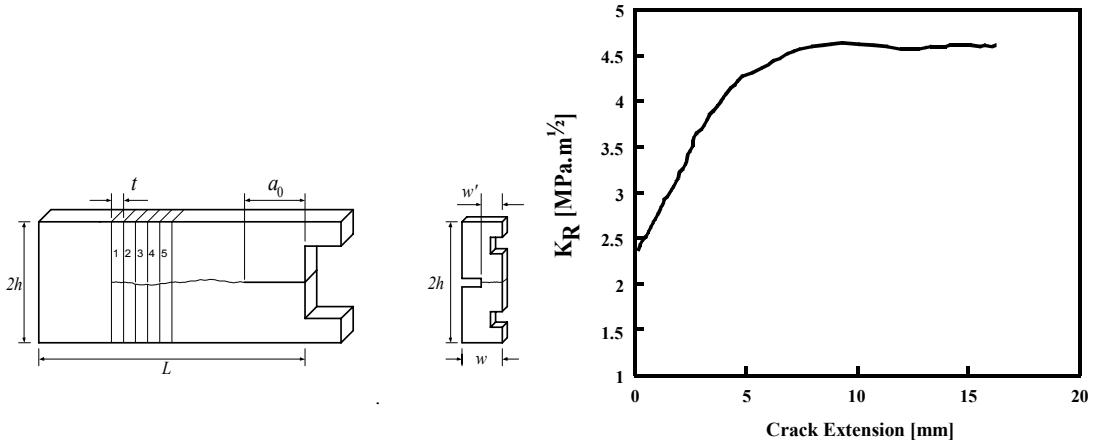

(a) (b)

Figure 2: Schematic of DCB and PFT specimens (a), R-curve behavior of the alumina tested (b).

Details of the experimental setup and data collection techniques will not be elaborated upon here as they have been extensively outlined in previous publications [24-27]. For these particular results, three PFT specimens have been fatigued to obtain information on load-cycling effects at room temperature and high temperature. Two came from the position nearest the crack tip, which we call PFT#1and PFT#2 (refer to Figure 2a) and the other came from the fifth position away from the tip, which we call PFT#5. All PFT specimens were subjected to series of cyclic tests.

RESULTS AND DISCUSSION

In Figure 3(a), load-displacement data for the #1 PFT specimen is presented for two maximum loading conditions. From this data, it is evident that this specimen exhibits the same linear elastic type behavior at maximum load of 0.32 Kg before (Test1) and after (Test 2) 10,000 cycles, and the compliance remains constant at approximately 0.11 μm/kg. Immediately following this test, PFT#1 was sinusoidally loaded to a higher maximum load of 0.72 kg and unloaded (Test 3), as shown in Figure 3(a). During this test we observe an interesting behavior evidenced by the formation of a hysteresis loop. Starting from the premise that the existence of this loop indicates the presence of some type of energy loss mechanism, we further assert that a damage mechanism, related to the fracture of the elastic ligaments and the sliding of the bridging grain, have been activated when the applied load or displacement reaches some critical value. Similar hysteretic behavior has been observed by Vekinis, *et al* [22] Dauskardt [10] in alumina and by Gilbert, *et al* [17] in silicon nitride.

The effects of cycling an additional 10,000 times to the same maximum load, 0.72 kg, are presented in Figure 3(b). From this data, two interesting points of note become

evident. Firstly, the initial elastic compliance remains unchanged at 0.11 μm/kg. However, the load at which the behavior becomes non-linear has been reduced from 0.41 kg to 0.32 kg. This indicates that cycling the specimen a further 10,000 times at 0.72 Kg has reduced the effectiveness of the elastic bridging (Test 4). Secondly, as we approach the maximum load of the cycle, we observe a greater increase in the specimen compliance. In first cycle, this compliance reached 0.22 μm/kg. However, after 10,000 cycles, it has increased quite substantially to 0.63 μm/kg (refer to Test 4). These results indicate that a damage mechanism may have been activated due to the combination of fracture of elastic ligaments observed under the SEM and continuous sliding of the bridging grains. Those mechanisms, therefore, have the effect of degrading the bridging capacity and hence the toughening ability of this alumina has been reduced.

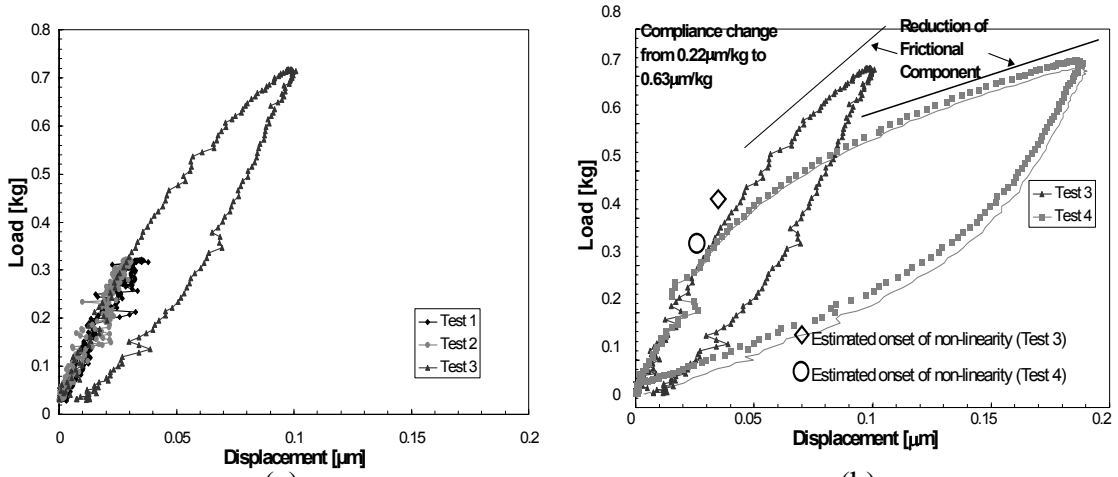

Figure 3: Load increase effect (a) and high cyclic loading effect (b)

The PFT procedure was used to investigate temperature effects on the wake zone behavior of alumina. Here, an isolated wake zone element obtained from a DCB was subjected to load cycling at various temperatures. A temperature interrupted PFT test was adapted to elucidate the effects of Thermal Expansion Anisotropy (TEA). The test consisted of initially testing a PFT at room temperature to obtain the load-displacement behavior. Continuation of the procedure then evaluated load-displacement behavior at 600 and 800 °C, follow by a repetition of the room temperature test. The results of a temperature interrupted PFT test is shown in Figure 4(a). All the tests were performed to the same test load level.

The room temperature test primarily shows linear-elastic behavior. Following the room temperature result, the specimen is evaluated at 600 °C. The increased compliance with temperature and the formation of a nearly-closed hysteresis loop at 600 °C is related to the reduction of the misfit strain associated with thermal expansion anisotropy. This causes a relaxation of the clamping forces on bridging grains and lowers the bridging stress. Continuing to 800 °C, it is observed that the deformation behavior then develops to a gross-slip condition.

Low cyclic loading tests were performed on a #5 PFT specimen, taken from about 7 mm behind the crack tip in a region of larger initial COD than the #1 PFT specimen. The #5 specimen therefore exhibits a lower stiffness and a lower peak load capacity than the #1 specimen[24]. Thus lower maximum load values were chosen for fatigue testing of this specimen. Figure 4(b) shows all of the test data obtained on the #5 PFT. As before, the material exhibits linear elastic behavior up to a maximum load of 0.15 Kg. The compliance also remains the same indicating that no fatigue degradation occurred up to this point in our test procedure.

However, by increasing the maximum load to 0.25 kg, we observe the formation of open loops indicating the predominant sliding mechanism activity discussed previously. We mention here the appearance of residual opening displacement that get larger as the load increases. It is also worth to mention that the stiffness of the loading and the unloading parts remain approximately the same, which means, from the contact point theory that even though sliding occurred during this set of tests (residual opening displacement), the distribution of contact point stays the same.

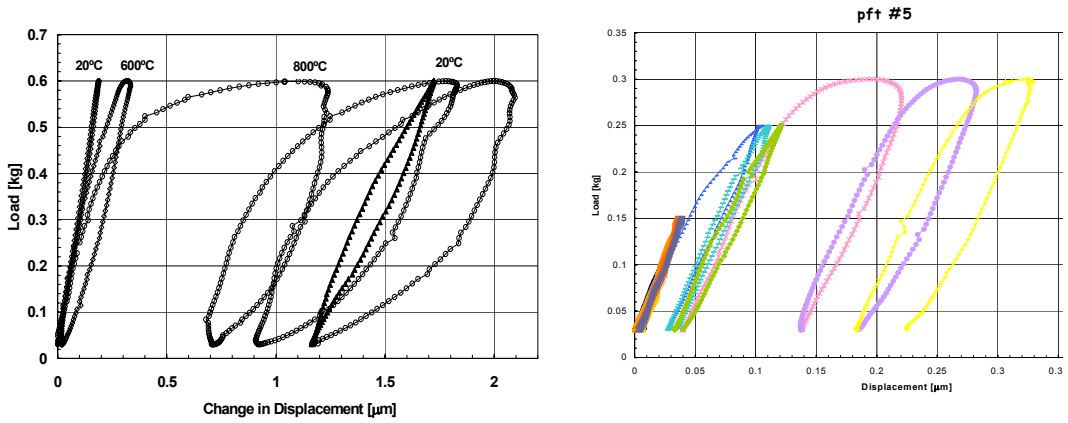

Figure 4: Effects of cyclic loading of PFT #5 (a) and of high temperature on PFT #2 (b)

CONCLUSIONS

The post-fracture-tensile (PFT) technique has been successfully applied to an investigation of cyclic fatigue of wake zone processes in a commercial alumina at room and high temperature. At room temperature, when the peak loads and number of cycles were held below the critical values which cause frictional sliding of the grains, no fatigue damage was observed. Below these threshold points the material behaved linear elastically and no compliance changes were observed as a result of cycling. Above the threshold values, however, fatigue damage resulted from the fracture of the elastic ligaments and continuous sliding action of the grains. Also, the load at which non-linear behavior begins was seen to be reduced and the final loading compliance increased quite substantially. Final Results indicate that a frictional wear mechanism is activated after a certain number of cycles depending on the applied loads, allowing the bridging grains to slide in their sockets. This cumulative process reduces the effectiveness of the elastic

contact points of the wake mechanism as evidenced by the reduction in the length of the initial elastic region. Also, the frictional bridging stress was degraded which resulted in an increased compliance towards the end of the loading cycle. In PFT #5, situated far from the crack tip, it was clear from the results obtained that frictional sliding was the only bridging mechanism active, which is generally associated with residual crack opening displacements

Finally, the effects of temperature indicated some interesting properties of the TEA. Increasing the test temperature caused the reduction of the misfit strain associated with TEA. One can conclude that temperature increase caused the relaxation of the normal forces due to the softening behavior of the grain boundary phase. This effect was clear at 800 ^{o}C by the development of gross slip behavior or residual crack opening displacement.

Acknowledgement- Financial support for the initial formulation of this concept provided by USAFOSR Project #F49620-93-1-0210. All results and development of this approach were supported by DOE grant DE-FG03-96ER45577.

REFERENCES

1. Evans, A. G., and Fuller, E. R., *Metall. Trans.*, 1974, **5** 27.
2. Krohn, D.A., Hasselman, D.P.H., *J. Am. Ceram. Soc.*, 1972, **55**(4), 208.
3. Guiu, F., *J. Mat. Sci. Lett.*, 1978, **13,** 1357.
4. Lathabai, S., Mai, Y-W., Lawn, B.R., *J. Am. Ceram. Soc.*, 1989, **72(**9), 1760.
5. Reece, M.J., Guiu, F., Sammur, M., *J. Am. Ceram. Soc.*, 1989, **72(**2), 348.
6. Kishimoto, H., Ueno, A., Okawara, S., *J. Am. Ceram. Soc.*, 1994, **77(**5), 1324.
7. Guiu, F., Li, M., Reece, M.J., *J. Am. Ceram. Soc.*, 1992, **75(**11), 2976.
8. Dauskardt, R.H., James, M.R., Porter, J.R., Ritchie, R.O., *J. Am. Ceram. Soc.*, 1992, **75(**4), 759.
9. Hu, Z-H, Mai, Y-W., *J. Am. Ceram. Soc.*, 1992, **75(**4), 848.
10. Dauskardt, R. H., *Acta. Metall. Mater.*, 1993, **41(**9), 2765.
11. Gilbert, C. J., Petrany, R. N., Ritchie, R. O., Dauskardt, R. H. and Steinbrech, R. W., *J. Mater. Sci.,* 1995, **30,** 643.
12. Gilbert, C. J. and Ritchie, R. O., *Fatigue Fract. Engng. Mater. Struct*, 1997, **20** [10] 1453.
13. Dauskardt, R. H., *Trans. of ASME – J. Eng. Mat. and Tech*, 1993, **115** 244.
14. Jacobs, D.S., Chen, I-W., *J. Am. Ceram. Soc.*, 1995, **78(**3), 513.
15. Jacobs, D.S., Chen, I-W., *J. Am. Ceram. Soc.*, 1994, **77(**5), 1153.
16. Suresh, S., Han, L.X., Petrovic, J.J., *J. Am. Ceram. Soc.*, 1988, **71(**3), 158.
17. Gilbert, C. J., Dauskardt, R. H. and Ritchie, R. O., *J. Am. Ceram. Soc*., 1995, **78**(9) 2291.
18. Buresch, F.E., Pabst, R., *Science Of Ceramics*, 1973, **6(**XVI), 3.
19. Steinbrech, R.W., Knehans, R., Schaarwachter, W., *J. Mater. Sci.*, 1983, **18,** 265.
20. Mai, Y.W., Lawn, B.R., *J. Am. Ceram. Soc.*, 1987, **70**(4), 289.
21. Swanson, P., Fairbanks, C.J., Lawn, B.R., Mai, Y.W., Hockey, B.J., *J. Am. Ceram. Soc.*, 1987, **70(**4), 279.
22. Vekinis, B., Ashby, M.G., Beaumont, P.W.R., *Acta metall. mater.*, 1990, **38(**6), 1151.
23. Lathabai, S., Rödel, J., Lawn, B.R., *J. Am. Ceram. Soc.*, 1991, **74(**6), 1340.
24. Hay, J.C., White, K.W., *J. Am. Ceram. Soc.*, 1995, **78**(4), 1025.
25. Hay, J.C., White, K.W., *Acta. Mater.*, 1997,.**45(**9), 3625.
26. Hay, J.C., White, K.W., *J. Am. Ceram. Soc.*, 1997, **80**(5), 1293.
27. White, K.W., Hay, J.C., *J. Am. Ceram. Soc.*, 1994, **77(**9), 2283.
28. Steinbrech, R.W., Deuerler, F., Reichl, A., Schaarwachter, W., *Science of Ceramics*, 1988, **14,** 659.
29. Reichl, A., Steinbrech, R., *J. Am. Ceram. Soc.*, 1988, **71(**6), C299.
30. Hay, J.C., White, K.W., *J. Am. Ceram. Soc.*, 1993, **76(**7), 1849.

DETERMINING LOAD HISTORY EFFECTS ON HCF CRACK GROWTH THRESHOLDS

Monty A. Moshier[1], Theodore Nicholas[2], and Ben M. Hillberry[3]

[1]Anteon Corporation, Dayton, OH 45431
[2]Air Force Research Laboratory, Materials and Manufacturing Directorate (AFRL/MLLM)
Wright-Patterson AFB, OH 45433-7817.
[3]Purdue University, School of Mechanical Engineering, West Lafayette, IN 47907.

ABSTRACT

The effect of load history on the fatigue crack growth threshold in Ti-6Al-4V at room temperature was evaluated using two specimen configurations. Short crack tests were conducted on notched specimens under load control to produce low cycle fatigue surface precracks in the size range 25 μm – 600 μm at R=0.1 and R=-1. The threshold for high cycle fatigue (HCF) crack propagation was then determined at 600 Hz using a step loading procedure. Long crack tests were conducted on C(T) specimens by subjecting them to constant high ΔK controlled prior cracking at R=0.1 and then determining the threshold using a procedure comprising an increasing ΔK, constant R, step-load method. In both test types, stress-relief annealing (SRA) is applied to some of the specimens after the load history has been applied but before the threshold determination. While the load history is seen to effect the subsequent threshold in the form of an underload or overload effect, results show that SRA removes all load history effects and produces a true material threshold which is independent of the load history. This true threshold is found to be slightly lower than the value obtained using C(T) specimens and standard load shed techniques.

KEY WORDS

High cycle fatigue, Load history effects, Small cracks, Overloads, Threshold

INTRODUCTION

Many HCF failures in gas turbine engines are the result of in-service damage due to fretting, foreign object damage (FOD), LCF, or others [1]. In the presence of damage and due to the large numbers of cycles applied in short periods of time the idea of a threshold below which HCF does not occur is necessary. Damage tolerance for HCF when initial cracks are present would therefore require the determination of a crack growth threshold applicable to the conditions under which the crack was formed. This study investigates the high cycle fatigue (HCF) threshold of a typical fan blade material, Ti-6Al-4V, when naturally initiated fatigue cracks, which have been created using different LCF loading sequences, are present.

EXPERIMENTS

All specimens were machined from forged Ti-6Al-4V plate. The titanium alloy had an alpha-beta microstructure of approximately 60% primary alpha with the remainder transformed beta. The mechanical properties of the Ti-6Al-4V plate are σ_y = 930 MPa and σ_{UTS} = 980 MPa.

Small Crack Testing

Double notch tension test specimens were stress relieved after machining and then electro-polished in the gage section in the vicinity of the notches. The two notches had the same depth but different notch root radii, thereby producing almost no bending when applying fixed grip axial

loading. The notch geometries were chosen so that failure could be confined to the more severe notch having an elastic stress concentration factor, K_t, of 2.2.

LCF was conducted at stress ratios of –1.0 and 0.1 under load control to initiate a crack using a sinusoidal wave form at a frequency of 10 Hz with a superimposed hold time of 0.5 s on each cycle during which the DCPD measurements could be made. Maximum stress levels (430 MPa at R=0.1 and 265 MPa at R=-1.0) were chosen which corresponded to approximately 250,000 cycles to failure. Cracks were typically detected with DCPD at cycle counts between 20,000 and 100,000 at which point the tests were stopped and the specimens inspected in the SEM to confirm the existence of a crack.

To fully characterize the geometry of these cracks in order to determine ΔK_{th}, the crack shape was determined by heat tinting the LCF cracked specimens at 400°C for four hours prior to HCF threshold testing. Heat tinting marks the crack profile for post fracture measurement of the crack geometry without affecting any subsequent crack growth properties.

The LCF cracked specimens were then tested in HCF using a step loading procedure to determine the failure stress [2]. The tests were conducted in a custom built HCF apparatus at a frequency of 600 Hz. The thresholds in the form of values of ΔK were determined from the load for crack extension to occur, and from the measurements of the initial crack size using heat tinting. K values were determined using the finite element method to modify existing solutions developed for a semi-elliptical surface crack and corner crack in a single edged notch tension specimen. In this work, ΔK_{th} is defined as the value of ΔK where propagation begins from a no-growth state. It was interpolated using the average of the load where no crack extension occurred and the load at which crack extension was observed. From the crack measurements made from the fracture surfaces, the interpolated threshold stress and the modified stress intensity factor solution, a value of ΔK_{th} was determined which represents the onset of crack propagation.

Long Crack Testing

Threshold testing was conducted on C(T) specimens under K-controlled conditions using a sinusoidal waveform at a frequency of 50 Hz using a step load procedure similar to that used in the HCF testing [2] in order to determine at what K level crack extension occurs. The method involves subjecting a specimen to 200,000 cycles at a K level below which crack extension was anticipated to occur. The 200,000 cycles was determined to be sufficiently large so that crack extension would be detected. If crack extension is not detected within the block of 200,000 cycles the level of K is increased 0.2 MPa$\sqrt{m}$ and the test repeated until the crack extension occurs. The threshold is defined to be the average of the K levels where no crack extension occurs and where crack extension first occurs. Because the increments are 0.2 MPa$\sqrt{m}$, the error is at worst 0.1 MPa$\sqrt{m}$.

RESULTS AND DISCUSSION

Small Cracks

Cracks initiated under LCF were measured under load in a SEM to determine the surface crack length, 2a. The depth of the crack was determined from the fracture surface that showed the heat tinted pattern of the crack after LCF but before HCF. Figure 1 shows the linear fit of the “a” and “c” crack data. The values of “a” from the heat tinted surface, covering a range from 25 to 400 μm, were in general agreement with the surface crack measurements in the SEM.

One method for evaluating threshold crack growth data is to compare stresses for a given crack size against crack length for LCF generated cracks and data extrapolated from a long crack growth threshold test. Such information can be presented in the form of a Kitagawa diagram [4], which plots stress against crack size. Using logarithmic scales, a crack growth threshold for a geometry where K is proportional to $\sqrt{c}$ (c is flaw size) produces a straight line of slope=-0.5 while the endurance limit of an uncracked material is a line of constant stress.

For any given geometry, all combinations of crack length and stress corresponding to a K solution equal to the threshold value establish the threshold crack growth line. This line now represents the fracture mechanics solution down to arbitrarily short crack lengths and makes no assumptions about the lack of validity of the solution for such short cracks. The short crack anomaly is easily demonstrated because the threshold value from the K solution produces stress levels for arbitrarily short cracks that are above the endurance limit yet below the crack growth threshold. Much more important is the concept of data points below the endurance limit and below the threshold ΔK for short cracks of a particular size. It is clear that such cracks could not be

naturally initiated since they develop under stress levels that are below the endurance limit. It follows, therefore, that data plotted on a Kitagawa diagram representing a crack length and stress below the endurance limit generally represent a condition where the crack was initiated above the endurance limit. An alternate explanation might be that a complex stress field allows the initiation, but not propagation of a crack. In this case, the simple K solution that produces the line of constant K is no longer valid and the actual K solution has to be represented in the diagram. With this in mind, the question is raised as to whether any point on a Kitagawa diagram is unique or, instead, is dependent on the history of loading in getting to that point. The long crack threshold is clearly an example of a data point which is dependent on load shed history. While standards have been set for determining this threshold by following a predetermined history, the history dependence and the existence of a unique long crack threshold still have to be questioned.

The data for the HCF threshold after a LCF crack was initiated are plotted in a Kitagawa type diagram in Figure 2. In the figure, a line is drawn representing the long crack threshold of K_{max}=5.1 MPa√m for R=0.1. The line represents the stresses calculated from the long crack thresholds above and the linear fit from the a/c data (Fig. 1). The horizontal line represents the experimentally determined endurance limit for the notched specimens corresponding to 10^7 cycles. It can be seen that the data which were obtained using LCF at R=-1.0 (triangles) tend to fall slightly below the projected long crack threshold, the type of effect being representative of what one would expect when a material sees an underload during prior cycling. Conversely, the circles which represent data obtained under LCF at R=0.1 show what appears to be equivalent to an overload effect since the threshold values of stress are consistently above the long crack threshold.

Also shown are small solid circles and triangles which represent specimens which were cracked in LCF, stress relief annealed (SRA), and then tested in HCF. The small circles represent specimens which were cracked using the same stress level as the larger circles (R=0.1) while the small triangles represent specimens which were cracked at the same level as the larger triangles (R=-1.0). The data indicate that the stress relief annealing process, which eliminates residual stresses, provides a baseline threshold level for different crack lengths, independent of load history.

Long Cracks

Long crack threshold testing was conducted to determine the effect of different K_{max} prior history on the measured long crack thresholds. The range of K_{max} used for precracking was 6 to 25 MPa√m. The resulting measured K_{max} thresholds, covering the range 4.6 to 11.2 MPa√m, vary linearly with the K_{max} used for the precrack (Fig. 3). Additionally, identical tests were conducted on specimens subjected to SRA. The long crack K_{max} threshold measurements for these specimens were 4.5 to 4.9 MPa√m for R=0.1 regardless of the prior ΔK level. These data provide a nearly constant estimate of the threshold that is slightly lower and more conservative than the long crack threshold, measured by standard load shed techniques, of 5.1 MPa√m. Similar experiments were conducted at R=0.5. The results are shown in Fig. 3 where the SRA threshold is 5.6 MPa√m, which is only slightly lower than the long crack threshold, from standard load shedding, of 5.8 MPa√m

Small Crack / Long Crack Threshold

The short crack threshold data from the DE(T)specimens can be plotted in the same format as the long crack data using the final crack length and stress amplitude necessary to initiate the cracks to calculate the K_{max} precrack. The K_{max} precrack ranged from 3.6 to 24.7 MPa√m and the measured K_{max} threshold ranged from 4.1 to 10.8 MPa√m. The small crack data (the open circles and open triangles in Fig. 4) appear to follow the same trend as the long crack data for the HCF thresholds produced at R=0.1. The SRA short crack specimen data (filled circles and triangles) produce thresholds that are near the measured SRA long crack thresholds. The K_{max} thresholds for the small cracks appear to be independent of the crack lengths that are related to the K_{max} of the precrack. The crack sizes of the small crack threshold data (Fig. 4) correspond to the data shown on the Kitagawa diagram (Fig. 2). The smaller cracks have lower K_{max} precracks due to the constant maximum applied stress (430 MPa at R=0.1 and 265 MPa at R=-1.0) that was used for the LCF crack initiation. It is important to note that because of this, the plastic zone sizes for the small crack data are much smaller than the cracks. It is also important to mention that the LCF R=-1.0 HCF threshold data (open triangles in Fig. 4) follow the same trend as the SRA HCF threshold data, indicating that R=-1.0 appears to be an appropriate stress ratio for initiating small cracks without loading histories. It is speculated that the compression portion of the R=-1.0 loading may remove closure effects, similar to what occurs when periodic underloads are applied.

CONCLUSIONS

Threshold values obtained on notched short crack specimens which are precracked in LCF at R=0.1 and R=-1.0 show a definite load history effect. LCF conducted at R=0.1 prior to HCF produces an overload effect which, in turn, increases the subsequent HCF threshold. On the other hand, LCF at R=-1.0 produces a slightly lower threshold than that from standard load shedding.

These results, when plotted in the form of a Kitagawa diagram, indicate that values of crack growth threshold are not unique but instead depend on the loading history used to produce the cracks. The small crack threshold data collected by initiating cracks in LCF and subsequent SRA and the threshold data collected by first initiating cracks in LCF at R=-1.0 appear to follow the same trend. These data are below the long crack load shed threshold on the Kitagawa diagram, indicating that load history free small crack data can be collected by either initiating at R=-1.0 or using SRA.

Load-history free threshold measurements in the C(T) specimen can be made by first precracking the specimen with subsequent SRA and threshold testing. In addition to the measurements being load history free, many tests can be completed with one specimen resulting in a significant time savings when the stress relief annealed step test is used.

REFERENCES

[1] Nicholas, T. and Zuiker, J.R., "On the Use of the Goodman Diagram for High Cycle Fatigue Design," *International Journal of Fracture*, **80**, 1996, pp. 219-235.

[2] Maxwell, D.C. and Nicholas, T., "A Rapid Method for Generation of a Haigh Diagram for High Cycle Fatigue," *Fatigue and Fracture Mechanics: 29th Volume*, *ASTM STP 1321*, T.L. Panontin and S.D. Sheppard, Eds., American Society for Testing and Materials, West Conshohocken, PA, 1999, pp. 626-641.

[3] Frost, N.E., "Notch Effects and the Critical Alternating Stress Required to Propagate a Crack in an Aluminum Alloy Subject to Fatigue Loading," *J. Mech. Eng. Sci*., **2**, 1960, pp. 109-119**.**

[4] Kitagawa, H. and Takahashi, S., "Applicability of Fracture Mechanics to Very Small Cracks or the Cracks in the Early Stage," *Proc. of Second International Conference on Mechanical Behaviour of Materials*, Boston, MA, 1976, pp. 627-631.

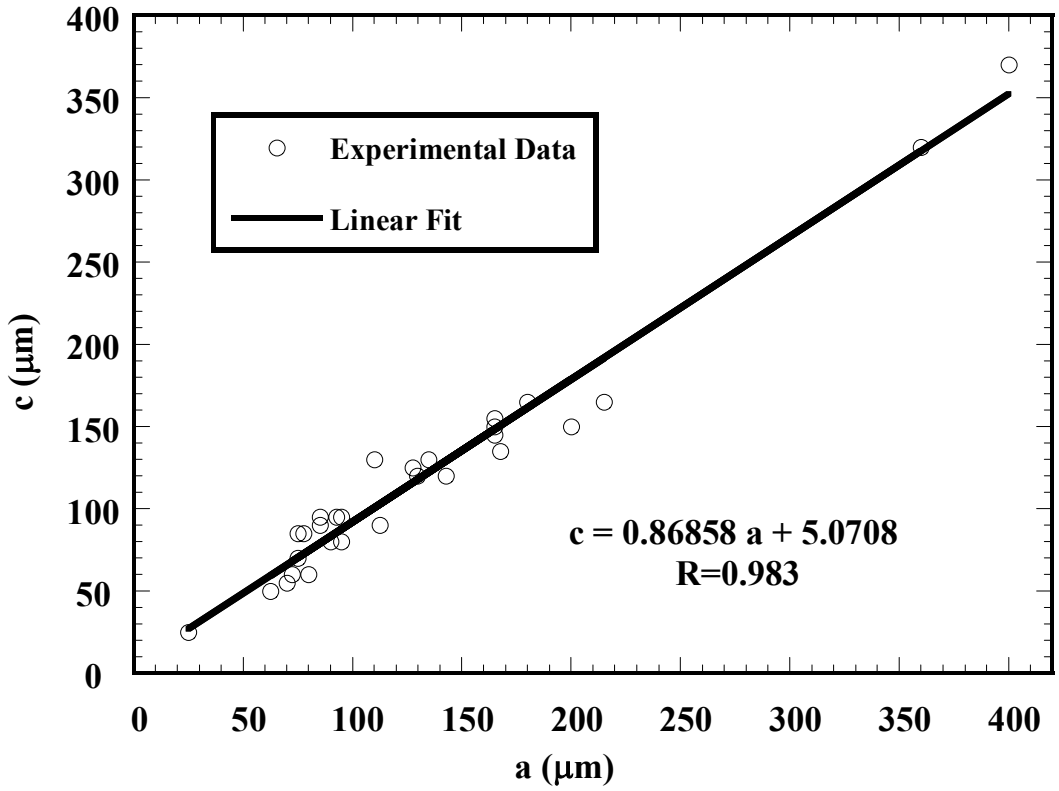

Figure 1 Experimental results for measured crack geometries.

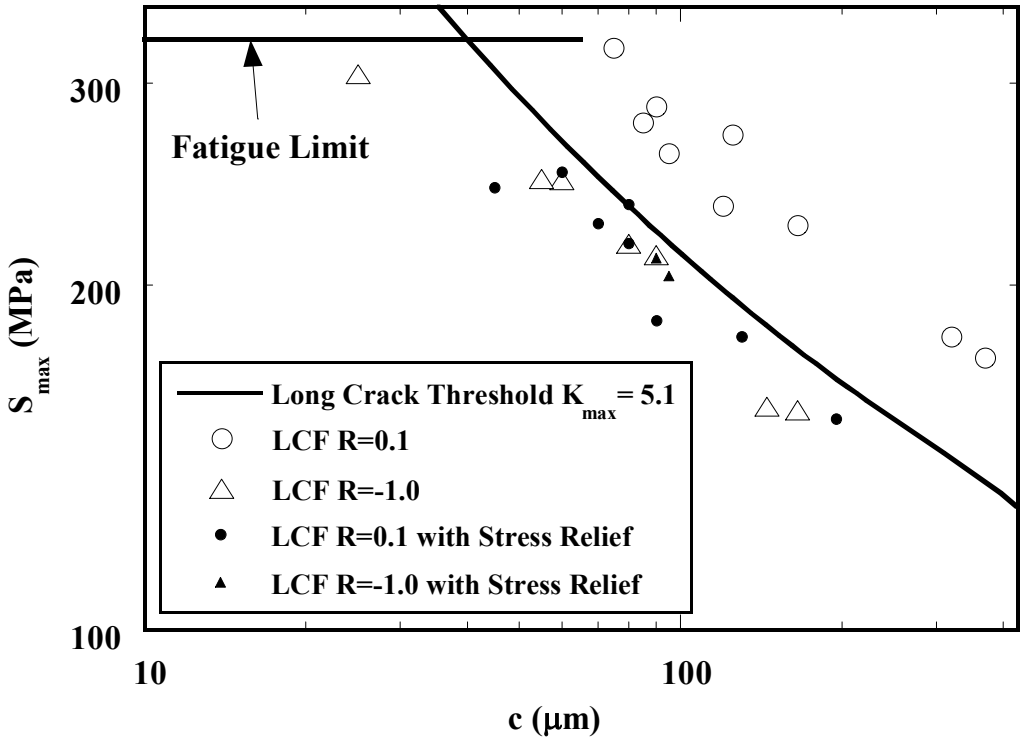

Figure 2 HCF thresholds at R=0.1 on a Kitagawa type diagram plotted versus "c".

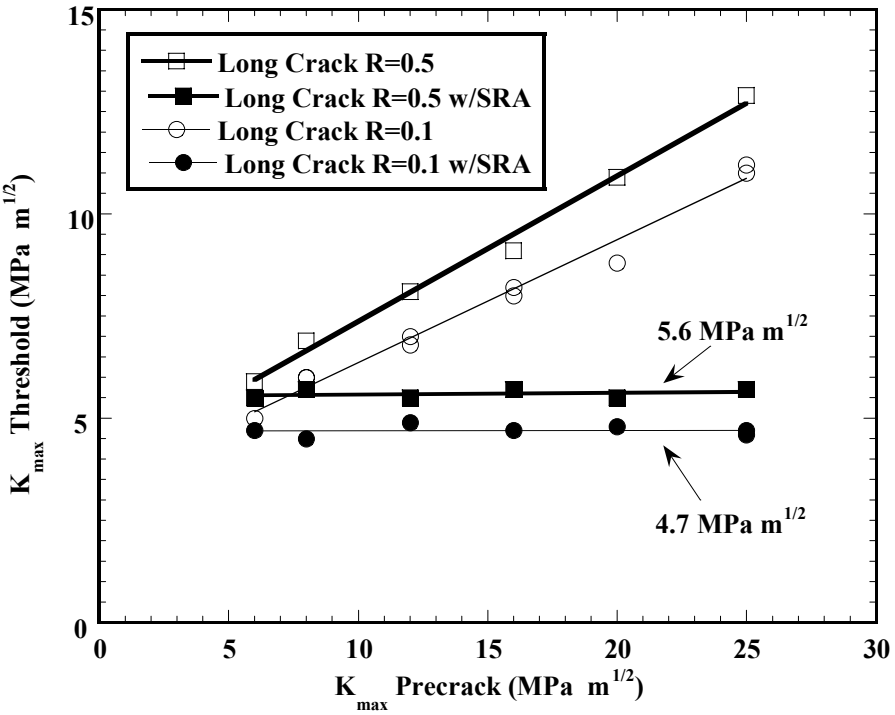

Figure 3 Long crack threshold data R=0.1 and R=0.5.

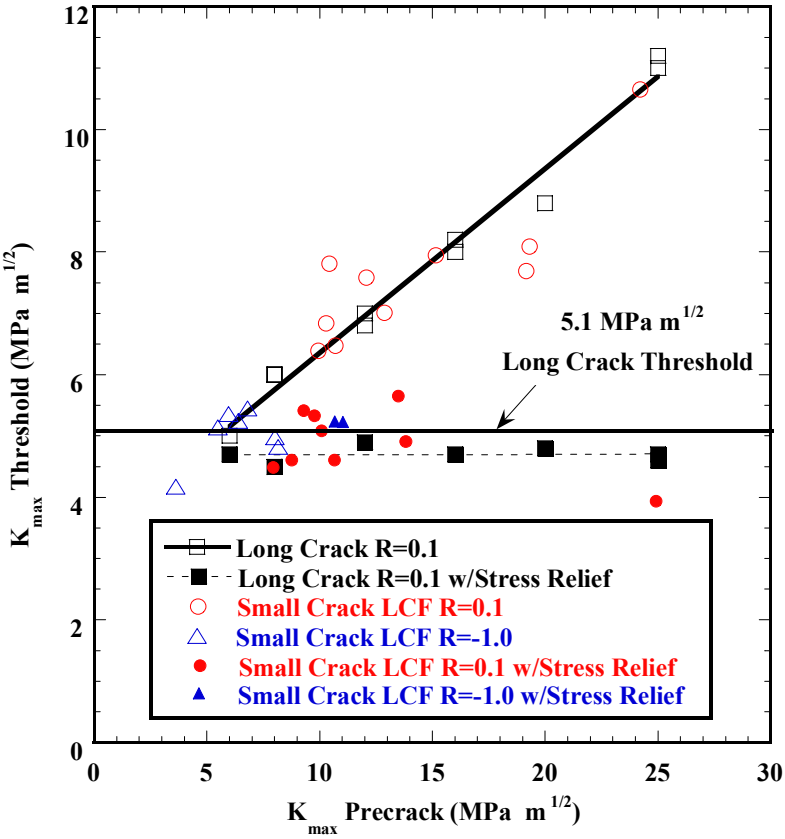

Figure 4 Long and small crack threshold data trends R=0.1.

OROAL/POSTER REFERENCE: ICF100674OR

DETRIMENTAL EFFECT OF HYDROGEN ON THE FRACTURE STRENGTH OF SINGLE-WALLED CARBON NANOTUBES

S.Q. Shi[1,@] and L.G. Zhou[2]

[1]Department of Mechanical Engineering, Hong Kong Polytechnic University, Hong Kong, China
[2]Institute of Metal Research, Chinese Academy of Sciences, Shenyang 110016, China

ABSTRACT

Molecular dynamics simulations have been performed to study the mechanical properties of single-walled carbon nanotube under tensile loading with and without hydrogen storage. Advanced bond order potentials were used in the simulations. (10,10) armchair and (17,0) zigzag carbon nanotubes have been studied. Two deformation stages of armchair carbon nanotube were found. In the first stage, the elongation of nanotube was primarily due to the altering of angles between two neighbor carbon bonds. The Young's Modulus observed in this stage is comparable with experiments. In the second stage, the lengths of carbon bonds were extended up to break point due to the increase of tensile loading. The tensile strength in this stage is higher than that observed in the first stage. Similar result was also found for the zigzag carbon nanotube. Hydrogen molecules stored inside and/or outside of nanotubes reduced the fracture strength of both types of carbon nanotubes. The competition in formation of hydrogen-carbon and carbon-carbon bonds was found to be responsible for the detrimental effect. During the deformation, some carbon-carbon bonds were broken and reconstructed. If hydrogen molecules were around, H atoms would compete with the carbon atoms, to form hydrogen-carbon bonds.

KEYWORDS

Carbon nanotubes, hydrogen, fracture, simulation

INTRODUCTION

A single-walled carbon nanotube (SWNT) can be described as a graphene sheet rolled into a cylindrical shell and is a quasi one-dimensional system [1]. Apart from the well-known electrical property [2] of SWNT, its remarkable mechanical properties and potentially high hydrogen-storage capacities are also intensively studied. Due to the nanosize of SWNT, a direct measurement of its mechanical properties is rather difficult. However, this extreme size is very suitable for performing atomistic simulations. Currently, the atomistic simulations on hydrogen in SWNTs are mainly focused on two issues: how much hydrogen can be stored and where the atoms are stored. An interesting question is, since carbon nanotubes are both promising for

[@] mmsqshi@polyu.edu.hk

use in structure and hydrogen storage, what is the effect of hydrogen on mechanical properties of carbon nanotubes? In this article, we report our MD simulations on single-walled nanotubes under a tensile loading with hydrogen storage.

METHODOLOGY

Brenner's hydrocarbon potential, a bond order potential, is used in this simulation [3-5]. Nanotubes in this paper are $(10,10)\times 100_u$ armchair type and $(17,0)\times 58_u$ zigzag type, respectively. The subscript u denotes a repeat unit of SWNT along the axial direction. These units were chosen so that the two types of nanotubes have a similar diameter and tube length.

To simulate the tubes under tensile loading, we followed two steps. First, the tubes were annealed at simulation temperature for 5,000 MD steps. The time interval between two MD steps is 0.5 fs. Then, the tube was pulled in axial direction (i.e., z-direction) with a strain of 5×10^{-4}. Following each step of pulling, some additional MD steps were used to relax the structure. A periodic boundary condition has been used along the axial and horizontal directions and the simulations were performed at 300 K and 600 K, respectively.

Unlike the continuum shell model, SWNT is constructed by hexangular carbon rings so that its mechanical p roperties are strongly depended on its chiral directions. Bond angle and bond length are the two crucial factor s that control the deformation. For armchair SWNT, the elongation of tube due to the altering of bond angles can be up to 15 % if the C-C bonds are assumed to be rigid. While for zigzag SWNT, one-third of the C-C b onds are parallel to the axis. The loading force is then directly acting on these bonds so that they are easy to b reak. Fig.1 shows the tensile force (F_z) along the axial direction of the armchair (10,10) and zigzag (17,0) S WNTs as a function of strain (F_z-ε curve) without hydrogen. The tensile force F_z is deduced from an early w ork [6] by changing the volume to tube length.

RESULTS AND DISCUSSION

A detailed examination of nanotube structures in Fig. 2 reveals that the elongation of the (10,10) nanotube is initially due to the altering of bond angles (Stage 1). Under further pulling, the contribution from the elongation of the C-C bonds becomes significant and plays the main role (Stage 2). When the strain is up to a critical level, some groups of the C-C bonds are broken. Then, the tube starts necking and the force F_z decreases dramatically (Stage 3).

Compared with the (10,10) SWNT, the (17,0) zigzag SWNT has significantly smaller maximum strain and maximum tensile force. Here, we define the maximum strain (MS) and the maximum tensile force F_z (MTF) at the turning point on F_z-strain curve that has the highest value of F_z. Due to the nature of the hexagonal carbon ring, pulling the zigzag tube along its axial direction would cause some second nearest neighbor C-C atoms to become closer and to form new C-C bonds. In the local regions of these newly formed bonds, some old carbon-carbon bonds have to break due to the saturation of covalent bonds. This would lead to the necking and breakage of the zigzag SWNT.

A range of 4~10wt% of hydrogen stored in SWNT were reported [7]. In the following simulations, the armchair (10,10) and zigzag (17,0) SWNTs were used again for comparison. In our simulation, these SWNTs were pre-stored with 4.17 or 8.34 wt% of hydrogen gas (H_2), both are in the reported range. The absorption of hydrogen in carbon nanotubes has been theoretically studied [8, 9]. In the current simulation, however, the details of the absorption procedure are not of primary concern. We place H_2 molecules into tubes directly. The initial positions and the orientations of H_2 molecules in the tubes are chosen randomly. To avoid the overlap of atom positions, atomistic relaxation was performed. When this is done, 5000 MD steps were used to anneal the structures of carbon and hydrogen atoms at simulation temperatures and the

tensile loading were then carried out. The results show that the maximum tensile force and the maximum strain both decreased due to the storage of H_2, see Figures 3(a) and (c).

The effect of stored molecular hydrogen on mechanical properties of SWNT was found to strongly depend on temperature. It can be seen from Figures 3(a) and (c) that the reductions of MS and MTF caused by hydrogen storage at 600K are much larger than that at 300K. As proposed in the following text, the competition between the carbon-carbon bonds and the carbon-hydrogen bonds are believed to be the main reason that causes the reductions in MS and MTF. The effect of H_2 on the zigzag (17,0) SWNT seems not as significant as on the armchair (10,10) one (Figures 3(b) and (d)).

The interstitial channels between adjacent nanotubes in a rope of SWNTs may also be the possible sites to accommodate H_2, although there are still some debates at present on this issue. Motivated by this possibility, we also studied the case in which H_2 is stored in outside surface of the tubes. The simulation procedure is as follows. A $(10,10)\times 100_u$ SWNT was placed in the center of a box of 3nm×3nm in length and width. The height of the box was set equal to the length of the SWNT. H_2 molecules were stored in the box, while the space inside the tube was kept empty. In order to compare to those tubes with H_2 stored inside, the molar fractions of H_2 were chosen to satisfy that the pressure of the hydrogen gas outside the tubes is equal to that of those tubes with H_2 stored inside (4.17 and 8.34 wt%). Periodic boundary conditions were used in the X, Y and Z directions of the box. The simulation temperature was 300K. Compared to the hydrogen-free SWNT, the reductions in the maximum force are 37.7eV/Å and 82.7eV/Å for 4.17 and 8.34 wt% hydrogen storage, respectively, see Figure 3(c). The increase in reduction of MTF might be due to the increase in effective contact area between H_2 and the nanotube surface, because the outer surface area of the nanotube is larger than the inner surface area.

There may be a couple of reasons that had caused the reduction of strength of nanotubes by hydrogen storage. One of reasons might be the high pressure of H_2 acting on the wall of the tubes. Take the (10,10) armchair tube with 4.17 wt% stored hydrogen as an example. The atomic ratio of H/C is 1:2. If we assume that all hydrogen atoms stored inside the tube are in the gas phase, the pressure of gas would be 95.2 MPa at 300K. Such high pressure of hydrogen gas acting on the wall of tubes would change the loading mode of the tube. In addition, under the high-strain tensile loading, some bonds in the carbon rings were broken and this created local defect regions on the wall. The pressure of hydrogen gas would drive molecular hydrogen passing through these defect regions and cause the regions to extend into holes. Another important reason comes from the competition in formations of the hydrogen-carbon and the carbon-carbon bonds. Fig.4 shows the total number of the C-H bonds during the tensile deformation. In this figure one can find that the number of the C-H bonds is significantly increased when the tube necking starts. Since some C-C bonds were elongated and broken during the deformation, hydrogen atoms were likely to "catch" some of the free carbon bonds to generate the C-H bonds (see Fig.5), so that the fracture of SWNT was then accelerated.

CONCLUSIONS

MD simulations based on a new bond order potential have been performed to study the mechanical properties of SWNT under tensile loading with and without hydrogen storage. The results show that:
(1) The tensile deformation of SWNTs up to the point of necking experiences two stages, controlled by altering of the C-C bond angle and the C-C bond length, respectively;
(2) Hydrogen storage in SWNT reduces the maximum tensile strength of the tube as well as the maximum tensile strain; and
(3) The competition between the formations of the H-C and the C-C bonds may be responsible for the reduction in the mechanical strength of the SWNT with H_2 storage.

ACKNOWLEDGEMENT

The MD program used in current simulations was modified from that of Brenner's. The authors are grateful to Prof. Donald W. Brenner for allowing us to share his program. This work was supported by a research grant from the Hong Kong Polytechnic University (A-PC04).

REFERENCES

1. R. Saito, G. Dresselhaus, M.S. Dresselhaus, Physical Properties of Carbon Nanotubes, Impreial College Press, London, 1998.
2. J.W.G. Wildoer, L.C. Venema, A.G. Rinzler, R.E. Smalley, C. Dekker, Nature, 391 (1998) 59; T.W. Odom, J.-L. Huang, P. Kim, C.M. Lieber, Nature, 391 (1998) 62.
3. R.C. Mowrey, D.W. Brenner, B.I. Dunlap, J.W. Mintmire, C.T.J. White, Phys.Chem. 95 (1991) 7138.
4. D.H. Robertson, D.W. Brenner, C.T.J. White, Phys. Chem., 96 (1992) 6133.
5. B.I. Dunlap, D.W. Brenner, G.W.J. Schriver, Phys. Chem., 98 (1994) 1756.
6. J. M Haile, Molecular dynamics simulation: elementary methods, A Wilry-Interscience Publication, 1992.
7. V.V. Simonyan, P. Diep, J.K. Johnson, J. Chem. Phys., 111 (1999) 9778.
8. M.S. Dresselhuas, K.A. Williams, P.C. Eklund, MRS Bulletin, November (1999) 45.
9. F. Darkrim and D.Levesque, J. Chem. Phys., 109 (1998) 4981.

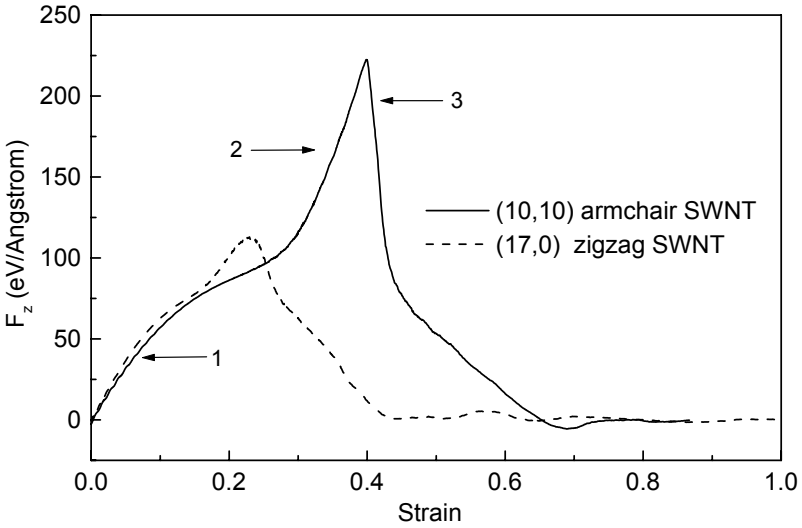

Figure 1. Tensile force along axes of the armchair (10,10) and zigzag (17,0) SWNT as a function of strain. The numbers 1, 2 and 3 denote the three deformation stages of armchair SWNT under tensile loading.

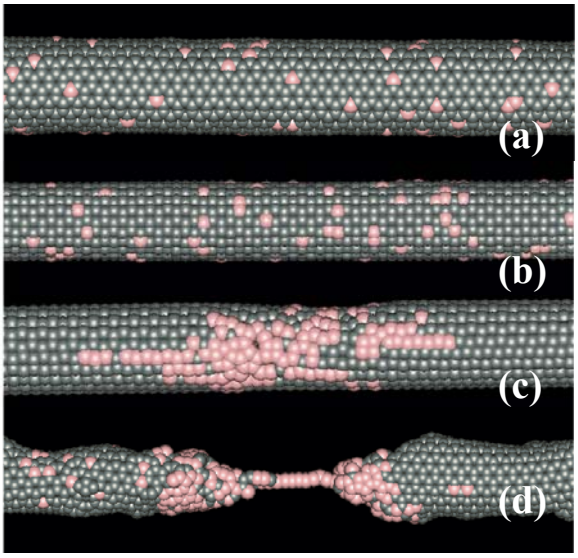

Figure 2. Typical snapshots of the armchair (10,10) SWNT without hydrogen during tensile deformation. Brighter color denotes higher kinetic energy of the carbon atoms.

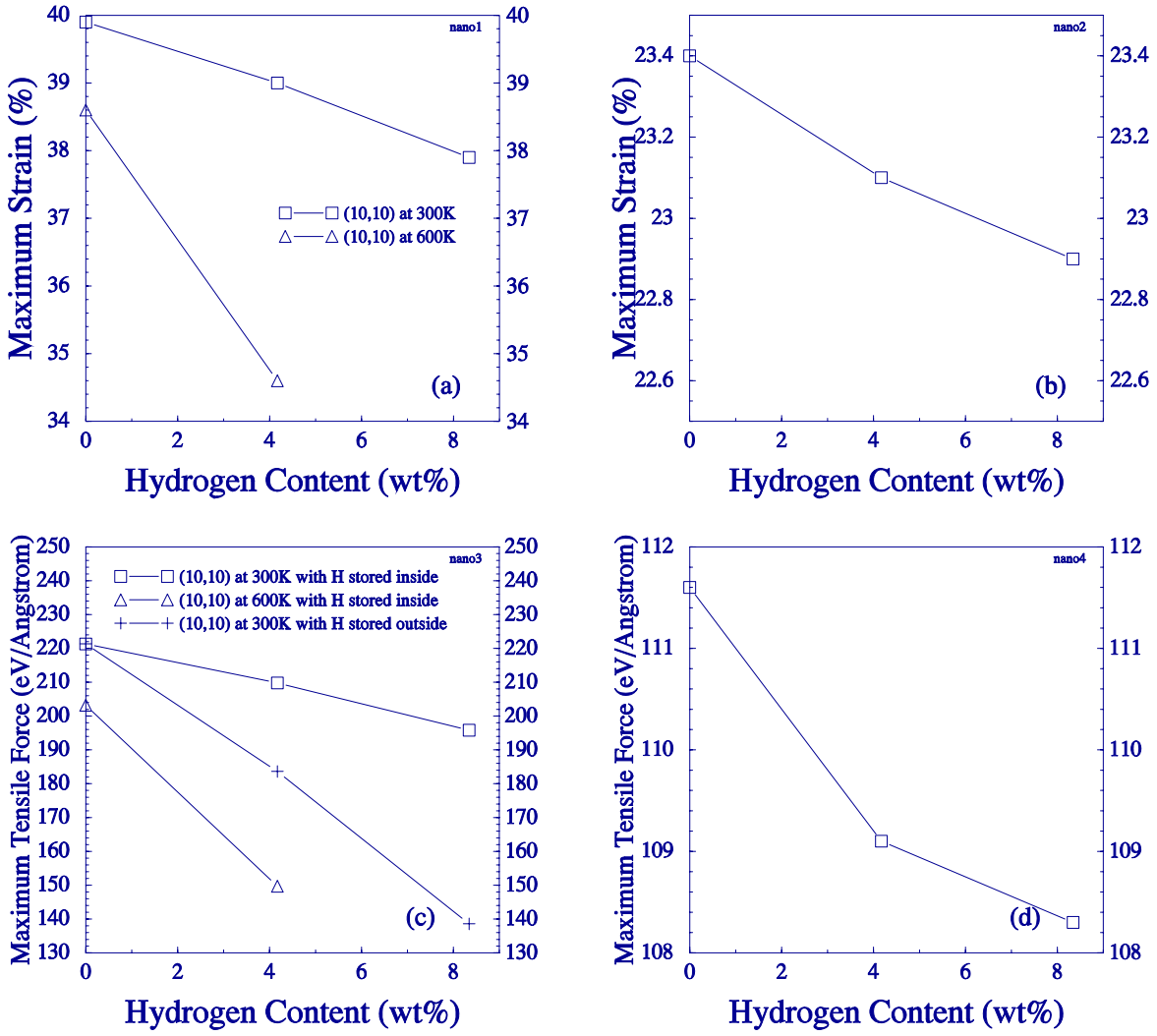

Figure 3. (a) maximum strains of (10,10) nanotubes; (b) maximum strains of (17,0) nanotubes at 300 K; (c) maximum tensile forces of (10,10) nanotubes; and (d) maximum tensile forces of (17,0) nanotubes at 300 K.

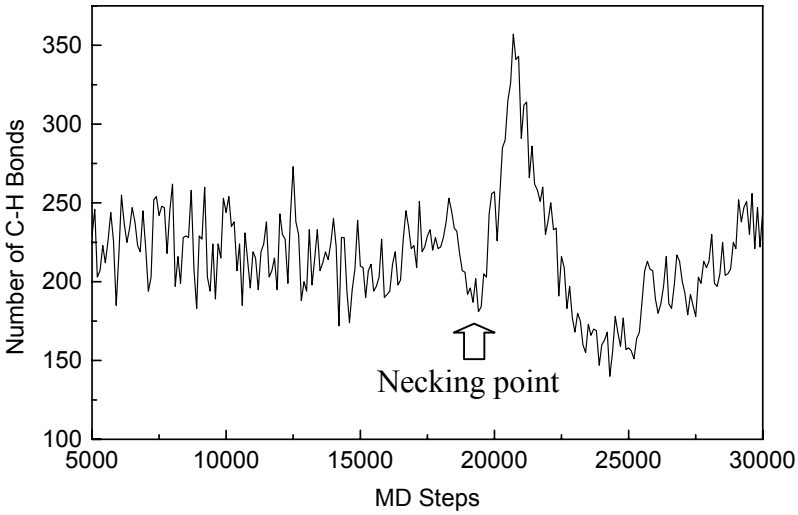

Figure 4. The variation in the number of the C-H bonds in the (10,10) armchair SWNT stored with 4.17wt% hydrogen during tensile deformation.

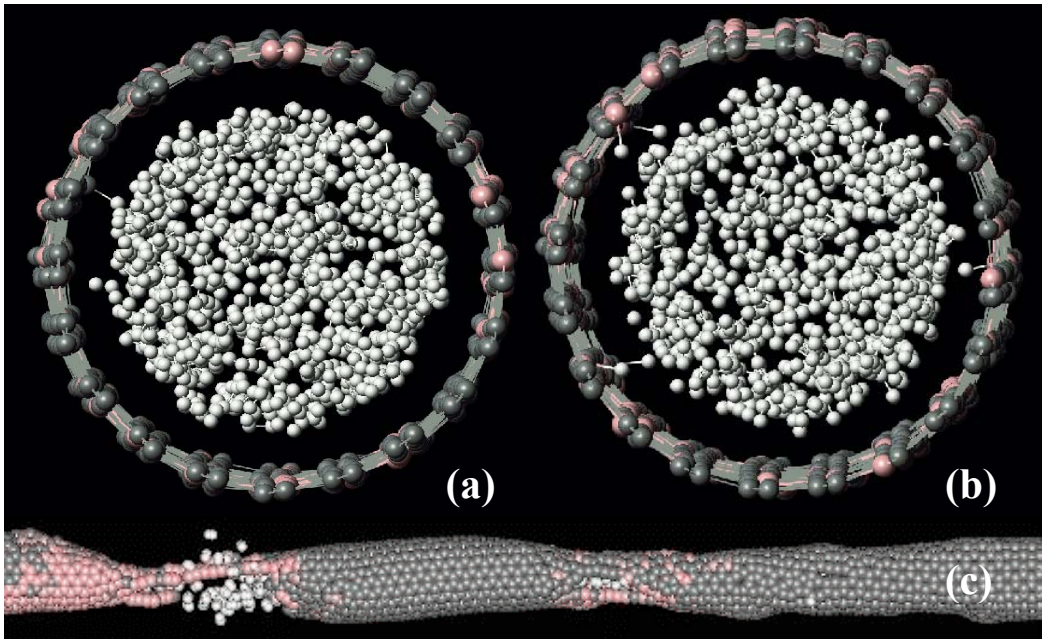

Figure 5. Snapshots of the (10,10) SWNT with 4.17wt% hydrogen storage: (a) a cross section at 4.7ps; (b) the same cross section at 7.6ps; and (c) a view at the point of fracture. Small white balls are hydrogen molecules or atoms.

DEVELOPMENT AND VALIDATION OF A ROBUST FRACTURE MECHANICS METHODOLOGY FOR DAMAGE TOLERANCE OF ROTORCRAFT

Satya N. Atluri[1], Gennadiy Nikishkov[1], Dy Le[2], Charles Harrison[3], and Mel F. Kanninen[4]

[1] Center for Aerospace Research & Education, UCLA, Los Angeles, CA 90095
[2] FAA William J. Hughes Technical Center, Atlantic City Int'l. Airport, NJ 08405
[3] FAA Rotorcraft Directorate, Ft. Worth, TX 76137
[4] Galaxy Scientific Corporation, San Antonio, TX 78229

ABSTRACT

The research presented in this paper is aimed at overcoming a major obstacle that currently slows effective damage tolerance assessments of rotorcraft fuselage and drive system components. Because cyclic loads are accumulated at a very high rate in rotorcraft, a substantial portion of the fatigue crack growth lifetime can be associated with cracks that do not lend themselves well to conventional fracture mechanics analyses. Accordingly, this effort was undertaken to address the small, arbitrarily shaped and warped, intrinsic, fabrication and service-induced cracks that can initiate fatigue crack growth in rotorcraft components. The resulting methodology is based on an innovative approach in which a symmetric Galerkin boundary element method (SGBEM) alternates with a finite element method (FEM). This technology is uniquely able to provide stress intensity factors (and, when appropriate, elastic-plastic crack tip criteria), to enable accurate and efficient fatigue crack growth predictions to be obtained for conditions pertinent to the full range of rotorcraft applications. This paper outlines the computational fracture mechanics analysis procedure that was developed. It also reviews the validations of the resulting methodology that were made in terms of critical comparisons with existing literature solutions for complex crack shapes. In addition, to illustrate the potential for practical applications of the methodology for rotorcraft, and for other applications where the safe operating lifetime is dictated by load cycles that are amassed at an ultra high rate, example computational results are presented for progressive fatigue crack growth from an elliptical crack initially inclined to the loading direction.

KEYWORDS

Damage tolerance, rotorcraft, fatigue crack growth, non-planar cracks, SGBEM, alternating FEM

INTRODUCTION

The damage tolerance (DT) methodology, largely spearheaded in work initiated over three decades ago by the U.S. Air Force, is now firmly based and widely applied for life determinations and for setting inspection intervals in both military and commercial aircraft. Applications of the DT methodology to a given aircraft structural component require comparable technological capabilities in four distinct areas: (1) performing nondestructive inspections to detect, or postulate, the existence of a crack-like defect, (2) anticipating the applied cyclic loads, (3) measuring the characteristic fatigue crack growth and fracture properties of the material, and (4) devising fracture mechanics analysis techniques for quantifying fatigue crack growth and the ultimate failure state. As concluded in a recent international workshop focused on rotorcraft damage tolerance (RCDT), the currently existing capabilities in all of these four areas are insufficient for RCDT applications [1]. The main reason is the combination of complex structural configurations with very rapid accumulations of cyclic loads. For example, there would be one, four and eight load cycles per blade revolution in the main rotor system that is shown in Figure 1 for which the rotational speed would be about 300 rpm.

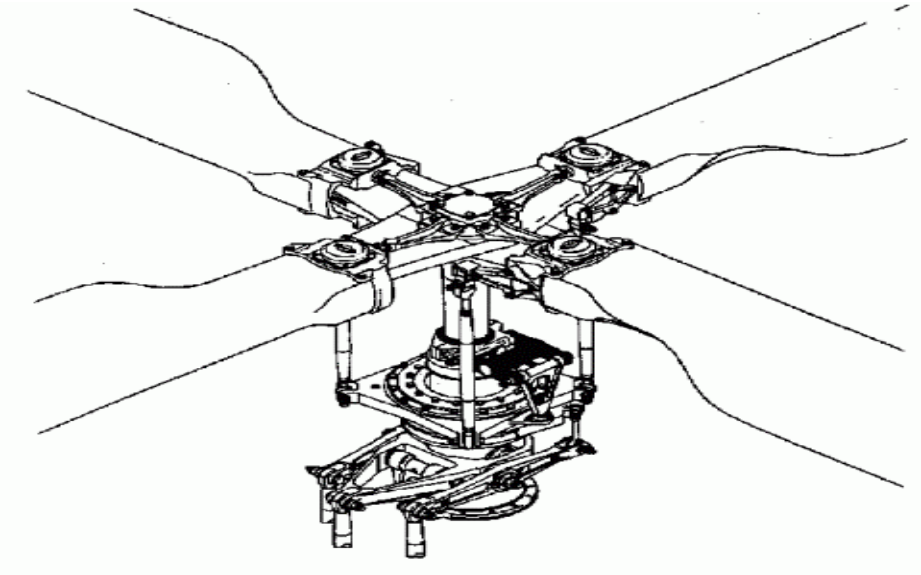

Figure 1: A typical rotorcraft drive and blade system

Because rotorcraft structural components accumulate cyclic loads at very high rates, very small arbitrarily shaped and warped cracks will often be the initiators of fatigue crack growth. Other barriers to practical RCDT applications also exist; e.g., rotorcraft structures make extensive use of surface treatments to retard fatigue crack growth, and they also are generally operated in ways that require highly variable and complex flight load spectra to be used for fatigue life predictions. Notwithstanding, with limited resources available for rotorcraft research, a simultaneous attack on all of the outstanding issues is not possible. To accelerate the practical implementation of RCDT, the Federal Aviation Administration (FAA) has focused its research on advancing the accuracy and efficiency of fracture mechanics calculations. While fuselage structure is certainly a concern for RCDT, the more challenging problem is involved with the dynamic components in the drive system; c.f., Figure 1. This paper describes an innovative fracture mechanics approach aimed at providing the basis for RCDT applications for this class of components.

ANALYSIS METHODOLOGY

An efficient and highly accurate technique utilizing a combination of the symmetric Galerkin boundary element method (SGBEM) and the finite element method (FEM) was developed for the analysis of three-dimensional non-planar cracks. This methodology addresses not only the initiation of growth, but also the subsequent unconstrained growth (i.e., as exclusively dictated by the deformation state existing at and near to the current crack tip) in structural components of non simple geometries. In this approach the crack is modeled by the SGBEM as a distribution of displacement discontinuities, as if in an infinite medium. The FEM is used to perform the stress analysis for the uncracked body only. The solution for the structural component containing the crack is obtained in an iteration procedure, which alternates between FEM solution for the uncracked body and the SGBEM solution for the crack in an infinite body. Numerical procedures, and the attendant Java code, are developed for the evaluation of crack tip parameters and fatigue crack growth modeling.

The SGBEM, originated by Bonnet et al. [2], is a way of satisfying the boundary integral equations of elasticity in a Galerkin weak form, as opposed to the method of collocations that is generally used to satisfy the integral equations in the traditional BEM. The SGBEM is characterized by weakly singular kernels. After a special transformation that removes the singularity from the kernels, the boundary element matrices can be integrated with the use of conventional Gaussian quadrature. The crack is modeled as a distribution of displacement discontinuities with the crack surface discretized by quadratic eight-node boundary elements. Quarter-point singular elements are placed near the crack front. With the use of the SGBEM/FEM alternating procedure, the crack tip parameters for planar and non-planar cracks in infinite media, and for embedded and surface cracks in finite bodies, can be calculated.

More specifically, for an infinite three-dimensional body containing a non-planar crack of arbitrary geometry, consider that a distributed load is applied at the crack surface. The crack can then be described by a distribution of displacement discontinuity for which the following weakly-singular boundary integral equation is valid for the crack; c.f., [2-4]:

$$-\int_S\int_S D_\alpha u_i^*(\mathbf{z}) C_{\alpha i\beta j}(\xi-\mathbf{z}) D_\beta u_j(\xi) dS(\xi) dS(\mathbf{z}) = \int_S u_k^*(\mathbf{z}) t_k dS(\mathbf{z}) \qquad (1)$$

where $S = S_+$ is one of crack surfaces; u_i are displacement discontinuities for the crack surface; u_i^* are the components of a continuous test function; and t_k are crack face tractions. Using Eqn. (1), the SGBEM models an arbitrary non-planar crack in an infinite body under external loading. The FEM solution for an uncracked finite body then enables a solution for a finite body with a crack to be obtained by superposition. While this can be done with a direct procedure, the alternating method advanced by Atluri [5] provides for a more efficient solution without the need for assembling the joint SGBEM-FEM matrix.

The basic steps of the SGBEM-FEM alternating iteration procedure are (1) using FEM, obtain the stresses at the location of the hypothetical crack in a finite uncracked body that is subjected to given boundary conditions, (2) using SGBEM, solve the problem of a crack, the faces of which are

subjected to the tractions found from FEM analysis of the uncracked body, (3) determine the residual forces at locations corresponding to the outer boundaries of the finite body that result from the displacement discontinuities at the crack surface, (4) using FEM, solve a problem for a finite uncracked body under residual forces from SGBEM analysis, and (5) obtain the stresses at the location of the crack corresponding to FEM solution. Steps 2 to 5 are repeated until the residual load is sufficiently small. Usually, less than 10 iterations are enough for convergence. Then, by summing all the appropriate contributions, the total solution for a finite body with the crack is obtained. This procedure is described in detail by Nikishkov et al. [6].

Having the converged solution, the next step is to compute the crack tip parameters associated with fatigue crack growth. For simplicity, consider mode I fracture for which the SGBEM/FEM alternating procedure solution is used to evaluate:

$$K_I = \frac{E}{(1-\nu^2)} \frac{u_3}{4\sqrt{2r/\pi}} \tag{2}$$

where, as usual, K_I is the mode I stress intensity factors; E is the elastic modulus, ν is the Poisson's ratio, r is the distance from a point on the crack surface to the crack front, and u_3 is the normal component of the displacement discontinuity at that point. For modeling fatigue crack growth it is only necessary to add another element layer to the existing crack model. To advance a point at the front of a nonplanar crack it is necessary to know the direction and extent of crack growth. Cherepanov's formulation [7] of the J-integral has been found to provide the most effective criterion for fatigue crack growth according to which the crack grows in the direction of the vector $\Delta\vec{J}$ with the crack growth rate determined by the relative magnitude of ΔJ using a conventional fatigue crack growth relationship (e.g., from the NASGRO database).

The procedure for the advancement of the front of a nonplanar crack is (1) using the SGBEM-FEM alternating method, solve the problem for the current crack configuration and determine ranges for the stress intensity factors for the element corner nodes located at the crack front, (2) for each corner node determine the crack front coordinate system by averaging the coordinate axis vectors determined at the corner points of two neighboring boundary elements, (3) for each corner node, calculate the crack advance Δa and the crack growth direction, (4) move each corner node in the local crack front coordinate system and transform the movement to the global coordinate system, (5) find the locations of crack front midside nodes, using cubic spline interpolations for corner nodes from several neighboring elements, and (6) shift the quarter-point nodes of the previous crack front elements to midside positions on the element sides normal to the crack front. After terminating the crack growth procedure, the total number of cycles N is calculated as a sum of the ΔN_i's.

This algorithm has been implemented as a Java code because its numerous attractive features (e.g., object-oriented nature, simplicity, reliability and portability) despite its somewhat slower speed in comparison to C and Fortran. A comparison of finite element codes written in C and Java shows that in many cases Java provides comparable performance as the C language [8]. While the manual tuning that is required for Java requires some additional effort, the use of Java leads to an overall development time reduction in comparison to other languages because of easier programming and debugging.

VALIDATIONS OF THE METHODOLOGY

To assess the accuracy of the methodology, the Java SGBEM-FEM alternating code, displacement discontinuity finite element alternating method, (DDFEAM) was applied to the solution of complex crack shape problems taken from the open literature. For these comparisons, 8-node quadrilateral boundary elements were used for the crack surface discretization, and the Gaussian integration rule was used with three points in each of the four directions employed for computing boundary element matrices for regular and singular cases. Quarter-point singular elements were placed at the crack front. The finite element models consisted of 20-node brick-type finite elements. The following open literature solutions were examined:

- Penny-shaped crack under tensile and shear loading -- compared with exact solutions given by Sneddon [9] and by Kassir and Sih [10].
- Inclined elliptical crack under tension – compared with exact solution for 45^o inclination given by Kassir and Sih [10].
- Circular arc crack under tension – compared with exact solution by Cotterell and Rice [11].
- Spherical penny-shaped crack under internal pressure and tension – compared with numerical solution given by Xu and Ortiz [12] and by Li, Mear and Xiao [13].
- Embedded circular crack in a cylindrical bar and in a cube – compared with numerical solution given by Li, Mear and Xiao [13].
- Semi-elliptical surface cracks – compared with numerical solution given by Wu [13].
- Inclined semi-circular surface crack in a plate – compared with numerical solutions given by Shivakumar and Raju [14], and by He and Hutchinson [15].

Good to excellent agreement was obtained in all cases. A detailed description of these comparisons can be found in the paper of Nikishkov et al. [6].

APPLICATION OF THE METHODOLOGY

As a first step in testing the practicality of the methodology for a representative drive system component of a rotorcraft. The analysis that was made was for a small planar crack in a much larger body under mixed-mode loading conditions. The initiating defect was taken to be an elliptical crack inclined at 45^o to the direction of a remote applied tensile loading. The minor/major semi-axis ratio a/c was taken as 0.5. The crack was discretized by 68 quadratic boundary elements. For simplicity, a Paris Law fatigue relation model was used in which $C = 1.49 \cdot 10^{-8}$ and $m = 3.321$ to represent 7075 Aluminum. The elliptical initial crack was analyzed and the stress intensity factors K_I, K_{II} and K_{III} calculated for each of the nodes along the crack front. Then, in accord with the calculated J-integral vector orientation and magnitude at each individual point, the crack front was advanced to new positions via scaling to the maximum crack advance $(\Delta a)_{max}$. A new layer of elements was then generated between the old and the new crack front lines, and the process repeated. The stress intensity factors that were determined inn this process were normalized to the reference value $K_o = \sigma\sqrt{\pi a}$. The values along the crack periphery that resulted from each of six individual crack advance increments, each with $(\Delta a)_{max}/a = 0.1$, are shown in Figure 2. A three-dimensional view of the crack after all six increments of growth have been completed is presented in Figure 3.

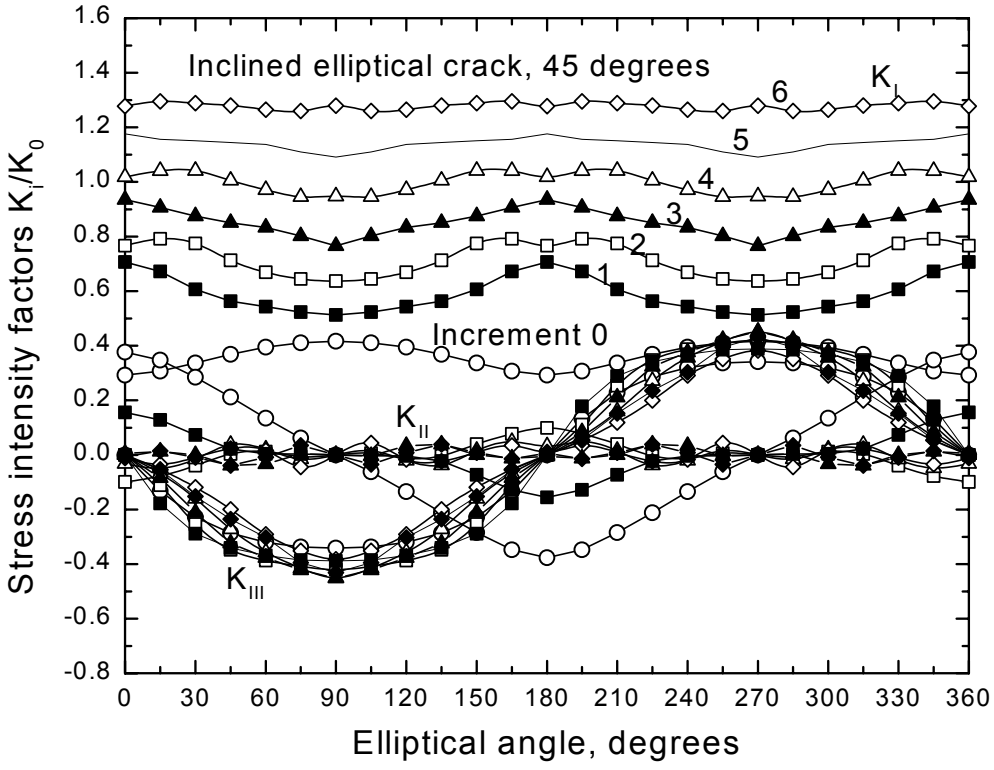

Figure 2: Calculated results for the stress intensity factors along the front of the initial crack, and along each of six subsequent crack fronts, for simulated fatigue crack growth from an initial elliptical crack oriented at 45^o to the direction of a remote tensile loading

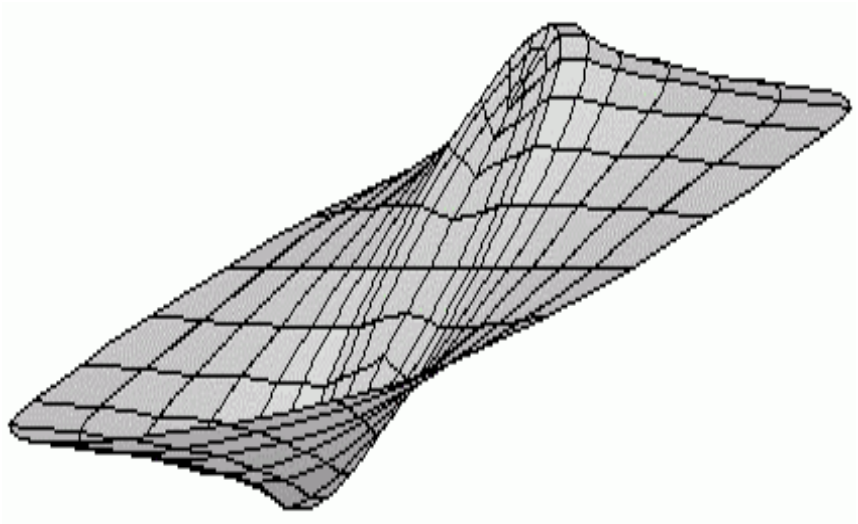

Figure 3: Three-dimensional view of the crack face after six crack growth increments

SUMMARY AND CONCLUSIONS

To help meet the demanding conditions associated with rotorcraft damage tolerance (RCDT), an SGBEM-FEM alternating method has been developed for predicting fatigue crack growth from non-planar cracks. The accuracy of the procedure was demonstrated by critical comparisons with a variety of solutions for complex cracks. To demonstrate its potential for attacking practical problems, fatigue crack growth from an inclined elliptical initial crack was calculated. While the results presented in Figures 2 and 3 are certainly in good qualitative agreement with observations of fatigue crack growth (e.g., crack growth takes place with K_{II} =0), it is not possible to directly assess the computed results using experimental data. However, some checks can be made by comparing with other numerical solutions. Such comparisons show that the distributions of the stress intensity factors along crack front during crack growth are similar to those obtained by Mi and Aliabadi [16], while the shape of the final crack is similar to crack shapes obtained both by them and by Forth and Keat [17]. Hence, while the progress that has been described in this paper is still at a preliminary stage, it is believed that an excellent start has been made towards overcoming the full range of the research challenges that need to be met for the implementation of a practical RCDT approach.

ACKNOWLEGEMENTS

The research reported in this paper was performed under contract with the FAA William J. Hughes Technical Center. Background knowledge on rotorcraft operations was provided by member companies of the Rotorcraft Industry Technology Association.

REFERENCES

1. *Workshop on Damage Tolerance in Helicopters*, 4-5 April 2000, Cranfield University, UK.
2. Bonnet, M., Maier, G. and Polizzotto, C. (1998) *Appl. Mech. Rev.*, **51**, 669-704.
3. Li, S., Mear, M.E. and Xiao, L. (1998) *Comp. Meth. Appl. Mech. Eng.*, **151**, 435-459.
4. Xu, G. and Ortiz, M. (1993) *J. Num. Meth. Eng.*, **36**, 3675-3701.
5. Atluri S.N. (1997) *Structural Integrity and Durability*, Tech Science Press, Forsyth, GA.
6. Nikishkov, G. P., Park, J. H., and Atluri, S. N. (2001) *Comp. Modeling in Eng. & Sci.*, **2**.
7. Cherepanov, G.P. (1979) *Mechanics of Brittle Fracture*, McGraw-Hill, New York.
8. Nikishkov, G.P. (2000) *Advances in Computational Engineering & Sciences 2000 (Ed. S.N.Atluri and F.W.Brust), V.1*. Tech Science Press, Palmdale, CA, 264-269.
9. Sneddon, I.N. (1946) *Proc. Royal Society of London*, Series A **187**, 229-260.
10. Kassir, M.K. and Sih, G.C. (1966) *J. Appl. Mech.*, **33**, 601-611.
11. Cotterell, B. and Rice, J. R. (1980) *Int. J. Fracture*, **16**, 155.
12. Xu, G. and Ortiz, M. (1993) *Int. J. Num. Meth. Eng.*, **36**, 3675-3701.
13. Li, S., Mear, M.E. and Xiao, L. (1998) *Comp.. Meth. Appl. Mech. Eng.* **151**,435-459.
14. Wu, X.R. (1984) *Eng. Frat. Mech.*, **19**, 387-405.
15. Shivakumar, K.N. and Raju, I.S. (1992) *Eng. Frat. Mech.*, **42,** 935-959.
16. He, M.Y. and Hutchinson, J.W. (2000) *Eng. Frat. Mech.*, **65**, 1-14.
17. Mi, Y. and Aliabadi, M.H. (1994) *Computers & Structures*, **52**, 871-878.
18. Forth, S.C. and Keat, WD (1997) *J. Eng. Gas Turbines & Power*, **119**, 964-968.

Development of cohesive models from the study of atomic scale fracture processes

P.A. Klein [a] J.A. Zimmerman [a] E.P. Chen [a]

[a] *Sandia National Laboratories, Livermore, CA 94550*

Abstract

In this work, we make a comparison of continuum simulations using a cohesive modeling approach with the predictions of atomistic simulations. Cohesive approaches to modeling fracture differ from classical approaches by embedding the physics of the fracture process directly in the simulation procedure. Cohesive zone methods use a traction-separation relationship to provide the constitutive relations for the localized failure mode of deformation. For modeling brittle fracture, the form of these traction-separation relations is typically based on simple physical arguments and motivation from semi-empirical atomistic potentials. First, we derive the parameters for the cohesive relations based on evaluation of Griffiths condition with the atomistic system. We then compare the fracture behavior predicted by this cohesive model with the results of atomistic simulations under quasistatic and dynamic loading conditions. We find that while cohesive approaches adequately reproduce the atomistic results under quasistatic loading, dynamic conditions reveal the significant effects dispersion has on the behavior of dynamically propagating cracks.

Key words: fracture simulation; atomistic simulation; cohesive modeling; multiscale modeling

1 Introduction

As early as 1933, Prandtl[3] employed a cohesive traction relation, motivated by atomistic considerations, to analyze debonding between two slender beams. Cohesive approaches to modeling fracture replace the point singularity model of the crack tip with a stress or traction response that incorporates a finite cohesive strength and a finite work to fracture. These approaches promise to reproduce the behavior of propagating cracks more accurately because the dissipation mechanisms associated growth may be directly incorporated in the cohesive relations. The approach of restricting the mechanisms of cohesive fracture to act only across discrete surfaces is gaining wide acceptance in the fracture modeling community. A finite element implementation of the cohesive surface approach was introduced by Needleman [2]. Ironically, while cohesive

approaches admit a very detailed description of crack tip processes, these processes are largely unobservable due to the small length scales involved and the relative inaccessibility of the fracture process zone. In this work, we attempt to validate the cohesive surface approach by comparison with a model atomistic system. Atomistic simulation provides physically realistic energetics and dynamics of crack growth processes that can be readily analyzed.

Depending on the material system, the fracture processes may be numerous and complicated. For this work, we consider only brittle fracture, which we define to mean that all dissipation during the fracture process is associated directly with the creation of new free surfaces. Accordingly, our continuum simulations employ a rate and history independent bulk constitutive model. The atomistic system used in this study is similar to the one considered by Farid et al. [1] to study the behavior of crack growth under severe loading conditions. Given sufficient driving force, this system activates additional mechanisms of dissipation during fracture. These include increasing the fracture surface area through roughening and relieving stresses through dislocation emission. In this study, crack driving forces are maintained below a level at which these dissipation mechanisms are activated. Therefore, we expect to understand the fracture behavior in terms of the surface dissipation and the transport of strain energy by elastic waves or dispersion by phonons for the atomistic system.

The strip geometry used in this study is illustrated in Figure 1. If the strip is

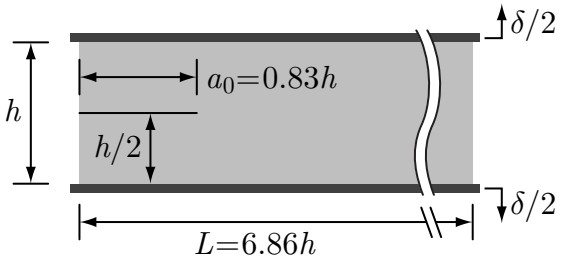

Fig. 1. Geometry of the two-dimensional strip.

sufficiently long in the lateral dimension, a J-integral analysis can be used to determine the static crack driving force under plain stress as

$$G = \frac{E\,h\,\epsilon^2}{2\,(1-\nu^2)}, \tag{1}$$

where E is Young's modulus, ν is Poisson's ratio, and $\epsilon = \frac{\delta}{h}$ is the nominal applied strain. This quasistatic analysis only applies to the onset of crack growth. Accurate predictions of the response of either the continuum or atomistic system during dynamic propagation remains a challenge for analysis.

2 Methods

Over a domain Ω with a boundary Γ, the variational form of the dynamic equation of equilibrium in the absence of body forces may be written as

$$\int_{\Omega} \rho \frac{\partial^2 \mathbf{u}}{\partial t^2} \cdot \delta\mathbf{u}\, d\Omega + \int_{\Omega} \boldsymbol{\sigma} : \delta\boldsymbol{\epsilon}\, d\Omega + \int_{\Gamma_{\text{int}}} \mathbf{t}(\boldsymbol{\Delta}) \cdot \delta\boldsymbol{\Delta}\, d\Gamma = \int_{\Gamma_h} \mathbf{t} \cdot \delta\mathbf{u}\, d\Gamma, \tag{2}$$

where ρ is the mass density, $\mathbf{u}$ is the displacement field, $\boldsymbol{\epsilon} = \frac{1}{2}\left(\nabla\mathbf{u} + (\nabla\mathbf{u})^{\mathrm{T}}\right)$ is the infinitesimal strain tensor, and the Cauchy stress $\boldsymbol{\sigma}$ and traction $\mathbf{t}$ are related through the normal $\mathbf{n}$ as $\mathbf{t} = \boldsymbol{\sigma}\mathbf{n}$. Contributions from surface tractions in (2) appear over regions of the boundary $\Gamma_h \subseteq \Gamma$ with externally applied tractions and over pairs of internal surfaces Γ_{int} due to the variation in the surface opening displacement $\delta\boldsymbol{\Delta}$. For this study, we use a model traction-separation relation similar to the one introduced by Tvergaard and Hutchinson [4]. The magnitude of the cohesive traction is expressed as a function of a nondimensional effective opening displacement

$$\Delta = \sqrt{\left(\Delta_t/\delta_t^*\right)^2 + \left(\Delta_n/\delta_n^*\right)^2}, \tag{3}$$

where δ_t^* and δ_n^* represent the characteristic tangential and normal opening displacements, respectively. As illustrated in Figure 2(a), the tri-linear magnitude of the traction $\hat{t}(\Delta)$ depends on a single shape factor Δ^*. The traction response is assumed to be reversible up to $\Delta = \Delta^*$, after which the surface is assumed to have failed. Defining a traction potential

$$\varphi(\boldsymbol{\Delta}) = \delta_n^* \int_0^{\Delta} \hat{t}(\xi)\, d\xi \tag{4}$$

yields the rate-independent, mixed-mode traction-separation relation

$$\mathbf{t}(\boldsymbol{\Delta}) = \frac{\partial\varphi(\boldsymbol{\Delta})}{\partial\boldsymbol{\Delta}} = \delta_n^*\, \hat{t}(\Delta)\, \frac{\partial\Delta}{\partial\boldsymbol{\Delta}} \tag{5}$$

and a fracture energy

$$G_c = \frac{1}{2}\sigma_c\delta_n^*. \tag{6}$$

The cohesive surface relation (5) is not intended to represent the response of any specific material. Surrounded by an elastic medium, the detailed shape of the relationship is not expected to have a significant effect. The relationship simply introduces a well-defined fracture energy into the simulation procedure with a clear point of complete failure in a form that facilitates analytical study. The stress response of the bulk is defined by

$$\sigma_{ij} = \left[\mu\, \delta_{ij}\delta_{rs} + \lambda\left(\delta_{ir}\delta_{js} + \delta_{is}\delta_{jr}\right)\right] \epsilon_{rs}, \tag{7}$$

where μ and λ are Lamé constants.

The approach for the atomistic simulations similarly makes use of a model system. The single crystal sample is constructed from a two-dimensional, hexagonal lattice bound by the Lennard-Jones 6-12 potential

$$\phi_{LJ}(r) = 4\,\varepsilon\left[-\left(\sigma/r\right)^6 + \left(\sigma/r\right)^{12}\right], \tag{8}$$

where σ sets the length scale of the potential and $-\varepsilon$ is the depth of the potential well. In order to allow us to control the range of influence of the potential without introducing abrupt behavior at a cut-off distance, we use the modified potential

$$\phi(r) = \phi_{LJ}(r) - \phi_{LJ}(r_c) - (r - r_c)\,\phi'_{LJ}(r_c)\,, \tag{9}$$

where r_c is the distance at which the potential and its first derivative pass through 0. This cut-off distance is selected to include up to the fifth nearest neighbors in the undeformed configuration. The crystal is oriented with lattice vectors

$$\mathbf{r}^{(1)} = r_0 \begin{Bmatrix} 1 \\ 0 \end{Bmatrix} \qquad \text{and} \qquad \mathbf{r}^{(2)} = \frac{r_0}{2} \begin{Bmatrix} 1 \\ \sqrt{3} \end{Bmatrix}, \tag{10}$$

where r_0 is the interatomic spacing. We choose $\frac{h}{r_0} = 212$ to distance the fracture process zone from the rigidly imposed boundary conditions. The characteristic dimension of the finite elements near the cleavage plane is $h_{\min} = r_0$.

3 Results and discussion

The parameters for the continuum and atomistic systems are selected to correspond with each as closely as the differing descriptions permit. Due to the centrosymmetry of the undeformed lattice, the initial elastic properties of the crystal display Cauchy symmetry, for which $\lambda = \mu$. The shear modulus μ is matched to the elastic properties calculated for the crystal, and the density ρ is selected to correspond with the mass and atomic volume of the undeformed lattice. The fracture properties of the systems cannot be compared so directly. The fracture energy ϕ is not solely dependent on ε, the energy of a single bond, and the effective opening displacement Δ (3) does not correspond to the bond length r.

The fracture parameters in the cohesive relation $\mathbf{t}(\boldsymbol{\Delta})$ (5) are selected in order to match the traction distribution on the cleavage plane of the strip model at the critical boundary displacement. The critical displacement is identified by applying Griffith's condition to the atomistic system. The boundaries are displaced until the static, uncleaved configuration of the strip is no longer energetically favored. Comparing the bond energy per undeformed volume "far" ahead of the pre-crack with the reference energy of the crystals yields the fracture energy G_c. The traction distribution for the atomistic system is calculated from the force in all bonds crossing the cleavage plane, averaged over segments of length r_0 along the fracture surface. This calculation yields a peak traction

of approximately $E/18$, where E is Young's modulus of the crystal. Matching just these two characteristics yields traction distributions illustrated in Figure 2(b). Quasistatic analysis of the strip configuration yields a failure strain

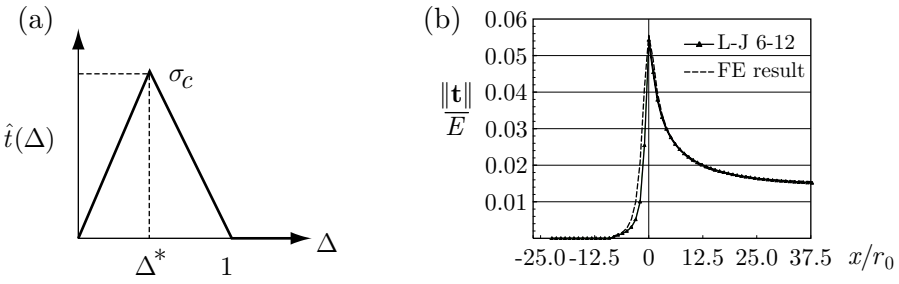

Fig. 2. (a) the traction-separation relation and (b) a comparison of the traction distribution on the cleavage plane.

$\epsilon_c = \frac{\delta}{h} \approx 1.5\ \%$. The continuum simulation cleaves at a strain within 1% of the predicted value. Correcting the Griffith analysis to account for the compliance of the cohesive surface layer reveals that the continuum simulation reproduces the expected failure strain to within nearly 0.1%. These results indicate that model has sufficient extent both ahead and behind the crack tip to match the steady-state cracking assumptions and that the tractions are well resolved over the elements in the fracture process zone. The atomistic model cleaved at a strain approximately 4% higher than that predicted by the Griffith analysis, which we attribute to the nonlinear response of the interatomic potentials. Figure 2(b) illustrates that the region on the traction distribution behind the peak is a tail that decays over a distance of approximately $10\, r_0$, and the stresses ahead of the tip stay well above the farfield values to a distance of nearly $25\, r_0$.

For the dynamic simulations, the continuum and atomistic system are loaded from near their critical strains with a constant velocity of $c_d/\dot{\delta} = 7500$, where c_d is the dilatational wave speed in the material. The atomistic system is loaded to near the critical strain using molecular statics, and an energy conserving conserving time integration scheme is used for the dynamic phase of the simulations. The variation of the crack velocity as a function of crack length is shown in Figure 3(a). The velocity is normalized by the Rayleigh wave speed c_{R}, the limit speed for cracks propagating under mode I loading. While the crack speed in the continuum simulation steadily climbs towards the limiting speed with increasing driving force, the crack speed in the atomistic simulation does not exceed approximately 20% c_{R}. Figure 3(b) reveals the markedly different energetics associated with crack growth for each system. The figure shows the rate of kinetic energy generation with crack extension $\frac{\Delta T}{\Delta a}$ as a function of crack length. The continuum simulation shows that approximately 3% of the strain energy required for quasistatic crack growth is converted to kinetic energy for $1 < \frac{a}{h} < 4$, corresponding to $0.2 < \frac{\dot{a}}{c_{\mathrm{R}}} < 0.7$. For $\frac{a}{h} > 4$, acceleration of the crack slows and the rate of kinetic energy gener-

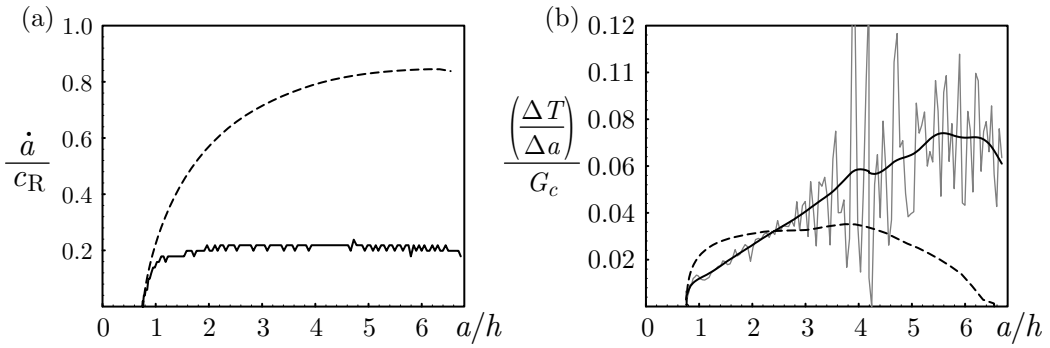

Fig. 3. Comparison of the continuum simulations with a cohesive surface interface (dashed lines) with atomistic simulations (solid lines).

ation decreases although the driving force continues to increase. The smoothed results from the atomistic simulation (dark, solid line in Figure 3(b)) reveal a steadily increasing rate of kinetic energy generation. The results suggest that the terminal crack speed for the continuum simulation is determined largely by limits in the driving strain energy release rate, while the terminal crack speed in the atomistic system is controlled by an intrinsic limit on the rate of bond breaking at the crack tip. Excess energy is converted to kinetic energy rather than increasing the speed of fracture.

In summary, we have compared the response of a continuum and atomistic system under conditions of quasistatic and dynamic fracture. Under quasistatic conditions, the cohesive surface approach reproduces the predicted response of the strip model. This result is expected since traction potential (4), with a simple change of variables, is equivalent to the J-integral evaluated on a contour over crack surfaces surrounding the tip. Under dynamic conditions, simply adopting a cohesive approach cannot reproduce crack dynamics of an atomistic system even when restricted to purely brittle propagation. We are currently assessing methods in which the continuum simulation approach can be improved to account for the dispersive behavior displayed by the atomistic system.

References

[1] F.F. Abraham, D. Brodbeck, R.A. Rafey, and W.E. Rudge. Instabilities dynamics of fracture: a computer simulation investigation. *Physics Review Letters*, 73:272–275, 1994.

[2] A. Needleman. A continuum model for void nucleation by inclusion debonding. *Journal of Applied Mechanics*, 54:525–531, 1987.

[3] L. Prandtl. Ein Gedankenmodell für den Zerreißvorgang spröder Körper. *Zeitschrift für angewandte Mathematik und Mechanik*, 13:129–133, 1933.

[4] V. Tvergaard and J.W. Hutchinson. The influence of plasticity on mixed mode interface toughness. *Journal of the Mechanics and Physics of Solids*, 41:1119–1135, 1993.

ORAL REFERENCE: ICF100502OR

Digital Speckle Correlation Test for Fracture of Thin Film

Huaiwen Wang and Yilan Kang

School of Mechanical Engineering, Tianjin University,
Tianjin, 300072, China

ABSTRACT

The digital speckle correlation method (DSCM) is a rapidly developing new photomechanics technique used to measure the surface deformation. With its advantages of non-contact, real time, whole field and direct measurement, it can be used from macro-scale area to nano-scale area. This paper describes the use of this method in the experiment of the fracture of copper thin film. The displacement field and strain field in a crack tip region of a thin film are measured. Based on the displacement field and strain field of the crack tip region, the figure of plastic zone is determined. The experimental results indicate that DSCM is a useful method for studying the fracture behavior of thin film.

KEYWORDS

Digital Speckle Correlation, Thin Film, Displacement Field, Strain Field, Plastic Zone

INTRODUCTION

With the rapid development of microelectronics and communication technology, the thin film finds wide applications in microelectromechanical system, microelectronics and molectron, etc. As the mechanical behaviors of film materials are different from which of normal materials and they are directly relevant to the life span and the reliability of the subassembly, the study on mechanical behaviors of films, including fracture behavior, have become a necessary research field. Several techniques have developed to evaluate the mechanical properties of thin film, hardness, Young's modulus and fracture strength , Poisson's ratio [1,2,3], etc., but the study of the crack tip region of thin film remain not sufficiently documented. The difficulty lies in there's few techniques can be applied to thin film material. The formulae and theories of fracture mechanics yielded from macro-scale bodies and the traditional experimental measuring methods are also not always available for thin film materials as the influence of geometrical scale. Therefore, the study on displacement field and strain field in crack tip region of thin film material by experimental means is essential. How to measure the displacement fields and strain fields in crack tip region of thin film material is an unresolved issue till now. The DSCM is used in this paper to test the fracture behavior of thin film.

THE DIGITAL SPECKLE CORRELATION METHOD

The digital speckle correlation method was proposed in 1982 [4,5]. It can measure directly the surface displacement vector and strain tensor to subpixel accuracy [6,7,8,9] and captures wide attention in the

development of experimental mechanics recently. This method involves recording, digitizing and processing a pair of speckle patterns of a specimen in different deformation states, one before deformation and another after deformation. If a speckle area in the speckle field before deformation is defined as reference subset and the speckle area corresponding to the subset after deformation is defined as object subset, what is required is to identify the corresponding relation between the two subsets. The difference between the two subsets includes the deformation information of the specimen. Then DSCM becomes a job of comparing subsets between the two digital patterns and the measurement process is converted to a calculation process.

The method for comparing the two subsets is commonly given by use of the correlation coefficient. The correlation coefficient for the two random variables $f(x, y)$ and $g(x^*, y^*)$ can be written in the discrete form as

$$S(\mathbf{X})=1.0-\frac{\Sigma f(x,y)\cdot g(x^*,y^*)}{\sqrt{\Sigma f^2(x,y)\cdot \Sigma g^2(x^*,y^*)}} \tag{1}$$

in which (x, y) and (x^*, y^*) are Cartesian coordinates of a material point in the subset of the undeformed pattern and deformed pattern, respectively. $f(x, y)$ and $g(x^*, y^*)$ are light intensities of that point in the corresponding pattern subsets. The correlation coefficient S(X) shows how closely the two random variables $f(x, y)$ and $g(x^*, y^*)$ are related with S(X)=0 corresponding to perfect correlation.

In general, the coordinates (x, y) are taken at a pixel location, but (x^* ,y^*) are normally not. The relations between x and x^*, y and y^* are given by the following equations:

$$\begin{aligned} x^* &= x+u+\frac{\partial u}{\partial x}\Delta x+\frac{\partial u}{\partial y}\Delta y \\ y^* &= y+v+\frac{\partial v}{\partial x}\Delta x+\frac{\partial v}{\partial y}\Delta y \end{aligned} \tag{2}$$

in which u and v are the in-plane displacement components of the center point of a subset, $\partial u/\partial x$、$\partial u/\partial y$、$\partial v/\partial x$ and $\partial v/\partial y$ are displacement gradients, and Δx and Δy are components of a distance vector between (x, y) and the subset's center point (x_0, y_0).

EXPERIMENT

The double edge-cracked specimen used in the test was made of copper that was produced in Shanghai smeltery. Its thickness was 40μm. The chemical composition of it is shown in Table 1. The film was made into double-edge cracked specimen in the rolling direction. Its geometry and dimensions are shown in Figure 1. In order to obtain a high quality speckle pattern and improve the sensitivity and accuracy, the speckle was made artificially. A random speckle pattern is shown in Figure 2.

TABLE 1
CHEMICAL COMPOSITION OF EXPERIMENTAL MATERIAL (%)

Cu	Fe	Zn	O	Pb	S	Ni
99.91	0.0035	0.001	0.003	0.001	0.001	0.001

The specimen was placed into the specially designed clamp. Then the locations of the CCD camera, lens and light source were adjusted until the speckle pattern was satisfied. The imaging system for the tests is shown in Figure 3. In order to diminish the out-of-plane displacement, an initial load F_0 was applied. Then the digital

speckle pattern was recorded before and after a load F_1, respectively. The couple digital patterns were the original data for the digital speckle correlation method. The digital correlation technique was then applied to analyze the digital images.

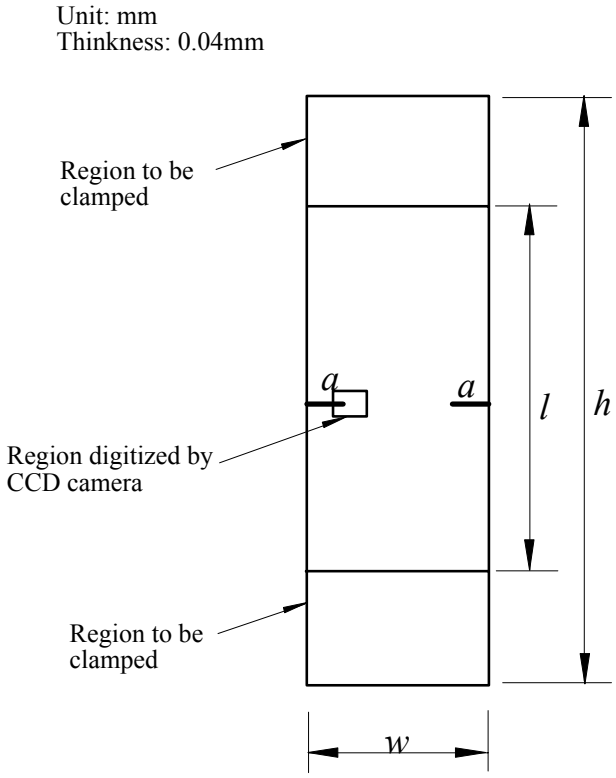

Figure 1: Dimensions of the specimen
(In which a =5, w=25, h=80 and l=50.)

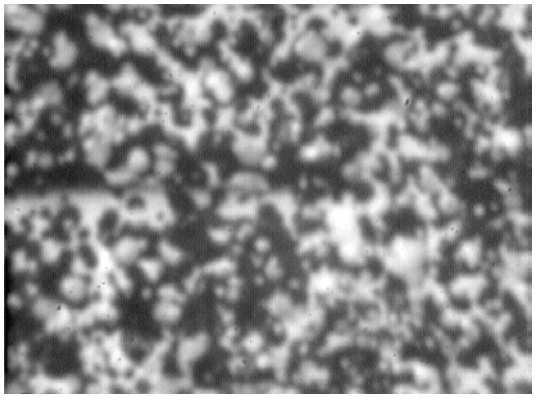

Figure 2: A Speckle pattern

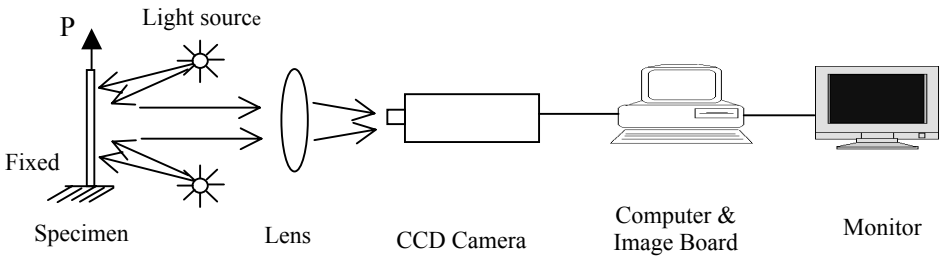

Figure 3: Image system used in the test

It is necessary to know the displacement field and strain field during studying the crack tip region and the plastic zone is the area of interest. Firstly, a pre-load 6.6N was applied, then the first speckle pattern was recorded. Secondly, a load 188.1N was applied and the second speckle pattern was recorded. At last, the digital correlation technique was applied to analyze the first and second digital images. The digitized region and the region calculated by DSCM are shown in Figure 1 and Figure 4. The distributions of the displacement v(x, y) and the normal strain ε_y of the crack tip region were obtained, as shown in Figure 5.

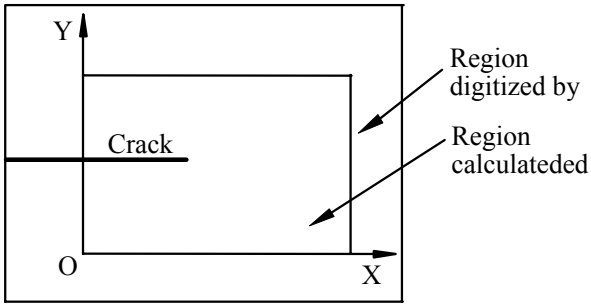

Figure 4: Illustration of the region calculated by DSCM

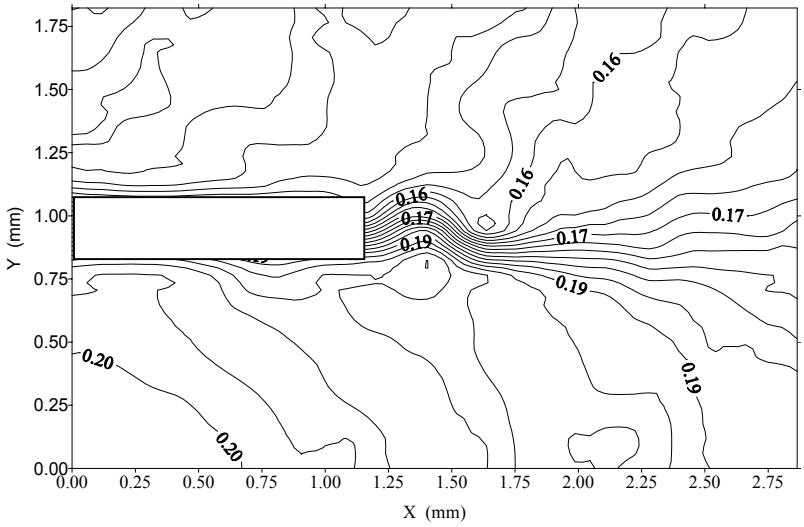

(a) Contour of displacement V field

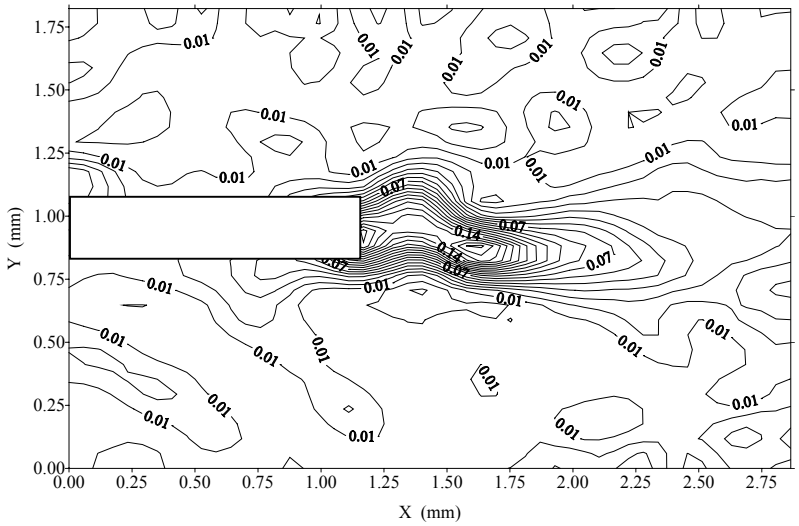

(b) Contour of strain ε_y field

Figure 5: Distribution of displacement field and strain field at the crack tip

From Figure 5, we can see the shape and the size of the plastic zone at the crack tip under given a given load.

CONCLUSION

In this paper the digital speckle correlation method is applied to the experiment of mechanical properties of the copper film. The measurement of displacement field and strain field of the crack tip region is achieved and the contour maps of displacement field and strain field of the crack tip region under given load are shown. The figure and size of the plastic zone are also determined. The present experimental results indicate that DSCM is a useful test technique in studying the fracture behavior of thin film material in future. And it is possible using this technique to study the propagating of the plastic zone in the crack tip region with the loading increase.

ACKNOWLEDGE

The authors would express their thanks to National Natural Science Foundation of China (NO.19972046) for its support of the project.

REFERENCE

1 Stone, D. S. (1989) Thin Film, 130, 105.

2 Sharpe, W. N. Jr., Yuan, B. and Edwards, R.L. (1997) J. Microelectromechanical System, 6, 193.

3 Vlassak, J. J. and Nix, W. D. (1992) J. Materials Res. 7, 3242.

4 Peters, W. H. Rason, W. F. (1982) Opt. Eng. 21, 427.

5 Yamaguchjc, I. (1982) Opt. Acta. 28, 1359.

6 Bruck, H. A. McNeill, S. R. Sutton, M. A. and Peters, W. H. (1989) Exp. Mech. 29, 261.

7 Sutton, M. A. Cheng, M. Q. (1988) Image And Vision Computing. 4, 145.

8 Kang, Y. L. Gao, Y. J. and Zhao, Z.G. (1997) Transaction of Inner Mongolia Polytechnic Univ. 16, 65.

9 Gao, Y. J. (1997) Digital Speckle correlation Method And Its Application in Studying Mechanical Behavior of New Materials. Master's Degree Dissertation of Tianjin Univ.

Oral Presentation: ICF100189OR

DIRECT COMPARISON OF ELASTIC-PERFECTLY-PLASTIC INTERFACIAL FREE-EDGE AND CRACK-TIP SINGULAR FIELDS

L. Marsavina[1] and A. D. Nurse[2]

[1] Department Strength of Materials, Bv. M. Viteazul,
Nr.1 Timisoara 1900, ROMANIA, msvina@mec.utt.ro
[2] Wolfson School of Mechanical and Manufacturing Engineering,
Loughborough University, Loughborough, LE11 3TU, U.K.
a.d.nurse@lboro.ac.uk

KEYWORDS

Interfacial stresses, Elasto-plastic behaviour, Plastic slip-line fields, Crack initiation, Crack propagation.

ABSTRACT

The problem of the elastic and perfectly-plastic plane-strain asymptotic fields for the interfacial free-edge joint singularity is examined and compared with the interfacial crack tip. The geometries are idealised as isotropic elastic and elastic-perfectly-plastic materials bonded to a rigid elastic substrate. Under elastic behaviour it is difficult to compare directly the asymptotic fields between the joint and the crack due to the difference in singularity order and stress distributions. The elastic-perfectly-plastic fields for the interfacial free-edge joint were determined as polar stress components and as idealised plastic slip-line sectors. A fourth-order Runge-Kutta numerical method provides solutions to fundamental equations of equilibrium and compatibility that are verified with those of a highly focused finite element (FE) analysis. A successful attempt to show that a direct comparison between the solutions for the interfacial free-edge joint and the Mode I interfacial crack exists if the deviatoric stresses are considered.

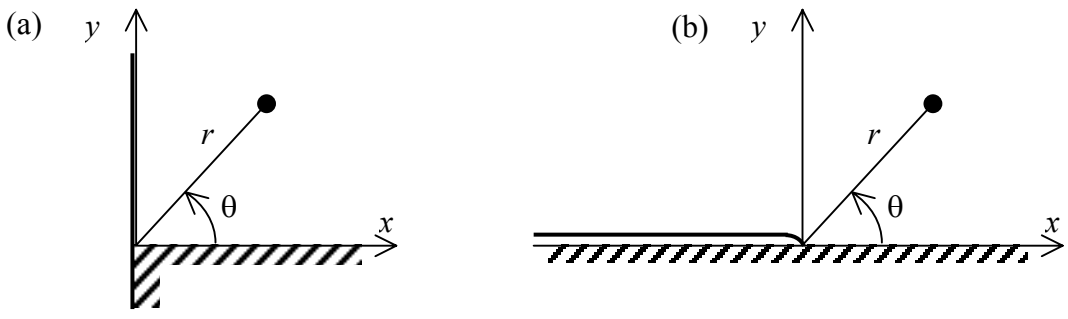

Figure 1: Schematic (a) interfacial free-edge joint and (b) interfacial crack-tip geometries including polar and Cartesian co-ordinate schemes.

INTRODUCTION

Interface-controlled fracture is the initial microscopic event leading to ultimate macroscopic rupture in many polycrystalline and composite materials. Failure frequently initiates within the interfacial free-edge singularity being the source of unbounded elastic stresses and/or a plastic zone. The fracture process continues through propagation of an interface crack driven by complex stress intensity factors (SIFs). However, the actual events that take place between the former (initiation) and latter (propagation) are not well understood. From a design perspective, one may choose to prevent initial debonding of the interfacial joint or to prevent crack propagation. To add to the confusion though, it has been shown by Klingbeil and Bleuth [1] that conflicting solutions are obtained if designing to prevent debonding of the interfacial free-edge and subsequent propagation of the interfacial crack. Thus far, at least, it has been shown by Akinsaya and Fleck [2] that in the interim stage between initiation and propagation that an interface crack has SIFs amplified if it is embedded in a free-edge singularity field. This may seem an issue related only to interfacial systems but considering that the vast majority of structural materials are either polycrystalline metals or composite materials it is more fundamental than perhaps first considered.

One approach to understand the events that take place between crack initiation at the interfacial free edge and propagation of an interface crack would be to examine the change in stress state from the initiating stage to the final stage. However, to link the two fields in terms of *elastic* stresses and strains is problematic due to the general difference in singularity orders and resulting angular distributions. From an asymptotic perspective, the problem is incomprehensible given that one either has a free edge (Figure 1a), or one has a crack (Figure 1b); there is no in-between stage. Furthermore, most structural materials are also known to undergo, in general, small-scale yielding (SSY) before failure. Consequently, there seems little point attempting to establish a direct link between crack initiation and propagation in the purely elastic regime. It seems more important to link the asymptotic fields of the interfacial free-edge joint and interfacial crack tip under elasto-plastic (SSY) conditions. Our understanding of the toughness of interfacial systems would be then be increased with this link between the events of crack initiation, i.e. debonding of the interfacial free-edge joint and the propagation of an interfacial crack.

In this paper, the structure of the asymptotic field at the interfacial free-edge is determined for an elastic-perfectly-plastic material bonded perfectly to a rigid elastic material forming a half plane. Stresses and displacements in the asymptotic fields are numerically calculated in an approach similar to Sharma and Aravas [3] and are verified by finite element (FE) analysis. To determine a pathological link between crack initiation at the interfacial free-edge and growth of an interface crack the two fields are compared directly. To compare for a range of possibilities the distributions of polar stress components are determined for the interfacial free-edge and crack-tip singular fields for the purely elastic and perfectly-plastic cases. In the latter case, direct comparisons are possible since the singularities are removed by material yielding except in the case of the radial shear strain. The plastic slip-line field for the interface crack-tip characterised by Zywicz and Parks [4] is used to show that the interfacial free-edge joint solution is very similar to its counterpart the crack-tip having a null elastic wedge sector.

FORMULATION OF THE PROBLEM

The singularity order of the interfacial crack tip under elastic conditions is always -0.5 in comparison to the free-edge joint that varies according to the elastic properties of the two materials. In general, the interface crack between two isotropic materials suffers a singularity stress field characterised by the complex SIF, $K=K_1+iK_2$, and is of the form:

$$\sigma_{ij}(r,\theta) = Kr^{-0.5+i\varepsilon} g_{ij}(\varepsilon,\theta) \tag{1}$$

where ε is the oscillatory index and g_{ij} are known non-dimensional functions. A singularity at the interfacial free-edge is predicted by Bogy [5] to be of order depending on the elastic constants of the materials. For the interfacial free-edge joint the stress singularity corresponds to the form:

$$\sigma_{ij}(r,\theta) = Hr^{\lambda-1} f_{ij}(\lambda,\theta) \tag{2}$$

where H is its intensity, λ-1 is the singularity order, and f_{ij} are known non-dimensional functions of (λ,θ). The order of the singularity λ is dependent on the degree of material mismatch and the intensity H depends on the far-field geometry and loading. For the purposes of this study the singularity order for the elastic case is assumed to be λ-1=-0.28.

A fracture mechanics' description of the critical state prior to separation using continuum-based mechanics usually involves the elastic solution for the crack. It is of limited use for describing materials that yield and undergo inelastic deformation at high strains. The elasto-plastic interfacial crack problem has received considerable attention in the last decade enabling a thorough understanding to be developed. Using a J-integral argument Rice and Rosengren [6], and Hutchinson [7] have shown that crack problems under SSY conditions result in a $1/r$ singularity in the strain-energy density and the radial shear strain fields. The analysis of interfacial free-edge is just as important to our understanding of crack initiation and growth though in comparison to its counterpart the interface crack it has received far less attention. It appears no effort has been made to understand the elasto-plastic behaviour of the free-edge singularity.

The constitutive behaviour of a homogeneous isotropic elasto-plastic material may be characterised by the J_2 deformation theory for a Ramberg-Osgood uniaxial stress-strain behaviour, i.e.:

$$\varepsilon_{ij} = \frac{1+\upsilon}{E} s_{ij} + \frac{1-2\upsilon}{3E}\sigma_{kk}\delta_{ij} + \frac{3}{2}\alpha\varepsilon_{\mathrm{o}}\left(\frac{\sigma_e}{\sigma_{\mathrm{o}}}\right)^{n-1}\frac{s_{ij}}{\sigma_{\mathrm{o}}} \tag{3}$$

where ε_{ij} is the infinitesimal strain tensor, σ_{o} is the yield stress, σ_e is the Mises equivalent stress, $\varepsilon_{\mathrm{o}} = \sigma_{\mathrm{o}}/E$, and s_{ij} is the deviatoric stress. Also, n is the power-law hardening exponent $(1 \le n \le \infty)$, E is the Young's moduli, δ_{ij} is the Kronecker delta, and α is a material constant. Putting n=∞ then the behaviour is elastic-perfectly-plastic.

Asymptotic solutions to the crack-tip behaviour under elastic-perfectly-plastic conditions may be obtained in polar co-ordinate form (r,θ) using the expansion form given by Sharma and Aravas [3]. To obtain the asymptotic solution the problem is formulated in terms of the leading order stresses $\tilde{\boldsymbol{\sigma}}^{(0)}$ and displacements $\mathbf{u}^{(0)}$ that are substituted into the governing equations of equilibrium, compatibility, and stress-strain relationship. Terms having like powers of radius r are collected and hierarchy of problems is obtained. The leading order problem that defines $\boldsymbol{\sigma}^{(0)}$ and $\mathbf{u}^{(0)}$ consists of five non-linear ordinary differential equations, where s is the stress singularity order:

$$\begin{aligned}
(s+1)\tilde{\sigma}_{rr}^{(0)} - \tilde{\sigma}_{\theta\theta}^{(0)} + \frac{\mathrm{d}\tilde{\sigma}_{r\theta}^{(0)}}{\mathrm{d}\theta} &= 0 \\
\frac{\mathrm{d}\tilde{\sigma}_{\theta\theta}^{(0)}}{\mathrm{d}\theta} + (s+2)\tilde{\sigma}_{r\theta}^{(0)} &= 0 \\
(sn+1)\tilde{u}_r^{(0)} - \frac{3}{2}\tilde{\sigma}_e^{(0)n-1}\tilde{s}_{rr}^{(0)} &= 0 \\
\tilde{u}_r^{(0)} + \frac{\mathrm{d}\tilde{u}_\theta^{(0)}}{\mathrm{d}\theta} - \frac{3}{2}\tilde{\sigma}_e^{n-1}\tilde{s}_{\theta\theta}^{(0)} &= 0 \\
\frac{1}{2}\left(\frac{\mathrm{d}\tilde{u}_r^{(0)}}{\mathrm{d}\theta} + sn\tilde{u}_\theta^{(0)}\right) - \frac{3}{2}\tilde{\sigma}_e^{(0)n-1}\tilde{\sigma}_{r\theta}^{(0)} &= 0
\end{aligned} \tag{4}$$

The focus of the paper is the leading order solution for the interfacial free-edge joint and its similarities with that of the crack tip where s=-1(1+n).

DEVELOPMENT OF THE ELASTIC-PERFECTLY-PLASTIC FIELD FOR THE INTERFACIAL FREE-EDGE JOINT

A fourth-order Runge-Kutta solution to the equations (4) was obtained for an elastic-perfectly-plastic hardening exponent (n>1000), using the proprietary software *Mathcad* (v.2000), distributed by Adept Scientific Ltd. An iteration scheme was used to determine the solution s to the non-linear eigenvalue problem and the subsequent distributions for the stresses and displacements that satisfy the governing equations and imposed boundary conditions. This asymptotic solution was verified by a FE analysis performed using the software *Lusas* (v13.3, distributed by FEA Ltd., Kingston, UK). Highly-focused, refined meshes for the interfacial free-edge joint were prepared using four-noded linear elements until satisfactory convergent results were obtained.

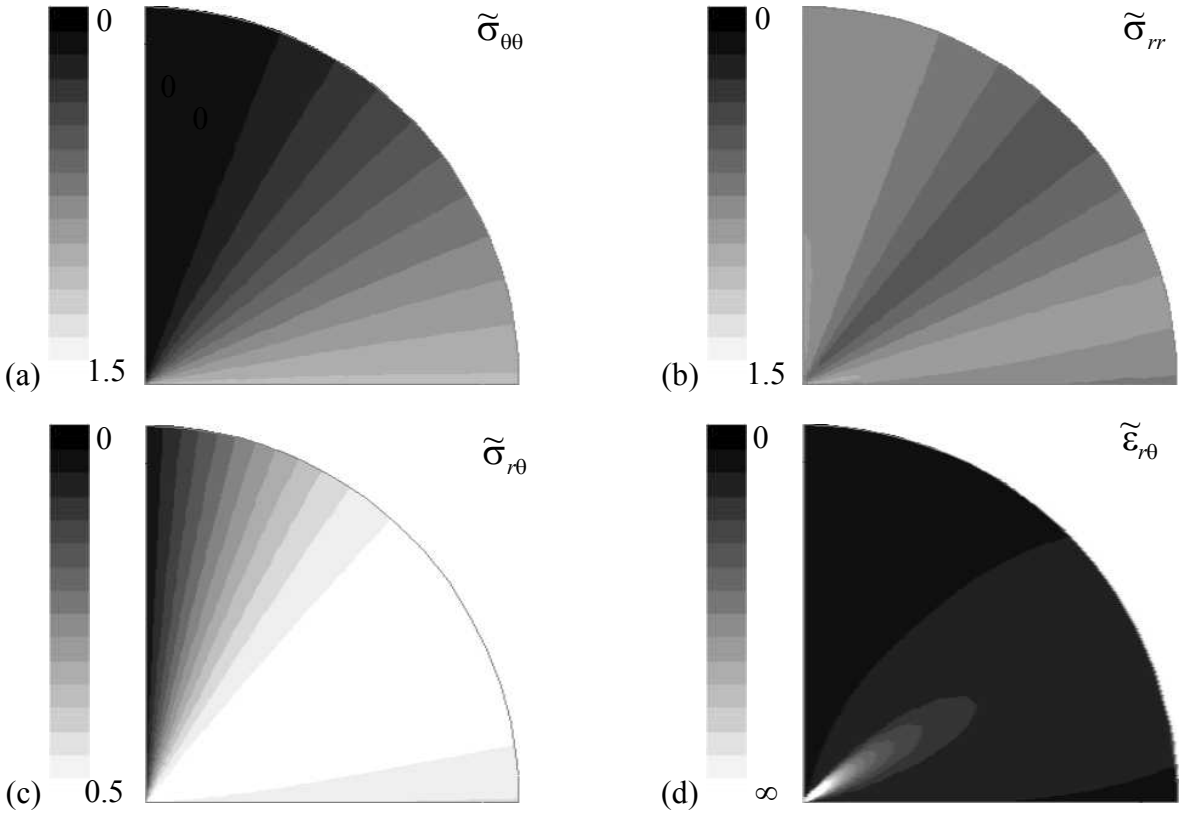

Figure 2: Contoured plots showing results of a FE analysis for an elastic-perfectly-plastic upper region bonded to a rigid elastic lower region.

Results of the FE analysis under SSY elastic-perfectly-plastic conditions are shown in Figure 2 as contour plots for the region $-10^{-5} \le r/r_p \le 10^{-3}$ where r_p is the maximum extent of the plastic zone defined by $\sigma_e = \sigma_o$. Figure 3(a) shows the angular variation of the polar components of stress for the interfacial free-edge joint. Nodal values of the polar components of stress from the FE analysis are plotted as symbols for the radius $\log(r/r_p) = -2$. The results are normalised so that the maximum value of the equivalent stress σ_e in the angular variation is unity, i.e.:

$$\left[1.5\tilde{s}_{ij}^{(0)}\tilde{s}_{ij}^{(0)}\right]_{\max}^{1/2} = 1 \qquad (5)$$

The fourth-order Runge-Kutta solution to the angular variations satisfying (4) and the imposed boundary conditions has been superimposed onto the FE results to enable them to be validated. In all cases of the polar components of stress the agreement is excellent between the asymptotic solution and the FE results.

The rigid-slip-line field solution for the interfacial free-edge may be characterised using the notation of Zywicz and Parks [4]. The three inelastic crack-tip sectors admissible are the centered fan, constant-state

sector, and the quasi-constant-state sector [4]. Elastic crack-tip sectors are also admissible and asymptotically they behave as semi-infinite elastic wedges loaded by constant surface tractions. The solution for the plastic slip-line field was determined and is shown in Figure 3(b). A quasi-constant-state sector exists at the interface followed by comparatively large angular distributions of centered fan and constant state. A characteristic of the centered fan region is a singularity in the shear strain as seen in Figure 2(d) and the order was found to be approximately –0.8 (c.f. –1 for the crack).

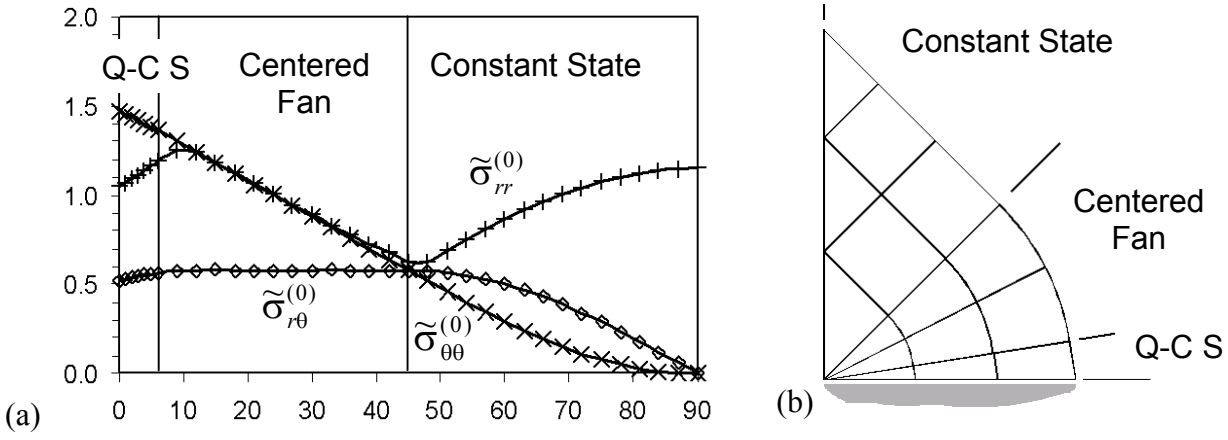

Figure 3: Rigid-slip-line field solution at an interfacial free-edge singularity for an elastic-perfectly-plastic upper region bonded to a rigid elastic substrate.

COMPARISONS OF INTERFACIAL FREE-EDGE JOINT AND CRACK-TIP ASYMPTOTIC FIELDS

Figure 4(a) and (b) shows the normalised solutions for the polar and deviatoric stress components for the two geometries assuming purely *elastic* behaviour. Asymptotic solutions assuming elastic-perfectly-plastic behaviour, that satisfy (4), were produced for both geometries under remote Mode I loading. It was considered here that there may be some similarity between the inelastic behaviour at the interfacial free-edge joint and the Mode I interfacial crack since the latter case includes an elastic sector between $90^\circ \le \theta \le 180^\circ$ [4]. That is, both are inelastic between $0^\circ \le \theta \le 90^\circ$ and the plasticity is confined to the same quarter. The normalised results for the polar components of stress for the interfacial crack and those for the free-edge joint (as in Figure 3a) are shown together in Figure 4(c) to enable comparisons to be made. The "elastic sector" indicated is the solution for a 90° elastic wedge and not those of equations (4).

For the elastic solutions, there is some similarity between the forms of the polar components of stress for the two geometries between 0° and 90°. The deviatoric stresses demonstrate, however, that there is still some major differences between the two geometries; it should also be emphasised that the singularity orders are –0.28 and –0.5 for the interfacial free-edge joint and crack tip respectively. Under perfectly-plastic behaviour, instead, the singularity orders are –0.8 and –1 for shear strain for the interfacial free-edge joint and crack tip respectively. There is no singularity for the stresses in both cases. The resulting distributions for the polar components of stress shown in Figure 4(c) compare very favourably in form. A more obvious similarity is obtained when the deviatoric stresses are plotted as in Figure 4(d). Here the two sets of curves cannot be distinguished for the region $0^\circ \le \theta \le 45^\circ$. One may surmise that upon development of an interfacial crack from an interfacial free-edge joint the asymptotic deviatoric stress field does *not* have to change in the region $0^\circ \le \theta \le 45^\circ$ for an elastic-perfectly-plastic material. In other v o' crack-tip will exist at the interfacial free-edge that h sses as for the interfacial crack. The close similarity e nt undergo a transition from centered fan to constant s 0°.

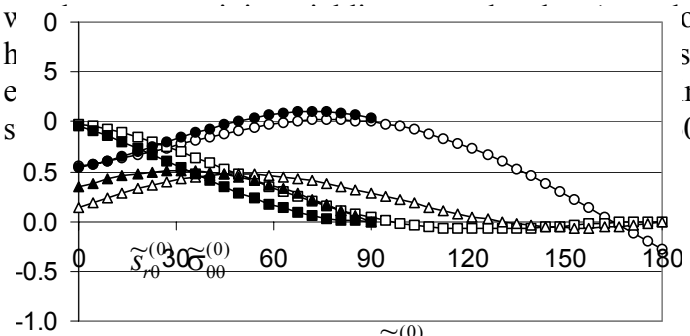

(a) Polar elastic stress components

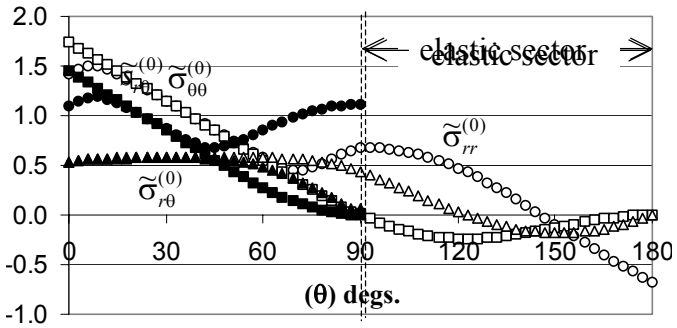

(b) Deviatoric elastic stress components

(c) Polar perfectly-plastic stress components

(d) Deviatoric perfectly-plastic stress components

Figure 4: Comparison of the asymptotic normalised plane-strain stress components for the interfacial free-edge and crack-tip under elastic-perfectly-plastic slip conditions.

CONCLUSIONS

The plastic-slip-line field has been sectorally assembled for elastic-perfectly–plastic behaviour at the interfacial free-edge joint. This is found to be in agreement with a Mode I solution for the interfacial crack. In comparing field stress solutions for the interfacial free-edge joint with that of the crack, involving an elastic sector between $90^\circ \le \theta \le 180^\circ$, it is seen that the normalised deviatoric stress field is indistinguishable between the two geometries for the region $0^\circ \le \theta \le 45^\circ$. Consequently, it would appear that the asymptotic deviatoric stress field that drives many forms of crack propagation does not need to change structure upon initiation of an interfacial crack at the free-edge joint.

ACKNOWLEDGEMENTS

This work was supported by the Government of Romania who sponsored a Visiting Scholarship awarded to Dr Marsavina to study at Loughborough University.

REFERENCES

1. Klingbeil, N. W. and Beuth, J. L. (2000) *Engng. Fract. Mech.* 66, pp93-110.
2. Akisanya, A. R. and Fleck, N. A. (1997) *Int. J. Solids Structures* 34, pp1645-1665.
3. Sharma, S. M. and Aravas, N. (1991) *J. Mech. Phys. Solids* 39, pp1043-1072.
4. Zywicz, E. and Parks, D. M. (1992) *J. Mech. Phys. Solids* 40, pp511-536.
5. Bogy, D. B. (1971) *J. Appl. Mechs.* 38, pp377-386.
6. Rice, J. R. and Rosengren, G. R. (1968) *J. Mech. Phys. Solids* 16, pp01-Dec.
7. Hutchinson, J. W. (1968) *J. Mech. Phys. Solids* 16, pp13-31.

ORAL/POSTER REFERENCE: ICF 100177OR

DIRECT EVALUATION OF ACCURATE SIF WITH PUM

B.L. Karihaloo [a] and Q.Z. Xiao [a, b]

[a] School of Engineering, Cardiff University, Cardiff, CF24 3TB,UK
[b] Department of Modern Mechanics, University of Science and Technology of China, Hefei, 230026, China

ABSTRACT

An alternative approach to the extended finite element method (XFEM) and generalised finite element method (GFEM) is introduced to enrich the finite element approximation of the crack tip node as well as its surrounding nodes. These nodes are enriched with not only the first term but also the higher order terms of the crack tip asymptotic field using a partition of unity method (PUM). The first term only is used in the XFEM to enrich the surrounding nodes, and in the GFEM to enrich the crack tip node. This approach also differs from the XFEM in that the additional coefficients of the enriched nodes are the actual coefficients of the crack tip asymptotic field. Numerical results show that together with a reduced quadrature rule, the current approach predicts accurate stress intensity factors directly after constraining the enriched nodes properly but without extra post-processing.

KEYWORDS

Crack tip asymptotic field, partition of unity method (PUM), stress intensity factor (SIF)

INTRODUCTION

For crack problems, Tong and Pian [1] have shown that, in general, the convergence rate for the finite element (FE) method is dominated by the nature of the solution near the point of singularity, and the error from the elements immediately adjacent to the point is of the same order as that of the remainder of the elements. Hence neither the use of the regular high accuracy elements using high order polynomials as interpolation functions nor finer elements improve the accuracy efficiently. In order to improve the convergence rate of the FE solution, various singular elements have been introduced to account for the required crack tip singularity [2-4]. Recently, Belytschko et al. [5-7] proposed the extended finite element method (XFEM) for modelling cracks in the FE framework, which seems promising for fracture problems since it avoids using a mesh conforming with the crack as is the case with the traditional FEM. By using XFEM, a standard FE mesh for the problem is first created without accounting for the crack. A crack is then represented independently of the mesh by enriching the standard displacement approximation with both discontinuous displacement fields along the crack face and the singular asymptotic fields at nodes surrounding the crack tip through a partition of unity method (PUM). The additional coefficients at each enriched node are independent. Strouboulis et al. [8] also discussed the possibility of enriching the crack tip node with the asymptotic field in their generalised finite element method (GFEM). The difference between the XFEM and the GFEM is that the former enriches the surrounding nodes instead of the crack tip, while the latter only enriches the crack tip. The weakness of most singular elements as well as the XFEM and the

GFEM is that they predict accurate global displacements but not accurate SIFs at the crack tip. The SIF has to be evaluated with the help of energy related parameters such as the *J*-integral by a post-processing procedure. This limits the application of singular elements, XFEM or GFEM in fracture simulation.

In order to determine the SIF directly without extra post-processing, an alternative approach is introduced to enrich the FE approximation of the crack tip node as well as its surrounding nodes with not only the first term but also the higher order terms of the crack tip asymptotic field using the PUM. It differs from the XFEM in that the enriched fields are the actual crack tip asymptotic fields and the additional coefficients of the enriched nodes are the relevant coefficients of this expansion. Sensitivity to the quadrature rule and number of retained terms, as well as the effect of constraining the enriched nodes, are studied. The computed SIFs of typical cracked specimens will be validated with results available in the literature.

ENRICHING THE CRACK TIP FE APPROXIMATION USING PUM

For our purposes and without loss of generality, we consider only Mode I crack problems. The truncated N terms of the displacement expansions near the tip of a crack can be written as [3, 4]

$$u_a(r,\theta) = \sum_{n=1}^{N} a_n f_{1n}(r,\theta), \qquad v_a(r,\theta) = \sum_{n=1}^{N} a_n f_{2n}(r,\theta) \tag{1}$$

where (r, θ) are the polar coordinates with the origin at the crack tip, and the angular functions

$$f_{1n}(r,\theta) = \frac{r^{n/2}}{2\mu}\left[\left(\kappa + \frac{n}{2} + (-1)^n\right)\cos\frac{n}{2}\theta - \frac{n}{2}\cos\left(\frac{n}{2}-2\right)\theta\right] \tag{2}$$

$$f_{2n}(r,\theta) = \frac{r^{n/2}}{2\mu}\left[\left(\kappa - \frac{n}{2} - (-1)^n\right)\sin\frac{n}{2}\theta + \frac{n}{2}\sin\left(\frac{n}{2}-2\right)\theta\right] \tag{3}$$

The coefficient of the first term is related to the mode I SIF K_I as $a_1 = K_I / \sqrt{2\pi}$.

In order to use higher order terms, r is normalised as

$$\bar{r} = r / r_m \tag{4}$$

where r_m is a characteristic length of the elements with enriched nodes, e.g., the length of a side or of the diagonal of a rectangular element. Taking into account of (4), displacements (1) become

$$u_a(\bar{r},\theta) = \sum_{n=1}^{N} a'_n f_{1n}(\bar{r},\theta), \qquad v_a(\bar{r},\theta) = \sum_{n=1}^{N} a'_n f_{2n}(\bar{r},\theta) \tag{5}$$

with the coefficients being related as

$$a'_n = a_n r_m^{n/2} \tag{6}$$

For an element near a crack tip (cf. Figure 1), the approximation of displacements enriched with the truncated crack tip asymptotic fields (5) using the PUM can be written as

$$\begin{Bmatrix} u^h(x) \\ v^h(x) \end{Bmatrix} = \sum_{i\in I} \boldsymbol{f}_i(x) \begin{Bmatrix} u_i \\ v_i \end{Bmatrix} + \sum_{j\in E\cap I} \boldsymbol{f}_j(x) \begin{Bmatrix} u_a(\bar{r},\theta) \\ v_a(\bar{r},\theta) \end{Bmatrix} = \sum_{i\in I} \boldsymbol{f}_i(x) \begin{Bmatrix} u_i \\ v_i \end{Bmatrix} + \sum_{j\in E\cap I} \sum_{n\in N} \boldsymbol{f}_j(x) \begin{Bmatrix} f_{1n}(\bar{r},\theta) \\ f_{2n}(\bar{r},\theta) \end{Bmatrix} a_n \tag{7}$$

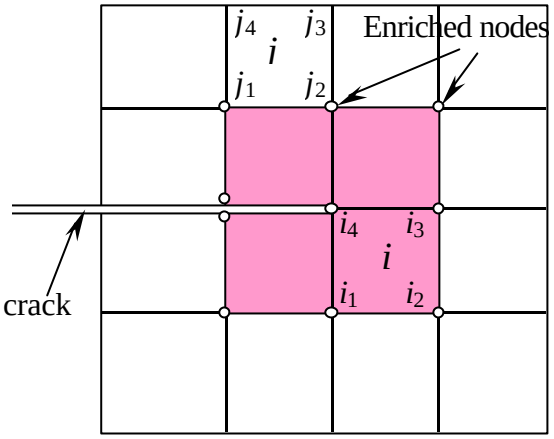

Figure 1: A schematic picture of the elements and enriched nodes near a crack tip

where I is the node set of an element, e.g., for elements i and j in Figure 1, $I=\{i_1 \quad i_2 \quad i_3 \quad i_4\}$ and $\{j_1 \quad j_2 \quad j_3 \quad j_4\}$, respectively. E is the set of the enriched nodes of the element, $E=\{i_1 \quad i_2 \quad i_3 \quad i_4\}$ for element i, and $E=\{j_1 \quad j_2\}$ for element j. Approximation (7) may be simplified in actual cases. For an element which includes the crack tip, e.g. element i in Figure 1, $I=E$. Noting the consistency condition $\sum_{i\in I} f_i(x) = 1$ we have from (7) the displacement approximation

$$\begin{Bmatrix} u^h(x) \\ v^h(x) \end{Bmatrix} = \sum_{i\in I} f_i(x) \begin{Bmatrix} u_i \\ v_i \end{Bmatrix} + \sum_{n\in N} \begin{Bmatrix} f_{1n}(\bar{r},q) \\ f_{2n}(\bar{r},q) \end{Bmatrix} a'_n \tag{8}$$

While for an element which does not include the crack tip, e.g. element j, we have

$$\begin{Bmatrix} u^h(x) \\ v^h(x) \end{Bmatrix} = \sum_{i\in I} f_i(x) \begin{Bmatrix} u_i \\ v_i \end{Bmatrix} + \left(f_{j_1}(x) + f_{j_2}(x)\right) \sum_{n\in N} \begin{Bmatrix} f_{1n}(\bar{r},q) \\ f_{2n}(\bar{r},q) \end{Bmatrix} a'_n \tag{9}$$

If all enriched nodes are constrained, i.e., the nodal displacements are set to be zero, the displacement approximation for elements including the crack tip (e.g., shaded elements in Figure 1) become the truncated crack tip asymptotic field. The outer ring of elements surrounding these elements actually match the crack tip field with the standard FE approximation. However, the current approach differs from all existing singular elements in that higher order terms have been taken into account.

From (7), we have the strain vector

$$\begin{Bmatrix} \varepsilon_x \\ \varepsilon_y \\ \gamma_{xy} \end{Bmatrix} = \begin{bmatrix} \partial/\partial x & 0 \\ 0 & \partial/\partial y \\ \partial/\partial y & \partial/\partial x \end{bmatrix} \begin{Bmatrix} u^h(x) \\ v^h(x) \end{Bmatrix} = Bq + \bar{B}a' \tag{10}$$

where q is the general nodal displacement vector, and $a'^T = \{a'_1 \quad a'_2 \quad \cdots \quad a'_N\}$. The additional matrix

$$\bar{B} = \begin{bmatrix} \bar{B}_1 & \bar{B}_2 & \cdots & \bar{B}_n & \cdots & \bar{B}_N \end{bmatrix} \tag{11}$$

with its nth element or column being

$$\overline{B}_n = \sum_{j\in E\cap I} \begin{bmatrix} \dfrac{\partial}{\partial x}\left(\phi_j(x) f_{1n}(\bar{r},\theta)\right) \\ \dfrac{\partial}{\partial y}\left(\phi_j(x) f_{2n}(\bar{r},\theta)\right) \\ \dfrac{\partial}{\partial y}\left(\phi_j(x) f_{1n}(\bar{r},\theta)\right)+\dfrac{\partial}{\partial x}\left(\phi_j(x) f_{2n}(\bar{r},\theta)\right) \end{bmatrix} \qquad (12)$$

With the use of the enriched strain-displacement relation (10), the element stiffness matrix can be formed in the general way.

NUMERICAL EXAMPLES

A single edge crack in a finite rectangular plate (SEC) shown in Figure 2 is chosen first as a benchmark problem. The coefficient of the singular term a_1 computed by the present method will be compared with the reference K_I solution given in [9]

$$\frac{K_I}{K_0} = 1.12 - 0.23\frac{c}{b} + 10.6\left(\frac{c}{b}\right)^2 - 21.7\left(\frac{c}{b}\right)^3 + 30.4\left(\frac{c}{b}\right)^4, \qquad K_0 = \sigma\sqrt{\pi c} \qquad (13)$$

which is claimed to be accurate to within 1 for $h/w \geq 1$ and $c/w \leq 0.6$. An eccentric through crack in a finite rectangular plate (Figure 3) is analysed next to show the potential of the present method in treating multiple crack tips. For both specimens, h=w=1 are used. As the coefficients in the asymptotic expansions (1) are independent of the material constants, in the computations Young's modulus E is set at 1, and Poisson's ratio at 0.25. The load (Figures 2 and 3) is chosen as =1 with its units consistent with that of E. A state of plane stress is considered and the thickness is assumed to be unity.

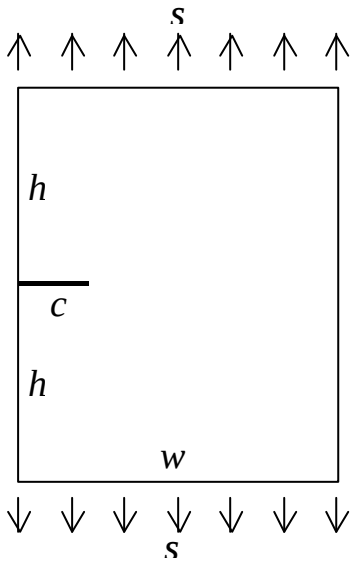

Figure 2: A single edge crack in a finite rectangular plate

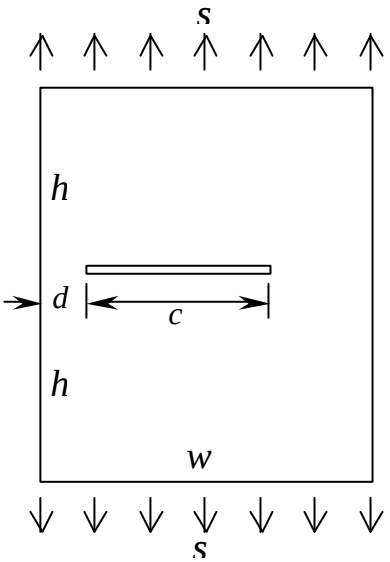

Figure 3: An eccentric through crack in a finite rectangular plate

Only the upper half of the plate in Figure 2 or 3 is considered and divided into 10 10=100 regular elements because of symmetry. The bilinear 4-node isoparametric element is used together with a 2 2 Gauss quadrature. The normal nodal displacements are fixed on the axis of symmetry. r_m=$0.1\sqrt{2}$ is used throughout the computations.

For the SEC with c/w=0.3, the computed a_1 with N=42 and various ngaus, order of Gauss quadrature, is plotted in Figure 4. The results obtained with or without constraining the enriched nodes are included. Obviously, results obtained by constraining the enriched nodes and a reduced integration (ngaus=2) are the most accurate. Quadratures higher than order three give almost identical results. Hence in the following we will constrain the enriched nodes. But the quadrature rule will be tested extensively.

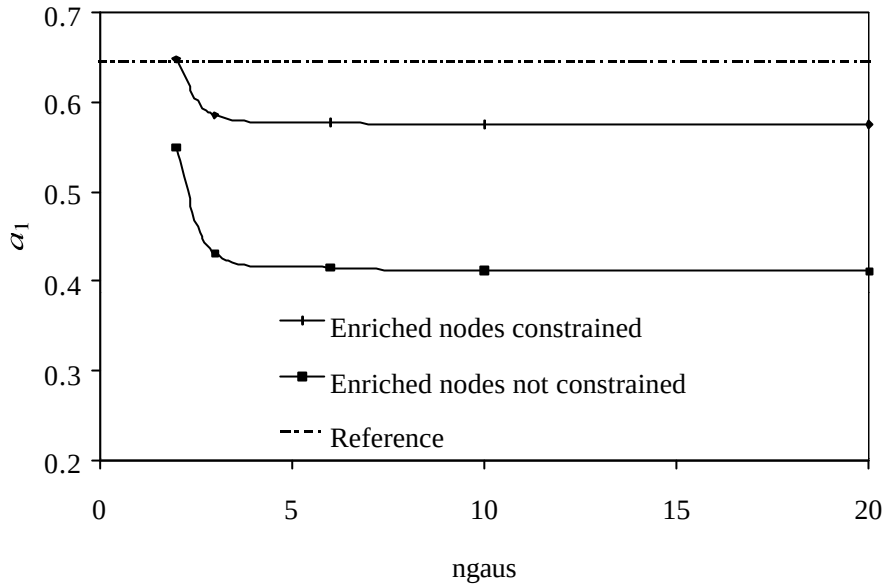

Figure 4: Computed a_1 for various quadrature orders with different constraints on the enriched nodes

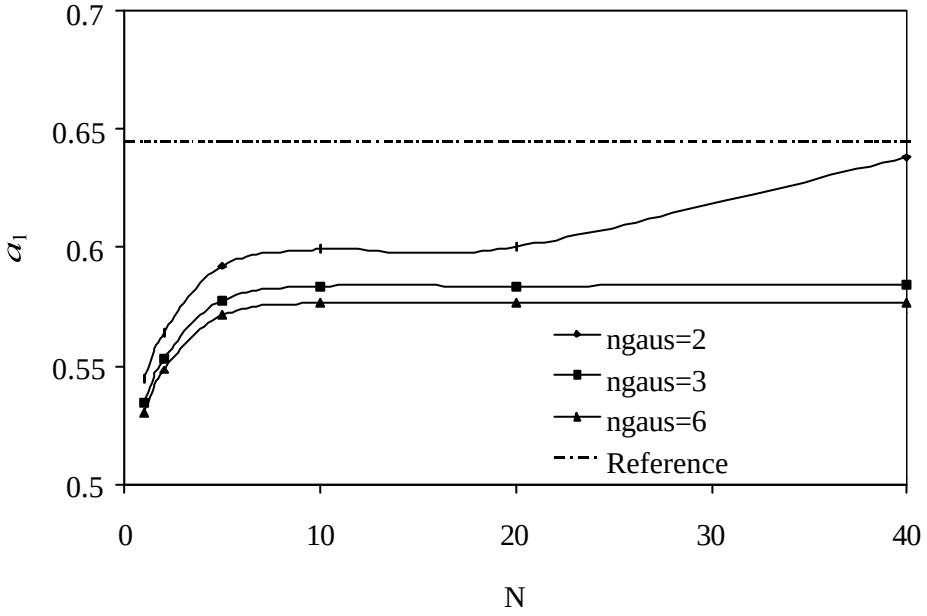

Figure 5: Convergence of the computed a_1 with an increase in the number of retained terms

Again for the SEC with c/w=0.3, the convergence of the computed a_1 with an increase in the retained terms N of various integration orders is studied and reported in Figure 5. It is clear that the second order Gauss integration again gives the most accurate results. Using only the first term or a few higher order terms improves the accuracy but not by much. Desirable accuracy has been maintained by using 40 terms.

By retaining 40-50 terms (a deeper crack needs more terms) and choosing ngaus=2, the computed a_1 for various crack lengths is listed in Table 1 and compared with the solution given by (13). It is clear that very high accuracy (about 1%) has been obtained by the present method.

TABLE 1
COMPUTED a_1 FOR VARIOUS CRACK LENGTHS FOR THE SEC

c/w	0.2	0.3	0.4	0.5	0.6	0.7	0.8
Computed a_1	0.433	0.648	0.936	1.404	2.165	3.554	5.668
(13)	0.434	0.645	0.945	1.421	2.219	3.555	5.731

The eccentric crack in Figure 3 can be easily treated by the present method. d=0.2, c=0.4 and ngaus=2 are used and 43 terms are retained. The computed a_1 for the left and right tips are 0.453 and 0.337, respectively.

The stiffness matrix of an enriched element as well as the system is generally rank deficient. This problem cannot be overcome completely by accurate integration. However, this kind of rank deficiency can be taken care of numerically [8]. In our computations, we used the program given in [10].

DISCUSSION AND CONCLUSIONS

By enriching the FE approximation of the crack tip node as well as its surrounding nodes with not only the first term but also the higher order terms of the crack tip asymptotic field, accurate SIFs are determined directly without extra post-processing. To maintain high accuracy, 40-50 terms in the crack tip asymptotic field should be retained, a reduced quadrature (2 2 Gauss quadrature used in this paper) is desirable, and the enriched nodes should be constrained properly.

Since the general bilinear interpolation cannot improve the approximation of the crack tip field, constraining the enriched nodes improves the condition of rank deficiency and thus the accuracy of the results.

2 2 Gauss quadrature provides the most accurate results because the truncation errors are mainly compensated by the higher order terms, while using accurate integration the errors are averaged among all terms.

Although only Mode I cracks are reported, it is straightforward to employ this method to more complicated crack configurations and/or loading conditions, especially together with the method for incorporating discontinuous displacement fields across the crack face away from the crack tip [5-7].

REFERENCES

1. Tong, P. and Pian, T.H.H. (1973) On the convergence of the finite element method for problems with singularity. *Int. J. Solids Struct.* 9, 313.
2. Liebowitz, H., Moyer, E.T. (1989) Finite element methods in fracture mechanics. *Comput. Struct.* 31, 1.
3. Owen, D.R.J., Fawkes, A.J. (1983). *Engineering fracture mechanics: numerical methods and applications*. Pineridge Press Ltd., Swansea UK.
4. Karihaloo, B.L. and Xiao, Q.Z. (2001) Accurate determination of the coefficients of crack tip asymptotic field by a hybrid element with p-adaptivity. *Engng. Fract. Mech.* (in press).
5. Belytschko, T. and Black, T. (1999) Elastic crack growth in finite elements with minimal remeshing. *Int. J. Numer. Meth. Engng.* 45, 601.
6. Moes, N., Dolbow, J. and Belytschko, T. (1999) A finite element method for crack growth without remeshing. *Int. J. Numer. Meth. Engng.* 46, 131.
7. Daux, C., Moes, N., Dolbow, J., Sukumar, N. and Belytschko, T. (2000) Arbitrary branched and intersecting cracks with the extended finite element method. *Int. J. Numer. Meth. Engng.* 48, 1741.
8. Strouboulis, T., Babuska, I., Copps, K. (2000) The design and analysis of the generalized finite element method. *Comput. Meth. Appl. Mech. Engng.* 181, 43.
9. Rooke, D.P., Cartwright, D.J. (1976). *Compendium of stress intensity factors*. HMSO, London.
10. Bathe, K.J. (1996). *Finite element procedures*. Englewood Cliffs, Prentice-Hall.

Discontinuous Crack Growth of Polyimide Resin,

Effect of Molecular Weight

M. Notomi[1], K. Kishimoto[2], T. Shibuya[2], H. Inaba[3] and A. Morita[3]

[1]Department of Mechanical Engineering, Meiji University, 1-1-1 Higashimita, Tama-ku, Kawasaki, Kanagawa, 214-8571, JPN
[2]Graduate School of Science and Engineering, Tokyo Institute of Technology, 2-12-1, O-okayama, Meguro-ku, Tokyo, 152-8552, JPN
[3]Mitsui Chemical Co.Ltd., 1190, Kasama-Cho, Sakae-ku, Yokohama, Kanagawa, 247-8567, JPN

ABSTRACT

The effects of molecular weight on fatigue crack propagation of polyimide (PI) are investigated for four kinds of molecular weight (Mw) from 2.5×10^4 g/mol to 3.8×10^4 g/mol. The rate of fatigue crack growth follows the Paris law under the ΔK range tested, and decreases with the increase of Mw. Except for the highest Mw case, the discontinuous crack growth (DCG) bands were observed on the fracture surfaces under lower ΔK. The width of DCG bands is almost independent of ΔK and increases with increase of Mw. The number of cycles needed to form one DCG band increases with increase of Mw, which is cause of the higher fatigue resistance for higher Mw. The critical values of craze stress at the onset of crack jump in DCG are estimated by Dugdale's model and are smaller for higher Mw. This result suggests that materials with higher Mw sustain more damage accumulation.

KEYWARDS

Discontinuous Crack Growth, Polyimide, Fatigue, Crack Propagation, Molecular Weight, SEM observation

INTRODUCTION

Polyimide (PI) is one of most useful engineering plastics and we have already investigated the effect of molecular weight on some mechanical properties, e.g. Young's modulus, J_{IC} and so on [1]. For applying the structural components, the behavior of fatigue crack propagation (FCP) of PI might be estimated. In some polymers, the crack does not propagate on one load cycle in spite of following the Paris law. This FCP process is called as discontinuous crack growth (DCG) [2]. For instance, Takemori [3] has investigated the DCG mechanism of amorphous polymer, e.g. PC. Although he indicated that this behavior occurs as a consequence of both crazing and shear banding ahead of the crack tip, there is little consideration about the width of DCG. While, Skibo [4] studied the fatigue [illegible] of DCG bands was the same as the length of craze regio[illegible] of molecular weight on the FCP of PI and discussed t[illegible]

METHOD

Table 1 Material properties of specimens.

Type	Molecular weight [g/mol]	Young's modulus [GPa]	Tensile strength [MPa]	Poisson's ratio	J_{IC} [kN/m]
A	2.5×10^4	3.18	88.3	0.399	3.6
B	2.8×10^4	2.98	88.3	0.399	5.7
C	3.0×10^4	3.14	86.6	0.390	6.6
D	3.8×10^4	3.68	110.0	0.382	7.8

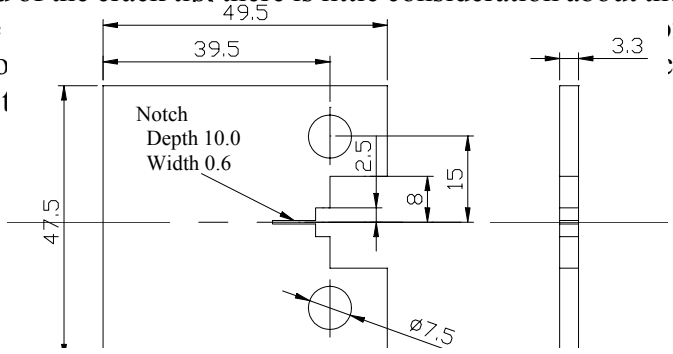

Fig. 1 Dimensions of CT specimen.

Thermoplastic polyimides with four kinds of molecular weight are used. They are called as Type A, B, C and D for convenient. Table 1 shows molecular weight, Young's modulus, tensile strength and elastic-plastic fracture toughness, J_{IC} of these material [1]. The dimensions of compact tension specimen are shown in Figure 1, which is cut from the plate made by the injection molding. An initial notch with 0.6 mm width is introduced by a precision cutting blade machine.

Procedure

Fatigue tests were performed with electrohydraulic closed-loop testing machine at room temperature. Frequency was 7.5Hz and stress ratio R was 0.1. K-decreasing procedure and constant-load-amplitude procedure were applied at the lower and higher ΔK, respectively, according to ASTM E647-95. The length of crack was measured with a traveling microscope.

Stress Intensity Factor Range and Crack Propagation Rate

Stress intensity factor range ΔK is calculated by,

$$\Delta K = \frac{\Delta P}{BW^{1/2}} f(\alpha)$$

$$f(\alpha) = \frac{(2+\alpha)(0.886 + 4.64\alpha - 13.32\alpha^2 + 14.72\alpha^3 - 5.6\alpha^4)}{(1-\alpha)^{3/2}} \quad (2)$$

$$\alpha = a / W \quad (3)$$

where ΔP, B, W and a are the range of load, the thickness and the width of specimen and the length of crack, respectively.

The crack propagation rate *da/dN* is obtained as follows,

$$\left(\frac{da}{dN}\right)_{\bar{a}} = \frac{a_{i+1} - a_i}{N_{i+1} - N_i} \quad (4)$$

where a_i and N_i are the crack length and the number of load cycle on i th. In addition, the average crack length, $\bar{a} = (a_{i+1} + a_i)/2$ is used to obtain ΔK.

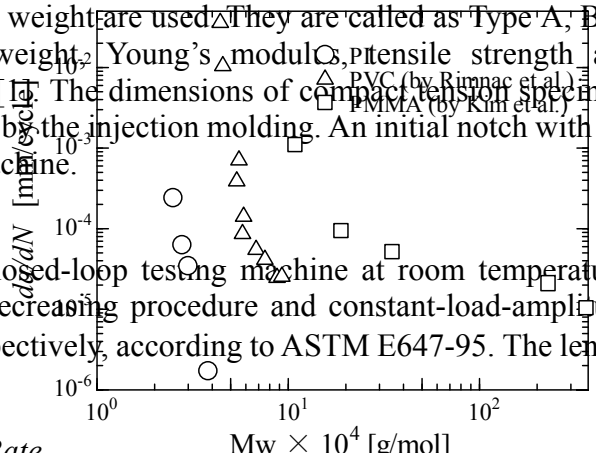

Fig.3 The effect of molecular weight on *da/dN* at ΔK = 0.7 MPa$\sqrt{m}$. Those of PVC by Rimnac et

RESULTS and DISCUSSION

Fatigue crack propagation properties

The relationship between the ΔK and *da/dN* are shown in Figure 2 and satisfy the Paris law:

$$\frac{da}{dN} = C(\Delta K)^m \quad (5)$$

where C and m are material constants and are given in Table 2. The fatigue crack extension resistance increases with the increase of Mw. The values of *da/dN* at ΔK = 0.7 MPa$\sqrt{m}$ are shown in Figure 3. The value for type D is estimated by the extrapolation of the measured data. For the comparison, the results of PVC by Rimnac[5] and PMMA by Kim[6] are also shown in the figure. It can be seen that the fatigue properties of PI is excellent.

SEM observation

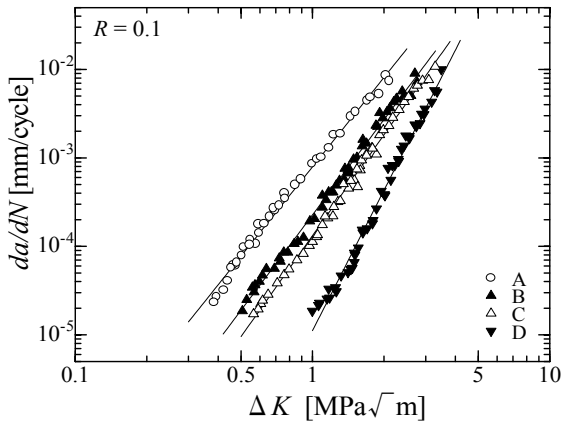

Fig. 2 Influence of molecular weight on fatigue crack propagation.

The typical fracture surfaces of type B by scanning electron microscope (SEM) are shown in Figure 4. The cracks on all photos propagate from bottom to top. Figure 4(d) indicates the observation point of each photo on the Δ*K*-*da/dN* relation. The typical DCG bands of PI are shown in Figure 4(a). In Figure 4(b) the DCG bands disappear with the advance of the crack. This is the transition of the fracture process from DCG to continuous crack growth (CCG). Since the width of DCG bands is almost constant during the process, the width might be almost independent of Δ*K*. (Please take care the different of mag nification

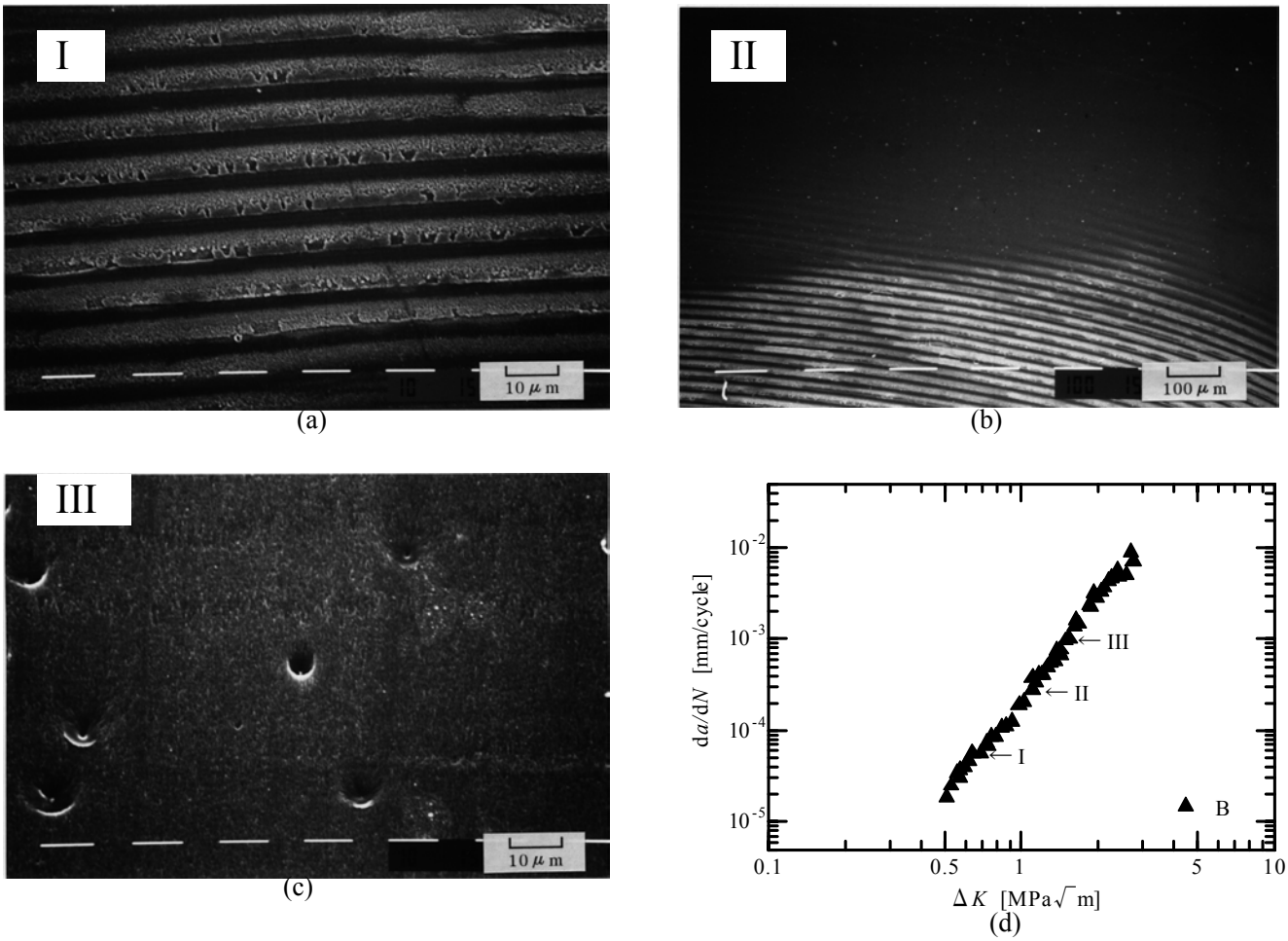

Fig. 4 SEM fractograph showing the DCG (a), the transition from DCG to FCP process (b) and the FCP process(c). The diagram (d) shows the observation point on Δ*K*-*da/dN* relation for each photo.

Table 2 Coefficients of Paris law for each specimen.

Type	A	B	C	D
C	7.93×10^{-4}	2.27×10^{-4}	1.32×10^{-4}	1.12×10^{-5}
m	3.35	3.58	3.79	5.26

Table 3 The space of DCG bands and the number of loading cycles for making DCG band. In addition, the critical fracture craze stress is derived from the Dugdale model.

Type	DCG band spacing [μm]	Number of Cycles	σ_c [MPa]
A	3.6	10	231
B	8.6	100	150
C	9.2	240	145

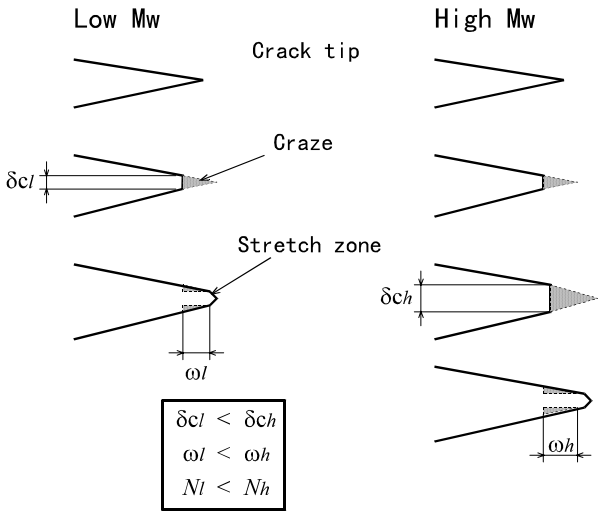

Fig. 5 Schematic diagram showing the discontinuous crack growth in each Mw.

between photos (a) and (b).) Any striation can't be seen on the fracture surface during CCG as shown in Figure 4(c). These behaviors are the same as that of type A and C. While, the morphology of the type D fracture surface is different from the others and DCG bands can't be seen on the any fracture surfaces.

Discontinuous Crack Growth

Several studies [4,6,7] have shown that the Dugdale formulation,

$$\omega = \frac{\pi}{8}\frac{\Delta K^2}{\sigma_C^2} \tag{5}$$

gives the relationship between the critical fracture craze stress σ_c at the crack jump due to damage accumulation and the width of DCG bands ω. The ω at $\Delta K = 0.7$ MPa$\sqrt{\text{m}}$ measured by the SEM photos, the number of cycle for a crack jump and σ_c by Eq. (5) are shown in Table 3. The ω increases with the increase of Mw. Figure 5 shows a schematic figure of the craze region of a DCG band. With the increase of Mw the more damage accumulates at the craze region of the higher Mw specimen for a crack jump. Subsequently, the craze region can be extended at crack tip, that is $\omega_h > \omega_l$. While, σ_c decreases with the increase of Mw because of this damage accumulation. This decrease of σ_c needs the more number of cycles for a crack jump, that is $N_h > N_l$. Consequently, *da/dN* decreases with the increase of Mw.

REFERENCES

1. Notomi, M. Kishimoto, K. Shibuya, T. Inaba, H. and Morita, A. (1999). *Tran. Jap. Soc. Mech. Engineers,* A, **65**, 629, pp.67-71. (in Japanese)
2. Hertzberg, R. W. (1996). *Deformation and Fracture Mechanics of Engineering Materials 4th ed.*, John Willy & sons, New York.
3. Takemori, M. T. (1990). *Advances in Polym. Sci.* 91/92 pp. 263-300.
4. Skibo, M. D. Hertzberg, R. W. Manson, J. A. (1976). *J. Mater. Sci.* 11, pp. 479-490.
5. Rimnac, C. Manson, J. A. Hertzberg, R. W. and Skibo, M. D. (1981). *J. Macromol. Sci. Phys.* B19 3, pp. 351-375.
6. Kim, S. L. Skibo, M. Manson, J. A. and Hertzberg, R. W. (1977). *Polym. Eng. Sci.* 17 3, pp. 194-203.
7. Clark, T. R. Hertzberg, R. W. and Mohammadi N. (1993). *J. Mater. Sci.* 28, pp. 5161-5168.

DISCRETE DISLOCATION ANALYSES OF CRACK GROWTH

V.S. Deshpande[1], A. Needleman[1] and E. Van der Giessen[2]
[1]Brown University, Division of Engineering, Providence, RI 02912, USA.
[2]University of Groningen, Dept. of Applied Physics
Nyenborgh 4, 9747 AG Groningen, The Netherlands.

ABSTRACT
Monotonic and cyclic loading of a plane strain mode I crack under small scale yielding are analyzed using discrete dislocation dynamics. The dislocations are all of edge character and are modeled as line singularities in an elastic solid. At each stage of loading, superposition is used to represent the solution in terms of the stress and displacement fields for edge dislocations in a half-space and a non-singular complementary solution that enforces the boundary conditions, which is obtained from a linear elastic, finite element model. The lattice resistance to dislocation motion, dislocation nucleation, interaction with obstacles and annihilation are incorporated into the formulation through a set of constitutive rules. A cohesive surface ahead of the initial crack tip is employed, with either reversible or irreversible relations between the opening traction and the displacement jump in order to simulate cyclic loading in a vacuum and in an oxidizing environment, respectively. It is found that crack growth can occur under cyclic loading conditions above a certain threshold value of ΔK_I; this value is higher in the case of the reversible cohesive law, in line with experimental observations.

KEYWORDS
discrete dislocation plasticity, crack growth, fatigue, environmental effects

INTRODUCTION
The interaction between plastic flow and the actual process of material separation plays an important role in setting the fracture response of structural materials under both monotonic and cyclic loading conditions. In particular, when structural components are subject to high frequency, low amplitude loading, even a typical near-threshold crack growth rate of 10^{-8} mm/cycle prompts designs to be based on the fatigue threshold, $\Delta K_{\rm th}$, of the metal. While threshold values for various metals are well documented, $\Delta K_{\rm th}$ values are known to be sensitive to the microstructure and particularly environmental conditions [1, 2]. Under near-threshold conditions, plastic zone sizes are small and discrete dislocation effects become prominent.

Previous simulations of cyclic crack growth using discrete dislocation models have been carried out, e.g. [3, 4], to gain insight into the mechanisms involved. Such models are specifically geared to cyclic loading, with dislocations nucleated from the crack tip being allowed to glide on specific slip planes around the crack tip. Thus, crack growth in [3, 4] is taken to be deformation controlled in that the crack is assumed to grow by emitting dislocations from the crack tip. In these works, environmental effects are simulated by reducing the stress intensity factor at which a dislocation is emitted from the crack tip.

In this paper, we carry out analyses of crack growth under both monotonic and cyclic loading conditions using the same discrete dislocation framework as in [5, 6]. The fracture properties of the material are embedded in a cohesive surface constitutive relation, and crack initiation and crack growth emerge as natural outcomes of the boundary value problem solution. As emphasis is placed on the environmentally sensitive near-threshold fatigue behavior, both reversible and irreversible cohesive traction-separation relations are employed to investigate cyclic loading in a vacuum and in an oxidizing environment, respectively. The main focus of this study is to ascertain whether the dislocation rearrangement due to cyclic loading can induce crack growth at levels of the applied stress intensity factor lower than needed for crack growth to occur under monotonic loading conditions.

THEORY

The formulation and numerical method follow that in [5, 6] where further details and additional references are given. We consider an infinitely long crack in a two-dimensional single crystal subjected to far field mode I loading, see Fig. 1a. The orientation of the crack is taken to be symmetric to the slip planes in the crystal, so that we need to consider only half of the crystal. Assuming small-scale yielding conditions, a process window

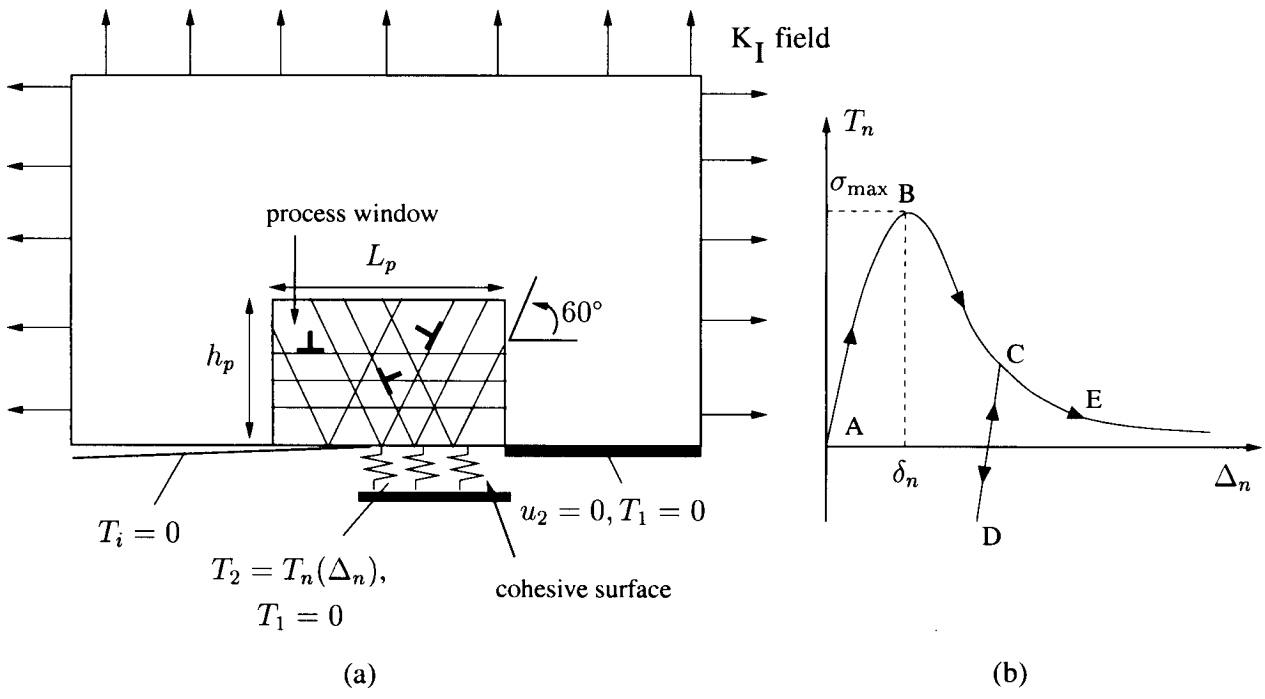

Figure 1: (a) Mode I crack problem with the imposed boundary conditions (b) Irreversible cohesive law.

is centered around the initial crack tip position in which dislocations live on a set of slip systems. The rest of the crystal remains elastic with isotropic properties, specified by the shear modulus $\mu = 26.3$ GPa and Poisson's ratio $\nu = 0.3$. Inside the process window, we assume three slip systems, two with planes at $\pm 60°$ from the crack plane $x_2 = 0$ and one parallel to this plane. The slip plane spacing is $86b$. Only edge dislocations are considered, with Burgers vector $b = 0.25$nm.

Initially, the crystal is assumed to be free of mobile dislocations, but to contain a random distribution of dislocation sources and point obstacles. The sources mimic Frank-Read sources and generate a dislocation dipole when the magnitude of the shear stress exceeds a critical value of $\tau_{\text{nuc}} = 50$MPa during a period of time $t_{\text{nuc}} = 10$ns. The obstacles, which could be small precipitates or forest dislocations, pin dislocations and will release them once the shear stress attains the obstacle strength $\tau_{\text{obs}} = 150$MPa. Annihilation of two dislocations with opposite Burgers vector occurs when they approach each other within a critical annihilation distance $L_{\text{e}} = 6b$. We present calculations for a material with a source and obstacle density $\rho_{\text{src}} = 60/\mu\text{m}^2$ and $\rho_{\text{obs}} = 290/\mu\text{m}^2$, respectively in the process region.

Loading is prescribed in terms of displacements corresponding to the isotropic elastic mode I singular field remote from the crack tip. There is a single cohesive surface [7] that extends over a distance x_c in front of the initial crack (the constitutive equations of the cohesive surface are detailed later in the paper). Ahead of the cohesive surface, symmetry conditions are prescribed. At each time step, an increment of the mode I stress intensity factor $\dot{K}_I \Delta t$ is prescribed. At the current instant, the stress and strain state of the body is known, and the forces on all dislocations can be calculated. On the basis of these forces we update the dislocation structure, which involves the motion of dislocations, the generation of new dislocations, their mutual annihilation, their pinning at obstacles, and their exit into the open crack. After this, the new stress and strain state can be determined. For this purpose, we use superposition [8],

$$u_i = \tilde{u}_i + \hat{u}_i\,, \quad \epsilon_{ij} = \tilde{\epsilon}_{ij} + \hat{\epsilon}_{ij}\,, \quad \sigma_{ij} = \tilde{\sigma}_{ij} + \hat{\sigma}_{ij}\,. \tag{1}$$

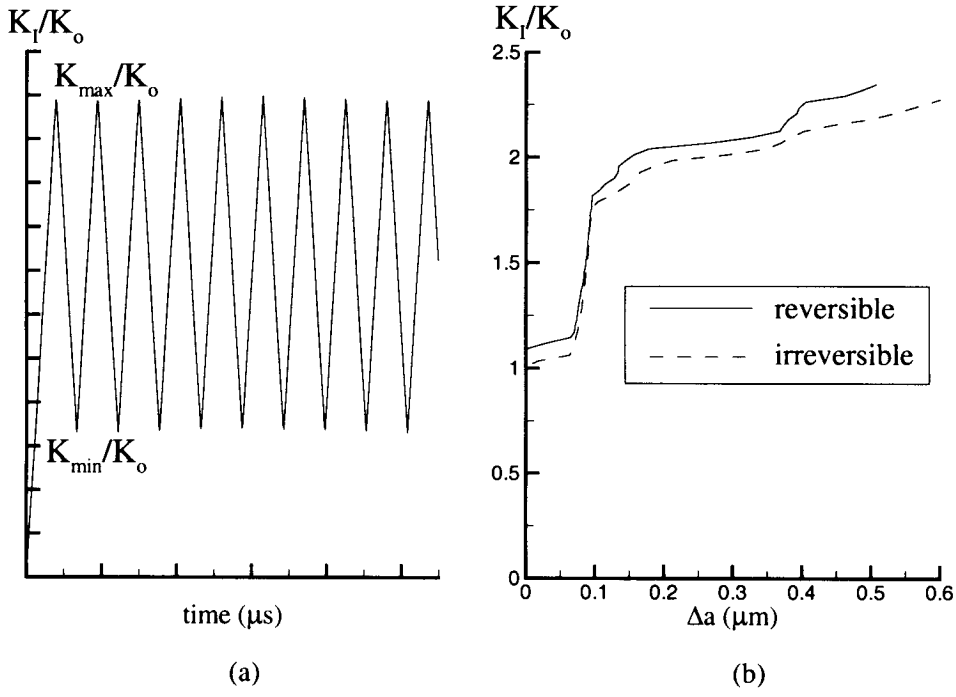

Figure 2: (a) Schematic of the applied stress intensity factor as a function of time (b) Applied stress intensity factor K_I/K_o versus crack extension Δa for monotonic loading with the reversible and irreversible cohesive surface laws.

The $\tilde{(\ )}$ fields are the superposition of the singular fields of the individual dislocations in their current configuration while the $\hat{(\ )}$ fields represent image fields that correct for the actual boundary conditions. For the former we use the fields of an edge dislocation in a half-space [9], with the traction-free surface corresponding to the crack plane $x_2 = 0$.

The sum of the $\tilde{(\ )}$ and the $\hat{(\ )}$ fields in (1) gives the solution that satisfies all boundary conditions. Since the $\hat{(\ )}$ fields are smooth in the region of interest, the boundary value problem for them can conveniently be solved using a finite element method. The size of the region analyzed is 1000μm $\times$ 500μm and a finite element mesh of 120×100 bilinear quadrilateral elements is used. The process window in Fig. 1a is specified by $L_{\rm p} = 10\mu$m and $h_{\rm p} = 12.5\mu$m and is discretized with a fine mesh of 80×80 quadrilateral elements.

With the decomposition (1), the Peach-Koehler force $f^{(k)}$ acting on the kth dislocation is given by

$$f^{(k)} = n_i^{(k)} \left(\hat{\sigma}_{ij} + \sum_{m \neq k} \sigma_{ij}^{(m)} + \Sigma_{ij}^{(k)} \right) b_j^{(k)} . \tag{2}$$

Here, $n_i^{(k)}$ is the slip plane normal, $b_j^{(k)}$ is the Burgers vector and $\Sigma_{ij}^{(k)}$ is the image field on dislocation k due to the traction-free surface, i.e. the difference between the half-space and infinite medium fields. The direction of the Peach-Koehler force is in the slip plane and normal to the dislocation line. The rules for dislocation nucleation and motion are based on this force as the driving force. Dislocation motion is assumed to occur only by glide with no cross slip. The magnitude of the glide velocity $v^{(k)}$ of dislocation k is taken to be linearly related to the Peach-Koehler force $f^{(k)}$ through the drag relation $f^{(k)} = Bv^{(k)}$. The value for B is taken as $B = 10^{-4}$Pa s, which is representative for aluminum [10].

The centerpiece of the present approach is the inclusion of both reversible and irreversible cohesive traction-displacement relations to simulate cyclic loading in non-oxidizing (vacuum) and oxidizing environments, respectively. We start by considering monotonic opening of the crack. The opening is resisted by cohesion at

the atomistic scale and we assume that the normal cohesive traction T_n has the universal binding form [11],

$$T_n(\Delta_n) = e\sigma_{\max}\frac{\Delta_n}{\delta_n}\exp(-\frac{\Delta_n}{\delta_n}), \tag{3}$$

where Δ_n is the total separation of the cohesive surface, $\Delta_n = 2u_2(x_2 = 0)$, and T_n is the traction normal to the cohesive surface. As the cohesive surface separates, the magnitude of the traction increases, reaches a maximum and then approaches zero with increasing separation. In a vacuum, there is no oxidation of the newly formed surface and it is expected that this relation is followed in a reversible manner. However, even in normal atmospheric conditions the newly formed surfaces oxidize and the cohesive law will not follow the above universal binding relation in a reversible manner. We model the effect of the formation of the oxide layer and the subsequent surface contact during unloading by specifying unloading from and reloading towards the monotonic cohesive law to occur according to the incremental relation

$$\dot{T}_n(\Delta_n) = \frac{e\sigma_{\max}}{\delta_n}\dot{\Delta}_n. \tag{4}$$

An example of a typical T_n–Δ_n path for the irreversible cohesive law is shown schematically in Fig. 1b.

The parameters used in this study are $\sigma_{\max} = 0.6\,\text{GPa}$ and $\delta_n = 4b$ giving a work of separation $\phi_n = e\sigma_{\max}\delta_n$ of 1.63 J/m^2. The work of separation can be related to a reference stress intensity factor K_0 defined by

$$K_0 = \sqrt{\frac{E\phi_n}{1-\nu^2}}, \tag{5}$$

where for the material parameters here $K_0 = 0.358\,\text{MPa}\sqrt{\text{m}}$. Note that crack growth in an elastic solid with the given cohesive properties takes place at $K_I/K_0 = 1$. The value of $\sigma_{\max}$ used is about a factor of four smaller than would be appropriate for aluminum. This small value of the strength was used for numerical convenience, since the length scale over which large gradients occur is proportional to $(E/\sigma_{\max})\delta_n$.

RESULTS

In the calculations presented here the applied stress intensity was varied with time between $K_{\min}$ and $K_{\max}$ as shown schematically in Fig. 2a. The calculations were carried out for a loading rate of $\dot{K}_I = 100\text{GPa}\sqrt{\text{m}}/\text{s}$. This rather high loading rate was chosen to reduce the computer time needed for the crack growth calculations because resolving the dislocation dynamics requires a small time step of $\Delta t = 0.5\text{ns}$. For comparison purposes, calculations with K_I monotonically increasing were also carried out. The monotonic crack growth behavior with both the reversible and irreversible cohesive laws are approximately the same. Crack growth initiates at $K_I/K_0 \approx 1.0$. This is followed by substantial plasticity and a sharp rise in the resistance to crack growth (Fig. 2b).

The near-threshold fatigue behavior of metals is known to be sensitive to the stress ratio $R = K_{\min}/K_{\max}$. We present results for $R = 0.3$, but for various values of ΔK_I. First we consider the reversible cohesive surface law. Figure 3a shows the time evolution of crack growth, Δa, under cyclic loading conditions. For both values of ΔK_I, there is an initial "burst" of crack growth. Subsequently, for the case with $\Delta K_I/K_0 = 1.12$ the behavior settles down to an incremental crack growth of the order of $10^{-4}\mu$m/cycle. This corresponds to a crack growth of about one lattice spacing per cycle and is the commonly used operational definition of the threshold crack growth rate [1]. However, for the lower value of $\Delta K_I/K_0 = 0.98$, no cycle-by-cycle crack growth is seen. Further insight into this behavior is gained by examining the evolution of the dislocation density (Fig. 3b). For the case with $\Delta K_I/K_0 = 1.12$ the dislocation density is seen to slowly accumulate with the number of cycles. On the other hand, with $\Delta K_I/K_0 = 0.98$, plastic shakedown takes place resulting in no cycle-by-cycle increase in the dislocation density. Thus, we see that irreversibility of the dislocation motion above a certain threshold value of ΔK_I results in an evolving dislocation structure with cyclic loading; this permits the crack to grow to different lengths during different loading cycles.

Next, we consider cyclic loading with the irreversible cohesive law. Figure 4 shows the time evolution of crack growth with $\Delta K_I/K_0 = 0.77$ and 0.90. We see that incremental crack growth of the order of

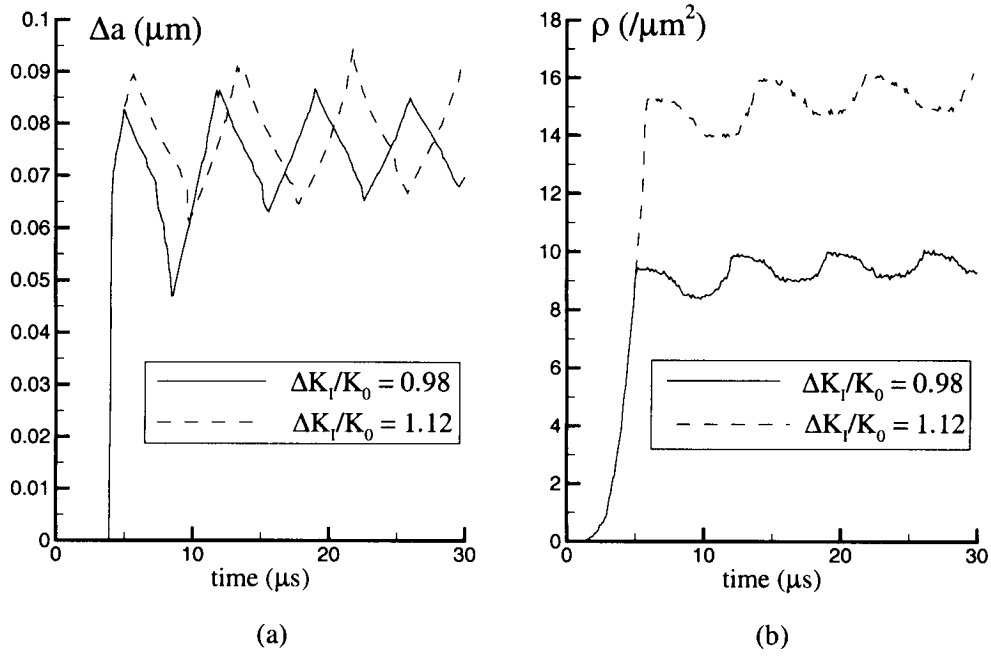

Figure 3: (a) Time evolution of the crack growth and (b) time evolution of the dislocation density for the case with the reversible cohesive surface law ($R = 0.3$).

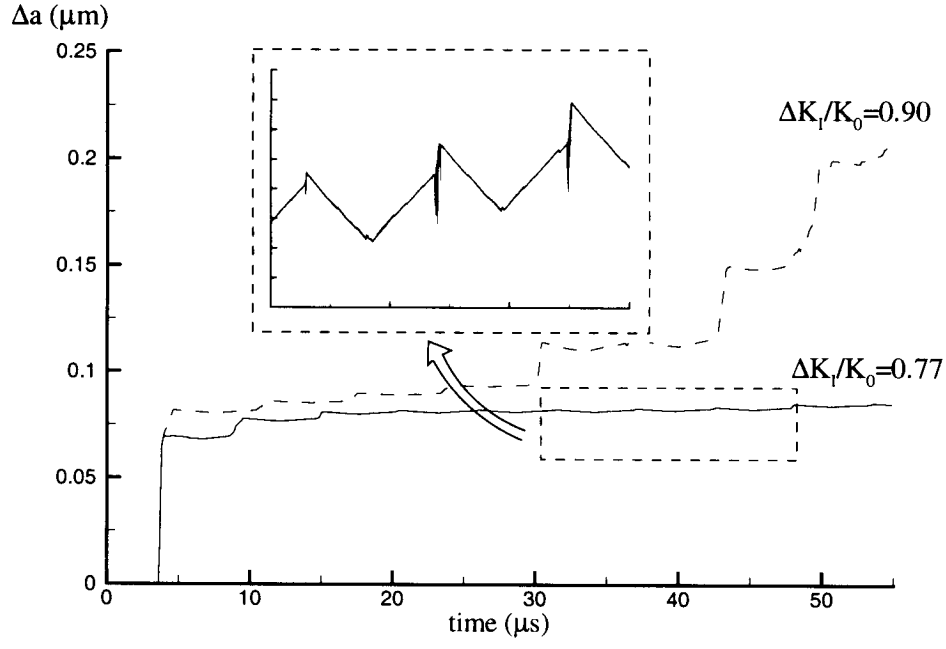

Figure 4: Time evolution of the crack growth with the irreversible cohesive surface law ($R = 0.3$).

$10^{-4}\mu$m/cycle (see inset Fig. 4) occurs in this case at the much lower value of $\Delta K_I/K_0 = 0.77$: a close examination of the inset in Fig. 4 reveals that the incremental crack advance in this case takes place due to a "spurt" of crack growth which occurs towards the end of every loading cycle. It is these "spurts" that result in the incremental cycle-by-cycle crack growth. On the other hand, with $\Delta K_I/K_0 = 0.90$, we are well above the fatigue threshold and crack growth is accelerating. Further calculations are needed to check whether or not

crack growth settles down to a "steady-state" value. It is worth emphasizing that we get continued crack growth under cyclic loading at a value of $K_{\max}$ at which the crack would have arrested under monotonic loading. This is best illustrated by the case with $\Delta K_I/K_0 = 0.90$ ($K_{\max}/K_0 \approx 1.29$ and $K_{\min}/K_0 \approx 0.39$): the crack grows by about 0.2μm after 8 cycles (Fig. 4). However, as seen in Fig. 2b, $K_I/K_0 \approx 2.0$ is needed for the crack to grow by that length under monotonic loading conditions.

CONCLUSIONS

Results of plane strain analyses of mode I crack growth under monotonic and cyclic loading conditions have been presented where plastic flow arises from the motion of large numbers of dislocations. The only difference between the analyses for monotonic and cyclic crack growth is in the specification of the applied loading. The material has three slip systems and is initially dislocation free. Dislocation nucleation occurs from Frank-Read sources distributed randomly in the material, with no special dislocation nucleation from the crack tip. Cyclic loading in a vacuum and in an oxidizing environment are simulated by employing a reversible and an irreversible cohesive law, respectively. Results have been presented for a stress ratio, $R = (K_{\min}/K_{\max}) = 0.3$: the fatigue threshold was calculated by reducing ΔK_I until no cycle-by-cycle crack growth was obtained. Crack growth rates of about $10^{-4}\mu$m/cycle corresponding to typical threshold values were seen with $\Delta K_I/K_0 = 1.12$ and 0.707 for the reversible and irreversible cohesive laws, respectively. Plastic shakedown with no incremental crack growth was observed for ΔK_I lower than these threshold values. In line with experimental observations we found that the fatigue threshold value was higher in a vacuum than in an oxidizing environment.

Fatigue was seen to emerge in the simulations as a consequence of the evolution of internal stresses associated with the irreversibility of the dislocation motion: the dislocation structure and density were different at the beginning and end of each cycle and it was this that permitted cycle-by-cycle crack growth. Moreover, continued crack growth under cyclic loading occurred at a value of $K_{\max}$ for which the crack would have arrested under monotonic loading.

Acknowledgements

Support from the AFOSR MURI at Brown University on *Virtual Testing and Design of Materials: A Multiscale Approach* (AFOSR Grant F49620-99-1-0272) is gratefully acknowledged.

References

[1] Suresh S. (1991). *Fatigue of Materials*, Cambridge University Press, Cambridge UK.

[2] Vasudevan A. K., Sadananda K. and Louat N. (1994). *Mat. Sci. Engin. A* 188, 1-22.

[3] Riemelmoser F. O. and Pippan R. (1997). *Mat. Sci. Engin. A* 234-236, 135-137.

[4] Wilkenson A. J., Roberts S. G. and Hirsch P. B. (1998). *Acta Mat.* 46, 379-390.

[5] Cleveringa H.H.M., Van der Giessen E. and Needleman A. (2000). *J. Mech. Phys. Solids* 48, 1133-1157.

[6] Van der Giessen E., Deshpande V.S., Cleveringa H.H.M. and Needleman A. (2001). *J. Mech. Phys. Solids*, in press.

[7] Needleman A. (1990). *J. Mech. Phys. Solids* 38, 289-324.

[8] Van der Giessen E. and Needleman A. (1995). *Modeling Simul. Mater. Sci. Eng.* **3**, 689-735.

[9] Freund L.B.(1994). *Adv. Appl. Mech.* 30, 1-66.

[10] Kubin L.P., Canova G., Condat M., Devincre B., Pontikis V. and Bréchet Y. (1992). *Solid State Phenomena* 23-24, 455-472.

[11] Rose J.H., Ferrante J. and Smith J.R. (1981). *Phys. Rev. Lett.* 47, 675-678.